**CONFERENCE PROCEEDINGS**

SB3C

biomechanics.
bioengineering.
biotransport.

# *2022 Summer Biomechanics, Bioengineering, and Biotransport Conference*

June 20th -23rd, 2022
Eastern Shore, Maryland

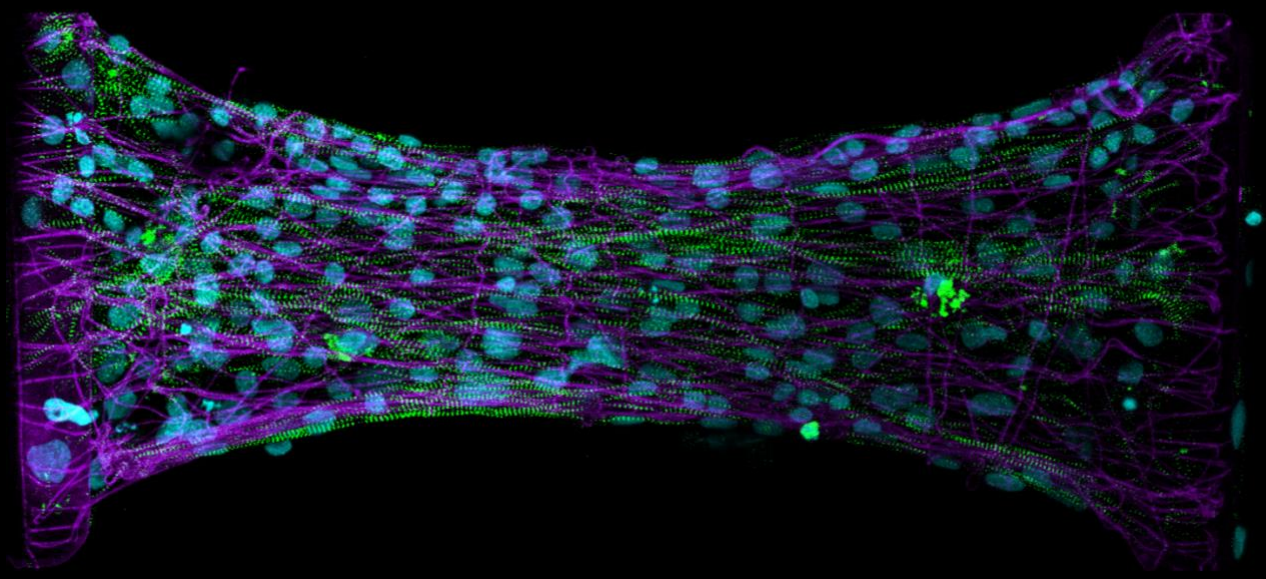

## *Reconnecting Networks in Biomechanics, Bioengineering and Biotransport*

Funding for this conference was made possible (in part) by the National Science Foundation's Civil, Mechanical, and Manufacturing Innovation Division (Biomechanics and Mechanobiology) 2209028. Funding for this conference was also made possible (in part) by R13EB033191A from the National Institute of Biomedical Imaging and Bioengineering. The views expressed in written conference materials or publications and by speakers and moderators do not necessarily reflect the official policies of the Department of Health and Human Services; nor does mention of trade names, commercial practices, or organizations imply endorsement by the U.S. Government. Prizes and other support for the Student Paper Competition were provided by the Bioengineering Division of the American Society of Mechanical Engineers.

**The 2022 Summer Biomechanics, Bioengineering, and Biotransport Conference ($SB^3C$) organizers gratefully acknowledge the support of the National Science Foundation, the National Institutes of Health, and American Society of Mechanical Engineers.**




Congratulations to the 2021 Cover Art Contest Winner:

**Samuel DePalma, University of Michigan**
*Title: Mechanical Cues Drive the Robust Assembly of Microfabricated Stem Cell-Derived Cardiac Tissues*
Description: Engineered cardiac microtissue composed of induced pluripotent stem cell derived cardiomyocytes on a synthetic fibrous matrix (violet) suspended between two elastomeric cantilevers. Sarcomeric Z-discs were visualized via cardiomyocytes encoding fluorescently tagged endogenous Titin (green). Cell nuclei were stained with DAPI (turquoise).



**ISBN 978-1-7351808-4-7**

# SB³C 2022 Meeting Scientific Podium Sessions

| Monday, June 20 | 9:30AM – 11:00AM EDT |
|---|---|

## Machine Learning and Artificial Intelligence

**Chesapeake A-D**

**Session Chairs: Hadi Wiputra,** *University of Minnesota*
**Kritika Iyer,** *University of Michigan*

**9:30AM** **Statistical Shape Representation of Ascending Thoracic Aortic Aneurysms: Accounting for Major Branches of the Aortic Arch** SB³C2022-312
Hadi Wiputra[1], Shion Matsumoto[2], Jessica E. Wagenseil[3], Alan C. Braverman[3], Victor H. Barocas[1]
*[1]University of Minnesota, [2]University of Michigan, [3]Washington University*

**9:45AM** **A Bayesian Approach for Inverse Problems on Patient-Specific CFD Simulation of Aorta Using an MI-Based Surrogate Model** SB³C2022-162
Pan Du, Jian-xun Wang
*University of Notre Dame*

**10:00AM** **AI-Accelerated Multiscale Modeling for Platelet Adhesion Dynamics and Multi-Platelet Aggregation at Millisecond and Molecular Resolutions** SB³C2022-262
Peineng Wang, Yicong Zhu, Jawaad Sheriff, Peng Zhang, Changnian Han, Yuefan Deng, Danny Bluestein
*Stony Brook University*

**10:15AM** **A Deep Learning Method for 3D Vessel Reconstruction Using Uncalibrated X-Ray Angiography Images: Application to Coronary Hemodynamics** SB³C2022-223
Kritika Iyer, Noah C. Stevens, Brahmajee K. Nallamothu, C. Alberto Figueroa, Raj R. Nadakuditi
*University of Michigan*

**10:30AM** **Learning Whole Heart Mesh Generation from Patient Images for Computational Simulations** SB³C2022-440
Fanwei Kong, Shawn Shadden
*University of California Berkeley*

**10:45AM** **Denoising and Super-Resolving 4D Flow MRI Using Physics-Guided Neural Networks** SB³C2022-259
Neal Patel, Emily Bartusiak, Hemanth Devarapalli, Sean Rothenberger, Amy Schwichtenberg, Edward Delp, Vitaliy Rayz
*Purdue University*

| Monday, June 20 | 9:30AM – 11:00AM EDT |
|---|---|

# Vascular Mechanics I

**Chesapeake E**

**Session Chairs: Vijay Vedula,** *Columbia University*
**Bryan Good,** *University of Tennessee*

**9:30AM** **Automatic Estimation of Mechanical and Geometrical Parameters of Abdominal Aortic Aneurysms Using 3D+T Ultrasound for Understanding Aneurysm Progression** SB³C2022-211
Esther Maas[1], Arjet Nievergeld[1], Judith Fonken[1], Mirunalini Thirugnanasambandam[1], Marc van Sambeek[2], Richard Lopata[1]
*[1]Eindhoven University of Technology, [2]Catharina Hospital Eindhoven*

**9:45AM** **Batch-Process Optimization of Kink-Resistant Vascular Grafts with High Compliance** SB³C2022-315
David Jiang[1], Andrew Robinson[2], Elizabeth Cosgriff-Hernandez[2], Lucas Timmins[1]
*[1]University of Utah, [2]University of Texas at Austin*

**10:00AM** **Biomechanical Analysis of Local Mural Defects in Angiotensin-II-Induced Thoracic Aortopathies** SB³C2022-475
Dar Weiss[1], Aaron S. Long[1], George Tellides[1], Stéphane Avril[2], Jay D. Humphrey[1], Matthew R. Bersi[3]
*[1]Yale University, [2]Mines Saint-Étienne, [3]Washington University*

**10:15AM** **Effects of Nitroglycerin Induced Vasodilation on Elastic versus Muscular Artery Stiffness in Older Veterans** SB³C2022-213
Ryan Pewowaruk[1], Amy Hein[1], Cynthia Carlsson[1], Claudia Korcarz[2], Adam Gepner[1]
*[1]William S. Middleton Memorial Veterans Hospital, [2]University of Wisconsin*

**10:30AM** **Investigation of The Regional Variations in the Mechanical Properties and Microstructure of Porcine Left Anterior Descending Artery** SB³C2022-117
Sergio A. Pineda-Castillo, Santiago Aparicio-Ruiz, Chung-Hao Lee
*University of Oklahoma*

**10:45AM** **Prediction of Analog Thrombi Mechanical Properties, Composition, and Contraction Using Computed Tomography Imaging** SB³C2022-219
Janneke Cruts[1], Jo-Anne Giezen[2], Kim van Gaalen[1], Robert Beurskens[1], Yanto Ridwan[1], Marcel Dijkshoorn[1], Heleen van Beusekom[1], Nikki Boodt[1], Aad van der Lugt[1], Frank Gijsen[1], Rachel Cahalane[1]
*[1]Erasmus Medical Center, [2]Delft University of Technology*

| Monday, June 20 | 9:30AM – 11:00AM EDT |
|---|---|

# Mineralized Tissue Mechanics

**Chesapeake F**

**Session Chairs: Natasha Case,** *Saint Louis University*
**Hannah Dailey,** *Lehigh university*

**9:30AM** **In-Situ Bone Fracture Mechanics Assessed by 3D-Xray Microscopy** SB³C2022-360
Glynn Gallaway[1], Rachel Surowiec[2], Matthew Allen[2], Joseph Wallace[2], Laura Pyrak-Nolte[1], Thomas Siegmund[1]
*[1]Purdue University, [2]Indiana University*

**9:45AM** **Prediction of Microarchitecture and Anisotropic Elastic Behaviour of Trabecular Bone Using a QCT-Based Deep Learning Model** SB³C2022-129
Pengwei Xiao, Eakeen Haque, Tinghe Zhang, Yufei Huang, Xiaodu Wang
*University of Texas at San Antonio*

**10:00AM** **Optimizing and Validating Soft Callus Mechanical Properties in Ovine Bone Fracture Healing Models with Biomechanical Data** SB³C2022-179
Brendan Inglis[1], Peter Schwarzenberg[1], Karina Klein[2], Brigitte von Rechenberg[2], Salim Darwiche[2], Hannah Dailey[1]
*[1]Lehigh University, [2]University of Zurich*

**10:15AM** **High-Fat Diet Concurrently Alters Bone Microstructure and Nanostructure** SB³C2022-438
Yoshihiro Obata[1], Neha S. Dole[2], Claire Acevedo[1], Tamara Alliston[2]
*[1]University of Utah, [2]University of California, San Francisco*

**10:30AM** **Enthesis Mechanical Properties and Composition Are Dependent on Movement And Development** SB³C2022-370
Kaitlin McCreery, Olivia Tonti, Callan Luetkemeyer, Corey Neu, Sarah Calve
*University of Colorado Boulder*

**10:45AM** **A Comparative Study of Bone Tissue Growth Between Bioinspired and Square Scaffolds** SB³C2022-394
Marco Fielder, Arun Nair
*University of Arkansas*

| Monday, June 20 | 9:30AM – 11:00AM EDT |
|---|---|

# Biomechanics of the Eye, Pelvic Floor, and Reproductive Track I

**Chesapeake G**

**Session Chairs: Ian Sigal,** *University of Pittsburgh*
**Megan R. Routzong,** *University of California*

**9:30AM** **Radiation Cystitis Results in Compromised Urinary Function and Decreased Bladder Distensibility** SB³C2022-397
Bernadette Zwaans[1], Marissa Grobbel[2], Laura Lamb[1], Sara Roccabianca[2]
*[1]Beaumont Health, [2]Michigan State University*

**9:45AM** **Simulations of The Gravid Human Uterus and Cervix for Patients at High- And Low-Risk for Preterm Birth** SB³C2022-384
Erin Louwagie[1], Mirella Mourad[1], Michael House[2], Ronald Wapner[1], Kristin Myers[1]
*[1]Columbia University, [2]Tufts Medical Center*

**10:00AM** **Dependence of Vaginal Tissue Creep Behavior On Applied Load** SB³C2022-29
Justin Dubik[1], David Dillard[1], Kristin Miller[2], Raffaella De Vita[1]
*[1]Virginia Tech, [2]Tulane University*

**10:15AM** **Simulation of Uterus Active Contraction During Fetus Delivery in Ls-Dyna** SB³C2022-22
Ru Tao, Michele Grimm
*Michigan State University*

**10:30AM** **Intraocular Pressure-Induced Lamina Cribrosa Deformations are Larger and More Inhomogeneous Between Quadrants in an Experimental Glaucoma Eye than in Healthy Eye** SB³C2022-381
Bingrui Wang[1], Fuqiang Zhong[1], Junchao Wei[1], Yi Hua[1], Juan Reynaud[2], Brad Fortune[2], Ian Sigal[1]
*[1]University of Pittsburgh, [2]Legacy Health Research*

**10:45AM** **Shear Properties of Collagen Crosslinked Porcine Cornea** SB³C2022-375
H Hatami-Marbini, M.E Emu
*University of Illinois*

| Monday, June 20 | 9:30AM – 11:00AM EDT |
|---|---|

# Joint & Spine Biomechanics

**Clipper A-C**

**Session Chairs: Sagar Singh,** *University of Pennsylvania*
**Anita Singh,** *Widener University*

**9:30AM** **Why Don't Bats Tear Their Rotator Cuffs Despite Repetitive Overhead Motion** SB³C2022-411
Iden Kurtaliaj[1], Jennifer Kunes[1], Michael Rowley[2], Lynn Ann Forrester[1], Mikhail Golman[1], Guy Genin[3], Sharon Swartz[4], Stavros Thomopoulos[1]
*[1]Columbia University, [2]California State University, [3]Washington University St. Louis, [4]Brown University*

**9:45AM** **Radiofrequency Ablation of the Medial Nerve for Facet Joint Pain Alters the Biomechanics of The Spine - A Computational Study** SB³C2022-261
Faris A. Amalki, Daniel H. Cortes
*Penn State University*

**10:00AM** **Pre-Exposure to a Painful Stretch Increases Both Strains & Neuronal Calcium Activity in Neuron-Collagen Constructs across Physiologic & Supraphysiological Stretch** SB³C2022-190
Sagar Singh, Prabesh Ghimire, Beth Winkelstein
*University of Pennsylvania*

**10:15AM** **Progressive Disc and Bone Adaptations Due to Posterolateral Tethering in a Porcine Model of Scoliosis** SB³C2022-286
Axel Moore[1], Adriana Barba[2], Harrah Newman[1], Kyle Meadows[1], Benjamin Sinder[3], Alessandra Fusco[2], Rachel Hillard[2], Sriram Balasubramanian[4], Edward Vresilovic[1], Brian Snyder[5], Patrick Cahill[3], Thomas Schaer[2], Dawn Elliott[1]
*[1]University of Delaware, [2]University of Pennsylvania, [3]Children's Hospital of Philadelphia, [4]Drexel University, [5]Boston Children's Hospital*

**10:30AM** **The Influence of Personal Protective Equipment on Male and Female Spinal Loads in Vertical Impact** SB³C2022-460
Sagar Umale, Prashant Khandelwal, John Humm, Narayan Yoganandan
*Medical College of Wisconsin*

**10:45AM** **Degeneration of the Lumbar Facet Joint Occurs in Both the Facet Capsular Ligament and the Facet Joint Articular Cartilage** SB³C2022-172
Jill Middendorf, Victor Barocas
*University of Minnesota*

| Monday, June 20 | 9:30AM – 11:00AM EDT |
|---|---|

# Mechanobiology

**Galleon A-C**

**Session Chairs: Eno Ebong,** *Northeastern University*
**Spencer Szczesny,** *Penn State University*

**9:30AM** **Increased Nuclear Compliance Enables Rapid Confined Migration in Mesenchymal Glioblastoma** SB³C2022-120
Landon Teer, Neha Anil, Dominic Armagno, Marco Munoz, Shah Tarun, Samuel Vielee, Joseph Chen
*University of Louisville*

**9:45AM** **Periventricular White Matter Hyperintensities Associated with Mechanical Changes of the Ependymal Wall** SB³C2022-21
Andreia Caçoilo[1], Madison Grigg[2], Henry Rusinek[3], Johannes Weickenmeier[1]
*[1]Stevens Institute of Technology, [2]West Virginia University, [3]New York University*

**10:00AM** **Mechanical Cues from The Environment Make Mesenchymal Stromal Cell Population Heterogeneous** SB³C2022-128
Samantha Kaonis, Soham Ghosh
*Colorado State University*

**10:15AM** **Microenvironmental Stiffness Modulates Responsiveness and Communication with Mesenchymal Stromal Cells** SB³C2022-336
Sung Yeon Kim, Edward Bonnevie, Carla Scanzello, Robert Mauck
*University of Pennsylvania*

**10:30AM** **Heterogeneity in Cell Distribution Due to Collective Organization Leads to Localized Higher Stresses** SB³C2022-469
Mahvash Jebeli, Samantha Lopez, Qi Wen, Kristen Billiar
*Worcester Polytechnic Institute*

**10:45AM** **Glaucomatous Stressors Drive Schlemm s Canal Cell Pathobiology Via Elevated Yap Activity** SB³C2022-49
Haiyan Li[1], Megan Kuhn[2], Daniel Stamer[2], Preethi Ganapathy[1], Samuel Herberg[1]
*[1]Suny Upstate Medical University, [2]Duke University*

| Monday, June 20 | 9:30AM – 11:00AM EDT |
|---|---|

# Transport in Diagnostics

**Schooner A-B**

**Session Chairs: Lyle Hood,** *University of Texas at San Antonio*
**Zhenpeng Qin,** *University of Texas at Dallas*

**9:30AM** **Development of a Multi-Timestep Approach for Microparticle and Erythrocyte Image Velocimetry** SB³C2022-400
Simon Tupin, Joseph van Batenburg-Sherwood
*Imperial College London*

**9:45AM** **Characteristic Impedance with Exercise Testing Correlates with Right Ventricular-Pulmonary Arterial Coupling in Isolated Postcapillary Pulmonary Hypertension** SB³C2022-30
Christopher Lechuga[1], Farhan Raza[2], Naomi Chesler[1]
*[1]University of California, Irvine, [2]University of Wisconsin*

**10:00AM** **Characterization of Porcine Pancreas Tissue Plasmonic Photothermal Heating at 808 And 1064 Nm Wavelengths** SB³C2022-321
Forhad Akhter[1], Andrea Smith[1], Santiago Manrique-Bedoya[1], Chris Moreau[2], Yusheng Feng[1], Kathryn Mayer[1], Lyle Hood[1]
*[1]University of Texas at San Antonio, [2]UT Health San Antonio*

**10:15AM** **A Deep Learning Approach to Investigate the Hidden Links Between Cannabis and Cardiovascular Health** SB³C2022-459
Joseph C. E. Messou, Francis Oparaocha, Hasan Imanli, James A. Perry, Timm-Michael L. Dickfeld, Jean Jeudy, Eleonora Tubaldi
*University of Maryland*

**10:30AM** **Elucidating the Impact of Plasmonic Nanoparticle Shape on Infectious Virus Diagnosis** SB³C2022-478
Yaning Liu[1], Haihang Ye[1], Tingting Zhang[1], Qi Cai[1], Hoang Dinh Huynh[2], Jeffery Kahn[2], Zhenpeng Qin[1]
*[1]University of Texas Dallas, [2]University of Texas Southwestern Medical Center*

**10:45AM** **Patient-Specific Modeling of Obstructed Ventriculoperitoneal Shunt Performance** SB³C2022-37
Sung Min Kwon, Stephanie TerMaath
*University of Tennessee*

| Monday, June 20 | 9:30AM – 11:00AM EDT |
|---|---|

# Rehab and Assistive Technologies

**Cutter A-B**

**Session Chairs: Sara Roccabianca,** *University of Michigan*
**Ria Mazumdar,** *Widener University*

**9:30AM** **Patient-Specific Models Reveal High Interfragmentary Strain in Distal Femur Fracture Fixation** SB³C2022-181
Jordan Inacio[1], Peter Schwarzenberg[2], Richard Yoon[3], Andrew Kantzos[4], Ajith Malige[4], Chinenye Nwachuku[4], Hannah Dailey[1]
*[1]Lehigh University, [2]AO Foundation Davos, [3]Jersey City Medical Center, [4]St. Luke's University*

**9:45AM** **Exercise Therapy Improves Glenohumeral Joint Function when Reaching Behind the Back in Individuals with Rotator Cuff Tears** SB³C2022-301
Luke Mattar, Rachel McLoughlin, Adam Popchak, William Anderst, Volker Musahl, James Irrgang, Richard Debski
*University of Pittsburgh*

**10:00AM** **Predicting Joint Torque Using sEMG and Deep Neural Networks** SB³C2022-304
Heath Boyea, J. Miles Canino
*Rose-Hulman Institute of Technology*

**10:15AM** **Design and Mechanical Testing of a Shoulder-Assistive Exosuit** SB³C2022-355
Kaleb Burch, Jill Higginson
*University of Delaware*

**10:30AM** **An Analysis of Octopus Curvature for Application in Soft Robotic Prostheses** SB³C2022-113
Garrett Weidig, Emily Kelly, Brittany Bush, Galit Pelled, Tamara Reid Bush
*Michigan State University*

**10:45AM** **Evaluating the Capabilities of a Novel Device Designed to Preserve Whole Pancreases Via Oxygenated Perfusion** SB³C2022-43
Daniel Portillo, Jose Gonzalez, Carorina Villareal, Sophia Salazar, Lyle Hood
*University of Texas at San Antonio*

| Monday, June 20 | 11:15AM – 12:45PM EDT |
|---|---|

# Patient Specific Flow and Physiology

**Chesapeake A-D**

**Session Chair: Jamasp Azarnoosh,** *Medical College of Wisconsin*
**Vijay Vedula,** *Columbia University*

**11:15AM** **Image-Based Temporal Quantification of Aortic Coarctation Within the Range of Severities and Durations Seen Clinically** SB³C2022-282
Jamasp Azarnoosh, Arash Ghorbannia, John F. LaDisa Jr.
*Medical College of Wisconsin*

**11:30AM** **Aortic Coarctation Assessment - In Vitro 4D Flow MRI Approach** SB³C2022-393
James Rice[1], Labib Shahid[1], Haben Berhane[2], Cynthia Rigsby[3], Joshua Robinson[3], Lindsay Griffin[3], Michael Markl[2], Alejandro Roldan-Alzate[1]
*[1]University of Wisconsin-Madison, [2]Northwestern University, [3]Lurie Children's Hospital*

**11:45AM** **Personalized Ultrasound-Based Fluid-Structure Interaction Modeling of Abdominal Aortic Aneurysms: From Model Development to Ex-Vivo Verification** SB³C2022-205
Judith Fonken[1], Esther Maas[1], Arjet Nievergeld[1], Floris Verheijen[1], Hein de Hoop[1], Marc van Sambeek[2], Frans van de Vosse[1], Richard Lopata[1]
*[1]Eindhoven University of Technology, [2]Catharina Hospital Eindhoven*

**12:00PM** **Computational Fluid Dynamics Model of Embryonic Heart and Supporting Vasculature Illustrates Temporal and Spatial Variation in Wall Shear Stress During Cardiac Cycle** SB³C2022-123
Kirsten Giesbrecht, Simone Rossi, Boyce Griffith
*University of North Carolina- Chapel Hill*

**12:15PM** **Analysis of Tracheal Air Flow Dynamics in Infant Tracheal Stenosis Before and after Repair Using 3D Printing and Computational Fluid Dynamics Modeling** SB³C2022-406
Clare Richardson[1,2], Michael Barbour[1], Seth Friedman[2], Randall Bly[1,2], John Dahl[1,2], Kaalan Johnson[1,2], Alberto Aliseda[1]
*[1]University of Washington, [2]Seattle Children's Hospital*

**12:30PM** **Analysis of Upper Airway Flow Dynamics in Infants with Robin Sequence Using 4-Dimensional Computed Tomography and Computational Fluid Dynamics Modeling** SB³C2022-398
Michael Barbour[1], Clare Richardson[1,2], Michael Bindschadler[2], Seth Friedman[2], Randall Bly[1,2], John P. Dahl[1,2], Alberto Aliseda[1]
*[1]University of Washington, [2]Seattle Children's Hospital*

| Monday, June 20 | 11:15AM – 12:45PM EDT |
|---|---|

## Vascular Mechanics II

**Chesapeake E**

**Session Chairs: Chiara Bellini,** *Northeastern University*
**Lucas Timmins,** *University of Utah*

**11:15AM** **Critical Pressure of Intramural Delamination in Aortic Dissection** SB³C2022-191
Ehsan Ban, Cristina Cavinato, Jay Humphrey
*Yale University*

**11:30AM** **Effect of Renal Denervation on the Biomechanical Properties of Common Carotid Arteries in Rats** SB³C2022-365
Anastasia Gkousioudi, Margherita Razzoli, Jesse Moreira, Gianluca Harbert, Richard Wainford, Katherine Zhang
*Boston University*

**11:45AM** **Inter-Donor Variability in the Tensile and Compressive Behaviour of In Vitro Human Thrombi** SB³C2022-224
Rachel Cahalane, Judith de Vries, Moniek de Maat, Kim van Gaalen, Heleen van Beusekom, Aad van der Lugt, Ali Akyildiz, Frank Gijsen
*Erasmus Medical Center*

**12:00PM** **Measurement of stent retriever removal forces in an experimental model of acute ischemic stroke** SB³C2022-104
Demitria Poulos, Bryan Good
*University of Tennessee*

**12:15PM** **Using a Tissue-Engineered Model to Investigate the Impact of Collagen Orientation on the Local Mechanical Behavior of Atherosclerotic Plaque Caps** SB³C2022-280
Hanneke Crielaard[1], Tamar Wissing[2], Su Guvenir Torun[1], Pablo de Miguel[1], Ranmadusha Hengst[3], Gert-Jan Kremers[1], Frank Gijsen[1], Kim van der Heiden[1], Ali Akyildiz[1]
*[1]Erasmus Medical Center, [2]Eindhoven University of Technology, [3]Delft University of Technology*

**12:30PM** **Mechanical Remodeling of Murine Thoracic Aorta During Pregnancy** SB³C2022-470
Ana I. Vargas, Samar Tarraf, Rouzbeh Amini, Chiara Bellini
*Northeastern University*

| Monday, June 20 | 11:15AM – 12:45PM EDT |
|---|---|

# Tendon & Ligament Mechanics

**Chesapeake F**

**Session Chairs: Benjamin Wheatley,** *Bucknell University*
**Jill Middendorf,** *University of Minnesota*

**11:15AM** **A Soft Tissue Grasping Device for Enhanced Rotator Cuff Repair Inspired By Python Teeth** SB³C2022-232
Iden Kurtaliaj[1], Ethan Hoppe[2], Yuxuan Huang[2], Mark Lipkin[2], Thomas Gardner[1], Liana Tedesco[1], Sohil Desai[1], Silvio Bentacur[1], Linda Effiong[1], William Levine[1], Guy Genin[2], Stavros Thomopoulos[1]
*[1]Columbia University, [2] Washington University*

**11:30AM** **Shear Wave Speed as a Measure of Regional Tendon Stress** SB³C2022-366
Jonathon Blank[1], Darryl Thelen[1], Matthew Allen[2], Joshua Roth[1]
*[1]University of Wisconsin-Madison, [2]Brigham Young University*

**11:45AM** **Injury Criteria: Defining Mechanical Thresholds for Collagen in Soft Tissues** SB³C2022-380
Callan Luetkemeyer[1], Kaitlin McCreery[1], Kathryn Jacobson[2], Corey Neu[1], Sarah Calve[1]
*[1]University of Colorado Boulder, [2]Purdue University*

**12:00PM** **Differences in Porcine ACL Morphology and Function are Minor Between Boars and Barrows at Early Adolescence** SB³C2022-404
Jacob Thompson[1,2], Danielle Howe[1,2], Lauren Schnabel[1], Matthew Fisher[1,2]
*[1]North Carolina State University, [2]University of North Carolina-Chapel Hill*

**12:15PM** **Biological Response of Rabbit Anterior Cruciate Ligaments To Mechanical Loading is Sex-Specific** SB³C2022-329
Lauren Paschall, Aman Dhawan, Spencer Szczesny
*Penn State University*

**12:30PM** **Effect of Mechanical Loading on the Microstructure and Diffusion Imaging Properties of Ligament-Mimicking Fibers** SB³C2022-116
Roberto Pineda Guzman, Noel Naughton, Bradley Sutton, Mariana Kersh
*University of Illinois*

| Monday, June 20 | 11:15AM – 12:45PM EDT |
|---|---|

## Biomechanics of the Eye, Pelvic Floor, and Reproductive Track II

**Chesapeake G**

**Session Chairs: Andrew Feola,** *Emory University and Atlanta VA Medical Center*
**Cyrus Rezvanifar,** *University of Minnesota*

**11:15AM** **Mechanical Anisotropy of the Equatorial Sclera Does not Concur with the Primary Collagen Fiber Orientations** SB³C2022-349
Yi Hua[1], Samuel Salinas[2], Marissa Quinn[1], Fengting Ji[1], Rouzbeh Amini[2], Ian A. Sigal[1]
*[1]University of Pittsburgh, [2]Northeastern University*

**11:30AM** **The Effects of Negative Periocular Pressure on Biomechanics of the Optic Nerve Head And Cornea: A Computational Modeling Study** SB³C2022-306
Babak Safa[1], John Berdahl[2], C. Ross Ethier[1]
*[1]Georgia Institute of Technology, [2]Vance Thompson Vision*

**11:45AM** **The Strain Response of the Human Lamina Cribrosa from Intraocular Pressure Decrease** SB³C2022-354
Cameron Czerpak[1], Michael Kashaf[2], Brandon Zimmerman[1], Harry Quigley[1], Thao Nguyen[1]
*[1]Johns Hopkins University, [2]University of California San Diego*

**12:00PM** **Vaginal Biomechanical Function and Composition in Premenopausal Women with and Without Pelvic Organ Prolapse** SB³C2022-347
Qinhan Zhou[1], Benard Ogola[1], Jasmine Kiley[1], Shelby White[1], Lyndsey Buckner[2], Laurephile Desrosiers[2], Leise Knoepp[2], Sarah Lindsey[1], Kristin Miller[1]
*[1]Tulane University, [2]Ochsner Health System*

**12:15PM** **Time-Dependent Material Properties of Nonpregnant and Pregnant Human Uterus Under Spherical Nanoindentation** SB³C2022-284
Daniella Fodera[1], Shuyang Fang[1], Michelle Oyen[2], Kristin Myers[1]
*[1]Columbia University, [2]Washington University in St. Louis*

**12:30PM** **Female Pelvic Morphological Variation in the Generation of Geometries for Simulations of Vaginal Childbirth** SB³C2022-196
Megan Routzong[1], Steven Abramowitch[2]
*[1]University of California, San Diego, [2]University of Pittsburgh*

| Monday, June 20 | 11:15AM – 12:45PM EDT |
|---|---|

# Brain & Injury Mechanics I

**Clipper A-C**

**Session Chairs: Johannes Weickenmeier,** *Stevens Institute of Technology*
**Brittany Coats,** *University of Utah*

**11:15AM** **In Vivo Quantification of Relative Skull-Brain Motion Using MR Elastography** SB³C2022-253
Alexa Diano[1], Grace McIlvain[1], Suhas Vidhate[2], Andrew Knutsen[2], Dzung Pham[2], Curtis Johnson[1]
*[1]University of Delaware, [2]Henry M. Jackson Foundation*

**11:30AM** **Recent Updates on the GHBMC Human Head Finite Element Model- Development of Crash Injury Index for Multiple Brain Injuries** SB³C2022-442
Ding Lyu, Shirin Phadke, Abhijeet Kumbhare, Liying Zhang
*Wayne State University*

**11:45AM** **On-Field Evaluation of Mouthpiece- And Helmet-Mounted Sensor Data from Head Kinematics in Football** SB³C2022-314
Ty Holcomb, Madison Marks, Stewart Pritchard, Logan Miller, Jillian Urban, Joel Stitzel
*Wake Forest School of Medicine*

**12:00PM** **Simulation of Murine Brain Deformation During Chimera Impacts** SB³C2022-414
Connor Bradfield, Liming Voo, K.T. Ramesh
*Johns Hopkins University*

**12:15PM** **Multi-Dimensional Morphometric Analysis of Posterior Fossa to Study Type I Chiari Malformation** SB³C2022-228
Ya-Chen Chuang[1], Alejandro Carrasquilla[2], Aymeric Pionteck[1], Javid Abderezaei[1], Addison Quinones[2], Gizem Bilgili[1], William H. Shuman[2], Shan Zhao[2], Raj K. Shrivastava[2], Mehmet Kurt[1]
*[1]University of Washington, [2]Icahn School of Medicine*

**12:30PM** **Effect of Helmet Size and Velocity on Cervical Spine Segmental Responses Under Rear Impact Acceleration** SB³C2022-419
Yuvaraj Purushothaman, Hoon Choi, Narayan Yoganandan
*Medical College of Wisconsin*

| Monday, June 20 | 11:15AM – 12:45PM EDT |
|---|---|

# Cardiovascular Tissue Engineering

**Galleon A-C**

**Session Chairs: Zhijie Wang,** *Colorado State University*
**Will Richardson,** *Clemson University*

**11:15AM** **Vascular Smooth Muscle Cells Upregulate Glycolytic and Contractile Phenotype Genes in the Presence of Glutamine** SB$^3$C2022-362
Pattie Mathieu, Alisa Clyne
*University of Maryland College Park*

**11:30AM** **Development of an In Vitro Experimental Model to Study Endothelial Dysfunction from Coarctation of the Aorta** SB$^3$C2022-352
Dylan Schock[1], Hilda Martinez Ramirez[1], Joy Lincoln[1], Abdel Alli[2], John LaDisa[1,3]
*[1]Medical College of Wisconsin, [2]University of Florida, [3]Herma Heart Institute, Children's Wisconsin*

**11:45AM** **A Structural Bio-Chemo-Mechanical Model for Traction Force Microscopy of Vascular Smooth Muscle Cells** SB$^3$C2022-40
Shannon Flanary, Victor Barocas
*University of Minnesota*

**12:00PM** **Mechanical Cues Such as Shear Stress and Piezo1 Activation Generate Red Blood Cell Extracellular Vesicles** SB$^3$C2022-192
Gurneet Sangha, Callie Weber, Ryan Sapp, Morgan Pettebone, Alisa Clyne
*University of Maryland College Park*

**12:15PM** **Perturbed Cyclic Strain in Cardiac Fibroblast Cultures Results in a Mechanically-Induced Senescent Phenotype** SB$^3$C2022-418
Stephanie E. Schneider, Adrienne K. Scott, Corey P. Neu
*University of Colorado at Boulder*

**12:30PM** **Microfabricated Anisotropic Tissue Bundles for the Production of 3D Cardiac Tissue at Scale** SB$^3$C2022-332
Maggie Jewett, Amanda Bluem, Samuel DePalma, Brendon Baker
*University of Michigan*

| Monday, June 20 | 11:15AM – 12:45PM EDT |
|---|---|

## Transport in Hemodynamics and Lymphatics

**Schooner A-B**

**Session Chairs: Ellie Rahbar,** *Wake Forest University*
**Jifu Tan,** *Northern Illinois University*

**11:15AM** **Material Property Changes of Polymerized Red Blood Cells in Sickle Cell Disease** SB³C2022-100
Dillon Williams, David Wood
*University of Minnesota*

**11:30AM** **Regional Differences in Perivascular Adipose Tissue Following Angiotensin II-Induced Hypertension** SB³C2022-474
Yujun Xu, J. Caleb Snider, Niyousha Karbasion, Matthew R. Bersi
*Washington University in St. Louis*

**11:45AM** **Linking Circulatory Turbulence and the Pathophysiology of Sickle Cell Disease** SB³C2022-160
Eudorah Vital[1], Alice Liu[2], Christina Caruso[3], David Bark[2], Wilbur Lam[1]
*[1]Georgia Institute of Technology, [2]Washington University in St. Louis, [3]Emory University*

**12:00PM** **Perivascular Cerebrospinal Fluid Flow is a Major Source of Interstitial Fluid and its Clearance in the Rat Brain** SB³C2022-210
Kristian Mortensen[1], Tuomas Lilius[1], Marko Rosenholm[1], Björn Sigurđsson[1], Douglas Kelley[2], Maiken Nedergaard[1]
*[1]University of Copenhagen, [2]University of Rochester*

**12:15PM** **Efflux of Cerebrospinal Fluid Through Cervical Lymph Vessels is Reduced in Aged Mice** SB³C2022-271
Aditya Raghunandan, Ting Du, Virginia Pla-Requena, Yara Izhiman, Guojun Liu, Maiken Nedergaard, Douglas Kelley
*University of Rochester*

**12:30PM** **Plasmonic Lamp: Highly Specific and Sensitive Detection of SARS-CoV-2 by Plasmonic Sensing of Isothermally Amplified Nucleic Acids** SB³C2022-310
Haihang Ye, Chance Nowak, Yaning Liu, Yi Li, Tingting Zhang, Leonidas Bleris, Zhenpeng Qin
*University of Texas at Dallas*

| Monday, June 20 | 11:15AM – 12:45PM EDT |
|---|---|

# Mechanics in Multi-Tissue Networks

**Cutter A-B**

**Session Chairs: Jacqueline Cole,** *University of North Carolina and North Carolina State University*
**Christopher Price,** *University of Delaware*

**11:15AM** **Evaluating the Effect of Pufas on Hepatic Stellate Cell Activation in a 3D Tissue Engineered Model of Hepatic Fibrosis** SB³C2022-57
L. Madison Kirk[1], Nathaniel Hauser[1], Lucy J. Price[1], Chia-Chi Chuang Key[1], Aleksander Skardal[2], Elaheh Rahbar[1]
*[1]Wake Forest University, [2]Ohio State University*

**11:30AM** **Functional Hyperemia Increases Influx of Cerebrospinal Fluid to the Brain** SB³C2022-130
Yiming Gan[1], Stephanie Holstein-Rønsbo[2], Douglas Kelley[1], Maiken Nedergaard[1]
*[1]University of Rochester, [2]University of Copenhagen*

**11:45AM** **Expression of the Injury Marker Activating Transcription Factor-3 After Exposure to MMP-1 is Decreased in a Neuron Collagen Co-Culture with Phospholipase A2 Inhibition** SB³C2022-279
Sagar Singh, Prabesh Ghimire, Beth Winkelstein
*University of Pennsylvania*

**12:00PM** **Investigating Structural Changes of Neonatal Brachial Plexus Post-Stretch** SB³C2022-431
Virginia Orozco[1], Rachel Magee[1], Mital Sahni[2], Sriram Balasubramanian[1], Anita Singh[3]
*[1]Drexel University, [2]Sunrise Children's Hospital, [3]Widener University*

**12:15PM** **Determining Effects on Pig Gait after Induced Traumatic Brain Injury: Initial Assessments** SB³C2022-187
Sloan Kanat, Paige Cordts, Alesa Hughson, Galit Pelled, Tamara Reid Bush
*Michigan State University*

**12:30PM** **Early Removal of the Infrapatellar Fat Pad in a Spontaneous Rodent Model of Osteoarthritis May Beneficially Alter the Development of Osteoarthritis** SB³C2022-165
Tammy Haut Donahue[1], Mary Afzali[2], Nicole Vigon[3], Ryan Ek[3], Gerardo Narez[3], Kelly Santangelo[2]
*[1]University of Memphis, [2]Colorado State University, [3]University of Massachusetts-Amherst*

| Tuesday, June 21 | 9:30AM – 11:00AM EDT |
|---|---|

# PhD-Level Student Paper Competition Session 1: Biofluid Mechanics and Cardiovascular Imaging

**Chesapeake A-D**

**Session Chairs: Elaheh Rahbar,** *Wake Forest University*
**Joseph van Batenburg-Sherwood,** *Imperial College London*

**9:30AM** **Radiomics Features on Contrast-Enhanced and Non-Enhanced MRI are Associated with Intracranial Aneurysmal Risk** SB³C2022-105
Sricharan Veeturi, Nandor Pinter, Adnan Siddiqui, Vincent Tutino
*University at Buffalo*

**9:45AM** **A Smart-PIV Approach for In Vitro Evaluation of Coronary Hemodynamics** SB³C2022-31
Elena Torta, Giuseppe Carlo Alp Caridi, Claudio Chiastra, Diego Gallo, Umberto Morbiducci
*Politecnico di Torino*

**10:00AM** **Global and Regional Quantification of Cardiotoxicity due to Radiotherapy Using Cardiac Magnetic Resonance Imaging: A Pilot Study in Lung Cancer** SB³C2022-151
Alireza Omidi, Mihaela Rosu-Bubulac, Georgia Thomas, Elisabeth Weiss, John S. Wilson
*Virginia Commonwealth University*

**10:15AM** **Predicting Hemodynamic Indices in Coronary Artery Aneurysms Using Response Surface Method: An Application in Kawasaki Disease** SB³C2022-118
Alireza Asadbeygi[1], Simon Lee[2], John Kovalchin[2], Hoda Hatoum[1]
*[1]Michigan Technological University, [2]Nationwide Children Hospital*

**10:30AM** **Patient-Specific Finite Element Modeling to Predict Clinical Risks of Percutaneous Pulmonary Valve Implantation** SB³C2022-94
Carly Donahue, Varun Aggarwal, Victor Barocas
*University of Minnesota*

**10:45AM** **Computational Modeling of Cryoballoon Ablation for Pulmonary Vein Isolation** SB³C2022-55
Tejas Patel[1], Chris Li[1], Farshad Raissi[2], Ghassan Kassab[3], Tong Gao[1], Lik Chuan Lee[1]
*[1]Michigan State University, [2]University of California, [3]California Medical Innovations Institute*

| Tuesday, June 21 | 9:30AM – 11:00AM EDT |
|---|---|

# PhD-Level Student Paper Competition Session 2: Tendon, Ligament, and Joint

**Chesapeake E**

**Session Chairs: Brianne Connizzo,** *Boston University*
**Guy Genin,** *Washington University in St. Louis*

**9:30AM** **Mechanical and Structural Changes Due to Tendon Overload in a Rat Model of Synergist Ablation** SB³C2022-112
Ellen Bloom, Lily Lin, Justin Parreno, Karin Gravare Silbernagel, Dawn Elliott
*University of Delaware*

**9:45AM** **Collagen Hybridizing Peptides Extend the Retention Time of Imaging Markers in Healthy and Osteoarthritic Rat Stifle Joints** SB³C2022-139
Emma Luke, Michael Yu, Jeffrey Weiss
*University of Utah*

**10:00AM** **Elastic Strength and its Relation to Mineral Density in Juvenile Equine Bones of the Lower Limb** SB³C2022-41
Sara Moshage, Annette McCoy, Mariana Kersh
*University of Illinois*

**10:15AM** **Mouse Supraspinatus Tendon Mechanical and Structural Properties are Dependent on Region and Age** SB³C2022-17
Michael DiStefano, Patrick Paglia, Stephanie Weiss, Snehal Shetye, Andrew Kuntz, Louis Soslowsky
*University of Pennsylvania*

**10:30AM** **Collagen Fibrils from Positional Tendons Exhibit Increased Amounts of Denatured Collagen Upon Reaching the Yield Point** SB³C2022-134
Allen Lin[1], Steven Eppell[2], Seungju Yu[1], Jeffrey Weiss[1]
*[1]University of Utah, [2]Case Western Reserve University*

**10:45AM** **Partial ACL Injury Location Impacts Biomechanics and Tissue Remodeling in a Skeletally Immature Porcine Model** SB³C2022-91
Danielle Howe[1,2], Jacob Thompson[1,2], Andre Bautista[1,2], Lauren Schnabel[1], Jeffrey Spang[2], Matthew Fisher[1,2]
*[1]North Carolina State University, [2]University of North Carolina- Chapel Hill*

| Tuesday, June 21 | 9:30AM – 11:00AM EDT |
|---|---|

# PhD-Level Student Paper Competition Session 3: Tissue Engineering, Remodeling, and Emerging Areas

**Chesapeake F**

**Session Chairs: Raffaella De Vita,** *Virginia Tech*
**Andrew Feola,** *Emory University and Atlanta VA Medical Center*

**9:30AM** **Epithelial Fluid Secretion and Luminal Pressure Regulate the Patterns of Proliferation that Sculpt the Developing Bronchial Tree** SB³C2022-145
Shelby Mohr-Allen, Victor Varner
*University of Texas at Dallas*

**9:45AM** **The Heterogenous and Anisotropic Mechanics of the Airway Tree** SB³C2022-13
Samaneh Sattari, Crystal Mariano, Mona Eskandari
*University of California Riverside*

**10:00AM** **PDGF-BB Disrupts the Stiffness-Dependent Myofibroblastic Differentiation of Corneal Keratocytes in Response to TGF-B1** SB³C2022-141
Krithika Shankar Iyer[1], David Schmidtke[1], Matthew Petroll[2], Victor Varner[1]
*[1]University of Texas at Dallas, [2]University of Texas Southwestern Medical Center*

**10:15AM** **Cervical Material Remodeling in Pregnancy Using a Nonhuman Primate Model** SB³C2022-125
Shuyang Fang[1], Lei Shi[1], Ivan Rosado-Mendez[2], Helen Feltovich[3], Timothy Hall[2], Kristin Myers[1]
*[1]Columbia University, [2]University of Wisconsin-Madison, [3]Intermountain Healthcare*

**10:30AM** **An Experimental and Numerical Investigation of Cardiac Tissue-Patch Interrelation** SB³C2022-76
Gozde Basara, Gokhan Bahcecioglu, Xiang Ren, Pinar Zorlutuna
*University of Notre Dame*

**10:45AM** **Patterns of Tissue Stiffness Correlate with Distributions of Proliferation and Yap Activity Along the Embryonic Ureteric Tree** SB³C2022-154
Somdutta Chakraborty[1], Thomas Carroll[2], Victor Varner[1]
*[1]University of Texas at Dallas, [2]UT Southwestern Medical Center*

| Tuesday, June 21 | 9:30AM – 11:00AM EDT |
|---|---|

# Valves

**Chesapeake G**

**Session Chairs: Jonathan Wenk,** *University of Kentucky*
**Lakshmi Dasi,** *Georgia Institute of Technology*

**9:30AM** **Measuring the Efficacy of Right Atrial Appendage Tissue to Withstand Pulmonary Hypertensive Conditions as a Functional Pulmonary Valve** SB³C2022-188
Kate Appleman[1], Katarina Lettner[1], Andrew Behrmann[1], Pirooz Eghtesady[2], Shamik Bhattacharya[1]
*[1]Missouri State University, [2]Washington University in St. Louis*

**9:45AM** **Texas TriValve 1.0: A Reverse-Engineered, Open Model of the Human Tricuspid Valve** SB³C2022-435
Mrudang Mathur[1], William Meador[1], Marcin Malinowski[2], Tomasz Jazwiec[2], Tomasz Timek[3], Manuel Rausch[1]
*[1]University of Texas at Austin, [2]University of Silesia, [3]Spectrum Health*

**10:00AM** **Bioprosthetic Leaflet Stress Following Transcatheter Aortic Valve Replacement in Bicuspid Aortic Valves** SB³C2022-424
Breandan Yeats[1], Aniket Venkatesh[1], Milad Samaee[1], Pradeep Yadav[2], Venkateshwar Polsani[2], Vinod Thourani[2], Lakshmi Dasi[1]
*[1]Georgia Institute of Technology, [2]Piedmont Hospital*

**10:15AM** **Dynamic In-Vivo Motion of the Mouse Aortic Heart Valve** SB³C2022-457
Xinzeng Feng[1], Daniel Gramling[2], Aletea vanVeldhuisen[2], David McComb[3], Christopher Breuer[4], Craig Goergen[2], Michael Sacks[1]
*[1]University of Texas at Austin, [2]Purdue University, [3]Ohio State University, [4]Nationwide Children's Hospital*

**10:30AM** **An Experimental Approach to Quantify the Pre-Strains of the Tricuspid Heart Valve Leaflets** SB³C2022-405
Devin Laurence, Chung-Hao Lee
*University of Oklahoma*

**10:45AM** **Multiscale Modeling of Cardiac Valve Disease Using Cell-Level Signals to Drive Myocardial Growth** SB³C2022-42
Hossein Sharifi, Austin Wellette-Hunsucker, Charles Mann, Kenneth Campbell, Jonathan Wenk
*University of Kentucky*

| Tuesday, June 21 | 9:30AM – 11:00AM EDT |
|---|---|

# Brain & Injury Mechanics II

**Clipper A-C**

**Session Chairs: Mehmet Kurt,** *University of Washington*
**Sarah Bentil,** *Iowa State University*

**9:30AM** **Network-Based Modeling of Alzheimer's Disease Assessing Impact of Connectome Measures on Progression Patterns** SB³C2022-110
Shima Jalalian[1], Oren Civier[2], Johannes Weickenmeier[1]
*[1]Stevens Institute of Technology, [2]Swinburne University of Technology*

**9:45AM** **Denoising Instrumented Mouthguards for Accurate Traumatic Brain Injury Detection with Convolutional Neural Network** SB³C2022-8
Xianghao Zhan, Yuzhe Liu, Olivier Gevaert, David Camarillo
*Stanford University*

**10:00AM** **Development of a Parameterized Microscale Axonal Injury Model** SB³C2022-26
Chaokai Zhang, Songbai Ji
*Worcester Polytechnic Institute*

**10:15AM** **Spatial Gradient in Frontal Lobe Stiffness During Brain Maturation** SB³C2022-333
Kyra Twohy, Grace McIlvain, Curtis Johnson
*University of Delaware*

**10:30AM** **Relationships Between Athletic Performance Measures and Head Kinematics in Youth Ice Hockey** SB³C2022-378
Abigail Swenson[1], N. Stewart Pritchard[1], Logan Miller[1], Chesney Oravec[1], Jason Mihalik[2], Jillian Urban[1], Joel Stitzel[1]
*[1]Wake Forest School of Medicine [2]University of North Carolina- Chapel Hill*

**10:45AM** **Infant Skull Fracture Pattern Characteristics from Low-Height Falls** SB³C2022-476
Yousef Alsanea, Tagrid Ruiz-Maldonado, Brittany Coats
*University of Utah*

| Tuesday, June 21 | 9:30AM – 11:00AM EDT |
|---|---|

## Soft Tissue Biomechanics

**Galleon A-C**

**Session Chairs: Chiara Bellini,** *Northeastern University*
**Babak Safa,** *Georgia Institute of Technology*

**9:30AM** **Carpal Arch Space Augmentation by Volarly Applied Force on the Skin Surface- A Finite Element Study** SB³C2022-14
Hui Zhang, Zong-Ming Li
*University of Arizona*

**9:45AM** **A Discrete-Fiber Model for Understanding Cellular Mechanoadaptation** SB³C2022-247
Ryan Mahutga, Patrick Alford
*University of Minnesota*

**10:00AM** **Precise Measurement of Microparticle Viscoelastic Properties Using a Microfluidic Extensional Flow Device** SB³C2022-465
Sara Ghanbarpour Mamaghani, Joanna Dahl
*University of Massachusetts Boston*

**10:15AM** **Cortical Thickness Correlates with Cortical Morphology Among Human and Non-Human Primate Brains** SB³C2022-52
Nagehan Demirci, Maria Holland
*University of Notre Dame*

**10:30AM** **A Novel Approach for Mapping 3D Extracellular Matrix Mechanics at the Cellular Scale Using Magnetic Microparticles** SB³C2022-256
Adil Khan, Jacopo Ferruzzi
*University of Texas at Dallas*

**10:45AM** **Comparative Study of Chemical and Nanomechanical Properties of Cat and Rat Vibrissae** SB³C2022-324
Davin Sim, Donna Ebenstein
*Bucknell University*

| Tuesday, June 21 | 9:30AM – 11:00AM EDT |
|---|---|

# Transport in Drug Delivery and Discovery

**Schooner A-B**

**Session Chairs: Govind Srimathveeravalli,** *University of Massachusetts Amherst*
**Malisa Sarntinoranont,** *University of Florida*

**9:30AM** **An Physiological On-Chip Vessel Platform to Study Vascular Transport of Circulating Tumor Cells** SB³C2022-146
Yue Wu, Yuyuan Zhou, Ratul Paul, Yaling Liu
*Lehigh University*

**9:45AM** **Drug Discovery for Selective Targeting of Pancreatic Cancer Cells Using Microfluidic Tumor-Stroma Model** SB³C2022-447
Hye-ran Moon[1], Mark R. Kelley[2], Melissa L. Fishel[2], Bumsoo Han[1]
*[1]Purdue University, [2]Indiana University*

**10:00AM** **3D Microfluidic Cell Arrays with Recirculation and Tumor-Stroma Interaction for the Development of Immunotherapeutic Drug** SB³C2022-461
Chun-Wei Chi[1], Yeh-Hsing Lao[2], A.H. Rezwanuddin Ahmed[1], Kam W. Leong[2], Sihong Wang[1]
*[1]CUNY City College of New York, [2]Columbia University*

**10:15AM** **Molecular Design of Polyelectrolyte Complex Micelles for Nucleic Acid Delivery** SB³C2022-292
Alexander Marras, Jeffrey Vieregg, Matthew Tirrell
*University of Chicago*

**10:30AM** **Minimally Invasive Blood-Spinal Cord Barrier Modulation for Drug Delivery** SB³C2022-243
Zhenghong Gao[1], Eric David[1], Tiffany Wei Leong[1], Xiaoqing Li[1], Qi Cai[1], Monica Giannotta[2], Elisabetta Dejana[2], John Wiggins[1], Sharada Krishnagiri[1], Robert Bachoo[3], Theodore J. Price[1], Zhenpeng Qin[1]

*[1]University of Texas at Dallas, [2]FIRC Institute of Molecular Oncology Foundation, [3]University of Texas Southwestern Medical Center*

**10:45AM** **Simple Analytic Model for Peristaltic Flow and Mixing** SB³C2022-51
Ruy Ibanez, Mohammad Shokrian, Jong-Hoon Nam, Douglas Kelley
*University of Rochester*

| Tuesday, June 21 | 9:30AM – 11:00AM EDT |
|---|---|

## Cartilage Mechanics & Musculoskeletal Imaging

**Cutter A-B**

**Session Chairs: Deva Chan,** *Purdue University*
**Mohammad Islam,** *University of Pittsburgh*

**9:30AM** **Superficial Zone Chondrocytes can get Compacted Under Physiological Loading: A Multiscale Finite Element Analysis** SB³C2022-455
Kimberly Kroupa, Katherine Spack, Lianna Gangi, Nadeen Chahine, Clark Hung, Gerard Ateshian
*Columbia University*

**9:45AM** **Effects of Compromised Synovial Fluid on Articular Cartilage Tribological Rehydration and Lubrication** SB³C2022-323
Shamimur Akanda, David Burris, Christopher Price
*University of Delaware*

**10:00AM** **A Chemo-Mechano-Biological Model of Evolving Osteoarthritis** SB³C2022-147
Muhammed M. Rahman[1], Paul N. Watton[2], Thomas S. E. Öst[3], Corey P. Neu[4], David M. Pierce[1]
*[1]University of Connecticut, [2]University of Sheffield, [3]Swedish Defense Research Agency, [4]University of Colorado Boulder*

**10:15AM** **Novel In Vivo Articular Cartilage Elastography Pipeline to Determine Mechanical Properties from Dynamic MRI Deformation Analysis** SB³C2022-36
Emily Miller[1], Hongtian Zhu[1], Woowon Lee[1], Stephane Avril[2], Corey Neu[1]
*[1]University of Colorado Boulder, [2]Univ Lyon Univ Jean Monnet*

**10:30AM** **Ultrasonic Analysis Reveals Layer-Dependent Shear Wave Propagation in the Patellar Tendon and Superficial Tissues** SB³C2022-343
Stephanie Cone, Lauren Welte, Darryl Thelen
*University of Wisconsin*

**10:45AM** **Accelerated Acquisition of In Vivo Cartilage Strain using Compressed Sensing and Spiral DENSE MRI** SB³C2022-185
Woowon Lee, Emily Miller, Hongtian Zhu, Corey Neu
*University of Colorado Boulder*

| Tuesday, June 21 | 11:15AM – 12:45PM EDT |
|---|---|

# PhD-Level Student Paper Competition Session 4: Cardiovascular Mechanics

**Chesapeake A-D**

**Session Chairs: Sara Roccabianca,** *Michigan State University*
**Matthew Bersi,** *Washington University in St. Louis*

**11:15AM** **Aortic Structural and Functional Remodeling in Response to Chronic E-Cigarette or Cigarette Exposure in the Apoe-/- Female Mouse** SB³C2022-149
Yasmeen Farra, Jacqueline Matz, Jessica Oakes, Chiara Bellini
*Northeastern University*

**11:30AM** **Multiscale Modeling of Restenosis after Percutaneous Transluminal Angioplasty: Towards a Patient-Specific Analysis** SB³C2022-33
Anna Corti[1], Monika Colombo[2], Cemre Çelikbudak[1], Philippe Büchler[3], Francesco Migliavacca[1], Scott Berceli[4], Stefano Casarin[5], Jose Felix Rodriguez Matas[1], Claudio Chiastra[6]
*[1]Politecnico di Milano, [2]ETH Zurich, [3]University of Bern, [4]University of Florida, [5]Houston Methodist Hospital, [6]Politecnico di Torino*

**11:45AM** **Tricuspid Valve Annulus Mechanics and Geometry in Newborns with Hypoplastic Left Heart Syndrome** SB³C2022-9
Colton Ross, Elizabeth Trimble, Arshid Mir, Harold Burkhart, Chung-Hao Lee
*University of Oklahoma*

**12:00PM** **Assessing Arterial Stiffness in Human Blood Pressure Waveform Using Harmonic Distortion** SB³C2022-95
Nicholas Milkovich[1], Gary Mitchell[2], Béla Suki[1], Yanhang Zhang[1]
*[1]Boston University, [2]The Framingham Heart Study*

**12:15PM** **A 3D Computational Model of Aortic Valve Interstitial Cell Contractile Behavior within a Peg Hydrogel Medium** SB³C2022-93
Alex Khang, John Steinman, Xinzeng Feng, Michael Sacks
*University of Texas at Austin*

**12:30PM** **Post-Stretch Behavior of Vascular Smooth Muscle Cells Depends on Strain-Rate and Actomyosin Interactions** SB³C2022-23
Samuel Boland, Patrick Alford
*University of Minnesota*

| Tuesday, June 21 | 11:15AM – 12:45PM EDT |
|---|---|

# PhD-Level Student Paper Competition Session 5: Orthopaedic Bioengineering and Mechanotherapeutics

**Chesapeake E**

**Session Chairs: Kyoko Yoshida,** *University of Minnesota*
**Manuel Rausch,** *University of Texas at Austin*

**11:15AM** **Large Animal Model of Meniscus Injury and Repair Shows Chondroprotection and Partially Restores Joint Kinematics as Measured via MRI** SB³C2022-24
Kyle Meadows[1], Brendan Stoeckl[2], John Peloquin[1], Adriana Barba[2], Eddie Bonnevie[2], Sonia Bansal[2], David Steinberg[2], Miltiadis Zgonis[2], Thomas Schaer[2], Robert Mauck[2], Dawn Elliott[1]
*[1]University of Delaware, [2]University of Pennsylvania*

**11:30AM** **Inhibiting Epigenetic Modifiers Rescues Chondrocyte Fate Following Cell Expansion for Cartilage Regeneration** SB³C2022-131
Adrienne Scott, Katie Gallagher, Stephanie Schneider, Corey Neu
*University of Colorado Boulder*

**11:45AM** **Mechanotherapeutics to Modulate the Foreign Body Response** SB³C2022-98
Niamh Ward[1], William Whyte[2], Debkalpa Goswami[2], Ruth Levey[1], Garry Duffy[1], Ellen Roche[2], Eimear Dolan[1]
*[1]National University of Ireland, [2]Massachusetts Institute of Technology*

**12:00PM** **Stimulating the Hedgehog Signaling Pathway to Improve Zonal Tendon-To-Bone Integration** SB³C2022-80
Timur Kamalitdinov, Keitaro Fujino, Xi Jiang, Sinaia Keith Lang, Mary Evans, Miltiadis Zgonis, Andrew Kuntz, Nathaniel Dyment
*University of Pennsylvania*

**12:15PM** **In Vivo Human Knee Varus-Valgus Loading Apparatus for Analysis of MRI-Based Intratissue Strain and Relaxometry** SB³C2022-152
Hongtian Zhu, Emily Miller, Woowon Lee, Robert Wilson, Corey Neu
*University of Colorado Boulder*

**12:30PM** **Hyaluronan, PRG4, and Cytokine Production in Synoviocytes is Sensitive to Cyclic Strain Magnitude** SB³C2022-67
Meghana Pendyala[1], Paige Woods[2], Douglas Brubaker[3], Elizabeth Blaber[1], Tannin Schmidt[2], Deva Chan[3]
*[1]Rensslaer Polytechnic Institute, [2]University of Connecticut, [3]Purdue University*

| Tuesday, June 21 | 11:15AM – 12:45PM EDT |
|---|---|

# PhD-Level Student Paper Competition Session 6: Growth & Remodeling in Injury and Disease

**Chesapeake F**

**Session Chairs: Maria Holland,** *University of Notre Dame*
**Jacopo Ferruzzi,** *University of Texas at Dallas*

**11:15AM** **APOE E4 Genotype Decreases Barrier Function and Glucose Uptake in Induced Pluripotent Stem Cell-Derived Brain Microvascular Endothelial Cells** SB³C2022-73
Callie Weber, Sophia Zic, Alisa Clyne
*University of Maryland College Park*

**11:30AM** **A Multiparameter Whole Blood Hemostasis Assessment Using a Highly Sensitive Flexible Carbon Nanotube Paper-Based Capacitance Sensor** SB³C2022-148
Praveen Kaliappan Sekar, Ye Jin, Dayong Gao
*University of Washington*

**11:45AM** **Progressive Mechanical and Structural Changes in Anterior Cerebral Arteries with Alzheimer□s Disease** SB³C2022-81
Xiaozhu Liu, Samuel Halvorsen, Nathan Blanke, Irving Bigio, Yanhang Zhang
*Boston University*

**12:00PM** **Comparison of Oscillatory Deformation Patterns Excited in the Human Brain In Vivo by Harmonic and Impulsive Skull Motion** SB³C2022-47
Jordan Escarcega[1], Andrew Knutsen[2], Ahmed Alshareef[3], Ruth Okamoto[1], Philip Bayly[1]
*[1]Washington University in St. Louis, [2]Henry M. Jackson Foundation, [3]Johns Hopkins University*

**12:15PM** **Rate and Region-Dependent Mechanical Properties of G□ttingen Minipig Brain Tissue in Oscillatory Shear** SB³C2022-6
Gregory Boiczyk[1], Noah Pearson[1], Aravind Sundaramurthy[2], Jose Rubio[2], Dhananjay Subramaniam[2], Ginu Unnikrishnan[2], Jaques Reifman[2], Kenneth Monson[1]
*[1]University of Utah, [2]Department of Defense Biotechnology High-Performance Computing Software Applications Institute*

**12:30PM** **The Relationship Between Cardiac Cycle Induced Strain in the Brainstem and Chiari Malformation Type I Symptomatology** SB³C2022-135
Mohamad Motaz Fouad Al Samman[1], Alaaddin Ibrahimy[2], Blaise Simplice Talla Nwotchouang[3], John N. Oshinski[4], Daniel L. Barrow[4], Philip A. Allen[3], Rouzbeh Amini[1], Francis Loth[1]
*[1]Northeastern University, [2]Yale University, [3]University of Akron, [4]Emory University*

| Tuesday, June 21 | 11:15AM – 12:45PM EDT |
|---|---|

# Special Session in Honor of Dr. Ajit Yoganathan

**Chesapeake G**

**Session Chairs: Lakshmi Dasi,** *Georgia Institute of Technology*
**Keefe Manning,** *Pennsylvania State University*

**11:15AM** **Flow Dynamic Differences Between Self-Expanding and Balloon Expandable Transcatheter Aortic Valves** SB³C2022-330
Hoda Hatoum[1], Milad Samaee[2], Janarthanan Sathananthan[3], Stephanie Sellers[3], Maximilian Kuetting[4], Scott Lilly[5], Abdul Ihdayhid[6], Philipp Blanke[3], Jonathon Leipsic[3], Vinod Thourani[7], Lakshmi Prasad Dasi[2]
*[1]Michigan Technological University, [2]Georgia Institute of Technology, [3]University of British Columbia, [4]New Valve Technology, [5]Ohio State University, [6]Harry Perkins Institute, [7]Piedmont Hospital*

**11:30AM** **A Novel Bi-Ventricle Mechanical Support Configuration for the Failed Fontan Circulation** SB³C2022-283
Emrah Sisli[1], Canberk Yildirim[2], Ibrahim Basar Aka[3], Osman Nuri Tuncer[4], Yuksel Atay[4], Mustafa Ozbaran[4], Kerem Pekkan[2]
*[1]Osmangazi University, [2]Koc University, [3]Istanbul Bilgi University, [4]Ege University*

**11:45AM** **The Interplay Between Transcatheter Aortic Valve Replacement Complications and Coronary Artery Disease** SB³C2022-198
Seyedvahid Khodaei, Zahra Keshavarz-Motamed
*McMaster University*

**12:00PM** **Predicting Valve Performance Using Logistic Regression** SB³C2022-218
Brennan Vogl[1], Yousef Darestani[2], Juan Crestanello[3], Brian Lindman[2], Mohamad Alkohouli[3], Hoda Hatoum[1]
*[1]Michigan Technological University, [2]Vanderbilt University Medical Center, [3]Mayo Clinic*

**12:15PM** **Hemodynamic Impact of Anterior Leaflet Laceration in Transcatheter Mitral Valve Replacement** SB³C2022-374
Keshav Kohli[1], Zhenglun Alan Wei[2], Vahid Sadri[1], Andrew Siefert[1], Philipp Blanke[3], Emily Perdoncin[1], Adam Greenbaum,[1] Jaffar Khan[4], Robert Lederman[4], Vasilis Babaliaros[1], Ajit Yoganathan[1], John Oshinski[1]
*[1]Georgia Institute of Technology and Emory University, [2]University of Massachusetts, [3]University of British Columbia, [4]National Institutes of Health*

**12:30PM** **Toward Subject-Specific Biomechanics of the Right-Noncoronary Bicuspid Aortic Valve and its Association with Molecular Gene Expression** SB³C2022-59
Hail Kazik[1], Kandail Harkamaljot[2], Benjamin Goot[3], Joy Lincoln[3], John LaDisa[1], El-Sayed Ibrahim[3]
*[1]Marquette University, [2]Cardio Consulting, [3]Medical College of Wisconsin*

| Tuesday, June 21 | 11:15AM – 12:45PM EDT |
|---|---|

# Mechanobiology and Pathology

**Clipper A-C**

**Session Chairs: Mitchel Colebank,** *University of California, Irvine*
**Giuseppe De Nisco,** *Politecnico di Torino*

**11:15AM** **A Computational Analysis of Experimental Designs to Study Pulmonary Hypertension and Right Ventricular Function** SB³C2022-20
Mitchel Colebank, Naomi Chesler
*University of California, Irvine*

**11:30AM** **Computational Fluid-Solid-Interaction Modeling of Normotensive and Angiotensin-II Infused Hypertensive Mice** SB³C2022-214
Sara Hopper[1], Dar Weiss[2], Federica Cuomo[1], Jay D. Humphrey[2], C. Alberto Figueroa[1]
*[1]University of Michigan, [2]Yale University*

**11:45AM** **Computational 13C Metabolic Flux Analysis Indicates Endothelial Cells Attenuate Metabolic Perturbations by Modulating TCA Cycle Activity** SB³C2022-161
Bilal Moiz[1], Jonathan Garcia[2], Sarah Basehore[2], Angela Sun[1], Andrew Li[1], Surya Padmanabhan[1], Kaitlyn Albus[1], Cholsoon Jang[3], Ganesh Sriram[1], Alisa Clyne[1]
*[1]University of Maryland College Park, [2]Drexel University, [3]University of California, Irvine*

**12:00PM** **Fluid-Structure-Based Computational Model of Hemodynamics-Driven Aortic Growth for FBLN4SMKO Mice** SB³C2022-68
Marisa S. Bazzi[1], Casey D. Hokanson[1], Jessica E. Wagenseil[2], Victor H. Barocas[1]
*[1]University of Minnesota, [2]Washington University*

**12:15PM** **Wall Shear Stress Topological Skeleton Variability Predicts Atherosclerotic Plaque Growth in Human Coronary Arteries** SB³C2022-237
Giuseppe De Nisco[1], Eline Hartman[2], Valentina Mazzi[1], Diego Gallo[1], Claudio Chiastra[1], Joost Daemen[2], Jolanda Wentzel[2], Umberto Morbiducci[1]
*[1]Politecnico di Torino, [2]Erasmus Medical Center*

**12:30PM** **Changes in CD44 and Drug Resistance in Ovarian Cancer Cells with Differing Mechanical Presentation of Hyaluronic Acid** SB³C2022-293
Maranda Tidwell, Gillian Huskin, Molly Buckley, Mary Sewell-Loftin, Joel Berry
*University of Alabama at Birmingham*

| Tuesday, June 21 | 11:15AM – 12:45PM EDT |
|---|---|

## Cancer & Morphogenesis

**Galleon A-C**

**Session Chairs: Karen Kasza,** *Columbia University*
**Victor Varner,** *University of Texas at Dallas*

**11:15AM** **Spatiotemporal Dynamics of Epithelial Cell Packings and Tissue Mechanics During Morphogenesis** SB³C2022-107
Christian Cupo, Cole Allan, Andrew Pomposelli, Karen Kasza
*Columbia University*

**11:30AM** **Actomyosin Contractility Controls Organ-Scale Buckling in the Developing Small Intestine** SB³C2022-340
John Durel, Hyunjee Lim, Nandan Nerurkar
*Columbia University*

**11:45AM** **An In Vitro Model of the Tumor Microenvironment Shaped by Cancer-Associated Fibroblasts** SB³C2022-268
Sarah Shelton[1], Brandon Piel[2], Tran Thai[2], Huu Tuan Nguyen[1], Jochen Lorch[2], Kartik Sehgal[2], David Barbie[2], Roger Kamm[1]
*[1]Massachusetts Institute of Technology, [2]Dana Farber Cancer Institute*

**12:00PM** **Examining Ovarian Cancer HSP27 Regulation Via Mechanotransduction Signaling in a 3D Model** SB³C2022-132
Molly Buckley, Joel Berry, Mary-Kathryn Sewell-Loftin
*University of Alabama at Birmingham*

**12:15PM** **Core-Shelled Microcapsules Produce Tumor Aggregates with Greater Sphericity and Drug Resistance than Gold-Standard Liquid Overlay Technique in HER2+ Breast Cancer Cells** SB³C2022-70
Cassandra Roberge[1], Margarida Barroso[2], David Corr[2]
*[1]Rensselaer Polytechnic Institute, [2]Albany Medical College*

**12:30PM** **A Gravity-Driven Multi Micro Physiological System to Study Tissue Responses to Cancer Therapeutics** SB³C2022-158
Pouria Rafsanjani Nejad, Hossein Tavana
*University of Akron*

| Tuesday, June 21 | 11:15AM – 12:45PM EDT |
|---|---|

# Lung Biomechanics

**Schooner A-B**

**Session Chairs: Ed Sander,** *University of Iowa*
**Mona Eskandari,** *University of California Riverside*

**11:15AM** **MicroRNA Therapies to Prevent Ventilator Induced Lung Injury During the Acute Respiratory Distress Syndrome** SB³C2022-234
Samir Ghadiali, Qinqin Fei, Basia Gabela-Zuniga, Tricia Oyster, Vasudha Shukla, Megan Ballinger, Joshua Englert
*Ohio State University*

**11:30AM** **Mapping Strain Amplification in Lung Cancer: A Geometric Model to Test How Altered Mechanics Could Promote Tumor Progression** SB³C2022-452
Rebecca Zitnay, Keith Carney, Michael Herron, Jeffrey Weiss, Michelle Mendoza
*University of Utah*

**11:45AM** **Murine Lung Mechanics in Response to Varying Inflation Volumes and Frequencies** SB³C2022-19
Kathrine Anduaga[1], Talyah Nelson[1], Samaneh Sattari[1], Crystal Mariano[1], Arzu Ulu[1], Edward Dominguez[1], Tara Nordgren[2], Mona Eskandari[1]
*[1]University of California, [2]Colorado State University*

**12:00PM** **Image-Based Dynamic Strain Estimation of Alveolar Microstructures During Ex Vivo Mechanical Ventilation** SB³C2022-240
Jacob Herrmann, Sarah Gerard, Edward Sander
*University of Iowa*

**12:15PM** **A Novel Fibrous Finite Element Model of Soft Tissues** SB³C2022-335
Mohammad R Islam, Fengting Ji, Manik Bansal, Yi Hua, Ian A. Sigal
*University of Pittsburgh*

**12:30PM** **Reducing Skin Injuries Induced by Prolonged Usage of Respirator Masks** SB³C2022-122
Rikeen Jobanputra, Kian Kun Yap, Manoj Murali, Margarita Santos, Marc Masen
*Imperial College London*

| Tuesday, June 21 | 11:15AM – 12:45PM EDT |
|---|---|

# Biomechanics of Human Motion

**Cutter A-B**

**Session Chairs: Sriram Balasubramanian,** *Drexel University*
**Lyle Hood,** *University of Texas at San Antonio*

**11:15AM** **Thumb Metacarpal Kinematics: A Volumetric Perspective** SB³C2022-239
Adam Chrzan[1], Nicole Arnold[1], Kevin Chan[2], Tamara Reid Bush[1]
*[1]Michigan State University, [2]Spectrum Health*

**11:30AM** **The Impact of Stiffness Gain on Spine Stability** SB³C2022-427
Valerie Jardon, Sara Wilson
*University of Kansas*

**11:45AM** **Tri-Compartment Knee Loading 3 Months after ACL Reconstruction** SB³C2022-305
Jack Williams, Kelsey Neal, Abdulmajeed Alfayyadh, Ashutosh Khandha, Kurt Manal, Lynn Snyder-Mackler, Thomas Buchanan
*University of Delaware*

**12:00PM** **Lateral Distance as a Measure of Balance During 90 Degree Pre-Planned and Late-Cued Turns** SB³C2022-124
Mitchell Tillman, Antonia Zaferiou
*Stevens Institute of Technology*

**12:15PM** **Regulation of Whole-Body Angular Momentum in Persons with Parkinson Disease when Transitioning from a Regular to an Irregular Surface** SB³C2022-295
Nicholas Gomez, Kelton Gubler, Andrew Merryweather
*University of Utah*

**12:30PM** **Handrim Biomechanics and Wheelchair Fit Measures in Pediatric and Emerging Adult Manual Wheelchair Users** SB³C2022-289
Samantha Schwartz[1], Alyssa Schnorenberg[1], Hannah Frank[1], Matthew Hanks[1], Shubhra Mukherjee[2], Brooke Slavens[1]
*[1]University of Wisconsin-Milwaukee, [2] Shriners Hospital for Children-Chicago*

| Wednesday, June 22 | 1:45PM – 3:15PM EDT |
|---|---|

# Vascular Mechanics III

**Chesapeake A-D**

**Session Chairs: Chung-Hao Lee,** *University of Oklahoma*
**Heather Hayenga,** *University of Texas at Dallas*

**1:45PM** **Clinical Imaging Derived Aortic Stiffness as an Aortic Dissection Risk Stratification Metric** SB$^3$C2022-339
Ronald Fortunato[1], Thomas Gleason[2], David Vorp[1], Spandan Maiti[1]
*[1]University of Pittsburgh, [2]University of Maryland*

**2:00PM** **Stochastic Optimization of a Porohyperelastic Bilayered Vascular Graft to Improve Hemocompatibility** SB$^3$C2022-87
Ali Behrangzade[1], Bruce Simon[2], William Wagner[1], Jonathan Vande Geest[1]
*[1]University of Pittsburgh, [2]University of Arizona*

**2:15PM** **Collagen Waviness Regulates the Damage of Vein Tissue** SB$^3$C2022-82
Xuehuan He, Jia Lu
*University of Iowa*

**2:30PM** **The Interplay Between Elastin and Proteoglycans and their Effect on Ascending Aortic Aneurysmal Biomechanics** SB$^3$C2022-428
Miriam Nightingale, Amy Bromley, Jehangir Appoo, Elena Di Martino
*University of Calgary*

**2:45PM** **The Influence of Plaque Structural Stress and Wall Shear Stress on Human Coronary Plaque Progression** SB$^3$C2022-177
Aikaterini Tziotziou, Jolanda Wentzel, Ali Akyildiz
*Erasmus Medical Center*

**3:00PM** **Pulmonary Artery Mechanics in Murine Models of Ageing** SB$^3$C2022-311
Abhay Ramachandra, Edward Manning, Jay Humphrey
*Yale University*

| Wednesday, June 22 | 1:45PM – 3:15PM EDT |
|---|---|

# Ventricular Mechanics I

**Chesapeake E**

**Session Chairs: Zhijie Wang,** *Colorado State University*
**Emma Lejeune,** *Boston University*

**1:45PM** **Computational Modeling of the Passive Anisotropic Viscoelastic Behavior of Ovine Right Ventricles** SB³C2022-249
Wenqiang Liu[1], Kevin Labus[1], Matt Ahern[1], Reza Avazmohammadi[2], Christian Puttlitz[1], Zhijie Wang[1]
*[1]Colorado State University, [2]Texas A&M University*

**2:00PM** **Effect of Geometrical and Microstructural Remodeling on Ventricular Mechanics in Hypertrophic Cardiomyopathy** SB³C2022-290
Joy Mojumder[1], Lei Fan[1], Thuy Nguyen[2], Julius Guccione[2], Theodore Abraham[2], Lik Chuan Lee[1]
*[1]Michigan State University, [2]University of California San Francisco*

**2:15PM** **Modeling Ventricular Mechanics in Patients with Obstructive Hypertrophic Cardiomyopathy (HOCM)** SB³C2022-391
Lei Shi, Hiroo Takayama, Vijay Vedula
*Columbia University*

**2:30PM** **A Novel Model for Passive Myocardium that Incorporates Complete Diffusion Tensor Information** SB³C2022-392
Christian Goodbrake, Kenneth Meyer, Michael Sacks
*University of Texas at Austin*

**2:45PM** **Measuring the Anisotropic Mechanical Properties of Single Neonatal Mouse Cardiac Myocytes** SB³C2022-361
Taylor Rothermel, Patrick Alford
*University of Minnesota*

**3:00PM** **Myosin and Myofibril Dynamics Drive Hypertrophic Cardiomyopathy Disease Mechanisms** SB³C2022-479
Alison Vander Roest[1], Kathleen Ruppel[1], James Spudich[1], Beth Pruitt[2], Daniel Bernstein[1]
*[1]Stanford University, [2]University of California Santa Barbara*

| Wednesday, June 22 | 1:45PM – 3:15PM EDT |
|---|---|

# Muscle and Spine Tissue Mechanics

**Chesapeake F**

**Session Chairs: Mariana Kersh,** *University of Illinois*
**Stephanie Cone,** *University of Wisconsin*

**1:45PM** **Transcriptional Profiling of Mouse Skeletal Muscle Following Daily Bouts of Optogenetic Stimulation** SB³C2022-84
Syeda N. Lamia[1], Elahe Ganji[2], Iman Bhattacharya[2], Megan L. Killian[1]
*[1]University of Michigan, [2]University of Delaware*

**2:00PM** **Muscle Immobilization Prevents Functional Development of Embryonic Tendons But Does Not Affect Collagen Crosslinking** SB³C2022-27
Benjamin Peterson, Spencer Szczesny
*Pennsylvania State University*

**2:15PM** **Estimating Gastrocnemius Muscle Volume by Using Panoramic Ultrasound Images in Orthogonal Planes** SB³C2022-197
Shabnam Rahimnezhad[1], Karin G. Silbernage[2]l, Daniel H. Cortes[1]
*[1]Pennsylvania State University, [2]University of Delaware*

**2:30PM** **Intervertebral Disc Geometry and Hydration are Altered From In Vivo to Segment Preparation for Mechanical Tests** SB³C2022-298
Harrah Newman[1], Natalie Thurlow[2], Kyle Meadows[1], Adriana Barba[3], Thomas Schaer[3], Edward Vresilovic[1], Dawn Elliott[1]
*[1]University of Delaware, [2]University of Florida, [3]University of Pennsylvania*

**2:45PM** **Contribution of Elastin and Collagen to the Mechanical Behavior of Bovine Nuchal Ligament** SB³C2022-86
Samuel Halvorsen, Ruizhi Wang, Yanhang Zhang
*Boston University*

**3:00PM** **Three-Dimensional Strain Assessment of the Lumbar Facet Capsular Ligament During Dynamic Motion** SB³C2022-142
Matthew MacEwen, Rebecca Abbott, Victor Barocas, Arin Ellingson
*University of Minnesota*

| Wednesday, June 22 | 1:45PM – 3:15PM EDT |
|---|---|

# Emerging Methods in Biofluid Mechanics

**Chesapeake G**

**Session Chairs: Keshavarz-Motamed,** *McMaster University*
**Karol Cal□,** *Politecnico di Torino*

**1:45PM** **Comparison of Velocity and Flow-Based Methods to Calculate Wall Shear Stress from 4D Flow CMRI Data** SB³C2022-388
Elliott Hurd[1], Elizabeth Iffrig[2], John Oshinski[2], Lucas Timmins[1]
*[1]University of Utah, [2]Emory University*

**2:00PM** **4D Flow MRI Study of Large-Scale Hemodynamics Correlation Persistence in the Healthy Human Aorta Using Network Science** SB³C2022-206
Karol Calò[1], Andrea Guala[2], Diego Gallo[1], Jose Rodriguez Palomares[3], Stefania Scarsoglio[1], Luca Ridolfi[1], Umberto Morbiducci[1]
*[1]Politecnico di Torino, [2]Universitat Autonoma de Barcelona, [3]University Hospital Vall d'Hebron*

**2:15PM** **Automated Tuning of a Lumped Parameter Model for Simulating Resting Cardiovascular Physiology** SB³C2022-102
Akash Gupta, Aseem Pradhan, Surya Sharma, Tyler Schmidt, Ethan Kung
*Clemson University*

**2:30PM** **Calibration of Cardiopulmonary and Systemic Circulation Models in Pulmonary Arterial Hypertension and Cardiac Transplant Patients** SB³C2022-382
Christopher Tossas-Betancourt[1], Nathan Y. Li[1], Sheikh M. Shavik[2], Adam L. Dorfman[1], Seungik Baek[1], Lik C. Lee[1], C. Alberto Figueroa[1]
*[1]University of Michigan, [2]Bangladesh University*

**2:45PM** **Real-Time MRI-Based Computational Modeling of Urinary Flow in Urethra** SB³C2022-168
Labib Shahid, Juan Pablo Gonzalez-Pereira, Cody Johnson, Alejandro Roldán-Alzate
*University of Wisconsin-Madison*

**3:00PM** **Using Smart Phones to Select Household Fabric for Making Face Coverings: A Case Study by FDA, NIST and High School Students** SB³C2022-300
Alexander Herman[1], Matthew Staymates[2], Salvatore Trupia[3], Victoria Guerrier[3], Glenda Garcia[3], Gloria Guerrier[3], Suvajyoti Guha[1]
*[1]US FDA, [2]National Institute of Standard and Technology, [3]West Hempstead High School*

| Wednesday, June 22 | 1:45PM – 3:15PM EDT |
|---|---|

## Thrombosis, Hemolysis and Mechanical Circulatory Support

**Clipper A-C**

**Session Chairs: Colleen Witzenburg,** *University of Wisconsin-Madison*
**Simon Tupin,** *Imperial College London*

**1:45PM** **Assessment of Interlaboratory Computational Simulations of the FDA Benchmark Blood Pump** SB³C2022-101
Sailahari Ponnaluri[1], Prasanna Hariharan[2], Luke Herbertson[2], Richard Malinauskas[2], Keefe Manning[1], Brent Craven[2]
*[1]Pennsylvania State University, [2]US FDA*

**2:00PM** **Experiment-Led Continuum Modelling of Microscale Blood Flow** SB³C2022-328
Simon Tupin[1], Stavroula Balabani[2], Joseph van Batenburg-Sherwood[1]
*[1]Imperial College London, [2]University College London*

**2:15PM** **Preliminary Modeling and Experimental Study of Thromboembolism: Effects of Shear Stress on Thrombus Behavior** SB³C2022-238
Arash Azimi, Eathan DiTullio, Keefe Manning
*Pennsylvania State University*

**2:30PM** **Platelet Adhesion is Dominated by Large Von Willebrand Factor Multimers at Device Relevant Shear Rates** SB³C2022-200
Connor Watson, Keefe Manning
*Pennsylvania State University*

**2:45PM** **In Silico Investigation of Contralateral Embolic Stroke Risks from Carotid Artery Disease** SB³C2022-425
Ricardo Roopnarinesingh, Debanjan Mukherjee
*University of Colorado Boulder*

**3:00PM** **Effect of Venous Valve Morphology on Flow Conditions Conducive to Thrombosis** SB³C2022-236
Jacob Biesinger, Matthew Ballard
*Utah Valley University*

| Wednesday, June 22 | 1:45PM – 3:15PM EDT |
|---|---|

# Musculoskeletal Tissue Engineering

**Galleon A-C**

**Session Chairs: Alix Deymier,** *University of Connecticut Health Center*
**Arun Nair,** *University of Arkansas*

**1:45PM** **Functional Cartilage Tissue Engineering Does Not Require Culture Media Replenishment** SB³C2022-201
Tianbai Wang, Yanli Lyu, Yue Liu, Michael Albro
*Boston University*

**2:00PM** **Fabrication and Drug Release Kinetics Characterisation of Poly(Glycerol Sebacate Urethane) Anisotropic Scaffolds** SB³C2022-176
Andreas Samourides, Zacharoula Xenou, Irene Louca, Konstantinos Kapnisis, Andreas Anayiotos
*Cyprus University of Technology*

**2:15PM** **Dose- And Time-Dependent Effects of Collagenase Clostridium Histolyticum Injection on Stiffness and Thickness of In Vitro Transverse Carpal Ligament** SB³C2022-16
Jocelyn Hawk, Sohail Daulat, David Margolis, Zong-Ming Li
*University of Arizona*

**2:30PM** **Mechanical Anchoring Drives Stem Cell Differentiation and Tissue Maturation in Tissue Engineered Ligament-To-Bone Entheses** SB³C2022-467
Ethan Brown, Sophia Murphy, Lais Morandini, Rene Olivares-Navarrete, Jennifer Puetzer
*Virginia Commonwealth University*

**2:45PM** **Ultrasound as a Stimulus for Transdermal, Hydrogel-Based Bone Repair** SB³C2022-215
Fayekah Assanah[1], Kevin Grassie[1], Hanna Anderson[1], Will Linthicum[1], Bryan Huey[1], Yusuf Khansh[2]
*[1]University of Connecticut, [2]UCONN Health*

**3:00PM** **Development of Porous, Mineralized Collagen-Chitosan Scaffolds to Recreate the 3D Cancellous Bone Microenvironment** SB³C2022-267
Sandra Stangeland-Molo, Kathryn Benedict, Jacqueline Cole
*University of North Carolina-Chapel Hill and North Carolina State University*

| Wednesday, June 22 | 1:45PM – 3:15PM EDT |
|---|---|

## Growth, Remodeling, and Repair

**Schooner A-B**

**Session Chairs: Kyoko Yoshida,** *University of Minnesota*
**Kristin Myers,** *Columbia University*

**1:45PM** **A Hybrid Discrete-Continuum Analysis of Remodeling In Arteries: An Assessment of Microscopic Features from Macroscopic Observables** SB³C2022-250
Ryan Mahutga, Elizabeth Gacek, Victor Barocas
*University of Minnesota*

**2:00PM** **A Constrained Mixture Model of Thoracic Aortic Aneurysm Growth** SB³C2022-216
David Li[1], Marcos Latorre[2], Jay Humphrey[1]
*[1]Yale University, [2]Universitat Politècnica de València*

**2:15PM** **Effects of Scaffold Degradation Behavior on Tissue Engineered Vascular Graft Growth and Remodeling** SB³C2022-377
Jason Szafron[1], Yuichi Matsuzaki[2], Stephanie Lindsey[3], Christopher Breuer[2], Jay Humphrey[4], Alison Marsden[1]
*[1]Stanford University, [2]Nationwide Children's Hospital, [3]University of California San Diego, [4]Yale University*

**2:30PM** **Effect of Smooth Muscle Tone and Age on Biaxial Mechanics of the Murine Vagina** SB³C2022-357
Shelby White, Qinhan Zhou, Kristin Miller
*Tulane University*

**2:45PM** **In Vivo Large Animal Evaluation of a Mechano-Responsive Fibrous Patch for Anti-Inflammatory Drug Delivery to Promote Repair after Disc Herniation** SB³C2022-48
Ana Peredo, Chet Friday, Hannah Zlotnick, George Dodge, Daeyeon Lee, Michael Hast, Sarah Gullbrand, Harvey Smith, Robert Mauck
*University of Pennsylvania*

**3:00PM** **Calibrating Mechanoregulatory Models of Fracture Repair and Remodeling Using Imaging Data from Sheep** SB³C2022-89
Tianyi Ren, Hannah Dailey
*Lehigh University*

| Wednesday, June 22 | 1:45PM – 3:15PM EDT |
|---|---|

# Undergraduate Design Competition

**Cutter A-B**

**Session Chairs: Anita Singh,** *Widener University*

**1:45PM** **Clinical Need is the Mother of Biomedical Innovation** SB3C2022
Sriram Balasubramanian
*Drexel University*

**2:00PM** **Commode for Neurogenic Bowel: A Mechanism for Achieving The Squatting Position** SB$^3$C2022-534
John Bates, Chastity Chavez, Madison Lang, Alexander Rivera, Camila Ruiz Vega, Amy Lerner, Scott Seidman, Richard Waugh
*University of Rochester*

**2:15PM** **Sixth Sense - A Hands Free and Haptic Feedback Navigation Tool for the Visually Impaired** SB$^3$C2022-509
Alyssa Taylor, Joseph Lahmann, Miles Canino
*Rose-Hulman Institute of Technology*

**2:30PM** **Dynamic Hand Brake for Manual Wheelchairs** SB$^3$C2022-495
Joshua Coombs, Nicholas Johnson, Nicholas Oram, Shelley Osterhout, Zev Sun, Noelle Tenney, Andrew Merryweather
*University of Utah*

**2:45PM** **Temperature Assessment Enabled Simulation Mannequin** SB$^3$C2022-518
Emily Eisele, Mason Klaus, Jessica Guarino, Amelia Wellmon, Sean Blade, Ria Mazumder
*Widener University*

**3:00PM** **Developmental Dysplasia of the Hip Pediatric Medical Trainer** SB$^3$C2022-514
Seth Eaby[1], Sheridan Perry[1], Joseph Sauerbrun[1], Victor Huayamave[1], Charles Price[2]
*[1]Embry-Riddle Aeronautical University, [2]International Hip Dysplasia Institute*

| Wednesday, June 22 | 3:30PM – 5:00PM EDT |
|---|---|

# Vascular Mechanics IV

**Chesapeake A-D**

**Session Chairs: Matthew Bersi,** *Washington University in St. Louis*
**Jonathan Vande Geest,** *University of Pittsburgh*

**3:30PM** **Identification of Intramural Stress Distribution in Cerebral Aneurysms Using Patient Specific Wall Thickness Maps** SB³C2022-413
Ronald Fortunato[1], Piyusha Gade[1], Juan Cebral[2], Anne Robertson[1], Spandan Maiti[1]
*[1]University of Pittsburgh, [2]George Mason University*

**3:45PM** **Effect of Breaking Calcification on the Compliance of Coronary Arteries Brain** SB³C2022-451
Yasamin Seddighi[1], Aleksandra Gruslova[2], Drew Nolen[2], Deborah Vela[2], L. Maximilian Buja[2], Marc Feldman[2], Hai-Chao Han[1]
*[1]University of Texas at San Antonio, [2]University of Texas Health Science Center at Houston*

**4:00PM** **Open-Source Automation of Patient-Specific Atherosclerotic Arteries Reveals Key Biomechanically Driven Remodeling** SB³C2022-119
Jeremy Warren, John Yoo, Federico Bernardoni, Brandon Boren, Clark Meyer, Stefano Leonardi, Heather Hayenga
*University of Texas at Dallas*

**4:15PM** **Tissue-Engineered Collagenous Fibrous Cap Models to Explore Atherosclerotic Plaque Rupture** SB³C2022-208
Tamar Wissing[1], Kim van der Heiden[1], Sheila Serra[2], Anthal Smits[3], Carlijn Bouten[3], Frank Gijsen[1,2]
*[1]Erasmus Medical Center, [2]TU Delft, [3]TU Eindhoven*

**4:30PM** **Local Structural and Rupture Characteristics of Atherosclerotic Human Carotid Arteries Through Second Harmonic Imaging, Tensile Testing and Digital Image Correlation** SB³C2022-209
Su Guvenir Torun, Pablo de Miguel Munoz, Hanneke Crielaard, Hence J.M. Verhagen, Aad van der Lugt, Gert J. Kremers, Ali C. Akyildiz
*Erasmus Medical Center*

**4:45PM** **Ultrasound-Based Volume-Time Curves of the Lumen, Thrombus and Vessel Wall for Estimating In-Vivo Thrombus Compressibility and Wall Stiffness** SB³C2022-226
Arjet Nievergeld[1], Esther Maas[1], Judith Fonken[1], Frans van de Vosse[1], Marc van Sambeek[2], Richard Lopata[1]
*[1]University of Technology Eindhoven, [2]Catharina Hospital Eindhoven*

| Wednesday, June 22 | 3:30PM – 5:00PM EDT |
|---|---|

# Ventricular Mechanics II

**Chesapeake E**

**Session Chairs: Lik Chuan Lee,** *Michigan State University*
**Michael Sacks,** *University of Texas at Austin*

**3:30PM** **Role of Microtubules in Right Ventricle Anisotropic Viscoelasticity with Pulmonary Hypertension Development** SB³C2022-358
Kristen LeBar, Wenqiang Liu, Kellan Roth, Matt Ahern, Erith Evans, Jassia Pang, Jessica Ayers, Adam Chicco, Zhijie Wang
*Colorado State University*

**3:45PM** **A Constitutive-Based Deep Learning Model for the Identification of Active Contraction Properties in the Ventricular Myocardium** SB³C2022-111
Igor Nobrega, Wenbin Mao
*University of South Florida*

**4:00PM** **Assessing Diastolic Function Using Mathematical Modeling of the EDPVR Curve** SB³C2022-126
Salla Kim[1], Naomi Chesler[1], Benjamin Randall[2]
*[1]University of California Irvine, [2]University of Michigan*

**4:15PM** **Construction and Initial Experience with a Four-Chambered Fluid-Structure Interaction Model of the Heart** SB³C2022-44
Marshall Davey[1], Charles Puelz[2], Simone Rossi[1], Margaret Anne Smith[1], David Wells[1], Boyce Griffith[1]
*[1]University of North Carolina-Chapel Hill, [2]Baylor College of Medicine*

**4:30PM** **Sepsis-Driven Inflammatory Responses in Cardiac Micro-Tissues** SB³C2022-331
Connor Virgile, Elise Corbin
*University of Delaware*

**4:45PM** **Automated Image Analysis of Human Induced Pluripotent Stem Cell Derived Cardiomyocytes and Cardiac Microtissue** SB³C2022-233
Hiba Kobeissi, Saeed Mohammadzadeh, Emma Lejeune
*Boston University*

| Wednesday, June 22 | 3:30PM – 5:00PM EDT |
|---|---|

# Cartilage Modeling & Characterization

**Chesapeake F**

**Session Chairs: Michael Albro,** *Boston University*
**Sonia Bansal,** *University of Pennsylvania*

**3:30PM** **Independent and Synergistic Effects of Interstitial Hydration and Synovial Fluid Presence on Cartilage Lubrication** SB³C2022-344
Emily Lambeth, Meghan Kupratis, David Burris, Christopher Price
*University of Delaware*

**3:45PM** **Frictional Forces do not Cause Wear in Human Articular Cartilage** SB³C2022-422
C.V. Sise, Courtney A. Petersen, Brenna Carbone, Clark T. Hung, Gerard A. Ateshian
*Columbia University*

**4:00PM** **Parameters to Model Cartilage as Osteoarthritis Progresses** SB³C2022-255
Xiaogang Wang, David Pierce
*University of Connecticut*

**4:15PM** **Verification of Biphasic Material Parameter Identifiability by Fully Automated Sensitivity Analysis and Error Checking** SB³C2022-369
John Peloquin, Harrah Newman, Dawn Elliott
*University of Delaware*

**4:30PM** **Raman Spectroscopy Probe Assessments of Cartilage Composition and Functional Mechanical Properties** SB³C2022-430
Masumeh Kazemi[1], Dev Mehrotra[1], Juncheng Zhang[1], Chenhao Yu[1], Diya Desai[1], Mark Grinstaff[1], Brian Snyder[2], Mads Bergholt[3], Micheal Albro[1]
*[1]Boston University, [2]Beth Israel Deaconess Medical Center, [3]King, Äôs College London*

**4:45PM** **Cartilage Mechanical Properties of Developmental Dysplasia of the Hip in a Porcine Model** SB³C2022-410
Kate Benfield[1], Amevi Semodji[1], Vidyadhar Upasani[2], Christine Farnsworth[2], Derek Nesbitt[1], Erin Mannen[1], Trevor Lujan[1]
*[1]Boise State University, [2]Rady Children's Hospital San Diego*

| Wednesday, June 22 | 3:30PM – 5:00PM EDT |
|---|---|

# Device and Treatment Implications

**Chesapeake G**

**Session Chairs: Milad Samaee,** *Georgia Institute of Technology*
**Ryan Pewowaruk,** *University of Minnesota*

**3:30PM** **Performance of The Balloon-Expandable Valve in a Self-Expanding Valve at Different Implantation Heights** SB³C2022-445
Milad Samaee[1], Huang Chen[1], Pradeep Yadav[2], Vinod Thourani[2], Lakshmi Prasad Dasi[1]
*[1]Georgia Institute of Technology, [2]Piedmont Heart Institute*

**3:45PM** **Effect of Aortic Curvature on Bioprosthetic Aortic Valve Performance** SB³C2022-220
Brennan Vogl[1], Rajat Gadhave[1], Zhenyu Wang[2], Juan Crestanello[3], Mohamad Alkohouli[3], Hoda Hatoum[1]
*[1]Michigan Technological University, [2]Ohio State University, [3]Mayo Clinic*

**4:00PM** **Design and Initial Optimization of a Centrifugal Left Ventricular Assist Device** SB³C2022-408
Huang Chen, Shweta Ashishkumar Karnik, Jeyan Kirtay, Lakshmi Prasad Dasi
*Georgia Institute of Technology*

**4:15PM** **A Computational Study of Aortic Dynamic Occlusion in Type B Dissection** SB³C2022-96
Taeouk Kim, Pieter van Bakel, Nitesh Nama, Himanshu Patel, David Williams, C. Alberto Figueroa
*University of Michigan*

**4:30PM** **Quantifying the Impact of Hemorrhagic Shock and Reboa on the Endothelial Glycocalyx Layer** SB³C2022-97
Antonio Renaldo, Aravindh Ganapathy, Nathaniel Hauser, Magan Lane, James Jordan, Lucas Neff, Timothy Williams, Elaheh Rahbar
*Wake Forest School of Medicine*

**4:45PM** **Simulated Performance of a Bioprinted Pulsatile Fontan Conduit** SB³C2022-320
Zinan Hu, Erica Schwarz, Jessica Herrmann, Mark Skylar-Scott, Alison Marsden
*Stanford University*

| Wednesday, June 22 | 3:30PM – 5:00PM EDT |
|---|---|

# Microfluidics, Optical and CSF

**Clipper A-C**

**Session Chairs: William Polacheck,** *University of North Carolina-Chapel Hill & NC State University*
**Jifu Tan,** *Northern Illinois University*

**3:30PM** **Feature Tracking Microfluidic Analysis Reveals Differential Roles of Viscosity and Friction in Sickle Cell Blood** SB³C2022-275
Hannah Szafraniec[1], Jose Valdez[1], Elizabeth Iffrig[2], Wilbur Lam[2], John Higgins[3], Philip Pearce[4], David Wood[1]
*[1]University of Minnesota, [2]Emory University, [3]Harvard University, [4]University College London*

**3:45PM** **Microfluidic Approach for Quantifying Vascular Permeability in the Presence of Transmural Flow** SB³C2022-138
Stephanie Huang, William Polacheck
*University of North Carolina-Chapel Hill & NC State University*

**4:00PM** **Transmural Solute Permeability, But Not Hydraulic Conductance, Increases in a Mouse Model of Ascending Thoracic Aortic Aneurysm** SB³C2022-11
Christie Crandall[1], Sean Kim[2], Jessica Wagenseil[1]
*[1]Washington University in St. Louis, [2]Saint Louis University*

**4:15PM** **Direct Numerical Simulation of Blood Flow with Cells in Retina Vascular Network** SB³C2022-468
Kacper Ostalowski, Jifu Tan
*Northern Illinois University*

**4:30PM** **Comparison of CSF Flow Resistance and Brainstem and Cerebellum Displacement for Chiari Malformation Type 1** SB³C2022-150
Saeed Mohsenian[1], Alaaddin Ibrahimy[2], John Oshinski[3], Blaise Simplice Talla Nwotchouang[4], Daniel Barrow[3], Rouzbeh Amini[1], Francis Loth[1]
*[1]Northeastern University, [2]Yale University, [3]Emory University, [4]University of Akron*

**4:45PM** **The Effect of Fluid Flow on the Leptomeningeal Cells of the Subarachnoid Space** SB³C2022-245
Mannthalah Abubaker, David Newport, John Mulvihill
*University of Limerick*

| Wednesday, June 22 | 3:30PM – 5:00PM EDT |
|---|---|

## Emerging Tools in Tissue and Cellular Engineering

**Galleon A-C**

**Session Chairs: Ed Sander,** *University of Iowa*
**L. Grace Zhang,** *George Washington University*

**3:30PM** **Characterization of Bioengineered Tissues by Digital Holographic Vibrometry and Machine Learning** SB$^3$C2022-433
Colin Hiscox, Juanyong Li, Ziyang Gao, Dmitry Korkin, Cosme Furlong, Kristen Billiar
*Worcester Polytechnic Institute*

**3:45PM** **Dynamic Mechanical Loading of Photopolymerized Hydrogels as a Tool for Studying Pulmonary Fibrosis** SB$^3$C2022-143
Qi Wang, Jacob Herrmann, Edward Sander, Kristan Worthington
*University of Iowa*

**4:00PM** **Evaluating Bio-Sourced Photoinitiators Efficiency for Use in Sustainable 3D Bioprinting** SB$^3$C2022-53
Rion Wendland, Kristan Worthington
*University of Iowa*

**4:15PM** **Overcoming the Force-Dependent Inhibition of Collagenase Using Macrophages** SB$^3$C2022-75
Ryan Jamieson, Suzanne Stasiak, Ralston Augspurg, Nihal Bharath, Seyed Mohammad Siadat, Jeff Ruberti, Hari Parameswaran
*Northeastern University*

**4:30PM** **DNA-Based Micropatterning Approach to Create Tissues of Defined Size, Shape, and Cellular Composition** SB$^3$C2022-203
Louis Prahl, Alex Hughes
*University of Pennsylvania*

**4:45PM** **A Novel Machine Learning-Based Framework to Predict The Anisotropic Mechanical Properties in Soft Materials Using Anisotropic Indentation** SB$^3$C2022-241
Habibeh Ashouri Choshali, Juanyong Li, Taylor Paradis, Nima Rahbar, Kristen Billiar
*Worcester Polytechnic Institute*

| Wednesday, June 22 | 3:30PM – 5:00PM EDT |
|---|---|

# Transport in Thermal Therapy

**Schooner A-B**

**Session Chairs: Fatemeh Hassanipour,** *University of Texas at Dallas*
**Sihong Wang,** *City College of New York*

**3:30PM** **Single Pulse Heating of Nanoparticle Array for Biological Applications** SB³C2022-115
Chen Xie, Peiyuan Kang, Zhenpeng Qin
*University of Texas at Dallas*

**3:45PM** **Incorporating Vascular Stasis Based Perfusion to Predict the Thermal Signatures of Cell Death Using Modified Arrhenius Equation with Regeneration of Living Tissues** SB³C2022-159
Manpreet Singh
*University of Maryland Baltimore County*

**4:00PM** **Feedback Temperature Control for Magnetic Hyperthermia Therapy to Treat Glioblastoma** SB³C2022-182
Avesh Jangam[1], Julian Low[1], Aiman Ahmad[1], Anirudh Sharma[2], Robert Ivkov[2], Anilchandra Attaluri[1]
*[1]Pennsylvania State University, [2]Johns Hopkins University*

**4:15PM** **Mitigation of Injury to Nerves During Prostate Cancer Cryoablation Using Cryoprotective Agents** SB³C2022-193
Pegah Ranjbartehrani[1], David Ramirez[1], Franz Schmidlin[2], Michael Etheridge[1], Paul Iaizzo[1], Qi Shao[1], John Bischof[1]
*[1]University of Minnesota, [2]Hirslanden Grangettes Group Geneva*

**4:30PM** **Bioheat Transfer Basis of Human Thermoregulation: Principles and Applications** SB³C2022-307
Laura Namisnak[1], Shahab Haghayegh[2], Sepideh Khoshnevis[1], Kenneth Diller[1]
*[1]University of Texas at Austin, [2]Harvard Medical School*

**4:45PM** **Characterization of Cellular Response to Endovascular Ablative Therapies** SB³C2022-463
Sean Brocklehurst[1], Danielle Stolley[2], Neda Ghousifam[1], Erik Cressman[2], David Fuentes[2], M. Nichole Rylander[1]
*[1]University of Texas at Austin, [2]MD Anderson Cancer Center*

| Wednesday, June 22 | 3:30PM – 5:00PM EDT |
|---|---|

## Emerging Methods and Multiscale Mechanics

**Cutter A-B**

**Session Chairs: Sara Roccabianca,** *Michigan State University*
**Ryan Pewowaruk,** *William S. Middleton Memorial Veterans Hospital*

**3:30PM** **Predicting Temperature Field During Thermal Ablations Using Deep Neural Networks** SB³C2022-202
Hanife Tugba Kumru[1], Anilchandra Attaluri[1], Vitaly Gordin[2], Daniel H. Cortes[1]
*[1]Pennsylvania State University, [2]Hershey Medical Center*

**3:45PM** **Automated 4D Meshing of Ex-Vivo Filling of the Murine Urinary Bladder** SB³C2022-432
Eli Broemer, Sara Purdue, Pragya Saxena, Nathan Tykocki, Sara Roccabianca
*Michigan State University*

**4:00PM** **Tensile Response of the Murine Uterosacral Ligament is Nonlinear and Spatially Inhomogeneous** SB³C2022-183
Lea Savard, Catalina Bastias, Kathleen Connell, Sarah Calve, Callan Luetkemeyer, Virginia Ferguson
*University of Colorado*

**4:15PM** **Developing a Precision-Cut Tissue Sectioning Protocol for Fresh Porcine Colonic Tissue for Downstream Mechanical Analysis** SB³C2022-180
Cliona McCarthy, Kieran McGourty, Michael Walsh, John Mulvihill
*University of Limerick*

**4:30PM** **Quantifying Tissue-Specific Differences in Compressive Material Behavior of Porcine Gastrointestinal Tissue** SB³C2022-434
Samantha Barr, Alexander McGuigan, Caroline Karczewski, Alexander Caulk
*Medtronic*

**4:45PM** **The Lasso Stitch: A Novel Suturing Technique for High-Tension Wound Repair in Plastic and Reconstructive Surgery** SB³C2022-303
Chung-Hao Lee, Colton Ross, Bradley Miyake, Henry Marsh, Parker Bryant, Guilherme Barreiro
*University of Oklahoma*

# Poster Sessions

Posters will be presented in two sessions as listed below. Please see the "Instructions for Poster Presenters' on Page 9 of the Program Book. The poster viewing area is located in the Choptank Ballroom and will be open throughout the conference.

| | |
|---|---|
| **Poster Session I** | **Monday, June 20, 12:45PM – 2:15PM EDT** |
| **Poster Session II** | **Tuesday, June 21, 12:45PM – 2:15PM EDT** |

## BS-Level Student Paper Competition Session 1: Biofluid and Cardiovascular Mechanics

**P1** **Blood Clot Removal Pressures in An Experimental Model of Aspiration Thrombectomy** SB³C2022-493
Nicole Beautz[1], Noah Robison[1], Michael Froehler[2], Bryan Good[1]
*[1]University of Tennessee, [2]Vanderbilt University Medical Center*

**P2** **4D Flow MRI Comparison of Surgical Grafts for Correction of Pulmonary Artery Aneurysms: A Case Study** SB³C2022-489
Tea Cohen[1], Melody Dong[1], Arshid Azarine[2], Francois Haddad[1], Olaf Mercier[3], Alison Marsden[1]
*[1]Stanford University, [2]Groupe Hospitalier Paris Saint-Joseph, [3]Marie Lannelongue Hospital*

**P3** **Investigating the Role of Aspirin on the Geometries and Mechanical Properties of Experimental Blood Clots** SB³C2022-504
Nolan Corbitt, Bryan Good
*University of Tennessee*

**P4** **Design and Validation of a Bioreactor for Dynamic Biaxial Mechanical Stimulation of Engineered Tissue Vascular Grafts** SB³C2022-521
Luke Dague[1,2], Hayden Nothacker[2], Sarah Saunders[2], Johane Bracamonte[2], Joao Soares[2]
*[1]Georgia Institute of Technology, [2]Virginia Commonwealth University*

**P5** **Vascular Smooth Muscle Cell Alignment on Micropattern Alters Glucose Metabolism** SB³C2022-515
Yusuf Mastoor, Pattie Mathieu, Alisa Clyne
*University of Maryland College Park*

**P6** **Estimation of Flow Data from Angiographic Time Series** SB³C2022-523
Noah Stevens, Kritika Iyer, Brahmajee Nallamothu, C. Alberto Figueroa
*University of Michigan*

**P7** **A Measure of Platelet Activation and Aggregation Across Two Flow Regimes to Minimize Thromboembolic Events in Blood Pumps** SB³C2022-510
Hannah Sturgis, Nicolas Tobin, Keefe Manning
*Pennsylvania State University*

**V1** **The Role of Actin Corralling in the Formation of Cell-Cell Adhesions** SB³C2022-497
Payton J Thomas, Tamara Bidone
*University of Utah*

**P8** **Assessment of Pressure Gradient and Recovery Following Transcatheter Aortic Valve Replacement in Bicuspid Aortic Valves** SB³C2022-529
Aniket Venkatesh[1], Breandan Yeats[1], Atefeh Razavi[1], Pradeep Yadav[2], Venkateshwar Polsani[2], Vinod Thourani[2], Lakshmi Dasi[1]
*[1]Georgia Institute of Technology, [2]Piedmont Hospital*

**P9** **Characterizing the Mechanical Heterogeneity of Porcine Carotid Artery Bifurcations** SB³C2022-492
Claire Westman, Carly Donahue, Victor Barocas
*University of Minnesota*

## BS-Level Student Paper Competition Session 2: Devices, Design, and Cell & Tissue Engineering

**P10** **Mechanical Improvement and Haptic Quantification of Digital Extenders Intubation Device** SB³C2022-499
Tristan Arias[1], Lyle Hood[2], Emma Treadway[1],
*[1]Trinity University, [2]University of Texas San Antonio*

**P11** **Establishing an Optimized Annuloplasty Ring Type Using In Vivo and Ex Vivo Biomechanical Analyses** SB³C2022-490
Katelynne Berland[1], Sanchita Bhat[1], Andrew Siefert[1], Maeve Janecka[1], Shelley Gooden[1], Beatrice Ncho[1], Takayuki Kawashima[2], Mori Kazuki[2], Satoshi Kozaki[2], Robert Gorman[2], Joseph Gorman[2], Ajit Yoganathan[1]
*[1]Georgia Institute of Technology, [2]University of Pennsylvania*

**V2** **The Influence of Emboli Size and Density on their Transport in a Cardiopulmonary Bypass Flow Loop** SB³C2022-513
Amy Chandler, Bryan Good
*University of Tennessee*

**P12** **Prediction of Diabetes Mellitus Progression using Supervised Machine Learning** SB³C2022-326
Apoorva Chauhan, Mathew Varre, Kenneth Izuora, Mohamed Trabia, Janet Dufek
*University of Nevada Las Vegas*

**P13** **Low-Intensity Vibrations Induce Changes in Microtubule Dynamics In Vitro** SB³C2022-527
Chase Crandall, Nina Nikitina, Gunes Uzer
*Boise State University*

**P14** **EMG Analysis of Vastus Lateralis and Vastus Medialis with Different Bicycle Crank Lengths, Pedaling Rate, and Pedal Speed** SB³C2022-531
Jackson Crovella, Karoline Wucherer, Christiane O'Hara
*California Polytechnic State University*

**P15** **Open-Source System for Real-Time Functional Assessment of Engineered Multicellular Filtration Barriers** SB³C2022-498
Tess Fallon[1], Alan Stern[2], Nanditha Anandakrishnan[2], Ilse Daehn[2], Evren Azeloglu[2]
*[1]Columbia University, [2]Icahn School of Medicine*

**P16** **Optimization of ECM/Gelatin Solution in a Near Field Electrospinning System for Engineering Tendon** SB³C2022-508
Aasim Hussain, Zachary Davis, Matthew Fisher
*University of North Carolina-Chapel Hill & North Carolina State University*

**V3** **In Vitro Human Lung Fibroblast-To-Myofibroblast Transition from Profibrotic Growth Factor Stimulation** SB³C2022-484
Catherine Sano, Julie Leonard-Duke, Shayn Peirce-Cottler
*University of Virginia*

**P17** **IPSC-Derived Brain Microvascular Endothelial Cells Increase Glycolysis and Glucose Transport in Hyperglycemia** SB³C2022-511
Sophia Zic, Callie Weber, Alisa Clyne
*University of Maryland College Park*

## BS-Level Student Paper Competition Session 3: Solid Mechanics

**P18** **Gadolinium-Infused Silicone: A New Material for Cyclically Deforming MRI Phantoms** SB³C2022-526
Andrew Baldassarre[1], Caroline Buckley[1], Sebastian Ardila[1], Francis Loth[1], John Oshinski[2], Rouzbeh Amini[1]
*[1]Northeastern University, [2]Emory University*

**P19** **The Effect of Pregnancy on Mechanical Injury Criteria in Murine Uterosacral Ligaments** SB³C2022-488
Catalina Bastias, Lea Savard, Kathleen Connell, Sarah Calve, Callan Luetkemeyer, Virginia Ferguson
*University of Colorado*

**P20** **Laboratory and On-Field Evaluation of a Padded Football Helmet Shell Cover** SB³C2022-528
Ashlyn Callan, Nicholas Cecchi, Yuzhe Liu, Landon Watson, Xianghao Zhan, Gerald Grant, Michael Zeineh, David Camarillo
*Stanford University*

**P21** **Visual Characterization of Aponeurosis Microstructure** SB³C2022-491
Olivia Dyer[1], Mark Seeley[2], Benjamin Wheatley[1]
*[1]Bucknell University, [2]Geisinger Medical Center*

**P22** **Physiochemical Mechanisms of Bone Dissolution Play a Significant Role in Regulating Bone Composition and Function in Acidosis** SB³C2022-494
Margaret Easson, Stephanie Wong, Mikayla Moody, Tannin Schmidt, Alix Deymier
*University of Connecticut Health Center*

**P23** **The Impact of Hyperglycemia and Ovariectomy on Host Response to Vaginal Prolapse Mesh Implants** SB³C2022-520
Abigail Fisk[1], Gabrielle King[2], Kristina Weber[2], Rui Liang[1]
*[1]University of Pittsburgh, [2]Magee Women's Research Institute*

**P24** **The Relationship Between Intramuscular Pressure and Compression of Skeletal Muscle** SB³C2022-487

Sabrina Lorza[1], Pierre-Yves Rohan[2], Mark Seeley[3], Benjamin B Wheatley[1]
*[1]Bucknell University, [2]Arts et Métiers, [3]Geisinger Medical Center*

**P25** **Exercise Therapy Does Not Alter Kinematic Repeatability in Individuals with Rotator Cuff Tears when Reaching Behind the Back** SB³C2022-530
Rachel McLoughlin, Luke Mattar, Adam Popchak, William Anderst, Volker Musahl, James Irrgang, Richard Debski
*University of Pittsburgh*

**P26** **Effect of Development Slow Elongation in Driving Hierarchical Collagen Fiber Formation in Engineered Tissues** SB³C2022-524
Kelly Ott, Jennifer Puetzer
*Virginia Commonwealth University*

**P27** **Development of 3D Brain Structures from Histology Images** SB³C2022-482
John Sayut, Maria Holland
*University of Notre Dame*

## MS-Level Student Paper Competition Session 1: Solid and Biofluid Mechanics of Cardiovascular, Lung, and Soft Tissues

**P28** **An Iterative Approach to Assign Tumor-specific Flow Boundary Conditions for Liver Cancer Using Multi-modal Image Analysis** SB³C2022-477
Summer Andrews, Premal Trivedi, Debanjan Mukherjee
*University of Colorado*

**P29** **Spectral Analysis of Kinetic Energy in a Healthy Aorta** SB³C2022-99
David Büchner[1], Emily Manchester[2], Xiao Yun Xu[2]
*[1]University of Stuttgart, [2]Imperial College London*

**P30** **Bioengineered Three-Dimensional Lung Airway Model To Study Neonatal Intratracheal Surfactant Delivery** SB³C2022-186
Hannah Combs, Hossein Tavana
*University of Akron*

**P31** **Phosphorylation Patterns of Vascular Endothelial Growth Factor Receptor-2 and Angiogenesis are Driven by Biomechanical Forces** SB³C2022-342
Bronte Miller, Molly Buckley, McKenzie Johnson, Joel Berry, M.K. Sewell-Loftin
*University of Alabama*

**P32** **Layer-Specific Aortic Aneurysm Biomechanics Suggest Relationship Between Medial Stiffness and Interfacial Strength in Patients with Bicuspid Aortic Valve** SB³C2022-423
Louise Neave[1], Tais Sigaeva[2], Paul Fedak[1], Elena Di Martino[1]
*[1]University of Calgary, [2]University of Waterloo*

**P33** **Fabrication and Characterization of 3D-Printed Anisotropic, Hydrogel Lattices** SB³C2022-269
Margrethe Ruding, Daniel Yoon, Charlotte Guertler, Annabella Mascot, Philip Bayly
*Washington University in St. Louis*

**P34** **Predictive Urodynamics of Bladder Voiding Using MRI-Based CFD: A Pilot Study** SB³C2022-167
Labib Shahid[1], Juan Pablo Gonzalez-Pereira[1], Cody Johnson[1], Yanheng Li[2], David Rowinski[2], Alejandro Roldán-Alzate[1]
*[1]University of Wisconsin-Madison, [2]Convergent Science, Inc.*

**P35** **Hemodynamic Changes in the Aortic Root Upon Transcatheter Aortic Valve (Tav) Implantation** SB³C2022-401
Hunter Tashman[1], Mia Bonini[1], Marc Hirschvogel[2], Yunus Ahmed[1], George Deeb[1], Stanley Chetcuti[1], Nicholas Burris[1], David Nordsletten[1]
*[1]University of Michigan-Ann Arbor, [2]King's College London*

## MS-Level Student Paper Competition Session 2: Musculoskeletal and Cardiovascular Mechanics, Tissue Engineering, and Biosensors

**V4** **Development of a Continuum Damage Model to Predict Accumulation of Sub-failure Damage in Tendons** SB³C2022-78
Alexandra Allan, Jared Zitnay, Steve Maas, Jeffrey Weiss
*University of Utah*

**P36** **Flow and Pressure Calibration of Polyvinylidene Fluoride Polymer for Biosensor Applications** SB³C2022-399
Matthew Danley, Jack Kloster, Ping Zhao, Victor Lai
*University of Minnesota Duluth*

**P37** **Non-Muscle Myosins are Critical Regulators of Skeletal and Connective Tissue Formation** SB³C2022-390
Mary Kate Evans[1], Tonia Tsinman[1], Xi Jiang[1], Ellie Ferguson[1], Joel Boerckel[1], Lin Han[2], Eiki Koyama[3], Robert Mauck[1], Nathaniel Dyment[1]
*[1]University of Pennsylvania, [2]Drexel University, [3]Children's Hospital of Philadelphia*

**P38** **Assessment of Bladder Biomechanics Using MRI** SB³C2022-353
Juan Gonzalez-Pereira, Cody Johnson, Wade Bushman, Shane Wells, Alejandro Roldan-Alzate
*University of Wisconsin-Madison*

**P39** **Disc Geometry Measurement Methods Alter Reported Compressive Mechanics by Up To 65%** SB³C2022-12
Shiyin Lim, Reece Huff, Joanna Veres, Divya Satish, Grace O'Connell
*University of California, Berkeley*

**P40** **Computational Modeling of iPSC-Derived Engineered Cardiac Microtissues** SB³C2022-364
Jason Lo, Javiera Jilberto, Samuel DePalma, Brendon Baker, David Nordsletten
*University of Michigan*

**V5** **Continuous Separation of Biological Cells Using a New Type of Dielectrophoresis-Based Microfluidic Device** SB³C2022-173
Yoshinori Seki[1], Aoi Nagasaka[1], Tsukushi Gondo[1], Masanori Eguchi[2], Shigeru Tada[1]
*[1]National Defense Academy, [2]National Institute of Technology Kure College*

**P41 Macromolecular Uptake affects Cartilage Mechanics and Chondrocyte Vulnerability** SB$^3$C2022-195
Yingjie Wu, Alexander Kotelsky, Mark Buckley
*University of Rochester*

## Biotransport

**P43 Carrier Solution Composition affects Recovery of Cpa-Perfused Rat Hearts** SB$^3$C2022-246
Casey Kraft, Baterdene Namsrai, Diane Tobolt, Zhe Gao, Michael Etheridge, Erik Finger, John Bischof
*University of Minnesota*

**P44 Cysteine Chemical Modifications as the Regulatory Response to Dimethyl Sulfoxide Exposure** SB$^3$C2022-458
Neda Ghousifam, Mahboobeh Rezayeeyazdi, Chris Riley, Dwight Romanovicz, Marissa Nichole Rylander, Matthew Uden
*University of Texas at Austin*

**P45 Spinal Cord Injury Increases Arterial Stiffness and Perivascular Adipose Tissue Inflammation in Mice** SB3C2022-178
Ryan Sapp[1], Swathi Swaminathan[2], Pattie Mathieu[1], Annie Barnes[1], Gurneet Sangha[1], Valerie Bracchi-Ricard[2], Alisa Clyne[1]
*[1]University of Maryland College Park, [2]Drexel University*

**P46 Transcranial Blood-Brain-Tumor Barrier Modulation for Enhancing Drug Delivery To Glioblastoma** SB3C2022-309
Qi Cai[1], Xiaoqing Li[1], Hejian Xiong[1], Xiaofei Gao[2], Ryan Margolis[1], Monica Giannotta[3], Kenneth Hoyt[1], Robert Bachoo[2], Zhenpeng Qin[1]
*[1]University of Texas at Dallas, [2]University of Texas Southwestern Medical Center, [3]FIRC Institute of Molecular Oncology*

**P47 Probing Molecular Diffusion in the Brain and Tumor Extracellular Space by the Fast Release from Plasmonic Nanovesicles** SB3C2022-385
Hejian Xiong[1], Blake Wilson[1], Aditi Naik[2], Sabina Hrabetova[2], Robert Bachoo[3], Zhenpeng Qin[1]
*[1]University of Texas, [2]SUNY Downstate Health Sciences University, [3]University of Texas Southwestern Medical Center*

**P48 A Timescale-Guided Microfluidic Synthesis of Hydrophobic Drug Nanoparticles with Metal-Phenolic Network Coatings** SB3C2022-403
Yingnan Shen, Simseok Yuk, Yoon Yeo, Bumsoo Han
*Purdue University*

**P49 Digital Plasmonic Nanobubble Detection (Diamond): Improved Nanoparticle Formulation for Clinical Sample Testing** SB3C2022-114
Yaning Liu[1], Haihang Ye[1], Hoang D. Huynh[2], Jeffrey S. Kahn[2], Zhenpeng Qin[1]
*[1]University of Texas at Dallas, [2]University of Texas Southwestern Medical Center*

**P50 A Hydraulic Resistance Model for Interstitial Fluid Flow in the Brain** SB$^3$C2022-338
Helena E. Schreder, Jia Liu, Douglas H. Kelley, John H. Thomas, Kimberly A. S. Boster
*University of Rochester*

**P51** **PCR-Based Approach to Measure Intravasation and Metastasis of Mouse Cancer Cells in the Chick Chorioallantoic Membrane Assay** SB$^3$C2022-260
Molly Brennan, Susan Leggett, Celeste Nelson
*Princeton University*

**P53** **Mathematical Model for Combined Effects of Heat Transfer and Pressure in Causing Soft Tissue Injury** SB$^3$C2022-308
Gary McGregor[1], Bruno Rego[2], Kenneth Diller[1]
*[1]University of Texas at Austin, [2]Yale University*

**P54** **Performance of Skin Cooling Device in Cooling Penetration in Tissue-Experiments and Simulations** SB$^3$C2022-242
Manpreet Singh, Jacob Lombardo, Alexander Caporale, Liang Zhu
*University of Maryland Baltimore County*

**P55** **Design and Development of In Vitro Medical Induction Heating System** SB$^3$C2022-270
Robert Yasalonis, Julian Low, Ahmad Aiman, Ma'Moun Abu-Ayyad, Matthew Garner, Anilchandra Attaluri
*Pennsylvania State University*

**P56** **Role of Thermal Contact Resistance in Induction Heating of Implants** SB$^3$C2022-276
Aiman Ahmad, Nathan Werkheiser, Ma'Moun A. Abu-Ayyad, Matthew R. Garner, Anilchandra Attaluri
*Pennsylvania State University*

**P57** **Influence of Vascular Stasis Based Blood Perfusion on Magnetic Nanoparticles Migration Using Modified Thermal Damage Model: An Illustration of Thermal By-Stander Effect** SB$^3$C2022-285
Manpreet Singh
*University of Maryland Baltimore County*

**P58** **Mathematical Modeling of PAR2 Signaling and Receptor Photoinactivation with Molecular Hyperthermia** SB$^3$C2022-426
Blake Wilson, Chen Xie, Xiaoqian Ge, Peiyuan Kang, Theodore Price, Zhenpeng Qin
*University of Texas at Dallas*

**V6** **Laser-Induced Calcium Influx and Propagation for Temporary Blood-Brain Barrier Opening** SB$^3$C2022-106
Xiaoqing Li, Ayesha Ahmad[1], Qi Cai[1], Monica Giannotta[2], Elisabetta Dejana[2], Robert Bachoo[3], Theodore Price[1], Zhenpeng Qin[1]
*[1]University of Texas at Dallas, [2]FIRC Institute of Molecular Oncology, [3]University of Texas Southwestern Medical Center*

## Design, Dynamics and Rehabilitations

**P59** **The Biomechanics of Low and High Impact Loading on the ACL And MCL in Adolescent Populations** SB$^3$C2022-64
Alexandria Mallinos[1], Kerwyn Jones[2], Brian Davis[1]
*[1]Cleveland State University, [2]Akron Children's Hospital*

**P60** **On Predicting Ground Reaction Force from Thigh and Shank Imu Data During Jump Landings: An In Vitro Study** SB$^3$C2022-79

Mirel Ajdaroski, Amanda Esquivel, James A. Ashton-Miller, So Young Baek
*University of Michigan-Dearborn*

**P61 Understanding Thumb Joint Movement and How Age Contributes to its Changes** SB$^3$C2022-273
Nicole Arnold, Tamara Bush
*Michigan State University*

**P62 Designing a Sustainable In-Clinic Protocol to Expand Postural Stability Data Collection** SB$^3$C2022-288
Rita Patterson, Mai Dinh, Alec Doederlein, Shawn Kennedy, Rajesh Nayak, Sanya Gupta, Fan Zhang, David Mason, Yein Lee
*University of North Texas Health Science Center*

**P63 A Case Study to Evaluate Pediatric Gait Speed and Effects of Chiari Malformation** SB$^3$C2022-481
Tayluer Streat-Ricchiuti, Doug Wajda, Brian Davis
*Cleveland State University*

**P64 In Silico Fatigue Optimization of Tavr Stent Designs with Physiological Motion in a Beating Heart Model** SB$^3$C2022-244
Kyle Baylous[1], Ryan Helbock[1], Brandon Kovarovic[1], Oren M Rotman[1], Marvin Slepian[2], Danny Bluestein[1]
*[1]Stony Brook University, [2]University of Arizona*

**P65 Novel Patient-Specific Computer Modelling of Stent Retriever Thrombectomy** SB$^3$C2022-383
S. Mostafa Mousavi J. S.[1], Danial Faghihi[2], Muhammad Waqas[2], Andre Monteiro[2], Ciprian Ionita[2], Elad Levy[2], Adnan Siddiqui[2], Vincent Tutino[2]
*[1]Canon Stroke and Vascular Research Center, [2]University at Buffalo*

**P66 Development of Fiber Optic Probes to Detect Visceral Arteries for In Situ Fabrication of Stent-Grafts** SB$^3$C2022-472
Timothy Chung, Nicholas Lagerman, Cyrus Darvish, Mohammad Eslami, David Vorp
*University of Pittsburgh*

**P67 Effects of Micropipette Handle Diameter and Inclusion of Finger Rest on Basilar Thumb Joint Contact Mechanics** SB$^3$C2022-235
Nolan Norton, Kenneth Fischer
*University of Kansas*

**P68 Pressure Injuries and Wheelchair Users: Understanding the Role of Friction Between Pant Fabrics and the Seat** SB$^3$C2022-229
Archana Lamsal, Tamara Reid Bush
*Michigan State University*

**P69 Analysis of Air Flowrate Standards for Portable Suction Devices** SB$^3$C2022-133
Saketh Ram Peri, Robert A. De Lorenzo, Robert Lyle Hood
*University of Texas at San Antonio*

**P70 Seated Shear Forces are Affected by Pants and Cushion Cover Materials** SB$^3$C2022-230
Justin Scott, Tamara Reid Bush

*Michigan State University*

**P71 Though I Walk Through the Shadow of The Valley Of Death... Hard Lessons Learned Through Development of the DREEM Machines** SB³C2022-337
Alan Eberhardt
*University of Alabama at Birmingham*

## Education

**P72 Comparing In-Person Biomedical Engineering Laboratory Teaching to Virtual Reality Teaching Approach** SB³C2022-429
Anita Singh[1], Sriram Balasubramanian[2]
*[1]Widener University, [2]Drexel University*

**P73 A Stand-Alone Module to Introduce Medical Image Segmentation into the BME Curriculum** SB³C2022-389
Donna Ebenstein, James Baish, Christine Buffinton
*Bucknell University*

**P74 Community Based Capstone Design Projects at The University of South Floria (USF)** SB³C2022-351
Stephanie Carey, Stephen Sundarrao, Rajiv Dubey
*University of South Florida*

**P75 Confidence Expression in Personal Statements from a Biomedical Engineering REU Site** SB³C2022-496
Elisabeth Reed, Daniella Cotto, Stephanie George
*East Carolina University*

## Fluids

**P77 ViT-FNO□A Robust Model For Tracking Motion in 4D-MRI** SB³C2022-421
Agamdeep Chopra[1], Aymeric Pionteck[2], Javid Abderezaei[2], Mehmet Kurt[2]
*[1]Stevens Institute of Technology, [2]University of Washington*

**P78 Automated Vascular Design and Simulation For 3D Bioprinting** SB³C2022-437
Zachary Sexton[1], Jessica Herrmann[1], Andrew Hudson[2], Jonathan Pham[1], Mark Skylar-Scott[1], Adam Feinberg[2], Sean Wu[1], Alison Marsden[1]
*[1]Stanford University, [2]Carnegie Mellon University*

**P79 Real-Time Shape Optimization of the Total Cavopulmonary Connection in Fontan Surgical Planning Via Reduced Order Modeling** SB³C2022-367
Imran Shah[1], Lakshmi Dasi[1], Traian Iliescu[2], Omer San[3], Alessandro Veneziani[4]
*[1]Georgia Institute of Technology, [2]Virginia Tech, [3]Oklahoma State University, [4]Emory University*

**P80 Effect of Bulging Sinus on Hemodynamic Performance of Polymeric RV-PA Conduit for Pediatric and Adult Patients** SB³C2022-444
Srujana Joshi[1], Hieu Bui, Milad Samaee[1], Susan James[2], Lakshmi Prasad Dasi[1]
*[1]Georgia Institute of Technology, [2]Colorado State University*

**P81 Flow Dynamics Assessment in a Physiological Aortic Arch Using a Validated Computational Framework** SB³C2022-231

Zhenyu Wang[1], Brennan Vogl[2], Ahmed El Shaer[3], Juan Crestanello[3], Mohamad Alkohouli[3], Hoda Hatoum[2]
*[1]Ohio State University, [2]Michigan Technological University, [3]Mayo Clinic*

**P82 Microbiome Metabolic Network Expansion Following Muscadine Grape Extract Intervention of Hypertensive Rats** SB³C2022-266
Brian Westwood, Pooja Patil, Ann Tallant, Patricia Gallagher
*Wake Forest University*

**P83 Fluid Structure Interaction Modeling of the Migration and Trapping of Physically Realistic Blood Clots in an Inferior Vena Cava Filter** SB³C2022-345
Ebrahim M. Kolahdouz[1], Brent A. Craven[2], Kenneth I. Aycock[2], Boyce E. Griffith[3]
*[1]Flatiron Institute, [2]US Food and Drug Administration, [3]University of North Carolina*

**P84 An In-Vitro Study of the Flow Past a Transcatheter Aortic Valve Using Time-Resolved 3D Particle Tracking** SB³C2022-409
Huang Chen[1], Yasaman Farsiani[2], Lakshmi Prasad Dasi[1]
*[1]Georgia Institute of Technology, [2]Nationwide Children's Hospital*

**P85 Evaluation of Shear Stress Variability along Capillaries in Angiogenic Rat Mesenteric Microvascular Networks** SB³C2022-448
Nien-Wen Hu[1], Lomel Banks[1], Peter Balogh[2], Walter L. Murfee[1]
*[1]University of Florida, [2]New Jersey Institute of Technology*

**P86 Restructuring of the Endothelial Glycocalyx after Pneumonectomy** SB³C2022-517
Taylor Paradis[1], Natasha Cruz-Calderon[1], Lydia Masse[1], Gillian Miller[1], Samantha Raskind[1], Aaron Waxman[2], Solomon Mensah[1]
*[1]Worcester Polytechnic Institute, [2]Brigham and Women's Hospital*

**P87 Fabrication of Polymeric Heart Valves Through Additive Manufacturing** SB³C2022-449
Hieu Bui, Adam Verga, Srujana Joshi, Scott Hollister, Lakshmi Prasad Dasi
*Georgia Institute of Technology*

**P88 Left Atrial Hemodynamics after Catheter Ablation** SB³C2022-58
Brennan Vogl[1], Ahmed El Shaer[2], Martin Van Zyl[2], Ammar Killu[2], Mohamad Alkohouli[2], Hoda Hatoum[1]
*[1]Michigan Technological University, [2]Mayo Clinic*

**P89 An Open Loop System for the Computational Investigation of Suspected Coronary Disease with the Patient-Specific CT-Data** SB³C2022-83
Sumit Kumar[1], BV Rathish Kumar[1], Sanjay Kumar Rai[1], Om Shankar[2], Ashish Verma[2]
*[1]Indian Institute of Technology (BHU), [2]Institute of Medical Sciences*

**P91 Fusiform Vs. Saccular Intracranial Aneurysms: Image-Based Blood Flow Simulations can Help to Understand Formation and Treatment Effects** SB³C2022-227
Jana Korte[1], Laurel Morgan Miller Marsh[2], Sylvia Saalfeld[1], Janneck Stahl[1], Daniel Behme[3], Philipp Berg[1]
*[1]Research Campus STIMULATE, [2]University of Washington, [3]University Hospital Magdeburg*

**P92 Subjects with Carotid Webs Exhibit Different Hemodynamic Flow Patterns than Subjects with Atherosclerotic Lesions** SB³C2022-263
Alireza Sharifi, Retta Al Sayed , Charlie Park, Diogo Haussen, Jason Allen, John Oshinski

*Emory University*

**P93 An Ultrasound Based One-Dimensional Modeling Framework for the Assessment of Peripheral Arterial Disease** SB³C2022-396
Milan Gillissen[1], Frans van der Vosse[1], Marc van Sambeek[2], Richard Lopata[1]
*[1]University of Technology Eindhoven, [2]Catharina Hospital Eindhoven*

**P94 Evaluation of Pressure Drop Across Aortic Coarctation: A Comparison of Zero-Dimensional and Three-Dimensional Models** SB³C2022-439
Priya Nair, Martin Pfaller, Seraina Dual, Daniel Ennis, Doff McElhinney, Alison Marsden
*Stanford University*

**P95 Analysis of the Short-Term Effects of Inhaled Nitric Oxide on Pulmonary Artery Hemodynamics Time-Resolved 1D and 3D Phase-Contrast Magnetic Resonance Imaging** SB³C2022-443
Johane Bracamonte, Nickolas Roberts, Raymond Hang, Daniel Grinnan, Elizabeth Sonntag, Janet Pinson, Uyen Truong, Joao Soares
*Virginia Commonwealth University*

**P96 Hemodynamics and Vascular Wall Mechanics of the Pulmonary Artery in Patients with Pulmonary Hypertension and Arteriovenous Fistula** SB³C2022-450
Fatemeh Bahmani[1], Daniel Pearce[2], Ali Vahdati[1], Veeranna Maddipati[1], Stephanie George[1]
*[1]East Carolina University, [2]University of Wisconsin-Madison*

**V7 The Analysis of Urethral Biomechanics During Voiding Using MRI** SB³C2022-506
Maxwell Kounga, Cody Johnson, Juan Gonzalez-Pereira, Shane Wells, Wade Bushman, Alejandro Roldan-Alzate
*University of Wisconsin-Madison*

**P98 Computational Modeling of Arteriovenous Fistula Hemodynamics in Pulmonary Hypertension Patients** SB³C2022-512
Kaitlin Southern, Veeranna Maddipati, Stephanie George, Fatemeh Bahmani
*East Carolina University*

**P99 Computational Nucleotyping in Acute Ischemic Stroke Clot Histopathology is Predictive of Underlying Etiology** SB³C2022-153
Briana Santo, Tatsat Patel, Andre Monteiro, Muhammad Waqas, John Tomaszewski, John Kolega, Adnan Siddiqui, Vincent Tutino
*University at Buffalo*

**P100 Simulation of Thrombus Formation in Microfluidic Constriction at Supraphysiologic Shear Rate** SB³C2022-257
Rodrigo Méndez Rojano, Grant Rowlands, Samuel Schirmacher, James Antaki
*Cornell University*

**P101 Hemodynamics Describing the Localization of Clot Formation in Patients with Carotid Web** SB³C2022-264
Alireza Sharifi, Retta El Sayed, Charlie Park, Diogo Haussen, Jason Allen, John Oshinski
*Emory University*

**V8 Correlation Between Anosmia and Airflow in the Nasal Cavity** SB³C2022-169
Shashwat Shah[1], Zachary Soler[2], Ethan Kung[1]

[1]*Clemson University,* [2]*Medical University of South Carolina*

**V9** **The Impact of Disturbed Flow-Induced Arterial Stiffness on Mechanotransduction in Endothelial Cells** SB³C2022-502
Andrea Alonso, Mahsa Dabagh
*University of Wisconsin-Milwaukee*

**V10** **Post-Operative Vena Cava Boundary Condition Prediction for Fontan Surgical Planning** SB³C2022-2
Wenyuan Song[1], Reena Ghosh[2], Mark Fogel[2], David Frakes[1]
[1]*Georgia Institute of Technology,* [2]*Children's Hospital of Philadelphia*

**V11** **Two Way Coupled FSI Analysis of Patients' Specific Stenosed Left Coronary Artery (LCA) with Multiphase Pulsatile Blood Flow** SB³C2022-171
Abdulgaphur Athani[1], Nik Nazri Nik Ghazali[1], Irfan Anjum Badruddin[2]
[1]*University of Malaya,* [2]*King Khalid University Abha*

**V12** **Patient-Specific Computational Fluid Dynamic Simulation of Cerebrospinal Fluid Flow in the Intracranial Space** SB³C2022-103
Patrick Fillingham, Michael Levitt, Swati Rane Levendovszky
*University of Washington*

## Solids- Cardiovascular

**P102** **Vessel Wall Enhancement is Associated with Increased Wall Stress in Intracranial Aneurysms** SB³C2022-395
Sricharan Veeturi, Seyyed Mostafa Mousavi Janabeh Sarayi, Ammad Baig, Andre Monteiro, Adnan Siddiqui, Vincent Tutino
*University at Buffalo*

**P103** **Image-Based 3D Anatomical Models for Characterization and Surgical Planning of Biatrial Drainage and Sinus Venosus Atrial Septal Defects** SB³C2022-441
Raymond Hang, Johane Bracamonte, Nickolas Roberts, Uyen Truong, Scott Gullquist, Thomas Yeh, Joao Soares
*Virginia Commonwealth University*

**P104** **A Doppler-Exclusive Non-Invasive Computational Framework for Personalized Valve Dynamics in Patients with Aortic Stenosis and Transcatheter Aortic Valve Replacement** SB³C2022-166
Nikrouz Bahadormanesh, Zahra Keshavarz-Motamed
*McMaster University*

**P105** **Effect of Residual Stress on Ring-Test Mechanical Analysis** SB³C2022-334
Manoj Ghosh, Marissa Grobbel, Lik Chuan Lee, Sara Roccabianca
*Michigan State University*

**P106** **Mitral Valve Parameterization** SB³C2022-356
Shelley Gooden[1], Mani Vannan[2], Konstantinos Boudoulas[3], Vinod Thourani[2], Pradeep Yadav[2], Lakshmi Dasi[1]
[1]*Georgia Institute of Technology,* [2]*Piedmont Heart Institute,* [3]*Wexner Medical Center*

**P107** **Mitral Valve Leaflet Coaptation in the Post-Myocardial Infarction Heart** SB³C2022-376

Natalie T. Simonian[1], Hao Liu[1], Alison M. Pouch[2], Joseph H. Gorman III[2], Robert C. Gorman[2], Michael S. Sacks[1]
*[1]University of Texas at Austin, [2]University of Pennsylvania*

**P108 A Computational Rule-Based Semi-Automatic Method for Creating Left Atrial Fiber Architecture** SB³C2022-417
Simone Rossi, Laryssa Abdala, Boyce Griffith
*University of North Carolina*

**P109 Estimation of Myocardial Material Parameters in Developing Zebrafish Using Inverse Finite Element Analysis** SB³C2022-420
Aaron Brown[1], Lei Shi[2], Vijay Vedula[2], Tzung Hsiai[3], Alison Marsden[1]
*[1]Stanford University, [2]Columbia University, [3]UCLA*

**P110 Computational Analysis of Papillary Muscle Approximation for Functional Mitral Regurgitation Repair** SB³C2022-453
Gediminas Gaidulis, Daisuke Onohara, Muralidhar Padala
*Emory University*

**P111 Replacement Heart Valve Simulations Using a Neural Network Finite Element Surrogate Model** SB³C2022-454
Shruti Motiwale, Christian Goodbrake, Wenbo Zhang, Michael Sacks
*University of Texas at Austin*

**P112 Topographical Micropatterning Induces an Anti-Inflammatory Endothelial Transcriptome** SB³C2022-62
Meghan Fallon, Anthony Barnes, Monica Hinds
*Oregon Health & Science University*

**P113 Changes in Anisotropic Viscoelasticity of Right Ventricle with Pulmonary Hypertension Development** SB³C2022-204
Kellan Roth, Wenqiang Liu, Kristen LeBar, Matt Ahern, Zhijie Wang, Adam Chicco
*Colorado State University*

**P114 Nuclear Morphology of Valve Interstitial Cells in the Presence and Absence of Native Elastin in Porcine** SB³C2022-456
Samuel Salinas, Julia Clarin, Rouzbeh Amini
*Northeastern University*

**P115 Active/Passive Mechanical Properties of Aorta Explants from a Mouse Model of Diet-Induced Medial Arterial Calcification** SB³C2022-92
Breanna Pederson, Mengistu G. Gebere, Mohamad Azhar, Narendra R. Vyavahare, Susan M. Lessner, John F. Eberth
*University of South Carolina*

**P116 Computational Modeling of Connectivity-Driven Cortical Scaling and Folding** SB³C2022-287
Xincheng Wang, Maria Holland
*University of Notre Dame*

**P117 The Effects of Formation Conditions on Embolus Analog Nonlinear, Time-Dependent Mechanical Properties** SB³C2022-184

Jose Monclova, Gretchen Hiller, Priyanka Patki, Francesco Costanzo, Keefe Manning
*Pennsylvania State University*

**P118 Factors Causing Interventricular Interactions in the Heart Implanted with Left Ventricular Assist Device** SB³C2022-189
Lei Fan[1], Jenny Choy[2], Ghassan Kassab[2], Daniel Burkhoff[3], Lik Chuan Lee[1]
*[1]Michigan State University, [2]California Medical Innovations Institute, [3]Cardiovascular Research Foundation*

**P119 Determining the Risk of Post-TAVR Cardiac Conduction Abnormalities in Tricuspid and Bicuspid Valves in a Beating Heart Using a Computational Approach** SB³C2022-199
Salwa Anam[1], Symon Reza[1], Brandon Kovarovic[1], Matteo Bianchi[1], Ashraf Hamdan[2], Rami Haj-Ali[3], Danny Bluestein[1]
*[1]Stony Brook University, [2]Rabin Medical Center, [3]Tel-Aviv University*

**P120 A Predictive Simulation of Core Valve Implantation in a Patient with Three Bioprosthetic Valves in Place - A Case Study** SB³C2022-322
Fateme Esmailie[1], Breandan Yeats[1], Huang Chen[1], Milad Samaee[1], Atefeh Razavi[1], Sri Krishna Sivakumar[1], Pradeep Yadav[2], Venkateshwar Polsani[2], Vinod Thourani[2], Lakshmi Prasad Dasi[1]
*[1]Georgia Institute of Technology / Emory University School of Medicine, [2]Piedmont Hospital*

**P121 Reduced Order Modeling Framework for Rapid Simulations of Transcatheter Aortic Valve Replacement Procedures** SB³C2022-363
Imran Shah[1], Milad Samaee[1], Atefeh Razavi[1], Fateme Esmailie[1], Alessandro Veneziani[2], Lakshmi Dasi[1]
*[1]Georgia Institute of Technology, [2]Emory University*

**P122 Changes in the In-vivo Functional State of the Mitral Valve in Percutaneous MitraClip Repair** SB³C2022-446
Hao Liu[1], Natalie Simonian[1], Sneha Vakamudi[1], Mark Pirwitz[1], Joseph Gorman[2], Robert Gorman[2], Michael Sacks[1]
*[1]University of Texas at Austin, [2]University of Pennsylvania*

**P123 Predictive Modeling of Coronary Artery Occlusion During Transcatheter Aortic Valve Replacement** SB³C2022-473
Sri Krishna Sivakumar[1], Breandan Yeats[1], Atefeh Ravazi[1], Ignacio Santos[2], Susan O'Neil[3], Scott Lilly[3], Pradeep Yadav[4], Venkateshwar Polsani[4], Vinod Thourani[4], Lakshmi Dasi[1]
*[1]Georgia Institute of Technology, [2]HCU Valladolid, [3]Ohio State University-Wexner Medical Center, [4]Piedmont Heart Institute*

**P124 Carotid Artery Stiffness Mechanisms Associated with Cardiovascular Disease Events and Incident Hypertension: The Multi-Ethnic Study of Atherosclerosis (MESA)** SB³C2022-212
Ryan Pewowaruk[1], Claudia Korcarz[2], Yacob Tedla[3], Gregory Burke[4], Philip Greenland[5], Colin Wu[6], Adam Gepner[1]
*[1]William S. Middleton Memorial Veterans Hospital, [2]University of Wisconsin, [3]Vanderbilt University, [4]Wake Forest School of Medicine, [5]Northwestern University, [6]National Heart, Lung, and Blood Institute*

**P125 Machine Learning Prediction of Abdominal Aortic Aneurysm Wall Strength and Evaluating Factor Sensitivity** SB³C2022-140
Pete Gueldner, Isabelle Chickanosky, Timothy Chung, David Vorp

*University of Pittsburgh*

**V13 Biomechanical and Microstructural Characterizations of Human Healthy and Hypertrophic Septal Tissues** SB³C2022-316
Katherine Copeland[1], Uday Chintapula[1], Alan Taylor[1], Yi Hong[1], Kytai Nguyen[1], Matthias Peltz[2], Pietro Bajona[3], Jun Liao[1]
*[1]University of Texas at Arlington, [2]University of Texas Southwestern Medical Center, [3]Allegheny Health Network*

**V14 Evaluation of Tachycardia Pacing Therapy Response in a Whole Heart HFpEF Model: Therapy Design Implications** SB³C2022-258
Kevin Sack, Josh Blauer, Richard Cornelussen, Troy Jackson
*Medtronic, Inc*

**V15 Dimensional Variability in Tensile Strength of the Tricuspid Annulus** SB³C2022-7
Andrew Behrmann, Anya Anokhin, Shamik Bhattacharya
*University of Missouri*

**V16 Assessing Local Delivery Capability of a Novel Septal Ablation System via an Ex Vivo Pig Heart Model** SB³C2022-317
Katherine Copeland[1], Uday Chintapula[1], Joyita Roy[1], Yi Hong[1], Liping Tang[1], Matthias Peltz[2], Pietro Bajona[3], Kytai Nguyen[1], Jun Liao[1]
*[1]University of Texas at Arlington, [2]University of Texas Southwestern Medical Center, [3]Allegheny Health Network*

**V17 Biomechanical Wall Thickness and Stiffness Uncertainty Quantification in an Idealized Model of the Pre-stretched Dissected Aorta** SB³C2022-88
Lise Gheysen[1], Lauranne Maes[2], Mathias Peirlinck[3], Annette Caenen[1], Nele Famaey[2], Patrick Segers[1]
*[1]Ghent University, [2]KU Leuven, [3]Delft University of Technology*

## Solids- Growth and Remodeling

**P126 Simulations of Cellular Guidance by 3D Matrix Orientation and Anisotropy Via Deformable Continuous Fibril Distributions** SB³C2022-291
Steven LaBelle, Steve Maas, Adam Rauff, Jeffrey Weiss
*University of Utah*

**P127 Computational Modeling of Brain Bilayer Under Cerebrospinal Fluid Pressure** SB³C2022-302
Fatemeh Jafarabadi, Maria Holland
*University of Notre Dame*

**P128 Multiscale Model of Pregnancy-Induced Heart Growth Applied to Postpartum Recovery** SB³C2022-66
Molly Kaissar, Kyoko Yoshida
*University of Minnesota*

**P129 A Multilayer Mechanical Cellular-Potts Model of Migrating Mesendoderm** SB³C2022-252
Tien Comlekoglu[1], Gustavo Pacheco[1], Bette Dzamba[1], David Shook[1], T.J. Sego[2], James Glazier[2], Shayn Peirce-Cottler[1], Douglas DeSimone[1]
*[1]University of Virginia, [2]Indiana University*

**P130 Multiscale Modeling of Tissue Growth and Remodeling Coupled with Mechanosensitive Cell-scale Systems Biology** SB³C2022-313
Mohammadreza Soltany Sadrabadi[1], Seungik Baek[2], Mohammad R. K. Mofrad[3], Amirhossein Arzani[1]
*[1]Northern Arizona University, [2]Michigan State University, [3]University of California*

**P131 A Combined Mechanical and Biological Approach to Quantify Failure in Human Skin** SB³C2022-34
Jack Hayes, Claire Higgins, Marc Masen
*Imperial College London*

**P132 Distortional Strain Definition for Finite Element Fracture Healing Algorithm** SB³C2022-296
George Morgan, Hana Fox, Lucas Low, Arul Ramasamy, Spyros Masouros
*Imperial College London*

**P133 Overstretch-Induced Softening is Independent of Strain Rate in Cerebral Arteries** SB³C2022-359
Noah Pearson, Gregory Boiczyk, Kenneth Monson
*University of Utah*

**V18 Modeling of Organ-Specific Tumor Microenvironments to Analyze Cell-To-Cell Interactions** SB³C2022-500
Morgan Connaughton, Mahsa Dabagh
*University of Wisconsin-Milwaukee*

## Solids- Injury and Brain Biomechanics

**P134 A Continuum Model for Transition Between Cell-Dense and Cell-Sparse Tissues: Application to Cerebral Aneurysms** SB³C2022-50
Elizabeth Shih, Ryan Mahutga, Victor Barocas, Patrick Alford
*University of Minnesota*

**P135 A Study on the Triaxial Mechanical Properties of Silicone Elastomers for Potential Use as a Brain Tissue Surrogate** SB³C2022-71
Ahsanul Torza, Johannes Weickenmeier
*Stevens Institute of Technology*

**P136 Mechanical and Structural Characterization of the Human Meninges and Falx** SB³C2022-221
Darragh Walsh, David Newport, John Mulvihill
*University of Limerick*

**P137 Recent Updates on the GHBMC Human Head Finite Element Model- A New Visco-hyperelastic Brain Material Model and Brain Strain Validation** SB³C2022-278
Ding Lyu, Runzhou Zhou, Liying Zhang
*Wayne State University*

**P138 How Signal-To-Noise Ratio Impacts the Apparent Stiffness of Brain Tissue in MR Elastography At 7T** SB³C2022-297
Emily Triolo[1], Oleksandr Khegai[2], Jelle Veraart[3], Akbar Alipour[2], Priti Balchandani[2], Mehmet Kurt[1]

[1]*University of Washington,* [2]*Icahn School of Medicine,* [3]*New York University*

**P139 Regional Maximum Principal Strain Response of an Anatomically Accurate Finite Element Human Brain Model** SB³C2022-350
Tyler F. Rooks, Jamie L. Baisden, Narayan Yoganandan
*Medical College of Wisconsin*

**P140 Creating a Platform to Study Headbanging Patterns in a Virtual Heavy Metal Concert Environment** SB³C2022-436
Aymeric Pionteck[1], Devlin Stein[2], Javid Abderezaei[1], Lyndia Wu[3], Mehmet Kurt[1]
[1]*University of Washington,* [2]*Stevens Institute of Technology,* [3]*University of British Columbia*

**P141 Computational Assessment of Stress Distribution in the Brain: Biomarkers of White Matter Lesion Formation** SB³C2022-466
Tyler Diorio[1], Kevin McIver[1], Noah Mehringer[1], Sean Bucherl[1], Eric Nauman[2], Yunjie Tong[1], Vitaliy Rayz[1]
[1]*Purdue University,* [2]*University of Cincinnati*

**P142 Novel Biomechanical Approach to Improve Controlled Cortical Impact Testing for Studying Rodent Closed-Head Traumatic Brain Injury** SB³C2022-35
Emilie Potts[1], Lihong Lu[1], Xiaoyun Xu[2], Arthur Brown[2], Haojie Mao[1]
[1]*University of Western Ontario,* [2]*Robarts Research Institute*

**P143 A Multi-Method Approach for Assessing Non-Lethal Cutaneous Impact Injuries** SB³C2022-155
Omar Elsafty, Christopher Berkey, Reinhold Dauskardt
*Stanford University*

**P144 Head Acceleration Measurement in Youth Football Athletes Using a Mouthpiece-Based Sensor** SB³C2022-281
Madison Marks, Ty Holcomb, N. Stewart Pritchard, Logan Miller, Joel Stitzel, Jillian Urban
*Virginia Tech & Wake Forest University*

**P145 A Hybrid Paradigm to Develop Regional Throaco-Abdominal Criteria for Behind Armor Blunt Trauma** SB³C2022-294
Narayan Yoganandan[1], John Humm[1], Brian Stemper[1], Cameron Bass[2], Salzar Robert[3], Joseph McEntire[4]
[1]*Medical College of Wisconsin,* [2]*Duke University,* [3]*University of Virginia,* [4]*USAARL*

**P146 Development and Validation of Two-Dimensional Finite Element Model of the Neonatal Brachial Plexus** SB³C2022-54
Sarah Trapp, Michele Grimm
*Michigan State University*

**P148 Identifying Micro-indentation Testing Parameters Suitable for Brain Tissue Testing** SB³C2022-46
Xuesong Zhang, Johannes Weickenmeier
*Stevens Institute of Technology*

**V19 I-PREDICT: Developing a Full Human Body Model in FEBio** SB³C2022-348
Lance Frazer[1], Dan Nicolella[1], Brian Stemper[2], Rob Salzar[3], Narayan Yoganandan[2], Dale Bass[4], Matthew Davis[5], Tim Bentley[6], Barry Shender[7]

*[1]Southwest Research Institute, [2]Medical College of Wisconsin, [3]University of Virginia, [4]Duke University, [5]Elemance LLC, [6]Office of Naval Research, [7]Naval Air Warfare Center Aircraft Division*

**V20 The Correlation Study of Brain Tissue Between Mechanical Frequency Properties and Microscopic Structures** SB³C2022-327
Suhao Qiu[1], Linghan Kong, Runke Wang[1], Fuhua Yan[2], Yuan Feng[1]
*[1]Shanghai Jiao Tong University, [2]Ruijin Hospital*

## Solids- Joint and Spine

**P149 Finite Element-Based, Kinematically-Driven, Subject-Specific Model of Human Cervical Facet Capsule Ligaments** SB³C2022-77
Maryam Nikpasand, Rebecca Abbott, Craig C. Kage, Victor H. Barocas, Arin M. Ellingson
*University of Minnesota*

**P151 The Risk of Recurrent Disc Herniation Following Decompression Surgery with Surgical Detachment of the Posterior Extensor Muscles** SB³C2022-346
Stephanie Rossman[1], Eric Meyer[2], Jorge Isaza[3], Steven Rundell[1]
[1]*Explico Engineering, [2]Lawrence Technological University, [3]Spine Specialist of Louisiana*

**P152 Implementation of a Low-Cost System to add Spine Bending to a Uniaxial Compression Device** SB³C2022-379
Axel Moore, Harrah Newman, Raith Nowak, Sean Magee, Gabriela Carlisle, Imani Carter, Justin Bouyer, Edward Vresilovic, Dawn Elliott
*University of Delaware*

**P153 Effect of Stature and Lordosis on Female Lumbar Spine Loads in Vertical Impact** SB³C2022-462
Sagar Umale, Prashant Khandelwal, John Humm, Narayan Yoganandan
*Medical College of Wisconsin*

**V21 Role of Midlevel Constraint in Reducing Midflexion Laxity after Additional Distal Femoral Resection in Posterior Stabilized TKA** SB³C2022-402
Shady Elmasry, Brian Chalmers, Cynthia Kahlenberg, Peter Sculco, Timothy Wright, Michael Cross, David Mayman, Geoffrey Westrich, Carl Imhauser
*Hospital for Special Surgery*

## Solids- Lung

**P154 Regional Strains Evaluated from Digital Image Correlation of Mechanically Ventilated Healthy and Fibrotic Murine Lungs** SB³C2022-18
Talyah Nelson, Kathrine Anduaga, Crystal Mariano, Samaneh Sattari, Arzu Ulu, Edward Dominguez, Tara Nordgen, Mona Eskandari
*University of California, Riverside*

**P155 Analyzing Elastase and Collagenase Treated Mechanical Behavior of Porcine Airways** SB³C2022-56
Crystal Mariano, Samaneh Sattari, Mona Eskandari
*University of California, Riverside*

**P156 A Physics-Based Multi-Scale Modeling Pipeline for Simulation of Ventilation in Advanced COVID-19** SB³C2022-194
Shea Middleton, Elizabeth Dimbath, Anup Pant, Stephanie George, Veeranna Maddipati, M. Sean Peach, Kaida Yang, Andrew Ju, Ali Vahdati
*East Carolina University*

## Solids- Musculoskeletal

**P157 How Cartilage Tribomechanics is Compromised by Elevated Contact Stresses and Inactivity** SB³C2022-39
Shamimur Akanda, Jamie Benson, Arnab Bhattacharjee, David Burris, Christopher Price
*University of Delaware*

**P158 Robust Articulation-Induced Cartilage Rehydration is Sustained Following Proteoglycan Loss** SB³C2022-45
Meghan E. Kupratis, Atia Rahman, Elise A. Corbin, David L. Burris, Christopher Price
*University of Delaware*

**P160 Effects of Interface Material on Cartilage Fluid Load Support In The Migrating Contact Area** SB³C2022-412
Jamie Benson, David Burris
*University of Delaware*

**P161 The Mechanics of Networked, Type II Collagen Fibers from Cartilage** SB³C2022-109
Phoebe Szarek, David M. Pierce
*University of Connecticut*

**P162 The Long Head of the Biceps Tendon Undergoes Multiaxial Deformation During Shoulder Motion** SB³C2022-299
S. Cyrus Rezvanifar, JJ Lamb, Miles Wing, Arin Ellingson, Paula Ludewig, Victor Barocas
*University of Minnesota - Twin Cities*

**P163 Examining the Effects of Localized ACL Damage on the Neighboring Ligaments of the Knee via Finite Element Analysis** SB³C2022-341
Alexander Knapp, Lakiesha Williams
*University of Florida*

**P164 Application Force Feedback Reduces the Measurement Variability of a Shear Wave Tensiometer** SB³C2022-25
Lesley Arant, Joshua Roth
*University of Wisconsin-Madison*

**P165 Quantification of Intervertebral Disc Strain from High-Resolution Ultrasound Imaging During Dynamic Loading** SB³C2022-225
Elnaz Ghajar-Rahimi[1], Shiyin Lim[2], Conner Earl[1], Reece Huff[2], Grace O'Connell[2], Craig Goergen[1]
*[1]Purdue University, [2]University of California Berkeley*

**P166 Comparison of Disc Designs and Outcomes in Cervical Disc Arthroplasty Using Multiscale Modeling** SB³C2022-318
Yuvaraj Purushothaman, Jamie Baisden, Hoon Choi, Narayan Yoganandan
*Medical College of Wisconsin*

**P167 Exploring 3D Printed Scaffold Designs for Meniscal Replacement** SB³C2022-371
Kevin Eckstein, Lawrence Smith, Robert MacCurdy, Virginia Ferguson, Kristine Fischenich
*University of Colorado at Boulder*

**P169 Tensile Stiffness of Skeletal Muscle Under Uniaxial Versus Biaxial Stretch** SB³C2022-486
Minhaj Bhuiyan, Benjamin Wheatley
*Bucknell University*

**P170 Characterizing Regional Anisotropy in a Commercial Soft Tissue Analog** SB³C2022-61
Daniel Pearce, Colleen Witzenburg
*University of Wisconsin-Madison*

**P171 Biomechanical Responses of Neuron-Collagen Constructs for Fast Strain Rate Loading to Failure** SB³C2022-248
Siitinon Nuethong, Sagar Singh, Beth Winkelstein
*University of Pennsylvania*

**P172 A Novel MATLAB Script for the Analysis of Mechanical Characterization Data** SB³C2022-254
Emily King, Michael Bramson, David Corr
*Rensselaer Polytechnic Institute*

**V22 Relationship Between Lumbar Intervertebral Disc Degeneration and Spatial Distribution of T1rho Relaxation Times** SB³C2022-207
Anika Kumar, Noah Bonnheim, Ravi Chachad, Jiamin Zhou, Thomas Link, Roland Krug, Aaron Fields
*University of California San Francisco*

## Solids- Skin

**P173 Modeling Indentation of Skin Using a Thin-Layer Nonlinear Hyperelastic Model** SB³C2022-85
Luli Li, Marc Masen
*Imperial College London*

**P174 The Failure Mechanism of Mouse Skin: A Multiscale Perspective** SB³C2022-121
Nathan Witt[1], Alan Woessner[2], Kyle Quinn[2], Edward Sander[1]
*[1]University of Iowa, [2]University of Arkansas*

## Solids- Reproductive

**P175 3-Dimensional Imaging of the Murine Vagina Using TO-PRO-3 Iodide and Eosin with Dual Inverted Selective Plane Illumination Microscopy** SB³C2022-407
Jasmine Kiley, Mari Domingo, Guang Li, Diego Gatica, Jonathon Brown, Kristin Miller
*Tulane University*

**P176 Comparison of Reduced Order Modeling Methods for Vaginal Tissue Tearing** SB³C2022-10
William Snyder, Traian Iliescu, Raffaella De Vita
*Virginia Tech*

**P177 A Semi-supervised Learning Algorithm for Efficient and Accurate MRI-based 3D Geometric Model Reconstruction of Pelvic Organs** SB³C2022-32
Fei Feng[1], James A. Ashton-Miller[2], John O.L. DeLancey[2], Jiajia Luo[3]
*[1]Shanghai Jiao Tong University, [2]University of Michigan, [3]Peking University*

**P178 3D Ultrasound Imaging of the Murine Cervix During Pregnancy Using Preterm Birth Models** SB³C2022-485
Riley Holloway, Jennifer Anderson, Craig Goergen
*Purdue University*

**P179 Three-dimensional Deformations of Swine Apical Vaginal Support** SB³C2022-38
Kandace Donaldson, Joseph Thomas, Sherrie Clark-Deener, Yizheng Zhu, Raffaella De Vita
*Virginia Tech*

## Solids- Ocular

**P180 An Experimental Investigation on Bending Response of Sclera Tissue Under Electrical Stimulation** SB³C2022-136
Hamed Hatami-Marbini, Jafar Arash Mehr
*University of Illinois at Chicago*

**P181 Finite Element Simulation of Electroactive Mechanical Response of Sclera Using a Multi-Physics Chemo-Electro-Mechanical Model** SB³C2022-137
Jafar Arash Mehr, Hamed Hatami-Marbini
*University of Illinois at Chicago*

**P182 Characterizing the Mechanical Response of Cornea Using Biaxial Tests** SB³C2022-464
M.E Emu, H Hatami-Marbini
*University of Illinois at Chicago*

## Solids- Emerging Topics

**P183 Multiscale Analysis of the Structure-Mechanics Relationship of Mycelium-Based Composites** SB³C2022-325
Zhao Qin, Libin Yang
*Syracuse University*

**P184 Three-Dimensional Reconstruction and Analysis of the Median Nerve Using Robot-Assisted Ultrasonography** SB³C2022-15
David Jordan, Hui Zhang, Zong-Ming Li
*University of Arizona*

**P185 Stiffness Mapping for Early Detection of Breast Cancer: Sensitivity to Errors in Modulus** SB³C2022-164
Lorraine Olson, Robert Throne
*Rose-Hulman Institute of Technology*

**P186 The Biotribology of Touch - Numerically Modelling Tactile Perception** SB³C2022-174
Rikeen Jobanputra[1], Gustavo Luengo[2], Marc Masen[1]
*[1]Imperial College London, [2]L'Oreal*

**P187 A Performance Comparison of a Novel Endotracheal Tube System and Current Clinical Standard Endotracheal Cuff** SB³C2022-415
Carlos Bedolla, James White, Robert De Lorenzo, David Restrepo, Robert Hood
*University of Texas at San Antonio*

## Tissue and Cellular Engineering

**P188 An Integrated Study of Orchestrated Neuronal Migration and Cortical Folding** SB³C2022-65
Shuolun Wang[1], Kengo Saito[2], Hiroshi Kawasaki[2], Maria Holland[1]
*[1]University of Notre Dame, [2]Kanazawa University*

**P189 Extracting and Building with the Engineering Principles of Kidney Development** SB³C2022-170
John Viola, Catherine Porter, Jiageng Liu, Ananya Gupta, Mariia Alibekova, Louis Prahl, Alex Hughes
*University of Pennsylvania*

**P190 The Effects of Cell-Cell Cooperation in 3D Breast Cancer Spheroids** SB³C2022-222
Carolina Trenado, Celeste M. Nelson
*Princeton University*

**P191 Dose-Dependent Chemical Reaction Kinetics for Modeling of TGF-beta Delivery in Cartilage Tissue Engineering** SB³C2022-251
Sedat Dogru, Gabriela Alba, Kirk Pierce, Tianbai Wang, Michael Albro
*Boston University*

**P192 Acute Targeting of Immune Cell Mechanotransduction Improves Healing and Prevents Fibrosis** SB³C2022-372
Kellen Chen, Michelle Griffin, Dominic Henn, Clark Bonham, Katharina Fischer, Dharshan Sivaraj, Geoffrey Gurtner
*Stanford University*

**P193 Evaluation of a Carrageenan Based Hydrogel Confinement Approach to Increase Collagen Deposition for In Vitro Tissue Development** SB³C2022-480
Joseph Krebs, Alyssa Brown, Samuel Stealey, Silviya Zustiak, Natasha Case
*Saint Louis University*

**P194 An Investigation of the Change in pH Following Administration of Pulsed Electrical Fields** SB³C2022-144
Zaid Salameh, Kenneth Aycock, Melvin Lorenzo, Rafael Davalos
*Virginia Tech*

**P195 Multi-node Cardiac Muscle-cell-based Coupled Bio-oscillator Network for Collective Computing** SB³C2022-157
Jiaying Ji[1], Xiang Ren[1], Mohammad Khairul Bashar[2], Jorge Gomez[1], Nikhil Shukla[2], Suman Datta[1], Pinar Zorlutuna[1]

[1]*University of Notre Dame,* [2]*University of Virginia*

**P196 Design and Hemodynamic Performance of a Fetal Valve Prototype Designed for Implantation in Utero** SB³C2022-217
Sanchita S Bhat[1], Hieu T Bui[1], Anna Farnan[1], Christopher K Breuer[2], Aimee K Armstrong[2], Lakshmi Prasad Dasi[1]
[1]*Georgia Institute of Technology,* [2]*Nationwide Children's Hospital*

**P197 Effects of Fiestin on Triple-Negative Breast Cancer Invasion** SB³C2022-69
Jacob Heiss, Nina Treacher, Hossein Tavana
*University of Akron*

**P198 In Vitro Culture of Human Lung Adenocarcinoma Patient-Derived Organoid Towards Expedited Growth and Drug Evaluation** SB³C2022-163
Xiaochen Qin, Yuyuan Zhou, Yaling Liu
*Lehigh University*

**P199 Modeling Macrophage-Regulated Pulmonary Fibrosis with Engineered Membraneous Lung Microtissues** SB³C2022-272
Ying Xu, Ruogang Zhao
*University at Buffalo*

**P200 Development of A 3D Microfluidic Liver Construct Model for Assessing the Effect Of PUFA Diets** SB³C2022-368
Nathaniel Hauser, L. Madison Kirk, Elaheh Rahbar
*Wake Forest School of Medicine*

**P201 Non-Destructive Evaluation of Regional Cell Density within Tumor Aggregates Following Drug Treatment** SB³C2022-386
Cassandra Roberge[1], Ling Wang[2], Margarida Barroso[2], David Corr[1]
[1]*Rensselaer Polytechnic Institute,* [2]*Albany Medical College*

**P202 The Roles of Shear Stress and Heparan Sulfate Degradation in Endothelial Cell Activation** SB³C2022-90
Nicholas O'Hare[1], Ian Harding[1], William Cisneros[1], Ira Herman[2], Eno Ebong[1]
[1]*Northeastern University,* [2]*Tufts University*

**P203 Pro-angiogenic Potential of Mesenchymal Stromal Cells Regulated by Matrix Stiffness and Anisotropy Mimicking Right Ventricles** SB³C2022-127
Michael Nguyen-Truong[1], Seungil Kim[2], Soham Ghosh[1], Peiman Hematti[3], Raghavan Chinnadurai[4], William R. Wagner[2], Zhijie Wang[1]
[1]*Colorado State University,* [2]*University of Pittsburgh,* [3]*University of Wisconsin,* [4]*Mercer University*

**P204 Roles of Polarized Membrane Trafficking in Breast Cancer Cell Migration** SB³C2022-265
Emily Chan, Yasaman Madraki, Jonathan Song, Comert Kural
*Ohio State University*

**P205 Mechanical and Biological Monitoring of Tissue Stiffness in Three-Dimensional Fibroblast Culture** SB³C2022-274
David Csordas, Junru Zhang, Julie Leonard-Duke, Paul DeCostanza, Blake Johnson, Shayn Peirce-Cottler

*University of Virginia*

**V23** **Porcine Neonatal Heart ECM-Based Hydrogel as a Cardiac Injectable Biomaterial** SB³C2022-319
Karla Perez[1], Alan Taylor[1], Jiazhu Xu[1], Diana Alatalo[2], Tam Nguyen[1], Rachel Claus[3], J Ryan Butler[3], Pietro Bajona[4], Matthias Peltz[5], Fatemeh Hassanipour[2], Kytai Nguyen[1], Yi Hong[1], Jun Liao[1]
*[1]University of Texas at Arlington, [2]University of Texas at Dallas, [3]Mississippi State University, [4]Allegheny Health Network, [5]University of Texas Southwestern Medical Center*

**V24** **Mechano-adaptation in Micropatterned MDCK Tissues** SB³C2022-108
Bernard Cook, Patrick Alford
*University of Minnesota*

## Undergraduate Design Competition

**P206** **Development of a Sensor-Imbedded Transmetatarsal Foot Amputation Prosthetic (TMAP)** SB³C2022-483
Jenna Munshi, Vinod Rangaprasad, Simon Hasik
*Purdue University*

**P207** **Pediatric Heart Assist Device Monitor** SB³C2022-503
Rachel Hillner, Luke Perry, Yuzhong Gong, Abdulaziz Khayat, Venkat Chivukula
*Florida Institute of Technology*

**P208** **A Novel, Portable, Nonelectronic, and Versatile Oxygenating Perfusion System for Multi-Organ Preservation** SB³C2022-519
Sophia Salazar, Anjelyka Fasci, Jessica Oseghale, Mariana Garcia, Anis Khalil, Brandt Wearden, Leslie Muenchow, Jose Gonzalez, Carorina Villareal, Daniel Portillo, R. Lyle Hood
*University of Texas at San Antonio*

**P209** **The-Franny** SB³C2022-525
Zahin Akif[1], Ryan Jose[1], Lazaros Papa[1], Francisca Vallejo[1], Winston Yuen[1], Parisa Saboori[2]
*City College of New York, [2]Manhattan College*

**V25** **Silent Speech Interface for Augmented Reality Devices** SB³C2022-505
Tania Rivas, Gianna Distefano, Victor Huayamave, Christine Dailey Walck
*Embry-Riddle Aeronautical University*

**V26** **Dynamic Ankle Brace for Ankle Sprain Recovery** SB³C2022-516
Amulya Bajracharya, Caitlin Brumley, Victor Huayamave
*Embry-Riddle Aeronautical University*

# CONFERENCE ABSTRACTS

# POST-OPERATIVE VENA CAVA BOUNDARY CONDITION PREDICTION FOR FONTAN SURGICAL PLANNING

**W. Song (1), R. Ghosh (2), M. Fogel (2), D. Frakes (1,3)**

(1) School of Electrical and Computer Engineering, Georgia Institute of Technology, Atlanta, Georgia, USA
(2) Cardiology, Children's Hospital of Philadelphia, Philadelphia, Pennsylvania, USA
(3) Wallace H. Coulter Department of Biomedical Engineering, Georgia Institute of Technology and Emory University, Atlanta, Georgia, USA

## INTRODUCTION

The Fontan procedure was introduced as surgical repair for single ventricle patients such as those with hypoplastic left heart syndrome and tricuspid atresia [1-3]. It is a palliation creating a univentricular circulation that channels caval return directly into the pulmonary arteries bypassing the heart altogether. Although the development of imaging and simulation technologies has given rise to opportunities for clinicians to pre-operatively select among surgical options for the optimal geometry of the systemic venous pathway to the lungs, the robust prediction of boundary conditions, i.e., realistic characterizations of post-operative flows into the Fontan connection, remains a critical issue. Because of the dissimilarity between the pre-operative and post-operative flows, it would be useful to predict post-operative conditions rather than use pre-operative conditions as boundary conditions for computational fluid dynamics (CFD) simulations aimed at surgical planning [4]. Our research proposes for the first time the application of machine learning to predict post-operative vena cava flows based on pre-operative vena cava flows from cardiac magnetic resonance (CMR) imaging.

## METHODS

We began by configuring our patient cohort data for machine learning. The data sets consist of both pre-operative and post-operative inferior vena cava (IVC) and superior vena cava (SVC) velocity maps (magnitude and phase images), organized as time series over a single cardiac cycle. Data were available for 6 serial pediatric patients having had Fontan surgeries. For each CMR sequence, manual segmentations of either the IVC or SVC region were executed on each magnitude image, and the resultant caval flow velocity over the cycle was tracked from the corresponding phase image by decoding the grey values of the pixels within the region. An example of a segmentation is presented in Figure 1.

We then resampled each flow sequence to uniformly have 30 datapoints and stacked the sequences into two 6 × 30 matrices paring the pre-operative data with post-operative data for both IVC and SVC training. A two-layer stacked LSTM network [5] with 100 units in each layer, followed by a 30-unit fully connected layer, was adopted as our machine learning model that underwent leave-one-out-cross-validation (LOOCV) to elevate reliability given the small training cohort. A total of 12 independent predictors were generated as a result of the LOOCV procedure, where each of the 6 patients was left out to generate a predictor for both IVC and SVC, respectively.

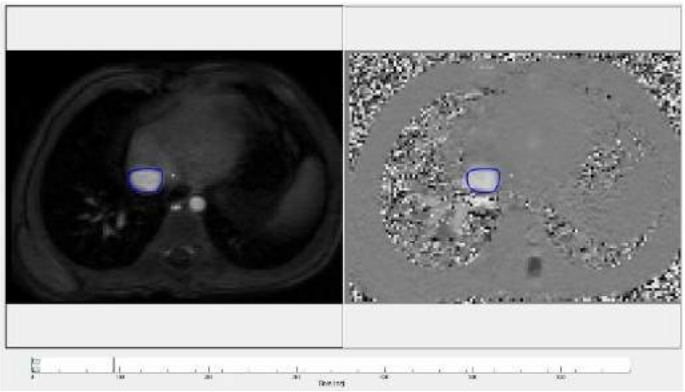

**Figure 1: IVC segmentation example (captured in Medviso AB's Segment v3.2 R8531). The region of interest was first outlined (in blue) manually on the magnitude image (left panel), then automatically transferred to the associated phase image (right panel) to track the flow velocity.**

## RESULTS

As we are motivated to use post-operative vena cava boundary conditions in lieu of pre-operative ones towards Fontan surgical planning, we need to determine if post-operative flow is predictable from pre-operative flow, i.e., to determine if our machine-learning-based post-operative predictions appear to be more similar to the measured post-operative flow curves than pre-operative flow curves. An intuitive comparison in the case of IVC prediction is demonstrated in Figure 2, where the six patients are sequentially left out of training and used for validation, as mentioned in the LOOCV procedure above. Notably, we have applied 5-order polynomial fitting to all the prediction curves to reduce noise.

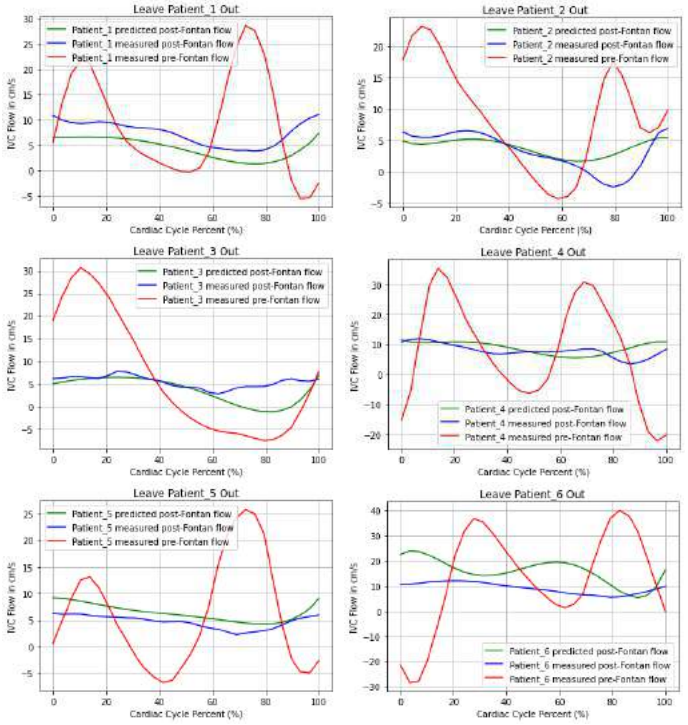


**Figure 2: Post-operative IVC flow velocity prediction and comparison. Each of the 6 patient-specific models shows the prediction's (green) greater similarity to the measured post-operative flow (blue) than the measured pre-operative flow (red), which indicates the predictability of post-operative boundary conditions with machine learning methods.**

In Table 1, we quantify flow curve similarities by calculating the mean-square errors (MSE) between flow curves for each of the 12 predictors. Results show that the overall MSE (averaged across all LOOCV-produced models) between post-operative measurements and predictions is smaller (marked in bold) in both IVC and SVC cases, which is aligned with the intuitive results from the plots above. Specifically, the MSE (cm/s) is 16.10 between the post-operative predictions and the post-operative measurements, and 224.18 between the former and the pre-operative measurements in the case of IVC, and those values become 56.81 and 67.53 in the case of SVC. It is also interesting to note that the gaps in the case of SVC are small compared to those in IVC, and that the similarity comparison may even reverse in isolated cases (an example is given by the 2nd patient in the table). This is aligned with, and explainable by the finding in our previous research where we implemented least square (LS) method to predicting post-operative flow from pre-operative flow using transfer functions in the frequency domain. The transfer functions simulating the Fontan procedure act as a damping system for the IVC, while appear to be flat for the SVC, which indicates that the SVC flow after surgeries does not change much in each time frame within the cardiac cycle, so the predictors do not add additional information [6].

**Table 1: Quantitative description of the similarities between post-operative predictions and measurements across all LOOCV models in both IVC and SVC cases.**

| Vena Cava (cm/s) | MSE between the predicted post-operative flow and the measured … | | | |
|---|---|---|---|---|
| Left-out patient ID | pre-operative flow | | post-operative flow | |
| | IVC | SVC | IVC | SVC |
| 1 | 139.14 | 58.46 | **9.58** | **18.38** |
| 2 | 84.93 | **166.00** | **4.64** | 238.11 |
| 3 | 130.22 | 86.25 | **8.38** | **43.25** |
| 4 | 306.25 | 18.33 | **6.88** | **9.77** |
| 5 | 114.44 | 54.51 | **3.50** | **17.14** |
| 6 | 570.11 | 21.60 | **63.63** | **14.21** |
| Average | 224.18 | 67.53 | **16.10** | **56.81** |

## DISCUSSION

This study introduces a machine learning method to predict post-operative caval return from pre-operative caval flows toward CFD-based surgical planning in Fontan patients. Evaluations of both IVC and SVC cases indicate the predictions' similarity to the post-operative states and thus justify their predictability from pre-operative states. The study shows potential for shifting the current surgical planning paradigm in which pre-operative states are often used as post-operative boundary conditions. We foresee that a more robust predictor will be developed as we enrich the training data, and will advance to pixel level for more detailed boundary condition specification in Fontan surgical planning. Future work will also quantify the impact of the proposed boundary condition prediction approach on key surgical planning metrics extracted from CFD such as hepatic flow split.


## ACKNOWLEDGEMENTS

The authors would like to acknowledge the Additional Ventures Fund for their generous support of this work.


## REFERENCES


[1] Y. Koeken, T. Arts and T. Delhaas, "Simulation of the Fontan circulation during rest and exercise," *2012 Annual International Conference of the IEEE Engineering in Medicine and Biology Society*, 2012, pp. 6673-6676, doi: 10.1109/EMBC.2012.6347525.

[2] M. Bingler, "The Fontan Procedure," July 2021. Accessed on: Dec. 16, 2021. [Online]. Available: kidshealth.org/en/parents/fontan.html

[3] E. N. Rubtsova, C. Alina and T. Dmitry, "A Mathematical Model of the Univentricular Fontan," *2019 IEEE Conference of Russian Young Researchers in Electrical and Electronic Engineering (EIConRus)*, 2019, pp. 2337-2340, doi: 10.1109/EIConRus.2019.8656894.

[4] Trusty, Phillip M., et al. "Fontan surgical planning: previous accomplishments, current challenges, and future directions." *Journal of cardiovascular translational research* 11.2 (2018): 133-144.

[5] S. Hochreiter and J. Schmidhuber, "Long Short-term Memory". *Neural computation*, 1997, 9. 1735-80. 10.1162/neco.1997.9.8.1735.

[6] M. Fogel, J. Plasencia, et al. "Predicting caval return in single ventricle patients after Fontan from pre-operative caval flow: a cardiac magnetic resonance serial study." *2017 AAP National Conference & Exhibition*, 2017, doi: 10.1542/peds.142.1_MeetingAbstract.25.

# RATE AND REGION-DEPENDENT MECHANICAL PROPERTIES OF GÖTTINGEN MINIPIG BRAIN TISSUE IN OSCILLATORY SHEAR

**Gregory M. Boiczyk (1), Noah Pearson (2), Aravind Sundaramurthy (3,4), Jose E. Rubio (3,4), Dhananjay Radhakrishnan Subramaniam (3,4), Ginu Unnikrishnan (3,4), Jaques Reifman (3), Kenneth L. Monson (1,2)**

(1) Department of Biomedical Engineering, University of Utah, Salt Lake City, UT, United States
(2) Department of Mechanical Engineering, University of Utah, Salt Lake City, UT, United States
(3) Department of Defense Biotechnology High Performance Computing Software Applications Institute, Fort Detrick, MD, United States
(4) Henry M. Jackson Foundation for the Advancement of Military Medicine, Inc. Bethesda, MD, United States

## INTRODUCTION

Blast-induced traumatic brain injury (TBI) is a major cause of injury and death in the US military [1]. Finite-element simulations allow investigation of brain strain distribution during blast exposure, but accurate material models of brain tissue are needed for these simulations to achieve a high degree of biofidelity. Experimentally derived constitutive models should be validated over a range of strain rates which can be on the order of several hundred per second in blast injury [2]. To date, high-rate characterization of brain tissue in shear is lacking, with much of the literature focusing on low oscillatory frequencies and strain rates [3] or high oscillatory frequencies but low strains, resulting in peak strain rates below 100 $s^{-1}$ [4].

A major post-mortem finding of severe TBI is axonal injury in regions of white matter within the brain [5]. This suggests that modeling of deformations in these regions is critical to better understanding TBI. White matter is structurally different from gray matter, consisting of myelinated axons which often travel in a highly aligned direction. It can thus be hypothesized that axons may act as a reinforcing fiber in the tissue with a preferred loading direction along the fibers. This is further backed up by the influence of myelin content on brain tissue stiffness [6]. Tissue in the brainstem has previously been shown to be transversely isotropic [7] in shear. To date, no study has conclusively demonstrated anisotropy or isotropy in the cerebrum or cerebellum.

In this work, brain tissue from the cerebrum and cerebellum was harvested from Göttingen minipigs and tested via oscillatory frequency sweeps between strain rates of 0.025 and 250 $s^{-1}$. Tissue was tested in three perpendicular directions to define anisotropy.

## METHODS

Brain tissue from 20 adolescent male Göttingen minipigs (age 23-25 weeks) was harvested immediately after euthanization. All animal protocols were approved by the University of Utah IACUC and the Department of Defense ACURO. Dissected tissue was immersed in a 7.5% polyethylene glycol buffered saline solution and cut into 8 x 8 x 5 mm samples corresponding to one of three fiber orientations (**Figure 1**).

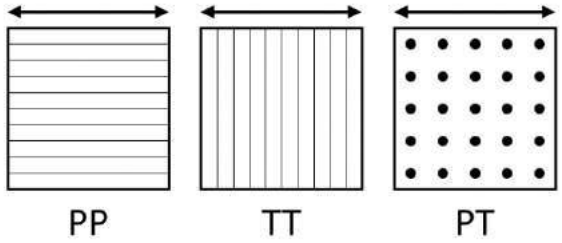


**Figure 1** | Fiber direction for the Parallel-Parallel (PP), Transverse-Transverse (TT), and Parallel-Transverse (PT) directions

Tissue samples were subjected to simple-shear frequency sweeps about a mean strain of K = 0 with a shear strain amplitude of K = 0.2 (strains of K = -0.2 to K = 0.2) at 8 strain rates ranging from 0.025 to 250 $s^{-1}$ (5 cycles each). Mean strain was then increased to K = 0.05 and held for two minutes of stress relaxation. Following stress relaxation, another set of frequency sweeps was performed around a mean strain of K = 0.05 (strains of K = -0.15 to K = 0.25). The same procedure was then repeated for a mean strain of K = 0.1 (strains of K = -0.10 to K = 0.3). Strains did not exceed K = 0.3 during these tests, which was below the failure strain of K = 0.35 observed in high-rate shear tests we have previously performed on brain tissue [8].

Load and displacement data were converted to stress and strain and then averaged within each group to create average stress and strain vs. time curves. To evaluate anisotropy, the average dynamic modulus was computed for each oscillation within a group. Using strain rates and directions as independent variables, two-way ANOVA were performed to identify differences in moduli. Where statistical significance was detected, pairwise comparisons were performed using a Bonferroni adjusted p-value of 0.025.

## RESULTS

Average ± standard deviation dynamic modulus vs strain rate plots for all directions of the cerebrum and cerebellum around a mean strain of K = 0 are shown in **Figure 2**. For both the cerebrum and cerebellum, the tissue shows a trend towards stiffer responses up to a strain rate of 50 $s^{-1}$ after which there is a slight drop off in stiffness. In the cerebrum the tissue is stiffest at a rate of 50 $s^{-1}$ before softening at higher strain rates, while in the cerebellum the tissue is stiffest at 250 $s^{-1}$. Overall, the preferred direction in the cerebrum (PP) is stiffer than the preferred direction in the cerebellum (TT) at all rates.

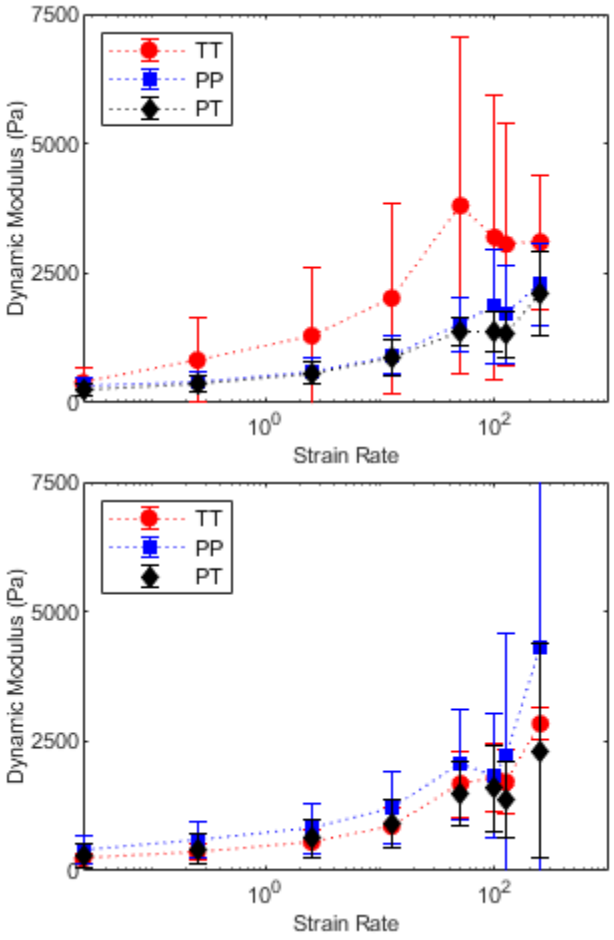


**Figure 2** | Dynamic moduli vs oscillatory strain rate around a mean strain of K = 0 for the cerebrum (N = 11-12, top) and cerebellum (N = 13-15, bottom)

The ANOVA showed a significant effect of direction ($p < 0.001$) on dynamic moduli. Further statistical characterization via pairwise comparisons in the cerebrum showed a statistically significant difference between the Transverse-Transverse (TT) direction and both the Parallel-Parallel (PP) and Parallel-Transverse (PT) directions ($p < 0.001$), with the tissue being stiffest in the TT direction. No significant difference was present between the PP and PT directions ($p = 0.58$). In the cerebellum a statistical difference was present between the PP direction and the PT direction ($p < 0.01$) but no difference between the PP and TT directions ($p = 0.08$) or the PT and TT directions ($p = 0.76$). However, the PP direction was noticeably stiffer than the PT and TT directions. The ANOVA showed no significant difference for region ($p = 0.18$) or the combination of rate and region ($p = 0.32$)

## DISCUSSION

Both the cerebrum and cerebellum showed pronounced rate stiffening with increasing strain rates up to a rate of 50 $s^{-1}$, as would be expected with a viscoelastic material. Interestingly, both regions then show a subsequent decrease in dynamic modulus at higher rates. At higher rates, the displacement waveform starts to show larger variations, contributing to larger variations in loads, potentially reducing the mean stiffness. This can be further seen from the larger standard deviations above a rate of 50 $s^{-1}$. This may also be a physical phenomenon of the tissue itself, warranting further evaluation through finite element simulations and constitutive modeling.

Generally, the mean dynamic moduli in the preferred direction in the cerebrum (TT) (299.5 ± 232.8 to 3803 ± 3242 Pa) was greater than that in the cerebellum (PP) (390.2 ± 270.8 to 2317.5 ± 2052 Pa) for all strain rates below 250 $s^{-1}$. This phenomenon could possibly be explained by increased white matter content in cerebral samples versus cerebellar samples, though we did not quantify the relative proportion of white and gray matter in each region in this work. It should be noted that higher variability was present for this direction in the cerebrum as indicated by the larger standard deviations. Results show that both regions had one direction that was statistically stiffer than at least one other direction. The stiffest directions were the Transverse-Transverse (TT) direction for the cerebrum and the Parallel-Parallel (PP) direction for the cerebellum. In a single fiber family model in simple shear, only the TT direction should show fiber contributions. This suggests that the assumption of predominant fiber angle was correct in the cerebrum (fibers running in the rostral-caudal direction) but incorrect in the cerebellum, where fibers appear to predominantly run in the medial-lateral direction as opposed to running perpendicular from the brainstem as hypothesized.

The work presented in this abstract represents the first characterization of the response of porcine brain tissue in the cerebrum and cerebellum in harmonic oscillation over a range of strain rates and strain levels relevant to injury modeling. Future work with this experimental data will be used to develop constitutive models and finite element simulations of the experiments.

## DISCLAIMER

The opinions and assertions contained herein are the private views of the authors and are not to be construed as official or as reflecting the views of the U.S. Army, the U.S. Department of Defense, or The Henry M. Jackson Foundation for Advancement of Military Medicine, Inc. This abstract has been approved for public release with unlimited distribution.

## ACKNOWLEDGMENTS

Funding for this project was provided by the Henry M. Jackson Foundation for the Advancement of Military Medicine, Inc.

## REFERENCES

[1] Tanielian T. et al., *RAND Corp*. 60. 2008.
[2] Bell E.D. et al. *J Biomech Eng. 140*. 2018
[3] Hrapko M. et al. *Biorheology* 45. 663–676. 2008.
[4] Nicolle S. et al. *Biorheology* 42, 209–223. 2005.
[5] Smith D.H. et al. *Neuroscientist* 6. 483–495. 2000.
[6] Weickenmeier J. et al. *J. Mech. Behav. Biomed. Mater.* 76. 2017.
[7] Arbogast K.B.et al. *J Biomech*. 31. 801–807. 1998.
[8] Sundaramurthy, A. et al, J. *Front. Bioeng. Biotechnol.*, 2021.

# DIMENSIONAL VARIABILITY IN TENSILE STRENGTH OF THE TRICUSPID ANNULUS

**Andrew J. Behrmann (1), Anya Anokhin (1), Shamik Bhattacharya (3)**

(1) School of Medicine, University of Missouri, Columbia, MO, United States
(2) Department of Engineering and Technology, Southeast Missouri State University, Cape Girardeau, MO, United States

## INTRODUCTION

Geometric changes of the tricuspid annulus can lead to functional tricuspid regurgitation, a heart valve disease associated with high morbidity and mortality rates. These geometric changes include dilation of the tricuspid annulus as well as flattening of the annulus to a point that it loses its native bimodal saddle shape and becomes planar [1]. Previous studies have investigated the tensile strength of the three distinct tricuspid annulus segments (septal, anterior, posterior) and found the annulus has the lowest elastic moduli at the points showing the highest amounts of dilation in the clinical setting, the posterior and anterior free wall segments. Collagen content of each annulus portion was directly correlated with tensile strength, finding the highest strength and collagen content in the septal segment of the annulus [2]. This determined tensile strength when stretching the annulus in the circumferential dimension but did not answer anything about the longitudinal plane of the annulus that becomes flattened in the pathologic state [2,3]. Thus, the current study aimed to determine if there was a difference in tensile strength of tricuspid annulus tissue when it is stretched in the longitudinal dimension compared to being stretched in the circumferential dimension. This may be used to better inform the design of tricuspid annuloplasty rings and percutaneous repair devices by determining which section of the annulus needs greater support and in which annular plane that support is needed; circumferential or longitudinal. These results may also better inform computational models of tricuspid regurgitations and right ventricular remodeling.

## METHODS

Ten porcine hearts were stored at -80℃ and thawed in a warm saline bath the day of experiments to a temperature of 37℃. The tricuspid annuli were removed from the porcine hearts using a scalpel and surgical scissors. The annulus was then divided into its three distinct segments, anterior, posterior, and septal which corresponds with the three leaflets of the tricuspid valve. Annulus segments were trimmed into segments measuring 32 mm in length, 8 mm in width, and 2 mm in thickness. Thickness was measure with Vernier calipers along the entire sample to ensure a uniform thickness was achieved. These annulus segments were then divided into a 24 mm long segment to be stretch circumferentially, and a shorter 8 mm by 8 mm square of annulus tissue to be stretched in the longitudinal dimension (figure 1A). Tensile testing was performed using a U-stretch precision uniaxial tensile machine (CellScale) with samples immersed in 37℃ saline solution and pierced with bio-rake tines (figure 1B).

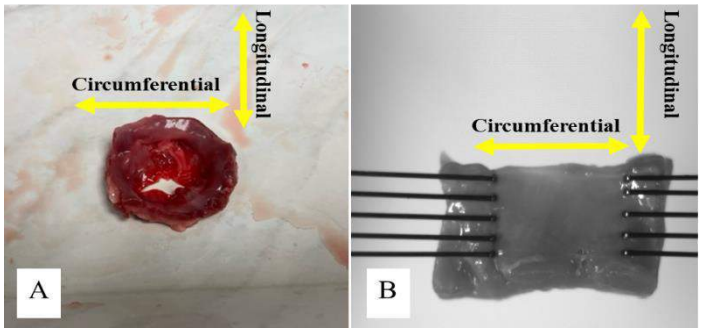


**Figure 1: A) Resected tricuspid annulus and valve with arrows denoting circumferential and longitudinal directions. B) Annulus sample loaded in U-stretch tensile testing machine.**

**Equation 1:** $Stress = \frac{Force\ required\ to\ stretch\ the\ sample}{Initial\ cross\ sectional\ area\ of\ the\ sample}$

All tissue samples were preconditioned at a load rate of 1 mm/s to 10% strain. Following preconditioning, samples were stretched at a rate of 0.2 mm/s to 20% strain [1]. This was performed in tissues that were stretched in the circumferential and longitudinal axes, respectively.

Strain was measured using video extensometery, and stress was calculated using equation 1. Stress-strain curves were developed from these results and the modulus of elasticity was calculated from these curves for all samples between strain ranges of 8% to 13% ($R^2 > 0.99$). The stress-strain curves for all samples are shown in figure 2. A students t-test was performed in R statistical software to determine the differences in longitudinal versus circumferential tensile strength in each of the three respective annulus segments. A one-way ANOVA was performed in R to compare the elastic moduli of the three annulus segments in the longitudinal dimension, and a second one-way ANOVA to compare the elastic moduli of each annulus section in the circumferential dimension.

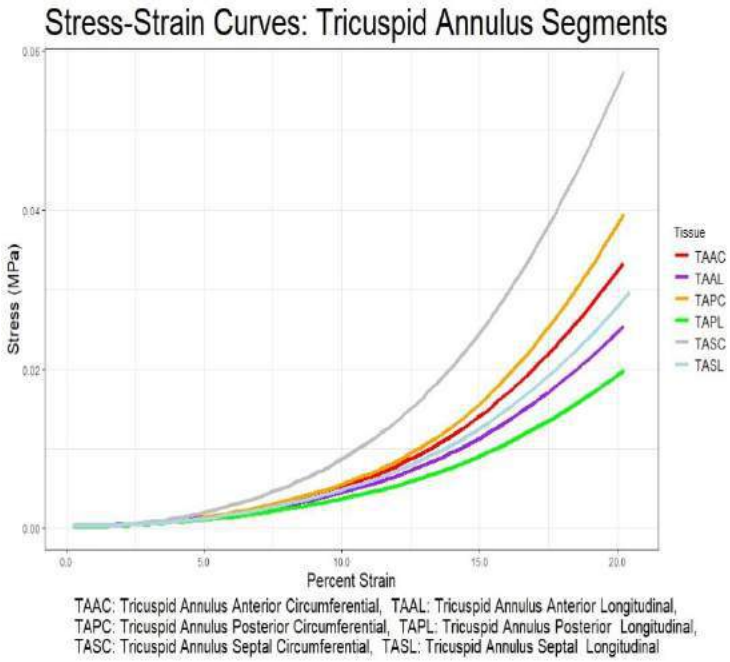


**Figure 2: Stress-strain curves of annulus segments.**

## RESULTS

The average elastic moduli of the tricuspid annulus segments in the longitudinal direction were 0.123±0.019 MPa in the anterior segment, 0.081±0.013 MPa in the posterior segment, and 0.140±0.020 MPa in the septal segment. The average circumferential elastic moduli of each segment was 0.173±0.028 MPa for the anterior segment, 0.188±0.020 MPa in posterior segment, and 0.140±0.020 MPa in septal segment (figure3). Each annulus segment's circumferential elastic modulus is significantly higher ($p<0.05$) than its longitudinal modulus. In the one-way ANOVA that was performed on each segment, septal segment moduli were significantly greater in both circumferential and longitudinal directions than each of the other segments' respective moduli (figure 3). The average elastic modulus in the longitudinal plane of the posterior annulus was significantly less than both anterior and septal segments. Average modulus values of all tissue sample for each directionality can be found in table 1.

| | Septal Moduli (MPa) | Anterior Moduli (MPa) | Posterior Moduli (MPa) |
|---|---|---|---|
| Circumferential | 0.268±0.036 | 0.173±0.028 | 0.188±0.020 |
| Longitudinal | 0.140±0.020 | 0.123±0.019 | 0.081±0.013 |

**Table 1: Average elastic modulus values.**

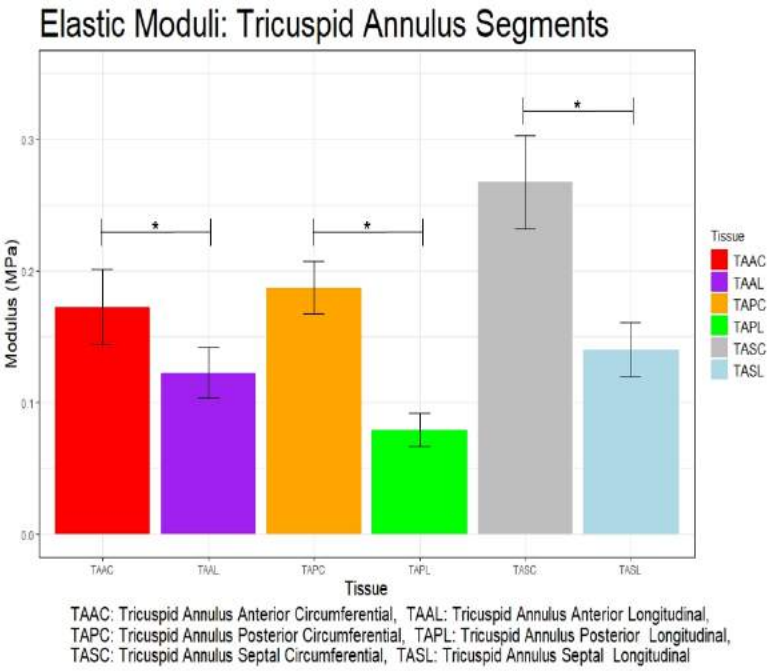


**Figure 3: Average elastic moduli of tricuspid annulus segments. * Indicates $p<0.05$**

## DISCUSSION

These preliminary results suggest that there is a significant difference ($p < 0.05$) in tensile strength of all three tricuspid annulus segments when comparing circumferential versus longitudinal planes. Thus, this is the first study to report that the tricuspid annulus differs in tensile strength depending on the tissue plane being studied. The weakest point of longitudinal tensile strength corresponds to the tricuspid annulus' two high points that fall into a flattened planar shape upon annular dilation. This may indicate a greater amount of vertical support in the longitudinal plane from tricuspid annuloplasty rings is needed within these regions in order to maintain or re-establish the taut bimodal saddle shape of the native annulus. These findings may also be used to inform computational models of tricuspid annulus dilation and ventricular remodeling seen in right heart failure. This study used bio-rake tines that pierced the tissue in order to avoid crushing and slipping of the tissue that may occur when clamping the tissue for uniaxial tensile testing, but this may come with its own end effects on the tissue's strength. These studies were performed in anatomically normal porcine hearts and there may be a pathologic difference in tensile strength of hearts undergoing tricuspid annulus dilation compared to unaffected hearts. Porcine tricuspid annulus mechanics may also differ from human. In conclusion, this study aimed to add a new dimension to the understanding of the tricuspid annulus and has provided another variable to be considered when designing tricuspid annuloplasty rings and other percutaneous tricuspid annulus repair techniques.


## ACKNOWLEDGEMENTS

This project was funded by the Funding For Results Grant of Southeast Missouri State University.


## REFERENCES


[1] Ton-Nu, T et al. *Circulation*, 114:143-149, 2006.
[2] Basu, A et al. *Cardiovasc. Eng. Technol*, 9(2):217-225, 2018.
[3] Alenezy, D. *World J Cardiovasc. Surg*, 5:115-123 2015.

SB³C2022
Summer Biomechanics, Bioengineering and Biotransport Conference
June 20-23, Eastern Shore, MD, USA

# DENOISING INSTRUMENTED MOUTHGUARDS FOR ACCURATE TRAUMATIC BRAIN INJURY DETECTION WITH CONVOLUTIONAL NEURAL NETWORK.

**Xianghao Zhan (1), Yuzhe Liu(1), Olivier Gevaert (2), David B. Camarillo (1)**

(1) Department of Bioengineering, Stanford University, Stanford, CA, USA
(2) Department of Biomedical Data Science, Stanford University, Stanford, CA, USA

## INTRODUCTION

Traumatic brain injury (TBI) has become a global health threat. In 2016, over 27 million cases of TBI were reported globally [1]. The fast diagnosis and early warning approaches of TBI are significant to helping prevent repetitive sport-related TBI [2]. Conventionally, brain injury criteria (BIC) have been developed to estimate TBI risks [3]. More recent studies have shown brain strain (maximum principal strain, MPS) and strain rate (MPS rate, MPSR) based on brain-physics-based finite element modeling (FEM) are promising mechanical parameters well correlated with TBI pathologies including blood-brain-barrier disruption and axonal injury. The head kinematics are the input to compute BIC, brain strain and strain rate. Researchers have developed wearable sensor technologies to precisely measure the head kinematics with systems like head impact telemetry system (HITS), Xpatch and instrumented mouthguard [4]. The instrumented mouthguard attaches the sensors to the dentition and enables the rigid coupling with the skull for more precise measurement of the head rotation.

Although the instrumented mouthguards showed the capability to precisely measure the head kinematics [4] that correlates well with TBI results, the measurement are deviated from the reference kinematics measured by sensors directly implanted into the anthropomorphic test dummy (ATD) head due to the potential loosening of the mouthguard and electronic noises of the sensors. For example, Liu et al. compared five different types of instrumented mouthguards on laboratory impacts [5]. With the measurement of ATD sensors as the reference, the mouthguards show an average of 2.5% to 32.4% relative error in peak of magnitude (REPM) in linear acceleration measurements and an average of 2.3% to 7.6% REPM in angular velocity measurement. The errors in the kinematics can further lead to ~10% errors in the estimation of 95th percentile MPS. In this study, we apply the deep learning to denoise the mouthguard kinematics to better represent head kinematics measured by sensors in dummy head.

## METHODS

With a pneumatic impactor system and anthropomorphic test dummy (ATD) headform [5], we collected two datasets with 163 independent impacts in total. The ATD headform was impacted at the locations including front, facemask, oblique, side and back (dataset 1) and at every 15° from front to back (dataset 2). The impact velocities ranging from 3 m/s to 9.3 m/s were used considering the impact velocity in NFL helmet testing protocol [6]. . The impacts were measured with kinematics sensors both in instrumented mouthguards and in the ATD head. Linear acceleration at the head center of gravity (Lin. Acc.) and angular velocity (Ang. Vel.) were measured in three anatomical axes (x: posterior-to-anterior, y: left-to-right, z: superior-to-inferior) respectively. Two different types of instrumented mouthguards were used to collect the data and the sensor measurement in the ATD head was referred to as the reference kinematics signals as the target.

We then partitioned the datasets into the training (113 impacts), validation (25 impacts) and test datasets (25 impacts). To improve the model accuracy, we augmented the training data by partitioning the impacts into 100ms frames using a sliding window (width: 100ms, stride: 5ms). Each validation or test impact was partitioned into 2 100ms impacts for model testing. We then used the training dataset to train a one-dimensional convolutional neural network (1D-CNN) to predict the ATD sensor kinematics with the mouthguard measurement as the input. Considering the different physics mechanisms of noises, we modeled the six channels of Lin. Acc. and Ang. Vel. independently. To further optimize the accuracy, we tested out two different modeling methods: 1) to predict the ATD sensor kinematics from the mouthguard kinematics; 2) to predict the difference between the two kinematics and add the difference onto the input mouthguard kinematics. The validation dataset was used to tune the hyperparameters of the 1D-CNN model and choose the modeling method. The test dataset was used to assess the model performance on unseen impacts. We evaluated the model accuracy on the test dataset on three levels: 1) kinematics level: we calculated mean absolute error (MAE), root mean squared error

(RMSE), coefficient of determination ($R^2$), peak absolute error (PAE) and signal-to-noise ratio (SNR); 2) BIC level: we computed Head Injury Criterion (HIC[7]), Kinematic rotational brain injury criterion (BRIC[8]), Generalized acceleration model for brain injury threshold (GAMBIT[9]) and Kleiven's linear combination (KLC[10]), and evaluate $R^2$ and RMSE over test impacts; 3) strain and strain rate level: we used KTH head model [10] to compute the whole-brain peak MPS and MPSR and computed the brain-element-wise absolute error, with the MPS/MPSR calculated by ATD sensor kinematics as the reference.

## RESULTS

The kinematics-level results are shown in Fig. 1. After denoising, the kinematics signals better correlate with the reference, with smaller MAE, RMSE and higher $R^2$ and SNR. The RMSE and PAE are significantly reduced with the 1D-CNN denoising models for all six channels of linear acceleration and angular velocity ($p<0.05$, Wilcoxon signed-rank test). The example linear acceleration from three test impacts before and after denoising is visualized in Fig. 2, which shows the effectiveness of the denoising: the denoised kinematics are closer to the reference ATD sensor measurement.

| Kinematics | Axis | Model | MAE | RMSE | R2 | Peak-MAE | Peak-RMSE | Peak-R2 | SNR |
|---|---|---|---|---|---|---|---|---|---|
| Angular Velocity | X | Denoised | **0.938** | **1.544** | **0.965** | **0.976** | **1.447** | **0.989** | **12.281** |
| Angular Velocity | X | Raw | 1.952 | 2.784 | 0.929 | 3.706 | 4.381 | 0.903 | 4.898 |
| Angular Velocity | Y | Denoised | **1.445** | **2.206** | **0.942** | **2.026** | **2.622** | **0.900** | **14.195** |
| Angular Velocity | Y | Raw | 1.699 | 2.557 | 0.924 | 2.887 | 3.894 | 0.779 | 12.658 |
| Angular Velocity | Z | Denoised | **0.749** | **1.235** | **0.938** | **0.862** | **1.315** | **0.978** | **9.812** |
| Angular Velocity | Z | Raw | 0.956 | 1.440 | 0.920 | 1.427 | 1.827 | 0.957 | 8.456 |
| Angular Velocity | Magnitude | Denoised | **1.023** | **1.656** | **0.954** | **1.231** | **1.692** | **0.972** | **21.514** |
| Angular Velocity | Magnitude | Raw | 1.445 | 2.100 | 0.935 | 2.022 | 2.468 | 0.940 | 18.296 |
| Linear Acceleration | X | Denoised | **2.694** | **4.762** | **0.499** | **4.598** | **5.874** | **0.881** | **6.921** |
| Linear Acceleration | X | Raw | 4.018 | 6.558 | -0.288 | 8.979 | 13.864 | 0.336 | 3.208 |
| Linear Acceleration | Y | Denoised | **1.521** | **2.705** | **0.793** | **2.692** | **3.646** | **0.974** | **5.782** |
| Linear Acceleration | Y | Raw | 3.017 | 4.891 | 0.158 | 8.216 | 10.484 | 0.787 | -0.496 |
| Linear Acceleration | Z | Denoised | **1.469** | **2.559** | **0.490** | **2.964** | **3.891** | **0.664** | **6.921** |
| Linear Acceleration | Z | Raw | 3.298 | 6.044 | -2.313 | 10.866 | 19.226 | -7.196 | -0.018 |
| Linear Acceleration | Magnitude | Denoised | **2.107** | **3.863** | **0.727** | **3.449** | **4.562** | **0.932** | **12.918** |
| Linear Acceleration | Magnitude | Raw | 4.495 | 7.952 | -0.788 | 11.336 | 18.727 | -0.146 | 6.966 |

**Figure 1. The model performance metrics on the kinematics level.**

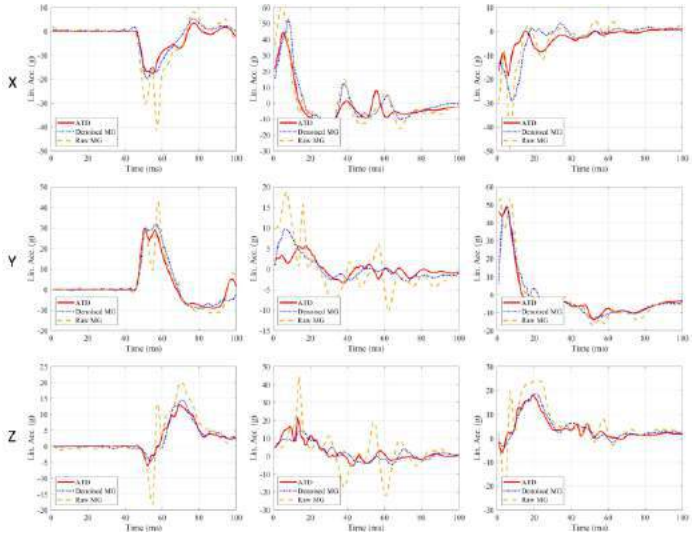


**Figure 2. The denoising effect on three example impact kinematics.**

On the BIC level, according to results in Fig. 3, the estimation error is significantly reduced ($p<0.001$). On the strain and strain rate level, the results are shown in Fig. 4 where we plotted the distribution of absolute error of the MPS and MPSR calculated by the raw mouthguard measurement and denoised measurement respectively. The denoising 1D-CNN models significantly reduced the MPS and MPSR errors ($p<0.001$). The mean error was reduced from 0.011 to 0.009 for MPS and from 3.895 to 2.286 for MPSR.

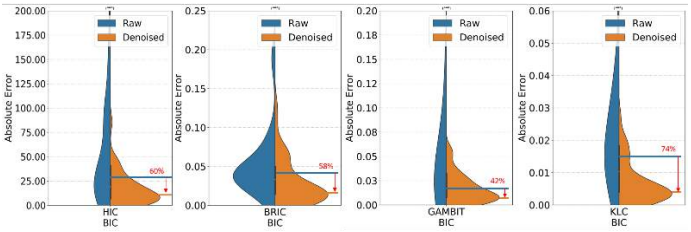


**Figure 3. The denoising effect on the BIC estimation error with percent reduction in median shown in the figure.**

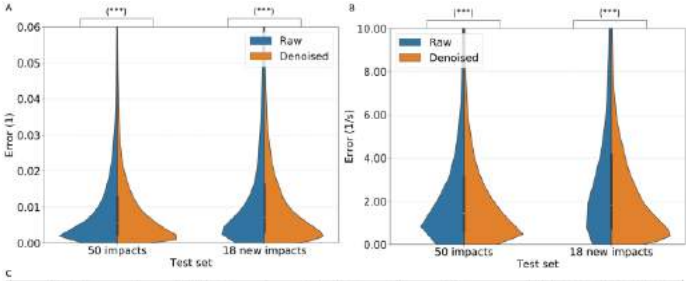


| Metric | Method | Median | Mean | Standard Deviation |
|---|---|---|---|---|
| MPS Error | Raw | 0.006 | 0.011 | 0.015 |
| MPS Error | Denoised | 0.006 | 0.009 | 0.010 |
| MPSR Error | Raw | 1.377 | 3.895 | 8.477 |
| MPSR Error | Denoised | 1.497 | 2.286 | 2.563 |

**Figure 4. MPS and MPSR estimation error with denoising.**

## DISCUSSION

We develop 1D-CNN models to denoise the mouthguard measurement of head impact kinematics with the reference kinematics measured by the sensors implanted in dummy test head. The models are effective in generating kinematics better correlated with the reference kinematics. The error between the denoised kinematics and the reference kinematics is significantly smaller than that between the raw mouthguard measurement and the reference kinematics. Furthermore, the 1D-CNN denoising models significantly reduce the errors of brain injury criterion (BIC) calculation and the brain strain and strain rate calculation based on the kinematics measurement, which enables more accurate brain injury risk estimation and early warning for potential patients of TBI. Following on this study, future studies could develop similar deep learning models to denoise the helmet sensors and skin-patch sensors for broad applications in clinical TBI management.


## ACKNOWLEDGEMENTS

This work was supported by the Department of Bioengineering at Stanford University and the Office of Naval Research Young Investigator Program (N00014-16-1-2949).


## REFERENCES


[1] James, S. *et al. Lancet Neur.* 18(1):56-87 (2016)
[2] G¨uiza F. *et al. Neurosurgery.* 45(3):e316-e320 (2017)
[3] Zhan X. *et al. IEEE Trans. Biomed. Eng.* (2021)
[4] Camarillo D. *et al. Ann. Biomed. Eng.* 41(9):1939-1949 (2013)
[5] Liu Y. et al. Ann. Biomed. Eng. 48(11):2580-2598 (2020)
[6]Funk J,et al.Biomechanics Consulting and Research, LLC (2017).
[7] Versace J. *SAE Tech. Pap.* (1971)
[8] Takhounts E. *et al. Proc. 22nd Enhanced Safety Veh. Conf.* (2011)
[9] Newman J. *et al. Proc. Int. IRCOBI Conf.* (1986)
[10] Kleiven S. *et al. SAE Tech. Pap.* (2007)

SB³C2022
Summer Biomechanics, Bioengineering and Biotransport Conference
June 20-23, Eastern Shore, MD, USA

# TRICUSPID VALVE ANNULUS MECHANICS AND GEOMETRY IN NEWBORNS WITH HYPOPLASTIC LEFT HEART SYNDROME (HLHS)

**Colton J. Ross (1), Elizabeth J. Trimble, (2), Arshid Mir (3), Harold M. Burkhart (2), and Chung-Hao Lee (1)**

(1) Biomechanics and Biomaterials Design Laboratory, School of Aerospace and Mechanical Engineering, The University of Oklahoma, Norman, OK, USA
(2) Department of Surgery, The University of Oklahoma Health Sciences Center, Oklahoma City, OK, USA
(3) Department of Pediatric Cardiology, The University of Oklahoma Health Sciences Center, Oklahoma City, OK, USA

## INTRODUCTION

Hypoplastic left heart syndrome (HLHS) is a congenital defect affecting 1 in every 3,841 newborns in the United States and is associated with a 20.6% mortality within the first two weeks of life [1]. HLHS is characterized by an underdevelopment of the left ventricle, mitral valve, and/or the ascending aorta, which consequently inhibits the systemic blood circulation. Cardiac palliation for HLHS is initiated immediately after birth and progresses over three stages during the first 2-3 years of life of the newborn. Throughout the three cardiac palliation stages, tricuspid regurgitation (TR) arises in 32% of newborns before the second palliation stage (Glenn operation) and is associated with a high mortality rate [2]. The occurrence of TR may be due to adverse tissue remodeling instigated by surgical corrections during the palliation stages. One avenue to improve HLHS treatments, including inter-staged TV repair, is to identify the geometric and biomechanical differences between the healthy (functional) and HLHS-afflicted tricuspid valve (TV) to better replicate a more desirable TV function.

Previous studies have quantified the unique features of the right-side heart anatomy and function in HLHS, as compared to the healthy patients. For example, the ventricular cavity is more circular in the HLHS condition due to a change in intraventricular septum shape, and the septal leaflet is supported by additional free-standing papillary muscles [3]. The circumferential strains of the right ventricle have also been found to be similar between healthy and HLHS newborns; however, the longitudinal strains are reduced in HLHS [4]. Despite these advances in our knowledges of congenital patients, the information on the biomechanical and geometric features of the HLHS-afflicted TV annulus remains lacking.

Thus, in the present work we present an *in vivo* TV annulus analysis pipeline for HLHS and healthy patients using 4-dimensional echocardiograms. This framework allows for quantification of the clinical/geometric indices for the TV annulus (e.g., the annular area) and the biomechanics metrics such as the strain rate and curvature. **Our objective** is to provide insight into the fundamental differences in those functional metrics between healthy and HLHS-afflicted TV annuli.

## METHODS

The study protocol was reviewed and approved by the University of Oklahoma Health Sciences Center institutional review board (IRB#14112). The patient cohort consisted of $n$=8 HLHS patients without TR and $n$=4 healthy patients. For all patients, 4D full-volume transthoracic echocardiographic data was collected for a full cardiac cycle (Philips EPIQ ultrasound machine). The imaging data was then imported to the open-source 3D Slicer software for segmentation of the TV annulus (**Fig. 1a**, next page), which was performed through manual point placement within the 3D Slicer GUI, targeting a resolution of 8°-9° between each segmentation point to capture the unique annular shapes. The three commissure locations were also identified: anterior-septal (AS), posterior-septal (PS), and the anterior-posterior (AP). The segmentation process was repeated at five distinct timepoints over the cardiac cycle: the right ventricular minimum pressure ($RVP_{min}$) chosen as the reference configuration in the subsequent strain analysis, end diastole (ED), end isovolumetric contraction (EIVC), end systole (ES), and end isovolumetric relaxation (EIVR).

The ($X$,$Y$,$Z$) coordinates from image segmentation were imported to MATLAB (MathWorks, MA) for curve fitting and geometric and biomechanical quantification. In brief, the segmented 3D point cloud of the TV annulus was fitted using 1D moving least-squares (MLS) shape functions $\Psi$ in a cylindrical coordinate system $(r, \theta, z)$ [5]:

$$C(X,Y,Z) = \left(\sum_{j=1}^{NP} \Psi_j(\theta) r_j\,,\ \theta,\ \sum_{j=1}^{NP} \Psi_j(\theta) z_j i\right), \qquad (1)$$

where $NP$ is the set of discrete points representing the annulus curve.

SB³C2022-009

Then, using the fitted curve, 300 uniformly spaced material points were generated around the TV annulus circumference (**Fig. 1b**), and the following engineering metrics were determined:

$$\text{Strain: } \varepsilon_i = s_i^t / s_i^0, \tag{2}$$

$$\text{Strain Rate: } \dot{\varepsilon}_i = \Delta s_i / \Delta t = (s_i^{t_2} - s_i^{t_1})/(t_2 - t_1), \tag{3}$$

$$\text{Curvature: } \kappa_i = \frac{|\boldsymbol{d}^{(1)}(X,Y,Z)_i \times \boldsymbol{d}^{(2)}(X,Y,Z)_i|}{|\boldsymbol{d}^{(1)}(X,Y,Z)_i|^3}, \tag{4}$$

where $t$ denotes a timepoint in the cardiac cycle, $\mathbf{d}^{(1)}$ and $\mathbf{d}^{(2)}$ are the first- and second-order derivatives of the annulus curve, and $i$=1~300.

For the geometric indices, we also quantified the AP diameter ($D_{AP}$) and the septal-lateral diameter ($D_{SL}$), annular height, bending angle, circumference, area, and sphericity ($D_{AP}/D_{SL}$), see **Fig. 1c** [6]. All geometric quantities were normalized by the patient's body surface area for comparisons between patients.

All quantities are reported as mean±SEM. Due to data normality and uneven variances, the Welch's $t$-test was used in statistical analysis between healthy and HLHS patients with $p$<0.05 considered significant.

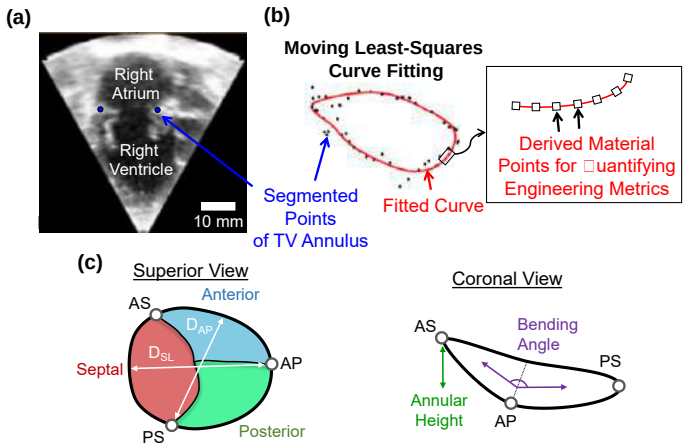


**Figure 1: (a) Echocardiogram from HLHS newborn. Schematic: (b) moving least-squares curve fitting, and (c) geometric indices.**

## RESULTS

For the geometric indices (**Fig. 2**), the TV annulus of the HLHS patients was found to become more circular during the valve closure (EIVC), as evidenced by a decreased $D_{AP}$ (−12.9±4.0%). At the same time, the annulus became more "bent" (143.9°±8.1°). Comparing the HLHS and healthy newborns, the annular circumference was smaller for the healthy patients at all five timepoints (20-30% smaller, 0.001<$p$<0.040). We also found that the healthy newborns had a more elliptical annulus with the major axis along the $D_{SL}$ direction (i.e., $D_{AP}/D_{SL}$<1) as compared to the HLHS newborns having a more circular annulus (i.e., $D_{AP}/D_{SL}$≈1) (0.017<$p$<0.040).

In terms of the quantified biomechanics-focused metrics, the HLHS patients had the largest strains in the posterior and septal annulus segments at ED (−5.7±2.2% and −8.7±3.8%, respectively), whereas the anterior segment underwent the smallest strain during the cardiac cycle (<5% at all timepoints) (**Fig. 3**). For the strain rate, the largest changes were at EIVC: posterior segment, 5.2±63.0%/s; anterior segment, 60.9±66.6%/s; septal segment, −158.8±96.1%/s. The greatest change in the curvature was found to be in the septal segment, with variations within ±2.0mm$^{-1}$. In addition, comparing the HLHS and healthy and newborns, we only observed significant differences in the strain of the anterior segment (HLHS vs. healthy): −0.1±2.6% vs. −13.3±2.9% at ED ($p$=0.010), and −1.7±3.0% vs. 6.8±0.9% at EIVR ($p$=0.026).

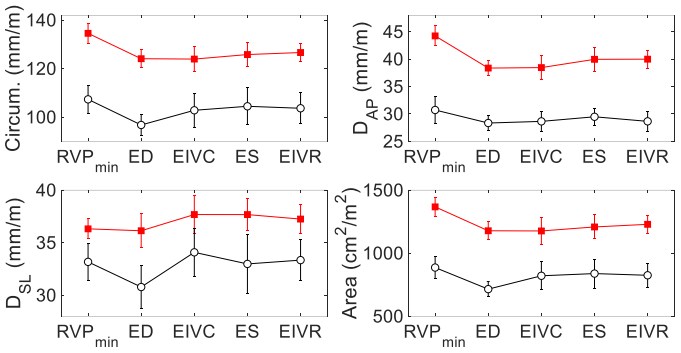


**Figure 2: Quantified geometric indices of the TV annulus (■ HLHS, $n$=8; ○ Healthy, $n$=4). Values are reported as mean±SEM.**

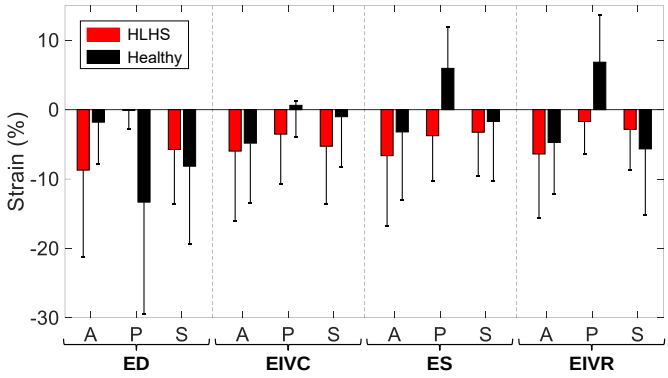


**Figure 3: Quantified strain in each TV annulus segment for: (a) the HLHS newborns ($n$=8), and (b) the healthy patients ($n$=4). Values are mean±SEM. (A: Anterior, P: Posterior, S: Septal)**

## DISCUSSION

We have presented a *novel*, comprehensive TV annulus analysis framework based on 4D echocardiographic images. This framework has been shown to be potentially useful for completing our understanding of the annulus biomechanics. For example, we have found that the HLHS-afflicted TV annulus is significantly larger and geometrically distinct from the healthy ones; however, the tissue strains are similar, suggesting that in both scenarios the tissue may maintain a homeostatic strain state during embryonic development. While a larger cohort is warranted to validate this postulation, *the implication of our findings* is that constriction of the TV annulus in HLHS may disrupt the homeostatic tissue strain, and alternative repairs may be necessary to avoid adverse TR initiation and development. Further, our framework serves as an important foundation for future longitudinal studies and determination of *biomechanics-based TR factors for risk stratification*.


## ACKNOWLEDGEMENTS

This work was supported by the Presbyterian Health Foundation Team Science Grant, and the National Science Foundation Graduate Research Fellowship (GRF 2020307284).


## REFERENCES


[1] Mai, CT, *et al.*, *Birth Defects Res*, 111:1420-1435, 2019.
[2] Colen, T, *et al.*, *J Am Soc Echocardiogr.*, 31:624-633, 2018.
[3] Stamm, C, *et al.*, *Eur J Cardiothorac Surg.*, 12:587-592, 1997.
[4] Petko, C, *et al.*, *J Am Soc Echocardiogr.*, 24:1226-1232, 2011.
[5] Chen, J-S, *et al.*, *Comput Meth Appl Mech Eng.*, 139:195-227, 1996.
[6] Nguyen, AV, *et al.*, *J Am Soc Echocardiogr.*, 32(5):655-666, 2019.

# COMPARISON OF REDUCED ORDER MODELING METHODS FOR VAGINAL TISSUE TEARING

**William D. Snyder (1), Traian Iliescu (2), Raffaella De Vita (1)**

(1) Department of Biomedical Engineering and Mechanics, Virginia Tech, Blacksburg, Virginia, USA
(2) Department of Mathematics, Virginia Tech, Blacksburg, Virginia, USA

## INTRODUCTION

Nearly 80% of women who undergo vaginal delivery will experience some degree of laceration of the vagina and surrounding tissues.[1] To make recommendations for preparatory treatment or an alternative mode of delivery (i.e. cesarean section), obstetricians need real-time computational tools which can predict the trauma from vaginal delivery. While the mechanics of birth-related vaginal lacerations have been investigated experimentally[2], computational methods have not been applied to the modeling and prediction of said trauma. Unfortunately, performing such predictions using sophisticated finite element (FE) models of the reproductive system is computationally expensive, making it impractical for real-time interventions. In this study, we propose reduced order modeling (ROM) techniques to capture the deformations of a torn vaginal canal, showing the potential of these techniques as real-time predictive tools for maternal birth trauma.

## METHODS

For this study, we used the commercial FE software, *Abaqus*, to create an FE full order model (FOM) simulation of the vagina undergoing inflation. The FOM geometry and boundary conditions were chosen to resemble the experimental setup used by McGuire et al. to investigate vaginal inflation and rupture.[2] Figure 1(a) displays the FOM geometry, which resembles a hollow prolate spheroid, with an initial outer diameter at mid-span of 10.2 mm, a uniform thickness of 0.3 mm, and a height of 12 mm. The inner diameter at the top surface was 4.2 mm and the inner diameter at the bottom surface was 5.16 mm. An elliptical hole was placed on the geometry's surface to represent a tear in the vagina. The tear was 5.4 mm long and 1.08 mm wide at mid-span.

For our material model, we selected the Holzapfel-Gasser-Ogden strain energy (c=6 kPa, D=0.05, $k_1$= 10 MPa, $k_2$=10, κ=0.25, N=2) with fiber orientations that differed in three equally sized regions along the longitudinal axis of the vagina (the anterior, middle, and posterior vagina).[3,4] Fiber families' orientations, $\beta$, were defined with hoop direction of the vagina representing 0° in the anterior and middle regions, and the longitudinal direction representing 0° in the posterior region. Within a given region, the orientation angle of one family of fibers would be positive and the other would be negative, but both families would have the same magnitude (either $\|\beta_1\| = \|\beta_2\| = 35^\circ$ or $\|\beta_1\| = \|\beta_2\| = 25^\circ$). These two fiber orientation angle magnitudes varying across the three regions of the vagina yielded eight total fiber orientation combinations. Each combination was used to simulate 30 internal pressure steps in equal increments from 2.5 to 75 kPa to produce the 240 solutions which made up our FOM snapshots. One representative solution is shown in Figure 1 (b).

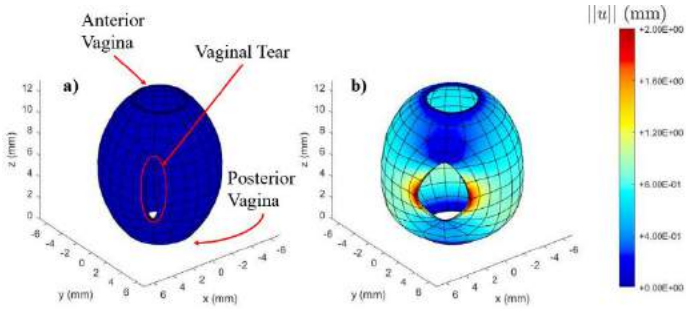


**Figure 1. (a) Undeformed FOM geometry and (b) fully deformed FOM geometry ($p_i$ = 75 kPa; $\beta$ = 35° in all regions).**

For our first reduction method, Galerkin ROM (G-ROM), we used the proper orthogonal decomposition (POD) method[5] to determine the POD basis of rank $l$ for the set of displacement vectors spanned by our snapshots, $\{\boldsymbol{u}_1, \boldsymbol{u}_2, \ldots, \boldsymbol{u}_n\}$ in $\mathbb{R}^m$ ($m$ = 10,257; $n$ = 240; $l \leq \min\{m, n\}$). Let $\boldsymbol{U}$ be the $m$ x $n$ matrix whose columns are the snapshots: $\boldsymbol{U} = [\boldsymbol{u}_1, \ldots, \boldsymbol{u}_n]$. Let $\boldsymbol{\Psi}$ be the $m$ x $l$ matrix whose columns are the POD

basis: $\boldsymbol{\Psi} = [\boldsymbol{\psi}_1, \dots, \boldsymbol{\psi}_l]$. The snapshot matrix, $\boldsymbol{U}$, is then approximated by the $m$ x $n$ matrix $\boldsymbol{U}^{ROM} = [\boldsymbol{u}_1^{ROM}, \dots, \boldsymbol{u}_n^{ROM}]$ with

$$\boldsymbol{u}_i^{ROM} = \boldsymbol{\Psi}\boldsymbol{\zeta}, \tag{1}$$

where $\boldsymbol{\zeta}$ is an unknown $l$ x 1 column vector.

The substitution of the $\boldsymbol{u}_i^{ROM}$ into the finite element system of equations, $\boldsymbol{K}\boldsymbol{u} = \boldsymbol{f}$, where $\boldsymbol{K}$ is the $m$ x $m$ stiffness matrix, $\boldsymbol{u}$ is the $m$ x 1 displacement vector, and $\boldsymbol{f}$ is the $m$ x 1 load vector, yields: $\boldsymbol{K}\boldsymbol{\Psi}\boldsymbol{\zeta} = \boldsymbol{f}$. By multiplying both sides of said equation by $\boldsymbol{\Psi}^T$we obtain

$$\boldsymbol{\Psi}^T\boldsymbol{K}\boldsymbol{\Psi}\boldsymbol{\zeta} = \boldsymbol{\Psi}^T\boldsymbol{f}. \tag{2}$$

On the left side of Eq. (2), $\boldsymbol{\Psi}^T\boldsymbol{K}\boldsymbol{\Psi}$ is an $l$ x $l$ matrix, and on the right side, $\boldsymbol{\Psi}^T\boldsymbol{f}$ is an $l$ x 1 column vector, so Eq. (2) can be solved to find an $l$ x 1 column vector, $\boldsymbol{\zeta}$. Thus, the $m$-dimensional FOM (FE) system of equations is reduced to the $l$-dimensional system of equations (2) ($l \ll m$). We then solve for $\boldsymbol{\zeta}_i$ and $\boldsymbol{u}_i^{ROM}$ for $i = 1, \dots, n$.

Next, we leveraged the *data-driven variational multiscale ROM* (DD-VMS-ROM) framework to increase the accuracy of the ROM at a modest computational overhead. In addition to $\boldsymbol{\Psi}$, we introduce the $m$ x ($d$ – $l$) matrix, $\boldsymbol{\Psi}' = [\boldsymbol{\psi}_{l+1}, \dots, \boldsymbol{\psi}_d]$ of additional POD basis functions where $d > l$. Thus, Eq. (1) becomes

$$\boldsymbol{u}_i^{ROM} = \boldsymbol{\Psi}\boldsymbol{\zeta} + \boldsymbol{\Psi}'\boldsymbol{\zeta}', \tag{3}$$

where $\boldsymbol{\zeta}'$ is a ($d$ – $l$) x 1 vector of unknowns corresponding to $\boldsymbol{\Psi}'$. Substituting Eq. (3) into the FE equations and performing Galerkin projection onto the space spanned by the POD basis, we get

$$(\boldsymbol{\Psi}^T\boldsymbol{K}\boldsymbol{\Psi})\boldsymbol{\zeta} + (\boldsymbol{\Psi}^T\boldsymbol{K}\boldsymbol{\Psi}')\boldsymbol{\zeta}' = \boldsymbol{\Psi}^T\boldsymbol{f}. \tag{4}$$

We then make the following ansatz:

$$(\boldsymbol{\Psi}^T\boldsymbol{K}\boldsymbol{\Psi}')\boldsymbol{\zeta}' \approx \widetilde{\boldsymbol{\Psi}}\boldsymbol{\zeta}, \tag{5}$$

where $\widetilde{\boldsymbol{\Psi}}$ is an $l$ x $l$ matrix which we can use data-driven modeling[6] to solve for via least-squares:

$$\min_{\widetilde{\boldsymbol{\Psi}} \in \mathbb{R}^{l \times l}} \sum_{i \in \{1,\dots,n\}} \left\| (\boldsymbol{\Psi}^T\boldsymbol{K}_i\boldsymbol{\Psi}')\boldsymbol{\zeta}_i'^{\boldsymbol{FOM}} - \widetilde{\boldsymbol{\Psi}}\boldsymbol{\zeta}_i^{\boldsymbol{FOM}} \right\|^2, \tag{6}$$

$$\boldsymbol{\zeta}_i^{\boldsymbol{FOM}} = \boldsymbol{\Psi}^T\boldsymbol{u}_i \text{ for } i = 1, \dots, n, \tag{7}$$

$$\boldsymbol{\zeta}_i'^{\boldsymbol{FOM}} = (\boldsymbol{\Psi}')^T\boldsymbol{u}_i \text{ for } i = 1, \dots, n. \tag{8}$$

Thereafter, $\boldsymbol{\zeta}_i$ for the DD-VMS-ROM can be determined by

$$(\boldsymbol{\Psi}^T\boldsymbol{K}_i\boldsymbol{\Psi} + \widetilde{\boldsymbol{\Psi}})\boldsymbol{\zeta}_i = \boldsymbol{\Psi}^T\boldsymbol{f}_i. \tag{9}$$

From the DD-VMS-ROM framework, we also construct the ideal ROM (I-ROM) which represents the ideal performance of the DD-VMS-ROM. The I-ROM is determined by solving Eq. (9) assuming $\widetilde{\boldsymbol{\Psi}}\boldsymbol{\zeta}_i^{\boldsymbol{FOM}} = (\boldsymbol{\Psi}^T\boldsymbol{K}_i\boldsymbol{\Psi}')\boldsymbol{\zeta}_i'^{\boldsymbol{FOM}}$ rather than solving for $\widetilde{\boldsymbol{\Psi}}$ via Eq. (6).

## RESULTS

Normalized $L^2$-norm error was calculated between the ROM solutions and the projection of the FOM solutions onto the POD basis. Errors for G-ROM, DD-VMS-ROM, and I-ROM were recorded for a range of POD bases with rank $l = 1, \dots, 150$ (Figure 2). Both the G-ROM and DD-VMS-ROM exhibited severe diminishing returns in error improvements for $l$ > 50. Neither method achieved the full potential suggested by the I-ROM with the given POD bases.

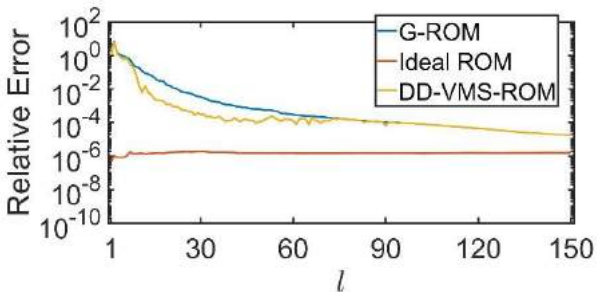


**Figure 2. $L^2$-norm error of ROM solutions vs. FOM projection for $\boldsymbol{l = 1, \dots, 150}$.**

In addition to the accuracy of our ROM methods, we compared their computational costs. We chose to measure such costs by the ratio of FOM on-line time to the on-line time of each ROM method which we call the Speed-up Factor (SUF). Table 1 shows SUFs for our ROM methods using POD bases of various ranks.

**Table 1. Comparison of SUFs for G-ROM and DD-VMS-ROM at selected values of $l$ from 1 to 150.**

| | Speed-up Factor | |
|---|---|---|
| $l$ | G-ROM | DD-VMS-ROM |
| $l$ = 1 | $5.34i \times i10^6$ | $4.32i \times i10^6$ |
| $l$ = 30 | $2.72i \times i10^6$ | $4.57i \times i10^5$ |
| $l$ = 60 | $1.15i \times i10^6$ | $2.15i \times i10^3$ |
| $l$ = 90 | $7.42i \times i10^5$ | $1.16i \times i10^3$ |
| $l$ = 120 | $1.69i \times i10^5$ | $6.30i \times i10^2$ |
| $l$ = 150 | $1.25i \times i10^5$ | $4.50i \times i10^2$ |

## DISCUSSION

We have successfully implemented a proof-of-concept for applying G-ROM and DD-VMS-ROM methods to an FE model of a vagina with a tear. The DD-VMS-ROM outperformed the G-ROM in terms of $L^2$ error for POD bases of rank $l = 10, \dots, 70$, after which our ansatz (5) did not appear to hold (Figure 2). We also noted the drastic increase in computational cost of the DD-VMS-ROM over the G-ROM as $l$ increased (Table 1), which indicated that the DD-VMS-ROM is only applicable in real-time for lower values of $l$. Given these limitations, our future work will involve either the improvement of our ansatz or pivoting to a new approach to model reduction, such as machine learning, for improving the accuracy and reducing computational costs of our FOM approximations.


## ACKNOWLEDGEMENTS

This research is supported by the National Science Foundation under Grant No.~1929731.


## REFERENCES


[1] Samuellson, E. et al., *Acta Obstetricia et Gynecologica Scandinavica*, vol. 81, no. 1, p. 44-49, 2002.

[2] McGuire, J.A. et al., *Interface Focus*, vol. 9, no. 4, p. 20190029, 2019.

[3] Gasser, T.C. et al., *Journal of the Royal Society Interface*, vol. 3, no. 6, p. 15–35, 2006.

[4] McGuire, J.A. et al., *Acta Biomaterialia*, vol. 127, p. 193-204, 2021.

[5] Volkwein, S., Lecture Notes, University of Konstanz, p. 5-12, 2013.

[6] Brunton, S.L. et al., *Journal of Physics: Materials*, vol. 2, no. 4, p. 044002, 2019.

# TRANSMURAL SOLUTE PERMEABILITY, BUT NOT HYDRAULIC CONDUCTANCE, INCREASES IN A MOUSE MODEL OF ASCENDING THORACIC AORTIC ANEURYSM

**Christie L. Crandall (1), Sean Y. Kim (2), and Jessica E. Wagenseil (1)**

(1) Mechanical Engineering and Materials Science, Washington University in St. Louis, St. Louis, MO, USA
(2) Biomedical Engineering, Saint Louis University, St. Louis, MO, USA

## INTRODUCTION

Aortic aneurysms are ballooning or weakening of the aortic wall. Aneurysms occur in the thoracic or abdominal region, but rupture of thoracic aortic aneurysms (TAAs) accounts for twice as many deaths as abdominal aortic aneurysms[1]. Disruption of the extracellular matrix proteins, particularly the elastic fibers, are common in aneurysm walls[2]. Mutations in genes that regulate synthesis of the elastic fiber network are directly associated with TAAs[3].

Previously, we found that genetic and chemical disruption of the elastic fibers altered transmural fluid and solute transport in carotid arteries. Ascending thoracic aortas (ATAs), where genetic TAA are located, have a much higher elastin content and number of elastic fiber layers (called laminae) compared to the carotid artery. We hypothesized that similar disruption of the elastic fibers in TAAs may lead to altered fluid and solute transport and contribute to aneurysm growth, rupture, or be leveraged for local treatment options.

Here we investigated mass transport using a genetic mouse model of TAA caused by a heterozygous missense mutation in the lysyl oxidase gene that was identified in human patients. We present data from experiments which measured fluid flux values from solute present and solute absent in the ATA wall. Using measurements of solute flux we were also able to optimize values of tissue solute permeability and reflection coefficients to better understand wall mass transport.

## METHODS

**Mouse model.** A mouse line with a heterozygous missense mutation in lysyl oxidase (c.857T>G encoding M292R) was used in this study[3]. Male and female $Lox^{M292R/+}$ mice (n = 17) were compared to wild-type control $Lox^{+/+}$ (n =13). Mice were sacrificed at 4 months of age and the ATA was isolated by dissection.

**Solute Absent.** Each ATA was mounted in a 37°C PBS bath of a myograph (DMT) using 7-0 sutures. A pressure column was attached to the fluid inlet and the ATA was pressurized to 100 mmHg. The fluid column was filled with PBS and a bubble was introduced along the tubing. Length was measured using the myograph micrometer and the ATA was stretched to a 1.1x stretch ratio. Loaded diameter was additionally measured using a microscope. Assuming one-dimensional flow in the radial direction, fluid flux, $J_v$, was calculated directly from tracking the bubble displacement over time and the ATA dimensions[4].

**Solute Present.** Fluid in the pressure column was replaced with a solution of 5 mg/mL 4 kDa fluorescein isothiocyanate (FITC) Dextran (#46946, Sigma-Aldrich Co.). The ATA was allowed to equalize for 30 minutes, then rinsed with PBS and transferred, still mounted at 100 mmHg, to a bath of fresh PBS. Samples of the external bath concentration were taken every 10 minutes for 70 minutes. Solute flux, $J_s$, was calculated using the change in concentration of the bath over time and ATA dimensions[4]. During these 70 minutes, bubble displacement in the tubing was also tracked and $J_v$ was calculated.

**Solute Permeability.** Mass transport by advection and diffusion were considered by a 1-D transmural flow in response to a pressure ($\Delta P$) and solute ($\Delta c$) gradient. Hydraulic conductance ($L_p$) can be measured by the solute absent experiment ($\Delta c = 0$) using the equation below[5];

$$J_v = L_p(\Delta P - i\sigma RT\Delta c), \quad (1)$$

where $\sigma$ is the reflection coefficient, and $R$ and $T$ are the gas constant and temperature, respectively. Solute diffusivity is determined by the material's solute permeability ($\omega$). Combining this with the average concentration of solute ($c_s$) moved by advection we can calculate solute flux ($J_s$)[5],

$$J_s = \omega RT\Delta c + (1 - \sigma')c_s J_v, \quad (2)$$

where $\sigma'$ is a reflection coefficient. Eqn. 2 was evaluated both by placing the solute absent experimental value of $L_p$ into Eqn. 1 with the

experimental parameters, and by using the values of $J_v$ from the concentration present experiment ($\Delta ci \neq 0$). Relative errors of the squared calculated values for $J_s$ were used in an error function to solve for solute permeability and the two reflection coefficients.

**Statistics.** Outliers were first removed using ROUT in GraphPad Prism. All statistical comparisons shown were done using a single comparison in an ordinary one-way ANOVA and p-values <0.05 were considered significant.

## RESULTS

When pressurized to 100 mmHg on the myograph system and loaded at a 1.1x axial stretch ratio, length and diameter of the ATAs were measured. Although measurements in the *Lox*$^{M292R/+}$ group trended higher, there were no significant differences (Fig 1).

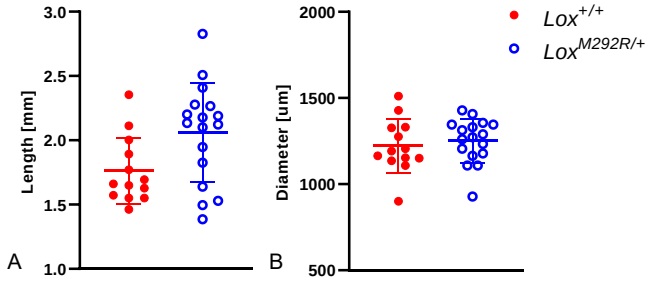


**Figure 1: Length (A) and diameter (B) of dissected ATAs loaded at 1.1x stretch ratio and 100 mmHg internal pressure.**

Using the bubble tracking system to measure fluid flux in both a solute absent and present experiment, the solute absent data were used in Eqn. 1 to solve for hydraulic conductance. No significance difference was found when comparing the hydraulic conductance, however, fluid flux when solute was present, $J_{v_s}$, was significantly higher by 115% in the *Lox*$^{M292R/+}$ group compared to wildtype (Fig. 2).

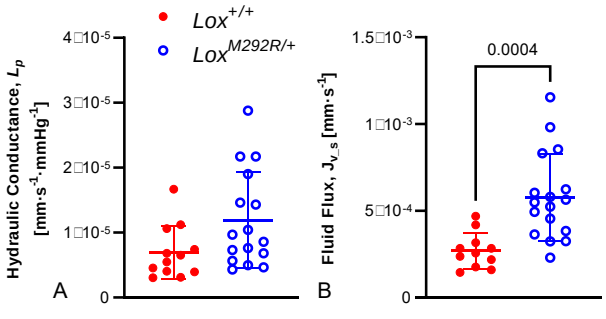


**Figure 2: Hydraulic conductance (A) and fluid flux (B) from solute absent and solute present experiments.**

With solute present, the change in concentration of the external bath was measured and used to solve for solute flux. The bath concentration was significantly higher in *Lox*$^{M292R/+}$ ATAs beginning at 30 minutes, which resulted in a 146% higher solute flux (Fig. 3). Using the data from Figs. 2 and 3 in Eqns. 1 and 2, we were able to optimize parameters of solute permeability and reflection coefficients. The *Lox*$^{M292R/+}$ group had a 147% higher permeability and 0.9% lower reflection coefficients (data not shown).

## DISCUSSION

The *Lox*$^{M292R/+}$ mutation is associated with TAA due to disrupted

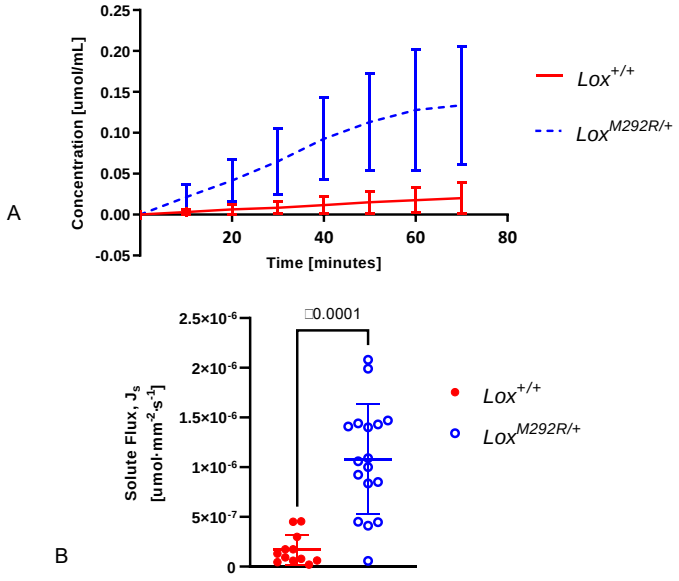


**Figure 3: Concentration of the external PBS bath over time (A) and calculated solute flux through the wall (B).**

elastic laminae organization[3], which we hypothesized would affect mass transport. Here, we measured properties of both fluid and solute transport through the wall of ATAs with and without the TAA model mutation. Our measured geometry values were not significantly different, indicating no aneurysm formation in this model. Previously, additional conditions like hypertension were used to push the aneurysm phenotype[3]. Despite the lack of aneurysm formation, the *Lox*$^{M292R/+}$ group had greater solute permeability.

Determining the contributions of advection and diffusion in mass transport can be useful in understanding TAA pathology and potential drug delivery. Peclet numbers were calculated for all experiments and were < 1 in 65% of the *Lox*$^{M292R/+}$ ATAs compared to 0% of the wildtype ATAs. This means that diffusion dominated in most of the *Lox*$^{M292R/+}$ ATAs, but not in the wildtype ATAs. Combined with a lower reflection coefficient in *Lox*$^{M292R/+}$ ATAs, this indicates that the flow of solute is less dependent on fluid flow in the TAA model.

Our study provides an initial understanding of transmural mass transport in the ATA for wildtype mice and a TAA model. Future investigations will examine differences in the laminae wall structure to identify mechanisms for the increase in solute permeability. Elastic laminae have fenestrations that could differ in the TAA model and allow for more mass transport. There may also be differences in proteoglycan content, which provide pathways of transport for molecules and growth factors. We additionally will study other TAA models to determine if alterations in mass transport are a common finding that may contribute to TAA pathology or be leveraged for disease treatments.


## ACKNOWLEDGEMENTS

Funding for this research was provided by The American Heart Association Award #19TPA-34910047.


## REFERENCES


[1] Hiratzka, L. et al, *Circulation*, 121:13:266-369, 2010.
[2] Carmo, M. et al, *Eu J. Vasc.& Endovasc. Surg.*, 23:6:543-549, 2002.
[3] Lee, V.S., et al, *JCI Insight*, 5(15):e122748, 2019.
[4] Cocciolone, A. et al. *J. Biomedical Enge*, 142:02013-1-10, 2019.
[5] Kedem, O., et al. A, *Biochim. Biophys Acta*, 27(2):.229–246, 1958.

SB³C2022
Summer Biomechanics, Bioengineering and Biotransport Conference
June 20-23, Eastern Shore, MD, USA

# DISC GEOMETRY MEASUREMENT METHODS ALTER REPORTED COMPRESSIVE MECHANICS BY UP TO 65%

**Shiyin Lim (1), Reece D. Huff (1), Joanna E. Veres (2), Divya Satish (2), Grace D. O'Connell (1,3)**

(1) Department of Mechanical Engineering, University of California, Berkeley, Berkeley, CA, USA
(2) Department of Bioengineering, University of California, Berkeley, Berkeley, CA, USA
(3) Department of Orthopaedic Surgery, UCSF, San Francisco, CA, USA

## INTRODUCTION

Lower back pain (LBP) is a common and often debilitating condition that affects between 70% and 80% of adults[1], with socioeconomic costs totaling over $100 billion a year[2]. In many cases, LBP is caused by intervertebral disc degeneration, a progressive condition that is thought to be triggered by mechanical overloading[3]. Mechanical testing has been performed extensively on human and animal disc joints to better understand disc degeneration, develop detailed computational models[4,5], and guide biological repair strategies[6]. However, obtaining material properties is not always straightforward, as slight deviations in sample preparation or testing methodology can greatly impact reported findings[7].

Disc geometry is a necessary metric for normalizing material properties, but disc area and height are measured using different techniques. While some research groups use magnetic resonance imaging (MRI), computed tomography (CT), or X-ray imaging, others may rely on excising the disc to measure disc area. Because this removes constraining boundary conditions, we hypothesized that the method used to measure disc area and height would have a significant impact on reported material properties of the disc joint. To test this hypothesis, we evaluated three different methods for measuring disc height and six methods for measuring disc area. Axial compressive testing was conducted, and material properties were calculated using different disc geometry measurements for comparison.

## METHODS

**Sample Preparation.** Skeletally mature bovine tails were sourced from a local abattoir (n = 12). Surrounding musculature was removed and vertebrae were cut at the mid-transaxial plane to create bone-disc-bone motion segments, which were potted in polymethyl methacrylate (PMMA) to ensure plano-parallel loading faces. During sample preparation, discs were wrapped in gauze soaked with 0.15M phosphate buffered saline (PBS) to prevent dehydration. After joint segment preparation, disc geometry was measured at six different points.

**Geometry Measurement.** After potting, joint segments were CT scanned at 0.092 mm resolution to measure pre-swell height and area (Pre.CT). Segments were then hydrated in 0.15M PBS for 18 hours at 4°C and immediately rescanned to measure post-swell height and area prior to mechanical testing (Pos.CT). After testing, the disc width was measured *in situ* with calipers (In.Cal). The disc was then carefully excised using a scalpel, and disc height and width were remeasured (Ex.Cal). The transverse plane of the excised disc was imaged with a millimeter scale (Ex.ImJ). Finally, the disc was cut to the mid-transverse plane using a freezing stage microtome and reimaged (Mt.ImJ).

**Table 1. Geometry measurement methods.**

| Name | Method | Outcome |
|---|---|---|
| Pre.CT | Pre-swell CT scan | Area, Height |
| Pos.CT | Post-swell CT scan | Area, Height |
| In.Cal | Disc measured *in situ* with calipers | Area |
| Ex.Cal | Disc measured *ex situ* with calipers | Area, Height |
| Ex.ImJ | Disc measured *ex situ* with ImageJ | Area |
| Mt.ImJ | Disc microtomed, measured with ImageJ | Area |

Disc height and area were collected from CT scans using a custom written MATLAB code[8]. Briefly, disc area was measured in the mid-transverse plane and disc height was measured by dividing the midsagittal cross-sectional area by the midsagittal disc width. ImageJ was used to calculate the disc area from images of excised and microtomed discs. Unless otherwise specified, measurements were taken in triplicate using digital calipers, and average widths were used to calculate area assuming a circular cross section[9].

**Mechanical Testing**. A 50N compressive preload was applied for 5 minutes before applying cyclic compression between 0-10% strain (based on Pre.CT height; 0.5 Hz, 15 cycles). Sample dehydration was prevented by wrapping segments with saline soaked gauze. The last loading cycle was used for analysis, and data was adjusted for machine compliance. Conversions to stress and strain were calculated using

SB³C2022-012

different combinations of geometry measurement. Stress-strain curves were generated and normalized compressive modulus was calculated as the slope of the linear region between 0.4 MPa and 0.6 MPa[10].

**Statistical Analysis.** Because data was paired and did not fit a Gaussian distribution, comparisons between groups were made using Friedman tests with Dunn's multiple comparisons adjustment. Statistical significance was assumed at $p \leq 0.05$.

## RESULTS

**Disc Geometry.** CT scanning of the bone-disc-bone segment resulted in an average disc height of 10.7±2.1 mm prior to swelling and 11.6±1.9 mm after swelling. There were no significant differences between Pre.CT and Pos.CT height (adj. p-val. = 0.3074), but Ex.Cal height was significantly smaller than both Pre.CT (-36%, adj. p-val. = 0.0128) and Pos.CT height (-44%, adj. p-val. < 0.0001; Fig. 1A). Disc area measurements demonstrated clear increasing trend, as boundary conditions were removed (Fig. 1B). Disc areas for Ex.ImJ and Mt.ImJ were both greater than Pre.CT area (+31%, p=0.0049 and +52%, p <0.0001, respectively; Fig. 1B).

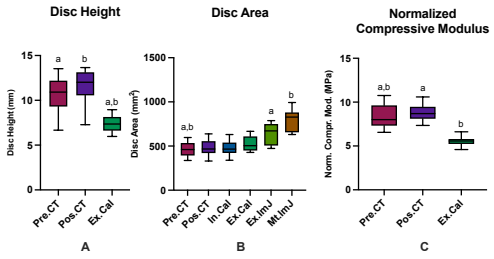


**Fig. 1. (A) Disc height and (B) disc area differences by method. (C) Normalized compressive modulus based on measurement method. Groups with the same letter represent p < 0.05.**

**Mechanics.** Due to variations in disc height between samples, the maximum applied load varied between 285N and 1250N (mean=655±341N). When load and displacement were transformed to stress and strain using Pre.CT values, normalized compressive modulus was 8.39±1.38 MPa. This was not significantly different when load and displacement were transformed using Pos.CT values (8.79±0.91 MPa, p = 1.0). However, the compressive modulus decreased significantly when load and displacement were transformed using Ex.Cal values (5.52±0.54 MPa, p=0.004; Fig. 1C). Figure 2 shows the effect of disc area measurement and disc height measurement on the calculated normalized compressive stress. When holding height constant, modulus calculated with Mt.ImJ area was 25% lower than the modulus calculated with Pre.CT area (8.39MPa vs 6.51MPa, p<0.0001), while modulus calculated with Ex.ImJ area was 13% lower (8.39 MPa vs. 7.36 MPa, p=0.0177). On average, using Ex.Cal disc height resulted in a 36% difference between reported modulus values when compared to Pre.CT height (Fig. 2, light grey vs. black bordered bars).

## DISCUSSION

Mechanical testing is an important measurement of disc health and function but comparing between studies can be challenging. This study investigated the contribution of methods for measuring disc geometry on compressive modulus.

Disc heights reported in the literature vary widely from ~5.5 mm to over 9 mm, partly due to differences in measurement approach[7,9-12]. Our values were closest to those reported by Beckstein *et al.* (9.18±0.65mm), who utilized fluoroscopic imaging of the disc joint; however, CT or X-ray imaging does not always correspond to greater disc heights. Disc height measured from CT images of intact bovine tails (6.8±0.90[9] mm and 6.90±0.35 mm[11]) are closer to disc height measurements reported after excising the disc (7.01±1.23mm[12] and 7.44±0.97mm). This may be due to disc expansion once surrounding soft tissue is removed and residual stresses are released[13].

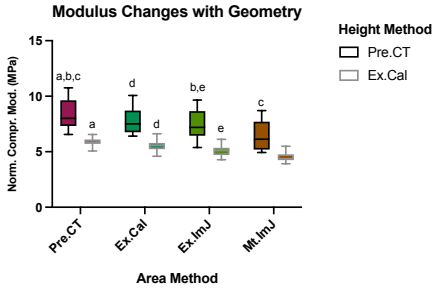


**Fig. 2. Modulus calculated with different height-area combinations. Groups with the same letter represent p < 0.05 (comparisons are made within groups – i.e., between solid fill groups and dark versus light bordered groups).**

While disc area measurements also varied by method, measurements were consistent while the disc remained bound by vertebral bodies. Pre.CT (465±79mm$^2$), Pos.CT (483±96mm$^2$), and In.Cal (480±89mm$^2$) area measurements agreed well with existing literature[7]. Area increased once the disc was excised and imaged, resulting in significantly higher measurements partly because disc boundary delineation is more challenging on an image. The highest disc area was reported when microtomed to the mid-transverse plane and measured using ImageJ (794±121 mm$^2$), which agreed well with publications that utilized the same method. While previous work by O'Connell *et al.* used this approach to compare disc geometry across species, the reported values have since been used to calculate disc mechanics.

The decrease in disc area and increase in disc height observed here had a significant effect of lowering the calculated compressive modulus (Fig. 2). Thus, we recommend using CT or X-ray imaging after preparing the motion segment to determine disc geometry, as it gives the best approximation at time of testing. If imaging is prohibitive, measuring the excised disc height at the outermost boundary may provide the closest approximation of disc height. Similarly, disc area can be measured *in situ* and approximated based on disc geometry, depending on species (*i.e.,* circle or ellipse).

Mechanical testing has been invaluable for understanding disc health and degeneration, but utilizing existing works requires a thorough understanding of the methods used and how those methods may impact reported values. As most studies report comparisons within a study, differences discussed here do not impact comparative outcomes. However, reliable comparisons between studies are valuable for reducing the need to re-test study groups in future studies. In summary, findings from this study showed that differences in reported moduli up to 65% may be attributed to differences in measuring geometry and not inherent mechanical properties.


## ACKNOWLEDGEMENTS

This study was supported in part by the NSF (1751212, GDO).



**REFERENCES** [1] Rubin, D.I., *Neurol Clin,* 25: 353–371, 2007. [2] Katz, J.N., *JBJS,* 88:Suppl 2:21-4, 2006. [3] Adams, M., et al*., Spine*, 31(18):2151-216, 2006. [4] Zhou, M., et al., *Front Bioeng Biotech,* 9:685799, 2021. [5] Adam, C., et al*., J Biomech*, 48(16): 4303-4308, 2015. [6] Schmitz, T., et al., *Act Biomat,* 114:1-15, 2020. [7] Newell, N., et al. *JOR Spine*, 3(3):1-9, 2020. [8] O'Connell, G., et al., *JMMBM,* 4(7): 933-942, 2011. [9] O'Connell, G., et al., *Spine*, 32(3):328-333, 2007. [10] Beckstein, J., et al., *Spine*, 33(6):166-173, 2008, [11] Newell, N., et al., *JMMBM,* 65:824-830, 2017. [12] Bezci, S.E., et al., *JBME*, 137(10):1-8, 2015. [13] Bass, E., et al., *Spine*, 22(24): 2867-76, 1997.

SB³C2022
Summer Biomechanics, Bioengineering and Biotransport Conference
June 20-23, Eastern Shore, MD, USA

# THE HETEROGENEOUS AND ANISOTROPIC MECHANICS OF THE AIRWAY TREE

**S. Sattari (1), C.A. Mariano (1), M. Eskandari (1,2,3)**

(1) Department of Mechanical Engineering, University of California, Riverside, CA, USA
(2) Department of Bioengineering, University of California, Riverside, CA, USA
(3) BREATHE Center, School of Medicine, University of California, Riverside, CA, USA

## INTRODUCTION

Pulmonary diseases lead fatalities worldwide and annually cost more than $50 billion in the United States alone [1,2]; these staggering statistics exclude the respiratory impact of the ongoing COVID-19 pandemic. Exploring lung tissue characterization and its remodeling due to pathologies are necessary to better understand and prevent pulmonary diseases. While most previous airway characterization studies have been limited to the trachea [3], the distal airways are the main site of pulmonary pathologies and remain understudied [4]. Furthermore, due to the lack of experimental investigations, most computational analyses seeking to predict airway occlusion behavior in order to understand diseases, such as asthma and chronic obstructive pulmonary disease (COPD), model airways as an isotropic and homogenous material and are limited to extrapolating trachea properties for use in whole bronchial tree analyses[4].

To fill this major knowledge gap, we investigate the heterogenous and anisotropic material properties of airway tree, including proximal and distal airways, using biaxial mechanical tensile testing for the first time. Here we present quantified airway mechanics as assessed by measures of elasticity (initial and ultimate stiffness moduli) and energetics (hysteresis and energy loss) to examine the differences between circumferential and axial tissue orientations in four regions: the trachea, trachealis muscle, large bronchi, and small bronchi. This experimental data can inform computational predictive models and establish the much needed baseline for future examinations of healthy versus diseased bronchial mechanics.

## METHODS

Fresh lungs from seven pigs (200-250lb) were obtained from local abattoir and were tested within 75hrs, storing the whole lung in 1X phosphate-buffered saline (PBS) until testing [4]. The samples were collected from three levels of the airway tree including the trachea, large bronchi, and small bronchi with inner diameters averaging $18.57\pm2.6$, $8.39\pm1.45$, $4.94\pm0.96$mm, respectively. Tracheal specimens were obtained from two locations of the proximal ring: the posterior region which included the trachealis muscle, and the contralateral region termed as the trachea in this study [5]. Three samples were collected from each region of each pig and a total of 147 specimens were analyzed (excluding specimens which exhibited obvious tearing and damage during testing). The specimens were prepared by isolating the soft tissue from the cartilage and dissecting a square testing sample using a scalpel similar to past works [4,6]. The two orthogonal circumferential and axial orientation of the airway tissue was noted.

Specimens were loaded in a commercial planar biaxial machine (BioTester, CellScale Biomaterials Testing) and were hydrated using 1XPBS bath at 37°C [7]. Four cycles of preconditioning to 60% strain followed by a fifth cycle for analysis were implemented at a strain rate of 1%/s. The first Piola-Kirchhoff engineering stress and engineering strain were calculated.

Similar to past studies, the initial and ultimate moduli were defined as the slopes of the beginning and final portions of the bilinear stress-strain curves, fitted by setting the coefficient of determination $R^2$ to >0.90 [8]. Hysteresis was calculated as the area between the fifth loading and unloading stress-strain cycle, and it was further normalized by the area under the loading curve to define the energy loss.

Statistical comparisons of the circumferential and axial directions were performed by using one-way analysis of variance, and regional group comparisons were executed using two-way analysis of variance (MATLAB Statistics Toolbox, MathWorks Inc.). Significance was defined as $p<0.05$ with p-values reported in Figures 1 and 2.

## RESULTS

Figure 1 illustrates the regional dependance of airway tree for both circumferential and axial directions in terms of initial and ultimate moduli, as well as hysteresis and energy loss. Amongst specimens in the circumferential direction, the trachea was the stiffest overall (Figure

1A-B), with the greatest degree of hysteresis (Figure 1C) compared to other regions of the large bronchi, small bronchi, and trachealis muscle. The circumferential trachealis muscle exhibited the greatest energy loss compared to other circumferential regions (Figure 1D). Axial results were similar to that of the circumferential direction, where the trachea was significantly different compared to other regions in terms of the

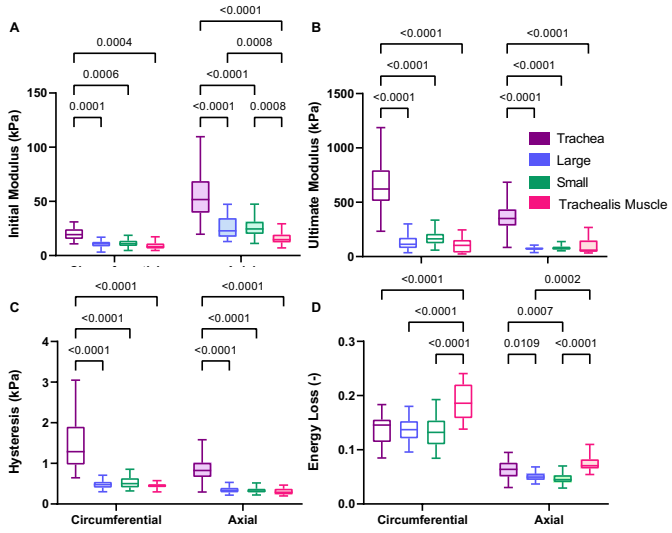


**Figure 1: The heterogeneity of airway tree elasticity (initial and ultimate modulus) and energetics (hysteresis and energy loss).**

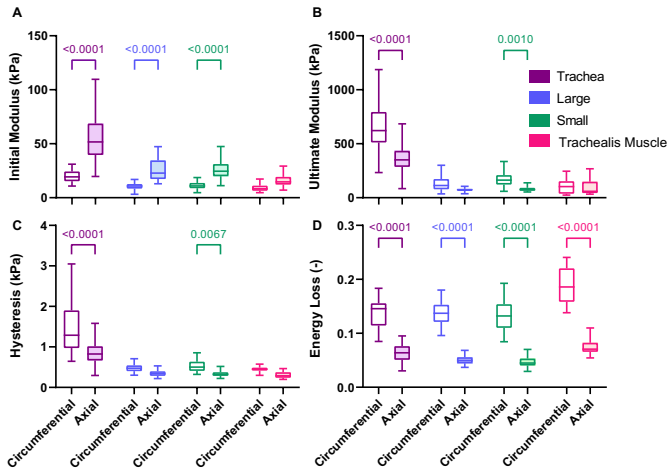


**Figure 2: The anisotropy of the airway tree assessed as measures of the initial modulus, ultimate modulus, hysteresis, and energy loss.**

initial modulus, ultimate modulus, and hysteresis (Figures 1A, 1B, 1C). Interestingly, while the trachea was the stiffest region both circumferentially and axially, its posterior region, the trachealis muscle, was significantly more compliant (Figure 1A-B). The axial trachea and trachealis muscle also exhibited the greatest energy loss compared to axial distal airways (Figure 1D).

The circumferential and axial mechanics of the airways were also evaluated as shown in Figure 2. The initial modulus of the specimens was observed to be stiffer axially compared to their circumferential counterparts (Figure 2A). However, the ultimate modulus transition demonstrated the reverse trend: the circumferential stiffness surpassed that of the axial direction, albeit this difference was only significant in the trachea and small bronchi samples (Figure 2B). When the directions were compared energetically, specimens had greater hysteresis in the circumferential orientation compared to the axial direction, with statistical significances noted in the trachea and small bronchi (Figure 2C). Energy loss was also found to be significantly greater in the circumferential rather than axial orientation for all four regions (Figure 2D).

## DISCUSSION

This study characterizes the biaxial mechanical properties of the bronchial tree for the first time, analyzing heterogeneous and anisotropic tendencies via measures of elasticity and energetics. Our results demonstrate significant directional and regional dependencies, highlighting current assumptions of airway isotropy and homogeneity to be an improper representation of respiratory mechanics. Furthermore, our findings emphasize the fact that the trachea cannot accurately exemplify the mechanics of the airway network. Additionally, the notable difference within tracheal ring underscores the importance of specifying regionality within tracheal specimens and motivates further histological assessments to understand the differences between the trachea and trachealis muscle.

Regional comparisons demonstrate that the trachea exhibits markedly different mechanics compared to the distal airways, both circumferentially and axially (Figure 1). This is in contrast to our past uniaxial experiments, which reported no regional dependency among axial specimens [4]. This difference may be attributable to biaxial versus uniaxial mechanics of testing, and histological differences observed between the trachea and distal airways: glycosaminoglycan (GAG) concentration is significantly decreased in proximal airways compared to distal bronchi [9]. Moreover, collagen and elastin fibers constituents are more taut and straightened in small bronchi, while they appear crimped in the trachea [1,9].

Our previous uniaxial investigations of the whole airway tree reported anisotropy with more compliant behavior in the circumferential direction [4]. The biaxial measurements reported in this work are in agreement (Figure 2A), with the initial modulus values consistent with previous values reported at 15% strain [4]. Notably, the circumferential stiffness of the trachea and small bronchi significantly increases to greater values than axial counterparts at greater strains, as measured by the ultimate modulus (Figure 2B). Conversely, the trachealis muscle is rather isotropic with similar initial and ultimate moduli in both circumferential and axial directions (Figure 2A, 2B). Specimens from all regions are more energy efficient axially compared to circumferentially, likely attributable to the axial orientation of the collagen and elastin fibers [4,10].

This first biaxial characterization of the airway tree serves as a foundation for future studies to explore deviations due to remodeling and diseased states, and facilitates computational modeling.

## REFERENCES


[1] Sattari, S. et al., *J Mech Behav Biomed Mater*, 110:103824, 2020.
[2] Guarascio, SM. et al. *Clin Outcomes Res*, 5:235-245, 2013.
[3] Safshekan, F. et al. *J Biomech Eng*, 139: 1-9, 2017.
[4] Eskandari, M. et al. *J Appl Physiol*, 125: 878-888, 2018.
[5] Teng, Z. et al. *J Biomech*, 45: 1717-1723, 2012.
[6] Noble, PB. et al. *J Appl Physiol*, 99:2061-2066, 1985.
[7] Duginski, GA. et al. JMBBM, 101: 103438, 2020.
[8] Smith, LJ. et al. *Ann Biomed Eng*, 36: 214-223, 2008.
[9] Eskandari, M. et al. *Acta Biomater*, 97: 513-523, 2019.
[10] Kamel, KS. et al. *Clin Anat*, 22: 689-697, 2009.

SB³C2022
Summer Biomechanics, Bioengineering and Biotransport Conference
June 20-23, Eastern Shore, MD, USA

# CARPAL ARCH SPACE AUGMENTATION BY VOLARLY APPLIED FORCE ON THE SKIN SURFACE—A FINITE ELEMENT STUDY

**Hui Zhang, Zong-Ming Li**

Hand Research Laboratory, Departments of Orthopaedic Surgery and Biomedical Engineering,
University of Arizona, Tucson, AZ, United States

## INTRODUCTION

The carpal tunnel is a confined space that encases the median nerve and nine flexor tendons. Its narrow structure predisposes the median nerve to compression. If the compression continued, the nerve impair may deteriorate and eventually devolve into carpal tunnel syndrome. The standard surgical treatment is to transect the tunnel's volar boundary, i.e., the transverse carpal ligament (TCL). Meanwhile, non-surgical solutions serve as alternatives for patients who are not suitable for surgeries (e.g., mild or temporary symptoms). For example, manipulating carpal tunnel mechanics without transecting the TCL—either by radioulnar wrist compression [1, 2] or thenar muscle loading [3, 4]—was demonstrated effective to expand the tunnel and to provide additional space for the median nerve. In like manner, we proposed a new carpal tunnel augmentation approach by applying external dorsal-to-volar force on the volar skin surface of the wrist. The force influence may be propagated to the TCL through the connective tissues (such as fat or muscles) between the skin and TCL, bowing the ligament to enlarge the area under the ligament-formed carpal arch. Thus, the purpose of this study was to examine the effects of this carpal arch space augmentation approach by volarly applied force. We hypothesized that the carpal arch could be expanded by volarly applied forces on the wrist skin, and the arch morphological changes (quantified by carpal arch area, width, and height) would vary with respect to the force magnitude.

## METHODS

To obtain precise control of the force magnitude, we adopted finite element analysis. Moreover, considering that the median nerve at distal carpal tunnel is more prone to compression than other tunnel levels [5], our focus was narrowed down to the distal carpal arch. Therefore, we used a 2D finite element model of the distal carpal arch previously developed and validated in our laboratory [6]. To build the model, a cadaveric hand (male; left; age 74 years; BMI 30.3kg/m$^2$) was imaged by ultrasonography at distal carpal tunnel to obtain a cross section at the hook of hamate level. The image was segmented to obtain the geometrical information of the hamate, trapezium, thenar muscles, skin, fat, and TCL (Figure 1A). Then the cross section was extruded with 1-mm thickness.

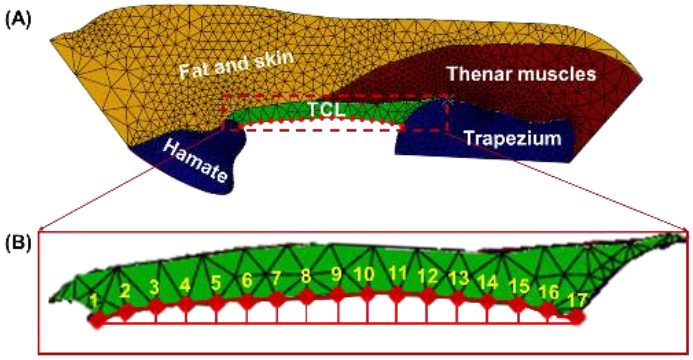


**Figure 1: Finite element model of the distal carpal arch with components and zoomed transverse carpal ligament (TCL). (A) Model components: the hamate, trapezium, thenar muscles, fat and skin, and TCL. (B) Nodes on the dorsal surface of the TCL.**

Material properties of these structural components were set on the basis of literature [6, 7]. In particular, the ligament's anisotropic modulus was implemented by adding tension-only nonlinear springs to strengthen the transverse modulus. To compensate for the missing of wrist bones, intercarpal ligaments and their functions, strings were added between the hamate and trapezium to simulate structural stiffness of the carpal arch based on a previous study [7]. As for boundary conditions, a tie constraint was set for all the interfaces with an assumption of ''no-slip" contact. All components had displacement boundary condition free in-plane but fixed out-of-plane. The hamate, along with the bottom edge of the fat-skin tissue adjacent to the hamate, was rigidly fixed. Pressure at 24 mmHg was applied to the dorsal surface of the TCL to simulate physiological intratunnel pressure.

A mesh convergence analysis was performed using h-refinement method. Three mesh sizes—the medium mesh, medium to fine mesh,

SB³C2022-014

and fine mesh—were tested on the TCL, thenar muscles, and skin-fat tissue with the same boundary conditions and material properties. The carpal arch's tensile strain and area were evaluated among the three meshes. The carpal arch's tensile strain was defined as the ratio of the TCL's dorsal length change to its original length. The deformed carpal arch area (under 24 mmHg) was normalized with respect to the corresponding initial arch area (0 mmHg). Among the three mesh sizes, the largest error for tensile strain was 1.9%, and for normalized carpal arch area the value was 1.8%. Therefore, the medium mesh was considered adequate. The validation process of the model was described in our previous paper [6].

To simulate dorsal-to-volar forces on the skin surface, we assumed that the force was evenly distributed on the wrist's volar surface, a squire of 20 mm × 20 mm (20 mm is the tunnel's length). As the model represented one slice (the distal level with 1-mm thickness) of the entire carpal tunnel, the magnitude of force applied on the model would be 1/20 of the total force on the wrist. Given five levels of forces on the wrist (from 2 to 10 N with an increment of 2 N), the corresponding force magnitudes on the distal carpal arch were from 0.1 to 0.5 N with an increment of 0.1 N. These forces were applied on the volar surface of the fat-skin tissue as pressure.

To quantify morphological changes of the carpal arch, the arch's area, height, and width were analyzed. The carpal arch area (CAA) was defined as the area enclosed by the TCL's volar edge and the line connecting node 1 and node 17 (Figure 1B). The carpal arch height (CAH) was defined as the distance from the most palmar node (node 10) on the TCL to the line connecting node 1 and node 17. The carpal arch width (CAW) was defined as the distance from TCL's node 1 to node 17. Moreover, the distances from rest nodes (nodes 2-16) to CAW were used to measure carpal arch bowing.

## RESULTS

The initial CAA without volarly applied forces was 13.15 mm$^2$. CAA increased under volarly applied forces, and the area increased more as the force magnitude increased (Figure 2A). The largest CAA was 22.96 mm$^2$, at 10 N force application. Similarly, CAH was increased during volar force application, and the height change increased as the force magnitude increased (Figure 2B). Under 10 N force application, CAH was increased from 1.13 mm to 2.03 mm. CAW, however, decreased under volarly applied forces (Figure 2C). The largest decrease in CAW occurred at 10 N was 0.27 mm (from 17.35 mm to 17.08 mm).

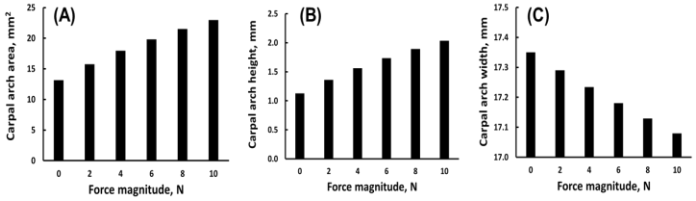


**Figure 2. Carpal arch area (A), height (B), and width (C) for different force magnitudes.**

The TCL was more bowed, shown by increases in the distance between the TCL's volar surface's nodes and CAW (Figure 3). All the nodes (except its two ends: node 1 and node 17) on the TCL's dorsal surface were volarly migrated, and the migration increased as the force magnitude increased. The greatest displacement of the TCL was 0.90 mm at its midpoint, and the displacement decreased towards the ligament's two ends.

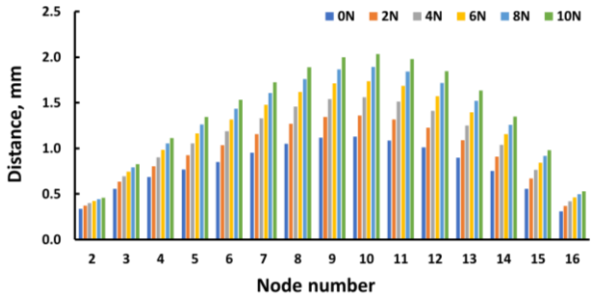


**Figure 3. Distance between the nodes and the CAW line at different force levels.**

## DISCUSSION

The simulation demonstrated that the carpal arch can be expanded by volarly applying forces on the skin surface of the wrist. As the force was applied, the fat and skin, thenar muscles, and TCL were pulled volarly. In the dorsal-volar direction, the largest displacement occurred at the skin surface where the force was applied. Then the force effect started to diminish dorsally as the influence propagated towards the TCL via connective tissues between the skin and ligament (such as fat or muscles). On the TCL, the force deforming effect still remained. The largest displacement on the TCL happened in the middle section and tapered down towards the ligament's two ends, which can be explained by the ligament's two ends being restrained by the hamate and trapezium (Figure 3). These displacements resulted in the increase in CAH and the decrease in CAW, which leads to an increase in CAA and to an expansion of the carpal arch.

Regarding carpal tunnel manipulation, many factors impact the mechanical effect on the carpal arch morphology, such as mechanical properties of the soft tissues, intratunnel pressure level, magnitude of the manipulation force [6]. As for volarly applied force on the skin surface, these factors may still affect carpal arch changes. In this simulation, we focused on the factor force magnitude. Within the current range of force magnitudes, larger forces deformed the carpal arch morphology more, shown by further increases in CAA and CAH and decreases in CAW as the force magnitudes increased. Moreover, larger forces further increased the bowing of the TCL, shown by larger volar displacements of the nodes on the ligament's volar surface. We expect these changes, however, may finally reach a plateau due to biomaterials' nonlinear mechanical properties.

The study has some limitations. First, the model is two-dimensional, which limits its findings to the distal level of the carpal tunnel. To get a comprehensive evaluation of the force effects on the entire carpal tunnel, future studies should expand the current model to a three-dimensional one. Second, *in vitro* or *in vivo* experiments can help confirm the current findings. In these experiments, we should apply volar force onto the wrist and image the carpal tunnel simultaneously. Furthermore, the experimental results could be used to validate future three-dimensional models.


## ACKNOWLEDGEMENTS

The study was supported by NIAMS/NIH R01AR068278.


## REFERENCES


[1] Li ZM et al., *Clin Biomech*, 28(4):402-407, 2013.
[2] Marquardt TL et al., *Clin Biomech*, 30(3):248-253, 2015.
[3] Shen ZL et al., *J. Appl. Physiol.*, 114(2):225-229, 2013.
[4] Zhang H et al., *J. Biomech. Eng.*, 143(10): 101003, 2021.
[5] Buchberger W et al., *AJR Am J Roentgenol*, 159(4):793-798, 1992.
[6] Yao Y et al., *J. Biomech.*, 73:210-216, 2018.
[7] Gabra JN and Li ZM, J. Biomech., 49(1):53-59, 2016.

SB³C2022
Summer Biomechanics, Bioengineering and Biotransport Conference
June 20-23, Eastern Shore, MD, USA

# THREE-DIMENSIONAL RECONSTRUCTION AND ANALYSIS OF THE MEDIAN NERVE USING ROBOT-ASSISTED ULTRASONOGRAPHY

**David Jordan, Hui Zhang, Zong-Ming Li**

Hand Research Laboratory, Department of Orthopaedic Surgery, University of Arizona College of Medicine, Tucson, Arizona, US

## INTRODUCTION

Carpal tunnel syndrome is a compression neuropathy that affects a large portion of the population[1] and is characterized by the compression of the median nerve within the carpal tunnel. The degree of nerve compression is often determined using two-dimensional ultrasonography, whereby an ultrasound probe is positioned transversely at the wrist crease with a fixed position and inclination angle. Given the subjective positioning of the probe, the resulting two-dimensional outcomes can vary between examiners. The discrete nature of the measurements also limits the extent of the available analysis methods. These limitations can potentially be overcome by utilizing a method which can accurately reconstruct the three-dimensional median nerve geometry using ultrasonography.

The two-dimensional properties of the median nerve within the carpal tunnel of healthy individuals have been studied with respect to a variety of influences and compared to the outcomes for individuals with carpal tunnel syndrome. These measurements include nerve cross-sectional area which has been shown to be larger for individuals with carpal tunnel syndrome[2]. Changes in transverse nerve position, perimeter and circularity resulting from active finger motion have also been quantified[3,4]. These studies have shown the difference in median nerve properties between healthy and patient groups. Near the carpal tunnel, these measurements are often taken at the distal or proximal wrist crease.

The properties of the median nerve outside the carpal tunnel have also been evaluated and proposed as a potential comparison tool for the nerve conditions within the tunnel. These studies include using a wrist-to-forearm cross-sectional area ratio as a potential evaluation measure, showing that individuals with carpal tunnel syndrome have a significantly larger ratio[5]. These studies highlight the complexity of the nerve properties within the carpal tunnel and along the forearm.

In order to advance the analysis methods of the median nerve relevant to the understanding of carpal tunnel syndrome, a method which can accurately reproduce the three-dimensional nerve geometry would be useful. This method would need to minimize the subjectivity of probe positioning and produce a continuous nerve model of arbitrary length which can be analyzed for a variety of anatomic measurables at any location along the nerve.

## METHODS

The subject was seated with their arm lying supine on a table with their elbow flexed at ninety degrees. A custom fixation device was used to secure the arm in this stable position and prevent forearm and finger motion. An ultrasound probe was attached to a six degree of freedom COBOTTA robot (Figure 1). The initial position of the robot and probe was set at the distal carpal tunnel, where a clear image of the median nerve and hook of hamate could be visualized.

A custom LabView program was used to control the motion of the robot. The motion of the robot was defined with respect to a coordinate system approximately centered at the location of the median nerve within the participant wrist. The coordinate axes were defined as +y distal, +x ulnar and +z dorsal (Figure 1).


**Figure 1. Robot and ultrasound scanning configuration**

The prescribed motion consisted of a series of 1 mm proximal translations in -y. At each proximal translational increment, the robot

rotated the ultrasound probe ±5˚ about the x-axis (transverse axis). At each position, an ultrasound image was programmatically taken. This continued for a total proximal translation of 30 mm, resulting in 341 ultrasound images (31 translations x 11 rotations).

Using a custom MATLAB script, the median nerve was manually segmented from each image. Images where the nerve could not be distinguished were discarded. The two-dimensional segmentation coordinates (u,v) measured with respect to the ultrasound imaging plane, were then transformed into three-dimensional coordinates (x,y,z) measured with respect to the robot base coordinate system. This was done using Equation (1), where $[T_{EI}]$ and $[T_{RE}]_i$ were the kinematic transformations from the respective coordinate systems of the ultrasound image to the robot end-effector (EI) and from the robot end-effector to the robot base (RE), for probe position i.

$$\begin{bmatrix} x \\ y \\ z \\ 1 \end{bmatrix} = [T_{RE}]_i [T_{EI}] \begin{bmatrix} u \\ v \\ 0 \\ 1 \end{bmatrix} \quad (1)$$

The transformed discrete data was then meshed and smoothed in order to produce the three-dimensional nerve model (Figure 2). The centroidal data of the segmentations was used to form the centroidal curve of the nerve. This curve was parameterized in the form of Equation (2). Equations (3) and (4) were then used to make measurements of nerve curvature κ and centroidal nerve length s. At any length s, the cross-sectional area of the nerve mesh was measured in a plane whose normal vector was parallel to the tangent vector of the centroidal curve*. The area distribution A(s), calculated for the entire nerve, was used to compute the nerve volume $\mathcal{V}$, between any two nerve lengths $s_a$ and $s_b$ (Equation 5). Nerve circularity $\mathcal{C}$, was calculated as shown in Equation (6), where P(s) was the nerve perimeter.

$$\mathbf{r}(t) = h(t)\hat{\mathbf{i}} + g(t)\hat{\mathbf{j}} + f(t)\hat{\mathbf{k}} \quad (2)$$

$$\kappa = \frac{|\mathbf{r}'(t) \times \mathbf{r}''(t)|}{|\mathbf{r}'(t)|^3} \quad (3)$$

$$s = \int_{t_a}^{t_b} \left[ \left(\frac{dh(t)}{dt}\right)^2 + \left(\frac{dg(t)}{dt}\right)^2 + \left(\frac{df(t)}{dt}\right)^2 \right]^{\frac{1}{2}} dt \quad (4)$$

$$\mathcal{V} = \int_{s_a}^{s_b} A(s)\,ds \quad (5)$$

$$\mathcal{C} = P(s)^2 / 4\pi A(s) \quad (6)$$

## RESULTS

Figure 2 shows the results for the three-dimensional nerve mesh, centroidal curve and parametric basis vectors ($\hat{\mathbf{e}}_1$-tangent, $\hat{\mathbf{e}}_2$-normal, $\hat{\mathbf{e}}_3$-binormal) at a given location of total nerve length.

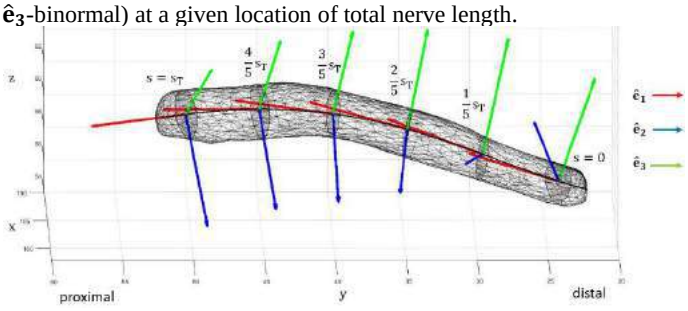


**Figure 2. Three-dimensional median nerve.**

Tables (1) gives the results for two-dimensional nerve measurements taken at given locations of the total nerve length. Table (2) gives the volume results for the corresponding nerve segments.

**Table 1. Median nerve CSA, curvature and circularity.**

| Nerve Length | $s = 0$ | $\frac{1}{5}s_T$ | $\frac{2}{5}s_T$ | $\frac{3}{5}s_T$ | $\frac{4}{5}s_T$ | $s = s_T$ |
|---|---|---|---|---|---|---|
| CSA [mm²] | 8.82 | 9.85 | 11.72 | 11.55 | 12.00 | 10.53 |
| Curvature [mm⁻¹] | 0.0512 | 0.039 | 0.035 | 0.031 | 0.024 | 0.017 |
| Circularity | 1.267 | 1.29 | 1.18 | 1.17 | 1.12 | 1.11 |

**Table 2. Median nerve volume.**

| Nerve Length Segment | $[0, \frac{1}{5}s_T]$ | $[\frac{1}{5}s_T, \frac{2}{5}s_T]$ | $[\frac{2}{5}s_T, \frac{3}{5}s_T]$ | $[\frac{3}{5}s_T, \frac{4}{5}s_T]$ | $[\frac{4}{5}s_T, s_T]$ |
|---|---|---|---|---|---|
| Volume [mm³] | 48.31 | 58.96 | 63.06 | 66.33 | 59.78 |

## DISCUSSION

The scanning method provided a thorough means of collecting ultrasound images of the median nerve. The sequential probe translation along the proximal direction and rotation around the transverse axis helped to reduce some of the positional biases commonly experienced with taking a limited number of single images. The large collection of images, combined with the three-dimensional transformation process, helped to generate a comprehensive reconstruction of the three-dimensional median nerve.

Reconstruction of the three-dimensional nerve provided a continuous model which helped to reduce the limitations experienced with taking traditional discrete measurements. With the continuous model, measurements can be taken at any location along the nerve. The parameterization of the centroidal curve and the calculation of nerve length, allowed for the measurement of nerve cross-sectional area, curvature and circularity at any fraction of the total nerve length. Describing the results with respect to position along the nerve, as opposed to position along the forearm, is important because the nerve may not be entirely straight within the forearm, as quantified by the curvature. The parameterized basis vectors provide a dynamic right-handed system (Frenet Frame) which can be used to describe the in-vivo nerve orientation.

With traditional imaging, it can be difficult to obtain a standardized representation of the nerve cross-section between individuals. With the continuous model, the nerve cross-section can be mathematically defined and consistently reproduced between subjects. The measurements of nerve volume can potentially be used as a three-dimensional evaluation criteria of nerve compression by observing how the volume of the nerve changes along the nerve length.

In conclusion, this work provides a method for generating a three-dimensional model of the median nerve, for which continuous measurements of nerve features relevant to the evaluation of carpal tunnel syndrome can be made. Limitations include the inherent errors associated with manual segmentation, automated surface generation and surface correction operations. Although the large collection of images can help to minimize these errors, they are likely to still be present and affect the nerve shape and measurement results.


## ACKNOWLEDGEMENTS

NIH/NIAMS R01AR068278


*Yury(2022). mesh_xsections (https://www.mathworks.com/matlabcentral/fileexchange/70238-mesh_xsections), MATLAB Central File Exchange, Retrieved January 4, 2022.

## REFERENCES


[1] Atroshi, I et al., *JAMA*, 281:153-158, 1999.
[2] Klauser, A et al., *J Radiology*, 250:171-177, 2009.
[3] Yoshii, Y et al., *J Orthop Res*, 31:1876-1880, 2013.
[4] Filius, A et al., *J Orthop Res*, 33:1332:1340, 2015.
[5] Hunderfund, A et al., *Muscle Nerve*, 44:485-491, 2011.

# DOSE- AND TIME-DEPENDENT EFFECTS OF COLLAGENASE CLOSTRIDIUM HISTOLYTICUM INJECTION ON STIFFNESS AND THICKNESS OF IN VITRO TRANSVERSE CARPAL LIGAMENT

**Jocelyn Hawk, Sohail Daulat, David Margolis, Zong-Ming Li**

Department of Orthopaedic Surgery, University of Arizona, Tucson, AZ, USA

## INTRODUCTION

The transverse carpal ligament (TCL) is a band of tissue constituted by collagen fibers types I and III and is relevant to carpal tunnel syndrome due to its volar restriction of the median nerve. The most common surgical procedure for carpal tunnel syndrome is to transect the TCL, which can disrupt the important biomechanical functions of the TCL and result in side effects such as pillar pain and hand weakness [1]. A possible alternative to surgery is to decompress the median nerve by biochemically altering TCL stiffness and thickness.

Collagenase Clostridium Histolyticum (CCH) is an enzyme that breaks down collagen fibers, and has previously been used in injection to treat Dupuytren's contracture, a condition characterized by formation of collagen cords in the hand, causing finger contractures and impaired hand function [2]. Similar to its use for Dupuytren's contracture, CCH injection to the TCL could potentially be used as a treatment for carpal tunnel syndrome. In order to decrease TCL stiffness and thickness without disrupting the anatomy of the TCL, determining an effective and safe dose of CCH to deliver to the TCL is needed. Therefore, the objective of this study was to assess the time- and dose-dependent effects of CCH on the stiffness and thickness of the TCL in vitro.

## METHODS

The TCLs of 9 fresh-frozen cadaveric hands were removed from the hand and each sutured to a fabric platform. On each TCL specimen, five injection points were marked on the volar surface of the TCL using tissue marking dye. These points were the center of the TCL (O), and four radial (A), ulnar (B), distal (C), and proximal (D) to the center by 5mm, respectively. The platform was then rigidly fixed in an incubator with the temperature set to 37ºC.

A coordinate system for each injection point was established by digitizing each of the five injection points using a MicroScribe digitizer (Figure 1). The x-axis was defined as the AB vector, the z-axis as the cross product of vectors AB and CD, and the y-axis as the cross product of the z-axis and x-axis.

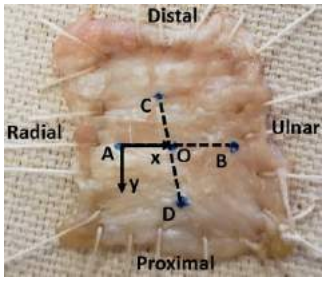


**Figure 1. A TCL specimen and one of the five injection point coordinate systems**

An 18L6 linear array transducer (SuperSonic MACH 30, Hologic Inc., Marlborough, MA, USA) was rigidly fixed to a 6-degree of freedom robot using a custom-made probe mount. A footprint coordinate system was established with its origin at the center of the probe footprint, its x-axis aligned with the horizontal axis of the image, its z-axis aligned with the vertical axis of the image, and its y-axis determined by crossing the z-axis with the x-axis.

CCH with a specific activity ≥125 Collagenase Digestion Units/mg solid (Sigma-Aldrich, St. Louis, MO) was dissolved in phosphate buffered saline to create five solutions of different concentrations such that the units of CCH per 5µL of each solution were 50U, 100U, 150U, 200U, and 250U, respectively. A microliter syringe with a 30G needle was used to inject 5µL of each solution into one of the five marked injection points at the middle of the TCL thickness.

A thin layer of ultrasound gel was applied to the surface of the TCL, and an ultrasound scan was done of each injection point immediately, 2 hours, 4 hours, 6 hours, 8 hours, and 24 hours after

injection (Figure 2). For each scan, the robot was programmed to move the probe to an initial position by superimposing the footprint coordinate system with each injection point coordinate system, except that the footprint coordinate system was offset 5mm in the negative-z direction. After the probe was moved to each initial position, the robot translated the probe 2mm in the positive and 2mm in the negative y-directions in the injection point coordinate system in 0.2mm steps. A shear wave elastography image and B-mode image were captured at each step.

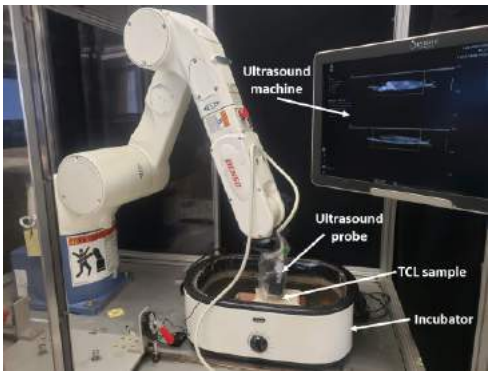


**Figure 2. Experimental setup for scanning procedure**

A region of interest for each injection point was defined as a rectangular prism centered on the injection point with a width of x=1mm, a length of y=1mm, and a height z that contained the entire TCL thickness. A custom LabVIEW program was used to determine the average shear wave speed of the TCL within the region of interest for each injection point from the shear-wave elastography images collected at each timepoint. TCL thickness was measured at each injection point from the B-mode image taken at that point using ImageJ.

Two-way repeated measures ANOVAs were performed with factors of dose and time using SigmaPlot 14 (Systat Software Inc. Chicago, IL). Analyses were performed with an alpha level of 0.05.

## RESULTS

Figure 3 shows shear wave speeds of each dose over time. There were no significant changes in shear wave speeds from time zero to any of the following timepoints within the doses of 50U, 100U, or 150U. For the dose of 200U, shear wave speeds decreased from time 0 by 12.05% and 18.70% at 8 and 24 hours, respectively. For the dose of 250U, shear wave speed decreased from time 0 by 11.96%, 11.46%, 11.20%, 13.92%, and 20.01% at 2, 4, 6, 8, and 24 hours.

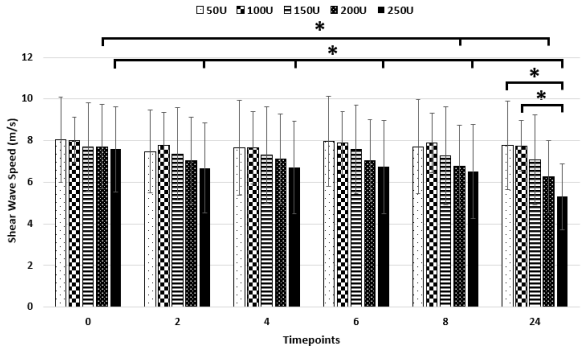


**Figure 3. Shear wave speed of individual doses at different timepoints**

Figure 4 shows the TCL thicknesses of each dose over time. TCL thickness for the 50U and 100U doses did not significantly change from time zero to any timepoint. For the 150U dose, TCL thickness significantly decreased after 8 hours and 24 hours by 4.74% and 7.28%, respectively. For the 200U dose, TCL thickness significantly decreased after 8 hours and 24 hours by 6.78% and 10.97%, respectively. For the 250U dose, TCL thickness significantly decreased after 6 hours, 8 hours, and 24 hours by 6.06%, 11.75%, and 14.92%, respectively.

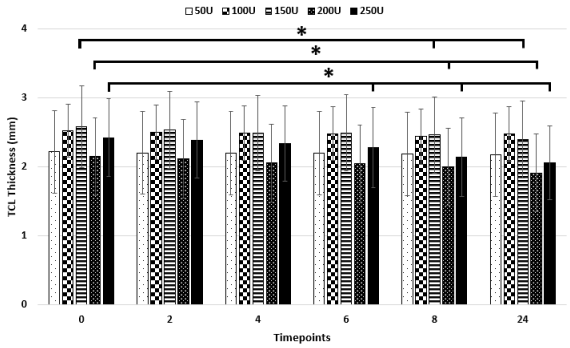


**Figure 4. TCL thickness of individual doses at different timepoints**

## DISCUSSION

As the first steps in assessing CCH injection as a viable treatment for carpal tunnel syndrome, we examined the dose- and time-dependent effects of CCH on TCL stiffness and thickness using isolated TCLs from cadaveric hands. Robot-assistance allowed for precise and accurate probe positioning, and shear-wave elastography imaging was used to measure shear-wave speeds within the TCL. Because elastic modulus can be determined by multiplying shear-wave speed with tissue density, changes in TCL stiffness could be represented by changes in shear-wave speed.

For injection of doses less than 150U, the enzymatic activity is not apparent as there were no significant changes in shear wave speed at any timepoints. As the dose increases to 200U and 250U, the tissue breaks down as indicated by decrease in shear wave speed. None of the doses of CCH resulted in high enough degradation to visibly change the outer surface of the TCL or break through the entire TCL thickness and create holes, suggesting that the effects of the CCH were contained within the boundaries of the TCL. Too much degradation not contained within the boundaries of the TCL could affect the biomechanical function of the TCL or allow the CCH to leak out and affect the surrounding structures.

This study found that higher doses of CCH result in greater and faster degradation of the TCL. Furthermore, injecting 150U or less of CCH has no significant impact on the mechanical properties of the TCL. Injecting 200U of CCH decreased TCL stiffness and thickness after a prolonged time (greater than 8 hours). A dose of 250U was the most effective for TCL degradation, significantly decreasing stiffness after 2 hours and thickness after 6 hours, as well as having the greatest percent decrease in stiffness and thickness after 24 hours. Future studies can investigate the effect of multiple CCH injections to the TCL on carpal arch morphology in situ.

## ACKNOWLEDGEMENTS

NIH R21AR075402A1

## REFERENCES

[1] Boya H. Özcan, Ö., Özteki N, *Muscle Nerve*, 38:1443-1446, 2008.
[2] Soreide, E. et al. *Bone Jt. J.* 100-B:1138-1145, 2018.

SB³C2022
Summer Biomechanics, Bioengineering and Biotransport Conference
June 20-23, Eastern Shore, MD, USA

# MOUSE SUPRASPINATUS TENDON MECHANICAL AND STRUCTURAL PROPERTIES ARE DEPENDENT ON REGION AND AGE

**Michael S. DiStefano (1), Patrick L. Paglia (1), Stephanie N. Weiss (1), Snehal S. Shetye (1), Andrew L. Kuntz (1), Louis J. Soslowsky (1)**

(1) McKay Orthopaedic Research Laboratory
University of Pennsylvania
Philadelphia, PA, USA

## INTRODUCTION

Musculoskeletal pathologies such as rotator cuff tendon disorders of the shoulder are prevalent in the aging population[1]. Dysregulation of tendon homeostasis due to aging can result in premature sub-rupture damage accumulation, degeneration, and ultimately injury. Such changes occur primarily in regions of high and complex stresses, such as at the supraspinatus tendon insertion site of the shoulder[2]. While recent studies in patellar tendons showed inferior dynamic structural response to load, reduced elastic and viscoelastic mechanical properties, and altered fibril structure with aging[3], region and age dependent changes in the rotator cuff of the shoulder remain unknown. Therefore, the objective of this study was to elucidate region-dependent mechanical and structural differences in aging mouse supraspinatus tendon. We hypothesized that aging would result in region-specific mechanical and structural changes, such as inferior elastic and viscoelastic mechanical properties as well as altered collagen fiber realignment and fibril morphology, with larger alterations at the insertion site due to the complex functional demands in this region[2].

## METHODS

Animals: Forelimbs were collected from male wildtype mice sacrificed at either 300 (P300, n=20) or 570 (P570, n=20) days of age (UPenn IACUC approved), corresponding to ~40 and ~65 years of age in human[4], respectively. Elastic and Dynamic Viscoelastic Mechanics: All mice for mechanical testing were frozen at -20ºC until the day of testing. Mice were thawed at room temperature and the supraspinatus tendon-humerus complex from the left limb of each mouse was carefully dissected to remove extraneous tissue. Stain lines were applied for optical strain tracking of the insertion and midsubstance regions and a laser device was used to measure cross-sectional area of the supraspinatus tendon. The myotendinous junction was placed between two sandpaper tabs with cyanoacrylate glue to prevent slippage. The humerus was secured in a custom construct with polymethyl methacrylate and the construct was mounted on a material testing machine (Instron 5848). All testing was conducted in a phosphate buffered saline bath at 37ºC. Each sample was preloaded to 0.025N. The testing protocol consisted of 10 cycles of preconditioning, followed by stress relaxations at 3%, 5%, and 7% strain. Following each stress relaxation, frequency sweeps of 10 cycles of 0.125% amplitude sinusoidal strain at 0.1, 1, 5, and 10 Hz were performed. Following a 10-minute rest at zero displacement, a quasistatic ramp-to-failure at a strain rate of 0.1%/s was completed. Data were collected at 100Hz. Elastic parameters stiffness, modulus, maximum load, and maximum stress were quantified. Viscoelastic parameters dynamic modulus (E*), phase shift (tan $\delta$), and percent relaxation were quantified for each stress relaxation and frequency sweep. Fiber Re-Alignment: Throughout mechanical testing, dynamic collagen fiber realignment was quantified using cross-polarization imaging, and regional fiber alignment data was interpolated in MATLAB with a polynomial fit as a function of strain from the load-displacement data. Images were also used to optically measure strain and modulus in the insertion and midsubstance regions. Transmission Electron Microscopy: Supraspinatus tendons (n=4/age group) were isolated, fixed, and embedded in epon resin blocks. 85nm sections were cut using an ultramicrotome, stained with uranyless and phosphotungstic acid, and imaged at 60,000x using a transmission electronic microscope (JEOL 1010). Fibril diameter frequency distribution was quantified. Statistics: Region-specific tendon elastic mechanical properties and collagen fiber realignment were compared using two-way ANOVAs across age and region followed by Bonferroni post-hoc tests. Viscoelastic properties were compared using two-way ANOVAs across age and strain levels followed by Bonferroni post-hoc tests. Fibril diameter distributions were compared using Kolmogorov-Smirnov tests. Significance was set at $p<0.05$.

## RESULTS

Elastic and Viscoelastic Mechanics (Fig. 1): Cross-sectional area was greater at the insertion than in the midsubstance region in both age

groups. Stiffness and modulus were lower at the insertion than in the midsubstance region in both age groups. Midsubstance modulus had an interaction and decreased with age. The viscoelastic response was preserved with aging across strain levels. Specifically, there were differences in stress relaxation and dynamic modulus at 5 and 7% strain relative to 3% strain with aging. P300 tendons exhibited more relaxation at 3% relative to both 5 and 7% strain than P570 tendons. Phase shift was not altered across strain levels for either age group. As expected, all supraspinatus tendon samples failed at their insertion sites.

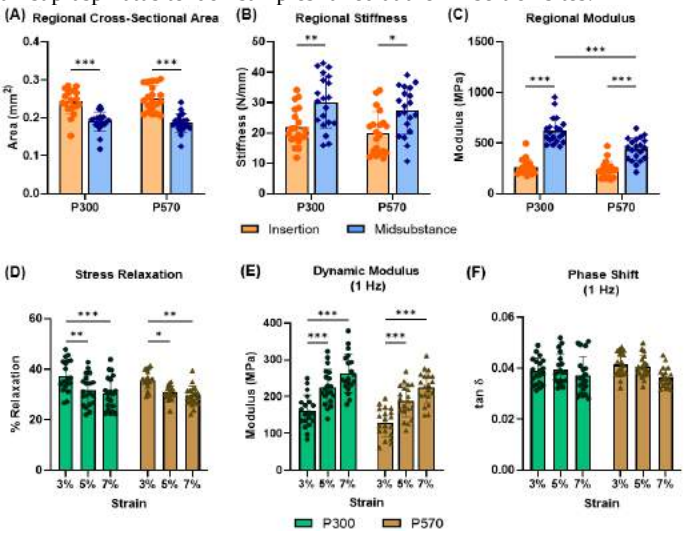


**Figure 1: Insertion regions demonstrated greater (A) cross-sectional area while midsubstance regions had greater (B) stiffness and (C) elastic modulus for both age groups. Elastic modulus was (C) reduced with aging. Viscoelastic properties were conserved with aging with similar differences across strain levels in (D) stress relaxation and (E) dynamic modulus and no differences across strain level in (F) phase shift in both age groups. Data as mean ± standard deviation (*p≤0.05, **p≤0.01, ***p≤0.001).**

Collagen Fiber Realignment (Fig. 2): Collagen fiber realignment had a significant interaction with region, but not age, in both age groups. Specifically, normalized circular variance was greater in the insertion than in the midsubstance region (indicative of less fiber alignment) between 3 and 9% strain in both the P300 and P570 age groups.

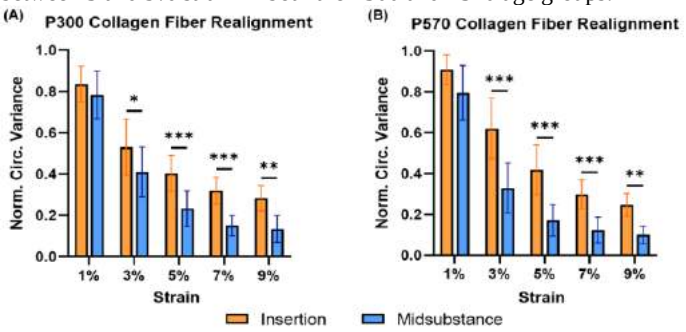


**Figure 2: Insertion regions demonstrated lower collagen fiber realignment (greater normalized circular variance) at strain values between 3 and 9% in the (A) P300 and (B) P570 age groups. Data as mean ± standard deviation (*p≤0.05, **p≤0.01, ***p≤0.001).**

Fibril Morphology (Fig. 3): Fibril distributions were significantly different across region and age with smaller diameter fibrils at the insertion compared to the midsubstance within each age group. Insertion region fibrils had narrower distributions compared to the midsubstance fibril whereas midsubstance fibrils demonstrated typical bimodal distributions for both age groups. Aging resulted in a shift towards smaller diameter fibrils in the midsubstance region.

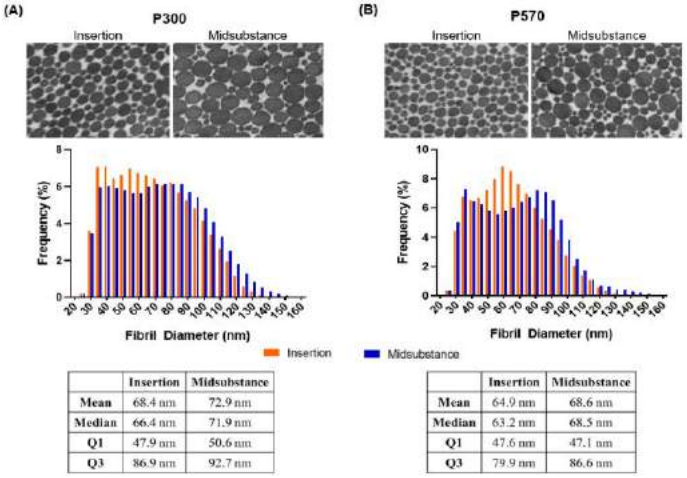


| | Insertion | Midsubstance |
|---|---|---|
| Mean | 68.4 nm | 72.9 nm |
| Median | 66.4 nm | 71.9 nm |
| Q1 | 47.9 nm | 50.6 nm |
| Q3 | 86.9 nm | 92.7 nm |

| | Insertion | Midsubstance |
|---|---|---|
| Mean | 64.9 nm | 68.6 nm |
| Median | 63.2 nm | 68.5 nm |
| Q1 | 47.6 nm | 47.1 nm |
| Q3 | 79.9 nm | 86.6 nm |

**Figure 3: Fibril diameter distributions for (A) P300 and (B) P570 age groups are similar with shifts towards smaller diameter fibrils in the insertion compared with the midsubstance region. Aging also resulted in a shift towards smaller fibrils in the midsubstance.**

## DISCUSSION

We studied regional properties in aging mouse supraspinatus tendons. Supporting our hypothesis, insertion regions exhibited inferior elastic mechanical properties and reduced collagen fiber realignment compared to midsubstance regions. Additionally, insertion region fibril size distributions shifted towards smaller fibril diameters. Previous studies in flexor tendons demonstrated that mechanical properties and fibril diameter distributions can differ from the bone-tendon junction to the myotendinous junction[5]. Interestingly, aging did not influence regional and whole tendon elastic and viscoelastic properties and collagen fiber realignment but did influence fibril morphology.

Multiscale regression analyses have shown that two strong predictors of mechanical properties at the insertion and midsubstance regions were collagen fiber realignment and fibril diameter[6]. Our results suggest potential multiscale structure-function mechanisms relating macroscale tissue mechanical behavior to microscale collagen fiber realignment and nanoscale fibril morphology. Specifically, in the insertion regions, decreased collagen fiber realignment, indicative of a reduction in dynamic structural response to load, in conjunction with smaller diameter fibrils unable to withstand the same loading magnitude results in inferior mechanical properties relative to the midsubstance region. This induces earlier accumulation of damage at the fiber and fibril levels propagating to the macroscale, ultimately leading to premature tendon failure at the tendon insertion[2], as observed in all supraspinatus tendon samples. Clinically, these structure-function mechanistic findings may further explain why supraspinatus tendon tears predominantly occur at its insertion on the proximal humerus[7].

This study reveals critical mechanical and structural differences in supraspinatus tendon region and age. Future studies will consider additional region-specific multiscale structural, functional, and compositional mechanisms in aging supraspinatus tendons.


## ACKNOWLEDGEMENTS

We thank Ashley Fung and Thomas Leahy for their assistance. This study was supported by NIH/NIAMS (AR070750) and the Penn Center for Musculoskeletal Disorders (NIH/NIAMS, P30 AR069619).


## REFERENCES


[1] Buckwalter et al., *JBJS*, 2003. [2] Connizzo et al., *Interface Focus*, 2016. [3] Dunkman et al., *Matrix Bio*, 2012. [4] Fox et al., *The mouse in biomedical research*. Elsevier, 2007. [5] Watanabe et al., *CTR*, 2007. [6] Connizzo et al., *J Biomech*, 2016. [7] Bell et al., *JOR*, 2015.

SB³C2022
Summer Biomechanics, Bioengineering and Biotransport Conference
June 20-23, Eastern Shore, MD, USA

# REGIONAL STRAINS EVALUATED FROM DIGITAL IMAGE CORRELATION OF MECHANICALLY VENTILATED HEALTHY AND FIBROTIC MURINE LUNGS

**T.M. Nelson (1), K.A.M. Anduaga (1), C.A. Mariano (1), S. Sattari (1), A. Ulu (2,3), E.C. Dominguez (2,3), T. M. Nordgren (2,3), M. Eskandari (1,2,4)**

(1) Department of Mechanical Engineering, University of California, Riverside CA, USA
(2) BREATHE Center, School of Medicine University of California, Riverside CA, USA
(3) Division of Biomedical Sciences, School of Medicine, University of California, Riverside CA, USA
(4) Department of Bioengineering, University of California, Riverside CA, USA

## INTRODUCTION

In recent decades, pulmonary diseases, such as chronic obstructive pulmonary disease (COPD), have become one of the most common causes of death around the globe [1]; COPD alone is the third leading cause of death in the United States, with an $800 billion estimated cost in direct medical expenses over the next 20 years [2]. And now, COVID-19's impact on lung function is the most recent respiratory threat [3]. Various types of pulmonary diseases impact lung mechanical behavior differently: for instance, the fibrotic lung exbibits greater stiffness than the healthy lung, due to its increase in collagen fiber deposition [4]. These remodeling and disease effects, in turn, influence pulmonary function, and are assessed by global (bulk) lung mechanics. However, local lung behaviors and tissue level alterations can offer insights to better understand the effect of respiratory pathologies compared to global assessments [5]. These key considerations are thus far absent in the field. As such, we interface digital image correlation (DIC) with a custom pressure-volume ventilation device to simultaneously characterize local strain and associated global lung measures [6].

In this study, we quantify tissue level strain in healthy and diseased murine pulmonary specimens over a range of volumes and breathing rates for the first time. We hypothesize that lungs with fibrosis will be less distensible than that of healthy counterparts, and thus will exhibit decreased strain contours, particularly when compared at higher inflation volumes. To characterize the difference between healthy and fibrotic lung strains, we systematically section regions of interest (ROI) across specimens to evaluate potential disparate stretch capabilities that may manifest due the spatial arrangement of matrix constitutive elements in disease [7].

## METHODS

Male C57BL/6J mice (ages 8-12 weeks old) were procured from Jackson Laboratory (Bar Harbor, ME, USA). For 21 weeks, subjects were intranasally exposed three-times weekly to agricultural dust, per an established fibrosis disease manifestation in-vivo model protocol [8]. Mice were euthanized and sacrificed (IACUC approved), and lungs were removed. Tracheal cannulation was performed to allow for inflation testing. Lungs were speckled to enable collection of DIC data and were tested within 8 hours post-sacrifice. During tests, specimens' hydration was maintained with 1X phosphate-buffered saline solution to minimize deterioration. The test sequence, executed via our electromechanical, volume-controlled, pressure-measuring ventilation apparatus, included an initial preload of the lung specimens to 5cm$H_2O$ to create a common datum state between specimens [9]. Similar to previous studies [4], various inflation volumes of 0.3, 0.5, 0.7ml were applied at rates of 5 and 20 breaths per minute (BPM) using three inflation-deflation preconditioning cycles followed by an analyzed cycle. During ventilation, an imaging system was used to collect DIC data [Trilion Quality Systems, King of Prussia, PA, USA]. Additionally, the global maximum change in lung volume response (which is always lower than the applied volume due to air compressibility and is accounted for in real-time by our device), was examined, as well as local displacement and strain contrasts between healthy and diseased lungs.

Tissue specimens' principal major strain means, ranges, and maximums were obtained via DIC at peak inflation stages for varying rates and volumes [10, 11]. Each lung lobe was sectioned into 3x3 ROI divisions, using the cranial-caudal length of the specimen as the orienting axis to ensure positioning independence across each murine sample and equidistant sections. Healthy versus diseased specimens' metrics were assessed for each rate and volume using a two-way ANOVA with a significance level of $p<0.05$ [GraphPad Prism, San Diego, CA, USA].

## RESULTS

Figure 1 illustrates the strain contour of a representative specimen and the associated nine ROIs used for the left, superior and inferior

lobes. Healthy and fibrotic whole lung strain distributions were both observed to be spatially heterogeneous (Figure 1A). Direct ROI comparisons between healthy versus diseased specimens for mean strain, range, and maximum revealed limited regions with significant differences across all considered breathing volumes and rates. ROI 9 of the healthy specimens' inferior lobe exhibited significantly higher strain measures in for an applied volume of 0.5ml and a frequency of 20 BPM ($p<0.05$, shown in Figure 2). At the same applied volume and slower rate of 5 BPM, ROI 8 of the superior lobe also yielded significantly higher strain range and maximum for healthy specimens ($p<0.01$, not shown).

While no other significant differences at other breathing volumes or rates were revealed, there was a general tendency for healthy specimens' mean strain to be higher than their fibrotic specimen counterparts. In diseased specimens, there were intermittent regions that experienced a sharp increase in maximum strain, as well as strain range.

Despite shared applied volumes between healthy and diseased specimens, differences in the global lung volume change were observed between groups: albeit statistically insignificant, healthy specimens tended to exhibit greater changes in lung volumes compared to diseased lungs, particularly for the slower rate (5 BPM) and greatest applied volume (0.7ml).

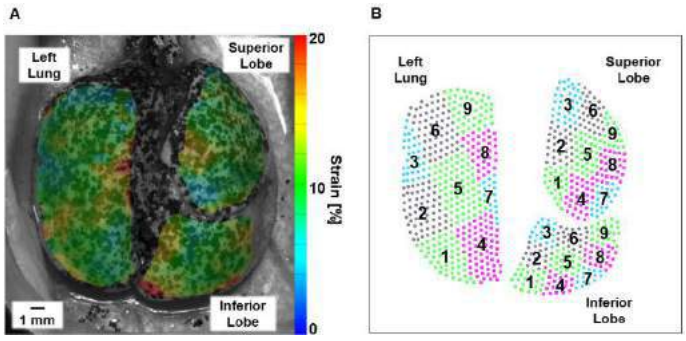


**Figure 1. A: Representative murine lung's topological strain contour map. B: Corresponding ROIs illustrating nine sections per lobe to compare each region's strains in healthy versus fibrotic specimens.**

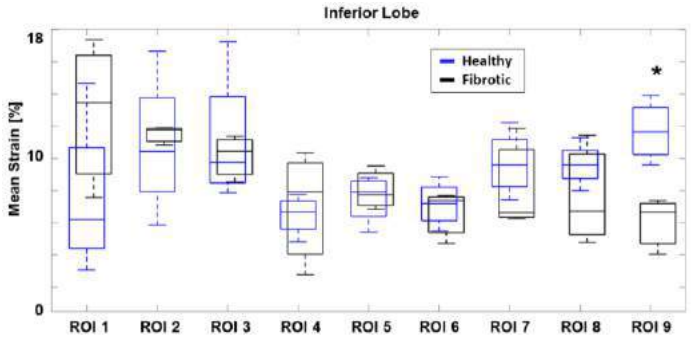


**Figure 2. Box plot representation of healthy and fibrotic specimens' inferior lobe surface mean strain for each ROI, at peak inflation for an applied volume of 0.5ml and breathing rate of 20 BPM. Healthy and fibrotic specimens are depicted in blue and black, respectively.**

## DISCUSSION

In this study, we provide a novel exploratory comparison of tissue strains in ventilated healthy versus fibrotic murine lungs under varying applied volumes and frequencies in order to assess potential differences. One limitation of this study is the ventilation system's reduced ventilation frequency capabilities compared to murine physiological breathing; nonetheless, our testing capabilities are faster than previous studies [4, 12]. We observe that fibrotic specimens generally tend to exhibit a reduction in mean tissue strain values in comparison to healthy counterparts, as hypothesized by other studies [13]. Furthermore, fibrotic lungs tend to reach lower global maximum lung volumes than healthy counterparts when delivered the same amount of air, and often exhibit greater inflation pressures. Together, these findings suggest that healthy tissues have greater adaptability and distention capabilities when ventilated. These local and global outcomes align with previous observations of increased stiffness and reduction in lung volume in fibrotic lungs [4, 7].

The spatial organization of fibers in the fibrotic lung is thought to influence mechanical behaviors, especially as regions of high collagen content cause an imbalance in expansion [7], translating to over- or underinflated regions [14]. Such regions are susceptible to increased deformation, often associated with ventilator induced lung injury (VILI) [13]. This behavior is reflected in the varying levels of strain experienced for different regions in the lung tissue (Figure 2): occasional spikes in the maximum and range of strain are observed, which may be attributable to these areas of varying inflatability and highlight areas that may be prone to injury. Our segmentation method and analysis of tissue strain data via ROIs lays the groundwork for future comparison of regions to one another to methodically evaluate the imbalance of expansion in fibrotic lungs. This will enable unique insights regarding the compromised pathological material response of other prominent pulmonary illnesses, such as asthma or COVID-19, as well.

From this study, healthy and fibrotic lungs' regional tissue strains are not observed to significantly differ, and the few instances of significance warrant future studies to more closely inspect these specific regions and augment mechanical measurements with histological analyses to evaluate the underlying constitutive material and pathological remodeling cause. However, the indications that the fibrotic lung is seemingly less stretchable and subject to more areas of intense deformation yields important insights for considerations of VILI, particularly in respiratory patients undergoing mechanical ventilation, considering their abnormal lung function.


## ACKNOWLEDGEMENTS

Authors would like to thank support from the Hellman Fellows Program to Dr. Mona Eskandari, and the University of California Riverside Dean's Biomed Collaborative Seed Grant awarded to Drs. Mona Eskandari and Tara Nordgren.


## REFERENCES


[1] Burney, P G J et al., *Eur Clin Respir J,* 45 (5): 1239–47, 2015. [2] Zafari, Z et al., *Chest,* 159 (4): 1400–1410, 2021. [3] Stokes, E K et al., *MMWR,* 69 (24): 759–65, 2020. [4] Limjunyawong, N et al., *J Vis Exp,* 95:52376, 2015. [5] Rubin, J M et al., *Ultrasound Med Biol,* 42 (11): 2525–31, 2016. [6] Mariano, C A et al., *Front Physiol,* 11 (December): 600492, 2020. [7] Manali, E D et al., *BMC Pulm Med,* 11 (May): 33, 2011. [8] Nordgren, T M et al., *Trans Res J Lab Clin Med,* 166 (1): 57–69, 2015. [9] Sattari, S et al., *Front Bioeng,* 8: 1183, 2020. [10] Nelson, T M et al., SB$^3$C, 2021. [11] Nelson, T M et al., *Front Physiol,* 2021, (under review). [12] Robichaud, A et al., *J Appl Physiol,* 123 (4): 746–56, 2017. [13] Marchioni, A et al., *Ann Intensive Care,* 10 (1): 13, 2020. [14] Fine, R et al., *J Appl Physiol,* 47 (1): 138–44, 1979.

# MURINE LUNG MECHANICS IN RESPONSE TO VARYING INFLATION VOLUMES AND FREQUENCIES

**K.A.M. Anduaga (1), T.M. Nelson (1), S. Sattari (1), C.A. Mariano (1), A. Ulu (2,3), E. C. Dominguez (2,3), T.M. Nordgren (2,3), M. Eskandari (1, 2, 4)**

1. Department of Mechanical Engineering, University of California, Riverside, CA, USA
2. BREATHE Center, School of Medicine, University of California, Riverside, CA, USA
3. Division of Biomedical Sciences, School of Medicine, University of California, Riverside, CA, USA
4. Department of Bioengineering, University of California, Riverside, CA, USA

## INTRODUCTION

Chronic pulmonary diseases are costly lifelong conditions affecting over 600 million people worldwide [1]. A large portion of the disadvantageous expenses associated with these conditions relate to diagnosis and treatment, which often focus on locating and defining the altered state of biological responses, such as lowered oxygenation levels or reduced available lung volume. While disease dangerously diminishes biological function, changes are not often unique enough to aid in exact diagnosis, requiring expensive imaging to ascertain damage level and type. The root of the experienced decreased function stems from the altered internal structure of the lung, which also changes the mechanics of the breathing cycle. Investigation of the modified mechanics tendencies in diseased subjects, as contrast to diminished biological outputs, could reveal insightful information and aid in furthering the development of more efficient diagnostic and treatment practices.

Mice are often used as valuable testing specimens to advance diagnostic development. However, accurate measurement of murine mechanics has historically been difficult due to the small physical size. Recent innovations in non-discrete and real-time measurement devices have facilitated material characterization, which has thus far been absent [2-4]; our custom-designed electromechanical apparatus allows continuous volume inflation control and measurement of actual real-time lung volume and transpulmonary pressure [4].

Here we utilize our apparatus to study healthy mice specimens and establish baseline measurements that can later be compared to diseased samples to identify possible energetic or elastic dependent mechanics. Examination of mechanical trends in response to varying controllable ventilation settings, such as inflation volume and cycling frequency, will provide comprehensive respiratory mechanics insights, much needed in the field.

## METHODS

Five mouse lungs (C57BL/6J, male, 29-33 weeks old, 31.3 ± 4.5g) (Jackson Laboratory, Bar Harbor, ME, USA) were collected after sacrifice by anesthesia overdose. To prevent airway collapse, a 1ml syringe was used to push 0.5ml of air into the trachea. Within 3 hours after sacrifice, the lung was placed in our custom apparatus for testing [4]. Establishment of volume history was done via three preconditioning inflation-deflation cycles prior to each test cycle. To achieve a shared datum state and evaluate a range of testing conditions, a preload pressure, 5cm$H_2O$, was applied prior to cycling and twelve flow combinations were tested: four volumes (0.3, 0.5, 0.7, 0.9ml) and three breathing frequencies (5, 10, 20 breaths per minute, BPM).

Figure 1A demonstrates compliance of deflation $C_{def}$ [5] and hysteresis calculations: $C_{def}$ was calculated as a tangent via linear regression ($R^2$>0.99) using MATLAB [6]. Hysteresis was defined as the enclosed area of the pressure-volume (PV) curve for volumes of 0.5, 0.7, 0.9ml. Hysteresis was normalized to account for varied PV size and defined as energy loss. Statistical analysis of mean +/- standard deviation of all samples was investigated by one-way ANOVA with repeated measures in R Studio (*p<0.05, **p<0.01, ****p<0.0001) [7].

## RESULTS

Deflation compliance decreased as cycling rate increased. This was significant at 0.3, 0.5, and 0.7ml for the transition between 10 and 20 BPM as shown in Figure 1B. Differing volume dependencies were found depending on frequency tested: deflation compliance increased with volume at 5 and 10 BPM between 0.5-0.9ml, and at 20 BPM increased between 0.3-0.7ml. Percent relaxation tended to increase with increasing volume (except for the decrease from 0.7 to 0.9ml), significant at only 5 BPM between 0.5-0.7ml. No cycling frequency dependency was found for percent relaxation (Figure 1C). Figure 1D and 1E demonstrate significantly increasing hysteresis across all

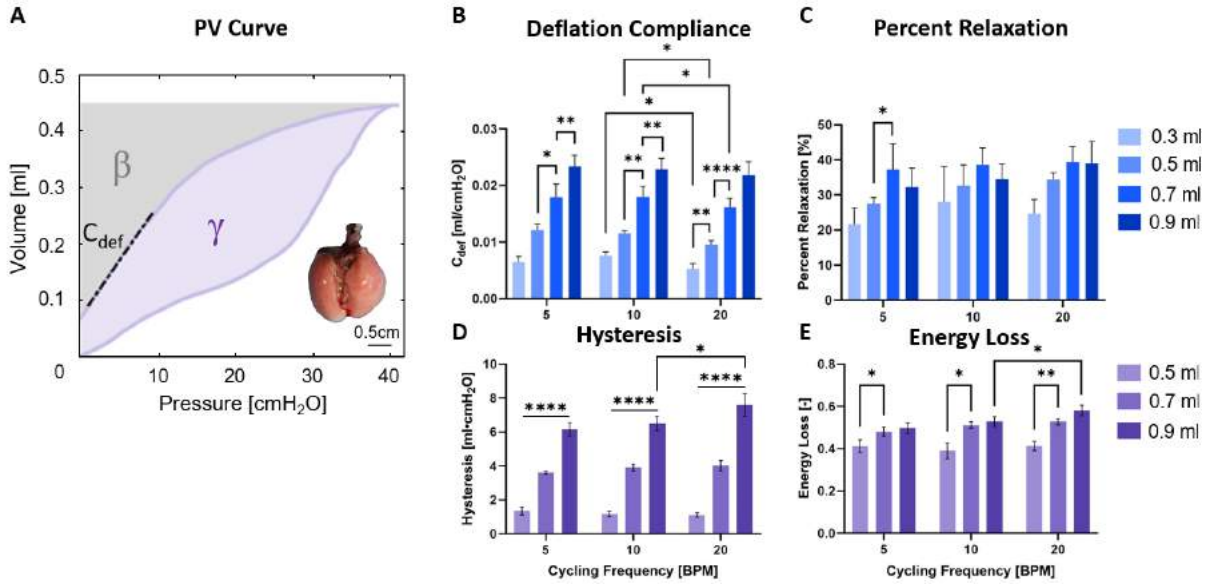


**Figure 1: (A) Quasi-static PV curve demonstrating calculation of $C_{def}$, hysteresis [γ], and energy loss [γ/(γ +β)]. Values on bar graphs are plotted as mean ± standard deviation for (B) deflation compliance, (C) percent relaxation, (D) hysteresis, and (E) energy loss.**

inflation volumes, while energy loss significantly increased across a single volume transition: 0.5 to 0.7ml. Cycling frequency significantly increased both energetic measurements at 0.9ml from 10 to 20 BPM.

## DISCUSSION

Deflation compliance ($C_{def}$) is commonly used as the measurement of murine lung compliance, and yet the effect of varying volume and frequency are understudied [3,8]. In our study, $C_{def}$ decreases with increasing BPM consistent with static and dynamic compliance, which exhibit this behavior in cat and dog lungs and diseased human lungs [9-11]. This frequency dependence may well only be present in ex vivo specimens due to the absence of the chest wall and may be partially attributable to the viscoelastic nature of lung [12].

Tissue viscoelasticity and the presence of surfactant give rise to the observed breathing cycle hysteresis [13]. In our study, we further observe the role of volume on frequency dependencies, contradictory to previous works. Previous investigation by Grotberg and Hildebrandt in dog lobes and cat lungs, respectively, resulted in differing findings [9,11]: Grotberg detected, as we do, that a volume dependency exists for frequency trends in isolated individual lobes, while Hildebrandt found no such tendency for the whole organ despite testing a range of values. Grotberg hypothesized that this distinction occurred because of the divergent nature of testing individual lobes versus the bulk intact organ. However, we find a slight volume dependency consistent with Grotberg, despite testing the whole organ similar to Hildebrandt.

In addition to analyzing hysteresis, we investigated energy loss to normalize the effect of inflation volumes. Frequency dependent trends of energy loss were comparable to hysteresis, indicating the observed frequency trends were not influenced by the growing PV loop. However, normalization resulted in fewer energy loss volume dependencies such that increasing the inflation volume only significantly increased energy loss across the transition from 0.5 to 0.7ml at all three BPMs.

Whole lung viscoelastic relaxation has been previously documented as a sharp decline that quickly asymptotes partially due to the documented stress relaxation of constituents (i.e., parenchyma and airway tissues) [12-15]. Previous viscoelastic investigations have focused on biological responses, including cytokine production and body temperature, with a few studies focusing on mechanical alterations [15-17]. One such study examining the influence of varying inflation volumes in rabbits found the percent relaxation of the asymptotic portion increases with inflation volume [15]. In this study, we similarly note a volume dependent trend (most were statistically insignificant). We also find percent relaxation tends to increase with increasing volume up to the 0.7 to 0.9ml transition where percent relaxation is then observed to decrease for all breathing frequencies. In contrast, the aforementioned previous study found percent relaxation continued to increase with increasing volume until specimen rupture. Discrepancies may be due to our extended two-minute hold in accordance with previous methods [4] compared to their one-second hold, our inclusion of the initial decrease in pressure, or expected differences in tissue response considering the mice versus rabbits.


## ACKNOWLEDGEMENTS

Authors thank support from the Hellman Fellows Program to Dr. Mona Eskandari, and the University of California Riverside Dean's Biomed Collaborative Seed Grant awarded to Drs. Mona Eskandari and Tara Nordgren.


## REFERENCES


[1] International Respiratory Coalition. https://www.ersnet.org/advocacy/international-respiratory-coalition/ (2021). [2] Irvin, C. G. & Bates, J. H. T. Respir. Res. 4, 4 (2003). [3] Limjunyawong, N., et al. Vis. Exp. 52376 (2015). [4] Sattari, S. et al. Front. Bioeng. Biotechnol. (2020) [5] Takeuchi, M. et al. Am. J. Respir. Crit. Care Med. 164, 1225–1230 (2001). [6] Robichaud, A. et al. Am. J. Physiol. Lung Cell. Mol. Physiol. 321, L204–L212 (2021). [7] Anduaga, K.A.M. et al., Under Review [8] Devos, F. C. et al. Respir. Res. 18, 123 (2017). [9] Grotberg, J. B. & Davis, S. H. J. Biomech. 13, 905–912 (1980). [10] Mitzner, W. Compr. Physiol. 1, 2009–2027 (2011). [11] Hildebrandt, J. J. Appl. Physiol. 27, 246–250 (1969). [12] Eskandari, M., et al. J. Appl. Physiol. 125, 878–888 (2018). [13] Sattari, S. et al. J. Mech. Behav. Biomed. Mater. 110, 103824 (2020). [14] Bates, J. H., et al. Ann. Biomed. Eng. 22, 674–681 (1994). [15] Hughes, R. et al. Physiol. 146, 85–97 (1959). [16] Rubini, A. Respir. Physiol. Neurobiol. 175, 255–260 (2011). [17] Rubini, A. Cytokine 51, 266–273 (2010).

# A COMPUTATIONAL ANALYSIS OF EXPERIMENTAL DESIGNS TO STUDY PULMONARY HYPERTENSION AND RIGHT VENTRICULAR FUNCTION

**Mitchel J. Colebank (1), Naomi C. Chesler (1)**

(1) University of California Irvine – Edwards Lifesciences Foundation Cardiovascular Innovation and Research Center, and Department of Biomedical Engineering, University of California, Irvine, Irvine, CA, USA

## INTRODUCTION

Computational modeling of the cardiovascular system can provide significant insight into disease mechanisms. When combined with *in-vivo* experimental data, model parameters can be estimated and correlated with disease severity [1,2]. This is especially important for pulmonary hypertension (PH), an understudied disease that draws heavily from animal disease models. PH affects both the pulmonary vasculature and the right ventricular (RV), leading to RV failure if left untreated. A computational model of hemodynamics and biventricular interaction can provide insight into RV failure and the progression of disease [1,2]. *In-silico* modeling can provide insight into which *in-vivo* designs are most informative, reducing uncertainty in model forecasts.

In this study, we use a multiscale cardiovascular model that simulates sarcomere shortening, ventricular interaction, and zero-dimensional hemodynamics in mice. We consider four experimental designs common for *in-vivo* models of PH research, and study parameter identifiability using sensitivity analyses, profile-likelihood confidence intervals, and Markov chain Monte Carlo (MCMC). We extend our analysis by providing uncertainty bounds in model forecasts and contrast predictive uncertainty across different experimental designs. With this approach, we optimize the synergy between *in-silico* and *in-vivo* approaches to ensure the most informative experimental design.

## METHODS

The computational model includes a phenomenological model of cardiac contractility and sarcomere shortening, a three-segment model of biventricular function and interaction [1], and a zero-dimensional model of the systemic and pulmonary circulations [2]. The model has 49 parameters, 18 differential equations, and 2 algebraic constraints. We consider four experimental designs for *in-vivo* data collection: (1) dynamic RV pressure only, (2) dynamic RV pressure-volume (PV) data, (3) dynamic RV PV data and systolic and diastolic pressure and volume data in the LV, and (4) dynamic PV data in both ventricles. Parameters are scaled to match parameter magnitudes typically found in mice [3].

We use Morris screening to quantify parameter importance by constructing coarse approximations of model sensitivity, $\mathrm{EE}_{i,f}^{i} \approx df/d\theta_i$ [2,3], where $f$ is the output for a given design and $\boldsymbol{\theta}$ are the parameters. Parameters are fixed if they are consistently non-influential using the following indices

$$\mu_{i,f}^{*} = \frac{1}{K}\sum_{j=1}^{K}\left|\mathrm{EE}_{i,f}^{j}\right|, \qquad \sigma_{i,f}^{2} = \frac{1}{K-1}\sum_{j=1}^{K}\left(\mathrm{EE}_{i,f}^{j} - \mu_{i,f}\right)^{2} \tag{1}$$

where $K$ is the number of samples. We subsequently use a derivative based local sensitivity analysis to test for parameter inter-dependence and reduce the subset [1,3]. Structural identifiability is tested by constructing 95% profile-likelihood confidence intervals

$$CI(\theta_i) = \left\{\theta_i \middle| -2PL\left(\theta_j\right) \leq -2\mathrm{LL}(y|\boldsymbol{\theta}) + icdf(\chi_1^2, 0.95)\right\} \tag{2}$$

where $PL(\theta_i)$ is the likelihood for fixed $\theta_i$, $\mathrm{LL}(y|\boldsymbol{\theta})$ is the data likelihood given model-generated data $y$, and $icdf(\chi_1^2, 0.95)$ is an upper bound constructed from the chi-squared distribution with one degree of freedom. After reducing the full 49 parameter set to a smaller, identifiable, and influential subset, we test for practical identifiability using MCMC. We first generate noise-corrupted data from the model and then estimate parameters using the delayed rejection adaptive Metropolis (DRAM) algorithm. DRAM constructs the parameter posterior distributions, providing information about parameter uncertainty for each experimental design. We run DRAM with 12 random initializations to ensure consistency in our results. Lastly, we sample from the posteriors and quantify forecast uncertainty in PV loops and LV, RV, and septal wall (S) engineering strain.

## RESULTS

The global and local sensitivity analysis reduces the original 49 parameter subset to a common set of 13 influential parameters for all

four experimental designs. Table 1 displays the profile-likelihood confidence interval width for 4 of the parameters describing LV and RV wall volume ($V_{wall}$) and reference area ($A_{m,ref}$). The confidence intervals are finite and bounded for all 13 parameters, suggesting that all are identifiable. In addition, confidence interval bounds shrink as more data are included in the experimental design. Figure 1 illustrates 3 of the 12 posterior distributions obtained using the DRAM algorithm. The true parameter values, shown in red, are contained within each posterior, and the posterior variances decrease with more data in the experimental design. Parameter realizations are drawn from the posteriors in Figure 1 to generate uncertainty in model simulations. Figure 2(a) shows that uncertainty in LV and RV PV loops decrease with increased data. LV, RV, and S engineering strain uncertainty is provided in Figure 2(b), and also decreases with more informed experimental designs.

## DISCUSSION

This study investigates parameter identifiability and model uncertainty for four different experimental designs in which *in-vivo* data relevant to PH and RV function are collected. Using a combination of local and global sensitivity analyses, a reduced subset of model parameters is determined as done previously [1-3]. We thoroughly test

| | Confidence interval width | | | |
|---|---|---|---|---|
| Parameters | Design 1 | Design 2 | Design 3 | Design 4 |
| $V_{wall,LV}$ ($mm^3$) | 5.86e-3 | 7.70e-4 | 1.16e-3 | 5.70e-5 |
| $V_{wall,RV}$ ($mm^3$) | 3.48e-3 | 8.40e-5 | 8.39e-5 | 1.80e-5 |
| $A_{m,ref,LV}$ ($cm^2$) | 1.39e-2 | 4.18e-3 | 3.53e-3 | 2.00e-4 |
| $A_{m,ref,RV}$ ($cm^2$) | 1.27e-2 | 8.00e-4 | 5.10e-4 | 4.85e-4 |

**Table 1: Profile-likelihood confidence interval widths.**

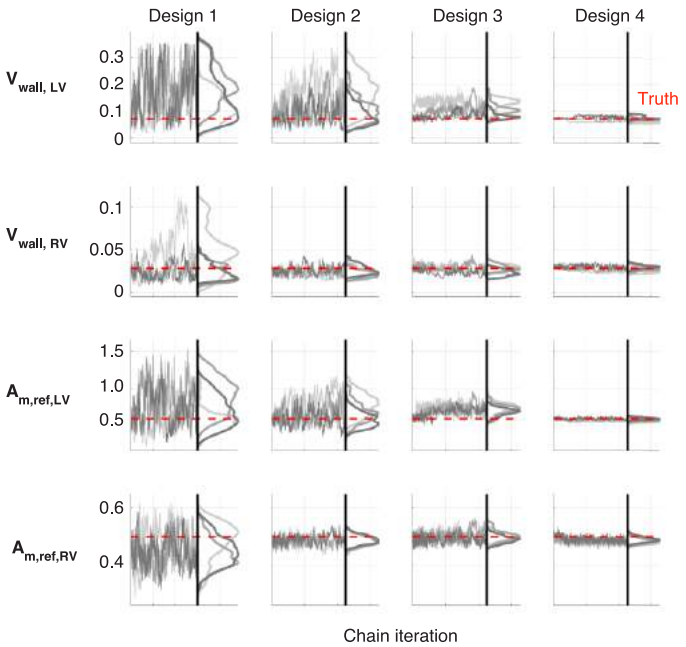


**Figure 1: Posterior chains and density estimates from 4 of 13 parameters using MCMC.**

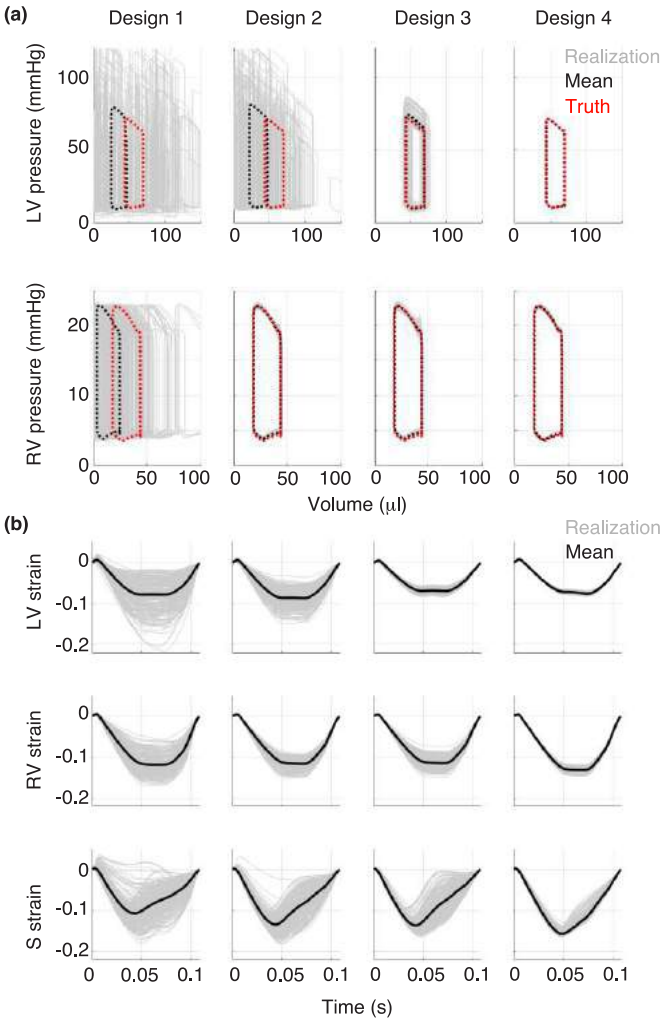


**Figure 2: (a) Uncertainty in LV and RV PV loops. (b) Uncertainty in chamber wall engineering strain.**

for structural identifiability using profile-likelihood confidence intervals, which decrease in width with more informative experimental designs. DRAM results show that designs with PV data in both ventricles reduced parametric and output uncertainty. These results suggest that a coupled *in-silico, in-vivo* investigation of PH and RV failure is optimal when RV PV loops are coupled with LV data. Moreover, *in-silico* forecasts of wall strain are better informed with additional LV data, and may provide more insight into the mechanisms of RV failure during PH. We conclude that biventricular functional data is pivotal in matching model predictions to *in-vivo* data. Designs with RV and LV data minimize the forecast uncertainty in biventricular interactions; hence these designs should be used when investigating the progression of RV failure due to PH using *in-vivo* experiments [2].


## ACKNOWLEDGEMENTS

This work was supported in part by NIH R01 HL154624 and R01 HL147590.


## REFERENCES


[1] Walmsley, J et al. *PLOS Comput Biol*, 11(7):e1004284
[2] Colunga, A et al. *J Physiol*, 598(15):3203-3222
[3] Colebank, M et al. *Int J Numer Meth Biomed Engng*, 37:e3242

SB³C2022
Summer Biomechanics, Bioengineering and Biotransport Conference
June 20-23, Eastern Shore, MD, USA

# PERIVENTRICULAR WHITE MATTER HYPERINTENSITIES ASSOCIATED WITH MECHANICAL CHANGES OF THE EPENDYMAL WALL

**A. Caçoilo (1), M. Grigg (2), H. Rusinek (3), J. Weickenmeier (1)**

(1) Department of Mechanical Engineering, Stevens Institute of Technology, Hoboken, NJ, USA
(2) Department of Biomedical Engineering, West Virginia University, Morgantown, WV, USA
(3) Department of Radiology, New York University Grossman School of Medicine, New York, NY, USA

## INTRODUCTION

Areas of high signal intensity on fluid-attenuated inversion recovery (FLAIR) magnetic resonance imaging (MRI) are known as white matter hyperintensities (WMHs). WMHs are classified into periventricular white matter hyperintensities (pvWMHs) or deep white matter hyperintensities (dWMHs) regions. PvWMHs are characterized by their unique locations near the boundary of the lateral ventricles (LVs), while dWMHs are diffusely spread out in deep white matter (WM) tissue [1]. Throughout the life, tissue degeneration causes cerebral atrophy which results in ventricular enlargement. With age, this causes structural changes in the ependyma and surrounding brain tissue. With the expansion of the ventricles, stretching of the ependymal surface occurs with flattening and compression of the ependymal cells, leading to rupture and degradation of the ependymal epithelium in specific locations along the ventricular surface [2]. Some authors believe that the onset of pvWMHs is linked to a progressive disruption of the ependymal cell wall, also known as ependyma [3,4]. With the ependyma degradation, fluid exchange between the ventricles and the brain substance is not regulated, facilitating the entry of CSF into the brain tissue and leading to the formation of edema in WM tissue [6]. The expansion of the ventricles also results in areas of gliosis, which can lead to glial scar development where the ependymal cells are replaced by dense astrocytic patches [2,6]. Shook *et al.* stated that the astrocytic ribbon layer is consistently thicker in regions with decreased ependymal cell coverage; consequently, the deterioration of the ependymal wall compromises the periventricular ISF homeostasis and disrupts trans-ependymal bulk flow mechanisms required to clear proteins and metabolites from the brain parenchyma [7]. The presence of WMHs is commonly associated with older subjects with cognitive impairment and neurological pathologies, such as stroke or dementia, and their severity has been shown to be correlated with age [8]. Some studies proposed that WMHs are associated with an increase of tissue water content, demyelination and axonal damage due to small vessel disease [9]. In this study, it is hypothesized that the mechanical loading on the ependymal cells of the ventricular wall leads to the emergence and gradual growth of pvWMHs due to the wall's disruption and subsequent CSF leakage into the brain tissue. Computational models were developed to simulate ependymal cell stretch at peak hemodynamic loading, aiming to predict the onset location of pvWMHs.

## METHODS

Brain images used in this work were obtained from cognitively normal subjects in the database of the New York University Alzheimer's Disease Research Center. From a cohort of healthy patients, four male and four female subjects were sorted by cerebrospinal fluid volumes ($20^{th}$, $40^{th}$, $60^{th}$ and $80^{th}$ percentile of the CSF volume distribution), aiming to capture a wide range of ventricular shapes. A finite element model (FEM) of the brain based on a semi-automatic segmentation approach was developed from the respective MR images. The MPRAGE images were used for segmenting the different regions of interest in the brain, such as the LVs, WM, the gray matter (GM), and the subarachnoid space (SAS), using the ScanIP software environment of Simpleware (Synopsis Inc., Mountain View CA) (see Fig. 1(a)). The segmentation process was then manually adapted to make it suitable for conversion to a FE model. Segmentation masks are converted into a volumetric model discretized by tetrahedral elements, as shown in Fig. 1(b). The FE program Abaqus (Dassault Systèmes SE) was used to simulate the mechanical loading of the ventricular wall and its surrounding tissues at peak ventricular pressure during the hemodynamic cycle. A normal pressure was applied to the ventricular wall and the GM-SAS interface to reproduce the effects of the CSF pulsations in the cranial cavity, which occur due to the periodic beating heart. Thus, a pressure of 300 Pa was applied on the LVs and a pressure of 290 Pa was applied on the GM-SAS interface. These values are line with findings available in the literature [10,11,12]. The skull is

SB³C2022-021

replaced here by applying zero displacement boundary conditions on the outer surface of the SAS layer, as can be seen in Fig. 1(c).

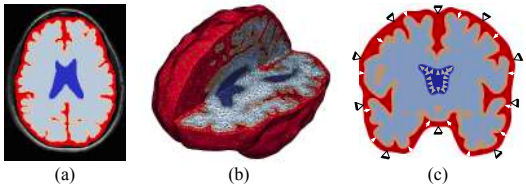


**Figure 1: (a) Segmentation of the subarachnoid space (red), gray matter (orange), white matter (light blue), as well as the lateral ventricles (dark blue); (b) assembling of the 3D FEM of the brain; (c) boundary conditions applied to the ventricular wall and to the outer GM-SAS surface.**

GM and WM tissues were modeled as an Ogden-type hyperelastic material and was implemented in a user-defined material subroutine (UMAT). The material was assumed to be nearly incompressible, with a Poisson's ratio of 0.45, and a white-gray matter stiffness ratio of 2 was assumed [13]. The CSF in the SAS was modeled as a soft compressible material with a Young's modulus of 1 Pa and a Poisson's ratio of 0.30 [13]. For all eight subjects, WMHs were segmented on FLAIR images. As for pvWMHs, Chen *et al.,* Milhorat *et al.* and Fazekas *et al.* reported that although they are more frequently found at anterior and posterior horns, they can also be found in the body of the LV and temporal horns [1,2,14], and that finding was also observed in this study, as shown in Fig. 2.

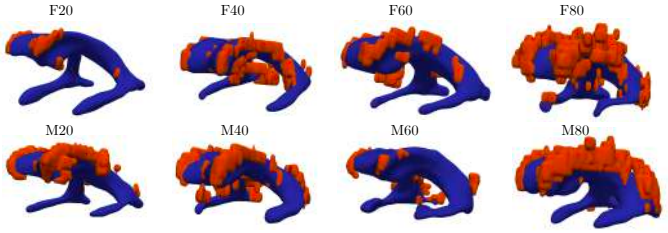


**Figure 2: Reconstruction of the lateral ventricles (in dark blue) and the pvWMHs (in red).**

## RESULTS

Maximum tangential stretch is 1.138, 1.099, 1.100, and 1.113 for female subjects F20 through F80, and 1.133, 1.133, 1.123, and 1.125 for male subjects M20 through M80. The maximum ependymal cell tension for F20 and M20 models is approximately 1.13, which represents an elongation of the ependymal cells of 13%. Peak stretches of models with smaller CSF volume (F20 and M20) are higher compared to the models with larger CSF volumes. The maximum tangent stretch plots, as can be seen in Fig. 3, show consistency with respect to spatial stretch distributions across all the models, and it is visible that the peak stretch is mostly located in the central part of the lateral ventricles. Despite pronounced variations in lateral ventricle geometry across all subjects, peak cell tension is consistently located between the anterior and posterior horns (upper part of the LVs). All other locations of the ventricular wall experience negligible cell stretch, with values around 1.

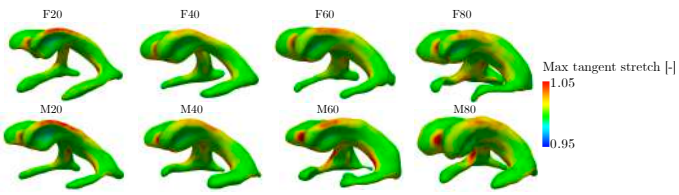


**Figure 3: Distribution of maximum tangent stretch for all subjects.**

A comparison with the location of pvWMHs along the ventricular wall reveals that tissue stretching co-localizes in regions of peak cell stretches. Figure 4 shows mean curvature of all eight models to illustrate the spatial correlation between ventricular wall geometry and the location of pvWMHs, by highlighting surface patches exposed to pvWMHs. Maximum mean curvature is 0.8 $mm^{-1}$, 0.78 $mm^{-1}$, 0.63 $mm^{-1}$, and 1.0 $mm^{-1}$ for female models (F20 to F80); and 0.95 $mm^{-1}$, 0.95 $mm^{-1}$, 1.37 $mm^{-1}$, and 0.64 $mm^{-1}$ for male models (M20 to M80). Thus, the smallest ventricles, i.e., F/M20 and F/M40, exhibit higher mean curvatures along the edges of the main body in comparison to larger models, i.e., F/M60 and F/M80. This is key to the hypothesis that mechanical loading of ependymal cells is one of the most important factors in pvWMH formation and the early growth phase. Inferior horns exhibit very high mean curvature values without corresponding pvWMHs. It appears that elevated mean curvature and high stretch must coincide to create a mechanical loading state that exceeds the physiological limit of the ependymal cells to prevent CSF leakage.

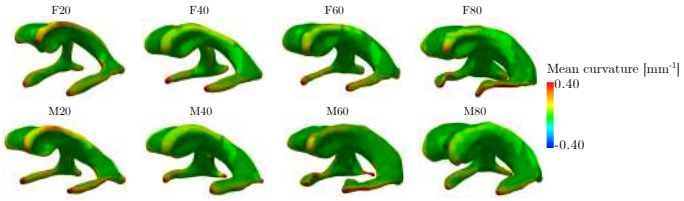


**Figure 4: Mean curvature across the ventricular wall is a geometric property that serves as a marker for regions of elevated LV loading.**

## DISCUSSION

The present work tests the hypothesis that mechanical loading of the ventricular wall is a critical factor for the emergence of white matter hyperintensities. The models included here cover a broad range of ventricular geometries representative of ventricular enlargement observed across a large age-span and provide extensive insight into ventricular wall loading. Ventricular curvature is a surrogate for mechanical loading and showed good spatial agreement with pvWMH locations. In summary, ependymal cell loading along the ventricular surface may serve as a mechanomarker for pvWMH onset locations. The eight subject-specific finite element models consistently demonstrated that peak mechanical loading of the ventricular wall spatially overlaps with pvWMHs locations for a broad spectrum of ventricular shapes and volumes.

## ACKNOWLEDGEMENTS

This research was supported by the National Institute on Aging of the National Institutes of Health under award R21AG067442.

## REFERENCES

[1] Chen J. *et al. Acad Radiol* 28(12):1699-1708, 2020.
[2] Milhorat T. *et al. Arch Neurol* 22(5):397-407, 1970.
[3] Jiménez A. J. *et al. Tissue barriers* 2(1):e28426, 2014.
[4] Hase Y. *et al. J Neurochem* 144(5):617-633, 2018.
[5] Sze G. *et al. AJR Am J Roentgeol* 147(2):331-7, 1986.
[6] Todd K.L. *et al. Front Aging Neurosci* 12(9):445, 2018.
[7] Shook B.A. *et al. Aging Cell* 13(2):340-50, 2014.
[8] Wardlaw J.M. *et al. J Am Heart Assoc* 4(6):001140, 2015.
[9] Chen J. *et al. Acad Radiol* 28(12):1699-1708, 2021.
[10] Evensen K. and Eide P. *Fluid Barriers CNS* 17(1):1-34, 2020.
[11] Penn R. *et al. J Neurosurg* 102(6):1069-75, 2005.
[12] Linninger A. *et al. IEEE Trans Biomed Eng* 52(4):557-65, 2005.
[13] Weickenmeier J. *et al. Acta Biomater* 42:265-272, 2016.
[14] Fazekas F. *et al. AJR Am J Roentgenol* 149(2):351-356, 1987.

SB³C2022
Summer Biomechanics, Bioengineering and Biotransport Conference
June 20-23, Eastern Shore, MD, USA

# SIMULATION OF UTERUS ACTIVE CONTRACTION DURING FETUS DELIVERY IN LS-DYNA

**R. Tao (1), M. Grimm (1,2)**

(1) Department of Mechanical Engineering, Michigan State University, East Lansing, MI, US
(2) Department of Biomedical Engineering, Michigan State University, East Lansing, MI, US

## INTRODUCTION

Normal biomechanical function and regulation of the uterus is vital for childbirth. Poor quality uterine contractions contribute to many labor problems, including labor dystocia (a delay in labor progression), which has proven to be a significant reason for the rising Caesarean section rate [1]. In addition, the interaction of the uterus, the fetus, and the maternal pelvis results in both the normal cardinal movements of labor and abnormalities of descent that can result in a shoulder dystocia (delay in delivering the shoulders after the head delivers). Therefore, it is important to be able to model uterine contraction behavior during the delivery process in order to better understand the pathomechanics.

The uterine wall consists of three layers: the endometrium, the myometrium, and the perimetrium (from inside to outside). The myometrium is composed of millions of smooth muscle cells (SMC). Such SMCs are organized in different directions to resemble fibers that contribute to uterine contraction [2]. The contraction behaviors of the uterus are summarized in Grimm's review [3]. The typical contraction pattern of the uterus resembles a bell-like curve [4], which takes on average 60 s for one cycle [5]. The active contraction is a force wave that is initiated from the fundus and then propagates to the lower part of the uterus, which takes 10 to 20 seconds [6]. While the contraction in different regions starts at different times, the peak force occurs almost at the same time and then relaxation occurs synchronously [6].

Due to ethical issues, human experiments during labor and delivery are difficult to conduct. Computer modelling has become a promising way to investigate uterine behaviors; however, simulation of uterine contraction is still a relatively new research area. In 2009 and 2013, Buttin *et al*. [7-8] established an FEM model of the female reproductive system containing the pelvis, uterus, and fetus to investigate how the different forces influence the fetus delivery process. However, in these simulations, the uterus's active contraction was not simulated directly, but rather an external force was applied through the uterus to the rigid fetal model to simulate what was assumed to be the resulting force. In 2015, Cochran *et al*. [9] developed a 3D electro-mechanical coupling model of the uterus to calculate the mechanical and electrical properties and the peak uterine pressure. A similar model was developed by Yochum *et al*. [10] in 2016, where the mechanical and electrical behaviors were analyzed on multiple scales. However, the geometries were highly simplified, and the strain was too small to represent the large deformation of the uterus during delivery. In 2019, Pouca, *et al*. [11] developed a chemo-mechanical coupling model to simulate uterine contraction and fetal delivery. However, the effects of fibers contributing to the contraction were not considered. Overall, the existing models in this area still include many limitations.

In this study, we developed an FEM uterus model in LS-DYNA to simulate the uterine active contraction, where the contraction forces were driven by contractile fibers. Multiple mechanical contraction properties of the uterus were included in this model.

## METHODS

The geometry of the uterus was designed in NX software with a length of 35 cm, a maximum width of 15.6 cm, a thickness of 1 cm, and diameter of 10 cm at the cervix, as shown in Figure 1a. Meshing was done in Hypermesh software using hexahedral elements (Figure 1b), which was then exported to LS-DYNA. Each element was bonded with four truss beam elements oriented in the longitudinal direction. These beams were assigned to one of seven regions in LS-DYNA (Figure 1c. These beams were used to provide the contraction force based on the Hill material model [12] (MAT_156 in LS-DYNA). The activation curves for the seven beam regions were assumed (Figure 1d), where the starting time for region one was at time 0 s. Each of the subsequent regions began contracting 2 s later than the previous region to simulate the propagation of the contraction wave, and all of the regions reached the fully activated status and began to relax synchronously based on physiologic behavior [6]. At time = 50 s, the activation returned to zero. The solid portion of the model, representing the non-contractile portions

SB³C2022-022

of the tissue, had a Young's modulus of 2 kPa and a Poisson's ratio of 0.495. For the boundary conditions, the nodes on the cervix were fixed in x, y, z translation directions. No external loads were applied.

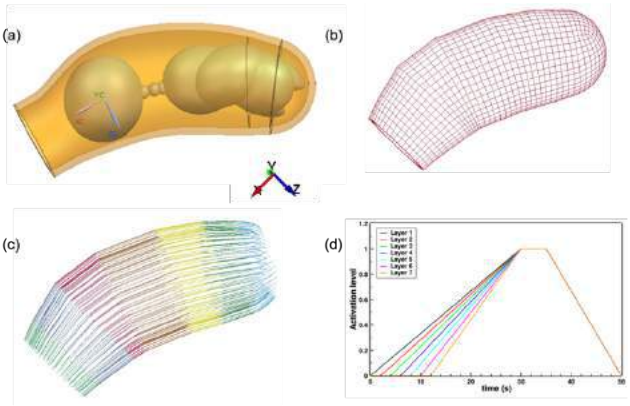


**Figure 1: Modeling details: (a) uterus geometry; (b) meshwork; (c) seven regions of beams; and (d) activation level curves.**

## RESULTS

The simulation result is shown in Figure 2. At t = 0 s, there is no deformation (Figure 2a). After that, the uterus starts to contract from the top, fundus region and the contraction wave starts to propagate to the lower part. By t = 5 s, the first three regions have started to contract, which causes the uterus to shorten in the longitudinal direction while expanding slightly in the transverse direction in these three layers. There is no deformation for the lower uterus, and the largest effective strain is 9.5% (Figure 2b). By t = 10 s, the contraction wave has propagated to the first five regions, causing the contracting portion of the uterine structure to further shorten in the longitudinal direction and expand more in the transverse plane. The largest strain was 17.2% (Figure 2c). By t =15 s, all of the regions have started to contract, and the largest strain is 23.5% (Figure 2d). The entire uterus continues to contract until about 32 s, where the largest stain is 36.1%. The uterus becomes much shorter and wider. From 35s, with the decrease of the activation level, the uterus starts to relax due to the elastic response of the non-contractile tissue. At t = 50 s, the uterus has almost returned to its initial state, and the largest strain was 3.8%.

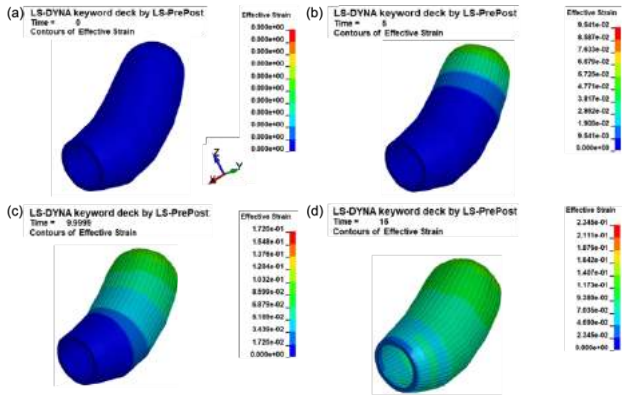


**Figure 2: Representation of the deformation for the uterus at times of (a) 0 s, (b) 5 s, (c) 10 s, and (d) 15 s.**

## DISCUSSION

In this study, we developed a uterus FEM model with contractile fibers. Our model can simulate active contraction directly rather than applying external loading conditions. Existing multi-scale electro-mechanical coupling models are usually mathematically complex, physiologically complicated, and computationally intensive [9-10], and therefore would need an extremely large amount of computer memory and high computational speeds to predict macro-level mechanical behavior. Due to these challenges, these models highly simplified their geometries and were not able to simulate big deformation, while our model can perform large deformation simulation on a complicated geometry. It is known that the variation of the fibers' orientation through the muscle thickness has a significant effect on uterine behavior [2]. The fibers in our current model were organized only in the longitudinal direction, which caused an expansion in the transverse direction during contraction that is not seen clinically. The results also demonstrate how important it is for the simulation to consider the arrangement of the fibers inside the uterus wall, which we plan to investigate with our model in future work. Moreover, our model includes more aspects of uterine mechanical behaviors -- such as the contraction wave propagation phenomenon, synchronous arrival at the peak force for different regions through the uterus, and synchronous relaxation -- by defining multiple regions and independent activation curves for each region.

One limitation of our model is that it is not linked to the cellular level models to study how electrical, chemical, and mechanical behaviors influence tissue and organ-level behaviors. However, such cellular-level models could be incorporated into the Hill muscle model to develop a new multi-scale constitutive model in the future. In addition, the propagation wave is not continuous through the uterus in this version of our model. More regions should be defined to make the propagation smoother. However, this is an important step forward in the simulation of macro-scale contraction behavior of the uterus.


## ACKNOWLEDGEMENTS

This project was supported by NSF Award CBET-2028474.


## REFERENCES


[1] Alrubaii, B et al., *Medical Journal of Babylon*, 2(1), 2005.
[2] Myers, K et al. *Wiley Interdisciplinary Reviews: Systems Biology and Medicine*, 9(5):e1388, 2017.
[3] Grimm, M, *Annals of Biomedical Engineering*, 1-17, 2021.
[4] Smith, R et al., *American Journal of Obstetrics and Gynecol*ogy 213:181–185, 2015.
[5] Steer, P et al., *American Journal of Obstetrics and Gynecol*ogy, 82:433–441, 1975.
[6] Caldeyro-Barcia, R et al., *Triangle*, 2:41–52, 1955.
[7] Buttin, R et al., *Annual International Conference of the IEEE Engineering in Medicine and Biology Society*, 5263-5266, 2009.
[8] Buttin, R et al., *Computer methods and programs in biomedicine*, 111(2):389-401, 2013.
[9] Cohran, A et al., *Mathematics and Mechanics of Solids*, 20(5):540-564, 2015.
[10] Yochum, M et al., *Computers in biology and medicine*, 77:182-194, 2016.
[11] Pouca, M et al., *Biomechanics and modeling in mechanobiology*, 18(3):829-843, 2019.
[12] Hill, V. *Proceedings of the Royal Society of London. Series B-Biological Sciences*, 126(843):136–195,1938.

# POST-STRETCH BEHAVIOR OF VASCULAR SMOOTH MUSCLE CELLS DEPENDS ON STRAIN-RATE AND ACTOMYOSIN INTERACTIONS

**Samuel F. Boland (1), Patrick W. Alford (1)**

(1) Department of Biomedical Engineering, University of Minnesota – Twin Cities, Minneapolis, MN, USA

## INTRODUCTION

Vascular smooth muscle cells (VSMCs) encircle blood vessels and modulate blood flow through active contraction in response to chemical and mechanical cues. In the vasculature, VSMCs are exposed to deformation at rates ranging from 1% per year during aneurysm growth[1] to 1000% per second during traumatic brain injury (TBI).[2] Though VSMC function and gene expression have previously been linked to applied stretch[3,4], our understanding of VSMC response to rate of deformation is still fundamentally lacking. Here, we utilize cellular microbiaxial stretching (C$\mu$BS) to benchmark VSMC mechanical behavior following stretch at different rates. We hypothesized that VSMCs will display viscoelastic characteristics with higher stress following high strain-rate stretch. Surprisingly, we find the opposite to be true: VSMCs generate lower stress following high strain rate stretch. Subsequently, we utilize pharmacological agents to identify actin-myosin binding affinity as a key factor of decreased stress generation following high strain-rate stretch.

## METHODS

**Substrate Fabrication and Cell Culture.** Human umbilical artery VSMCs were micropatterned with aspect ratio 1:4 (AR4) on a fluorescent-bead-doped polyacrylamide (PA) gel with a Young's modulus of 13.5 kPa (Fig. 1A) as previously described[3,5]. VSMCs were cultured using a standard protocol to induce a physiological phenotype[3,5].

**Cellular Microbiaxial Stretching (C$\mu$BS).** C$\mu$BS experiments were performed using a custom-built microscope-mounted device to perform traction force microscopy (TFM) experiments (Fig. 1B). VSMCs were stretched to an engineering strain of 0.15 at rates of 0.001 $s^{-1}$ or 0.1 $s^{-1}$. Following stretch, cells were imaged at 40X using a confocal microscope to obtain traction images. VSMCs were imaged once per second in a time lapse, with the stretch time and imaging time totaling 5 minutes for each condition (Fig. 2A). For example, for cells stretched at 0.001 $s^{-1}$, the time to stretch to a strain of 0.15 is 2 min and cells are imaged for 3 min while the cell is held at a strain of 0.15. Brightfield images were acquired of the VSMC at the first timepoint and fluorescent images were taken of the respective underlying bead layer in the PA gel at every timepoint. Cells were then returned to a strain of 0 and the same imaging protocol was performed. Three cycles of stretch were performed on each cell. The cells were then lysed with SDS and the bead layer of the gel was imaged again at the location of each cell at 0 and 0.15 strain.

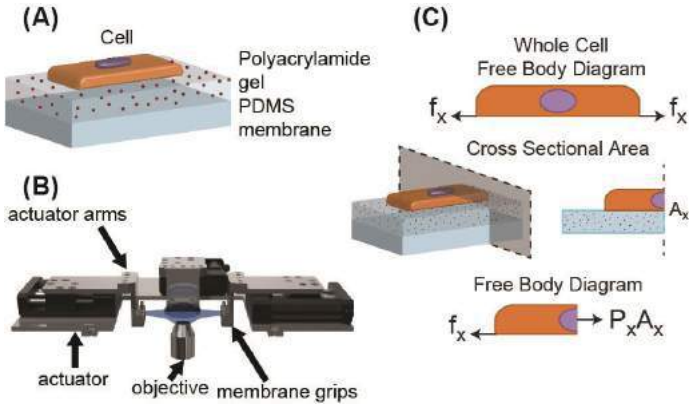


**Figure 1: (A) AR4 VSMC micropatterned on PA gel. (B) Section view of C$\mu$BS apparatus. (C) $P_x$ calculation from VSMC free body diagram. Adapted from Win et al.[5] and Rothermel et al.[3]**

Traction forces at each timepoint were calculated using previously described methods[5,6]. The first Piola-Kirchoff stress, represented by $P_x = f_x/A_x$, where $f_x$ is the total traction force and $A_x$ is the undeformed cell cross-sectional area, was calculated at the mid-plane of the cell (Fig. 1C). Stress is presented as normalized $P_x$, where stress at any time point is normalized to the basal stress at $t$ = 0 s prior to stretch.

**Pharmacological Treatment.** VSMCs were treated with one of four pharmacological agents to induce changes in the cytoskeleton: 20 $\mu$M nocodazole to inhibit polymerization of microtubules, 1 $\mu$M paclitaxel to inhibit microtubule disassembly, 0.1 nM calyculin-A to inhibit myosin dephosphorylation (promote actin-myosin binding), or 3 $\mu$M Y-27632 to promote myosin phosphorylation (inhibit actin-myosin binding). Cells were treated 30 minutes prior to undergoing the stretch protocol.

**RESULTS**

VSMCs were strained at either 0.001 $s^{-1}$ or 0.1 $s^{-1}$ according to the protocol in Fig. 2A. Prior to stretch, VSMCs generate a non-zero basal stress (Fig. 2B(i)). Immediately following strain to 0.15, stress shows a sharp increase (Fig. 2B(ii)) and gradually decreases over time as the cell is held at a constant strain (Fig. 2B(iii)). When cells are returned to 0 strain, stress shows a sharp decrease (Fig. 2B(iv)) and gradually increases over time as the cell is held at 0 strain (Fig. 2B(v)). VSMCs display stress relaxation-like behavior, as displayed in the full normalized $P_x$ vs. time plot for a representative cell (Fig. 2C).

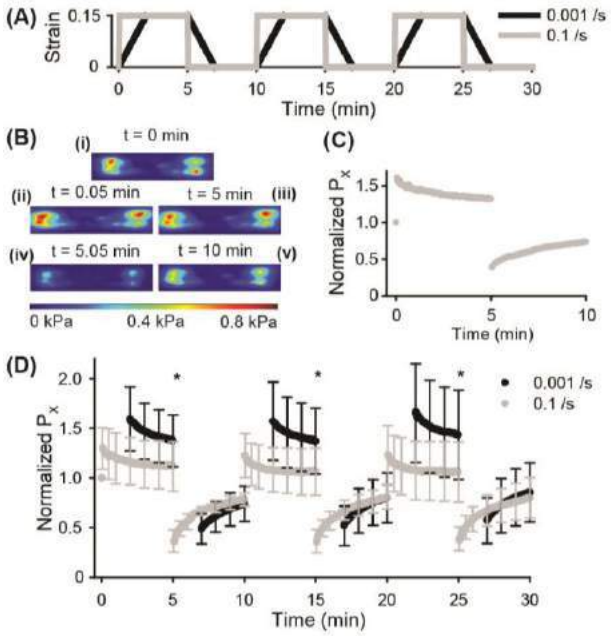


**Figure 2: (A) VSMC strain protocol at 0.001 $s^{-1}$ (black) and 0.1 $s^{-1}$ (gray). (B) Traction stress maps of a cell strained at 0.1 $s^{-1}$ before strain (i), immediately after strain (ii), after being held at 0.15 strain (iii), immediately after return to 0 strain (iv), and after being held at 0 strain (v). (C) Normalized $P_x$ vs. time plot for the cell shown in (B). (D) Average normalized $P_x$ vs. time plots for VSMCs stretched at 0.001 $s^{-1}$ (n=18) or 0.1 $s^{-1}$ (n=20). * = p<0.05**

Surprisingly, VSMCs stretched at 0.1 $s^{-1}$ consistently generated lower stress than cells stretched at 0.001 $s^{-1}$ (Fig. 2D), conflicting with predictions of viscoelastic models commonly used for representing contractile cells. Stress generation is significantly different at the end of the relaxation phase ($t$ = 5, 15, 25 min) but there is no significant difference in stress at the end of the recovery phase ($t$ = 10, 20, 30 min).

VSMCs treated with microtubule-affecting drugs nocodazole or paclitaxel showed stress vs. time plots roughly identical to Fig. 2D (data not shown). After treatment with 0.1 nM calyculin-A, the stress vs. time plots for VSMCs stretched at 0.001 $s^{-1}$ or 0.1 $s^{-1}$ show similar trends independent of strain rate (Fig. 3A). VSMCs treated with 3 $\mu$M Y-27632 show more pronounced differences in stress between cells stretched at 0.001 $s^{-1}$ or 0.1 $s^{-1}$, and display decreased stress with each successive stretch cycle (Fig. 3B). The ratio of stress produced by cells strained at 0.001 $s^{-1}$ compared to cells strained at 0.1 $s^{-1}$ immediately after stretching and after 5 minutes of relaxation is shown in Fig. 3C and 3D, respectively. Calyculin treatment decreases the difference in stress between cells strained at 0.001 $s^{-1}$ or 0.1 $s^{-1}$ compared to untreated VSMCs, while Y-27632 treatment slightly increases the difference.

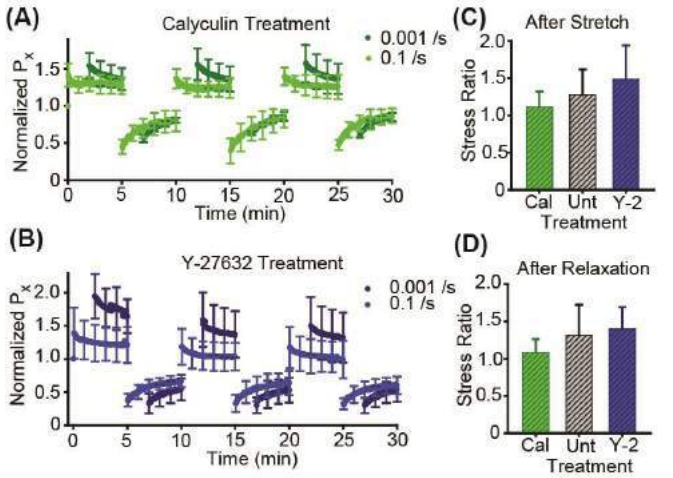


**Figure 3: (A) Average normalized $P_x$ vs. time plot for VSMCs treated with calyculin-A and stretched at 0.001 $s^{-1}$ (dark green, n=5) or 0.1 $s^{-1}$ (light green, n=5). (B) Average normalized $P_x$ vs. time plot for VSMCs treated with Y-27632 and stretched at 0.001 $s^{-1}$ (dark blue, n=5) or 0.1 $s^{-1}$ (light blue, n=5). (C) Average ratio of $P_x$ for cells strained at 0.001 $s^{-1}$ over cells strained at 0.1 $s^{-1}$ immediately after stretch for untreated (Unt), calyculin-A-treated (Cal), and Y-27632-treated (Y-2) VSMCs. (D) Average ratio of $P_x$ for cells strained at 0.001 $s^{-1}$ over cells strained at 0.1 $s^{-1}$ after 5 minutes of relaxation.**

**DISCUSSION**

In this study, we demonstrate that VSMCs show decreases in stress following stretch at high strain-rates. This finding directly contradicts conventional viscoelastic interpretations of contractile cells. Treatment with calyculin-A, which reinforces actin-myosin binding, decreased the difference between stress in VSMCs strained at 0.001 $s^{-1}$ vs. 0.1 $s^{-1}$, while Y-27632 treatment slightly increased the difference. This suggests that decreases in stress generation due to high strain-rate stretch may result from decreased actin-myosin binding. We intend to develop a new model based on our Hill-type active fiber model[7,8] incorporating strain-rate dependent instantaneous rupture and gradual reformation of actomyosin bonds. Understanding how VSMC contractile function depends on rate of applied stretch will help better understand cerebrovascular dysfunction following TBI[9] and may inform the development of long-term arterial remodeling models.

**ACKNOWLEDGEMENTS**

This work was supported by the National Science Foundation (CMMI-193583, CMMI-1553255) and the National Institutes of Health through the Cardiovascular Engineering Training Program at the University of Minnesota (T32-HL139431).

**REFERENCES**

[1] Marwick, T, *J Am Coll Cardiol*, 47(7), 1313-1327, 2006. [2] Miller, S et al., *Front Neurol*, 12(5), 1-15, 2021. [3] Rothermel, T et al., *J Biomech*, 111(2020), 110005, 2020. [4] Szczesny, S & Mauck, R, J Biomech Eng, 139(2), 1-16, 2017. [5] Win, Z et al., *J Biomech Eng*, 139(7), 1-10, 2017. [6] Tseng, Q et al., *Proc Natl Acad Sci USA*, 109(5), 1506-1511, 2012. [7] Win, Z et al., *Biophys J*, 115(11), 2044-2054, 2018. [8] Rothermel et al., *J Biomech Eng*, 143(12), 1-11, 2021. [9] Gama Sosa, M et al., *Acta Neuropathol Commun*, 9(1), 1-27, 2021.

# LARGE ANIMAL MODEL OF MENISCUS INJURY AND REPAIR SHOWS CHONDROPROTECTION AND PARTIALLY RESTORES JOINT KINEMATICS AS MEASURED VIA MRI

**Kyle D. Meadows (1), Brendan D. Stoeckl (2,3), John M. Peloquin (1), Adriana Barba (4), Eddie D. Bonnevie (2), Sonia Bansal (2), David R. Steinberg (2,3), Miltiadis H. Zgonis (2), Thomas P. Schaer (4), Robert L. Mauck (2,3), Dawn M. Elliott (1)**

(1) Biomedical Engineering, University of Delaware, Newark, DE, USA
(2) McKay Orthopaedic Research Laboratory, University of Pennsylvania, Philadelphia, PA, USA
(3) Translational Musculoskeletal Research Center, CMC VA Medical Center, Philadelphia, PA, USA
(4) School of Veterinary Medicine, University of Pennsylvania, Philadelphia, PA, USA

## INTRODUCTION

The meniscus serves key functions in knee loadbearing and in protecting the underlying articular cartilage. The meniscus is commonly injured, which in turn impairs its ability to distribute loads and predisposes the joint to developing osteoarthritis (OA). Surgical meniscus repair is chondro-protective and can delay OA but does not halt degeneration for many patients. The unknown altered joint kinematics with meniscus injury and repair are a barrier to addressing this clinical problem. While joint contact measurements do show improved load distribution [1], these methods disrupt the joint capsule and are a 1D measurement. Therefore, a 3D non-invasive MRI-based method that applies physiologic loads to an intact joint is needed [2]. Large animal models of medial meniscus injury develop similar cartilage pathology as humans [3, 4, 5], yet it remains unknown whether surgical repair in these models can restore meniscus function and prevent cartilage OA. Therefore, the objective of this study was to evaluate joint kinematics and cartilage degeneration following injury and repair in a large animal surgical model. We hypothesized that repair would restore near-intact kinematics and prevent cartilage degeneration. Establishing the relationship between joint kinematics and cartilage OA is critical for improving clinical outcomes of meniscus repair.

## METHODS

Meniscus injury and repair were performed in Yucatan minipig joints in 1) a cadaver model (n=3 knees, 18 months old, ~70 kg) and 2) an established surgical model with sacrifice at 6 weeks post-op (n=4 knees per group, 12 months old, ~50 kg), with IACUC approval. The three treatment groups were Intact, Injury, and Repair. The injury was performed by cutting the anterior attachment of the medial meniscus; in the *in vivo* surgical model this cut removed 5 mm of attachment en bloc. The repair was made using a suture anchor. Joint kinematics were quantified using a custom MRI-compatible loading device that compressed the intact knee joint at 30° flexion and held that position during imaging. MRIs were acquired for each joint at 50 N (Preload) and 1X body weight (Full Load) using a 0.2 mm isotropic T1 VIBE sequence. Meniscus motion (kinematics) was calculated from MRI between Preload and Full Load by aligning the tibia, labeling the meniscus boundary, and then calculating its displacement between loads. Initial meniscus position was calculated at Preload relative to the medial intercondylar tubercle ("+" in Fig 1B). Meniscus displacement and position were averaged across the anterior and mid-body (Fig 1B); the posterior meniscus had little motion (Fig 1B), so it was not included.

In the surgical model, additionally, a T2 CPMG image was acquired at Preload, and cartilage T2 time was calculated using noise corrected exponential decay as a measure of degeneration [6]. After MRI, knee joints were dissected, and tibial plateaus were assessed for cartilage wear using India Ink. Further, cartilage indentation testing was performed using a 2mm spherical indenter at four locations, two each on cartilage regions previously covered by the meniscus or on more central uncovered regions. These are denoted as the cartilage-meniscus (C-M) and cartilage-cartilage (C-C) contact regions, respectively. Fifteen-minute duration creep tests at a 0.1N load were fitted to a model of Hertzian biphasic creep [7], and values for compressive modulus, tensile modulus, and permeability were determined. Values for the C-M and C-C contact regions were averaged. Synovium sections were stained with Hematoxylin & Eosin. Osteochondral tissues were scanned via μCT at 70kVp, 85μA, with a voxel size of 10.3μm. Trabecular thickness and bone volume fraction were calculated for 3mm diameter cylindrical regions of interest just below (0-1mm) the C-M and C-C contact regions. Decalcified osteochondral sections were stained with Safranin O/Fast Green.

Cadaveric data was compared between treatment groups by one-way ANOVA followed by a paired t-test with pooled variance. All surgical data was compared with one-way ANOVA followed by post-hoc Tukey HSD; significance was set at $p<0.05$.

## RESULTS

In cadaver knees, large meniscus displacements occurred with load in the Injury group and were restored to near-Intact levels in the Repair group (Fig 1A,B). Quantitatively, the initial position at preload was not different between groups ($p>0.05$ for anterior and medial distance, Fig 2A, circles). Compared to Intact, Injured menisci displaced more medially with loading ($p<0.05$), although anterior displacement was not different (Fig 1C and vectors in Fig 2A). The Repair displacement was not significantly different from Intact (Fig 1C and vectors in Fig 2A).

In the surgical model after 6 weeks, the initial meniscus positions for Injury and Repair were 3 mm more medial than Intact ($p<0.05$) and, for Injury, 1 mm more anterior ($p>0.05$, Fig 2B, circles). However, for Repair, initial position along the anterior axis was similar to Intact (Fig 2B). Displacement with load (Fig 2B, arrow length + direction) was not statistically different between treatments.

In the cartilage 6 weeks after surgery, quantitative MRI T2 trended higher in Injury vs. Intact ($p=0.08$, Fig 3A,B), indicating degeneration. Injury showed more macroscopic signs of degeneration than Intact, with a significantly greater area of the medial tibial plateau positive for India ink staining. Qualitatively, Repair showed less wear than Injury and was not significantly different from the Intact group. Histologically, the Injury group showed more degeneration and greater proteoglycan loss compared to the Intact or Repair groups (Fig 3C), and the synovium in the Injury group showed the greatest signs of inflammation. From indentation tests, tensile and compressive moduli were not significantly different between groups, but the C-C contact region permeability trended higher ($p=0.084$) in the Injury vs. Intact and in Repair the permeability was the same as Intact (Fig. 4). The bone volume fraction in the C-M contact region subchondral bone of the Injury group was significantly higher than that of the Intact group, and trended higher than that of the Repair group ($p=0.054$). Intact and Repair were not significantly different.

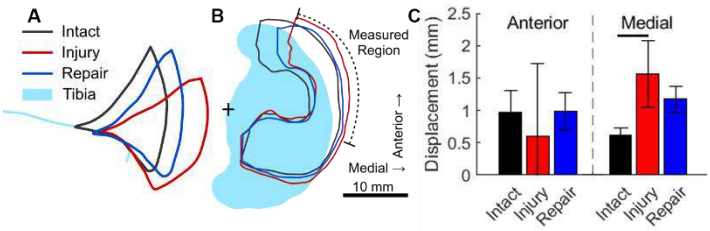


**Figure 1: Cadaver displacement with load. A,B) representative meniscus and tibia boundary, and C) anterior and medial displacement of meniscus (mean ± std dev).**

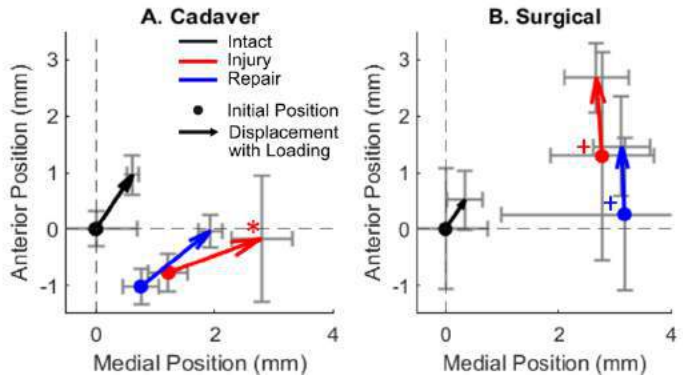


**Figure 2: A) Cadaver and B) surgical meniscus displacement relative to initial preload positions. Error bars are std dev. Significant vs. Intact: * for displacement and + for initial position.**

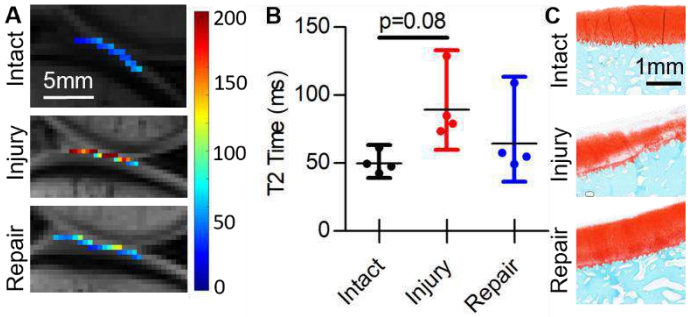


**Fig 3: A) Representative T2 MRI maps, B) T2 times, and C) histology of C-C contact region (surgical model; mean ± 95% CI).**

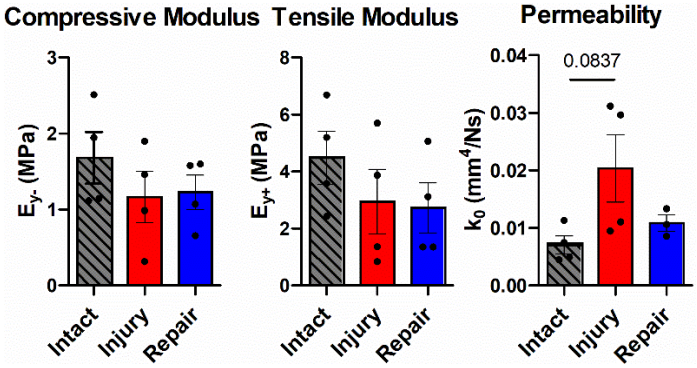


**Figure 4: Compressive and tensile moduli and permeability of the tibial C-C contact region (surgical model; mean ± std dev).**

## DISCUSSION

This study evaluated changes in meniscus kinematics and cartilage changes in a porcine animal model of meniscus injury and repair. Overall, our data support that surgical repair provides some restoration of meniscus kinematic and cartilage protection at 6 weeks. Acutely, severing the meniscus attachment caused large displacements under physiological load, while suture repair re-established meniscus kinematics nearer to intact values. 6 weeks after surgical injury and repair, the meniscus position at preload was near-normal anteriorly but was displaced medially, and displacements during loading were not different from injury. Despite this, the repair was protective of the cartilage, based on T2 times, gross morphology, histology, mechanical testing and μCT. Ongoing work will address limitations in sample size and add longer post-surgical time points. The significance of this work is that we used an MRI-based technique to quantify physiological knee kinematics and changes with meniscus injury and repair in an intact joint. Combined with a large animal model, we demonstrated that meniscus repair was chondroprotective and established a platform to quantify kinematics after meniscus injury and repair.


## ACKNOWLEDGEMENTS

This work was supported by the NIH and the Department of Veterans Affairs.


## REFERENCES


[1] Bedi, A et al., J Bone Joint Surg Am., 92(6):1398-408. 2010.
[2] Schwer, J et al., Front. Bioeng. Biotechnol., 8:582055. 2020.
[3] Bansal, S et al., J Orthop. Res., 38(12):2696-2708. 2020.
[4] Bansal, S et al., Tissue Engineering Part C: Methods, 23(11):661-672. 2017.
[5] Waller, K et al., Am J Sports Med, 45(7):1512-1521. 2017.
[6] Raya, J et al., Magn Reason Med, 63(1):181-193. 2010.
[7] Moore, A et al., J Tribol., 138(4): 041405. 2016.

# APPLICATION FORCE FEEDBACK REDUCES THE MEASUREMENT VARIABILITY OF A SHEAR WAVE TENSIOMETER

**Lesley R. Arant (1), Joshua D. Roth (2, 3)**

(1) Department of Biomedical Engineering, University of Wisconsin-Madison, Madison, WI, USA
(2) Department of Orthopedics and Rehabilitation, University of Wisconsin-Madison, Madison, WI, USA
(3) Department of Mechanical Engineering, University of Wisconsin-Madison, Madison, WI, USA

## INTRODUCTION

Although proper ligament tensioning plays a key role in the success of ligament reconstructions [1] and total knee arthroplasties [2], surgeons do not have the tools they need to directly and noninvasively measure ligament tension. To meet this need, our research group is developing a shear wave tensiometer that uses the speed of shear waves propagating along a ligament to gauge its tension [3,4].

Our tensiometer is a handheld device composed of a piezoelectric tapper and two downstream miniature accelerometers. The tapper excites shear waves in the ligament and the downstream miniature accelerometers track the shear wave propagation. Similar to the sensitivity of shear wave elastography measurements to ultrasound probe pressure [5], measured shear wave speeds are sensitive to the application force of the tensiometer components against the specimen [6,7]. As such, variable forces applied by a user can result in erroneous measurements of shear wave speed and thus ligament tension.

Although application force is a determinant of tensiometer accuracy [7], current tensiometer designs do not have onboard, real-time application force monitoring. Furthermore, the effect of application force on the *variability* of measured shear wave speeds remains unknown. Achieving small variability is important for measuring ligament tension with high precision and repeatability, as required for a clinically translatable tensiometer.

Accordingly, the objectives of this work were to 1) incorporate application force monitoring into our ligament tensiometer, and 2) use this monitoring to determine the effect of application force user-feedback on the variability of measured shear wave speeds. We hypothesized that providing users with real-time feedback on their application force would decrease the variability of measured shear wave speeds.

## METHODS

We incorporated an application force monitor into our tensiometer using a Hall effect sensor, spring, magnet, brass rod, and 3D printed tip in series (Figure 1) [8]. When a user holds the tensiometer against the specimen, the spring compresses, causing the magnet to move closer to the Hall effect sensor and change the sensor's output voltage. We used the voltage-distance calibration curve for the Hall effect sensor to determine the spring displacement. Using this spring displacement and the spring constant, we computed the application force based on Hooke's law. We placed two such application force monitors in parallel to monitor the application force of the contact points of the two accelerometers used to track shear wave propagation (Figure 1).

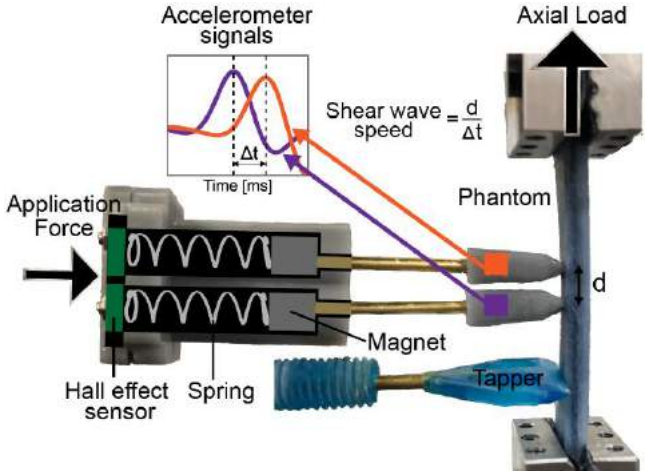


**Figure 1: Schematic showing the tensiometer used to measure shear wave speeds and the onboard application force monitors.**

We measured shear wave speeds in a yarn-silicone ligament phantom because it is less variable than a biological ligament [9,10]. A handheld piezoelectric tapper excited shear waves in the phantom using a 50% bandwidth Gaussian wavelet with a 700 Hz center frequency. We embedded an accelerometer into each of the two 3D printed tips to track the shear waves. We cross-correlated the transient portion of the accelerometer signals at each tap event to find the time delay between wave arrivals. We then computed the shear wave speed by dividing the spacing of the tips (7.25 mm) by the time delay (Figure 1) [3].

We recruited five users to measure shear wave speeds in the phantom under application forces and axial loads that varied following a full factorial design of experiments (Figure 2). First, each user measured shear wave speeds during 15-second trials at phantom axial loads of 100 N, 200 N, and 300 N using a self-selected application force without knowing the magnitude of that force. Then, at the same phantom axial loads, each user measured shear wave speeds using target application forces of 2 N, 5 N, and 8 N in a randomized order. During these trials, two dials displayed the target and measured application forces on each tip in real-time (Figure 2).

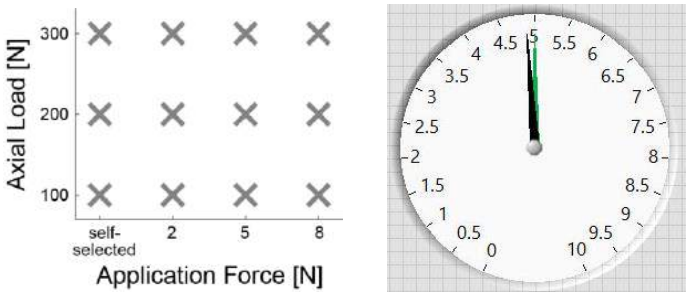


**Figure 2: Full factorial experimental design for application force and axial load (left). Dials provided a real-time display of the target (green) and measured (black) application forces (right).**

For the self-selected application force trials, we averaged the measured application forces across the 15-second static hold and across both application force monitors to yield one application force per user per axial load level. We then computed the range of these average application forces across users at each axial load level to quantify the variability in the self-selected application force across users. For all application force trials, we computed the mean and standard deviation of the measured application forces pooled across all users for each axial load – target application force combination. We also computed the standard deviation of the measured shear wave speeds across all users for each axial load – target application force combination.

For each axial load level, we applied Levene's test to determine whether the standard deviation of shear wave speeds across all users was significantly different for at least one of the four application forces. We also applied Levene's test with Bonferroni correction for pairwise comparisons of the standard deviation of shear wave speeds between each target application force and the self-selected application force.

## RESULTS

Across users, the average self-selected application forces ranged from 0.4 to 2.6 N, 0.5 to 2.5 N, and 0.4 to 2.6 N at axial loads of 100 N, 200 N, and 300 N, respectively. Small differences between the target and average measured application forces indicate that users were able to control application force with high accuracy (Table 1). However, both the bias and precision errors of the measured application forces tended to increase with increases in the target application force (Table 1).

There was a statistically significant difference in the standard deviation of the shear wave speeds for at least one of the four application forces ($p < 0.001$ for all axial loads) and between each target application force and the self-selected application force ($p < 0.001$ for all pairwise comparisons for all axial loads) (Table 1). The standard deviation of shear wave speeds tended to decrease with increases in application force (Table 1).

**Table 1: Statistics quantifying the measured application forces and the variability of shear wave speeds. Asterisks (*) indicate significant differences in the standard deviation of the shear wave speeds between the target and self-selected application forces.**

| Axial Load | Target Application Force | Measured Application Force [N] | | Shear Wave Speed [m/s] |
|---|---|---|---|---|
| | | Mean | Std. Dev. | Std. Dev. |
| 100 N | self-selected | 1.1 | 0.8 | 40.7 |
| | 2 N | 2.0 | 0.1 | 9.7* |
| | 5 N | 4.9 | 0.2 | 4.6* |
| | 8 N | 7.8 | 0.3 | 3.0* |
| 200 N | self-selected | 1.1 | 0.7 | 63.3 |
| | 2 N | 2.0 | 0.1 | 8.2* |
| | 5 N | 5.0 | 0.2 | 5.8* |
| | 8 N | 7.7 | 0.4 | 4.6* |
| 300 N | self-selected | 1.1 | 0.8 | 139.9 |
| | 2 N | 2.0 | 0.1 | 38.7* |
| | 5 N | 5.0 | 0.2 | 3.0* |
| | 8 N | 7.8 | 0.4 | 2.3* |

## DISCUSSION

We found that users tended to apply self-selected forces to the tensiometer that were lower than the target application forces and variable from user to user. With application force feedback, each user accurately achieved the target application forces, suggesting that the design of the application force monitor facilitates precise control.

Consistent with our hypothesis, shear wave speeds were highly variable when the users did not have application force feedback. Interestingly, although higher target application forces were more difficult to control (i.e., larger bias and precision errors), they yielded the least variable shear wave speeds. This may be because higher application forces provide a better coupling between the motions of the specimen and the accelerometers. To determine the cause of the high variability in shear wave speeds at the self-selected application forces, we plan to explore the effects of feedback at lower application forces better matched to user-selected forces. We also plan to incorporate application force monitoring into the tapper.

Previous work found that application force affects measured shear wave speeds [6] and the accuracy of shear wave tensiometers [7]. We extend upon these findings by identifying that self-selected application forces vary between users and that controlling application force decreases the variability of measured shear wave speeds. These insights underscore the importance of providing users with application force feedback to reduce the measurement variability of the tensiometer.

## ACKNOWLEDGEMENTS

We gratefully acknowledge support from the Draper Technology Innovation Fund (TIF), administered by Discovery to Product (D2P) at UW–Madison.

## REFERENCES

[1] Tohyama, H et al., *Knee Surg Sports Traumatol Arthrosc*, 6:S30-S37, 1998. [2] Babazadeh, S et al., *Orthop Rev (Pavia)*, 1:e26, 2009. [3] Martin, JA et al., *Nat Commun*, 9:1592, 2018. [4] Blank, JL et al., *J Mech Behav Biomed Mater*, 105:103704, 2020. [5] Vachutka, J et al., *Ultrason Imaging*, 40:380-393, 2018. [6] Blank, JL et al., *CMBBE*, 2020. [7] Arant, LR et al., *ORS*, 2022. [8] Singal, K et al., *IEEE Trans Biomed Eng*, 62:426-437, 2015. [9] Arant, LR et al., *J Mech Behav Biomed Mater*:104984, 2021. [10] Pineda Guzman, RA et al., *J Mech Behav Biomed Mater*, 118:104339, 2021.

SB³C2022
Summer Biomechanics, Bioengineering and Biotransport Conference
June 20-23, Eastern Shore, MD, USA

# DEVELOPMENT OF A PARAMETERIZED MICROSCALE AXONAL INJURY MODEL

**C. Zhang (1), S. Ji (1,2)**

(1) Department of Biomedical Engineering, Worcester Polytechnic Institute, Worcester, MA, USA
(2) Department of Mechanical Engineering, Worcester Polytechnic Institute, Worcester, MA, USA

## INTRODUCTION

Traumatic brain injury (TBI) is a serious public health threat that occurs across the length scales from the whole brain to individual cells . Diffuse axonal injury (DAI) is one of the most common types of injury leading to damages to neuronal axons. However, its injury mechanism at the microscale, cellular level, remains elusive. Experimental observations have led to various hypotheses, such as microtubules (MTs) tear [1], strain concentration around the Ranvier node, [2] and interaction among various axonal substructures [3], among others.

To-date, studies on axonal injury mechanisms are limited to specific geometries of selected axonal substructures. Different axonal models have adopted different subsets of substructures, and for common substructures, they do not always have the same geometry either. This makes it difficult to compare findings across studies.

To enhance the understanding of axonal injury mechanism at the microscale, here we develop a parameterized finite element (FE) axonal injury model, where parameters regarding the geometry of each axonal substructures can be specified and adjusted. This allows automatic generation of a model with details of axonal substructures adaptable according to specific needs and/or anatomical regions. Finally, we report results of model validation and injury risks to the microtubules in typical axonal stretches.

## METHODS

A representative volume element (RVE) of an axonal injury model was developed, including major substructures such as microtubules (MTs), microtubule-associated protein (MAP), tau, neurofilament (NF) network, Axolemma, myelin sheath, and the Ranvier node. The baseline model uses average geometrical parameters for each substructure according to the literature [2–4]. Their values are reported in (Table 1). Values for each continuous geometrical parameter are adjustable. The number of MTs across the axonal cross-section is a discrete number. The baseline model choses to use 7 so that to allow a hexagonal staggering, which corresponds to the axon of a female subject [5].This parameter can also be adjusted to 19 when two layers of MTs are present (corresponding to the axon of a male subject). The MT length was found to have a range [6]. Their gaps are then randomly generated based on the statistic distribution that each microtubule has an average length of 4.02 ±5.28 um [6].

**Table 1 | Geometrical features of Axon substructures**[2–4]

| Axolemma radius | # of MTs | MT. spacing | MT inner radius | MT outer radius | g-ratio* |
|---|---|---|---|---|---|
| 200 nm | 7 | 20 nm | 7 nm | 12.5 nm | 0.5 |

*g-Ratio: The ratio of the inner axonal diameter to the total outer (myelin sheath) diameter

Each axon model is composed of hexahedral elements for the MTs, axolemma, myeline sheath, as well as connector elements for tau, NF, and NF-MT connections. Most axonal substructures were assigned with linear viscoelastic material properties based on the literature [2,3].

Nevertheless, material properties for the neurofilament have not been well-characterized. Therefore, we calibrated the NF stiffness by replicating the hertz contact experiment conducted with AFM [7]. Specifically, the indenter tip reaction force was collected and compared with the AFM data to calibrate the NF stiffness. Finally, considering that the connector components play an import role on maintaining the integrity of axonal substructures, a failure model was also included to prescribe the behaviors of the connectors, where a strain failure threshold was set to be 100% strain [1].

After calibration of the NF material properties, the model was validated against in-vivo experimental tension dataset [8]. Axonal model was then used to simulate axonal stretch from a real-world impact. Specifically, a strain history curve in the corpus callosum obtained by simulating a concussive NFL head impact using the anisotropic

SB³C2022-026

Worcester Head Injury Model V1.0 was used as the boundary condition to drive the baseline axonal injury model. The strain curve was scaled so that its peak axial strain was 18%, corresponding to an average injury threshold found from an *in vivo* animal injury model. The peak strain rate for the loading and unloading phases were $\dot{\epsilon}$ = 9.5 $s^{-1}$ and $\dot{\epsilon}$ = -19 $s^{-1}$ respectively. The strain history was then applied as a periodic boundary condition (PBC) to the axonal RVE model.

To further explore how the MT gap configurations affect peak MT strains, we randomly generated 1000 female axonal models with the MT gap locations along each bundle independently following a normal distribution. We then used a range of "critical lengths" to count how many MTs within the given length had a gap. Effectively, this was also to count how many MTs remained intact a within the given length. The classification was based on the first occurrence of maximum number of MTs having gaps in the given length. The critical lengths were chosen as discrete percentages of the average MT length, ranging from 5% to 25%, with a step size of 5%. Then, we used stratified sampling to select 250 from the 1000 total gap configurations to apply the same PBC for numerical simulations.

Due to the extremely small dimension of the axonal models, all simulations were performed in SIMULIA Abaqus Standard using the implicit non-linear FEA solver (32 CPUs, 64GB).

## RESULTS

Figure 1 shows MT undulation pattern of a female (7 MTs) and a male (19 MTs) model (**Fig. 1a**) occurring during unloading. Qualitatively, this matched well with the experiment result observed from dynamic stretch injury analysis (**Fig. 1b**) [4]. We found that unloading (i.e., strain from peak to zero) was critical for the undulation, which did not happen during the loading phase. We also found that gaps along MT bundles critical for the formation of undulation, without which no undulation was observed (**Fig. 1c**). In addition, MT deformation strongly depended on the gap configuration (**Fig. 1d**).

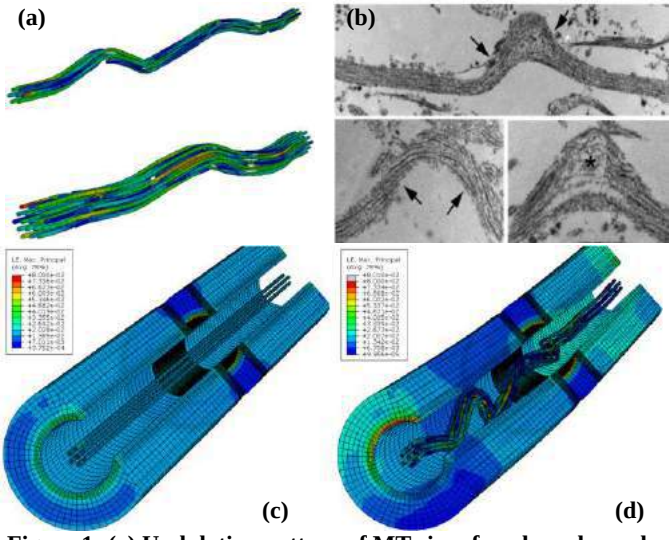


**Figure 1: (a) Undulation pattern of MTs in a female and a male axonal injury model; (b) MT undulation in dynamic stretch injury test [6]; (c) No undulation if no gaps along MT bundles; (d) Undulation strongly depends on MT gap configuration.**

Figure 2 summarizes peak MPS of the MT bundles resulting from the 250 random axonal models. Each grid represents a gap configuration, i.e., within x% of the MT as the critical length, how many MTs having gaps. The numerical values indicate the average peak MPS of those corresponding models. Evidently, the more MTs having gaps within a shorter range, or, equivalently, the less MTs remaining intact within a shorter range, the higher peak strains would occur. Some grids had no peak strain values, because there were no models satisfying the specified MT gap configuration, due to the random nature of how axonal models were generated following the statistical model.

The highest MT peak strain was 32.4%, when there were 5 MTs having gaps within a critical length of 10% of the average MT length. This represented an 80% increase of the peak input strain of 18%. When fewer MTs having gaps within a larger critical length, peak MPS was much reduced, to about 10% higher than the peak input strain.

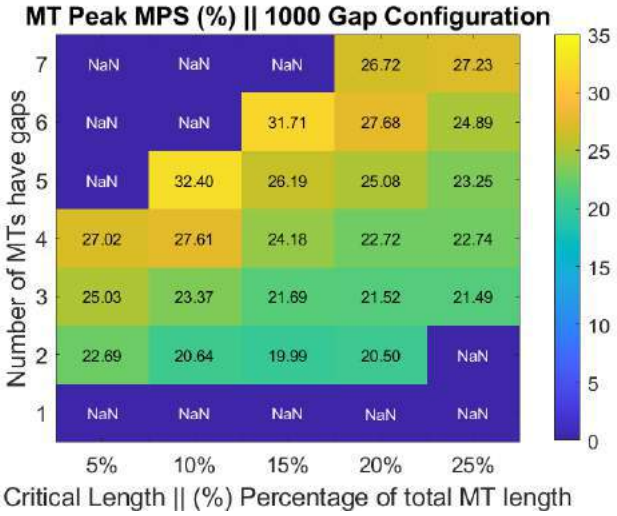


**Figure 2: Peak MPS of MT bundles disaggregated by gap configuration from 250 numerical simulations.**

## DISCUSSION

Our parameterized axonal injury model offers an efficient approach for future large-scale studies of axonal substructural damages. We find that unloading is critical to the formation of MT undulation, which has not been reported previously. In addition, we find that the MT gap configuration plays an important role in peak strain amplification. The strain amplification map (**Fig. 2**) indicates that the more MTs having gaps (or equivalently, the less intact MTs) within a shorter length, the higher the peak strain amplification. This is consistent with expectation, and suggests the effectiveness of our classification strategy of the MT gap configurations. These findings may lead to improved understanding of injury mechanisms of microscale axonal injury.


## ACKNOWLEDGEMENTS

Funding is provided by NIH Grant R01 NS092853 and NSF CMMI 2114697. Simulations were conducted using a high-performance computing system acquired through the NSF MRI grant DMS-1337943 to WPI.


## REFERENCES


[1] Montanino, A. et al., *Front. Neurol.* **9**, 1–12 (2018).
[2] Zhu, F. et al., *Arch. Phys. J. Neurotrauma* **33**, 859–870 (2016).
[3] Peter, S. J. et al., *Arch. Biophys. J.* (2012)
[4] Ahmadzadeh, H. et al., *Biophys. J.* **106**, 1123–1133 (2014).
[5] Dollé, J. P. et al., *Exp. Neurol.* **300**, 121–134 (2018).
[6] Yu, W. et al., *J. Neurosci.* **14**, 2818–2829 (1994).
[7] Ouyang, H. et al., *J. Biol. Eng.* **7**, 1 (2013).
[8] Rajagopalan, J. et al., *Biophys. J.* **99**, 3208–3215 (2010)

SB³C2022
Summer Biomechanics, Bioengineering and Biotransport Conference
June 20-23, Eastern Shore, MD, USA

# MUSCLE IMMOBILIZATION PREVENTS FUNCTIONAL DEVELOPMENT OF EMBRYONIC TENDONS BUT DOES NOT AFFECT COLLAGEN CROSSLINKING

**Benjamin E. Peterson (1), Rebecca A. Rolfe (2), Paula Murphy (2), Spencer E. Szczesny (1,3)**

(1) Department of Biomedical Engineering, Pennsylvania State University, University Park, PA.
(2) Department of Zoology, Trinity College Dublin, The University of Dublin, Ireland
(3) Department of Orthopaedics & Rehabilitation, Pennsylvania State University, Hershey, PA, USA

## INTRODUCTION

To date, no tissue engineered tendon construct has successful replaced a tendon or ligament in a human patient[1]. Understanding how tendon naturally develops can provide critical insights into advancing tissue engineering strategies. In particular, chick tendons experience a critical period during late embryonic development in which there is a rapid increase in the tissue multiscale mechanics[2,3,4]. While various structural changes contribute to this behavior, our recent work suggests that this transition is mediated by less interfibrillar sliding and increased fibril loading due to collagen fibril lengthening[4]. Additionally, both the change in tissue mechanics and collagen fibril lengthening were dependent on muscle activity[4]. However, it's unclear what other structural changes may contribute to tendon development. For example, lysyl-oxidase (LOX) activity, which mediates collagen crosslinking, also increases during late embryonic development and is dependent on muscle activity[5]. Still, it's unclear whether the effects of muscle paralysis on tendon tensile mechanics are due to reduced collagen crosslink formation. Therefore, the objective of this study was to measure the change in functional collagen crosslinking following muscle paralysis and investigate the effects of LOX inhibition on the tensile multiscale mechanics of developing tendons. We hypothesize that muscle paralysis and LOX inhibition will reduce the macroscale mechanics but paralysis will decrease the fibril:tissue strain ratio (i.e., increase fibril sliding) while LOX inhibition will increase the fibril:tissue strain ratio (i.e., increase fibril strain). Additionally, we hypothesize that muscle paralysis will not alter the enthalpy or temperature required to denature embryonic tendons, suggesting that functional crosslinking is not dependent on muscle activity. This study will provide essential knowledge regarding the structure-function processes driving tendon development, which will aid the advancement of tissue engineered tendon constructs.

## METHODS

Chicken eggs were obtained under IACUC approval and windowed at embryonic day 3 (E3). Rigid or flaccid paralysis was induced by an injection of decamethonium bromide (DMB) or pancuronium bromide (PB), respectively. Specifically, at E13 eggs were given 100 ul of a 0.02% DMB or PB, followed by daily 50 ul injections from E14-E19 of the same concentration. LOX mediated crosslinking was inhibited with 2 mg of BAPN at E15. Controls for both groups consisted 3of saline injections with matching treatment protocols. Embryos were sacrificed at E20 for testing.

Mechanical testing was conducted using a custom micotensile device mounted atop a confocal microscope[5]. The flexor brevis tendon was dissected and stained with 5 µg/ml DTAF. Samples were mounted at a gauge length of 10 mm and preloaded to 0.1 g. Image stacks were acquired to measure the major/minor diameter to calculate the cross-sectional area assuming an elliptical cross-section. Three sets of photobleached lines (PBL) (4 lines, 80 µm apart) were bleached at the sample center and ±1.5 mm from the center. Samples were then loaded to failure in 2% grip-to-grip strain increments. After each increment, samples were allowed 20 min of stress relaxation and then image stacks were acquired at all PBL locations. The stage positions of the two peripheral PBL sites were used to calculate the macroscale tissue strain. Fibril strains were calculated using custom MATLAB code as the change in distance between the individual photobleached lines at each site[5]. The fibril:tissue strain ratio was calculated by dividing the mean fibril strain by the bulk tissue strain at each increment.

Differential scanning calorimetry (DSC) was performed to determine the degree of functional collagen crosslinking in developing tendons and paralysis/BAPN treatments[7]. Samples were hermitically sealed in an aluminum pan, equilibrated at 30°C, and then ramped to 80°C at 3°C/min. Endotherms were analyzed using TA Universal Analysis software for peak denaturation temperature and total enthalpy of denaturation (ΔH). The percentage of enthalpy absorbed at a lower peak temperature (Peak 1 ΔH / Total ΔH) was calculated to assess the relative amount of collagen with reduced crosslinking.

SB³C2022-027

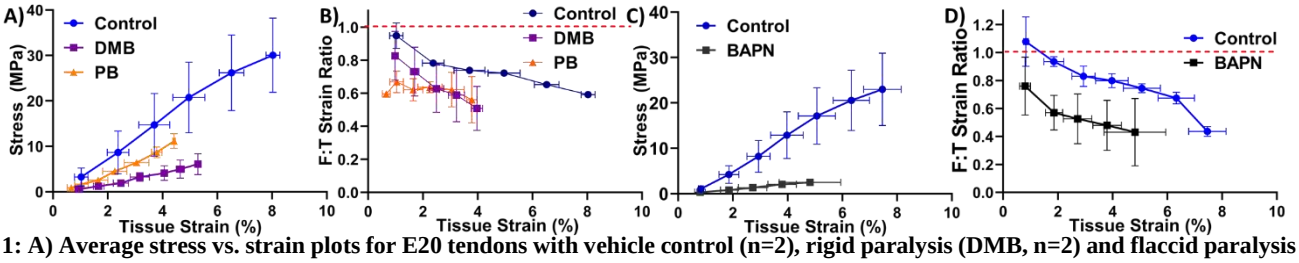


**Figure 1: A) Average stress vs. strain plots for E20 tendons with vehicle control (n=2), rigid paralysis (DMB, n=2) and flaccid paralysis (PB, n=2). B) The decrease in the fibril:tissue strain ratio with applied strain with paralysis was not significant (DMB: p = 0.32, PB: p = 0.35) C) Average stress vs. strain plot for E20 tendons with vehicle controls (n=2) and LOX inhibited (BAPN, n=4) treatment. D) The fibril:tissue strain ratio was significantly reduced with LOX inhibition (p < 0.01).**

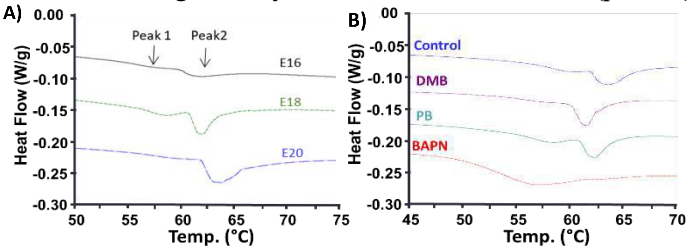


**Figure 2: A) Representative endotherms as a function of development. Arrows mark the two peaks of enthalpy absorption. B) Representative endotherms of E20 tendons after rigid paralysis (DMB), flaccid paralysis (PB), or LOX inhibition (BAPN).**

Statistical differences in fibril:tissue strain ratio were evaluated using a linear mixed model with strain as a covariate. A one-way ANOVA with a Dunnett's post-hoc test was used to evaluate differences in modulus and thermal properties with respect to paralysis or BAPN treatments. A one-way ANOVA with a Tukey's post-hoc test was used to evaluate differences in thermal properties as a function of development. Significance was set at $p < 0.05$.

## RESULTS

Both forms of skeletal paralysis significantly reduced the macroscale modulus of developing tendons (Control: 462 ±86.2 MPa, DMB: 125 ± 49.0 MPa p<0.001, PB: 249.8 ± 19.3 MPa p< 0.05) (**Fig. 1A**); however, there was no change in the fibril:tissue strain ratio (DMB: p=0.31, PB: p=0.35). BAPN treatment significantly impaired the macroscale modulus (51.41 ± 31.84 MPa, p<0.001) (**Fig.1C**) and reduced the fibril:tissue strain ratio in comparison to vehicle control (p< 0.01) (**Fig. 1D**). With development, increases in the total enthalpy (p<0.05) and the peak temperatures (p<0.01) were observed (**Fig. 2A, Table 1**). Paralysis treatments resulted in no change in total enthalpy, but PB treatment increased the proportion of enthalpy absorbed by temperature peak 1 (p<0.05). Both PB & DMB paralysis reduced peak denaturation temperatures ($T_{Peak}$) (p<0.05) in comparison to controls (**Table 1**). BAPN treatment created a large shift in the endotherm curve (**Fig. 2B),** characterized by a significant increase in the relative enthalpy absorbed in peak 1 (p<0.001) and a reduction in peak temperatures (p<0.05) despite no net change in total enthalpy.

## DISCUSSION

This study has demonstrated that, while tendon development requires musculoskeletal activity and LOX mediated crosslinking, they are independent of each other. That is, while both paralysis and BAPN treatments caused similar effects on tendon multiscale mechanics, they exhibited very different effects on functional crosslinking as measured via DSC. This is evident from the endotherm curves (**Fig. 2B**) and the amount of enthalpy absorbed at the lower temperature peak (**Table 1**). Specifically, nearly 90% of the enthalpy required for denaturation occurred in peak 1 for BAPN treated tendons, which is characteristic of an abundant population of collagen with reduced crosslinking[7].

**Table 1: Thermal properties of embryonic tendons as a function of development or paralysis/crosslink inhibition. Statical comparisons for development are done with respect to E20 timepoint and treatments are compared to respective controls. * p< 0.05, ** p<0.01, *** p<0.001**

| | *ΔH(J/g)* | | *$T_{peak}$ (°C)* | |
|---|---|---|---|---|
| | Total ΔH | Peak1 ΔH/TotalΔH(%) | Peak 1 | Peak 2 |
| *E20 (n=4)* | 2.56±0.46 | 6.39±4.95% | 59.67±0.33 | 63.05±0.57 |
| *E18 (n=4)* | 1.97±0.22 (ns) | 20.86±2.0%(*) | 58.47±0.23(*) | 62.29±0.30(*) |
| *E16 (n=4)* | 0.88 ±0.18 (**) | 16.4±7.97% (ns) | 57.02±0.15(***) | 61.46±0.22(***) |
| *Control (n=4)* | 2.06±0.48 | 7.28%±5.99% | 59.46±0.38 | 63.18±0.46 |
| *PB (n=3)* | 1.67±0.06 | 24.87%±9.76%(*) | 57.77±0.17(**) | 62.04±0.25(*) |
| *DMB (n=3)* | 1.91±0.59 | 4.25%±2.18% (ns) | 57.61±0.47(**) | 61.74±0.36(**) |
| *Control (n=3)* | 2.53 ±0.43 | 3.11%±1.03% | 57.93±0.95 | 63.60±0.25 |
| *BAPN (n=3)* | 2.88±0.43(ns) | 88.04%±5.99%(***) | 57.28±0.64(ns) | 62.85±0.04(*) |

Consistent with prior studies showing a decrease in LOX activity after paralysis[5], there was an increase in the Peak 1 ΔH / Total ΔH in the PB treated animals. However, the overall net effect is minimal in comparison to the direct LOX inhibition. This suggests that functional collagen crosslinking is not dependent on muscle activity and that the effect of muscle paralysis on tendon mechanics is not due to decreased crosslinking. This further reinforces the conclusion from previous work that impaired tendon development with loss of muscle activity is due to an impairment of collagen fibril elongation.

Interestingly, rigid muscle paralysis (DMB treatment) at E13 resulted in a significant reduction in the macroscale modulus (**Fig. 1A**). This conflicts with our prior findings that induced paralysis two days later at E15[4], suggesting that embryos in our earlier work were not fully immobilized. The similar effect of both rigid and flaccid paralysis suggests that there is no difference between complete unloading and static tendon loading and that limb motility is the stimulation driving tendon development. While the reduction in the fibril:tissue strain ratio was not significant for both paralysis treatments, this was likely due to a small sample size (n=2)[4]. It was also interesting that BAPN treatment significantly reduced the fibril:tissue strain ratio, indicating that collagen crosslinking is necessary to transmit load between the fibrils. It is possible that this is due to a weakening of small diameter collagen fibrils that possibly transfer load between the larger diameter collagen fibrils in tendon[8]. Additional work is required to characterize the unique effects of muscle paralysis and crosslink inhibition on the hierarchical collagen network and the mechanisms of interfibrillar load transfer.


## ACKNOWLEDGEMENTS

This work was funded by the NIH (R21 AR075941).


## REFERENCES


[1] Shearn et al., *JMNI*, 2011; 1**1(2)**: 163-73
[2] McBride et al., *Int. J. biol. Macromol*., 1998; **10(4):**194-200
[3] Birk et al., *Dev. Dyn*., 1995: **202(3)**:229-43
[4] Peterson et al., *Fron. Cell Dev. Biol., 2021:* **2471**
[5] Peterson et al., *Acta Biomat*., 2020; **117**:302-3
[6] Pan et al., Phil. *Trans. R. Soc. B*., 2018; **373** 20170325
[7] Horgan et al., *Arch. Biochem. Biophys.*, 1990; **281**(1):21-26
[8] Szczesny et al., *J. Orthop. Res.*, 2017; **35**(10):2127-2134

# A NEONATAL PULSE OXIMETER DESIGNED FOR RAPID AND SAFE ATTACHMENT IN THE RESUSCITATION ROOM

**I. Salafian (1), C. Klunk (2), C. Rylander (1)**

(1) Department of Mechanical Engineering
The University of Texas at Austin
Austin, TX, USA

(2) Department of Pediatrics
The University of Texas at Austin – Dell Medical School
Austin, TX, USA

## INTRODUCTION

Red blood cells carry hemoglobin molecules in the bloodstream, delivering oxygen to peripheral tissues and returning to the lungs where deoxygenated hemoglobin can again bind to oxygen. Pulse oximeters measure the percentage of absorbed light in circulating hemoglobin bound to oxygen, or the ratio of oxygenated to deoxygenated hemoglobin. Pulse oximeters emit two frequencies of light through the hand, foot, and ear of infants or fingertip of adults, then, a sensor on the other side of the appendage detects how much light and of what frequency was absorbed by the hemoglobin in the bloodstream [1]. The sensors' data is then displayed to an external reader showing the percentage of the patient's hemoglobin that is bound to oxygen of the patient.

Pulse oximetry is commonly used in delivery rooms, especially during the resuscitation of newborns requiring some assistance to begin breathing at birth. Around 10 million of 136 million babies born annually require assistance to breathe at birth. Each year 1.03 million neonatal deaths result from complications of prematurity and 814,000 from intrapartum-related events in term babies (previously "birth asphyxia") [2]. Within the first minutes of an infant's life, doctors must obtain an accurate oxygen saturation level and electrocardiogram (ECG) signals as well as provide adequate thermoregulatory, respiratory and circulatory support, and administer intravenous medications and fluids as needed. Both oxygen saturation levels and the ECG determine the next course of action for the infant's treatment. As the provider works through the neonatal resuscitation algorithm, if any of these aspects are below standard, the doctor must quickly support the establishment of breathing and circulation [3]. The initial rapid establishment of adequate oxygenation and ventilation is of such importance to neonates that this first sixty seconds of resuscitative effort has been named "the Golden Minute."

During the resuscitation process, there are several problems in obtaining an accurate and reliable reading from the pulse oximeter. The main problem is to provide a secure and rapid attachment of the pulse oximeter device to the infant's hand or foot. Most pulse oximeters for neonatal applications use an adhesive band to secure the device as shown in Figures 1a, b. [4].


**Figure 1a.: Hand attachment of a Masimo Pulse Ox band**


**Figure 1.b: Foot attachment of a Masimo Pulse Ox band**

In the hand attachment method, a natural response from infants after birth is to ball their hands into a fist. Opening the infant's hand to attach the device can be difficult, dangerous to fingers, and time-consuming. Both in hand and foot attachment, the alignment of the emitter with the sensor on each side is difficult to achieve because of the difference in body size of each infant. Even though the balled hand problem does not exist in the foot attachment, the adhesive (in both hand and foot) is often ineffective because of the presence of some combination of vernix, amniotic fluid, blood, and meconium [5]. Cleaning away these substances can be time-consuming in a situation where time is of the essence. The adhesive can also be dangerous to neonate's skin,

especially premature neonates during the removal. In addition, when the device is fully attached, a consistent contact pressure of sensor and the emitter is required for reliable and accurate reading. Extraneous motion can detach the sensor and cause false alarms and erroneous readings from the device [5]. In neonates, extraneous movement can include kicking, stretching, crying, and flexing, as well as the movement created by providers administering cardiopulmonary resuscitation to an otherwise unresponsive patient. Other reasons a pulse oximeter may give inaccurate readings include ambient light interruption and low light perfusion [6]. Inaccuracies in pulse oximetry can leave providers in the dark making their determination of correct treatment method very difficult. Lastly, the previously mentioned Pulse Ox band requires two hands from the neonatologist or nurse for attaching the device to the baby's hand or foot.

In this paper, we developed and prototyped a pulse oximeter device with a clamping mechanism for rapid, secure, and safe attachment to the infant's hand or foot. Using this device, the neonatologists can attach the sensors with only one hand, ensuring a perfect alignment of sensors at all times with consistent contact pressure.

## METHODS

As mentioned in the last section, an accurate and reliable reading of pulse oximeter sensors requires adequate alignment of emitter and sensor, minimizing the movement of sensors, and providing a consistent sensor contact on the skin to maintain light transmission from the emitter to the detector. This also serves to protect fragile skin and soft tissue. In addition, in a neonatal resuscitation process, a fast while safe attachment of sensors may be lifesaving. To meet all the requirements above, we developed a spring-loaded (0.879 in.lbs) parallel clamping mechanism where the top clamp is padded (using medical-grade silicone gel) and the bottom clamp is a solid bar with round edges and a soft and smooth surface to help to open a balled (fist) hand if needed (Figure 2). Each clamp has a sensor mounted on the surface. The hook and loop band at the tip of the clamps ensures the device is not sliding out of the infant's hand due to the sudden movements during the reading.

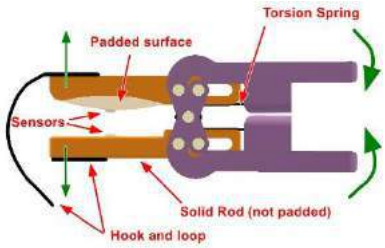


**Figure 2.a: Our clamping Pulse Ox when open**

**Figure 2.b: Clamping Pulse Ox when closed**

The main risk associated with our device is the amount of force applied to the infant's hand. Our device is designed to provide a gentle pressure to avoid any damage to the skin, bones, or underlying soft-tissue while maintaining contact. To measure the force created by the clamps, a Sparkfun SEN-09376 force sensitive resistor is placed between the clamps and the analog signal is measured using an Arduino Mega 2560. The same experiment is conducted on a Masimo neonate Pulse Ox and a Face Lake fingertip Pulse Ox (Fig 3a, b, and c).

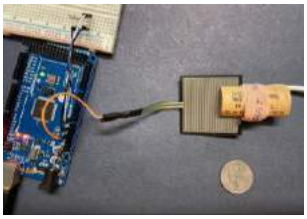

**Figure 4.a: Masimo neonate Pulse Oximeter**

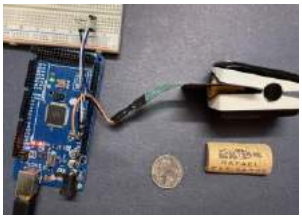

**Figure 4.b: Face Lake fingertip pulse oximeter**

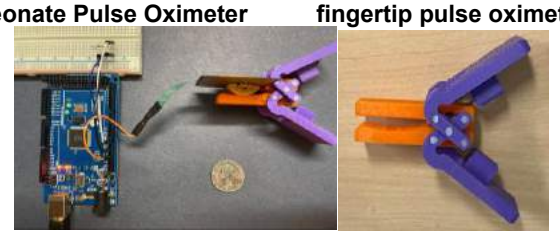

**Figure 3.c: Our parallel clamp device prototype**

## RESULTS

The results of these experiments showed that the force from the Masimo device was 0.05 lb., the Face Lake device was 0.524 lb. and our device was 1.75 lb. These results show that our force is larger than the other two devices and needs to be lowered down to a safe value by choosing a lighter spring while providing a secure connection during the reading. The 0.05 lb. from the Masimo Pulse Ox band is not adequate to provide consistent pressure. Therefore, we decided to use the 0.5 lb. force value from the fingertip device as our baseline for choosing the new torsion spring since our attachment mechanism is more similar to this device where it ensures that the device won't slide off the patient's finger during the screening process. Since the load value needs to be reduced to 0.5 lb. from 1.75 lb. (3.5 times less), the torsion spring load should be lowered to 0.879/3.5=0.251 in.lbs. Using this spring, we ensure that a secure connection with consistent pressure is provided while the baby's hand is protected.

## DISCUSSION

Our pulse oximeter device provides fast, easy, secure, and reliable attachment of the sensors to the infant's hand during the resuscitation process. Unlike the hinged fingertip device that touches the skin in a slope with varied force (higher closer to the hinge), our device with parallel attachment mechanism always provides consistent pressure across the contact surface. Also, our device can be easily mounted by one hand with no adhesives to avoid damaging the infant's skin in a wet environment.

## ACKNOWLEDGEMENTS

A special thanks to Emily Cazes and Sarah Cheatham, undergraduate students at the University of Texas at Austin, for their collaboration in this project.

## REFERENCES

[1] Lee, A, et al., *BMC public health*, 10.1186/1471-2458-11-S3-S12, 2011.
[2] Wyckoff, M. H., et al., *Neonatal Resuscitation*, 10.1161/CIR.0000000000000267, 2021.
[3] (Newborn Critical Congenital Heart Disease (CCHD), https://www.masimo.com/siteassets/us/documents/pdf/plm-10060a_sales_tool_cchd_screening_adhesive_sensor.pdf
[4] Petterson, M. T., et al., *Anesthesia and analgesia*, 10.1213/01.ane.0000278134.47777.a5, 2007.
[5] Dawson, J. A., et al., *Archives of disease in childhood. Fetal and neonatal edition*, 10.1136/adc.2006.102749, 2007.

# DEPENDENCE OF VAGINAL TISSUE CREEP BEHAVIOR ON APPLIED LOAD

**J. Dubik (1), D. Dillard (1), K. Miller (2), R. De Vita (1)**

(1) Department of Biomedical Engineering and Mechanics, Virginia Tech, Blacksburg, Virginia, United States of America
(2) Department of Biomedical Engineering, Tulane University, New Orleans, Louisiana, United States of America

## INTRODUCTION

Of the nearly 4 million women who give birth each year in the U.S., roughly a third undergo Cesarean delivery [1], where the baby is delivered via an abdominal incision rather than vaginally. This rate is one of the highest in the world, more than double that of the global average and the upper limit on medically necessary Cesarean deliveries as estimated by the WHO [2]. Cesarean deliveries introduce risk of maternal morbidities [3]. While the United States Department of Health and Human Services has identified a need to reduce the number of Cesarean procedures performed in the United States, there are currently no scientific-based criteria for their recommendation or administration [4].

Cesarean procedures are intended for cases when the mechanically intensive process of vaginal delivery is not possible or safe for a mother, avoiding trauma to the vaginal canal such as lacerations. As such, knowledge on the mechanical properties of vaginal tissue could provide a basis for deciding when Cesarean sections are recommended and performed. There is currently a paucity of knowledge on the viscoelastic properties of the vaginal canal. In this study, we utilize free-extension inflation to characterize the creep behavior of the rat vagina under biaxial loading.

## METHODS

The vaginal canals of 10-week-old virgin female Sprague Dawley rats were isolated via dissection. Cross-sectional images were captured under dissection microscope, from which vaginal radius and thickness were measured using ImageJ (NIH, Bethesda, MD). Specimens (n=13) were mounted onto vertically aligned concentric dispensing needles as described in [5], such that one needle could freely extend from the other as the vagina was inflated (Figure 1). Once mounted, the specimens were speckled with spray paint to create a pattern for non-contact strain measurements using digital image correlation (DIC).

Specimens were submerged in a phosphate buffered saline (PBS) bath during testing. Specimens were preconditioned to 150% of their initial volume and back for 20 cycles by a computer-controlled syringe pump. After a 600 second rest period, the specimens were then inflated with PBS to 4 psi for 50 minutes (creep test 1), then immediately to 8 psi for 50 minutes (creep test 2), then immediately to 12 psi for 50 minutes (creep test 3). There was no rest period between creep tests. Throughout testing, two CMOS cameras (Basler ace acA2440-75$\mu$m, Basler Inc., Exton, PA) captured images of the dorsal wall of the specimens at a rate of 2 Hz as the pressure increased and 0.2 Hz under constant pressures.

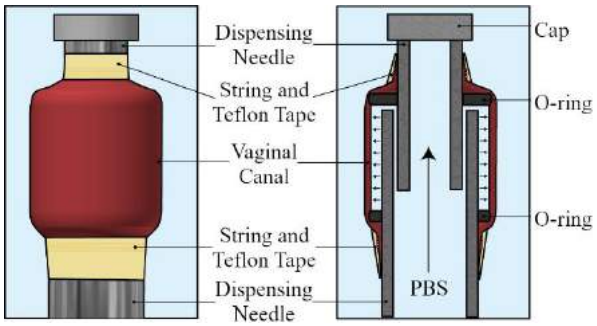


**Figure 1: Vaginal tissue clamped between two concentric needles as described in [5].**

Using these images, 3D DIC software (Vic-3D, version 8, Correlated Solutions, Columbia, SC) was used to calculate the normal axial Lagrangian strains in the longitudinal direction (LD) and circumferential direction (CD) of the vagina. Nominal normal stresses in the LD and CD were calculated assuming the specimens behave as a cylindrical pressure vessel, using the collected pressure data and measured dimensions. A map of the local normal Lagrangian strains in the LD and CD for a representative specimen is shown in Figure 2. As these strains varied across the surface of each specimen, a small circular region with a diameter <1 mm was selected, and the average (across this region) were computed.

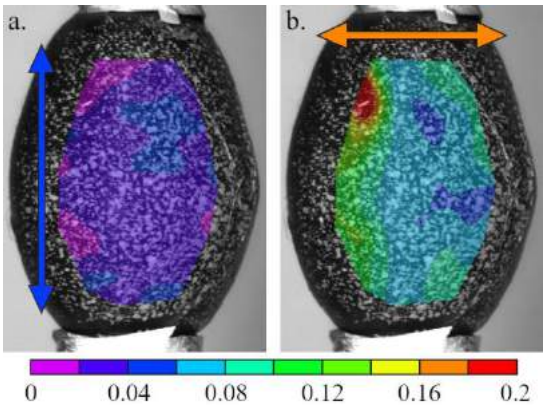


**Figure 2: Maps of axial strains in the LD (a) and CD (b) for a representative vaginal specimen. Blue and orange arrows indicate the orientation of the LD and CD respectively.**

## RESULTS

The average increase in strains over time in the LD and CD from the beginning to the end of each creep test is shown in Figure 3 (n=13).

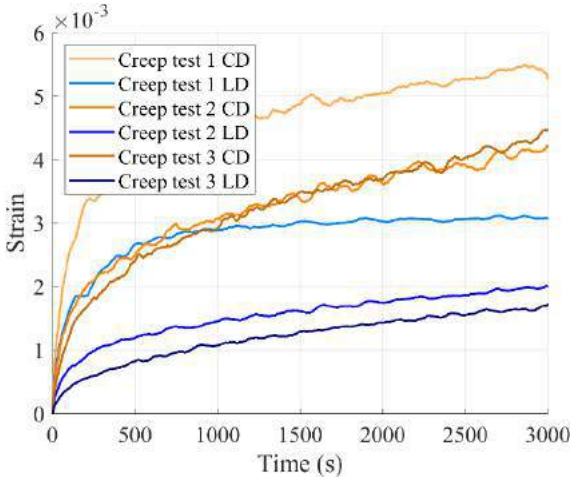


**Figure 3: Average increase in strain over time throughout creep tests 1, 2, and 3 in the CD and LD (n=13).**

The mean increase in strains in the LD and CD at 3000 s into each creep test are reported in Table 1 (n=13). Under paired t-test, the change in strain at 3000 s into each creep test was significantly higher in the CD than in the LD ($p < 0.05$). In the LD, the increase in strain during creep test 1 was significantly higher than the increase in strain during creep test 2 or 3. In the CD, the increase in strain during creep test 1 was significantly higher than the increase in strain during creep test 2. Other comparisons were not statistically significant under paired t-test.

**Table 1: Average (mean ± s.e.m.) increase in strain in the LD and CD at 3000 s into each creep test (n=13).**

| | LD | CD |
|---|---|---|
| Creep test 1 | 0.00309 ± 0.00045 | 0.00534 ± 0.00090 |
| Creep test 2 | 0.00188 ± 0.00021 | 0.00411 ± 0.00045 |
| Creep test 3 | 0.00167 ± 0.00016 | 0.00438 ± 0.00045 |

## DISCUSSION

This study presents the first biaxial study of the creep behavior of rat vaginal tissue at multiple and consecutive levels of pressure/stress. The vaginal specimens were found to strain consistently more in the CD than the LD. The increase in strain was higher during creep test 1 than during creep test 2 or 3. It is likely that the organization and architecture of the collagen fibers, which dictate the mechanical behavior of vaginal tissue, play an important role in reducing the strain experienced by the tissue during creep in the LD and at subsequent pressures/stresses.

In agreement with Clark-Patterson et al. [6], our experimental data showed that increasing pressure/stress does not lead to a proportional increase in strain during creep. Although the results are not included in this data set, several specimens ruptured during creep at 12 psi (creep test 3). This could indicate that the structural mechanism which acts to decrease the amount of strain from the first to second creep test fails at higher pressure/stress, possibly due to tissue damage.

This work represents a crucial first step in understanding the complex mechanical behavior of vaginal tissue. Investigations which pair further viscoelastic mechanical studies with microstructural investigations will provide critical key insights into why and how the behaviors observed in this study occur. Furthermore, future studies will investigate how the mechanical properties investigated here change throughout pregnancy to anticipate childbirth. This in turn will provide information for setting universal criteria for the recommendation and administration of Cesarean procedures.

## ACKNOWLEDGEMENTS

This work was supported by NSF grant no. 177844. Rats were provided for testing by the Jarome Lab at Virginia Tech.

## REFERENCES

[1] Martin, J. et al., *Natl Vital Stat Rep*, 2019, 68(13)
[2] Gibbons, L. et al., *World Health Report*, 2010, 30
[3] Maconges, G. et al., *Am J Obstet Gynecol*, 2005, 193:1656-1662
[4] WHO Childbirth Recommendations, 2018
[5] McGuire, J. et al., *Interface Focus*, 2019, 9(4)
[6] Clark-Patterson, G. et al., *J Biomech Eng*, 2021, 143:121008

# CHARACTER IMPEDANCE WITH EXERCISE TESTING CORRELATES WITH RIGHT VENTRICULAR-PULMONARY ARTERIAL COUPLING IN ISOLATED POSTCAPILLARY PULMONARY HYPERTENSION

**Christopher G. Lechuga (1), Farhan Raza (2), Naomi C. Chesler (1)**

(1) University of California, Irvine Edwards Lifesciences Foundation Cardiovascular Innovation and Research Center and Department of Biomedical Engineering University of California, Irvine Irvine, CA, USA

(2) Division of Cardiovascular Medicine University of Wisconsin - Madison Madison, WI, USA

## INTRODUCTION

Pulmonary hypertension (PH) is present in ~70 million people globally and almost always leads to a mismatched right ventricular (RV)-pulmonary arterial (PA) relationship (RV:PA uncoupling), resulting in right heart failure (RHF) [1]. The gold standard method of PH diagnosis involves right heart catheterization (RHC) to measure mean pulmonary arterial pressure (mPAP), pulmonary arterial wedge pressure (PAWP), and pulmonary vascular resistance (PVR) [2]. However, during early disease stages at rest, the pulmonary vasculature can compensate, leading to misdiagnosis and an average three-year diagnosis/treatment delay [3]. Recently, exercise testing has been shown to detect and diagnose at these early stages of PH, improving clinical intervention and prognosis [3].

Even when PH assessment incorporates exercise testing, however, diagnosis relies on PVR, which is primarily based on steady pulmonary hemodynamics, ignoring the innate pulsatile component in pulmonary vasculature [4]. By contrast, pulmonary vascular impedance (PVZ) captures the relationship between pulsatile pressure and flow, which depends on arterial stiffness and lung compliance [5, 6]. To date, only a few studies have quantified PVZ during exercise [7, 8] and none have investigated correlation with RV:PA uncoupling.

Therefore, our goal was to measure and analyze the relationship between metrics of PVZ, including characteristic impedance ($Z_C$), and RV:PA coupling during exercise in subjects with PH. We hypothesize that increases in $Z_C$ with exercise will correlate with RV:PA uncoupling.

## METHODS

**Subject Population.** 10 adult subjects (5 female, 5 male) referred for invasive cardiopulmonary exercise testing (iCPET) were enrolled in a multi-step, rest-to-exercise-to-recovery study protocol. Enrolled subjects were in WHO Group I (pulmonary arterial hypertension; PAH, n = 3), II (PH due to left heart disease; PH-LHD, including both Ipc-PH and Cpc-PH, n = 5), and IV (PH due to chronic thromboembolism; PH-CTEPH, n = 1) or did not have PH (n = 1). The study protocol was described to all subjects, who provided informed consent (IRB ID: 2019-1184).

**Invasive CPET & Echocardiogram.** All subjects underwent iCPET in the semi-recumbent position utilizing a cycle ergometer [9]. This assessment included simultaneous RHC at rest and exercise, with simultaneous pulsed-wave Doppler (PWD) echocardiography of the right ventricular outflow tract (RVOT). Then, subjects performed exercise with 2-minutes of unloaded peddling, followed by an incremental ramp protocol at 10 Watts/min (60 RPM on ergometer at all times). At every 25 Watts, the incremental protocol was held at that stage, and simultaneous PAP (via Millar catheter) and RVOT PWD were acquired. After peak symptom-limited exercise, simultaneous PAP and echocardiographic doppler data were acquired 5-minutes into recovery.

**Real-Time Pressure-Volume Loop Acquisition.** Simultaneous pressure-volume (PV) data were obtained with a high-fidelity conductance catheter (CD Leycom, Zoetermeer, Netherlands) inserted and advanced into the RV cavity near the apex [10].

**Pulmonary Vascular Impedance Analysis.** From the continuously obtained, time-dependent, PA pressure (P) and flow (Q) waveforms, the time domain characteristic impedance ($Z_C$) at rest, exercise, and recovery was estimated by the "up-slope" method of the P-Q relationship during early systole for varying threshold percentages of the maximum flow rate ($Q_{max}$), which was based on an iterative linear fit and sum of squares process [5]. $Q_{max}$ threshold percentages ranged from 40-80%, with a mean threshold of 56%.

**Right Ventricular, Pulmonary Arterial Coupling Analysis.** RV:PA coupling was determined by the ratio of end-systolic to arterial elastances ($E_{es}/E_a$), which were derived from RV PV loops and pressure waveforms, for each subject at all stages of protocol following the second derivative single beat method [11, 12].

**Statistical Analysis.** Linear regression and two-tailed Pearson's correlation coefficient analyses were used to assess the relationship and significance between $Z_C$ and RV:PA coupling during exercise. p-value $\leq 0.05$ was considered significant. $R^2 \leq 0.40$ was considered a weak linear relationship, $0.40 \leq R^2 \leq 0.70$ was considered a moderate linear relationship, and $R^2 \geq 0.70$ was considered a strong linear relationship.

## RESULTS

**Association Between $Z_C$, RV:PA Coupling, and Exercise.** The small sample sizes for Cpc-PH (n = 1) and No PH (n = 1) prevented statistical analysis and drawing conclusions for these groups. There was a significant negative relationship between RV:PA coupling and $Z_C$ in the Ipc-PH group during exercise (**Fig. 1A;** slope = -28.94, $R^2 = 0.48$, $p \leq 0.05$), which was absent in the pre-capillary PH group (**Fig. 1B**). Moreover, in the pre-capillary PH group, $E_{es}/E_a$ was weakly positively correlated with $Z_C$ during exercise (slope = 13.03, $R^2 = 0.08$). When only focusing on the exercise segments of the protocol (i.e., excluding rest and recovery stages), RV:PA coupling correlated even more strongly with $Z_C$ in the Ipc-PH group ($R^2 = 0.73$, $p \leq 0.05$) but remained non-significantly correlated with $Z_C$ in the precapillary PH group ($R^2 = 0.08$, $p > 0.05$).

## DISCUSSION

The current study confirms that measuring impedance and ventricular pressure-volume loops during exercise provide a comprehensive assessment of cardiopulmonary disease that can be used to better understand the pathophysiology of disease. Our main finding is that $E_{es}/E_a$ and $Z_C$ exhibit a significant, strong inverse correlation in Ipc-PH, but not pre-capillary PH (**Fig. 1**). The lack of relationship between $E_{es}/E_a$ and $Z_C$ in pre-capillary PH is supported by recent findings from Ravallette, which investigated 47 PAH subjects that were grouped based on disease severity [13]. However, these findings were limited to analyses at rest. Further interpretation of our results reveals that in Ipc-PH there may be a threshold (~0.016 mmHg*s/mL), above which $Z_C$ negatively correlates with $E_{es}/E_a$. In our data, below this threshold, the correlation is weaker, the data are more spread out, and all Ipc-PH subjects were at rest or in recovery. Alternatively, exercise may generate a unique relationship between $Z_C$ and RV:PA coupling in Ipc-PH, further supporting exercise's diagnostic impact.

Furthermore, in the Ipc-PH subjects, it appears that as exertion increases, the change in pulsatile hemodynamics deteriorates the RV:PA relationship, which is intact at rest. Recently, two unrelated studies had similar findings, where $Z_C$ increased with exercise in PAH and RV:PA coupling decreased with exercise in PH-LHD [8, 14]. Thus, our study marries these two concepts and reveals a unique uncoupling trend in Ipc-PH with $Z_C$ during exercise. Moreover, our study provides novel correlative information. Finally, in the event that invasive PV data cannot be collected either at rest or exercise, our findings suggest that Ipc-PH subjects whose $Z_C$ increases with exercise experience RV:PA uncoupling with exercise, and thus warrant closer monitoring.

The current study has two main limitations: 1) small sample size for all groups and 2) not all subjects achieved all stages of exercise.

Overall, our findings suggest metrics of pulsatile hemodynamics with exercise reveal distinctive relationships within two PH subgroups, which may not be present at rest. The causal factors responsible for these correlations have yet to be determined.

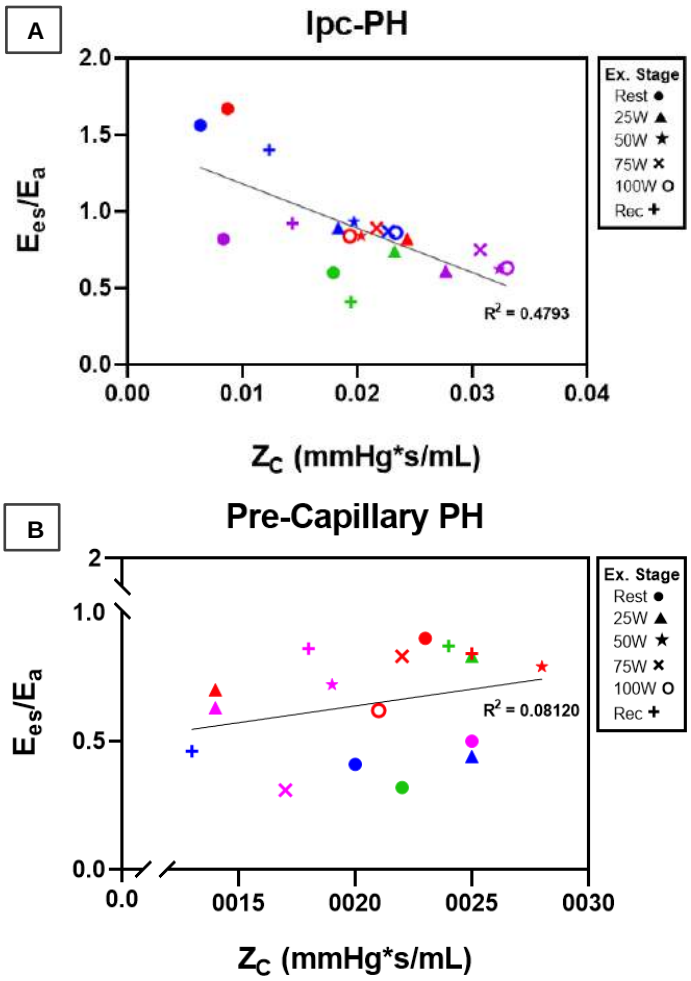


**Figure 1: Correlation comparison between RV:PA coupling ($E_{es}/E_a$) and characteristic impedance in the time domain ($Z_C$) for A. Ipc-PH (n = 4) and B. pre-capillary PH (n = 4). In each group, every subject is shown using a distinct color symbol.**


## ACKNOWLEDGEMENTS

Research reported in this publication was supported by the National Heart, Lung, And Blood Institute of the National Institutes of Health under Award Number T32HL116270.


## REFERENCES


[1] Rosenkranz, S et al., *Circulation*, 141(8):678-693, 2020. [2] Al-Omary, MS et al., *Hypertension*, 75(6):1397-1408, 2020. [3] Sabbahi, A et al., *Expert Review of Respiratory Medicine*, 14(3):317-327, 2020. [4] Vanderpool, RR et al., *Annals of Biomedical Engineering*, 38(5):1854-1861, 2010. [5] Qureshi, MU et al., *Physiol Meas*, 39(1):014004-014004, 2018. [6] Chesler, NC et al., *Annu Int Conf IEEE Eng Med Biol Soc*, 2009:177-180, 2009. [7] Naeije R, Chesler N, *Comprehensive Physiology*, 2(1):711-741, 2011. [8] Karvasarski, E et al., *Canadian journal of cardiology*, 37(10):S63, 2021. [9] Berry, NC et al., *Pulm Circ*, 5(4):610-618, 2015. [10] Tran, T et al., *J Hear Lung Transplant*, 40(2):128-137, 2020. [11] Bellofiore, A et al., *J Appl Physiol*, 124(2):283-290, 2018. [12] Vanderpool, RR et al., *Heart (British Cardiac Society)*, 101(1):37-43, 2014. [13] Ravallette K, Bachelor's Thesis, The University of Arizona, 2020. [14] Bellofiore, A et al., *Heart (British Cardiac Society)*, 103(6):421-427, 2017.

SB³C2022
Summer Biomechanics, Bioengineering and Biotransport Conference
June 20-23, Eastern Shore, MD, USA

# A SMART-PIV APPROACH FOR IN VITRO EVALUATION OF CORONARY HEMODYNAMICS

**Elena Torta (1), Giuseppe C. A. Caridi (1), Claudio Chiastra (1), Diego Gallo (1), Umberto Morbiducci (1)**

(1) Polito$^{BIO}$Med Lab, Department of Mechanical and Aerospace Engineering, Politecnico di Torino, Turin, Italy

## INTRODUCTION

In the last two decades, Particle Image Velocimetry (PIV) has become a reliable measurement technique for the in vitro characterization of the local fluid dynamics in presence of cardiovascular pathologies (e.g. atherosclerosis, aneurysms) or implantable medical devices (e.g. stent, aortic valve). PIV-based experimental measurements play a fundamental role in validating/verifying in silico models and/or in the design/optimization of cardiovascular devices, contributing to the minimization of safety and ethical issues associated with animal and human experiments [1,2,3]. The wide use of PIV in cardiovascular applications is hampered by the high costs of its components, i.e. high-power lasers, high speed cameras and synchronization units (order of magnitude of 100 k€). Recently, attempts have been made to use alternative test benches adopting e.g. video cameras embedded inside commercial smartphones [4]. A further strength point of turning to lower-cost PIV systems whenever possible is given by the possibility to adopt low-energy light sources requiring much less energy as well as less safety procedures and standards (EN 207 in EU; ANSI z136 in US) than pulsed lasers commonly used in standard PIV applications (the latter belonging to Class 4, IEC 60825-1 i.e. the highest and most dangerous class of laser). In this regard, the feasibility of adopting the combination of a smartphone camera and a continuous wave laser for reliable velocity measurements has been already demonstrated in air and water flows [4]. These alternative approaches, when applicable, have allowed a scaling down of the costs to an order of magnitude of 1 k€.

The present study explores the feasibility of adopting a test bench based on the use of smartphone cameras and low energy light source (referred to as smart-PIV approach in the following) for cardiovascular applications. In detail, (1) smart-PIV is adopted to analyze the flow field in realistic phantoms of healthy and stenotic coronary arteries, and (2) the hemodynamic results are compared with the ones obtained from standard PIV measurements.

## METHODS

The adopted smart-PIV experimental set up is presented in Figure 1. The study was conducted in realistic silicone phantoms of coronary arteries manufactured applying a molding technique by Elastrat (Geneva, Switzerland). One phantom consisted in a patient-specific replica of a healthy left circumflex coronary artery with a diameter of 3mm reconstructed from angiographic images (healthy case). The second phantom represented a diseased condition, through an artificially generated 67% diameter stenosis obtained by locally reshaping the healthy model (stenotic case).

Measurements were carried out under steady state flow conditions, spanning flow rates within a range of 80-100 mL/min for the healthy model and of 10-80 mL/min for the stenotic one, according to in vivo measurements [5]. An ultrasonic flow meter (Transonic, Ithaca, NY, USA) was used to monitor the flow rate. A 60/40 water to glycerin mixture was used as a working fluid in order to match the kinematic viscosity and density of blood. Polyamide particles (density 1030 kg/m$^3$, diameter 60 μm) were used as tracers. In the smart-PIV set-up, a smartphone camera and a low-power continuous laser (30mW) were used. Specifically, the camera of a Samsung Galaxy S9+ (12800x720 pixels, 960 Hz) smartphone was adopted for the time-resolved, high frame rate image acquisition, resulting in an image resolution of 34 μm/pixel (healthy case) and of 26 μm/pixel (stenotic case) and a temporal resolution of 1040 μs. In the standard PIV set-up (Dantec Dynamics A/S, Denmark), one HiSense Zyla camera (CMOS, 2560x2160 pixels) and the Bernoulli 200-15 Dual Pulsed Nd:YAG laser (nominal pulse energy of 200 mJ at 15 Hz) were adopted. The image pair interval Δt ranged between 90-900 μs, while the image resolution was of 20 μm/pixel (healthy case) and of 16 μm/pixel (stenotic case). The MATLAB® (MathWorks, Natick, MA, USA) toolbox PIVlab was adopted to postprocess the acquired images using the ensemble-correlation method [5].

SB³C2022-031

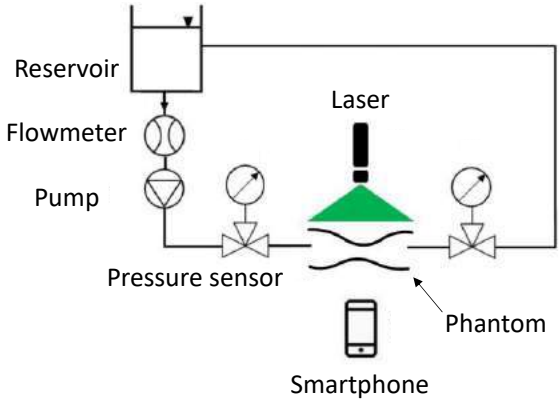


**Figure 1: Experimental smart-PIV set-up. The same hydraulic circuit is maintained for the standard PIV measurements.**

## RESULTS

The comparison between smart-PIV and standard PIV measured 2D velocity vector fields in the healthy and stenosed coronary artery phantoms is shown in Figure 2. In detail, the smart-PIV approach is capable to capture the main flow features identified by the conventional PIV approach, in particular those acceleration regions (one in proximal segment and one in the distal segment) locally dictated by the irregular shape of the healthy vessel phantom (Figure 2-a). The agreement between measurements, which is satisfactory in the central region of the vessel, is moderate in the near wall region. The two PIV-based approaches catch the flow features of the stenotic vessel with a very good agreement (Figure 2-b), in particular (1) the increase in fluid velocity caused by the area reduction in the stenotic region, where the classical jet-like flow configuration is properly detected, and (2) the typical post-stenotic recirculation region. The capability of the smart-PIV approach in identifying local flow features in the stenotic vessel is testified by the results displayed in Figure 3, where the expected expansion/stretching of a stable recirculation region distal to the stenosis in consequence of an increasing flow rate is properly measured.

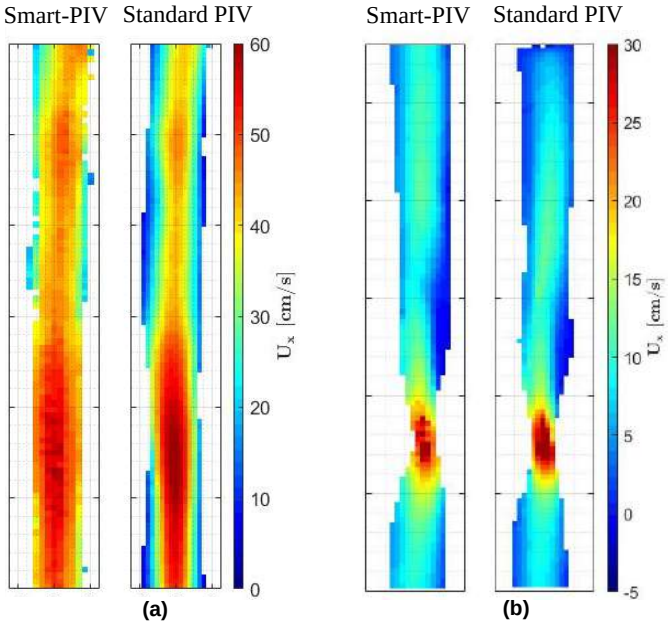


**Figure 2: Axial velocity maps in (a) healthy LCX phantom ($Q_{inlet}$= 80mL/min), and (b) stenotic LCX phantom ($Q_{inlet}$= 30mL/min).**

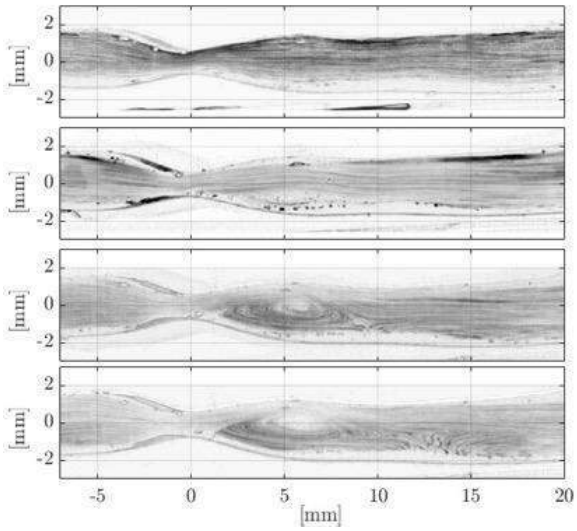


**Figure 3: Flow patterns visualization in the stenotic LCX phantom at (from top to the bottom): 10-30-50-80 mL/min.**

## DISCUSSION

In this study the feasibility of using a smart-PIV approach for the in vitro characterization of healthy and stenosed coronary flows in patient-specific phantoms is explored. Corroborated by standard PIV measurements, the findings of this work support the possibility of employing a low-cost, low-energy consumption, easily maneuverable acquisition system for the characterization of cardiovascular flows [4]. In the very next years, the expected speed up of smartphone-based technologies could allow to use the experimental test bench proposed here for e.g. the rapid and economic characterization of more complex flow fields such as the ones observed in the presence of implantable devices. At this stage of the investigation, the limited smartphone camera image acquisition frame-rate still hampers the wide application of the proposed set-up to the in vitro characterization of e.g. prosthetic heart valves. In relation to the presented coronary artery flow characterization, the limitation in the smartphone camera acquisition frame-rate explains the strong reported agreement between smart-PIV and standard PIV at low-to-moderate flow regimes in the stenotic phantom, while it underwent measurement degradation in the stenosis region at the highest flow regimes, where blur particles generated by continuous illumination and intense spatial gradients might affect the quality of the measured flow field (data not shown).

In conclusion, an easily reproducible and maneuverable, secure, low-cost and low-energy consumption set-up for the in vitro characterization of cardiovascular flow is proposed. Thanks to the decrease in terms of costs and the increase in terms of security, the smart-PIV system can be used for educational and research purposes for low-cost practical investigations, thus expanding the use of PIV in biomedical applications.

## REFERENCES

[1] Geoghegan, P.H. et al., *Fluids*, 54:1528, 2013
[2] Medero, R. et al., *Ann Biomed Eng*, 48:2484-2493, 2020
[3] Freidoonimher, N. et al., *Fluids*, 62:133, 2021
[4] Cierpka, C. et al., *Fluids, 57(6):1-10*, 2016
[5] Kessler, W. et al., *Int J Card Imaging*, 14(3):179-186, 1998

# A SEMI-SUPERVISED LEARNING ALGORITHM FOR EFFICIENT AND ACCURATE MRI-BASED 3D GEOMETRIC MODEL RECONSTRUCTION OF PELVIC ORGANS

**Fei Feng (1), James A. Ashton-Miller (2), John O. L. DeLancey (3), Jiajia Luo (4)**

(1) University of Michigan-Shanghai Jiao Tong University Joint Institute
Shanghai Jiao Tong University
Shanghai, China

(2) Department of Mechanical Engineering
University of Michigan
Ann Arbor, MI, USA

(3) Department of Obstetrics and Gynecology
University of Michigan
Ann Arbor, MI, USA

(4) Biomedical Engineering Department
Peking University
Beijing, China

## INTRODUCTION

Pelvic organ prolapse is a common condition requiring surgery in 1 of 7 women. High operative failure rates of 25% occur because of a limited understanding of its pathophysiology. Important progress in identifying causal mechanisms has come from 3D analysis of magnetic resonance (MR) images as well as finite element analysis of prolapse, but obtaining a geometric model is an essential but time-consuming step that mainly depends on the image segmentation process. Deep learning methods such as convolutional neural networks (CNNs) have shown advantages in improving the accuracy and efficiency of biomedical image segmentation. Training data are crucial for model performance, but large datasets are difficult to collect and the annotation of biomedical images is expensive, tedious, and time-consuming, further limiting the number of labeled images used for training. Therefore, there is a need to find an approach to reduce the annotation burden for CNN training in biomedical applications.

Since there are usually more images that are not annotated, some researchers have investigated how to utilize unlabeled data through unsupervised learning methods[1-4]. Self-supervised learning (Self-SL) is one of the unsupervised learning methods that uses only unlabeled data to learn general knowledge by creating proxy tasks. But if a few labeled training data are available, these can be used as a reference to guide the CNN training and to evaluate the model performance. So the present method utilizes both labeled and unlabeled data making it a semi-supervised learning (semi-SL) method. The semi-SL method not only reduces the need for labeled data, but also ensures that the model can learn knowledge from manual annotations[5], which is promising for biomedical applications[6].

In this work, we aimed to investigate a semi-supervised algorithm for 3D geometric model reconstruction of pelvic organs using MR images. More details are elaborated below.

## METHODS

To take advantage of both labeled data and unlabeled data, a semi-SL framework was designed (Fig. 1). The training framework had two stages. In the first stage, CNN 1 was trained using the unlabeled MR images for the image restoration task. Next, CNN 2 was trained using the pre-trained weights of CNN 1 to segment using labeled MR images to end the first stage. In the second stage, CNN 2 was used to perform pseudo-label prediction on the unlabeled images. In this stage, the training process of CNN 3 utilized both unlabeled data and labeled data. CNN 3 was also initialized with weights of CNN 1 at the beginning of training. During the forward propagation, CNN 3 was used for the prediction of labeled and unlabeled data. During the backward propagation, the total loss included both the supervised loss and the unsupervised loss, and the CNN 3 weights were updated according to the total loss. These steps are described in detail below.

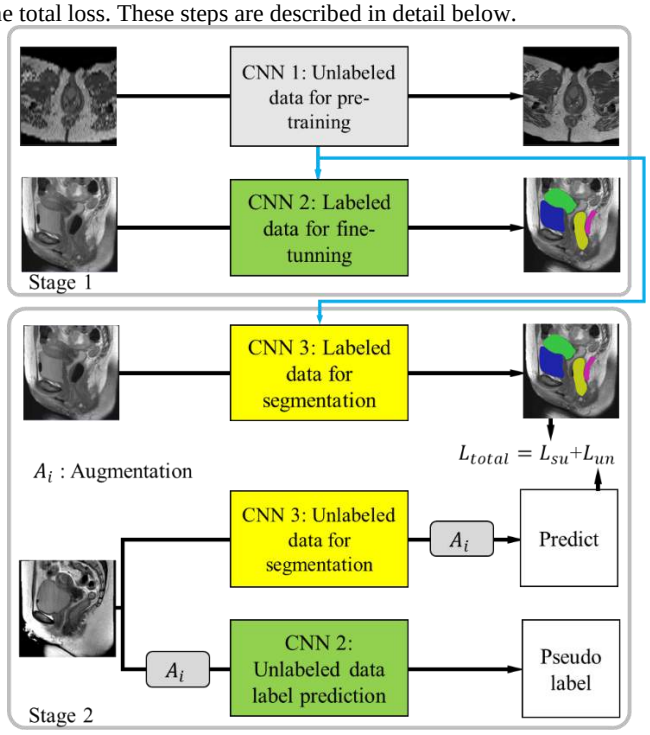


Figure 1: The semi-SL framework for pelvic organ segmentation. Notes: CNNs 1-3 share the same model structure but different weights. $A_i$: Augmentation of rotation and scaling.

In the self-SL step, the image restoration task was used as a proxy task. The image degradation equation was expressed as follows:

$$I^{d}_{\downarrow r_x S_y}(x,y) = I(x \cdot r_x, S(y)) \quad (1)$$

where $I^d$ is the degraded image and $I$ is the original high-resolution image. $r_x$ represents the downsampling ratio and $S(\cdot)$ is the shuffle operator. During downsampling, the downsampling ratio was set to 1:4, 1:6, and 1:8, respectively. The loss function, L1 loss, was defined as:

$$Loss_{CNN1} = \frac{1}{MN}\sum_{m,n}^{M,N} |g_{mn} - r_{mn}| i \quad (2)$$

where $M$ and $N$ are the length and width, respectively. $g_{mn}i$ and $\dot{r}_{mn}$ are the pixel values of the high-resolution image and the predicted image of CNN 1, respectively.

Then CNN 2 was trained using the labeled segmentation data. The loss function is the cross entropy (CE), which was defined as:

$$\text{CE} = \sum_{l=1}^{L}\sum_{n} -t_{ln}\, log(m_{ln}) \quad (3)$$

where $L$ is the total segmentation classes. $t_{ln}$ represents the pixel values of the ground truth and $m_{ln}$ represents the segmentation mask of the $l^{th}$ class at the $n^{th}$ position. CNN 1 trained in the previous step was used for the model initialization of CNN 2.

Next, the weights of CNN 1 weights were used for the initialization of CNN 3. In the semi-supervised training, there are two branches, namely the labeled branch and the unlabeled branch. The total loss was represented as follows:

$$L_{total} = L_{su} + L_{un} \quad (4)$$

where $L_{total}$ represents the total loss, $L_{su}$ represents the supervised loss, and $L_{un}$ represents the unsupervised loss. $L_{su}$ is computed by evaluating the difference between the prediction and the manual annotation. $L_{un}$ was calculated by evaluating the difference between the prediction and the pseudo label predicted by CNN 2. The unsupervised branch was trained using the mean square error (MSE) loss defined as follows:

$$MSE = \frac{1}{L*N}\sum_{l=1}^{L}\sum_{n}(t_{ln} - m_{ln})^2 \quad (5)$$

where $N$ represents the number of pixels for output.

Finally, the segmentation performance was evaluated using the Dice similarity score (DSC), defined as follows:

$$DSC = 2\frac{\sum_{l=1}^{N}\sum_{n} t_{ln} m_{ln}}{\sum_{l=1}^{N}\sum_{n}(t_{ln}+m_{ln})} \times 100 \quad (6)$$

An Adam optimizer was used for training on an NVIDIA TITAN RTX graphics card with 24 GB of computational memory. The CNN was trained for 800 epochs with a learning rate of 0.0002.

To explore the effectiveness of the semi-SL, we used a dataset that included 48 MR series (4103 images), from the Michigan Pelvic Floor Research Collection with ethical approval, scanned in the axial, coronal, and sagittal planes. From the total, 16 MR series (1442 images) were selected for uterus and urinary bladder annotation, and 32 MR series (2661 images) remained unsegmented for self-SL. The labeled MR images were divided into model training (902 images) and testing (540 images) sets. In the testing dataset, 180 images were used for the optimal model validation. Besides, the segmentation performance of vanilla UNet-based baseline[7], self-SL, and semi-SL were compared using different numbers of training images (182, 362, 542, and 722 images).

## RESULTS

A comparison of segmentation performance is shown in Fig. 2. It shows that the segmentation results of semi-SL were consistently better than those of baseline and self-SL when the same number of images were used for training. It also shows that when semi-SL was performed using data from six subjects, the performance was close to the segmentation results of the baseline using data from ten subjects. Similarly, when using the same number of images, self-SL always had better segmentation performance than the baseline. This also shows that the segmentation performances of all three methods improve as training images increases.

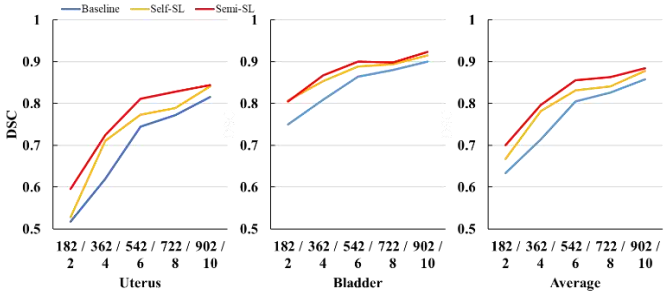


Figure 2: Segmentation performance using U-Net with a different number of training images. 902/10 refers to 902 images from 10 subjects.

For individual organs, the DSCs of the bladder were always better than those of the uterus with the same number of training images. However, the DSC of the uterus improved significantly with the number of images.

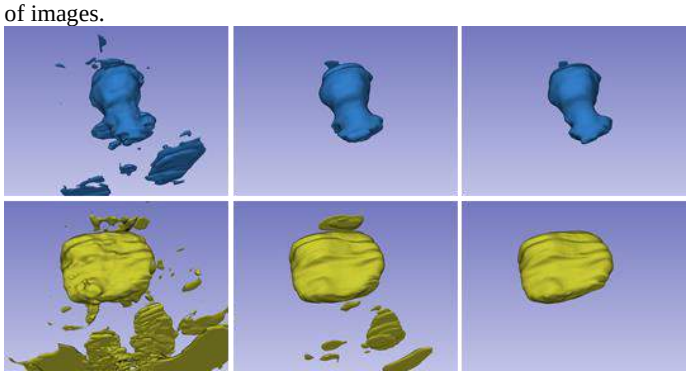

Figure 3: Comparison of the results of the 3D geometric model reconstruction of the uterus (Blue) and urinary bladder (Yellow). The first column shows the baseline results with 542 images. The second and third columns are the results of semi-SL with 542 images and 902 images, respectively.

Fig. 3 shows the results of the 3D geometric model reconstruction for three different configurations. When training with 542 images, the semi-SL (second column) clearly reduced artifacts compared to baseline (first column). The results in the second column are similar to those in the third column, which also demonstrates the effectiveness of the proposed method for reconstruction with less training data. Besides, the average segmentation time for a single MR image is 0.022 seconds.

## DISCUSSION

A semi-SL algorithm was designed to improve the segmentation performance of pelvic organs by utilizing both labeled and unlabeled data. This algorithm proved efficient and accurate for the segmentation and 3D geometric model reconstruction of pelvic organs. In the future, we plan to evaluate the effectiveness of its extension in clinical settings.


## ACKNOWLEDGEMENTS

We appreciate the following financial support: NSFC 31870942, Peking University Clinical Medicine Plus X-Young Scholars Project PKU2020LCXQ017 and PKU2021LCXQ028, PKU-Baidu Fund 2020BD039, NIH R01 HD038665 and P50 HD044406 grants.


## REFERENCES


[1] Doersch, C., *et al. ICCV* 2015. [2] Chen, X., *et al.* arXiv:2003.04297, 2020. [3] Chen, T., *et al.* arXiv:2006.10029, 2020. [4] Chen, T., *et al.* arXiv:2002.05709, 2020. [5] French, G., *et al.* arXiv:1706.05208, 2017. [6] Li, X., *et al.*, IEEE TNNLS, 2021. **32**(2): p. 523-534. [7] Ronneberger, O., *et al. MICCAI 2015*.

# MULTISCALE MODELING OF RESTENOSIS AFTER PERCUTANEOUS TRANSLUMINAL ANGIOPLASTY: TOWARDS A PATIENT-SPECIFIC ANALYSIS

**A. Corti (1), M. Colombo (1,2), C. Celikbudak (3), P. Büchler (4), F. Migliavacca (1), S. A. Berceli (5,6), S. Casarin (7,8,9), J. F. Rodriguez Matas (1), C. Chiastra (1,10)**

(1) Dept. of Chemistry, Materials and Chemical Engineering “Giulio Natta”, Politecnico di Milano, Milan, Italy
(2) Institute for Chemical and Bioengineering, Dept. of Chemistry and Applied Biosciences, ETH Z□rich, Switzerland
(3) □cole polytechnique fédérale de Lausanne, Lausanne, Switzerland
(4) Institute for Surgical Technology and Biomechanics, University of Bern, Bern, Switzerland
(5) Dept. of Surgery, University of Florida, Gainesville, FL, USA
(6) Malcom Randall VAMC, Gainesville, FL, USA
(7) Dept. of Surgery, Houston Methodist Hospital, Houston, TX, USA
(8) Center for Computational Surgery, Houston Methodist Research Institute, Houston, TX, USA
(□) Houston Methodist Academic Institute, Houston, TX, USA
(10) PoliTo$^{BIO}$Med Lab, Dept. of Mechanical and Aerospace Engineering, Politecnico di Torino, Turin, Italy

## INTRODUCTION

Restenosis is a frequent complication of percutaneous transluminal angioplasty (PTA) in the femoral arteries, which is responsible for the low primary patency rate at 1-year follow-up (~60%) [1]. The PTA-induced injury (i.e., endothelial denudation and arterial wall damage) has been recognized to trigger the inflammatory-driven arterial wall response, characterized by vascular cell activation leading to abnormal tissue re-growth [2]. Moreover, altered hemodynamics after the intervention modulates vascular cell activity, contributing to the overall remodeling of the arterial wall [3]. Besides the biomechanical factors, different systemic and biological events are involved in the complex multifactorial and multiscale process that determines the arterial wall response to PTA, whose complete understanding is lacking. Multiscale computational modeling, integrating continuum- with agent-based methods, has the potential to improve the current knowledge of the underlying pathological pathways by simulating the interrelated mechanobiological events [4]. Accordingly, the present work proposes a fully-automated multiscale agent-based modeling framework that replicates arterial wall remodeling after PTA by integrating the effects of the PTA-induced wall damage and post-intervention hemodynamics on cellular activities.

## METHODS

Figure 1 shows schematically the developed multiscale framework of restenosis following PTA. The framework was applied to an idealized model of a diseased femoral artery and consists of three modules, namely: (i) a PTA module, in which a finite element (FE) analysis of PTA was performed and the post-PTA arterial configuration and wall damage were determined; (ii) a hemodynamics module, in which the wall shear stress (WSS) of the deformed arterial configurations was computed using computational fluid dynamics (CFD) simulations; (iii) a tissue remodeling module, in which a 2D agent-based model (ABM) first replicates arterial wall remodeling of several cross-sections by simulating cellular and extracellular matrix (ECM) dynamics in response to the computed arterial wall damage and WSS, and in a second step reconstructs the 3D arterial lumen geometry from the ABM outputs.

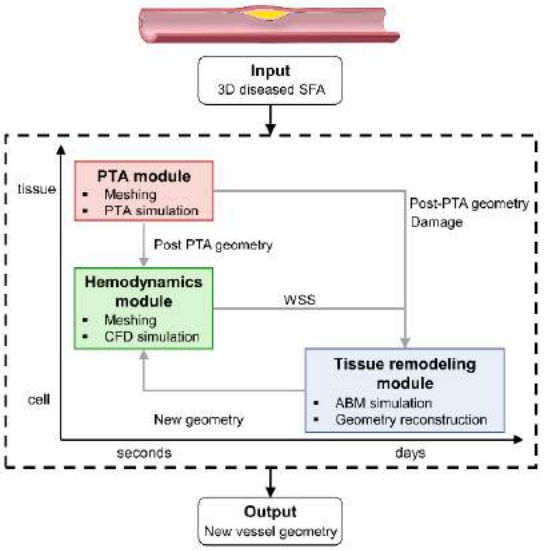


**Figure 1: Multiscale framework of restenosis after PTA.**

The framework was applied for a follow-up time of 3 months. At each simulated post-operative month, the hemodynamics and tissue remodeling modules are coupled, so that the hemodynamics is calculated in the current remodeled arterial geometry and the WSS input to the cellular activities is updated.

For the PTA module, hyperelasticity was considered to model the arterial wall tissues. The material properties were derived from experimental data of human femoral arteries [5],[6]. The ductile damage model available in Abaqus (Dassault Systèmes Simulia Corp.) was adopted to compute the amount of damage of each intima element. Regarding the hemodynamics module, steady-state CFD simulations were performed in the deformed artery models using Fluent (Ansys Inc.) to compute the WSS profile along the luminal wall. A parabolic velocity profile (flow-rate of 200 mL/min [7]) was applied at the inlet, while a reference pressure was applied at the outlet. An ABM for 19 evenly-spaced arterial cross-sections was created using Matlab (MathWorks) by adapting our previously developed ABM of atherosclerosis to the restenosis scenario [8]. Specifically, a three-layered arterial wall ABM structure was created by importing the nodal coordinates of the 19 cross-sections from the FE model. Each layer was populated with cells, ECM and plaque (in the intima of the diseased portion) agents. Probabilistic rules were defined to control the behavior of cells and ECM according to their local damage and WSS inputs. As for the damage-related input (*Dinput*), the FE-computed damage was considered as a weight of a generic post-operative inflammatory curve [9], according to the hypothesis that regions exposed to higher trauma (i.e., higher damage) lead to a more intense inflammatory response. Regarding the WSS-related input (*WSSinput*), luminal regions exposed to low WSS were associated to a high *WSSinput*, which promotes increased cellular activity.

After 1 simulated month, the ABM simulations were stopped, a new 3D arterial geometry was reconstructed from the ABM outputs and the hemodynamics – tissue remodeling modules sequence was repeated until the desired follow-up time (3 months).

## RESULTS

The virtual PTA resulted in an increase in lumen area of ~25% in the treated vessel portion and caused a mild damage (up to ~0.35), with the largest values localized at the plaque side in the intima layer. The hemodynamics in the post-operative arterial configuration presented three regions, namely (i) the healthy extremities were characterized by WSS ~ 0.5 Pa, (ii) the central atherosclerotic portion with a WSS > 1 Pa, and (iii) the region downstream of the plaque with a WSS < 0.05 Pa. Both the PTA-induced damage and the WSS were used to initialize the ABM, simulating the monthly post-operative remodeling of the arterial wall. Figure 2 shows details of the ABM evolution of 2 explanatory arterial cross-sections and the remodeled arterial geometry obtained at month 3. The most important intimal growth was observed at the most vulnerable regions (i.e., those with elevated damage levels and low WSS), with a lumen area reduction of ~25% at plane 10 (plane with the highest damage) and of ~50% at plane 15 (plane exposed to very low WSS). Overall, a median restenosis of 27% was obtained at 3 months, with the greatest reduction in lumen area occurring during the first post-operative month. Moreover, a heterogeneous lumen area reduction was found along the artery, due to the development of a focal restenosis pattern, in particular at month 3 (Figure 2).

## DISCUSSION

A novel multiscale framework of restenosis at the cell-tissue scale was developed to mimic the 3-month arterial wall remodeling following PTA procedure in an idealized, diseased SFA model. The framework captured the early inflammatory-driven cellular activation due to the PTA-induced wall damage and the long-lasting hemodynamic-driven arterial wall remodeling. In particular, the combination of the 2 biomechanical factors allowed us to detect relevant features of the vascular adaptation process to PTA, namely: (i) localization of the greatest intimal growth in the regions exposed to high damage and low WSS; (ii) a 3-month lumen area restenosis of 27%, in accordance with clinical observations in femoral arteries [10]; and (iii) temporal dynamics of the lumen area characterized by 3 phases (early severe reduction of the lumen area, followed by stabilization and late focal narrowing), as observed in stented femoral arteries [11].

Based on these promising results, the application of the framework to patient-specific cases of SFAs treated with PTA is ongoing, as shown in Figure 3 for an explanatory patient-specific arterial cross-section. Accordingly, the present study lays the foundation for an in-silico model of restenosis that can be used to predict the remodeling of the entire lumen area following endovascular interventions in patient-specific scenarios.

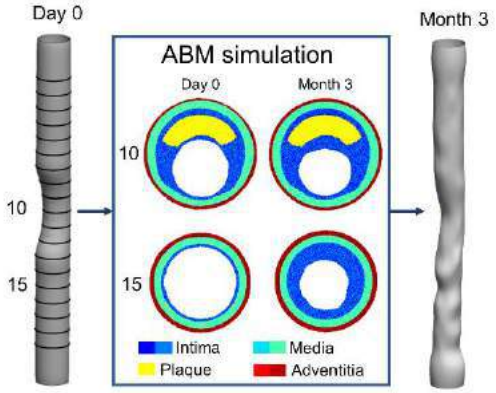


**Figure 2: Arterial wall remodeling along 3 post-operative months.**

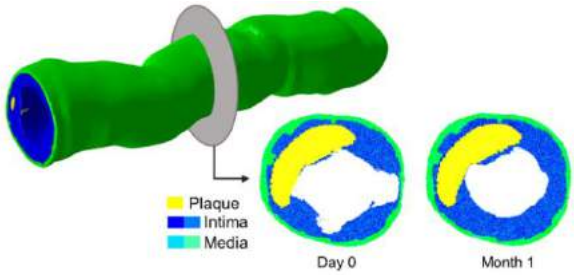


**Figure 3: Patient-specific application of the multiscale framework.**


## ACKNOWLEDGEMENTS

The work has been supported by Fondazione Cariplo, Italy (Grant number 2017-0792, TIME).


## REFERENCES


[1] Katsanos, K. et al. *Cardiovasc. Intervent.Radiol.* 37: 592–603, 2014.
[2] Parmar, J. H. et al. *Ann. Vasc. Surg.* 23: 569–576, 2009.
[3] Chistiakov, D. A. et al. *Acta Physiol. (Oxf).* 219: 382–408, 2017.
[4] Corti, A. et al. *Front. Bioeng. Biotechnol.* 9: 744560, 2021.
[5] Prendergast, P. J. et al. *J. Biomech. Eng.* 125: 692–699, 2003.
[6] Cunnane, E. M. et al. *Acta Biomater.* 11: 295–303, 2015.
[7] Holland, C. K. et al. *Ultrasound Med. Biol.* 24: 1079–1086, 1998.
[8] Corti, A. et al. *Comput. Biol. Med.* 118: 103623, 2020.
[9] Edelman, E. R. et al. *Am. J. Cardiol.* 81: 4E-6E, 1998.
[10] Wyttenbach, R. et al. *Circulation* 110: 1156–1161, 2004.
[11] Colombo, M. et al. *Ann. Biomed. Eng.* 2021.

SB³C2022
Summer Biomechanics, Bioengineering and Biotransport Conference
June 20-23, Eastern Shore, MD, USA

# A COMBINED MECHANICAL AND BIOLOGICAL APPROACH TO QUANTIFY FAILURE IN HUMAN SKIN

**J. Hayes (1), C. Higgins (2), M. Masen (1)**

(1) Department of Mechanical Engineering, Imperial College London, London, UK
(2) Department of Bioengineering, Imperial College London, London, UK

## INTRODUCTION

Lower limb prosthetics have proven to be an extremely successful intervention, providing mobility to people with congenital limb deficiencies and traumatic amputations. However, retention rates among lower limb amputees are very low, with 22% of amputees abandoning their prosthesis within 1 year and 29% of amputees using their prosthetic only indoors after 1 year [1]. It is generally accepted that device abandonment associated with high levels of injuries from usage, with 63% of amputees reporting one or more skin problems [1]. Injury of the residuum skin at the socket interface is a commonly reported issue among prosthesis users [2]. Prosthesis wear time 4 months after amputation is reported as less than 8 hours per day and mean time walking on the device is 3.4 hours a day [3], this low wear time is consistent with high reports of skin injuries in lower limb amputees [4]. Current prosthetics research puts heavy emphasis on manufactured components, i.e., socket and joint articulation, not much work has been undertaken to understand how the skin interacts in the coupling with the prosthetic device. To achieve adequate function, a lower limb prosthetic requires extreme resilience from the skin on the limb stump. During use, all loads are transferred through the socket-skin interface, meaning the skin is subjected to significant loading through shear stresses. These increased demands on the skin may result in a variety of injuries, as non-plantar skin is not specialised for loading. In this study we look to find tissue tolerance levels by quantifying the response to mechanical loading through cellular mechanisms like apoptosis.

## METHODS

In this study we look at how loading type and duration affect tissue viability, as quantified by cleaved caspase-3 expressed in the compressed and the uncompressed case. We use 8 mm punches of human abdominal skin sampled from tissue discarded after abdominoplasty.. The samples are then transferred to the top of a 0.45 µm nylon membrane placed on a nonwoven gauze in a 35 mm dish. William's E media (1.5 ml) supplemented with 1% Penicillin/Streptomycin 2 mM L-glutamine, 10 µg/ml insulin and 10 ng/ml hydrocortisone is added to the nonwoven gauze in each well.[5]

Prepared samples are subjected to loading through biomomentum indentation and use of a novel nanotribometer [6] for shear loading. Specimens are embedded in optimal cutting temperature compound (OCT compound) and sectioned at 14 µm and mounted onto microscope slides. Analysis of caspase expression is achieved with immunofluorescent microscopy techniques using a confocal microscope for image acquisition and Icy for post processing image analysis.

We aim to determine the difference in cell death compared to a control specimen; cell death is quantified with use of cleaved caspase-3 (a protein used to execute programmed cell death in response to increasing cell damage).

## RESULTS

Figures 1 and 2 show fluorescent microscopy images of fixed human abdominal skin sections, with figure 1 showing the unloaded sample and figure 2 the sample after mechanical loading. The composite fluorescent microscopy images presented show intact nuclei (Blue), Collagen VII (Green) and Cleaved Caspase-3 (Red).

Structural changes can be observed between the compressed and uncompressed case. The dermal-epidermal junction is ruptured (arrow), as shown by the basement membrane (green line) in figure 2, indicating that the barrier function of the skin would be compromised, and the tissue may become necrotic.

In both results caspase-3 expression overlaps with the nuclear stain. This is consistent with caspase-3 being translocated to the nucleus during apoptosis, in order to cleave nuclear substrates [7].

In figure 1 (uncompressed case) caspase-3 induced apoptosis is localised close to the dermal-epidermal junction but the remainder of the cells do not express caspase-3. In contrast in figure 2 (compressed

case) caspase-3 expression is found most cells throughout the depth of the tissue section, suggesting a global commitment to apoptosis in the skin as a result of being compressed.

.

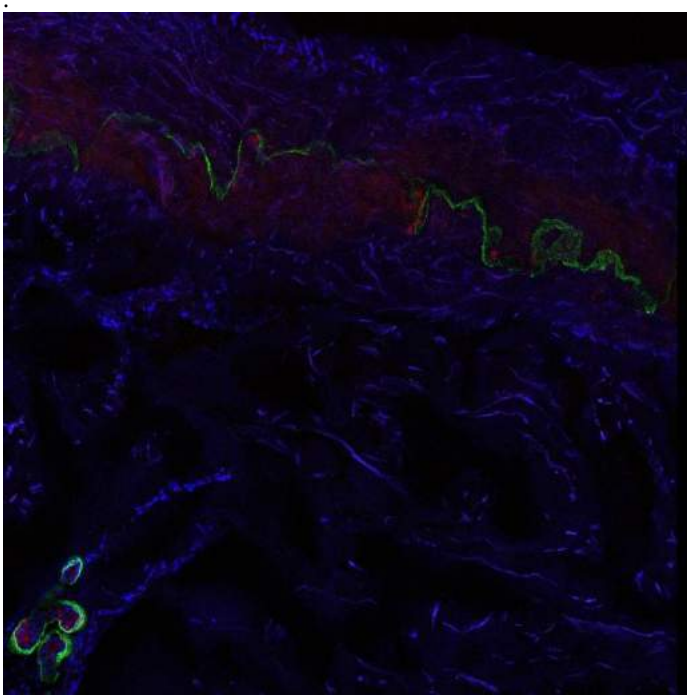

**Figure 1: Uncompressed control immunofluorescent confocal image on 14 µm section of abdominal human skin. Section stained for Nuclei (blue), Collagen 7 (green) and Cleaved Caspase-3 (red)**

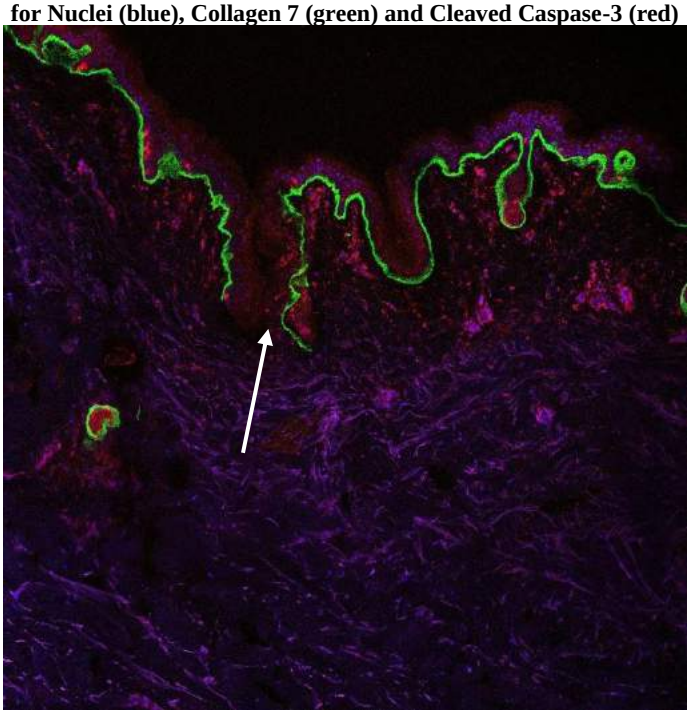

**Figure 2: Compressed control immunofluorescent confocal image on 14 µm section of abdominal human skin. Section stained for Nuclei (blue), Collagen 7 (green) and Cleaved Caspase-3 (red)**

The first set of results indicate that compressive stress has resulted in an upregulation of nuclear caspase-3, indicating an increase in apoptosis. that would suggest that a stress related mechanism of regulated cell death must exist.

## DISCUSSION

The results presented highlight the effects of 6 hours of loading onto human skin and may help explain the high injury prevalence in prosthesis users. We found that loading causes an increase in apoptosis in cells across the tissue, when compared to an uncompressed baseline. In this study we looked at entire tissues in contrast to previous studies on skin load ability, which were performed on single cell layers, thus distorting the stress field for the cells. Therefore, the results presented have more relevance to in vivo applications and provide a meaningful conclusion on how to quantify failure in skin from mechanical insults. A limitation of the study is the small sample size of skin tested, and the unique setup of the experiment prevents direct comparison to the literature. A methodology for assessing cell viability is important and needs to utilise engineering testing procedures with biological failure mechanisms. This study will outline how different loading and time domains effects using the method discussed.

In conclusion increasing the mechanical stimuli causes an upregulation of apoptotic genes and commitment to cell-death by individual cells within the tissue. There is, however, a lack of critical understanding on whether a critical stress level exists, and if so, what this critical stress level would be. Current work focuses on how duration of mechanical insults affect tissue viability and how the presence of shear affects cell death, as these are two factors of great importance in current prosthesis technology. Better understanding on how stress-initiated apoptosis occurs is pivotal to improving regenerative medicine and prosthesis technology to prevent skin failure from prosthesis wear.


## ACKNOWLEDGEMENTS

EPSRC Centre for Doctoral Training (CDT) in Prosthetics and Orthotics (P&O), a combination of the Universities of Salford, Strathclyde, Southampton and Imperial College.


## REFERENCES


[1] LeMoyne, R., *Advances for prosthetic technology*, 2016.

[2] Koc, E et al., *International journal of dermatology*, *47*(5), pp.463-466. 2008.

[3] Balk, E.M et al., *Comparative Effectiveness Review, No. 213 Report No.: 18-EHC017-EF*. 2018.

[4] Dudek, N.L et al., *Archives of physical medicine and rehabilitation*, 86(4), pp.659-663, 2005.

[5] Topouzi, H et al., *Journal of Investigative Dermatology*, *140*(5), pp.1075-1084. 2020.

[6] Cobb, J.A et al., *Biotechnology letters*, *30*(5), pp.801-806. 2008.

[7] Luo, Met al., *Cell research*, *20*(2), pp.211-222. 2010

SB³C2022
Summer Biomechanics, Bioengineering and Biotransport Conference
June 20-23, Eastern Shore, MD, USA

# NOVEL BIOMECHANICAL APPROACH TO IMPROVE CONTROLLED CORTICAL IMPACT TESTING FOR STUDYING RODENT CLOSED-HEAD TRAUMATIC BRAIN INJURY

**Emilie A. Potts (1), Lihong Lu (2), Xiaoyun Xu (3), Arthur Brown (3), and Haojie Mao (1, 2)**

(1) Biomedical Engineering, University of Western Ontario, London, ON, Canada
(2) Mechanical and Materials Engineering, University of Western Ontario, London, ON, Canada
(3) Robarts Research Institute, Western University, London, ON, Canada

## INTRODUCTION

Researchers have relied on animal studies for decades, particularly for traumatic brain injury (TBI) studies. These types of studies have aided researchers in obtaining a better understanding of the after-effects and repercussions of the brain following a TBI [1]. Numerous testing methods have been utilized in the past, which can be broken into two categories, open- and closed-head impact systems. Closed-head impact (CHI) systems use either a mechanical force or gravity to conduct an impact on the skull, not penetrating the brain directly, while open-head impact models directly impact the brain. Controlled cortical impact (CCI) and fluid percussion injury (FPI) are popular open-head impact models for rodent studies [2].

Further growth of the CHI model has developed neurotrauma models that report both head kinematics and brain pathology, such as the one called CHIMERA (Closed-Head Impact Model of Engineered Rotational Acceleration) [2]. This model was created to address the gap in knowledge between the translation of animal studies and human cases [2]. Other types include an improved weight drop model to deliver a weight to an animal placed on a foam [3]. With these improved testing methods, researchers can yield a variety of brain-related deficits found in human cases in an animal application. These brain-related deficits can include memory impairment, diffuse axonal injury (DAI), inflammation, and tau accumulation [2], which all can account for life-altering effects.

The CCI testing method has been deeply developed over the past 40 years and is now used to gather a better understanding of the biomechanical properties surrounding brain injuries[1][3][4], specifically investigating the relationship between engineering parameters and biological damage [6]. This testing tool utilizes a mechanical force onto the exposed surface of the brain creating repeatable injuries such as axonal damage, contusions, and neuronal death [4][6]. CCI is chosen over other testing methods as it has a high rate of repeatability, scalability, and user adaptability and control [5]. This device offers the researcher to select different parameters such are depth, velocity, and site of impact [5], allowing the researchers to simulate the severity of TBI that they desire. Although CCI testing has been proven to be a reliable method over the decades, there is always room for improvement for closed-head TBI, and that is where this study comes into play.

In our previous closed-head mild TBI model using the CCI device, mouse heads were placed on a plate, restricting large rotations [7]. Repeated impacts to the head were found to induce mild TBI such as altered levels of synaptic proteins and behavioural deficits in attention and spatial memory [7]. In this study, a new CCI-based model is developed, primarily focused on the rotational properties, as it has been proven that the angular motion of the brain has worsened biological repercussions. When comparing the repercussions of linear motion to angular motion, angular motion significantly outweighs linear motion. In addition, large head rotations were observed in real-world human head impacts and hence were mimicked in this study.

## METHODS

### *Experimental setup*

Similar to traditional CCI tests, a pneumatic CCI impactor machine was utilized to impact the mice head at the bregma, where the coronal suture bisects the midline. Each impact was then recorded with the aid of two highspeed cameras, each camera obtaining a different angle, from lateral and frontal views. To ensure optimal filming conditions, two floodlights were used to illuminate the testing field. The height of the camera and floodlights were adjusted to be the same height as the testing surface. The cameras were placed directly in front of the desired view, while the floodlights were off to the side, with the light beam directed at the subject. A schematic diagram is depicted below in Figure 1. Before testing, the camera settings were adjusted accordingly, and the camera view was zoomed in to eliminate unneeded background to ensure easy tracking of the mouse movement in later steps.

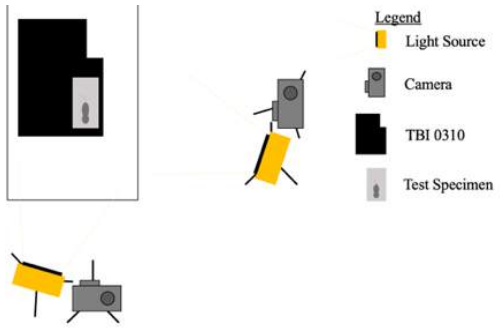


**Figure 1: Schematic diagram of experimental setup**

***Testing Specimen Preparation***

Each mouse was anesthetized with ketamine (80mg/kg)/xylazine (10mg/kg) and was placed in a custom-designed head cover with trackable dots. The mouse was then placed on a transparent plastic film that was secured to a transparent container and moved into the testing field.

***Data Collection***

Before each impact, the cortical impactor (Traumatic Brain Injury Device (TBI) 0310) was calibrated and centered over the intended impact site. Each impact was recorded by two observers to eliminate movement between cameras, as excessive movement would introduce vibrations to the video. After each impact, the recorded video was trimmed to the impact event to limit the amount of memory being used.

Once the impact occurred, the plastic film supporting the mouse would break due to the force of the impact, and the mouse would freefall on to a cushion at the bottom of the container. An example of the movement can be seen in Figure 2. The container and supporting film were transparent to ensure tracking of the mouse movement was not obscured during the recording.

For initial 5 m/s, single-impact tests, four small female and two large male mice were tested. For 3.5 m/s, triple-impact tests four small female and 16 small male mice were tested, and each mouse was impacted three times; the three impacts were done in consecutive days (one hit per day for 3 days), resulting in all three hits being conducted within 48 hours. One video recording was lost due to human error (Mouse 0210907-5).

**Figure 2: Example of the tracking of the mice in the lateral (left) and frontal (right) views.**

The set of X and Y values for each point tracker was exported from Tracker and imported into Microsoft Excel (Redmond, Washington: Microsoft Corporation), and later imported into MATLAB (Natick, Massachusetts: The MathWorks Inc.) for further analysis. With the use of MATLAB codes, the angular and linear properties of the mouse head were calculated for 10 ms following impact. The linear data will be presented elsewhere.

## RESULTS & DISCUSSION

A total of 66 laboratory impacts were recorded and preliminary data were analyzed. High-speed videos confirmed large head rotations (>60 degrees) for all impacts. The average angular velocity was determined for three studies. The 5 m/s impact speed study resulted in a 316 rad/s velocity. While the two 3.5 m/s impact speed studies resulted in 287 rad/s for the female mouse study, and 343 rad/s for the male mouse study.

The most significant difference between the described CCI setup and other CCI setups reported in the literature lies in the break-away transparent platform used to support the mouse at impact. In traditional setups, the mouse is rested on a fixed platform, such as a desktop, while the setup herein described has the mouse supported on a tear-away plastic film. The break-away platform promotes more realistic post-impact head movements.

Simulating more organic head movements allows for more clinically relevant data. As seen in Figure 3, this method allows for peak acceleration and velocity at the time of impact to be calculated. However, with this realistic model of concussive injuries, there are factors to be taken into consideration such as impact distance and speed. In traditional CCI testing, impact distance varies between 0.5 to 2 mm as the testing specimen is on a fixed surface and the brain cannot exceed the confines of the skull cavity [3][6]. This present method has an impact distance of 8 mm as the unfixed platform allows the testing specimen to move away from the impactor to prevent serious damage to the brain. Also, regarding impact speed, both 5 and 3.5m/s were tested. However, it was found that 5m/s was too forceful and included lots of axonal staining after single impacts. Despite setting the machines to a specific speed, deviation in speed during the impacts was also noted and needs to be considered in future subject-specific injury analysis.

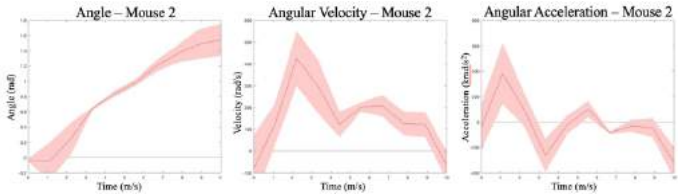


**Figure 3: Standard deviation graphs for Mouse 2, angle (left), angular velocity (center) and angular acceleration (right)**

Having numerous views of the impact is ideal as it allows for verification that the head is rotating along desired axis. The frontal view confirms that the head is moving in a linear downwards motion in the majority of cases. As buckling of the head or moving on a diagonal may introduce more axes of rotation, they are not accounted for in our calculations.

This proposed method shows promise to simulate more realistic head movements following experimental TBI. The unfixed break-away platform allows natural head movements and rotations post-impact, which generates more realistic after-effects when compared to standard CCI testing. Our method has the potential to improve the clinical relevance of CCI small animal (rodent) testing using CCI devices by using popular CCI devices to induce closed-head, large-rotation TBIs.

## REFERENCES

[1] Osier, N. D. et al., *Methods in Molecular Biology*, 1462:177-192, 2016.
[2] Namjoshi, D. R. et al., *Molecular neurodegeneration*, 9:55, 2014.
[3] Li, Y. et al., *Journal of the Neurological Sciences*, 359:280–286, 2015.
[4] Chen, Y. C. et al., *Frontiers in Neurology*, 5:100, 2014.
[5] Osier, N. D. et al., *Frontiers in Neurology*, 7:134, 2016.
[6] Dixon, C. E. et al., *Journal of Neuroscience Methods*, 39:253-262, 1991.
[7] Xu, X. et al., *Acta Neuropathologica Communications*, 9, 2021.

SB³C2022
Summer Biomechanics, Bioengineering and Biotransport Conference
June 20-23, Eastern Shore, MD, USA

# NOVEL *IN VIVO* ARTICULAR CARTILAGE ELASTOGRAPHY PIPELINE TO DETERMINE MECHANICAL PROPERTIES FROM DYNAMIC MRI DEFORMATION ANALYSIS

**Emily Y. Miller (1), Hongtian Zhu (2), Woowon Lee (2) Stephane Avril (3) Corey P. Neu (1,2)**

(1) Biomedical Engineering Program, University of Colorado Boulder, Boulder, CO, USA
(2) Paul M. Rady Department of Mechanical Engineering, University of Colorado Boulder, Boulder, CO, USA
(3) Mines Saint-□tienne, Univ Lyon, Univ Jean Monnet, INSERM, U 105□ Sainbiose, Centre CIS, Saint-□tienne, France

## INTRODUCTION

Elastography is a non-invasive imaging approach that is commonly used to quantify the average and spatially-resolved stiffness of soft tissues of the body. Quantification of material stiffness can provide a powerful approach to understanding structure-function relationships in soft tissues, including load-bearing tissues such as cartilage. In cartilage, softening and decreased stiffness is a functional hallmark of osteoarthritis (OA) pathogenesis due to structural changes to the collagen network and depletion of proteoglycans [1]. Moreover, OA is a degenerative joint disease that is a leading cause of joint pain, disability, and health care costs worldwide. However, diagnosing early-stage OA can be difficult due to a lack of validated outcome measures for individuals with early knee OA [2]. As post-traumatic OA may progress from an initial injury in the superficial zone of cartilage to more widespread biochemical and mechanical changes throughout the zonal tissue cartilage, quantifying changes to cartilage material properties non-invasively *in vivo* is of substantial interest. While elastography seems like an ideal approach to accomplish this, current conventional elastography methods, most commonly using ultrasound, lack the ability to penetrate stiff musculoskeletal tissues such as cartilage due to the dissipation of high frequency shear waves [3].

MRI is unique among imaging tools as it can characterize tissues with high spatial detail, has a deep penetration depth, and can assess tissues non-invasively [4]. Recently, spiral displacement encoded stimulated echo MRI (spiral DENSE) has been used to calculate pixel level full field displacement maps of soft tissues under repetitive motion [5]. In this work, we coupled spiral DENSE MRI to displacement under applied loading MRI (dualMRI) to capture *in vivo* full field displacement and mechanical strain maps of the human knee during varus loading. Material property characterization leveraging full-field information was accomplished by combining both the virtual fields method (VFM) and a constrained FEBio-based optimization method [6, 7]. In summary, we present a proof of concept for one human subject of a combined MRI experimental method and processing pipeline to acquire *in vivo* full field cartilage displacements, and non-invasively quantify cartilage stiffness and Poisson's ratio.

## METHODS

*Varus Loading of Human Knee:* 1 adult female subject, age 25, with a healthy left knee was recruited. An MRI-compatible loading apparatus that provides a varus-valgus load to the tibiofemoral cartilage of the knee was manufactured and validated, leading to compression of the medial femoral condyle (**Fig 1A**). Momentum conservation was used to calculate the load applied on the foot to be equivalent to one-half body weight of load applied at the knee. Following validation, the subject was imaged in a clinical MRI system (3T; Siemens Prisma$^{fit}$) using a cyclic loading regime (pneumatic, 25N load at foot, 1s load,1s unload) to mimic a walking cadence.

*Spiral DENSE MRI:* Spiral displacement-encoded MRI was collected following preconditioning to a quasi-steady-state load-displacement response (**Fig 1B**). A steady-state response was achieved by applying 8 minutes of cyclic loading to minimize the viscoelastic response of articular cartilage. 27 time-sequenced coronal plane DENSE MR images were collected using 8 averages, 10 spiral interleaves, and a temporal resolution of 40ms. Echo time (TE) was 2.5ms and relaxation time (TR) was 20ms. Field of view, slice thickness, and displacement encoding gradient were 125×125μm$^2$, 1.7mm and 0.64cycles/mm, respectively. Total imaging time was 13.6 minutes.

*Displacement and Strain Calculation:* Cartilage and bone regions of interests (ROIs) were manually segmented and binary masks were created to represent the articular cartilage/menisci regions and bone. MRI phase data was unwrapped using a custom Goldstein branch-cut phase unwrapping algorithm [8]. Displacements for each pixel within the cartilage ROIs were determined from unwrapped phase data [9] and

smoothed (**Fig 1C**) using a locally weighted Gaussian filter with a kernel size of 3. A nearest neighbor transform was used to minimize bias at the ROI edges during smoothing [10]. In-plane Green-Lagrange strains were calculated from the smoothed displacements.

*Inverse Modeling to Derive Material Properties:* The virtual fields method (VFM) was applied to determine the Poisson's ratio of the medial femoral cartilage region. To apply the VFM, the main orientations of the cartilage were defined, and a kinematically admissible virtual displacement field and the associated virtual strain field were determined [6]. Assuming both plane strain and Hooke's law, Poisson's ratio was calculated using the principle of virtual work. To determine Young's modulus, cartilage and bone material elements from the segmented MRI image were mapped to a pseudo 2D hexahedral finite element mesh. The tibia was modeled at full length based upon the experimentally measured leg length of each participant. Linear elastic springs were incorporated into the models to represent the collateral ligaments. MRI-derived displacements were prescribed to nodes within the medial and lateral cartilage (**Fig 1D**). Boundary conditions were assigned to the FE model to mimic the varus-valgus load. An inverse parameter optimization on the medial cartilage Young's modulus was performed (FEBio) using the experimentally known force at the base of the tibia (25N) as the optimization function.

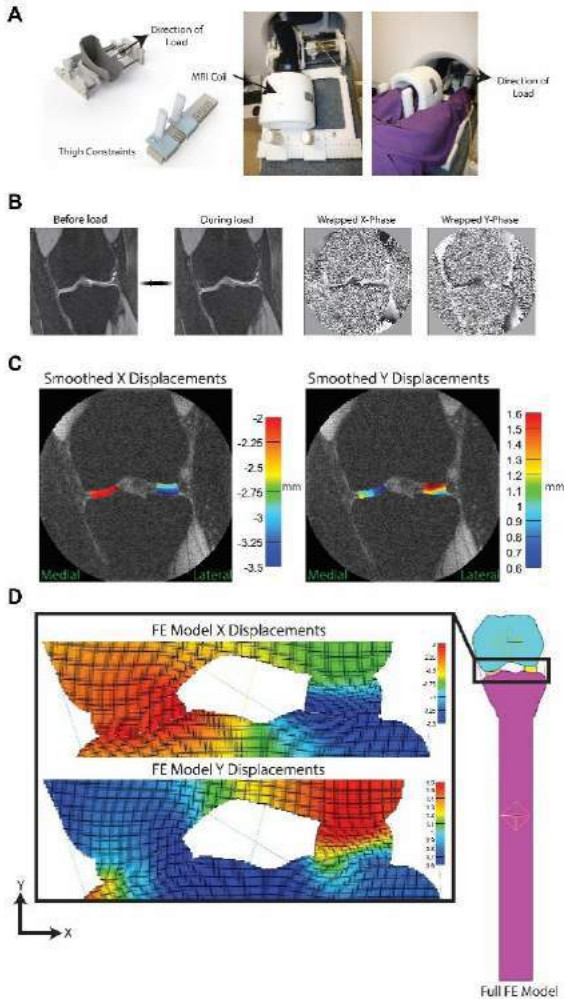


**Figure 1: (A) Varus-valgus MRI compatible loading device. (B) Magnitude and phase images of the knee undergoing varus load. (C) Smoothed displacements obtained by DENSE MRI. (D) FE Model used for inverse parameter optimization of medial cartilage**

## RESULTS

The knee joint translated gradually both in *x* and *y* (**Fig 1B**) due to varus loading applied at the foot. In the medial cartilage, displacement in *x* was spatially uniform while *y* displayed higher values near the medial side and lower near the lateral side. Optimization required approximately 5 minutes of solution time on a 240 GB computing cluster. Final converged material properties in the medial cartilage were a Young's modules of 0.62 MPa and a Poisson's ratio of 0.48.

## DISCUSSION

This work provides a single-subject proof of concept of a MRI framework to non-invasively determine cartilage stiffness and Poisson's ratio. While other work has determined cartilage material properties *ex vivo*, we believe this is the first work to do so *in vivo* using standard clinical 3T MRI. Additionally, while previous work has calculated relative stiffness within cartilage [3], our method allows us to calculate an absolute stiffness value. To further investigate this method, additional subjects with both healthy and pathological knees will be added to this study. Future work will also include further validation and sensitivity studies. Ultimately, we plan to expand this work to identify heterogeneous distributions of the Young's modulus within cartilage [6]. We hypothesize based upon *ex vivo* cartilage mechanical studies that changes in stiffness to the medial cartilage middle and deep zones are potential biomarkers for osteoarthritis pathogenesis [8]. Ultimately, we hope this framework can provide a way forward to measure cartilage material properties in a clinical MRI setting and could potentially be extended to other load-bearing musculoskeletal tissues, including ligament and intervertebral disc.

## ACKNOWLEDGEMENTS

This work was supported by NIH grant 2 R01 AR063712.

## REFERENCES

[1] Chan D.D. and Neu C.P., *J R Soc Interface.*, 10:78, 2013.
[2] Hafezi-Nejad N. et al., *Skeletal Radiol.*, 44:11, 2015.
[3] Cai, L. et al., *Sci Rep*., 10:7980, 2020.
[4] F. Eckstein et al., *Nat. Rev. Rheumatol*., 8:10, 2012.
[5] Zhong, X. et al.. *Med. Phys*., 36:1, 2009.
[6] Yue M. and Avril S., *Int J Solids Struct.*, 178:1, 2019.
[7]. Maas et al., *J. Biomech. Eng*.., 134:1, 2012.
[8] Chan, D.D., et al., *Sci Rep*., 6:19220, 2016.
[9] Chan D.D., et al., *Comput. Methods Biomech. Biomed. Eng.*,16:8, 2013
[10]. Luetkemeyer C. M., et al., *Extreme Mechanics Letters*., 19:1, 2018.

SB³C2022
Summer Biomechanics, Bioengineering and Biotransport Conference
June 20-23, Eastern Shore, MD, USA

# PATIENT SPECIFIC MODELING OF OBSTRUCTED VENTRICULOPERITONEAL SHUNT PERFORMANCE

**Sung Min Kwon (1), Stephanie C. TerMaath (1)**

(1) Mechanical, Aerospace and Biomedical Engineering, University of Tennessee, Knoxville, TN, USA

## INTRODUCTION

Hydrocephalus is a condition in which an excessive amount of cerebrospinal fluid (CSF) is accumulated in the ventricular system, resulting in elevation of intracranial pressure (ICP). Elevated ICP can damage brain tissue and cause many serious symptoms including headaches, nausea, papilledema, cognitive difficulties, motor skills impairment, incontinence, and even death if left untreated. Approximately 1 of every 500 infants is born with hydrocephalus making it the most common reason for neurosurgery in children in the US [1]. While there is no cure, the most common treatment for hydrocephalus is insertion of a device called a ventriculoperitoneal (VP) shunt. This shunt drains excess CSF from the ventricular system and directs the fluid to the abdomen where it can be absorbed. While essential to patient treatment, this implantable medical device has a high failure rate. Most of the patients who receive shunt insertion require additional neurosurgeries to revise or replace the VP shunt within 10 years.

VP shunts have been used for over 50 years, yet there is no notable solution to prevent shunt failure. One of the most common reasons for shunt malfunction is obstruction of the ventricular catheter (VC) that transports CSF from the lateral ventricle (LV) to the valve. Reducing the obstruction rate of the VC requires understanding a complex CSF dynamics scenario characterized by patient specific anatomy and physiological conditions. In addition to the high dimensional parameter space needed to characterize shunt performance, it is also challenging to mimic the in-vivo environment experimentally. Computational fluid dynamics (CFD) using validated models is a method to rapidly model and investigate the effects of the large number of parameters on CSF behavior and shunt performance. The objective of this research is to model patient specific in-vivo conditions and characterize CSF transport through obstructed VC from an obstructed LV to the valve. In addition to the model, a physically realistic apparatus has been created to collect validation data. This research studies the interacting effects of VC insertion location, lateral ventricle (LV) and choroid plexus (CP) geometry, boundary conditions (BC), obstructions, and in-vivo operating conditions on CSF dynamics through an obstructed VC. The results provide essential information to characterize CSF transport using a patient specific 3D computational model to inform VC optimization studies to reduce failure rates.

## METHODS

The computational simulation, parameter studies, and sensitivity analysis follows the approach shown in Figure 1 and described below.

**Patient Specific LV model:** The open-source 3D printing software, Slicer, and Computer Aided Design (CAD), Solidworks, are utilized to model patient specific LVs. A total of five different LV CAD models are constructed from CT scans. The choroid plexus is a unique shaped tissue within the brain that produces the majority of CSF, and its location can vary for all patients. The shape and size of the CP implemented in the LV model are based on Madhukar et al [2].

**VC model:** The baseline VC has 4 rows and 4 holes on each row with each drainage hole measuring 3 mm apart. The side holes appear in a zigzag pattern. The length of the catheter is 200 mm and the inner and outer diameters are 1.2 mm and 2.5 mm respectively. Each drainage hole is tapered.

**Modeling and Simulating CSF Flow:** The open-source CFD software OpenFOAM® is utilized for the computational simulations. Several assumptions included incompressible flow, Newtonian fluid, and steady-state. A range of intracranial pressure (ICP) and intra-abdominal values for both normal and hydrocephalus patients are applied as the inlet and outlet BCs. Wall shear stress is capturing using extra grid layers near the drainage holes. Postprocessing was conducted using the open-source multiple-platform application, Paraview to obtain quantified data, particularly streamlines, outflow from the VC, and wall shear stresses.

SB³C2022-037

**Experimental validation:** A test apparatus is constructed to collect data to validate the computational model. Patient specific pediatric LV and skull models are extracted from CT scans and fabricated using a mold and 3D printing respectively. Water is used to represent the CSF. The skull is filled with aloe vera gel to replicate fluid structure interaction. The experiment is conducted under steady-state conditions with a constant water pressure.

**Parameter studies and sensitivity analysis:** The effects of LV shape, BCs, and VC locations (Fraizer's and Kocher's point) on CSF flow are investigated. Shunt performance is measured relative to outflow and wall shear stress (WSS) (known to correlate to obstruction propensity). Sensitivity analysis to determine the relative influence of model parameters is performed using a surrogate model created with machine learning to calculate Sobol Indices.

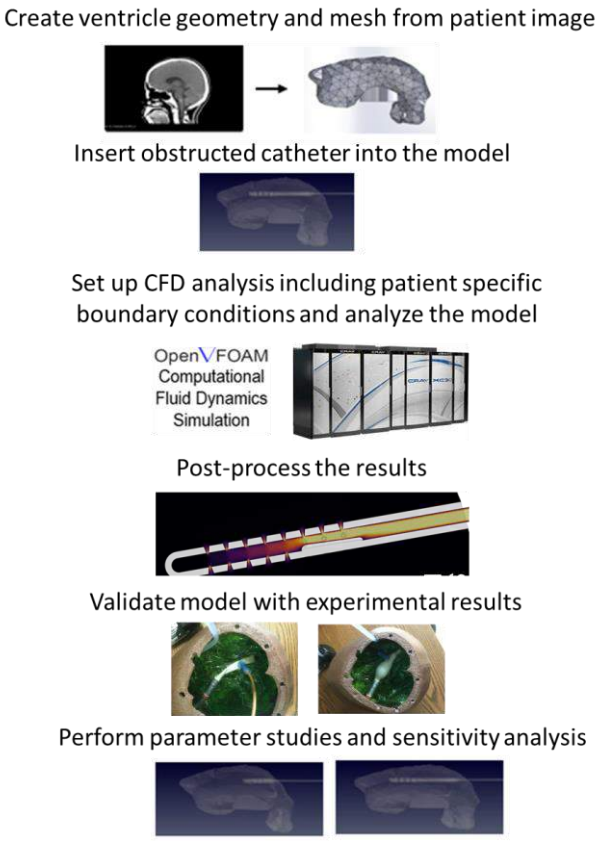


**Figure 1: Patient Specific modeling and CSF analysis process**

## RESULTS

Pressure and flow rate values were obtained experimentally and compared to the 3D computational model results. Varying catheter locations and BC for five different LV models were simulated. Some primary results include the following. No significant change in WSS and outflow was identified relative to LV shape and catheter location for constant BC. The detail results of WSS for varying VC will be shared during the presentation. However, the streamlines of CSF flow from the CP to the catheter exhibit significant differences due to LV shape and catheter location (Fig. 2 and 3). As typically observed in the literature, more than 50 percent of CSF flow passes through the proximal drainage hole (Fig. 4). The effects of VC obstruction are highly correlated to obstruction size, porosity, and location (Fig 5). Detailed results of this study including sensitivity analysis will be provided in the presentation.

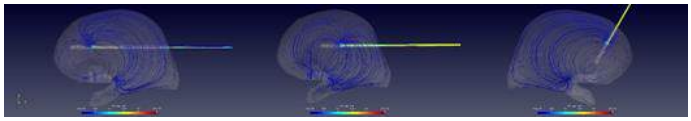

**Figure 2: Representative comparison of streamline for varying VC locations in an enlarged LV**

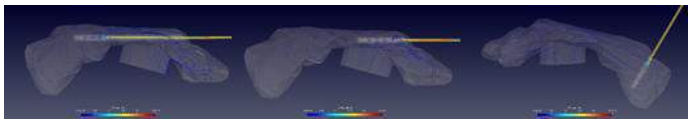

**Figure 3: Representative comparison of streamline for varying VC locations in a slit LV**

**Figure 4: The majority of CSF flows through the proximal holes**

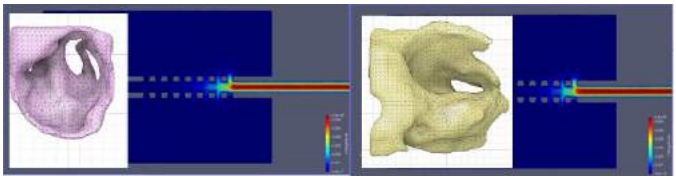

**Figure 5: Representative comparison of obstruction porosity and size effects**

## DISCUSSION

CFD application has been widely and successfully used as an analytical tool in the biomedical field to model biofluid flow phenomena. This paper investigates the effects of patient specific geometric, in-vivo BC, and VC obstruction on shunt performance as measured by outflow and wall shear stresses using parameter studies and sensitivity analysis. It should be noted that this study was based on steady state flow. In the future, physically realistic in-vivo operating conditions will be added to the computational model including pulsatile effects, transient effects due to valve opening and closing, turbulence effects in the CP, and fluid structure interaction to characterize more realistic in-vivo CSF dynamics.

## REFERENCES

[1] More Facts About Hydrocephalus, National Hydrocephalus Foundation. Available: http://nhfonline.org/MoreHydrocephalusFacts.pdf

[2] Madhukar, Megha et al. "Choroid plexus: normal size criteria on neuroimaging." Surgical and radiologic anatomy: SRA vol. 34,10 (2012): 887-95. doi:10.1007/s00276-012-0980-5

[3] Paff M., Alexandru-Abrams D., Muhonen M., Loudon W. Ventriculoperitoneal shunt complications: a review. Interdisciplinary Neurosurgery. 2018; 13:66–70. doi: 10.1016/j.inat.2018.04.004.

# THREE-DIMENSIONAL DEFORMATIONS OF SWINE APICAL VAGINAL SUPPORT

**K. Donaldson (1), J. Thomas (2), S. Clark-Deener (3), Y. Zhu (2), and R. De Vita (1)**

(1) Department of Biomedical Engineering and Mechanics, Virginia Tech, Blacksburg, VA, USA
(2) Bradley Department of Electrical and Computer Engineering, Virginia Tech, Blacksburg, VA, USA
(3) Department of Large Animal Clinical Sciences, Virginia Tech, Blacksburg, VA, USA

## INTRODUCTION

Pelvic floor disorders, including pelvic organ prolapse which involves the descent of the pelvic organs into the vagina, affect up to 50% of U.S. adults with female pelvic anatomy, sometimes causing severe physical and psychological symptoms [1,2]. The uterosacral ligaments (USLs), often targeted as native tissue supports in pelvic surgeries, are the most important support structures of the apical vagina, cervix, and uterus. Despite their mechanical importance to normal pelvic organ support and their role in correcting prolapse, the USLs remain understudied from a mechanistic perspective. In particular, the viscoelastic mechanical properties of the USLs must be elucidated in order to understand how these disorders occur as well as how they may be treated. The objective of this study is to characterize the three-dimensional deformations of the USLs under equibiaxial loading.

## METHODS

USLs were excised from 5 healthy gilts (virgin swine) immediately post sacrifice. Since the USLs *in vivo* are membrane-like in nature, the main loading axes were defined in the direction from the distal attachment at the cervix to the proximal attachment at the sacrum (the main *in vivo* loading direction, or MD) and the direction perpendicular to it (the perpendicular direction, or PD). Specimens of 1.5 cm by 1.5 cm were isolated, suspended with hooks, and loaded into a custom-built biaxial testing apparatus equipped with two 8.9 N-capacity load cells. Specimens were immersed in PBS and preloaded to 5 mN along the MD and PD. They were then equibiaxially preconditioned between 0.01 N and an upper value of 1, 1.5 or 2 N at a rate of 10 μm/sec for 10 cycles. Following preconditioning, specimens were loaded quasi-statically to their upper load at 5 μm/s and then held at a constant load and allowed to creep for 40 minutes. During this time, images were taken at a rate of 1 Hz for digital image correlation calculation of the (Lagrangian and normal) strain fields in both the MD and PD. Optical coherence tomography (OCT) was used to collect through-thickness images at discrete time points throughout the tests. Deformation data were compared between the MD and PD using paired Student's t-tests. Creep strains in the MD and PD were fit to the exponential equation:

$$\varepsilon = \alpha t^n. \quad (1)$$

where ε is strain, α is a material constant and *n* is the rate of creep.

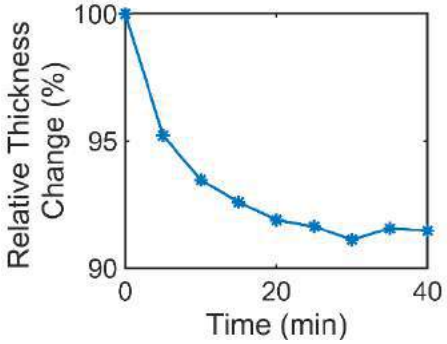


**Figure 1: Average relative thickness change for one representative USL specimen during creep.**

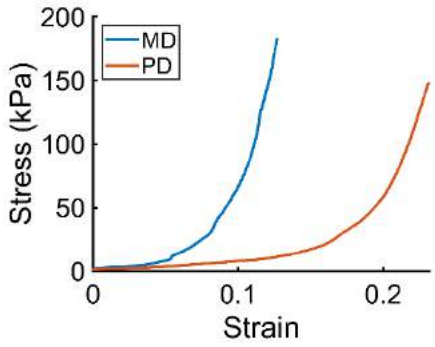


**Figure 2: Stress-strain curves in the MD (blue) and PD (orange) for a representative specimen during quasi-static testing.**

## RESULTS

Thickness data were successfully computed using OCT for a subset of 8 specimens out of the total 15 tested, which were used to calculate the (nominal and normal) stresses both in the MD and PD for each of these specimens during the pre-creep and creep loading phase of the testing protocol. These specimens were found to be significantly stiffer in the MD than in the PD when strains were compared at equivalent values of stress in each loading direction: 50 kPa ($p$=0.036), 100 kPa ($p$=0.025), and 150 kPa ($p$=0.025). The OCT images showed that the specimens consistently got thinner during quasi-static loading, but during creep, some specimens got thinner while others increased in thickness or stayed the same. The creep behavior of the 15 total specimens was not different between the two loading directions. The specimens did not strain much in either direction during creep, and the rates of creep in the MD and PD were very similar ($p$=0.71)

## DISCUSSION

The gilt USLs demonstrated some anisotropy during quasi-static testing with the specimens straining less in the MD than in the PD at equivalent values of stress. However, we found that the

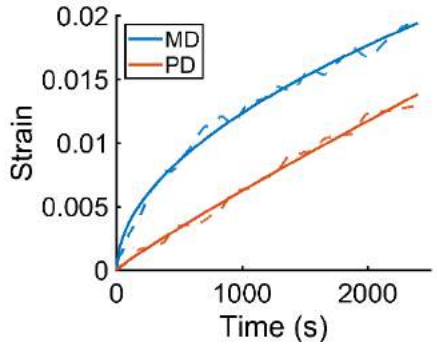


**Figure 3: Moving average (dashed lines) and curve fitting (continuous lines) of (normal, Lagrangian) strain over time during creep testing in the MD (blue) and PD (orange) for one representative specimen.**

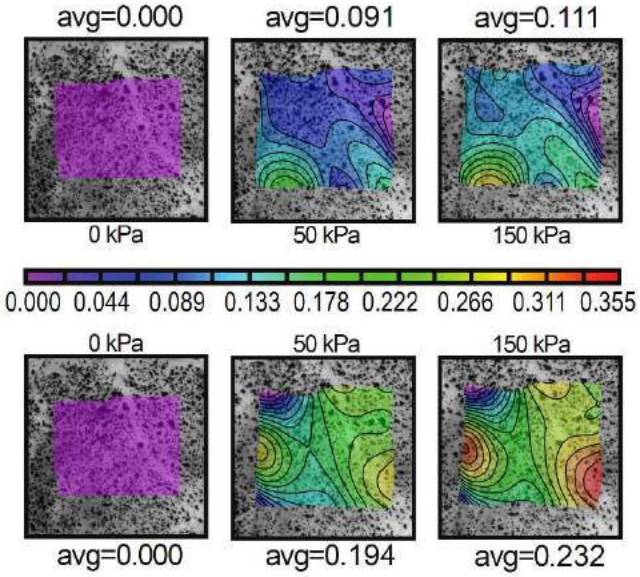


**Figure 4: Map of (normal, Lagrangian) strains and average strains in the MD (top) and PD (bottom) at (nominal) stress levels of 0 kPa, 50 kPa, and 150 kPa in each respective direction during quasi-static testing.**

creep properties were not different between the two loading directions. The gilt USLs experienced less creep than the swine USLs which were previously tested by our lab (Baah-Dwomoh et al. 2018) [3]. This is potentially due to increased damage of the swine USLs during pregnancy when they must support the increased weight of the uterus. The OCT images showed variability in specimen thickness change over the course of creep, with some specimens getting thinner and some thicker over time. This likely reflects competing effects of tensile forces and swelling. Collectively, these data could allow us to better understand the *in vivo* behavior of the USLs and ultimately inform surgeries for prolapse correction which use the USLs to restore pelvic organ support.

## ACKNOWLEDGEMENTS

Funding was provided by NSF Grant No. 1804432. J.T. thanks the Bradley Department of Electrical and Computer Engineering at Virginia Tech for the support of the Bradley Fellowship.

## REFERENCES

[1] M. Barber and C. Maher, Int Urogynecol J. 24(11):1783-1790, 2013.
[2] J. Jelovsek and M. Barber, Am J Obstet Gynecol. 194(5):1455-1461, 2006.
[3] A. Baah-Dwomoh, et al., Ann. Biomed. Eng. 46(12):2036-2047, 2018.

SB³C2022
Summer Biomechanics, Bioengineering and Biotransport Conference
June 20-23, Eastern Shore, MD, USA

# HOW CARTILAGE TRIBOMECHANICS IS COMPROMISED BY ELEVATED CONTACT STRESSES AND INACTIVITY

**Shamimur R. Akanda (1), Jamie M. Benson (2), Arnab Bhattacharjee (1), David L. Burris (1), Christopher Price (1,2)**

(1) Mechanical Engineering, University of Delaware, Newark, Delaware, USA
(2) Biomedical Engineering, University of Delaware, Newark, Delaware, USA

## INTRODUCTION

Articular cartilage, the tissue that lines our diarthrodial joints, sustains, near frictionless lubrication over millions of articulations annually. This phenomenal behavior derives from the tissue's biphasic properties. When initially loaded, cartilage generates high interstitial fluid pressures and fluid load support that limit tissue compression and interfacial frictions. However, static loading drives time-dependent fluid exudation from cartilage, compromising its fluid load support, allowing substantial tissue compression and loss of lubricity.

Thus, cartilage can, on the one hand, withstand transient contact pressures (~10-20 MPa during walking and running) that far exceed its compressive modulus (~0.5-1 MPa) without compromising lubricity.[1-3] On the other hand, cartilage is habitually exposed to non-zero quasi-static average contact stresses (~0.2-2 MPa)[4] that cannot be overlooked as a primary influencer of tissue function. Indeed, how habitual average stresses influence fluid exudation, tissue compression, and loss of fluid load support, and how the joint compensates for their detrimental consequences provides key insights into joint lubrication and how modifiable human factors could impact joint health/longevity.

Habitual non-zero joint contact stresses invariably lead to time dependent cartilage compressions and loss of fluid load support. To maintain cartilage's critical fluid pressure-dependent functions our joints must counteract these losses, by recovering interstitial fluid. Fortunately, *in vivo* and intact joint studies demonstrate joint articulation to be a strong modulator of fluid recovery.[5] Such recovery has been thought to occur solely through 'passive' mechanisms, during cartilage unloading and 'bath exposure'.[6] Recently, we've identified an alternative mechanism by which articulation promotes active interstitial fluid recovery. Using the convergent stationary contact area (cSCA) benchtop testing configuration, we've shown that interfacial sliding, by generating hydrodynamic pressures within sliding contact interfaces, drives robust fluid recovery.[7-9] Importantly, this 'tribological rehydration', which rescues tissue compression and lubricity, is governed by a competition between load-induced fluid exudation and sliding speed-mediated rehydration.

Subsequently, we've established, for physiologically relevant sliding speeds (80mm/s), that optimal tribological rehydration occurs at contact stresses of ~0.5MPa in healthy cartilage; above ~1.0MPa, tribological rehydration is significantly compromised, if not abolished.[10] Furthermore, we've shown how '*daily*' sliding activity patterns influence '*diurnal*' interstitial fluid exudation and recovery, tissue compression, and frictional behaviors. Sliding patterns mimicking frequent daily activity promote significantly reduced tissue compressions and friction exposures under modest compressive stresses (~0.25MPa) than more sedentary patterns.[11] These results suggest that elevated joint contact stresses and increasing levels of inactivity, which are associated with obesity and rapidly increasing in prevalence, could serve to significantly, and synergistically compromise activity mediated fluid recovery within cartilage, and thus tissue functionality/health.

The objective of the present work was to investigate the influence of both elevated cartilage contact stresses and sedentary activity patterns, both modifiable osteoarthritis risk factors, on sliding-mediated tribological rehydration using the cSCA testing configuration. OwHo

## METHODS

In *study 1* (**Fig. 1A**), ovine femoral condyle cSCA explants (Φ = 12 mm) were subjected to tribological characterization under different activity patterns simulating a human '*day*' of fixed activity volume.[11] Each day contained a 22 min '*awake*' period, comprising 15 '*sedentary*' min (static loading) and 7 '*active*' min (80mm/s sliding), and a 13 min '*sleep*' period of nominal contact unloading. These times were scaled, based upon contact size, to match the exudative dynamics of the human knee.[11] Different loads (2 & 7N) and three activity patterns (1, 3-, or 15-equally distributed bouts) were investigated in each explant (n = 6).

In *study 2* (**Fig. 1B**), *daily* sliding volume was reduced (3.5 min) or increased (10.5 min), with *sedentary* time adjusted accordingly, to

determine the effect of *daily* activity volume on *tribological rehydration* under elevated applied loads (7N, n = 6).

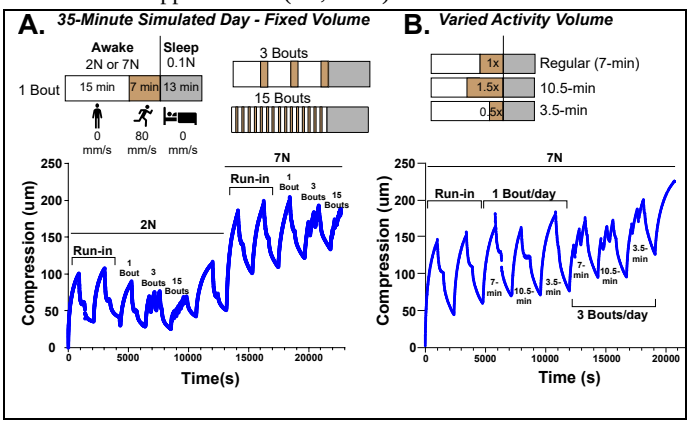


**Fig. 1: Experimental design to investigate the effects of A) activity patterning (w/ fixed activity volume) and applied load, and B) activity volume at elevated loads on tribological rehydration.**

## RESULTS

In study 1, the effects of daily activity patterning and contact stress (~0.25 vs. 0.5 MPa) on tribological rehydration and tissue compression were clear (**Fig. 2**). For a fixed sliding volume (7.5 min), all activity patterns and loads supported tribological rehydration to some degree (**Fig. 2A, B**). However, activity patterns having less-frequent sliding exhibited significantly elevated compressions at the start- and end-of-sliding and when averaged across each *day* (**Fig. 2C, D**); 1x > 3x > 15x.

Modest increases in contact stresses compromise tribological rehydration. [10] Here, we show that they also greatly exacerbate activity pattern-influenced compression accumulation. When thrice daily activity was simulated for five 'days', an ~2-fold increase in contact stress caused an ~2-fold increase in tissue compression (**Fig. 2E**), suggesting that increased activity frequency alone might not fully restore rehydration under elevated contact stresses.

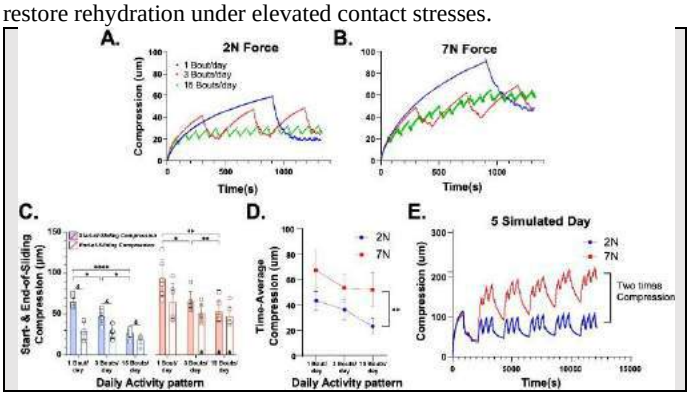


**Fig. 2: Representative compression traces for a cSCA explant subjected to three different '*activity*' patterns at A) 2 vs. B) 7N. Summary of C) start- & end-of-sliding, and D) time-averaged cSCA compression outcomes for different loads and activity patterns. E) Compression response of a cSCA explant across 5-days of simulated thrice daily activity at 2 vs. 7N.**

Indeed, while we found, in study 2, that a 50% increase in activity volume (to 10.5 min) could improve activity-mediated compression recovery in the presence of elevated loads (7N, or 0.5-0.6MPa; **Fig 3**), these gains were modest. Increasing the prescribed activity ratio from ~33 to 50% of the '*awake*' day resulted in only a 10% suppression of compression accumulation under elevated contact stresses compared to '*normal*' activity (**Fig. 3C, D**). The effect of halving *daily activity volume* (to 3.5 min) resulted in predictable increases in compression accumulation due to reduced sliding-mediated tribological rehydration.

For the sake of brevity, only tribological rehydration/compression outcomes have been shown; frictional responses were far less sensitive to the applied stresses and activity patterns explored here (not shown).

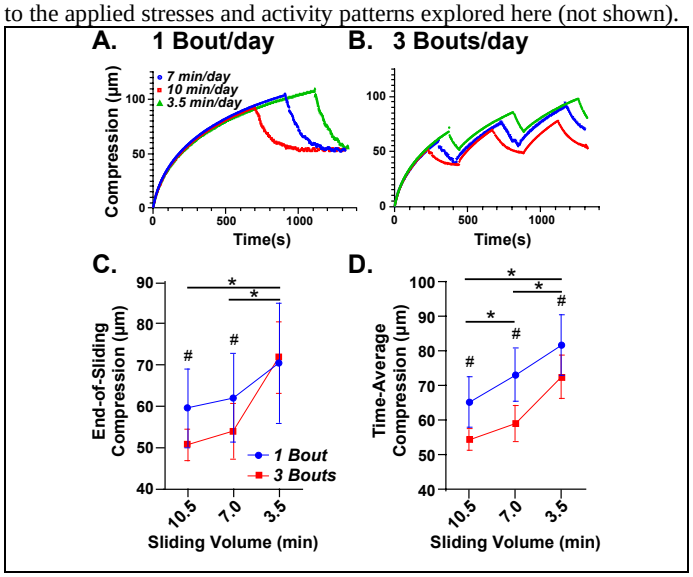


**Fig. 3: Representative explant compression under different volumes of A) once vs. B) thrice '*daily*' sliding activity at elevated (~0.5MPa) contact stresses. C) End-of-sliding and D) time-averaged compression outcomes (* p<0.05 for indicated comparisons, # p<0.05 between 1 vs 3 bouts/day).**

## DISCUSSION

Recently, osteoarthritis (OA), has been discussed as an evolutionary mismatch disease, rooted in our joints being poorly adapted to the environment we now live in. Obesity and inactivity, prevalent yet modifiable risk factors associated with OA, have been suggested as prime 'mismatch' candidates. Yet, how they contribute to elevated OA risk/prevalence is unclear. Through our benchtop activity studies, a plausible mechanism by which obesity and inactivity might directly and physically compromise articular cartilage function can be found.

Cartilage function depends upon maintaining high levels of interstitial fluid load support. Joint activity, it appears, supports cartilage function by providing robust mechanisms to passively (e.g., bath exposure) and actively (i.e., tribological rehydration) recover interstitial hydration. It also appears that the elevated contact stresses and reduced activity levels experienced by joints in obese and sedentary individuals likely compromise the balance between fluid exudation (increased) and imbibition (decreased) needed to maintain optimal interstitial hydration, tissue strains, and tribomechanical functions.

Future work is needed to establish the links between obesity and inactivity-linked tribomechanical behaviors and disease etiology, both *in vitro* and *in vivo*. However, the present work does suggest, that beyond the established biochemical effects of obesity and sedentariness on cartilage health, these easily modifiable risk factors of might also have more simply understood, and possibly more detrimental, effects on basic cartilage function.

## REFERENCES


[1] Mansour, *Kinesiology*, 2003. [2] Ateshian, *J Biomech*, 2009. [3] Mow, *J Biomech Eng*, 1980 [4] Brand, *Iowa Orthop J.*, 2005. [5] Chan, *Sci Reports*, 2016. [6] Caligaris, *OA&C*, 2008. [7] Burris, *OA&C*, 2017. [8] Burris, *Tribo Letters*, 2019. [9] Farnham, *JMBBM*, 2020. [10] Akanda, *SB3C* 2021. [11] Graham, *Connect Tissue Res*, 2020.

# A STRUCTURAL BIO-CHEMO-MECHANICAL MODEL FOR TRACTION FORCE MICROSCOPY OF VASCULAR SMOOTH MUSCLE CELLS

**Shannon M. Flanary, MSE (1), Victor H. Barocas, PhD (2)**

(1) Department of Chemical Engineering & Materials Science, University of Minnesota – Twin Cities, Minneapolis, MN, USA
(2) Department of Biomedical Engineering, University of Minnesota – Twin Cities, Minneapolis, MN, USA

## INTRODUCTION

Traction force microscopy (TFM) is a vital tool to quantify the contractility of many cell types, including vascular smooth muscle cells (VSMCs). Although seeming simple and easily qualified, TFM involves a complex interplay among biological, chemical, and mechanical processes. To interpret and apply TFM data, we require computational models informed by the real-life complexity.

Previous simulations of TFM experiments were continuous and treated the cell as a black box.[1–3] These attempts did not consider how a contractile signal is generated, how actomyosin stress fibers interact, nor how the elastic substrate deforms. A realistic model of TFM cannot be formulated without consideration of how these phenomena interact.

Therefore, we developed a comprehensive model that builds upon previous studies within and beyond biomedical engineering to simulate TFM (Figure 1). This simulation utilizes previous advances in systems biology to model ECM deposition and phenotype switching to predict actomyosin activation.[4–6] Additionally, a result from tribology was used to model substrate displacement due to focal adhesion forces.[7] This new model is intended to predict the two-dimensional contractile behavior of VSMCs under various experimental conditions.

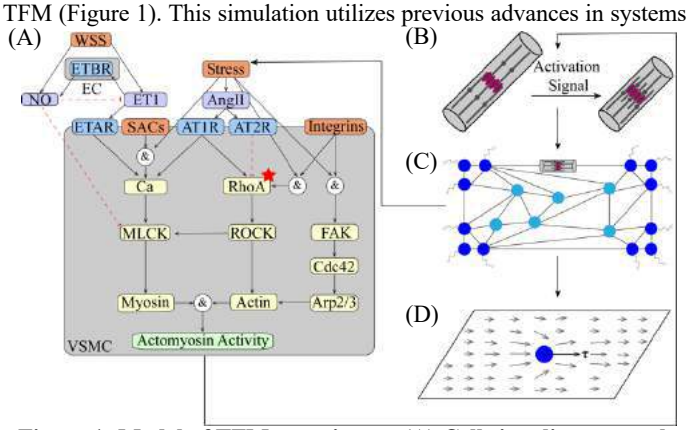


**Figure 1: Model of TFM experiment. (A) Cell signaling network. Star denotes node manipulated in case study. (B) Stress fiber contraction. (C) Cytoskeletal network of stress fibers. (D) Displacement of elastic substrate.**

## METHODS

The model consists of four components: *cell signaling* (Fig. 1A) drives *stress fiber contraction* (Fig. 1B), and the stress fibers interact with one another via a *cytoskeletal network* (Fig. 1C). Focal adhesions transmit cytoskeletal forces to the substrate, inducing *substrate deformation* (Fig. 1D). The model also includes feedback between cytoskeletal stress and biochemical signaling.

*Cell Signaling Network*: A VSMC signaling network was constructed by isolating nodes of interest from a published model.[4] The relationships between nodes were modeled as ordinary differential equations based on a normalized (0-1) Hill function for activation of each species in the network.[8] The calculated steady-state actomyosin activity set the maximum fiber activation level in the fiber-level model.

*Stress Fiber Contraction:* Actomyosin bundle contraction and stress were modeled following Deshpande et al.[1], with fiber bundle activation ($\eta$) described by a first-order kinetic equation:

$$\frac{d\eta}{dt} = (1-\eta)\frac{k_f C_{max}}{\theta}\exp\left(\frac{-t}{\theta}\right) - \left(1-\frac{\sigma}{\sigma_0}\right)\frac{k_b}{\theta}\eta \qquad (1)$$

where $C_{max}$ is the maximum actomyosin activity based on the signaling network results, $\sigma/\sigma_0$ is the normalized fiber stress, $k_f$ and $k_b$ are rate parameters for formation and dissociation of fibers, and $\theta$ the activation signal decay time. The normalized active fiber stress was described[1] as:

$$\frac{\sigma}{\sigma_0} = \left(1+\exp\left(-5.301\left(\frac{k_v\dot{\lambda}}{\eta}-\frac{\eta}{2k_v}\right)\right)\right)^{-1} \qquad (2)$$

where $k_v$ describes the reduction in fiber stress with increased shortening rate $\dot{\lambda}$ and $\sigma_0$ is the product of the fiber activation level and maximum stress allowed by biochemistry. The passive fiber stress was given by:

$$\sigma_p = \frac{E}{B}\left(\exp\left(B\frac{\lambda^2-1}{2}\right)-1\right) \quad (3)$$

where $\lambda$ is the stretch, and $E$ and $B$ are material constants.

*Cytoskeletal Network:* A Delaunay network of 50 randomly seeded interior nodes and 7 uniformly spaced boundary nodes in each corner of the 127 $\mu$m x 32 $\mu$m region was constructed to simulate an actomyosin stress fiber network. Boundary nodes were designated as focal adhesions, linking the VSMC to the substrate. Equilibrium positions of the fiber network nodes were determined by setting the sum of all fiber forces and the spring force due to substrate displacement (for focal adhesions) to zero (i.e., mechanical equilibrium for each node).

*Substrate Displacement:* Each focal adhesion was modeled as a circular contact displacing tangentially on a linear elastic half-space.[7] The superposition of all focal adhesion forces and displacements determined the overall substrate deformation.

## RESULTS

The bio-chemo-mechanical model operates by combining inputs from biochemical signaling and mechanical stress generation. The model captures dynamic contraction of the stress fiber network following a single activation signal. To capture steady-state behavior, the model can be modified to respond to recursive signaling. Without additional activation signals, the fiber stress peaks uniformly after a delay associated with penetration of the activation signal into the network (Figure 2). Fiber stress is approximately uniform due to biochemical signaling being modeled as uniform throughout the cell. Additionally, the substrate displacement is concentrated near focal adhesions.

The integration of biochemical signaling into the model allows the comparison to experimental results from genetically-modified VSMCs. Work completed by Porter et al.[9] has demonstrated that a knockdown of SUN1 results in a decrease in traction force through a reduction in RhoA, a positive regulator of ROCK-mediated contraction, activity.[10] When the maximum activation level of the RhoA node in the signaling network (starred in Fig. 1A for reference) was reduced, the model recapitulated the 40-50% reduction in VSMC traction stress demonstrated by Porter et al. (Figure 3A).[9]

In addition to direct biochemical modulation, VSMCs are also mechanosensitive and adapt their contractility in response to changes in substrate stiffness. In work examining circular dorsal ruffle formation, Huynh et al.[11] illustrated that traction force is positively correlated with substrate stiffness in VSMCs. When only the shear modulus of the substrate was changed in the model, the traction force rose as seen experimentally, but the stiffness-dependence was much less pronounced (Figure 3B). VSMCs also respond to increased substrate stiffness by increasing focal adhesion size and number.[12] When the number of

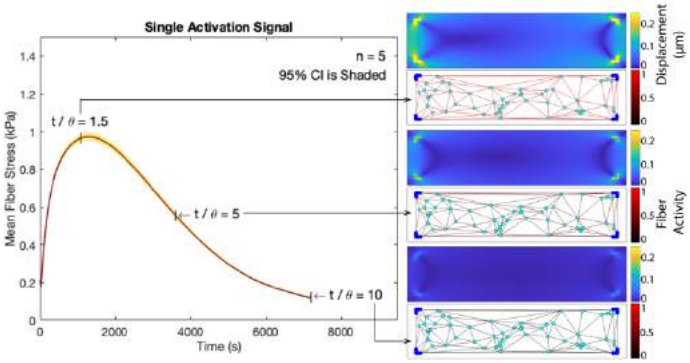


**Figure 2: Dynamics of (left) actomyosin fiber stress after a single activation signal and (right) resulting substrate displacement (top) and fiber network (bottom) of a simulated VSMC on 12 kPa substrate over time.**

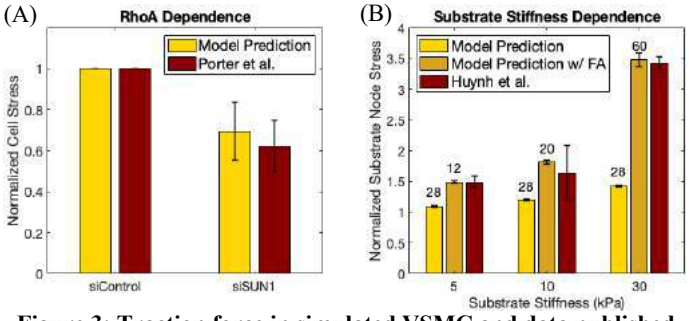


**Figure 3: Traction force in simulated VSMC and data published by (A) Porter et al.[9] and (B) Huynh et al.[11] Cases are normalized to siControl and 2.5 kPa substrate. Text above is focal adhesion number and error is 95% confidence interval.**

simulated focal adhesions was scaled with substrate stiffness, the computational model matched the experimentally-observed changes in cell traction with no other adjusted parameters.

## DISCUSSION

This new model of traction force microscopy recapitulates data from published VSMC experiments. The level of biochemical node activation in the cell signaling network component does not map directly to experimental measures of expression due to the use of normalized values, and therefore the model responds to changes in a qualitative, but not necessarily quantitatively similar, manner.[4–6] The solution to rectify this discrepancy would sacrifice the benefit of not defining large numbers of rate constants and biochemical binding parameters. Thus, for more complex signaling networks, it is not beneficial to quantitatively match the reaction weights directly.

When the number of simulated focal adhesions was not modulated to respond to substrate stiffness, the model did not match experimental data published by Huynh et al.[11] However, it is well established that cells on stiff substrates increase the size and number of focal adhesions.[12] When the number of substrate nodes was modeled to respond to substrate stiffness, the simulated response matched experimental data. The distinct advantage of the model relying on feedback from focal adhesions allows the number and distribution of focal adhesions to respond dynamically over time in future applications.

This simulation of a TFM experiment benefits from its ability to draw upon feedback from both chemical and mechanical signals. Unlike previous models that do not consider the biochemical signal cascades, this version can capture the behavior of VSMCs from a variety of genetic sources and biochemical treatments. A discrete approach also provides the possibility of matching fiber anisotropy seen in VSMC micropatterning.[13] Additionally, the discrete fiber formulation allows an accurate representation of the substrate displacement resulting from focal adhesion point forces. The presented bio-chemo-mechanical model offers a powerful tool for predicting the dynamic contractile behavior of VSMCs *in vitro*.


## ACKNOWLEDGEMENTS

Funding provided by NIH NHLBI grant U01-HL139471.


## REFERENCES


[1] Deshpande, VS et al., *PNAS*, 103:14015-14020, 2006. [2] Barrasa-Fano, J et al., *Acta Biomater*, 126:326-338, 2021. [3] Soiné, J et al., *PLOS Comput Bio*, 11:1-16, 2015. [4] Irons, L et al., *PLOS Comput Biol*, 16:1-22, 2020. [5] Estrada, AC et al., *Biomech Model Mechanobiol*, 20:293-307, 2021. [6] Ziegler, AC et al., *J Mol Cell Cardiol*, 94:72-81, 2016. [7] Menga, N et al., *Eur J Mech A/Solids*, 73:137-143, 2019. [8] Kraeutler, MJ et al., *BMC Syst Biol*, 4:157, 2010. [9] Porter, L et al., *Cells*, 9:1-17, 2020. [10] Ahmed, S et al., *Vessel Plus*, 3:36, 2018. [11] Huynh, J et al., *Cell Mol Bioeng*, 6:138-147, 2013. [12] Balaban, NQ et al., *Nat Cell Biol*, 3:466-472, 2001. [13] Rothermel, TM et al., *J Biomech*, 111:110005, 2020.

SB³C2022
Summer Biomechanics, Bioengineering and Biotransport Conference
June 20-23, Eastern Shore, MD, USA

# ELASTIC STRENGTH AND ITS RELATION TO MINERAL DENSITY IN JUVENILE EQUINE BONES OF THE LOWER LIMB

**Sara G. Moshage (1), Annette M. McCoy (2), Mariana E. Kersh (1,3,4)**

(1) Dept. of Mechanical Science and Engineering, University of Illinois Urbana-Champaign, Urbana, IL, USA
(2) Dept. of Veterinary Clinical Medicine, University of Illinois Urbana-Champaign, Urbana, IL, USA
(3) Beckman Institute for Advanced Science and Technology, University of Illinois Urbana-Champaign, Urbana, IL, USA
(4) Carle Illinois College of Medicine, University of Illinois Urbana-Champaign, Urbana, IL, USA

## INTRODUCTION

Most fatal musculoskeletal injuries in racing horses occur in the lower limb, particularly the third metacarpal/tarsal (MC3/T3) and proximal phalanx (P1) bones, and are a significant welfare issue for racehorses [1,2]. Mechanical loading via exercise has proven to be a viable means for inducing bone adaptation to mitigate fractures [3] but determining the amount and type of exercise remains a challenge [3,4]. Computational models allow for pre-clinical, non-invasive predictions of the mechanical loads of bone in vivo [5] under different exercise modes. Critical to these predictions is accurate material properties, such as the Young's modulus, which can be assessed empirically from computed tomography based apparent mineral density [6,7]. Currently, no such relationship has been reported for juvenile equine bone.

While the growth plates in the distal MC3 and proximal P1 close at nearly the same time [8] and these regions form a congruous joint, whether their mineralization rates and therefore properties are the same is not known. Further, density-modulus relationships vary by anatomical location and are known to be anisotropic [6,7]. Therefore, the objectives of this study were to (1) determine whether the longitudinal and transverse Young's modulus in the P1 and MC3 are different and (2) develop a density-modulus relationship for juvenile equine bone.

## METHODS

**Specimens** – Intact bones (P1:8, MC3:3, MT3:1) were collected from young horses (age: 3-day (n=1), 4-weeks (n=6)) euthanized for reasons unrelated to this study. The bones were wrapped in PBS soaked gauze and stored in plastic bags at -20°C.

**Intact Sample Imaging** – Bones were cleaned of soft tissue and imaged with overlapping microCT (μCT) scans (isotropic resolution = 144 μm, 90 kVp, 177 μV, Rigaku CTLab GX130) acquired along the bone length and merged (Fig. 1A, Amira 2020.1). The bones and mineral density phantoms (range: 25-750 mg HA/cm$^3$, CIRS) were then scanned in a clinical CT scanner (LightSpeed16, GE Medical Systems) with the same protocols used for live horses (resolution=0.875 x 0.875 x 0.625 mm, 120 kVp, 200 mA).

**Bone Core Preparation** – Bone sections perpendicular to the longitudinal axis were cut using a water-irrigated diamond band saw. Trabecular cores were removed in the longitudinal (n=81, Fig. 1B) and dorsal-palmar transverse (n=53) directions using a water-irrigated diamond sintered coring bit (diameter = 5mm) mounted on a drill press. Bone marrow was left intact [9] and the cores were fixed in custom Delrin endcaps using 2-part epoxy (exposed length =12.29±1.57 mm). Samples were wrapped in PBS-soaked gauze and refrigerated at ~2°C for 18 hours before testing.

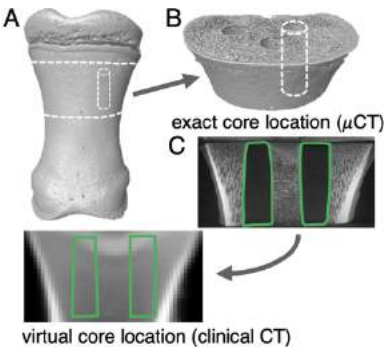

**Figure 1: (A) P1 showing cut lines. (B) Longitudinal core. (C) Bone cores in the intact image stack.**

**Bone Core Imaging** – Importantly, the CT density of intact bone is known to be different from cut samples [10]; therefore, we developed a method to identify virtual cores. The bone sections that remained following core extraction were μCT scanned and aligned to the intact CT data to locate each core within the clinical CT data set (Fig. 1C, Amira 2020.1).

**Compression Testing** – Cores were brought to room temperature and hydrated with PBS. Compression tests were performed on a tabletop test frame (Instron 5967) using a fixed lower platen and a self-aligning, spherical seated upper platen. Embedded cores were pre-loaded to 5N, pre-conditioned for 5 cycles by loading to 0.001 strain at 0.01 strain/s, and loaded till failure at 0.01 strain/s. Force and crosshead displacement

were recorded after adjusting for machine compliance using the direct technique [11]. Data were sampled at 100 Hz.

**Young's Modulus Calculation** – Stress was calculated by dividing force by each sample's cross-sectional area and strain by dividing displacement by exposed length for each sample. Young's modulus was calculated as the slope of the linear regression of all data between two points on the elastic portion of the stress-strain curve.

**Density Calculation** – The clinical CT scan and phantoms were used to calculate average CT density ($\rho_{CT}$) for each core. Ash density (g/cm$^3$) was calculated using Eq. 1 [12].

$$\rho_{ash} = (\rho_{CT} + 0.09)/1.14 \quad (1)$$

**Statistical Analysis** – MT3 and MC3 samples were combined (herein referred to as MC3). Normality of Young's modulus and ash density was tested using a Shapiro-Wilks test. Distributions of Young's modulus between groups were compared using a Mann-Whitney-Wilcoxon test. For each bone, Young's modulus and ash density were log transformed and their relationship was examined using linear regressions. The slope and intercept were used to define the exponential and leading coefficient terms, respectively, in the function relating modulus to ash density. The interaction effect of sample orientation with ash density on experimental modulus was evaluated using an analysis of variance. All analyses were performed in R (v3.5.2).

## RESULTS

The MC3 group had 48 longitudinal and 27 transverse samples, while the P1 group had 33 longitudinal and 26 transverse samples. The transverse modulus of MC3 samples was lower (Mdn=197 MPa) than samples from the P1 (Mdn=250 MPa, Fig. 2) and these distributions differed significantly (p=0.04). In contrast, there was no significant difference between longitudinal samples from the MC3 and P1 (Mdn E=458 MPa and 394 MPa, respectively). The median longitudinal modulus was 132% higher than the median transverse modulus in the MC3 (Fig. 2A) and 57% higher in the P1 (Fig. 2B); these distributions differed significantly (p<0.001 and p=0.0015, respectively).

Bone type (MC3 vs P1) significantly affected the leading coefficient (p<0.001) but not the exponent (p=0.07) of the density-modulus relationships. Both the leading coefficient and exponent (p<0.001) were sensitive to sample orientation for the MC3. In contrast, orientation only affected the leading coefficient (p<0.001) for the P1.

Overall, longitudinal modulus is better predicted in the P1 than the MC3 by a factor of ~4 ($R^2$ of 0.64 and 0.14, respectively, Fig. 3 orange lines). However, our predictions of modulus in the transverse direction are more robust, with density predicting 84% of the variability in the P1 and 75% of the variability in the MC3 (Fig. 3 blue lines).

## DISCUSSION

We found that the longitudinal modulus in the MC3 and P1 was not significantly different, while the transverse modulus in the P1 was higher than the MC3 reflecting a tendency towards more isotropic material properties in the P1. These differences may be because the loading modes of the MC3 and P1 are different. It's likely the MC3 undergoes bending due to its long slender structure, whereas the cuboidal P1 would be more resistant to bending. Variation in surface strain modes between the distal MC3 (compression) and the P1 (shear) has been reported [13]. The density-modulus relationship derived in our study, combined with computational models of musculoskeletal loading, provides the groundwork for testing our hypotheses regarding the nature of bone loading during movement.

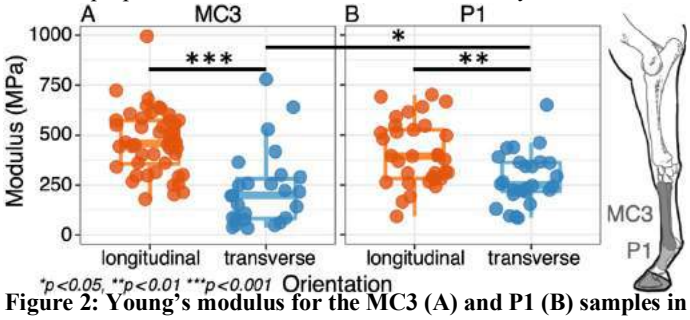


**Figure 2: Young's modulus for the MC3 (A) and P1 (B) samples in the longitudinal (orange) and transverse (blue) directions.**

In terms of predicting modulus from ash density, bone type influenced the leading coefficient but not the exponent and is consistent with differences in density-modulus relationships between anatomic locations for human trabecular bone [7]. The prediction of elastic modulus using density alone was stronger in the P1 compared to the MC3. Further work is needed to confirm whether mineralization rates are different between the two bones as well as the influence of microstructure and non-mineral composition on the elastic modulus.

When the density-modulus relationship derived from mature horses [14] was applied to our longitudinal MC3 samples, the Young's modulus root mean squared error (RMSE) was nearly double the RMSE in this study (RMSE=269 vs 147 MPa). However, over 80% of the samples tested by Les et al. were cortical bone though they reported no difference in the density-modulus relationship between cortical and trabecular bone. Our samples are trabecular and may explain some of the differences between $E_{Les1994}$ and $E_{long}$ (Fig. 3A). Current work involves testing cortical bone samples.

Our data highlight the sensitivity of elastic modulus to bone type and orientation. The incorporation of these data into computational models will allow for more rigorous predictions of the mechanical environment of bone and therefore the potential for bone adaptation.


## ACKNOWLEDGEMENTS

Beckman Institute Graduate Research Fellowship (SGM). Project funded by UIUC Campus Research Board and Grayson Jockey Club. Thanks to Griffin C Sipes for assistance with mechanical tests.


## REFERENCES


[1] Verheyen, K et al., *Equine Vet J,* 36(2):167-173, 2004. [2] Georgopoulos, S et al., *Prev Vet Med*, 139:99-104, 2017. [3] Firth, E et al., *The Vet J*, 190:383-389, 2011. [4] van Weeren, P et al., *Equine Vet J Suppl*, 31:4-8, 1999. [5] Kersh, M et al., *JBMR*, 33(11):1999-2006,2018. [6] Keyak, J et al., *J Biomed Mat Res*, 28:1329-1336, 1994. [7] Morgan, E et al., *J Biomech*, 36:897-904, 2003. [8] Smallwood, J et al., *Vet Radiology*, 30(3):98-110, 1989. [9] Zhao, S et al., *Bone Joint Res*, 7:524-538, 2018. [10] Drum, M et al., *Am J Vet Res*, 69(7):891-893, 2008. [11] Kalidindi, S et al., *Exp Mech*, 37(2):210-215, 1997. [12] Schileo, E et al., *J Biomech*, 41:2483-2491, 2008. [13] Singer, E et al., *J Biomech*, 123:110455, 2021. [14] Les, C et al., *J Ortho Res*, 12:822-833, 1994.


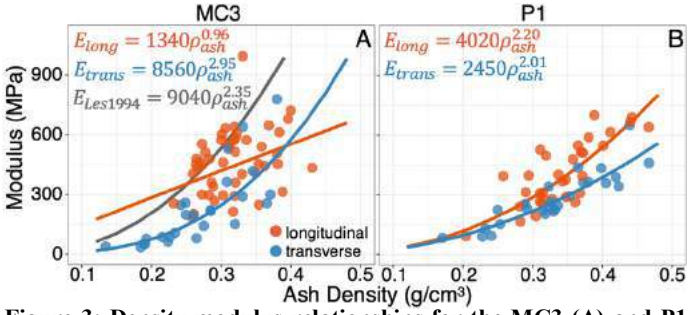


**Figure 3: Density-modulus relationships for the MC3 (A) and P1 (B) samples in the longitudinal (orange) and transverse (blue) directions.**

SB³C2022
Summer Biomechanics, Bioengineering and Biotransport Conference
June 20-23, Eastern Shore, MD, USA

# MULTISCALE MODELING OF CARDIAC VALVE DISEASE USING CELL-LEVEL SIGNALS TO DRIVE MYOCARDIAL GROWTH

**Hossein Sharifi (1), Austin G. Wellette-Hunsucker (2), Charles K. Mann (1), Kenneth S. Campbell (2), Jonathan F. Wenk (1,3)**

(1) Department of Mechanical Engineering, University of Kentucky, Lexington, Kentucky, USA
(2) Department of Physiology & Division of Cardiovascular Medicine, University of Kentucky, Lexington, Kentucky, USA
(3) Department of Surgery, University of Kentucky, Lexington, Kentucky, USA

## INTRODUCTION

Multiscale models of the cardiovascular system are emerging as effective tools for investigating the mechanisms that drive ventricular growth and biological remodeling. Such models can be used to evaluate the effects of molecular-level mechanisms on organ-level function, which could provide new insights for improving patient care. PyMyoVent is a multi-scale computer model that simulates a left ventricle (LV) pumping blood around a systemic circulation by bridging from molecular to organ-level mechanisms. In previous work, we implemented baroreflex control of arterial pressure by using feedback to regulate heart rate, intracellular $Ca^{2+}$ dynamics, the molecular-level function of both the thick and the thin myofilaments, and vascular tone.

Davis et al. [1] have suggested that cardiac growth correlates with the magnitude of tension developed by myofilaments over time, which reflects the work done by the heart. Therefore, cellular level mechanisms that are associated with altered work demand in the heart could be potential driving signals for concentric growth. In this study, we hypothesize that the energy used by cells, to perform the work required by the heart, could be an alternative signal in driving concentric growth.

Valvular diseases, such as mitral insufficiency, lead to overstretching of the sarcomeres and thus increasing of the passive stress within a cell. The alteration in the intracellular passive stress can be sensed by proteins located near the end of sarcomeres. In particular, titin, which spans from the Z disk to the M line, contains an elastic structure within the I band that interacts with other proteins on the Z disk. This provides the passive stiffness of the sarcomeres by storing strain energy during diastole [2]. Therefore, in the current framework, the intracellular passive stress, which reflects the stress within titin, is assumed to drive the serial deposition of sarcomeres and eccentric growth of the LV.

## METHODS

In this work, we extend PyMyoVent with concentric growth (wall thickening / thinning) and eccentric growth (chamber dilation / constriction) driven by cell and molecular-level signals (Figure 1). Specifically, concentric growth is controlled by the energy used by cells during contraction (expressed as myosin ATPase normalized to myofibrillar volume), while eccentric growth responds to intracellular passive stress. The new framework's ability to predict LV growth was tested by simulating two types of valvular disease, namely aortic stenosis and mitral insufficiency.

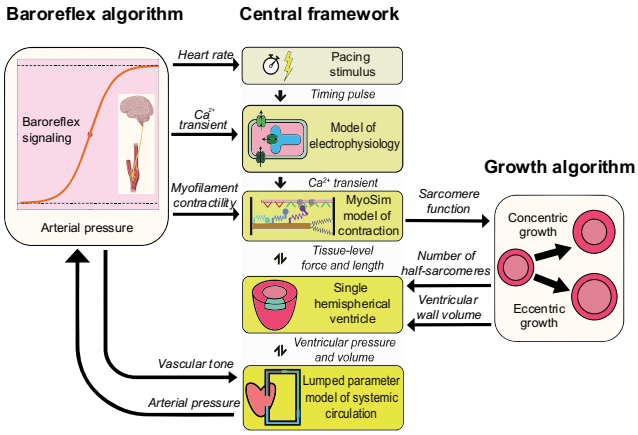


**Figure 1. Overview of the PyMyoVent framework.** Adapted from Campbell et al. [3].

The growth module algorithm was inspired by the underlying biology. In vivo, growth stimuli signals trigger a complex pathological downstream signaling pathway that promotes cell growth and

ventricular enlargement. In the current model, a growth stimulus signal ($S_i$) transduces into a normalized growth signal $G_{a,i}$ that represents the net result of triggered upstream signals within the cell. The rate of change in $G_{a,i}$ is defined as

$$\frac{dG_{a,i}(t)}{dt} = \begin{cases} k_{a,i}\dfrac{\left(S_i - S_{i,set}\right)}{S_{i,set}}\left(1 - G_{a,i}(t)\right) & S_i \geq S_{i,set} \\ k_{a,i}\dfrac{\left(S_i - S_{i,set}\right)}{S_{i,set}}\left(G_{a,i}(t)\right) & S_i < S_{i,set} \end{cases} \quad (1)$$

where i represents the growth type (i.e. concentric or eccentric), $k_{a,i}$ is a rate constant and sets the speed at which $G_{a,i}$ responds to a change in $S_i$. $S_{i,set}$ is the homeostatic setpoint for the stimulus signal $S_i$. During positive feedback, $G_{a,i}$ tends towards one when $S_i$ is greater than $S_{i,set}$ and towards zero when $S_i$ is less than $S_{i,set}$. In vivo, these bounds mimic the saturated levels of phosphorylation and dephosphorylation of underlying proteins by protein kinase.

The control signal $G_{c,i}$ reflects the net result of downstream signals and governs how the effector parameters (i.e. wall volume or the number of half-sarcomeres) should respond to the normalized growth signal $G_{a,i}$. The rate of change in $G_{c,i}$ is defined as

$$\frac{dG_{c,i}(t)}{dt} = \begin{cases} \gamma_{growth,i}\dfrac{\left(G_{a,i}(t) - 0.5\right)}{0.5} & G_{a,i} \geq 0.5 \\ \gamma_{anti\ growth,i}\dfrac{\left(0.5 - G_{a,i}(t)\right)}{0.5} & G_{a,i} < 0.5 \end{cases} \quad (2)$$

where $\gamma_{growth,i}$ and $\gamma_{anti\ growth,i}$ are rate constants that set the speed at which the effector parameters would grow or shrink according to $G_{a,i}$. Finally, eccentric growth was implemented by changing the number of serial half-sarcomeres around the circumference of the left ventricle. Concentric growth was modeled by changing the left ventricular wall volume to mimic the parallel deposition of half-sarcomeres.

## RESULTS

Figure 2 summarizes the simulated response to two types of valvular dysfunction wherein each column represents one case. All simulations started with model parameters set to default values that mimic the LV function of an adult human with no valvular disease.

Aortic stenosis (left-hand column) was modeled by increasing the aortic resistance parameter. In response to such a perturbation, LV wall volume increased by ~30%, end-diastolic LV cavity volume decreased by ~8%, but end-systolic LV cavity volume remained nearly unchanged. These changes led to thickening of the LV wall by ~21% and ~29% at end-systole and end-diastole, respectively, suggesting the occurrence of concentric growth.

Mitral insufficiency (right-hand column) was modeled by allowing retrograde blood flow through the mitral valve during systole. A ~60 ml regurgitant volume resulted in the LV wall volume increasing by ~50% and dilation of the LV cavity (~57% at end-diastole and ~68% at end-systole). Due to these changes, the LV wall hypertrophied by ~12% at end-diastole and 10% at end-systole. Furthermore, simulations for each valvular disorder regained LV size and function (reversal of growth) once the disease-mimicking perturbation was removed.

## DISCUSSION

The new framework simulated concentric growth (wall thickening / thinning) and eccentric growth (chamber dilation / constriction) in response to two types of valvular disorder. The results were consistent with changes in LV dimension reported in the literature for patients with aortic stenosis and mitral insufficiency. In conclusion, the simulations suggest that myosin ATPase normalized to myofibrillar volume and intercellular passive stress can be used to drive concentric and eccentric growth in simulations of valve disease.

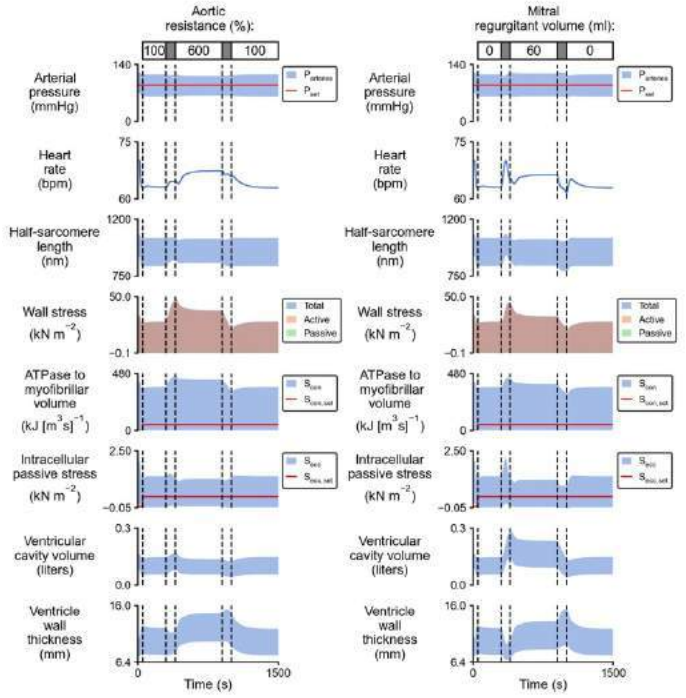


**Figure 2. Predicted LV growth in response to two types of valvular disorders.** Each column summarizes the simulated response to a valvular disease (left, aortic stenosis; right, mitral insufficiency). In each column, $P_{arteries}$ is arterial pressure, $P_{set}$ is the baroreflex setpoint which is set to 90 mmHg, $S_{con}$ and $S_{con,set}$ refer to the driving signal and setpoint for concentric growth, respectively, $S_{ecc}$ and $S_{ecc,set}$ refer to the driving signal and setpoint for eccentric growth, respectively. The growth module was activated at 50 s (first vertical line from left on all panels) when the system was at steady state using default parameters. The disease-mimicking perturbations were gradually applied (between second and third vertical lines) by altering the relevant model parameters. Once the growth simulations were at steady state, the underlying perturbations were removed (between fourth and fifth vertical lines) to capture the reversal of growth. Variables that are pulsatile during a cardiac cycle are shown by an envelope containing the extreme values.


## ACKNOWLEDGEMENTS

Supported by NIH HL133359 to KSC and JFW, NIH 148785 and TR0001998 to KSC, and AHA TP135689 to KSC.


## REFERENCES


1. Davis, J., et al., *A Tension-Based Model Distinguishes Hypertrophic versus Dilated Cardiomyopathy.* Cell, 2016. **165**(5): p. 1147-1159.
2. Lyon, R.C., et al., *Mechanotransduction in cardiac hypertrophy and failure.* Circ Res, 2015. **116**(8): p. 1462-1476.
3. Campbell, K.S., B.S. Chrisman, and S.G. Campbell, *Multiscale Modeling of Cardiovascular Function Predicts That the End-Systolic Pressure Volume Relationship Can Be Targeted via Multiple Therapeutic Strategies.* Front Physiol, 2020. **11**: p. 1043.

SB³C2022
Summer Biomechanics, Bioengineering and Biotransport Conference
June 20-23, Eastern Shore, MD, USA

# EVALUATING THE CAPABILITIES OF A NOVEL DEVICE DESIGNED TO PRESERVE WHOLE PANCREASES VIA OXYGENATED PERFUSION

**Daniel J. Portillo (1), Jose Gonzalez (1), Carorina Villareal (1), Sophia Salazar (1), R. Lyle Hood (1,2)**

(1) Department of Mechanical Engineering, The University of Texas at San Antonio, San Antonio, TX, USA
(2) Department of Biomedical Engineering, The University of Texas at San Antonio, San Antonio, TX, USA

## INTRODUCTION

Although there are over 1,000 pancreas transplants performed in the US every year, that number is slowly declining as more donors are presenting higher-risk organs for transplantation [1]. Recent research focused on preserving pancreases using machine perfusion (MP), as opposed to static cold storage (the current gold standard), has shown that MP offers significantly improved preservation outcomes [1]. The benefits of MP for pancreas preservation include nutrient delivery, toxic waste removal, and reduced rates of ischemic reperfusion injury [1]. Leemkuil *et al.* also demonstrated that supplying oxygen to the perfusion solution is feasible and can further increase pancreatic tissue viability [2]. Despite those benefits, there are currently no devices on the market that are designed to preserve pancreases via MP.

Fortunately, a cost-effective, versatile oxygenating perfusion system (VOPS) has been previously designed by our group [3]. The novel design of the VOPS incorporates the oxygenator and perfusion pump into one embodiment. That embodiment contains small silicone tubes, which are cyclically inflated/deflated with compressed oxygen. The expanding and contracting tubes act as a diaphragm-style pump that displaces and circulates the perfusion solution throughout the device. Since oxygen permeates through silicone, the tubes also supply oxygen to the circulating perfusion solution. Thus far, our group has successfully demonstrated that the VOPS is capable of supplying perfusion pressures, flow rates, and oxygenation rates used in previous kidney, liver, and heart preservation studies [3].

The focus of this work was to evaluate the VOPS's ability to supply perfusion parameters used by previous groups to preserve pancreases. Since perfusion pressure is the most reported perfusion parameter in pancreas preservation [4], we hypothesized that the VOPS could achieve perfusion pressures between 15 – 60 mmHg while pumping against a phantom element that mimicked the vascular resistance of a pancreas.

## METHODS

Preliminary tests were conducted to measure the rate that each silicone tube length expanded and contracted, which determined the rate that they were pulsed. Three different lengths of silicone tubing (Silastic® Laboratory Tubing, DuPont de Nemours, Inc.) were evaluated in the VOPS; they had a constant inner diameter of 0.058 in. and lengths of 10, 30, or 50 ft. Various compressed oxygen pressures were used to inflate and deflate the tubes, ranging from 2 – 12 psi (increments of 2 psi). In total, 90 trials were conducted (three silicone tubes, 6 oxygen pressures, n=5). Phosphate-buffered saline (PBS, Sigma-Aldrich) was used as the perfusion solution and a flexible polyvinyl chloride (PVC) tube was installed in the perfusion loop to mimic the vascular resistance of a pancreas (0.76 mmHg/mL/min) [5].

The perfusion pressures were measured with pressure transducers (PX309-030G5V, Omega Engineering, Inc.) and the flow rate was measured with an ultrasonic flow sensor (2PXL-TS410, Transonic Systems Inc.). All sensors were read simultaneously using a custom LabVIEW virtual interface (NI 9221 and NI USB-9162, LabVIEW 2019 SP1, National Instruments). The oxygenation rate ($\dot{O}_2$) was calculated using Equation 1 (Van 't Hoff equation) and relied on an oxygen solubility constant ($H_c$), the volume of solution in the VOPS

($V_{sol}$), and the pressure increase in the device ($P_{dev}$) over the time of the trial ($t_{trial}$).

$$\dot{O}_2 = H_c V_{sol} \left(\frac{\Delta P_{dev}}{t_{trial}}\right) \quad (1)$$

## RESULTS

Figure 1 illustrates the peak perfusion pressures attained by different silicone tube lengths across the range of oxygen supply pressures. The peak perfusion was linearly correlated to the oxygen supply pressure and inversely proportional to the length of silicone tubing. All three lengths of silicone tubing achieved adequate perfusion pressures when operating with oxygen pressures between 4 – 10 psi. Figures 2 and 3 illustrate the mean flow rates (7.1 – 20.6 mL/min) and mean oxygenation rates (5.5 – 90.2 µmol/min), respectively, that were achieved while the VOPS was operating within ideal perfusion pressures [4].

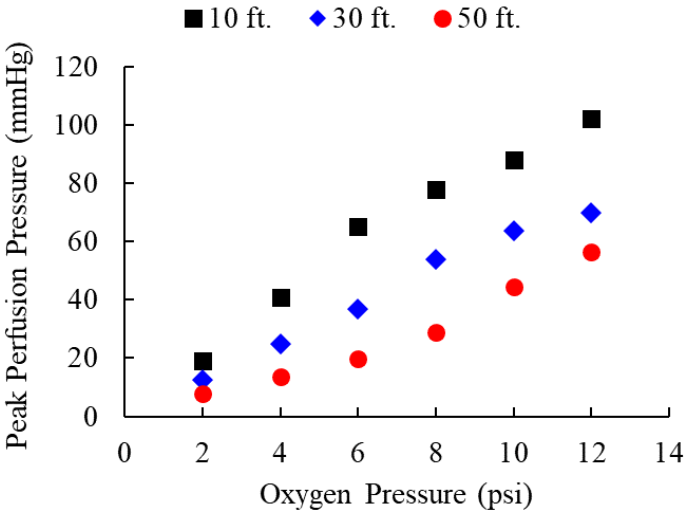


**Figure 1. Peak perfusion pressures produced by different lengths of tubing at various oxygen pressures.**

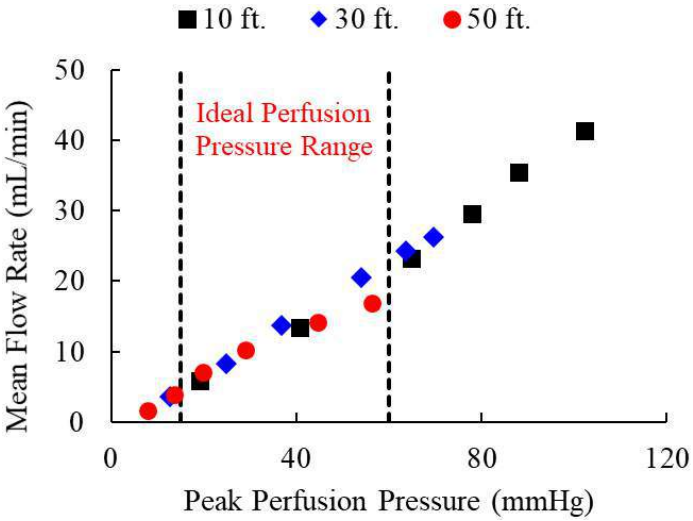


**Figure 2. Mean flow rates and peak perfusion pressures produced by the VOPS for various silicone tubes.**

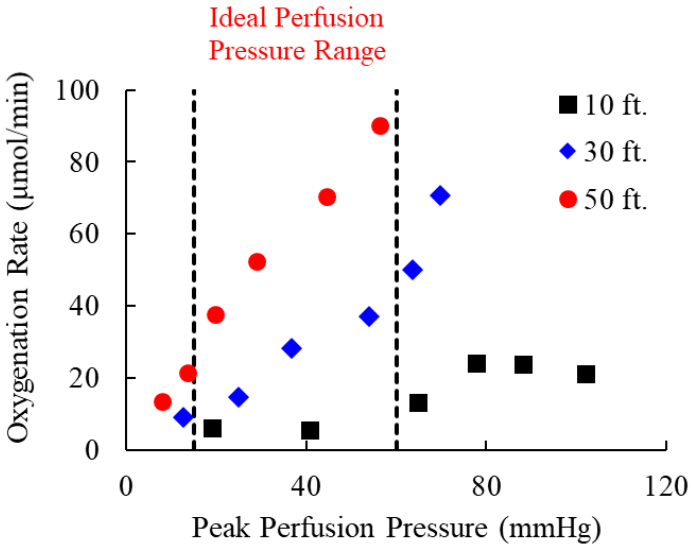


**Figure 3. Oxygenation rates and peak perfusion pressures produced by the VOPS for various silicone tubes.**

## DISCUSSION

The results confirmed our hypothesis by demonstrating that the VOPS produced a wide range of flow rates and oxygenation rates when performing at ideal perfusion pressures (15 – 60 mmHg) [4]. Although all tube lengths produced equivalent flow rates, the shorter tube lengths produced higher perfusion pressures and lower oxygenation rates. This study strengthens the notion that *versatile* oxygenating perfusion systems could exist and would facilitate wider use compared to the current organ-specific preservation devices. Future work will focus on characterizing the VOPS across different viscosities of common perfusion solutions, creating computational models to simulate the VOPS performance, and *ex vivo* studies to evaluate the preservation efficacy of the VOPS.


## ACKNOWLEDGEMENTS

This work was funded through a Department of Defense PRMRP; Award Number: W81XWH-18-1-0640. The authors would like to thank Dr. Endor Finol and Dr. Chris Combs for providing data acquisition equipment.


## REFERENCES


[1] Hamaoui, K. *et al.*, "Machine perfusion and the pancreas: will it increase the donor pool?," *Current Diabetes Reports*, 19 (8):1-12, 2019.

[2] Leemkuil, M. *et al.*, "Hypothermic oxygenated machine perfusion of the human donor pancreas," *Transplantation Direct*, 4(10), 2018.

[3] Portillo, D.J. *et al.*, "Characterizing and tuning perfusion parameters within an innovative versatile oxygenating perfusion system," *Annals of Biomedical Engineering*, 2021.

[4] Prudhomme, T. *et al.*, "Ex situ perfusion of pancreas for whole-organ transplantation: is it safe and feasible? A systematic review," *Journal of Diabetes Science and Technology*, 14(1):120-134, 2020.

[5] Hamaoui, K. *et al.*, "Development of pancreatic machine perfusion: translational steps from porcine to human models," *Journal of Surgical Research*, 223:263-274, 2018.

# CONSTRUCTION AND INITIAL EXPERIENCE WITH A FOUR-CHAMBERED FLUID-STRUCTURE INTERACTION MODEL OF THE HEART

**Marshall R. Davey (1), Charles Puelz (2-3), Simone Rossi (4), Margaret Anne Smith (4), David Wells (4), Boyce E. Griffith (4)**

(1) Bioinformatics and Computational Biology, UNC-Chapel Hill, Chapel Hill, NC, USA
(2) Pediatrics-Cardiology, Baylor College of Medicine, Houston, TX, USA
(3) Computational and Applied Mathematics, Rice University, Houston, TX, USA
(4) Mathematics, UNC-Chapel Hill, Chapel Hill, NC, USA

## INTRODUCTION

Cardiovascular disease is the leading cause of death in the United States, and the estimated annual cost associated with heart diseases in the U.S. alone is over $200B [1]. The current paradigms for in vivo cardiovascular diagnosis and research is imaging and catheterization, but imaging can be expensive, catheterization is invasive, and both are inadequate with respect to capturing certain measurements, such as local stresses within the myocardium [2].

Computational modeling can assist researchers and clinicians by providing insight into data inaccessible to imaging modalities [3]. The heart lends itself to macro-scale, whole organ computational modeling because the myocardium can be described as a continuum, and the blood acts as an incompressible fluid at the organ scale [4]. Fluid-structure interaction (FSI) methods, in which the fluid dynamics inform the structural deformations and the stresses from the structures impact the fluid velocity, have the potential to provide the most accurate and predictive description of the blood-organ relationship as neither the structure motions nor fluid dynamics are prescribed [4].

We are only aware of two previous FSI models of the entire heart, but these models either lack physiologic valves [5] or model the myocardium in a way non-conducive to extracting meaningful data about stresses and strains [6]. The immersed finite element (IFE) method [7] is an FSI method that enables modeling studies of biological tissues, including cardiac chambers coupled with valves [8, 9]. This study employs the IFE method to construct a comprehensive model of the entire heart, including physiologic valves. This model of the heart will ultimately be used as a platform for valve replacement and repair studies that cannot be conducted using prior models because of the capabilities of the FSI methods used.

## METHODS

Our IFE method relies on a finite element (FE) mesh for all of the structures fully inscribed within a cuboid computational fluid domain. The myocardial structure in our model was generated using computed tomography (CT) data from a male in his 30s. The segmentation process results in surface representations of most of the cardiac structures that must be thickened to physiologic values. For the ventricles, however, the myocardium is thick enough to capture the inner and outer surfaces which can be attached to capture the in vivo wall thickness. In contrast the valves are difficult to capture using CT data [2]. Consequently, the structures of all four valves and the valve complexes were constructed using measurements from previous studies on valve anatomies [10, 11]. Fig. 1 shows the resulting FE geometry.

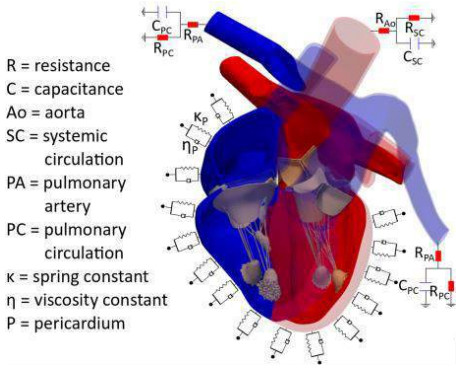


**Figure 1: The structure of the model includes all of the chambers and valve complexes. The pericardium, modeled by a spring-dashpot model, acts to tether the structure, and the Windkessel model informs the outflow boundary conditions.**

The passive mechanics of the structures are generally anisotropic because of the myosin and actin fibers within the myocardium and the collagen fibers within the valves [12]. To capture this anisotropy within our model, we defined three orthogonal fiber fields within the

FE mesh [12]. We identified constitutive equations that relied on fiber orientations for the structures based on studies that used human tissue for parameter estimation via stress-strain experiments [13-15]. The contraction of the heart is generated using an active strain model [16] using waveforms based on chamber pressure plots. The effects of the pericardium are modeled using a spring and dashpot in parallel tethered to the epicardial surface [17], as seen in Fig. 1.

The fluid in the IFE method is modeled using the incompressible Navier-Stokes equations. The boundary of the fluid domain is defined with traction free boundary conditions (BCs) except where the outflow vessels of the structure meet the edge of the domain. The outflow pressure BC is controlled by a three-element Windkessel (WK) model [18], shown in Fig. 1, that uses the flux through the outflow boundary of the fluid domain to inform the pressure. The left and right heart fluid flows and pressures are not currently connected, so during atrial filling we rely on a fluid source within the atria to generate fluid. The entire model was built using the IBAMR software platform [19].

## RESULTS

We ran full simulations of the model over consecutive cycles to test the efficacy of our methods. Fig. 2 shows snapshots of one of the model iterations at key points within the cardiac cycle, which helps to verify that the valves are working and the fluid is being pumped as anticipated during each phase of the cycle.

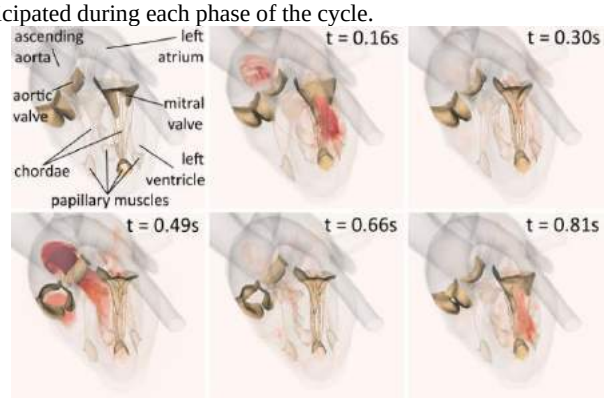


**Figure 2: Heat map of the velocity magnitude (0-120 cm/s) during different phases of the cardiac cycle.**

A particularly useful diagnostic tool is the pressure-volume (P-V) relation in the left ventricle (LV) throughout the entire cycle (Fig. 3). LV is the focus of our results as the most data exists for the LV, and the LV is subject to the highest stresses and strains. Plotting the P-V relationship over successive cycles can also show if the model is converging to a steady-state with regards to the LV performance. From the P-V relation we can also extract general data about the cardiac cycle to assess performance including the end diastolic volume (EDV), end systolic volume (ESV), and stroke volume (SV) (Fig. 3).

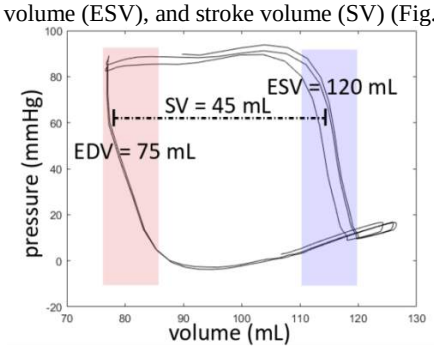


**Figure 3: Pressure-volume loop over 3 consecutive cycles with labelled isovolumetric contraction (blue) and relaxation (red) phases. Loops are formed counter-clockwise in time. End diastolic volume (EDV), end systolic volume (ESV), and stroke volume (SV), have been labelled for clarity.**

## DISCUSSION

The results demonstrate that the IFE method can be used to model whole-heart fluid and structural dynamics across full cardiac cycles. Our model intrinsically captures the isovolumetric contraction and relaxation phases of the cardiac cycle, and it reaches a steady state with respect to the LV P-V relationship within two-to-three cardiac cycles (Fig. 3). This is significant in that no prescriptive motion is defined and the fluid is only externally influenced by the WK model at the boundary and a fluid source in the atria during atrial filling.

The flow dynamics also capture the important posterior-to-anterior washout jet of fluid during the ventricular filling phase after contraction (Fig. 2). Our model is unique in that it captures these features while also using a physiologic description of the valves. The SV is 45 mL (Fig. 3), which leads to a cardiac output (CO) of 2.7 L/min given that the simulation was running at 60 bpm. This is significantly lower, however, than a healthy cardiac output of 5 L/min, where the SV should be closer to 80 mL [20].

In its current condition the model can be improved with respect to SV and CO. However, results from previous iterations show that changing the contraction magnitude, tuning the WK parameters, and adjusting the contraction waveforms significantly affects the P-V relationship in a predictable way. We are confident that we can use these features to replicate a fully physiologic cycle of a healthy human heart.

With these results we have also shown that the model has potential, after tuning, to be used in valve replacement and repair studies where FSI is needed in addition to physiologic valves. Specifically we plan to use this model to conduct the first FSI studies of edge-to-edge repair devices and transcatheter mitral valve replacement devices used as interventions for mitral regurgitation. With this model we can query the stresses these devices place on the heart and the valve leaflets, as well as identify any changes in flow patterns these devices cause.

## ACKNOWLEDGEMENTS

We acknowledge funding from the NIH (Awards R01HL117063, U01HL143336, and R01HL157631) and NSF (Awards OAC 1450327, OAC 1652541, OAC 1931516, and CBET 1757193).

## REFERENCES

[1] https://www.cdc.gov/heartdisease/facts.htm. 2021.
[2] Di Carli, MF et al., *Circulation*, 133(25):2640-2661, 2016.
[3] Ben Zerky, S et al., *Circ Cardiovasc Imaging*, 9(1):e003254, 2016.
[4] Hirschhorn, M et al., *Med Eng Phys*, 78:1-13, 2020.
[5] Kariya, T et al., *Ann Biomed Eng*, 48(6):1740-1750, 2020.
[6] McQueen, DM et al., *Mechanics for a New Mellennium*, 2002.
[7] Griffith, BE et al., *Int J Numer Method Biomed Eng*, 0:1-32, 2017.
[8] Liuyang, F et al.,*Int J Numer Method Biomed Eng*, 35:e3254, 2019.
[9] Gao, H et al., *Med Eng Phys*, 47:128-136, 2017.
[10] Swanson, MS et al., *Circ Res*, 35(6):871-882, 1974.
[11] Lim, KH et al., *J Heart Valve Dis*, 14(3):386-392, 2005.
[12] Rossi, S et al., *Eur J Mech A Solids*, 48:129-142, 2014.
[13] Pham, T et al., *Acta Biomater*, 54:345-355, 2017.
[14] Gültekin, O et al., *Comput Methods Biomech Biomed Engin*, 19:1647-1664, 2016.
[15] Augustin, CM et al., *Biomech Model Mechanobiol*, 19:1015-1034, 2020.
[16] Ambrosi, D et al., *J Elasticity*, 107:199-212, 2012.
[17] Pfaller,MR et al.,*Biomech Model Mechanobiol*,18:503-529, 2019.
[18] Stergiopulos, N et al., *Am J Physiol*, 276(1):H81-89, 1999.
[19] Griffith, BE, https://ibamr.github.io/, 2002.
[20] Katz, DH et al., *Cardiovascular Hemodynamics: An introductory Guide*, Ch. 4:51-60, 2019.

SB³C2022
Summer Biomechanics, Bioengineering and Biotransport Conference
June 20-23, Eastern Shore, MD, USA

# ROBUST ARTICULATION-INDUCED CARTILAGE REHYDRATION IS SUSTAINED FOLLOWING PROTEOGLYCAN LOSS

**Meghan E. Kupratis (1), Atia Rahman (2), Elise A. Corbin (1,3), David L. Burris (2), Christopher Price (1,2)**

(1) Biomedical Engineering
University of Delaware
Newark, DE, USA

(2) Mechanical Engineering
University of Delaware
Newark, DE, USA

(3) Materials Science & Engineering
University of Delaware
Newark, DE, USA

## INTRODUCTION

Articular cartilage is a highly-hydrated connective tissue that facilitates load dissipation and nearly frictionless motion at diarthrodial joints. Nonetheless, cartilage is susceptible to osteoarthritis (OA), a progressive, irreversible disease that is a leading cause of disability among U.S. adults.[1] Healthy cartilage consists primarily of interstitial fluid (68-85% by weight). The remainder is comprised of a deformable matrix of anionic proteoglycans (PG) and fibrillar collagen (5-10% and 10-20% wet weight, respectively).[2] Degradation of these matrix constituents is a hallmark of OA that increases tissue compliance and permeability. Indeed, biochemical approaches, such as enzymatic digestion of proteoglycans and/or collagen, stimulate OA-like changes *ex vivo,* including decreased modulus and elevated permeability.[3-5]

Benchtop tribological studies suggest that ECM degradation impairs cartilage's lubrication behaviors, including friction coefficients and fluid load support (FLS).[4-5] However, such studies have been confined to sliding environments interrogating only a portion of the lubrication modes accessible to cartilage, namely boundary (sliding speeds ≤1 mm/s) and mixed mode lubrication (~10 mm/s). Recently, we found that sliding at higher—and more physiological—speeds (≥40 mm/s) promotes interstitial fluid recovery. Under these conditions, interstitial lubrication is sustained through a hydrodynamically-mediated mechanism termed *tribological rehydration*.[6] In the context of tribological rehydration, our findings suggest cartilage's exceptional *in vivo* frictional behaviors ($\mu$<0.01) depend on the maintenance of high FLS via articulation-driven fluid recovery. Furthermore, we recently discovered that healthy cartilage's ability to support tribological rehydration at speeds ≥40 mm/s is largely insensitive to tissue property variations across five model species.[7] Here, we extended our studies of articulation-mediated interstitial fluid recovery to compromised tissues using controlled digestion of articular cartilage via chondroitinase-ABC (chABC). Using this model, we assess whether moderate levels of PG removal (consistent with OA progression in humans) have adverse effects on articulation-induced tribological rehydration.

## METHODS

Osteochondral explants (∅19mm) were harvested from the femoral condyles of mature bovine stifle joints. Biphasic tissue properties were measured by microindentation with a ∅4mm spherical probe under creep relaxation. Hertz biphasic theory[8] was used to calculate the effective contact modulus ($E_c$), tensile modulus ($E_t$), and equilibrium contact modulus ($E_{c0}$). Tribological characterization consisted of 30 minutes of static compression at 0.25 MPa followed by 15 minutes of reciprocal sliding at 80 mm/s under the same stress. Compression magnitudes ($\delta$) and friction coefficients ($\mu$) were recorded in LABVIEW and analyzed via MATLAB.

Indentation and tribological characterization were repeated following enzymatic digestion with 0.1 units/mL chondroitinase ABC (chABC) in 50 mM Tris-HCl, 60 mM sodium acetate, and 0.02% bovine serum albumin.[4] Explants were digested for 40 min, washed, indented, and tribologically characterized. Explants then were digested for an additional 3 hr and 20 min (for total enzyme exposure time of 4 hr) and characterized a third time. These incubation times were chosen based on preliminary studies that aimed to generate modulus and permeability values consistent with, and then exceeding those of arthritic human cartilage.[9] Differences among groups were assessed via two-way ANOVA with significance at multiple comparison-adjusted $p < 0.05$.

## RESULTS

Biphasic tissue properties were characterized via Hertzian indentation. As evidenced in **Fig. 1A**, 40 minutes of chABC digestion had little influence on deformation relative to naïve samples under equivalent normal loads (~160mN; $p = 0.71$). In contrast, a sharp

increase in deformation was observed following 4 hours of digestion ($p < 0.0001$). As expected, equilibrium contact moduli ($E_{c0}$), which describes the compressive stiffness of the ECM at steady state, decreased significantly with each digestion period (**Fig. 1B, left**). Average equilibrium contact moduli decreased by 24% and 60.5% (from 0.56 ± 0.24 MPa for naïve tissue to 0.44 ± 0.18 and 0.30 ± 0.13 MPa) following 40 minutes and 4 hours of chondroitinase digestion, respectively ($p < 0.0001$). Chondroitinase digestion had no significant impact on $E_c$ (**Fig. 1B, right**), which depends upon contributions of both fluid load support and solid matrix integrity, or on $E_t$ ($p > 0.20$).

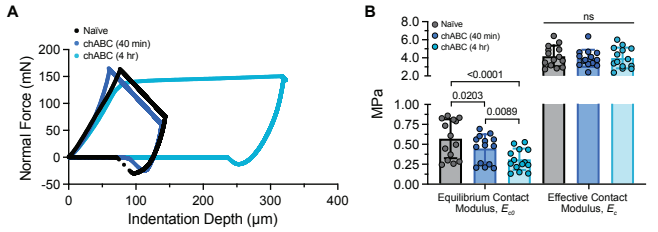


**Fig. 1. Mechanical characterization. (A) Force vs. deformation response of a representative sample before and after digestion. (B) Digestion led to decreases in equilibrium contact moduli (left) but no differences in effective contact moduli (right).**

The tribological rehydration of a representative sample prior to and following 40 minutes and 4 hours of enzymatic digestion via chondroitinase are shown in **Fig. 2**. Data summarizing the strain recovery and friction behaviors of n = 7 longitudinally digested cSCA explants are shown in **Fig. 3**. While strain at the start- and end-of-sliding were significantly elevated following 4 hours of enzymatic degradation ($p = 0.0001$ and 0.024 vs. naïve tissue for start- and end-of-sliding, respectively), no differences in strain recovery among groups were observed ($p = 0.20$). This indicated sustained capacity for tribological rehydration even following 4 hours of PG digestion (**Fig. 2A**). Similarly, friction coefficients did not differ significantly among groups, despite exhibiting a modest rise with longitudinal chABC digestion (**Fig. 2B**).

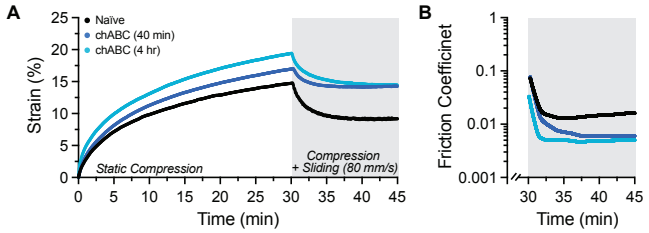


**Fig. 2. Tribological rehydration behavior of a representative before and after proteoglycan digestion.**

## DISCUSSION

Our findings demonstrate that cartilage can retain rather remarkable tribological rehydration and lubrication capacity following proteoglycan digestion. Consistent with prior work,[4] chABC digestion led to substantial loss of compressive stiffness (>50%) and increases in permeability (18%, not shown), but had little effect on collagen network integrity (as assessed by tensile modulus). Despite substantial reductions in compressive modulus, chABC-digested cartilage exhibited marked strain recovery and concomitant decreases in friction coefficients (to ~0.01) during high-speed sliding. In contrast, preliminary assessments of tribological rehydration following collagenase degradation indicate deleterious effects of compromised tensile stiffness on tissue function, namely reduced strain recovery and

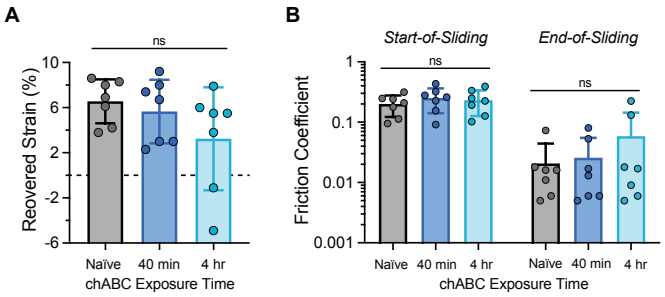


**Fig. 3. Chondroitinase digested explants retained the capacity for robust tribological rehydration, as indicated by the strain recovery (A) and friction behavior (B). Tribological rehydration produced significant decreases in friction coefficients between start- and end-of-sliding in all conditions ($p < 0.002$, paired t-test).**

elevated equilibrium friction coefficients (≥0.1). These findings suggest that the collagen network's ability to resist lateral expansion under compressive load plays a crucial role in tribological rehydration. This mirrors work from Soltz and Ateshian, who found that high tension-compression nonlinearity is required to sustain high FLS in cartilage.[10] However, our results also hint at a compressive property floor below which interstitial lubrication is significantly impacted. **Fig. 3A** shows two explants failed to exhibit interstitial fluid recovery following the second chABC digestion. Interestingly, these samples had the lowest equilibrium contact moduli both initially (~0.25 MPa, vs. ~0.4-0.9 MPa for the remaining samples) and after the second digestion (~0.1 MPa).

Broadly, this study provides important insights regarding OA etiology and treatment strategies. That cartilage can support tribological rehydration in the face of significant proteoglycan loss and compromised compressive resistance might inform the natural timeline of OA progression. While PG loss is considered an early sign of OA onset, the disease can remain asymptomatic for many years following such identification. This may be, at least in part, because cartilage appears capable of supporting robust hydration recovery and interstitial lubrication well after PG loss is initiated. Furthermore, PG loss is thought to precede collagen loss in the OA cascade. It has been suggested that interactions of aggrecan and other PGs with collagen create a macromolecular coating that protects collagen from proteolytic degradation.[11] Thus, only once extensive PG loss has occurred might the collagen network become vulnerable to physical and/or biological degradation. Together with our present findings, this suggests that PG repair/reinforcement, such as by a PG-mimetic interpenetrating network (IPN)[12] may be a promising strategy to slow OA-associated degradation of both PG and collagen. Our ongoing work will investigate whether PG-based reinforcement can restore FLS and tribological rehydration in digested cartilage.

## REFERENCES


[1] Leifer *et al*., *OA&C*, 30: 10-16, 2022.
[2] Ateshian, *J Biomech*, 9(42): 1163-1176, 2009.
[3] Han *et al., Sci Rep*, 11:9527, 2021.
[4] Basalo *et al., J Biomech Eng*, 128: 131-134, 2006.
[5] Bonnevie *et al., JOR,* 36(5): 1456-1464, 2018.
[6] Moore & Burris, *OA&C,* 25: 99-107, 2017.
[7] Kupratis *et al.*, *Acta Biomater*, 138: 375-389, 2022.
[8] Moore & Burris, *J Biomech,* 47: 148-153, 2014.
[9] Graham *et al.*, *JOR*, 36(12): 3256-3267, 2018.
[10] Soltz & Ateshian, *J Biomech*, 122:576-586, 2000.
[11] Pratta *et al*. *J Biol Chem*, 278(46): 45539-45545, 2003.
[12] Cooper *et al*., *Biomaterials*, 181:210-226, 2018.

# IDENTIFYING MICRO-INDENTATION TESTING PARAMETERS SUITABLE FOR BRAIN TISSUE TESTING

**Xuesong Zhang (1), Johannes Weickenmeier (1)**

(1) Department of Mechanical Engineering
Stevens Institute of Technology
Hoboken, NJ, United States

## INTRODUCTION

Mechanical properties of soft tissues play an important role in maintaining their physical and biological function. It is well understood that the mechanical environment of cerebral tissues influences everything from neuronal development to neurodegeneration [1,2]. For example, Goriely et al. have summarized and concluded the importance of mechanical factors, including deformation, stretch, strain, strain rate, pressure, and stress on regulating both brain geometry and functions [3].

Brain tissue is considered as extremely soft and most complex organ in the body, which can be divided into gray matter and white matter. Specifically, gray matter consists of neurons, some axons. While white matter is made up of glial cells and bundles of myelinated axons. Also, both white matter and gray matter have remarkable water content. The microstructural nature of brain tissue leads brain to be a nonlinear, anisotropic, poroviscoelastic, and spatially heterogeneous material [4].

Indentation is one of the most popular experimental techniques to determine the mechanical properties of a wide array of soft biological tissues. Despite its frequent use, however, some experimental design factors must be determined for each application including variations from repeated measurements in the same location, indentation speeds, indentation depths, bead size, testing conditions such as dry or submerged, and the model use to analyze the force-displacement data. In the present study, we investigated the impact of these indentation parameters on stiffness and report indentation results for fresh mouse brain experiments.

## METHODS

**Sample Preparation.** We used fresh mouse brain tissue (with a focus on the corpus callosum, cortex, cingulum, and hippocampus) and the brain-mimicking material gelatin methacrylate (GelMA) hydrogel. Specifically, 5% (weight/volume) GelMa was cured by UV light for 2 minutes, which has been widely used in biomedical applications, including 3D bioprinting brain-like constructs [5]. Fresh mouse brains were harvested from 6-week-old female mice from Jackson Laboratory. We cut 1000 um thick slices, glued them into a Petri dish, and submerged our samples in three different fluids to test their impact on the indenter-tissue interaction: deionized (DI) water, phosphate-buffered saline (PBS) solution, and contact lens (CL) solution. GelMA bioink was prepared from ready lyophilized GelMA foam (Allevi Inc., PA, USA). 0.5% Lithium phenyl-2,4,6-trimethylbenzoylphosphinate (LAP, Allevi Inc., PA, USA) and 5% GelMA foam were mixed thoroughly with PBS at 60°C for over an hour in the dark. When the final GelMA bioink solution is well homogenized and dissolved, it is stored overnight in the dark at 4°C. When needed, GelMA is melted down in a warm water bath (37 °C) and crosslinked after use under 365nm UV light.

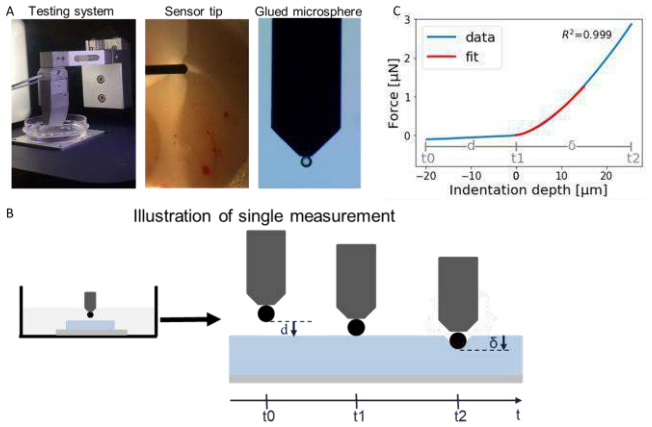


**Fig.1. Illustration of the machine setup, testing protocol, and the resulting force-depth data. (A) Machine setup. (B) Testing method. (C) The resulting force-indentation depth data and the model fitted curve.**

**Indentation Measurement and Data Analysis.** We performed a sensitivity analysis with 5% GelMa and a fresh mouse brain slice and varied six parameters: number of measurements in the same location (1 to 9), indentation speed (5, 10, 15, 20μm/s), indentation depth (4 to

20µm), bead diameter (50 and 100µm), tissue surfactant (PBS, DI water, and CL solution), and fitting model (Hertzian contact model, Neo-Hookean, and Ogden). We used our FT-MTA03 testing device (FemtoTools AG) equipped with a FT-S200 sensing probe (Fig.1A). Our testing protocol, as shown in Fig.1B, is as follows: we position the tip over the sample 20µm and further indent the sample until it reaches the mentioned indentation depths at the proposed speeds. We fit our force-displacement data to three previously mentioned material models and report resulting stiffness parameters. We subsequently performed Student T-tests to analyze statistical significance between individual groups (* indicates $p < 0.05$, ** indicates $p<0.01$, and *** indicates $p<0.001$).

## RESULTS

We summarize the results of our sensitivity analysis with 5% GelMa in Figure 2. Averaged GelMa stiffness is 1.3±0.07 kPa and is independent of the number of measurements in the same location (Fig.2A). Due to the nonlinearity of the sample, stiffness increases with indentation depth (Fig.2B). Average stiffness is higher at an indention speed of 20µm/s (1.37±0.08 kPa) in comparison to 5µm/s (1.26±0.09 kPa) due to the viscosity of the material (Fig.2C). Average stiffness decreases with bead size because of the nonlinearity of the material (Fig.2D). The strain is smaller when we use a larger bead diameter according to equation $\varepsilon i = i0.2 * i\sqrt{d/R}$, with strain ε, indentation depth d, and bead radius R [6]. Furthermore, the different fitting models (Fig.2E) result in young's moduli of 1.3±0.09 kPa for the Hertzian contact model, 1.03±0.08 kPa for the Neo-Hookean material model, and 1.06±0.12 kPa for the Ogden model; goodness of fit, measured by the $R^2$ value (>0.998), was similar for all three models (Fig.2F). Lastly, the surfactant has a great influence on indentation testing; contact lens solution gives the least resistance (Fig.2F) for the indenter when compared to PBS and DI water due to the decreased surface tension of CL solution [7].

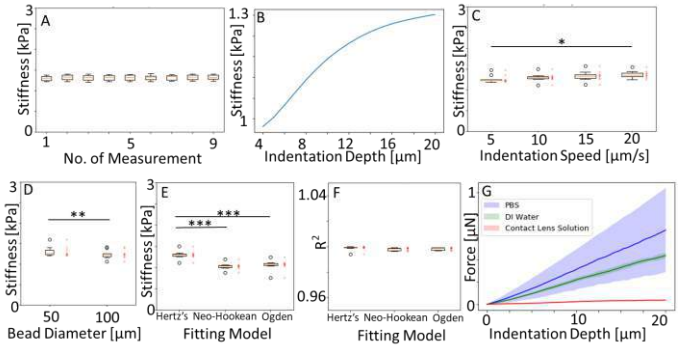


**Fig.2. The sensitivity analysis of parameters in indentation testing for 5% GelMa. (A) The number of measurements at the same location. (B) Indention depths. (C) Bead sizes. (D) Indentation speeds. (E) Fitting models. (F) The $R^2$ values of the fitting models. (G) The mean and standard deviation curve for different surfactants.**

For fresh mouse brain, stiffness of cortex is decreasing from 4.02±0.52 kPa to 3.4±0.59 kPa when we compare the first measurement and the fourth measurement in the same location (Fig.3A). This might be caused by surface damage resulting from repeated measurements and the poro-viscoelastic property of brain tissue. The stiffness continuously increases with indentation depth (Fig.3B). Moreover, the cortex is stiffer when we used a larger diameter bead (Fig.3C), the reason is might because the smaller bead we used, the less water was confined under the bead during testing. Averaged stiffness increases from 3.73±0.7 kPa to 5.06±0.91 kPa with increasing indentation speed from 5µm/s to 20µm/s (Fig.3D), suggesting highly viscous tissue properties. Like 5% GelMa, different fitting models result in different young's modulus (Fig.3E), however, the non-linear models (Neo-Hookean and Ogden) show better $R^2$ values (Fig.3F) than Hertz's linear contact model.

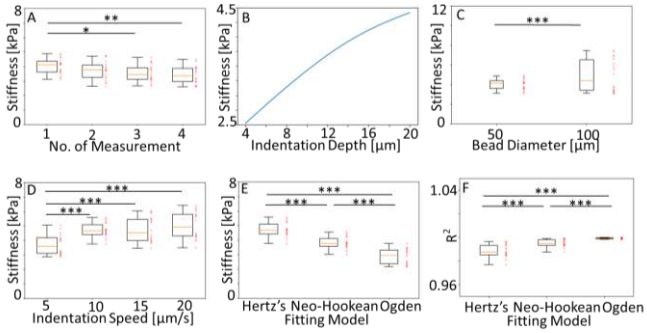


**Fig.3. The sensitivity analysis of parameters in indentation testing for fresh brain cortex. (A) The number of measurements at the same location. (B) Indention depths. (C) Bead sizes. (D) Indentation speeds. (E) Fitting models. (F) The $R^2$ values of the fitting models.**

## DISCUSSION

The influence of testing parameters in indentation experiments was investigated and resulted in a testing protocol suitable for fresh mouse brain tissue. Our results also confirmed that fresh tissue is more heterogeneous, viscous, and behaves more nonlinearly than 5% GelMa.

We already successfully applied our protocol to fresh hippocampal mouse tissue and are able to create localized stiffness maps that align with anatomical subregions as shown in Fig.4. Going forward, we will use our testing protocol to determine the impact of individual microstructural brain constituents on tissue-level mechanical behavior.

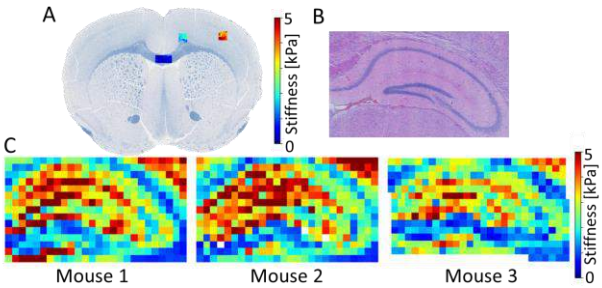


**Fig.4. Application of indentation on fresh soft tissues. (A) The stiffness heterogeneity in mouse corpus callosum, cingulum, and cortex. (B) Hematoxylin and eosin stain result for mouse hippocampus. (C) The stiffness heterogeneity in mouse hippocampus.**

## REFERENCES


[1] Franze, K et al., *Development* 140.15 2013.
[2] Weickenmeier, J et al., *Acta Biomater* 42 2016.
[3] Goriely, A et al. *Biomech Model Mechanobiol* 14.5 2015
[4] Budday, S et al. *Arch. Comput. Methods Eng* 27.4 2020
[5] Li, Y et al., *Biofabrication* 13.1 2020.
[6] Lin, D et al., *Biomech. Model. Mechanobiol*. 8.5 2009
[7] Dalton, K et al., *Optom Vis Sci*, 85.2 2008

SB³C2022
Summer Biomechanics, Bioengineering and Biotransport Conference
June 20-23, Eastern Shore, MD, USA

# COMPARISON OF OSCILLATORY DEFORMATION PATTERNS EXCITED IN THE HUMAN BRAIN IN VIVO BY HARMONIC AND IMPULSIVE SKULL MOTION

**J.D. Escarcega (1), A.K. Knutsen (2), A.A. Alshareef (3), R.J. Okamoto (1), P.V. Bayly (1)**

(1) Mechanical Engineering and Materials Science, Washington University, St. Louis, MO, USA
(2) Henry M. Jackson Foundation for the Advancement of Military Medicine, Bethesda, MD, USA
(3) Electrical and Computer Engineering, Johns Hopkins University, Baltimore, MD, USA

## INTRODUCTION

Traumatic brain injury (TBI) is widespread and associated with the possibility of debilitating emotional and cognitive deficits. TBIs are caused by rapid brain deformations that arise from skull acceleration. The mechanics of TBI are incompletely understood; improved insight and ability to simulate injury could help reduce, diagnose, and treat TBI.

The mechanical behavior of the human brain is difficult to characterize *in vivo*; previous studies have relied on computational and animal models to study brain biomechanics [1, 2, e.g.]. However it is challenging for computer models to capture the nonlinear, viscoelastic, and anisotropic response of the brain, and animal models cannot completely recapitulate human brain behavior due to differences in structure and size. Recently, experimental techniques such as tagged MRI (tMRI) and MR elastography (MRE) have emerged as tools to study low-amplitude, dynamic deformation in the human brain *in vivo*. These imaging methods provide high-resolution data complementing animal and cadaver studies of brain biomechanics.

In previous work we analyzed tMRI images using dynamic mode decomposition (DMD) [3] and identified dominant low frequency modes of oscillation (~7-11 Hz) in which the brain may be vulnerable to injury. MRE is used in our lab [4] to harmonically excite motion in the human brain. The objective of this research is to compare (i) the low frequency modes found by tMRI of impulsive skull motion to (ii) deformation modes excited by harmonic skull motion using MRE.

## METHODS

3D displacement (Fig 1a) and strain data were acquired by tMRI (18 ms/frame 1.5×1.5×5 mm voxels) in two subjects (S1, M 32 yrs; S2, F 37 yrs) undergoing mild impulsive, rotational deceleration in the axial plane (neck rotation). To produce the impulsive loading, the subject voluntarily rotates their head towards the left shoulder until arrested by a soft impact. tMRI images are acquired by a custom sequence synchronized with motion. Displacement and strain were estimated from the motion of tag planes [5]. These data are also on the Brain Biomechanics Imaging Repository on the NeuroImaging Tools and Resources Collaboratory (NITRC) site [6]. Strain fields were analyzed by DMD [3] to find the dominant oscillatory mode of 3D deformation, defined by a complex 3D strain tensor at each voxel. (Fig 1b).

MR elastography was used to image brain deformation in two different human subjects (S3, F 57 yrs; S4, M 55 yrs) undergoing harmonic skull motion at 10 Hz and 50 Hz. Skull motion was driven by an inflatable silicone actuator pre-loaded against the side of a subject's head. A pneumatic driver (Resoundant, Rochester, MN for 50 Hz or customized PL-300 sub-woofer, BIC America, Anaheim CA for 10 Hz) was used to deliver harmonic pressure waves to the actuator. A custom MRE sequence [6] was used to obtain all components of 3D harmonic displacement (3×3×3 mm voxels, Fig 1a), which were numerically differentiated to estimate 3D strain tensors at each voxel (Fig 1b).

To compare strains in dominant modes from tMRI of impulsive motion to harmonic strains from MRE in different subjects, we performed a series of spatial transformations (Fig 1). Anatomical T1-weighted images (Fig 1c) were used to rigidly register each subject's brain to a standard structural template (MNI152 T1-weighted 0.8 mm brain atlas) using Advanced Normalization Tools (ANTS) [7] (Fig 1d) T1- and T2-weighted images were rigidly registered to the MNI-152 space [8] using the Advanced Normalization Toolkit (ANTs) v2.2 [9], resampled to 0.8 mm isotropic resolution.

Strain tensor components were re-computed in the rigidly registered space based on the rotation matrix associated with the rigid registration. The radial-circumferential ($\varepsilon_{r\theta}$) strain component was computed in the rigidly registered space using the centroid of the brain volume as the origin (Fig 1d). This strain component was chosen because radial-circumferential shear is the dominant mode of deformation in neck rotation [5].

The nonlinear transform from each subject's T1 volume to the MNI152 template was calculated using the cross-correlation standard

SB³C2022-047

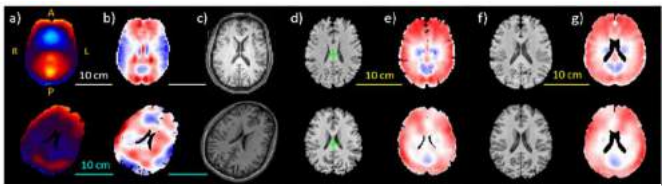


**Figure 1. Comparison of oscillatory strain fields in the brain from MRE during harmonic skull motion (top row) and from DMD of tMRI during impulsive skull motion (bottom row). (a) Displacement $u_x$ (x=LR, y=AP). (b) Cartesian ($\varepsilon_{xy}$) strain fields. (c) T1 images in their respective "native" spaces. (d) Rigidly registered T1 images (centroids in green). (e) Strain ($\varepsilon_{r\theta}$) fields after rigid registration. (f) T1 images registered to MNI atlas. (g) $\varepsilon_{r\theta}$ strain fields after nonlinear registration to MNI atlas. Scale bars 10 cm: white (MRE), cyan (tMRI), yellow (MNI).**

symmetric normalization (SyN) transformation model in ANTS (Fig 1f). The SyN transformation matrix was applied to the $\varepsilon_{r\theta}$ strain (Fig 1g) for each set of tMRI or MRE data. A mask was applied to each set of strain data to remove voxels in the ventricles.

Comparisons between data sets were performed either over the entire brain volume or slice-by-slice. In the whole volume comparison, strain fields are normalized using the $L_2$ norm as shown in Eq. (1a). A dot product is then taken between each normalized strain field ($\hat{\varepsilon}_{r\theta}$), giving a correlation value between 0 and 1 (Eq. (1b)). A correlation magnitude of 1 indicates identical strain fields. The slice-by-slice comparison is analogous; but performed in each slice independently.

$$\hat{\varepsilon}_{r\theta,i} = \frac{\varepsilon_{r\theta,i}}{\sqrt{\sum_n |\varepsilon_{r\theta,n}|^2}} \quad (1a) \qquad CV = \hat{\varepsilon}^{(1)}_{r\theta} \cdot \hat{\varepsilon}^{(2)}_{r\theta}. \quad (1b)$$

## RESULTS

Transformed $\varepsilon_{r\theta}$ strain fields in the MNI atlas space are shown in Fig 2, for the dominant modes of oscillation from DMD of impulsive motion (Fig 2ab), MRE of harmonic motion at 10 Hz (Fig 2cd), and MRE of harmonic motion at 50 Hz (Fig 2ef). Slice-by-slice comparisons between (i) the dominant DMD mode from tMRI of impulsive motion and (ii) a strain field from MRE of 10 Hz harmonic motion show a large region of high similarity throughout the cerebrum (Fig 3a) as well as lower similarity in the cerebellum. In whole-volume comparisons (Fig 3c) relatively high correlation scores (>0.60) are found between DMD modes of impulsive motion and strain fields from MRE of 10 Hz harmonic motion. Relatively low correlation values (<0.50) were found between DMD modes from impulsive motion and MRE of harmonic motion at 50 Hz. Notably, similar low values were found between strain fields from MRE of harmonic motion at 10 Hz and 50 Hz.

## DISCUSSION

Dominant modes of oscillatory, 3D deformation in the human brain induced by impulsive motion of the skull are similar to the patterns of deformation induced by low-frequency (10 Hz) harmonic excitation of the skull. In contrast, both the dominant modes of oscillation caused by impulsive excitation, and the patterns of deformation due to low-frequency (10 Hz) skull motion, differ from the deformation patterns induced by high-frequency (50 Hz) harmonic skull motion.

To perform comparisons between strain fields obtained by different imaging methods (tMRI and MRE), caused by different motion types (impulsive or harmonic), in different subjects, we leveraged the ANTS registration suite to transform fields into a common MNI atlas space. Once in this space, quantitative comparison is straightforward. The approach used here to find correlations between scalar fields can be readily extended to vector or tensor fields.

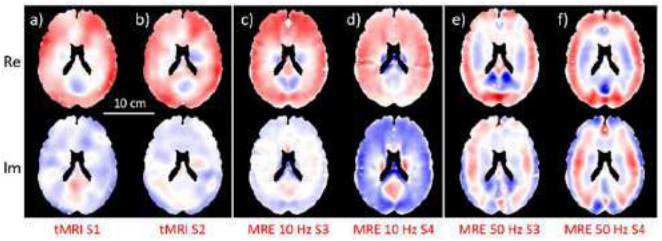


**Figure 2. Dominant oscillatory modes of brain deformation induced by impulsive and harmonic skull motion. Strain fields ($\varepsilon_{r\theta}$) are shown on a representative axial slice after registration to the MNI atlas (slice location is denoted by the dashed blue line in Fig 3b). (a-b) Mode shapes from DMD of tMRI of impulsive motion in subjects S1 & S2. (c-d) Strain fields from MRE of harmonic motion at 10 Hz in subjects S3 & S4. (e-f) Strain fields from MRE of harmonic motion at 50 Hz in S3 & S4.**

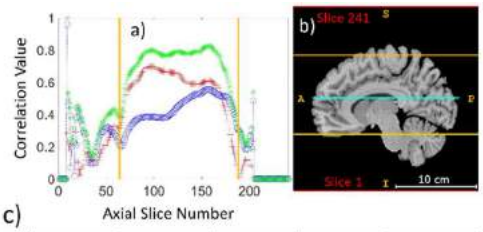


| | tMRI S1 | tMRI S2 | MRE10 S3 | MRE10 S4 | MRE50 S3 | MRE50 S4 |
|---|---|---|---|---|---|---|
| tMRI S1 | 1.00 | 0.73 | 0.75 | 0.70 | 0.31 | 0.45 |
| tMRI S2 | | 1.00 | 0.69 | 0.62 | 0.37 | 0.48 |
| MRE10 S3 | | | 1.00 | 0.81 | 0.35 | 0.49 |
| MRE10 S4 | | | | 1.00 | 0.28 | 0.48 |
| MRE50 S3 | | | | | 1.00 | 0.61 |
| MRE50 S4 | | | | | | 1.00 |

**Figure 3. (a) Slice-by-slice comparison of oscillatory deformation modes in subjects S1 (impulsive loading) and S3 (harmonic loading at 10 Hz). Red +: Real($CV$); blue -: Imag($CV$); green*: $|CV|$. (b) Sagittal cross-section of S3 brain mapped to MNI atlas. (c) Whole-volume correlation magnitudes computed between oscillatory modes shown in Fig 2.**

We acknowledge some limitations. Data from only 4 subjects were used, and the subject ages in tMRI and MRE differed substantially. With age, the human brain shrinks and ventricle size increases. The MNI-152 atlas is not ideal, as it was constructed using subjects aged 18-44 yrs. In future studies we plan to compare brain deformation patterns in groups of subjects of similar age and sex. Nevertheless, this study shows the importance of low-frequency modes in the response of the brain to impulsive loading, and that these modes are uncovered by MRE.

## ACKNOWLEDGEMENTS

Research was supported by NIH grant U01 NS112120.

## REFERENCES

[1] Wu, T et al., J Neuro Tr, 37(2):410-422, 2020
[2]Xiong, Y et al., *Nat Rev Neurosci,* 14(2):128-142, 2013
[3]Escarcega, JD et al., *J Biomech*, Vol:119, 2021
[4] Okamoto, RJ et al., *J Exp Neurosci*, Vol: 12, 2019
[5] Knutsen, AK et al., *Brain Multi Phys*, Vol: 1, 2020
[6] Bayly, PV et al., *Ann Biomed Eng*, 49(10):2677-2692, 2021
[7] Avants, BB et al., *Neuro Img*, 54: 2033-2044, 2011
[8] Fonov, VS et al., *Neuro Img*, 42:S102, 2009
[9] Avants, BB et al., *Insight J*, 2:1-35, 2009

SB³C2022
Summer Biomechanics, Bioengineering and Biotransport Conference
June 20-23, Eastern Shore, MD, USA

# IN VIVO LARGE ANIMAL EVALUATION OF A MECHANO-RESPONSIVE FIBROUS PATCH FOR ANTI-INFLAMMATORY DRUG DELIVERY TO PROMOTE REPAIR AFTER DISC HERNIATION

**A.P. Peredo (1,2,4), C.S. Friday (1), H.M. Zlotnick (1,2,4), G.R. Dodge (1,4), D. Lee (3), M.W. Hast (1,4), S.E. Gullbrand (1,4), H.E. Smith (1,4), R.L. Mauck (1,2,4)**

(1) Department of Orthopaedic Surgery, University of Pennsylvania, Philadelphia, PA, USA
(2) Department of Bioengineering, University of Pennsylvania, Philadelphia, PA, USA
(3) Department of Chemical and Biomolecular Engineering, University of Pennsylvania, Philadelphia, PA, USA
(4) Translational Musculoskeletal Research Center, Philadelphia VA Medical Center, Philadelphia PA, USA

## INTRODUCTION

Symptomatic intervertebral disc (IVD) herniations cause debilitating numbness and pain. While resection of the herniated tissue can alleviate these symptoms, the remaining compromised annulus fibrosus (AF) is left unrepaired, providing an uninterrupted path for aberrant scar infiltration, nociceptive nerve ingrowth, and recurrent herniation [1]. The low AF cellularity, high density, and avascularity prevent endogenous healing and predispose the disc to degeneration.

Numerous approaches have attempted to seal the AF injury or deliver biologics to enhance repair [2-3]. Although some of these approaches have partially restored IVD biomechanics, the inflammation-mediated loss of extracellular matrix (ECM), that exacerbates degeneration, has not yet been addressed. Therefore, there is a need for an annular repair device that provides both physical reinforcement and closure of the AF tear while simultaneously mitigating inflammation to prevent the degenerative loss of ECM.

Upon herniation of the disc, local expression of the proinflammatory cytokine interleukin-1β (IL-1β) increases, contributing to the acute loss of ECM post-injury. Elevated IL-1β also causes an increase in nerve growth factor (NGF) - a chemotactic signal that increases the infiltration of nociceptive neurites into the disc [4-5]. Thus, blocking IL-1β signaling may prevent the inflammation-mediated loss of ECM and prevent recurrent pain.

Mechanically-activated microcapsules (MAMCs) are drug-encapsulating depots that have tunable mechano-activation and degradation properties, thus representing an ideal localized drug delivery system for the load-bearing IVD [6]. The goals of this study were to (1) develop and optimize a mechano-responsive annular repair scaffold and (2) assess the delivery, retention, and performance of the AF repair device in a goat cervical spine herniation model. We hypothesized that repairing the torn AF post-herniation and blocking local IL-1β signaling would prevent the loss of AF ECM, decrease neurite and scar infiltration, and improve IVD biomechanics.

## METHOD

MAMC Fabrication: MAMCs were fabricated to encapsulate a model drug (bovine serum albumin, BSA) or the IL-1 receptor antagonist, Anakinra (Sobi) [6].

Drug Bioactivity Assessments: To test the effects of increasing Anakinra concentrations on cell viability, Alamar Blue cell viability assay was performed on AF cells from healthy human donors (Articular Eng.) after 3 days of culture with soluble Anakinra. To assess drug bioactivity after encapsulation in MAMCs, the contents of Anakinra-loaded MAMCs or soluble Anakinra was added to human AF cells ± IL-1β (10ng/mL) for 3 days. qPCR was performed after treatment to assess changes in catabolic gene expression.

Patch Fabrication: Aligned polycaprolactone (PCL) – polyethylene oxide (PEO) nanofibrous scaffolds were fabricated via electrospinning [7]. Annular repair devices were fabricated by heating up 3D-printed metal stamps to 80ºC and melt-stamping MAMCs between two scaffold sheets. Metal stamps with varied lengths of the longest rhombus diagonal (δ: 3-5 mm) were tested.

Scaffold Tensile Loading: Dynamic uniaxial tension cycles (6% strain, 1Hz) were applied to MAMC-laden scaffolds along the fiber direction using a custom-built bioreactor, after which MAMC imaging was performed to quantify MAMC mechano-activation. To determine scaffold mechanical properties, scaffolds were subjected to uniaxial tension to failure with optical strain tracking of local deformation [8].

In Vivo Annular Repair: With IACUC approval, 8 goats underwent annular injury and/or patch repair at C2-3 and C3-4, with the C4-5 level used as a healthy control. Annular injury consisting of a partial-thickness AF laceration followed by full thickness needle puncture was performed. Scaffold groups received either a BSA-MAMC control patch (repair) (l:10 mm, w: 3.5 mm, δ=4) or an Anakinra-loaded patch (Anakinra) that was sutured over the injury. Animals were euthanized at 4 weeks. Cervical spines were subjected to MRI at 3T for quantitative T2 mapping. Following MRI, motion segments were subjected to

SB³C2022-048

compressive testing (0 to -100 N, 0.24MPa) to determine biomechanical properties. Motion segments were then fixed, decalcified, and processed for paraffin histology. Mallory-Heindenhain staining was performed, and collagenous infiltration was quantified using ImageJ.

Statistical Analyses: Significant differences were assessed via parametric or non-parametric one- or two-way ANOVA ( * $p \leq 0.05$, ** $\leq 0.01$, ***$\leq 0.001$, ****$\leq 0.0001$).

## RESULTS

Anakinra-loaded MAMCs were effectively fabricated (**Fig. 1a-b**). Anakinra concentrations of up to 1000 ng/mL did not have a detrimental effect on AF cell viability (**Fig. 1c**) and caused a concentration-dependent decrease in the expression of MMP3 and LCN2. Furthermore, the contents retrieved from Anakinra-loaded MAMCs demonstrated a comparable effect to that of soluble Anakinra (**Fig. 1d**).

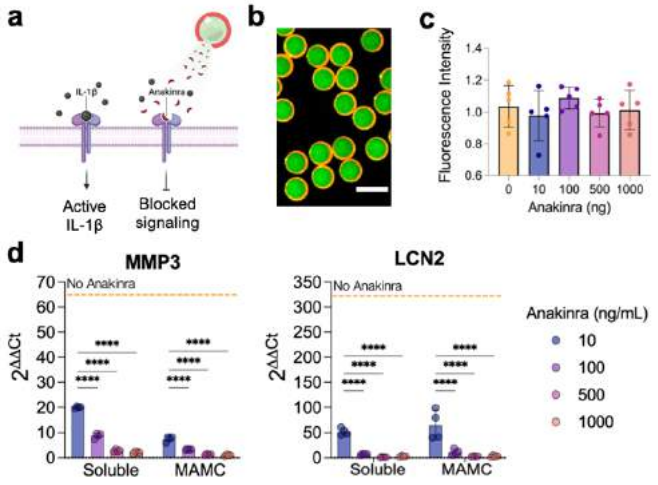


**Figure 1: (a) Anakinra delivery blocks IL-1$\beta$ signaling. (b) Anakinra-loaded MAMCs (scale: 50$\mu$m). (c) Alamar Blue viability assay for cells treated with Anakinra. (d) MMP3 and LCN2 expression after treatment with soluble Anakinra or Anakinra extracted from crushed MAMCs in the presence of IL-1β.**

Annular repair scaffolds were formed by melt-stamping MAMCs between two fibrous scaffold layers (**Fig. 2a**). Dynamic tensile loading of scaffolds resulted in increasing mechano-activation of MAMCs with increasing number of loading cycles (**Fig. 2b**). $\delta$=4 and 5 mm stamp patterns created comparable MAMC mechano-activation profiles while the $\delta$=3 pattern resulted in less activation with loading. Melt stamping increased the tensile modulus of the scaffolds compared to an unstamped scaffold of comparable thickness (**Fig. 2c**).

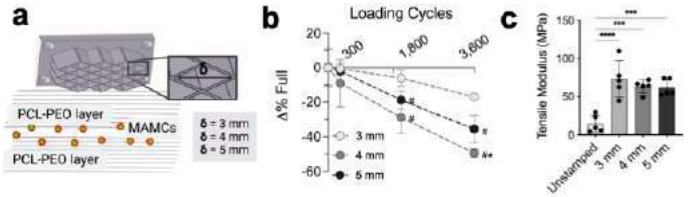


**Figure 2. (a) Schematic of melt-stamped scaffolds. (b) MAMC mechano-activation with tensile loading (# vs. 0 cycles, * vs 3 mm) and (c) scaffold tensile modulus.**

After 4 weeks *in vivo*, annular repair patches remained secured at the injury site. Average T2 maps showed greater signal in the AF for injury and repair (empty scaffold) groups compared to uninjured controls and the Anakinra scaffold group (**Fig. 3a-b**). Repair with an empty patch maintained the disc linear modulus at uninjured levels, while stiffening occurred in the injury group (**Fig. 3b-c**). Empty patch delivery also reduced the collagenous infiltration observed on the anterior and posterior AF of injured discs (**Fig. 3d-f**). Disc biomechanical testing and histology (including immunohistochemistry for neurites and catabolic factors) for animals treated with Anakinra-loaded scaffolds is currently in progress.

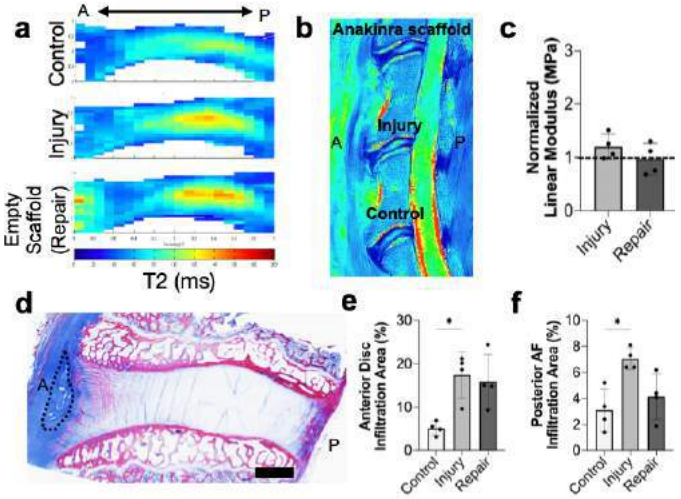


**Figure 3: (a) Average MRI T2 (A: anterior, P: posterior). (b) Representative T2 for Anakinra scaffold, injury, and control. (c) Linear modulus normalized to healthy control (dashed line). (d) Mallory Heindenhain-stained section for empty scaffold repair (dashed line) (scale: 1mm). Fibrous tissue infiltration area in the (e) anterior and (f) posterior AF.**

## DISCUSSION

Anakinra potently blocked IL-1β signaling, attenuating the upregulation of catabolic genes in human AF cells in a dose-dependent manner. Therefore, the localized delivery of MAMCs with bioactive Anakinra may be used to provide therapeutically effective concentrations at the target injury site. MAMCs could be integrated into annular repair patches and mechano-activated in response to dynamic loading. The repair patches remained in place after 4 weeks *in vivo*. Interestingly, empty patch delivery prevented the stiffening of injury-only groups, potentially by decreasing the robust scar infiltration and collagenous remodeling observed after injury. While further analysis of Anakinra-loaded patch groups is in progress, the effects of Anakinra treatment *in vitro* and the T2 signal observed for the Anakinra patch group indicate that the simultaneous provision of structural reinforcement and anti-inflammatory molecules may potentially prevent catabolic remodeling and loss of disc function post-herniation.


## ACKNOWLEDGEMENTS

This work was supported by the NIH (R01 AR071340) and the VA (IK6 RX003416, IK2 RX003118, IK2 RX001476, I01 RX002274, I21 RX003447).


## REFERENCES


[1] Kokubo, Y et al., *J Neurosurg*, 9(3):285-95, 2008.[2] Peredo, AP et al., *Tissue Eng Part B Rev*, 27(4): 295-312, 2021. [3] Peredo, AP et al., *JOR Spine*, 4(1): e1133, 2021. [4] Johnson, ZI et al., *Eur Cell Mater*, 30: 104-16, 2015. [5] Abe Y et al., *ORS Annual Conference* 2006, #1194 [6] Peredo, AP et al., *Biomaterials,* 265: 120255, 2021. [7] Ashinsky, BG et al., *Acta Biomater,* 111:232-241, 2020. [8] Baker, BM et al., *Biomaterials*, 29(15): 2348-58, 2008.

SB³C2022
Summer Biomechanics, Bioengineering and Biotransport Conference
June 20-23, Eastern Shore, MD, USA

# GLAUCOMATOUS STRESSORS DRIVE SCHLEMM'S CANAL CELL PATHOBIOLOGY VIA ELEVATED YAP ACTIVITY

**H. Li (1,2,3), M. Kuhn (4), WD. Stamer (4,5), PS. Ganapathy (1,3,6), S. Herberg (1,2,3,7,8)**

(1) Department of Ophthalmology and Visual Sciences, SUNY Upstate Medical University, Syracuse, NY, USA
(2) Department of Cell and Developmental Biology, SUNY Upstate Medical University, Syracuse, NY, USA
(3) BioInspired Institute, Syracuse University, Syracuse, NY, USA
(4) Departments of Ophthalmology, Duke Eye Center, Duke University, Durham, NC, USA
(5) Department of Biomedical Engineering, Duke University, Durham, NC, USA
(6) Department of Neuroscience and Physiology, SUNY Upstate Medical University, Syracuse, NY, USA
(7) Department of Biochemistry and Molecular Biology, SUNY Upstate Medical University, Syracuse, NY, USA
(8) Department of Biomedical and Chemical Engineering, Syracuse University, Syracuse, NY, USA

## INTRODUCTION

Primary open-angle glaucoma (POAG) is a leading cause of irreversible vision loss worldwide, and elevated intraocular pressure (IOP) is the primary modifiable risk factor [1-5]. Elevated IOP results from increased resistance to aqueous humor (AH) outflow in the juxtacanalicular region of the conventional outflow pathway where the trabecular meshwork (TM) and Schlemm's canal (SC) inner wall cells interact [6]. Extracellular matrix (ECM) stiffening and increased transforming growth factor beta2 (TGFβ2) in the AH are strongly associated with outflow tissue dysfunction [7]. Yes-associated protein (YAP), a central player in mechanotransduction, has emerged as key contributor to glaucoma pathogenesis [8,9]; a recent genome-wide study identified *YAP1* among novel glaucoma risk loci [10]. However, the precise role of SC cell YAP signaling in response to known glaucomatous stressors is poorly understood. Here, we investigate how ECM stiffness/composition and TGFβ2 regulate YAP activity in human SC cells using biomimetic hydrogels [11] with tunable stiffness, and whether pharmacologic YAP inhibition increases *ex vivo* outflow facility.

## METHODS

ECM hydrogels were fabricated by photocrosslinking functionalized collagen type I (3.6 mg/ml [all final concentrations]), elastin-like polypeptide (2.5 mg/ml), and hyaluronic acid (0.5 mg/ml, 0.025% (w/v) photoinitiator Irgacure® 2959) [11]. Bioinert alginate (4 mg/ml) was added to facilitate $Ca^{2+}$ (100 mM)-mediated hydrogel stiffening and alginate lyase (50 μg/ml)-mediated softening (**Fig. 1A**). Fibronectin (FN) was used to coat ECM hydrogels (10 $\mu g/cm^2$). Human Schlemm's canal (HSC) cells were isolated from surgical discard corneal rims and validated according to accepted standards in the field. Four HSC cell strains were used for the experiments in this study. Donor demographics were as follows: Male/33-years-old; M/46; F/46; F/68. HSC cells were plated on hydrogels and stimulated with TGFβ2 (2.5 ng/ml), ROCK inhibitor (Y27632; 10 μM), or latrunculin B (Lat B; 2 μM). YAP signaling in SC cells cultured on hydrogels was inhibited with verteporfin (VP; 0.5 μM). YAP transcriptional activity, cytoskeletal organization, fibrotic marker levels, and ECM remodeling were quantified. Outflow facility with ocular perfusion of VP (10 μM) was measured in enucleated eyes from 3-6-month-old C57BL/6J mice using *iPerfusion* [12].

## RESULTS

ECM-alginate hydrogel stiffness was increased ~3-fold upon $Ca^{2+}$ crosslinking ($p<0.001$); alginate lyase treatment restored soft baseline levels (**Fig. 1B**). ECM stiffening increased YAP activity and F-actin levels in HSC cells ($p<0.001$), which was fully restored by matrix softening (**Fig. 1D-G**). Nuclear YAP completely translocated to the cytoplasm within 3 h after ECM softening; F-actin levels reached baseline after 24 h ($p<0.0001$). FN coating enhanced HSC cell YAP activity and actin cytoskeleton/ECM remodeling. TGFβ2 increased nuclear YAP and its downstream effectors transglutaminase-2 (TGM2) and connective tissue growth factor ($p<0.001$). This was found to be dependent on cytoskeletal integrity; Y27632 or Lat B co-treatment potently interrupted aberrant YAP signaling. VP treatment fully blocked TGFβ2-driven YAP activation in HSC cells ($p<0.0001$) and largely restored FN, TGM2, F-actin, α-smooth muscle actin, and phospho-myosin light chain levels ($p<0.001$) – all implicated in POAG pathogenesis. Importantly, 6/10 mouse eyes displayed ~15-80% increased outflow facility with VP perfusion.

SB³C2022-049

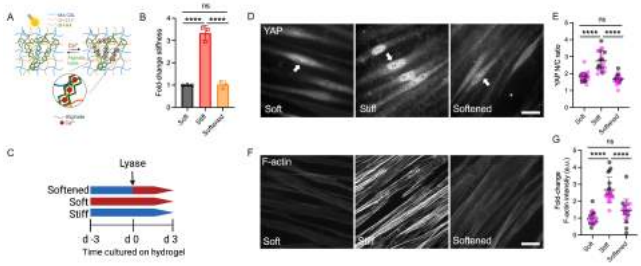


**Fig. 1. ECM hydrogel softening decreases F-actin and nuclear YAP in HSC cells.** (A) Schematic of hydrogel stiffening by incorporating alginate and hydrogel softening using alginate lyase. (B) Fold-change stiffness of hydrogels (N = 3 replicates/group). (C) Schematic showing time course of hydrogel softening experiments with HSC cells (D) Representative fluorescence micrographs of YAP in HSC cells on hydrogels (YAP = grey). Scale bar, 20 μm. (E) Analysis of YAP nuclear/cytoplasmic ratio (N = 20 images from 2 HSC cell strains with 3 biological replicates per cell strain). (F) Representative fluorescence micrographs of F-actin in HSC cells on hydrogels (F-actin = grey). Scale bar, 20 μm. (G) Analysis of F-actin intensity (N = 20 images per group from 2 HSC cell strains with 3 replicates per HSC cell strain). Symbols with different colors represent different cell strains. The bars and error bars indicate Mean ± SD. Significance was determined by one-way ANOVA using multiple comparisons tests (***p < 0.001; ****p < 0.0001).

## DISCUSSION

The mechanosensitive transcriptional coactivator YAP plays important roles in mechanotransduction, a process through which cells translate external biophysical cues into internal biochemical signals. YAP modulates target gene expression profiles across many cell and tissue types [8,9]. Through this mechanism, YAP signaling regulates critical cellular functions and normal tissue homeostasis; imbalance or failure of this process is at the core of various diseases [13]. A recent genome-wide meta-analysis identified *YAP1* among 44 previously unknown POAG risk loci [11]; this observation provides strong new evidence that YAP may play a prominent role in glaucoma pathogenesis. However, the detailed mechanisms underlying YAP modulation in HSC cells under glaucomatous conditions (i.e., elevated ECM stiffness/composition and increased growth factors in AH) remain to be elucidated. To model this, we used ECM-alginate hydrogels with tunable stiffness to study the roles of YAP in HSC cells in response to stiffened matrix, FN deposition and TGFβ2. As summarized in **Fig. 2**, our data support that YAP is a critical regulator of HSC cellular responses to ECM stiffening/composition and elevated TGFβ2 seen in POAG; we propose that increased YAP activity may drive further HSC cell contractility and actin/ECM remodeling to exacerbate disease pathology conditions. This conclusion is supported by the findings that (i) ECM stiffening elevates YAP activity and F-actin, which is completely reversed by matrix softening; (ii) TGFβ2 induces YAP transcriptional activity; F-actin relaxation/depolymerization abolishes TGFβ2-induced aberrant YAP signaling. (iii) YAP inhibition with verteporfin increases actin cytoskeletal/ECM remodeling and cell contractile properties; and (iv) ocular perfusion of verteporfin increases outflow facility.

Our data suggest that YAP modulates HSC cell dysfunction in response to known glaucomatous stressors, and that pharmacologic YAP inhibition has promising potential to improve outflow tissue dysfunction.

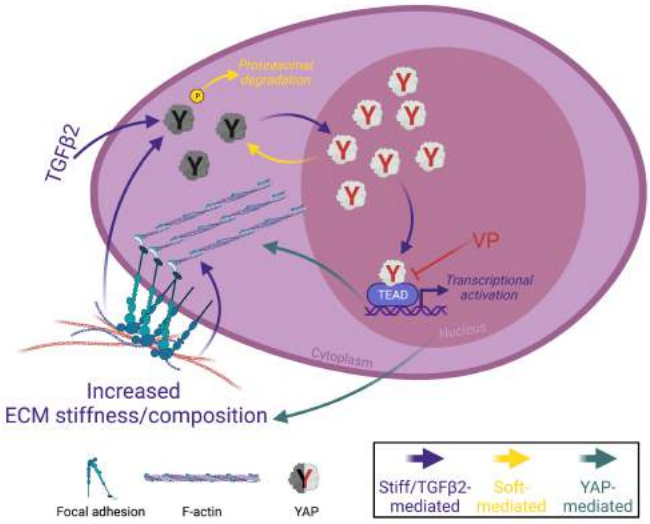


**Fig. 2. Schematic illustration of the effects elicited by ECM stiffness/composition and TGFβ2 that modulate YAP activity in HSC cells.** Stiffened matrix elevates YAP activity (purple arrows = stiff/TGFβ2-mediated), which can be reversed by matrix softening (yellow arrows = soft-mediated). TGFβ2 increases nuclear YAP contingent on cytoskeletal integrity; actin cytoskeleton relaxation/depolymerization decrease nuclear YAP. YAP activation induces HSC cell contractility and actin/ECM remodeling (green arrows = YAP-mediated), which together may induce ocular hypertension in POAG. Created with BioRender.com.

## ACKNOWLEDGEMENTS

This project was supported in part by National Institutes of Health grants R01EY031710, K08EY031755 (W.D.S., and P.S.G), an American Glaucoma Society Young Clinician Scientist Award (to P.S.G.), a Syracuse University BioInspired Seed Grant (to S.H.), unrestricted grants to SUNY Upstate Medical University Department of Ophthalmology and Visual Sciences from Research to Prevent Blindness (RPB) and from Lions Region 20-Y1, and RPB Career Development Awards (to P.S.G. and S.H.). We thank Dr. Robert W. Weisenthal and the team at Specialty Surgery Center of Central New York for assistance with corneal rim specimens. We also thank Dr. Nasim Annabi at the University of California – Los Angeles for providing the KCTS-ELP, Dr. Alison Patteson at Syracuse University for rheometer access, Drs. Audrey M. Bernstein and Mariano S. Viapiano, and Neuroscience Microscopy Core at Upstate Medical University for imaging support.

## REFERENCES

[1] Quigley, H.A. et al., *N Engl J Med*, 328(15): p. 1097-106, 1992.
[2] Quigley, H.A. et al., *Br J Ophthalmol*, 90(3): p. 262-7, 2006.
[3] Kwon, Y.H., et al., *N Engl J Med*, 360(11): p. 1113-24, 2009.
[4] Tham, Y.C., et al., *Ophthalmology*, 121(11): p. 2081-90, 2014.
[5] Tamm, E.R. et al., *Prog Mol Biol Transl Sci*, 134: p. 301-14, 2015.
[6] Brubaker, R.F., *Invest Ophthalmol Vis Sci*, 32(13): p. 3145-66, 1991.
[7] Wang, K., et al., *IOVS*, 58(11): p. 4809-4817, 2017.
[8] Dupont, S., et al., *Nature*, 474(7350): p. 179-183. 2011
[9] Boopathy, G.T.K. et al., *Front Cell Dev Biol*, 7(49). 2019.
[10] Gharahkhani, P., et al., *Nat Commun*, 12(1): p. 1258, 2021.
[11] Li, H., et al. *Exp Eye Res*, 205: 108472, 2021.
[12] Sherwood J.M. et al., *PLoS One*, 11(3):e0150694. 2016
[13] Panciera, T., et al., *Nat Rev Mol Cell Biol*, 18(12): p. 758770, 2017.

# A CONTINUUM MODEL FOR TRANSITION BETWEEN CELL-DENSE AND CELL-SPARSE TISSUES: APPLICATION TO CEREBRAL ANEURYSMS

**Elizabeth D. Shih (1), Ryan M. Mahutga (1), Victor H. Barocas (1), Patrick W. Alford (1)**

(1) Department of Biomedical Engineering
University of Minnesota – Twin Cities
Minneapolis, MN, USA

## INTRODUCTION

During initial cerebral aneurysm (CA) formation, the tissue is cell dense, but as the CA progresses, vascular smooth muscle cells (VSMCs) undergo apoptosis and the tissue becomes cell sparse (1) (**Fig. 1A**). VSMCs are primarily responsible for maintaining tissue integrity through cellular contraction and structural regulation of its surrounding extracellular matrix. Understanding the role of VSMCs in aneurysms is integral to examining CA mechanics during growth and remodeling (G&R) to determine rupture risk. In our models of G&R, we assume G&R to be a function of VSMC stress (3). The most common continuum method for modeling G&R is using the constrained mixture (CM) theory, which assumes that all constituents strain equally (4) (**Fig. 1B**). There have been other models that consider cell-sparse tissues, in which the cell does not strain equally with its matrix, but these models assume an infinite matrix volume (5). We hypothesize that in intermediate cell density conditions, neither of these models accurately represents the stress state of the cells in the tissue. Here, we study tissue models with intermediate cell density and determine how much error is introduced by the existing models and what characteristics introduce the most error (**Fig. 1C-D**). Based on these studies, we propose a new modified strain factor model for intermediate-cell-density tissues and evaluate its efficacy against our simulated data.

## METHODS

**Finite Element Model (FEM).** A cube was created in FEBio with a cell modeled in the center of a box, representative of matrix (6) (**Fig. 1C**). Different cell volume fractions ($\phi_{cell}$), morphologies, material properties, and matrix material properties were assigned to the model. Cauchy stresses of the system ($\boldsymbol{\sigma_{tot}}$), cell ($\boldsymbol{\sigma_{cell}}$), and matrix ($\boldsymbol{\sigma_{mat}}$) were calculated at each time step during an unconstrained uniaxial stretch in the 1-direction. A total of 160 simulations were examined.

**Constrained Mixture (CM) Analysis.** CM models assume that all constituents comprising a tissue strain equally, and that the stresses of the constituents can be weighted against their respective volume fractions and summed together to determine the total stress of the tissue (**Fig. 1D**). In our analysis, we simplify the tissue into two components: the cell and the matrix.

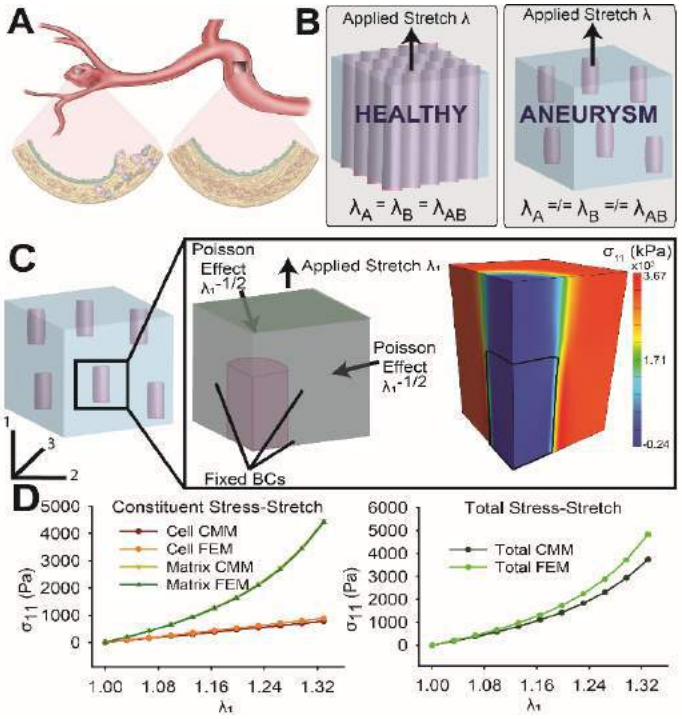


**Figure 1. A. Illustration of CA versus healthy arterial structure (2). B. Deformations of VSMCs in healthy arteries and CAs. C. Schematic of FEM, with example simulated. D. Example FEM and CM stress-stretch curves.**

$$\boldsymbol{\sigma_{tot}} = \phi_{cell}\boldsymbol{\sigma_{cell}} + [1 - \phi_{cell}]\boldsymbol{\sigma_{mat}} \quad (1)$$

where $\boldsymbol{\sigma_{cell}}$ and $\boldsymbol{\sigma_{mat}}$ are both functions of the applied strain ($\boldsymbol{\varepsilon_{app}}$). We derived stresses for the components and the total mixture for comparison against the FEM results.

**Marquez Strain Factor (SF) Analysis.** Marquez *et. al*. evaluated the relationship between cell and matrix strain and derived a strain factor (SF) from Eshelby's theory, which solves for a strain field of an inclusion of some geometry in an infinite matrix (5, 7)

$$\boldsymbol{A^{Marquez}} = [\boldsymbol{I} + \boldsymbol{E}(\boldsymbol{C^m})^{-1}(\boldsymbol{C^c} - \boldsymbol{C^m})]^{-1} \quad (2)$$

where $\boldsymbol{I}$ is the identity tensor, $\boldsymbol{E}$ is the Eshelby tensor, which describes the geometry of the inclusion, and $\boldsymbol{C^c}$ and $\boldsymbol{C^m}$ are the stiffness tensors of the cell and the matrix, respectively. Under uniaxial strain, $\boldsymbol{A^{Marquez}}$ is simplified into a scalar term $SF^{Marquez}$, which acts as a coefficient to the applied strain $\varepsilon_{app}$ to solve for the cell strain $\varepsilon_{cell}$

$$\varepsilon_{cell} = SF^{Marquez}\varepsilon_{app} \quad (3)$$

For each of our simulations, we calculated $\boldsymbol{E}$ given the cell geometry, derived the $SF^{Marquez}$, and found the subsequent $\varepsilon_{cell}$. We re-calculated the Cauchy stress of the cell in Eq. 1 using $\varepsilon_{cell}$ and compared the values against the simulated results. Additionally, we fit a 'true' SF to each simulation to evaluate the Marquez value against a true value.

**Modified SF Model.** $SF^{Marquez}$ incorporates the effects of cell geometry ($\boldsymbol{E}$) and cell ($\boldsymbol{C^m}$) and matrix ($\boldsymbol{C^{im}}$) stiffnesses but not the effects of cell volume fraction ($\phi_{cell}$). We fixed the listed variables to evaluate how $\phi_{cell}$ influences $\varepsilon_{cell}$. As $\phi_{cell}$ increases, the true SF approaches 1, reflective of a dense system where a SF is unnecessary. To account for this, we incorporated a weighting term on the SF that is nonlinearly dependent on $\phi_{cell}$:

$$SF^{modified} = \left(e^{-a\phi_{cell}}\right)SF^{Marquez} + (1 - e^{-a\phi_{cell}}) \quad (4)$$

where $a$ was fit to a value of 5.38. The weighting term pulls the SF towards 1 as density increases, where SF=1 indicates equal strain between constituents. Like the above analyses, we compared our new model against FEM data.

## RESULTS

**Sparsity influences cell stress.** Cell stresses predicted by the FEM and the CM model were compared for varying cell geometries (**Fig. 2Ai**) and cell/matrix stiffnesses (**Fig. 2Aii**) at different $\phi_{cell}$'s. The error between CM and our FEM data is minimized as the aspect ratio approaches 1, where the cell percolates through the matrix, deforming similarly with the matrix. As stiffness ratios deviate from 1, where both constituents have the same material properties, errors are observed to increase. Notably, errors consistently increase as $\phi_{cell}$ decreases, indicative of decreasing cell density. This supports our hypothesis that sparse systems require a modified CM law.

**Sparse-cell models do not replicate cell stresses at intermediate cell density.** We applied Marquez's SF to the total strain to find the cell strain, and the resulting stress was compared against FEM data (**Fig. 2Bi-ii**). Contrary to the CM model, the Marquez model showed high accuracy at low volume fractions but was less accurate as cell density increased. These data show that the Marquez SF does not fully capture the effects of semi-sparse tissues. An $R^2$ of 0.79 was obtained from linear regression of the true SFs against the Marquez SFs (**Fig. 2Dii**).

**Modified SF improves stress calculations.** We modified the SF to adjust for the nonlinear effects of $\phi_{cell}$ and compared the results against our FEM data. A substantial decrease in error was observed across the board for all simulations (**Fig. 2Ci-ii**), and an $R^2$ of 0.92 demonstrated the improved goodness of fit (**Fig. 2Diii**).

## DISCUSSION

Here, we demonstrate that neither the CM model nor the Marquez SF application capture cell stress at intermediate cell densities. We modify the SF to account for these conditions and find that the model is substantially improved when compared to simulated data.

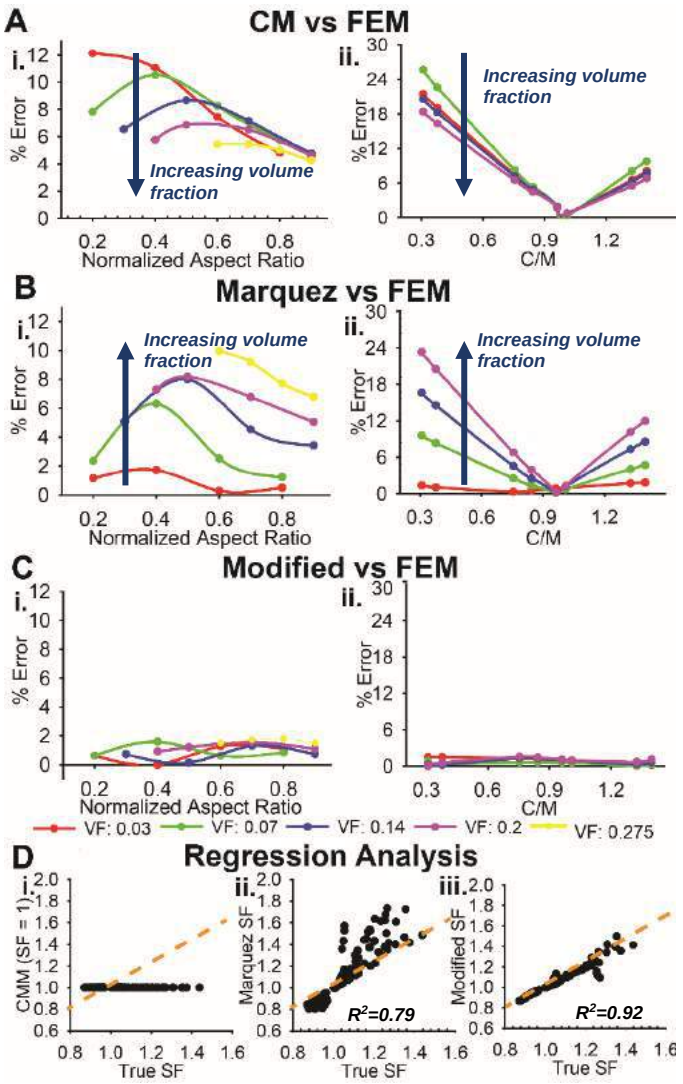


**Figure 2. A: Error plots of CM model against FEM results when (i) C/M is fixed at 0.75 and when (ii) CH is fixed at 0.6. Bi-ii.: Corresponding plots with Marquez SF. Ci-ii.: Corresponding plots with modified SF. D. Regression analyses for each model.**

This modification has significant implications to the determination of cell stress we believe to drive G&R (3). This is particularly relevant for CAs which have a lower cell density than that of healthy arteries (1-2). We will continue to investigate how our model for intermediate cell density systems describe how mechanical stimuli drive VSMC mechanoadaptation of its surrounding matrix, and how that influences stress at the tissue-scale. This will help us elucidate how heterogeneous and multiscale mechanics in diseased arteries evolve aneurysm stability under load.

## ACKNOWLEDGEMENTS

We acknowledge financial support by NSF (CMMI 1553255).

## REFERENCES

[1] Hara, A, et al. *Neurol Res*, 20(2):127-130. 1998. [2] Jung, KH. *Neuroint*, 13(2). 2018. [3] Alford, PW. et al., *BMMB*, 7(4). 2008. [4] Humphrey, JD. et al., *Math Mod Meth Appl Sci*, 12(3). 2002. [5] Marquez, JP, et al. *Biophys J*, 88(765-777). 2005. [6] Maas, S, et al., *JBiomech Eng.*, 134(1). 2012. [7] Eshelby, J.D. *Proc Roy Soc A*, 241:346-396. 1957.

# SIMPLE ANALYTIC MODEL FOR PERISTALTIC FLOW AND MIXING

**R. Ibanez (1), M. Shokrian (1), J.-H. Nam (1), D. H. Kelley (1),**

(1) Mechanical Engineering, University of Rochester, Rochester, New York, USA

## INTRODUCTION

Peristaltic flows occur when a fluid channel is subjected to periodic, traveling deformations at its boundaries. This type of flow is found in numerous biological systems [1-3]. One area of particular interest is the inner ear, where the fluid homeostasis plays an important role for healthy hearing [1].

We present an analytic approach to modeling peristaltic flow and mixing properties, with particular interest toward biophysical peristalsis. We show that experimental and computational results validate our analytic approach. We demonstrate that the assumptions we made are valid for the parameter regime of the inner ear, and that peristalsis should play a role in enhancing the rate of chemical diffusion in the inner ear.

## METHODS

To analytically model the problem, we consider a simplified two-dimensional system seen in figure 1. The simplified domain is an infinite two-dimensional channel of mean width $L$. It is periodic in the x-direction, with a spatial period $\lambda$. Fluid flows because one boundary is deformed in a periodic shape $\eta(x,t)$ moving with constant speed c in the x-direction and characteristic amplitude $A$. The viscosity of the fluid is given by $\nu$.

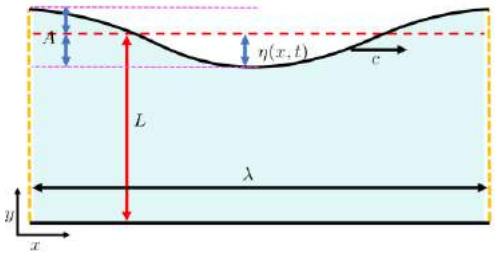


**Figure 1: Sketch of the analytic model's domain.**

We find an analytic solution to the problem for high Reynolds flows (where $Re = cL^2/\nu\lambda \gg 1$), amplitude is small $\epsilon = A/Li \approx 0$ and the wavelength is long $\lambda/Li \gg 0$.Then we apply a viscous correction.

The inviscid approach consists of defining a stream function $\psi$ where the x velocity is $\partial\psi/i\partial x = -u$ and y velocity is $\partial\psi/i\partial x = v$. Then, solving equation (1) using separation of variables and applying the boundary conditions of the problem.

$$\frac{\partial^2\psi}{\partial x^2} + \frac{\partial^2\psi}{\partial y^2} = 0 \qquad (1)$$

The viscous correction is implemented by solving Stokes' second problem. Where we solve equation (2) near $y = 0$ and $y = \mathrm{L}$ using the boundary conditions derived from the inviscid solution.

$$\frac{\partial \mathrm{u}}{\partial \mathrm{t}} = \nu \frac{\partial^2 \mathrm{u}}{\partial y^2} \qquad (2)$$

A solution is obtained that can be used to determine a generalized Lagrangian mean flow, which describes the material transport properties of the flow. This is useful for determining the mixing properties of peristalsis.

For validation we use numerical simulations using a finite element method in the COMSOL Multiphysics software. We also use experimental measurements to validate the analytic model. The experiment consists of a transparent long square channel (2.54cm x 2.54cm x 91.4 cm), where one of the walls is flexible. The flexible wall is actuated using an array of stepper motors. Figure 2 shows a diagram of the experimental setup. To measure the induced flow, we use particle imaging velocimetry (PIV) processed via PIVlab [4] and particle tracking velocimetry via a MATLAB based predictive tracking algorithm [5]. PIV is used to obtain velocity fields and Eulerian data form the flow. PTV is used to obtain Lagrangian measurements of the flow to determine mass transport properties of the flow.

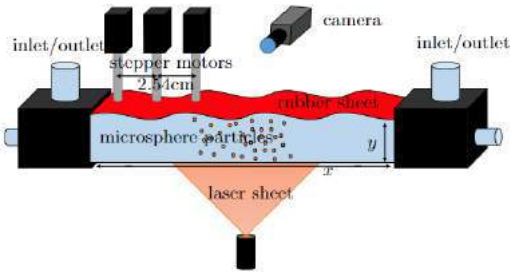


**Figure 2: Sketch of the experimental apparatus. Flow is driven via the actuation of the stepper motors, which deform the rubber sheet to produce a shape that closely approximates a periodic wave traveling with constant speed in the x-direction.**

Finally, we compare the analytic model and numerical results when applied to microfluidics in the context of the inner ear. We show using a combination of our analytic results and numerical diffusion simulations that peristalsis enhances mixing in a channel.

## RESULTS

We show validation results in figures 3 and 4. Figure 3 compares the root mean squared velocity for different parameters between different methods, results agree between methods suggesting our analytic model is accurate. Figure 4 compares Lagrangian drift velocities, the agreement suggests that the analytic model accurately captures the Lagrangian properties of the flow. Having validated the analytic model, we show using the Lagrangian measurements and modeling that peristalsis can enhance mixing. Figure 5 demonstrates the effects on chemical concentration during peristalsis in the parameter range of the inner ear. Our validated model suggests that the effects of peristalsis enhance the rate of mixing significantly due to the Lagrangian properties of the flow when compared to pure diffusion.

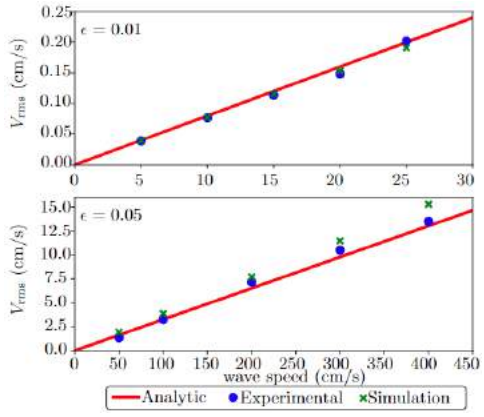


**Figure 3: Comparison of the root-mean-square velocity in the bulk flow region in experiments, modeling, and simulations. The wavelength was held constant at λ = 30 cm.**

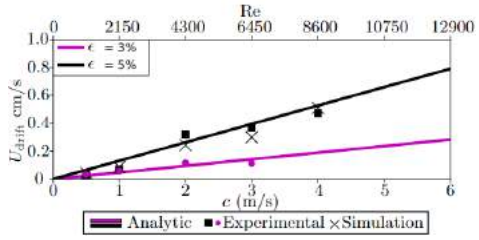


**Figure 4: Variation of the mean drift velocity $U_{drift}$. The wavelength was held constant at λ = 30 cm.**

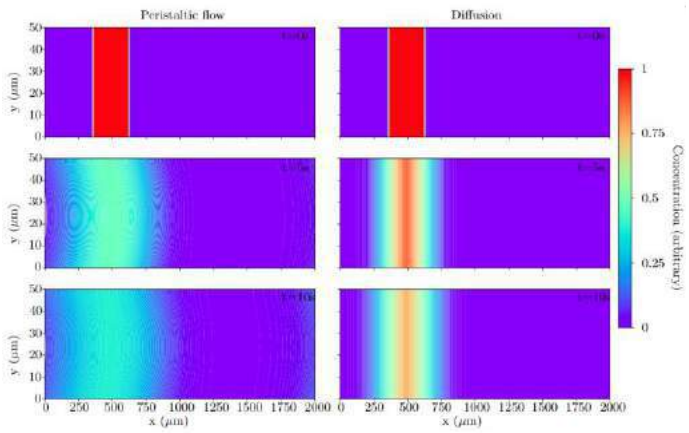


**Figure 5: Change of the concentration of a passive scalar subjected to both diffusion and the modeled Lagrangian mean flow, or subjected to diffusion alone.**

## DISCUSSION

The simplicity of our analytic model and range of parameters makes it a useful tool to be employed in a diverse set of biophysical problems. The simplicity of the analytic model makes it a useful tool for understanding the role of peristalsis in biophysical flows, particularly where mixing effects are of interest.


## ACKNOWLEDGEMENTS

This work was supported by the National Science Foundation under award number CMMI-1661413 and by the US Army under award number MURIW911NF1910280.


## REFERENCES


[1] M. Shokrian, C. Knox, D. H. Kelley, and J.-H. Nam, Mechanically facilitated micro-fluid mixing in the organ of Corti, *Sci. Rep.* , 1 (2020).

[2] H. Mestre, J. Tithof, T. Du, W. Song, W. Peng, A. M. Sweeney, G. Olveda, J. H. Thomas, M. Nedergaard, and D. H. Kelley, Flow of cerebrospinal fluid is driven by arterial pulsations and is reduced in hypertension, *Nature communications* 9, 1 (2018).

[3] A.H. Shapiro, M. Y. Jaffrrin, and S. L. Weinberg, Peristaltic pumping with long wavelengths at low reynolds number, *Journal of Fluid Mechanics* 37, 799{825 (1969).

[4] W. Thielicke and E. J. Stamhuis, Pivlab { towards user-friendly, affordable and accurate digital particle image velocimetry in matlab, *Journal of Open Research Software 2*, 10.5334/jors.bl (2014).

[5] D. H. Kelley and N. T. Ouellette, Using particle tracking to measure flow instabilities in an undergraduate laboratory experiment, *Am. J. Phys.* 79, 267 (2011).

SB³C2021
Summer Biomechanics, Bioengineering and Biotransport Conference
June 20-23, Eastern Shore, MD, USA

# CORTICAL THICKNESS CORRELATES WITH CORTICAL MORPHOLOGY AMONG HUMAN AND NON-HUMAN PRIMATE BRAINS

**Nagehan Demirci (1,2), Maria A. Holland (1,2)**

(1) Aerospace and Mechanical Engineering
(2) Bioengineering Graduate Program
University of Notre Dame
Notre Dame, Indiana, USA

## INTRODUCTION

The typical human brain has a highly folded superficial layer, i.e. the cerebral cortex, with gyral ridges and sulcal valleys. Although each brain is unique, one morphological feature of the cortex is common for each individual; gyri are universally thicker than sulci [1]. This characteristic thickness distribution has been partially explained by biological and mechanical factors. Cellular processes and mechanical forces generated during growth have been shown to lead to these consistent variations in cortical thickness between gyri and sulci [2]. In our recent study, we found a strong correlation between cortical thickness and shape by analyzing 501 typical human brains [3]. We showed that cortical thickness varies in a gyral-sulcal spectrum, with the cortex consistently thickest for convex shapes, thinnest for concave shapes and in the middle for saddle shapes. In this study, we investigate this pattern of the cortex among non-human primate brains with varying shapes and sizes and compare with the human data. We hypothesize that the mechanical forces that emerge during the development of the brain might lead to this systematic morphological trait of the cortex, therefore, we expect to observe a similar outcome. We used our open-source computational pipeline [4] to investigate cortical thickness variations both globally and locally among 12 different primate species ranging from the Senegal Galago to humans. The pipeline takes in cortical surface meshes as an input and outputs many quantitative measures including curvature (mean curvature, Gaussian curvature, and shape index), thickness, depth, and area at each vertex.

## METHODS

We used publicly available neuroimaging resources in this study (Table 1).

Many automated pipelines that perform tissue classification (gray and white matter) and surface reconstruction (pial and white surfaces) are optimized for humans, and struggle to process non-human brains due to their varying shapes and sizes. Therefore, we have used a variety of different tools to find an optimal solution for segmentation and surface reconstruction for each species (Table 1).

**Table 1: Primate species used in this study along with their total number of subjects, sources, and processing tools.**

| Species | Subject # | Source | Processing Tool(s) |
|---|---|---|---|
| Human | 501 | ABIDE [5, 6] | Freesurfer [7] |
| Chimpanzee | 54 | NCBR [8] | CAT12 in SPM12 with Juna-Chimp Template [9] |
| Rhesus Macaque | 26 | INDI-PRIME [10] | AFNI and ANTs with NMT Template [11] |
| Bonobo | 1 | NCBR [8] | BrainVisa Morphologist [12] |
| Gorilla | 1 | NCBR [8] | BrainVisa Morphologist [12] |
| Others | 1 per species | [13] | Freesurfer [7] |

Then, by using our open-source computational pipeline [4], we analyzed the pattern of cortical thickness variations in each species with respect to local topology (concave, saddle, and convex shaped local points). Additionally, we developed an open-source pipeline to reduce manual interventions on reconstructed surfaces after tissue segmentation, automate topology corrections, and smoothen the initial surface generated. This pipeline will be shared in the near future for use by other researchers.

SB³C2022-052

## RESULTS

We present the cortical thickness variations throughout the cortex as a Gaussian kernel density distribution. To determine the shape at each point of the surface mesh we used a non-dimensional surface measure, i.e. shape index [14], which has a value between -1 and 1 that corresponds to a perfect cup and a perfect cap respectively. We found a strong correlation between cortical thickness and cortical topology not only for humans but also for non-human primate species, which might be suggesting a universal physical law (Fig. 1).

Additionally, we calculated the total area of the pial surface for each species. We plotted mean cortical thickness in the order of increasing surface area (Fig. 2). We observe that there is a significant correlation between surface area and cortical thickness. The most noticeable outcomes are: 1) general increase of cortical thickness with surface area, in line with previous findings; 2) excellent correlation of cortical thickness with local shape; 3) relatively larger cortical thickness of the Rhesus Macaque compared to its neighbors; and 4) increased difference of average cortical thickness between convex, concave, and saddle shape with increases in surface area.

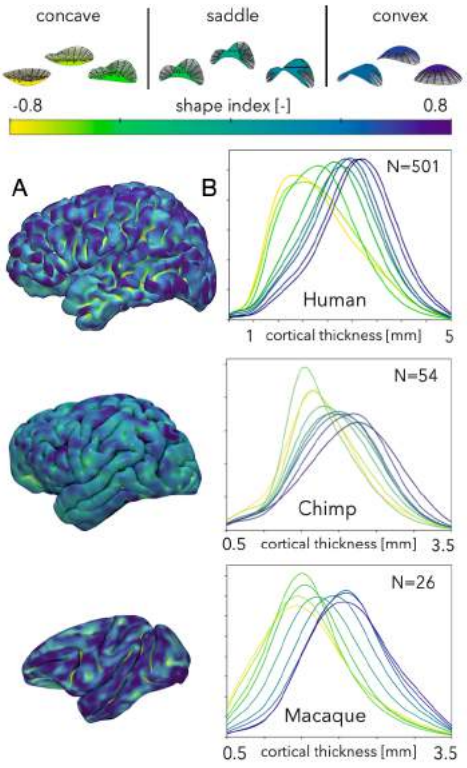


**Fig. 1: Correlation of cortical thickness with cortical topology. (a) Shape index overlaid on pial surface (b) Cortical thickness kernel density distribution profile with respect to local shape.**

## DISCUSSION

In this study we comprehensively investigated the correlation between cortical thickness and cortical morphology among human and non-human primate brains with varying shapes and sizes. The main conclusion of this study is the well-organized variation of cortical thickness in a gyral-sulcal spectrum for all species; convex shape is thickest, concave shape is thinnest, and saddle shape is in the middle consistently. This result might be suggesting a universal physical law of cortical folding. The physical forces generated during growth and development of the cortex might strongly be affecting the final cortical morphology and its relationship with cortical thickness. As a secondary note, cortical thickness noticeably correlates with the size of the cortex, increasing with surface area. Interestingly, we found a relatively thicker cortex on a global scale for Rhesus Macaque compared to other species with comparable sizes, which requires further consideration.

As part of our future work, we will thoroughly compare our results with the data in the literature and expand our dataset by including more species. Next, we will explore the correlations of cortical thickness with sulcal depth and folding index, as these quantitative measures might also vary significantly among different species. Finally, considering the current challenges of analyzing non-human primate MRI datasets, we will enhance our computational pipeline and develop algorithms to effectively process multiple brains with varying shapes and sizes.

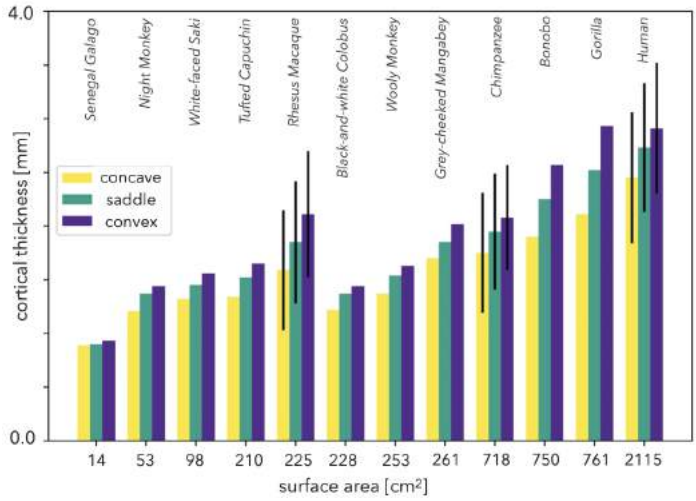


**Fig. 2: Mean cortical thickness of all concave, saddle, and convex shaped points with respect to total pial surface area. Note that, subject size is greater than one for rhesus macaque (N=24), chimpanzee (N=56), and human (N=501) species.**


## ACKNOWLEDGEMENTS

This work was supported by NSF Grant No. IIS1850102 and authors acknowledge support from NCBR by NIH grant No. NS092988.


## REFERENCES


[1] Holland, MA. et al., *Phys Review Letters* 121 (22): 228002, 2018.
[2] Wang, S. et al., *Biomech. Model Mechanobiol*, 20(2):555-567, 2021.
[3] Demirci, N. and Holland MA, *Hum Brain Mapp*, 2022 (in press).
[4] https://github.com/mholla/curveball
[5] Di Martino, A. et al., *Molecular Psychiatry* 19 (6): 659–67, 2014.
[6] Craddock, C. et al., *Frontiers in Neuroinformatics*, 7, 2013.
[7] Fischl, B., *NeuroImage* 62 (2): 774–81, 2012.
[8] https://www.chimpanzeebrain.org
[9] Vickery, S. et al., *ELife* 9 (November): e60136, 2020.
[10] Milham, M. P. et al., *Neuron* 100 (1): 61-74, 2018.
[11] Seidlitz, J. et al., *NeuroImage* 170 (April): 121–31, 2018.
[12] Cointepas, Y. et al., *NeuroImage* 13 (6): 98, 2001.
[13] Ardesch, D. J. et al., *Cerebral Cortex*, 00:1-12, 2021.
[14] Koenderink, J et al., *Image and Vision Comp.* 10 (8): 557–64, 1992.

SB³C2022
Summer Biomechanics, Bioengineering and Biotransport Conference
June 20-23, Eastern Shore, MD, USA

# EVALUATING BIO-SOURCED PHOTOINIATORS EFFECIENCY FOR USE IN SUSTAINABLE 3D BIOPRINTING

**Rion J. Wendland (1), Kristan S. Worthington (1,2)**

(1) Roy J. Carver Department of Biomedical Engineering, University of Iowa
Iowa City, IA, United States
(2) Department of Chemical and Biochemical Engineering, University of Iowa
Iowa City, IA, United States

## INTRODUCTION

Photopolymerization has emerged as a key fabrication technique in biomedical engineering, with applications ranging from drug delivery, tissue engineering, bioprinting, microfluidics, and more. Many of these applications leverage photopolymerization's precise spatial and temporal control to construct highly detailed and consistent polymer structures. However, recent studies have demonstrated that commonly used, synthetic photoinitiators, coupled with UV light exposure, may have toxic effects on cells and can disrupt cell signaling. [1-3] Bio-sourced photoinitiators may be more biocompatible, nontoxic, and biodegradable than their synthetic counterparts. [4-6] In this work, we determined the effectiveness of several bio-sourced initiator systems using light-based photo-rheology. Our results help to advance the use of bio-sourced initiators for biomedical applications and establish a procedure for using rheology to determine photoinitiator effectiveness.

## METHODS

*Prepolymer Formulations*

Bio-sourced initiators (curcumin, Curc; riboflavin, Ribo; and β-carotene, Bcar) were added to poly(ethylene) glycol dimethacrylate 750 (PEGDMA) at a final concentration of 0.2 wt%. Groups containing potential amine synergists (histidine, Hist; adenosine, Adeno; or 2-(diethylamino)ethyl methacrylate, DEA) were added at 0.2 wt%. The synthetic photoinitiator I369 was included as a positive control; I369 was dissolved in acetone at 100 mg/mL and used at a final concentration of 0.1 wt%.

*Photo-rheology*

Photo-rheology was performed using a Kinexus Ultra+ (Netzsch, Selb, Germany) coupled with a violet ($\lambda$ = 410 nm) LED light source (3-Watt High Intensity LED Spotlight, Oznium). This wavelength was chosen as it is close to the wavelength used in many bioprinters. For all solutions, a single-frequency strain controlled oscillatory sequence was performed using an 8 mm upper geometry, a gap height of 0.05 mm, a frequency of 1 Hz, and a strain rate of 1%. Data points were collected every 5 seconds over a 30-minute run.

For each sample, shear storage modulus data were collected over time to evaluate the polymerization kinetics and properties. This approach leverages the dependence of modulus on extent of reaction (crosslinking). Two primary metrics were extracted from storage modulus profiles: 1) rise time, defined as the time at which the modulus increased from baseline, and 2) final modulus, calculated as the average storage modulus at the end of the light exposure window (29 min).

## RESULTS AND DISCUSSION

To determine bio-sourced initiator systems with the greatest photopolymerization potential, we used a model polymer (PEGDMA) and real-time photo-rheology. As the samples polymerized under violet light, rheological behavior was recorded, and the extent of the reaction was observed via the evolution of the storage modulus (**Fig. 1A-B**). In these experiments, the photoinitiation efficiency of four groups (control – no initiator, curcumin, riboflavin, and β-carotene) with four additional additives (Hist, Adeno, DEA, and I369) were evaluated. Of the three initiator candidates, curcumin had the shortest rise time as well as a comparable final modulus to the positive control (**Table 1**). The modulus profiles of the riboflavin formulation do not appear to be substantially different than the negative control, in which some spontaneous crosslinking occurs. Meanwhile, B-carotene seems to hinder PEGDMA crosslinking by violet light. These results indicate that curcumin may be an appropriate photoinitiator for crosslinking using the violet range, while riboflavin and B-carotene are not efficient photoinitiators on their own in this system.

SB³C2022-053

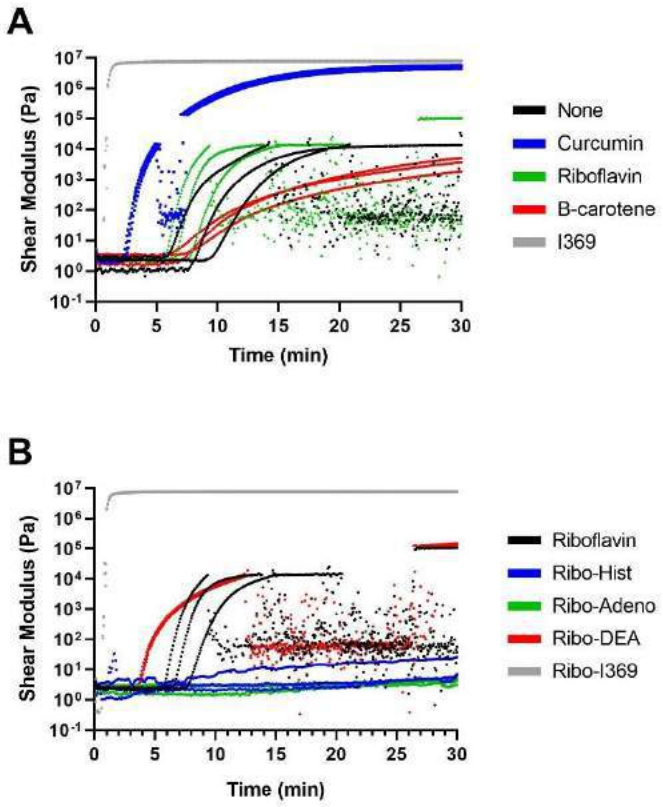


**Figure 1.** Graphs of the shear modulus evolution upon violet light exposure for the bio-sourced initiator systems. A) Comparison of the bio-sourced initiator samples with positive (I369) and negative (no initiator) controls. B) Riboflavin initiator group with potential synergist additives, similar trends were observed across all initiator groups. In all runs, the violet light was on for 29 minutes, with a thirty second delay at the start of the run. N=3 for all samples.

**Table 1.** Rise times of the various bio-sourced initiators and controls as well as the rise times of the potential synergists added to the riboflavin group. Note: DNR stands for 'Did Not Rise', and a rise time of 0 seconds indicates the sample's modulus increased within 5 seconds of the light being turned on. Data is shown as mean ± standard deviation.

| | None | Curc | Ribo | Bcar | I369 |
|---|---|---|---|---|---|
| Rise Time (s) | 520 ± 130 | 130 ± 10 | 400 ± 70 | 810 ± 150 | 0 ± 0 |
| | | | | | |
| | Ribo | Ribo - Hist | Ribo-Adeno | Ribo-DEA | Ribo-I369 |
| Rise Time (s) | 400 ± 70 | DNR | DNR | 220 ± 5 | 0 ± 0 |

When comparing the polymerization effectiveness of the bio-sourced initiators with potential amine synergists, the addition of the synergists actually decreased the extent of reaction in most cases (**Fig 1B**). Like the initiators, the synergists in this experiment were chosen as an evaluation of potential bio-sourced synergists. Here, histidine is an amino acid and adenosine in a sugar-attached nucleic acid, both with tertiary amines groups (most synthetic synergists are molecules with tertiary amines). The synthetic synergist (DEA) included in the groups proved the exception; the addition of DEA seemed to slightly improve the polymerization reaction across the samples. We hypothesize that the bio-sourced synergists are instead acting as inhibitors to the reaction, possibly through less defined side-reactions which use up many of the free-radicals generated upon light exposure and decrease the overall extent of crosslinking. Moving forward, we plan to evaluate other possible bio-sourced synergists to potentially improve the polymerization effectiveness of the bio-sourced initiators.

In most samples throughout this study, we observed a region during the reaction where the storage modulus profile exhibited a sudden and drastic inconsistency: storage modulus appeared to drop, and the signal became noisy before returning to an expected profile. This phenomenon seems to have occurred in approximately the same range of modulus values (while not necessarily the same timepoint in the run) for different samples. The phenomenon is also correlated with extremely high harmonic distortions (data not shown), which could indicate the data are not an accurate representation of the sample's modulus. While sample slipping is a possible explanation, consistent resumption of the modulus profile would be unlikely in this case. As an alternative explanation, we hypothesize that the sample is undergoes a structural phase separation event as pockets of crosslinked material grow and become immiscible in the unpolymerized phase. [7] Our future work will focus on testing this hypothesis using atomic force microscopy and dynamic scanning calorimetry.

Overall, the results presented here describe the use of photo-rheology to evaluate the polymerization effectiveness of bio-sourced initiator systems. Our findings indicate that curcumin alone is the most promising bio-sourced initiator under violet light, based on both rise time and final polymerized storage modulus. Current work is now moving forward to use curcumin-initiated systems in 3D bioprinting applications. Namely, while curcumin was the most effective bio-sourced initiator, photopolymerization parameters such as exposure time and light intensity must still be tuned for structural design fidelity to be achieved, and curcumin's cytocompatibility in this context needs rigorous evaluation. However, the use of photo-rheology as a method to first test the effectiveness of initiator systems provides a more precise starting point for selecting printing parameters. In the long run we anticipate that our findings will be translatable to many biomedical applications that leverage light-based 3D printing to fabricate cellular, tissue, and medical devices and products.

## ACKNOWLEDGEMENTS

Support for this work is provided by the University of Iowa Institute for Vision Research, the University of Iowa College of Engineering, and the University of Iowa Roy J. Caver Department of Biomedical Engineering.

## REFERENCES

1. Lindberg, G.C.J., et al., Applied Physics Reviews, 2021. **8**(1).
2. Zeng, B.N., et al., Toxicology in Vitro, 2021. **72**.
3. Li, J., et al., Environmental Science & Technology, 2019. **53**(18).
4. Zhao, J.C., et al., Polymer Chemistry, 2015. **6**(28).
5. Noirbent, G., et al., European Polymer Journal, 2021. **142**.
6. Zaborniak, I., et al., European Polymer Journal, 2021. **142**
7. Forney, B.S., et al., Macromolecules, 2010. **43**(20).

# DEVELOPMENT AND VALIDATION OF TWO – DIMENSIONAL FINITE ELEMENT MODEL OF THE NEONATAL BRACHIAL PLEXUS

**Sarah J. Trapp (1), Michele J. Grimm (1,2)**

(1) Department of Biomedical Engineering, Michigan State University, East Lansing, MI USA
(2) Department of Mechanical Engineering, Michigan State University, East Lansing, MI USA

## INTRODUCTION

Neonatal brachial plexus palsy (NBPP) occurs during the birthing process in approximately 1.5/1,000 total births[1]. When the injury persists past 12 months of age, continuing outcomes may include joint subluxation, muscle weakness, and sensory dysfunction[2]. Until the early 1990's, it was thought that NBPP solely occurred due to trauma induced by lateral neck traction caused by the birthing attendant (exogenous force). Since then, clinical evidence has demonstrated that NBPP may occur due to other mechanisms of injury. Factors affecting the mechanism of injury may include bending of the neck, fetal malpositioning, labor induction, labor abnormalities, operative vaginal delivery, and shoulder dystocia[1].

NBPP injuries are difficult to research clinically due to ethical issues that surround the venerable subject group - infants. Finite element models (FEM) present an opportunity to investigate different aspects of NBPP. Currently, there is no FEM model in the literature of a neonatal brachial plexus and spinal cord. The objective of this study was to create a two-dimensional model of the neonatal brachial plexus that could be used to investigate how the stress and strain develop in the various roots of the brachial plexus when loads and displacements are applied. This first phase of the project focuses on development and validation of the model.

## METHODS

ABAQUS software was used to design, mesh, and analyze the brachial plexus and spinal cord model of a neonate. The brachial plexus is divided into five sections – roots, trunks, divisions, cords, and terminal nerves. Our 2D model was constructed solely of the roots and trunks due to the 3D anatomical complexity that occurs within the division section.

The model was based on dimensions measured during primary reconstructive surgery. These dimensions are provided in Table 1 and include the length of the sections as well as both the transverse and cranial-caudal dimensions of each nerve root. The cranial caudal dimensions were used to depict the thickness of the nerves in this 2D model, as that dimension falls within the plane of analysis.

**Table 1: Average Dimensions (mm) for Infant Brachial Plexus**

| Dimensions | C5 | C6 | C7 | C8 | T1 |
|---|---|---|---|---|---|
| **Cranial Caudal** | 3 | 3.1 | 3.8 | 2.7 | 2.5 |
| **Transverse** | 1.1 | 1.3 | 1.6 | 1.4 | 1.4 |
| **Spinal root to dorsal root ganglion** | 7.5 | 7.5 | 7.5 | 7.5 | 7.5 |
| **Dorsal root ganglion to end of bony foramen** | 9 | 8 | 7 | 5.5 | - |
| **Foramen to formation of trunk** | 14 | 15.5 | 19 | 7 | 6 |

Two cases were developed to analyze the difference between quasistatic stretch (0.01 mm/second) and dynamic stretch (10 mm/second) of the nerves, as seen in Table 2. Within ABAQUS software boundary conditions and loads were established. The boundary conditions were the same for both cases, including an encastré condition to the midline of the spinal cord and XYSMM condition to the superior and inferior portions of the five nerves. The encastré boundary condition constrains all active structural degrees of freedom within the edge selected and the XYSMM boundary condition allows the nerve to stretch in the plane of the model when loads were applied.

To date, there has been no assessment of the mechanical properties of neonatal brachial plexus. The Young's modulus and Poisson's ratio were taken from neonatal piglets, as seen in Table 2[3,4]. Due to lack of clinical research on neonatal spinal cord and brachial plexus mechanical properties, in our 2D model, the same Young's modulus was used for both the brachial plexus and spinal cord.

Two different loading conditions were examined with the model, as summarized in Table 2. Both simulated a pulling force applied to the

nerves at the distal end of the trunk, as would occur with the depression of the shoulder while the head and neck remained aligned with the axis of the spine. Two different loading rates were used, to match experimentally available data for validation – and these affected both the Young's modulus and the maximum load applied, which increase at higher loading rates due to the viscoelastic nature of nerves.

Loading was modeled as an applied stress at the distal end of each nerve trunk – at the junction with the division. The tensile stress was calculated based on the maximum load (Table 2) normalized by the estimated cross-sectional area of the nerve root. This cross-sectional area was calculated based on an ellipse with the major and minor axes equal to the cranial-caudal and transverse dimensions (Table 1). The force used to calculate the applied stress to the C5/C6 and C8/T1 trunks was twice as high as that applied to C7, due to the fact that the latter structure includes the axons of only the single nerve root.

**Table 2: Mechanical Properties of the Neonatal Brachial Plexus and Spinal Cord – Measured in Piglets at Two Loading Rates[3,4]**

| Case | Loading Rate (mm/second) | Maximum Load (N) | Young's Modulus (MPa) | Poisson's Ratio |
|---|---|---|---|---|
| 1 | 0.01 | 1.08 | 1.48 | 0.4 |
| 2 | 10 | 2.12 | 2.02 | 0.4 |

## RESULTS

Tables 3 and 4 provide the values of each type of stress and displacement predicted by the model for both loading cases, with all measurements taken at the proximal end of the nerve root, where it intersects with the spinal cord.

Our model was validated through comparison with the results of Dr. Anita Singh[3]. Dr. Singh calculated a stress in the piglet brachial plexus corresponding to the failure load. For Case 1, the maximum stress found experimentally was 0.20 MPa, and for Case 2 it was 0.45 MPa. In our model, the maximum Von Mises stress for Case 1 was 0.255 MPa, and for Case 2 it was 0.444 MPa.

**Table 3: Results of Case 1 Model (Low Loading Rate Properties)**

| | Von Mises Stress (MPa) | Max Principal Stress (MPa) | Tresca Stress (MPa) | Displacement Magnitude at end of trunk (mm) |
|---|---|---|---|---|
| **C5** | 0.173 | 0.174 | 0.177 | 8.764 |
| **C6** | 0.255 | 0.254 | 0.225 | |
| **C7** | 0.077 | 0.086 | 0.110 | 4.382 |
| **C8** | 0.157 | 0.151 | 0.157 | 8.764 |
| **T1** | 0.155 | 0.159 | 0.169 | |

**Table 4: Results of Case 2 Model (High Loading Rate Properties)**

| | Von Mises Stress (MPa) | Max Principal Stress (MPa) | Tresca Stress (MPa) | Displacement Magnitude at end of trunk (mm) |
|---|---|---|---|---|
| **C5** | 0.329 | 0.324 | 0.350 | 5.609 |
| **C6** | 0.444 | 0.442 | 0.461 | |
| **C7** | 0.199 | 0.161 | 0.161 | 3.569 |
| **C8** | 0.277 | 0.295 | 0.295 | 5.609 |
| **T1** | 0.315 | 0.310 | 0.310 | |

The results are presented visually for Case 2 in Figure 1. The pattern of stresses was the same for Case 1 and Case 2, as the nerve roots were modeled as homogeneous, linear elastic materials.

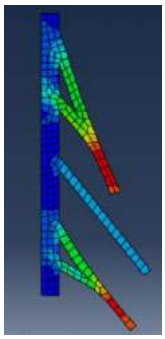

**Figure 1: Case 1 results for Von Mises stresses**

## DISCUSSION

Clinical patterns of injury and some experimental work demonstrates that C5 and C6 experience higher stress under initial loading of the brachial plexus than do the lower roots[5]. Our study also demonstrates that pattern of injury, as seen in Table 3 and 4. Our goal of this study was to validate the model against previous literature and replicate the findings and similar stress values.

When it comes to any finite element analysis, limitations exist and must inform the application of the results. In our model, the first limitation stems from the fact there are no neonatal mechanical property values of the human infant brachial plexus and spinal cord, thus the needed use of neonatal piglets. The second limitation is the inability to model the complete brachial plexus in two dimensions. The need to stop at the division level limits our ability to study the entirety of the brachial plexus model.

While this model is not a complete model of the brachial plexus, it does provide opportunity to investigate how normal variations in nerve anatomy (e.g., root diameter and angle) affect the stress developed at the nerve roots. This 2D model is the first step towards developing a complete 3D model of the neonatal brachial plexus. This will provide the opportunity to more accurately assess the effect of the birth process and biological variation's structure and properties on the risk of NBPP.

## ACKNOWLEDGEMENTS

We thank our colleagues from Lynda Yang's neurosurgery team at the University of Michigan, who provided insight and expertise that assisted the research – including the infant nerve dimensions. This project was supported through NSF Award CBET 2028474.

## REFERENCES

1. Gherman, R. B. *et al. Neonatal brachial plexus palsy*. *Obstetrics and Gynecology* vol. 123 (2014).
2. Narendran, L. M. *et al.* Predictors of neonatal brachial plexus palsy subsequent to resolution of shoulder dystocia. *J. Matern. Neonatal Med.* **0**, 1–7 (2021).
3. Singh, A., Shaji, S., Delivoria-Papadopoulos, M. & Balasubramanian, S. Biomechanical Responses of Neonatal Brachial Plexus to Mechanical Stretch. *J. Brachial Plex. Peripher. Nerve Inj.* **13**, e8–e14 (2018).
4. Nishida, N. *et al.* Mechanical properties of nerve roots and rami radiculares isolated from fresh pig spinal cords. *Neural Regen. Res.* **10**, 1869–1873 (2015).
5. Metaizeau, J. P., Gayet, C. & Plenat, F. [Brachial plexus birth injuries. An experimental study (author's transl)]. *Chir. Pediatr.* **20**, 159–163 (1979).

SB³C2022
Summer Biomechanics, Bioengineering and Biotransport Conference
June 20-23, Eastern Shore, MD, USA

# COMPUTATIONAL MODELING OF CRYOBALLOON ABLATION FOR PULMONARY VEIN ISOLATION

**Tejas Patel (1), Chris Li (1), Farshad Raissi (3), Ghassan Kassab (4), Tong Gao (1, 2), Lik Chuan Lee (1)**

(1) Department of Mechanical Engineering, Michigan State University, East Lansing, MI, USA
(2) Department Computational Mathematics, Science and Engineering, Michigan State University, East Lansing, MI, USA
(3) Department of Medicine, University of California, San Diego, CA, USA
(4) California Medical Innovations Institute, San Diego, CA, USA

## INTRODUCTION

Cryoballoon Ablation (CBA) is a promising treatment for atrial fibrillation (AF). Since the release of CB2 (second-generation Arctic Front Advance Pro cryoballoon) by Medtronic [1] in 2020, the efficiency of CBA surgery has increased drastically. During CBA, a cryoballoon (CB) is first positioned at the pulmonary vein (PV) ostium that connects the left atrium (LA). Liquid nitrous oxide is then injected into the CB, and a phase change gradually absorbs heat and freezes the targeted region in the LA. When the temperature in the targeted region falls below $-20^0$C, lesion formation is initiated at the balloon-tissue contact region. Isolation is confirmed by the loss of PV potentials, and the time taken to achieve this isolation is called time to isolation (TTI). After TTI the CB is held in place as per recommended dosing protocols for about 2 to 4 minutes per freeze.

The effectiveness and safety of CBA, however, depend on multiple factors, such as the cooling rate, leakages, minimal temperature, and the isotherm distribution. Some of the underlying issues with CBA include the possibility of phrenic nerve injury as well as determining the optimal CB position and dosing time to get a contiguous lesion. In addition, the presence of leakage also reduces the efficacy of CBA, which necessitate further lowering of the CB temperatures and increase hold times.

Given these issues, there is a need to investigate factors affecting the temperature (and flow) field in the area surrounding the PV ostium to help optimize the treatment. On the other hand, only a few highly idealized numerical models [1,2] have been developed to simulate CBA. As such, the goal here is to develop a patient-specific computational modeling framework to investigate blood flow and temperature field during CBA surgery in a realistic LA geometry. Specifically, we seek to investigate how the presence of a CB affects hemodynamics in the LA, and how the presence of leakage affects temperature distribution at the PV ostium, which directly affects the lesion formation.

## METHODS

Hemodynamics and heat transfer in the LA are described by solving the continuity, incompressible Navier-Stokes and energy conservation equations. Non-dimensional numbers governing the physics are the Reynolds number $Re = \frac{V_{sc} L_{sc}}{\upsilon}$ and Prandtl number $Pr = \frac{\upsilon}{\alpha}$, where $\upsilon$ is the kinematic viscosity and $\alpha$ is the thermal diffusivity of blood. Laminar flow is assumed here and the complete non-dimensional boundary value problem in the LA fluid domain, is given as follows:

$$\frac{\partial \boldsymbol{u}}{\partial \tau} + \boldsymbol{u} \cdot \nabla \boldsymbol{u} - \nabla \cdot \boldsymbol{\sigma} - \boldsymbol{f} = \boldsymbol{0}, \tag{1}$$

$$\nabla \cdot \boldsymbol{u} = \boldsymbol{0}, \tag{2}$$

$$\frac{\partial \mathrm{T}}{\partial \tau} + \boldsymbol{u} \cdot \nabla \mathrm{T} - \frac{\nabla^2 \mathrm{T}}{Pe} - Q = 0. \tag{3}$$

In the above equations, $\boldsymbol{u}, p, \mathrm{T}$ are the velocity, pressure, and temperature fields, respectively, whereas $\boldsymbol{\sigma}(\boldsymbol{u}, p) = -p\boldsymbol{I} + \frac{1}{Re}(\nabla \boldsymbol{u} + (\nabla \boldsymbol{u})^T)$ is the stress tensor for a Newtonian fluid and $Pe = Re \cdot Pr$ is the Peclet number.

The finite element (FE) method is used for spatial discretization of Eqs. (1) – (3). A closer look at the physical properties of blood and the velocity at the PV ostium reveals that the flow is advection dominated. Numerical stability to capture sharp spatial gradients is achieved by applying Streamline-Upwinding (SUPG) and crosswind stabilization[3] schemes to the weak form. To further increase stability and accuracy, we include two additional stabilization terms, namely a Least-Squares on Incompressibility Constraint (LSIC) and a penalty-based backflow stabilization term[4]. The latter confines the flow to be in the normal direction and helps to avoid numerical

instabilities arising from flow reversal at the mitral valve (MV). Lastly, we also employ the Pressure-Stabilizing Petrov Galerkin (PSPG) stabilization to suppress the node-to-node pressure oscillations.

The standard first order forward Euler scheme is used for time-discretization of the inertia term in Eq. (1) and (3) along with the unconditionally stable crank Nicolson scheme for the advection, temperature diffusion and viscous terms. We employ the Taylor-Hood elements for velocity/pressure and quadratic elements for temperature. The Incremental Pressure Correction Scheme is used to decouple the equations and the resultant time-discretized weak form of the governing equations (with $\boldsymbol{v}$ , $q$, $w$ as test functions) is given below:

$$\left\langle \frac{\boldsymbol{u}^{*}-\boldsymbol{u}^{\theta}}{\Delta\tau}, \boldsymbol{v} \right\rangle + \left\langle \boldsymbol{u}^{\theta}\cdot\boldsymbol{\nabla}\boldsymbol{u}_{\boldsymbol{ck}}^{*}, \boldsymbol{v} \right\rangle + \left\langle \boldsymbol{\sigma}\left(\boldsymbol{u}_{\boldsymbol{ck}}^{*}, p^{\theta}\right), \boldsymbol{\nabla}\boldsymbol{v} \right\rangle - \left\langle \boldsymbol{\sigma}\left(\boldsymbol{u}_{\boldsymbol{ck}}^{*}, p^{\theta}\right)\cdot \boldsymbol{n}, \boldsymbol{v} \right\rangle_{\partial\boldsymbol{\Omega}} - \langle \boldsymbol{f}, \boldsymbol{v} \rangle + \int_{\Omega} \gamma_{SUPG}\left(\boldsymbol{u}^{\theta}\right) i P\left(\boldsymbol{u}^{\theta}, \boldsymbol{v}\right)\cdot\left(\frac{\boldsymbol{u}^{*}-\boldsymbol{u}^{\theta}}{\Delta\tau} + \boldsymbol{u}^{\theta}\cdot\boldsymbol{\nabla}\boldsymbol{u}_{\boldsymbol{ck}}^{*} - i\overline{\boldsymbol{\nabla}}\cdot\boldsymbol{\sigma}\left(\boldsymbol{u}_{\boldsymbol{ck}}^{*}, p^{\theta}\right) - \boldsymbol{f}\right) dx + \int_{\Omega} \left(\gamma_{CW}\left(\boldsymbol{u}^{\theta}\right) i\Lambda\left(\boldsymbol{u}^{\theta}, \boldsymbol{u}^{*}\right)\right) : \boldsymbol{\nabla}\boldsymbol{v}\, dx + \int_{\Omega} \gamma_{LSIC}\, i(\boldsymbol{\nabla}\cdot\boldsymbol{u}^{*}) i(\boldsymbol{\nabla}\cdot\boldsymbol{v})\, dx + \langle 10^{4} i(\boldsymbol{I}-\boldsymbol{n}\otimes\boldsymbol{n}) i\boldsymbol{u}^{*}, \boldsymbol{v} \rangle_{\partial\Omega_{D}^{p}} = \boldsymbol{0} \quad (4)$$

$$\left\langle \nabla\left(p^{\theta+1}-p^{\theta}\right), \nabla q \right\rangle + \frac{1}{\Delta\tau}\langle \boldsymbol{\nabla}\cdot\boldsymbol{u}^{*}, q \rangle + \int_{\Omega} \gamma_{PSPG}(\boldsymbol{u}^{*}) i\overline{\nabla} q \cdot \left(\frac{\boldsymbol{u}^{\theta}-\boldsymbol{u}^{\theta-1}}{\Delta\tau} + \boldsymbol{u}^{\theta}\cdot\boldsymbol{\nabla}\boldsymbol{u}_{\boldsymbol{ck}}^{\theta} - \boldsymbol{\nabla}\cdot\boldsymbol{\sigma}\left(\boldsymbol{u}_{\boldsymbol{ck}}^{\theta}, p^{\theta}\right) - \boldsymbol{f}\right) dx = 0 \quad (5)$$

$$\left\langle \frac{\boldsymbol{u}^{\boldsymbol{\theta+1}}-\boldsymbol{u}^{*}}{\Delta\tau}, \boldsymbol{v} \right\rangle + \left\langle \nabla\left(p^{\theta+1}-p^{\theta}\right), \boldsymbol{v} i \right\rangle = 0 \quad (6)$$

$$\left\langle \frac{\mathrm{T}^{\theta+1}-\mathrm{T}^{\theta}}{\Delta\tau}, w \right\rangle + \left\langle \boldsymbol{u}^{\boldsymbol{\theta+1}}\cdot\nabla \mathrm{T}_{ck}, w \right\rangle + \frac{1}{Pe}\left[\langle \nabla \mathrm{T}_{ck}, \nabla w \rangle - \langle \overline{\mathrm{T}}_{\omega} i, w \rangle_{\partial\Omega_{N}^{\mathrm{T}}}\right] - \langle Q, w \rangle + \int_{\Omega} \gamma_{SUPG}\left(\boldsymbol{u}^{\boldsymbol{\theta+1}}\right) i P\left(\boldsymbol{u}^{\boldsymbol{\theta+1}}, w\right)\cdot\left(\frac{\partial \mathrm{T}^{\theta+1}}{\partial\tau} + \boldsymbol{u}^{\boldsymbol{\theta+1}}\cdot\nabla \mathrm{T}_{ck} - \frac{\nabla^{2}\mathrm{T}_{ck}}{Pe} - Q\right) dx + \int_{\Omega} \left(\gamma_{CW}\left(\mathrm{T}^{\theta}\right) i\Lambda\left(\boldsymbol{u}^{\boldsymbol{\theta+1}}, \mathrm{T}^{\theta+1}\right)\right) : \nabla w\, dx = 0 \quad (7)$$

In the above, $P(\boldsymbol{u}, \boldsymbol{m}) = \boldsymbol{u}\cdot\boldsymbol{\nabla}\boldsymbol{m}$ and $i\Lambda(\boldsymbol{u}, \boldsymbol{\phi}) = \boldsymbol{\Gamma}(\boldsymbol{u})\cdot\boldsymbol{\nabla}\boldsymbol{\phi}$ are the SUPG and crosswind operators and $\gamma$ is the stabilization constant.

We use the open-source FE library FEniCS [5] to solve the weak forms in Eqs. (4) – (7). Simulations are performed on a patient specific LA geometry with an oblate CB with a major diameter of 23 mm that occludes the right-inferior PV (RIPV) inlet (**Fig. 1**). Model dimensions [6] are listed in Table 1. PV isolation is simulated by applying a temperature of -70ºC on the CB. Patient specific PV flow rate measurements[7] and blood perfusion rate in the LA wall are imposed as boundary conditions in the model. At the LA wall, Eq. (3) reduces to the Pennes Heat conduction equation. Initial blood temperature is set as 37ºC and the problem is solved for 40 heart cycles on a FE mesh consisting of a total of 1.86 mi DOF's with a Courant number < 0.25.

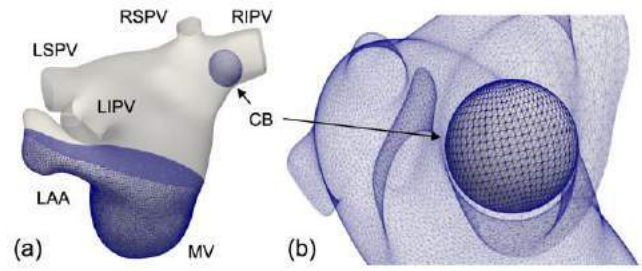


**Figure 1: (a) A schematic of patient specific LA with an oblate CB at the RIPV (b) Fine uniform mesh at CB.**

**Table 1: Areas and diameters of PV's extracted from MRI data**

| | LSPV | LIPV | RSPV | RIPV |
|---|---|---|---|---|
| Area ($mm^{2)}$ | 322.5 | 209.9 | 188.35 | 437.6 |
| Av. Dia. (mm) | 20.26 | 16.34 | 15.48 | 23.6 |

## RESULTS

**Fig. 2a** shows the temperature distribution at the RIPV ostium after a periodic steady state is reached. This occurs in less than 30 seconds. Once, the lesion thickness remains unchanged with time, we stop the simulation. **Fig. 2b** shows the region at the RIPV ostium where the temperature is less than $-20^{0}$C (i.e., threshold at which the lesion is formed). The maximum lesion thickness at the PV ostium is found out to be 6.8 mm. The heat transfer rate across the CB also flattens out once a steady state is reached, and the average value is about -2150W. **Fig. 2c** shows the gap measured at various points between the CB to the RIPV ostium and the corresponding temperature at the RIPV ostium. Next, we simulate different positions of the CB. We observe that no lesion is formed if there is considerable leakage around the gap (defined by a threshold value of 2mm), which causes advection of the cold energy from the CB downstream. Hence, a contiguous balloon-tissue contact area with minimum leakage throughout is highly important for optimum lesion formation.

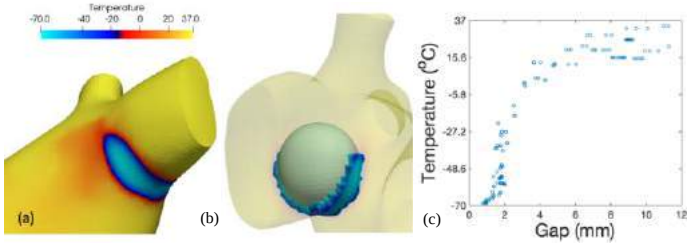


**Figure 2: (a) Periodic steady state temperature at the RIPV ostium. (b) Mesh cells at the lesion where temperature is $< -20^{0}$C (c) Temperature vs gap (between the CB and RIPV ostium).**

## DISCUSSION

Here, we have developed a novel computational framework to simulate CBA. Our model is used to predict lesion formation at the PV ostium. For CBA, we show that the LA wall temperature (and effectiveness of PV isolation) is sensitive to the leakage at the PV ostium. We also found that a minimum gap of 2mm is necessary for lesion to form on the LA wall. The developed computer framework will be applied in future studies for understanding and patient-specific optimization of the CBA. The framework will be used also to determine the conditions (e.g., at different PV velocities) at which lesions will form. At present, there are some limitations associated with this study. First, motion of the LA wall is not considered here. Second, we do not account for a closed MV. In future, we intend to improve on our framework by incorporating a fluid-structure interaction model.


## ACKNOWLEDGEMENTS

We acknowledge National Science Foundation grant no. 1702987.


## REFERENCES


[1] Getman, M.K. et al., *J. Cardiovas. Electr.*, 30(11): 2274-2282, 2019.
[2] Yuantong, X. et al., *Appl. Ther. Eng.*, 142: 524-529, 2018.
[3] Codina, R., *Comput Meth Appl Mech Eng* 110, 3-4 (1993):325-342.
[4] Moghadam, M. E. et al., *Comput. Mech.* 48, 3 (2011): 277-291.
[5] Logg, Anders, et al. *The FEniCS book. Vol. 84. Springer*, 2012.
[6] Fastl T.E., et al. *Medical Image Analysis* 47: 180-190, 2018.
[7] Lantz, J., et al. *Annals of Biomedical Engineering*, 47(2): 413-424, 2019.

SB³C2022
Summer Biomechanics, Bioengineering and Biotransport Conference
June 20-23, Eastern Shore, MD, USA

# ANALYZING ELASTASE AND COLLAGENASE TREATED MECHANICAL BEHAVIOR OF PORCINE AIRWAYS

**Crystal A. Mariano (1), Samaneh Sattari (1), Mona Eskandari (1,2,3)**

(1) Mechanical Engineering, University of California, Riverside, Riverside, CA, USA
(2) Bioengineering, University of California, Riverside, Riverside, CA, USA
(3) BREATHE Center, School of Medicine, University of California, Riverside, Riverside, CA, USA

## INTRODUCTION

Respiratory diseases, known to be one of the leading causes of death worldwide, are primarily characterized by compromised lung constituents. Specifically, the connective tissues of elastin and collagen are responsible for the recoil and structural integrity of the lung [1,2]. Studies have shown that the cause for chronic obstructive pulmonary disease (COPD) is attributable to the damage of elastin fibers [3,4]; moreover, excessive collagen deposition leads to tissue stiffening diseases, such as cystic fibrosis and asthma [5]. Investigations characterizing the imbalance of these constituents have previously been done on guinea pig and dog lung [6,7] but are limited to parenchymal strips, not isolating pulmonary airways, which are a major site of lung function compromise and occlusion in disease.

Here we introduce the first biaxial tensile tests on lung airways to compare the degenerative effects of collagen and elastin. This study directly compares the mechanics of treated and untreated specimens, examining these effects through the lens of tissue anisotropy by analyzing both circumferential and axial material properties, and additionally assessing heterogeneity by comparing proximal to distal airways via the comparative material behaviors of the trachea, large bronchi, and small bronchi. This experiment provides airway tissue mechanical insights in diseased states and furthers our understanding of the role of these structural constituents.

## METHODS

Airway tissue samples from four pigs obtained from an abattoir and cut into squares with an effective testing size of 5.1 +/-0.2mm. Since the cartilage layer is significantly stiffer than the soft tissue, it was removed to assess solely the behavior of the connective tissue, similar to methods described in past studies [8]. The dissected samples were comprised of three regions based on their extra- or intra-parenchymal location and inner diameter [9]: the trachea (>16mm), the large bronchi (>7mm), and the small bronchi (>3mm). A mark made on the corner of the tissue designated the circumferential orientation. Samples were placed in a 1X phosphate-buffered saline (PBS) bath and refrigerated until the day of testing.

Elastase and collagenase (Worthington Biochemical Corp.) solutions were prepared: the elastase solution consisted of 0.001mg/ml Trypsin inhibitor and deionized water to obtain a concentration of 0.1units/ml, while the collagenase solution had a concentration of 96units/ml [10]. Both solutions were mixed using a thermal shaker at 100RPM. Each untreated sample was placed in PBS at ambient room temperature for 30min [11], then tested and subsequently treated for direct comparison with either a 1ml bath of elastase for 1 hour or collagenase for 30 min [12]. Biaxial tensile testing was conducted using 1.5N load cells, cycling each specimen to 60% strain in both loading directions at a rate of 1%/s. The protocol consisted of five preconditioning cycles and a final test cycle which was analyzed.

The engineering stress-strain loading curve for each bronchial region, treated and untreated, was analyzed. Due to the curve's bilinear transition between small and large strains, the slopes were calculated based on the initial modulus ($E_I$) and ultimate modulus ($E_U$) as in prior studies using a linear fit with $R^2 > 0.90$ [13]. From four pigs, 36 untreated specimens (12 per trachea, large bronchi, and small bronchi regions) were tested; of those, half of each region's samples were subsequently collagenase or elastase treated groups, designating six samples per region per un/treated categories for equal group statistical comparisons. A two-way ANOVA with post-hoc Bonferroni was used to compare the effects of tissue treatment with a defined significance of $p<0.05$, where *$p<0.05$, **$p<0.01$, ***$p<0.001$, and ****$p<0.0001$.

## RESULTS

The circumferential and axial stress-strain loading curves (average +/- standard deviation) of the untreated and treated regions of the lung are shown in Figure 1. Overall, the untreated small and large bronchi regions were most similar to each other: the untreated trachea response

was statistically disparate, stiffer than other regions both axially and circumferentially. Once treated, the small and large bronchi regions continued to exhibit comparable behaviors to one other. The trachea samples became most similar to its bronchial counterparts after collagenase treatment in the circumferential direction only, but remained distinct otherwise.

For all three airway regions, collagenase and elastase tissue treatment resulted in lower stresses for the same induced strains compared to untreated counterparts. This degenerated response was noted to be statistically significant for collagenase treatments in all regions. In fact, collagenase treated samples experienced a 64-89% reduction of maximum stress from its pre-treated state, whereas elastase treated samples experienced a 44-63% stress reduction compared its untreated state.

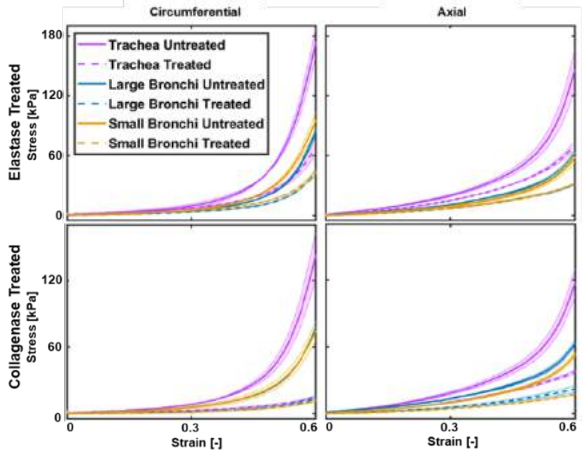


**Figure 1: Average +/- standard deviation of the stress-strain loading profiles of untreated versus elastase and collagenase treated lung regions in the circumferential and axial directions.**

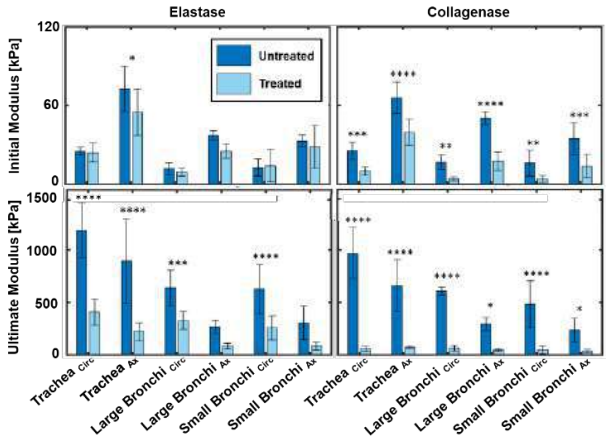


**Figure 2: Average +/- standard deviations of the initial ($E_I$) and ultimate ($E_U$) moduli of each airway region, and circumferential or axial orientation.**

Airway tissue stiffness, observed via the initial and ultimate moduli values displayed in Figure 2, decreased significantly over all regions and directions of the collagenase treated samples compared to the untreated states. The elastase treated samples collected from the trachea demonstrated a significant decrease in the axial direction for both moduli, but other regions did not exhibit this significant axial degeneration; however, the circumferential response of all regions did significantly decrease with elastase treatment for the ultimate modulus. Tissue compliance tended to increase in most treated samples, however the change due to elastase was not as substantial as the collagenase treated tissues: the initial modulus of the collagenase treated tissues experienced a 40-76% decrease, whereas the elastase treated samples exhibited only a 4-33% reduction. The elastase treatment also had less effect on the ultimate modulus as well compared to the collagenase treatment, with a 49-74% reduction compared to an 84-94% decrease respectively.

## DISCUSSION

Our findings observe an overall increase in tissue compliance after the degeneration of airway constitutive collagen and elastin fibers. Albeit the degree of induced damage remains to be quantified via planned upcoming histological assessments, this study provides the first mechanical characterization of degenerated airways as observed in pulmonary disease. When elastin and collagen are damaged in COPD [14], lung tissue softens and exhibits reduced recoil, aligning with our findings. The converse, where increased collagen deposition in the airways as a result of disease causes tissue stiffening [5,15], also supports our findings.

An interesting outcome within the collagenase treated samples in the circumferential direction is how bronchial regions nearly converged to the same stress-strain curve. This could possibly be due to the structure of the lung constituents, where the weave of the trachea's axially aligned fibers differ from that of the large and small bronchi [16], and thus, upon degeneration, the underlying matrix in the circumferential direction behaves similarly across all regions.

Higher instances of degeneration in the collagenase treated group compared to the elastase group may be attributable to our utilization of a 1000-fold greater treatment concentration in order to be able to measurably degrade collagen, since collagen fibers have a greater elastic modulus than elastin and are present in greater abundance in the airway network [16,17]. Our preliminary studies found that if elastase treatment activation levels used for the aorta [10] or parenchyma [18] were employed, the resulting elastase treated stress-strain curve would be completely flat and insensitive to loading between the physiological 0-60% strain regime, whereas the collagenase treated specimens were responsive. Future work will utilize confocal imaging to measure the damage imposed upon the elastin and collagen network to yield insights regarding the comparative pulmonary mechanical role for each constituent.


## ACKNOWLEDGEMENTS

This work was supported by the Hellman Faculty Fellows Program.


## REFERENCES


[1] Mecham, R.P. et al., *Matrix Biol,73:6-20, 2018* [2] Suki, B. et al., *J Appl Physiol,* 98:1892-99, 2005 [3] Vindin, H.J. et al., *Curr Opin Biotechnol,* 74:1-6, 2022 [4] Merrilees, M.J. et al., *Respir Res,* 9:41, 2008 [5] Liu, L. et al., *Bioeng*, 8:1-13, 2021 [6] Yuan, H. et al., *J Appl Physiol,* 89:3-14, 2000 [7] Vawter, D.L. *J Appl Physiol*, 45(2):261-69, 1978 [8] Noble P.B. et al., *J Appl Physiol*, 92:1119-11124, 2002 [9] Sattari, S. et al., *J Mech Behav Biomed Mater*, 110:1-10, 2020 [10] Ross, C.J. et al., *Acta Biomater,* 135:425-40, 2021. [11] Safshekan, F. et al., *Materials*, 9(6):456, 2016. [12] Yuan, H. et al., *J Appl Physiol,* 89:3-14, 2000 [13] Smith, LJ. et al. *Ann Biomed Eng*, 36: 214-223, 2008 [14] Novak, C.J. et al., J *Biomech Eng,* 143(110801):1-15, 2021 [15] Setlakwe, E.L. et al., *J Physiol Lung Cell Mol Physiol,* 307:L252-60, 2014 [16] Eskandari, M. et al., *Acta Biomater,* 97:513-23, 2019 [17] Mead, J. *Physiol Rev,* 41(2):281-330, 1961 [18] Sata, M. et al., *J Appl Physiol,* 78(1):239-246, 1995

SB³C2022
Summer Biomechanics, Bioengineering and Biotransport Conference
June 20-23, Eastern Shore, MD, USA

# EVALUATING THE EFFECT OF PUFAS ON HEPATIC STELLATE CELL ACTIVATION IN A 3D TISSUE ENGINEERED MODEL OF HEPATIC FIBROSIS

**L. Madison Kirk (1,2), Nathaniel Hauser (1), Lucy J. Price (1), Chia-Chi Chuang Key (3) Aleksander Skardal (4), Elaheh Rahbar (1,2)**

(1) Department of Biomedical Engineering, Wake Forest School of Medicine, Winston Salem, NC
(2) Virginia Tech – Wake Forest University School of Biomedical Engineering and Sciences
(3) Department of Internal Medicine, Section of Molecular Medicine, Wake Forest School of Medicine, Winston Salem, NC
(4) Department of Biomedical Engineering, The Ohio State University, Columbus, OH

## INTRODUCTION

Chronic liver conditions resulting from prolonged hepatic inflammation and fibrosis have been indicted as the cause of 2 million deaths each year [1]. Liver fibrosis is a dynamic process characterized by the scarring and accumulation of extracellular matrix (ECM) components resulting from chronic liver injury, including choleostatic and metabolic diseases. Activation of hepatic stellate cells (HSCs) has been shown to be the primary driver of hepatic fibrosis in both experimental and clinical models of liver injury, and therefore a key target for anti-fibrotic therapy. Extracellular signals from the ECM (e.g., stiffness) and adjacent hepatic cells including hepatocytes and liver sinusoidal endothelial cells (LSECs) and have been sown to modulate HSC activation and play a role in the progression of hepatic fibrosis. The increasingly stiff ECM and upregulation of integrins increases the formation of focal adhesions, triggering intracellular signaling that further sustain the fibrotic state, such as p21-activated kinases (PAK), focal adhesion kinase (FAK), and yes-associated protein (YAP) - mediated upregulation of genes associated with ECM deposition and inflammation.

It is well known that the dietary intake of omega-3 (n-3) polyunsaturated fatty acids (PUFAs) exerts strong anti-inflammatory and anti-oxidative stress effects and has been beneficial within the context of cardiac, kidney and pulmonary fibrosis and non-alcoholic hepatic steatosis. Less is known if n-3 PUFAs could be used to treat non-lipid associated hepatic fibrosis. Studies by Zhang et al. suggest that n-3 PUFAs can reduce HSC proliferation and activation by upregulating YAP/TAZ degradation [2]. As YAP/TAZ nucleation has been linked to cell-ECM signaling, we aim to harness a 3D tissue engineered hepatic model to evaluate the influence of both ECM and PUFAs on FAK activation and ultimately its effect on modulating HSC activation. We hypothesize that hepatic constructs formed in hydrogels functionalized with RGD peptides will exhibit improved viability, function and phenotype compared to malHA only, due to increased FAK activation. Furthermore, feeding of dietary PUFAs will attenuate HSC activation and we aim to show that this is at least partially dependent upon the degree of FAK activation.

## METHODS

Hepatic constructs were formed by suspending a 3:1 ratio of HepG2s (hepatocyte-like cell line) (ATCC) to LX-2s (hepatic stellate cell-like cell line) (ATCC), in un-crosslinked maleimide-modified hyaluronic acid (malHA) hydrogel, as previously reported [3-4]. The addition of 5 kDa dithiol PEG crosslinked the gels around the cells, resulting in 25 µL constructs that were prepared in a 48-well plate. All hepatic constructs were maintained for 14 days and supplemented with Dulbecco's Modified Eagle Medium. All assays were performed in triplicate.

Viability was assessed using ATP quantification (Promega CellTiter Glo 3D). Cell viability and organization was visualized using calcein-ethidium homodimer staining and imaging on a macro-confocal microscope. RNA was isolated using TRIzol reagent and utilized in qPCR to quantify the expression of CYP1A1, FAK, YAP, TAZ, and connective tissue growth factor (CTGF). Immunofluorescence (IF) was used to visualize hepatocyte polarization, by staining for zonula occludin-1 (ZO-1), a tight junction protein, and multidrug resistance protein 2 (MRP2), which is expressed on the apical domain of hepatocytes.

The capacity of the constructs to generate lipids de novo was quantified through feeding of [$C^{14}$]-acetate at 1 µCi/mL, extracting the total lipids with hexane:isopropanol, sorting them into classes through thin-layer chromatography, and quantifying the amount of [$C^{14}$] in each class using a scintillation counter. Results were normalized to total DNA. The PUFA-processing capacity was demonstrated by feeding the constructs with the essential dietary n-6 PUFA linoleic acid (LA), extracting lipids from the constructs out to 8 hours post-feed, and

SB³C2022-057

quantifying the production of long-chain PUFAs through the formation of fatty acid methyl esters and gas chromatography.

To test the effect of PUFAs on HSC activation and the FAK pathway, hepatic constructs were stimulated with 10 ng/mL TGF-β, and then supplemented with n-6 PUFA (GLA) or n-3 PUFA (EPA) in the media with and without the presence of a FAK inhibitor (25 uM, FAK inhibitor 14, Fisher Scientific) was applied to the hepatic constructs in conjugation with media changes. The activation state of the LX-2s were quantified through staining of α-smooth muscle actin and qPCR quantification of *Col1A1* expression. Statistical analysis was performed using 2-way ANOVA with post-hoc Tukey tests in GraphPad.

## RESULTS

Inclusion of RGD peptides in the malHA hydrogel increased cell viability, while the inhibition of FAK resulted in significantly reduced viability as quantified through the production of ATP ($p = 0.0082$) (Fig1). Cellular aggregates were shown to develop within the constructs containing RGD as the culture time progressed (constructs were imaged out to 14 days) (Fig1). This effect was lessened in constructs formed without RGD peptides or treated with the FAK inhibitor.

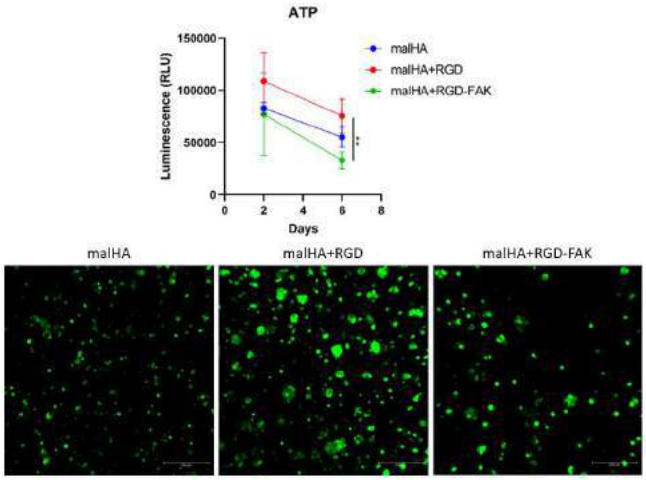


**Figure 1. Construct viability as demonstrated by ATP output through 6 days and live-dead imaging after 14 days of culture.**

CYP1A1 expression levels were also impacted by the inhibition of FAK. Expression levels increased between days 2 and 6 regardless of the presence of RGD peptides, though in a non-significant manner. The inhibition of FAK resulted in a trend toward decreased CYP1A1 expression. The production of albumin was increased significantly on day 6 of culture when RGD peptides were present in the scaffolds compared to no RGD present ($p=0.014$).

Successful conversion of [$C^{14}$]-acetate into the complex lipid species phospholipids, free cholesterol, triglycerides, and cholesterol esters indicate that the constructs could perform *de novo* lipogenesis (**Fig. 2A**). We also successfully demonstrated that upon feeding of LA, the constructs not only contained increased levels of LA (**Fig. 2B**) compared to those fed with only the human serum albumin vehicle control, but also increased levels of the product long-chain PUFAs dihomo-gamma linolenic acid (DGLA) (**Fig. 2C**) and arachidonic acid (ARA) (**Fig. 2D**). In our preliminary assays (n=3/group), we observe an increasing trend that requires further study. ($p=0.162$, $p=0.134$, and $p=0.1137$ for the diet effects of LA, DGLA, and ARA respectively). This is consistent with the dietary effects we demonstrated in a similar model of monocultured primary human hepatocytes [5].

When hepatic constructs were stimulated with TGF-β, we observed decreased viability and function (albumin and urea) compared to those that were not stimulated [4]. We further anticipate increased expression of *Col1A1* and α-SMA. We expect that in constructs exposed, then treated with the n-3 PUFA EPA, there will be a decrease in this inflamed phenotype. Additional experiments are needed.

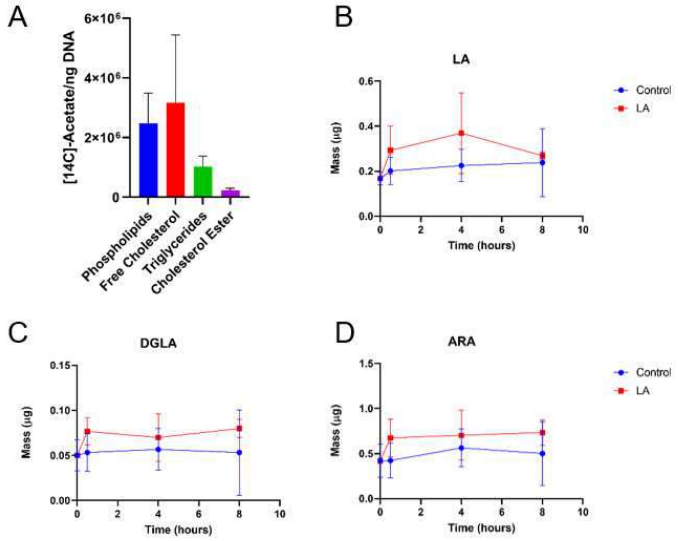


**Figure 2. De novo lipogenic and PUFA processing capacity of the hepatic constructs as demonstrated through feeding experiments.**

## DISCUSSION

Preliminary findings confirm our hypothesis that viability and hepatic functional markers were enhanced in the presence of RGD peptides, and that this effect was negated when FAK phosphorylation was inhibited. Furthermore, we successfully demonstrated that 3D hepatic models were capable of processing acetate into complex lipid species, as is done in the liver during states of energy excess. Upon supplementation with the n-6 PUFA LA under normal conditions, n-6 PUFAs DGLA and ARA increased, as expected. This is an indication that LA was successfully metabolized into the long chain PUFAs. When hepatic constructs were stimulated with TGF-β we observed activation of LX-2s and this was exacerbated in the presence of n-6 PUFAs. This study reveals some interesting insights about how dietary PUFAs can affect early HSC activation and fibrotic pathways. Further studies are needed with primary cells (rather than cell lines). We anticipate that this tissue engineered platform will enable exploration into more mechanistic effects of PUFA and lipid diets on HSC activation and involvement in hepatic fibrosis progression.

## ACKNOWLEDGEMENTS

Funding for this study was provided by Dr. Rahbar's laboratory start-up funds, NIH K25 HL133611 and HL13361-04S1 and NSF REU Award #1950281. We would like to acknowledge the assistance of Dr. Susan Sergeant and Matt Davis with the fatty acid methyl extraction. HepG2 and LX-2 cell lines were provided by Dr. Shay Soker.

## REFERENCES

[1]Asrani, SK et al, *J Hepatol*, 2019, doi: 10.1016/j.jhep.2018.09.014,.
[2] Zhang, K et al, *Sci Rep*, 2016, doi: 10.1038/srep30029.
[3] Yoo, KM et al, *Gels*, 2021, doi: 10.3390/gels7010013.
[4] Mazzocchi, A et al, *Biomed Mat*, Accepted 2021.
[5] Kirk, LM et al, *PLOS1*, Accepted 2021.

SB³C2022
Summer Biomechanics, Bioengineering and Biotransport Conference
June 20-23, Eastern Shore, MD, USA

# LEFT ATRIAL HEMODYNAMICS AFTER CATHETER ABLATION

**B. Vogl (1), A. El Shaer (2), M. Van Zyl (2), A. Killu (2), M. Alkhouli (2), H. Hatoum (1,3)**

(1) Biomedical Engineering Department, Michigan Technological University, Houghton, MI, USA
(2) Department of Cardiovascular Medicine, Mayo Clinic, Rochester, MN, USA
(3) Health Research Institute, Center of Biocomputing and Digital Health and Institute of Computing and Cybernetics, Michigan Technological University, Houghton, MI

## INTRODUCTION

Atrial fibrillation (AF) is the most common arrythmia affecting 3-6 million individuals in the USA alone[1]. AF is associated with numerous adverse outcomes including heart failure, stroke and reduced survival. Catheter ablation has gained increased popularity given its improved efficacy and acceptable safety profile. The effect of ablation on the left atrial flow dynamics has not been studied extensively. It has been proposed that tissue remodeling and clinical outcomes of various cardiovascular procedures are mediated by the impact of these procedures on cardiac fluid dynamics[2]. Some studies reported hemodynamic deterioration, worsening of mitral regurgitation and impaired diastolic function after radiofrequency ablation. Conversely, positive effects on hemodynamics have been reported with restoration and maintenance of sinus rhythm after radiofrequency ablation and improvement of outcomes with some variability depending on AF duration, comorbidities, extent of ablation, and ablation energy. To address these knowledge gaps, we performed an exploratory study with full geometric and flow dynamics assessment of 10 patients who underwent AF ablation.

## METHODS

Contrast-enhanced computed tomography (CT) and echocardiographic images of 10 patients (labeled patient 1 to 10) pre- and post-ablation were obtained from Mayo Clinic, Rochester, MN. The 10 datasets included full cardiac cycles (20 subsets), and echocardiographic studies. The overall workflow adopted in this study is shown in **Figure 1**. The CT images were imported into Mimics Research 23.0 (Materialise, Belgium) and segmented to generate the 3D digital models. All the phases of the 20 subsets were segmented. In order to determine the inflow boundary conditions (BC) and the phase that corresponds to the E-wave with minimal approximations and in order to account for the specific shape of the atrium during that phase (as the atrium contracts), we extracted and plotted versus time the ventricular volumes, depending on each heart rate (HR) of each patient. After that, the derivative of the volume with respect to time was performed to obtain the flow variations. The mitral valve saddle shape was segmented using a different threshold limit in Mimics Research 23.0 and the area was calculated using a spline function in Mimics. The area obtained from the saddle shape was conserved during the extraction of the LA geometry. The LV flow waveform variation with time was converted to velocity versus time by dividing by the MV area. The first peak obtained after the LV volume starts increasing (as it is filling) was chosen to be the phase that corresponds to the E-wave. This process was used to select the appropriate **geometry** of the LA at the E-wave. Echocardiographic waveforms were used to extract the appropriate boundary conditions (BC) at the MV outlet corresponding to the E wave. A constant pressure equal to 0 was imposed at the PVs. Rigid walls and no slip BCs were imposed on the LA surface. The segmented geometry was imported into Ansys Workbench 2020 R1, where extensions equivalent to 10 times the vessel diameters were applied to overcome entrance effects and to have an appropriate velocity profile. The LA models were then meshed with polyhedral meshes after mesh independent results were performed and an element size of 1.2mm was selected (~2,700,000 elements). The computational fluid dynamic (CFD) simulations were performed using Ansys Fluent.

Blood was simulated as an incompressible Newtonian fluid with a density of 1060 kg/m$^3$ and a dynamic viscosity of 0.0035 Pa.s. As the Reynolds number, estimated from peak MV at the E-wave and the MV diameter, was for all cases always below 2000, a laminar model was chosen. Three transient simulations were carried out to ensure stability and overcome transition effects. For data analysis, the final cycle was used for stability. We compared the results obtained from the CFD with available PV echo data showing velocity waveforms. We found close agreement with the values obtained from CFD and from echocardiography. Our study documented several flow dynamic characteristics before and after AF ablation: (1) blood velocities and

SB³C2022-058

velocity streamlines, (2) wall shear stress (WSS), and (3) vorticity. Where vorticity is further defined by the q-criterion and circulation.

## RESULTS

Velocity: In 6 patients (1, 2, 3, 5, 6, and 9), an increase in velocity post-ablation was noted whereas in the other 4 (4, 7, 8 and 10), a decrease in velocity magnitude was noted. **Figure 2** shows velocity streamlines pre- and post-ablation for each patient. The average velocity pre-ablation was 0.82±0.45 m/s and 1.01±0.53 m/s (p = 0.39) post-ablation.

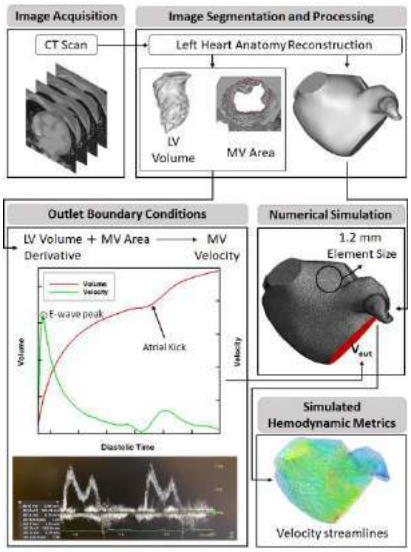


**Figure 1. Overall project workflow.**

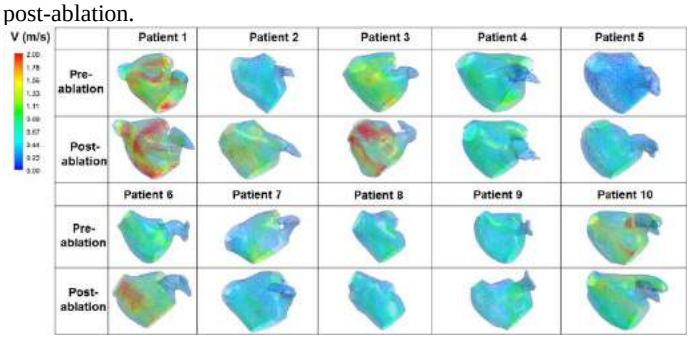


**Figure 3. Velocity streamlines in the left atrium pre- and post-ablation for the 10 patients.**

Vorticity: To visualize and appreciate the 3-dimensional structures of the simulated flow that grow and evolve, we used the q-criterion. Regions with q>0 are dominated by rotation and are occupied by vortex structures. From pre- to post-ablation, different vortex tubes, and different vortex locations are noted in all patient cases, but there was no unique vortex pattern that unified the LA flow dynamics after ablation. To visualize the effect of ablation on the hemodynamic structures, we showed vorticity, and vortex structures on a plane right below the four pulmonary veins and right above the left atrial appendage (LAA). **Figure 3** shows the velocity streamlines in the plane, highlighting the formed vortices. The plane pre-ablation is characterized, in each patient case by clear vortices rotating clockwise and counterclockwise. After ablation in some cases, these vortices get divided into smaller and multiple ones of different rotational directions such as the case with 5 patients (1, 5, 7, 8 and 9). In 3 other cases, several vortices pre-ablation get reduced to one vortex (patients 2, 4 and 6). Patient 3 shows a clear vortex before ablation and no discernable vortex structure after ablation. In same plane, the circulation (Γ) was also calculated (**Table 1**).

| Γ (m²/s) | Pt 1 | Pt 2 | Pt 3 | Pt 4 | Pt 5 | Pt 6 | Pt 7 | Pt 8 | Pt 9 | Pt 10 |
|---|---|---|---|---|---|---|---|---|---|---|
| Pre-ablation | 0.978 | 0.226 | 0.516 | 0.524 | 0.201 | 0.421 | 0.31 | 0.243 | 0.342 | 0.716 |
| Post-ablation | 0.895 | 0.558 | 0.638 | 0.442 | 0.357 | 0.576 | 0.246 | 0.212 | 0.374 | 0.455 |
| %Change | -8.49 | 146.90 | 23.64 | -15.65 | 77.61 | 36.82 | -20.65 | -12.76 | 9.36 | -36.45 |

**Table 1. Circulation calculated in the plane under the pulmonary veins (PV) and above the left atrial appendage (LAA).**

Circulation was found to increase post-ablation in 5 patient cases and decrease in the other 5.

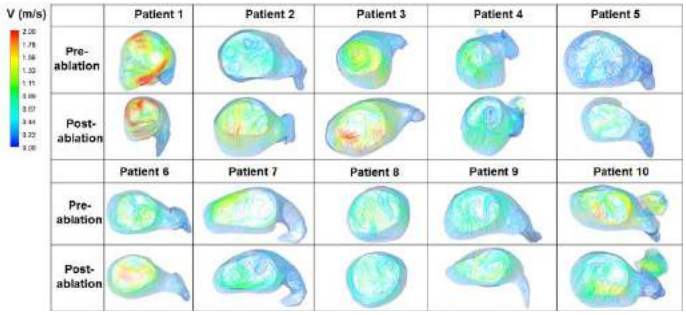


**Figure 2. Velocity streamlines in a plane above the LAA and below the pulmonary veins pre- and post-ablation for the 10 patients.**

Geometrical variations: From a geometrical perspective, there were considerable differences in pre and post ablation LA volumes and PV. Post-ablation, the LA volumes were found to decrease in all but one patient. The percentage of increase differed among the patients and ranged from 5.96% (lowest with patient 8) to 28.83% (highest with patient 9). There was an average decrease in LA volume (11.58±15.17%), after ablation.

## DISCUSSION

In this exploratory study, with heterogeneity in the population and small size, there were no uniform trends in the change in hemodynamics and geometries after the ablation procedure. However, a few general themes were notable and warrant further research. LA volumes decreased after AF ablation. Catheter ablation has been repeatedly shown to reduce LA size without necessarily affecting LA systolic function[3]. The mechanism underlying this change remains poorly understood. The impact on overall LA velocity distribution was not uniform amongst the patients, as 4 patients showed a decrease and 6 showed an increase in overall velocity distribution. In some studies, a decrease in the E-wave velocity of the MV was observed after ablation[4], whereas an increase was observed in others[5]. There was more flow unsteadiness and distinctive vortex patterns after ablation as evidenced in **Figure 2**. These observations were evident in the streamlines and the q-criterion results that demonstrated a prevalence in rotational structures in the atrium in addition to multiple division and coupling of vortices. In some studies, it was demonstrated that vortices are slow in propagating in less compliant geometries compared to more compliant ones[6]. The slow motion may lead to more mixing and disintegration of the vortex structure with the surrounding flow, leading to the resulting unsteadiness. Incoherent, broken, and unstable vortices are the result of either impaired flow or stiffening of the surrounding walls[7]. The calculated circulation (Γ) in the plane located between PVs and above LAA consistently decreased when the velocities decreased. This was expected as geometrical changes occurred on the PV ostia influencing flow mixing and entrainment into the atrium and on the overall LA volume, affecting therefore the rotational aspects of the blood flow and the entrainment of the vortices. Further exploration of the impact of catheter ablation on intracardiac flow dynamics is warranted to discern general and uniform patterns that may correlate with clinical outcomes.

## REFERENCES


[1] Kornej J, Circ Res, 127(1):4-20, 2020
[2] Pedrizzeti G, Nat Rev Cardiol,11:545-553, 2014
[3] Xiong B, PLoS One, 6;10(7):e0129274, 2015
[4] You L, Sci Rep, 22, 9(1):7695, 2019
[5] Compier M, EP Europace, 19(4):560-567, 2017
[6] Brum J, Proc. Mtgs. Acoust., 38:020010, 2019
[7] Pedrizzetti G, Phys Rev Lett., 95(10):108101, 2005

# TOWARD SUBJECT-SPECIFIC BIOMECHANICS OF THE RIGHT-NONCORONARY BICUSPID AORTIC VALVE AND ITS ASSOCIATION WITH MOLECULAR GENE EXPRESSION

**Hail B. Kazik. (1), Harkamaljot S. Kandail (2), El-Sayed Ibrahim (3), Benjamin H. Goot (4,5), Joy Lincoln (4,5) and John F. LaDisa Jr. (1,4,5)**

(1) Department of Biomedical Engineering, Marquette University and Medical College of Wisconsin, Milwaukee, WI, USA
(2) Cardio Consulting, Warwick, United Kingdom
(3) Department of Radiology, Medical College of Wisconsin, Wauwatosa, WI, USA
(4) Department of Pediatrics, Medical College of Wisconsin, Wauwatosa, WI, USA
(5) Section of Pediatric Cardiology, Herma Heart Institute, Children's Wisconsin, Wauwatosa, WI, USA

## INTRODUCTION

Bicuspid aortic valve (BAV) is the most common congenital cardiovascular defect (1-2% of all live births) and is characterized by the abnormal formation of two rather than three cusps.[1] Approximately 50% of young adults with BAV develop premature calcification leading to aortic stenosis by age 35, and this is particularly prominent with fusion of the right and noncoronary (R/NC) cusps.[2] The mechanistic etiology of premature calcification in BAV is poorly understood, but studies, primarily on adult cohorts after the onset of calcification, have used computational models, cardiac imaging, and bench-top methods to speculate that BAV-associated alterations in mechanical stimuli contribute to calcification (Fig 1).

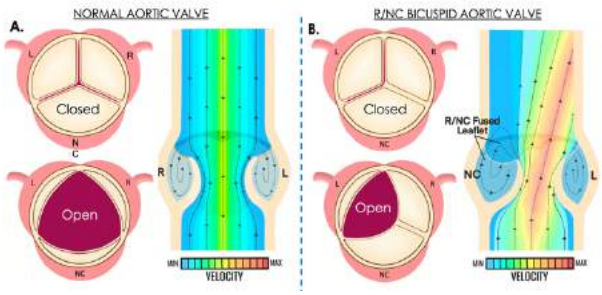


**Figure 1. Aortic Valve Flow Patterns. Compared to the TAV (A), cusp fusion in R/NC BAV (B) leads to a smaller, elliptical opening that results in a high velocity jet skewed to the ascending aorta and creating asymmetrical flow patterns in the sinus. L, left coronary; R, right coronary; NC, noncoronary.**

However, contributions to the field lack evidence supporting a link between the valvular biomechanical environment and molecular changes that promote premature calcification in the setting of R/NC BAV in the pediatric population. Therefore, our objective is to create fluid-structure interaction (FSI) simulations of young BAV patients to elucidate BAV-induced mechanical stimuli prior to calcification. In addition, we use a murine model of R/NC BAV to correlate mechanical stimuli with temporal and spatial transcriptomic changes indicative of calcification processes in valve cell populations during early stages of the disease.[3]

## METHODS

Magnetic resonance imaging (MRI) of 23 y/o patients with R/NC BAV and a healthy tri-cuspid aortic valve (TAV) were conducted after IRB approval. Aortic and coronary artery morphology were extracted using SimVascular (simvascular.github.io). Valve cusps were constructed in SolidWorks (Dassault Systems) using dimensions made patient-specific by scaling to sinus geometry.[4] Physiologic boundary conditions (BCs) were implemented including measured pressure at the aortic inlet, a lumped-parameter model of downstream physiology at the aortic outlet, and flow imposed at coronary artery outlets (Fig 2A). Hyperelastic anisotropic properties based on Gasser-Ogden-Holzapfel's model were applied using biaxial tensile results of human valve cusps from a 20 y/o.[5,6] FSI simulations were performed by coupling

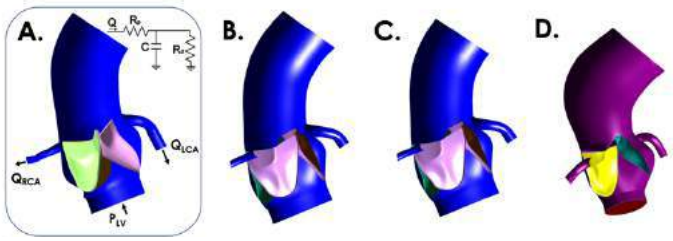


**Figure 2. FSI Simulation Test Cases. TAV and BC setup (A), Virtual R/NC BAV w/ same BCs (B), Virtual R/NC & tuned BCs (C), and patient-specific R/NC BAV (D)**

FlowVision (Capvidia) with Abaqus/Explicit (Dassault Systems). Three cases were conducted from the TAV patient including (1) TAV, (2) virtual R/NC fusion with the same BCs to elucidate the impact of BAV alone, and (3) R/NC fusion with tuned BCs mimicking physiologic compensation to BAV (Fig 2). A validation case (4) included fusion from the R/NC BAV patient. Quantification of mechanical stimuli such as wall shear stress (WSS) and von Mises stress were then extracted.

Endocardial-specific heterozygous deletion of *exocyst 5 (Exoc5)* (*NfatC1$^{cre(+)}$/Exoc5$^{f/+}$*) is reported to lead to aortic valve degeneration in 100% of mice, which includes R/NC in ~45% with secondary calcification present by ~5-6 weeks.[3] Aortic valve function and anatomical dimensions are currently being determined in experimental and genotype controls (*NfatC1$^{cre-}$/Exoc5$^{f/+}$*) using echocardiography and 4D Flow MRI. This is assessed during early (~4 weeks) and later (10-12 weeks) stages of the calcification process. In parallel, aortic valve tissue is being collected and prepared for spatial gene expression studies to determine differential mRNA differences between genotypes correlative to biomechanical profiles.

## RESULTS

Preliminary FSI results from virtual fusion of the R/NC cusps in case 2 revealed reduced systemic pressure requiring tuning of BCs in case 3 to match clinical values. Both R/NC BAV cases showed similar alterations in mechanical stimuli, with differences due to tuning of BCs. Compared to TAV, the fused BAV cusp in case 2 experienced overall higher WSS throughout the fibrosa/aortic surface during systole while WSS was mostly isolated to the tip region on the nonfused cusp (Fig 3).

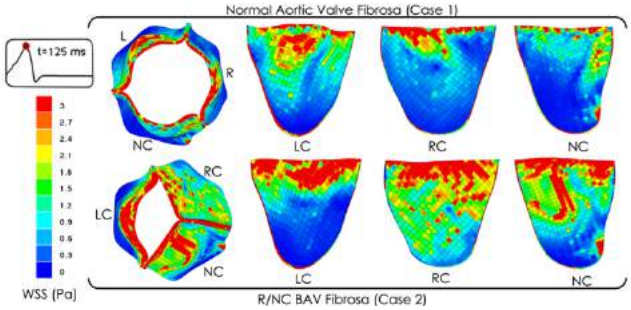


**Figure 3. Wall Shear Stress (WSS). Virtual fusion of R/NC cusps imposes higher WSS magnitude (red) on the aortic/fibrosa surface of BAV cusps. LC, left coronary; RC, right coronary; NC, noncoronary.**

Compared to TAV, the R/NC BAV in case 2 also features regions of high von Mises stress concentrated to the fusion site, which are not present on TAV cusps (Fig 4).

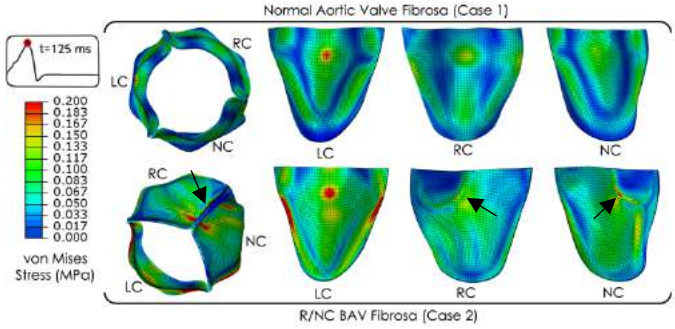


**Figure 4. von Mises Stress. Virtual R/NC fusion leads to high von Mises stress at the cusp fusion site (black arrows) not present in TAV. LC, left coronary; RC, right coronary; NC, noncoronary.**

Out of n=15 *NfatC1$^{cre(+)}$/Exoc5$^{f/+}$* mice that are genetically predisposed to developing R/NC BAV, 3 have demonstrated increased mean velocity gradients (>1000 mm/s) across the aortic valve as well as increased mean pressure gradients (> 4 mmHg) via echocardiography. Development of an optimized protocol for 4D Flow MRI of the aortic valve in mice is currently underway to confirm our echocardiographic findings and serve as a tool for FSI model construction. Figure 4 shows a four-chamber view of a wild-type heart obtained using a 9.4T Bruker MRI scanner with a cardiac and respiratory gradient-echo sequence.

**Figure 5. Magnetic resonance imaging (MRI) of murine heart. Preliminary images of *NfatC1$^{cre+}$/Exoc5$^{f/+}$* mice in a four-chamber view.**

## DISCUSSION

To our knowledge these are the first FSI simulations to characterize the mechanical stimuli for a young adult with R/NC BAV prior to calcification. Our models are *technically* innovative with the implementation of realistic material properties and inclusion of coronary artery flow, which are known to affect flow in the cusp sinuses.[8] Therefore, these methods allow for robust assessment of mechanical stimuli on the valve cusps and thus may ultimately allow us to further characterize the spatiotemporal mechanical changes in both human pediatric and murine BAV subjects leading up to calcification. By examining molecular gene expression changes of the aortic valve over time in the mouse model, which is not possible in humans, we will be able to correlate spatial transcriptomics studies in response to BAV-induced mechanical stimuli leading up to calcification. Additionally, these findings may complement and validate other computational studies using calcification progression models.[7]


## ACKNOWLEDGEMENTS

This work was supported by NIH/NHLBI R01HL132801 and R01HL127033 (JL), 1R01HL142955 (JFL), and Advancing a Healthier Wisconsin (9520519) (JL).


## REFERENCES


[1] Menon V, Lincoln J. The Genetic Regulation of Aortic Valve Development and Calcific Disease. Frontiers in Cardiovascular Medicine. 2018;5.

[2]. Tzemos N. Outcomes in Adults With Bicuspid Aortic Valves. JAMA. 2008;300(11).

[3]. Fulmer D, et al. Defects in the Exocyst-Cilia Machinery Cause Bicuspid Aortic Valve Disease and Aortic Stenosis. Circulation. 2019;140(16):1331–1341.

[4]. Thubrikar MJ. The Aortic Valve. 1st ed.; 1990.

[5]. Van Geemen, D., et. al (2016). Age-dependent changes in geometry, tissue composition and mechanical properties of fetal to adult cryopreserved human heart valves. *PLoS ONE*, *11*(2).

[6]. Gasser TC, Ogden RW, Holzapfel GA. Hyperelastic modelling of arterial layers with distributed collagen fibre orientations. Journal of the Royal Society Interface. 2006;3(6):15–35.

[7] Arzani, A., et. al. (2017). A strain-based finite element model for calcification progression in aortic valves. *Journal of Biomechanics*, *65*, 216–220.

[8] Flemister, D. C. (2020). Effect of Left and Right Coronary Flow Waveforms on Aortic Sinus Hemodynamics and Leaflet Shear Stress: Correlation with Calcification Locations. *Annals of Biomedical Engineering*.

# CHARACTERIZING REGIONAL ANISOTROPY IN A COMMERCIAL SOFT TISSUE ANALOG

**Daniel P. Pearce (1), Colleen M. Witzenburg (1)**

(1) Department of Biomedical Engineering
University of Wisconsin Madison
Madison, Wisconsin, USA

## INTRODUCTION

TissueMend (TEI Biosciences and Stryker Corporation) is a Class II FDA-approved surgical patch intended to reinforce damaged soft tissues (Figure 1). The patch is composed of non-denatured, non-crosslinked collagen derived from fetal bovine skin, exhibits good biocompatibility, and is most commonly used in rotator cuff, patellar, and Achilles tendon repair surgeries [1]. Groups have studied the uniaxial mechanical behavior of TissueMend and compared it to other surgical patches and tendons. Aurora et al. [2] and Derwin et al. [3] reported TissueMend to have a Young's modulus of approximately 15.2 ± 3.5 MPa and 20 – 30 MPa, respectively. Despite having a higher hydroxyproline content than its competitors [3], these moduli are lower than but still comparable to those of similar products; however, they fall short of the 1 – 2 GPa modulus range generally associated with tendons [4–6].

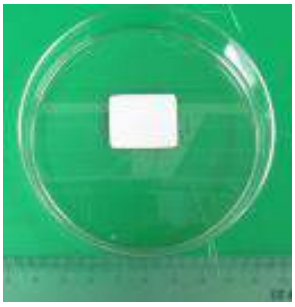

**Figure 1. The uncut, unhydrated TissueMend sample.**

Quantifying the directional mechanical behavior of surgical products, such as TissueMend, intended to reinforce and repair damaged tendons is of the utmost importance since tendons exhibit pronounced anisotropy due to strong collagen fiber alignment [6,7]. There have been no reported biaxial mechanical characterizations of TissueMend, however, or other attempts to quantify its mechanical anisotropy. We have developed a Generalized Anisotropic Inverse Mechanics (GAIM) method capable of quantifying regional variations in stiffness and anisotropy of soft tissues [8–11]. In this study, we used biaxial testing and GAIM to improve the understanding of TissueMend's anisotropic mechanical behavior.

## METHODS

**Sample Preparation.** Prior to testing, the TissueMend sample was covered in phosphate buffered saline (PBS) for ~10 minutes to hydrate. The sample was then trimmed into a cruciform shape (~15x15 mm) and scanned by a LJ-V7080 laser micrometer (Keyence) at 20 Hz to obtain a 3D thickness profile. To determine full-field displacement, we speckled the sample with India ink (Speedball Arts) using an airbrush at an air pressure of 40 psi and a sample-to-nozzle distance of about six inches. The sample was placed in a custom gripping system and secured to the biaxial testing machine (574E2, TestResources). For this experiment, a combination of axial (WF12S; TestResources) and six degree of freedom (Nano 17; ATI) load cells were used to record in-plane normal and shear forces. The sample was immersed in PBS throughout mechanical testing and images of the sample's surface were acquired at a frequency of approximately 7 Hz.

**Mechanical Testing.** The TissueMend sample was cut so that the long-axis (Figure 1) aligned with the horizontal testing axis. Preload (~0.24 N) was added to each arm of the sample and it was preconditioned with 10 equibiaxial stretches of ~15% strain at a strain rate of 1%/s [12,13]. Subsequent biaxial testing consisted of a series of extensions designed to generate shear stresses in the sample and included equibiaxial, two-arm, three-arm, and strip biaxial tests [9]. Testing concluded with one final equibiaxial extension used to confirm no damage was inflicted during the atypical extensions and that the sample's state of pseudoelasticity was unchanged.

**Data Analysis.** The GAIM method directly solves the stress balance using the measured boundary forces and full-field

displacements determined by digital image correlation. The components of the fourth-order neo-Hookean generalization of the linear elasticity tensor, $K_{ijkl}$, are fit for a state of static equilibrium as shown in Equations 1 and 2:

$$S_{ij} = K_{ijkl}E_{kl} \quad (1)$$

$$\left(F_{mi}K_{ijkl}E_{kl},\right)_j = 0 \quad (2)$$

where $S_{ij}$ is the second Piola-Kirchhoff stress, $E_{kl}$ is the Green strain, and $F_{mi}$ is the deformation gradient [13]. The Galerkin finite element method relates nodal forces to the stiffness constants for each individual element (Equation 3) as follows:

$$\boldsymbol{G = MK} \quad (3)$$

where $\boldsymbol{G}$ is a vector of nodal forces, $\boldsymbol{K}$ is a vector of elastic constants, and $\boldsymbol{M}$ is a collection of leftover terms from the discretized form of Equation 2. By assuming the sample domain is comprised of homogeneous partitions, Equation 3 becomes an overdetermined linear system solvable with a least-squares approach. For a state of plane stress, solution of the inverse problem results in six stiffness tensor constants for each partition. The eigentensors of $\boldsymbol{K}$ represent principal states of stress and strain [14]. The first Kelvin modulus corresponds to the largest eigenvalue and represents stiffness in the sample's stiffest direction. The associated eigenvectors enable estimation of relative mechanical anisotropy ($r$) and preferred stiffness directions ($\theta$) [9]. Relative mechanical anisotropy ranges from 0 for a totally isotropic material to 1 for a totally anisotropic material and is comparable to the retardation metric produced by polarized light microscopy [12].

## RESULTS

Table 1 includes mechanical characterizations from GAIM for the TissueMend sample with increasing numbers of partitions. In all cases, the first Kelvin modulus, relative mechanical anisotropy, and the preferred stiffness direction were similar. The TissueMend sample exhibited roughly uniform stiffness with an average Kelvin modulus of about 11 MPa across the sample surface and a low spatial standard deviation ranging from 5.1 to 6.2 MPa. It exhibited marked, uniform anisotropy with an average relative anisotropy of about 0.8 (indicating the sample was roughly nine times stiffer in the preferred direction) and a spatial standard deviation of 0.16 to 0.19. The average preferred stiffness direction was about $\theta$ = -13º relative to the horizontal axis, with a spatial standard deviation of about 16º. This average roughly corresponds with the horizontal. This was consistent with gross inspection of the TissueMend sample, which suggested collagen fibers were predominately oriented along the long-axis. Low spatial variability of mechanical properties suggested homogeneity and is apparent in Figure 2, which illustrates the similar relative anisotropy and preferred stiffness direction for 1 partition and 64 partitions throughout the bulk of the sample.

## DISCUSSION

TissueMend is a commercial product intended to support weak or damaged tendons and while it has been shown to perform similarly to its competitors in uniaxial tests, few efforts have been made to quantify its biaxial mechanical properties. The sample tested here had a Kelvin modulus of approximately 11 MPa, which agrees reasonably well with reported values from uniaxial tests [2,3]. We found that TissueMend had pronounced anisotropy and was approximately nine times stiffer in the horizontal direction than the vertical direction. This level of mechanical anisotropy is similar to the physiological levels of anisotropy in tendons tested by Hoffmeister [6], and is, to our knowledge, the first attempt to quantify homogeneity and anisotropy in TissueMend samples.

**Table 1. GAIM results for a TissueMend sample using a varying number of partitions.**

| Partitions | Kelvin Modulus (MPa) | $r$ | $\theta$ (degrees) |
|---|---|---|---|
| **1** | 13.2 | 0.83 | -12.5 |
| **16** | 11.5 ± 5.1 | 0.78 ± 0.17 | -14.5 ± 15.5 |
| **32** | 11.3 ± 5.3 | 0.81 ± 0.19 | -13.5 ± 16.0 |
| **52** | 11.1 ± 5.8 | 0.79 ± 0.16 | -12.4 ± 15.6 |
| **64** | 10.7 ± 6.2 | 0.78 ± 0.18 | -12.6 ± 16.4 |

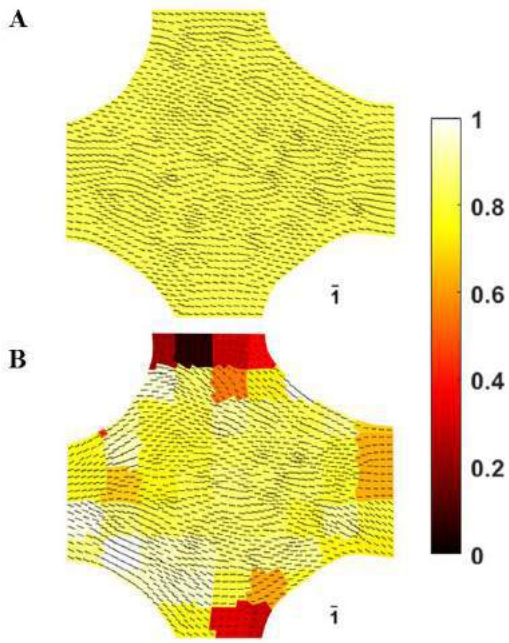


**Figure 2. Relative mechanical anisotropy and preferred stiffness direction computed for a TissueMend sample with A.) one partition and B.) 64 partitions.**


## ACKNOWLEDGEMENTS

This work was funded by a grant from the NSF to C.M.W (2030173). The authors would also like to thank Michael Chiariello, Elizabeth Gunderson, Jiujiu Pan, Riley Pieper, and Mark Nemcek for their assistance.


## REFERENCES


[1] FDA 2002. [2] Aurora, A. et al. *J. Shoulder Elb. Surg.*, 2007. [3] Derwin, K. A et al. *J. Bone Jt. Surg. - Ser. A*, 2006.[4] Ker, R. et al. *J. Zool.*, 1988. [5] Bennett, M. B et al. *J. Zool.*, 1986. [6] Hoffmeister, B. K et al. *Cit. J. Acoust. Soc. Am.*, 1996. [7] Lynch, H. A et al. *J. Biomech. Eng.*, 2003. [8] Raghupathy, R. et al. *J. Biomech. Eng.*, 2010. [9] Raghupathy, R et al. *J. Biomech. Eng.*, 2012. [10] Witzenburg, C. et al. *J. Biomech.*, 2012. [11] Shih, E. D. et al. *J. Vasc. Res.*, 2021. [12] Fung, Y. et al. *Hear. Circ. Physiol.*, 1979. [13] Demer, L. L. et al. *J. Physiol.*, 1983. [14] Thomson, W., *Philos. Trans. R. Soc. London*, 1856.

SB³C2022
Summer Biomechanics, Bioengineering and Biotransport Conference
June 20-23, Eastern Shore, MD, USA

# TOPOGRAPHICAL MICROPATTERNING INDUCES AN ANTI-INFLAMMATORY ENDOTHELIAL TRANSCRIPTOME

**Meghan E. Fallon (1), Anthony P. Barnes (2), Monica T. Hinds (1)**

(1) Department of Biomedical Engineering, Oregon Health & Science University, Portland, Oregon, USA
(2) Knight Cardiovascular Institute, Oregon Health & Science University, Portland, Oregon, USA

## INTRODUCTION

A leading cause of cardiovascular disease is atherosclerosis, a chronic inflammatory disease characterized by the progressive thickening and hardening of arterial walls. Early in the atherogenic process, endothelial dysfunction is induced by disturbed fluid shear stress (FSS) acting on the vessel wall. In these regions, endothelial cells (ECs) maintain a rounded morphology with an unaligned cytoskeleton. ECs exposed to disturbed FSS express an athero-prone and inflammatory phenotype that promotes monocyte adhesion and translocation. Conversely, athero-protective regions of the vasculature where laminar FSS is persistent contain ECs with an anti-inflammatory phenotype that are elongated and aligned with the direction of blood flow. The complex molecular basis for these distinct endothelial phenotypes *in vivo* remains unclear. One regulatory candidate is the transcription factor Yes-associated protein (YAP), which functions as a mechano-transducer that regulates endothelial phenotype and gene expression in response to the mechanical environment. In cells exposed to laminar FSS, YAP becomes inactivated through phosphorylation by the Hippo signaling pathway and is retained within the cytoplasm. However, oscillatory FSS activates YAP via dephosphorylation and subsequent nuclear translocation. The induction of activated YAP is associated with upregulated inflammatory EC target genes which are all highly expressed within atherosclerotic plaques [1].

The differential response of ECs and YAP activation to various flow regimes has been extensively studied within literature, but it is still largely unclear exactly how ECs convert mechanical stimuli into biochemical responses. Previous studies have correlated endothelial morphology and cytoskeletal alignment, independent of FSS, to the regulation of EC function and phenotype [2,3]. However, the in-depth transcriptional signature of an elongated and aligned endothelial monolayer within static culture has yet to be investigated and is needed in order to further understand endothelial mechanotransduction.

## METHODS

Micropattern Fabrication: Topographical micropatterned and planar substrates were fabricated as previously described [2,4]. Briefly, micropatterned PDMS submasters with ridge and groove widths of 3 µm were fabricated by soft lithography. Planar PDMS submasters were fabricated using petri dishes as a master. Polyurethane was then dispensed on top of the submasters and covered by a glass coverslip. The culture substrates were cured by using 2 J of long-wave UV light. Substrates were demolded and sterilized prior to cell culture.

Cell Culture: Baboon carotid artery endothelial cells (BaCaECs) at passage 3 were cultured in complete endothelial growth medium and seeded on substrates for 24 hrs for RNA-sequencing (RNA-seq) experiments. For subsequent experiments, BaCaECs (passage 4) were seeded for 48 hrs.

RNA Isolation and Sequencing: After 24 hr of static culture on substrates, BaCaECs were lysed and total RNA was purified using a Qiagen RNeasy Mini Kit following the manufacturer's protocol. RNA quality assessment and sequencing was performed by OHSU's MPSSR core. Briefly, quality and quantity of total RNA were assessed with an Agilent 2100 Bioanalyzer with all samples having a RIN $\geq$ 9.9. RNA-seq fastq files were aligned with STAR (v2.7.9a) to the Ensembl baboon reference genome Panu_3.0.104 by OHSU's Epigenetics core. Differential analysis was performed with edgeR (v3.28.0). P-values were adjusted by the Benjamini-Hochberg procedure. Enrichr was used to identify pathways regulated by micropatterning.

Image Analysis: BaCaECs were stained for YAP, VE-cadherin, and nuclei. Samples were imaged on a Zeiss LSM 880 scanning confocal microscope (20X, NA = 0.8). Three images per pattern per

SB³C2022-062

sample were collected for quantitative image analysis. Cells were randomly traced using a 4x4 grid overlaying the VE-cadherin color channel. Whole cell morphology was determined by calculating shape index, where 0 equals a perfect line and 1 equals a perfect circle. The nuclear/cytoplasmic YAP intensity ratio was determined by manually drawing ROIs for the cellular nucleus and VE-cadherin border. The YAP intensity ratios were calculated as previously described [1].

Statistical Analysis: Data are presented as mean ± standard deviation. Statistical significance was determined using a Student's t-test between substrate types. Results were considered statistically significant with a *p*-value < 0.05.

## RESULTS

**Identification of mechano-sensitive genes in BaCaECs due to micropatterning.** We investigated the transcriptional profile of BaCaECs on micropatterned surfaces using RNA-seq global gene expression analysis of ECs cultured on either micropatterned or planar substrates. We find 1302 differentially expressed genes in micropatterned BaCaECs with 888 genes were significantly up-regulated and 914 genes were significantly downregulated relative to planar substrate cells (**Fig. 1**). Notably, YAP transcriptional targets (ANKRD1, VCAM1, ICAM1, CTGF, CYR61, and IL-6) that are associated with atherosclerotic plaques were significantly down-regulated for micropatterned BaCaECs. Enrichr pathways analyses were next performed using the significantly downregulated gene set. This algorithm identified multiple pathways significantly downregulated by micropatterned substrates including: NF-κB, lipid and atherosclerosis, TNF, and IL-17 inflammatory signaling pathways (**Fig. 2**, p < 0.00001).

**Micropatterning modulates endothelial morphology and phenotype**. We also observe significant elongation for micropatterned cells induced by topographical micropatterning. Micropatterned cells exhibit shape indices of 0.51 ± 0.01 compared to planar cells with shape indices of 0.61 ± 0.03 (data not shown, p < 0.05). YAP activation was significantly downregulated for micropatterned cells compared to planar cells with nuclear/cytoplasmic as determined YAP nuclear localization with intensity ratios of 2.01 ± 0.13 and 3.04 ± 0.35 (p < 0.05), respectively (**Fig. 3**), consistent with previous studies and our transcriptional analysis.

## DISCUSSION

Topographical micropatterning is an effective technique to align and elongate endothelial monolayers in the absence of fluid shear stress but FSS-independent, mechano-sensitive athero-protection has yet to be fully investigated. Our current study used bulk RNA-seq to reveal the transcriptional difference produced by micropatterning that modulates endothelial mechanotransduction pathways to induce an anti-inflammatory phenotype. We find a subset of YAP target genes significantly downregulated in micropatterned ECs. We also find that micropatterning regulates YAP activation by downregulating nuclear translocation using single-cell image analysis techniques. Taken together, our data supports micropatterning as a potential cardiovascular device surface modification to improve biocompatibility via modulating endothelial morphology and genetically altering inflammation transduction mechanisms.


## ACKNOWLEDGEMENTS

This work was supported by the National Institutes of Health R01HL130274 and R01HL144113.


## REFERENCES


[1] Wang, KC, et al., *PNAS*, 113(41):11525-111530, 2016.

[2] Fallon, M.E. et al., *Biochem Biophys Res Comm*, 555:160-167, 2021.

[3] Vartanian K.B. et al., *Am J Physiol Cell Physiol*, 298: C333-C341, 2010.

[4] Hagen, M.W. et al., *Tissue Eng Part A*, 27(3-4):270-281, 2021.


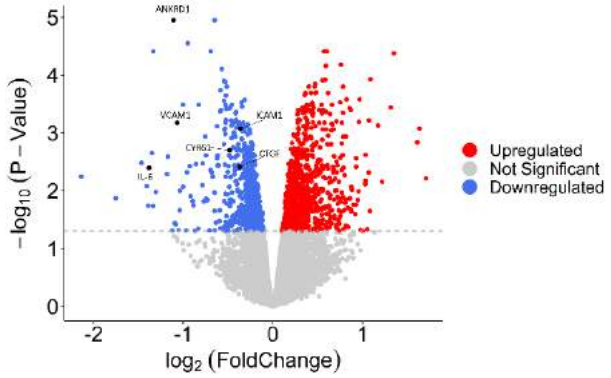


**Figure 1. Volcano plot of the fold change of transcripts in micropatterned BaCaECs compared to planar BaCaECs. Red and blue dots represent significantly upregulated or downregulated genes in micropatterned BaCaECs compared to planar BaCaECs, respectively. Genes represented in black indicate signature YAP target genes. Significance was determined for p < 0.05, n=4.**

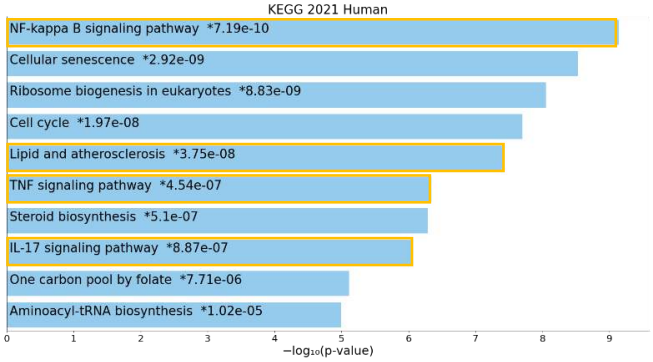


**Figure 2. Top 10 of the 43 enriched pathways associated with significantly downregulated genes in micropatterned BaCaECs compared to planar BaCaECs. Numbers indicate the *p*-value of the respective pathway.**

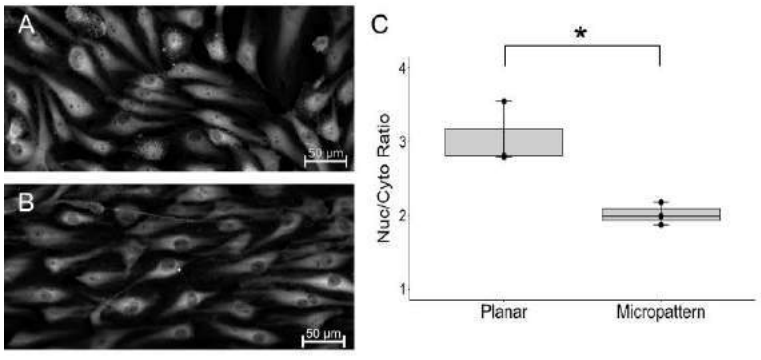


**Figure 3. Micropatterning regulates YAP nuclear localization and activity. Fluorescent images of planar (A) and micropatterned (B) BaCaECs. Scale bar indicates 50 μm. YAP nuclear/cytoplasmic intensity ratio is significantly downregulated for micropatterned cells compared to planar cells (C).**

# THE BIOMECHANICS OF LOW AND HIGH IMPACT LOADING ON THE ACL AND MCL IN ADOLESCENT POPULATIONS

**Alexandria D. Mallinos, MSOP (1), Kerwyn C. Jones, MD (2), Brian L. Davis, PhD (3)**

(1) Department of Biomedical Engineering, Cleveland State University, Cleveland, Ohio, USA
(2) Department of Orthopedic Surgery, Akron Children's Hospital, Akron, Ohio, USA
(3) Department of Mechanical Engineering, Cleveland State University, Cleveland, Ohio, USA

## INTRODUCTION

Combinations of loads that the knee experiences during different levels of activity can place an individual at greater risk for ligament injury. This is especially evident in adolescents, as high impact sports such as football and soccer have all been associated with Anterior Cruciate Ligament (ACL) ruptures. These are due to high impact loads caused from side cutting maneuvers, even in non-contact scenarios.

Advancements in finite element technology have made it possible to develop patient-specific models that can accurately predict the *in vivo* environment of the knee. Despite adolescents making up the majority of ACL reconstructions, never has this methodology been applied to this core demographic. The goal of this research project was to determine how different loading conditions experienced through high and low impact sports influence the biomechanics of the ACL and Medial Collateral Ligament (MCL) in adolescents.

## METHODS

A total of 22 CT images of juvenile knees were utilized (ages: 9-18, m: n=16, f: n=6). 3D Slicer was used to convert the CT images into a three-dimensional representation of the bony anatomy. FEBio was used to construct each tibiofemoral joint and perform the finite element analyses (Figure 1).

The developed knee models were validated through simulations replicating the anterior drawer and pivot shift test. The predicted anterior tibial displacement determined by the finite element models were shown to accurately represent what has been established experimentally with these clinical tests [1-2].

Front knee baseball hitting [3] (low impact) and side cutting [4] (high impact) kinetic adolescent experimental data was used to replicate the two different loading scenarios (Table 1).

Since anterior force and internal rotation torques were not reported in the adolescent side cutting experimental data, one of the assumptions made for this study is that adolescent side cutting kinetics are proportional to those experienced in adults [5].

A 95% confidence interval (CI) was taken to determine statistical significance.

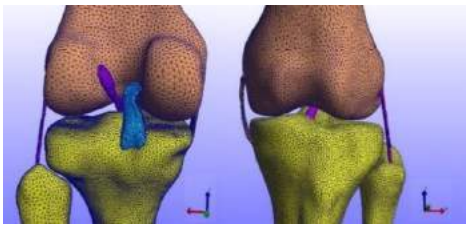

**Figure 1: Frontal plane views of the adolescent model.**

**Table 1: Kinetic experimental loading conditions used in the high and low impact simulations.**

| | Baseball Hitting Kinetics [3] | Side Cutting Kinetics [4] |
|---|---|---|
| *Internal Rotation (Nm)* | 6.3 | 43.4 |
| *Valgus Torque (Nm)* | 11 | 63.5 |
| *Anterior Force (N)* | 86.2 | 395.5 |

## RESULTS

The high impact side cutting maneuver resulted in greater ligament displacement compared to the low impact baseball swing simulation for both the ACL and MCL (Table 2).

**Table 2: Descriptive statistics for ACL and MCL displacement.**

| | ACL Displacement | | MCL Displacement | |
|---|---|---|---|---|
| | *Baseball Hitting* | *Side Cutting* | *Baseball Hitting* | *Side Cutting* |
| N | 22 | 22 | 22 | 22 |
| Mean | 4.7 | 9.5 | 4.1 | 6.0 |
| SD | 2.1 | 4.5 | 1.8 | 2.3 |

A 95% confidence interval on the predicted ligament displacements was performed (Table 3). It can be observed that there is no overlap of the confidence intervals between the baseball hitting and side cutting displacements for both ligaments.

**Table 3: 95% CI for ACL and MCL baseball hitting and side cutting loading scenarios.**

| ACL Displacement | MCL Displacement |
|---|---|
| *Baseball Hitting 95% CI (mm)* | *Baseball Hitting 95% CI (mm)* |
| 3.85 - 5.56 | 3.29 - 4.82 |
| *Side Cutting 95% CI (mm)* | *Side Cutting 95% CI (mm)* |
| 7.65 - 11.42 | 5.0 - 6.94 |

As expected, the peak first principal stress of the ACL and MCL increased significantly when subject to higher loading conditions. When analyzing ratios of peak stress increases, both ligaments experienced over a two-fold increase when undergoing the side cutting maneuver compared to the baseball hitting simulation (Table 4).

**Table 4: Ratio of peak 1st principal stress for the ACL and MCL.**

| Ratio of Peak 1st Prinicpal Stress (Side Cutting : Baseball Hitting) | |
|---|---|
| *ACL* | *MCL* |
| 2.14 : 1 | 2.5 : 1 |

## DISCUSSION

Ligament displacements increased significantly when the input parameters replicated a high impact loading environment for both the ACL and MCL. This follows trends that have been established experimentally, as knee ligaments have been shown to experience greater displacement when subject to increasing force levels [3-4].

Furthermore, the 95% confidence intervals between the low and high impact loading scenarios did not overlap for ACL and MCL displacement demonstrating that the difference between sporting maneuvers is statistically significant. This shows that knee loading experienced in high impact sports places more strain on the ligaments ultimately increasing the likelihood of ruptures.

One limitation of the proposed models is the inability to directly quantify the predicted stress against known literature values. This is in part due to the differences in experimental and computer simulated methodologies in calculating ligament biomechanical properties. Many experimental tensile testing methods rely on calculating nominal stress values over a simplified, uniform geometry [6]. In contrast, however, the finite element models calculate the stress of each individual tetrahedron within the mesh of a specific ligament resulting in non-uniform stress/strain distributions which are more representative of the *in vivo* biomechanics.

Notwithstanding the discrepancies between the finite element modeling and experimental methodologies, the predicted peak stress values of the models provide valuable insight into the effect that various loading conditions have on the knee ligament biomechanics. In particular, ratios of stress increases can be extracted from the data revealing the consequence of high impact loading on the ligaments. Both the ACL and MCL experienced over a two-fold increase in peak first principal stress when undergoing the side cutting maneuver compared to the baseball swing. This demonstrates that participating in higher intensity activities places greater stress on the ligaments thus increasing the chance of the athlete developing an injury in the future.

Although the ACL is the most commonly injured ligament in the knee, MCL injuries are often experienced during ACL ruptures. In adolescent populations, isolated ACL injuries occur at a rate of 78% where as two-ligament injuries (ACL and MCL) occur at a rate of 17% [7]. ACL injuries are predominately due to anterior forces being combined with valgus and internal rotation torques resulting in a pivot shift movement [8]. Pivot shift mechanisms are found in baseball hitting and side cutting activities and this combination of loading is primarily resisted by the ACL [9]. The ACL's resistance to these motions is evident in the modeling as higher loading parameters resulted in increases in ACL displacement and stress.

The MCL is also impacted by these movements because the axis of the pivot shift mechanism is located about the MCL [9]. When the forces are applied to the knee, movements at the medial side of the tibia are restricted by the tension in the MCL [9]. This rise in MCL tension is depicted in the FEBio models such that both displacement and peak principal stress increase when subject to higher impact loading. Both the ACL and MCL experienced comparable displacement in the lower impact simulation. However, it is during the side cutting maneuver that the displacements between the ACL and MCL are found to be statistically significant. This is consistent with the findings in the literature that conclude that pivot shift movements are predominantly resisted by the ACL as overall, it experienced the greatest average displacement.

It is interesting to note that the MCL had a greater ratio increase in peak stress than the ACL despite having a lower average displacement. This suggests that high impact forces place *both* ligaments in a vulnerable position for injury. In doing so, this further supports clinical findings that higher external valgus moments such as those experienced during side cutting maneuvers are predictive of ACL injury as higher loading resulted in higher predicted ligament displacement and stress [8]. Thus, it can be concluded from the models that side cutting increases the likelihood of a coupled ACL/MCL injury compared to lower impact activities such as hitting a baseball.

Despite limitations of the study, the proposed models were able to demonstrate how increasing loads experienced in high impact sports can lead to ruptures of the ACL and MCL – the two ligaments that are often affected during knee injuries [10]. This provides a solid foundation by which to assess and understand the biomechanical consequences of various sporting maneuvers.

Developing models that quantify the changes in the biomechanics of the knee ligaments during different sporting activities can be utilized by orthopaedic surgeons in justifying alterative activities for patients who have had a prior ACL reconstruction or may be prone to ACL injury given their bony anatomy risk factors.

## ACKNOWLEDGEMENTS

This research is funded by the Cleveland State University Cellular and Molecular Medicine Fellowship.

## REFERENCES

[1] Diermann et al., *Arch Orthop Trauma Surg*, 129(3), 353-358, 2009.
[2] Highgenboten et al., *Am J Sports Med*, 20(4), 450-454, 1992.
[3] Giordano et al., *J Sports Med*, 42(09), 847-852, 2021.
[4] Celebrini et al., *J Strength Cond Res*, 26(12), 3406, 2012.
[5] McLean et al., 2004. *Clin Biomech,* 19(8), 828-838.
[6] Woo et al., *Am J Sports Med*, 19(3), 217-225, 1991.
[7] Lee et al., *Orthop J Sports Med*, 6(11), 1-5, 2018.
[8] Bencke et al., *Knee Surg Sports Traumatol Arthrosc*, 21(8), 1876-1881, 2013.
[9] Matsumoto, H., *Bone Surg*, *72*(5), 816-821, 1990.
[10] Barber FA. *Arthroscopy*. 8(1):19-22, 1992.

SB$^3$C2022
Summer Biomechanics, Bioengineering and Biotransport Conference
June 20-23, Eastern Shore, MD, USA

# AN INTEGRATED STUDY OF ORCHESTRATED NEURONAL MIGRATION AND CORTICAL FOLDING

**Shuolun Wang (1), Kengo Saito (2), Hiroshi Kawasaki (2), Maria A. Holland (1,3)**

(1) Department of Aerospace and Mechanical Engineering, University of Notre Dame, IN, USA
(2) Department of Medical Neuroscience, Kanazawa University, Ishikawa, Japan
(3) Bioengineering Graduate Program, University of Notre Dame, IN, USA

## INTRODUCTION

Brain development involves precisely orchestrated genetic, biochemical, and mechanical events. At the cellular level, neuronal proliferation in the innermost zone of the brain followed by migration towards the outermost layer results in a rapid increase in brain surface area, outpacing the volumetric growth of the brain, and forming the highly folded cortex. Atypical neurodevelopment and cortical malformation are associated with neurological disorders such as autism spectrum disorder [1], schizophrenia [2], and epilepsy [3]. Hence, a deeper understanding of neurodevelopment is of great interest and could prove essential for increased knowledge, improved diagnostics, and effective treatments of developmental disorders.

Here we aim to provide mechanistic insights into the process of brain development and cortical folding using a biomechanical model that couples cell division and migration with volumetric growth. Unlike phenomenological growth models, our model tracks the spatio-temporal development of cohorts of neurons born at different times. Each cohort is modeled separately as an advection-diffusion process, and the total cell density determines the extent of volume growth. We numerically implement our model in Abaqus/Standard (2020) [4] by writing user-defined element (UEL) subroutines. On the experimental side, we apply *in utero* electroporation (IUE) to ferret brains to visualize and track cohorts of neurons born at different stages of embryonic development, which is used to calibrate our model. The calibrated simulations of cortical folding align qualitatively with the experiments.

## METHODS

***In utero* electroporation** We conducted our well-established IUE procedure on ferret brains to visualize the distribution of migrating neurons over time [5,6]. We consider N=8 ferret brain sections, covering different imaging dates and different IUE dates, corresponding to distinct cohorts of neurons (Fig 1). We select a consistent rectangular region from each brain section as the region of interest (ROI), in which the cell migration dominates in the vertical direction. The cell counting of each ROI is done via ImageJ [7] and is used later for model calibration (Fig 2, circles).

**Mathematical modeling** Unlike previous models [8,9,10], we track the cell density of *i*th cohort of neurons, $c_i$. The advection-diffusion process governs the neuronal cell density,

$$\dot{c}_i + c_i \frac{\dot{J}}{J} = f_i^c + \mathrm{div}\mathbf{q}_i \,, \tag{1}$$

where $J$ is the volumetric change, $f_i^c$ is the rate of neurogenesis, and $\mathbf{q}_i$ describes how neurons migrate along with the velocity field $\mathbf{v}$ and spread out in space via diffusion.

Next, to take the growth-related growth into account, our total deformation could be decomposed into elastic and growth counterparts,

$$\mathbf{F} = \mathbf{F}^e\mathbf{F}^g. \tag{3}$$

According to the literature [11,12], the neurons that migrate along glial fibers at the early stage contribute to radial expansion. In contrast, the tangential expansion dominates when neurons reach their destinations in the cortical plate. Thus, we take the growth deformation tensor as a linear combination of the two modes,

$$\mathbf{F}^g = \vartheta^{\parallel}(c)\mathbf{N}\otimes\mathbf{N} + \vartheta^{\perp}(c)(\mathbf{1} - \mathbf{N}\otimes\mathbf{N}), \tag{4}$$

where $\vartheta^{\parallel}(c)$ and $\vartheta^{\perp}(c)$ are functions that relate to the cell density, and $\mathbf{N}$ is a unit vector that indicates the direction of glial fiber at the reference state. The ferret brain is modeled as standard neo-Hookean material,

$$\psi_R(\boldsymbol{C}^e, J^e) = \frac{\mu}{2}[\mathrm{tr}(\boldsymbol{C}^e) - 3 - 2\ln(J^e)] + \frac{L}{2}\ln^2(J^e), \tag{5}$$

where $\mu$ and $L$ are Lamé constants. Note that only elastic deformation ($\boldsymbol{C}^e = \boldsymbol{F}^{eT}\boldsymbol{F}^e$, $J^e = \det(\boldsymbol{F}^e)$) contributes to the stress.

## RESULTS

We calibrate our model to a 1-D cell density profile from N=8 ferret brains via a genetic algorithm, and the results show a good agreement between simulations and experiments. Some material parameters are constrained within the reasonable range reported by the literature. Note that only calibration results of cohort 2 are shown here (Fig 2).

We then simulate cortical folding with the parameters obtained from the model calibration. Our simulation with both 2-D and 3-D settings -- we only show 2-D case here -- are qualitatively in line with our experiments (Fig 3). As expected, cohorts of neurons generated at E31, E33-34, and E36-37 gradually reside at the cortex's lower, medium, and upper layers, respectively.

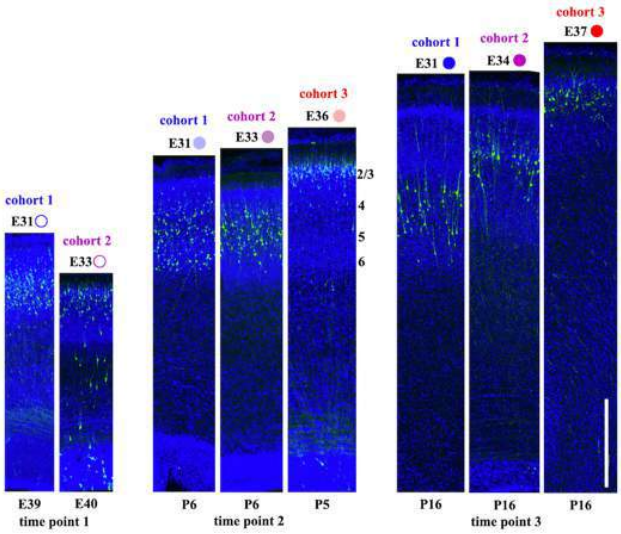


**Fig 1: Regions of interest taken at consistent locations of N=8 typically developing ferret brains, grouped based on IUE and imaging times. Neurons are labeled with EGFP (bright green). Scale bar: 500 µm.**

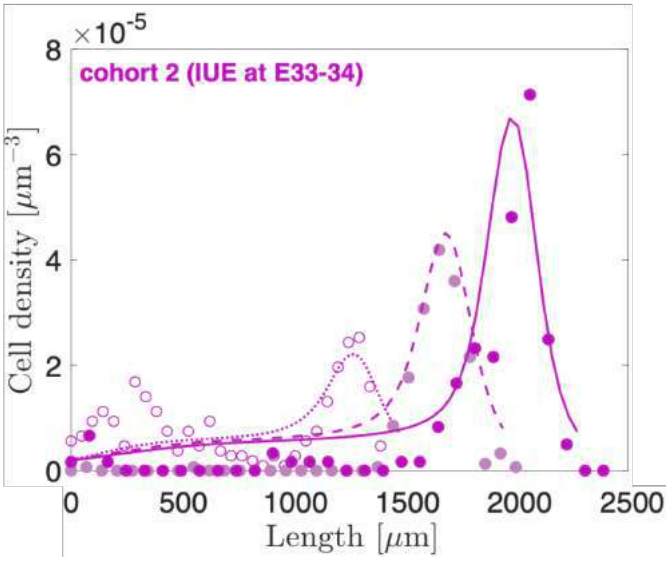


**Fig 2: Comparison between experiments (circles) and model (lines) of cohort 2 at three different imaging dates.**

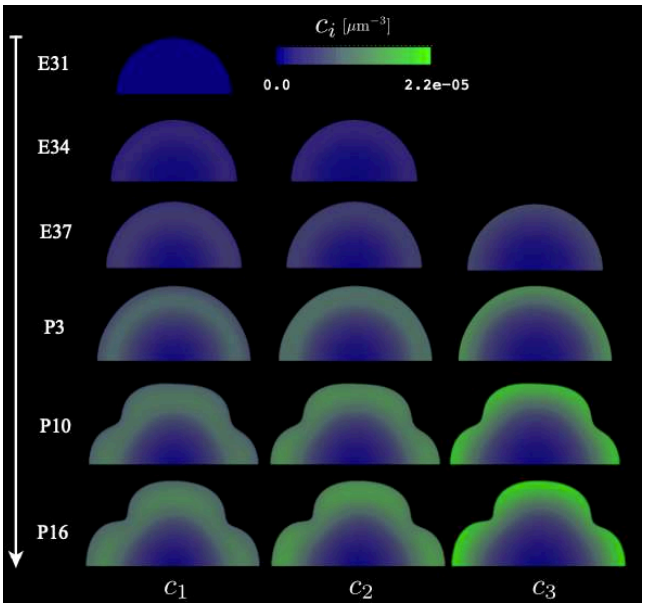


**Fig 3: Simulations of cortical folding with contour denoted as cell density $c_i$.**

## DISCUSSION

In this work, we have developed a biomechanical model for numerical simulations of brain development. The model extends the earlier works to account for the spatial-temporal development of multiple cohorts of neurons, each modeled as an advection-diffusion process. The model was implemented numerically by writing customized finite elements in the commercial finite-element program Abaqus/Standard (2020) [4]. We also conducted novel experiments on ferret brains via IUE, used for model calibration. Our simulations qualitatively agree with the experiments on ferret brains.

Our results suggest significant opportunities for further extensions and improvements in future work. First, the current work accounts for only three cohorts of neurons for simplicity. Secondly, we assumed constant mechanical properties throughout the brain. Finally, our work could potentially be used to study atypical-developing brains.


## ACKNOWLEDGEMENTS

This work was supported by a Notre Dame International Asia Research Collaboration Grant.


## REFERENCES


[1] Wu, C et al., *J Neuroscience*, 27(43):11725-11735, 2007.
[2] Jou, R et al., *Schizophrenia Research*, 75(2-3):309-313, 2005.
[3] Harvey, A et al., *J Neurology*, 84(20):2021-2028, 2015.
[4] Abaqus/Standard. *Abaqus Reference Manuals*. Dassault Systemes Simulia, Providence, RI, 2020.
[5] Kawasaki, H et al., *Molecular Brain*, 5(1):1-7, 2012.
[6] Kawasaki, H et al., *Biology Open*, 2(1):95-100, 2013.
[7] Schneider, C et al., *Nature methods*, 9(7):671-675, 2012.
[8] Verner, SN et al., *Extreme Mechanics Letters*, 18:58-69, 2018.
[9] Rooij, R et al., *JMPS*, 112:563-576, 2018.
[10] Zarzor, M et al., *Brain Multiphysics*, 2:100025, 2021.
[11] Rakic, P et al., *Science*, 241(4862):170-176, 1988.
[12] Rakic, P et al., *Experimentia*, 46(9):882-891, 1990.

SB³C2022
Summer Biomechanics, Bioengineering and Biotransport Conference
June 20-23, Eastern Shore, MD, USA

# MULTISCALE MODEL OF PREGNANCY–INDUCED HEART GROWTH APPLIED TO POSTPARTUM RECOVERY

**Molly S. Kaissar (1), Kyoko Yoshida (1)**

(1) Department of Biomedical Engineering, University of Minnesota, Minneapolis, MN, USA

## INTRODUCTION

Pregnancy stands at the interface of mechanics and biology – continuous loading from the growing fetus combined with drastic shifts in circulating hormones induce rapid soft tissue remodeling. The adaptations of a pregnant patient's cardiovascular system include an expanding blood volume, rising cardiac output, and decreasing vascular resistance [1, 2]. These changes coupled with an increase in circulating hormone concentrations culminate in the patient's heart growing approximately 30% in both mass and cavity volume by term pregnancy [3]. Following delivery, the patient's heart then regresses to its pre-pregnant size within 3–6 months [3].

Cardiovascular disease accounts for 35% of pregnancy-related mortality, with pregnancy-associated heart failure causing 32% of deaths between 43 days to one year postpartum [4]. Heart growth is driven by a combination of mechanical and hormonal cues, yet the mechanisms that cause this remodeling during pregnancy and postpartum are not well characterized. Uncovering these remodeling mechanisms is necessary to understand how pregnancy-induced physiological changes can lead to heart failure during postpartum recovery. Thus, our aim is to investigate the interactions of the hormonal and mechanical cues that drive left ventricular (LV) remodeling during the postpartum period.

Towards this objective, we applied our existing multiscale model of LV growth during pregnancy to normal postpartum remodeling [5]. We simulated 21 days of normal rat pregnancy followed by 21 days of postpartum-induced changes in hemodynamics and hormones and compared our predictions to the available data. We then manipulated the activity of different signaling network model inputs to determine their influence on cardiac remodeling during postpartum recovery. Our analysis suggests that hemodynamic changes are important drivers of postpartum LV remodeling.

## METHODS

*Multiscale Model of Cardiac Growth*

To simulate pregnancy-mediated cell-level growth, we used an intracellular signaling network model that predicts cardiomyocyte hypertrophy in response to key reproductive (*Progesterone, P4; Estrogen, E2*) and cardiovascular *(Angiotensin II, AngII*) hormones and a generalized stretch term (*Stretch*) (Fig. 1a). The activity level of each species was represented as a value between 0 and 1, where 0 indicates no signaling activity and 1 represents maximal activation. At each time step, the network model simulated 5 hours of growth to predict changes in cardiomyocyte size (*CellArea*).

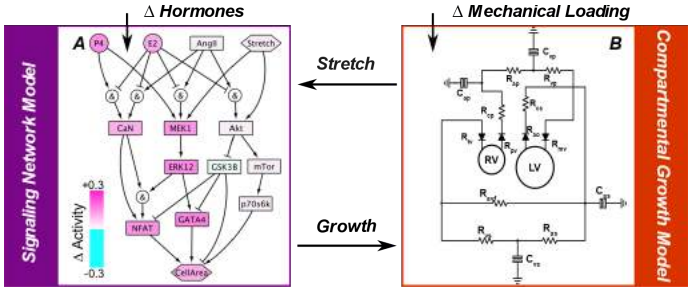


**Figure 1: Multiscale cardiac growth model for pregnancy.** A schematic of the cell-level intracellular signaling network model (*A*) coupled to the organ-level compartmental growth model (*B*).

To simulate organ-level growth, we used a mechanical compartmental model of the rat heart and circulation that predicts cardiac hypertrophy in response to hemodynamic changes (Fig. 1b). This model uses a kinematic growth framework that calculates the total stretch experienced by the heart ($F_{tot}$) as a product of the growth stretch ($F_g$) and the elastic stretch ($F_e$), $F_{tot} = F_g \times F_e$. $F_g$ is related to the

network model output *CellArea* through $J_g = 2 \times CellArea$, where $J_g = \det(F_g)$. The maximum elastic fiber stretch, $\max(F_{e,f})$, is calculated by the compartmental model and fed back into the signaling network model input, *Stretch*, to complete the loop between the two models. We previously calibrated the multiscale model parameters by matching the individual effects of volume overload (VO) and hormonal infusions of AngII, E2, and P4 on LV growth and demonstrated this model's ability to correctly predict LV growth during pregnancy [5].

*Simulating Postpartum Remodeling*

To simulate postpartum remodeling, we extended the growth simulation to include the postpartum period. To capture hemodynamic changes, we optimized the stressed blood volume input in the compartmental model to match the reported mean arterial pressure. We simulated cardiac remodeling in non-lactating and lactating rats since non-lactating rats return to pre-pregnant cardiac output and hormones within days of weaning, whereas lactating rats exhibit elevated cardiac output and P4 with suppressed E2 while nursing [6, 7].

*Contributions of Mechanics vs. Hormones on Postpartum Remodeling*

As our previous modeling work identified P4 and hemodynamics as the primary drivers of growth during pregnancy [5], we investigated their influence on postpartum remodeling. To understand the relative contributions of each parameter on postpartum remodeling, we re-ran the simulated the 21 days of postpartum-induced changes while maintaining either *P4* or *Stretch* at the activity level it reached at the end of pregnancy.

## RESULTS

During the 21-day postpartum period in rats, our model predicted a decrease in LV mass in the non-lactating group, but an increase in LV mass in the lactating group (Fig. 2). These results suggest that the elevated cardiac output and circulating P4 concentration induce additional heart growth as rats nurse their pups.

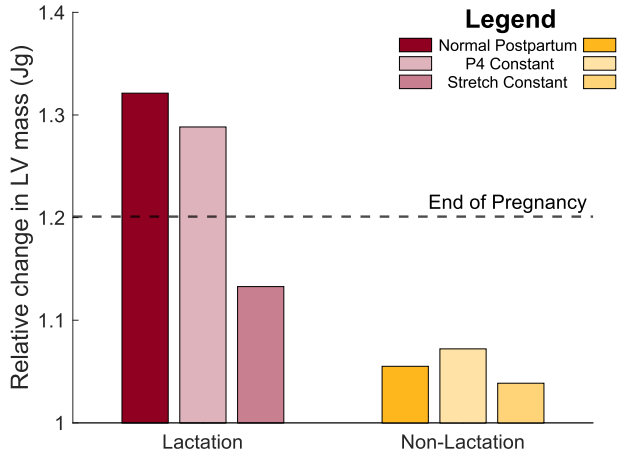


**Figure 2: Predicted changes in left ventricular (LV) mass in the non-lactating and lactating groups.** Bars represent changes in LV mass with respect to the pre-pregnant LV mass.

To assess the relative contributions of P4 and hemodynamic changes on postpartum cardiac remodeling, we repeated the postpartum simulations with either the *P4* or *Stretch* network model inputs maintained at the activity levels reached at the end of pregnancy. Maintaining either *P4* or *Stretch* at these constant levels underpredicted growth. In both the non-lactation and lactation groups, maintaining *Stretch* at a constant activity had a greater impact on the predicted LV mass (Fig. 2, rightmost bar in each group) and cardiomyocyte size (Fig. 3, *CellArea*) compared to maintaining *P4*. These results suggest that hemodynamic changes play a bigger role during postpartum remodeling in our model compared to changes in circulating P4 concentration.

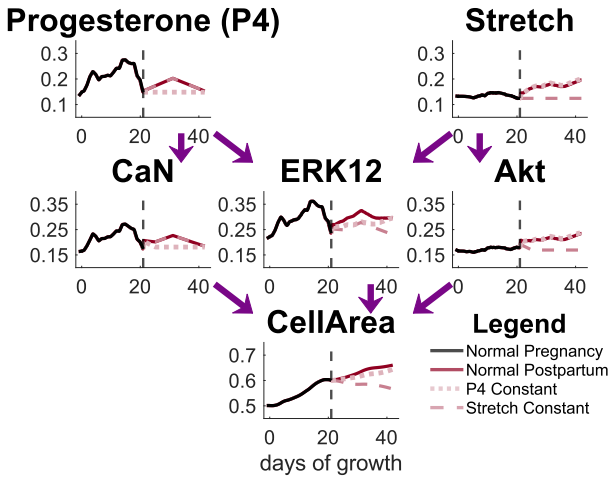


**Figure 3: Signaling network model predictions for the lactation group during pregnancy and postpartum recovery.** Arrows represent interactions between species, where intermediate species are influenced by *P4*, *Stretch*, or *P4* + *Stretch*.

## DISCUSSION

The objective of this work was to determine how hormonal and mechanical cues influence LV remodeling during postpartum recovery. The elevated cardiac output and progesterone in the lactation group led to increased LV mass in our multiscale model of cardiac growth. We further demonstrated that the mechanical signal *Stretch* played a larger role compared to hormonal signal *P4* during postpartum-mediated cardiac remodeling. Together, our results indicate hemodynamics as a primary driver of growth during postpartum recovery in our model.

During postpartum recovery, human patients, regardless of breastfeeding status, experience similar decreases in cardiac output to non-lactating rats [8] – likely due to the differences in the typical number of offspring per pregnancy (1-2 babies in humans vs. 8-12 pups in rats) and the resulting demand on the mammary glands [6, 9]. Therefore, the non-lactating simulation presented here is likely a better representation of human postpartum cardiac remodeling.

Future work will focus on applying this model to understand normal and abnormal postpartum-induced cardiac remodeling. Towards this goal, we will simulate postpartum remodeling in hypertensive pregnant rats and genetically modified mice that experience postpartum heart failure, better known as peripartum cardiomyopathy.

## ACKNOWLEDGEMENTS

This work was supported by the National Heart, Lung, and Blood Institute of the National Institutes of Health (T32-HL139431).

## REFERENCES

[1] Pritchard, J et al., *Anesthesiology*, 26:393-399, 1965.
[2] Tulchinsky, D et al., *Am. J. Obstet. Gynecol.*, 112:1095-1100, 1972.
[3] Savu, O et al., *Circ. Cardiovasc. Imaging*, 5:289-297, 2012.
[4] Declercq, E et al., *Commonw. Fund Fund Rep.*, 2020.
[5] Yoshida, K et al., *bioRxiv*, 2020.
[6] Hanwell, A et al., *J. Physiol.*, 233:93-109, 1973.
[7] McNeilly, A et al., *Marshall's Physiology of Reproduction*, 1994.
[8] Robson, S et al., *BJOG: Int. J. Obstet.*, 94:1028-1039, 1987.
[9] Thoresen, M et al., *Acta. Obstet. Gynecol. Scand.*, 67:741-745, 1988.

# HYALURONAN, PRG4, AND CYTOKINE PRODUCTION IN SYNOVIOCYTES IS SENSITIVE TO CYCLIC STRAIN MAGNTIUDE

**Meghana Pendyala (1), Paige Woods (2), Douglas K Brubaker (3), Elizabeth A Blaber (1), Tannin Schmidt (2), Deva D Chan (1,3)**

(1) Department of Biomedical Engineering, Rensselaer Polytechnic Institute, Troy, NY, USA
(2) Department of Biomedical Engineering, University of Connecticut Health Center, Farmington, CT, USA
(3) Wheldon School of Biomedical Engineering, Purdue University, West Lafayette, IN, USA

## INTRODUCTION

Synovial fluid works to lubricate the surfaces and maintain the macroenvironment of the joint [1]. Hyaluronan (HA) and PRG4 (proteoglycan-4) are major components of synovial fluid and are produced by fibroblast-like synoviocytes in the synovial membrane [2]. In healthy joints, synovial fluid contains high molecular weight HA and PRG4 [1], but in osteoarthritis (OA), HA concentration, HA molecular weight, and PRG4 concentration decreases [3,4]. Changes to cytokine concentrations in the synovial fluid have also been used as biomarkers to determine disease state [5]. Despite our knowledge on changes to proteoglycan and cytokine content within the joint, the effect of mechanics on these changes has not been thoroughly assessed.

HA is produced by three isoenzymes, hyaluronan synthase 1, 2, and 3 (HAS1, -2, -3) [6]. Hyaluronidases, which have been shown to increase activity during OA, break down HA chains into fragments [7]. Promoting *HAS2* expression has been shown to increase HA concentration [8], making synthase activity an ideal target for improving HA content. PRG4 is a vital component of synovial fluid, working to maintain its viscosity and to modulate cellular function [9], highlighting the need to improve PRG4 concentration within an OA joint.

Synoviocytes also modulate the inflammatory state within the synovial fluid. Chronic synovial inflammation is typically found in osteoarthritic joints, along with increased concentrations of pro-inflammatory cytokines, such as TNF-alpha, IL-6, IL-8, and IL-12, within the synovial fluid [10].

Mechanical stimulation, from exercise [11] to applied loading to cells [12], has been shown to alleviate OA symptoms, improve overall production of HA and other proteoglycans, and alter the expression of inflammatory molecules. The goal of our study is to determine the extent to which cyclic loading affects HA, PRG4, and cytokine content from synoviocytes. Our hypothesis is that high strain magnitudes will promote HA and PRG4 production and decrease pro-inflammatory cytokine secretion.

## METHODS

Human synovial sarcoma fibroblasts (SW982, ATCC) were cultured and seeded onto silicone membrane well-plates at a density of 3-4 x $10^4$ cells/cm$^2$. After 24h, cells were subjected to 0%, 5%, 10%, and 20% peak strain magnitude at a frequency of 1 Hz (sinusoidal waveform) for 3 hours using the Flexcell FX6000T Tension System (Figure 1). Cells were also plated on tissue culture plastic (TCP) as a control.

Four hours after the end of loading, media was removed and cell layers were lysed for RNA isolation. TaqMan®-based qRT-PCR was used to measure expression of *HAS1*, *HAS2*, *HAS3*, *HYAL1* (hyaluronidase 1), *HYAL2* (hyaluronidase 2), *CEMIP* (cell migration inducing hyaluronidase), *TMEM* (cell surface hyaluronidase), relative to *GAPDH*.

From separate wells, 24 hours after the end of loading, media was removed for HA and PRG4 concentration quantification using ELISA and cytokine concentration using a multiplex panel. Cell layers were fixed and stained for HA (HA binding protein with Alexa Fluor-488) and counterstained with DAPI.

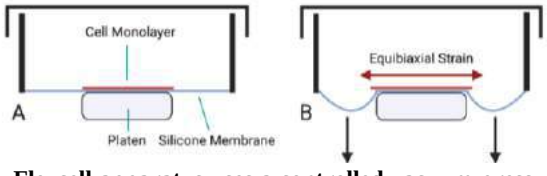


**Figure 1. Flexcell apparatus uses a controlled vacuum pressure to apply strain.** A) Cells are seeded onto a silicone membrane, B) which is stretched when subjected to a controlled loading parameter.

## RESULTS

Synoviocytes cultured on the silicone membranes had significantly lower *HYAL1* and *TMEM* expression when compared to cells cultured on TCP. Hyaluronan synthase gene expression was not significantly affected by substrate stiffness, and only *HAS3* expression was significantly different among the loaded groups (Figure 2). Cells strained to 20% strain showed higher *HAS3* ($p = 0.043$). 5% strain and 20% strain had significantly lower abundance of *HYAL1* and *HYAL2*. Cells strained to 10% strain had lower *HYAL2*, *TMEM* expression than 5% ($p = 0.01$) and 20% strain ($p = 0.003$).

All cyclic loading groups had lower HA concentration than the unloaded group, with the 5% strain group having the highest concentration among loaded groups (Table 1). Immunofluorescence imaging revealed that all stained HA was localized intracellularly. When comparing PRG4 concentrations of loaded groups, 5% strain resulted in a significant percent increase from the unloaded group (Table 1), while 10% and 20% strain decreased the amount of PRG4 in the conditioned media.

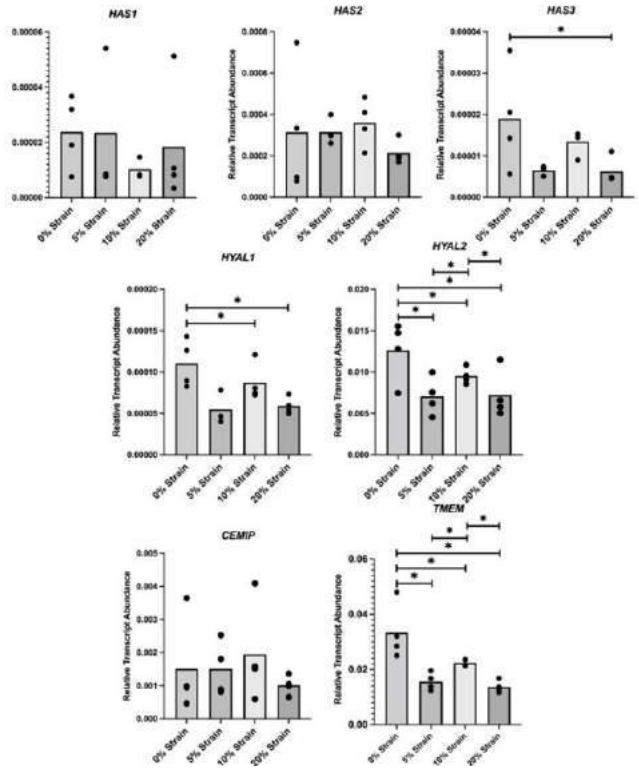


**Figure 2. Gene expression of hyaluronan turnover genes**. Relative transcript abundance measured as $2^{-\Delta Cq}$, where $\Delta Cq$ is the difference in quantification cycle from the gene of interest to *GAPDH*. Black circles represent replicates and significant difference (*, $p < 0.05$) between groups are shown with brackets.

**Table 1. Percent change concentrations of hyaluronan (HA) and PRG4 calculated against the 0% strain group**. Shown as mean ± standard deviation. Significance between groups shown by an asterisk ($p < 0.05$).

| | *HA Concentration* | *PRG4 Concentration* |
|---|---|---|
| **5% Strain** | -32.4% ± 0.09 | 26.3% ± 0.37 * |
| **10% Strain** | -11.1% ± 0.31 | -64.3% ± 0.20 * |
| **20% Strain** | -18.2% ± 0.15 | -38.2% ± 0.10 * |

Media from synoviocytes cultured on silicone membranes had significantly higher cytokine concentrations when compared to media from the TCP group. 5% strain had lower IL-5 concentration than 10% strain ($p = 0.035$), lower IP-10 concentrations than 0% ($p = 0.035$), 10% ($p = 0.030$) and 20% strain ($p = 0.005$) and RANTES concentrations than 10% ($p = 0.029$) and 20% strain ($p = 0.017$).

## DISCUSSION

Cyclic loading impacted HA turnover gene expression, decreasing *HAS3* and hyaluronidase expression. The softer silicone substrate stiffness also resulted in a hyaluronidase expression., and hyaluronidase expression was affected by substrate stiffness. However, strain magnitude did not demonstrate a consistent effect on HA turnover gene expression.

Previous studies have shown that static stretch of synoviocytes result in minimal changes to synthase expression [13], highlighting that cyclic loading impacts synoviocyte response differently that static stretch. However, changes to the expression of HA degrading enzymes have not been measured in previous mechanical stimulation studies. In this study, *HYAL1*, *HYAL2*, and *TMEM* expression was upregulated in a magnitude-dependent manner. This coincides with the reduction in overall HA concentration from the media and the presence of intracellular HA, which is indicative of HA reuptake and breakdown [14]. Cyclic tensile strain has been shown to depolymerize HA from chondrocytes, which supports the idea that cyclic strain may be increasing HA breakdown. 5% cyclic strain also increased PRG4 concentration in the media, consistent with studies that show cyclic compression increases PRG4 secretion in chondrocytes [15].

Cytokine concentration was sensitive to strain magnitude, with 5% strain reducing the concentration of pro-inflammatory markers, such as IL-5, IP-10, and RANTES, while 10% and 20% strain increased concentrations of these cytokines, compared to the unloaded group. Previous studies have shown that the effect of cyclic tensile strain affect cytokine production in synoviocytes is dependent on loading parameters, i.e. short-term or long-term exposure to stimulation [16, 17]. This variability suggests that cytokine production from synoviocytes is highly sensitive to changes in the mechanical environment, shown here by the significant increase in all cytokine concentration from culture on a silicone membrane and the sensitivity to strain magnitude.

Our data reveal that hyaluronidase expression and concentrations of HA, PRG4, and cytokines were sensitive to cyclic strain. Taken together, these results underscore the importance of mechanical stimulus of the synovium in regulating the joint environment.

## ACKNOWLEDGEMENTS

This work is supported by the National Science Foundation (1944294).

## REFERENCES

[1] Schmidt, T et al., *Arthritis Rheum*, 56(3):882-91, 2007
[2] Smith, M., *Open Rheumatol J*, 5:100-6, 2011
[3] Temple-Wong et al., *Arthritis Res Ther*, 18:18, 2016
[4] Ludwig, T et al., *Arthritis Rheum*, 64(12):3963-71, 2012
[5] Altobelli et al., *Curr Rheumatol Rev*, 13(3):170-79, 2017
[6] Itano N et al., *IUBMB*, 54(4):195-9, 2002
[7] Yoshida M et al., *Arthritis Res Ther*, 6(6):R514-20, 2004
[8] Yang YM et al., *Sci Transl Med*, 11(496), 2019
[9] Martin-Alarcon et al., *Biorheology*, 53(2):49-67, 2016
[10] Wojdasiewicz et al., *Mediators Inflamm*, 2014:561459, 2014
[11] Säämämen et al., *Connect Tisse Res*, 30(3):191-201, 1994
[12] Uehara et al., *Cytotechnology*, 67(1):19-26, 2015
[13] Momberger et al., *Matrix Biol*, 24(8):510-9, 2005
[14] Skandalis et al., *Semin Cancer Biol*, 62:20-30, 2020
[15] Jeon JE et al., *Osteoarthritis Cartilage*, 20(8):906-15, 2012

SB³C2022
Summer Biomechanics, Bioengineering and Biotransport Conference
June 20-23, Eastern Shore, MD, USA

# FLUID-STRUCTURE-BASED COMPUTATIONAL MODEL OF HEMODYNAMICS-DRIVEN AORTIC GROWTH FOR *FBLN4$^{SMKO}$* MICE

**Marisa S. Bazzi (1), Casey D. Hokanson (2), Jessica E. Wagenseil (3), Victor H. Barocas (2)**

(1) Chemical Engineering and Materials Science Department, University of Minnesota, Minneapolis, MN, USA
(2) Department of Biomedical Engineering, University of Minnesota, Minneapolis, MN, USA
(3) Department of Mechanical Engineering and Materials Science, Washington University, St. Louis, MO, USA

## INTRODUCTION

Thoracic aortic aneurysms (TAAs) are bulging enlargements of the aorta. They affect approximately 15,000 people in the US per year and can be fatal in 80% of the cases when ruptured [1]. Studies have suggested genetic connective tissue disorders that affect extracellular matrix (ECM) proteins [2] as well as blood flow dynamics features, such as altered luminal pressure, wall shear stress, and intramural stress, are linked to the disease [3].

Blood fluid dynamics features have been correlated with aneurysm outcome[4]. However, computational models aortic growth and remodeling often simplify the hemodynamically-driven stress along the aorta [5]. This simplification can lead to inaccuracy in longitudinal and axial growth, since it doesn't account for inhomogeneous growth of the tissue resulting from inhomogeneous fluid stress fields.

We studied hemodynamically-driven heterogeneous growth in the aortic wall of *FBLN4*$^{SMKO}$ mice. To perform the study, we use a combination of subject-specific fluid-solid-interaction (FSI) models, longitudinal data obtained from medical scans during the mouse lifetime, and a local stress-driven growth model.

## METHODS

**Mouse models:** Mouse models with TAA caused by deletion of the ECM fibulin-4 gene in smooth muscle cells (*Fbln4$^{SMKO}$*) were used in the study. TAA growth in each animal was monitored throughout the early disease stages by magnetic resonance angiography (MRA). The scans were collected at two-, four- and six-months of age. After the mice died naturally or were sacrificed at roughly 24 months of age, biaxial tests were used to obtain material properties of the aortic tissues.

**FSI simulations:** MRA scans of mice at age 2 months were used to generate mouse-specific models via the SimVascular image processing features. The wall thickness was considered to be constant and based on experimental measurement. The aortic wall was described using the Holzapfel-Gasser-Ogden (HGO) model to account for anisotropic tissue mechanics; HGO parameters were specified for each mouse based on postmortem measurements. A Newtonian model (viscosity 3.5 cP) was used for the blood. A waveform from an earlier mouse study was used as inlet boundary condition [6] and was assumed to be the same for all mice. For the brachiocephalic, left common carotid, and left subclavian arteries, as well as for the outlet at the distal end of the aorta, windkessel models with values based on literature were used as boundary conditions [6]; the same windkessel parameters were used for all mice. Simulations were performed for ten cardiac cycles using SimVascular [7] at the Minnesota Supercomputer Institute (MSI).

**Local stress-driven growth model:** The local stress-driven growth was solved for each element in the finite element mesh. The growth model is based on that of Alford and Tabor [8]

$$\frac{\dot{\lambda_r}}{\lambda_r} = \frac{1}{T_r}\left(\frac{\sigma_r}{\widehat{\sigma_r}} - 1\right); i\frac{\dot{\lambda_\theta}}{\lambda_\theta} = \frac{1}{T_\theta}\left(\frac{\sigma_\theta}{\widehat{\sigma_\theta}} - 1\right) + \frac{1}{T_\tau}\left(\frac{\tau_w}{\widehat{\tau_w}}\right); i\frac{\dot{\lambda_a}}{\lambda_a} = \frac{1}{T_a}\left(\frac{\sigma_a}{\widehat{\sigma_a}} - 1\right) \quad (1)$$

where $\dot{\lambda}_i i\text{and}i\dot{\lambda}_i$ are the growth stretch rate and the stretch ratio respectively.$i\hat{\tau}_w$ is the target wall shear stress, $\tau_w$ is the hemodynamics-driven wall shear stress, $\widehat{\sigma_i}$ is the target stress, $\sigma_i$ is the hemodynamics-driven stress and $T_i$ is a time constant for i-direction (r, θ, z).

**Finite Element Growth:** Kinematic growth of the aorta was defined locally by a growth tensor $\mathbf{G}$=diag$(\lambda_r, \lambda_\theta, \lambda_z)$ at time relative to the reference state, t=T$_0$. For this study, T$_0$ was taken to be at 2 months and the geometry was prestressed during the FSI simulation to account for the residual stress from the initial growth. The macroscale change in the geometry is solved using *Prestrain* plugin [9] of *FEBio Studio* 3.5 [10].

**Model tuning and validation:** Time constants were based on longitudinal measurement of aortic diameter. Fig. 1 on the next page shows the validation and tuning scheme. The ascending aortic geometry (Fig. 1b) was extracted from MRA scans of 2 month-old mice (Fig. 1a). FSI simulation were performed on the extracted geometry, and von Mises stress distributions were calculated (Fig. 1c). A ring around the maximum diameter region was extracted from the full geometry (Fig. 1d), and the G&R model was solved (Fig 1e) by adjusting the time constants so radial growth matched the experimental trends (Fig 1f).

SB³C2022-068

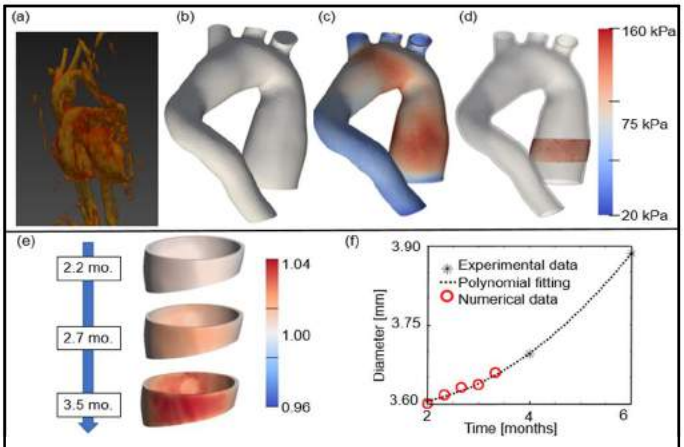


**Figure 1: (a)** MRA scans of *FBLN*$^{SMKO}$ mice taken at 2 month old**. (b)** 3D model generated from the scans. **(c)** von Mises stress distribution from the FSI simulations**. (d)** Aortic ring around the largest diameter region used to solve the **(e)** local growth or the aortic tissue and **(f)** validate the model based on the change in diameter over time.

## RESULTS

Five *FBLN4*$^{SMKO}$ mice were used for this study. Figure 2a below shows the *in vivo* change in the aortic diameter observed across 16 weeks. The data were fitted to a polynomial curve to obtain the growth trend between experimental data points. The inset of Figure 2a shows the changes in aortic diameter for the first few weeks obtained from the G&R model and compared against the experimental observations. The G&R model describes the initial radial growth process (from of 8 to 12 weeks) reasonably well for all the five models. Fig 2c shows the adjusted time constants for all five mice. As expected, smaller values of the radial and tangential time constants were observed for geometries with a larger growth in the first weeks.

Using the fitted time constants, the stress-driven G&R model was solved for full aortic geometry of two mice. The Von Mises stress was obtained from the mouse-specific FSI simulation, as shown on Fig. 3a and 3e. Figures 3b-3d and 3f to 3h display the computed growth along the aorta due to the inhomogeneous stress distribution. The growth process presents longitudinal and axial heterogeneity. As expected, more growth occurs in the ascending aorta.

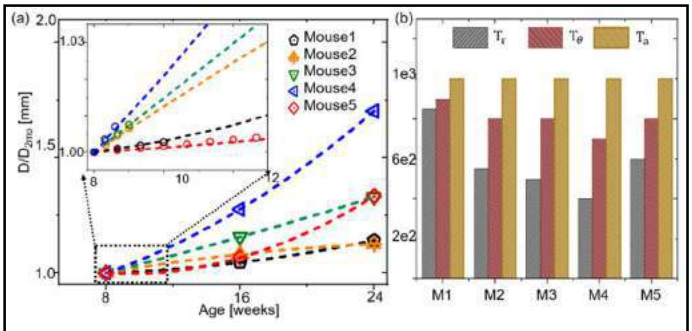


**Figure 2: (a)** Change in maximum aortic diameter for 5 *FBLN*$^{SMKO}$ mice models**.** Markers are measurements obtained from MRA scan and dashed lines are the polynomial fitting of the experimental. The inset figure shows the change in the diameter obtained from the G&R model (open circles) compared against the trend observed experimentally (dashed lines)**.** 3D model generated from the scans. **(b)** Time constants obtained from tuning the G&R model for each mouse model.

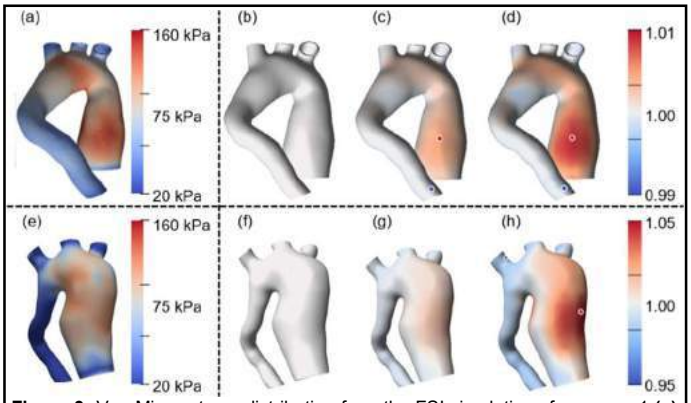


**Figure 3:** Von Mises stress distribution from the FSI simulations for mouse 1 **(a)** and mouse 4 **(e).** Total aortic growth driven by the stress distribution at **(a/f)** 1 weeks**, (b/g**) 2 weeks and **(d/h**) 4 weeks relative to the reference state.

## DISCUSSION

Five aortic models for Fbln4$^{SMKO}$ mice at the age of two months were created based on MRA. Mouse-specific material properties and wall thickness were combined with generic boundary conditions for blood flow in the FSI simulations. Results for von Mises stress were used as input to solve the local stress-driven G&R model. The G&R was compared to the trend of the change in diameter measured *in vivo*. The model qualitatively matched the experimentally observed radial growth for the first 3-12 weeks relative to the initial state.

Results for full aortic growth show substantial heterogeneity of the growth process along the length of the aorta, as a direct consequence of the inhomogeneous stress distribution along the aortic wall. Those results reinforce the importance of using anatomically realistic models, rather than simplified models, when a complex geometry such as the aorta is being considered.

The study is performed with only five mice and involved only two mouse model. Further analysis is necessary to determine additional limitations of the subject-specific growth model, and its translatability to human subject. Nevertheless, as it becomes more and more possible to acquire geometric and mechanical data from patients [11] and to do complex, detailed computer simulations, multi-physics models will provide new insight into growth and development of aneurysms.

## ACKNOWLEDGEMENTS

This work was supported by NIH U01HL139471 and by the Marfan Foundation. Special thanks to Dr. Vijay Vedula for his help. We appreciate the support from the Minnesota Supercomputing Institute (MSI) at the University of Minnesota.

## REFERENCES

[1] B. Zhou *et al.*, *Lancet*, vol. 389, no. 10064, pp. 37–55.
[2] J. Kim, *et al., Am. J. Physiol. - Hear. Circ. Physiol.*, vol. 309, 2015.
[3] D. P. J. Howard, *et al., Br. J. Surg.*, vol. 102, no. 8, pp. 907–915.
[4] "Bazzi *et al.*," *Cardiovasc. Eng. Technol.*, vol. accepted, 2022.
[5] R. R. Mahutga *et al. J. Biomech. Eng.*, vol. 142, no. 11, 2020.
[6] F. Cuomo, *et al.Ann. Biomed. Eng.*, vol. 43, no. 7, pp. 1555–1570, 2015.
[7] H. Lan, A. *et al. J. Biomech. Eng.*, vol. 140, no. 2, pp. 1–11, 2018.
[8] P. W. Alford and L. A. Taber, *"Comput Methods Biomech Biomed Eng*," vol. 11, no. 5, pp. 525–538, 2009.
[9] S. A. Maas, *et al. J. Mech. Behav. Biomed. Mater.*, vol. 61, pp. 499–510, 2016.
[10] S. A. Maas, *et al.J. Biomech. Eng.*, vol. 134, no. 1, Feb. 2012.
[11] S. Farzaneh, *et al.*," *Ann. Biomed. Eng.*, vol. 47, no. 4, pp. 1038–1050, 2019.

SB³C2022
Summer Biomechanics, Bioengineering and Biotransport Conference
June 20-23, Eastern Shore, MD, USA

# EFFECTS OF FISETIN ON TRIPLE NEGATIVE BREAST CANCER INVASION

**Jacob Heiss (1), Nina Treacher (1), Hossein Tavana (1)**

(1) Biomedical Engineering, The University of Akron, Akron, OH, USA

## INTRODUCTION

Triple negative breast cancer (TNBC) is a highly aggressive disease that often metastasizes to other organs [1]. Metastasis involves local invasion of cancer cells into the adjacent tissue to access circulation [2]. Although targeted therapies of cancers have increased the efficacy of treatments while reducing systemic toxicity, a lack of hormone receptors and HER2 amplification on TNBC cells significantly limits targeted therapies for this disease. Currently, chemotherapy is the mainstay treatment for TNBC. However, because chemotherapeutics are toxic to normal cells and do not prevent invasion of cancer cells, other treatment options are being explored. We report that fisetin, a naturally occurring plant flavanol, has anti-invasion properties blocks the extracellular matrix invasion of TNBC cells in a three-dimensional in vitro tumor model.

## METHODS

Four TNBC cell lines were used in this study: MDA-MB-231, SUM159, MDA-MB-157, and BT-549. Tumor spheroids were created from each cell line using an aqueous two-phase system cell patterning technology [3]. Each spheroid was encapsulated in 2.7 mg/ml human-derived type I collagen to simulate the extracellular matrix. Incubation resulted in the formation of a collagen hydrogel containing the spheroid. The spheroids were treated dose-dependently with fisetin in a concentration range of 0-200 μM. After sufficient invasion of cells under no treatment (three days for MDA-MB-231, SUM159, and MDA-MB-157, and six for SUM159), confocal microscopy was used to image cell invasion. For each dose and cell line combination, five spheroids were imaged in replicate. In order to see the cells with confocal microscopy, the MDA-MB-231 and SUM159 cell lines were transfected to stably produce a green fluorescent protein and the MDA-MB-157 and BT-549 cells were stained with a Calcein AM dye. Matrix invasion of cells was quantified by measuring the total pixel area of the invading cells from the collapsed z-stack image for each spheroid. The invading areas were used to create a dose-response curve and find the 50% inhibitory concentration (IC50) for each cell line.

## RESULTS

We selected a 2.7 mg/ml collagen concentration to give a stiffness of ~2.5 kPa to reproduce stiffness of human breast tumors [4]. While all four TNBC cell lines effectively invaded the collagen matrix under no treatment, fisetin significantly decreased the invasiveness of all four cell lines (Fig 1). Fisetin showed a maximum inhibition of TNBC invasiveness by 98%, 100%, 93%, and 100% for MDA-MB-231, SUM159, MDA-MB-157, and BT-549 cell lines, respectively. In addition, we found the IC50 value for each cell line to be 11.23 μM for MDA-MB-231, 40.57 μM for SUM159, 51.57 μM for MDA-MB-157, and 26.29 μM for BT-549 (Fig 2).

SB³C2022-069

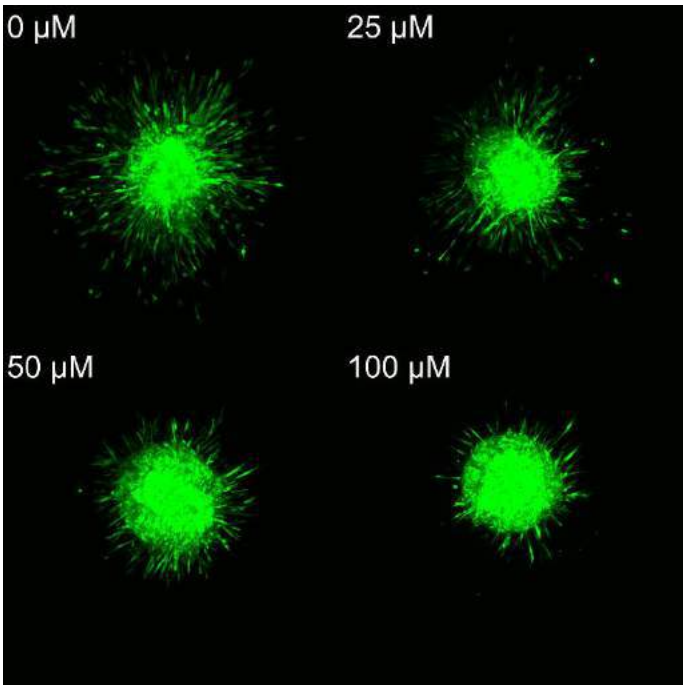


**Figure 1: Confocal images of SUM159 spheroids treated with at 0, 25, 50, and 100 µM of fiestin.**

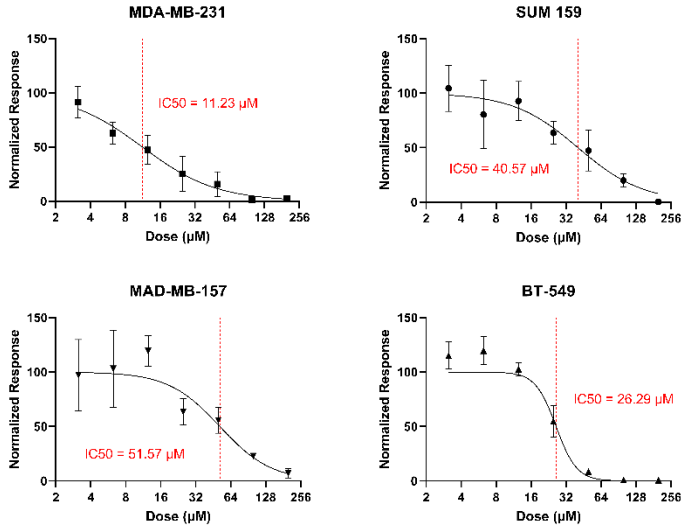


**Figure 2: Dose-response curves of fisetin treatment for each cell line. IC50 values marked in red.**

## DISCUSSION

We demonstrated that fisetin effectively reduces the matrix invasion of TNBC cells. This finding is consistent with a previous study from our group that fisetin interferes with signaling of PI3K/Akt and MAPK/ERK pathways, which are highly active in TNBC cells [5]. Our finding suggests that fisetin may provide additional benefits in treating TNBC. To further establish this finding, we plan to test this effectiveness of fisetin in more complex tumor models that contain other components of tumor stroma, such as cancer associated fibroblasts and critical matrix proteins in TNBC tumors such as hyaluronan and fibronectin, as well as in animal models.

## ACKNOWLEDGEMENTS

Financial support was provided by NIH grant CA225549 and NSF grant 1801591.

## REFERENCES

1. Bianchini, G., et al., *Triple-negative breast cancer: challenges and opportunities of a heterogeneous disease.* Nature Reviews Clinical Oncology, 2016. **13**(11): p. 674-690.
2. Stuelten, C.H., C.A. Parent, and D.J. Montell, *Cell motility in cancer invasion and metastasis: insights from simple model organisms.* Nature Reviews Cancer, 2018. **18**(5): p. 296-312.
3. Atefi, E., et al., *High Throughput, Polymeric Aqueous Two-Phase Printing of Tumor Spheroids.* Advanced Functional Materials, 2014. **24**(41): p. 6509-6515.
4. Singh, S., et al., *Organotypic breast tumor model elucidates dynamic remodeling of tumor microenvironment.* Biomaterials, 2020. **238**: p. 119853.
5. Shahi Thakuri, P., et al., *Phytochemicals inhibit migration of triple negative breast cancer cells by targeting kinase signaling.* BMC Cancer, 2020. **20**(1): p. 4.

SB³C2022
Summer Biomechanics, Bioengineering and Biotransport Conference
June 20-23, Eastern Shore, MD, USA

# CORE-SHELLED MICROCAPSULES PRODUCE TUMOR AGGREGATES WITH GREATER SPHERICITY AND DRUG RESISTANCE THAN "GOLD-STANDARD" LIQUID OVERLAY TECHNIQUE IN HER2+ BREAST CANCER CELLS

**Cassandra L. Roberge (1), Margarida Barroso (2), and David T. Corr (1)**

(1) Department of Biomedical Engineering, Rensselaer Polytechnic Institute, Troy, NY USA
(2) Department of Molecular and Cellular Physiology, Albany Medical College, Albany, NY USA

## INTRODUCTION

3D tissue-engineered *in vitro* models, particularly multicellular tumor spheroids (MCTSs), are being increasingly used to explore disease progression and novel therapeutic strategies, especially for oncological applications. Once grown to 0.03-0.5mm$^3$ in volume, these avascular constructs begin mimicking several key aspects of *in vivo* tumors, such as 3D structure and pathophysiological gradients [1,2]. However, a lack of standardization of MCTS fabrication has led to a large variety of "spheroid" or "organoid" models, many of which are unable to achieve the necessary morphology (i.e., size, sphericity) for physiologically-representative behavior. This poses a particular challenge for drug-screening MCTS applications, where inaccurate models may overestimate the efficacy of a given drug. Indeed, improper screening models have already been implicated in the high percentage of investigated drugs that later fail in clinical trials [3].

Previously, our lab has used Optical Coherence Tomography (OCT), a non-destructive structural imaging modality, to assess 3D morphologies of MDA-MB-231 breast cancer MCTSs formed via liquid overlay, the current gold standard method of fabrication [4]. We demonstrated that in liquid overlay cultures the addition of Matrigel (solubilized basement membrane derived from mouse sarcoma) was required for the formation of 3D spheroids, even for cells that have an innate ability to self-aggregate [4]. In other work, we demonstrated the ability to form highly spherical aggregates, without requiring Matrigel, by growing these same cells in microcapsules [5,6]. Lastly, we have shown that the OCT-based technique used to assess model morphology can also accurately estimate cell density within these 3D aggregates, and provide a systematic and non-destructive measure of cell viability throughout aggregate growth, and in response to drug [4].

Herein, we non-destructively assess the differences in drug response between HER2+ tumor aggregate models created in microcapsules and those created via liquid overlay, highlighting the influence of morphology on model behavior and the importance of model selection for *in vitro* drug-screening applications.

## METHODS

Following established methods, cell-loaded microcapsules were prepared using electrostatic bead generation [7,8]. Briefly, AU565 HER2+ breast cancer cells (5e6 cells/mL) were suspended in 1.5% alginate (Sigma, #9005-38-3) and extruded into a 2% CaCl2 bath using an electrostatic droplet generator to form calcium alginate gel beads. The gel beads were incubated with 0.16% w/v chitosan (Spectrum MFG, C1569) to form alginate-chitosan membranes around each bead, and subsequently incubated with sodium citrate to chelate the alginate bead cores. This produced cell-loaded core-shelled capsules 300-350 µm in diameter. Cells began to aggregate after 14 days in culture, and formed spheroids matching the capsule diameter by 27 days. On day 27, matured spheroids were drugged with 50ug/mL Trastuzumab, a clinically-used chemotherapeutic, and cultured for 5 days.

Control aggregates were formed via liquid overlay (L.O.), the current gold standard method for aggregate production. Cells were seeded (2.5 x10$^4$ cells/well) in non-adherent U-shaped 96-well plates and cultured for 4 days either with or without the addition of 2.5% Matrigel [9]. On day 4, matured aggregates were drugged with 50ug/mL Trastuzumab and cultured for 5 days.

Following our previously published technique [4], 3D volume scans of full tumor aggregates were collected via OCT at key timepoints of 0h, 24h, and 120h (5d) post-drug addition. Imaris image analysis software was used to count the number of cell-sized objects present in each scan, which when normalized to the measured aggregate volume, provides a systematic estimation of cell density at each timepoint, ***within each aggregate*** throughout the drug timecourse. Statistical comparisons were made using Student's t-test, and data are shown as means ± SD, with $p < 0.05$ used as significance cutoff.

## RESULTS

Morphologically, aggregates grown with liquid overlay were quite flat, while those grown with the addition of Matrigel became thicker and more disk-like (**Figure 1A+B**). Sphericities for these samples were 0.34 ± 0.01 and 0.57 ± 0.03, respectively, (with 0 representing a plane and 1.0 a perfect sphere). Neither of these L.O. fabricated aggregates met the 0.8 cutoff characteristic of good tumor spheroid models [10]. However, those grown via microcapsule grew to be quite round (**Figure 1C**) with an average sphericity of 0.79 ± 0.09, ranging approximately at the cutoff value. Thus, spheroid shape for this cell line was rescued by growing these cells within capsules, which boast better size and shape control than liquid overlay, even in AU565 cells that have been reported to have little to no innate ability to self-aggregate.

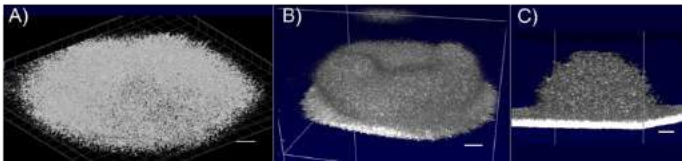


**Figure 1: Representative OCT volume scans of matured AU565 tumor aggregates fabricated via A) liquid overlay, B) liquid overlay with Matrigel, or C) microcapsule, highlighting differences in morphology. Scale bars = 100 µm.**

Cell aggregates exhibited increased drug resistance with greater model dimensionality; with more cell death observed in flatter aggregates than in the 3D spheroids (**Figure 2**). When treated with drug for 5 days, aggregates grown via liquid overlay saw a severe drop in the number of viable cells throughout the timecourse. The addition of Matrigel imparted a significant increase in drug resistance at both timepoints assessed, possibly due to the Matrigel itself or the increase in aggregate thickness. Of the models tested, capsule-based spheroids were most resistant to the drug, which was particularly evident at the final timepoint.

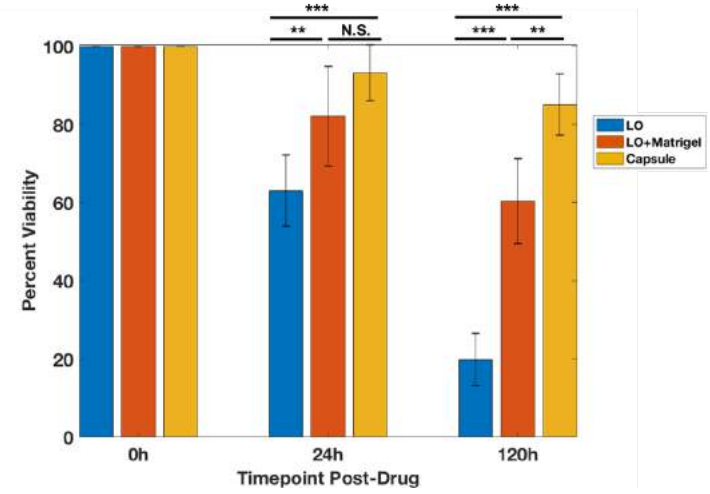


**Figure 2: Longitudinal quantification of tumor aggregate percent cell viability in response to anti-cancer drug indicates increased drug resistance in more spherical aggregates (L.O. n=6, capsule group n=3)(** = p < 0.001, *** = p < 0.0001).**

## DISCUSSION

Our goal was to quantify the drug response of a known chemo-therapeutic on HER2+ *in vitro* tumor aggregate models fabricated in core-shelled microcapsules and via liquid overlay with and without Matrigel, using our non-destructive, OCT-based approach to assess viability. Our data show that these different approaches produced AU565 aggregates of different dimensionality (2D, 2.5D, and 3D), and that cells grown to tumor spheroids within capsules (3D) are significantly more resistant to drug than those grown via the gold standard L.O. method, with (2.5D) or without (2D) Matrigel. Within the liquid overlay models, Matrigel addition increases aggregate thickness, which is expected to create larger diffusion gradients and thus limit the penetration of the drug into the aggregate, which may explain why these models were more resistant than those grown without Matrigel. This same reasoning could explain the even greater drug resistance observed in 3D capsule-based spheroids. Future work should also investigate possible shielding effects from the capsule wall, which may be further protecting the cells from the drug.

Given that *in vivo*-like gradient formation and drug response are functions of spheroid morphology, it is likely that 3D aggregates with high sphericities will provide much more accurate surrogates for drug discovery than their low-sphericity counterparts. Taken together, these findings emphasize the importance of using 3D models in drug-screening applications and demonstrate the utility of electrostatic bead generation for engineering 3D tumor spheroids, even in a cell line with little to no known ability to self-aggregate.


## ACKNOWLEDGEMENTS

This work was funded, in part, by NIH R01 BRG CA207725 (MB/DTC) and NIH R01 CA233188 (MB/DTC).


## REFERENCES


[1] Hirschhaeuser F, Menne H, Dittfeld C, West J, Mueller-Klieser W and Kunz-Schughart L A, *J. Biotechnol*. 148 3–15, 2010.

[2] Mueller-Klieser W, *J Cancer Res Clin. Oncol.* 113 101–22, 1987.

[3] Langhans S A, *Front. Pharmacol*. 9 1–14, 2018.

[4] Roberge C L *et al.*, *Acta Biomater*. 117 322–34, 2020.

[5] Kingsley D M *et al., Acta Biomater*. 95 357–70, 2019.

[6] Kingsley D M, Dias A D and Corr D T, *Biotechnol. Bioeng*. 113 2264–74, 2016.

[7] Bugarski B, Smith J, Wu J and Goosen M F A, *Biotechnol. Tech.* 7 677–82, 1993.

[8] Zhang X *et al., Biotechnol. Prog*. 21 1289–96, 2005.

[9] Nagelkerke A, Bussink J, Sweep F C G J and Span P N. *Anal. Biochem*. 437 17–9, 2013.

[10] Noto A *et al.*, *Cell Death Dis.* 4 e947-11, 2013.

SB³C2022
Summer Biomechanics, Bioengineering and Biotransport Conference
June 20-23, Eastern Shore, MD, USA

# A STUDY ON THE TRIAXIAL MECHANICAL PROPERTIES OF SILICONE ELASTOMERS FOR POTENTIAL USE AS A BRAIN TISSUE SURROGATE

**Ahsanul Torza (1), Johannes Weickenmeier (1)**

(1) Department of Mechanical Engineering
Stevens Institute of Technology
Hoboken, NJ, United States

## INTRODUCTION

Freshly isolated human tissue samples are difficult to obtain for several logistical and regulatory reasons [1]. Thus, researchers use animal models and elastomers to measure the mechanical response in various applications including traumatic brain injury, neurosurgical procedures, and mechanobiology experiments [2]. To ensure bio-fidelity in predicting behavior in either finite element or physical surrogate brain models, accurate material properties of the brain are necessary. Measurements of human and animal brain tissue properties have been recorded using various ex vivo methods. There is a significant discrepancy in reported property values due to differences in experimental parameters such as postmortem time, temperature sensitivity, and brain region [3].

The human brain is a nonlinearly elastic porous material and shows rate-dependent characteristics. This behavior can be attributed to interaction between interstitial fluid and the solid matrix of the tissue. As a result, brain deformations during trauma (fast rate), palpation (medium rate), and brain shift (slow rate) differ [4]. Hyperelastic constitutive models are currently used to express the mechanical behavior of brain materials under strain and are typically calibrated using data from a single deformation mode (compression, tension, or shear). It has been shown, however, that this approach is insufficient for materials whose strain-stress response varies significantly between deformation modes [5]. Therefore, constitutive models of brain behavior should include multiple deformation modes for optimal parameter calculation.

A wide range of artificial brain tissue simulants has been proposed in literature, including agarose, gelatin, hydrogels, and silicone elastomers. In recent years, Polydimethylsiloxane (PDMS Sylgard 184) has been proposed as the preferred surrogate brain material [4,6]. The stiffness of PDMS can be altered by adjusting the ratio of the base to the curing agent. However, it is unknown what is the optimal ratio to produce PDMS comparable to fresh human brains. Previous work aiming at determining a suitable mixing ratio is limited because their constitutive model parameters were calibrated based on only a single mode of deformation [4].

The purpose of this study is to assess and contrast mechanical properties of fixed bovine brains with silicone elastomers using the same experimental device and testing in 4 different deformation modes without altering the sample, enabling a direct comparison of the materials.

## METHODS

In soft materials such as the brain and PDMS, loads higher than a few hundred kilopascals (kPa) will cause irreversible damage [7]. To account for this, we developed a custom-built triaxial testing device (Fig. 1a) to measure forces experienced by soft materials. Three orthogonally arranged translational stages can displace the 2N load cell attached to a pin containing the test sample. To create the control and acquisition system, LabView was used. This system allows the number of cycles, distance traveled by each stage, and strain rate on each axis to be controlled independently.

It has been shown that PDMS at a ratio of 1:80 shows similar compression properties as fresh porcine brains [4]. On that account, we created PDMS in a custom-built aluminum mold with a varying ratio of 1:80, 1:100, and 1:120. Every PDMS ratio was prepared as follows: 30 minutes of mixing followed by one hour in a vacuum chamber to remove air bubbles, then two hours to cure in an incubating chamber at 100 degrees °C, and finally 24 hours of cooling before extraction.

7 cubic samples for each PDMS ratio and 7 bovine brain samples from different locations were prepared. Sample size was set to 5x5x5 mm and 1 loading-unloading cycle at 0.03 mm/s in compression, tension, and two shear directions were performed. Since brain tissue exhibits a different behavior during loading and unloading, both curves were averaged for each test (Fig 1b).

SB³C2022-071

The behavior of brain tissue is frequently modeled using Ogden model-based-hyperelastic constitutive equations [7]. In this case, the shear modulus μ and nonlinearity parameter α are material dependent parameters that were determined via a customized inverse finite element scheme (iFEM) implemented in ABAQUS and python, that simultaneously fitted all four deformation modes, see Fig 3a.

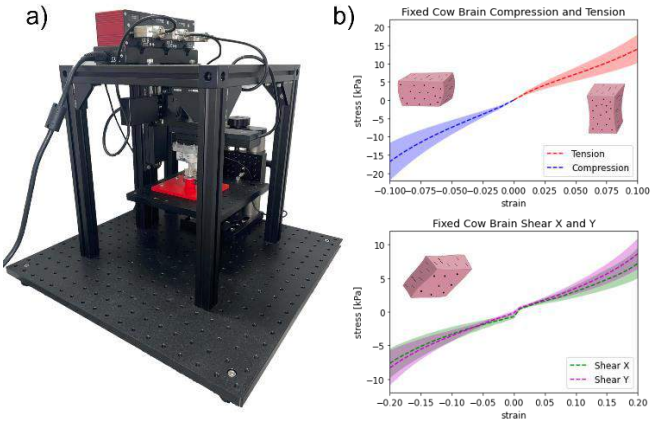


**Figure 1. a) Triaxial testing device. b) Standard deviation and mean of the average curves for 7 bovine brain samples under 4 deformation modes (compression, tension, shear x, and shear y)**

## RESULTS

For all three PDMS ratios, mean and standard deviation of the stress-strain curves were calculated for each mode of deformation (Fig. 2). The results show that the PDMS with a mixture ratio of 1:80 falls within the standard deviation of fixed cow brain behavior in all 4 modes of deformation. For increasing PDMS ratio, stiffness decreases, indicating a softer elastomer more closely representative of fresh brain stiffness. When tension is applied, both materials reach a lower stress level compared to compression. In addition, the shear stress values for both materials were similar in each respective strain directions.

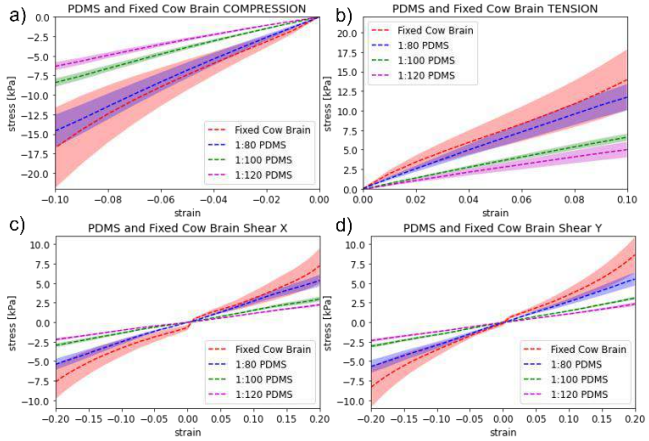


**Figure 2. Mean and standard deviation of seven PDMS with varying ratio and fixed bovine cubes in a) compression, b) tension, c) shear x, and d) shear y.**

Using the iFEM approach, model parameters were obtained by fitting against fixed brain data, see Fig 3b. Shear modulus and nonlinearity parameters describing the 4 deformation modes of the 1:80 PDMS and fixed bovine brain simulations differed by 4.86 kPa and 1.07, respectively.

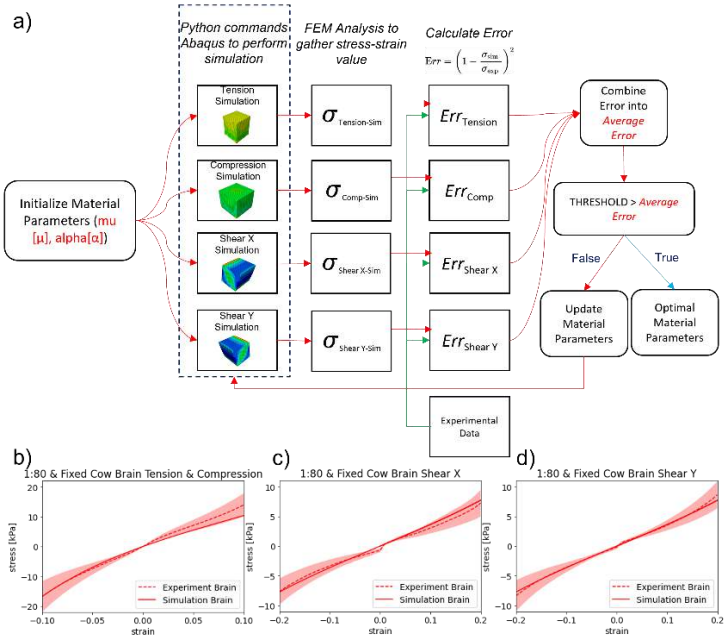


**Figure 3. a) Overview of inverse finite element model and b) plot of simulation and experiment of fixed bovine brain in compression and tension, c) shear x, d) shear y**

## DISCUSSION

Our triaxial testing device and iFEM results show that PDMS with a 1:80 mixture ratio has a similar stiffness to fixed bovine brain tissue. Furthermore, the iFEM provided a way to characterize the behavior of PDMS and fixed bovine brain in tension, compression, and shear with one set of parameters.

Our results for PDMS with ratio 1:80 differed from data reported in literature as they left their mold inside the over for 2 days, and they used 0.083 mm/s to test their material under compression [4]. A speed of 0.03 mm/s was used in our work to achieve a quasi-static process [7]. In an additional test, after curing PDMS 1:80 for 2 days, a significantly stiffer behavior was observed compared to fixed bovine brain tissue.

In this study, we demonstrate that the curing time, mixing ratio, and strain rate affect the mechanical response of PDMS, and that the Ogden model successfully reproduces the mechanical response of four different deformation modes with a single parameter set.

## ACKNOWLEDGEMENTS

This work was supported by the “Frank, Sr and Mary Jane Semcer Fellowship” to A. Torza.

## REFERENCES

[1] W. Grizzle et al. *Cancer Biomarkers* 2011: *9*(1–6), 531–549.
[2] D. Stewart et al. *PLoS ONE* 2017: *12*(6).
[3] D. Singh et al. *Journal of Biomechanics* 2019: *92*, 84–91.
[4] L. Zhang et al. *Journal of the Mechanical Behavior of Biomedical Materials* 2019: *95*, 180–190.
[5] K. Upadhyay et al. *International Journal of Engineering Science* 2020: *154*.
[6] S. Bentil et al. *Experimental Mechanics* 2016: *56*(5), 759–769.
[7] S. Budday et al. *Acta Biomaterialia* 2017: *60*, 315–329.

SB³C2022
Summer Biomechanics, Bioengineering and Biotransport Conference
June 20-23, Eastern Shore, MD, USA

# APOE ε4 GENOTYPE DECREASES BARRIER FUNCTION AND GLUCOSE UPTAKE IN INDUCED PLURIPOTENT STEM CELL-DERIVED BRAIN MICROVASCULAR ENDOTHELIAL CELLS

**Callie M. Weber (1), Sophia M. Zic (1), Alisa Morss Clyne (1)**

(1) Fischell Department of Bioengineering
University of Maryland
College Park, MD USA

## INTRODUCTION

5.8 million Americans have Alzheimer's disease (AD), and with the aging population, that number is predicted to triple by 2050. With no effective treatments to prevent or slow AD, it is currently the seventh leading cause of death in the United States [1]. The cause of AD is unknown, but people homozygous for the apolipoprotein E (APOE) ε4 allele have a more than 25 times higher odds ratio for AD compared to those with the ε3 or ε2 allele [2]. It is therefore essential to understand how the APOE ε4 allele contributes to AD development.

One of the first detectable AD biomarkers is brain glucose hypometabolism [3]. Glucose entry into the brain is modulated through the selective transporter GLUT-1 in brain microvascular endothelial cells (BMEC) [4]. BMEC GLUT-1 density is directly correlated with glucose uptake into the brain [5]. Isolated BMEC from transgenic APOE ε4 mice demonstrated decreased glucose flux through glycolysis compared to APOE ε3 cells [6]. However, BMEC from mice and humans are demonstrably different in their barrier function [7], [8], indicating that animal cells do not accurately recapitulate human cell function. The goal of this study was to determine how the APOE ε4 genotype affects barrier function and glucose uptake in a human BMEC model. We hypothesized that BMEC homozygous for the APOE ε4 genotype would demonstrate decreased glucose uptake and barrier function compared to APOE ε3 cells.

## METHODS

**CRISPR/Cas9:** IMR90 human induced pluripotent stem cells (iPSC) homozygous for the APOE ε3 genotype were dissociated from Matrigel-coated plates into a single cell suspension and combined with Cas9, sgRNA, ssODN, and a homology-directed repair enhancer. Cells were electroporated using a Neon system. Cells were replated, and CRISPR efficiency was evaluated using Sanger sequencing. Individual cell colonies were produced, and colonies determined to have the APOE ε4 genotype were expanded, along with unedited isogenic controls.

**Cell Culture:** APOE ε3 and APOE ε4 iPSC were maintained in mTESR-plus medium. Cells were differentiated into iPSC-BMEC following previously established protocols [8]. Briefly, cells were cultured in E6 medium for 4 days, then switched to human endothelial serum free medium (hESFM) supplemented with 50x B27, basic fibroblast growth factor (bFGF), and retinoic acid (RA) for 48 hours. Cells were then dissociated into single cells and replated on 6-well plates or glass coverslips coated with collagen IV and fibronectin in hESFM with B27, bFGF, and RA for another 24 hours. Finally, cells were switched to hESFM with B27 for experiments.

**Immunocytochemistry:** Tight junction proteins in iPSC-BMEC seeded on glass coverslips were analyzed by labeling with a primary antibody for the tight junction protein zonula occludin-1 (ZO-1) and Hoechst (nuclei). Cells were then imaged using a spinning disk confocal microscope (Nikon). Images were analyzed for continuous junctions, indicating barrier fidelity, using a junction analyzer program (JAnaP) [9]. GLUT1, the primary BMEC glucose transporter, was also labeled with a primary antibody and imaged by confocal microscopy. GLUT1 was quantified by analyzing fluorescent intensity using ImageJ and normalizing to the number of nuclei.

**Metabolic Analysis:** Following differentiation, iPSC-BMEC were seeded in 6-well plates and cultured for 2 days. At 0- and 24-hours following a medium change, 200 µL media aliquots were collected and analyzed for glucose and lactate concentration on a YSI 2950 Bioanalyzer. Glucose uptake, lactate production, and lactate-to-glucose ratio were then calculated.

**Statistical Analysis:** Statistical analyses were completed in GraphPad using a Mann-Whitney test, with $p < 0.05$ being significant.

## RESULTS

We first determined how the APOE genotype impacted iPSC-BMEC barrier function. Tight junction continuity, as measured by JAnaP analysis of ZO-1, was nearly 85% lower in iPSC-BMEC with the APOE ε4 genotype as compared to iPSC-BMEC with the APOE ε3

SB³C2022-073

genotype. GLUT1 fluorescence intensity also decreased by 22% in the APOE ε4 compared to APOE ε3 iPSC-BMEC (Fig. 1B).

To determine if decreased GLUT-1 correlated with reduced glucose uptake in APOE ε4 iPSC-BMEC, we analyzed media glucose and lactate concentrations with a YSI Bioanalyzer. Glucose uptake significantly decreased by 28% in APOE ε4 iPSC-BMEC compared to those with the APOE ε3 genotype (Fig. 2A). Interestingly, lactate production was similar between the cells regardless of genotype (Fig. 2A). The lactate:glucose ratio, which should be two if every glucose is metabolized to lactate via glycolysis, was slightly below two for the APOE ε3 iPSC-BMEC. However, the lactate:glucose ratio was above two for the APOE ε4 iPSC-BMEC (Fig. 2B).

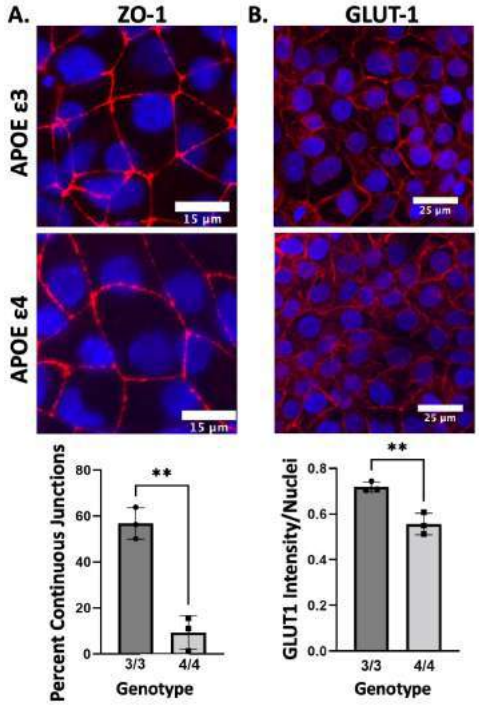


**Figure 1. APOE ε4 genotype decreased iPSC-BMEC tight junction continuity and GLUT1 compared to APOE ε3 genotype.** A. Representative confocal microscopy images of ZO-1 (red) and nuclei (blue) in APOE ε4 and APOE ε3 iPSC-BMEC. Quantification of continuous junctions by JAnaP. B. Representative confocal microscopy images of GLUT1 (red) and nuclei (blue) in APOE ε4 and APOE ε3. Fluorescent intensity analyzed using ImageJ. ** $p < 0.001$.

## DISCUSSION

We now show that the APOE ε4 allele decreases tight junction continuity and glucose uptake in iPSC-BMEC. Decreased ZO-1 continuity in APOE ε4 compared to APOE ε3 iPSC-BMEC likely contributes to decreased barrier function, which has also been observed via decreased trans-endothelial resistance (TEER) in immortalized BMEC from transgenic mice [6]. However, the effect of APOE ε4 had not yet been demonstrated in a human BMEC model, which has higher barrier strength than mouse BMEC. We will use JAnaP to further quantify barrier continuity of other BMEC tight junction proteins, including occludin and VE-cadherin [9]. We will also assess barrier function using TEER and a dextran permeability assay.

APOE ε4 iPSC-BMEC had decreased GLUT1 compared to APOE ε3 iPSC-BMEC, which correlated with decreased glucose uptake. This is congruent with research in immortalized BMEC from transgenic mice, in which APOE ε4 BMEC produced less ATP from glycolysis than APOE ε3 BMEC [6]. Interestingly, APOE ε4 iPSC-BMEC had similar levels of lactate production as APOE ε3 cells, despite their decreased glucose uptake. This could indicate that APOE ε3 iPSC-BMEC shunt more glucose into branch pathways of glycolysis such as the hexosamine biosynthesis pathway (HBP), thereby producing less lactate per glucose molecule. Since APOE ε4 iPSC-BMEC produce more than two lactate per glucose molecule, there must be another lactate source. This could indicate that APOE ε4 cells undergo increased rates of reductive carboxylation of glutamine, in which glutamine enters the TCA cycle and goes backwards through the TCA cycle to produce lactate (Fig. 2C). Alternatively, APOE ε4 cells may mobilize glucose stores such as glycogen to produce more lactate. In future experiments, we will investigate the fate of glucose and other metabolites in iPSC-BMEC by metabolic mass spectrometry. We will also measure metabolite transport by culturing iPSC-BMEC on Transwell filters to demonstrate how APOE genotype alters glucose transport.

Overall, these experiments give novel insight into how the APOE ε4 genotype decreases BMEC tight junction continuity and glucose uptake in a human derived BMEC model, which could inform how the APOE allele contributes to AD development via cerebral glucose hypometabolism.

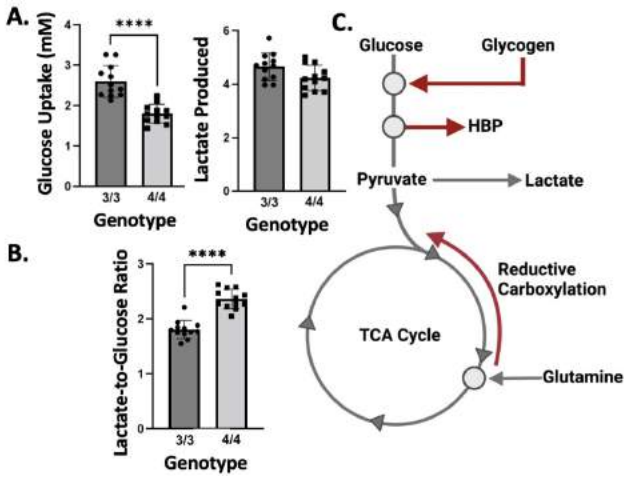


**Figure 2. APOE ε4 iPSC-BMEC took up less glucose but produced similar amounts of lactate compared to APOE ε3 iPSC-BMEC.** A. Glucose and lactate concentrations were measured in the cell culture media at 0 and 24 hours by YSI bioanalyzer. B. Lactate-to-glucose ratio calculated from glucose and lactate concentrations. C. Metabolic pathways that may contribute to altered lactate:glucose ratios. **** $p < 0.00001$.


## ACKNOWLEDGEMENTS

This research was funded by a seed grant from the Brain and Behavior Initiative at the University of Maryland, NIH R01HL140239 to ASMC, the NSF GRFP under Grant No. DGE 1840340 to CMW, and the ASPIRE Undergraduate Research Fellowship to SMZ.


## REFERENCES


[1] 2021 Alzheimer's Disease Facts and Figures Report. [2] Saddiki, H. et al., *PLoS One,* 17(8):e1003289, 2020. [3] Sanabria Diaz, G. et al., *PLoS One,* 8(7): e68860, 2013. [4] Simpson, I. A. et al., *J. Cereb. Blood Flow Metab.*, 28(11):1766-1791, 2007. [5] Zeller, K. et al., *J. Cereb. Blood Flow Metab.*, 17(2):204-209, 1997. [6] Marottoli, F. M. et al., *Front. Cell Dev. Biol.*, 9:1-20, 2021. [7] Förster, C. et al., *J. Physiol.*, 565(2):475-486, 2005. [8] Neal, E. H. et al., *Stem Cell Reports*, 12(6): 1380–1388, 2019. [9] Gray, K. M. et al., *Fluids Barriers CNS*, 17(1):1-20, 2020.

SB³C2022
Summer Biomechanics, Bioengineering and Biotransport Conference
June 20-23, Eastern Shore, MD, USA

# OVERCOMING THE FORCE-DEPENDENT INHIBITION OF COLLAGENASE USING MACROPHAGES

**R.R. Jamieson, S.E. Stasiak, R.D. Augspurg, N. Bharath, S.M. Siadat, J.W. Ruberti and H. Parameswaran**

Department of Bioengineering, Northeastern University, Boston, MA, U.S.

## INTRODUCTION

Excessive deposition of fibrillar collagens is associated with a wide range of diseases including cancer[1] and fibrosis, cardiovascular[2], lung[3], eye[4] and age-related diseases. In all these diseases, it is becoming increasingly apparent that collagen deposition is not merely a byproduct of disease progression, but an important factor that drives disease progression[5]. Thus far attempts to restore collagen homeostasis have focused on genetic and molecular signaling pathways that regulate collagen synthesis[6]. However, in addition to these, there are *mechanical* factors that can play a crucial role in driving fibrosis. One such factor that has not received much attention is the force-dependent inhibition of the collagenase enzymes that degrade collagen[7,8].

In healthy tissue, collagen is maintained in a homeostatic balance between processes that regulate production and organization of collagen and the activity of collagenase enzymes and their inhibitors that regulate collagen degradation. This homeostatic balance can be disrupted in disease, especially in inflammatory environments. The resulting changes in the composition and mechanics of the local extracellular environment are sensed by cells, causing them to switch their physical connections from cell-cell contacts to integrin-based cell-matrix contacts[9,10]. This switch in connectivity increases the strain on the collagen fibers within the extracellular matrix, slowing down the rate of collagen degradation. Collagen deposition also causes an increase in matrix stiffness which can increase the force that cells exert on the collagen fibers, leading to a further decrease in the rate of collagen degradation. Thus, the force-dependent inhibition of collagenase is a critical factor that can create a detrimental, self-sustaining feedback loop that promotes more collagen deposition and disease progression.

Here we report that the force-dependence of collagen fiber degradation can be overcome using macrophages and a milk fat protein Mfge8. We show that in contrast to collagenase, tensile strain on collagen fibers accelerates the degradation of fibrillar collagen by macrophages and Mfge8.

## METHODS

Collagen degradation was quantified as the normalized change in the stiffness of collagen gels over time. To measure stiffness, gels were mounted on a dual-mode lever arm force transducer system capable of stretching gels uniaxially. First, gels were preconditioned using five triangular displacement stretch-relaxation cycles with a maximum displacement of 2.2mm to eliminate viscoelastic effects, then baseline force-length measurements were collected (t=0 min). Stress-strain curves were generated by dividing force output during stretch by the cross-sectional area of each gel to obtain stress and dividing the displacement of the gel by the initial gel length to obtain strain. Stiffness was reported as the Young's modulus of gels measured at 6% strain. For collagenase experiments, collagen gels were held at either 0% strain or 7.5% strain during 45 minutes of treatment with bacterial collagenase (*Clostridium histolyticum*, 34 μg/ml, pH = 7.4). Stiffness was measured every 15 minutes and normalized by the stiffness of each gel at baseline prior to the addition of collagenase.

To measure collagen degradation by macrophages, MH-S murine alveolar macrophages were treated with 0.25 μg/ml lipopolysaccharide (LPS) and 10 μg/ml recombinant human Mfge8 protein and incubated with collagen gels at a density of 200,000 cells/gel for up to 1 hour. Experiments were performed within custom 3D-printed collagen stretcher devices that were designed to hold collagen gels stretched during incubation with macrophages. After incubation, gels were removed from the devices and stiffness measurements were collected. At each time point, degradation was quantified as the stiffness of gels incubated with macrophages normalized by the stiffness of control gels incubated under the same conditions without any macrophages present. To inhibit force in macrophages, cells were pretreated with the Rho-associated kinase (ROCK) inhibitor Y-27632 at 100 μM for 1 hour. After 1 hour of pretreatment, macrophages were incubated with collagen gels for 1 hour in the stretcher devices in the presence of Mfge8, LPS, and 100 μM Y-27632.

SB³C2022-075

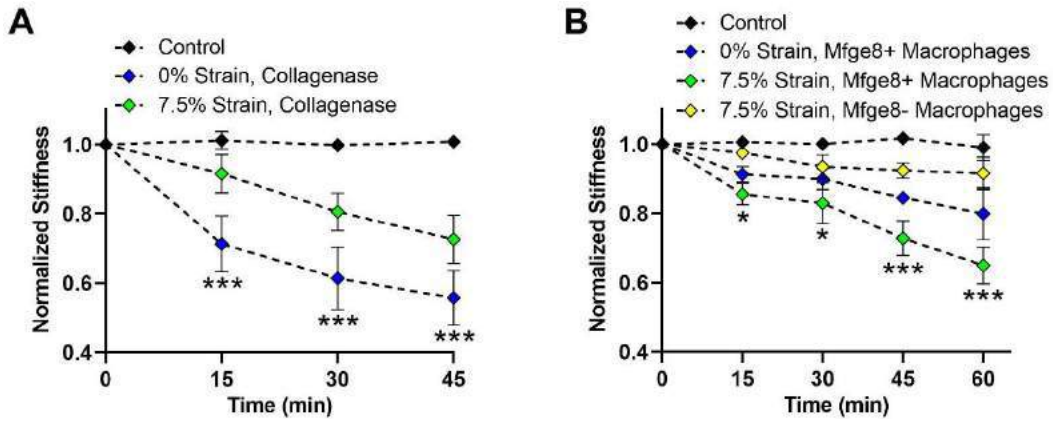


**Fig. 1 - (A) Normalized stiffness over time for untreated control gels (black, N=5), gels held at 0% strain during collagenase treatment (blue, N=6), and gels held at 7.5% strain during collagenase treatment (green, N=6). (B) Normalized stiffness over time for untreated control gels (black diamonds, N≥3), gels held at 0% strain during incubation with Mfge8-treated macrophages (green, N≥5), gels held at 7.5% strain during incubation with untreated macrophages (yellow, N≥4), and gels held at 7.5% strain during incubation with Mfge8-treated macrophages (blue, N≥5). Statistical significance is represented by (*) for P<0.05, (**) for P<0.01, and (***) for P<0.001.**

## RESULTS

***Tensile strain on collagen fibers inhibits degradation by collagenase enzymes, but accelerates degradation by macrophages and Mfge8:***

**Figure 1A** shows the change in normalized stiffness over time for untreated control gels (black), gels held at 0% strain (blue), and gels held at 7.5% strain (green) during collagenase treatment. A two-way ANOVA test with time and strain as the independent factors confirmed that time and strain both had a significant effect on normalized gel stiffness (time: P<0.001, strain: P<0.001), and the effect of time was dependent on whether strain was present (P<0.001). Unstrained gels experienced a significantly larger decrease in normalized stiffness compared to gels held at 7.5% strain during collagenase treatment at every time point (Tukey test, 15 min: P<0.001, 30 min: P<0.001, 45 min: P<0.001, **Fig. 1A**). This was an expected result, since evidence demonstrating the strain-dependence of collagenase activity has been previously demonstrated[7,8]. Although the strain-dependence of collagenase activity has been previously reported, the effect of strain on the degradation of fibrillar collagen by macrophages has not been explored. Here, we applied strain to collagen gels during incubation with macrophages treated with Mfge8 and measured the change in gel stiffness over the course of 1 hour. **Figure 1B** displays the results from these experiments, where the normalized stiffness of gels from each treatment group are displayed as a function of time. A two-way ANOVA analysis with time and strain as the independent factors revealed that time and strain both significantly affected normalized gel stiffness (time: P<0.001, strain: P<0.001), and the effect of time was dependent on whether strain was present (P = 0.002). At every time point, collagen gels held under tension experienced a larger decrease in gel stiffness after incubation with Mfge8-treated macrophages (Tukey test, 15 min: P=0.034, 30 min: P=0.015, 45 min: P<0.001, 60 min: P<0.001, **Fig. 1B**).

***Cytoskeletal tension is necessary for macrophages to degrade strained collagen fibers:***

Our experiments using Mfge8-treated macrophages to degrade collagen fibers under tension revealed that strain within collagen networks led to a higher degree of degradation by macrophages, which directly contrasts the results of our experiments using collagenase. Based on this finding, we hypothesized that if the degradation of fibrillar collagen by Mfge8-treated macrophages is enhanced when force is applied to collagen fibers, then eliminating the ability of macrophages to generate force should diminish the effect of strain on collagen degradation. To test this hypothesis, we incubated Mfge8-treated macrophages with strained collagen gels for 1 hour in the presence of 100μM of the ROCK inhibitor Y-27632. Y-27632 reduces force generation in cells by inhibiting myosin light chain phosphorylation and removing ROCK-mediated inhibition of myosin light chain phosphatase[11]. The results from this experiment revealed that incubating Mfge8-treated macrophages with Y-27632 diminished the effect of strain on gel stiffness after 1 hour (Mann-Whitney Rank Sum test, P=0.005, N=8).

## DISCUSSION

Degrading excess collagen deposited in fibrotic tissue is challenging due to the strain-dependent inhibition of collagenase enzymes that degrade fibrillar collagen. In this study, we show that macrophages can degrade strained collagen fibers in the presence of the milk fat protein Mfge8. Further, we demonstrate that the force-dependence of collagen fiber degradation is reversed in the case of Mfge8 and macrophages, with strain accelerating the degradation of fibrillar collagen. We conclude that if macrophage degradation of collagen is enhanced by the presence of force, the combination of Mfge8 and macrophages could serve as a potential therapy to counteract pathological collagen remodeling in fibrosis.

## ACKNOWLEDGEMENTS

This work was supported by the NSF CAREER grant #2047207 [HP].

## REFERENCES

[1] Alowami, S., et al., *Breast Cancer Res*, 5:R129-135, 2003. [2] Hoffman, J., et al., *Am J Physiol Lung Cell Mol Physiol*, 308: L1002–L1013, 2015. [3] Mostaco-Guidolin, L.B., et al., *Am J Respir Crit Care Med*, 200:431-443, 2019. [4] Zhao, X., et al. *Investig Opthalmol Vis Sci*, 45:4023-4034, 2004. [5] Jamieson, R.R., et al., *J Appl Physiol*, 6:1635-1645, 2021. [6] Hostettler, K.E., et al., *Respir Res*, 15: 1571-1579, 2014. [7] Bhole, A.P., et al., *Philos Trans R Soc A Math Phys Eng Sci*, 367:3339-3362, 2010. [8] Flynn, B.P., et al., *PLoS One*, 5:e12337, 2010. [9] Polio, S.R., et al. *Sci Rep*, 9:9564-9576, 2019. [10] Krishnan, R., et al. *Am J Physiol Cell Physiol*, 300: C146-C154, 2011. [11] Ishizaki, T., et al. *Mol Pharmacol*, 5:976-983, 2000.

SB³C2022
Summer Biomechanics, Bioengineering and Biotransport Conference
June 20-23, Eastern Shore, MD, USA

# AN EXPERIMENTAL AND NUMERICAL INVESTIGATION OF CARDIAC TISSUE-PATCH INTERRELATION

**G. Basara (1), G. Bahcecioglu (1), X. Ren (1), P. Zorlutuna (1,2)**

(1) Department of Aerospace and Mechanical Engineering, University of Notre Dame, Notre Dame, Indiana, USA
(2) Department of Chemical and Biomolecular Engineering, University of Notre Dame, Notre Dame, Indiana, USA

## INTRODUCTION

Myocardial infarction (MI) is one of the most common cardiovascular diseases and results in damaged cardiac tissue. The limited healing capacity, specific fibrillar structure and the electrical conduction of the adult cardiac tissue make the damaged myocardium regeneration one of the most challenging topics in regenerative medicine. Tissue-engineered cardiac patches have great potential as a therapeutic treatment for MI. However, heart regeneration through patches is still limited, due to electromechanical coupling and resemblance with the heart tissue, and high durability of the patch.

Many studies have focused on assessing the effect of the patches on the damaged tissue by evaluating the promotion of angiomyogenesis, through reduction of the scar tissue size, and improvement of cardiac functions [1]. Yet, the mutual interaction of cardiac patches with the healthy tissues has not been completely explored, which is crucial to understand in order to enhance the therapeutic effect of cardiac patches.

Here, we investigated the impact of the cell-free or cellular patch on the healthy beating tissue underneath, as well as the effect of this beating tissue on the cells encapsulated in the patch. As the cell source, we used human induced pluripotent stem cells (hiPSCs)-derived cardiomyocytes (iCMs), which have recently become an attractive therapeutic solution to replace the lost cardiac tissue [2]. In this study our aim is to 1) investigate the effect of placing the cell-free patch on the beating and phenotypical characteristics of the underlying iCMs (the beating tissue), 2) encapsulate iCMs in the patch and observe their effect on the beating tissue, 3) create a numerical model to understand the effect of cyclic contraction and relaxation (cardiac cycle) of the beating tissue on the patch, and 4) investigate the consequences of this cardiac cycle on the encapsulated iCMs in the cardiac patch.

## METHODS

hiPSCs were differentiated to iCMs following a well-established protocol [3]. iCMs seeded on 12 mm glass coverslips were used as the underlying healthy beating tissue. Gel patches were prepared from a solution containing gelatin methacryloyl (GelMA) (10%) and visible light photoinitiators, ruthenium, and sodium persulfate (2%) in PBS. To test the effect of cell-free patch on the beating tissue, a 7 mm ring-shaped polydimethylsiloxane (PDMS) mold was placed on the healthy tissue and GelMA solution (17 µL) was placed in the mold, crosslinked using visible light (3s), and further crosslinked enzymatically using microbial transglutaminase (8 % *w/v* in cell culture media, 30 mins at 37 °C). To observe the effect of the cellular patch on the healthy tissue, iCMs were mixed with GelMA solution (40 mil/mL) prior to placing on top of the beating tissue and crosslinking the gel. To test the effect of the beating healthy tissue on the encapsulated iCMs, a dynamic cell culture model was created by placing the cellular patch on the beating tissue. To prepare the static cell culture model, cellular patches, were placed on non-beating iCMs on 12 mm glass coverslips. The samples were kept for 7 days or 21 days in culture before doing any experiments with media changes every 3 days. Immunostaining was performed by following the manufacturer's instructions and the samples were stained for sarcomeric alpha-actinin. Sarcomere length was then quantified using ImageJ. For beating characterization, brightfield videos were taken and analyzed using an in-house MATLAB code adapting a block-matching algorithm to identify the beating velocity and frequency. To study the effect of the contraction of the beating tissue on the gel deflection, a simple numerical model was created using COMSOL Multiphysics. The force applied by the beating tissue on the gel when contracted was measured using a nano-indenter through dwell experiments.

For the synchronization analysis of the patch and the healthy tissue, the $Ca^{2+}$ flux staining was performed, and videos were taken at the boundary of underlying beating iCMs and cellular patch on top while keeping the focus on the underlying beating cells. The videos were then analyzed using a custom-made MATLAB code. The mean ± standard deviation was reported. The student's t-test was used to find any

SB³C2022-076

statistically significant differences and $p<0.05$ was considered statistically significant.

## RESULTS

When the cell-free patch was placed on the beating tissue, the sarcomere length of the underlying iCMs increased significantly ($p = 0.0014$), while the beating velocity and frequency decreased ($p = 0.0010053$ and non-significant respectively) (**Figure 1**). On the other hand, when iCMs were encapsulated in the patch, the beating velocity and the frequency of the underlying healthy tissue increased to a healthy beating velocity (8 µm/s) and frequency (0.67 Hz) level of iCMs which has been previously reported [4] (**Figure 2**). A numerical model was used to understand the deformation exerted by the contraction of the healthy beating tissue on the cell-free gel placed on top as a patch. When the underlying iCMs contracted, the total displacement of the patch was 850 µm on the bottom surface of the gel, and 94.6 µm on the top surface (data not shown). The maximum total displacement measured at the bottom surface corresponds to an approximately 12% strain. Experimentally, using a video showing the deflection of the patch, the difference between the contracted and the relaxed gel was measured, and the strain was calculated as 12.5%, validating the numerical model. When the cellular patches were placed on the healthy beating tissue, the beating velocity and the frequency of the encapsulated cells improved compared to patches in static condition on both day 7 and day 21 ($p < 0.01$ for day 21 frequency result) (**Figure 3**). The $Ca^{+2}$ transient profiles revealed synchronized beating of the iCMs encapsulated in the patch and the healthy beating tissue underneath, which is crucial for gel-healthy tissue integration (**Figure 4**).

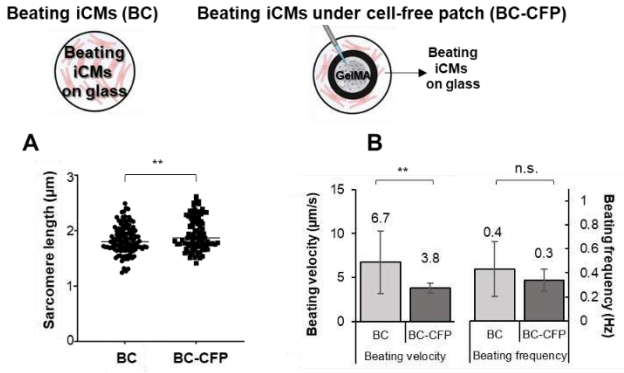


**Figure 1:** (A) Sarcomere length quantification in µm. (B) Average beating velocity and frequency of BC and BC-CFP.

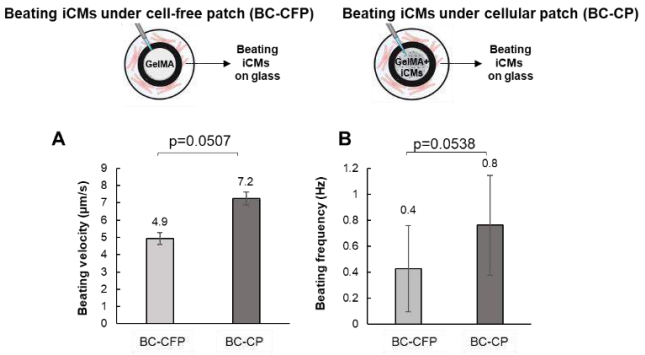


**Figure 2:** Evaluation of the effect of the cells encapsulated in the patch on the beating tissue D7. (A) Beating velocity of beating iCMs under the acellular patch (BC-CFP) and the cellular patch (BC-CP), (B) Beating frequency of BC-CFP and BC-CP.

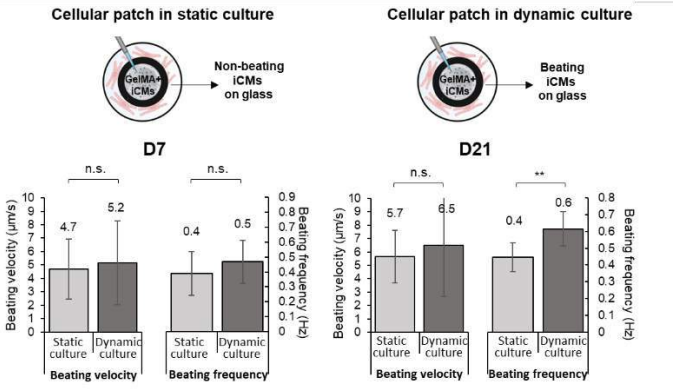


**Figure 3:** Average beating velocity and frequency of encapsulated iCMs in the static and dynamic culture at day 7 and day 21.

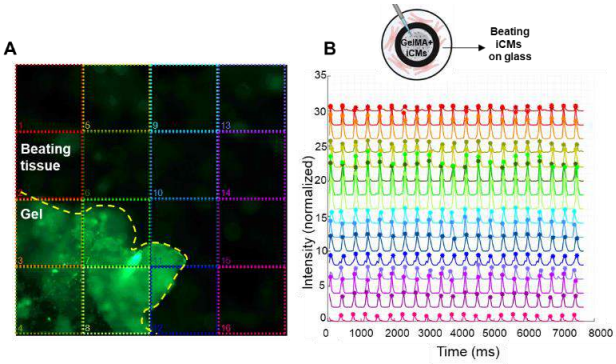


**Figure 4:** Synchronization analysis on D7. (A) A representative snapshot from calcium flux time-lapse recording (the image was divided into 16 groups and each group was represented with a different color), (B) $Ca^{2+}$ transient profile of each designated group as extracted from these time-lapse recordings.

## DISCUSSION

Although, placing the cell-free patch on the healthy tissue had an adverse effect on the beating characteristics of the underlying healthy tissue, encapsulating iCMs in the patch improved these characteristics. This observation is in parallel with the findings from the literature [5] and most likely resulting from the released secretion and the beating of the encapsulated iCMs. We hypothesized that the cyclic deformation caused by the healthy beating tissue on the patch would result in the maturation of the encapsulated iCMs. We observed some improvement in the beating characteristics; however, the change was not significant. The strength of this paper is to evaluate each aspect of the patch and healthy tissue separately while also investigating the patch-tissue integration. One limitation of this paper may be focusing only on the relation of the patch with beating heart tissue and not having scar tissue.


## ACKNOWLEDGEMENTS

This study was funded by NIH Award #1 R01 HL141909-01A1, NSF Award #1651385.


## REFERENCES


[1] Tang, J., et al., *Science Advances*, 4, 2018.
[2] Ishida, M. et al., *Transplantation*, 103:291-298,2019.
[3] Lian, X. et al., *Nature Protocols*, 8:162-175, 2013.
[4] Huebsch, N., *Tis. Eng. Part C*, 21: 467-479, 2014.
[5] Mei, X. et al., *Front. Cardiovasc. Med.*, 7, 2020.

SB³C2022
Summer Biomechanics, Bioengineering and Biotransport Conference
June 20-23, Eastern Shore, MD, USA

# FINITE ELEMENT-BASED, KINEMATICALLY-DRIVEN, SUBJECT-SPECIFIC MODEL OF HUMAN CERVICAL FACET CAPSULE LIGAMENTS

**M. Nikpasand (1), R. Abbott (2), C. C. Kage (2), V. H. Barocas (3), A. M. Ellingson (2)**

(1) Mechanical Engineering, University of Minnesota, Minneapolis, MN, USA
(2) Rehabilitation Medicine, University of Minnesota, Minneapolis, MN, USA
(3) Biomedical Engineering, University of Minnesota, Minneapolis, MN, USA

## INTRODUCTION

Neck pain is a leading cause of activity limitation and years lived with disabilities [1]. Many sources for neck pain have been recognized, including the highly innervated facet capsular ligament (FCL) [2]. To understand the FCL's role in neck pain, the interactions between the FCL and other spinal components must be examined. One approach is to develop a finite element (FE) model of the cervical spine segment, simulating the motion segment and its components' behaviors under physiological loading conditions. This approach can be particularly attractive when patient anatomical and kinematic data are available.

The goal of this study was to develop and demonstrate a method to create 3D subject-specific models of the lower cervical spine (C4-C7), with focus on FCL biomechanics. This model incorporates spine geometry and replicates individual vertebral kinematics.

## METHODS

In this study, a kinematically-driven, subject-specific model of a healthy 23-year-old female's cervical FCL was developed and simulated in FEBio Studio [3]. The geometries of C4–C7 vertebrae were created by segmenting the skeletal surfaces out from the Computed Tomography (CT) scans (0.22x0.22x0.6 mm; 1.8 mSv; Siemens AG, Munich, Germany) of the participant's cervical spine. The FCL geometries were generated by morphing an existing FCL model [4] to the extracted facet joint geometry following [5].

The fiber structures and material characteristics of the tissue were extracted from available cervical FCL data [6–8] and were incorporated in a hybrid multiscale model [9] to generate fiber characteristics that are subsequently used in FEBio to define tissue material.

To generate kinematic data for the FE model, the participant performed flexion-extension, axial rotation, and lateral bending (three trials each) during biplane videoradiography acquisition (160mA, 70kV, 30Hz, 0.32mSv/trial). Undistortion (DSX Suite, C-Motion Inc., USA) and calibration [10] were completed, and volumetric shape-matching was performed for levels C4-C7 [11]. Data were filtered with a moving average filter and relative kinematics were extracted (Kinematics Toolbox v4.0, Becky Lawrence, PT, PhD).

### *3D volumetric mesh of vertebral bodies*

The CT image stack was imported into an image processing software (Materialise Mimics, v23, Materialise NV, Belgian) and the 3D vertebral shells of C4-C7 were segmented out using an automatic threshold mask based on pixel intensity, followed by manual refinement. The resulting 3D surface meshes (triangle with 3 nodes – tri3) were created and exported in the stereolithography (STL) format using a custom MATLAB program which ensures retaining the same coordinate system between the extracted geometries and the shape-matching images. The 3D surface meshes were then re-meshed (4 nodes tetrahedral – tet4) in Materialise 3-Matic (v15, Materialise NV, Belgian) to construct volumetric geometries of the cervical vertebrae. The 3D volumetric meshes of vertebral bodies were imported into the FEBio Studio software as rigid bodies (Fig.1 on next page).

### *3D geometry of FCLs*

Extraction of FCL geometry from participants *in vivo* is not feasible. Therefore, we used Zarei et al.'s method [5] to morph an existing L3-L4 FCL geometry [4] (Fig. 1a) onto the facet joint areas of our model. Briefly, the area that FCL attaches to the joint's bones on the new model (Fig. 1b) were picked such that they match the corresponding insertion regions on the available micro-CT geometry. Then a set of linear equations was solved to map every point on the reference geometry (micro-CT) to its corresponding node on the target geometry (new geometry) (Fig. 1c-i). The insertion points on the bones were used as known boundary conditions to solve these equations. Then, a re-meshing technique [12] was used to generate high quality 4-node quadrilateral (quad4) elements (Fig. 1j). Finally, the new surface mesh was extruded to an average thickness of $0.42 \pm 0.07$ mm (mean $\pm$ std) for cervical FCL [8] to generate a volumetric 8-node hexahedron (hex8) mesh for each FCL (Fig. 1k).

SB³C2022-077

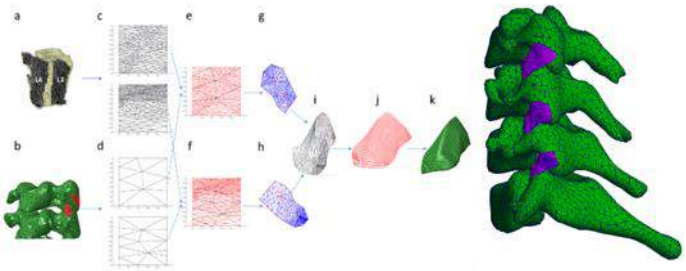

**Figure 1: FCLs FE development. (a) Micro-CT of reference geometry. (b) Insertion regions of target geometry. (c-i) Mapping points of the reference geometry to its corresponding node on the target geometry. (j) High quality quad4 elements. (k) Final FCL FE mesh. (l) FE model of C4-C7 and corresponding FCLs**

***Fiber structures and material properties for FCLs***

The cervical FCL is a collagenous tissue with high spatial heterogeneity in its collagen organization [8]. To incorporate fiber heterogeneity into our continuum FE model, we used a hybrid method [9]. First, a set of previously inferred fiber structures from quantitative polarized light imaging (Fig. 2a) [6,7] was used to generate fiber alignment maps and morph them onto the FCL surface mesh (Fig. 2c) [5,13]. Next, structural information for each finite element was used to generate a 3D Delaunay network in MATLAB (R2019a, MathWorks, Natick, MA) to serve as a representative volume element (RVE). Additional details on network generation and its governing equations are available in [14]. Each RVE network then underwent the network-to-continuum scheme that was described in [9] to calculate the fiber parameters for a three-orthogonal-fiber-family strain energy density function for that network. This fiber-based strain energy density function was combined with a neo-Hookean ground matrix in FEBio to form a coupled solid mixture material for each element (Fig. 2d).

***Loading and boundary conditions***

Prescribed displacements were applied to the bone geometries to mimic the kinematics extracted from biplane videoradiography. To simulate each motion in FEBio, the C7 vertebra was held fixed and the relative motions of C4-C6 vertebrae were calculated with respect to it. Since FEBio defines the rotation of a rigid body in terms of quaternion angles, the relative Euler angles measured for each vertebral body were converted to their corresponding quaternion angles and imported into FEBio as load curves. The FCL-bone attachment areas were defined as tied connections controlled by the bone motion.

## RESULTS

We demonstrated a successful implementation of this method to generate nine 3D, subject-specific FE models of a healthy 23-year-old female's cervical spine and simulated them in axial rotation, flexion-extension, and lateral bending motions to calculate the stress field over the FCLs. Fig. 3a, b shows the average of von Mises stress and the average of the top one percent von Mises stress over the FCLs when the head is in its ultimate position in these motions. Error bars in this figure represent the range of von Mises stresses across three trials for each motion. Fig 3c is a representative image of the von Mises stress distribution in left FCLs and vertebrae position for extension.

As can be seen in Fig. 3a, b, the results were, as expected, roughly symmetric between the right and left sides (e.g., the stresses in the C4-C5 and C5-C6 FCLs were high in ipsilateral axial rotation), but some differences were also observed (the von Mises stress was higher on the left C4-C5 FCL for both left and right lateral bending), and there was an asymmetry in the flexion-extension response, with larger stresses on the left side.

## DISCUSSION

The primary limitations of the proposed approach stem from the fact that FCL fiber organization and geometry cannot be captured accurately with available imaging technologies. To address these limitations, we rely on *ex vivo* structural data from literature along with the fact that the FCL encapsulates the facet joint and must conform to joint geometry, which is reliably derived from CT. Nevertheless, it is clear that there are significant individual differences that cannot be measured *in vivo* at present.

Despite these limitations, the current study provides a methodology to create a subject-specific model of the cervical FCLs (C4-C7) and can investigate various clinical questions by coupling experimental kinematics with multiscale computational models.

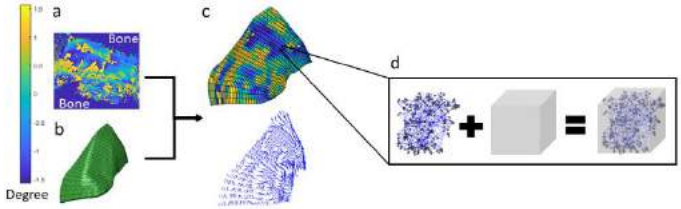


**Figure 2: FCLs fiber structure. (a) Fiber orientation from quantitative polarized light images. (b) FE meshes of left C4-C5 FCL. (c) Mapped fiber orientation over FE mesh. (d) The solid mixture material for each element.**

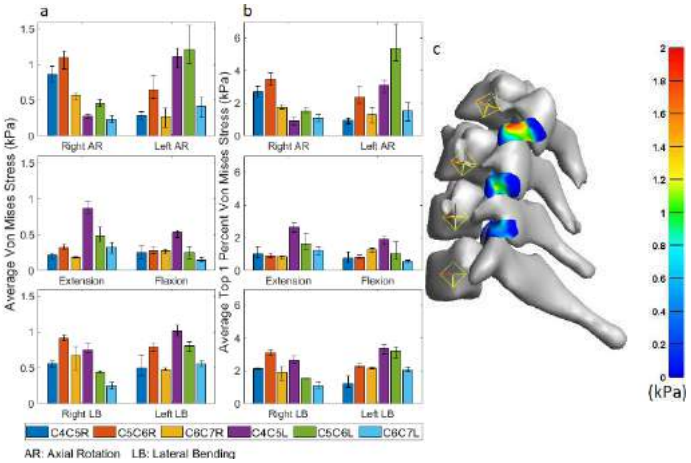


**Figure 3: Comparison between von Mises stress over FCLs in different motions and different levels. (a) Average of von Mises stress. (b) Average of top one percent von Mises stresses. Error bars in this figure represent the range of von Mises stresses across three trials for each motion. (c) Von Mises stress in extension for the 3rd trial. Colorbar is in kPa.**


## ACKNOWLEDGEMENTS

Funding was provided by NIH grants U01 AT010326, R03 HD09771, and T32 AR050938.


## REFERENCES


[1] Safiri, S. et al., BMJ, 2020. [2] O'Leary, S. A. et al., Annu. Rev. Biomed. Eng. , 2018. [3] Maas, S. A. et al., J. Biomech. Eng., 2012. [4] Claeson, A. A. et al., Spine J., 2017. [5] Zarei, V. et al., J. R. Soc. Interface, 2018. [6] Quinn, K. P. et al., J. Biomed. Opt., 2009. [7] Quinn, K. P. et al., Ann. Biomed. Eng. 2011. [8] Ban, E. et al., J. Biomech. Eng., 2017. [9] Nikpasand, M. et al., J. Elast., 2021. [10] Brainerd, E. L. et al., J. Exp. Zool. A. Ecol. Genet. Physiol., 2010. [11] Akhbari, B. et al., J. Biomech., 2019. [12] Liang, L. et al., Biomech Model Mechanobiol, 2017. [13] Zarei, V. et al., J. Biomech. Eng., 2000.

SB³C2022
Summer Biomechanics, Bioengineering and Biotransport Conference
June 20-23, Eastern Shore, MD, USA

# DEVELOPMENT OF A CONTINUUM DAMAGE MODEL TO PREDICT ACCUMULATION OF SUB-FAILURE DAMAGE IN TENDONS

**Alexandra N. Allan (1, 2), Jared L. Zitnay (1, 2), Steve Maas (2), Jeffrey A. Weiss (1, 2, 3)**

(1) Department of Biomedical Engineering & Scientific Computing and Imaging Institute, University of Utah, Salt Lake City, Utah, USA
(2) Scientific Computing and Imaging Institute, University of Utah, Salt Lake City, Utah, USA
(3) Department of Orthopaedics & School of Computing, University of Utah, Salt Lake City, Utah, USA

## INTRODUCTION

Many painful and physically debilitating conditions involve sub-failure mechanical damage to seemingly intact connective tissues such as tendons and ligaments. We found that the amount of denatured collagen in rat tail tendon (RTT) fascicles increased over experiments of cyclic loading to a constant load level (creep cyclic fatigue) with fluorescently tagged collagen hybridizing peptides (CHPs) that bind to denatured collagen (Fig. 1A). The results for collagen denaturation during the cyclic loading of tendons combined with CHP staining provides us with valuable information to formulate constitutive models that predict sub-failure damage in tendons through the mechanism of collagen molecular damage.

Therefore, the objective of this study was to develop, implement, and test the ability of a new CDM that produces the sub-failure damage behavior seen in our RTT fascicle creep cyclic fatigue loading data. The damage model was designed to predict the specific damage mechanisms seen in our experimental creep cyclic fatigue stress-strain data collected by Zitnay et al. (Fig. 1B) [1]. It encompasses a modified version of the combination discontinuous and continuous damage model presented originally by Balzani et al. [2], convolved with the elastic undamaged material used to describe a tendon material. The damage formulation was accurately able to capture the sub-failure damage accumulation seen in the creep cyclic fatigue and provide predictions for other loading scenarios.

## METHODS

The constitutive model in the present study was created to describe the two softening mechanisms seen in our stress-strain creep cyclic fatigue experimental data (Fig. 1B) conducted by Zitnay et al. [1]. During the experiment, 6 month old rat tail tendon (RTT) fascicles were fatigue loaded to 40% of their UTS at 0.4, 4, or 40% $s^{-1}$ until failure (Fig. 1A) [1]. We plotted and analyzed the stress-strain data from the 0.4% $s^{-1}$ experiments and characterized the damage behavior through two mechanisms. The first mechanism during this experiment was defined as the preconditioning effect in which the fibers in the RTT fascicle completely straightened out from their crimped formation (Fig. 1B, 1). The second mechanism was characterized as collagen damage (Fig. 1B, 2). The collagen damage is thought to have occurred over the entire experiment, however, it has a small contribution up until the fibers become un-crimped and are able sustain their maximum load.

In our finite element (FE) models, the RTT fascicle undamaged elastic constitutive material was composed of a matrix and fibers described by the Coupled Veronda-Westmann and exponential-linear materials within our finite element program, FEBio. This undamaged elastic material was convolved with a modified CDM model adapted from Balzani et al. [2]. Specifically, the internal damage variable $D$ scaled the initial strain energy of the fibers $\Psi_f^0$, while the stress free configuration $c$ was subtracted off to shift the stress strain curve to the right for increasing cycles:

$$\Psi_f = (1-D)\Psi_f^0 - c \text{ with } c = \Psi_f^0\left(\boldsymbol{C} = \boldsymbol{I}\right), \quad (1)$$

where $\boldsymbol{C}$ is the right Cauchy Green deformation tensor (a function of the deformation gradient $\boldsymbol{F}$).

The novelty of the Balzani damage model is the inclusion of two interrelated mechanisms described as continuous and discontinuous damage. The continuous damage formulation accumulated damage in the loading and reloading portion of each cycle. It was mathematically described as the change in the undamaged effective strain energy of the fibers over time:

$$\beta = \left\langle \tilde{\beta} - \tilde{\beta}^{ini} \right\rangle, \quad \tilde{\beta} = \int_0^t \left\langle \dot{\Psi}_f^0(s) \right\rangle ds \cdot \quad (2)$$

Here the internal variable $\beta$ is the measure of the continuous damage function and $\tilde{\beta}_{ini}$ is the value of $\tilde{\beta}$ at the initial damage state to ensure the damage evolution only begins to accumulate when the strain energy

increases above its initial state. The variable $t$ is the time associated with the current loading situation, while the variable $s$ is the time associated with the loading history, where $t \in \mathbb{R}^+$ and $s \in \mathbb{R}^+$. On the other hand, the discontinuous damage function accumulated damage based on the maximum strain energy achieved in the loading history up to the current state:

$$\gamma = \max_{s\in[0,t]} \left\langle \Psi_f^0 - \Psi_{f,ini}^0 \right\rangle \cdot \tag{3}$$

Here, $\Psi_{f,ini}^0$ is the strain energy density of the fibrils at their initial state [13]. We modified the Balzani damage model formulations to represent increases in damage by the addition of the preconditioning effect $D_1$ and collagen damage $D_2$ mechanisms seen in RTT fascicles through:

$$D(\beta,\gamma) = D_1(\beta,\gamma) + D_2(\beta,\gamma) \cdot \tag{4}$$

We then optimized our material parameters to the creep cyclic fatigue experimental data and used this model to predict other common tendon loading scenarios.

## RESULTS

All models were able to predict the creep cyclic fatigue damage over the number of cycles with a small standard deviation amongst models (Fig. 2A, grey shading). The continuous damage function for all models linearly increased until it began to incline near the failure point (Fig. 2B, purple line). The discontinuous damage function increased slowly in a sigmoid fashion up to failure (Fig. 2B, green line). The standard deviation for the continuous damage grew from minimal to marginal over the number of cycles (Fig. 2B, purple shading), while the discontinuous damage standard deviation remained fairly large through the entire test (Fig. 2B, green shading). When comparing to experimental stress-strain data, the models were able to closely reproduce the experimental creep cyclic fatigue experimental stress-strain curve by Zitnay et al. (Fig. 2C & 2D).

## DISCUSSION

The model validation for the creep cyclic fatigue loading provides us with confidence in our experimental and computational methodologies. To our knowledge, there are no comparable studies in the literature that model creep cyclic fatigue sub-failure damage accumulation in tendons with the combined continuous and discontinuous damage formulations. This new CDM provided the ability to more closely inspect the different mechanisms present during cyclic fatigue damage accumulation by mathematically separating the preconditioning effect and collagen damage mechanisms.

The novelty of this CDM formulation came from adapting the mathematics from the Balzani damage model to simulate tendon sub-failure damage, while also providing the ability to convolve the damage model with other undamaged constitutive materials in FEBio. The Balzani damage model equipped us with the means to capture continuous and discontinuous damage. However, unlike the Balzani damage model and other common models in the literature [2-4], the total damage function scaled the strain energy of the fibers, instead of being more intricately inserted in the calculation of the strain energy density function, allowing different material models to be used. This allows the total damage function to be separate from the undamaged constitutive model, providing flexibility in the FEBio implementation to use any undamaged constitutive material that has a fiber term.

We have created a new continuum damage mechanics model that accurately reproduces and predicts the damage accumulation in tendons over cyclic fatigue loading conditions. The verification models, formulations, user manual, and finite element software are open to the public on the FEBio website, allowing others to expand this damage model to their specific tendon or ligament modeling needs. Thus, this project is advancing our capabilities to model damage accumulation which will increase our understanding of damage mechanisms, prevention strategies, and treatments for tendon-related pathologies.

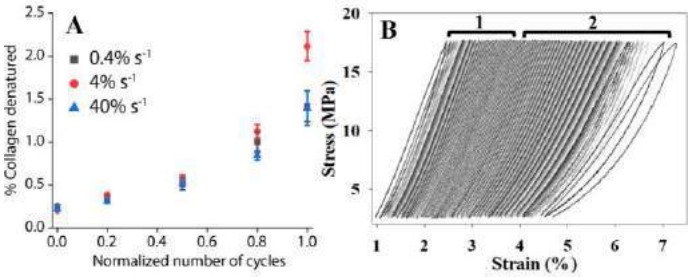


**Figure 1. (A) % collagen denatured from CHP staining and imaging of RTT fascicles subjected to creep cyclic fatigue at 3 different strain rates. Figure adapted from Zitnay et al. [1] (B) The stress-strain curve for the creep cyclic fatigue test with the 1. preconditioning effect and 2. collagen damage mechanisms indicated.**

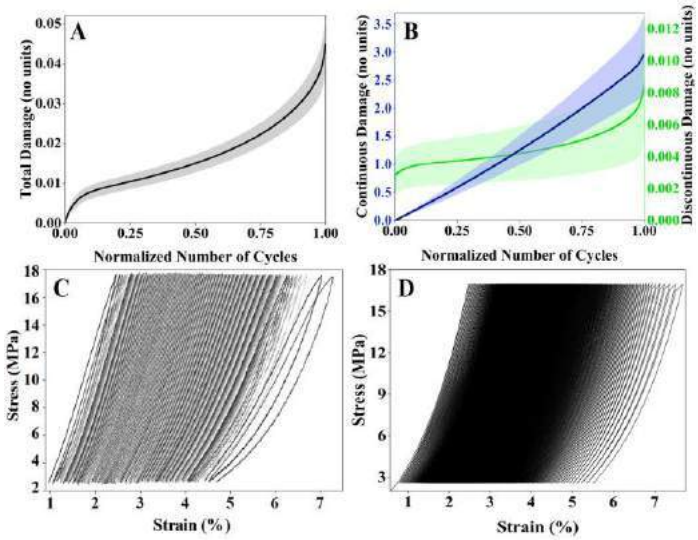


**Figure 2. Creep cyclic fatigue simulation results. (A) Total average damage over the normalized number of cycles for n=4 models with standard deviation from the mean. (B) Average continuous and discontinuous damage over the normalized number of cycles for n=4 models with standard deviation from the mean. (C) Experimental stress strain curves during cyclic creep loading for sample #1. (D) Predicted stress strain curves for the model fit to experimental data from sample #1.**


## ACKNOWLEDGEMENTS

Funding support from NIH #R01AR071358 and #R01GM083925 are gratefully acknowledged.


## REFERENCES


[1] Zitnay J. L. et al., *Sci Adv*, 6(35):eaba27952020. [2] Balzani D., *Comput Methods Appl Mech Eng*, 213-216:139-151, 2012. [3] Marino M., *J Mech Behavior Biomed Mtls*, 97, 2019. [4] Liao H., *J Biomech*, 32(2):183-188, 1999.

SB³C2022
Summer Biomechanics, Bioengineering and Biotransport Conference
June 20-23, Eastern Shore, MD, USA

# ON PREDICTING GROUND REACTION FORCE FROM THIGH AND SHANK IMU DATA DURING JUMP LANDINGS: AN IN VITRO STUDY

**Mirel Ajdaroski (1), So Young Baek (2), James A. Ashton-Miller (2), Amanda Esquivel (1)**

(1) Mechanical Engineering, University of Michigan-Dearborn, Dearborn, MI, United States
(2) University of Michigan- Ann Arbor, Ann Arbor, MI, United States

## INTRODUCTION

In recent years, the development of wearable sensors has emerged as a useful alternative to camera-based laboratory motion capture methods for gait analysis and rehabilitation research (Arif and Kattan). One type of wearable sensor, an inertial measurement unit (IMU), consisting of orthogonal accelerometers, rate gyroscopes and magnetometers allows for the direct measurement of a body segment's linear acceleration, angular velocity, and environmental magnetic field strength. Within the context of sports, for example, the development and application of post-collection equations are required if IMUs are to be used for the direct assessment of the forces or torques causing injuries like ACL ruptures. Several studies have reported upon the correlation between linear acceleration and ground reaction force (GRF) and have then attempted to develop models relating IMU linear acceleration to GRF (Elvin et al.; Meyer et al.). However, these studies have employed linear models. It may be that the relationship between IMU linear acceleration and GRF is not purely linear and is instead more complex and affected by multiple variables either directly or indirectly. So, the purpose of this study was to develop a mathematical model that can be applied to an IMU's data to obtain more accurate and reliable GRF estimates.

## METHODS

Cadaveric knee specimens were used for this experiment. An in-depth explanation of how specimens were prepared can be found in a previous study (Ajdaroski et al.). Specimens were rigidly fixed in a custom-built testing rig designed to apply different magnitudes of simulated one-legged jump landing GRF in multiples of body weight (xBW); this rig included simulated trans-knee muscle forces and has been validated in previous studies (Ajdaroski et al.; Lipps et al.). Pairs of knee specimens were used, with one knee being randomly selected to be tested under lower (nominally 1-2xBW) GRF, and the other knee tested under higher (nominally 3-4xBW) GRF conditions.

Two, 6-axis load cells (MC3A-1000, AMTI, Watertown, MA) were used to record 3D forces, one at the end of the mid-tibia and the other at the end of the mid-femur. The sampling rate for each load cell was 2 kHz. Using two IMU sensors (APDM Wearable Technologies, Portland, OR), one sensor was rigidly attached to the medial aspect of the mid-tibia stripped of soft tissue, and likewise the other directly to the lateral aspect of the mid femur using Co-flex bands and elastic ties to mitigate potential motion between IMU and bone. IMU sampling rate was 200 Hz. The IMUs were calibrated through the predefined calibration conditions recommended for use with the Moveo Mobility software from APDM. An in-depth overview of the testing procedure can be found in a previous study (Ajdaroski et al.). A fourth order, zero-lag, low pass Butterworth filter was applied to all accelerometer and gyroscope data. Based on the findings of previous studies. which show there is a strong correlation between linear acceleration and GRF, it was assumed that peak vertical linear acceleration (pVLA) occurred at the same time as peak vertical force (pVF) (Elvin et al.).

Because testing resulted in a clustered data set, development of a mathematical model relating values as measured by the IMUs to the GRF was accomplished through the implementation of mixed effect modeling (MEM). A grouping based on specimen was used to account for inter-specimen differences which may arise from body muscle-to-fat ratio, age, sex, weight, and height. Furthermore, because of the lack of usefulness of the random effects in terms of contributing to a useable model, only fixed effects terms were utilized in the construction. The pVF was assumed to be the outcome variable with potential predictor variables assumed to be the 6-axis linear and angular acceleration data from both upper and lower IMUs, as well as body mass. Various combinations, as well as potential interactions between one or more predictor variables were considered. The efficacy of the MEM was determined based on how accurate and how reliable the MEM's predicted values were compared to the measured values. This was assessed through mean absolute percent error (MAPE) values and associated limits of agreements from Bland-Altman plots (LoAs).

SB³C2022-079

## RESULTS

Of the constructed MEMs observed, the best model (Equation 1), consisted of the vertical linear acceleration of the lower leg ($x$), rotational angular acceleration of the lower leg ($y$), the flexural angular acceleration of the lower leg ($w$), and the linear acceleration of the upper leg ($z$) along with a random intercept term.

$$62.5x - \frac{y}{100}(30.5 + 0.539x) + \frac{z}{100}(1.83y + 3w + 0.068yw) - 340 \quad \textbf{(1)}$$

**Table 1: The absolute difference ("ABS. xBW") and the mean absolute percent error (MAPE) between predicted and measured GRF (in units of body weights, xBW) for each xBW range. N denotes the number of observed trials in each xBW range, and SD the standard deviation.**

| xBW Range | N | ABS. xBW ± SD | MAPE ± SD |
|---|---|---|---|
| **0-1** | 162 | 0.07 ± 0.06 | 7.8 ± 5.8% |
| **1-2** | 235 | 0.15 ± 0.10 | 9.9 ± 6.5% |
| **2-3** | 443 | 0.15 ± 0.11 | 6.0 ± 4.5% |
| **3+** | 20 | 0.22 ± 0.12 | 7.4 ± 4.2% |
| **Mean** | | 0.14 ± 0.11 | 7.5 ± 5.6% |

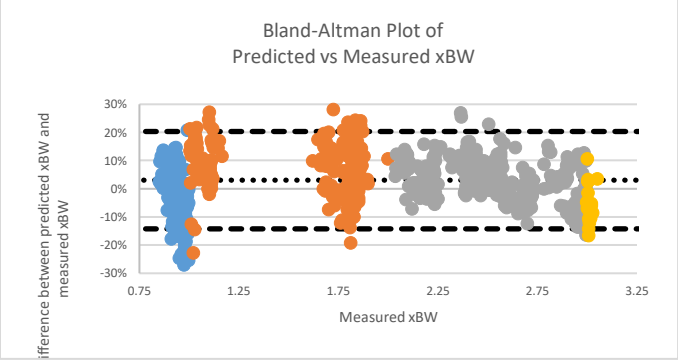


**Figure 1: Bland-Altman plot of the % difference between the predicted and measured xBW (y-axis) and the measured GRF (in units of xBW (x-axis)). Colors represent xBW range**

## DISCUSSION

The purpose of our study was to develop a mathematical model that could accurately and reliably predict GRF using wearable sensors. The results show there was a MAPE of 7.5% between the predicted and measured ground impact force in xBW, indicating our model shows potential in accurately estimating xBW based on IMU data. However, the Bland-Altman LoA (LoA: Lower Limit, -14.2%; Upper Limit, 20.4%) show that the model may not be reliable in its predictive capabilities under all conditions. Importantly, as the landing force was increased in magnitude, the % difference range between predicted and measured decreased. This indicates that model reliability was better for large GRFs than small GRFs (Figure 1). It should be noted that because we removed the soft tissue between the bone and each IMU, these results were not affected by the usual soft tissue artefacts that complicate IMU measurements in living individuals (when IMUs are placed over skin and muscle overlying bone).

A model has been developed to estimate peak GRF (pGRF) via accelerometer data from an IMU during youth gait (Neugebauer et al.). pVGRF was modeled using both a MEM in which a subject-specific random effect was used, as well as a generalized regression model. They reported that the MEM resulted in a MAPE between actual and predicted pGRF of 5.2 ± 1.6% which is lower than that observed in our study. This may be due to the inclusion of speed of action (i.e., running vs walking) as a fixed effect. However, in on-field studies, quantification of speed of an action may not be possible. Alcantara et al. examined the accuracy of a linear regression model to predict pGRF via sacral-mounted accelerometer data across multiple running speeds (Alcantara et al.). Construction of the linear regression model was accomplished using linear acceleration obtained from the IMU, the subject's body mass, step frequency, and running speed as the predictor variables. They reported a MAPE of 4.04 ± 2.57%, lower than that observed by either Neugebauer et al. or in our study. However, like the Neugebauer et al. study, the use of subject's step frequency and running pose on-field difficulties in quantification. Furthermore, neither study reported the reliability of their models, either through the determination of LoAs or by some other means. Reporting the reliability of a model's predictive capability may be essential, because even if the model demonstrates a high level of accuracy (low MAPE), the reliability may be such that predictive values can range from ± 20% of measured value.

Overall, the low MAPE value in our model using only IMU derived data shows the potential for predicting GRF from an IMU, particularly in sports involving large landing forces. However, the large LoA shows the model's reliability needs improvement. Future research might include factors like sex and height to help develop a more robust model.


## ACKNOWLEDGEMENTS

This material is based upon work supported by the National Science Foundation under grant no 2003434 and the National Institutes of Health under award number AR054821. The authors wish to thank Dr. Melanie Beaulieu for her assistance with data collection


## REFERENCES


Ajdaroski, M. et al. "Testing a Quaternion Conversion Method to Determine Human 3d Tibiofemoral Angles During an in Vitro Simulated Jump Landing." *J Biomech Eng*, 2021, doi:10.1115/1.4052496.

Alcantara, R. S. et al. "Sacral Acceleration Can Predict Whole-Body Kinetics and Stride Kinematics across Running Speeds." *PeerJ*, vol. 9, 2021, p. e11199, doi:10.7717/peerj.11199.

Arif, M. and A. Kattan. "Physical Activities Monitoring Using Wearable Acceleration Sensors Attached to the Body." *PLoS One*, vol. 10, no. 7, 2015, p. e0130851, doi:10.1371/journal.pone.0130851.

Elvin, N. G. et al. "Correlation between Ground Reaction Force and Tibial Acceleration in Vertical Jumping." *J Appl Biomech*, vol. 23, no. 3, 2007, pp. 180-9, doi:10.1123/jab.23.3.180.

Lipps, D. B. et al. "Anterior Cruciate Ligament Fatigue Failures in Knees Subjected to Repeated Simulated Pivot Landings." *Am J Sports Med*, vol. 41, no. 5, 2013, pp. 1058-66, doi:10.1177/0363546513477836.

Meyer, U. et al. "Validation of Two Accelerometers to Determine Mechanical Loading of Physical Activities in Children." *J Sports Sci*, vol. 33, no. 16, 2015, pp. 1702-9, doi:10.1080/02640414.2015.1004638.

Neugebauer, J. M. et al. "Estimating Youth Locomotion Ground Reaction Forces Using an Accelerometer-Based Activity Monitor." *PLoS One*, vol. 7, no. 10, 2012, p. e48182, doi:10.1371/journal.pone.0048182.

SB³C2022
Summer Biomechanics, Bioengineering and Biotransport Conference
June 20-23, Eastern Shore, MD, USA

# STIMULATING THE HEDGEHOG SIGNALING PATHWAY TO IMPROVE ZONAL TENDON-TO-BONE INTEGRATION

**Timur B. Kamalitdinov (1), Keitaro Fujino (1,2), Xi Jiang (1), Sinaia Keith Lang (1), Mary K. Evans (1), Miltiadis H. Zgonis (1), Andrew F. Kuntz (1), Nathaniel A. Dyment (1)**

(1) Department of Orthopaedic Surgery, University of Pennsylvania, Philadelphia, PA, USA
(2) Department of Orthopedic Surgery, Osaka Medical College, Takatsuki, Osaka Prefecture, Japan

## INTRODUCTION

Zonal enthesis formation involves anchoring collagen fibers, creating proteoglycan-rich fibrocartilage, and mineralizing part of this fibrocartilage. During development, Hedgehog (Hh) signaling promotes fibrocartilage production and maturation, leading to these distinct zones [1]. Despite this important developmental role, it is not known whether the Hh pathway plays a similar function in adult tendon-to-bone repair. To address this gap in knowledge, we modulated the Hh pathway in a murine anterior cruciate ligament reconstruction (ACLR) model [2,3] to assess its role in tendon-to-bone integration between the implanted tendon graft and adjacent bone. Our objective is to genetically and pharmacologically stimulate the Hh pathway in α-smooth muscle actin (αSMA)-expressing bone marrow stromal cells (bMSCs), which give rise to zonal fibrocartilaginous attachments [2], to promote tunnel integration. Our central hypothesis is that the Hh pathway promotes zonal fibrocartilage formation in the adult, similarly to its role in growth and development.

## METHODS

All animals and procedures were approved by UPenn's IACUC. Experimental Design. ACL reconstructions were performed on 60 transgenic mice. *Genetic Hh Activation Study*. αSMACreERT2 mice [4] were crossed with constitutively active SmoM2 mice [5] (Gt(ROSA)26Sor$^{tm1(Smo/EYFP)Amc}$/J) to yield SMACre;SmoM2 (SmoCA) mice with increased Hh signaling and Cre-negative controls. Mice were sacrificed at 28 days post-surgery and assigned to cryohistology (n = 7-13/group) or biomechanics (n = 5-7/group). Tamoxifen injections (80 mg/kg) were given on the day of surgery and every other day thereafter for a total of five injections to constitutively activate Smo in αSMA-expressing cells. *Pharmacologic Hh Activation Study*. Mice received either Hh agonist (20mg/kg Hh-Ag1.5 [6]) or PBS injections 5X per week. Mice were sacrificed at 28 days post-surgery and assigned to cryohistology (n = 6-8/group) and biomechanics (n = 7/group). Calcein was given 7 days before sacrifice and Demeclocycline was given 1 day before sacrifice to help define the mineralized fibrocartilage (MFC) zones of attachments. ACL Reconstruction. The ACL was excised near the femoral insertion. Bone tunnels were drilled with 27G needles. A tail tendon autograft was passed through the tunnels and anchored to the femoral and tibial outer cortices with stainless steel washers [2,3]. Mineralized Cryohistology. Knees were fixed in formalin, embedded, sectioned undecalcified with cryofilm, and imaged on the Zeiss Axio Scan.Z1. Tunnel Pullout Test. Femurs were potted in PMMA and gripped such that the tunnel was parallel to the linear actuator. A suture was passed through the washer and loaded to failure. Image Quantification. MFC area/total length, percentage of tunnel length containing MFC, and percentage of MFC produced in the last week were measured to assess the extent and timing of zonal integration at day 28. Bone area fraction (BAF), mineral apposition rate (MAR), mineralizing surface/bone surface (MS/BS), and alkaline phosphatase+ surface/bone surface (AP/BS) were measured in the newly formed bone 400μm from the tunnel interface at day 28 using OsteoMeasure. Statistics. Treated and control groups were compared via Student's t-tests ($p < 0.05$). Data presented as mean ± SD.

## RESULTS

SmoCA and Hh agonist-treated groups did not display any adverse systemic effects throughout the duration of the study. Hh Pathway Positively Regulated Tunnel Integration and Strength. When targeting the αSMA-expressing amplifying progenitor pool, SmoCA mice had 45% greater MFC compared to controls at day 28 (Fig. 1F, $p < 0.01$) resulting in 58% greater pullout strength (Fig. 2B, $p = 0.25$). Mice that received Hh agonist for four weeks had 25% more MFC (Fig. 1G, $p = 0.15$) resulting in 48% greater pullout strength (Fig. 2C, $p = 0.03$). Hh Pathway Activation Increased Attachment Sites and Area in the Last Week. Since Hh-stimulated mice showed greater MFC formation at 28 days, we next sought to identify the mechanism that led to this improved integration: increased number of attachments along the tunnel length or increased mineral apposition within each attachment. We found that

16% more of the tunnel length contained MFC in the SmoCA mice (Fig. 3B, p = 0.01) and 17% more in Hh agonist-treated mice (Fig. 3C, p = 0.04) compared to respective controls after 28 days. Additionally, there was 37% greater MFC produced in the last week in SmoCA mice compared to controls (Fig. 3E, p < 0.01) while Hh agonist-treated mice had comparable levels of MFC produced in the last week with controls (Fig. 3F, p = 0.45). Both SmoCA and Hh agonist-treated mice had comparable BAF, MS/BS, and AP/BS with their respective controls at 28 days after surgery in the newly formed bone surrounding the tunnels (n = 5-13 for each measure, p > 0.1). SmoCA mice had 11% lower MAR compared to controls (n = 4-13, p = 0.03) while Hh agonist-treated mice had comparable MAR compared to controls after 28 days (n = 3-4, p > 0.1)

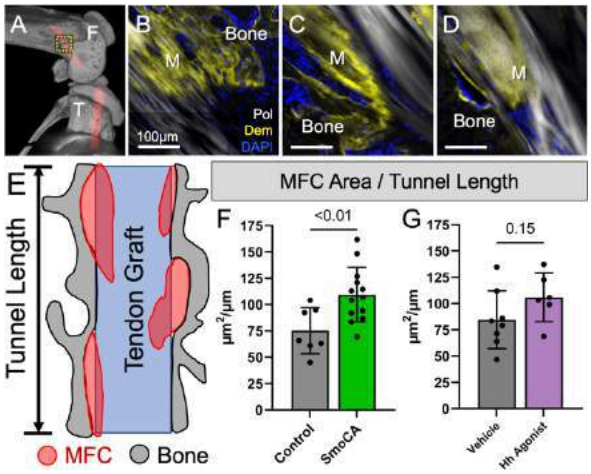


**Figure 1: Hh stimulation promoted MFC formation after 28 days. A) μCT of mouse knee showing tunnel placements (red) in femur (F) and tibia (T). B-D) Representative images of mineralized fibrocartilage (M) with adjacent bone from control (B), SmoCA (C) and Hh agonist-treated mice (D) from femoral tunnel (dashed box in A). E) Schematic of MFC quantification strategy with MFC area (red) normalized by tunnel length. F-G) MFC area in SmoCA (F) and Hh agonist-treated mice (G) at day 28. Pol – polarized light, Dem – demeclocycline.**

## DISCUSSION

Following ACL reconstruction, bMSCs must expand and infiltrate the periphery of the tendon graft, then assemble collagen and zonal fibrocartilage to properly anchor the tendon to adjacent bone. Similar to enthesis development, we demonstrated that Hh signaling promoted mineralized fibrocartilage formation (Fig. 1) leading to greater pullout strength (Fig. 2). While Hh signaling improves fracture repair via improved osteogenesis and angiogenesis [6], we found in this study that Hh promoted fibrocartilage formation with minimal effects on adjacent bone at day 28. Since a higher percentage of the tunnel length contained MFC in the treated vs. control groups (Fig. 3A-C), Hh may promote the initiation of attachment sites along the length of the tunnel. The SmoCA mice continued to mineralize more than controls in the later stages of healing (Fig. 3D-F), unlike the agonist treated group, which may indicate that the agonist treatment lost its effectiveness with time. Therefore, our results indicate that the increased MFC formation may, at least partially, be due to increased commitment of the bMSC progeny to initiate the attachments and if the cells maintain elevated levels of Hh signaling (i.e., SmoCA) during later stages, they will continue to produce elevated levels of MFC.

An improved understanding of the signaling pathways that regulate zonal insertion formation in the adult will be crucial to developing new therapies to improve repair outcome. If the Hh pathway is harnessed therapeutically, it could result in a paradigm shift in the treatment of these debilitating injuries, especially in more challenging scenarios that require reformation of the enthesis, such as rotator cuff repair.


## ACKNOWLEDGEMENTS

Work supported by NIH R00AR067283, NIH P30AR069619, NIH R01AR076381, NIH F31AR079840, the Thomas B. McCabe and Jeannette E. Laws McCabe Fund at UPenn, and startup funds from the Department of Orthopaedic Surgery at UPenn.


## REFERENCES


[1] Dyment, N et al., *Dev Biol, 405*(1), 96–107, 2015.
[2] Kamalitdinov, T et al., *J Orthop Res*, 38(1), 105–116, 2020.
[3] Hagiwara, Y et al., *Ann N Y Acad Sci*, 1460(1), 57-67, 2020.
[4] Grcevic, D et al., *Stem Cells*, 30(2), 187-196, 2012.
[5] Liu, C-F et al., *PLoS ONE*, 8(6), e65411, 2013.
[6] McKenzie, J et al., *J Orthop Res*, *37*(1), 51–59, 2019.


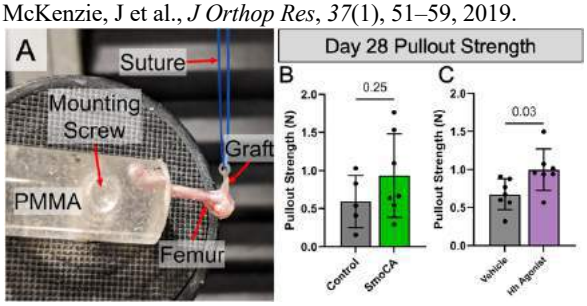


**Figure 2: Hh stimulation improved tunnel integration strength. A) Tunnel pullout test setup with femur potted in PMMA and suture attached to washer and linear actuator. B-C) Tunnel pullout strength in SmoCA (B) and Hh agonist-treated mice (C) at day 28.**

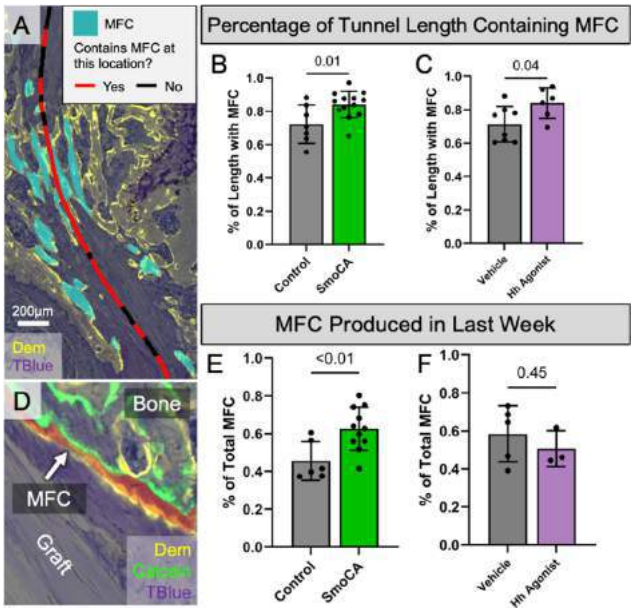


**Figure 3: Hh stimulation increased % of tunnel length containing MFC as well as MFC produced in the last week after 28 days. A) Schematic for measuring % of tunnel length (black line) containing MFC (red). B-C) Percentage of tunnel length containing MFC in SmoCA (B) and Hh agonist-treated mice (C) at day 28. D) Schematic for measuring MFC produced in the last week (red) between the calcein (green) mineral label given 1 week before and demeclocycline (yellow) given 1 day before sacrifice. E-F) % of MFC produced in the last week normalized to total MFC produced after 28 days in SmoCA (E) and Hh agonist-treated mice (F).**

SB³C2022
Summer Biomechanics, Bioengineering and Biotransport Conference
June 20-23, Eastern Shore, MD, USA

# PROGRESSIVE MECHANICAL AND STRUCTURAL CHANGES IN ANTERIOR CEREBRAL ARTERIES WITH ALZHEIMER'S DISEASE

**Xiaozhu Liu[1], Samuel Halvorsen[1], Nathan Blanke[2], Irving J. Bigio[2,3,4], and Yanhang Zhang[1,2,5]**

[1]Department of Mechanical Engineering, Boston University, Boston, MA
[2]Department of Biomedical Engineering, Boston University, Boston, MA
[3]Department of Electrical and Computer Engineering, Boston University, Boston, MA
[4]Department of Medicine, Boston University, Boston, MA
[5]Division of Materials Science & Engineering, Boston University, Boston, MA

## INTRODUCTION

Alzheimer's Disease (AD) is a neurodegenerative disease and the most prevalent cause of dementia[1]. Brain atrophy due to AD leads to gradual cognitive decline, personality changes, and eventually inability to sustain one's daily activities independently. Previous studies have shown that cerebrovascular changes are common neuropathologic findings in aged subjects with dementia[2]. Despite the importance of cerebrovasculature in brain function, compared with studies on the degeneration and alteration of neurons, cerebrovascular remodeling during the progression of AD and the neurovascular relationships in the brain are less delineated. To establish an understanding of the changes in structure and function of cerebrovascular arteries with AD progression, biaxial inflation-extension tests were performed on anterior cerebral arteries (ACAs) from normal control and pathologically diagnosed AD groups, from which the stress-stretch relationships in circumferential and longitudinal directions were obtained. Additionally, histology studies, multiphoton imaging, and polarized light microscopy were carried out to examine structural integrity of the ACAs.

## METHODS

**Biomechanical Characterization.** A total of 28 human ACAs were obtained from NIH NeuroBioBank. Based on pathological Braak stage, samples were divided into early AD (Braak I-II), intermediate AD (Braak III-IV), and advanced AD group (Braak V-VI). Biaxial inflation-extension tests were performed using a pressure Myograph (DMT 110P XL, Denmark). Samples from the 2nd segment of ACA were canulated at both ends, stretched axially to *in vivo* stretch ratio, and then inflated. After preconditioning, biaxial inflation-extension tests were performed from 0 - 80mmHg, the mean arterial pressure of ACA[3], at 10 mmHg increments. The inlet and outlet pressure P, axial force $f_T$, and the outer radius $r_o$ of the artery during the procedures were recorded. ACA rings were cut from the arteries after the biaxial inflation test to measure the undeformed inner radius $R_i$ and outer radius $R_o$. Assuming incompressibility and using a thin wall model, the circumferential and longitudinal stress, $\sigma_\theta$ and $\sigma_z$, respectively, can be calculated as:

$$\sigma_\theta = \frac{Pr_i}{r_o - r_i}, \text{ and } \sigma_z = \frac{f_T + P\pi r_i^2}{\pi(r_o - r_i)(r_i + r_o)} \quad (1)$$

where $r_i = \sqrt{r_o^2 - (R_o^2 - R_i^2)/\lambda_z}$ is the inner radius, and $\lambda_z$ is the axial stretch.

**Structural Characterization.** After biomechanical characterization, rings about 1mm in length were cut from the ACAs and fixed with paraformaldehyde, embedded in paraffin, cut into 5 μm slices, and collected on slides. Half of the slides were stained with Movat's stain for histological analysis and the other half were deparaffined for label-free imaging with quantitative birefringence microscopy (qBRM). For qBRM, the unstained sections were imaged with a monochromatic red LED source. First, A cross-circular polarized setup with a 20× objective lens (Olympus UPLFLN20XP) was used to acquire full-sample images. A horizontally-aligned region of the arterial wall was then selected and imaged with the same objective to generate quantitative images with the rotating linear polarizer and circular analyzer method[4]. A set of six images were taken during stepwise rotation of the linear polarizer at 30° increments. In the resulting image sets, the intensity variation of each pixel can be analyzed as a function of the angle of the rotating polarizer[5], providing quantitative birefringence parameter maps of relative retardance and in-plane optic-axis orientation.

For multiphoton imaging, the circumferential cross-sections of ACA rings were imaged using a Zeiss LSM 710 NLO Microscope with a 20× water immersion objective lens. An 810nm Ti:sapphire laser was used to generate second harmonic generation from collagen (417/80 nm) and two-photon-excited fluorescence from elastin (525/45 nm). Images were taken at 1 μm intervals to a depth of approximately 50 μm.

## RESULTS

As AD develops, the mechanical response of ACAs changes progressively. Compared to the control, the axial force in the early AD stage doubled, and nearly tripled in the intermediate and advanced stages (Fig. 1a). The longitudinal stress in the AD groups showed similar extent of increase in the AD groups (Fig. 1c). AD progression also leads to a left shift of the pressure-diameter curves (Fig. 1b). The toe region of the circumferential stress-stretch curves shortened, and the curves become steeper at a lower stretch (Fig. 1d). The left-shift of the stress-stretch curve demonstrates a continuous reduction in compliance of ACAs with AD progression, which becomes more

pronounced in the intermediate and advanced stages.

Progressive structural changes were also observed in ACAs. Presented in Figure 2 are ACAs from a 72-year-old control, a 66-year-old with early AD pathology (Braak I-II), a 69-year-old with intermediate AD pathology (Braak IV), and a 62-year-old with advanced AD pathology (Braak VI). Movat's stain revealed that ACAs exhibit decreased medial layer thickness and loss of smooth muscle cells (Figs. 2b-d). Medial layer thickness reduced by nearly half for ACA with advanced AD pathology (Fig. 2d). As a result of smooth muscle cell atrophy, an empty band appeared between the medial and adventitial layer, indicating compromised structural integrity of the arterial wall with the loss of elastic fibers and smooth muscles cells.

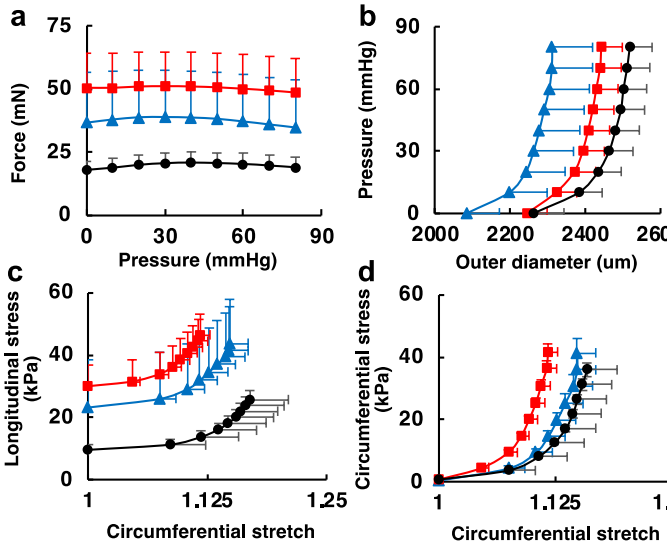


**Figure 2. Mechanical response of ACAs from biaxial inflation-extension tests at in vivo axial stretch. (a) Axial force – pressure; (b) pressure – diameter; (c, d) longitudinal and circumferential stress vs. circumferential stretch, respectively. Control (●), early AD (▲), and intermediate & advanced AD groups (■).**

Structural degeneration in elastin was further revealed from the multiphoton images (Figs. 2e-h) taken at different stages of AD progression. The loss of elastic fibers becomes evident with an empty band appearing at the media-adventitia interface. Additional observation can be made in the qBRM images (Figs. i-l). In the normal control (Figure 2i), the structural integrity of the arterial wall is evident from the compaction of the layers and the relatively uniform color of the orientation map. The corresponding images of the AD cases (Figures 2j-l), on the other hand, exhibit clear signs of structural breakdown and delamination. In the medial layer, this can be seen by a steady decline in the quantity of birefringent elastin fibers and smooth muscle cells as AD progresses. Moreover, in the adventitial layer, the collagen fibers become progressively more disorganized in AD arteries, as evidenced by the colorful orientation map (Figure 2l).

## DISSCUSSION

Current understanding of cerebrovascular remodeling in AD is limited. Smooth muscle atrophy in posterior cerebral artery has been reported[6], however, changes in human cerebrovascular function and extracellular matrix in AD have not been studied. Our study shows that with pathological progression of AD, human ACAs undergo progressive stiffening, elastin and collagen structural breakdown, and smooth muscle cell atrophy.

The ACAs become stiffer as AD develops (Fig. 1). Arterial stiffening has been reported in AD and other dementia cases using noninvasive measurements such as pulse wave velocity method, but the reason remains unclear [7][8]. The collagen disorganization in AD, which can be clearly seen in our birefringence images (Figures 2j-l), can potentially cause early collagen recruitment and contribute to cerebral artery stiffening. The elastin degradation, accompanied by smooth muscle cell deprivation, leads to the overall media atrophy and this progresses with pathological AD stages (Figs. 2f-h).

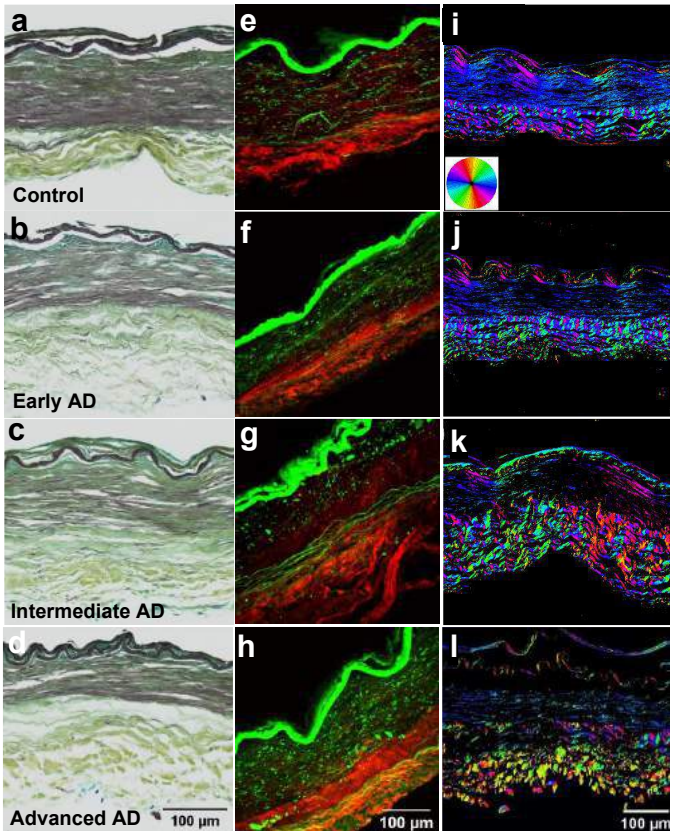


**Figure 1. Circumferential cross section of ACAs from a control, early AD, intermediate AD, and advanced AD subject. (a-d) Histological images with Movat's stain which stains nuclei and elastin black, GAGs blue, and collagen yellow. (e-h) multiphoton images showing elastin green and collagen red. (i-l) Birefringence images showing the optic-axis orientation maps obtained with qBRM. The inset in *i* shows the color coding for the orientation of the optic axis. Scale bars, 100 µm. Intimal layer is facing up in all images.**

Cerebrovascular dysfunction can render the brain more susceptible to pulse pressure and lead to blood brain barrier (BBB) breakdown[9]. With an impaired BBB and vascular contractibility, Amyloid-β is more likely to deposite in brain tissues and the cerebrovascular system[10], resulting in smooth muscle cells atrophy, causing further decrease of vascular contractability and cerebral blood flow.

In summary, our study demonstrated, for the first time, progressive structural changes in human ACAs during the development of AD, including elastin degradation, smooth muscle cell atrophy and collagen disorganization. These structural changes compromise arterial wall integrity and lead to cerebrovascular stiffening as AD progresses. Future studies are underway to quantify these structural changes and their correlations with AD progression.

## ACKNOWLEDGMENT

The authors acknowledge the funding support from NIH (3R01 HL098028-06S1 to YZ) and NIH NeuroBioBank for providing the tissue samples.

## REFERENCE

[1] Alzheimer's Assoc., *Alzheimer's & Dementia* 15:321-387, 2019.
[2] Marlatt, W et al., *J Alzheimer's Dis*, 15:199-210, 2008.
[3] Rosenberg, A et al., *Pediatr Res*, 19: 67-70, 1985.
[4] Glazer, AM et al., *Proc R Soc Lond*, 452: 2751-2765, 1996.
[5] Blanke, N et al., *Neurophotonics*, 8:1-15, 2021.
[6] Perry, G et al., *Brain Res*, 791: 63–66, 1998.
[7] Rabkin, S and Jarvie, G, *Blood Press*, 20: 274-283, 2011.
[8] Rivera-Rivera, L et al., *Cereb Blood Flow Metab*, 41: 298-311, 2021.
[9] Kisler, K et al., *Rev Neurosci*, 18: 419-434, 2017.
[10] Austin, B et al., *J Alzheimers*, 26: 123-133, 2011.

SB³C2022
Summer Biomechanics, Bioengineering and Biotransport Conference
June 20-23, Eastern Shore, MD, USA

# COLLAGEN WAVINES REGULATES THE DAMAGE OF VEIN TISSUE

**XH. He, J. Lu**

Department of Mechanical Engineering
The University of Iowa
Iowa City, Iowa, United States

## INTRODUCTION

Coronary artery disease (CAD) is a prevalent cause of morbidity and mortality worldwide. Human saphenous vein (SV) is routinely used as a coronary arterial bypass graft (CABG) in treating CAD. SV segment harvested for graft often undergoes a distension procedure in which the segment is pressurized beyond the venous pressure. Many saphenous vein CABGs were found to fail in service. The failure has been attributed to factors including elevated pressure in the service condition, and structural remodeling caused by damage during distension [1]. The present study aims to investigate the role of collagen fiber waviness in regulating the damage of vein tissue. To this end, a constitutive model considering collagen waviness and damage, with layer-specific properties, is proposed. The descriptive capability of the model is evaluated against reported experimental data. The model is then applied to examine the change of tissue properties induced by distension. Eventually, the uniaxial properties of the SV and the human abdominal aortic(AA) tissue are characterized using this model, and further compared through performing statistical analysis.

## METHODS

### *Modelling recruitment and dispersion*

Although much thinner walled than arteries, the vein also consists of three layers: intima, media and adventitia. The media and adventitia layers can be regarded as a fibrous composites with wavy collagen fibers embedded in isotropic ground substance. In our previous studies [2], a two-layer version microstructurally-motivated constitutive model is proposed to consider different waviness, direction distribution and stiffness characteristics of the media and adventitia layer for the vascular tissue. The strain energy density function (SEDF) consists of contribution from the lumped ground matrix and collagen fibers ($W_f$) in both layers:

$$W = \frac{\mu_1}{2}(\mathrm{I}_1 - 3) + \sum_{j=M,A} W_{f,j} \qquad (1)$$

For each layer, the fibers are assumed to be dispersed and the directional density follows von Mises distribution. After applying a four-point integration scheme to discrete the continuous distribution, we obtain an expression for fiber energy in each layer

$$W_f = \mu_{2i}[\kappa^2 w_b(\theta_0^1) + \kappa(1-i\kappa)\big(w_b(\theta_0^1) + w_b(\theta_0^3)\big) + (1-\kappa)^2 w_b(\theta_0^4)] \qquad (2)$$

where $w_b\big(\theta_0^i\big)$ is the strain energy of a fiber bundle oriented in the quadrature directions $\theta_0^i$. At the fiber-level, the undulation of a single wavy fiber is quantified by a straightness parameter $p$. Beta distribution function $\psi(p)$ is employed to describe the random distribution of the fiber straightness within the fiber bundle. The beta distribution is parameterized by a mean straightness parameter $e$ and a concentration parameter $s$. Cauchy stress at the fiber bundle level then follows as

$$\sigma_b = \lambda\frac{dw_b}{d\lambda} = \mu_{2i}\lambda\int_{\lambda^{-1}}^{1}(\lambda\rho - 1)\psi(p; ie, s)\,d\mathrm{p} = i\mu_{2i}\lambda(\bar{\lambda} - 1) \qquad (3)$$

Here $\bar{\lambda}$ is a kinematic average variable "*effective stretch*" introduced by the authors in [3] to account for the true stretch of the fiber bundle after factoring out the uncrimping effect.

### *Modelling damage*

We introduce a damage variable $D_f$ for the fiber energy function such that the fiber bundle strain energy $w_b$ in (2) is updated as $(1 - D_f)w_b$. $D_f$ is assumed to be a function of the effective stretch $\bar{\lambda}$. This is motivated by a recent study [4] which found that the rupture stretches of human ascending aortic aneurysms tissue are closely clustered $\bar{\lambda}$ =1.1, suggesting that the inelastic behavior of fiber

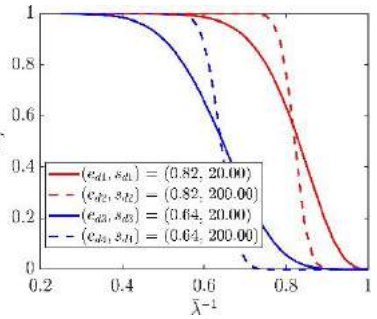


**Figure 1: Influence of $(e_d, s_d)$ on $D_f$**

SB³C2022-082

bundles may be intrinsically described by the effective stretch. Further, we assume that $D_f$ is given by beta distribution of $1/\bar{\lambda}$:

$$D_f = \int_{\bar{\lambda}^{-1}}^{1} \psi(\eta; e_d, s_d)\, d\eta \qquad (7)$$

where $e_d$ and $s_d$ are two damage parameters. As illustrated in Fig. 1, $ie_d$ controls the position of the damage evolution curve while $s_d$ affects the local damage rate.

***Constitutive fitting***

This model is applied to fit the uniaxial tensile test data (with damage) of four SV samples harvested along the circumferential and longitudinal directions [5]. The uniaxial data obtained in each direction is treated as a biaxial case by assuming the stretch in the transverse direction as $\lambda_t\ i = i1/\sqrt{\lambda_{exp}}$.

***Change of waviness after distention***

We hypothesis that the manual pressure distension mainly changes the collagen waviness. A partially joint fitting (PJF) is then conducted over the biaxial response data (without damage) of SV with and without manual pressure distension [6]. PJF employs two groups of waviness and ground stiffness parameters and one group of other parameters to fit both specimens jointly.

***Difference of uniaxial properties between vein and artery***

The stress function (3) is fitted to uniaxial response data (up to yield) from 30 human SV samples published in [5,7] and 93 human abdominal aortic (AA) samples published in [8]. Statistical analyses are performed to investigate the differences of fitted constitutive parameters as well as the ultimate stress $\sigma_u$, ultimate stretch $\lambda_u$ and ultimate effective stretch $\overline{\lambda_u}$ in two data groups. A primary normality test finds that the data do not follow the normal distribution. Hence, a nonparametric test, namely Mann Whitney U test, is performed to determine whether significant differences exists between the parameters in these two groups. Parameters with p-value less than 0.05 are deemed to be significantly different.

## RESULTS

The response of four SVs with damage are accurately captured using the proposed model with $R^2$ reaches 0.998 (Fig. 2a).

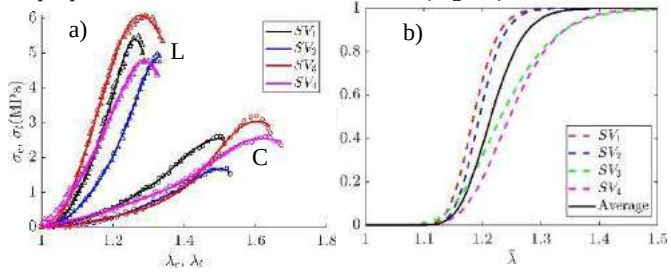


**Figure 2: a) Fitted response. b) damage evolution versus $\bar{\lambda}$**

The damage evolutions using fitted damage parameters and the calculated mean values with respect to the effectives stretch are illustrated in Fig. 2b. Despite the damage rates are varied, nonnegligible damage value $D_f$ occurs in all SV samples when effective stretch reaches around 1.1.

The PJF approach yields an excellent fitting of the biaxial response data for both the normal and distended SV (Fig. 3). The fitted waviness parameters are presented in Table 1. As expected, evident reduction of waviness is observed in both layers in the distended case. At the same time, the stiffness parameter of the ground substance reduced. The change of waviness could be partially caused by the breakage of collagen fibers, or disruption of the elastin network.

**Table 1: Fitted parameters**

| Parameter | Normal | Distend |
|---|---|---|
| $e_A$ | 0.678 | 0.804 |
| $e_M$ | 0.849 | 0.918 |
| $s_A = s_M$ | 21.048 | 110.889 |
| $\mu_1(MPa)$ | 0.013 | 0.009 |

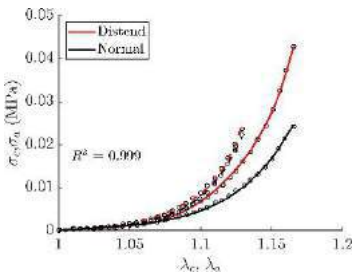


**Figure 3: Fitted biaxial response**

Statistical results of variables obtained from the SV and the AA are presented in Table 2. Compared to the ultimate stress and stretch which are much higher in SV, the ultimate effective stretches are centered around 1.11 within a small interquartile range in both SV and AA. This result is consistent with the observed clustering of damage initiation effective stretch. Among the fitted parameters, there are significant differences in collagen waviness $(e, s)$ and collagen stiffness $(\mu_2)$ between SV and AA. The SV is associated with higher $e$ and $\mu_2$, indicating much wavier and higher content of collagen.

**Table 2: Fitted parameters in median [interquartile range]**

| | SV (n =30) | AA (n = 93) | p-value |
|---|---|---|---|
| $e$ | 0.60 [0.54, 0.70] | 0.84 [0.73, 0.89] | **2.46e-08** |
| $s$ | 43.68[7.22, 86.13] | 73.17 [ 40.28, 136.94] | **1.12e-03** |
| $\mu_1$ | 0.079[0.06, 0.08] | 0.070 [ 0.045, 0.099] | 0.247 |
| $\mu_2$ | 33.52[11.74,90.89] | 4.43[ 2.59, 7.65] | **3.27e-12** |
| $\overline{\lambda_u}$ | 1.11[ 1.07, 1.14] | 1.11 [ 1.08, 1.14] | 0.411 |
| $\lambda_u$ | 1.80[1.48, 1.93] | 1.33 [ 1.25, 1.52] | **5.90e-07** |
| $\sigma_u$ | 4.48[ 3.09, 8.40] | 0.67 [ 0.41, 1.09] | **1.78e-15** |

## DISCUSSION

The constitutive model proposed in current study accurately capture the stress response and damage in SV tissue under tensile loading. The observed similar $\bar{\lambda}$ at damage initiation suggests that the collage waviness plays a significant role in regulating vein damage. It is found that the change of response characteristics induced by manual distension could be attributed to the reduction of fiber waviness. The SV is found to have much wavier collagen fibers than the AA tissue. The adventitia layer has been reported to have much higher content and undulation of collagen fibers than the media layer. Therefore, waviness of fibers in the adventitia layer could dominate the distensibility of the entire wall. Thus the SV collagen tissues are much wavier than AA may shed light on understanding the failure of the CABG when the SV is exposed to arterial pressure.

The current study embodies some limitations. Firstly, response data with damage from only four samples are used in the constitutive fitting. There is a need to accumulate more data to validate our model. Secondly, the predicted waviness parameters should be validated experimentally. This could be accomplished using the optical imaging methods. Although limitations exist, current study reveals the importance of collagen waviness in regulating the damage of venous tissue.

## REFERENCES


[1] Vekilov, D. et al. (2018). *Methodist Debakey Cardiovasc. J.*, 14, 182-187. [2] He, X. et al. (2022) *J Mech Phys Solids*. (Under review). [3] Lu, J., *Biomech Model Mechanobiol* 20, 1833–1850 (2021). [4] He, X., (2021). *Acta Biomat*, 136, 306-313. [5] Hamedani, B. A., Navidbakhsh, M., & Tafti, H. A. (2012). *Biomed*, 11(1), 1-15. [6] Zhao J. et al. *J Biomech*, 2007, 40(10): 2268-2276. [7] Rassoli, A. et al. *Biomed.*, 27(05), 1550050. [8] Gomes, V. C. et al. (2021). *Ann. Vasc. Surg*, 70, 517-527.

# AN OPEN LOOP SYSTEM FOR THE COMPUTATIONAL INVESTIGATION OF SUSPECTED CORONARY DISEASE WITH THE PATIENT SPECIFIC CT-DATA

**Sumit Kumar (1) BV Rathish Kumar (2) Sanjay Kumar Rai (3) Om Shankar (4) Ashish Verma (5)**

(1) School of Biomedical Engineering, Indian Institute of Technology (BHU), Varanasi, UP, India
(2) Department of Mathematics and Statistics, Indian Institute of Technology, Kanpur, UP, India
(3) School of Biomedical Engineering, Indian Institute of Technology (BHU), Varanasi, UP, India
(4) Department of Cardiology, Institute of Medical Sciences, (BHU), Varanasi, UP, India
(5) Department of Radiodiagnosis and Imaging, Institute of Medical Sciences, (BHU), Varanasi, UP, India

## INTRODUCTION

Coronary Artery Disease (CAD) is the most frequently reported cardiovascular disease (CVD) and is one the primary causes of death today. CAD involves myocardial ischemia due to atherosclerotic build-up, which narrows the arterial lumen. There is an estimate by the Indian Heart Association that approx. 60% of the world and CVD load will happen in the South Asian countries in spite of accounting for only 20% of the entire world population. However, early prognosis and diagnosis of CAD could reduce this high morbidity rate and thus decrease the mortality rate. In recent times, for computing cardiovascular hemodynamics, some assessment tools have been developed. These cardiovascular assessment tools provide awareness to physicians to assist CVD diagnosis by allowing them to use the CFD based computational indicators/markers to CVD. In the patients with questionable CVD conditions these tools help in identifying the coronary lumen plaque and shape property during their initial clinical visits [1,2]. Currently, to evaluate the intensity of coronary stenosis from (CAD-RADS) database, the fractional flow reserve (FFR) is extensively used, with the target of verifying the impact of the stricture (stenosis) on the myocardial ischemia [3]. In CAD patients, hemodynamics plays a vital role in the progression, evaluation, and treatment of cardiovascular disease. For personalized treatment planning, suitable blood flow-based markers like shear stress of wall, deformation of the vessel wall, blood pressure, streamlines, and velocity are used to explore the impact of mechanical stimuli in CVD. Standardized person-specific and region-specific reporting will be helpful to reduce the variability of CADs among practitioners for maximizing the clinical impact of coronary computed tomography angiogram (CCTA). Therefore, it is crucial to know the hemodynamics characteristics of patients having chest pain in the initial visit. This study performed a detailed blood flow analysis of suspected coronary artery diseases using CFD and an open-loop system. This study will provide the medical practitioner with some theoretical support for diagnoses and treatments of CADs.

## METHODS

In this study, a CCTA scanning examination was done for one of the hospitalized patients of age 51 yrs. having chest pain for diagnosis of coronary artery disease (CAD) at a 128 slice CT scan center, SSH, Institute of Medical Sciences BHU, Varanasi, India

The study was supervised in conformity with the principles of the declaration of medical ethics requirements. The ethical review committee of the Institute of Medical Sciences, BHU, Varanasi, India. To generate a patient-specific anatomic model based on CT angiography image data, the geometry of coronary arteries and aorta was first reconstructed from the patient image data using open-source [5]. The design details of the model are depicted in Figure 1.

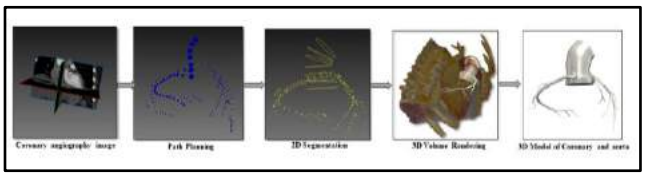


**Figure 1: - (a) Complete step by step process for coronary arteries modelling using CT-image data**

To analyze the various hemodynamic parameters like Pressure Drop, Velocity Profile, WSS, TASSS, OSI, FFR and streamline a three-dimensional (3D) finite element model of the coronary arteries from CCTA, was used as shown in Fig 1(b). In the study, blood was assumed to be a Newtonian fluid with a density of (1.06 g/mL) and dynamic viscosity of (0.04 dyne. s/cm$^2$) for all simulations. Blood vessel walls were assumed to be rigid in all cases. A time-step size of 0.001 ms was chosen to satisfy the stability condition. Simulations were run for 3 cardiac cycles until the pressure fields at the inlet and outlet did not change more than 1% from the previous cycle. Blood flow was modelled using the incompressible Navier–Stokes equations NSEs and the corresponding governing equations for NSEs given below:

$$\rho\vec{v},ti+i\rho\vec{v}i.\nabla\vec{v}\,i=i-\nabla p+div(\tau)+i\vec{f} \quad (1)$$

$$divi(\vec{v})=0\ddot{u}fori(\vec{x},t)\,i\in\Omega i\times i(0,T) \quad (2)$$

$$\text{Where}\quad \tau=\mu(\nabla\vec{v}+i(\nabla\vec{v})^T) \quad (3)$$

To assess the wall shear stress acting on the lumen wall under pulsating flow in human heart circulation, Time Average Wall Shear Stress

(TAWSS), Oscillatory Shear Index (OSI) and Relative Residence Time (RRT) were considered.

## RESULTS & DISCUSSION

In this study all the numerical simulations pertaining to the patient with chest pain have been carried out using CFD methods. The various hemodynamic parameters were investigated after three cardiac simulations and validated with the previous work [6]. The critical regions of TAWSS, OSI and RRT as shown in Figure 2 are also analyzed. Velocity contour and streamlines of blood flow in the coronary model are shown in Figs 2 and 3. Astoundingly, the patient classified as (CAD-RADS0) had abnormal hemodynamic characteristics that could not be ascertained from the CCTA directly. The results recommended that this patient should also have been treated well at the time of their initial visit to avoid future adverse effects. Also, patient-specific hemodynamic characteristics may play as vital a role as changes in coronary artery morphology in the prognosis of patients with coronary stenosis.

The present work was focused on single-patient data. However, based on this preliminary study, our future research will emphasize the following: (1) Does the degree of coronary stenosis have a strong effect on coronary blood supply and less of an effect on the blood flow disorder? and (2) Does the location of stenosis have a strong effect on intra-luminal blood flow disorder?

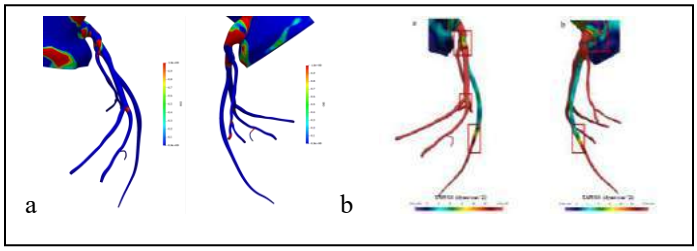


**Figure 2:(a) Oscillatory Shear index (OSI) distribution contour map on vessel wall 3D model including LCA & RCA (b) Time average wall shear stress (TAWSS) a) 3D model including LCA & RCA**

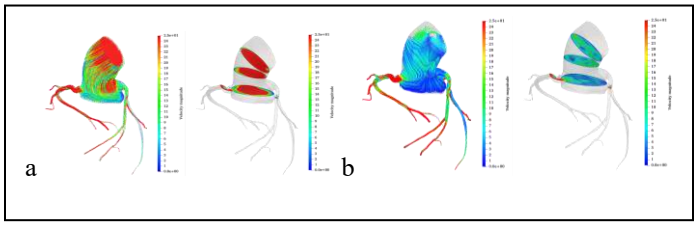


**Figure 3:(a) Velocity contour and streamline visualization at peak of systole (b) end of diastole**

Fig 3 (a) and (b) depicts the blood flow velocity contour and flow pattern during systolic and diastolic phase, the maximum magnitude of blood flow is shown in color legend of visualization and also others hemodynamics parameters were analyzed and few of them shown.

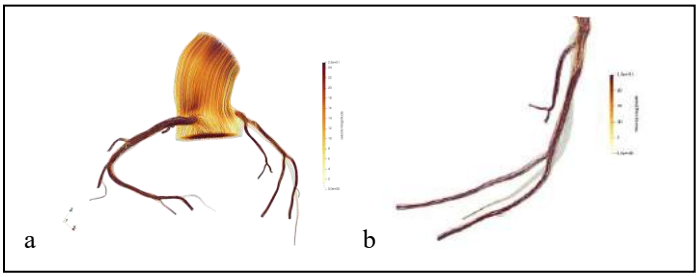


**Figure 3: (a) Velocity streamline during the peak of systole (b) Magnified view of left coronary arteries during peak systole**


## ACKNOWLEDGEMENTS

The authors would like to acknowledge simvascular (https://simtk.org) for open-source support, IMS BHU, for CT scan data support and Indian Council of Medical Research, Government of India, for funding and support, Project File [No: GIA/2019/000607/PRCGIA IRIS cell, ICMR, ID.No. 2020-9527]


## REFERENCES:


[1] R.H. Helfant, H.G. Kemp, R. Gorlin, Coronary atherosclerosis, coronary collaterals, and their relation to cardiac function., Ann. Intern. Med. 73 (1970) 189–193. https://doi.org/10.7326/0003-4819-73-2-189.

[2] S. Motoyama, M. Sarai, H. Harigaya, H. Anno, K. Inoue, T. Hara, H. Naruse, J. Ishii, H. Hishida, N.D. Wong, R. Virmani, T. Kondo, Y. Ozaki, J. Narula, Computed Tomographic Angiography Characteristics of Atherosclerotic Plaques Subsequently Resulting in Acute Coronary Syndrome, J. Am. Coll. Cardiol. 54 (2009) 49–57. https://doi.org/10.1016/j.jacc.2009.02.068.

[3] E. Hulten, C. Pickett, M.S. Bittencourt, T.C. Villines, S. Petrillo, M.F. Di Carli, R. Blankstein, Outcomes after coronary computed tomography angiography in the emergency department: A systematic review and meta-analysis of randomized, controlled trials, J. Am. Coll. Cardiol. 61 (2013) 880–892. https://doi.org/10.1016/j.jacc.2012.11.061.

[4] H.J. Kim, I.E. Vignon-Clementel, J.S. Coogan, C.A. Figueroa, K.E. Jansen, C.A. Taylor, Patient-specific modeling of blood flow and pressure in human coronary arteries, Ann. Biomed. Eng. 38 (2010) 3195–3209. https://doi.org/10.1007/s10439-010-0083-6.

[5] A. Updegrove, N.M. Wilson, J. Merkow, H. Lan, A.L. Marsden, S.C. Shadden, SimVascular: An Open-Source Pipeline for Cardiovascular Simulation, Ann. Biomed. Eng. 45 (2017) 525–541. https://doi.org/10.1007/s10439-016-1762-8.

[6] H. Cao, Y. Li, Y. Zhao, T. Xiong, Z. Liu, T. Zheng, M. Chen, Hemodynamic Characteristics of Patients with Suspected Coronary Heart Disease at Their Initial Visit, Front. Physiol. 12 (2021) 1–9. https://doi.org/10.3389/fphys.2021.714438.

SB³C2022
Summer Biomechanics, Bioengineering and Biotransport Conference
June 20-23, Eastern Shore, MD, USA

# TRANSCRIPTIONAL PROFILING OF MOUSE SKELETAL MUSCLE FOLLOWING DAILY BOUTS OF OPTOGENETIC STIMULATION

**Syeda N. Lamia (1, 2), Elahe Ganji (3), Iman Bhattacharya (4), Megan L. Killian (1)**

(1) Department of Orthopaedic Surgery, University of Michigan, Ann Arbor, Michigan, USA
(2) Department of Mechanical Engineering, University of Michigan, Ann Arbor, Michigan, USA
(3) Department of Mechanical Engineering, University of Delaware, Newark, Delaware, USA
(4) Department of Bioinformatics, University of Delaware, Newark, Delaware, USA

## INTRODUCTION

Exercise is a major stimulus that drives structural and metabolic changes to skeletal muscle as well as systemic changes in cardiovascular health. The response of muscle to exercise depends on the type of stimulus [1] and understanding muscle adaptation in response to exercise is challenging due to the coupled effect of both local (e.g., muscle fiber) and systemic (e.g., metabolism) adaptation. We have recently developed a novel exercise model using optogenetic stimulation (opto stim) of the skeletal muscle to elicit isometric muscle contraction in transgenic mice without the simultaneous effect of systemic metabolic changes associated with aerobic or resistance exercise. In this study, we first measured in vivo ankle torque produced by opto stim of the triceps surae muscle in young mice daily for two weeks using our established protocol [2]. We then identified if and how transcriptional profiles of muscle change after 5 and 12 days of daily opto stim using RNA sequencing (RNAseq).

## METHODS

The Unit for Laboratory Animal Medicine at the University of Michigan approved all animal procedures.

*Ankle torque measurements*: Right triceps surae muscles of doxycycline-treated 4-week-old Acta1-Cre; Ai32 (AA) homozygous male mice (n = 8) were subjected to daily bouts of *in vivo* opto stim (455 nm light) at 10 Hz (70 msec on; 30 msec off) for two weeks (20 min/day; 5 days/week; 10 bouts total). The hindlimb was stabilized via knee clamp and the foot was positioned on a pedal to measure isometric ankle joint torque (Aurora Scientific) (2). The maximum ankle torque over the 20 min-period was normalized to body weight (nMAT). nMATs were averaged for each sample per week, repeated measure ANOVA was performed between days, and students t-test was performed to compare nMATs between weeks using GraphPad Prism ($p < 0.05$).

*RNAseq experiment*: In a separate experiment, we repeated daily bouts of opto stim of the right triceps surae muscles on a cohort of 3-week-old AA male mice (n = 6) using the same stimulation protocol without the force measurement system. Daily bouts were repeated for 5 days (5 bouts) or 12 days (10 daily bouts) (n = 3/time point; contralateral limb was unstimulated control). Mice were euthanized three hours after the last bout and triceps surae muscles were dissected, snap-frozen, and stored at -80 ºC. Muscles were pulverized using steel beads in Trizol and total RNA was isolated with on-column DNA digestion (PureLink RNA Mini Kit, Invitrogen). RNA integrity was > 9.0 for all samples. Poly-A mRNA library preparations and next-generation sequencing were performed using Illumina NovaSeq Shared platform followed by Snakemake pipeline analysis [3] for quality control and sequence alignment. Differential expression (DE) of genes was determined from the count matrix with paired design in DESeq2 in R/Bioconductor [4]. A 1.25-fold change threshold was applied with Wald tests of significance and p-values were corrected for multiple testing using the Benjamini and Hochberg method, with significance set at p-adjusted < 0.05. For pathway analyses and identifying upstream regulators, two gene lists (5 days and 12 days) were input separately using Ingenuity Pathway Analysis (Qiagen). A cut-off of p-adjusted < 0.1 was applied and significance was set at enrichment $|z| \geq 2$ with Fisher's exact $p < 0.05$ and $< 0.01$ for pathways and regulators, respectively.

## RESULTS

nMAT generated by opto stim did not change significantly during the experiment (Fig. 1). After 5 bouts of daily isometric contraction, 326 genes were upregulated, and 110 were downregulated in the stimulated muscle compared to contralateral controls (Fig. 2A). After 12 days, 56 genes were downregulated, and 116 genes were upregulated (Fig. 2B). We identified 99 DE genes conserved between both time points. Five days of stimulation led to enriched pathways related to immune response, cellular development, nuclear receptors, metabolism, and inhibition of matrix metalloproteases (Fig. 3). Pathway enrichment was reduced after 12 days with only 6 significantly enriched pathways relating to cellular development, nuclear receptor signaling, and immunological response (Fig. 3B). Numerous transcription regulators

SB³C2022-084

were identified as upstream regulators at the 5-day time point, but only two were found to be activated after 12 days of stimulation (Fig. 3A).

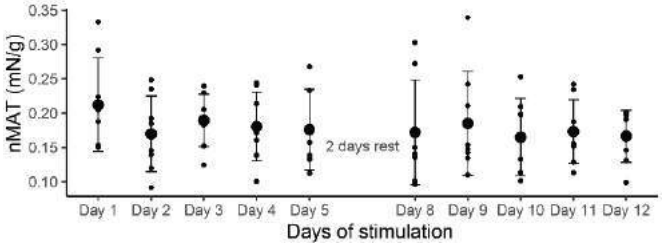


**Figure 1: nMAT for each 20 min bout of daily opto stim. Average nMAT did not change throughout the experiment. Data shown are biological replicates (small dots), average (large dots) with standard deviation (bars).**

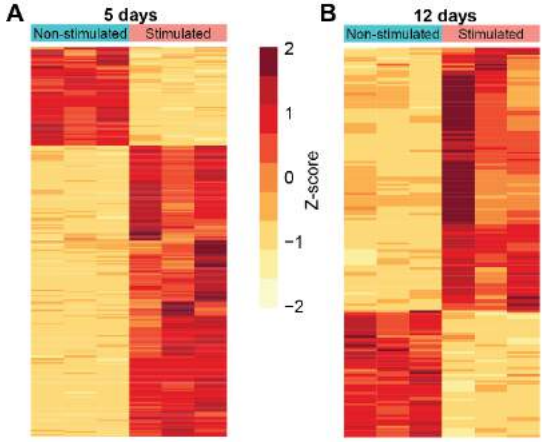


**Figure 2. RNAseq revealed consistent changes in DE genes within groups after (A) 5 and (B) 12 days following opto stim of muscle compared to unstimulated controls.**

## DISCUSSION

This study explored 1) the repeatability of opto stim induced torque production and 2) the transcriptional changes in skeletal muscle following daily bouts of opto stim in young mice. Opto stim has the following advantages over traditional exercise methods, e.g., treadmill running or electrical stimulation: opto stim is non-invasive and locally contracts skeletal muscle independent of nerve activation; opto stim minimizes systemic/organism-scale metabolic adaptation; and opto stim provides a controlled experimental approach for paired (intra-animal) comparisons. Myogenic (*Ankdr2, Cspr3, MyoD1*), anti-myogenic (*Tead4, Tnfrsf12a*), adipogenic (*Adipoq, Cebpa, Lpl*, etc.), inflammatory (*Il1r1*), and fibrotic (*Lox*) genes were DE over the stimulation period. *Runx1*, a transcription factor active during muscle regeneration, was identified as an upstream regulator following opto stim at 5-days [5]. *Nfkbia* was also activated, which may explain the reduced immune response at the transcriptional level at 12 days [6]. *Myod1,* which is responsible for muscle cell proliferation, differentiation, and transformation, was activated only after 12 days of stimulation. Besides inflammatory responses, opto stim activated p38 MAPK, PKA, and FAK signaling, which are active during the differentiation of myogenic cell lines in response to exercise stimuli [7, 8], and also activated CREB, VDR/ RXR, and GM-CSF signaling which may indicate muscle regeneration [9-11]. Opto stim also led to HIF1a signaling enrichment, which plays a critical role in exercise-induced muscle metabolism [12]. Surprisingly, PPAR signaling, a pathway related to mitochondrial biogenesis and often elevated by exercise [13], was inhibited by opto stim, suggesting the volume and intensity of muscle contraction may not be adequate to induce or maintain structural changes [14]. A decreased number of DE genes, upstream regulators, and enriched pathways after 12 days also indicate transcriptional adaptation to our opto stim protocol [1, 14].

These findings support our hypothesis that opto stim of skeletal muscle is a repeatable and effective exercise protocol that elicits differential transcriptional responses and activates known pathways associated with inflammation, muscle regeneration, and differentiation. Future studies should focus on the transcriptional profile in aged mice following opto stim, the structural changes to muscle following acute and repeated opto stim, as well as comparing our transcriptional findings to that of "gold standard" exercise regimens (e.g., treadmill running) and injury (e.g., denervation).

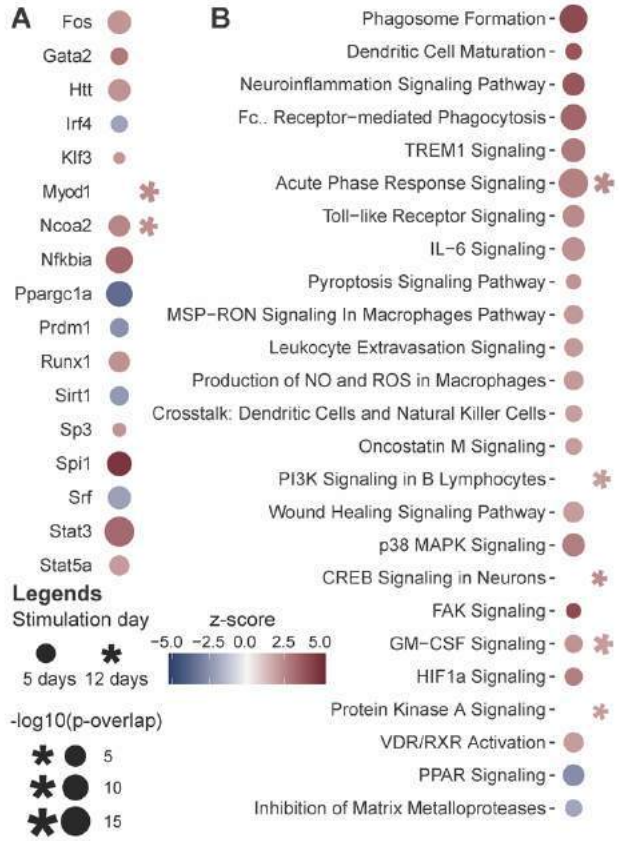


**Figure 3. (A) Upstream transcription regulators and (B) canonical pathways, identified using Ingenuity Pathway Analysis, which were enriched by opto stim. Positive & negative z-scores = activated and inhibited pathways, respectively.**

**ACKNOWLEDGEMENTS:** NSF CAREER Award 1944448 (MLK); NIH R01AR079367 (MLK). Advanced Genomics Core at UMich carried out next-generation sequencing and preliminary alignments.

**REFERENCES:** [1] Qaisar et al., *Free Radic Biol Med*, 98:56-67, 2016; [2] Ganji et al., *Connective Tiss Res*, 62(1):15-23, 2021; [3] Zhang & Jonassen, *BMC Bioinformatics*, 21:110, 2020; [4]. Love et al., *Genome Biology*, 15:550, 2014; [5] Umansky et al., *PloS Genet*, 11(8): e1005457, 2015; [6] Vella et al., *Am J Physiol Regul Integr Comp Physiol*, 302(6):R667-73, 2012. [7] Kramer & Goodyear, *J Appl Physiol*, 103:388–395, 2007; [8] Graham et al., *J Muscle Res Cell Motil*, 36(0):305–315, 2015; [9] Stewart et al., *PLoS One* 6(9):e24714, 2011; [10] Wright et al., *Mediators Inflamm*, 2017:7517350, 2017; [11] Latham et al., *Front Physiol*, 12:660498, 2021; [12] Mason et al., *PLoS Biology*, 2(10):e288, 2004; [13] Egan et al., *J Physiol*, 588(10):1779-90, 2010 [14] MacInnis & Gibala, *J Physiol*, 595(9):2915-30, 2017.

# MODELLING INDENTATION OF SKIN USING A THIN-LAYER NONLINEAR HYPERELASTIC MODEL

**L. Li (1), M. Masen (1)**

(1) Department of Mechanical Engineering, Imperial College London, London, United Kingdom

## INTRODUCTION

A full understanding of the mechanical properties of skin tissue is crucial for exploring the tissue behaviors and tolerance in all kinds of activities, as well as designing improved medical and clinical devices. Hertz' theory, as the classical contact mechanics theory, is commonly used to define the mechanical parameters from indentation tests on a range of soft tissues, by assuming the tissue follows linear elastic behavior, with small deformation. However, most soft tissues express nonlinear properties during indentation tests. This nonlinear behavior does not only depend on the intrinsic hyperelastic properties of the tissue, but also originates from geometric confinement, for instance most tissue specimens used in mechanical tests only have a small thickness and are supported by a hard or rigid specimen holder. Hayes' model provides a numerical solution to describe such substrate effects during indentation tests but is still based on the linear elastic field equations, meaning it cannot be used to describe the behavior for soft tissues with hyperelastic properties and at large deformations. Ogden's model has been proven to provide a good description for hyperelastic behavior of soft tissues, including skin.

In this study, a computational model based on Ogden's material model was established to describe thin skin tissue with nonlinear hyperelastic properties during spherical indentation. Following a similar procedure as the Hayes model, two correction functions were introduced to account for the effect of geometric confinement due to both the substrate and indenter geometry. The correction functions are defined based on the radius of the spherical indenter, the thickness of the indented sample and the depth of indentation into the tissue. Additionally, a parameter defining the relationship between the contact radius and indentation conditions, as quantified the indenter size and the sample thickness, was defined to consider the nonlinear behavior of the soft tissue under large deformation. The numerical simulations obtained were compared with experimental data, providing a good match.

## METHODS

Hayes model as shown in Eq. (1) is commonly used to describe the contact force $P$ during indentation of thin layered homogeneous isotropic soft materials on a solid substrate. It was established based on a representation of the underlaying boundary value problem in terms of potential functions [1].

$$P = \frac{2\kappa\sqrt{\chi}ER^{\frac{1}{2}}\omega_0^{\frac{3}{2}}}{1-\nu^2} \tag{1}$$

where $P$ is contact force, $E$ is the elastic modulus, $\nu$ is the Poisson's ratio and $\omega_0$ is the indentation depth. $\kappa$ and $\chi$ are correction parameters used to account for the geometric confinement due to the boundary condition and indenter geometry, respectively. They were determined by the explicit solution of the Fredholm integral equation $\omega$, as Eq (2) and (3).

$$\kappa = \frac{P(1-\nu)}{4aG\omega_0} = \int_0^1 \omega(\tau)\mathrm{d}\tau \tag{2}$$

$$\chi = \frac{a^2}{\omega_0 R} = \frac{-\omega_1(1)}{\omega_2(1)} \tag{3}$$

in which $\omega$ could be obtained as follows:

$$\begin{aligned}
&\xi = \frac{x}{a}, \quad \tau = \frac{t}{a} \\
&\omega(\xi) = \omega_1(\xi) + \frac{a^2}{\omega_0 R}\omega_2(\xi) \\
&\omega_1(\xi) = 1 - \frac{1}{\pi}\int_0^1 \omega_1(\tau)\left[K(\tau+\xi) + K(\tau-\xi)\right]\mathrm{d}\tau \\
&\omega_2(\xi) = -\xi^2 + \frac{1}{\pi}\int_0^1 \omega_2(\tau)\left[K(\tau+\xi) + K(\tau-\xi)\right]\mathrm{d}\tau
\end{aligned} \tag{4}$$

From Eq. (2), two correction parameters $\kappa$ and $\chi$ are related to the contact radius $a$,the indentation depth $\omega_0$ and the indenter radius $R$. In

classical Hertz' model, there is $\kappa = 3/2$ and $\chi = 1$. Therefore, the contact radius $a$ could be written as Eq. (5).

$$a = \omega_0^{\frac{1}{2}} R^{\frac{1}{2}} \tag{5}$$

Extending this to hyperelastic material and following the approach followed by Lin [2], we assume a similar relationship using the Hayes correction parameter $\chi$.

$$a = \sqrt{\chi}\,\omega_0^{\,m} R^{1-m} \tag{6}$$

In Ogden's model, the stress σ relates to the strain, quantified in terms of the stretch ratio λ, as defined in Eq. (7), following an exponential relationship with an exponent of $\alpha$-1 [2]. For hyperelastic materials these expressions can be combined to derive a relationship between force and indentation depth for small deformations. To accommodate large deformation, the contact force was further modified following Fessel's [3] method, to finally provide Eq. (9), describing the relationship between force and indentation for a hyperelastic material under large deformation.

$$\sigma = \frac{2\mu}{\alpha}\left(\lambda^{\alpha-1} - \lambda^{-\alpha/2-1}\right) \tag{7}$$

$$\lambda = 1-\varepsilon, \quad \varepsilon = u_z + \frac{1}{2}u_z^{\,2}, \quad u_z = \omega_0 - \psi(r) \tag{8}$$

$$P = \frac{2\kappa\sqrt{\chi}ER^{1-m}\omega_0^{\,(\alpha-1+m)}}{\left(1-\nu^2\right)\left(1-\omega_0/h\right)^n} \tag{9}$$

In these equations, $\mu$ *and* $\alpha$ are the Ogden material parameters, $\lambda$ is the stretch ratio, $\varepsilon$ the strain, *u the* displacement and *h* the sample thickness. The correction factors $\kappa$, $\chi$, *m* and *n* relate to the indenter radius *R*, the indentation depth $\omega_0$ and the sample thickness *h*.

## RESULTS

The FEA model is shown in Figure 1, where both the substrate and the indenter were defined as steel.

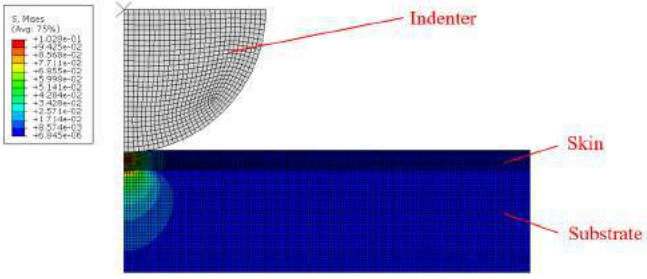


**Figure 1: Overview of the Finite Element Model, showing the stress distribution in the tissue and the substrate during indentation**

An initial estimate of the Ogden material parameters ($\mu$ = 0.2566 and $\alpha$ = 1.9942) was obtained from literature [2]. Subsequently, a series of numerical simulations was conducted with these material properties in which the indenter radius was varied between 4 mm and 8 mm in intervals of 0.5 mm. From these simulations, curves describing the relationship between contact radius *a* and indentation depth $\omega_0$ were extracted as shown as the blue circles in Figure 2. From this data, the parameters $\chi$ and *m* were obtained, curve fitting Eq. (6) shown as the red curves in Figure 2. The obtained values are listed in Table 1. For reference, the green curves in Figure 2 represent the assumed material behaviour for $m = n = 0.5$, representing the Hertz solution of Eq. (5).

**Table 1: The parameters *m* and $\chi$ obtained from simulations**

| ***R* [mm]** | 4.0 | 4.5 | 5.0 | 5.5 | 6.0 | 6.5 | 7.0 | 7.5 | 8.0 |
|---|---|---|---|---|---|---|---|---|---|
| ***m*** | 0.6067 | 0.6054 | 0.6054 | 0.6038 | 0.6054 | 0.6044 | 0.5888 | 0.6044 | 0.6027 |
| **$\chi$** | 7.7494 | 7.0541 | 6.4912 | 5.9983 | 5.6212 | 5.4150 | 4.9974 | 4.8354 | 4.7214 |
| **$\kappa$** | 0.5763 | 0.6337 | 0.6981 | 0.7614 | 0.8284 | 0.8885 | 0.9016 | 1.0221 | 1.0545 |
| ***n*** | 1.5 | 1.5 | 1.5 | 1.5 | 1.5 | 1.5 | 1.5 | 1.5 | 1.5 |

Whilst *m* takes a fairly constant value of 0.6 irrespective of indenter radius *R*, $\chi$ reduces substantially with increasing value of *R*. Substituting this into Eq. (5) provides the following relation between contact radius, indenter size and indentation depth, $a = \sqrt{\chi}\,\omega_0^{\,0.6} R^{0.4}$, where $\chi$ follows Table 1. With $\chi$ and *m* known, values for $\kappa$ and *n* can be obtained from curve fitting eq. (8) through the numerically determined relationship between contact force *F* and indentation depth $\omega_0$.

Finally, the skin Ogden modulus $\mu$ and material parameter $\alpha$ were updated by curve fitting Eq. (9) through physical experimental results obtained on skin tissue using the Biomomentum soft tissue indenter, resulting in $\mu = 0.37 \pm 0.24$ MPa and $\alpha = 1.98 \pm 0.09$.

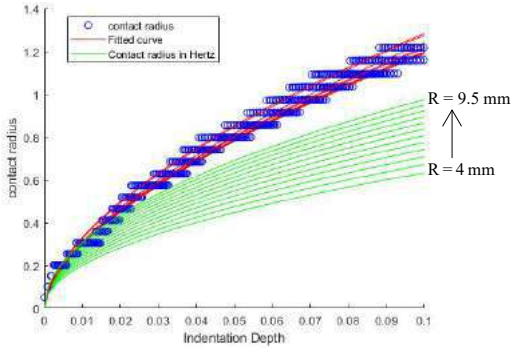


**Figure 2: Relationship between a and $\omega_0$ for different indenter radii.**

## DISCUSSION

To accurately describe the indentation behaviour of thin soft tissue, we employ two correction functions $\kappa$ and $\chi$ to account for the limited thickness of the specimens, in combination with two hyperelastic correction parameters *n* and *m.* The result is a semi-analytical model describing the hyperelastic behavior of thin specimens of soft tissue in indentation tests. The relationship between force and indentation as obtained using this model provides a more accurate description of experimental results. The material parameters extracted from experimental results, at present show a relatively large variation.

## REFERENCES

[1] Hayes W C, Keer L M, Herrmann G, et al. *Journal of biomechanics*, 1972, 5(5): 541-551.
[2] Lin D C, Shreiber D I, Dimitriadis E K, et al. *Biomechanics and modeling in mechanobiology*, 2009, 8(5): 345-358.
[3] Fessel A, Döbereiner H G. *Biomechanics and modeling in mechanobiology*, 2018, 17(2): 419-438.

SB³C2022
Summer Biomechanics, Bioengineering and Biotransport Conference
June 20-23, Eastern Shore, MD, USA

# CONTRIBUTION OF ELASTIN AND COLLAGEN TO THE MECHANICAL BEHAVIOR OF BOVINE NUCHAL LIGAMENT

**S. Halvorsen (1), R. Wang (1), Y. Zhang (1,2,3)**

(1) Mechanical Engineering, Boston University, Boston, Massachusetts, United States
(2) Biomedical Engineering, Boston University, Boston, Massachusetts, United States
(3) Division of Materials Science & Engineering, Boston University, Boston, Massachusetts, United States

## INTRODUCTION

Bovine nuchal ligament, or *ligamentum nuchae*, is a highly elastic structure often used in tissue research for its abundance of the structural protein elastin. Located in the dorsal cervical region, the *ligamentum nuchae* stabilizes the head and neck. The ligament comprises two distinct regions – a lamellar portion and a paired funiculus, which extend from the external occipital protuberance of the skull and gradually unite to form the stiffer supraspinous ligament that runs along the spine [1]. The funiculus has an organized structure of closely interwoven elastic fibers and collagen fibrils, the two most abundant structural proteins in the body. These fibers are almost entirely oriented along the direction of the spine [2].

Elastic fibers provide elasticity and resilience while collagen provides strength and stiffness, and a balance between these proteins is necessary for physiological functions of *ligamentum nuchae*. Elastic fibers make up approximately 70% of the ligament [3], while collagen content is split between types I and III collagen with small amounts of types IV, V, and VI [2]. Understanding bovine *ligamentum nuchae* structure and mechanics is necessary to consider tissue grafting. Previous studies demonstrate the effectiveness of autografting equine *ligamentum nuchae* for digital flexor tendon healing in donkeys [4].

To better understand the structure and mechanical behavior of *ligamentum nuchae*, this study combines imaging and mechanical testing to quantitatively examine the elastin and collagen microstructure and their individual contribution to the nonlinear stress-strain behavior of the tissue. Additionally, a transversely isotropic structure-based constitutive model that considers the structural organization of elastic and collagen fibers is presented.

## METHODS

*Sample Preparation*

Bovine nuchal ligaments excised from male Holstein calves aged 2-14 days old were frozen in a -20°C freezer before experiments. Rectangular samples ($n = 5$) approximately 30×8×3 mm in size were cut from the ligaments and sandpaper tabs were glued at the ends. For purified elastin network, ligament samples were treated with cyanogen bromide (CNBr) in 70% formic acid to remove all constituents apart from the elastin network [5]. Sandpaper tabs were then re-attached for further mechanical testing.

*Uniaxial Tensile Testing*

Samples were tested before and after CNBr treatment in uniaxial strain-control at 0.5 mm/s up to 1.35 stretch for 12 cycles using an Instron testing device equipped with a 10 N load cell. Force and displacement were recorded. Assuming incompressibility, Cauchy stress $\sigma$ was calculated using Eq. 1:

$$\sigma = F\lambda/A_o \quad (1)$$

where $A_o$ is the undeformed cross-sectional area and $\lambda$ is the stretch. Tangent modulus was calculated as the slope of the unloading stress-stretch curve using *gradient* function in MATLAB.

*Histological Study*

Intact and elastin network samples oriented in both longitudinal and transverse directions ($n = 4$) were stained with Movat's Pentachrome for histological study. Histological slides were imaged under an Olympus VS120 Slide scanner at 40× magnification.

*Multiphoton Imaging*

Multiphoton imaging was performed to study the structure of elastic and collagen fibers in *ligamentum nuchae* using a Carl Zeiss LSM 710 NLO microscope with a 20× water immersion objective. Samples were immersed in 1× PBS for imaging. The femtosecond infrared 810 nm pulse laser generated two-photon excited fluorescence from elastin (525/45 nm) and second harmonic generation from collagen (417/80 nm) [5]. Z-stack images were acquired with an interval of 1 μm with total depths ranging from 50 to 100 μm.

SB³C2022-086

*Constitutive Modeling*

Structure-based constitutive models that consider the organization of elastic and collagen fibers were developed and used to describe the mechanical behavior of intact *ligamentum nuchae* and purified elastin network that was assumed to be transversely isotropic. Modified from Holzapfel et al. [6], the elastin network is modeled using a single-fiber family model, with the strain energy function shown below in Eq. 2:

$$W_E = C_{10}(\bar{I}_1 - 3) + \frac{k_{1E}}{2k_{2E}} \exp[k_{2E}\langle \bar{I}_4 - 1\rangle^2] - 1 \quad (2)$$

The model contains three parameters: $C_{10}$, $k_{1E}$, and $k_{2E}$, which represent the ground substance response, a stress-like parameter, and a unitless parameter, respectfully. $\bar{I}_1$ and $\bar{I}_4$ are the first and fourth invariants, respectively. The strain energy function for the intact *ligamentum nuchae* tissue considers the contribution from both elastic and collagen fibers by incorporating a second fiber family for collagen, described by two new parameters: $k_{1C}$ and $k_{2C}$, and is shown in Eq. 3 as:

$$W_C = W_E + \frac{k_{1C}}{2k_{2C}} \exp[k_{2C}\langle \bar{I}_4 - 1\rangle^2] - 1 \quad (3)$$

Cauchy stress is derived from the strain energy function as:

$$\sigma_m = -pI + 2F * \frac{\partial W}{\partial C} * F^T \quad (4)$$

where $I$ is the identity tensor and $p$ the Lagrange multiplier. Both models were fitted simultaneously to the stress-stretch responses of elastin network and intact tissue using the *fminsearch* function in MATLAB to minimize an objective function. Goodness of fit was measured by the root mean square error [7].

## RESULTS

Figure 1a shows averaged stress-stretch response for intact *ligamentum nuchae* and elastin network under uniaxial tension. The stress-stretch responses of the two groups of samples are similar prior to 1.25 stretch, at which point the intact tissue stiffens. A similar trend was observed in the tangent modulus in Fig. 1b, increasing from 0.5 MPa to nearly 8 MPa between 1.25 and 1.35 stretch for the intact tissue.

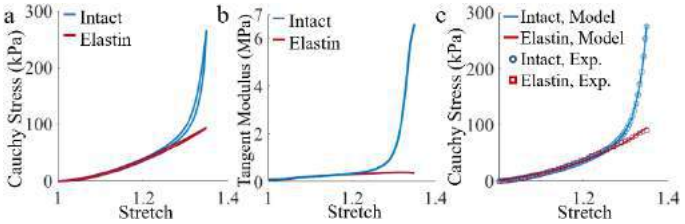


**Figure 1. (a) Averaged stress-stretch responses and (b) averaged tangent modulus for *ligamentum nuchae* and elastic network samples. (c) Representative results showing the fitting of the stress-stretch response of elastin network and *ligamentum nuchae* using the constitutive models in Eqs. 2 and 3.**

Figure 1c contains a representative plot demonstrating the fitting capability of the constitutive models. Material parameters for the hyperelastic behavior of *ligamentum nuchae* and elastin network are $C_{10}$=0 kPa, $k_{1E}$=26.277 kPa, $k_{2E}$=0.269, $k_{1C}$=0.0715 kPa, and $k_{2C}$=9.965. The model RMS error of the sample is 0.0371 with an $R^2$ value of 0.98.

Histological stains of intact tissue and elastin network shown in Figures 2a and 2b depict the longitudinal cross-sections of the tissue samples, respectively. Figure 2a shows longitudinally oriented wavy elastin and collagen fibers with the presence of ground substance, while only elastin fibers are shown in Figure 2b due to the removal of other constituents, as evidenced by the white empty spaces.

Figures 2c and 2d contain a multiphoton image and Z-stack image, respectively, of the transverse cross-section view of *ligamentum nuchae*. The dotted pattern seen in Figure 2c is due to the elastic fibers coming out of the page. Collagen is generally sparse in comparison to elastin fibers, with few visible in Figure 2c. Localized collagen-rich

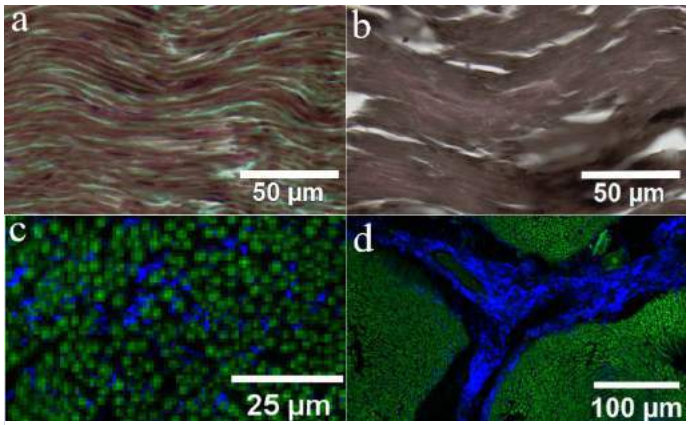


**Figure 2. (a,b): Histological images of *ligamentum nuchae*. Movat's Pentachrome stains elastin grey, collagen yellow, and ground substance blue-green. (c,d) Multiphoton images of *ligamentum nuchae*, with elastin shown in green and collagen in blue.**

regions exist throughout the ligament, as shown in a maximum intensity projection of a 75 μm deep Z-stack in Figure 2d.

## DISCUSSION

In this study, we examined the contributions of elastic and collagen fibers of *ligamentum nuchae* by combining uniaxial tension data with multiphoton imaging and histological studies. Our study demonstrates elastic fibers are responsible for undertaking the mechanical loading under 1.25 stretch, after which the engagement of collagen fibers results in significant stiffening behavior (Fig. 1). Removal of collagen inhibits sample stiffening. The delay in stiffening implies an elastic extension of the ligament in physiological range with lower resistance. Collagen recruitment acts as a protection point to prevent overextension of cattle neck, possibly leading to tissue damage. Purified elastin uniaxial stress-stretch data is comparable with that from Green et al. [8]. Age- and disease-induced reorganization and degradation of the elastic and collagen fibers may affect both the contribution of elastin to deformation of *ligamentum nuchae* and the collagen recruitment process due to their closely interwoven structure.

The transversely isotropic constitutive models developed in this study (Eqs. 1 and 2) effectively capture the mechanical behavior of purified elastin network and intact tissue. The contribution of strain energy due to ground substance is much smaller compared to the fiber families, suggesting that the elastin and collagen are the main contributors to sustain the mechanical loading.

In conclusion, our study reveals the sequential roles of elastin and collagen fibers in contributing to the mechanical response of *ligamentum nuchae*. The mechanical behavior of *ligamentum nuchae* was well captured by a transversely isotropic structure-based constitutive model that considers the contribution of elastic and collagen fiber families.


## ACKNOWLEDGEMENTS

This research was supported in part by 2R01HL098028.


## REFERENCES


[1] Budras and Havel, *Bovine Anatomy*, 58, 2003.
[2] Morocutti, M et al., *J Anatomy*, 178:145–154, 1991.
[3] Jackson, DS et al., *Biochemical Journal*, 96:813-817, 1965.
[4] Khajeh, A et al., *Vet. Res. Forum*, 12(1):53-61,2021.
[5] Yu, X et al., *J. Mech Behavior of Biomed Mats*, 77(2018):745-753.
[6] Holzapfel, G et al., *J. Elast*, 61(1):1-48, 2000.
[7] Holzapfel et al., *Am. J. Phys. Heart. C.*, 289(5):H2048-2058, 2005.
[8] Green, EM et al., *Interface Focus*, 4(2):20130058, 2014.

SB³C2022
Summer Biomechanics, Bioengineering and Biotransport Conference
June 20-23, Eastern Shore, MD, USA

# STOCHASTIC OPTIMIZATION OF A POROHYPERELASTIC BILAYERED VASCULAR GRAFT TO IMPROVE HEMOCOMPATIBILITY

**A. Behrangzade (1), B.R. Simon (4), W.R. Wagner (1, 3,5), J.P. Vande Geest (1,2,5)**

(1) Department of Bioengineering, University of Pittsburgh, Pittsburgh, PA, USA
(2) Department of Mechanical Engineering and Material Science, University of Pittsburgh, Pittsburgh, PA, USA
(3) Department of Chemical Engineering, University of Pittsburgh, Pittsburgh, PA, USA
(4) Department of Aerospace and Mechanical Engineering, University of Arizona, Tucson, AZ, USA
(5) McGowan Institute for Regenerative Medicine, Pittsburgh, PA, USA

## INTRODUCTION

Cardiovascular disease (CVD) is the leading cause of mortality in the U.S. and globally (1). Atherosclerosis is a form of CVD that is characterized by the formation of a fatty plaque inside the artery. In this disease, the fatty plaque blocks the blood flow and can potentially cause myocardial infarction and stroke. The availability of autologous blood vessels such as saphenous vein and radial artery is limited for bypass surgery. Synthetic grafts like expanded polytetrafluoroethylene (ePTFE) and Dacron have high failure rates specifically in small-diameter applications. Thrombosis and Intimal Hyperplasia (IH) are two main failure mechanisms of vascular grafts. The onset of thrombus formation is linked to deviation from homeostatic hemodynamic condition where activated platelets and polymerized fibrin create a thrombosis that can ultimately lead to arterial occlusion (2). During IH, different factors including compliance mismatch between the graft and native tissue cause smooth muscle cell migration toward the lumen which thickens the vascular wall and causes stenosis (3). A variety of methods have been researched to prevent stenosis, however, it has yet remained a clinical problem. In porous vascular grafts, blood can penetrate through the structure during systole and can be reversed during diastole. We hypothesized that a large luminal reversal fluid velocity (LRFV) carries a momentum that can repel the platelets and reduce the incidence of thrombosis and matching the compliance reduces the likelihood of IH. In this study, we determined the material, geometrical, and transport properties of a bilayered vascular graft that maximize the LRFV while simultaneously matching the compliance to a target artery. A multi-objective function was minimized using a particle swarm optimization algorithm to find the optimized graft properties.

## METHODS

We developed a porohyperelastic (PHE) finite element framework to model a bilayered and porous vascular graft. We used ABAQUS solver to run the simulations. In this solver, transport in a deformable porous media is governed by Darcy's law (4).

$$v_i{}^{fr} = -\frac{k_A}{\gamma_f}\frac{\partial p^f}{\partial x_i} \quad (1)$$

$v_i{}^{fr}$ is the relative fluid velocity, $k_A$ is the apparent permeability, $\gamma_f$ is the specific weight of the permeating fluid (water), and $p^f$ is the pore fluid pressure. A compressible Neo-Hookean model was utilized to model the material behavior.

$$U^{eff} = C_{10}(\bar{I}_1 - 3) + \frac{1}{D_1}(J-1)^2 \quad (2)$$

$U^{eff}$ is the effective drained strain energy potential per unit of reference volume, $J$ is the total volume ratio, $I_1$ is the first deviatoric strain invariant. $C_{10}$ and $D_1$ are material parameters. $C_{10}$ and Poisson's ratio $(v)$ were defined as open-fit parameters and the relationship between $C_{10}$ , $D_1$ and $v$ was used to calculate $D_1$ in each simulation.

$$D_1 = \frac{3(1-2v)}{2C_{10}(v+1)} \quad (3)$$

A 2D axisymmetric model was developed in this study (Figure 1) and the dimensions were matched to rat aorta (internal diameter of 1.2mm, thickness of 100µm and a cardiac cycle duration of 0.15s). There were three steps in our simulations: 1) internal ramping pressure from zero to 100mmHg 2) consolidation 3) cyclic pressure between 80 and 120mmHg. A mesh convergence study was implemented with a criterion of less than 1% difference in the luminal reversal flow. The results revealed that a 0.5-micron element size in the radial direction is appropriate. All rotational degrees of freedom, displacements in the axial direction and pore pressure at the outer surface of the graft wall were set to zero.

SB³C2022-087

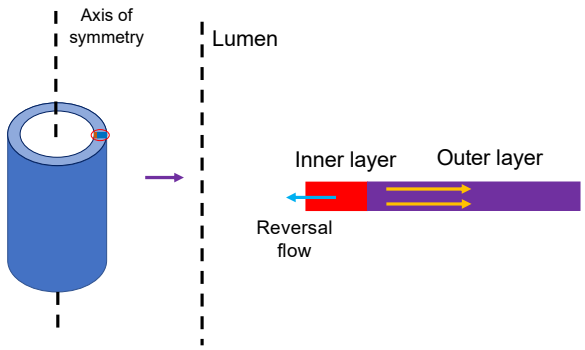


**Figure 1. Geometry of the vascular graft in the 2D Axisymmetric model**

A two-step particle swarm optimization algorithm (MATLAB) was utilized to minimize the objective functions (5). The results of the first step of the optimization were used as the initial guess for the second step. In single-objective optimization, we focused on maximizing the luminal reversal flow using the following function.

$$f_{so} = e^{v^{fr}} \tag{4}$$

For multi-objective optimization, we simultaneously maximized the LRFV and matched the compliance to rat aorta (C=0.0014) using the following function.

$$f_{mo} = \sqrt{s_1\left(\frac{e^{v^{fr}} - {f_{so}}^{opt}}{{f_{so}}^{opt}}\right)^2 + s_2\left(\frac{f_c - C_{ratiaorta}}{C_{ratiaorta}}\right)^2} \tag{5}$$

$s_1$ and $s_2$ are scaling factors, ${f_{so}}^{opt}$ is the minimized single-objective function and $f_c$ is the graft compliance in each simulation. $C_{10}$, $v$, $k_A$ and t for each layer were the open-fit parameters except for the outer layer thickness which was calculated based on the overall thickness and the thickness of the inner layer. Table 1 summarizes the optimization constraints.

**Table 1. Optimization constraints**

| | $C_{10} i(kpa)$ | $v$ | $k_A(m/s)$ | t (μm) |
|---|---|---|---|---|
| Lower bound | 80 | 0.3 | $1e^{-3}$ | 10 |
| Upper bound | 1000000 | 0.49 | $1e^{-12}$ | 90 |

## RESULTS

Figure 2 represents the LRFV and compliance of the vascular graft in both optimizations. In single-objective optimization, we achieved a maximum LRFV of 168 μm/s. In this optimization, the graft compliance was approximately 5 times larger than that of rat aorta. In multi-objective optimization, imposing mechanical constraints to match the compliance resulted in a lower LRFV of 49 μm/s. The graft compliance was precisely matched to the target artery. Table 2 summarizes the optimized parameters for both optimizations. These results indicate the significance of increasing the thickness of a highly permeable inner layer and a low-permeability outer layer in a compressible soft vascular graft to increase the LRFV. $C_{10}$ value of the outer layer in the multi-objective optimization was optimized to match the compliance to rat aorta. Poisson's ratio values are all at the bounds indicating the effect of high compressibility on the LRFV.

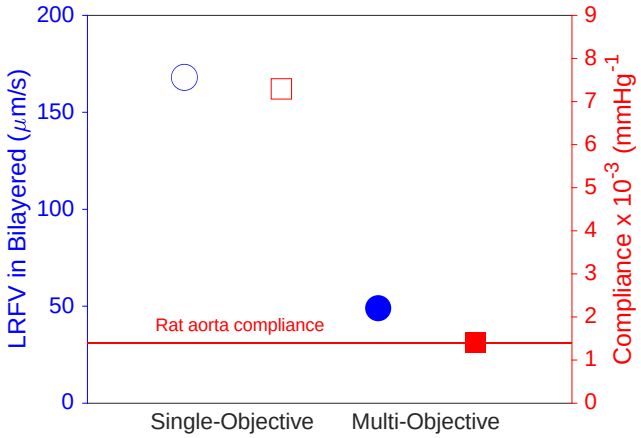


**Figure 2. LRFV and compliance in single and multi-objective optimizations**

**Table 2. Optimized parameters in both optimizations. ($C_{10}$ is in $kpa$, $k_A$ is in $m/s$ and thickness is in μm)**

| | Inner layer | | | | Outer layer | | | |
|---|---|---|---|---|---|---|---|---|
| | $C_{10}$ | $v$ | $k_A$ | t | $C_{10}$ | $v$ | $k_A$ | t |
| SO | 80 | 0.3 | $7.6e^{-4}$ | 90 | 80 | 0.3 | $\mathbf{1.5e^{-11}}$ | 10 |
| MO | 80 | 0.3 | $1e^{-3}$ | 90 | $\mathbf{1.1e^{-3}}$ | 0.3 | $1e^{-12}$ | 10 |

## DISCUSSION

In this research, we optimized the material, geometrical, and transport properties of a porohyperelastic bilayered vascular graft to maximize the LRFV which can potentially repel the platelets. We achieved an LRFV of 168 μm/s and 49 μm/s in the single-objective and multi-objective optimization, respectively. In multi-objective optimization, we accurately matched the graft compliance to rat aorta. Soldani et. al., have shown that a highly permeable inner layer and a highly impermeable outer layer can reduce thrombus formation in-vivo (6), which is consistent with our optimization results. Ayyalasomayajula et. al, have also captured luminal reversal flow in an abdominal aortic aneurysm computational model (7). We used a compressible Neo-Hookean material to perform this study. More complex constitutive models and incorporation of anisotropy into our model can potentially alter the optimization results. Thrombosis in both acute and chronic form has long been a major clinical problem. Although we require in-vitro and in-vivo data to support our hypothesis, our computational findings open a new avenue to address this clinical need.

## ACKNOWLEDGEMENTS

This study was supported by the American Heart Association award 20PRE35211036 and NIH award R01HL157017.

## REFERENCES

[1] Heart diseaes and stroke statistics, *Circ.*, 2021.
[2] Lippi, G et al., *Nat Rev Cardiol*, 2011.
[3] Ballyk, P et al., *J Biomech*, 1998.
[4] Vande Geest, J et al., *J Biomech Eng*, 2011.
[5] Kennedy, J et al., *Morgan Kaufmann Publisher Inc*, 2001.
[6] Soldani, G et al., *Biomaterials*, 2009.
[7] Ayyalasomayajula, A et al., *J Biomech Eng*, 2010.

SB³C2022
Summer Biomechanics, Bioengineering and Biotransport Conference
June 20-23, Eastern Shore, MD, USA

# BIOMECHANICAL WALL THICKNESS AND STIFFNESS UNCERTAINTY QUANTIFICATION IN AN IDEALIZED MODEL OF THE PRE-STRETCHED DISSECTED AORTA

**Lise Gheysen (1), Lauranne Maes (2), Mathias Peirlinck (3), Annette Caenen (1), Nele Famaey (2), Patrick Segers (1)**

(1) Electronics and Information Systems, Ghent University, Ghent, Belgium
(2) Mechanical Engineering, KU Leuven, Leuven, Belgium
(3) Biomechanical Engineering, Delft University of Technology, Delft, The Netherlands

## INTRODUCTION

Despite a high short-term success rate of thoracic endovascular aortic repair (TEVAR) for type B aortic dissections, the desired mid- and long-term outcome, i.e. the formation of a fully thrombosed false lumen, is often not obtained. Instead, for 30% of the patients aortic expansion within the first year is observed [1]. Up to now, it has not been elucidated how to predict which patients will benefit from TEVAR on the long-term. Consequently, more insight into the effect of TEVAR on the dissected aortic wall may be required to further optimize the current treatment on a patient-specific level. In order to fully understand the effect of this treatment, it is needed to accurately capture the biomechanical response of the stent graft deployment on the blood flow and the dissected aortic wall. Such insight may be acquired from computational biomechanical studies, but dissected wall models are currently fairly limited and, to the best of our knowledge, do not include anisotropy combined with constituent-specific residual stretches in the soft tissue [2]. Besides, the influence of both geometrical, e.g. wall thickness, and material modeling parameters on the resulting wall displacement remains largely unknown. With the long-term goal to predict the patient-specific outcome of TEVAR, it is essential to know the influence of variations in these parameters, especially for those parameters that cannot be retrieved from clinical CT scans.

Therefore, this study aims to develop a computational framework of an idealized dissected aortic wall, including anisotropy and residual stresses, which is used to estimate the uncertainty on the predicted wall displacements.

## METHODS

The finite element model framework for the idealized dissected aortic wall was developed in Abaqus\Standard (Dassault Systèmes, France). The model was generated, starting from a cylinder, with a diameter of 27.3 mm and length of 60 mm, that contained a false lumen, with a length of 40 mm, and tears in the dissected membrane (DM), both with a predefined size and location [3]. The wall consisted of a medial and an adventitial layer, both modelled as an anisotropic hyperelastic material according to the Gasser-Ogden-Holzapfel (GOH) model [4]. The deposition stretches of elastin and collagen were included using a Matlab (The MathWorks Inc., Natick, MA, USA) implementation of the algorithm presented by Famaey et al. for an intact thick-walled cylinder without false lumen or tears [5]. Firstly, these deposition stretches were applied and the true and false lumen were subsequently loaded to diastolic (80 mmHg) and systolic (120 mmHg) pressure. A mesh sensitivity study was performed to ensure a mesh independent outcome and resulted in a model with 36 000 hexahedral elements.

The uncertainty related to the unknown total wall (1.3-2.5 mm), medial (65-85% of total wall thickness) and DM (50-90% of medial thickness) thickness and material properties ($c_{10}$ = 0.005-0.025 MPa , $k_1$ = 0.0002-1.0 MPa, $k_2$ = 4.0-35.0, $\alpha$ = 0-90°, $\kappa$ = 0-1/3) was estimated, using a Latin hypercube with 40 samples and input ranges based on a literature study. The conventional material properties of the GOH model were converted into a single clinically tangible functional stiffness parameter, i.e. the pulse wave velocity (PWV), which was assessed for a reference tube with the same material parameters. PWV at 80 mmHg was limited to the physiological range of 4 to 12 m/s. As the dissected wall deformation is of interest, the maximal displacements of the remaining wall (RW) and DM, relative to the intact configuration, at diastolic and systolic pressure were taken as output parameters.

## RESULTS

From the 40 samples of the Latin hypercube, 39 fulfilled Abaqus's convergence criteria. Each of the converged cases resulted in a typical dissected configuration with a narrowed true lumen and a false lumen that is bulging out, as shown in figure 1. The box plots, based on these 39 cases, of the maximal displacements of RW and DM at diastolic and systolic pressure are presented in figure 2, as well as the corresponding absolute difference in maximal displacement between diastole and

systole. For RW, median maximal displacement values of 2.21 mm and 2.78 mm were found at diastolic and systolic pressure, respectively. For DM, median maximal displacements of 5.76 mm in diastole and 6.10 mm in systole were observed. Considering the absolute difference of the maximal displacements at diastolic and systolic pressure, median values of, respectively, 0.62 mm and 0.23 mm were observed for RW and DM.

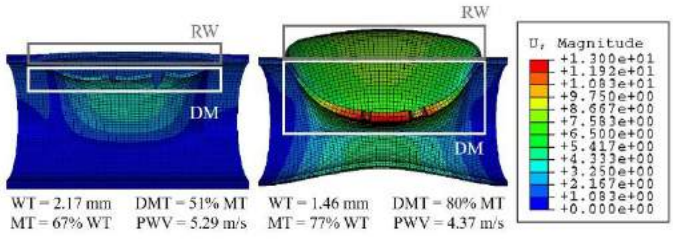


**Figure 1: Deformed systolic configurations for two samples that represent the extent to which the bulging in and out of the dissected membrane (DM) and remaining wall (RW) varies. The applied input parameters – wall thickness (WT), media thickness (MT), dissected membrane thickness (DMT) and pulse wave velocity (PWV) – for both samples are indicated too. The displacement magnitude (U) is given in mm.**

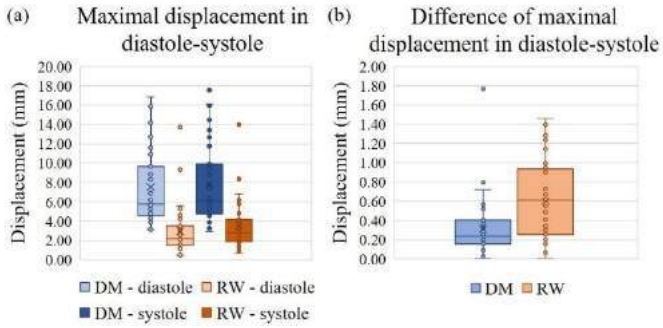


**Figure 2: Boxplots of (a) the maximal displacements of the dissected membrane (DM) and remaining wall (RW) at diastolic and systolic pressure and (b) the absolute difference between these displacements of DM and RW, based on the 39 converged samples.**

Based on the minimal and maximal results, uncertainty ranges of [-79; 524]% and [-75; 417]% of the corresponding median value were found for the maximal displacement of RW in diastole and systole. Similarly, variations of [-45; 195]% and [-51; 190]% were found for DM at diastolic and systolic pressure, respectively. By using the interquartile range, the following variations w.r.t. the corresponding median value were found in diastole and systole, respectively: [-33; 56]% and [-33; 49]% for RW; [-20; 62]% and [-21; +58]% for DM.

## DISCUSSION

From the 40 simulated Latin hypercube samples, based on large though physiologically relevant ranges for the considered input parameters, only one case with a total wall thickness of 1.35 mm diverged. This points out that a robust model framework was developed for an idealized dissected aortic wall.

The median maximal displacement is larger for DM compared to RW, both in diastole and systole. By considering the differences between diastole and systole, an estimation is made for the expected displacement throughout the cardiac cycle, although no pressure waves are taken into account and the locations of the maxima might differ. The simulations with this idealized model yielded a median DM displacement of 0.23 mm from diastolic to systolic pressure, with values ranging from 0.01 mm to 1.77 mm. Baumler et al. observed a maximal DM displacement of 0.6 mm in the cardiac cycle based on 4D MRI data for a patient-specific case, while Ganten et al. observed a median maximal DM displacement of 1.3 mm [2,6]. There is, thus, still a discrepancy between the model results and the experimental data, which is suggested to be mainly caused by the difference in dissection length. Indeed, the dissection extended from the thoracic to the abdominal aorta in the experimental data whereas the dissection length in the idealized model was only 40 mm. However, a similar order of magnitude was obtained, especially when comparing to the data of Baumler et al. [2].

Although the median maximal RW displacement has a lower magnitude, it seems to result in higher variations between systolic and diastolic pressure, i.e. a median difference of 0.62 mm, compared to DM. Taking into account that the same pressure load is applied to the true and false lumen, it is intuitive that RW displacement is more susceptible to variations in pressure.

The full uncertainty ranges based on the minimal and maximal displacement results, over all cases, show large variations, in particular for RW. The uncertainty based on the interquartile ranges is remarkably smaller, with a total variation of 80-90% of the corresponding median maximal displacement for RW and DM. Although a smaller range is expected, the large differences in upper boundary might indicate that the full uncertainty ranges overestimate the uncertainty for the majority of the cases. However, it is important to keep in mind that these extreme cases can, although rarely, occur as well.

For both types of uncertainty ranges, no large differences were observed between systole and diastole, suggesting that the applied pressure load will influence the uncertainty results only up to a limited extend. It might, therefore, be sufficient to consider one loading state when looking into the uncertainty imposed by unknown wall thicknesses and material parameters.

This study presented a robust model framework of the soft tissue behavior in an idealized aortic dissection. Although the geometry was idealized, an advanced material model including constituent-specific residual stresses was applied. This framework was used to quantify the uncertainty on the biomechanical response of the aortic dissection to inflation, taking into account the physiological variability of geometrical and constitutive material parameters that cannot be determined from clinical CT scans. It was shown that this variability strongly influences the predicted maximal displacements of DM and RW. It is, therefore, essential to report and further investigate the outcome uncertainty when developing dissected wall models. Given that the resulting uncertainty in wall displacement strongly depended on the exact uncertainty metric, a more advanced technique might be required to provide a more accurate estimate. It is, therefore, envisaged to combine the obtained result with a Gaussian process.

## ACKNOWLEDGEMENTS

L. Gheysen is funded by a doctoral grant (1S48920N) of the research foundation-Flanders.

## REFERENCES

[1] Fattori R. et al., Jacc-Cardiovascular Interventions **6**, 876 (2013).
[2] Bäumler K. et al., Biomechanics and Modeling in Mechanobiology, 1 (2020).
[3] Yamauchi T. et al., Cardiovasc Surg Res Grp, Journal of the American Heart Association **7**, e009196 (2018).
[4] Gasser T. C. et al., in *J. R. Soc. Interface*2006), pp. 15.
[5] Famaey N. et al., ZAMM-Zeitschrift fur Angewandte Mathematik und Mechanik (2018).
[6] Ganten M. K. et al., European Journal of Radiology **72**, 146 (2009).

SB³C2022
Summer Biomechanics, Bioengineering and Biotransport Conference
June 20-23, Eastern Shore, MD, USA

# CALIBRATING MECHANOREGULATORY MODELS OF FRACTURE REPAIR AND REMODELING USING IMAGING DATA FROM SHEEP

**Tianyi Ren, MS (1) and Hannah L. Dailey, PhD (1)**

(1) Department of Mechanical Engineering and Mechanics, Lehigh University Bethlehem, PA, USA

## INTRODUCTION

One of the most common misconceptions about bone repair pertains to remodeling. Traditionally, fracture healing is described as a sequence of four phases starting with an inflammation phase, followed by two repair phases consisting of soft callus formation and hard callus formation, and completed via a remodeling phase. Most numerical models assume that remodeling occurs after bridging and can therefore be neglected in favor of capturing the process of woven bone deposition in the callus. The potential drawback of this four-phase model is that it does not consider the often-significant temporal overlap between the different phases. The key barrier to developing new mechanoregulatory models that can consider coupled repair and remodeling is the lack of available *in vivo* validation data. Therefore, the objectives of this study were to: 1) measure remodeling activity during fracture healing using micro-computed tomography (μCT) scans of osteotomized ovine tibiae, and 2) use this *in vivo* data to calibrate a mechanoregulatory simulation of fracture repair with coupled remodeling. To achieve this, we developed an image-processing technique to noninvasively quantify structural remodeling adaptations at the bone-callus boundary and adapted an established strain-based numerical simulation framework to predict fracture repair with remodeling.

## METHODS

### *Image-Based Measurement of Remodeling During Fracture Healing*

Twenty-six adult female Swiss alpine sheep (average body weight 68 kg, range 63-76 kg) were part of previously completed research studies with tibial osteotomies stabilized by two different medial plates. Group 1 consisted of a 3-mm gap tibia osteotomy stabilized with a 12-hole stainless steel plate. Group 2 consisted of data from animals with a 17 mm gap tibia defect stabilized with a 12-hole stainless steel plate and augmented with autografts. After sacrifice at nine (Group 1) or twelve (Group 2) weeks, both tibiae (operated and intact) from each animal were excised and stripped of soft tissue. The stabilizing plate and screws were carefully removed from the operated tibia. Both tibiae were wrapped in saline-soaked gauze and μCT was scanned at 60.7 μm isotropic resolution.

The radiodensity data across the cortical-callus boundary was sampled from the images using our recently published method [1]. In brief, radial arrays of profile lines were created from the medullary canal through the callus. This process was repeated for sets of transverse planes containing 20 sequential slices each. Data points were sampled from the underlying pixels using bicubic interpolation, resulting in at least 170,000 data points in each region of interest (ROI). For this study, one ROI was sampled at the midshaft of each intact contralateral limb. Two ROIs were sampled for osteotomies, one just distal to the osteotomy line and one at the distal extent of the callus. Data from each profile line was registered to set its local linear coordinate system to zero at the bone-callus boundary (if osteotomized) or at the pericortical surface (if intact). Negative linear coordinates were normalized to the local cortex thickness; positive linear coordinates were normalized to the doubled local callus thickness. Radiodensity was normalized to the median cortical bone density in the untreated limb for each sheep. Multi-objective optimization in MATLAB was used to fit the parameters of a piecewise generalized sigmoid function describing the gradients in mineralization from cortical bone to callus. Fit parameters obtained for all 26 animals were then compared between the three ROIs. Two-tailed paired-samples t-tests was used to analyze if the fitting function constants and the evaluated slope of the fitting function at the pericortical boundary ($x$=0) were significantly different between the operated and contralateral limbs and between the central and peripheral callus. All statistical analyses were performed using SPSS Statistics 27 (IBM Corp; Armonk, New York, USA).

SB³C2022-089

### *Mechanoregulation Simulations with Coupled Repair & Remodeling*

Iterative simulations of bone healing with coupled remodeling were carried out in ANSYS with the mechanoregulation model controlled in MATLAB (R2021A; Mathworks, Inc.) using the Fuzzy Logic Toolbox (v. 2.3.1). Model parameters without remodeling activity were established in our previous studies [2,3]. Healing simulations were run with a fuzzy engine comprising 16 linguistic rules to control tissue differentiation based on dilatational and distortional strains, the volume fractions of connective tissue, cartilage, and bone at the previous iteration, and proximity to the fracture line. For this new work, remodeling was incorporated into our fuzzy logic framework by introducing a new tissue type (cortical bone, $E_{cb}\,i{=}\,i12.5iGPa$) with remodeling rules that activate only for cortical bone and woven bone elements, which were allowed to have density-dependent properties. The new regulatory remodeling model describes three levels of strain stimuli: resorption, quiescence, and formation. To capture the coupled remodeling of both cortical bone and callus, we adapted a published strain energy density-based description of the remodeling stimulus [4].

## RESULTS

### *Remodeling Occurs in Tandem with Early Fracture Healing*

The radiodensity sampling data clearly showed evidence of remodeling activity in the cortical wall bounded by callus (Fig. 1D). At the proximal and distal ends, there was an average decrease in density of 1-2% in the operated limbs compared to the intact contralateral limbs. At the midshaft, the preexisting increase in radiodensity toward the pericortical boundary seen in the intact bones (Fig. 1C) disappeared in the osteotomized bones (Fig. 1C/D). Comparing intact versus operated limbs, there were statistically significant differences in all obtained radiodensity profile fitting function parameters that describe the extent of remodeling ($p \leq 0.001$). At the pericortical boundary bounded by callus, these changes corresponded to a 23.4% drop on average from the peak density of the native cortical wall.

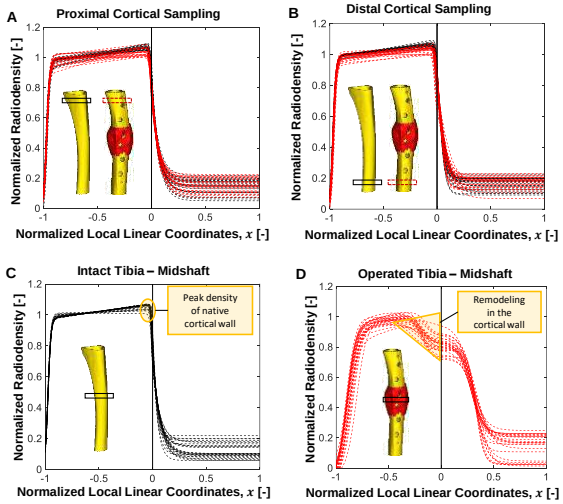


**Figure 1: Profilometry curves were fitted from data sampled at the proximal end (A) or distal end (B) of intact tibiae (black curves) and operated tibiae (red curves). Data was also sampled at the midshaft of intact tibiae (C, black curves) and operated tibiae (D, red curves). Early remodeling caused a 23% average reduction in density in the cortical wall bounded by callus.**

### *Calibration of Mechanoregulatory Healing Models with Remodeling*

Without remodeling, the fracture healing simulation produced bridging with no changes in density in the cortical wall and achieved a steady-state callus size and material distribution. With remodeling, both increasing callus mineralization and loss of cortical wall density were observed in the models. The remodeling rate constants and strain energy density thresholds were systematically varied to study the sensitivity of the model results to these parameters. When the remodeling rate constants were set too high, extreme non-physical remodeling occurred, resulting in a total erosion of the cortical wall in consistent with the experimental observations. However, with calibration, the results achieved a qualitatively good match of callus shape, callus propagation, and remodeling extent when compared with the animal data (Fig. 2).

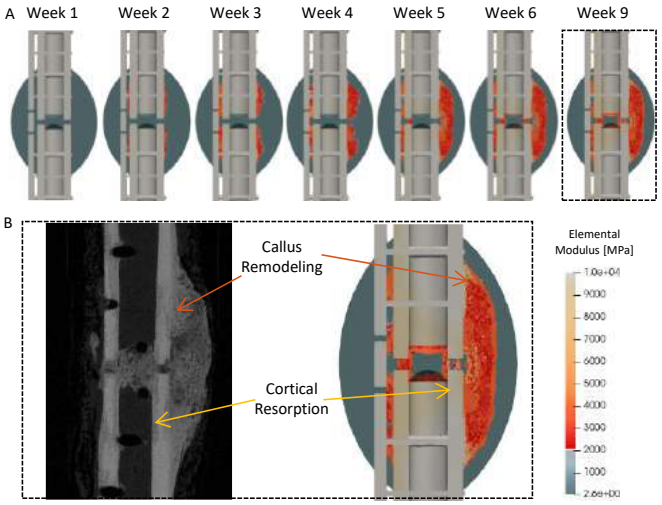


**Figure 2: A) Elastic modulus contour plots at selected timepoints for the mechanoregulation model with remodeling. B) Model prediction compared to coronal slice view from a µCT scan of an ovine tibial osteotomy at 9 weeks post-op.**

## DISCUSSION

The results of this study showed that remodeling occurs in the cortical tissue adjacent to the repair zone early in the healing process, in tandem with bridging. The image analysis methods were successful in quantifying the extent of these changes. The *in vivo* data also provided a framework for incorporating and calibrating remodeling terms in a mechanoregulatory simulation of fracture healing. These methods are unique in their use of *in vivo* datasets for numerical model development. The results suggested that incorporating remodeling activity is critical for the development of numerical simulations that match the physiologic patterns of callus development *in vivo*. The work also provided a basis for future investigations that will explore the mechanical and biological stimuli that drive late-stage callus resorption.


## ACKNOWLEDGEMENTS

We thank Karina Klein, Brigitte von Rechenberg, and Salim Darwiche for their collaboration on this work. The preclinical studies from were funded by the Johnson & Johnson Family of Companies. This work was also supported by the National Science Foundation under Grant No. 1943287. Any opinions, findings, and conclusions or recommendations expressed in this material are those of the author(s) and do not necessarily reflect the views of the Johnson & Johnson Family of Companies or the National Science Foundation.


## REFERENCES


[1] Ren, T *et al.*, *Biomech and Modeling in Mechanobiology*, 2022. https://doi.org/10.1007/s10237-021-01553-2

[2] Ren, T and Dailey HL, *Biomech and Modeling in Mechanobiology*, 2020. https://doi.org/10.1007/s10237-020-01340-5

[3] Schwarzenberg, P*, Ren, T*, *et al.*, *J Biomech*, 118, 2021. https://doi.org/10.1016/j.jbiomech.2021.110300 (*equal contribution)

[4] McNamara, L *et al.*, *J Biomech*, 40:1381-1391, 2006. https://doi.org/10.1016/j.jbiomech.2006.05.007

SB³C2022
Summer Biomechanics, Bioengineering and Biotransport Conference
June 20-23, Eastern Shore, MD, USA

# THE ROLES OF SHEAR STRESS AND HEPARAN SULFATE DEGRADATION IN ENDOTHELIAL CELL ACTIVATION

**Nicholas R. O'Hare (1), Ian C. Harding (2), Ira M. Herman (3, 4), Eno E. Ebong (1,2,5)**

(1) Department of Chemical Engineering, Northeastern University, Boston, MA, USA
(2) Department of Bioengineering, Northeastern University, Boston, MA, USA
(3) Department of Developmental, Molecular, and Chemical Biology, Tufts Sackler School of Graduate Biomedical Sciences, Boston, MA, USA
(4) Center for Innovations in Wound Healing Research, Tufts University School of Medicine, Boston, MA, USA
(5) Department of Neuroscience, Albert Einstein College of Medicine, New York, NY, USA

## INTRODUCTION

Endothelial activation characterized by the increased production of reactive oxygen species (ROS) and a shift towards a pro-inflammatory state is associated with numerous cardiovascular diseases including atherosclerosis[1,2]. Endothelial phenotype, and thus activation, is regulated by the application of shear stress, an example of endothelial mechanotransduction. The endothelial glycocalyx (GCX), a glycoprotein-proteoglycan layer extending from the endothelial membrane, is a known mechanotransducer that promotes proper function of endothelial cells[4]. Major GCX components implicated in mechanotransduction include its core proteins, mainly syndecan and glypican, the protein receptor CD44, and the attached glycosaminoglycans heparan sulfate (HS), hyaluronic acid, and chondroitin sulfate. Elucidating the role of a healthy GCX and normal shear stress in deterring endothelial activation remains critical to combatting a wide range of cardiovascular diseases.

Interestingly, it was previously reported that GCX degradation, particularly of the HS and sialic acid components, leads to increased ROS production[5]. Yet, these findings have not been further validated and the molecular mechanism behind the relationship remain unknown. While GCX degradation is associated with classical markers of pro-inflammatory EC activation (e.g., increased adhesion molecule expression), high-throughput analyses on the impact of HS degradation on endothelial phenotype have not been performed but would provide a deeper understanding of the full impacts of the GCX in regulating endothelial function. Furthermore, studies investigating the impact of shear stress on ROS production have generated contradicting results and the full extent to which flow regulates endothelial inflammation is unclear. Thus, the goal of this research was to identify the roles of both shear stress application and HS expression on endothelial activation with specific regards to ROS production and the expression of inflammatory genes.

## METHODS

To analyze the effects of HS and shear stress on endothelial activation, Human aortic endothelial cells were exposed to shear stress in a parallel-plate flow chamber (adapted from previous work)[6] with either intact or enzymatically degraded glycocalyx layers. For all shear stress experiments, cells were exposed to flow for 24 hours at an eventual 14 dynes/cm$^2$, administered using a peristaltic pump. The HS component of the endothelial glycocalyx was enzymatically degraded using 250 μIU/mL (micro international units) of heparinase III (Ibex; Montreal, Canada) for 24 hours in either static or flow conditions. Optimal HepIII concentration was determined through a dose response and subsequent immunocytochemistry (ICC) of HS.

Once the cells were conditioned, a variety of biological assays were performed to determine the effects of HS degradation and shear stress, including ROS probes, RNA sequencing (RNA-seq), western blotting, and ICC. For all assays, four groups of samples were analyzed: (i) static conditioned, (ii) flow exposed, (iii) Hep III-treated and static conditioned, and (iv) Hep III-treated and flow exposed. Two ROS assays, dihydroethidium, to identify mainly superoxide, and 6-chloromethyl-2', 7'-dichlorodihydrofluorescein diacetate (H2DCFDA), a more general indicator of ROS including hydrogen peroxide (H2O2), were performed to identify ROS production. RNA-seq was applied to assess the presence, quantity, and dynamic expression of genes associated with either the endothelial redox state or endothelial inflammatory response. Finally, western blotting and/or ICC was performed on a variety of anti/pro-oxidant and anti/pro-inflammatory proteins including HS, Nrf2, Nf-κB-p65, Nox2/4, ICAM-1, E-selectin, and KLF2.

Data pertaining to fluorescent imaging and western blotting was analyzed using one-way ANOVAs with post hoc Tukey's multiple comparison tests with an alpha value of 0.05. Additionally, with the exception of RNA-seq data, data was normalized to control groups in each experiment to eliminate any bias introduced by inter-experiment

SB³C2022-090

differences such as cell passage number. For RNA-seq data, differential expression was assessed using the Wald test implemented in the DESeq2 R package. Correction for multiple hypothesis testing was accomplished using the Benjamini-Hochberg false discovery rate (FDR). To identify changes in expression of entire gene sets, Gene Set Enrichment Analysis (version 2.2.1) was used.

## RESULTS

To initially evaluate the impact of uniform flow on EC redox state, a combination of fluorescent ROS probes, ICC, and western blotting was utilized. Using the fluorescent ROS indicator $H_2$DCFDA, we found that the application of 24 hours of uniform flow reduced total ROS levels by approximately 30% compared to static controls. Furthermore, the reduction in total ROS was accompanied by a significant 2.5-fold increase in the activation of the antioxidant transcription factor Nrf2 as determined by ICC. Increased Nrf2 activation and decreased total ROS also correlated with significant reductions in the oxidant enzymes Nox2 and Nox4 to approximately 10% and 54% of their static expression, respectively, as indicated by western blots. Regarding the GCX's role in the redox state, we found that HS degradation had no significant effect on overall ROS production or anti/pro-oxidant protein expression.

RNA-seq was utilized to further investigate the impact of uniform flow and the endothelial glycocalyx, particularly its HS component, on endothelial redox state while also identifying key genes implicated in these relationships. Out of 41 antioxidant genes with significant expression (>1000 counts) that had previously been implicated in endothelial redox regulation, we observed increased expression in 23 of these genes after exposure to uniform flow in non-enzyme (non-Hep III) conditions. Specifically, significant increases in the expression of antioxidant genes including GSTO-1, HMOX-1, NQO1, NRF2, PRDX1, SELENOS, TXN, and TXNRD1 were observed to increase after flow exposure. With regard to oxidant genes, uniform flow exposure reduced the expression of the oxidant genes CYBA, a Nox protein subunit, and MAOA while simultaneously increasing NOX4 expression. Additionally, RNA-seq supported our fluorescent and western blot redox analysis, finding no impact of HS degradation on redox gene regulation.

Increased production of ROS, such as hydrogen peroxide and superoxide, occurs during pro-inflammatory endothelial activation associated with cardiovascular diseases such as atherosclerosis[7]. Thus, we utilized RNA-seq, ICC, and western blot data to identify relationships between uniform flow or heparan sulfate degradation and inflammation related to endothelial activation. Uniform flow exposure led to a significant upregulation of anti-inflammatory genes. Specifically, flow led to increased expression of 15 out of 22 investigated anti-inflammatory genes. These included genes associated with Nf-kb inhibition such as CHUK, IKBKG, NFKBIA, and NFKBIE as well as the KLF transcription factor family, of which KLF2 and KLF4 have been strongly implicated in anti-inflammatory endothelial function. Additionally, out of 60 pro-inflammatory genes associated with activation, 30 of these genes had significantly decreased expression after uniform flow exposure, including the adhesion molecules ICAM-2 and VCAM-1; the transcription factor HIF1A; the cytokines IL1A, IL1B, and IL33; the immune receptor TLR3; the glycoprotein VWF; and the endopeptidase MMP14.

HS was also found to regulate gene expression related to pro-inflammatory EC activation. Specifically, the RNA-seq results demonstrated upregulation in pro-inflammatory genes after HS degradation, correlating with the increased expression of 42 out of the 60 investigated genes. These included the adhesion molecules ICAM-1, SELE, and VCAM-1; the cytokines IL1A and IL1B; MMP14; and the Nf-kb subunits NFKB2 (p52/100) and RELB. The observed increase in pro-inflammatory gene expression after HS degradation occurred in both static (untreated static vs. Hep III-treated static) and flow (untreated flow vs. Hep III-treated flow) conditions. These increases were also interestingly accompanied by a significant increase in anti-inflammatory gene expression, suggesting a complex relationship between HS degradation and inflammatory state.

To support findings from RNA-seq data, protein-level analysis was performed on a known inflammatory (ICAM-1) and anti-inflammatory (KLF2) marker. Western blotting identified a significant 86.6% increase in total ICAM-1 protein expression when comparing static and Hep III treated static conditions. Furthermore, ICC imaging identified a significant 63.0% increase in Hep III uniform flow ICAM-1 expression, compared to static conditions. Altogether, protein-level analysis supports RNA-seq findings of enzymatic degradation of HS increasing inflammation. On the other hand, uniform flow led to a significant 22.3% and 21.1% upregulation in KLF2 expression via ICC between Hep III flow and static conditions as well as Hep III flow and Hep III static respectively. Additionally, uniform flow exhibited an 11.8% (although statistically insignificant) increase in KLF2 mean fluorescence intensity, compared to static conditions.

## DISCUSSION

Collectively, findings from this study implicate the beneficial roles of shear stress exposure on endothelial activation via a shift towards anti-oxidant and anti-inflammatory gene expression while identifying a pro-inflammatory response induced by HS degradation, in agreement with previous research[8,9]. However, to our knowledge, no previous study has utilized RNA-seq or similar high-throughput modalities to study the role of HS degradation on activation. RNA-seq paired with more traditional protein-level analysis illustrates the complexity of the endothelial redox response that involves not several but dozens of genes, suggesting that future studies investigating endothelial redox state may require high-throughput analysis to accurately identify the complete effects. Ultimately, data from this study may be used to develop therapeutics combating ROS production, inflammation, and other modes of endothelial activation associated with several cardiovascular diseases such as atherosclerosis.

## ACKNOWLEDGEMENTS

Funding: Northeastern University Department of Chemical Engineering (graduate student stipend to Nicholas R. O'Hare), the American Heart Association (18PRE33960461 to Ian C. Harding), National Institute of Health (HL125499 to Eno E. Ebong), and the National Science Foundation (CMMI-1846962 to Eno E. Ebong).

## REFERENCES

[1] Mudau, M, et al., *Cardiovasc J Afr*, 23(4):222-231, 2012.
[2] Sima AV, et al., *Cell Tissue Res*., 335(1):191-203., 2009.
[3] Guzik TJ, et al., *Circ Res*, 86(9):E85-90, 2000.
[4] Tarbell JM et al., *Sci Signal*, 1(40), 2008.
[5] Kumagai R, et al., *Free Radic Biol Med*. 47(5):600-7. 2009.
[6] Harding IC, et. al., *J Transl Med*., 16(1):364, 2018.
[7] Guzik TJ, et al., *Circ Res*. 86(9):E85-90. 2000.
[8] McDonald KK, et al.,, *PLoS One*., 11(12), 2016
[9] Hwang J, et al., *J Biol Chem*., 278(47):47291-8, 2003

SB³C2022
Summer Biomechanics, Bioengineering and Biotransport Conference
June 20-23, Eastern Shore, MD, USA

# PARTIAL ACL INJURY LOCATION IMPACTS BIOMECHANICS AND TISSUE REMODELING IN A SKELETALLY IMMATURE PORCINE MODEL

**Danielle Howe (1), Jacob D. Thompson (1), Andre Bautista (1), Lauren V. Schnabel (2), Jeffrey T. Spang (3), Matthew B. Fisher (1,3)**

(1) Joint Department of Biomedical Engineering, North Carolina State University and University of North Carolina at Chapel Hill, Raleigh, NC, USA
(2) Department of Clinical Sciences, North Carolina State University, Raleigh, NC, USA
(3) Department of Orthopaedics, University of North Carolina at Chapel Hill, Chapel Hill, NC, USA

## INTRODUCTION

Approximately 25% of diagnosed ACL injuries are partial tears, which can be concentrated in either the anteromedial (AM) or posterolateral (PL) bundle of the ACL [1]. While full-thickness ACL tears typically lead to two-fold greater anterior knee joint laxity, partial tears lead to more subtle increases [2]. For this reason, there is not a consensus regarding treatment of partial tears, particularly in pediatric patients [3]. Some advocate for non-operative management to avoid the risk of disrupting growth plates as well as any further trauma to the joint. Others argue that surgical reconstruction is needed to restore joint stability and avoid subsequent injury to the menisci and cartilage. Furthermore, some opt for single-bundle surgical augmentation while conserving the intact bundle. To improve clinical decision-making, it is important to determine whether partial ACL injury leads to degenerative changes to the joint, and particularly to cartilage. Additionally, it would be valuable to determine whether these changes differ between injuries concentrated in the AM or PL bundle. Large exploratory studies with pediatric patients are difficult and rare. As such, the pig has been established as a model of the human ACL since the AM and PL bundles function similarly in mature humans and pigs [4]. Additionally, porcine ACL size and bundle function throughout skeletal growth have been well characterized [5,6]. Furthermore, the porcine model can be paired with clinically translatable tools to non-invasively study joint health and remodeling, such as T2* (indicative of collagen organization) and T1rho (indicative of proteoglycan content) mapping via MRI. Therefore, the objective of this study was to evaluate the effect of partial injury location in a juvenile porcine model on joint function as well as remodeling of the remaining ACL bundle and cartilage.

## METHODS

All experimental protocols were approved by the NC State University IACUC. A total of 16 juvenile (3 month old) Yorkshire cross-breed pigs underwent unilateral arthroscopic transection of the AM bundle (n=4 female, n=4 male) or the PL bundle (n=4 female, n=4 male) and a sham operation in the contralateral joint. After 24 weeks, animals were euthanized, and hind limbs were collected for analysis. T1rho mapping (FLASH, FA:10°, TR:8.74ms, TE:4.6 ms, ST: 1.5 mm, TSL: 2, 10, 20, 30, 40 ms) and T2* mapping (T2 SWI, FA:12°, TR:31ms, TE: 3.3, 7.01, 11.35, 15.68, 20, 24.4 ms, ST: 0.8mm) were performed on all stifle (knee) joints at full extension using a Siemens PRISMA 3T MRI system. Relaxation maps were created by fitting mono-exponential curves on a voxel-by-voxel basis using MATLAB. Articular cartilage was manually segmented from T1rho images to calculate the median T1rho value for the medial and lateral femoral and tibial compartments. The bundles of the ACL were segmented from T2* images to calculate the median T2* value of each bundle. ACL models segmented from T2* images were also analyzed using MATLAB to calculate the cross-sectional area (CSA) of each bundle [5,6].

Next, joints were biomechanically tested using a universal force-sensing robotic testing system (Kuka, SimVitro) [5,6]. 100 N of anterior-posterior (AP) drawer was applied to stifle joints at 60° of flexion while recording translations. The kinematics were then replayed while recording forces. Kinematics were repeated while recording forces after removing the capsule followed by the AM, then PL bundle (or only the remaining bundle in injured joints). Joint laxity was calculated as the AP tibial translation (APTT) under AP drawer. The force contributions of each bundle under maximum anterior translation were calculated using the principle of superposition [7].

Joint laxity, bundle contribution, bundle CSA, and bundle T2* values were compared between injured and contralateral joints using paired t-tests with Holm-Sidak correction for multiple comparisons ($\alpha$=0.05). The difference in median T1rho values between paired injured and contralateral joints was compared between injury types using unpaired t-tests ($\alpha$=0.05) and compared to zero using one-sample t-tests ($\alpha$=0.025). Data presented as mean overlaid with individual data points.

SB³C2022-091

## RESULTS

At 24 weeks post-surgery, mean force-translation curves were nearly indistinguishable between intact and PL-deficient (PL-) joints, while curves from AM-deficient (AM-) joints extended substantially further, with a shallower appearance (Fig. 1B). APTT was 50% greater in AM- joints compared to contralateral controls (adjusted [adj.] p=0.001), but within 9% (not significant) for PL- joints (Fig. 1C).

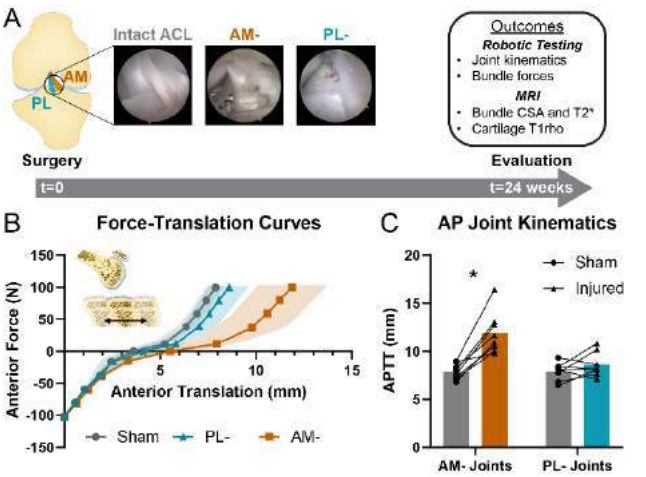


**Figure 1: (A) Joints were evaluated at 24 weeks after arthroscopic AM or PL bundle transection. (B) Average anterior-posterior (AP) force-translation curves. Shading represents 95% CI. (C) AP tibial translation (APTT). Lines connect data points from paired joints. *statistical significance from paired t-test.**

The force contribution of the remaining bundle to anterior drawer restraint was greater in AM- joints (166%↑, adj. p=0.004) and PL- joints (53%↑, adj. p=0.011) compared to the corresponding bundle in contralateral joints. (Fig. 2A). Correspondingly, the remaining bundle remodeled such that the CSA of the remaining bundle was larger compared to the healthy contralateral bundle for both AM- joints (28%↑, adj. p=0.005) and PL- joints (25%↑, adj. p=0.001) (Fig. 2B). T2* values of the remaining bundle in injured limbs did not significantly differ (<3ms) from the contralateral pair for either injury case (Fig. 2C).

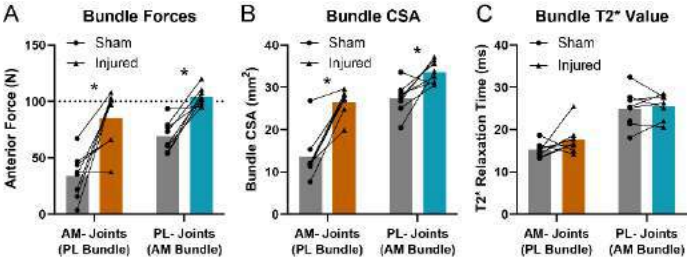


**Figure 2: Remaining bundle (A) force contributions under maximum anterior translation (dotted line represents applied load), (B) cross-sectional area, and (C) T2* value compared to contralateral joints. *statistical significance from paired t-test.**

The difference in T1rho value between paired injured and contralateral joints averaged larger for AM- joints than PL- joints, although not significantly different, for lateral femoral (2.7ms, p=0.27), medial femoral (4.6ms, p=0.06), lateral tibial (3.9ms, p=0.12), and medial tibial (0.8ms, p=0.84) cartilage, respectively (Fig. 3). Additionally, means were not statistically different from zero (control) for PL- joints (p=0.3-0.9) or AM- joints (p=0.04-0.6).

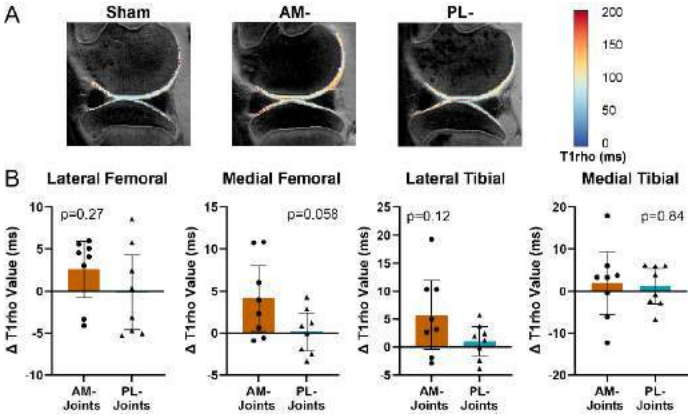


**Figure 3: (A) Representative T1rho maps of medial cartilage for each case. (B) Difference in median T1rho values between paired injured and contralateral joints for the medial and lateral femoral and tibial articular cartilage. Error bars represent 95% CI. P-values from t-test between injury types shown in graph.**

## DISCUSSION

In this study, functional outcomes varied by injury location at 24 weeks after partial ACL injury. The remaining bundle remodeled for both injuries, but AM- joints had increased joint laxity while PL- joints had similar laxity to intact joints. Additionally, cartilage T1rho was elevated in AM- joints but not PL- joints, though differences were not statistically significant for the current sample size. Ongoing work will increase the sample size. Joint function and bundle data from intact legs in the present study are consistent with values reported in mid- to late-adolescent (6-18 month) pigs [5,6]. These results point to potential clinical challenges in diagnosing PL- injuries but indicate that AM- injuries may be detectable via anterior drawer or Lachman tests. In PL- joints, near-intact levels of joint laxity, the ability of the remaining bundle to remodel by increasing in size, and little evidence of abnormal cartilage remodeling suggest that conservative treatment may be adequate for partial injuries concentrated in the PL bundle in young patients. However, AM- joints showed measurably increased joint laxity and the potential for abnormal cartilage remodeling, suggesting reconstruction or single-bundle augmentation may be necessary to restore stability and prevent cartilage degeneration. Although clinical data from pediatric partial tears are rare, one study with 45 patients found PL-concentrated tears were more likely to experience re-injury than AM-concentrated tears [8], contrary to the present study. However, it is not clear whether factors such as injury severity or joint laxity differed between groups at the onset of the study. Additionally, the study excluded patients with a Lachman test showing >5mm side-side difference. From our data, it is possible that more AM tears were excluded and that the results suffer from survivor bias. Ongoing and future work will compare between ages and sexes.


## ACKNOWLEDGEMENTS

We would like to thank Laboratory Animal Resources (NC State) and the Biomedical Research Imaging Center (UNC-CH) for their contributions to this work. Funding provided by NIH (R01 AR071985, F31 AR077997) and NSF (DGE-1746939).


## REFERENCES


[1] Colombet, P +, *Orthop Traumatol-Surg*, 2010. [2] Dejour, MD +, *Arthroscopy*, 2013. [3] McClincy, MP +, *The Pediatric Anterior Cruciate Ligament,* 2018. [4] Xerogeanes, JW +, *Ann Biomed Eng*, 1998. [5] Cone, SC +, *CORR*, 2019. [6] Howe, D +, *JOR,* 2021. [7] Rudy, TW +, *J Biomech*, 1996. [8] Kocher, MS +, *AJSM*, 2002.

# ACTIVE/PASSIVE MECHANICAL PROPERTIES OF AORTA EXPLANTS FROM A MOUSE MODEL OF DIET-INDUCED MEDIAL ARTERIAL CALCIFICATION

**Breanna Pederson (1), Mengistu G. Gebere (2), Mohamad Azhar (2), Narendra R. Vyavahare (3), Susan M. Lessner (1,2), John F. Eberth (1,2)**

(1) Biomedical Engineering Program, University of South Carolina, Columbia, South Carolina, USA
(2) Cell Biology and Anatomy, University of South Carolina School of Medicine, Columbia, South Carolina, USA
(3) Biomedical Engineering, Clemson University, Clemson, South Carolina, USA

## INTRODUCTION

Arterial calcification occurs in most individuals above 60 years of age and is a well-known clinical predictor of all-cause mortality.[1,2] Unlike atherogenesis that originates in the intima, medial arterial calcification (MAC) is the mineralization of the musculo-elastic middle layer of large arteries leading to progressive stiffening, increased pulse pressure, and eventual heart and kidney damage. MAC is particularly prominent in patients with chronic kidney disease and diabetes due to dysregulated metabolic processes.[3] In MAC, vascular smooth muscle cells (VSMC) undergo a phenotypic switch into osteoblast-like cells, losing smooth muscle-specific markers.[4] A high-adenine and high-phosphate diet (adenine-diet) was previously shown to induce chronic kidney disease and MAC in rats. Still, this model has had limited translatability to other species thus far.[5] With several genetic mouse models available to researchers to study aortopathic conditions, extension of the adenine-diet to mice could provide a tool to understand the human condition better and to test potential therapeutic strategies. Distinguishing the role of extra-cellular-matrix stiffening in MAC from the reduced contractile capacity of the VSMCs is a crucial step in model characterization. Thus, in this study, we confirm the effectiveness of the adenine-diet to produce MAC in mice and test the active and passive mechanical properties to quantify the biomechanical consequences this diet has on extra-cellular-matrix remodeling and altered VSMC tone.

## METHODS

Explanted mouse abdominal aortas, taken from five-month-old C57BL6 male mice fed an adenine (n=3-4) or standard chow (n=7, control) diet, were biaxially tested in our lab. Due to limited tissue availability, qualitative histology was performed on females of the same age and diet groups as their male counterparts. Inflation-extension testing was performed over a pressure range of 10-160 mmHg and an axial stretch ratio of ±10% of the *in vivo* axial stretch ratio, defined as the ratio at which axial force is pressure-invariant. Two contractile states were investigated: first with VSMCs maximally contracted using phenylephrine ($10^{-5}$ M), next with the cells fully relaxed through the addition of sodium nitroprusside ($10^{-4}$ M). Both tests were performed in a 37 deg-C temperature-controlled and oxygenated medium. Isometric decomposition delineated the active stress from the total (contracted) and passive (relaxed) stress state of arteries at a common biaxial stretch ratio (details provided in Zhou et al. 2018). Using two-tailed t-tests, differences between discrete data were considered at $p<0.10$ and $p<0.05$ as indicated in the figures by * and **, respectively.

## RESULTS

The active-passive biaxial inflation-extension properties (**Figure 1**) of aortic explants were successfully tested using our custom-designed Mouse Aortic Active Response Tester (MAARTy). The adenine-diet group was found to have a lower *in vivo* axial stretch ratio (Ad = 1.49 ± 0.11, Ct = 1.65 ± 0.06; p=0.05), decreased passive outer diameter (Ad = 0.70 ± 0.01, Ct = 0.78 ± 0.08, $p<0.05$), and decreased passive area compliance (Ad = 0.002 ± 0.0002, Ct = 0.003 ± 0.0009 $mm^2$/mmHg; $p<0.10$) compared to controls (**Figure 2**). Moreover, the active stress

generation revealed adenine-diet hypo-contractility (Ad = 33.54 ± 9.72, Ct=63.26 ± 29.00 kPa; $p<0.10$) compared to controls (**Figure 3**). Although trending towards a lower value in the adenine-diet group, passive circumferential stretch was not statistically different between the two groups.

Histological composition analysis using Alizarin Red revealed a heterogeneous distribution of calcific nodules (deep red) in the media that lacked circumferential and axial uniformity. A representative sample of this heterogeneity can be seen in **Figure 4**. Additionally, each mouse demonstrated considerable specimen-to-specimen variation despite identical diets.

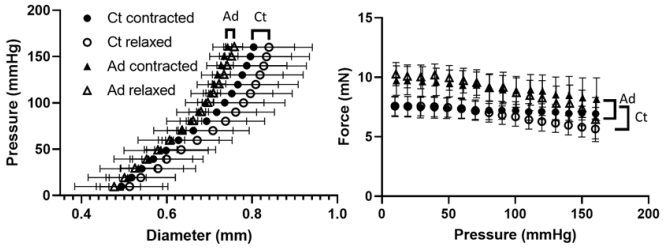


**Figure 1: Continuous A) pressure-diameter and B) force-pressure for fully contracted and fully relaxed VSMC tone in control (Ct) and adenine diet (Ad) mice. All data at *in vivo* axial stretch ratio.**

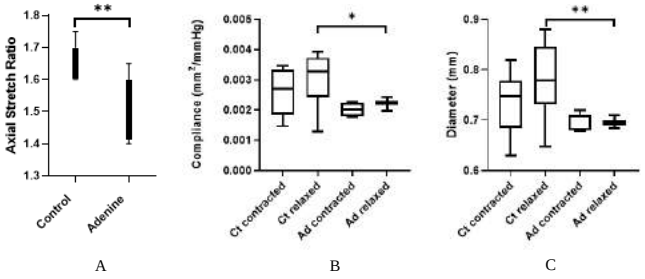


**Figure 2: A) In vivo axial stretch ratio, B) area compliance, and C) diameter for control and adenine diet mice. Panels B-C at 100 mmHg using fully contracted and fully relaxed VSMCs.**

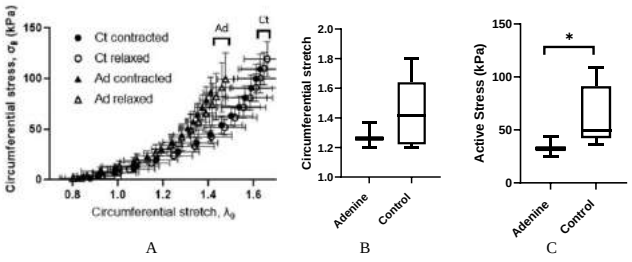


**Figure 3: A) Continuous stress-stretch relationships for fully contracted and fully relaxed VSMCs using control (Ct) and adenine diet (Ad) mice. B) Circumferential stretch ratio at 100 mmHg in the fully contracted configuration and C) active stress generation at the average stretch ratios described in B using isometric decomposition.**

**Figure 4: Alizarin-Red staining of aortas taken from two female adenine-diet mice illustrate considerable spatial heterogeneity and sample-to-sample variation, especially in female mice. Calcific nodules are indicated by the deep red staining areas.**

## DISCUSSION

Through histomechanical characterization of explanted mouse aortas we have confirmed the presence of calcific nodules in our diet-induced mouse model of MAC and preliminarily characterized the biomechanical phenotype of these mice. Our results indicate significant regional and animal-to-animal variations in calcification, thus highlighting the need to correlate specimen-specific calcium scoring with an individual vessel's mechanical properties. In terms of passive properties, biaxial mechanical testing indicated a reduction in caliber and extra-cellular-matrix stiffening in the adenine-diet explants. These tissues also demonstrated hypo-contractility with decreased VSMC vasoreactivity compared to controls. Thus, the extra-cellular-matrix properties and the contractile capacity of aortas were pathologically altered in adenine-diet mice. Overall, our findings suggest that the adenine-diet mouse model of MAC is successful, but with significant variability.


## ACKNOWLEDGEMENTS

This project was funded by NIH RO1 HL145064.


## REFERENCES


1. Demer LL, Tintut Y. Vascular calcification: Pathobiology of a multifaceted disease. Circulation. 2008;117(22):2938-2948.
2. Shanahan CM, Cary NRB, et al. Medial localization of mineralization-regulating proteins in association with Monckeberg's sclerosis: Evidence for smooth muscle cell-mediated vascular calcification. Circulation. 1999;100(21):2168-2176.
3. Shanahan CM, Crouthamel MH, et al. Arterial calcification in chronic kidney disease: key roles for calcium and phosphate. Circ Res. 2011;109(6):697-711.
4. Abedin M, Tintut Y, Demer LL. Vascular calcification: Mechanisms and clinical ramifications. Arterioscler Thromb Vasc Biol. 2004;24(7):1161-1170.
5. Diwan V, Brown L, Gobe GC. Adenine-induced chronic kidney disease in rats. Nephrology. 2018;23(1):5-11.
6. Zhou B, Prim DA, et al. Contractile Smooth Muscle and Active Stress Generation in Porcine Common Carotids. J Biomech Eng, Jan. 2018, 140 (1), pp. 0145011-0145016.

SB³C2022
Summer Biomechanics, Bioengineering and Biotransport Conference
June 20-23, Eastern Shore, MD, USA

# A 3D COMPUTATIONAL MODEL OF AORTIC VALVE INTERSTITIAL CELL CONTRACTILE BEHAVIOR WITHIN A PEG HYDOGEL MEDIUM

**Alex Khang (1), John Steinman (1), Xinzeng Feng (1), Michael S. Sacks (1)**

(1) James T. Willerson Center for Cardiovascular Modeling and Simulation, The Oden Institute and Department of Biomedical Engineering, The University of Texas at Austin, Austin, Texas, United States of America

## INTRODUCTION

Aortic valve interstitial cells (AVICs) oversee extracellular matrix (ECM) maintenance and turnover in the aortic valve (AV) and take on an activated phenotype in diseases such as bicuspid AV (BAV) disease, in which the AV has two instead of the normal three leaflet tissues. AVIC activation is characterized by increases in ECM production, remodeling, and contractility via expression of alpha-smooth muscle actin stress fibers (SFs). Currently, we have a limited understanding of the intrinsic differences between AVICs from structurally normal AVs and BAVs and how these differences contribute toward an increased rate of disease progression in the BAV population. Moreover, we have a limited understanding of AVIC contractile behaviors, which play a critical role in mechanosensing and ECM remodeling and reflect AVIC activation levels and biophysical state. This is partly because individual SF forces and their orientation are difficult to measure directly due to their small feature size (~7 nm). Previous studies of AVIC mechanics have heavily utilized 2D culture environments out of convenience and ability to visualize the AVICs directly. However, these environments do not recapitulate the 3D nature of the AV, resulting in unrealistic SF structures. Herein, we used experimental and computational methods to estimate AVIC SF architecture and contractile forces in tissue-emulating 3D hydrogels. Ultimately these techniques will be used to study differences in AVICs from normal AVs and BAVs.

## METHODS

**3D traction force microscopy (3DTFM)**. Porcine AVICs and fluorescent microbeads were seeded in peptide-modified, poly (ethylene glycol) hydrogels for 72 hours before experimentation. The sample was incubated in Tyrode's Salt before obtaining an image stack of a single AVIC and surrounding fluorescent microbeads. Afterwards, Cytochalasin D was added to elicit cell relaxation through actin depolymerization and a second z-stack of the same FOV was obtained. The images were analyzed with our software, FM-track [1], which outputted an AVIC surface mesh and field displacements (Fig. 1). The displacements were interpolated onto the AVIC surface mesh, resulting in a 1:1 mapping between the initial and final AVIC shapes.

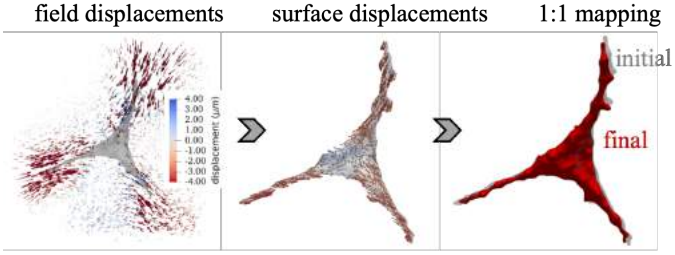


**Figure 1: 3DTFM experimental data. Field displacements and AVIC surface meshes are generated by our software FM-track [1]. Field displacements are interpolated onto the AVIC surface mesh to establish a 1:1 mapping to the final configuration.**

**Finite element mesh**. The hydrogel, AVIC cytoplasm, and AVIC nucleus were modeled (Fig. 2). AVIC geometry and spatial position was informed by 3DTFM data. Average nuclear geometry and spatial position was informed by immunostaining images from prior studies. The mesh consisted of ~50,000 linear tetrahedral elements.

**Modeling the mechanical behavior of the hydrogel**. The hydrogel domain was modeled as a Neo-Hookean solid with the following strain energy density function:

$$\psi = \frac{\mu}{2}(I_1 - 3 - 2\ln J) + \frac{\kappa}{2}(J-1)^2\,, \qquad (1)$$

where $\mu$ is the shear modulus, $I_1$ is the first invariant of the right Cauchy-Green deformation tensor, $J$ is the determinant of the deformation gradient tensor, and $\kappa$ is the bulk modulus. To account for cell-induced degradation [2] or strengthening of the gel, $\mu$ was allowed to vary spatially from the experimentally measured value of 108 Pa.

SB³C2022-093

**Modeling AVIC SF contraction**. The cytoplasm and nuclear domains were modeled as Neo-Hookean using eq. 1 with shear moduli of 750 and 7500 Pa, respectively, as informed by literature values [3,4]. SFs were modeled in the cytoplasm with total Cauchy stress given as:

$$\boldsymbol{T}^{sf} = \mathrm{H}(I_4 - 1)\left(2\frac{I_4}{J}\frac{\partial \psi_p^{sf}}{\partial I_4}\boldsymbol{m}\otimes\boldsymbol{m}\right) + \mathrm{f}\bar{\phi}_{sf}\frac{I_4}{J}\boldsymbol{m}\otimes\boldsymbol{m}, \quad (2)$$

where the first and second terms account for the passive and active stress produced by the SFs, respectively, $H()$ is a Heaviside step function that ensures SF passive stress arises only in tension ($I_4 > 1$), $I_4$ is the SF stretch, $\psi_p^{sf}$ is the SF strain energy density function:

$$\psi_p^{sf} = \frac{\mu_{sf}\bar{\phi}_{sf}}{2}(I_4 - 1)^2, \quad (3)$$

where $\mu_{sf}$ and $\bar{\phi}_{sf}$ are the SF modulus and expression level, respectively, $\boldsymbol{m}$ is the SF orientation, and $f$ is the contractile strength per unit SF. Parameters $\mu_{sf}$ and $f$ are set to 390 and 1590 Pa, respectively [3,4]. We backed out $\boldsymbol{m}$ and $\bar{\phi}_{sf}$ by minimizing the error between the simulated and experimental hydrogel displacements.

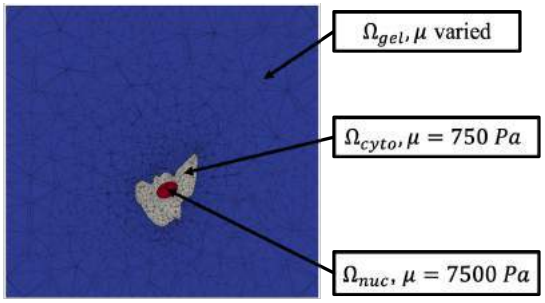


**Figure 2: A cross section of the 3D finite element mesh containing the hydrogel matrix, the AVIC cytoplasm, and the AVIC nucleus.**

## RESULTS

**Gel-model predicts hydrogel stiffening by AVICs.** Stiffening the hydrogel material near the AVIC surface resulted in better qualitative agreement in displacement magnitude with experiment than a homogenous model (Fig. 3A). The model estimated a non-linear stiffness profile in relation to distance from the AVIC surface (Fig. 3B). Stiffening also resulted in better quantitative agreement in displacement and principal stretch profiles with experimentation (Fig. 3C&D). Measurements were made along the arrows shown in Fig. 3A.

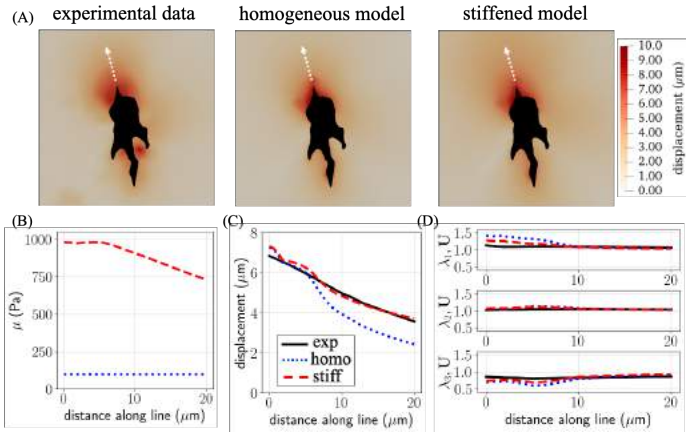


**Figure 3: (A) Plane slices depicting displacement magnitude for the experiment and both the homogeneous and stiffened simulations. (B,C,D) The shear modulus, displacement, and principal stretch profiles measured along the arrows shown in panel (A).**

**AVIC model predicts SF orientation.** The model successfully predicted SF orientations ($\boldsymbol{m}$) within the AVIC cytoplasm (Fig. 4). In addition, the model successfully predicted SF expression levels ($\bar{\phi}_{sf}$) and total stress ($\boldsymbol{T}^{sf}$), which showed that the highest SF expression level, and therefore total stress, was localized at the AVIC protrusions (Fig. 4A&B). The simulated AVIC shape in the final configuration (red) showed good agreement with experiment (green) (Fig. 4C).

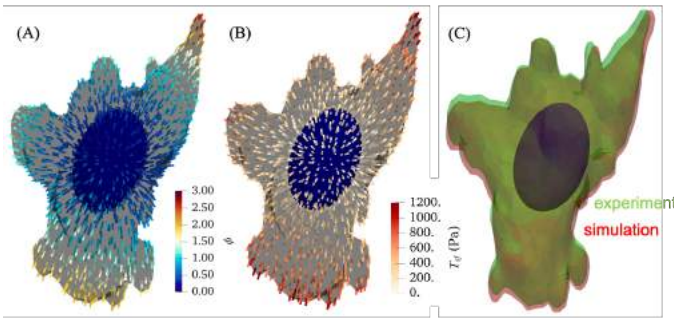


**Figure 4: SF orientation depicted by lines. (A) SF expression level. (B) Total SF stress. (C) The simulated (red) and experimental (green) AVIC shapes in the final configuration.**

## DISCUSSION

To our knowledge, we present for the first time the ability to predict 3D SF architecture and contractile strength in AVICs embedded within a 3D medium. This novel experimental and computational approach allows for unprecedented insight into AVIC SF structure, expression levels, and contractile forces in full 3D, which reflect AVIC biophysical state and phenotypic activation level. Moreover, our simulation was able to predict that AVICs strengthen and do not meaningfully degrade the hydrogel, contrary to previous reports in the literature [2]. This is likely a result of the AVICs excreting nascent ECM components that reinforce the PEG hydrogel material and lead to an increase in local moduli.

Looking forward, these approaches are currently being extended to study intrinsic differences between human AVICs derived from patients with structurally normal AVs and BAVs. Specifically, this model will enable us to quantify differences in AVIC biophysical state and activation levels between the two groups. This will provide key insight into cell-level differences that may lead to increased disease progression in BAV patients, which is critical toward identifying cell-level targets for therapy.

## ACKNOWLEDGEMENTS

We acknowledge our funding sources: NSF-GRFP grant no. DGE-1610403 and NIH grant no. F31HL154654 awarded to AK. NIH grant no. R01 HL142504 awarded to MSS. We thank the Anseth Research group at the University of Colorado Boulder for their help with the hydrogel chemistry.

## REFERENCES

[1] Lejeune, E et al., *Software X,* 2019.
[2] Song et al., *Comput. Methods Appl. Mech. Engrg*., 2020.
[3] Sakamoto et al., *J Mech Behav Biomed Mater*, 2016.
[4] Sakamoto et al., *J Biomech Eng*, 2017.

SB³C2022
Summer Biomechanics, Bioengineering and Biotransport Conference
June 20-23, Eastern Shore, MD, USA

# PATIENT-SPECIFIC FINITE ELEMENT MODELING TO PREDICT CLINICAL RISKS OF PERCUTANEOUS PULMONARY VALVE IMPLANTATION

**Carly L. Donahue (1), Varun Aggarwal, MD (2), Victor H. Barocas, PhD (1)**

(1) Department of Biomedical Engineering, University of Minnesota, Minneapolis, MN, USA
(2) Department of Pediatrics, University of Minnesota, Minneapolis, MN, USA

## INTRODUCTION

Almost 20% of congenital heart disease patients have right ventricular outflow tract (RVOT, Fig. 1a) dysfunction [1], which can be treated non-surgically by percutaneous pulmonary valve implantation (PPVI). During PPVI, a replacement valve is delivered via catheter and anchored by a stent. Stent oversizing may cause distortion of a nearby vessel, a risk currently assessed via balloon angioplasty prior to stent deployment. Aortic valve insufficiency (AVI) due to aortic root (AR) distortion is seen in up to 10% of patients during balloon angioplasty [2]. Additionally, around 5% of PPVI patients experience coronary artery compression [3,4] which can result in myocardial ischemia. Both of these potential outcomes can be disastrous.

Imaging [5,6] and 3D printing vessel anatomy [7] have been explored to assess the feasibility of stent placement but are unable to evaluate the effects of stent expansion. Finite element (FE) analysis of patient-specific PPVI models has been used to evaluate coronary compression risk in two studies [8,9], with one group reporting run times of 300hr on 16 CPUs [8]. The time-consuming nature of complex FE models makes them impractical for the clinical setting. To this end, we created a simpler, faster FE model to assess the risks of PPVI, aid in procedural planning, and potentially prevent unsuitable candidates from undergoing unnecessary procedures.

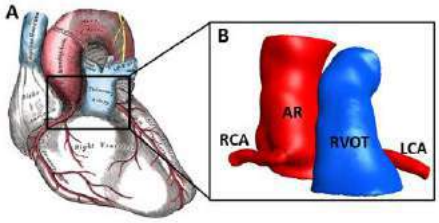


**Figure 1: A) Human Heart Illustration showing the proximity of the RVOT to the AR and coronary arteries [10]. B) 3D model of a patient's vascular anatomy constructed from a CT scan.**

## METHODS

**3D Model Generation:** Patient-specific models (e.g., Fig. 1b) were constructed from segmented CT scans of the RVOT, AR, and coronary arteries. Vessel wall thicknesses were set to 1.5 mm, 1.8 mm, and 0.7 mm. The space between vessels was filled with a compressible solid representing adipose tissue. Element volumes for vessels and adipose tissue were 0.06-0.20 $mm^3$ and 0.91-2.83 $mm^3$, respectively.

**Material Models:** Material models for each anatomical component were based on available data for healthy, human tissue [11–14]. The RVOT was modeled as an incompressible, anisotropic Holzapfel-Gasser-Ogden material [15] with strain energy $W$ given by

$$W = i\frac{c}{2}i(I_1\, i - i3)\, i + i\frac{k_1}{2k_2}\sum_{\alpha=1}^{2}(\exp(k_2\langle E_\alpha\rangle^2)\, i - i1) \quad (1)$$

where $E_\alpha = i\kappa(I_1 - i3)\, i + i(1i - i3\kappa)(I_{4\alpha} - i1)$, $C$ is the right Cauchy-Green deformation tensor, $I_1 = itr(C)$, $I_4 = ia_{\alpha r} \cdot C \cdot a_{\alpha r}$, and $\alpha = 1, 2$. There are two fiber families along vectors $a_{\alpha r}$ in the local $\{e_1, e_2\}$ plane making an angle $\pm i\gamma$ with the circumferential direction $e_1$. The model constants are $c$, $k_1$, and $k_2$. The AR and coronaries were modeled using an incompressible, isotropic Ogden model [16] with strain energy $W$ given by eqn. (2). Adipose tissue was modeled as neo-Hookean, equivalent to eqn. (2) with $m_1=2$.

$$W = i\frac{c_1}{m_1^2}i\left(\lambda_1^{m_1}\, i + i\lambda_2^{m_1}\, i + i\lambda_3^{m_1}\, i - i3\right)i \quad (2)$$

**FE Simulation of PPVI:** Simulation was performed using the FE solver FEBio [17]. Based on the RVOT geometry, a custom MATLAB code identified a 2 cm long RVOT segment with the smallest luminal diameter as the target for stenting. Lumen surface nodes in the stented region were displaced radially to achieve 30% oversize relative to the vessel diameter. Following stent expansion, the interaction between the RVOT and the surrounding vessels was analyzed for potential complications.

**Retrospective Analysis of PPVI:** Nine PPVI cases from the catheterization lab were analyzed using the FE code, and the model predictions were compared to clinical observation. To prevent bias, the engineering analysis for each case was blinded to the clinical outcome.

## RESULTS

Model results agreed with the retrospective clinical outcomes. In patients that experienced AVI and/or coronary compression in the catheterization lab, the affected vessels showed increased displacement, stress, and strain as a result of PPVI in the model. The change in the cross-sectional inscribed circle diameter is the most clinically relevant output due to its direct implication in AVI and reduced coronary blood flow (Fig. 2).

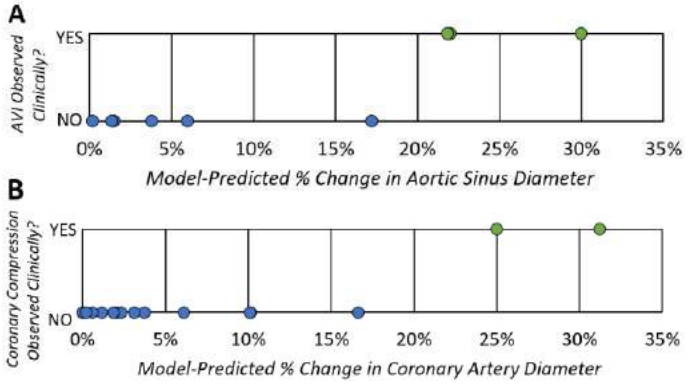


**Figure 2: A) Correlation between the FE-calculated change in aortic sinus inscribed circle diameter and clinically observed AVI. B) Correlation between the FE-calculated change in coronary inscribed circle diameter and clinically observed compression.**

In the three patients that experienced AVI in the catheterization lab, the FE model of PPVI showed that the aortic sinus diameter decreased by at least 21%. Five of the six models from patients that did not experience AVI clinically had diameter changes less than 6%. An example of AVI observed in a FE simulation is shown in Fig. 3.

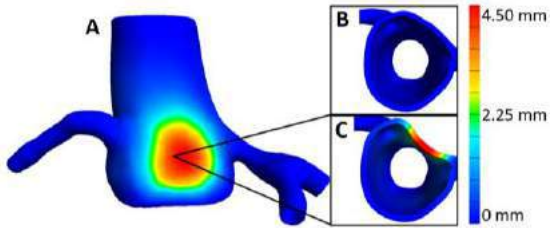


**Figure 3: A) Color map showing displacement as a result of stent oversizing in the aortic sinus. B) Cross-sectional view of the aortic sinus before stent expansion. C) Cross-sectional view showing the distorted aortic sinus after PPVI.**

In the two patients that experienced left coronary artery compression clinically, the model showed the coronary lumen diameter decreased at least 26%. In both simulations, the 30% stent oversizing created conflicting boundary conditions between the stent and the fixed boundary condition under the coronary artery where it is embedded in the heart tissue. This error indicated coronary compression, but to achieve model convergence, the stent oversize condition was lowered to 20%. In 14 of 15 coronary arteries (left and right) that were not compressed in the catheterization lab, the FE model showed diameter changes of less than 11%. An example of modeled coronary artery experiencing compression resulting from PPVI is shown in Fig. 4.

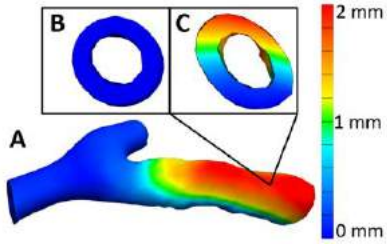


**Figure 4: A) Color map showing compression of the left coronary artery as a result of stent oversizing. B) Cross-sectional view of the coronary artery before stent expansion. C) Cross-sectional view showing the distorted artery after PPVI.**

## DISCUSSION

These results demonstrate the ability of our workflow to identify risks of AVI and coronary compression during PPVI in a computationally efficient manner. To our knowledge, this is the largest study using FE analysis to predict PPVI risks, and our model is the first to predict the occurrence of AVI in addition to coronary compression. Our simulations have run times of less than 5 minutes on a desktop computer, making them much faster than previous models and eliminating the need for a supercomputer. This improvement in efficiency creates the potential for the clinical implementation of pre-procedural FE analysis for PPVI risk evaluation.

Two limitations should be considered while interpreting results. First, the materials used in the model are inherently not patient-specific. As a result, the model is unable to predict the asymmetric expansion of the RVOT due to inhomogeneity, calcification, or scarring. Additionally, varying stiffness in the AR and/or coronaries would also impact how the vessels resist deformation. Second, while the run times of our FE analysis are significantly faster than previous studies, image segmentation and model generation are still relatively slow processes. Combining the proposed FE workflow with an automatic image segmentation technique would result in an improved clinical tool for assessing the risks of PPVI.

## ACKNOWLEDGEMENTS

This work was supported by the NIH (T32-HL139431, U01-HL139471), and the Andrew David Sit Foundation Innovators Fund.

## REFERENCES

[1] Krasuski, R.A. et al., Circ., 134:110–113, 2016.
[2] Torres, A.J. et al., J. Interv. Cardiol, 29:197–207, 2016.
[3] Morray, B.H. et al., Circ. Cardiovasc. Interv., 6:535–542, 2013.
[4] Fraisse, A. et al., Cath. Cardiovasc. Interv., 83:E260-E268, 2014.
[5] Malone, L. et al., Ped. Cardiol., 38:746–753, 2017.
[6] Tezza, M. et al., Eur. J. Radiol., 110:88–96, 2019.
[7] Chung, R. et al., Circ. Cardiovasc. Imaging, 7:182–189, 2014.
[8] Caimi, A. et al., J. Biomech., 79:135–146, 2018.
[9] Capelli, C. et al., Interface Focus, 8, 2018.
[10] Gray, H. et al., "Anatomy of the Human Body", 1918.
[11] Cabrera, M.S. et al., J. Biomech., 46:2075–2081, 2013.
[12] Azadani, A.N. et al., Ann. Thorac. Surg., 93:87–94, 2012.
[13] Karimi, A. et al., Tissue Cell, 47:152–158, 2015.
[14] Comley, K. et al., Int. J. Solids Struct., 47:2982–2990, 2010.
[15] Gasser, T.C. et al., J. R. Soc. Interface, 3:15–35, 2006.
[16] Ogden, R.W. et al., J. Mech. Phys. Solids, 26:37–57, 1978.
[17] Maas, S.A. et al., J. Biomech., 134, 2012.

SB³C2022
Summer Biomechanics, Bioengineering and Biotransport Conference
June 20-23, Eastern Shore, MD, USA

# ASSESSING ARTERIAL STIFFNESS IN HUMAN BLOOD PRESSURE WAVEFORM USING HARMONIC DISTORTION

**Nicholas M. Milkovich (1), Gary F. Mitchell (2), Béla Suki (3), Yanhang Zhang (1,3)**

(1) Department of Mechanical Engineering, Boston University, Boston, Massachusetts, USA
(2) The Framingham Heart Study, Framingham, Massachusetts, USA
(3) Department of Biomedical Engineering, Boston University, Boston, Massachusetts, USA

## INTRODUCTION

Blood pressure (BP) is routinely used as a measure of cardiovascular function. BP is also a key indicator of hypertension (HT), which is closely associated with stiffening of arteries[1]. Stiffening of central elastic vessels, such as the aorta and the carotid arteries, results in a pressure augmentation from the propagating and reflected waves, components of the BP waveform (BPW)[2]. Therefore, the BPW is also associated with arterial stiffness. Commonly used indexes to assess arterial function includes augmentation index (AI) and pulse wave velocity (PWV). Interestingly, AI and PWV have proven to not be strongly correlated with one another[3]. This could imply that not all BP information responsible for distorting the BPW via wave reflection is being considered in these calculations. Recently we have developed a new index from the BPW, harmonic distortion (HD), that showed promise in assessing arterial stiffness in a mouse model[4]. We hypothesize that this index can be used to further characterize arterial stiffness in human BPWs collected clinically. In this study, BPWs from the Framingham Heart Study (FHS) participants were analyzed for HD and compared with existing indexes.

## METHODS

*Human BPWs:* BPWs of 10-20 sec in length collected via over-skin carotid artery tonometry from 400 male and female participants (≥18 years of age), enrolled at the FHS, were used in this study with approval from the FHS Executive Committee and Boston University's Institutional Review Board. De-identified data such as age, sex, height, weight, BPs, carotid-femoral PWV, AI, prior cardiovascular disease (CVD), and HT were also collected for these patients.

*Harmonic distortion:* To quantify the shape of BPW, we calculated HD, defined as[4]:

$$HD = \sum_{k=2}^{8} \frac{|A_k|^2}{|A_1|^2} \quad (1)$$

where $|A_k|^2$ are the Fourier coefficients of a single BPW multiplied by their complex conjugates. Thus, HD is essentially the ratio of energy above the fundamental frequency to that at the fundamental frequency of the waveform. Fourier coefficients higher than the 8th were found to be negligible and do not contribute significantly to HD. For an ideal sinusoidal wave, the HD is 0. To obtain HD, individual heartbeat cycles isolated from the 10-20 sec BPW recordings (Fig. 1a) were processed using custom MATLAB code according to Equation (1). As an illustration, the normalized power spectrum (PS), $|A_k|^2/|A_1|^2$, were obtained for the BPW and plotted in Figure 1b. The HD value and the corresponding BPW's systolic BP (SBP) were recorded.

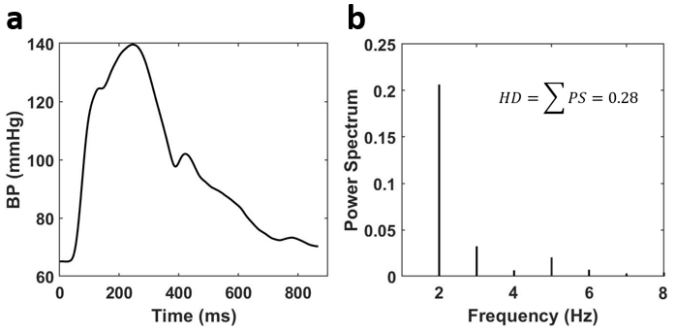


**Figure 1: (a) A single human BPW from carotid artery tonometry and (b) normalized power spectrum of the BPW.**

HD values from all patients were then pooled for further analysis. HD data was further processed by generating evenly sized BP bins and HD values outside two standard deviations of the average were removed from that bin. The average HD and SBP for each bin were then plotted for age groups (≥ 50 and < 50 years) and with and without HT. Linear regressions were then performed on the HD-SBP data separately according to HT diagnosis and age being above or below 50 years.

SB³C2022-095

*Statistical analysis*: HD-SBP data was confirmed non-Gaussian via the Kolmogorov-Smirnov test. A Wilcoxon Rank Sum test was performed on HD data between 90-160 mmHg for participants by HT and age groups. This BP range was chosen for the overlapping range of SBP value in all groups. Regression statistics (estimate, variance, degrees of freedom) were used to find significance between regression coefficients. Backward stepwise regressions were performed on HD, PWV, and AI, recursively eliminating non-significant variables, including age, height, weight, mean arterial pressure (MAP), SBP, diastolic BP (DBP), sex, and prior cardiovascular disease (CVD). The indexes were then introduced as independent factors to the linear model to determine any correlation with one another ($^{*}P < 0.05$).

## RESULTS

Figure 2 shows the HD vs. SBP relations obtained from BPWs by HT and age groups. HD shows a negative linear relationship with SBP. This trend varies distinctly according to HT and age. Further, regression slopes are significantly different by HT and age (HT: $p = 0.038$, Age: 0.009). In the HT groups (Fig 2a.) the hypertensive patients appear to have higher HD values from 100-150 mmHg, though the HD values between both groups are not statically significant ($p = 0.083$). The young group (< 50 yrs) has significantly higher HD values (Fig. 2b), regardless of SBP ($p < 0.001$). Both the HT group and old group (≥ 50) contain the highest observed SBPs (~150-175 mmHg) and lowest measured HD values (~0.3-0.2).

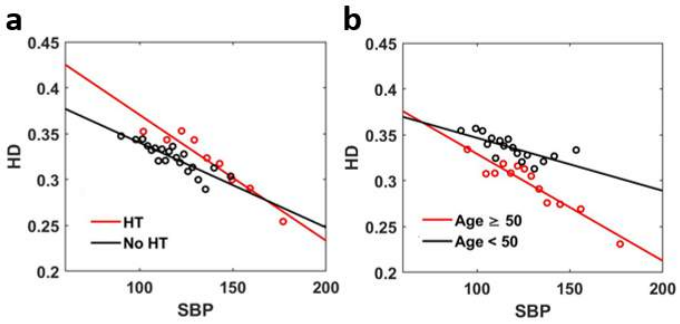


**Figure 2: Linear regressions between average HD and average SBP for participants by HT diagnosis (a) and by age (b).**

Table 1 shows the results of stepwise regressions for select *in vivo* indexes with respect to independent variables. These indexes include PWV and AI, as well as the new index HD. All variables were highly significant to the index calculations ($p \leq 0.007$) if not eliminated by the recursive regression. AI is the only index that differs by sex and PWV by height. When introducing the indexes in to each regression, PWV and AI were found to be significant with HD with $p = 0.021$ and $p < 0.001$, respectively, however PWV and AI were found to not be significant with one another ($p = 0.058$).

**Table 1: p Values from Backward Stepwise Regression showing Stiffness Index Significance to Patient Data**

| | HD | PWV | AI |
|---|---|---|---|
| Age (yr) | <0.001 | <0.001 | <0.001 |
| Height (m) | - | 0.007 | - |
| Weight (kg) | <0.001 | - | - |
| Sex (M/F) | - | - | <0.001 |
| MAP (mmHg) | <0.001 | - | - |
| SBP (mmHg) | <0.001 | <0.001 | <0.001 |
| DBP (mmHg) | <0.001 | - | - |
| prior CVD (Y/N) | - | <0.001 | 0.002 |
| R Value | 0.521 | 0.782 | 0.660 |

## DISCUSSION

BPWs contain information from the coupled interactions between forward and reflected waves, and arterial wall mechanics. With increased arterial stiffness, the BPW peak is augmented due to the overlapping of the forward and reflected waves[2]. At higher BPs, there is an increase in arterial stiffness due to the gradual recruitment of collagen fibers in the adventitia[5]. The inverse linear *relationship* between HD and SBP (Fig. 2) suggests that HD is sensitive to changes in arterial stiffness. Further, our study consistently show that HD decreases with age (Fig. 2b), as increase in arterial stiffness with aging is well documented[2,5]. Also, the significant difference in HD slope (Fig. 2) illustrates a marked change in HD's SBP dependence with HT and aging. The reason that the HD values between HT arteries and the non-HT ones are not significantly different is not clear and requires further investigation.

Addressing the efficacy of the three *in vivo* indexes begins with the R values, a metric of correlation, from the backwards stepwise regressions. PWV has proven to have the highest correlation ($R = 0.782$) suggesting it is the best fit for this model and database. The large variance of HD data observed during our analysis could be responsible for its lower R value (Table 1). However, the HD index is still highly significant with its independent factors showing sensitivity to age, weight, and BPs. Interestingly, only HD is significant with all BP information and weight (Table 1). This is unexpected due to PWV and AI having previously established correlation with cardiovascular risk factors such as BP and weight[6,7]. However this could due to the relatively small number of participants in this study.

Our study further highlights that PWV and AI are not correlated. However, HD is strongly correlated with both AI and PWV, implying its sensitivity to a combination of factors measured independently in PWV and AI. Study shows that PWV and AI are both sensitive to aging, but PWV is primarily sensitive to arterial stiffening risk in older individuals (> 50) while AI is sensitive to risk in younger individuals (< 50)[3]. Our results suggest HD has greater sensitivity to older individuals (Fig. 2b) but can also effectively differentiate between age groups. AI is the only index showing high significance with sex (Table 1), which supports the finding that higher AI values in females compared to males of the same age[7]. Taken together, our study suggests that HD provide a more comprehensive analysis of the BPW.

## CONCLUSION

In this study we studied the effectiveness of HD in assessing arterial stiffness using human BPWs. HD's sensitivity to BP measures, age and HT suggests that HD provides a comprehensive assessment of the BPWs. HD is also shown to be correlated with both PWV and AI. BPWs obtained using tonometry is readily available clinically. Hence, our results demonstrate that HD can potentially be used to clinically assess arterial function in patients with various diseases.


## ACKNOWLEDGEMENTS

This research was supported in part by Translational Research in Biomaterials Fellowship Program (TRB) at Boston University (T32 EB006359), 2R01HL098028 to YZ, and U01 HL-139466 to BS.


## REFERENCES


[1] Weisbrod, R., et al., *Hypertension*, 62:1105-10, 2013.
[2] van Varik, B., et al., *Front. Genet*., 3:1-10, 2012.
[3] McEniery, C., et al., *J Am Coll Cardiol*, 46:1753-1760, 2005.
[4] Milkovich, N., et al., Harmonic Distortion of Blood Pressure Waveform as a Measure of Arterial Stiffness. *Submitted 2021.*
[5] Chow, M., et al., *Biophys. J*., 106:2684–2692, 2014.
[6] Blacher, J., et al., *Hypertension* 33:1111-1117, 1999.
[7] Ayer, J., et al., *J Hypertension,* 28:306–313, 2010.

# A COMPUTATIONAL STUDY OF AORTIC DYNAMIC OCCLUSION IN TYPE B DISSECTION

**T. Kim (1), P. Bakel (2), N. Nama (3), H. Patel (2), D. Williams (4), and C.A. Figueroa (1,3)**

(1) Department of Biomedical Engineering, University of Michigan, Ann Arbor, MI, USA
(2) Department of Cardiac Surgery, University of Michigan, Ann Arbor, MI, USA
(3) Department of Surgery, University of Michigan, Ann Arbor, MI, USA
(4) Department of Radiology, University of Michigan, Ann Arbor, MI, USA

## INTRODUCTION

Type B Aortic dissection (TBAD) is the most frequent acute descending thoracic aortic pathology [1]. A tear occurs in the aortic wall, resulting in a sudden split of the vessel into a true lumen (TL) and a false lumen (FL). TBAD are characterized by a significant rate of aneurysm formation and high 10-year mortality rates [2]. Several computational studies have explored the factors determining the long-term fate of TBAD, including size and number of entry and exit tears, FL thrombosis, and hypertension [3-5].

A serious complication in TBAD is dynamic occlusion (DO) of the TL due to motion of the intimal flap, resulting in blockage of blood supply toward a vital organ, i.e. kidney, inducing malperfusion, which is the second most fatal complication of aortic dissection after rupture [6]. In a large fraction of patients in our clinical experience, global blood pressure (BP) changes are associated with DO. Global increases in BP have been shown to trigger DO, whereas pharmacologically induced reductions in BP restored the patency of the TL (Figure 1). The mechanisms by which the dynamic motion of the flap results in DO remain poorly understood and unexplored.

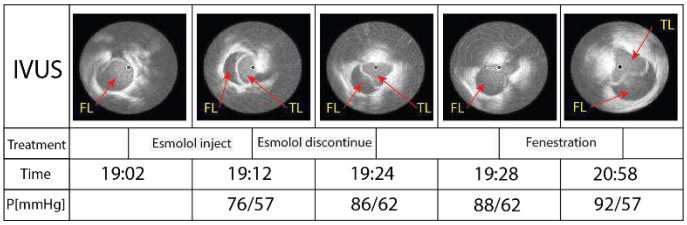


**Figure 1: Timeline of DO with drug and fenestration treatments. IVUS: intravascular ultrasound. P: global blood pressure.**

In this work, we aim the explore the biomechanical and hemodynamical factors driving DO. We hypothesize that relatively small pressure differentials between TL and FL experienced during global changes in BP in DO are sufficient to displace the flap to induce occlusion or to restore TL patency. To test this hypothesis, we developed a Fluid-structure interaction (FSI) model of aortic DO.

## METHODS

An idealized 3D model of a TBAD was constructed by assuming uniform aortic diameter (30 mm), a single entry tear (20 mm diameter), and an intimal flap (100 mm length) with uniform thickness (1 mm), resulting in TL and FL areas of 100 and 580 mm$^2$, respectively (see Figure 2 (a)). There was no re-entry tear on the intimal flap.

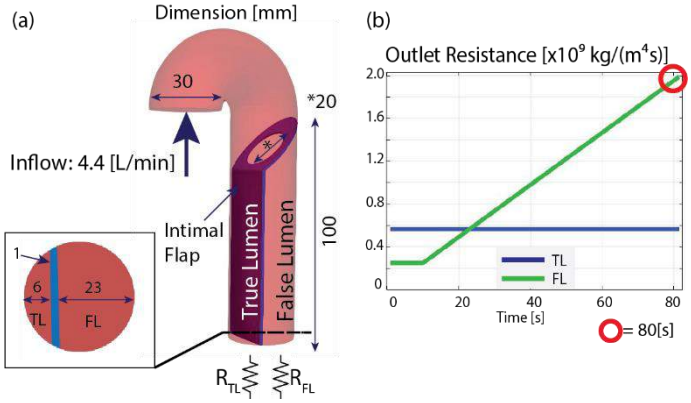


**Figure 2: (a) Idealized 3D TBAD geometry and (b) Imposed histories of outlet resistance in TL and FL over the course of 80 s.**

A Neo-Hookean constitutive model was used for the intimal flap with stiffness parameter of 180 kPa. This value is more compliant than typical stiffness values of the whole aortic wall [7] due to its correspondence with the intima and inner-most media segments of the aorta. The remaining (outer) aortic walls were modeled as rigid. Given that DO occurs over the course of several minutes, hemodynamic simulations were run under mean flow conditions. Outflow boundary

conditions for TL and FL were set by imposing dynamic changes in zero-dimensional resistors ($R_{TL}$ and $R_{FL}$) which trigger global changes in BP. FSI simulations were run using COMSOL Multiphysics.

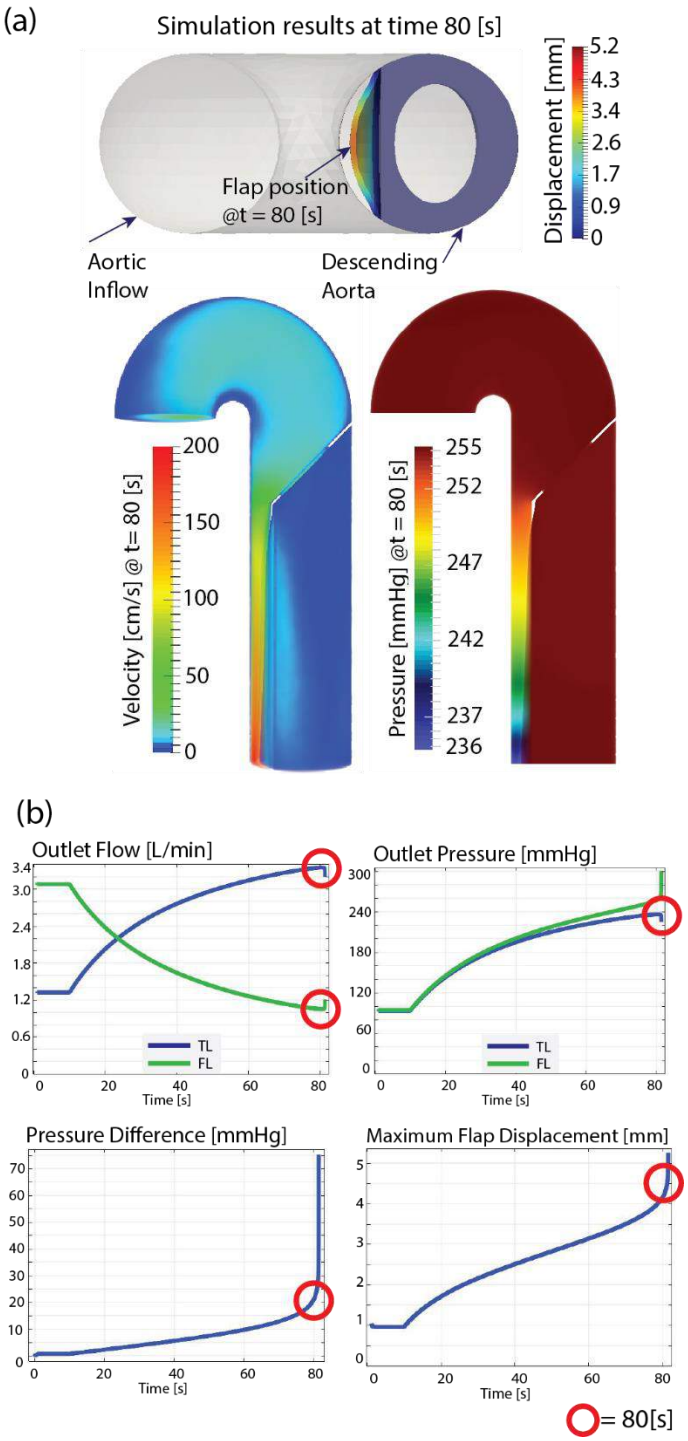


**Figure 3: (a) Flap displacement, pressure, and velocity simulation results at t = 80 seconds and (b) Time histories of Outlet flow, outlet pressure, pressure difference between TL and FL, and maximum flap displacement**

## RESULTS

TL resistance was kept constant, and FL resistance was increased over 80 seconds (Figure 2 (b)). These resistance changes resulted in an overall increased in BP, as well as motion of the flap towards the TL wall, ultimately resulting in DO (Figure 3 (a)), consistent with clinical findings (Figure 1). Blood flow decreased in the FL and increased in the TL, resulting in high TL velocities (Figure 3 (a)). Both TL and FL pressures were increased during the simulation. However, there was a relatively small (<20 mmHg) pressure differential between TL and FL during most of the simulation (Figure 3 (b)). As this pressure differential increased, flap displacement towards the TL aortic wall also increased. Maximum flap displacement was located at the distal part of the model due to the pressure difference between TL and FL. TL pressure and flow dropped suddenly once the flap almost got in contact with the TL wall, at time = 81seconds (Figure 3 (b)).

## DISCUSSION

A simplified FSI model of TBAD was used to study DO. With increased FL resistance, dynamic increases in global BP resulted in flap motion and TL collapse, as reported in our clinical data. Our results demonstrated our hypothesis that relatively small differences in TL and FL pressures are enough to induce the flap motion.

The simulation was stopped right before contact between the flap and TL aortic wall occurred. This would have required using a contact model in the analysis. However, despite this limitation, sudden drops in TL pressure and flow were observed as the TL area got closer and closer to zero. At this point (t>80 s.), most of the blood flowed through the FL.

Further limitations of this model include the lack of re-entry tears in the flap, which have been shown to induce significant changes in hemodynamics [8], the rigid wall assumption for the outer aortic walls, and the lack of side branches. Despite these limitations, this simple FSI model has enabled us to successfully test the hypothesis that relatively small pressure differentials between TL and FL are enough to drive flap motion in DO.

## REFERENCES


[1] Olsson C, et al., Thoracic aortic aneurysm and dissection: increasing prevalence and improved outcomes reported in a nationwide population-based study of more than 14 000 cases from 1987 to 2002, *Circulation*, 114.24: 2611-2618, 2006

[2] Luebke T. and Jan B., Type B aortic dissection, *Aorta*, 2.06: 265-278, 2014

[3] Menichini C, et al., Predicting false lumen thrombosis in patient-specific models of aortic dissection, *Journal of The Royal Society Interface*, 13.124: 20160759, 2016

[4] Cheng Z, et al., Initial findings and potential applicability of computational simulation of the aorta in acute type B dissection, *Journal of vascular surgery*, 57.2: 35S-43S, 2013.

[5] Cheng Z, et al., Geometric and flow features of type B aortic dissection: initial findings and comparison of medically treated and stented cases, *Annals of biomedical engineering*, 43.1: 177-189, 2015

[6] Yang B, et al., Management of type A dissection with malperfusion, *Annals of Cardiothoracic Surgery*, 5.4: 265, 2016

[7] Roccabianca S, et al., Quantification of regional differences in aortic stiffness in the aging human, *Journal of the mechanical behavior of biomedical materials*, 29: 618-634, 2014

[8] Dillon-Murphy D, et al., Multi-modality image-based computational analysis of haemodynamics in aortic dissection, *Biomechanics and modeling in mechanobiology*, 15.4: 857-876, 2016

# QUANTIFYING THE IMPACT OF HEMORRHAGIC SHOCK AND REBOA ON THE ENDOTHELIAL GLYCOCALYX LAYER

**Antonio C. Renaldo (1,2), Aravindh S. Ganapathy MD (3), Nathaniel Hauser, MS (1,2), Magan R. Lane (3), James E. Jordan, PhD (3), Lucas P. Neff, MD (4), Timothy K. Williams, MD (5), Elaheh Rahbar, PhD (1,2)**

(1) Department of Biomedical Engineering, Wake Forest School of Medicine, Winston-Salem, NC
(2) Virginia Tech-Wake Forest University School of Biomedical Engineering and Sciences
(3) Department of Cardiothoracic Surgery, Wake Forest School of Medicine, Winston-Salem, NC
(4) Department of General Surgery, Section of Pediatric Surgery, Wake Forest School of Medicine, Winston-Salem, NC
(5) Department of Vascular and Endovascular Surgery, Wake Forest School of Medicine, Winston-Salem, NC

## INTRODUCTION

The vascular endothelium is lined by a mechano-sensitive glycocalyx (GCX) layer comprising of glycosaminoglycans (GAGs), glycoproteins and proteo-glycan complexes. The main components of the GCX are hyaluronic acid (HA), syndecan-1 (SDC-1), heparan sulfate and chondroitin sulfate. Under normal physiologic conditions, the GCX is intact and maintains a homeostatic balance. However, when physiologic flow is altered (e.g., high flow, high shear environment), there is a disruption in the GCX [1,2]. The shedding of the endothelial GCX after injury results in an increase in vascular permeability, platelet adhesion, and in worse cases endothelial dysfunction. In particular, shock-induced endotheliopathy (SHINE) is a growing concern as increasing levels of circulating GCX components (e.g., HA and SDC-1) are associated with hypercoagulability, in-hospital complications, and poor patient outcomes [3,4].

The phenomenon of shear-dependent changes in the endothelial GCX is emerging to play an important role in endovascular medical interventions. For example, Resuscitative Endovascular Balloon Occlusion of the Aorta (REBOA) is an emerging technique aimed to minimize internal bleeding by creating a temporary aortic occlusion. This lifesaving intervention prolongs survival until definitive surgical hemostasis can be achieved [5]. However, one of the greatest limitations to REBOA is the ischemia-reperfusion (I/R) injury and subsequent renal failure that manifests after imposing a full aortic occlusion. As a result, partial REBOA (p-REBOA) and other endovascular hemorrhage control (EHC) devices that allow for variable levels of occlusion have been developed [4]. While p-REBOA may attenuate the degree of ischemia imposed, there is still concern about the vascular endothelial damage and end-organ damage that may arise as a consequence of altered hemodynamics and prolonged periods of tissue hypoperfusion [6, 7].

We have previously shown with computational fluid dynamics (CFD) simulations that REBOA and p-REBOA results in significant hemodynamic alterations, including areas of high shear proximal and around the site of occlusion which could lead to potential GCX damage [Fig. 1, 8]. In this study, we aimed to quantify the degree of vascular endothelial GCX damage, *in vivo*, induced by full and partial REBOA. We hypothesize p-REBOA will cause more GCX damage than REBOA. We performed a pilot study that analyzes circulating blood biomarkers of shed GCX components and endothelial integrity from local tissue in a porcine hemorrhage model.

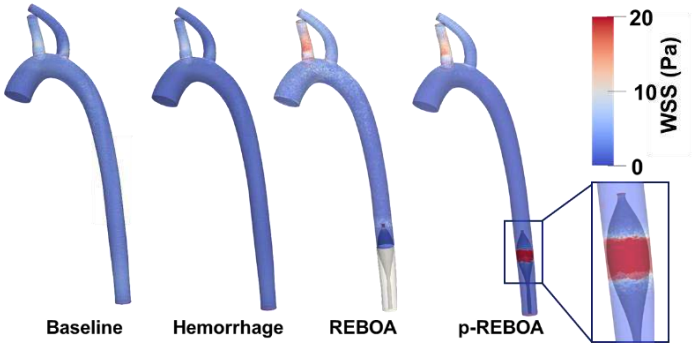


**Figure 1. Wall shear stress (WSS) distribution. Areas of high shear stress are identified in the brachiocephalic artery during full REBOA and around the p-REBOA balloon [8].**

## METHODS

**Porcine Hemorrhage Model:** 10 male and female Yorkshire swine were subjected to 20% hemorrhage (by blood volume) then randomized to either receive a full or partial aortic occlusion (i.e.,

REBOA vs. p-REBOA, n=5/group) for 20 minutes and subsequently resuscitated with a standardized critical care protocol for 4 hours.

To quantify the degree of GCX damage, we serially collected serum over the duration of the experiment and vascular tissue samples were collected after euthanasia. Specifically, we focused on 4 time points: baseline (T0), end of hemorrhage (T30), end of aortic occlusion (T60), and 10 minutes post-occlusion (T75). Enzyme-linked immunosorbent assays (ELISA) for pig serum were used to quantify circulating hyaluronic acid (HA, Echelon Biosciences) and syndecan-1 (SDC-1, Bluegene biotech) as the two key components of the GCX. We used a repeated measures two-way ANOVA to assess differences in GCX biomarkers over time and between groups; significance was set at 0.05 level.

To quantify any histological changes to the vascular endothelium, tissue samples were harvested at the end of each experiment. Specifically, we collected tissue from five key areas that were potentially affected by high shear or distal ischemia; 1) proximal to the REBOA placement, 2) at the site of REBOA, 3) distal to REBOA, 4) the brachiocephalic trunk, and 5) the left renal artery. All samples were fixed in paraformaldehyde. At the time of submission, the histological characterization of the tissue is ongoing with plans to perform H&E staining for morphology, and immunohistochemical (IHC) staining of CD138 (i.e. SDC-1), E-selectin, and thrombomodulin, to quantify local changes in the integrity of the endothelium and GCX.

## RESULTS

We observed significant changes in circulating levels of HA (Fig. 2) over time, consistent with prior reports of SHINE. Maximal levels of shed HA were observed after full REBOA intervention. Animals receiving p-REBOA tended to exhibit lower HA levels in comparison to REBOA at the end of aortic occlusion (T60, 943.8 ng/ml vs. 747.7 ng/ml) and 10 minutes post occlusion (T75, 1238 ng/ml vs. 655.1 ng/ml), though not statistically significant. Additionally, at T75 minutes HA levels in REBOA trended up in contrast to p-REBOA which trended downwards. Further experiments are needed to confirm these trends.

Unlike HA, circulating levels of SDC-1 were relatively constant over time (Fig. 3). The highest levels were actually detected at baseline in the REBOA pigs, suggesting that instrumentation of the pigs may influence the level of SDC-1. Overall, these circulating biomarkers suggests that there is less systemic shedding of the endothelial GCX damage imposed by p-REBOA.

While the vascular tissue processing is ongoing at this time, we aim to quantify the local variations in GCX and endothelial integrity. We expect that vascular areas of high shear will exhibit the most GCX damage.

## DISCUSSION

Our preliminary findings reveal higher trends of systemic shedding of HA with full REBOA compared to p-REBOA. We did not detect any differences in circulating SDC-1 levels between REBOA and p-REBOA. These preliminary findings suggest that there may be other factors influencing GCX shedding in full REBOA compared to p-REBOA. For example, an increase in oscillatory flow and pulsatility within the supraaortic region may affect GCX integrity. Alternatively, higher levels of ischemia in full REBOA compared to p-REBOA [9,10] can be contributing to the increase in HA shedding.

Furthermore, it is important to note that these systemic biomarkers may not be concordant with local markers of GCX shedding or damage. Our histological analysis of tissue damage may offer insight on why these differences occur as well as the direct impact of the balloon itself on the endothelial GCX layer. While preliminary findings indicate full. REBOA results in more circulating HA than p-REBOA, further studies are needed to confirm this phenomenon.

Ultimately, this pilot study offers interesting insight on the impact of an aortic occlusion during hemorrhagic shock on the vascular endothelium and poses interesting questions for future studies. We anticipate to build on these findings and leverage GCX integrity as a metric to better characterize the use of REBOA and p-REBOA as a clinical intervention, as well as to guide resuscitation strategies post-REBOA to accelerate the restoration of the GCX.

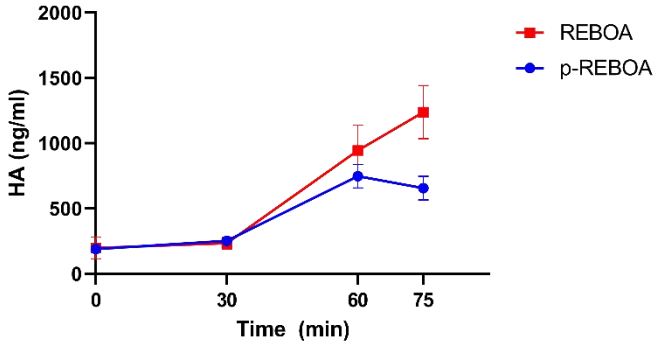


**Figure 2. Preliminary serum HA levels are trending higher after full aortic occlusion (REBOA) compared to a partial occlusion (p-REBOA), 15 minutes after occlusion is imposed (i.e. T75 min).**

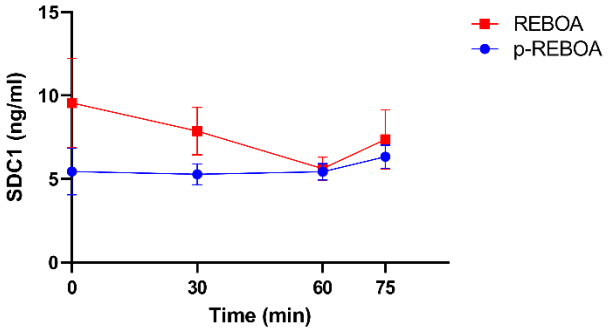


**Figure 3. Preliminary serum SDC-1 levels are similar between REBOA and p-REBOA.**


## ACKNOWLEDGEMENTS

This study was supported by the National Science Foundation (Awards#1559700, #1950281), the Critical Illness Injury Recovery Research Center (CIIRRC) Pilot Award (PI: Rahbar), and the US Army Medical Research and Development Command. (W81XWH-18-0072, Neff and Williams).


## REFERENCES


[1] Ebong, Eno E., et al. *Integrative Biology* 6.3 (2014): 338-347., [2] Yao, Yu et al. *American Journal of Physiology-Heart and Circulatory Physiology* 293.2 (2007), [3] Fu, BM et al., *Wiley Interdisciplinary Reviews: Systems Biology Medicine.* 5(3):381-390, 2013, [4] Johansson, P et al., *Critical Care* 21(1):1-7, 2017., [5] Johnson, MA et al., *Journal of Trauma and Acute Care Surgery*, 81(5):S133-S137, 2016, [6] Williams, TK et al., *Journal of Trauma Acute Care Surgery*, 81(2):294, 2016., [7] Kozar, Rosemary A. et al., *Anesthesia and analgesia* 112(6): 1289, 2011, [8]Renaldo et al., Submitted to Journal, Under review, 2022, [9] Russo, R.M., et al. *Journal of the American College of Surgeons* 223(2)359-368, 2016, [10] Kauvar, David S., et al. *Journal of Trauma and Acute Care Surgery* 87(5) 1026-1034, 2019

SB³C2022
Summer Biomechanics, Bioengineering and Biotransport Conference
June 20-23, Eastern Shore, MD, USA

# MECHANOTHERAPEUTICS TO MODULATE THE FOREIGN BODY RESPONSE

**Niamh A. Ward (1), William Whyte (2), Debkalpa Goswami (2), Ruth E. Levey (3), Garry P. Duffy (3), Ellen T. Roche (2), Eimear B. Dolan (1)**

(1) Department of Biomedical Engineering, School of Engineering, College of Science and Engineering, National University of Ireland, Galway, Ireland
(2) Institute of Medical Engineering and Science, Massachusetts Institute of Technology, Cambridge, MA, USA
(3) Department of Anatomy, School of Medicine, College of Medicine, Nursing & Health Sciences, National University of Ireland, Galway, Ireland

## INTRODUCTION

The long-term performance of implanted medical devices is hindered by the foreign body response (FBR). This is a complex cascade of events that is initiated upon implantation of a foreign object, such as a medical device, to protect the body from this foreign object. The FBR is initiated by the adsorption of proteins to the surface of the implant. The presence of protein receptors enables the adhesion of monocytes which secrete pro-inflammatory cytokines and chemokines, stimulating further inflammatory cell infiltration [1, 2]. Inflammatory cytokines also initiate the differentiation of fibroblast cells to collagen-producing myofibroblasts, which deposit a hypopermeable, collagen-rich fibrotic capsule (FC) around the implant [3]. In many instances, this is an advantageous response, as the FC forms a protective barrier between the body and a potentially harmful foreign object. However, this is detrimental to medical devices that rely on molecular exchange, such as devices that encapsulate cells or include biosensing components, as the FC impedes diffusion of essential molecules between the device and surrounding tissue [4].

Our group previously demonstrated that mechanical actuation of an implanted reservoir for 14 days in a rat model caused a significant reduction in thickness of the formed FC ($p = 0.0005$). Additionally, there was a significant reduction ($p = 0.0036$) in myofibroblast cells at the implant site, suggesting that mechanical loading may affect cell differentiation and/or proliferation. In this study, implanted devices were actuated at a frequency of 1 Hz for 5 minutes every 12 hours at a pressure of 6.9 – 13.8 kPa, and FC thickness was compared to non-actuated controls [5].

For this mechanotherapeutic platform to reach its full potential, we must explore the reproducibility of these promising results in a different animal model and with a different device geometry, as varying applications of this technology will necessitate a wide range of device design requirements. One potential application of this platform is to serve as a cell encapsulation device for the treatment of type 1 diabetes (T1D). Cell therapies have shown promise in restoring glucose responsiveness in T1D patients [6], but currently necessitate lifelong immunosuppression to overcome rejection by the host immune system. In this instance, the device must provide immunoprotection, and a large surface area to volume ratio to reduce the diffusion distance of essential nutrients to the encapsulated cells [7]. Alternatively, arrays of smaller, interconnected actuatable reservoirs may be preferred for reducing FC formation around implantable pacemaker leads [5]. We must also identify the precise cellular interactions that modulate the FBR when actuation is applied. Whilst it is widely understood that mechanical loading can affect cell differentiation and signaling, there is no clear consensus on how applied forces can influence cell behavior in relation to the FBR. For example, mechanical stretch has been attributed to both up- and down- regulation of markers of fibrosis [4,5]. This work uses a combined approach of analytical modelling and *in vitro* and *in vivo* studies to demonstrate reproducibility of this FBR modulating technology and improve our understanding of actuation mediated FBR modulation at the cellular level.

## METHODS

Analytical models of the tissue-interfacing membrane of actuatable devices were designed based on Von Kármán plate theory and analytical approximations for clamped circular and rectangular plates proposed by Timoshenko and Woinowsky-Krieger [10] and Zhang *et al*. [11]. These models predict the surface strain of different configurations of thermoplastic polyurethane (TPU) membranes during actuation. In this study we explored the use of devices with both hemispherical and rectangular geometries.

Actuatable devices were manufactured using TPU sheets (HTM-8001-M and HTM-1001 polyether TPU film, American Polyfilm, Inc). Vacuum thermal forming was used to form sheets of 0.3 mm thickness, which were sealed with TPU sheets of 0.076 or 0.15 mm thickness using a heat-press. A Micro-Renathane® catheter was inserted between the

SB³C2022-098

sheets, creating an actuatable reservoir (hemispherical configuration shown in Figure 1).

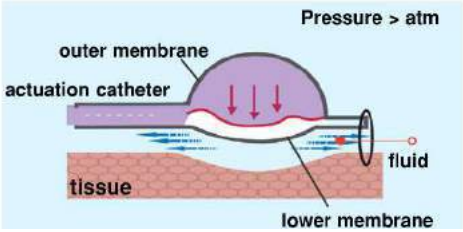


**Figure 1** Hemispherical actuatable device, adapted from Dolan *et al.* 2019 [5]

In the previous *in vivo* study we investigated hemispherical devices in a rat model for 14 days [5]. Here, rectangular actuatable devices were implanted in C57BL/6 mice and actuated using the above regime at a pressure of 13.8 kPa. After 14 days, actuation was ceased, and devices remained implanted for a further 8 days. After 23 days, devices were explanted *en bloc* and stained with phosphomolybdic acid before imaging using Scanco Medical MicroCT 100. FC thickness was quantified using Materialise MIMICS and 3-matic Research software. The thickness of the FC was compared to non-actuated controls using an unpaired, one-tailed, two-sample t-test (OriginLab Corp.).

To explore these responses at a cellular level and investigate the effect of actuation on collagen production, myofibroblast cell line WPMY1 were seeded on lower membrane (actuating membrane) of hemispherical devices (see Figure 1) and cultured for 14 days *in vitro.* Devices were connected to a pressurized air supply and actuated using the previously described actuation regime at an increased pressure of 27.5 kPa. Collagen production was measured using a Sircol Soluble Collagen Assay (Biocolor Ltd.), and collagen production by cells in the actuated group were compared to non-actuated controls using an unpaired, two-tailed, two sample t-test with Welch's correction (GraphPad Software, Inc.).

## RESULTS

Our models predict actuation of a clamped rectangular TPU plate (12 mm x 6 mm) induces a maximum in plane principal strain ($\varepsilon_p$) of 9.7% (mean $\varepsilon_p$ =2.07%) when a uniform pressure of 13.8 kPa is applied (Figure 2A). Following 14 days actuation of a device with the above dimensions in a mouse model, there was a significant reduction ($p<0.0001$) in FC thickness surrounding the device on day 15 when compared to non-actuated controls. This effect was sustained, although attenuated, at day 23 ($p=0.02453$) despite ceasing actuation (Figure 2B).

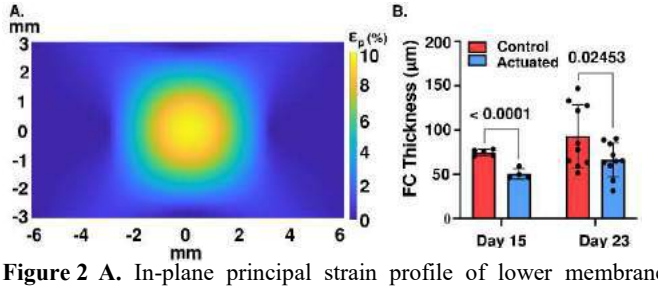


**Figure 2 A.** In-plane principal strain profile of lower membrane during actuation at 13.8 kPa **B.** FC thickness (μm) surrounding implanted devices after 14 days actuation *in vivo*. Data is presented as mean ± standard error of the mean.

Modeling predicts that actuation of a clamped circular TPU plate (Ø = 7.2 mm) induces maximum surface strains of 3.9% in the radial ($\varepsilon_r$) and tangential directions when pressurized to 27.5 kPa (Figure 3A). At the same applied pressure (27.5 kPa), there was a significant reduction in collagen production by WPMY-1 (myofibroblast cell line) cells after 9 ($p = 0.01409$) and 14 ($p = 0.02729$) days actuation *in vitro* when compared to non-actuated controls (Figure 3B).

## DISCUSSION

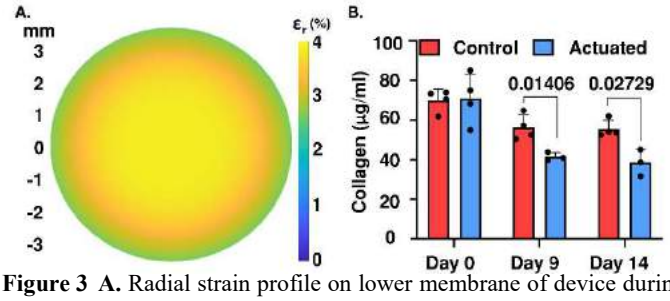


**Figure 3 A.** Radial strain profile on lower membrane of device during actuation at 27.5 kPa **B.** Collagen production (μg/ml) by WPMY-1 cells *in vitro*. Data is presented as mean ± standard deviation.

Here, we show that periodic cyclical loading at a low membrane strain magnitude *in vivo* for a 14 day period can significantly reduce FC formation in a mouse model. This builds upon our previous work where we demonstrated a significant reduction in FC thickness in a rat model using the same actuation regime. Importantly, we show reproducibility of actuation mediated FBR modulation in different animal models and with multiple device geometries. This mechanotherapeutic platform holds great promise for a range of applications, including improving targeted drug delivery, and extending the longevity of biosensors.

However, we must first improve our understanding of how mechanical actuation modulates the FBR at the cellular level. Whilst it is difficult to recapitulate the highly complex immune response using an individual cell type *in vitro*, our work suggests that mechanical actuation can modulate the host FBR through a reduction in myofibroblast presence at the implant site, and a reduction in collagen production by these cells. We hypothesize that this effect is driven by mechanical strain applied at the device interface, or by inducing extracellular fluid flow around the device during actuation. Strain has been shown to reduce myofibroblast differentiation [9], which may lead to a reduction in collagen-producing cells around an implant. It is also understood that fluid flow can aid clearance of inflammatory cells [12], curtailing recruitment of fibroblasts to the implant site. Future work will aim to identify the specific signaling pathways that are disrupted by actuation. Whilst strain and fluid flow are inherently linked, we aim to fully decouple these to identify the mechanism driving this response.

## ACKNOWLEDGEMENTS

The authors acknowledge funding from the Science Foundation Ireland Royal Society University Research Fellowship (URF\R1\191335) and a Pilot and Feasibility Grant from the Juvenile Diabetes Research Fund (1-PNF-2019-778-S-B).

## REFERENCES

[1] J. M. Anderson *et al., Seminars in Immunology*, vol. 20, pp. 86-100, 2008 [2] O. Veiseh and A. J. Vegas, "*Advanced Drug Delivery Reviews*, vol 144, p148-161, 2019 [3] W. K. Ward, *Journal of Diabetes Science and Technology*, vol. 2, pp. 768–777, 2008, [4]A. A. Sharkawy, *et al., J. Biomed. Mater. Res.*, vol. 37, pp. 401–412, 1996 [5] E. B. Dolan *et al.*, *Sci. Robot.*, vol. 4, 2019 [6] A. Ramzy *et al.*, *Stem Cell*, vol. 28, pp. 2047-2061, 2021 [7] D. Goswami *et al.*, "*Adv. Sci.*, vol. 8, pp. 1–19, 2021 [8] J. Lee *et al.*, *Nat. Biomed. Eng.*, vol. 5, pp. 89–102, 2021[9] M. E. Blaauboer *et al., Biochem. Biophys. Res. Commun.*, vol. 404, pp. 23–27, 2011[10]S. Timoshenko and S. Woinowsky-Krieger, McGraw-Hill, 1959 [11] Y. Zhang, *Sci. China Physics, Mech. Astron.*, vol. 59, pp. 1–11, 2016 [12] B. R. Seo *et al.*, *Sci. Transl. Med.*, vol. 13, 2021

SB³C2022
Summer Biomechanics, Bioengineering and Biotransport Conference
June 20-23, Eastern Shore, MD, USA

# SPECTRAL ANALYSIS OF KINETIC ENERGY IN A HEALTHY AORTA

**David Büchner (1), Emily L. Manchester (2), Xiao Y. Xu (2)**

(1) University of Stuttgart, Stuttgart, Germany
(2) Imperial College London, London, United Kingdom

## INTRODUCTION

Detailed analysis of turbulence and transition in blood flow has become more relevant, as advanced experimental and numerical resources have enabled us to quantify turbulence parameters and link them with different cardiovascular diseases. Nevertheless, physiological blood flow in vessels, such as the aorta, has been assumed to be predominantly laminar. It is surprising that this assumption is still widely accepted and rarely questioned even though the presence of disturbed flow and flow instabilities in the aorta is well known [1,2,3]. While the discussion on the actual state of flow in healthy human aortas and other blood vessels is ongoing, relatively little effort has been spent on the development of a holistic understanding of it. A recently reported study seeks to provide further clarification by employing powerful tools from general fluid dynamics [4]. Using Womersley's analytical solution of the Navier-Stokes equations as well as Doppler ultrasound measurements of healthy carotid arteries they demonstrate that the flow is sensitive to initial conditions, globally unstable, and exhibits a kinetic energy cascade; all three being major characteristics of turbulence. However, their study remains limited to the carotid arteries and thus calls for similar investigations also in other vessels, especially the aorta. The present work takes on this motivation and conducts a spectral analysis of kinetic energy (KES) for the flow field obtained by an extensive Large Eddy Simulation (LES) of an anatomically realistic aorta under normal physiological conditions.

## METHODS

The aorta, as the vessel of interest in this study, has complex geometric features. To fully capture the true state of flow it is necessary to perform investigations using anatomically realistic models. For this reason, following the workflow described in [5], a subject-specific aorta model was reconstructed from MRI scans of a healthy volunteer. The modelled geometry includes the ascending and descending aorta, aortic arch, and the main branching arteries as shown in Figure 1.

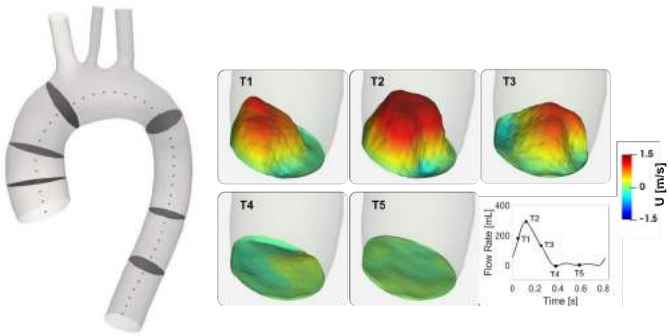


**Figure 1: Reconstructed 3D geometry of the aorta and locations of the selected cross-sections (left) and 3D time-resolved inlet velocity profiles (right).**

As described in [5], the LES model was implemented in OpenFOAM with blood being assumed to be Newtonian and the aortic walls rigid. At the inlet 3D time-resolved velocity profiles, reconstructed from 4D-flow MRI (Figure 1), were applied while a three-element Windkessel model was used for all outlet boundary conditions. Following mesh and time-step sensitivity studies, the simulation was run for 23 cardiac cycles and the resolved velocity field was validated against 4D-flow MRI data.

From the computed flow field in the modelled aorta, velocities at six cross-sections (defined in Figure 1) were extracted; proximal- and mid-ascending aorta, entry to the arch, proximal- and mid-descending aorta, and entry to the distal-descending aorta. At every grid point within the cross-sections, the velocity components were transformed

from the global Cartesian coordinate system to a point-wise local coordinate system in the axial, circumferential, and radial directions. Fourier decomposition was then conducted and the KES was calculated for every point and direction, both for the entire time-trace as well as for every cardiac cycle individually, following the method proposed in [6]. Moreover, for every harmonic the energy was integrated over the cross-sections, allowing a more holistic qualitative assessment of the spectral distribution of the kinetic energy at the selected locations.

## RESULTS

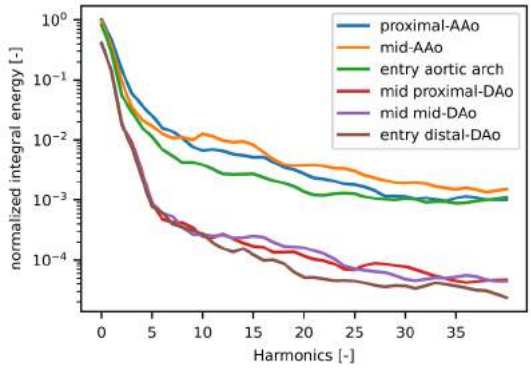


**Figure 2: Energy amplitudes of the harmonics integrated over the respective cross-section for flow in the axial direction. Frequency of the fundamental harmonic is 1.23 Hz.**

The distribution of integrated kinetic energy over the first 40 harmonics resolves a distinctive reverse exponential course as depicted in Figure 2. The course is similar in shape for all locations; a steep decline of energy contained until around the 5th harmonic, followed by a gradual and less steep decrease towards higher harmonics. However, the steep decline is much less pronounced at locations in the ascending than in the descending aorta. As a result, the range of a more gradual decline is, although of a similar shape at all locations, almost two orders of magnitudes lower in the descending aorta. In other words, in the descending aorta considerably less energy is contained in high-frequency components, thus fluctuations, of the flow. Moreover, the contained energy is normalized also by the total area of the cross-sections thereby eliminating the effect of narrowing cross-sections and energy leaving the system through the arch branches. Consequently, the overall decrease of energy can be attributed to the transport and dissipation of turbulent kinetic energy.

In order to better understand this integral distribution, the kinetic energy amplitudes of the individual frequency ranges are plotted over the cross-sections. Figure 3 shows the results for the summed 8 highest harmonics evaluated. Evidently, the highest amplitudes are reached in the mid ascending aorta, also explaining the highest integral values in this frequency range, as observed in Figure 2. Similar plots of other frequency ranges and velocity magnitudes reveal the presence of larger coherent structures in this region. They form during systolic acceleration and break down during systolic deceleration and diastole, releasing turbulent kinetic energy into the system. With decreasing strength, this process continues towards the arch. Although most of the turbulent kinetic energy is dissipated when the descending aorta is reached, secondary effects, such as radial forces and flow separation, introduce new but weaker fluctuations mainly in the inner area of the aortic curvature. The turbulent kinetic energy introduced by this then slowly dissipates again, as can be seen by the lower amplitudes and less energy contained at the cross-section located at the entry to the distal aorta.

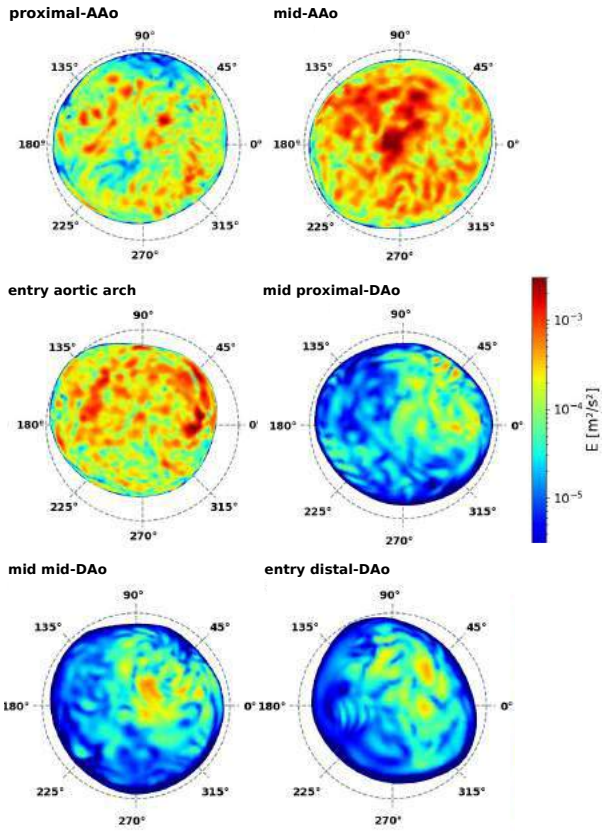


**Figure 3: Pseudocolormaps of the amplitude of the combined 8 highest harmonics considered, respectively 43.21 to 50.62 Hz.**

## DISCUSSION

The obtained results are in overall agreement with previous findings of flow instabilities in the aorta [1,2] and demonstrate that they cause high-frequency fluctuations thus turbulent like flow patterns along the entire aorta. Moreover, the spectral analysis performed shows that in the aorta, similar to in the carotid artery [4], transport of kinetic energy between different frequency components as well as dissipation takes place; this primary characteristic of turbulent flow is present in a healthy aorta under normal physiological conditions.

For now, this study is confined to flow in one individual aorta, and results, therefore, cannot be generalized to make universal statements. In addition, the non-Newtonian effect and wall compliance should be taken into account in future analysis.


## ACKNOWLEDGEMENTS

MR images of the aorta were provided by Prof D.P. O'Regan of Hammersmith Hospital, MRC London Institute of Medical Sciences Imperial College London.


## REFERENCES


[1] Hansen, K. L. et al., *Ultrasound in Medicine and Biology*, 42.4:899-908, 2016.

[2] Stalder, F. et al., *Journal of Magnetic Resonance Imaging*, 33.4:839-846, 2011.

[3] Stein, P. D. et al., *Circulation Research*, 39:58-65, 1976.

[4] Saqr, K. M. et al., *Scientific Reports*, 10.1:1-12, 2020.

[5] Manchester, E. L. et al., Cardiovascular Engineering and Technology, 2021

[6] Kahn, M. O. et al., Journal of Biomechanics, 52:179-182, 2017.

SB³C2022
Summer Biomechanics, Bioengineering and Biotransport Conference
June 20-23, Eastern Shore, MD, USA

# MATERIAL PROPERTY CHANGES OF POLYMERIZED RED BLOOD CELLS IN SICKLE CELL DISEASE

**Dillon C. Williams (1), David K. Wood (2)**

(1) Biomedical Engineering, University of Minnesota, Minneapolis, MN, United States
(2) Biomedical Engineering, University of Minnesota, Minneapolis, MN, United States

## INTRODUCTION

Sickle cell disease (SCD) is an autosomal recessive blood disorder that arises from a single nucleotide mutation in the β-globin gene; a GAG codon is switched to a GTG codon causing a glutamine to be replaced by a valine [1]. This leads to a mutated hemoglobin, known as HbS, which has lower oxygen affinity than healthy HbA and can bind to other HbS proteins under deoxygenated conditions. When HbS proteins bind they form polymer domains that can develop into long inflexible strands that deform the red cell and give it the characteristic sickle shape. Sickled red blood cells are the main driver of the adverse effects of SCD [2].

Sickle cell disease is an enormous global health burden. SCD affects roughly 13 million people worldwide; the polymerization of HbS under low oxygen tension leads to a multitude of adverse effects. The mechanical and morphological changes and decreased oxygen carrying capabilities of polymerized red cells disrupt bulk flow, create vascular occlusions, and increase inflammation and cell adhesion. Over time this can lead to thrombosis, stroke, ischemia, hemolytic anemia, and organ failure. In the United States, patients with SCD have an average life expectancy of 54 years versus the healthy average of 76 years [3].

Though the underlying mechanism of SCD has been well studied, the link between hemoglobin aggregation and altered red cell mechanical properties is not well understood. When polymer domains form in the deoxygenated red cells the cells undergoes drastic changes in material properties. In bulk flow SCD patient samples exhibit altered fluid proprieties due to these mechanical changes [4]. The work in this study aims to quantify specific material and chemical changes in the red blood cells as they undergo sickling. Novel microfluidic platforms and optical instruments have been developed to quantify single cell saturation, morphology, and mechanical properties. The advances from this study will fill in knowledge gaps connecting changes at the molecular scale to single cell changes that ultimately lead to the SCD pathologies. This information will provide the necessary foundation for more focused design and testing of treatments.

## METHODS

To measure single cell properties, SCD patient blood samples were analyzed using two assays. The first assay, Quantitative Absorption Cytometry (QAC), builds off previous work published by Di Caprio et al [5] to quantify the saturation and morphology of single RBCs in high throughput under variable oxygen tension. In this assay, a custom built optical set up utilizes a constant red LED to quantify cell thickness, and two alternating blue LEDs in the Soret Band to leverage the optical absorption proprieties of oxygenated and deoxygenated hemoglobin and quantify the ratio of the two species. Single cell images are recorded to calculate saturation from the ratio of oxy and dexoyhemoglobin, and the morphology of the cells is analyzed by a convolution neural net to determine if the cells are polymerized or soluble. The outputs of this assay are fractions of soluble and polymerized cells at each oxygen tensions and saturation curves for both species.

The second assay utilizes microfluidic techniques to perform a controlled stress relaxation test at the single cell level for RBCs in high throughput under variable oxygen tension. Red cells are forced through a 4x6μm capillary channel under controlled pressure. In the capillary section cells undergo consistent deformation and upon exit relax back to a steady state geometry. A high speed camera uses image based auto triggering to capture cells undergoing this process. A custom python image analysis tool kit tracks the cells to determine shape and location, and from this the relative changes in circularity, C, can be determined.

$$C = \frac{2\sqrt{\pi(area)}}{perimeter} \quad (1)$$

The distribution of relative circularity changes in a sample gives a qualitative measure of the distribution of cell stiffness values.

## RESULTS

Results from one sample show the heterogeneous nature of red blood cells in SCD. The saturation measurements in the QAC assay show polymerized RBCs display a lower saturation at a given oxygen tension compared to soluble cells (fig. 1).

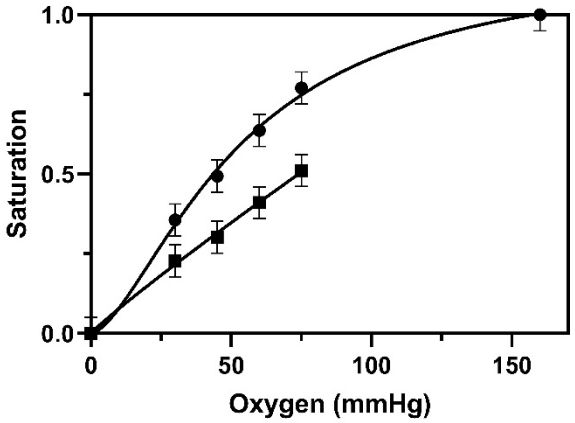


**Figure 1: Saturation curves of soluble population (circles) and polymerized population (squares). Soluble hemoglobin has a higher oxygen affinity resulting is high saturation for a given oxygen tension. There are no polymerized cells at 160mmHg**

QAC also measures the fraction of soluble cells at a given oxygen tension. This is shown in figure 2 (right y-axis). The fraction of soluble cells increases with increasing oxygen content as polymer melts in the cells. Figure 2 also shows the distribution of normalized deformation from the Single Cell Deformation assay (left y-axis).

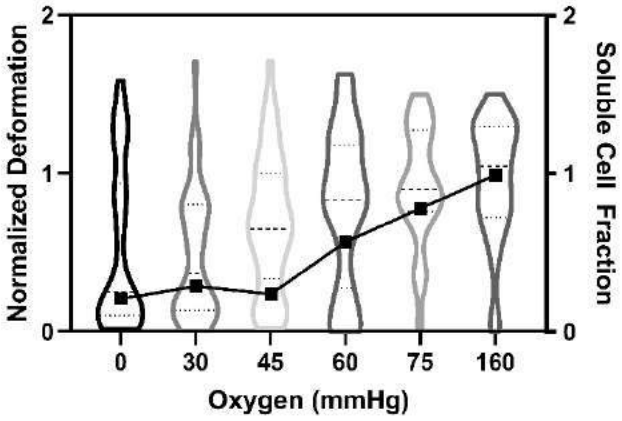


The soluble cell fraction has been overlaid on the distribution of normalized deformation to highlight the relationship between the two. At low oxygen tensions the fraction of soluble cells is low as a large portion of the cells are polymerized. Similarly, the deformation distribution is shifted towards zero at low oxygen tensions suggesting a higher fraction of stiff cells. As oxygen tension increases the soluble cell fraction increases, and the deformation distribution shifts towards one suggesting a higher fraction of pliant cells. These two independent assays, QAC and Single Cell Deformation, have been compared with a Paired T-Test and give a p value of 0.04.

## DISCUSSION

Many studies have presented data on the increased stiffness of sickle red blood cells. The data in this project so far agrees with the current understanding of SCD physiology. As oxygen decreases hemoglobin in sickle RBCs will polymerize, and as a result oxygen carrying capacity will decrease and cell stiffness will increase [6]. This study adds a measure of granularity to the data. Previous work has quantified cells as either polymerized or soluble with binary measures of material properties. However, at intermediate oxygen tensions it is unknown if polymerized RBCs act the same as those under fully deoxygenated conditions. A higher saturation of a polymerized cell could lead to less aggregation of hemoglobin and a more intermediate stiffness. These cells would not align with material properties of fully polymerized cells at 0mmHg or fully soluble cells at 160mmHg, and would suggest that the stiffness of polymerized RBCs exist on a continuum.

The preliminary data in this study suggests that this is a possibility. In figure 2 the comparison of soluble fraction to distribution of deformation shows strong agreement at both ends of the oxygen spectrum, but less so in the intermediate oxygen tensions. At 45 and 60 mmHg the soluble fraction is considerably less than the median of the normalized deformations, which suggests that some of the polymerized cells are not as stiff as those found in deoxygenated conditions.

The relative changes in mechanical properties are an important biomarker for SCD. As it is hypothesized that stiff, polymerized cells are responsible for vascular occlusion and endothelial damage [2], this biomarker is an excellent target for measuring efficacy of treatment.

## ACKNOWLEDGEMENTS

Portions of this work were conducted in the Minnesota Nano Center, which was supported by the National Science Foundation through the National Nano Coordinated Infrastructure Network (NNCI) under Award No. ECCS-1542202. This work was supported by the NHLBI under Grant Nos. HL130818 and HL132906.

## REFERENCES

[1] Stuart MJ, Nagel RL. Sickle-cell disease. *The Lancet*, 364(9442):1343–1360, 2004.

[2] Henry ER, Cellmer T, Dunkelberger EB, Metaferia B, Hofrichter J, Li Q, Ostrowski D, Ghirlando R,Louis JM, Moutereau S, et al. *Proceedings of the National Academy of Sciences*, 117(26):15018–15027, 2020.

[3] Lubeck D, Agodoa I, Bhakta N, Danese M, Pappu K, Howard R, Gleeson M, Halperin M, Lanzkron S. *JAMA*, 2(11):e1915374–e1915374, 2019

[4] Bazzi MS, Valdez JM, Barocas VH, Wood DK. *Biophysical Journal,* 119(11):2307–2315, 2020.

[5] Di Caprio G, Schonbrun E, Gonc ̧alves BP, Valdez JM, Wood DK, Higgins JM. *Proceedings of the National Academy of Sciences,* 116(50):25236–25242, 2019.

[6] Li X, Dao M, Lykotrafitis G, Karniadakis GE. *Journal of biomechanics*, 50:34–41, 2017

# ASSESSMENT OF INTERLABORATORY COMPUTATIONAL SIMULATIONS OF THE FDA BENCHMARK BLOOD PUMP

**Sailahari V. Ponnaluri (1,2), Prasanna Hariharan (2), Luke H. Herbertson (2), Richard A. Malinauskas (2), Keefe B. Manning (1,3), Brent A. Craven (2)**

(1) Department of Biomedical Engineering, The Pennsylvania State University, University Park, PA, USA
(2) Division of Applied Mechanics, Office of Science and Engineering Laboratories, Center for Devices and Radiological Health, U.S. Food and Drug Administration, Silver Spring, MD, USA
(3) Department of Surgery, Penn State Hershey Medical Center, Hershey, PA, USA

## INTRODUCTION

Computational fluid dynamics (CFD) modeling is a widely used predictive tool in the design and assessment of medical devices. However, to be relied upon to inform regulatory decision making, the credibility of computational predictions must be demonstrated by performing verification and validation [1,2]. Toward this end, the U.S. Food and Drug Administration (FDA) collaborated with academic researchers to establish a benchmark centrifugal blood pump model for CFD validation. An open interlaboratory study was conducted in which participants from around the world submitted CFD simulation results of the benchmark blood pump for comparison with experimental data [3,4]. A total of 24 CFD simulations were submitted. In this study, we report the complete results of the interlaboratory study including comparisons of the CFD predictions in the pump with experimental velocity and hemolysis measurements at several different pump operating conditions.

## METHODS

The centrifugal blood pump (Figure 1) was designed with simple geometric features and could operate across a wide range of flow and pressure conditions. Details of the pump geometry are available at: https://nciphub.org/wiki/FDA_CFD/ComputationalRoundRobin2Pump. Interlaboratory experiments were conducted to provide an experimental benchmark dataset for CFD validation. Specifically, inlet and outlet pressure values were acquired and the velocity field was measured using particle image velocimetry (PIV) at six pump conditions with flow rates ranging from 2.5–7.0 L/min and rotational speeds of 2500–3500 rpm (Figure 2). The PIV methodology and results obtained from three independent labs are detailed in Hariharan *et al* [4]. The hemolytic potential of the blood pump was determined through *in vitro* tests using porcine blood at one lab [3].

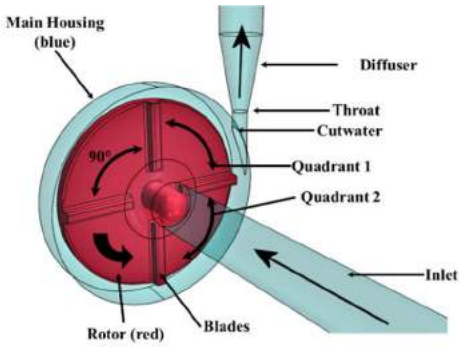


**Figure 1: Schematic illustration of the FDA benchmark blood pump.**

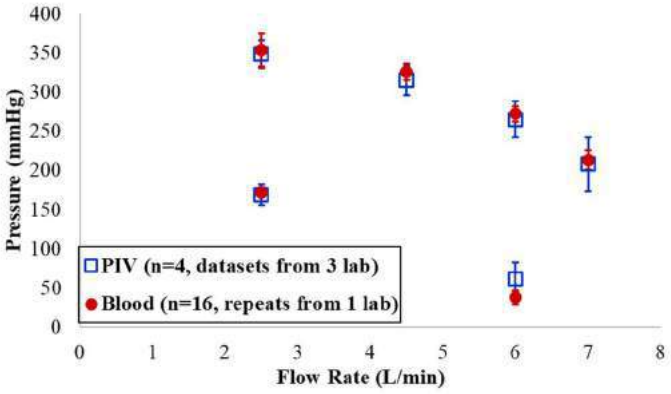


**Figure 2: Experimental measurements of pump pressure head versus flow rate for the FDA benchmark blood pump. The PIV data are from interlaboratory measurements in three labs and the blood data were acquired in one lab with 16 repeats.**

The interlaboratory CFD study was conducted by participants in a blinded fashion prior to the publication of the experimental data. The participants were only provided the geometry of the pump, the fluid properties, and the measured inlet velocity profiles and turbulence intensities, and they were asked to simulate six pump operating conditions. Beyond this, the participants were free to choose the specific CFD solver, mesh resolution, boundary conditions, turbulence model, and other simulation choices.

Here, we performed detailed analyses of the interlaboratory CFD results for three test conditions: (i) 2.5 L/min at 3500 rpm, (ii) 6.0 L/min at 2500 rpm, and (iii) 6.0 L/min at 3500 rpm. To prevent bias, the participant data were anonymized for the analyses. In particular, we compared the CFD predictions to the experimental results to assess computational performance in terms of the pump pressure head, velocity distributions throughout the pump and the outlet diffuser, and hemolysis. For scalar quantities, a percent error was calculated for the CFD predictions of pressure and hemolysis. As each of the individual modelers used different computational meshes, to evaluate the velocity field, we interpolated the simulation results and the PIV data onto a common high-resolution mesh using Kriging interpolation (Figure 3). To quantify the overall error in the velocity field predictions compared with the PIV measurements, we calculated a relative comparison error ($\varepsilon$) in different pump regions (Figure 1: Quadrants 1 and 2, and the diffuser region), defined as

$$\varepsilon = \sqrt{\frac{1}{n}\sum_{i=1}^{n}\left(\frac{u_{CFD,i}-u_{exp,i}}{u_{exp,max}}\right)^2} \qquad (1)$$

where $u_{CFD,i}$ is the local CFD velocity magnitude at each spatial location, $u_{exp,i}$ is the corresponding experimental value at the same location, and $u_{exp,max}$ is the maximum experimental value in the entire region of interest.

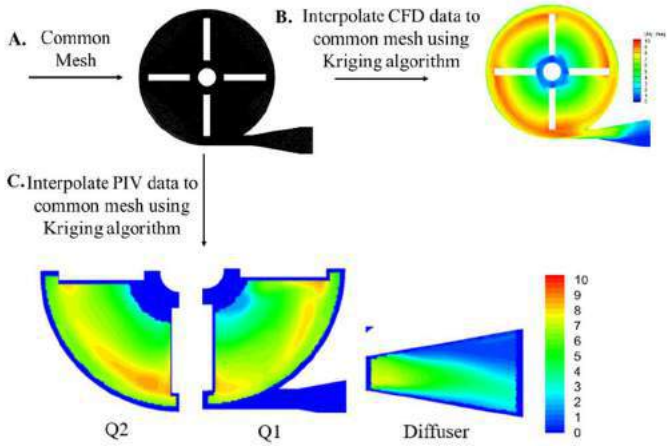


**Figure 3: Data analysis pipeline including A. the common interpolation mesh, B. interpolation of participant CFD submissions, and C. interpolation of PIV results.**

## RESULTS

The interlaboratory study participants submitted results from 14 steady-state and 10 transient simulations using a wide range of CFD solvers, reference frame formulations, mesh resolutions, and turbulence models. In general, there was not a strong correlation between mesh resolution or turbulence model with CFD accuracy compared to the experimental pressure and velocity measurements. Most CFD predictions of the pump pressure head were within two standard deviations of the mean experimental data, except at the 6.0 L/min, 2500 rpm condition for which only 16 of 23 submissions were within this range (Figure 4). The unsteady simulations of the velocity field agreed more closely with the experiments within the rotor region of the pump, but showed little advantage over the steady simulations in the outlet diffuser region. Predictions of hemolysis varied widely for the eight participants who submitted results.

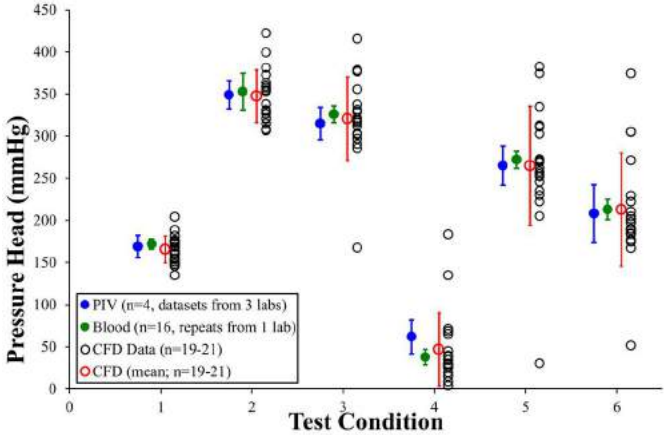


**Figure 4: Summary of pressure head from PIV experiments, blood experiments, and the interlaboratory CFD study simulations.**

## DISCUSSION

This study provides insight into the accuracy of CFD simulations of the FDA benchmark blood pump from a wide range of users in the medical device community. While the number of participants using different options and approaches was insufficient to determine definitive trends, there were some valuable observations. Most notably:

- CFD accuracy was not strongly correlated with the choice of turbulence model
- Transient simulations were more accurate than steady simulations in the rotor region of the pump
- Flow field predictions in the outlet diffuser were generally much less accurate than in the rotor region

We also note that, while a number of CFD submissions accurately predicted a single operating condition, few of the participants in the study were able to accurately predict the pump performance at all three conditions analyzed. This highlights the need to validate CFD modeling of mechanical circulatory support devices across a range of operating conditions, especially at off-design conditions that are more challenging to accurately predict.


## ACKNOWLEDGEMENTS

We thank Steven Day of the Rochester Institute of Technology who led the design and fabrication of the pump model in collaboration with RAM. This study was funded by the FDA CDRH Critical Path program and, in part, by a National Science Foundation INTERN supplement through NSF CMMI-2017805.


## REFERENCES


[1] ISO 14708-5:2020. Implants for surgery — Active implantable medical devices — Part 5: Circulatory support devices.

[2] ASME V&V 40-2018. Assessing credibility of computational modeling through verification and validation: Application to medical devices.

[3] Malinauskas, R.A., et al., *ASAIO Journal*, 63(1):150-160, 2017.

[4] Hariharan, P., et al., Cardiovascular Engineering and Technology, 9(4):623-640, 2018.

# AUTOMATED TUNING OF A LUMPED PARAMETER MODEL FOR SIMULATING RESTING CARDIOVASCULAR PHYSIOLOGY

**Akash Gupta (1), Aseem Pradhan (1), Surya Prakash Sharma (3), Tyler Schmidt (1), Ethan Kung (1,2)**

(1) Department of Mechanical Engineering, Clemson University, South Carolina, The United States
(2) Department of Bioengineering, Clemson University, South Carolina, The United States
(3) Department of Electrical and Computer Engineering, Clemson University, South Carolina, The United States

## INTRODUCTION

Lumped Parameter Network (LPN) models have provided a powerful tool for modelling the cardiovascular system, and have been used for medical device design, surgical planning, as well as education and training[1]. However, the determination of appropriate LPN component values has traditionally required extensive manual tuning and presents a practical barrier to using this tool. Several studies have attempted to address this practical barrier by developing automated tuning procedures, but a majority of these automated tuning procedures apply to highly simplified models of the cardiovascular system[2], [3]. Several studies provide automated tuning protocols for more sophisticated LPN models but apply to patients with congenital heart defects or only determine a limited set of cardiovascular parameters such as the elastance, end diastolic volume of the left ventricle, and systemic vascular resistance[4], [5].

To the best of our knowledge, there exists no protocol that can automatically provide a full set of component values for a sophisticated closed-loop model of the healthy cardiovascular system at rest, such that the hemodynamics simulated match a target set of multiple hemodynamic quantities. To address this, we develop a protocol which can automatically generate the full set of component values for an LPN model according to the desired set of hemodynamic parameters to be simulated. This desired (target) set of hemodynamics includes the mean aortic pressure, systolic and diastolic aortic pressures, cardiac output, as well as the systolic and diastolic ventricular volumes for both ventricles. In addition, the protocol also ensures that the resulting simulated mean pulmonary artery pressure and the mean atrial pressures are realistic for a typical healthy subject at rest.

## METHODS

Our protocol determines all LPN component values needed to obtain a set of target hemodynamic parameters (THP) in an LPN model derived from previous work (Figure 1). We divide all the LPN component values into three categories based on the procedure used to determine them. The first category of LPN component values includes LPN components governing the ventricles, the capacitance of the aorta and are determined using a neural network with an architecture specifically designed for non-linear regression[6]. The data required for training the neural network was obtained by running the LPN with 300,000 combinations of the LPN component values in the first category and recording the corresponding hemodynamic outputs.

The second category includes all of the remaining LPN component values except for the ventricular reference volumes. The values for the second category are predicted by scaling a reference set of LPN component values. The reference set of LPN component values reflect clinically nominal hemodynamics and were obtained by manual tuning. From the THP and using clinically nominal values for mean atrial pressures, the systemic vascular resistance (SVR) and the pulmonary vascular resistance (PVR) can be calculated. All of the reference values for the systemic and pulmonary resistances are then scaled to match the target SVR and PVR. To adjust for body size, the capacitances are scaled according to equation 1, similar to previous work[5], [7].

$$\frac{C}{C_i} = \left(\frac{TVR}{TVR_i}\right)^{-\frac{4}{3}} \quad (1)$$

Where $C$ and $C_i$ represent the scaled capacitance and reference capacitance, respectively. Similarly, $TVR$ and $TVR_i$ represent the target and the reference LPN total vascular resistance, respectively.

Finally, the third category which includes the ventricular reference volumes, are calculated using equations 2 and 3 based on information in the THP. The end systolic pressures are estimated using equations 4 and 5[8].

$$Vlv_0 = LVESV - \frac{LVESP}{E_{maxLV}} \quad (2)$$

$$Vrv_0 = \left(RVESV - \frac{RVESP}{E_{maxRV}}\right) + 15 \quad (3)$$

$$LVESP = \frac{mean(P_{ao})}{0.8721} - SV * 0.051565 \quad (4)$$

$$RVESP = \frac{2}{3} * \left(mean(P_{pa}) + sPAP\right) \quad (5)$$

Where $Vlv_0$ and $Vrv_0$ are the left and right ventricular reference volumes respectively. $LVESV$ and $RVESV$ are the left and right ventricular end systolic volumes respectively. $LVESP$ and $RVESP$ represent the left and right ventricular end systolic pressures. $mean(P_{ao})$ refers to the mean pulmonary artery pressure, $mean(P_{pa})$ the mean PA pressure, and $sPAP$ the systolic pulmonary artery pressure. All pressures are in mmHg, and volumes in ml.

To test protocol performance, we used 500 realistic sets of THP generated from previous work reflecting resting physiology of healthy subjects and compared the protocol output to the THP [9]. We have used the normalized root mean square error (NRMSE) to quantify the difference between the target values and the simulated hemodynamics.

## RESULTS

Simulation results show that waveforms for critical hemodynamic parameters were physiologically realistic (one example shown in Figure 2A) and within clinically normal ranges. The NRMSE between the target and simulated hemodynamics ranged between 0.63% and 14.2%. The highest NRMSE corresponds to systolic left ventricular volume for which the maximum absolute difference between the target and simulation was 9.6 ml. The NRMSE for all other parameters was below 8.2% (Figure 2B). In all test cases, the mean pulmonary artery pressure, both the left and right mean atrial pressures also lie within clinically normal ranges (< 25, <15, and < 10 mmHg, respectively).

## DISCUSSION

Our automated protocol can significantly shorten the time-consuming and labor-intensive process of tuning LPN models. The simulated pressure and flow waveforms from our protocol are clinically realistic, and match very closely to the desired tuning targets. The ability of our protocol to automatically generate appropriate LPN component values lowers the barrier-to-entry for other researchers to adopt powerful LPN modelling tools for their work.


## ACKNOWLEDGEMENTS

This work is supported by an award from the National Science Foundation (1749017) and by the department of Mechanical Engineering at Clemson University. Clemson University is also acknowledged for their generous allotment of compute time on the Palmetto cluster.


## REFERENCES


[1] Y. Shi, P. et al. doi: 10.1186/1475-925X-10-33.
[2] T. L. Ruchti, et al. doi: 10.1007/BF02368178.
[3] A. Cappello et al. doi: 10.1007/BF02368323.
[4] X. Xiao et al. doi: 10.1114/1.1484217.
[5] E. Kung et al. doi: 10.1115/1.4027271.
[6] D. Chen, F. Hu et al. doi: 10.3390/e22020193.
[7] C. Corsini et al. doi: 10.1080/10255842.2012.758254.
[8] M. I. Monge Garcia, Z. et al. doi: 10.1007/s10877-018-0236-y.
[9] A. Pradhan et al. doi: 10.1007/s13239-021-00582-3.


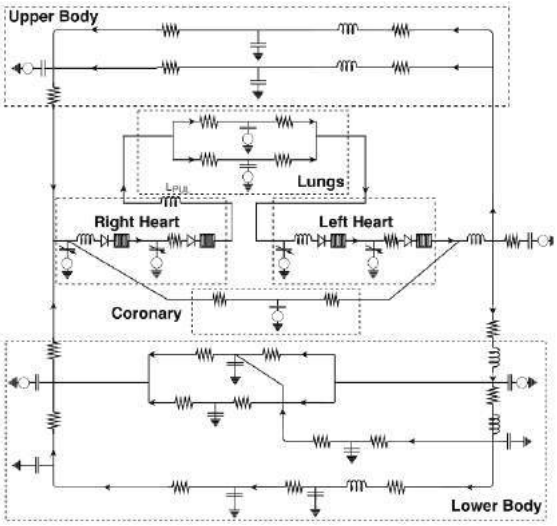


**Figure 1: The Lumped Parameter Network Model**

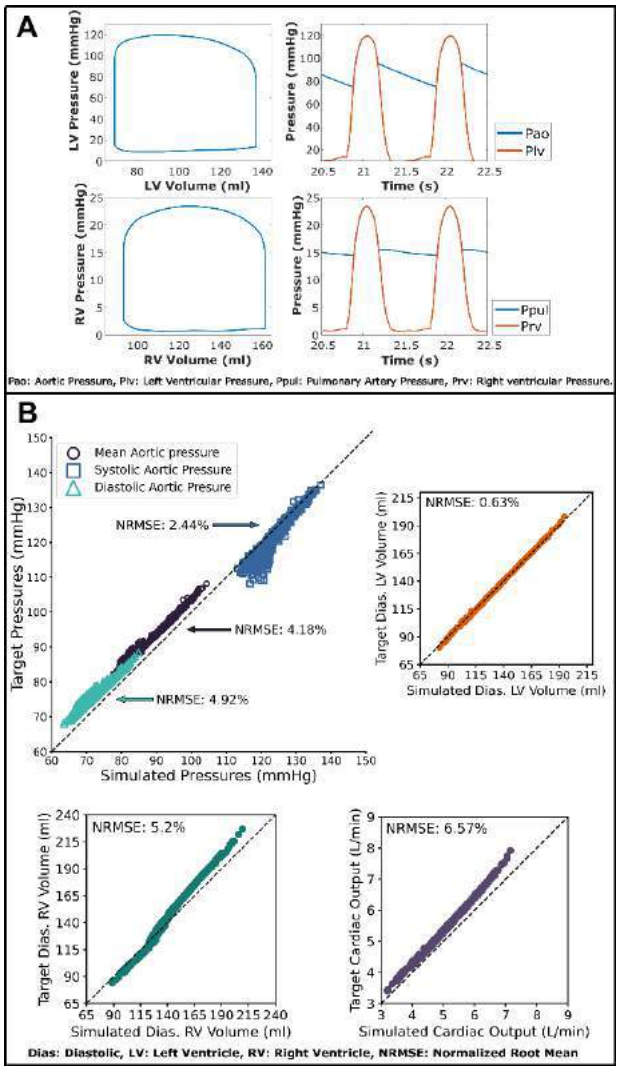


**Figure 2: (A) One example of hemodynamics simulated by the LPN from the test set; (B) A comparison of the target and simulated hemodynamics from the protocol test set.**

SB³C2022
Summer Biomechanics, Bioengineering and Biotransport Conference
June 20-23, Eastern Shore, MD, USA

# Patient-specific computational fluid dynamic simulation of cerebrospinal fluid flow in the intracranial space

**Patrick Fillingham (1), Swati Rane Levendovszky(2), Michael Levitt (1)**

(1) Department of Neurological Surgery, University of Washington, Seattle, WA, USA
(2) Department of Radiology, University of Washington, Seattle, WA, USA

## INTRODUCTION

Abnormal cerebrospinal fluid (CSF) flow is associated with a variety of poorly understood neurological disorders such as Alzheimer's Disease[1, 2] and hydrocephalus[3]. The lack of comprehensive understanding of the fluid and solid mechanics of CSF flow remains a critical barrier in the development of diagnostic assessment and potential treatment options for these diseases. We have developed a whole brain, patient-specific computational fluid dynamics (CFD) simulation of CSF flow in the cranial cavity, incorporating patient specific pulsatile brain deformation as boundary conditions, as a step towards comprehensive understanding of CSF dynamics and how they relate to neurodegenerative diseases.

## METHODS

A patient-specific 3D geometry of the CSF filled spaces was segmented from structural MRI. Patient-specific flow boundary conditions were measured and calculated using phase contrast MRI and conservation of mass. Patient specific pulsatile deformation along the surface of the cerebrum and cerebral ventricles is measured using amplified MRI. A three-dimensional CFD simulation was conducted using only patient-specific waveforms as boundary conditions. Phase contrast MRI measurement of maximum velocity at the cerebral aqueduct was used to validate the simulation with excellent agreement.

## RESULTS

The CSF dynamics across the cardiac cycle are presented, (a preview shown in Figure 1) illustrating the relationship between arterial flow and CSF flow. Flow in and out of the ventricles was shown to have a slight phase delay (~20% of the cardiac cycle) from flow in the subarachnoid space. Intracranial pressure dynamics are presented, with pressure in the Lateral Ventricles demonstrating less significant transient effects than pressure in the subarachnoid space.

## DISCUSSION

This work presents a quantitatively validated whole-brain simulation of CSF flow for a single healthy subject. The computational methodology improves over the state of the art by eliminating non-physiological boundary conditions and unnecessary assumptions about the mechanical properties of brain tissue, providing an essential step towards clinically useful tools for assessing the development of neurodegenerative disorders.

## ACKNOWLEDGEMENTS

This work was made possible by the generous support of the Catchot Family.

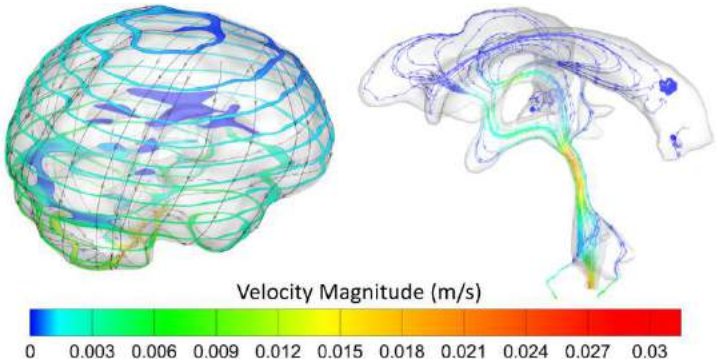


**Figure 1.** Velocity contours at ten axial slices with overlaid streamlines (left). Streamlines in the ventricles colored by velocity magnitude (right).

**REFERENCES**


[1] M. D. Sweeney, A. P. Sagare, and B. V. Zlokovic, "Cerebrospinal fluid biomarkers of neurovascular dysfunction in mild dementia and Alzheimer's disease," (in eng), *J Cereb Blood Flow Metab,* vol. 35, no. 7, pp. 1055-68, Jul 2015, doi: 10.1038/jcbfm.2015.76.

[2] K. Blennow and H. Zetterberg, "Biomarkers for Alzheimer's disease: current status and prospects for the future," (in eng), *J Intern Med,* vol. 284, no. 6, pp. 643-663, Dec 2018, doi: 10.1111/joim.12816.

[3] A. A. Linninger, M. Xenos, D. C. Zhu, M. R. Somayaji, S. Kondapalli, and R. D. Penn, "Cerebrospinal fluid flow in the normal and hydrocephalic human brain," (in eng), *IEEE Trans Biomed Eng,* vol. 54, no. 2, pp. 291-302, Feb 2007, doi: 10.1109/tbme.2006.886853.

# MEASUREMENT OF STENT RETRIEVER REMOVAL FORCES IN AN EXPERIMENTAL MODEL OF ACUTE ISCHEMIC STROKE

**Demitria A. Poulos (1), Bryan C. Good (1)**

(1) Mechanical, Aerospace, and Biomedical Engineering
University of Tennessee
Knoxville, TN, USA

## INTRODUCTION

Large vessel occlusions (LVOs) are the cause of approximately 40% of strokes worldwide, and acute ischemic stroke (AIS) due to LVO accounts for 90% of 6-month post-stroke mortality [1]. The standard treatment for an AIS due to LVO is a mechanical thrombectomy (MT), and when compared to therapeutic treatments indicates an improvement in patient outcomes [2]. Current MT procedures require the use of stent retrievers (SRs) or aspiration techniques to restore blood flow. Despite its clinical success, nearly 2 out of 3 patients who had an AIS experience adverse outcomes [3]. To improve the degree of revascularization, the interaction between a SR and thrombus, as well as the thrombus removal force needs to be understood. These findings can improve clinical training and inspire new SRs to further improve patient outcomes [3].

## METHODS

To determine the required removal forces of embolus analogs (EAs) in experimental models of AIS, two protocols were used. In the first, EAs were created *in situ* from bovine blood collected in CPDA-1 anticoagulated bags. The blood was centrifuged to separate red blood cells and platelet rich plasma, reconstituted to achieve a hematocrit of 50%, and $CaCl_2$ was introduced to promote coagulation. Two types of tubing (Tygon medical tubing and PVC tubing) were used in both bare and collagen-coated states to mimic a range of vascular surface interactions. Type-I bovine collagen was diluted with HCl and DI water and allowed to incubate within the tubes at room temperature. After the addition of $CaCl_2$, the blood was allowed to statically clot for 1.5 hours in one of the vascular models. A Solitaire2 Revascularization Device (Medtronic) was inserted and deployed in the tube across each EA to mimic SR MT. To measure clot removal force, the tubing and SR were attached to a Single Column Material Testing System (Instron), and the SR wire was pulled at a constant 2 mm/s until the crosshead displaced 20 mm and the SR and EA were removed from the tubing (**Fig. 1A**). The length of each EA was measured with digital calipers after each experiment. Additional tests were performed for each model without an EA, as a control test to determine the friction between the SR and each surface.

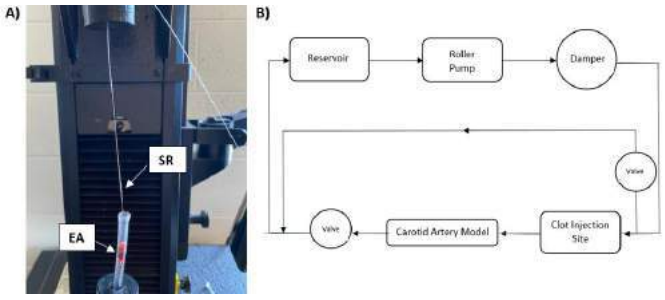


**Figure 1: Experimental setup of the A) Instron stent removal test and B) diagram of the benchtop circulatory flow loop.**

To more accurately represent how EAs originate and lodge in AIS patients, a benchtop circulatory flow loop was developed with a constricting cerebral artery model (**Fig. 1B**), which tapered from 5.5 to 3.3 mm in diameter. For this experiment, 6 mm diameter tubing and a Chandler loop were used to create EAs of 50% hematocrit under dynamic flow conditions for approximately 1.5 hours. The EAs were removed from the Chandler loop, cut to size, and inserted into the flow

loop upstream of the artery model. The EAs were allowed to lodge downstream within the carotid artery model for roughly 15 minutes under cerebral flow rate and pressure conditions. The model and lodged EA were removed from the flow loop and transferred to the Instron machine, the SR was deployed, and the Instron protocol from the previous experiments was followed to measure the EA removal forces.

## RESULTS

As displayed in **Fig. 2**, the measured force ramps up as the SR is pulled by the Instron machine until the EA eventually detaches from the tubing. The downward slope after detachment represents residual friction between the SR and tubing. Peak removal forces (**Table 1**) ranged between 0.1 to 0.5 N.

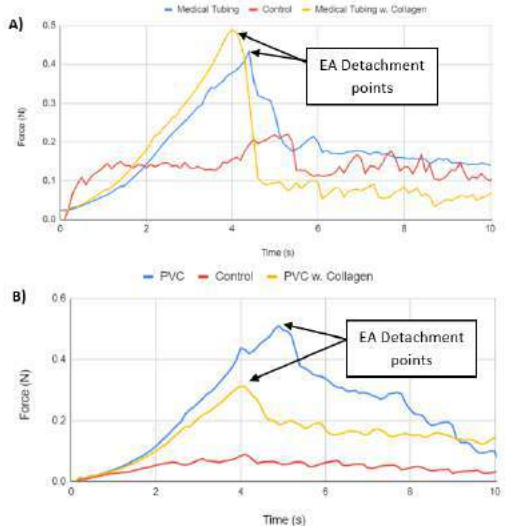


**Figure 2: Force vs. time data for EA removal in A) Tygon and B) PVC tubing with and without collagen compared to controls.**

From **Fig. 3** it can be observed that EA length correlated with lower removal forces. The average EA lengths for PVC bare and collagen coated tubes were approximately 27.1 and 25.4 mm and 22.9 and 24.1 mm for Tygon bare and collagen coated tubes. The introduction of collagen only had a minor effect on the EA removal forces shown in **Table 1**.

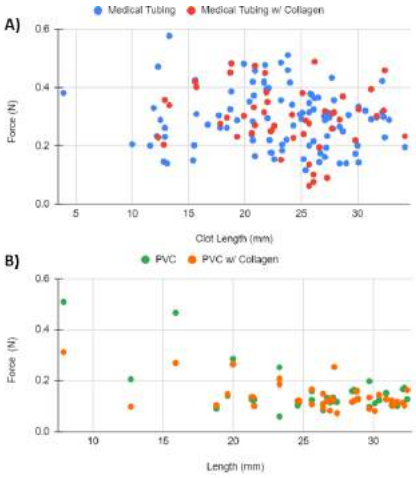


**Figure 3: Relationship between maximum removal force and EA length formed *in situ* in A) Tygon medical and B) PVC tubing.**

**Table 1: Sample size and removal forces for each test parameter**

| Test Parameter | Sample Size | Average Max. Force (N) |
|---|---|---|
| Tygon Medical Tubing | 102 | 0.295±0.1 |
| Tygon Medical Tubing with Collagen | 57 | 0.293±0.1 |
| PVC Tubing | 44 | 0.151±0.08 |
| PVC Tubing with Collagen | 51 | 0.132±0.05 |

A total of 5 EAs were tested in the circulatory flow loop, and the average removal force was 0.304±0.1 N. Similar trends were present in all 5 tests (example shown in **Fig 4**), the initial accumulation of force is a result of the SR pulling through the EA. Once the EA detaches it begins to curl on itself and the SR vacates the tube, pulling the EA accumulation with it.

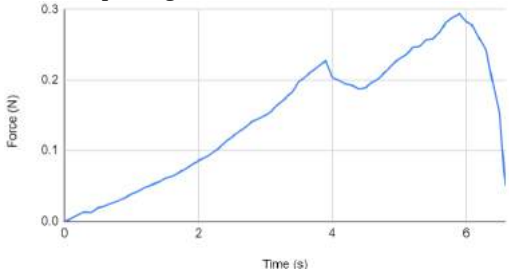


**Figure 4: Example of force (N) vs. time (s) data of an EA lodged in the circulatory flow loop cerebral artery model.**

## DISCUSSION

These results indicate that surface coating influences EA adhesion and can affect the maximum detachment forces. To accurately represent the formation and adhesion of EAs in AIS, further experiments will be performed with other concentrations of collagen and tubing surfaces. The simple vascular models, however, provided a basis for a more complex representation created by the constricting artery model and flow loop. When comparing the data across all experiments it is observed that the forces required to remove EAs from the circulatory flow loop model were greater than that of EAs formed statically in various vascular models. Since the flow loop was a more realistic representation of the formation of EAs, we can assume that data collected from this experiment can be compared to clinical settings. Further studies are needed to understand the complete range of thrombus removal forces. More data will be collected with the constricting carotid artery model, and other physiological cerebral models will also be introduced to the flow loop to observe the relationship between arterial geometry and SR removal forces.


## ACKNOWLEDGEMENTS

We thank Dr. Michael Froehler from the Vanderbilt University Medical Center for providing the SR used in this study.


## REFERENCES


[1] Hui, W et al., *AHA Journals*, 51:2026-2035, 2020.
[2] Pérez, MA et al., *Journal of NeuroInterventional Surgery*, 2011.
[3] Luraghi, G et al., *Journal of Biomechanics*, 127, 2021.

# RADIOMICS FEATURES ON CONTRAST-ENHANCED AND NON-ENHANCED MRI ARE ASSOCIATED WITH INTRACRANIAL ANEURYSMAL RISK

**Sricharan S Veeturi (1,2), Nandor K Pinter (3), Adnan H Siddiqui (1, 3), Vincent M Tutino (1,2,4)**

(1) Canon Stroke and Vascular Research Center, University at Buffalo, Buffalo, NY, USA
(2) Department of Mechanical and Aerospace Engineering, University at Buffalo, Buffalo, NY, USA
(3) Department of Neurosurgery, University at Buffalo, Buffalo, NY, USA
(4) Department of Biomedical Engineering, University at Buffalo, Buffalo, NY, USA

## INTRODUCTION

Vessel wall enhancement (VWE) in intracranial aneurysms (IAs) is a phenomenon where a distinctly higher signal intensity is observed in T1-MRI image after injection of gadolinium-based contrast, as compared to the image before contrast injection. This is a potential imaging biomarker for risk stratification of IAs and has been associated with aneurysm instability. Clinical studies have associated VWE with growing/unstable aneurysms in the past and found that unstable aneurysms were more likely to exhibit VWE than stable aneurysms [1]. Currently, VWE assessment is done manually via visual inspection of non-enhanced MRI (NE-MRI) and contrast-enhanced MRI (CE-MRI) images and is characterized as focal/circumferential. To aid in more objective evaluation of enhancement, metrics have been developed in recent years to quantify the overall degree of enhancement. For example, $CR_{stalk}$ is the ratio of the maximal signal intensity on the aneurysm wall to the pituitary stalk intensity in the CE-MRI image. However, metrics like $CR_{stalk}$ are single values that are computed for each aneurysm case and may not consider the complex variations of intensity across the aneurysm sac that reflect differences in tissue behavior and biology.

Radiomics has emerged as a promising tool for analyzing and quantifying complex textural variations in signal intensities among different modalities of images [2]. This is a technique where images are converted into a mineable high dimensional space using automatically extracted data-characterization algorithms. In this study, we investigated if radiomics features (RFs) derived from NE-MRI and CE-MRI images could assist in better risk stratification of IAs. To do this, we performed radiomics analysis on NE-MRI and CE-MRI image pairs of aneurysms to extract 293 RFs and classified them as high or low-risk using their 5-year ISUIA scores as a risk surrogate. We built a multivariate regression model using the RFs that are significantly different between high and low risk aneurysms which could potentially help in better risk stratification of IAs.

## METHODS

Time of flight (TOF) MR angiography, NE-MRI and CE-MRI images from patients imaged between September 2019 and July 2020 were acquired. We excluded images which were at the cavernous segment of the ICA due to the presence of high intensity imaging artifact in the cavernous sinus region [2]. Additionally, we also excluded aneurysms that had a perpendicular height < 2 mm due to image resolution constrictions.

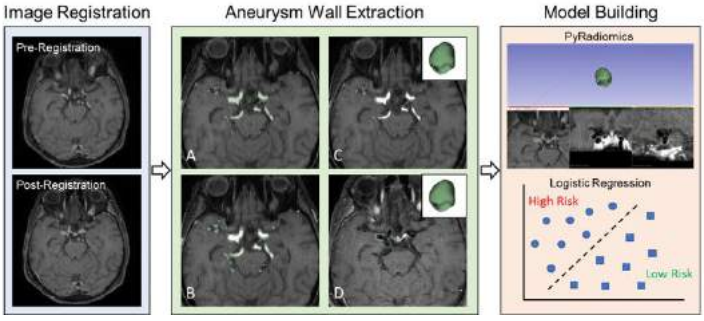


**Figure 1: Pipeline for extraction of radiomics features.** NE-MRI and CE-MRI images were registered in 3D slicer.

The pipeline for extracting RFs from the features shown in Figure 1. This was all performed in 3D slicer (www.slicer.org). We extracted RFs from the NE-MRI and CE-MRI using the masks as the region of interest, and also computed the difference in the RFs. An interactive PyRadiomics (https://radiomics.io) add-in was used in Slicer 3D to compute the RFs in all the images. The MRI images had an anisotropic

resolution (0.375 mm X 0.375 mm X 0.4 mm) hence, for more robust computation of RFs, the original images were resampled into an isotropic resolution of 0.5 mm X 0.5 mm X 0.5 mm [4]. We computed a total of 293 RFs for each aneurysm. The details are shown in table 1.

**Table 1: Radiomics Features computed for each aneurysm.**

| | Method | NE-MRI | CE-MRI | Diff. |
|---|---|---|---|---|
| Shape and Size | Aneurysm wall mask morphology | 14 | | |
| Intensity Distribution Metrics | Intensity Distribution Metrics | 18 | 18 | 18 |
| High level textural features | Gray-level co-occurrence matrix (GLCM) | 24 | 24 | 24 |
| | Gray-level size zone matrix (GLSZM) | 16 | 16 | 16 |
| | Gray-level run length matrix (GLRNM) | 16 | 16 | 16 |
| | Neighborhood gray-tone difference matrix (NGTDM) | 5 | 5 | 5 |
| | Gray level dependence matrix (GLDM) | 14 | 14 | 14 |
| | | | **Total: 293** | |

For risk categorization, we computed the 5-year ISUIA score for each case which were assumed to be representative of the risk [5]. Following feature extraction, we performed univariate analysis on all the RFs obtained. For normally distributed parameters, a two-tailed student t-test was used to assess statistical difference and from non-normally distributed parameters, we performed a non-parametric Mann-Whitney U test. A parameter was assumed to be significantly different if $p<0.05$ from the univariate analysis.

To evaluate the potential utility of RFs in risk stratification of aneurysmal lesions, we built a multivariate logistic regression model using the significant different RFs identified above. Aneurysms having a an ISUIA score>2.5 were considered high risk lesions. The co-linear RFs were first removed by performing a correlations analysis. Features having a correlation coefficient >0.8 were removed and a logistic regression model was trained using ISUIA scores as the independent variable. The logistic regression model was built using scikit-learn libraries in python. We implemented a leave-one-out cross validation due to small sample size. We compared the performance of the regression model with $CR_{stalk}$ alone as the metric for risk stratification.

## RESULTS

A total of 25 aneurysms from 23 patients were collected for this study. Using ISUIA as the clinical score, a total of 6 RFs were significantly different between high and low risk lesions of which 3 were RFs extracted from CE-MRI and 3 RFs from the difference. Correlation, Informational Measure of Correlation 2 (IMC2), and maximal correlation coefficient (MCC) were computed using the GLCM filter in the CE-MRI images. The coarseness computed using the difference in NGTDM values between NE-MRI and CE-MRI were significantly lower in high-risk aneurysms, whereas IMC1 computed using the GLCM filter and Busyness computed using the NGTDM filter in the CE-MRI were significantly higher in high risk aneurysmal lesions.

Using ISUIA as the clinical score, we ended up with 5 independent RFs which we used to train the logistic regression model. A heatmap of the correlation matrices is shown in figure 2. ROC analysis of the logistic regression model built using ISUIA scores showed a very good predictive value with ROC of 0.88. The model had an accuracy of 84%, a sensitivity of 75% and a specificity of 88%. Upon calculating the odds ratio, we found that the NGTDM busyness in the CE-MRI image had the highest odds ratio (1.05) followed closely by GLCM IMC1 (1.04). This shows that both the complexity of signal intensities as well as the gradients in signal intensities in CE-MRI images are higher in high-risk IAs. Gradients and complexity of signal are higher in aneurysms exhibiting VWE which is characteristic of high-risk aneurysms.

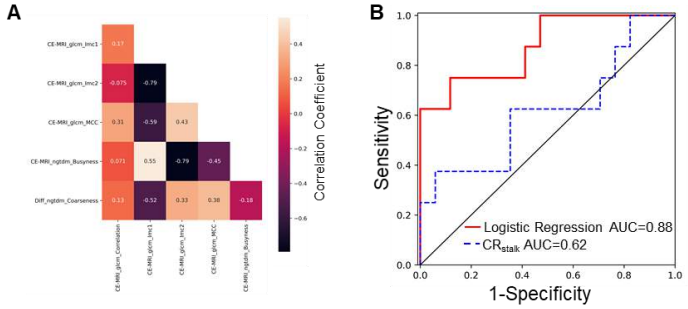


**Figure 1: Statistical models for predicting high risk lesions. A)** A heat map showing the final 5 independently associated RFs used to build the logistic regression model. **B)** Assessment of performance using of the logistic regression model and an existing metric $CR_{stalk}$ using ROC analysis.

## DISCUSSION

In this preliminary study we explored the feasibility of using radiomics features derived from NE-MRI and CE-MRI images in risk stratification of intracranial aneurysms. Over the years, it has been observed that ruptured and growing IAs demonstrate significantly higher contrast enhancement in the CE-MRI images as compared to stable IAs [1]. Indeed, our observations in the current study resonate with such previous studies. We observed that high-risk aneurysms were characterized by lower GLCM correlation, IMC2 and MCC in the CE-MRI image. In different ways, all these features quantify the complexity of the texture of the image. This suggests that high-risk aneurysms tend to have higher "complexity" or higher variations in in MRI signal intensity as compared to low-risk aneurysms in the CE-MRI image. This could potentially be due to the presence of vessel wall enhancement in certain parts of aneurysms. Additionally, we also observed that high-risk IAs had a lower difference in NGTDM Coarseness, which is a measure of the gradient of intensities of surrounding voxels from the center voxel, between NE and CE-MRI images. A potential explanation to the lower difference in high-risk IAs is that high-risk IAs tend to exhibit enhancement throughout the whole aneurysm which would lead to lower gradients and thus lower difference in coarseness values from NE-MRI images when compared to low risk aneurysms. Similarly, we also observed that the NGTDM busyness, which quantifies the rapidly changing signal intensities, was higher in case of high-risk IAs.

We also observed that statistical models built from RFs outperform current clinical metrics of assessing risk. Thus, RFs derived from NE and CE-MRI images could potentially be added as a quantitative tool for risk stratification in the current clinical pipeline.

## REFERENCES:

[1] Edjlali, M et al., *Neuroradiology*, 289:181-187, 2018.
[2] Aerts, H et al., *Nat Comm*, 5, 2014.
[3] Lindenholz, A et al., *Radiology*,286: 12-28. 2018
[4] van Timmeren, J et al., *Insights Imaging*,11: 91, 2020
[5] Wiebers, D et al., *Lancet*,362: 103-110, 2003

# LASER-INDUCED CALCIUM INFLUX AND PROPAGATION FOR TEMPORARY BLOOD-BRAIN BARRIER OPENING

**X. Li (1), A. Ahmad (2), Q. Cai (3), M. Giannotta (4), E. Dejana (4), R. Bachoo (5,6,7), T. Price (2,8), Z. Qin (1,3,8,9)**

(1) Department of Bioengineering, University of Texas at Dallas, Richardson, TX 75080, USA
(2) School of Behavior and Brain Sciences, University of Texas at Dallas, Dallas, TX 75080, USA
(3) Department of Mechanical Engineering, University of Texas at Dallas, Richardson, TX 75080 USA
(4) FIRC Institute of Molecular Oncology Foundation (IFOM), 20139 Milan, Italy
(5) Department of Internal Medicine, University of Texas at Southwestern Medical Center, Dallas, TX 75390 USA
(6) Harold C. Simmons Comprehensive Cancer Center, University of Texas at Southwestern Medical Center, Dallas, TX 75390 USA
(7) Department of Neurology, University of Texas Southwestern Medical Center, Dallas, TX75390, USA
(8) Center for Advanced Pain Studies, University of Texas at Dallas, Richardson, TX 75080, USA
(9) Department of Surgery, University of Texas Southwestern Medical Center, Dallas, TX75390, USA

## INTRODUCTION

To maintain a stable microenvironment for brain homeostasis, the blood-brain barrier (BBB) acts as a physical barrier to protect the brain parenchyma from the toxic effects of blood components but also poses a formidable challenge to the delivery of therapeutics[1]. Therefore, safe and effective approaches to open the BBB are essential to deliver therapeutics for CNS diseases. We have developed a novel method to reversibly open the BBB *in vivo* by picosecond-laser excitation of gold nanoparticles (AuNPs) modified by a antibody targeting JAM-A, one of the tight-juntion proteins along the BBB, and delivered human IgG, viral vector AAV and cargo-laden liposome successfully *in vivo*[2].

$Ca^{2+}$ influx and signaling have been shown to increase BBB permeability by several pathways including ERK1/2 phosphorylation to modulate the integrity of BBB. We investigated this hypothesis with an *in vitro* transwell BBB model (**Fig. 1**). We showed that picosecond-laser stimulation of targeted AuNPs causes a drop in the tranendothelial electrical resistance (TEER) and an increase in the permeability, both reversibly. We further observed $Ca^{2+}$ influx, propagation and recovery after laser stimulation. The phosphorylation of ERK1/2, one of the candidates on the $Ca^{2+}$ signaling pathway, maximized at 0.5 hr and recovered at 6 hr after laser tretament. These results suggest that the mechanism involves $Ca^{2+}$ influx and propagation.

## METHODS

*Nanoparticle synthesis and functionalization:* Gold nanoparticles (AuNPs) were synthesized and functionalized with BV16 (anti-human JAM-A) to target JAM-A or *lycopersicon esculentum* lectin (LEL) to target glycoprotein by previous reported method[2].

*In vitro experiments:* Human cerebral microvessel endothelial cell/D3 (hCMEC/D3) cells were seeded on collagen-coated transwell inserts and cultivated approximately 1 week to form cellular monolayer. The monolayers were incubated with AuNP-BV16 (0.5 nM) followed by laser treatment. To measure the permeability, the media with 1 mg/ml FITC-dextran was added to the upper chambers. At selective time points, 100 µl media were aspirated from the bottom chamber. The fluorescent intensity of FITC-dextran was detected with excitation at 490 nm and emission at 540 nm. The permeability (cm/sec) was calculated by rate of FITC-dextran quantity change over time (dQ/dt), divided by the initial concentration of dextran (C) and the membrane area (A) (Eq. 1). To detect $Ca^{2+}$, the monolayers were treated with 3 µM fluo-4 ($Ca^{2+}$ indicator) for 0.5 hr, followed by real-time imaging. The percentage change (%) of fluo-4 was calculated by the change in intensity, $\Delta I$ (the intensity at a time $t$, $I_t$, minus the baseline intensity, $I$), divided by the baseline intensity $I$ (Eq. 2). To detect phospharylation level of proteins, RIPA buffer was used to extract protein for western blot assay.

$$P_{app} = \frac{\frac{dQ}{dt} * 1}{A * C} \quad (1)$$

$$\text{Intensity change}(\%) = \frac{I_t - I}{I} = \frac{\Delta I}{I} \quad (2)$$

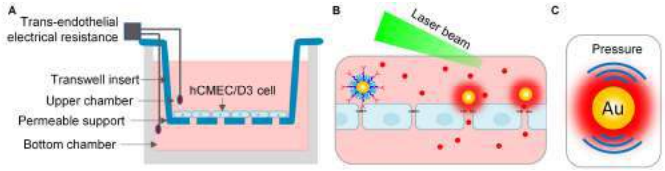


**Fig.1. Schematic of BBB opening *in vitro*.** (A) An *in vitro* transwell BBB model. (B) The targeting AuNPs on the cell membrane activated by picosecond laser. Red dots represent FITC-dextran molecules for permeability test. (C) Activated AuNP generates pressure variations.

## RESULTS

### Nanoparticle targeting and optical opening of the BBB

We examined the targeting of AuNP-BV16 using immunocytochemistry (ICC) staining. The results show similar distribution of free BV16 (positive control) and AuNP-BV16 on the cell boundaries, in contrast to control group (AuNP-PEG) (**Fig. 2A**), indicating that AuNP-BV16 targets JAM-A *in vitro*. Picosecond-laser excitation of AuNP-BV16 on monolayers temporarily decreases the TEER and increases the permeability (**Fig. 2B**). TEER drop suggests that the BBB opening involves the paracellular pathway to allow the passage of substances from top chamber to bottom chamber through intercellular clefts.

To improve the targeting efficiency, we modified the AuNPs with LEL for targeting glycoprotein. The results show that the targeting efficiency was improved by around 40-fold (**Fig. 2C**). AuNP-LEL (0.02 nM) resulted in the comparable TEER and permeability change when compared with 0.5 nM AuNP-BV16 (**Fig. 2D**).

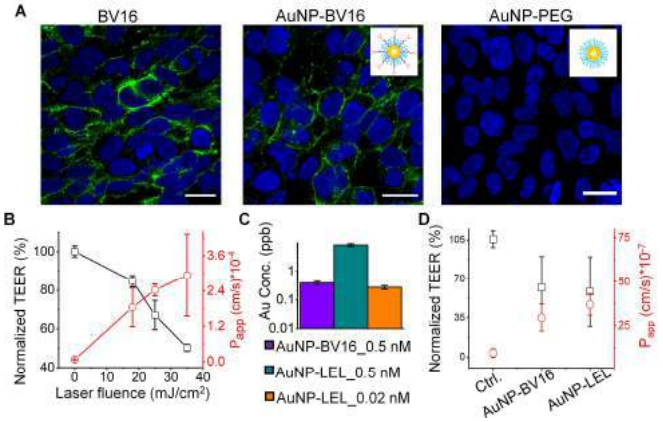


**Fig. 2. Picosecond-laser stimulation of cell-targeting nanoparticles opens the BBB reversibly.** (A) AuNP-BV16 distribution on the D3 monolayers by ICC staining. (B) Picosecond-laser stimulation of AuNP-BV16 on monolayers cause TEER drop and permeability increase (5 pulses). (C) Comparison of AuNP-BV16 and AuNP-LEL using Inductively Coupled Plasma Mass Spectrometry. (D) Comparison of TEER and permeability change between AuNP-BV16 (0.5 nM) and AuNP-LEL (0.02 nM). 35 mJ/cm$^2$, 5 pulses. Scale bar: 20 μm.

### Laser-induced $Ca^{2+}$ increase and propagation

Previous study reported that mechanical force can cause $Ca^{2+}$ increase in endothelial cells[4]. Picosecond-laser excitation of AuNPs leads to mechanical pressure variation, known as photoacoustic effect. To understand the mechanism of the BBB opening, we tested the $Ca^{2+}$ signal of the cells upon nanoparticle binding and laser irridiation. The result suggests that $Ca^{2+}$ were transiently increased after laser stimulation as indicated by the increase of fluo-4 intensity (**Fig. 3A**). More importantly, the analysis shows that $Ca^{2+}$ signal propagated after laser irradiation (**Fig. 3B and C**). When stimulating half area of the inserts, there is no significant difference of TEER drop compared with the full area irradiated by laser, indicating propagation (data not shown).

Taken together, these findings suggest the optical BBB opening (TEER drop) involves temporary $Ca^{2+}$ increase and propagation.

### Phosphorylation of ERK1/2

The influx of $Ca^{2+}$ into endothelial cell can activate second-messenger cascade and ultimately leads to the BBB opening[3]. Phosphorylation of ERK1/2 is one of the important activities in the $Ca^{2+}$-sensitive signaling cascades that causes cytoskeletal contraction to modulate the integrity of the BBB[3]. In our study, the western blot results show the phosphorylation of ERK1/2 can be detected at 5 min,

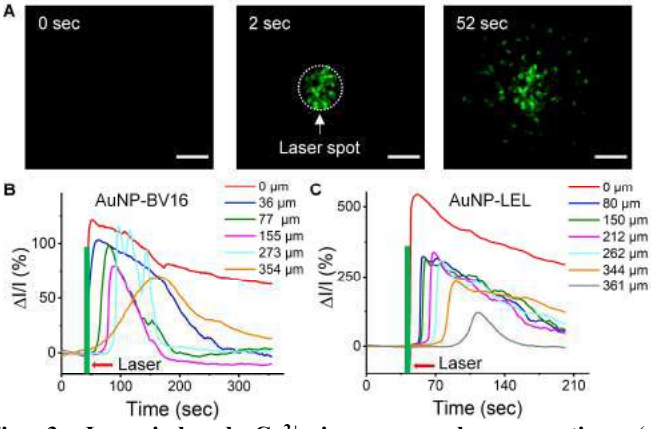


**Fig. 3. Laser-induced $Ca^{2+}$ increase and propagation.** (A) Represetive images of the intensity change of fluo-4 ($Ca^{2+}$ indicator ) after laser stimulation of AuNP-LEL. (B-C) Analysis of $Ca^{2+}$ increase and propagation after laser excitation of AuNP-BV16 (B) and AuNP-LEL (C). 35 mJ/cm$^2$, 1 pulse. Scale bar: 100 μ m.

maximized at 0.5hr and recovered at 6 hr after laser treatment (**Fig. 4**). Furthermore, the ERK1/2 inhibitor blocked the phosphorylation, further confirming that the $Ca^{2+}$ increase activated the phosphorylation of ERK1/2.

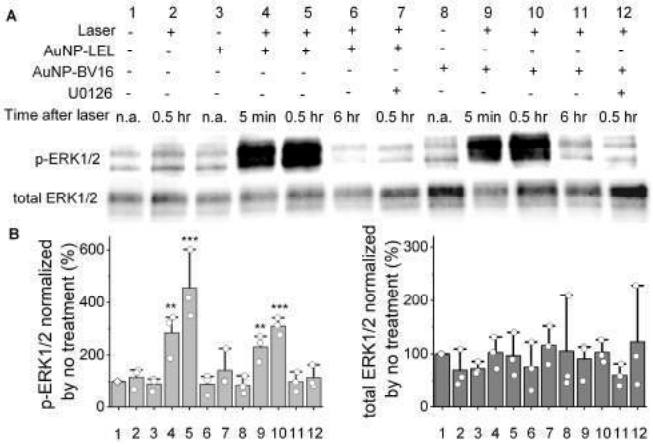


**Fig. 4. Phosphorylation of ERK1/2.** (A) The phosphorylated and total ERK1/2 detected by western blot. (B) The quantification analysis of (A). 35 mJ/cm$^2$, 5 pulses. One-way ANOVA. **: P<0.01, ***: P<0.001.

## DISCUSSION

In this study, we investigated the cellular signaling of the optical BBB opening. Our results suggest picosecond-laser stimulation of cell-targeting AuNPs triggers a $Ca^{2+}$ influx and propagation, which in turn causes temporary phosphorylation of second-messenger ERK1/2, ultimately leading to the reversible increase in the BBB permeability. Targeting glycoprotein by *lycopersicon esculentum* lectin advances this work with low concentration of AuNPs to reach comparable efficacy.


## ACKNOWLEDGEMENTS

We acknowledge funding support from Cancer Prevention & Research Institution of Texas (RP160770, RP180846).


## Reference:


1. Arvanitis, C.D., *et al*. *Nat Rev Cancer* 20, 26-41 (2020).
2. Li, X., *et al.* Nano Lett 21(20), 9805-9815 (2021).
3. Brown, R.C. Metal Ion in Stroke. 129-163 (2012).
4. D'hondt C., *et al.* J Vis Exp 77, 50443 (2013).

# SPATIOTEMPORAL DYNAMICS OF EPITHELIAL CELL PACKINGS AND TISSUE MECHANICS DURING MORPHOGENESIS

**Christian M. Cupo (1), Cole J. Allan (1), Andrew Pomposelli (1) Karen E. Kasza (1)**

(1) Department of Mechanical Engineering
Columbia University
New York, NY, USA

## INTRODUCTION

The ability for epithelial tissues to remodel and flow during development is essential to generating functional tissue structure and shape. Coordinated cellular movements allow collections of cells to rearrange positions so that the tissue can remodel and flow as a fluid-like material during development (1-3). *Drosophila* body axis elongation is a dramatic example of a rapid tissue flow that drives embryo morphogenesis. This convergent and extension process doubles the length of the germband epithelial tissue in about 30 min and is driven by local cell rearrangements that require anisotropic myosin II activity (Fig. 1). Recent work from our group and others has revealed that the germband tissue becomes more fluid-like at the onset of body axis elongation, which is likely to help accommodate rapid cell rearrangements and tissue flow (4). However, it is not understood how local features of a tissue might control tissue mechanics and influence the likelihood for a cell rearrangement to occur at a particular location. Here, we develop a framework for analyzing local cell packings within the germband epithelium as a foundation for ultimately studying spatiotemporal tissue mechanics and the links to underlying protein activity and gene expression patterns in developing embryos.

## METHODS

**Fly Stocks.** Fly stocks were from the Bloomington Drosophila Stock Center (BDSC). The cell membrane was visualized with gap43-mCherry, and myosin II was visualized with sqh-GFP, a GFP-tagged myosin regulatory light chain.

**Time-Lapse Imaging.** Embryos were generated at 23ºC and collected for analysis at stage 6. Embryos were dechorionated for 2 min in 50% bleach and washed with distilled water for 2 min. Embryos were mounted between a glass slide and an oxygen-permeable membrane in a 50:50 mixture of halocarbon oil 27:700. Confocal imaging was performed on the ventrolateral region of the embryo at 0.7µm z-steps and 15 s time intervals using a Zeiss LSM880 laser-scanning confocal microscope.

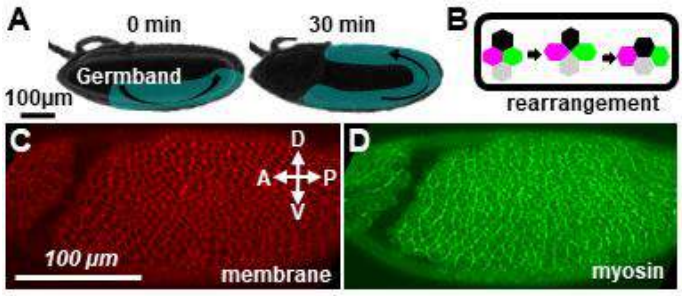


**Figure 1. During *Drosophila* body axis elongation, the germband epithelium extends to twice its initial length in 30 min via a rapid tissue flow.** Tissue flow (A) is driven by myosin-dependent oriented cell rearrangement events (B) that narrow and elongate the tissue. Images of cell outlines (C) and myosin II (D) during axis elongation.

**Image Processing and Quantification.** Analysis was performed on maximum intensity projections of 3 z-slices at the apical side of the tissue at the level of adherens junctions. Cell membrane networks were initially mapped by combining a watershed algorithm (5) with a mask in MATLAB and then resolving errors manually using the SEGGA tissue segmentation and analysis software (6). The cell shape index is defined as the cell perimeter ($P$) divided by the square root of the cell area ($A$):

$$p = P/\sqrt{A}$$

The corrected shape index $p_{\mathrm{corr}}$ accounts for packing disorder, as previously described (4). The cell shape alignment index $Q$ was

determined by triangulating the centers of all cells and finding the area-weighted average of the triangle alignment tensors, as previously described (7). Calculations were performed in MATLAB, unless otherwise noted. The time point $t = 0$ corresponds to the onset of tissue elongation.

## RESULTS

To explore how cell packings and tissue mechanics contribute to tissue flows at a local level, we determined the geometric configurations of cells in the germband and locally quantified these configurations. To visualize cell outlines, we used existing *Drosophila* lines expressing gap43-mcherry to tag cell membranes and then imaged the germband of developing embryos by confocal microscopy. To segment the tissue and extract the cell membranes network, we developed a custom MATLAB-based code to trace fluorescence intensity as described in Methods.

First, we analyzed the cell shape index $p$ and the cell shape alignment index $Q$, which have previously been reported to predict the solid-fluid behavior of the germband when analyzed at the tissue-level. To study these metrics at the local level, the cell shape index was calculated for each individual cell, and the shape alignment index was calculated for each cell and a corona of one cell neighbor outward. To visualize the local patterns of cell packings and inferred tissue mechanics, we color mapped the corrected shape index (Fig. 2A) and shape alignment index (Fig. 2B) for each cell. We find that both parameters vary spatially and temporally across the tissue, suggesting that spatially varying tissue mechanics might correlate with underlying protein localization or gene expression patterns.

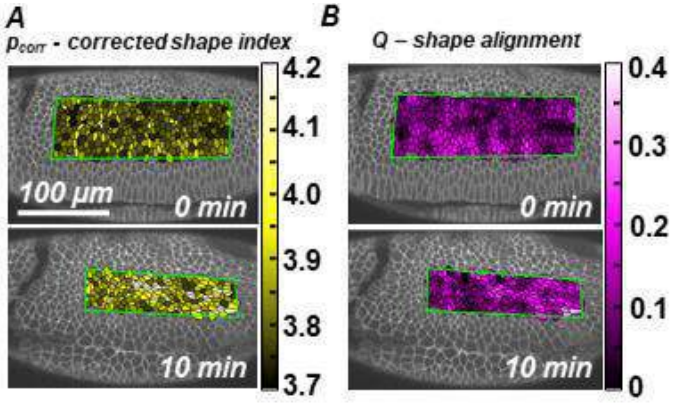


**Figure 2. Spatiotemporal variation of cell packings as a readout of local tissue mechanics in the germband.** To infer local tissue mechanics in the germband, we mapped the local corrected cell shape index $p_{corr}$ (A) and cell shape alignment $Q$ (B) in the ventrolateral region of the germband. Here, we show cell packings at 0 min and 10 min.

Next, we inferred the local solid-fluid tissue mechanical properties using a recently described anisotropic vertex model that predicts whether a tissue will behave as a solid (finite energy barriers to cell rearrangement) or a fluid (vanishing rearrangement energy barriers) (4). Within this framework, two metrics of cell packings in the tissue, $p$ and $Q$, predict the mechanical behavior of the tissue. This approach has been used successfully to predict the onset of rapid cell rearrangements and tissue flow in the germband (4). Above the predicted solid-fluid transition line in the $p$-$Q$ parameter space, there are vanishing energy barriers to cell rearrangement and fluid-like behavior, and below the transition line there are high energy barriers and solid-like behavior (Fig. 3A). We analyzed the trajectory of the germband in the $p$-$Q$ space over time, and found that at the whole tissue level, the germband becomes more fluid-like during axis elongation, consistent with previous reports (4). As a metric for local tissue mechanical behavior and rearrangement energy barriers, we measured the distance from the solid-fluid transition line in $p$-$Q$ space for each cell based on the local $p$ and $Q$ values at each time point. To visualize these data, we color-mapped at cell resolution the distance from the transition line (Fig. 3B). Notably, we observe spatial heterogeneities in this metric that also vary over time (Fig. 3B). This suggests that the mechanical properties of the tissue are spatially heterogeneous and that these spatial patterns of mechanics evolve over time as the germband transitions from solid-like to fluid-like during this developmental process.

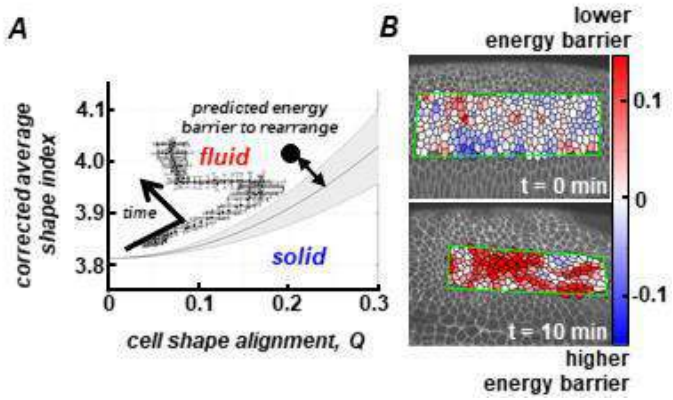


**Figure 3. Spatiotemporal patterns of predicted solid-fluid tissue mechanical properties and energy barriers to cell rearrangements.** As a metric for solid-fluid tissue mechanical behavior, we analyzed the distance from the predicted solid-fluid transition line in $p$-$Q$ space in the vertex model framework, with more fluid-like behavior associated with low energy barriers to rearrangement and more solid-like behavior associated with high energy barriers to rearrangement. (A) Tissue-scale behavior of the germband cell packings over time. (B) Local behavior of cell packings at t = 0 and 10 min reveals spatial and temporal patterns of tissue structure and predicted mechanical behavior.

## DISCUSSION

In this paper, we analyzed local cell packings in the germband epithelium and found that these packings are heterogeneous and evolve over time during axis elongation. In future work, we will connect these local cell packings to tissue mechanics and analyze how these spatial patterns evolve over time. Furthermore, we will correlate local tissue mechanics with cell rearrangement events and determine the influence of each packing parameter. Finally, we will connect spatiotemporal tissue mechanics to the underlying myosin II localization patterns and gene expression patterns in the developing embryo.

**ACKNOWLEDGEMENTS** This work was supported by a Columbia Blavatnik Fellowship to CMC, the Eunice Kennedy Shriver National Institute of Child Health & Human Development of the National Institutes of Health under Award Number F31HD105405 (CMC), and NSF CMMI-1751841 grant (KEK). KEK is the recipient of a Burroughs Wellcome Fund Career Award at the Scientific Interface and a Packard Fellowship for Science and Engineering.

**REFERENCES** [1] Bryant, D, et al. Nature Reviews. Molecular Cell Biology. 9.11 (2008): 887-901. [2] Chung, S, et al. Wiley Interdisciplinary Reviews: Developmental Biology 3.4 (2014): 281-300. [3] O'Brien, L.E., et al. Nature Reviews Molecular Cell Biology 3.7 (2002): 531-537. [4] Wang, X, Merkel, M, et al. Proceedings of the National Academy of Sciences 117 (2020): 13541-13551. [5] Vincent, L, et al. IEEE 13(6), (1991): 583–598. [6] Farrell, D.L., et al. Development. (2017). 144:1725–1734. [7] Merkel, Matthias, et al. Physical Review E 95.3 (2017): 032401.

# MECHANO-ADAPTATION IN MICROPATTERNED MDCK TISSUES

**Bernard L. Cook (1), Patrick W. Alford (1)**

(1) Department of Biomedical Engineering, University of Minnesota, Minneapolis, MN, USA

## INTRODUCTION

Many live tissues sense and respond to their mechanical state by changing form and function, or mechano-adapting. Mechano-adaptation may result in adaptive changes (e.g., an increase in muscle mass following routine weightlifting) or maladaptive changes (e.g., left ventricular hypertrophy following hypertension) in mature tissues. Further, mechano-adaptation helps sculpt embryonic tissues during morphogenesis. Because mechano-adaptation is prevalent in a variety of tissue remodeling contexts, it is important to develop experimental and computational tools to characterize this process.

Previously, we used our *in vitro* Cellular Microbiaxial Stretching (CμBS) assay to demonstrate that mechano-adaptation in an isolated cell depends on cellular architecture, which was captured by a continuum-based growth law [1]. However, mechano-adaptation in tissues is inherently a multicellular process. In addition to mechano-adaptive behaviors observed in a single cell, like cytoskeletal remodeling, mechano-adaptation in multicellular tissues can manifest through changes in proliferation and cell-cell contacts, among other behaviors. Here, we extend our work in single cells by using CμBS to experimentally characterize mechano-adaptation in 2D tissues comprised of micropatterned Madin Darby canine kidney (MDCK) cells and find that mechano-adaptation depends on cellular architecture and proliferation. Ultimately, this work will yield an experimental and computational framework that can be used to study mechano-adaptation *in vitro* in more specific contexts, such as embryonic heart looping.

## METHODS

**Stretching device.** The CμBS device [2] consists of a silicone membrane secured between metal clamps fastened to linear actuators. Bead-doped polyacrylamide gels are chemically bonded to the membrane, onto which cells are micropatterned. The device is fixed above an inverted microscope and housed within a chamber maintained at physiological conditions. The linear actuators are used to precisely stretch micropatterned cells, while the microscope is used to quantify cell-generated forces, architecture, and proliferation (Fig 1A, B).

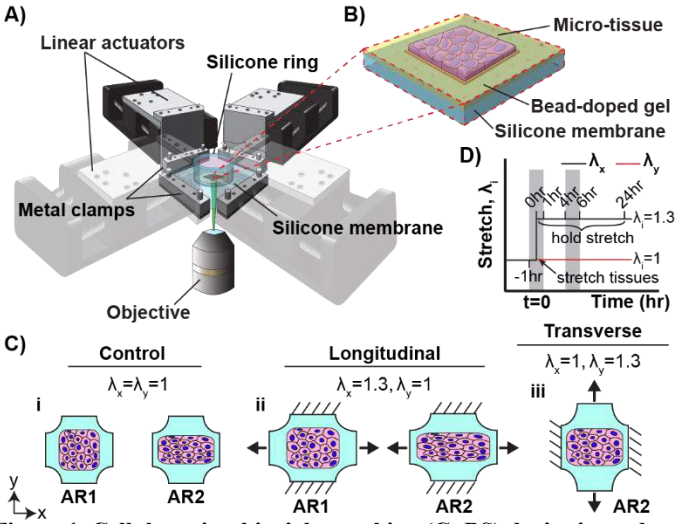


**Figure 1. Cellular microbiaxial stretching (CμBS) device is used to assess tissue mechano-adaptation. A) CμBS device. B) MDCK tissue patterned onto bead-doped gel bonded to the CμBS membrane. C) Stretching configurations. D) Stretching protocol. Data is collected between times highlighted by grey boxes.**

**Micropatterning.** For all experiments, MDCKs were micropatterned into aspect ratio 1 (AR1) or 2 (AR2) tissues (8000 $\mu m^2$) on CμBS substrates and cultured in cell growth medium.

**Stretching.** Tissues were uniaxially strained to 30% (applied stretch ratio $\lambda_i$=1.3) at 2%/s and held for 24 hrs (Fig 1C, D). To characterize tissue anisotropy, AR2 tissues were strained longitudinally

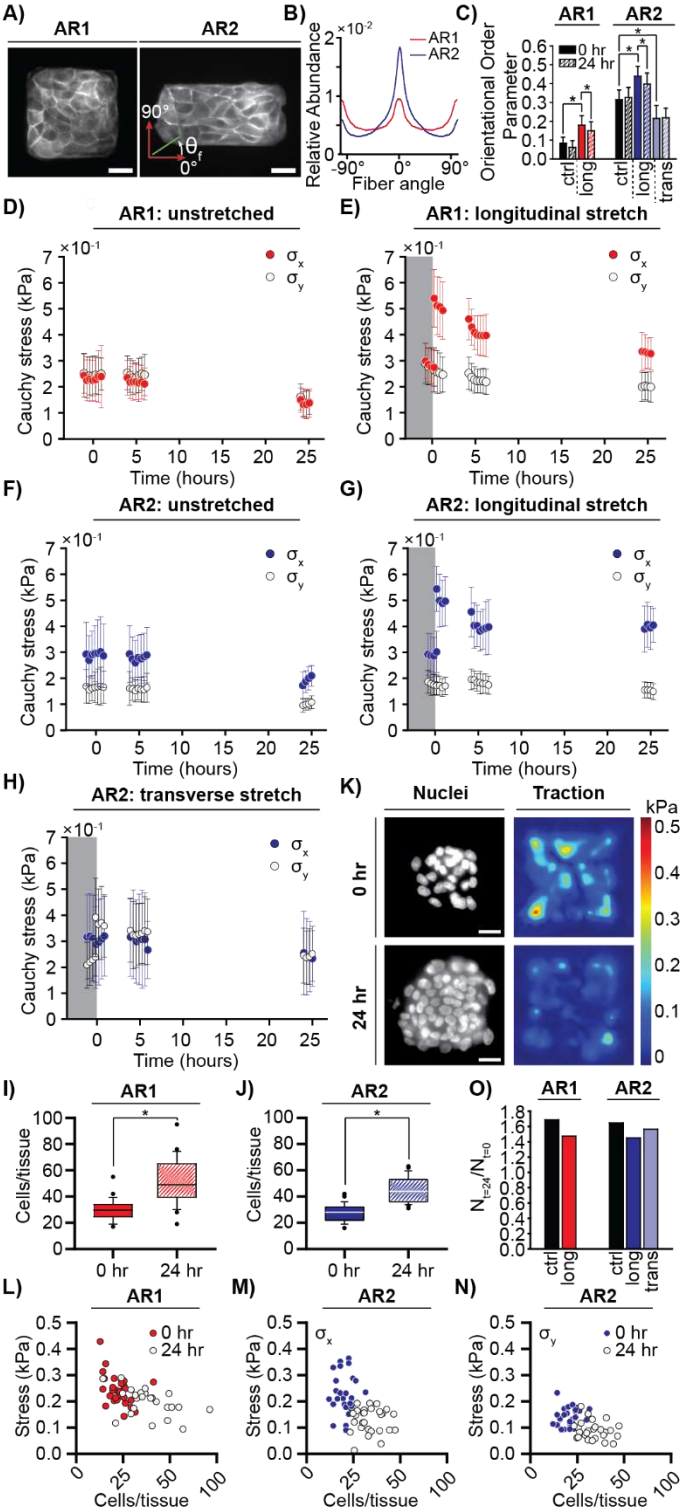


**Figure 2. Experimental measurements of mechano-adaptation. A) Tissues stained for F-actin. B) Probability density function of fiber alignment measured from tissues like those in (A). C) OOP of fiber alignment. D-H) Tissue stress behavior in mechano-adaptation experiment. In (E), (G), and (H), grey box highlights data taken before stretch. I-J) Cell density and tractions (K) over time in unstretched tissues. L-N) Tissue stress vs. cell density in unstretched tissues. O) Change in cell density. Scale: 40 μm.**

($\lambda_x$=1.3, $\lambda_y$=1) or transversely ($\lambda_x$=1, $\lambda_y$=1.3). Stresses in unstretched ($\lambda_x$=1, $\lambda_y$=1) tissues were assessed as a control (Fig 1C).

For stress experiments, fiducial bead images were captured to quantify tissue-induced bead displacements used to calculate tissue traction stress. For architecture experiments, MDCKs were stained with phalloidin (F-actin) and DAPI (nuclei) using immunocytochemistry.

**Cell stress and structure.** Midplane Cauchy stresses were calculated from tissue traction stresses and tissue geometry [1]. A ridge detection algorithm was applied to images of tissues stained for F-actin to quantify architecture alignment. Alignment was quantified with an orientational order parameter (OOP), which measurements relative alignment on a scale of 0 (unaligned) to 1 (perfectly aligned).

**Cell density.** Cell density was measured by counting nuclei in stained tissues using a custom MATLAB program. To characterize if cell density correlated with tissue stress, unstretched MDCKs were stained with Hoechst 33342 and traction stresses assessed simultaneously to measure nuclei per tissue and tissue stress, respectively. To characterize if changes in density depended on tissue shape or stretch, relative change in density for each stretch-shape condition was taken as $N|_{t=24}/N|_{t=0}$, where $N|_{t=24}$ and $N_{t=0}$ are mean cell densities at 24 and 0 hrs post-stretch for a given condition, respectively.

**Stats.** A one-way analysis of variance (ANOVA) was applied to OOP and cell density measurements to determine pairwise significance between groups. Significance was taken at $p < 0.05$.

## RESULTS

Without stretch, F-actin fibers in AR2 tissues were more aligned than in AR1 tissues (Fig 2A-B). Over time, this relationship was retained because the cytoskeleton did not significantly reorganize (Fig 2C). Following stretch, F-actin became more aligned and reorganized over time in tissues stretched longitudinally (Fig 2C). In AR2 tissues stretched transversely, F-actin became less aligned and did not reorganize, demonstrating an anisotropic mechanical response (Fig 2C).

In stretched tissues, stress increased in the direction of stretch and slowly decreased over time (Fig 2E, G, H), demonstrating an adaptation to stretch. However, it was not clear how tissues adapted to stretch. Stress patterns in unstretched tissues demonstrated that stress evolved without applied loading (Fig 2D, F), which was suspected to result from proliferation. We then sought to characterize tissue proliferation, its influence on stress behavior, and whether this was mechano-sensitive.

Without stretch, tissues experienced a significant increase in cell number that was consistent across tissue shapes (Fig 2I, J, O). Increase in cell number correlated with a decrease in tissue stress (Fig 2L-N). Interestingly, proliferation appeared to depend on applied loading inversely from what was expected: increased stress resulted in decreased proliferation in tissues of each shape (Fig 2O).

## DISCUSSION

Here, we used CμBS to demonstrate that mechano-adaptation in micropatterned tissues depends on architecture and proliferation. Interestingly, we found that the rate of proliferation decreases when tissues are stretched, which contradicts previous findings [3]. Further work will be performed to elucidate whether constraints from micropatterning or the timescale of the experiment yield these discrepancies. Moving forward, we seek to develop a continuum model that captures mechano-adaptation in these tissues. The experimental work here is a step towards developing this model. Together, these experiments and model will provide a framework for characterizing mechano-adaptation in specific contexts such as in the developing heart.

**ACKNOWLEDGEMENTS** We acknowledge support from the U.S. National Science Foundation (NSF): CMMI-156319 (P.W.A.)

**REFERENCES** [1] Cook, B et al., *J Biomech Eng*, 143(10): 101002, 2021. [2] Win Z et al., *J Biomech Eng*, 139(7):0710061, 2017. [3] Gudipaty et al., *Nature*, 543(7643):118-121, 2017.

# THE MECHANICS OF NETWORKED, TYPE II COLLAGEN FIBERS FROM CARTILAGE

**Phoebe Szarek (1), David M. Pierce (1,2)**

(1) Department of Biomedical Engineering, University of Connecticut, Storrs, CT, USA
(2) Department of Mechanical Engineering, University of Connecticut, Storrs, CT, USA

## INTRODUCTION

Collagen, a key load-bearing molecule essential to the function of most soft tissues and load-bearing organs, is the most abundant protein in the mammalian world [1]. Understanding the mechanics of collagen is thus critical to understanding the biomechanics of soft tissues and organs. Type I collagen is the most abundant collagen in the human body (e.g. in dermis, tendons, and arteries), so researchers have extensively characterized the mechanics of type I collagen [2]. Type II collagen forms networks and is the second most abundant type in the human body (e.g. in hyaline cartilage and intervertebral discs), but *no data exist* on the tensile mechanical response of individual type II collagen fibers. Experimental testing of individual fibers of type II collagen poses many difficulties due to their small size (Ø 20-200 nm) and due to the complexity of *in vitro* fibrillogenesis [3,4].

We aim to quantify the mechanics of individual type II collagen fibers via inverse analyses of fiber networks with measurable bulk responses and fiber arrangements. Specifically, we aim to 1) identify an appropriate constitutive model for the stress-strain response of type II collagen fibers, 2) identify an appropriate failure model (criteria) for individual type II collagen fibers, and 3) determine the parameters for these models by leveraging our diverse experimental data.

## METHODS

*Specimen Preparation.* Following established protocol, we extracted 10×20 mm full-thickness specimens from bovine patella-femoral grooves (< 36 m old) [5]. We microtomed 140 or 160 µm slices from the superficial zones (SZ) and punched out dumbbell-shaped specimens (gauge width = 3 mm, length = 4 mm). We incubated these in phosphate buffered saline (PBS) with 0.5 mg/mL trypsin for 18 hrs at 37 °C to remove >95% of the proteoglycan (PG), then rinsed.

*Uniaxial Tension Testing.* We performed uniaxial tension tests using a custom microtensile device (20 N capacity with 0.3 mN resolution, 12.5 mm range with 2.5 µm resolution) at a displacement rate of 300 or 600 µm/min until failure in PBS at room temperature [5].

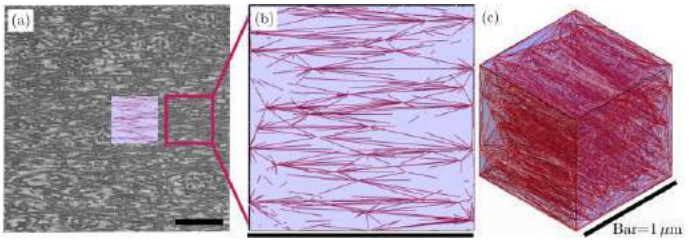


**Figure 1. Representative Statistically-Equivalent Representative Volume Element (SERVE) for modeling networks of collagen fibers. a) Transmission electron microscope image of collagen within the superficial zone of human cartilage. b) Cross section of a fiber-network SERVE model. c) RVE with statistically equivalent orientation, dispersion, and volume fraction of collagen fibers [7].**

*Statistically-Equivalent Representative Volume Elements.* We modeled a 1 µm$^3$ cube, i.e. a statistically-equivalent representative volume element (SERVE), at the center of the gauge region of the tensile specimen using FEBio (University of Utah) [6]. We used data on the orientation, diameter, and volume fraction of type II collagen fibers within the SZ (measured via Transmission Electron Microscope images [7]) to create statistically-equivalent networks of fibers within multiple SERVEs (Fig. 1). We modeled fibers as springs (selecting from five different constitutive models) and we modeled the PG-depleted interfibrillar space using a biphasic neo-Hookean model ($Gi = E_{\mathrm{iso}}/3$).

*Constitutive Models.* We used five different constitutive models for individual fibers: 1) linear, 2) exponential [8,9], 3) bilinear (i.e. toe and linear regions [10]), 4) exponential-linear, and 5) linear-exponential. We tested each of these models by fitting the stress-strain responses of networked collagen to data using inverse finite element modeling. Leveraging each of these constitutive models we fit the responses of the each SERVE to measured data. We assessed the model fits using both the coefficient of determination $R^2$ and number of parameters required.

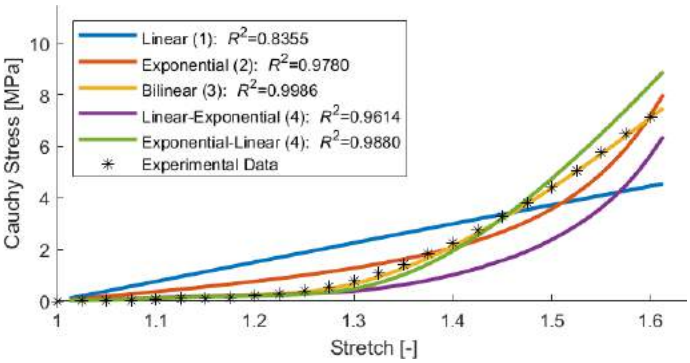


**Figure 2. Representative best fits of five constitutive models. The bilinear model provided the best fit to the experimental data even compared against models with more parameters (in parentheses).**

*Failure Models.* To model failure of individual type II collagen fibers we extended the constitutive models to include failure, and tested two failure criteria: 1) critical stress and 2) critical stretch. In the first failure criterion, e.g. if the stress exceeds a critical value the fiber is removed from the network. We rerun each time step of the simulation up to ten times to redistribute the total load, remove fibers, and stabilize the results. We assessed both failure models within SERVEs to establish which better predicted the network responses measured experimentally.

*Data Analyses.* We performed inverse fitting of the experimental data ($n$ = 10) using the parameter optimization module in FEBio. We fit the first 10% of the experimental data to establish the stiffness (shear modulus) of the isotropic matrix. We then fit the stress-strain data up to bulk softening (i.e. decrease in slope) using the different SERVEs with fibers ($n$ = 3) to fit the parameters of the individual fiber response. Finally, we fit the failure criteria using the complete data to rupture.

*Statistical Analyses.* Grouping all the data we used $t$-tests to discard SERVEs with responses significantly different from all others. We used two-way ANOVAs to assess the variance due to both experiments and network models (SERVEs). We used $p$ = 0.05 as our level of significance and reported median and interquartile range (M + IQR).

## RESULTS

*Constitutive Models.* Figure 2 shows a representative network response and the best-fits of the models. We found that a bilinear model

$$\sigma = \begin{cases} E_1(\lambda - 1) & \text{if } \lambda < \lambda_t \\ E_2(\lambda - \lambda_t) + E_1(\lambda_t - 1) & \text{if } \lambda \geq \lambda_t \end{cases}, \qquad (1)$$

where $E_1 < E_2$ are the slopes of the bilinear fiber model which transition at the stretch $\lambda_t$, provided the simplest and best-fit for the response of single fibers. Table 1 shows the resulting parameters after fitting all of the experimental data with the bilinear model. We found that responses from the SERVEs were statistically equivalent and had no effect on the model parameters. The fiber parameter most affected by the SERVEs, albeit not significantly, was the transition stretch.

**Table 1. Bi-linear Model Parameters for Type II Collagen Fibers.**

| | $E_{\text{iso}}$ [MPa] | $E_1$ [MPa] | $E_2$ [MPa] | $\lambda_t$ [-] |
|---|---|---|---|---|
| M | 1.015 | 0.9526 | 23.27 | 1.138 |
| IQR | 0.8100 | 0.9558 | 4.919 | 0.0649 |

*Failure Models.* Figure 3 shows the effects of adding mechanical criteria to model individual fiber failures within the networked collagen. Failure based on critical fiber stress more accurately captured the bulk network responses measured experimentally versus critical fiber stretch.

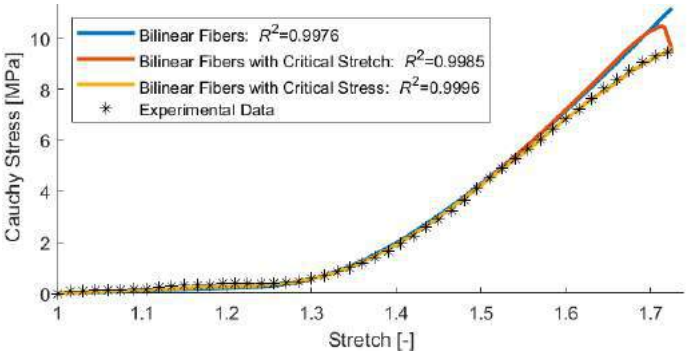


**Figure 3. Representative best fits including fiber failure. Maximum fiber stress more accurately captured the bulk network response measured experimentally versus maximum fiber stretch.**

## DISCUSSION

We propose a new fitted model for networked, type II collagen fibers within cartilage, and potentially within other soft tissues containing type II collagen. The bilinear model for a single fiber is comparable to the toe and linear regions seen in highly aligned collagenous structures. We model each fiber with zero-order continuity, but obtain a first-order continuous network response due to progressive recruitment of fibers. While we tested and modeled tension to rupture, physiological stretches are often less extreme, possibly explaining the usability of the common exponential model. Our model parameters also indicate that type II collagen may not be as stiff as type I collagen, cf. [2]; differences in testing methods may also explain the discrepancies.

Introducing fiber failure into our constitutive model allowed fitting of the complete experimental data and a better estimation of fiber and network responses at large strains. In our experimental data, we identified cases where networks abruptly failed making fitting of individual fiber failures difficult. Fiber failure with a stress-based criterion better represented network failure with softening but a stretch-based failure may better represent catastrophic network failure.

Limitations of this work include difficulty in decoupling the isotropic stiffness and the low-strain stiffness of the collagen fibers. Unfortunately, we are unable to run simulations with very low stiffness PG (e.g. the networks collapse) or past complete rupture (indeterminate solution). While it is primarily type II, collagen within cartilage is also heterotypic with small quantities of other types of collagen.

We introduce a new mechanical model for type II collagen fibers, a key load-bearing molecule in the human body. Our findings may serve to improve current modeling approaches and introduce opportunities for multiscale modeling. Including a failure criterion for individual fibers results in a better fit to experimental (data for networks tested to failure), a more accurate fiber response for physiological models, and the possibility to model softening under cyclic loading.

## ACKNOWLEDGEMENTS

NSF CAREER 1653358, NSF 1662429, GE Fellowship.

## REFERENCES

[1] Sherman, VR et al., *J. Mech. Behav. Biomed. Mater.* 52:22-50, 2015. [2] Yang, L et al., *J. Mech. Behav. Biomed. Mater.* 6:148-158, 2012. [3] Gottardi, R et al., *PLoS One*, 11:e0163552, 2016. [4] Kadler, K et al., *Curr. Opin. Cell Biol*., 20:495-501, 2008. [5] Szarek, P et al., in preparation. [6] Maas, SA et al., *J Biomech. Eng.*, 134:e0110005, 2012. [7] Szarek, P et al., *Osteoarthritis Cartilage Open*, 2:e100086, 2020. [8] Holzapfel, GA et al., *J. Elast.*, 61:1-48, 2000. [9] Pierce, DM et al., *Biomech. Model Mechanobiol.*, 15:229-244, 2016. [10] Roeder, BA et al., *J. Biomech Eng.*, 124: 214-222, 2002.

SB³C2022
Summer Biomechanics, Bioengineering and Biotransport Conference
June 20-23, Eastern Shore, MD, USA

# NETWORK-BASED MODELING OF ALZHEIMER'S DISEASE: ASSESSING IMPACT OF CONNECTOME MEASURES ON PROGRESSION PATTERNS

**Shima Jalalian (1), Oren Civier (2), Johannes Weickenmeier (1)**

(1) Mechanical Engineering, Stevens Institute of Technology, Hoboken, NJ, USA
(2) Swinburne Neuroimaging, Swinburne University of Technology, Melbourne, VIC, Australia

## INTRODUCTION

The increasing availability of large functional and structural brain connectivity datasets has led to a better understanding of the healthy and the diseased brain. One example is the attempt to correlate the propagation of toxic proteins with cerebral atrophy and cognitive decline associated with neurodegenerative diseases.

When treating the brain as a discrete network of nodes, which represent individual brain regions, and their connections, representing axonal white matter tracts, we obtain a simplified network model to simulate biomarker spread using graph theory. At the core of these models is the brain connectome, or the matrix representing the brain connectivity network, and a reaction-diffusion equation that describes the production and spreading of any respective biomarker [1,2]. Previous studies have shown that this connectome is organized according to a small-world topology [3], i.e., many specialized highly interconnected communities [4] and a highly effective level of integration of information between these communities throughout the brain. Some nodes are critical to this integration and segregation, which are called hubs. Hub nodes generally have a high number of connections (degree centrality) or a high level of betweenness centrality [5]. Meta-analysis on different brain disorders suggests grey matter lesions concentrate in brain network hubs regardless of the disorder [6]. It has also been shown that brain regions with strong anatomical connectivity are at increased risk of high toxic protein exposure [3]. Despite the good qualitative agreement between these models and data from pathology, however, the fact that each study uses a different approach to determine the adjacency matrix that represents their brain connectome is making direct comparisons between studies very challenging.

Here, we selected 100 subjects from the Human Connectome Project (HCP) [7] and quantify the differences between commonly used adjacency matrices by means of critical graph theory-based properties and results from biomarker progression simulations. We also proposed our anatomically corrected weighted streamline adjacency matrix, which is based on SIFT2 correction of diffusion MRI tractography [8], and compared it to the currently used connectomes. Streamlines are defined as pathways between two regions in the brain that assumes to follow the trajectory of biological axon fibers. SIFT2 is a widely used method in the structural connectomics community to reduce the biases caused by the reconstruction of the streamlines, which causes them not to accurately represent the density of underlying fiber bundles [8]. Using this method a cross-sectional area multiplier is applied to each streamline, which permits the use of the resulting weighted streamline count (S) as a more valid biological marker than the original non-weighted streamline count (N) of how strong each fiber bundle connects the two brain regions at its ends [8].

## METHODS

Prion-like diffusion of toxic protein within the brain network is well described by the following reaction-diffusion model:

$$\frac{dc_I}{dt} = \mathrm{k}\sum_{J=1}^{N} L_{IJ}c_J + \alpha c_I[1-c_I], \quad (1)$$

where $c_I$ is the nodal biomarker level, parameter k controls diffusivity, and parameter $\alpha$ characterizes the growth rate, i.e., the conversion rate of healthy into toxic protein. The graph Laplacian in (1) is defined as:

$$L_{IJ} = D_{IJ} - A_{IJ} \text{ with } D_{IJ} = \mathrm{diag}\sum_{J=1, I\neq J}^{N} A_{IJ}\,. \quad (2)$$

To determine adjacency matrix A, we used preprocessed connectome data from 100 healthy subjects in the HCP [7]. For each subject, we compute the four commonly used forms of the adjacency matrix and differentiate between matrices defined by (1) the number of streamlines between regions over the average length of streamlines (N/L), (2) weighted streamline count over the average length of streamlines (S/L) [8], as well as both number of streamlines and weighted streamlines count, divided by the average length of

streamlines squared ($N/L^2$ and $S/L^2$, respectively). Borrowing from basic graph theory, we calculated the following well-established graph measures to determine network differences for our four adjacency matrices: degree centrality, betweenness centrality [5], and global efficiency [9]. These measures quantify localized connectivity, between community connectivity, and efficiency of distant information transfer, respectively.

## RESULTS

Figure 1 shows the degree and betweenness centrality measures. Superior frontal, precentral, superior parietal, precuneus, postcentral brain regions appear to be critical hubs across all subjects. We also observe that hub location is mostly unaffected by the denominator of the adjacency matrices, i.e., division of N and S by L or $L^2$.

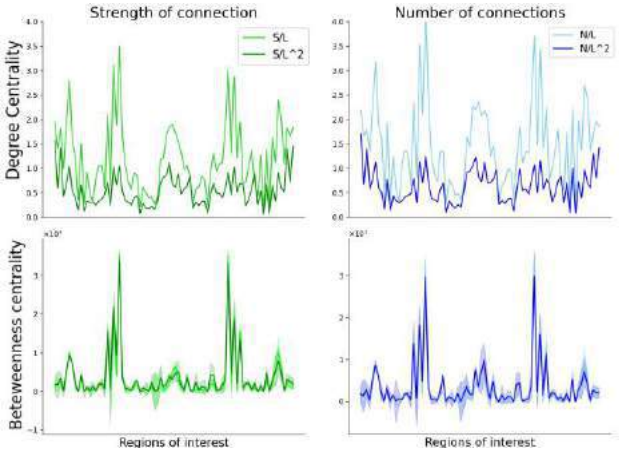


**Figure 1: Hubs of degree centrality (provincial hubs) and betweenness centrality (connector hubs) in our four connectomes.**

Figure 2 shows the global efficiency for our adjacency matrices. The value of global efficiency accounts for the network capacity for parallel information transfer. We observe that the values for the number of streamlines are larger than the values for the weighted number of streamlines and also by dividing both measures to the higher orders of length the value of the global efficiency reduces.

Figure 3 illustrates the change in the mean of one hundred biomarker curves with different graph construction methods in the A) precentral gyrus, one of the aforementioned brain hubs and a symptom node for loss of motor control in Alzheimer's disease and B) in all the other identified hubs of the brain network. For this simulation the misfolded proteins ($c_0$) were seeded of in the entorhinal cortex nodes of both hemispheres. The weighted number of streamlines-based simulations shifts the biomarker wavefront to the left in comparison to the number of streamline-based graphs. It can also be seen that the division by higher magnitudes of length shifts the curve to the right.

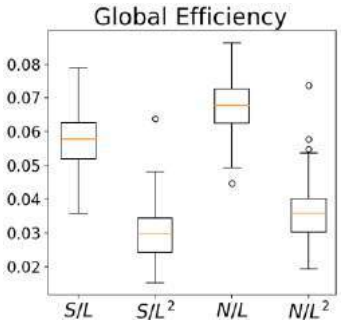


**Figure 2: Global efficiency of our four different adjacencies. This measure shows transmissibility between nodes.**

## DISCUSSION

Here we studied the location of brain hubs and the graph-theoretical measurements of two widely used brain connectomes and two proposed anatomically corrected connectomes. We saw that the hub regions were unaffected by the different methods of adjacency matrix definition that we used here. And the determined hub locations are consistent with previous works on studying structural brain hubs [5].

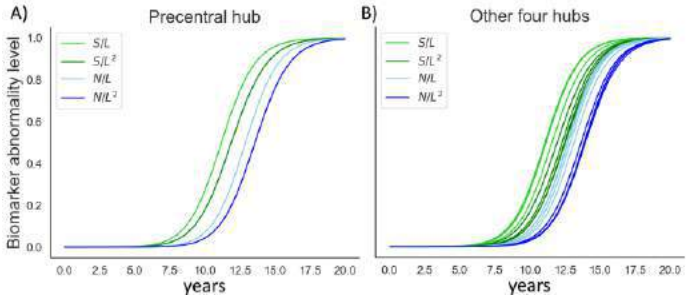


**Figure 3: Pattern of biomarker concentration change in A) precentral cortex and B) in Superior frontal, superior parietal, precuneus, postcentral in the different connectomes**

In Figure 2, we could see that using S/L results in lower global efficiency than N/L. This is due to the fact that the SIFT2 algorithm weighted down the streamlines that represent the major fiber bundles in the brain; these bundles are the main factor deciding global efficiency and are usually over-represented by tractography algorithms [10].

We could also see that the method of adjacency matrix calculation marginally impacted the biomarker progression pattern. The only major difference was that abnormality level curves are shifted horizontally. The slope of the curves and the time to reach the full toxicity are only marginally affected.

Also, according to Figure 2, based on the values of the global efficiency we would expect N/L to lead to quicker spread of toxic proteins than S/L, but the opposite is observed in Figure 3. This is due to the fact that global efficiency is not a direct representative of the efficiency in the neighborhood of a specific region, but rather a general representation of transmissibility of the whole connectome.

As a recommendation for future studies in the field, we suggest using the weighted number of streamlines. The correction for cross-sectional area used to define the weighted streamline count adds an additional step in our reconstruction process. It has been proven to be more anatomically informed, however, and therefore increases agreement between our disease progression simulations based on these connectomes and underlying pathology of the disease observed from patient data.


## ACKNOWLEDGEMENTS

The authors acknowledge the facilities and scientific and technical assistance of the National Imaging Facility, a National Collaborative Research Infrastructure Strategy (NCRIS) capability, at Swinburne Neuroimaging, Swinburne University. This work was also supported through NIH grant #R21AG067442 to Johannes Weickenmeier.


## REFERENCES


[1] Thompson, T. B. *et al.*, *PLoS Comput. Biol.*, 16, (2020).
[2] Schäfer, A. *et al.*, *Front. Neurosci.*, 14, (2020).
[3] Iturria-Medina, Y. *et al.*, *PLoS Comput. Biol.*, 10, (2014).
[4] Bullmore, E. *et al.*, *Nat. Rev. Neurosci. 2009 103*, 10, (2009).
[5] Van den Heuvel, M. P. *et al.*, *Trends Cogn. Sci.*, 17, (2013).
[6] Crossley, N. A. *et al.*, *Brain*, 137, (2014).
[7] Sotiropoulos, S. N. *et al.*, *Neuroimage*, 80, (2013).
[8] Smith, R. E. *et al.*, *Neuroimage*, 119, (2015).
[9] Rubinov, M. *et al.*, *Neuroimage*, 52, (2010).
[10] Yeh, C. H. *et al.*, *Neuroimage*, 142, (2016).

# A CONSTITUTIVE-BASED DEEP LEARNING MODEL FOR THE IDENTIFICATION OF ACTIVE CONTRACTION PROPERTIES IN THE VENTRICULAR MYOCARDIUM

**Igor A. P. Nobrega, Wenbin Mao**

Department of Mechanical Engineering
University of South Florida
Tampa, FL, USA

## INTRODUCTION

Cardiovascular disorders are the primary cause of death, comprising for more than 40% of all human fatalities [1]. Engineering, computer science, and data mining advancements have paved the way for new insights of soft tissue mechanical properties and their physiological responses. The examination of elastic properties of soft biological tissue [2] can uncover early indicators of illness or physiological complications [2] as these are entangled with its internal microstructure [3], which regulates its macroscopic behavior and mechanical functions. Moreover, to better comprehend the mechanical activities of the myocardial structure, accurate representations of myocardial structure utilizing constitutive models are essential.

Although various models have been constructed to depict both passive and active contraction of myocardial tissues, most of them are unsuitable outside the research setting; they often need substantial computing resources and time, limiting their use in clinical applications. Thus, the use of artificial intelligence and machine learning offers significant benefits over conventional techniques.

The primary goal of this study was to develop a constitutive-based deep learning method for evaluating and predicting the behavior of an active contraction model of the left ventricular myocardium during a cardiac cycle by autonomously selecting the best-fitting material parameters from patient-specific clinical conditions.

## METHODS

The active and passive reactions of myocardium are coupled as an additive decomposition of the Cauchy stress tensor $\sigma = i\sigma_p + \sigma_a$. In this definition, $\sigma_p$ identifies the passive stress component, which describes the myocardium's reaction when the muscle is not active. $\sigma_a$ defines the component of active stress that is induced by electrical stimulation of the myocardial tissue [4].

The passive model was based on Holzapfel-Ogden's extensively recognized depiction of the passive myocardial tissue [5]. Given that the ventricular wall is a multilayered structure with transmural variation in the direction of its myocytes, the modeling of fiber distribution throughout layers of the myocardium is a fundamental benefit of the chosen model. The passive stress function is composed of eight material parameters a, b, $a_f$, $a_s$, $b_f$, $b_s$, $a_{fs}$ and $b_{fs}$, and is given as follows:

$$\sigma_p\, i = \mathrm{a} e^{\mathrm{b}(\mathrm{I}_1 i - i3)}\mathbf{B} - i\rho \mathrm{I} + 2\mathrm{a}_f\left(\mathrm{I}_{4f} - 1\right)e^{\mathrm{b}_f\left(\mathrm{I}_{4f} i - i1\right)^2}\boldsymbol{f}\otimes\boldsymbol{f} + i2\mathrm{a}_s(\mathrm{I}_{4s} - 1)e^{\mathrm{b}_s(\mathrm{I}_{4s} i - i1)^2}\boldsymbol{s}\otimes\boldsymbol{s} + \mathrm{a}_{fs}\mathrm{I}_{8fs}e^{b_{fs}I_{8fs}^2}(\boldsymbol{f}\otimes\boldsymbol{s} + \boldsymbol{s}\otimes\boldsymbol{f}) \quad (1)$$

The active model adopted was proposed by Pezzuto et al. [4]. This model is advantageous due to its simple yet effective formulation. The active model considers the multiplicative decomposition of the deformation gradient by adding just one new parameter, $\gamma$, preserving the ellipticity of the stress tensor and yielding a "active strain" approach [4]. The model is defined by:

$$\sigma_a\, i = i(1-\gamma)i\boldsymbol{f}_0\otimes\boldsymbol{f}_0\, i + i\frac{1}{1-\gamma}(\mathbf{I}i - i\boldsymbol{f}_0\otimes\boldsymbol{f}_0) \quad (2)$$

, where $\boldsymbol{f}_0$ denotes the unit vector of fiber axis. The constitutive model was implemented in the open-source Finite Element (FE) solver FEBio [6], and was validated by comparing with the analytical solutions of a solid cube under simple shear and biaxial deformations [4][5]. In addition, we utilized two principal geometries of the left ventricle: an idealized truncated ellipsoid (Fig 1a) and a patient-specific one (Fig 1c). Mesh independence was performed for each geometry and the best configuration was used for all FEA simulations. Furthermore, to calculate the fiber orientation for each element, we adopted an rule-based reconstruction algorithm using Poisson interpolation proposed by Wong & Kuhl [7], which is commonly used in the field when clinical DT-MRI data is unavailable. As can be seen in figures 1b and 1d, the muscle fiber orientations properly change with position through the

wall: from a positive angle ($\alpha_{epi}$) in the sub-epicardial region to nearly 0◦ in the mid-wall to a negative angle ($\alpha_{endo}$) in the sub-endocardial region.

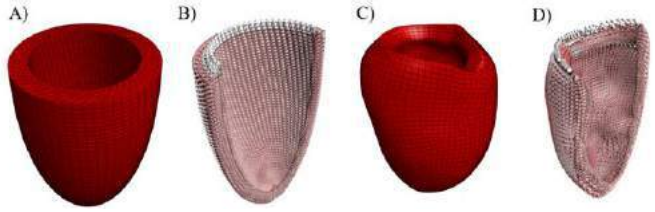


**Figure 1: Left ventricular myocardium meshes and fiber orientations: (a) and (b) idealized, and (c) and (d) patient specific.**

Our deep learning (DL) model (Fig. 2) consisted of two functional modules: (a) a convolution network (CNN) devoted to extracting features from a PV loop and clinical metrics to estimate the best set of fiber orientations (FO); and (b) a recurrent network (RNN) designed to estimate the γ waveform for an entire cardiac cycle. The inputs of the model are 5 clinical metrics: longitudinal and radial shortening, wall thickening, longitudinal and circumferential strains, and a PV loop; while the outputs are: $\alpha_{epi}$ and $\alpha_{endo}$ orientations and γ waveform.

How to generate adequate training data for the model? The pressure-volume (PV) loop data was obtained through a lumped-parameter simulator representing a wide spectrum of physiological and pathological waveforms. Other training data were generated by two pretrained neural network regressors: GR model and GC model to obtain the **γ** value and clinical metrics, respectively (dataset generator in Fig. 2). The training data for the regressors were obtained from FE simulations with variant γ value (0 ~ 0.3) and fiber orientations (from -40 to -80 degrees for $\alpha_{endo}$ and 40 to 80 degrees for $\alpha_{epi}$) using linearly increasing pressure loads from 0 to 20 kPa. We recorded the corresponding cavity volume and geometric characteristics from the deformed myocardium for each pressure value. Because the predictions of the regressors are very accurate, we treat the generated synthetic data from them as the gold standard for the final model.

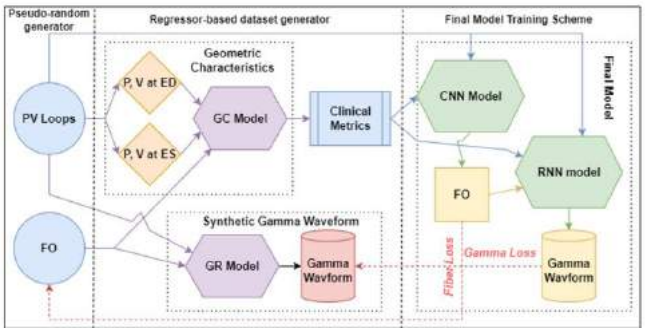


**Figure 2: Deep learning approach schematics.**

This procedure reduced the number of FE simulations required to obtain a suitable dataset for our final model. As such, our method used less than 1100 FE simulations to provide over 220,000 synthetic datasets. The traditional method of extracting training data straight from FE simulations would take significantly more time and memory.

## RESULTS

Each regressor was independently trained and evaluated to ensure high accuracy on their respective tasks. The final Mean Squared Error (MSE) for the GR and GC model was 1.38e-5 and 4.38e-6, respectively. Uniform accuracy distribution was observed for the entire testing dataset. Lastly, the final DL model reached an overall 1.583e-6 MSE and was observed to generate smooth **γ** waveforms.

To assess the final model's efficiency, we evaluated the accuracy of clinical metrics and volume waveforms obtained from the FE model with the predicted fiber orientation and gamma waveform parameters by the DL model. We first generated 50 sets of PV loops and fiber orientations. They were utilized to produce the clinical metrics by our GC regressor as input, along with the corresponding PV loop for the final DL model. With the predicted fiber orientation and gamma waveform, we conducted these FE simulations, and the simulation-obtained volumetric waveforms and clinical metrics were compared to the original inputs (Fig. 3). The predicted γ waveform is highest around peak systole, representing the strongest active contraction; followed by a gradual decrease to zero at the end of diastole. The volume waveform calculated from FE closely matches the input value. The relative error between these curves is less than 0.5%. Additionally, the mean absolute error for all clinical metrics was 0.7%.

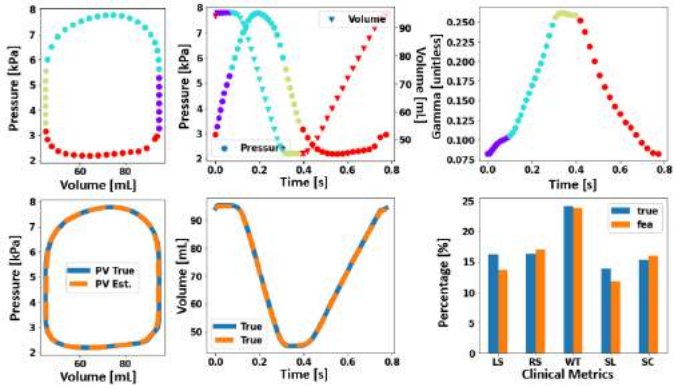


**Figure 3: A representative case for the comparison of FE simulation and the DL model prediction. First row: PV loop as inputs of the DL model and the predicted gamma waveform. Second row: Comparison of true (inputs of the DL model) and FE simulated volume waveforms and clinical metrics.**

## DISCUSSION

We were able to accurately capture the mechanical response of the left ventricular myocardium using a few clinically relevant measures and a predetermined pressure-volume curve by designing a constitutive-based machine learning model. Our model exhibits great accuracy for a variety of pressure-volume curves and is applicable to both idealized and patient-specific left ventricle geometries. The combination of artificial intelligence with constitutive-based models enables the autonomous selection of challenging model parameters facilities their usage for patient-specific geometries.


## ACKNOWLEDGEMENTS

This work was supported by the AHA 19CDA34660003 grant.


## REFERENCES


[1] Göktepe, S., et al., *Wiley-Blackwells: Great Britain*, p. 1, 2011.
[2] S. Rao., et al., *Clinical Biomechanics*, 69: p. 127-140, 2019.
[3] Gasser, T.C., et al., *J R Soc Interface*, p. 15-35, 2006.
[4] Pezzuto, S., et al., *Eur J Mech A Solids*, 48: p. 83-96, 2014
[5] Holzapfel Gerhard, A., et al., *Philos Trans A Math Phys Eng Sci*, 367(1902): p. 3445-3475 2009.
[6] Maas, S.A., et al., *J. Biomech. Eng.*, 134(1): p. 11005, 2012.
[7] Wong, J., et al., *Computer Methods in Biomechanics and Biomedical Engineering*. 17(11), p.1217-1226, 2014.

# MECHANICAL AND STRUCTURAL CHANGES DUE TO TENDON OVERLOAD IN A RAT MODEL OF SYNERGIST ABLATION

**Ellen T. Bloom (1), Lily M. Lin (1), Justin Parreno (2), Karin Grävare Silbernagel (3), Dawn M. Elliott (1)**

(1) Biomedical Engineering, University Delaware, Newark, DE, USA
(2) Biological Sciences, University of Delaware, Newark, DE, USA
(3) Physical Therapy, University of Delaware, Newark, DE, USA

## INTRODUCTION

Altered loading in tendon can lead to tendinosis and tendinopathy, however the mechanisms for clinical tendon disorders are not well understood and progressive changes following altered loading remain undetected until pain or rupture occur. Perhaps the most common animal model to overload tendons uses treadmill running to induce tendinopathy by increasing loading and frequency [1]. A rodent model of synergist ablation (SynAb), which overloads the plantaris tendon without altering loading frequency by ablating the synergist Achilles tendon, was recently evaluated for tendon remodeling via histology and gene expression up to 4 weeks [2,3]. However, the mechanical and structural changes and long-term effects remain unknown. The objective of this study was to quantify the progressive changes due to overload in plantaris tendon area (using *in vivo* MRI), fibril microstructure, and mechanical behavior in the rat SynAb model. For fibril microstructure, we utilized serial block face scanning electron microscopy (SBF-SEM) to obtain 3D image stacks [4] and developed a machine learning algorithm to evaluate several thousand collagen fibrils. We hypothesize that the tendon and collagen fibrils will show remodeling (increased tendon cross-sectional area) and will be more disorganized (larger fibril diameters and lower fibril density) after overload compared to sham and intact controls. We also hypothesize that overload from SynAb will induce a decrease in mechanical properties.

## METHODS

Bilateral plantaris tendons of 7-month-old Long-Evans female rats were studied according to three groups: SynAb (synergist ablation, where the Achilles was excised to overload the plantaris), Sham, and Intact controls. 3D T1-weighted MR images were acquired of rat hind limbs in vivo on a 9.4T Bruker Biospec scanner before surgery, at 4 weeks (Sham and SynAb only), and at sacrifice at 8 weeks (n=8/group) and 12 weeks (n=2/group). MR images were segmented, and the plantaris tendon cross-sectional area (CSA) median value was calculated across all slices. SEM images of one tendon from each group was acquired along 30 µm of tendon length with 200 nm section thickness, resulting in over 150 slices along the length (FEI Apreo VolumeScope SEM, Thermo Fisher Scientific). Auto-segmentation of collagen fibrils was performed using a deep convolutional neural network (U-Net) run on a GPU node of a high-performance computing cluster [5]. The average fibril diameter, circularity, and fibril % area for each slice were calculated across all slices. Differences between groups were evaluated with a two-way repeated measures (MRI) or one-way (SEM) ANOVA and means compared with Tukey HSD post hoc ($p < 0.05$).

A separate set of 4- to 8-month-old Long-Evans male rats were used to quantify mechanical behavior at 8 weeks (n=2) and 16 weeks (n=2) after SynAb. Sham and intact controls were pooled as no difference was observed with either treatment or time (n=4). Testing used an established protocol on a custom uniaxial device. At the reference length a 0.1 N preload was measured, and each sample was preconditioned with 5 cycles to 5% grip strain. After cyclic ramps to 10, 20, and 30%, a ramp to failure was applied and used for analysis. Parameters quantified included transition point (end of toe region), inflection point (yield), and linear region modulus [6].

## RESULTS

MRI images were able to clearly define tendon structures (Fig 1A-B) and the void was filled with granulation tissue after Achilles resection (Fig 1B). The SynAb CSA was significantly larger than intact and sham at 8 weeks post-surgery (Fig 1C). The SynAb had a 30% larger CSA at 8-weeks post-surgery, while intact and sham CSA did not change over time. The U-Net convolutional neural network prediction successfully segmented the collagen fibrils throughout the image stack (Fig 2A-B). In total, the analysis auto-segmented 5,000-7,000 fibrils in each image stack. Thus ~750,000 fibril diameters were identified for each sample (ongoing efforts are registering fibrils tracks along the tendon length). The average fibril diameter for SynAb was 3% and 19%

larger than Sham and Intact, with Sham also larger than Intact (Fig 2C). The average collagen fibril circularity (with 1.0 portraying a perfect circle) for SynAb was 14% and 25% higher than Sham and Intact, with also Sham higher than Intact (Fig 2D). The fibril % area (e.g., fibril density) for SynAb was 7% and 23% lower than Sham and Intact, with Sham also lower than Intact (Fig 2E).

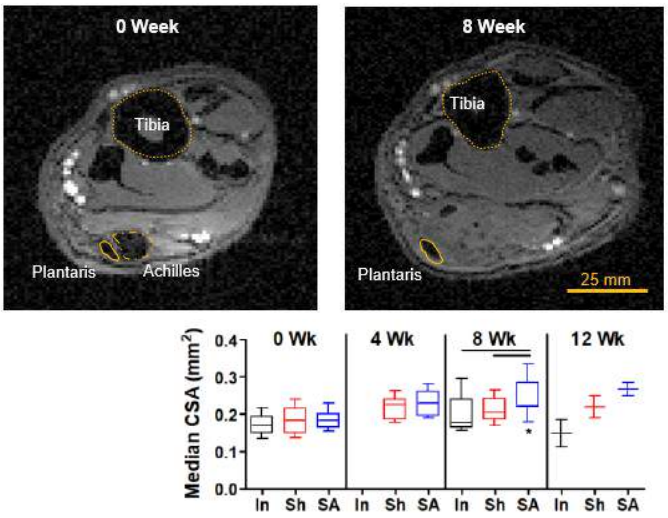


**Figure 1:** A-B) Representative MRI in SynAb at 0- and 8-weeks showing anatomy. C) Median (SD) CSA In=Intact, Sh=Sham, SA=SynAb. Line (between group) and * (over time) show p<0.05.

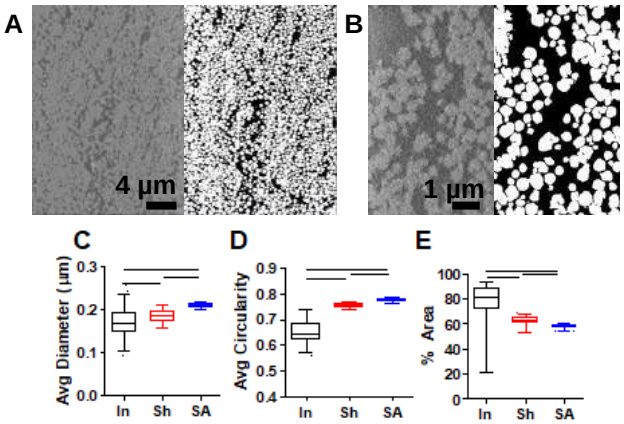


**Figure 2:** A-B) Representative SynAb SEM raw image and U-Net segmentations. C) Average diameter, D) average circularity, and E) fibril % area across image stacks. Lines show p<0.05.

Compared to control, SynAb modulus was lower at 8 weeks, but by 16 weeks returned toward control values (Fig 3A). The transition strain during the ramp to failure showed no differences between the groups (Fig 3B); however, the inflection point strain was higher for the SynAb 16-week samples (Fig 3C).

## DISCUSSION

This study demonstrated multiscale structural and mechanical changes in an animal model where the tendon was subjected to overload without increasing frequency. The SynAb model is a novel way to increase tendon loading to induce multiscale tendon remodeling without directly injuring the tendon. It is complementary to repetitive loading models that use treadmill running to alter tendon loading [1]. The geometry changes leading to larger diameters and more circular

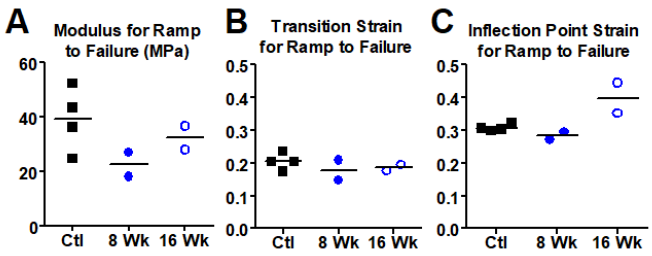


**Figure 3:** A) Modulus, B) transition strain, and C) inflection point strain from ramp to failure for control, 8-week, and 16-week SynAb.

collagen fibrils in the overloaded tendons suggests adaptation as the tendon attempts to increase its load-bearing capacity to meet the increased load demand. Decreased fibril density in the SynAb tendons may correspond to a degenerative response to the increased load. The SynAb tendons also showed a decrease in modulus compared to control, which indicates degeneration. However, the modulus for SynAb at 16 weeks was closer to control values, which may indicate positive adaptation by 16 weeks to meet the increased mechanical demand on the plantaris. Similarly, the high inflection point strain for the 16-week SynAb also suggests an adaptation to increase in load capacity for the tissue in the longer post-surgery time point. These possibly contradictory changes (increased CSA and fibril diameter vs. decreased fibril density and modulus) correspond to a transitory downturn in mechanical properties at 8 weeks followed by possible increase in tendon load capacity between 8 and 16 weeks, further illuminating the complex structural and mechanical changes that occur with altered tendon loading states.

This work shows machine learning can be successfully utilized to automatically segment large images sets of fibrils of dense collagenous tendon from SBF-SEM. The U-Net convolutional neural network was able to segment thousands of fibrils from the entire image stack spanning 30 µm. Following U-Net training, image stacks were fully segmented in ~15 minutes on a GPU node. Manual segmentation at a similar scale would take hundreds of hours. Further, the segmented diameters for the control fibrils are like those previously reported [7]. Previous investigations of tendon 3D volumes involved a much smaller number, ~50 fibrils [4]. In ongoing work, these comprehensive data of fibril geometry are being reconstructed along the length to investigate the 3D fibril structure. The success of these segmentations helps open a door to evaluating the complex 3D microstructure of collagen in tendon and other tissues.

Future work will add histological analyses, microscale mechanics, and increased sample numbers. In summary, the observed mix of changes following overload that includes possible early degeneration followed by later adaptation is intriguing and motivates next steps.


## ACKNOWLEDGEMENTS

Delaware Bio-Imaging Center. Supported by NIH-NIAMS via F31 AR078005-02 and NIH-NIGMS via DE INBRE (P20 GMI03446) & shared instrumentation grant (S10 OD025165).


## REFERENCES


[1] Hast, M et al., *Bone Joint Res*, 3:193-202, 2014. [2] Gumucio, J et al., *J App Phys*, 11:1-21, 2014. [3] Flood, M et al., *FASEB J*, 26:1142-1152, 2012. [4] Safa, B et al., *J. R Soc Interface*, 16:20190407, 2019. [5] Ronneberger, O et al., *Lec Notes in Comp Science*, 9351:234-241, 2015. [6] Bloom, E et al., *Annals Biom Eng*, 49:1058-1068, 2020. [7] Kastelic, J et al., *Conn Tissue R*, 6:11-23, 1978.

SB³C2022
Summer Biomechanics, Bioengineering and Biotransport Conference
June 20-23, Eastern Shore, MD, USA

# AN ANALYSIS OF OCTOPUS CURVATURE FOR APPLICATION IN SOFT ROBOTIC PROSTHESES

**G. Weidig (1), E. Kelly (1), B. Bush (1), G. Pelled PhD (1), T. Reid Bush PhD (1)**

(1) Department of Mechanical Engineering
Michigan State University
East Lansing, MI, USA

## INTRODUCTION

Upper limb loss is accompanied by loss of range of motion, loss of independence, financial burden, and other traumatic effects [1]. Smart prostheses, through the application of soft robotics, are devices that have the potential to fully restore function. They rely on the remaining, intact muscle groups to drive function. The ideal case is that they are capable of the range of motion of the extremities that they are replacing. At the very least, these devices must be able to restore the range of motion necessary for completing everyday tasks so that users can regain independence.

Unfortunately, current myoelectric smart devices have challenges that on average result in 30% of users abandoning them [2]. They are slow, uncomfortable, expensive ($60,000-$100,000), and rely heavily on a connection to the brain and body [3]. This dependence on connection accounts for long adjustment periods, malfunction, and the crossing of signals inputted to the device, which decreases their utility.

Therefore, there is a need for upper limb prostheses to be simpler, more intuitive, and function without complex input from the brain, while still providing necessary function to the user. To do this, inspiration can be drawn from an animal whose movements meet these criteria: the octopus.

The octopus is a muscular hydrostat which allows its arms to create unique movements and curvatures using nearly infinite degrees of freedom (DOFs). The octopus also has axial nerves in each of the arms that allow them to often move without the brain's input. They are even capable of completing some of the everyday activities that humans do, such as opening a jar or reaching and grasping for food. Existing motion data of octopus arms have been limited to largely 2D analysis. However, a smart prosthesis must be capable of 3D movements, which require more complex analysis.

Therefore, the goal of this work was to determine how to characterize 3D octopus movement data so that it can be used to influence an octopus arm-like prosthesis.

## METHODS

A four-camera underwater motion capture system was used to collect 3D movement data on amputated octopus arms, species *Octopus bimaculoides*. Five single retroreflective markers were attached to the skin of the amputated arm, and the arm was manually moved underwater to replicate octopus arm curvature (Figure 1). This involved moving the arm along a long, narrow elliptical path.

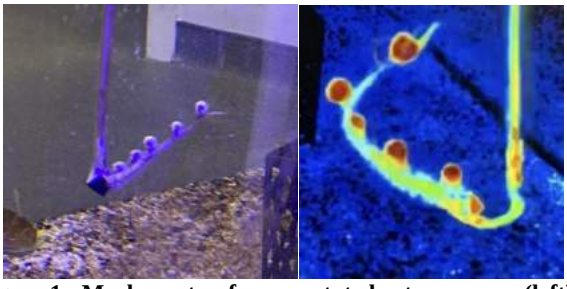

**Figure 1: Marker setup for amputated octopus arms (left) and motion capture display where the five dark red circles are the markers (right).**

The position data from the markers were used to calculate the overall curvature of the arm. The fields of robotics and biomechanics have different ways of computing curvature which makes relating the data to device design even more difficult. The robotics curvature, $(k_r)$ is

defined as $\frac{1}{R}$, where R is half the distance between the first and last marker. The biomechanical curvature (θ) is defined by the angle between the two vectors created by the first, middle, and last markers.

Finally, the planes of motion were investigated to understand the orientation of the octopus arm throughout these motions. A vector normal to the plane created by the first, middle, and last markers was calculated for three time points. These time points correspond to before curvature was initiated, during, and after (based on the path of motion).

## RESULTS

Figure 2 provides the results from the amputated arm for the robotic curvature analysis and for the biomechanical curvature analysis.

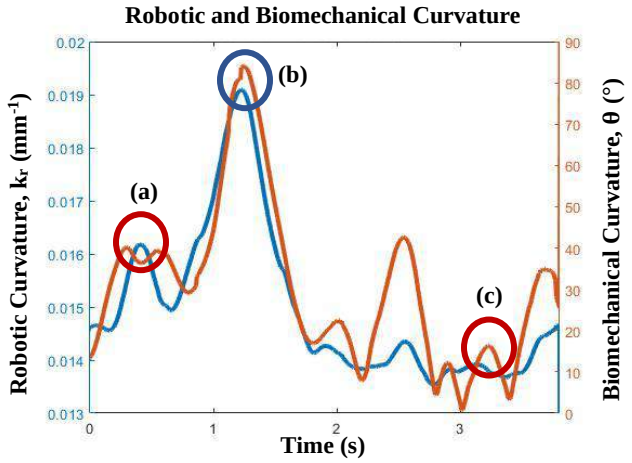


**Figure 2: Comparisons of two methods for curvurature calculation for the amputated octopus arm. Points a, b, and c will be used for analysis in Figure 3.**

Figure 3 shows the results of the planar analysis for three time points: before curvature was initiated, during, and after.

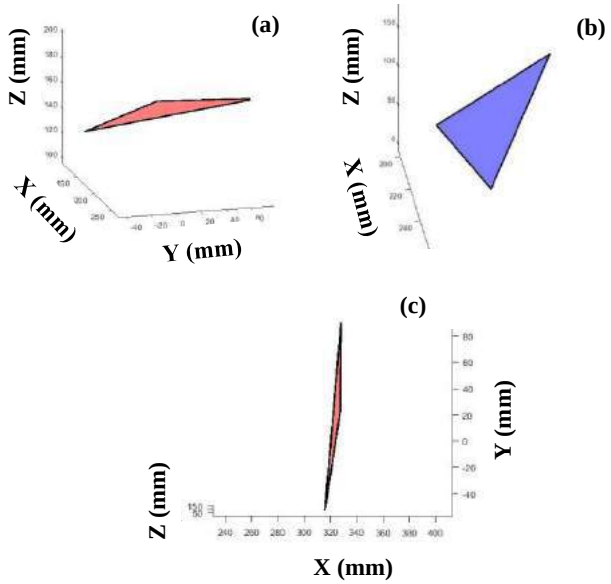


**Figure 3: Planes identify the orientation of the arm in space and correspond to three time points (a) before curvature was initiated, (b) during, and (c) the after.**

Based on Figure 2, in both analyses, straighter movements result in curvature values closer to 0 and more curved movements result in higher curvature values. The robotic curvature varies between 0.013 and 0.019 $mm^{-1}$ during the straight portions and the turning portions, respectively. Also, the biomechanical curvature reports ranges from 0 to 84° of movement during the straightaway and turning portions, respectively.

The planes of motion (Figure 3) were analyzed to determine the orientation of the curvature measurements in the octopus arm. The planes of motion move from Figure 3a to 3b to 3c. Note that together with the curvature, the plane orientation provides a complete description of arm movement. In addition to the overall leg orientation, larger curvature creates a larger planar area. The planes have areas of 843 $mm^2$, 1282 $mm^2$, and 341 $mm^2$, respectively.

## DISCUSSION

Methods used in soft robotics and biomechanics were applied to the curvature of the octopus leg to determine which one would be the most appropriate to describe it's movement. Since many soft robots only have one degree of freedom, the method to determine curvature is largely two dimensional. Although this analysis may be necessary to drive smart robotics, it is not intuitive or comprehensive enough to describe true human movements. The biomechanical analysis is better equipped to intuitively describe the magnitude of the curvature and it is more sensitive to movement. However, both analyses are unable to explain the orientation of the curvature in space.

The planar analysis describes the orientation of the octopus arms using planes. Current techniques for defining octopus movement have assumed that the curvature occurs in one plane. However, this analysis clearly demonstrates the multiple planes of movement. The straight portions of the movement actually have side-to-side curvature, which is shown by Figures 3a and 3c; and the turning portions have flexion-like curvature, shown in Figure 3b. Also, computation of the area component of the plane provides even more detail that may be beneficial to the description of movement.

The differences between movement definitions must be determined for advancement of biomechanics and soft robotics. Also, to be able to implement a multi-planar functioning octopus arm-like prosthesis, the added complexity of the planar movements must be better understood, as it has not been investigated or quantified. Future work will include a full planar analysis for all time points of octopus movement, and the best method for communicating curvature and orientation for the design of smarter and less expensive prostheses will be determined.


## ACKNOWLEDGEMENTS

This work was supported by NIH grant UF1NS115817 and is under IACUC# PROTO201800092.


## REFERENCES


[1] Bowrey, S et al., *Disability and Rehab.*, 26:831-836, 2009.
[2] Biddiss and Chau,Am J Phys Med Rehabil., 86:997-87, 2007.
[3] Raiche, K et a., *J. Rehab. Research & Dev.*, 45:961-972, 2008.

# DIGITAL PLASMONIC NANOBUBBLE DETECTION (DIAMOND): IMPROVED NANOPARTICLE FORMULATION FOR CLINICAL SAMPLE TESTING

**Y. Liu (1), H. Ye (1), H. Huynh (2), J. Kahn (2), Z. Qin (1, 3, 4, 5)**

(1) Department of Mechanical Engineering, University of Texas at Dallas, Richardson, Texas 75080, U.S.
(2) Department of Pediatrics & Microbiology, University of Texas Southwestern Medical Center, Dallas, TX 753□0, U.S.
(3) Department of Bioengineering, University of Texas at Dallas, Richardson, Texas 75080, U.S.
(4) Center for Advanced Pain Studies, University of Texas at Dallas, Richardson, Texas 75080, U.S.
(5) Department of Surgery, University of Texas Southwestern Medical Center, Dallas, Texas 753□0, U.S.

## INTRODUCTION

Digital immunoassays are capable of quantifying analytes in a calibration-free manner and detecting them at single-molecule level.[1] The major barriers to its widespread use are the time-consuming protocols (e.g., sample partition and signal amplification) and laboratory infrastructures.[2] Here we developed digital plasmonic nanobubble detection (DIAMOND) technique to overcome some of these bottlenecks. Specifically, we designed an optofluidic setup to flow the gold nanoparticle (AuNP)-based samples in a micro-capillary, where two aligned laser beams synchronically activate and detect the plasmonic nanobubbles (PNBs) generated from nanoscale heating of AuNPs (**Fig. 1a**). Since the PNBs are transient events and have no crosstalk between laser pulses, DIAMOND creates microscale "virtual detection zones" of about 16 pL and counts the "on" and "off" signals in a compartment-free manner (**Fig. 1b, c**). We demonstrated that DIAMOND can be implemented on a homogeneous immunoassay and does not require additional sample washing, separation, and signal amplification steps. On the other hand, DIAMOND does not require chip preparation or on-chip reaction and can be performed with less assay time (i.e., within 30 minutes) compared to other digital assays. Using antibody-modified gold nanoparticle (AuNP) probes with bovine serum albumin (BSA) backfilling, we demonstrated DIAMOND could specifically detect respiratory syncytial virus (RSV) in nasal swab samples and achieves a detection limit of ~100 PFU/mL or 1 RNA copy/μL equivalent. We also discussed several further improvements to this technology to bring it to a broad range of labs and practical applications in clinics.

## METHODS

*Preparation of antibody-coated AuNPs with BSA backfilling.* In brief, DTSSP as a crosslinker was first reacted with Synagis as detection antibody, followed by an overnight membrane dialysis at 4 ºC and incubation with AuNPs and 0.1% of DTSSP-BSA. The product was then washed and centrifuged before re-dispersed in 2 mM borate buffer.

*Detection of virus in complex sample matrix*. We used BD Universal Viral Transport Collection Kits to collect nasal swab samples from the nostrils of healthy adults following the manufacturer's instruction. The unpurified virus suspensions including respiratory syncytial virus (RSV), human metapneumovirus viruses (hMPV), parainfluenza viruses (PIV), and influenza virus type A (IVA) were then spiked into the as-prepared nasal swab healthy control samples and used as clinical samples. The use of human nasal swab samples was approved by Institutional Review Board (IRB) at University of Texas at Dallas (ID: 20MR0093).

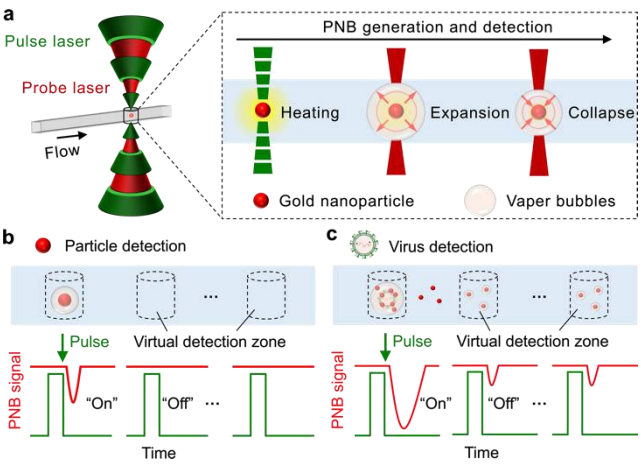


**Figure 1. Concept of digital plasmonic nanobubble detection (DIAMOND).** (a) The schematic illustration of the transient plasmonic nanobubble (PNB) events. Pump-probe laser configuration allows PNB

generation and detection simultaneously. (b, c) The principle of digital counting of "on" and "off" PNB signals for particle detection (b) and virus detection (c).

## RESULTS

We previously found that the antibody-modified AuNP probes had limited detection specificity for control viruses, including PIV, IVA, and hMPV (**Fig. 2a, b**). This is because those viruses were dispersed in culture fluids without purification and the impurities like cell debris involved in the medium could cause non-specific aggregation of AuNP probes. As a result, they led to positive counts and thereby false positive. To address this issue, we used bovine serum albumin (BSA) to backfill the AuNP probes. The BSA has been frequently used in immunoassays as block reagent and can prevent the non-specific binding for improved detection specificity.[3] To evaluate the performance of BSA-backfilled AuNP probes, we incubated them with respiratory viruses spiked in nasal swab samples and subjected the complete assay solution to the DIAMOND test. The viral transport medium (VTM), hMPV, PIV, and IVA were used as negative controls, and all viral titers were kept the same as $10^5$ PFU/mL. **Fig. 2c, d** show the virus detection results using BSA-backfilled probes, where the positive PNB signals from the control viruses were significantly reduced, while the PNB signals from RSV can be easily distinguished from the control samples, yielding $f_{on}$=100% that matches well with the theoretical probability. In contrast, the non-backfilled probes still cause non-specific aggregation upon detection. This result suggests that DIAMOND has a better detection specificity when utilizing BSA-backfilled probes. These probes also enabled sensitive detection of spiked RSV in nasal swab samples with a detection limit of 102 PFU/mL (**Fig. 2e, f**), equivalent to 1 RNA copy/μL as validated by digital isothermal amplification (data not shown). Taken together, these results demonstrated that implementing DIAMOND on a homogeneous immunoassay allows sensitive analysis of viral samples in the human specimen matrix and supports the potential clinical applications.

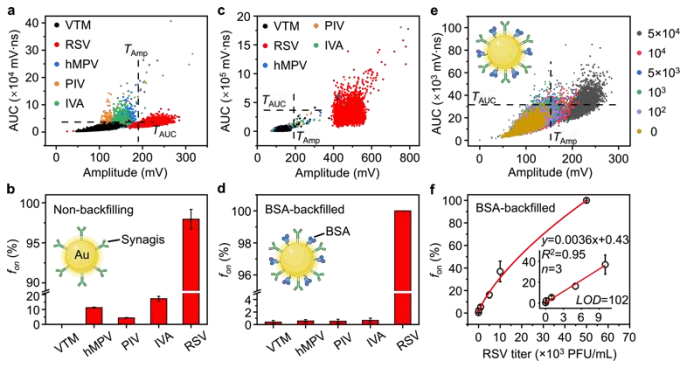


**Figure 2. Detection of RSV among closely related respiratory viruses by DIAMOND.** Detection and quantification results for (a, b) control viruses and RSV in culture fluids using non-backfilled AuNP probes; (c-f) control viruses and RSV spiked in *complex sample matrix* using BSA-backfilled AuNP probes.

## DISCUSSION

We envision several further improvements to this technology in order to bring it to a broad range of labs and practical applications. Current implementation of DIAMOND relies on a research-grade pump laser, which is too bulky to perform tests out of a lab. It is important to explore the feasibility of DIAMOND using a small benchtop device. As a first step, we used a portable nanosecond (ns) laser (Wedge-HB-532, RPMC) that can be integrated into a benchtop device (15×15×6 inches, **Fig. 3a**). Evaluation of PNB generation and detection by this ns laser shows robust results across a range of AuNP concentrations (**Fig. 3b-d**). More importantly, the ns laser provides a repetition rate up to 2,000 Hz and allows a much faster readout and thus more efficient event counting. Taking advantage of the high-throughput ns laser and a focusing flow, we expect to increase the event counting (e.g., 1 million readings within 10 minutes, similar to flow cytometer). This will improve the detection range and sensitivity of DIAMOND, because the digital counting performance essentially relies on the number of counted events.[4]

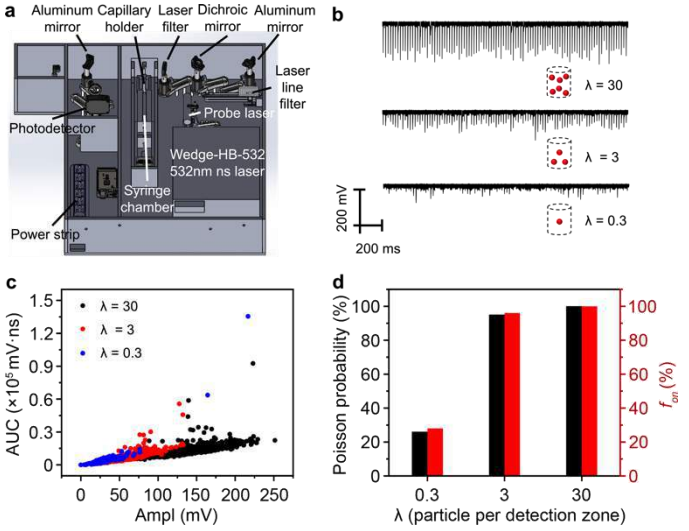


**Fig. 3. Detection of 75 nm AuNPs by DIAMOND using a nanosecond laser (Wedge-HB-532, RPMC).** (a) SOLIDWORKS model built for benchtop device. (b) PNB signal traces (100 pulses) generated from ns laser for 75 nm AuNP suspensions with different particle concentrations, where λ refers to the number of NPs per detection zone. (c) PNB signal analysis of amplitude and area under the curve (AUC) extracted from 3,000 pulses for the three samples in (b). (d) Bar plot of experimental frequencies ($f_{on}$) as determined in (c) and theoretical probability predicted by Poisson statistics for the given λ.

In summary, we have developed DIAMOND for virus detection via the AuNPs-based homogeneous immunoassay. DIAMOND allows digitizing a homogeneous assay without sample washing. Importantly, DIAMOND can specifically detect RSV among different respiratory viruses in complex matrix and achieve a detection limit of ~100 PFU/mL (or 1 RNA copy/μL). Compared with other digital assays, DIAMOND counts events in a compartment-free manner and utilizes a one-pot protocol for sample handling at room temperature. Our study provides a digital counting platform for rapid and ultrasensitive diagnostics of intact viruses at their early representation.


## ACKNOWLEDGEMENTS

This research is partially supported by National Institute of Health grants R21AI140462 and R01AI151374, and DOD grant PR192581.


## REFERENCE:


[1] Wilson, D. H., et al. *J. Lab. Autom.* **2016**, 21, 533-547.
[2] Chang, L., et al. *J. Immunol. Methods*. **2012**, 378, 102-115.
[3] Xiao, Y., et al. *J. Immunol. Methods*. **2012**, 384, 148-151.
[4] Kim, S. H., et al. *Lab Chip*. **2012**, 12, 4986-4991.

# SINGLE PULSE HEATING OF NANOPARTICLE ARRAY FOR BIOLOGICAL APPLICATIONS

**C. Xie (1), P. Kang (1), Z. Qin (1, 2, 3, 4)**

(1) Department of Mechanical Engineering, University of Texas at Dallas, Richardson, Texas, USA
(2) Department of Bioengineering, University of Texas at Dallas, Richardson, Texas, USA
(3) Department of Surgery, University of Texas at Southwestern Medical Center, Dallas, Texas, USA
(4) Center for Advanced Pain Studies, University of Texas at Dallas, Richardson, Texas, USA

## INTRODUCTION

Nanoparticles (NPs) have found an essential role in various biomedical applications due to their capabilities to efficiently absorb external energy excitation and convert that energy to heat[1]. Heating generated by NPs broadly falls into one of two modes: nanoscale-confined heating (NCH) and macroscale-collective heating (MCH)[2]. Efforts had been made on revealing the transition between these heating modes[3-5]. Keblinski et al. highlighted the role of the duration of energy excitation in controlling the transition between NCH and MCH[3]. Baffou et al. systemically investigated how the geometry of an NP array affects the temperature confinement[4]. While these efforts advanced our understanding of nanoparticle heating, there is an important gap in understanding how single pulsed NP heating affects biological systems through protein denaturation or activation.

In this study, we developed a computational model to systematically investigate the single-pulsed heating of NP array and corresponding protein denaturation/activation. We found that NCH may lead to targeted protein denaturation, however, NCH does not lead to nanoscale selective TRPV1 channel activation. The excitation duration and NP concentration are primary factors that determine a window for targeted protein denaturation, and together with heating power, we defined quantified boundaries for targeted protein denaturation. Our results improve our understandings of NCH and MCH under realistic physical constraints and provide robust guidance to customize biomedical platforms with NP heating.

## METHODS

For NP array heating, we solve the problem by superposition of the analytical solution of single nanoparticle heating:

$$\Delta T_{multi}(\mathbf{r},t) = \sum_{i=1}^{N} \Delta T_{single}^{i}(\mathbf{r},t) \quad (1)$$

The single spherical particle heat conduction model in spherical system was analytically solved by Laplace transform[6].

The protein denaturation was treated as a first-order kinetic model, and the reaction rate was determined by the Arrhenius model[7]:

$$k = Ae^{\frac{-E_a}{RT_m}i} \quad (2)$$

where $T_m$ is the temperature of NP array heating.

For the TRPV1 channel, the activation can be determined by two-state model and the opening rate $k_{on}$ is estimated by[8]:

$$k_{on} = Ae^{\frac{-\Delta H - T_m \Delta S}{RT_m}i} \quad (3)$$

All solutions were calculated in Matlab 2019b software.

## RESULTS

We first constructed and validated the modeling framework for NP array heating and protein thermal denaturation: 10 μm ×10 μm 2D square arrays composed of 30 nm gold nanoparticles (AuNP) immersed in an aqueous solution(Fig. 1). To connect NP heating to the protein denaturation, we analyzed protein denaturation using α-chymotrypsin. Additionally, we analyzed NP heating-induced protein activation with the TRPV1 channel. Here we consider the NP-water interface ($P_1$) and the mid-point between NPs ($P_2$) as two representative locations. We will use $P_1$ and $P_2$ to indicate these locations, along with $\Delta T_1$, $\Delta T_2$ and $D_1$, $D_2$ and $O_1$, $O_2$ to indicate temperature increase ($\Delta T$), normalized protein denaturation ($D$), and normalized TRPV1 activation ($O$) at $P_1$ and $P_2$ respectively.

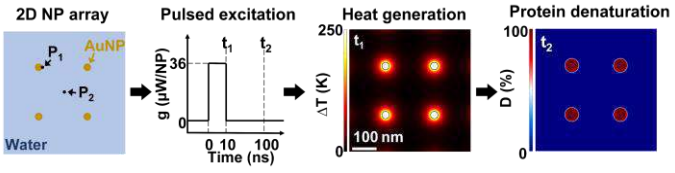


**Figure 1. Analysis framework for nanoparticle heating-induced protein denaturation.**

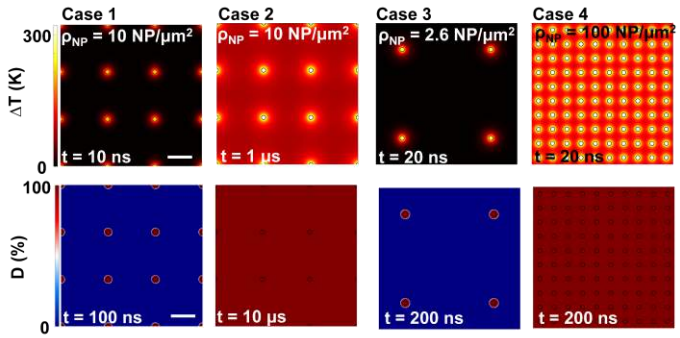


**Figure 2. Effects of excitation duration and NP area density on the heating and protein denaturation.** Heating power (g) = 36 μW/NP Scalebar represents 200 nm.

Secondly, we investigated the role of excitation duration and NP area density ($\rho_{NP}$) in transition from NCH to MCH, and from targeted to widespread denaturation respectively. Here we adopt $D_2/D_1$ to characterize the denaturation profile. High $D_2/D_1$ indicate uniform denaturation profiles, while low $D_2/D_1$ indicate heterogeneous profiles, which is necessary for selective denaturation. By comparing thermal responses and protein denaturation with NP array heating under different excitation durations (Fig. 2, case 1&2), and with NP arrays that have different $\rho_{NP}$ (Fig. 2, case 3&4), we found the excitation duration and $\rho_{NP}$ are key factors that driving transition from NCH to MCH, and from heterogeneous denaturation ($D_2/D_1 \sim 0$ % for case 1&3) to uniform denaturation ($D_2/D_1 \sim 100$ % for case 2&4).

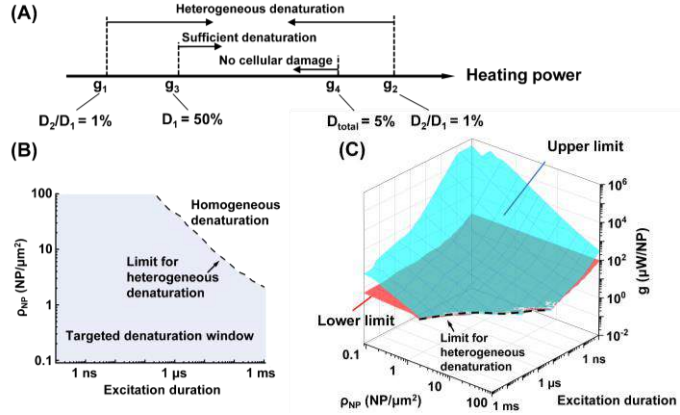


**Figure 3. Limits and window for targeted protein denaturation.** (A) Schematic of critical heating powers $g_1$, $g_2$, $g_3$ and $g_4$. (B) Excitation duration and $\rho_{NP}$ determines the targeted protein denaturation window. (C) Lower limit (red surface) and upper limit (blue surface) for targeted protein denaturation in terms of excitation duration and $\rho_{NP}$.

Next, we analyzed the effect of heating power ($g$) on protein denaturation. We found that as $g$ increases, $D_2/D_1$ drops from 100 % to ~0 % at certain heating power $g_1$, and dramatically increases back to 100 % at $g_2$. Here $g_1$ and $g_2$ represent the boundaries for heterogeneous protein denaturation zone (Fig. 3A), where targeted denaturation is possible. Importantly, we found the limits for this targeted denaturation window are determined by excitation duration and $\rho_{NP}$ (Fig. 3B), *i.e.,* targeted protein denaturation is possible only when NCH is established. Within this targeted denaturation window, we further define critical heating powers $g_3$ and $g_4$ to quantify the limits of targeted denaturation in terms of g, *i.e.,* sufficient denaturation around NP ($g_3$, $D_1 = 50\%$) without widespread cellular damage ($g_4$, $D_{total} = 5$ %, less than 5 % total protein denaturation; Fig. 3A). Considering all these factors we determined the quantified limits for targeted protein denaturation in terms of excitation duration, $\rho_{NP}$, and $g$ (Fig. 3C).

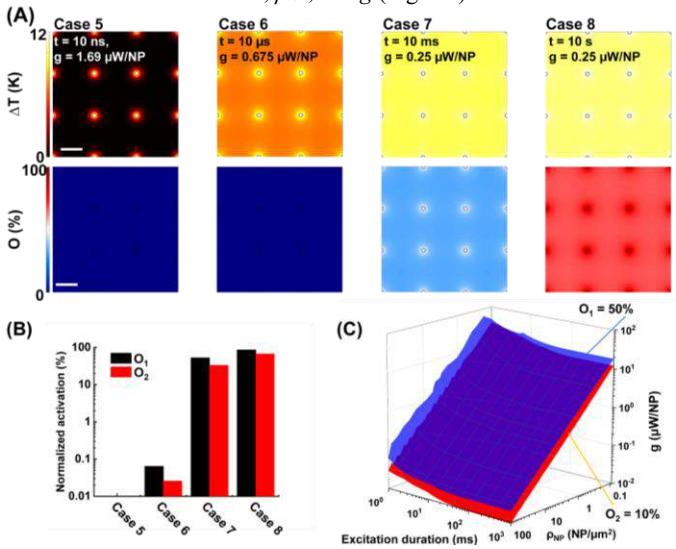


**Figure 4. Analysis of TRPV1 channel activation by NP array heating.** (A) $\Delta T$ profile and $O$ profile for case 5-8, $\rho_{NP}$ = 9 NP/μm$^2$, scalebar represents 200 nm. (B) $O_1$ and $O_2$ for case 5-8. (E) Threshold for on-target TRPV1 activation ($O_1$ = 50%, blue surface) and off-target TRPV1 activation ($O_2$ = 10%, red surface).

Lastly, we investigated whether NP array heating could selectively activate the TRPV1 channel. Following the similar framework in Fig. 1, NCH is observed with short excitation duration(Fig. 4 A&B, case 5&6). However, due to the mismatch between the nanosecond excitation durations required for NCH and the millisecond timescale needed for channel activation[8], there is no obvious TRPV1 activation for case 5&6. As excitation duration increases, MCH is established (Fig. 4 A&B, case 7&8), resulting in widespread TRPV1 activation. Here we set a threshold of on-target TRPV1 activation ($O_1$ = 50 %), and off-target TRPV1 activation ($O_2$ = 10 %). Fig. 4C shows the threshold for on-target TRPV1 activation (blue surface) is always higher than off-target activation (red suface), indicating that either no TRPV1 activation or widespread TRPV1 activation is possible by NP array heating.

## DISCUSSION

In this study, we found nanoscale selective activation of TRPV1 is not feasible based on our current understanding of its millisecond activation kinetics. It should be noted, however, that it is unclear if TRPV1 can be activated at faster rates at a higher temperature. According to molecular dynamics simulations, channel opening was not observed within 200 ns at temperatures of 60 and 72 ° C, suggesting that TRPV1 activation may be unlikely to occur at nanosecond timescale[9].

## ACKNOWLEDGEMENTS

We acknowledge the support from National Science Foundation (1631910), National Institute of Health (R35GM133653).

## REFERENCES

[1] Park J, et al., *J. Phys. Chem. C*, 116:26335-26341,2012.
[2] Qin Z, et al., *Chem. Soc. Rev.*, 41:1191-1217, 2012.
[3] Keblinski P, et al., *J. Appl. Phys.*, 100:054305,2006.
[4] Baffou G, et al., *ACS Nano*, 7:6478-6488,2013.
[5] Xie C, et al., *J. Heat Transfer*, 2021.
[6] Goldenberg H., et al., *Br. J. Appl. Phys.*, 3:296,1952.
[7] Kang, P., et al., *ACS nano*, 13:12487-12499,2019.
[8] Yao J, et al., *J. Biophys.*, 99:1743-1753,2010.
[9] H. Wen, et al., *Biophys. J.*, *114*:40-52,2018.

# EFFECT OF MECHANICAL LOADING ON THE MICROSTRUCTURE AND DIFFUSION IMAGING PROPERTIES OF LIGAMENT-MIMICKING FIBERS

**Roberto A. Pineda Guzman (1), Noel M. Naughton (2), Bradley P. Sutton (2,3), Mariana E. Kersh (1,2,4)**

(1) Department of Mechanical Science and Engineering, University of Illinois Urbana-Champaign, Urbana, IL, USA
(2) Beckman Institute for Advanced Science and Technology, University of Illinois Urbana-Champaign, Urbana, IL, USA
(3) Department of Bioengineering, University of Illinois Urbana-Champaign, Urbana, IL, USA
(4) Carle Illinois College of Medicine, University of Illinois Urbana-Champaign, Urbana, IL, USA

## INTRODUCTION

Over 120,000 Anterior Cruciate Ligament (ACL) injuries occur in the United States every year [1] and the rate of ACL reconstruction surgeries is steadily increasing [2]. The choice of graft used in ACL reconstruction influences the resulting knee loading following ACL reconstruction, and may contribute to increased rates of osteoarthritis [3]. The patellar tendon is the most common graft used as an ACL replacement, but has different microstructural [4] and mechanical properties [5] than those of the ACL. To better guide the selection of ACL grafts, *in vivo* imaging techniques that can provide microstructural information to better match the native tissue are required.

Diffusion Tensor Imaging (DTI) measures the diffusion properties of water through tissue [6] thereby inferring the underlying microstructure [7] governing the diffusion. In order to translate the quantitative data provided by DTI into relevant biomechanical information, it's important to establish relationships between the parameters measured by DTI and the mechanical structure-function relationships of soft collagenous tissues. However, doing so in biological tissues presents challenges due to the natural heterogeneity and complexity in the microstructure of ligaments and tendons.

Previously, we used spun fibers as a mimic of the microstructure of collagen-based tissues to develop material constructs of ligaments [8]. These constructs have tensile [8] and shear properties [9] similar to those of ligaments and tendons, with the benefit that their microstructure is controllable and more homogeneous. As a first step to understand the diffusion-structure-function relationships, the objective of this study was to evaluate the effects of mechanical loading on fiber microstructure and DTI parameters using ligament-mimicking fibers. We hypothesized that fiber diameter and ply-angle would change with loading and result in differences in diffusion properties.

## METHODS

*Yarn samples.* Ten fiber (Caron, 570 tex) samples (5 pre-loaded, 5 loaded, length = 10 cm) were used for mechanical loading and imaging.

*Mechanical loading and sample preparation.* All samples were pre-loaded to 0.3 N to standardize the initial length. Five samples were held at the pre-load value and fixed using water-resistant epoxy in a custom imaging container (Figure 1). Next, five samples were pre-conditioned to 30N (50 cycles, rate = 106 mm/min) loaded to 10 N (rate = 106 mm/min) and the tensioned samples were secured with water-resistant epoxy into the imaging containers.

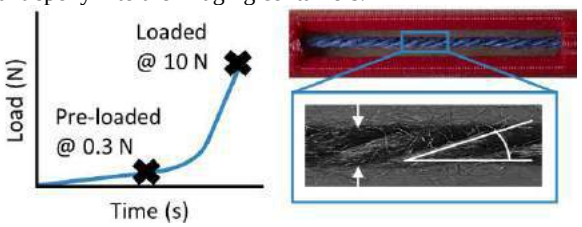


**Figure 1: Points on load curve at which the samples were imaged (left). Measurement of the yarn diameter and ply twist angle from the high-resolution images (right).**

*High-resolution structural imaging.* The fiber samples were imaged using a high-resolution camera (100MP, PhaseOne, Denmark). Apparent fiber diameter and twist angle was measured from the images using custom Matlab code. For diameter, the fiber was segmented from the background, binarized, and the mean distance between the fiber edges was calculated. Grey scale versions of the images were used to measure the ply twist angle based on textural differences between the plies. The central region of the fiber was isolated and the gradient structure tensor was calculated from which the eigenvectors were determined. The ply twist angle was defined as the principal eigenvector.

*Diffusion Tensor Imaging.* The fiber samples were next submerged in water and imaged using a 9.4T MRI system (Bruker, MA, USA). DTI

was performed using an echo-planar imaging sequence (TE/TR = 180/4200 ms, 12 directions, 12 averages, and $b$ = 600 s/mm$^2$). Twenty slices were acquired for each fiber (slice thickness = 375 µm, in-plane resolution = 150 x 150 µm, field of view = 19.2 x 19.2 x 7.5 mm). Fractional anisotropy (FA), apparent diffusion coefficient (ADC), and radial diffusivity (RD) were calculated from the DTI images using MRtrix3 (https://www.mrtrix.org/) and custom Python code. Fiber tractography was performed using DSI Studio (https://dsi-studio.labsolver.org/).

*Statistical Analysis.* Normality of the microstructural and DTI metrics was tested and confirmed using a Shapiro-Wilks test. An unpaired t-test was used to evaluate differences in the microstructural and DTI metrics between the pre-loaded and loaded samples.

## RESULTS

Loading decreased the diameter of the fibers by 32% ($p < 0.001$), while no significant change was observed in ply twist angle (Table 1). The FA in loaded samples increased by 5% ($p < 0.01$) while RA and ADC decreased by 30% ($p < 0.01$) and 25% ($p < 0.01$), respectively. Local differences in FA and RD and diametrical compression of the loaded samples were observed in the fiber tractography (Figure 2).

**Table 1: Mean ± standard deviation values of fiber structural parameters (*** = $p < 0.001$)**

| Structural Parameter | Pre-loaded | Loaded |
|---|---|---|
| Yarn Diameter (mm) | 1.85 ± 0.09 | 1.25 ± 0.08*** |
| Ply twist angle (°) | 16.26 ± 3.59 | 14.25 ± 1.77 |

## DISCUSSION

We have used a combination of high-resolution structural imaging and MRI to evaluate the structure-function relationships of ligament mimicking fibers under different load states. Our data indicate that loading has a greater effect on fiber compaction than angular rearrangement. During the early pre-load (toe) phase, diametrical fiber compression results in an increase in fiber density in agreement with theoretical models [10].

The lack of change in ply twist angle suggests that angular rearrangements of fibers may occur outside the bounds measured by our study - either at loads lower than 0.3 N or greater than 10N. Fiber compaction correlated with changes observed in the DTI metrics: loading resulted in increased FA and both the RD and ADC decreased. Highly aligned fiber networks present more barriers for water molecules to diffuse since fiber density is increased and result in more anisotropic diffusions [11]. The diffusion directions obtained from the fiber tractographies agree with the alignment direction of the fibers and support our interpretation.

One limitation of our study is that our optical image measurement of fiber rearrangement was limited to ply angles and it is possible that smaller scale rearrangements may occur such that the fibers within a given ply may change orientation in response to loading. This lower length scale variation is more readily seen in the visualization of FA and RD where local heterogeneities are observed. The presence of air bubbles was also noted in some images and care was taken to avoid using DTI measures in those regions when possible.

Our results show that DTI is sensitive to the microstructural changes in ligament-mimicking fibers. Importantly, MRI is a clinically viable technique and the use of DTI will open new opportunities for the assessment of musculoskeletal tissues. These diffusion-structure relationships can bridge *in vitro* findings of collagen fiber alignment on knee ligament mechanics [12] and *in vivo* clinical images of knee ligaments [13-15]. With an enhanced clinical characterization of ligament microstructure and mechanics, appropriate graft selection and improved outcomes for ACL reconstructions are possible.


## ACKNOWLEDGEMENTS

This research was completed with the support of the Jump ARCHES endowment through the Health Care Engineering Systems Center of the University of Illinois Urbana-Champaign.


## REFERENCES


[1] Kaedig, CC et al., *Clin Sports Med*, 36:1-8, 2017. [2] Sanders, TL et al., *Am J Sports Med*, 44:1502-1507, 2016. [3] Dare, D & Rodeo, S, *Curr. Rheumatol. Rep.*, 16:1-5, 2014. [4] Yahia, LH & Drouin G, *J. Mater. Sci.*, 23:3750-3755, 1988. [5] Chandrashekar, N et al., *Clin Biomech*, 23:918-925, 2008. [6] Roberts, TPL & Schwartz, ES, *Pediatr. Radiol.*, 37:739-748, 2007. [7] Kakkad, S et al., *Neoplasia*, 18:585-593, 2016 [8] Pineda Guzman, RA & Kersh, ME, *J Mech Behav Biomed Mater*, 118:104339, 2021. [9] Arant, LR & Roth, JD, *J Mech Behav Biomed Mater*, 104984, 2021. [10] Le, C & Phillips, D, *J. Test. Inst.*, 98:421-429, 2007. [11] Tourell, MC et al., *J. Phys. D*, 46:455401, 2013. [12] Skelley, NW et al., *Am J Sports Med*, 43:928-936, 2015. [13] Van Dyck, P et al., *J. Magn. Reson. Imaging*, 46:1423-1432, 2017. [14] Van Dyck, P et al., *Eur. Radiol.*, 30:6673-6684, 2020. [15] Van Dyck, P et al., *J. Orthop. Res.*, 39:1318-1330, 2021.


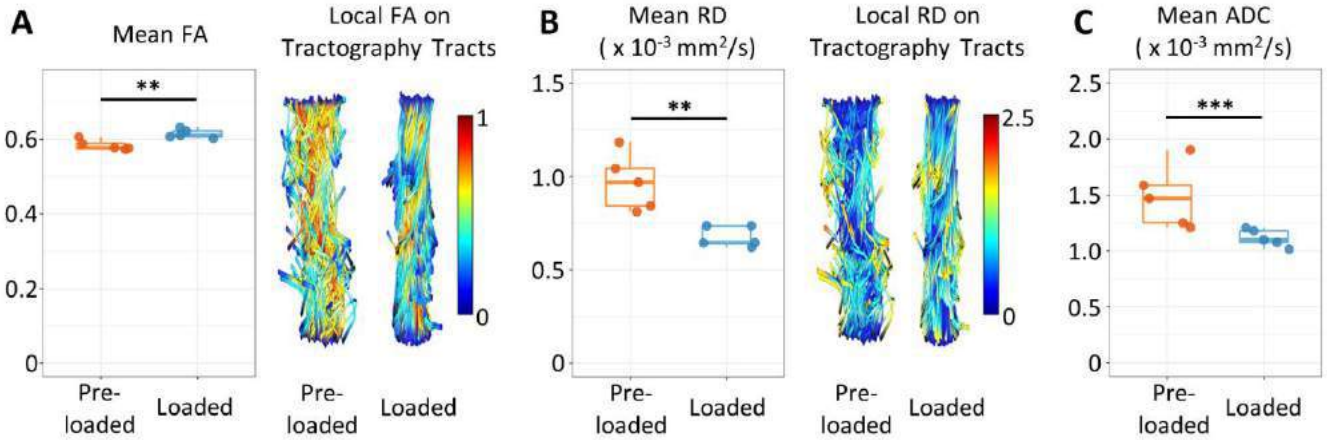


**Figure 2: Mean FA (A), RD (B), and ADC (C) of all pre-loaded and loaded samples (** = $p < 0.01$, *** = $p < 0.001$). A and B include a rendering of the tractography tracts of one pre-loaded and one loaded sample showing local FA and RD**

# INVESTIGATION OF THE REGIONAL VARIATIONS IN THE MECHANICAL PROPERTIES AND MICROSTRUCTURE OF PORCINE LEFT ANTERIOR DESCENDING ARTERY

**Sergio A. Pineda-Castillo (1,2), Santiago Aparicio-Ruiz (1), Chung-Hao Lee, PhD (1,3)**

(1) Biomechanics & Biomaterials Development Laboratory, School of Aerospace and Mechanical Engineering, University of Oklahoma, Norman, OK, USA
(2) Stephenson School of Biomedical Engineering, University of Oklahoma, Norman, OK, USA
(3) Institute for Biomedical Engineering, Science & Technology, University of Oklahoma, Norman, OK, USA

## INTRODUCTION

Coronary heart disease (CHD) is the cause of mortality for about 300,000 Americans each year [1]. Treatment of CHD includes medication, angioplasty, and, for severe vessel occlusion, coronary artery bypass grafting (CABG) that is a procedure requiring the use of an autologous vein or artery from the patient's body. Autologous grafts can frequently become unavailable, necessitating the need for fabricating non-autologous grafts. Tissue-engineered vascular grafts (TEVGs) aim at mimicking the microstructure and mechanical properties of the native coronary artery [2]; however, current TEVGs fail to replicate these properties due to a lack of understanding in the mechanical and structural requirements of the target vessel. In addition, surgeons frequently select anastomotic sites based on different factors, resulting in the variability in the portion (proximal, medial, or distal) of the artery connected to the graft [3]. Thus, it is of a paramount importance that the local tissue microstructural and mechanical properties are characterized for the development of TEVGs. In this study, we aim to characterize the porcine left anterior descending artery (LADA) via biaxial testing, polarized light imaging and multiphoton microscopy. Our findings demonstrate the unique regional properties of the vessel, creating the need for biomaterials for CABG that can potentially mimic the unique properties of native coronary artery tissue.

## METHODS

*Tissue Preparation & Dissection*: Healthy porcine hearts (n=14) were obtained from a local abattoir (Chickasha Meat Company, OK). Upon arrival at our lab, hearts were dissected through the following procedures: (i) excising surrounding tissue of the LADA and sectioning the artery immediately next to the branching of the left coronary artery, (ii) delicately exposing the complete artery by cutting open the epicardium and surrounding fatty tissue, (iii) delicately removing connective tissue, and (iv) cutting the excised artery in thirds. Each third was then stored as proximal, medial, and distal specimens.

*Biaxial Testing*: The CellScale BioTester system was used in the biaxial tissue mechanical characterization. The tissue circumferential (C) and longitudinal (L) directions were aligned with the device *x*- and *y*-axes. Once mounted via four BioRakes, glass beads were glued to the surface of the specimen as fiducial markers for the quantification of in-plane strains [4]. All testing was performed in phosphate-buffered saline at 32°C, and the specimens were subjected to 15 preconditioning cycles, followed by a series of biaxial tension ratios: $T_{CC}$:$T_{LL}$ = 1:1, 1:0.75, 1:0.5, 1:0.25, 0.25:1, 0.5:1, 0.75:1. Tissue strains were then calculated using digital image correlation together with a single bilinear finite element, and the first Piola-Kirchhoff stress tensor was calculated by $\mathbf{P} = \mathrm{diag}[T_{CC}, T_{LL}]/t$, where $t$ is the tissue thickness measured by a non-contact laser sensor. The stress-stretch curves were used to calculate several derived mechanical parameters. (**Fig. 1**).

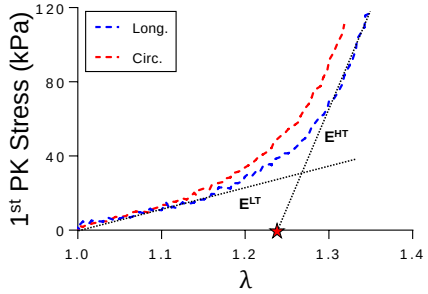


**Figure 1: Biaxial stress-stretch data of a representative porcine left anterior descending artery (LADA), for deriving the low- and high-tension moduli ($E^{LT}$ and $E^{HT}$) and tissue extensibility $\lambda^*$.**

*Polarized Spatial Frequency Domain Imaging (pSFDI):* The specimens were illuminated using an LED projector coupled with a light polarizer. The back-scattered light intensity response was imaged at a series of polarization states (0°-180°, every 5°) at several loading points of the biaxial tension ratios. The reflective intensity of each loading state

was fitted with a 3-term Fourier series in MATLAB (MathWorks) to determine the degree of optical anisotropy (DOA, that describes the collagen fiber alignment). Changes in the DOA were also quantified to explore an increase/decrease in the collagen fiber alignment [5].

*Multiphoton Microscopy*: The specimens were optically cleared in a graded 1:2 BABB solution (50/50% ethanol/BABB and 100% BABB, each solution for 30 min, twice). The specimens were then imaged using a confocal microscope (Leica SP8) with a multiphoton laser for autofluorescence imaging (excitation: 830 nm, emission: 500-550 nm). The vascular wall was imaged in a 2 µm thickness resolution and a field of view of 290x290 µm.

*Statistical Analysis*: Quantities are shown as mean±standard error of the mean. The data was tested for normality and compared using applicable statistical tests, such as ANOVA or aligned rank transform. $p < 0.05$ was considered as statistically significant. All analyses were performed in R software v4.1.1.

## RESULTS

*Arterial Geometry*: The thicknesses for the arterial wall were: 388±27 µm (proximal), 439±42 µm (medial), and 289±10 µm (distal), where the distal region was significantly thinner than the others. The LADA diameter was reduced along the proximal-to-distal direction ($p<0.001$): 3.05±0.06 mm, 2.58±0.07 mm, and 2.27±0.11mm for the proximal, medial, and distal regions, respectively.

*Biaxial Stress-Stretch Behavior*: The LADA tissues exhibited a non-linear anisotropic response, with minimal hysteresis [6]. The specimens were compliant at low levels of stress, before reaching a transition point, where the stress increased exponentially. The longitudinal peak stretch ($\lambda^P$) did not vary across the LADA regions (average: 1.31±0.01), while the circumferential $\lambda^P$ was 1.30±0.02, 1.25±0.02, and 1.27±0.03 for the proximal, medial, and distal regions. Further, $\lambda^*$ was homogeneous across regions and loading directions with an average of 1.19±0.01. The distal region was the least extensible.

For the $T_{CC}$:$T_{LL}$= 1:0.5 loading ratio, which accurately mimics the stresses of thin-walled vessel models, $\lambda^*$ was 1.24±0.02, 1.19±0.02 and 1.21±0.02 for the proximal, medial, and distal regions. On the other hand, $\lambda^*$ in the circumferential direction was significantly greater than the one in the longitudinal direction (1.21±0.01 vs. 1.14±0.01; $p < 0.001$). The general average of $E^{LT}$ was 217.53±20.26 kPa, which did not vary across the loading directions and regions, whereas $E^{HT}$ for the circumferential direction was 1986.37±110.43 kPa, greater than the longitudinal $E^{HT}$ of 881.05±64.28 kPa ($p < 0.001$). In addition, the distal region exhibited greater $E^{HT}$ than the other LADA regions, but significance was not reached ($p = 0.14$).

*Microstructure Results*: pSFDI allowed the quantification of the *load-dependent* changes in the collagen architecture of LADA tissues. We observed that the DOA increases in all regions from Loading Point 1 (unloaded) to Loading Point 5 (peak biaxial tensions), $p < 0.001$. Further, DOA increase was more pronounced in the distal-to-proximal-direction ($p < 0.001$), indicating a higher degree of fiber recruitment in response to the load (**Fig 2.**). Moreover, multiphoton microscopy allowed us to understand the microscopic collagen/elastin organizations for the tissue. The tunica adventitia of the proximal region exhibited the traditional random distribution of fibers (**Fig. 3**). However, the tunica media exhibited a transition where the fibers became better aligned towards the longitudinal direction. This re-orientation further progressed into the distal region, where the fibers were found to be almost parallel in this direction. This behavior was observed throughout the entire layer depth, as demonstrated in the heatmaps (**Fig. 3**).

## DISCUSSION

The LADA tissue wall mechanics have been previously reported using a myriad of methods. However, its regional variations have not been fully characterized, limiting a comprehensive understanding of the regional requirements for the design of TEVGs for CABG that accurately mimic the native LADA. Given the significant geometrical differences between the LADA regions, we have characterized a uniquely varying microstructure of the vessel. These changes may be attributed by a series of factors: (i) the LADA, as all other coronary arteries, is of proepicardial origin and they penetrate the aorta at the last stages of the heart development, indicating that the proximal region, being the connection to the main left coronary artery, may serve as a transition to a LADA-specific microstructure; (ii) the LADA inward motion during the cardiac cycle [7] might induce a reorientation of the fibers of the adventitia at the distal section.

Previously, the LADA microstructure was assumed to have a homogeneous fiber arrangement in the entire artery. In this study, we demonstrate the unique mechanical, microstructural and load-dependent properties of the LADA across the vessel length. Our novel findings in this work elucidate the importance of the subtle microstructure, mechanical properties, and geometry that need to be holistically considered for the design of effective and durable TEVGs.

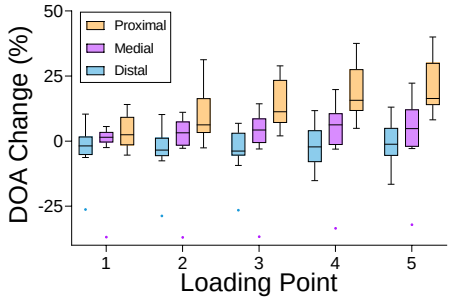


**Figure 2: Load-dependent changes of the fiber alignment (DOA) in the characterized LADA specimens – $T_{CC}$:$T_{LL}$= 1:0.5 loading ratio.**

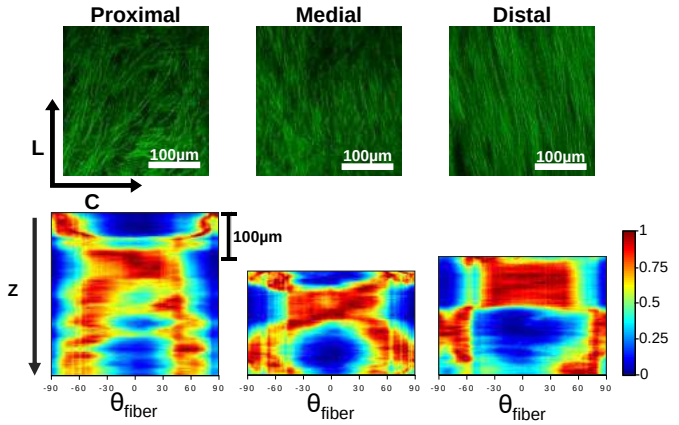


**Figure 3: (*top*) Multiphoton microscopy images of the tunica adventitia of the LADA regions. (*bottom*) Heatmap representation of the normalized fiber frequency across the depth of LADA.**


## ACKNOWLEDGEMENTS

OU's VPRP Institutional Support is greatly appreciated.


## REFERENCES


[1] Virani *et al. Circulation*. 141(9): e139-e596, 2020.
[2] Dimitrievska *et al. Cold Spring Harb Persp Med*. 8: a025742, 2018.
[3] Ravulapalli *et al. Ann Card Anaesth.* 13(3) 231-235, 2010.
[4] Jett *et al. J Mech Behav Biom Mat.* 87. 155-171, 2018.
[5] Jett *et al. Acta Biomater*. 102. 149-168, 2020
[6] Holzapfel *et al. Am J Physiol Heart Circ Physiol*.289.248-258, 2005.
[7] Shechter *et al. IEEE Trans Med Imaging.* 25(3): 369–375, 2006.

# PREDICTING HEMODYNAMIC INDICES IN CORONARY ARTERY ANEURYSMS USING RESPONSE SURFACE METHOD: AN APPLICATION IN KAWASAKI DISEASE

**A. Asadbeygi (1), S. Lee (2), J. Kovalchin (2), and H. Hatoum (1,3)**

(1) Department of Biomedical Engineering, Michigan Technological University, Houghton, Michigan, United States
(2) Department of Pediatrics, Nationwide Children's Hospital, Columbus, Ohio, United States
(3) Health Research Institute, Center of Biocomputing and Digital Health and Institute of Computing and Cybernetics, Michigan Technological University, Houghton, MI, USA

## INTRODUCTION

Coronary artery aneurysms (CAA) describe local dilatations of the coronary artery that exceed 1.5 the neighboring artery diameter. The prevalence of CAA ranges from 0.3 to 5% [1]. The pathogenesis of CAA is not well understood however, several factors come into play such as certain vasculitic and connective tissue diseases such as the Kawasaki disease (KD) [1]. CAAs are mostly not accompanied by symptoms and their finding is usually incidental. However, clinical symptoms can appear due to the presence of concomitant atherosclerotic disease or local thrombosis in the large CAAs among others causes, leading to angina and myocardial infarction [1].

Literature has shown that the blood flow stagnation and sluggish flow are correlated with thrombosis and atherosclerosis [2]. Several patient-specific computational fluid dynamics (CFD) and experimental investigations to analyze the flow and risk level of CAA cases based on hemodynamic indices were performed [3,4,5]. However, the effect of different aneurysm shape indices and resulting flow parameters on local hemodynamics in CAAs is not systematically investigated yet.

The goal of this study was to investigate the effect of CAA shape indices on local hemodynamics using the response surface method (RSM) through considering KD applications at rest (normal conditions) and during exercise. CFD was performed on idealized controlled geometries where different aspect ratios were considered. Regression models of time averaged wall shear stress (TAWSS), oscillatory shear index (OSI), and relative residence time (RRT) were developed. These models can be used as valuable tools to obtain a real-time assessment of CAA local hemodynamics and resulting risk stratification based on fusiform aneurysm shape indices.

## METHODS

An idealized aneurysm 3D model defined by a sinus curve was designed based on three geometrical parameters, similar to the works of Martufi et al. [6]. After that, the maximum and minimum values of these parameters were set according to previous clinical measurements in KD patients [7] (Table1). Then a Central Composite Design (CCD) design of experiments consisting of 15 cases was created in MINITAB software, and the corresponding geometries were generated in SOLIDWORKS (Figure1). A, B, and C are the linearly scaled parameters of Dneck, Dmax/Dneck, and L/Dmax in the interval [-1,1], respectively.

**Table 1: Maximum and minimum values of shape indices. A, B, and C are the scaled parameters of Dneck, Dmax/Dneck, and L/Dmax in the interval [-1,1], respectively.**

| | Levels | | | | |
|---|---|---|---|---|---|
| **Parameters** | 1 | 2 | 3 | 4 | 5 |
| A,B,C | -1 | -0.594 | 0 | 0.594 | 1 |
| Dneck(mm) | 2 | 2.6 | 3.5 | 4.39 | 5 |
| Dmax/ Dneck | 1.2 | 1.97 | 3.1 | 4.22 | 5 |
| L/ Dmax | 1 | 1.3 | 1.75 | 2.195 | 2.5 |

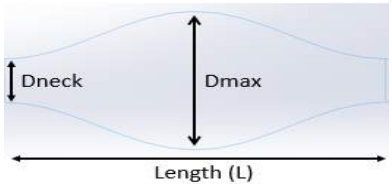


**Figure 1: schematic of idealized CAA.**

To develop the CFD simulations, CAA models were imported to ANSYS MESH and the computational domains were discretized. Then ANSYS CFX package was used to run the simulations. Velocity and pressure waveforms of the left coronary from Kim et al. [8] works were extracted and set as the inlet and outlet boundary conditions, respectively. In order to investigate the hemodynamic alteration in

exercise conditions, all the simulations at rest "normal" conditions (75 bpm) were repeated using new boundary conditions scaled to 120 bpm with an average velocity of 1.5 times the previous one. The arterial wall was assumed to be rigid, and the Carreau model was used to model the non-Newtonian behavior of blood [9]. TAWSS (Pa), OSI, and RRT ($Pa^{-1}$) are the most common hemodynamic indices studied in the literature, which are defined by the following equations with T being the cardiac cycle duration in seconds:

$$TAWSS = \frac{1}{T} \int_0^T |WSS| \, dt \quad (1)$$

$$OSI = \frac{1}{2}\left(1 - \frac{\left|\int_0^T WSS \, dt\right|}{\int_0^T |WSS| \, dt}\right) \quad (2)$$

$$RRT = \frac{1}{(1-2\times OSI)\times TAWSS} \quad (3)$$

In order to have a quantitative assessment of hemodynamics in CAAs, these indices were calculated in each case. For TAWSS and RRT, the thresholds adopted were 0.4 Pa and 4.15 $Pa^{-1}$, respectively[10]. These thresholds are correlated with the risk of thrombosis and atherosclerosis and were applied to the numerical values using RSM. Ideally, high TAWSS and low OSI and RRT are desired.

## RESULTS

Based on the obtained results for the CCD, full quadratic regression models were developed for each of the hemodynamic indices using RSM analysis in MINITAB. These models and the respective $R^2$ values are shown in Table 2. Based on analysis of variance for TAWSS and RRT models, B and A were found to be the most significant parameters with P-values of 0.0001 and 0.002 respectively ($p<0.05$). Hence, we plotted the contours that show the variations of TAWSS and RRT as A and B vary. We would like to emphasize that A and B should be in the linearly scaled format (ranging from -1 to 1 as explained in the methods section). The contour plots highlighting the effect of two input parameters (Dneck and Dmax/Dneck) on the mean TAWSS and mean RRT in exercise conditions is shown in Figure 2. For TAWSS and RRT, the thresholds adopted were 0.4 Pa and 4.15 $Pa^{-1}$, respectively[10]. It is clear from Figure 2 that exercise conditions lead to different effects as compared to normal or at rest conditions. For a Dmax/Dneck ratio less than 2 (considered defining of small aneurysms, and equivalent to B < -0.594 in the linearly scaled system), the TAWSS was shown to increase under exercise conditions irrespective of the absolute neck size (Figure 2, top row). Meanwhile, for the RRT, exercise conditions led to an increase of mean RRT for Dmax/Dneck ratios less than 2, depending on the absolute neck size as shown in Figure 2, bottom row. For Dmax/Dneck ratios > 2, higher mean RRT were generally obtained, however, also dependent on neck size. TAWSS generally increased under exercise conditions regardless of the geometry.

## DISCUSSION

In this study, a parametric CFD quantification of CAA was performed, and regression models of 2 hemodynamic metrics (Table 2) under normal at rest conditions and under exercise conditions were developed using the response surface method. The analysis of variance illustrates that the diameter of the artery before and within the aneurysm area is the most significant shape index affecting the local hemodynamics. This fact strongly highlights the importance of coronary Z-score as the gold standard in KD assessment of severity and treatment [11]. Our results show that the small aneurysms (low Dmax/Dneck) experience very high RRT values under exercise conditions (Figure 2), which is a neglected risk factor in Z-score criteria. The elevated RRT in small aneurysms lends credence to the recommendation to continue aspirin treatment in case of diagnosis, even in small aneurysms. These findings highlight the importance of computational tools to achieve a general understanding of the hemodynamics in CAA. Although some patient-specific studies in KD have been done in recent years, there is not any fast and affordable computational framework for real-time evaluation of hemodynamics in CAA. The proposed regression models can be used as a fast and straightforward estimator to assess the severity and risk level of CAAs, especially in KD patients. It's worth mentioning that these results are limited to idealized symmetric aneurysm models. This methodology can be implemented in more complicated asymmetric models in future works. Ongoing work includes model development using patient-specific data.

**Table 2: Regression models (N: Normal, at rest E: Exercise).**

| | | Regression models | $R^2$ |
|---|---|---|---|
| Mean TAWSS (Pa) | N | 0.803 - 0.2861 A - 0.5522 B + 0.0363 C + 0.136 A*A + 0.297 B*B - 0.072 C*C+ 0.119 A*B + 0.064 A*C + 0.048 B*C | 97.21 |
| | E | 1.347 - 0.5006 A - 0.9775 B + 0.1011 C + 0.268 A*A + 0.563 B*B - 0.096 C*C+ 0.300 A*B - 0.039 A*C - 0.064 B*C | 97.9 |
| Mean RRT (1/Pa) | N | 4.586 + 2.677 A + 5.256 B - 1.289 C + 0.402 A*A + 1.930 B*B + 1.316 C*C+ 3.563 A*B - 1.225 A*C - 3.139 B*C | 98.2 |
| | E | 4.86 + 16.54 A + 15.78 B - 7.38 C + 14.7 A*A + 11.8 B*B - 2.0 C*C + 22.47 A*B - 16.48 A*C - 19.04 B*C | 89.76 |

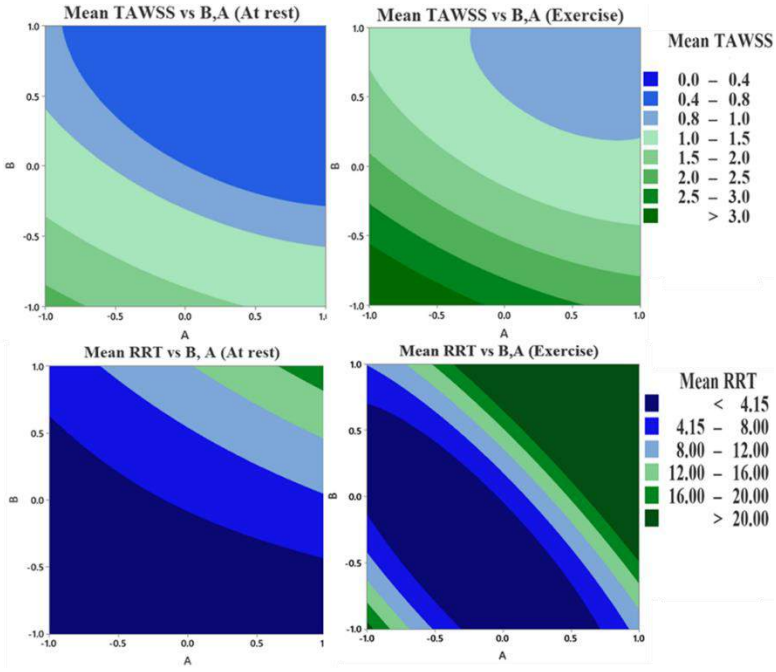


**Figure 2: Mean TAWSS and RRT vs B and A in normal (at rest) and in exercise conditions.**

## REFERENCES


[1] Kawsara, Akram, et al. JACC: Cardiovascular interventions (2018)
[2] Abou Sherif, Sara, et al. Frontiers in cardiovascular medicine (2017)
[3]Grande Gutierrez, N et al., Glob Cardiol Sci Pract. 2017.
[4] Sengupta, D, et al. BMMB (2014)
[5] Kung, E, et al. CVET (2014).
[6] Martufi, G et al.,ASME. J Biomech Eng. June 2009.
[7] Bang, JS et al., Korean Circ J. 2017 Jul;47(4):516-522.
[8] Kim, H et al.,Annals of biomedical engineering. 38. 3195-209.
[9] Lockie, T et al., *J Invasive Cardiol*, *25*, 549-550.
[10] Chiastra, C et al., J Biomech. 2017 Jun 14; 58:79-88.
[11] McCrindle BW, et al. Circulation 2017; 135:e927.

# OPEN-SOURCE AUTOMATION OF PATIENT-SPECIFIC ATHEROSCLEROTIC ARTERIES REVEALS KEY BIOMECHANICALLY DRIVEN REMODELING

**Jeremy Warren (1), John Yoo (1), Federico Bernardoni (2), Brandon Boren (2), Clark Meyer (1), Stefano Leonardi (2), Heather Hayenga (1)**

(1) Department of Bioengineering, University of Texas at Dallas, Dallas, Texas, United States
(2) Department of Mechanical Engineering, University of Texas at Dallas, Dallas, Texas, United States

## INTRODUCTION

Despite advancements in early detection, imaging, and innovative treatments, atherosclerosis remains the leading cause of death across all cardiovascular disease (CVD). Clinical treatment decisions rarely consider biomechanics of the stenosed lesion due to the difficulties in obtaining this information; Even though biomechanical analysis of atherosclerotic lesions has been linked to increased likelihood of an adverse cardiovascular event [1]. Understanding the inherent biomechanics in atherosclerotic plaques is critical and a deeper interpretation will pave the way for more effective treatment plans, medication, and overall quality of life for coronary artery disease (CAD) patients. Previously, finite element analysis (FEA) has been used to determine stresses and strains within linear 2D artery models and non-linear materials or homogenous approximations of heterogenous tissues. Our novel, open-source tool automates the creation of anatomically accurate 3D models of arterial geometry with volumetric plaque composition using patient-specific virtual histology-intravascular ultrasound (VH-IVUS) data. The arterial geometry is integrated with in-house computational fluid dynamics (CFD) code to model hemodynamics and leukocyte transport, FEBio to model the internal stresses via FEA, and an agent-based model for growth and remodeling. Understanding patient-specific arterial mechanics can aid in personalized treatment care and the livelihood of patients.

## METHODS

A 6-month longitudinal dataset of 20 patients, with angiogram data and VH-IVUS images, were provided by Emory University. This dataset was used for creating our mesh creation code and validation. The following subsections outline mesh creation and FEA and CFD setup.

### Mesh Creation

Before FEA and CFD can be performed, a mesh of the patient's arterial geometry must be generated. To do so, VH-IVUS images are filtered to remove background noise and the plaque constituent data is extracted. The lumen and outer profiles are outlined, oriented along the 3D centerline, and lofted sequentially to create the surface mesh. This mesh is smoothed and resampled to create a uniformly distributed triangular surface mesh [**Figure 1**]. The surface mesh is then tetrahedralized to generate the volumetric finite elements necessary for FEA. These finite elements are assigned materials using data extracted from the VH-IVUS images.

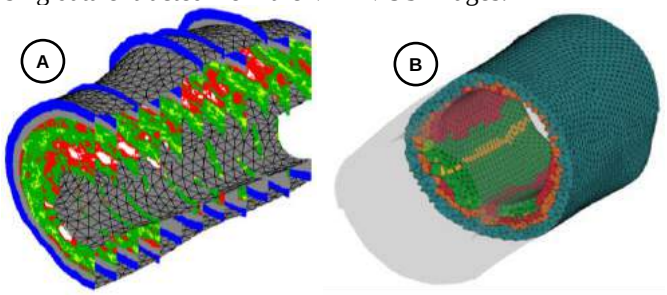


**Figure 1: Surface and Volumetric Mesh Generation**
**A**. The outer and luminal surface profiles extracted from VH-IVUS images are used to create the surface mesh. **B**. The surface mesh is tetrahedralized using open-source TetGen and the resulting elements are assigned a material using the VH-IVUS data.

## FEA Setup

Once associated with a tissue type, we use literature-derived values for Neo-Hookean materials [**Table 1**]. Although literature has shown that Mooney-Rivlin material models are best suited for describing the shear deformation in elastic materials [2], Neo-Hookean material models are acceptable for non-contact simulations. Boundary and loading conditions for the analysis consist of fixed nodes on inlet and outlets surfaces of the mesh, and a physiological pressure of 16 kPa on the lumen surface.

| Tissue Type | Young's Modulus [MPa] | Poisson's Ratio |
|---|---|---|
| Arterial | 0.3 | 0.48 |
| Fibrotic | 0.6 | 0.48 |
| Fibrofatty | 0.5 | 0.48 |
| Calcium | 10 | 0.48 |
| Necrotic | 0.02 | 0.48 |

**Table 1: Material Properties**

Neo-Hookean material properties used in the FE model.

## CFD Setup

The luminal surface mesh is passed to the in-house CFD code which solves the Navier-Stokes and continuity equations using a finite difference scheme coupled with a Runge Kutta algorithm for the time integration. Immersed Boundaries [3] are used to model the real geometry of the artery. The results from CFD are combined with a set of literature-derived rules to model leukocyte adhesion and transendothelial migration (TEM) [4].

## RESULTS

In a representative patient, mean von-mises effective stress was ~210 kPa with a peak stress of 597 kPa [**Figure 2**].

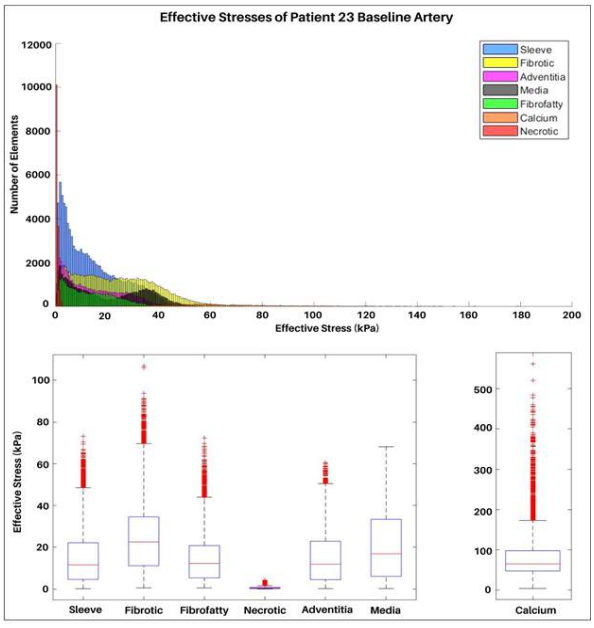


**Figure 2: Effective Stress Results**

Calcium elements present the highest average stress. When stiff calcium elements are adjacent to significantly softer tissues, large strains develop between them, resulting in higher stress in these areas.

## FEA

Areas of high stresses reside only around calcium while stresses around other tissues averaged below 100 kPa. In determining potential rupture, calcium content and location in the artery wall help identify potential sites of rupture. In addition to calcium, we use the widely accepted threshold of 300 kPa to determine regions where a rupture can occur. For this particular patient, the mean stress for micro and macro-calcifications were below the rupture threshold and were generally located >65μm from the lumen. Since this patient's plaque did not rupture, this suggests that plaque rupture is dependent on location, magnitude of stress, and calcium content.

## CFD

Post-analysis of CFD results revealed regions with low wall shear stress (WSS), below 4 kPa, correlated with increased rates of leukocyte adhesion and plaque growth over 6 months [5].

## DISCUSSION

Preliminary results from FEA reflect stresses seen in other studies and the leukocyte adhesion and hemodynamics agree well with clinical data inferred from baseline and six-month follow-up exam of the same artery [6]. Our current aim is to determine the impact of wall mechanics and biological factors on plaque remodeling. We plan to fully couple the CFD, ABM, and FEA to develop a comprehensive, well informed multi-physics growth and remodeling model. In addition, we plan to incorporate more patient-specific data as input to the model and validate our post-analysis techniques when determining potential rupture regions. A better understanding of the underlying factors and how they affect each other will validate previous models and drive future research on other frameworks.

## ACKNOWLEDGEMENTS

Authors gratefully acknowledge funding for this work provided by the American Heart Association (17SDG33400239) and by the National Heart, Lung, And Blood Institute of the National Institutes of Health under Award Number R01HL136776. The content is solely the responsibility of the authors and does not necessarily represent the official views of the National Institutes of Health. Emory University (ClinicalTrials.gov; Identifier: NCT00576576) for the data set used in this study. UTD (University of Texas of Dallas) Department of Bioengineering for startup funds. Vascular Mechanobiology Lab for providing opportunity to work on this research through the guidance of Dr. Hayenga, the lab director.

## REFERENCES

[1] Kelly-Arnold A. et al, *Proc Natl Acad Sci*, 2013.
[2] Zahnd, G. et al, *Int J CARS*, 11:1779–1790, 2016.
[3] Orlandi, P & Leonardi, S., *Journal of Fluid Mechanics*, 2008.
[4] Bhui, R. & Hayenga, H., *PLoS Computational*. 13:5, 2017.
[5] U. Ciri et al., *Scientific reports*, 11:12680, 2021.
[6] Bailey AM. et al., *Ann Biomed Eng*, 35(6):916, 2007.

SB³C2022
Summer Biomechanics, Bioengineering and Biotransport Conference
June 20-23, Eastern Shore, MD, USA

# INCREASED NUCLEAR COMPLIANCE ENABLES RAPID CONFINED MIGRATION IN MESENCHYMAL GLIOBLASTOMA

**Landon Teer (1), Neha Anil (1), Dominic Armagno (1), Marco Munoz (1) Shah Tarun (1), Sam Vielee (2) Joseph Chen (1,2)**

(1) Department of Bioengineering, University of Louisville, Louisville, KY, USA
(2) Department of Pharmacology and Toxicology, University of Louisville, Louisville, KY, USA

## INTRODUCTION

Glioblastoma (GBM) is an incurable and highly aggressive cancer with a dismal prognosis of 15-months. [1] GBM progression is coupled with a proneural-to-mesenchymal transition (PMT), a molecular event consisting of a phenotypic shift that leads to heightened invasive potential and disease evolution. These events mirror the epithelial-to-mesenchymal transitions (EMT) seen in other types of cancers, which lead to increased metastasis and poorer prognosis. [2] Increased invasiveness in mesenchymal GBM notably occurs despite the presence of tight, physical barriers in the dense brain parenchyma, suggesting potential biophysical alterations that have yet to be elucidated. Recent studies have revealed that more invasive cells can navigate these confined microenvironments by significantly deforming their cell body; however, the details underlying these physical changes remain unclear. Here, we examine this phenomenon through a biophysical lens by investigating the relationship between mesenchymal transformation in GBM and mechanical alterations and its subsequent functional effect on confined migration.

We hypothesize that TGF-β1 promotes efficient confined migration by activating mesenchymal pathways to induce PMT, which may result in mechanical softening of the cells, especially in their nuclear regions, thus allowing them to rapidly bypass the tight, natural barriers in the brain microenvironment. In this study, we induced mesenchymal transitions via TGF-β1 and evaluated changes in cytoskeletal and nuclear protein expression, mechanical rigidity, and functional confined migration. Our data suggests an important role of the nucleus in enabling cell deformation and confined migration. These data reveal the biophysical alterations that arise from mesenchymal transformation, providing new insights into mechanical features of aggressive glioblastoma.

## METHODS

GBM cells were treated with 10 ng/mL TGF-β1 for 72 hours preceding all experiments. Western blots were used to confirm mesenchymal pathway activation (pSmad2, pSTAT3, ZEB1), and evaluate nuclear and cytoskeletal protein expression (Lamin A/C, F-Actin/G-Actin). To assess changes in biophysical properties, AFM was utilized to quantify the effect of mesenchymal transitions on the nucleus and cytoskeleton mechanics. The functional consequence of cellular stiffness changes was examined via PDMS microchannel platforms consisting of 1D channels at multiple widths (5 μm, 10 μm, 20 μm, and 50 μm). Confined migration experiments were conducted via time lapse microscopy on a Nikon Eclipse TE2000-U.

## RESULTS

TGF-β1 was sufficient to induce mesenchymal transitions within GBM cell lines. First, we verified TGF-β1 activation via Smad2 phosphorylation (Figure 1A). Then, we evaluated mesenchymal marker Stat3 and mesenchymal transcription factor ZEB1. As expected, TGF-β1 led to significant increases in both Stat3 phosphorylation and ZEB1 expression (Figure 1B, C), indicating a mesenchymal phenotype. To assess the biophysical changes that may be attributed to mesenchymal transitions, we wondered how structural proteins in the nucleus and cytoskeleton may be affected. TGF-β1 treatment led to decreases in Lamin A/C expression, although the difference was not significant (Figure 1D); however, we observed unexpected pore-like structures in the nuclei of the TGF-β1 treated cells that were not seen in the non-treated (NT) cells (Figure 1E). Further, we found that the ratio of F-actin to G-actin was dramatically reduced in treated cells, indicating that TGF-β1 treatment disrupted cytoskeletal organization and increased pools of depolymerized actin (Figure 1F).

SB³C2022-120

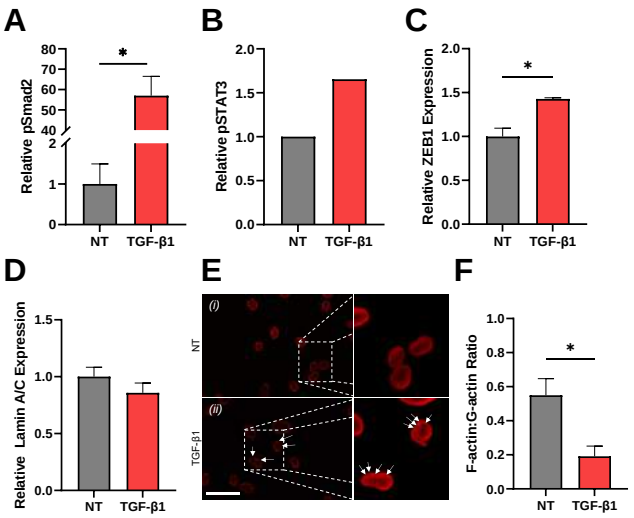


**Figure 1: TGF-β1 activates canonical signaling (A) and STAT3 signaling (B), leading to increases in ZEB1, a mesenchymal transcription factor (C). Additionally TGF-β1 cells displayed reduced Lamin A/C expression and aberrant organization (D, E) along with a significant decrease in F-actin/G-actin ratio (F).**

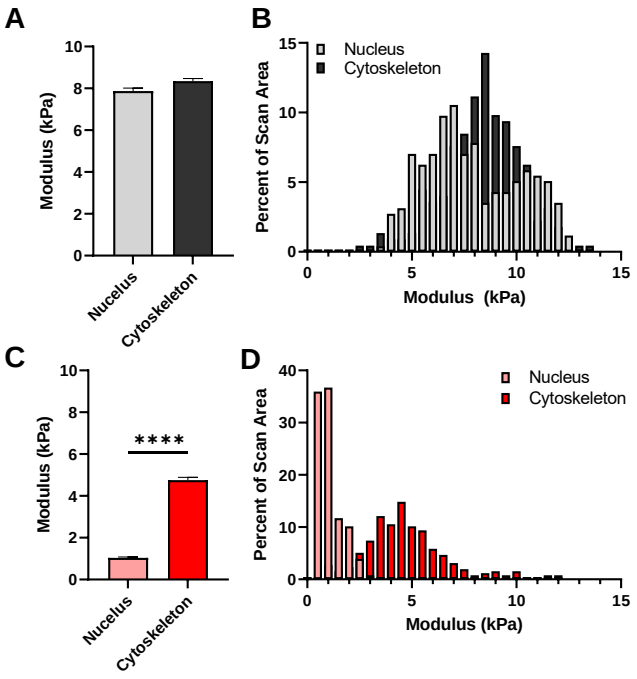


**Figure 2: AFM analysis reveals that TGF-β1 treatment significant reduces nuclear and cytoskeletal stiffness (A,C). Histograms illustrate that nuclear stiffness is more dramatically reduced in treated groups with > 60% of the scan area exhibiting a stiffness of < 1 kPa (B,D).**

We employed AFM to determine how protein level changes to the nucleus and cytoskeleton might affect cell rigidity. We found that cellular stiffness was reduced in the TGF-β1 treated group in both the nucleus and the cytoskeleton (Figure 2 A-D). Intriguingly, the relative nuclear stiffness was dramatically reduced while the decrease in cytoskeletal stiffness was less pronounced (Figure 2 B, D).

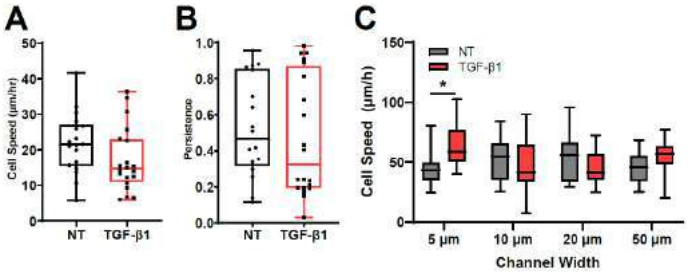


**Figure 3: 2D motility assays show minimal differences between NT and TGF-β1 treated GBM cells (A, B); however, microchannel platforms reveal that upon encountering tight physical constrictions in 5 μm channels, TGF-β1 treated cells exhibit a significant increase in cell speed whereas NT cells displayed a reduction in cell speed (C).**

We then evaluated the functional changes in NT and TGF-β1 treated cells using 2D motility assays and microchannel platforms. Interestingly, 2D cell speed and persistence did not change significantly in TGF-β1 treated groups (Figure 3 A, B). Using microchannel platforms, we found that while NT cells struggled to migrate under tight constriction (5 μm), TGF-β1 cells surprisingly displayed enhanced migration speed in 5 μm channels (Figure 3 C).

## DISCUSSION

In this study, we demonstrate that TGF-β1 induced mesenchymal transitions are coupled with changes to the nucleus and cytoskeleton, with reductions in Lamin A/C expression and F-actin G-actin ratios. Moreover, we provide evidence that the nuclear organization is altered with the presences of pores surrounding the nuclear membrane. Further, we demonstrate via AFM mapping that TGF-β1 treatment reduces cell rigidity in both nuclear and cytoskeletal compartments. Notably, the nuclear stiffness was reduced more substantially when compared to the cytoskeleton, which may provide the basis for efficient migration through confined spaces. We then show through microchannel platforms that TGF-β1 treated cells more easily navigate constrained environments by exhibiting more rapid cell migration speed under these conditions.

This study uncovers a novel relationship between mesenchymal transitions and mechanical rigidity and adds to the growing appreciation for the impact of cell mechanics on cancer aggressiveness. Deeper investigations of this relationship may aid in the development of novel diagnostic tools and help identify new targets for pharmacological intervention.

## ACKNOWLEDGEMENTS

The authors gratefully acknowledge the Huson Imaging & Characterization Laboratory at the University of Louisville.

## REFERENCES

[1] Omuro, A. and DeAngelis, L.M., JAMA, 310(17): 1842-50, 2013
[2] Fedele, M., et al. International Journal of Molecular Sciences, 20(11): 2746, 2019

SB³C2022
Summer Biomechanics, Bioengineering and Biotransport Conference
June 20-23, Eastern Shore, MD, USA

# THE FAILURE MECHANISM OF MOUSE SKIN: A MULTISCALE PERSPECTIVE

**Nathan J. Witt[1], Alan E. Woessner[2], Kyle P. Quinn[2], Edward A. Sander[1]**

[1]Department of Biomedical Engineering,
University of Iowa, Iowa City, IA, 52242, USA

[2]Department of Biomedical Engineering,
University of Arkansas, Fayetteville, AR, 72701,
USA

## INTRODUCTION

The skin's biomechanical properties are dependent primarily on organization of collagen and other extracellular matrix (ECM) proteins in the dermis. With aging or disease, significant changes to the dermal layer can occur, altering the skin's mechanical function and the mechanobiological conditions necessary for normal ECM turnover. For example, as skin ages the dermal layer experiences fragmentation of the collagenous microstructure [1], a reduction in ECM remodeling [2], and an increased susceptibility to tissue injury and failure [3]. We have combined multiscale experiments of mouse skin with image-based multiscale mechanical models (MSM) that can predict the non-affine fiber kinematics observed under uniaxial tension prior to and during the progression of tissue failure. We are now using these models to understand and predict the age-dependent tissue failure observed experimentally in mouse skin and the corresponding mechanical basis for the loss of mechanical function.

## METHODS

**Experiments:** Dog-bone shape murine skin was gripped in a bioreactor mounted on a multiphoton microscope (MPM) [4]. The samples were notched in the gauge region to promote failure at the location where microstructural MSM imaging occurred. Samples were deformed uniaxially at a rate of 0.2 mm/min until failure. At each half mm of displacement, stretching was paused, and MPM image stacks of the collagen microstructure were acquired to create a mosaic of the region between the inner fiducial markers (Fig. 1). Quantification of tissue kinematics and changes in microscale directional variance (DV) were also made [ 5].

**Simulation:** To-scale image-based multiscale models (MSMs) were created from the geometry of the inner gauge region of the sample prior to testing as in previous work [6,7]. These models link the macroscopic domain of the model to microscopic fiber networks representative of the collagen microstructure via volume averaging theory [8]. A finite element (FE) mesh of 89 linear hexahedral FEs was then generated (one FE through the thickness). At the microscale, the volume fraction of the fibers and their DV approximated the average of the tissue's microstructure at 24% and 0.68, respectively. To represent the skin's non-collagenous matrix an additive stress from a compressible neo-Hookean material (G = 3.0 kPa, ν = 0.1) was included. Failure at the microscale was implemented by removing fibers when their stretch ratios exceeded 2.35. Parameters in the fiber-level constitutive equation were chosen to closely match the experimental loading curve.

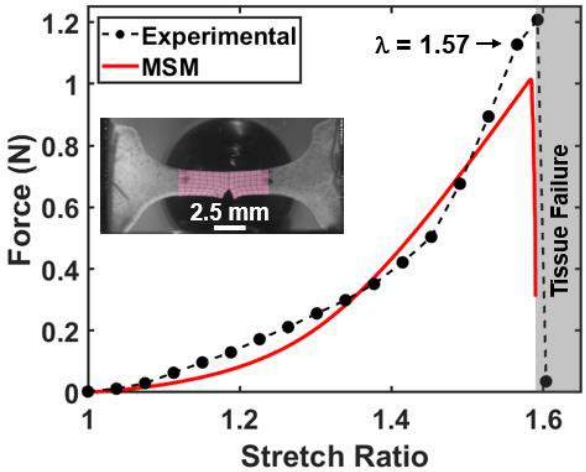


**Fig. 1. The multiscale model predicted a similar force curve and stretch ratio at which failure occurred as in the experiment. The last MPM image of the microstructure occurred at λ = 1.57.**

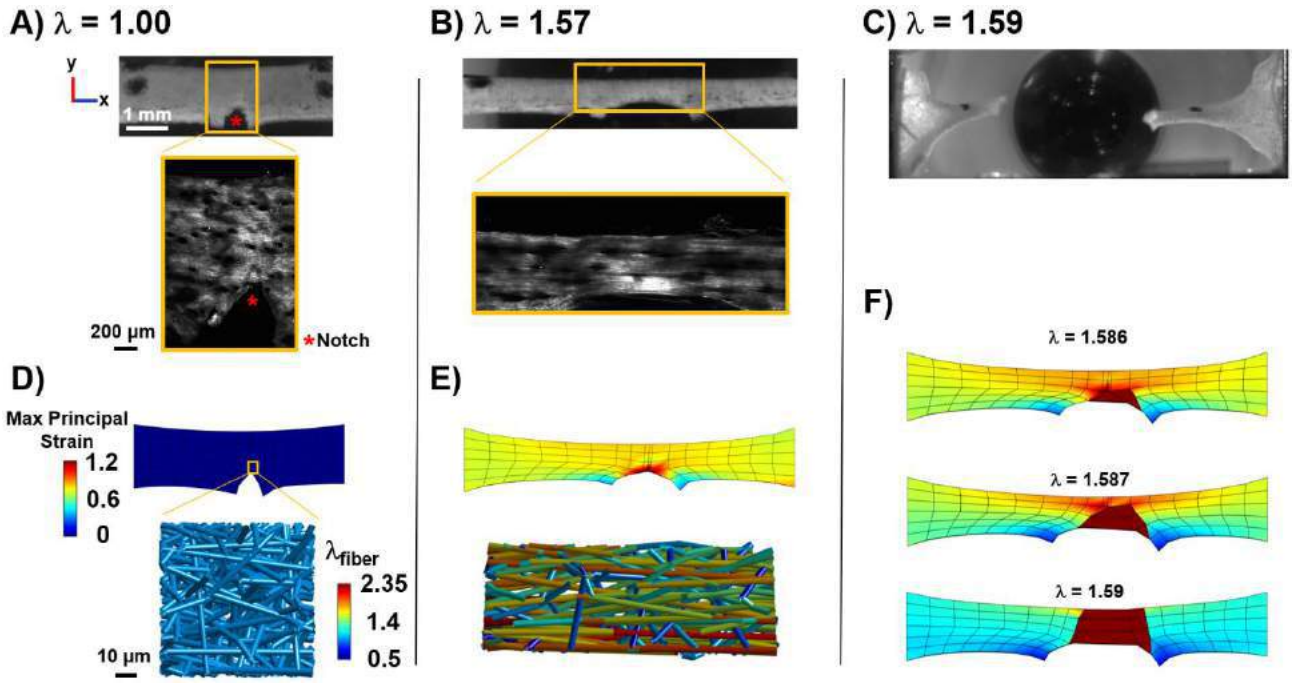


**Fig 2. (A) Macro- and microscale images of a sample show the notch and the organization of collagen. (B) As the tissue stretches collagen aligns in the direction of loading until (C) failure occurs. (D) Model predictions show the maximum principal strain and fiber stretch ratios for experimentally equivalent levels of stretch are concentrated (E) at and around the notch. (F) A zipper like tear from the notch is predicted to occur over a short period.**

## RESULTS

Macroscopically, the model deformed similarly to the sample (Fig. 2), including the manner in which the notch stretched before eventually tearing. Microscopically, and at a location adjacent to the apex of the notch, collagen reorientation into the directional of loading progressively increased while the tissue resisted tearing, consistent with experimental observations. Furthermore, the model predicted the largest maximum principal strains at the notch apex, where failure proceeded with a zipperlike tear at a similar stretch ratio to the experimental results. The mechanism of tear-resistance predicted by the model was a gradual recruitment of network-fibers into the direction of stretch, followed by increasing axial stretch and then rapid fiber failure (Fig. 3). Once the adjacent networks failed, the load propagated transversely to the next adjacent elements and quickly repeated the process until a complete tear formed. Interestingly, average fiber stretch levels were lower in the elements directly above the element adjacent to the notch (*c.f.*, Fig. 3), suggesting that stress shielding was occurring.

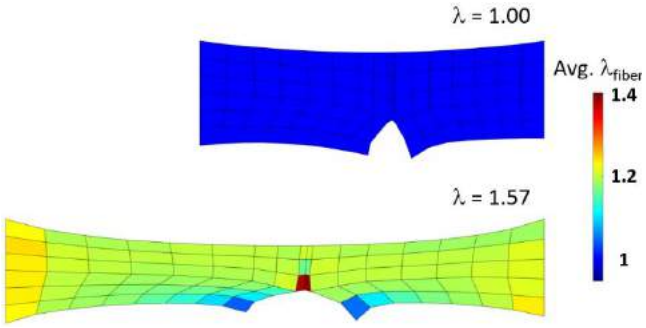


**Fig. 3. The multiscale model predicted large fiber level stretching concentrated at the apex of the notch at λ = 1.57. Comparatively, other regions experienced less fiber-level stretching while fibers at the base of the notch remained relatively unloaded.**

## DISCUSSION

Model predictions produced comparable deformations to the notched sample and reasonably predicted the experimental force at which failure occurred. Tear propagation at the notch was resisted by the ability of the collagen to reorient before recruitment into the direction of tissue stretch. We hypothesize that the increased risk of tissue tearing with aging could arise from a diminished capacity for fiber recruitment. Our combined experimental and computational approach is providing more insight into the mechanical effect of aging on skin and its susceptibility to injury and failure.


## ACKNOWLEDGEMENTS

Support for this work was provided by R01 AG056560. Computational resources were provided by the University of Iowa Argon HPC Cluster.


## REFERENCES


1. Marcos-Garces, V. et al, J Anat., 225(1):98-108, 2014
2. Haydont, V. et al, Mech. Ageing Dev, 117:150-156, 2019
3. Blair, M.J. et al, Adv Wound Care, 9(3):127-143, 2020
4. Woessner, A.E. et al, Front Bioeng Biotechnol, 9:642866, 2021
5. Liu, Z et al., J Biomaterials, 116:34-47, 2017
6. Hadi, M.F. et al, J Biomech Eng., 134(9):091005, 2012
7. Witt, N.W. et al, J Biomech Eng., 144(4):041008, 2022
8. Stylianopoulos, T. et al, JCMA, 196: 2981-2990, 2007

SB³C2022
Summer Biomechanics, Bioengineering and Biotransport Conference
June 20-23, Eastern Shore, MD, USA

# REDUCING SKIN INJURIES INDUCED BY PROLONGED USAGE OF RESPIRATOR MASKS

**R.D. Jobanputra, K.K. Yap, M. Murali, M. Santos, M.A. Masen**

Department of Mechanical Engineering
Imperial College London
United Kingdom

## INTRODUCTION

The prolonged use of respirator masks, such as worn by medical staff during the COVID-19 pandemic and by patients with respiratory conditions, can result in a range of skin issues. These include irritation and injuries such as urticaria, skin tears and pressure injuries, ranging from isolated indentation marks to deep tissue level bruising across a larger area (Fig. 1). The cause of such device-related pressure injuries are the prolonged shear stresses inside the tissue as a result of the interaction between skin and the respirator mask. High friction conditions are elevating these shear stresses further: mask-related skin injury is strongly correlated with heavy sweating and the use of high grade, tight-fitting masks [1]. Healthcare organizations have suggested the application of topical creams and hydrocolloid dressings to reduce skin injury [2]. The purpose of this current study is to evaluate these suggestions and offer more specific solutions to mitigate respirator mask-related skin injury.

**Figure 1: Skin damage following excessive PPE-skin interaction. Source: www.instagram.com/covid_nurses**

Our combined experimental and computational approach consists of three phases:

1) Conducting parametric studies to observe the effects of modifying the respirator mask's geometric, material, and interfacial properties on the skin's damage propensity.
2) Assessing short- and long-term skin friction levels against silicone following the application of commercially available moisturizers/lubricants.
3) Use these results to develop tailor-made, optimized lubricants to reduce interfacial shear forces at the skin-PPE boundary.

## A NUMERICAL INVESTIGATION OF FACE MASKS

### Method

A finite element model was developed [3] to assess the local maximum strain energy density (SED) in the dermis as the result of loading. The SED has been shown to be an indicative measure of skin injury occurring [4], whilst the focus of the investigation is the dermis, because skin bruising, and damage typically involve the rupturing of blood vessels in this skin layer. By performing a parametric study, the effect of changes to the design of the face mask in terms of material (elastic modulus, Poisson's ratio), geometry (thickness and area of skin-mask contact) and the interfacial friction coefficient are investigated.

### Results Summary

All investigated mask properties affect the dermal SED. Figure 2 shows the calculated effects of modulus and friction. The SED reduces when employing softer mask materials, whilst the interfacial friction has a very pronounced effect: reducing the friction in the skin-mask interface strongly reduces friction. Additional findings are that the contact area between the mask and skin should be maximized, whilst the use of a material that exhibits incompressible behaviour (e.g. many elastomers) should be avoided.

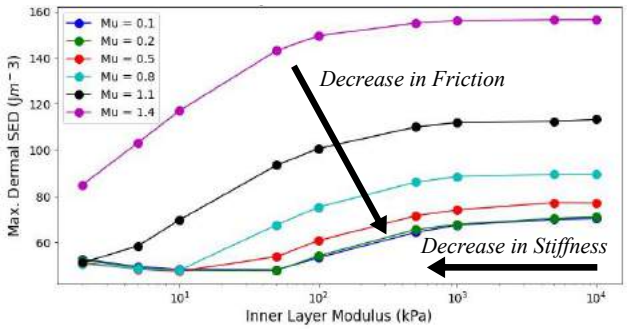


**Figure 2: Effect of changing the modulus and frictional coefficient of the mask's inner layer on the max. dermal SED.**

Friction in the interface between skin and mask was found to be having the largest effect on the SED. There are various methods to reduce the friction, including the application of micro-textures to the mask interface, controlling the humidity in the interface and by applying a lubricant, such as a cream. Whilst the first two options require significant design alterations and are therefore longer-term options, lubricants can be easily implemented.

## ANALYSING COMMERCIALLY AVAILABLE LUBRICANTS

### Method

An extensive literature review identified a range of potential commercially available products that may reduce friction. A custom-built, portable tribometer was used to evaluate the lubricating performance of the substances *in-vivo*. Commercial lubricants were applied to forearm skin before loading the test site with 1.1 N in order to replicate the contact pressures applied by respirator masks. A polydimethylsiloxane (PDMS) probe was rotated against the skin in order to observe friction levels immediately after application of the lubricant, as well as 5 to 10 mins and 4 hours after application.

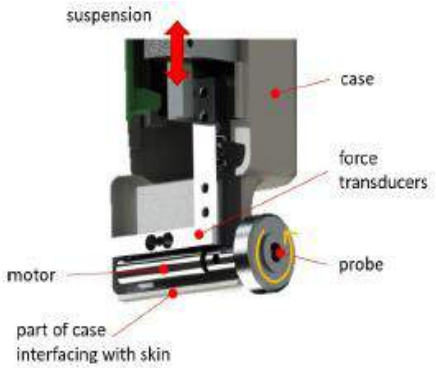


**Figure 3: The portable tribometer**

### Results Summary

Most products provided a strong initial reduction in friction, however only few products provided a long-lasting lubrication effect. Talcum powder, a lubricant comprising a mixture of petrolatum and lanolin, and waxy substance containing coconut oil, cocoa butter and beeswax showed excellent long-term performance. Whilst the short-term performance of the lubricants mainly depends on the shear strength of the applied substance, the longer-term performance also depends on the persistence of the applied product and the response of the skin to the product. Many moisturizing creams function by causing occlusion of the skin, resulting in water retention. This increases friction and should therefore be avoided. Wax-oil lubricants were identified as having the potential to offer significant long term reduced friction, thus reducing the risk of skin injury. The next step is therefore to investigate a range of wax-oil lubricants that provide long-term friction reduction in the skin-respirator interface.

## DEVELOPING AN OPTIMIZED LUBRICANT

### Method

Various wax and oil combinations were created by mixing paraffin wax, beeswax, mineral oil, and olive oil. *In-vivo* friction measurements were performed on 7 participants by sliding a PDMS probe against the volar forearm to simulate the skin-respirator interaction. The maximum static friction coefficient was measured immediately after application of the lubricant, as well as 4 hours after application.

### Results Summary

Figure 4 shows selected results, indicating that endured reduced friction is possible, but this depends strongly on the composition of the lubricant. The friction coefficient is predominantly governed by the ratio of wax and oil, as well as the thermal stability of the wax. Additionally, the absorption of oil into the respirator material must be considered. The best performing lubricant comprises 20 wt% beeswax, 40 wt% olive oil, and 40 wt% mineral oil. In contrast to unlubricated skin, this provides a 87% (P = 0.0006) reduction in friction immediately after application, and a 59% (P = 0.0015) reduction 4 hours after application.

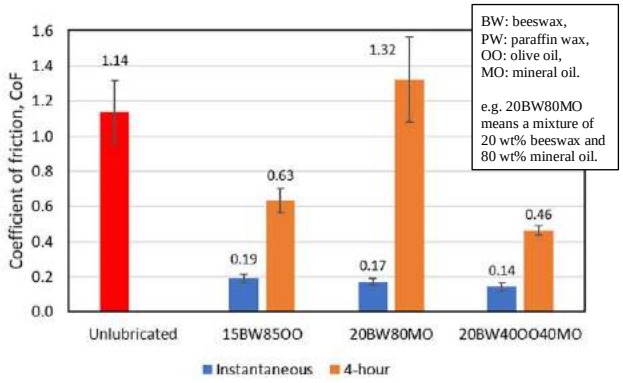


**Figure 4: Instantaneous and 4h friction performance of selected lubricants.**

## DISCUSSION & CONCLUSION

Based on an initial numerical study, friction was identified as the major parameter affecting the strain energy density in the tissue, and therefore directly affecting the risk of injury. Experimental investigations showed that excellent long-term friction performance can be achieved using a lubricant comprising 20% beeswax, 40% olive oil and 40% mineral oil. It needs noting that these results were obtained on the volar forearms of a limited number of subjects. The next step in this project will therefore be the implementation of the developed solutions in a clinical trial using respirator masks.


## ACKNOWLEDGEMENTS

The authors gratefully acknowledge support from the Imperial College London COVID-19 response fund.


## REFERENCES


[1] NHS England, Publication reference 001559 2020
[2] Jiang Q, et al. Advanced Wound Care 2020; 9(7):1–8.
[3] Jobanputra, RD et al., Scientific Reports, 11:16248, 2021.
[4] Oomens CW, et al. Computational Methods in Biomechanics and Biomedical Eng. 2003; 6(3):171–180.

SB³C2022
Summer Biomechanics, Bioengineering and Biotransport Conference
June 20-23, Eastern Shore, MD, USA

# COMPUTATIONAL FLUID DYNAMICS MODEL OF EMBRYONIC HEART AND SUPPORTING VASCULATURE ILLUSTRATES TEMPORAL AND SPATIAL VARIATION IN WALL SHEAR STRESS DURING CARDIAC CYCLE

**Kirsten B. Giesbrecht (1), Simone Rossi (1), Boyce E. Griffith (1)**

(1) Department of Mathematics, University of North Carolina at Chapel Hill, Chapel Hill, NC, USA

## INTRODUCTION

Intracardiac hemodynamics factors, such as blood velocity, blood pressure, and wall shear stress, are well recognized epigenetic factors contributing to congenital defects[1-11], but the relationship between blood flow and cardiac development remains poorly understood. Congenital heart defects (CHDs) are the most common congenital defect and are present in approximately 1% of newborns[12]. Only 20-30% of CHDs can be traced to genetic or environmental causes, while altered hemodynamic environments account for the pathogenesis of many CHDs[1-6].

Despite the recognition that hemodynamics plays a critical role in the pathogenesis of a variety of CHDs, there has been very little research on investigating regular hemodynamic patterns in both the early cardiac and circulatory systems. Specifically, establishing typical temporal and spatial patterns of wall shear stress, blood velocity, and blood pressure throughout both the embryonic heart, aortic arches, and dorsal aorta is critical to distinguishing between normal and pathogenic hemodynamic patterns, yet has proven to be difficult to obtain experimentally. Particularly, measuring wall shear stress in the developing heart *in vivo* is challenging due to the minuscule size of the developing heart and constant motion of the heart from beating. Often wall shear stress is roughly approximated by averaging blood velocity or pressure data[9,13]. In contrast, computational fluid dynamics models of the blood flow through the early heart and surrounding vasculature can reveal precise patterning of intracardiac wall shear stress. This study establishes a profile of wall shear stress, blood velocity, and blood pressure throughout the developing heart and surrounding vasculature using a computational fluid dynamics embryonic chick heart model.

## METHODS

Chick (*Gallus gallus*) embryos are an ideal system to study hemodynamics during cardiac development. The chick embryonic heart has a similar order of developmental events, such as cardiac looping and valvulogenesis[2,11], as well as a similar size to the fetal human heart, and it is easy to manipulate and visualize[14,15]. A stage HH16 embryonic chick heart and surrounding vasculature including the aortic arches and dorsal aorta were imaged using light-sheet fluorescence microscopy. Next, the images were segmented to obtain three-dimensional anatomic models and meshed. Then, blood was modeled to flow through the model using computational fluid dynamics described by the governing equations:

$$\rho\left(\frac{\partial u}{\partial t} + u \cdot \nabla u\right) = -\nabla p + \nabla \cdot \frac{\mu}{2}(\nabla u + \nabla u^T) \quad (1)$$

$$\nabla \cdot u = 0 \quad (2)$$

In which $\rho$ = 1.06 kg · mm$^{-3}$ is the fluid density, $\mu$ is the dynamic viscosity, and $p$ and $u$ are the fluid pressure and velocity fields, respectively. Where (2), the continuity equation, describes blood as an incompressible fluid. Blood is a non-Newtonian fluid. A rheological study on embryonic avian blood shows that embryonic avian blood can be closely described as a Carreau fluid[16] in which the dynamic viscosity depends on the shear rate, $\dot{\gamma}$ (3).

$$\mu(\dot{\gamma}) = \mu_{\text{inf}} + (\mu_0 - \mu_{\text{inf}})(1 + (\lambda\dot{\gamma})^2)^{\frac{n-1}{2}} \quad (3)$$

In this model, $\mu_{\text{inf}}$ = 3.7 Pa· s is the fluid viscosity at infinite shear rate, $\mu_0$ = 7.4 Pa· s is the fluid viscosity at zero shear, $\lambda$ = 0.033 s is the relaxation time, and $n=0$ is the power index[16]. No slip boundary conditions are imposed on intracardiac and vessel walls ($u$ = 0), and sinusoidal pressure profiles of distinct amplitudes and periods are assigned to the inflow and outflow boundaries.

## RESULTS

Laminar flow is observed with a roughly parabolic velocity profile (Fig. 1). As expected, the peak velocity is at the center of the luminal

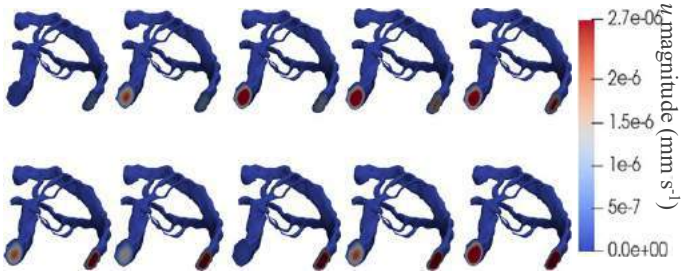


**Figure 1: Laminar flow is observed and velocity fluctuates as the pressure drop changes over time. Each time frame is taken an average of 2.7 ms apart.**

cross section and altered as the pressure drop varies from the imposed dynamic pressure boundary conditions at the inlet and outlet (Fig. 2) throughout the cardiac cycle.

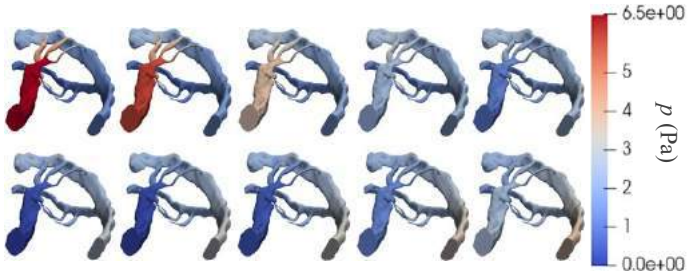


**Figure 2: Distinct sinusoidal pressure functions imposed at the inlet and outlet leads to variation in pressure drop and change in peak velocity over time. Each time frame is taken an average of 2.7 ms apart.**

Peak wall shear stress values are observed in the aortic arches, rather than in the heart (Fig. 3). Wall shear stress varies greatly throughout the embryonic heart and connected vessels, both spatially and temporally.

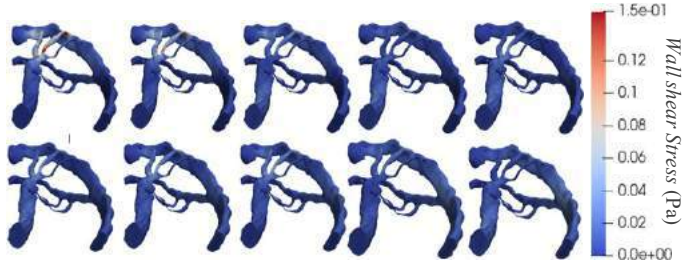


**Figure 3: Wall shear stress during the cardiac cycle had peak values in the aortic arches, rather than in the developing heart. Each time frame is taken an average of 2.7 ms apart.**

## DISCUSSION

This study illustrates the advantage of computational fluid dynamics models in estimating wall shear stress throughout the fluid domain over time. This model demonstrates the variation in wall shear stress both spatially and temporally during HH16 in embryonic chick hearts, which would be lost if averaging wall shear stress over space or time. Accurately describing the minimum and maximum wall shear stress values is critical to examining mechanosensitive developmental pathways since studies have shown that often high levels of shear stress or prologued exposure to shear stress are required to stimulate mechanosensitive pathways[17]. Describing the location, duration, and magnitude of peak wall shear stress values during development stages is critical to understanding the influence of wall shear stress on congenital heart defects.

Additionally, few computational models include both the developing heart and surrounding vasculature in the fluid domain. This model demonstrates that utility of including both the heart and vessels in the fluid domain, as peak wall shear stress was observed in the aortic arches, but could have eventual downstream impacts on heart development. Future directions include expanding this model to a fluid structure interaction (FSI) model to account for the motion from the beating heart.

## ACKNOWLEDGEMENTS

This research is supported through the NIH IVB training program at UNC-Chapel Hill (Award T32HL069768-19).

## REFERENCES

[1] Dyer LA, Rugonyi S. *J Cardiovasc Dev Dis.* 2021;8(8):90.
[2] Alser M, et al. *J Cardiovasc Dev Dis*. 2021;8(4):32.
[3] Midgett M, et al. *Am J Physiol-Heart Circ Physiol.* 2017;312(3):H632-H642.
[4] Midgett M, et al. *Front Physiol.* 2017;8:56.
[5] Hogers B, et al. *Cardiovasc Res*. 1999;41(1):87-99.
[6] Menon V, et al. *J Cardiovasc Dev Dis*. 2015;2(2):108-124.
[7] Espinosa MG, et al. *Dev Dyn*. 2018;247(7):914-923.
[8] Kalogirou S, et al. *Cardio Res.* 2014;104(1):49-60.
[9] Biechler SV, et al. *Front Physiol*. 2014;5:225.
[10] Hogers B, et al. *Circ Res.* 1997;80(4):473-481.
[11] Lindsey SE, et al. *Front Physiol*. 2014;5:318.
[12] Hoffman JI, Kaplan S.. *J Am Coll Cardiol*. 2002;39(12):1890-1900.
[13] Leatherbury L, et al. *Ann N Y Acad Sci*. 1990;588(1 Embryonic Ori):305-313. doi:10.1111/j.1749-6632.1990.tb13220.x
[14] Vilches-Moure JG. *Comp Med.* 2019;69(3):184-203.
[15] Korn MJ, Cramer KS. *JoVE J Vis Exp*. 2007;(8):e306.
[16] Al-Roubaie S, et al. *Am J Physiol-Heart Circ Physiol*. 2011;301(6):H2473-H2481.
[17] Dekker RJ et al. *Blood.* 2002;100(5):1689-1698. doi:10.1182/blood-2002-01-0046.

SB³C2022
Summer Biomechanics, Bioengineering and Biotransport Conference
June 20-23, Eastern Shore, MD, USA

# LATERAL DISTANCE AS A MEASURE OF BALANCE DURING 90 DEGREE PRE-PLANNED AND LATE-CUED TURNS

**Mitchell A. Tillman (1), Antonia M. Zaferiou (1)**

(1) Biomedical Engineering, Stevens Institute of Technology, Hoboken, NJ USA

## INTRODUCTION

Turning while walking comprises up to 50% of all steps [1]. The increased dynamic requirements of turns relative to straight-line gait likely challenges balance during the turn [2] especially in the frontal plane which requires more active balance control than in the sagittal plane [3]. Turns can be executed in either a pre-planned or late-cued manner, depending on the environment or the movement intent. Pre-planned turns are performed when the cue to turn is perceived early with respect to movement execution. Late-cued turns are required when the cue to turn is perceived later, therefore the movement planning duration is shorter. There is emerging evidence that turn kinematics may be affected by late cues, including increased maximum center of mass (COM) acceleration during the turn [4] and shifting turn execution methods from foot placement based in pre-planned turns to frontal-plane rotation during late-cued turns [5].

Balance control is often modulated by foot placement relative to the COM horizontal position [6], most typically quantified using the margin of stability metric proposed by [7]. However, the inverted pendulum assumption that this method relies on to compute the "extrapolated" COM may not be appropriate during different types of turns [2]. One prior study of pre-planned turning has removed the inverted pendulum assumption, using the "lateral distance" between the edge of the base of support (BOS) and horizontal COM position as a measure of balance [8]. When using either metric to assess balance, the smaller the value, the more precarious the balance state is thought to be, due to the COM being close to or outside of the bounds of the BOS.

The purpose of this study was to understand how frontal-plane balance is regulated during straight-line gait and 90-degree pre-planned and late-cued turns, quantified by the lateral distance between the COM and the frontal-plane lateral edge of the BOS. We hypothesized that minimum lateral distance decreases during late-cued and pre-planned turns vs. straight-line gait, and during late-cued vs. pre-planned turns.

## METHODS

Ten healthy adults (3 f, 7 m; 25.2±4.2 yrs; 73.9±14.8 kg; 1.79±0.1 m) provided informed consent according to the IRB standards. All participants indicated that they were free of pathologies and pain that would impair their ability to walk and turn during daily life.

We simulated the conditions of a grocery store using tape on the floor in a T-shape to emulate two aisles 0.91 m wide forming a perpendicular intersection. A 2.03 m screen at the end of the intersecting aisle served as the aisle's signage. Participants were asked to imagine that they were in a grocery store walking at a comfortable pace in three contexts: walking straight, pre-planned turns, and late-cued turns. First, they walked straight five times down the 10 m aisle. Next, they performed 10 pre-planned turns to the left, followed by 10 late-cued turns to the left. The foot that initiated gait was randomized evenly during turn trials. During pre-planned turns, the participants were instructed ahead of time that they should always turn 90 degrees left to walk down the intersecting aisle because it contained the item of interest, as though they were familiar with its location in the grocery store. In late-cued turns, participants knew there was a 50% chance they needed to turn left into the aisle, as though they were unfamiliar with this store and needed to check the signage to determine whether to turn. The monitor displayed green broccoli indicating to turn, or a red "NO" symbol (circle with line through it) to continue straight. Retroreflective markers were placed on participants to record motion data (200 fps, NaturalPoint, Corvallis, OR USA) and all analyses were conducted in MATLAB (Mathworks, Natick, MA USA)

Lateral distance is defined as the horizontal distance in the frontal-plane of COM position relative to the lateral edge of the BOS. It is negative when the COM is positioned lateral of the lateral edge of the BOS. COM position was computed using a whole-body model [9]. To quantify the BOS, markers on the foot were deemed in contact with the ground and part of the BOS (modeled by a convex hull) if they were

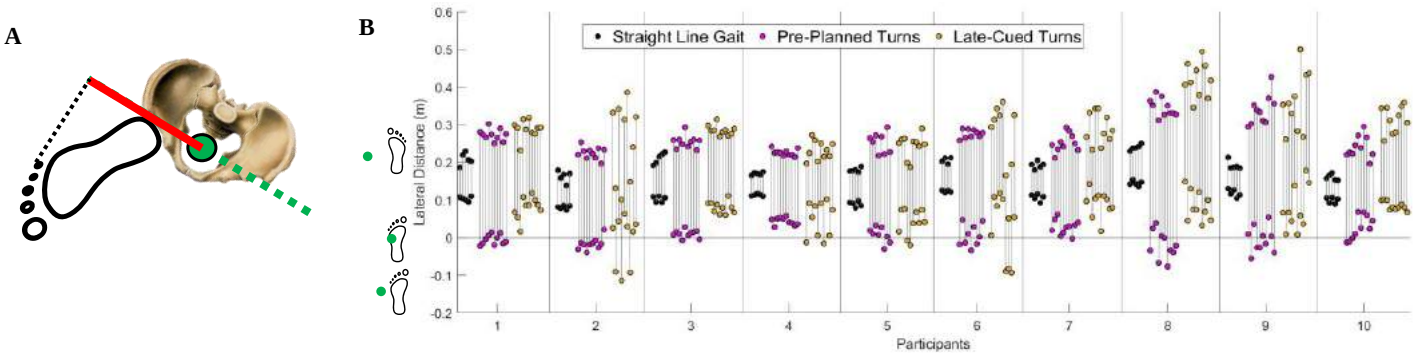


**Figure 1. (A) Horizontal-plane view illustrating the lateral distance. The red line indicates the lateral distance as the horizontal distance from the COM (green circle) to the lateral edge of the BOS in the frontal plane, defined by the pelvis mediolateral axis (green dotted line). (B) Lateral distance max & min for all trials in straight-line gait (black), pre-planned turns (purple), and late-cued turns (gold).**

below the height threshold established during quiet standing. During double support, only the front foot was considered as the COM velocity is always anteriorly directed. To define the frontal plane, we used a pelvis-fixed reference frame computed with respect to the global vertical and pelvis mediolateral axis [8]. Finally, the horizontal distance between the COM position and the lateral edge of the BOS in the frontal plane was the lateral distance (Figure 1A), computed throughout the phase of interest. For straight-line gait, the phase of interest was when the COM was within the center 3 m of the walkway. In turn trials, the turn phase was defined by when the pelvis began and finished rotating (when the pelvis heading angle passed three times the standard deviation of straight-line gait pelvis heading angles). We computed the median lateral distance for each trial and used the sign test to conduct all pairwise comparisons of the three tasks across participants ($\alpha$=0.05).

## RESULTS

Across all trials in all participants, lateral distance ranged from 0.07 to 0.25 m (straight-line), -0.08 to 0.43 m (pre-planned), and -0.11 to 0.5 m (late-cued) (Figure 1B). We found a significant decrease in minimum lateral distance in each turn type compared to straight-line gait (p=0.002 for each), and a larger minimum lateral distance in late-cued turns vs. pre-planned turns (p=0.002). We also found larger lateral distance maxima in each turn type vs. straight-line gait (p=0.002 for each) and in late-cued vs. pre-planned turns (p=0.022). We observed that negative lateral distances during a left turn indicate that the COM is positioned to the left of the left foot during single support, while the large positive lateral distances indicated that the COM was very far to the left of the right foot during single support. Qualitatively, we also observed a much larger variance in many participants' extrema values during late-cued vs. pre-planned turns and straight-line gait.

## DISCUSSION

This study focused on understanding how frontal-plane positioning of the center of mass relative to the base of support relates to balance maintenance during straight-line gait, pre-planned turns, and late-cued turns. We found a significant increase in lateral distance maxima and decrease in minima during each turn type vs. straight-line gait, as the COM translated in the direction of the turn (left) towards the inside (left) foot, which yielded lateral distance minima. COM translation in the direction of the turn (left), away from the outside (right) foot, yielded lateral distance maxima. During turns, lateral distance minima occurred during inside (left) foot single stance phase, and maxima during outside (right) foot single stance.

We theorize that the larger lateral distance minima and maxima in late-cued vs. pre-planned turns relate to distinct roles of each footfall. We found emerging evidence in both pre-planned and late-cued turns that more horizontal-plane body rotation occurs during the inside (left) foot single stance phase, and more COM trajectory redirection occurs during the outside (right) foot single stance phase. Thus, lateral distance minima are associated with more body rotation while the lateral distance maxima are associated with COM trajectory redirection towards the new direction of travel. We postulate that the role of each footfall becomes more distinct during late-cued turns due to the fewer number of footfalls used vs. pre-planned turns (median 3.25 vs. 4, p<0.01).

During late-cued turns, when the outside (right) footfall occurred first after the cue was presented, the outside foot typically redirected the COM trajectory within one single stance phase, leading to large lateral distance maxima. If the inside (left) footfall occurred first, the outside foot made contact with the ground earlier with a "half-step" that also resulted in large lateral distance maxima.

The benefit of increased lateral distance minima during inside (left) foot single stance phase of late-cued turns is still unclear. It may aid in horizontal-plane body rotation and/or facilitate balance.

This study expands on previous work on the role of relative COM and BOS positioning in straight-line gait [6] and pre-planned turns [5] and also provides evidence that late-cued turn execution induces changes in this relationship relevant to maintaining balance control. These findings encourage implementing late cues in turning while walking in clinical balance training paradigms. Future research should examine this phenomenon in balance impaired populations and explore its relationship to other factors of balance control.

## ACKNOWLEDGEMENTS

This work is supported by NSF CAREER Award #1944207. We also thank Jun Ming Liu for his assistance with data collection.

## REFERENCES

[1] Glaister, B et al., *Gait & Posture*, 25:389-294, 2007.
[2] Nolasco, L et al., *Gait & Posture*, 70:12-19, 2019.
[3] Bauby, C et al., *J Biomech*, 33:1443-1440, 2000.
[4] Dixon, P et al., *Gait & Posture*, 61:257-262, 2018.
[5] Patla, A et al., *Exp Brain Res*, 129:629-634, 1999.
[6] Bruijn, S et al., *J R Soc Interface*, 15:1-11, 2018.
[7] Hof, A et al., *J Biomech*, 38:1-8, 2005.
[8] Dixon, P et al., *Clinical Biomech*, 32:286-294, 2016.
[9] Dumas, R et al., *J Biomech*, 40:543-553, 2007.

# CERVICAL MATERIAL REMODELING IN PREGNANCY USING A NONUMAN PRIMATE MODEL

**S. Fang (1), L. Shi (1), I. Rosado-Mendez (2,3), T. Hall (2), H. Feltovich (2,4), and K. Myers (1)**

(1) Department of Mechanical Engineering, Columbia University, NYC, NY, USA
(2) Department of Medical Physics and (3) Radiology, University of Wisconsin-Madison, Madison, WI, USA
(4) Maternal Fetal Medicine, Intermountain Healthcare, Salt Lake City, UT, USA

## INTRODUCTION

A timely remodeling of the cervix is crucial for a healthy pregnancy because premature cervical softening can result in preterm birth (PTB), a serious medical condition [1-2]. A better characterization of cervical material properties is critical to uncovering the mechanisms behind premature cervical softening. Previous studies of the mechanical properties of the human cervix have characterized its fiber architecture and shown the impact of this architecture on its material behaviors, which manifested a large asymmetry between tensile and compressive loadings [3-5]. *In vivo* study of the human cervix is difficult, however, so only tissues at endpoints (nonpregnant [NP] and term-pregnant [PG]) were assessed. We explore mid-gestation properties using a nonhuman primate model (Rhesus macaque) for its similarities in anatomy and pregnancy physiology [6]. We combine spherical indentation and uniaxial tension tests with digital image correlation (DIC) and inverse finite element analysis (IFEA) to study the evolution of the equilibrium material properties of the macaque cervix throughout gestation.

## METHODS

Tissue preparation: We collected two disk-shaped cervical tissue samples (~4 mm in thickness and 25.25±5.06 mm in diameter) from the internal (proximal) and external (distal) cervical os of a group of Rhesus macaques at four different gestation points of the ~25 week gestation (nonpregnant [NP, n = 3], week 10 [n = 3, *early 2nd], week 16 [n = 3, *early 3rd], and weeks 20 and 23 [n = 7, *late 3rd]; * correspondence to human trimesters). We cut each sample into four quadrants and stored them in a -80°C freezer immediately after. Prior to testing, we equilibrated the samples in a 4°C phosphate-buffered saline (PBS) solution for 18 hours and flattened them using a microtome to create an even testing surface. To enable deformation tracking of the testing surface using DIC, we speckled the samples with water-insoluble ink.

Mechanical testing and data collection: We performed spherical indentation tests using a 2.5-mm diameter indenter and uniaxial tension tests to investigate tissue behaviors under compressive and tensile

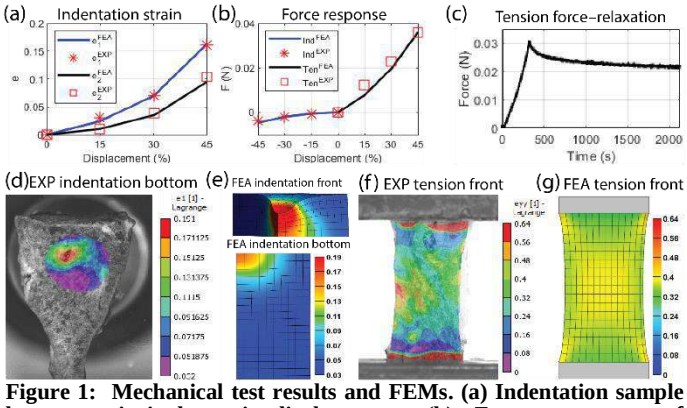


**Figure 1: Mechanical test results and FEMs. (a) Indentation sample bottom principal strain–displacement. (b) Force responses of indentation and tension. (c) Tension force–relaxation response to ramp–hold. (d)(e) The first Lagrange principal strain of one sample under indentation test and FEA. (f)(g) The vertical Lagrange principal strain of the same sample under tension test and FEA.**

loadings. We used a PBS-filled bath for tissue hydration and performed our tests on a universal testing machine (Instron). For both testings, we prescribed a three-level ramp–hold protocol similar to our human study [7]. For indentation, a front camera captured the sample bottom surface reflected by a prism located under the bath chamber; for tension, two orthogonal cameras captured the sample from the front and the side for geometry and surface deformation tracking. We collected force–extension–time data and calculated surface strain using DIC for both testings (Fig. 1(e)(g)).

FEM and IFEA: We created finite element models for both testings, where we modeled the sample and tension grips as rectangular cuboids, and the indenter as a rigid sphere (Fig. 1(f)(h)). For indentation, we adopted a quadrant model to reduce computational complexity (Fig. 1(f)). We meshed the geometries with hexahedron elements and applied

appropriate boundary conditions. We proposed a constitutive material model with an anisotropic continuous fibrous network embedded in an isotropic compressible ground substance. Briefly, the ground substance is described by a bulk modulus $\kappa$. The fiber network is the summation of entropic fibers, individually described by Langevin chain statistics, with the following material parameters: locking stretch $\zeta$, initial fiber stiffness $\xi_f$, preferential fiber direction $\theta$, and fiber dispersion $b$. For fiber direction $\theta$, we adopted a circumferential fiber alignment based on previous literature [8]. To fit our model to the experimental data, we performed IFEA. We used the first and second principal Lagrange strains of the indentation sample bottom surface and the force response of both indentation and tension tests as the fitting objectives, and optimized the four material parameters ($\kappa$, $\zeta$, $\xi_f$, and b) using a genetic algorithm for over 100 generations until the fitness criterion (5%) was reached. For indentation strains, we averaged the data within a 1-mm diameter circle under the indenter as our FEA showed an almost uniform stress distribution across that area.

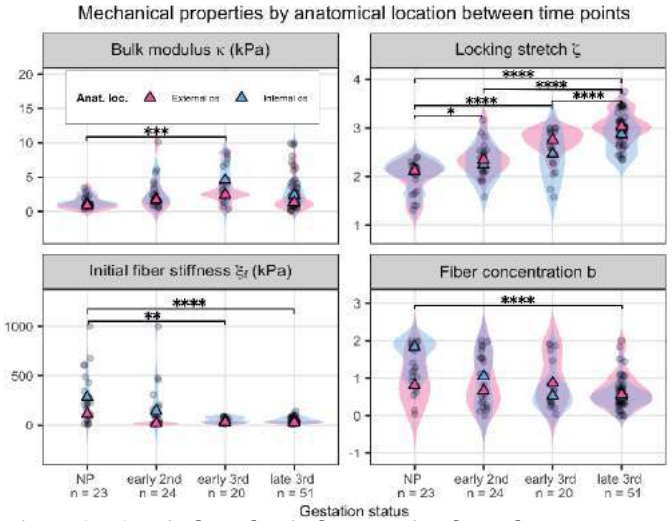


**Figure 2: Cervical mechanical properties throughout pregnancy. Triangles represent the medians of each data series. Statistical significance: * $p \leq 0.05$, ** $p \leq 0.01$, *** $\leq 0.001$, **** $p \leq 0.00001$**

Model validation: To examine the validity of the material model, we compared two forward predictions by the IFEA-fitted model with the experimental data that were not used for IFEA. For indentation, we compared the principal strains of the sample bottom surface within a 2-mm diameter circle under the indenter between the model prediction and experimental data; for tension, we compared the stretch ratios in both the width and thickness dimension between the model prediction and experimental data.

Statistical analysis: We performed a Shapiro-Wilk test to assess the data normality and a Kruskal-Wallis ANOVA to assess the statistical significance among different comparison groups such as gestational time points and anatomical locations (internal vs. external os).

**Table 1: Best-fit material parameters of all samples by IFEA**

| Gestational time point | Bulk modulus (kPa) | Locking stretch | Initial fiber stiffness (kPa) | Fiber concentration |
|---|---|---|---|---|
| NP | 1.37±0.84 | 2.01±0.33 | 272±257 | 1.29±0.61 |
| early 2nd | 3.19±3.68 | 2.33±0.35 | 152±223 | 0.94±0.69 |
| early 3rd | 3.87±2.53 | 2.55±0.43 | 46.2±27.4 | 0.83±0.62 |
| late 3rd | 2.81±2.60 | 2.98±0.33 | 44.3±28.7 | 0.62±0.43 |

## RESULTS

We observe the macaque cervical tissue exhibits (1) a nonlinear anisotropic strain response to the indentation displacement (Fig. 1(a)); (2) a nonlinear force–displacement relationship under both indentation and tension; (3) a large asymmetry between the indentation and tension stress responses (Fig. 1(b)); (4) a force–relaxation response to the ramp–hold displacement under both indentation and tension (Fig. 1(c)).

The best-fit material properties by IFEA are listed in Table 1 and plotted in Figure 2. We find that as gestation progresses: (1) in the early second and the early third trimester, the uterus presents a higher bulk modulus compared to in NP and the late third trimester; (2) the locking stretch increases significantly; (3) the initial fiber stiffness decreases significantly; (4) the fiber concentration (the reciprocal of dispersion) decreases from NP to the late third trimester; (5) values of the locking stretch, fiber stiffness, and the fiber concentration between the internal and external os converge.

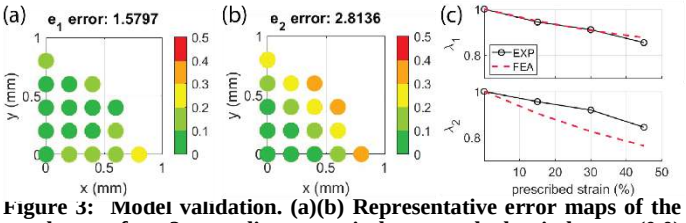


**Figure 3: Model validation. (a)(b) Representative error maps of the quadrant of a 2-mm diameter circle around the indenter (0,0) generated between the principal strain fields of experiment and FEA. (c) Representative stretch ratios of the width ($\lambda_1$) and thickness ($\lambda_2$) compared between the experiment and FEA.**

Our model captures the first and second principal strains of the indentation sample under the indenter well in terms of both magnitude and pattern, and captures the stretch ratios well under tension (Fig. 3).

## DISCUSSION

In this study, we characterized the evolution of the equilibrium mechanical properties throughout gestation using a nonhuman primate cervix. Our results suggest with the progression of pregnancy, cervical collagen fibers become more extensible and compliant. This is likely due to an increase in the proportion of immature crosslinks in the tissue. The ground substance stiffness increases from the beginning to mid-gestation and decreases into late gestation. Throughout pregnancy, the collagen fiber dispersion increases, indicating that its arrangement moves from aligned to randomly oriented; the bulk modulus, fiber stiffness, and locking stretch between the internal and external os all converge, indicating a material homogenization of the organ. These findings agree with previous studies on the human and murine cervix [4,9]. We recognize that the cervical tissue exhibits time-dependent behaviors which are also important for understanding tissue remodeling, such as poro-elasticity under indentation and visco-elasticity under tension. Therefore, a parallel study is currently underway to investigate these time-dependent and rate-dependent behaviors.


## ACKNOWLEDGEMENTS

Research reported in this publication was supported by the NIH R01HD091153 to KM and R01HD072077 to TJH, HF & KM. The content is solely the responsibility of the authors and does not necessarily represent the official views of the NIH.


## REFERENCES


[1] Li, Q. et al., *Am. J. Obstet. Gynecol*., 212(2): 145-156, 2015.
[2] WHO. Preterm Birth fact sheet, 2015.
[3] Yao, W. et al., *PLoS ONE*, 11(11): e0166709, 2016.
[4] Shi, L. et al., *J. Biomech. Eng.*, Sep, 141(9): 171-173, 2019.
[5] Myers, K. et al., *J. Biomech. Eng.*, Feb, 132(2): 003-018, 2010.
[6] Esch, V. et al., *Toxicol. Pathol*., 36: 171-172, 2008.
[7] Fang, S. et al., *Ann. Biomed. Eng.*, 49, 1923-1942, 2021.
[8] Vink, J. Y. et al., *Orig. Res. Ob.*, 215(4): 478, 2016.
[9] Yoshida, K. et al., *Acta Biomaterialia.*, May, 36: 195-209, 2016.

SB³C2022
Summer Biomechanics, Bioengineering and Biotransport Conference
June 20-23, Eastern Shore, MD, USA

# ASSESSING DIASTOLIC FUNCTION USING MATHEMATICAL MODELING OF THE EDPVR CURVE

**Salla M. Kim (1), Naomi C. Chesler (1), E. Benjamin Randall (2)**

(1) University of California Irvine - Edwards Lifesciences Foundation Cardiovascular Innovation and Research Center and Department of Biomedical Engineering, University of California Irvine, Irvine, CA, USA
(2) Molecular and Integrative Physiology, University of Michigan, Ann Arbor, Michigan, USA

## INTRODUCTION

Patients with heart failure with preserved ejection fraction (HFpEF), where an ejection fraction of >50% is maintained, exhibit a wide range of phenotypes [1]. Thus, HFpEF is difficult to diagnose, and the mechanisms of the disease are not well defined. Left ventricular (LV) diastolic dysfunction is a key component HFpEF involving incomplete filling of the LV due to stiffening of the heart [2]. Therefore, good understanding of diastolic dysfunction is needed to uncover aspects of HFpEF. Mathematical modeling facilitates this by allowing the input of patient data to conduct in silico experiments and make predictions that are either difficult to conduct in vivo or otherwise not possible. In this study, we use routine patient data as inputs to conduct total blood volume loading experiments. We chose to use the LV, right ventricle (RV), septum three-segment "TriSeg" model [3] of biventricular function in conjunction with a cardiovascular system (CVS) and atrial elastance model because of the TriSeg model's ability to simulate interventricular dependence. However, when simulating diastolic function with this model, there are discrepancies between the simulated end-diastolic pressure-volume relationship (EDPVR) curve and the expected EDPVR curve. The EDPVR is an indicator of diastolic function, and an upward, leftward shift in the EDPVR of a subject indicates ventricular stiffening. So, being able to appropriately simulate the EDPVR in the model is important to the study of diastolic dysfunction. Thus, in this study we develop a modified TriSeg model that appropriately predicts the EDPVR curve in a healthy subject.

## METHODS

Klotz et al. [4] observed that the EDPVR curve may be represented by the same exponential formulation across species. Hence, they derived a method of normalizing the EDPVR curves by the end diastolic volumes (EDV). From their ex vivo studies on volume-loaded human hearts with different etiologies, they found that the normalized EDPVR curves were nearly identical independent of etiology. We employ their methodology to ensure the EDPVR curve produced by our model has the appropriate behavior.

Our modified TriSeg heart in conjunction with an atrial and CVS model comprises 8 arterial, venous, ventricular, and atrial compartments. The TriSeg model approximates the ventricles as semi-spherical and thick-walled: the LV free wall (LW), the RV free wall (RW), and the septal wall (SW). The CVS model is a 0D electrical circuit analog in which volume is conserved, flow is formulated using Ohm's law, heart valves are diodes, and vascular pressures are linear with respect to volume. This model incorporates routine patient data as inputs (systolic and diastolic blood pressures, heart rate, etc.) for patient-specific predictions; however, for this study we are using representative hemodynamic data as pseudodata.

Nominal parameters are calculated using end-diastolic and end-systolic pressures and volumes to determine passive and active stress scaling parameters, respectively. The passive stress, $\sigma_{pas,i}$, coincides with the formulation from [4], i.e.,

$$\sigma_{pas,i} = k_{pas}\left(L_{s,i} - L_{sc0}\right)^{\gamma} \quad (1)$$

where $i = LW, SW,$ and $RW$, $k_{pas}$ is the passive stress scaling parameter, $L_{s,i}$ is the sarcomere length, $L_{sc0}$ is the contractile element length when active stress is zero, and $\gamma$ is a dimensionless steepness parameter. $L_{s,i}$ depends on an estimated reference midwall surface area, $A_{m,ref}$, that is highly influential and analogous to the size of the heart.

To assess the EDPVR model prediction, we performed two experiments: (1) total blood volume loading, and (2) volume loading with morphological changes to the heart. Experiment (1) was performed on both the TriSeg and our modified model. Volume loading was induced by incrementally increasing the circulating volume. Experiment (2) is an in vivo simulation of the Klotz et al. experiments, where hearts of different sizes, adjusted by scaling $A_{m,ref}$, for both the LV and RV simultaneously, are volume loaded to obtain the EDPVR

curves. Ventricular volumes were normalized to determine normalized EDPVR curves as in [4].

## RESULTS

The TriSeg model exhibits unconstrained increases in chamber volume with minimal increases in pressure with volume loading as seen in **Figures 1A** and **1C**. In panel **C**, the solid curves are the approximation of the EDPVR curve using the Klotz formulation based on a "normal" total blood volume of 5 L. The EDPVR curve of the TriSeg model is linear rather than exponential in shape. In comparison, **Figures 1B** and **1D** show that our modified model exhibits exponential increases in pressure with incremental increases in volume. In fact, the model-predicted EDPVR closely follows the predicted Klotz EDPVR curve without optimization (**Figure 1D**).

Our modified model also exemplifies how Klotz normalization of the EDV across several heart sizes leads to similar normalized EDPVR curves as seen in **Figure 2**. In **Figures 2A** and **2B,** hearts of different sizes are volume loaded to produce their respective LV and RV EDPVR curves, which exhibit differing behavior across heart sizes. **Figures 2C** and **2D** show the same data from **2A** and **2B**, respectively, with normalized EDVs, resulting in normalized EDPVR curves that exhibit similar behavior across the different hearts for both the LV and RV.

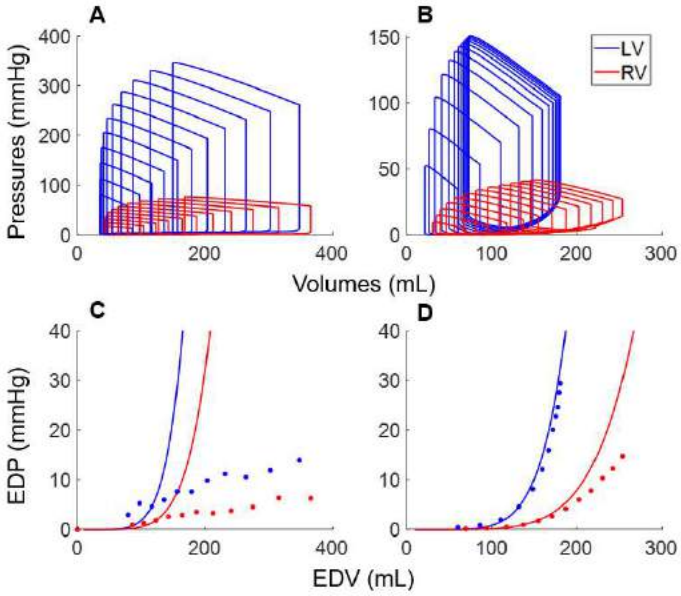


**Figure 1: A. and B. Pressure-volume (PV) loop progressions for the left (LV, blue) and right (RV, red) ventricles with increasing circulating volume for the TriSeg model [3] and the modified model developed in this study, respectively. C. and D. Model-predicted end-diastolic pressure-volume relationship (EDPVR) points from panels A and B superimposed with the Klotz EDPVR curve approximation [4] for the TriSeg and modified models, respectively. EDP – end-diastolic pressure. EDV – end-diastolic volume.**

## DISCUSSION

Our modified model slightly simplifies the passive stress formulation from the TriSeg model while maintaining similar function in the rest of the heart, producing appropriate EDPVR and Frank-Starling relationship curves with our few modifications. The normalized EDPVR curves for the LV and RV exhibit similar behavior (**Figures 2C** and **2D**), agreeing with the ex vivo studies by Klotz that show normalized EDPVR curves following the same curve across different hearts. There is some discrepancy between the approximated Klotz EDPVR curve and our model-predicted points for the RV as seen in **Figure 1D**. However, the Klotz EDPVR curve estimation was determined only for the LV; thus, it is possible that the RV exhibits slightly differing behavior. Regardless, there is a significant improvement of the RV EDPVR in our modified model compared to the TriSeg model.

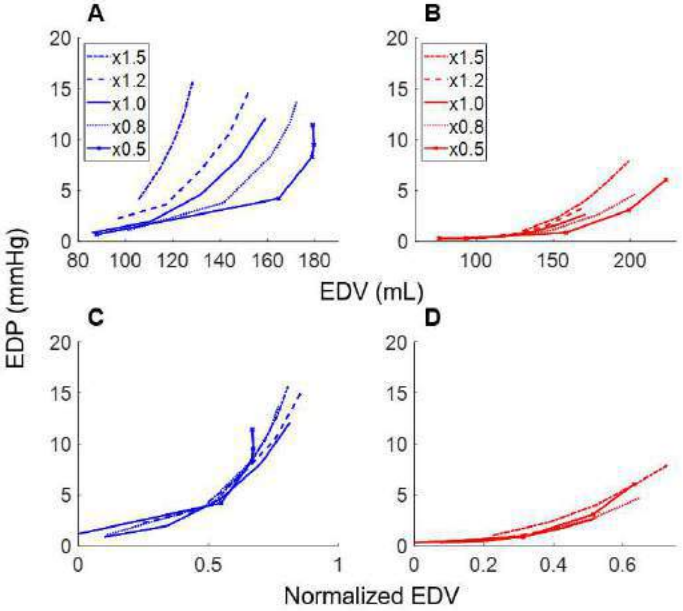


**Figure 2. A. and B. Model-predicted end-diastolic pressure-volume relationship (EDPVR) curves for the left ventricle (LV, blue) and right ventricle (RV, red), respectively, as the midwall reference area, $A_{m,ref}$, for both ventricles are scaled from 0.5-1.5 the normal blood volume. C. and D. EDPVR curves from A and B with normalized end-diastolic volume (EDV). EDP – end-diastolic pressure.**

Limitations of this modeling framework include assumptions and limitations propagated from the TriSeg model, such as the assumptions of spherical ventricular geometry and sarcomere lengths determined from isolated rat cardiac muscles [3]. In addition, in Experiment (2), we perform in vivo simulations whereases the Klotz study conducts ex vivo experiments. Also, we used representative hemodynamic data as input pseudodata for this study; however, our model is formulated for patient-specific modeling in the future.

This study establishes a modified TriSeg model that appropriately predicts a EDPVR in a healthy virtual patient across various heart sizes. Now, with understanding of the diastolic behavior in a healthy patient, we can investigate LV diastolic dysfunction that typically occurs in HFpEF patients.


## ACKNOWLEDGEMENTS

The authors would like to acknowledge Filip Jezek and Dan Beard for their contributions. This research was supported in part by NIH T32HL116270 and T32HL00785322.


## REFERENCES


[1] Lekavich, C et al., *Heart Fail Rev*, 20:643-653, 2015.
[2] Jones, E et al., *J Physiol*, 599:4991-5013, 2021.
[3] Lumens, J et al., *Ann Biomed Eng*, 37:2234-55, 2009.
[4] Klotz, S et al., *Am J Physiol Heart Circ Physiol*, 291:H403-12, 2006.

# PRO-ANGIOGENIC POTENTIAL OF MESENCHYMAL STROMAL CELLS REGULATED BY MATRIX STIFFNESS AND ANISOTROPY MIMICKING RIGHT VENTRICLES

**Michael Nguyen-Truong (1), Seungil Kim (2,3), Soham Ghosh (1,4), Peiman Hematti (5), Raghavan Chinnadurai (6), William R. Wagner (2,3), Zhijie Wang (1,4)**

(1) School of Biomedical Engineering
Colorado State University
Fort Collins, CO, USA

(2) McGowan Institute for Regenerative Medicine
University of Pittsburgh
Pittsburgh, PA, USA

(3) Department of Surgery
University of Pittsburgh
Pittsburgh, PA, USA

(4) Department of Mechanical Engineering
Colorado State University
Fort Collins, CO, USA

(5) Department of Medicine
University of Wisconsin, Madison-School of Medicine and Public Health
Madison, WI, USA

(6) Department of Biomedical Sciences
Mercer University School of Medicine
Savannah, GA, USA

## INTRODUCTION

Right ventricle (RV) failure is common in the advanced stage of pulmonary hypertension and is a useful predictor of mortality in these patients [1]. It has been noted that the RV becomes stiffer and more anisotropic with pressure overload [2,3]. Mesenchymal stromal cells (MSCs) are highly active paracrine cells with pro-angiogenic function, which has been found in various *in vivo* studies and is beneficial for reversing capillary rarefaction often observed in failing RV [4]. As a result, it is of great clinical interest to offer novel regenerative therapies for various diseases including RV failure.

Previous *in vitro* studies have further shown that MSC behavior and function are dependent on substrate stiffness. However, those investigations are limited to a narrow stiffness range (0.5-200 kPa) that does not encompass the complete range of RV tissue stiffness obtained *ex vivo* [5], especially with regards to RV end-diastolic stiffness at high strains. Only one study has examined the effect of anisotropy on MSC pro-angiogenic function, but the substrate stiffness was not quantified [6]. Thus, it remains unclear how RV-specific mechanics affect MSC pro-angiogenic properties. Motivated by the knowledge gaps and clinical needs, the aim of this study is to investigate the effects of the RV-like stiffness and anisotropy on MSC pro-angiogenic function. We hypothesize that the isotropic, diseased RV-like stiffness leads to the highest pro-angiogenic potential in individual MSCs.

## METHODS

To fabricate scaffolds, polyester urethane urea (PEUU) [7] was dissolved (6 or 12 w/v%) in hexafluoro-2-propanol and then electrospun into fibrous scaffolds using a custom electrospinning apparatus with a rotating mandrel (speed: 100-1250 rpm; diameter: 7.46 cm). In some scaffolds, 6% PEO was blended with the PEUU solution to alter nanofiber fusion and anisotropic behavior. The fixed parameters used for electrospinning all scaffold groups include: voltage: 16 kV, injection flow rate: 1.5 mL/h, and distance from collector: 9-10 cm. The Young's moduli ($E$) of the scaffolds along the fiber and cross-fiber directions were obtained by biaxial tensile tests at room temperature after 24 h of phosphate buffered saline soak. The degree of anisotropy was quantified as the ratio of the $E$ in the fiber direction to the $E$ in the cross-fiber direction (anisotropy index (AI)). Human bone marrow MSCs through passage 6 were cultured in 24-well plates at 10,000 cells/cm$^2$ on the sterilized scaffolds or tissue culture plastic (TCP). Human vascular endothelial growth factor (VEGF) expression in the MSC-derived conditioned medium (CM) was determined by ELISA (Invitrogen) after 48 h. Cell counts were determined via hemocytometer at 48 h. The overall pro-angiogenic potential was then evaluated by a tubulogenesis assay. Human umbilical vein endothelial cells (HUVECs) were plated on Geltrex (Thermo-Fisher) and cultured in collected MSC-derived CM at 20,000 cells/well (96-well plate). Images were taken of neovessel (tube) formation after 22 h and the total tube length was used as an indicator of angiogenesis. Data are presented as mean ± SEM. A one-way ANOVA (the data were normally distributed) and the appropriate post-hoc tests were performed: Tukey (equal standard deviations) or Dunnett's T3 (variable standard deviations). $p<0.05$ was statistically significant.

## RESULTS

To represent the end-diastolic stiffness of the RV, we fabricated the scaffolds with the Young's modulus in the fiber direction at ~550 kPa to mimic healthy RVs and at ~1.1 MPa to mimic diseased RVs [2,3]. Moreover, the scaffolds at the same stiffness range were fabricated with and without anisotropy to decouple the effects of stiffness and anisotropy on MSC behavior. Mechanical test data confirmed the mechanical differences in these scaffold groups (Table 1). The Norm scaffold groups had significantly lower Young's moduli

(p<0.05) than the Fail scaffold groups. The anisotropic index was ~1.0 in the isotropic groups and ~1.7 in the anisotropic groups, with the two anisotropic groups showing significantly (p<0.05) larger ratios versus isotropic groups with the same stiffness range.

**Table 1. Four electrospinning scaffold groups with altered stiffness that represent healthy and diseased RVs at end-diastole, with or without anisotropy. *p<0.05 vs. Norm group within the same anisotropy; §p<0.05 vs. Iso group within the same stiffness range.**

| | Isotropic (Iso) | Anisotropic (Ani) |
|---|---|---|
| **Normal RV Stiffness (Norm)** | *E*: 580±42 kPa<br>AI: 1.0±0.16 | *E*: 532±73 kPa<br>AI: 1.9±0.21§ |
| **Failing RV Stiffness (Fail)** | *E*: 1269±144 kPa*<br>AI: 1.0±0.09 | *E*: 983±83 kPa*<br>AI: 1.5±0.09§ |

After 48 h of culture on the scaffolds or TCP, we measured the total VEGF concentration in CM and the VEGF expression per cell (Fig. 1). There was a trend (p=0.09) of higher total VEGF production in the Norm&Ani group compared to the Norm&Iso group (Fig. 1A). But when we examined the VEGF production per cell, the Fail&Iso group had the largest value among all scaffold groups, and it had significantly higher VEGF production per MSC than the Norm&Iso group (p<0.05, Fig. 1B). Lower MSC counts in the Fail&Iso scaffold group were noted, although the difference was insignificant, and all other three groups had similar number of cells (data not shown). Finally, the stiffer scaffolds (Fail&Iso, Fail&Ani) tended to have higher VEGF production per cell compared to the soft scaffolds (Norm&Iso, Norm&Ani) in general (Fig. 1B).

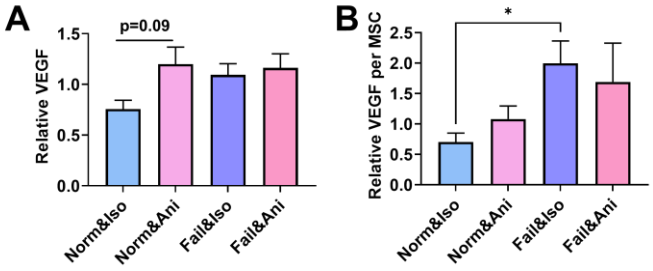


**Figure 1: Effects of stiffness and anisotropy on total VEGF production and VEGF per MSC normalized with TCP after 48 h. (A) Trend of higher total VEGF expression in Norm&Ani group versus Norm&Iso group. (B) VEGF expression per MSC is significantly higher in Fail&Iso group compared to Norm&Iso group. *p<0.05.**

Since there are other pro-angiogenic factors produced by MSCs besides VEGF, we further examined the overall pro-angiogenic potential of the MSC-derived CM by examining *in vitro* tube formation of HUVECs. There were no significant differences between the groups in terms of the total tube length (Fig. 2A). But when examining the total tube length formed per MSC, different pro-angiogenic potentials were found for MSCs cultured in different mechanical conditions. MSCs from the Fail&Iso group had the most pronounced pro-angiogenic function and led to significantly more pro-angiogenic potential compared to MSCs from the Norm&Iso group (p<0.05, Fig. 2B). There was also a strong trend (p=0.07) of greater pro-angiogenic potential made by MSCs from the Fail&Iso group compared to the Fail&Ani group (Fig. 2B). Therefore, similar to the VEGF production per MSC result (Fig. 1B), the Fail&Iso scaffold's mechanical environment led to the strongest pro-angiogenic potential for individual MSCs.

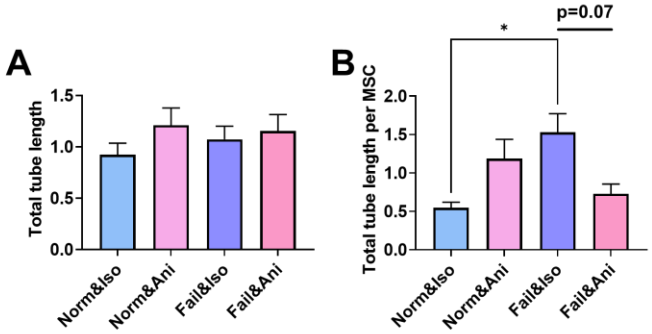


**Figure 2: (A) Total tube length and (B) total tube length/MSC normalized with TCP after 22 h. *p<0.05.**

## DISCUSSION

In this study, we assessed how these two mechanical factors - RV-like end-diastolic stiffness and anisotropy - affect MSC pro-angiogenic potential. By fabricating PEUU matrices that had varied matrix stiffness and anisotropy, we were able to use this *in vitro* platform to delineate the MSC behavior in response to the varied mechanical conditions.

From our data on the collective and individual MSC's pro-angiogenic properties, we found that this paracrine function and cell proliferation were not parallel. Despite the enhanced pro-angiogenic function per MSC in the Fail&Iso group (Figs. 1B&2B), the overall pro-angiogenic potential was limited by the low cell counts in this scaffold group. Actually, this group tended to have the lowest cell numbers after 48 h of culture, which indicated minimal cell proliferation. The 'opposite' effects of this mechanical environment (isotropic, stiff RV) on cell proliferation and pro-angiogenic function seemed to mirror that of the mechanical regulation on MSC phenotype and proliferation observed in TCP culture (versus hydrogel/polydimethylsiloxane) [8,9].

Moreover, there may be some synergistic effect of matrix stiffness and anisotropy on individual MSC behavior, but the effect is stiffness-dependent. In all experimental data (total VEGF production, VEGF/cell, tube length, and tube length/cell) from the Norm groups (when the stiffness was that of healthy RVs), the addition of anisotropy consistently led to a trend of higher value compared to the isotropic scaffold. But in the data from Fail groups (when the stiffness was that of diseased RVs), the 'beneficial' effect of anisotropy disappeared and the tube length result suggested a reduced pro-angiogenic function in anisotropic matrix.

Taken together, our results originally reveal the evidence of mechanical regulation of the MSC angiogenesis property in the context of RV mechanics and tissue anisotropy, which will help to inspire the development of tissue-specific, MSC-based therapies for heart failure patients.

## REFERENCES

[1] Lahm T et al., *Am J Respir Crit Care Med*, 198:15-43, 2018.
[2] Liu W et al., *J Integr Cardiol*, 6:1-6, 2020.
[3] Jang S et al., *J Am Heart Assoc*, 6(9):e0060084, 2017.
[4] Nguyen-T M, *Am J Physiol Heart Circ Physiol*, 321: 112-27, 2021.
[5] Nguyen-Truong M et al., *Bioengineering*, 7(4): 122, 2020.
[6] Su N et al., *Biomaterials*, 141:74-85, 2017.
[7] Gu X et al., *Biomaterials*, 133:132-43, 2017.
[8] Gerardo H et al., *Sci Rep*, 9(1):9086, 2019.
[9] Rao V et al., *Bioeng Transl Med*, 4(1): 51:60, 2018.

SB³C2022
Summer Biomechanics, Bioengineering and Biotransport Conference
June 20-23, Eastern Shore, MD, USA

# MECHANICAL CUES FROM THE ENVIRONMENT MAKE MESENCHYMAL STROMAL CELL POPULATION HETEROGENEOUS

**Samantha M. Kaonis (1,3), Soham Ghosh (1,2,3)**

(1) School of Biomedical Engineering, Colorado State University, Fort Collins, Colorado, United States
(2) Department of Mechanical Engineering, Colorado State University, Fort Collins, Colorado, United States
(3) Translational Medicine Institute, Colorado State University, Fort Collins, Colorado, United States

## INTRODUCTION

Multipotent mesenchymal stromal cells (MSC) from different sources such as bone marrow and adipose tissue are highly promising candidates for tissue engineering and regenerative medicine. Despite having multi-differentiation ability, immunomodulatory and trophic properties, scalable application of MSC at the clinical endpoint is limited. To achieve a clinically relevant number of MSCs, a small amount of autologous MSCs must be expanded to millions of MSCs. However, in vitro expansion of MSCs results in gradual differentiation into a heterogeneous population of senescent osteoprogenitor cells through activation of the Runx2 pathway, causing the loss of MSC attributes [1]. Mechanics of the culture substrate is a potential candidate among several factors that might promote this loss of the MSC phenotype [2]. Cells exert contractile forces on their culture substrate and the substrate elasticity can alter the cell behavior, promoting the formation of cell-cell contacts [3]. We hypothesize that neighboring cells can communicate by force transduction through the soft growth substrate to maintain the MSC phenotype and stemness thus resulting in population level homogeneity. Our objective in this work is to understand how substrate mechanics in combination with seeding density plays a role in maintaining the MSC phenotype by examining nuclear morphology and chromatin architecture in human BM-MSCs.

## METHODS

*Cell culture*: Primary human MSC derived from bone marrow (BM-MSC) were cultured (PT-2501, Lonza). Passage 3 and 4 cells were cultured on either a soft PDMS substrate (Sylgard 527, Dow) or a stiff substrate: polymer with same mechanical property as tissue culture plastic, both coated with type I collagen for MSC adhesion.

*Imaging and analysis of nuclear morphology and chromatin architecture:* Cells were fixed with 4% PFA, washed in 1X PBS, and stained with DAPI (Thermo Fisher) then imaged using a confocal microscope (Zeiss LSM 980). Custom MATLAB code was used for the nuclear morphology analysis. Chromatin segregation index was calculated using a previously established technique [4].

*Statistics*: Student's t-test was used to compare different groups. *p value of $<0.05$ represents statistically significant difference. Heterogeneity of MSC population level phenotype was quantified using the interquartile range (IQR) of the data (Q3-Q1).

## RESULTS

At earlier passages, most adherent BMSCs are small, spindle shaped, exhibiting the well characterized MSC phenotype. Figure 1A demonstrates the significant cell spreading MSCs experience over passaging on the stiff TCP substrate, showing a more flattened, fibroblast-like phenotype with considerable actin stress fiber formation. Meanwhile cells on the soft substrate generally maintained the spindle-like shape and diffuse actin in the cytoskeleton. Upon quantification of nuclear shape parameters (Figure 1B), nuclei on the stiff substrate were significantly larger and more circular from P3 to P4 becoming more fibroblast-like. When cells were cultured on the soft substrate, nuclei did not show any significant change in area but became significantly more elongated, demonstrating the typical MSC phenotype. The MSC phenotype was preserved over a single passage on the soft substrate whereas cells became increasingly more fibroblast-like, and more heterogeneous on the stiff substrate.

Next, we examined how substrate stiffness in conjunction with seeding density can affect the nucleus phenotype and chromatin architecture. Cell density had a significant effect on nuclear morphology with 5-10,000 cells/cm2 having the most MSC-like phenotype whereas the low seeding density of 100 cells/cm2 had an extremely wide range of nucleus morphologies (Figure 2 A,B) spanning from fibroblast to MSC phenotypes. Examining the intranuclear chromatin architecture showed that chromatin segregation was significantly affected by seeding density, with cells grown on the soft substrate at high seeding densities showing overall more chromatin segregation (Figure 2 C,D).

SB³C2022-128

The stiff substrate and a low seeding density resulted in a diffuse chromatin architecture, deviating from MSC nuclear phenotype.

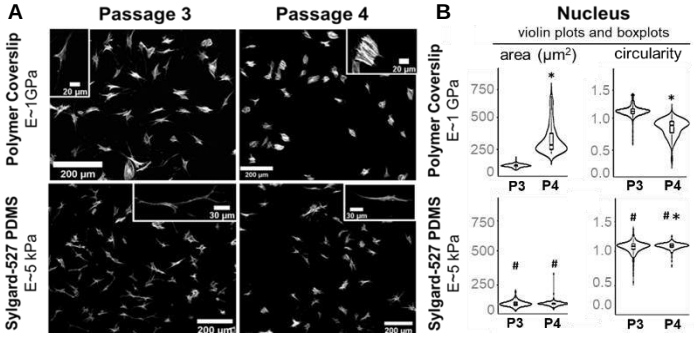


**Figure 1. (A) MSC phenotype was maintained on the soft gel over one passage. (B) Violin plots of nuclear geometrical parameters from one technical replicate. *represents significance between passages and # represents significance between substrates. n = 1000.**

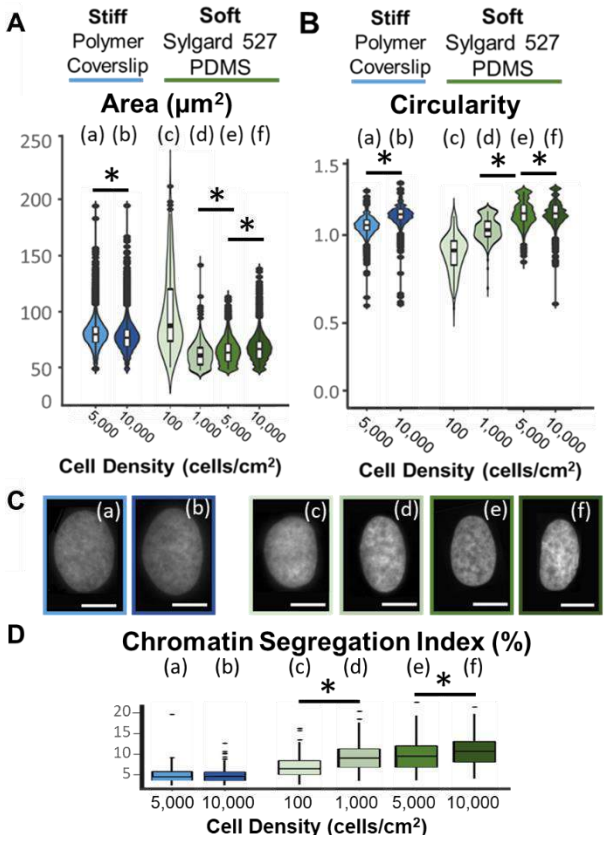


**Figure 2. (A,B) Violin plots of nuclear geometrical parameters from one technical replicate. n = 1000 (C) Representative nuclei from each experiment group to demonstrate the degree of chromatin condensation. (D) Quantification of the percent chromatin segregation within nuclei. n = 40.**

To understand if better substrate-mediated cell-cell mechanical communication leads to a more homogeneous population of MSCs we examined the IQR values for the nuclear shape quantification. It was found that a soft substrate leads to decreased heterogeneity in passage 4 (Figure 3A). One of two mechanics inhibitors that either stopped further actin formation or blocked actin-myosin contractions were applied to P4 cells grown on a stiff substrate (results not shown). This disruption of F-actin led to the same improved nucleus morphology changes as cells grown on a soft substrate, but surprisingly had no significant effect on the MSC population heterogeneity. This suggests that stiffness-dependent heterogeneity does not rely on actin formation and actin-myosin contractions as we previously thought. Seeding density did not have a largely significant effect on maintaining a consistent MSC-like population at densities between 1,000-10,000 cells/cm$^2$. However, when cells were grown at a very low seeding density of 100 cells/cm$^2$, the nuclear phenotype was extremely varied as indicated by the large IQR values, signifying higher heterogeneiy.

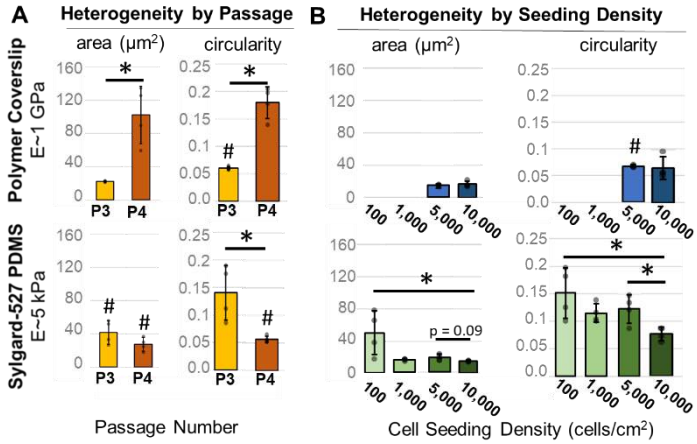


**Figure 1. Soft substrates in P4 and with a higher seeding density show a decreased heterogeneity. IQR values from 4 technical replicates for cells grown on stiff and soft substrates over a single passage (A) or with varying cell seeding densities (B).**

## DISCUSSION

In vitro expansion of MSCs results in gradual differentiation into a heterogeneous population of senescent osteoprogenitor cells through activation of the Runx2 pathway, that do not retain MSC attributes. Culturing MSCs on a soft substrate to avoid unintended differentiation may aid in maintaining a homogeneous population during in vitro passaging. We saw that when cells are cultured on soft substrates at a high enough cell density, they display the classic MSC phenotype and the soft culture substrate helps aid in maintaining this phenotype over a single passage, appearing to be a relatively homogeneous population of MSCs. Surprisingly, cell seeding density had a significant effect on the chromatin architecture. The open chromatin architecture seen on soft substrates at higher cell seeding densities is associated with transcriptional activation and is a hallmark of stem cells [5]. This is consistent with the literature in other cell types that also exhibit a uniform cell response in extremely soft environments that show a small cell diameter that are multipotent [1,5]. Consistent with our study results' small diameter and open chromatin architecture displayed by MSC when cultured on a soft substrate, we anticipate that MSCs will also demonstrate an increase in pluripotency markers. Further mechanistic and MSC based preclinical studies might reveal how the substrate mechanics functionally alters the MSC, opening novel possibilities to intervene such mechanism.

## REFERENCES


[1] Chang, L. et al., *Nature*, 563: 265-269,2018.
[2] Kim, D. et al., *Biomed. Reports*, 6(3):300-306, 2017.
[3] Reinhart-King, C.A. et al. *Biophys J*., 95(12):6044-6051, 2008.
[4] Irianto, J. et al., *Med. Engr. Phys*., 36: 412-417, 2014.
[5] Gaspar-Maia, A. et al., *Nat. Rev. Mol. Cell. Biol.* 12(1): 36-47.

# PREDICTION OF MICROARCHITECTURE AND ANISOTROPIC ELASTIC BEHAVIOUR OF TRABECULAR BONE USING A QCT-BASED DEEP LEARNING MODEL

**P. Xiao (1), E. Haque (1), T. Zhang (2), Y. Huang (2), X. Wang (1)**

(1) Department of Mechanical Engineering, University of Texas at San Antonio, San Antonio, Texas, USA
(2) Department of Electrical and Computer Engineering, University of Texas at San Antonio, San Antonio, USA

## INTRODUCTION

Bone osteoporotic fractures have been a great concern as its high prevalence in US population aged older than 50 or postmenopausal women [1]. Current clinical prognosis/diagnosis of bone fracture risks mainly relies on DXA image-based measurement of bone mineral density (BMD). However, BMD can only explain around 50% of variance in bone fractures as such fractures are also sensitive to the deterioration of trabecular bone microstructure. Recent successes of deep learning in biomedical image-based diagnosis/prognosis of diseases have motivated us to investigate the possibility of using Deep learning (DL) techniques to build high-fidelity predictive models to assess bone fracture risks. Our previous study showed that a high-fidelity DL model could be trained using 2D DXA images in multiple three-orthogonal projections to predict the histomorphometric parameters and elastic behavior of trabecular bone [2,3]. However, it is impractical to acquire three-orthogonal DXA images in clinical applications. As an alternative, quantitative computed tomography (QCT) images, which is a common 3D image modality for measuring BMD, could be used to train a DL model to evaluate 3D bone microarchitecture and anisotropic elastic behavior. Thus, this study was performed to determine whether a high fidelity QCT image-based DL model could be trained to predict the histomorphometric parameters and anisotropic elastic behavior of trabecular bone.

## METHODS

A total of 1,015 trabecular bone cubes (6mm × 6mm × 6mm) were acquired from six human cadaver proximal femurs of diverse ages (ranged from 22 to 79 years old, with an average age of 48.5 years) and different genders (three females and three males). These proximal femurs were scanned using a micro-CT system (SkyScan 1173) with a resolution of 35 μm, which is sufficient to capture the microstructural details of trabecular bone. The digitized trabecular cubes were then analyzed using ImageJ and BoneJ to determine the following six histomorphometric parameters: Degree of Anisotropy (DA), Connectivity Density (Conn.D), Bone surface (BS), Structure Model Index (SMI), Bone Volume Fraction (BV/TV) and Trabecular Thickness (Tb.Th). Furthermore, the anisotropic elastic behavior of trabecular bone was assessed using the apparent stiffness tensor. Firstly, trabecular cubes were aligned with the three orthogonal principal directions defined using their fabric tensor (**Fig. 1**). Secondly, three uniaxial compression tests in the three principal axes and three pure shear tests in the three principal planes were conducted using ABAQUS (2019/Standard software package) to assess the apparent elastic modulus ($E_{apparent}$), apparent shear modulus ($G_{apparent}$), and the Poisson's ratio of each trabecular cube in its three principal directions. Lastly, the apparent stiffness tensor of trabecular bone cubes can be described using the following equations:

$$\sigma_{ij} = C_{ijkl}\varepsilon_{kl} \tag{1}$$

$$C = \begin{bmatrix} C_{11} & C_{12} & C_{13} & 0 & 0 & 0 \\ C_{21} & C_{22} & C_{23} & 0 & 0 & 0 \\ C_{31} & C_{32} & C_{33} & 0 & 0 & 0 \\ 0 & 0 & 0 & C_{44} & 0 & 0 \\ 0 & 0 & 0 & 0 & C_{55} & 0 \\ 0 & 0 & 0 & 0 & 0 & C_{66} \end{bmatrix} = \begin{bmatrix} \frac{1}{E_1} & \frac{-\nu_{21}}{E_2} & \frac{-\nu_{31}}{E_3} & 0 & 0 & 0 \\ \frac{-\nu_{12}}{E_1} & \frac{1}{E_2} & \frac{-\nu_{32}}{E_3} & 0 & 0 & 0 \\ \frac{-\nu_{13}}{E_1} & \frac{-\nu_{23}}{E_2} & \frac{1}{E_3} & 0 & 0 & 0 \\ 0 & 0 & 0 & \frac{1}{G_{23}} & 0 & 0 \\ 0 & 0 & 0 & 0 & \frac{1}{G_{31}} & 0 \\ 0 & 0 & 0 & 0 & 0 & \frac{1}{G_{12}} \end{bmatrix}^{-1} \tag{2}$$

Where $\sigma_{ij}$ is the stress tensor, $\varepsilon_{kl}$ is the strain tensor, $C$ is the apparent stiffness tensor, $\nu_{12}$, $\nu_{13}$, $\nu_{21}$, $\nu_{23}$, $\nu_{31}$, $\nu_{32}$ are the Poisson's ratio in the orthotropic principal planes, and $E_1$, $E_2$, $E_3$ are the elastic modulus in three principal directions, while $G_{23}$, $G_{31}$, $G_{12}$ are the shear modulus in the three orthotropic principal planes, respectively. It should be noted that the trabecular cubes with significantly low BV/TV and trabecular number, as well as significantly high trabecular separation will be removed from assessing the apparent stiffness tensor, as some unknown errors will occur under these extreme conditions, thus influencing the calculation of apparent stiffness tensor of trabecular cubes.

Then, simulated QCT images of trabecular cubes with the resolution of 0.33 × 0.33 ×0.33 $mm^3$/voxel were digitally generated from the micro-CT images of the trabecular cubes that were aligned with the three orthogonal principal directions using ImageJ. A 3D convolutional neural network (CNN) model with subsequent 3D convolution filters and pooling layers was developed and trained to predict the histomorphometric parameters and apparent stiffness tensor of trabecular bone cubes using the simulated QCT images. During the training process, 85% of the entire dataset were randomly selected from as the *training data*, which include the QCT image and corresponding microarchitectural properties and apparent stiffness tensor for each trabecular cube. Of the training date, 80% were used for training the model and 20% for verifying the performance of the 3D CNN model. The remaining 15% of the entire dataset were used as the *testing dataset* to evaluate the efficacy of the 3D DL model in prediction of the histomorphometric parameters and apparent stiffness tensor, and compared with our previous DXA image-based DL models [2,3]. Among the DXA models, **Model 1** used nine projections of DXA images, whereas **Model 2** used only one projection of DXA image.

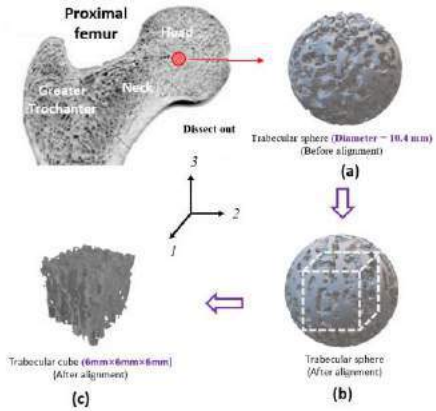


**Figure 1: Schematic representation of dissecting out trabecular bone cubes**

## RESULTS

In order to evaluate the efficacy of the QCT-based DL model in prediction of the histomorphometric parameters and apparent stiffness tensor of trabecular bone, linear regressions were performed to determine the Pearson correlation coefficients ($R^2$) between the DL model predicted and the measured histomorphometric parameters (**Table 1**) and elastic constants of the apparent stiffness tensor (**Table 2**). The results indicated that QCT-based DL model had high accuracy in predicting the histomorphometric parameters BV/TV, BS, Tb.Th and SMI, with the Pearson correlation coefficient ($R^2$) being 0.98, 0.95, 0.86 and 0.85, and had reasonable accuracy in prediction of Conn.D ($R^2$ =0.76) and DA ($R^2$=0.72). Furthermore, the QCT-based DL model demonstrated a high fidelity in predicting the apparent stiffness tensor, with Pearson correlation coefficients ($R^2$) being 0.94, 0.94, 0.94, 0.98, 0.97,0.97, 0.93, 0.94 and 0.93 for $C_{11}$, $C_{22}$, $C_{33}$, $C_{44}$, $C_{55}$, $C_{66}$, $C_{21}$, $C_{31}$ and $C_{32}$, respectively, thus verifying that QCT-based DL model could have high fidelity in predicting the histomorphometric parameters and anisotropic elastic behavior of trabecular bone.

**Table 1: Prediction accuracy in histomorphometric parameters using QCT-based DL model and DXA-based DL models**

| DL model | Pearson Correlation Coefficient (R2) | | | | | |
|---|---|---|---|---|---|---|
| | BV/TV | BS | Tb.Th | SMI | Conn.D | DA |
| QCT-based DL model | 0.98 | 0.95 | 0.86 | 0.85 | 0.76 | 0.72 |
| DXA-based DL model 1 | 0.99 | 0.94 | 0.95 | 0.76 | 0.69 | 0.64 |
| DXA-based DL model 2 | 0.90 | 0.87 | 0.90 | 0.62 | 0.61 | 0.61 |

Note: DXA-based DL model 1 uses nine projections of DXA images as input
DXA-based DL model 2 uses one projection of DXA images as input

**Table 2: Prediction accuracy in apparent stiffness tensor using QCT-based DL model and DXA-based DL models**

| DL model | Pearson Correlation Coefficient (R2) | | | | | | | | |
|---|---|---|---|---|---|---|---|---|---|
| | C11 | C22 | C33 | C44 | C55 | C66 | C21 | C31 | C32 |
| QCT-based DL model | 0.94 | 0.94 | 0.94 | 0.98 | 0.97 | 0.97 | 0.93 | 0.94 | 0.93 |
| DXA-based DL model 1 | 0.94 | 0.96 | 0.94 | 0.95 | 0.95 | 0.97 | 0.93 | 0.90 | 0.91 |
| DXA-based DL model 2 | 0.80 | 0.83 | 0.83 | 0.86 | 0.84 | 0.87 | 0.77 | 0.75 | 0.73 |

Note: DXA-based DL model 1 uses nine projections of DXA images as input
DXA-based DL model 2 uses one projection of DXA images as input

## DISCUSSION

This study investigated the feasibility of using QCT-based DL model techniques to predict the histomorphometric parameters and anisotropic elastic behavior of trabecular bone cubes. The results provide convincing evidence that QCT images assisted by DL model have great potential for clinical prognosis of osteoporotic bone fracture risks.

The results (**Table 1**) showed that QCT-based DL model had significantly higher accuracy ($R^2$=0.72-0.98) than that ($R^2$=0.61-0.90) of DXA image-based DL model (using one projection of DXA image as input) in prediction of BV/TV, BS, SMI, Conn.D and DA (**Table 1**). It is not a surprise that the QCT-based DL model could have high fidelity in prediction of the microstructure of trabecular bone since QCT images contain 3D information whereas DXA is 2D. Our previous results showed that the accuracy of DXA-based DL model in predicting histomorphometric parameters will increase as the number of orthogonal projections of DXA increase. Nonetheless, QCT-based DL model still have higher accuracy in predicting SMI, Conn.D and DA and have similar accuracy in predicting BV/TV and BS compared with those of DXA image-based DL model with nine projections (**Model 2**). These results suggest that QCT-based DL model always has a higher fidelity in prediction of histomorphometric parameters of trabecular bone compared to the DXA image-based DL models.

The QCT-based DL model also show significantly higher accuracy ($R^2$=0.93-0.98) than that of DXA-image based DL models ($R^2$=0.73-0.87 for Model 2 and $R^2$=0.90-0.97 for Model 1) in prediction of the apparent stiffness tensor of trabecular cubes. These results indicate that QCT-based DL model has a higher fidelity in prediction of anisotropic elastic behavior of trabecular bone cubes than DXA image-based DL model.

In Summary, it is clinically impractical to acquire orthogonal projections of DXA images, thus limiting the application of DXA image-based DL model to clinical prognosis of bone fracture risks. However, the results of this study indicate that QCT-based DL model could be an alternative to DXA image-based DL model in predicting bone microarchitecture and anisotropic elastic behavior.

## ACKNOWLEDGEMENTS

The authors are grateful of Mr. James Schmitz at UT Health San Antonio for technical assistance in acquisition of micro-CT scans of human cadaveric proximal femur samples.

## REFERENCES

[1] Wright, N. C., et al., *J. Bone Miner. Res*, 29(11):2520-2526, 2014.
[2] Xiao, P., et al., *Bone Rep*, 100295, 2020.
[3] Xiao, P., et al., *J Mech Behav Biomed Mater*, 104834, 2021.

SB³C2022
Summer Biomechanics, Bioengineering and Biotransport Conference
June 20-23, Eastern Shore, MD, USA

# FUNCTIONAL HYPEREMIA INCREASES INFLUX OF CEREBROSPINAL FLUID TO THE BRAIN

**Yiming Gan (1), Stephanie Holstein-Rønsbo (2), Douglas H. Kelley (1), Maiken Nedergaard(2,3)**

(1) Department of Mechanical Engineering, University of Rochester, Rochester, NY, USA
(2) Center for Translational Neuromedicine, University of Copenhagen, Copenhagen, Denmark
(3) University of Rochester Medical Center, Rochester, NY, USA

## INTRODUCTION

Neurons have little storage of energy metabolites, and are, therefore, highly dependent on tight regulation of blood flow. Upon neuronal activation, local consumption of metabolites increases. In response, cerebral blood flow increases to supply oxygen and metabolites to the depleted area, a process called neurovascular coupling or functional hyperemia. The neurovascular coupling involves arterial dilation, which displaces cerebrospinal fluid (CSF) and drives flow in perivascular spaces(PVS) around cerebral arteries. Flows of CSF in PVSs are believed to couple to a network of brain-wide fluid transport pathways known as the glymphatic system, which facilitates waste clearance [1]. It was speculated that reciprocal interchanges of blood and CSF volumes within the rigid cavity of the skull were responsible for initiating the movement of CSF[2]. Here, we hypothesize large vasomotions as a major driver of CSF flow in the perivascular space.

In this study, we employ a complementary range of optical imaging approaches to assess the effects of unilateral whisker stimulation on glymphatic system fluid transport of mice. In an intact skull preparation, we find via transcranial imaging that sensory stimulations result in a larger glymphatic influx to the stimulated hemisphere. Additionally, we find that functional hyperemia, induced by puffing air across the whiskers for 20 minutes, causes faster clearance of fluorescent tracer from the stimulated hemisphere. Using optogenetics, we induced artery constriction and found that manipulation of arterial diameter can accelerate glymphatic influx in the absence of neural activation. We used particle tracking to measure the velocity of CSF microspheres and found that arterial diameter change is negatively correlated to the CSF flow velocity. Lastly, we proposed an impedance pumping model that might explain our experimental observation of the vasomotion-driven flow. Altogether, our results demonstrate that changes in arterial diameter are important for CSF flow. We hypothesize that the glymphatic system is activated to clear away metabolites produced by the increased neuronal activity in response to sensory stimulation. Low glymphatic activity is associated with a buildup of metabolic waste [3], so maintaining high sensory stimulation to induce functional hyperemia could protect against age-related glymphatic impairment.

## METHODS

We used a mixture of male and female mice for the studies. For optogenetic experiments, we bred mice expressing channelrhodopsin in smooth muscle cells. Mice were anesthetized with a ketamine/ xylazine. The cisterna magna was exposed and a 30GA needle was inserted. The air puffs were delivered by a pneumatic pressure pump controlled by a digitizer. The air puffs were delivered for 30 seconds.

A cranial window was made above a branch of the middle cerebral artery. Just before imaging, an i.v. tracer was injected to visualize the artery. Red fluorescent microspheres were injected into the cisterna magna during 2-photon imaging. We recorded at a frame rate of 29.6 fps.

We used a custom-built, automated particle tracking software in MatLab to measure CSF flow velocity from the recordings. A Matlab algorithm was used to measure the artery and perivascular space width changes[4].

We used the IB2D, an open-source immersed boundary simulation tool to simulate CSF flow driven by the motion of the elastic artery in 2D[5][6][7].

For the awake mice studies, the anesthetized mouse was injected with the xylazine reverser atipamezole. This caused rapid elevation of heart and respiration rate, and when it had stabilized, we began whisker stimulation.

## RESULTS

### Whisker stimulation causes functional hyperemia through neuronal activation in the barrel field cortex

Whisker air puffing activates barrel cortex neurons and causes an increase in local blood flow. Using lightly anesthetized mice, we here found stable whisker-induced neuronal Ca2+ in the stimulated hemisphere(Figure 1).

### Functional hyperemia increases the glymphatic influx

We combined whisker stimulation with in vivo imaging of the glymphatic CSF tracer transport under anesthesia. The tracers appeared in both hemispheres, at which point air puff stimulations

were started. Glymphatic tracer signal continuously increased in both hemispheres as the tracer entered the perivascular space, yet the whisker stimulations consistently triggered a higher net tracer influx compared to the unstimulated hemisphere, demonstrating that sensory stimulation increases glymphatic influx.

**Whisker stimulation increases glymphatic clearance**

We let the tracer circulate for 30 minutes to saturate the perivascular spaces before air puffing the whiskers for 20 minutes. We found that whisker stimulation causes faster clearance of tracer from the stimulated hemisphere.

**Functional Hyperemia transiently decreases the CSF flow velocity**

To quantify CSF flow, we next injected fluorescent microspheres and imaged their transport using 2-photon excitation followed by particle tracking analysis. As the artery dilated, we found that the downstream velocity of the microspheres decreased indicating that glymphatic inflow is transiently impaired during whisker stimulation.

**Vasomotion changes the volume of the PVS**

From diameter measurement, we observed that the perivascular space width during hyperemia decreases as the artery dilates. We did not observe any movement of the outer perivascular space membrane, suggesting that the outer boundaries of the perivascular space are rigid.

**Vasomotion increases the glymphatic influx in the absence of neural activation**

We used Optogenetic mice to test the importance of vasomotion as a driver of CSF influx in the absence of neural activation[8]. We induced vasoconstriction by photostimulation of the arterial trunk. We found that the photostimulation increased the tracer signal in the perivascular space of the MCA compared with the unstimulated hemisphere.

The results show that both sensory stimulation and artificial manipulation of the arterial diameter result in an increased influx of CSF tracer confirming that vasomotion is a driver of glymphatic inflow.

**Impedance pumping simulation may reveal the mechanism of vasomotion-driven flow in the PVS**

We used the 2D numerical Immersed Boundary Method to simulate vasomotion-driven flow. We set the PVS outer boundaries to be rigid and the artery as a flexible tissue with both ends fixed to the Cartesian mesh. A net flow in the PVS is observed when we induce periodic vasomotion to the system, which matches our experimental observations in detail.

Upon the change of the PVS volume caused by vasomotion, we expect the local hydraulic resistance to change proportionally. A substantial increase in the PVS volume may attract fluid from both ends of the dilating area causing an inflow at one end and backflow at the other and vice versus. In the meanwhile, vasomotion wave reflections happen at both ends of the vasculature non-simultaneously, causing a unidirectional net flow component that is independent of the flow component driven by the local hydraulic-resistance change or the mass conservation law, which is described as impedance pumping in previous literature[9]. Our in-vivo experiments and simulation results suggest that impedance pumping may play an important role in the CSF flow.

**Functional hyperemia does not drive CSF flow in awake mice**

Earlier studies have shown that wakefulness strongly suppresses glymphatic influx[10]. Therefore, we woke up the anesthetized mice with atipamezole. Then, we began whisker stimulation and tracer measurement. The results showed that whisker stimulation caused no detectable changes in glymphatic influx.

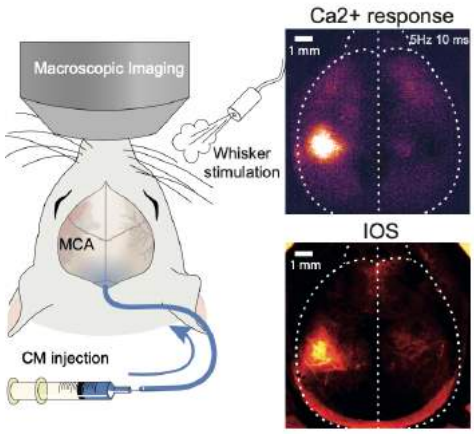


**Figure 1: Whisker stimulation setup and the response in the stimulated(Left) hemisphere**

**DISCUSSION**

Our study presents the first direct evidence that functional hyperemia accelerates CSF influx in anesthetized mice. The increased CSF transport is not only noticeable for the glymphatic influx, but causes also faster clearance of glymphatic tracer in response to whisker stimulation. In an optogenetic mouse model, we demonstrate that it is not neuronal activation per se that increases CSF influx, but rather changes in arterial diameter. To detail the CSF flow changes occurring in response to vasomotion, we used a unique custom-built velocity tracking software to yield kinetic data of injected microspheres in the perivascular spaces. We find a rapid velocity change in response to arterial diameter changes. Altogether, we observe vasomotion to greatly affect the CSF flow in the perivascular space, and that vasomotion is a major driver of CSF transport.

In this study, we present an impedance pumping model with the assumption of a non-distensible external layer. The inner tubing is elastic, and large waves, as those caused by functional hyperemia, can propagate along the arterial wall and causes the cerebrospinal fluid to move in a specific direction. Our data demonstrate an anti-correlation between arterial diameter and CSF flow velocity.

Our study on awake mice suggests that functional hyperemia drives no influx when the glymphatic system is suppressed by wakefulness.

**ACKNOWLEDGEMENTS**

This project has received funding from the Novo Nordisk Foundation, Lundbeckfonden, the NIH National Institute on Aging through grant RF1AG057575, and the Army Research Office through grant MURI W911NF1910280. We would like to thank Dan Xue for help with graphical design and Hajime Hirase for providing GLT1-GCaMP7 mice.

**REFERENCES**

[1] Iliff, JJ et al., *Science translational medicine* 4.147 :147ra111-147ra111, 2012.
[2] Fultz, E et al. *Science* 366.6465:628-631, 2019.
[3] Kress, T et al., *Annals of neurology* 76.6: 845-861, 2014.
[4] Mestre, H et al., *Nature communications* 9(1):1-9, 2018.
[5] Battista, NA et al., *Integ. Comp. Biol.* 55(5):901-911, 2015.
[6]Battista, NA et al., *Bioinspiration and Biomemetics* 12(3): 036003, 2017
[7] Battista, NA et al., *Appl. Sci.* 41:8455-8480, 2018
[8] Madisen, L et al., *Nature neuroscience* 15.5: 793-802, 2012.
[9] Avrahami, ID et al., *Journal of Fluid Mechanics* 608: 139-160, 2008.
[10] Xie, L et al., *science* 342.6156: 373-377, 2013.

# INHIBITING EPIGENETIC MODIFIERS RESCUES CHONDROCYTE FATE FOLLOWING CELL EXPANSION FOR CARTILAGE REGENERATION

**Adrienne K. Scott (1), Katie M. Gallagher (1), Stephanie E. Schneider (1), Corey P. Neu (1)**

(1) Mechanical Engineering, University of Colorado Boulder, Boulder, CO, U.S.

## INTRODUCTION

Increasing evidence links spatial organization of the genome to gene function and cell fate. For example, work from our lab has recently shown that different cell types have specific nuclear architectures [1]. A critical component of nuclear architecture is the lamina-associated domain (LAD) at the periphery of the nucleus. Genes localized in the LAD are generally repressed and not necessary to carryout cell-type specific functions. H3K27me3 and H3K9me3 are two histone modifications that are critical for repressing genes in the LAD. When the enrichment of H3K27me3 and H3K9me3 in the LAD is disrupted, variable reactivation of genes can occur leading to maladaptive states, such as cancer [2] or cardiac pathologies [1].

Our work explores how the disruption of the peripheral enrichment of H3K27me3 and H3K9me3 to the nuclear envelope leads to maladaptive cell states in cartilage regeneration procedures. Current cartilage regeneration procedures (e.g. MACI, ACI) require a cell expansion process of autologous chondrocytes to generate sufficient cells that can be transferred to damaged regions of cartilage to promote repair and regeneration of the tissue. However, during the expansion process, chondrocytes dedifferentiate leading to loss of the native chondrocyte phenotype and emergence of a fibroblast-like cell. How the dedifferentiation process is regulated, and methods to restore the native chondrocyte phenotype post expansion, are unknown. Thus, the objective of this study is to determine the extent to which H3K27me3 and H3K9me3 play a role in regulating chondrocyte dedifferentiation, and how these modifications could be disrupted to rescue the chondrogenic phenotype to improve cartilage regeneration procedures.

## METHODS

***2D and 3D Culture***: Bovine chondrocytes were isolated (N=3-6 animals) and plated on Tissue Culture Plastic (TCP) or encapsulated into 3D HA-PEGDA hydrogels directly (PD0-3D). Cells plated on TCP were cultured for 8 population doublings (PD8) and 16 population

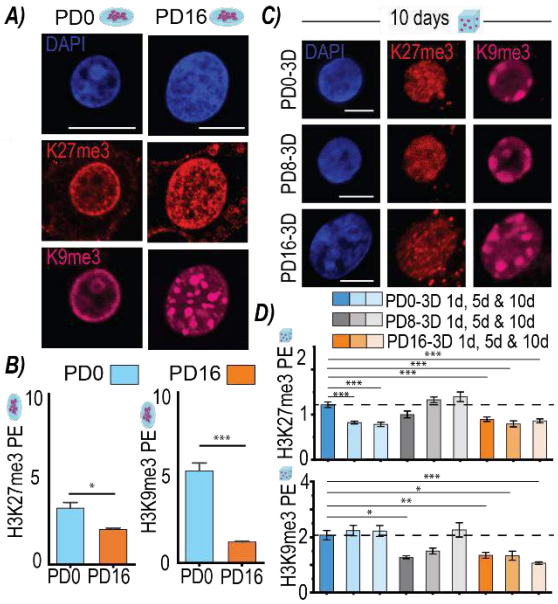


**Figure 1: Retention of chromatin architecture of expanded chondrocytes in 3D culture depends on time in 2D culture. A) Chromatin architecture of H3K27/K9me3 remodels and B) peripheral enrichment (PE) of H3K27/K9me3 is lost with increased population doublings of chondrocytes. scale= 10µm C) After 0, 8 and 16 population doublings (PD0, PD8, PD16), cells were transferred to 3D hydrogels and imaged. scale= 5µm D) PE levels of PD16-3D cells remained low in 3D culture, however, after 10 days in 3D culture the PE levels of PD8-3D cells returned to levels similar to PD0-3D cells. ±sem, *p<0.05, **p<0.01, ***p<0.001**

doublings (PD16) before collection for analysis or transfer to 3D hydrogels (PD8-3D and PD16-3D) for 1, 5, and 10 days. **Microscopy**: All samples were stained and imaged to visualize DNA (DAPI:405nm), H3K27me3 (561nm) and H3K9me3 (640nm). Additionally, 3D hydrogel samples were stained with calcein-AM and ethidium homodimer-1 to assess cell viability. **Peripheral Enrichment Analysis**: A custom MATLAB code was used to analyze nuclei (n>15 nuclei/treatment/animal) to calculate the ratio of relative intensity of outer H3K27/K9me3 signal to inner H3K27/K9me3 signal (Peripheral Enrichment: PE). **Gene Expression:** RT-qPCR was used to assess gene expression, normalizing to reference genes HPRT1 and GAPDH. **Epigenetic Treatments:** Cells were treated with inhibitors of epigenetic modifiers: Ezh2 inhibitor, GSK343 (2μM), to disrupt the methylation of H3K27; KDM4 inhibitor, ML324 (10μM), to influence methylation of H3K9; or DMSO (vehicle control). **Statistics:** A linear mixed effect model with a type III sum of squares ANOVA was used.

## RESULTS

While cultured on TCP, chondrocytes dedifferentiated, marked by a loss in the chondrocyte phenotype and cell morphology. At the same time, the chromatin architecture of H3K27me3 and H3K9me3 remodeled. H3K27 and H3K9 trimethylated chromatin enriched the periphery of PD0 cells (Fig. 1A,B). However, by PD8 and PD16 this peripheral enrichment (PE) of epigenetically marked chromatin decreased (Fig. 1A,B). When PD8 and PD16 chondrocytes were encapsulated in 3D hydrogels to mimic the change in environment after cell expansion in cartilage regeneration procedures, the alterations in chromatin architecture persisted (Fig. 1C). While PD8-3D cells regained the PE levels similar to PD0-3D cells after 10 days, the PD16-3D cells did not (Fig. 1C,D). After treating chondrocytes with GSK343, we found that the PE of H3K27me3 increased compared to PD16 DMSO treated controls (Fig. 2A). At the same time, GSK343 significantly decreased levels of H3K9me3 PE of PD16 cells compared to PD16 DMSO controls. Treating chondrocytes with ML324 did not change the PE of H3K27me3 for PD16 cells, but did restore PE of H3K9me3 of PD16 cells to similar levels of H3K9me3

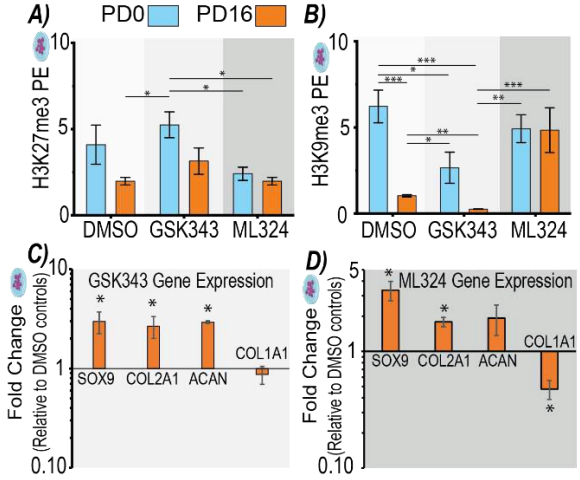


**Figure 2: Inhibiting epigenetic modifiers of H3K27me3 and H3K9me3 alters chromatin architecture and increases chondrogenic gene expression in 2D culture. A) While PE of H3K27me3 decreases with increased population doublings with DMSO treated cells, the PE of H3K27me3 increased with the GSK343 treatment. B) Treatment with ML324 maintains the high PE of H3K9me3. C) GSK343 and D) ML324 increased expression of chondrogenic genes. ±sem, *p<0.05, **p<0.01, ***p<0.001**

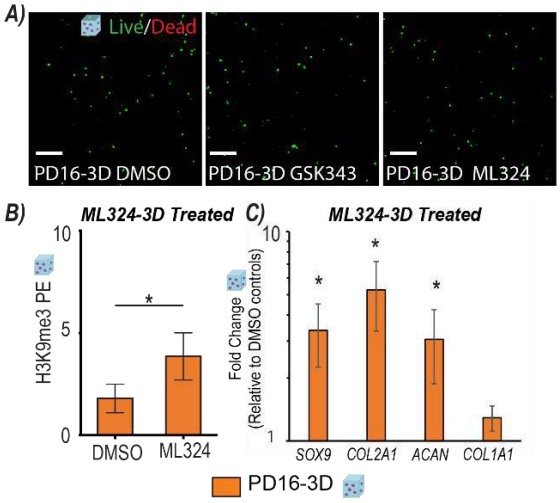


**Figure 3: Epigenetic treatments during 2D culture do not influence cell viability and enhance the chondrogenic phenotype when cells are encapsulated in 3D culture. A) PD16 cells treated with GSK343, ML324 or vehicle control (DMSO) were encapsulated into hydrogels and stained for live for cell viability. scale bar= 200μm B) H3K9me3 PE of PD16-3D cells previously treated with ML324 increased compared to DMSO PD16-3D cells. C) Chondrogenic gene expression of PD16-3D cells treated with ML324 increased compared to DMSO controls. ±sem, p<0.05**

PE of PD0 cells (Fig. 2B). Additionally, both inhibitor treatments increased expression of chondrogenic genes (Fig. 2C,D). Next, we encapsulated PD16 cells treated with GSK343 and ML324 and showed that the treated cells remained viable (Fig. 3A). The PE of H3K9me3 of ML324 treated cells in 3D hydrogels increased compared to encapsulated PD16-3D DMSO control cells (Fig. 3B). In addition, chondrogenic gene expression of ML324 treated PD16-3D cells increased compared to DMSO PD16-3D cells (Fig. 3C).

## DISCUSSION

We found that the chromatin architecture, specifically quantified as the PE of H3K27me3 and H3K9me3, remodels during chondrocyte dedifferentiation, supporting previous findings that disruption of the LAD leads to aberrant gene expression [3]. Additionally, chromatin architecture of H3K27me3 and H3K9me3 is retained even when chondrocytes are transferred to a different (3D) environment. The persistence of chromatin architecture overtime in 3D culture suggests that a memory from the previous environment is retained. Treating chondrocytes with epigenetic inhibitors, such as GSK343 and ML324, presents a promising method to prevent the memory from the expansion process and increase the therapeutic potential of chondrocytes [4]. More work is needed to assess how treatments of ML324 and GSK343 influences the chondrocyte phenotype when cultured in 3D hydrogels for longer time periods and if these treatments influence long-term matrix deposition to avoid fibrous matrices that often result from cartilage defect repairs [4]. Overall, understanding epigenetic regulation of chondrocytes could lead to chondrocyte reprogramming methods to improve strategies for cartilage defect repair.

## ACKNOWLEDGEMENTS

This work was supported by funding from NIH and NSF.

**REFERENCES** [1] Seelbinder, B. et al., *Nat BME*, 5:1500-16, 2021. [2] Lochs, S.J.A. et al., *Cells*, 8:271, 2019. [3] Joffe, B. et al., *Curr Opin Genet Dev*, 20:562-69, 2010. [4] Armiento, A. et al., *Adv Drug Deliv Rev*, 146:289-305, 2019.

SB³C2022
Summer Biomechanics, Bioengineering and Biotransport Conference
June 20-23, Eastern Shore, MD, USA

# EXAMINING OVARIAN CANCER HSP27 REGULATION VIA MECHANOTRANSDUCTION SIGNALING IN A 3D MODEL

**Molly S. Buckley (1), Joel L. Berry (1,2), Mary-Kathryn Sewell-Loftin (1,2).**

(1) Biomedical Engineering, University of Alabama at Birmingham, Birmingham, AL, USA
(2) O'Neal Comprehensive Cancer Center, University of Alabama at Birmingham, Birmingham, AL, USA

## INTRODUCTION

Ovarian cancer is the deadliest malignancy of all gynecological cancers with a 5-year survival rate of 49.1% [1], primarily due to the chemoresistant qualities of ovarian cancer cells which lead to high rates of recurrence. The current standard of care for epithelial ovarian cancer (EOC) patients is primary debulking surgery followed by a combination of taxane-based and platinum-based chemotherapies [2]. These therapeutic agents target the biochemical signaling that promotes cancer growth, but not the biomechanical signaling that is involved. Pathologic biomechanical forces within the tumor microenvironments (TMEs) of epithelial tumors of all types are emerging as potent regulators of cancer progression; these forces include compression at the tumor interior [3], tension at the tumor periphery [4] and altered or insufficient blood flow in the tumor vasculature due to high interstitial shear stresses [5]. When cells in a tumor sense these dynamic mechanical forces, a biochemical signaling response occurs called mechanotransduction [6].

Mechanotransduction studies of all epithelial cancer types have increased in number in the past 20 years, but few EOC mechanotransduction studies exist – and none have specifically focused on the effect of tensile stress on EOC chemoresistance. To address this gap in knowledge, this project studied the biomechanical regulation of EOC chemoresistance due to applied tensile strain using a 3D microfluidic device that is physiologically relevant to human EOC. The molecular relationship between the mechanotransduction response of EOC cells and their subsequent chemoresistance was examined through the expression and activation of the mechanosensitive heat shock protein 27 (HSP27). HSP27 is expressed and activated under stress conditions such as heat shock, hypoxia, and increased shear stress [7-9], is found to be upregulated in ovarian cancer [10], and has been shown to lead to increased chemoresistance in ovarian cancer cells [11, 12]. While these studies are a promising start to elucidating the role of HSP27 in ovarian cancer and determining its function as a possible biomarker or therapeutic target, determining how HSP27 is regulated in EOC through mechanotransduction signaling pathways that are modified by increasing tensile stress has not yet been explored. We hypothesized that tensile strain applied to the EOC cell line SKOV-3 and the chemoresistant EOC cell line SKOV-3.tr would increase HSP27 expression. A 3D microfluidic model of EOC with a fully formed vasculature was then developed with appropriate matrix components to further study the effect of tensile strain on EOC cells in a 3D environment.

## METHODS

Human epithelial ovarian cancer cell line SKOV-3 and the chemoresistant cell line SKOV-3.tr (taxane resistant) were seeded at 5 x $10^5$ cells/well (one cell type per plate) in 6-well collagen type I coated Flexcell plates with a flexible silicone membrane on the bottom of the well. Once seeded, the plates were placed in an incubator (37°C, 5% $CO_2$) for 24 hours such that an ~80% confluent monolayer was formed. The well plates were placed in the Flexcell FX-6000T tension system where an oscillatory tensile force of 10% strain and a frequency of 0.3 Hz was applied for 15 and 30 minutes. These cells were lysed and protein expression of HSP27 was determined through Western Blot analysis.

Next, a previously developed 3D microfluidic model was used [13] with EOC cells to create a physiologically relevant model of EOC. Briefly, a 3-chamber microfluidic model was used in which a 2:1 ratio of human microvascular epithelial cells (HMECs) to normal human lung fibroblasts (NHLFs) was seeded in conjunction in the middle chamber with a matrix of fibrin and collagen to create a fully formed vasculature network similar to that found in a tumor. SKOV-3 (n=3) cells were placed in the side chambers with the same matrix

components. Two concentrations of a fibrin: collagen mixture were used: 9:1 and 6:4, for a total of 10 mg/mL ECM protein. These devices were allowed to grow for eight days after which they were stained for CD31, collagen, and DAPI and imaged using immunofluorescence.

## RESULTS

A Western Blot analysis of SKOV-3 and SKOV-3.tr cells after application of oscillatory tension (Figure 1) showed differences in HSP27 expression between cell lines in each condition (experiment or control) at each time point. Trends towards a change in HSP27 expression over time within the same cell type under the different conditions were found.

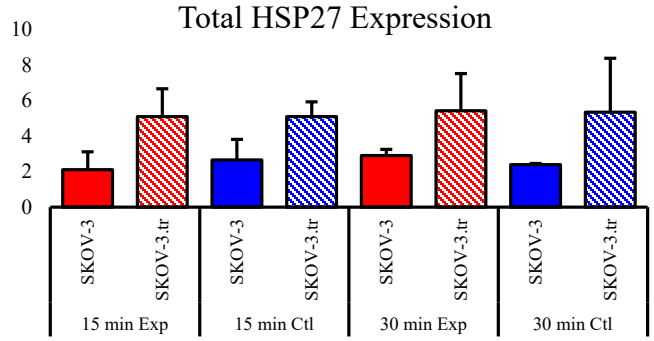


**Figure 1: Western Blot analysis of SKOV-3 and SKOV-3.tr cells placed under tensile strain for 15 and 30 minutes. N=2.**

Immunofluorescent staining and imaging were performed to analyze CD31 (TXRED), Collagen I (GFP), and DAPI expression (Figure 2A-B) in devices set up using the methods described above. Blood vessel formation was analyzed using the TXRED channel (Figure 2C-D) to determine if the collagen addition would hinder blood vessel development. This image was then analyzed in AngioTool using the skeletonization feature (Figure 2E-F) to highlight the fully formed vasculature network.

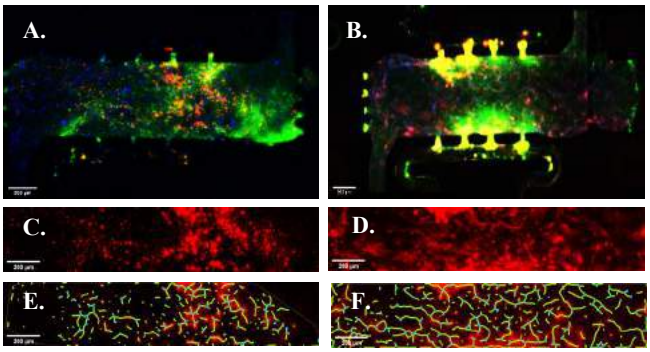


**Figure 2: 3D microfluidic devices with SKOV-3 cells with (A) 6:4 and (B) 9:1 ratio of fibrin: collagen matrix. Blood vessel formation in devices with (C) 6:4 and (D) 9:1 ratio of fibrin: collagen. AngioTool analysis of blood vessel formation with (E) 6:4 and (F) 9:1 ratio of fibrin: collagen. N=3 of each matrix composition**

## DISCUSSION

In previous studies with this particular 3D microfluidic device [13] the relationship between micro-strains in the ECM and angiogenesis was studied using endothelial cells and fibroblasts. The next step in developing this 3D model to study the biomechanics of cancer was to introduce cancer cells into these experiments as well as using the relevant ECM associated with cancer. Collagen type I is the most prevalent structural protein in EOC [14], therefore using it in conjunction with fibrin in this device would increase the physiological relevance of these experiments. However, collagen is an extremely stiff and contractile substance and replacing fibrin entirely with collagen in a microfluidic device needed to be tested to confirm a blood vessel network would still develop. Indeed, after testing the highest (6:4) and lowest (9:1) ratio of fibrin: collagen it was observed and quantified that blood vessel formation was hindered with a higher collagen concentration and flourished with a lower collagen concentration. Future experiments where different collagen concentrations in between the maximum and minimum to determine the optimum ratio will be needed.

As shown in Figure 1, there is a possible biomechanical signaling relationship between tensile strain, the chemoresistant quality of certain types of cancer cells, and the expression of HSP27. HSP27 expression increased after 30 minutes of tensile stretch in both SKOV-3 and SKOV-3.tr cells as opposed to 15 minutes of stretch, whereas the cells that were plated on the same plates but not stretched did not show much difference. Also, there is a stark difference between the total HSP27 expression in SKOV-3 cells vs. SKOV-3.tr cells. These results suggest that HSP27 expression is increased in chemoresistant cell types. As mentioned above, HSP27 is upregulated in many cancers including ovarian cancer and is implicated in EOC resistance of both paclitaxel and cisplatin [11, 12]. HSP27 is also highly sensitive to changing mechanical environments, such as heat shock, hypoxia, and increased shear stress [7, 9, 15]. Similar stresses, with the addition of compression and tension, are present in EOC. Studies are ongoing to determine the correlation between increased tensile stress and changes in HSP27 activation. Therefore, studying differences in HSP27 expression in cells that are first exposed to tensile strain then placed in the 3D microfluidic device provides the opportunity to explore changes in HSP27 expression and subsequent chemoresistant behaviors in a physiologically relevant 3D model which will have more insight than a standard 2D assay.

A unique aspect of this microfluidic model is that it allows for examination of cellular function without the added variable of soluble factors. The media in these devices is changed daily and flow is unidirectional each day, allowing for the influence of one single variable, in this case increased tensile strain, to be examined at a time. We will use this system to examine the differences in cells pre-treated with strain or without strain and compare HSP27 expression patterns and responses to chemotherapy to elucidate the relationship between increased tensile strain, HSP27 and EOC chemoresistance.

In conclusion, a connection between increased tensile strain and HSP27 expression was quantified. A previously designed 3D microfluidic device was further developed to be used for studies of EOC and their relationship with different mechanical stressors. Future experiments will further define the appropriate ratio of fibrin: collagen to be used in these devices, determine a link between HSP27 and tensile stress in a 3D environment, and elucidate a relationship between HSP27, tensile stress, and chemoresistance in EOC. This project helps generate sufficient understanding of the mechanisms of action of HSP27 expression or activation in EOC due to a mechanotransduction response that results in chemoresistance using a system where mechanical forces can be controlled, and the resultant cellular response is quantified.


## ACKNOWLEDGEMENTS

Funding for this work was provided by the NIH T32 Fellowship (T32-EB023872 M.B.), R00-CA230202 (M.K.S.L), IMPACT Award, O'Neal Comprehensive Cancer Center (M.K.S.L).


## REFERENCES


[1] Siegel, R.L., et al., CA: A Cancer Journal for Clinicians, 2021. **71**(1): p. 7-33. [2] Ozols, R.F., et al., J Clin Oncol, 2003. **21**(17): p. 3194-200. [3] Tse, J.M., et al., PNAS, 2012. **109**(3): p. 911-916. [4] Samuel, M.S., et al., Cancer Cell, 2011. **19**(6): p. 776-791. [5] Jain, R.K., Cancer Metastasis Rev, 1987. **6**(4): p. 559-93. [6] Jaalouk, D.E. and J. Lammerding, Nat Rev Mol Cell Biol, 2009. **10**(1): p. 63-73. [7] Rogalla, T., et al., Journal of Biological Chemistry, 1999. **274**(27): p. 18947-18956. [8] Lianos, G.D., et al., Cancer Lett, 2015. **360**(2): p. 114-8. [9] Zhang, B., et al., Biomolecules, 2019. **9**(2). [10] Langdon, S.P., et al., Clinical Cancer Research, 1995. **1**: p. 1603-1609. [11] Song, T.F., et al., J Int Med Res, 2009. **37**(5): p. 1375-88. [12] Lu, H., et al., Oncol Res, 2016. **23**(3): p. 119-28. [13] Sewell-Loftin, M.K., et al., Lab Chip, 2020. **20**(15): p. 2776-2787. [14] Cho, A., V.M. Howell, and E.K. Colvin, Frontiers in oncology, 2015. **5**: p. 245. [15] Arrigo, A.-P. and X. Préville, 1999, Springer. p. 101-132.

# ANALYSIS OF AIR FLOWRATE STANDARDS FOR PORTABLE SUCTION DEVICES

**Saketh R. Peri (1&3), Robert A. De Lorenzo (1,2,3), R. Lyle Hood (1,2,3)**

(1) Department of Biomedical Engineering, University of Texas at San Antonio, San Antonio, Texas, USA
(2) Department of Mechanical Engineering, University of Texas at San Antonio, San Antonio, Texas, USA
(3) Department of Emergence Medicine, University of Texas Health Science Center San Antonio, San Antonio, Texas, USA

## INTRODUCTION

Airway clearance is one of the primary functions performed during emergency or trauma situations. Airway obstruction is a major priority in prehospital emergency care and is also the second leading cause of preventable battlefield death [1]. Suction devices, also termed aspirators, are powered or unpowered devices employed to remove infectious materials from wounds or fluids from a patient's airway or respiratory support system [2]. Unfortunately, many of these commercial portable suction devices have not been scientifically validated for key performance measures relevant to prehospital care [3, 4]. The majority of suction devices advertised for use in prehospital tactical environments were well within the specifications dictated by the ISO 10079-1 standards, yet no device on the market meets even the most basic field requirements on size, weight, and suction performance [2, 5]. The current ISO 10079-1 standard for primary performance is maximum free air flow rate [5]. This is problematic, as maximum air flowrate overestimates the capability of the device. Peak flow rate at a single instant does not necessarily correlate to its performance for volume evacuation over time. Manufacturers maintain compliance with ISO – 10079-1 by reporting the peak/maximum air flowrate. The focus of this study was to measure and compare air flowrates of four (4) different commercially available suction devices, as well as assess their claims of instantaneous peak flowrate against their actual evacuation performance over a clinically relevant period of time.

## METHODS

The four (4) portable medical suction devices were Laerdal LCSU 4 & SSCOR Quickdraw, which were battery operated suction devices, and Laerdal V-VAC & AMBU RES-QUE, which were manually operated suction devices. The portable suction devices were selected based on their frequency of use among current first responders and their weight (<1.5 kg). A microelectromechanical system (MEMS) air flow sensor (Omron MEMS Air Flow Sensor - D6F-50A61-000) was used to measure the instantaneous air flowrate drawn by the suction device. The air flow sensor was powered with 12 V DC voltage and was connected to digital acquisition system (DAQ) (National Instruments 9221) to log the sensor output (Figure 1). The DAQ was connected to a laptop, where mathematical programming software, MATLAB, was used to record and analyze the data. The airflow sensor outputs the data in the form of volts which was converted to air flowrate unit, liters/minute (l/min), by a quadratic relation using MATLAB. All four (4) suction devices were tested using the experimental setup described in the diagram shown in Figure 1. The suction devices were operated for 30 seconds, where the air flow sensor captures the air drawn by the suction device for a period of 30 seconds at 100 Hz. All suction devices were operated at their respective peak settings. Each device was tested for 5 trials. Manual suction devices were operated by a single operator for 5 trials.

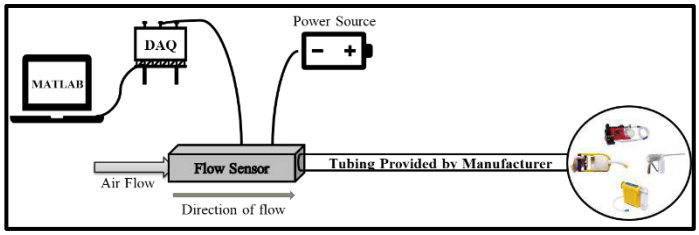


**Figure 1: Air Flowrate Experimental Setup**

## RESULTS

Tests were repeated 5 times for each suction device as described. Data was recorded via the DAQ and analyzed with MATLAB. Figure 2 shows the peak air flowrates of each suction device for 5 trials.

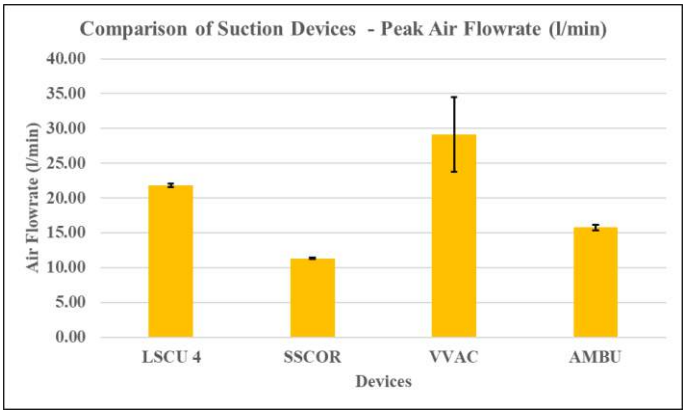


**Figure 2: Peak Air Flowrates of the Suction Devices**

The recorded flowrates were integrated with respect to time to determine the total volume of air drawn the by the suction device over the 60 second experimental timeframe. Figure 3 shows the total volume of air drawn in 60 seconds by each suction device for 5 different trials.

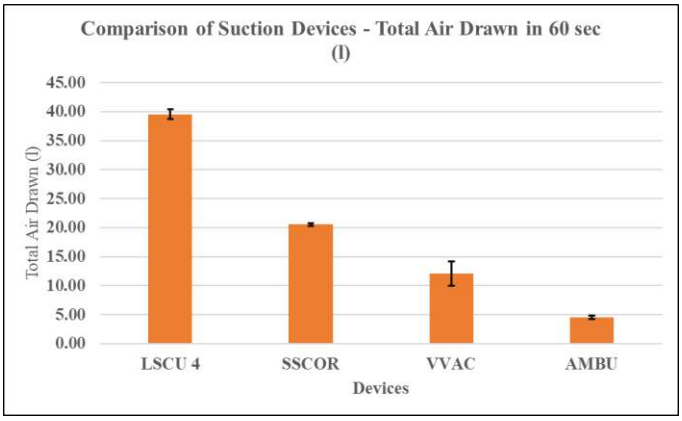


**Figure 3: Total Air Drawn (l) in 60 sec**

## DISCUSSION

Comparison of total air flowrate and instantaneous flowrate for manual suction devices show that, although the manual suction devices offer high instantaneous flowrate, the total airflow rates over time were far less. Peak instantaneous air flowrate is not a meaningful or relevant specification as it cannot provide information on total amount of air drawn by the suction device, which is of course an implied correlation to the liquid flowrate. Total airflow for 60 seconds, is more likely to imply liquid flowrates than peak air flowrate.

Performance of manually operating suction devices naturally changes with the user. In our test, a single user operated the manual devices. Observing the VVAC and AMBU peak flowrates and total volume of air drawn, one can infer that intra-operator variability is increased for VVAC relative to the AMBU as shown in Figure 4. Our results did not assess inter-operator variability, which is most likely significant.

Use of the peak/maximum air flowrate metric allows the manually operated suction devices to claim comparable, or even superior, performance to their battery-powered counterparts. As per the data herein, this is untrue and misleading to purchasers and users of these portable suction systems. Based on this data, we recommend total airflow rate over 60 seconds as an improved specification for analyzing the performance of the suction device. In addition, our data suggests that peak air flowrates reported by manufacturers may not be reproducible in the field.

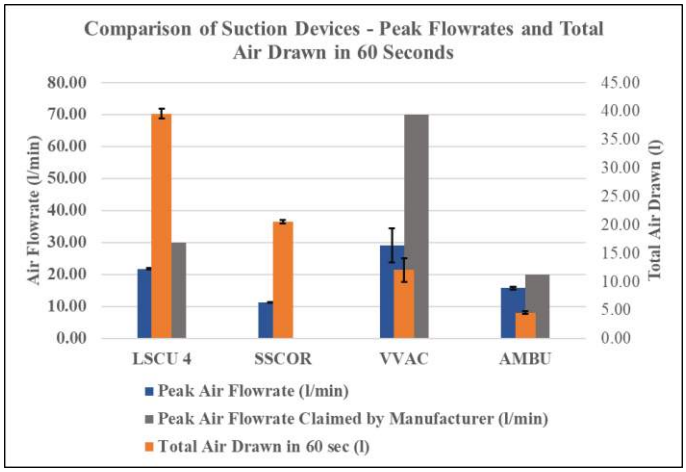


**Figure 4: Comparison of Peak Air Flowrates and Total Air Drawn for 60 seconds by Suction Devices for 5 Trials**


## ACKNOWLEDGEMENTS

The authors acknowledge funding support under a Sponsored Project from the Norwegian company Excitus AS towards the investigation of the current portable suction units on the commercial market.


## REFERENCES


1. De Lorenzo, R.A., et al., *Summary of Findings and Recommendations for Suction Devices for Management of Prehospital Combat Casualty Care Injuries*. 2017, TEXAS UNIV MEDICAL SCHOOL AT SAN ANTONIO SAN ANTONIO United States.
2. Jain, P., et al., *Airway Clearance Using Suction Devices in Prehospital Combat Casualty Care: A Systematic Review.* Prehospital and Disaster Medicine, 2020. **35**(6): p. 676-682.
3. De Lorenzo, R.A., *A Report on Deliverable Four: Develop a specifications list for a portable, lightweight prehospital suction device*. 2017, TEXAS UNIV MEDICAL SCHOOL AT SAN ANTONIO SAN ANTONIO United States.
4. Kozak, R.J., B.E. Ginther, and W.S. Bean, *Difficulties with portable suction equipment used for prehospital advanced airway procedures.* Prehospital Emergency Care, 1997. **1**(2): p. 91-95.
5. Standardization, I.O.f., *ISO 10079-1: 2015*, in *Medical suction equipment — Part 1: Electrically powered suction equipment*. 2015.
6. Paulsen, A.W., L. Wanstreet, and I.J.A.N. West Frankfort, *Are There Guidelines For Anesthesia Suction.* 2015. **29**(3): p. 41-64.

SB³C2022
Summer Biomechanics, Bioengineering and Biotransport Conference
June 20-23, Eastern Shore, MD, USA

# COLLAGEN FIBRILS FROM POSITIONAL TENDONS EXHIBIT INCREASED AMOUNTS OF DENATURED COLLAGEN UPON REACHING THE YIELD POINT

**Allen H. Lin (1,2), Steven J. Eppell (3), Seungju M. Yu (1,4), Jeffrey A. Weiss (1,2,5)**

(1) Department of Biomedical Engineering, University of Utah, Salt Lake City, UT, USA
(2) Scientific Computing and Imaging Institute, University of Utah, Salt Lake City, UT, USA
(3) Department of Biomedical Engineering, Case Western Reserve University, Cleveland, OH, USA
(4) Department of Pharmaceutics and Pharmaceutical Chemistry, Salt Lake City, UT, USA
(5) Department of Orthopaedics, University of Utah, Salt Lake City, UT, USA

## INTRODUCTION

Collagen is the most abundant protein in mammals, and is the main structural constituent of musculoskeletal tissues such as tendon [1]. The base unit of collagen, the collagen molecule, can become denatured during injury and disease [1]. Our lab has recently demonstrated that sub-failure levels of tensile stretch in tendons can cause collagen damage in the form of denaturation, as indicated by collagen hybridizing peptide (CHP) binding [1,2]. Specifically, collagen denaturation is initiated at the yield point of the stress-strain curve regardless of tendon type [2]. However, questions remain about how load is transferred throughout the collagen hierarchy when tendons are stretched.

In this study, we characterized collagen denaturation in fibrils relative to features of the stress-strain curve using a microelectromechanical system (MEMS) device. We selected fibrils because they are the main structural unit in collagenous tissues and one level up from the collagen molecule in the physical hierarchy, allowing more direct assessment of how tensile load affects the collagen molecule. It's been previously shown that collagen fibrils exhibit denatured collagen as indicated by CHP binding when stretched to sub-failure levels of strain [3] and to failure [4]. We hypothesized that collagen fibrils would exhibit increased denatured collagen upon reaching the yield point of the stress-strain curve. This is based on coarse-grain models of collagen fibrils that predict collagen enzymatic crosslinks resist intermolecular sliding of collagen α-helices until the yield point, at which point the α-helices slide out, allowing CHPs to bind [5].

## METHODS

The MEMS devices were fabricated using published techniques [6]. Briefly, silicon on insulator (SOI) wafers with device and oxide thicknesses of 4 and 2 µm, respectively, were purchased. Photoresist was applied to the wafers, and the MEMS devices were patterned using photolithography. The polysilicon was etched using $SF_6$ plasma followed by wet etching with hydrofluoric acid. The MEMS devices were rinsed with isopropyl alcohol then critical point dried.

Collagen fibrils were isolated from rat tail tendon (RTT) fascicles from 12-16 week old male Sprague-Dawley rats using published methods [7]. Individual collagen fibrils were removed from solution using glass micropipettes, placed on the MEMS device, and adhered with epoxy droplets. The fibril and droplets were positioned such that a portion of the fibril was stretched, while a separate portion of the fibril was not stretched, providing a control region (Figure 1). The epoxy was allowed to cure overnight; the next day, endogenous biotin was blocked using a commercial kit (E21390, Invitrogen, Waltham, MA).

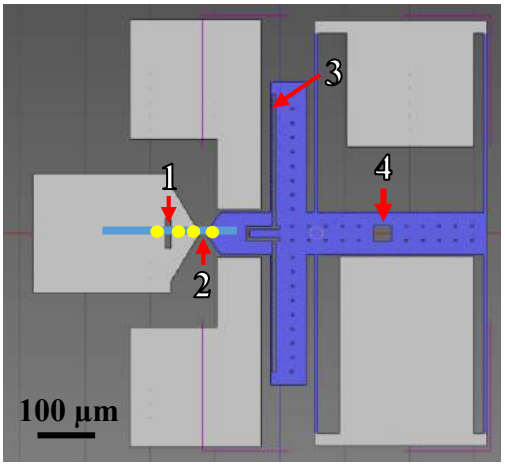


**Figure 1**: **Schematic of the MEMS device. The blue and gray portions represent the moveable and fixed pads, respectively. The blue line represents a collagen fibril adhered with yellow epoxy droplets. (1) Control region. (2) Test region. (3) Force gauge beam. (4) Porthole.**

The baseline amount of denatured collagen in the fibrils was quantified using CHPs. The MEMS device was stained in 3 mL of 15 µM biotinylated CHP (B-CHP, 3-Helix Inc., Salt Lake City, UT) in PBS overnight at 4°C. Excess B-CHP was removed by rinsing in 3 mL of 4°C PBS for ten min, three times. The MEMS device was subsequently stained with 3 mL of a 5 µg/mL solution of Streptavidin-Alexa Fluor 488 (S11223, Invitrogen, Waltham, MA) in 1% bovine serum albumin for two hrs. Excess Streptavidin-Alexa Fluor 488 that had not bound to B-CHP was removed by rinsing in 3 mL of 4°C PBS for ten min, ten times. Collagen fibrils were imaged with an upright microscope (BX51WI, Olympus, Center Valley, PA) in PBS with a 60× objective. Fluorescence intensity of the tested region of the fibril was quantified to measure the amount of denatured collagen.

The MEMS device was then adhered to a piezoelectric stage (Nano-H100, Mad City Labs, Madison, WI) and immersed in PBS. A tungsten probe was placed in a porthole on the moveable pad of the MEMS device to hold it in place, while the rest of the device was displaced at a rate of 0.05 µm/s. The test was recorded at a rate of 4 frames/second. The stretched region of the fibril was attached to a force-gauge beam, where its deflection was quantified and used to calculate the force applied to the collagen fibril. Therefore, the displacement of the piezoelectric stage was the sum of the displacement of the force gauge beam and that of the collagen fibril.

After stretching the collagen fibrils, the B-CHP and Streptavidin-Alexa Fluor 488 staining and imaging protocols were repeated. The post-stretch fluorescence intensity was divided by the pre-stretch intensity for each individual collagen fibril to calculate the increase in denatured collagen following tensile stretch, referred to as the relative fluorescence increase (RFI). The MEMS device was sputter coated with 5 nm of Au-Pd, and the control region was imaged using scanning electron microscopy (SEM) to measure the fibril cross-sectional area.

Image processing was performed on the video recordings of the tests. The images were thresholded and line tracking was used to calculate the displacements of the sample and the force gauge beam. We analyzed a finite element model of the MEMS device during stretch using FEBio to calculate the force that was applied to the collagen fibril. These results were used to construct a stress-strain curve for each fibril; the yield point was defined as the point where the linear region modulus reduced to 50% of its value.

The collagen fibrils were divided into two groups: those that reached the yield point, and those that did not. The mean RFI of the two groups were compared using a two-tailed t-test with $\alpha$=0.05.

## RESULTS

A total of n=8 collagen fibrils were tested. The initial length of the fibrils was 6.15±1.95 µm (mean±s.d.). The final strain levels of the eight fibrils ranged from 0% to 122.4% (Figure 2). Ultimately, n=3 fibrils reached their yield point, while n=5 fibrils did not. One collagen fibril failed at 70.3% strain.

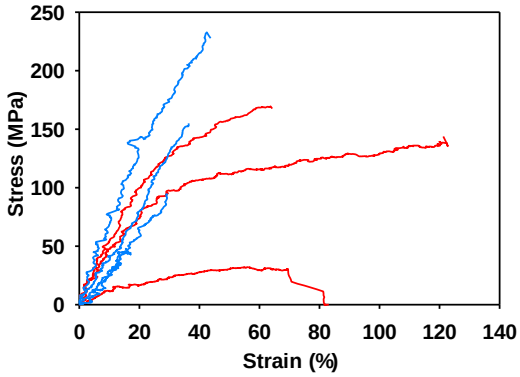


**Figure 2: Stress-strain plots for stretched collagen fibrils. Red lines represent samples that reached a yield point. Blue lines represent samples that did not reach a yield point.**

The three collagen fibrils that reached the yield point were stretched to the three highest strain levels in the dataset. The RFI of these three fibrils increased with increasing strain levels. The five fibrils that did not reach the yield point all had an RFI value that remained at a baseline level of ~2.0 (Figure 3). The mean±s.d. RFI for collagen fibrils that did and did not reach the yield point were 25.09±15.79 and 2.16±0.94, respectively. The difference between the mean RFI values of these two groups was statistically significant (p=0.0139).

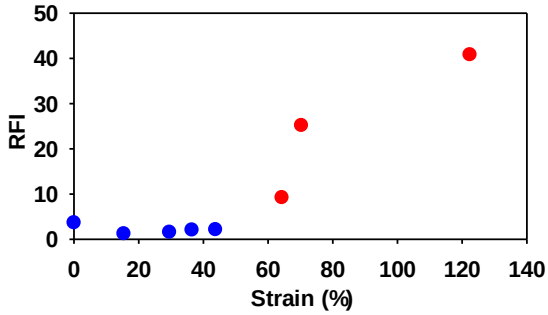


**Figure 3: Relative fluorescence intensity (RFI) of collagen fibrils, indicating denatured collagen increases with applied strain. Red circles represent fibrils that reached the yield point. Blue circles represent fibrils that did not reach the yield point.**

## DISCUSSION

The results of this study demonstrate that collagen fibrils exhibit increased levels of collagen denaturation only after reaching the yield point of the stress-strain curve. This is similar to results found at the tissue level [2] and coarse-grained models of collagen fibrils [5]. Depalle et al [5] predicts that crosslinks resist intermolecular sliding until the yield point, at which point the collagen molecules uncoil, leading to collagen chains sliding, exposing binding sites for CHPs. This is additional evidence that the shear-dominant loading mechanism is the mode of failure in collagen fibrils [1].

An interesting result of this study is that while our strain levels are consistent with strain levels when the same MEMS device was previously used [6], the observed strain levels were significantly higher than those reported by other studies that stretched fibrils [3,4]. Possible reasons for this could be due to the gauge length of the fibrils and the testing methods. The MEMS technique has relatively short gauge lengths (5-10 µm) compared to other methods that used the bowstring methods on much longer samples of ~50 µm [3,4]. Greater sample lengths increase the probability that local point weaknesses exist along the fibril length, leading to reduced failure strains [8]. Regardless, the overall shape of the stress-strain curves in this study is consistent with other studies that investigated collagen fibrils from positional tendons.

This study provides important insights into how load is transferred throughout the collagen hierarchy, the role of enzymatic collagen crosslinks, and how tendons ultimately fail during tension. Understanding these different mechanisms will lead to improved understanding of musculoskeletal injuries.

## ACKNOWLEDGEMENTS

Financial support from NIH #R01AR071358.

## REFERENCES

[1] Zitnay, JL et al., *Nat. Commun.* 8:14913, 2017. [2] Lin, AH et al., *Acta Biomater.* 18:153-160, 2020. [3] Iqbal, S.M. et al., *Soft Matter*. 15:6237-6246, 2019. [4] Quigley, A et al., *Sci. Rep.* 8:4409, 2018. [5] Depalle, B et al., *JMBBM.* 52:1-13, 2015. [6] Liu, Y et al., *Interace Focus.* 6(1):20150080, 2016. [7] Liu, Y et al., *J. Biol. Methods.* 3(4):e54. 2016. [8] Svensson, RB et al., *Acta Biomater.* 70:270-280. 2018.

# THE RELATIONSHIP BETWEEN CARDIAC CYCLE INDUCED STRAIN IN THE BRAINSTEM AND CHIARI MALFORMATION TYPE I SYMPTOMATOLOGY

**Mohamad Motaz Fouad Al Samman (1), Alaaddin Ibrahimy (2), Blaise Simplice Talla Nwotchouang (3), John N. Oshinski (4), Daniel L. Barrow (5), Philip A. Allen (6), Rouzbeh Amini (7), and Francis Loth (7)**

(1) Department of Bioengineering, Northeastern University, Boston, Massachusetts, USA
(2) Department of Biomedical Engineering, Yale University, New Haven, Connecticut, USA
(3) Department of Biomedical Engineering, The University of Akron, Akron, Ohio, USA
(4) Radiology & Imaging Sciences and Biomedical Engineering, Emory University School of Medicine, Atlanta, Georgia, USA
(5) Department of Neurosurgery, Emory University, Atlanta, Georgia, USA
(6) Conquer Chiari Research Center, Department of Psychology, University of Akron, Akron, Ohio, USA
(7) Department of Mechanical and Industrial Engineering, Department of Bioengineering, Northeastern University, Boston, Massachusetts, USA

## INTRODUCTION

The goal of this study is to explore the relationship between Chiari malformation I (CMI) symptoms and cardiac cycle induced strain on the vestibulospinal tract (VST). Milhorat found 89 out of 126 CMI patients with Otoneurological disturbances [1]. The most common ones are tinnitus (81%), vertigo (69%), unsteadiness (49%), and dizziness (18%) [2,3,4]. It has been evident that CMI patients suffer from a significant impaired postural control in the anterior-posterior (AP) direction compared to healthy controls [4]. It is thought that impaired balance may be a result of traction and distortion of cerebellar pathways due to hindbrain (pons, medulla, and cerebellum) descent [5]. This article emphasizes the function of lateral VST (lVST) that ensures the coordination of different muscle groups during postural control [6]. In this work, the authors proposed a tool in which motion and strain in sub-sections of the vestibular circuitry can be investigated using DENSE MRI. We hypothesize that CMI subjects have higher VST strain than controls, and this higher strain impacts their postural control and balance.

## METHODS

Participants: 55 adult CMI subjects and 25 healthy adult controls were scanned at Emory University School of Medicine between 2017 and 2020 according to its institutional review board-approved protocol [7]. Symptomatology was collected via interviewing CMI subjects at the time of presurgical MRI scan. Those without clinical data were excluded from the correlation (n = 24). We examined symptoms relevant to vestibulocochlear nerve: vertigo (n = 14), imbalance (n = 12), tinnitus (n = 8), dizziness (n = 7), and nausea or vomiting (n = 14).

Imaging Protocol: Sagittal T1 and T2 weighted images of the brain were acquired using a PrismaFit 3T MRI scanner (Siemens Healthcare, Erlangen, Germany) employing a 20-channel head coil. DENSE scans were acquired in the midsagittal plane using a 2D spiral cine technique and peripheral pulse unit gating with spatial and temporal resolution [7]. Pixel size was 0.9 x 0.9 mm, and the slice thickness was 8 mm [7].

Processing: An in-lab developed MATLAB code (Mathworks, Natick, MA) was used to process DENSE images in midsagittal plane, neglecting the 3rd dimension (through plane) based on Pahlavian's reporting [7,8]. Further, the 2D displacement encoded in DENSE was used to calculate strain.

Region of Interest: There are 4 pairs of vestibular nuclei (superior, lateral, medial, and inferior) that are located along the lateral floor of the 4th ventricle in the lower pons [9]. Those nuclei are connected to the spinal cord through the medial VST (mVST) and lVST [6]. lVST originates from lateral and inferior vestibular nuclei and projects to the entire ipsilateral (same side) spinal cord through its anterior funiculus (white matter anterior to the anterior grey horn) [6]. Due to the very close proximity of lVST and mVST at vestibular nuclei and in the cervical spinal cord, they are considered one tract (VST) for the sake of the analysis. VST was analyzed using 2 investigational boxes placed along the structure in the midsagittal plane (Figure 1).

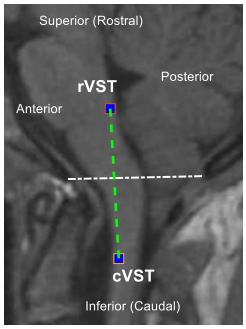


**Figure 1: Location of the region of interest (blue boxes) on an anatomical MRI of a CMI patient at the midsagittal plane.**

The rostral VST (rVST) box was placed at the start of the tract (most posterior aspect of the lower pons), and the caudal VST (cVST) was placed approximately 5-7 cm inferior to the rVST (most anterior aspect of the spinal cord at the level of C1/C2). Each box is a mask of 3 x 3 pixels in the midsagittal plane corresponding to a 3D displacement field measures 2.7 x 2.7 x 8 mm in the cephalo-caudal (CC or y-dir), anterior-posterior (AP or x-dir), and mediolateral (through-plane or z-dir) directions, respectively. Due to documented cardiac cycle-induced regional brain tissue motion [7], the displacement field changes with the cardiac cycle, so does the position vector which is the summation of location of the mask (box) and the displacement in each phase on each direction. Furthermore, the length ($d$) of the line, distance between the 2 boxes, changes throughout the cardiac cycle as well. The length is calculated using the equation (1). Lengthening ($L$) and strain ($\varepsilon$) are calculated using equations (2), and (3), respectively. Statistical Analysis: independent samples t-test was used to compare the maximum strain in CMI (n = 55) and control (n = 25). Correlation test was used to correlate the maximum strain on VST of CMI (n = 24) and imbalance. Correlation with the rest of symptoms is not appropriate because of the lack of strain data on the vestibular and cochlear nuclei.

## EQUATIONS

$$d(t) = i\sqrt{(X_{rVST} - X_{cVST})^2 + (Y_{rVST} - Y_{cVST})^2} \quad (1)$$

$$L = d_{max} - id_{min} \quad (2)$$

$$\varepsilon_{max} = \left(\frac{L}{d_{min}}\right) * 100 \quad (3)$$

## RESULTS

The brain tissue motion of rVST and cVST was traced over the cardiac cycle and the path was illustrated in Figure 2. This motion implies the motion and the lengthening that VST experiences over the cardiac cycle.

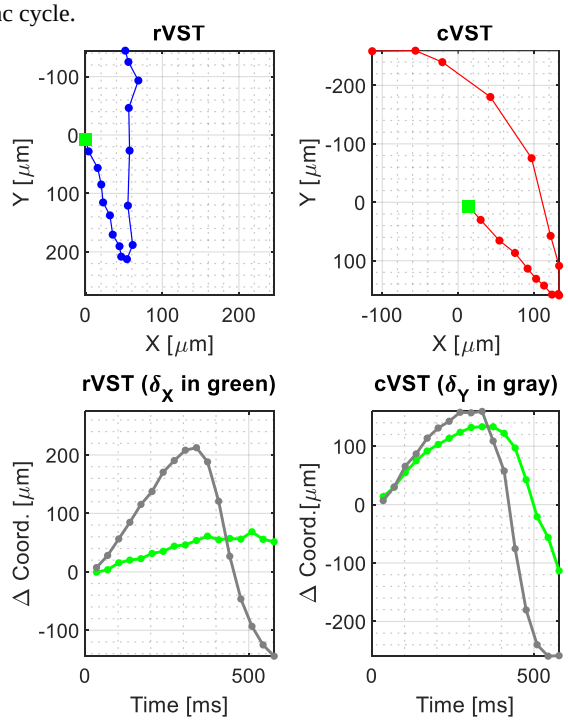


**Figure 2: Top: Brain tissue motion path of rVST and cVST for one CMI subject (the green box is the starting point). Bottom: The position time trace of rVST and cVST over the cardiac cycle.**

There is a statistically significant difference between the maximum strain on VST in Chiari and on that of the control ($p$-value = 0.009). The maximum strain on the VST in CMI, and control were 0.58 ± 0.38 %, and 0.36 ± 0.23 %, respectively.

A nonsignificant trend between the maximum strain on VST in CMI and the vestibulocochlear symptoms was seen. This nonsignificant trend varied from one symptom to another. While dizziness and tinnitus showed a positive trend with strain, vertigo and nausea or vomiting did not. A weaker nonsignificant trend was seen between imbalance and strain. This weak strain-imbalance trend is illustrated in the bar chart (Figure 3) where strain with imbalance is plotted in green, and strain without imbalance in grey. Finally, there was no significant correlation between maximum strain and imbalance (r = 0.282, $p$-value = 0.182).

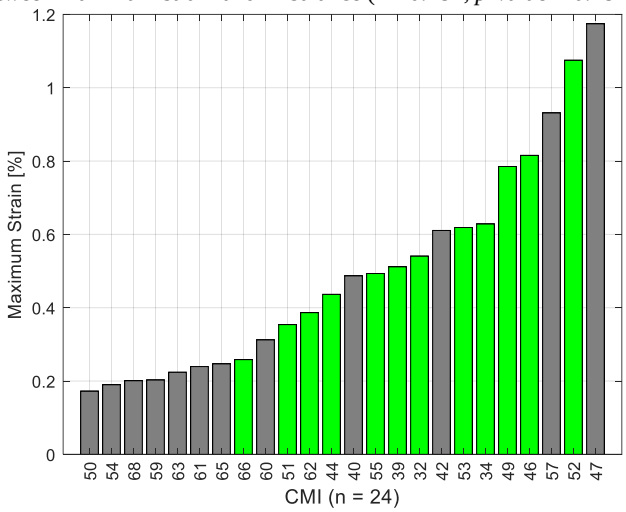


**Figure 3: Distribution of maximum strain for the VST in CMI subjects (green = with imbalance, grey = without imbalance).**

## DISCUSSION

We demonstrated that the cardiac cycle induced strain on the VST in CMI patients was significantly higher than that of the healthy control. We found no correlation between maximum VST strain in CMI subjects and imbalance. This may be due to the small strain values we observed (< 1 % for both CMI and controls). Based on our definition of lengthening and strain, strain was considered only in tension (Note: zero strain lengthening is unknown). Because the locations and dimensions of each subject's neuroanatomical structures are not known, anatomical landmarks were used to estimate their location. Due to a reduction in the signal-to-noise ratio at the end of the cardiac cycle caused by T1 decay, only the first two-thirds of each cardiac cycle are reliable [7]. Therefore, the rVST and cVST position at the end of the cycle does not match the start location.


## ACKNOWLEDGEMENTS

The authors would like to thank Conquer Chiari and the National Institutes of Health, NINDS R15 (Grant No. 1R15NS109957-01A1) for providing funding for this research work.


## REFERENCES


[1] Milhorat, T H et al., *Neurosurgery*, 44:1005-1017, 1999.
[2] Sperling, N M et al., *Otol Neurotol*, 22:678-681, 2001.
[3] Jiménez, G G et al., *Acta Otorrinolaringol*, 66:28-35, 2014.
[4] Sommers, B N et al., *Gait & Posture*, 88:280-285, 2021.
[5] Paul, K S et al., *J Neurosurg*, 58:183-187, 1983.
[6] Mihailoff, G A et al., *Fundamental Neuroscience*, 5th ed,2018.
[7] Nwotchouang, B S T et al., *Annals of Biomed Eng*, 2021.
[8] Pahlavian, S H et al., *J Biomech Eng*, 140:1-13, 2018.
[9] Fernández-Gil, Á et al., *Sem. in Ultras, CT, MRI*, 31:196-219, 2010.

SB³C2022
Summer Biomechanics, Bioengineering and Biotransport Conference
June 20-23, Eastern Shore, MD, USA

# AN EXPERIMENTAL INVESTIGATION ON BENDING RESPONSE OF SCLERA TISSUE UNDER ELECTRICAL STIMULATION

**Hamed Hatami-Marbini (1), Jafar A. Mehr (1)**

(1) Mechanical and Industrial Engineering, University of Illinois at Chicago, Chicago, Illinois, USA,
Email. hatami@uic.edu

## INTRODUCTION

The sclera is the shell surrounding the eyeball attached to the cornea. It is a dense connective tissue constituting more than 80% of the eye's wall. The tough nature of the sclera protects the eye from serious damages as well as also providing a solid support for the extraocular muscles. From the microstructure point of view, the main compositions of the sclera include collagen, proteoglycans (PG) and elastin. PGs are polysaccharides units which are attached to glycosaminoglycans (GAGs) side chains. The GAGs play a key role in determining hydration, elasticity and resiliency of the sclera tissue. The main chemical compositions in the GAGs structure are carboxyl (i.e., $COO^-$) and sulfate (i.e., $SO_3^-$) groups. Within the physiological pH range (pH≅7.0) the GAGs are negatively charged, and the sclera tissue is considered as a natural polyelectrolyte hydrogel [1]. When an electroactive hydrogel is placed in a salt solution (e.g., NaCl) between two electrodes, upon the application of electrical voltage to the electrodes, the hydrogel bends towards one of the electrodes. The direction of the bending depends on the sign of the electrical charge inside the samples; a negatively charged gel bends to the cathode while a positively charged hydrogel bends to the anode. The sclera is a negatively charged tissue, so it is expected to behave like an electroactive polyanionic hydrogel, i.e. show a mechanical response when subjected to external electrical stimulations. The objective of the present work was to perform experiments and test the above hypothesis.

The electrical stimulation leads to water transportation due to migration of the counterions of the fixed charges inside the hydrogel (i.e., electroosmosis) [2]. The mechanism proposed for this electroactive bending response is the transient alteration in concentration of mobile ions (e.g., $Na^+$ and $Cl^-$) at the boundaries of the hydrogel and surrounding solution leading to local swelling/shrinking at the gel-solution interfaces. Aside from the content of the fixed charge, mechanical properties of the hydrogel, strength of the electrical field, the pH of the surrounding medium are other important contributing factors in electromechanical bending response of a polyelectrolyte hydrogel.

In the present study, we conducted experimental measurements to demonstrate the electro-responsiveness of sclera and investigate the effects of magnitude of the electrical filed on bending response of the tissue.

## METHODS

Fresh porcine eyes were collected from slaughterhouse (n = 18). After cleaning the globes by removing the fat and muscle, the globes were dissected, and sclera strips with dimensions of 2.5 mm × 20 mm were excised from the posterior of the eye globe in superior-inferior direction with 2 mm distance from the optic nerve head. The sclera strips were dried in desiccator for 24 hours. After measuring the weight of the dried samples, the strips were placed in 0.15M NaCl solution. The weight of the samples was monitored in time and their hydration H was calculated as

$$H = \frac{\mathrm{W_s} - \mathrm{W_d}}{\mathrm{W_d}}$$

where $\mathrm{W_s}$ is the wet weight of samples and $\mathrm{W_d}$ is their dry weight. After the samples reached to hydration of 2 mg water / mg dry weight, they were mounted in experimental setup. For conducting the experiments, we designed a container with two carbon electrodes 5 cm apart along with clamps for fixing the tissue from one side inside the container. We used a DC power supply for applying the electric voltage. In addition, we used a digital microscope to track the electromechanical bending response of the sample inside the container filled with NaCl solution (0.15M concentration). For this purpose, we developed a program in Python in order to capture the movement and calculate the

bending angle of the sample in real time. The main components of the experimental setup are shown in Figure 1. The bending angle of the samples was defined as deviation of their tip from the initial position as shown in Figure 2.

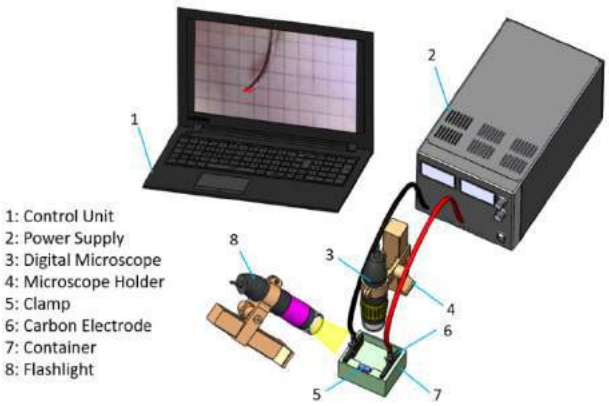


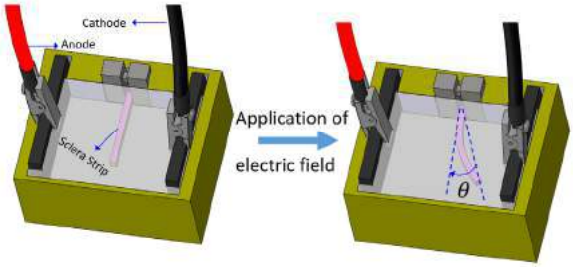


**Figure 2: Illustration of different components of the experimental setup. Sclera strips were mounted in the setup immersed in NaCl solution and their deformation was captured by a digital camera. The bending angle θ quantifies the amount of their bending under electrical stimulations.**

It is expected that the bending angle of the samples to depend on the pH of the solution since any change in the solution pH could change the amount of fixed charges inside the tissue. Upon applying the voltage, pH waves will be generated because of electrolysis of water. We used a universal pH indicator to monitor propagation of pH waves inside the container under different voltages.

## RESULTS

It was seen that with increasing the voltage, the pH waves propagate faster into the solution. For example, it took more than 2 minutes for pH waves propagating from the electrodes to reach the center of the container when an electrical voltage 15 V was used. It is also known that speed of pH wave propagation is proportional to the magnitude of the applied voltage. Since 15 V was the maximum voltage that we applied in the present work, we limited the duration of our experiments to 60 seconds in order to limit the pH variation inside the solution surrounding the samples.

The bending deformation of a typical sample under electric voltage is shown in Figure 1. Furthermore, the electromechanical bending response of scleral strips at 5 V, 10 V and 15 V of electrical stimulations was plotted as a function of time in Figure 2. It is seen that with increasing the voltage and time, the bending angle increases. The rate of scleral bending was fast in the beginning and it slowed down with increasing time.

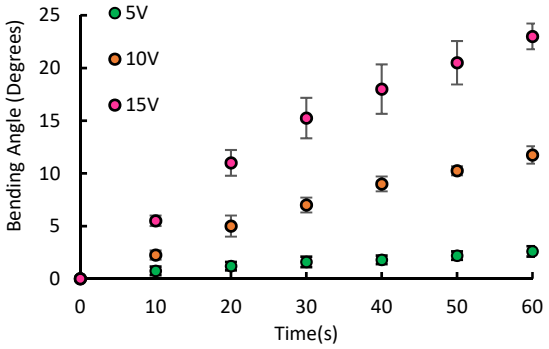


**Figure 2: The bending angle of scleral strips subjected to 5 V, 10 V and 15 V as a function of time.**

## DISCUSSION

The scleral samples showed mechanical bending response to the external electric voltage. We observed that samples subjected to 5V, 10V and 15V for 60 seconds reached to a maximum bending angle of nearly 3°, 10° and 23°, respectively. Thus, it is concluded that the deformation of sclera was significantly dependent on the magnitude of the applied external electrical field. This observation is in agreement with previous studies on the electroactive bending behavior of electroactive hydrogels [3]. This dependence on the strength of the electrical field is because increasing the voltage leads to increasing the speed of movement of the ions inside the solution. Subsequently, differential osmotic pressure at the boundaries of the samples and solution is created more quickly, which in turn increases the mechanical bending response of the tissue. The present experiments had some limitations. For example, the electrolysis of water and creation of pH gradient in the solution may have affected the electromechanical response of the tissue. This is because the pH waves alter the net electrical charges inside the tissue. In the present work, the strength of electrical field and time of electrical stimulation were limited to minimize the possible effects of pH gradient on electromechanical bending response of the samples. The present work characterized the electromechanical response of the sclera and its findings revealed some of the biochemical as well of biomechanical properties of this ocular tissue. We have also developed numerical models and tuned them against the experimental data [4]. We are currently working on applying the experimental framework of the present study to other biological tissue containing fixed electrical charges in order to increase our understanding of their electromechanical properties.

## ACKNOWLEDGEMENTS

The authors would like to acknowledge the support in part by National Science Foundation: Grant No. 1635290.

## REFERENCES

[1] Elliott, G.F., Hodson, S.A. Cornea, and the swelling of polyelectrolyte gels of biological interest. Reports on Progress in Physics 61:1325, 1998
[2] De Rossi, D., et al., Electrically induced contractile phenomena in charged polymer networks: preliminary study on the feasibility of muscle-like structures, Trans Am Soc Artif Intern Organs 31 (1985) 60-65
[3] Kim, S.Y., et al. Properties of electroresponsive poly (vinyl alcohol)/poly (acrylic acid) IPN hydrogels under an electric stimulusJ applied polymer science 73:1675-83, 1999.
[4] Mehr, J.A, Hatami-Marbini, H. Experimental and numerical analysis of electroactive characteristics of scleral tissue, Acta Biomaterialia, accepted.

SB³C2022
Summer Biomechanics, Bioengineering and Biotransport Conference
June 20-23, Eastern Shore, MD, USA

# FINITE ELEMENT SIMULATION OF ELECTROACTIVE MECHANICAL RESPONSE OF SCLERA USING A MULTI-PHYISICS CHEMO-ELECTRO-MECHANICAL MODEL

**Jafar A. Mehr (1), Hamed Hatami-Marbini (2)**

(1) Mechanical and Industrial Engineering, University of Illinois at Chicago, Chicago, Illinois, USA, Email. hatami@uic.edu

## INTRODUCTION

Electroactive hydrogels have gained great interest in the last years due to their wide range of applications from robotic and artificial muscles to drug delivery systems and biosensors. They can directly transform the electrical energy into mechanical work if placed in an electrical field. A polyelectrolyte hydrogel contains electrical charges which is bound to its polymeric network. According to the electroneutrality principle, when a charged electroactive hydrogels is placed inside a salt solution (e.g., NaCl), the unbalance between the electrical charges, causes the gel to swell. When an electrical voltage is applied to the electrodes, the local ionic strength is altered. The transient accumulation and transient depletion of mobile ions (e.g., $Na^+$ and $Cl^-$) at hydrogel and solution boundaries near the cathode side and anode side, in addition to causing swelling or shrinkage of the hydrogel-solution interfaces, create transient mechanical bending response of the electroactive hydrogel [1]. The purpose of this study is to propose and implement a numerical model for electro-actuation of the scleral tissue in support of recent experimental studies which showed that the sclera deforms when subjected to the electrical stimulations [2]. The sclera is composed of negatively charged proteoglycans and collagen fibers and we showed that it behaves like an electroactive polyanionic hydrogel. In these experiments, scleral strips were placed between two electrodes in a NaCl solution. We observed that the scleral strips bend in response to the electrical stimulations. Here, computational modelling will be used to understand and estimate the effects of various parameters on the electromechanical response of the sclera.

In the course of last decades, theoretical and computational models have been developed to study the electromechanical response of the electroactive hydrogels such as finite element models. These models are built based on principles of continuum mechanics and microscale level properties of hydrogels and their surrounding bathing fluid. In this work, we created a coupled chemo-electro-mechanical (CEM) model to investigate the electromechanical bending response of scleral tissue [3].

## METHODS

Figure 1 shows the numerical representation of the experimental studies of the sclera. The scleral strips of thickness of about 1.3 mm were clamped from one side inside the 0.15M NaCl solution at the center between two electrodes 5-cm away from each other; the same dimensions were used in the numerical simulations. The nonlinear coupled Poisson-Nernst Planck (PNP) system of equations are written as:

$$\frac{\partial c_i}{\partial t} + \nabla.\left(-D\nabla c_i - z\mu F c_i \nabla \emptyset\right) = 0 \qquad (1)$$

$$\nabla^2 \emptyset = -\frac{F}{\varepsilon_0 \varepsilon_r}\sum(z_i c_i) \qquad (2)$$

where $c_i$ is the concentration of mobile ionic species, D is diffusion constant of the ions, $\mu$ is mobility of the ionic species, R is universal gas constant, T is temperature, F is Faraday constant, $\emptyset$ is electric potential, z is the valence of the ions, $\varepsilon_0$ is vacuum permittivity, and $\varepsilon_r$ is the relative permittivity of the medium. We derived the weak form equations of the PNP system by multiplying the equations in appropriate test functions and integration by parts. The resulting PNP system of equations was solved using an open-source finite element platform (FEniCS) [4]. For this purpose, GMSH software was used to generate the domains and mesh [5]. As it is shown in Figure 1, the mesh was refined near the boundaries of the sample and solution to be able to capture the steep gradient of the ion concentrations at the sample-solution interfaces.

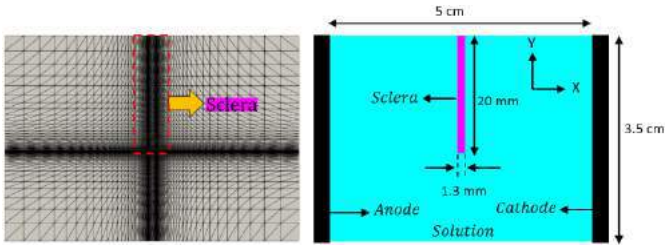


**Figure 1: Illustration of the mesh and computational domains.**

Furthermore, the equations of equilibrium are given by:

$$\sigma_{ij,j} + F_i = \frac{\partial^2 u_i}{\partial t^2} \qquad (3)$$

Where $\sigma_{ij}$ is the stress tensor, $u_i$ is the displacement vector, and $F_i$ corresponds to the body force. We defined the body force by introducing the osmotic pressure:

$$\Delta\pi = RT\sum[(c_i)_{Sclera} - (c_i)_{Solution}] \qquad (4)$$

In equation 4, $c_i$ represents the concentration of $i^{th}$mobile specie. Finally, the body force was defined as gradient of normalized differential osmotic pressures at the vicinity of anode side ($\Delta\pi_1$) and cathode side ($\Delta\pi_2$):

$$F_i = \frac{1}{RT}\nabla(\Delta\pi_2 - \Delta\pi_1) \qquad (5)$$

We used implicit backward Euler method to discretize the equations in time. We first validated our implementation of PNP equations in the FEniCS by reproducing the results of the reference paper [3]. The Young's modulus of the sclera, temperature, were taken equal to 0.2 MPa and 293K, respectively. The diffusion constants of the mobile ions, relative permittivity, and other constants were obtained from the literature. The simulation was performed for 60 seconds under 10 V of electrical voltage.

## RESULTS

The bending angle was defined as the angle that the tip of the sample makes with respect to the initial position that was calculated in each time step. The variation of the bending angle versus time along with deformation of the tissue in time are shown in Figure 2.

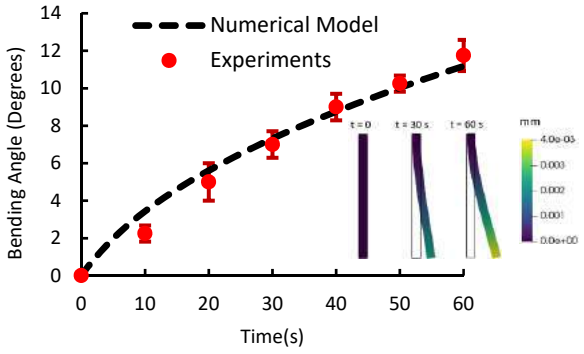


**Figure 2: The numerical results of the variation of the bending angle in time are compared with the experiments. The deformation of the sample along with contour of displacement are also shown.**

In this figure, the symbols show the experimental results. From fitting the model to the experimental data, the fixed charge density of 10 mM inside the tissue was found.

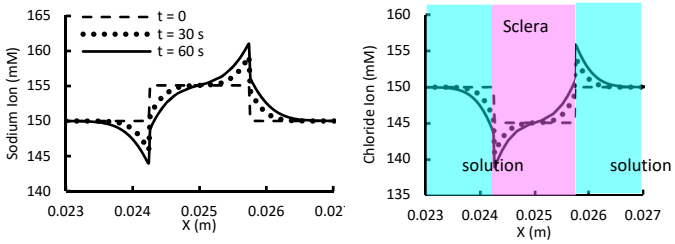


**Figure 3: Concentration of the sodium (Left) and chloride (Right) ions in different times under 10V of electrical stimulation along the horizontal line**

## DISCUSSION

We developed and implemented a CEM model for the simulation of electroactive bending behavior of polyelectrolyte hydrogels. The focus of our study was to use this computational model for investigating the electromechanical response of the sclera.

By looking into the variation of the mobile ion concentrations in time, we observe a step-shaped of distribution of the concentration of both ions along the width of the domains before applying the electrical voltage and in equilibrium state. Once the voltage is applied, these concentrations decrease in time at the anode side (i.e., left electrode) while they increase at the cathode side (Figure 3). This is in agreement with the theory of depletion polarization [6] demonstrating the bending of the sclera to the cathode based on generation of the differential osmotic pressure at the interfaces of the sclera and solution domains.

It should be noted that we simplified this simulation to a 2D geometry in order to reduce the computational cost. However, it could be extended to a more complex 3D geometry to achieve more realistic results in future. In addition, the linear elastic material model was employed in this study for simplicity. However, the sclera is fibrous tissue and orientation of the collagen fibers plays an important role in its mechanical response. This is another important fact that we are currently working on, i.e. using a nonlinear material model for the sclera. The numerical framework of the present study could be used to estimate to model the electroactive mechanical response of both electroactive biological tissue and hydrogels.

## ACKNOWLEDGEMENTS

The authors would like to acknowledge the support in part by National Science Foundation: Grant No. 635290.

## REFERENCES

1. Doi, M., M. Matsumoto, and Y. Hirose, *Deformation of ionic polymer gels by electric fields.* Macromolecules, 1992. **25**(20): p. 5504-5511.
2. Mehr, J.A. and H. Hatami-Marbini, *Experimental and numerical analysis of electroactive characteristics of scleral tissue.* Acta Biomaterialia, accepted.
3. Wallmersperger, T., B. Kröplin, and R.W. Gülch, *Coupled chemo-electro-mechanical formulation for ionic polymer gels—numerical and experimental investigations.* Mechanics of Materials, 2004. **36**(5-6): p. 411-420.
4. Logg, A., K.-A. Mardal, and G. Wells, *Automated solution of differential equations by the finite element method: The FEniCS book*. Vol. 84. 2012: Springer Science & Business Media.
5. Geuzaine, C. and J.F. Remacle, *Gmsh: A 3-D finite element mesh generator with built-in pre-and post-processing facilities.* International journal for numerical methods in engineering, 2009. **79**(11): p. 1309-1331.
6. Kwon, I.C., Y.H. Bae, and S.W. Kim, *Characteristics of charged networks under an electric stimulus.* Journal of Polymer Science Part B: Polymer Physics, 1994. **32**(6): p. 1085-1092.

# MICROFLUIDIC APPROACH FOR QUANTIFYING VASCULAR PERMEABILITY IN THE PRESENCE OF TRANSMURAL FLOW

**S. Huang (1,2), W. Polacheck (1,2,3)**

(1) Department of Biomedical Engineering, UNC-NC State, Chapel Hill, NC, USA
(2) McAllister Heart Institute, UNC, Chapel Hill, NC, USA
(3) Cell Biology and Physiology, UNC, Chapel Hill, NC, USA

## INTRODUCTION

Endothelial cells (ECs) form the innermost layer of all blood vessels, and act as a barrier between blood and tissue to direct the transport of essential compounds within the body. These cells mediate transvascular transport in response to a variety of chemical and mechanical microenvironment including inflammation and shear stress [1,2]. Endothelial dysfunction, resulting in compromised vascular barrier function, is a hallmark of and contributes to the pathogenesis of various diseases including chronic kidney disease and cancer [3,4]. To quantitatively characterize vascular barrier function, two metrics are commonly employed: 1) the diffusive permeability ($P_d$), a measure of the barrier to molecular diffusion, and 2) the hydraulic conductivity (HC), a measure of the resistance to convection [5,6]. $P_d$ governs the rate of mass transport of a given solute across the vascular wall in response to a gradient in solute concentration, while HC governs fluid velocity in response to a transmural pressure gradient [5,6]. Previous work by our group and others have quantified $P_d$ in engineered vascular models as a measure of barrier integrity [7,8]. Here, leveraging a microfluidic model of the vasculature and live imaging techniques, we demonstrate a technique to determine the role of HC in governing transmural flux.

## METHODS

A microfluidic device featuring two parallel, cylindrical channels within a type I collagen hydrogel derived from rat tail was designed and fabricated as previously described (Fig. 1A) [7]. After seeding one channel with human umbilical vein endothelial cells (HUVECs), devices were placed either on a laboratory rocker (30 angle at 5 cycles/minute) or a static shelf within an incubator to precondition ECs with luminal flow applying a peak wall shear stress of 3 dynes/cm$^2$ or static culture, respectively (Fig. 1B). Devices were then flooded with 200 µg/ml 10 kDa Cascade Blue dextran. We then applied a defined concentration and pressure gradient across the vessel wall by emptying the non-seeded channel and adding a cocktail of 125 µg/ml 70kDa Fluorescein or Texas Red dextran and 200 µg/ml 10kDa Cascade Blue dextran to the seeded channel. Specific volumes of the dextran cocktail were added to generate pressure gradients of 0, 0.5, 5, and 50 Pa/mm across the two channels (Fig 2A). The endothelialized

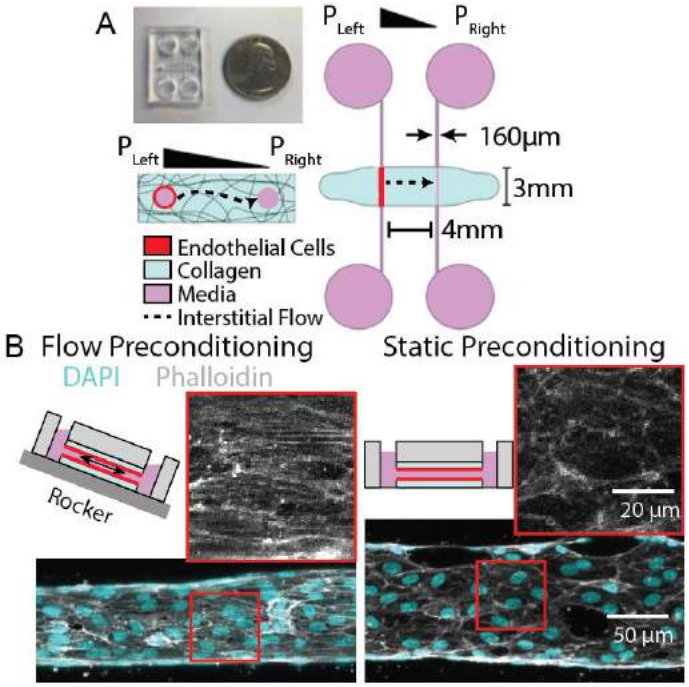


**Figure 1: Microfluidic blood vessel on chip. A) Schematic of two channel microfluidic platform B) Schematic of flow and static preconditioning, as well as representative vessels**

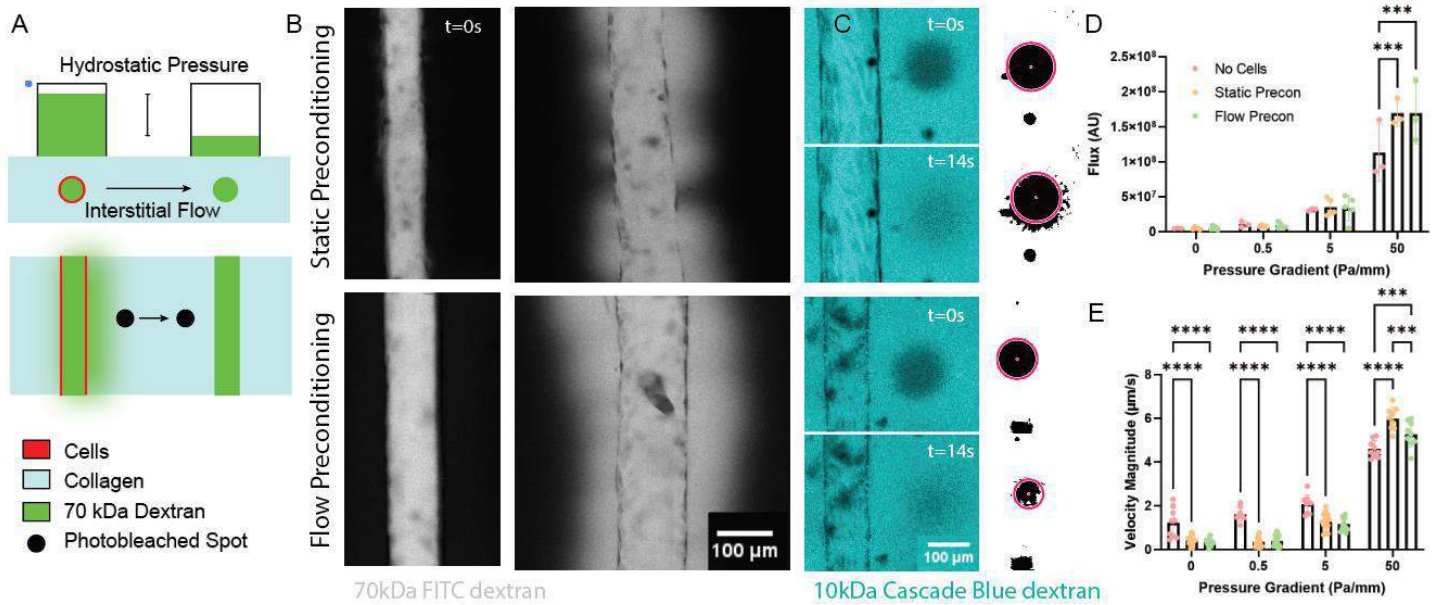


**Figure 2: Assay to measure transluminal flux in a blood vessel. A) Experimental setup to measure transluminal flux and interstitial velocity. B) Bulk extravasation of 70 kDa dextran out of microfluidic vessels cultured under flow and static conditions for a 5Pa/mm pressure gradient. C) Fluorescence recovery after photobleaching illustrates dextran displacement over time for a 5Pa/mm pressure gradient. Binary images display photobleached circle identified and used to quantify displacement using a custom Matlab code. D) Bulk flux of 70kDa dextran for a given pressure gradient. E) Interstitial velocity for various pressure gradients. ***p < 0.001 *** p < 0.0001**

channel was imaged every second for 1 minute as dextran entered the vessel and extravasated into the subluminal collagen matrix (Fig. 2B). Total transluminal flux of 70 kDa dextran was quantified as previously described [7]. Fluorescence recovery after photobleaching (FRAP) was then utilized to bleach a circular region of the 10kDa dextran, and the resulting bleached region was imaged every 0.25 seconds for 30 seconds. A Matlab code was written to track the displacement of the bleached region and to calculate the interstitial fluid velocity (Fig. 2C).

## RESULTS

ECs cultured on a rocker formed confluent monolayers, and the cytoskeletal structure of ECs aligned in the direction of flow; whereas, ECs cultured in static conditions demonstrated pericellular gaps, and ECs did not align in any direction (Fig. 1B). For applied pressure gradients up to 5 Pa/mm, the presence of ECs and flow preconditioning did not have an effect on total flux of 70 kDa dextran (Fig. 2D). At 50 Pa/mm, transluminal flux of 70 kDa dextran exceeded the magnitude of flux in unseeded channels, and transluminal flux was not a function of flow preconditioning (Fig. 2D). At pressure gradients less than and including 5 Pa/mm, interstitial velocity magnitude was significantly higher in unseeded channels, and velocity magnitude in seeded channels was not a function of flow preconditioning (Fig. 2E). When subjected to a 50 Pa/mm pressure gradient, interstitial flow velocity magnitude was highest in vessels with static preconditioning, followed by vessels with flow preconditioning, and vessels with no cells (Fig. 2E).

## DISCUSSION

The changes in EC actin alignment with the direction of flow, and a confluent endothelial monolayer, are consistent with previous studies on ECs cultured under applied shear stress [7,9]. While the pressures applied (0-200 Pa) and resulting pressure gradients (0-50 Pa/mm) are smaller in magnitude than physiological transluminal pressures (130-400 Pa) and pressure gradients (20,000 Pa/mm), we achieve transluminal velocity magnitudes similar to those found *in vivo* of 0.1-2 µm/s [10-12]. These results imply superphysiological HC values, which can be attributed to the reductionist nature of the assay –vessels are comprised of only ECs in a type I collagen hydrogel, whereas native vasculature is comprised of layers of surrounding mural cells and dense basement membrane [13]. We found the presence of ECs reduced fluid velocity magnitude, except at high (50 Pa/mm) transmural pressure gradients, where seeded vessels demonstrated increased fluid velocity magnitude compared to empty channels. The fluid velocity magnitude (> 4µm/s) at these pressures is greater than what is seen in healthy tissue [14], and the increased flow may be caused by flow-induced expression of matrix metalloproteinases [15] and resultant collagen degradation [16]. Future work entails isolating diffusive and convective contributions to transluminal flux of 70 kDa dextran. The resulting technique can be utilized to quantify and probe the underlying mechanisms that govern regulation of vascular barrier function in physiological and pathophysiological settings.

## ACKNOWLEDGEMENTS

This work was supported by NIH Grant T32HL69768 and by a UNC Computational Medicine Pilot Award. Device fabrication was performed in the Chapel Hill Analytical and Nanofabrication Laboratory, CHANL, a member of the North Carolina Research Triangle Nanotechnology Network, RTNN, which is supported by the National Science Foundation (ECCS-2025064), as part of the National Nanotechnology Coordinated Infrastructure, NNCI.

## REFERENCES

[1] Park, S.A. et al., *J Anal Methods Chem.*, 2-7, 2018. [2] Hillsley, M.V. et al., *Biochem Biophys Res Commun.*, 293:1466-1471, 2002. [3] Terpstra, M.L. et al., *World J Nephrol.*, 5:378-388, 2016. [4] Huang, Y. et al., *Cancer Res.*, 19:7529-7538, 2009. [5] Meijer, E.F. et al., *Methods Mol Biol.*, 176:139-148, 2016. [6] Curry, F.E. et al., *J Vis Exp.*, 103:1-10, 2015. [7] Polacheck, W.J. et al., *Nat Protoc.*, 14:1425-1454, 2019. [8] Frost, T. et al., *Micromachines*, 10:533, 2019. [9] Gong, X. et a.l, *Microsc. Microanal.*, 23:1013-1023, 2017. [10] Heldin, C.H. et al., *Nat Rev Cancer*, 4:806-813, 2004. [11] Swartz, M.A. et al., *Annu Rev Biomed.*, 9:229-256, 2007. [12] Wiederhielm, C., *J. Gen. Physiol.*, 52:29-63, 1968. [13] Potente, M. et al., *Nat. Rev*, 18:477-494, 2017. [14] Polacheck, W.J. et al., *Lab Chip*, 13:2252-2267, 2013 [15] Galie, P. et al., *PNAS*, 111:7968-7973, 2014. [16] Davis, G. et al., *Circ. Res.*, 97:1093-1097, 2005.

SB³C2022
Summer Biomechanics, Bioengineering and Biotransport Conference
June 20-23, Eastern Shore, MD, USA

# COLLAGEN HYBRIDIZING PEPTIDES EXTEND THE RETENTION TIME OF IMAGING MARKERS IN HEALTHY AND OSTEOARTHRITIC RAT STIFLE JOINTS

**Emma N. Luke (1,2), S. Michael Yu (1,3), Jeffrey A. Weiss (1,2,4)**

(1) Department of Biomedical Engineering, University of Utah, Salt Lake City, UT, USA
(2) Scientific Computing and Imaging Institute, University of Utah, Salt Lake City, UT, USA
(3) Department of Pharmaceutics and Pharmaceutical Chemistry, University of Utah, Salt Lake City, UT, USA
(4) Department of Orthopaedics, University of Utah, Salt Lake City, UT, USA

## INTRODUCTION

Osteoarthritis (OA) is a degenerative joint disorder that leads to the breakdown of protective cartilage on bone, inflammation in the joint capsule, and pain [1]. OA is the most common form of arthritis and affects 32.5 million adults in the US [2]. Current treatments for OA include non-surgical intervention, surgery, and the administration of therapeutics. While there are some promising results using locally injected therapeutics to treat OA, they currently provide only short-term pain relief and fail to remain in the joint space for periods long enough to provide long-term benefits for patients [3].

The overall goal of this research is to develop a new strategy to extend the retention time of therapeutics, such as hyaluronic acid, within the joint space to slow disease progression and deliver long-term analgesic effects. To extend the retention time of therapeutics within the joint, we propose using collagen hybridizing peptides (CHPs), which are small, synthetic peptides that selectively bind to denatured collagen. CHPs can be conjugated to different functional groups, including therapeutics and imaging markers [4]. To better understand how CHPs behave following an intra-articular injection, CHPs were conjugated to near-infrared fluorophores (NIRF; excitation: 675 nm, emission: 720 nm) and the retention time of CHPs in healthy and osteoarthritic joints of a rat model was examined over two weeks using fluorescence imaging. Peptide with a scrambled sequence was used as a control. We hypothesize that the targeted CHPs (t-CHPs) will remain in the joint longer than the scrambled-sequence CHPs (ss-CHPs) since the targeted CHP can bind to denatured collagen within the joint.

## METHODS

Male Sprague Dawley rats (N=16) weighing 126-150 g were kept in accordance with the approved IACUC protocol through the University of Utah. Animals were assigned to one of four groups (n=4 per group): OA, t-CHP; OA, ss-CHP; healthy, t-CHP; or healthy, ss-CHP.

CHP (1 nmol in 25 µL of saline) and monosodium iodoacetate (MIA; 10 mg/mL in saline) solutions were prepared in a sterile environment.

Animals were anesthetized using isoflurane and the stifle joints were shaved. The skin was sterilized using isopropanol. Using a sterile 27-gauge/0.5-inch needle, a single intra-articular injection of 25 µL of MIA was administered to induce OA [5]. OA developed for one week before the respective CHP solutions, activated by heating for 10 min at 80°C and quenching for 30 sec on ice, were injected into the joint space under isoflurane. Healthy animals received only a single CHP injection.

Following the CHP injection, animals were kept under isoflurane and imaged (<2 hr following CHP injection) using an in vivo imaging system (IVIS; Perkin Elmer, Waltham, MA). During each subsequent imaging session (6, 12, 24, 48, 72, 120, 168, 240, and 336 hr), animals were anesthetized using isoflurane and imaged using the IVIS. During each imaging session, regions of interest (ROIs) were selected to encapsulate the stifle joint and a background measurement was taken over the shaved fur. Measurements of total radiant efficiency were collected and analyzed. Area under the curve (AUC), representative of "solution available," was calculated (Eq. 1) for both t-CHP groups.

$$AUC = \sum_1^n \frac{(C_{n-1} - C_n)}{2} * (t_n - t_{n-1}), \quad (1)$$

where $n$ is the time point number, $C$ is total radiant efficiency ($\frac{p/\sec/cm^2/isr}{\mu W/cm^2}$) measured, and $t$ is time (hours).

Sample size was calculated using an alpha of 0.05, power of 0.9, and comparing pilot signal intensities between t-CHP groups. Between the t-CHP groups, total radiant efficiency at each time point was compared using two-tailed t-tests to compare independent means in Stata (College Station, TX, USA).

To confirm the development of OA, stifle joints were harvested following euthanasia and fixed in 10% neutral buffered formalin for 120

hr. Joints were then decalcified, paraffin embedded, sectioned, and stained using Safranin-O and Fast Green.

## RESULTS

Primary outcomes of this study included differences in retention time between t-CHP and ss-CHP, as well as between healthy and OA animals. Analysis began at the 12-hr mark when IVIS signal became stable. The t-CHP signals were present throughout the imaging period and were still measurable at the 336-hr time point (Fig. 1, top two rows). However, signal from ss-CHP was already nearly cleared from the joint at the 12-hour mark (Fig. 1, bottom two rows).

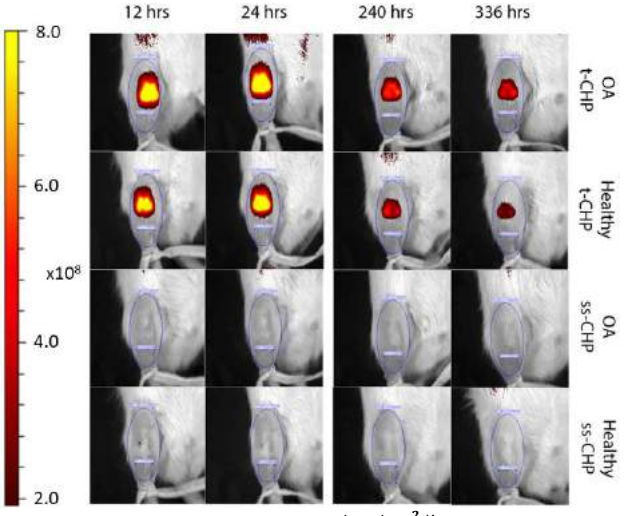


**Figure 1. Total radiant efficiency ($\frac{p/sec/cm^2/isr}{\mu W/cm^2}$) results from IVIS NIRF-imaging. Representative animal selected for each group. Time points 48-168 hr not pictured. Color bar ranges from 1.69E+10 to 8.0E+10.**

Independent t-tests comparing t-CHP between OA and healthy groups resulted in statistical significance ($p<.05$) for each time point (Fig. 2). Furthermore, AUC (mean±SD) between t-CHP groups was found to be statistically significantly different ($p=.0035$), where $AUC_{OA}$ = (2.41E+12) ± (3.31E+11) and $AUC_{healthy}$ = (1.62E+12) ± (7.68E+10).

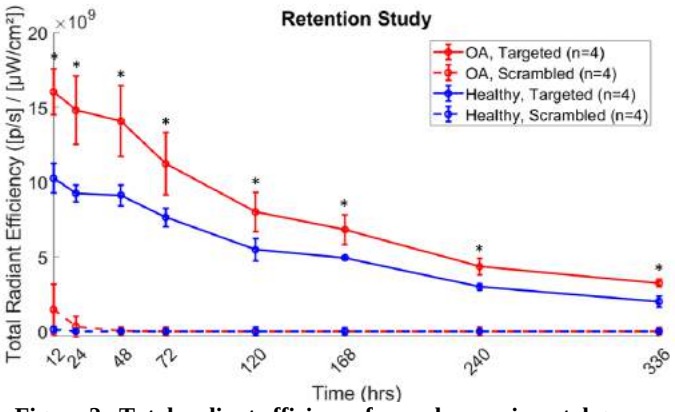


**Figure 2. Total radiant efficiency for each experimental group. Each time point represents mean±SD. * indicates $p<.05$ between OA targeted and healthy targeted at corresponding time point.**

Safranin-O and Fast Green staining showed a loss of proteoglycan content, hypocellularity, and an increase in calcified cartilage at the osteochondral interface in OA joints compared to healthy joints (Fig. 3).

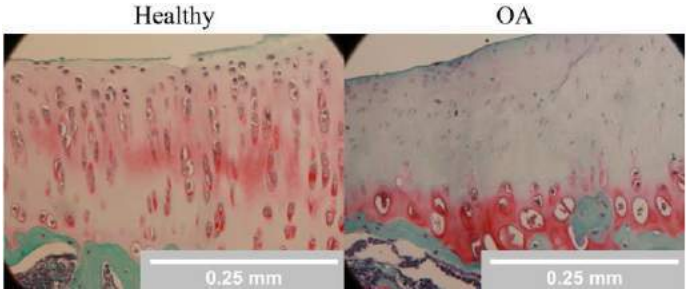


**Figure 3. Safranin-O and Fast Green staining of representative tibial plateaus. OA joints show a loss in proteoglycan staining (red) through the cartilage thickness, loss of chondrocytes (dark circles with surrounding white area), and an increase in calcified cartilage (dark red stain at osteochondral interface).**

## DISCUSSION

By longitudinally monitoring CHP presence through the use of NIRF markers (Fig, 1 and 2), we determined that t-CHPs remain in the joint space longer than ss-CHPs, confirming our initial hypothesis. This indicates that t-CHPs are, in fact, binding to collagen within the joint and remaining in the joint for the entire imaging period of 336 hr. On the other hand, ss-CHPs cleared quickly, within 12 hr of injection, as they do not bind to collagen and were cleared through the blood and lymphatics.

Further, between the t-CHP groups, OA joints retained the CHPs for a longer time than healthy joints. This is likely due to an increase in damaged and denatured collagens present in the OA joints, which are the primary targets that CHPs bind to. The CHPs stably bind to the collagen strands undergoing remodeling due to OA and remain in the joint for a longer period of time.

Through statistical analysis of the t-CHP groups, we determined that AUC, representative of "solution availability" in pharmacokinetic studies, was greater in OA joints than in healthy joints. This indicates that there is potential for an increased therapeutic availability in OA joints in future studies involving extended retention time of therapeutics.

Finally, through histological staining (Fig. 3), the development of OA was confirmed. Several features similar to OA seen in humans were present, including a loss of proteoglycans through the cartilage thickness, hypocellularity of chondrocytes, and an increase in calcified cartilage at the osteochondral interface.

IVIS imaging of NIRF-CHPs enables the longitudinal monitoring of CHP presence. This study represents a step towards establishing a method for extending the retention time of therapeutics within the joint space using CHPs functionalized with therapeutics to treat OA.

## ACKNOWLEDGEMENTS

Supported by NIH R01AR071358 and NSF GRFP No. 1747505.

## REFERENCES

[1] Arden, N et al., *Best Practice & Research Clinical Rheumatology*, 20:3-25, 2006.
[2] US Bone and Joint Initiative, *BMUS*, 4, 2018.
[3] Ruane, J et al., *Practical Pain Management*, 11, 2015.
[4] Hwang, J et al., *Acta Biomaterialia*, 53: 268-278, 2017.
[5] Janusz, M et al., *Osteoarthritis and Cartilage*, 9:751-760, 2001.

SB³C2022
Summer Biomechanics, Bioengineering and Biotransport Conference
June 20-23, Eastern Shore, MD, USA

# MACHINE LEARNING PREDICTION OF ABDOMINAL AORTIC ANEURYSM WALL STRENGTH AND EVALUATING FACTOR SENSITIVITY

**Pete H. Gueldner (1), Isabelle K. Chickanosky (1), Timothy K. Chung (1), David A. Vorp (1,2,3,4,5,6,7)**

(1) Department of Bioengineering, University of Pittsburgh, Pittsburgh, Pennsylvania, USA
(2) Department of Mechanical Engineering and Materials Science, University of Pittsburgh, Pittsburgh, Pennsylvania, USA
(3) McGowan Institute for Regenerative Medicine, University of Pittsburgh, Pittsburgh, Pennsylvania, USA
(4) Department of Surgery, University of Pittsburgh, Pittsburgh, Pennsylvania, USA
(5) Department of Chemical and Petroleum Engineering, University of Pittsburgh, Pittsburgh, Pennsylvania, USA
(6) Department of Cardiothoracic Surgery, University of Pittsburgh, Pittsburgh, Pennsylvania, USA
(7) Clinical and Translational Sciences Institute, University of Pittsburgh, Pittsburgh, Pennsylvania, USA

## INTRODUCTION

Abdominal aortic aneurysm (AAA) is the permanent expansion of the terminal aorta by more than 50% of its native healthy size and rupture is the 13th leading cause of death in the United States[1]. AAA rupture is a biomechanical event when the pressures induced wall stress exceeds the strength of the aorta to withstand the pressure. Researchers in the field of biomechanics have spent years trying to understand when rupture occurs and likely locations of where rupture could occur. Rupture potential index is defined as the ratio of the wall stress to wall strength to identify where rupture will occur in an AAA [2,3]. Experimentally measured material properties comprise constitutive models, which the stress model is based on. Assessing patient-specific wall strength is performed *ex vivo* through tissue extraction and subsequent mechanical testing. However, these destructive techniques cannot be performed *in vivo*. To address the need for a non-invasive assessment of wall strength, our lab previously developed a stochastic equation in 2006. This equation was derived using multiple regression to estimate wall strength from clinical factors, image-based indices, and experimental mechanical strength [4].

The purpose of the current study is to explore whether machine learning (ML) can more accurately predict the localized AAA wall strength. In addition, we will independently interrogate the sensitivity of individual factors (sex, smoking, and family history) in our model with the predicted wall strength values.

## METHODS

*Experimental Testing:* The previous mechanical testing and patient/imaging data from 23 patients and 83 tissue specimens were utilized [4]. The binary clinical factors gathered from each patient are sex, smoking status, and family history, as shown in **Table 1.** The tissue specimen was excised and CT image sets were used to measure the specimen diameters. The excised specimen was cut into 1.5 cm wide x 4 cm long sections and was uniaxially extended to failure.

**Table 1: Binary factors representation in the specimen cohort.**

| Factor | Number of Specimen | |
|---|---|---|
| **Sex** | 30% Male (n = 25), | 70% Female (n = 58) |
| **Non-Smokers** | 73% Smoker (n = 61), | 27% Non-smoker (n = 22) |
| **Family History** | 21% with Family History (n = 18), | 79% without Family History (n = 65) |

*Multiple Regression:* The multiple regression model (ranging up to 150 N/cm$^2$) as previously described by Vande Geest et al [4]. The factors considered in **Equation 1** are intraluminal thrombus thickness (in cm), the local normalized diameter (ratio 0–1), family history of AAA, represented by either no family history (-0.5) or family history of AAA (0.5), similarly, sex is striated by female (-0.5) or male (0.5).

$$Strength = 71.9 - 37.9 \times (\sqrt{ILT} - 0.81) - 15.6 \times (NORD - 2.46) - 21.3 \times HIST + 19.3 \times SEX \quad (1)$$

*Machine Learning:* A ML regression model, XGBoost, was used to fit the patient set (training set of 72 specimen, and 11 randomly selected validation specimen) which considers 13 variables: age, smoking history, local AAA diameter, maximum AAA diameter, proximal AAA diameter, three separate diameter ratios, predicted stress (from stochastic equation), and the four variables considered by the stochastic equation, from **Equation 1** [4]. To test the sensitivity of the algorithm, incorrect individual factors (from **Table 1**) were predicted.

*Statistical Comparisons:* The results of the wall strength predictions by the stochastic equation and ML model were compared by their correlation coefficients and $R^2$ values (using a zero y-intercept). Residuals were also compared between the previous stochastic model and trained ML model. The residuals of the wall strength predictions of individual factors were also compared to investigate if any binary factors have better predictions than their binary counterparts. Lastly, ANOVA was run with Dunnett's post-hoc to test the sensitivity of incorrect factors with the original ML predictions.

## RESULTS

The stochastically equation produced an R-value of 0.60 for the prediction of wall strengths below 150 N/cm$^2$ [4]. As shown in **Figure 1A**, ML predicted wall strength compared to experimentally measured wall strength below 150 N/cm$^2$ reports an R-value of 0.70 shown in **Figure 1B**, the residuals plots, the average error for the ML model estimating strengths below 150 N/cm$^2$ was 5.04 N/cm$^2$. When the curve is extended to 325 N/cm$^2$ the R-value increases to 0.83, but the average error increased to 9.89 N/cm$^2$.

Additionally, individual factors were inputted incorrectly to monitor how sensitive the algorithm is to binary factors. It can be seen in **Figure 2** that for both sex (0.36 ± 6.60 N/cm$^2$, correlation coefficient = 0.993, $R^2$ = 0.914) and smoking status (-0.17 ± 0.54 N/cm$^2$, correlation coefficient = 1.022, $R^2$ = 0.999), that the predicted wall strength is not statistically significant. Lastly, the predictions of family history (3.34 ± 14.17 N/cm$^2$, correlation coefficient = 0.938, $R^2$ = 0.694) are affected the most. It is important to note that statistically, none of these values are changed significantly different from the ML predictions.

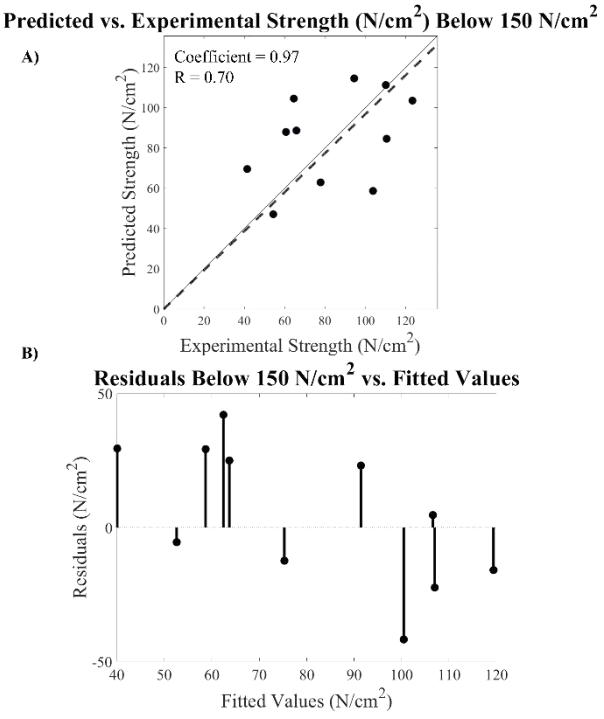


**Figure 1: A)** Plot of ML model's predicted versus measured wall strength below 150 N/cm$^2$ where R = 0.70. **B)** Residuals for ML predictions below where average error equals 5.04 N/cm$^2$.

## DISCUSSION

ML improved wall strength predictions compared to the previous stochastic model while also analyzing wall strengths up to 300 N/cm$^2$. The multiple regression equation was best suited for wall strengths up to 150 N/cm$^2$, whereas the ML model modeled wall strength predictions up to 300 N/cm$^2$. The ML predicted wall strengths below 150 N/cm$^2$ showed an improved R-value and decreased average error by 49% when compared to the ML predictions of wall strengths up to 300 N/cm$^2$.

In this study we find that the ML model is not sensitive to any factor. Particularly sex and smoking show nearly no effect on the estimated wall strength values. Family history is the factor that changed the ML prediction most. While it did not statistically change the predictions, it did lower the $R^2$ value (to 0.694). A study of the sensitivity of the stochastic model by Rengarajan et al., recently showed that family history was the most important factor to significant changes in the maximum RPI, and that the other three factors of wall strength stochastically (intraluminal thrombus thickness, NORD, and sex) did not significantly change the maximum wall strength predicted values, in the stochastic equation[5]. This suggests that the ML algorithm is less dependent on family history than the stochastic formulation was. While there is not a statistical difference in our results, trend-wise, incorrect family history led to the largest deviation of the predicted stress values.

This work is limited by a small data set. Therefore, future work will focus on data expansion techniques will be used to train our ML model on a larger variety of patient types. Future studies will incorporate this ML wall strength prediction into our rupture potential index pipeline, coupled with finite element models.

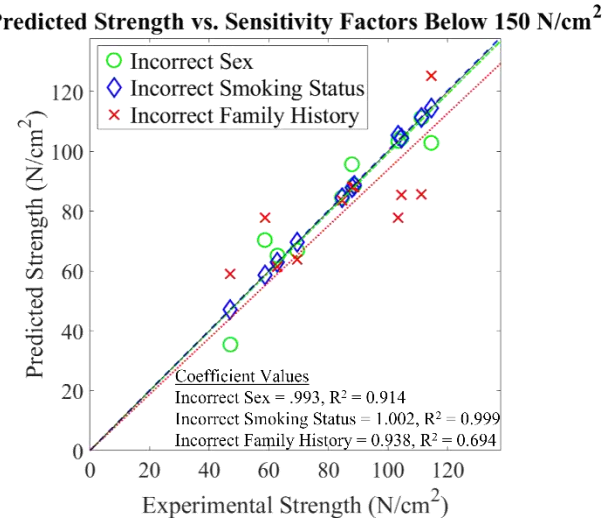


**Figure 2:** Plot of each incorrect factor mapped versus the original ML predictions of wall strength.


## ACKNOWLEDGEMENTS

This experimental dataset gathered in this work was supported by NIH award R01HL060670.

Additionally, this material is based upon work supported by the National Science Foundation Graduate Research Fellowship Program under Grant No. 1747452. Any opinions, findings, and conclusions or recommendations expressed in this material are those of the author(s) and do not necessarily reflect the views of the National Science Foundation.


## REFERENCES


[1] Vorp, D., *J. Biomech.*, 40(9), 1887-1902, 2007.
[2] Vande Geest, J., et al., *Ann. N Y Acad. Sci.*, 1085.1: 11-21, 2006.
[3] Maier, A et al., *Ann. Biomed. Eng.*, 38:3124-3134, 2010.
[4] Vande Geest, J., et al., *Ann. Biomed. Eng.*, 34(7), 1098-1106, 2006.
[5] Rengarajan, B., et al., *SB3C*, p171-172., 2021.

SB³C2022
Summer Biomechanics, Bioengineering and Biotransport Conference
June 20-23, Eastern Shore, MD, USA

# PDGF-BB DISRUPTS THE STIFFNESS-DEPENDENT MYOFIBROBLASTIC DIFFERENTIATION OF CORNEAL KERATOCYTES IN RESPONSE TO TGF-β1

**Krithika S. Iyer (1), David W. Schmidtke (1), W. Matthew Petroll (2), Victor D. Varner (1,3)**

(1) Department of Bioengineering, University of Texas at Dallas, Richardson, Texas, United States
(2) Department of Ophthalmology, UT Southwestern Medical Center, Dallas, Texas, United States
(3) Department of Surgery, UT Southwestern Medical Center, Dallas, Texas, United States

## INTRODUCTION

The cornea is the soft transparent tissue located at the anterior aspect of the eye, which helps bend light towards the retina [1]. It contains three distinct cellular layers (the endothelium, epithelium, and stroma), but the stromal compartment accounts for the majority of the tissue thickness. The corneal stroma contains a highly organized extracellular matrix (ECM) that consists of lamellae of aligned type I collagen fibrils [2], which imbue the tissue, in part, with its transparent optical properties [3].

In the healthy cornea, a population of cells called corneal keratocytes maintain this highly ordered ECM but remain otherwise mechanically quiescent [3]. Following injury or refractive surgery, however, damage to the cornea causes growth factors, such as transforming growth factor beta-1 (TGF-β1) and platelet derived growth factor-BB (PDGF-BB) to be released into the stromal space [4]. This process activates keratocytes into a repair phenotype and is associated with changes in tissue stiffness [5]. Previous work has shown that the TGF-β1-mediated myofibroblastic differentiation of corneal keratocytes depends on the mechanical properties of the ECM [6], but it is unclear if changes in ECM stiffness also regulate the response of keratocytes to other growth factors, such as PDGF-BB, or to combinations of growth factors like TGF-β1 and PDGF-BB.

Here, we used a polyacrylamide (PA) gel system to determine if changes in substratum stiffness regulate the proliferation and motility of primary corneal keratocytes treated with PDGF-BB, since PDGF-BB has been shown to promote both these phenotypes in cultured cells [7]. We also investigated how treatment with TGF- β1 and PDGF-BB influences the stiffness-dependent myofibroblastic differentiation of these cells.

## METHODS

PA substrata with an elastic modulus of either 1 kPa (soft) or 10 kPa (stiff) were fabricated to mimic the mechanical properties of either normal or fibrotic corneal tissue and then functionalized with unpolymerized type I collagen.

Primary rabbit corneal keratocytes (NRKs), harvested from rabbit eyes, as described previously [8], were plated on either the functionalized PA substrata or on collagen-coated glass coverslips and cultured in defined serum-free media. In some experiments, the media was supplemented with either PDGF-BB, TGF-β1, or a combination of both growth factors.

We used a freeze injury model to assay changes in keratocyte motility [9]. Briefly, a circular wound, approximately 1.5 mm in diameter, was created by holding a liquid nitrogen-cooled aluminum rod against the underside of the culture dish. The samples were then placed in a stage-top incubator, where time-lapse phase contrast images were captured at 1-hr intervals for 4 days. We used the Click-iT EdU Imaging Kit to quantify rates of cell proliferation. In other experiments, cells were fixed and stained with phalloidin and DAPI, to label F-actin and nuclei, respectively, as well as for alpha-smooth muscle actin (α-SMA), a marker for myofibroblastic differentiation, or phosphorylated myosin light chain (pMLC), a marker for active actomyosin contractility. To compute cell-generated traction stresses, we also performed traction force microscopy (TFM) experiments. Confocal images of fixed samples were captured on a Zeiss LSM 800, and quantitative image analysis was performed in ImageJ.

## RESULTS

In the presence of PDGF-BB alone, cultured NRKs exhibited stiffness-dependent differences in morphology and proliferation. In serum-free conditions, on substrata of all stiffnesses, the cells retained the branched, dendritic morphology indicative of a mechanically quiescent phenotype, as well as negligible amounts of EdU incorporation. In the presence of PDGF-BB, however, NRKs cultured on stiff PA substrata (or collagen-coated glass coverslips) exhibited a

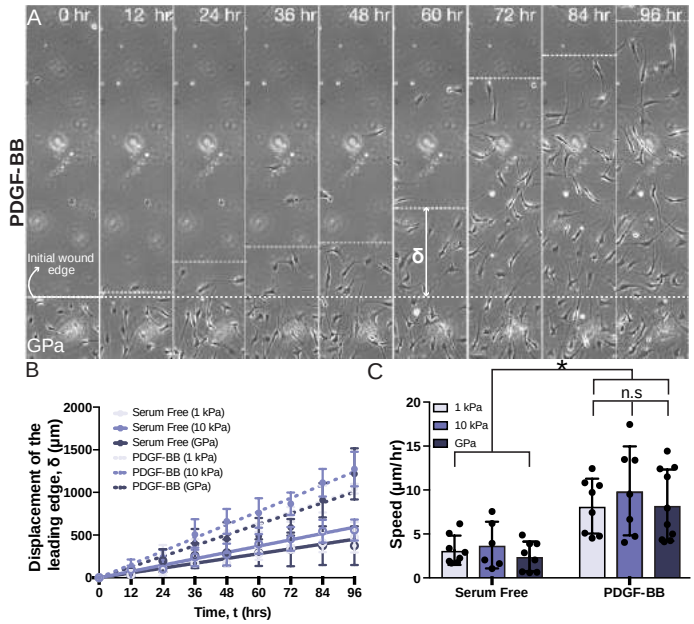


**Figure 1. PDGF-BB-treated keratocytes do not exhibit stiffness-dependent differences in motility. (A) Kymograph depicting the motion of the leading edge of a freeze-injury-induced wound. (B-C) Quantification of the (B) displacement, δ, and (C) speed of the leading edge of the wound.**

more highly spread and elongated morphology, as well as a higher rate of proliferation than cells cultured on soft PA gels (data not shown).

Changes in substratum stiffness, however, did not affect the migratory behavior of PDGF-BB-treated keratocytes. We created freeze injuries on both soft (1 kPa) and stiff (10 kPa) PA substrata, as well as collagen-coated glass coverslips (GPa), and quantified cell motion into the decellularized wounds. On substrata of all stiffnesses, PDGF-BB-treated cells migrated further into the wound and exhibited faster migration speeds than their counterparts in serum-free conditions, as assayed by both the tracked displacements of individual cells (data not shown), as well as the motion of the leading edge of the wound (Fig 1A-B). We did not, however, observe stiffness-dependent differences in the motility of keratocytes cultured in the presence of PDGF-BB (Fig. 1C).

We also cultured keratocytes in the presence of both TGF-β1 and PDGF-BB to determine how combinations of soluble cues impact stiffness-dependent differences in cell behavior. Surprisingly, we found that treatment with PDGF-BB disrupts the effect of substratum stiffness on the TGF-β1-mediated myofibroblastic differentiation of these cells (Fig. 2). In the presence of TGF-β1 alone, NRKs exhibited decreased α-SMA immunofluorescence on soft PA substrata as opposed to the elevated levels observed on stiff PA or collagen-coated glass coverslips, consistent with previous work (Fig. 2A) [6]. When treated simultaneously with PDGF-BB, however, we no longer observed stiffness-dependent differences in levels of myofibroblastic differentiation; elevated levels of α-SMA immunofluorescence were seen on substrata of all stiffnesses (Fig. 2B-C). No α-SMA-positive cells were observed in either serum-free media or when treated with PDGF-BB alone (Fig. 2C).

## DISCUSSION

Taken together, these data indicate that PDGF-BB modulates the stiffness-dependent behavior of corneal keratocytes. Changes in substratum stiffness alter the proliferation and morphology but not the motility of cells cultured in the presence of PDGF-BB alone. In addition, somewhat surprisingly, treatment with PDGF-BB disrupted the stiffness-dependent myofibroblastic differentiation of keratocytes also treated with TGF-β1. These data are suggestive of potential mechanotransductive crosstalk between the signaling pathways downstream of TGF-β1 and PDGF-BB. Indeed, previous work has shown that the TGF-β1-induced myofibroblast differentiation of corneal fibroblasts requires synergistic signaling between TGF-β1 and PDGF-BB [10], but the influence of biophysical cues on this process is completely unexplored. In vivo, corneal keratocytes are subjected to a multiplicity of soluble cues, and future work will be necessary to investigate how changes in ECM stiffness influence keratocyte behavior in response to combinations of different growth factors.

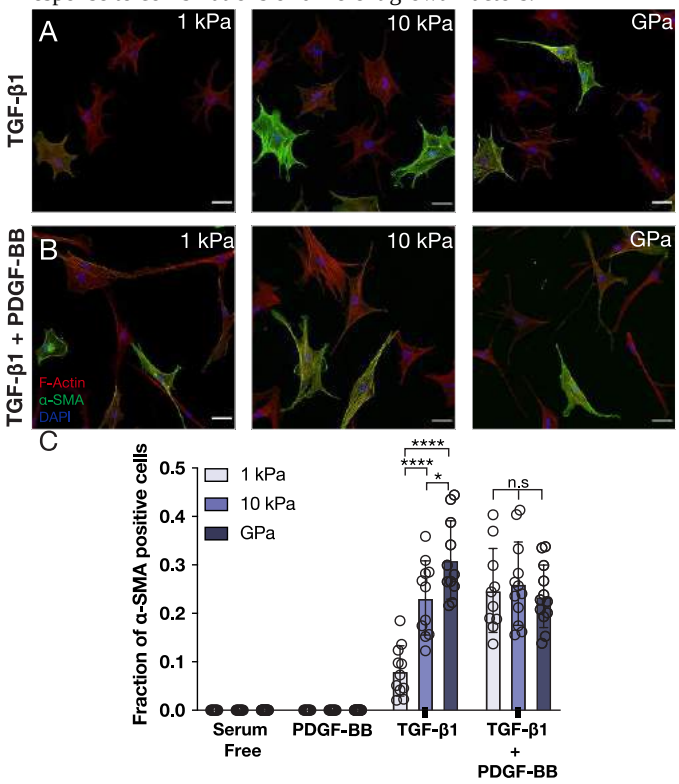


**Figure 2. Treatment with PDGF-BB disrupts stiffness-dependent differences in myofibroblastic differentiation. (A-B) Confocal images of phalloidin, DAPI, and α-SMA immunofluorescence. Scale bar = 50 μm. (C) Quantification of the fraction of α-SMA-positive cells on substrata of varying stiffnesses in the presence of TGF-β1 and/or PDGF-BB.**


## ACKNOWLEDGEMENTS

This work was supported by the NIH grants R01 EY030190 and P30 EY030413, as well as an unrestricted grant from Research to Prevent Blindness.


## REFERENCES


[1] Fini, M. E., *Prog Retin Eye Res*, 18:529 – 551, 1999.
[2] Meek, K.M., *Prog Retin Eye Res*, 28:369 – 392, 2009.
[3] Hassell, J. R., *Experimental Eye Research*, 91:326 – 335, 2010.
[4] Torricelli, A. A.M., *IOVS*, 54: 6390 – 6400, 2013.
[5] Thomasy, S. M., Acta *Biomaterialia*, 10:785 – 791, 2014.
[6] Maruri, D P., *Biophysical journal*, 119.9: 1865-1877, 2020.
[7] Lakshman, N., *IOVS*, 53:1077-1086, 2012.
[8] Jester, J. V., *Cornea*, 15:505-516, 1996
[9] Kivanany, P. B., *Journal of functional biomaterials*, 9, 2018.
[10] Jester, J. V., *Experimental eye research*, 75(6), 645-657, 2002.

# THREE-DIMENSIONAL STRAIN ASSESSMENT OF THE LUMBAR FACET CAPSULAR LIGAMENT DURING DYNAMIC MOTION

**Matthew R. MacEwen (1), Rebecca E. Abbott (2), Victor H. Barocas (1), Arin M. Ellingson (2)**

(1) Biomedical Engineering, University of Minnesota-Twin Cities, Minneapolis, MN, USA
(2) Rehabilitation Medicine, University of Minnesota-Twin Cities, Minneapolis, MN, USA

## INTRODUCTION

Low back pain (LBP) is a wide-spread, debilitating ailment that is currently listed as the leading cause of disability in the world[1]. It hinders the quality of life of roughly 80% Americans during their lifetime.[1] As a result, the disability has a high cost both from a health and a socioeconomic perspective. Root causes of LBP are challenging to diagnose and only a select few pathologies can be localized to a specific etiology. The facet joints have been identified as a potential origin of LBP, and studies confirm this idea with evidence of nociceptors in the facet capsular ligament (FCL)[2-4]. Mechanical nociceptor activation necessitates that a deformation and strain analysis be performed on the ligament to determine its potential contribution to LBP. An orthopaedic test known as the Kemp's test has shown the potential to specifically assess facet joint pain via a multiplanar motion that attempts to load the joint and recapitulate sympotomology.[5] **This study aims to quantify the three-dimensional strain fields across the FCL during dynamic activities.** The outcome of the study will relate dynamic activities to FCL strains, and lead to a better understanding of the mechanical environment surrounding the neurons.

## METHODS

One osteoligamentous lumbar spine (male, age 73) was obtained by the University of Minnesota Anatomy Bequest program and screened for spinal abnormalities. The L4 and L5 segment was scanned via a 3T MRI (Siemens MAGNETOM, Germany) utilizing T1 volumetric interpolated breath-hold examination sequences where the facets were scored with the Fujiwara scoring metric.[6] The left was scored a 3 for sclerosis and the right was scored a 2 for joint narrowing. Four 2mm tantalum beads were then embedded into each transverse process and into the vertebral bodies of L4 and L5. The spinal unit was then imaged with a CT scanner utilizing a B60 kernel scan sequence to maximize contrast between the bone and the surrounding tissue (Siemens Biograph PET/CT, Germany). Following imaging, the superior and inferior portion of segment was potted in polymethyl methacrylate in preparation for testing, and micro-dissected to expose the FCL. The specimen was then loaded into a calibrated Spine Kinetic Simulator (8821 Biopuls, Instron, USA), retroreflective markers were rigidly adhered to each vertebral body, and the ligament was speckled with an ultraviolet reflective paint to reduce glare and enhance contrast (Figure 1). The tissue remained hydrated using a saline soaked gauze.

Pure moments of up to 7Nm were applied to the segment in axial rotation, flexion/extension, and lateral bending at 0.015Hz for 3 cycles of preconditioning and 1 cycle for data analysis. Motion capture data was recorded at 100Hz, and three digital single-lens reflex (DSLR) cameras recorded videos of the ligament at 20fps. A multiaxial Kemp's test was simulated through 7Nm of extension and 6Nm of both axial and lateral bending. The Kemp's was performed to the ipsilateral and contralateral side and data were analyzed for both the right and left FCL.

**Figure 1: Experimental Set Up: The spine (circled) is shown loaded in the spine kinetic simulator while the optical motion capture cameras (yellow arrow) and DSLR system (gray arrow) recorded its motion.**

The CT scans were segmented within Mimics Software (Materialise NV, Leuven, Belgium). Anatomic landmarks were identified at adjacent surfaces of each endplate, and their relationships to the position of the tantalum beads within the CT coordinate system were established. Spine tester and optical motion capture data underwent a spatial frequency analysis to determine lowpass Butterworth cutoff frequencies and were filtered at 15Hz and 1.75Hz, respectively. The optical motion capture system, spine tester, and DSLR cameras were all time synchronized. The synced kinematic data collected via optical motion capture were transformed to the anatomic landmarks via a custom MATLAB code using the digitized beads to bridge the coordinate systems. The range of motion (ROM) was established to provide context for the recorded strain of the FCL.

The videos for digital image correlation (DIC) were converted into images and inverted to allow tracking. The images were decimated down to 0.5Hz and loaded into the MultiDIC MATLAB package.[7] To ensure an accurate measure of strain, an image of the ligament under zero load was used as the neutral frame. DIC analysis quantified the three-dimensional 1st principle Lagrangian strain fields across the FCL throughout each induced motion.

## RESULTS

Table 1 displays the segments ROM and translations for each activity. Figure 2 displays both the left and right FCLs at the maximum torque for each of the applied motions. A strain between 0.05 and 0.40 is shown between the interface of the joint consistently while the surrounding areas experienced little to no strain for all the motions. The ligament strained across the joint (i.e. in the bone-to-bone direction) with an oblique influence driven by the direction of primary motion. The Kemp's trial proved successful at deforming the ipsilateral FCL and created a lesser strain on the contralateral ligament.

## DISCUSSION

The results from this collected specimen showcase the feasibility of the introduced protocol. The areas of the highest strain for this specimen are near the articular surfaces and this is likely due to the orientation of the joint surfaces, direction of motion, and the FCL's predominant role in stabilization.[8] There is also an association between amount of motion of the segment and the corresponding strain of the ligament, as kinematic motions with a higher ROM had a larger strain.

A major limitation for this study is the use of a single specimen without active musculature and axial loading. Other limitations of the work are the inability to record the dynamic response of the FCL due to the quasi-static natures of the testing protocol, and the limits on speckle resolution due to spatial constraints.

The preliminary kinematic data aligns well with what has been recorded in the literature and we see ROM and strain that fall within expected ranges.[9-12] We plan to establish resultant strain field trends moving forward and isolate regions with consistent levels of high strain. Localizing these regions will be crucial in developing our understanding of the FCL's role in mechanical LBP.

**Table 1:ROM and Translations for each applied motion**

| | Rotations (°) | | | Translations (mm) | | |
|---|---|---|---|---|---|---|
| | Axial | Flexion | Lateral | Antero-posterior | Superior-inferior | Medio-lateral |
| Axial Rotation | 3.97 | 0.29 | 0.97 | 0.96 | 0.53 | 2.13 |
| Flex/ Ext | 1.61 | 6.63 | 1.00 | 6.42 | 0.97 | 1.96 |
| Lateral Bending | 1.31 | 0.61 | 5.73 | 2.08 | 0.85 | 2.94 |
| Kemps Left | 1.71 | 1.78 | 4.04 | 1.90 | 1.12 | 2.82 |
| Kemps Right | 2.32 | 3.49 | 4.34 | 2.37 | 0.49 | 3.42 |

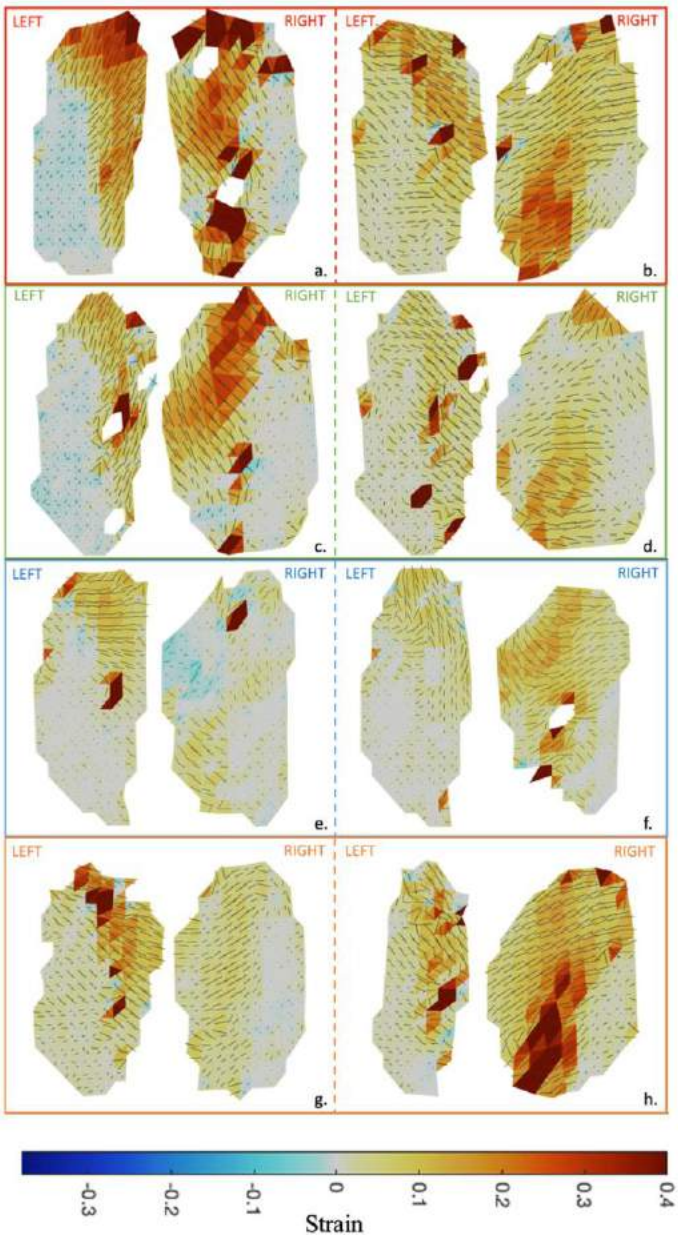


**Figure 2: 1st Principle Lagrangian Strain fields at motion maxima (a) flexion, (b) extension, (c) lateral bend-left, (d) lateral bend-right, (e) axial rotation-left, (f) axial rotation-right, (g) Kemp's test-left, and (h) Kemp's test-right**


## ACKNOWLEDGEMENTS

This work was supported by the National Institutes of Health (U01-AT010326).


## REFERENCES


[1] Andersson, G., et al., *Lancet* 354:581-85, 1999, [2] Cavanaugh, JM., et al., J *Biomech* 29: 1117-1129, 1996, [3] Beaman DN, *Spine* 18: 1044-1049, 1993, [4] Jaumard, N., et al, *J. of BME* 133, 2011, [5] Stuber, K., et al., *J Can Chiropr Assoc* 58:3, 2014, [6] Fujiwara, A., et al, *Eur Spine* 8:396-401, 1999, [7] Solav, D., et al., *IEEE Access* 6:30520-30535, 2018, [8] Sharma, M., et al, *Spine* 20:4, 1995 [9] Jaramillo, H., et al., *J. of Biomech* 49:1248-1254, 2016, [10] Ianuzzi A., et al., *The Spine Journal* 4: 143-152, 2004, [11] Claeson, A., et al., *Spine J*.17: 109-119, 2017, [12] Bermel, E., et al., *J Biomech* 105: 109814, 2020.

SB³C2022
Summer Biomechanics, Bioengineering and Biotransport Conference
June 20-23, Eastern Shore, MD, USA

# DYNAMIC MECHANICAL LOADING OF PHOTOPOLYMERIZED HYDROGELS AS A TOOL FOR STUDYING PULMONARY FIBROSIS

**Qi Wang (1, 2), Jacob Herrmann (1), Edward A. Sander (1) Kristan S. Worthington (1)**

(1) Roy J. Carver Department of Biomedical Engineering, University of Iowa, Iowa City, IA, USA
(2) Medical Scientist Training Program, Roy J. and Lucille A. Carver College of Medicine, University of Iowa, Iowa City, IA, USA

## INTRODUCTION

Pulmonary fibrosis is a hallmark and final consequence of several lung diseases including idiopathic pulmonary fibrosis and post-COVID-19 pulmonary fibrosis. Although these diseases have distinct etiologies, the outcome is fibrogenesis that leads to impaired pulmonary function. Fibrotic lesions and scarring of the lung connective tissue are a result of alterations in extracellular matrix (ECM) composition and biochemistry. Current treatments, such as nintedanib and pirfenidone, have been shown to slow the progression of idiopathic pulmonary fibrosis. However, they cannot stop or reverse lung fibrosis.

Mechanosensing pathways can potentially mitigate lung fibrosis. However, animal models do not allow for isolated study of mechanical or chemical cues. Reductionist cell culture systems are essential for understanding the molecular mechanisms of fibroproliferative response and resolution of fibrosis. However, the lung is a dynamic environment in which cells experience cyclic mechanical loading in addition to biochemical and static mechanical cues from the extracellular matrix (ECM). Thus, a new *in vitro* culture system that allows for precise manipulation of mechanical and biochemical cues is needed to advance our understanding of how changes in the ECM influence fibrotic lung disease progression, so that better therapies can be developed.

Photopolymerized hydrogels are useful substrates for the study of cellular responses to ECM alterations. The composition and concentration of pre-polymer mixtures can be tuned to yield desired biochemistry and stiffness of hydrogels, respectively. In addition, the crosslinking of methacrylated polymers using UV light provides superior spatial and temporal control. These hydrogels are also biocompatible, and some can be used with no additional coating for cell attachment. They can also be attached to a bioreactor that applies dynamic mechanical loading. In this study, we describe how these elements can be combined to produce alveolar ECM mimics that serve as simple model systems of the native lung ECM.

## METHODS

Fabrication of hydrogels

Methacrylated gelatin (GelMA), methacrylated hyaluronan (HAMA) and non-methacrylated gelatin (Gel) were mixed in various concentrations as base materials. Hydrogels were formed via ultraviolet light (1W/cm2), with Irgacure-2959 used at 1% vol as a photoinitiator.

Material property measurements using Photo-rheology

Rheology was performed during the photo-crosslinking process using Kinexus Ultra+ (Malvern Panalytical) fitted with an Omnicure S2000 UV light source. Storage modulus during polymerization ($G'$) was fitted to **Equation 1** to determine final storage modulus ($G'_\infty$ ). Crossover point ($t_c$) was defined as the point in which storage modulus is greater than loss modulus ( $G''$)1

$$G' = G'_\infty\left(1 - \exp\left[-\alpha\left(\frac{t}{t_c - 1}\right)^\beta\right]\right) \quad (1)$$

Hydrogel biocompatibility

IMR-90 human fetal lung fibroblasts were seeded on polymerized hydrogels overnight. Standard viability assay was performed according to manufacturer's protocol. Cells were imaged and analyzed using ImageJ. Statistical analysis was performed using Graphpad PRISM.

Application of dynamic strain to hydrogels

Pre-polymer mixtures were applied to custom attachments designed for the bioreactor (ADMET Inc.) before photopolymerization at pre-determined photopolymerization times. The hydrogels were then deformed cyclically at physiological rates and over amplitudes spanning 5% and 80% strain.

## RESULTS

Photo-rheology results (**Fig 1A**) demonstrate that by changing the initial concentration of GelMA and Gel, the final storage modulus of photopolymerized hydrogels can be manipulated to fit desired substrate stiffnesses between 10 and 100 kPa. Photopolymerized hydrogels also allow precise spatial control of the biochemistry within the hydrogel,

such as shown in **Fig 1B**, where GelMA with rhodamine was photopolymerized with drops of HAMA approximately 2 mm in diameter. HAMA volume can be calibrated or 3D printed to achieve higher precision in the future.

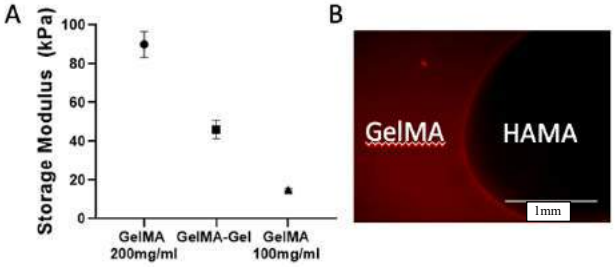


**Figure 1: Precise control of hydrogel stiffness and spatial composition**

Pre-polymer mixtures can also be applied to surfaces and polymerized to allow for attachment. **Fig 2C** demonstrates how these hydrogels can be attached on a bioreactor fitted with a servo-controlled linear actuator to apply prescribed waveforms. Five-second cycles (12 breaths per minute) were applied to photopolymerized hydrogels over amplitudes spanning 5% to 80% strain (**Fig 2A**). Force displacement curves were also obtained (**Fig 2B**). The gels exhibited nearly linear elasticity over this strain range.

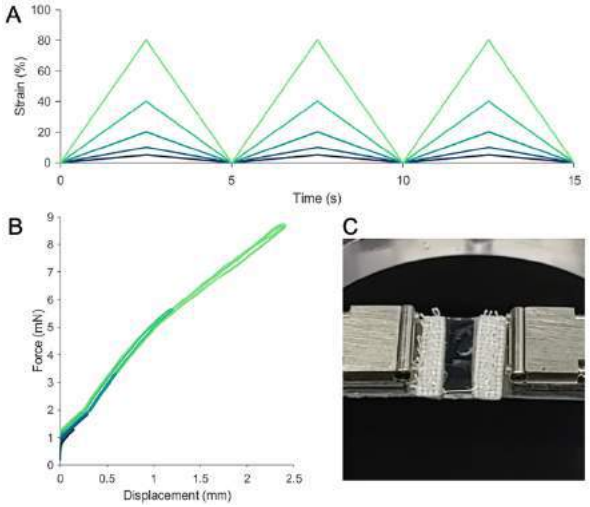


**Figure 2: Cyclic strain can be applied to hydrogels at controlled frequencies and strains**

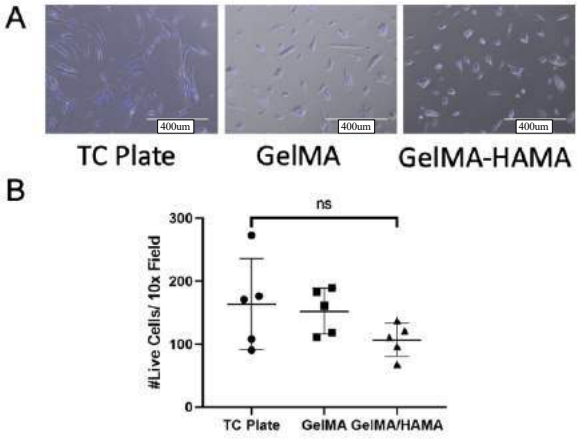


**Figure 3: Photopolymerized hydrogels allows for cell attachment without additional coating and are biocompatible**

IMR 90 fibroblasts were seeded overnight on GelMA and GelMA/HAMA (70/30) photopolymerized hydrogels. Qualitatively, seeding on tissue culture plastic (TC) caused more cell spreading compared to seeding on hydrogels, an observation consistent with the idea that cell area increases with substrate stiffness (**Fig 3A**). Live-dead viability assays were also performed and the number of live (blue) and dead (green) cells were analyzed using ImageJ. Despite the morphological differences observed, no statistical differences in cell viability were found between surfaces (**Fig 3B**).

## DISCUSSION

Overall, our results demonstrate that photopolymerized hydrogel stiffness, biochemistry and spatial composition can be precisely controlled to facilitate the study of ECM alterations in pulmonary fibrosis. The ability to manipulate stiffness with the addition of Gel not only allows for a wider range of hydrogel stiffness but also maintains similar number of Arg-Gly-Asp (RGD) binding sites at lower moduli. This capability is important for the study of pulmonary fibrosis because previous studies have demonstrated that inhibition of RGD binding sites ameliorates fibrosis.[2] The ability to include hyaluronan homogeneously or as concentrated foci is also important, as various studies of patients with fibrotic lung disease have shown an increase in hyaluronan deposition.[3] Hyaluronan is also a component of fibrotic foci, which is a hallmark of idiopathic pulmonary fibrosis.

Under physiological conditions, lung cells are continuously subjected to mechanical stimulation and in some instances, the mechanical stimuli can promote fibrogenesis.[4] This is the case for mechanical ventilation, which saves patient lives, but can also lead to ventilator induced lung injury, and thereby to pulmonary fibrosis. The ability to apply strain to photopolymerized hydrogels is therefore important for the study of cell behavior in the lung. As demonstrated by our results, photopolymerized hydrogels can be strained up to 80%. This is important for studying injurious ventilation associated with overdistension; our calculations suggest that dynamic conditions should include a 35% pre-strain and additional 20% cyclic strain.

Inherent cytocompatibility of these hydrogels is also an advantage for this application. Inconsistency in stiffness between coating and bulk material can impact strain experienced by cells. Conversely, the use of photopolymerized hydrogels composed of GelMA allows for direct cell attachment and showed no toxicity.

In our future work, we will use this system to identify individual contributions of stiffness and ECM composition in diseased lungs to the progression of lung fibrosis. Specifically, we will subject IMR90 fibroblasts to strain and strain frequencies modeling physiologic breathing and mechanical ventilation. Photopolymerized hydrogels ranging from 2kPa to 16kPa will be used to represent healthy to fibrotic lungs. We will then analyze these fibroblasts using an RT-qPCR panel of 32 genes. These experiments are expected to answer many questions regarding the relative contributions of ECM stiffness, composition, and cyclic mechanical loading to the progression of lung fibrosis.


## ACKNOWLEDGEMENTS

Support for this work was provided by the National Institute of Health (NIH T32 GM007337, NIH T32 HL144461) and the Roy J. Carver Department of Biomedical Engineering Carver Graduate Fellowship.


## REFERENCES


[1] Wendland R.J. et al. Exp. Eye. Rrsch, 207, 108566, 2021
[2] Basta, J. et al. Physiol Rep 8, e14329, 2020.
[3] Booth, A.J. et al. Am. J. Respir. CCM. 186, 866-876, 2012.
[4] Marchioni, A. et al. Int. J. Mol. Sci. 22, 6443, 2021.

SB³C2022
Summer Biomechanics, Bioengineering and Biotransport Conference
June 20-23, Eastern Shore, MD, USA

# AN INVESTIGATION OF THE CHANGE IN pH FOLLOWING ADMINISTRATION OF PULSED ELECTRICAL FIELDS

**Zaid S Salameh, Kenneth N Aycock, Melvin F. Lorenzo, Rafael V. Davalos**

Biomedical Engineering and Mechanics, Virginia Tech, Blacksburg, VA, USA

## INTRODUCTION

Irreversible electroporation (IRE) is an electric field-based treatment in which cell death is triggered by creating pore formations across the cell membrane.[1] It is well established that the non-thermal ablation treatment generates electrochemical effects.[2,3] In some instances, the electrolytic effects of pulsed electrical fields (PEFs) are intentional and combined with electroporation to maximize ablation volumes in a treatment termed E2.[4] However, these electrochemical effects can also disturb physiological pH, which may lead to unwanted side effects in surrounding tissue. These effects are thought to be more pronounced in monopolar pulses as compared to bipolar pulses. The second generation of IRE, known as high-frequency irreversible electroporation (H-FIRE)[5] utilizes shorter pulses of alternating polarity, which are known to mitigate these electrochemical effects. As different clinical treatments have their unique objective for these effects, there is a need to establish a relationship between treatment paradigms of PEFs and their subsequent electrochemical effects. Here, we utilize an agar solution and bromothymol blue, a pH indicator, to investigate and compare pH disturbances from treatments with different pulse parameters and in tissue phantoms with varying electrical conductivities.

## METHODS

*Experiment 1:* A 1% weight/volume agar solution was prepared with DI water and a 1/10 ratio of bromothymol blue. Bromothymol blue is a pH indicator that turns from green (pH 7.0) to dark blue (pH > 7.6). The solution was boiled, stirred, and split into three groups with varying concentrations of NaCl: 0%, .25%, and .5%. The solutions were pipetted into a 12 well culture plate (1 mL per well) and allowed to solidify for 24 hours. The same treatment was applied in each well using an ECM 830 Square Wave Electroporator (Harvard Apparatus, Holliston, MA): 100 V, 1 ms pulse width, and 99 pulses applied at 1 Hz. Current readings were collected using a wideband current monitor (Pearson Electronics, Palo Alto, CA) connected to an oscilloscope (Wavesurfer 3024z, Teledyne LeCroy, Chesnut Ridge, NY). Treatment was applied using a custom single needle-grounding ring electrode configuration. Photographs were captured and ImageJ (NIH, Bethesda, MD) was used to quantify pH disturbance area. pH disturbance areas were defined as areas with a pH greater than 7.6 after treatment, with the initial pH being neutral (pH 7). *Experiment 2:* The solution was prepared in the same manner as experiment 1. Applied voltage was adjusted between different groups to normalize the current using Ohm's law. A single diagnostic pulse (100 V, 50 µs) was applied to determine initial resistance. There are no significant electrochemical effects from this single pulse. The resistance of each group was used to find the necessary voltage unique to each group to normalize current to 250 mA. Treatment was administered identically to Experiment 1, but with different voltages applied to achieve this target current across each group. *Experiment 3:* The solution was prepared in the same fashion but with constant NaCl concentrations across all groups (.25%). The solution was added to a 12 well plate and 3 different treatments were applied. The treatments were uniform in applied electrical dose but varied in pulse width and voltage. The dose was kept constant using equation 1 with $E$=electrical field, $\eta =$ pulse number, and $\tau$ = pulse width.

$$Dose = E^2 * \eta * \tau \quad (1)$$

Voltage ($V$) can be substituted for the electrical field ($E$) because the electrical field is dependent on the geometry of the electrodes and our geometry is constant. Treatment consisted of 99 monopolar pulses applied at 1 Hz. The groups were treated with 500, 158, and 50 V with pulse widths of 100 µs, 1 ms, and 10 ms, respectively. *Experiment 4:* Experiment 3 was repeated, with the on-time, frequency, and conductivities of each treatment kept constant but the pulses were set to be bipolar. Treatment was applied via 50-10-50 µs pulses (positive pulse–delay–negative pulse) with 1, 10, and 100 being the number of cycles per burst for the 3 treatments. Each burst correlates with a pulse width group in experiment 3, hence constant on-time.

For each group, the conductivity was computed with equation 2. The shape factor k is from the analytical equation of two finite concentric cylinders (equation 3).

$$\sigma = \mathrm{k} * \frac{I}{\mathrm{V}} \quad (2)$$

$$k = {2\pi L}\Big/{\ln\left(\frac{r_2}{r_1}\right)} \quad (3)$$

*Statistical Analysis:* An ordinary one-way ANOVA and post-hoc Tukey's multi-comparison test was used to assess differences in pH disturbance sizes.

## RESULTS

The experiments were designed to investigate the effects of voltage, current, conductivity, pulse width, polarity, and ionic concentration on pH change. The goal of the first experiment was to isolate the effects of induced electric current by varying the tissue phantom's electrical conductivity. A significant increase in pH disturbance area was observed among all treated tissue phantoms as shown in Figure 1A. The change in pH area was 61.83 $mm^2$ between 0.050 A and 0.350 A ($p<0.001$) and 21.54 $mm^2$ between 0.350 A and 0.700 A ($p<0.001$). Experiment 2 was necessary to isolate the effects from the concurrent change in conductivity and ionic concentration. Voltage was adjusted to normalize the current through each tissue phantom, and we recorded a statistically insignificant difference among all tissue phantom groups as seen in Figure 1B.

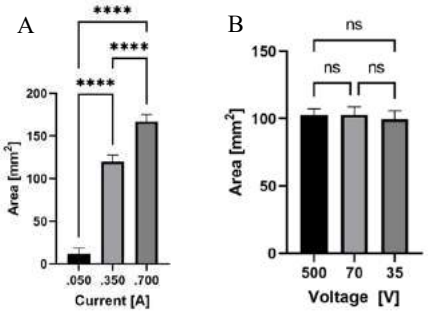


**Figure 1: A) Increased conductivity resulted in an increased current, which correlates with a greater pH disturbance. Conductivities were found to be 0.1, 0.7, and 1.4 S/m from left to right. (n=4) B) Area of pH disturbance generated by constant-current treatment (0.250 A) within tissue phantoms of different electrical conductivities. (n=4)**

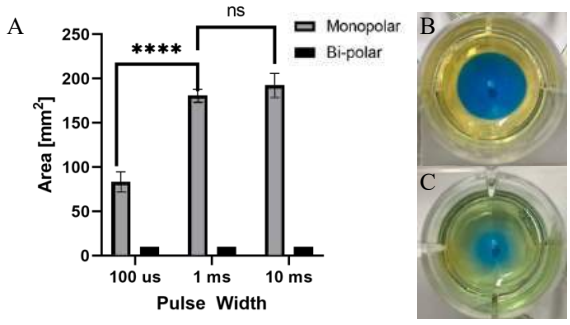


**Figure 2: A) Increased pulse width increases area of pH disturbance in dose matched treatments. Voltage decreases from left to right [500, 158, 50 V] to ensure constant dose. The bipolar pulsing method show minimal effects on pH. (n=4) B) Tissue phantom treated with 10 ms monopolar pulse width applied at 50 V. C) Tissue phantom treated with 100 µs monopolar pulse width applied at 500 V.**

To isolate and investigate the effects of pulse width and voltage, the total dose was kept constant in accordance with equation 1, with pulse width increasing inversely with voltage. The change in pH area was statistically significant from 100 µs to 1 ms ($p<0.001$) and statistically insignificant from 1 ms to 10 ms. Figure 2A shows minimal change in pH across the bipolar treatment groups when compared with each other and are negligible when compared with their correlating monopolar group. Figures 2B – 2C provide visuals of the tissue phantoms dyed with bromothymol blue following monopolar treatment. The yellow, green, and blue coloring represent pH of less than 6.0, between 6.0 and 7.6, and greater than 7.6, respectively. The tissue phantoms were green prior to treatment (pH 7.0).

The results from switching the needle's polarity from the anode to cathode show the anode generates an acidic pH and the cathode generates a basic pH. These effects are equal and opposite. These data show current and pulse width dominate the electrical field in generating electrochemical effects.

## DISCUSSION

These data offer new insight into the electrochemical effects of PEFs and demonstrates pH change is driven from the flow of electrons. Tissue phantoms in experiment 1 were all treated with the same pulse parameters while the conductivity was varied by increasing concentrations of the electrolyte NaCl. This experiment was able to show a statistically significant increase in pH disturbance area although the voltage was constant. In translation, as electrical properties vary drastically between different tissue types[6], organ-specific protocols will need to be developed if these pH changes are to be used for therapeutic purposes. Experiment 2 furthers this notion by demonstrating a statistically insignificant difference in pH disturbance area among groups with different voltages. Experiment 3 demonstrates a significant increase in pH disturbance area as pulse width increases inversely with voltage, followed by experiment 4 which confirms bipolar pulses have a significantly smaller effect on pH than monopolar pulses. However, due to the broad pH threshold of the dye (pH 6.0 – 7.6) we were limited in investigating the extent of bipolar pH changes which most likely occur within that margin. The results of this study show that in monopolar pulses, current and pulse width dominate the subsequent electrochemical effect, suggesting that electrochemical effects are less dependent on the electrical field. H-FIRE is a competitive treatment for applications in which pH change is unwelcome because of its bipolar pulsing mechanism. These data provide insight for applications of PEFs which seek to leverage these electrochemical effects, such as to increase ablation volumes with the combination of electroporation and electrochemical effects.[4] This study evaluates the driving mechanisms behind electrochemical effects of monopolar pulses and can provide guidance in modulating these effects for clinically relevant treatment paradigms.

## ACKNOWLEDGEMENTS

This project was supported by the National Institutes of Health (Bethesda, MD) under award R01-CA240476.

The authors acknowledge support from the Center for Engineered Health and Institute for Critical Technology and Applied Science at Virginia Tech.

## REFERENCES

[1]. Davalos, R.V et al., *Ann Biomed Eng,* 33:223, 2005
[2]. Turjanski P et al., *PLOS ONE* 6(4): e17303, 2011
[3]. Maglietti F et al., *PLOS ONE* 8(11): e80167, 2013
[4]. Klein N et al., *PeerJ,* 5:e3190, 2017
[5]. Arena, C.B. et al., *BioMed Eng OnLine* 10:102, 2011
[6]. Gabriel S et al., P*hysics in medicine & biology*, 41(11):2251, 1996

SB³C2022
Summer Biomechanics, Bioengineering and Biotransport Conference
June 20-23, Eastern Shore, MD, USA

# EPITHELIAL FLUID SECRETION AND LUMINAL PRESSURE REGULATE THE PATTERNS OF PROLIFERATION THAT SCULPT THE DEVELOPING BRONCHIAL TREE

**Shelby R. Mohr-Allen (1), Victor D. Varner (1,2)**

(1) Department of Bioengineering, The University of Texas at Dallas, Richardson, TX, USA
(2) Department of Surgery, UT Southwestern Medical Center, Dallas, TX, USA

## INTRODUCTION

The development of numerous organs in the body, including the lung, kidney, and salivary gland, involves a series of branching events referred to collectively as branching morphogenesis. In the embryonic lung, this process constructs the bronchial tree, a ramified architecture that facilitates the transport of air to the distally located alveoli, where gas exchange occurs [1]. Normal airway branching depends crucially on cell proliferation, and several signaling pathways, including those downstream of sonic hedgehog (Shh), Wnt, and various fibroblast growth factors (FGFs), have been shown to regulate this process. Recent work, however, has shown that mechanical forces can also influence airway branching. The embryonic airways are fluid-filled, and changes in luminal fluid pressure can modulate rates of branching morphogenesis in cultured embryonic lungs [2]. The embryonic airway epithelium is secretory, and fluid pressure is controlled by the amount of fluid secreted into the luminal space. Even so, it is completely unclear how changes in epithelial fluid secretion and luminal fluid pressure impact the patterns of proliferation that sculpt the bronchial tree.

Here, we focus on lateral branching morphogenesis and use as a model system the embryonic avian lung, which forms exclusively via lateral branching, wherein daughter branches form along the length of the parent branch. We thus used pharmacological modulators of epithelial fluid secretion to alter the transmural pressure in cultured embryonic chicken lungs. These experiments were then combined with quantitative fluorescence microscopy to determine how changes in fluid secretion affect patterns of proliferation during the formation of lateral branches. We also microinjected a small volume of biologically inert oil into the lumen of some lungs to locally dilate the embryonic airway. These explants were then cultured and quantified for changes in proliferation in the neighborhood of the locally distended lumen.

## METHODS

Fertilized White Leghorn chicken eggs were incubated at 37°C in a forced-draft incubator to Hamburger and Hamilton stage 26. Embryonic lungs were dissected in phosphate-buffered saline (PBS) using fine forceps and cultured for 24 hr on Nucleopore membranes at the air/liquid interface in DMEM/F12 medium supplemented with 5% fetal bovine serum (FBS) and antibiotics. In some experiments, the culture medium was supplemented with either an agonist (10 μM forskolin, 100 μM CPT-cAMP) or antagonist (200 μM bumetanide, 100 μM CFTR inhibitor-172) of epithelial fluid secretion. In other experiments, to locally (and more directly) alter epithelial tension, a pulled glass micropipette was filled with biocompatible oil and inserted into the lumen of the embryonic airway. A small amount of oil was then injected into the lumen with the use of a pneumatic pump.

Bright-field images of cultured explants were captured at 0 and 24 hr. We used the Click-iT EdU Imaging Kit to quantify rates of epithelial proliferation. Samples were pulsed with EdU 20 min prior to fixation. Fixed explants were then co-stained with LCAM immunofluorescence and DAPI, to label the airway epithelium and nuclei, respectively, and then optically cleared. Confocal fluorescence images of whole-mount explants were then captured using a laser scanning confocal microscope. Quantitative image analysis was performed using ImageJ.

## RESULTS

To determine how changes in fluid secretion impact branching and proliferation during early lung development, we used pharmacological modulators of epithelial fluid secretion to alter the transmural pressure in cultured embryonic chicken lungs. Treatment with forskolin, an activator of cAMP and agonist of fluid secretion, caused the embryonic airways to dilate dramatically and produced a significant decrease in the formation of new branches (Fig. 1). Similar results were obtained using explants treated with 100 μM CPT-cAMP, another activator of cAMP

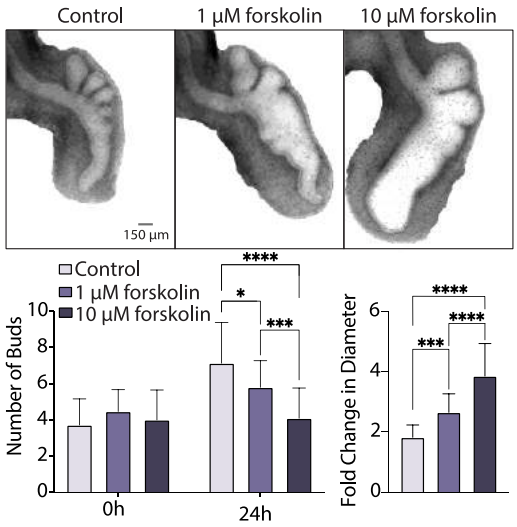


**Figure 1: Embryonic chicken lungs treated with forskolin, an agonist of fluid secretion, show decreased branching morphogenesis.**

and agonist of fluid secretion. Then, to determine if the observed decrease in branching was associated with a concomitant change in proliferation, we quantified rates of EdU incorporation in explants cultured in the presence of forskolin. Increased levels of fluid secretion modified patterns of proliferation along the airway epithelium (Fig. 2), increasing slightly the rate of proliferation in the nascent buds and, more surprisingly, elevating levels of proliferation in non-branch-forming regions along the ventral epithelium. Proximal regions of the airway, which remained undilated after treatment with forskolin, did not show dose-dependent changes in proliferation, suggesting that proliferative

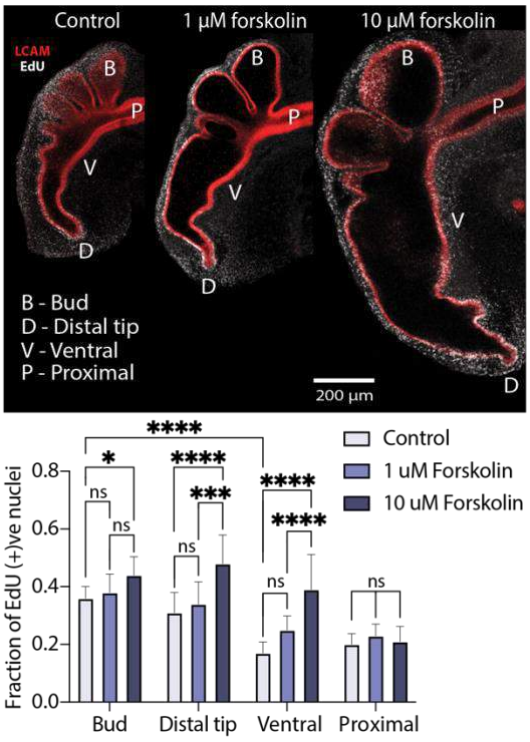


**Figure 2: Increased luminal pressure promotes proliferation in a non-branch-forming region of the embryonic chicken airway epithelium.**

differences along the dilated epithelium were caused by increased fluid pressure, as opposed to other off-target effects associated with increased cAMP activity.

To more locally perturb the transmural pressure, we also microinjected a small volume of flourinert FC-70, a biocompatible oil, into the lumen of the embryonic airway in other explants (Fig. 3). Each localized distension of the airway inhibited the formation of new epithelial buds (Fig. 3) and produced a localized increase in EdU incorporation around the dilated lumen, consistent with our fluid secretion experiments (data not shown).

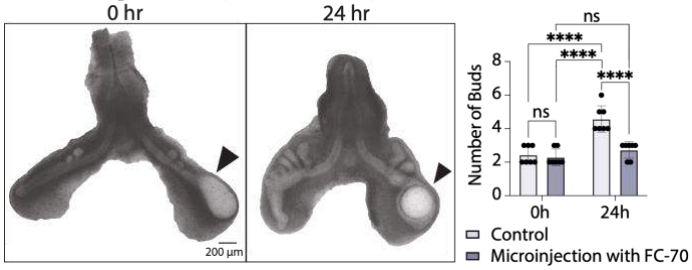


**Figure 3: Microinjection with bioinert oil produces local dilation of airway epithelium leading to disrupted branching morphogenesis.**

Lastly, to determine the effect of decreased fluid pressure on branching morphogenesis, we cultured other explants in the presence of either 200 μM bumetanide or 100 μM CFTR inhibitor-172 to inhibit epithelial fluid secretion. Treatment with each of these inhibitors caused the embryonic airways to collapse and increased the number of new epithelial buds. Taken together, these data suggest that changes in fluid secretion and luminal fluid pressure can modulate proliferation and branching morphogenesis within the developing bronchial tree.

## DISCUSSION

Many congenital lung malformations, including pulmonary hypoplasia and congenital diaphragmatic hernia (CDH), are associated with defects in the mechanical environment surrounding the fetal lung [3]. To treat patients with CDH, surgeons perform a risky surgery known as fetoscopic endotracheal occlusion (FETO), which involves inserting and inflating a balloon in the fetal trachea to increase the fluid pressure within the lung. This operation can rescue the hypoplastic lung phenotype by increasing lung growth, but it is unclear if changes in fluid pressure impact the patterns of proliferation that underlie airway branching morphogenesis. Our experiments suggest that increased epithelial fluid secretion, and thus luminal fluid pressure, alters the spatial pattern of proliferating cells in cultured embryonic lungs. Previous studies using embryonic mouse lungs have shown that elevated fluid pressure can increase rates of branching morphogenesis [2]. Our experiments, using cultured embryonic chicken lungs, however, suggest the opposite. Since avian lung development depends exclusively on lateral branching, whereas branching morphogenesis in the mammalian lung involves both lateral branches and bifurcations, these results suggest that particular branching modes may be affected differently by changes in luminal fluid pressure.

## ACKNOWLEDGMENTS

This work was supported, in part, by the NIH grant R01HL145147 to VDV.

## REFERENCES

[1] Cardoso WV, Lü J, *Development*, 133:1611-1624, 2006.
[2] Nelson CM, et al., *Development*, 144:4328-4335, 2017.3
[3] Smith NP, et al., *Arch. Dis. Childh*, 90:426-428, 2005

# AN PHYSIOLOGICAL ON-CHIP VESSEL PLATFORM TO STUDY VASCULAR TRANSPORT OF CIRCULATING TUMOR CELLS

**Yue Wu[1], Yuyuan Zhou[1], Ratul Paul[2], and Yaling Liu[1, 2, *]**

[1]Bioengineering Department, Lehigh University, Bethlehem, Pennsylvania, 18015, USA
[2]Mechanical Engineering and Mechanics Department, Lehigh University, Bethlehem, Pennsylvania, 18015, USA
[*]Author to whom correspondence should be addressed: yal310@lehigh.edu

## INTRODUCTION

Cancer is a major public health problem in the world and metastasis is the direct culprit of most cancer related deaths[1]. By releasing the circulating tumor cells (CTCs), primary solid tumor can initiate the metastasis process and disseminate to distant organs (Fig.1)[2]. Among them, blood vessels function as highways for CTCs transportation[3,4]. Due to the rarity of the event and limited *in vivo* characterization techniques, the cancer metastasis still remains enigmatic.

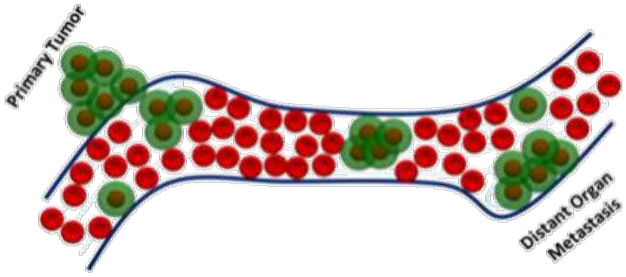


Figure 1. Vascular transport of CTCs from primary tumor to distant dissemination.

To date, microfluidics has become a powerful modeling and screening platform to investigate cancer biology and develop cancer therapy[5–7]. Here, we report an microphysiological vessel platform. With facile on-chip modelling of vessels, vascular transport of CTCs can be recapitulated and characterized *in vitro*. As a demonstration, the influence of vascular glycocalyx (VGCX) status on CTC adhesion was investigated. It is believed that our microphysiological vessel platform will not only help address critical steps in complicated metastatic cascades but also contribute to advanced cancer therapy development.

## METHODS

Human umbilical vein endothelial cells were cultured in EGM-2 medium (Lonza). Prostate cancer cell, PC3, were cultured in F-12K medium (ATCC). All cells and experiments were incubated at 37 °C with 5% CO2.

The microfluidic devices were fabricated using standard soft lithography techniques (Fig. 2A). A PDMS rod was used as mold and loaded in the chamber[8]. Then, fibrinogen solution was mixed with thrombin and injected into the device through side ports. After hydrogel polymerization, the rod was extracted and HUVEC suspension was seeded int the tubular channel. The channel endothelialization can be finished in 24 hours.

Suspended PC3 cells were perfused through the vessels of different VGCX thickness and the adhered cancer cells were counted. The VGCX was labeled with biotinylated wheat germ agglutinin (WGA; Vector Labs) lectin. Neuraminidase (Neur) enzyme in PBS was used for VGCX degradation[9].

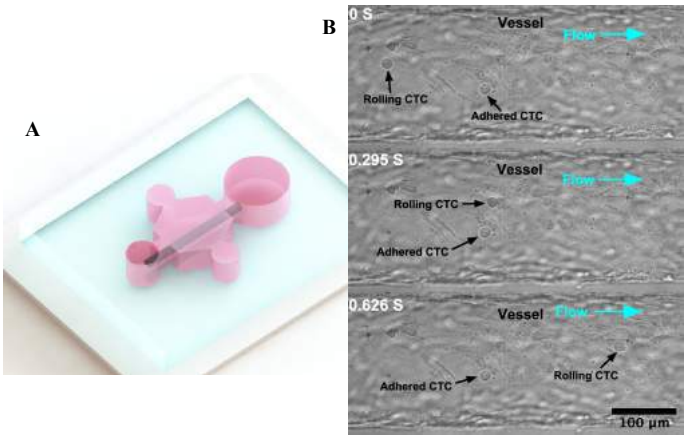


Figure 2. Microfluidic on-chip vessel platform. A) Schematic of microfluidic device. B) Representative images of CTCs transport on the vessel. CTCs move on the vessel inner surface in a rolling manner.

## RESULTS

With high-speed camera recording, CTCs were observed to move on the inner surface of the blood vessel in a rolling manner (Fig. 2B). Once adhered, the CTC would stop movement and not be detached easily by

flow within a certain flow rate. Our observation is consistent with some theories which claim that hematogenous metastatic behavior of CTCs maybe similar to leukocyte transport in the bloodstream, during the inflammatory response[10].

Furthermore, as the VGCX thickness decreased, the number of adhered CTCs increased significantly (Fig. 3). The potential explanation would be that degraded VGCX increase the probability of direct contact between various adhesion receptors, such as integrins, immunoglobulins, and selectins[11] with ligands on CTCs.

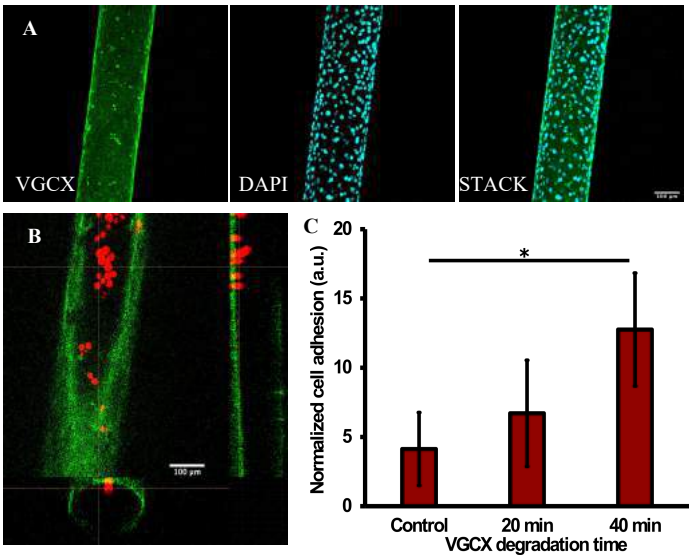


Figure 3. CTC adhesion result on vessels under various VGCX conditions. A) VGCX characterization of the on-chip vessels. Fluorescent staining of VGCX (green). The VGCX was labelled by WGA, which targets some main components of VGCX, including sialic acid and N-acetylglucosamine. DAPI signal (blue) stains cell nuclei. B) Confocal scanning of adhered CTCs on VGCX. VGCX were labeled with WGA (FITC). C) Normalized rate of adhered CTCs on the vessels with VGCX degradation treatment of different times.

## DISCUSSION

In addition to the above-mentioned biophysiological factors, we will also study the effect of biomechanical factors such as flow rate and vascular geometry on CTC transport on this platform. As a demonstration, a stenotic vessel model will be constructed on-chip and CTCs' movement in the resulted hemodynamic disturbed flow will be probed in real-time. Moreover, cancer intravasation and extravasation of vessel will be modelled *in vitro*. By recapitulating these key steps of cancer metastatic cascade, our adaptable vessel-on-a-chip platform is envisioned to facilitate cancer metastasis interpretation and has potential for personalized therapy screening.

## ACKNOWLEDGEMENTS

This work was supported by National Institute of Health grant R01HL131750, National Science Foundation grant CBET 2039310, Pennsylvania Department of Health Commonwealth Universal Research Enhancement Program (CURE), and Pennsylvania Infrastructure Technology Alliance (PITA).

## REFERENCES

(1) Siegel, R. L.; Miller, K. D.; Fuchs, H. E.; Jemal, A. Cancer Statistics, 2021. *CA Cancer J. Clin.* **2021**, *71* (1), 7–33.
(2) Plaks, V.; Koopman, C. D.; Werb, Z. Cancer. Circulating Tumor Cells. *Science* **2013**, *341* (6151), 1186–1188.
(3) Wu, Y.; Zhou, Y.; Qin, X.; Liu, Y. From Cell Spheroids to Vascularized Cancer Organoids: Microfluidic Tumor-on-a-Chip Models for Preclinical Drug Evaluations. *Biomicrofluidics* **2021**, *15* (6), 061503.
(4) McDonald, D. M.; Baluk, P. Significance of Blood Vessel Leakiness in Cancer. *Cancer Res.* **2002**, *62* (18), 5381–5385.
(5) Chen, M. B.; Whisler, J. A.; Fröse, J.; Yu, C.; Shin, Y.; Kamm, R. D. On-Chip Human Microvasculature Assay for Visualization and Quantification of Tumor Cell Extravasation Dynamics. *Nat. Protoc.* **2017**, *12* (5), 865–880.
(6) Zhang, Q.; Liu, T.; Qin, J. A Microfluidic-Based Device for Study of Transendothelial Invasion of Tumor Aggregates in Realtime. *Lab Chip* **2012**, *12* (16), 2837.
(7) Thomas, A.; Wang, S.; Sohrabi, S.; Orr, C.; He, R.; Shi, W.; Liu, Y. Characterization of Vascular Permeability Using a Biomimetic Microfluidic Blood Vessel Model. *Biomicrofluidics* **2017**, *11* (2), 024102.
(8) Virumbrales-Muñoz, M.; Chen, J.; Ayuso, J.; Lee, M.; Abel, E. J.; Beebe, D. J. Organotypic Primary Blood Vessel Models of Clear Cell Renal Cell Carcinoma for Single-Patient Clinical Trials. *Lab Chip* **2020**, *20* (23), 4420–4432.
(9) Harding, I. C.; Mitra, R.; Mensah, S. A.; Herman, I. M.; Ebong, E. E. Pro-Atherosclerotic Disturbed Flow Disrupts Caveolin-1 Expression, Localization, and Function via Glycocalyx Degradation. *J. Transl. Med.* **2018**, *16* (1), 364.
(10) Coussens, L. M.; Werb, Z. Inflammation and Cancer. *Nature* **2002**, *420* (6917), 860–867.
(11) Weinbaum, S.; Tarbell, J. M.; Damiano, E. R. The Structure and Function of the Endothelial Glycocalyx Layer. *Annu. Rev. Biomed. Eng.* **2007**, *9* (1), 121–167.

SB³C2022
Summer Biomechanics, Bioengineering and Biotransport Conference
June 20-23, Eastern Shore, MD, USA

# A CHEMO-MECHANO-BIOLOGICAL MODEL OF EVOLVING OSTEOARTHRITIS

**Muhammed M. Rahman (1), Paul N. Watton (2), Thomas S. E. Öst (3), Corey P. Neu (4), David M. Pierce (1,5)**

(1) Department of Mechanical Engineering, University of Connecticut, Storrs, Connecticut, USA

(2) Insigneo Institute for in silico Medicine and Department of Computer Science, University of Sheffield, Sheffield, UK

(3) Department of Weapons, Protection and Security, FOI – Swedish Defense Research Agency, Stockholm, Sweden

(4) Department of Mechanical Engineering, University of Colorado Boulder, Boulder, Colorado, USA

(5) Department of Biomedical Engineering, University of Connecticut, Storrs, Connecticut, USA

## INTRODUCTION

Osteoarthritis (OA) is a multifactorial disease of synovial joints with degeneration and loss of articular cartilage as a hallmark feature. Nearly 20% of the US population suffers from OA, affecting quality of life through pain, functional limitations, lost earnings, anxiety, and depression. While mechanical stimuli is essential to maintain healthy cartilage, overloading (e.g. trauma) and reduced loading (e.g. immobilization) induce molecular and microstructural changes that lead to mechanical softening, fibrillation, and erosion [1].

In response to mechanical stimuli, chondrocytes (the cells within cartilage) express chemicals (e.g. cytokines, growth factors, collagenase, and aggrecanase) which promote degradation or production of structural constituents, e.g. collagen and proteoglycan. Existing investigations on effects of mechanical loading on cartilage – including both *in vitro* experiments with human cartilage and *in vivo* animal models – fall short of true human physiological relevance [2]. Current mathematical models of signaling pathways lack mechanical effects while biomechanical models lack the chemical effects [3].

To facilitate better understanding of the coupled chemo-mechano-biological evolution of OA in cartilage, we seek coupled functional forms among intra-tissue mechanics and cell-driven mass/volume changes mediated by cytokines and chemical species. Here we establish a framework incorporating the evolution of chemical, mechanical, and biological constituents generating anisotropic volumetric changes in cartilage. We leverage our established constitutive model of cartilage [4] and adapt a biochemical pathway model [5] to predict the evolution of relevant cellular and biomolecular species during OA. We demonstrate our framework by predicting the effects of immobilization and overloading on the progression of OA (and relative to homeostasis).

## METHODS

*Constitutive Model.* To capture the nonlinear mechanics of cartilage, we employ an additive decomposition of the superimposed solid Helmholtz free energy $\psi^{\mathrm{S}}$ into $\psi^{\mathrm{S}}_{\mathrm{IM}}$ and $\psi^{\mathrm{S}}_{\mathrm{FN}}$, representing an isotropic matrix and a distributed, fiber network respectively as [5]

$$\psi^{\mathrm{S}} = (1-\nu)\psi^{\mathrm{S}}_{\mathrm{IM}}(J_{\mathrm{S}}, I_1) + \nu\psi^{\mathrm{S}}_{\mathrm{FN}}(I_4, \mathbf{M}) \,, \tag{1}$$

where $\nu$ is the volume fraction of collagen to total solid, $J_{\mathrm{S}}$ is the Jacobian, $I_1 = \mathrm{tr}(\mathbf{C}_{\mathrm{S}})$ with $\mathbf{C}_{\mathrm{S}}$ the right Cauchy-Green tensor, and $\mathbf{M}$ is the reference fiber orientation with $I_4 = \mathbf{M}\cdot\mathbf{C}_{\mathrm{S}}\mathbf{M}$. We modeled the densely packed proteoglycan using a neo-Hookean strain energy function for $\psi^{\mathrm{S}}_{\mathrm{IM}}$. We modeled the network of collagen fibers as [5]

$$\psi^{\mathrm{S}}_{\mathrm{FN}} = \frac{1}{\rho^{\mathrm{S}}_{0\mathrm{S}}}\int_{\Omega}\rho(\mathbf{M})\frac{k_1}{2k_2}\left\{e^{[k_2(I_4-1)]^2-1}\right\}\mathcal{H}(I_4-1)\,\mathrm{d}\Omega \tag{2}$$

where $\rho(\mathbf{M}), k_1, k_2$ are an orientation distribution function and two model parameters, respectively, and $\mathcal{H}$ is a Heaviside function.

*Anisotropic Volumetric Growth and Remodeling.* We defined the target volume change $\hat{v} = \nu\hat{m}_{\mathrm{co}} + (1-\nu)\hat{m}_{\mathrm{pg}}$, where $\hat{m}_{\mathrm{co}}$ and $\hat{m}_{\mathrm{pg}}$ are the normalized mass of type II collagen and proteoglycan, respectively. We exploit the very different time scales between daily activities, e.g. walking ($t$ in sec), and progression of OA ($\tau$ in mos), which allows iterative rather than simultaneous solutions. We define the overall deformation gradient $\mathbf{F}$ by a multiplicative decomposition of $\mathbf{F}(\tau,t) = \mathbf{F}^{\mathrm{e}}(t)\mathbf{F}^{\mathrm{g}}(\tau)$ [6]. Here, we define anisotropic cartilage loss as $\mathbf{F}^{\mathrm{g}} = \mathbf{I} + (1-\hat{v})\mathbf{n}\otimes\mathbf{n}$, where $\mathbf{n}$ is a unit vector normal to the articular surface.

*Signaling Pathways Biochemical Model.* In health and with moderate daily activities, chondrocytes maintain cartilage homeostasis and do not proliferate. In OA, and both in immobilization and overloading, homeostasis is lost and chondrocytes express catabolic and anabolic cytokines, along with structural proteins. We propose the following system of ODEs to model the key components in cartilage

$$\frac{\mathrm{d}\hat{n}_{\mathrm{c}}}{\mathrm{d}\tau} = \left(r^{\mathrm{c}}_1 + r^{\mathrm{c}}_2\hat{c}_\beta\right)\hat{n}_{\mathrm{c}} - \left(r^{\mathrm{c}}_3 + r^{\mathrm{c}}_4 f(\sigma_{\mathrm{sh}})\hat{c}_\beta + r^{\mathrm{c}}_5\hat{c}_{\mathrm{p}}\right)\hat{n}_{\mathrm{c}} \tag{3}$$

$$\frac{\mathrm{d}\hat{n}_{\mathrm{hc}}}{\mathrm{d}\tau} = r^{\mathrm{hc}}_1 f(\sigma_{\mathrm{sh}})\hat{c}_\beta\hat{n}_{\mathrm{c}} - r^{\mathrm{hc}}_2\hat{n}_{\mathrm{hc}} \tag{4}$$

$$\frac{\mathrm{d}\hat{m}_{\mathrm{co}}}{\mathrm{d}\tau} = \left(r_1^{\mathrm{co}} + r_2^{\mathrm{co}}\hat{c}_\beta\right)\hat{n}_{\mathrm{c}} - \left(r_3^{\mathrm{co}} f(\sigma_1) + r_4^{\mathrm{co}}\hat{c}_{\mathrm{ca}}\right)\hat{m}_{\mathrm{co}} \quad (5)$$

$$\frac{\mathrm{d}\hat{m}_{\mathrm{pg}}}{\mathrm{d}\tau} = \left(r_1^{\mathrm{pg}} + r_2^{\mathrm{pg}}\hat{c}_\beta\right)\hat{n}_{\mathrm{c}} - \left(r_3^{\mathrm{pg}} f(\mathrm{E}_3) + r_4^{\mathrm{pg}}\hat{c}_{\mathrm{ag}}\right)\hat{m}_{\mathrm{pg}} \quad (6)$$

$$\frac{\mathrm{d}\hat{c}_{\mathrm{ca}}}{\mathrm{d}\tau} = \left[\frac{r_1^{\mathrm{ca}} + r_6^{\mathrm{ca}}\hat{c}_{\mathrm{p}}}{1 + r_2^{\mathrm{ca}}\hat{c}_\beta}\right]\hat{n}_{\mathrm{c}} + r_3^{\mathrm{ca}}\hat{n}_{\mathrm{hc}} - \left(r_4^{\mathrm{ca}} + r_5^{\mathrm{ca}}\hat{c}_{\mathrm{i}}\right)\hat{c}_{\mathrm{ca}} \quad (7)$$

$$\frac{\mathrm{d}\hat{c}_{\mathrm{ag}}}{\mathrm{d}\tau} = \left[\frac{r_1^{\mathrm{ag}} + r_6^{\mathrm{ag}}\hat{c}_{\mathrm{p}}}{1 + r_2^{\mathrm{ag}}\hat{c}_\beta}\right]\hat{n}_{\mathrm{c}} + r_3^{\mathrm{ag}}\hat{n}_{\mathrm{hc}} - \left(r_4^{\mathrm{ag}} + r_5^{\mathrm{ca}}\hat{c}_{\mathrm{i}}\right)\hat{c}_{\mathrm{ag}} \quad (8)$$

$$\frac{\mathrm{d}\hat{c}_{\mathrm{i}}}{\mathrm{d}\tau} = \left(r_1^{\mathrm{i}} + r_2^{\mathrm{i}}\hat{c}_\beta\right)\hat{n}_{\mathrm{c}} - \left(r_3^{\mathrm{i}} + r_4^{\mathrm{i}}\hat{c}_{\mathrm{ca}} + r_5^{\mathrm{i}}\hat{c}_{\mathrm{ag}}\right)\hat{c}_{\mathrm{i}} \quad (9)$$

$$\frac{\mathrm{d}\hat{c}_{\ell\beta}}{\mathrm{d}\tau} = \left(r_1^{\ell\beta} + r_2^{\ell\beta}\hat{c}_\beta\right)\hat{n}_{\mathrm{c}} - \left[r_4^{\ell\beta} + r_5^{\ell\beta} f(\sigma_{\mathrm{sh}})\right]\hat{c}_{\ell\beta} \quad (10)$$

$$\frac{\mathrm{d}\hat{c}_{\beta}}{\mathrm{d}\tau} = r_1^{\beta} f(\sigma_{\mathrm{sh}})\hat{c}_{\ell\beta} - r_2^{\beta}\hat{c}_\beta \quad (11)$$

$$\frac{\mathrm{d}\hat{c}_{\ell\mathrm{p}}}{\mathrm{d}\tau} = \left[\frac{r_1^{\ell_{\mathrm{p}}} + r_2^{\ell_{\mathrm{p}}}\hat{c}_{\mathrm{p}}}{1 + r_3^{\ell\mathrm{p}}\hat{c}_\beta}\right]\hat{n}_{\mathrm{c}} - \left[r_4^{\ell\mathrm{p}} + r_5^{\ell\mathrm{p}} f(\sigma_1)\right]\hat{c}_{\ell\mathrm{p}} \quad (12)$$

$$\frac{\mathrm{d}\hat{c}_{\mathrm{p}}}{\mathrm{d}\tau} = r_1^{\mathrm{p}} f(\sigma_1)\hat{c}_{\ell_{\mathrm{p}}} - r_2^{\mathrm{p}}\hat{c}_{\mathrm{p}} \quad (13)$$

where, $\hat{n}_{\mathrm{c}}$, $\hat{n}_{\mathrm{hc}}$, $\hat{c}_{\mathrm{ca}}$, $\hat{c}_{\mathrm{ag}}$, $\hat{c}_{\mathrm{i}}$ $\hat{c}_{\ell\beta}$, $\hat{c}_\beta$ $\hat{c}_{\ell\mathrm{p}}$, $\hat{c}_{\mathrm{p}}$, are the normalized living cells, hypertrophic cells, collagenases (MMP-3,13, etc.), aggrecanases (ADAMTS-4,5, etc.), tissue inhibitors of metalloproteinase (TIMP), latent growth factors (TGF-$\beta$, BMP, etc.), active growth factors, latent pro-inflammatory cytokines (IL-1, TNF-$\alpha$, etc.) and active pro-inflammatory cytokines, respectively. We define $f(\sigma_{\mathrm{sh}})$, $f(\sigma_1)$ and $f(E_1)$ as well-shaped, double-sigmoidal functions of shear stresses, first principal stresses, and third principal Green-Lagrange strains, respectively. The $r_i^X$ are rate parameters for the variables, where $i \in \{1,2,3,\dots,N\}$ and $X \in \{\mathrm{c}, \mathrm{hc}, \mathrm{co}, \mathrm{pg}, \mathrm{ca}, \mathrm{ag}, \mathrm{i}, \ell\beta, \beta, \ell\mathrm{p}, \mathrm{p}\}$.

*Cartilage in Homeostasis, Immobilization, and Overloading.* We simulated cartilage undergoing physiological loading (i.e. normal daily activities), immobilization, and overloading for 30 months duration. We defined ($f(\sigma_{\mathrm{sh}})$, $f(\sigma_1)$ and $f(E_1)$) following literature [7].

*Numerical implementation.* In the constitutive model we used $\mu^S = 1i\mathrm{MPa}$, $k_1 = 0.43i\mathrm{MPa}$, $k_2 = 8i[-], i\ \nu = 0.8i[-]$ [4]. The initial conditions for the coupled pathway model are $\hat{n}_{\mathrm{c}} = \hat{c}_{\mathrm{ca}} = \hat{c}_{\mathrm{ag}} = \hat{c}_i = \hat{c}_{\ell\beta} = i\hat{c}_{\ell\mathrm{p}} = 1$ and $\hat{c}_\beta = \hat{c}_{\mathrm{p}} = \hat{n}_{\mathrm{hc}} = 0$, and we estimated the rate parameters following literature. We implemented the chemo-mechano-biological framework in Matlab R2021b (The Mathworks, USA) and solved the system of ODEs using a backward-finite-difference Euler approach with a fixed step size of $\mathrm{d}\tau = 0.1$ months.

## RESULTS

During the moderate loading of normal daily activities cartilage remained in homeostasis, i.e. no changes in the constituents or cytokines (dashed lines in **Fig. 1**). During immobilization we predicted a reduction in living cells (-16%), proteoglycan (-25%), and collagen (-28%) (**Fig. 1(a)**). We also predicted gradual increases in collagenase, aggrecanase, latent growth factors, and latent pro-inflammatory cytokines, all which remained upregulated (**Fig. 1(b)**). However, TIMP followed the opposite pattern due to its inverse relationship with both collagenase and aggrecanase. Active growth factors and active pro-inflammatory cytokines increased and stabilized at ~10% and ~6% with respect to the latent forms, respectively (**Fig. 1(c)**). We also predicted volume loss (-28%) consistent with experimental measurements (**Fig. 1(d)**) [8]. In overloading we observed greater volume loss (results not shown).

## DISCUSSION

We introduced a modeling framework for cartilage considering the chemo-mechano-biologically induced turnover of key constituents in resulting from mechanical loading and/or biochemical activity. We included the complex chemical and mechanobiological mechanisms within cartilage, and addressed the key constituents in formulating our model. With representative rate parameters, our simulations for immobilization successfully predicted the loss of cartilage volume quantified experimentally as loss of thickness [8]. The upregulation of pro-inflammatory cytokines and the growth factors in immobilization is also consistent with to the experimental studies [9]. There is a lack of data quantifying the long-term effects of overloading human cartilage, but we simulated the evolution of constituents supported by *in vitro* and *in vivo* experiments leveraging animal models [10]. Both immobilization and overloading caused the progression of OA, demonstrating the potential of our framework to predict degradation.

*Limitations and outlook.* We considered only a subset of known signaling pathways, while many more exist [11]. We also, as a starting point to establish our framework, combined the chemical species into classes based on their roles, although not all members within each class have the same effect on cartilage homeostasis. We aim to implement our chemo-mechano-biological framework for finite element analyses, thus enabling advanced understanding of patient-specific pathological changes due to biomechanical factors, improved clinical diagnostics and therapies [12], and new methods for non-invasive diagnosis and pre-/post-operative decision making.

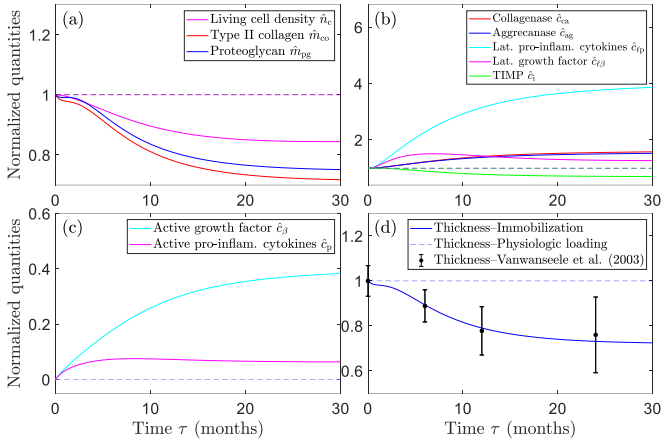


**Figure 1: Cartilage evolving in homeostasis and immobilization. Normalized quantities of (a) structural components (living chondrocytes, collagen and proteoglycan), (b) cytokines and growth factors (collagenase, aggrecanase, TIMP, latent growth factor and latent pro-inflammatory cytokines), (c) active cytokines and growth factors, and (d) cartilage thickness. Dashed and solid lines represent moderate and reduced loading, respectively.**


## ACKNOWLEDGEMENTS

NSF 1662429.


## REFERENCES


[1] Goldring, MB and Marcu, KB, *Arthr Res Ther*, 11:224, 2009. [2] Halloran, JP et al., *Ann Biomed Eng*, 40:2456-74, 2012. [3] Baker, M et al., *J Math Biol*, 75:985-1024, 2017. [4] Pierce, DM et al., *Biomech Model Mechanobiol*, 15:229-44, 2016. [5] Aparício, P et al., *J Biomech*, 49:2321-30, 2016. [6] Grytsan, A et al., *Materials*, 10:1-19, 2017. [7] Kuster, MS et al., *J Bone Jt Surg*, 79:109-13, 1997. [8] Vanwanseele, B et al., *Arthritis Rheum*, 48:3377-81, 2003. [9] Haapala, J et al., *Int J Sports Med*, 21:76-81, 2000. [10] Hosseini, SM et al., *Osteoarthritis Cartilage*, 21:136-43, 2013. [11] Fang, T et al., *Int Orthop.*, 45:1125-36, 2021. [12] Nakamura, H et al., *Sci Rep*, 10:1-9, 2020.

# A MUTIPARAMETER WHOLE BLOOD HEMOSTASIS ASSESSMENT USING A HIGHLY SENSIVITE FLEXIBLE CARBON NANOTUBE PAPER-BASED CAPACITANCE SENSOR

**Praveen K. Sekar (1), Ye Jin (1), Yanyun Wu (1), Dayong Gao (1,2)**

(1) Department of Mechanical Engineering
University of Washington
Seattle, WA, USA

(1) Department of Bioengineering
University of Washington
Seattle, WA, USA

## INTRODUCTION

Rapid and accurate assessment of hemostasis is imperative in various clinical settings to diagnose, treat, and monitor patients with impaired hemostasis[1].Over 15 million people worldwide receive oral anticoagulant therapy to prevent and treat life-threatening thromboembolic events[2]. Despite their effectiveness in lowering the risk of acute thrombosis, effective anticoagulation management in these patients remains challenging because of the narrow therapeutic window between either increased risk of thromboembolic events or higher probability of dangerous hemorrhage and life-threatening organ failure, which is influenced by numerous factors[3]. Therefore, patients require frequent laboratory testing of blood clotting status to ensure appropriate selection of anticoagulant agent and dosing, which imposes a staggering service load on health care providers.

Traditional laboratory-based clotting assays and devices are limited to not only time-consuming and expensive, but also insufficient information due to partial analysis of various individual facetted clotting elements, such as coagulation function (aPTT, PT, TT), fibrinogen, platelet function (PFA, LTA) or blood cellularity (hematology analyzers), or lack sensitivity and specificity to key clotting parameters such as platelet dysfunction (viscoelastic assays- TEM, TEG). As a result, each current assay or testing technology has provided an incomplete assessment of bleeding and thrombosis status and risks[4]. This has also stymied the fields of clinical and experimental hematology given the interdependence among the clotting elements.

In this study, we present a novel capacitance-based approach for blood permittivity measurement using a carbon nanotube-paper composite (CPC) capacitance sensor. A major advancement of the proposed approach is that the capacitance signal obtained from a single measurement could provide three parameters with distinctive sensitivity towards coagulation function, platelet count or function, and hematocrit. The CPC sensor exhibited high fringing field to detect permittivity changes in a blood sample placed in a glass vial on top of the sensor, eliminating the need for physical electrical contact. The feasibility and sensitivity of this approach was demonstrated using clinically relevant human blood samples. The results were compared against a conventional TEG analyzer to validate the effectiveness of the sensor.

## METHODS

### CPC sensor and capacitance measuring system

The experimental setup used for capacitance measurement consists of two CPC capacitance sensors, FDC 2214 capacitance evaluation module (Texas Instruments, TX, U.S.A), glass vials (Agilent Technologies, CA, U.S.A), 3D printed plastic fixtures and orbital shaker. A blood sample in glass vials was precisely positioned using plastic fixtures on top of the crack region in the sensor.

### Clotting assay protocol & Data Analysis for signal parameters

A baseline capacitance was measured for 5 min with the glass vials placed on the sensors. Then, 325 µL of the blood sample was added to the reference sensor. Immediately, 300 µL of the same blood was added to the detector sensor and 80-rpm orbital shaking was applied. The glass vial on the detector sensor was prefilled with 25 µL of 162.5 mM $CaCl_2$ solution (final $Ca^{2+}$ concentration: 12.5 mM) for recalcification of the blood sample. Differential capacitance was measured for an additional 30 min after activation. From the capacitance signal, three parameters were chosen for analysis ($T_{Cpeak}$, $\Delta C1$ and $\Delta C2$; *Fig 1a*). $T_{Cpeak}$ was the timepoint for maximum capacitance value after activation. $\Delta C1$ was evaluated as the magnitude decrease in capacitance from peak to a steady state value. Steady state capacitance was the averaged value between 28-30 min after activation. $\Delta C2$ was the maximum capacitance value after activation.* denotes a $p < 0.05$, ** $p < 0.01$. Pearson's coefficient ($r$) was used to evaluate linearity between the pairs of data. $p$ values calculated from ANOVA.

## RESULTS

Whole blood based hemostasis assessments were conducted on clinically relevant human whole blood samples. We found that $T_{Cpeak}$ decreased with increasing $CaCl_2$ concentration (Fig. 1b), which indicated a trend in $T_{Cpeak}$ and coagulation time ($p < 0.00001$). For the remaining studies, 12.5 mM $CaCl_2$ was used to activate clotting in the samples. When we tested blood samples with a predefined platelet count, we found that *ΔC1* linearly increased with increasing platelet count (Fig. 1c). From measurements using blood samples incubated with aspirin, which inhibits platelet activation, we found that *ΔC1* dose-dependently decreased with increasing aspirin concentrations (Fig. 1d). Together, the above two results (Fig. 1c, d) showed that *ΔC1* was sensitive to both platelet count and function. When we tested blood samples with a predefined hematocrit, we found that *ΔC2* linearly increased with increasing hematocrit (Fig. 1e). Collectively, the above results showed that the sensor can offer a multiparameter assessment of hemostasis by providing concurrent information on coagulation function, platelet count or function, and hematocrit.

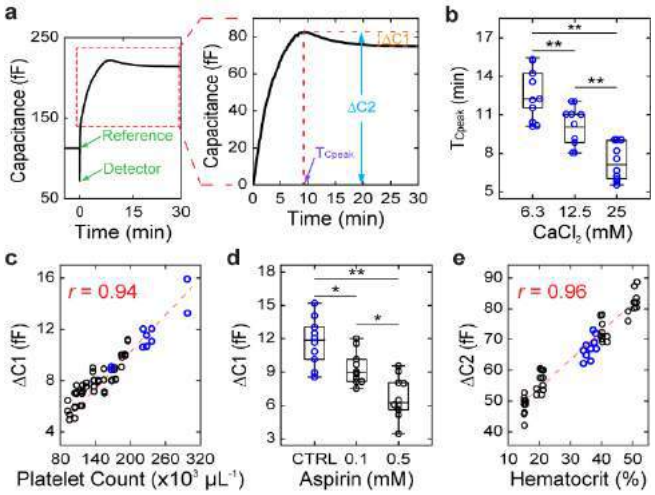


***Figure 1.*** *(a) Left: A representative overall capacitance signal for a blood sample, Right: Zoom-in view of the region of interest (b) $T_{Cpeak}$ decreases with increasing concentration of activating CaCl2 (mM). (c) ΔC1 linearly increases with platelet count (d) ΔC1 decreases dose-dependently with aspirin treatment. (e) ΔC2 linearly increases with hematocrit, n = 5 healthy donors with two replicate measurements.*

To evaluate the potential clinical utility of our sensor, we compared the coagulation time and platelet parameters with the clinically relevant diagnostic parameters of citrate native thromboelastography (CN-TEG) assay. Results illustrated a strong positive correlation between $T_{Cpeak}$ and Reaction time (*R-time)* (Fig. 2a). The obtained data validated the effectiveness of the presented sensor in evaluating coagulation function and is in good agreement with the viscoelastic TEG assay. However, there was a relatively less degree of correlation between *ΔC1* and Maximum Amplitude (*MA)* (Fig. 2b). The reason for such discrepancy is likely because the *MA* parameter, which measures clot strength, may be affected by both the number of cells in the clot and passive fibrin elasticity[5]. To examine the hypothesis, we rearranged the data as illustrated in Fig. 2c. Interestingly, a much stronger correlation between *ΔC1* and platelet count than to *MA* was observed, suggesting *ΔC1* may be solely dependent on the platelet count. This also implies that *ΔC1* might be a better alternative in evaluating platelet count-related diseases as it may have a higher sensitivity and specificity to platelet count. Our results suggests that the proposed sensor could potentially eliminate the need of using additional specialized inhibitors to assay platelets in whole blood, which could further minimize the chances of pre-analytical errors that complicate existing assays.

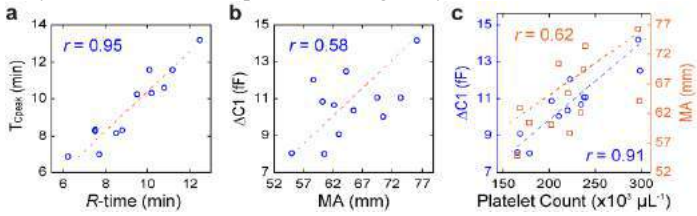


***Figure 2.(a)*** *$T_{Cpeak}$ shows a strong positive correlation with the Reaction time (R-time) parameter* ***(b)*** *Less degree of correlation between ΔC1 and Maximum Amplitude (MA).* ***(c)*** *ΔC1 shows a stronger positive correlation with platelet count in comparison to MA. n = 12 healthy donors with single replicate measurement*

## DISCUSSION

Motivated by the importance of having a rapid, accurate and convenient hemostasis assessment device, we have developed the first reported capacitance-based approach with a unique ability to multiplex the assessment of coagulation function, platelets and hematocrit in a single measurement. The CPC capacitance sensor described here provides several attractive advantages over existing clinical assays and devices as summarized in Table 1. Its ease of use without the necessity of extensive sample preparation or highly trained laboratory personnel, and additional benefits, such as non-contact, high reusability and low cost, makes it an ideal tool to readily evaluate clotting status while significantly reducing the financial burden on primary care resources.

| Features | **Presented System** | Viscoelastic assays | Traditional laboratory Assay | Blood gas or handheld analyzers |
|---|---|---|---|---|
| Provide global assessment of hemostasis and evaluate bleeding risk in a single device | ✓ | | | |
| Provide global assessment of hemostatic status (coagulation time + platelet function) | ✓ | ✓ | | |
| Can measure platelet count | ✓ | | ✓ | |
| Can measure hematocrit | ✓ | | ✓ | ✓ |
| Rapid Turnround Time (TAT) | ✓ | ✓ | | ✓ |
| Ease of use and cost efficient (reusability): | ✓ | | | ✓ |

***Table 1.*** *Potential advantages of the presented system over current approaches*


## ACKNOWLEDGEMENTS

This work was supported in part by the University of Washington - CoMotion Innovation Fund.


## REFERENCES


[1] Jackson, S.P., 2011. Nat. Med. 17, 1423–1436.
[2] Chen, A., et.al. 2020. J. Am. Heart Assoc. 9, 17559.
[3] Penning-VB, F.J.A. et.al.,2001.Thromb. Haemost. 86, 569–574.
[4] Tynngård, N., et.al., 2015. Thromb. J. 13, 8.
[5] Gottumukkala, V.N.R, et.al., 1999. Anesth. Analg. 89, 1453–1455.

# AORTIC STRUCTURAL AND FUNCTIONAL REMODELING IN RESPONSE TO CHRONIC E-CIGARETTE OR CIGARETTE EXPOSURE IN THE APOE$^{-/-}$ FEMALE MOUSE

**Yasmeen M. Farra (1), Jacqueline Matz (1), Jessica M. Oakes (1), Chiara Bellini (1)**

(1) Bioengineering, Northeastern University, Boston, MA, USA

## INTRODUCTION

Notwithstanding a decline in prevalence, cigarette smoking remains the principal cause of preventable death worldwide[1]. Electronic cigarettes have recently emerged as a popular alternative for both current and former smokers[1], and continue to attract novice users[2]. While a causative link between smoking and cardiovascular disease exists[1], the long-term effects of e-cigarette use are unknown and will take decades to observe in humans. Animal models of e-cigarette exposure are therefore necessary to identify the health hazard of this practice, with cigarette smoking as a requisite condition for comparison. To address this need, we present here the structural and functional characterization of the Apoe$^{-/-}$ mouse aorta following chronic inhalation of combustible and electronic cigarette aerosols.

## METHODS

We exposed adult, female Apoe$^{-/-}$ mice daily to either filtered air (AIR, N=15), cigarette smoke (CS, N=8), or e-cigarette aerosols (JUUL, N=10) for 24 weeks. To evaluate vascular ageing over the treatment window, we also analyzed mice at baseline (BASE, N=5). We tracked blood pressure and body mass weekly in awake mice. At the end of the exposure period, we dissected the suprarenal abdominal aortas (SAAs) for mechanical testing. We performed passive inflation/extension tests using a computer-controlled device that measures luminal pressure, outer diameter, axial force, and axial length. We fit a microstructurally-motivated constitutive relationship to the experimental data by nonlinear regression and used the estimated parameters to predict mechanical metrics at systolic pressure[3]. Finally, we analyzed tissue microstructure using histological assays. Data is presented as mean ± SEM. ANOVA was used to determine statistical significance ($p < 0.05$).

## RESULTS

While systolic blood pressure in AIR-exposed mice remained close to baseline, CS and JUUL-exposed mice experienced a progressive increase in systolic blood pressure over the first half of treatment, then stabilized around values that were modestly but significantly elevated from AIR control (by 22% in CS mice and by 15% in JUUL mice; Figure 1A). Although body mass increased from baseline in all groups over the 24 weeks, growth was significantly blunted in CS and JUUL-exposed mice when compared to AIR controls (Figure 1B), resulting in lower body mass at the time of sacrifice (AIR: 23.9 ± 0.4g, CS: 22.3 ± 0.4g, JUUL: 22.9 ± 0.2g). Change in body mass from baseline was not significantly different between CS and JUUL-exposed mice at any time over the duration of exposure ($p = 0.235$).

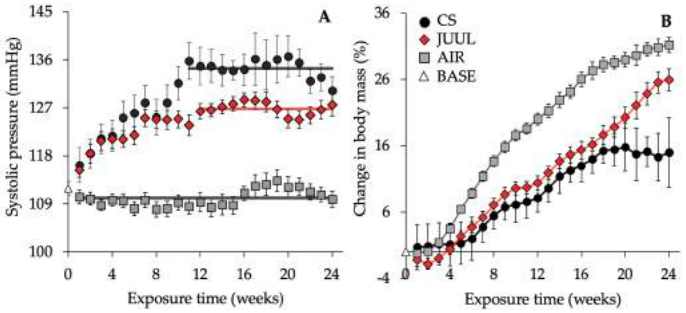


**Figure 1: (A) Systolic pressure and (B) body mass at baseline (white) or with exposure to AIR (grey), CS (black), or JUUL (red).**

The mechanical behavior of the AIR-exposed abdominal aorta did not significantly differ from baseline (Figure 2). At any given level of stress, aortic tissues from CS and JUUL-exposed mice experienced larger deformations than AIR-exposed and baseline tissues. However, the rightward expansion of the stress vs. stretch response was more pronounced in the CS compared to the JUUL group.

Consistently, the circumferential stretch at systolic pressure was significantly larger in both exposure groups when compared to control,

but there was also a significant difference between samples from CS and JUUL-exposed mice (AIR: 1.56 ± 0.02, CS: 1.89 ± 0.05, JUUL: 1.68 ± 0.03; Figure 3A). In part because of this differential effect, JUUL exposure alone compromised the ability of aortic tissues to store elastic energy (CS: 52 ± 2 kPa, JUUL: 44 ± 1 kPa, AIR: 50 ± 1 kPa, Figure 3B). Nevertheless, the overall softening of the material response contributed to maintaining the intrinsic stiffness of tissues near control values in both the CS and JUUL groups, despite larger hemodynamic loads (data not shown). However, the aorta from mice exposed to either CS or JUUL aerosols was significantly thicker than AIR control (AIR: 39 ± 1 μm, CS: 46 ± 1 μm, JUUL: 49 ± 1 μm at systole, Figure 3C). As a result, both exposure groups experienced a significant decline in aortic distensibility when compared to AIR control (AIR: 20 ± 1 $MPa^{-1}$, CS: 14 ± 1 $MPa^{-1}$, JUUL: 12 ± 1 $MPa^{-1}$, Figure 3D).

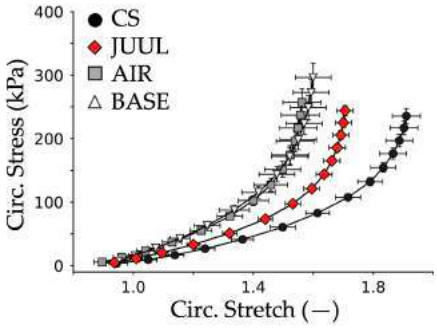


**Figure 2: Circumferential stress vs. stretch response of tissues.**

Microstructural analysis indicated that chronic exposure to either CS smoke or JUUL aerosols significantly increased adventitial collagen when compared to AIR control (Figure 4). Additionally, collagen was significantly more abundant in the media of JUUL-exposed aortas but remained similar to control levels in CS-exposed samples. The increased collagen content of the media contributed to a significant decline in the area fraction of elastin in JUUL-exposed samples, compared to the AIR and CS-exposed groups (AIR: 0.25 ± 0.01, CS: 0.24 ± 0.02, JUUL: 0.20 ± 0.01). Finally, both CS and JUUL-exposed mice developed larger atherosclerotic lesions than AIR controls. Lesion progressed to a vulnerable phenotype with thinner fibrous cap, less collagen, and more macrophages in the CS group.

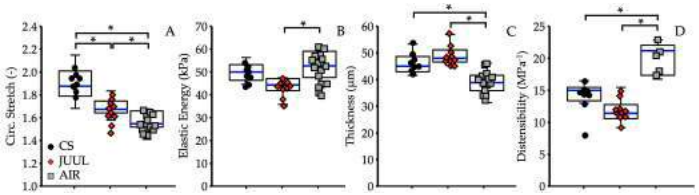


**Figure 3: Mechanical parameters of (A) thickness, (B) circumferential stretch, (C) elastic energy, and (D) distensibility.**

## DISCUSSION

Although the public continues to perceive e-cigarettes as less harmful than combustible cigarettes[4], levels of particulate emissions in the two aerosols are similar[5]. Furthermore, pod e-cigarette devices contain high concentrations of nicotine that is easier to inhale than cigarette smoke[6], increasing their addictive potential[7]. Answering the need for preclinical data that elucidate the long-term cardiovascular outcomes of vaping, we assessed changes in the passive structure and function of the abdominal aorta following 24 weeks of daily exposure to JUUL aerosols, with CS as a necessary comparison[8].

While exposure to both CS and JUUL aerosols caused systolic blood pressure to rise, the increase was smaller with JUUL (Figure 1A). Similarly, both CS and JUUL-exposed mice gained less weight than controls, though more so in the CS group (Figure 1B). These findings suggest that the adverse cardiovascular effects of vaping may be less severe than those of smoking, or that they may take longer to manifest.

Consistent with previous animal studies[9], chronic inhalation of CS and JUUL aerosols promoted aortic thickening via collagen deposition, in part as a mechanoadaptive response to increased blood pressure[10] (Figure 3A). While CS-exposed samples contained more collagen in the adventitia alone, exposure to JUUL aerosols promoted collagen deposition in both media and adventitia (Figure 4), causing the area fraction of elastin to decrease. In addition to lower blood pressure, more abundant collagen in the media may have contributed to limit the systolic circumferential stretch in JUUL aortas compared to CS samples, though it remained above control values in both exposure groups (Figures 2, 3A). Furthermore, larger systolic circumferential deformation in CS aortas may have compensated for the decline in axial stretch (data not shown), preventing the loss of elastic energy storage that occurred with JUUL exposure (Figure 3B).

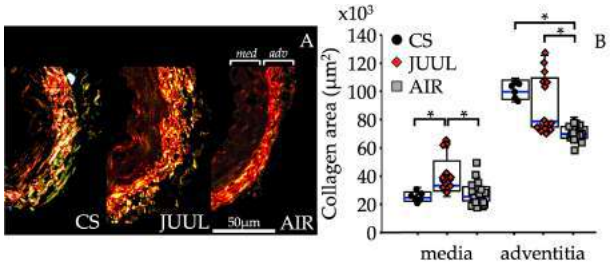


**Figure 4: (A) Picrosirius red stained aortic cross-sections for collagen and (B) plots of medial and adventitial collagen content.**

Finally, coupled with wall thickening (Figure 3C), elevated central blood pressure reduced the distensibility, or increased the structural stiffness, of CS and JUUL-exposed samples (Figure 3D). Structural stiffening of the aorta increases the workload on the heart and has been previously reported in animal models of chronic exposure[11] and recapitulates clinical findings in smokers[12].

In conclusion, our study offers new insights on how vaping and smoking may contribute to cardiovascular disease. Our findings suggest that chronic JUUL e-cigarette use may lead to cardiovascular complications comparable to those of smoking. This data may help inform regulators seeking to provide guidance and limit the potential hazards of chronic e-cigarette use over the coming decades.


## ACKNOWLEDGEMENTS

Our funding sources include R03 HL142472-01 and NSF GRFP.


## REFERENCES


[1] Creamer, M et al., *Morb Mortal Wkly Rep*, 68(45):1013-1019, 2019.
[2] Leventhal, A et al., *JAMA*, 314(7):700-707, 2021.
[3] Bellini, C et al., *J Biomech*, 48:113-121, 2015.
[4] Huerta, T et al., *Am J Prev Med*, 52(3):339-346, 2016.
[5] Ingebrethsen, B et al., *Inhal Toxicol*, 24(14):976-984, 2012.
[6] Talih, S et al., *Tob Control*, 28(6):678-680, 2019.
[7] Jackler, R et al., *Tob* Control, 28(6):623-628, 2019.
[8] Farra, Y et al., *Am J Physiol*, 320(6):H2270-H2282, 2021.
[9] El-Mahdy, M et al., *Am J Physiol*, 320(5):H2112-H2129, 2021.
[10] Humphrey, JD et al., *Hypertension*, 52:195-200, 2008.
[11] Olfert, M et al., *J Appl Physiol*, 124:573-582, 2017.
[12] Doonan, R et al., *Hypertens Res*, 33(5):398-410, 2010.

# COMPARISON OF CSF FLOW RESISTANCE AND BRAINSTEM AND CEREBELLUM DISPLACEMENT FOR CHIARI MALFORMATION TYPE 1

**Saeed Mohsenian (1), Alaaddin Ibrahimy (2), John N. Oshinski (3), Blaise Simplice Talla Nwotchouang (4), Daniel L. Barrow (5), Rouzbeh Amini (6) and Francis Loth (7)**

(1) Department of Bioengineering, Northeastern University, Boston, Massachusetts, USA
(2) Department of Biomedical Engineering, Yale University, New Haven, Connecticut, USA
(3) Radiology & Imaging Sciences and Biomedical Engineering, Emory University School of Medicine, Atlanta, Georgia, USA
(4) Department of Biomedical Engineering, The University of Akron, Akron, Ohio, USA
(5) Department of Neurosurgery, Emory University, Atlanta, Georgia, USA
(6) Department of Mechanical and Industrial Engineering, Department of Bioengineering, Northeastern University, Boston, Massachusetts, USA
(7) Department of Mechanical and Industrial Engineering, Department of Bioengineering, Northeastern University, Boston, Massachusetts, USA

## INTRODUCTION

Chiari malformation type 1 (CMI) is a neurological disease characterized by elongation of the cerebellar tonsils five millimeters or more below the foramen magnum [1] and when a part of the brain (the cerebellum) bulges through the spinal canal at the back of the skull, causing pressure on the brain and spinal cord. Often patients who have the radiological definition of CMI, do not experience any symptoms. However, in some cases, CMI patients experience signs and symptoms such as severe headaches, neck pain, unsteady gait, poor hand coordination, numbness and tingling of the hands and feet, dizziness, difficulty swallowing, sometimes accompanied by gagging, choking, and vomiting, and speech problems, such as hoarseness. People with symptomatic CMI usually experience severe headaches, neck pain, unsteady gait, poor hand coordination, numbness and tingling of the hands and feet, dizziness, difficulty swallowing, sometimes accompanied by gagging, choking, and vomiting, and speech problems, such as hoarseness.

In addition to altered brain morphology, CMI patients have more resistance to cerebrospinal fluid (CSF) motion [2] and have increased tissue motion in the cerebellum and brainstem [3]. To quantify the CMI patients' resistance to CSF, a hydrodynamic property called *longitudinal impedance* (LI) is defined as the ratio of pressure harmonic to the flow harmonic at the same frequency. To obtain the *integrated longitudinal impedance* (ILI), which represents the overall CSF resistance, the resulting LI is integrated from 1 to 8 Hz.

The present study considers the interaction of CSF motion and brainstem/cerebellum tissue displacement to understand the severity of the CMI disease in the patients. The relationship between ILI and tissue displacement at the brainstem and the cerebellum was examined.

## METHODS

The MRI exams were acquired at Emory University under an IRB-approved research protocol. Twenty-three CMI patients were analyzed by determining ILI and displacement in the brainstem and cerebellum. All patients had cerebellar tonsillar position (CTP) greater than *5mm.*

To calculate ILI, axial T2 weighted images were used with axial slice thickness 0.9 mm and pixel spacing 0.85 mm to segment the subarachnoid space into a 3D model of CSF space.

*ANSYS ICEM CFD* was used to generate the mesh for the CSF space. Depending on the shape and size of the flow geometry, the mesh ranged between 0.75 to 1.1 million tetrahedral elements. The following conditions were considered as the boundary limits: *velocity inle*t for the inlet, *pressure outlet* for the outlet, and *wall* for the wall. The commercial finite volume solver *Ansys Fluent* was used to run computational fluid dynamics (CFD) simulations of CSF motion. ILI was calculated using a MATLAB program.

To quantify brain tissue motion, a MATLAB program was employed (DENSEPro) which utilized DENSE phase images to compute the average displacement of the brain tissue over the cardiac cycle [4]. A *30 mm²* circular ROI was automatically identified in sections with the greatest amount of displacement or principal strains to obtain a more homogeneous representation of maximum displacement and principal strain in each brain region. The decision to use *30 mm²* was based on the previous findings, which showed that DENSE MRI requires approximately 80 averaged voxels to provide a reliable displacement measurement [4]. The average of the peak displacements within each circular area for all brain regions was used to determine the maximum displacement in each circular area. An example case taken from Nwotchouang et a. [4] is shown in Figure 1.

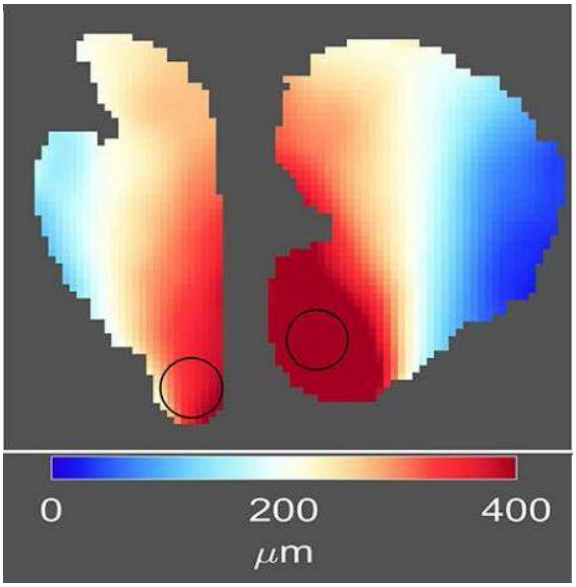


**Figure 1: Two-dimensional Eulerian displacement maps of the brainstem and the cerebellum of a CMI subject [4]**

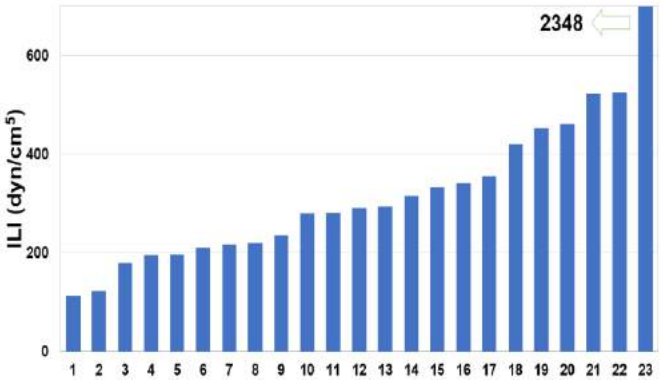


**Figure 2: ILI (resistance to CSF flow) distribution**

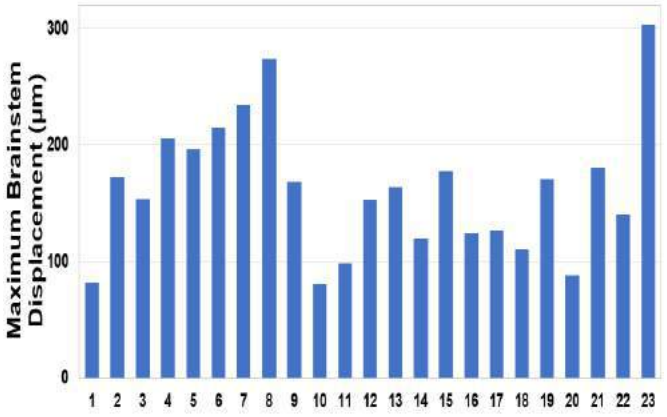


**Figure 3: Maximum displacement at the brainstem**

## RESULTS

Figure 2 shows the ILI for all 23 subjects (note that this figure is scaled and the ILI for the final patient is *2348 dyn/cm*$^5$). The corresponding maximum displacement for brainstem is shown in Figure 3, and for cerebellum in Figure 4. There was a weak correlation between ILI and the displacement at the brainstem (*r=0.14, p=0.03*) and the cerebellum (*r=0.47, p=0.02*).

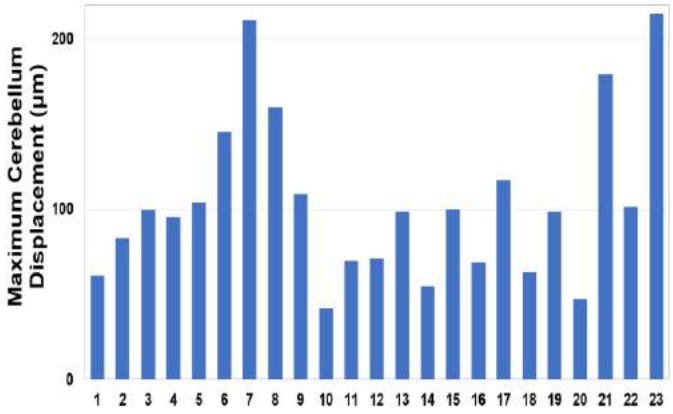


**Figure 4: Maximum displacement at the cerebellum**

## DISCUSSION

Subjects with CMI have tonsillar herniation which often results in an increase in resistance to CSF motion between the cranium and spinal canal. The magnitude of ILI provides a quantitiate measure of this resistance. ILI and brain tissue motion have both been shown to be elevated for CMI subjects [2, 3]. Thus, we postulated there was a connection between resistance and tissue motion. However, this study demonstrates only a weak correlation between ILI and brain tissue displacement. Thus, brain tissue motion is not necessarily related to the increased pressure caused by an increase in resistance in the spinal canal (spinal canal blockage). One case that a had a particularly large ILI (*2348 dyn/cm*$^5$) also had a large tissue displacement both for the brainstem and cerebellum. However, several subjects also had large displacements but with ILI values near that of healthy controls (*220 dyn/cm*$^5$) indicating that ILI alone does not dictate brain tissue motion magnitude [5]. Elevated brain tissue motion has been associated with elevated brain tissue strain and may imply nerve damage [3, 4]. Thus, understanding the underlying biomechanics present in cardiac induced brain tissue motion/strain could help further understand the how various clinical symptoms arise. While ILI clearly plays a role in the unsteady pressure environment within the spinal canal, the relationship between ILI and tissue motion requires further study.

## ACKNOWLEDGEMENTS

The authors would like to thank Conquer Chiari and the National Institutes of Health, NINDS R15 (Grant No. 1R15NS109957-01A1) for providing funding for this research work.

## REFERENCES

[1] Milhorat et al., *Neurosurgery.,* 44(5):1005–1017, 1999.
[2] Ibrahimy et al., *J. of Biomech. Eng.*, 143 (5), 051003, 2020.
[3] Pahlavian, et al., *J. of Biomech. Eng.*, 140: 2018.
[4] Nwotchouang, B., *Ann. of Biomed. Eng.,* 49: 1462–1476, 2021.
[5] Shaffer et al., *ASME J. Biomech. Eng.*, 136(2), 021012, 2014.

# GLOBAL AND REGIONAL QUANTIFICATION OF CARDIOTOXICITY DUE TO RADIOTHERAPY USING CARDIAC MAGNETIC RESONANCE IMAGING: A PILOT STUDY IN LUNG CANCER

**Alireza Omidi (1), Mihaela Rosu-Bubulac (2), Georgia Thomas (3), Elisabeth Weiss (2), John S. Wilson (1,4)**

(1) Department of Biomedical Engineering, Virginia Commonwealth University, Richmond, Virginia, United States of America
(2) Department of Radiation Oncology, Virginia Commonwealth University Health System, Richmond, Virginia, United States of America
(3) Department of Internal Medicine, Virginia Commonwealth University Health System, Richmond, Virginia, United States of America
(4) Pauley Heart Center, Virginia Commonwealth University Health System, Richmond, Virginia, United States of America

## INTRODUCTION

Cancer is the second leading cause of death after cardiac disease globally [1], [2]. These two drivers of mortality intersect in the field of cardio-oncology. As the number and longevity of cancer survivors continues to increase, clinicians and scientists have become increasingly aware of the need to understand, diagnose, mitigate, and ultimately prevent cancer therapy induced cardiotoxicity [3], [4]. Meeting this need begins with serial assessment of patient-specific cardiac structure and function before, during, and after cancer therapy (e.g., chemotherapy and radiotherapy (RT)). In current clinical practice, cardiac function is primarily assessed by global metrics such as left ventricular ejection fraction (LVEF) [5] and global longitudinal strain (GLS) [6]; however, global metrics may not detect local and/or early myocardial changes, which are more likely to be reversible if detected soon after the initiation of therapy when the damage is limited.

The main aim of this pilot study is to assess the use of advanced quantitative MRI-based metrics to monitor cardiac structure and function, both globally and regionally, before and after radiotherapy, to detect early changes, and to evaluate correlations between radiation doses and MRI-derived metrics.

## METHODS

Four lung cancer patients who received ≥5 Gy of radiation to ≥10% of the heart were recruited for this study. Each patient underwent cardiac magnetic resonance (CMR) at baseline (before RT) and 3 months following RT. The CMR protocol contained standard cine MRI to measure LVEF and calculate strain (radial, circumferential, longitudinal) by feature-tracking algorithm, T1/T2 mapping for tissue characterization, late gadolinium enhancement (LGE) MR to evaluate scar tissue, and T1 volumetric breath hold examination (VIBE) forimage registration purposes. All CMR examinations were done using a 3T Magnetom Avanto Scanner (Siemens, Munich, Germany).

To map iso-dose lines onto MR sequences, radiation dosimetry maps from each patient's clinical CT planning dataset were registered onto the T1-VIBE MR images and subsequently registered from T1-VIBE onto the other MR sequences (e.g., T1/T2 mapping, LGE MRI) using MIM software (MIM Software Inc, Cleveland, OH) (Figure 1). Further post-processing and analysis were performed on cvi42 (Version 5.10.1, Circle Cardiovascular Imaging; Calgary, Canada). Statistical analyses (ANOVA, t-test, and Pearson correlation) were performed on JMP software (version Pro 14, SAS Institute Inc.) using a significance of $P < 0.05$.

## RESULTS

In this small pilot study, no significant differences in global metrics were detected (Table 1), though a decrease in GLS magnitude neared significance ($P = 0.06$). In regional evaluation of MRI-derived metrics, mean regional T1 signal showed an insignificant increase at 3 months FU (1287 ± 64.6 ms) compared to baseline (1283.7 ± 72.9 ms). Mean regional T2 values remained unchanged (43.5 ± 4.5 - 43.7 ± 3.9 ms). Interestingly, regional radial strain (RRS) showed a significant increase ($P = 0.04$) from 31.95 ± 13.8 to 35.12 ± 18.4. Regional circumferential strain (RCS) and regional longitudinal strain (RLS) demonstrated insignificant increase in magnitude between (-18.3 ± 4.7 to -18.9 ± 6) and between (-15 ± 7.1 to -15.7 ± 5.7), respectively. Notably, regional percent enhanced LGE areas were significantly higher at 3 months FU (10.2% ± 13.5) compared to baseline (7.4% ± 9.5), $P = 0.04$. Figure 2 shows enhanced LGE areas (pointed by an arrow) at highly radiated regions before and after RT treatment.

In addition to evaluation of individual global/regional metrics, significant percent changes of regional metrics (i.e., the difference of 3 mo. metrics from baseline values divided by baseline values) at highly irradiated regions (>30 Gy) and low irradiated areas (<30 Gy) were compared. No significant differences were noted for T1 signal changes

at either region. However, T2 signal showed significant differences (P = 0.013) between changes at high dose regions (mean T2 signal +5.5% at >30 y regions) and low dose regions (mean T2 signal +0.04% at <30 Gy regions). Interestingly, RRS and RCS values demonstrated significant increase (P = 0.012 and P = 0.009) at high radiated regions (mean RRS +38.9%, mean RCS +22.8%) compared to low radiated areas (mean RRS +7.6%, mean RCS +3.8%). No significant differences were found for changes in RLS (P = 0.25). Surprisingly, no significant changes were found in LGE between the high-dose and low-dose regions despite greater increase of mean percent LGE area in >30 Gy regions (+10.3%) compared to <30 Gy regions (+2%).

Finally, Pearson correlation test results between percent changes of regional MRI-derived metrics and the maximum RT dose at corresponding segmental regions demonstrated no correlation between changes of T1/RLS/LGE and the maximum dose. However, segmental correlations were noted for percent changes in T2, RRS, RCS and the maximum dose (T2: r = 0.3, P =0.025; RRS: r = 0.28, P = 0.024; RCS: r = 0.3, P = 0.016).

**Table 1. Mean ± SD global metric values at baseline and 3 months follow-up (FU) along with P-values**

| Metric | Baseline | 3 months FU | P value |
|---|---|---|---|
| **LVEF (%)** | 53.5±11.4 | 53±14 | 0.36 |
| **T1 (ms)** | 1285.4±50.4 | 1287.4±45.2 | 0.43 |
| **T2 (ms)** | 43.7±3.7 | 44.3±4 | 0.3 |
| **GRS** | 25.1±7.8 | 26.8±13 | 0.56 |
| **GCS** | -16.1±3.2 | -16.2±4.6 | 0.43 |
| **GLS** | -16.1±5.2 | -15.1±2.1 | 0.06 |
| **LGE (%)** | 8.03±2 | 9.5±1.6 | 0.37 |

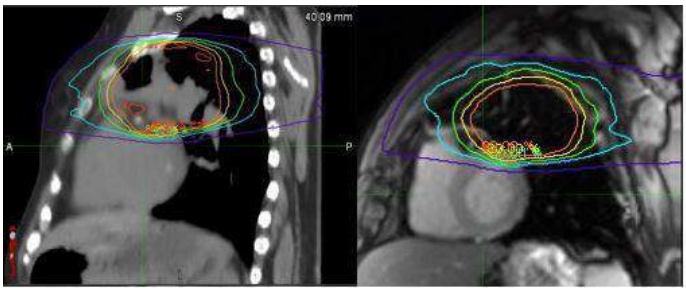

**Figure 1: Registration of the dosimetry map from CT planning (left) onto MR T1 map (right).**

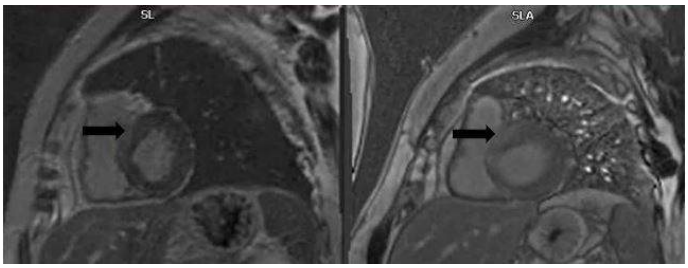

**Figure 2: LGE MR images of the same patient and LV basal cross-section in Figure 1 at baseline (left) and 3 months follow up (right). Arrows show focal areas of LGE in the basal anterior and basal anteroseptal wall where radiation dose was high.**

## DISCUSSION

Even though small changes were observed in global metrics 3-months following RT, none reached significance. Given that some of the changes were in opposite directions (e.g., GLS decreasing while GRS increases) while LVEF was maintained suggests that the heart may be able to functionally compensate for early minor deficiencies in myocardial contraction in the longitudinal direction.

As opposed to global metrics, significant changes were found in a few regional metrics. Notably, percent enhanced areas of LGE images were significantly increased (7.4 to 10.2%, P = 0.04), suggesting that regional fibrosis [8] may precede global functional changes of myocardium. The potential increase of mean regional T1 signal (1283.7 ms to 1287 ms), though not significant, supports this interpretation as T1 increase is also associated with fibrosis [7]. Significant increase of RRS might be in compensation to damages in other cardiac substructures to keep the same global function/output. A similar effect could be responsible for elevated RRS and RCS at highly irradiated regions. At this point, further investigations are required to fully examine this matter. Apart from strain, greater increases of T2 value at highly radiated areas compared to lower radiated regions may introduce a dose-dependency relation between T2 signal changes and radiation doses. Correlations were noted for changes of T2 signal and maximum dose (r = 0.3, P = 0.025). Quantitative T2 relaxation time may represent regions of myocardial edema [7], with higher signal values potentially reflecting greater tissue damage. Finally, we note that the lack of significance in the increase of regionally enhanced LGE areas at highly irradiated regions may be due to missing LGE MR images for one of the patients who received the highest radiation doses to the heart.

Though larger sample sizes are required for confirmation, this early pilot study suggests that regional metrics may be more suitable in detection of early cardiac dysfunction/abnormalities. Moreover, it shows that the abnormalities are mostly found in structural variations of tissue rather than functional changes at 3 months following RT. Despite valuable findings of this study in early quantitative assessment of cardiotoxicity, further investigations with larger cohort of patients are required to fully monitor changes over longer time periods and find the possible relationships between dose and MRI-derived metrics.

## ACKNOWLEDGEMENTS

This study was supported by pilot funding from the VCU Massey Cancer Center and Pauley Heart Center.

## REFERENCES

[1] Global Burden of Disease Cancer Collaboration *et al., JAMA Oncol*, vol. 3, no. 4, pp. 524–548, 2017
[2] M. Tibaut *et al., Cardiovasc. Hematol. Agents Med. Chem.*, vol. 14, no. 3, pp. 150–159, 2016
[3] I. Harries *et al., JACC CardioOncology*, vol. 2, no. 2, pp. 270–292, 2020
[4] C. Jaworski *et al., J. Am. Coll. Cardiol.*, 2013
[5] A. Scatteia *et al., J. Pers. Med.*, vol. 11, no. 11, p. 1153, 2021,
[6] O. A. Smiseth *et al., Eur. Heart J.*, vol. 37, no. 15, pp. 1196-1207b, 2016
[7] P. K. Kim *et al., Korean J. Radiol.*, vol. 18, no. 1, pp. 113–131, 2017
[8] A. Ricco *et al., Cardio-Oncology*, vol. 6, no. 1, pp. 1–9, 2020

SB³C2022
Summer Biomechanics, Bioengineering and Biotransport Conference
June 20-23, Eastern Shore, MD, USA

# *IN VIVO* HUMAN KNEE VARUS-VALGUS LOADING APPARATUS FOR ANALYSIS OF MRI-BASED INTRATISSUE STRAIN AND RELAXOMETRY

**Hongtian Zhu (1), Emily Y. Miller (2), Woowon Lee (1), Robert L. Wilson (1), Corey P. Neu (1,2)**

(1) Paul M. Rady Department of Mechanical Engineering, University of Colorado Boulder, Boulder, CO, USA

(2) Biomedical Engineering Program, University of Colorado Boulder, Boulder, CO, USA

## INTRODUCTION

Varus-valgus stress testing is a commonly used clinical method to assess the integrity and laxity of the knee joint [1]. This method has also been useful in assessing osteoarthritis (OA) to probe for weakened tibiofemoral cartilage [2-4] and ligaments [5]. However, varus-valgus stress tests are mostly performed by physicians manually, and the assessment is more qualitative rather than quantitative. Here, with the help of a customized magnetic resonance imaging (MRI-) compatible varus-valgus loading apparatus, the same exam can be done automatically in combination with modern imaging techniques, where the mechanical behavior and material properties of the tibiofemoral cartilage can be revealed by functional analysis. Therefore, the status of the knee cartilage can be accessed by physicians with more quantitative and precise insights.

The primary objective of this study was to design, validate, and verify the varus-valgus loading apparatus for use in a common 3 Tesla (T) MRI scanner. One part of the validation and verification process of the apparatus was done using an independent laser-based displacement sensor, while another part was performed using specialized MRI methods, including spiral Displacement ENcoded Stimulated Echo MRI (spiral DENSE) sequences. Besides spiral DENSE, we also acquired T1, T2, T2*, and T1ρ weighted data before and after loading. We developed a functional MRI-compatible loading apparatus for varus-valgus stress test on human patients, which may assist in the quantitative diagnosis of OA.

## METHODS

*Varus-valgus Loading Apparatus:* A customized MRI-compatible varus-valgus loading apparatus was designed (**Fig. 1A**) based on defined design parameters. The device was geometrically compatible with both a SIEMENS Prisma$^{fit}$ 3T MRI scanner and a QED 15-channel knee coil. Major parts were designed in-house and machined by ProtoLabs®, while other parts were either commercially purchased from manufacturers or fabricated in-house. The apparatus provides loading either the left or right knee with a quick-release structure, while the flex angle of the knee was also adjustable on the device. All parts were made from MRI-compatible materials. The load magnitude of the cylinder was pre-calibrated for both varus and valgus loading conditions over a range of 0-400N force.

*In-Lab Validation and Verification:* The performance of the apparatus was validated and verified in the lab. Three individuals (2 male and 1 female) with healthy left knees were recruited to perform repeatability and precision testing. Independent displacement data was collected during loading using a laser-based displacement sensor system (Keyence). Here, the participant was placed in a neutral position first, with the mock MRI gantry and knee coil put in place, followed by varus loading. Three individual (20 min) tests were performed on each participant, with two 10-min intervals in between (**Fig. 1B**). We applied 25N cyclic loading to the ankle at a frequency of 0.5Hz (1s loading session, 1s unloading) to mimic a walking cadence, resulting in approximately 0.5 times body weight at the knee. The sensor captured displacement versus time. Statistical analysis of the data was conducted using customized software (MATLAB).

*MRI Validation and Verification:* The performance of the apparatus was additionally validated using MRI. Here, a 25-year-old female with a healthy left knee was recruited for MRI mechanical and relaxivity analysis using a 3T MRI system. To conduct the validation and verification process, we obtained DESS (proton density weighted; morphology) images, in additional to images with T1, T2 [6], T2* [7], T1ρ [8] weighting, before and after applying 25N loading. Additionally, spiral DENSE MR images were acquired under repetitive varus loading. The spiral DENSE sequence was capable of capturing *in vivo* full-field displacement and strain fields within the tibiofemoral cartilage while under repetitive varus-valgus loading conditions [9]. Before running the spiral DENSE session, the geometry of the tibia was measured and a moment balance was applied to calculate the desired output force from the apparatus.

The loading scheme was controlled using a customized digital control system. During the spiral DENSE sequence, we loaded the medial condyle using cyclic force for varus loading conditions, and the images were captured only during the loading portion of the cycle. The loading regime was identical to the in-lab session, but with calculated force from the tibial geometry and customized for the patient. Before the scanning session, 8 min of preconditioning was applied to the knee to eliminate the viscoelastic response of the tissue.

*Displacement and Strain Mapping:* Using the phase data from the spiral DENSE sequence, in-plane smoothed displacements ($d_x$, $d_y$) and 2D Green-Lagrange strains ($E_{xx}$, $E_{yy}$, $E_{xy}$) were calculated on a pixel-by-pixel basis [10] using customized software (MATLAB).

## RESULTS

The data from the laser system demonstrated that the pooled standard deviation of the displacement during cyclic loading among all 3

participants was 270 μm, which corresponded to 16 μm displacement in cartilage, noticeably lower than the pixel size (360 μm). We also observed an increase (from 16 to 19 μm) in displacement error if data acquired during a typical preconditioning period was used. Additionally, the loading device did not prevent acquisition of relaxometry (e.g., T1, T2, T2*, and T1ρ weighted) images, which depicted the motion of the tibia as well as the value changes in cartilage (**Fig. 1**). Meanwhile, the increase of displacement and strain values with respect to time was observed, as well as the increase of values from the lateral side to the medial side of the medial cartilage for both displacement (**Fig. 1**) and strain (**Fig. 2**) fields.

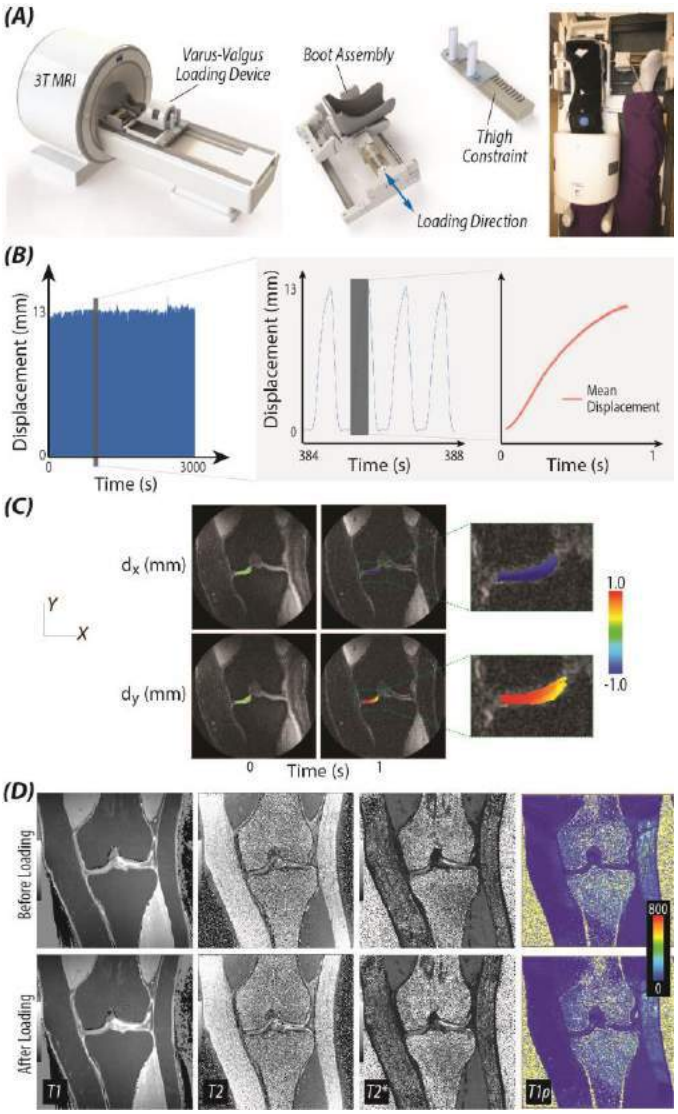


**Figure 1: Validation and verification of an MRI-compatible *in vivo* knee varus-valgus loading apparatus using in-lab and MRI sessions. (A) Assembly of the apparatus in a 3 Tesla MRI system. (B) In-lab validation and verification process. Multiple repeated loading cycles were applied for each participant. Data was gathered using a laser displacement sensor. (C) MRI-based displacements were obtained using a spiral DENSE sequence, with full-field maps captured at the beginning and the end of loading cycle. (D) Relaxometry (weighted) images were obtained before and after applying a loading.**

## DISCUSSION

Previous work from our lab has demonstrated that intratissue displacement and strain maps of cartilage can be acquired *in vivo* under pure compressive loading [9]. Here, we provide a clinically-relevant, varus-valgus loading scheme, which can be used to examine cartilage strain, ligament weakness, and joint instability, all early indicators of OA in the early stage [5,11]. Additionally, we found that patients more comfortably prefer varus-valgus loading over direct compression. The MRI data collected under varus-valgus loading scenario will also likely provide us a deeper insight into material property alternations of articular cartilage during OA pathogenesis, and may reveal potential biomarkers of early OA detection.

In this work, the standard deviation of the displacement during the scanning session proves this apparatus can provide a stable, robust, and precise platform for image-based mechanics. Increased displacement errors were found when adding the data from the precondition session, supporting the idea that it is essential to load the joint prior to the scanning session in order to obtain high-quality data. The pattern of the displacement and strain demonstrates the apparatus is capable of applying varus and valgus loading conditions to the knee. We believe this work is the first to implement varus and valgus stress test in a clinical 3T MRI setup to acquire *in vivo* full-field displacement and strain maps of the tibiofemoral cartilage at the pixel level, and obtain relaxometry values under load. Further steps will include recruitment of additional participants with healthy and OA knees, examining the behavior of ligaments and other load-bearing cartilages under the motion with a similar concept, and linking *in vivo* MRI results with *ex vivo* pathological analysis of the damaged articular cartilage to identify the potential biomarkers of OA. By doing so, we would hope that we can establish novel diagnostic methods to evaluate disease therapies.

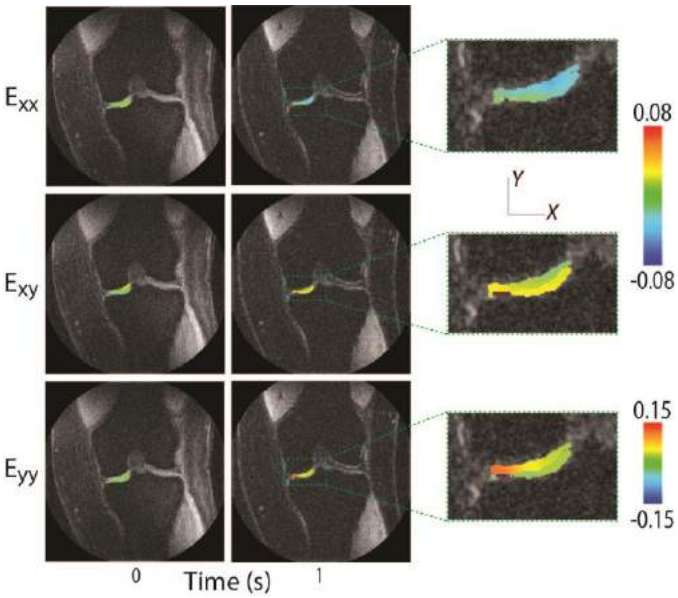


**Figure 2: *In vivo* cartilage strain in the medial femoral condyle and tibial plateau was obtained during varus loading of the knee. Here, strain values at time step 0 (0.0 seconds) and 27 (1.0 seconds) are shown, with heterogeneous strain magnitudes approaching +/-8% in $E_{xx}$ and $E_{xy}$, and +/-15% in $E_{yy}$.**


## ACKNOWLEDGEMENTS

This study was supported by NIH grant 2 R01 AR063712.


## REFERENCE


[1] Calmbach+ *American Fam Phys* 68.5 (2003): 907-912. [2] Freisinger+ *J Knee Surg* 30.05 (2017): 440-451. [3] Gibson+ *JBJS* 68.4 (1986): 608-609. [4] Waldstein+ *J Arth* 32.3 (2017): 788-792. [5] Wheaton+ *J Prolother* 2.1 (2010): 294-304. [6] Dunn+ *Radiology* 232.2 (2004): 592-598. [7] Bittersohl+ *Osteo & Cart* 20 (2012): 653-660. [8] Wang+ Eur *J Rad* 81.9 (2012): 2329-2336. [9] Chan+ *Sci Rep* 6 (2016): 1-14. [10] Chan+ *Comp Methods Biomech Biomed Eng* 16.8 (2013): 852-860. [11] Fleming+ COOR 16.5 (2005): 354.

# COMPUTATIONAL NUCLEOTYPING IN ACUTE ISCHEMIC STROKE CLOT HISTOPATHOLOGY IS PREDICTIVE OF UNDERLYING ETIOLOGY

**Briana A. Santo (1,2), Tatsat R. Patel (1,3), Andre H. Monteiro (4), Muhammad Waqas (4), John Tomaszewski (2), John Kolega (2), Adnan H. Siddiqui (1,4), Vincent M. Tutino (1,2,3,4)**

(1) Canon Stroke and Vascular Research Center, University at Buffalo, NY, USA
(2) Department of Pathology and Anatomical Sciences, University at Buffalo, NY, USA
(3) Department of Mechanical and Aerospace Engineering, University at Buffalo, NY, USA
(4) Department of Neurosurgery, University at Buffalo, Buffalo, NY

## INTRODUCTION

Acute Ischemic Stroke (AIS) remains a leading cause of morbidity and mortality. Clinical trials have shown that mechanical thrombectomy (MT), a recent innovation for clot retrieval, is associated with improved functional outcomes in patients after AIS. Following treatment, secondary stroke prevention is the chief clinical concern. In cryptogenic cases, which comprise 20-40% of strokes, this is problematic as, etiology identification could have aided in management of future ischemic events. Recent studies indicate that the biologic composition of the occlusive clot, retrieved during MT, may be related to the underlying etiology, since the origin of the thrombotic material is different for different types of stroke. However, prior histological studies correlating clot composition and etiology have produced mixed results; reported proportions of red blood cell and fibrin-platelet components for clots of similar origins have often been disparate. Further, many of these studies overlooked white blood cells (WBCs), a key component that can affect pro-thrombotic mechanisms and structural components during clotting. In this study, we hypothesized that WBC diversity in clot histopathology would correlate with etiology and designed the following computational study.

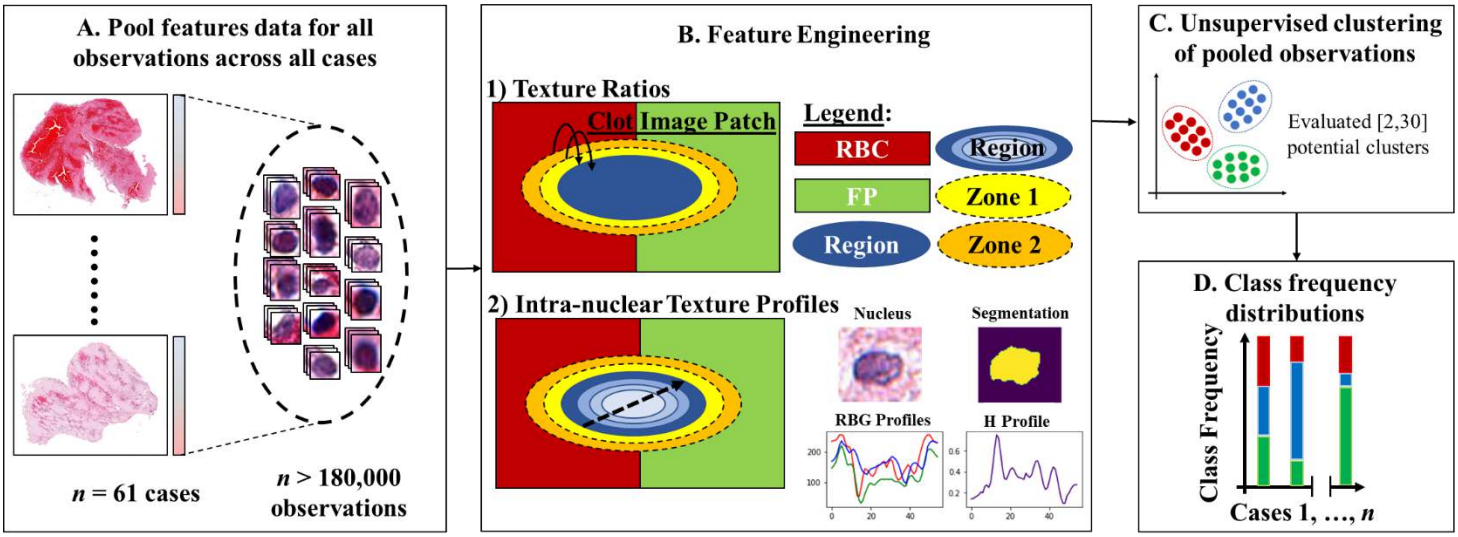


**Figure 1: Determining Distribution Frequencies of Unsupervised Classes of WBCs. A.** Pool features for all WBC instances across all WSI images. **B.** Extract texture ratios and intra-nuclear texture profile-based features for each WBC instance. **C.** Perform unsupervised clustering of pooled observations using texture ratios and texture-profile based features. **D.** Calculate frequency distribution of each class per WSI.

## METHODS

Histological sample preparation, H&E staining, and whole-slide scanning were completed to produce a digital histopathology dataset comprised of 61 whole-slide images (WSIs) of AIS clot samples collected via MT between 11/2018 and 7/2021 at the Gates Vascular Institute in Buffalo, NY (UB institutional review board study 00002092). The underlying etiology of each AIS clot was identified using the Trial of org 10172 in Acute Stroke Treatment (TOAST) score. This TOAST classification denoted the following subtypes of AIS: large artery atherosclerosis (LAA) ($n$ = 11), cardiac embolism (CE) ($n$ = 34), other determined etiology (e.g. hypercoagulable states) ($n$ = 4), and cryptogenic (undetermined etiology) ($n$ = 12). LAA and CE cases were the primary focus in this work.

WBC nuclei were segmented from each WSI using a H&E stain deconvolution approach [1], resulting in ~180,000 unique WBC instances. For each WBC, computational image analysis was used to engineer 645 quantitative histomorphometric features from intra- and extra- nuclear regions (***Fig 1***). To quantify intra-nuclear texture, red-green-blue (RGB) and hematoxylin (H) intensity profiles were extracted from WBC nuclei and analyzed (***Fig1B-2***). To quantify extra-nuclear texture, statistical and structural texture features were extracted from computationally-defined zones (***Fig1B-1***) using PyRadiomics [2]. WBC histomorphometrics were then pooled across all 61 cases and filter-based feature selection was applied to reduce the dimensionality of the feature set. Using the reduced feature space, unsupervised, k-means clustering was completed for k = [2,30] (***Fig1C***) and the optimal number of clusters was identified based on the Davies-Bouldin Index [3]. Within the context of this work, each cluster represented a unique, computationally defined WBC nucleotype or class. From the optimal clustering experiment, the WBC class distribution frequency (CDF) per case was computed as input for supervised classification tasks (***Fig1D***).

WBC nucleotypes differentially enriched in the LAA and CE clot subset were identified and ranked using uni- and multi- variate statistical analysis ($\alpha$ = 0.05), including Mann-Whitney U tests and SHapley Additive exPlanations (SHAP) [4]. The capacity of WBC class frequencies to predict LAA and CE was assessed using linear support vector machine (SVM) trained with five-fold cross validation.

## RESULTS

Filter-based selection reduced the dimensionality of the feature set from 645 to 94 features. The minimum Davies-Bouldin Index was achieved for a k-means model trained with 23 potential clusters. Therefore, CDFs were computed per case assuming 23 distinct WBC nucleotypes. Statistical comparison using univariate statistics identified seven WBC nucleotypes that were significantly different between LAA and CE etiologies (***Fig2***). Multivariate SHAP Analysis identified the five most significant WBC classes (***Fig2***). A linear SVM trained to classify LAA vs. CE using the CDFs of the five most significant WBC classes achieved mean AUCs of 0.87±0.02 and 0.85±0.1 in training and cross-validation testing, respectively (***Fig3***). These computational observations suggested that WBC instances in AIS are diverse and can be classified based on intra- and extra-nuclear texture. Further, the frequency of unique WBC instances in AIS clots was predictive of and may be tied to underlying etiology.

## DISCUSSION

Computational nucleotyping has demonstrated tremendous potential for improved prognostication of diseases with structurally complex histopathology [5]. Unfortunately, biological interpretation of prognostically relevant nucleotypes remains difficult due to the use of deep-learning for feature extraction. In this study, for the first time, we present a novel approach for computational nucleotyping in AIS clot histopathology that harnesses image processing, featuring engineering, and classical machine learning to produce interpretable, quantitative histomorphometrics for (i) WBC subtyping based on nuclear attributes, and (ii) prediction of underlying stroke etiology. While preliminary, these findings suggest that WBC structural diversity in clot histopathology has clinical potential and warrants further study. Future work for conference presentation includes qualitative and quantitative interpretation of WBC instances representative of each class.

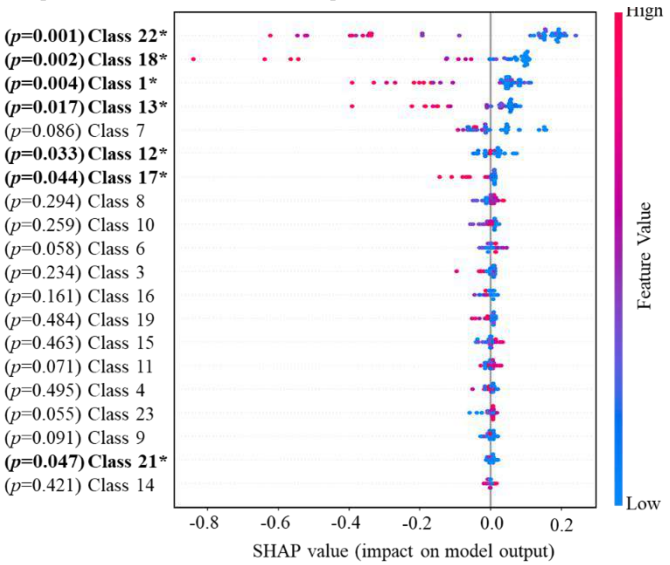


**Figure 2: Significant WBC Classes between LAA and CE.** Univariate statistics and SHAP Analysis were used to rank WBC classes based on their differential enrichment in LAA and CE clot WSIs. *Asterisks mark significantly different class frequencies

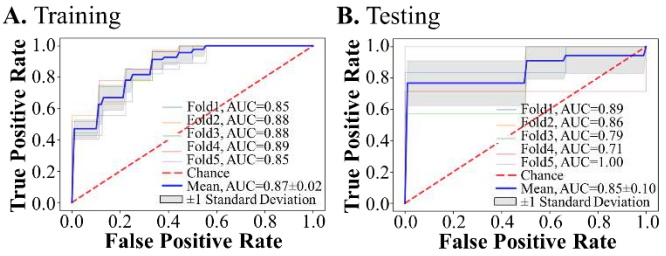


**Figure 3: The frequency of distinct WBC nucleotypes in AIS clot histopathology is predictive of underlying etiology.** Linear SVMs trained to classify LAA v CE based on the five most significant WBC class frequencies for five-fold cross validation achieved mean AUCs of (A) 0.87 in training, and (B) 0.85 in testing.


## ACKNOWLEDGEMENTS

Research reported in this publication was supported by the National Center for Advancing Translational Sciences of the National Institutes of Health under award number KL2TR001413 to the University at Buffalo. The content is solely the responsibility of the authors and does not necessarily represent the official views of the NIH.


## REFERENCES


[1] Ruifrok, A. C. et al., X, 23: 291-299, 2001.
[2] Van Griethuysen, J. J. et al., *Cancer Research*, 77: 104-107, 2017.
[3] Xiao, J. et al., *Intell. Data Anal*, 21: 1327-1338, 2017.
[4] Lundberg, S. M. et al., *NeurIPS*, 4768-4777, 2017.
[5] Li, H. et al., *Breast Cancer Research*, 21: 1-16, 2019.

SB³C2022
Summer Biomechanics, Bioengineering and Biotransport Conference
June 20-23, Eastern Shore, MD, USA

# PATTERNS OF TISSUE STIFFNESS CORRELATE WITH DISTRIBUTIONS OF PROLIFERATION AND YAP ACTIVITY ALONG THE EMBRYONIC URETERIC TREE

**Somdutta Chakraborty (1), Thomas J. Carroll (2), Victor D. Varner (1,3)**

(1) Department of Bioengineering, The University of Texas at Dallas, Richardson, TX, USA
(2) Departments of Internal Medicine (Nephrology) and Molecular Biology, UT Southwestern Medical Center, Dallas, TX, USA
(3) Department of Surgery, UT Southwestern Medical Center, Dallas, TX, USA

## INTRODUCTION

The kidney is a highly complex organ that maintains the volume and composition of fluids in the body. It does so, in part, using a tree-like network of collecting ducts, which forms during embryonic development via a process known as branching morphogenesis. The embryonic kidney originates as a simple ureteric bud, which then undergoes a series of branching events to build the ureteric tree, the tips of which interact with cells in the metanephric mesenchyme to direct the formation of developing nephrons [1]. Branching morphogenesis is thus intimately tied to nephron number, and defects in this process can lead to congenital abnormalities that compromise renal function.

Proper renal branching morphogenesis depends crucially on proliferation, and elevated levels of proliferation are thought to be localized to the morphogenetically-active tips of the branching ureteric tree [2]. It is unclear, however, how the spatial patterns of proliferation that sculpt the ureteric tree are developmentally patterned. Mechanical forces are known to regulate the morphogenesis of other branched organs, such as the lung and mammary gland [3], but the role of biophysical cues during renal branching morphogenesis is completely unexplored. Recent experiments have shown that the embryonic renal interstitium is highly patterned [4] with distinct spatial differences in the expression of several ECM-modifying genes which modulate ECM crosslinking and stiffness. It is unknown if there are regional differences in stiffness within the embryonic kidney and, if so, whether these differences impact spatiotemporal patterns of proliferation, along the ureteric tree.

Here, we used microindentation to quantify spatial patterns of tissue stiffness within embryonic mouse kidneys. These distributions were then compared to patterns of proliferation and sub-cellular localization of Yap along the developing ureteric tree, since disrupted Yap signaling is associated with renal branching defects [5]. Finally, we used a polyacrylamide (PA) gel system to determine if changes in substratum stiffness were sufficient to regulate the proliferation and sub-cellular localization of Yap in cultured collecting duct epithelial cells.

## METHODS

*Embryonic kidney dissection and culture:* Embryonic kidneys were dissected from timed-pregnant CD1 mice between embryonic day 13 and 16. In some experiments, E13 kidneys were cultured at 37°C at the air-fluid interface in DMEM/F12 medium supplemented with 5% fetal bovine serum (FBS) and antibiotics. In other experiments, E16 kidneys were fixed in 4% PFA solution, dehydrated in 30% sucrose in PBS, embedded and frozen in OCT compound for cryosectioning. We used a cryostat to obtain 10 μm sections, which were processed for antigen retrieval and stained.

*Microindentation:* We used the CellScale MicroSquisher to measure tissue stiffness within E16 mouse kidneys. Briefly, we created thick (~400 μm) mid-sagittal sections of the kidneys (Fig. 1A) by embedding them in a 6% w/v solution of low temperature gelling agarose and sectioning with a Vibratome. A 70 μm-diameter cylindrical microindenter was used to probe tissue stiffness at different locations along the cortical-medullary axis.

*Polyacrylamide gel fabrication:* PA gels of varying stiffnesses were fabricated on glass coverslips, as described previously [6]. These substrata were then functionalized with 50 μg/ml of fibronectin and plated with inner medullary collecting duct epithelial cells (IMCD3).

*Confocal microscopy:* Confocal stacks of stained samples were obtained using a Zeiss LSM 800. Quantitative image analysis was performed using ImageJ and Imaris.

## RESULTS

We observed clear regional differences in the stiffness of the tissue along the cortical-medullary axis in mid-sagittal sections of E16 mouse kidneys (Fig. 1). The cortical region, where branching morphogenesis

occurs, was significantly stiffer than locations within the medullary zone of the kidney.

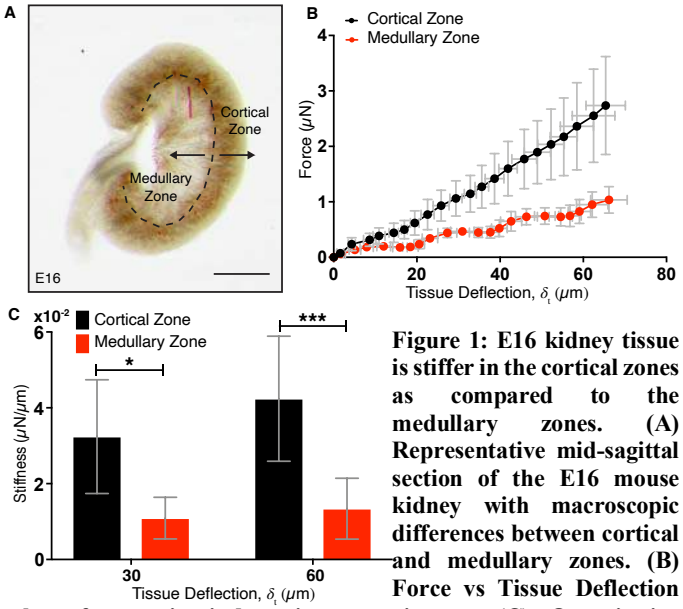


**Figure 1: E16 kidney tissue is stiffer in the cortical zones as compared to the medullary zones. (A) Representative mid-sagittal section of the E16 mouse kidney with macroscopic differences between cortical and medullary zones. (B) Force vs Tissue Deflection plots from microindentation experiments. (C) Quantitative differences in tissue stiffness between the cortical and medullary zones.**

To compare the measured regional differences in stiffness to patterns of proliferation along the ureteric tree, we cultured embryonic kidney explants ex vivo for up to 72 hr and measured distributions of EdU incorporation along the ureteric epithelium (Fig. 2A). Elevated levels of proliferation were observed in the distal-most generations of branches, which were situated within the cortical zone of the kidney, where our microindentation data indicated increased tissue stiffness.

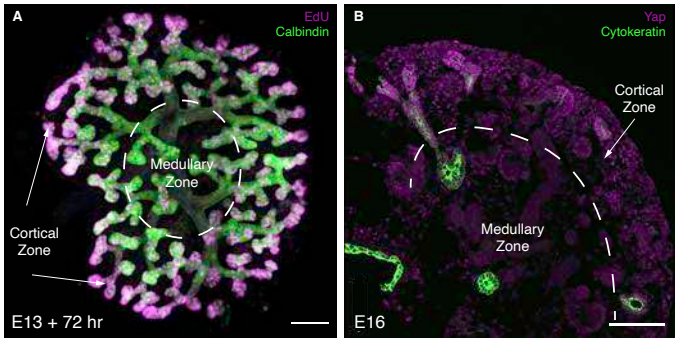


**Figure 2: Proliferation and sub-cellular localization of Yap is patterned in the developing kidney (A) 3D confocal imaging of an E13 kidney, cultured for 72 hr and stained for EdU and calbindin (B) Stained cryosections of E16 kidneys show that Yap is localized to the nucleus in cells at the branching regions of the ureteric epithelium and to the cytoplasm in cells along the non-branching, stalk region of the ureteric epithelium.**

Since Yap signaling is essential for proper renal branching morphogenesis, we also compared these patterns of proliferation to distributions of the sub-cellular localization of Yap along the ureteric tree, as assayed by Yap immunofluorescence in cryosections of E16 mouse kidneys stained for both Yap and calbindin, a marker for the ureteric epithelium (Fig. 2B). In the cortical region of the kidney, Yap was localized nuclearly within cells at the tips of the ureteric tree, but cytoplasmic within cells along the stalk regions. Taken together, these data indicate that proliferation, stiffness and Yap activity are correlated in different regions of the ureteric tree. In the cortical zone, where branching occurs, proliferation and tissue stiffness are elevated and Yap is localized to the nucleus of ureteric epithelial cells. In the medullary zone, these trends are reversed: stiffness and proliferation are reduced and Yap is sequestered in the cytoplasm.

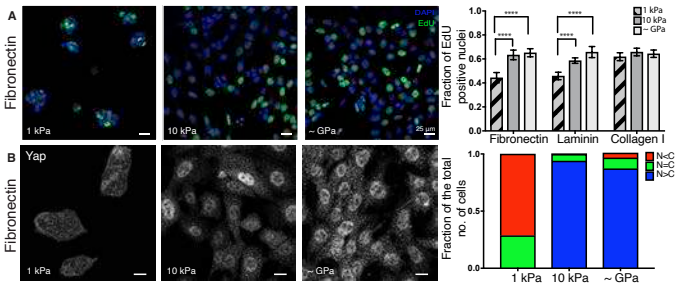


**Figure 3: Proliferation and sub-cellular Yap localization in IMCD3 cells depends on substrate stiffness (A) EdU and DAPI co-staining and quantification of proliferation of cells seeded on Fibronectin coated polyacrylamide gels of 1 kPa, 10 kPa and glass coverslips of ~GPa stiffness (B) Yap staining and quantification.**

To determine if differences in stiffness sufficiently regulate the proliferation and sub-cellular localization of Yap in collecting duct cells, we cultured IMCD3 cells on PA gels of different stiffnesses. Proliferation was elevated on stiff (10 kPa) substrata, as well as on ECM-coated glass coverslips, but lower on soft (1 kPa) gels (Fig 3A), trends consistent with our observations in embryonic kidneys. We also observed stiffness-dependent differences in the sub-cellular localization of Yap. Yap was preferentially localized to the nucleus in cells seeded on stiff substrata but absent from the nuclues in cells on soft PA gels (Fig. 3B). When Yap signaling was disrupted using either verteporfin or genetically ablating Lats 1/2, the kinases that phosphorylate Yap to modulate its activity, we no longer observed stiffness-dependent differences in proliferation (data not shown).

## DISCUSSION

Taken together, these data suggest that regional differences in stiffness are present within the embryonic kidney, which correlate with the patterns of proliferation and Yap activity along the developing ureteric tree. Previous studies have shown that changes in stiffness can modulate the differentiation of progenitor cells in vitro, but there have been little efforts to apply these ideas to organogenesis. Embryonic kidneys with disrupted Yap activity undergo abnormal renal branching morphogenesis [5] and it would be interesting to determine whether altering patterns of ECM stiffness in the embryonic kidney can recapitulate this phenotype. Future work will investigate how ectopic patterns of ECM stiffness modulate branching dynamics in embryonic kidneys cultured ex vivo.


## ACKNOWLEDGEMENTS

This work was supported, in part, by the NIH grant R01HL145147 to VDV, as well as The UT Southwestern O'Brien Kidney Core Center (NIH P30DK079328)


## REFERENCES


[1] Costantini F, Kopan R, *Developmental cell*, 18:698-712, 2010.
[2] Michael L, Davies JA, *Journal of anatomy*, 204:241-255, 2004.
[3] Varner VD, Nelson CM, *Development*, 141:2750-2759, 2014.
[4] England AR, et al. *Biorxiv,* 2020.03.02.973966 (2020).
[5] Reginensi, Antoine, et al. *PLoS Genet.* 9.3 (2013): e1003380.
[6] Maruri D et al. *Biophysical journal* 119.9 (2020): 1865-1877.

SB³C2022
Summer Biomechanics, Bioengineering and Biotransport Conference
June 20-23, Eastern Shore, MD, USA

# A MULTI-METHOD APPROACH FOR ASSESSING NON-LETHAL CUTANEOUS IMPACT INJURIES

**Omar Elsafty (1), Christopher Berkey (2), Reinhold H. Dauskardt (1,2)**

(1) Department of Mechanical Engineering, Stanford University, Stanford, CA, USA
(2) Department of Materials Science and Engineering, Stanford University, Stanford, CA, USA

## INTRODUCTION

Cutaneous wounds have the highest incidence of all bodily injuries in survivors of blast debris [1]. Even after survival, there is an increased risk of mortality due to wound infection, and a possible decline in a person's well-being due scar formation which can have long lasting functional, aesthetic, and psychological effects on the wounded. These non-lethal cutaneous wounds are not only prevalent in military settings, but they are also often observed in civilian life due to natural disasters and construction accidents [2]. However, while their significance is clear, a thorough understanding of these types of injuries has yet to be achieved, as emphasis in the research field has been on lethal injuries [3]. To design for the treatment and prevention of these injuries, a high-fidelity model that can accurately predict the ensuing damage caused under distinct circumstances is necessary.

Recently, we quantitatively characterized the damage mechanisms that occur for non-lethal cutaneous injuries for single projectile impact using experimental techniques and a high-fidelity 3D finite element (FE) damage model. However, a transition to multi-projectile analysis is needed to accurately assess these injuries and to relate them to specific settings, since the injury severity is highly dependent on the impact angle, impact velocity, and projectile attributes. Furthermore, the analysis will often need to be performed in real-time, and so, developing a finite element model for multi-projectile impact on a full body would be too time-consuming and computationally costly. Here we develop a multi-method approach that utilizes FE analysis, machine learning, and 3D computer graphics to analyze injury severity variability under customizable circumstances.

## METHODS

Three multi-class classification machine learning algorithms were developed to assess injury severity, which can be characterized by evaluating wound area, wound depth, and wound shape. The features used for each neural network were the impact angle, cross-sectional kinetic energy at impact, cross-sectional area, and coefficient of friction between the projectile and the skin. As for our output parameters, wound area and wound depth were discretized into ranges of 5.0mm2 and 200um, respectively, and had upper limits of 35.0mm2 and 2000um, respectively. To characterize wound shape, we used our recently developed wound damage index for spherical projectiles, see Figure 1, providing a score of 0 to 11 based on the expected wound shape. In addition, the predictions of the wound area and wound depth algorithms were also used as features for the wound shape algorithm, constructing a machine learning pipeline in the process, see Figure 2a. To have adequate data to train the models, we ran several FE simulations, see Figure 2b, and performed experimental tests under various input conditions. Furthermore, owing to the high variability of these injuries, and the clinical need to differentiate between them, the models provide the two most probable results to ensure the appropriate treatment can be performed.

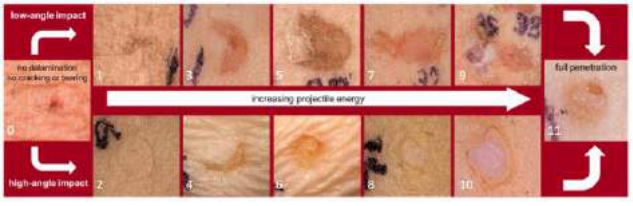


**Figure 1: Wound damage index for non-lethal cutaneous injuries.**

A multi-projectile full-body model was developed using Python API on Blender. The model positions a meshed human body, see Figure 2c, a user-defined distance away from the blast source and distributes fragments equidistantly across the surface of the blast source. Considering drag, the model uses Newtonian physics-based equations to derive the projectile path for each fragment that could be in the vicinity of the human body. The initial projectile angle is taken to be the

angle between the ray connecting the fragment position and blast center and the XZ-plane where the blast center is located. Once the projectile path intersects the body, the incident angle is measured between the projectile path ray and the triangular mesh element that the ray intersected. The velocity at the point of impact is also calculated and used to obtain the cross-sectional kinetic energy at impact. Using the calculated impact angle, cross-sectional kinetic energy, and the user-defined fragment parameters, the model utilizes the multi-class classification algorithms to assess the injury severity at each impact location.

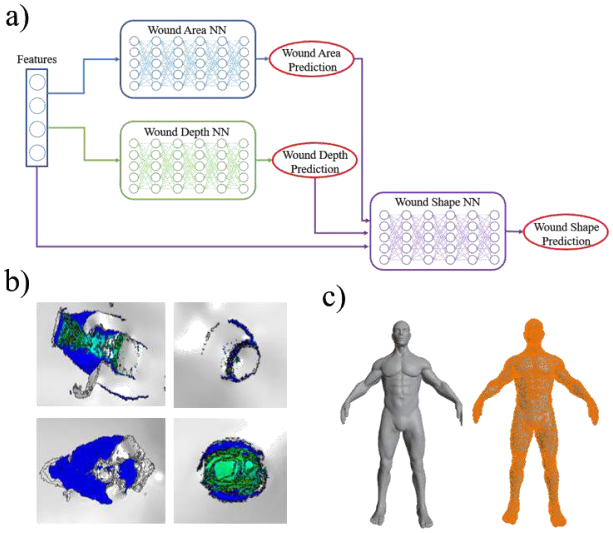


**Figure 2: a) Neural network pipeline b) Injury results from finite element simulations. c) The meshed full body human model.**

## RESULTS

After training and model optimization, accuracies of 71.99%, 71.76%, and 83.2% were obtained for the wound area, wound depth, and wound shape multi-class classification algorithms, respectively, indicating that these models can be used with good fidelity.

In Figure 3, we show features of the multi-method approach for the example of a 1.8m person standing 5m and 8m away from a spherical blast source of 64mm diameter. Owing to the variability of the debris impact, the diameter, mass, and initial velocity of each fragment was randomized within the ranges of 3-5mm, 0.1-0.4 g, and 100-150m/s, respectively, since fragment velocity can vary by up to 50% [4].

The model identified 8 impact points and 4 impact points for the 5m and 8m distance, respectively. After appropriate calculations of the impact angle and impact velocity, the model provided its top two predictions regarding the injury severity parameters at each point, and we provide the average values of these predictions, see Table 1. The maximum time taken to run one complete simulation was 4.86 minutes without the use of high-performance computing.

## DISCUSSION

In this study, we developed a customizable multi-method model to investigate injury severity of a full human body for high-speed debris impact. The model allows for real-time analysis of non-lethal injuries and can be tailored to a specific setting, as the fragments, blast source, and the target can all be adjusted by the user. In the example scenario, the model accurately predicted a significant reduction in wound distribution and injury severity with increasing distance away from the blast site. It should be noted that the average wound area increased with increasing distance due to a reduction in full-penetration wounds, which are commonly associated with small wound areas and large wound depths. These results illustrate the model's capability to simulate realistic injury distributions, a step beyond single projectile impact currently observed in the literature.

Further improvements to the model await more extensive data sets, including quantitative analysis of injuries caused by irregularly shaped projectiles, since current analysis has focused on regular shaped projectiles such as spheres and cylinders.

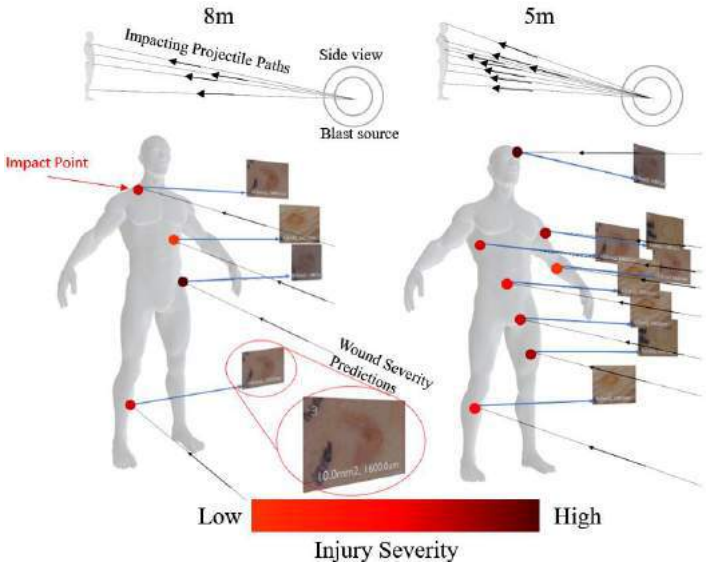


**Figure 3: Resulting injury severity and distribution at 8m and 5m from blast source.**

**Table 1: Average Injury severity predictions at each distance**

| Distance (m) | Number of Impact Points | Wound Area (1st) ($mm^2$) | Wound Area (2nd) ($mm^2$) | Wound Depth (1st) ($\mu m$) | Wound Depth (2nd) ($\mu m$) | Wound Shape (1st) | Wound Shape (2nd) |
|---|---|---|---|---|---|---|---|
| 5 | 8 | 8.125 | 6.25 | 1450 | 1175 | 6.375 | 7.25 |
| 8 | 4 | 12.625 | 11.25 | 1290 | 1075 | 5.875 | 8.05 |

The model provides visual and quantitative investigations of the injury severity and distribution for non-lethal cutaneous injuries. As such, we believe it will be highly advantageous for the advancement of wound treatment methods and for the development of protective equipment, as it can be readily customized to suit the design space.


## ACKNOWLEDGEMENTS

This work was supported by the Irregular Warfare Technical Science Directorate, an affiliate of the U.S. Department of Defense, under Contract N4175620C3013.


## REFERENCES


[1] Sen, C. et al., Human skin wounds: A major and snowballing threat to public health and the economy. *Wound Repair And Regeneration*, 17:763-771, 2009.

[2] Kecojevic, V., & Radomsky, M., Flyrock phenomena and area security in blasting-related accidents. *Safety Science*, 43:739-750,2005.

[3] Hollerman, J., et al., Gunshot wounds: 1. Bullets, ballistics, and mechanisms of injury. *American Journal Of Roentgenology*, 155:685-690, 1990.

[4] Liao, W et al., Effect of the end cap on the fragment velocity distribution of a cylindrical cased charge. *Defence Technology*, 17:1052-1061, 2021.

SB³C2022
Summer Biomechanics, Bioengineering and Biotransport Conference
June 20-23, Eastern Shore, MD, USA

# MULTI-NODE CARDIAC MUSCLE-CELL-BASED COUPLED BIO-OSCILLATOR NETWORK FOR COLLECTIVE COMPUTING

**Jiaying Ji (1), Xiang Ren(1), Mohammad K. Bashar (3), Jorge Gomez (2), Nikhil Shukla (3), Suman Datta (2), Pinar Zorlutuna (1)**

(1) Department of Aerospace and Mechanical Engineering, University of Notre Dame, Notre Dame, IN, USA
(2) Department of Electrical Engineering, University of Notre Dame, Notre Dame, IN, USA
(3) Department of Electrical and Computer Engineering, University of Virginia, Charlottesville, VA, USA

## INTRODUCTION

The inefficiencies of modern computers in energy become apparent when dealing with large amounts of data or performing computationally hard problems, such as combinatorial optimization problems [1]. Vertex coloring problem, defined as assigning colors to each vertex such that every two adjacent vertices have different colors, is an archetypal combinatorial optimization problem. Recently, coupled oscillator systems have been reported to provide a new computational platform to address combinatorial optimization problems [2-3]. Inspired by the biological system's natural ability to minimize their energy to reach a ground state, we present new hardware for the coupled oscillator system, cardiac muscle-cell-based bio-oscillator network, for solving vertex coloring problems (Figure 1).

## METHODS

We used neonatal rat ventricular cardiac cells isolated from 2-day-old Sprague-Dawley rat hearts as the model cell source. The isolated cell mixture of rat cardiomyocytes (rCMs) and rat cardiac fibroblasts (rCFs) was preplated to enrich the rCMs, and the ratio of rCM to rCF was about 7:3. The cell mixture was suspended in the culture medium and used as the cell source throughout the study.

To create a well-defined network of the bio-oscillators, we started by patterning the rCMs and rCFs on the micro-electrode array (MEA) substrate. We used PDMS blockers to partially cover a cell adhesive protein micropattern. After seeding, the rCMs within the clusters started to beat after one day of culture. Then, the blocker was carefully removed. rCFs in the cell mixture would proliferate and migrate to fill in the gap, therefore bridging the beating cell clusters. After cells began to beat, the cell membrane potential was continuously measured by the MEA-2100 system. The optical videos were recorded using a microscope and the impedance was measured with a potentiostat.

## RESULTS

In the proposed cardiac cell-based bio-oscillator system, we mapped the graph of coloring problem into the bio-oscillator network, such that each vertex (or node) of the graph is represented by a bio-oscillator, a cardiac cell cluster composed of rCMs and rCFs. Any two nodes connected by an edge in the graph are coupled in the bio-oscillator system by an rCF bridge. We fabricated pairwise bio-oscillators (Figure 2a) and a more complex multi-node bio-oscillator network using a simple cell-patterning method. Immunofluorescence staining results of the multi-node network (Figure 2b) were used to observe cell distribution and rCF growth. No troponin T signals (rCM marker) but only vimentin signals (rCF marker) in the bridges verify blockers successfully obstructed the initial rCM attachment, and rCF proliferated in the empty bridge sections.

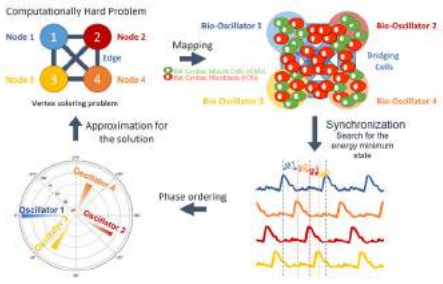


**Figure 1: The schematic of cardiac muscle cell-based bio-oscillator network for vertex coloring problem.**

Computing of oscillator systems is driven by the coupling (i.e., synchronization) of oscillators. We studied the coupling dynamics of the pairwise bio-oscillators with different rCF length. After coupling, the synchronization dynamics of cardiac cell-based bio-oscillators was recorded using the MEA system. The waveforms, fast Fourier transform

(FFT) and the long-term dynamics are shown in the Figure 2. Although there is a variation in the extracted phase–frequency points, we can conclude in a statistically significant fashion that the phase between the clusters is modulated by the rCF length and the frequency. In order to understand the electric nature of the synchronization dynamics, we measured the impedance between the two oscillators and the Nyquist plot reveals that the rCF bridge can be regarded as a resistor parallel with a capacitor and provides an RC-type coupling between two oscillators (Figure 3a-b). To further studied the relation between phase and frequency, we re-ploted long-term dynamics as the figure 3c. We can see that for a higher length, at any frequency, the resistance increases; therefore, the capacitance coupling dominates, and the phase difference becomes bigger. On the other hand, the smaller coupling length increases the conductance, thus reducing the phase difference between oscillators.

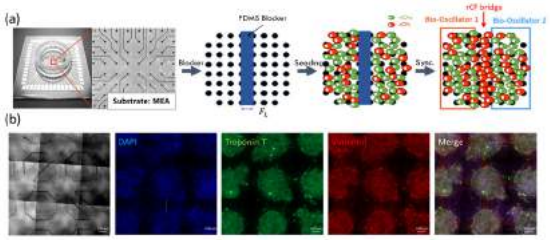


**Figure 2: Cell-patterning approach for constructing a well-defined network of bio-oscillators and rCF bridges.**

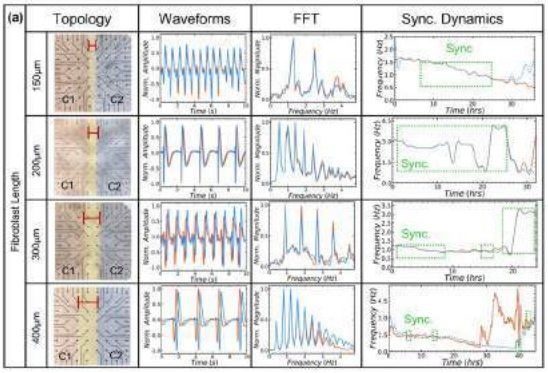


**Figure 3: (a) The synchronization dynamics of two cardiac cell clusters (C1 (red) and C2 (blue)) connected by an rCF bridge (yellow) of different lengths.**

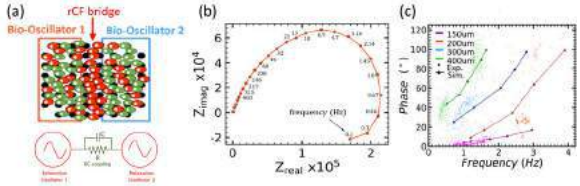


**Figure 4: (a) Electric nature of the rCF coupling. (b) Nyquist plot of rCF coupling. (c) The relation between phase and synchronization frequencies at different rCF length.**

Based on the pairwise bio-oscillator results, we selected 300 μm of rCF length to implement the three-clusters bio-oscillator network. The topology and the dynamics are shown in Figure 5. We used C1 as the reference cluster to measure the phase differences of C2 and C3. Figure 5b shows the phase evolutions of C2 and C3 over the entire experiment in a polar histogram, displaying that the three separated bio-oscillators present a stable phase lock.

Figure 6 simulates the application of the rCF-coupled cardiac cell-based bio-oscillators to solve the minimum vertex coloring problem in a 9-node graph. The equivalent circuit models of bio-oscillator and rCF connection are described in figure 6a-b. The resulting steady-state sequence of the bio-oscillators represents a unique ordering of phases (Figure 6c-f) which can subsequently be partitioned into three independent sets using a simple polynomial time operation [4]. Assigning each set a color implies that a minimum of three colors are required which is the optimal solution to "color" the 9-node graph. We further mapped the same 9-node graph onto the cardiac cell clusters to demonstrate the potential of the bio-oscillator network to be scaled up to a larger number of nodes. The experiment results are shown in Figure 6g-h which shows the exact same optimal solution of simulation.

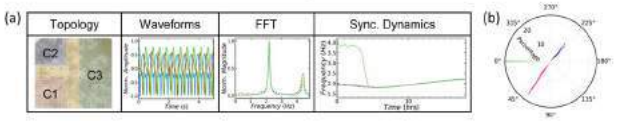


**Figure 5: (a) The synchronization dynamics of three cardiac cell clusters. (b) Polar plot of the phase differences over time**

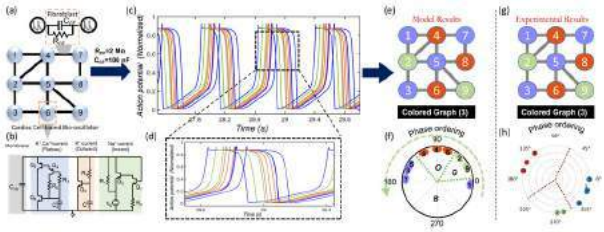


**Figure 6: (a) The representative graph of a 9-node coloring problem. (b) The equivalent circuit model of cardiac cell-based bio-oscillator. (c-d) Time domain waveforms of the equivalent circuit. (e-h) Resulting coloring solution obtained from the simulated and experimental phase ordering of the bio-oscillators**

## DISCUSSION

Combinatorial optimization problems are often regarded as energy minimization problems that can be implemented by the coupled oscillator system. Here, we used a simple cell-patterning method to encode the coloring problem into the cardiac cell-based bio-oscillator network, following the rules that each graph vertex is represented by a bio-oscillator, a cardiac cell cluster, while the edge is represented by an rCF bridge. The bio-oscillators interconnect with each other with the rCF bridge which provides an RC-type coupling between the separated bio-oscillators. As the bio-oscillators coupled, the network naturally searches for the minimum energy state through the mutual interaction. The final steady state of the bio-oscillator network exhibits ordered phase differences which can be used to approximate the solution of the minimum vertex coloring problem.

In this paper, we have demonstrated the potential of cardiac muscle cells as an oscillatory building block to implement the multi-node bio-oscillator systems for solving coloring problem.


## ACKNOWLEDGEMENTS

This work is supported by National Science Foundation (NSF) Electrical, Communication & Cyber Systems under award number 1807551; and Semiconductor Research Corporation (SRC) under award number 2841.001. The fabrication processes are conducted in the Notre Dame Nanofabrication Facility (NDNF).


## REFERENCES


[1] Csaba, G et al., *Applied Physics Reviews*, 7: 011302, 2020.
[2] Wu, C. W. et al., *IEEE Trans. Circuits Syst. I*, 45(9): 974–978, 1998.
[3] Parihar, A et al., *Sci. Rep.*, 7: 911, 2017.
[4] Ren, X et al., *Advanced Intelligent Systems*, 3(4): 2000253, 2021.

SB³C2022
Summer Biomechanics, Bioengineering and Biotransport Conference
June 20-23, Eastern Shore, MD, USA

# A GRAVITY-DRIVEN MULTI MICRO PHYSIOLOGICAL SYSTEM TO STUDY TISSUE RESPONSES TO CANCER THERAPEUTICS

**Pouria Rafsanjani Nejad (1), Hossein Tavana (1)**

(1) Department of Biomedical Engineering, The University of Akron, Akron, OH, USA

## INTRODUCTION

Multi Micro Physiological Systems (MMPS) provide relevant in vitro models to study systemic drug responses in preclinical studies [1]. However, many MMPS technologies are complex, and their assembly is time-consuming. Additionally, existing MMPS platforms often have a low throughput and do not meet the research need for testing and identifying of effective therapeutics while minimizing systemic toxicity for diseases such as cancer. We have developed a multi-well MMPS that is similar to standard 96-well plates. Our system has three main compartments that represent liver, tumor, and bone marrow. We selected liver and bone marrow because they are both common sites of off-target toxicity from cancer therapeutics and because liver is a major site of drug metabolism. Our system is facile, utilizes 3-dimesional extracellular matrix-embedded cells, captures tissue toxicities, and is compatible with automated liquid handling. This model will facilitate evaluating effects of cancer therapeutics on both tumor and normal tissues in preclinical studies.

## METHODS

The MMPS was designed in SolidWorks. The distance between the wells match that of a standard 96-well plate. The wells are fluidically connected via microchannels (d=800 µm) that reside higher than the well surface. Fluid flow among different tissue compartments is driven by the pressure difference between two end reservoirs caused by gravity and tilting of the device. The device is placed on top of a plate rocker to tilt ± 7 degrees at 1-minute intervals and is kept inside a cell culture incubator. Partial removal of media from the device stops the fluidic connection of wells and enables individual assessment of wells using metabolic assays such as Prestoblue (ThermoFisher). Fluidic flow and mass transport in the device were simulated using COMSOL Multiphysics. The device was fabricated using a polymethyl methacrylate (PMMA)-based biocompatible resin (BMCL) with a Form-3B (Formlabs) 3D printer. To enable high-resolution imaging, the device was printed without a bottom layer. A single sheet of sealer film was then used to seal the bottom of the wells.

Ten MMPSs were generated on each plate and each MMPS has five linearly-connected wells (Fig 1a, b). Out of the five wells, the outer two were used as media reservoir and the inner three were used as tissue compartments. Human cell lines HEPG2/C3A, MDA-MB-231, and HS-5 were used in these compartments to represent liver, tumor, and bone marrow stroma, respectively. Spheroids of cancer cells were formed prior to placing them in the device using our previously established aqueous two-phase system (ATPS) [2]. The spheroids were harvested from their original plate and suspended in a 4 mg/ml rat tail collagen I solution (VitroCol, advanced biomatrix) in the tumor compartment. Liver and bone marrow cells were suspended as single cells in 25 µl of collagen and at a density of $10^4$ cells/well in their respective compartments. MDA-MB-231 cells were previously transfected to produce GFP. Cells in all the wells were stained with Calcein AM (ThermoFisher) prior to confocal microscopy. A chemotherapy drug, Fluorouracil (5FU) (100 µM) and its prodrug, Tegafur (200 µM), were used to test the drug response of different cells over 4 days of culture. Tegafur was mixed with uracil at a 1:4 molar ratio, also known as a UFT cocktail, to prevent 5FU break down by hepatic cells [3]. Each experiment had 4 replicates. Statistical significance was calculated using two-way ANOVA in GraphPad Prism.

## RESULTS

Fluid flow in the MMPS was simulated using an estimated pressure function. The simulation shows that metabolites are transported well across different compartments by the cyclical advective flow. Fig. 1c shows how a hypothetical compound (200 µM, 12.5 µl, $D=10^{-9}$ $m^2/s$) introduced in one of the reservoirs is evenly distributed among the compartments in about 20 minutes. Following the computational validation, we fabricated the two-layer device. There was no leakage

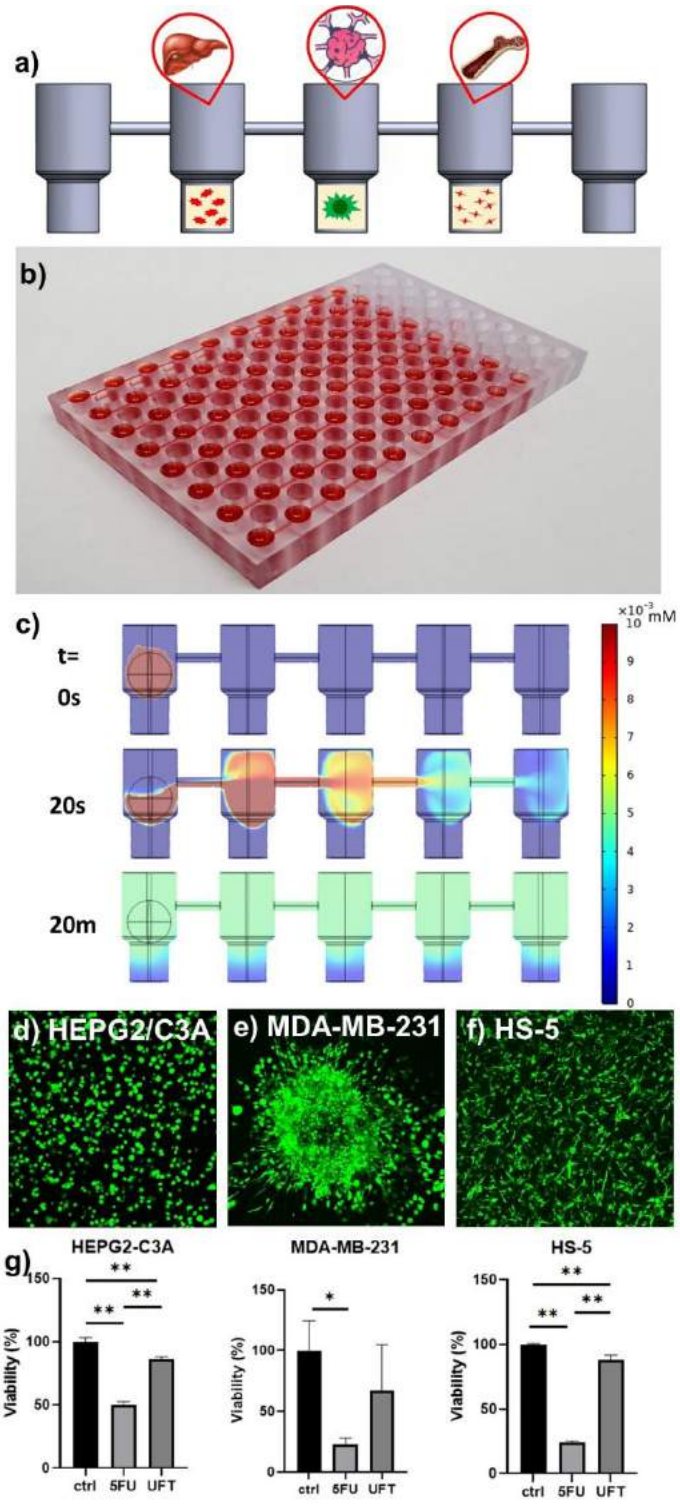


**Figure 1. (a) schematics of a single MMPS (b) image of a 3D printed array of MMPS on a plate filled with food coloring (c) transport simulation of a compound (200 µM, 12.5 µl, D=10-9 m2/s) administered in one of the reservoirs (d-f) Confocal images of cells from liver, tumor, and bone marrow compartments on day 4 in the device (g) responses of cells in each compartment to 50 µM 5-FU and 200:800 µM Uracil: Tegafur (UFT), *p<0.05, **p<0.01**

between the adhesive layer and the printed plate during two weeks of incubation with culture media. After 4 days of culture, all the compartments had highly viable populations of cells (Fig. 1d-f). Cancer cells invaded from the spheroid into the collagen matrix, and single-cell cultures had uniform distribution in collagen. Next, we measured the toxicity of 5FU and UFT to cells in all compartments (Fig. 1g). Viability of cells dropped to 50.4%, 22.6%, and 23.9%, respectively, for HEPG2/C3A, MDA-MB-231, and HS-5 cells when exposed to 5FU and 86.6%, 67.3%, and 87.8% when exposed to UFT.

## DISCUSSION

**W**e presented a new MMPS to study the effects of chemotherapeutics on cells from multiple interconnected tissue compartments simultaneously. Our design builds upon our previously established tumor model [4] and connects it with other tissues in a way that is compatible with automated liquid handling. The gravity-assisted flow avoids complexities associated with tubing needed in pump-driven flows and bubble entrapments. Furthermore, our design is based on PMMA and avoids lipophilic compound absorptions associated with silicone. We demonstrated sustainability of cells in our MMPS in short-term experiments. Our future studies will test the feasibility for longer-term cultures. We also showed responses of tissue compartment to a classic chemotherapy agent. While the response to 5FU was as expected, reduction in the viability with the UFT treatment was less than that predicted based on available literature. We intend to further investigate this issue by optimizing culture conditions of the liver compartment, drug doses, and molecular analysis of the metabolized media. Finally, we aim to present an MMPS that can be utilized for screening cancer treatments earlier in the drug discovery process by further developing this system to include cancer associated fibroblasts and immune components.

## ACKNOWLEDGEMENTS

This work was sponsored by the NIH grant CA225549 and NSF grant 1801591.

## REFERENCES

1. Skardal, A., T. Shupe, and A. Atala, *Organoid-on-a-chip and body-on-a-chip systems for drug screening and disease modeling.* Drug Discovery Today, 2016. **21**(9): p. 1399-1411.
2. Atefi, E., et al., *High Throughput, Polymeric Aqueous Two-Phase Printing of Tumor Spheroids.* Adv Funct Mater, 2014. **24**(41): p. 6509-6515.
3. Nakayama, T. and S. Noguchi, *Therapeutic usefulness of postoperative adjuvant chemotherapy with Tegafur-Uracil (UFT) in patients with breast cancer: focus on the results of clinical studies in Japan.* The oncologist, 2010. **15**(1): p. 26-36.
4. Singh, S., et al., *Organotypic breast tumor model elucidates dynamic remodeling of tumor microenvironment.* Biomaterials, 2020. **238**: p. 119853.

SB³C2022
Summer Biomechanics, Bioengineering and Biotransport Conference
June 20-23, Eastern Shore, MD, USA

# INCORPORATING VASCULAR STASIS BASED PERFUSION TO PREDICT THE THERMAL SIGNATURES OF CELL DEATH USING MODIFIED ARRHENIUS EQUATION WITH REGENERATION OF LIVING TISSUES

**Manpreet Singh**

Department of Mechanical Engineering,
University of Maryland Baltimore County,
Baltimore, MD, USA

## INTRODUCTION

The thermal damage predictions by first-order Arrhenius kinetic rate equation gives us monotonic degradation of living tissues alongwith cancerous lesions. For low temperature hyperthermia (T≤41℃) i.e. at diathermic temperatures, biological tissues shows an accelerated tissue recovery and repair with an evident rise in blood perfusion levels and associated metabolic demands. At the temperature range of 40-42℃, some transformations and molecular-level changes in tumour cells might have been already initiated. According to the hypothesis of Dombrovsky et al., 2015 [1]; continuous regeneration of living human tissues due to the continuous supply of oxygen through arterial blood must be taken into account to counter balance the thermal degradation at quasi-static thermal conditions. However, previous studies [2-3] implemented regeneration term into Arrhenius formulation; however, to incorporate the effect of hyperemic region through vascular stasis (fractional injury) based non-linear perfusion change [4-5] is not addressed for such regeneration based model. This study aims to investigate this issue in the context of magnetic nanoparticle assisted thermal therapy.

## METHODS

Pennes Bioheat Transfer Equation (PBHTE) [6] is used to compute the temperature field distribution in both the healthy tissue and cancerous tissue domain as per **equations (1a)** and **(1b)** respectively;

$$\rho_h c_h \frac{\partial \mathrm{T}_h}{\partial \mathrm{t}} = k_h \nabla^2 \mathrm{T}_h + \omega_{h,0} \rho_b c_b (\mathrm{T}_b - \mathrm{T}_h) + Q'''_{met,h} \quad (1a)$$

$$\rho_c c_c \frac{\partial \mathrm{T}_c}{\partial \mathrm{t}} = k_c \nabla^2 \mathrm{T}_c + \omega_{c,0} \rho_b c_b (\mathrm{T}_b - \mathrm{T}_c) + Q'''_{met,c} + Q'''_{source} \quad (1b)$$

Here, the subscripts, *h* and *c* represents healthy and cancerous tissue domains respectively. Also, *met* represents metabolic *b* represents blood and *source,* is the heat source contribution of heterogeneously distributed magnetic nanoparticles [6] known as Specific Absorption Rate (SAR) mapped at different tumour locations (refer **fig.1**).

It is well known that during heating, the blood perfusion rate first increases at hyperthermic temperature due to vasodilation of vessels and then starts decreasing due to total collapse of vasculature due to thermal damage. This phenomenon is known as "*degree of stasis*" [5]. In this problem formulation, the blood perfusion of cancerous lesion is defined as a piecewise function of vascular stasis as per **equation 2** and **fig. 2**;

$$\omega_{c,0}(t) = \begin{cases} \omega_{b,o}(1 + 30 \cdot \Theta); \text{ if or } 0 < \Theta \leq 0.02 \\ \omega_{b,o}(1.86 - 13 \cdot \Theta); \text{ if or } 0.02 < \Theta \leq 0.08 \\ \omega_{b,o}(0.884 - 0.79 \cdot \Theta); \text{ if or } 0.08 < \Theta \leq 0.97 \\ \omega_{b,o}(3.87 - 3.87 \cdot \Theta); \text{ if or } 0.97 < \Theta \leq 1.00 \\ 0; \text{ if or } \Theta > 1.00 \end{cases} \quad (2)$$

Here, the baseline value of blood perfusion, $\omega_{b,o}$ is extracted from the thermal infrared imaging by adjusting the metabolic heat generation rates and blood perfusion values using inverse heat transfer analysis to match the thermal maps of infrared images [6]. The degree of vascular stasis (collapse of vasculature) can be calculated as per **equation (3)**;

$$\Theta(\mathrm{x}, \mathrm{y}, \mathrm{z}, \mathrm{t}) = 1 - \exp(-\Omega(\mathrm{x}, \mathrm{y}, \mathrm{z}, \mathrm{t})) \quad (3)$$

As per the traditional Arrhenius equation, the spatio-temporal thermal cell-death parameter, Ω (dimensionless), can be computed as per **equation (4)**;

$$\Omega(x, y, z, \tau) = \ln\left\{\frac{C(0)}{C(\tau)}\right\} = \int_0^{\tau} A e^{-E_a/R_g T(x,y,z,t)}\, dt \quad (4)$$

where, $C$ represents concentration of cells, $R_g$ is the universal gas constant ($8.314 J/(mol \cdot K)$), $\tau$ is the duration of exposure(s), T is the temperature (K). The thermal damage parameter, $\Omega = 1$ represents 63.21% of denaturation of proteins sufficient to initiate coagulation. It should be noted that the induced thermal damage is zero before the onset of nanoparticle assisted heating. According to Rai and Srivastava, 2009 [7]; Ω=0 represents no burn, Ω=0.5 first degree burn, Ω=1 shows

approaching second degree burn and $\Omega=10^4$ represents third degree burn. The Arrhenius kinetic coefficients used to evaluate the degree of vascular stasis, $\Theta$ are summarized in **Table-I**. It is to note that these coefficients of vascular collapse or vascular shut-down are specific to perfusion changes and must not be compared with thermal damage coefficients reported in this context of work on thermal ablation [4-5].

**Table-I**: Arrhenius coefficients considered in this study [1-5].

| Parameters | Symbol [Units] | Vascular Stasis | Thermal damage |
|---|---|---|---|
| Frequency factor | $A$ [$s^{-1}$] | $1.98 \times 10^{106}$ | $3.1 \times 10^{98}$ |
| Activation Energy | $E_a$ [$Jmol^{-1}$] | $6.67 \times 10^5$ | $6.28 \times 10^5$ |

The Arrhenius kinetic equation is recently modified by Dombrovsky and Timchenko, 2015 [1] and later revisted and implemented by Kumar and Rai, 2016 [2] and Liu and Chen, 2021 [3]. One additional term is introduced in Arrhenius equation to account for regeneration of the healthy cells. Thermophysical properties can be referred from **Table-II.**

$$\frac{d\Omega(\mathrm{x,y,z,t})}{d\mathrm{t}} = A\big(1-\Omega(x,y,z,t)\big)\exp\left(\frac{-E_a}{R_g T(x,y,z,t)}\right) - B\omega_{c,o}\Omega(x,y,z,t) \qquad (5)$$

where, B is a dimensionless coefficient= $9 \times 10^{-3}$[2].

**Table-II**: Thermophysical properties [6].

| Property | Symbol [Units] | Healthy Tissue | Cancerous Tissue | Blood |
|---|---|---|---|---|
| Thermal conductivity | $k_i$[W/(m K)] | 0.5 | 0.5 | 0.55 |
| Density | $\rho$ [kg/m$^3$] | 1060 | 1060 | 1060 |
| Specific heat capacity | $c$ [J/(kg K)] | 3780 | 3780 | 3780 |
| Baseline blood perfusion | $\omega_b$ [m$^3$/(s m$^3$)] | 0.00285# | 0.00111# | - |
| Metabolic heat generation | $Q_{met}$ [W/m$^3$] | 9265# | 3602# | - |

*#extracted from thermal imaging using inverse heat transfer analysis*.

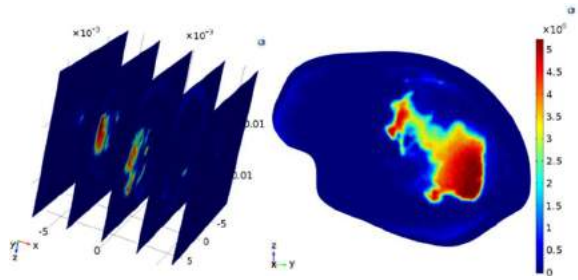

**Figure 1.** Heterogeneously distributed magnetic nanoparticles-SAR.

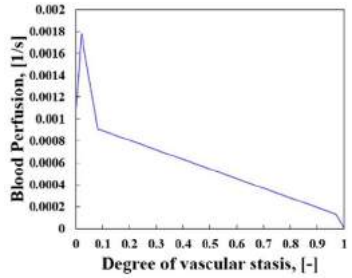


**Figure 2.** Perfusion dependence on stasis.

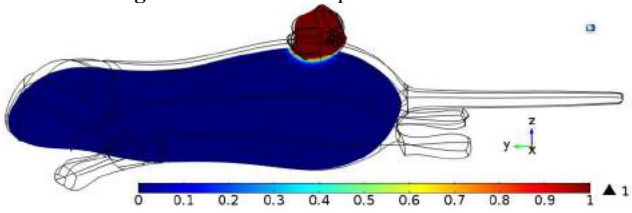

**Figure 3.** Modified thermal damage incorporating the effect of regeneration term thereby preserving healthy tissues at interface.

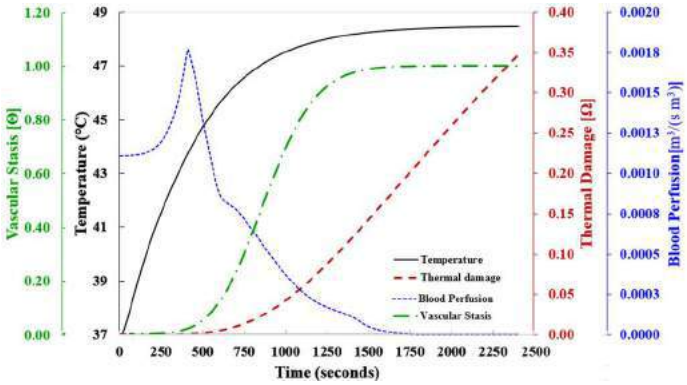


**Figure 4.** Perfusion, Vascular stasis, Thermal damage, Temperature variations at minimal temperature location of tumour.

## RESULTS AND DISCUSSION

Perfusion mediated heat-sink impairs the efficacy of cancer treatment. Vascular stasis based perfusion variation is a predictive indicator of cancer response to the thermal treatment. **Fig. 4** demonstrates spatio-temporal variation of parameters: $\omega_{c,0}$,$i\Theta$, $\Omega$ and T at the minimum temperature location. Modified thermal damage is computed via **equation (5)** (shown in **fig. 3**) is in agreement with the results of Dombrovsky et al., 2015 [1]. The inclusion of regeneration of living tissues to compute the thermal signatures of cell-death suggests that the modified Arrhenius equation seems to restrict within the damage limits of $\Omega = 1$ (63.21% denaturation of protein). The physical interpretation of this regeneration term implies that thermal damage would not propagate deep inside the healthy tissue fringes. Thus, it can inferred that regeneration phenomenon prevents and suppress the collateral thermal damage spread at the interface which is in agreement with the findings of literature [3-5]. We speculate that for a tumour needs to be treated within the hyperthermic temperature range, it will not only predict accurate ablation volumes but also restricts the damage propagation front to cross the fringe layers at the interface of tumour and healthy tissue. Such a model based on vascular shunt-off is a real assessment of the thermal damage spread within bound of $\Omega = 1$. The implication of this work would help design better heating protocol designs in future. However, more experimental exploration is needed in this context. Similar simulation approach can be utilized by the physicians in clinical treatment planning to address the likelihood of achieving complete thermal ablation at cancerous lesion while sparing the critical surrounding organs. For the deadliest cancers like Glioblastomas, or chest wall recurrence (CWR) where the clinical margins are not enough to be sacrificed, these estimates will aid in better treatment planning.


## ACKNOWLEDGEMENTS

The author would like to thank the Graduate School, UMBC for conferring the award of Dissertation Fellowship towards the progress of Doctorate degree and the Department of Mech. Engg. for the usage of computational facilities.


## REFERENCES


[1] Dombrovsky, L, et al., *Therm. Proc. Eng.,*7:24-36, 2015.
[2] Kumar, D, and Rai, KN, *J. Therm. Biol.,* 62:170-180, 2016.
[3] Liu, K-C, and Chen, T-M, *J. Therm. Biol.,* 98: 102907, 2021.
[4] Prakash, P, and Diederich, CJ, *Int. J. Hyperthermia,* 28:69-86, 2012.
[5] Schutt, DJ, and Haemmerich, D, *Med. Phys.,* 35: 3462, 2008.
[6] Singh, M et al., *Int. Comm. In Heat Mass Trans.,* 126:105393, 2021.
[7] Rai, KN, and Srivastava, V, *Int. J. Mech. Eng.,* 14:489-500, 2009.

# LINKING CIRCULATORY TURBULENCE AND THE PATHOPHYSIOLOGY OF SICKLE CELL DISEASE (SCD)

**E. Vital (1), A. Liu (2), C. Caruso (3), D. Bark (2,4), W. Lam (1,3)**

(1) Wallace H. Coulter Department of Biomedical Engineering, Georgia Institute of Technology and Emory University, Atlanta, Georgia, USA
(2) Department of Biomedical Engineering, Washington University in Saint Louis, Saint Louis, Missouri, USA
(3) Aflac Cancer and Blood Disorders Center of Children's Healthcare of Atlanta and Department of Pediatrics, Emory University School of Medicine, Atlanta, Georgia, USA
(4) Department of Pediatrics Division of Hematology and Oncology, Washington University in Saint Louis, Saint Louis, Missouri, USA

## INTRODUCTION

Sickle Cell Disease (SCD) is a chronic and clinically heterogeneous disease that is characterized by high levels of hemolysis, which gives rise to anemia and an unpredictable course of vaso-occlusion, pain crises, and stroke[1]. In the context of venous circulation, the dynamics of SCD have been well characterized. However, there remains a gap in the understanding of the root of the arterial pathologies that arise in SCD, such as stroke.

While arterial flow is primarily laminar, fluctuations in blood flow velocity and viscosity can cause turbulence[2]. Turbulent regimes are typically transient, but chronic exposure to them can negatively impact the blood and arterial condition[3,4]. Previous studies have suggested that anemic conditions, exhibit a higher propensity for turbulence, due to their lowered hematocrit values and thus reduced viscosities[5]. As mentioned, chronic exposure to turbulent flow is known to increase the red blood cell (RBC) susceptibility to damage, though no data exists for the extent to which this affects sickle RBCs (sRBCs). Considering the presumed propensity for turbulence in SCD, and the major role hemolysis plays in the pathophysiology of SCD, *it is critical* to investigate the connection between circulatory turbulence and its impacts on sRBCs and the downstream arterial and thromboembolic phenomena seen in SCD, which likely occur downstream of turbulence[6].

Determining the direct impact turbulence has on the sRBC, the local vessel endothelium, and the distal endothelium will improve our understanding of SCD vasculopathy and the anatomic regions that will be most likely be impacted. However, blood turbulence is challenging to study due to the lack of convenient technologies to investigate these processes. Here we demonstrate an easy paradigm for doing so.

## METHODS

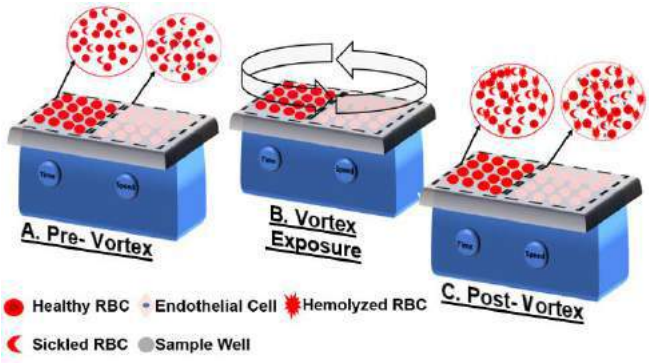


**Figure 1. Experimental set-up.**
**The schematic above demonstrates the experimental set-up for exposing small volumes of RBCs to turbulence. This method can be applied to test as many conditions as there are wells in parallel for various vortex speeds and times. (A) Baseline hemolysis levels are measured[7]. (B) Turbulent conditions are introduced by applying set speeds for desired durations of exposure. (C) Post- vortex exposure hemolysis levels are measured and subsequent cellular imaging and endothelial labeling for desired targets are conducted.**

RBCs from healthy and sickle cell donors were isolated from their plasma and resuspended in a physiological buffer to achieve target hematocrit levels. Turbulent flow regimes were applied to healthy and sickle RBCs using a multi-well plate vortex-mixer (Figure 1). Hemolysis percentages were quantified via obtaining absorbance measurements of free hemoglobin levels in the supernatant of the experimental well plate following the vortex condition and

centrifugation. Concurrently, of the above wells, some were endothelialized to observe the local impacts of turbulent sickle cells on the endothelium. Sickle and healthy RBC hemolysate from the turbulent vortex conditions were saved and perfused through endothelialized straight channel microfluidic devices to observe the impacts of turbulence on the distal vessel endothelium. Glycocalyx stains were used to assess endothelial damage. The damage was quantified via measurement of total pre- and post-perfusion fluorescence of Wheat Germ Agglutinin, a fluorescent glycocalyx stain.

## RESULTS

Figure 2 displays the change in percent hemolysis that in sRBCs and healthy RBCs at varied hematocrits and from unique donors, following exposure to laminar (1000RPM) and Turbulent (2000RPM and 2300RPM). All RBC groups exhibited an increase in hemolysis when exposed to turbulent regimes. The greatest increase in hemolysis was seen in sRBCs exposed to "high turbulence" magnitudes (2300RPM). In figure 3, our preliminary microfluidic experiments assessing the distal impacts of the hemolysate on the endothelium suggest that sRBC hemolysate (vortexed sRBCs) result in the highest amount of endothelial disruption glycocalyx, as indicated by the lowest amount of total WGA fluorescence. Experiments assessing the localized impacts of turbulent sickle cells suspensions are ongoing.

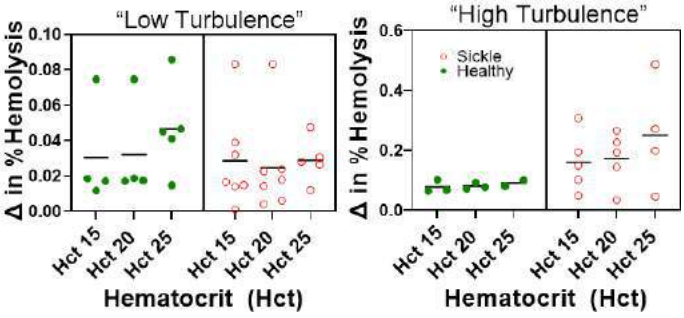


**Figure 2. Hemolysis Profile of sRBCs and Healthy RBC.**
**Magnitude of sRBC and healthy RBC percent hemolysis increase resulting from exposure to "high" (2000RPM) and "low" (2300RPM) magnitude turbulence conditions relative to baseline laminar regime (100RPM).**

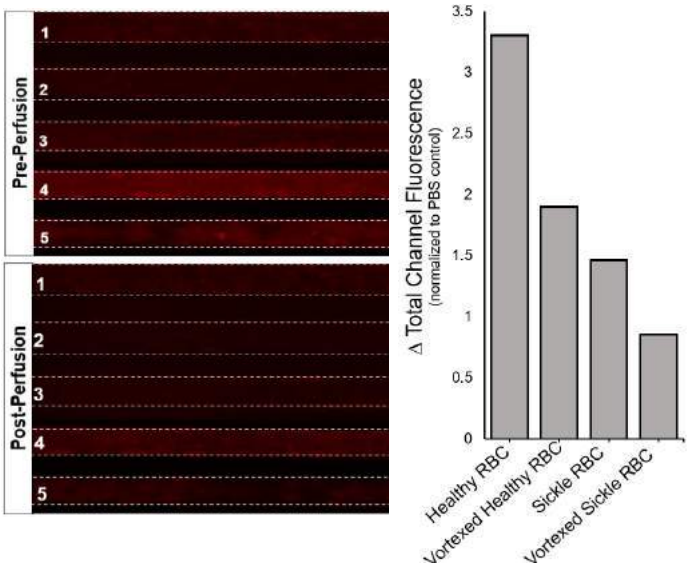


**Figure 3. Turbulence-exposed sRBCs Disrupt the Endothelial Glycocalyx.**
**Fluorescence microscopy image of a microvasculature-on-chip system stained with Wheat Germ Agglutinin (WGA) to label endothelial glycocalyx. Images were captured before and after perfusion with 1. Physiologic Buffer Saline (PBS), 2. healthy RBCs suspended in PBS (Hct 10%), 3. healthy RBCs exposed to vortex-induced turbulence (Hct 10%), 4. sickle RBCs resuspended in PBS (Hct 10%), and 5. vortexed sRBCs resuspended in PBS (Hct 10%). (right) Glycocalyx reduction was quantified by measuring the total fluorescence of the channels prior to perfusion and afterwards. The change in total fluorescence was normalized to the PBS control channel.**

## DISCUSSION

Traditional assays do not allow for the observation of the cellular processes that result from turbulent sRBCs traveling through the vasculature. Thus, we have adopted a multi-well-plate vortex mixer paradigm to subject small volumes of sickle cell blood to turbulence with the advantage of assaying multiple cellular and temporal conditions. The contributions of this investigation are two-fold. First, by better understanding the dynamic conditions that cause sickle cell hemolysis we can begin to predict when and where it will occur in the vascular network and how to mitigate it. As the lifespan of SCD patients increases, these patients are at heightened risk of vascular conditions that can alter their physiologic flow regimes. This data can inform treatment guidelines for this population. Second, characterizing how turbulent sickle cells affect the endothelium can provide more insight into the mechanisms of endothelial dysfunction observed in SCD.

Extensive computational modeling and experimental validation to truly characterize turbulence in this simple benchtop system are ongoing. Once the turbulent conditions that induce sRBC hemolysis and endothelial dysfunction are determined, our future work includes locating those pathologic areas in circulation based on existing published data to develop a predictive arterial map for sRBC hemolysis. This information can then encourage the development of a novel modality for identifying hotspots for potential arterial disease in SCD patients which can inform treatment regimes and improve the overall care for this aging patient population.

## ACKNOWLEDGEMENTS

The authors would like to acknowledge the members of the Lam and Bark labs for contributing to this work. This research is supported by the National Heart, Lung and Blood Institute under the following awards: R35HL145000, R01HL140589, 1F31HL158223.

## REFERENCES

[1] Kato, G.J. et al., *J Clin Investig*, 127:750-760,2013
[2] Pappano, A. et al., Cardiovasc *Physiol*, 10:119-134, 2013
[3] Chiu, J et al., *Physiol Rev*, 91:327-387,2011
[4] Kameneva, M et al., *ASAIO J*, 50:418-423, 2004
[5] Blick, H et al., *Simp Turbul Liq*, 14, 1975
[6] Stein, P et al., *J Appl Physiol*, 40:60-66,1976
[7] Evans, B.C. et al, *J Vis Exp*,73, 2013

# COMPUTATIONAL 13C METABOLIC FLUX ANALYSIS INDICATES ENDOTHELIAL CELLS ATTENUATE METABOLIC PERTURBATIONS BY MODULATING TCA CYCLE ACTIVITY

**Bilal Moiz (1), Jonathan Garcia (2), Sarah Basehore (2), Angela Sun (1), Andrew Li (1), Surya Padmanabhan (1), Kaitlyn Albus (1), Cholsoon Jang (3), Ganesh Sriram (4), Alisa Morss Clyne (1)**

(1) Department of Bioengineering, University of Maryland, College Park, MD 20742, USA
(2) School of Bioengineering, Science, and Health Systems, Drexel University, Philadelphia, PA 1□104, USA
(3) Department of Biological Chemistry, Chao Family Comprehensive Cancer Center, University of California Irvine, Irvine, CA □26□7, USA
(4) Department of Chemical and Biomolecular Engineering, University of Maryland, College Park, MD 20742, USA

## INTRODUCTION

Disrupted endothelial cell metabolism is linked to vascular dysfunction and cardiovascular disease [1]. Recent efforts have focused on manipulating endothelial metabolism to alter cell signaling pathways and thereby cell function [2]. However, the cellular metabolic network consists of interlinked metabolite and reactions. Therefore, supposedly targeted inhibition in specific metabolic pathways could have unexpected effects on glycolysis, the tricarboxylic acid (TCA) cycle, and other metabolic pathways [3].

Although glucose primarily fuels glycolysis to generate pyruvate, it can enter side branch pathways such as the pentose phosphate pathway (PPP) and the polyol pathway. In glycolysis, glucose is metabolized into glucose-6-phosphate (G6P), which can continue down the glycolytic pathway or enter the PPP. The PPP is vital for generation of nucleotide precursors as well as the reducing agent NADPH. PPP activity increases during cell proliferation or oxidative stress [4]. The polyol pathway reduces excess glucose into sorbitol in a step that generates NADP+ from NADPH. This pathway has been implicated in diabetic neuropathy and endothelial dysfunction [5].

Although each of these pathways plays vital roles in cellular function, the impact of targeted inhibition of these pathways remains unclear. Reductionist approaches focused on specific pathways do not fully account for the interconnected nature of metabolic networks, which limit understanding of off-target or compensatory mechanisms that occur during inhibition. Thorough understanding of systemic metabolic changes requires advanced analytical and computational tools that can contextualize metabolomic data within a network-based context. Isotope-assisted metabolic flux analysis (iMFA) is a computational approach that utilizes isotope labeling experiments and mathematical representations of metabolic networks to quantify systems-level metabolic activity [6].

The goal of this study was to utilize iMFA to understand how inhibiting glycolytic side branch pathways impacted endothelial metabolism at a systems-level. We utilized pharmacological inhibitors of the polyol pathway (fidarestat) and PPP (dehydroepiandosterone, DHEA) to determine whether inhibition triggered off-target or compensatory metabolic changes. Human umbilical vein endothelial cells (HUVECs) were treated with metabolic inhibitors and analyzed using mass spectrometry and iMFA. Our results demonstrate that each of these inhibitors incurred systemic metabolic changes. This study highlights the need to study systemic metabolic therapeutic effects as well as the potential for data-driven, computational approaches in improving our understanding of cardiovascular health and disease.

## METHODS

HUVECs were cultured to confluence and then treated with either 0.1% DMSO as solvent control, 25 µM DHEA or 18 µM fidarestat in endothelial basal media for 24 hours. Following treatment, cells were labeled with DMEM containing 5 mM [$U^{13}$-$C_6$] glucose for 24 hours. Metabolites were extracted and analyzed via liquid chromatography-mass spectrometry. Mass spectrometer data was corrected for natural isotope abundance. Extracellular metabolite concentration changes were quantified with the YSI Bioanalyzer 2900. Metabolic fluxes in the network were determined using the INCA metabolic flux analysis software suite. A metabolic network map was manually constructed to include TCA cycle, glycolysis, PPP, and hexosamine biosynthetic (HBP) pathways. Isotopomer mass spectrometer and external flux data were incorporated into the model. Steady-state metabolic fluxes were estimated through an iterative process where flux estimates are used to simulate isotope distributions that are then compared to experimentally derived isotopes. At each iteration, goodness-of-fit is assessed and used to refine the flux estimate until it reaches a sufficient error threshold. The flux distribution that results in simulated isotopomers that optimally fit experimental isotopomers are returned as the best flux estimate.

## RESULTS

We first measured extracellular flux changes in all three groups. Interestingly, there were no significant changes in glucose consumption, lactate secretion, or glutamate secretion. However, fidarestat-treated HUVECS significantly increased glutamine intake (Figure 1). DHEA-treated cells also increased uptake of glutamine, although this effect was not statistically significant.

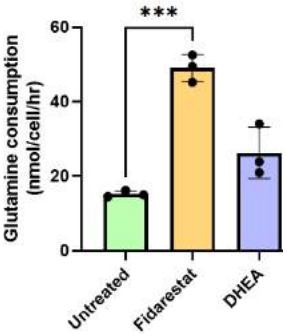


Figure 1. Glutamine intake significantly increased in fidarestat-treated HUVECs. Statistical significance was determined with one-way ANOVA followed by Dunnett's multiple comparison test. * $p < 0.05$; ** $p < 0.01$

We then created a baseline endothelial mode using extracellular flux and isotope labeling data from control groups to quantify metabolic fluxes in untreated HUVECs. Initial results showed that TCA cycle activity was approximately 20% the rate of incoming glucose flux.

We then analyzed each inhibitor individually by refitting the baseline model to data from the treated groups. iMFA of fidarestat-treated and DHEA-traated cells estimated a significant decrease in PPP fluxes and increases in overall carbon intake, primarily into the TCA cycle. As a result, all TCA cycle fluxes increased. In fidarestat-treatment, activity of the malate-pyruvate shuttle reversed direction from mitochondrial import towards mitochondrial export (Figure 2).

## DISCUSSION

These results demonstrate the importance of assessing the system-wide effects of targeted metabolic inhibition. In this work, we identified systemic metabolic changes that occurred with inhibition of glycolytic side branches.

Fidarestat treatment resulted in increased TCA cycle and PPP activity. Interestingly, fidarestat is known to increase SIRT1 which promotes glutamine uptake [7,8]. This may have been one of the driving forces in increased glutamine uptake and TCA cycle activity. Fidarestat inhibits aldose reductase, the enzyme that metabolizes glucose and NADPH into sorbitol and NADP+. Therefore, fidarestat treatment may result in NADPH accumulation, which can allosterically downregulate the PPP.

Similar changes were observed in DHEA-treated cells. However, in this case, decreased PPP fluxes are likely to be due to direct downregulation by DHEA. This may have driven DHEA-treated cells to drive NADPH production through malic enzyme activity, which is an important generator of NADPH. Increased glutamine intake may have been used to supply malic enzyme activity. This simultaneously could have increased overall TCA cycle activity.

These results demonstrate that HUVECs may attenuate metabolic disturbances by dramatically modifying TCA cycle activity. Furthermore, these inhibitors dramatically affect pathways beyond their intended targets, which suggests that the off-target effects of these drugs should be further investigated. Together, this work highlights the powerful application of metabolic flux analysis to quantify systemic metabolic changes and its potential to elucidate off-target effects of pharmacological compounds.

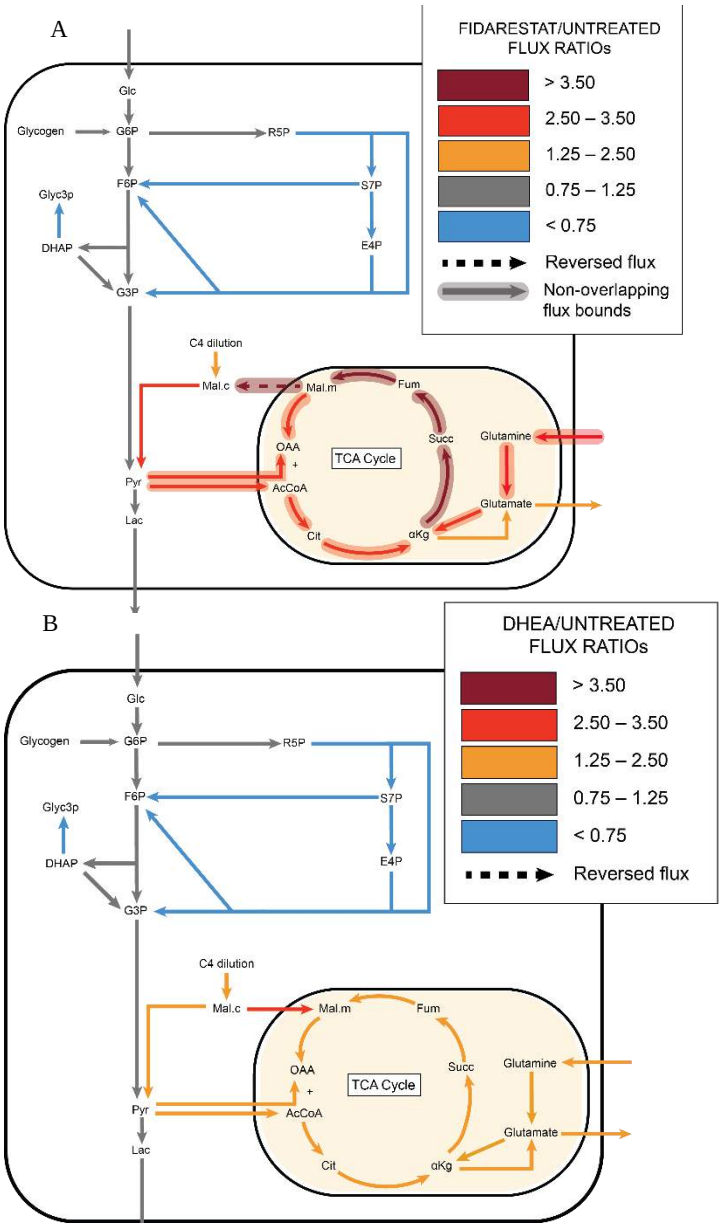


**Figure 2.** Metabolic flux analysis demonstrates that (A) fidarestat and (B) DHEA treatment elevate PPP and TCA cycle fluxes


## ACKNOWLEDGEMENTS

This research was funded by NIH 1R01HL140239 to AC and NSF DGE-1632976 to BM.


## REFERENCES


1. G. Eelen, P. De Zeeuw, M. Simons, and P. Carmeliet, "Endothelial cell metabolism in normal and diseased vasculature," *Circ. Res.*, vol. 116, no. 7, p. 1231, Mar. 2015
2. X. Li, X. Sun, and P. Carmeliet, "Hallmarks of Endothelial Cell Metabolism in Health and Disease," *Cell Metabolism*, vol. 30, no. 3. Cell Press, pp. 414–433, 03-Sep2019
3. J. H. Tsai et al. "Glucosamine inhibits decidualization of human endometrial stromal cells and decreases litter sizes in mice," *Biol. Reprod.*, vol. 89, no. 1, 2013,.
4. Verdegem, D.; Moens, S.; Stapor, P.; Carmeliet, P. Endothelial cell metabolism: Parallels and divergences with cancer cell metabolism. *Cancer Metab.* 2014, *2*, 19.
5. Luengo, A.; Gui, D.Y.; Vander Heiden, M.G. Targeting Metabolism for Cancer Therapy. *Cell Chem. Biol.* 2017, *24*, 1161–1180.
6. M. R. Antoniewicz, "A guide to (13)C metabolic flux analysis for the cancer biologist.," *Exp. Mol. Med.*, vol. 50, no. 4, p. 19, Apr. 2018
7. Corbet, C., et al., *The SIRT1/HIF2alpha axis drives reductive glutamine metabolism under chronic acidosis and alters tumor response to therapy.* Cancer Res, 2014.
8. Pal, P.B., et al., Aldose reductase regulates hyperglycemia-induced HUVEC death via SIRT1/AMPK-alpha1/mTOR pathway. J Mol Endocrinol, 2019. 63(1): p. 11-25.

SB³C2022
Summer Biomechanics, Bioengineering and Biotransport Conference
June 20-23, Eastern Shore, MD, USA

# A BAYESIAN APPROACH FOR INVERSE PROBLEMS ON PATIENT-SPECIFIC CFD SIMULATION OF AORTA USING AN ML-BASED SURROGATE MODEL

**Pan Du (1), Jian-xun Wang (1)**

(1) Department of Aerospace and Mechanical Engineering,
University of Notre Dame,
Notre Dame, IN, U.S.

## INTRODUCTION

Cardiovascular disease (CVD) remains the first leading cause of death and morbidity in the U.S., posing a major healthcare concern. Physically principled computational modeling, often combined with medical imaging, plays an important role in the diagnosis of CVD by virtue of its capability of providing comprehensive hemodynamic flow information (e.g., blood flow velocity, pressure, wall shear stress) [1-2]. The ever-growing computational capability and understanding of cardiovascular fluid mechanics spur the development of more realistic and sophisticated CFD models, yet bring many challenges to inverse optimization and uncertainty quantification (UQ) of unknown/uncertain model parameters due to large number of uncertain inputs and excessive computational burden. Many attempts have been done to solve inverse UQ problems of cardiovascular flow under the Bayesian framework [3-4]. Direct coupling of Markov Chain Monte Carlo (MCMC)-based posterior sampling approach and non-trivial forward CFD modeling involves numerous expensive trials which can easily be computationally prohibitive especially for complex flows. As a result, surrogate models for cardiovascular simulation (e.g., lumped parameter models, multi-fidelity CFD simulation, neural networks) are introduced to reduce the online cost of the forward propagation step. Neural network (NN) is a highly preferred choice for surrogate models because it is capable of approximating complex high-order nonlinear mapping between inputs (geometry, boundary conditions, parameters, etc.) and field outputs, and features a fast online prediction speed. However, building interpolation-based surrogate models such as neural networks requires a significant amount of sample points. Therefore, more efficient sampling strategies are needed to achieve the same accuracy with fewer samples. Iterative ensemble Kalman method (IEnKM), for example, is more efficient in terms of sampling compared to fully Bayesian methods such as MCMC.

Moreover, besides common parameters (e.g., viscosity, Re, velocity, etc.), quantifying the uncertainty of 3-D geometries is quite challenging especially for complex cardiovascular systems. Graph neural network (GNN) or dimensionality-reduction methods such as primary component analysis (PCA) are typically used for the parameterization of complex 3-D geometries. GNN learns a point-to-point mapping between input and output but requires considerable computational resources when the mesh resolution is large. The latter one is more efficient since it directly encodes the 3-D mesh into a lower-order latent space, reducing the complexity of the neural network in the surrogate model if present.

In this study, we propose a novel deep learning solution to address these challenges and enable scalable geometric UQ and optimization. Specifically, a statistical generative model for 3-D patient-specific shapes will be constructed based on a handful of available baseline patient geometries. An unsupervised shape correspondence solution is used to enable geometric morphing and a compact geometric design space can then be constructed by the statistical generative shape model. In order to build a fast forward map between geometric input space to the solution space of functional information, we propose a supervised deep learning solution. With the fast surrogate model, we ran test cases to demonstrate its application in shape optimization and UQ analysis in a massively scalable manner.

## METHODS

### 1). Aorta geometry dataset parameterization

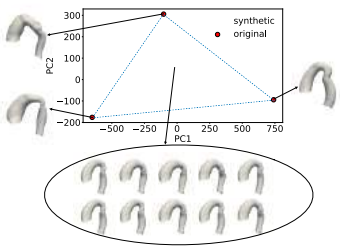


**Figure 1: geometry parameterization and synthesis**

Eight 3-D aorta geometries are reconstructed from MRI scans of patients with Coarctation of the aorta (COA) conditions at the German Heart Institute Berlin [5]. A statistical shape model (SSM) is built and performed to parameterize input geometric space and synthesize virtual shapes to form a large-size aorta geometry dataset.

**2). Automatic CFD routine**

A python program is built to automatically conduct CFD simulations on each aorta sample to produce the desired fluid quantities (e.g., pressure, velocity and wall shear stress).

**3). ML-based surrogate model**

The shape inputs and field outputs are encoded into a latent space using PCA transform and an MLP is used to learn the non-linear relationship in between. Once the training is done, the surrogate model will be able to predict the 3-D hemodynamic flow information within a split second for any new aorta shape.

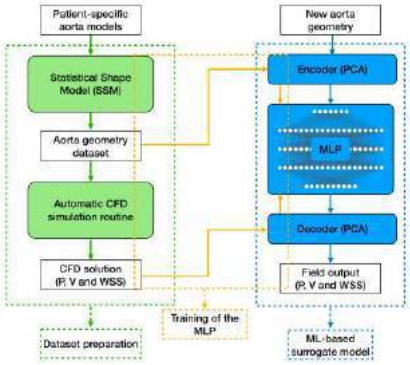


**Figure 2: Diagram of the surrogate model**

**4). Hybrid Bayesian approach**

The proposed surrogate model is embedded into a hybrid Bayesian method to quantify geometry uncertainty. The observation data is sparse measurements of the velocity field and a prior is assumed for the PCA encoded vector. The hybrid Bayesian method operates in two phases: the IEnKM coupled with full-resolution CFD modeling is used to find the posterior mean; A ML-based surrogate model is built by sampling around the found mean and importance sampling incorporating the surrogate model is performed to quantify the uncertainty.

**RESULTS**

Among the eight patient-specific aorta geometries, one aorta is randomly selected as the template and seven diffeomorphisms are calculated from the template to the rest of the geometries using the SSM, which yields seven deformed geometries replacing the original ones. Later, the synthesizing method expands the eight original geometry set to a dataset containing 1000 samples. The samples are then passed to a CFD solver to generate field outputs. All CFD simulation cases were run in parallel (4 CPUs per case) using the Simple solver in OpenFOAM. Each simulation takes about 20 minutes to reach convergence.

The learning of the MLP was conducted on an Nvidia RTX A6000 card and a minimum of 2000 epochs were executed for each MLP to ensure convergence. The average relative mean squared error (ARMSE) of the predicted flow fields with respect to the ground truth is reported in Table 1. A visualization of the field outputs is shown in Figure 3.

| | Pressure | Velocity | Wall shear stress |
|---|---|---|---|
| ARMSE | 1.336% | 0.640% | 1.203% |

**Table 1: Error of prediction of the surrogate model**

Figure 4 shows the first phase of the hybrid Bayesian approach. The ensemble size is 18 and samples for the first and second iterations are displayed.

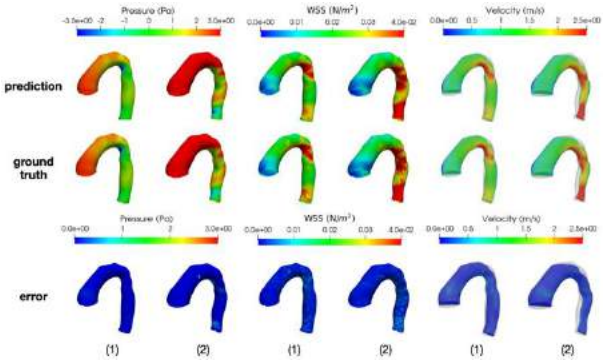


**Figure 3: Comparison of prediction and ground truth**

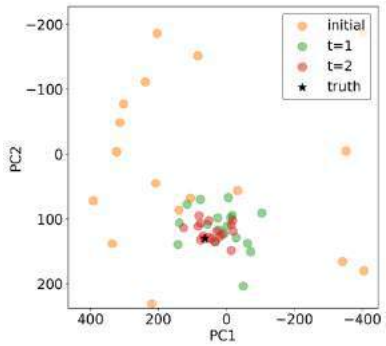


**Figure 4: Determination of posterior mean via IEnKF**

**DISCUSSION**

In this study, a set of patient aorta geometries is collected and an SSM is built to parameterize the 3-D topological space of the aorta shapes and synthesize virtual aorta geometries. An ML-based Surrogate model is proposed to predict desired field outputs.

The prediction errors in Table 1 are small, indicating a great prediction accuracy for the proposed ML-based surrogate model. The visualization (Figure 3) also proves that the proposed model is in good agreement with the ground truth generated from CFD simulation. However, certain discrepancies are inspected near the stenosis of the descending aorta, exposing the inherent limitations of neural networks in capturing local details. For uncertainty quantification, the first phase of the hybrid Bayesian method successfully found an ensemble close the truth after 2 iterations. In future work, phase two will be implemented, where a local surrogate model will be built around the found mean and importance sampling will be utilized to calculate the posterior of the input shape. A good agreement between the posterior and the truth is expected.

**ACKNOWLEDGEMENTS**

I would like to express my gratitude to my advisor Prof. Jian-xun Wang for providing insights and guidance in building up the workflow. Many thanks to my colleagues including Han Gao, Luning Sun, and Xinyang Liu who shared their thoughts and suggestions with me.

**REFERENCES**

[1] Romarowski, Rodrigo M., et al. *International journal for numerical methods in biomedical engineering*, 34.11: e3134, 2018

[2] Dillon-Murphy, Desmond, et al. *Biomechanics and modeling in mechanobiology*, 15.4: 857-876, 2015.

[3] Schiavazzi, D. E., et al. *International journal for numerical methods in biomedical engineering*, 32.3 (2016): e02737.

[4] Chen, Peng, et al. *International journal for numerical methods in biomedical engineering*, 29.6 (2013): 698-721

[5] Brüning, Jan, et al. *Cardiovascular engineering and technology*, 9.4 (2018): 582-596.

# IN VITRO CULTURE OF HUMAN LUNG ADENOCARCINOMA PATIENT DERIVED ORGANOID TOWARDS EXPEDITED GROWTH AND DRUG EVALUATION

**Xiaochen Qin[1], Yuyuan Zhou[1], Yaling Liu[1,2,*]**

(1) Department of Bioengineering, Lehigh University, Bethlehem, PA, USA
(2) Department of Mechanical Engineering & Mechanics, Lehigh University, Bethlehem, PA, USA
*Corresponding contact yal310@lehigh.edu

## INTRODUCTION

Patient-derived organoids contains more heterogeneity and tissue architecture of the parental tumor than tumor cell-lines and therefore provide the possibility for an in vitro personalized prediction on the anticancer drug responses. Lung cancer remains one of the most challenging diseases due to the heterogeneities in the medical treatment procedures. As the current 2D culturing methods have been provided poor physiological relevance to clinical therapeutics, therefore, 3D models are being developed to better reproduce physiological responses. 3D culturing methods often require large initial cell populations and a long growth period before the organoid models are ready for therapeutic testing. As a solution, a 3D culturing system has been developed capable of producing physiologically relevant organoid modal in an expedited fashion while only requiring a small number of initial tumor cells for the prediction of therapeutic response. The expedited growth of organoids has been facilitated by our inhouse developed bi-layer microfluidic system through active convective nutrition supply and toxin removal. Furthermore, we demonstrated the utility of lung adenocarcinoma organoid lines as a model for drug testing to advance personalized medicine.

## METHODS

The human samples were sectioned with sterile blades into 1-2mm size on ice. Transferred 6-8 pieces of sectioned tissues and washed three times with cold adDMEM/F12 medium (ThermoFisher) and were incubated with 0.001% DNase (Sigma-Aldrich, MO, USA), 1 mg ml$^{-1}$ collagenase/dispase (Roche, IN, USA), 200 U ml$^{-1}$ penicillin, 200 mg ml$^{-1}$ streptomycin, and 0.5 mg ml$^{-1}$ amphotericin B (2% antibiotics, Sigma) in DMEM/F12 medium (Lonza) at 37 °C for 2 h with on roter. After incubation, the suspensions were repeatedly triturated by pipetting and passed through 70 µm cell strainers (BD Falcon, CA, USA). The strained cells were centrifuged at 1300 RPM for 5 min, and the pellet was resuspended in 100 µl Matrigel (serum-free medium DMEM/F12 supplemented with 20 ng ml$^{-1}$ of bFGF (Invitrogen, CA, USA), 50 ng ml−1 human EGF (Invitrogen), N2 (Invitrogen), B27 (Invitrogen), 10 µM ROCK inhibitor (Enzo Life Sciences, NY, USA), and 1% penicillin/streptomycin (Gibco, OK, USA).

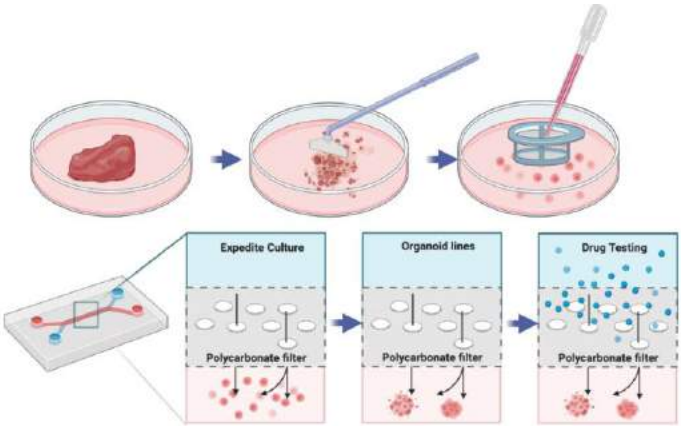


**Figure 1:** Schematic of bi-layer microfluidic model for lung adenocarcinoma patient-derived organoid expedited growth and drug evaluation

To ensure sufficient nutrition and oxygen supply and optimized metabolite clearance, the microfluidic devices were designed as shown in Fig. 1. Both apical and basal pieces were made with PDMS, and the embedded channels were formed from a pre-obtained silicon wafer by photolithography. The two pieces were separated by a semipermeable membrane, which usually has dense 200–800 nm pores, allowing for water, nutrient, oxygen, and metabolite diffusion, while preventing cell transportation. Four outlets (diameter = 2 mm) on the apical piece were matched to the four circle areas for the apical and basal channels. The two channels share the same size (500 µm width and 200 µm height), and they have more than 80% overlapping area, as shown in Fig. 1. Since the two PDMS pieces are separated by the semipermeable polyurethane membrane, which has a surface that cannot be activated by plasma treating, an additional thin layer of PDMS was applied onto the whole membrane, excluding the channel area to ensure strong bonding.

Paclitaxel was used as a model drug for the Lung Adenocarcinoma organoid. The drug displays a remarkable efficacy on the organoid after 1 day under 100 nM of drug concentration. The drug was applied using hydraulic force through a pipette tip that inserted at the inlet of the device.

## RESULTS

To establish the lung adenocarcinoma organoid lines, we received surgical discard from Cooperative Human Tissue Network (CHTN). The organoid establishment and drug efficacy tests can be assessed using dead and live staining and confocal microscopy. Small organoid has started forming after 3 days and reach 100um after day 7, as shown in Fig. 2. The growth of the organoid can be measured directly under confocal imaging using Cell Tracker green stain. The application of the flow has generated by hydraulic force with pipette tip fixed at the inlet. The various flow rates withing the microfluidic devices were controlled with the amount of medium loaded in the tip.

In our previous published work [1]-[2], Paclitaxel of a high concentration has negative effects on the HCT116 cells and the cocultured EC cells. In order to evaluate the efficacy of the patient-derived organoid to the anticancer drugs, we perfused the Paclitaxel as the model drug into the system for 24 hours. The organoids were treated one day and stained with live/dead stains. In Fig. 3, it shows that the organoid was sensitively responded in the device to as little as 10nM of drug concentration.

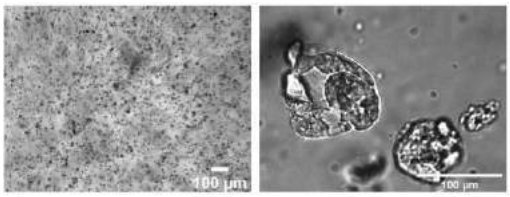


**Figure 2:** Bright field image of Lung adenocarcinoma patient-derived cell seeding and established organoid.

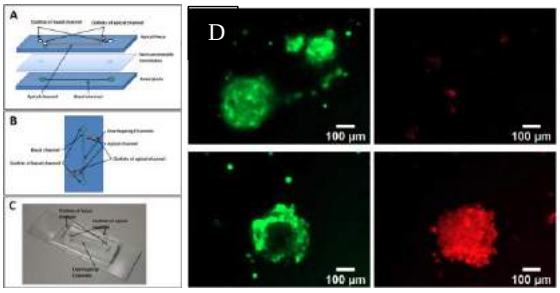


**Figure 3:** Diagram of the microfluidic device using PDMS molds with basal and apical channels. (a) Layer diagram, (b) top view, and (c) photo of the microfluidic device, (d) Fluorescent images of organoids subjected to 1-day 100 nM paclitaxel (Pac) treatment. The organoids were stained with Calcein AM and propidium iodide (PI) (live/dead)

## DISCUSSION

The expedite growth and drug testing of the lung adenocarcinoma organoid provide an opportunity to bridge the gap between traditional c ell lines and patient-derived xenograft animal models. The in vitro antitumor drug-screening platform presented that consisted of two layers with two channels and a semipermeable membrane. The membrane between channels has allowed the infiltration of medium and drugs, and showed both permeability and resistance to several molecules, including drugs. Additionally, direct seeding of tumor-derived cells more closely mimicked the in vivo nature of tumors, while the Matrigel served as a scaffold for the tumor organoid, which functioned as ECM. The drug efficacy has been expressed by the viability of tumor cells, which can be quantified by dead/live staining using confocal microscopy. More drugs will be selected for our bi-layer microfluidic system based on their clinical relevance. The half-maximal inhibitory concentration (IC50) will be presented. Since both the cell culture in the microfluidic device and the drug screening characterization techniques can be automated, we believe this work can dramatically increase the efficiency with shorter turnaround time and cost on antitumor drug screening.

## ACKNOWLEDGEMENTS

This work was supported by National Science Foundation grant CBET 2039310, National Institute of Health grant R01HL131750, Pennsylvania Department of Health Commonwealth Universal Research Enhancement Program (CURE), and Pennsylvania Infrastructure Technology Alliance (PITA).

## REFERENCES

[1] Liu, Y et al., *Biomicrofluidics*, 13, 044108, 2019.
[2] Liu, Y et al., *Lab Chip*, 19, 1458-1470, 2019.

SB³C2022
Summer Biomechanics, Bioengineering and Biotransport Conference
June 20-23, Eastern Shore, MD, USA

# STIFFNESS MAPPING FOR EARLY DETECTION OF BREAST CANCER: SENSITIVITY TO ERRORS IN MODULUS

**Lorraine G. Olson (1), Robert D. Throne (2)**

(1) Department of Mechanical Engineering, Rose-Hulman Institute of Technology, Terre Haute, Indiana, USA
(2) Department of Electrical and Computer Engineering, Rose-Hulman Institute of Technology, Terre Haute, Indiana, USA

## INTRODUCTION

Early detection of breast cancer is crucial for improving patient survival rates. Manual breast exams and mammograms are currently the most effective and widely used early detection techniques. Manual breast exams depend on tissue stiffness but are limited in their ability to detect tumors. Mammograms, while effective, expose the patient to radiation. In addition, mammograms are sensitive to tissue density rather than stiffness, so identifying cancerous sites in the half of women over 40 with dense breasts can be challenging.

Our ultimate goal is to develop a system that automates/refines the manual breast exam process to detect the roughly 10x stiffness difference between healthy and cancerous tissues. An electro-mechanical device will gently indent the tissue surface in various locations, recording the forces required and the tissue surface deflections on the remainder of the surface. This force and deflection data will be used with inverse techniques involving finite element methods and genetic algorithms to provide detailed 3D maps of the elastic modulus of the interior of the breast tissue.

We have developed 3D mapping algorithms and have conducted experiments on tissue phantoms to validate our approach [1]. Figure 1 shows a prototypical 3D stiffness map. We tested 14 tumor-free phantoms and 14 tumor-containing phantoms. Using a combination of 10% force data and 90% displacement data we could correctly classify all phantoms as tumor-containing or tumor-free, which was substantially more robust than either measurement modality alone.

These experiments were conducted with a background phantom stiffness (Young's modulus) $E_h$= 3.3 kPa and a tumor phantom stiffness $E_c$=22 kPa, which closely mimics experimental data for healthy and cancerous breast tissues reported in the literature [2]. The computations assumed $E_h$ =3.2 kPa and $E_c$ = 22.6 kPa – effectively the correct values. In actual applications we will not know the stiffnesses yet we would still like to correctly classify phantoms as tumor-containing or tumor-free.

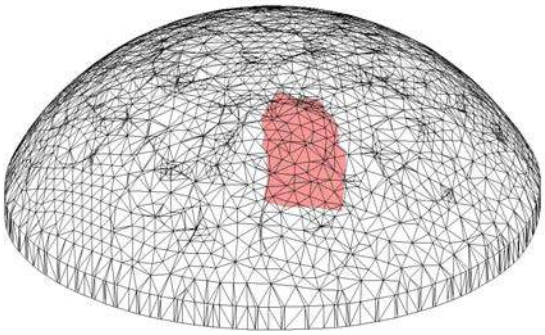

**Figure 1: Prototypical 3D Stiffness Map. (Stiff Cancerous Tissues are Red, Normal Healthy Tissues are Transparent.)**

In this abstract we study the sensitivity of the tumor presence/absence classification to errors in the assumed modulus in the computations.

## METHODS

Experimental Methods. Before we review the computational methodology – which is the focus of this abstract – it is useful to understand the data collection.

Figure 2 shows the experimental set-up. The phantom sits on a turntable underneath the indenter. The phantoms themselves are made of silicone and are for average-sized (180g) breasts. The tumors are 2g which would correspond to a 100% 5-year relative survival rate for the patient. A structured light scanner is used to capture the initial phantom geometry. The indenter has 4 possible locations on the arc and the turntable rotates to 9 positions for a total of 36 measurement sites.

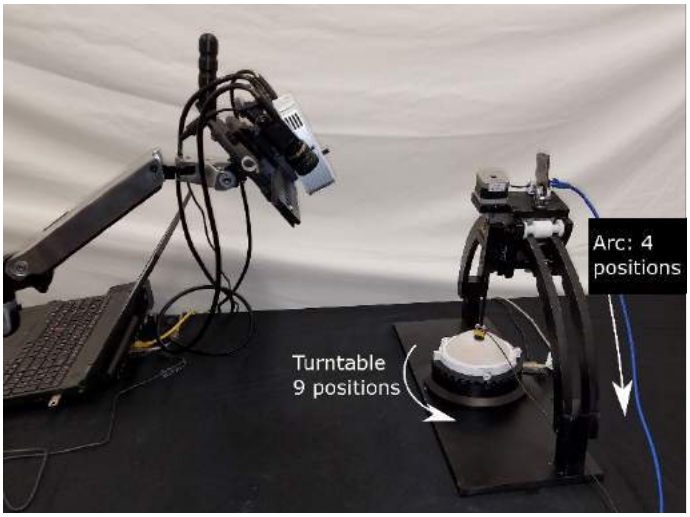


**Figure 2: Experimental Setup. (Structured light scanner is attached to arm at left. Arc positions indenter above phantom. White phantom sits on turntable below indenter.)**

At each measurement site we indent the tissue 5 mm and measure the force required to produce that indentation. At the same 36 indentation sites, we use the structured light scanner to capture "before indentation" and "after indentation" geometries. These geometries allow us to estimate the normal displacement of points on the phantom surface.

Computational Methods. The initial phantom geometry, the forces from the 36 indenter sites, and the normal displacements of points on the surface (36 sets of them) are the inputs to the computational algorithm. The cost function to be minimized balances the error in the match to the measured data and the size of the tumor:

$$\begin{aligned} \text{Cost} = \quad & (1-\alpha)*(\text{Error in Forces}) \\ & + \alpha*(\text{Error in Displacements}) \\ & + w*(\text{Tumor Radius}) \end{aligned} \qquad (1)$$

α adjusts the relative importance of errors in the force data and errors in the displacement data. $w$ is the weighting that adjusts the balance between the errors in the match to the measured data and the tumor size, which regularizes the problem, and choosing $w$ appropriately is important. The output is the 3D stiffness map.

Our experimental validation indicated that $\alpha = 0.9$ gave the best balance between force and displacement data. $w$ in the range from 0.4 to 0.7 correctly classified all samples as tumor-containing or tumor-free. These results were obtained with the correct values of the moduli in the computational algorithm.

We then varied the moduli in the computational model to examine how sensitive our stiffness mapping algorithm is to having the correct moduli. In doing this, we held α at 0.9 and $w$ at 0.6. We first varied the tumor modulus in the computational model while holding the healthy modulus at 3.2 kPa. Next we held the tumor modulus fixed at 22.6 kPa and varied the healthy modulus.

## RESULTS

Figure 3 shows the results. Notice that the horizontal axis is the ratio of the tumor modulus to the healthy tissue modulus in the computational model – the results for a given ratio were the same regardless of whether we varied the tumor modulus or the healthy tissue modulus. The vertical axis gives $w_{cross}$ for each test—this is the value for which a given test crosses from being correctly classified to being incorrectly classified. Red lines indicate results for tumor-containing phantoms and blue lines indicate results for tumor-free phantoms.

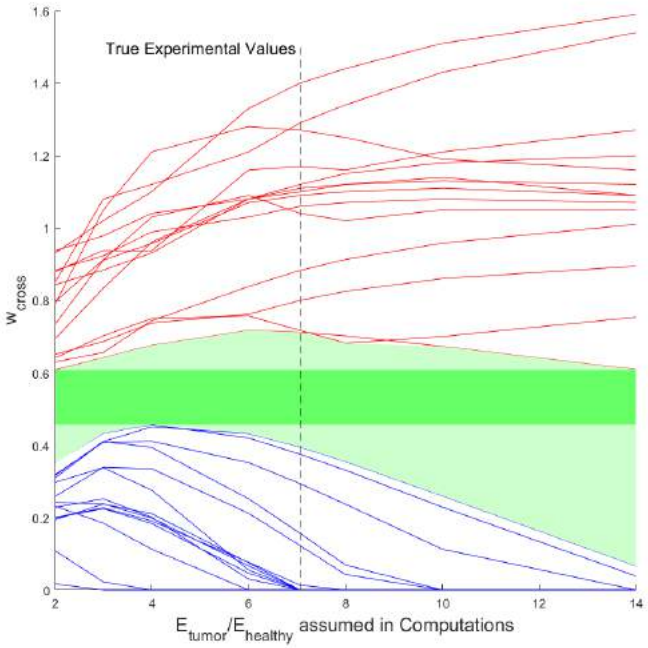


**Figure 3: Correct classification of tumor-free and tumor-containing (light green region) is robust to errors in the assumed computational stiffness ratio. (Dark green region: correct classification over all tested stiffness ratios.)**

## DISCUSSION

Figure 3 shows that method is quite robust over a range of modulus ratios– when the ratio is at the true value of approximately seven we see almost the same performance as when the ratio is 14 or even 2. The dark green region represents the range of w's for which we would correctly classify all samples over the entire range of modulus ratios. This range is w = 0.46 to w = 0.61. Thus, choosing $w = 0.55$ along with $\alpha = 0.9$ would give good results even with errors in the assumed stiffnesses.

It is important to note that this does not mean that we can experimentally detect tumors at stiffness ratios of 2 or 14 – it means that when the data is collected from one of our samples (stiffness ratio of 7) we do not need to have the correct ratio in our computational algorithm to make a correct prediction of the presence or absence of a tumor.

It is also important to realize that this insensitivity to the modulus ratio means that we will almost certainly be unable to predict the stiffness of the tumors – merely presence/absence.

## ACKNOWLEDGEMENTS

This work was supported by generous contributions to the Lawrence J. Giacoletto endowment. This work used the Extreme Science and Engineering Discovery Environment (XSEDE), which is supported by National Science Foundation grant number ACI-1548562. Resources were obtained through the Texas Advanced Computing Center at the University of Texas at Austin.

## REFERENCES

[1] Olson, L et al, *Inverse Probl Sci Eng*, 29:2239-2273, 2021.
[2] Samani, A. et al, *Phys Med Biol*, 52:1565-1576, 2007.

# EARLY REMOVAL OF THE INFRAPATELLAR FAT PAD IN A SPONTANEOUS RODENT MODEL OF OSTEOARTHRITIS MAY BENEFICIALLY ALTER THE DEVELOPMENT OF OSTEOARTHRITIS

**Tammy L. Haut Donahue (1), Mary F. Afzali (2), Nicole Vigon (3), Ryan J. Ek (3), Gerardo E. Narez (3), Kelly S. Santangelo (2,3)**

(1) Biomedical Engineering, University of Memphis, Memphis, TN, USA
(2) Department of Microbiology, Immunology and Pathology, Colorado State University, Fort Collins, CO, USA
(3) Department of Biomedical Engineering, University of Massachusetts, Amherst, MA, USA

## INTRODUCTION

Adipose depots described in the knee joint include the infrapatellar fat pad (IFP), the posterior knee fat pad, the quadriceps fat pad, and the pre- femoral fat pad [1]. The IFP is the largest of these and is found in the anterior aspect of the joint in the space shaped by the patella, femoral condyles, and tibial plateau. While the exact functions of the IFP are not completely understood, it is thought to facilitate the distribution of synovial fluid and absorbs loads through the knee [2.3].

Osteoarthritis (OA) is a painful, debilitating disease often found in the elderly population. While the exact mechanisms of OA development are not well understood, recent studies suggest a strong inflammatory role of the IFP in OA. Additionally, resection of the IFP in human cadavers was shown to decrease tibial external rotation, increase medial translation of the patella, reduce retro patellar contact pressure and decrease patellofemoral contact area and force [4].

Only a few studies have documented the change in biomechanical properties of the knee as a whole, as well as tissues such as cartilage, meniscus and bone, following removal of the IFP from this joint. We have previously shown that, after resection of the IFP in the Hartley Guinea pig model of spontaneous OA, a fibrous connective (FCT) was formed in its place [5] (Figure 1). Thus, the goal was to investigate the biomechanical behavior of cartilage, meniscus, and bone following removal of the IFP and compare it to the native joint.

## METHODS

All procedures were approved by the University's Institutional Animal Care and Use Committee and were performed in accordance with the NIH Guide for the Care and Use of Laboratory Animals. Male Hartley guinea pigs (n=8) were purchased at 2 months of age to allow acclimation for 4 weeks. Surgical removal of the IFP was performed at 3 months of age (prior to the development of OA) on one limb while the contralateral limb had a sham surgery.

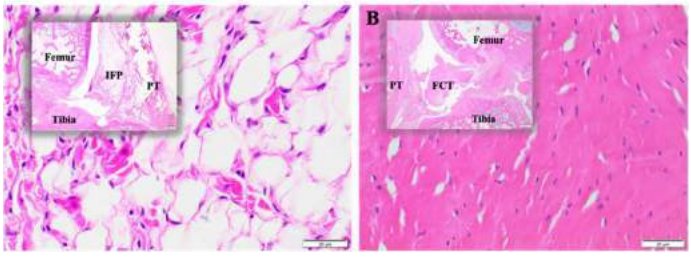


**Figure 1. Representative mid-sagittal H&E photomicrographs of a stifle joint from a sham control (A) and IFP removal (B) guinea pig. 40X objective for main photo; 2X objective for inset. (A) Control joint from 7-month-old guinea pig depicting the normal histoanatomic features of IFP in its native state. (B) Knee joint from a 7-month-old guinea pig, which demonstrates the dense, collagenous nature of the replacement FCT.**

Whole knee joints were scanned using a Bruker Skyscan 1276 for micro-computed tomography (uCT). Osteophytic bone was identified by its reduced bone mineral density compared to the native bone, as well as being outside the original joint margins. Osteophytes then manually outlined every 10 slides such that representative volumes could be determined.

Cartilage and menisci from both native IFP and FCT knee joints were subjected to indentation relaxation tests in a phosphate buffered saline bath to determine instantaneous and equilibrium moduli. The bath was mounted to a two degree of freedom camera mount and an X-Y stage to allow for the indentation surface to be oriented normal to the indenter tip. Both the femoral and tibial cartilage was indented on the medial and lateral plateaus, which is a location where there would be cartilage on cartilage contact. To test the cartilage, the tibia was potted distally and adjusted to indent perpendicular to the surface. The cartilage was assumed to be 0.5 mm thick on the femur and 0.75 mm

thick on the tibia and following a pre-load of 50 mN, indentation was conducted to 10% strain in 1 second and held for 420 second to reach equilibrium. The menisci were extracted off the tibial plateau at the anterior and posterior root attachments. They were then glued onto a plexiglass mounting plate to allow the proximal surface to be mounted perpendicular to the indenter tip. The medial and lateral menisci were indented at both the anterior and posterior locations. Menisci were assumed to be 1.2 mm thick and, following a preload of 50mN, menisci were indented to 10% strain (0.12 mm) in 1 second and held for 900 seconds to reach equilibrium. Hertzian contact between an elastic half space (meniscus) and a rigid sphere (indenter) was assumed [6,7]. A custom MATLAB algorithm (Mathworks, Natick, MA) was used to calculate the instantaneous and equilibrium moduli from the collected data.

## RESULTS

Osteophyte volume was significantly decreased in the limbs containing the replacement FCT compared to the contralateral limb (Figure 2). The equilibrium modulus of the medial hemijoint articular cartilage and the instantaneous modulus of the lateral hemijoint articular cartilage were significantly decreased in the FCT limbs compared to the contralateral limbs with the native IFP (Figures 3,4). The only significant change in meniscal properties between the FCT and IFP limbs was the medial posterior meniscus equilibrium modulus (Figure 5).

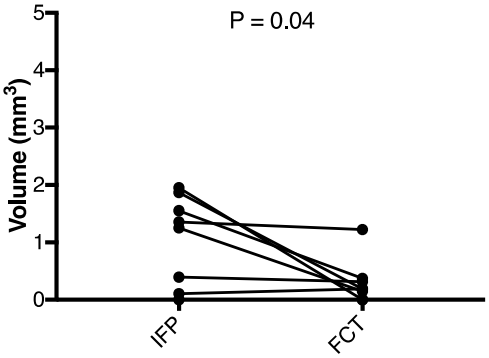


**Figure 2. Osteophyte volume for IFP and FCT limbs.**

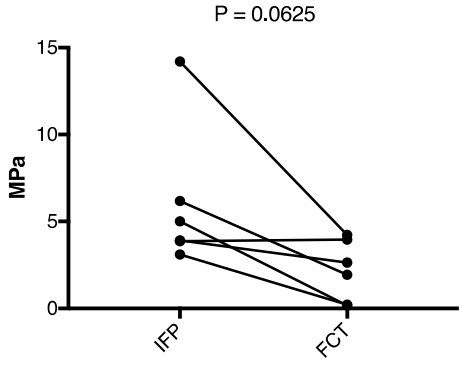


**Figure 3. Equilibrium modulus for the medial tibial plateau articular cartilage.**

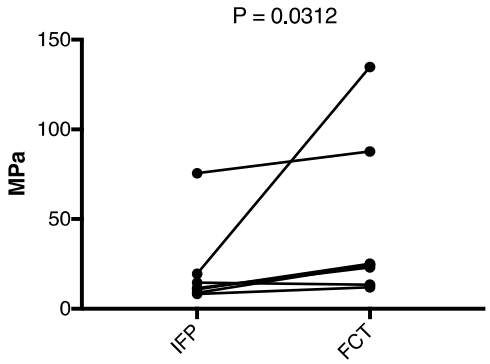


**Figure 4. Instantaneous modulus for the lateral tibial plateau articular cartilage.**

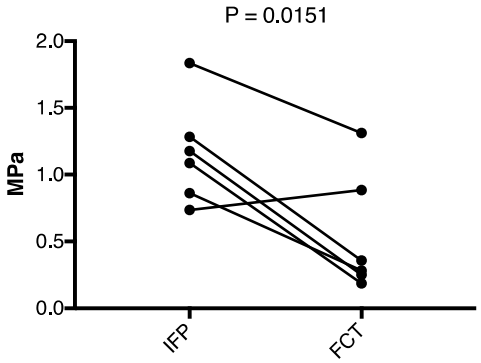


**Figure 5. Equilibrium modulus for the medial posterior region of the meniscus.**

## DISCUSSION

Removal of the native IFP and replacement by the FCT results in significant changes in the bone, cartilage, and menisci of the knee. The fact that the instantaneous and equilibrium modulus were decreased in the FCT-containing joint could imply an altered loading environment in these tissues, perhaps as a result of unloading of the of soft tissue of the joint in favor of more load through the FCT. This is the first data to report biomechanical changes in joint tissues following early removal of the IFP. The results of this study elude to the role of the IFP in OA and thus warrants further investigation as to the mechanism by which the IFP may influence joint health.


## ACKNOWLEDGEMENTS

NIH R21 AR073972 provided funding to support the acquisition, analysis, and interpretation of data.


## REFERENCES


[1] Clockaerts et al., *OA&C*, 18(7):876-882. 2010, [2]Santangelo et al., Horm Mol Biol Clin Investig, 26(2):97-108, 2016. [3]Macchi et al., *J. Anat.,* 233:146-154. 2018, [4]Bohnsack et al., *AJSM*, 32(8):1873-1880, [5] Afzali, et al., ORS, Phoenix, AZ, 2020. [6] Fischenich et al., *J. Biomech.*, 48(2):346-253,2015, [7] Li et al., *JOR*, 16(1):122-127, 1998.

# A DOPPLER-EXCLUSIVE NON-INVASIVE COMPUTATIONAL FRAMEWORK FOR PERSONALIZED VALVE DYNAMICS IN PATIENTS WITH AORTIC STENOSIS AND TRANSCATHETER AORTIC VALVE REPLACEMENT

**Nikrouz Bahadormanesh (1), Zahra Keshavarz-Motamed (1,2,3)**

(1) Department of Mechanical Engineering, McMaster University, Hamilton, Ontario, Canada

(2) School of Biomedical Engineering, McMaster University, Hamilton, Ontario, Canada

(3) School of Biomedical Engineering, McMaster University, Hamilton, Ontario, Canada

## INTRODUCTION

Transcatheter aortic valve replacement (TAVR) is an emerging treatment alternative to surgical aortic valve replacement that covers a range of patients suffering from moderate to severe aortic stenosis (AS). AS is one of the most common and serious cardiovascular problems and if left untreated, often leads to death. Surgical valve replacement remains the standard treatment method for AS, however, many patients suffering from this pathology are at a high risk for surgery and may suffer death or other complications [1].

TAVR is a growing alternative for intervention of AS patients across a broad risk spectrum and has lower death rates in severe cases compared to a surgical approach. Although TAVR has critical benefits for surgical high-risk patients, there are several drawbacks that patients may experience [2]. *Given the associated risks with TAVR, it is crucial to determine: how the implant will affect the cardiac function? when is the proper timing for intervention? Will TAVR improve or worsen the outcome of the patient [3].*

The condition of the heart valves heavily relies on the geometry and material properties of the leaflets as well as the interaction between the flow and the valve [3,4,5,6]. Valvular disease, including AS, often results in, or is a result of abnormal stress and strain distributions on aortic valve leaflets for both pre- and post-interventional cases.

In this study, we developed a highly innovative non-invasive Doppler-exclusive computational-mechanics framework that can function as a diagnostic tool to assess aortic valve dynamics in pre and post-TAVR states at no risk to the patients. The developed diagnostic tool is able to dynamically couple the local valve dynamics with the global circulatory system [4] which provides a platform for testing intervention scenarios (e.g. TAVR) and evaluating their effects.

## METHODS

We developed a Doppler-based computational mechanics diagnostic framework to non-invasively investigate the dynamic behavior of the aortic valve (e.g., transient 3-D distribution of stress and displacement field, 3-D deformed shape of leaflets, geometric orifice area, angular positions of leaflets, stiffness, etc.). This framework is based on a Doppler-based patient-specific lumped parameter algorithm (LPM) [4] along with a 3-D Doppler-based nonlinear (using anisotropic hyper elastic) finite element solver CalculiX with some supplements. The developed LPM algorithm [4] consists of a parameter estimation algorithm and a lumped-parameter model that includes several sub-models allowing analysis of any combination of complex valvular, vascular and ventricular diseases. A Doppler-based parametric method was developed to construct the 3-D geometry of the asymmetric aortic valve leaflets. Calculations of this Doppler-based computational mechanics diagnostic framework were validated against clinical Doppler echocardiography data in patients with AS.

## RESULTS

In patients with aortic stenosis, the healthy instantaneous LV pressure and/or volume are altered which ultimately overloads the heart. We investigated metrics of cardiac function (global hemodynamics) computed by our Doppler-based lumped parameter algorithm to determine the effects of TAVR on patient condition. The impacts of the TAVR on the aortic valve pressure gradient were not always be associated with reduction in LV function parameters, e.g., LV workload, normalized LV workload to stroke volume and maximum LV pressure. LV hemodynamics metrics worsened in some patients, and they were not significantly improved in the others (Figure 1, panel c)

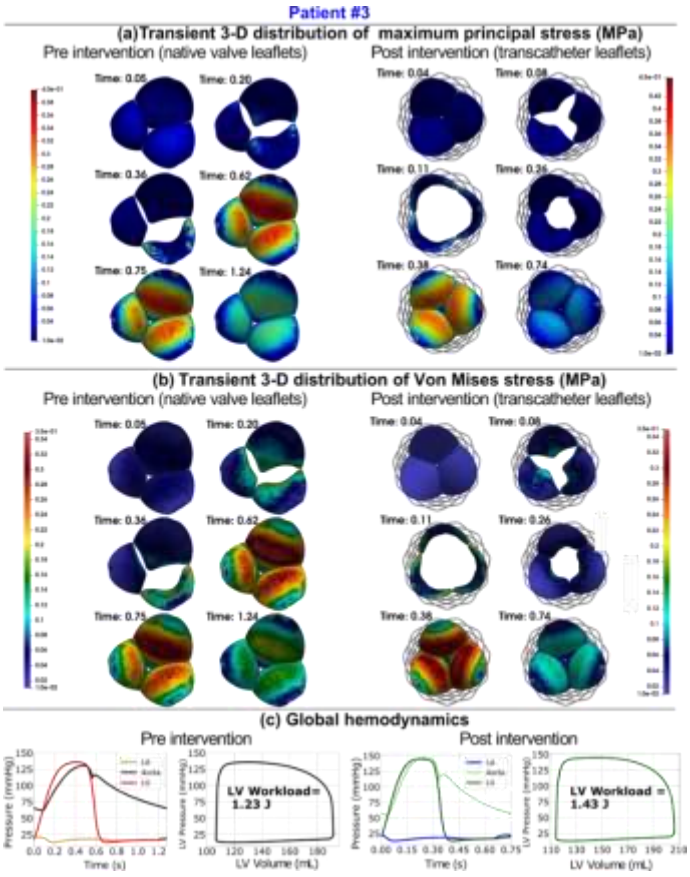


**Figure 1. Changes in valve dynamics and global hemodynamics in patient #3 between baseline and 90-day post-TAVR.**

Biomechanical factors resulting from hemodynamic loads are a common dominator of a variety of vascular diseases. Various mechanical metrics including 3-D Mises stress (the derivative format of principle stress), 3-D major principal stress (the maximum value of the three principal stresses), as well as displacement magnitude resulted from our Doppler-based computational framework reveled that TAVR worsened valve dynamics in some patients. Indeed, mechanical forces are the driving force behind the degeneration and failure of prosthetic heart valves and must be measured regularly to prevent the deterioration of the replacement valve.

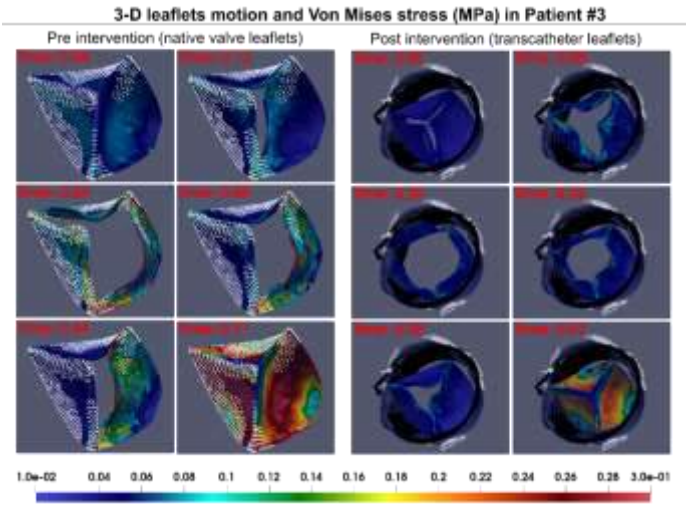


**Figure 2. 3D motion and 3D distribution contours of Mises stress in patient #3 at six time points throughout the cardiac cycle in both pre- and post-intervention states**

## DISCUSSION

TAVR does not always improve cardiac function metrics. LV hemodynamics metrics worsened in some patients, and they were not significantly improved in the others. TAVR does not always improve valve dynamics metrics. Valve dynamics post-intervention should be quantified and monitored to ensure the improvement of patient conditions and prevent any further complications. Improper evaluation of biomechanical valve features pre-intervention as well as post-intervention may result in harmful effects post-TAVR in patients including paravalvular leaks, valve degeneration, failure of TAVR and heart failure.


## ACKNOWLEDGEMENTS

This work was supported by NSERC Discovery Grant (RGPIN-2017-05349).


## REFERENCES


[1] Pibarot, P et al., *JACC Cardiovasc Imaging*, 8:340–360, 2015.
[2] Ben-Assa, E et al, *Sci Transl Med*, 1(509): eaaw0181, 2019.
[3] Keshavarz-Motamed Z, et al, *J Am Heart Assoc*, 9:e015063, 2020.
[4] Keshavarz-Motamed Z, *Sci Rep*, 10:1–19, 2020.
[5] Khodaei S, et al, *Sci Rep*, 11:10888, 2021.
[6] Khodaei S, *Int J Mech Sci*, 202–203:106506, 2021.

# PREDICTIVE URODYNAMICS OF BLADDER VOIDING USING MRI-BASED CFD: A PILOT STUDY

**Labib A. Shahid (1), Juan Pablo Gonzalez-Pereira (1), Cody J. Johnson (2), Yanheng Li (3), David Rowinski (3), Alejandro Roldán-Alzate (1,2,4)**

(1) Department of Mechanical Engineering, University of Wisconsin-Madison, Madison, WI, USA
(2) Department of Radiology, University of Wisconsin-Madison, Madison, WI, USA
(3) Convergent Science, Inc., Madison, WI, USA
(4) Department of Biomedical Engineering, University of Wisconsin-Madison, Madison, WI, USA

## INTRODUCTION

Benign prostatic hyperplasia (BPH) is the nonmalignant growth of the prostate, commonly observed in aging men. Lower urinary tract symptoms (LUTS) is the most common manifestation of BPH. Over 50% of men aged over 60 years suffer from BPH, and 15%-30% of these men have LUTS [1]. Multi-channel urodynamic studies are performed to measure bladder pressure and flow during voiding, and when coupled with 2D fluoroscopy, allows visualization of urine flow. However, these techniques are invasive and do not provide sufficient information on biomechanical properties, bladder anatomy, and detrusor muscle function in BPH/LUTS [2]. Image-based computational fluid dynamics (CFD) has been used to study biomechanics in cardiovascular diseases [3]. Our group has investigated MRI-based CFD, with a focus on cardiac flows as well [4]. In this study, we expand the tools we developed and apply them to urinary flows. Here, we present an MRI-based computational method that enables in-silico CFD simulation of bladder voiding.

## METHODS

In-vivo MRI studies were performed on two male volunteers with no history of LUTS following an IRB-approved HIPAA-compliant protocol. Subject 1 was 29 years old and Subject 2 was 55 years old. Both subjects were scanned on a clinical 3T scanner (Premier, GE Healthcare, Waukesha, WI, USA) using 3D Differential Subsampling with Cartesian Ordering (DISCO) Flex sequence. Before the scan, the subject was equipped with a condom catheter to allow the void event while scanning, and volumetric dynamic images of the bladder were collected throughout the void. The MR images were manually segmented using semiautomatic segmentation software Mimics and 3-matic (Materialise NV, Leuven, Belgium), providing an anatomical geometry of the bladder at each time instant, i.e., each MR temporal phase during the voiding event. Each anatomical geometry was represented as a surface, composed of discrete triangular elements. We developed a novel algorithm that maps one surface to another by calculating displacements and building a transformation matrix. Figure 1 shows a schematic of the mapping algorithm.

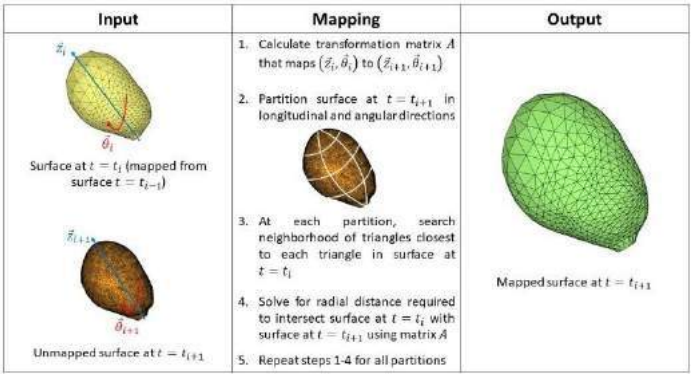


**Figure 1: Steps of the novel mapping algorithm.**

This algorithm is executed between each MR time phase and provides surfaces of the bladder wall that have the same topology. The surfaces in this sequence are applied as a moving wall boundary condition into the CFD software package CONVERGE 3.1 (Convergent Science, Inc., Madison, WI, USA), which automatically constructs the finite volume mesh according to the instantaneous surface position. The mesh consisted of 1 mm × 1 mm × 1 mm cubic elements. The Pressure-Implicit with Splitting of Operators (PISO) algorithm was used as the Navier-Stokes solver. Pressures at the outlet, i.e., bladder neck, were determined from separate CFD simulations of the urethra anatomies. Wall motion was set as the transition from one mapped surface to the next, and the motion rate was determined by the time resolution of the MRI scan. Figure 2 illustrates the stages of our methods, starting from

in-vivo MRI to CFD. Tecplot 360 EX (Tecplot, Inc., Bellevue, WA, USA) was used to visualize and quantify the in-silico results.

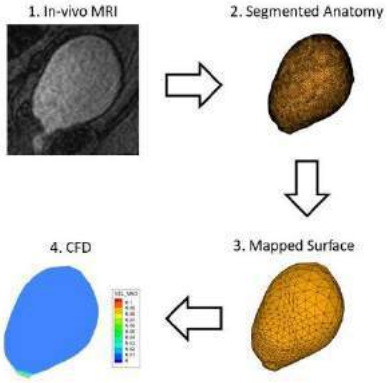


**Figure 2: Schematic of methods.**

## RESULTS

Both healthy subjects were successfully imaged and time-resolved contrast-enhanced images of the bladder during voiding were obtained in a single MRI session for each subject. The time resolution was 3.7 seconds. The total void times were 74 seconds for Subject 1 and 81 seconds for Subject 2. After implementing the mapping algorithm, we executed two CFD simulation for the two subjects using MRI-based wall motion. Velocity, pressure, and wall shear stress were calculated from CFD results and are visualized in Figures 3 and 4.

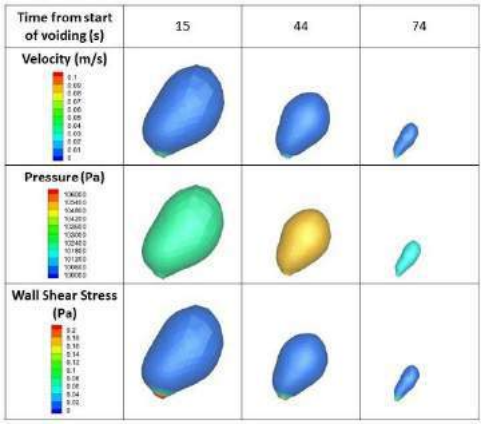


**Figure 3: CFD results for Subject 1.**

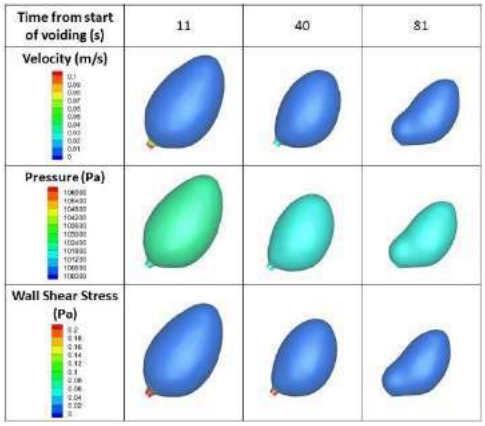


**Figure 4: CFD results for Subject 2.**

CFD predicted the maximum urine flow rate, $Q_{max}$, and detrusor pressure at maximum flow, $P_{det}Q_{max}$. For Subject 1, $Q_{max}$ = 19.23 $cm^3/s$ and $P_{det}Q_{max}$ = 38.45 $cmH_2O$, and for Subject 2, $Q_{max}$ = 15.12 $cm^3/s$ and $P_{det}Q_{max}$ = 9.13 $cmH_2O$. Values for Bladder Outlet Obstruction Index (BOOI) and Bladder Contractility Index (BCI) were calculated. These indices are defined as flows, BOOI = $P_{det}Q_{max}$ - 2*$Q_{max}$ and BCI = $P_{det}Q_{max}$ + 5*$Q_{max}$, where $P_{det}Q_{max}$ is in $cmH_2O$ and $Q_{max}$ is in $cm^3/s$. For Subject 1, BOOI = -0.01 and BCI = 134.6, and for Subject 2, BOOI = -21.11 and BCI = 84.73. The CFD simulations were executed on a high performance computing cluster with 40 CPU cores. The runtime was about 4 hours per simulation.

## DISCUSSION

The goal of this study was to implement a non-invasive methodology to comprehensively assess bladder biomechanics using MRI-based CFD. Previously, bladder biomechanics, including BOOI and BCI, were measured using invasive multi-channel urodynamics. The in-vivo MRI results only showed real-time images of the bladder at different instants but provided no information on urine flow dynamics or bladder contraction dynamics. Coupling CFD with MRI has enabled a non-invasive method to characterize bladder biomechanics by quantifying and visualizing urodynamics. To impose bladder motion in our CFD simulation, we developed an algorithm that maps the bladder wall surfaces (from MR images) at successive time phases. Execution of CFD simulations is a result of the successful surface mapping algorithm. The subjects in this study did not present BPH/LUTS and our results show no obstruction in their bladder outlet or urethra since BOOI < 20. Subject 1 showed normal bladder contractility because BCI was between 100 and 150. Subject 2 showed impaired bladder contractility because BCI < 100. This is due to the subject's inability to void completely while in the scanner. Image-based CFD has primary focused on cardiovascular flows. We expanded the computational tools to simulate urinary flows and introduced a new application for MRI-based CFD.


## ACKNOWLEDGEMENTS

The authors acknowledge support from the NIH (R01 DK126850-01).

GE Healthcare, which provides research support to the University of Wisconsin.

UW-Madison Center For High Throughput Computing (CHTC) in the Department of Computer Sciences.


## REFERENCES


[1] A. Thorpe and D. Neal, "Benign prostatic hyperplasia," in *Lancet*, Apr. 2003, vol. 361, no. 9366, pp. 1359–1367. doi: 10.1016/S0140-6736(03)13073-5.

[2] R. Pewowaruk, D. Rutkowski, D. Hernando, B. B. Kumapayi, W. Bushman, and A. Roldán-Alzate, "A pilot study of bladder voiding with real-time MRI and computational fluid dynamics," *PLoS ONE*, vol. 15, no. 11 November, p. e0238404, Nov. 2020, doi: 10.1371/journal.pone.0238404.

[3] A. L. Marsden and J. A. Feinstein, "Computational modeling and engineering in pediatric and congenital heart disease," *Current Opinion in Pediatrics*, vol. 27, no. 5. NIH Public Access, pp. 587–596, Jan. 01, 2015. doi: 10.1097/MOP.0000000000000269.

[4] R. Pewowaruk and A. Roldán-Alzate, "4D Flow MRI Estimation of Boundary Conditions for Patient Specific Cardiovascular Simulation," *Annals of Biomedical Engineering*, vol. 47, no. 8, pp. 1786–1798, 2019, doi: 10.1007/s10439-019-02285-2.

# REAL-TIME MRI-BASED COMPUTATIONAL MODELING OF URINARY FLOW IN URETHRA

**Labib A. Shahid (1), Juan Pablo Gonzalez-Pereira (1), Cody J. Johnson (2), Alejandro Roldán-Alzate (1,2,3)**

(1) Department of Mechanical Engineering, University of Wisconsin-Madison, Madison, WI, USA
(2) Department of Radiology, University of Wisconsin-Madison, Madison, WI, USA
(3) Department of Biomedical Engineering, University of Wisconsin-Madison, Madison, WI, USA

## INTRODUCTION

Benign prostatic hyperplasia (BPH) is the nonmalignant growth of the prostate, commonly observed in aging men. Lower urinary tract symptoms (LUTS) is the most common manifestation of BPH. Over 50% of men aged over 60 years suffer from BPH, and 15%-30% of these men have LUTS [1]. Standard imaging techniques to assess urethral abnormalities are retrograde urethrography (RUG) and voiding cystourethrography (VCUG) [2]. However, both RUG and VCUG have become uncommon and the limited exposure of radiologists to these examinations can make it challenging to interpret results [3]. Image-based computational fluid dynamics (CFD) has been used to study biomechanics of cardiovascular diseases [4]. Our group has investigated MRI-based CFD with a focus on cardiac flows as well [5]. In this study, we expand the tools we developed and apply them to urinary flows. The purpose of this study was to develop and implement a non-invasive MRI-based computational methodology for the simulation of urinary flow inside urethra.

## METHODS

In-vivo MRI studies were performed on five male subjects (51 ± 19 years old) with no history of BPH/LUTS following an IRB-approved HIPAA-compliant protocol. Subjects were scanned on a clinical 3T scanner (Premier, GE Healthcare, Waukesha, WI, USA) using 3D Differential Subsampling with Cartesian Ordering (DISCO) Flex sequence. 15 minutes prior to the start of the imaging session, 1/3 of a single weight-based dose (0.1 mmol/kg) of gadolinium-based contrast was slowly hand injected intravenously outside and the subjects were asked to walk around to ensure enhancement of the urine. Right before the scan, each subject was equipped with a condom catheter to allow the void event while scanning, and volumetric dynamic images of the bladder and urethra were collected throughout the void. The MR images were manually segmented using the semiautomatic segmentation software packages Mimics and 3-matic (Materialise NV, Leuven, Belgium). For the computational simulations, anatomical models of the urethra at the moment of maximum flow were generated from the segmented images for all subjects. To determine, the inlet boundary conditions, bladder volumes were segmented and the urinary flow rate in the urethra was calculated as the rate of change in volume of the bladder over time. The outlet boundary condition was atmospheric pressure. The CFD simulations were executed on software package CONVERGE 3.1 (Convergent Science, Inc., Madison, WI, USA) [6]. Tecplot 360 EX (Tecplot, Inc., Bellevue, WA, USA) was used to visualize the in-silico results. Figure 1 shows age, MR images, urethral anatomy, and calculated flow rates of all subjects.

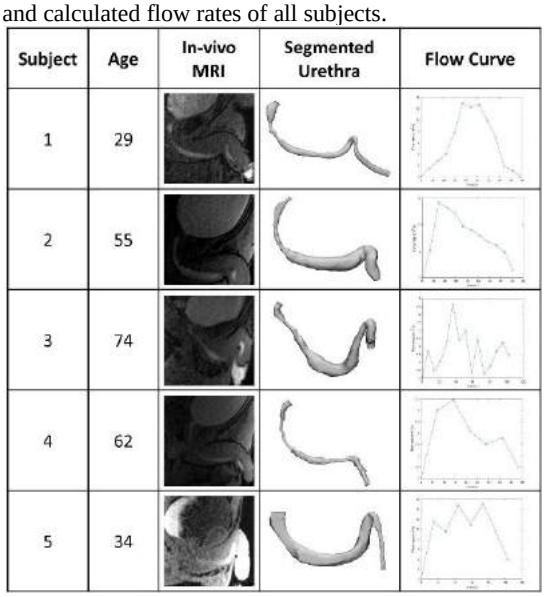


**Figure 1: Age, MRI scans, urethra anatomies, and flow rates.**

## RESULTS

Contrast-enhanced MRI studies provided real-time anatomies of urethra and bladder during voiding. The flow rates and geometries extracted from the in-vivo studies were used to successfully simulate the urine flow inside each subject's urethra during voiding. The CFD simulation results are visualized in Figure 2.

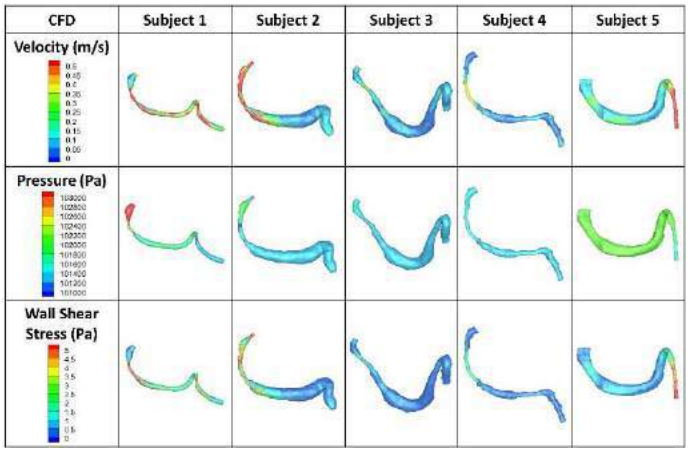


**Figure 2: Velocity, pressure, and wall shear stress from CFD.**

The flow curves in Figure 1 show that Subjects 1 and 2 voided the largest volumes. This is reflected in our CFD results, with these two subjects having the highest velocities. For Subjects 1 to 4, the membranous urethra was the narrowest section of the urethra, and that corresponded to the peak wall shear stress. For Subject 5, the peak wall shear stress was at the penile urethra, which was the narrowest section for this subject. Furthermore, CFD predicted the pressure drops in the prostatic, membranous, and penile urethra for all subjects. The pressure drops are plotted in Figure 3.

In Subjects 1 and 4, the pressure drop across the membranous urethra is larger than pressure drop across prostatic urethra. In Subjects 2 and 3, the pressure drop across the prostatic urethra is larger. For Subjects 1 to 4, the pressure drop in the penile urethra is the smallest, corresponding to the thickest section of the urethra for these subjects. Since the penile urethra is the narrowest section for Subject 5, the pressure drop across the penile urethra is the largest.

## DISCUSSION

Real-time MRI data alone does not provide any insight into the flow dynamics of urine. Our method combines MRI of the urinary system with CFD to present a computational methodology that quantitatively and qualitatively characterizes urine flow in the urethra. Furthermore, the MRI-based CFD simulation calculates the pressure required at the bladder neck (start of the urethra) to flow urine at a prescribed rate. Information on the pressure at the bladder neck is useful because it can be imposed as the outlet boundary condition when simulating the bladder voiding process. Unlike the current procedures used to measure urine flow in the urethra, namely RUG and VCUG, our MRI-based approach is non-invasive and provides not only anatomical but functional information not available with any other diagnostic method.

This study shows that MRI-based CFD can be expanded to study pathological flows in the urinary system. Comparing urine flow dynamics in healthy subjects versus subjects with BPH/LUTS is of interest in future studies. Our simulations assumed the urethra to be rigid, which is anatomically unrealistic. Future studies should include the motion of the urethra wall in their model extracted from the real time MR images and fluid-structure interaction. Further studies should compare results from our method with results from benchmark clinically used techniques.

## ACKNOWLEDGEMENTS

The authors acknowledge support from the NIH (R01 DK126850-01).

GE Healthcare, which provides research support to the University of Wisconsin.

UW-Madison Center For High Throughput Computing (CHTC) in the Department of Computer Sciences.

## REFERENCES

[1] A. Thorpe and D. Neal, "Benign prostatic hyperplasia," in *Lancet*, Apr. 2003, vol. 361, no. 9366, pp. 1359–1367. doi: 10.1016/S0140-6736(03)13073-5.

[2] J. C. Flanagan, R. Batz, S. M. Nordeck, G. E. Lemack, and C. Brewington, "Urethrography for assessment of the adult male urethra," *Radiographics*, vol. 38, no. 3. pp. 831–832, 2018. doi: 10.1148/rg.2018170131.

[3] P. Bach and K. Rourke, "Independently interpreted retrograde urethrography does not accurately diagnose and stage anterior urethral stricture: The importance of urologist-performed urethrography," *Urology*, vol. 83, no. 5, pp. 1190–1194, 2014, doi: 10.1016/j.urology.2013.12.063.

[4] A. L. Marsden and J. A. Feinstein, "Computational modeling and engineering in pediatric and congenital heart disease," *Current Opinion in Pediatrics*, vol. 27, no. 5. NIH Public Access, pp. 587–596, Jan. 01, 2015. doi: 10.1097/MOP.0000000000000269.

[5] R. Pewowaruk and A. Roldán-Alzate, "4D Flow MRI Estimation of Boundary Conditions for Patient Specific Cardiovascular Simulation," *Annals of Biomedical Engineering*, vol. 47, no. 8, pp. 1786–1798, 2019, doi: 10.1007/s10439-019-02285-2.

[6] K. J. Richards, P. K. Senecal, and E. Pomraning, "CONVERGE 3.1." Convergent Science, Madison, WI, 2021.

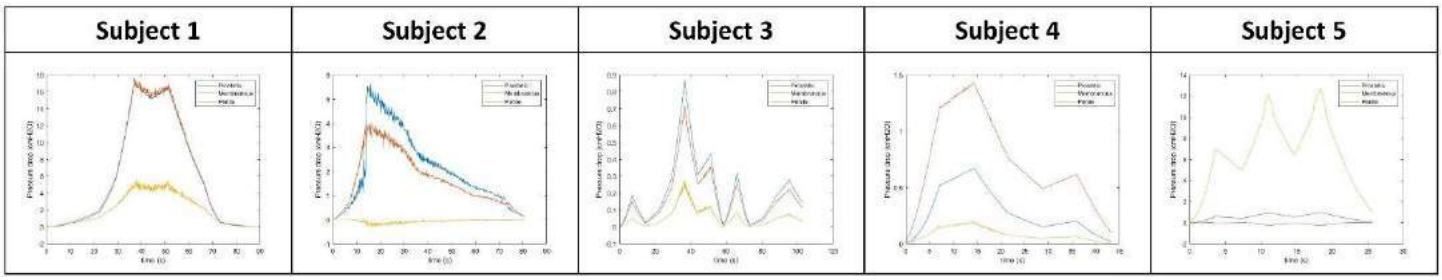


**Figure 3: Pressure drops predicted from CFD simulations.**

SB³C2022
Summer Biomechanics, Bioengineering and Biotransport Conference
June 20-23, Eastern Shore, MD, USA

# CORRELATION BETWEEN ANOSMIA AND AIRFLOW IN THE NASAL CAVITY

**Shashwat Shah (1), Zach Soler (2), Ethan Kung (1,3)**

(1) Mechanical Engineering Department, Clemson University, Clemson, South Carolina, USA
(2) Otolaryngology Department, Medical University of South Carolina, Charleston, South Carolina, USA
(3) Bioengineering Engineering Department, Clemson University, Clemson, South Carolina, USA

## INTRODUCTION

Anosmia is a medical condition where the patient loses their sense of smell. It can be temporary or permanent; a permanent and severe condition can lead to a loss of sense of taste. Identifying the causes of anosmia can help doctors diagnose it more accurately and decide operational procedures accordingly. Researchers have studied the effect of odorant particles in the nasal cavity by different experimental and numerical methods. With evolving technology in 3D imaging and segmentation, creating an anatomically accurate representation of the Nasal Cavity is now more accessible than ever. With the help of the latest meshing techniques, a very fine and precise mesh can be generated for simulation. This study aims to correlate anosmia with airflow in the olfactory cleft region simulated using computational fluid (CFD) dynamics.

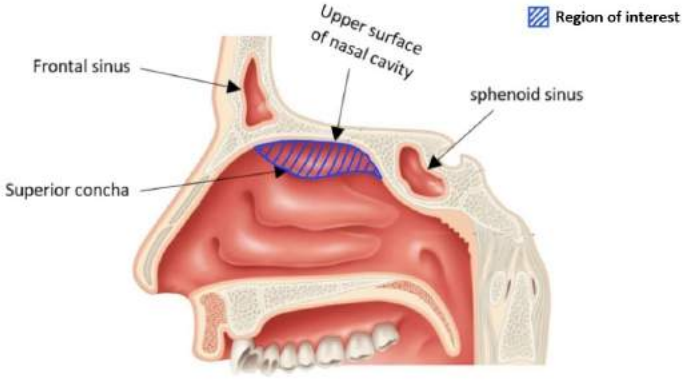


## METHODS

6 Test subjects of different ages and genders were chosen, three each with and without anosmia. In this study, we performed CFD simulations to simulate realistic air flow conditions using ANSYS Fluent. Boundary conditions were prescribed based on the flow rate of normal breathing for an adult human, with the inlet being 5 m/s velocity and outlet being zero-gauge pressure. In all cases, convergence criteria of $10^{-4}$ residual for continuity equation and velocities were reached with the k-omega SST turbulence model. Since olfactory sensors are located in the olfactory bulb, we analyzed the flow data within the corresponding region bounded by the upper surface of nasal cavity (superior), the superior concha (inferior), the frontal sinus (anterior) and the sphenoid sinus (posterior) as shown in Fig-1. The study's primary objective was to find patterns in the flow parameter that can differentiate between people with and without anosmia.

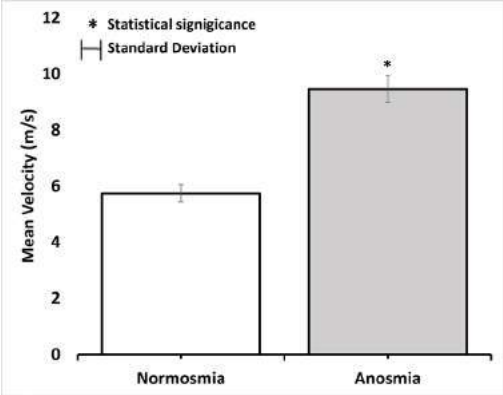

## RESULTS

Flow velocity provides a good surrogate on how long odorant particles may stay in the olfactory cleft region without the need for calculating more resource-intensive residence time. Nasal cavities associated with anosmia demonstrated a statistically significant increased average velocity (9.4667 m/s) near the olfactory bulb region, compared to those not associated with anosmia (5.74 m/s, $p = 0.0029$) (Fig-2). This represents a ~60% increase in flow velocity for the subjects with anosmia than in those without.

## DISCUSSION

Higher velocity implies less contact between odorant particles and olfactory sensors, leading to partial or total loss of smell. Going forward, further examination of other flow parameters can give more insights on flow patterns inside the nasal cavity with deformities and assist anosmia diagnosis and treatment planning.

## ACKNOWLEDGEMENTS

We thank Mr. Maitreya Bhagwat for his help with meshing process in HyperMesh.

SB³C2022
Summer Biomechanics, Bioengineering and Biotransport Conference
June 20-23, Eastern Shore, MD, USA

# EXTRACTING AND BUILDING WITH THE ENGINEERING PRINCIPLES OF KIDNEY DEVELOPMENT

**John M. Viola (1), Catherine M. Porter (1), Jiageng Liu (1), Ananya Gupta (1), Mariia Alibekova (1), Louis S. Prahl (1), Alex J. Hughes (1,2,3)**

(1) Department of Bioengineering, University of Pennsylvania, Philadelphia, PA, USA
(2) Department of Cell & Dev. Bio., University of Pennsylvania, Philadelphia, PA, USA
(3) Institute for Regenerative Medicine, University of Pennsylvania, Philadelphia, PA, USA

## INTRODUCTION

The intricate branching of the kidney's urinary collecting duct tree occurs in response to tightly choreographed cues passed between ureteric epithelial tubules and surrounding tissue layers during development. The tips of this epithelial network are then the engines that drive formation of the 200,000-2 million nephron filters present in adult kidneys. However, the engineering principles governing the remarkable development of this tubule network are not well understood. Thus, there is massive potential to study and apply new engineering rules that would shed light on the wide variability in nephron number between individuals, which correlates with adult disease, and to build large enough kidney tissues for functional replacement.

## METHODS

All mouse experiments followed NIH guidelines and were approved by the Institutional Animal Care and Use Committee of the University of Pennsylvania. Embryos were collected from timed pregnant CD-1 mice (Charles River) at developmental stages between embryonic day (E)14 and E18, dissected and processed for live analysis or studied by confocal immunofluorescence. Physical modeling was performed in the Kangaroo Physics environment in Rhino 3D software.

Kinomorphs were created through photolithographic DNA-programmed assembly of cells (pDPAC). Briefly cells were incubated with lipid-ssDNAs and attached to polyacrylamide substrates bearing complementary ssDNAs photopatterned onto them. These cell patterns were then transferred to Collagen-1/Matrigel hydrogel sheets in microfluidic flow cells, before floating them into culture for cell-directed folding and tubule formation. Model-guided design of morphogenesis trajectory was performed in MATLAB and Kangaroo Physics.

## RESULTS

Epithelial organs perform diverse functions - lung alveoli exchange gases, kidney tubules exchange water and ions, and mammary acini secrete milk. However, little is known about how developmental constraints and compromises affect adult organ function per unit volume.

However, while some organs like the lung fill 3D space during branching, ureteric branching occurs at the kidney surface. This should create a conflict between the available organ surface area and exponentially increasing tip number. How then does the kidney navigate this conflict?

We first cast tubule network formation in the developing mouse kidney as a packing problem using organ explants and physical models [1]. Our data indicate that developing kidneys visit only a narrow range of possible tubule packing solutions and highlight two classes of packing defects – tip burial within deeper tissue layers or "short circuits" through adjacent tip fusion – examples of which can be found in published literature. Furthermore, they suggest that internal, radially oriented forces on tubules are required to avoid these defects and for tubule trees to resolve into vertically packed arrays. We validate this by perturbing live kidney explants and matching outcomes to our physical models.

We next outline a route to synthetically create ureteric tubule networks by drawing parallels between programmed strain in micropatterned tissues and the ureteric branching program [2]. We reconstitute these mechanics in tissue scaffolds that progressively encode 3D extracellular microenvironments by programmed shape change.

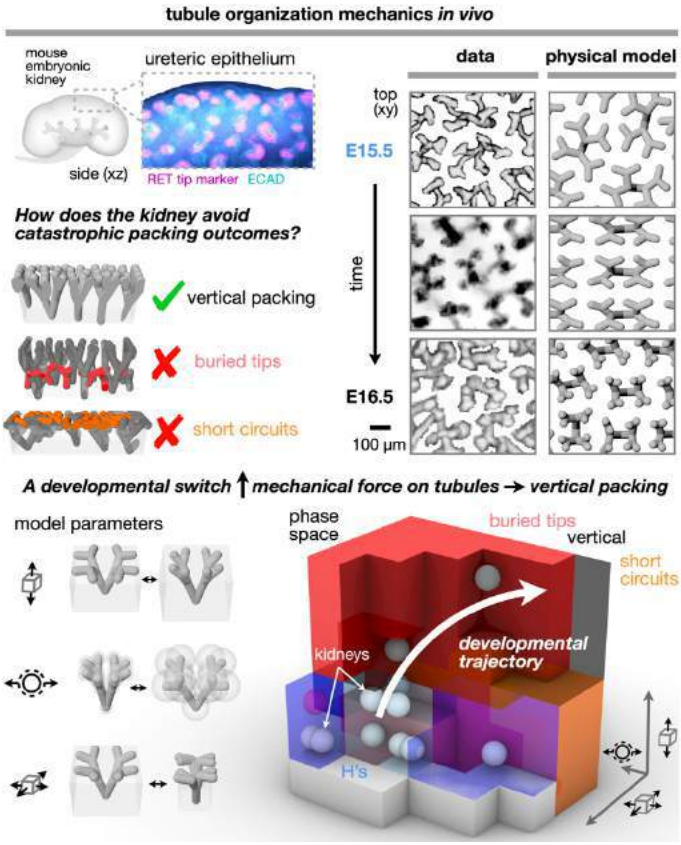


**Figure 1: The ureteric epithelium forms a tree-like network, where tips induce and fuse with nephrons. We studied this as a packing problem, discovering several phases of packing geometry, including two forbidden ones found in mutants. We show that active mechanical tension on tubules is required for developing kidneys to traverse the packing phase space without entering forbidden phases.**

We first noted that mechanical compaction of floating sheets of Collagen-1/Matrigel ECM by randomly seeded MDCK kidney epithelial cells tended to lead to fusion of nearby spheroids and tubule formation. We therefore sought to control the spatial patterning of tubules formed by self-organization through the initial cell pattern by pDPAC. Creating this photolithographic cell assembly technology allowed us to pattern millions of adhesive ssDNA spots over large areas (~size of a postage stamp). Transfer of adhered cells to ECM sheets then creates folds due to cell traction mechanics in prescribed regions, generating mountain or valley folds according to custom mechanical modeling. In analogy with origami paper folding, we generated complex fold networks called flashers that emanate from a single point, similar to the ureteric collecting duct network. Indeed, patterned MDCKs condensed and created polarized and lumenized tubules along hundreds of folds, verified by immunofluorescence staining. We are currently extending this technology for iPSC-derived ureteric epithelial and early nephron lineages, towards production of long-range ureteric networks spanning cm length-scales. These arrays have strong potential applications in iPSC-derived models of human kidney disease, and for kidney replacement therapies.

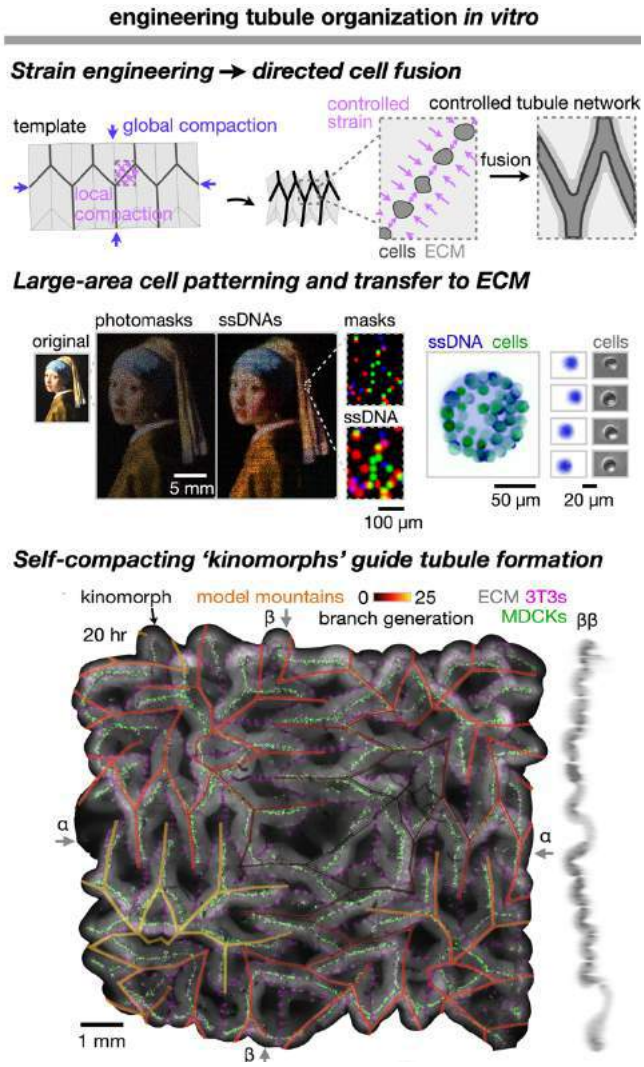


**Figure 2: Synthetic creation of cm-scale kidney tubule networks in "kinomorphs" – autonomous shape-change hydrogels driven by active cell mechanics. Cells are patterned precisely and at massive scale by pDPAC into ECM sheets. Cells actuate folding and formation of tubule niches at creases in the sheet, and self-organize as polarized and lumenized tubule networks.**

## DISCUSSION

By integrating microfluidic cell and matrix patterning, kinematic models, and tubule engineering, we describe a vision for encoding long-range patterning in next-generation kidney organoids.


## ACKNOWLEDGEMENTS

We would like to thank Hughes lab members and instructors and students of the 2021 MBL Embryology. We are grateful K. Sasaki, and Y. Sakata for technical assistance with kidney dissections. This work was supported by NIH grants F32 to LSP, T32 to JMV, R35 MIRA to AJH; NSF GRFP to CMP, NSF CAREER award to AJH.


## REFERENCES


[1] Prahl, L.S. et al., *BioRxiv*, 2021.
[2] Viola, J.M. et al., *Adv. Mater.*, 2002195, 2020.

# TWO WAY COUPLED FSI ANALYSIS OF PATIENT'S SPECIFIC STENOSED LEFT CORONARY ARTERY (LCA) WITH MULTIPHASE PULSATILE BLOOD FLOW

**Abdulgaphur Athani (1), Nik Nazri Nik Ghazali (2), Irfan Anjum Badruddin (3)**
**Correspondence email: althani0102@gmail.com**

(1) Mechanical Engineering, University of Malaya, Kuala Lumpur, Kuala Lumpur, Malaysia
(2) Mechanical Engineering, University of Malaya, Kuala Lumpur, Kuala Lumpur, Malaysia
(3) Mechanical Engineering, King Khalid University, Abha, Kingdom of Saudi Arabia

## INTRODUCTION

In developed and developing countries, atherosclerotic coronary artery disease is a significant cause of illness and death due to cardiac arrest [1]. Atherosclerosis shows the primary distribution, implying that various parameters caused by blood flow can contribute towards its development. Coronary arteries are a clinically important anatomical region because of their high risk of developing atherosclerotic plaque, the constriction of coronary arteries, which affects cardiac perfusion, and the related risk of heart failure. The synchronised presence of double plaques and disturbed flow in anatomical regions with more complex geometries, such as arterial bifurcations, has indicated that hemodynamic (HD) stresses play a significant role in atherosclerosis pathogenesis. In this context, computer-aided engineering (CAE) in connection with diagnostic imaging (CT-scan), which enables patient-specific computational fluid dynamics (CFD) and fluid structure interaction (FSI) simulations and other computational modelling [2] were implemented, that provides a broad application for identifying potential links between local flow patterns, RBC behaviours, artery wall elasticity [3]. The objective of this research was to perform a preliminary CFD on the impact of using two way coupled FSI simulations on HD near wall as well as intravascular flow descriptors on the reconstructed patient's specific left coronary artery. No study has previously conducted by considering stenosis with multiphase (RBC and Plasma) pulsatile blood flow in LCA with side branches. The syndrome associated with this disease occurs at rest and with a temporary alteration of the electrocardiogram (ECG). However, with the patients involved; may or may not have coronary atherosclerosis, may have stable and unclear data, but they encountered ischemia, atria and ventricles block, and coronary heart death in extreme cases were also found [4].

## METHODS

The 2D images of CT scan (DICOM formatted) report converted into 3D model using image processing software (**MIMICS Materialise NV, a Belgian)**. The patient's pulsatile blood flow given as inlet boundary condition and outlet is maintained as outflow. The carreau non-Newtonian viscosity model is preferred for the simulation of LCA [3]. The FSI is created between blood domain and wall of elastic artery. The frictionless support was assigned at outer area of artery wall structure. The two ways coupled FSI analyses transfers the forces initially which occurred initially from blood domain to target defined structure and vice versa. The governing equations are solved for LCA model using software **(ANSYS Inc. Canonsburg, PA, USA).**

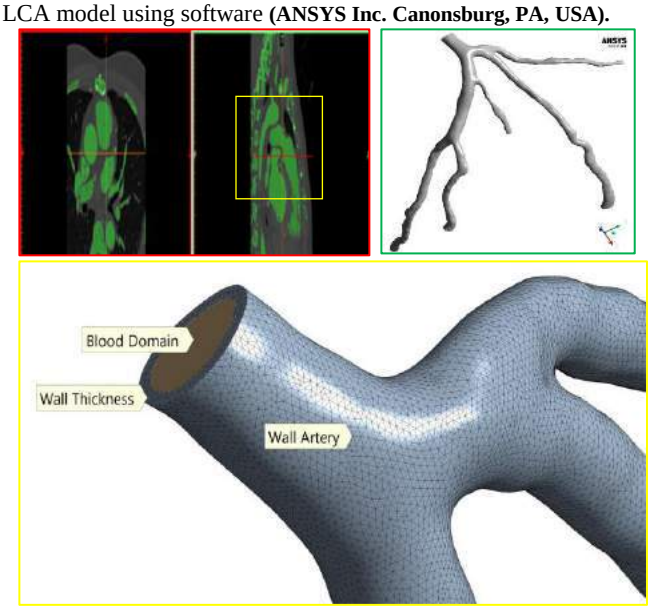


**Figure 1: a)2D CT-Scanned data in MIMICS window (Red outline); b).stl format reconstructed LCA 3D-model(Green**

**outline); c) Fluid and Solid mesh model's close-up view (Yellow outline labeled) with tetrahedral elements of LCA model.**

***Material properties:*** The structural properties of the arterial wall required for establishing FSI simulations and the fluid properties mimicking blood composed of blood Plasma and RBCs are adopted from an earlier study [3].

**RESULTS AND DISCUSSION**

In the current study, hemodynamic parameters such as Velocity, WSS, and pressure are calculated for the patient's left coronary stenosed artery. The structural results like deformation and von-misses stresses were also estimated for the flexible artery wall.

As mentioned before, the current analysis objectives are to simulate left coronary artery model with the FSI model. The pressure drop was extreme across the stenosis area compared to other regions of artery model. The velocity streamlines represent the flow direction of mimic of blood with respect to irregular diameter of LCA. The results show that, high areas of stenosis regions have high blood velocity (~3.59m.s) due to reduction of diameter in artery. It was also observed that, velocity streamlines are visible more after the exact stenosed area which is shown in square box in fig 2a. The maximum pressure drop was found at high stenosed region by 16217.54 to 6357.43 Pa. whereas a slight difference in wall pressure was noted across the second bifurcation regions as shown in fig 2b.

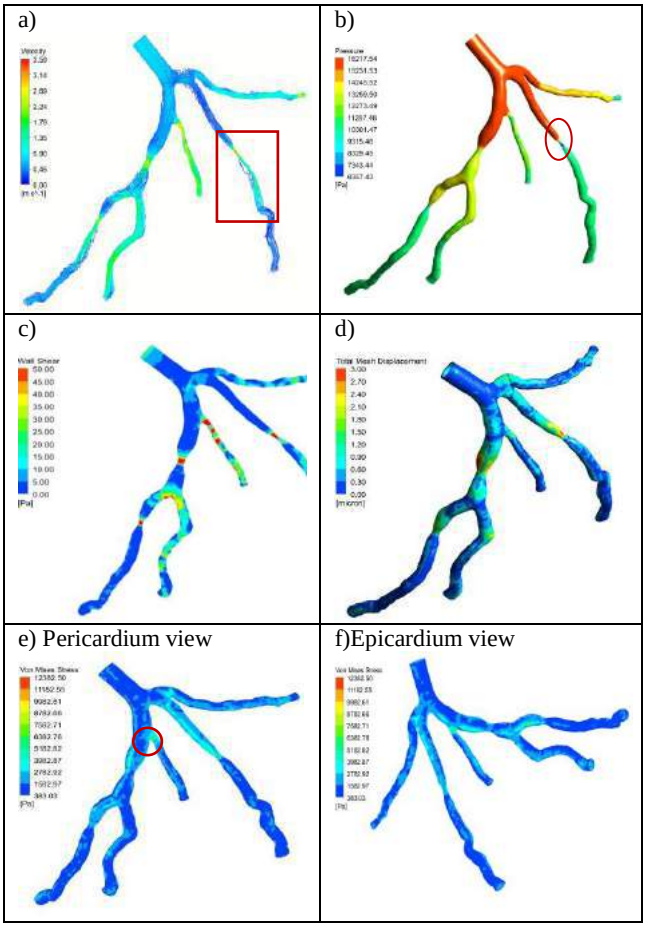


**Figure 2: a) Velocity streamlines; b) Wall Pressure; c) Wall Shear Stress (WSS); d) Displacement e) and f) Von-misses stresses for Epicardium and Pericardium views respectively.**

The wall shear stress is an important factor in determining the artery's strength, and it's thought that a larger wall shear stress may aid in arterial wall rupture. The cumulative WSS in the segmented left coronary artery (LCA) varies slightly depending on the artery model's area decrease (percentage of stenosis). It is observed that, the highest WSS at the high area stenosis was found in the range of 40 to 50 Pa as shown in fig 2c. At the bifurcation or compared to LAD and LCx branches the WSS at $LC_X$ regions are more because of its more complex artery. The side branches LAD and $LC_X$ also plays important role hence it is necessary to simulate always the complete model to achieve the accurate results.

The wall structure results help to determine the initiation of cracks in the artery models. The various results can predict the failure of artery wall such as Deformation and von-misses stresses. In the present study we have also calculated the deformation and von-misses stress for LCA model. It is clearly visible that, the maximum deformation of 3µm is observed before the highest stenosed region. Whereas at smaller reduction area or less stenosed artery areas the deformation is negligible that indicates the less chances of rupture of artery compared to the highest stenosed surrounded area as shown in fig 2d.

The blood flows inconsistently if there is stenosis in the artery. The wall is flexible elasticity properties hence the future study for crack initiation will be more important sector to determine the artery wall failures.

The von-misses stresses are also evaluated in the present case. The von-misses stresses are highest at before the stenosed areas. The highest von-misses observed are at the bifurcation area which is around 5182.82 Pa and lowest of 383.03 Pa at the ends of artery where the pressure is lesser as shown in figure 2e and 2f. There is additional advantage of multiphase blood flow simulations compared to single phase blood flow. This method gives the clear results for two separate fluids which are present in the whole blood (such as RBC and Plasma volume fractions) [3].

As a result, it is concluded that a large increase in velocity and a recirculation region around the stenosis may lead to stenosis growth and development. As a result, artery wall results play a crucial part in accurate WSS estimations. Furthermore, stenosis of greater degree may necessitate an emergency interventional therapy to cure the condition.

**ACKNOWLEDGEMENT**

No any funding or financial support provided for this research work.

**REFERENCES**

[1] Okrainec, K., Banerjee, D.K. and Eisenberg, M.J., 2004. Coronary artery disease in the developing world. *American heart journal*, *148*(1), pp.7-15.

[2] Walpole, J., Papin, J.A. and Peirce, S.M., 2013. Multiscale computational models of complex biological systems. *Annual review of biomedical engineering*, *15*, pp.137-154.

[3] Athani, A., Ghazali, N. N. N., Badruddin, I. A., Usmani, A. Y., Kamangar, S., Anqi, A. E., & Ahammad, N. A. (2021). Two-Phase Non-Newtonian Pulsatile Blood Flow Simulations in a Rigid and Flexible Patient-Specific Left Coronary Artery (LCA) Exhibiting Multi-Stenosis. *Applied Sciences*, *11*(23), 11361.

[4] Picard, F., et al., *Vasospastic angina: A literature review of current evidence.* Archives of cardiovascular diseases, 2019. **112**(1): p. 44-55.

SB³C2022
Summer Biomechanics, Bioengineering and Biotransport Conference
June 20-23, Eastern Shore, MD, USA

# DEGENERATION OF THE LUMBAR FACET JOINT OCCURS IN BOTH THE FACET CAPSULAR LIGAMENT AND THE FACET JOINT ARTICULAR CARTILAGE

**Jill M. Middendorf (1), Victor H. Barocas (1)**

(1) Department of Biomedical Engineering, University of Minnesota, Minneapolis, MN

## INTRODUCTION

Despite the importance of the facet joint to the stability and pain-free function of the lumbar spine, degeneration of the facet joint, including the facet capsular ligament and the articular cartilage, is poorly understood. Clinically, degeneration of the lumbar spine is often characterized using magnetic resonance imaging (MRI) to quantify intervertebral disc (IVD) health (Pfirrmann grade) and facet joint health (Fujiwara score) using standard scoring systems [1,2]. Increased IVD degeneration and increase facet joint arthritis as characterized using MRI have been associated with decreased stiffness of the IVD and decreased stiffness of various spinal ligaments [3].

However, mechanical changes in the facet joint cartilage and facet capsular ligament are not well understood with respect to MRI scores of the lumbar spine. This correlation is made more difficult to explore by the fact that reliability of Fujiwara scores can be characterized as fair at best [4,5]. Nevertheless, this study explored which mechanical changes in the facet capsular ligament and the facet joint articular cartilage can be associated with MRI scores of the lumbar spine. Additionally, decreases in the stiffness of one spinal soft tissue may cause altered loading and degeneration of another spinal tissue [6]; therefore, degeneration of the facet joint as a whole was characterized by examining the relationship between facet capsular ligament stiffness and the modulus of facet joint cartilage.

## METHODS

A total of 7 human cadaveric lumbar spines were obtained through the University of Minnesota Anatomy Bequest Program. These cadavers ranged in age from 62 to 98, with 2 males and 5 females. 3T MRI were taken of each lumbar spine using T1- and T2-weighted scans with a knee coil. Then, three spine researchers independently scored the L2-L3, L3-L4 and L4-L5 IVDs and facet joints using standard Pfirrmann grades [2] and Fujiwara scores [1].

A linear inverse mechanics approach [7] was used to characterize the anisotropic tensile mechanics of the capsular ligament. First, the ligament was removed from the facet joint and loaded into a biaxial testing system with independently actuated arms. During testing, videos of the ligament motion were recorded so DIC analysis could be performed and a strain field across the surface of the ligament could be determined. Using this strain field and the forces on the boundary, the average 2D generalized linear stiffness tensor $C_{ijkl}$ was determined. The coordinate system was defined such that the 1 direction was roughly parallel to the joint surface and the 2 direction was roughly bone-to-bone. These defnition allows the $C_{2222}$ component to be a measure of stiffness in the bone-to-bone (primary fiber) direction and $C_{1111}$ to be a measure of the transverse stiffness. The $C_{1111}$ and $C_{2222}$ stiffnesses were plotted against the Pfirrmann and Fujiwara scores.

The mechanical behavior of the facet joint cartilage was assessed using unconfined compression. Osteochondral plugs with 5mm diameters were taken from the lateral side of the facet joint. The thickness of the articular cartilage was measured. Then, each osteochondral plug was compressed to a total of 25% strain in 5% increments. The articular cartilage was allowed to relax for 5 min between each pair of loading steps. The Young's Modulus of the articular cartilage was calculated from the slope of the stress-strain curve and compared to Pfirrmann grades and Fujiwara scores.

Finally, a joint-based correlation between the Young's modulus of articular cartilage and the FCL stiffness parameters was created. A linear ($C_{1111}$) or a log based ($C_{2222}$) correlation was used to compare the Young's modulus of cartilage to the FCL stiffness.

Some facet joints contained large amounts of bone growth, which caused fusion of the joint and made cartilage testing impossible.

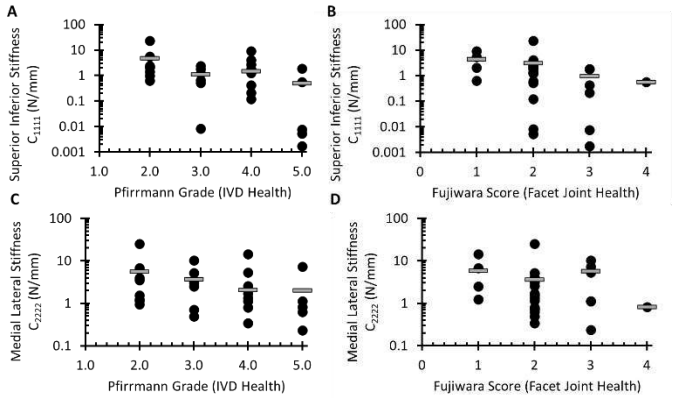


**Figure 1: Stiffness of the facet capsular ligament decreases with increased signs of lumbar spine degeneration. A) medial lateral stiffness versus Pfirrmann grade; B) medial lateral stiffness versus Fujiwara score; C) superior inferior stiffness versus Pfirrmann grade; D) superior inferior stiffness versus Fujiwara score. (gray bars = average; black dots = individual sample values)**

## RESULTS

Stiffness of the facet capsular ligaments decreased slightly with increases in both the Pfirrmann and Fujiwara scores (Fig 1A). Stiffness in the superior-inferior direction ($C_{1111}$, transverse direction) decreased by an order of magnitude between Pfirrmann grades of 2 and 5, and it decreased by a factor of 4 between Fujiwara scores of 1 and 4. Similarly, stiffness in the medial-lateral direction ($C_{2222}$, primary direction) decreased by a factor of 2.5 between Pfirrmann grades of 2 and 5 and decreased by a factor of 6 between Fujiwara scores of 1 and 4. However, all groups contained large error bars which reduced the statistical significance of these changes.

The Young's modulus of the facet joint cartilage did not change with increases or decreases in the Fujiwara or Pfirrmann grade. (Fig 2A & 2B). This lack of change may be the result of small sample sizes in the highest and lowest Pfirrmann grades (1,2 and 5) and Fujiwara scores (1 and 4).

In contrast, facet capsular ligament stiffness and the articular cartilage Young's modulus were correlated with each other. First, the superior-inferior stiffness (transverse direction, $C_{1111}$) showed a linear correlation with the Young's modulus of the facet joint cartilage ($R^2$ = 0.55, $p < 0.01$, Fig 3A). The slope of the linear fit is 0.11 MPa of cartilage for every 1N/mm increase in ligament stiffness. Similarly, the facet capsular ligament stiffness in the bone-to-bone (primary, medial-lateral, $C_{2222}$) direction, correlated with the Young's modulus of facet joint cartilage ($R^2$ = 0.16, p = 0.18, Fig 2B). The relationship between this stiffness parameter of the FCL and the facet joint cartilage is logarithmic, indicating the Young's modulus of facet cartilage approaches a plateau value at large FCL stiffnesses .

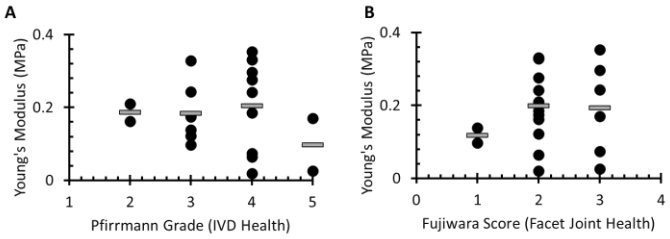


**Figure 2: Young's Modulus of facet joint articular cartilage does not correlate with MRI scores of lumbar spine degeneration: A) Pfirrmann grade and B) Fujiwara score. (gray bars = average; black dots = individual sample values)**

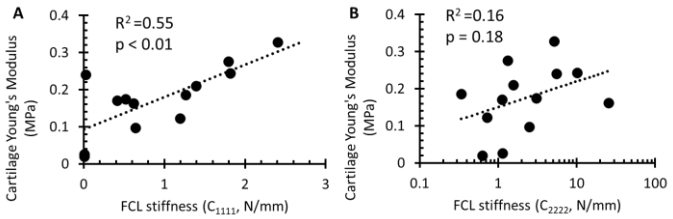


**Figure 3: Correlations between the Stiffness of the facet capsular ligament and the Young's Modulus of the facet joint articular cartilage were strongest for A) $C_{1111}$ versus Young's Modulus and weaker for B) $C_{2222}$ versus Young's Modulus**

## DISCUSSION

In this study, we showed how multiple stiffness parameter of the facet capsular ligament correlate with the Young's modulus of the articular cartilage. This result indicates that degeneration of the lumbar facet capsule may be a joint-scale process, associated with both degeneration of the articular cartilage and decreased stiffness in the facet capsular ligament. However, this study did not explore the mechanisms that cause these changes. Patient-specific loading patterns or biochemical factors, including facet joint inflammation, may contribute to the observed correlations [8].

Pfirrmann grades and Fujiwara scores are imperfect measures of facet joint articular cartilage health. The lack of correlation between articular cartilage and the FUiwara or Pfirrmann grade was unexpected and may be caused by the low sample size of the healthy (low Pfirrmann and Fujiwara scores) and very degenerated spines (high Pfirrmann and high Fujiwara scores). Healthy cadaveric spines are difficult to obtain, while severe degeneration of the facet joint usually implies boney growth and fusion of the vertebral bodies at the facet joint. Additionally, current T1- and T2-weighted MRI may not be sensitive enough to characterize the heterogeneity of facet joint articular cartilage. Depth-dependent mechanical properties of articular cartilage may be causing differences in cartilage stiffness that cannot be measured by the current MRI techniques. Further non-destructive evaluation of the facet joint may be necessary to understand lumbar spine degeneration more accurately.


## ACKNOWLEDGEMENTS

This work was supported by the Minnesota Supercomputing Institute (MSI), and NIH grant U01 AT010326. Lumbar cadaveric spines were made available through the UMN Bequest program.


## REFERENCES


[1] Fujiwara+ *European Spine Journal* 1999
[2] Pfirrmann+ *Spine* 2001
[3] Cornaz+ *Spine 2021*
[4] Stieber+ *Spine* 2009
[5] Andreisek+ *American Journal of Roentgenology.* 2013
[6] Bermel+ *Comput Methods Biomech Biomed Engin*. 2018
[7] Raghupathy+ *Journal of Biomechanical Engineering.* 2010
[8] Perolat+ *Insights into Imaging* 2018

# CONTINUOUS SEPARATION OF BIOLOGICAL CELLS USING A NEW TYPE OF DIELECTROPHORESIS-BASED MICROFLUIDIC DEVICE

**Yoshinori SEKI(1), Aoi NAGASAKA(1), Tsukushi GONDO(1), Masanori EGUCHI(2), Shigeru TADA(1)**

(1) National Defense Academy, Yokosuka, Kanagawa, Japan
(2) National Institute of Technology, Kure College, Kure, Hiroshima, Japan

## INTRODUCTION

Separation of target cells from a diverse population is crucial to many biomedical applications [1]. For example, isolation of circulating tumor cells (CTCs) from a blood sample may allow reliable early detection of cancer. Cell separation using Dielectrophoresis (DEP) technology has been attracted attention as a non-invasive method with less mechanical damage to cells. However, significant technical challenges arise in applying DEP for clinical application when it comes to process extremely large numbers of cells with high throughput. In the present study, a novel DEP device is proposed to effectively separate nonviable cells from viable cells by exploiting their different behaviors in response to AC electric fields. We conducted experiment of cell-separation to evaluate the performance of the proposed device.

## METHODS

In this study, live and dead human mammary epithelial (MCF10A) cells were used. Cells were cultured in a 5 % $CO_2$ incubator and cells of 10-15 passages of the cell culture were used for the experiment. To distinguish live cells from dead cells in the separation process, live cells were labeled with fluorescent calcein and then suspended in a 300 mM mannitol solution together with dead cells. After the cell separation, the sample solution was collected and the cell-separation ratio was obtained by flow cytometry analysis.

Figure 1 shows the experimental setup. The flow channel of dimensions 0.5 (H) ×40 (L)*i*× 10 (W) mm was constructed with parallel top and bottom glass plates separated by 0.5 mm with a silicon rubber spacer. Thin-film aluminum counter-interdigitated electrodes of thickness 300 nm were vacuum-deposited on a glass substrate by standard photolithography. The width of the electrode finger was 50 µm. A sinusoidal AC voltage of 20 $V_{pp}$ was applied to the electrodes by a wave generator. A digital syringe pump was used to provide a continuous flow of the cell suspension. Cells behaviors were monitored using a CCD camera equipped on the microscope and movies were recorded. Cells collected at the exit of the flow channel before and after the voltage application were analyzed by a flow cytometer. Cell-separation ratio was calculated using the following equation.

$$\text{Separation Ratio}(\%) = \frac{\text{Live cell \% } (before-after) \text{ separation}}{\text{Live cell \% before separation}} \times 100 \quad (1)$$

In order to evaluate in detail how the various parameters affect the cell-separation performance, experiments were conducted by varying the frequency *f*; 20, 200, 2000 kHz, the volumetric flow rate *Q*; 5, 10, 20 mL/h and the distance between electrodes; 50 µm (Type A), 75 µm (Type B) (Fig 2). Live and dead cells with the ratio of 1:1 suspended in the mannitol solution having an electric conductivity of 1mS/m were introduced into the device. The cell density of the sample solution was ~$6 \times 10^6$ cells/mL.

## RESULTS AND DISCUSSION

Figure 3 shows the cell's behavior in the flow channel before and after the voltage application for $f$=20 kHz. In the range of AC frequency 20-2000 kHz, dead cells experience n-DEP and move away from electrodes while live cells experience p-DEP and attach to electrodes. We confirmed that live cells attached to electrodes while dead cells went through the flow channel without being trapped on electrodes.

Figure 4 shows the ratio of live and dead cells in the collected sample solution, before and after the separation. In the graph, graph bars on the left are the cell ratio before separation and bars on the right are after separation. Results demonstrated that the cell-separation ratio was frequency dependent and it dropped down significantly for extremely high frequency (not shown). It is because the magnitude of DEP force maybe reduced for high frequencies [2]. The highest cell-separation ratio attained was ~ 90 % for $f$ = 20 kHz and $Q$ = 10 mL/h.

Results of the separation experiment using the type A and the type B electrodes with the fixed frequency $f$ = 200 kHz and the flow rate $Q$ = 10 mL/h are shown in Fig.5. Cell-separation using the type A electrode showed higher separation efficiency than type B. This implies that the non-uniform electric field generated by the type A electrode induced stronger DEP force on cells than the type B electrode. Figure 6 shows distributions of square of the electric field strength for 2 types of electrode, type A and B, obtained by numerical simulations. Areas of large electric-field strength generated by the type A electrode is wider than those of the type B electrode, resulting in higher separation efficiency for the type A electrode.

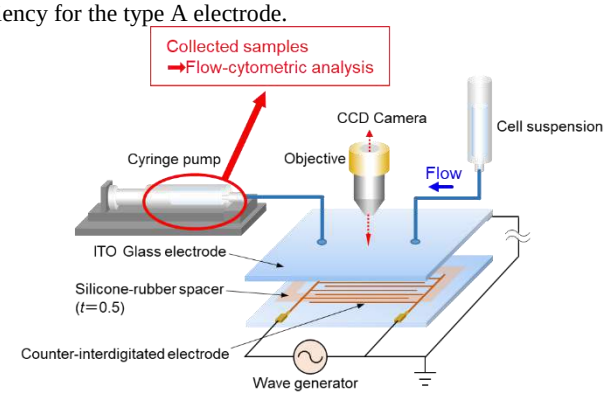


**Figure 1: Experimental setup**

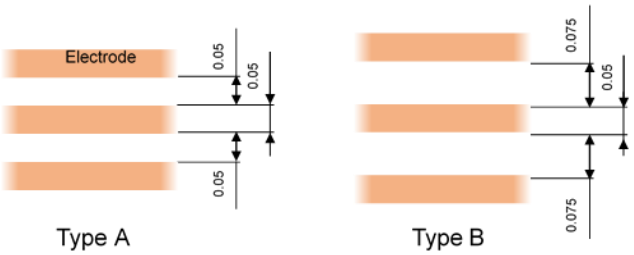


**Figure 2: Schematic of the two types of electrodes**

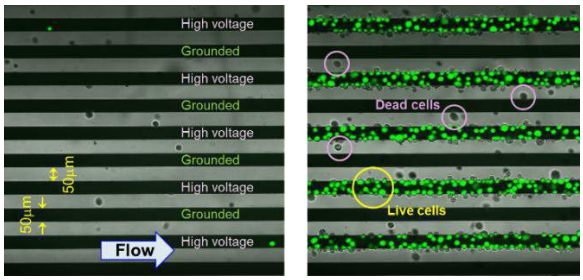


**Figure 3: Cells behavior before and after the voltage application**

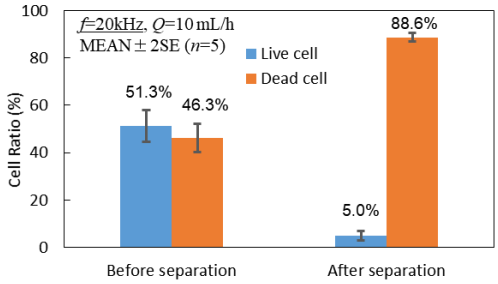


**Figure 4: Result of the cell separation experiment for $f$ = 20 kHz and $Q$ = 10 mL/h**

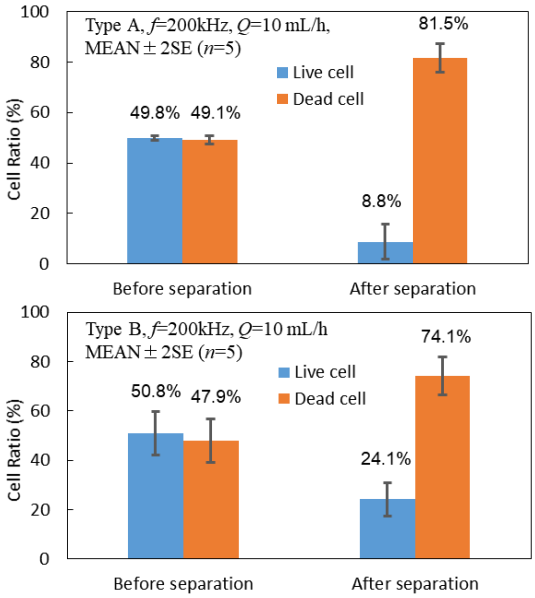


**Figure 5: Effect of the electrode spacing on the cell separation**

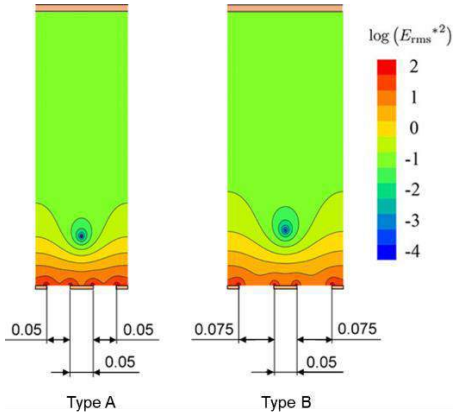


**Figure 6: Electric field distributions in the cross-section of the flow channel for type A and B electrodes**

## SUMMARY

The performance of the DEP device proposed in the present study was evaluated and the optimum operation condition of the present device was explored by varying dominant physical parameters. It was found that the cell-separation ratio of 90 % was attained by the proposed device. In the future, we will improve the structure of the device and adjust values of dominant parameters to achieve higher cell-separation efficiency necessary for separation of rare cells from large population.

## ACKNOWLEDGEMENTS

This work was supported by JSPS KAKENHI Grant Number JP17K06176.

## REFERENCES

[1] Rahman NA et al. (2017). *Sensors*, **17**: 449.
[2] Gascoyne P.R.C., Noshari J., Anderson T.J., Becker F.F., Isolation of rare cells from cell mixtures by dielectrophoresis. Electrophoresis, 2009, 30(8), 1388-1398.

SB³C2022
Summer Biomechanics, Bioengineering and Biotransport Conference
June 20-23, Eastern Shore, MD, USA

# THE BIOTRIBOLOGY OF TOUCH: NUMERICALLY MODELLING TACTILE PERCEPTION

**R. D. Jobanputra (1), G. Luengo (2), D. Dini (1), M. A. Masen (1)**

(1) Department of Mechanical Engineering, Imperial College London, United Kingdom
(2) L'Oréal Research & Innovation, Paris, France

## INTRODUCTION

Touch is fundamentally a biomechanics problem that is not fully understood. A better understanding of tactile perception has implications in a variety of fields including product design, the treatment of skin injuries, artificial skins and robotics, and cosmetic products.

The propagation of stimuli such as pressures and vibrations, from the skin-surface boundary to the sites of our mechanoreceptors is obscure due to the complexity of the skin. Mechanically, the skin can be characterized by its inhomogeneity, non-linearity and viscoelasticity. Each layer of the skin possesses different mechanical and structural properties; in addition to having different functional roles. The outermost layer, the stratum corneum, is the major load bearing component of the skin. The fingerprints filter and amplify vibrations, which, in addition to applied stresses and strains, propagate through the viable epidermis to the dermal mechanoreceptors.

The space-time variation of stress, strain and energy fields throughout the skin causes the mechanoreceptors to deform and respond with corresponding variations in their discharge rates (Fagiani et al., 2012). This triggers our neurological response by causing an influx of ions into the receptors via voltage and stretch-gated channels within the axon. The influx is a prerequisite for the release of synaptic transmitters which prompt the receptors to fire action potentials to the central nervous system (Halata, Grim & Baumann, 2010; Hamann, 1995).

Researchers have previously described how surfaces that are smoother than the fingerprint geometry are perceived as more desirable than their rougher counterparts. The duplex theory of tactile perception (Bergmann Tiest, 2010) describes how surface roughness features of different magnitudes are distinguished and discriminated during sliding contact against textures. Fine textures with transverse spatial periods below 100 microns are perceived dynamically by vibrations induced through sliding contact against the fingerprint ridges. Coarse textures can be perceived statically as uneven pressure distributions and textures with spatial periods above 200 microns are perceived by spatial code generated by the firing variation of mechanoreceptors. Within the characteristic region of 100 to 200 microns, both spatial and temporal mechanisms play an important role in tactile perception

Previously, a microscale finite-element finger skin model was used to test the effects of biomechanical skin ageing on tactile perception (Jobanputra et al., 2020). This two-dimensional, hyperelastic model was employed to examine the stress, strain and energy fields at the locations of the Type-1 (high spatial resolution) mechanoreceptor in response to age-related mechanical and geometric skin alterations. In the current study, we incorporate viscoelasticity into the model, before conducting a parametric study to investigate the effect of altering the surface roughness on the mechanical state of the dermal mechanoreceptors.

This newly developed model enables the observation of the mechanoreceptors' stress, strain and energy fields in response to changing the amplitude and wavelength of rigid sinusoidal rough surfaces during a parametric study. Surface design engineers can use the outputs of this investigation to generate product surfaces to manifest desirable sensations amongst consumers.

## MATERIALS & METHODS

ABAQUS CAE 2021 was used to develop a skin model comprising the stratum corneum, viable epidermis, dermis and hypodermis. Quadric, quadrilateral, hybrid, plane strain elements were used to mesh the model. To simulate tactile perception, the model was compressed with a uniformly distributed load of 1 N and before sliding against a geometrically rough counter surface at 20 mm/s, whilst a coefficient of friction of 0.5 was applied at the skin-surface interface. Non-linear behavior of skin was represented using an Ogden model (Eq. 1.) whose moduli $\mu$, and exponents $\alpha$, were established experimentally, by compressing and shear-loading glabrous skin (Boyle et al., 2019).

$$U = \sum_{i=1}^{N} \frac{2\mu}{{\alpha_i}^2}\left({\lambda_1}^{\alpha_i} + {\lambda_2}^{\alpha_i} + {\lambda_3}^{\alpha_i} - 3\right) + \sum_{i=1}^{N} \frac{1}{D_i}(J-1)^{2i} \quad Eq.\ 1.$$

Viscoelastic characteristics were implemented into the material model using a Prony series (Eq. 2.) using data presented by Wu et al., 2006.

$$g_R(t) = g_0 - \sum_{i=1}^{N} g_i \cdot \left[1 - e^{-\frac{t}{T_i}}\right] \quad Eq.\ 2.$$

In this investigation, the wavelength and amplitude of the sinusoidal countersurface are independently altered during sliding contact to observe the effect on the Type-1 mechanoreceptor sites (Merkel and Meissner receptors) along the dermal-epidermal junction (DEJ – Fig. 1). The wavelength of the countersurface was varied between 0 and 500 μm, whilst the amplitude wave varied between 10 and 80 μm.

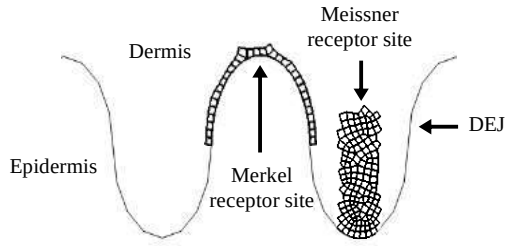


**Figure 1: Finite element mesh at the locations of the Merkel and Meissner receptors.**

From literature, it is reported that the Type-1 receptors are particularly sensitive to localized stretch and deformation (i.e. strain), deviatoric (Von Mises) stresses, and strain energy density (SED) (Wang & Hayward, 2008; Pham et al., 2017; Johnson, 2001). Consequently, these responses were monitored as the finger model was brought into sliding contact against a range of rigid rough surfaces.

## RESULTS

The mechanical stimuli recorded at the receptor sites following sliding against each counter surface exhibited oscillatory behavior due to the periodicity of the surface topology. These stimuli were decomposed into the average and range (max-min) for each surface. Figure 2 illustrates the effects of altering surface wavelength on the deviatoric stresses at the Meissner site, for different surface amplitudes.

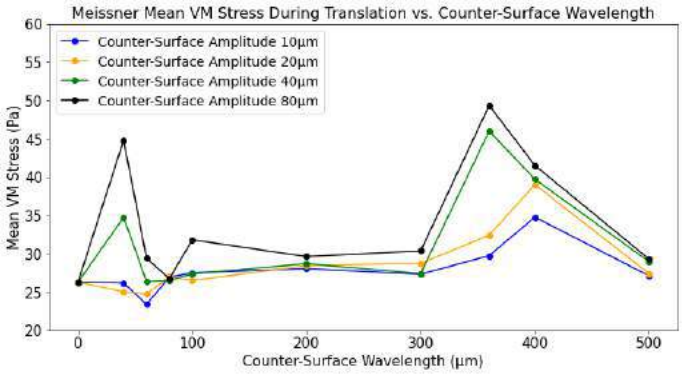


**Figure 2: Average deviatoric stress at the Meissner site following translation against surfaces with different wavelengths.**

Overall:

- For surface wavelengths above 100 μm, increases in roughness amplitude resulted in increases in average stimuli magnitude and oscillation range at the receptor sites.
- For surface wavelengths above 100 μm, further increases in wavelength resulted in increases in stimuli range (oscillatory response) at the receptor sites.
- Mechanoreceptor responses to surfaces with spatial periods below 100 μm cannot be explained by surface roughness alone.
- Surface wavelengths approaching that of the fingerprint (360 μm), result in peaks in average stress and oscillatory behaviour.

## DISCUSSION & CONCLUSION

The results show the effect of altering microscale topological features on stimuli propagation to the sites of our Type-1 mechanoreceptors. For textures with wavelengths above 100 μm, increasing amplitude increases stimulus magnitude and oscillatory behavior at the receptor sites. Furthermore, as the surface periodicity approaches that of the fingerprint, resonant and interlocking effects occur, increasing friction and mechanoreceptor response. For finer textures, below 100 microns, countersurface geometry alone cannot explain stress field at the location of the receptor. This finding confirms neuropsychological experiments reported in literature concerning the duplex theory of tactile perception and current research focuses on the spectral analysis of the elicited mechanical vibrations.

## REFERENCES


Bergmann Tiest, W.M. (2010) Tactual perception of material properties. *Vision Research*. 50 (24).

Boyle, C.J., Plotczyk, M., Villalta, S.F., Patel, S., Hettiaratchy, S., Masouros, S.D., Masen, M.A. & Higgins, C.A. (2019) Morphology and composition play distinct and complementary roles in plantar skin's tolerance to load. *Science Advances*. 5 (10).

Fagiani, R., Massi, F., Chatelet, E., Costes, J.P. & Berthier, Y. (2012) Contact of a finger on rigid surfaces and textiles: Friction coefficient and induced vibrations. *Tribology Letters*. 48 (2), 145–158.

Halata, Z., Grim, M. & Baumann, K.I. (2010) Current understanding of Merkel cells, touch reception and the skin. *Expert Review of Dermatology*. 5 (1), 109–116.

Hamann, W. (1995) Mammalian Cutaneous Mechanoreceptors. *Progress in Biophysics and Molecular Biology*. 64 (1), 81–104.

Jobanputra, R.D., Boyle, C.J., Dini, D. & Masen, M.A. (2020) Modelling the effects of age-related morphological and mechanical skin changes on the stimulation of tactile mechanoreceptors. *Journal of the Mechanical Behavior of Biomedical Materials*. 112.

Johnson, K.O. (2001) The roles and functions of cutaneous mechanoreceptors. *Current Opinion in Neurobiology*. 11 (4).

Pham, T.Q., Hoshi, T., Tanaka, Y. & Sano, A. (2017) Effect of 3D microstructure of dermal papillae on SED concentration at a mechanoreceptor location. *PLoS ONE*. 12 (12).

Wang, Q.I. & Hayward, V. (2008) Tactile Synthesis and Perceptual Inverse Problems Seen from the Viewpoint of Contact Mechanics. *ACM Transactions on Applied Perception*. 5 (2).

Wu, J.Z., Krajnaj, K., Welcome, D.E. & Dong, R.G. (2006) Analysis of the dynamic strain in a fingertip exposed to vibrations: Correlation to the mechanical stimuli on mechanoreceptors. *Journal of Biomechanics*. 39 (13), 2445–2456.

# FABRICATION AND DRUG RELEASE KINETICS CHARACTERISATION OF POLY(GLYCEROL SEBACATE URETHANE) ANISOTROPIC SCAFFOLDS

**A. Samourides (1), Z. Xenou (1), I. Louca (1), K. Kapnisis (1), A. Anayiotos (1)**

(1) Department of Mechanical Engineering and Materials Science and Engineering, Cyprus University of Technology, Limassol 3036, Cyprus

## INTRODUCTION

Injuries of tendons are characterized with painful, slow healing time and usually insufficient, in terms of restoring its strength and various functions. Tendon tissue engineering has presented a promising approach to promote tendon healing or its replacement [1]. This approach is usually based on the use of three-dimensional porous scaffolds, combined with biological factors such as cells and growth factors, to support the tendon temporarily. The scaffold ideally mimics the structure and the physical properties of the native tissue until its regeneration [2].

A promising biodegradable, biocompatible material that has suitable physical properties for use in tendon tissue engineering is poly(glycerol sebacate urethane) (PGSU). Furthermore, PGSU was found to be angiogenic and to promote tissue ingrowth depending on the ratio of the reactants [3]. In this study, three different PGSU scaffolds, with different ratios of HDI and polymer concentration, were fabricated and investigated for specific physical properties such as: microstructure, pore size, swelling ratio and drug release kinetics.

## METHODS

PGSU scaffolds were fabricated as described by Samourides et al. [2] with HDI ratios of 0.8 and 1.0 and polymer concentrations (w/v%) equal to 10% and 15% which were found to exhibit the highest mechanical properties between the other PGSU scaffolds that were synthesized. Briefly, the PGS pre-polymer was dissolved in 1,4-dioxane at the required w/v concentration and HDI was added at 0.8 or 1.0 ratio to glycerol. The solution was left to react for 5 hours at 55 ºC. The solution was then frozen in an in-house customized mold (see [2]) and freeze dried for 16 hours. PGSU scaffolds were characterized for their microstructure using scanning electron microscopy (SEM) (SEM Quanta 200, FEI, United States). The hydrophilicity was studied using contact angle and swelling ratio calculations. Finally, the scaffolds were studied for their ability to be loaded with bovine serum albumin (BSA) and the drug release rate was subsequently derived.

**Pore size:** The pore size of the samples was measured from the SEM images using ImageJ and the free hand selection tool. Images were taken from all views and 50 fully defined pores were used to determine the average pore size of the top view, cross section and bottom view of the PGSU scaffolds.

**Swelling ratio:** The swelling ratio of the scaffolds was measured to determine their swelling ability in phosphate buffered solution (PBS). The samples were dried, weighted and soaked in PBS for a total of 24 hours. Mass measurements of the scaffolds were taken at multiple time points to calculate their swelling ratio according to Eq. (1):

$$SR_i(\%) = \frac{W_w - W_d}{W_d} i x i 100 \qquad \text{Eq. (1)}$$

with $W_w$ and $W_d$ to be the sample's wet weight at different time points and the sample's dry weight, respectively. The experiment was repeated three times in technical triplicates.

**Drug loading:** The PGSU scaffolds were loaded with BSA using an in-house dynamic vacuum loading method. A BSA solution was prepared at 500 μg/ml in PBS and 200 μl of the solution was placed on top of the scaffolds. The samples were moved into a vacuum chamber where the vacuum pressure was increased until air bubbles began to form and rapidly ventilated to atmospheric pressure. This cycle was repeated 12 times. The drug loaded scaffolds were then submerged in PBS and placed on a rocker at 100 rpm for 28 days. Samples were collected at various time points throughout the study and a bicinchoninic acid (BCA) assay was used to quantify the amount of protein that was released over time.

**Statistical Analysis:** All experiments were repeated three times and the statistical analysis was performed using two-way ANOVA in

GraphPad Prism 8. Results are shown as mean ± standard deviation and the statistical significance was considered at $p < 0.05$.

## RESULTS

Figure 1 shows representative macroscopic and microscopic images of the scaffold fabricated using ice-templating and freeze-drying.

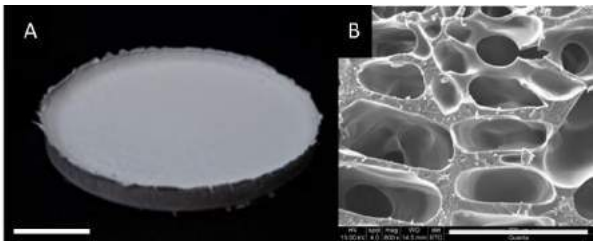


**Figure 1: Representative macroscopic and microscopic images of the PGSU scaffolds. Scale bars for A = 10 mm, B = 200 µm.**

The assessment of the pore size showed that the scaffolds exhibited a range of pore sizes, from 54.6 ± 18.3 to 66.1 ± 23.7 µm depending on the polymer concentration and HDI ratio (see Figure 2). The PGSU scaffolds fabricated with 1.0 HDI ratio had the most uniform pore sizes between the different viewing angles.

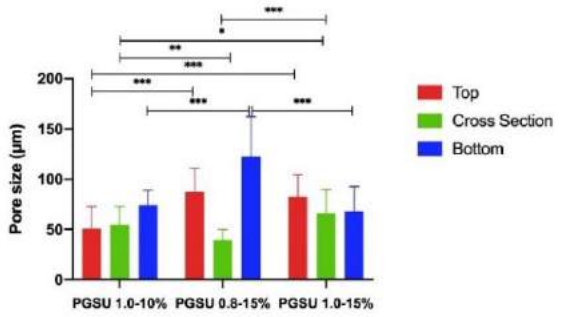


**Figure 2: The pore sizes of the PGSU scaffolds viewed from different angles using SEM. * when $p < 0.05$, ** when $p < 0.01$ and *** when $p < 0.001$.**

The measurements for the swelling ratio are shown in Figure 3 and at 24 hours it ranged between 71.3 ± 7.3%, 115.9 ± 7.1% and 140.8 ± 15.5%. for PGSU 1.0-10%, 0.8-15% and 1.0-15% respectively. The samples showed statistical difference and the swelling ratio increased with the increase of polymer concentration and HDI ratio.

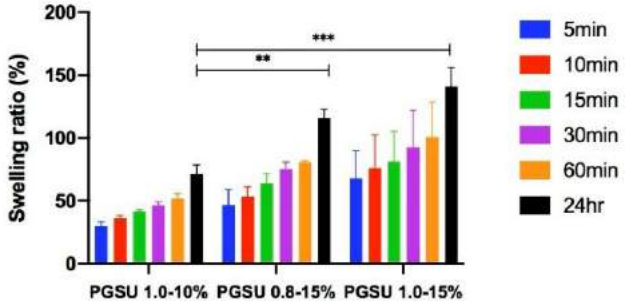


**Figure 3: The swelling ratio measurements for the samples. ** when $p < 0.01$ and *** when $p < 0.001$.**

Finally, the drug release rate of BSA loaded into the PGSU scaffolds was examined using a BCA assay. A linear release rate was found and almost all samples withheld and released the protein over a period of at least 19 days.

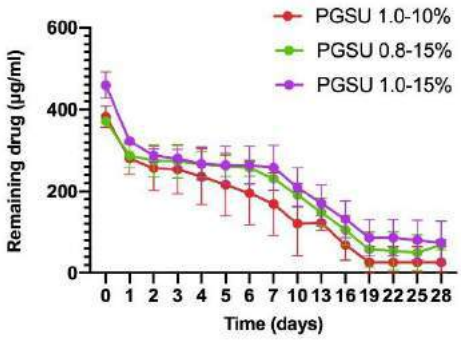


**Figure 4: Drug release rate of the PGSU scaffolds over a period of 28 days using BCA assay.**

## DISCUSSION

Large PGSU scaffolds were fabricated, and a controlled pore orientation was achieved using ice-templating and freeze drying. The scaffolds exhibited significantly different pore sizes between sample groups. However, a uniform microstructure in terms of pore size was achieved from the scaffolds that were synthesized using 1.0 HDI (PGSU 1.0-10% and PGSU 1.0-15%). Furthermore, a linear swelling rate was also observed from the swelling testing of the scaffolds which is considered an advantage in drug loading because a uniform distribution of the drug within the scaffold construct is promoted. The PGSU scaffolds have also shown a fairly linear release of the BSA over time which correlates with our previous swelling and degradation studies in [3] and further adds to the advantages of the anisotropic PGSU scaffolds that were fabricated in this study. The loading and steady release of proteins that can stimulate the biological response for tendon regeneration indicated no significant difference between the examined PGSU scaffolds. Finally, the drug loading technique that was developed by our group for this purpose allowed us to load BSA at approximately the 3-folds the mass of the scaffold with an average of 75% loading efficiency. This method can be modified to be used with almost any scaffold.

## ACKNOWLEDGEMENTS

This work was co-funded by the European Regional Development Fund and the Republic of Cyprus through the Research and Innovation Foundation (Grant number: OPPORTUNITY/0916/MSCA/0017).

## REFERENCES

1. Testa, S., et al., *Combination of biochemical and mechanical cues for tendon tissue engineering.* Journal of cellular and molecular medicine, 2017. **21**(11): p. 2711-2719.
2. Samourides, A., et al., *Fabrication of Hierarchical Multilayer Poly(Glycerol Sebacate urethane) Scaffolds Based on Ice-Templating.* Applied Sciences, 2021. **11**(11): p. 5004.
3. Samourides, A., et al., *The effect of porous structure on the cell proliferation, tissue ingrowth and angiogenic properties of poly(glycerol sebacate urethane) scaffolds.* Materials Science and Engineering: C, 2020. **108**: p. 110384.

# THE INFLUENCE OF PLAQUE STRUCTURAL STRESS AND WALL SHEAR STRESS ON HUMAN CORONARY PLAQUE PROGRESSION

**Aikaterini Tziotziou (1), Eline Hartman (1), Suze-Anne Korteland (1), Antonius F.W. van der Steen (1), Joost Daemen (2), Jolanda Wentzel (1), Ali C. Akyildiz (1,3)**

(1) Department of Biomedical Engineering, Erasmus Medical Center, Rotterdam, the Netherlands
(2) Department of Cardiology, Erasmus Medical Center, Rotterdam, the Netherlands
(3) Department of Biomechanical Engineering, Delft University of Technology, Delft, the Netherlands

## INTRODUCTION

Atherosclerosis, defined as plaque formation within the arterial wall, is one of the most widespread diseases in our cardiovascular system. It is a primary cause of death as its progression and rupture can lead to myocardial attack or stroke [1]. Atherosclerotic plaque progression over time in coronary arteries is affected by local hemodynamic and biomechanical factors, such as the Wall Shear Stress (WSS) and the Plaque Structural Stress (PSS) [2]. WSS is due to the friction caused by blood flow on the endothelial surface of the arterial lumen and low WSS is known to be associated with plaque progression [3]. PSS is stress developed within atherosclerotic plaque tissue due to the blood pressure and there are no well-established scientific findings revealing the association between PSS and plaque progression yet. Furthermore, the combination of different values of WSS and PSS, and their association with plaque progression is yet to be examined [3]. In this work, we aimed to study the influence of PSS and WSS on human coronary plaque progression over time.

## METHODS

Data Acquisition

Forty-nine non-stented, non-culprit coronary arteries from 48 patients with acute coronary syndrome were imaged at two time points (baseline and one-year follow-up) using near-infrared spectroscopy intravascular ultrasound (NIRS-IVUS) and optical coherence tomography (OCT) imaging techniques, within the protocol of the earlier reported IMPACT study [4]. The baseline and follow-up images of the coronary arteries with at least 30 mm length were segmented (lumen, plaque and necrotic core) (Figure 1), and 2D plaque geometries and 3D lumen surfaces were generated based on the combined IVUS and OCT frames.

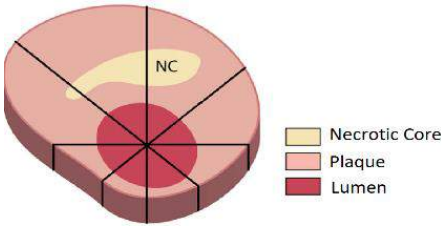


**Figure 1: Every cross-section is divided into 8 sectors with 1,5mm thickness based on the center of the lumen [4].**

Plaque Structural Stress

The 2D patient-specific plaque cross-sections, generated from the combined IVUS-OCT frames via MATLAB scripts, were transferred to the finite element software ABAQUS. An adventitia layer (not visible in IVUS or OCT) of uniform thickness (0.15 mm) [5] was added to plaque geometry. The material properties of the individual plaque components (i.e., NC, plaque and adventitia) were obtained from literature [3, 6]. Since, the IVUS-OCT images were obtained from coronary arteries under blood pressure, the backward incremental method was applied to calculate the initial stresses within the plaque structure [6]. The 2D finite element analyses in ABAQUS was performed under plane strain assumption and eight PSS parameters under the intraluminal pressure loading of 120 mmHg were computed. These parameters included the maximum and average of Max Principal and von Mises stresses on the lumen surface and in the plaque tissue.

Wall Shear Stress

WSS of the coronary data set was calculated previously [4]. Briefly, computational fluid dynamics simulations (Fluent, ANSYS) were performed for every patient-specific 3D lumen geometry, implementing blood flow as an incompressible, homogeneous, Carreau

fluid. Time averaged wall shear stress (TAWSS) was calculated along all coronary arteries.

Statistical Analysis

The impact of PSS and WSS on the human coronary plaque progression was estimated using Linear Mixed Model (Regression) in SPSS Software. The 3D artery geometries were divided into 1,5mm/45º sectors (Fig.1) and the statistical analyses were based on the PSS and WSS values per sector. A p-value < 0.05 was considered significant. The plaque thickness change from the baseline to the follow-up was used as the parameter to quantify plaque progression in the analyses.

## RESULTS

A representative patient-specific case is illustrated in Figure 2. Figure 2A demonstrates the max principal stress distribution of a cross-section. The results show greater stresses in the thin wall region and in the plaque cap region, which separates the NC from the lumen. Figure 2B demonstrates the average max principal within the plaque tissue per sector for the entire 3D artery geometry. The large range of values indicate the non-uniform stress distribution over the geometry. Figure 2C is the cut-open demonstration of the 3D stress distribution. Similar representation is provided for TAWSS in Figure 2D.

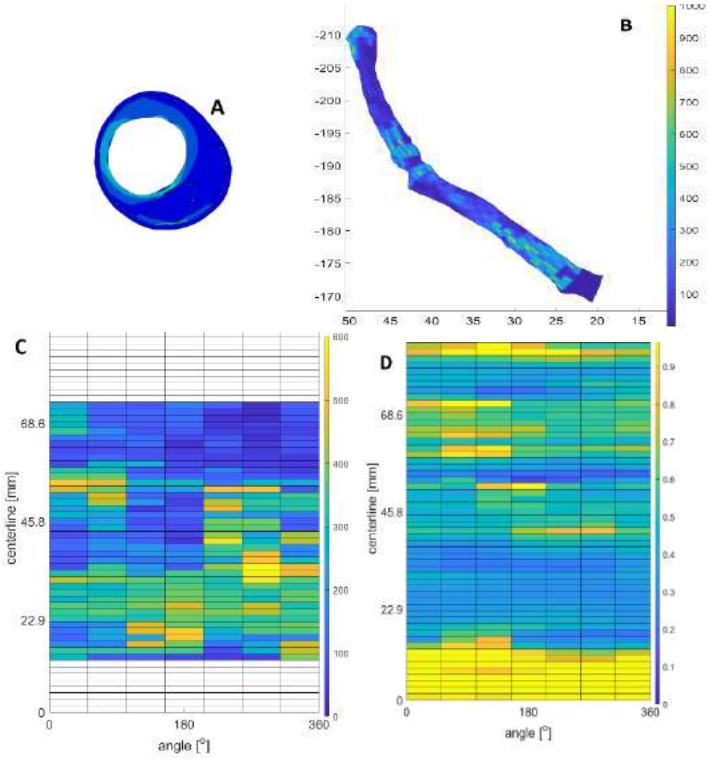


**Figure 2: (A) Max principal stress distribution on a 2D cross-section. (B) Average max principal stress distribution in 3D vessel model. (C) Max principal stress distribution and (D) TAWSS distribution in the cut-open demonstration of 3D artery geometry.**

So far, the analyses of 17 patients have been finalized. Based on the obtained results, of the 8 PSS metrics, many correlated with each other statistically significantly, except the maximum max-principal stress on the lumen and maximum max-principal stress in the plaque tissue. Hence, these two PSS metrics were further used in the statistical analyses.

All stress categories were divided into three groups (tertiles: low, mid, high) for the linear mixed models. According to the statistical analysis, the effect of TAWSS, PSS on the lumen and PSS in the plaque individually, and the effect of their combination on the plaque thickness change over time were statistically significant. Specifically, as demonstrated in Figure 3A, low lumen PSS associated with plaque regression (negative plaque thickness change) while high lumen PSS associated with plaque growth (positive plaque thickness change). Figure 3B shows the combined impact of lumen PSS and WSS on plaque thickness change: high lumen PSS combined with low TAWSS correlated with maximum plaque progression whereas low lumen PSS with high TAWSS correlated with maximum plaque regression.

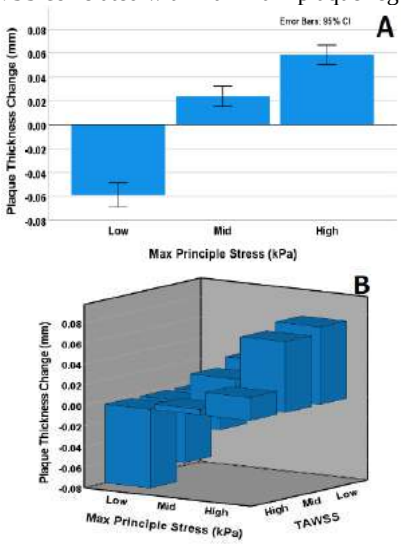


**Figure 3: (A) Impact of Max Principal stress on the lumen only and (B) Impact of Max Principal stress on the lumen and TAWSS combined on plaque thickness change over 1-year follow up time.**

## DISCUSSION

In this work, we have generated 2D and 3D patient-specific coronary computational models to investigate the influence of PSS and WSS on atherosclerotic plaque change over time, from a unique data set of IVUS and OCT combined. We calculated the PSS on the lumen and within the plaque tissue as they are regions with high interest regarding plaque progression. The analyzed cross-sections included healthy and diseased sectors and based on the results the higher PSS were mainly observed in the healthy sectors. Our analysis of the first 17 coronaries already showed the statistically significant impact of PSS and WSS on plaque change over time individually and combined. Next immediate step of our study is to finalize the analyses of the entire data set of 49 coronaries. We also plan to further analyze the relatively healthy-sectors and the diseased-sectors separately. These will unravel the important correlation of PSS and WSS with plaque progression (or regression) and provide great insights for better understanding the plaque growth mechanisms and for developing plaque progression prediction models.


## ACKNOWLEDGEMENTS

This project has received funding from the European Research Council, Brussels, Belgium # 310457.


## REFERENCES


[1] Shah, P et al., *Thrombosis*, 2015:634983, 2015. [2] Wang, L et al., *J Biomech.*, 68:43-50, 2018. [3] Costopoulos, C et al., *Eur Heart J.*, 40:1411-1422, 2019. [4] Hartman, E et al., *J. of Cardiovasc. Trans. Res.*, 14:416–425, 2021. [5] Akyildiz, A C et al., *Biomed. Eng. Online*, 10:25, 2011. [6] Akyildiz, A C et al., *Computer. Methods in Biomech. and Biomed. Eng.*, 19: 771–779, 2016.

# SPINAL CORD INJURY INCREASES ARTERIAL STIFFNESS AND PERIVASCULAR ADIPOSE TISSUE INFLAMMATION IN MICE

**Ryan M. Sapp (1), Swathi Swaminathan (2), Pattie S. Mathieu (1), Annie Barnes (1), Gurneet S. Sangha (1), Valerie Bracchi-Ricard (2), Alisa M. Clyne (1)**

(1) Fischell Department of Biomedical Engineering, University of Maryland, College Park, MD, USA
(2) Department of Biology, Drexel University, Philadelphia, PA, USA

## INTRODUCTION

Progressive stiffening of large arteries underlies the development of cardiovascular disease (CVD), the primary global cause of mortality [1]. Spinal cord injury (SCI) causes accelerated arterial stiffening, contributing to the disproportionate ~2-fold greater risk for CVD in SCI patients [2]. The mechanisms underlying arterial stiffening in SCI are incompletely understood, but the chronic inflammation characteristic of SCI [3] may contribute by promoting vascular smooth muscle cells (VSMC) to switch from a healthy, contractile to a synthetic phenotype. It is not only important to determine the mechanisms underlying arterial stiffening in SCI patients to develop preventative interventions specific to this population, but SCI may serve as a unique model to investigate inflammation and arterial stiffness.

Perivascular adipose tissue (PVAT) directly surrounds almost all arteries in the body and regulates vascular health via the release of paracrine factors to adjacent VSMCs [4]. In response to CVD risk factors, PVAT can become dysfunctional and alter its paracrine secretions, which may contribute to arterial stiffening and CVD development [4]. Specifically, dysfunctional PVAT is inflamed and releases more pro-inflammatory cytokines and less anti-inflammatory adipokines [5]. Thus, our overarching hypothesis is that SCI induces PVAT inflammation, which causes dysfunctional paracrine signaling and initiates a pro-inflammatory feedback loop promoting a synthetic VSMC phenotype and arterial stiffening.

In this study we used a mouse model of SCI and *ex vivo* cultured PVAT to determine 1) how SCI affects PVAT inflammation, 2) how inflammation impacts PVAT secretions, and 3) how paracrine factors released from inflamed PVAT affect VSMC phenotype.

## METHODS

SCI was induced in female C57Bl/6 mice by moderate contusive injury to the thoracic spinal cord (T9) at 14-15 weeks of age. Females were used as they are less susceptible to complications after SCI (e.g. bladder infection) and we showed similar arterial stiffening to males. Mice were euthanized 1, 3, 7, or 14 days after SCI. The aorta was collected and portions of it stored separately for atomic force microscopy (AFM), staining, or RNA isolation. Blood was collected and centrifuged to collect serum, which was stored at -80°C until analysis. Age-matched uninjured mice were used as controls because sham-operated mice do not have increased aortic stiffness.

AFM was used to assess aortic stiffness. Macrophage infiltration into PVAT surrounding the aorta was determined by immunofluorescent staining for CD68. PVAT area was determined by Oil Red O staining. Serum was analyzed in triplicate for the levels of 16 cytokines and chemokines via multiplex ELISA (Quansys Biosciences).

For *ex vivo* experiments, thoracic aortic PVAT was obtained from euthanized uninjured mice and cultured for generation of conditioned media (CM). PVAT was cultured in DMEM at 5 mg / 250 µl with 100 ng/ml TNFα (TNFα-treated) or without (untreated) for 24 hours. The resulting media was then collected as CM and stored at -80°C. Aortas were also collected and used to isolate VSMC by enzymatic digestion. VSMC were cultured and expanded for later experiments.

CM generated from PVAT of four mice was pooled to determine the expression of 38 adipokines using the Proteome Profiler Mouse Adipokine Array kit (R&D Systems). Separate dotblot membranes were incubated with CM from either the untreated or TNFα-treated PVAT, imaged, and analyzed using ImageJ (NIH). ELISAs (Raybiotech) were used to verify levels of adiponectin, IL-6, and lipocalin-2. CM samples for both conditions were generated from four mice and analyzed in duplicate. To determine the effects of CM on VSMC gene expression, mouse VSMC were treated with 25% CM for 24 hours. CM of both conditions generated from three mice was tested on triplicate wells of VSMC. Gene expression of both aortas and VSMC was determined using RT-qPCR.

Statistical analyses were performed using Prism Graphpad 8. Groups were compared using nonparametric tests with $p<0.05$ considered statistically significant. Kruskal-Wallis tests were used for comparisons of three or more groups with adjusted Mann-Whitney tests used for post-hoc comparisons or comparisons of two groups.

## RESULTS

SCI significantly increased mouse aortic stiffness ($p<0.0001$), as demonstrated by AFM (Figure 1). Four weeks after SCI, elastic modulus of the thoracic and abdominal aortae were 5.5 and 7.5-fold greater, respectively, compared to uninjured controls.

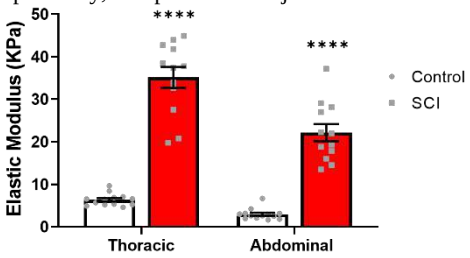


**Figure 1. Aortic stiffness increased in response to SCI, as measured by AFM. n=12-13. ****p<0.0001**

Up to two weeks after SCI, PVAT quantity did not increase with SCI ($p=0.59$; Oil Red O). However, PVAT macrophage infiltration into PVAT increased two weeks after SCI ($p=0.02$), as signified by increased number of CD68+ cells (Figure 2).

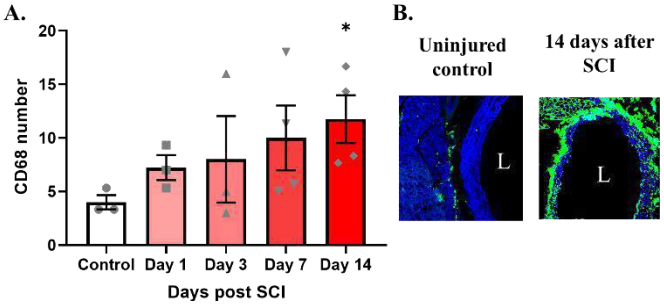


**Figure 2. CD68+ macrophages increased in PVAT two weeks after SCI. A) Macrophage quantification and B) Immunofluorescent images (green: CD68; blue: nuclei). L = lumen. n=3-4. *p<0.05.**

Aortic MMP12 gene expression was significantly decreased ($p=0.03$) by 44% on day one and 49% by day three after SCI, before returning to baseline. Conversely, aortic collagen ($p=0.07$) and adiponectin ($p=0.48$) gene expression were not significantly affected by SCI. Compared to control mice, SCI mice exhibited significant elevations in serum circulating concentrations of pro-inflammatory cytokine IL-6 ($p=0.03$, 1 and 7 days post SCI) and chemokines CXCL1 ($p=0.02$, 1 day post SCI) and CCL1 ($p=0.05$, 1 and 7 days post SCI). Other circulating proteins, including IL-1b, IL-2, IL-3, IL-4, IL-12, IL-13, CCL2, and GM-CSF, were not significantly affected ($p>0.05$) up to two weeks after SCI.

Using dot blots, 15 proteins were detected in CM from either untreated or TNFα-treated PVAT. The three proteins with the highest concentrations in both conditions were adiponectin, MCP-1, and serpin E1. TNFα was present only in the TNFα-treated PVAT CM while VEGF, IGFBP-3, IGFBP-6, and M-CSF were present only in the untreated PVAT CM. Other proteins exhibiting the greatest differences between the untreated and TNFα-treated PVAT CM were TIMP-1 (2.6-fold), IL-6 (1.9-fold), RBP4 (1.8-fold), and lipocalin-2 (1.6-fold). Protein-specific ELISAs confirmed that adiponectin decreased by 38% ($p=0.002$) and IL-6 increased by 50% ($p=0.05$) in CM from PVAT treated with TNFα (Figure 3), while the difference in lipocalin-2 was not confirmed ($p=0.55$).

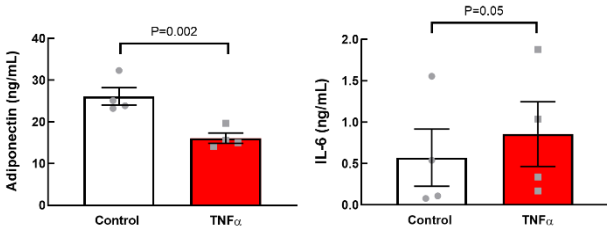


**Figure 3. ELISAs confirmed a decrease in adiponectin and increase in IL-6 in conditioned media of PVAT treated with TNFα. n=4**

There were no significant differences in gene expression of alpha smooth muscle actin (ACTA2), smooth muscle myosin heavy chain (MYH11), calponin (CNN1) (Figure 4), collagen (COL1A1), or MMP-12 (MMP12) (all $P>0.05$) in mouse VSMC following 24 hours of culture with CM from untreated versus TNFα-treated PVAT.

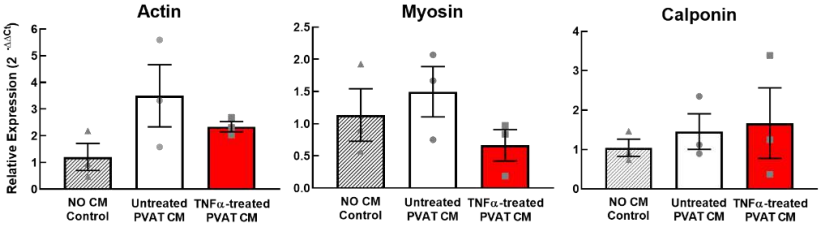


**Figure 4. Conditioned media (CM) from PVAT ± TNFα had no significant effect on VSMC phenotype-related gene expression. n=3**

## DISCUSSION

The primary findings of our study were that SCI increased aortic stiffness and markers of inflammation in the blood and thoracic aortic PVAT. Inducing inflammation in PVAT *ex vivo* using TNFα caused changes in the release of paracrine factors including an increase in the inflammatory cytokine IL-6 and a decrease in the anti-inflammatory adipokine adiponectin. These pro-inflammatory changes in paracrine factors would be expected to promote a shift in VSMC phenotype from contractile to synthetic. However, CM from inflamed PVAT had no significant effects on VSMC gene expression related to either synthetic or contractile phenotype. Still, further experiments, using more functional measures, are needed to better determine VSMC phenotype after treatment with PVAT CM before conclusions can be made.

The increased aortic stiffness and systemic inflammation following SCI that we observed in mice are in line with previous studies in humans [2, 6]. Increased macrophage infiltration in PVAT following SCI is also a novel finding of our study that adds to the current understanding of chronic inflammation associated with SCI. A limitation is that we did not perform experiments with CM from SCI mice PVAT, and this is a future direction of study. Further studies using CM from SCI mouse PVAT will provide insights on how PVAT modulates arterial stiffness.


## ACKNOWLEDGEMENTS

This study was supported by NSF grant (1916814) to AMC. RMS was supported by NIH postdoctoral training grant (5T32HL007698-26). GSS was supported by a UMD Presidential Postdoctoral Fellowship.


## REFERENCES


[1] Virani, SS et al, *Circulation*, 141(9):e139-e596, 2020.
[2] Lee, AHX et al, *J Neurotrauma*, 34(6):1129-1140, 2017.
[3] Allison, DJ et al, *Spinal Cord*, 53(1):14-8, 2015.
[4] Queiroz, M et al, *Ageing Res Rev*, 59:101040, 2020.
[5] Nosalski, R et al, *Br J Pharmacol*, 174(20):3496-3513, 2017.
[6] Hellenbrand, DJ et al, *J Neuroinflammation*, 7;18(1):284, 2021.

# OPTIMIZING AND VALIDATING SOFT CALLUS MECHANICAL PROPERTIES IN OVINE BONE FRACTURE HEALING MODELS WITH BIOMECHANICAL DATA

**Brendan J. Inglis (1), Peter Schwarzenberg (1), Karina Klein (2), Brigitte von Rechenberg (2,3), Salim Darwiche (2,3) Hannah Dailey (1)**

(1) Mechanical Engineering, Lehigh University, Bethlehem, PA, United States
(2) Musculoskeletal Research Unit (MSRU), Vetsuisse Faculty University of Zurich, 8057 Zurich, Switzerland
(3) Center for Applied Biotechnology and Molecular Medicine (CABMM), University of Zurich, 8057 Zurich, Switzerland

## INTRODUCTION

There is an unmet clinical need to diagnose poorly healing fractures using imaging-based methods. In a recent ovine study, we demonstrated that a virtual torsion test outperforms subjective methods like radiographic scoring for predicting the progress of healing and that it is a reliable surrogate for postmortem physical torsion testing in intact tibiae [1]. The key to success in reliable virtual torsion testing of bone mechanics is the use of appropriate scaling laws for converting the radiodensity (gray value) in each voxel of the scan to a Young's modulus, $E$. Our previous ovine study found that extending a density-modulus scaling law developed for cortical bone to include regions of callus produced strong correlations between virtual and physical biomechanical tests, but that the virtual tests over-predicted the measured torsional rigidity in osteotomized specimens by an average of 58% [1]. This over-prediction of rigidity when callus is present suggests that a material model derived for cortical bone does not completely capture the mechanical behavior of callus and that more work is needed to virtually replicate the in-vivo biomechanics of healing fractures. Therefore, the purpose of this investigation was to develop a new constitutive mechanics model for fracture callus that captures its dual nature—hard and soft—and to test this method for assigning material properties in finite element models of healing ovine long bones.

## METHODS

Thirty-three adult female Swiss alpine sheep (2-3 years old, weighing 59-87 kg) were part of previously completed research studies [1]. All animal experiments were conducted according to the Swiss laws of animal protection and welfare. All animals had postmortem biomechanical testing and CT scans available for analysis. CT scans were processed to create the virtual models using Materialize Mimics (21.0, Plymouth, MI). and virtual mechanical testing was performed in ANSYS (2020 R2, Canonsburg, PA). Virtual torsional rigidity ($VTR = ML/\phi$) was calculated using moment reaction ($M$), segment length ($L$), and angle of twist ($\phi$) and compared the biomechanical rigidity (GJ) from postmortem bench testing of each sample.

Density-dependent material properties were assigned on an elementwise basis, with the baseline material model being a linear function optimized for ovine cortical bone [1]. The dual soft-hard material model was implemented using a piecewise function:

$$E = \begin{cases} E_{sc} & \rho_{QCT} < \rho_{cut} \\ 10{,}225\rho_{QCT} & \rho_{QCT} \geq \rho_{cut} \end{cases} \quad (1)$$

where the elemental modulus, $E$ [MPa], depends on the local bone mineral density ($\rho_{QCT}$). Above a to-be-determined density cutoff ($\rho_{cut}$), tissue within the callus was modeled as bone using a scaling function derived for ovine tibial cortical bone [1]. Below the cutoff, elements were considered soft tissue with a modulus ($E_{sc}$) ranging from 0.5 to 500 MPa based on literature reports.

The 33 animals were divided into a Training group (N = 17) and a Testing group (N = 16) and an optimization procedure encompassing 2,363 simulations was used to determine $E_{sc}$ and $\rho_{cut}$ that produce best agreement between VTR and GJ from physical testing (Fig. 1).

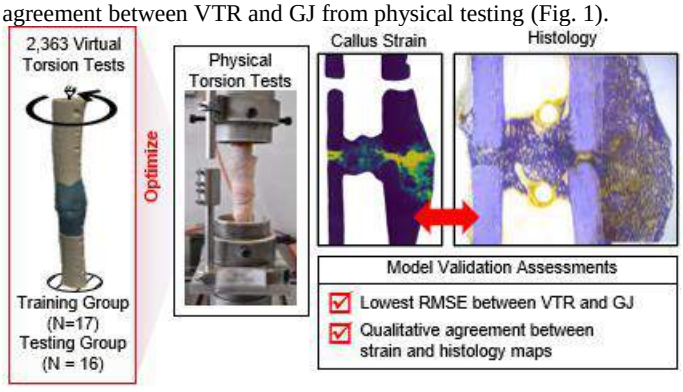


**Fig. 1: Dual-zone material model optimization study.**

Predictive validity was evaluated by calculating the root-mean-square error (RMSE) between VTR and GJ. Success was defined as virtual tests producing RMSE less than the standard deviation of the datum set (GJ) across training and validation stages. Qualitative comparisons of predicted callus strains and stained histology sections (Toluidine Blue) were also used to evaluate model performance. Statistical analysis was performed in IBM SPSS 27 (Armonk, NY).

## RESULTS

The optimization was successful in identifying a value for $\rho_{cut}$ at each level of $E_{sc}$ that minimized the difference in torsional rigidity between the virtual and physical biomechanical tests. Compared to the single-zone material model from our previous study [1] (Fig. 2a), the dual-zone model produced had better absolute agreement between physical and virtual torsion tests (Fig. 2b).

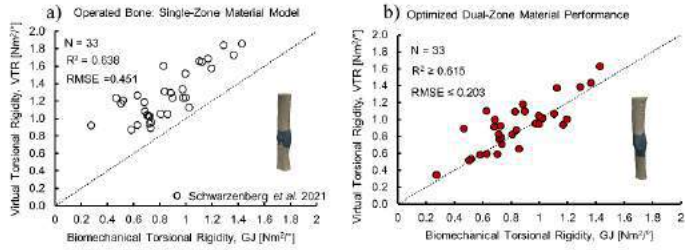


**Fig. 2: (a) Modeling callus using a single-zone material model derived for cortical bone overpredicts the rigidity of healing ovine tibiae. (b) Predictive accuracy was greatly improved by the dual-zone model (Equation 1) for callus in both the training set (shown) and testing set (not shown).**

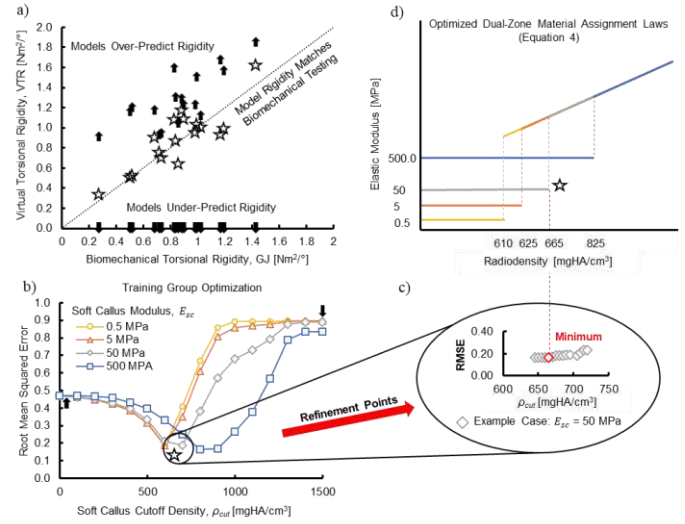


**Fig. 3: (a) The single-zone material model (Eq. 3, up arrows) overpredicted the rigidity of osteotomized ovine tibiae. When the soft callus density cutoff was set too high (example shown: $E_{sc}$ = 50 MPa, $\rho_{cut}$ = 1500 mgHA/cm$^3$) rigidity was clearly underpredicted (down arrows). At the optimized soft callus cutoff value (example shown: $E_{sc}$ = 50 MPa, $\rho_{cut}$ = 665 mgHA/cm$^3$ (stars), the dual-zone material model out-performed the single-zone material model. (b) The minimum RMSE between the VTR and GJ was identified for each $E_{sc}$ level by sweeping the $\rho_{cut}$ space. (c) Refinement point simulations about the initial minimum were performed to identify the optimized $\rho_{cut}$ value (red diamond) (d) The resulting four optimized combinations of soft callus modulus and density cutoff can all be represented using Equation (1).**

At all tested levels of soft callus modulus, the optimized dual-zone material models produced moderate-to-strong correlations between VTR and GJ with absolute agreement that met our defined success criteria for material model validation (all $R^2 \geq 0.558$ and RMSE $\leq 0.248$ versus datum SD = 0.268).

Evaluation of strain contour plots showed that increasing $\rho_{cut}$ was associated with increasing concentrations of strain in and around the fracture gap. Below the optimized $\rho_{cut}$, strain was low throughout the callus volume. Above the optimized $\rho_{cut}$ value, non-physical strain artifacts began to appear in the solution, originating at the defect line (data not shown). At the optimized combinations of $E_{sc}$ and $\rho_{cut}$, the regions filled with soft material in the finite element models and the resulting strain contours were qualitatively well-matched with the localization of less-mature callus in the histological sections.

## DISCUSSION

The development of a clinically relevant, reliable, scalable, non-invasive test to detect problems in bone healing earlier could have profound impacts on the care of nonunion fractures. Image-based virtual mechanical testing shows promise for addressing this need, but one key problem is the material modeling in fracture callus. Unlike native bone, the mechanical properties of callus cannot be studied in human cadavers, so our understanding of the material mechanics and structural organization of this tissue must be strongly informed by observations from large animals.

The results of this study clearly demonstrate that the material properties of the tissues in the callus region for ovine long bones are not monolithic and should therefore not be treated as such. From a structural mechanics perspective, soft tissues within the callus are not functioning simply as low-density bone. This can be inferred because using a bone-derived radiodensity scaling law to assign their mechanical properties leads to a systematic over-prediction of limb rigidity.

The data from this study showed that virtual mechanical testing with a dual-zone material assignment law that captures both the hard and soft nature of callus out-performs single-zone material modeling when validated to physical biomechanical data. To rule out any potential for dependency on randomization in assignment to the training and testing groups, a cross-validation of the optimization was performed. The conclusions were unchanged and the results met our validity criteria based on RMSE.

Future work will be needed to translate the dual-zone material model for callus to other species. A current study in progress seeks to determine a similar density cutoff in human tibiae. It should be noted that the dual-zone material model is not limited to a linear association between mineralized tissue density and modulus and a constant value to model soft callus tissue. The two zones of the material model are not required to be coupled and theoretically could be defined using any equations that are appropriate for the species and anatomic site of interest. Further exploration of combinations of curve segments is warranted.


## ACKNOWLEDGEMENTS

This material is based upon work supported by the National Science Foundation (NSF) under Grant No. CMMI-1943287. The animal work was completed with support and funding from the Johnson & Johnson Family of Companies and Biomech Innovations. Any opinions, findings, and conclusions or recommendations expressed in this material are those of the author(s) and do not necessarily reflect the views of the Johnson & Johnson Family of Companies or the National Science Foundation.


## REFERENCES


[1] Schwarzenberg et al., *J. Orthop. Res.* **39**, 727-738 (2021)

# DEVELOPING A PRECISION-CUT TISSUE SECTIONING PROTOCOL FOR FRESH PORCINE COLONIC TISSUE FOR DOWNSTREAM MECHANICAL ANALYSIS

**Clíona M. McCarthy (1,2), Michael T. Walsh (1,2,3), Kieran D. McGourty (1,4), John J.E. Mulvihill (1,2,3)**

(1) Bernal Institute, University of Limerick, Limerick, Ireland
(2) School of Engineering, University of Limerick, Limerick, Ireland
(3) Health Research Institute, University of Limerick, Limerick, Ireland
(4) Chemical Sciences, University of Limerick, Limerick, Ireland Ireland

## INTRODUCTION

Cancer is among the leading obstacles to improving life expectancy worldwide. Specifically, colorectal cancer accounts for 1 in 10 cancer cases and deaths, making it the third most common cancer with the second highest mortality rate [1]. More specifically, there is a 90% survival rate among patients over a 5 year period in Stage 1. This drops to a 10% survival rate in Stage 4 [2] There is increasing evidence to suggest that mechanical changes to microenvironment elicit an oncogenic response. However, this pathway has yet to be investigated in detail [3] and there has been no robust mechanical analysis of the colon at a microscale. It has been established that diseases of the colon are associated with a failure of the colonic biomechanics [4]. Therefore, in order to truly understand the disease process it is necessary to characterise the biomechanics of healthy colonic tissue.

While macroscale mechanical characterisation obtains the bulk properties of tissue, it does not capture the heterogeneity of soft biological tissues at the microscale. However, microscale mechanical characterisation requires tissue to be sectioned into compatible sizes. The gold standard for tissue sectioning is cryosectioning, but this procedure requires the tissue to be fixed and snap frozen beforehand, leading to the loss of some of the native mechanical properties. Therefore, the aim in this study is develop a protocol for sectioning fresh biological tissue, using a Compresstome® VF-210-0Z for downstream mechanical analysis of fresh tissue, avoiding deleterious freezing of the tissue. Ultimately, this protocol can lead to the creation of a microscale map of fresh tissue to better understand the mechanics of tissue on this scale.

The aim of this study is to carry out a robust biomechanical characterisation of porcine colon tissue. This will involve at both the macroscale and microscale mechanical characterisation for both fresh and frozen tissue. The information gained from this analysis should lend itself to a realistic profile of the physiological mechanical properties of the healthy tissue.

## METHODS

**Tissue Sectioning Protocol** Porcine colonic tissue is sourced from a local abattoir (n=6), cut into 1 $cm^2$ sections, and kept at 4 $^oC$ until required. Three technical samples of tissue per pig are prepared (n=3). Certain conditions remain constant across the majority of studies. The embedding reagents used are cooled to 37 $^oC$ before embedding to prevent heat shock [5]. Once this step is complete, the buffer temperature is maintained at between 0-4 $^oC$ to promote tissue viability.

The variable chosen to optimize for the study is reagent concentration. Three different agarose concentrations (2%, 2.5% and 3%) and 3 gelatin concentrations (1%, 1.5% and 2%) will be tested (n=3 per concentration combination). Section thickness achieved is between 250 – 400 µm.

**Nanoindenter Protocol** Fresh and frozen porcine colon tissue layers were nanoindented using the Optics 11 Chiaro Nanoindenter, which is designed for fresh soft biological tissue mechanical analysis. This will be compared to macroscale compression testing of fresh and frozen porcine colon tissue using the Mecmesin 2.5-dV. The optimised protocol of 2.5% Agarose and 1.5% is used to section the fresh and frozen porcine colons. The approach and retraction speed was set to 2 µm/s as it has been demonstrated that for speeds $\leq$ 2 µm/s tissue

demonstrates elastic behaviour [6]. For this study, the probe used to perform this analysis was probe 0.32 N/m cantilever stiffness and 52.0 µm radius spherical tip. The analysis is performed at room temperature in PBS x1. The tissue was kept hydrated with X1 PBS at room temperature for approximately 30 mins prior to sectioning. Approximately 20 indents are carried out on each tissue sample, beginning at the serosa layer, and then indenting the muscle and mucosal layer. This provides a surface area map of an Effective Young's Modulus (E.$eff$) of the tissue section using the Hertzian Model. The Hertzian contact model follows the fit of the loading curve using the following equation:

$$F = \frac{4}{3} E_{eff} \sqrt{R_i} \cdot h^{3/2} \quad (1)$$

Where $F$ is the force applied, $E_{eff}$ is the Effective Young's Modulus, $R_i$ is the spherical tip radius and $h$ is the indentation depth [7]. $E_{eff}$ values were calculated using the Optics 11 Piuma DataViewer v2.4.13 software. The Hertz contact model was fitted to 50% of the indentation loading curve. The software outputs both $E_{eff}$ and $E$ values, but as the Poisson's ratio for the tissue was unknown the $E_{eff}$ values are used [7].

## RESULTS and DISCUSSION

The preliminary data of the ongoing study is presented in Figure 1 is of a frozen colon tissue sample, and it shows a unique profile for each layer with a statistical difference seen between the mucosa and muscle layers; the serosa (61.68 kPa ±9.302 kPa); the muscularis propria (88.85 kPa ±16.48 kPa); and the mucosa layer (32.65 kPa ±3.62 kPa). The muscularis propria appears to be the stiffest layer with the greatest variability and the mucosa layer is the softest layer with the least variability.

The study highlights that fresh porcine colonic tissue in can be sliced to between 250 – 400 µm which allows for accurate mechanical testing of the native tissue environment on a microscale. It is not recommended to cut tissue sections less than 100 µm as this damages the cells and therefore would not be a true representation of the native microenvironment [5].

The concentration at which agarose is used varies across studies, and is important to ensure precise tissue section cuts. For example, concentrations range from 0.5% to 4% for the preparation of precision cut lung slices [5, 8]. Agarose combined with gelatin preserves the native microenvironment of cells and tissue viability, and allows the tissue to remain flat once sectioned [9] this is useful for downstream microscale mechanical analysis. This optimised protocol for soft biological tissue is the first step in robust microscale mechanical characterisation. A fresh tissue analysis should lend itself to a more realistic profile of the native mechanical microscale properties of the tissue to help develop our understanding of the effects of disease on tissue structure.

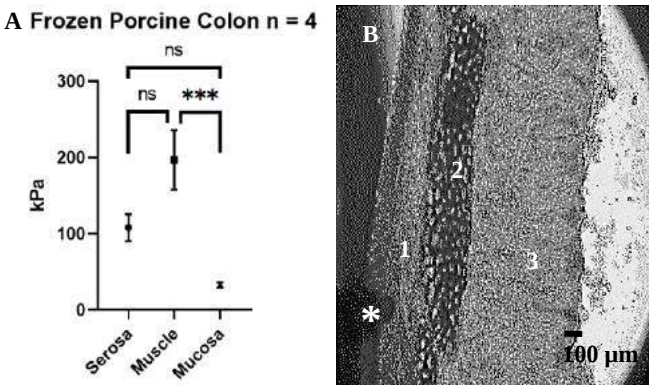


**Figure 1 A) Results from nanoindentation of frozen porcine colon sections (n=4). Significant difference between the 3 layers of the colon depicted B) Nanoindentation of frozen porcine sample *Probe tip 1. Serosa 2.Muscularis propria 3. Mucosa**


## ACKNOWLEDGEMENTS

Irish Research Council Enterprise Partnership Scheme with Becton Dickinson EPSPG/2020/467.

The authors wish to acknowledge Fitzgerald's Butchers for the provision of the porcine colon tissue characterised in this study.


## REFERENCES


[1] Bray, F *et al.*, *CA Cancer J Clin*, vol. 68, no. 6, pp. 394-424, Nov 2018, doi: 10.3322/caac.21492.

[2] CancerResearchUK. "Survival." Cancer Research UK. https://www.cancerresearchuk.org/about-cancer/bowel-cancer/survival (accessed 17/08/2021, 2021).

[3] Li, M *et al.*, *Expert Opin Drug Metab Toxicol*, vol. 12, no. 2, pp. 175-90, 2016, doi: 10.1517/17425255.2016.1125882.

[4] Siri, S *et al. Bioengineering*, vol. 7, no. 4, 2020, doi: 10.3390/bioengineering7040130.

[5] I. A. de Graaf *et al.*, "Preparation and incubation of precision-cut liver and intestinal slices for application in drug metabolism and toxicity studies," (in eng), *Nat Protoc*, vol. 5, no. 9, pp. 1540-51, Sep 2010, doi: 10.1038/nprot.2010.111.

[6] Islam, MR *et al.*, *Journal of Biomechanics*, vol. 113, p. 110090, 2020/12/02/ 2020, doi: https://doi.org/10.1016/j.jbiomech.2020.110090.

[7] Optics11Life, "User Manual Chiaro Nanoindenter ", ed: Optics11Life, 2020.

[8] M. J. Sanderson, *Pulm Pharmacol Ther*, vol. 24, no. 5, pp. 452-65, Oct 2011, doi: 10.1016/j.pupt.2011.05.001.

[9] Jones MV *et al.*, *Biotechniques*, vol. 42, no. 5, pp. 569-70, May 2007, doi: 10.2144/000112456.

# PATIENT-SPECIFIC MODELS REVEAL HIGH INTERFRAGMENTARY STRAIN IN DISTAL FEMUR FRACTURE FIXATION

**J. Inacio (1), P. Schwarzenberg (1), R. Yoon (2), A. Kantzos (3), A. Malige (3), C. Nwachuku (3), H. Dailey (1)**

(1) Department of Mechanical Engineering and Mechanics, Lehigh University, Bethlehem, PA, USA
(2) Department of Orthopaedic Surgery, Jersey City Medical Center – RWJ Barnabas Health, Jersey City, NJ, USA
(3) Department of Orthopaedic Surgery, St. Luke's University Health Network, Bethlehem, PA, USA

## INTRODUCTION

Despite extraordinary recent advances in unraveling the genetic and molecular mechanisms of bone fracture healing, clinical fracture care remains fraught with guesswork. The goal of surgery is to assemble an implant construct that will be strong enough to avoid fatigue failure, yet compliant enough to generate mechanical strain at the fracture site and stimulate bone healing. However, strain is impossible to measure *in vivo*, so surgeons rely on rules of thumb developed over decades of practice to help guide intra-operative construct selection.

Modern ideas about mechanoregulation of bone healing have their roots in Stephan Perren's seminal 1979 paper [1,2]. From this work, the widely reported strain limits for secondary bone healing are 2-10%, with strain greater than 10% predisposing a fracture to nonunion. Since the introduction of this strain rule, several preclinical studies, including a study coauthored by Stephan Perren himself, have demonstrated that fracture healing can occur at strains far greater than 10% [3,4], which is contrary to what surgeons are taught to believe in their clinical training.

Therefore, the purpose of this study was to use patient-specific finite element modeling to virtually measure the interfragmentary strain environment in clinically realistic fractures. The hypothesis of this study was that in the early post-operative period, the tissues in and around the fracture gap can tolerate a state of strain greatly in excess of 10%.

## METHODS

Patients with distal femur fractures (OTA/AO 33-A/B/C) treated in a single Level I trauma center over a ten-year period were retrospectively reviewed. Eight representative cases (6 males, 2 females; ages 22-95 years), all treated with lateral bridge plating, were selected for virtual mechanical testing. Routine preoperative computed tomography (CT) scans were imported into Mimics (v23.0, Materialise, Leuven, Belgium) for segmentation (Fig. 1A). As described in an earlier study, a lower threshold of 160 Hounsfield Units (HU) was used to isolate the distal femur fragments from the neighboring bones and soft tissue [5]. These fragments were individually identified (Fig. 1B). The proximal portion of the fractured femur, which is missing in routine pre-operative imaging of distal femur fractures, was virtually reconstructed using an intact femur (Fig. 1B-D).

Bone fragments were then virtually realigned to represent the surgical reconstruction. A minimum fracture gap of 2.5mm was created between all fragments, across all models. Where applicable, the articular surface was completely reduced and fused, representing standard clinical practice for articular reconstruction. A 3D interfragmentary strain visualization region was added to calculate strains within and around the fracture gaps. Each anatomically reduced model was then virtually fixated using a 4.5mm variable angle (VA) curved condylar locking compression plate (LCP) (DePuy Synthes, Pennsylvania, USA) (Fig. 1E). A physical plate was used as a reference to recreate the 3D virtual plate model in SolidWorks 2020 (Dassault Systemes SolidWorks Corps., Massachusetts, USA). Post-operative X-rays and the VA LCP surgical technique guide were both referenced to match each model to the clinical scenario for each case.

All finite element meshes were generated using 3-Matic (v15.0, Materialise, Leuven, Belgium). A quadratic tetrahedral (tet-10) element type with a maximum edge length of 1.5 mm was applied to both the surfaces and volumes of every model (Fig. 1F). Radiodensity [HU] in the scans was converted to bone mineral density using a phantom calibration, which in turn was used to calculate apparent density, $\rho_{app}$, and then Young's modulus, $E$, using a power-law scaling equation [7]:

$$E = 8.92 * i\rho_{app}^{1.83} \quad (1)$$

This material assignment relationship, along with a Poisson's ratio, $\nu$ = 0.3 was applied for all the elements (Fig. 1G).

Finite element simulations were carried out in ANSYS Workbench (vR2020, ANSYS Inc., Canonsburg, PA, USA). For each model, three different axial loads (20%, 60%, and 100% body weight (BW)) were

applied through the centroid of the femoral head, directed distally along the mechanical axis, replicating a common bench-test condition for single-leg stance (Fig. 1H). The axial displacement [mm] of the femoral head along the z-axis was recorded and used to calculate construct axial stiffness [N/mm]. The pre- and post- deformed locations of the medial-most nodes on the distal and proximal fracture surfaces were recorded for gap closing strain calculations.

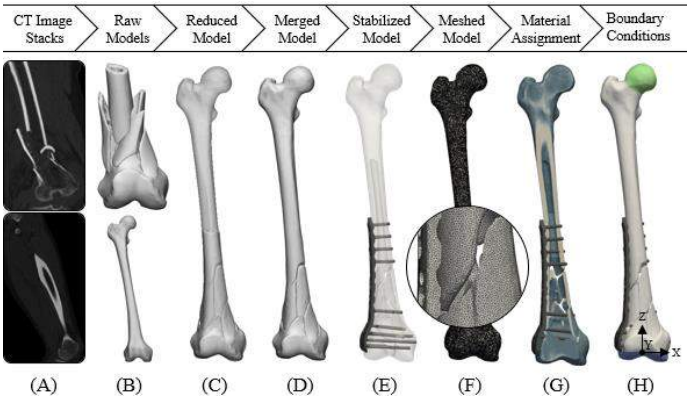


**Figure 1: Work flow for building a patient-specific finite element model of a plated distal femur fracture.**

## RESULTS

Models for the eight clinical cases are shown in Fig. 2A. Bridge spans (distance between screws across the fracture line) ranged from 21 to 126 mm. Elements with von Mises strains >10% are shown in Fig. 2 for the 100% body weight loading condition. For the three loading scenarios (20%, 60%, and 100% BW), as the bridge span increased, so did the maximum von Mises strain within the strain visualization region and the total volume of elements with strains greater than 10%. This behavior can be better visualized in the results shown in Figure 3. The average gap closing strain (mean ± SD) for all patient-specific models at each body weight (20%, 60%, and 100%) was 8.6% ± 3.9%, 25.8% ± 33.9%, and 39.3% ± 33.9%, respectively, while the corresponding max von Mises strain was 42.0% ± 29%, 110.7% ± 32.7%, and 168.4% ± 31.9%.

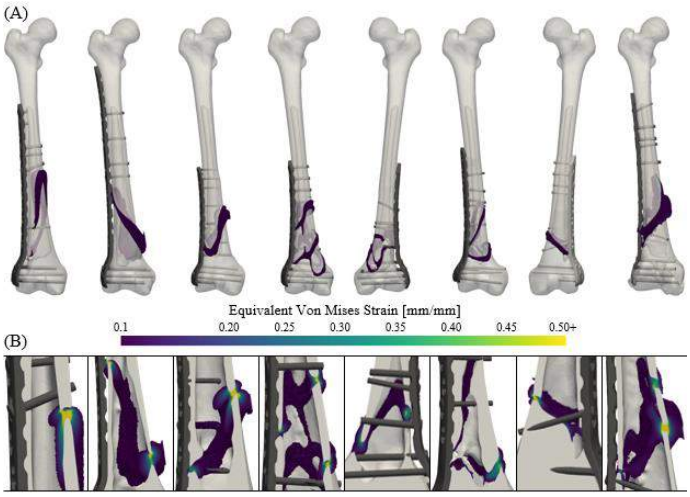


**Figure 2: (A) Anterior-posterior view of elements with strains >10%. (B) Magnified section views of each model illuminating the large strain values within the fracture gap. Note: Models were scaled to the same height for illustration purposes.**

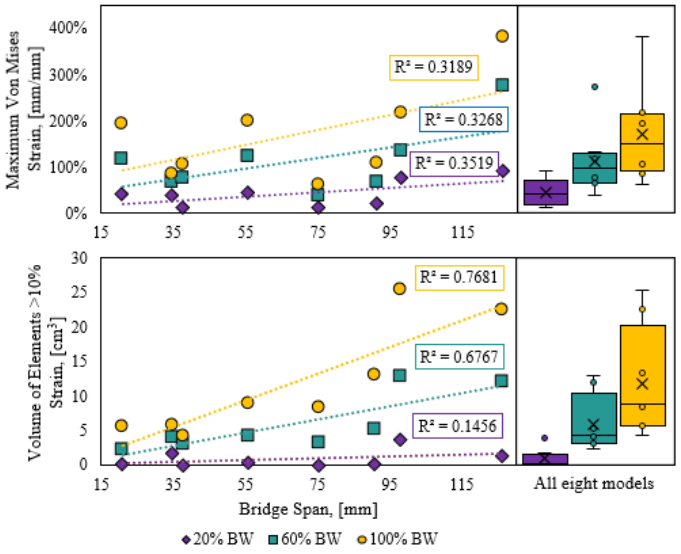


**Figure 3: The max von Mises strain and volume of elements with strains greater than 10% for three loading scenarios (20%, 60%, and 100% BW) across the eight models.**

## DISCUSSION

This study showed that strains in and around the fracture gap stayed in the 2-10% range only for the lowest load application level (20% BW). Moderate loading of 60% BW and above caused gap strains that far exceeded the upper limit of the classical strain rule (i.e., <10% strain for bone healing). Since all of the patients included in this investigation resulted in successful unions, these findings indicate that *in vivo* healing of distal femur fractures may be more robust to localized strains greater than 10%. Additionally, to better characterize the complex interfragmentary strain environment, the von Mises strain was evaluated in our study. Unlike the traditional, one-dimensional gap strain measurement, the method developed herein gives greater insight into the true strain environment which regulates fracture healing. Gap strain measures the motion between axially opposing points across an idealized fracture line, whereas the von Mises strain allows characterization of the full strain field throughout fracture pattern (see Fig. 2A). Gap strain is frequently reported because it is easily measured in both virtual and physical osteotomy models, but this parameter only assesses axial motion and disregards the associated shear strains entirely. This study showed that shear-dominated conditions can exist for the tissues in and around the fracture line, even without large gross shearing motions of the bone fragments. Excessive shear motion has been shown to be detrimental to the fracture repair process compared to axial motion [8], but this study revealed that shear-dominated strains may be much higher than has been previously appreciated and that this does not necessarily predispose a fracture to nonunion. These findings may have significant implications for the development of orthopedic implants because allowable fracture-site motion has long been a key design input, but the target specifications may be over constrained.

## REFERENCES


[1] Perren, S.M. et al., *Clini. Orthop. Relat. Res.*, 138:175-196, 1979.
[2] Perren, S.M. et al., *J. Bone Jt. Surg.*, 84(8):1093-1110, 2002.
[3] Claes, L.E. et al., *Clin Biomech.*, 10(5):227-234, 1995.
[4] Hente, R.W. et al., *J. Biomech.* 125:110576. 2021.
[5] Inacio, J.V. et al., *Clin. Biomech.* 67:20-26. 2019.
[6] Schileo, E. et al., *J. Biomech*. 41(11):2483-2491.
[7] Morgan, E.F. et al., *J. Biomech.* 36(7):897-904.
[8] Augat, P. et al., *J. Orthop. Res.*, 22(5):1156-1157, 2004.

# FEEDBACK TEMPERATURE CONTROL FOR MAGNETIC HYPERTHERMIA THERAPY TO TREAT GLIOBLASTOMA

**A. Jangam (1), J. Low (1), A. Ahmad (1), A. Sharma (2), R. Ivkov (2), A. Attaluri (1)**

(1) Department of Mechanical Engineering, The Pennsylvania State University Harrisburg, Harrisburg, PA, United States
(2) Department of Radiation Oncology and Molecular Radiation Sciences, Johns Hopkins University School of Medicine, Baltimore, MD, USA

## INTRODUCTION

Glioblastoma (GBM) is a common and one of the most lethal types of brain tumor in adults [1]. Current treatment procedures for GBM are surgical resection followed by a combination of fractionated radiation and chemotherapy [1,2]. The main issue with current GBM treatment methods is that it recurs due to the infiltrated cancer cells which reside away from the tumor bulk, close to the tumor margins [1]. These cancer cells are found to be resistant to both chemotherapy and radiation therapy [1]. To overcome this problem, we propose the combined use of magnetic hyperthermia therapy (MHT) with chemotherapy and radiation therapy. MHT inhibits DNA-damage repair and enhances drug distribution through increased perfusion. MHT is a process of increasing the tumor temperature within the range of 41-46°C, from heat deposited by magnetic nanoparticles (MNPs) through magnetic hysteresis, when exposed to radiofrequency (RF) magnetic fields. The goal for MHT is to achieve a uniform isoeffect thermal dose of CEM 43 °C ~ 60-90 mins for ≥ 90% of tumor volume [1,3]. However, heterogeneous MNP distribution within the tumor results in non-uniform temperature and thermal dose distribution. Additionally, non-specific eddy current-based heating can result in damage of healthy tissue. In this study, we present the use of a feedback control system that achieves the target temperature and thermal dose through proportional-integral-derivative (PID) control of field amplitude and pulse width modulation (PWM) control of power to minimize heating of healthy tissue.

## METHODS

### a. 1.2 kW System-Small Animals

A 1.2 kW induction system was used for the small animal testbed. The system consists of the following main components: an induction system and custom coil, the temperature sensors, and the controls system hardware. The experimental setup is as shown in Figure 1.


**Figure 1: Experimental setup of the 1.2 kW system**

The signals from the fiber optic probe (FISO Technologies) consisting of four gallium arsenide (GaAs) temperature sensors–spaced 2 cm apart–are sent to the signal generator (FISO EVO-RM-8 Rack-Mount with FISO FPI-HR modules) which converts the raw data to voltage signals. A National Instruments (NI) CompactRIO (NI cRIO 9042) with the Multifunction I/O module (NI 9381) converts the voltage signals to temperature data in °C. The cRIO 9042 also controls the power output of the 1.2 kW induction power supply (Ambrell EASYHEAT 0112) with a 0-5V analog signal.

The closed-loop temperature feedback control model (*Figure 2*) and graphical user interface (GUI) (*Figure 3*) were developed in NI LabVIEW. A PID controller is used to maintain the probe temperature ($T_{probe}$) at the setpoint value ($T_{ref}$). The temperature error:

$$e(t) = T_{ref} - T_{probe} \quad (1)$$

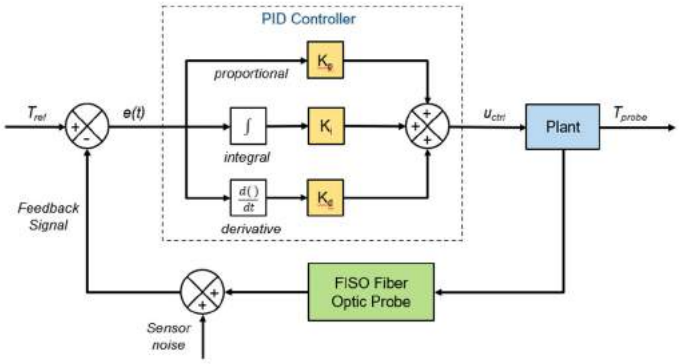


**Figure 2: Feedback controller block diagram**

was used to control the power output of the induction heating system by the following governing equation:

$$u_{ctrl} = K_p e(t) + K_i \int_0^t e(t)\,dt + K_d \frac{d}{dt} e(t) \qquad (2)$$

where $u_{ctrl}$ is the controller output. The initial gains ($K_p$, $K_i$, $K_d$) were determined with manual tuning.

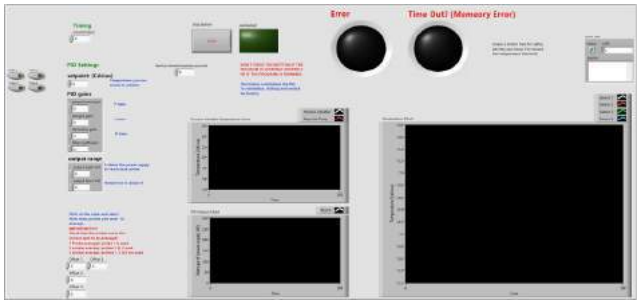

**Figure 3: GUI of the control system with user defined setpoint temperature, PID gain values, sensor selection and offset values.**

**b. 120 kW System-Large Animals**

The PID controller verified on the small animal testbed was implemented on a large animal system consisting of a 20 cm diameter water cooled modified Maxwell-type induction coil powered by a 120 kW induction power supply. Figure 4 shows the setup of the control system for large animals.

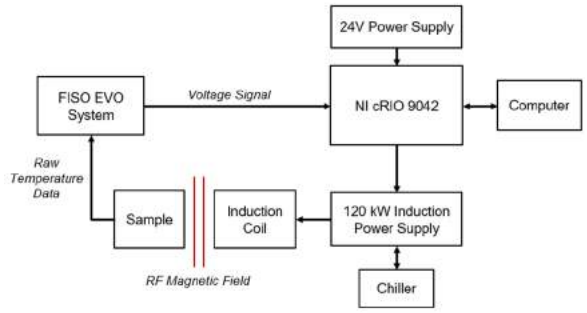


**Figure 4: Schematic of the 120 kW large animal system**

Initial evaluation of the developed closed-loop temperature feedback controlled 120 kW medical induction heating system was performed by heating a uniform distribution of MNPs in agarose gel in an Eppendorf tube. The FISO fiber optic probe was placed at the center of the gel with MNPs sample. A set point of 25°C was used. Commercial finite element (FE) software, COMSOL Multiphysics, was used to develop a coupled electromagnetic-thermal model. An initial set of PID gains ($K_p$ = 10, $K_i$ = 0.5, and $K_d$= 1) were obtained based on the FE simulation.

## RESULTS

Figure 5 shows the setpoint temperature, measured temperature of MNPs in agarose gel and the voltage response from the PID controller. The PID controller achieved setpoint temperature (25 °C) in 53 sec with a 0.08% error, overshoot < 0.034°C (0.13 %), and a shorter settling oscillation time (< 10 ms). The inset in Figure 5 shows the overshoot and stabilizing response of the temperature measurement.

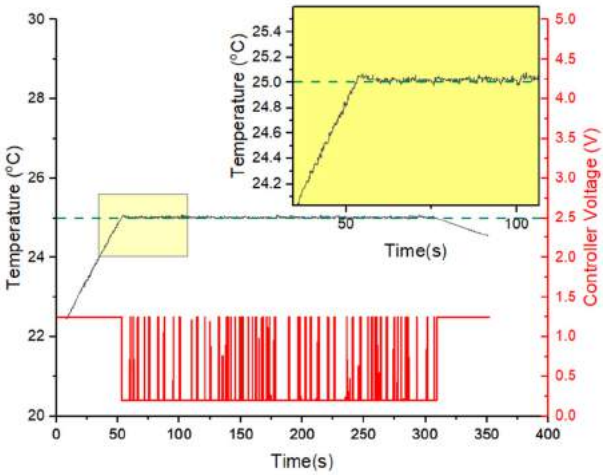


**Figure 5: Temperature of MNPs in agarose gel at 2.5 mg Fe/ml with time. Modulation of heating power using a PID controller to achieve and maintain $T_{ref}$ of 25 °C at the probe location.**

## DISCUSSION

The experimental results show that the experimental induction setup can successfully heat and maintain the heat source at the setpoint temperature. The developed PID controller achieved the target specifications of ±0.525°C within 200 sec. The controller also acted to minimize overshoot and stabilize the temperature response of the system. However, the controller fluctuation between the maximum and minimum voltage values still presents an issue. Fine tuning the PID gain parameters will help achieve optimization between target temperature control and eddy current heating. Future work will include an analytical approach to calculating the gain values, and additional safety features in compliance with FDA device design guidelines. A copper strip in agarose gel will be used for the validation and verification of the system.

## ACKNOWLEDGEMENTS

This project was made possible through the National Institute of Health (NIH) Research Project Grant Project (R01) 5R01CA247290-02. We would also like to thank Mr. Nathan Werkheiser for his technical inputs.

## REFERENCES

[1] Mahmoudi, K et al., *Int. J. Hyperthermia,* 34(8):1316-1328, 2018.
[2] Stupp, R et al., *N Engl J Med,* 352:987-996, 2005.
[3] Attaluri, A et al., *Int J Hyperthermia,* 31:359-374, 2015.
[4] Attaluri, A et al., *J. Nanotechnol. Eng. Med.*, 4(1):011006, 2013

# TENSILE RESPONSE OF THE MURINE UTEROSACRAL LIGAMENT IS NONLINEAR AND SPATIALLY INHOMOGENEOUS

**Lea M. Savard (1), Catalina Bastías (2), Kathleen Connell (3)**
**Sarah Calve (1, 2, 4), Callan M. Luetkemeyer (1), Virginia L. Ferguson (1, 2, 4)**

(1) Department of Mechanical Engineering, University of Colorado at Boulder, Boulder, CO, USA
(2) Biomedical Engineering Program, University of Colorado at Boulder, Boulder, CO, USA
(3) Department of Obstetrics and Gynecology, University of Colorado Anschutz, Aurora, CO, USA
(4) BioFrontiers Institute, University of Colorado at Boulder, Boulder, CO, USA

## INTRODUCTION

In the United States, 12% of women undergo gynecological surgery to treat Pelvic Organ Prolapse (POP) [1]. POP is characterized by the descent of the pelvic organs, including the bladder, uterus, and rectum, causing lower intestinal and urinary tract disorders, as well as general discomfort [2]. Multiple factors known to be associated with POP include aging, increasing BMI, and parity (i.e., the number of times a woman has given birth), all of which decrease the mechanical integrity of the reproductive system support tissues [2,3]. These support tissues include the uterosacral ligament (USL), which is the primary structure for apical vaginal support. Damage to and failure of the USL due to biomechanical injury results in the protrusion of the uterus and/or vagina, or POP [2].

Traditional prolapse surgical techniques using native tissue repair have poor short-term outcomes, with up to 30% recurrent prolapse at 2 years postoperatively, due in part to insufficient knowledge on how to properly repair these damaged support tissues [1]. Histological studies have demonstrated decreased total collagen and elastin fiber content in the reproductive connective tissues following delivery and POP, suggesting diminished strength and impaired extensibility, but there lacks data and methodology to describe the tissue's change in mechanical behavior [3]. In combination with histological and proteomic data, this mechanical information will elucidate the relationship between structure and function in the USL which can help to better identify who is most at risk for POP, how we might mitigate their risk, and inform new POP treatment strategies. In this study, we developed a method to evaluate the mechanical properties of the murine USL. Mouse models are advantageous for studying the USL and POP due to their short gestation times and many genetically modified lines, which will help us study how pregnancy and extracellular matrix composition, respectively, affect USL behavior and injury.

## METHODS

Female mice (one nulliparous and two multiparous) were obtained and euthanized according to the University of Colorado Boulder's Animal Care and Use Committee. In each mouse, the bony pelvis, and the attached USLs and cervix were isolated. The cervical end of one USL was tied with a 5-0 polyglactin suture and the uterus was removed, leaving only the cervix attached to prevent the suture from sliding off the tissue. The other USL was removed, such that only one USL remained attached to the sacrum, which is within the extracted pelvic tissue. The freshly harvested cervix-USL-pelvis sample was placed in Ghost Dye Red 780 (Tonbo Biosciences) and NucBlue Reagent (ThermoFischer Scientific) stain for 2 hours at 4°C.

A custom loading chamber with a PBS bath was mounted under a confocal microscope (Leica STELLARIS), attached to a Femtotools actuator and an in-line 10 N load cell (Futek). Two custom 3D printed grips were fabricated to secure the cervix and pelvis in the loading apparatus (Fig. 1). Once secured, the actuator was positioned to remove all slack from the USL, with approximately a 0.01 N preload, which we referred to as the reference configuration.

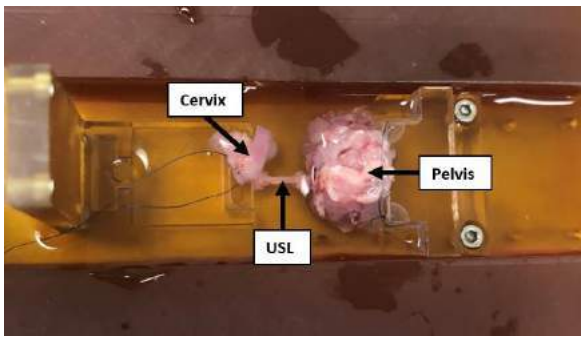


**Figure 1. Cervix-USL-pelvis in custom loading chamber**

The surface of the USL was imaged at 10× magnification in its reference configuration. Each USL was then subjected to three stress relaxation tests, coming back to its reference position following each test. Applied displacements were 1000 µm, 2000 µm, and 3000 µm, applied at 50 µm /s. Each stretched configuration was held for 10 minutes while the specimen's surface was imaged again at 10×. The confocal images of the stained USL were used to map deformation with the Matlab function 'imregdemons'.

Preliminary assessment of the viscoelastic behavior of the USLs was performed using macroscopic displacement and force data. Percent force relaxation was calculated as:

$$\frac{F_{max}-F_{eq}}{F_{eq}} \times 100\% \quad (1)$$

where $F_{max}$ is the maximum force and $F_{eq}$ is the equilibrium force.

## RESULTS

Our preliminary results demonstrate that deformation in the USL is inhomogeneous and the tensile response is nonlinear. Figure 2 shows the Lagrange strain fields of one USL from a multiparous mouse at an applied displacement of 1000 µm. The maximum strain experienced was 0.18 in the axial direction, and there was heterogeneous compression and extension experienced in the transverse (perpendicular) direction to loading. The strain is not uniform across the ligament, and there appears to be a periodicity to the strain in the main $E_{11}$ loading direction.

Moreover, global normalized force vs. time curves indicate that the USL is a nonlinear viscoelastic material (Fig. 3). The multiparous mouse USL held larger forces than the nulliparous USL at each global displacement state, with maximum forces of 0.156 N and 0.075 N respectively, both at the 3000 µm stretch. For both specimens, the equilibrium forces increased nonlinearly with increasing displacement. Over the three stretch states, the nulliparous USL exhibited 43.7% relaxation on average, and the multiparous USL experienced 31.7% relaxation on average. The amount of relaxation varied with each stretch state.

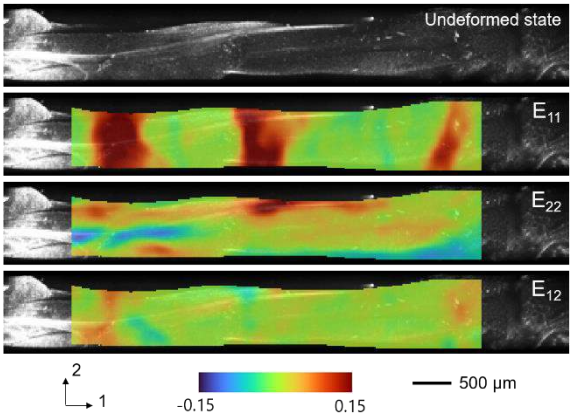


**Figure 2. Reference configuration and associated strain fields for a multiparous murine USL at an applied displacement of 1000 µm**

## DISCUSSION

The USL from the nulliparous mouse used in this study exhibited more viscoelastic relaxation than the USL from the multiparous mouse, despite lower overall loads. This finding is congruent with work from Yao et al. that demonstrates nonpregnant mice cervixes experience larger relaxation than pregnant mice [4]. The nulliparous USL also displayed a more nonlinear response than the multiparous USL, as determined by the larger disparity in loads and relaxations in each stretch state. Understanding how the viscoelastic and nonlinear properties of the USL change during pregnancy and postpartum may help in clinical settings to determine who is most at risk for POP. However, due to the heterogeneity of the strain field, strain homogeneity cannot be assumed for material modeling.

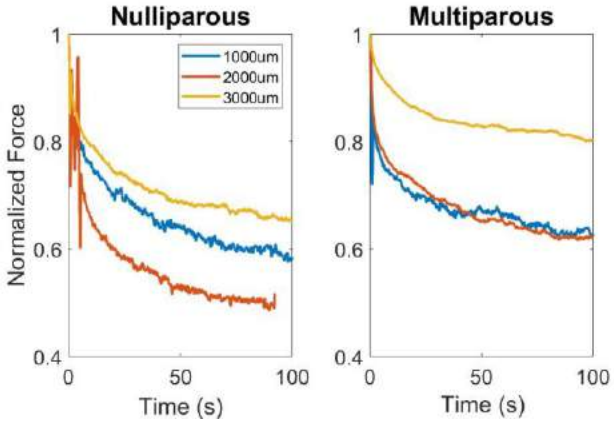


**Figure 3. Normalized force relaxation curves at applied displacements of 1000 µm, 2000 µm, and 3000 µm for a nulliparous (left) and a multiparous (right) murine USL**

The experimental methods developed and presented here will allow for the identification of USL viscoelastic properties from tensile tests with heterogeneous and multimodal strain. Nonlinear viscoelastic behavior will be confirmed and fully characterized. Full-field deformation maps like those shown in Fig. 2 will be used in conjunction with full-field inverse methods to build constitutive models and damage criteria for the USL in future work.

The work provided above reflects preliminary work, where the mice that have been tested were not age- or strain-matched. Future studies will control for these additional factors. Limitations of this preliminary study are in the small number of samples, the difference in USL length and preload in its reference state, and inconsistent staining. The planned future study will have n=8 mice in each group, will be more consistent in preload measures, and will use a newly constructed staining chamber to ensure the entire length of the USL is stained to improve deformation tracking.

We will use this new technique to examine how the mechanical properties of the murine USL change during pregnancy, post-partum, and after multiple births. In combination with proteomics and histology, this work will lend insight into new treatment and prevention strategies for POP.

## ACKNOWLEDGEMENTS

This work was supported by the NSF Graduate Research Fellowship (LS), the Schmidt Science Fellowship (CL) and other funding provided by the University of Colorado Innovative Grant Program and the Anschutz Boulder AB Nexus Seed Grant Program.

## REFERENCES

[1]: Danso, EK *et al*., *Sci Rep*, 10:1-14, 2020.
[2]: Jelovsek, JE *et al*., *Lancet*, 369:1027-1038, 2007.
[3]: Kerkhof, MH *et al*., *Int Urogynecol J Pelvic Floor Dysfunct*. 20:461-474, 2009.
[4]: Yao, W *et al*., *Journal of the Mechanical Behavior of Biomedical Materials*, 34:18-36, 2014.

SB³C2022
Summer Biomechanics, Bioengineering and Biotransport Conference
June 20-23, Eastern Shore, MD, USA

# THE EFFECTS OF FORMATION CONDITIONS ON EMBOLUS ANALOG NONLINEAR, TIME-DEPENDENT MECHANICAL PROPERTIES

**Jose L. Monclova (1), Gretchen E. Hiller (1), Priyanka Patki (1), Francesco Costanzo (1,2), Keefe B. Manning (1,3)**

(1) Department of Biomedical Engineering, University Park, Pennsylvania, USA
(2) Department of Engineering Science and Mechanics, The Pennsylvania State University, University Park, Pennsylvania, USA
(3) Department of Surgery, Penn State Hershey Medical Center, Hershey, Pennsylvania, USA

## INTRODUCTION

Stroke and cardiovascular disease, conditions caused by thromboembolization, are leading causes of death in the United States [1]. Recent studies suggest that, in addition to embolus morphology, their mechanical properties contribute to complications in removal procedures [2,3]. Mechanical characterization of emboli is critical to the design of new procedures and techniques to improve clinical outcomes. However, the study of emboli removed from patients is complicated due to the time lapse between embolus removal and characterization in a lab. For this reason, embolus analogs (EAs) are commonly used in a laboratory setting and are often paired with computational modeling to bridge the gap to clinical applicability. EAs and clinical emboli are most commonly modeled as nonlinear viscoelastic tissues [refs. Irish group]. However, our recent experiments indicate that EAs discharge fluid when mechanically loaded, suggesting that their behavior might be poroelastic, as seen in brain tissue [4]. The goal of this project is to characterize the behavior of EAs with varied hematocrit when loaded in compressive relaxation and cyclic loading.

## METHODS

**EA formation conditions:**

To study the effect of EA composition and storage conditions on their load bearing properties, EAs were created using bovine blood, following approved institutional IACUC protocols. Briefly, extracted whole blood was anticoagulated with 6.45% wt. citrate-phosphate-dextrose with adenine (CPDA). Blood was separated into red blood cells, platelet rich plasma (PRP), and platelet poor plasma (PPP) via centrifugation. Blood was reconstituted to 214 x $10^6$ platelets per mL. Hematocrit was varied in EAs by addition of 0%, 20%, 40%, and 60% vol. red blood cells. To counter the effects of the anticoagulant, blood was recalcified with 11 mM calcium chloride ($CaCl_2$). Recalcified blood was mixed and injected into 24-well plates to form cylindrical clots for mechanical testing. To study the effect of static versus dynamic formation of EAs, blood was left in a warm room and formed statically on a benchtop or dynamically on a rocking plate. Blood was left for 24 hours at 37°C for EAs to form.

**EA mechanical testing:**

All EAs were tested in compression using an Instron (Norwood MA, USA) uniaxial load frame. To investigate the time dependent properties of EAs under the various conditions, EAs were removed from well plates and loaded at a rate of 5% strain per second to 10% strain and held for 30 seconds. Percent relaxation and peak stresses were calculated from the resultant curves. To investigate the time dependent effects of cyclic loading, EAs were compressed cyclically to 10% strain for 50 cycles, at 5% strain per second. Area between the loading-unloading curves were computed as an indicator of energy loss over time in the material.

**Statistics:**

Due to variability in coagulation, clot contraction, and other factors, multiple sources (n = 6) were collected with replicates (n = 6) tested for each source. For this reason, mean values were computed with standard error of the mean, and t-tests were performed between samples to determine significant changes in parameters.

## RESULTS

For the compressive relaxation tests, peak stresses for statically formed EAs were 0.55 ± 0.02, 0.49 ± 0.02, 0.48 ± 0.01, and 0.55 ± 0.01 kPa for 0, 20, 40, and 60% hematocrit, respectively. For the dynamically formed EAs, the peak stresses were 0.65 ± 0.04, 0.61 ± 0.02, 0.63 ± 0.02, and 0.73± 0.04 kPa for 0, 20, 40, and 60% HCT, respectively. The percent relaxation for static EAs was 100 ± 0, 100 ± 0, 100 ± 0, and 99.09 ± 0.67 kPa for HCTs from 0% to 60%, respectively. For dynamic EAs, the percent relaxation after 30 seconds was 100 ± 0, 100 ± 0, 100 ± 0, and 97.75 ± 0.67 for 0, 20, 40, and 60% HCT, respectively. These data were calculated as the final stress over the peak stress from the relaxation curves shown in **Figure 1.**

Preliminary data for area under the curve from **Figure 2.** were calculated from the area between the loading and unloading curves. The change in area from the previous cycle falls below 3% after roughly 25 cycles for all hematocrits.

## DISCUSSION

Peak stresses for each hematocrit decreased significantly, from 0% to 60% HCT, suggesting a softening of the material due to increased red blood cell content. However, no significant differences in peak stresses were observed between static and dynamic EAs, suggesting negligible differences between groups. This implies that the fiber distribution is similar for both formation protocols. From the percent relaxation data, complete relaxation was observed for nearly all hematocrits, except for the 60% HCT static and dynamic EAs. This suggests a high degree of relaxation, possibly related to the addition of highly viscous red blood cell content with increased hematocrit. This is similar to Boodt et al. who demonstrated no significant changes in lower elastic moduli in clinical EAs until hematocrit was above 60% [3].

The cyclic loading tests demonstrate an overall decrease in area between curves, with changes in area from cycle to cycle falling below 3% around cycle 25 for each hematocrit. This suggests an overall loss of energy stored in the EAs after repeated loading. Additionally, we observed fluid excretion at the end of each test, suggesting that the EAs hold fluid in a sponge-like manner until a stress is applied. Further investigation is needed to determine if fluid is reabsorbed after stress is released.

Overall, these data suggest a softening of these materials due to an increase in hematocrit content, and a corresponding decrease in hysteretic energy loss over time, as indicated by **Figure 2.** The static versus dynamic EAs showed no significant differences in peak stresses or percent relaxation, an indication that there is little difference in their load bearing properties. Finally, the cyclic loading demonstrates a behavior somewhat different from current understanding. Along with the observed EA leakage, the decrease in hysteretic energy loss suggests EAs behave more like a poroelastic material rather than a purely viscoelastic material. Future work will focus on the comparison of these two models and their relevance to modeling emboli.

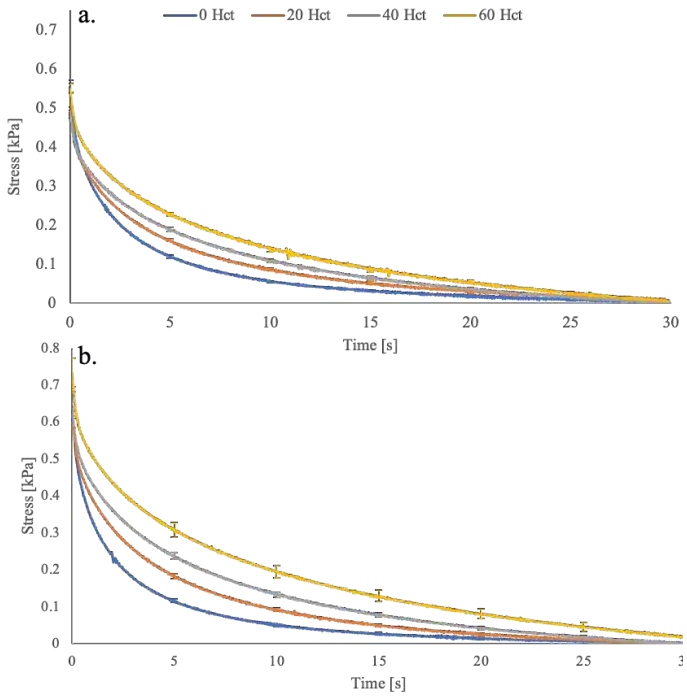


**Figure 1:** Relaxation curves for **a.** statically formed EAs and **b.** dynamically formed EAs with varied hematocrit.

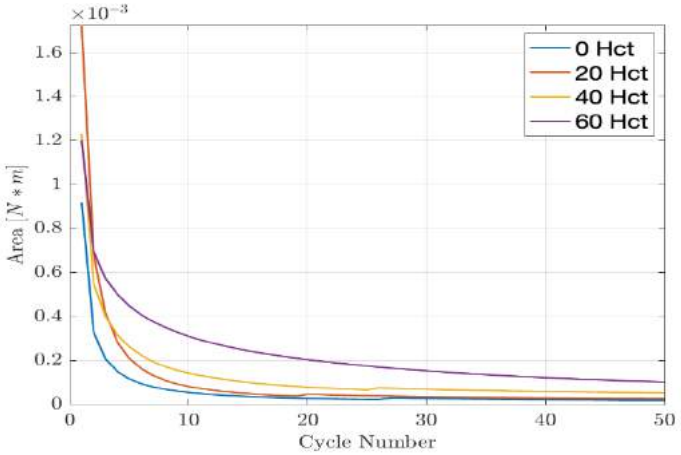


**Figure 2:** Area between loading and unloading curves for 50 compression cycles.


## ACKNOWLEDGEMENTS

This research was supported by NIH Grant HL146921, an Alfred P. Sloan Scholarship, and a Gates Millennium Scholarship.


## REFERENCES


[1] Murphy, S. *et al., NCHS Data Brief*, 38:4-5, 2017.
[2] Liu, Y. *et al., J. of Stroke and Cerebr. Diseases*, 29, 2020.
[3] Boodt, N. *et al., Stroke,* 52:2510-2517, 2021.
[4] Comellas, E. *et al., Comp. Methods in Applied Mech. And Eng.*, 369, 2020.

# ACCELERATED ACQUISITION OF *IN VIVO* CARTILAGE STRAIN USING COMPRESSED SENSING AND SPIRAL DENSE MRI

**Woowon Lee (1), Emily Y. Miller (2), Hongtian Zhu (1), Corey P. Neu (1,2)**

(1) Paul M. Rady Department of Mechanical Engineering, University of Colorado Boulder, Boulder, CO, USA
(2) Biomedical Engineering Program, University of Colorado Boulder, Boulder, CO, USA

## INTRODUCTION

Displacement encoding with stimulated echoes (DENSE) MRI provides deformation maps on a pixel level non-invasively, and is critical for analyzing the biomechanics of soft tissues [1]. Adapting *k*-space spiral scanning enhances the temporal resolution which ultimately extracts high resolution time-course displacement maps [2]. This approach allows for measurement of mechanical properties of soft tissue under rapid loading and motion such as walking, leading to potentially useful biomarkers for early joint degeneration. However, to gather high quality MR images using DENSE MRI, long scanning times are needed resulting in high cost, patient discomfort, and misregistration errors. To accelerate the imaging speed, we examine the use of compressed sensing (CS) on DENSE MR images collected on *in vivo* human knees. Subjects underwent varus loading at the ankle leading to compressive loading on tibiofemoral cartilage while the knee joint was imaged. Quantitative measures including signal-to-noise ratio (SNR) and displacement are compared between non-CS (NCS) and CS images, and we find that CS can reduce the MRI scanning time at least twofold while maintaining comparable image quality.

## METHODS

*Cyclic Varus Loading:* Six adults (3 males, 3 females, 25-35 years old) with no history of knee joint damage were recruited. A custom-built varus loading device was mounted on the clinical MRI (3T; Siemens Prisma$^{fit}$), and varus loading was applied on the ankle. We used a moment balance to make the varus load on ankle be equivalent to half body weight of force applied on the knee joint. Varus loading was applied on a cyclic fashion (100 ms delay, load 1 s, unload 1 s) leading to a loading frequency comparable with a walking cadence.

*Spiral DENSE MRI:* Multiple frames (27) of DENSE MR images were collected in magnitude and phase during varus loading. We used ten spiral interleaves to generate images, and two interleaves were collected for each loading cycle. An electric pulse triggered the MRI system to initiate and synchronize data acquisition. Imaging parameters were as follows: TE/TR=2.5/20ms, spatial resolution=360×360μm$^2$, slice thickness=1.7mm, displacement encoding gradient =0.32cycles/mm, and the number of image averages=8 (for high SNR images). Prior to spiral DENSE MRI acquisition, the loading cycle was applied for 8 minutes to achieve a quasi-steady state response [3], and high SNR doubled echo steady state (DESS) images were collected. The *k*-space data was archived to perform CS analysis.

*Displacement and Strain Calculation:* Articular cartilage regions of interest (ROIs) were manually segmented using custom software (MATLAB) and binary masks were created on the medial and lateral cartilage. Displacements for each pixel within the ROIs were determined from phase data [1]. Displacements were manually phase unwrapped followed by smoothing with a locally weighted scatterplot smoothing (LOWESS) filter for 10 cycles. Finally, in-plane Green-Lagrange strains were calculated from the smoothed displacements.

*Compressed Sensing:* We extracted the spiral trajectory and *k*-space data along the trajectory for each channel and image average. Subsequently the trajectory, *k*-space data, and the channel sensitivity map were analyzed using the Berkeley Advanced Reconstruction Toolbox [4] (BART) to run Parallel Imaging and Compressed Sensing (PICS) command for reconstructing the images. The regulation parameter was 0.01 and all processes underwent five iterations. The process was repeated for each image average and later were averaged after the reconstruction.

*Data and Statistical Analysis:* SNR of the DENSE MR images was calculated by analyzing regions depicting the medial condyle and background. We measured the average intensity for both regions and calculate the ratio. To measure the discrepancy of displacements with respect to the average 8 images, we calculated the root mean square error (RMSE) on selected ROIs for both NCS and CS images. To determine which image average was comparable with NCS average 8, we applied one-tailed paired t-test on the RMSEs for all averages of CS (n=6) with the RMSE of NCS average 7.

## RESULTS

Displacement and strain maps were collected on 27 time-lapse images during 1 s of loading. The DESS images reflected the displacement of the joint caused by varus load applied on ankle (Figure 1). Higher number of averages resulted in increased SNR, and additionally was linearly correlated with the scanning time (1 average=1.7 minutes, 8 averages=13.6 minutes). The displacement and strain in the medial condyle displayed heterogeneous patterns (Figure 2A). Low average displacement maps had an irregular pattern with more

noise compared to high average images laying out a smooth displacement pattern. CS reduced the roughness in displacement map. This displacement affected the strain measurement where clear compressive strain ($E_{yy}$) was observed on the medial condyle in the high average and CS images, but did not appear in the low average images.

We found that CS enhanced the image SNR and reduced the RMSE with respect to average 8 images (Figure 2B). SNR was consistently higher in CS images with any average than NCS images, while raw and smoothed RMSE were substantially lower in CS images. RMSE of both NCS and CS images gradually improved with averages. We found that the RMSE of average 4 CS image was 0.13mm, which was similar with the average 7 NCS image. The *p*-values comparing CS with NCS average 7 RMSE had a peak at average 3 and started to decline at average 4 indicating the non-significant difference with NCS average 7 and diverging starting from average 4.

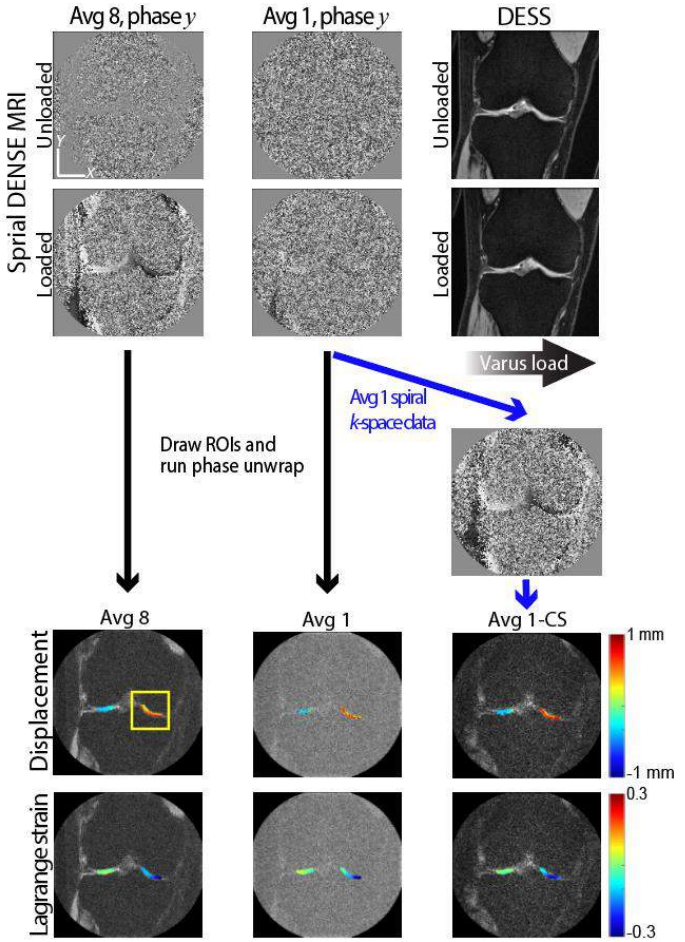


**Figure 1: Displacement and strain maps captured by spiral DENSE MRI with CS. DESS images show the translation of the knee due to varus load. To obtain the displacement maps, ROIs were drawn and we ran phase unwrapping on both low and high average images. CS was applied on the spiral *k*-space data, and followed the same process for obtaining displacement maps. Further analysis was conducted on the medial condyle (labeled in yellow box).**

## DISCUSSION

In this study, we explored the effects of CS on displacement and strain calcuation using sprial DENSE MRI. We confirmed CS can improve the image SNR and provides comparable results with high average images while needing half the scanning time (6.8 minutes). Further in-depth quantitative analysis is needed to assess the performance of CS on DENSE MRI. Nevertheless, this study demonstrates that CS applied on spiral DENSE MRI can significantly reduce the imaging time. As future work, this method can be applied to patients of different level of joint disease (e.g. in articular cartilage following ACL reconstruction), benefiting from the shortened imaging time, and can potentially discover biomarkers of tissue degeneration processes [5].

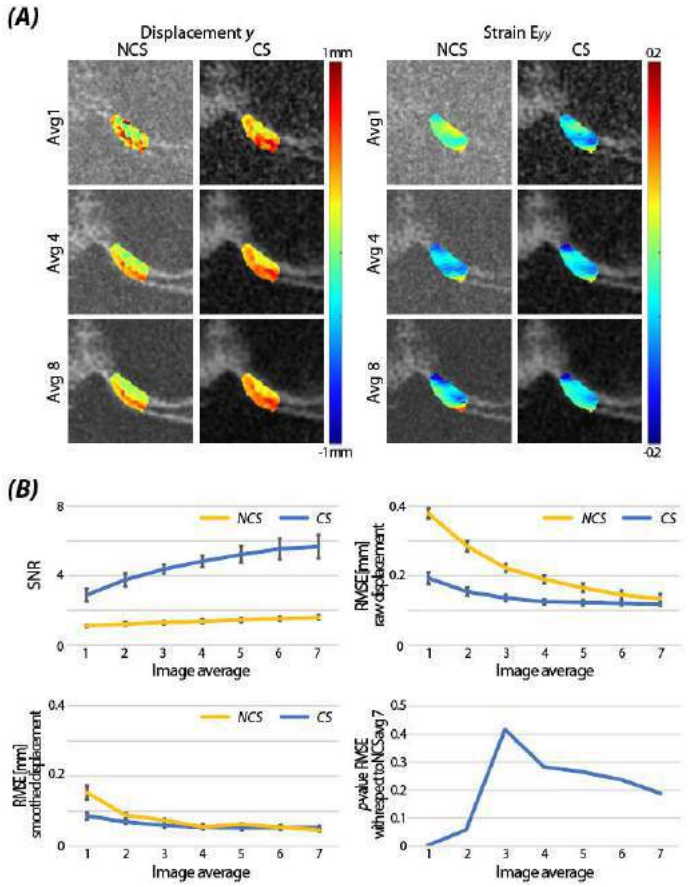


**Figure 2: NCS and CS comparison on displacement and strain. (A) Displacement *y* maps compared on frame 27 show SNR increases with more averages and applying CS smooths the displacement field. Compressive $E_{yy}$ strain is not observed in low average NCS images. (B) Quantitative analysis shows SNR increased and RMSE decreased after applying CS. Error bars represent the standard error.**


## ACKNOWLEDGEMENTS

The authors gratefully acknowledge NIH 2 R01 AR063712.


## REFERENCES


[1] Chan DD. et al., *Sci Rep*. 6, 19220, 2016
[2] Zhong X, et al., *Med. Phys*. 36, 3413–3419, 2009
[3] Neu CP, et al., *J Biomech Eng*. 125, 180-188, 2003
[4] Tamir JI, et al., *ISMRM Workshop*, 2016
[5] Khajehsaeid H, et al., *Biomechanics*. 1, 225-238, 2021

SB³C2021
Summer Biomechanics, Bioengineering and Biotransport Conference
June 14-18, Virtual

# BIOENGINEERED THREE-DIMENSIONAL LUNG AIRWAY MODEL TO STUDY NEONATAL INTRATRACHEAL SURFACTANT DELIVERY

**Hannah M. Combs (1), Hossein Tavana (1)**

(1) Department of Biomedical Engineering
The University of Akron
Akron, Ohio, USA

## INTRODUCTION

The lung contains a series of branching airways that lead to the respiratory zone. The respiratory zone houses the respiratory bronchioles and alveolar sacs. A low surface tension at the air-liquid interface of the alveolar sacs is critical to allow for the alveoli to remain open and facilitate gas exchange.[1] A low surface tension is maintained by the pulmonary surfactant secreted by mature alveolar cells. Pre-term infants have under-developed lungs and insufficient pulmonary surfactant production, causing breathing irregularities and potential lung collapse. This condition is known as Neonatal Respiratory Distress Syndrome (NRDS).[2] NRDS treatment consists of the intratracheal delivery of exogenous surfactant into the lungs in surfactant replacement therapy (SRT). Despite its benefits,[2] there is a high non-response rate of up to 35% to SRT, potentially due to inhomogeneous distribution of instilled surfactant. The optimization of delivery condidions is crucial to ensure a uniform distribution and increased efficieny that improves the outcomes of SRT. The goal of this study was to develop a 3D, biomimetic neonate lung model and study the distribution of surfactant in airways and the delivery efficiency.

## METHODS

A 3D computational lung model was designed in Solidworks using morphometric data from human lungs. The design began by constructing the trachea (z=0) with a diameter of 3.5 mm and a length of 17.5 mm.[3] The diameter of the trachea was designed to taper 13.5% to ensure for a smooth transition into the next generation. A bifurcation zone between each parent airway and daughter airways emerging from it was designed with an angle of $\theta$=80° and was rotated 90° in the gravitational space starting at z=3. The subsequent genrations were constructed following this strategy to create an eight generation model, i.e., z=0-7, of continuously branching airways (Figure 1a).[3,4] Physical models were fabricated using 3D printing. Prior to experiments, the model was subjected to oxygen plasma (Harrick Plasma) for 10 minutes to render the interior of airways hydrophilic. The model was pre-wetted with DI water. Then, a 140 µL plug of Infasurf (ONY, Inc) surfactant was instilled into the tracheal tube. The plug was propagated through the airways at a Capillary number of 0.016. The lung model was positioned at four different roll angles of $\alpha$=0º, 30º, 60º and 90º to simulate rolling of a neonate during SRT. A distribution index was quantified for the four lobes, upper right (UR), lower right (LR),

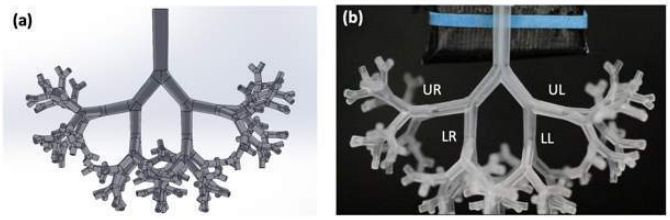


**Figure 1.** a) Computational multi-generation (z=0-7) neonate lung model developed in SolidWorks. b) Semi-transparent printed model. Four different lobes are labeled.

SB³C2022-186

lower left (LL), and upper left (UL) (Figure 1b) and an efficiency index was quantified using surfactant volume in z=5 airways.

## RESULTS

We found that rolling the model away from its center line at $\alpha$=0º to $\alpha$=30º, 60º, and 90º resulted in a significant increase in surfactant distribution to the UR lobe a decrease to the LL and UL lobes ($p < 0.05$). Our results indicate that as the roll angle increased, the gravitational force increased the fluid flow to the UR and LR lobes (Figure 2). We also found that the sum of the distribution indices for the four lobes increased as the model was rolled gradually to 90º. This result indicates that as the model was rolled, the surfactant passed through fewer airways, thus depositing less volume onto the walls and delivering more further down the airway tree.

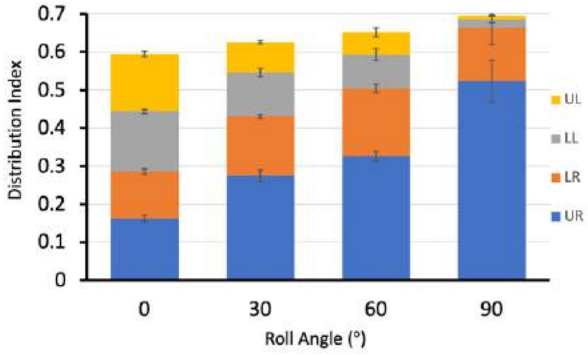


**Figure 2.** The distribution index for each lobe at various roll angles, representing the volume of surfactant to reach z=2 in each lobe.

We quantified volume of plugs in the distal airways (z=5) to determine the efficnecy of delivery when the model was rolled away from the horizontal plane. The efficiency was defined as the percentage of the total volume delivered to z=5 to the instilled dose in the z=0 airway. Our results showed that the efficieny increased significantly when the model was rolled from $\alpha$=0º to 60º, and 90º ($p < 0.05$). At $\alpha$=0º and $\alpha$=30º the efficiency was 43.0% ± 0.67 and 42.1% ± 0.67. As we increased the roll angle to 60º, the effiency increased significantly to 46.1% ± 0.67 ($p < 0.05$). A maximum efficieny of 60.1% ± 0.67 was found at $\alpha$=90º. The efficiency index indicates that a neonate positioned 90º on their side would receive a greater amount of surfantant to the distal airways than in any other position. We then evaluated how much of the instilled dose at a $\alpha$=0º was in certain regions of the lung model at z=5 for $\alpha$=0º and $\alpha$=90º. At $\alpha$=0º the right lung received 50.3% ± 2.46 of surfactant while the left lung received 49.7% ± 1.58 (Figure 3). At $\alpha$=90º the right lung receives 100% of the surfactant and the left lung received 0% (Figure 3). Although the maximum efficiency occurs at a $\alpha$=90º, fewer distal airways received surfactant in this orientation than at $\alpha$=0º. At a roll of 90º, the only lobe to receive surfactant was the UR lobe. The increase in effeicncy was due to the surfactant passing though fewer airways than at $\alpha$=0º but clearly indicates that the majority of the lung does not receive any surfactant, potentially decreasing the effectiveness of SRT at a roll angle of 90º.

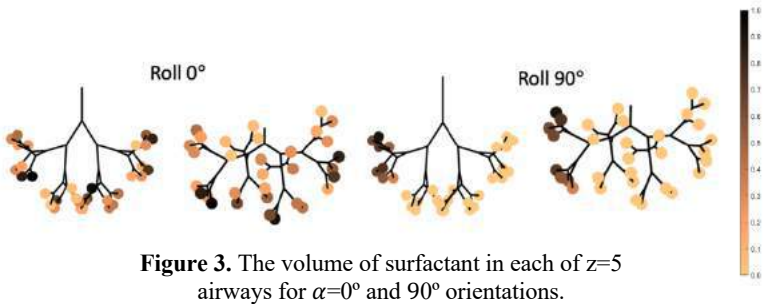


**Figure 3.** The volume of surfactant in each of z=5 airways for $\alpha$=0º and 90º orientations.

## DISCUSSION

Our 3D, eight-generation neonate lung airway model enabled simulating surfactant delivery. This case study suggests that when delivering surfactant during SRT, orientation should be considered prior to the delivery. Our findings showed that surfactant loss dependence on orientation could affect the clinical success of SRT. This study successfully demonstrated the utility of the model to study intratracheal therapeutics delivery taking into account orientation, hydrophilicity of airways, and flow rate of surfactant plugs. Our study presents a more elaborate understanding of SRT and validates previous computational studies in regard to the effects of orientation during SRT.[5] This model has the potential to advance drug delivery studies with respect to simulated environments and offers a device to study therapeutics effects at a cellular level. With the continuous use of these models, varies respiratory disorders may be studied for delivery methods, fluid dynamics, and the overall effects on the respiratory system.


## ACKNOWLEDGEMENTS

Support and Funding provided by The University of Akron to H.T and a grant 1904210 from the National Science Foundation (NSF).


## REFERENCES


[1] H. Tavana et al., *Lab. Medicine.* 40 (2009) 203-209.
[2] T. Stevens et al., *Chest.* 121 (2007) 1577-1582.
[3] E.R. Weibel et al., *Science* 137 (1962) 557-585.
[4] A. Copploe, et al., *Ann. of Biomed. Eng.* 47 (2019) 1435-1445.
[5] Grotberg. J et al., *Three-dimenstional model of surfactant replacement therapy*, 112:9287-9292, 2015.

# DETERMINING EFFECTS ON PIG GAIT AFTER INDUCED TRAUMATIC BRAIN INJURY: INTITAL ASSESSMENTS

**Sloan Kanat (1), Paige Cordts (1), Alesa Hughson (2), Galit Pelled, PhD (1), Tamara Reid Bush, PhD(1)**

(1) Department of Mechanical Engineering, Michigan State University, East Lansing, MI, United States
(2) Department of Biomedical Engineering, Michigan State University, East Lansing, MI, United States

## INTRODUCTION

It has been estimated that 1.7 million traumatic brain injuries (TBIs) occur annually in the US [1]. Additionally, there were over 50,000 deaths and almost 300,000 hospitalizations related to TBIs annually from 2002-2006. [1]. TBIs have been shown to have lasting negative effects on a person's health, learning, sociability, work, and relationships [2]. There are a vast range of causes of TBIs, with motor vehicle accidents making up the largest number of reported TBIs in adults, followed by falls [3]. In children, sports are a major contributor to TBIs, with falls being the second leading cause [4].

Due to many causes and severities of TBIs, it is difficult to classify them. A mild TBI could have symptoms such as balance or concentration problems. Mild TBIs are challenging to diagnose in people because the symptoms can be mistaken for other health problems, such as anxiety or headaches [5]. More severe TBIs are easier to diagnose since they have more significant symptoms. Evidence also shows that repeated small TBIs can lead to chronic traumatic encephalopathy [6], which has symptoms such as depression, dementia, and overall cognitive impairment [6]. Smaller TBIs can go undetected and can lead to long-term cognitive issues, so it is important to have a way of diagnosing smaller TBIs.

Since it is difficult to obtain quantitative human TBI data, the pig brain provides a reasonable comparison to the human brain. The size, organization, and makeup of a pig brain is closer to that of a human brain compared to the usual animal surrogates, which are rodents [7].

Previous research has shown that there are notable parameters for TBIs in pig gait. Pressure mats have been the most popular method of data collection and have yielded evidence to support gait changes after TBIs [8]. Pressure mats alone do not provide hoof height or 3-D data that can be used in gait analysis. This study builds on previous research by adding unique 3-D data including relative rotations between shoulders and hips with the head.

The goals of this study were to determine new methods and identify possible measures that can be used to study pig gait pre- and post-TBI.

## METHODS

This study investigated two Yucatan minipigs. The pigs were studied pre-TBI and then underwent a clinical induction of a TBI, after which they were studied again. The TBI was induced by a controlled drop indenter.

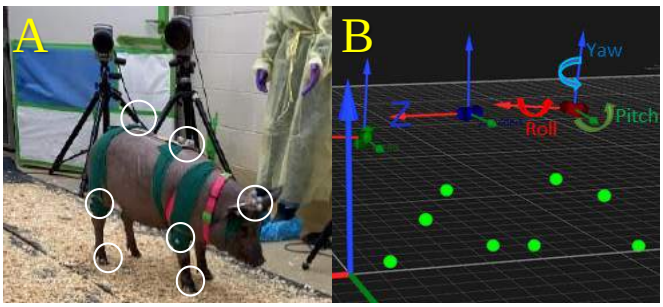


**Figure 1: A) Pig with markers on in motion capture testing space. Coban tape was used to secure rigid bodies and single markers, circled in white, to the pig. The hoof markers were secured using double-sided tape. B) Qualisys Motion Capture view of markers in 3-D space. Green markers show the knee and hoof markers. Three rigid bodies seen in dark green (head), dark blue (shoulders) and red (hips).**

Reflective markers were placed on anatomical locations of the pigs. Marker pods with four markers on each (referred to as rigid bodies) were used. The rigid bodies were placed at three locations: on top of the pigs' head; on the back between the shoulders; and on the hips. Individual markers were placed laterally on each knee joint and on the

outside of each hoof. The 3D locations of the marker were collected using a motion capture system at 100Hz. The vertical height of each hoof was determined and reported for each trial. The rigid bodies on the head, shoulder and hips were used to calculate the rotations of the shoulders and hips relative to the rotation of the head during each trial. Rotation of the x-axis (roll), y-axis (pitch) and z-axis (yaw) are labeled. The x-axis goes from the back of the pig to head, the y-axis is left to right side of pig, and the x-axis is vertical from the pig (Figure 1 B)

For each trial, the pigs were led by a trainer through the calibrated motion capture space. The trainers used treats to maintain the pigs' attention as they walked through the space. The trainer walked the pig through the calibrated space at a consistent pace. The number of times the pigs walked through the space varied depending on the cooperation and mood of the pig, which each time walking through the space counted as a trial.

## RESULTS

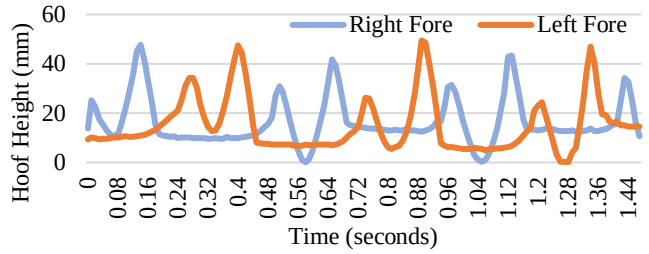


**Figure 2: Fore-leg hoof height variation with time for pig C post-TBI.**

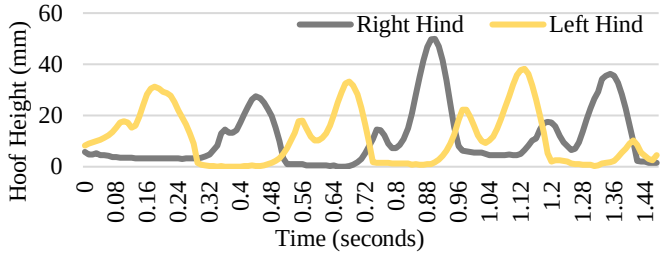


**Figure 3: Hind-leg hoof height variation with time for pig C post-TBI.**

Figures 2 and 3 present the heights of each hoof, timing of steps, and comparison between the right and left side of the pig gait for one trial of pig C. The fore legs had an average swing time of 0.290±0.014 seconds, and the hind legs had an average swing time of 0.283±0.039 seconds.

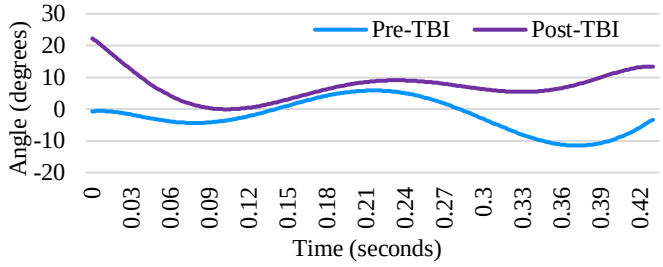


**Figure 4: Shoulder rigid body pitch rotation angles for pre- and post-TBI of pig B. The timing of the pre- and post-TBI data were scaled to show a full gait cycle starting with a right fore-leg step from 0-0.22 seconds and a left fore-leg step from 0.22-0.42 seconds.**

The pitch angles showed a parabolic pattern through the swing of each leg. The maximum rotation angles of shoulders and hips relative to the head during each trial are presented in Table 1. There was a decrease in the yaw deviation angles from both the shoulders to head and hips to head between the pre- and post-TBI pig

**Table 1: Maximum deviation angles (in degrees) from neutral position pre- and post-TBI of the shoulder relative to the head, and the hips relative to the head for one pass of pig B.**

| | | Pre-TBI (degrees) | Post-TBI (degrees) |
|---|---|---|---|
| Shoulders to Head | Roll | 18.020 | 13.052 |
| | Pitch | 11.847 | 13.891 |
| | Yaw | 18.148 | 12.142 |
| Hips to Head | Roll | 14.710 | 18.172 |
| | Pitch | 21.087 | 14.334 |
| | Yaw | 22.428 | 19.850 |

## DISCUSSION

This study investigated methods to assess pig gait and explored measurements of that gait to be used to evaluate quantitative signs of TBI.

Because of the complexity of evaluating the gait of pigs, the majority of the published research has focused on hoof contact patterns. There is limited TBI related gait research, particularly with the inclusion on relative movements between body segments. This work demonstrates the ability to gather hoof height, timing of each leg during gait and relative motions between body segments. All of these measures have the potential to provide insights to changes in movements pre- and post-TBI. Determining not only magnitude of movements, but timing of these movements will add to our understanding of functional changes in gait patterns. This is the initial step for a full evaluation of multiple pigs pre- and post-TBI injury.

This is an important first step. Measurement of pig gait was challenging as it was unclear how the pigs would tolerate the marker systems and if they would accept an environment with cameras. Interestingly, the pigs have very sensitive hooves, so initial attempts at full spherical markers on were unsuccessful. The small, flat hoof markers were well tolerated and able to be viewed for the entire trial with our system.

Additionally, the rigid body marker pods stayed securely on the animal during all trials. These rigid body pods successfully captured relative movement between the three segments.

Future work on this research will begin with three new cohorts of pigs introduced throughout 2022. The full pre- and post-TBI gait analysis will be conducted at least twice. First, once the pigs are trained to walk through the motion capture space and second, after the induction of the TBI. In addition, this study aims to combine the full gait analysis with pig play and behavioral changes pre- and post-TBI to create a more extensive list of TBI markers that could be adapted to human TBI assessments to improve diagnostic criteria for smaller TBI's that otherwise may go unnoticed.


## ACKNOWLEDGEMENTS

A portion of the work was supported by the National Institutes of Health grants UF1NS115817.


## REFERENCES


[1]Faul M., et al., *Injury Prevention*, 16:A268, 2010
[2] Dijkers MP., *Archives of Phy Med Rehab*, 21-35, 2004
[3] Majdan M., et al., *Brain Injury*, 797-805, 2011
[4] Thurman DJ., *Journal of Child Neurology*, 20-27, 2014
[5] CDC TBI and Concussion
[6] Mckee AC., *Brain*, 43-64, 2013
[7] Kinder HA., et al., *Neural Regen Res*, 413-24, 2019
[8] Wang H., et al., *Neural Regen Res*, 338-344, 2021

# MEASURING THE EFFICACY OF RIGHT ATRIAL APPENDAGE TISSUE TO WITHSTAND PULMONARY HYPERTENSIVE CONDITIONS AS A FUNCTIONAL PULMONARY VALVE

**Kate E. Appleman (1), Katarina E. Lettner (1), Andrew J. Behrmann (2), Pirooz Eghtesady (3), and Shamik Bhattacharya (4)**

(1) Department of Biology, Southeast Missouri State University, Cape Girardeau, MO, USA
(2) School of Medicine, University of Missouri, Columbia, MO, USA
(3) Department of Cardiothoracic Surgery, Washington University School of Medicine, St. Louis, MO, USA
(4) Department Engineering and Technology, Southeast Missouri State University, Cape Girardeau, MO, USA

## INTRODUCTION

Tetralogy of Fallot (TOF) is a congenital heart defect that affects blood flow to the lungs. There are four deformities associated with TOF: right ventricular outflow tract obstruction (RVOTO), ventricular septal defect, overriding aorta, and right ventricular hypertrophy. The focus of this study is on RVOTO. This deformity is associated with both pulmonary stenosis and pulmonary atresia. Pulmonary stenosis occurs when the pulmonary valve does not open properly, while pulmonary atresia is when the pulmonary valve fails to form at all [1].

During TOF repair, it is vital to prevent pulmonary insufficiency (PI). PI is a condition in which the function of the pulmonary valve is compromised and causes backflow. A new repair technique has been introduced that uses right atrial appendage (RAA) tissue from the patient to create a neo-pulmonary valve [2]. The aim of this study is to further the understanding of the efficacy of the neo-RAA valve to withstand increased pressurization conditions.

## METHODS

Adult porcine hearts were used in this experiment. Storage and thawing methods were adopted from a previous study [3]. To prepare the hearts, the right atrial appendage was resected, and then the right ventricle outflow tract (RVOT) was completely removed from the heart. The native pulmonary leaflets were then extracted from the RVOT. A portion of the RAA tissue was then dissected to form a bicuspid pulmonary valve [4]. The valve was then sutured into the pulmonary trunk (PT). Figure 1 shows the neo-RAA valve sutured into the PT from different angles.

The RVOT with its neo-RAA valve was then placed into a Plexiglass container that contained a hydrostatic pressure system. The hydrostatic pressure system was fabricated to induce pressurization of the pulmonary artery (PA). The reservoir for the system was set at various elevations to produce pressurization levels that ranged from 20 mmHg to 140 mmHg. A zip tie was used to secure the PA to the system's cannula to prevent backflow.

The PA was then pressurized to 20 mmHg to test the function of the bicuspid RAA valve. Pressurization was then increased by factors of 20 mmHg until reaching 100 mmHg, and then by increments of 10 mmHg thereafter. The PA was pressurized for ten seconds at each stage of pressurization to measure the efficacy of the bicuspid RAA valve. This was done until the bicuspid valve failed to withstand the pressurization.

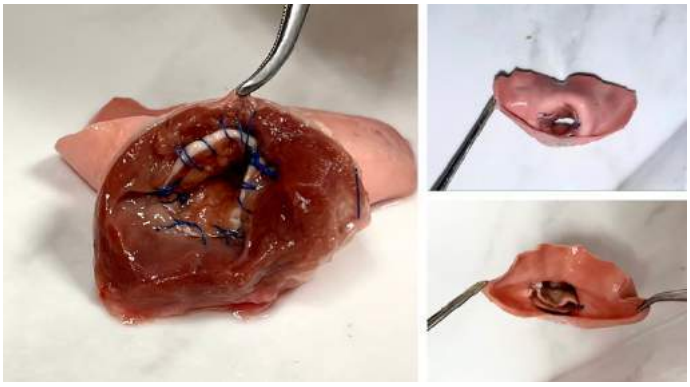

**Figure 1: Pulmonary valve replaced with bicuspid right atrial appendage valve in the right ventricle outflow tract.**

## RESULTS

Peak systolic and severe pulmonary hypertension (PH) conditions were simulated in the pulmonary artery and the RVOT [5]. The neo-RAA bicuspid valve was pressurized to close at various pressurizations, until it was no longer able to withstand the pressure exerted on it. The study revealed that the bicuspid valve functioned at 20 mmHg, 40

mmHg, 60 mmHg, 80 mmHg, and 100 mmHg. The valve failed at 110 mmHg. Therefore, the efficacy of the bicuspid RAA valve fell between the range of 100 and 110 mmHg. This clearly demonstrates that RAA tissue is able to function properly and withstand considerable PH conditions. Figure 2 demonstrates the PA and neo-RAA being pressurized to failure.

**Figure 2: Pulmonary artery and the right atrial appendage valve being pressurized to failure.**

## DISCUSSION

In this study, we evaluated the efficacy of RAA tissue for usage as a pulmonary valve. We found that the bicuspid RAA valve was able to withstand pressurization that exceeded 100 mmHg. A normal PA pressure has been found to be between 14 to 20 mmHg. Therefore, our results show that RAA tissue is able to function at pressures five times greater than the pressure the PA usually experiences [5]. This discovery is important because it shows us that as someone ages, the neo-RAA valve will be able to withstand PH that may develop overtime as the patient grows and develops.

Several limitations were present in this study. The first is that porcine heart tissue was used over human heart tissue. Porcine tissue may differ from the tissue of human hearts; however, porcine and human hearts do have similar characteristics [6]. The second limitation deals with the system used to induce pressurization on the pulmonary valve. The system used in the experiment was static, not a dynamic pressurization system. The third limitation is that a bovine patch was not used to repair the PT after the neo-RAA valve was placed. However, the PT was sutured closed with carefully placed sutures.

In conclusion, the results of the project are significant for furthering the understanding of the efficacy of RAA tissue being used as a pulmonary valve. Additionally, the current results reinforce the idea that RAA tissue is a good alternative material for reconstruction of the RVOT. Therefore, the experiment allowed us to quantify the pressure that the neo-RAA valve is able to withstand normal and severe PH conditions. With more experiments, the results could potentially lead us to the betterment of the surgical procedures used to correct the RVOT and PI.

## ACKNOWLEDGEMENTS

These studies were supported by the Faculty Mentored Student Research Grant from Southeast Missouri State University's Provost Office.

## REFERENCES

[1] R. Wilson, O. Ross, and M. J. Griksaitis, "Tetralogy of Fallot." *BJA Educ*, 19(11):362-369, 2019.

[2] I. S. Onan *et al.*, "Early Results of Neopulmonary Valve Creation Technique Using Right Atrial Appendage Tissue." *J. Card Surg.*, 35(10):2640-2648, 2020.

[3] A. Behrmann, K. Appleman, P. Eghtesady, and S. Bhattacharya, "Tricuspid Annulus Cinching Force Under Pulmonary Hypertensive Right Ventricle Conditions: An Ex Vivo Study." *J Biomech.*, 123:110488, 2021.

[4] A. Amirghofran *et al.*, "Surgical Repair of Tetralogy of Fallot Using Autologous Right Atrial Appendages: Short-to Mid Term Results." *Eur J Cardiothorac Surg.*, 59(3):697-704, 2021.

[5] E. Lau *et al.*, "Resting Pulmonary Artery Pressure of 21-24 mmHg Predicts Abnormal Exercise Haemodynamics." *Eur Respir J*, 47(5):1436-1444, 2016.

[6] P. P. Lelovas, N. G. Kostomitsopoulos, and T. T. Xanthos, "A comparative Anatomic and Physiologic Overview of the Porcine Heart." *J Am Assoc Lab Anim Sci.*, 53(5):432-438, 2014.

# FACTORS CAUSING INTERVENTRICULAR INTERACTIONS IN THE HEART IMPLANTED WITH LEFT VENTRICULAR ASSIST DEVICE

**Lei Fan (1), Jenny S. Choy (2), Ghassan S. Kassab (2), Daniel Burkhoff (3) Lik Chuan Lee (1)**

(1) Department of Mechanical Engineering, Michigan State University, East Lansing, MI, USA
(2) California Medical Innovations Institute, San Diego, California, USA
(3) Cardiovascular Research Foundation, New York, NY, USA

## INTRODUCTION

Mechanical circulatory support devices such as the left ventricular assist device (LVAD) has been increasingly used to treat patients with end-stage heart failure. The incidence of right ventricular (RV) failure is common and is associated with substantial morbidity and mortality after LVAD implantation. The occurrence of RV failure has been hypothesized to be due to the alterations of mechanical interdependence between the left ventricle (LV) and RV, which refers to the effects of LV function on RV function and vice versa. The effects of LVAD on interventricular interactions have been observed in the clinic to vary between patients. The underlying mechanisms that cause such a variation is, however, unclear [1]. This is especially so when there are many possible factors contributing to an alteration in the interventricular interactions in LVAD patients. To address this issue, we develop computational models to investigate the effects of different factors on interventricular interactions.

## METHODS

An idealized biventricular finite element (FE) model is coupled with a closed loop lumped parameter circulatory model that describes both the systemic and pulmonary circulations (**Fig. 1a**). There are eight compartments with four cardiovascular components each in the systemic and pulmonary circulations. Conservation of total mass of blood in the circulatory model requires the change of inflow and outflow rates of each compartment be related to the rate of change of the volume. The functional relationship between the LV and RV pressures and volumes (i.e., $P_{LV,RV} = f(V_{LV,RV}, t)$) is obtained by minimizing a Lagrangian function consisting of myocardial tissue strain energy function and terms associated with the enforcement of constraints on **1)** myocardial tissue incompressibility, **2)** zero-mean rigid body translation and rotation, and **3)** cavity volume [2]. Mechanical behavior of the biventricular is modeled using an active stress formulation, in which the passive and active mechanical behaviors are described, respectively, by a Fung-type strain energy function and a modified time-varying elastance model [3]. The left atrium and right atrium are described by time-varying elastance models [4].

To model the LVAD, a pressure gradient-flow characteristics of a commercially available LVAD (Thoratec Corporation HeartMate III) is prescribed with an operating pump speed between 4k to 6k rpm (**Fig. 1b**). The LVAD pumps blood from the LV to the aorta at a flow rate that is determined by the aorta-LV pressure gradient and the operating pump speed based on the pump characteristics curve.

The modeling framework is first calibrated to obtain LV and RV pressure-volume (PV) loops that agree with clinical measurements from a patient with heart failure (HF). After model calibration, the model is

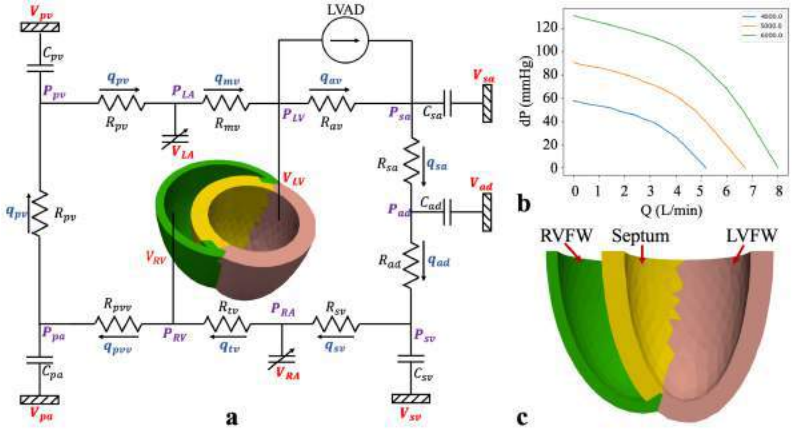


**Fig. 1**: **a.** Schematic of the coupled biventricular FE in a closed loop modeling framework; **b.** Pump characteristics curve used to model the LVAD; **c.** Schematic of the contours associated with the RVFW, septum and LVFW.

applied to investigate the effects of **1)** LVAD pump speed, **2)** myocardial contractility at 3 regions defined in **Fig. 1c**, and **3)** septal wall thickness (swt) on the LV and RV PV loops and interventricular interactions. Systolic and diastolic interventricular interactions are characterized, respectively, by changes in end-systolic pressure-volume relationship (ESPVR) and end-diastolic pressure-volume relationship (EDPVR) under different loading conditions. Specifically, ESPVR and EDPVR are obtained by connecting end-systolic and end-diastolic points in the RV PV loops with different RV preload. Changes in the gradient of ESPVR ($E_{es}$) and the RV volume at zero RV pressure ($V_0$) with different pump speeds are used to evaluate systolic interaction, while changes in RV volume at RV pressure of 20 mmHg ($V_{20}$) at different pump speeds is used to evaluate diastolic interaction.

## RESULTS

**Fig. 2** shows the effects of pump speed on the LV and RV PV loops, and the effects of pump speed regional contractility and swt on EDPVR and ESPVR. Without LVAD, the LV and RV PV loops predicted by the model show good agreement with clinical measurements from a HF patient (**Fig. 2a-b**). Implantation of LVAD resulted in a loss of isovolumic phases in the LV PV loop. When the pump speed was increased from 4k to 6k rpm, peak LV pressure was reduced from 104 to 71 mmHg. The LV PV loop shifted leftward (**Fig. 2a**) and became more triangular, indicating that the LV was increasingly unloaded. On the other hand, the RV PV loops shifted rightward toward higher volumes with elevated end-diastolic pressure (**Fig. 2b**). An increase in pump speed increased $E_{es}$ and $V_0$ of the RV ESPVR, indicating that the RV contractile function is affected by the LVAD (**Fig. 2c**). The quantity $V_{20}$ in the RV EDPVR was increased with increasing pump speed, implying that the RV passive chamber stiffness was reduced with LVAD (**Fig. 2c**). A reduction in contractility by 60% in either the LVFW, septum or RVFW (**Fig. 2d-f**) affects $V_0$ and $E_{es}$ in the RV ESPVR with respect to that at the same pump speed in baseline (**Fig. 2c**), suggesting alteration in systolic interaction. Conversely, EDPVR and $V_{20}$ are not affected, suggesting diastolic interaction is not affected. On the other hand, an increase in swt from 0.6cm in swt0 (**Fig. 2g**) to 3.0cm in swt3 (**Fig. 2h**) increases systolic interaction on ESPVR but reduces diastolic interaction on EDPVR.

## DISCUSSION

In this work, a biventricular computational modeling framework was developed to investigate the factors affecting interventricular interactions in the heart implanted with LVAD. The model predicted the LV and RV PV loops agree with the clinically measured data from a HF patient. The key findings of this work are listed as follows. **First**, with increasing pump speed, the LV PV loop became more triangular shaped with reduced LV peak pressure and volumes while RV volumes were increased with elevated RV filling pressure. **Second**, the model predicts that swt affects both systolic and diastolic interactions while regional contractility only affects the systolic interaction. These key findings, which clarifies the factors altering interventricular interactions in HF patients with LVAD, may have clinical implications in terms of patient selection for this treatment.

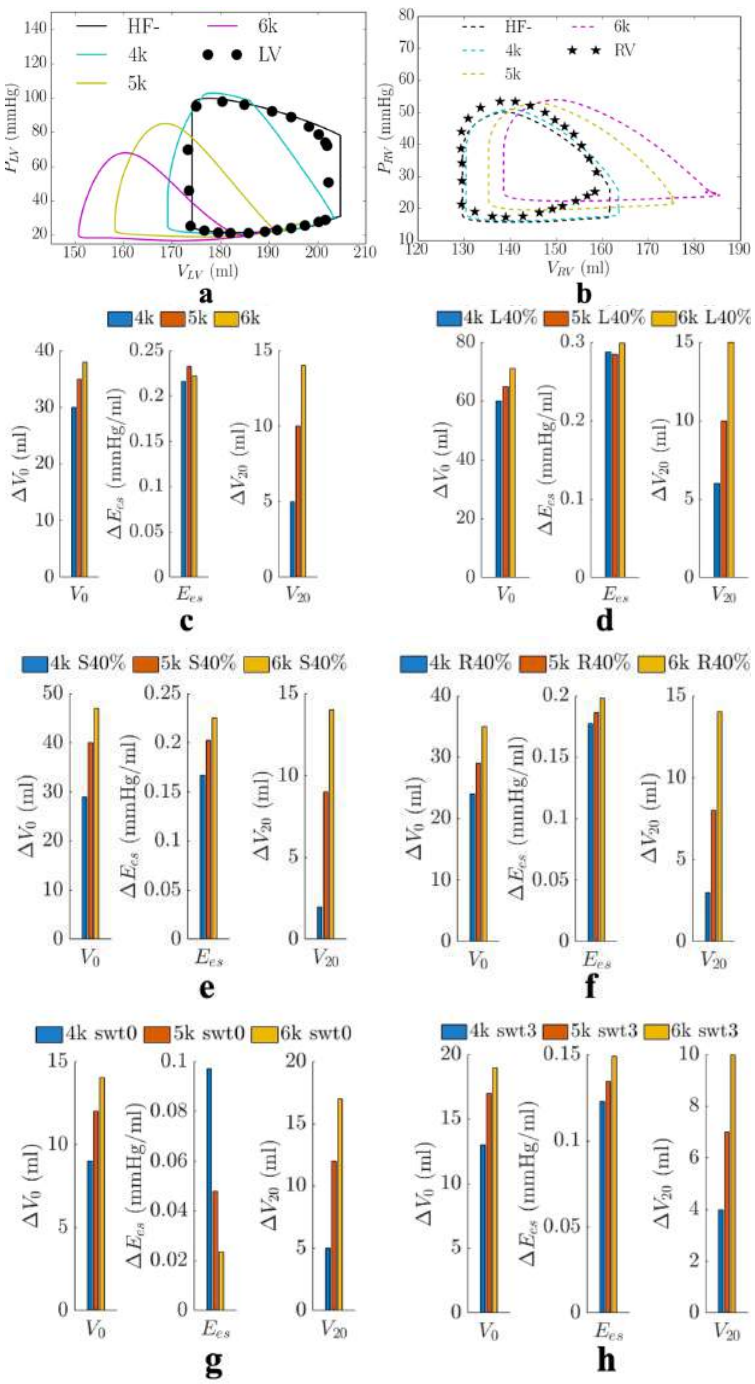


**Fig. 2**: Model predicted effects of the LVAD pump speed on the **a.** LV and **b.** RV PV loops are plotted together with clinical measurements from a patient with HF [1]; Effects of **c.** pump speed; reduction of regional contractility in **d.** LVFW; **e.** septum; **f.** RVFW; and **g.** reduced swt; and **h.** increased swt on systolic interaction indexed by $V_0$ and $E_{es}$, and diastolic interaction indexed by $V_{20}$. 'ED' and 'ES' denote EDPVR and ESPVR.


## ACKNOWLEDGEMENTS

This work was supported by the National Institute of Health (R01 HL134841) and American Heart Association Postdoctoral Fellowship (AHA 835298).


## REFERENCES


[1] Brener. M. et al., J. Card. Fail., 27: 9, 2021
[2] Shavik, S. M. et al., *Front. Physiol.*, 11: 2, 2020.
[3] Guccione, J. M. et al., *J. Biomech.*, 28, 1167–1177, 1995.
[4] Fan, L. et al., *Am. J. Physiol. - Hear. Circ. Physiol.*, 2021.

# PRE-EXPOSURE TO A PAINFUL STRETCH INCREASES BOTH LOCAL STRAINS & NEURONAL CALCIUM ACTIVITIY IN NEURON-COLLAGEN CONSTRUCTS ACROSS PHYSIOLOGIC & SUPRAPHSYIOLOGICAL STRETCH

**Sagar Singh (1), Prabesh Ghimire (1), Beth A. Winkelstein (1,2)**

(1) Department of Bioengineering, University of Pennsylvania, Philadelphia, PA, USA
(2) Department of Neurosurgery, University of Pennsylvania, Philadelphia, PA, USA

## INTRODUCTION

The capsular ligament that encloses the facet joints of spinal vertebrae is comprised of collagen fibers and is innervated by afferent neurons [1]. Loading to the capsular ligament both directly and indirectly loads the embedded afferents via collagen fiber reorganization [2,3]. Supraphysiological loading of the capsular ligament activates nociceptive nerve fibers and increases calcium ion ($Ca^{2+}$) influx into the neuronal cytoplasm [4,5]. Further, repeated non-injurious distractions of the capsular ligament separated has been shown to be sufficient to induce pain [6,7], suggesting the initial stretch may lower the threshold for injury and neuronal activation. Despite these suggestions, it is unclear how afferent calcium activity is affected by a mechanical pre-exposure.

Primary afferents in the capsular ligament have mechanoreceptors that respond to matrix deformation [8]. Local strains that are at or below physiologic loading (~7%) are sufficient to upregulate and induce transport of NMDA receptor ion channels from the soma to extrasynaptic regions that would transport calcium ions intracellularly [9]. Although supraphysiological loading of afferents increases substance P and ATF3 expression after distraction [10,11], the extent to which a pre-stretch sufficient to induce pain may sensitize a neuron to subsequent stretch is unknown. Further, since local mechanical environment affects load transmission to afferents [11,12], defining relationships between neuronal activity and local strains after a pre-exposure provide important context.

The goal of this study is to examine the effects of a mechanical pre-exposure on modulating the local strains and neuronal calcium activity for different stretch scenarios within and exceeding the physiologic range. Neuron-collagen constructs (NCC) that mimic the microstructural environment of the capsular ligament were fabricated and a painful stretch was used a pre-exposure followed by another stretch after 2 days to allow for any transcriptional changes that may occur in the neuron [13-15]. NCCs were then exposed to macroscopic loading matching physiological, painful, and supraphysiological stretches experienced by the native ligament, and local strains and neuronal calcium activity were measured.

## METHODS

NCCs (n=9) were fabricated from 2mg/mL collagen and DRG neurons ($3x10^5$cells/mL) from embryonic day 18 rats [2,11]. The collagen solution was mixed with fluorescent microspheres (40nm dia; 558nm emission; 1:500; ThermoFisher) and self-assembled before plating neurons on the gel [16,17]. A DRG explant was also plated on each gel to serve as a reference for image tracking and analyses. After plating, neurons were cultured with neurobasal medium supplemented by 1% GlutaMAX, 2% B-27, 1% fetal bovine serum, and 10ng/mL 2.5S nerve growth factor (ThermoFisher). On day in vitro (DIV) 2, neurons were transduced with an AAV expressing GCaMP6f in the feeding media (1:5000 dilution) which causes them to transiently fluoresce at 488nm with calcium influx [18,19]. At DIV6, additional collagen (150µL) with fluorescent beads was added to encapsulate neurons in the NCC. For testing, NCCs were cut into a single strip (21mm x 7mm).

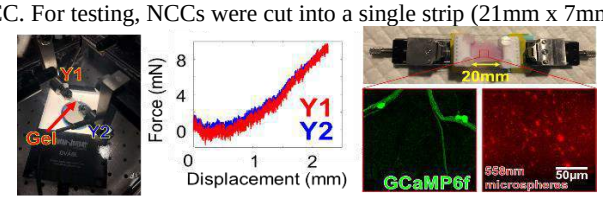


**Figure 1: NCCs were pre-exposed to painful PS before manual stretch measuring microsphere displacements & $Ca^{2+}$ activity.**

On DIV7, a subset of gels (n=5) was exposed to a uniaxial prestretch (PS) with each end clamped in a planar biaxial testing machine (TestResources) and displaced 2.3mm (Fig. 1) to induce strain (~22%) corresponding to capsular ligament distraction known to induce pain in vivo [20]. Distraction was applied at 0.06mm/s to match the rate of stretch applied manually during calcium imaging. Force and displacement data were acquired at 500Hz; a high speed camera

(500Hz; Phantom v9.1) tracked strains for each NCC. After prestretch, NCCs were transferred to fresh culture media supplemented by 1% penicillin-streptomycin for 48 hours.

On DIV9, PS (n=5) and unstretched (US; n=4) gels were clamped in a custom-built loading device for controlled manual stretch (Fig. 1). The device was placed on the stage of a Leica inverted spinning disc confocal microscope. A 20x water immersion objective imaged 2 fields of view (FOVs) for each gel. Image series (60s; 1024x1024 pixels$^2$) were taken at 20fps to visualize the initial position of the microspheres and baseline neuronal calcium activity as reference without any applied stretch [21]. The FOV x-y position of the microscope stage was stored; NCC were distracted to 3 relevant macroscopic stretch magnitudes as a proportion of its length: 10% (physiological), 25% (painful), and 40% (supraphysiological) [22]. At each stretch level, FOVs were imaged to capture microsphere positions and calcium activity. Microsphere displacements were tracked with ProAnalyst (Xcitex) and 4-node elements (n=139 PS; n=147 US) were generated; local maximum principal strain (MPS) was calculated for each element at reference and each stretch. Average elemental MPS was calculated and compared across stretch levels and group by a 2-way repeated measures ANOVA.

The custom MATLAB script, FluoroSNNAP, was used to segment neurons, and quantify the number of calcium events for each neuron (n=95 PS; n=71 US) in each FOV at each stretch level. Neurons were identified by a grader blinded to group and stretch level and segmented using each neuron's soma. The same neurons were analyzed throughout and the frequency of calcium events for each neuron was captured by a template-matching algorithm [23]. Average neuronal activity was calculated at each stretch level and compared using a 2-way repeated measures ANOVA. Histograms of neuronal activity were generated and distributions were compared using a non-parametric Mann-Whitney U test. The proportions of neurons with no or any calcium activity were also calculated and compared using Pearson's chi-squared tests.

## RESULTS

The prestretch generates macroscopic strains of 23.1±1.2% and a maximum force of 4.7±1.8N. NCCs exposed to prestretch experience greater ($p<0.04$) local strains at physiological (14.6±5.8%), painful (31.8±10.8%), and supraphysiologic (48.3±14.1%) stretch than gels that do not undergo the prestretch (13.3±3.8%; 26.0±12.5%; 39.4±16.4%) (Fig. 2). For both exposure groups, painful stretch generates greater ($p<0.01$) strains than the physiological stretch, and supraphysiological strains are greater ($p<0.01$) than those at painful stretch.

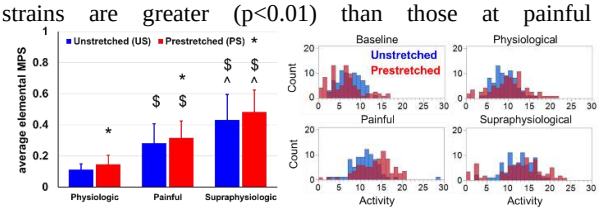


**Figure 2: Prestretched NCCs exhibit greater (*p<0.04) strains & calcium activity than unstretched NCCSs. Strain increases with stretch level for both groups ($^p<0.01).**

Although baseline calcium activity does not differ ($p=0.8$) between US (6.8±2.6), and PS (5.7±2.9), neuronal activity does differ ($p<0.01$) between exposure groups at all stretch levels. Also, the distributions of calcium activity differ between unstretched and prestretched NCCs, with more prestretched neurons exhibiting a greater frequency of calcium events (Fig. 2). This rightward shift compared to unstretched neurons is evident at each of physiological ($p=0.03$), painful ($p=0.04$), and supraphysiological ($p<0.01$) stretch (Fig. 2).

The proportion of neurons with increased activity between baseline and physiological stretch is greater ($p=0.04$) in unstretched NCCs (80%) than prestretched NCCs (76%) (Fig. 3). This trend differs at painful stretch where a greater proportion of neurons in prestretched gels than unstretched gels increase their activity over levels at physiologic stretch (US 62%, PS 72%; $p<0.001$) (Fig. 3). Yet, at supraphysiological stretch, the reverse occurs, with a smaller proportion of neurons experiencing increased activity from painful ($p<0.01$) to supraphysiological stretch in the prestretched (47.4%) group than the unstretched NCCs (Fig. 3).

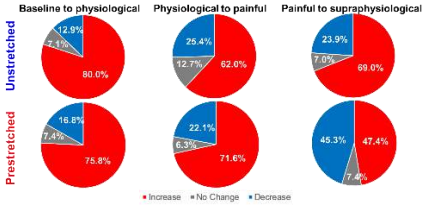


**Figure 3: Proportions of neurons that experience change in activity differs between pre-exposure groups ($p<0.04$).**

## DISCUSSION

The findings that a prestretch sufficient to induce pain (23%) imposed before mechanical stretch increases both the local strains and neuronal activity (Figs 2 & 3) is consistent with other in vivo and ex vivo studies reporting laxity in ligaments [6,24,25]. Since painful ligament loading can upregulate enzymes that remodel the extracellular matrix [26], the larger local strains in the pre-stretched specimens may be expected. Although the NCCs are primarily neuronal preparations, other cell types, like glia and fibroblasts, may be present due to isolation procedures and they can also upregulate matrix metalloproteinases and other digestive enzymes that may affect fiber-level kinematics, and bind selectively to neuronal receptors [17,21]. The increase in local strains and calcium activity observed in the PS gels (Figs. 2 & 3) could be attributed to increased receptor expression and/or enzymatic activity.

Painful prestretch also increases neuronal calcium activity (Fig. 2), which is not surprising since painful injuries increase neuronal hyperexcitability of afferents in loaded ligaments [8]. In fact, the prestretch magnitude in this study exceeds the threshold for neuronal activation via pERK upregulation (~11%) [2]. So, pre-exposed neurons would be expected to be sensitized and have a more robust response to loading [27]. Although immunohistochemistry was not performed here, studies probing associated mechanistic cellular responses are needed. Because local strains are greater in prestretched gels (Fig. 2), determining whether increased neuronal activity is due to more calcium channels, and/or changes in local mechanics is also needed.

## ACKNOWLEDGEMENTS

Funding from NCCIH (AT010326) and Catharine Sharpe Foundation.

## REFERENCES

[1] Yamashita T et al, *Spine* 21:538-43, 1996 [2] Zhang S et al, *J Biomech Eng* 138(021013-1):1-12, 2016 [3] Singh S et al, *SB3C*, #219, 2017 [4] Chen C et al, *Spine*, 30(12):1367–72,2005 [5] Laplaca M & Prado G, *J Biomech*, 43(1):71–8, 2010 [6] Kartha S et al, *J Biomech Eng* 140:1-8, 2018 [7] Singh S et al, *Clin Biomech* 64:122-30, 2019 [8] Chen Y et al, *JBJS* 88:1807-16, 2006 [9] Singh S & Winkelstein B, *BMMB*, submitted. [10] Zhang S et al, *JOR* 36(2):770-77, 2018 [11] Singh S & Winkelstein B, *8th WCB Mtg* 1, 2018 [12] Ban E et al, *J Biomech Eng* 139:071009, 2017 [13] Nascimento D et al, *PLoS One* 9(9), 2014 [14] Dong L et al, *Neurosci* 193:377-86, 2011 [15] Su J et al, *J Comp Neurol* 523:1505-28, 2015 [16] Kimura F et al, *Meas Sci Technol* 17:1254-60, 2006 [17] Singh S & Winkelstein B, *SB3C* 17-18, 2021 [18] Chen T et al, *Nature* 499(7458):295–300, 2013 [19] Nguyen J et al, *PNAS* 9:33, 2015 [20] Lee K & Winkelstein B, *J Pain* 10:436-45, 2009 [21] Ita M et al, *Sci Rep* 10:1-15, 2020 [22] Dong L et al, *Brain Res* 1461:51-63, 2012 [23] Patel T et al, *J Neurosci Methods* 243:26-38, 2015 [24] Quinn K et al, *Stapp Car Crash J* 51:169-87, 2007 [25] Ivancic P et al, *Clin Biomech* 23:159-65, 2008 [26] Ita M et al, *J Orthop Sports Phys Ther* 47:450-61, 2017 [27] Gao Y & Ji R, *Open Pain J*, 2(2):11-7, 2009.

SB³C2022
Summer Biomechanics, Bioengineering and Biotransport Conference
June 20-23, Eastern Shore, MD, USA

# CRITICAL PRESSURE OF INTRAMURAL DELAMINATION IN AORTIC DISSECTION

**Ehsan Ban (1), Cristina Cavinato (1), Jay D. Humphrey (1)**

(1) Department of Biomedical Engineering, Yale University, New Haven, CT, USA

## INTRODUCTION

Aortic dissection is a deadly disease of the ascending aorta, where blood delaminates the arterial media as observed upon medical imaging after the acute onset of disease. Margot Roach et al. [1] performed seminal controlled experiments on porcine aortas and reported delamination of the aortic wall by ink injection using submillimeter-sized needles at ~547 mmHg (Fig 1a). The reported pressure is notably higher than normal blood pressure but could be within the range of the swelling pressure of glycosaminoglycans and proteoglycans by the Gibbs-Donnan effect [2]. The mechanics of tearing in the mentioned experiments have not been quantitatively analyzed. Here, we extended our previous model [3] of injection into a cut-open tissue to a cylindrical artery to model the mentioned experiments and assess the theoretical aspects of aortic delamination by fluid injection. We repeated the cited experiments to complement and verify our computational observations.

## METHODS

We computationally modeled the delamination process using a hydraulic fracturing phase-field finite element model [4]. The model consisted of ~500,000 elements and accounts for the deformation of medial elastin and smooth muscle, and four families of collagen fiber in the adventitia. The strain energy density of the wall is

$$W = \frac{\bar{c}}{2}(\lambda_1^2 + \lambda_2^2 + \lambda_3^2 - 3) + \sum_{i=1}^{4} \frac{c_1^i}{4c_2^i}\left(\exp\left(c_2^i\left((\lambda^i)^2 - 1\right)^2\right) - 1\right). \quad (1)$$

$\lambda_i$'s and $\lambda^i$ are principal stretch ratios and stretch ratios along one of the four families of fibers, axial, circumferential, and two diagonal directions within the axial-circumferential plane. $c$'s are material constants determined from previous experiments on diseased aortic tissue [5].

Our contribution to the computational model was in the application of loading. We controlled the volume of injection or damage by adding the following term to the energy of the system, which was minimized to determine damage and deformation,

$$E_{\text{pressurized-fluid}} = mi\left(i\int_V \phi\lambda_1\lambda_2\lambda_3 idV - V_{\text{injection}}\right), \quad (2)$$

where $m$ is a global Lagrange multiplier. $\phi \in [0,1]$ is the tissue damage, and $V_{\text{injection}}$ is the prescribed volume of intramural fluid.

We performed complementary experiments by repeating the approach of Roach et al. [1]. Briefly, needles of two different sizes, 30- and 25-gauge, were used to assess the effect of the insult size on critical pressure. Eighteen descending aortic sections were harvested from Yorkshire pigs, used in separate studies, which did not affect the biomechanics of the aorta. Those studies were performed in accordance with protocols approved by the Institutional Animal Care and Use Committee of Yale University. The experiments included the injection of India ink within the medial layer of the aorta. As in the finite element model, the aortas were initially extended axially (to stretch ratios of 1.1 and 1.3) and pressurized to physiologic levels (130 mmHg), then injected locally with ink [4].

## RESULTS

The computational model reproduced the pressure-volume curves and shapes of the false lumens reported by Roach et al. (Fig. 1b and c). Moreover, the computational model indicated an increase of the critical pressure of tearing with increasing luminal pressure and decreasing size of the false lumen size (Fig. 2). The computational results were explained by a Griffith-type simplified analytical model (Fig. 2a, *inset*), indicating

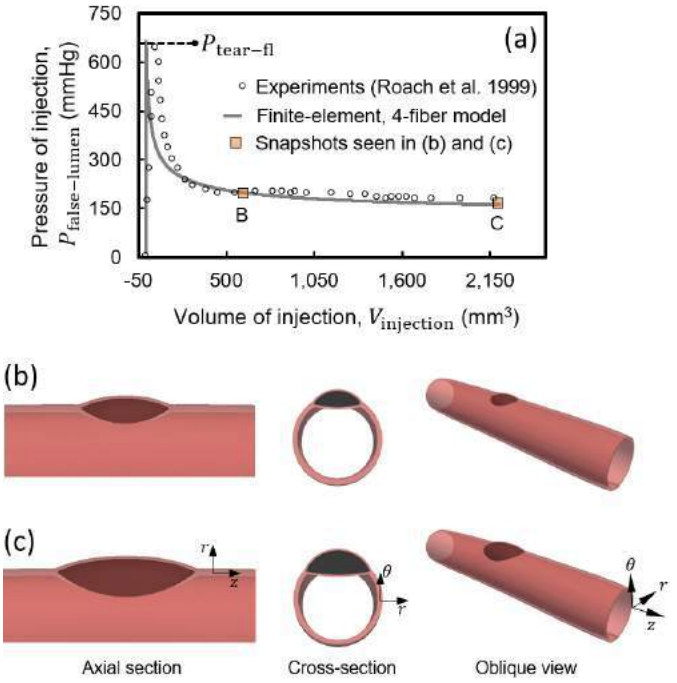


**Figure 1: Finite element hydraulic fracturing model of aortic delamination by fluid injection. (a) The pressure versus volume of injection, and (b and c) deformed and torn shapes of the aorta.**

$$P_{\text{tear-fl}}^{\eta} + (P_{\text{tear-fl}} - P_{\text{true-lumen}})^{\eta} = c^2 \propto K_t^{\alpha} G_c^{\beta} / A_{\text{torn}}^{\gamma}, \quad (3)$$

where, $P_{\text{tear-fl}}$ is the critical pressure of delamination, $K_t$, $G_c$, and $A_{\text{torn}}$ are related to tissue stiffness and strength and the size of the false lumen. $\alpha$, $\beta$, and $\gamma$ are positive exponents. The decrease of delamination pressure with increasing false lumen size was further verified by our complementary experiments (1.9-fold change between the 25- and 30-gauge needles, images in Fig 2b, *inset*).

## DISCUSSION

Unexpectedly, the results indicate a drastic drop in the pressure of delamination with increasing size of the false lumen. The critical pressure decreases from ~600 mmHg to ~200 mmHg as the tear size increases from less than a millimeter to 1 cm. While a large pressure is needed to initiate a weakening within the wall, this result confirms that an elevated pressure of blood may propagate centimeter-sized dissections. The tear propagation is unstable. As the tear propagates, the torn area becomes larger, and the pressure of delamination becomes smaller. This effect is consistent with the common observation of acute onsets of dissection.

The computational model did not restrict the path of tear propagation to any specific direction. But the tears propagated circumferentially in this model. This result agrees with the previous experiments [1] and our complementary ones (Fig. 2b, *inset*). Our additional computations using inhomogeneous wall properties confirmed the possibility of radial deviation of tears from the axial-circumferential plane by weakening or strengthenings in wall properties [4].

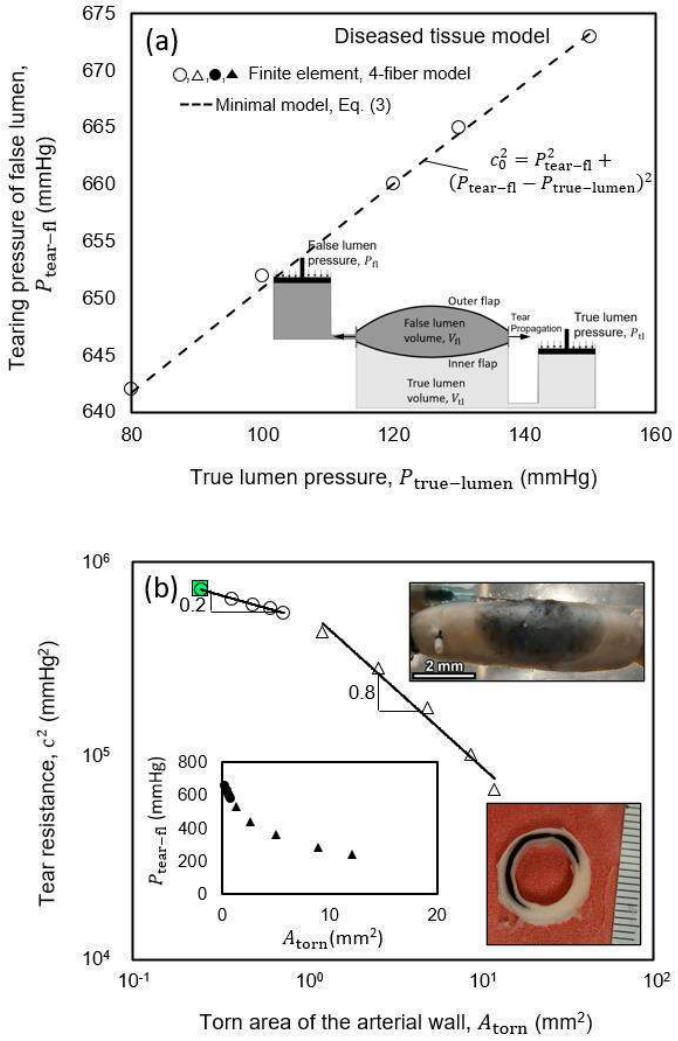


**Figure 2: Critical pressure of delamination versus (a) vessel pressure and (b) size of the torn tissue or the false lumen. Insets show (a) an schematic of the simplified analytical model, (b) and experimental images of tear propagation.**


## ACKNOWLEDGEMENTS

We thank the Sinusas Lab at Yale University for providing us with aortic tissue samples. This work was supported, in part, by a grant from the US National Institutes of Health (U01 HL142518).


## REFERENCES


[1] Roach, M R et al., *Can J Cardiol*, 15:569–575, 1999.
[2] Humphrey, J D, *J Vasc Res*, 50:1–10, 2013.
[3] Ban, E, et al., *Biomech Model Mechanobiol*, 20:895–907, 2021.
[4] Ban, E, et al., *Ann Biomed Eng*, 2022 (*In press*).
[5] Gultekin, et al., *Biomech Model Mechanobiol*, 18:1607–1628, 2019.

# MECHANICAL CUES SUCH AS SHEAR STRESS AND PIEZO1 ACTIVATION GENERATE RED BLOOD CELL EXTRACELLULAR VESICLES

**Gurneet S. Sangha (1), Callie M. Weber (1), Ryan M. Sapp (1), Morgan E. Pettebone (1), Alisa M. Clyne (1)**

(1) Fischell Department of Bioengineering, University of Maryland, College Park, MD, USA

## INTRODUCTION

Red blood cells (RBCs) can affect vascular health by releasing extracellular vesicles (EVs), lipid-bound particles that facilitate intercellular signaling by transporting cargo (e.g., proteins, RNA) to other cells. RBC-EVs generated in pathological conditions, such as obstructive sleep apnea [1], sickle cell disease [2], or blood storage [3] exacerbate endothelial dysfunction, the initial hallmark of vascular disease. These atherogenic RBC-EV effects are partly attributed to hemoglobin, which can decrease endothelial nitric oxide synthase phosphorylation, scavenge nitric oxide, and increase oxidative stress [4]. However, healthy RBCs also lose 20% of their volume in the form of RBC-EVs throughout their 120-day lifecycle [5]. It is unclear how RBC-EVs generated in nonpathological conditions affect endothelial function and subsequent vascular health.

Shear stress may trigger RBC-EV production in nonpathological conditions by stimulating piezo1, a mechanosensitive ion channel that increases RBC $Ca^{2+}$ influx [6]. Indeed, RBC $Ca^{2+}$ influx caused by $Ca^{2+}$ ionophore treatment is a well-established method for RBC-EV production [7]. Furthermore, piezo1 activation also decreases RBC volume, possibly due to RBC-EV formation, and increases ATP [8], increasing atheroprotective nitric oxide in endothelial cells. Based on this evidence, we hypothesize that healthy RBCs undergoing capillary shear stress generate atheroprotective RBC-EVs through piezo1 induced $Ca^{2+}$ influx.

Here, we investigate whether shear stress generates RBC-EVs through piezo1 stimulation. To do this, we provide evidence that healthy RBCs generate RBC-EVs under shear stress conditions. We then show that chemical RBC piezo1 stimulation triggers RBC-EV production. Finally, we begin establishing methods to maximize piezo1 RBC-EV production and minimize protein contamination for future mechanistic studies. This research lays the groundwork needed to study the effects of healthy shear stress-induced RBC-EVs on endothelial function *in vitro*.

## METHODS

RBCs were pooled from two male and two female subjects and washed four times to remove the buffy coat consisting of white blood cells and platelets. RBCs were then resuspended in 50 mL PBS supplemented with 99 mg/dL glucose and 1 mM $CaCl_2$ at pH 7.4. All blood draws were approved by the University of Maryland Institutional Review Board.

To generate RBC-EVs via shear stress, RBCs (6% hematocrit) were sheared through a 2 inch, 25G needle 15 times. RBC-EVs were then concentrated from 50 mL to 400 µL using Amicon Ultra-15 centrifugal filter units (100 kDa molecular weight cut off). EV markers were detected in concentrated RBC-EVs samples by Western blot. Briefly, RBC-EVs were lysed by sonicating three times for 15 seconds and then loaded into NuPAGE 4-12% Bis-Tris protein gels. Proteins were then transferred to polyvinylidene difluoride membranes and detected using primary antibodies for ALIX (Santa Cruz; sc-53538), TSG101 (Santa Cruz; sc-7964), CD63 (Santa Cruz; sc-5275), and GAPDH (Cell Signaling, 2118S), along with the appropriate secondary antibodies. Lipid-bound EV particle size and concentration was quantified using tunable resistive pulse sensing (TRPS; qNano, IZON Science). CPC100 beads (mode diameter: 100nm) were used to calibrate NP100 nanopores to detect RBC-EVs between 50-330 nm. At least 500 particles were counted, using particle rate between 200-1500 particles/minute, at 5 and 10 mBar pressure.

To generate RBC-EVs via piezo1 stimulation, RBC (6% hematocrit) were treated with 100 µM piezo1 agonist yoda1 for 2 hours. 100 µM $Ca^{2+}$ ionophore was the positive control, and 0.28% DMSO was the vehicle control. RBC supernatant was centrifuged at 600xg for 20 min, 1600xg for 15 min, 3260xg for 15 min, and 10,000xg for 30 min to remove cell debris. The RBC supernatant was then ultracentrifuged two times at 100,000xg to concentrate and wash the RBC-EVs. RBC-EV size, concentration and EV markers were quantified as previously described. RBC-EVs were visualized using transmission electron microscopy (TEM).

To optimize the hematocrit % and yoda1 incubation time and concentration needed to generate piezo1 RBC-EVs, we treated 1) 1, 3, 6, 18% hematocrit with 100 µM yoda1 for 2 hours; 2) 6% hematocrit with 100 µM yoda1 for 0.5, 1, 2, 24 hours; and 3) 6% hematocrit with 1, 10, 100 µM yoda1 for 30 min. RBC-EV size and concentration, and EV markers were quantified as previously described. RBC-EV purity was calculated as the ratio between RBC-EV concentration measured using TRPS and total protein concentration measured using bicinchoninic acid assay.

Shapiro-Wilk normality test was performed on all datasets. We then performed a one-way analysis of variance (ANOVA) with a Tukey post-hoc test to determine statistical significance amongst groups. Data are shown as mean ± standard deviation.

## RESULTS

Needle shearing RBCs generated lipid-bound particles that contain EV markers. RBC needle shearing generated $6.3e^9$ particles/mL with a diameter of 101 ± 45.7 nm (**Figure 1a**). When RBC-EV were incubated with Triton X-100, which should lyse EVs, particle concentration decreased more than 10X to $3.7e^8$ particles/mL (**Figure 1a**). Western

blot confirmed that cytoplasmic EV markers ALIX and TSG101, and surface marker CD63 were present in shear stress RBC-EV (**Figure 1b**).

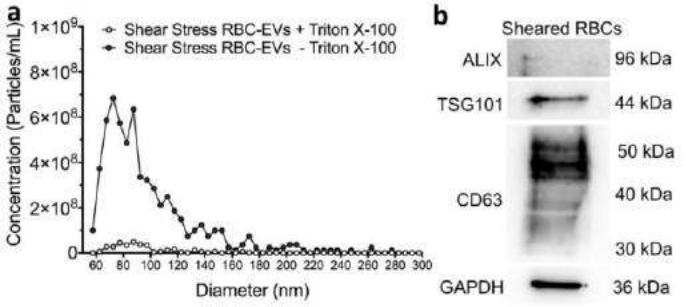


**Figure 1: RBC shear stress triggers RBC-EV production. TRPS measurement shows a decrease in lipid-bound particles after Triton X-100 treatment (a). Western blot confirms presence of cytosolic EV markers ALIX and TSG101 and surface EV marker CD63 (b).**

Chemical stimulation of mechanosensitive RBC piezo1 triggered RBC-EV production. RBC treated with piezo1 agonist yoda1 produced $2.8e^{12}$ RBC-EVs/mL at diameter 115 ± 49 nm. In contrast, $Ca^{2+}$ ionophore treatment produced EVs of similar size ($3e^{12}$ RBC-EVs/mL; 122 ± 52 nm diameter), while DMSO vehicle control produced 1000X less EVs of smaller size ($7e^{9}$ particle/mL; 78 ± 24 nm diameter; **Figure 2a**). Piezo1 RBC-EVs showed a biconcave morphology (**Figure 2b**) and were more enriched in ALIX and CD63 (**Figure 2c**; $p<0.05$) compared to $Ca^{2+}$ ionophore RBC-EVs.

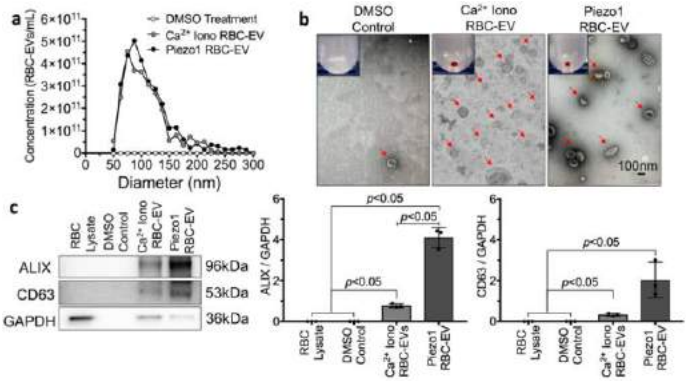


**Figure 2: Piezo1 activation produces unique RBC-EVs. RBC-EV size and concentration measured by TRPS (a). RBC-EVs visualized by TEM (b). Panel B inset shows RBC-EV pellet after ultracentrifugation. Red arrows highlight RBC-EVs. Western blot confirmed presence of EV markers ALIX and CD63 (c).**

Finally, we optimized our methods to generate piezo1 RBC-EVs using ultracentrifugation. While 1, 3, and 6% hematocrit showed increasing RBC-EV concentration ($2e^{11}\pm8e^{10}$, $6.7e^{11}\pm3e^{11}$, and $4.7e^{12}\pm2e^{12}$ particles/mL, respectively), 18% hematocrit did not generate significantly more RBC-EV than 6% hematocrit ($1e^{13}\pm6e^{12}$ particles/mL) when RBCs were treated with 100 µM yoda1 (**Figure 3a**). RBC-EV purity was greater in samples produced from 6% or 18% hematocrit than 1% or 3% hematocrit (**Figure 3b**). Yoda1 treatment for 30 min produced similar RBC-EV concentrations as 1, 2, and 24 hours treatments (**Figure 3c**). RBC-EV concentration did not increase when using yoda1 concentration above 10 µM (**Figure 3d**). Incubation time and yoda1 concentration did not affect RBC-EV purity. There were no significant differences in RBC-EV size when comparing the different hematocrit %, yoda1 incubation time, and yoda1 concentration conditions.

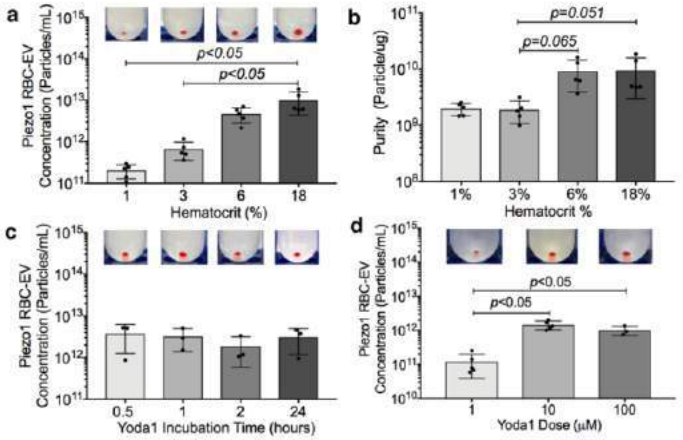


**Figure 3: Optimization of experimental parameters to generate piezo1 RBC-EVs. Both 6% and 18% hematocrit produced greater RBC-EV concentration (a) and purity (b) than 1 and 3% hematocrit. RBC yoda1 incubation time did not significantly affect RBC-EV concentration between 30 min and 24 hours (c). 10 µM Yoda1 maximized RBC-EV production (d).**

## DISCUSSION

This study provides evidence that shear stress may trigger RBC-EV production by stimulating mechanosensitive RBC piezo1. Furthermore, comparison of size, morphology, and EV biomarkers suggests that piezo1 RBC-EVs may be different from RBC-EVs generated by $Ca^{2+}$ ionophore or pathological conditions. Finally, 6% hematocrit treated with 10 µM yoda1 for 30 min yields the purest RBC-EVs isolated using standard ultracentrifugation.

In our future work, we will needle shear RBCs treated with piezo1 inhibitors to verify that piezo1 simulation during shear stress produces RBC-EVs. We will then perform functional assays to quantify how piezo1 RBC-EVs affect endothelial reactive oxygen species, inflammation, barrier function, and nitric oxide production. Understanding how shear stress-induced RBC-EVs affect endothelial function can lead to clinical biomarkers that improve cardiovascular disease diagnosis, treatment, and prognosis.

## ACKNOWLEDGEMENTS

Funding support was provided to G.S.S through the University of Maryland Presidential Postdoctoral Fellowship, C.M.W. through the National Science Foundation Graduate Research Fellowship Program (DGE 1840340), R.M.S through the National Institutes of Health Postdoctoral Institutional Training Grant (5T32HL007698-26), and A.M.C through a National Institute of Health grant (R01HL140239–0).

## REFERENCES

[1] Peng, L. et al., *Cardiovasc. Drugs Ther*, 35:901–913, 2020.
[2] Jana, S. et al., *JCI insight*, 3:e120451, 2018.
[3] Straat, M. et al., *Transfusion*, 56:3012–3020, 2016.
[4] Michel, J.-B et al., *Int. J. Mol. Sci*, 21:6756, 2020.
[5] Werre, J. M et al., *Cell. Mol. Biol*, 50:139–145, 2004.
[6] Gottlieb, P. A., *Curr. Top. Membr*, 79:1–36, 2017.
[7] Usman, W. M. et al., *Nat. Commun*, 9:1–15, 2018.
[8] Cahalan, S. M. et al., *Elife*, 4:e07370, 2015.

# MITIGATION OF INJURY TO NERVES DURING PROSTATE CANCER CRYOABLATION USING CRYOPROTECTIVE AGENTS

**P. Ranjbartehrani (1), D. Ramirez (2), F. Schmidlin (3), M. Etheridge (1), P. Iaizzo (2,4,5), Q. Shao (1), J. Bischof (1,2,5)**

1 Department of Mechanical Engineering, University of Minnesota, United States
2 Department of Biomedical Engineering, University of Minnesota, United States
3 Urology Center Hirslanden Grangettes Group Geneva, Switzerland
4 Department of Surgery, University of Minnesota, United States
5 Institute for Engineering in Medicine, University of Minnesota, United States

## INTRODUCTION

Prostate cancer (PCa) is the most frequently diagnosed cancer and the second leading cause of cancer death for men in the United States [1]. Radical treatments such as prostatectomy and radiation therapy are primary treatment options, but complications including erectile dysfunction (ED) and urinary incontinence are very common. Focal therapies are an emerging treatment modality that offer similar curative outcome but fewer side effects. Among them, cryosurgery represents an effective focal therapy treatment method for all stages of PCa [2]. One major complication associated with PCa cryosurgery is ED, caused by cryoinjury to the cavernous nerve in the neurovascular bundle (NVB), which is in close proximity to the prostate and is therefore directly exposed to freezing temperatures during cryosurgery. The use of cryoprotective agents (CPAs) to protect nerves against freezing temperatures is a method that has been used in nerve cryopreservation [3]. While existing literature establishes the idea of using CPAs to prevent nerve damage, there is still a lack of experimental data and quantitative models to study the effect of CPAs in preventing nerve cryoinjury during prostate cryosurgery. Moreover, no comprehensive study has assessed both the toxicity of CPA exposure to the nerve and the cryoprotective effectiveness within a repeatable and relevant biological model.

In this work, we developed an ex-vivo nerve model as representative of the NVB to investigate the toxicity and efficacy of a number of cryoprotective agent (CPA) in protecting the NVB from cryoinjury. The CPA cocktails includes different concentrations of DMSO-based, alcohol-based, and sugar-based cryoprotective agents.

## METHODS

**Prostate Cryosurgery Modeling:** To determine the thermal conditions experienced by the NVB during the PCa cryosurgery, we developed a model in COMSOL Multiphysics (Version 5.3) that mimics the conditions applied in a cryosurgery treatment of PCa. The 3D prostate model was reconstructed based on MRI images of a PCa patient. Four cryoprobes (P1-4) along with a urethral warmer (UW) are placed in the prostate as shown in Figure 1 A. The relative positions of the probes to the tumor and the NVB is shown on Figure 1 B. In order to find the temperature distribution within the prostate and on the NVB, Equation (1) was solved.

$$\rho c_p(T)\frac{\partial T}{\partial t} - \nabla(k(T)\vec{\nabla}T) + w_b c_b(T - T_a) = Q_{met} \qquad (1)$$

Where where T and t are temperature and time; $\rho$, $c_p$ and k are density, specific heat, and thermal conductivity of the biological tissues; $\rho_b$, $c_b$, $w_b$, $T_a$ and $Q_{met}$ represent blood density, specific heat, and perfusion rate, and arterial temperature and metabolic heat generation, respectively. Material properties used for the biological tissues in this model were taken from the literature [4,5]. The boundary conditions of the cryoprobe are determined by matching the isotherm (0, -20 and -40°C) diameters of the numerical model to those disclosed by the manufacturer, in a separate model.

***Ex vivo* Assessment of Neural Response to CPAs:** Freshly procured porcine phrenic nerves, supplemented with rat sciatic nerves, were rested in oxygenated modified Krebs-Henseleit buffer (KHB) before the experimental conditions were applied. There were 4 experimental groups: (1) control (No CPA exposure and no freezing) , (2) direct freezing (No CPA exposure, only freezing), (3) toxicity testing (No freezing, only CPA exposure) and (4) treatment (Both CPA exposure and freezing). The timeline of the experiment and the experiment setup are further elaborated in Figure 2. For CPA exposure, the nerves were exposed to oxygenated KHB mixed with CPA for 30 minutes before they were rinsed with the original KHB. The freezing condition was applied on the nerve using a cryostage (BCS 196, Linkam Scientific). The applied temperature profile, which is derived from the PCa cryosurgery model, was simplified and set as following: cooling to -10 °C with a cooling rate of -10 °C/min and thawing to room temperature with a warming rate of 10 °C/min. All nerves were further

incubated in oxygenated KHB at 37°C for 3 hours for recovery. To quantify acute cryoinjury, the AP was measured before and after the CPA exposure, right after the freezing and during 3 hours of recovery from freezing. The impact of the freezing was quantified by comparing the AP collected on the recording leads distal to the freezing point over time. The AP amplitude was normalized using the baseline of the AP amplitude of the first AP measurement, measured before CPA exposure or freezing. Normalized AP is the key indicator of the continuity of AP conduction, with 0 indicating complete blockage of the evoked AP at the freezing site.

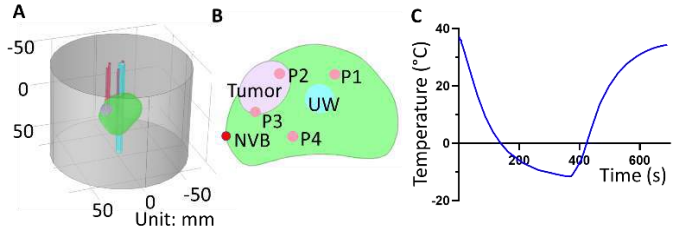


**Figure 1: A) Modeling geometry B) relative position of the probes, UW, tumor and NVB C) Temperature profile on the NVB**

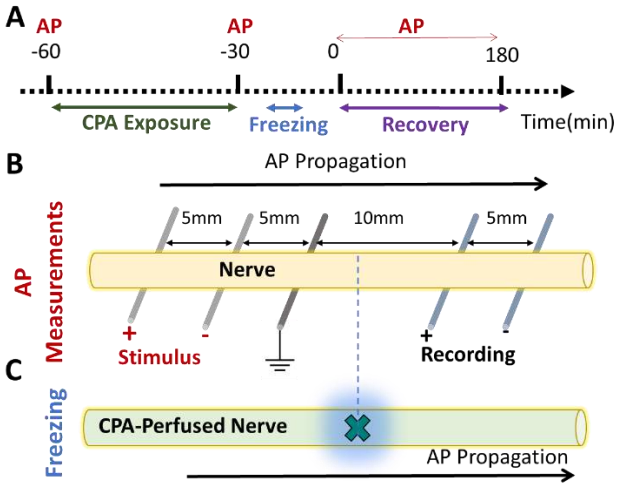


**Figure 2: A) Experiment timeline B) AP measurement setup C) Freezing location**

## RESULTS

The freezing condition that the NVB is experiencing during the cryosurgery is found by the modeling and is shown on Figure 1 C.

In both porcine phrenic and rat sciatic nerve models, the action potentials did not change substantially over time when the nerves were not exposed to freezing conditions or CPA, as confirmed by the positive control groups in Figure 3A (porcine phrenic nerve) and 3B (rat sciatic nerve). Exposing "Direct Freezing" group nerves (i.e. no CPA with freezing) result in an AP conduction halt and no recovery after freezing (AP amplitude =0 between 0 and 180 min) as shown in Figures 3A and 3B.

The CPAs which were tested on porcine phrenic nerves are listed on Figure 4A and 4B, along with their toxicity and cryoprotective efficacy. The CPA cocktail containing 5% DMSO and 7.5% Trehalose was non-toxic and showed the highest AP recovery ratio (0.48) at 180 min after freezing. The CPAs which were tested on the rat sciatic nerves are listed in Figure 4C and 4D, along with their toxicity and cryoprotective efficacy. Among all the CPAs evaluated, 5% M22 was not toxic to the nerves and showed the highest averaged AP amplitude after the freezing condition.

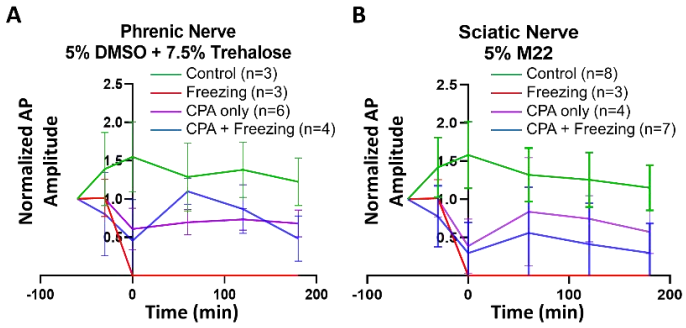


**Figure 3: Normalized AP amplitudes change over time for 4 experimental groups in A) porcine phrenic and B) rat sciatic nerve**

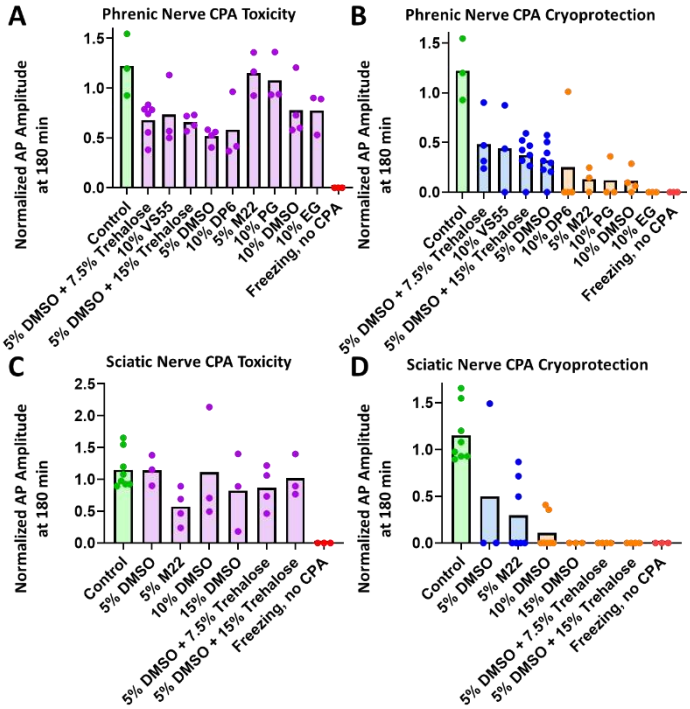


**Figure 4: Comparison of CPAs by their neural toxicity and cryoprotective efficacy.**

## DISCUSSION

In this work, we demonstrated preliminary feasibility of an approach to use cryoprotective agents to prevent cryoinjury to the nerves. This nerve-sparing approach have potential application in preventing cryoinjury to the NVB during prostate cryoablation. We developed an ex-vivo nerve model and tested different concentrations of several CPAs in terms of their toxicity and cryoprotective effects after freezing. The results show 5% DMSO and 7.5% Trehalose and 5% M22 are the most effective CPAs for protecting porcine phrenic and rat sciatic nerves after freezing, respectively. In-vivo and clinical studies will also be needed to confirm the efficacy and safety of this method.


## ACKNOWLEDGEMENTS

This work is funded by Medical Immersion Technology (MIT) Sàrl.


## REFERENCES


[1] Siegel et al., Cancer J Clin, 2021
[2] Baust et al., *Medical Research Archives*, 2020
[3] Asher et al., Cryobiology 1972
[4] Rabin et al., Cryoletters 2002
[5] Thaokar et al., Cryobiology 2012

# A PHYSICS-BASED MULTI-SCALE MODELING PIPELINE FOR SIMULATION OF VENTILATION IN ADVANCED COVID-19

**Shea T. Middleton (1), Elizabeth Dimbath (1), Anup Pant (1), Stephanie M. George, PhD (1), Veeranna Maddipati, MD (2), M. Sean Peach, MD-PhD (3), Kaida Yang, PhD (3), Andrew W. Ju, MD (3), Ali Vahdati, PhD (1)**

(1) Department of Engineering, East Carolina University, Greenville, North Carolina, USA
(2) Department of Pulmonary and Critical Medicine, Brody School of Medicine, East Carolina University, Greenville, North Carolina, USA
(3) Department of Radiation Oncology, Brody School of Medicine, East Carolina University, Greenville, North Carolina, USA

## INTRODUCTION

COVID-19 disease, generated by a coronavirus called SARS-CoV-2, has caused a deadly worldwide pandemic. The viral infection can result in extensive tissue and organ damage, particularly in the lungs. Computed tomography (CT) images are valuable for analyzing heterogenous COVID-19 lung injuries such as ground-glass opacities (GGO) and areas of consolidation[1].

Physics-based computer models of the lung offer a virtual hypothesis-testing platform to gain a deeper understanding of pulmonary ventilation dynamics in healthy and disease states [2]. *In silico* modeling of COVID-19-afflicted lung mechanics may provide valuable insights into the multi-scale interactions of heterogenous acinar damage with lobar and whole-lung function.

This research aims to develop a physics-based multi-scale computational modeling pipeline for COVID-19-afflicted lungs by coupling airflow and lung tissue mechanics [3]. To this end, this study develops an *in silico* multi-scale workflow for simulating heterogenous patient-specific lung damage using a meso-scale acinar model coupled to a reduced-order conducting airway model.

## METHODS

This study utilized a 4D CT scan obtained during tidal breathing of a male patient hospitalized in Vidant Medical Center (Greenville, North Carolina, USA) with an advanced case of COVID-19. The methodology used in this paper was approved by the East Carolina University and Medical Center Institutional Review Board (UMCIRB) with study ID 20-001447. Informed consent was obtained from the patient.

The geometry of the first several airway generations visible in CT images and the lung lobes were segmented from the end-inspiratory and end-expiratory phase using Mimics 23.0 (Materialise NV, Belgium) and the Chest Imaging Platform in 3D Slicer [4]. A space-filling airway generation algorithm with random heterogeneity was then used to create 16 generations of conducting airways [5]. The model included 30,142 acini, each coupled to a terminal bronchiole. 3D Slicer was also used to segment the aerated, GGO, and consolidated COVID-19 regions using the Hounsfield values in the CT images [6].

The C++ simulation package CHASTE (Cardiac, Heart, and Soft Tissue Environment) was used to establish the multi-scale coupling between the macroscale airflow and the meso-scale acinar mechanics model[7]. The airflow equation was presented as a modified Poiseuille flow with corrections to dynamic resistance [3].

Airflow was driven by changes in acinar volume of each of the approximately 30,000 acini as a function of the fluctuating pleural pressure of the lung. Pleural pressure varied based on Equation 1:

$$P_{pl} = P_{plimax} + \frac{\Delta P_{pl}}{2}\left(1 - \cos\left(\frac{2\pi t}{T} + \Phi\right) + \pi\right) + P_g \qquad (1)$$

where $P_{pl}$ is pleural pressure, t is simulation time, T is the inspiration-to-inspiration breathing period (four seconds for this simulation), Φ is a phase shift, and $P_g$ is pressure due to gravity

Acinar mechanics were represented by a sigmoidal transpulmonary pressure-volume relationship, incorporating different levels of tissue damage through increased surface

tension and decreased compliance [8,9]. The coefficients for the sigmoidal acinar model were selected based on patient-specific characteristics, including patient sex, height, and age. A hypothetical healthy lung simulation without any tissue damage and a COVID-19-afflicted lung simulation with heterogeneously-distributed damage were run for 12 seconds (three breathing cycles) on a workstation with 128 GB of RAM and a 14-core Intel Xeon CPU.

## RESULTS

Our image analysis based on segmentation of CT images showed that the right middle lobe exhibited the least amount of COVID-19-induced damage (29.6% of the lobe volume was made of GGO and consolidated regions), while the right lower lobe had the highest COVID-19-induced damage presence (78.2% of the lobe volume was made of GGO and consolidation areas). In our simulations, the least damaged lobe (right middle) demonstrated a far more minor change in tidal volume and flow between healthy and diseased simulation scenarios (Figure 1).

Furthermore, the COVID-19 simulation scenario demonstrated a re-distribution of ventilation from the most injured lobes (right upper, right lower, and left lower) to the least injured lobes (right middle and left upper lobes). The pressure distributions in the lung for each simulation are shown in Figure 2. These images show that the diseased case simulation demonstrated more heterogeneity in air pressure distribution throughout the lung with lower pressure magnitude on average.

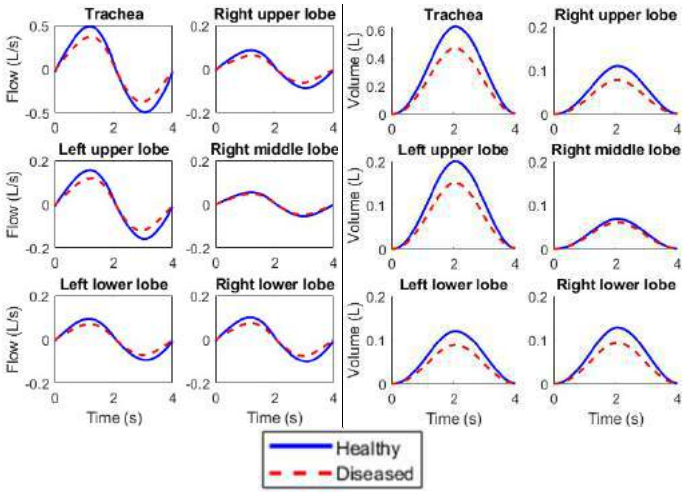


**Figure 1: Whole lung and lobar tidal airflows (left) and tidal volumes (right) for the healthy and diseased simulation scenarios.**

## DISCUSSION

This study presents a multi-scale modeling pipeline to simulate patient-specific heterogeneous COVID-19-induced damage and compares the results to a hypothetical healthy lung simulation scenario.

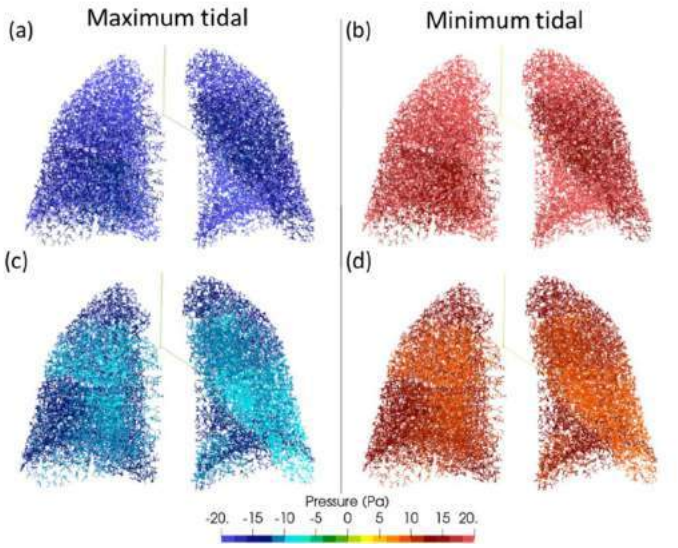


**Figure 2: Pressure distribution in coronal view of the healthy (a,b) and diseased (c,d) lung simulation scenarios at maximum inspiration and expiration.**

Our simulation results show that as damage manifested in the patient's right upper, right lower, and left lower lobes, ventilation was redistributed to the patient's less damaged lobes (right middle and left upper lobe), which is in agreement with recent clinical observations [10]. Moreover, our multi-scale model reasonably simulated a decrease in overall tidal volume as a consequence of tissue injury and surfactant loss in the meso-scale acinar mechanics model.

The presented *in silico* study is a step towards building digital twins of the human lung incorporating subject-specific heterogenous tissue damage to gain a deeper understanding of pulmonary ventilation and eventually individualized treatment strategies.

## ACKNOWLEDGEMENTS

This material is based on the work supported by the National Science Foundation under 9. Special thanks to nurses and respiratory therapists at Vidant Medical Center for their help with this study and to Vidant Radiation Oncology (Greenville, North Carolina, USA) for the use of CT scanner in the facility. Special thanks to Rafel Bordas for insightful email correspondence on lung model generation.

## REFERENCES

[1] Barisione, E, *Virichows Arch,* 478:471-485, 2020
[2] Ma, H, *Front. Physiol.*, 11:941, 2020
[3] Bordas, R, et al. *PLoS One*, 10, 2015
[4] Fedorov, A, et al. *Magn. Reason. Imaging*, 30, 2012
[5] Tawhai, M, et al. *J. Appl Physiol*, 97:2310-2321, 2004
[6] Kassin, M, et al. *Sci. Reports,* 11:1-13, 2021
[7] Cooper, F, et al. *J. Open Source Softw.* 5:1848, 2020
[8] Venegas, J, et al. *J. Appl. Physiol.*, 84:389-395, 1998
[9] Fujioka, H, et al. *J. Biomech*, 46:319-328, 2013
[10] Cobes, N, et al. *Eur. J. Nucl. Med. Mol. Imaging 47, 2020.*

SB³C2022
Summer Biomechanics, Bioengineering and Biotransport Conference
June 20-23, Eastern Shore, MD, USA

# MACROMOLECULAR UPTAKE AFFECTS CARTILAGE MECHANICS AND CHONDROCYTE VULNERABILITY

**Y. Wu (1), A. Kotelsky (2), M. Buckley (2)**

(1) Materials Science Program, University of Rochester, Rochester, New York, USA
(2) Department of Biomedical Engineering, University of Rochester, Rochester, New York, USA

## INTRODUCTION

Articular cartilage (AC) covers and protects the ends of long bones in synovial joints, enduring roughly a million loading cycles every year for multiple decades. AC is surrounded by synovial fluid, a thick, viscous liquid that lubricates and provides nutrients for the tissue. While the lubricating properties of synovial fluid are mostly due to the presence of hyaluronic acid, since synovial fluid is formed from filtered blood plasma, it is also replete with plasma proteins such as albumin (the most abundant molecule in synovial fluid [1]). These macromolecules can freely diffuse into cartilage interstitial fluid (CIF), the liquid component of cartilage that comprises >70% of the tissue and provides most of the tissue's resistance to mechanical load [2]. Interestingly, concentrations of albumin and other plasma proteins are markedly increased in joints affected by osteoarthritis (OA) [3], a devastating disease whose most prominent feature is progressive cartilage degeneration. However, it is not known how soluble macromolecules (such as albumin) in CIF affect cartilage function and whether they may contribute to OA pathogenesis.

To begin to address this knowledge gap, the objective of this research was to determine how soluble macromolecules that accumulate in cartilage influence its mechanical properties and, consequently, the vulnerability of cartilage cells (chondrocytes) to loading. Since the size of albumin is close to the average size of cartilage pores, we hypothesized that albumin-sized macromolecules in cartilage would interfere with interstitial fluid flow and reduce permeability $k$, a measure of the ease with which fluid is squeezed from compressed cartilage. Given that fluid outflow diminishes fluid load support, we further hypothesized that soluble macromolecules would ultimately make chondrocytes in loaded cartilage less vulnerable to injury for short loading durations by slowing fluid exudation.

## METHODS

Mechanical testing was performed on a total of 168 C57BL/6 mouse humeral cartilage-on-bone specimens from 84 <10-month-old mice using our established method [4-5]. This method enables visualization of cell death in mouse cartilage-on-bone explants subjected to prescribed mechanical forces under controlled *in vitro* conditions. The explant is placed cartilage-side-down on a glass slide, and a prescribed load is applied on the opposite side by a weight directed by a guide block. The cartilage – which is stained with fluorescent live dead cell indicators – is imaged through the objective of an inverted fluorescence microscope under the glass slide. We previously showed that 1N loading generates a circular area of cell death in humeral explants whose area correlates strongly with peak cartilage strain.

In the current study, we used this method to assess chondrocyte death induced by 1N loading sustained for 20s or 5min in explants that had been cultured under varying conditions to facilitate uptake or release of soluble macromolecules into or out of the cartilage prior to mechanical testing. We investigated several soluble macromolecules, including albumin and both 40 kDa and 270 kDa dextran (a polysaccharide with a similar structure to hyaluronic acid) at concentrations ranging from 3 to 30 mg/mL. Explants were incubated in solutions containing high or low concentrations these macromolecules to drive them into or out of the tissue via concentration gradients. For specimens incubated in high concentrations of dextran, fluorescence micrographs of explants after incubation confirmed infiltration of this macromolecule into the tissue (not shown).

After mechanical testing, we used inverse finite element modeling (iFEM) to determine the biphasic/poroelastic material properties (permeability $k$ and solid matrix Young's modulus $E$) of tested specimens from select treatment groups based on the extent of cell death 20s and 5min (respectively) after 1N loading. First, we calculated the "experimentally measured" peak strain in each specimen (for a given loading duration) by converting cell death area to peak tissue strain using our previously established relationship between these parameters. Next, we simulated the loading experiment using a finite element model generated in FEBio and varied $k$ and $E$ until the peak strain output by

the model at 20s and 5min (respectively) matched the experimentally measured peak strains for these loading durations.

We also performed experiments to determine how diffusivity of small molecules – a measure related to tissue permeability – is influenced by macromolecular infiltration. First, humeral cartilage-on-bone explants were incubated in a solution of low MW (3kDa) fluorescent dextran, after which the tissue appeared bright under fluorescent illumination due to infiltration of the solute. Next, explants were incubated in solutions with larger macromolecules including 40kDa dextran, albumin, and polyethylene glycol (PEG). Finally, a 1N force was applied onto each specimen and removed after a prescribed duration. Immediately after *unloading*, a circular, dark (non-fluorescent) area appeared due to tissue intake of non-fluorescent buffer from the surrounding bath. This dark region briefly grew, reaching its maximum size in about 3s before shrinking as fluorescent 3kDa molecules diffused in from the edges, a process that lasted tens of seconds. Based on the speed of fluorescence recovery, the diffusion constant of 3 kDa FITC-dextran in the tissue was determined.

**RESULTS**

In experiments to test the relationship between area of cell death and loading time, as expected, we found that for both fresh explants and explants cultured for 2 days in standard media (2-day culture w/o dextran, used to desorb interstitial solutes present at baseline), significantly more cell death was induced for 5min loading (assumed to reflect the equilibrium state without load supported only by the solid matrix) than for 20s loading (**Fig. 1a**). However, cell death area in explants cultured for 2 days in media with 30mg/mL 40 kDa dextran (2-day culture w/ dextran) prior to 1N loading was not different for 20s and 5min loading durations. Moreover, cell death area for 20s loading in explants cultured with dextran was significantly higher than fresh explants and explants cultured without dextran. In contrast, cell death area for 5min loading was not affected by incubation in media with or without dextran. Using iFEM, we found that the solid matrix Young's modulus $E$ was not significantly altered by 2-day culture w/ or w/o dextran (**Fig. 1b**). However, 2-day culture w/o dextran led to decreased $k$, while explants subjected to 2-day culture w/ dextran had higher $k$ than both fresh explants and explants subjected to 2-day culture w/o dextran (**Fig. 1c**). The effects of 2-day culture with other macromolecular solutes including albumin (not shown) were similar to 40 kDa dextran (increased cell death area for 20s loading, but no change in cell death area for 5min loading). Moreover, the effects were reversible (not shown) and were not reproduced when a small solute (the ionic compound NaCl) replaced the tested macromolecules in the incubation media, even at high osmotic concentrations (485 mOsm for NaCl compared to 335 mOsm for 40kDa dextran).

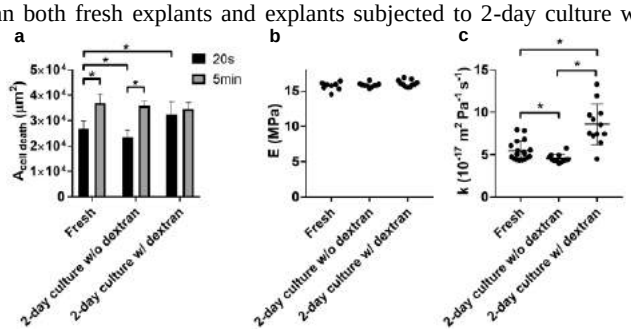


**Fig. 1: (a) Comparison of cell death area for 20s and 5min loading across treatment groups. Data are mean ± SD. (b-c) Comparison of (b) Young's modulus $E$ and (c) permeability $k$ across treatment groups as determined through iFEM.**

In experiments assessing the diffusion constant $D$ of cartilage for a small solute (3kDa dextran), we found that like $k$, $D$ was significantly increased by infiltration with macromolecular solutes including 40kDa dextran and albumin (data not shown).

**DISCUSSION**

Our data suggest that, contrary to our hypothesis, uptake of large (~40kDa) macromolecules into articular cartilage *increased* tissue permeability, while desorption of solutes from fresh explants *decreased* permeability. Increased permeability likely explains the measured increase in cell death area induced by 1N/20s loading after absorption of different macromolecular solutes. Under a constant load, fluid is gradually squeezed out of cartilage, leading to a progressive increase in tissue strain (creep) as fluid load support is lost. When permeability increases, this process is faster and tissue strain is higher for a given (short) loading duration. Thus, chondrocytes become more susceptible to injury after 20s loading. In contrast, our data suggest that macromolecular uptake does not affect equilibrium tissue properties (e.g., $E$). Specifically, cell death area for long loading durations (5min) that extend into the steady state – i.e., when fluid flow ceases and fluid support is absent – was not influenced by these molecules.

A limitation of this study is that permeability was not directly measured, but was rather inferred based on load-induced cell death area in combination with inverse finite element modeling. However, our finding of increased permeability is corroborated by our separate diffusion constant measurements, which demonstrate that macromolecular infiltration increased small molecule diffusivity – a metric that generally scales with permeability.

It does not appear that our unexpected findings can be explained by current models, which suggest macromolecules at the concentrations studied (orders of magnitude lower than the concentration of ions such as $Na^+$ in cartilage) should have a negligible effect on tissue mechanics. For example, biphasic solute/triphasic models (constructed in FEBio) did not reproduce the phenomenon we observed (data not shown). Moreover, the finding that permeability was not similarly altered by small molecules (ionic compounds) suggests the origin of the observed phenomenon was not tissue-wide alterations in osmolarity. Thus, we developed an analytic model that accounts for pore-size-dependent penetration of large macromolecules into the cartilage ECM, leading to osmotic pressure gradients that alter pore dimensions and modify tissue permeability. Our model assumes the tissue has a heterogeneous pore structure, consistent with findings of prior work [6]. We further assumed that because the size of the tested macromolecules is close to the average pore size in cartilage, these solutes can only infiltrate the widest pores, generating an osmotic pressure that in turn grows these pores at the expense of narrow pores and alters tissue permeability. Values of most model parameters were taken from the literature. A model parameter dependent on unknown variables (such as the pore tortuosity) was set to a value that ensured consistency with the measured tissue permeability after 2 days of culture in standard media without large solutes ($k^{measured}_{w/o i dextran} = 4.0 \times 10^{-17}\,\frac{m^2}{Pa \cdot s}$), when the tissue was assumed to be macromolecular solute-free. According to a calculation based on our model, we found that $k^{predicted}_{w/i dextran} = 7.9 \times 10^{-17}\,\frac{m^2}{Pa \cdot s}$, consistent with out experiments that yielded $k^{measured}_{w/i dextran} = 8.5 \times 10^{-17}\,\frac{m^2}{Pa \cdot s}$ with a range of $4.5 \times 10^{-17}\,\frac{m^2}{Pa \cdot s}$ to $13.2 \times 10^{-17}\,\frac{m^2}{Pa \cdot s}$.

**ACKNOWLEDGEMENTS**

We thank Dr. Whasil Lee for help with osmolarity measurements.

**REFERENCES**

[1] Bergmann, T et al., *J Proteome Res*, 13:4377-4387, 2014. [2] Soltz, MA et al., *J Biomech*, 31:927-934, 1998. [3] Gobezie, R et al., Arthritis Res Ther, 9:R36, 2007. [4] Kotelsky, A et al., *J Vis Exp*,143:1-7, 2018. [5] Kotelsky, A et al., *Connect Tissue Res*, 61:360-374, 2020. [6] Majda D et al., *Microporous Mesoporous Mater*, 241:238-245, 2017.

SB³C2022
Summer Biomechanics, Bioengineering and Biotransport Conference
June 20-23, Eastern Shore, MD, USA

# FEMALE PELVIC MORPHOLIGCAL VARIATION IN THE GENERATION OF GEOMETRIES FOR SIMULATIONS OF VAGINAL CHILDBIRTH

**Megan R. Routzong (1, 2), Steven D. Abramowitch (1)**

(1) Department of Bioengineering, University of Pittsburgh, Pittsburgh, PA, U.S.
(2) Department of Obstetrics, Gynecology & Reproductive Sciences, University of California, San Diego, La Jolla, CA, U.S.

## INTRODUCTION

After aging, vaginal childbirth is the greatest risk factor for the development of pelvic floor disorders[1,2], which may result from acute injury or accumulated microdamage sustained by the pelvic floor tissues during vaginal delivery in conjunction with alterations to tissue architecture and function associated with aging and menopause. During vaginal childbirth, pelvic floor tissues must stretch to accommodate the fetus, peaking during fetal crowning which is when injury likely occurs.

It is apparent that the shape of the female pelvic anatomy plays a role in vaginal childbirth mechanics. Studies have shown that cephalopelvic disproportion (referring to the fetal head and maternal pelvis) can cause obstructed labor—when the fetus cannot physically fit through the obstetric outlet of the maternal pelvis[3]. While existing literature has predominantly focused on the shape of the bony pelvis, it is probable that the shape of the pelvic floor muscle complex would also impact childbirth biomechanics.

This study aimed to evaluate the influence of variation in maternal pelvic morphology on the biomechanics of vaginal childbirth—specifically, pubovisceral muscle and perineal body strains, which are common sites of maternal birth injury. We hypothesized that variation in specific shape attributes—quantified by principal component analysis (PCA)—would significantly impact predicted strains.

## METHODS

The 6 geometries in this study were outputs of a statistical shape model of the combined bony pelvis–pelvic floor muscle complex of pregnant women. This model was built based on imaging data from 34 pregnant women (17 in the 1st/2nd trimester and 17 in the 3rd trimester, ranging in age from 20-49 years and in race/ethnicity)[4]. PC scores (parameters that define the 3D shape) were chosen using Latin Hypercube Sampling[5]. The resulting geometries were imported into Houdini FX (SideFX, Toronto, CA) for computation and simulation.

Regions of interest were defined by the corresponding surface mesh vertices from the statistical shape model. Then volume meshes were created. Each coccyx was made of ~10,000 tetrahedral elements, the sacrum and innominate bones as a unit of ~50,000 tetrahedral elements, and the pelvic floor muscle complexes of ~28,000 tetrahedral elements. The fetal head—identical for each simulation—was a sphere with a diameter of 90 mm[6,7] and composed of 8,048 tetrahedrons.

The sacrum and innominate bones were fixed in all degrees of freedom. The superior coccyx was fixed to the last sacral vertebrae which allowed rotation about the sacrum, while the lower tip of the coccyx was fixed to nearby vertices of the pelvic floor muscle complex. The pelvic floor muscle complex was fixated to the bony pelvis at the ischial spines, inferior ischiopubic rami, pubovisceral muscle entheses, and at the location of the clitoral ligament. Contact was defined between all parts of the fetal head, pelvic floor muscle complex, and bony pelvis and optimized to minimize penetration between meshes.

The fetal head and bony pelvis were treated as rigid bodies, with Lamé parameters 3 orders of magnitude larger than the soft tissues. Pelvic floor muscle material properties were determined by approximating the slope of stress-strain curves from literature (obtained from *ex vivo* uniaxial tensile testing of younger human female cadaveric pelvic floor muscles)[8]. The estimated Young's modulus of 200 kPA and a selected Poisson's Ratio of 0.49 were converted to Lamé parameters. The anococcygeal ligament material properties were set as the secant modulus of human uterosacral ligament uniaxial testing along the main loading direction[9]. This resulted in a modulus of 8 MPa and a selected Poisson's Ratio of 0.49, which were also converted to Lamé parameters.

Each geometry underwent 2 simulations: 1) A force-driven simulation to determine a geometry-dependent fetal head path and, 2) A displacement driven simulation with a fully prescribed fetal head path from which strains were calculated (Figure 1). This workflow allowed for geometry-specific fetal head paths while increasing simulation stability and reducing penetration issues.

Strain was not measured at the element level in this study as issues with negative Jacobians are still being resolved. Pubovisceral muscle length was averaged across the left and right muscles and defined as the distance from the midpoint of the enthesis to the centroid of the perineal body. Perineal length was defined as the sum of the distance from the left edge to the centroid and the right edge to the centroid. Both lines were calculated as the perineal body bends significantly around the fetal head during childbirth (see Figure 1). Strain was defined as the change in length over the original length and peak strains were determined. Bivariate correlations analyzed relationships between shape (defined by a set of 7 PC scores) and pubovisceral muscle and perineal body strain.

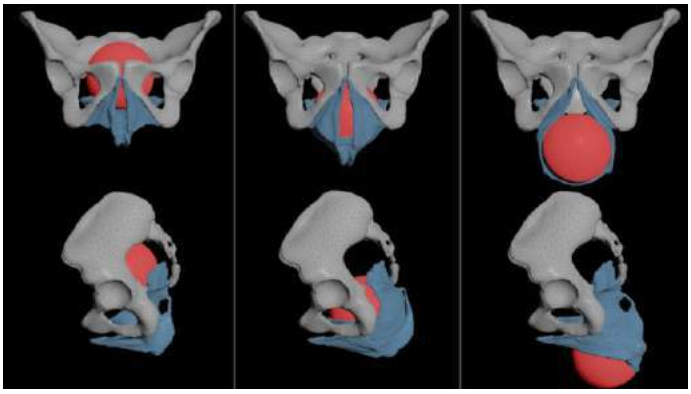

**Figure 1: A vaginal childbirth simulation from inferior (top row) and left, sagittal (bottom row) views. The fetal head (red), bony pelvis (gray), and pelvic floor muscle complex (blue) are shown at time 0 (left column), the halfway point (middle column), and at peak strain (right column).**

## RESULTS

Pubovisceral muscle and perineal body strains varied across the 6 simulations (Figure 2). PC 2 and 3 scores were significantly correlated with perineal body strains ($\rho$ = -0.747 and 0.811 and p = 0.044, and 0.025, respectively). PC 3 was significantly correlated with pubovisceral muscle strains ($\rho$ = 0.759 and p = 0.040). These PCs describe variation in the curvature of the bulbocavernosus muscle, relative location of the perineal body, iliococcygeus muscle convexity/concavity, and relative size of the coccyx. These correlations between strains and PC scores suggest that perineal body and pubovisceral muscle strains were higher when there was less anterior bulging of the bulbocavernosus muscle, a more superior perineal body, greater iliococcygeus convexity, and a proportionally larger coccyx.

## DISCUSSION

This study demonstrates that anatomical variation in the maternal bony pelvis and pelvic floor muscle complex morphology significantly impacts predicted strains in simulations of vaginal childbirth. This indicates that the shape of pelvic anatomy with respect to pregnancy and childbirth should be studied further and that studies need to consider morphological variation (or lack thereof in their work) when drawing conclusions from finite element simulations of vaginal childbirth.

The posterior and inferior displacement of the fetal head, and, therefore, the corresponding displacement of the pelvic floor tissues, is going to meaningfully impact the strains those tissues experience. As such, it is logical to assume the initial shape of the pelvic floor muscle complex would also impact resulting strains. For example, if the iliococcygeus muscle is in a more convex configuration at the onset of labor, that muscle will need to be pushed further posteriorly and inferiorly (resulting in increased strains) compared to a more concave iliococcygeus to accommodate a fetal head of comparable size. This explains how soft tissue morphology (alone, but also in conjunction with bony pelvis shape) influences pelvic floor muscle complex strains.

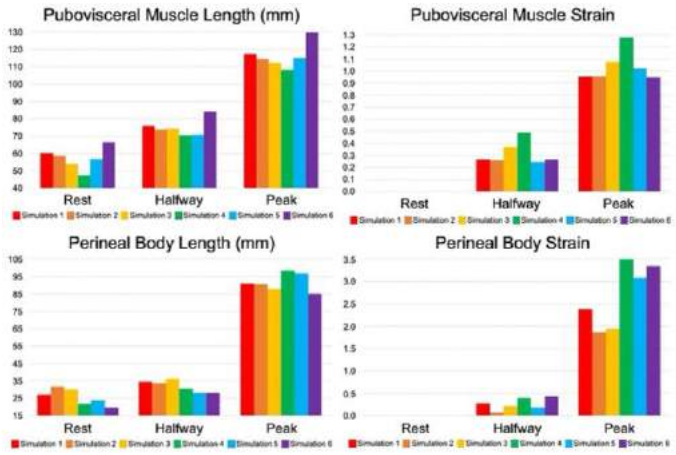


**Figure 2: Histograms demonstrating the variation in the length and strain (distension) measures calculated for each simulation.**

Strain was not measured directly in this preliminary study due to the presence of negative Jacobians (which ongoing efforts aim to resolve). However, Houdini is able to reasonably simulate gross motion and mechanics even in the presence of such issues, allowing for the use of the described approximate strain measures. With the resolution of these issues and the addition of more unique geometries, these results can be more robustly validated. Additionally, the statistical shape model these geometries were generated from only considered pregnant anatomy. Many existing simulations of vaginal delivery use nonpregnant, older, or even cadaveric data when building the geometry for such simulations, which likely results in even more disparity in predicted strain values than demonstrated here.

In its current form, this study demonstrates the utility of a combined statistical shape—finite element modeling workflow, which allows for more consistency across multiple geometries while still allowing for geometry-specific effects. This was a novel endeavor demonstrating that both bony pelvis and pelvic floor muscle complex shape play an important role in the biomechanics of vaginal childbirth.

## ACKNOWLEDGEMENTS

This material is based upon work supported by the National Science Foundation Graduate Research Fellowship Program under Grant #1747452. Any opinions, findings, and conclusions or recommendations expressed in this material are those of the author(s) and do not necessarily reflect the views of the National Science Foundation.

## REFERENCES

[1] Handa, VL et al., *Obstet. Gynecol.*, 118(4):777, 2011.
[2] Mant J et al., *BJOG*, 104(5): 579-585, 1997.
[3] Dolea C et al., *WHO*, 2003.
[4] Routzong MR, *Univ. Pittsburgh*, 2021.
[5] Martinez JM et al., *pyDOE*, 2017.
[6] Li X et al., *Biomech. Model. Mechanobiol.*, 10(4):485-494, 2011.
[7]. Lien KC et al., *Obstet. Gynecol.*, 103(1): 31-40, 2004.
[8] Burnett LA et al., *J. Biomech.*, 98:109436, 2020.
[9] Baah-Dwomoh A et al., *Ann. Biomed. Eng.*, 46(12):2036-2047, 2018.

SB³C2022
Summer Biomechanics, Bioengineering and Biotransport Conference
June 20-23, Eastern Shore, MD, USA

# ESTIMATING GASTROCNEMIUS MUSCLE VOLUME BY USING PANORAMIC ULTRASOUND IMAGES IN ORTHOGONAL PLANES

**Shabnam Rahimnezhad (1), Karin G. Silbernagel (2), Daniel H. Cortes (1)**

(1) Mechanical Engineering Department
Penn State University
State College, PA, USA

(2) Department of Physical Therapy
University of Delaware
Newark, DE, USA

## INTRODUCTION

Among all the morphological parameters, muscle volume has a good correlation with muscle strength[1]. Patients with Achilles tendon injuries experience structural changes of their tendons and significant atrophy of calf muscles[2]. Understanding the morphology of the gastrocnemius muscle and measuring muscle volume is important to determine the effectiveness of treatments and rehabilitation strategies for Achilles' tendon rupture. Currently, Magnetic Resonance Imaging (MRI) is the most precise imaging method for measuring muscle volume in vivo. While MRI provides detailed data, the employment of MRI technology is not free of cons. Obtaining MRI images is time-consuming, and it is more expensive comparing other imaging methods. In addition, MRI is not a convenient method for individuals with metal implants and other contraindications to MRI. 3D ultrasound (3DUS) is another technique that can be used to quantify muscle volume by combining multiple 2D cross-sections of the muscles [2, 3]. Requiring multiple cross-sectional images and time for combining these images make 3DUS hard to use for routine checkups. The second way of estimating the muscle volume is based on morphological parameters like a cross-section area, length, and thickness of the muscle. These morphological parameters can be obtained by ultrasound and/or panoramic ultrasound (PU) imaging. Since the muscles do not have simple geometries, the geometrical parameters must be 'calibrated' by shape factors to have an acceptable estimation of the volume of the muscles. Bandholm et al utilized ultrasound techniques for measuring the thickness and length of the muscle to estimate the gastrocnemius and soleus volume [5]. Vanmechelena et al combined the anatomical cross-sectional area of the muscle and muscle length to suggest the simple equations estimating the muscle volume [6]. Due to the complex shape of the gastrocnemius muscles, additional morphological information may be required to obtain a better estimation of muscle volume. The objectives of this study are to use two panoramic ultrasound images to capture the cross-section areas in two orthogonal planes and to evaluate an equation to estimate the gastrocnemius muscle volumes (GMV).

## METHODS

This study was approved by the Penn State University IRB (STUDY00019121). Five healthy young adults (three females, two males, age=30.8±1.9, weight=67.6±15 kg, height=167±7 cm) participated in this study. Participants had no recent injuries, disease, surgeries, or metals in their lower limbs. Participants were asked to lay on a bed still but relax during the MRI imaging procedure. Wedges are used under the participants' ankles to eliminate the contact of the gastrocnemius muscle and the MRI table. 3T whole-body MRI system (Siemens Prima Fit) was used to gather the imaging data with the following parameters: T1-weighted, time to echo= 3.69 ms, time to repetition= 7.8 ms, 6 mm slice thickness. 3D Slicer 4.13.0 was used to create segmentations and construct the volumes (Figure 1). The panoramic ultrasound images of the gastrocnemius muscles of the participants were taken within 15 days of the MRI test using a SIEMENS (ACUSON P300™) Ultrasound System. Panoramic images in the axial and sagittal planes were taken three times, and the average of the results was used for analysis. Figure 2 shows the axial cross-section and sagittal section in one of the participants.

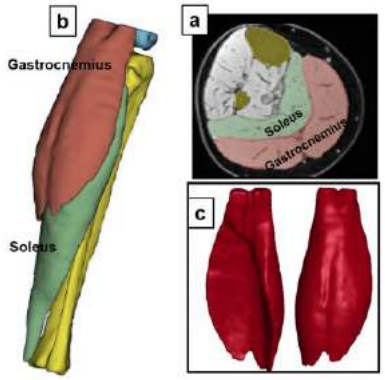


**Figure 1: a) Axial MRI image, b) Segmented volume in 3D slicer, c) Gastrocnemius muscle front and back view**

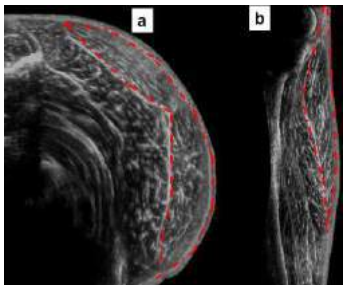


**Figure 2: a) Axial panoramic view of the gastrocnemius muscle, b) Sagittal view of the medial gastrocnemius muscle**

The equations that were suggested in the literature to estimate the muscle volume (MV) are based on the muscle length (ML), thickness (t), and anatomical cross-section area (ACSA) of the muscle, and generally can be illustrated as below [5, 6]:

$$MV = a + bi(ti \times ML) \quad (1)$$
$$MV = c + di(ACSAi \times ML) \quad (2)$$

Here we anticipate that the inclusion of a sagittal area (AS) of the muscle can result in a better estimation of the GMV (equation 3).

$$MV = e + fi\left(ACSA * \frac{AS}{t}\right) \quad (3)$$

Where a, b, c, d, e, f are constant parameters obtained from regression analysis. To understand the morphological changes of the GM among individuals, 'segment Geometry' modules of slicer are employed to get the graph of changes of the area in axial and sagittal planes from MRI 3D data.

## RESULTS

Figure 3 illustrates the normalized area over the length percentile in the axial direction, and figure 4 shows the normalized area over the width percentile in the sagittal direction from the MRI 3D data.

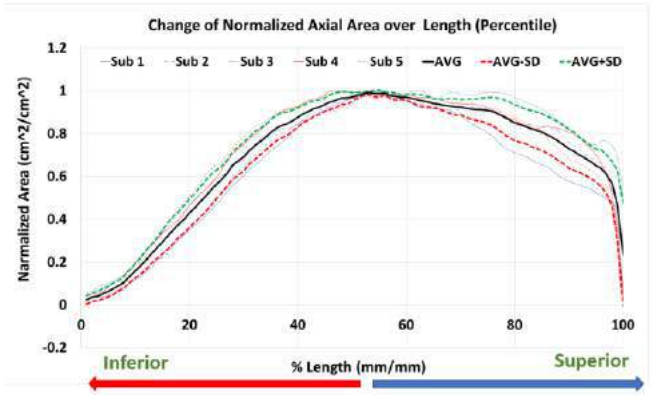


**Figure 3: Change of normalized axial area over Length percentile**

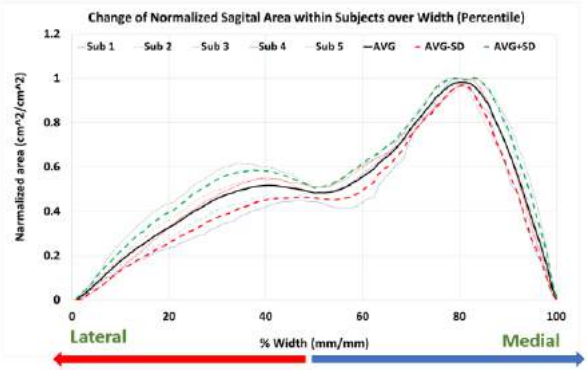


**Figure 4: Changes of the normalized sagittal area over width percentile**

Despite inter-individual differences, the normalized areas in two different directions for everyone had almost the same trends. Also, in both axial and sagittal planes, the graph of areas has minimum slopes around %50-60. This means that the areas do not change a lot around %50 of the length and %50 of the width of GM. Thus, obtaining panoramic ultrasound images in these locations can reduce the errors due to differences in probe location between trials.

Table 1 shows the parameters measured using ultrasound and MRI. Compared to MRI data, ultrasound data generally showed lower values.

**Table 1: Measured parameters by use of Ultrasound and MRI**

| | MRI data | | | | | Ultrasound data | | | | |
|---|---|---|---|---|---|---|---|---|---|---|
| Sub. No. | Volume of the GM $cm^3$ | Length of the Medial (Lm) $cm$ | ACSA $cm^2$ | As $cm^2$ | t $cm$ | Length of the Medial (Lm) $cm$ | ACSA $cm^2$ | As $cm^2$ | t $cm$ |
| 1 | 334.264 | 19.4 | 25.9 | 33.92 | 2.1 | 17 | 22 | 26 | 2.1 |
| 2 | 213.755 | 17.5 | 17.08 | 21.58 | 1.9 | 17.5 | 12.7 | 20.5 | 1.6 |
| 3 | 380.655 | 21.7 | 22.26 | 38.75 | 1.9 | 21 | 19 | 27 | 1.6 |
| 4 | 271.5 | 18.4 | 19.52 | 32 | 1.9 | 17.4 | 16.4 | 24.5 | 1.7 |
| 5 | 543.841 | 20 | 34.88 | 45.01 | 2.54 | 21.3 | 22 | 37 | 1.9 |

Table 2 demonstrates the regression analysis for differential equations in estimating the muscle volumes that were obtained from MRI data and segmentation in Slicer.

**Table 2: Regression analysis to estimate GMV**

| EQUATION | REGRESSION ANALYSIS MRI DATA | REGRESSION ANALYSIS ULTRASOUND DATA |
|---|---|---|
| $a + bi(ti \times ML)$ | a= -380.14, b=18.135 $R^2$ = 0.9816 | a= -454.27 b= 23.99 $R^2$ = 0.90 |
| $c + di(ACSAi \times ML)$ | c= -27.534 d=0.8037 $R^2$ = 0.9624 | c= -85.387 d= 1.24 $R^2$ = 0.91 |
| $e + fi\left(ACSA * \frac{AS}{t}\right)$ | e= 32.096 f= 0.7866 $R^2$ = 0.958 | e= -9.38 f= 1.26 $R^2$ = 0.98 |

## DISCUSSION

Normalized cross-sectional data of the muscle in sagittal and axial directions show that the healthy muscle has almost the same geometrical trends among individuals. And %50-%60 of the length and width are good places to capture the panoramic image since the sagittal and axial areas have the minimum changes in these positions. Our analysis showed that to reduce the possible errors, ultrasound measured values must be captured from these locations. Regression analysis showed that by use of MRI data all the suggested equations can potentially predict GMV accurately; since the use of freehand ultrasound data is not free of errors, our suggested method of combining sagittal and axial areas (and thickness) shows a slightly better estimation of muscle volume. This may be due to the additional morphological information captured in the two panoramic images. A limitation of this study is the difficulty in capturing the proximal insertion of the medial gastrocnemius muscle and obeying the curvature of the muscle without tilting the probe. In conclusion, this study showed the possibility of using simple equations, by choosing correct locations for obtaining the PU imaging.

**ACKNOWLEDGMENTS**: Research reported here was supported by NIAMS of the NIH under award number R21 AR077282.

## REFERENCES

[1] R. Akagi, et al., *Age and Ageing*, 38: 564–569, 2009.
[2] C. Rosso *et al., Surg., Sport. Traul. Arthro.*, 21: 1369–1377, 2013.
[3] O. Article *et al.*, Clin Anat, 2(3): 319-327,2019.
[4] L. B. Ã, R. Barrett, et al., Biomech, 42: 1313–1319, 2009.
[5] T. Bandholm, et al., Pediatr Neurol, 37(4): 263-9, 2007.
[6] I. M. Vanmechelen,et al., *Clin. Biomech.*, 51: 40–44, 2018.
[7] S. H. Schless *et al., Dev. Med. Child Neurol.*, 60(1): 81–87, 2018.

SB³C2022
Summer Biomechanics, Bioengineering and Biotransport Conference
June 20-23, Eastern Shore, MD, USA

# THE INTERPLAY BETWEEN TRANSCATHETER AORTIC VALVE REPLACEMENT COMPLICATIONS AND CORONARY ARTERY DISEASE

**Seyedvahid Khodaei (1), Zahra K. Motamed (1,4,5)**

(1) Department of Mechanical Engineering, McMaster University, Hamilton, Ontario, Canada

(2) School of Biomedical Engineering, McMaster University, Hamilton, Ontario, Canada

(3) School of Computational Science and Engineering, McMaster University, Hamilton, Ontario, Canada

## INTRODUCTION

Over the past several years, transcatheter aortic valve replacement (TAVR) has surpassed the traditional treatment method, surgical aortic valve replacement (SAVR), for patients who suffer from aortic stenosis, specifically those who are of a high-risk of an unsuccessful surgery. TAVR is becoming popular for patients who are of an intermediate or low risk, indicating that it may become the superior treatment modality for aortic stenosis for all patient types. Unfortunately, there are drawbacks to TAVR – one of them being the presence of paravalvular regurgitation (PVR) (1). In addition, since the coronary ostia are located superior to the aortic valve, the presence of PVR jets may impede blood flow into the coronary arteries. Coronary Artery Disease (CAD) is present in approximately 50% of the TAVR population (2), and the question, however, of if CAD should be treated or reduced in severity prior to TAVR is still being debated (2).

Fluid mechanics plays an essential role in the development, progression, diagnosis, and treatment of cardiovascular disease (3, 4) – Indeed, the essential sources of cardiovascular mortality and morbidity can be explained on the basis of adverse hemodynamics (4, 5). There has been an emerging conclusion by many researchers that valvular disease is a complex disease that also depends on the dictates of the ventricle and the vascular system (6–9).

In this study, we developed a computational-mechanics diagnostic framework to assess the effect of TAVR complications, such as PVL on the coronary arteries and aortic root in both pre and post TAVR states to quantify local and global hemodynamics. Currently only lumped-parameter models have the capabilities to quantify global hemodynamics due to the complexity of the cardiovascular system and the unmanageable computational cost of 3-D models of hemodynamics in the entire cardiovascular system. Our diagnostic framework, therefore, uses an image-based patient-specific lumped-parameter algorithm and a 3-D strongly-coupled FSI model to quantify both local and global hemodynamics in patients who underwent TAVR.

## METHODS

*Global hemodynamics (LV workload)*. We developed a patient-specific lumped-parameter model that considers interactions of the aortic valve, LV and arterial system to estimate the LV workload non-invasively in both pre and post intervention states. The model uses a limited number of input parameters all of which can be reliably obtained using Doppler echocardiography and a sphygmomanometer.

*Local hemodynamics (blood flow dynamics)*. We developed a fluid-solid interaction and lumped parameter modeling framework to calculate 3-D blood flow dynamics in the aortic root, neo-sinus and coronary arteries. As described above, the lumped parameter model in this framework used few input parameters all of which can be measured using Doppler echocardiography and a sphygmomanometer.

## RESULTS

***LV workload (global hemodynamics).*** The LV workload is an effective metric of the LV load and clinical state and represents the energy that the ventricle delivers to the blood during ejection plus the energy necessary to overcome the viscoelastic properties of the myocardium itself. Pre-TAVR, untreated AS increased the load on the LV due to the augmented flow resistance which caused a LV pressure overload. Although the flow resistance and consequently the LV pressure decreased greatly post TAVR, the LV workload did not improve because PVL contributed to a switch from a ventricular pressure overload to a ventricular volume overload (Figure 1).

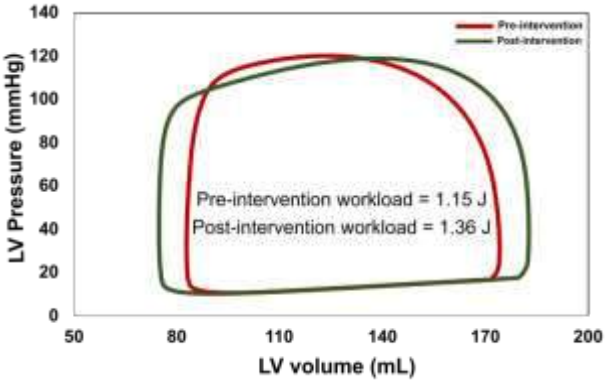


**Figure 1. LV workloads in a sample patient between baseline and 90 days post-TAVR. *Pre-TAVR*: severe aortic stenosis (EOA=0.6 cm2), coronary artery disease and dyslipidemia, diastolic dysfunction, ejection fraction: 38%, brachial pressures: 54 and 107 mmHg, forward LV stroke volume: 74 mL; *Post-TAVR*: aortic valve (EOA=1.8 cm2), diastolic dysfunction, ejection fraction: 51%, brachial pressures: 59 and 120 mmHg, forward LV stroke volume: 92 mL. *LV workload did not improve by TAVR.***

***Aortic root and coronary arteries fluid dynamics (local hemodynamics)***. It has been shown that for a TAVR without PVL, the coronary flow influences the flow patterns of aortic root and neo-sinus and favors the transfer of blood flow towards ostium during diastole (10). However, our results showed that in the presence of PVL, the aortic root vortices will not favor the transfer of blood flow towards ostium in the aortic root and neo-sinus region. We observed (figures 2) that in presence of PVL, considerable portion of the forward flow towards coronary ostium diverges towards the left ventricle, leading to a decreased coronary flow. TAVR can also disturb the vortical structures inside the Valsalva sinuses, which are essential for the washout of sinus flow and providing flow to the coronary arteries. Our findings demonstrate that PVL exacerbates the washout mechanism for the sinus and neo-sinus regions. Moreover, PVL leads to a significantly lower shear stress at the coronary walls due to the decreased blood supply during diastole after TAVR. This makes the coronary arteries susceptible to atherosclerosis, due to the low wall shear stress-induced inflammatory activation of endothelium mainly at the inner bend of curved arteries, ostia of branches and lateral walls of bifurcations

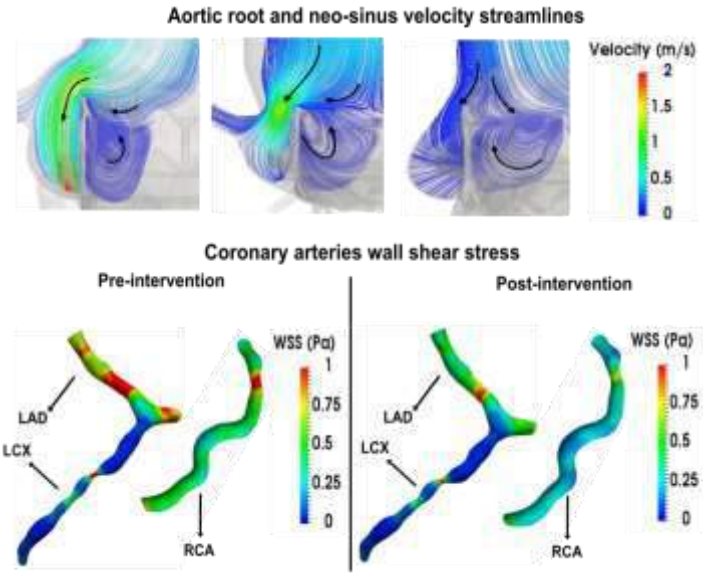


**Figure 2. Flow modeling in an Aortic root and coronary arteries with moderate to severe PVL in a sample patient. (a) Velocity vector during diastole. (b) Wall shear stress during diastole.**

## DISCUSSION

Concomitant CAD and PVL limit the benefit of TAVR: may increase the LV load, may potentially worsen coronary perfusion, and worsens heart failure. Atherosclerosis promotion through loss of physiological flow-oriented alignment of endothelial cells and its exacerbation by PVL will likely play an important hindering role in success of TAVR. The findings of this study suggest that beyond routine clinical indices for hemodynamic evaluation of the valvular disease (e.g, Doppler pressure gradients), valvular, vascular, and ventricular hemodynamics and their interactions should be clinically quantified and considered to better conduct the aortic valve management and treatment planning.


## ACKNOWLEDGEMENTS

This study were supported by NSERC Discovery Grant (RGPIN-2017-05349).


## REFERENCES


[1] Conte, S. M et al., *JACC: Case Reports* 1, 696–702 ,2019.
[2] Faroux, L et al., *JACC*: 74, 362–372 ,2019.
[3] Taylor, C. A et al., *Ann Biomed Eng* 38, 1188–1203 ,2010.
[4] Siebes, M et al., *Ann Biomed Eng* 38, 1216–1224 ,2010.
[5] Lieber, B. B et al., *Ann Biomed Eng* 33, 1695–1703, 2005.
[6] Keshavarz-Motamed, Z et al., *JAHA* 9, e015063 ,2020.
[7] Pibarot, P et al, *Heart* 93, 780–782 ,2007.
[8] Ben-Assa, E et al., *Sci Transl Med* 11 ,2019.
[9] Antonini-Canterin, F et al., *J Cardiovasc Echogr* 23, 91–95 ,2013.
[10] Madukauwa-David, I. D. et al., *Ann Biomed Eng* 48, 169–180, 2020.

# DETERMINING THE RISK OF POST-TAVR CARDIAC CONDUCTION ABNORMALITIES IN TRICUSPID AND BICUSPID VALVES IN A BEATING HEART USING A COMPUTATIONAL APPROACH

**S. Anam (1), S. Reza (1) B. Kovarovic (1), M. Bianchi (1), A. Hamdan (2), R. Haj-Ali (3), D. Bluestein (1)**

(1) Department of Biomedical Engineering, Stony Brook University, Stony Brook, New York, U.S.A
(2) Department of Cardiology, Rabin Medical Center, Faculty of Medicine, Tel Aviv University, Tel Aviv, Israel
(3) School of Mechanical Engineering, Tel-Aviv University, Tel Aviv, Israel

## INTRODUCTION

Transcatheter aortic valve replacement (TAVR) procedure is a minimally invasive procedure to treat patients with severe aortic stenosis. TAVR technology underwent a rapid evolution due to generational device design improvements, and the increase in the experience in TAVR procedures. However, few post-TAVR complications still remain persistent, with cardiac conduction abnormality (CCA) being one of the major ones. Post-TAVR cardiac conduction abnormality can occur due to any mechanical damage sustained by the atrioventricular conduction system located near the inter-leaflet triangle region between the non-coronary and the right-coronary leaflet. Conduction disturbances may eventually lead to permanent pacemaker implantation, abnormal cardiac function, and therefore to increased mortality[1]. This is particularly important in bicuspid aortic valve (BAV) patient population, as those tend to have higher risk of developing post-TAVR left bundle branch blockage (LBBB), which is a common form of conduction disturbance. BAV is the most common congenital cardiac defect, marked by an abnormal fusion of two aortic leaflets and often associated with early development of aortic stenosis. With the recent regulatory approval for TAVR in BAV, the number of younger patient cases receiving TAVR is likely to rise and requires to study the biomechanical aspects involved in TAVR deployment that may increase the risk of post-TAVR CCA development.

Several anatomical and biomechanical factors have been analyzed to assess the risk of CCA associated with TAVR. However, the effect of valvular calcium distribution on post-TAVR CCA development has not been conclusive and could be further analyzed using computational modeling approaches. The goal of this study was to first analyze the influence of tricuspid valvular calcification distribution on the TAVR device in dynamic physiological cardiac motion and the resulting risk of CCA throughout the cardiac cycle, then expanding our computational approach to BAV patients using patient-specific models to identify a strain threshold near LBB region which would help us identify BAV patients who are at the risk of developing post-TAVR CCA.

## METHODS

Five tricuspid models were created based on the most common shape and volume of annular calcium deposit[2] that were computationally incorporated into a dynamic beating, electromechanically coupled, 4-chamber adult male human heart model[3] (The SIMULIA Living Heart Model). Finite element (FE) simulation of the deployment of a 26 mm CoreValve (Medtronic plc, Minneapolis, MN) was performed using Abaqus Explicit 2019. Calcium deposits were tied to the aortic surface of the leaflets. In order to

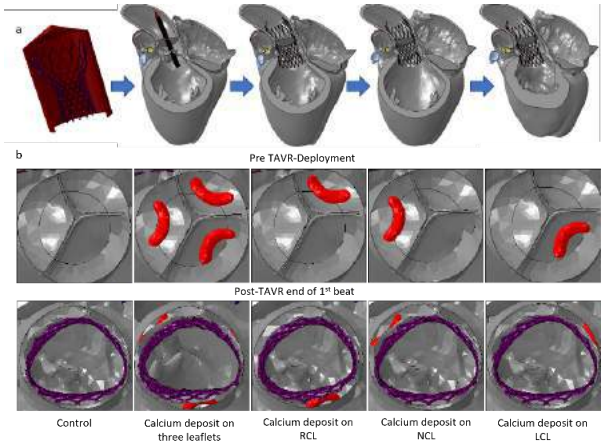


**Figure 1: (Tricuspid cases) TAVR deployment inside a 4-chamber beating heart model (tricuspid), (b) Control and 4 virtual patient model based on different valvular calcium deposit distribution; RCL - right coronary leaflet; NCL – non-coronary leaflet; LCL - left coronary leaflet**

quantify the strains that may trigger CCAs, area-weighted average maximum principle logarithmic strain (AMPLS) in the MS region of all the cases were measured during the TAVR deployment and two cardiac cycles.

For the patient-specific BAV study, we used de-identified cardiac CT scans (from Rabin Medical Center, Israel, with IRB approval) of 5 type I BAV patients who underwent TAVR procedure with self-expandable devices from Medtronic. Three patients had developed post-TAVR LBBB (LBBB patients) and the remaining did not develop any conduction disturbance (Control patients). Patient-specific stationary aortic root model preparation and FE simulation of TAVR procedure was performed based on our previous studies[4]. Clinical data and anatomical description found in the literature, were used to identify the approximate location of the LBB region in these patients.

**RESULTS:**

In the tricuspid valve cases, initial results demonstrated that the maximum AMPLS in the MS region of the patient cases with calcium deposits on non-coronary and right coronary leaflets (NCL and RCLs) were relatively lower during the deployment stage. Figure 2 (bottom row) demonstrates that the maximum AMPLS was higher for the calcium deposit on all three leaflets and RCL cases.

In majority of the BAV cases, highly eccentric stent deployments were observed (Figure 3 top row). Maximum principal logarithmic strain contour near the LBB region did not demonstrate any clear trend. However, the weighted AMPLS demonstrated a higher strain values (> 12.5%) near the LBB region in the LBBB patients (Figure 3 middle and bottom rows).

**DISCUSSIONS:**

Maximum AMPLS in the MS did not follow a similar trend during TAVR deployment and systole following TAVR deployment. The calcium deposits on RCL and NCL seemed to damp the impact of the TAVR prosthesis on the MS region during the deployment stage. Calcium deposit on the left coronary leaflet (LCL) seemed to push the

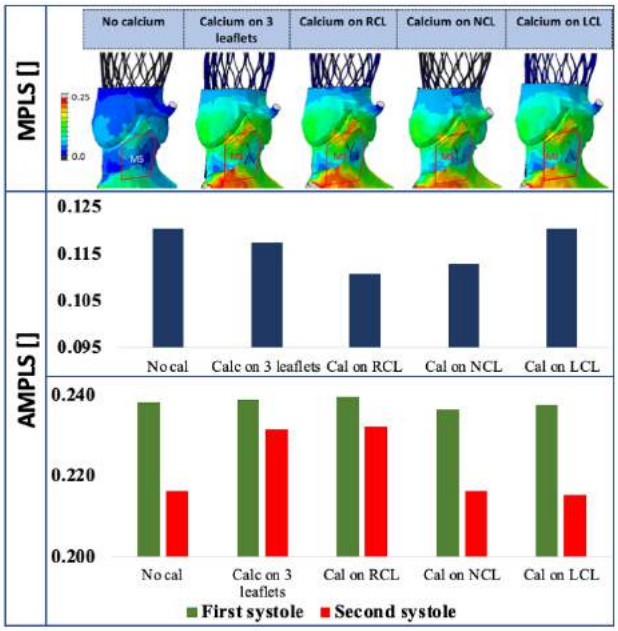


**Figure 2: (Tricuspid cases) Top row- Maximum principal logarithmic strain at the end of pre-load step in the MS region of 5 virtual patient cases; Middle and bottom rows – Maximum AMPLS in the MS during TAVR deployment and systoles following TAVR deployment, respectively**

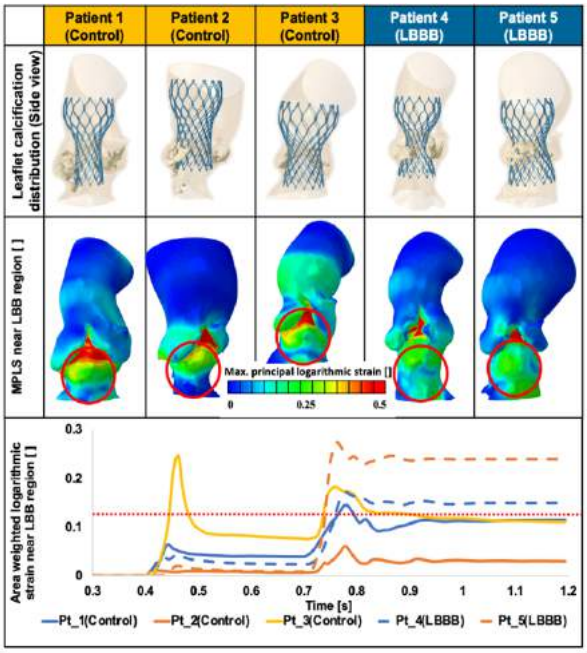


**Figure 3: (Bicuspid cases) Top row - Deployed TAVR device in each patient case; Middle row - Contour plot of maximum principal logarithmic strain on the aortic wall and the left ventricular outflow tract region. The MS and LBB regions are circled in red; Bottom row - Area-weighted AMPLS at the LBB region in each patient during different steps of TAVR simulation**

TAVR prosthesis towards the MS and resulted in relatively higher maximum AMPLS for cases with calcium deposits on all three leaflets and LCL (Figure 2-middle row). On the other hand, maximum AMPLS was higher for cases with calcium on three leaflets and RCL which was dictated by the location and the interaction between the calcium on the RCL and the TAVR prosthesis. Analysis was performed to understand the effect of the volume of calcium deposits on each leaflet. Further study on patient-specific beating heart is necessary to validate the novel technique of post-TAVR risk assessment.

For the BAV patient cases, *in-silico* data obtained from current patient models are consistent with clinical patient outcomes. All the control patients who did not have post-TAVR LBBB had lower strain values near LBB (~ <12.5%) compared to the LBB patients, making 12.5% a possible strain threshold for triggering CCA (Figure 3 bottom row– red dashed line) that may be used to identify the risk of post-TAVR LBBB - based on our area-weighted AMPLS approach. However, this threshold may vary with simulation parameters, and requires further investigation Future study will include analyzing the precision of this threshold using larger patient population and analyzing balloon-expandable cases in order to enhance the applicability of this method. Since BAV patients tend to have heavy and asymmetric leaflet calcification, the impact of leaflet calcification on the CCA would also be analyzed in future.

**ACKNOWLEDGEMENTS**

Funding provided by NIH-NIBIB U01EB026414 (DB). Industry Partners: ANSYS, Simulia Living Heart Project.

**REFERENCES**

[1] Houthuizen, P, et al., *Circulation*. 2012, 126:720–728
[2] Halevi, Rotem, et al. *J. Biomechanics* 48.3 (2015): 489-497.
[3] Baillargeon, Brian, et al, *E. J. Mechanics-A/Solids* 48 (2014): 38-47
[4] Anam, Salwa, et al. J Cardiovasc Transl Res. 2021

# PLATELET ADHESION IS DOMINATED BY LARGE VON WILLEBRAND FACTOR MULTIMERS AT DEVICE RELEVANT SHEAR RATES

**Connor T. Watson (1), Keefe B. Manning (1,2)**

(1) Department of Biomedical Engineering
The Pennsylvania State University
University Park, PA, USA

(2) Department of Surgery
Penn State Hershey Medical Center
Hershey, PA, USA

## INTRODUCTION

Platelet adhesion to bioreactive surfaces, while critical for hemostatic regulation, is also responsible for the onset of device-induced thrombosis [1]. Device-induced thrombosis is a potentially lethal complication that can be caused by either the supraphysiological high shear forces applied to blood by mechanical circulatory support (MCS) devices, or the absorption of proteins to device surfaces. These conditions permit platelet adhesion and the subsequent formation of occlusive thromboemboli. Device design is informed by a desire to prevent thrombus formation within the device domain. Careful consideration of device fluid mechanics and the use of non-thrombogenic biomaterials typically prevent intra-device thrombus deposition. However, thrombi often still form due to either protein surface absorption or downstream adhesion due to ultra shear forces within the device.

Platelet adhesion is mediated by fibrin binding to subendothelial proteins, as well as transient tethering by the von Willebrand Factor (vWF). While both mechanisms have been studied individually, it is unknown how these platelet receptors interact in the high shear flows characteristic of MCS devices [2,3]. Platelet-fibrin bonds, while strong, require longer formation times, and direct exposure by proximity to subendothelial proteins, making attachment difficult in high-shear flows. As a result, these bonds are typically formed in lower-shear environments, or as a stabilizing bond after platelet capture by vWF. Alternatively, vWF is important in arresting platelet transport in high shear flows, prior to the establishment of stronger fibrin-based bonds. The vWF unfurling mechanics, while tethered to the subendothelium, have been subject to much discussion [3-4]. Adhesion efficacy of vWF may be significantly altered by ADAMTS13, a cleaving enzyme within the blood that reacts with the exposed A2 domain to reduce vWF multimer length. Identification of the interaction between these mechanisms in conditions relevant to patients with MCS devices is critical to understanding downstream device-induced thrombosis. We hypothesize that a transitional shear range exists in which both vWF capture and platelet-surface interactions contribute to adhesion and that vWF begins to dominate deposition as shear rate increases past this range. By investigating the role of vWF and platelet-surface interactions in adhesion, novel targets can be identified for regulation of thrombosis due to pathological shear conditions.

## METHODS

The primary goal of this study was to observe vWF and platelet deposition as a function of shear rate and biochemistry. Polydimethylsiloxane (PDMS) microchannels were fabricated to act as a testing platform for shear-altered deposition. Channels were fabricated following standard soft lithography protocols for PDMS. A sudden expansion geometry was chosen to evaluate the effects on shear-mediated adhesion [5]. PDMS chips were cleaned in 70% ethanol and sealed to glass microslides using a plasma cleaner (Harrick Plasma, Ithaca NY). Shear rates were calculated in ANSYS FLUENT (ANSYS, Canonsburg PA) and verified by acquiring velocity data with a micro-PIV system (TSI Inc., Shoreview MN). Human blood was acquired in an IRB approved protocol for venipuncture and perfused through the microchannels with a Harvard syringe pump (Kd Scientific, MA). Channels were coated with human type I collagen (100 µg/mL) to create a reactive surface. Human vWF (Haematologic Technologies, Essex VT) was obtained and diluted to physiological concentrations of 12 µg/mL. Samples (n=6) were treated with ADAMTS-13 (0.5 µg/mL) and sheep anti-human vWF antibodies conjugated with AlexaFluor647 (Haematologic Technologies, Essex VT) in the case of vWF, and lipophilic dye $DiOC_6$ to stain platelets. During perfusion at 1,000, 5000, and 10,000 $s^{-1}$, real-time immunofluorescence images were acquired with an Olympus IX71 inverted microscope and DP74 camera (Olympus, Tokyo Japan). Images were converted to binary and processed in ImageJ (NIH, Bethesda MD) and MATLAB (Mathworks, Natick MA).

## RESULTS

Shear-mediated adhesion of platelets and von Willebrand Factor deposition onto a collagen surface within the sudden expansion. In total, deposition onto collagen at three shear rates was investigated for two biofluids, vWF and whole blood, under two conditions: ADAMTS-13 treated and untreated (n = 6 each). Shear rate was observed to be statistically significant ($p<0.001$) and was directly related to deposition of vWF and platelets. ADAMTS-13 also significantly diminished vWF deposition ($p<0.05$) at all shear rates **(Fig 1)**. However, the deposition of platelets was significantly affected by ADAMTS-13 only at 10,000 $s^{-1}$. This effect is summarized in **Figure 2**, where the relationship between adhesion of untreated vWF and platelets can be observed to follow a tight linear trend. While the deposition of vWF+ADAMTS-13 remained consistently low, platelet adhesion was unaffected by ADAMTS-13 until 10,000 $s^{-1}$.

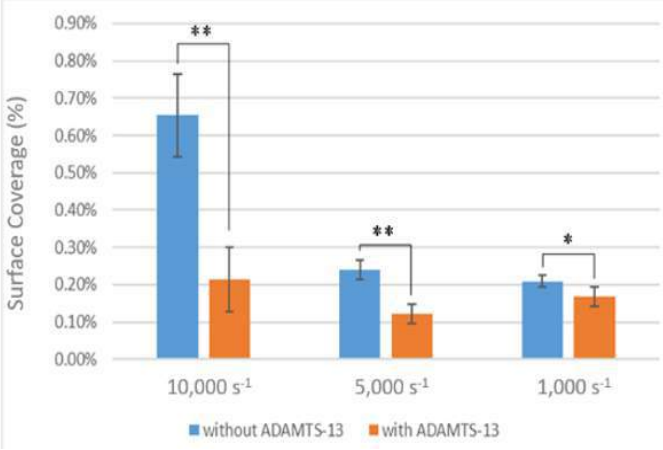


**Figure 1: Reduction of vWF adhesion and surface coverage due to ADAMTS-13 cleavage. Deposition was measured as % surface area covered. Data are presented as mean + SEM (n=6). Significance is denoted as * (p<0.05) or ** (p<0.01).**

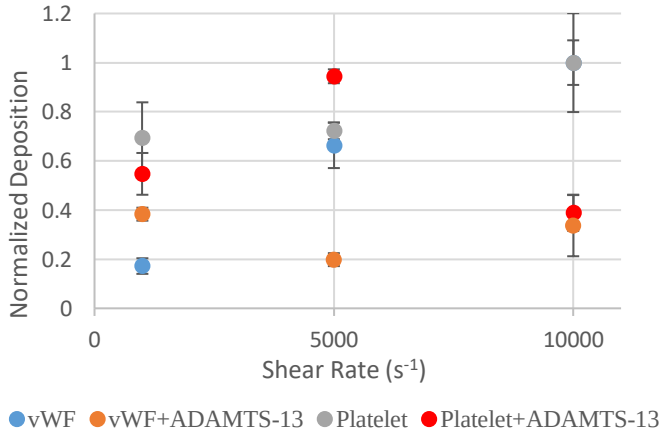


**Figure 2: Shear-mediated adhesion of platelets and vWF deposition. Deposition was measured as % surface area covered and normalized to the peak adhesion achieved for either metric, platelets or vWF. Data are presented as mean + SEM (n=6).**

## DISCUSSION

We observed that platelet and vWF deposition at high shear (10,000 $s^{-1}$) was hindered by ADAMTS-13, yet platelet deposition was not affected at lower shear rates (1,000-5,000 $s^{-1}$). vWF deposition was significantly diminished by ADAMTS-13 at all investigated shear rates. Shear rate was observed to have a significant effect on both untreated vWF and platelet deposition ($p<0.001$), while having no effect on the deposition of vWF treated with ADAMTS-13. A strong correlation between deposition of vWF and platelets was demonstrated *in vitro*.

The ADAMTS-13 protease inhibited vWF deposition at all shear rates, while only affecting platelet deposition at high shear. This indicates that at high shear, platelet adhesion is mediated by high molecular weight (MW) vWF multimers, while adhesion is possible through surface contact at lower shear rates. Low MW multimers have been shown to be ineffective in adhering and covering a functionalized surface *in vitro*, and this likely is true for platelet capture as well [6]. This study suggests the existence of a shear threshold between 5,000 and 10,000 $s^{-1}$ that requires uncleaved, high MW vWF multimers to facilitate platelet capture even on highly thrombogenic surfaces. These findings align with the range suggested by literature [7]. The behavior observed supports the hypothesis that the vWF-mediated mechanism of platelet capture is dominant only once a critical shear threshold has been reached. These findings match favorably with the current estimate of ~6,000 $s^{-1}$ [7]. The adhesion of enzymatically-treated platelets below this threshold is likely due to one of two mechanisms: the shear required for exposure of ADAMTS-13 reactive A2 domains within the vWF multimer has not been achieved, or that cleaved vWF multimers still mediate platelet adhesion at lower shear rates. Platelet adhesion at the investigated shear rates below this threshold (1,000 and 5,000 $s^{-1}$) is likely a result of contributions from both vWF and surface contact, rather than one mechanism dominating the other.

This study investigated mechanisms of platelet adhesion onto a thrombogenic protein surface and shed some light onto the contribution of vWF at various shear rates. To gain clearer insight, additional clinically relevant surfaces and shear rate conditions should be evaluated to determine if this behavior is conserved. Additionally, identification of the specific platelet integrins, such as GPVI and $\alpha_{2b}\beta_3$, that mediate surface contact adhesion would be useful in determining clinically relevant antiplatelet strategies. Further investigation of additional thrombogenic surfaces and platelet glycoprotein sites is necessary for deeper understanding of this phenomenon.


## ACKNOWLEDGEMENTS

This work is supported, in part, by NIH HL136369.


## REFERENCES


1. Manning, K. B., et al., *Curr Opin Biomed*, 2021.
2. Induruwa, Isuru, et al., *J. Thromb Haemost*, 2018
3. Westein, E., et al., *P Natl Acad Sci USA*, 2013.
4. Sadler, J. E, *Annu Rev Biochem*, 1998.
5. Jamiolkowski, M. A., et al., *Biomaterials*, 2016
6. Restle, D. J., et al., *Artificial Organs*, 2015.
7. Schneider, S. W., et al., *P Natl Acad Sci USA*, 2007

# FUNCTIONAL CARTILAGE TISSUE ENGINEERING DOES NOT REQUIRE CULTURE MEDIUM REPLENISHMENT

**Tianbai Wang (1), Yanli Lyu (1), Yue Liu (2), Michael B. Albro (1,2)**

(1) Materials Science and Engineering, Boston University, Boston, MA USA
(2) Biomedical Engineering, Boston University, Boston, MA USA

## INTRODUCTION

Cartilage tissue engineering (TE) is a promising osteoarthritis treatment strategy, whereby tissue constructs derived from cell-seeded scaffolds are fabricated for the repair of clinical cartilage defects. While the technology has exhibited growing clinical success, it continues to be encumbered—in both the clinical and research developmental stages—by the utilization of costly and laborious protocols needed to generate high quality tissues. Notably, for TE platforms, constructs are initially subjected to prolonged periods of *in vitro* cultivation (2-6 weeks) in chondrogenic media (CM) formulations to accelerate ECM biosynthesis [1]. While *in vitro* cultivation protocols beneficially give rise to functional constructs that can exhibit native composition and mechanical properties, they necessitate the use of frequent media replenishment procedures, constituting a significant time/cost burden for researchers and clinical technicians.

Periodic replenishment of culture medium is fundamental to cell/tissue culture applications, serving to restore cell-depleted nutrients (e.g., glucose, vitamins, amino acids), restore degraded signaling molecules (e.g., growth factors, hormones), and clear cell-secreted waste products (e.g., lactic acid). For *in vitro* cartilage TE protocols, the conventional paradigm to meet this need is to subject tissue constructs to relatively low media volumes but replenish the media frequently—daily or every other day. Interestingly, this convention is based on traditional cell culture protocols [2], rather than a fundamental understanding of the stability and cell consumption rates of constituents in media. As such, it is worth considering that state-of-the-art TE replenishment protocols may be far from optimized—i.e., it may be possible to generate functional engineered cartilage with larger media volumes and less frequent media replenishment or even to avoid replenishment entirely. Here, we hypothesize that the administration of larger media volumes can be used to: 1) mitigate the depletion of nutrients and accumulation of waste products in CM and, accordingly, 2) reduce the media replenishment frequency required to maintain construct viability and generate functional engineered cartilage. We examine this hypothesis through several experimental characterizations that consist of determining: 1) the minimum levels of media constituents and maximum levels of waste product accumulation that can achieve functional TE cartilage, 2) the depletion rates of critical CM constituents (insulin, ascorbic acid, and glucose) and accumulation rates of waste products (lactic acid assessed via pH) for different media volumes, and 3) the effect of varying culture medium volumes and replenishment frequencies on TE cartilage viability, composition, and material properties.

## METHODS

**Tissue constructs:** Immature bovine chondrocytes were seeded in 2% type VII agarose at $30\times10^6$ cells/mL. ∅4×2mm constructs were generated and cultured in serum-free CM, consisting of glucose, insulin, ascorbic acid, L-proline, sodium pyruvate, dexamethasone, and antibiotic–antimycotic [3]. To promote similar accelerated growth rates for all replenishment groups, all constructs were subjected to an initial 1-week exposure of 10ng/mL TGF-β3 with the media replenished (1mL/construct/media change) every other day. Varied media replenishment protocols and medium analysis of this study were subsequently performed in TGF-β-free medium over the next 6 weeks. **Requisite medium constituent levels:** Medium was administered to constructs with varied pH (7.6, 7.0, 6.8, 6.6, 6.4, 6.2) or varied constituent levels, relative to 1× CM standard concentrations (4.5mg/mL for glucose [GLU], 6.25μg/mL for insulin [INS], 50μg/mL for ascorbic acid 2-phosphate [AAP]) [4]: GLU (0.2×, 0.3×, 0.5×, 0.7×, 1×), INS (0×, 0.02×, 0.1×, 0.3×, 1×), and AAP (0×, 0.02×, 0.1×, 0.3×, 1×). **Media replenishment variation:** Media was administered over 6 weeks with parametric variation in replenishment frequency—thrice weekly [TW] (conventional frequency), weekly [W], biweekly [BW], or replenishment-free [RF], representing 17, 5, 2, and 0 replenishment points, respectively, over 6 weeks of culture—and cumulative media

volume (CMV) applied to each construct over the culture duration (3, 6, 9, 18 [conventional level], or 54mL). For each group, the administered media volume at each replenishment point can be computed as the CMV divided by the number of replenishments over the 6-week culture plus one for the initial day 0 supply. **Tissue analysis:** Constructs were analyzed for Young's modulus ($E_Y$), composition (GAG, DNA), viability (Live/Dead imaging/CellProfiler), and histology (Safranin O [Saf O]/Fast Green). **Medium constituent stability:** For RF groups and in the absence of tissue, medium was assayed at regular time points to monitor the decay of nutrient/constituent levels. Constituents for monitoring were selected based on those shown previously to be required to promote TE cartilage growth [4]: GLU (oxidase assay, Invitrogen), AAP [5], and INS (ELISA, R&D Systems)— Medium pH levels were also monitored.

## RESULTS

**Requisite medium constituent levels:** At day 49, constructs exhibited a decrease in $E_Y$ for levels of GLU below 0.5× ($p<0.05$), INS, AAP below 0.02× ($p<0.005$), and pH below 6.6 ($p<0.05$) (Fig 1). **Medium constituent stability:** In the absence of tissue, medium levels of GLU, AAP, and pH remained stable over 6 weeks (Fig 2A, 2C, 2D). In contrast, INS levels decreased by 38% over 35 days, indicating an intrinsic instability of the hormone (Fig 2B). In the presence of tissue, at low media volumes, all constituent levels (INS, AAP, GLU) and pH exhibited a more pronounced decrease. For GLU, INS, and pH, using higher media volumes mitigated this decrease.

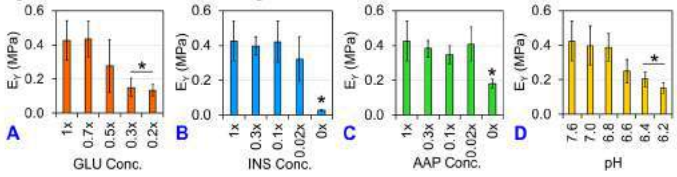


**Fig 1: Construct $E_Y$ after 7-week culture in response to varied levels of (A) GLU, (B) INS, (C) AAP, and (D) pH. * p<0.05: significant decrease below 1× level or pH 7.6.**

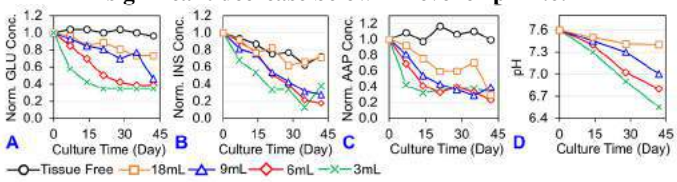


**Fig 2: Stability of (A) GLU, (B) INS, (C) AAP, and (D) pH over 6 weeks in un-replenished medium in the absence or presence of a TE construct for varying administered medium volumes.**

**Media replenishment variation:** At week 6, the conventional replenishment protocol of TW-18mL yielded constructs that reached native $E_Y$ (Fig 3A) and GAG (Fig 3B) levels. In general, $E_Y$ and GAG decreased to sub-native levels at lower CMVs and replenishment frequencies. However, at higher CMVs, lower media replenishment frequencies gave rise to increased $E_Y$ and GAG, with native levels reached for TW/BW/RF-18mL, and W/BW/RF-54mL. A similar trend was observed for cell density (Fig 3C) and viability measures (Fig 3D). Interestingly, for low CMV groups (TW-3mL & RF-3mL), viability loss was observed predominantly in the construct periphery, rather than the tissue interior (Fig 3F), suggesting that waste product accumulation, rather than nutrient depletion, serves as the limiting factor in requisite medium supply. Saf O staining showed consistent results, where reduction in GAG staining was observed for the low 3mL CMV groups but more intense staining was observed for high 18mL CMV groups (Fig 3E).

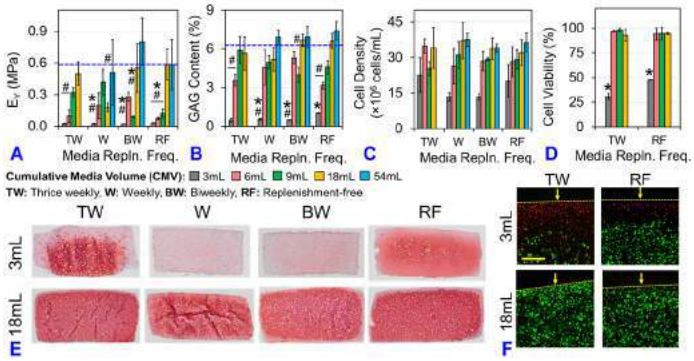


**Fig 3: (A) $E_Y$, (B) GAG, (C) cell density, (D) cell viability, (E) Saf O staining of TE constructs after 6-week culture for TW, W, BW, and RF replenishment frequencies and varied CMVs. Dashed line represents native level. * # p<0.05: significant decrease below TW-18mL and native levels, respectively. (F) Representative Live/Dead images of TW/RF-3/18mL constructs. Dashed lines and arrows depict media exposed surface. Scale bar: 300μm.**

## DISCUSSION

In contrast to serum-based media, the use of chemically-defined, serum-free CM formulations in TE culture protocols provides a unique opportunity to optimize replenishment protocols based on the inherent stability of defined medium constituents. Here, we demonstrate that several critical growth-inducing medium constituents (GLU, AAP) exhibit high levels of intrinsic stability while constituted in CM—constituent levels decreased by less than 5% over 45 days in the absence of TE constructs. When TE constructs are present, the temporal depletion of GLU, INS, AAP is far more pronounced—likely as a result of cell-mediation internalization/consumption processes. However, their depletion can be effectively mitigated by increasing the initial volume of media supplied to tissues (Fig 2). Similarly, the accumulation of lactic acid (assessed via decreasing pH) in culture medium can be mitigated by increasing medium volume. As such, one can increase the likelihood of maintaining constituent levels over the culture duration above the requisite threshold needed to maintain construct viability and achieve functional cartilage growth (Fig 1). Accordingly, by administering larger media volumes at the beginning of culture, functional cartilage with native-matched properties can be generated with fewer media replenishments, and remarkably, can even be generated with replenishment-free culture. It is important to note that while reducing replenishment frequency requires increasing the supplied media volume initially and at each replenishment point, it does not require increasing the cumulative media volume supplied over the entire culture duration. Essentially, functional cartilage can be generated by "front-loading" the entire 18mL CMV at the initiation of culture, rather than administering it serially with 18 × 1-mL replenishments over 6 weeks. Replenishment-free media culture platforms can advance a paradigm shift in cartilage TE technology by significantly reducing the time and cost burdens required to generate functional cartilage tissue specimens in clinical and research-based platforms.

**ACKNOWLEDGEMENTS**: This work was supported by the Musculoskeletal Transplant Foundation (MTF) Biologics, Boston University Materials Science & Engineering Innovation Award, and National Institutes of Health (NIH).

**REFERENCES:** **[1]** Huang BJ+ 2016 Biomaterials; 98:1-22. **[2]** Moore GE+ 1967 JAMA; 199:519-24. **[3]** Byers BA+ 2008 Tis Eng A; 14:1821-34. **[4]** Cigan AD+ 2013 Tis Eng A; 19:1941-48. **[5]** Vislisel JM+ 2007 Anal. Biochem; 365:31-39.

SB³C2022
Summer Biomechanics, Bioengineering and Biotransport Conference
June 20-23, Eastern Shore, MD, USA

# PREDICTING TEMPERATURE FIELD DURING THERMAL ABLATIONS USING DEEP NEURAL NETWORKS

**Hanife Tugba Kumru (1), Anilchandra Attaluri (2), Vitaly Gordin (3), Daniel H. Cortes (1)**

(1) Department of Mechanical Engineering, The Pennsylvania State University, State College, PA
(2) Department of Mechanical Engineering, The Pennsylvania State University, Harrisburg, PA
(3) Department of Pain Medicine, Hershey Medical Center, Harrisburg, PA

## INTRODUCTION

Chronic low-back pain (LBP) is one of the most common disorders causing long-term disabilities and approximately 15% to 45% of chronic back pain cases involve facet joints [1]. Monopolar radiofrequency ablation (RFA) of the medial branch of the dorsal rami is one of the treatments used to reduce facet joint pain. In this procedure, an electrode is placed near the medial branch and radiofrequency (RF) current is applied. Medial branch ablation induced thermocoagulation blocks pain signals to be sent from facet joint. However, there are a few mild to medium adverse effects associated with this procedure. Because the medial branch carries both the motor and the sensory nerves, RFA of medial branch not only destroys the sensory nerves but also damages the motor nerves innervating the multifidus muscle [2]. Denervation of the multifidus muscle is followed by the atrophy and fat infiltration observed after an RFA procedure [2,3]. Since the multifidus muscle plays an important role in spine stability, RFA of the medial branch nerve can alter the loading and biomechanics of the spine leading to other adverse effects such as disc degeneration [4]. Hence, while monopolar RFA may be beneficial in the short term, it may lead to the changes leading to other painful conditions in the spine in long term. To avoid multifidus muscle dysfunction, RFA can potentially be applied exclusively to the articular branch which provides sensation to the joint. By doing this, the motor nerves are going to be spared while the sensory nerves are going to be ablated to reduce facet joint pain. However, articular branches are smaller and a new RFA procedure would require a more precise control of the ablated volume. For this reason, temperature controlled bipolar RFA may be preferred. It is important to simulate RFA procedure to design a new RFA method targeting the articular branch and sparing the branch that innervates the multifidus muscle. During RFA procedure, spinal muscle is also being ablated since articular branch innervates the multifidus muscle. Commercial finite element analysis (FEA) software has been used to accurately simulate ablation process in several tissues [5],[6]; however, conventional FEA simulations have long run times in the order of hours to days. As an alternative method, neural networks can be used for the prediction of tissue temperature during RF procedure [7]. Apart from the work in [7] which predicts the midpoint temperature at three different antenna distances using the probe temperatures, to the best of our knowledge there exists no work predicting the temperature around the probes. In this study, we predict the final temperature field for several distances between probes positions using deep neural networks (DNNs). Our results show that our approach can accurately predict the tissue temperature.

## METHOD

### a. Finite Element (FE) simulation

COMSOL Multiphysics® modules, Bioheat Transfer and Electric Current, were used to couple the thermal and electrical effects of the RFA process. The model consisted of a cylinder of homogeneous muscle tissue (24 mm in diameter, 25 mm in height) with two parallel (bipolar) electrodes with an active length of 10 mm and diameter of 0.7 mm. Given the symmetry of the problem, 1/8$^{th}$ of the cylinder was modeled as shown in Figure 1. The initial temperature of the model was set to 21 °C and the initial voltage of the entire model was set to zero. While voltage of one of the electrodes was controlled by using a PI controller to keep the electrode temperature ($T_{electrode}$) at a target value ($T_{target}$), the symmetry plane was modeled as ground (V=0). Lastly, the temperature error (Eq. 1) was used to control the voltage of the active electrode by the following governing equation (Eq. 2):

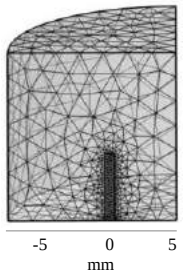

Figure 1: Model mesh distribution.

$$\text{iiie}(t) = T_{target} - T_{electrode} \quad (1)$$

$$V(t)\,i=iK_P\,ie(t)\,i+iK_i\,i\int_0^t e(\tau)d\,\tau i+iK_d\,i\frac{d}{dt}ie(t), \quad (2)$$

where $V(t)$ is the applied voltage (V). For this simulation, the optimal PID parameters were found as $K_p = 40$, $K_i = 0.01$ and $K_d = 0$ by parametric analysis. The target temperature is a function of time collected from ex-vivo experiments. Only the active tip of the electrode was modeled to make the model simpler and faster. Blood perfusion rate ($w_b$) was not considered. The mesh for the domain was generated using tetrahedral elements with a finer mesh size around the electrode to get a more sensitive temperature change [8].

## Deep Neural Network (DNN) Structure

Figure 2 shows the steps followed to train and verify the results from the DNN. FE simulations were used to generate the training dataset. Three different distances between probes were used, because the ablated region and the temperature distribution within the tissue is being affected by the probe locations. First, the FE model was run for three different distances between probe locations, 4 mm, 8 mm and 10 mm, to obtain the temperature distribution within the tissue. Second, a DNN that takes in features generated using the probe positions and outputs the temperature for a given probe position has been used. For a given sample $(i)$ with probe 1 position $p1(i)$, probe 2 position $p2(i)$, and the position of the target point $pt(i)$, the features $f_i$ are generated as follows:

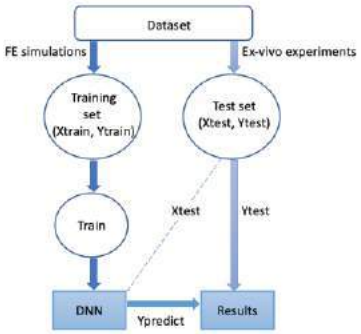


Figure 2: DNN prediction of tissue temperature after an RFA process.

$$f_i = [\ddot{u}correlate([p1(i) - \dot{p}t(i)]^T i[\dot{p}2(i) - \dot{p}t(i)]^T i \\ ||p1(i) - \dot{p}t(i)||i||p2(i) - \dot{p}t(i)i||)i \\ \ddot{u}\ddot{u}\ddot{u}\ddot{u}\ddot{u}\ddot{u}\ddot{u}\ddot{u}\ddot{u}\ddot{u}\ddot{u}\ddot{u}\ddot{u}\ddot{u}\ddot{u}\ddot{u}\ddot{u}\ddot{u}[p1(i) - \dot{p}t(i)]^T i[\dot{p}2(i) - \dot{p}t(i)]^T \ddot{u} \\ \ddot{u}\ddot{u}\ddot{u}\ddot{u}\ddot{u}\ddot{u}\ddot{u}\ddot{u}\ddot{u}\ddot{u}\ddot{u}\ddot{u}\ddot{u}\ddot{u}\ddot{u}\ddot{u}\ddot{u}\ddot{u}||p1(i) - \dot{p}t(i)||i||\dot{p}2(i) - \dot{p}t(i)||i]i^T.\ddot{u}\ddot{u} \quad (3)$$

$X_{train}i$ contains features for all the N samples, i.e., $X_{train} = [f_1, f_2, \dots, f_N]$ and the target point temperature $T_i$ at 100 seconds has been used as labels which are collected in $Y_{train}$ as $Y_{train} = [T_1, T_2, \dots, T_N].i$ The DNN consists of three hidden layers with 100 hyperbolic tangent activations, 20 rectified linear unit (ReLU) activations, and 20 ReLU activations; and the output layer has one linear activation. The DNN has been trained with $X_{train}$ and $Y_{train}$ with mean squared error as a loss function using Adam optimizer. After training, a separate data set was constructed using ex-vivo experiments to test the performance of the DNN, which is explained next.

## b. Ex-vivo experiments

RF ablations were performed with an RF generator (Stryker Multigen) on a porcine spinal muscle sample. A target temperature of 90 ℃ for 100 seconds for the two active probes was set. Two passive probes were inserted into the tissue to measure tissue temperatures at given locations near the active probes. Ultrasound imaging was performed to visualize the probe locations. A distance between active probes of 9.5 mm was measured. The temperature measurements collected at 100 seconds of tissue ablation were used as a test data set for the DNN. The temperature field was predicted using the trained DNN for a 9.5 mm distance. The predicted temperature values using DNN were compared with the ex-vivo measurements and FE simulations to validate the approach.

## RESULTS

Table 1 shows the temperature of the two probes at 100 seconds for three different methods. The comparison was done when the distance between the probes was 9.5 mm. While the run time of the simulation is 3 hours 45 min, the training time for the DNN is only 20 min (Table 1). The DNN prediction yields 0.43% error for Probe 1 and 1.14% error for Probe 2 when compared to ex-vivo experiments. Comparing to FE simulations, the algorithm yields 0.2% error for Probe 1 and 1.23% error for Probe 2. The temperature field predicted in Kelvin with the DNN, and the FE simulation is given in Figure 3 when the probe distance is 9.5 mm. The results shown in Table 1 and Figure 3 show that the proposed approach is in a good agreement with both ex-vivo experiment and the FE simulation.

Table 1: Temperature comparison for three different methods.

| | *Ex-vivo* | *DNN* | *FE simulation* |
|---|---|---|---|
| *Probe 1 [K]* | 335.65 | 334.22 | 335.13 |
| *Probe 2 [K]* | 327.65 | 331.38 | 331.67 |
| *Run time [min]* | N/A | 20 | 225 |

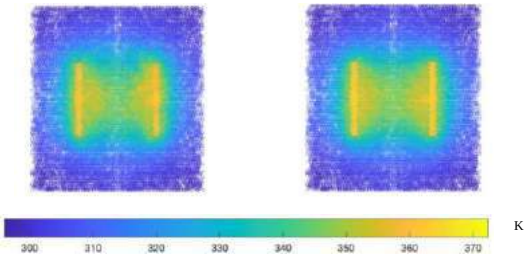


Figure 3: Temperature distribution around the electrode (a) DNN prediction, and (b) FE simulation.

## DISCUSSION

In this paper, a novel approach has been proposed using a DNN to predict tissue temperature at 100 seconds. Our work differs from [7] as our model takes in probe locations as inputs. The DNN takes in features generated from probe positions and the target probe positions and outputs the temperature. The DNN was trained using the data obtained from FE simulations and the efficacy of our algorithm was tested on a real life ex-vivo porcine tissue. The approach was matching well with the experimental and simulation results with as low as 0.2% error and reduced in run time by ~91% compared to FE simulation. For more complex geometry, FEA run time may increase to days or even weeks, but DNN run time might not change dramatically for the same DNN and the similar data size. The DNN approach presented has shown to be beneficial predicting the tissue temperature in a short time at a given point of choice. However, one of the limitations of this study is that it predicts the tissue temperature at 100 seconds only. As our ongoing work, the tissue temperature will be predicted for any given time. Predicting future tissue temperatures given the current probe temperatures and positions was kept as future work.

**ACKNOWLEDGEMENTS:** Grace Woodward pilot grant, PSU

## REFERENCES

[1] Kavita, N., et al., Pain physician, 11(1), 67-75, 2008.
[2] Smuck, M., et al., The Spine Journal, 15(6), 1415-1421, 2015.
[3] Bonython, M., et al., European Congress of Radiology-2019 ASM.
[4] Dreyfuss, P., et al., PM&R, *1*(8), 719-722.
[5] Trujillo, M., et al., International Journal of Hyperthermia, 29(6), 590-597.
[6] Hanks, B., et al., Journal of Medical Devices, 12(3).
[7] Phasukkit, P., et al., IEEE Access, vol. 9, pp. 79572-79587, 2021.
[8] Kumru, H. T., et al., SB3C, 2021.

SB³C2022
Summer Biomechanics, Bioengineering and Biotransport Conference
June 20-23, Eastern Shore, MD, USA

# DNA-BASED MICROPATTERNING APPROACH TO CREATE TISSUES OF DEFINED SIZE, SHAPE, AND CELLULAR COMPOSITION

**Louis S. Prahl (1), Alex J. Hughes (1,2,3)**

(1) Bioengineering, University of Pennsylvania, Philadelphia, PA, USA
(2) Cell & Developmental Biology, University of Pennsylvania, Philadelphia, PA, USA
(3) Institute for Regenerative Medicine, University of Pennsylvania, Philadelphia, PA, USA

## INTRODUCTION

Developing organs often consist of multiple cell types which interact through biochemical signaling and mechanical interactions to pattern tissue structures. In the kidney, epithelial-mesenchymal interactions pattern key functional structures such as the collecting duct network and nephrons [1]. For example, collecting duct patterning involves Ret-GDNF signaling interactions between the epithelium and nephron progenitors as well as inhibitory interactions from the surrounding stroma. Ret-GDNF signaling activates downstream signals such as the extracellular signal-related kinase (ERK) pathway that guide collective epithelial cell movements and proliferation [2]. Tools to reconstruct these epithelial-mesenchymal tissue interfaces *in vitro* would improve our understanding of Ret-related congenital kidney defects [3] and efforts to guide proper organization of tubule networks in organoid models.

We have modified a previously published cellular micropatterning approach [4] to support cell adhesion to photoactive polyacrylamide (pPA) hydrogel substrates. This approach uses photolithography to deposit single-stranded DNA (ssDNA), which serves as an intermediate adhesion ligand. Cells are labeled with lipid-modified antisense ssDNA [5] enabling multiplexed cell patterning with high precision (~10s of μm) and specificity. We first demonstrate patterning and long-term pattern retention of multiple cell types on pPA hydrogels. We use this to investigate ERK signaling dynamics and cell migration in freely expanding Ret-expressing epithelial colonies of defined initial size and shape.

## METHODS

**Cell culture.** MDCK epithelial cell lines were cultured in MEM containing 10% FBS. 3T3 mouse fibroblasts were cultured in DMEM containing 10% calf serum. All cell lines were maintained at 37°C and 5% $CO_2$. Cell lines expressing fluorescent histone 2B (H2B) constructs were generated by lentiviral transduction.

**pPA gels**. 30 μm thick pPA gel sheets were cast on methacrylate coated glass slides using SU-8 photoresist shims anchored to a hydrophilic silicon wafer as guides. pPA gel precursor solutions contained between 3-10%/0.035-0.25% acrylamide/bis-acrylamide, 3 mM benzophenone-methacrylate (BPMAC) photosensitizer and other components as previously described [4].

**ssDNA photolithography**. pPA gels were impregnated with ssDNA, sandwiched against photomasks, and grafted to the pPA gel surface. using 254 nm light transmitted through transparent patches on a 5”x5” quartz-on-chrome photomask.

**Fibronectin coating**. pPA gel surfaces were functionalized with a surface layer of bis-acrylamide and N-hydroxysuccinimide (NHS) ester groups using the photo-crosslinker LAP and 365 nm light [6]. NHS-functionalized surfaces were then passively coated in 20 μg $ml^{-1}$ fibronectin and washed before plating cells.

**Lipid-ssDNA labeling and cell patterning**. Cell membranes were passively labeled with lipid-ssDNA anchor, co-anchor, and antisense handle sequences [5]. Labeled cells were introduced to pPA gels enclosed within clip-on 8-well chambered slides and allowed to adhere to gel-bound ssDNA patches. Cells outside of ssDNA patches were removed by gently washing the pPA gel surface with DPBS.

**Immunofluorescence.** Cells were fixed in 4% paraformaldehyde, permeabilized in 0.5% Triton X-100 and methanol, and stained for phospho-ERK and DAPI [7].

**Imaging**. Images of cells and ssDNA were captured at 4x-10x magnification using a Nikon epifluorescence microscope equipped with LED illumination. Time-lapse and immunofluorescence image stacks of cell monolayers were acquired at 10x-20x magnification using a Nikon microscope equipped with a Yokugawa W1 spinning disk and environmental chamber to maintain cells at 37°C and 5% $CO_2$.

**Data analysis**. Phospho-ERK intensities were quantified using Fiji/ImageJ and CellProfiler [7]. All other image quantification was performed in Fiji/ImageJ.

## RESULTS

Here we show a scheme to pattern ssDNA on pPA hydrogel substrates by applying UV light through a photomask (**Figure 1a**). ssDNA patches mark sites of lipid-ssDNA-labeled cell capture using DNA "Velcro" (**Figure 1b**). We patterned arrays of 250 μm diameter circular ssDNA features and benchmarked the technique by showing efficient capture of 3T3 mouse fibroblasts bearing matched (base paired) ssDNA, but not cells bearing mismatched pairs (**Figure 1c**). Next, we show that this technique can be multiplexed by patterning two unique ssDNA sequences into alternating arrays of square features and using these to capture MDCK epithelial cells expressing histone 2B labels with different fluorescent markers (**Figure 1d**). MDCK cells subsequently adhered to fibronectin ligands on the pPA hydrogel surface following ssDNA patterning (**Methods**) and retained their approximate original positions after 16 hours, suggesting that this technique can be used to establish and study complex tissue patterning *in vitro*.

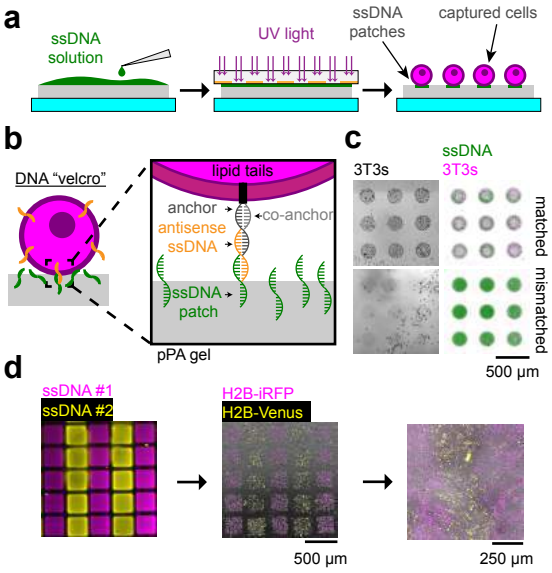


**Figure 1: ssDNA photolithography and cell capture on pPA gels.** **a.** Schematic of the ssDNA photolithography and cell capture process. **b**. Schematic of the DNA "Velcro" scheme used to specifically capture cells through base pairing. **c**. 3T3 fibroblasts captured on circular ssDNA patterns using DNA "Velcro". **d**. Multiplexed cell capture, adhesion, and long-term pattern formation of MDCK cells expressing fluorescent H2B reporters using multiple ssDNA sequences.

Since spatially regulated ERK signaling is involved in kidney tubule morphogenesis, we next used our micropatterning technology to study ERK signaling dynamics in patterned epithelial cell colonies (**Figure 2a**). We used MDCK epithelial cells expressing Ret [8] as a model of the ureteric epithelium, since application of exogenous GDNF activates the ERK signaling pathway in these cells (**Figure 2b**). Immunofluorescence staining of phosphorylated ERK reveals the spatial distribution of ERK within the tissue, with strongest activation near the colony edge. Furthermore, GDNF-treated MDCK colonies expanded at a faster rate than untreated controls (**Figure 2c**), suggesting that the spatially defined activation of ERK activates cytoskeletal machinery involved in collective cell migration.

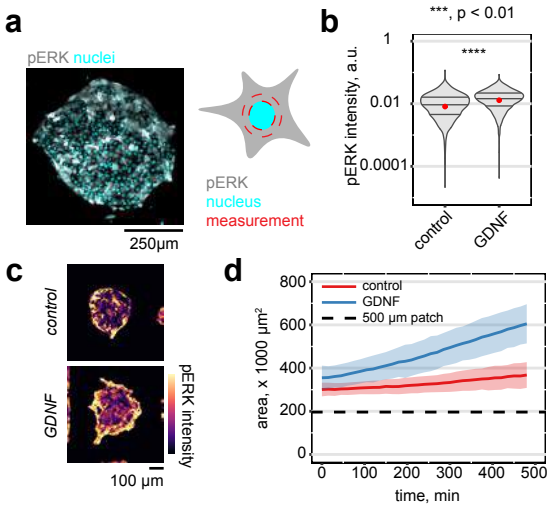


**Figure 2: ERK signaling within patterned epithelial tissues. a.** Immmunofluorescence image of phosphorylated ERK in a pattterned epithelial colony. **b-c.** Quantification of phosphorylated ERK intensity for cells stimulated with GDNF and controls. **d.** Area rate of expansion of patterned epithelial colonies treated with GDNF and controls.

## DISCUSSION

In this abstract, we introduce a technique for patterning cells across large (~cm$^2$) hydrogel surface areas with ~10-100 μm precision using ssDNA photolithography. Multiplexed cell patterning with unique ssDNA sequences allows the creation of long-term patterns within epithelial monolayers. We show that ssDNA photopatterning can be used to investigate signaling dynamics across epithelial colonies. GDNF activates leading edge ERK signaling and increases collective migration speed in patterned epithelial colonies. This technique is compatible with standard hydrogel chemistry, meaning that it can be applied to investigate combinatorial effects of colony size, geometry, cell-cell interactions, and substrate stiffness on cell behaviors. Future work will use this technique to test whether cell polarity proteins expressed in the kidney stroma are sufficient to restrict ERK signaling and erroneous branching of collecting duct cells [9]. Other future applications include modeling tumor-stroma interactions, and investigations into developmental patterning and boundary formation.


## ACKNOWLEDGEMENTS

We thank members of the Hughes, Bugaj, and Burdick laboratories for their helpful comments and assistance with experimental protocols. Thanks to G. Dressler for MDCK-RET cell lines. This work was supported by NIH grants F32 DK126385 (to LSP), R35 GM133380 (to AJH), and NSF CAREER award 2047271 (to AJH). This work was carried out in part at the Singh Center for Nanotechnology, which is supported by NSF grant NNCI-1542153.


## REFERENCES


[1] Costantini, F et al., *Dev. Cell*, 18:698-712, 2008.
[2] Fisher, CE et al., *Development*, 128:4329-38. 2001.
[3] Nicolaou, N et al., *Nat. Rev. Nephrol.*, 11:720-731, 2015.
[4] Viola, JM et al, *Adv. Mater.*, 32:e2002195. 2020.
[5] Weber, RJ, et al. *Biomacromolecules*, 15:4621-26, 2014.
[6] Lakins, JN et al., *Methods Mol. Biol.*, 916:317-50. 2012.
[7] Bugaj, LJ & Lim, WA. *Nat. Protoc.*, 14:2205-28. 2019.
[8] Tang, MJ et al., *Dev. Biol.*, 243:128-36. 2002.
[9] Zhang, H et al., *Dev. Cell*, 48:780-92. 2019.

# CHANGES IN ANISOTROPIC VISCOELASTICITY OF RIGHT VENTRICLE WITH PULMONARY HYPERTENSION DEVELOPMENT

**Kellan Roth (1), Wenqiang Liu (2), Kristen LeBar (1), Matt Ahern (1,2), Adam Chicco (3), Zhijie Wang (1,2)**

(1) Department of Mechanical Engineering, Colorado State University, Fort Collins, CO, USA
(2) School of Biomedical Engineering, Colorado State University, Fort Collins, CO, USA
(3) Department of Biomedical Sciences, Colorado State University, Fort Collins, CO, USA

## INTRODUCTION

An estimated 6.2 million Americans above 20 years old have heart failure (HF). It is known that the mechanical behavior of myocardium contributes to the diastolic function and the tissue mechanics change during HF development [1]. But there remains limited understanding of the alternation in anisotropic, viscoelastic behavior of myocardium in HF progression, particularly for the right ventricle (RV). To fill these gaps in knowledge, it is critical to investigate changes in RV tissue viscoelasticity during RV failure development.

To date, the only group that reported increased stiffness and viscous damping in pressure overloaded RVs investigated the papillary muscles [2,3]. But the one dimensional measurement of individual muscles cannot fully reveal the anisotropic properties of the entire myocardial wall. The **goal** of the study was to investigate the changes in the passive, anisotropic viscoelasticity of the RV in RV failure development. We **hypothesize** that the RV failure progression leads to increased viscoelasticity in the longitudinal direction and that the failing RVs exhibit more anisotropic behavior than the healthy RVs. Our results provide novel findings in the dynamic mechanical property changes of the RV with RV failure development, which brings a more complete understanding of the tissue's mechanical function in energy storage as well as energy dissipation in RV failure patients.

## METHODS

To test these hypotheses, ex vivo cyclic biaxial tests were performed on normal and PH rat RVs, using a monocrotaline (MCT) rat model of pulmonary hypertensive (PH). All procedures were approved by Colorado State University Institutional Animal Care and Use Committee. Monocrotaline (60 mg/kg) was injected (s.c.) into 6-week-old male rats for 3-4 weeks to induce PH. Similar healthy rats were used as the control group (CTL). Prior to tissue harvest, echocardiography was performed, and RV function was quantified. The establishment of RV failure in the MCT rats was confirmed by dilated RV and reduced fractional shortening (data not shown).

After harvest, the hearts were placed in cardioplegic solution (CPS) on ice. Prior to the mechanical tests, the RV tissue was excised, measured, and then placed in CPS combined with the 30 mM of 2,3-butanedione monoxime (BDM) solution at body temperature (26-37°C) for 30 minutes to ensure fully relaxation of cardiomyocytes. The outflow tract (OT) direction was the longitudinal direction. Each sample was marked with 4 equally spaced markers for strain analysis.

The samples were mounted on an in-house biaxial tester designed specifically for small animal viscoelasticity measurement. The samples were preloaded by approximately 0.05 N and underwent 15 cycles of equibiaxial stretch at 1Hz and 20% strain (physiological strain) for preconditioning. Then, cyclic equibiaxial tensile tests with 20% strain (at 0.1, 1, 2, 5, and 8Hz) were performed with sufficient resting periods between tests. 2$^{nd}$ Piola-Kirchhoff stress ($\sigma$) and Green's strain ($\varepsilon$) were calculated from the last cycle of stress-strain data. From the hysteresis loop, the stored energy ($W_S$) was calculated for RV elasticity, and the dissipated energy ($W_d$) was calculated for RV viscosity. These methods are described previously [4]. All data are shown as mean±SE. Statistical significance was determined as $p<0.05$ calculated with a student's t-test.

## RESULTS

**Different frequency-dependent viscoelastic behavior between MCT and CTL RVs.** First, we examined the elastic behavior of the RV at different frequencies. We found that there was a general trend of increasing stored energy ($W_S$) as frequency increased for both the CTL and MCT groups in the longitudinal direction, with the CTL group showing significant larger $W_S$ at 2 and 5Hz in the longitudinal direction (Fig. 1A). The similar frequency-dependent behavior was seen in the $W_S$ of CTL group in the circumferential direction with a larger $W_S$ at 1, 2, and 5Hz in the circumferential direction (Fig. 1B). However, the MCT group tended to have increased $W_S$ from 0.1 to 1Hz and then it

plateaued (Fig. 1B). Thus, PH led to a change in RV frequency-dependent elasticity in the circumferential direction.

From the viscosity measurement, we found that the dissipated energy ($W_d$) tended to increase with increasing frequency in the longitudinal direction for both MCT and CTL groups (Fig. 1C). But in the circumferential direction, the frequency-dependent increase in $W_d$ was seen in the CTL group (except for the 5Hz) whereas the MCT group barely showed frequency independency (Fig. 1D). Thus, the RV frequency-dependent viscosity in the circumferential direction was altered by PH development.

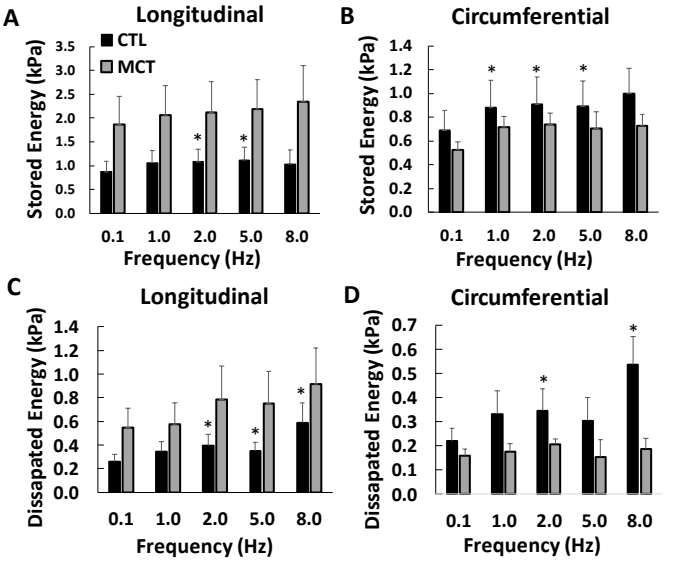


**Figure 1: Frequency-dependent viscous (A&B) and elastic (C&D) behavior of rat RVs in the longitudinal and circumferential directions. *P<0.05 vs. 0.1Hz in CTL group.**

**Reduced ratio of viscosity to elasticity in the circumferential direction and trends of increased viscoelasticity in the longitudinal direction in MCT RVs.** We then further compared the dynamic anisotropic viscoelastic changes of the RV during PH development. Because some data were incomplete at 5Hz (physiological heart rates), we presented the data obtained at 2Hz here. In the longitudinal direction, a trend of increased $W_S$ with PH development is seen, while the opposite trend in $W_S$ was shown in the circumferential direction with PH development (Fig. 2A). Therefore, our data suggest that in PH the RV is stiffer in the longitudinal direction but more compliant in the circumferential direction. As a result, the MCT RV became more anisotropic in elasticity than the CTL RV. Similar trends were observed for other frequencies (see Fig. 1A&B).

Examining viscosity through the dissipated energy ($W_d$) showed that with PH development, the RV tended to become more viscous in the longitudinal direction and less viscous in the circumferential direction (Fig. 2B). This led to a more anisotropic viscous behavior in the MCT group compared to the CTL group. Similar trends were observed for other frequencies (Fig. 1C&D). Moreover, when examining $W_d/W_S$ we found the ratio was reduced significantly in the MCT group in the circumferential direction (Fig. 2C).

## DISCUSSION

This study is the first to investigate the changes of RV passive, anisotropic viscoelastic properties with PH development by cyclic biaxial tests. The pilot data suggested that the MCT RV was stiffer and more viscous than the CTL RV in the longitudinal direction, while interestingly a decrease in circumferential viscoelasticity as well as decreased $W_d/W_S$ were found. Increased viscoelasticity is similarly reported in prior studies using RV papillary muscles [2,3]. These trends of increasing viscoelasticity in the longitudinal direction and decreasing viscoelasticity in the circumferential led to a more anisotropic viscoelasticity with the RV failure progression. During the early stage of HF, the myocardium adapts to its new environment to preserve cardiac output, which will often result in significant remodeling of the tissue [5]. But in late stage of HF, the remodeling can no longer maintain the cardiac output and it remains unclear what drives the transition from adaptation to maladaptation. Here, we suspect that an increase in anisotropy with a stronger viscoelasticity in the longitudinal direction will impair the RV function significantly as this is the main axis of shortening in normal conditions.

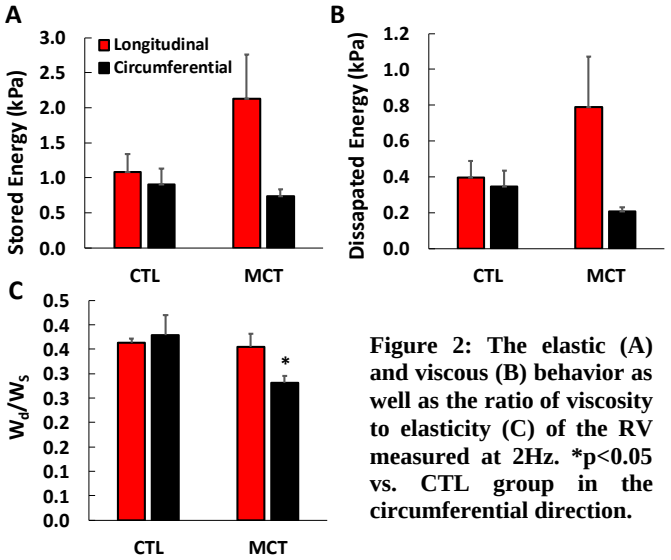


**Figure 2: The elastic (A) and viscous (B) behavior as well as the ratio of viscosity to elasticity (C) of the RV measured at 2Hz. *p<0.05 vs. CTL group in the circumferential direction.**

We also noticed altered frequency-dependent viscoelastic behavior in the circumferential direction in the MCT RV. PH seemed to result in a loss of frequency dependency at high frequencies (2-8Hz). This indicates that the pathological remodeling reduced the tissue's response to stretch-rate circumferentially, probably due to the fiber orientation change toward longitudinal direction as reported previously [6]. We speculate that the myofibers and collagen fibers are loaded differently in diseased tissues and it cannot be explained by 'collagen accumulation' alone. Further study should investigate the microstructures of RVs to study the underlying molecular mechanisms.

In summary, our study provides novel insight into the frequency-dependent and anisotropic viscoelasticity of RV during PH development. The results enhance our understanding of RV biomechanics by investigating both elasticity and viscosity and in different directions. Further study will involve more RV samples for mechanical tests and computational modeling analysis.


## ACKNOWLEDGEMENTS

We would like to thank Michael Nguyen-Truong and Katie Evans for assistance in experimental preparations.


## REFERENCES


[1] W. Liu, Z. Wang. *Bioengineering*, 2019.
[2] J.D. Stroud et al. *Heart & Circulatory Physiology*, 2002.
[3] T. S. Harris et al. *Heart & Circulatory Physiology*, 2002.
[4] Z. Wang et al. *BMMB*, vol. 12, no 1115-1125, 2013
[5] K.D. Dwyer et al.. *Bioactive Materials*, vol. 6, no. 2198-2220, 2021
[6] Hill M et al., *Ann Biomed Eng*, 42:2451-65, 2014.

# PERSONALIZED ULTRASOUND-BASED FLUID-STRUCTURE INTERACTION MODELING OF ABDOMINAL AORTIC ANEURYSMS: FROM MODEL DEVELOPMENT TO EX-VIVO VERIFICATION

**Judith H.C. Fonken (1,2), Esther J. Maas (1,2), Arjet H.M. Nievergeld (1,2), Floris B.T. Verheijen (1), Hein de Hoop (1), Marc R.H.M. van Sambeek (1,2), Frans N. van de Vosse (1), Richard G.P. Lopata (1)**

(1) Photoacoustics & Ultrasound Laboratory Eindhoven (PULS/e), Eindhoven University of Technology, Eindhoven, Netherlands
(2) Department of vascular surgery, Catharina hospital, Eindhoven, Netherlands

## INTRODUCTION

Currently, the prediction of rupture risk in abdominal aortic aneurysms (AAAs) solely relies on the maximum diameter. However, wall mechanics and hemodynamics have shown to provide better risk indicators. Research on abdominal aortic aneurysm development, growth and rupture risk requires a large, longitudinal, biomechanical study. Furthermore, a patient-specific assessment is required, based on fluid-structure interaction (FSI) models. Time-resolved 3-dimensional ultrasound (3D+t US) is the preferred image modality to extract the patient-specific geometry, since 3D+t US is safe, affordable and provides geometric information during the full cardiac cycle. A previous study has shown the feasibility of 3D+t US-based FSI simulations and the importance of incorporating the pre-stress [1].

Due to the limited field-of-view of 3D+t US, the aorto-iliac bifurcation is often not included in the 3D+t US acquisitions. It has been shown that the presence of the aorto-iliac bifurcation does not significantly influence the wall mechanics in the AAA region [2]. However, previous studies have shown that the bifurcation does influence the hemodynamics in the AAA. Part of our study aims at quantifying the influence of excluding the bifurcation in FSI simulations. Secondly, part of our study aims at experimentally verifying the obtained patient-specific FSI framework.

## METHODS

To quantify the influence of excluding the aorto-iliac bifurcation in the FSI simulations, patient-specific geometries including the bifurcation geometry from 20 patients were derived from CT-scans. The CT-based geometry was elongated by 3 cm in proximal and 2 cm in distal direction. The AAA wall geometry was obtained by extruding the inner-wall geometry by 2 mm. For each patient, an additional AAA geometry was obtained by replacing the bifurcation by a single outlet. For both FSI simulations, the same time-varying flow profile was prescribed at the inlet and a 3-element Windkessel (WK) model was used to prescribe the patient-specific outlet pressure. In the simulation with bifurcation, the flow division, needed for calculating the WK parameters, was approximated using Murray's law. The pre-stresses in the AAA wall geometry were estimated using the Backward Incremental Method. The FSI simulations were initialized with the patient-specific diastolic pressure and multiple cardiac cycles were modeled to ensure a stable, periodic solution. The last cycle was used for result evaluation. The results in the aneurysm region were compared to quantify the influence of excluding the bifurcation.

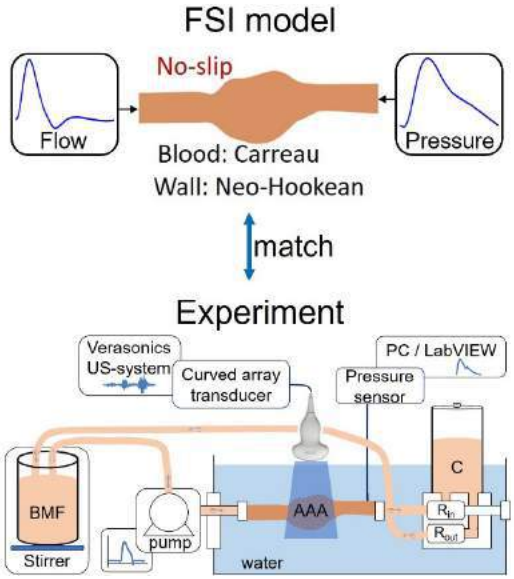


**Figure 1: Schematic representation of the experimental verification of the FSI model using a mock-loop circulation with blood mimicking fluid (BMF) and high-framerate US acquisitions.**

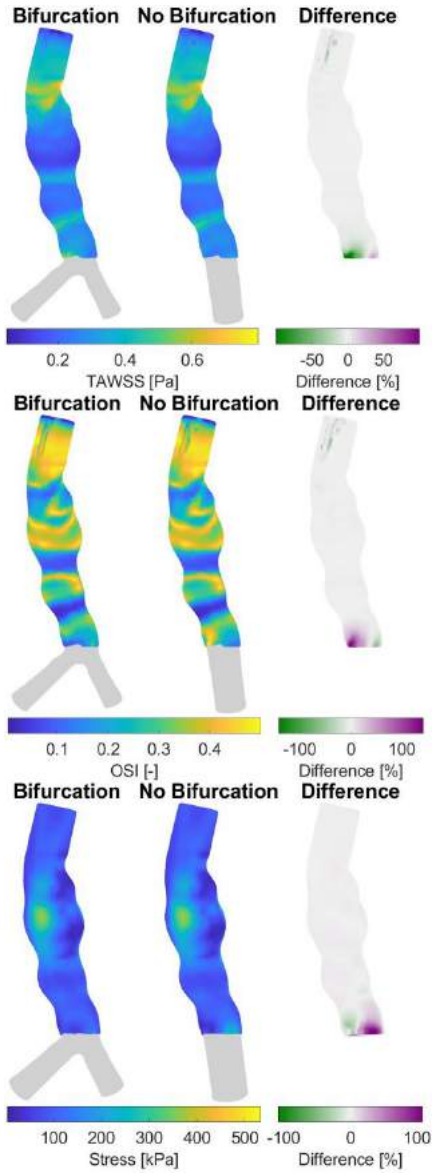


**Figure 2: Preliminary results of the influence of excluding the bifurcation on time-averaged wall shear stress (TAWSS, top) and oscillatory shear index (OSI, middle) and systolic wall stress (bottom) in the AAA region**

Experimental verification of the FSI framework will be performed using an experimental mock-loop circulation. In this study, an experimental set-up to mimic the in-vivo hemodynamics was developed (Fig. 1). An elastic, 3D-printed US-based AAA geometry was mounted in a mock-loop circulation [3]. A realistic inlet flow profile was supplied by a PC-controlled gear pump and physiological pressures were obtained using the 3-element Windkessel model at the distal side of the AAA geometry, consisting of a vertical column as compliance (C) and adjustable inlet ($R_{in}$) and outlet ($R_{out}$) resistances. During the experiment, high-framerate (~1300 Hz) US acquisitions were obtained and processed with a motion estimation algorithm to determine the wall strain and blood velocities. A blood-mimicking fluid (BMF) was used within the mock-loop circulation to ensure US speckle signals in the AAA lumen. The circulation was surrounded by water to suppress US signal around the AAA geometry.

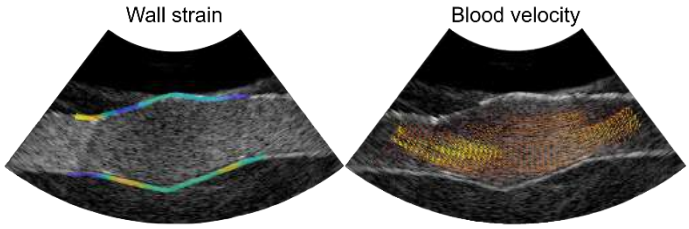


**Figure 3: Preliminary results of the experimental wall strain (left) and blood velocity (right) extracted from the ultrasound acquisitions in the mock-loop circulation.**

## RESULTS

Figure 2 shows the time-averaged wall shear stress (TAWSS), oscillatory shear index (OSI) and systolic wall stress for a single patient with and without the bifurcation geometry. Mean differences in the aneurysm region equaled 1.2% (std: 5.6%), 0.1% (std: 8.8%) and 1.3% (std: 6.3%) for the TAWSS, OSI, and systolic wall stress, respectively. The largest differences for all quantities were found in the most distal part of the aneurysm region.

Using the gear pump and the 3-element Windkessel system, physiological inlet flow and outlet pressure waveforms were obtained in the experimental set-up. With a mean flow of 0.97 L/min, the pressure ranged between 81 and 127 mmHg. US acquisitions with sufficient signal in the AAA lumen were obtained and (preliminary) wall strain and blood velocities in the AAA geometry were calculated (Fig. 3).

## DISCUSSION

In this study, the influence of excluding the aorto-iliac bifurcation was quantified. Preliminary results show only slight differences in hemodynamics and wall mechanics in the aneurysm region, except for the most distal part. FSI simulations for the remaining patients in the dataset should be executed and analyzed before any conclusions can be drawn regarding the influence of the bifurcation geometry.

Furthermore, an experimental mock-loop circulation to mimic the in-vivo hemodynamics was developed in this study. In ongoing research, improvements in US acquisition and processing are implemented. Moreover, the acquired flow and pressure waveforms will be used as boundary conditions for the FSI simulation (Fig. 1). Finally, the experimental results will be compared to the FSI results to verify the simulation.

In future studies, the FSI framework will be further personalized by including the patient-specific shear modulus [4] and inlet velocity profile. The envisioned framework for personalized 3D+t US-based FSI simulations paves the way for future longitudinal studies on AAA development, growth, and rupture risk.

## ACKNOWLEDGEMENTS

This work was supported by the Dutch Research Council (NWO) and received funding from the NWO talent program VIDI, awarded to R.G.P. Lopata.

## REFERENCES

[1] Fonken, J. et al., Front. Physiol., 1255, 2021.
[2] Disseldorp, E. et al., J. Biomech., 2405-2412, 2016.
[3] Hoop, H. et al., IEEE Trans. Med. Imaging., 3714-3724, 2020
[4] Disseldorp, E. et al., Eur.HeartJ.Cardiovasc.Imaging.,185-191, 2019

# 4D FLOW MRI STUDY OF LARGE-SCALE HEMODYNAMICS CORRELATION PERSISTENCE IN THE HEALTHY HUMAN AORTA USING NETWORK SCIENCE

**Karol Calò (1), Andrea Guala (2), Diego Gallo (1), Jose Rodriguez Palomares (2), Stefania Scarsoglio (1), Luca Ridolfi (1), Umberto Morbiducci (1)**

(1) Polito[BIO]Med Lab, Department of Mechanical and Aerospace Engineering, Politecnico di Torino, Turin, Italy

(2) Hospital Universitari Vall d'Hebron, Department of Cardiology, CIBER-CV, Vall d'Hebron Institut de recerca (VHIR), Universitat Autonoma de Barcelona, Barcelona, Spain

## INTRODUCTION

The quantitative characterization of the large-scale features of the aortic hemodynamics is currently based on spatially and/or temporally-averaged quantities which do not fully capture the four-dimensional complexity of real cardiovascular flows. Aiming at extracting as much information as possible from *in vivo* hemodynamic data, this study proposes a network-based approach [1] to analyze the spatiotemporal correlation of large-scale flows in a 4D flow MRI dataset of 42 healthy thoracic aortas [2]. In detail, the correlation between the flow rate waveform at the inflow of the ascending aorta (AAo) and the axial velocity waveforms obtained from measured phase velocities at each voxel of the aortic domain was used to build a subject-specific *"one-to-all"* network [3]. An ad-hoc network metric was introduced to quantify the anatomical length of persistence of the correlation between the inflow rate and the large-scale fluid structures along the main flow direction. The analysis was then completed with a geometric characterization of the investigated subjects, exploring possible links between aortic geometric attributes and the dynamic similarity between inflow rate and axial flow.

## METHODS

The adopted methods are summarized in **Fig. 1**. The study population comprises 42 healthy volunteers with a tricuspid aortic valve. All details on 4D flow MRI acquisition protocol and data processing are reported elsewhere [2,4]. The study was approved by the ethics committee of the Vall d'Hebron Hospital and written informed consent was obtained from all participants. Subject-specific 3D geometry of the thoracic aorta was semi-automatically reconstructed from an angiography derived from 4D flow MRI data using ITK-Snap and its centerline was computed using VMTK (www.vmtk.org). Anatomical landmarks of the sinotubular junction (STJ), first and last supra-aortic vessels and location of the pulmonary artery (PA) bifurcation were identified from co-registered 2D cine images. For each subject the time-resolved waveforms along the cardiac cycle of the three velocity components in each voxel were obtained as reported elsewhere [2], and 3D velocity data were exported using in-house Matlab code (MathWorks Inc, USA).

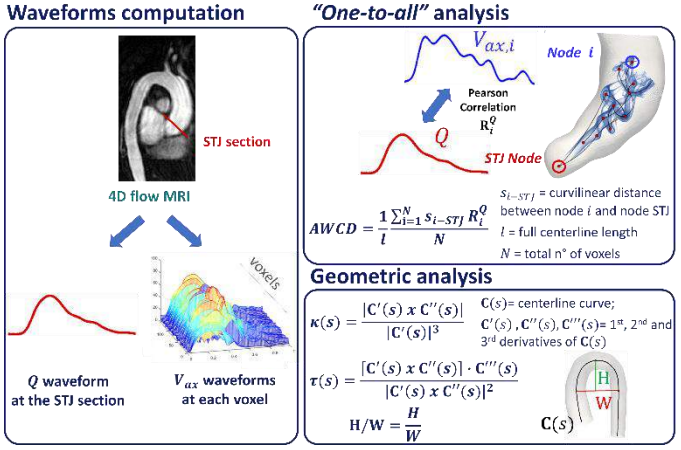


**Figure 1: Overview of study methods.**

The inflow rate $Q$ waveform was computed at the STJ cross-section and the (through-plane) axial velocity component $V_{ax}$ waveform in each voxel of the investigated aortic domain was obtained as proposed in [5]. Inspired by a previous *in silico* study on carotid bifurcation hemodynamics [3], here an *in vivo "one-to-all"* network approach was adopted to characterize the aortic large-scale intravascular hemodynamics by investigating the relationship between the shape of the subject-specific inflow rate waveform and that of the $V_{ax}$ component in each voxel. In this study, the nodes of the *"one-to-all"* network are represented by the center of the STJ section and by all the voxels of the

aortic domain. The link between the STJ node and each voxel was weighted by the Pearson correlation coefficient $R_i^Q$ between $Q$ and $V_{ax}$ waveform at the *i-th* voxel, which measures the dynamic similarity between the inflow rate and the axial velocity waveforms in the aorta. To quantitatively characterize the *"one-to-all"* network structure, the curvilinear distance $s_{i-STJ}$ between the STJ node and voxel $i$ was calculated along the centerline, weighted by the value of $R_i^Q$ and averaged over all the $N$ voxels, obtaining the ad-hoc network metric *Averaged Weighted Curvilinear Distance AWCD* [3] that quantifies the anatomical length of persistence of the $Q$ *vs.* $V_{ax}$ waveforms correlation *in vivo*:

$$AWCD = \frac{1}{l}\frac{\sum_{i=1}^{N} s_{i-STJ} R_i^Q}{N}. \qquad (1)$$

To account for the geometric variability of the investigated dataset, *AWCD* was normalized with respect to the full thoracic aorta centerline's length $l$. To complete the analysis, the aortic geometry was characterized in terms of average curvature $\bar{\kappa}$ and torsion $\bar{\tau}$ [6], width W of the aortic arch (3D distance between the points of the AAo and descending aorta (DAo) at the level of the right PA), height H of the aortic arch (maximal vertical distance between W and the highest point of the aortic arch) and height over width ratio (H/W).

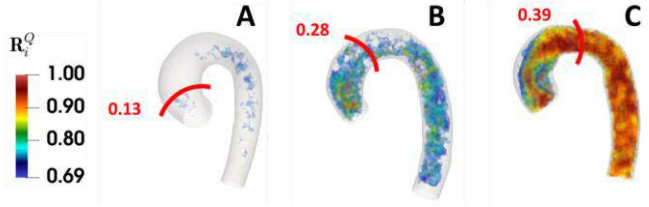


**Figure 2: $R_i^Q$ volumetric maps and *AWCD* (red line) for three representative subjects (presenting, respectively, the minimum, around the mean and the maximum $R_i^Q$ value). Only $R_i^Q$ values above the full dataset median value ($\widehat{R^Q} = 0.69$) are shown.**

## RESULTS

The influence of the subject-specific inflow rate on the aortic axial flow structures is presented in **Fig. 2**, where the volumetric maps of $R_i^Q$ values above the median ($\widehat{R^Q} = 0.69$) of the distribution pooled over the entire dataset is displayed. In detail, the three subjects presenting the minimum, around the mean and the maximum value of $Q$ *vs.* $V_{ax}$ correlation are presented here. Notably, it emerged that, in those subject with $R_i^Q$ mostly below the median, $Q$ and $V_{ax}$ waveforms are weakly correlated ($R_i^Q$ = 0.30 on average for case A), with a non-negligible amount of negative $R_i^Q$ values (i.e., indicative of retrograde axial flow [3]). In subject C, on the other hand, axial structures waveforms are strongly correlated with the inflow rate ($R_i^Q$ = 0.84 on average) and the negative correlations are mostly confined to the AAo inner wall. To quantify the anatomical persistence length of the $Q$ *vs.* $V_{ax}$ correlation, *AWCD* is reported in **Fig.2** and represented with a red line. Consistently with the $R_i^Q$ distribution, subject A presents the lowest *AWCD* with the correlation between $Q$ and $V_{ax}$ only persisting for 13% of the full thoracic aortic length, whereas in subject B the dynamical similarity between axial flow and inflow rate vanishes, on average, at the distal end of the AAo. In subject C, *AWCD* is among the highest in the dataset, with the $Q$ *vs.* $V_{ax}$ correlation propagating almost for the 40% of the full aortic length. Regarding the geometric analysis, as an example **Fig.3** displays *AWCD* box plots obtained after stratifying the 42 subjects in three groups based on H/W tertiles. In the range of H/W values ([0.31,0.64], median = 0.43) characterizing the healthy aortas, an increasing trend for *AWCD* emerged, even if not significant ($p$ = 0.62). Similarly, no significant links emerged between the *"one-to-all" AWCD* metric and all the other investigated geometric attributes.

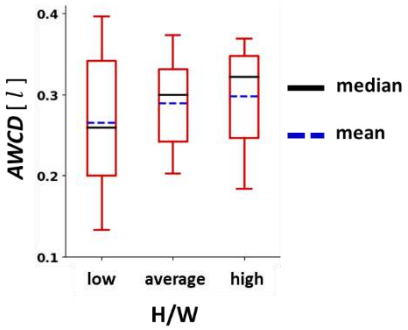


**Figure 3: Box plots of *AWCD* distributions obtained by dividing H/W in three groups based on tertile values.**

## DISCUSSION

In this study, a *"one-to-all"* network approach is adopted to quantitatively investigate the anatomical length of persistence of the similarity between the inflow rate at the STJ and the large-scale fluid structures along the main flow direction *in vivo* on a 4D flow MRI dataset of healthy human aortas. To do that, an ad-hoc network metric, the *AWCD*, was introduced to measure the anatomical persistence length of the correlation. The findings of the study suggest that in those healthy subjects where $R_i^Q$ values are low, the $Q$ *vs.* $V_{ax}$ correlation generally persists up to the mid AAo, whereas in cases where the correlations are higher their anatomical persistence length extend distally up to one third of the full thoracic aortic length (i.e., *AWCD* > 0.33) to include large portions of the aortic arch. No significant association emerged between the anatomical persistence length of the correlation and the geometric attributes, although a clear trend was observed between *AWCD* and H/W suggesting that the role of geometric features in transporting large-scale fluid structures dynamically similar to the inflow rate waveform downstream in the healthy aorta deserves further investigation. In conclusion, the here-proposed approach allows for the first time to evaluate the anatomical length of healthy aorta over which the subject-specific inflow rate waveform markedly shapes the large-scale fluid structures, thus providing a measure of the spatiotemporal aortic flow coherence *in vivo*. Besides investigating more in detail the role of geometric attributes on aortic flow heterogeneity, future studies should also adopt the here presented approach to analyze the impact that aortic stiffness and distensibility might have on large-scale hemodynamics.


## ACKNOWLEDGEMENTS

Guala A. has received funding from the Spanish Ministry of Science, Innovation and Universities (IJC2018-037349-I).


## REFERENCES


[1] Calò, K et al., *Ann Biomed Eng*, 49:2441-2453, 2021.
[2] Dux-Santoy, L et al., *Eur Heart J Cardiovasc Imaging*,34:1-11, 2019.
[3] Calò, K et al., *IEEE Trans Biomed Eng*, 67:1841-53, 2020.
[4] Johnson, KM et al., *Magn Reson Med*, 60:1329-1336, 2008.
[5] Morbiducci, U et al., *J Biomech*, 48:899-906, 2015.
[6] Gallo, D et al., *Ann Biomed Eng*, 43:68-81, 2015.

# RELATIONSHIP BETWEEN LUMBAR INTERVERTEBRAL DISC DEGENERATION AND SPATIAL DISTRIBUTON OF T1ρ RELAXATION TIMES

**Anika Kumar (1), Noah B. Bonnheim, Ph.D. (1), Ravi Chachad (1), Jiamin Zhou (1), Thomas M. Link, M.D., Ph.D. (2), Roland Krug, Ph.D. (2), Aaron J. Fields, Ph.D. (1)**

(1) Department of Orthopaedic Surgery, University of California, San Francisco, San Francisco, CA, USA
(2) Department of Radiology and Biomedical Imaging, University of California, San Francisco, San Francisco, CA, USA

## INTRODUCTION

Intervertebral disc degeneration in the lumbar spine is believed to be an important contributor to low back pain (LBP) in some patients [1]. Disc degeneration is associated with an overall loss of glycosaminoglycans (GAG), which help regulate disc swelling and biomechanical function [2]. However, the details regarding how GAG content changes throughout the disc at different stages of the degenerative process are not well understood. Such information could help elucidate the mechanisms and/or uncover unknown phenotypes of disc degeneration and possibly help identify new diagnostic and therapeutic targets for LBP.

The goal of this study was to quantify the spatial variation in GAG content in human discs at various stages of the degenerative process. To do this, we used T1ρ MRI because it provides an accurate, non-invasive estimate of GAG content [3]; additionally, T1ρ relaxation times decrease with increased degenerative grade [4].

The avascular discs receive their nutrients via diffusion from the vertebral capillaries terminating in the cartilage endplates [5]. Thus, we hypothesize that the early stages of disc degeneration begin in the center of the disc, farthest from the endplate nutrient sources.

## METHODS

Sagittal MRI data acquired using a T1ρ mapping sequence (slice thickness = 4 mm, FOV = 28x28 cm, acquisition matrix = 256x256, TE/TR = 12 ms/3,000 ms, 3 echoes per TR) [3] and standard clinical T1- and T2-weighted fast spin-echo sequences from $n$ = 80 patients with chronic LBP were utilized in this study. Discs were automatically segmented using a neural network [6] before voxel-by-voxel relaxometry was used to compute T1ρ relaxation times (ms) for all voxels in the L4/5 and L5/S1 discs. Separately, degenerative grade was scored by a trained radiologist using the Pfirrmann classification system [7] using the T2-weighted images. According to this system, Pfirrmann I represents a healthy (non-degenerate) disc, Pfirrmann V represents a fully degenerate disc, and the intermediate grades represent a progression of degeneration (Table 1). Patient-reported measures for disability and pain were collected using the Oswestry Disability Index (ODI) and Visual Analog Scale (VAS), respectively.

**Table 1: Patient demographic information. Values are mean ± SD.**

| Characteristic | $n$ = 80 patients | |
|---|---|---|
| Age (years) | 40.4 ± 12.2 | |
| Female, male | 38, 42 | |
| ODI | 26.77 ± 14.52 | |
| VAS | 6.55 ± 2.48 | |
| Pfirrmann Grade | L4/L5 | L5/S1 |
| I | 9 | 6 |
| II | 23 | 25 |
| III | 20 | 22 |
| IV | 19 | 17 |
| V | 9 | 10 |

Sagittal and axial line-scans bisecting the disc from a single mid-sagittal section were used to quantify T1ρ values as a function of anatomic location (Figure 1). For each disc, the sagittal/axial extents from the mid-sagittal section were divided into twelve equal regions (each region representing ~8% of the disc). The median T1ρ value of all voxels in each region was used to reflect the T1ρ value for that region (~5 voxels/region). Then, the median values in each region were averaged for each Pfirrmann grade. A mixed effects regression model accounting for multiple measurements per patient (from multiple spinal levels) followed by a Tukey post-hoc test was used to compare T1ρ values as a function of anatomic location between discs grouped according to Pfirrmann grade. In the sagittal direction, values were

compared between an anterior, central, and posterior location (sagittal 0%, 50%, and 100%). In the axial direction, values were compared between an inferior, central, and superior location (axial 25%, 50% and 75%).

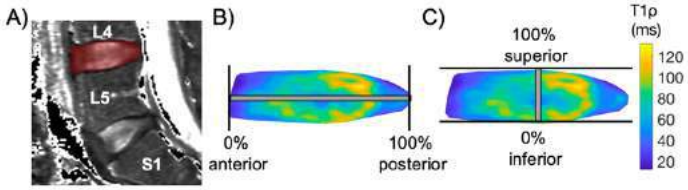


**Figure 1: A) Cropped T1ρ MR image showing segmentation of L4/L5 disc (red). T1ρ maps of disc with B) sagittal and C) axial line-scans. Grey bars annotate thickness and location of line-scans.**

## RESULTS

The spatial variation in T1ρ depended on Pfirrmann grade (Figure 2). T1ρ values tended to decrease with increased degenerative grade throughout the disc. Higher Pfirrmann grades (more severe degeneration) were also associated with a more homogenous T1ρ distribution both axially and sagittally. For example, in Pfirrmann I and II discs, the maximum difference in T1ρ as a function of sagittal locations was always above 48 ms, but for Pfirrmann III, IV, and V discs, this maximum difference was always below 16 ms.

Along the inferior-superior direction, in Pfirrmann grade II and III discs, T1ρ values in the disc center (50%) were lower than adjacent superior (75%; $p = 0.03$ and $< 0.0001$ for Pfirrmann II and III, respectively) and inferior regions (25%; $p = 0.002$ and 0.02). Differences in T1ρ between the disc center and these superior and inferior regions were not statistically significant in Pfirrmann grade IV and V discs ($p > 0.801$).

Along the anterior-posterior direction, Pfirrmann grade I, II, and III discs had significantly higher T1ρ values centrally compared to anteriorly (0%) and posteriorly (100%; $p \leq 0.0001$, 0.0001, and 0.0006 for Pfirrmann I, II, and III respectively). Statistically significant differences as a function of location were not detectable in for Pfirrmann IV and V discs. Sagittally, the differences in T1ρ values between the anterior/posterior regions of statistical comparison and the disc center were on average 43, 29, 10, 7, and 2 ms for Pfirrmann I, II, III, IV, and V respectively, demonstrating a more homogenous distribution of T1ρ values as degenerative grade increased.

## DISCUSSION

These data demonstrate that the distribution of T1ρ values both decreases and becomes more spatially homogenous with increased Pfirrmann grade, suggesting that GAG decreases and becomes more homogenous with increased disc degeneration.

The axial data for Pfirrmann II and III discs (mild and moderate degeneration) suggest that early-stage degeneration is characterized by diminished GAG content in the central region relative to adjacent superior or inferior regions. This finding supports the mechanistic hypothesis that disc degeneration may begin farthest from the vertebral capillary nutrient sources in the cartilage endplates (i.e., the region with the longest diffusion distance from the nutrient source).

The sagittal pattern in T1ρ values suggests that GAG content is greater in the nucleus pulposus than the annulus fibrosis, but that the differences in GAG content between those regions become much lower as the discs degenerate. Using published regression data relating dry weight of GAG content to T1ρ values [4], our estimated measurements of GAG in mildly and moderately degenerate discs range from 120-390 μg GAG/mg dry tissue: these data are consistent with the range of 50-400 μg GAG/mg dry tissue reported in a prior study of mildly and moderately degenerate discs in which GAG content was measured directly [8], supporting our computational methodology. Our data expand these prior works by estimating GAG distribution *in vivo* in a large number of LBP patients with varying disc degenerative grades.

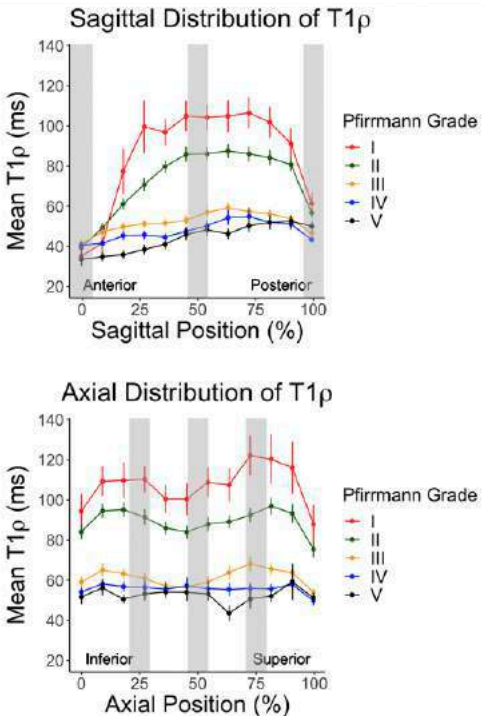


**Figure 2: Mean ± SE T1ρ relaxation times as a function of sagittal (top) and axial (bottom) location for each Pfirrmann grade. Grey vertical bars represent regions of statistical comparison.**

These data are limited in that the analysis was restricted to a single mid-sagittal cross-section and therefore neglects coronal variation in GAG content. However, the mid-sagittal region analyzed here is consistent with the Pfirrmann methodology relying primarily on mid-sagittal images [7]. Additionally, this study is inherently limited in its use of Pfirrmann grade to estimate degeneration, as it is a subjective, semi-quantitative measure of whole-disc degeneration.

Finally, these data reinforce the use of T1ρ-weighted MR imaging as a method for quantitatively, objectively, and non-invasively measuring and characterizing GAG content in lumbar intervertebral discs. Understanding the relationship between spatial distribution of GAG content in the disc and the progression of degeneration can be an important tool in the study of the etiology of disc degeneration.


## ACKNOWLEDGEMENTS

This research was supported by the National Institutes of Health through NIH HEAL Initiative awards UH2AR076719, UH3AR076719, and U19AR076737, and through R01AR070198.


## REFERENCES


**[1]** Urban, J et al., *J Biomech*, 102:109573, 2020.**, [2]** Hwang, d et al., *Quant. Imaging Med Surg.,* 6:744-755, 2016., **[3]** Auerbach J et al., *Eur Spine J.,* 15:338-344, 2006.**, [4]** Johannessen, W et al., *Spine*, 31(11): 1253-1257, 2010.**, [5]** Fields, AJ et al., *Curr Mol Biol Rep.,* 4:151-160, 2018.**, [6]** Iriondo, C et. al, *Magn Reson Med*, 84(3):1376-1390, 2020.**, [7]** Pfirrmann CWA et al., *Spine*, 26(17):1873-1878, 2001., **[8]** Iatridis, JC et al., *Spine*, 32(14): 1493-1497, 2007.

# TISSUE-ENGINEERED COLLAGENOUS FIBROUS CAP MODELS TO EXPLORE ATHEROSCLEROTIC PLAQUE RUPTURE

**Tamar B. Wissing (1,2), Kim van der Heiden (1), Sheilla Serra (1), Anthal Smits (2), Carlijn Bouten (2), and Frank Gijsen (1,3)**

(1) Department of Biomedical Engineering, Erasmus Medical Center, Rotterdam, the Netherlands

(2) Department of Biomedical Engineering, Eindhoven University of Technology, Eindhoven, the Netherlands

(3) Department of Biomechanical Engineering, Delft University of Technology, Delft, the Netherlands

## INTRODUCTION

Thin cap fibroatheromas are the plaque types that are most prone to rupture and are therefore termed "vulnerable" plaques. They are characterized by a soft lipid core embedded in a collagenous matrix, separated from the bloodstream by a fibrous cap[1]. The stability of a plaque largely depends on the integrity of this fibrous cap, but little is known about its mechanical properties and rupture mechanism.

The mechanical properties of the of fibrous cap are mainly determined by the fibrillar collagenous matrix. The mechanical properties of the collagenous matrix are subject to change, as production, remodeling, and degradation are known to be locally controlled by the mutual interplay between the cellular population and environmental cues, like mechanical strain [18–20].

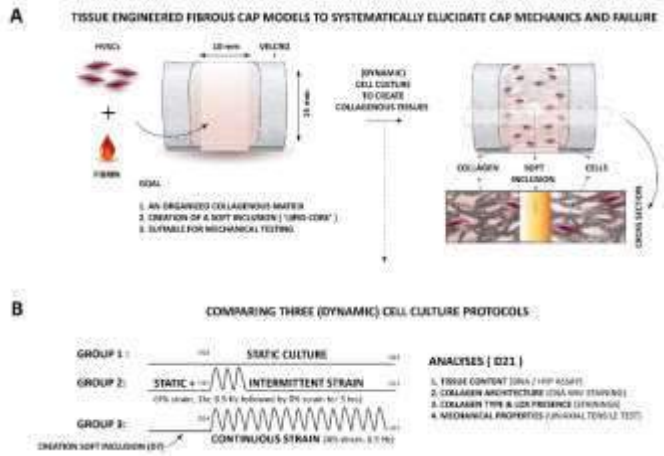


**Figure 1: Protocol for developing fibrous cap analogs.**

The cap strength values reported in literature very widely, at least partly reflecting the different cap failure mechanisms. Several failure mechanisms have been proposed[2]. However, due the paucity of experimental data, the conditions that underlie each failure mechanism remain still largely unknown.

Innovative models should be developed that aid in the systematic investigation of human cap rupture with high experimental control with relatively high throughput. Within this study, we take the first step in developing a human disease model for atherosclerotic plaques using concepts from the tissue engineering domain.

## METHODS

*Development of fibrous cap analogs*

Plaque analogs were created by seeding human vena saphena cells. The samples were statically cultured for 7 days, whereafter a 2 mm Ø soft inclusion (SI) was created by punching a core in the center of each analog and filling this core with fibrin (Fig 1A). This fibrin inclusion mimics the soft lipid core of atherosclerotic plaques. The analogs were statically cultured for 7 more days, after which they were exposed to 7 days of dynamic culturing using the Flexcell FX-4000T Three different loading protocols were applied (Fig 1B), static, intermittent strain (I-strain) and continuous strain (C-strain) with n=5 for each group. Velcro strips were added for mechanical testing[3].

*Collagen imaging*

At day 21, the samples were exposed to multiphoton microscopy (Leica TCS SP8X) with second harmonic generation to visualize the collagen architecture. The samples were incubated with CNA35 probe to visualize the collagen. Collagen fiber organization was quantified using second harmonic imaging. Fibrillar collagen or cell nuclei were visualized in cross-sections stained for Picrosirius Red (PSR) or Hematoxylin and Eosin (H&E), respectively[3].

*Uniaxial tensile tests and DIC*

After imaging, the samples were mechanically tested. A speckle pattern for digital image correlation (DIC) was applied to the top surface of each sample using an airbrush and a tissue dye. After pre-stretch (15 mN) and preconditioning (10 cycles of 10% strain), the samples were uniaxially strained until failure at a speed of 100%/min. The samples were strained in the direction, which biologically corresponds to circumferential strain. The nominal engineering stress-strain curves were derived from the force and displacement measurements utilizing the average initial thickness and width measurements. Data averaging was performed on the stress-strain data and the stiffness values were computed as the linear slopes at 2%, 5% and 10% strain based on the DIC analyses[3].

## RESULTS

*Collagen imaging*

Fig. 2 demonstrates the created organized collagenous tissues for the I-strain sample. All top regions analyzed exhibited isotropic collagen organizations irrespective of the culture protocol applied. The predominant fiber angles ranged between 74°degrees for the statically cultured samples up till 61° and 45° degrees when exposed to intermittent and continuous loading, respectively. Moving towards the shoulder and mid cap regions, the fibers appear more anisotropic in the direction of the Velcro constraints for the dynamically loaded samples. Those samples showed predominant fiber angles of 4° and 3° degrees in the shoulder region and 4° and 5° degrees in the mid cap region for the I-strain and C-strain respectively. The static control demonstrated a more isotropic collagen fiber distribution with a predominant fiber angle of 77° degrees in the shoulder and 35° degrees in the mid cap region. Increased collagen alignment was observed in the direction of the Velcro constraints when moving from the top to the shoulder and ultimately the mid-cap region, especially when loading was applied during culture.

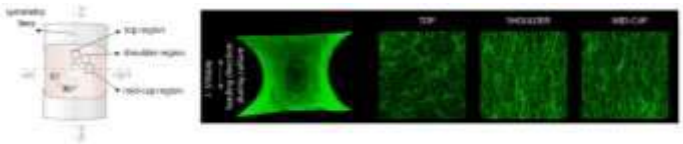

**Figure 2: Collagen fibre orientation**

Histological assessment of the tissue engineered fibrous cap models tissue content, demonstrated a similar collagenous architecture as observed in the fibrous cap of human atherosclerotic plaques, especially when loading was applied during culture (Fig.3). H&E and PSR staining shows a similar morphology, although the intensity of the H&E stain was less intense for the tissue engineered fibrous cap models in comparison to the human cap control.

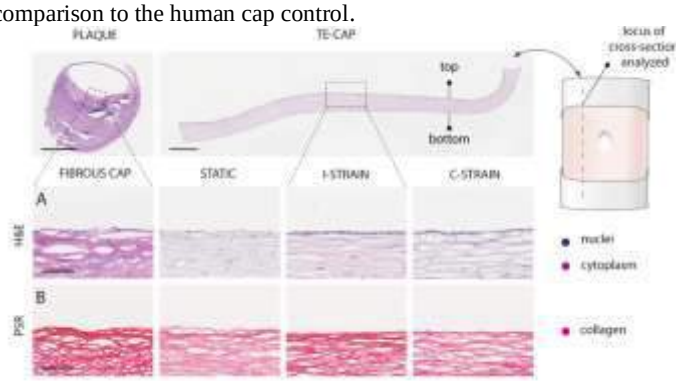


**Figure 3: Collagen fibre orientation**

*Uniaxial tensile tests and DIC*

Uniaxial tensile tests revealed that all engineered matrices demonstrated physiological strain stiffening responses (Fig.4A) with values that mimic plaque mechanical properties *ex vivo*. More specifically, stiffness values were 0.3 ± 0.2 (static), 0.3 ± 0.1 (I-strain) and 0.4 ± 0.2 (C-strain) MPa at 2% strain, 1.1 ± 0.5 (static) 1.1 ± 0.5 (I-strain) and 1.2 ± 0.4 (C-strain) MPa at 5% strain, and 2.3 ± 0.9 (static), 1.6 ± 0.3 (I-strain) and 2.2 ± 0.9 (C-strain) MPa at 10% strain (Fig.4B).

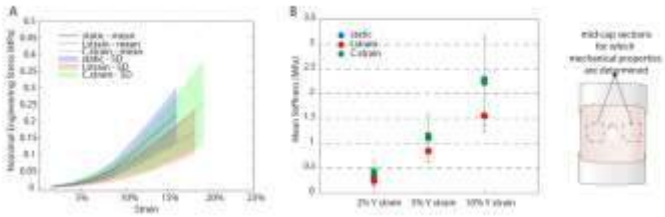

**Figure 4: Mechanical assessment of fibrous caps**

## DISCUSSION

In the newly developed platform, anisotropic collagen configurations, in the direction of loading, were observed. These matrix (re-)orientation responses are known to be a direct consequence of cellular (re-)orientations due to tissue constraints, contact guidance of the endogenous matrix and the magnitude and type of applied loads[4]. A predominantly isotropic collagen organization was detected in the top and base regions of the dynamically stimulated tissues illustrating that cellular (re-)orientation processes and consequent collagen fiber (re)distributions depend on the cumulative presence of constraints, matrix stiffness and local strain patterns. The histological analyses indicate that also the structural organization of the collagen mimics human cap composition adequately.

Although it is difficult to make a direct comparison to human caps, because of their complex composition and the variety of mechanical analyses performed in literature[5], all engineered tissues analyzed demonstrated physiological strain stiffening behavior and calculated stiffness values fell within the range reported for human carotid fibrous caps (i.e. 0.5-5 MPa) 5. Based on these initial data, we can conclude that not only the structural aspects of fibrous caps can be captured with this model, but we also generated a mechanical cap equivalent.

In conclusion, we present three tissue-engineered fibrous cap models that aid in the controlled and systematic investigation of the reciprocal relationships between cap composition and mechanical properties. By applying different (dynamic) cell culture protocols we were able to create reproducible naturally crosslinked tissues, with a tunable collagen content and organization, suitable for mechanical testing.

## ACKNOWLEDGEMENTS

TBW and KvdH are funded by an NWO-Vidi grant 18360.

## REFERENCES

[1] Libby et al., Nat Rev Dis Prim, 2019, 5(1)
[2] Cardoso et al, Journal of Bioemechanics 2014, 47(4)
[3]Wissing et al., *BioRxiv*. Preprint. 2021
[4] Foolen et al., Biomaterials 2021, 33.
[5] Akyildiz et al., Journal of Biomechanics 2014, 47(4) AC, Chai

# LOCAL STRUCTURAL AND RUPTURE CHARACTERISTICS OF ATHEROSCLEROTIC HUMAN CAROTID ARTERIES THROUGH SECOND HARMONIC IMAGING, TENSILE TESTING AND DIGITAL IMAGE CORRELATION

**S. Guvenir Torun (1), P. de Miguel Munoz (1,2), H. Crielaard (1), H.J.M. Verhagen (3), A. van der Lugt (4), G.J. Kremers (5), A.C. Akyildiz (1,2)**

(1) Department of Biomedical Engineering, Erasmus Medical Center, Rotterdam, Netherlands
(2) Department of Biomechanical Engineering, Delft University of Technology, Delft, Netherlands
(3) Department of Vascular Surgery, Erasmus Medical Center, Rotterdam, Netherlands
(4) Department of Radiology and Nuclear Medicine, Erasmus Medical Center, Rotterdam, Netherlands
(5) Erasmus Optical Imaging Center, Erasmus Medical Center, Rotterdam, Netherlands

## INTRODUCTION

Atherosclerotic plaque rupture, a major cause of cardiovascular events, is a local mechanical failure of the plaque tissue [1]. However, the current knowledge on rupture characteristics of the highly heterogeneous plaque tissue and the association of these to the underlying tissue structure is very scarce and limited to global, aggregate tissue properties [2]. In this work, we aim to characterize local heterogenous rupture properties of atherosclerotic human plaques by using tensile testing and digital image correlation (DIC), and investigated their association to the structural collagen architecture derived from second harmonic generation (SHG) microscopy imaging.

## METHODS

Tissue Collection and Structural Imaging

Nineteen atherosclerotic human carotid endarterectomy (CAE) samples were collected at Erasmus Medical Center, in Rotterdam. Initially, the samples were scanned with a micro-CT scanner (Quantum GX 2, Perkin Elmer) to identify non-calcified regions (Fig.1). Based on the scanning results, rectangular tissue strips (n=31) of fibrous plaque tissue were prepared. The tissue strips had their long-axis in the circumferential direction of the artery. Subsequently, the fibrillar collagen structure of tissue strips were imaged with a multiphoton microscope (Leica SP5) using SHG imaging (Fig.1). Before the imaging, a tile scan was performed per each sample. Each tile element consisted of 512 x 512 pixels and had the size of 738 x 738 µm. In selected tile elements, in-plane Z stack images were obtained with step size of 3 µm starting from the luminal surface up to approximately 150 µm tissue depth. The fibrillar collagen orientation (the predominant angle (pDA) ± standard deviation (SD)) and the anisotropic fraction (AF) within each scanned tile element was extracted by Gaussian Distribution fit histograms, obtained from the maximum intensity projection (MIP) images, using the Fiblab Software [3] (Fig.2). The AF indicated the anisotropy (0=isotropic, 1=anisotropic) of analyzed areas.

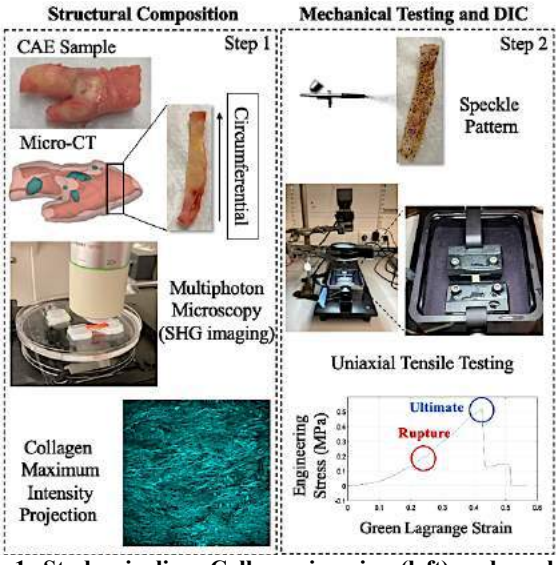


**Figure 1: Study pipeline: Collagen imaging (left) and mechanical testing combined with DIC (right) of plaque strips.**

Uniaxial Tensile Testing and Digital Image Correlation

After the structural imaging, a speckle pattern was applied to the luminal surface of the tissue strips. Then, the speckled tissue strips were placed into 37°C PBS filled in-house-built uniaxial tensile testing setup (Fig.1). A pre-load of 0.05N was applied. Then, the samples were preconditioned up to %10 strain for 10 cycles with a speed of 0.05mm/s. With constant speed, samples were continuously stretched along their long axis (circumferential direction of the artery) until complete rupture. The initial rupture was defined as the first failure detected in the gauge-length (GL) based stress-strain curve (Fig.1). Tissue deformation and

the local rupture(s) during the tests were recorded with a 5.3 MP CMOS camera (PL D 725, Pixelink). The local tensile strain (Green-Lagrange) within the tissue strips (excluding ~1 mm near-clamp regions) during the tensile testing were assessed from the camera recordings using a DIC software (Ncorr, version 1.2) [4] (Fig.3 (A)).

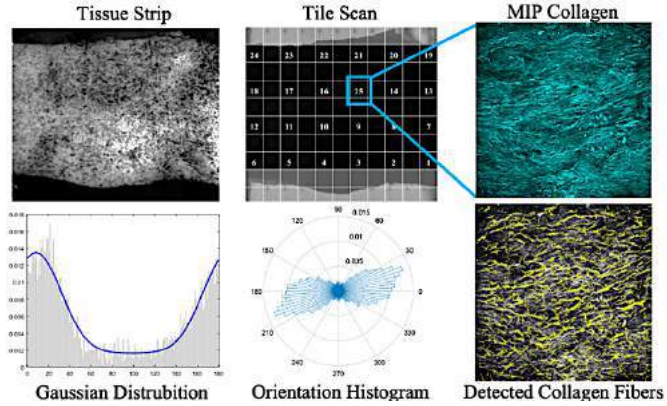


**Figure 2: SHG tile scan, MIP image and fiber detection to predict the local pDA and the SD of the peak.**

## RESULTS

Micro-CT scans, SHG based structural collagen imaging, uniaxial tensile testing and DIC of all samples were performed successfully. The pipeline was applied on 31 tissue strips from 19 CAEs, and the post-processing of 5 strips from 5 CAEs have been completed.

GL-based assessment revealed the average, global tensile strain properties of the tissue strips at the rupture initiation (range: 13-38% with a median of 22%) and the ultimate strains, at complete tissue separation (range:17-61% with a median of 28%). DIC analysis, on the other hand, enabled the local strain assessment: the plaque strips had a highly non-uniform, heterogenous strain distribution (a representative DIC map of CAE #3 demonstrated in Fig.3(A)). The averaged DIC based tensile strains at the rupture initiation time point for the whole strip (range:11-18%, median:16%) was lower than the global GL based measurements (Fig.3(B)). However, the DIC based local max strains at ROI (range:20-83%, median: 40%) was observed to be higher than both ultimate, and GL based global strain at the first rupture. Interestingly, 4 of 5 CAEs had a high or the maximum local DIC strain at the rupture.

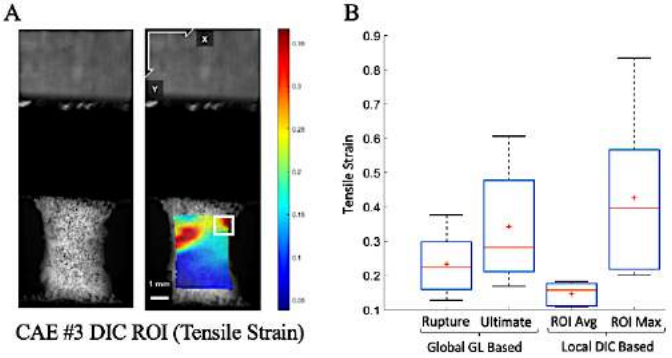


**Figure 3: (A) DIC based strain patterns of CAE (#3). The white square indicates the rupture. (B) Global GL based and DIC strains.**

Collagen Architecture of CAE Strips

All 5 CAEs were analyzed locally to obtain pDAs and SDs (Fig.4(A)), and AFs of each tile element. Mainly, all samples had circumferentially aligned pDAs (between -45° and 45°) with average ± SD of -34°±33°, 11°±34°, 0°±14°, 3°±14°, 11°±31° respectively for CAEs # 1, 2, 3, 4 and 5 (Fig.4(B)). The SDs (range:14° to 48°, mean:26) and AFs (range:0.10 to 0.82, mean: 0.53) of all CAEs demonstrated a variable anisotropy degree within and between samples.

The measured pDA ± SD and AF at rupture locations were 16° ± 29° and 0.72, 44° ± 21° and 0.43, -29° ± 26° and 0.44, -12° ± 26° and 0.59, and 30° ± 23° and 0.26 respectively for CAEs # 1, 2, 3, 4 and 5. All samples (n=5) were observed to have circumferential direction aligned pDAs at the rupture locations (Fig.4(B)).

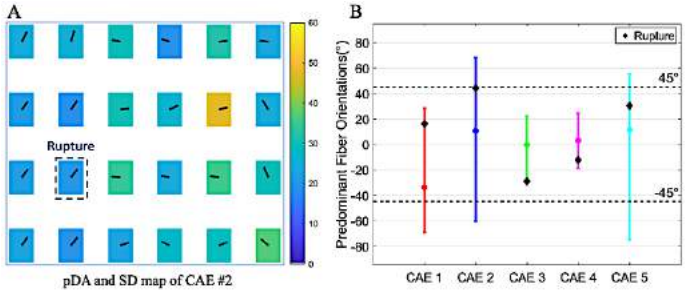


**Figure 4: (A) A representative pDA and SD map of CAE (#2). Black arrows and the colormap indicate the pDA and the SD within each tile element, respectively. (B) The pDA range of each CAE sample. Black diamonds indicate the pDA at the rupture locations.**

## DISCUSSION

In this work, we conducted a preliminary analysis of our pipeline developed to characterize the local mechanical rupture properties of atherosclerotic human carotid plaques, and their correlation with the underlying fibrillar collagen structure. The pipeline comprises pre-testing structural imaging, uniaxial tensile testing and DIC based local strain analysis. Thirty-one strips from 19 CAEs were tested, and the data of 5 strips from 5 CAEs have been analyzed. First, the commonly reported ultimate tensile strain, and the GL-based tensile strain at the first rupture were predicted. Yet, any GL-based strain assessment provides global, average tissue properties. Hence, we obtained DIC based strain measurements for observing the heterogenous nonuniform strain distribution of the plaque tissue. Our DIC-based average measurements were lower than the GL-based strains. This is likely due the exclusion of the near-clamp regions in the analysis, which show greater strains than the center region because of the clamping effects. However, DIC-based max strain measurements had a clear wide range of values within strips, up to ~80%, and was greater than both the ultimate and GL-based rupture initiation strains. Hence, the DIC based analysis was advantageous in avoiding overestimated averages due to the clamping, and the underestimated local high strains by the inherent homogeneity-based traditional ultimate analysis. Interestingly, the structural collagen analysis demonstrated predominant circumferential alignment at rupture regions, as well as for the rest of the tissue. However, the anisotropy varied inter- and intra- samples likely due to the heterogenous structure of plaque strips. For future work, all tested strips (n=31) will be analyzed to have a complete picture of structural and mechanical fingerprints of plaque rupture. This will provide us with unraveled insights of plaque rupture and as such, enable developing better treatment strategies for preventive medicine.


## ACKNOWLEDGEMENTS

This project is funded by the European Commission's Horizon 2020 under the Marie Skłodowska-Curie grant agreement # 749283.


## REFERENCES


[1] Cheng, G C et al., *Circulation*,87.4:1179-1187,1993. [2] Akyildiz A C et al., *J Biomech*,47.4:773-783,2014. [3] van Haaften, E et al., *Tissue Eng Part C:Methods*, 24:418-429,2018.[4] Blaber, J. et al., *Exp Mech,* 55.6:1105-1122,2015.

# PERIVASCULAR CEREBROSPINAL FLUID FLOW IS A MAJOR SOURCE OF INTERSTITIAL FLUID AND ITS CLEARANCE IN THE RAT BRAIN

**Kristian N. Mortensen (1), Tuomas Lilius (1,2,3,4), Marko Rosenholm (1), Björn Sigurðsson (1), Douglas H. Kelley (5), Maiken Nedergaard (1,6)**

(1) Center for Translational Neuromedicine, University of Copenhagen, Copenhagen, Denmark
(2) Department of Pharmacology, Faculty of Medicine, University of Helsinki, Helsinki, Finland
(3) Individualized Drug Therapy Research Program, Faculty of Medicine, University of Helsinki, Helsinki, Finland
(4) Department of Emergency Medicine and Services, University of Helsinki, Helsinki, Finland
(5) Department of Mechanical Engineering, University of Rochester, Rochester, NY, USA
(6) Center for Translational Neuromedicine, University of Rochester Medical Center, NY, USA

## INTRODUCTION

Brain metabolism produces waste, which must either be degraded or cleared from the brain tissue. Compounds that are not degraded and do not pass the blood-brain-barrier (BBB) are cleared by bulk efflux of interstitial fluid (ISF) [1]. The glymphatic model proposes that the driving mechanism behind bulk ISF efflux is influx of cerebrospinal fluid (CSF) from the subarachnoid space via arterial perivascular spaces (PVSs) [2]. This proposition has been challenged in subsequent studies and reviews [3,4], with differing anesthetic regimens as a possible confounding factor [5]. To assess the contribution of CSF influx to ISF clearance, we used magnetic resonance imaging (MRI) and single photon emission tomography (SPECT) to quantitatively measure both CSF influx and ISF efflux using different methods in rats under the same anesthetic regimen.

## METHODS

Experiments were carried out in male or female Sprague-Dawley rats (200-400g) under ketamine-dexmedetomidine anesthesia (K: 100 mg/kg, Dex: 0.5 mg/kg). MRI experiments were carried out on a Bruker BioSpec 94/30 USR magnet interfaced to a Bruker Advance III console using an 86 mm volume RF-transmit coil and a 4-channel phased array RF receiver coil (Bruker, Ettlingen, Germany). SPECT experiments were carried out on a Vector4CT (MILabs, Utrecht, Netherlands).

**CSF influx quantification.** We estimated CSF influx through the PVS surrounding the middle cerebral artery (MCA), which supplies a large portion of the cortex. We measured flow as the product of the cross-sectional PVS area ($A$, mm$^2$) and the flow velocity in the PVS ($v$, mm·min$^{-1}$). We then converted the flow measurement to perfusion ($Q$, µl·g$^{-1}$·min$^{-1}$) by dividing by the weight of the perfused brain tissue ($m$, g), i.e.:

$$Q = v \cdot A/m. \quad (1)$$

**Flow velocity.** Flow velocity was measured using dynamic contrast-enhanced MRI (DCE-MRI; FLASH3D; TE/TR/FA/matrix/FOV: 3ms/16ms/20°/ 280x173x380/28x20x38mm) with infusion of Gd-DTPA (50mM, 40µl, 2µl/min) in cisterna magna to trace the flow of CSF. Along the MCA, we measured arrival time and distance from the circle of Willis, and the flow velocity was estimated at the slope of the fit between the arrival time and distance (Fig. 1).

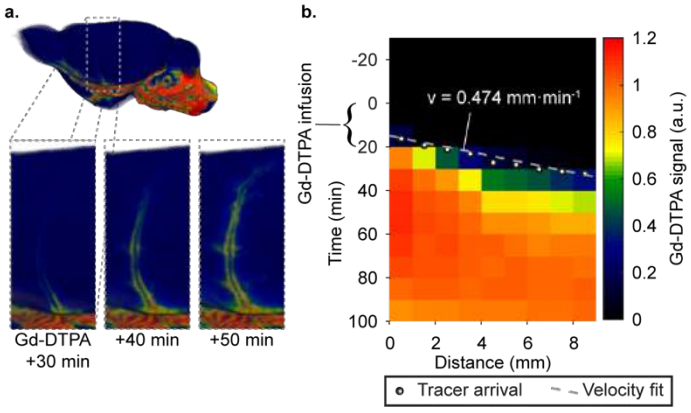


**Figure 1: Measurement of PVS flow velocity. a.** Visualization of Gd-DTPA distribution in PVS. **b.** Linear fit of arrival time over distance estimates the average flow velocity.

**PVS cross-sectional area.** Cross-sectional area was measured using high-resolution, long echo time T2-weighted MRI (TurboRARE, TE/TR/matrix/FOV/slices 24ms/16s/375x250/30x20mm/128, 8 repetitions) without contrast-enhancement. The images were converted to CSF partial-volume maps, and the cross-sectional area was estimated

as the summed CSF volume along the main trunk of the MCA divided by the length.

**Perfusion region mass.** We estimated the perfused area using quantitative DCE-MRI (FLASH3D; TE/TR/FA/matrix/FOV: 4ms/15ms/15°/128x128x128/ 30x32x30mm), to measure Gd-DTPA concentration quantitatively [6]. From these data, we calculated a voxel-wise tracer arrival-time map (Fig 2a), which allowed us to use a gradient-step algorithm to step against the direction of tracer distribution until reaching the subarachnoid or perivascular space (Fig 2b). Voxels from which the gradient-step algorithm reached the PVS of MCA were assigned to the MCA PVS perfusion region (Fig 2c), and finally the area of the region was multiplied by the density of rat brain (0.001045 g/mm$^3$) [7] to calculate $m$.

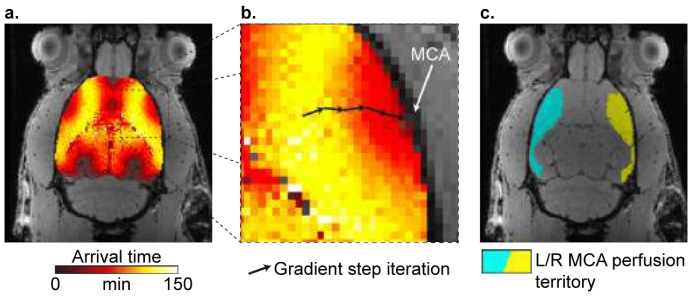


**Figure 2: Estimation of the perfusion territory. a.** Gd-DTPA arrival time map. **b.** Illustration of the gradient step algorithm. **c.** Example segmentation of left and right MCA perfusion territories.

Using these data, we further estimated whether a significant amount of the PVS flow bypassed the brain. To that end, we compared the accumulation of Gd-DTPA in the MCA perfusion territory to the cumulative amount of Gd-DTPA flowing through the MCA perivascular space in individual rats:

$$n_{\mathrm{CTX}}(T) = \int_{t=0}^{T} c_{\mathrm{PVS}}(t) \cdot v \cdot A \, \mathrm{dt}, \qquad (3)$$

where $n_{\mathrm{CTX}}(t)$ amount of Gd-DTPA in the MCA perfusion territory at time $t$, $c_{\mathrm{PVS}}(t)$ is the PVS Gd-DTPA concentration and $\dot{V}_{\mathrm{PVS}} = v \cdot A$ is the PVS flow.

**ISF clearance rate quantification.** To estimate the ISF clearance rate, we infused $^{99m}$Tc-DTPA through a chronically implanted cannula in striatum and measured the residual $^{99m}$Tc activity in the brain every ten minutes for 200 minutes using SPECT. After decay-correction we measured the tracer half-life ($T_{1/2}$) and converted it to a ISF clearance rate ($CL$) using the equation

$$CL = 0.693/T_{1/2} \cdot V_D \text{ [8]}, \qquad (2)$$

where $V_D$ is the distribution volume of the extracellular tracer, approximately 200 µl/g [9]

## RESULTS

Average flow velocity ($v$) was 0.61±0.17 mm·min$^{-1}$ (n=7), average PVS cross-sectional area ($A$) was 0.076±0.014 mm$^2$ (n=12), and average MCA PVS perfusion region mass ($m$) was 0.150±0.016 g (n=5). Applying eq. 1, we estimated CSF perfusion in the territory of the MCA ($Q$) to be 0.32±0.11 µl·g$^{-1}$·min$^{-1}$. Qualitative evaluation (Fig. 3) showed good agreement between Gd-DTPA accumulation and cumulative Gd-DTPA flow through PVS during the influx phase (0-100 min), indicating that the amount of flow bypassing the brain is negligible. The average ISF clearance was 0.471±0.053 µl·g$^{-1}$·min$^{-1}$ (n=12).

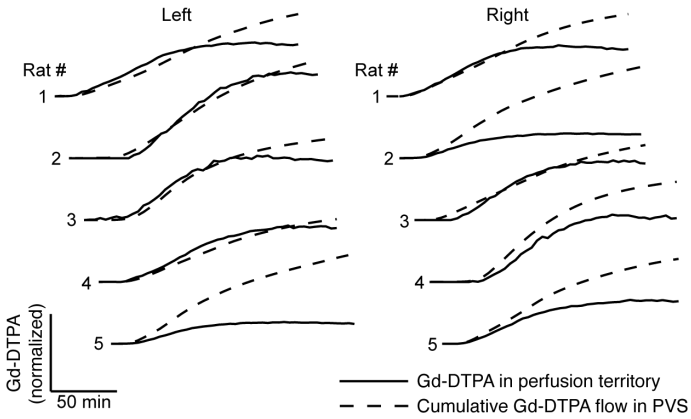


**Figure 3.** Qualitative assessment of CSF flow bypassing brain.

## DISCUSSION

We found a high degree of congruency between CSF influx and ISF clearance under the same anesthetic conditions despite applying very different measurement methods. These results indicate that CSF inflow is a major source of ISF and thereby of its clearance, contributing to the removal of metabolic waste from the brain tissue. We additionally found that PVS flow predominantly enters the brain parenchyma, that Gd-DTPA can freely enter the interstitium with CSF through PVSs, and that advection via PVS inflow is the dominant tracer influx mechanism.


## ACKNOWLEDGEMENTS

The work was supported by grants from the Lundbeck Foundation (R249-2017-1511, K. N. M), the U. S. Army (MURIW911NF1910280, M. N. and D. H. K.), and the NIH National Institute on Aging (RF1AG057575, M. N. and D. H. K.).


## REFERENCES


[1] Cserr, H et al., *Am J Physiol-Renal,* 240:319–328, 1981.
[2] Iliff, J et al., *Sci Transl Med,* 4:147ra111, 2012.
[3] Smith, A et al., *Elife,* 6:e27679, 2017.
[4] Abbott, N et al., *Acta Neuropathol,* 135:387–407, 2018.
[5] Hablitz, L et al., *Sci Adv,* 5:eaav5447, 2019.
[6] Lee, H et al., *Magnet Reson Med,* 79:1568–1578, 2018.
[7] DiResta, G et al. *J Neurosci Meth,* 39:245–251, 1991.
[8] Hladky, S et al., *Fluids Barriers CNS*, 15:30, 2018.
[9] Syková, E et al., *Physiol Rev,* 88:1277–1340, 2008.

SB³C2022
Summer Biomechanics, Bioengineering and Biotransport Conference
June 20-23, Eastern Shore, MD, USA

# AUTOMATIC ESTIMATION OF MECHANICAL AND GEOMETRICAL PARAMETERS OF ABDOMINAL AORTIC ANEURYSMS USING 3D+T ULTRASOUND FOR UNDERSTANDING ANEURYSM PROGRESSION

**Esther J. Maas (1,2), Arjet H.M. Nievergeld (1,2), Judith H.C. Fonken (1,2), Mirunalini Thirugnanasambandam (1), Marc R.H.M. van Sambeek (1,2), Richard G.P. Lopata (1)**

(1) Biomedical engineering, University of Technology Eindhoven, Eindhoven, the Netherlands
(2) Department of Vascular Surgery, Catharina Hospital Eindhoven, Eindhoven, the Netherlands

## INTRODUCTION

In current clinical practice, the rupture risk of abdominal aortic aneurysms (AAAs) is estimated from their maximal diameter. When a critical maximum diameter of 5.5cm is reached, surgery is performed to prevent rupture. However, some aneurysms rupture before this threshold is met, while others remain stable at larger diameters [1].

Previous research has shown the added value of additional rupture risk parameters, such as the AAA volume, curvature, elasticity and maximum wall stress [2-5]. These studies typically used computed tomography (CT) data, whose acquisition requires the use of radiation and nephrotoxic contract agents, preventing longitudinal studies. The current study focusses on the use of time-resolved 3D ultrasound (3D+t US), which non-invasive character and low cost make it the preferred imaging modality. Furthermore, 3D+t US gives information on the whole AAA geometry during different phases in the cardiac cycle, enabling the study of many parameters from a single image acquisition.

The aim of this study is to 1) develop a method to automatically determine rupture-risk related parameters from 3D+t US acquisitions and 2) apply this method in a follow-up study of AAA patients, to relate these parameters to the progression of the aneurysm.

## METHODS

3D+t US images of AAA patients were acquired during follow-up visits in the Catharina Hospital in Eindhoven. Each visit, the AAA outer-to-inner wall diameter is determined using 2D US ($D_{meas}$, current clinical workflow). A 3D+t US acquisition is performed during breath hold in a supine position, using a Philips IU22/Epiq US scanner with an X6 matrix array probe. The blood pressure is measured with an arm cuff.

The acquired 3D+t US images have a volume rate of 4-8 Hz and contain 15-35 frames. These images were processed offline using MATLAB R2021a. The segmentation of the inner aortic wall from the images was performed automatically on transverse slices using an in-house created adaptation of a Star-Kalman algorithm [6], followed by 3D deformable contours [7]. This segmentation was repeated on all time frames of the 3D+t data, allowing studying the motion of the aorta.

From the time-average segmentation, a centerline (CL) was created using a Dijkstra shortest path algorithm. Next, the segmentations of all time frames were resampled to obtain slices perpendicular to the CL with 1mm spacing between them. From this, the maximal inner-to-inner wall diameter ($D_{max,perp}$) and volume in a region of 60 mm around the maximal diameter ($V_{part}$) were determined. The point-wise curvature of the whole aortic inner wall was determined (mean of the principal components) using a finite differences approach [8], from which the median value over the AAA was taken. Furthermore, the elasticity (Ep) of the aortic wall was determined from systolic and diastolic diameter ($D_{sys}$ and $D_{dia}$) and the pulse pressure ($\Delta p$):

$$Ep = \frac{133.3 \cdot \Delta p}{(D_{sys} - D_{dia}) / D_{dia}} i \qquad (1)$$

In addition, the pressure-independent relative diastolic-to-systolic volume change was determined.

These parameters were determined in a preliminary analysis of 22 patients from our follow-up study, who had at least 3 follow-up measurements. The average growth rate was determined. Furthermore, the development of these parameters with the AAA progression was studied by investigating the linear regression of these parameters with the diameter. For the elasticity and relative volume change, box-and-whiskers plots for different diameter groups were created and groups were compared with a Wilcoxon rank sum test.

## RESULTS

An example of a AAA inner wall segmentation result on the US data is shown in Fig 1a, showing good correspondence to the image features. This also shows the location of the maximal diameter, whose variation over time is shown in Fig 1b. The curvature map is presented in Fig 1c, showing regions of high curvature at the ends of the aneurysm.

Segmentations were successful for 99 out of 113 datasets (visual check). Furthermore, the pulsatility was clearly visible in 83 of these acquisitions. Patients with unclear vessel pulsation (caused by poor image quality) were not further analyzed.

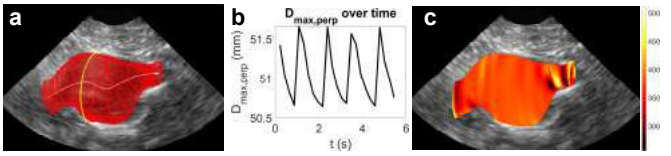


**Figure 1a: the segmentation plotted on the ultrasound data with the centerline (white), perpendicular slices with 5mm spacing (red) and the maximal diameter slice (yellow). b: The diameter variation over time. c: Curvature map of the geometry.**

Fig 2a shows the progression of the aneurysms over time. The growth rate of patients with at least 3 successful segmentations (N =15) was 2.2 [1.4-3.1] mm/year (median [IQR]), with a range of 1.0-6.0mm/year, indicating large variations between patients.

A clear relationship between $D_{meas}$ (outer-to-inner wall, from 2D US) and $D_{max,perp}$ (inner-to-inner wall, from 3D US) is shown in Fig 2b ($R^2$ =0.82). The average point-wise difference is 3.0mm, with IQR [1.4-4.7] mm, which is partially caused by wall thickness that is incorporated in $D_{meas}$. The differences seem slightly larger at larger diameters.

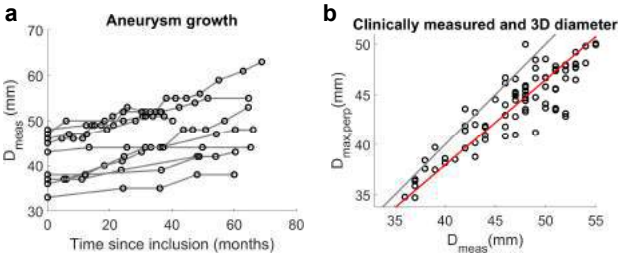


**Figure 2a: the growth of the aneurysm over time. For visualization purposes, only patients with at least 40 months of follow-up are shown (N = 9). b: relationship between $D_{meas}$ and $D_{max,perp}$; the identity line is indicated in grey and linear regression curve in red.**

The relation between $V_{part}$ and $D_{max,perp}$ is shown in Fig 3a, which demonstrates good correspondence ($R^2$ = 0.83) but also some spreading in the data. Fig 3b shows a negative correlation between the $D_{max,perp}$ and the median curvature of the AAA ($R^2$ =0.59, p <0.01).

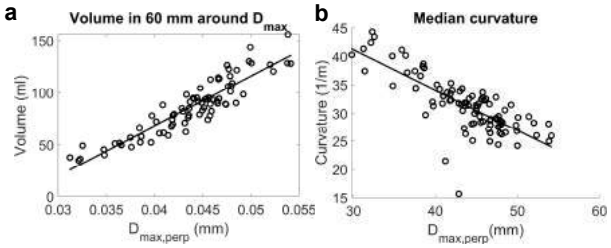


**Figure 3a: Relation between the maximal perpendicular diameter ($D_{max,perp}$) and volume in 30mm around $D_{max,perp}$. b:relation between $D_{max,perp}$ and curvature.**

The elasticity and relative volume change for different diameter groups are shown in Fig 4a and Fig 4b, respectively. The Wilcoxon rank sum test shows significant differences between the small and medium AAA group for both elasticity and volume change (P<0.01). There are no significant differences between the other groups. Both plots indicate that larger aneurysms pulsate less than smaller aneurysms, independent of whether the patient-specific blood pressure is taken into account.

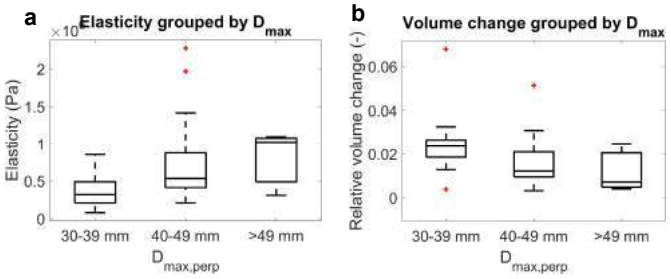


**Figure 4: Box-and-whiskers plots of the elasticity (a) and relative volume change (b) grouped by maximal diameter.**

## DISCUSSION

A tool to automatically determine many rupture-risk related parameters of AAA from a single 3D+t US acquisition has been developed. The good overlap between the clinically measured maximal diameter and diameter obtained from the automatic segmentation (Fig 2b) shows the accuracy of the segmentations. The good correlation between the volume and diameter is as expected, but the spreading in the data shows that investigation of the volume can add additional information about the state of the AAA.

The negative correlation between $D_{max,perp}$ and curvature could be explained by the increased proximal-distal size of the aneurysm with increasing diameter. The positive correlation between the diameter and elasticity corresponds to findings in research on 2D US [8], suggesting mechanical changes in the aneurysm wall occur as the dilatation progresses. Presence of an intraluminal thrombus could also play a role.

The next step in our research is to couple the workflow presented in this study to a method to determine the aortic stiffness and wall stresses using finite element modeling, which has already been developed in our group [10]. With this, more mechanical parameters can be investigated, including wall stress.

In conclusion, an important tool to study geometrical and mechanical parameters of AAAs has been developed, showing accurate geometrical results (Fig 2b), and expected correlation between geometry and elasticity (Fig 4). When applied to the whole dataset of 500 patients in our follow-up study, the predictive value of these parameters (volume, curvature, elasticity, and wall stresses) for AAA growth and rupture can be further investigated, to obtain more patient-specific rupture risk and growth predictors.


## ACKNOWLEDGEMENTS

This work is part of the MUSE project, which has received funding from the European Research Council (ERC) under the European Union's Horizon 2020 research and innovation programme (ERC starting grant 757958).


## REFERENCES


[1] Darling, R.C. et al, *Circulation,* 56:161-164, 1977.
[2] Lindquist Liljeqvist, M. et al., *J Vasc Surg*, 63:1434-1442, 2016.
[3] Lee, K. et al., *Ann Biomed Eng*, 41:562-576, 2013.
[4] Wilson, K. et al., *J Vasc Surg*, 37:112-117, 2003.
[5] Fillinger, M.F. et al. 2002, *J Vasc Surg*, 36:589-597,2002.
[6] Guerrero, J. et al, *Trans Med Im*, 26:1079-1090, 2007.
[7] Kass, M. et al, *Int J Comput Vision*, 1:321-331, 1988.
[8] Rusinkiewicz, S. *Proceedings. 2nd International Symposium on 3D Data Processing, Visualization and Transmission*, 486-493, 2004.
[9] Wilson, K. et al, *Eur J Vasc Endovasc Surg*, 15:472:477, 1998.
[10] Disseldorp, E.M.J. et al, *Eur J Vasc Endov Surg*, 52:635-642, 2016.

# CAROTID ARTERY STIFFNESS MECHANISMS ASSOCIATED WITH CARDIOVASCULAR DISEASE EVENTS AND INCIDENT HYPERTENSION: THE MULTI-ETHNIC STUDY OF ATHEROSCLEROSIS (MESA)

**Ryan J. Pewowaruk (1,2), Claudia Korcarz (1), Yacob Tedla (3), Gregory Burke (4), Philip Greenland (5), Colin Wu (6), and Adam D. Gepner (1,2)**

(1) University of Wisconsin School of Medicine and Public Health, Madison, WI, USA
(2) William S. Middleton Memorial Veteran's Hospital, Madison, WI, USA
(3) Vanderbilt University School of Medicine, Nashville, TN, USA
(4) Wake Forest School of Medicine, Winston-Salem, NC, USA
(5) Northwestern University Feinberg School of Medicine, Chicago, IL, USA
(6) National Heart, Lung, and Blood Institute, National Institutes of Health, Bethesda, MD, USA

## INTRODUCTION

Higher levels of arterial stiffness are associated with higher risk for hypertension, cardiovascular disease (CVD) events, and overall mortality [1]. The central, elastic arteries stiffen via two main mechanisms: 1) Load dependent stiffening due to elevated blood pressure increasing collagen fiber loading without an intrinsic change to the artery wall, and 2) Structural stiffening due to arterial remodeling which manifests as intima-media thickening, elastin fragmentation, and collagen accumulation. We previously quantified the age-associated longitudinal changes in structural and load-dependent carotid artery stiffness in the Multi-Ethnic Study of Atherosclerosis cohort [2]. Over a decade of aging, the vast majority of the age-associated increases in carotid artery stiffness were due to structural stiffening intrinsic to the arterial wall rather than being a concomitant effect of increased systolic BP with aging. However, there was high individual variability, with approximately 1/3$^{rd}$ of participants having more load-dependent than structural stiffening. The roles of load-dependent and structural stiffening in the development of hypertension and CVD events are still unknown. We hypothesized that structural stiffness would have the strongest association with CVD events because it is representative of intrinsic changes to the makeup of the artery wall material, leading to subclinical atherosclerosis and thus contributing to future CVD events. The Multi-Ethnic Study of Atherosclerosis (MESA) cohort provides a unique opportunity to better understand the mechanisms for large artery stiffening and test their hypothesized relationship with hypertension and CVD development.

## METHODS

The Multi-Ethnic Study of Atherosclerosis (MESA) is a longitudinal study of 6,814 men and women without CVD at enrollment, from 6 diverse communities in the United States [3]. MESA participants with B-mode carotid ultrasound and brachial BP at baseline Exam in (2000-2002) and CVD surveillance (mean follow up 14.3 years through 2018) were included (n=5873). Peterson's elastic modulus (PEM) was calculated to represent total arterial stiffness. Structural stiffness was calculated by adjusting PEM to a standard BP of 120/80 mmHg with participant-specific models [2,4]. Load dependent stiffness was the difference between total and structural stiffness.

Cox proportional hazard models were used to evaluate associations with incident CVD events and hypertension. Models were adjusted for traditional CVD risk factors including non-linear interactions.

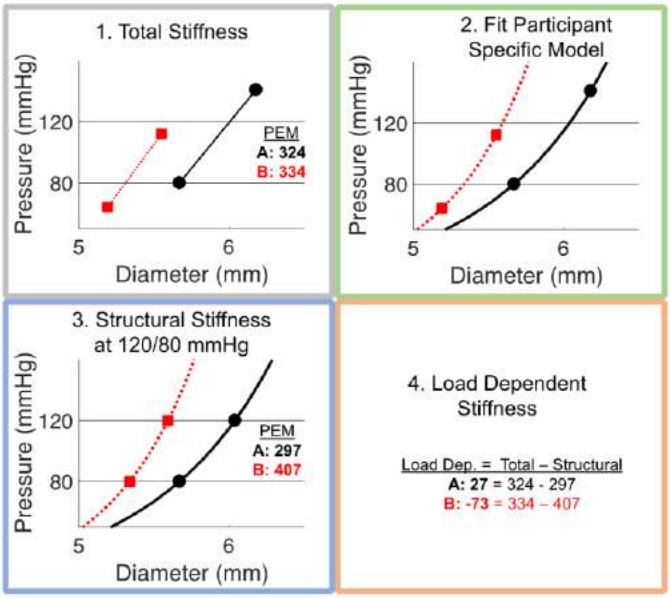


**Figure 1: Graphical representation for two participants of the methods to differentiate structural and load-dependent stiffness.**

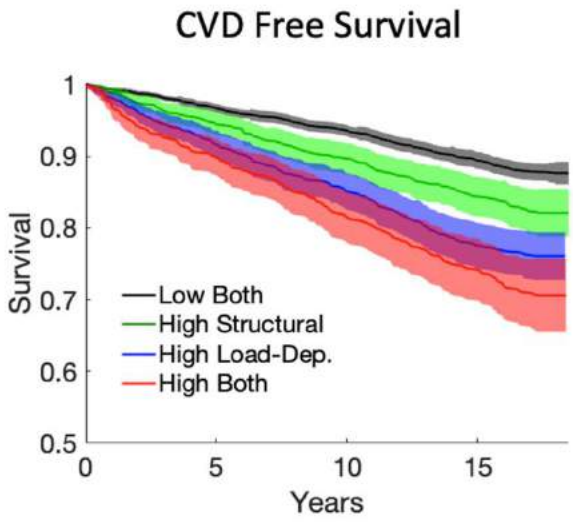


**Figure 2: Unadjusted Kaplan-Meier curves show that CVD free survival is greater for participants with high structural versus high load-dependent stiffness.**

## RESULTS

Based on 75th percentile cut-offs of PEM among these participants, groups of high structural, high load-dependent, high percentiles of both stiffness mechanisms, and low percentiles of both stiffness mechanisms were created for Kaplan-Meier curves (Figure 2). In this unadjusted analysis, CVD free survival was greater for participants with high structural stiffness versus high load-dependent stiffness.

In Cox models adjusted for traditional risk factors (Table 1), load-dependent stiffness was significantly associated with higher incidence of CVD events (hazard ratio per 100mmHg [HR] 1.21, 95% CI [1.09-1.34], p<0.001) events while higher structural stiffness was not (HR 1.03, 95% CI [0.99-1.07], p=0.10). Similar results were found for types of CVD events. Analysis of participants who were normotensive (BP < 130/80, no antihypertensives) at baseline exam (n=2122) found higher load-dependent stiffness was also associated with significantly higher incidence of hypertension (HR 1.53, 95% CI [1.35-1.75], p<0.001) while higher structural stiffness was not (HR 1.03, 95% CI [0.99-1.07], p=0.16).

**Table 1: Cox Models for Incident CVD and Hypertension**

| Events | Total PEM | | Structural PEM | | Load-Dep PEM | |
|---|---|---|---|---|---|---|
| | HR | p | HR | p | HR | p |
| CVD | 1.05 | 0.008 | 1.03 | 0.11 | 1.20 | <0.001 |
| Hard CVD | 1.04 | 0.08 | 1.01 | 0.59 | 1.26 | <0.001 |
| CHD | 1.04 | 0.08 | 1.03 | 0.26 | 1.17 | 0.017 |
| Stroke+TIA | 1.01 | 0.77 | 0.98 | 0.44 | 1.26 | 0.003 |
| Hypertension | 1.07 | 0.001 | 1.03 | 0.16 | 1.53 | <0.001 |

HR – Hazard ratio calculated per 100mmHg increment PEM, CHD – Coronary heart disease, TIA – transient ischemic attack

## DISCUSSION

Arterial stiffness is known to be an independent predictor of incident CVD [1]. The present study demonstrated that the underlying mechanisms of arterial stiffness were associated with both incident CVD events and incident hypertension. High load dependent carotid artery stiffness was significantly associated with future CVD events and hypertension, but that high structural carotid artery stiffness was not.

There are two primary advantages of using a participant specific model of arterial mechanics, as was done in this study, instead of a classical statistical adjustment based on blood pressure. The first advantage is that statistical adjustment is potentially correcting for two effects of BP on arterial stiffness at the same time, the chronic effect of increased BP due to remodeling and the acute effect of distending elevated blood pressure [5]. Using an exponential modeling approach these two mechanisms can be differentiated [2]. The second advantage is that the statistical adjustment for BP only gives the average effect of BP on arterial stiffness. Using participant specific models allows individual level correction for the effect of BP on arterial stiffness.

The results of this study support the idea that understanding the mechanism behind an individual's arteries are stiff is paramount. In heart failure, individuals receive different treatments based on etiology. This study presents a corollary regarding the mechanisms of arterial stiffness. We hypothesized that high structural stiffness would have the strongest association with CVD events because it is representative of intrinsic changes to the makeup of the artery wall material, leading to subclinical atherosclerosis and thus contributing to future CVD events. Instead, we found that higher load-dependent stiffness was significantly associated with future CVD events, but higher structural stiffness was not. Prior clinical studies have demonstrating that increased carotid artery stiffness in hypertension is primarily due to load dependent stiffening (from increased blood pressure) and not due to structural stiffening intrinsic to the vessel wall [6]. Taken together, these results suggest that the association of arterial stiffness and CVD risk in hypertension is due to load-dependent stiffening on a population level.

Measuring and treating arterial stiffness has not been used to improve CVD outcomes because there are no therapeutic strategies proven to reduce arterial stiffness independent of reducing blood pressure. This study provides valuable insight into the challenge of how arterial stiffness could best be used in in clinical practice. Recognizing and differentiating the mechanical components of arterial stiffness could provide a novel way to reduce CVD risk and personalize hypertensive care. Future trials focusing on improving load dependent arterial stiffness, either through personalized blood pressure goals or through specific antihypertensive regimens needs to be explored as a potential way to improve CVD outcomes. Our previous analysis in MESA suggests that, unlike structural stiffness, changes in load-dependent stiffness are modifiable through traditional CVD risk factors and individual hypertension management6. There is potential for elevated load-dependent carotid artery stiffness could be used as a threshold to initiate early hypertensive care.

These results provide valuable new insights into mechanisms underlying the association between arterial stiffness and CVD. Load-dependent stiffness was significantly associated with CVD events but structural stiffness was not.

## ACKNOWLEDGEMENTS

The authors thank the other investigators, the staff, and the participants of the MESA study for their valuable contributions (http://www.mesa-nhlbi.org). This work was supported by the Madison VA Hospital and T32 HL07936 (RP).

## REFERENCES

[1] Vlachopoulos, C et al., *JACC*, 55(13):1318-1327, 2010.
[2] Pewowaruk, R et al., *Hypertension*, 79(1):150-158, 2022
[3] Bild, D et al., *J Epidemiology*, 156(9):871-881, 2002
[4] Pewowaruk, R et al., *Hypertension*, E-pub, 2022
[5] Van Der Bruggen, M et al., *Am J Hypertension*, 34(7):737-743, 2021
[6] Bussy, C et al., *Hypertension*, 35(5):1049-1050, 2000

# EFFECTS OF NITROGLYCERIN INDUCED VASODILATION ON ELASTIC VERSUS MUSCULAR ARTERY STIFFNESS IN OLDER VETERANS

**Ryan J. Pewowaruk (1,2), Amy J. Hein (2), Cynthia M. Carlsson (1,2), Claudia E. Korcarz (1), Adam D. Gepner (1,2)**

(1) University of Wisconsin School of Medicine and Public Health, Madison, WI, USA
(2) William S. Middleton Memorial Veteran's Hospital, Madison, WI, USA

## INTRODUCTION

Studies of the biomechanics of the central elastic arteries like the aorta and carotid artery have predominately focused on passive contributions to arterial stiffness such as the extracellular matrix (ECM) and neglected active contributions to arterial stiffness from vascular smooth muscle (VSM). It has traditionally been believed that VSM and changes in VSM tone are unimportant to elastic artery stiffness [1] although recent studies have challenged this view [2,3]. In a recent retrospective analysis of several clinical studies, nitroglycerin (NTG) induced vasodilation was found to both increase and decrease arterial stiffness [2] depending on the ratio of passive-to-active stiffness along the continuum of young-to-old, healthy-to-diseased, and elastic-to-muscular arteries. Decreased VSM tone in the carotid artery of hypertensive individuals also bore striking resemblance to the effects of 10 years of aging [4], the carotid artery dilated and stiffened. These results suggest that VSM tone may be a key component of arterial aging and have different impacts on elastic versus muscular arteries. We performed the present study to test the responses of NTG induced vasodilation on arterial stiffness in the brachial and carotid arteries in older Veterans.

## METHODS

40 older Veterans (>60 years old), without known cardiovascular disease, were recruited for this study from the Madison VA Hospital (MVAH) and surrounding clinics. 20 were hypertensive and 20 were normotensive controls. Participants were administered 400mcg sublingual nitroglycerin NTG. NTG induced changes in arterial stiffness were measured locally with vascular ultrasound in the carotid and brachial arteries, and regionally by carotid-femoral pulse wave velocity (cfPWV) by tonometry.

Peterson's Elastic Modulus (PEM) of the carotid and brachial arteries were calculated:

$$PEM = \ddot{u}\frac{\Delta p D d^2}{(Ds^2 - Dd^2)} \quad (1)$$

where *Ds* is systolic diameter, *Dd* is diastolic diameter, and $\Delta p$ is pulse pressure. We used a recently developed arterial mechanics model based on pressure-diameter relationships to model the passive ECM and active VSM contributions to arterial stiffness for each participant [2].

Results are presented as mean and standard deviation. The arterial stiffness response to NTG was analyzed with a repeated-measures linear model with NTG administration as a within subjects factor and hypertension status as a between subjects factor. Results from modeling the active and passive contributions to arterial mechanics were compared using the Mann-Whitney U test due to non-normal distributions of some variables.

## RESULTS

Participant characteristics are shown in Table 1. Controls and hypertensive Veterans participating in this study were similarly matched for age (72.0±9.3 vs 70.8±6.6 year, p=0.64), sex (40% female vs 50% female, p=0.53), and smoking status. 85% of hypertensive participants were using antihypertensive medications and self-reported an average of 14.7±14.3 years since hypertension diagnosis (range: 2-60 years).

NTG decreased mean arterial pressure in control and hypertensive Veterans (NTG p<0.001, Figure 1). The carotid artery dilated more in control participants than hypertensive Veterans (Δ 0.54±0.19mm vs 0.42±0.12mm, p=0.022). Brachial artery dilation was similar, (Δ 0.55±0.26mm vs 0.51±0.20mm, p=0.46). With NTG, both control and hypertensive Veterans showed increased carotid PEM (Δ 66±90 vs 114±129 mmHg, NTG p<0.001) and cfPWV (Δ 1.1±2.2 vs 0.6±2.4 m/s, NTG p=0.020) NTG did not change brachial PEM in control and hypertensive Veterans (Δ 8±495 vs -82±476 mmHg, NTG p=0.69).

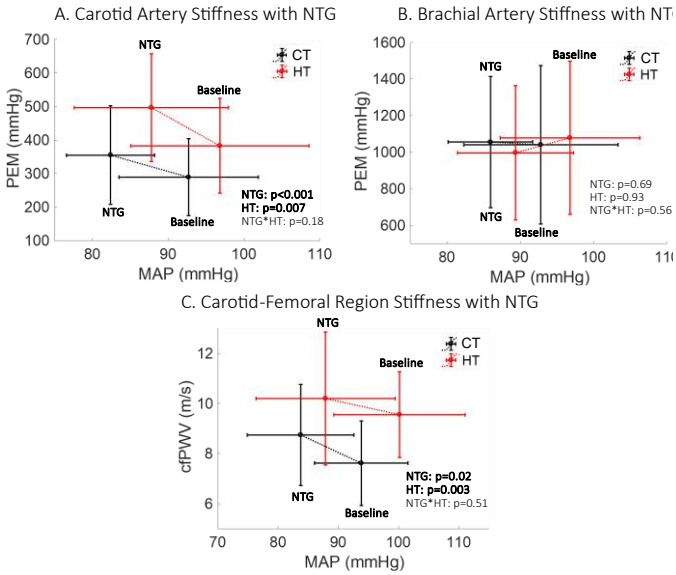


**Figure 1:** NTG A. increased carotid artery PEM, B. did not change brachial artery PEM, and C. increased carotid-femoral pulse wave velocity (cfPWV). CT – Control, HT – hypertensive

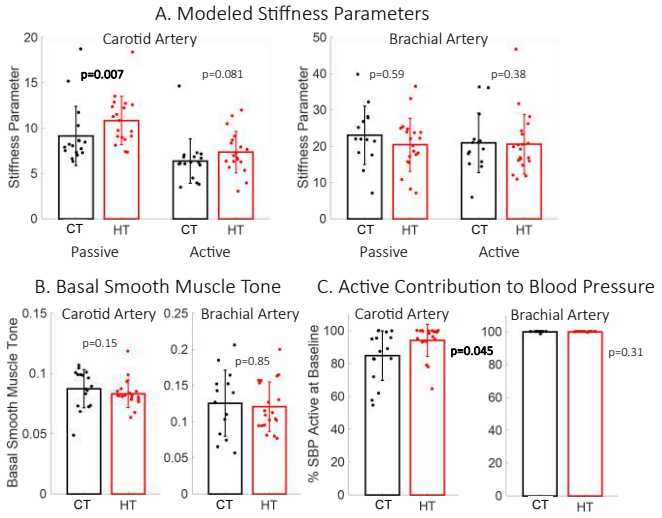


**Figure 2:** A. Carotid artery and brachial artery passive and active stiffness parameters. B. Basal smooth muscle tone for the carotid and brachial arteries. C. For the carotid artery, a greater percentage of baseline SBP was supported by active elements of the artery wall in hypertensive participants compared to control participants. For the brachial artery nearly all of baseline SBP was supported by active components of the artery wall for both groups.

Modeling results are shown in Figure 2. For the carotid artery, hypertensive participants had greater passive stiffness compared to control participants (10.8±2.7 vs 9.1±3.8, p=0.007) while active stiffness was not significantly different (7.3±2.3 vs 6.4±2.8, p=0.081). For the brachial artery, hypertensive and control participants had similar passive and active stiffness (Figure 4). Basal smooth muscle tone was similar between control and hypertensive participants (Carotid: 0.087± 0.026 vs 0.083 ± 0.011, p=0.15; Brachial: 0.115± 0.044 vs 0.121 ± 0.034, p=0.85). For the carotid artery, a greater percentage of baseline SBP was supported by active muscular elements of the artery wall in hypertensive participants compared to control participants (94.1±9.7% vs 84.8±24.7%, p=0.045).

## DISCUSSION

This study assessed the effects of nitroglycerin induced vasodilation on the stiffness of elastic and muscular arteries in older Veterans. The major finding was that the stiffness of central, elastic arteries significantly increased following sublingual nitroglycerin administration. Based on prior studies examining overall CVD risk associated with arterial stiffness parameters, this is a clinically significant observation that equates to an approximate increase of 15% in CVD risk [5]. In contrast to the carotid artery and carotid-femoral region, nitroglycerin did not change the stiffness of the muscular brachial artery.

In this study vasodilator administration decreased brachial BP by approximately 10 mmHg, but also had the negative effect of paradoxically increasing elastic artery stiffness. Awareness of the increase in arterial stiffness despite a decrease in BP is paramount, because it could offset some of the benefits of lowering BP in older patients who are prescribed vasodilators as an antihypertensive therapy. These results emphasize that vasodilators should only be 4th-5th line antihypertensive therapy options, particularly in older patients, and prompt the need to test the impact of other hypertensive therapies on active and passive stiffness parameters.

Nitroglycerin induced vasodilation also had different effects on the stiffness of elastic versus muscular arteries. Vasodilation increased elastic artery stiffness and did not change muscular artery stiffness. We hypothesize that these different findings are due to the ratio of passive and active contributions to arterial stiffness based on a Hill-type partition of passive-elastic and active-contractile forces [2]. When an artery has high passive stiffness, decreasing VSM tone will increase arterial stiffness. The elastic arteries of older individuals likely have higher passive stiffness due to mechanisms such as collagen accumulation and elastin fragmentation.

The arterial stiffness response to vasodilation is likely important in the development of CVD. Carotid artery VSM in hypertensive participants supported the majority of the load imposed on the arterial wall by blood pressure, limiting excess stress on passive, elastic elements of the carotid artery wall. Increased VSM tone has been shown to promote adaptive remodeling by the same mechanism in hypertensive rodents [3]. Our data in Veterans who have had hypertension for years suggests that basal VSM tone may be a long-term adaptation in humans with hypertension.

Limitations of this study include the relatively small number of subjects and is limited to an older, albeit less studied, patient population.

In older Veterans, without known cardiovascular disease, NTG induced vasodilation increased elastic artery stiffness and did not change muscular artery stiffness. Elastic artery stiffening with vasodilation may be important for antihypertensive medication selection and influence CVD development.

## ACKNOWLEDGEMENTS

This work was supported by the Madison VA Hospital, the VA IK2 CX001776 (AG) and NHLBI T32 HL07936 (RP).

## REFERENCES

[1] Lacolley, P et al., *Physiol Reviews*, 97(4):1555-1618, 2017.
[2] Pewowaruk, R and Gepner, A, *J Hypertension*, E-pub, 2021
[3] Spronck, B et al., *J R Soc Interface*, 18:1:11, 2021
[4] Pewowaruk, R et al., *Hypertension*, 79(1):150-158, 2022
[5] Vlachopoulos, C et al., *JACC*, 55(13):737-743, 2021

# COMPUTATIONAL FLUID-SOLID-INTERACTION MODELING OF NORMOTENSIVE AND ANGIOTENSIN-II INFUSED HYPERTENSIVE MICE

**Sara E. Hopper (1), Dar Weiss (2), Federica Cuomo (1), Jay D. Humphrey (2,3), C. Alberto Figueroa (1,4)**

1. Department of Biomedical Engineering, University of Michigan, Ann Arbor, MI, USA
2. Department of Biomedical Engineering, Yale University, New Haven, CT, USA
3. Vascular Biology and Therapeutics Program, Yale University, New Haven, CT, USA
4. Department of Surgery, University of Michigan, Ann Arbor, MI, USA

## INTRODUCTION

Hypertension, which contributes to neurologic, renal, and cardiac disorders, is a leading cause of death [1]. Aortic stiffening is both a cause and consequence of hypertension and occurs as a homeostatic response to increases in tensile stress from elevated blood pressure [2]. Because of this increase in structural stiffness, the compliance of the aorta decreases and pulse wave velocity (PWV) increases, resulting in a further increase in blood pressure, creating an insidious positive feedback loop. It is important to broaden our understanding of this interplay to potentially develop therapies that target this positive feedback loop.

Angiotensin II (AngII) is an important hormone in the renin-aldosterone-angiotensin-system (RAAS), which regulates blood pressure and fluid balance in vivo [4]. Improper control of the RAAS system has been clinically linked to hypertension, cardiac hypertrophy, and heart failure [4]. Infusion of AngII in murine models can be used to investigate the effects of hypertension and aortic stiffening on the cardiovascular system, as it increases blood pressure and inflammation [5]. In this study, we combined experimental and computational studies to characterize the relationship between arterial mechanics and hemodynamics in mice with chronic infusion of angiotensin II (AngII) and wild-type control mice.

## METHODS

**Experimental:** Animal protocols were approved by Yale University's Institutional Animal Care and Use Committee (IACUC). *In vivo* and *ex vivo* data were collected for 3 control mice and 3 mice following two weeks of AngII infusion (1000ng/kg/min). First, Doppler ultrasound was performed on the ascending thoracic aorta (ATA), infrarenal abdominal aorta (IAA), and the left carotid artery (LCA) to measure dynamic velocity and luminal area waveforms. Second, micro-computed tomography (μCT) scans were performed to collect anatomical data on the aorta and main branches. Third, Millar catheterization was performed to obtained ATA pressure waveforms. Finally, biaxial tissue testing was performed on excised vessels at 7 anatomical locations: ATA, proximal (pDTA) and distal (dDTA) descending thoracic aorta, suprarenal abdominal aorta (SAA), IAA, LCA, and right carotid artery (RCA).

**Computational:** FSI models were created using the open-source software CRIMSON [3]. 3D models of the AngII-infused (**Fig. 1, A1-A3**) and control (**Fig. 1, C1-C3**) mice were reconstructed from μCT images. Spatially-varying wall stiffness and thickness were derived from biaxial tissue testing data by linearizing around the *in vivo* diameter determined from μCT. ATA flow waveforms, measured with Dopper ultrasound, were imposed at the aortic inlet. Lumped parameter three-element Windkessel models were prescribed at each outlet branch to represent the distal vasculature and tuned to match ATA pressure waveform and LCA and IAA mean flow within 10%.

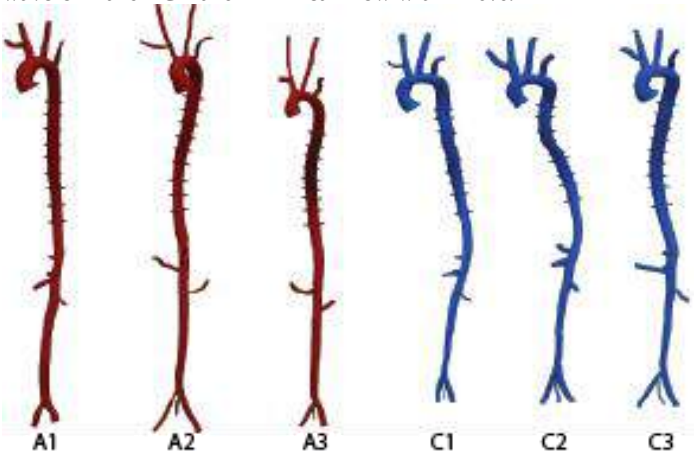


**Figure 1. Computational models for each mouse included in this study; AngII-infused: A; controls: C.**

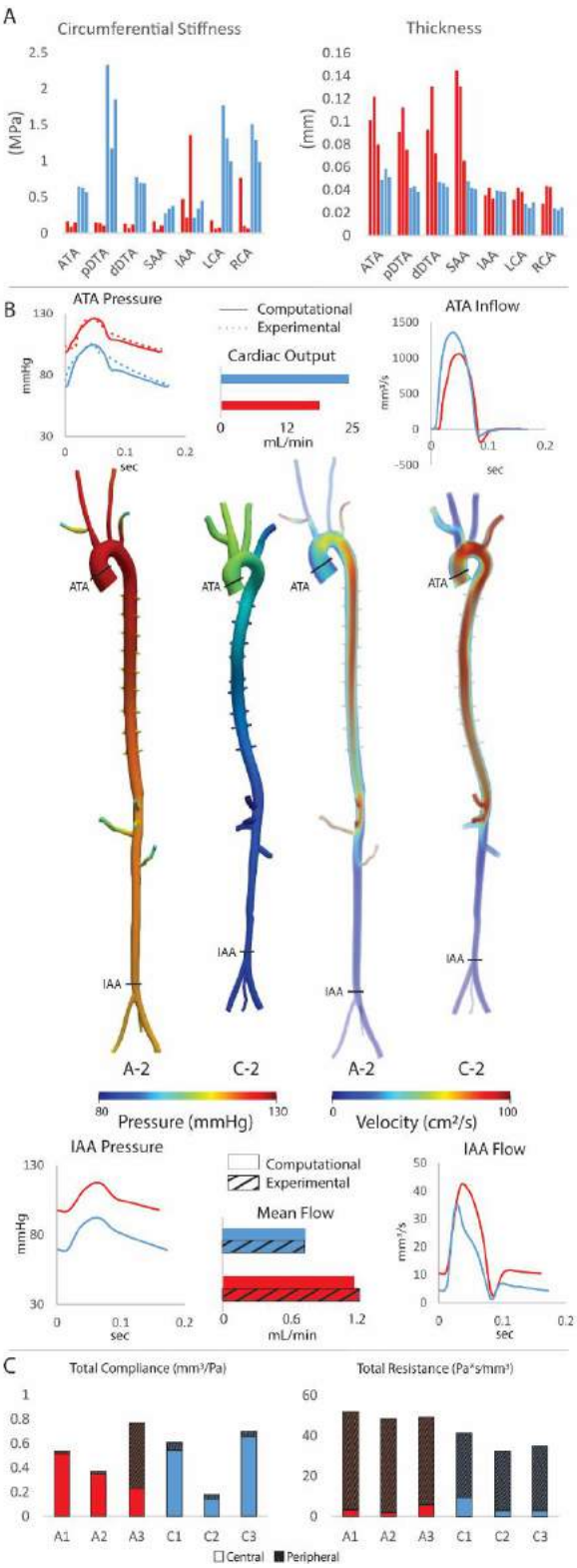


**Figure 2. (A) Measured arterial wall stiffness and thickness from biaxial testing. (B) Hemodynamic results of computational study. ATA and IAA pressure and flow waveforms were matched to the experimentally-acquired data. (C) Total resistance and compliance split into central (3D) and peripheral components.**

## RESULTS

**Experimental:** Mice infused with AngII exhibited a widely variable hypertensive phenotype compared to the controls (ATA mean arterial blood pressure (MAP): A1: 126 mmHg, A2: 109 mmHg, A3: 105 mmHg, C1: 88 mmHg, C2: 89 mmHg, C3: 105 mmHg; pulse pressure (PP): A1: 26 mmHg, A2: 28 mmHg, A3: 25 mmHg, C1: 37 mmHg, C2: 32 mmHg, C3: 32 mmHg). There were no differences in cardiac output (CO) between the AngII and control mice (A1: 24 mL/min, A2: 18 mL/min, A3: 15 mL/min, C1: 15 mL/min, C2: 22 mL/min, C3: 21 mL/min). In addition to having the most severe hypertensive phenotype, A1 also had an aortic dissection in the SAA. Biomechanical testing revealed that AngII mice (**Fig. 2A, blue**) had a higher wall thickness in the central aorta, but lower material and structural stiffness most aortic locations when compared to control mice (**Fig. 2A, red**).

**Computational:** The computational models successfully matched the mean, pulse, systolic and diastolic ATA pressures within 10%; mean flows at the LCA and IAA were also matched within 10%. Computational results for two representative mice (A-2, C-2) show that AngII mice had slightly lower cardiac output (CO) than control mice, but higher IAA flow (**Fig. 2B**). The AngII mice also had higher MAP but lower PP at all locations of the aorta. Furthermore, AngII mice had similar total arterial compliance and larger resistances than controls (**Fig. 2C)**. The observed increases in arterial resistance occurred largely in the peripheral arteries.

## DISCUSSION

Data-informed computational modeling allowed high-resolution examination of AngII-induced changes in hemodynamics, leading to new insights into effects of hypertension on aortic structure and function. Many of our results are consistent with known effects of AngII on the cardiovascular system [4]. An increase in mean arterial pressure is observed in the AngII-infused mice. Consistent with previous studies, AngII mice showed an increase in luminal thickness in all regions of the aorta, except for the IAA [5]. There is an increase in peripheral resistance in the AngII mice, which is attributed to known contraction of distal vasculature in response to AngII [4].

Previous studies of AngII-induced changes in aortic biomechanics have demonstrated no significant difference in circumferential material stiffness and an increase in structural stiffness [6], which is not consistent with our results. We show a decrease in material and structural stiffness consequent of AngII infusion, which contributes to the predicted decrease in PP along the aorta in these mice. However, it is important to note that we did not account for the possible changes in smooth muscle tone [7]. A possible explanation for the lower structural stiffness observed in the AngII-infused mice is that the anesthetic used for the *in vivo* measurements – isoflurane – had differential effects on the control and AngII-infused mice, which demands further study [8].

## ACKNOWLEDGEMENTS

This research was supported by grants from the NIH (R01HL105297; U01HL135842). Computing resources were provided by the NSF (Grant1531752).

## REFERENCES

[1] Mitchell, G.F., *J Appl Phys*, 105:1652-1660, 2008.
[2] Humphrey, J.D. *et al.*, *Circ Res*, 379-381, 2016.
[3] Arthurs, C.J. *et al.*, *PloS Comp Biol*, 2021.
[4] Sparks, M.A. *et al., Comp Phys*, 1201-1228, 2014.
[5] Bersi, M. *et al.*, *J R Soc Interface*, 14, 2017.
[6] Bersi, M. *et al.*, *Hypertension*, 67:890-896, 2016.
[7] Korneva, A. & Humphrey, J.D., *Am J Physiol Heart Circ Physiol*, 316: H265-H278, 2019.
[8] Qi, F. *et al.*, *Anesh and Analg*, 109:412-417, 2009.

# ULTRASOUND AS A STIMULUS FOR TRANSDERMAL, HYDROGEL-BASED BONE REPAIR

**Fayekah Assanah (1), Kevin P. Grassie (1), Hanna J. Anderson (1), Will Linthicum (2), Bryan D. Huey (2), Yusuf M. Khan (1,2,3)**

(1) Biomedical Engineering, UCONN, Storrs CT, USA

(2) Materials Science & Engineering, UCONN, Storrs CT, USA

(3) Orthopaedic Surgery, CT Convergence Institute, UCONN Health, Farmington CT, USA

## INTRODUCTION

Regenerative engineering has tremendous potential as an alternative to over 2 million bone grafting procedures performed annually [1]. Toward that end, we have merged regenerative engineering techniques with existing clinical therapies to develop a treatment strategy for large-scale bone defects. This approach combines hydrogel-based cell delivery with low-intensity pulsed ultrasound (LIPUS), an FDA approved treatment for fracture repair. Our strategy involves the delivery of cell-laden hydrogels to bone defects followed by the application of transdermal, LIPUS-derived acoustic radiation force (ARF). Physical forces applied to cell-hydrogel constructs would stimulate the cells within the defect site to promote bone formation without disrupting the unstable bone defect. We have demonstrated the efficacy of this technique by observing the upregulation of load-sensitive markers in cell-loaded collagen hydrogels [2, 3]. Here, we sought to better understand the impact of acoustic radiation force on encapsulated cells using traction force microscopy (TFM) to predict forces experienced by encapsulated cells, and both *in vitro* and *in vivo* techniques to evaluate cellular responses to them. Briefly, a 3-D TFM algorithm was developed in which the physical forces on and around fluorescent beads embedded in hydrogels were computed as a predictor of mechanical forces experienced by hydrogel-encapsulated cells subjected to ARF. Additionally, to determine the optimal combination of hydrogel stiffness and ultrasound intensity for rapid bone repair early and late stage phenotypic markers of osteoblastic behavior were evaluated. Finally, the *in vivo* healing of critical size mouse calvarial defects filled with cell-hydrogel constructs and stimulated transdermally with ARF was evaluated. Results suggest enhanced healing as a result of ARF stimulation.

## METHODS

***TFM Algorithm:*** The MATLAB algorithm developed reconstructs the force-density field by 1) 3D interpolation of displacement data to obtain a displacement field, and 2) Fourier-domain inversion of the Green's function solution to the general problem in 3D linear elasticity.[4] This approach approximates the hydrogels as linearly elastic, isotropic mediums under small deformations compared to the bulk dimensions. To test the algorithm's accuracy in force-density reconstruction, simulated displacement data were first computed from user-defined, randomized distributions of point-forces with varied magnitude ranges. The force-density fields were then reconstructed from the simulated data and compared to the known input fields. In hydrogels subject to varied ARF, fluorescent beads were embedded in 0.1% w/v Type I collagen hydrogels (detailed below) and displacements were measured using imaging and tracking procedures in Volocity software and the force-density fields reconstructed as mentioned.

***Cell-Hydrogel Construct Synthesis:*** Bone Marrow Stromal Cells (BMSCs) were harvested from the long bones of wild-type mice and cultured for 7 days on TCP. Adherent cells were then lifted, resuspended, and encapsulated in type I collagen hydrogels ($5x10^5$ cells/gel) using two different collagen concentrations, 0.3 and 0.5%. Cell-hydrogel constructs were then maintained in 37°C and α-MEM media (10% FBS 1% pen/strep) for analysis.

***In Vitro Analysis:*** LIPUS-derived ARF was applied to cell-hydrogel constructs (0.3, 0.5% collagen) using a 1 MHz unfocused immersion transducer, by submerging the transducer in media and placing it directly above the cell-hydrogel construct. A one-time ARF treatment (300 $mW/cm^2$) was applied to the cultures for 20 minutes. After one hour, media and cells were extracted to measure $PGE_2$ expression and of COX-2 gene expression with ELISA and qRT-PCR, respectively. For long-term studies cell-hydrogel constructs were

treated with ARF for 5 out of 7 days per week for 2 weeks and either extracted to measure COL1 and RUNX2 gene expression or left *in situ* for an additional two weeks of ARF treatment and stained with alizarin red stain to evaluate hydrogel mineral formation. One-way analysis of variance (Tukey post-hoc) was used to determine statistical significance between groups ($p<0.05$, $n=3$).

***In Vivo Analysis:*** For the *in vivo* studies, a unilateral critical size calvarial defect (size: 4mm) was created in NSG mice and a 4.8mm diameter collagen hydrogel (0.3%) encapsulating $1x10^6$ reporter BMSCs per hydrogel was placed inside the defect. ARF was applied transdermally to the defect site once per day for 20 minutes, 5 days per week, for 4 weeks, at which time animals were sacrificed and evaluated using x-ray radiographs. Qualitative assessment of bone healing was done by observing the opacity of tissue within the defect as an indication of mineralized bone formation.

## RESULTS

Figure 1 displays the associated 3D vector fields of reconstructed force-density for hydrogel regions from the 50% and 100% duty cycle conditions. Corresponding data (not shown) suggests that as the duty cycle of LIPUS stimulation (and therefore force magnitude) increases, larger average displacements are measured, and larger reconstructed force-densities are predicted. In general, for a fixed spatial intensity ($mW/cm^2$) of LIPUS, higher duty cycles correspond to an increased

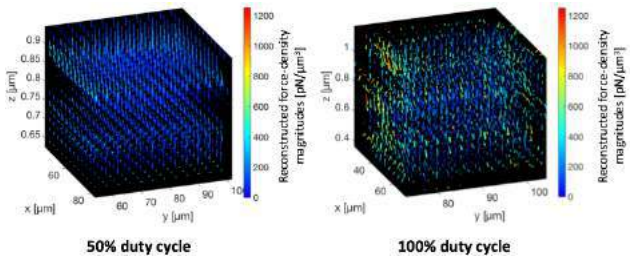


**Figure 1. 3D plots of the TFM-reconstructed force-density vector fields in the analyzed regions of 0.1% collagen hydrogels exposed to LIPUS at 50% (left) and 100% (right) duty cycles.**

time-averaged, apparent spatial intensity of ARF impinging upon cell-laden hydrogels. Therefore, these 3D-TFM experiments suggest that larger forces are transferred into hydrogels when exposed to greater apparent ARF (via higher duty cycle). Higher applied forces to the hydrogel resulted in higher measured forces within the hydrogel. This, it is theorized, would translate to greater forces being applied to encapsulated cells and would stimulate upregulations of key osteogenic markers commonly associated with bone repair. Indeed, when ARF was applied to cell-hydrogel constructs the forces to encapsulated cells increased, and expression levels of (figure 2A) COX-2 and (B) $PGE_2$ were upregulated when compared to control (no ARF) encapsulated cells. Interestingly just encapsulating cells in the 0.3% hydrogel (no ARF) upregulated COX-2 and $PGE_2$ when compared to cells on TCP (data not shown), but the combination of both encapsulation and ARF increased these expressions further. Similar trends were noted in gene expression for both type I collagen (2C) and RUNX2 (2D). Alizarin red staining showed that cells encapsulated within 0.3% gels had greater mineral formation over the other groups in response to ARF treatment after 3 weeks (figure 3) while *in vivo* analysis revealed that mechanically loading encapsulated cells resulted in better bone healing after 4 weeks (figure 4). X-ray radiographs show more bone formation with ultrasound (D-F)) than without (A-C).

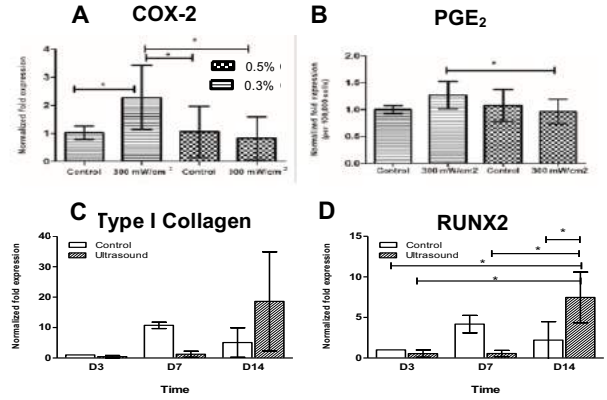


**Figure 2. Upregulation of early (A,B) and late (C,D) stage osteogenic markers indicate ARF influences the differentiation of encapsulated cells toward the osteoblastic phenotype.**

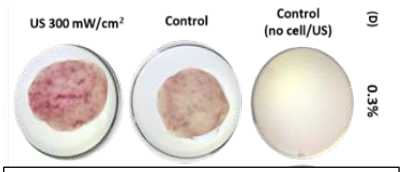


**Figure 3. Mineralization is enhanced from cells in 0.3% hydrogels exposed to ARF (left) vs. cells not exposed to ARF.**

## DISCUSSION

Here we propose a novel treatment for bone defects that delivers stem cells and mechanically stimulates them *in situ* through transdermal acoustic radiation force for the purpose of accelerating the healing of large scale bone defects. To that end, we have shown 3-D TFM simulations that suggest increasing force input to a cell-hydrogel construct results in increased physical forces experienced by encapsulated cells. This model will output forces

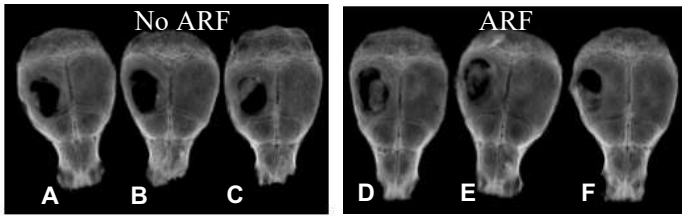


**Figure 4. Cell-hydrogel constructs implanted and subsequently exposed to ARF (right) showed more mineralized tissue than those not exposed (left), suggesting that ARF-derived forces stimulate rapid bone formation.**

applied to cells based on model input parameters such as ARF and hydrogel stiffness. *In vitro* and *in vivo* experiments demonstrate that increased forces result in elevated osteogenic expression by BMSCs, and that this translates to more rapid bone formation, which can be used to heal large scale bone defects. This may have far reaching clinical potential as a new tool in the clinical armamentarium.

## ACKNOWLEDGEMENTS

Research reported in this abstract was supported by National Institute of Arthritis and Musculoskeletal and Skin Diseases of the National Institutes of Health under award number R01AR073206.

## REFERENCES

[1] Giannoudis PV. Bone substitutes 2005; 36; S20-S2. [2] Veronick JA. Exp Biol Med 016; 241: 1149–1156. [3] Veronick JA. Tiss Eng Part A 2017; 00 1-10. [4] Schwarz, U.S. et al. Biochimica et Biophysica Acta (2015).

SB³C2022
Summer Biomechanics, Bioengineering and Biotransport Conference
June 20-23, Eastern Shore, MD, USA

# A CONSTRAINED MIXTURE MODEL OF THORACIC AORTIC ANEURYSM GROWTH

**David S. Li (1), Marcos Latorre (2), Jay D. Humphrey (1)**

(1) Department of Biomedical Engineering, Yale University, New Haven, CT, USA
(2) Center for Research and Innovation in Bioengineering, Universitat Politècnica de València, Valencia, Spain

## INTRODUCTION

Thoracic aortic aneurysms (TAAs), localized dilatations of the aortic vessel, increase the risk of aortic dissection or rupture and can be initiated from a variety of biomechanical and genetic factors. There is a pressing need to understand the complex roles of these factors in TAA development. While much has been learned through studies involving murine models and clinical data, risk factors are often present in combination and are challenging to isolate. Thus, computational models of aneurysm growth can offer insight by isolating the influence of individual effects on the progression of aneurysms.

Here, we apply a well-established computationally efficient mechanobiologically equilibrated constrained mixture model for arterial growth and remodeling (G&R) to describe the long-term evolution of TAAs arising from several predisposing factors investigated previously [1]. We contrast their effects on final aneurysm geometry and key biomechanical metrics and illustrate how preexisting hypertension and aging have dramatic impacts on disease progression.

## METHODS

*Constrained mixture model for arterial growth and remodeling*

The arterial wall is modeled as a mixture of three load-bearing constituents (elastin $e$, collagen $c$, and smooth muscle cells $m$) that undergo changes in mass (grow) and microstructure (remodel) in response to biomechanical stimuli. Each constituent $\alpha = e, c, m$ is governed by a mass density production rate $m^\alpha(\tau)$, survival (decay) function $q^\alpha(s,\tau)$, and stored energy density function $\widehat{W}^\alpha(s,\tau)$ that depends on its multiaxial deformation relative to its evolving natural configuration $\kappa_n(\tau)$, where $s$ is the current G&R time and $\tau \leq s$ is the time of deposition. We express production at time $\tau$ using a (potentially evolving) nominal rate $m_N^\alpha(\tau) > 0$ modulated by deviations from homeostatic set points in intramural stress $\sigma$ and wall shear stress $\tau_w$ by

$$m^\alpha(\tau) = m_N^\alpha(\tau)\left(1 + K_\sigma^\alpha \Delta\sigma(\tau) - K_{\tau_w}^\alpha \Delta\tau_w(\tau)\right) = m_N^\alpha(\tau)\Upsilon^\alpha(\tau) \quad (1)$$

where $K_i^\alpha$ are gain parameters controlling sensitivity to changes in stress $\Delta\sigma$ and $\Delta\tau_w$. These are summarized by the stimulus function $\Upsilon^\alpha$. Constituent removal is modeled by

$$q^\alpha(s,\tau) = \exp\left(-\int_\tau^s k_o^\alpha \left(1 + \omega\left(\Delta\sigma(t)\right)^2\right) dt\right) \quad (2)$$

where $k_o^\alpha$ is the basal removal rate and $\omega > 0$ is a gain parameter for stress changes. Lastly, the Cauchy stress at the tissue (mixture) level $\boldsymbol{\sigma}$ is described with passive contributions from each constituent along with an active stress $\boldsymbol{\sigma}^{act}$ from the smooth muscle cells

$$\boldsymbol{\sigma}(s) = -p(s)\mathbf{I} + \frac{2}{J(s)}\mathbf{F}(s)\frac{\partial W_R(s)}{\partial \mathbf{C}(s)}\mathbf{F}^{\mathrm{T}}(s) + \boldsymbol{\sigma}^{act}(s) \quad (3)$$

where $p$ enforces isochoric (transient) motion, $\mathbf{F}$ is the deformation gradient tensor for the tissue, $\mathbf{C} = \mathbf{F}^{\mathrm{T}}\mathbf{F}$, $J = \det \mathbf{F}$, and $W_R = \sum W_R^\alpha$ is the total (referential, with subscript $R$) stored energy of the mixture.

*Mechanobiologically equilibrated constrained mixture model*

In cases of TAA, where the characteristic timescale of G&R is frequently shorter than that of the biomechanical stimulus (e.g., elastin degradation or compromised collagen remodeling along with gradual hypertension or aging), G&R can be assumed to reach a quasi-static mechanobiological equilibrium at time $s$, thus allowing for a time-independent approach in which production balances removal $\forall s$. In particular, the stimulus function in Eq. 1 reduces to

$$\Upsilon_h^\alpha(\Delta\sigma_h, \Delta\tau_{wh}) = 1 \quad (4)$$

with $h$ denoting the evolved homeostatic state. This assumption allows for rule-of-mixtures expressions to be used for stored energy ($W_{Rh} = \sum \phi_{Rh}^\alpha \widehat{W}^\alpha$, where $\phi_{Rh}^\alpha$ are the referential constituent mass fractions) and

similarly Cauchy stress. Linearization of this formulation has been implemented in a finite element framework [1].

*Modeling TAA growth from prescribed mechanobiological insults*

Five types of contributors to TAAs are considered in this model: loss of elastic fiber integrity, compromised collagen cross-linking, dysfunctional smooth muscle contractility, loss of mechanosensing, and loss of mechanoregulation. Aneurysms were initiated by prescribing a localized insult in an individual predisposing factor onto an initially straight cylindrical vessel, with *in-vivo* geometric and mechanical properties derived from our previous studies [2]. Specifically, we modeled an insult defined in the $z_o$-$\theta_o$ (i.e., axial-azimuthal) plane by

$$\vartheta(z_o,\theta_o) = \vartheta_{end} + (\vartheta_{apex} - \vartheta_{end}) \exp\left(-\left|\frac{z_o - l_o/2}{z_{od}}\right|^{\nu_z}\right) \exp\left(-\left|\frac{\theta_o - \pi}{\theta_{od}}\right|^{\nu_\theta}\right) \quad (5)$$

where $z_o \in [0, l_o]$, $l_o$ is the initial axial length (15 mm), $\theta_o \in [0,2\pi]$, $z_{od}$ and $\theta_{od}$ are the axial and circumferential characteristic widths of the insult profile, respectively, $\nu_z$ and $\nu_\theta$ are decay parameters in the axial and circumferential directions, respectively, and $\vartheta_{end}$ and $\vartheta_{apex}$ are the values of the insult at the ends of the cylinder ($z_o = 0, l_o$) and the apex ($z_o = l_o/2$, $\theta_o = \pi$) of the profile, respectively.

We employed a 3D finite element model with 1x20x20 quadratic hexahedral elements in the radial, circumferential, and axial directions. Displacement of the vessel ends was fixed in the axial direction, and the vessel was pressurized and axially (pre-)stretched uniformly. The open-source software FEBio (febio.org) was used to perform the simulation and evaluate key biomechanical metrics related to aortic health such as stored energy and material stiffness. We also compared final remodeled states between insults applied uniformly throughout the geometry, axisymmetrically (variation along $z_o$ only), and asymmetrically (Eq. 5).

## RESULTS

For each of the factors considered, insult values ranging from mild to severe were simulated, all of which led to significant dilations of the vessel when applied nonuniformly. In Figure 1 we show the aneurysmal geometries and final stored energy resulting from mild and severe insults in elastic fiber integrity (analogous to a loss of functional elastin) and mechanosensing (representing an impaired ability of cells to sense changes in intramural stress).

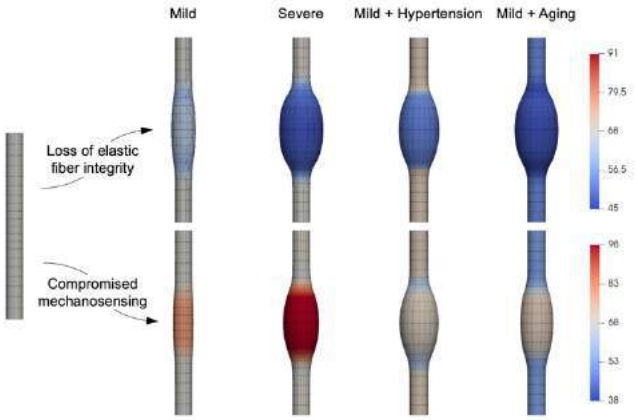


**Figure 1: Stored energy (kPa) for axisymmetric insults: (top) loss of elastic fiber integrity, (bottom) compromised mechanosensing; (left to right) mild, severe, mild + hypertension (1.5-fold pressure increase), mild + aging (30% uniform loss of functional elastin).**

In both cases, the location of the maximal change in stored energy coincides with the region of maximal dilatation; however, the two insults result in opposite trends in stored energy within the insult region, consistent with the stretching of compromised or functional elastic fibers. Additionally, each factor was modeled in combination with superimposed hypertension (increased blood pressure) or aging (diffuse loss of functional elastin), emphasizing how even a mild insult with modest dilatation can be exacerbated by the presence of risk factors.

Comparison of uniform, axisymmetric, and asymmetric insult profiles in Figure 2 highlights the importance of localized wall damage in aneurysm formation, where insults of the same value applied uniformly maintain their non-aneurysmal geometry. In the asymmetric cases, without total circumferential involvement of insult, the unaffected regions attenuate dilatation in the insult area, necessitating greater insult values to produce effects similar to the axisymmetric case.

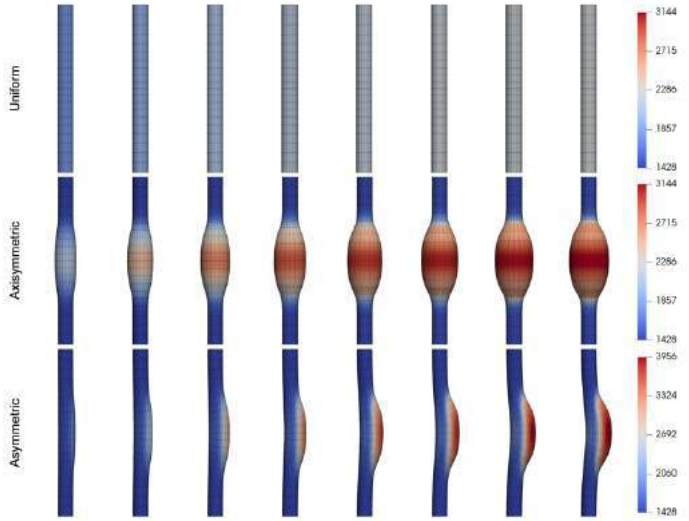


**Figure 2: Circumferential stiffness (kPa) for uniform, axisymmetric, and asymmetric losses of elastic fiber integrity from mild (left, 32%) to severe (right, 62–78%).**

## DISCUSSION

Herein we have presented an *in-silico* study on the effects of multiple combined predisposing and risk factors on the initiation and development of TAAs, demonstrating the feasibility of the model to capture a wide range of insult types and severities (Fig. 1) that can offer mechanistic insight into experimental findings. The progressive dilatation from mild to severe insults shown in Figure 2 provides an illustrative evolution of disease, in which an initially moderate loss of elastic fiber integrity progressively worsens, allowing this model to be easily parametrized for future longitudinal animal and clinical studies.

Ultimately, with increased *in-vivo* and *ex-vivo* data becoming available for human lesions, as well as the ability to couple tissue-level finite element models to cellular-level genetic models, we aim to further improve the applicability of such *in-silico* platforms to better inform the treatment of TAAs.

## ACKNOWLEDGEMENTS

National Institutes of Health (P01 HL134605, U01 HL142518, and R01 HL146723) to JDH.

## REFERENCES

[1] Latorre, M et al., *PLOS Comput Biol*, 16(10): e1008273, 2020.
[2] Bersi, MR et al., *Hypertension*, 67(5): 890–896, 2016.

SB³C2022
Summer Biomechanics, Bioengineering and Biotransport Conference
June 20-23, Eastern Short, MD, USA

# DESIGN AND HEMODYNAMIC PERFORMANCE OF A FETAL VALVE PROTOTYPE DESIGNED FOR IMPLANTATION *IN UTERO*

**Sanchita S. Bhat (1), Hieu T. Bui (1), Anna Farnan (1), Christopher K. Breuer (2), Aimee K. Armstrong (3), Lakshmi Prasad Dasi (1)**

(1) The Wallace H. Coulter Department of Biomedical Engineering
Georgia Institute of Technology
Atlanta, GA, USA

(2) Department of Pediatric Surgery
Nationwide Children's Hospital
Columbus, OH, USA

(3) The Heart Center
Nationwide Children's Hospital
Columbus, OH, USA

## INTRODUCTION

Single ventricle heart disease is a rare type of congenital heart defect affecting about five out of 10,000 newborns [1]. Traditionally, this is surgically palliated in three stages. Despite these procedures, the morbidity and mortality are high, and most will require heart transplantation [2]. Some fetuses with developing single ventricle heart disease are candidates for percutaneous transcatheter balloon valvuloplasty of the pulmonary valve or aortic valve in an attempt to prevent the development of hypoplastic right or left heart syndrome, respectively [3]. If the fetal intervention prevents single ventricle disease, the prognosis is thought to be improved, but the pulmonary or aortic valve ultimately needs to be replaced as restenosis or regurgitation develops. If this is done in childhood, the prosthetic valve often requires replacement due to somatic growth of the child, as well as degeneration of the valve, which can be hastened in a growing child. For instance, the average time to a second right ventricular to pulmonary artery valved conduit replacement in a child is 7.5 years [4].

A bioresorbable tissue-engineered heart valve (TEHV) that could be replaced by the patient's own tissue could allow the valve to grow with the patient and could preclude the need for multiple valve replacements during a patient's lifetime. The goal of a resorbable valve is for the tissue-engineered scaffold to serve as a template to direct tissue formation. As the scaffold degrades, the neotissue forms, ultimately creating a living autologous valve.

The central hypothesis driving this project is that a biodegradable TEHV will normalize the fetal hemodynamics in a way that the complexity and severity of the congenital heart defect formation may be mitigated or even eliminated. Further the highly regenerative potential of fetuses may serve as the perfect host and timing for intervention such that the neovalve takes over the function as a normal heart valve with the capacity to grow. Recent advancements from our group have demonstrated the efficacy of a fully resorbable fetal TEHV design [6] with the help of a fetal ovine model [5]. Due to the transcatheter nature of this valve deployment, the procedure may not be riskier than a traditional fetal valvuloplasty. However, restoration of normal valve function in utero holds the potential to restore biventricular anatomy and function.

## METHODS

**Valve design manufacturing.** We scaled down our adult valve design (after numerous computational simulations to establish an optimized design) to a fetal size of 5mm. A 2D drawing was developed from this 3D CAD design in order to laser-cut this design. A tube made of Cobalt-Chromium, specifically the L605 alloy (Vascotube, GmbH, Birkenfield, Germany) was used in this process. The stent was cut using an OPTEC Femtosecond laser (Optec Laser Group, Frameries, Belgium). To manufacture biodegradable resolvable leaflets, we created 0.75% wt/vol solutions of polycaprolactone (PCL) (Mn = 80,000 Da) (Sigma-Aldrich, St. Louis, MO) in chloroform. We used an in-house spray method to cast leaflets onto the laser cut stent prototype using 1.2mL of PCL solution.

**Valve testing.** A custom fetal flow loop was constructed to mimic right heart conditions. The flow loop consisted of a reservoir to simulate atrial function, a bladder pump controlled by compressed air that acted as the ventricle, a mechanical valve acting as a tricuspid valve and a pulmonary valve test chamber with a diameter of 7.5 mm, where the prototyped valve was deployed. A compliance chamber was connected in series with a resistance valve to simulate the compliance and resistance of the great arteries. The valve was tested in a working fluid of 60/40 water/glycerin (99% pure glycerin) at 0.5 L/min (cardiac output), 140 beats per minute (heart rate), 70/45 mm Hg (peak systolic/diastolic pulmonary artery pressure) for 100 consecutive cardiac cycles. Transvalvular pressure gradient (PG), regurgitation fraction (RF) and effective orifice area (EOA) were evaluated from this setup.

**Leaflet degradation studies**. Homogenous and heterogenous films were cast using the 0.75% wt./v. PCL/chloroform solution. Dried samples underwent accelerated degradation testing using a high-pH solution to understand the natural degradation of the PCL polymer. Samples were weighed to take the pre-degradation mass and then rinsed in dH2O. The samples were then submerged in 8M sodium hydroxide solution at room temperature. Samples were removed from the solution after 20, 30, 40, 60, 120 and 150 minutes. The sample films were rinsed in dH2O and placed in the oven to dry. Pre-degradation masses were

compared to the measurements taken after the samples dried to determine the remaining mass.

## RESULTS

**Valve design and manufacturing.** We successfully manufactured the valve stent from a 5mm tube of cobalt-chromium with our in-house adult stent design (as shown in Figure 1). The PCL was cast onto the laser cut stent and a trileaflet prototype was developed.

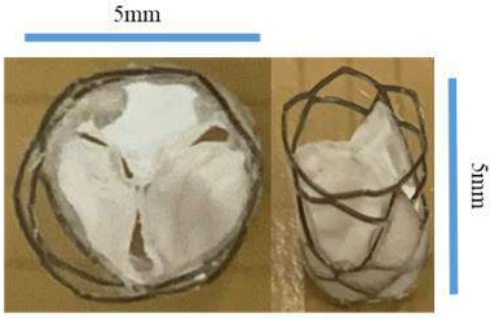


**Figure 1: Trileaflet fetal valve prototype**

**Valve testing.** Our prototype fetal valve was tested for 100 consecutive cardiac cycles in the fetal pulmonic conditions described in the methods. The valve had a regurgitant fraction of 3.9% with an effective orifice area (EOA) of 0.18 $cm^2$ and a mean transvalvular pressure gradient of 3.84mmHg, as shown in Figure 2. These values are in line with our previous studies and also show that the design and setup are robust, able to be tuned to varied fetal conditions.

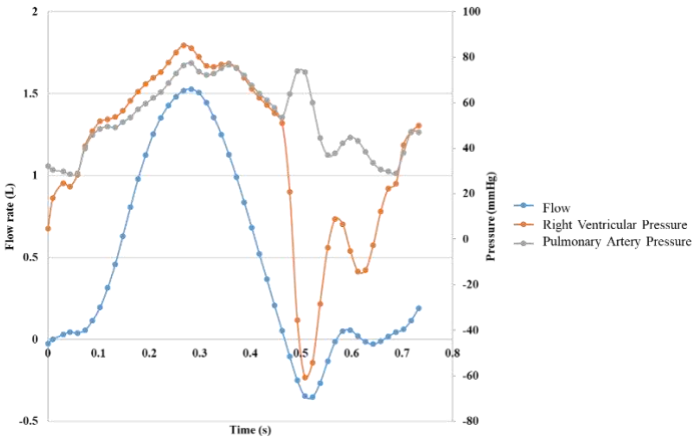


**Figure 2: Valve prototype performance characteristics**

**Leaflet degradation studies.** Our preliminary results did not show any significant differences in the 20 - 40 minute treatments, but we are currently running studies for the longer time periods in order to observe and document significant differences.

## DISCUSSION

This project is the first step to design, develop, and manufacture a fully biodegradable tissue-engineered valve for use *in utero.* Our current prototype, although developed from a non-resolvable metal alloy, provided the basis for design development and modifications. Our next iterations in the project will be using completely resolvable metal alloys. The current drawback in the lack of interventional techniques for cardiac anomalies can be overcome with the progress of such a replacement device. By establishing an in-house sutureless design, we are potentially alleviating the diastolic stresses on the leaflets and, therefore, premature failure of the device.

The ability to replace a stenotic fetal heart valve with a living autologous TEHV could, for the first time, enable the creation of a truly curative strategy for the complex cardiac anomalies that cause single ventricle physiology.

## ACKNOWLEDGEMENT

Funding is provided by Additional Ventures.

## REFERENCES

[1] Heaton J et. al, *Single Ventricle*, July 2018.
[2] Khairy P et.al, *Circulation*,117(1):85-92, 2008
[3] Guseh SH et. al, *Prenat Diagn*. 40(4):415-423, 2020
[4] *Huygens et. al, Annals of Thoracic Surg. 107(6):1845-1853, 2019*
[5] Zakko J et. al, *JACC Basic Transl Sci* 5(8):815-828, 2020
[6] Hatoum H et. al, *Ann Biomed Eng.*48(6):1683-1693, 2020

# PREDICTING VALVE PERFORMANCE USING LOGISTIC REGRESSION

**B. Vogl (1), Y. Darestani (2), J. Crestanello (3), B. Lindman (4), M. Alkhouli (3), H. Hatoum (1,5)**

(1) Biomedical Engineering Department, Michigan Technological University, Houghton, MI, USA
(2) Department of Civil, Environmental and Geospatial Engineering, Michigan Technological University, Houghton, MI, USA
(3) Department of Cardiovascular Medicine, Mayo Clinic, Rochester, MN, USA
(4) Structural Heart and Valve Center, Division of Cardiovascular Medicine, Vanderbilt University Medical Center, Nashville, TN, USA
(5) Health Research Institute, Center of Biocomputing and Digital Health and Institute of Computing and Cybernetics, Michigan Technological University, Houghton, MI

## INTRODUCTION

Aortic stenosis (AS) is one of the major causes of mortality, and its prevalence is estimated to increase in the next few years among the aging population. Bioprosthetic aortic valve replacement (AVR) procedures are currently the most efficient widely used approaches for aortic stenosis. AVR involves surgical aortic valve (SAV) replacement (SAVR) and transcatheter aortic valve (TAV) replacement (TAVR). While SAVR is highly invasive, TAVR is a less invasive therapy that recently has been approved for low-risk patients.

Although SAVR and TAVR procedures are effective, they are associated with adverse outcomes such as restenosis due to short durability, thrombus formation, coronary obstruction, among others. Several studies tried to predict (clinically, computationally, and experimentally) valve performance and implantation. For example, Yanagisawa et al.[1], through a clinical study, identified balloon-expandable valves as predictors of leaflet thrombosis. Simonato et al.[2] suggested that sub-annular deployments after TAVR are predictors of elevated pressure gradients. Hatoum et al.[3] derived a semi-empirical model to predict thrombus formation.

Despite the aforementioned efforts, a statistical model that can numerically estimate valve performance (without running extensive computational or experimental assessments) is still lacking. In this study, we aim to generate a data driven statistical predictive model based on experimental in-vitro data for valve performance (transvalvular pressure gradient (DP)) under different physiological conditions such as heart rate (HR) and blood pressure through the usage of a logistic regression method. The goal of this work is to provide a model where valve performance under different physiological conditions can be conveniently estimated using a simple equation obtained from logistic regression.

## METHODS

The hemodynamics of a 25mm Magna Ease (Edwards Lifesciences, Irvine, CA) SAV and a 23mm SAPIEN 3 (Edwards Lifesciences, Irvine, CA) TAV were assessed under different HRs, a constant cardiac output (5L/min), and systolic and diastolic blood pressure conditions (SBP and DBP, respectively) in a duplicating left heart simulator.

The left heart simulator consists of: (1) a reservoir where the blood analog (water/glycerin mixture 60 – 40% by volume) with properties similar to blood (density of 1060kg/m$^3$ and a kinematic viscosity of 3.5 cSt) was used, (2) a mechanical valve emulating the role of a mitral valve, (3) a custom-made bladder pump connected to compressed air and regulated by an in-house developed LABVIEW program, (4) an aortic valve chamber where the valves were deployed, (5) a compliance chamber, and (6) a resistance valve to control the flow rate. The pressure measurements were obtained using Millar Catheters (ADInstruments Inc., Colorado Springs CO) at the ventricular and aortic pressure ports. Instantaneous cardiac cycles of flow rate, aortic and ventricular pressures were collected and recorded at a sampling rate of 100 Hz for each condition (1,924 total cycles). In this study, we are looking at the DP to measure the performance of the valve.

Our reasoning is based on the fact that the performance of an aortic valve is affected by the output being greater or lower than a threshold such as stenosis criteria[4]. For such cases, the performance of the valve could be enumerated by a binary (0 or 1) event where 1 indicates the event of failure and 0 indicates the event of survival. The recommendations on the echocardiographic assessment of aortic valve stenosis define mild aortic stenosis as DP>20mmHg[4]. Therefore, DP values greater than 20mmHg indicate a failure event (1) in the valve, while values less than 20mmHg indicate a survival event (0) in the heart valve. For such binary events, when enough experimental or empirical data are available, a logistic regression model could be employed to estimate the probability of failure in the heart valve as a function of hemodynamic conditions of the valve. In this study, we employed logistic regression on a total of 1,924 input data for the conditions listed in Table 1, for each valve. The outputs were the probabilities of having

a DP, exceeding 20mmHg. The logistic regression model is computed using MATLAB.

To test the accuracy of the model with the original data that the logistic model was obtained from, one may have hardship in comparing probabilities with binary values. Since these probabilities cannot be directly compared with Zero and One values, a discrimination threshold is chosen such that any probability lower than the threshold is considered as Zero and any probability larger than the threshold is considered as One. To do so, in statistics, a confusion matrix is introduced.

| Valve | Cardiac Output (L/min) | Heart Rate (bpm) | Blood Pressure (mmHg) |
|---|---|---|---|
| 25 mm Magna Ease | 5 | 60, 120 | 100/60 |
| | | | 120/60 |
| | | | 140/60 |
| | | | 160/60 |
| | | | 180/60 |
| | | | 120/40 |
| | | | 120/60 |
| | | | 120/80 |
| | | | 120/90 |
| | | 60, 90, 120 | 100/80 |
| | | | 120/80 |
| | | | 140/80 |
| | | | 140/40 |
| | | | 140/60 |
| | | | 140/80 |
| | | | 140/100 |
| 26 mm SAPIEN 3 | | 60, 120 | 100/60 |
| | | | 120/60 |
| | | | 140/60 |
| | | | 160/60 |
| | | | 180/60 |
| | | | 120/40 |
| | | | 120/60 |
| | | | 120/80 |
| | | | 120/90 |
| | | 60, 90, 120 | 100/80 |
| | | | 120/80 |
| | | | 140/80 |
| | | | 140/40 |
| | | | 140/60 |
| | | | 140/80 |
| | | | 140/100 |

**Table 1. List of experimental conditions used for each valve.**

A logistic model that results in more true Ones and true Zeros and less false Ones and false Zeros are more accurate[5]. Commonly, to test the accuracy of the logistic model using confusion matrix, a discrimination threshold of 0.5 is selected, providing bias in the evaluation[8]. To eliminate this bias, in statistics, a receiver operation characteristics (ROC) curve is used. ROC curves plot the Sensitivity versus the Specificity. To estimate the accuracy of the logistic model, the area under the ROC curve (AUC) is measured. AUC ranges from 0 to 1. The closer it is to 1, the better the performance of the logistic model is. In this study, ROC curves were adopted to test the accuracy of the logistic regression models. Additionally, we performed experiments at SBP conditions that were not input in the model (110/80 mmHg and 130/80 mmHg) for both valves, collected 57 cardiac cycles for each, and compared the probabilities of DP>20mmHg between the experiment and the model.

## RESULTS

Based on the employed logistic regression model, the probability of DP>20mmHg in the valve follows the following equation (1):

$$P(DP > 20\text{mmHg}) = \frac{1}{1+\exp[-(a_0+a_1\times HR+a_2\times SBP+a_3\times DBP)]} \quad (1)$$

where $a_0$, $a_1$, $a_2$, and $a_3$ are the regression coefficients for linear log odds. The estimated values for each of these coefficients are provided in **Table 2.**

| Valves | Output | a0 | a1 | a2 | a3 | AUC |
|---|---|---|---|---|---|---|
| SAPIEN 3 | Pressure Gradient (DP) | -21.1905941 | -0.024493659 | 0.054906659 | 0.189990387 | 0.947 |
| | P-Value | N/A | 1.14E-10 | 3.33E-26 | 3.15E-76 | |
| Magna Ease | Pressure Gradient (DP) | -15.83684824 | -0.028063161 | 0.047635196 | 0.109735857 | 0.905 |
| | P-Value | N/A | 2.87E-09 | 1.19E-07 | 2.27E-33 | |

**Table 1. Parameters of SAPIEN 3 and Magna Ease logistic regression model (Eq 1). AUC denotes Area under the curve of the ROC curve. A p-value less than 0.05 is considered to be significant.**

**Figure 1** shows the 3D map contour of the probability of DP>20 mmHg for the SAPIEN 3 (A) and Magna Ease (B). In both models, for both valves, the AUC was found to be close to 1 (>0.90) (**Table 2**), and the p-values for each of the input parameters were < 0.05 (**Table 2**), indicating that each input variable (HR, SBP and DBP) significantly influences the results. The contours in **Figures 1** were plotted at HR = 60bpm. The figures show that at a specific SBP, increasing the diastolic pressure will lead to an increase in the probability of DP>20mmHg for both valves, which is consistent with the experimental data used. The logistic model presented in Eq. (1) also allows us to estimate the probability of DP>20mmHg for any other pressure condition. For instance, we can now obtain a probability for any DBP, SBP, and HR between those used For Eq. (1). In Eq. (1), HR values are valid between 60 and 120 beats per min, SBP values are valid between 100 and 180 mmHg, and DBP are valid between 40 and 100 mmHg. The experiments performed with 110/80 mmHg and 130/80 mmHg showed probabilities that agreed with the values obtained with the generated model.

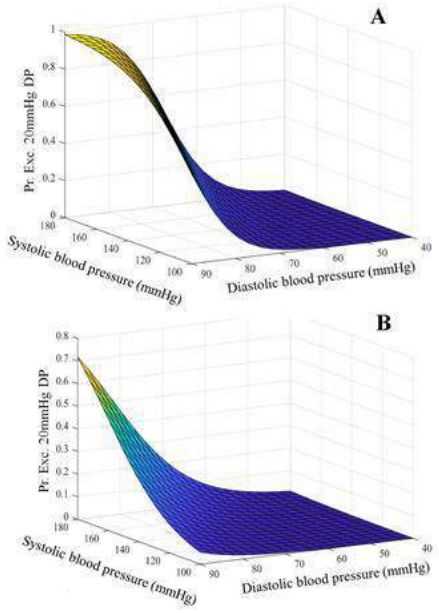


**Figure 2. Logistic regression plot of the SAPIEN 3 (A) and Magna Ease (B) shown in a 3D map contour format.**

## DISCUSSION

In this proof-of-concept study, we generated a probabilistic model that estimates the probability of a hemodynamic output (average DP) under different heart rates and blood pressure conditions (systolic and diastolic). The model was obtained based on logistic regression, and the results suggest that a logistic model with linear log odds function offers a good fit to the data. The importance of this model lies within its ability to quickly obtain an estimate of the hemodynamic parameters pertaining to the performance of aortic valves and to help in preprocedural clinical decision-making. Any testing condition within the limits of the input range based on which the model was generated can be interpolated. The model up to this point does not include numerous cardiac outputs or patient-specific variability in terms of various geometries and dimensions as previously mentioned. However, ongoing studies using clinical data aim at refining it. It should be also noted that the output parameters can be expanded to include a variety of desired outputs given enough experimental data are provided.

## REFERENCES

[1] Yanagisawa R, JACC Card. Img., 8:S1936-878X(16)30897-X, 2016
[2] Simonato M, Circ Cardio. Interv., 9(6):e003651, 2016
[3] Hatoum H, J am Coll Cardiol, 7(18):3405, 2021
[4] Baumgartner H, Eur Heart J Cardiovasc Img., 18(3):254-275, 2017
[5] Darestani Y, J. Perf. of Construct. Facilit., 35(16): 04021088, 2021

# PREDICTION OF ANALOG THROMBI MECHANICAL PROPERTIES, COMPOSITION, AND CONTRACTION USING COMPUTED TOMOGRAPHY IMAGING

**Janneke M.H. Cruts* (1), Jo-Anne Giezen* (2), Kim van Gaalen (1), Robert Beurskens (1), Yanto Ridwan (3,4), Marcel L. Dijkshoorn (3), Heleen M.M. van Beusekom (1), Nikki Boodt (3, 5, 6), Aad van der Lugt (3), Frank Gijsen (1,2), Rachel Cahalane (1)**

(1) Department of Biomedical Engineering, Erasmus Medical Center, Rotterdam, the Netherlands
(2) Department of Biomechanical Engineering, Delft University of Technology, Delft, the Netherlands
(3) Department of Radiology and Nuclear Medicine, Erasmus Medical Center, Rotterdam, the Netherlands
(4) Department of Molecular Genetics, Erasmus Medical Center, Rotterdam, the Netherlands
(5) Department of Neurology, Erasmus Medical Center, Rotterdam, the Netherlands
(6) Department of Public Health, Erasmus Medical Center, Rotterdam, the Netherlands

*Authors contributed equally

## INTRODUCTION

Endovascular thrombectomy (EVT) was recently proven to be an effective and safe treatment for a subset of patients with acute ischemic stroke (AIS) and is now the standard of care. However, improvement is needed since this treatment is not effective in 41% of the patients [1]. Studies on thrombi retrieved with EVT found that the main components are red blood cells (RBCs), fibrin, platelets, and white blood cells, and that the thrombus composition is an important factor influencing successful recanalization [2]. The exact reason for this is unknown, but it has been postulated that the thrombus composition and platelet-driven thrombus contraction affects the mechanical properties of thrombi, which in turn influences the interaction with the thrombectomy device [3, 4]. A pre-interventional estimation of the mechanical properties is hypothesized to aid in selecting the most suitable treatment on a case-by-case basis to improve success rates.

Computed Tomography (CT) imaging is the most commonly used imaging modality for diagnosis of AIS and could therefore potentially be useful in predicting the mechanical properties, composition, and contraction of cerebral thrombi [5]. While a link between mechanics and thrombus composition, as well as radiological imaging characteristics and thrombus composition have been determined, the direct relationship between thrombus mechanics, imaging characteristics, composition, and contraction has not been examined before [6].

## METHODS

Blood was drawn by venipuncture from four healthy human volunteers. Twenty thrombus analogs per donor were made by reconstituting the platelet rich plasma and RBCs in five different volumetric RBC percentages: 0%, 20%, 40%, 60% and 80%. To assess the extent of thrombus contraction, the weight of each thrombus was measured and expressed as a percentage of the weight of the original clotting mixture [4].

To determine the mechanical properties, unconfined compression tests were performed using a custom made compression tester [7]. For this, the thrombi were cut into 2 mm slices. The samples were 80% compressed, with a compression and retraction speed of 0,2 mm/s (10% strain/s). As a measure for the stiffness, the low strain (approximately initial 20%) and high strain (approximately final 2%) secant moduli were measured from the slopes of fitted straight lines of the non-linear nominal stress-strain curves [4].

Clinical CT was used to determine the thrombus imaging characteristics. First, a non-contrast computed tomography (NCCT) was made to study the density. Subsequently, an iodinated contrast agent was added and scans were made 5, 10, 15, and 20 minutes after administering the contrast in order to study the perviousness, which reflects the permeability of a thrombus. In each scan, three non-overlapping regions of interest with 1 mm diameter were defined in each thrombus, of which the mean density was measured in ImageJ [8].

The composition of the thrombi was analysed using histology. Hemotoxylin and Eosin (H&E) stain was used to identify the percentage of RBCs using Orbit Image Analysis software.

Spearman correlation tests and two-way ANOVA tests were performed to determine the relationship between the four thrombi characteristics. Within one thrombus composition group, t-tests were performed to assess differences in density between NCCT and contrast-enhanced CT imaging. A p-value lower than 0.05 was considered statistically significant.

## RESULTS

Figure 1 shows the histological results. Composition analysis showed that the initial volumetric RBC ratios of the clotting mixture of 0%, 20%, 40%, 60% and 80% produced thrombi with non-equivalent compositions of 0.0%, 91.0%, 93.5%, 95.1%, and 97.9% RBCs, respectively. This indicates that only 0% RBC and RBC-rich thrombi (>90% RBC) were produced.

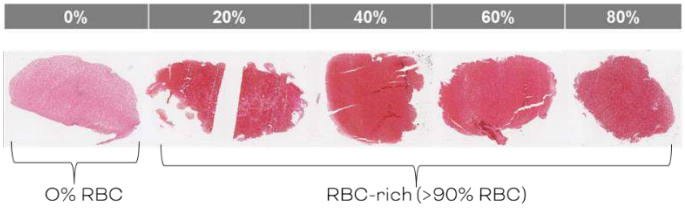


**Figure 1: Representative thrombus samples of the five volumetric RBC percentages of the clotting mixture, with resulting thrombus RBC content indicated at the bottom.**

Figure 2A and B show the thrombus mechanical properties. The mechanical tests showed that the low and high strain secant moduli decreased with increasing RBC content of the clotting mixture: e.g. for donor 1 we measured a high strain of 264, 84, 72, 27, and 13 kPa for increasing RBC content of the clotting mixture. Furthermore, a large variation between donors for thrombi with comparable composition was observed.

Figure 2C shows the results of the contraction measurements. A strong positive linear relationship was found between the degree of contraction and the volumetric RBC ratio of the clotting mixture ($r=0.98$, $p<0.001$). Furthermore, the relationship between the high strain stiffness and degree of contraction was observed, for which a strong negative correlation was found ($r=-0.68$, $p=0.006$).

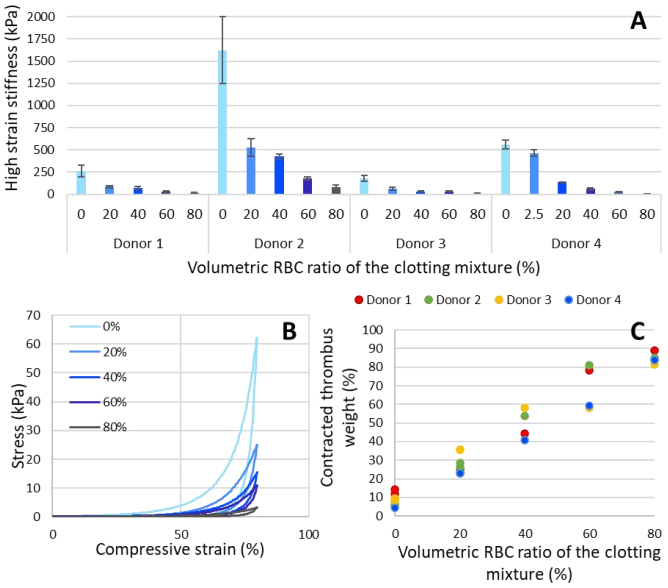


**Figure 2: Thrombus mechanics and contraction properties. (A) High strain stiffness of the five volumetric RBC ratios of the clotting mixture of the four donors. (B) Representative stress-strain loading and unloading curve for the five compositions. (C) Relative contracted thrombus weight (i.e. degree of contraction) per volumetric RBC ratio of the clotting mixture for the four donors.**

Figure 3 shows the CT imaging characteristics. On NCCT, the 0% RBC thrombi had a mean density of 34 HU, which was found to be significantly lower in density compared to the RBC-rich thrombi with a mean density higher than 78 HU ($p<0.001$). The increase in density, the perviousness, was significantly higher for the 0% RBC sample compared to the RBC-rich thrombi compositions after 10, 15, and 20 minutes ($p=0.002$, $p=0.001$, $p=0.005$).

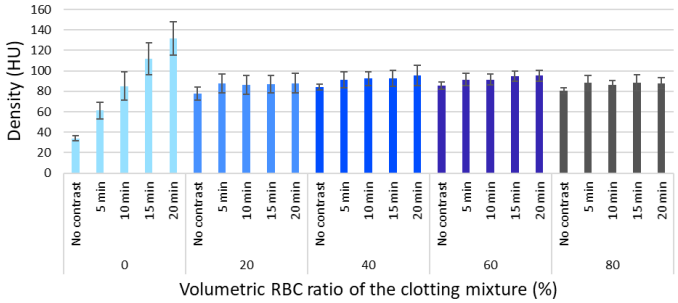


**Figure 3: Mean thrombus densities on NCCT baseline scans and 5, 10, 15, and 20 minutes after contrast administration.**

The relationship between thrombus mechanics (high strain stiffness), thrombus imaging characteristics (NCCT density and density increase after 20 minutes), and resulting thrombus RBC content was analysed. Stiffer thrombi were moderately correlated to a lower density and higher perviousness ($p=0.03$ and $p=0.02$, respectively). The density and perviousness were found to be more significantly correlated to the thrombus RBC content (both $p<0.001$).

## DISCUSSION

This is the first study to assess the thrombus mechanics of thrombi in conjunction with an analysis of CT density, contraction, and composition. Strong correlations were found between 1) the compressive high strain stiffness and the volumetric RBC ratio of the clotting mixture 2) the compressive high strain stiffness and the degree of thrombus contraction, 3) the degree of thrombus contraction and the volumetric RBC ratio of the clotting mixture, and 4) the CT density and perviousness, and thrombus RBC content.

Mechanics was not (strongly) associated with the imaging characteristics that were explored in this study, indicating that the thrombus mechanical properties cannot be directly predicted from CT imaging. However, thrombus contraction is hypothesized to be associated with perviousness [8]. Therefore, assessing the perviousness of thrombi and correcting for the RBC content through NCCT density may provide a measure for contraction on pre-interventional imaging. This could be clinically relevant since thrombus mechanics could then be predicted prior to the intervention.

Although the volumetric RBC ratios in the clotting mixture used in this study resulted in either RBC-rich or 0% RBC thrombi, the mechanical properties were different per volumetric RBC ratio. A possible explanation could be a difference in amount of fibrin or the degree of platelet-driven contraction. Future experiments will focus on creating clots with intermediate RBC and fibrin content and different levels of contraction in order to improve the understanding of the differences in mechanics.

## REFERENCES

[1] Jansen, I. et al., *BMJ*, 360: k949, 2018.
[2] Yuki, I. et al., *Am. J. Neuroradiol*, 33: 643–648, 2012.
[3] Johnson S. et al., *Ann. Biomed. Eng*, 45(11): 2494-2508, 2017.
[4] Johnson S. et al., *J. Neurointerv. Surg*, 12(9): 853-857, 2020.
[5] Simons, N. et al.,. *J. Neuroradiol*, 42: 86–92, 2015.
[6] Cahalane, R. et al., *J. Biomech*, 129: 110816, 2021.
[7] Boodt, N., Schauburg, P.R.W.S. Van, et al., *Stroke*, 1-120, 2021.
[8] Benson, J. C. et al., *J Neurointerv Surg*. 12(1):38-42, 2020.

# EFFECT OF AORTIC CURVATURE ON BIOPROSTHETIC AORTIC VALVE PERFORMANCE

**B. Vogl (1), R. Gadhave (1), Z. Wang (2,3), A. El Shaer (4), J. Crestanello (4), M. Alkhouli (4), H. Hatoum (1,5)**

(1) Department of Biomedical Engineering, Michigan Technological University, Houghton, MI
(2) Department of Mechanical Engineering, The Ohio State University, Columbus, OH
(3) Simulation Innovation and Modeling Center, The Ohio State University, Columbus, OH
(4) Department of Cardiovascular Medicine, Mayo Clinic, Rochester, MN
(5) Health Research Institute, Center of Biocomputing and Digital Health and Institute of Computing and Cybernetics, Michigan Technological University, Houghton, MI

## INTRODUCTION

Aortic stenosis (AS) is the most common valvular heart disease in developed countries, and is a major cause of heart failure[1]. A treatment approach for AS can be accomplished by replacement of the diseased valve with a bioprosthetic transcatheter aortic valve or surgical aortic valve. The performance and durability of these bioprosthetic valves have been related to postoperative mean transvalvular pressure gradient (ΔP). Echocardiography (ECHO) and catheterization (CATH) modalities are used to measure ΔP.

Discrepant differences in ECHO- and CATH-based measurements of ΔP have been reported. These discrepancies are a result of the different measurement locations for each modality in the pressure recovery zone. ECHO measurements do not account for pressure recovery unlike CATH measurements. Several attempts have been made (clinically, computationally, and experimentally) to quantify pressure recovery in these geometries and to understand its effect on postoperative ΔP measurements. Attempts have also been made to modify the simplified Bernoulli equation to account for pressure recovery as a function ascending aorta size[2]. Abbas et al.[3] investigated these modifications clinically. Samaee et al.[4] experimentally assessed the effects of the ascending aorta on ΔP by varying its diameter while keeping the annulus fixed. In a computational study by Keshavarz-Motamed et al.[5], pressure recovery in coarcted aortas was simulated in a U-shaped tube.

Despite the aforementioned efforts, pressure recovery assessment of physiological diameter, shape, and three-dimensional curvature of the ascending aorta and aortic arch is still lacking. In this study, we aim to assess pressure recovery in a physiological 3D aortic arch to determine its effects on valve performance and ultimately durability.

## METHODS

A 23mm SAPIEN 3 Ultra (Edwards Lifesciences, Irvine, CA) was hemodynamically assessed in a pulse duplicator left heart flow loop simulator under physiological flow and pressure conditions (cardiac output = 5L/min, heart rate = 60bpm, and systolic to diastolic pressures = 120/80mmHg). Briefly, the pulse duplicator was comprised of a reservoir for fluid storage, a mechanical mitral valve separating the fluid reservoir and pump, a bladder pump whose contraction is controlled by an in-house LabVIEW program, an aortic chamber (with arch and without), a compliance chamber to simulate arterial distensibility, and a gate valve to control the flow. The blood analog fluid used was a mixture of water-glycerin with a density of 1060kg/m$^3$ and a kinematic viscosity of 3.5cSt. Flow rate at the valve was measured using an ultrasound Clamp-on Flowsensor (Transonic Systems Inc., Ithaca, NY).

The rigid aortic chambers had two different geometries, curved and straight, but had the same aortic root dimensions. The curved chamber was designed using a physiological geometry detailed by Boufi et al.[6] Both chamber setups can be seen in **Figure 1**.

All pressure measurements were taken with Millar Pressure Catheters (Millar, Houston, TX). The measurements were made

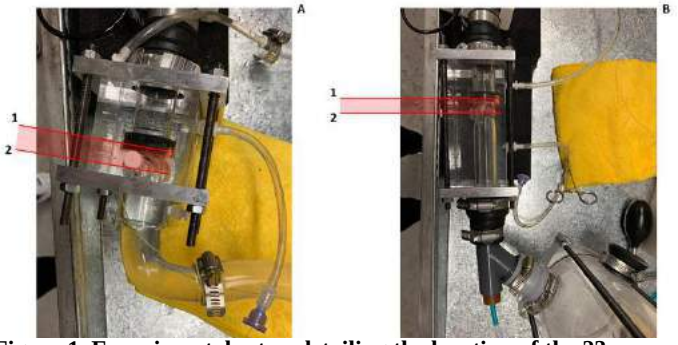


**Figure 1. Experimental setup detailing the location of the 23mm SAPIEN 3 Ultra in the curved (A) and straight (B) aortic root chambers. Locations 1 and 2 represent the valve entrance at 2.1mm and valve limit at 3.9mm, respectively.**

incrementally along the aortic model with intervals of 0.1cm, 0.2cm,

and 0.5cm downstream of the valve, at the valve, and upstream of the valve, respectively. In both models, the position 0cm corresponds to the most upstream measurement (ventricular) and the positions 12.2cm and 19.7cm are the last measurements made in the straight and curved models, respectively. Fifty consecutive cardiac cycles of pressure and flow data were recorded at a sampling rate of 100Hz. The mean pressure measurements were recorded at each incremental increase in catheter position. Peak flow was determined by the time point at which the flow was maximum (peak systole) in the generated curves. The mean transvalvular pressure gradient (ΔP) — defined as the average of positive pressure difference between the ventricular and aortic pressure curves during forward flow — was calculated for both aortic models. Values are presented as mean with standard deviations.

## RESULTS

The pressure measurements as a function of distance at different time points during systole in the curved model are plotted in The peak flow time point (peak systole) occurred at 0.28s into the cardiac cycle. Results from the pressure measurements are plotted starting from upstream (ventricular) of the valve and end downstream (aortic) of the valve. As the valve opens and flow begins, pressure decreases until the vena contracta (VC; 3.7cm). After passing VC, pressure gradually rises until the curvature of the aorta begins (3.7–11.2cm). This rise in pressure marks the beginning of pressure recovery. At the curvature of the aorta, pressure drastically decreases (11.2–14.7cm). After passing the curvature of the aorta (14.7cm), the pressure starts increasing gradually marking the beginning of a second pressure recovery zone. During peak flow, pressure was 118.66±4.49mmHg at the valve entrance, 121.83±4.75mmHg at VC, 129.04±3.86mmHg at the start of the curvature, and 127.852±3.47mmHg after the curvature (final measurement point). The final pressure measurement was taken at 19.7cm and the slope of the pressure curve indicates the pressure will continue recovering past this point.

The pressure measurements as a function of distance at different time points during systole in the straight model are plotted in **Figure 2B**. The peak flow time point (peak systole) occurred at 0.27s into the cardiac cycle. Results from the pressure measurements are plotted starting from the upstream (ventricular) of the valve and end downstream (aortic) of the valve. As the valve opens and flow begins, pressure decreases from the LVOT region until VC (3.1cm). After passing VC, pressure gradually rises (3.1–12.2cm). This rise in pressure marks the beginning of pressure recovery. The final pressure measurement was taken at 12.2cm.

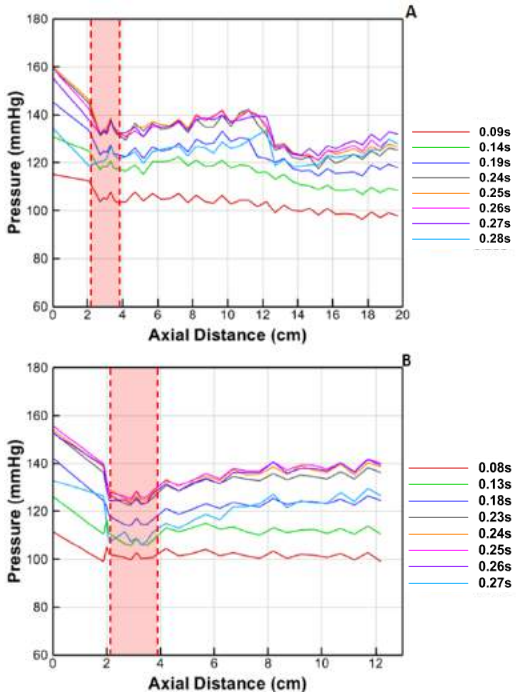


**Figure 2. Variation of pressure as a function of axial distance at the selected time points during systole for curved (A) and straight (B) aortas. The shaded regions represent the location of the valve.**

During peak flow, pressure was 107.04±5.07mmHg at the valve entrance, 108.62±4.05mmHg at VC, and 126.51±2.89mmHg at the final measurement point.

The ΔP as a function of axial distance in the curved model are shown in **Figure 3A**. ΔP is 7.71±1.03mmHg at the valve entrance, 13.08 ±0.27mmHg at VC, 21.15±0.31mmHg before the curvature, and 21.03±0.36mmHg after the curvature (final measurement point).

ΔP vs. axial distance in the straight model are shown in **Figure 3B**. ΔP is 12.08±0.67mmHg at the valve entrance, 17.45±0.41mmHg at VC, and 13.51±0.26mmHg from positions 3at the final measurement point.

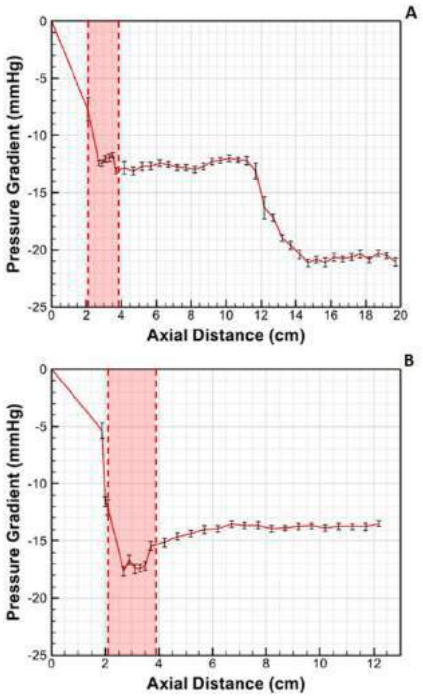


**Figure 3. Mean pressure gradient as a function axial distance with curved (A) and straight aortas (B). The shaded region represents the valve location, and the error bars represent standard deviation.**

## DISCUSSION

In this study, we measured pressure recovery in a physiological aortic arch in-vitro. The resulting pressure recovery curves for the straight model are consistent with those found in other studies[7]. In the curved model, we observed pressure recovery unlike the pattern seen in the straight model. This difference is due to minor losses associated with bending in internal flows. As the fluid passes through the bend, centrifugal forces cause a difference in pressure at the inner and outer bend, causing the formation of a recirculation zone containing Dean vortices[8]. These vortices cause the kinetic energy of the fluid to change, resulting in an energy loss downstream which is represented by pressure loss. Literature reporting ΔP in healthy aortic arch models is limited. However, some studies reported clinically significant pressure gradients in coarcted aorta models at the curvature[5]. This is consistent in our study, where we observe an increase in ΔP of about 9mmHg at the curvature. Clinically, where the catheter is positioned is important to assess accurately the pressure variation or the pressure drop. If the aorta curves where the tip of the catheter is located, the measurement may be influenced and the pressure drop may be overestimated. Based on the ΔP curves of this study, if a catheter measurement is made at the curvature, the resulting ΔP is going to be drastically higher than a measurement made in the recovery zone just after the valve. Ongoing work on other bioprosthetic valves and patient specific models assessing the effect of pressure recovery in the ascending aorta and aortic arch is underway.

## REFERENCES


[1] Nkomo, V et al., *The Lancet*, 368(9540):1005-1011, 2006
[2] Baumgartner, H et al., J Am Coll Cardiol, 33(6):1655-1661, 1999
[3] Abbas, A et al., Circ Cardiovasc Interv, 12(7): e007973, 2019
[4] Samaee, M et al., J Am Coll Cardiol, 77(18):1768-1768, 2021
[5] Keshavarz-Motamed, Z et al., Med Eng Phys, 33(3):315-24, 2010
[6] Boufi, M et al., Eur J Vasc Endovasc Surg, 53(5):663-670, 2017
[7] Hatoum, H et al., Ann Biomed Eng, 48(2):860-867, 2020
[8] Dean, Wo R. The London, Edinburgh, and Dublin Philosophical Magazine and Journal of Science 4.20 (1927): 208-223.

# MECHANICAL AND STRUCTURAL CHARACTERISATION OF THE HUMAN MENINGES AND FALX

**Darragh R. Walsh (1,2,3), David T. Newport (1,2,3), John J.E. Mulvihill (1,2,3)**

(1) Bernal Institute, University of Limerick, Limerick, Ireland
(2) School of Engineering, University of Limerick, Limerick, Ireland
(3) Health Research Institute, University of Limerick, Limerick, Ireland

## INTRODUCTION

The meningeal membrane is a critical composite tissue that protects the central nervous system. The incorporation of the meninges into finite element (FE) models of traumatic brain injury (TBI) is essential to ensure accurate injury prediction. Inaccurate modelling of the meninges can significantly impact FE model results [1]. There is a paucity of studies detailing the mechanical response of the cranial meningeal membrane. In particular, no mechanical analyses have been conducted on the falx cerebri tissue which projects between the two cerebral hemispheres. As a result of the anatomical location of the falx and its relatively large stiffness (approx. 1,000 fold the stiffness of the brain [2]), it is of significant importance when evaluating the mechanopathology of TBI. If efforts are to improve preventative measures of TBI and advance the design of protective equipment, an improved knowledge of meningeal tissue properties is required. Additionally, damage to the meninges is frequently incurred during both traumatic injuries and during surgical interventions [3]. In particular, angioplasty procedures are frequently conducted on the superior sagittal sinus (SSS) vessel of the meninges, with limited knowledge on how this circumferential stretch may damage the structure [4]. The study seeks to address these knowledge gaps by conducting biaxial tensile analysis of the meninges to characterise the tissues' stiffness and evaluating the sensitivity of the SSS structure to the effects of mechanical strain.

## METHODS

7 human meningeal tissues were acquired in collaboration with the Dublin Brain Bank at Beaumont Hospital, Ireland. Specimens from the dura mater, SSS and falx cerebri were prepared for biaxial tensile testing by first cutting specimens into square sections (of approx. 8 – 15 mm length). The thickness of specimens (for post-test stress calculation) was analysed using a noncontact photogrammetry technique [5]. Samples were then speckled in preparation for digital image correlation (DIC) analysis using an ABEST airbrush and a tissue-specific staining dye (Cancer Diagnostics Inc.). Samples were then placed in the biaxial tensile configuration, see Fig. 1 (A). Following 10 preconditioning cycles to 1% strain (preconditioning serves to allow test samples to settle into the testing apparatus and to return the tissue to its in situ stress configuration [6]), samples were stretched to a nominal strain of 20% for biaxial mechanical characterisation.

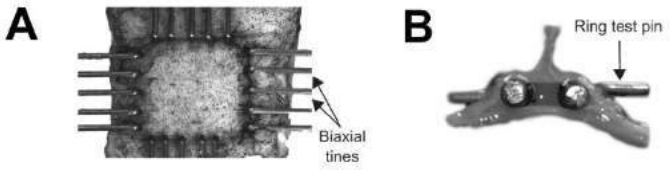


**Figure 1(A) Biaxial tensile setup with Cellscale BioRake system. (B) Ring test setup.**

Specimens from the SSS region were prepared for strain sensitivity analysis using a combination of uniaxial ring testing (to emulate the circumferential stretches the tissue may be subjected to during an angioplasty procedure, see Fig. 1 (B)) and a novel collagen hybridizing peptide (CHP) which enables detection of damaged collagen fibres [7]. Specimens were cut into rings of approx. 3 mm length. DIC was not possible for the SSS rings due to the limited cross-sectional thickness

for speckle application [8]. Samples were subjected to various magnitudes of subfailure stretch prior to structural analysis with CHP. Briefly, CHP analysis involved snap-freezing specimens, cryosectioning specimens into 20 µm sections, staining with CHP and imaging utilising immunofluorescent microscopy. Immunofluorescence images were quantified using CellProfiler software to quantify the extent of CHP binding in acquired images (indicative of the amount of collagenic damage in specimens [7]).

## RESULTS

Specimens from the SSS region were prepared for strain sensitivity analysis using a combination of uniaxial ring testing (to emulate the circumferential stretches the tissue may be subjected to during an angioplasty procedure, see Fig. 1 (B)) and a novel collagen hybridizing peptide (CHP) which enables detection of damaged collagen fibres [7]. Specimens were cut into rings of approx. 3 mm length. DIC was not possible for the SSS rings due to the limited cross-sectional thickness for speckle application [8]. Samples were subjected to various magnitudes of subfailure stretch prior to structural analysis with CHP. Briefly, CHP analysis involved snap-freezing specimens, cryosectioning specimens into 20 µm sections, staining with CHP and imaging utilising immunofluorescent microscopy. Immunofluorescence images were quantified using CellProfiler software to quantify the extent of CHP binding in acquired images (indicative of the amount of collagenic damage in specimens [7]).

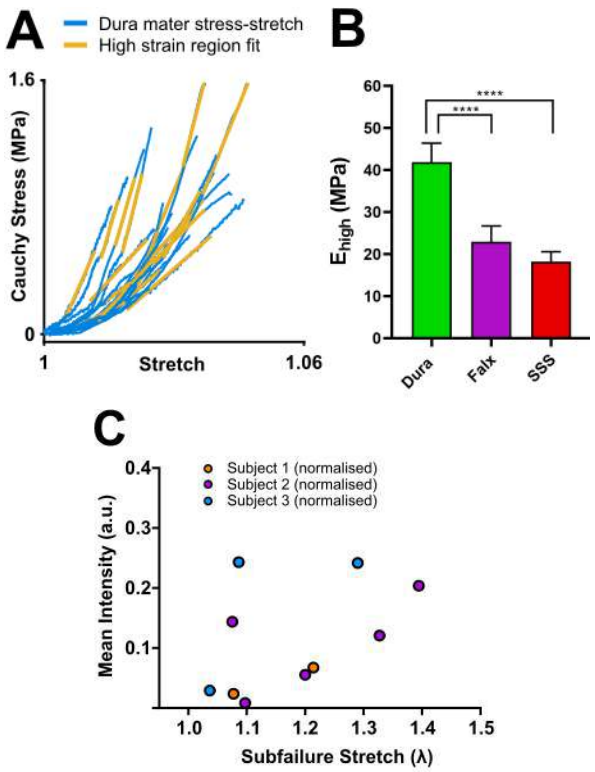


**Figure 2 (A) Stress stretch curves from dura mater region including linear fit for elastic modulus calculation. (B) Linear elastic modulus results. (C) Stretch sensitivity results for 3 human subject SSS tissues.**

## DISCUSSION

These results demonstrate that there are mechanical stiffness differences between the dura mater, falx cerebri and SSS tissues, in contrast to the assumption typically employed in FE head models that these tissues are mechanically homogeneous [2]. These results have important implications for FE head model design (particularly given the mechanopathological influence of these structures [9]) and may aid in improving FE biofidelity through direct implementation of the linear elastic values to head models. It is also demonstrated that the SSS undergoes circumferential strain-mediated damage at a relatively low value of subfailure stretch, at least when compared to cerebral arteries [7]. This finding suggests the structure may be particularly susceptible to angioplasty-mediated damage, which has the potential to induce permanent damage to targeted vessels [7]. Care should thus be taken during clinical procedures involving the SSS structure.


## ACKNOWLEDGEMENTS

Irish Research Council Government of Ireland Postgraduate Scholarship GOIP/2017/1816.

The authors wish to acknowledge Dublin Brain Bank the provision of the issue characterised in this study.


## REFERENCES


[1] Gu, L.X., Chafi, M.S., Ganpule, S., and Chandra, N. The influence of heterogeneous meninges on the brain mechanics under primary blast loading. Composites Part B-Engineering, 2012. 43(8): p. 3160-3166

[2] Ho, J., Zhou, Z., Li, X., and Kleiven, S. The peculiar properties of the falx and tentorium in brain injury biomechanics. Journal of Biomechanics, 2017. 60: p. 243-247

[3] Roth, T.L., Nayak, D., et al. Transcranial amelioration of inflammation and cell death after brain injury. NATURE, 2014. 505(7482): p. 223-8

[4] Teleb, M.S., Cziep, M.E., et al. Stenting and angioplasty for idiopathic intracranial hypertension: a case series with clinical, angiographic, ophthalmological, complication, and pressure reporting. Journal of neuroimaging : official journal of the American Society of Neuroimaging, 2015. 25: p. 72-80

[5] Walsh, D.R., Zhou, Z., et al. Mechanical Properties of the Cranial Meninges: A Systematic Review. Journal of Neurotrauma, 2020

[6] Walsh, M.T., Cunnane, E.M., et al. Uniaxial tensile testing approaches for characterisation of atherosclerotic plaques. Journal of Biomechanics, 2014. 47(4): p. 793-804

[7] Converse, M.I., Walther, R.G., et al. Detection and characterization of molecular-level collagen damage in overstretched cerebral arteries. Acta Biomaterialia, 2018. 67: p. 307-318

[8] Walsh, D.R., Lynch, J.J., O' Connor, D.T., Newport, D.T., and Mulvihill, J.J.E. Mechanical and structural characterisation of the dural venous sinuses. Scientific Reports, 2020. 10(1): p. 21763

[9] Gu, L., Chafi, M.S., Ganpule, S., and Chandra, N. The influence of heterogeneous meninges on the brain mechanics under primary blast loading. Composites Part B: Engineering, 2012. 43(8): p. 3160-3166

SB³C2022
Summer Biomechanics, Bioengineering and Biotransport Conference
June 20-23, Eastern Shore, MD, USA

# THE EFFECTS OF CELL-CELL COOPERATION IN 3D BREAST CANCER SPHEROIDS

**Carolina Trenado (1,2), Celeste M. Nelson (1,3)**

(1) Department of Chemical and Biological Engineering, Princeton University, Princeton, NJ, USA
(2) Lewis Sigler Institute of Integrative Genomics at Princeton University, Princeton, NJ, USA.
(3) Department of Molecular Biology, Princeton University, Princeton, NJ, USA

## INTRODUCTION

Breast cancer (BC) is the most frequent cancer in women and the second-leading cause of cancer deaths worldwide. Breast tumor development is the consequence of cell mutations manifested in the mammary glands that result in uncontrollable proliferation, and other properties such as survival strategies, invasiveness, and metastasis. New studies of cancer development are necessary to predict patient prognosis from the morphology of early-stage tumors and decrease cancer-related deaths. To this end, by taking advantage of 3D engineered culture models and computational models of breast tumors, we establish connections between morphology and dynamics of the primary tumor and cancer progression.

Considering all the above, we study the migratory behaviors and mechanical interactions between cancer cells that arise during tumor development. We also recognize the cellular mechanisms that promote tumor growth, cancer cell invasion, and cell dissemination from the primary tumor [1,2,3,4,5], which are necessary to clarify crucial aspects of cancer development **(Figure 1A**).

To help interpret our experimental findings, we consider a minimal continuum model that incorporates the main mechanisms driving cancer progression and escape.

## METHODS

We engineered 3D tumor spheroids of triple-negative breast cancer (TNBC) 4T1 murine mammary carcinoma cells. We embeebed the 3D spheroids in type I collagen to provide a physiologically relevant microenvironment in which to study cell behavior. Although spheroids can be generated using a variety of experimental techniques [6,7,8,9], we prepared the size-controlled 3D spheroids in agarose microwells. We fabricated PDMS masters with positive circular posts and stamped them on aqueous solution of 2% agarose. After gelation of the agarose, cells were seeded in the microwells and excess cells were removed by washing. Cells began to aggregate within a few hours and formed into spheroids within one day. After four days, we collected the spheroids and embedded them within collagen (**Figure 1B**).

## RESULTS

The 3D tumor spheroids allowed us to examine the dynamics of tumor-like anatomy and physiology. Using agarose microwells, our resultant spheroids were homogeneous in size and with a rounded shape. The size of the spheroids was controlled by the size of the well stamped into the agarose. Between days 4-6 we collected the spheroids and embedded them in collagen to study their growth rate and invasion.

We characterized the dynamical features of migratory response of individual cells within the tumor spheroids and analyzed the mechanical interaction between the cells to determine and

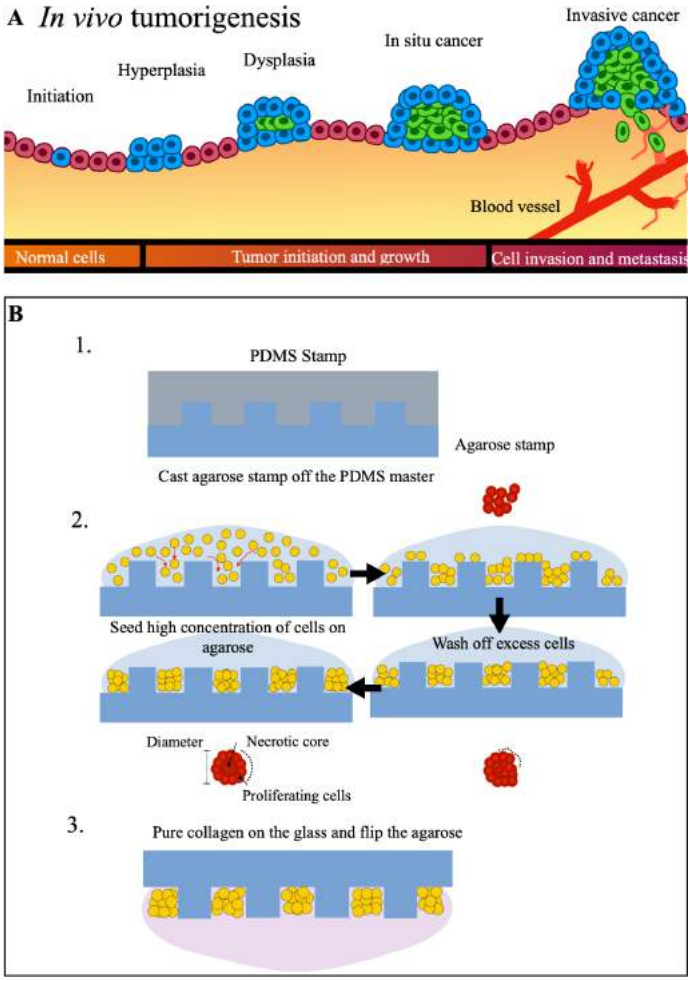


**Figure 1. A. Tumor development. B. Schematic of spheroid formation in agarose microwells.**

predict responses to therapeutic drugs. For this purpose, we studied the spreading of the spheroid by measuring its growth area and the effects of cellular forces. From the theory side, we propose a hydrodynamic active continuum model of the 3D growing tumor as an initial disordered network with embedded cells. We include growth and death, to understand the different types of stages during tumor development.

## DISCUSSION

Using agarose microwells, we were able to reproduce tumor spheroids that can be used to model tumor growth, invasion, and escape. Our approach allowed us to control the size of the spheroid, which is crucial to reproduce and analyze how the development of a tumor depends on its diameter, as well as to analyze how treatment with drugs affects the spheroids.

We investigate the growth rate of the spheroids by monitoring the area and volume over several days. These measurements provided the minimal parameters necessary to model the 3D spheroids using continuum theory. Overall, we performed experiments and simulations to study tumor growth, invasion, and the effects of cell-cell interaction. In addition, given that the mechanical properties of the tumor influence its morphogenesis, we were able to control the structural and shape evolution of the tumor through specific driving protocols that change during tumor growth or that are position-dependent.


## ACKNOWLEDGEMENTS

This work was supported in part by grants from the National Institutes of Health (CA187692, CA214292) and a Faculty Scholars Award from the Howard Hughes Medical Institute.


## REFERENCES


[1] Feng, Y., et al. (2018) Breast cancer development and progression: Risk factors, cancer stem cells, signaling pathways, genomics, and molecular pathogenesis. *Genes & diseases*, *5*(2), 77–106.

[2] Seyfried, T. N., & Huysentruyt, L. C. (2013). On the origin of cancer metastasis. *Critical Reviews™ in Oncogenesis*, *18*(1-2).

[3]Silver B.B., Zhang S.X., Rabie E.M., & Nelson C.M. (2021) Substratum stiffness tunes membrane voltage in mammary epithelial cells. *J. Cell Sci.*, 134: jcs256313

[4]Nerger B.A., Jaslove J.M., Elashal H., Mao S., Kosmrlj A., Link A.J., & Nelson C.M. (2021) Local accumulation of extracellular matrix regulates global morphogenetic patterning in the developing mammary gland. *Curr. Biol.*, 31: 1903-1917.

[5] Piotrowski-Daspit A.S., Nerger B.A., Wolf A.E., Sundaresan S., & Nelson C.M. (2017) Dynamics of tissue-induced alignment of fibrous extracellular matrix. *Biophys. J.,* 113: 702-713.

[6] Piotrowski-Daspit A.S. & Nelson C.M. (2016) Engineering three-dimensional epithelial tissues embedded within extracellular matrix. *JoVE,* 113: e54283.

[7] Nelson C.M., Inman J.L., & Bissell M.J. (2008) Three-dimensional lithographically-defined organotypic tissue arrays for quantitative analysis of morphogenesis and neoplastic progression. *Nat. Protoc.,* 3: 674-678.

[8] Foty R. (2011) A simple hanging drop cell culture protocol for generation of 3D spheroids. *Journal of visualized experiments : JoVE*, (51), 2720.

[9] Huang, Y. L., Ma, Y., Wu, C., Shiau, C., Segall, J. E., & Wu, M. (2020) Tumor spheroids under perfusion within a 3D microfluidic platform reveal critical roles of cell-cell adhesion in tumor invasion. *Scientific reports*, *10*(1), 1-11.

# A DEEP LEARNING METHOD FOR 3D VESSEL RECONSTRUCTION USING UNCALIBRATED X-RAY ANGIOGRAPHY IMAGES: APPLICATION TO CORONARY HEMODYNAMICS

**Kritika Iyer (1), Noah C. Stevens (1), Brahmajee K. Nallamothu (2), C. Alberto Figueroa (1,3), Raj R. Nadakuditi (4)**

(1) Biomedical Engineering, University of Michigan, Ann Arbor, MI, USA
(2) Cardiovascular Medicine, University of Michigan, Ann Arbor, MI, USA
(3) Surgery, University of Michigan, Ann Arbor, MI, USA
(4) Electrical Engineering and Computer Science, University of Michigan, Ann Arbor, MI, USA

## INTRODUCTION

The most widespread cause of heart disease is coronary artery disease (CAD) [1] , which manifests as narrowings, or stenoses, in the arteries that supply the heart muscle. The disease is diagnosed by visually inspecting X-ray coronary angiography images to estimate percent diameter reduction of the affected vessel. While diameter reduction is a useful metric, functional metrics of disease severity lead to better patient outcomes [2]. Fractional Flow Reserve (FFR) is a functional metric of CAD severity, defined as the ratio of pressures on both sides of the stenosis. FFR is typically measured via cardiac catheterization and traditionally requires the placement of coronary wires across stenoses; however, it can also be derived from CFD simulations in patient-specific 3D geometries.

Automatic geometric reconstruction of 3D coronary artery trees using a limited number of X-ray angiography images is a challenging task due to heart and respiratory motion, as well as angle orientation and calibration of the angiography system. Several approaches to reconstruct 3D coronary geometries have been developed, based on the principles of projective geometry. While these methods have demonstrated some success, their accuracy is limited, often requiring operator intervention or calibration of the angiography system [3]–[5].

In this work, we describe a calibration-free, angle-agnostic deep learning method to reconstruct 3D models of synthetically-generated vessel-like structures given two projection images. Furthermore, we present preliminary results on the effect of geometric reconstruction error on the pressure gradient, a surrogate measure for FFR.

## METHODS

A synthetic vessel generator was developed to produce 2,000 vessel-like structures with up to 3 random stenoses, informed by anatomical parameters (Fig 1). Stenosis geometry was determined by randomly sampling position, percent diameter reduction, and length from random uniform distributions. The generated ground truth vessel geometries mimicked the anatomy of the major branches of coronary vessels.

Each vessel was encoded as an Nx4 matrix, with N centerline points $(x, y, z)$ and radius $r$. Two projections of each synthetic vessel were created by randomly sampling spherical angles from uniform distributions. Finally, a Euclidean distance transform (EDT) was applied to the projection images to create a continuous array for neural network training. Of the 2,000 synthetically generated vessels, 1800 were used for training and 200 were used for validation.

Transformed projection images were input into a multistage neural network (Fig 1), which used features extracted by ResNet101 [6] to learn the corresponding vessel matrix. Mean squared error (MSE) was used as the loss function. The learned vessel matrix was used to reconstruct a NURBS-based centerline and an analytical vessel surface.

Steady-flow simulations were performed using CRIMSON [7] in two pairs of ground truth and predicted geometries, one with stenosis and one without (Fig 2). Each pair of vessels was modeled with identical boundary conditions: fixed inflow ($Q_{in}$ = 1200 mm$^3$/s) and fixed outlet resistance. The difference in pressure along the ground truth and predicted vessel centerlines were evaluated.

## RESULTS

The mean absolute error (MAE) of the $x$, $y$, and $z$ centerline coordinates for the 200 vessels in the validation set were 0.384±0.024mm, 2.219±0.039mm, and 1.196±0.030mm, respectively. MAE of the radius in the validation set was 0.0735±0.004mm.

For the two pairs of vessels chosen for CFD analysis, a comparison of the ground truth and predicted radii is shown in Fig 2A. In the stenotic

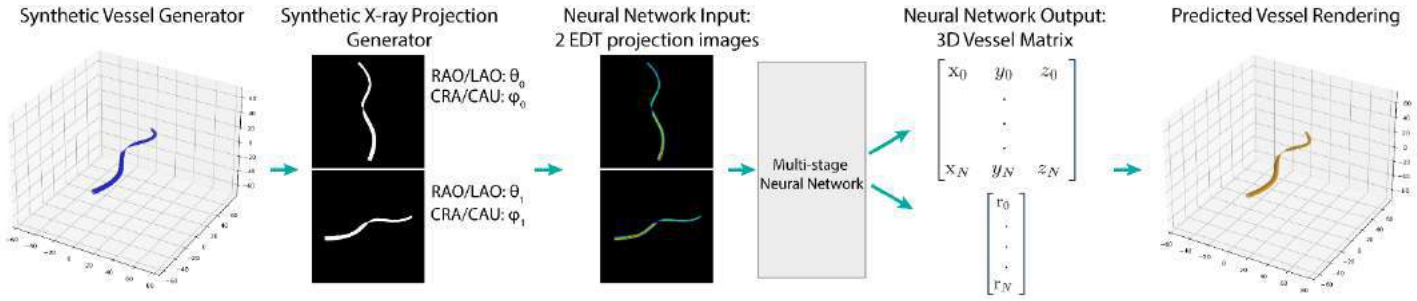


**Figure 1: Workflow of 3D vessel reconstruction. Ground truth synthetic vessels are generated and randomly projected to produce synthetic X-ray images. The images are transformed and input into a neural network, which predicts the 3D vessel geometry.**

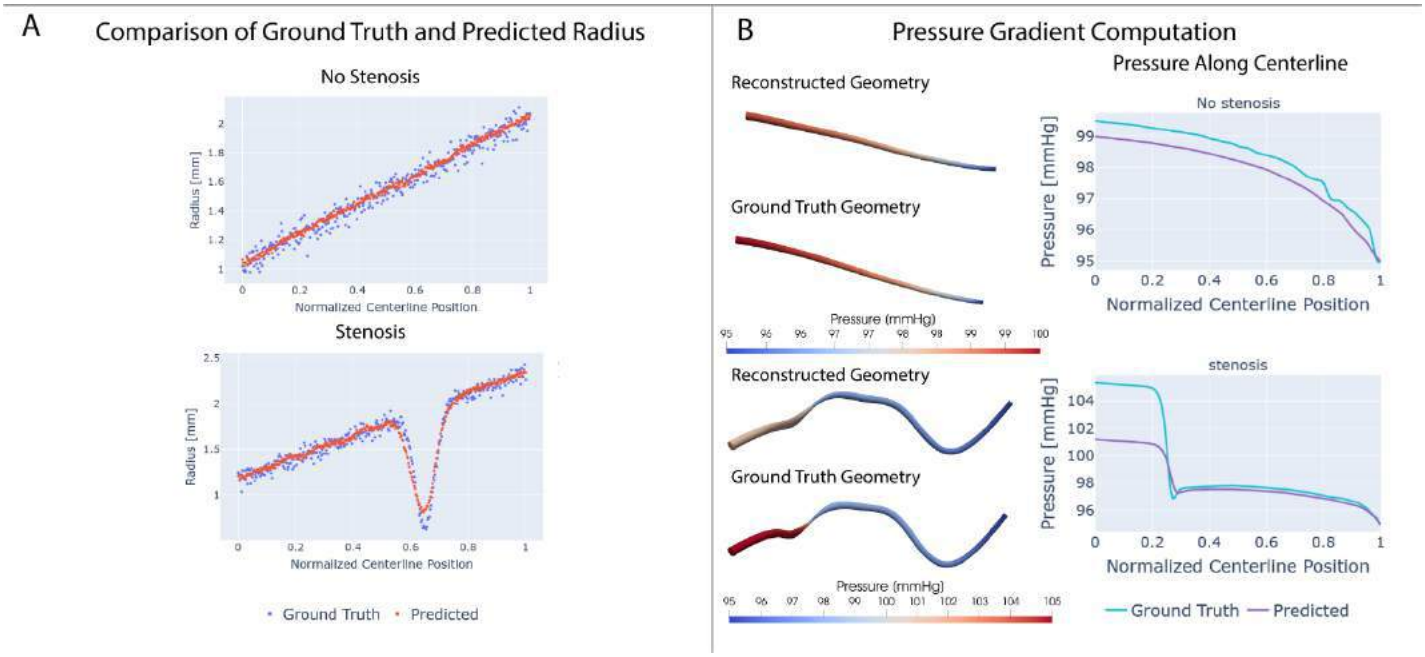


**Figure 2: Reconstruction results. 2A shows the radius along the centerline in the ground truth and predicted geometries. In 2B, the results of CFD simulations to measure the difference in pressure between ground truth and predicted vessel geometries are shown.**

case, the ground truth geometry had a maximum diameter reduction of 1.24mm or 66%, while the predicted geometry had a maximum diameter reduction of 1.09mm or 57%. In Fig 2B, the MAE of pressure along the centerline was 0.47mmHg in the non-stenotic case, with a maximum error of 0.58mmHg, and 1.17mmHg with a maximum error of 4.14mmHg in the stenotic case.

## DISCUSSION

This work is proof-of-concept that 3D vessel-like structures can be reconstructed from two projection images without any information about the geometry of X-ray image acquisition, including projection angle.

These results highlight that while the absolute error in the reconstructed path (0.384±0.024mm, 2.219±0.039mm, and 1.196±0.030mm for x,y, and z coordinates, respectively) was larger than errors in the reconstructed radius (0.0735±0.004mm), the impact of the radius error is (as expected) much larger on pressure gradient metrics. This is demonstrated by the CFD simulation results of the stenotic vessel. A 0.15mm difference in minimum vessel diameter at the region of stenosis leads to a 44% error in total pressure gradient. One major contributor to the error in radius is the discretization of the vessel radius into pixels on the projection images. One pixel typically represents 0.2-0.3mm in X-ray angiograms, thus limiting the accuracy of any reconstruction method, machine learning or otherwise.

Future work will focus on improving reconstruction accuracy by training on a larger and more varied synthetic vessel dataset. The synthetic vessel generator will also be improved to more closely resemble the geometry of coronary vessels, including the addition of branches.

## ACKNOWLEDGEMENTS

Funding for this work was provided by the National Science Foundation GRFP (DGE1841052) and Rackham Merit Fellowship.

## REFERENCES

[1] Gheorghiade, M. and Bonow, R. O. *Circulation*, 97:82–289, 1998.
[2] Tonino, P. A. L. et al., *N. Engl. J. Med.*, 360-3:213–224, 2009.
[3] Banerjee, A. et al. *IEEE Trans. Med. Imaging*, 39-4:1278–1290, 2020.
[4] Vukicevic, A. M. et al., *Sci. Rep.*, 8-1, 2018.
[5] Yang, J. *Phys. Med. Biol.*, 59-4:975–1003, 2014..
[6] He, K. et al., *arXiv*. 2015. http://arxiv.org/abs/1512.03385
[7] Arthurs, C.J., *et al.*, *PLOS Comput. Biol.*, 17-5:1008881, 2021.

# INTER-DONOR VARIABILITY IN THE TENSILE AND COMPRESSIVE BEHAVIOUR OF IN VITRO HUMAN THROMBI

**Rachel M.E. Cahalane (1), Judith J. de Vries (2), Moniek P.M. de Maat (2), Kim van Gaalen (1), Heleen M. van Beusekom (3), Aad van der Lugt (4), Ali C. Akyildiz (1,5) and Frank J.H. Gijsen (1,5)**

(1) Department of Biomedical Engineering, Erasmus Medical Centre, Rotterdam, the Netherlands.
(2) Department of Hematology, Erasmus Medical Centre, Rotterdam, the Netherlands.
(3) Experimental Cardiology, Erasmus Medical Center, Rotterdam, the Netherlands.
(4) Department of Radiology and Nuclear Medicine, Erasmus Medical Centre, Rotterdam, the Netherlands
(5) Department of Biomechanical Engineering, Delft University of Technology, Delft, the Netherlands.

## INTRODUCTION

Adequate reperfusion is still not achieved in 41% of endovascular thrombectomy (EVT) procedures [1]. These procedures are significantly influenced by the mechanical behaviour of the occluding thrombus [2], which is exposed to complex multi-axial loading conditions during retrieval [2]. While unconfined compression is commonly used to determine compressive thrombus mechanics, the difficulties in specimen handling has led to a shortage of data on thrombi in tension. In the limited tensile data available, there are conflicting reports of linear and non-linear stress-strain responses [3]. Moreover, composition alone cannot explain the observed variation in compressive stiffness values for thrombi retrieved from EVT procedures [4]. Although the majority of in vitro studies do not consider inter-donor variation in their design [5,6] or do not report it in their results [7–10]. data suggests that a mechanical variation exists between comparable thrombi from different donors [9,11,12]. Here, we report on the tensile and compressive behaviour of comparable thrombus analogues produced in a variety of compositions from the blood of human donors.

## METHODS

**In vitro Thrombi Production:** Thrombus analogues were prepared from the blood of 6 healthy human donors (3 males, 3 females). The different blood constituents were used to produce platelet-rich plasma (PRP), platelet-poor plasma (PPP), whole blood (WB) clots and clots with a range of red blood cell (RBC) concentrations (0%, 5%, 10%, 20%, 40%, 60% and 80% RBC volume with PRP in the clotting mixture). All specimens were formed under static conditions.

**Mechanical Characterisation:** Both uniaxial tensile and unconfined compression tests were performed using custom-built setups. Tensile stretching was conducted until failure. Compressive stretching was performed to 80% strain. Both tests were conducted at 5% strain per second. It was not possible to perform tensile testing on 80% RBC samples, as observed by the limits of specimen handleability in preliminary experiments. For both datasets, a low-strain stiffness value was acquired by applying a linear fit to the nominal stress-strain data between 0 and 10% strain. For tensile data, a high-strain stiffness value was acquired by applying a linear fit to the final 10% of the stress-strain curve (prior to sample failure). For compressive data, a high-strain stiffness value was acquired by applying a linear fit to the nominal stress-strain data between 70-80% strain.

**Composition, Microstructure, Contraction and Hemostasis:** Histology (hematoxylin & eosin [H&E], Martius Scarlet [MS] and CD42b) and scanning electron microscopy (SEM) were performed to determine the composition and microstructure of the thrombi, respectively. The degree of clot contraction was assessed gravimetrically. Complete blood cell counts and fibrinogen levels were also measured to appreciate the origin of any inter-donor variations.

## RESULTS

There is a strong negative (almost linear) relationship between the percentage of RBCs in the clotting mixture and the degree of clot contraction (Fig.1A). Additionally, the percentage of RBCs in the clotting mixture does not produce thrombi with a proportionate RBC content. The thrombus RBC content ranged from 0.03% (PRP [MS]) to 97% (40% RBC [MS]). Of note, a 5% RBC volume produces a thrombus with approximately 70% RBC content (Fig.1B).

There is pronounced asymmetry in the compression-tension behaviour of in vitro human blood clots for all compositions. A marked strain-stiffening compressive response is observed, in contrast to the approximately linear nominal stress-strain profiles under tension (Fig.2A). Of interest, there are overlapping behaviours for thrombi of different compositions from different donors (Fig.2B). Tensile low-strain stiffness values are approximately 15 times higher than compressive low-strain stiffness values (Fig.2C). Additionally,

compressive high-strain stiffness values are approximately 39 times higher than tensile high-strain stiffness values (Fig.2D).

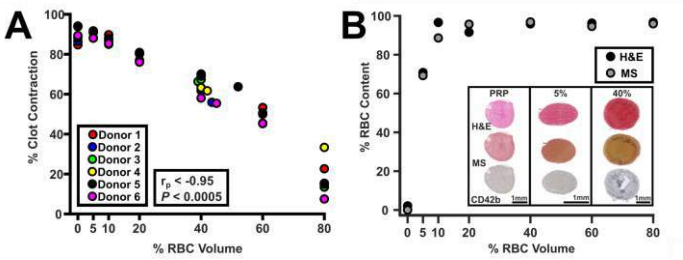


**Figure 1: Clot contraction and RBC content per RBC volume in the clotting mixture (or hematocrit for WB). (A) Clot contraction by weight. (B) Thrombus RBC content. Representative H&E, MS and CD42b stained section for PRP, 5% and 40% RBC clots.**

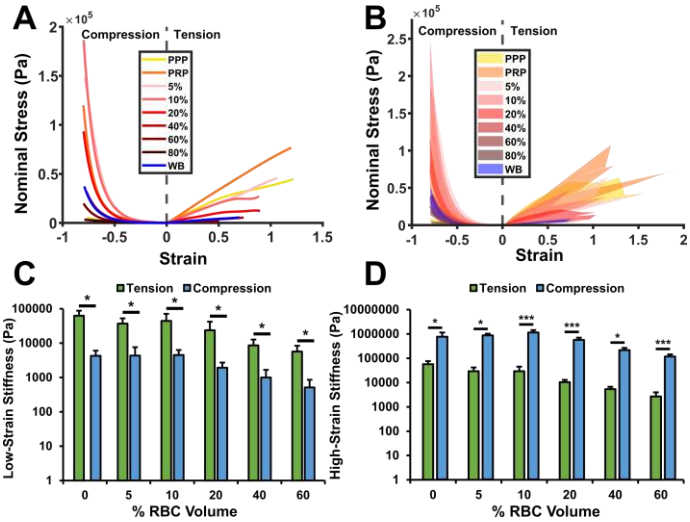


**Figure 2: (A) Nominal stress-strain midlines per composition. (B) Nominal stress-strain range per composition. (C) Tensile versus compression low-strain stiffness (log scale y-axis). (D) Tensile versus compression high-strain stiffness (log scale y-axis). Statistical significance: *$P$<0.05, ***$P$<0.0005.**

Thrombus tensile stiffness generally decreases for each increasing RBC volume (Fig.3A). In contrast, compressive stiffness increases from 0% to 5% and 10% RBC volumes, followed by a decrease in stiffness with subsequent RBC volumes (Fig.3B). By examining the microstructure of the samples with SEM, it is clear that PRP samples exhibit pores in the fibrin network (Fig.3C), while RBCs are tightly packed in the network for a 5% RBC sample (Fig.3D). The network becomes looser again for a 60% RBC sample (Fig.3E). Additionally, PRP clots are stiffer than PPP clots in compression (high-strain stiffness: 741 ± 359 vs. 31 ± 12 kPa, $P$ = 0.005). However, there are no significant differences in the tensile stiffness of PRP and PPP clots (high-strain stiffness: 57 ± 20 vs. 46 ± 12 kPa, $P$ = 0.28).

To further quantify the variations observed in Fig.2B we examined the coefficient of variances (CoV) for low- and high-strain stiffnesses of the WB clots between donors. High-strain compressive stiffness exhibited the lowest CoV (30%), followed by low-strain compressive stiffness (47%), low-strain tensile stiffness (48%) and high-strain tensile stiffness (49%). Pearson's correlation revealed trends towards significance between donor age, platelet cell counts and levels of fibrinogen with high-strain compressive stiffness. There was also a trend towards significance between the degree of clot contraction and low-strain compressive stiffness.

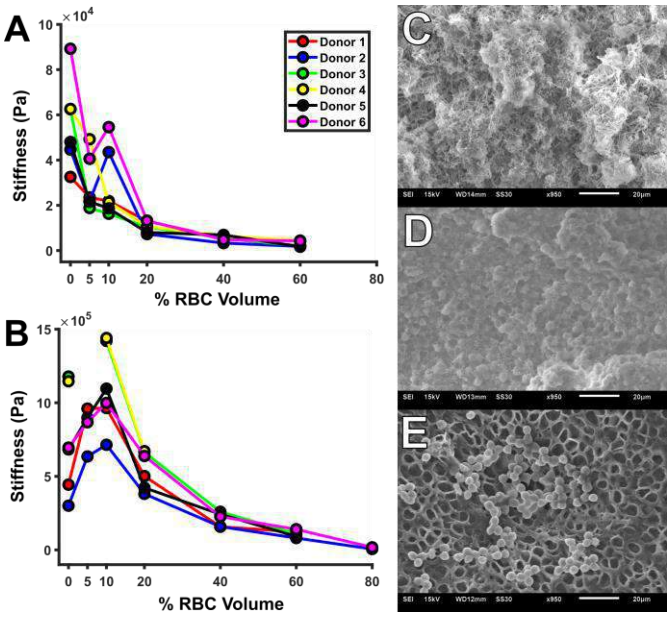


**Figure 3: Influence of composition on thrombus mechanics and SEM of microstructure. (A) Tensile and (B) compressive high-strain stiffness. (C) PRP, (D) 5% and (E) 60% RBC clot.**

## DISCUSSION

This is the first investigation of the stiffness properties of thrombus analogues made from the blood of healthy human donors in a range of compositions under both tensile and compressive loading. There is a distinct asymmetry in the tension-compression nominal stress-strain profiles of in vitro healthy human thrombi. Accordingly, different material models may be required to adequately capture the thrombus response to EVT. The effect of composition on stiffness also differs in tension versus compression. In line with previous findings [3,5], the tensile stiffness of clots decreases with increasing RBC content, but the compressive stiffness initially increases from 0 to 10% RBC content, then decreases with further amounts of RBCs. There is significant variation present in the stiffness of whole blood clots derived from different healthy human donors. Composition alone does not account for all the observed variation in retrieved clot mechanics [4]. Future studies should assess the utility of this mechanical variation in the prediction of EVT success in patients undergoing AIS treatment.


## ACKNOWLEDGMENTS

The authors acknowledge Robert Beurskens and Pablo De Miguel Muñoz for their assistance with the setups. This study is funded by the Convergence Health & Technology Alliance TU Delft.


## REFERENCES


[1] Jansen, I et al., *BMJ*, 360: k949, 2018.
[2] Yuki, I et al., *Am J Neuroradiol*, 33:643–648, 2012.
[3] Cahalane, R et al., *J Biomech*, 129:110816, 2021.
[4] Boodt, N et al., *Stroke*, 52:2510-2517, 2021.
[5] Johnson, S et al., *J Neurointerv Surg*, 12:853-857, 2019.
[6] Sugerman, G et al., *Soft Matter*, 16:9908–16, 2020.
[7] Windberger, U et al., *Molecules*, 25:3890, 2020.
[8] Machi, P et al., *Neurointerv Surg*, 9:257–63, 2015.
[9] Luo, Z et al., *J Vasc Interv Radiol*, 23:1077–1083, 2012.
[10] Weafer, F et al., *J Neurointerv Surg*, 11:891–7, 2019.
[11] Malone, F et al., *Cardiovasc Eng Technol*, 9:489–502, 2018.
[12] Merrit, W et al., *J Neurointerv Surg*, 10:1168–1173, 2018.

# QUANTIFICATION OF INTERVERTEBRAL DISC STRAIN FROM HIGH-RESOLUTION ULTRASOUND IMAGING DURING DYNAMIC LOADING

**Elnaz Ghajar-Rahimi (1), Shiyin Lim (2), Conner C. Earl (1), Reece D. Huff (2), Grace D. O'Connell (2), Craig J. Goergen (1)**

(1) Weldon School of Biomedical Engineering, Purdue University, West Lafayette, Indiana, USA
(2) Department of Mechanical Engineering, University California Berkeley, Berkeley, California, USA

## INTRODUCTION

Two-thirds of people experience lower backpain during their lifetime, with herniated discs commonly occurring in patients 20-40 years of age.[1,2] The intervertebral disc (IVD) separates adjacent spinal vertebrae. IVDs consist of an outer annulus fibrosus (AF) and an inner nucleus pulposus (NP). Herniated discs occur when the inner NP region of an IVD extrudes through a full-thickness annular tear and impinges on spinal nerves, often resulting in debilitating back and leg pain. Despite the high prevalence of herniated discs, the mechanical factors that drive annular tears are still poorly understood. More specifically, knowledge of the relationship between the AF and NP in IVD degeneration is limited.[3] This highlights the critical need for both investigating the mechanisms of disc herniation and developing diagnostic methods for characterizing disease progression. Previous studies have used magnetic resonance imaging to assess IVD strains in human samples.[4] However, ultrasound may be advantageous over other imaging modalities because of its fast acquisition time, lower equipment costs, and improved resolution. We aim to integrate advanced high-resolution ultrasound imaging and texture correlation to quantify strain profiles in the IVD under dynamic loading conditions. This study establishes a methodology for measuring IVD strain in bovine caudal spine with high-frequency ultrasound and establishes the foundation for future work quantifying strain profiles with texture correlation.

## METHODS

### Bone-Disc-Bone Segment Preparation

Two bone-disc-bone (BDB) segments were used for this study. Bovine caudal spine was acquired from a local abattoir (age 18-24 months; West Lafayette, IN). Tissue surrounding the spine was removed with a scalpel to isolate the IVDs. Three cuts were made along the mid-transverse plane of the top three vertebrae (C1-C3), and spinous processes were removed to create BDB segments (Figure 1A). The ends of the BDB segments were then potted in polymethyl methacrylate (PMMA; 2.08 g powder per mL liquid; Bosworth Fastray Custom Tray and Acrylic Base Plate) (Figure 1B). Prepared BDB segments were wrapped in gauze dampened with phosphate-buffered saline and stored at -20 ºC.

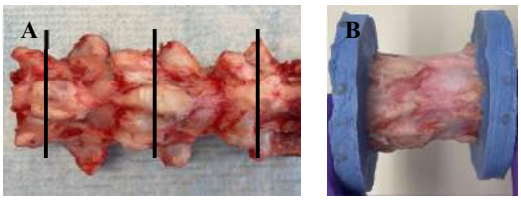


**Figure 1: A) Bovine caudal spine with tissue removed. Black lines demarcate vertebrae C1, C2, and C3 along which the sample was cut B) BDB segment with spinous processes removed and potted in PMMA**

### Loading System

A custom-built testing device was built to apply axial compression at one end of the BDB segments. The tester has five main components: a frame, motor, transmission, Arduino controller, and a power supply (Figure 2). The motor generates a rotational force which is converted into axial force by the transmission and applied to the potted BDB segment.

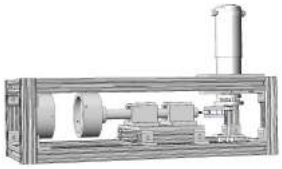

**Figure 2: Representative image of tester**

### Ultrasound Imaging

All data was collected using a 40 MHz center frequency ultrasound transducer (MX550D, Vevo3100, FUJIFILM VisualSonics) held in place by a linear step motor above the disc surface. Thawed BDB segments were loaded into the custom testing device. Ultrasound conductive gel was applied to the topside of the BDB segments. B-mode images and three-dimensional ultrasound volumes were collected along the transverse plane of the bovine caudal spine at 0 mm, 2 mm, and 4 mm of axial displacement. The transducer orientation relative to the sample is shown in Figure 3.

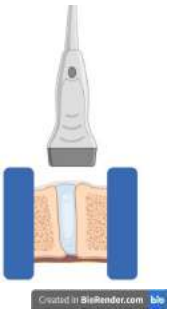

**Figure 3: Transducer orientation above potted sample**

### Disc Deformation

Disc height (distance between vertebral end plates) was measured 4 mm from the surface of the disc (VevoLab, FUJIFILM VisualSonics) with a linear measurement tool. Linear axial strain ($E_{Axial}$) was then calculated at 2 mm and 4 mm of compression using the linear definition of strain (Eq:1), where $\Delta H$ is change in height and $H_0$ is initial height of the disc:

$$E_{Axial} = \frac{\Delta H}{H_0} \quad (1)$$

## RESULTS

The vertebral end plates and IVD appeared clearly in the B-mode ultrasound images. The subcomponents of the IVD could be distinguished from one another, with visible striations in the AF. Vertebral end plates were black and contrasted against the white IVD. A labeled representative B-mode ultrasound image is shown in Figure 4.

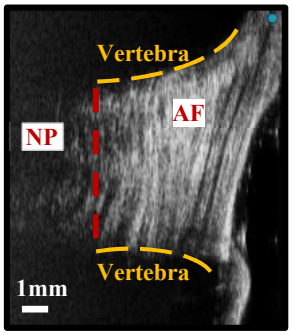


**Figure 4: Representative B-mode ultrasound image of BDB segment at 0 mm axial displacement, NP: nucleus pulposus, AF: annulus fibrosus**

Linear strain increased as axial displacement increased. The IVDs experienced an average compressive strain of 3.3% at 2 mm and 6.1% at 4 mm of displacement, respectively. Curvature of the disc also increased as axial displacement increased. The outward bulging of the disc is highlighted in Figure 5.

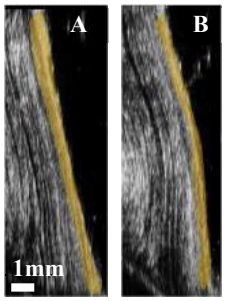


**Figure 5: BDB segment with visual evidence (yellow) of annulus fibrosus curvature increasing with axial displacement A) 0 mm displacement B) 2 mm displacement**

## DISCUSSION

Here we demonstrate the ability to measure axial IVD strain with high frequency ultrasound under dynamic loading. The results show that IVD axial strain increased by approximately two-fold with increased compression from 2 mm to 4 mm. IVD curvature also increased with compression. This method could be used to assess dynamic disc compression at varying frequencies and magnitudes to describe time-dependent behavior. The system is capable of cycling loading tissue up to 0.5 Hz. The clear delineation between the disc (white) and the adjacent vertebrae (black), as well as the clear striations in the AF, in the ultrasound images will be valuable when developing displacement fields.

One of the samples maxed out at 2 mm of axial displacement. Consequently, only one measurement could be taken at 4 mm of axial displacement by the tester. Non-uniform IVD anatomy throughout a given sample poses a limitation in measuring disc height. Therefore, determining or assigning a coordinate point to track within samples during compression would improve the accuracy of the calculated strains. After further validating this method in bovine specimens, the study will be expanded to assess human cadaveric-lumbar spine sections. We anticipate that the methods described in this work will lead to improved approaches for non-invasive image-based assessment of IVD herniation and add to our current understanding of herniation progression and treatment.

## ACKNOWLEDGEMENTS

The authors acknowledge Norvin Bruns at Purdue University for assisting in slicing the bovine caudal spine and sample preparation.

## REFERENCES

[1] Druss, B. G., Marcus, S. C., Olfson, M. & Pincus, H. A. The Most Expensive Medical Conditions In America. *Health Affairs* **21**, 105–111 (2002).

[2].Haro, H. Translational research of herniated discs: current status of diagnosis and treatment. *J Orthop Sci* **19**, 515–520 (2014).

[3].O'Connell, G. D., Vresilovic, E. J. & Elliott, D. M. Human Intervertebral Disc Internal Strain in Compression: The Effect of Disc Region, Loading Position, and Degeneration. *J Orthop Res* **29**, 547–555 (2011).

[4].O'Connell, G. D., Johannessen, W., Vresilovic, E. J. & Elliott, D. M. Human Internal Disc Strains in Axial Compression Measured Noninvasively Using Magnetic Resonance Imaging. *Spine* **32**, 2860–2868 (2007).

# ULTRASOUND-BASED VOLUME-TIME CURVES OF THE LUMEN, THROMBUS AND VESSEL WALL FOR ESTIMATING IN-VIVO THROMBUS COMPRESSIBILITY AND WALL STIFFNESS

**Arjet H.M. Nievergeld (1,2), Esther J. Maas (1,2), Judith H.C. Fonken (1,2), Frans N. van de Vosse(1), Marc R.H.M. van Sambeek(1,2), Richard G.P. Lopata(1)**

(1) Biomedical engineering, University of Technology Eindhoven, Eindhoven, the Netherlands
(2) Department of Vascular Surgery, Catharina Hospital Eindhoven, Eindhoven, the Netherlands

## INTRODUCTION

An abdominal aortic aneurysm (AAA) is a localized dilation of the aorta, which, in case of rupture, has a mortality rate of 80%. Current clinical guidelines for intervention are based on AAA diameter, which has been proven to be a non-optimal criterion for rupture risk prediction [1,2]. Biomechanical models can improve rupture risk prediction using patient-specific geometries obtained from imaging modalities such as computed tomography (CT) and ultrasound (US). US is safer than CT because of the lack of nephrotoxic contrast agents and radiation, especially when longitudinal studies are needed. Moreover, US imaging adds temporal information required for accurate mechanical characterization (elastography), which is important for rupture risk prediction. Those patient-specific mechanical properties can be used in combination with the patient-specific geometry for FE-based stress analysis for a more patient-specific rupture risk assessment [2].

Previous studies have shown that intraluminal thrombus (ILT) affects the rupture risk. Some studies showed that ILT attenuates oxygen diffusion from the lumen to the vessel wall, leading to increased inflammation, therefore weakening the vessel wall and increasing the rupture risk [3]. On the other hand, studies showed that ILT reduces the peak wall stress in the AAA, therefore decreasing the rupture risk [4]. Intraluminal thrombus should therefore be included in rupture risk assessment. Imaging thrombus using US is challenging, due to the limited contrast between lumen and thrombus.

Recently, a method was developed in-house to assess the geometry of ILT from 3D US images, for patient-specific measurements as well as modeling purposes. In this study, we investigate the feasibility of US-based mechanical characterization of both the thrombus and AAA vessel wall from 3D(+t) US data.

## METHODS

In this study 10 AAA patients were included, who all gave their informed consent. The 3D+t (volume rate 4-8 Hz) ultrasound images were acquired in the Catharina Hospital Eindhoven, The Netherlands. Time-resolved 3-D ultrasound data were acquired using a Philips iU22/Epiq system with X6-1 transducer. After the US exam, the brachial blood pressure was measured.

The thrombus and vessel wall geometries were segmented from the ultrasound images using an in-house developed fully automatic segmentation algorithm, which was validated using CT (Figure 1).

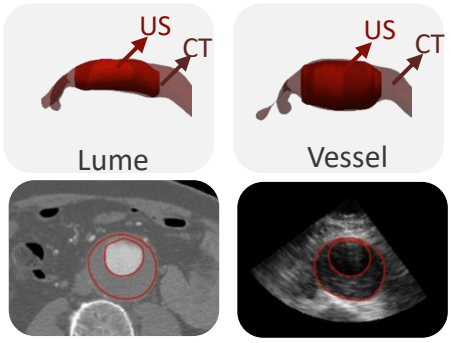


**Figure 1: US-based geometry of the lumen and the inner vessel wall and its comparison with CT**

Those time-varying geometries resulting from the US-based segmentations were used to determine the volume at each time-step using the Gibbon toolbox.

The volume-time curves resulting from those geometries (Figure 2) were used to calculate the in-vivo relative thrombus volume change

during the cardiac cycle using the systolic and diastolic thrombus volume ($V_{ILT,sys}$ and $V_{ILT,dia}$):

$$dV_{ILT} = \frac{V_{ILT,sys} - V_{ILT,dia}}{V_{ILT,dia}} \cdot 100\% i \qquad (1)$$

The circumferential stress can be calculated using Laplace's law with pressure (p), radius (a) and wall thickness (h). The radius was calculated from the volume and the length.

$$\sigma = \frac{p \cdot a}{h} \qquad (2)$$

The shear modulus can be calculated using the diastolic and systolic circumferential stress ($\sigma_{dia}$ and $\sigma_{sys}$) and Finger strain ($\varepsilon_F$).

$$Gi = i\frac{(\sigma_{sys} i - i\sigma_{dia})}{2 \cdot \varepsilon_F} \qquad (3)$$

## RESULTS

In Figure 2, the volume-time curves of the lumen, vessel and thrombus are shown. For the lumen and vessel a clear pulsatility is visible. However, for the thrombus volume no clear pulsation is seen.

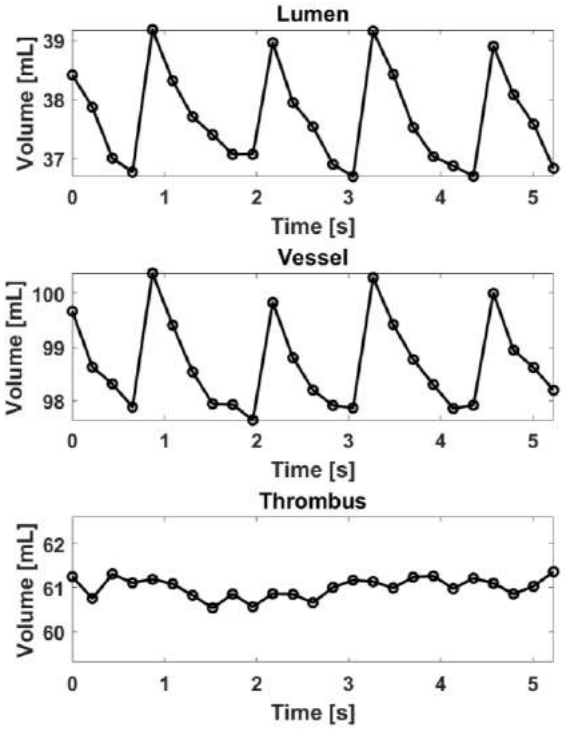


**Figure 2: Volume-time curves of the lumen, total artery, and intraluminal thrombus.**

In Figure 3, the volume change of the thrombus and shear modulus of the vessel wall are shown. The median thrombus volume change is 0.4 %, with an IQR of 1.5%. The median shear modulus of the vessel wall is 1.12 MPa, with an IQR of 0.8 MPa.

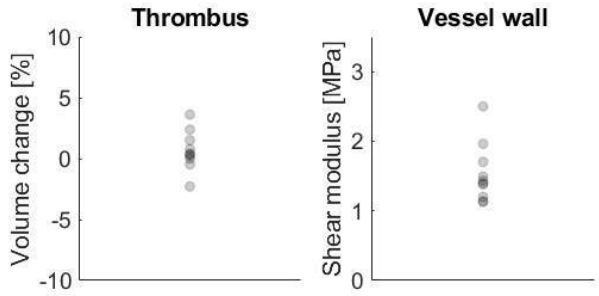


**Figure 3: Compressibility of the thrombus and shear modulus of the vessel wall resulting from the volume-time curves.**

## DISCUSSION

In this study the volume-time curves of the lumen, vessel and thrombus were acquired fully automatically from a 3D+t US acquisition. As shown in Figure 2, a clear pulsatility is seen for the lumen and vessel volume-time curve, which is promising for mechanical characterization. The volume-time curve of the thrombus was used to calculate the thrombus volume change. Kontopodis performed comparable measurements on 5 patients, using ECG-gated CT [5]. The results of the volume change (median 0.4% , IQR 3%), were comparable to the ones shown in Figure 3 [5]. Vorp et al. analyzed the thrombus area ratio using 2D-ultrasound (median 2%, IQR 2%) [6]. Those results were comparable to the volume-ratio obtained in this study. These and our results show that the assumption of incompressibility of the thrombus, which is often used in mechanical modeling, is valid.

In van Disseldorp et al [7], the shear modulus of the vessel wall was determined using 4D-ultrasound. In that specific study, 40 patients were analyzed and the displacements were determined using 3D speckle tracking. The stiffness was determined using inverse finite element analysis (FEA) and resulted in a median of 1.1 MPA (IQR, 0.7-1.4). The stiffness shown in Figure 3 are higher compared to the ones found in this study. Those deviations might be because of the assumptions made in Laplace's law for a thin-walled tube. However, this shear modulus is a good first estimate for the stiffness. In future, this shear modulus can be used as a first guess and input for inverse Finite Element Analysis.

This study showed that it is feasible to estimate mechanical parameters of the AAA and thrombus from 3D+t US using volume-time curves. The limiting factor remains the quality of the US data. Future research will focus on thrombus stiffness estimation using inverse finite element analysis. The patient-specific geometry in combination with the patient-specific stiffness of both thrombus and vessel wall can ultimately be used for FE-based stress analysis for more accurate, patient-specific rupture risk.

## REFERENCES

[1] vande Geest et al. Annals of Biomedical Engineering, 34(7):1098-1106, 2006
[2] Khosla et al., BJS, 101:1350-1357, 2014
[3] Vorp et al., J Biomech Eng., 120(5):579-83, 1998
[4] Riveros et al. Ann Biomed Eng. 43(9):2253-6, 2015
[5] Kontopodis, et al. EJVES Extra, 26(1):e4–e6,2013
[6] Vorp et al. Cardiovasc Surg, 4(6):732-9,1996
[7] van Disseldorp et al., JVES, 52(5):635-642, 2016

# FUSIFORM VS. SACCULAR INTRACRANIAL ANEURYSMS: CAN BLOOD FLOW BEHAVIOUR INDICATE FORMATION AND TREATMENT EFFECTS?

**Jana Korte (1,2), Laurel Miller Morgan Marsh (1,3), Sylvia Saalfeld (1,4), Janneck Stahl (1), Daniel Behme (1,5), Philipp Berg (1,2)**

(1) Research Campus *STIMULATE*, University of Magdeburg, Magdeburg, Germany
(2) Department of Fluid Dynamics and Technical Flows, University of Magdeburg, Magdeburg, Germany
(3) Department of Mechanical Engineering, University of Washington, Seattle, WA, USA
(4) Department of Simulation and Graphics, University of Magdeburg, Magdeburg, Germany
(5) Department of Neuroradiology, University Hospital Magdeburg, Magdeburg, Germany

## INTRODUCTION

Intracranial aneurysms (IAs) are categorized into non-saccular and saccular (SIA) shapes. Counting to non-saccular types, fusiform intracranial aneurysms (FIAs) occur in 3-13% among all IAs [1]. Subsequently, blood flow parameters in FIAs are less examined than in SIAs and more difficult to make assumptions about the rupture risk, since parameters concerning the aneurysm neck reference cannot be taken into account [2].

In this study the focus is on the difference from FIA to SIA concerning the occurring hemodynamic parameters. To analyze the treatment effectiveness onto each aneurysm model's flow, the virtual implantation of a stent is considered. On top of that the creation and investigation of their healthy counterpart is added to analyze the impact onto the aneurysm formation.

## METHODS

### Patient data and IA models

In this study, three FIA models from different patients were captured with 3D digital subtraction angiography (Case 1 and 3) and computer tomographic angiography (Case 2). Case 1 was found in the left middle cerebral artery (MCA), case 2 in the left vertebral artery and case 3 in the basilar artery [3].

To further elucidate the flow, three SIAs each at a similar location as one fusiform IA were chosen to be analyzed as a comparable basis.

### Virtual stenting and healthy model creation

For each aneurysm model a virtual flow-diverter stent was applied and a healthy counterpart was created manually. Hence, the efficacy of treatment and the blood flow differences between an IA and an equal vessel model without IA could be investigated. The flow diverting devices were deployed with an in-house software [3]. The IAs were extracted from the vessel geometry within the open-source software Blender 2.9 (Blender Foundations, Amsterdam, Netherlands).

### Hemodynamic simulation

In total 18 patient-specific image-based blood flow simulations were carried out using the fluid dynamic solver STAR-CCM+ 14.04 (Siemens Product Lifecycle Management Software Inc., Plato, TX, USA). The same simulation settings were used for each IA model and a spatial resolution of 0.15mm mesh size was enabled. Incoming flow was set to representative flow rates [4] and adapted according to the vessels' inlet diameter. An advanced outlet flow splitting method was used to apply realistic outlet boundary conditions [5].

### Analysis

Blood flow inside the FIA and SIA models was analyzed qualitatively and quantitatively examining the time- and spatially averaged hemodynamic parameters velocity (VEL), vorticity (ω), kinetic energy (KE) and time averaged walls shear stress (AWSS).

To create a comparable basis of the pathological aneurysm model to the stented and the manually created healthy model, the energy loss (EL) for each vessel geometry was considered [6]. The EL describes the difference of the energy at all inlets to the energy at all outlets. For calculating EL, cut planes were set at the inlet and outlet areas for each model at equal locations. The energy appearing at these cut planes was calculated (equation (1)) and then summarized (equation (2)) using velocity (V), area (A), fluid density ($\rho$) and static pressure (P). For summarizing the appearing energy, the temporal and spatial mean over the cut planes was considered.

$$E = V * A * ((0.5 * \rho * V^2 + P) \quad (1)$$

$$EL = i\sum E_{inlets} - i\sum E_{outlets} \quad (2)$$

## RESULTS

Figure 1 represents qualitative results of the velocity streamlines inside the IA models colored with the temporal mean velocity. The three examined FIA models are compared line-wise, together with their saccular comparative case. The different conditions (pathological, treated, healthy – in this order from top to bottom) are stated column-wise for each model. The streamlines within the pathological IAs show a higher variation in temporal mean velocity and in formation than

within the healthy and treated cases. Within the treated cases, the velocity value gets lower inside the IA but follows straight lines compared to the healthy cases.

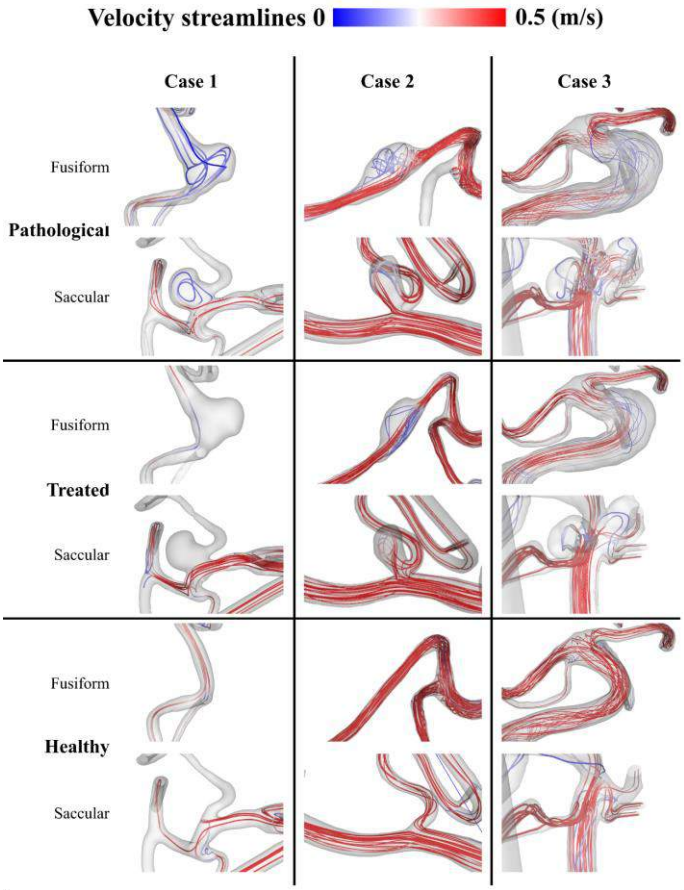


**Figure 1: Velocity streamlines of all aneurysm models.**

Concerning the aneurysm formation, the specific results for the parent vessel in the healthy and treated geometry are shown in Table 1 exemplary for case 1. The parent vessel is chosen to be the part of the vessel in flow direction before the aneurysm part. For the direct comparison, the results of the saccular comparative of case 1 are listed below the FIA results. The values show that the internal blood flow behavior (ω and KE) is decrease in the pathological model for FIAs and SIAs, respectively. Wall characteristics at the SIAs decrease as well and increase minimally FIA, respectively. The deviation from pathological to healthy is higher for SIA than for FIA.

**Table 1: Resulting hemodynamic parameters inside the parent vessel of case 1 (FIA and SIA) for the configurations pathological and healthy.**

| Hemodynamic parameter | | Pathological | Healthy | Pathological /Healthy |
|---|---|---|---|---|
| ω mean (1/s) | FIA | 798.27 | 803.37 | 0.994 |
| | SIA | 1505.43 | 1546.40 | 0.974 |
| KE mean (J) | FIA | 36.44 | 36.615 | 0.995 |
| | SIA | 158.04 | 164.51 | 0.961 |
| AWSS (Pa) | FIA | 6.24 | 6.23 | 1.001 |
| | SIA | 16.10 | 16.97 | 0.949 |

The visualization of the EL in figure 2 shows that especially the aneurysm treatment leads to a high loss of energy inside the vessel flow for all cases. The EL of the pathological compared to the healthy cases is slightly different in both directions (higher and lower).

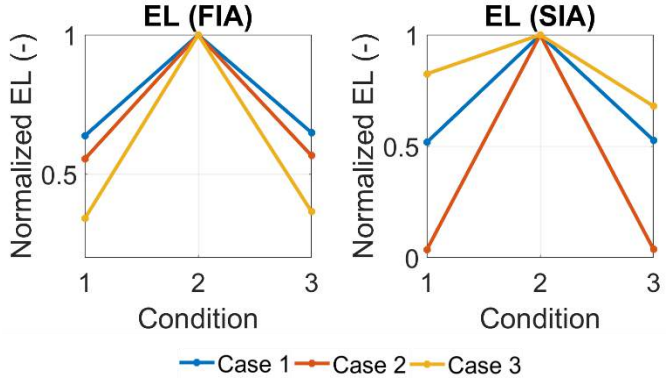


**Figure 2: Energy loss normalized by the highest value for each IA model shown for every condition (1- pathological, 2-treated, 3-healthy).**

## DISCUSSION

Models of FIA and SIA are chosen located at the vertebrobasilar system and MCA according to highest appearance in literature [1].

Qualitative results of the velocity streamlines reveal a high variation in flow structures and velocity value for both (FIA and SIA) compared to treated and healthy models [7]. Nevertheless, treated models show lower velocity values than the healthy ones. Comparing the healthy and pathological values in the parent vessel directly reveals that higher changes appear for SIA then for FIA which could indicate formation. Furthermore, the treatment shows undesirable effects onto the EL within each case [6]. Limitation of this study is the small number of cases analyzed. However, the amount of recorded and with computational fluid dynamics analyzed FIAs is yet rarely represented in the literature [8].


## ACKNOWLEDGEMENTS

We thank Dr. Oliver Beuing and Yurii Cherednychenko for the original draft preparation and the Federal Ministry of Education and Research in Germany within the Forschungscampus *STIMULATE* (grant number 13GW0473A) and the German Research Foundation (grant number SA 3461/3-1, BE 6230/6-1) for financial support.


## REFERENCES


[1] Park, S.-H.et al., *J Korean Neurosurg Soc* 44:116, 2008
[2] Raghavan, M. L., et. al., *J Neurosurg* 102: 355–362, 2009
[3] Janiga, G. et al., *J Bio Mech* 48: 3846-3853, 2015
[4] Berg, P. et. al., *J Biomech Eng* 136(4), 2014
[5] Saalfeld, S. et al., *I J CARS* 14: 1805-1813, 2019
[6] Hu, P. et al., *Int J Clin Exp Med.* 8(3): 4128–4133, 2015
[7] Zhang, Y. et. al., *BMC Neurology* 16: 231, 2016
[8] Barletta, E.A. et al., *Surg Neurol Int* 9: 189, 2018

# MULTI-DIMENSIONAL MORPHOMETRIC ANALYSIS OF POSTERIOR FOSSA TO STUDY TYPE I CHIARI MALFORMATION

**Ya-Chen Chuang, PhD (1), Alejandro Carrasquilla, MD (2), Aymeric Pionteck, PhD (1), Javid Abderezaei, PhD (1), Addison Quinones, BS (2), Gizem Bilgili, MD (1), William H. Shuman, BS (2), Shan Zhao, MD. PhD (3), Raj K. Shrivastava, MD (2), Mehmet Kurt, PhD (1)**

(1) Department of Mechanical Engineering, University of Washington, Seattle, WA 98195, USA
(2) Department of Neurosurgery, Icahn School of Medicine At Mount Sinai, New York, NY 10029, USA
(3) Department of Anesthesia, Icahn School of Medicine At Mount Sinai, New York, NY 10029, USA

## INTRODUCTION

Chiari Malformation type I (CM-I) is a complex neurological disorder, which occurs in children and adults [1]. The typical diagnostic criteria is cerebellar tonsillar descent for at least 5 mm below the Foreman magnum in adults and 3 mm in children [2], along with the diagnosis of clinical manifestations, such as syringomyelia, neurological symptoms, headache, back and neck pain, blurry vision, or, in children, scoliosis or sleep apnea. However, it has been shown that a substantial number of patients expressed symptoms without severe tonsillar herniation [3]. On the other hand, there are underestimated numbers of asymptomatic patients who meet the radiographic diagnostic criteria of tonsillar herniation [4].

Therefore, the measurement of tonsillar descent may be a limited marker as the CM-I diagnostic criteria. Even though other hindbrain regions in CM-1 keep their normal position, they may be slightly deformed and changed in size. Several studies analyzed the 2D morphometric characteristics of the posterior fossa and studied the correlation with CM-1 syndromes [5, 6]. However, 2D analysis may not be sufficient to explain complicated morphometric abnormalities and associated diseases. For example, syringomyelia, which involves the collection of cerebrospinal fluid (CSF) in a small cavity in the parenchyma of the spinal cord, is usually associated with CM-1 syndromes. The obstruction of CSF outflow may be caused from the deformation of 4$^{th}$ ventricle or to disturbance of CSF fluid dynamics due to tonsillar herniation [7, 8].

Here, we studied anatomical correlations in CM-1 patients using 3D volumetric analysis of posterior fossa, along with 2D length, surface and angle measurements, in an attempt to improve the understanding of the morphological abnormalities of other hindbrain regions, and thus further promote CM-1 diagnosis and surgical treatment.

## METHODS

The retrospective MRI scans obtained from 72 adult CM-1 patients (58 females and 14 males between 19 and 74 years of age, mean = 43.71 ± 13.13 years), as well as 26 healthy adult volunteers (13 females and 13 males between 24 and 60 years of age, mean = 42.35 ± 11.71 years) at Icahn School of Medicine at Mount Sinai were analyzed through IRB approval. Whole brain segmentation was done by Freesurfer, a brain imaging software package, to extract the 3D rendering of the cerebellum, brainstem and 4$^{th}$ ventricle automatically, followed by manual corrections. Brainstem and cerebellum segmentations were then used to create masks for the cerebellar lobular parcellation by SUIT (Fig. 1), a SPM toolbox run by MATLAB 3D volumetric results of cerebellum, tonsil and 4$^{th}$ ventricle were analyzed by Freesurfer, while 2D surface area analysis, angle and tonsil length analysis were performed by Horos.

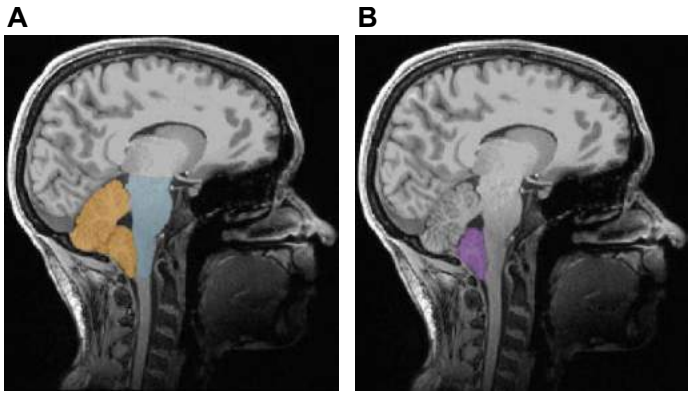


**Figure 1: Cerebellum and brainstem segmentation. Examples of (A) brainstem and cerebellum segmentation by Freesurfer, and (B) tonsil segmentation by SUIT.**

## RESULTS

We summarized some prevalent clinical symptoms in CM-1 patients (total $N$ = 72), and listed in Table 1. Most CM-1 patients experienced headache (72.2%), 2-fold higher than patients who experienced back or neck pain and burry vision. However, no significant age differences for patients exhibiting these symptoms.

**Table 1: Prevalence of symptoms in CM-1 patients.**

| | headache | back and neck pain | blurry vision |
|---|---|---|---|
| $N$ (%) | 52 (72.2%) | 28 (38.9%) | 22 (30.6%) |
| Mean age (σ) | 43.5 (12.8) | 46.2 (11.7) | 45.7 (10.8) |

In our 3D volumetric analysis of the posterior fossa, the mean cerebellar volume is lower in CM-1 patients than in healthy controls (133.19 ± 16.88 $cm^3$ vs. 144.17 ± 12.67 $cm^3$, $p$ = 0.003); while mean tonsillar volume is higher in CM-1 group (10.71 ± 2.71 $cm^3$ vs. 9.23 ± 2.11 $cm^3$, $p$ = 0.0099). The mean 4th ventricular volume was found to be significantly smaller in CM-1 patients (986.23 ± 422.31 $mm^3$ vs. 1433.86 ± 511.81 $mm^3$, $p < 0.0001$) (Fig. 2).

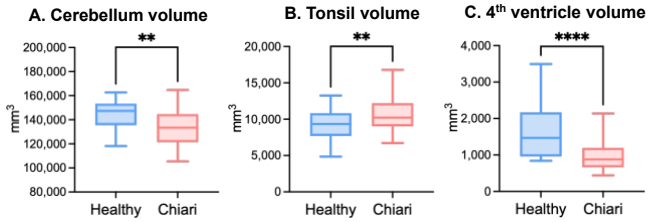


**Figure 2: 3D volumetric analysis of posterior fossa sub-regions. Volume comparison between Healthy subjects and CM-1 patients on (A) Cerebellum, (B) Tonsil, and (C) 4th ventricle.**

In 2D morphological measurements, we analyzed the mean length of tonsillar herniation length in CM-1 patients to be 9.48 ± 4.47 mm. The surface area of the foramen magnum ($A_F$), and areas of the cervicomedullary junction ($A_C$) and tonsils ($A_T$) at the foramen magnum (FM) were also analyzed. The ratio of neural tissue within the area of the FM $(A_C + A_T)/A_F$ was calculated. We found about 3-fold higher ratio in the CM-1 group (67.88 ± 9.73% vs. 18.44 ± 2.97%, $p < 0.0001$) (Fig. 3A), indicating more brain tissues occupied the FM in CM-1 patients.

To find the correlation between length of tonsillar herniation and crowding of the FM, we plotted tonsillar herniation length vs. the ratio of $(A_C + A_T)/A_F$, where we found a positive correlations ($p < 0.0001$) (Fig. 3B).

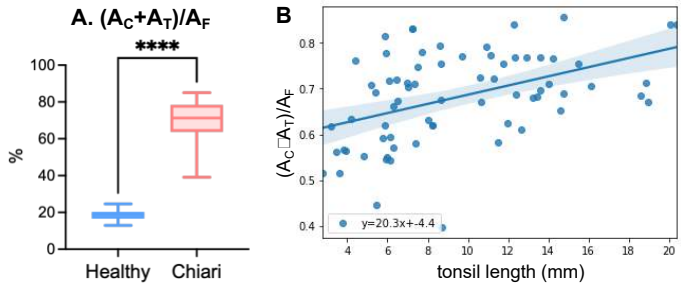


**Figure 3: 2D length and surface area analysis. (A) The comparison between healthy subjects and CM-1 patients of $(A_C + A_T)/A_F$ ratio. (B) A linear regression showing a positive correlation between $(A_C + A_T)/A_F$ ratio and tonsil length ($p < 0.0001$).**

## DISCUSSION

Various conditions can lead to CM-1 syndrome. One possible cause is incomplete development of the occipital bones and small posterior fossa resulting in overcrowding of the cerebellum, thus leading to tonsillar herniation [9]. These structural abnormalities may further cause volumetric changes not yet elucidated. Our 3D volumetric analysis demonstrated significantly larger tonsillar volumes in CM-1 patients compared to healthy controls. Additionally, CM-1 patients exhibited significantly smaller cerebellar volumes. Our 3D volumetric analysis found significantly smaller 4th ventricle volume and more brain tissue $(A_C + A_T)$ at the FM in the CM-1 group ($p < 0.0001$). In addition, a positive correlation between this ratio and tonsillar herniation length, indicates a correlation between tonsillar ectopic and the degree of brain tissue crowding at the FM. The results suggest that tonsillar herniation in CM-1 is also associated with other anatomical abnormalities in the posterior fossa.

Some studies suggest that abnormalities of CSF flow, such as reduced flow velocity, are present in CM-1 patients [10], and could be related to CM-1 symptomatology [3]. As a next step, we are currently investigating the relationships of morphometric characteristics with disturbance of CSF dynamics. The anatomic characteristics found in this study, namely smaller 4th ventricular volumes and increased crowding of the FM with greater tonsillar ectopia may contribute to irregular CSF flow. This may be an explanation for syringomyelia that is not infrequently found in CM-1 patients. Together, these factors may all compound to affect the clinical presentation of the CM-1 patient.

Follow on this research, we will expand more morphometric measurements, such as angle analysis of posterior fossa, to study more complicated morphometric correlations in CM-1 patients. In addition, we will explore more sophisticated correlations between CM-1 conditions and morphometric abnormalities of posterior fossa. This could improve the understanding of disease development, and could potentially build a more reliable model for CM-1 diagnosis.

## REFERENCES


[1] G. K. Bejjani, *Neurosurgical focus*, 11: 1-8, 2001.

[2] A. O. Aboulezz, K. Sartor, C. A. Geyer, M. H. Gado, *Journal of computer assisted tomography* 9: 1033–1036, 1985.

[3] R. F. Sekula, P. J. Jannetta, K. F. Casey, E. M. Marchan, L. K. Sekula, C. S. McCrady, *Cerebrospinal fluid research* 2: 1–7, 2005.

[4] M. C. Speer, D. S. Enterline, L. Mehltretter, P. Hammock, J. Joseph, M. Dickerson, R. G. Ellenbogen, T. H. Milhorat, M. A. Hauser, T. M. George, *Journal of Genetic Counseling* 12: 297–311, 2003.

[5] S. Thakar, V. Kanneganti, B. S. T. Nwotchouang, S. J. Salem, M. Eppelheimer, F. Loth, P. A. Allen, S. Aryan, A. S. Hegde, World Neurosurgery 157: 497–505, 2022.

[6] W. H. Shuman, A. DiRisio, A. Carrasquilla, C. D. Lamb, A. Quinones, A. Pionteck, Y. Yang, M. Kurt, R. K. Shrivastava, Neurosurgical Review 1–11, 2021.

[7] H. Chang, H. Nakagawa, *Journal of Neurology, Neurosurgery & Psychiatry* 74: 344–347, 2003.

[8] E. C. Clarke, D. F. Fletcher, M. A. Stoodley, L. E. Bilston, *Journal of biomechanics* 46: 1801–1809, 2013.

[9] B. Badie, D. Mendoza, U. Batzdorf, *Neurosurgery* 37: 214–218, 1995.

[10] C. Cai, W. J. Oakes, *Seminars in pediatric neurology* 4: 179–191, 1997.

# PRESSURE INJURIES AND WHEELCHAIR USERS: UNDERSTANDING THE ROLE OF FRICTION BETWEEN PANT FABRICS AND THE SEAT

**Archana Lamsal and Tamara Reid Bush, PhD**

Department of Mechanical Engineering, Michigan State University, East Lansing, MI, USA

## INTRODUCTION

Wheelchair users spend a large amount of time seated, and because of this, have a high risk of developing pressure injuries (PIs) particularly on the bottom of the buttocks. The World Health Organization estimates that 1% of the global population requires wheelchairs for increased mobility [1]. In 2010, there were 3.7 million wheelchair users in the USA and 264,000 in Canada [2]. Annually over 2.5 million people suffer from PIs in the US, and nearly 1 million in the UK [3], [4]. PIs are a global problem. PIs can lead to infections, sepsis, and potentially death [5]. Shear forces acting on the seat interface have been linked to PI formation. Shear forces are parallel to person's tissue and occur at the person-chair interface. A larger friction coefficient correlates to a larger capacity of generating shear force between the person and chair. Higher friction leads to larger shear forces which are related to increased risk of pressure injuries [6]. Thus, reducing the coefficient of friction between the seat interface and clothing material (specifically pants) can be a beneficial strategy to reduce the shear forces in wheelchair seating and therefore the incidence of PIs. This same reduction of friction and shear forces can also be beneficial to patients who need to be frequently repositioned in bed or, have chronic muscle spasms, and are thus at an elevated risk of developing a PI [6].

Research showed that the coefficient of friction of fabrics depends on various factors, such as the yarn material, type of weave and surface finish[7], [8]. Yarn with higher frictional properties have been generally known to produce fabrics with higher frictional properties [9]. However, different structure and finish of the fabrics have also been found to affect the friction properties of the material [7]. Because of the interaction of various factors, predicting the frictional property of a fabric is a complex task. Further, little is known about the frictional interactions of commonly used pant fabrics with the seat cover of wheelchair. So, the goal of this study was to determine the coefficient of friction between a vinyl seat cover (common cover coating for wheelchair seats and cushions) and seven commonly used pant fabrics.

## METHODS

A wooden block with cross section of 15 cm x 15 cm and thickness of one centimeter, called the 'sled' was used to carry a test weight during trials. A 110 N weight was attached to the top surface of the sled, and segments of the pant fabric were cut out and attached to the bottom surface of the sled (Figure 1). These fabrics were wrapped around the wooden surface and secured so they were taut (Figure 1a). Seven commonly used fabrics were tested: men's jeans (100% cotton, woven fabric), men's khakis (100% cotton, woven fabric), women's jeans (75% cotton, 24% polyester, woven fabric), women's khakis (93% cotton, 7% spandex, woven fabric), sweatpants (60% cotton, 40% polyester, knit fabric), basketball shorts (100% polyester, knit fabric), women's pull-on pants (100% polyester, woven fabric). The woven fabrics were all twill weaves. The fabric structures of all fabrics are shown in Figure 2.

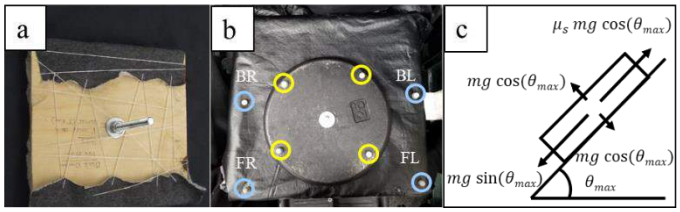


**Figure 1 (a) The top of the sled. Fabric was wrapped around the wooden surface and secured so they were taut (b) A round weight was positioned on top of the sled while on top of seat pan. Yellow circles denote the markers on the sled, and blue circles denote the seat pan markers. The seat pan markers were named front left (FL), back left (BL), front right (FR) and back right (BR). (c) Free body diagram for sled just before it starts to slide on the seat pan.**

Four reflective markers were attached to the weight on top of the sled (Figure 1b). A custom designed chair with a tilting seat-pan (0-45 degrees of tilt) was used. A vinyl seat cover was secured in the seat pan, and four reflective markers were attached to the articulating seat pan. The sled was placed on the seat pan, and the seat pan was tilted starting from 0 degrees (horizontal) until the sled started sliding. The data set was collected for 20 repetitions for each fabric.

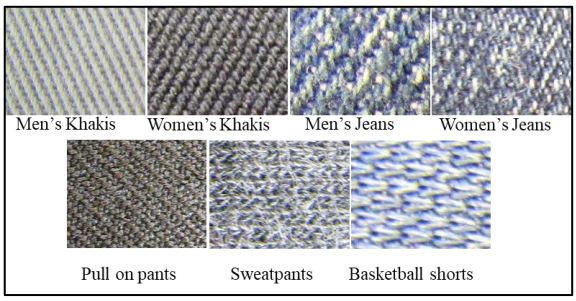


**Figure 2 Fabric structure of different pant fabrics tested. The sweatpants and basketball shorts were knit fabric, whereas the rest of the fabrics were woven with twill weave.**

A multi-camera motion capture system was used to capture the 3D positions of the markers at a sample rate of 100 Hz. The position of the sled ($\vec{s}$) was the average position of the four markers on the sled. The unit vector along the orientation of the seat pan ($\hat{e}$) was determined using two markers- front left (FL) and back left (BL). The position of the sled along the depth of the seat pan ($\vec{r}$) was calculated using Equation 1.

$$\vec{r} = \hat{e}i \cdot (\overrightarrow{FL} - \vec{s}i) \quad (1)$$

The angle of tilt of seat pan $\theta$ was determined using Equation 2.

$$\theta = \tan^{-1}\left(\frac{\hat{e}_z}{\hat{e}_y}\right) \quad (2)$$

The coefficient of static friction was determined using Newton's second law of motion. The free body diagram of the experimental setup just before the sled started sliding on the seat pan is shown in Figure 1c. Equation of motions to determine the coefficient of static friction are given in Equations 3 and 4.

$$\sum F_t = \mu_s mg\cos(\theta_{\max}) - mg\sin(\theta_{\max}) = 0 \quad (3)$$

$$\mu_s = \tan(\theta_{t,max}) \quad (4)$$

To determine the time point when the sled started to slide on the seat pan, a difference (d) between $\vec{r}$ and moving average of r (using 20 preceding data points) at each time point was calculated. The last point when the value of d was less than 1mm was determined as the point where the sled started to move. Thus, the coefficient of static friction was calculated at that point.

## RESULTS

The mean and standard deviations of the coefficients of static friction between the vinyl seat cover and seven different pant fabrics are presented in Table 1. Men's khakis and men's jeans, which were both 100% cotton twill weave fabrics, demonstrated small differences in their coefficients of friction. Women's jeans (75% cotton, 24% polyester) had a smaller friction coefficient compared to men's jeans. Women's jeans and sweatpants, both comprised of cotton-polyester blend, demonstrated similar coefficients. Women's pull-on pants and basketball shorts demonstrated large differences in their friction coefficient despite both being comprised of 100% polyester.

**Table 1 Means and standard deviations of static coefficients of friction ($\mu_s$)**

| Composition | Type of cloth | $\mu_s$ (Mean) | SD |
|---|---|---|---|
| 100% polyester | Women's pull-on pants | 0.46 | 0.01 |
| 93% cotton, 7% spandex | Women's khakis | 0.48 | 0.02 |
| 60% cotton 40% polyester | Sweatpants | 0.51 | 0.02 |
| 75% cotton, 24% polyester | Women's jeans | 0.53 | 0.02 |
| 100% cotton | Men's khakis | 0.54 | 0.03 |
| 100% cotton | Men's jeans | 0.57 | 0.01 |
| 100% polyester | Basketball shorts | 0.59 | 0.01 |

## DISCUSSION

This study determined the coefficient of friction between a vinyl, seat cover and seven common pant fabrics. Understanding the frictional properties of the seat interface is important, especially for wheelchair users who are seated the majority of the day and at high risk for PIs.

Since the reduction of friction and shear force is desired for wheelchair users, pure cotton fabrics such as denim and 100% cotton khakis are not the optimal choices due to their higher friction coefficient. Our data suggest that sweatpants and polyester pull-on pants may be better choices as they have lower frictional coefficients.

Our data have some interesting findings. For example, the basketball shorts and women's pull-on pants had large differences in their friction coefficients despite both consisting of 100% polyester. These differences between fabrics of the same composition could be due to the finish of the fabrics. There might also have been differences in the density and thickness of the yarn or tightness of the weave [10]. Literature has shown that the tighter fabric construction results in lower coefficients of friction [7].

Another interesting comparison was between women's khakis and the basketball shorts. Both fabrics were stretchy, but with a different composition. The stretch of the women's khakis was due to the material properties of spandex whereas the stretch of the shorts was due to the looser fabric construction. This could be one of the reasons behind higher friction coefficient of the shorts.

The results show that the coefficient of friction can vary with difference in content, construction, as well as finish. Pants normally chosen by the users might be producing high friction and increasing the risk of PI formation. Thus, there is a need for better guidelines and understanding of frictional behavior of pant fabrics for the wheelchair users. The results also indicate that pants designed for males (from our selection) mostly had higher friction coefficients than pants designed for females. So, the male wheelchair users might need to be more cautious in choosing their pants.

## REFERENCES


1. Williams E. et al., BMC Int. Health Hum. Rights, 17:1, 1-12, 2017
2. Torkia C. et al., Disab. Rehab. Assist. Tech., 10:3, 211-215, 2015
3. Gefen A., EWMA Journal, 19:2, 7-13, 2018
4. Wood J. et al., BMJ Open Qual., 8:3, 2019
5. Bryan C. et al., Arch. of Int. Med., 143:11, 2093-2095, 1983
6. Hanson D. et al., Adv Skin Wound Care, 23:1, 21-24, 2021
7. Ajayi J., Text. Res. J., 62: 2, 87–93, 1992
8. Ajayi J., Text. Res. J., 62:1, 52–59, 1992
9. Ajayi J., and H. M. Elder, J. Test. Eval., 22:5. 463–467, 1994
10. Jeddi A. et al., J. of Text. Instit., 79:2, 103-109, 2010

# SEATED SHEAR FORCES ARE AFFECTED BY PANTS AND CUSHION COVER MATERIALS

**J. Scott PhD and T.R. Bush PhD**

Department of Mechanical Engineering, Michigan State University, East Lansing, MI, USA

## INTRODUCTION

Over 3 million wheelchair users live in the United States, over half of whom will develop a pressure injury (PI) in their lifetime [1,2]. PIs are painful and disrupt the lives of those experiencing them because treatment includes unloading the affected body region, disengaging people from their lives. Not only are PIs disruptive, but expensive, costing the United States an estimated $27 billion per year [3].

Shear forces have been consistently cited as a risk factor for the development of PIs, particularly in tissues deeper than the skin [4]. These forces are present on the buttocks and thighs while seated, creating risk for PI development in those regions. Although back recline is the most popular repositioning strategy to reduce the risk of PIs in the buttocks and thighs, some studies have suggested that it may actually increase shear forces in those areas [5,6]. Thus, there is a need to evaluate the effects of back recline on shear and potential alternative ways to reduce shear at the buttock and thigh-to-cushion interface.

One potential way that shear forces on the buttocks and thighs may be mitigated is by using cushion covers that have low coefficients of friction when contacting typical clothing materials. Examples of applications where low friction materials are already applied include transfer sheets in hospitals. As such, this type of material may be used to reduce shear forces experienced on the buttocks while seated.

Therefore, the goals of this work were to 1) evaluate three cushion covers' abilities to reduce shear on the buttocks and thighs while in reclined position and 2) determine coefficients of friction for pairs of three cushion cover materials and two clothing materials.

## METHODS

10 able-bodied individuals (5 male, 5 female) volunteered for this study (IRB #16-681). An articulating chair was built with independently rotating seat pan and chair back supports. The supports were mounted on six-axis load cells and covered by a 1-inch layer of foam. Cushion cover materials were attached on top of the foam and included vinyl, one-layer nylon, and two-layer nylon covers. Pants materials included denim and sweatpants. Two different experiments were conducted in a motion capture space, with markers on the corners of the seat pan, on the back of the chair, and on participants' lateral epicondyles (Figure 1).

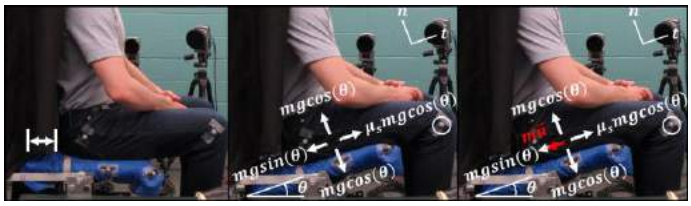


**Figure 1. A participant sitting on the chair without touching the back (left), a free body diagram of person before they begin sliding (middle), and while they are sliding (right). The coordinate system is in the top right and lateral epicondyle marker circled.**

The first experiment was to determine the effects of pants, cushion cover, and back recline angle on shear forces on the buttocks and thighs. Participants sat in the chair with their buttocks pushed back as far into the chair as possible. Motion capture and force data were collected while the back was reclined to 15° and then inclined back to 0° recline (vertical). Shear force data were collected at 5°, 10°, and 15° of back recline. The angle of the back recline was recorded by the markers on the back of the chair. A two-way repeated measures ANOVA and post-hoc Tukey tests were used to determine between-material pair and between-recline differences in shear forces.

The second experiment was to determine the coefficients of friction between the pants and cushion covers. The seat pan was covered with one of the cushion cover materials, and participants sat in the chair

wearing one of the pants materials with their back not contacting the back of the chair (Figure 1). The seat pan was tilted until the participant began sliding. Sliding along the anterior-posterior axis of the seat pan was tracked with markers on participants' lateral epicondyles and on the front and back left corners of the seat pan using Equations 1 and 2.

$$\hat{e_1} = \frac{\overrightarrow{FL} - \overrightarrow{BL}}{\|\overrightarrow{FL} - \overrightarrow{BL}\|} \quad (1)$$

$$\vec{q} = \hat{e_1} \cdot \left(\vec{k} - \overrightarrow{BL}\right) \quad (2)$$

Where $\overrightarrow{FL}$ was the front left marker on the seat pan, $\overrightarrow{BL}$ the back left, $\hat{e_1}$ the unit vector along the anterior-posterior axis of the seat pan, $\vec{k}$ the average position of the two markers on the lateral epicondyles, and $\vec{q}$ the position along the axis of the seat pan. The vertical and horizontal components of $\hat{e_1}$ were used to determine the angle of seat pan tilt ($\theta$), and $\vec{q}$ was used with the motion capture data collection frequency (60 Hz) to determine the acceleration of the participant by dividing the difference in $\vec{q}$ between frames by the frequency twice. The static and kinetic coefficients of friction were determined by Equations 3 and 4.

$$\mu_s = \tan(\theta_{max}) \quad (3)$$

$$\mu_k = i\tan(\theta_{max}) - \frac{|\vec{a}|}{g\cos(\theta_{max})} \quad (4)$$

Where $\theta_{max}$ was the maximum angle of tilt before the participant started sliding, and $|\vec{a}|$ was the magnitude of their acceleration.

## RESULTS

Shear forces at 5°, 10°, and 15° of back recline for all material pairs are displayed in Figure 2. Shear forces increased with back recline, regardless of cushion cover ($p < .0001$). Further, the largest shear forces occurred with sweatpants on vinyl. Though there were no significant between-pants differences in shear forces, shear forces on the two-layer nylon cover were reduced by 20% relative to the vinyl cushion cover.

The coefficients of friction for the material pairs including the one and two-layer nylon covers are displayed in Figure 3. Because of the large coefficients of friction for the material pairs that included the vinyl cushion cover, the participants never slid on the vinyl cover during coefficient of friction experiments. Instead, the seat pan tilt was too large for participants to keep their backs from contacting the chair. The coefficients of friction on the two-layer nylon cover were smaller than on the one-layer nylon cushion for both pants materials.

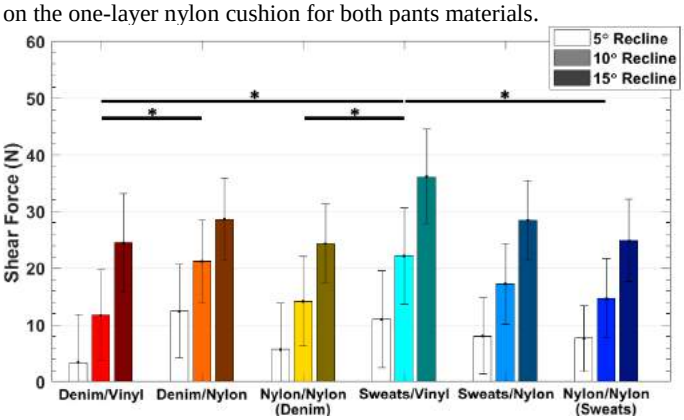


**Figure 2. Shear forces on the seat pan at three recline angles for all pairs of pants and cushion cover materials. Significant differences between shear on material pairs are indicated by asterisks (*).**

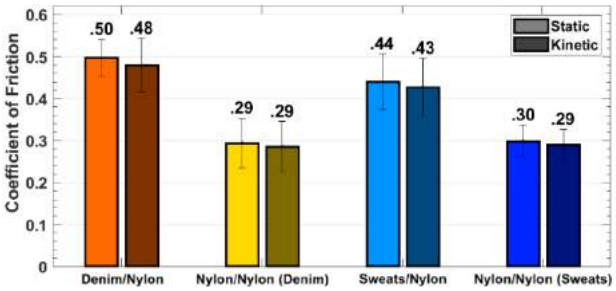


**Figure 3. Static and kinetic coefficients of friction between pants and cushion cover materials.**

## DISCUSSION

The goals of this work were to establish the coefficients of friction for material pairs that may be seen at the soft tissue-cushion interface and to evaluate their abilities to reduce shear forces on the buttocks and thighs while seated. This work is integral to mitigating the risk of developing PIs because it investigates a current repositioning method used to reduce PI risk and a potential method for reducing shear forces.

The data collected from this study indicated that increasing back recline angle increased the shear forces on the buttocks and thighs. This finding held true, regardless of the pants-cushion cover material pair. Moreover, this finding is of the utmost importance because of the ubiquity of using back recline as a pressure relief strategy. The data from this work suggest that increasing back recline angle may actually increase the risk of developing a PI instead of reducing it, which means that the most common repositioning strategy to relieve pressure might need to be reevaluated.

Our results also showed that the vinyl cushion cover had too large of coefficients of friction when paired with pants materials to be determined with the current method and that shear forces on the seat pan were larger with that cover than with the two-layer nylon cover. These findings suggest that materials used to make cushion covers are a potential mechanism by which shear forces can be reduced on the buttocks and thighs. Further, a specific material like the nylon material used in transfer sheets has the potential to reduce the shear forces on the buttocks and thighs. Such a strategy may be able to mitigate the increase in shear forces on the buttocks and thighs due to increases in back recline angle. Doing so may allow wheelchair users to continue using back recline with a smaller increase in risk in PI development.

Future work will need to consider the inclusion of wheelchair users in shear force studies and extension to real-world settings outside of the laboratory. These will be used to confirm that the results hold true in more realistic settings and applications.


## ACKNOWLEDGEMENTS

Funding for this project was provided by NSF grant CBET-1603646


## REFERENCES


[1] Brault, *US Census Bureau*, 2012.
[2] Hubli, et al, *Spinal Cord*, 2020.
[3] Padula & Delarmente, *Int. Wound J.*, 2019.
[4] Hoogendoorn, et al, *J. Tis. Via.*, 2017.
[5] Ding, D., et al., *J. Reh. Res.*, 45, 2008.
[6] Hobson, *J. Rehab. Res. Dev.*, 1992.

# FLOW DYNAMICS ASSESSMENT IN A PHYSIOLOGICAL AORTIC ARCH USING A VALIDATED COMPUTATIONAL FRAMEWORK

**Z. Wang (1,2), B. Vogl (3), R. Gadhave (3), A. El Shaer (4), J. Crestanello (4), M. Alkhouli (4), H. Hatoum (3,5)**

(1) Department of Mechanical and Aerospace Engineering, Ohio State University, Columbus, OH
(2) Simulation Innovation and Modeling Center, Ohio State University, Columbus, OH
(3) Department of Biomedical Engineering, Michigan Technological University, Houghton, MI
(4) Department of Cardiovascular Medicine, Mayo Clinic, Rochester, MN
(5) Health Research Institute, Center of Biocomputing and Digital Health and Institute of Computing and Cybernetics, Michigan Technological University, Houghton, MI

## INTRODUCTION

The flow in 3D curved pipes is much more complicated compared to that in straight pipes. All biological systems are characterized by curvatures and bifurcations that make the geometry more challenging to model. For simplification, the majority of experimental flow assessment studies did not account for the physiological 3D spatial curvature and geometry of the ascending aorta as opposed to the efforts done computationally especially with patient-specific geometries.

The existence of secondary flows in curved pipes was noted by Eustice 1910[1], and a complete assessment of the flow features pertaining to vortices in the ascending aorta was performed by Dean 1927[2]. Additionally, the additional pressure drop imposed by the curvature is important to assess for a complete ventricular pumping energy understanding and evaluation[3]. The locations of maxima and minima in the wall shear stress (WSS) are also of utmost importance in the aorta because these may represent sites for plaque buildup on vessel walls, and thus may play a major role in atherogenesis[3].

The aim of this work is to (1) validate the computational framework using in-vitro particle image velocimetry (PIV) experiments and (2) assess the flow dynamics in a physiologically curved aortic arch. The importance of validated computational assessment in this body of work is to allow the visualization and quantification of the 3D flow features that 2D PIV in experiments cannot capture.

## METHODS

Large Eddy Simulation (LES) was adopted in our study with the capability to resolve the wall regions that contain a wide range of scales of flow motion from both temporal and spatial domains. It can directly resolve the large scales of turbulence everywhere in the computational domain and model those small-scale motions in the near-wall region. The wall-adapting local-eddy viscosity (WALE) sub-grid scale model was used to account for the effects of small eddies on the resolved flow. All simulations were calculated using STAR-CCM+ (Siemens, Inc., Germany) with all y+ treatment. The wall y+ treatment method combines the high y+ wall treatment for coarse meshes and the low wall y+ treatment for fine meshes, which gives similar results to the low y+ treatment as y+≤1 and to the high y+ treatment for y+≥30. In addition, it is also designed to produce reasonable results within the buffer layer (i.e., 1<y+<30) for intermediate meshes. The working fluid has a density of 1060 kg/m$^3$ and a kinematic viscosity of 3.5cSt.

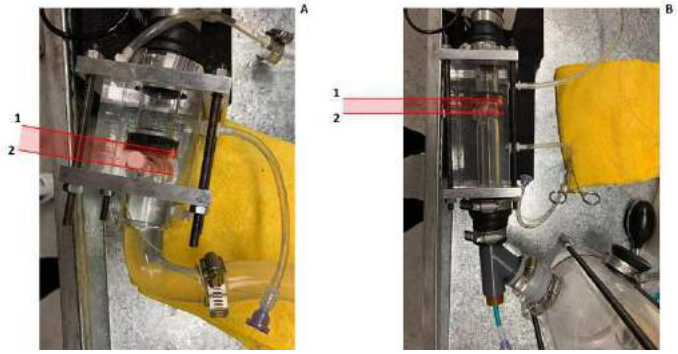


**Figure 1. Experimental setup detailing the location of the 23mm SAPIEN 3 Ultra in the curved (A) and straight (B) aortic root chambers. Locations 1 and 2 represent the valve entrance at 2.1mm and valve limit at 3.9mm, respectively.**

The boundary conditions adopted in this study were obtained from pressure and flow data obtained experimentally using an in-vitro model of the same computational one. Briefly, the experiments were performed using the curved aortic model along with a typical straight one under pulsatile physiological conditions. The cardiac output was 5 L/min, the heart rate was 60 beats per min and the pressures imposed were 120/80 mmHg in the presence of a 23 mm SAPIEN 3 Ultra valve. Several pressure measurements were taken using Millar catheters going from upstream to downstream of the valve. The velocity conditions right

at the valve leaflets were adopted as boundary conditions for the simulations. Figure 1 shows the experimental setup for both aortic models.

*Model Validation*

The model validation was performed between a straight aorta model experimentally through PIV experiments and computationally. Given the 3D complex geometry of the aortic arch, 2D PIV was not possible. Thus, in this study, we used the straight model for validation, and we show the results of the aortic curvature flow through computational modeling only. **Figure 2** shows the instantaneous velocity distributions in the central plane (i.e., z=0) at the acceleration, peak systole, and deceleration phases. The upper images are from experimental measurement and the lower ones are from simulation. Agreement was found between velocity magnitudes between the experiment and the simulation along with the overall general flow features.

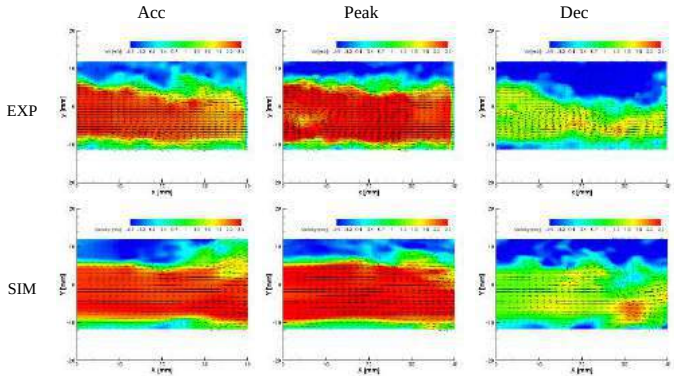


**Figure 2: Comparison of velocity contours at Acceleration (Acc), Peak Systole and Deceleration (Dec) phases: Experiment (upper row); Simulation (Lower row). The legend shows the velocity contours with magnitudes ranging from 0 to 2.5 m/s. EXP denotes experimental results and SIM denotes simulation results.**

## RESULTS

The velocity contours in the central plane of the curved aorta are shown

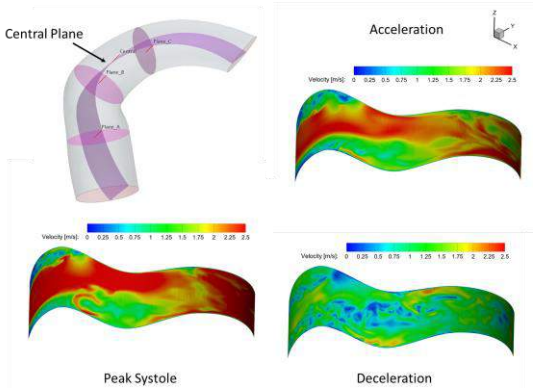


**Figure 3: Velocity contours at the center plane of the curved aorta at acceleration, peak systole, and deceleration phases of the cardiac cycle. Velocity legend ranges from 0 to 2.5 m/s.**

in Figure 3. The location of the maximum axial velocity is shifted toward the outer wall of the aorta. Figure 4 shows the velocity distribution in the cross section of each of the planes marked on the figure at peak systole. These planes indicate the locations where the curvature changes. With these geometric changes, different velocity patterns are seen as well. It is important to note that from construction

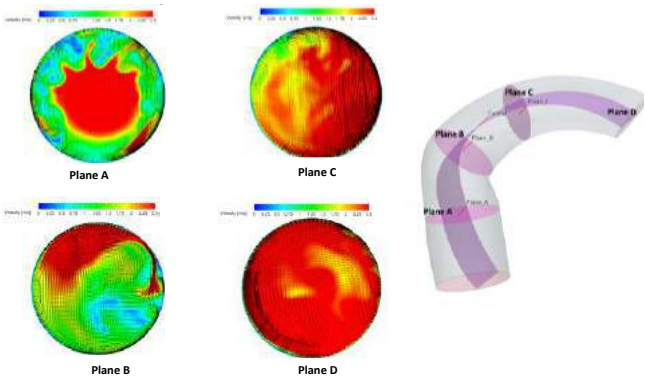


**Figure 4: Velocity contours and vectors in planes A, B, C and D at different curvatures of the ascending aorta during peak systole. The diameter at planes C and D is smaller than that in planes B and A, hence the increase in velocity magnitude. The velocity contours range from 0 to 2.5 m/s in magnitude.**

of the aortic arch[4], the diameter decreases as the descending aorta is reached. This decrease in diameter leads to an increase in velocity as shown in the figure. Additionally, on these planes, the shift in velocity maxima is also apparent. Figure 5 shows the WSS distribution in the straight and curved aortic arches. More concentrated WSS maxima are shown in the curved aortic model.

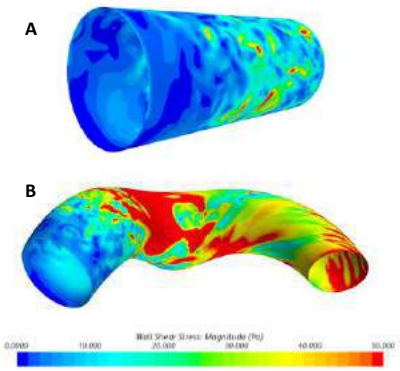


**Figure 5: Wall shear stress contours of the (A) straight and (B) curved aortic arches at peak systole.**

## DISCUSSION

In this study, we validated and established a computational framework to assess the flow dynamics in the ascending aorta with a 3D physiological curvature. We found great agreement with PIV results and CFD results in the straight aortic model and therefore, we extrapolated our computational framework to the aortic arch modeling. The results show the shift in axial velocity towards the outer wall, which is expected given the centrifugal effects induced by the aortic curvature[3]. The spatial and temporal effects of the 3D curvature leads to different velocity profiles. Additionally, the low velocities observed on one side of the aortic walls combined with the elevated non-physiological WSS results show are associated with atherosclerosis and plaque deposits[5,6].

## REFERENCES

[1] Eustice, J. 1910. Proc. R. Soc. London Set. A84:107-18
[2] Dean, Wo R. The London, Edinburgh, and Dublin Philosophical Magazine and Journal of Science 4.20 (1927): 208-223.
[3] Berger, S. A., et al. Annual review of fluid mechanics 15.1 (1983): 461-512.
[4] Boufi, M et al., Eur J Vasc Endovasc Surg, 53(5):663-670, 2017
[5] Kronzon, Itzhak, et al. Circulation 114.1 (2006): 63-75.
[6] Kojima, Keisuke, et al. Journal of Atherosclerosis and Thrombosis (2020): 56598.

SB³C2022
Summer Biomechanics, Bioengineering and Biotransport Conference
June 20-23, Eastern Shore, MD, USA

# A SOFT TISSUE GRASPING DEVICE FOR ENHANCED ROTATOR CUFF REPAIR INSPIRED BY PYTHON TEETH

**Iden Kurtaliaj (1), Ethan D. Hoppe (2), Yuxuan Huang (2), Mark Lipkin (2), Thomas Gardner (3), Liana Tedesco (3), Sohil Desai (1), Silvio Torres Betancur (1), Linda Effiong (3), William N. Levine (3), Guy M. Genin (2), Stavros Thomopoulos (1)**

(1) Department of Biomedical Engineering, Columbia University, New York, NY, USA
(2) NSF Science and Technology Center for Engineering Mechanobiology, Washington University, St. Louis, MO, USA
(3) Department of Orthopedic Surgery, Columbia University, New York, NY, USA

## INTRODUCTION

Rotator cuff tears are common, affecting more than 50% of patients over the age of 65 and resulting in pain and loss of shoulder function [1]. Rotator cuff repair is one of the most common shoulder procedures performed clinically. Recent literature shows healing after rotator cuff repair to be very unpredictable, with reported failure rates as high as 94% [2]. In the current standard double-row suture bridge repair, the suture punctures through bone and tendon at only two anchor points, concentrating stress so that sutures can cut through the tendon and cause the repair to fail (Fig. 1) [3]. Previously, inspired by the remarkable grasping ability of python teeth on their prey, we showed a strong relationship between tooth curvature and tendon grasping, and determined the optimal tooth shape for grasping soft tissue [4]. Furthermore, we identified an optimal tooth array design for a grasping device to augment rotator cuff tendon-to-bone repair [4]. In this study, we applied this biomimetic approach to augment rotator cuff repair. We hypothesized that a clinically relevant tooth array device interposed between tendon and bone can enhance tendon-to-bone repair mechanics through better load distribution across the repair site (Fig. 1). We performed 3D finite element models (FEM) to study stresses near the tip of the tooth and to determine the effect of tendon thickness on tooth gripping strength. We extended the single tooth and the tooth array optimization to the design of a rotator cuff-specific device. To assess the efficacy of the device, we tested its strength in a cadaveric rotator cuff repair model.

## METHODS

*Device design:* To translate the idealized model and shear lag test results from prior studies for clinical tendon-to-bone repair, a rotator cuff-specific device was designed using SolidWorks (Dassault Systèmes, Waltham, MA, USA). The device consisted of the optimized array of teeth placed in a curved, flexible base that matched the curvature and dimensions of the human humeral head supraspinatus tendon attachment site (0.67" x 0.4" footprint area [5]). The fit and qualitative grasping ability of the device were evaluated in human cadaver shoulders for 3 different device prototypes. To optimize fixation of the device into bone, 9 cadaveric shoulder rotator cuff repairs were completed with various iterations of the device. A series of device design changes were implemented based on hands-on feedback from orthopedic surgeons.

*Finite element model (FEM):* 3D finite element simulations were performed to interpret how the shape of the teeth affected the peak stresses in the tendon and the contact area between the tendon and the bone (Abaqus, Dassault Systèmes, Waltham, MA, USA). Consistent with models of healing tendon, transversely isotropic material properties were used (Young's modulus $E_1$=450 MPa, $E_2$=$E_3$=100 MPa, shear modulus $G_{12}$ = 0.1 $E_1$, Poisson ratio $\nu$=0.55); the tooth and base were isotropic with E=100 MPa and $\nu$=0.3. Periodic boundary conditions were applied on the four lateral faces, and a master-slave algorithm with a penalty for interpenetration was used to enforce frictionless contact boundary conditions between the tendon, tooth, and bone; tooth and bone were fully adherent. The upper surface was traction free. The tendon was displaced in the direction opposite that of the tooth. Convergence studies were performed.

*Human cadaver rotator cuff repairs:* To assess the device in a clinically relevant rotator cuff repair setting, paired human cadaver rotator cuff samples were used (Anatomic Gift Foundation, Inc., Hanover, MD). Clinically relevant supraspinatus tendon tears were created with a scalpel and then repaired using a double-row suture bridge technique, in a paired fashion either with or without the device (n=5 per group). After repair, humerus-supraspinatus tendon-muscle samples were carefully isolated and stored at 4 °C overnight.

*Biomechanical testing:* The humerus was secured in a pipe with two orthogonal k-wires and Rockite cement. The pipe was secured close to the humeral head to prevent flexion. The rotator cuff muscle was secured in a freezing clamp using liquid $N_2$. The humerus was angled at

120° relative to the tendon so that muscle was pulled parallel to the tendon fibers at the insertion. Repaired supraspinatus samples were held in tension at 15 N for 20 s and then pulled in uniaxial tension to failure at 0.5 mm/s. Force and grip displacement data were recorded (MTS, Eden Prairie, MN, USA), and maximum force, stiffness, and energy to failure were determined.

*Statistical analysis:* All data are shown as mean ± standard deviation. Paired t-tests were used to evaluate the efficacy of the device with statistical significance set to $p < 0.05$ (GraphPad Prism 7).

## RESULTS

FEM results showed that stresses in the tendon were elevated in the region of the tip of the tooth (Fig. 2a). Peak stresses in the tooth were dominated by flexure, and occurred approximately midway up the tooth (Fig. 2a). Peak stresses increased as tendon thickness increased relative to tooth size, and decreased with tendon curvature (Fig. 2b). When iterating on the design of the device, the amount of tissue in contact with the bone increased with increasing base curvature and tooth length.

The final design of the rotator cuff-specific device consisted of an array of teeth placed in a curved, flexible base that matched the curvature and dimensions of the human humeral head supraspinatus tendon attachment site (Fig. 1). Fixation of the device onto bone was accomplished through 4 suture holes, placed in the 4 corners of the rectangular base. Mechanical testing results revealed that testing of the device led to 28%, 43%, 62%, 139% and 141% improvements in strength (i.e., maximum force) relative to the paired repair without the device (average strength improvement of 83%; Fig. 3b). Consistent with this, energy absorption was significantly increased with use of the device (Fig. 3c). The trend towards increased repair stiffness with the device was not significant statistically (p=0.07; Fig. 3c).

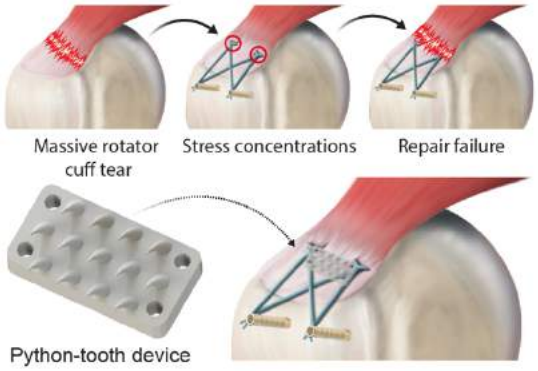


**Figure 1. Schematic of double row suture repair final (top) and implementation of device with current methods (bottom)**

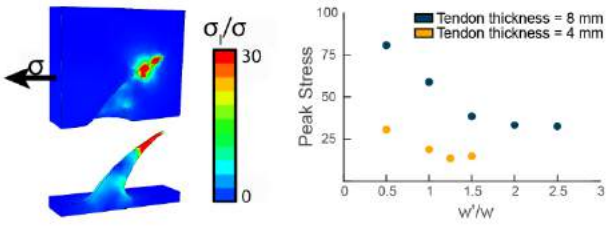


**Figure 2. (a) 3D FEM simulations showed elevated peak principal stress ($\sigma_1$) in the tendon near the tooth tip. (b) Peak stresses as a function of tendon thickness**

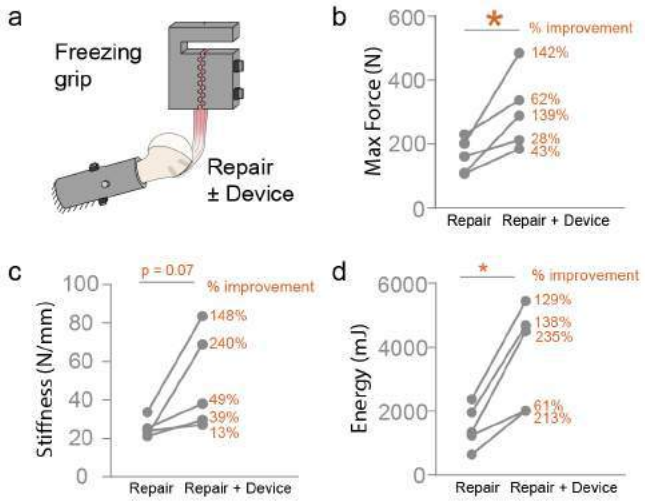


**Figure 3. (a) Setup of mechanical test (b-d). Effect of device on maximum force, stiffness and energy to failure.**

## DISCUSSION

Rotator cuff repair using current techniques and hardware has reached a limit. Therefore, there is a major clinical need to develop novel approaches for improving tendon-to-bone fixation and reducing failure rates after surgical repair.

Integrated experiments and modeling provided insight into how to adapt a concept based upon python teeth to tendon-to-bone reattachment. 3D modeling revealed that stresses in tendon were elevated in the region of the tip of the tooth, indicating that the tooth tip is crucial in maintaining maximum tendon grip. Modeling also showed that tooth size can be optimized to the thickness of a tendon to improve gripping strength. This is of particular interest as we apply these findings and adapt them to better repair other commonly injured tendons such as the patellar and Achilles tendons.

Human rotator cuff cadaver experiments indicated that the python-tooth-inspired device interposed between tendon and bone significantly enhanced rotator cuff repair mechanics. The base of the device must be made in various sizes to accommodate for variations in the size of the attachment footprints across patients.

The efficacy of the device was likely related to improvement of stress distribution. Instead of relying on a small number of suture anchor points, the device augmented the current repair through better load distribution by transferring stress between tendon and bone over the entire footprint area. Combined with current repair techniques, the proposed grasping device nearly doubled repair strength. Improving fixation of tendon to bone during rotator cuff repair by this amount would have a significant impact on outcomes after rotator cuff repair by reducing the high re-rupture rates currently observed.

## ACKNOWLEDGEMENTS

This work was supported by Nationals Institute of Health (EB016422).

## REFERENCES

[1] Sher, J et al., *J Bone Joint Surg Am,* 77(1):10-5, 1995
[2] Galatz, L et al., *J Bone Joint Surg Am,* 86-A:219-24, 2004
[3] Linderman, S et al. *Acta Biomater* 70:165-176, 2018
[4] Kurtaliaj, I et al., *ORS 2019*, Austin, TX
[5] Curtis, A et al *Arthroscopy: The Journal of Arthroscopic and Related Surgery*, 22(6):603-609, 2006

SB³C2022
Summer Biomechanics, Bioengineering and Biotransport Conference
June 20-23, Eastern Shore, MD, USA

# AUTOMATED IMAGE ANALYSIS OF HUMAN INDUCED PLURIPOTENT STEM CELL DERIVED CARDIOMYOCYTES AND CARDIAC MICROTISSUE

**H. Kobeissi (1), S. Mohammadzadeh (2), E., Lejeune (1)**

(1) Department of Mechanical Engineering, Boston University, Boston, MA, USA
(2) Department of Systems Engineering, Boston University, Boston, MA, USA

## INTRODUCTION

Heart disease is the leading cause of death worldwide [1]. Because of this pressing societal challenge, cardiac drug discovery and cardiac tissue engineering are highly active areas of research. There is not only a pressing need to discover new treatments for cardiac disease, but also a pressing need to understand unintended cardiac-related adverse effects of drugs used for other purposes [2]. Recently, there has been a growing focus on human induced pluripotent stem cell derived cardiomyocytes (hiPSC-CMs). This technology presents a feasible approach to acquiring human cells and future patient-specific treatment plans [3]. These cells can be studied either in isolation, or as components of tissue engineered constructs (Fig. 1). For example, hiPSC-CMs can self-assemble into beating microtissue. However, despite this functionality, hiPSC-CMs are both morphologically and functionally distinct from the cells in mature cardiac tissue (Fig. 1).

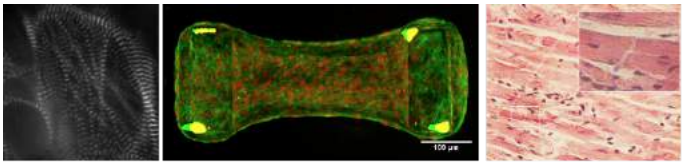


**Figure 1. Example of disordered myofibrils in hiPSC-CMs, a hiPSC-CM microtissue that formed between two flexible posts, and highly ordered mature cardiac tissue for contrast.**

The immature and non-linear structure of hiPSC-CMs makes it difficult to extract quantitative information from image-based assays. Recently, there has been significant work in this direction where z-disks in hiPSC-CMs are fluorescently labeled (Fig. 1) and advanced image processing and analysis software is used to segment and track sarcomeres and approximate their length with respect to time [3]. However, these state-of-the-art computational methods have room for improvement in both the efficacy of sarcomere segmentation and tracking under laboratory conditions, and strategies for comprehensive data analysis. Here we present our recent steps forward in automated quantitative analysis of beating hiPSC-CMs and cardiac microtissue constructs.

## METHODS

Here we introduce "Sarc-Graph," a computational framework to segment, track, and analyze sarcomeres in fluorescently tagged immature and non-linear hiPSC-CMs. Our framework includes functions to segment z-disks and sarcomeres, track z-disks and sarcomeres in movies of beating cells, and perform automated spatiotemporal analysis and data visualization. Here we briefly note a few key features of our framework. First, we created an algorithm to segment z-disks and sarcomeres (Fig. 2a). Of note, our algorithm does not require any input parameter tuning, and is able to reliably capture non-linear sarcomeres in the presence of noise. Then, we track z-disks and sarcomeres independently using the Python package trackpy which is based on the Crocker–Grier algorithm [4]. Finally, we use Gaussian process regression to interpolate data between lost movie frames when necessary and feasible [5]. The segmentation and tracking process take only a few minutes to run on a laptop computer.

Next, we introduce two novel analysis approaches. First, we treat tracked and segmented components (i.e., sarcomeres and z-disks) as fiducial markers and use them to compute the approximate deformation gradient of the entire tracked population. This represents a new quantitative descriptor of hiPSC-CM function (Fig. 2b). Second, we construct spatial graphs where z-disks correspond to nodes and sarcomeres correspond to edges. This makes measuring the network distance between each sarcomere straightforward and makes it possible to compute statistics that include information about the network structure (Fig. 2c). In addition, we provide additional analysis tools that compute descriptive metrics previously proposed in the literature such as the Orientational Order Parameter [6]. We showcase and validate our

approach with both synthetic and experimental movies of beating hiPSC-CMs. The Sarc-Graph software can be freely accessed through GitHub: https://github.com/elejeune11/Sarc-Graph [7]. Example data and code to generate and analyze synthetic data with a known ground truth are also included on GitHub.

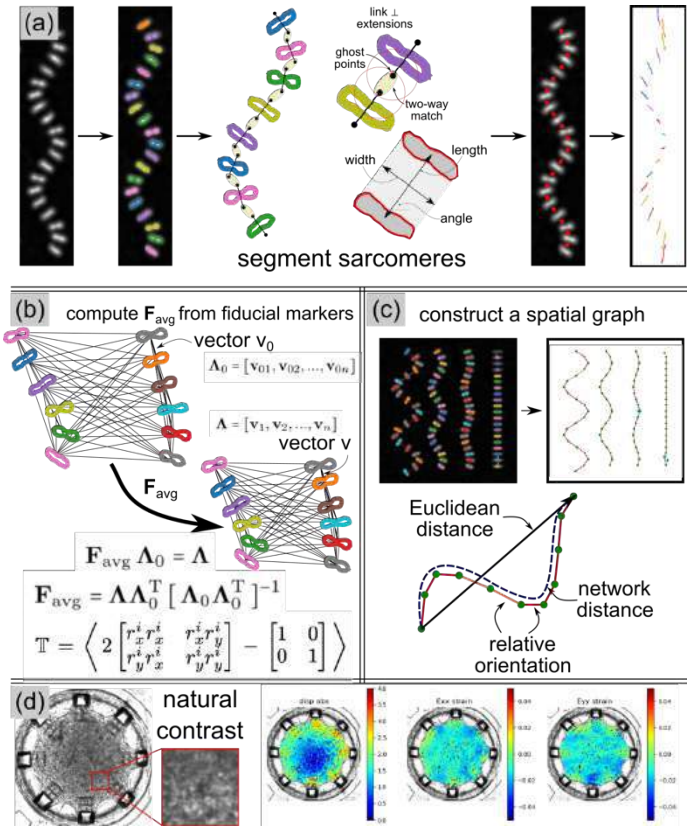


**Figure 2: Key aspects of our image analysis pipelines: (a) segmenting and tracking individual sarcomeres; (b) computing key quantities of interest such as average deformation and structure from images and movies; (c) constructing spatial graphs of myofibril structure; and (d) analyzing strain in movies of beating microtissue.**

Finally, we move up one spatial scale and create software to analyze cardiac microtissue. Specifically, we extend Sarc-Graph to analyze static 3D confocal images of hiPSC-CM based microtissue and we implement a digital image correlation approach to compute surface strains from movies of beating microtissue (Fig. 2d).

## RESULTS

Here we show one example of Sarc-Graph run on movies of beating hiPSC-CMs (Fig. 3, see also [7]). In this example, we are able to segment ≈800 sarcomeres per frame and successfully track 539 sarcomeres. The time series plot of normalized sarcomere length with respect to frame number show five distinct contraction events during the movie. Though the individual sarcomeres are clearly not perfectly in sync, there is enough of a unifying pattern for these peaks to emerge. These five distinct contraction events are also reflected in the average deformation plot. We also show the spatial graph representation of the example and a plot of normalized cross-correlation between pairs of individual sarcomere time series curves with respect to network distance. We note briefly that additional information, including movies, more experimental data examples, and validation examples on synthetic data, are available both on GitHub and in our manuscript [7].

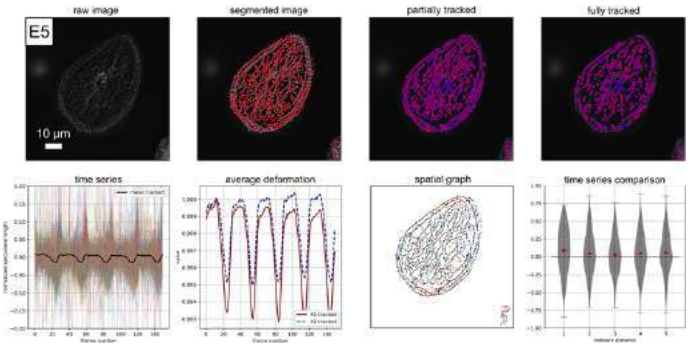


**Figure 3: Example set of results from running Sarc-Graph. For the corresponding movie, please see S5 Movie in [7].**

## DISCUSSION

These results clearly show the importance of developing computational tools and metrics to analyze this type of imaging data. From the raw data alone, it is not possible to either objectively discern collective sarcomere contraction in irregularly contracting hiPSC-CMs or quantify spatial and temporal patterns. With our software, we are able to both extract information about individual sarcomeres, and summarize mechanical behavior in a manner that is suitable for statistical comparison between groups.

The objective of this work was to provide an open source computational framework to quantitatively analyze images and movies of beating hiPSC-CMs on both the individual cell and microtissue spatial scales. With our framework, we are able to automatically segment and track a higher number of sarcomeres than other state of the art tools (see comparison in [7], appendix S4), and we introduce two important new approaches for the analysis of beating hiPSC-CM: a method for computing an average deformation gradient based metric, and a method for treating the hiPSC-CMs as spatial graphs. In addition, we have recently extended our Sarc-Graph software to 3D, where we can segment confocal z-stacks of regions of interest in cardiac microtissue (results forthcoming). Finally, we have created an open source digital image correlation pipeline for computing strain in movies of beating microtissue that relies solely on the natural contrast of bright field microtissue images (results forthcoming). Looking forward, we see this work as an important tool for substantial future study of hiPSC-CM behavior with applications ranging from drug discovery to tissue engineering. We encourage others to download and use our open source software for their own research purposes.

## ACKNOWLEDGEMENTS

This work was supported by the CELL-MET Engineering Research Center NSF ECC-1647837, the Boston University Hariri Junior Faculty Fellowship, the David R. Dalton Career Development Professorship, and an American Heart Association Career Development Award #856354.

## REFERENCES

[1] Murphy, Sherry L., et al. "Mortality in the united states, 2017," 2018.
[2] de Korte, Tessa, et al. *Annu Rev Pharmacol Toxicol.* 60: 529-551, 2020.
[3] Toepfer, Christopher N., et al. *Circ Res.* 124.8: 1172-1183, 2019.
[4] Allan, et al. soft-matter/trackpy: Trackpy v0.4.2 (Version v0.4.2). Zenodo. http://doi.org/10.5281/zenodo.3492186
[5] Pedregosa et al., *JMLR* 12:2825-2830, 2011.
[6] Morris, Tessa Altair, et al., *PLoS Computational Biology* 16.3 (2020): e1007676.
[7] Zhao, Bill et al., *PLOS Computational Biology* 17(10): e1009443.

# MICRORNA THERAPIES TO PREVENT VETILATION INDUCED LUNG INJURY DURING THE ACUTE RESPIRATORY DISTRESS SYNDROME

**Ghadiali S.N. (1,2,3), Fei, Q. (2), Gabela-Zuniga, B. (1), Oyster, T. (1), Shukla, V. (1), Ballinger, M. (2,3), Englert, J.A. (2,3)**

(1) Department of Biomedical Engineering, The Ohio State University, Columbus, Ohio, USA
(2) Davis Heart & Lung Research Institute, The Ohio State University, Columbus, Ohio, USA
(3) Department of Internal Medicine, Division of Pulmonary & Critical Care Medicine, The Ohio State University, Columbus, Ohio, USA

## INTRODUCTION

The global COVID19 pandemic has highlighted the lethality associated with the acute respiratory distress syndrome (ARDS) [1]. ARDS occurs when bacterial or viral infections cause excessive lung inflammation, disruption of the alveolar-capillary barrier and severe hypoxemia. ARDS patients often require mechanical ventilation (MV) and the mechanical forces generated during ventilation exacerbates lung injury and inflammation [2]. Since protective ventilation strategies are not able to eliminate the injurious mechanical stimuli, developing novel therapeutics that can prevent the mechanotransduction process responsible for ventilation induced lung injury (VILI) is a major area of research. Our group has used a novel combination of in-vitro organ-on-a-chip modeling, in-silico computational modeling and in-vivo animal and human studies to identify the biomechanical and molecular mechanisms responsible for VILI [3]. Specifically, we have identify mechanosensitive microRNAs and used nanotechnology gene delivery tools to demonstrated that over-expression of microRNA-146a (miR-146a) can be used to dramatically mitigate VILI.

## METHODS

As shown in Fig 1A, microfabrication technologies were used to develop a novel ventilator-on-a-chip (VOC) platform that incorporates co-cultures of primary human alveolar epithelial cells, endothelial cells and alveolar macrophages on an electrospun fibrous matrix. Specifically, primary cells obtained from human donors under IRB-2014H0367 or from commercial sources and/or human epithelial/endothelial/macrophage cell lines were seeded on electrospun matrices of collagen coated polyurethane. Platinum electrodes were used to monitor trans-epithelial electrical resistance (TEER) and fluorescent microscopy was used to quantify cell injury (plasma membrane rupture). In addition, ELISA was used to quantify pro-inflammatory cytokine levels in the apical and basal compartments. As shown in Fig 1B, cell were exposed to the major mechanical forces associated with MV, i.e. volutrauma (stretch), barotrauma (pressure) and atelectrauma (surface tension/shear). Standard lipofectamine transfection techniques were used to investigate how over-expression of miR-146a and miR-155 influenced the degree of barotrauma and atelectrauma respectively.

In-vivo animal studies utilized 7–9-week-old C57BL/6J wildtype and miR-146a knockout mice. Animals were subjected to an injurious ventilation protocol (12mL/kg tidal volume and 0 positive end expiratory pressure) for 4h [3,4]. The flexivent system was used to monitor changes in lung mechanics and bronchoalveolar lavage (BAL) fluid was analyzed for pro-inflammatory cytokine and total protein content. Cell pellets from the BAL as well as whole lung tissue were analyzed by PCR for miR-146a levels. Mice were pre-treated with a

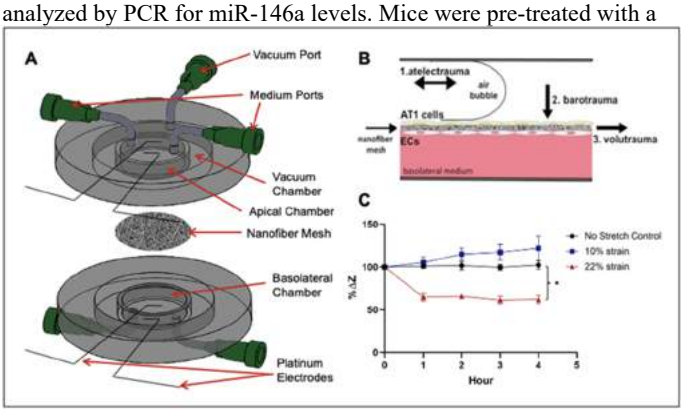


**Figure 1: A.** Schematic of ventilator-on-a-chip (VOC) **B**. Schematic of cell co-culture and application of injurious mechanical forces **C.** Effect of injurious strain (22%), physiologic strain (10%) and no stretch control (n=3/condition) on TEER measurements (data normalized to 0Hr. *p<0.05

solid lipid nanoparticle (LNP) containing a pre-miR-146a or scramble control construct 24h and 0h before ventilation. LNPs were prepared using an ethanol injection method [3].

Human studies were conducted by collecting bronchoalveolar lavage (BAL) fluid under an approved IRB protocol (IRB-2016H0009) from 15 control non-ventilated subjects, 11 ventilated subjects without ARDS and 10 ventilated subjects with ARDS. RNA was isolated from the cell pellet and PCR was used to quantify the expression of several microRNAs.

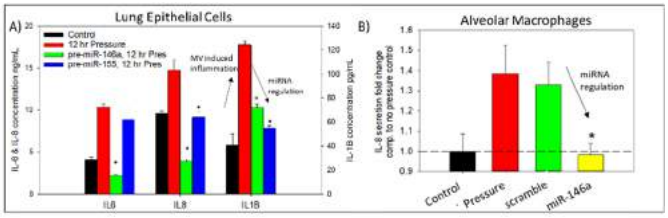


**Figure 2:** A) Over-expressing miR-146a (green) and miR-155 (blue) reduces pressure-induced IL-6, IL-8 and IL-1β cytokine secretion in primary human airway epithelial cells (EpC). *p<0.05 with respect to 12 hr pressure. B) Over-expressing miR-146a downregulates pressure-induced IL-8 secretion from AMs. *p<0.05 with respect to pressure control and scramble.

## RESULTS

As shown in Fig 1C, cyclic strain magnitude had a significant effect on barrier formation and disruption where low levels of physiologic strains (10%) promoted increased barrier resistance while large pathological strains (22%) promoted disruption of the barrier and reduced resistance. As shown in Figure 2, barotrauma experiments indicate that 12h of high transmural pressure results in increased pro-inflammatory cytokine secretion (IL-6, IL-8 and IL-1β) in both alveolar epithelial cells (Fig 2A) and alveolar macrophages (Fig 2B) and that over-expression of miR-146a in both epithelial cells and macrophages significantly reduces the inflammatory signaling caused by barotrauma. Atelectrauma experiments indicate that co-culture of AMs with EpCs exacerbates the cell injury/plasma membrane disruption caused during airway reopening (data not shown). Interestingly, overexpression of miR-155 in epithelial cells alters cytoskeletal structure and reduces atelectrauma but over-expression of miR-155 in macrophages exacerbates mechanically-induced inflammation and injury (data not shown).

Animal studies indicated that miR-146a knockout mice exhibit more inflammation (i.e. increased pro-inflammatory cytokine secretion, Figure 3AB) and lung injury (i.e. barrier disruption as measured by increased protein in the BAL, Figure 3C) during MV. Interestingly, wild-type mice exhibited a modest increase in miR-146a levels but still suffer from VILI as measured by increase pro-inflammatory cytokine secretion and barrier disruption (data not shown). Importantly, the use of a non-targeted LNP to delivery miR-146a resulted in a dramatic 100-1000x over-expression of miR-146a in both epithelial cells and macrophages (Figure 3D) and this resulted in a significant reduction in inflammation and injury during MV (Figure 3EF).

Finally, we investigated the expression of several miRs (miR-27b, miR-21, miR-33a, miR-144, miR-155 and miR-146a) in human patients and found that miR-146a and miR-155 levels were significantly higher in patients undergoing MV alone while the level of these miRs were not upregulated in patients suffering from ARDS. This data suggests that miR-146a/155 are mechanosensitive miRs in human subjects and that the failure to upregulate these anti-inflammatory miRs may play a role in the development of ARDS.

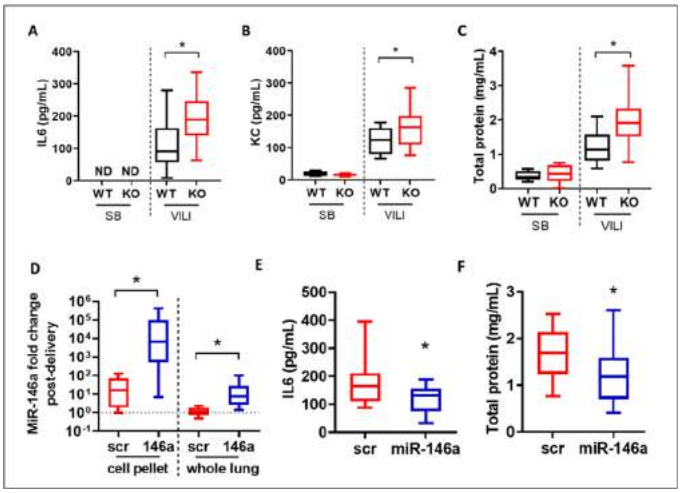


**Figure 3: Knock-out mice lacking miR-146a exhibit** AB) increased IL-6 and KC (IL-8 analogue) expression and C) increased barrier disruption as measured by BAL protein. Nanoparticle delivery of miR-146a resulted in A) dramatic over-expressing in cell pellet and whole long and E) reduced pro-inflammatory cytokine expression and F) reduced barrier disruption *p<0.05 with respect to wild-type and scramble controls.

## DISCUSSION

We have identified as set of mechanosensitive microRNAs (miR-146a and miR-155) in human subjects and have demonstrated using in-vitro and in-vivo animal models. Importantly, changes in miR expression during mechanical stress appears to be an insufficient compensatory response that doesn't mitigate VILI on its own. However, therapeutic over-expression of miR-146a to supra-physiological levels resulted in a significant reduction in lung injury and inflammation during MV. Therefore, nanoparticle mediated over-expression of miR-146a may represent a novel therapeutic way to reduce VILI during ARDS.


## ACKNOWLEDGEMENTS

NIH Grants: R56 HL142767, R01 HL142767-01A1 and Department of Defense Grant W81XWH-19-1-0210


## REFERENCES


[1] Lentz, S et al, Am J Emerg Med, 38(10):2194-2202, 2020.
[2] Beitler, JR et al, Clin Chest Med, 37(4):633-646, 2016.
[3] Bobba, C et al, Nat Commun, 12(1):289, 2021.
[4] Lee, H et al, JCI Insight, 6(14):e137708, 2021.

SB³C2022
Summer Biomechanics, Bioengineering and Biotransport Conference
June 20-23

# EFFECTS OF MICROPIPETTE HANDLE DIAMETER AND INCLUSION OF FINGER REST ON BASILAR THUMB JOINT CONTACT MECHANICS

**Nolan M. Norton (1), Kenneth J. Fischer (1,2)**

(1) Bioengineering Graduate Program
University of Kansas
Lawrence, KS, USA

(2) Mechanical Engineering
University of Kansas
Lawrence, KS, USA

## INTRODUCTION

The use of manual micropipettes has been associated with a high prevalence of upper extremity and work-related musculoskeletal disorders in laboratory workers [1]. This may be due to a combination of repetitive motions during pipetting and the amplification of forces from the thumb tip to the basilar thumb joint [2] that lead to tendonitis, carpal tunnel syndrome, other musculoskeletal injuries, and may increase risk of osteoarthritis (OA). These pathologies cause substantial physical pain/discomfort, increase health care costs, and cause employees to miss time at work. An investigation into ergonomic micropipette design could help to reduce these musculoskeletal pathologies and their consequent negative impacts.

One method to investigate micropipette design parameter effects on stresses within joints is magnetic resonance imaging (MRI) based modeling. This offers a non-invasive *in vivo* approach to estimate joint forces, contact pressures, contact area and contact location(s), and tissue stresses in joints during functional activities. MRI-based modeling allows for good soft tissue visualization and subject-specific geometries. It also minimizes assumptions for model boundary and loading conditions. This is accomplished through the collection of higher resolution unloaded scans (i.e. with a relaxed hand) for finite element model building. Then lower resolution loaded scans (i.e. during simulated pipetting) are used with image registration to obtain displacement boundary conditions for the finite element analysis [5-6].

A modular MRI-compatible micropipette simulator enabled analyses of the effects of base design parameters on contact measures within joints of the hand through MRI-based modeling. In this pilot study, the effects of handle diameter and the inclusion or exclusion of a finger rest on contact measures within the basilar thumb joint were examined. We hypothesized that increasing handle diameter would decrease contact measures in the basilar thumb joint. We also hypothesized that the inclusion of a finger rest would decrease contact measures in the basilar thumb joint.

## METHODS

***Micropipette Simulator and Handle Designs –*** The micropipette simulator was divided into multiple parts: a button to be pushed by the thumb, a carbon fiber plunger/rod to transfer force through a handle, an O-ring on the far end of the rod to prevent the rod and button from falling out of the handle, a two-piece spherical base, and a pneumatic rubber bulb inside the base. Each handle set (with button and push-rod) can be screwed onto the spherical base (with rubber bulb). The rubber bulb was attached via plastic connectors and tubing to a pneumatic pressure system with pressure regulator to assure consistent pre-pressure (before the pipette plunger is pushed) and a precision pressure transducer to assure consistent plunger force. This system was designed for minimal friction and a had a pressure precision of 0.001 psi. A custom LabVIEW code provided visual feedback to the subjects and allowed them to attain and hold the pressure near a specified target during the MRI scan.

**Figure 1. From left to right: 40 mm handles with and without a finger rest, 25 mm handles with and without a finger rest, and 12 mm handles with and without a finger rest. Each handle also has the plastic button, carbon fiber rod, and O-ring (not visible)**

A combination of three handle diameters (12 mm, 25 mm, and 40 mm) and the inclusion or exclusion of a finger rest resulted in six handles that were tested per subject (Figure 1). All the handles had a length of 127 mm.

***Subject Information and Imaging Protocol*** – Three male subjects (average age = 30 years, range = 28-33 years) and two female subjects (average age = 27.5 years, range = 27-28 years) were recruited for the study. MR image sets for each subject were acquired for two types of conditions. One image set was collected while the hand was in a relaxed state where the wrist and thumb ray were imaged at a high resolution (in-plane voxels 0.22 mm by 0.20 mm and out-of-plane thickness 0.5 mm) over a duration of 4.5 minutes. This image set was used to create finite element model geometries. The second group of image sets was collected while a subject was using the micropipette simulator (loaded state). The loaded state images were collected at a reduced resolution (in-plane voxel 0.31 mm by 0.31 mm and out-of-plane thickness 1.0 mm) over a duration of 188 seconds. These images were used to create kinematic transformations that placed the trapezium into the loaded position for the finite element models. A total of six loaded state image sets were collected per subject (one for each micropipette handle variation). A simulator target pressure of 1.125 psi was used for consistent micropipette plunger depression force during image collection. Handles without a finger rest were tested first due to concerns about subject fatigue limiting the number of possible tests. The image set of the relaxed state was collected next. Finally, the handles with a finger rest were tested. Within each type of handle, they were tests from smallest diameter to largest diameter. Subjects wore an MRI-compatible wrist brace with 20º wrist extension during testing to assure consistent hand/wrist position (and thus more consistent data overall) between subjects.

***Finite Element Model Definition and Statistical Analysis*** – MR images for both the relaxed and loaded states were segmented using ScanIP 7.1. The metacarpal and trapezium were isolated in the loaded state images. The metacarpal, trapezium, and their respective cartilages were isolated in the relaxed state images. ScanIP was also used to generate tetrahedra meshes of the bone and cartilage geometries from the relaxed state scan. Kinematic transformations for the trapezium were defined using image registration between loaded and unloaded scans [5-6]. Once the trapezium was in the loaded position, contact was eliminated for the start of the simulation, through an initial separation displacement. Displacements were then applied to the trapezium during the simulation to restore the trapezium to the loaded position. The cartilage was assumed to be a Neo-Hookean material with an effective relaxation modulus of 1 MPa and a Poisson's ratio of 0.2 (due to the length of the scans) with frictionless contact. Bone was assumed to be a rigid body. Contact area, contact force, and contact pressure were primary simulation outputs. Two-way repeated measures analysis of variance (ANOVA) and one-way repeated measures ANOVA were used to test for statistical differences in contact measures. Statistical significance was set at $p < 0.05$.

## RESULTS

Images from one female subject had poor image quality could not be processed. For the remaining subjects, contact force decreased with increasing handle diameter, and it increased with the presence of a finger rest (Figure 2). Contact area and peak contact pressures followed the same pattern for changes in handle diameter and finger rest.

Two-way repeated measures ANOVA results indicated that there were no significant interactions between the diameter and finger rest factors for contact area ($p = 0.9$), contact force ($p = 0.9$), or peak contact pressure ($p = 0.8$). There were significant differences between the levels of diameter for contact area ($p = 0.01$), contact force ($p = 0.01$), and peak contact pressure ($p = 0.004$). There were also significant differences between levels of finger rest for contact area ($p = 0.007$) and contact force ($p = 0.02$). One-way repeated measures ANOVA results indicated that significant differences only between the 12 mm handle diameter and 40 mm handle diameter for contact area ($p = 0.002$), contact force ($p = 0.007$), and peak contact pressure ($p = 0.03$). Contact pressure location was consistent within subjects.

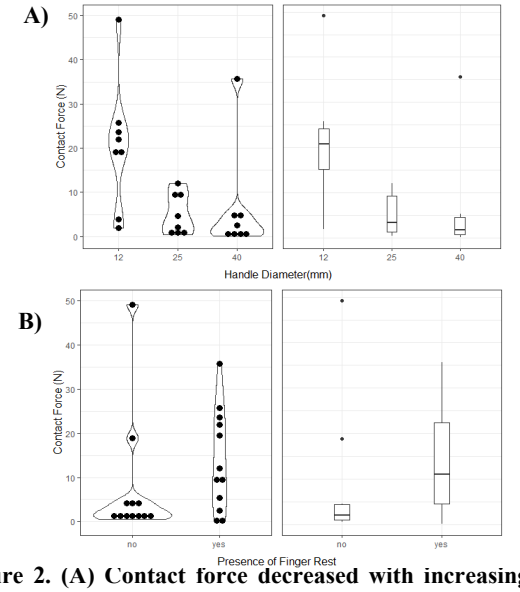


**Figure 2. (A) Contact force decreased with increasing handle diameter. (B) Contact force increased with the presence of a finger rest.**

## DISCUSSION

Decreasing contact measures with increasing handle diameter confirmed our first hypothesis. However, increased contact measures with the presence of a finger rest did not confirm our second hypothesis. This result likely resulted from the order of testing. All handles with a finger rest were tested after handles without a finger rest, so fatigue (which can increase co-contractions and overall force) may have contributed to increased contact measures. We expected that the finger rest would provide additional stabilization which would reduce the necessary grip strength and muscle tension. The chosen order put (assumed) easier handles later in the sequence, to help subjects complete tests with every handle. Future studies should randomize the order of micropipette handles and increase rest breaks between tests to reduce the effects of fatigue.

## ACKNOWLEDGEMENTS

We would like to thank the University of Kansas General Research Fund for support of this project. We would also like to thank the Hoglund Biomedical Imaging Center at the University of Kansas Medical Center.

## REFERENCES

[1] McKean, ML et al., *G. Ital. Med. Lav. Ergon*, 27(2):240-243, 2005.
[2] Wu, JZ et al., *J. Biomech. Eng.,* 137(8):084501/1-084501/7, 2015.
[3] Wu, JZ et al., *J. Biomech.,* 47(2):392-9, 2014.
[4] Wu, JZ et al., *Med Eng. Phys.,* 35(12):1801-10, 2013.
[5] Johnson, JE et al., *J. Orthop. Res.,* 31(9):1455-1460, 2013.
[6] Johnson, JE et al., *J. Biomech.,* 46:1548-1553, 2013.

# EFFECT OF VENOUS VALVE MORPHOLOGY ON FLOW CONDITIONS CONDUCIVE TO THROMBOSIS

**Jacob T. Biesinger (1), Matthew S. Ballard (1)**

(1) Mechanical Engineering, Utah Valley University, Orem, Utah, USA

## INTRODUCTION

Venous valves serve a vital role in the proper return of blood from the lower extremities. These valves open and close with pressure oscillations to enable blood to return to the heart against the pull of gravity. Thrombi are known to form in the regions near the venous valves, referred to as deep vein thrombosis (DVT). Once DVT develops, the thrombi may release from the vein wall and travel toward the lungs to become a pulmonary embolism (PE). PE is a major cause of death in the U.S. responsible for approximately 200,000 deaths annually, a figure that likely underestimates the effect of PE since it can be difficult to detect and thus often goes unnoticed [1]. DVT and PE are especially concerning for individuals who are immobile for an extended period of time, such as during a hospital stay, or long plane ride.

This study is an investigation of the effect of valve morphology on disease-conducive flow conditions. Specifically, mechanical properties of the valve, as well as the three-dimensional shape are varied to identify the effect on shear stress, residence time and fluid stasis. Results of this study will help to establish an understanding of how doctors can better identify at-risk patients for whom to take preventative measures against DVT and PE.

## METHODS

A model of the venous valve region is made by creating a rigid sinusoidal vessel which is then intersected by two planar membranes. The portion of the planes internal to the vessel forms the elastic valve, and the valve tips are trimmed to a crescent shape, as shown in Figure 1. The intersecting lines of the vessel and valve are fixed, simulating connection of the valve to the vessel wall. The vessel is filled with a viscous fluid, which is driven by a dynamically-oscillating pressure gradient.

To effectively model the dynamics of the valve and fluid, a fully-coupled, three-dimensional fluid-solid-interaction model is used. Fluid mechanics are solved using a lattice Boltzmann method (LBM), an effective method for simulation of incompressible viscous flows interacting with complex and moving boundaries [2]. Solid mechanics are modeled using a lattice spring method (LSM), modeling the solid valve leaflets as a network of mass points connected by harmonic springs [3]. The LBM and LSM models are fully-coupled via appropriate boundary conditions [4,5].

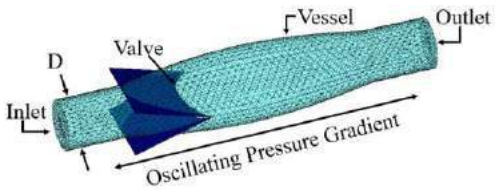


**Figure 1: Venous valve model with vessel and intersecting valve.**

Geometric parameters varied for this study are the valve length and the depth of the crescent at the valve tip. The stiffness of the valve is also varied using a dimensionless stiffness, K [5]:

$$K = \frac{4\,k_b}{\pi\,D^3 \Delta P} \tag{1}$$

## RESULTS

Flow in the vicinity of the valve can be seen in the normalized velocity magnitude plots given in Figure 2. Flow is driven past the valve by an oscillating pressure gradient. A favorable pressure gradient causes the valve to open and fluid to flow in the forward direction (left to right in Figure 2A). As the pressure gradient reverses, the valve closes (Figure 2B) and once fully-closed (Figure 2C) blocks any significant reverse flow from occurring. As seen in Figure 2D, this results in an overall flow rate waveform giving a significant amount of

forward flow followed by a short duration of negative flow when the pressure gradient is reversed but the valve has not yet closed, and finally very little flow once the valve has closed. Thus, a net positive flow effect is obtained.

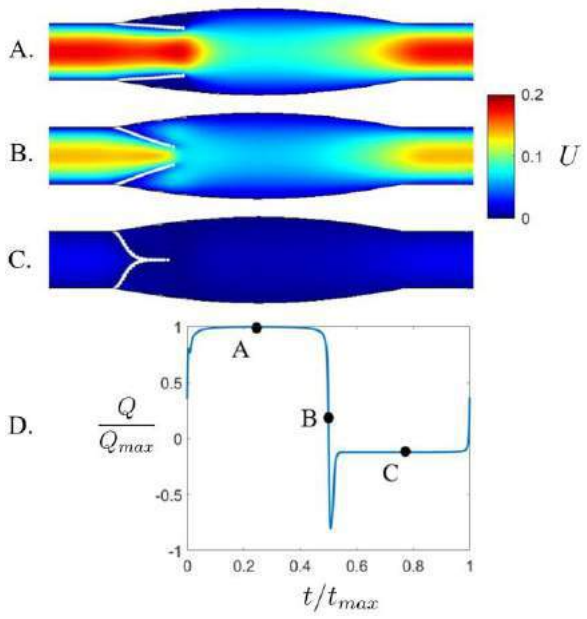


**Figure 2: Velocity profile of: A) fully open valve, B) closing valve, C) closed valve. D) flow rate versus time.**

Since shear stress is an important factor in thrombus formation, the fluid shear stress magnitude (normalized by the maximum shear stress in Poiseuille flow through a tube with diameter D) in the region of interest is plotted in Figure 3 for the same time snapshots as given in Figure 2.

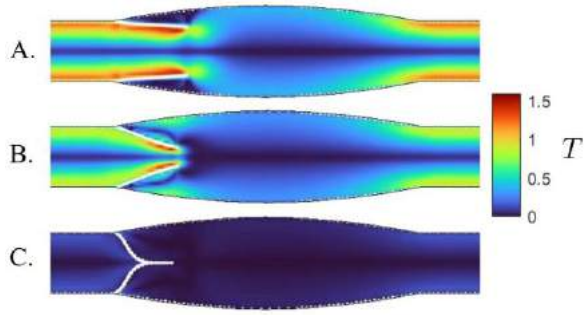


**Figure 3: Shear stress profile of: A) fully open valve, B) closing valve, C) closed valve.**

In this system, thrombi are likely to form in areas of low and oscillatory shear stress, high residence time, fluid stasis [6,7]. Figure 2 shows that the fluid behind the valve experiences low velocity, and presumably high residence time. Additionally, Figure 3 shows that the region behind the valve also experiences low shear stress, making this an area of concern.

While detailed quantification of shear stress, residence time and fluid stasis cannot be addressed in this abstract and will be addressed in the presentation, here we briefly show the effect of valve stiffness on the fluid shear stress distribution in the vicinity of the valve. Each column of Figure 4 represents simulation data with a different value of *K*, and gives the distribution of the fluid domain in the shear range given at left. Increasing valve stiffness gives a general decrease in shear stress. This increases the amount of the system that is at risk of thrombus formation due to low shear stress. This shift occurs due to the decrease in valve deflection allowing less flow, leading to reduced velocity and shear stress. Additionally, the region behind the valve is bigger for low deflection, as the valve cannot deflect as close to the vessel wall.

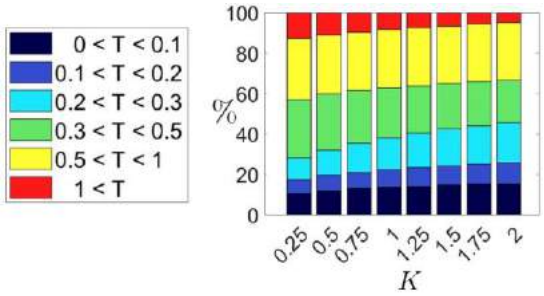


**Figure 4: Shear stress distribution with varying stiffness.**

## DISCUSSION

A fully-coupled FSI model was used to study the effect of venous valve morphology on resulting flow conditions. Low fluid velocity and low shear stress behind the valve indicate that it is an area likely to give conditions conducive to thrombosis. Further, valve stiffening reduces shear stress, also making thrombosis more likely. In the full version of this study, we investigate in more detail the effect of valve morphology on shear stress, as well as on residence time and fluid stasis. This study informs a deeper understanding of the effect of valve morphology on flow conditions conducive to thrombosis, and can help pave the way to improved risk analysis to inform measures for prevention of DVT and PE, especially in admitted hospital patients.


## ACKNOWLEDGEMENTS

We gratefully acknowledge the Utah Valley University Undergraduate Research Summer Institute Grant (UVU URSIG), UVU Undergraduate Research Scholarly and Creative Activities (URSCA), and the National Science Foundation (NSF) CMMI 2138836 grant for financial support.


## REFERENCES


[1] G.T. Gerotziafas, M.M. Samama, Prophylaxis of Venous Thromboembolism in Medical Patients, 2004.

[2] S. Succi, The Lattice Boltzmann Equation for Fluid Dynamics and Beyond, Oxford University Press, Oxford, 2001.

[3] G.A. Buxton, R. Verberg, D. Jasnow, A.C. Balazs, Phys. Rev. E 71 (2005) 56707.

[4] A. Alexeev, R. Verberg, A.C. Balazs, Macromolecules 38 (2005) 10244–10260.

[5] M. Ballard, K.T. Wolf, Z. Nepiyushchikh, J.B. Dixon, A. Alexeev, Biomech. Model. Mechanobiol. (2018) 1–14.

[6] S.P. Downie, S.M. Raynor, D.N. Firmin, N.B. Wood, S.A. Thom, A.D. Hughes, K.H. Parker, J.H.N. Wolfe, X.Y. Xu, Am J Physiol Hear. Circ Physiol 294 (2008).

[7] D.N. Ku, D.P. Giddens, C.K. Zarins, S. Glagov, Pulsatile Flow and Atherosclerosis in the Human Carotid Bifurcation Positive Correlation between Plaque Location and Low and Oscillating Shear Stress, 1985.

SB³C2022
Summer Biomechanics, Bioengineering and Biotransport Conference
June 20-23, Eastern Shore, MD, USA

# WALL SHEAR STRESS TOPOLOGICAL SKELETON VARIABILITY PREDICTS ATHEROSCLEROTIC PLAQUE GROWTH IN HUMAN CORONARY ARTERIES

**Giuseppe De Nisco (1), Eline Hartman (2), Valentina Mazzi (1), Diego Gallo (1), Claudio Chiastra (1), Joost Daemen (2), Jolanda Wentzel (2), Umberto Morbiducci (1)**

(1) PolitoBIOMed Lab, Department of Mechanical and Aerospace Engineering, Politecnico di Torino, Turin, Italy
(2) Department of Cardiology, Biomedical Engineering, Erasmus MC, Rotterdam, Netherlands

## INTRODUCTION

Although low wall shear stress (WSS) has become the consensus hemodynamic mechanism for coronary atherosclerosis, the exact biomechanical stimulus affecting atherosclerosis evolution is still undetermined [1]. In this regard, recently there is a marked in the topological skeleton analysis applied to the WSS vector field [2,3]. The WSS topological skeleton consists of fixed points, where the WSS vector vanishes, and manifolds, namely the regions connecting them, where the WSS vector field contracts or expands. The interest in such an analysis is dictated by its ability to (1) identify flow features usually classified as "disturbed flow", linked to atherosclerosis onset and development, and (2) quantify the contraction/expansion action exerted by the WSS on the endothelium. Very recent findings have demonstrated a link between the WSS topological skeleton features and adverse vascular response [4-7], showing its capability to concur to the identification of the complex biomechanical stimulus affecting atherosclerosis evolution [6,7].

Based on these pieces of evidences this study tests the ability of WSS topological skeleton features to predict the temporal evolution of coronary artery plaque burden (PB), a hallmark of atherosclerosis development, in 49 patient-specific computational models of human coronary arteries. The final aim is to probe whether hemodynamic quantities giving a direct measure of the variability of the contraction/expansion action exerted by the blood flow on endothelial cells are capable to predict longitudinal local PB changes.

## METHODS

**Patient population.** An overview of the methods is provided in Figure 1. Forty-eight hemodynamically stable patients from the IMPACT study data set [8] were used in the analysis. The IMPACT study enrolled patients with acute coronary syndrome and with at least one non-stented non-culprit coronary segment accessible for intracoronary imaging. The presence of previous coronary artery bypass graft surgery, 3-vessel disease, renal insufficiency (creatinine clearing < 50 ml/min), left ventricular ejection fraction < 30%, and atrial fibrillation, were considered as exclusion criteria. All patients underwent percutaneous coronary intervention of the culprit coronary vessel. After successful treatment, a non-culprit coronary segment (right - RCA, left anterior descending - LAD, or left circumflex - LCX coronary artery) was imaged by coronary computed tomography (CCTA) angiography and intravascular ultrasound (IVUS) at the time of the intervention (T1) and at 1 year follow-up (T2).

**Computational hemodynamics.** The lumen geometry of 49 imaged coronary arteries (18 RCA, 18 LAD, and 13 LCX,) was reconstructed at T1 [8]. IVUS images were segmented into lumen contours and stacked upon the 3D CCTA centerline. Luminal regions proximal and distal to the IVUS segment were added using lumen segmentations from the CCTA images. Transient computational fluid dynamics simulations were performed by using the finite volume method (Fluent, Ansys Inc.). Blood was modelled as non-Newtonian Carreau fluid. Patient-specific inflow and outflow boundary conditions were derived from ComboWire Doppler flow velocity measurements. If velocity-based flow measurements were inaccurate or not available, a generalized flow rate [9] was prescribed as inflow BC, while a proper diameter-based scaling law [9] was applied to estimate the flow ratio at the outflow sections.

**Wall shear stress-based descriptors.** The most widely adopted descriptors of WSS magnitude, multidirectionality and topological skeleton features were tested. In detail, three canonical WSS-based descriptors of "disturbed flow", i.e., TAWSS, OSI, and RRT, were computed. Additionally, the transverse WSS (transWSS), representing the average WSS component acting orthogonal to the time-average

WSS vector direction, was considered [10]. Moreover, the contraction/expansion action exerted by hemodynamic shear forces on the endothelium was quantified according to a Eulerian-based method for the analysis of the WSS topological skeleton based on the divergence of the WSS unit vector field ($DIV_{WSS}$) [2]. Negative (positive) $DIV_{WSS}$ values at the luminal surface identify WSS contraction (expansion) regions. Here the quantity Topological Shear Variation Index (TSVI) was used as a measure of the variability of the local contraction/expansion action exerted by the WSS along the cardiac cycle. Technically, the TSVI is defined as [4,5]:

$$TSVI = i\left\{\frac{1}{T}\int_0^T [DIV_{WSS} - \overline{DIV_{WSS}}]^2 dt\right\}^{1/2} \quad (1)$$

where T is the cardiac cycle duration.

**Statistical analysis.** The analysis was focused at the IVUS imaged arterial segments. Each IVUS segment was divided into 3mm/45° sectors [8]. In all IVUS frames at T1 and T2, lumen and external elastic membrane contours were semi-automatically segmented, and PB was assessed as the ratio between plaque area and total vessel area, multiplied by 100. The mean values of the difference between PB measurements at T2 and T1 was evaluated for each sector and used for the analysis (PB growth). Hemodynamic descriptors were averaged over each 3mm/45° sector and divided into artery-specific low, mid and high tertiles to perform a statistical difference analysis on the associated PB growth measurements. Significance was assumed for $p < 0.05$.

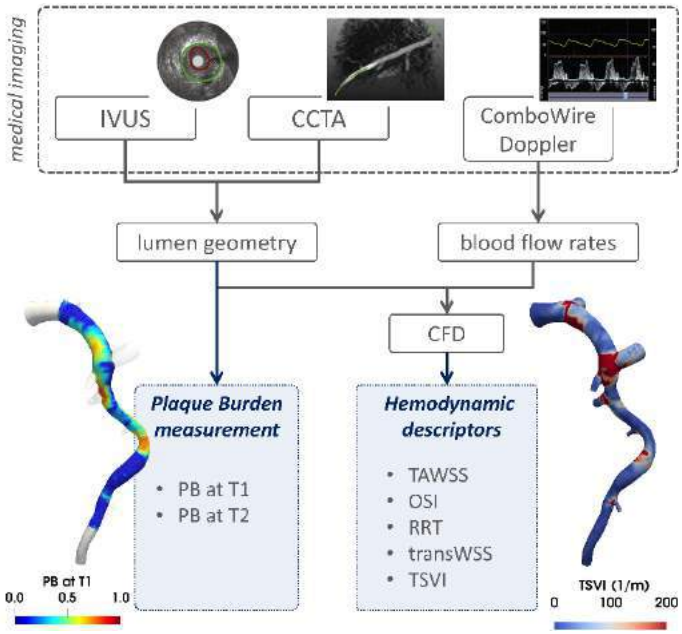


**Figure 1: Overview of study methods.**

## RESULTS

Figure 2 reports the (mean ± sem) PB growth values associated to low, mid, or high values of each hemodynamic descriptor. It clearly emerged that sector exposed to high TSVI values at T1 exhibited significantly higher PB growth in the T2-T1 time interval, compared to the exposure to low or mid TSVI at T1. As expected, a significant association emerged also for the exposure to low TAWSS at T1 and PB growth. Finally, an association between PB growth in the T2-T1 time interval and WSS multidirectionality at T1, quantified in terms of OSI and transWSS, emerged. However, the scarce multidirectional action of the WSS in the investigated coronary arteries (with OSI <0.01 and transWSS <0.15 Pa), suggests a secondary role for WSS multidirectionality in promoting aggravating biological events.

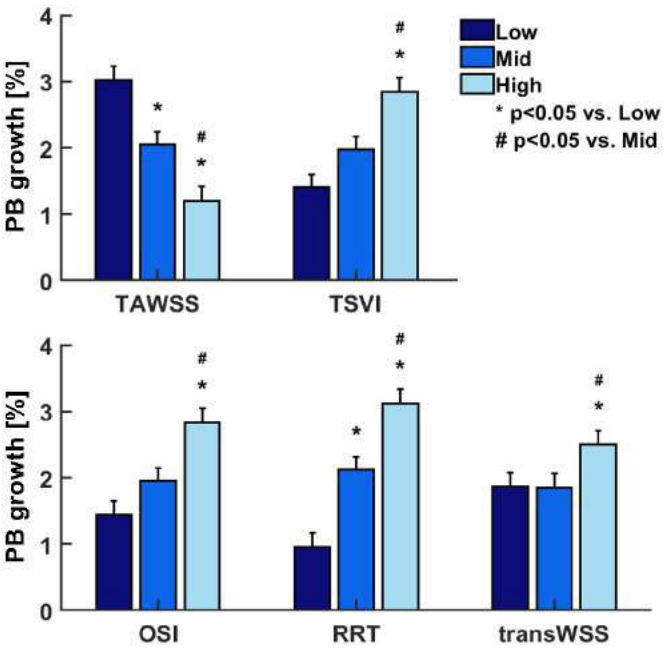


**Figure 2: Hemodynamic descriptors vs. estimated PB growth.**

## DISCUSSION

This study tested the capability of CFD-derived WSS topological skeleton features and canonical WSS-based descriptors of disturbed flow to predict local plaque burden temporal changes in human coronary arteries. The main results can be summarized as follows: (1) as confirmation, luminal sectors characterized by low TAWSS values at T1 exhibited significant plaque growth; (2) luminal exposure to high variability in the WSS contraction/expansion action was associated with significant PB growth. Physically, TSVI describes the variability of the contraction/expansion action exerted by WSS on the endothelium. Thus, it describes different features of the WSS vector field with respect to TAWSS and it represents a different hemodynamic stimulus to the endothelium. Translating this into mechanistic implications, the variability in the contraction/expansion action exerted by shear forces on endothelial cells reflects on intra- and inter-cellular tension variability that could lead to aggravating biological events. Recent results on a large dataset of 188 atherosclerotic coronary arteries confirm the effectiveness of TSVI as biomechanical biomarker able to identify intermediate coronary lesion site of subsequent myocardial infarction at 5-year follow-up [7].

In conclusion, high TSVI is a strong predictor of PB growth in the analyzed population, encouraging further clinical trials to enforce the presented results and translate this concept into clinical practice.

## REFERENCES


[1] Brown AJ et al., *Nat Rev Cardiol*, 13:210-220, 2016.
[2] Mazzi V et al., *Biomech Model Mechanobiol*, 19(5):1403-23, 2020.
[3] Arzani A et al., *J Biomech*, 73:145-152, 2018.
[4] Morbiducci U et al., *Ann Biomed Eng*, 48:2936-49, 2020.
[5] De Nisco G et al., *Med Eng Phys*, 82:119-129, 2020.
[6] Mazzi V et al., *Ann Biomed Eng*, 49:2606-2621, 2021.
[7] Candreva A et al., *Atherosclerosis*, 2021.
[8] Hartman EMJ et al., *Sci Rep*, 11:22086, 2021.
[9] van der Giessen AG et al., *J Biomech*, 44(6):1089-95, 2011.
[10] Peiffer V et al., *J Biomech*, 46:2651-2658, 2013.

SB³C2022
Summer Biomechanics, Bioengineering and Biotransport Conference
June 20-23, Eastern Shore, MD, USA

# PRELIMINARY MODELING AND EXPERIMENTAL STUDY OF THROMBOEMBOLISM: EFFECTS OF SHEAR STRESS ON THROMBUS BEHAVIOR

**Arash Azimi (1), Eathan S. DiTullio (1), Keefe B. Manning (1,2)**

(1) Department of Biomedical Engineering, The Pennsylvania State University, University Park, PA, USA
(2) Department of Surgery, Penn State Hershey Medical Center, Hershey, PA, USA

## INTRODUCTION

While thrombosis and thromboembolism in cardiovascular devices have been observed clinically, few studies related to thrombosis deformation and embolization are available. Thromboembolism can result in partial or full occlusion in blood vessels and implanted cardiovascular devices, which can be involved in life-threatening complications. Thus, to evaluate the stability of the thrombus and its behavior under different flow conditions, it is important to predict thromboembolism [1-4].

Coupled reactions among blood clot, flow regime, and surface increase the complexity of numerical modeling and require significant computational power. The shear stress can impact the thrombus and may result in partial or full embolization. Therefore, it is critical to understand the interplay between the thrombus and flow regimes. While the clot formation time is on the order of minutes, when embolization starts, it may occur on a time scale of seconds. Thus, any computational model must include this complex aspect. Furthermore, to assess the credibility of numerical simulations, *in vitro* experiments must be performed.

Taylor *et al.* [5, 6] introduced a continuum model to predict platelet adhesion and cardiovascular device-induced thrombosis. Fogelson and Guy [7] presented a continuum macroscale model of platelet aggregation and studied individual platelets and their interactions with fluid flow. This approach is used to model the thrombosis mechanics here using computational fluid dynamics (CFD). The principal objectives are to perform 3D numerical simulations and provide insight on thrombus behavior, deformation, and embolization under different flow conditions. Moreover, verification and calibration of the computational model are conducted by comparing to *in vitro* experimental data.

## METHODS

The governing equations to model thromboembolism include the equations of motion for fluid flow and cohesive stress equations to characterize the thrombosis viscoelasticity. To predict the turbulent motions, momentum equations for the fluid are modeled via large-eddy simulations (LES), which solves the spatially filtered Navier-Stokes (N–S) equations. Equations 1 and 2 represent the incompressible Newtonian flow governed by the continuum and N–S equations, respectively:

$$\nabla \cdot u = 0 \tag{1}$$

$$u_t + u \cdot \nabla u = -\frac{1}{\rho}\nabla P + \nu \nabla^2 u + \frac{1}{\rho}\nabla \sigma \tag{2}$$

where $u$ is flow velocity, $\rho$ is density, $t$ is time, $P$ is pressure, $\nu$ is kinematic viscosity, and $\sigma$ is cohesive stress tensor.

The thrombosis and thromboembolism mechanics are modeled in a way similar to [7]. This model incorporates two sets of evolution equations for the cohesive stress tensor $\sigma$ (Equation 3) and the cohesive link density $z_c$ (Equation 4).

$$\sigma_t + u \cdot \nabla \sigma = \sigma \nabla u + (\sigma \nabla u)^T + \alpha_2 \phi_a^2 I - \beta[Tr(\sigma)/(z_c)]\sigma \tag{3}$$

$$\frac{\partial z_c}{\partial t} + u \cdot \nabla z_c = \alpha_0 \phi_a^2 - \beta(Tr(\sigma)/(z_c))z_c \tag{4}$$

where $\alpha_0$ and $\alpha_2$ are constant growth rate coefficients, $\phi_a$ is activated platelets, $\beta$ is breakage rate, and $I$ is an intensity factor. To halt fluid flow in areas with thrombus, the divergence of the cohesive stress tensor is added as a body force. Figure 1a shows the computational domain and boundary conditions using OpenFOAM.

*In vitro* experimental validation is performed by using a tube geometry as depicted in Figure 1b. This geometry is designed to validate different aspects of the numerical simulations. The experimental flow loop is filled initially with phosphate buffered saline (PBS) solution with viscosity of 1 cP. The PBS is circulated using a peristaltic pump (Cole-Parmer, Vernon Hills, IL, USA) in the range of $1500 < Re <$

20000. The dimensions of the tube are 100 mm with inner diameter of 12.7 mm and made of clear polycarbonate (PC). Fresh whole bovine blood, collected through an approved IACUC protocol, is used to form a clot by adding 6.45% b/w calcium chloride ($CaCl_2$). We used this recalcified blood to inject into the tube and allowed it to form a clot for 1 hour, then slowly filled the loop with PBS. In both numerical simulations and experiments, a constant pressure boundary condition is set on the outlet of the tube, while a constant inlet velocity is set for the inlet boundary. After the loop is filled with PBS, the pump is set to a constant speed, and the embolization captured using high speed videography.

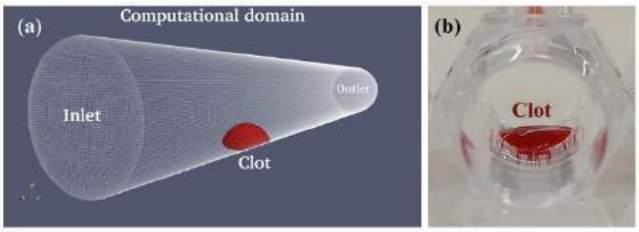


**Figure 1: The circular tube and blood clot: (a) the computational domain and (b) a clot formed in the tube.**

## RESULTS

For both numerical simulations and experiments, the results are presented for the mechanical interaction of pre-existing thrombus and fluid flow at different Reynolds number. Figure 2 shows the results for a 100 µL blood clot. The clot starts to separate from the surface due to the high inertial force induced by the fluid flow, resulting in embolization. The velocity and pressure contours along with the streamlines are presented for better graphical understanding of embolization.

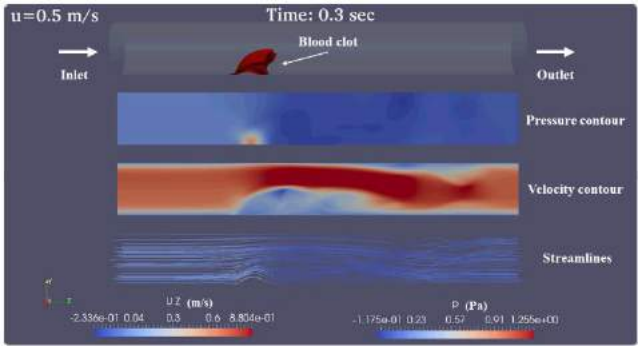


**Figure 2: The numerical results in terms of streamlines and contours for a pre-existing clot in a circular tube.**

Figure 3 shows the *in vitro* experimental validation of thromboembolism. The results show good agreement between simulations and experiments. Due to the high Reynolds number, the leading edge of the clot separates from its anchor point (Figure 3a-c) and then from the surface (Figure 3d). The same phenomenon can be observed experimentally.

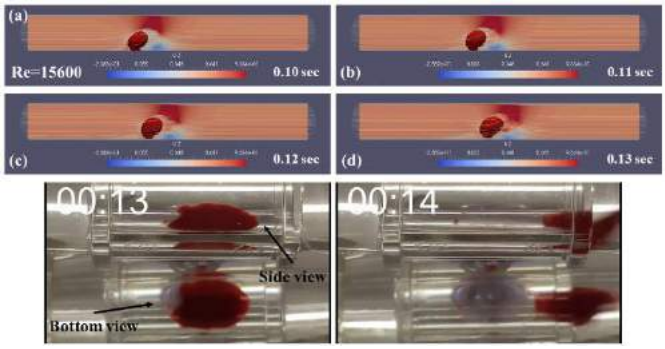


**Figure 3: The comparison of numerical simulations with experimental data at a Reynolds number (*Re*) of 15600.**

For the flow at Re=2000, the upstream flow kinetic energy dissipated during the impact with the leading edge of blood clot. This impact can cause a small separation of clot from the surface. Once this separation between the clot and surface is initiated, the wall shear stress amplifies the separation and results in full embolization. When the clot fully embolized, the downstream flow becomes chaotic due to perturbations induced by the clot. Therefore, our model is designed to capture this chaotic motion.

## DISCUSSION

In this study, a computational model has been improved to consider thromboembolism under different flow conditions. These numerical simulations provide a foundation to predict the embolization risk and physical behavior of the thrombus under different Reynolds numbers. The dynamic process of embolization is extremely brief ($< 0.3$ s), and thus, the numerical model can be used to understand the complexity of turbulent flow and physical behavior of thrombus, deformation, and embolization. Parameters for the numerical simulations such as fluid viscosity, density, Reynolds number, and clot volume can be provided with controlled experiments. The impact of shear stress is extremely important in turbulence regimes, which are considered in our CFD model. In addition, our simulation results can predict the chaotic motions and complex interplay between turbulent flow and physical behavior and characteristics of blood clots. Our simulations showed good agreement of clot embolization compared to experiments.


## ACKNOWLEDGEMENTS

Research reported in this publication was supported by the National Science Foundation under Grant CMMI-2017805. This work used the Extreme Science and Engineering Discovery Environment (XSEDE), which is supported by National Science Foundation grant number ACI-1548562.


## REFERENCES


[1] Wu, Wei-Tao et al., *Sci Rep* 7, no. 1:1-16, 2017.
[2] Goodman, Paul D. et al., *Ann Biomed Eng*, 33, no. 6:780-797, 2005.
[3] Xu, Shixin et al., *J Roy Soc Interface*, 14, no. 136, 2017.
[4] Du, Jian et al., *J Biomech*, 122: 110398, 2021.
[5] Taylor, Joshua O. et al., *J Biomech*. 50: 114-120, 2017.
[6] Taylor, Joshua O. et al., *Biomech Model Mechanobiol*.15, no. 6:1713-1731, 2016.
[7] Fogelson and Guy, *Comput Method Appl M*, 197, no. 25- 28: 2087-2104, 2008.

# THUMB METACARPAL KINEMATICS: A VOLUMETRIC PERSPECTIVE

**Adam J. Chrzan (1), Nicole D. Arnold (1), Kevin Chan, M.D. (2), Tamara Reid Bush, PhD (1)**

(1) Mechanical Engineering, Michigan State University, East Lansing, MI, USA
(2) Orthopedic Hand and Upper Extremity Surgery, Spectrum Health, Grand Rapids, MI, USA

## INTRODUCTION

Radiographic osteoarthritis (OA) of the hand is a condition characterized by radiographically visible damage to a joint's articular cartilage and underlying bone. Among Americans ages 50-54, more than 27% show signs of OA. The prevalence steadily increases with age to a rate of more than 84% when 70-74 years old [1].

OA in the thumb carpometacarpal (CMC) joint, located at the interface of the thumb metacarpal and trapezium, is of particular concern (Fig. 1). The thumb CMC joint is the most likely joint in the hand to develop OA (~32%) and the most likely to cause symptoms, such as decreased pinch strength, joint stiffness, and pain, which render daily tasks difficult (i.e. open jars, writing, etc.) and hinder the ability to live independently [1, 2].

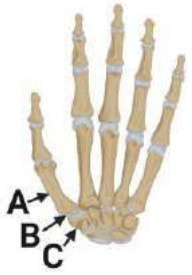


**Figure 1: A) Thumb metacarpal, B) CMC Joint, and C) Trapezium.**

Standard assessments of thumb kinematics include qualitative and goniometric measures, which are limited due to their subjective nature and single plane measurements, respectively. Some work has been conducted to characterize 3D kinematics of the healthy thumb, but these studies are bounded by small sample sizes, small age ranges, and by describing the thumb as a whole [4]. Thus, there is a need for research with a more detailed kinematic analysis of each bone in the healthy thumb, particularly the metacarpal where CMC OA surgeries occur.

A thorough understanding of healthy thumb kinematics will inform treatment options for OA patients and may lead to new treatment approaches. In severe cases of thumb CMC OA, loss of function and constant pain require surgical intervention [2]. Current standard-of-care treatments involve partial or complete removal of the damaged cartilage and bone in the CMC joint. While this and other available surgical procedures have been shown to reduce pain and increase thumb mobility, there is little evidence identifying which procedure, if any, yields superior postoperative thumb kinematics [3]. The goal of this work is to provide a more detailed 3D characterization of healthy thumb metacarpal kinematics as a point of comparison to better understand and improve the kinematic outcomes of thumb CMC OA surgeries.

## METHODS

Recruited participants had no history of significant hand injury, hand surgery, or diagnosis of arthritis, were right-hand dominant, and not pregnant. This work was approved by the university (IRB #00006111), and all participants gave written consent.

The 52 participants were segmented into the following groups, each containing 13 participants: young males (avg. age = 28.8 ± 5.6), young females (avg. age = 25.8 ± 5.1), older males (avg. age = 60.2 ± 11.4), older females (avg. age = 58.0 ± 9.3). 'Young' groups had individuals ages 18-39, and 'Older' groups ages ≥40. The lengths of

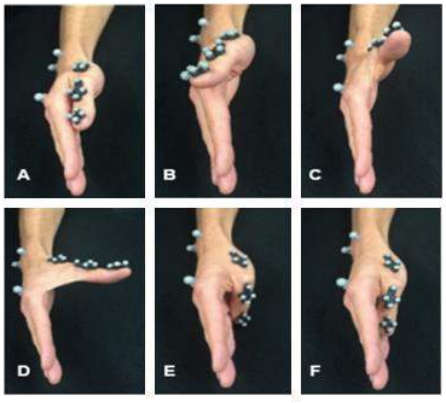


**Figure 2: Movement steps used to gather the metacarpal volume. A) starting position, B) adduction towards dorsal palm, C) maximum 'thumbs-up', D) largest arc to oppose to the pad of the fifth digit, E) completed opposition, F) sliding thumb laterally along finger pads. Rigid marker pods, each containing 4 markers, were fixed to the dorsal surface of the thumb metacarpal, proximal phalange, and distal phalange.**

participants' thumb bones were measured before testing. Thumb metacarpal (MC) kinematics were gathered using a six-camera motion capture system (Qualysis, Gothenburg, Sweden), which collected the positions of reflective markers at 100 Hz. Rigid marker pods and individual markers were used to identify thumb and hand movements (Fig. 2).

Participants performed the movement described in Figure 2 to scribe out the largest volume around which the thumb MC could move, or the MC volume. Each participant performed the motion three times.

Spherical coordinates were used to plot the outer surface of the MC volume, where the r-coordinate was the length of the MC (Fig. 3). The two angular coordinates were perpendicular to each other, and defined relative to the palm. Both angles were calculated for each time point during the motion and plotted to obtain the outer perimeter of the MC volume, or the path of the distal end of the MC during the motion. The MC volume was completed by sweeping from one side of the perimeter to the other and plotting angles internal to the perimeter.

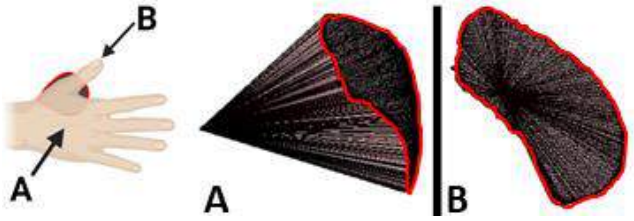


**Figure 3: A) Representative MC volume viewed from the back of the palm. The leftmost tip is the thumb CMC joint. B) The same volume viewed from the distal thumb. The outermost edge shows the MC perimeter.**

The MC volume was determined using the 'boundary' function in MATLAB (MathWorks), which calculates the volume enclosed by the plotted spherical coordinates. To normalize for MC length, each volume was divided by the participant MC length cubed. A two-way ANOVA and Brown-Forsythe tests were used to determine differences in normalized MC volume means and variances between groups, respectively.

## RESULTS

Normalized MC volume data showed no significant change due to age ($p = 0.88$) or sex ($p = 0.60$) (Fig. 4). In both younger and older groups, females had a slightly larger normalized MC volume than males. In both male and female groups, older participants had a larger normalized MC volume. Variances were similar across all groups ($p > 0.80$). Average perimeters for all groups were visually similar (Fig. 5).

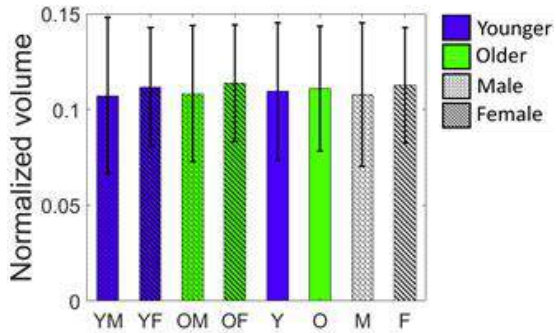


**Figure 4: Mean normalized metacarpal volume and standard deviation. Y = young(18-39), O = older(40+), M = male, F = female. Raw volume data was normalized by dividing by the cube of the MC length.**

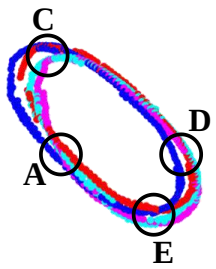


**Figure 5: Average metacarpal volume perimeter for each group viewed from the distal thumb. Red = YM, blue = YF, magenta = OM, cyan = OF. Letters correspond to Figure 2.**

## DISCUSSION

This work used the normalized metacarpal volume to characterize the complex 3D kinematics of the thumb metacarpal. Establishing baseline healthy kinematics using methods that offer more information than those typically seen in clinical settings is key to understanding and optimizing patient outcomes for CMC OA surgeries.

Our data suggest that, in a healthy population, age has a minimal effect on normalized MC volume, or may even increase it, while females show larger MC volumes than males. Increased CMC mobility may be of concern because it is linked to joint laxity, a known risk factor for CMC OA [5]. This increased risk in females and in older populations is consistent with increased prevalence among the same populations [1].

Average MC perimeters for all groups are comparable in size, which is consistent with volume numbers, shape, and position. Shape and position similarity implies groups have access to the same 3D space of movement.

This is the first work to use a volumetric approach to thumb kinematics that is normalized for thumb size. This is a vital step, as it enables comparisons between individuals, across groups, and provides the foundation for the MC volume to be a tool to evaluate the effects of surgical interventions. This is also the first work to use the volume of just the thumb metacarpal, instead of the whole thumb. Breaking down the volume of the entire thumb by each bone is key to identifying regions where therapeutic and surgical components can be targeted to provide optimal function post-surgery.

Future expansions of this work will include the normalized volume of the other bones of the thumb, and the thumb as a whole. Testing participants before and after a CMC OA surgery will also be conducted to gain a better understanding of post-operative thumb kinematics. Increased understanding will inform adjustments to surgical and therapeutic methods to optimize patient outcomes.

## ACKNOWLEDGEMENTS

Funding was received from the Spectrum Health – Michigan State University Alliance Grant.

## REFERENCES

[1] Haugen, I et al., *Ann Rheum Dis*. 70:1581-1586, 2011.
[2] Matullo, K et al., *Hand*. 2:232-239, 2007.
[3] Deutch, Z et al., *Hand*. 13:403-411, 2018.
[4] Curran, P et al., *Clinical Biomechanics*. 63:63-72, 2019.
[5] Wolf, J et al., *J. Am. Acad..Ortho. Surgeons*. 19:463-471, 2011.

# IMAGE-BASED DYNAMIC STRAIN ESTIMATION OF ALVEOLAR MICROSTRUCTURES DURING EX VIVO MECHANICAL VENTILATION

**Jacob Herrmann (1), Sarah E. Gerard (2), Edward A. Sander (1)**

(1) Roy J. Carver Department of Biomedical Engineering, University of Iowa, Iowa City, Iowa, USA
(2) Department of Radiology, University of Iowa, Iowa City, Iowa, USA

## INTRODUCTION

Breathing and mechanical ventilation cause deformation of lung tissues and cyclic strain fluctuations in alveolar ducts and septal walls. Injurious ventilation may induce or worsen lung injury associated with mechanical trauma via alveolar overdistension and/or repetitive collapse and reopening. Mechanical ventilation settings applied across the entire lung—such as positive end-expiratory pressure and driving pressure—result in heterogeneous alveolar dynamics due to regional variations in the mechanical properties of lung tissue. Thus, microscale investigations of alveolar dynamics during mechanical ventilation may reveal mechanisms of ventilator-induced lung injury associated with heterogeneity in alveolar mechanics and deformation.

Previous approaches to laser-scanning confocal microscopy of alveolar dynamics have relied on quasi-static conditions (i.e., holding the inflation pressure constant during imaging) to characterize the change in lung structure between an end-expiratory and end-inspiratory state [1,2]. However, quasi-static conditions may not accurately reflect dynamic conditions, especially if the lung does not reach mechanical equilibrium within the time allowed for inspiration or expiration. Videomicroscopy techniques allow rapid imaging of alveolar dynamics [3], but interpretation of specific alveolar structures is fraught with difficulty [4]. Optical coherence tomography enables volumetric imaging with high temporal resolution, but comes at the expense of a reduced signal-to-noise ratio and lower spatial resolution [5].

In this study, we developed a retrospectively gated laser-scanning confocal microscopy technique [6] that enabled us to reconstruct a sequence of two-dimensional images of alveolar deformation within a cross-section of lung tissue (Figure 1A). From these reconstructed images, we were able to quantify the dynamics of alveolar septal wall strain during pressure-controlled mechanical ventilation.

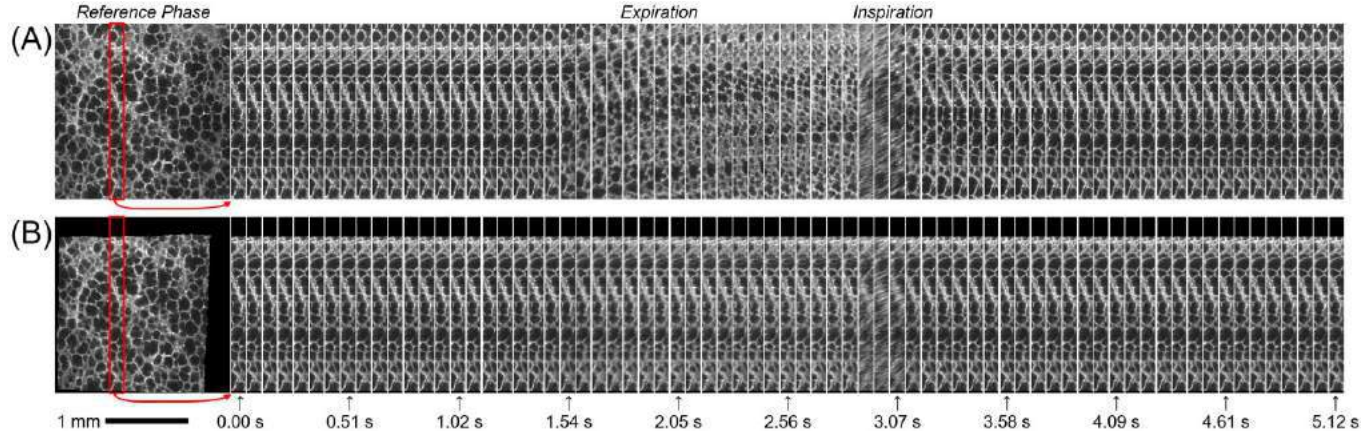


**Figure 1. (A) Slices of a reconstructed image sequence showing alveolar deformation throughout ventilator cycle. (B) Corresponding slices from the deformed image sequence after image registration, showing alveolar structures aligned with those of the reference image.**

## METHODS

Subsegmental regions of porcine lung tissue were dissected, carefully preserving intact airtight structure. Periodic pressure-controlled mechanical ventilation was simulated by a microcontroller-timed solenoid valve that switched the airway opening pressure between high and low states determined by adjustable pressure relief valves.

Imaging was performed on a Nikon A1 laser-scanning confocal microscope, using 561 nm excitation and 595 nm emission. Image frames were acquired continuously over a 2.12-mm field of view, without interrupting mechanical ventilation, and with a fixed 3-second time delay between the start of each frame's acquisition. Image reconstruction was performed retrospectively according to the ventilator rate [6]. Each pixel was associated with a phase of the periodic respiratory cycle. Pixels with the same respiratory phase but different spatial locations were assembled into phase-binned frames. Each frame thus described the structure of the lung sample at a single phase in the ventilation cycle, with minimal motion artifact. A sequence of these phase-binned frames was constructed to describe the dynamic motion of the lung sample throughout the ventilation cycle (Figure 1A).

Image registration was performed to estimate periodic spatial transformations that describe alveolar deformations during the ventilator cycle. A sequence of B-spline transformations between each frame and a common reference frame were estimated using the Elastix registration library [7]. All frames could then be deformed to align alveolar structures with those of the reference frame (Figure 1B). The resulting spatial transformations were queried to assess regional expansion and contraction at each ventilation phase.

Linear strain in each alveolar septal wall was approximated by first segmenting alveolar walls in the end-inspiratory reference frame, and then computing the change in distance between the endpoints of each wall after applying the spatial transformations corresponding to each ventilation phase. Exponential regression was performed to estimate time associated with relaxation of septal wall strain in response to step changes in airway opening pressure during expiration.

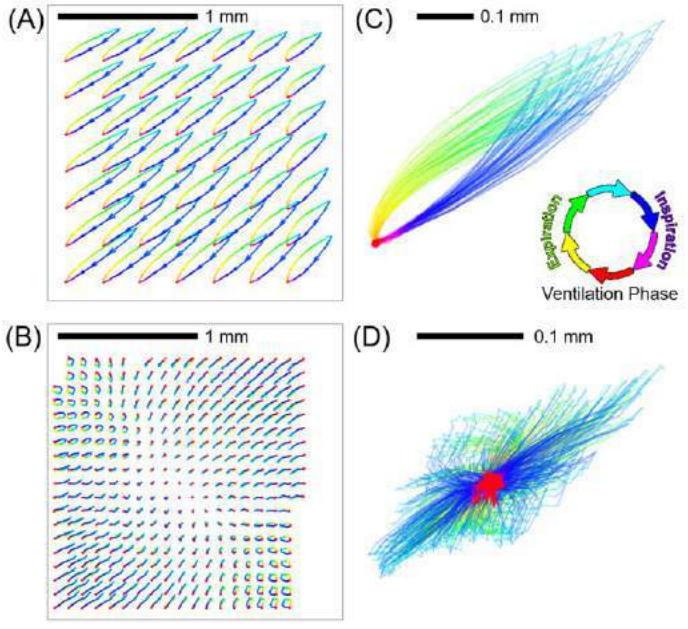


**Figure 2. Trajectories of tracked points within the 2.12-mm field of view before (A) and after (B) subtracting the mean translation at each phase. Superimposed trajectories (C, D) magnified for clarity. Color indicates phase of ventilation cycle.**

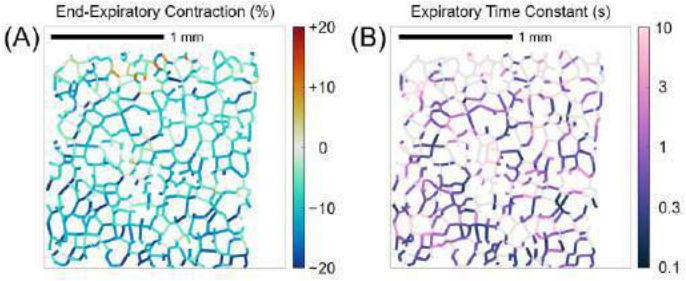


**Figure 3. (A) End-expiratory alveolar wall strain (relative to end-inspiratory state). (B) Exponential time constant associated with relaxation of alveolar wall strain after a stepwise decrease in airway pressure (gray indicates $R^2 < 0.8$ for exponential regression).**

## RESULTS

The reconstructed image sequence (Figure 1) contained 71 images throughout the 5.19-second ventilator cycle, for an effective temporal resolution of 73.1 ms. Image registration revealed hysteresis of spatial trajectories that varied throughout the sample (Figure 2). Substantial heterogeneity was observed even after subtracting the mean translation component of displacement, indicating nonaffine deformations (Figure 2C,D). Linear strain within alveolar septal walls demonstrated substantial heterogeneity, both in end-expiratory contraction (strain mean ± standard deviation: -9.1% ± 6.3%) (Figure 3A), and in the rate at which strain equilibrated to a step change in airway pressure (time constant percentiles 50$^{th}$ [25$^{th}$, 75$^{th}$]: 0.7 [0.4, 1.6] seconds) (Figure 3B).

## DISCUSSION

This study presents a microscale investigation of alveolar dynamics using retrospectively gated image reconstruction and image registration. Substantial mechanical heterogeneity of alveolar deformation and septal wall strain occurred even within a well-aerated region of the lung, consistent with previous findings in quasi-static conditions. However, imaging under dynamic conditions revealed that many alveolar structures are not in mechanical equilibrium by end-inspiration or end-expiration, but rather exhibit a wide range of relaxation time constants. There is also a large degree of hysteresis in the spatial trajectories of alveolar deformation. These findings underscore the importance of imaging alveolar dynamics without interrupting ventilation, especially for specialized modalities that rely on high respiratory rates or low exhalation times. Furthermore, these findings suggest the possibility of characterizing viscoelasticity for individual alveolar structures. The techniques developed herein enable future investigations to assess interactions between expiratory time, driving pressure, and end-expiratory pressure on heterogeneous microstructural dynamics in normally and poorly aerated lung tissues.


## ACKNOWLEDGEMENTS

Lung samples provided by Andrea F. da Cruz, Emmanuel A. Akor, and David W. Kaczka. Technical support provided by Nikon advanced imaging specialist Ali Strtak. Funding: NIH T32 HL144461.


## REFERENCES


[1] Perlman CE, Wu Y, *Am J Physiol Lung Cell Mol Physiol*, 307(4):1302-1310, 2014.
[2] Namati E, et al., *Am J Respir Cell Mol Biol*, 38(5):572-578, 2008.
[3] DiRocco JD, et al., *Intensive Care Med*, 32(1):140-148, 2006.
[4] Gaertner M, et al., *J Biomed Opt*, 20(6):066009, 2015.
[5] Schnabel C, Gaertner M, Koch E, *Appl Sci*, 7(3):287, 2017.
[6] Vinegoni C, et al., *Nat Protoc*, 10(11):1802-1819, 2015.
[7] Klein S, et al., *IEEE Trans Med Imaging*, 29(1):196-205, 2010.

SB³C2022
Summer Biomechanics, Bioengineering and Biotransport Conference
June 20-23, Eastern Shore, MD, USA

# A NOVEL MACHINE LEARNING-BASED FRAMEWORK TO PREDICT THE ANISOTROPIC MECHANICAL PROPERTIES IN SOFT MATERIALS USING ANISOTROPIC INDENTATION

**Habibeh Ashouri Choshali (1, 2, 3), Juanyong Li (2), Taylor Paradis (2), Nima Rahbar (3), Kristen L. Billiar (2)**

(1) Data Science, Worcester Polytechnic Institute, Worcester, MA, USA
(2) Biomedical Engineering, Worcester Polytechnic Institute, Worcester, MA, USA
(3) Civil Engineering, Worcester Polytechnic Institute, Worcester, MA, USA

## INTRODUCTION

Characterizing the mechanical properties of soft tissues and biomaterials is of intense interest as changes in mechanical properties in these materials can be a sign of disease and abnormalities. Many biological materials are anisotropic due to the alignment of the fibers in their internal structure which increases the difficulty in characterization (1, 2).

Characterization of anisotropic mechanical properties in soft materials is challenging due to the difficulties that exist in the nature of biological material, applying and measuring the mechanical loads, and the need to combine the data from multiple experimental protocols (3). Indentation is widely used to determine the local mechanical properties of soft materials due to the ability to test samples in their native state without harvesting (4, 5). However, a single indentation experiment with a symmetric (conical or spherical) probe is not sufficient to estimate the anisotropic mechanical properties; the force-displacement data need to be combined with other experimental and computational techniques such as tracking 3D deformations and inverse finite element model fitting (3, 4, 5).

Here, we develop a machine learning (ML)-based framework to predict the local anisotropic mechanical properties of anisotropic soft materials using two orthogonal indentation protocols with a novel anisotropic indenter. We demonstrate the applicability of the proposed framework using the experimental data for chicken breast and develop a normalization process and workflow which makes the approach applicable for a wide range of anisotropic materials from micro to macro scale.

## METHODS

Frozen chicken breasts were defrosted in air until they were able to be sliced into reproducible-sized slabs. The samples were cut to an average width and length of 25-40 mm and thickness of ~10 mm. Typical samples are shown in (Fig. 1a). Indentation experiments were performed with an anisotropic indenter made from a curved metal wire of major radius 3.5 mm and minor radius 0.5 mm at 0.1 mm/s to a maximum depth of 2 mm using an Instron EP1000 with 1N load cell (±1mN) (Fig. 1b). The maximum load was set between 0.15 N-0.3 N. The direction of fibers was determined visually for each sample. At each site, indentations were performed for two directions: 0-degree (the long axis of the indenter aligned with the fiber direction) and 90-degree. The indentation sites were chosen away from the sample edges to avoid the edge effects.

Finite element (FE) modeling (Abaqus) was used to generate a labeled dataset using the indentation simulation for different material property sets. The size of the sample is 40 by 30 mm with a thickness of 10 mm. Mesh convergence and optimization was performed. The elements were modeled as transversely isotropic material with values in Table 1. The whole process was automated.

We then extracted features for our ML model using the resultant normalized pair of force-displacement curves for each data point. For this purpose, each pair of curves was transformed to a feature vector which is constructed as follows: the range of the indentation for each pair of curves was split to a certain number of knots (the number of knots is a hyper-parameter that can be tuned to improve the performance of the model). The indentation value, the force corresponding to 0-degree alignment, and the force corresponding to 90-degree alignment were then extracted at each knot. These values were finally concatenated for all knots to construct the feature vector. To train the ML model, 80 percent of the dataset was used, and the remaining 20 percent was used for testing the model after shuffling. Linear regression, random forests, and fully connected neural networks were used to develop the ML models per aspect ratio, R. A max depth of 40 was used to build the random forests model. For the fully connected neural network model, we used 3 layers in which the first, second, and third layers had 20, 10, and 20 nodes respectively. Our activation function was ReLU.

## RESULTS

A total of 37 sets of orthogonal indentations were completed on 17 different chicken samples. The average of the results for each indentation angle was then measured, and the results are shown in (Fig. 1c). The results of indentation experiments as well as FE simulation with two different property sets are shown in Fig. 1d (black: $E_1 = 20$, $E_2 = 10$, $G_{12} = G_{23} = 10$; blue: $E_1 = 30$, $E_2 = 5$, $G_{12} = 15$, $G_{23} = 2.5$; $\nu = 0.47$ for both and moduli in kPa) showing an obvious difference for the predicted force-displacement curves in 0-deg and 90-deg for anisotropic elastic constants in agreement with the experimental results.

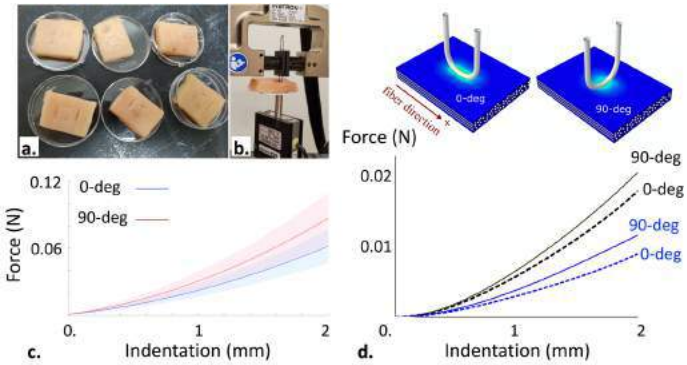


**Figure 1: a) Chicken breast samples post indentation. b) Experimental setup for indentation experiments. c) Average indentation results ± 1 SD with a shade of similar color for each direction. d) The results of FE simulation for two example material property sets, for 0- and 90- degree alignment (see text).**

After validation of the FE model using the Hertz contact theory for a spherical indentation into an isotropic material, 3568 pairs of orthogonal force-displacement (F-d) curves were simulated for each combination of the material properties presented in Table 1. The values of the material properties are taken from the literature as representative of a broad range of biological tissues (3, 5, 6). The F-d data were normalized to remove the scale dependency by dividing the displacement by the maximum indentation, $d_{max}$ and the force values by $d_{max}^{3/2}\sqrt{r}$ according to the Hertz contact rule where r is the smaller radius of the indenter.

**Table 1: Transversely anisotropic material properties and indenter geometry values for grid generation with $E_1 > E_2 = E_3$.**

| parameter | values |
|---|---|
| $E_1\ (kPa)$ | [1, 5, 10, 30, 50, 70, 90, 100] |
| $E_2 = E_3\ (kPa)$ | [1, 5, 10, 30, 50, 70, 90, 100] |
| $\upsilon_{12} = \upsilon_{13}$ | [0.3, 0.47] |
| $\upsilon_{23}$ | [0.3, 0.47] |
| $G_{12} = G_{13}\ (kPa)$ | [0.1, 0.5, 1, 5, 10, 20, 30, 40] |
| $G_{23}$ | $E_2\ /(2(1+\upsilon_{23}))$ |
| R (large:small indenter radius ratio) | [3.25, 5, 7, 10] |

The best overall performance achieved for the linear regression, random forests, and fully connected neural networks models are 0.63, 0.76, and 0.9 respectively. The performance of the ML framework in predicting the elastic constants for the training and test set using the fully connected neural networks for R=3.25 is presented in Fig. 2. The neural networks model shows the highest $R^2$ among all the ML techniques with the lowest overfitting meaning that it achieved the best performance. Random forests tended to over-fit the training set and the linear regression model achieved a very poor performance due to the complex pattern that exists between the dependent features and the response (elastic constants).

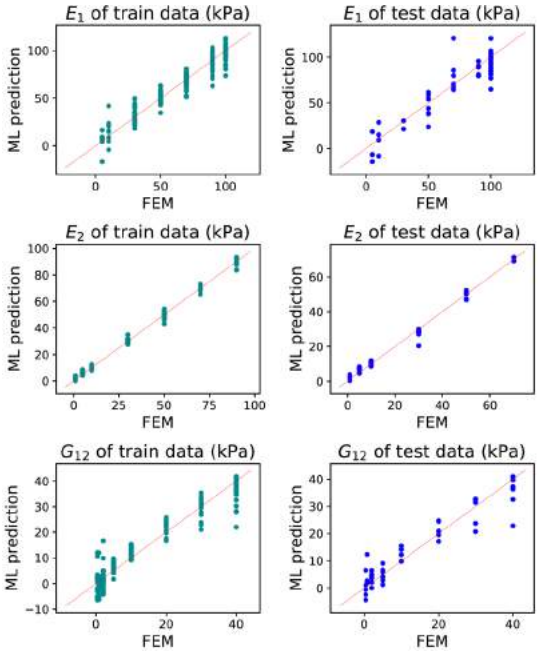


**Figure 2: Predictions on the training and test sets using neural networks. $R^2$= 0.94 for the training set and $R^2$= 0.9 for the test set.**

## DISCUSSION

For an anisotropic material, indentation with an anisotropic indenter along and perpendicular to the preferred mechanical axis (i.e., fiber direction) will result in different force-indentation behavior. Here, we proposed a novel ML-based methodology to predict the anisotropic mechanical properties of biological material using the difference between the force-displacement curves resulting from two asymmetric orthogonal indentations parallel and perpendicular to the fiber directions. The main application of the proposed framework is to determine anisotropic properties for biological materials for which performing multiple experiments such as biaxial testing and shear testing is not straightforward (e.g., living cells, in situ tissues). We built a computationally effective model that can determine the anisotropic mechanical parameters for a given material in just a few seconds on a standard desktop computer by using just one set of two indentation test results as input. This result is more significant if we compare it with the average time for running a single forward FE simulation for a pair of indentations (more than half an hour on a standard computer). Solving the inverse problem and finding the properties using the force-displacement curves using the available techniques requires multiple simulations and an optimization protocol e.g., genetic algorithm taking many hours. The proposed framework has the potential to be a powerful tool for quickly determining the anisotropic properties of biological materials with application in disease diagnosis.


## ACKNOWLEDGEMENTS

This work was supported by the NSF (CMMI 1761432) and ARMI BiofabUSA (T0137).


## REFERENCES


[1] Billiar, K.L. and Sacks, M.S., *J. Biomech. Eng.*, 122:23-30, 2000.
[2] Tower, T.T., et al., *Ann Biomed Eng*, 30(10):1221-1233, 2002.
[3] Namani, R., et al., *J. Biomech Eng.*, 134(6): 061004, 2012.
[4] Moghaddam, A.O., et al., *J Mech Behav Biomed Mater*, 103: 103539, 2020.
[5] Feng, Y., et al., *J Mech Behav Biomed Mater*, 65:490-501, 2017.
[6] Ding, Y., et al., *Sci. Rep.*, 7(1):1-8, 2017.

# PERFORMANCE OF SKIN COOLING DEVICE IN COOLING PENETRATION IN TISSUE – EXPERIMENTS AND SIMULATIONS

**Manpreet Singh (1), Jacob Lombardo (1), Alexander Caporale (1), Liang Zhu (1)**

(1) Department of Mechanical Engineering, University of Maryland Baltimore County, Baltimore, Maryland, USA

## INTRODUCTION

Placing a cooling device on the skin of a surgical site is one of the recommendations for patients after surgery to reduce inflammation and to alleviate pain.[1-2] Cooling may temporarily reduce nerve activity via disrupting the transmission of pain signals.[1-2] Unfortunately, unknown cooling penetration depth and uneven cooling on the surgical site are factors contributing to the discontinuous use of the cooling device by patients. Those patients often turn to take pain-killer medications to relieve pain, and this has led to the opioid epidemic in the country. Theoretical simulation is a valuable tool to predict cooling extent in targeted tissue region, however, its accuracy depends on physiological and physical parameter inputs. In this study, we performed experiments on healthy volunteers to record temperatures on skin surface under a cooling pad and then developed a whole-body heat transfer model to simulate the temperature field in the body tissue before and during cooling. Physiological parameters such as local blood perfusion rate and metabolism and heat transfer parameters such as lumped heat transfer coefficients will be extracted first. Then temperature field underneath the cooling pad will be simulated to evaluate both cooling penetration and the time duration needed to achieve the penetration.

## METHODS

A commercially available cooling device was evaluated in this study. Shown in Figure 1, it consists of a container with good insulation, a pump to induce water circulation, and a cooling pad suitable for cooling the lower extremities. The cooling pad was wrapped on both the thigh and leg of a human volunteer in a sitting position. An elastic belt was used to ensure good physical contact to the skin and an aluminum sheet was attached to the cooling pad to generate even cooling to the skin surface.

Two healthy volunteers were recruited to this study with local IRB approval. The baseline temperatures of the thigh were recorded by an infrared camera (TIS45, Fluke Corporation, Everett, WA), shown in Figure 1. Then the cooling pad was wrapped on the thigh and leg of the volunteer. A thermistor bead sensor with a nominal resolution of 0.001°C (0.8 mm dia., T-View system, Alpha Technics, Irvine, CA) was attached to the center of the cooling pad on the thigh to measure the temperatures before and during the cooling experiment. Water at approximately 1-2°C was circulating through the cooling pad and the total cooling time was 20 minutes. The oral temperature of the volunteer was also recorded before and after the cooling.

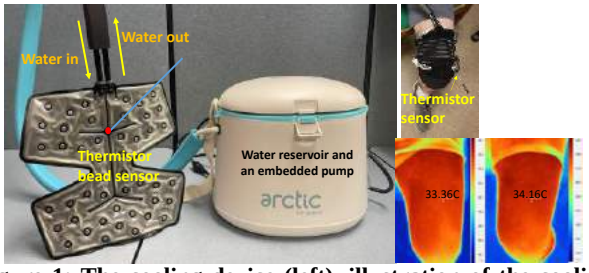


**Figure 1: The cooling device (left), illustration of the cooling pad wrapped on the thigh and leg of a volunteer (upper right), and recorded infrared images of two volunteers (lower right).**

A physical model based on realistic measurements of the volunteer was generated. As shown in Figure 2, the body (79 kg and 1.75 m tall) consists of three components: the brain, the rectangular column of the internal organ, and the muscle for the rest of the body. Each component has its own thermal and physiological properties. The Pennes bioheat equation[3] is used to model both the steady state and the transient temperature fields of the body as

$$\rho_t c_t \frac{\partial T_t}{\partial t} = k_t \nabla^2 T_t + \omega_t \rho_b c_b (T_a(t) - T_t) + Q'''_{met,t} \quad (1)$$

where $\rho$ is density, $c$ is specific heat, $k$ is thermal conductivity, $\omega$ is local blood perfusion rate, and $Q'''_{met}$ is volumetric heat generation rate due to metabolism. Initially, the body is exposed to an ambient environment, and the thermal resistances due to clothing layers and convection/radiation with the air are lumped as an overall heat transfer coefficient $h_{air}$. The boundary condition of the cooling pad is also lumped as an overall heat transfer coefficient $h_{water}$.

$h_{air}$ was determined considering free convection and radiation as 9.57 W/m$^2$K. We first adjusted the blood perfusion rate and metabolism in the muscle component (including the lower extremities) so that the recorded temperatures in the infrared image matched that predicted by the steady state simulation (Eq.1) before wrapping the cooling pad. Then the transient temperatures predicted by Eq. 1 during cooling were compared to that measured by the thermistor bead sensor, and $h_{water}$ was adjusted until the match between predictions and experimental data was achieved. Finally, local blood perfusion rate and metabolism, $h_{water}$, and other parameters were used to simulate temperature distribution inside the thigh and leg using the cooling pad with a water temperature at 0°C, a setting as recommended by the manufacturer.

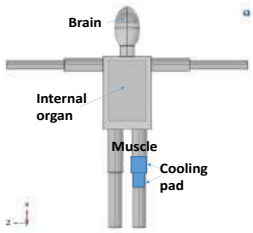


**Figure 2: Schematic diagram of the whole body model and location of the cooling pad.**

## RESULTS

Table 1 gives the physical and physiological properties needed in the model. The air temperature in the lab ($T_{air}$) was recorded as 22.1°C. The local blood perfusion rate and the metabolism of the muscle were determined and shown in Table 1, based on the infrared temperature recording (the emissivity was selected as 0.94). One notes that the two volunteers have similar $\omega$ and $Q'''_{met}$ values, with variations < 10%.

**Table 1 Physical and physiological properties[4,5], *: fitted results**

| **Properties** | Brain | Internal organ | Muscle | Blood |
|---|---|---|---|---|
| $k$, W/mK | 0.52 | 0.52 | 0.52 | 0.50 |
| $\rho$, kg/m$^3$ | 1060 | 1060 | 1060 | 1060 |
| $c$, J/kg K | 3800 | 3800 | 3800 | 3800 |
| $\omega$, 1/s | 0.009 | 0.0021 | **0.00054*,0.00050*** | |
| $Q'''_{met}$ W/m$^3$ | 9225 | 2198 | **543*, 498*** | |

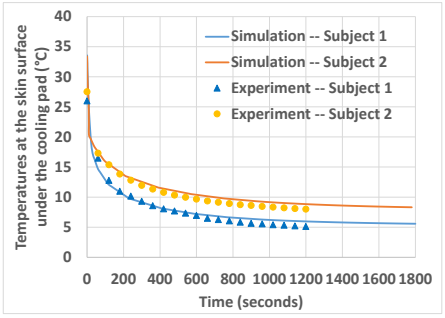


**Figure 3: Recorded temperatures by the thermistor bead sensor (symbols) and the simulation using the finalized $h_{water}$.**

The oral temperature of the volunteer changed slightly, as ±0.1°C from the baseline to that after the cooling. The transient temperatures recorded by the thermistor bead in both volunteers are shown by the symbols in Figure 3. Note that water temperatures in the reservoir did not change very much during the cooling (subject 1: 0°C-1.36°C; subject 2: 1.36°C-2.32°C). In the simulation, an average water temperature (0.68°C or 1.84°C) was used for each subject. While adjusting the overall heat transfer coefficient $h_{water}$ (subject 1: 223 W/m$^2$K, subject 2: 138 W/m$^2$K), one obtains the best match between the experimental data and simulation predictions, shown in Figure 3. The variation of $h_{water}$ from one subject to another may be due to how tight the elastic belt and/or measurement uncertainty.

The final task of this study is to simulate the transient temperature distribution based on the recommended cooling setting by the manufacturer. The water in the reservoir should be ice-water mixture ($T_{water}$=0°C) and the cooling time is set as 30 minutes. Figure 4 illustrates the baseline temperature contours, showing the maximal temperature of 37.3°C occurring in the brain and internal organ. After 30 minutes of cooling by the cooling pad ($T_{water}$=0°C), one can see significant cooling penetration to the deep tissue of the thigh and leg.

The transient temperature distribution along the horizontal line in the right panel of Figure 4 is plotted in Figure 5. The results show a relatively uniform temperature distribution inside the thigh before the cooling, varying from ~33°C at the skin to 37°C at the center. Once the 0°C water is circulating in the cooling pad, temperature decreases rapidly. Temperature profile in the tissue does not change very much after cooling of 20 minutes. Cooling penetrations of both volunteers are similar, even if the thigh diameter of the two volunteers are slightly different (0.12 m vs. 0.129 m). If the cooling front is defined as 33°C, the penetration depth is appropriately 28 mm.

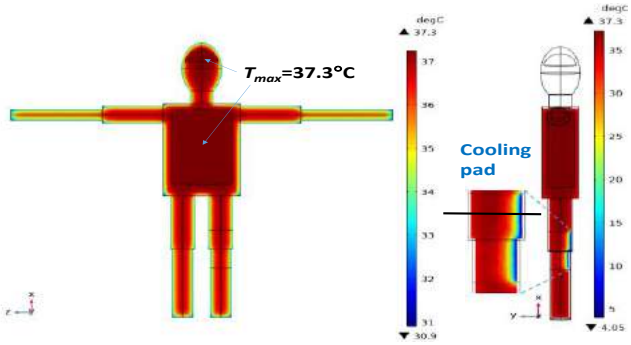


**Figure 4: Contours of the temperature field of the body before (left) and 30 minutes after surface cooling, $T_{water}$ = 0°C (right).**

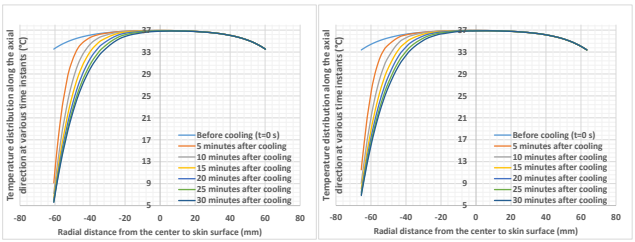


**Figure 5: Temperature distribution along a middle horizontal path (shown in Figure 4) at various time instants of cooling (left: subject 1; right: subject 2).**

## DISCUSSION

The current study shows feasibility of extracting physical and physiological parameters from measured temperatures at the skin surface of targeted cooling region using a cooling pad. The extracted parameters are within the range of normal physiology. The accuracy of theoretical model should be significantly improved with those extracted parameters. Based on the data, the model predicts a cooling penetration depth (<33°C) as 28 mm from the skin surface to the deep region. Further, the cooling penetration is almost unchanged after 20 minutes, suggesting possible shortened cooling duration for patients.


## ACKNOWLEDGEMENTS

This study was supported by an NSF S-STEM grant (DUE-1742170).


## REFERENCES


[1] Bech et al., *Physiotherapy Canada*, 67(1);48–55, 2015.
[2] Dhavalikar et al., *Journal of Exercise Science and Physiotherapy*, 5(1): 24-29, 2009.
[3] Pennes, *Journal of Applied Physiology*, 1:93–122, 1948.
[4] Zhu et al., *Advances in Numerical Heat Transfer*, 3:197-219, 2009.
[5] Lebrun et al., *Journal of Thermal Biology*, 62:129-137, 2016.

# MINIMALLY INVASIVE BLOOD-SPINAL CORD BARRIER MODULATION FOR DRUG DELIVERY

**Zhenghong Gao (*,#,1), Eric David (#,2), Tiffany Wei Leong (#,3), Xiaoqing Li (3), Qi Cai (1), Monica Giannotta (4), Elisabetta Dejana (4), John Wiggins (2), Sharada Krishnagiri (2), Robert Bachoo (5), Theodore J. Price (*,2,6), Zhenpeng Qin (*,1,6)**

(1) Department of Mechanical Engineering, University of Texas at Dallas, Richardson, TX 75080 USA.
(2) Department of Neuroscience, University of Texas at Dallas, Richardson, TX 75080, USA.
(3) Department of Bioengineering, University of Texas at Dallas, Richardson, TX 75080, USA.
(4) FIRC Institute of Molecular Oncology Foundation (IFOM), 20139 Milan, Italy.
(5) Department of Surgery, University of Texas Southwestern Medical Center, Dallas, TX 75390, USA.
(6) Center for Advanced Pain Studies, University of Texas at Dallas, Richardson, TX 75080, USA.

#These authors contributed equally to this work. *Corresponding should be addressed to zhenghong.gao@utdallas.edu, theodore.price@utdallas.edu, zhenpeng.qin@utdallas.edu

## INTRODUCTION

Systemic delivery of therapeutics to the spinal cord is restricted by the blood-spinal cord barrier (BSCB), which regulates the molecular transport from the blood into the spinal cord parenchyma via transcellular and paracellular pathways, only allowing small molecules crossing (<500 Da), such as oxygen, glucose, and water molecules [1-2]. BSCB represents a critical challenge in therapeutics delivery for treating various diseases/disorders affecting the spinal cord in humans. Innovative approach for effective and safe modulation of the BSCB is highly demanded for improving the drug delivery to the spinal cord [3-4]. Herein, we present a novel optical approach (refer as Opto-BSCB, Figure 1) for transiently modulating the BSCB permeability (works for the blood-brain barrier -BBB modulation in the brain as well) [5] and its utility for localized drug delivery with high spatial resolution into the spinal cord in a rodent model [6].

## METHODS

Opto-BSCB approach relies on the optical stimulation of spinal cord vascular tight-junction (TJ) protein, junction adhesion molecule-A (JAM-A) targeted plasmonic gold nanoparticle (AuNP) by ultrashort picosecond laser pulses (Figure 1A). AuNPs conjugated with vasculature protein targeted antibodies are administrated intravenously and stimulated by 532 nm picosecond laser [5]. An optimal method for delivering laser light to reach the spinal cord surface for modulating the BSCB permeability is developed by using an intrathecal injection cannula with an ultrasmall optic fiber inserted through the inner channel at the mouse lumbar region. The efficacy is evaluated by systemically delivering tracers including Evans blue (EB), 660 Da EZ-link biotin, 70 kDa FITC-dextran, and a small molecule peptide-bombesin through intravenous injection. Laser is delivered to lumber L4-5 though the intrathecal device. Behavior studies are carried out to assess the impact of bombesin, an itching causing peptide, after BSCB opening. The safety is examined by analyzing cell specific protein expression in spinal cord tissue after BSCB modulation and bombesin delivery.

## RESULTS

Significantly increased BSCB permeability were observed in the laser stimulated region as compared to region without laser (Figure 1B-E). Opto-BSCB enabled the transient opening of the BSCB within 24 hours for local delivery of biologics with sizes ranging of 660Da – 70kDa in mice.

To demonstrate whether the Opto-BSCB approach can be used for delivering therapeutics/biologics to the spinal cord without significant adverse effect, we used an itch-inducing peptide, namely bombesin (BBS, MW: 1.62 kDa), as a model molecule. After systemic administration following the BSCB modulation (Figure 2A), a rapid and transient itching behavior was observed in the mice with BSCB opening (Figure 2B). In contrast, only a slow and much lower itching behavior (due to the IT injection itself) was observed in the mice with intact BSCB (Figure 2B, $p<0.05$ at 5-10 minutes post-injection of BBS). The increased itching score lasted up to 10 minutes, consistent with the peptide clearance profile. These results suggest that small peptide drugs can be delivered to the spinal cord to introduce behavior-specific changes in rodent models. We then compared the major cellular activities by staining NeuN, IB4, and CGRP post-bombesin delivery in the mice with BSCB intact versus BSCB open (Figure 4C-F, and 4G-J, respectively). We observed no significant changes to IB4, CGRP, and NeuN (Figure 4K, no significance), reflecting the minimal invasiveness of Opto-BSCB-enabled drug delivery. Additional staining suggested no significant increase in GFAP (data not shown).

## DISCUSSION

With this integrated optical nanotechnology, BSCB can be opened efficiently as indicated by the enhanced EB distribution in the laser stimulated region in the mouse spinal cord. BSCB nonpermeable

molecules with sizes ranging from 600 Da to 70 kDa can be delivered into the spinal cord within a 24-hour time window post-laser stimulation. The rapid and transient increase to the itching behaviors is observed in mice upon systemic administration of bombesin within the optimal delivery window after local Opto-BSCB modulation. Opto-BSCB causes minimum impact on the protein expression on the major cell types in the spinal cord (neuron, astrocyte, and glial cells) and does not significantly alter animal behaviors (motor function, inflammation, and pain relevant behaviors, data not included).

Opto-BSCB as a novel minimally invasive BSCB modulation approach is promising for delivering a wide range of therapeutics to the spinal cord, and may have potential applications in improving the local concentration of therapeutics for facilitating the treatment of many diseases/disorders in the spinal cord. Opto-BSCB shows great potential for integrating with the intrathecal devices for bypassing issues of the ultrasound-BSCB opening approach, such as impact of the complicated vertebrae, overheating of bone, and standing waves generated in the narrow spinal canal [3].

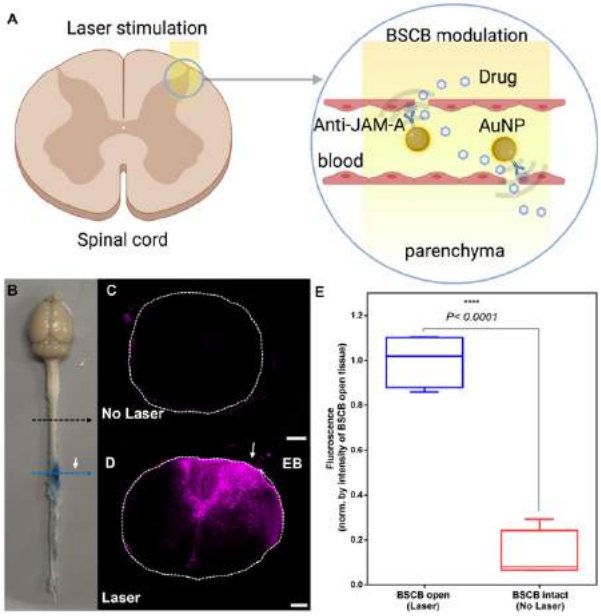


**Figure 1: Opto-BSCB modulation with the bulk laser beam (beam size of 6 mm in diameter).** (A) Schematic representation of the BSCB modulation via TJ protein (JAM-A)-targeted plasmonic AuNPs under laser pulse stimulation for drug delivery into the spinal cord. AuNPs are intravenously (I.V.) injected into the tail vein at a volume of 90 µL dispersed in PBS 1x at a final concentration of about 8.5 nM. 532 nm ps laser stimulation is applied by penetrating the intact tissue on top of the spinal cord to excite nanoparticles targeted to the TJ protein in the blood vessel. Tracer molecules or therapeutics will be I.V. administrated following BSCB opening for delivery to the spinal cord. (B) A macroscopic image of the mouse CNS shows the EB dye penetration in spinal tissue regions with (blue color) and without (natural color) laser stimulation. Laser pulse number of 10 at an intensity of 35 mJ/cm$^2$ measured at the fiber tip. (C) Fluorescence imaging of the cross-section of spinal cord tissue collected from the BSCB intact tissue (no laser), and (D) with BSCB open tissue (laser). Scale bar: 200 µm. (E) Quantitative comparison of the fluorescence in the spinal cord with BSCB open vs intact, showing a 7.7-fold higher fluorescence in the BSCB open tissue as compared to BSCB intact tissue (fluorescence is indicated as mean ± SD, normalized by the mean intensity at BSCB open tissue N=4, ****p<0.0001).

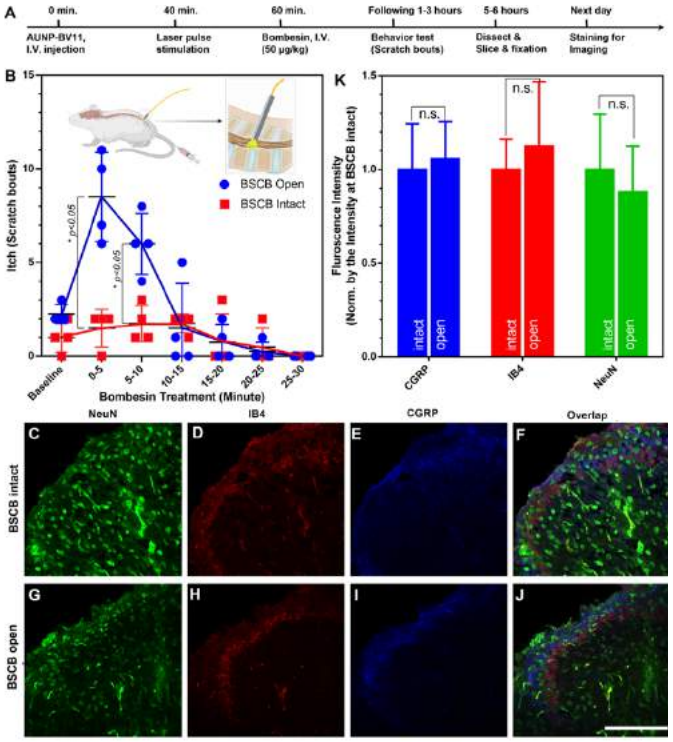


**Figure 2: Local drug delivery into the spinal cord post-Opto-BSCB modulation with the integrated intrathecal device.** (A) Schematic of Opto-BSCB modulation and stepwise experimental methods. (B) Increased itching behavior in mice with BSCB open (blue scatter/line) in comparison with control mice with BSCB intact (red scatter/line). Bombesin (BBS) is I.V. injected at the dose of 50 µg/kg body weight in mice tail vein at a volume of 100 µL. BSCB is opened by using an optic fiber injected through intrathecal injection in vivo at lumbar L4-L5, N=4 per group, $p<0.05$ at 0-5 and 5-10 minutes. Immunohistochemistry (IHC) staining of tissue from spinal cord regions with BSCB intact by (C) NeuN (green), (D) IB4 (red), (E) CGRP (blue), (F) Overlay; and tissue from regions with BSCB open by (G) NeuN (green), (H) IB4 (red), (I) CGRP (blue), (J) Overlay. (K) Quantification of NeuN, IB4, and CGRP on IHC images. Laser pulse number of 10 at an intensity of 35 mJ/cm$^2$ measured at the fiber tip. Scale bar: 100 µm.


## ACKNOWLEDGEMENTS

This research was supported by grants funded by the Department of Defense (DOD: W81XWH2110219, to Z. G), National Institutes of Health (NIH: NS065926, to T. P.), American Hospital Association (AHA: 19CSLOI34770004, to Z.Q.), and Cancer Prevention and Research Institute of Texas (CPRIT: RP190278, to Z.Q.).


## Conflict of interest

Z.G., E.D., T.P., and Z.Q. co-invented the system and method of Opto-BSCB. A US patent application (No. 63/253,543) has been filed through The University of Texas at Dallas.

## REFERENCES


[1] Bartanusz, V et al., *Ann Neurol*, 2011:70:194-206.
[2] Jin LY, et al., J Neurotrauma. 2021 1;38(9):1203-1224.
[3] Montero AS, et al., Ultrasound Med Biol. 2019;45(9):2417-2426.
[4] Fletcher SP, et al., Theranostics. 2020;10(17):7758-7774.
[5] Li X, et al., Nano Lett. 2021. doi: 10.1021/acs.nanolett.1c02996.
[6] Gao Z, et al., to be submitted.

# IN SILICO FATIGUE OPTIMIZATION OF TAVR STENT DESIGNS WITH PHYSIOLOGICAL MOTION IN A BEATING HEART MODEL

**K. Baylous (1), R. Helbock (1), B. Kovarovic (1), O.M. Rotman (1), M. Slepian (2), D. Bluestein (1)**

(1) Biomedical Engineering, Stony Brook University, Stony Brook, NY, USA
(2) Sarver Heart Center, University of Arizona, Tucson, AZ, USA

## INTRODUCTION

Transcatheter aortic valve replacement (TAVR) is a minimally invasive therapy used to treat severe aortic valve (AV) stenosis resulting from progressive calcific aortic valve disease (CAVD). With recent advances in the TAVR procedure and device design generations, TAVR is becoming a standard therapy that is rapidly expanding to younger and lower risk patients. This new patient cohort highlights the importance of long-term fatigue resistance of the device leaflets and stent frame as the device must remain safe and functional for a longer time or else risk the patient with repeat replacement surgeries.

The testing standards for TAVR devices, chiefly the ISO 5840-3 (2021) standard [1], was created by combining the hydrodynamic accelerated wear leaflet testing standards of surgical valves and the stent frame fatigue analysis of stent and graft devices. The leaflet structures are evaluated with various pressure loading conditions and various deployment configurations (under and over expanded, elliptical) at an accelerated frequency ensuring proper full opening and closing for a minimum of 200M cycles. Whereas the stent frame is required to withstand 400M cycles with the manufacturer subject to "identify and justify appropriate *in vivo* loading conditions" [1]. Some researchers have focused on induced strain on the stent frame from the flexure of the diastolic leaflets [2]. Others will use a similar protocol to stent grafts with *in vitro* testing the stent deployed within a compliant tube (representative of the vessel deployed against) with a cyclic pressure waveform inducing the cyclic strains within the stent frame. Others will select a uniform radial displacement that is measured with *in vivo* observations. Since TAVR devices are not deployed against only an artery, with potentially part of the stent in contact with ascending aortic artery, the calcific valve, and the dynamic aortic annulus, the TAVR stent is subject to the cardiac motion as well as the pressures.

Currently there is a paucity of longer term clinical studies data indicating the risk of stent fracture within patients, with most of the research focus on the structural valve degeneration of the leaflet tissues. In the following study, we present a more accurate stent fatigue analysis by utilizing the motion and interaction of the device with a full electro-mechanical coupled beating heart model to determine the *in vivo* loading conditions. The lack of this clinical focus is likely a result of yet to be established durability in these younger., longer-term patients. We additionally posit that the devices may be over engineered and their design iterated in order to achieve similar fatigue life of that acceptable in high-risk and shorter-term elderly patients – aimed at fewer other clinical complications (e.g. cardiac conduction abnormalities). Extended stent fatigue lifetimes will become more critical with the rapid development of polymeric TAVR

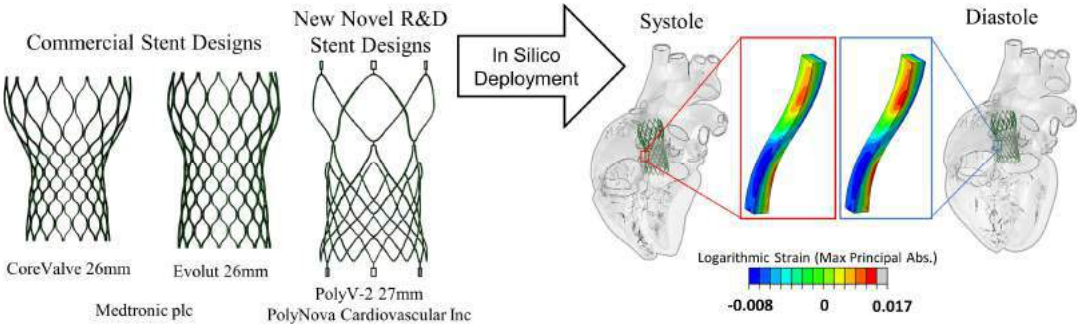


**Figure 1: Commercial stent models and experimental stent designs (left) are simulated deployments within a beating heart model (right). Inset features the change in strain on a single strut over the cardiac cycle.**

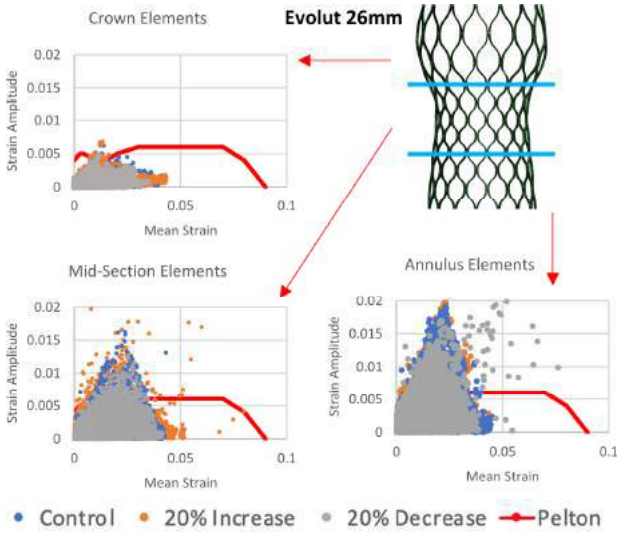


**Figure 3: Fatigue analysis of the Evolut model compared to 20% increase and decrease in strut width and split into different stent sections for comparison**

devices where SVD of tissue valves will not be present resulting in longer leaflet lifetimes [3].

**METHODS**

Commercial stent models were generated for self-expandable nitinol CoreValve 26mm and Evolut 26mm (Fig 1, Medtronic plc, Dublin, Ireland) devices. These models were generated with variable stent circumferential thicknesses as measured on the physical devices. In order to validate the models, finite element analysis (FEA) of the radial force and crush resistance of each model was compared to *in vitro* results. The nitinol material properties at 37°C were adjusted to achieve similar curves and mesh sensitivity/convergence was completed to optimize the simulations. Additionally, the novel polymeric PolyV-2 (Fig 1, 27mm, PolyNova Cardiovascular Inc, Stony Brook, NY) stent frame was analyzed in this study.

These models were deployed inside the Living Heart Model v.2019 (The Living Heart Project, Simulia, Dassault Systemes, Velizy, France) and simulated with ABAQUS Explicit v.2019. The stents are crimped to the appropriate diameter and the outer sheath is retracted with the device is deployed into the native aortic valve (simulating the deployment procedure). After the device is stabilized, the heart is allowed to beat and the deformation of the stent is tracked over 3 cycles until the deformation is repeatable.

In this study FEA is utilized to determine the fatigue resistance of the stent models with an analysis for nitinol materials defined by Pelton et al [4]. Given the unique hyperelastic material properties of self-expanding nitinol stents, both the mean strain (over the loading cycle) and the strain amplitude (change in strain over the cycle) of each element node is tracked. Pelton defines a unique curve (Fig 2 and 3) with limits of mean absolute principal strains over 8% failing and strain amplitudes over 0.4% (below the curve is considered no risk of fatigue failure).

**RESULTS**

The fatigue analysis of the Evolut model (Fig 2) is compared to modified Evolut models with 20% increase and decrease in circumferential strut thickness. Pelton et al indicate that an increase in strut width should result in larger strains in the standard fixed radial displacement analysis [4], however the opposite is observed in our analysis. The thinner strut models apply lower radial force against the contracting myocardium of LHM, thus displacing more and having a higher strain. In all the models, there were elements that would fail (above the Pelton curve) an indefinite fatigue lifetime.

The PolyV-2 design (Fig 3) was iterated to optimize achieving the highest radial force with a lower crimping volume of the stent (total volume must be reduced due to the incompressiblity of the polymer). The larger oversizing of the valve in comparison to the Evolut 26mm, resulted in higher mean strains in the analysis. The PolyV-2 struts were optimized to reduce the strain in stent joints and thus achieving better fatigue resistance in the top and mid element compared to the Evolut and similar fatigue in the annulus region.

**DISCUSSION**

This study demonstrates the utility of advanced *in silico* analysis of devices with the electro-mechanical coupled beating LHM. This analysis is able establish a more realistic study of the interaction of the device and the cardiac structure, as well as the resulting cardiac motion and stent motion. This offers a unique tool to analyze close to *in vivo* loading – bypassing the need for risky human or animal trials to obtain this motion, as well as establish a platform to study the impact of device design features on these results. There may be a discrepancy between this analysis that indicates a limited fatigue life of the commercial stents which has not been observed yet in current clinical reports. It may indicate an over estimation of strain amplitudes due to the explicit analysis or may highlight a clinical complication that may eventually develop as younger, lower-risk TAVR patients age. However, this protocol and analysis does establish a platform to iterate device designs with limited research cost to reduce other clinical complications while maintaining the expected fatigue lifetime. Additionally, with advancements in the LHM, in the future this analysis could be performed on patient-specific models to study the fatigue life in more extreme anatomies.

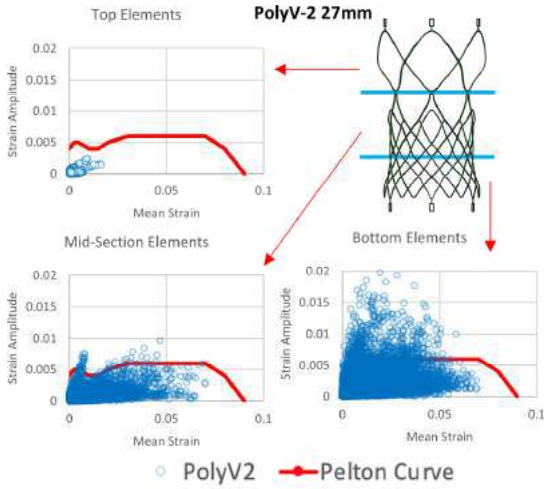


**Figure 2: Analysis of the PolyV-2 experimental stent after optimization to with reduction in mid-section (leaflet region) strains.**

**ACKNOWLEDGEMENTS**

Funding provided by NIH-NIBIB Phase II-U01EB012487 (DB); NIH-NIBIB 1U01EB026414-01 (DB). Industry Partners: ANSYS, Simulia Living Heart Project.

Disclosure: Author OMR and BK are consultants for PolyNova Cardiovascular Inc. Author DB and MS has an equity interest in PolyNova Cardiovascular Inc.

**REFERENCES**

[1] ISO 5840-3 (2021), ICS:11.040.40
[2] Xuan, Y et al., *Ann Thorac Surg,* 104(3):773-781 2017
[3] Rotman, O.M. et al., *Ann Biomed Eng.* 47, 113–125 (2019).
[4] Pelton, AR, *JMEPEG,* 20(4):613-61 (2011)

# THE EFFECT OF FLUID FLOW ON THE LEPTOMENINGEAL CELLS OF THE SUBARACHNOID SPACE

**Mannthalah Abubaker (1,2), David Newport (1,2,3), John Mulvihill (1,2,3)**

(1) Bernal Institute, University of Limerick, Limerick, Ireland
(2) School of Engineering, University of Limerick, Limerick, Ireland
(3) Health Sciences, University of Limerick, Limerick, Ireland

## INTRODUCTION

The Leptomeningeal cells (LMC) are cells that are part of the meninges and line the subarachnoid space (SAS). They function to form membranes that protect and support the brain, and barriers that ensure separation of the cerebrospinal fluid (CSF) from blood found in the vessels of the brain and the dura mater. Emerging evidence has started to show that these cells, previously only thought to have a supportive role in the CNS, are much more complex [1].

Research has so far focused on the role of LMC's developmentally and have shown that they are major sources of extracellular matrix components, growth factors and proteins which in turn make them integral to the formation of basement membranes such as the glial limitans, integral to the migration of the Cajal-Retzius cells, proliferation of cerebellar radial glial progenitor cells, cortical layer formation, cortical neurogenesis, and cerebrovascular development [2-6]. Thus, cells with such complex roles developmentally, should also retain some importance in the adult brain, especially as the LMC's cover the entire CNS and are in constant contact with CSF flow.

This preliminary study aims to understand the importance of the LMC's and their relationship with flow by characterizing the morphological changes of the LMC's. The LMC's will be examined under different flow conditions, imitating the SAS environment in homeostatic and pathophysiological instances, and their responses analysed. This study aims to give a deeper understanding of the potential consequences of altered flow in the CNS and the roles LMC's provide.

## METHODS

**Cell culture and flow experiments:** Primary Human Leptomeningeal Cells were obtained from Sciencell (SC1400, USA) and cultured per recommendations. For the preliminary rocker flow experimentation (Figure 1), 6 well plates were used with no coating and grown to confluence in normal LMC medium (SC1401, Sciencell, USA). A day before experimentation, serum-free medium was applied to minimise cell growth. Four 6-well plates were used, two plates for dynamic flow application and two plates for static control. The magnitude of shear applied was calculated using the peer reviewed ShearFast application [7]. A shear stress of 0.02 Pa was applied by setting the rocker to 30 RPM at a rocking angle of $\pm$ 7°. The wells were filled with 2 mL serum free medium. Flow was applied to the cells for 24 hours and 48 hours respectively in an incubator (37°C, 5%$CO_2$). This was a preliminary study to assess if cells reacted to the stimulus of flow.

**Immunofluorescence experiments:** To verify LMC's identity cells were stained for Vimentin (ab45939, Abcam, Netherlands), CRABP2 (NB100-2590, Bio-techne Ltd, England), S100a6 (NBP1-89388, Bio-techne Ltd, England) and E-cadherin (data not shown) (NBP2-19051, Bio-techne Ltd, England) [2]. Appropriate secondary antibody was used, either anti-mouse (ab150115, Abcam, Netherlands) or anti-rabbit (ab150077, Abcam, Netherlands). Cells were fixed in 4% paraformaldehyde (PFA) in 1x PBS for 15 minutes at room temperature followed by an hour incubation in blocking buffer made up of 1% fetal bovine serum (FBS) and 0.3% Triton x-100 in 1x PBS. Primary antibody diluted in blocking buffer was applied and left over-night at 4°C. The secondary antibody diluted in blocking buffer was applied the next day and left for an hour at room temperature in the dark. 1x PBS was applied to prevent drying and plates were covered to prevent light exposure. Samples were imaged using an IMX confocal high-content imaging system (Molecular devices, USA) at 20x widefield magnification.

## RESULTS

**Flow experiments:** A preliminary test run was performed to optimize the rocker experiment and to determine whether the LMC's were responsive to flow stimulus. This test showed that there could be

a potential response to flow. Two plates underwent a shear of 0.02 Pa. Their response to this shear (flow) was assessed using trypan blue cell counting. Figure 2 below shows the cell count and viability of the dynamic and static controls plates in this preliminary test. A p-value < 0.001 was observed between the 24 hour and 48-hour results for both dynamic and static results. The 48-hours run yielded a larger cell viability than the 24-hour run while the opposite was seen for the controls.

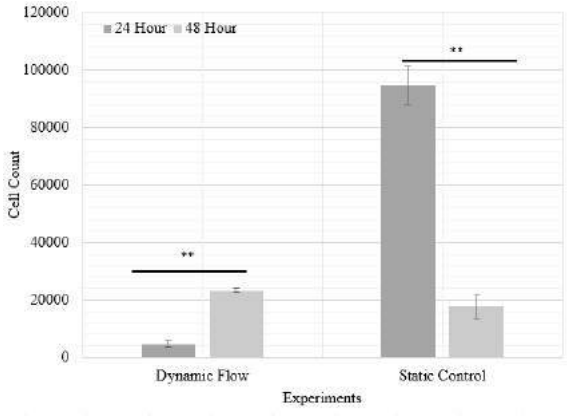


**Figure 2: The viability of the cells in the dynamic plates and static control plates after undergoing flow for 24 hours and 48 hours. **p<0.001**

**Immunofluorescence experiment:** Immunofluorescence staining for Vimentin, CRABP2, S100a6 were performed to characterise the cells and validate that they are LMC's (Figure 3). The cells stained positively for the three proteins which confirms that these are LMC's. Figure 3D highlights the elongated morphology of the LMC's under a static environment. This was also found in the immunofluorescent images with some cells displaying flat and large cell bodies (e.g., Figure 3A). CRABP and S100a6 stained as expected, as cytoplasmic protein, with CRABP2 staining with greater intensity around the nucleus in comparison to S100a6.

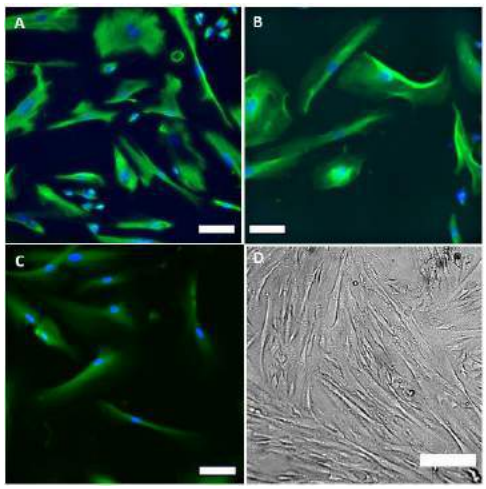


**Figure 3: (A) Vimentin (green) and DAPI (blue) immunofluorescence staining of LMC, scale bar 100µm. (B) CRABP2, scale bar 100µm. (C) S100a6, scale bar 100µm. (D) Brightfield of LMC at full confluency, scale bar 100µm.**

## DISCUSSION

We hypothesize that the LMC's play an important role in maintaining a functional CNS. For this preliminary study, we examined the response of the LMC's to a flow stimulus by inspecting the change in cell viability and performed immunofluorescence staining to confirm cell identity. It is hoped that this research will provide information that will aid in understanding the neurological environment more in-depth to be able to diagnose disease and offer better treatments.

In the preliminary rocker experiment, cell response to flow was observed by comparing cell viability in a flow applied dynamic plate to a no flow static control. The cells showed a higher viability after 48 hours of flow application in comparison to 24 hours but an opposite response in the static controls. This was hypothesised to be indicative of cell adaptation to the flow over time and that the cells may require a stimulation to retain viability as can be seen by comparing the 24-hour static plate to the 48-hour static plate which saw a large drop in cell number. However, the abrupt addition of serum-free media a day in advance of the test may have propagate cell death in both plates and thus influenced the overall results. To confirm this, more testing is required which will be achieved in the next stage of flow experimentation. Serum-free medium will be applied more gradually to the cells to ensure cells will only be impacted by flow. The next stage experimentation will also examine protein expression and cell morphology changes under different flows compared to the static.

The immunofluorescence experiment confirmed that the LMC's stained for three of the five proteins of interest that this study will focus on [1-2]. Figure 3A demonstrated vimentin protein structure of the LMC, showing the typical morphological structure expected of the LMC's. Figure 3B and 3C, CRABP2 and S100a6, both cytoplasmic proteins with functional roles in the LMC, were used to identify whether the LMC's originated from the arachnoid mater or pia mater. However, due to the LMC's staining for both, there is a possibility that these LMC's originate from both. To further confirm this, flow cytometry will be used to detect cell type. Similarly, further staining will be completed to fully characterise the cell morphology using GFAP, Cytokeratin, Claudin-11 and Nestin [1][8].

## ACKNOWLEDGEMENTS

This work is funded by the Irish Research Council, GOIPG/2020/1424.

## REFERENCES

[1] Weller, R et al., *Acta neuropathologica*, 135(3):363-85, 2018
[2] Siegenthaler, J et al., *Cell*, 139(3):597-609, 2009
[3] Bifari, F et al., *Frontiers in cellular neuroscience*, 9:383, 2015
[4] DeSito, J et al., *Dev Cell.*, 54(1):43-59, 2020
[5] Decimo, I et al., *The Neuroscientist*, 27(5):506-28, 2021
[6] Suter, T et al., *Dev Biol.*, 430(1):1-10, 2017
[7] Smith, T et al., *bioRxiv*, 2020
[8] Frank, E et al., *Experimental cell researcher*, 146(2):371-6, 1983

# CARRIER SOLUTION COMPOSITION AFFECTS RECOVERY OF CPA-PERFUSED RAT HEARTS

**C. Kraft (1), B. Namsrai (2), D. Tobolt (2), Z. Gao (3), M. Etheridge (3), E. Finger (2), J. Bischof (1) (3)**

(1) Department of Biomedical Engineering, University of Minnesota, Minneapolis, MN, USA
(2) Department of Surgery, University of Minnesota, Minneapolis, MN, USA
(3) Department of Mechanical Engineering, University of Minnesota, Minneapolis, MN, USA

## INTRODUCTION

Heart cryopreservation would revolutionize cardiac transplantation and regenerative medicine applications[1]. The only approach that can achieve indefinite cryopreservation is vitrification or cooling the organ into a glassy state[2]. While vitrification solutions have been developed that can be delivered to organs such that they can be successfully vitrified, the exposure to these solutions often causes injury[3], hindering recovery of organ function. Our group is focused on reducing toxicity and improving the delivery of these solutions in an isolated rat heart model thereby allowing functional recovery sufficient for both cryopreservation and eventual transplantation. A vitrification solution is a mixture of cryoprotective agents (CPAs) and a carrier solution which contains different salt, sugars, buffers, antioxidants and/or metabolites. A key finding is that while the carrier solution is a fraction of the overall osmolality of the cryoprotective solution, it has an oversize impact on toxicity. Through manipulation of the carrier solution we are able to demonstrate dramatic functional improvements that suggest recovery of contraction following vitrification and nanowarming will be possible.

## METHODS

To answer the research question of which vitrification solution is least toxic, we implemented two perfusion stages. In the "toxicity" stage, the rat heart was perfused with the test vitrification solution. In the "recovery" stage, the rat heart was perfused with a physiological solution, wherein any recovery of beating was observed. Perfusate was flowed retrograde into an aortic cannula[4], causing perfusion of the heart tissue via the coronary vasculature. To assess edema, the heart was weighed before and after each perfusion stage. To assess vascular resistance, flowrate was recorded at constant perfusion pressure. Every twenty minutes, samples were taken from the organ bath and analyzed for lactate dehydrogenase (LDH), a biomarker of injury. Afterwards, biopsies from each chamber were procured and analyzed for ATP, our key quantitative metric of viability. Other details are shown below (Fig. 1).

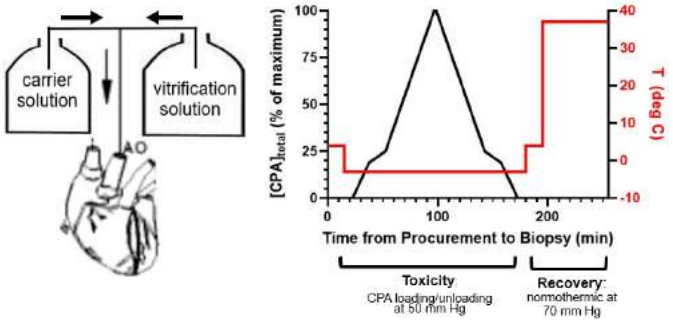


**Figure 1: To limit osmotic damage, CPA concentration was gradually increased until all flow originates from the vitrification solution reservoir at 83 min of hypothermic perfusion, then gradually decreased until all flow originates from the carrier solution reservoir at 158 min of hypothermic perfusion. Qualitative recovery of contractions was assessed at 37 °C during perfusion with Tyrode's, a blood-mimicking solution.**

Our study focused on four different carrier solutions: LM5[5], Euro-Collins (EC)[6], University of Wisconsin (UW)[7], and

Celsior[8]. Though these solutions have been investigated by others[9] as perfusates for hypothermic preservation, our study is the first to our knowledge to compare their utility as CPA "carriers" for vitrification.

## RESULTS

Our major result is that carrier solution selection is important. So important, in fact, that we found it made the difference between recovery of beating versus no recovery at all.

This "carrier solution screening" was conducted using VEG, a CPA cocktail consisting of 2.7 M ethylene glycol, 3.1 M dimethyl sulfoxide, and 3.1 M formamide[10]. The total CPA concentration in this cocktail is 8.9 M, and we found that this high concentration was extremely toxic if LM5 or EC was the chosen carrier (Fig 2.). For LM5, in fact, two rat hearts did not even recover beating at half the listed CPA composition (4.45 M). Both UW and Celsior, by contrast, enabled recovery of beating at the full 8.9 M.

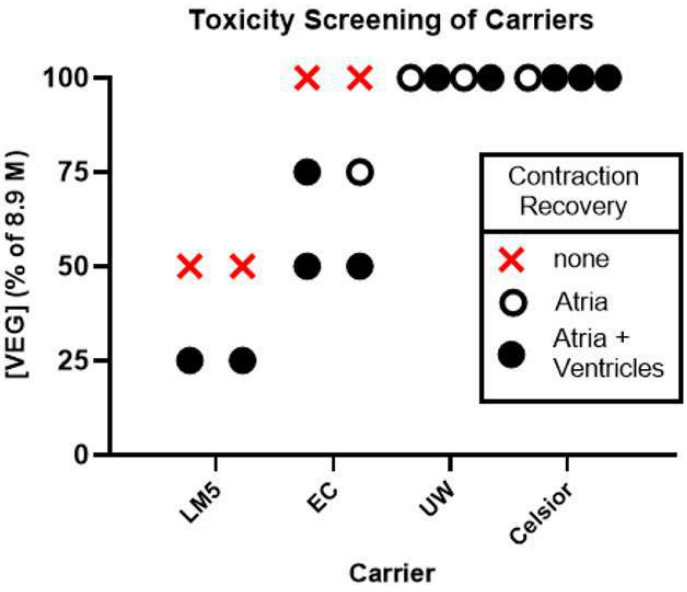


**Figure 2: The carrier solutions UW and Celsior confer better tolerance to VEG than LM5 and EC. Each data point represents one heart, and contraction recovery was ascertained visually.**

## DISCUSSION

In clinic, donor hearts are preserved by ischemic immersion in either UW or Celsior. One study in rats found that Celsior is slightly better[11], while another study in humans found that UW is slightly better[12]. These results extend this understanding of hypothermic perfusates to CPA-containing vitrification solutions. While a mechanistic explanation for the superiority of these solutions is incomplete, some insight may be gleaned by comparing the compositions of these solutions (Table 1).

**Table 1: Compositions of Tested Carrier Solutions**

| component | EC | UW | LM5 | Celsior |
|---|---|---|---|---|
| sodium | 10 | 25 | 10 | 100 |
| potassium | 115 | 125 | 35.4 | 15 |
| magnesium | | | | 13 |
| chloride | 15 | 20 | 29.2 | 41.5 |
| calcium | | | | .26 |
| glucose | 195 | | 90 | |
| lactose | | | 45 | |
| lactobionate | | 100 | | 80 |
| raffinose | | 30 | | |
| mannitol | | | 45 | 60 |
| glutathione | | 3 | 5 | 3 |
| allopurinol | | 1 | | |
| adenosine | | 5 | | |
| adenine | | | 1 | |
| glutamate | | | | 20 |
| phosphate | 50 | 25 | 7.2 | |
| bicarbonate | 10 | | 10 | |
| histidine | | | | 30 |
| HEPES | | | | |
| properties | | | | |
| pH | 7.4 | 7.4 | 7.4 | 7.3 |
| osmolality (mOsm/kg) | 365 | 320 | 283 | 340 |

We speculate that the low cation content of LM5 interfered with the transmembrane potential, leading to worse recovery. Perhaps UW and Celsior outperformed EC because of the inclusion of glutathione, a free radical scavenger. A better mechanistic understanding could be achieved by a cellular/molecular investigation.

Although Celsior and UW hearts did recover beating, their contractility was very low. Therefore, future work could involve improving these perfusates for the application of vitrification, or shift focus to minimizing CPA toxicity by adjusting temperature and/or exposure time, as well as preconditioning the heart to tolerate ischemia and CPA damage.

## ACKNOWLEDGEMENTS

This work was supported by an NIH T32 traineeship (T32HL139431), an NIH grant (R01HL135046-01A1), and an NSF ERC (EEC 1941543).

## REFERENCES

[1] Giwa S, et al., *Nat Biotechnol*, 35:530-542, 2001.
[2] Finger E, Bischof J., *Curr Opin Organ Transplant*, 23:353-360, 2018.
[3] Gao Z, et al., *Adv Mater Technol*,
[4] Langendorff O, *Arch Für Gesamte Physiol Menschen Tiere*, 61:291-332, 1895.
[5] Fahy GM et al., *Cryobiology*, 48:157-178, 2004.
[6] Collins GM, et al., *The Lancet*, 294:1219-1222,1969.
[7] Wahlberg JA, et al., *Transplantation*, 43:5-7, 1987.
[8] Menasche P, et al., *Eur J Cardiothorac Surg*, 8:207-213, 1994.
[9] Peltz M, et al., *Surgery*, 138:795-805, 2005.
[10] Fahy et al., *Cryobiology*, 48:22-35, 2004.
[11] Michel P, et al., *J Heart Lung Transplant*, 21:1030-1039, 2002.
[12] Li Y et al. *Artif Organs*. 40:489-496, 2016.

# A DISCRETE-FIBER MODEL FOR UNDERSTANDING CELLULAR MECHANOADAPTATION

**Ryan R Mahutga (1), Patrick W Alford (1)**

(1) Department of Biomedical Engineering, University of Minnesota, Minneapolis, MN, USA

## INTRODUCTION

Cells are the living component of tissues and are responsible both directly and indirectly for how tissues grow and remodel [1]. We know that cells actively adapt to their extracellular environment by changing both their morphology and their cytoskeletal architecture both of which affect the cellular mechanics as well as overall tissue mechanics. Particularly, cells tend to be at the initiation of mechanical dysfunction in disease like aortic aneurysm [2–4]. Thus, being able to understand how mechanical cues affect cells, and how cells adapt to those cues is important for predicting disease progression and assessing intervention outcomes.

Most models of tissue growth and remodeling (G&R) either treat the cells quite coarsely or neglect them altogether. In this work, we develop a multiscale model of cellular mechanoadaptation to simulate cellular microbiaxial stretching (CμBS) [5]. This model allows us to track the changes within the cell and the influences such changes have on the substrate. With this model system, we can readily alter actin dynamics simulating pharmacological treatments as an in-silico disease-on-a-chip model. This framework is also easily adapted to investigate cells in 3D environments, which can include both experimental gel-based systems and in vivo mimicking fibrous extracellular matrix.

## METHODS

Computational Model:

*Cell Mechanics:* We developed a model using a discrete actin stress fiber network that lies within a membrane domain (Fig. 1A). The actin stress fibers are defined as linear springs with modulus 150kPa. The membrane itself is a surface upon which hydrostatic pressure acts from within the cell. The cellular hydrostatic pressure is given by $P = k\phi$ where $k$ is 1kPa and $\phi$ is the fiber volume fraction of actin. The cell's homeostatic state is then calculated by finding the equilibrium between the hydrostatic pressure on all free surfaces and the force within constituent stress fibers using Newton iteration. We derive the Cauchy stress within the cell of arbitrary shape using volume-averaging theory [6] as

$$\sigma_{ij} = \frac{1}{V}\int \sigma'_{ij}\,dV = \frac{1}{V}\sum_f \sigma^f V^f n_i^f n_j^f = \frac{1}{V}\sum_f t^f l^f n_i^f n_j^f \quad (1)$$

where V is the cell volume, $\sigma'_{ij}$ is the local stress at any point within the cell, $f$ is an index for each fiber, $\sigma^f$ is the fiber stress, $V^f$ is the fiber volume, $n^f$ is the normal vector along a fiber, $t^f$ is the fiber force, and $l^f$ is the fiber deformed length. We can see from this relation that the cell can be any arbitrary shape, and the only geometric quantity we need from the cellular domain is the volume. Simply, we can define the membrane surface using triangular surface elements from which we can calculate an enclosed volume for the surface mesh. We define the edges of the membrane surface mesh to be intermediate filaments, serving the primary role of maintaining cellular structure. We prescribe these fibers as linear with modulus 15kPa.

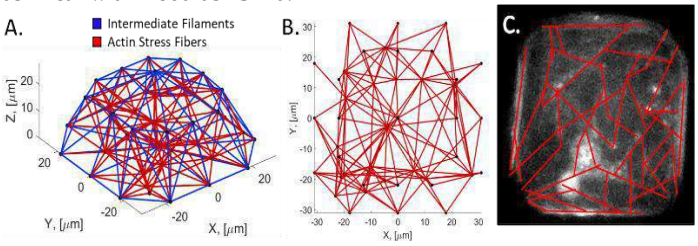


**Fig. 1. A.** 3D cell cytoskeletal network architecture immediately after substrate attachment. **B.** 2D projection of the actin stress fiber network. **C.** SIR live actin image of representative VSMC with overlay of identifiable fibers (red).

*Remodeling:* Actin fibers within cells are dynamic and assumed to exhibit tensional homeostasis, so we prescribe the remodeling law

$$dL^f/dti = 1/T^f\left(\sigma^f - \sigma^\infty\right)ïL^f \quad (2)$$

where $L^f$ is the fiber undeformed length, $T^f$ is the remodeling time constant (150 kPa h), and $\sigma^\infty$ is the fiber homeostatic (target) stress (35kPa). This remodeling equation is solved using a forward Euler

method to obtain the fiber lengths at each time point during remodeling. Because intermediate filaments are relatively stable in nondividing, nonmotile cells [7], we do not remodel them in this model system. Further, we prescribe a minimum fiber length of 3μm to prevent fibers from being removed (or becoming very short) which lead to instabilities in the computation.

Experimental Validation:

Human umbilical artery vascular smooth muscle cells (VSMCs) were cultured using standard methods [5], and were tested at passage six. Fibronectin micropatterns of aspect ratio one (L=62um,W=62um) were created on a fluorescent bead-doped 13.5kPa polyacrylamide gel affixed to a silicone membrane construct [5]. After gelling, the constructs were seeded with VSMCs, and incubated for 24h. The media was then changed to serum-free equivalent, and the constructs were incubated for 24h prior to experimentation.

The constructs were loaded into a custom apparatus mounted to a confocal microscope consisting of four high-resolution linear actuators. The actuators were used to stretch the construct to 30% grip strain. The construct was then imaged for a 0h timepoint. The construct was then placed in a custom bracket to maintain the stretch and moved to incubate until the next time point. At the next timepoint, the construct was imaged at the stretched state then returned to the incubator for the next time step. This process was repeated for time steps 2h and 4h. At 22h the sample was again placed in the scope in the stretch configuration and imaged. After this imaging, the sample was returned to zero grip strain where its position was recorded. The construct was then stretched back to 30% grip strain, and the cells were lysed from the construct using SDS. The sample was then imaged for a stretched, cell-free state. The construct was returned to the zero-strain state and imaged again for the undeformed, cell-free state.

Displacements and tractions were measured from the fluorescent bead images using ImageJ [5]. With displacements and tractions measured, stressed were calculated using a custom Matlab routine integrating the traction fields over the cellular cross-sections.

**RESULTS**

In this model system, we perform two stages of remodeling. In the first we apply no deformation to the cell, and simply let it equilibrate according to Eq. 2 taking the network from the initial state to the basal state. Next, we apply an instantaneous stretch to the cell and allow it to re-equilibrate taking it from the basal state to the stretched, remodeled state. The experiment we attempt to recapitulate with this model gave the local substrate stretch determined from the bead displacements (strains of 0.263±0.017 in X and -0.077±0.019 in Y). Fig. 2 shows the experiment compared to the model. The basal state is shown in the black box, and the remodeling comparison shows the model as dashed lines and the experiment as data points.

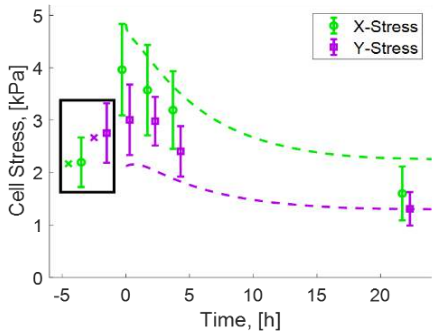


**Fig. 2.** Cellular mechanoadaptation comparison between experiments (circles and squares) and model (x's and dashed lines). The black box shows the basal state. (experiment: n=9, error bars: 95% confidence interval)

This model system further allowed us to investigate cellular morphology and individual fiber changes. For example, in Fig. 3A and 3B, we show the changes in fiber lengths and in fiber orientations respectively in the initial, basal, and stretched cases. The fiber length evolution (Fig. 3A) tends to form two populations: short fibers and long fibers. The stretched remodeled case shows a shift of the short fiber family to the right, indicating lengthening of these fibers. The fiber orientations in the plane of stretch (Fig. 3B) show realignment toward the X-direction in the stretched state as compared to the basal state.

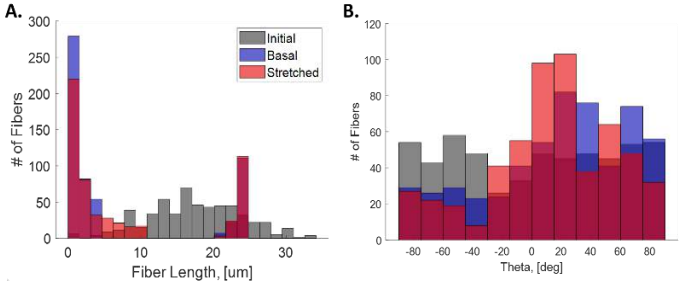


**Fig. 3. A.** Fiber length histograms showing initial state (grey), basal state (blue), and stretched state (red). **B.** Fiber orientation in the plane of stretch relative to the X-direction showing initial state (grey), basal state (blue), and stretched state (red).

**DISCUSSION**

The model described above is a new method for understanding cell mechanobiology. We show very good agreement in the cellular basal state between the experiment and the model (black box in Fig. 2) and match the qualitative trend of cell stress progression post-stretch (data points vs. lines in Fig. 2). The X-direction stress in the model is slightly elevated compared to the experiment, but the slopes of the evolution curve match quite well. The Y-direction stress in the model is slightly depressed as compared to the experiment, but we show similar behavior including an initial phase of relatively little change over the course of the first two hours, and a lower overall homeostatic stress state at the end of remodeling. Further, this model gives us increased structural insight into the cell such as the fiber orientations and growth of individual fibers (Fig. 3A, B). We see general lengthening of fibers in the stretched case as one would expect, as well as reorientation of the fibers toward the direction of stretch consistent with experimental observation [5].

*Limitations:* In its current state, the model assumes a rigid substrate. We mitigate the issues with this assumption by precisely prescribing the deformations the cell undergoes, but it will be important to include the substrate stiffness moving forward as we know there is an influence between stiffness and mechanoadaptation of cells. We have a framework developed to couple this discrete model to a finite-element mesh of the substrate where one can control the substrate behavior more accurately. We also neglect other fiber types (such as microtubules) and exclude the cell nucleus in the model in its current form. We could prescribe any number of different fiber constituents, as well as prescribing the nucleus in a method similar to the cell itself. The purpose of this study was to investigate the actin remodeling in cells, so we omit these structures for simplicity. Future work with this model will use the nucleus as a structural element that drives mechanoadaptation based on the stress experienced by the nucleus itself.

**ACKNOWLEDGEMENTS**

The authors acknowledge funding from the American Heart Association Postdoctoral Fellowship (Award 827242).

**REFERENCES**

[1] Qiu, J., et al. 2014, J. R. Soc. Interface, 11(90). [2] Perrucci, G. L., et al., 2016, Cell. Mol. Life Sci., 74. [3] Bunton, T. E., et al., 2001, Circ. Res., 88(1), pp. 37–43. [4] Hayashi, K., and Naiki, T., 2009, J. Mech. Behav. Biomed. Mater. [5] Mahutga, R., and Barocas, V. H., 2020, J. Biomech. Eng., 142(11). [6] Cook, B., et al. 2021, J. Biomech. Eng., 143(10). [7] Tang, D. D., and Gerlach, B. D., 2017, Respiratory Research, 18:54

SB³C2022
Summer Biomechanics, Bioengineering and Biotransport Conference
June 20-23, Eastern Shore, MD, USA

# BIOMECHANICAL RESPONSES OF NEURON-COLLAGEN CONSTRUCTS FOR FAST STRAIN RATE LOADING TO FAILURE

**Sittinon Nuethong (1), Sagar Singh (1), Beth A. Winkelstein (1,2)**

(1) Department of Bioengineering
University of Pennsylvania
Philadelphia, PA, USA

(2) Department of Neurosurgery
University of Pennsylvania
Philadelphia, PA, USA

## INTRODUCTION

The facet capsular ligament, which is primarily composed of collagen fibers arranged in the extracellular matrix (ECM) network with afferent neurons embedded in that ECM [1,2], is a common source of pain in both the cervical and lumbar spines [3,4]. Injury and/or damage to the capsular ligament has been shown in animal models to result from excessive stretch of the ligament, which induces laxity and collagen disorganization in the ligament [5,6] and induces pain and injury responses in afferent nerve fibers via mechanotransduction [4,7-8]. Those neuronal responses are rate-dependent [9]. Further, the local biomechanical environment surrounding afferents has been shown to alter their neuronal response [10] for systems like the capsular ligament. In addition, the biomechanical response of ligaments is also known to vary with loading rate [11-14]. Although the effect of loading rate has been studied for ligament injuries [12,13] and neuronal injury is rate-dependent [15-18], little is known about the effects of loading rate on neuronal activity and pain signaling.

Our lab has developed a neuron collagen gel construct (NCC) in vitro system that enables the integrated investigation of macroscale and local mechanics, along with neuronal responses, to better understand joint pain and injury [19-22]. That NCC system has been used to define relationships between local mechanics, collagen fiber responses and neuronal mechanisms relevant to nociception. In fact, collagen realignment, which likely modulates neuronal responses [10], occurs to a lesser extent when the rate of uniaxial tension is increased by 7-fold [19,20]. While that work suggests loading rate to be important, most work with the NCC system has been limited to a slow strain rate (i.e. 1%/s) [21,22]. However, ligament trauma is known to occur at much faster rates [13]. As such, this study aimed to define the macroscale biomechanical response and corresponding microscale regional strains for NCCs undergoing stretch at a high rate of loading (10.5mm/s), corresponding to an order of magnitude greater than previous work [19,22].

## METHODS

NCCs (n=11) were prepared using 2.0mg/mL of rat tail collagen I solution cast in 12-well plates as previously described [19-22]. Briefly, collagen gels self-assembled at 37°C in 5% $CO_2$ for at least 45 minutes and were seeded with DRG neurons ($3x10^5$ cells/mL) dissociated from embryonic day 18 rats [19]. After 3 days in vitro, more collagen was added to encapsulate the neurons and the NCCs.

On day-in-vitro 7, NCCs were transferred to sterile phosphate buffered saline (PBS) and cut into a strip (21mm x 8mm). A marker grid was drawn on each NCC surface to define smaller regions, allowing elemental strain analyses (Figure 1). Gels were submerged in a 37°C PBS bath, and each arm was fastened to microclamps of a planar testing machine (TestResources) that was integrated with a high-speed camera (Phantom-v9.1; Vision Research; Inc.) [19-22]. NCCs were stretched to failure uniaxially with each arm distracted at 10.5mm/s. Force and displacement data were recorded at 500Hz and synchronized with imaging data (500fps).

Force and displacement data were filtered using a 25-point moving average filter [19-22]; failure was defined as the maximum point of the force-displacement curve for each loading arm (Figure 1A). Stiffness was calculated as the slope of the force-displacement curve between 20% and 80% of maximum force [23] (Figure 1A). Each of the failure force and displacement, as well as stiffness, was averaged across both arms for each NCC. Elements of each NCC were defined using the fiducial markers as elemental nodes (Figure 1). Nodal displacements were measured using ProAnalyst software (Xcitex) and input into LS-DYNA (LSTC) to compute both the peak maximum principal strain

(MPS) from any element in each NCC and also the mean MPS across all elements for each NCC (Figure 1) [19-22].

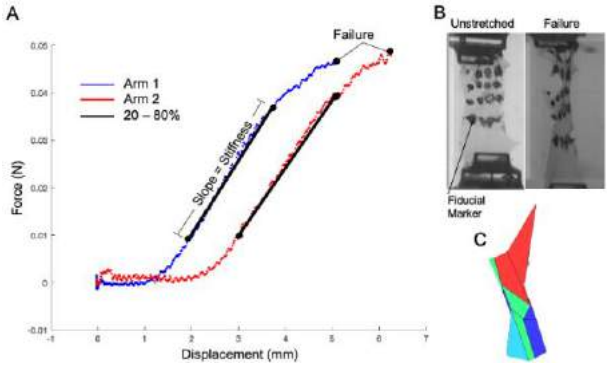


**Figure 1: (A) A representative force-displacement curve. (B) Representative images at reference (unstretched) and failure, with the (C) corresponding MPS map of the sample at failure.**

## RESULTS

The measured displacement rate across all NCCs is 9.7±0.6mm/s, corresponding to an imposed strain rate of 92.4±5.6%/s. At this rate of applied stretch, the NCCs fail at a force of 25.6±14.6mN and a displacement of 4.5±1.2mm. The corresponding stiffness for loading at this rate is 10.2±5.6mN/mm. Image data were available for strain analysis from only 6 of the total 11 NCCs due to poor image quality or asynchronous acquisition during the applied distraction. The mean elemental MPS in those NCCs is 0.47±0.20 and the peak MPS is 0.81±0.43 at failure (Figure 2). Failure was observed to occur at either the top or bottom edge of the gel in the majority (5 of the 6) of the NCCs with imaging, corresponding to the location where the peak MPS was calculated (Figure 1C).

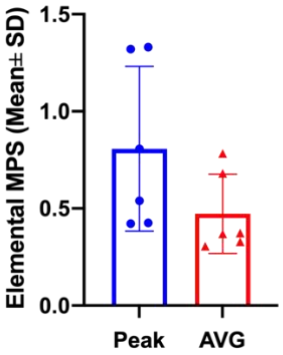


**Figure 2. Peak and average elemental MPS at failure, showing individual gel data points in circles and triangles for each outcome.**

## DISCUSSION

This is the first study to our knowledge defining the macro-scale biomechanical responses and microscale regional strains of NCCs. The force at failure is double, and the stiffness is nearly 3-fold greater than, corresponding values at failure with the same NCC system (12.6±7.3 mN; 3.1±1.1mN/mm) at a measured strain rate of approximately one-tenth (1%/s) of the rate used here [22]. This increase in macroscopic mechanical metrics is consistent with other work supporting increases in both force and stiffness with increasing loading rate for ligaments in the knee and spine stretched to failure [12,13].

However, the displacement (4.5±1.2mm in current study) at failure is similar despite the difference in loading rates (4.68±1.6mm for 1%/s).[22]. Interestingly, both the peak and average MPS are at least 3-4 times greater than the average MPS (0.12±0.07) found using a 1%/s distraction rate [22]. This difference is in contrast to reports that strain is independent of strain rate [12,13,19]. Also notable is that the standard deviation of both strain metrics (Figure 2) in the current study are relatively larger than those reported in prior studies using slower loading rates. That variability, together with the small group size for strain data may suggest the need for both more testing and more detailed investigation to define the collagen responses and micro-level mechanics.

The stiffening and strengthening of ligament tissues has been attributed to the stiffening of collagen fibrils and a reduction in fibril strain associated with matrix-debonding of inter-fibillar sidechains [24]. It is possible to integrate polarized light imaging during testing to simultaneously measure collagen kinematics in this test system [19-22], which would help not only to define reorganization of collagen but also help to better understand the strain response magnitude and regional variability. In addition, studies defining the neuronal responses in this system would help characterize the effects of traumatic loading on nerve injury, pain transmission and mechanotransduction in this unstudied high-rate loading paradigm. Nevertheless, this study demonstrates that the macroscale and microscale mechanics of NCCs is altered with increasing strain rate, exhibiting similar response to that observed in ligaments, and given the known relationship to cellular and neuronal mechanotransduction likely has implications for pain and injury.


## ACKNOWLEDGEMENTS

Funding for this study was provided by the NCCIH (AT010326).


## REFERENCES


[1] Yamashita T et al, *Spine J.*, 21(5):538–543, 1996.
[2] Yahia L & Garzon S, *Ann. Anat.*, 175(2):185–188, 1993.
[3] Lee K & Winkelstein B, *J. Pain*, 10:436-45, 2009.
[4] Kallakuri, et.al, *Eur. Spine J.*, 17(4):556–63, 2008.
[5] Quinn K et al, *J. Biomech.*, 43(10):1870-1875, 2010.
[6] Quinn K et al, *Stapp Car Crash J.*,51:169-187, 2007
[7] Chen, C et al, *J. Bone Joint Surg. Am.*, 88(8):1807–1816, 2006.
[8] Dong L & Winkelstein B, *J. Neurotrauma*, 27(1):163-174, 2010.
[9] Ahmadzadeh H et al, *Biophys. J.*, 106:1123–1133, 2014.
[10] Middendorf J et al, *Biomech Model Mechanobio*, 20(6):2269-2285, 2021.
[11] Bass C et al, *Spine J.*, 32(1): E7-E13, 2007.
[12] Noyes F et al, *J. Bone Joint Surg.*, 56(2):236–253, 1974.
[13] Stephen F et al, *J. Mech Behav Biomed Mater*, 10: 216-226, 2012.
[14] Yoganandan N et al, *Spine J.*, 14(10):1102-1110, 1989.
[15] Geddes D et al, *J. Neurotrauma*, 20(10):1039‑1049, 2003.
[16] Cullen D & LaPlaca M, *J. Neurotrauma*, 23(9):1304‑1319, 2006.
[17] Tang-Schomer M et al, *FASEB J.*, 24(5):1401‑10, 2010.
[18] Kochba E et al, *Sci. Rep.*, 6:1‑11, 2016.
[19] Zhang S et al, *J. Biomech. Eng.*, 138:021013, 2016.
[20] Zhang S & Winkelstein B, *SB3C*, 2016.
[21] Zhang S et al, *J. Orthop. Res.*, 36(2):770-7, 2018.
[22] Ita M & Winkelstein B, *J. Biomech. Eng.*,138(2):021013, 2019.
[23] Lee E et al, *J. Biomech.*, 39(7):256–1264, 2006.
[24] Karunaratne A et al, *Sci. Rep.*, *8*(1): 3707, 2018.

# COMPUTATIONAL MODELING OF THE PASSIVE ANISOTROPIC VISCOELASTIC BEHAVIOR OF OVINE RIGHT VENTRICLES

**Wenqiang Liu (1), Kevin M. Labus (2), Matt Ahern (1), Reza Avazmohammadi (3,4), Christian M. Puttlitz (1,2), Zhijie Wang (1,2)**

(1) School of Biomedical Engineering
Colorado State University
Fort Collins, CO, USA

(2) Department of Mechanical Engineering
Colorado State University
Fort Collins, CO, USA

(3) Department of Biomedical Engineering
Texas A&M University
College Station, TX, USA

(4) Department of Mechanical Engineering
Texas A&M University
College Station, TX, USA

## INTRODUCTION

Ventricle dysfunction is the most common cause of heart failure, which leads to high mortality and morbidity in the United States. However, compared to the left ventricle (LV), there is a lack of right ventricle (RV) treatment due to the poor understanding of the RV. In order to have a comprehensive view of the RV, thorough experimental and computational studies of the RV under physiological conditions are required. Our previous experimental data showed that the LV and RV exhibit different viscoelastic behaviors and the RV exhibited fully non-linear viscoelastic (NLV) behavior [1]. However, due to the complex nature of myocardium biomechanics, most computational models are hyperelastic and there is a lack of nonlinear viscoelastic models for the RV. Previous viscoelastic models on the LV adopted the quasi-linear viscoelastic (QLV) assumption and a formulation originally established by Fung [2,3]. To date, there is no computational study for the RV passive viscoelasticity using either QLV or NLV assumptions.

Therefore, the goal of the study was to characterize the RV passive viscoelastic behavior by computational modeling. We applied both QLV and NLV models to the biaxial experimental data from healthy adult ovine. Our results suggest that the NLV model is a more appropriate formulation to model the RV viscoelastic behavior, and the RV had strain–dependent, anisotropic relaxation behavior. The findings will assist the development of RV simulation to capture both energy storage and energy dissipation functions, which can help to reveal the RV failure mechanism and inspire new treatment development.

## METHODS

Details of our experimental work described in our previous study [1]. Briefly, eight fresh RVs from adult female ovine with no known cardiac disease were included. The outflow tract direction was marked as the longitudinal (L) direction and its perpendicular direction was the circumferential (C) direction. All samples underwent equibiaxial stress relaxation tests at different strain magnitudes (3, 6, 9, 12 and 15%).

We applied two viscoelastic models to the experimental data. 1) In the QLV model, stress relaxation data were fitted to Eq. 1. The instantaneous elastic stress $\sigma^e$ was derived from an anisotropic Ogden strain energy density function $W$ (Eq. 2). The reduced relaxation function ($G(t)$) with the Prony series and constraint was used to describe the relaxation response (Eq. 3), which is associated with the time constants $\tau_n$ fixed at decadal values and different $G_n$ represent the strength of the relaxation at the corresponding time constant [4,5]. A two-step fitting strategy was used in which we fitted the relaxation phase first, then fitted the entire data including the ramp phase. 2) To test the strain-dependence of the viscoelastic response, we first adopt a power law model previously used to describe tissue's NLV behavior (Eq. 4) [4,5]. A power law fitting procedure was used for the log-log scale of stress relaxation curves at different strain magnitudes [4]. From the fitting line, the initial stress ($\sigma_0$) (ordinate intercept) and the relaxation rate m (slope) were determined [4]. All fits were performed using MATLAB software.

$$\sigma(\varepsilon,t) = \int_0^t G(t-\tau)\frac{d\sigma^e(\varepsilon)}{d\varepsilon}\frac{d\varepsilon(\tau)}{d\tau}d\tau \quad (1)$$

$$W = \frac{2\mu}{\alpha^2}(\lambda_1^\alpha + \lambda_2^\alpha + \lambda_3^\alpha - 3) + \frac{2k\mu}{\alpha^2}(I_4^{\alpha/2} + 2I_4^{-\alpha/4} - 3) \quad (2)$$

$$G(t) = G_\infty + \sum_{n=1}^{3} G_n e^{-t/\tau_n}$$

and $G_1 + G_2 + G_3 + G_\infty = 1$ (3)

$$\sigma(\varepsilon,t) = \sigma_0(\varepsilon)t^{m(\varepsilon)} \quad (4)$$

where $\varepsilon$ is strain, $\tau_n$ are time constants, $G_1$, $G_2$, $G_3$ and $G_\infty$ are relaxation coefficients, $\mu$ is the infinitesimal shear modulus, $\alpha$ is nonlinearity parameter, $k$ is anisotropy parameter, $I_4$ is anisotropic invariance, $\sigma_0$ is the initial stress, and $m$ is the relaxation rate.

Data are presented as mean ± SE. Paired Student's t-test was performed and $p \leq 0.05$ was considered significant.

## RESULTS

**The relaxation function *G(t)*, shear modulus and nonlinearity were strain dependent.** At each individual strain magnitude, the QLV model fitted the experimental data well (Fig. 1). Next, we examined the effect of strain on relaxation function. We found in both directions $G(t)$ was strongly dependent on the strain magnitude (Fig. 2A&B). Furthermore, the RV's shear modulus increased with increased strain level and had altered nonlinearity as strain increased (Fig. 2C&D).

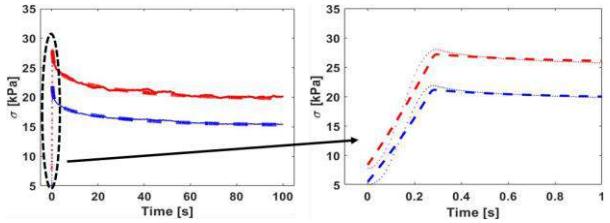


**Fig 1.** Representative fitting results of the QLV model.

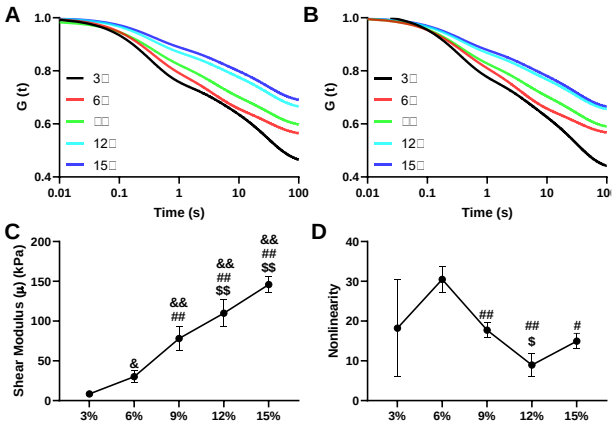


**Fig 2.** Averaged fitted reduced relaxation function *G(t)* in longitudinal (A) and circumferential (B) directions. (C&D) show the strain-dependent shear modulus and nonlinearity of the RV. $^{\&}$<.05, $^{\&\&}$<.01, $^{\#}$<.05, $^{\#\#}$<.01, $^{\$}$<.05, $^{\$\$}$<.01, vs 3, 6 and 9%, respectively.

**The *G(t)* coefficients were strain-dependent and $G_1$ and $G_3$ *i*differently contribute to relaxation response at low and high strains.** In both directions, the *G(t)* coefficients were strongly dependent on strain magnitudes (Fig. 3A&B). Interestingly, the $G_\infty$ was monotonically increasing with increased strains whereas the opposite behavior was observed for the $G_1$. At most strain levels, the relaxation coefficients did not differ between directions, except that at 15% of strain there was a larger $G_\infty$ in the L than C direction (Fig. 3A). Furthermore, we also observed that in both directions, $G_1$ and $G_3$ were both prominent at low strain (3%), whereas at high strain (15%) only $G_3$ was more prominent (Fig. 3C&D). This indicate that the dominant $G_n$ varied at different strain levels.

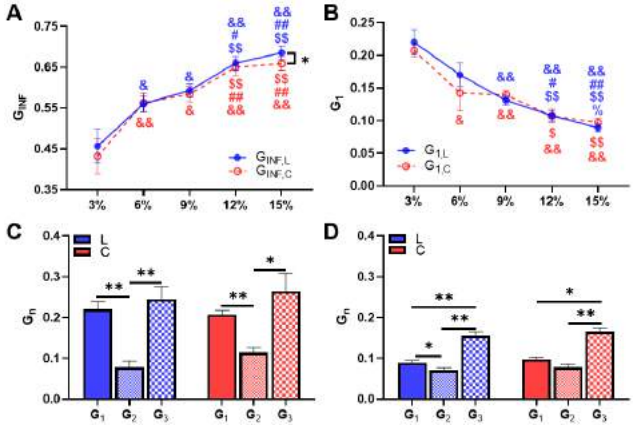


**Fig 3.** (A&B) $G_\infty$ (shown as $G_{INF}$) and $G_1$ vary with strain levels in both directions. At the fixed strain of 3% (C) and 15% (D), $G_n$ show varied values and the trends are similar between two directions. $^{\&}$<.05, $^{\&\&}$<.01, $^{\#}$<.05, $^{\#\#}$<.01, $^{\$}$<.05, $^{\$\$}$<.01, $^{\%}$<.05 vs 3, 6, 9 and 12%, respectively and $^{*}$<.05, $^{**}$<.01.

**The relaxation rate and initial stress were different between directions.** In both directions, with increased strain, the RV had a slower relaxation rate with larger initial stress (Fig. 4), this suggests fully nonlinear viscoelastic behavior. These relations were well fitted by a 2nd polynomial function, indicating a dependence on the square of strain [4]. Furthermore, the RV had different relaxation rate at 15% of strain and different initial stress at 6-12% of strain between L and C directions, which indicate an anisotropic relaxation behavior.

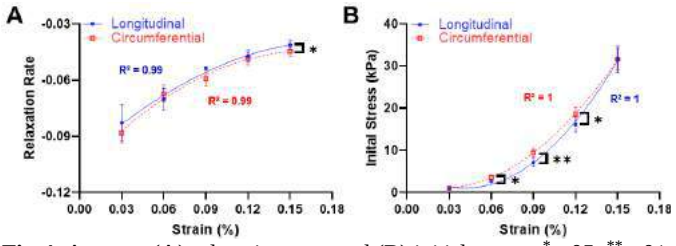


**Fig 4.** Average (A) relaxation rate and (B) initial stress. $^{*}$<.05, $^{**}$<.01.

## DISCUSSION

To best of our knowledge, this is the first study to model the RV passive viscoelastic behavior. In this study, we applied both QLV and NLV theories to the biaxial experimental data. Our results suggest that the relaxation function *G(t)* was strain-dependent and had a diverging behavior in both directions (Fig. 2A&B). Therefore, despite a good fitting of the QLV model at individual strains, an NLV constitutive formulation should be more appreciate to model the RV viscoelasticity.

Nevertheless, we found some interesting characters of the RV viscoelasticity based on the QLV model. As the strain increased, the RV had a larger shear modulus and initially increasing and then decreasing nonlinearity (Fig. 2C&D). This behavior may be linked to the recruitment process of the collagen fibers and different contributions of myofiber and collagen to RV viscoelasticity at different strains. When the collagen becomes gradually recruited from low to high strains, the monotonically increasing shear stress indicates an increasing contribution of collagen in load bearing. But the nonlinearity may be affected by collagen and myofiber orientation and inter-fibril sliding patterns, and thus the change was biphasic. We also observed anisotropic RV relaxation response at end-diastole (15% of strain), which is evidenced by a larger $G_\infty$ (Fig. 3A) and a slower relaxation rate (Fig. 4A) in the L direction. Since more collagen fibers are recruited at high strain, the anisotropic viscoelastic behavior may be attributed to collagen rather than myofibers. Furthermore, we observed that, at small strain (3%), the $G_1$ and $G_3$ had similar strength of the relaxation, whereas at the high strain (15%), $G_3$ had the largest strength of the relaxation than other coefficients (Fig. 3C&D). This implies different dominant $G_n$ at different strain levels. Overall, $G_1$-$G_3$ were reduced as the strain increased, and this agrees with the reduced relaxation response of RV at higher strains shown in Fig. 2A&B. We postulate that the dominant role of myofibers at low strains may explain the enhanced viscoelasticity at low strains. The potential molecular mechanisms that determines these $G_n$ awaits further investigation. Lastly, from the NLV model, we observed that the relaxation rate and initial stress were strongly correlated with the square of the strain rather than the strain (Fig. 4). These findings merit further study into RV structure-function relations responsible for the nonlinear viscoelasticity.

## REFERENCES

[1] Liu, W et al., *J Biomech Eng*,143,12,2021.
[2] Nordsletten, D et al., *Acta Biomater*, 135,Nov,2021
[3] Cansiz, F et al., *Comput Meth Biomech Biomed Engi* 18,2015
[4] Troyer K et al., *Acta Biomater*, 7,2011
[5] Troyer K et al., *Acta Biomater*, 8,2012

SB³C2022
Summer Biomechanics, Bioengineering and Biotransport Conference
June 20-23, Eastern Shore, MD, USA

# A HYBRID DISCRETE-CONTINUUM ANALYSIS OF REMODELING IN ARTERIES: AN ASSESSMENT OF MICROSCOPIC FEATURES FROM MACROSCOPIC OBSERVABLES

**Ryan R Mahutga (1), Elizabeth Gacek (1), Victor H Barocas (1)**

(1) Department of Biomedical Engineering, University of Minnesota, Minneapolis, MN, USA

## INTRODUCTION

The study of tissue growth and remodeling (G&R) remains an open question. Of particular interest in the biomedical space is predicting how a tissue will grow and remodel in response to various therapeutics. Traditional continuum-based computational growth and remodeling frameworks are an excellent and efficient method for understanding macroscopically observable phenomena (e.g. aneurysmal growth, cardiac hypertrophy) [1,2]. However, such frameworks lack the robustness to evaluate microstructural characteristics including fiber-by-fiber evolution within the extracellular matrix (ECM) and constituent cells, local mechanical heterogeneity in the tissue, and overall tissue strength in various physiological loading scenarios. Such factors are of particular importance in the evaluation of aortic aneurysm, where growth rate and overall size have historically been the only markers of risk, and have been shown to be inadequate in many cases [3]. In this work, we detail a technique using a discrete-microstructural network of the ECM to inform a continuum-based finite-element (FE) G&R model. We apply this model to aortic remodeling and assess clinically and experimentally observed phenomena including growth, tissue stiffness, and fiber volume fraction. We relate these features to microstructural evolution providing insight into the remodeling process.

## METHODS

We utilize microstructural discrete-fiber networks to represent a tissue's ECM (collagen and elastin), and cellular stress fibers (actin), as shown in Fig 1A. The networks are generated from a periodic Delaunay tessellation using the tetrahedron edges as fibers. Fibers are linked at the nodes of the tessellation tetrahedra via a pin joint. We define collagen fibers to have a nonlinear behavior based on a helical spring model, elastin fibers to be linear, compliant springs, and actin to be slightly stiffer, linear springs (for full details see [4]). To solve for the internal equilibrium of the network subject to a deformation, we use Newton-Raphson iteration to minimize the forces on all nodes.

Each fiber in each network remodels separately based on its own fiber stress. The assumption is made that the cells remodel the microstructure to approach a defined target stress for each individual fiber (local application of tensional homeostasis), which, in turn, results in a net tissue equilibrium state. This remodeling model is given by

$$\frac{dR^p}{dt} = \frac{1}{\tau}\left(\frac{\sigma^p}{\sigma_\infty} - 1\right) R^p i; \frac{dL^p}{dt} = k\frac{dR^p}{dt} \quad (1)$$

where $R^p$ is the fiber radius, $t$ is time, $\tau$ is the remodeling time constant, $\sigma^p$ is the fiber stress, $\sigma_\infty$ is the homeostatic fiber stress, $L^p$ is fiber initial length, and $k$ is a parameter relating fiber lengthening to fiber thickening. For our study, we used $\tau_{collagen} = 90 days$, $\sigma_{\infty,collagen} = 200 iMPa$, $\tau_{actin} = 4.5 idays$, $\sigma_{\infty,actin} = 750 kPa$, and $k = 60$. The elastin fibers do not remodel.

As the fibers remodel, the network zero-stress state is updated by finding a new deformation such that the average stresses in the network are zero. More precisely, we reduce the problem to finding the diagonal terms of $F^g_{kN}$, which are the growth stretches $\lambda^g_i$, such that the stresses on the diagonal of the volume-averaged Cauchy stress $\sigma_{ij}$ are zero, since the shear stresses are relatively small throughout the remodeling process and thus neglected. Further, to maintain network stability, we enforce an osmotic (or hydrostatic) pressure to prevent the network from collapsing. The expression for the osmotic pressure is

$$c_{fcd} = c_0 \phi i; P = RT\left(\sqrt{c_{fcd}^2 + 4c_*^2} - 2c_*\right) \quad (2)$$

where $c_{fcd}$ is fixed charge density, $c_0$ is a fixed charge scaling factor (70 mM), $\phi$ is the fiber volume fraction, $P$ is the osmotic pressure, $R$ is the universal gas constant, $T$ is the tissue temperature (310K), and $c_*$ is the external osmolarity (150 mM). Thus, the total stress in the fiber network system can be expressed as

$$\sigma_{ij}^{total} = \frac{1}{v}\sum_p f^p l^p \alpha_i^p \alpha_j^p - P\delta_{ij} \quad (3)$$

where $v$ is the volume of the network, $f^p$ is the force in fiber p, $l^p$ is the deformed length of fiber p, $\alpha^p$ is the direction vector of fiber p, and $\delta_{ij}$ is the Kronecker delta.

Using Eq. 3, we fit the behavior of our network using a continuum material 3-fiber family model with a strain-energy density

$$W = c_1(I_1 - 3) + \frac{K}{2}(ln(J))^2 + \sum_{i=1}^{3} \frac{c_2^i}{2c_3^i}\left[exp\left(c_3^i(I_4^i - 1)^2\right) - 1\right] \quad (4)$$

where $c_1$ is the modulus of the ground matrix, $I_1 = tr(C_{ij})$ is the first strain invariant of the right Cauchy-Green tensor C, $K$ is the bulk modulus, $c_2^i$ is the fiber modulus of family i, $c_3^i$ captures the nonlinearity of fiber family i, $I_4^i$ is the fourth strain invariant of C. This technique is further outlined in [5]. We take the fiber families to align with the axes of the microstructural element which are aligned as R, Θ, Z in the cylindrical case (Fig 1).

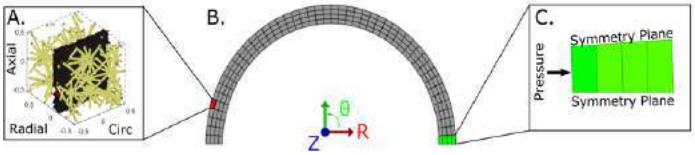


**Fig. 1: A.** Fiber network consisting of actin (yellow), elastin (black), and collagen (red) for **B.** vessel mesh element with **C.** applied boundary conditions.

The network growth and fitted material properties are model inputs into *FEBio 2.9.1* using the *Prestrain plugin* [6] where compatibility is enforced onto the macroscopic geometry based on the microstructural growth. The coupled hybrid process is shown in Fig. 2. Utilizing symmetry planes, a small wedge of the cylindrical mesh (Fig. 1) with an inner applied pressure of 100mmHg is remodeled for 235 days before pressure is increased to 150 mmHg. Circumferential stress, network fiber volume fraction, and growth stretches are analyzed throughout the 320 days of remodeling.

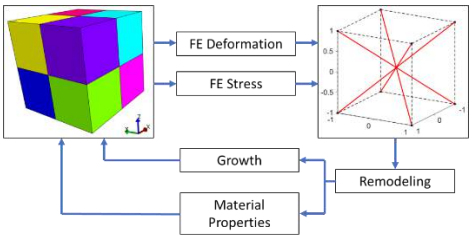


**Fig. 2:** Flowchart of coupling the finite element model of arterial inflation with the growth and remodeling scheme.

## RESULTS

We apply the model to remodel a thick-walled cylinder representing an arterial blood vessel. The vessel initially contracted going from its initial configuration (Fig 3A) to its homeostatic, normotensive (100mmHg) arterial pressure state (Fig. 3B). The vessel was then prescribed a 50% increase in pressure (150 mmHg), and allowed to re-equilibrate, where it grew in response (Fig. 3C).

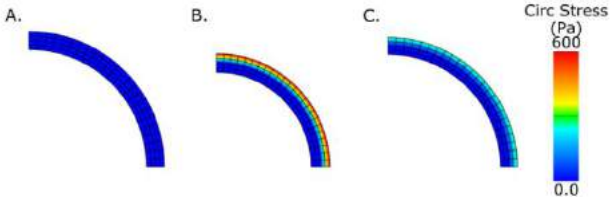


**Fig. 3:** Circumferential residual stress at **A.** t = 0, **B.** t = 235, and **C.** t = 320 days.

The main feature that makes this modeling technique so valuable is that one can observe the fiber network throughout the remodeling period. We monitor the growth of individual element networks shown in Fig. 4A where we observe through thickness variation in network growth. We also monitor the composition of the tissue shown in Fig. 4B. We note that elastin, while not being remodeled, increases in volume fraction because the tissue is compacting (Fig. 3A vs Fig. 3B). Upon the application of increased pressure, we note that the vessel grows (Fig. 3C) and, therefore, the elastin content decreases. We also see a drop in actin content and an increase in collagen content associated with this hypertensive remodeling scenario.

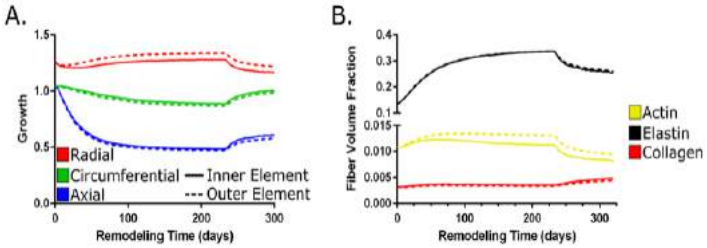


**Fig. 4: A.** Growth in the radial (red), circumferential (green), and axial (blue) direction at the inner (solid) and outer (dashed) radius. **B.** The fiber volume fraction for actin, elastin, and collagen. Pressure increased from 100 mmHg to 150 mmHg at t = 235 days.

## DISCUSSION

This technique is the marriage of two powerful and insightful computational strategies, one of which is extremely efficient (FE analysis) and one of which gives a high degree of structural detail (discrete microstructural analysis). The hybridizing of the two allows us to maintain structural detail without loss of computational efficiency by coarse graining the microscale mechanics in the macroscale simulation, but maintaining the detail in the actual remodeling process.

We analyze a standard problem in the G&R field in this work, and have a qualitative agreement with previously published models [7], as we see circumferential growth in response to increased pressure (Fig. 3C, Fig. 4A), and a decrease in actin and elastin content with an increase in collagen content (Fig. 4B).

This model not only captures the G&R behavior, but will allow us to investigate other pertinent properties that are often lost in standard continuum G&R approaches. For instance, we are particularly interested in tissue strength and the modes of failure in physiological loading. This approach is readily adapted to local failure assessment following [4], which will be insightful for analysis of therapies and surgical intervention.


## ACKNOWLEDGEMENTS

This work was supported by the National Institutes of Health (U01-HL139471, U01-AT010326, T32 AR050938). Computations were facilitated by a resources grant from the Minnesota Supercomputing Institute.


## REFERENCES


[1] Ateshian, G. A., and Humphrey, J. D., 2012, Annu. Rev. Biomed. Eng., 14(1), 97–111.

[2] Humphrey, J. D., and Rajagopal, K. R., 2003, Biomech. Model. Mechanobiol., 2(2), 109–126.

[3] Nardi, P., and Ruvolo, G., 2016, J. Vasc. Endovasc. Surg., 01(02).

[4] Mahutga, R., and Barocas, V. H., 2020, J. Biomech. Eng., 142(11).

[5] Nikpasand, M., et al., 2021, "J. Elast. 2021, 1–25.

[6] Maas, S. A., et al., 2016, J. Mech. Behav. Biomed. Mater., 61, 499–510.

[7] Alford, P. W., et al., 2008, Biomech. Model. Mechanobiol., 7(4), 245–262.

SB³C2022
Summer Biomechanics, Bioengineering and Biotransport Conference
June 20-23, Eastern Shore, MD, USA

# DOSE-DEPENDENT CHEMICAL REACTION KINETICS FOR MODELING OF TGF-β DELIVERY IN CARTILAGE TISSUE ENGINEERING

**Sedat Dogru (1), Gabriela M. Alba (2), Kirk C. Pierce (2), Tianbai Wang (3), Michael B. Albro (1,2,3)**

(1) Mechanical Engineering
(2) Biomedical Engineering
(3) Materials Science & Engineering
Boston University

## INTRODUCTION

Cartilage tissue engineering (TE) is a promising osteoarthritis treatment strategy whereby chondrogenic cells are embedded in scaffolds to generate cartilage replacement tissues. TGF-β is prominent cartilage TE growth mediator due to its efficacy in accelerating extracellular matrix (ECM) biosynthesis. An assortment of TGF-β delivery platforms are currently in development, varying by delivery mode (e.g. media supplementation, scaffold loading) and administered dose (0.3-2000ng/mL) [1]. Cells are highly sensitive to TGF-β dose—low doses may be insufficient to induce ECM enhancements and excessive doses can lead to fibrosis [2], hyperplasia [3], or biosynthetic suppression [4] As such, TGF-β delivery optimization may be critical for TE outcomes.

Methodology to optimize TGF-β exposure in delivery systems remain limited. Optimization predominantly consists of empirical measures of TGF-β desorption from acellular scaffolds with the goal of maximizing scaffold retention durations [1]. However, these assessments provide limited predictive capabilities and do not provide quantitative insights into TGF-β activity levels to which cells are exposed. As an alternative approach, reaction-diffusion modeling frameworks that account for chemical reaction kinetics in TE cartilage (e.g. scaffold/ECM binding, cell-mediated internalization, enzymatic degradation) can potentially be used to predict temporo-spatial distribution of different states of TGF-β in TE constructs that are important for clinical outcomes, including: 1) scaffold-bound TGF-β, 2) available free TGF-β, 3) cell-internalized TGF-β, and 4) TGF-β desorbed into synovial joint tissues. As such, modeling can be used to optimize scaffold design parameters to improve TE growth outcomes.

Here, we advance the development of predictive reaction-diffusion modeling frameworks by characterizing chemical reaction constitutive relations that can be influential of TGF-β delivery outcomes, including TGF-β-scaffold/ECM reversible binding and TGF-β cell-mediated internalization reactions. Characterizations are performed over the range of TGF-β doses used in TE applications (0.3-2000 ng/mL) and assessed in the absence or presence of intracellular TGF-β signaling processes. Lastly, finite element (FE) models are implemented to examine the impact of chemical reactions on the spatiotemporal distribution of TGF-β in TE constructs for media supplementation and scaffold loaded delivery platforms.

## METHODS

**Tissue source**: Immature bovine chondrocytes were seeded in 2% agarose ($45\times10^6$ cells/mL) to form ∅2×1mm TE constructs [5]. Freshly-cast constructs were maintained live in chondrogenic media (CM) [5] or subjected to an initial freeze-thaw cycle to induce rapid devitalization for reaction kinetic characterizations.

**Binding kinetics:** Devitalized constructs were exposed to a range of TGF-β3 doses (0.3-2000ng/mL) for 48h (n=3/dose). Bound TGF-β3 was extracted and measured via ELISA as performed previously [5]. Binding models were curve-fit to experimental data: 1) Langmuir isotherm (Eq.1)—accounting for reversible binding to construct binding sites, and 2) BET isotherm (Eq.2)—accounting for additional aggregation of TGF-β bound to binding sites:

$$C_{B_T} = \frac{C_F N_T}{C_F + K_o} \quad (1) \qquad C_{B_T} = \frac{N_T c x[1-(M+1)x^M + Mx^{M+1}]}{[1-x][1-x+cx-cx^{M+1}]} \quad (2) \qquad c = K_o/K_c \;\; x = C_F/K_c$$

where $C_{B_T}$ and $C_F$: bound and free TGF-β dose, respectively, $N_T$: surface binding site density, $M$: maximum number of aggregated TGF-β molecules at a binding site, $K_o$ and $K_c$: dissociation constant for scaffold-to-TGF-β binding and TGF-β-to-TGF-β binding, respectively. Uptake ratio, $R_U$, was calculated as the ratio of total TGF-β dose ($C_B$+$C_F$) within the construct to free TGF-β dose ($C_F$).

**Internalization rate kinetics**: Live constructs were exposed to TGF-β3 in CM (100 μL) at the aforementioned doses. The cell-mediated internalization rate, $V_i$, of TGF-β3 in constructs was determined by

monitoring the transient TGF-β3 concentration decrease in the bath over 48h and curve-fitting the response with our reaction-diffusion model, which accounts for TGF-β diffusion (Eq.3), scaffold/ECM reversible binding and TGF-β aggregation (Eq.4&5, respectively), and cell-mediated internalization (Eq.6) of TGF-β in constructs:

$$\frac{\partial C_F}{\partial t} = D\nabla^2 C_F \quad (3) \qquad \frac{\partial C_F}{\partial t} = k_r C_B - k_f C_F N_T \quad (4)$$

$$\frac{\partial C_F}{\partial t} = k_{r_1} \sum_{i=1}^{M-1} C_{B_{i+1}} - k_{f_1} C_F \sum_{i=1}^{M-1} C_{B_i} \quad (5) \qquad \frac{\partial C_F}{\partial t} = R_i C_F \quad (6)$$

where $D$: TGF-β diffusivity, $k_r$&$k_f$: reverse and forward binding constant, respectively, $R_i$: internalization rate constant. The transient TGF-β3 bath decrease was curve fit for $R_i$ using our measured binding parameters as performed previously [5]. The influence of intracellular TGF-β signaling dynamics was further assessed by repeating $R_i$ measurements in the presence of a TGF-β receptor kinase inhibitor (5μg/mL, LY364947). Subsequently, $V_i$, (internalized TGF-β molecules per cell per second [mol/cell/s]) was calculated as $R_i \times C_F$.

**TGF-β transport modeling: Media-supplemented delivery:** FE simulations were implemented using measured reaction kinetics parameters to predict the uptake of media-supplemented TGF-β in constructs (∅6×3mm) at a 10 or 800 ng/mL dose ± TGF-β internalization kinetics and ± intracellular TGF-β signaling.

**Affinity-scaffold-loaded delivery:** FE simulations were implemented to predict the retention of scaffold-loaded TGF-β (800ng/mL) in heparin-affinity scaffold constructs using previously measured heparin -to-TGF-β binding parameters ($k_r$:$9.2\times10^{-3}s^{-1}$&$k_f$:$1.0\times10^{5}(M.sec)^{-1}$)[6] and measured internalization rate ± TGF-β internalization kinetics.

## RESULTS

**Binding kinetics:** The TGF-β uptake ratio increased with dose, ranging from $R_U$=11.4 at 0.9 ng/mL to $R_U$=32.1 at 1400 ng/mL. While this binding response could not be described by the Langmuir model ($R^2$<0.01), it could be faithfully described by the BET isotherm model ($R^2$=0.99, Fig 1A).

**Internalization rate kinetics:** In the low dose regime (0.3-100ng/mL), $V_i$ exhibited a Michaelis-Menten relationship ($R^2$=0.96; Fig 1B), saturating at a rate of 2mol/cell/s. In the high dose regime (100-2000ng/mL), $V_i$ increased linearly with dose ($R^2$=0.96), reaching a rate of 504mol/cell/s at 2000ng/mL. For all doses in the high regime, TGF-β signaling inhibition induced a significant decrease in $V_i$ ($p<0.05$, Fig 1C).

**TGF-β transport modeling: Media-supplemented delivery:** Media-supplemented 10ng/mL TGF-β exhibited pronounced steady-state gradients in constructs in the presence of cell-mediated internalization whether or not TGF-β signaling dynamics were present (Fig 2). In contrast, 800ng/mL supplemented TGF-β exhibited pronounced steady-state gradients but gradients were mitigated upon TGF-β signaling inhibition (Fig 2). For both doses, gradients were greatly mitigated in the absence of cell-mediated internalization.

**Affinity-scaffold-loaded delivery:** Cell-mediated internalization led to a rapid loss of loaded TGF-β, exhibited by an 80% loss in the constructs after 2 days. In the absence of internalization, over 40% of TGF-β was retained in the construct after 20 days (Fig 3A&B).

## DISCUSSION

This work establishes novel quantitative relations of dose-dependent TGF-β chemical reaction kinetics and provides expanded insights into its biochemical behavior in TE systems. For characterizations of TGF-β binding kinetics, we observe that TGF-β binding to constructs increases with dose. This response contrasts with behavior predicted by Langmuir, in which the uptake ratio is expected to decay to a value near unity as tissue binding sites saturate, thus suggesting the occurrence of TGF-β aggregation events at tissue binding sites. This aggregation phenomenon is consistent with prior examination of TGF-β binding events [7] and can be predicted by a BET isotherm model, that accounts for multiple layers of aggregated TGF-β at each tissue binding site. For characterizations of TGF-β cell-internalization kinetics, we observe an intriguing interplay between TGF-β dose and intracellular TGF-β signaling dynamics. The internalization rate exhibits a unique biphasic response, following Michaelis-Menten kinetics at low doses (<100ng/mL), saturating as a value $V_i$=2.4 mol/cell/s, but increasing further with a linear relationship at higher doses (>100ng/mL). A striking aspect of this characterization is the remarkably high TGF-β internalization rates measured at high doses—reaching 500 mol/cell/s at 2000 ng/ml—particularly when considering the documented limited number of TGF-β receptors at the cell surface (~10k receptors) [8]. These elevated TGF-β internalization rates can be suppressed at high doses by blocking intracellular TGF-β signaling, thus suggesting a role of TGF-β signaling in upregulating internalization machinery to clear high doses of TGF-β from the extracellular space. Reaction kinetics are predicted to have a significant impact on the spatiotemporal distribution of delivered TGF-β to TE constructs. For conventional 10ng/mL media-supplemented delivery, TGF-β internalization kinetics give rise to pronounced steady state gradients in TE constructs with TGF-β penetrating less than 500μm into the tissue—remarkably, gradients are also present with an 800ng/mL dose due to elevated internalization rates resulting from intracellular TGF-β signaling. For scaffold delivery, while heparin affinity domains can promote long term TGF-β retention, retention is far reduced in the presence of TGF-β internalization kinetics as affinity domains compete for TGF-β with cell internalization machinery. Overall, this work demonstrated the potential significant impact of chemical reactions on the delivery of TGF-β in TE applications and sets the foundation for using reaction-diffusion frameworks to modulate delivery platform parameters to optimize TGF-β delivery to TE constructs.

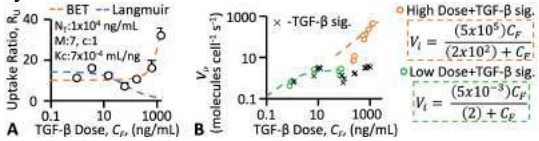


**Fig 1: (A)Uptake ratio ($R_U$) vs free TGF-β ($C_F$) dose and model fits. (B) Internalization rate for low and high TGF-β dose regime in the absence (+TGF-β sig) or presence (-TGF-β sig) of LY364947.**

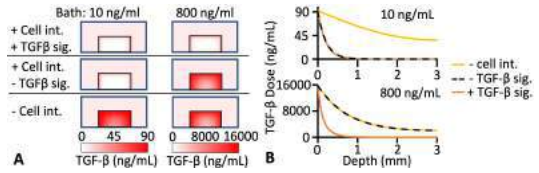


**Fig 2: Predicted distribution of media supplemented TGF-β in TE construct after 1-week ±cell internalization ±TGF-β signaling.**

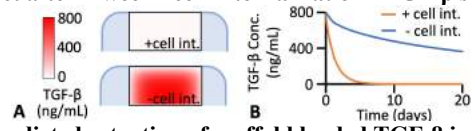


**Fig 3: Predicted retention of scaffold loaded TGF-β in heparin-affinity scaffolds after 20 days ±cell internalization**

**ACKNOWLEDGEMENTS:** Supported by NSF (CMMI 1906469)

**REFERENCES: [1]** Madry H+ 2013 Tis Eng PartB; 20.2: 106-125. **[2]** Van Beuningen, HM+ 2000 Osteoarthr. Cartil. 8.1:25-33; **[3]** Pearle AD+ 2005 Clin Sports Med. 24.1: 1-12. **[4]** Wang T+ 2018 WCB: Abstract No.3226; **[5]** Albro MB+ 2016 Biomaterials (77):173-85; **[6]** Zhang F+ 2019 Molecules 24.18:3360; **[7]** Tran V+ 2020 JPCB 124.43: 9497-9504 **[8]** Massague J+ 1985 JBC 260.5: 2636-2645

SB³C2022
Summer Biomechanics, Bioengineering and Biotransport Conference
June 20-23, Eastern Shore, MD, USA

# A MULTILAYER MECHANICAL CELLULAR-POTTS MODEL OF MIGRATING MESENDODERM

**Tien Comlekoglu(1,3), Gustavo Pacheco(1), Bette Dzamba(1), David R. Shook(1), T. J. Sego(2), James A. Glazier(2), Shayn Peirce-Cottler(3), Douglas DeSimone(1)**

(1) Department of Cell Biology, University of Virginia School of Medicine, Charlottesville, VA, USA
(2) Department of Intelligent Systems Engineering, Indiana University, Bloomington, IN, USA
(3) Department of Biomedical Engineering, University of Virginia, Charlottesville, VA, USA

## INTRODUCTION

Coordinated collective cell migration is a fundamental biological process particularly important for the proper formation of tissues and organs during embryonic development[1]. During vertebrate gastrulation, mesoderm and endoderm precursor cells associate to form a mesendodermal mass. Mesendoderm cells maintain adhesions to one another and exert tension between C-Cadherin complexes and integrin-dependent contacts with a fibrillar fibronectin matrix at the inner surface of the blastocoel roof (BCR), which serves as a migratory substratum[2]. Mesendoderm cells migrate collectively with front row leader cells polarized in the direction of travel and with follower cells dragged along by leader cells[2-3]. Leader cells extend monopolar protrusions forward on the fibronectin matrix and generate significant traction stresses, while follower cells form random transient attachments to the BCR substrate below them[4]. Prior studies of these movements utilized the Dorsal Marginal Zone (DMZ) explant from developing *Xenopus laevis* embryos[2]. However, these movements and mechanisms remain challenging to observe and measure *in-vivo* while *in-vitro* explants (e.g., DMZ) may not demonstrate the full range of behaviors that occur in the embryo. Because these mechanisms of cell migration and resultant tissue formation are difficult to investigate experimentally, computational methods may provide insight into the contributions of the multiple morphogenic mechanical mechanisms present as they drive embryonic development.

In-silico experiments have the potential to predict and/or reveal cellular dynamics that are difficult to observe in wet bench analysis and lead to new hypotheses that drive further *in-vivo* and *in-vitro* experimentation. In this work, we introduce a computational multicellular model developed in the Cellular-Potts framework to represent the mechanics of a tissue of collectively migrating cells, built to recapitulate observed behaviors of the *Xenopus laevis* DMZ explant. Our model represents a computational tool with which to perform in-silico experiments to further investigate fundamental mechanics of collective cell migration.

## METHODS

The Cellular-Potts Model framework (CPM, also known as the Glazier-Graner-Hogeweg model) as implemented in the open-source simulation environment Compucell3D was chosen to approximate the behavior of the DMZ explant because the method effectively captures the inherently stochastic behavior of biological cells and tissues. In the Cellular-Potts formulation, single cells are represented as a collection of pixels on a square lattice. These computational "cells" are given properties of predefined volume, contact affinity with surrounding cells and substrate, and spring-like mechanical objects called "links" representing properties of cell adhesion and formation of lamellipodia. These properties are defined mathematically in the Effective Energy function *H*, which is evaluated for every cell during each computational timestep[5]. To approximate the DMZ explant, a bilayer of tissue was created by pre-defining a tissue 8 cells in width, 4 cells in length, and 2 cells in height where each cell occupied 5x5x5 voxels (to represent approximately 30x30x30μm). Cells were placed upon a two-dimensional substrate consisting of 1x1x1 volumes of material so that simulated cells could form links to the simulated substrate to represent experimental cell-substrate attachments. The front row of cells was defined to be of the "leading edge" cell type. Equation (1) represents the Effective Energy function which imposes the physical properties of each cell in the model.

$$H = \sum_{i,j,neighbors} J\left(\tau_{(\sigma(i))}, \tau_{(\sigma(j))}\right)\left(1 - \delta_{\sigma(i),\sigma(j)}\right) + \lambda_{volume}\left(V_{cell} - V_{target}\right)^2 + \left(\sum_{i,j,cell\ neighbors} \lambda_{ij}\left(l_{ij} - L_{ij}\right)^2\right) \quad (1)$$

The first term models cell affinity for neighboring cells and surrounding medium governed by the contact coefficient *J* where *i*, *j*, denote neighboring lattice sites, $\tau$ denotes cell types, and $\sigma$ denotes individual cell ID's in the simulation. The second term imposes a

volume constraint $\lambda_{volume}$ on each cell. The third term represents the forces of elastic links which represent persistent cell-cell adhesion within the tissue, where $\lambda_{ij}$ represents the Hookean spring constant of a link between neighboring cells *i* and *j*, *l* represents the distance between the centers of mass of neighboring cells, and *L* is the target length of the spring-like link. Additional elastic links model the random attachments that passive cells form with their substrate. Leading edge cells have an additional term detailed in equation (2) to represent the constant-tension traction force between the cell's lamellipodium and the substrate.

$$Hi = \lambda_{Lamellipodia} * l \quad (2)$$

Lamellipodial extension and retraction behaviors are modeled as a Poisson process whereby the probability $P_\tau$ of an extension/retraction event occurring per timestep is approximated by equation (3)

$$P_\tau = 1 - e^{\lambda} \quad (3)$$

We calibrated the Poisson parameter λ to reflect observed mesendoderm lamellipodial cycling rates obtained from video data collected for the development of the model.

## RESULTS

The migration speed of leading-edge cells was calibrated to match literature migration speeds of 107 μm/hr[2]. The model recapitulates migrating mesendoderm at a temporal resolution of 5 seconds per Monte Carlo Step (MCS, the intrinsic timestep of the model's CPM methodology).

We applied our model to perform an in-silico experiment simulating the *in-vitro* experimental disruption of fibronectin binding by computationally disrupting lamellipodial links after 100 minutes. Our experiments reproduced observed "hold-fast" retraction behavior of living mesendoderm tissue after application of a function-blocking monoclonal antibody (mAB) directed against the "synergy site" of fibronectin as reported by Davidson et. al[2]. This behavior implies that migrating mesendodermal tissue is under anisotropic tension in the direction of migration during development. Figure 1. shows the "hold-fast" behavior whereby tissue retracts approximately one cell diameter both from a representative simulation and as observed *in-vitro*.

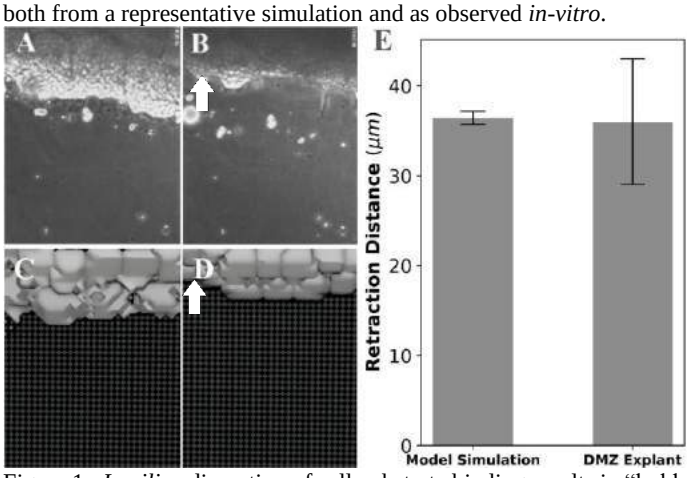


Figure 1: *In-silico* disruption of cell-substrate binding results in "hold-fast" behavior that has been observed in experiments. Top-down images from a representative experimental DMZ explant before (A) and after (B) disruption of cell-substrate binding via function-blocking mAB. Similar top-down images from a representative simulation before (C) and after (D) disruption of cell-substrate binding. White arrows represent the simulated (B) and experimentally observed (D) retraction direction. Quantitative comparison of measured retraction distances from 10 experiments each shown in (E).

## DISCUSSION

In this work, we present a novel multi-layered model of collective cell migration calibrated to experimental data of explant tissue removed from developing *Xenopus laevis* embryos. Our model employs the Cellular-Potts methodology to represent the multiple mechanical mechanisms underlying gastrulation movements in development as well as the stochastic nature of biological cells. The model reproduced experimentally measured migration speeds (data not shown). We also applied our model to observe the snap-back behavior previously demonstrated experimentally by blocking binding to the synergy site of fibronectin thus reproducing similar directional tissue tension characteristic of migrating mesendoderm tissue.

Few three-dimensional models characterize collective cell migration during early development. Prior efforts to investigate the mechanics contributing to collective cell migration often describe two-dimensional monolayers during important physiologic phenomena such as wound healing, re-epithelialization, or cancer metastasis[6-7]. Three-dimensional models are better suited to studying tissue morphogenesis as they can capture the mechanics of multiple layers of cells and developing cell types.

Our initial model recapitulates elements of physical cell and tissue mechanics and at present, offers limited insight into biochemical mechanisms of migration such as chemotaxis in response to morphogen gradients. Additionally, our model does not fully capture the complex geometry of the tissue when present in the embryo such as the toroidal shaped tissue that forms during late gastrulation in the *Xenopus laevis* embryo[2,4]. Future models will investigate how cellular mechanics give rise to tissue-level behaviors characteristic of these more complex geometric configurations. Modeling more elaborate tissue geometries will yield new insights into the emergence of complex tissue-scale dynamics occurring during development and morphogenesis.

## ACKNOWLEDGEMENTS

This work is supported by NIGMS R35 GM131865 to D. DeSimone

## REFERENCES

[1] Scarpa, E., Roberto M., *J Cell Biol* 212 (2): 143–155. 2016
[2] Davidson, L., et al. *Developmental Biology* 242(2):109-29. 2002
[3]Weber, G., et al. *Developmental Cell* 22(1): 104-115. 2012
[4] Sonavane, P., et al. *Development* 144(3): 4363-4376. 2017
[5] Maciej, S.H., et al. *Methods in Cell Biology* 110: 325-366. 2012
[6] Yang Y., et al. *Adv Exp Med Biol* 1146:1-11. 2019

# IN VIVO QUANTIFICATION OF RELATIVE SKULL-BRAIN MOTION USING MR ELASTOGRAPHY

**Alexa M. Diano (1), Grace McIlvain (1), Andrew K. Knutsen (2), Suhas Vidhate (3), Dzung L. Pham (2), Curtis L. Johnson (1)**

(1) Department of Biomedical Engineering, University of Delaware, Newark, DE, USA
(2) Henry M. Jackson Foundation, Bethesda, MD, USA
(3) Clinical Center, National Institutes of Health, Bethesda, MD, USA

## INTRODUCTION

Traumatic brain injury (TBI) is a leading cause of death and disability[1,2] that results from a direct impact or blast when the force applied to the head exceeds the protection provided by the skull-brain interface[3]. Despite the prevalence and severity of TBI, the brain's response to trauma and the mechanisms involved with injury remain unclear. Quantifying the relative motion between the brain and skull at this interface can help researchers better understand how skull acceleration leads to brain injury. Data on skull-brain coupling can be used to improve computational TBI models that will elucidate these mechanisms and aid in the design of protective equipment[4]. Magnetic resonance elastography (MRE) can measure brain deformation noninvasively to estimate brain mechanical properties but can also be used to measure the relative motion of the skull and brain *in vivo*[5,6]. Previous work introduced a method to separately measure the relative motion of the skull and brain by isolating signal from fat in the bone marrow[3]. In this study, we expand on that approach using a modified multishot spiral MRE sequence to simultaneously measure both skull and brain motion to ultimately quantify the transmission of motion from the skull to the brain.

## METHODS

**Imaging:** MRE displacement data of the brain and skull was acquired using a modified 2D multishot spiral MRE sequence[7]. We used a 12-shot constant-density spiral sequence with no fat suppression to see the fat signal while minimizing blurring through short data readout times. All scanning was conducted using a Siemens 3T Prisma MRI scanner and a 64-channel head coil. Vibrations were generated at 50 Hz and 100 Hz using a Resoundant pneumatic actuation system (Rochester, MN) and a passive pillow driver (Figure 1). Low motion encoding gradient strength (5 mT/m) was used to capture rigid body motion of both the skull and brain while avoiding temporal phase wrapping[3,5].

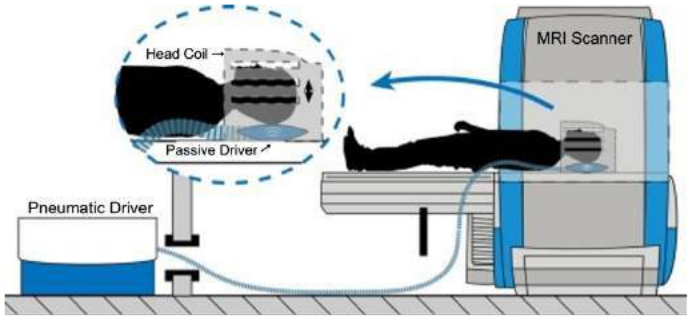


**Figure 1: Overview of MRE setup and acquisition showing the external mechanical driver inducing shear waves into the brain through inflation of the passive driver.**

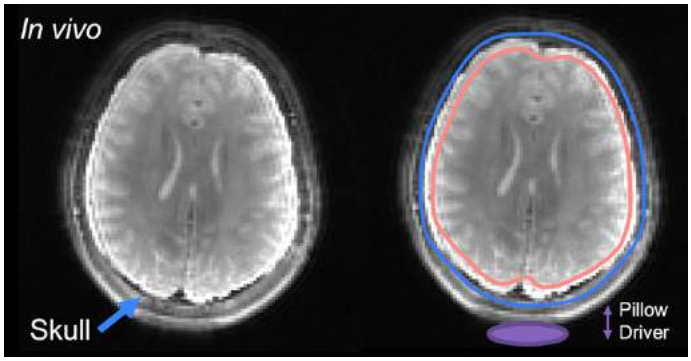


**Figure 2: Magnitude images from an adapted 2D multishot spiral MRE sequence. Both water and fat components are visible, and masks of the brain and skull are overlayed.**

***In vivo* Testing:** A single human subject (female, age 23) was scanned using the fat-water MRE sequence at both 50 Hz and 100 Hz vibration frequencies.

**Analysis:** Imaging data was iteratively reconstructed[8]. Phase images were processed to obtain maps of complex motion with sensitization in the x (left-right), y (anterior-posterior), and z (superior-inferior) directions. Representative masks were created at the interface of the skull and brain (Figure 2). Points around the circumference of the skull were defined in terms of polar coordinates and described by their polar angle, $\theta$. Displacement amplitude and relative phase of the harmonic motion was quantified for each point in both skull and brain.

## RESULTS

Our *in vivo* analysis of brain and skull motion showed an overall lower displacement amplitude of the brain relative to the skull, indicating reduced transmission of motion to the brain in all three directions (Figure 3). The skull motion amplitude appears to follow a sinusoidal pattern for each individual direction starting from the site of actuation and represents the rigid body motion in three dimensions. The brain shows a similar pattern but at a lower amplitude than the skull.

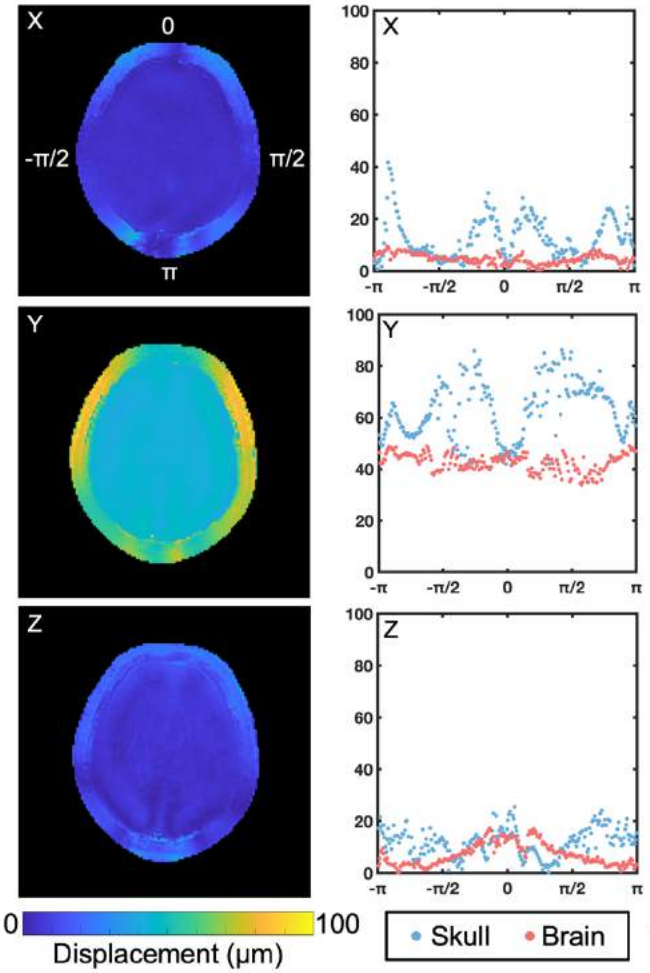


**Figure 3: Motion amplitude in the x, y, and z directions at 50 Hz.**

The phase plots show that the skull and brain are moving out of phase in both the x (left-right) and z (superior-inferior) directions while the brain and skull in the y direction (anterior-posterior) appear to remain in phase (Figure 4).

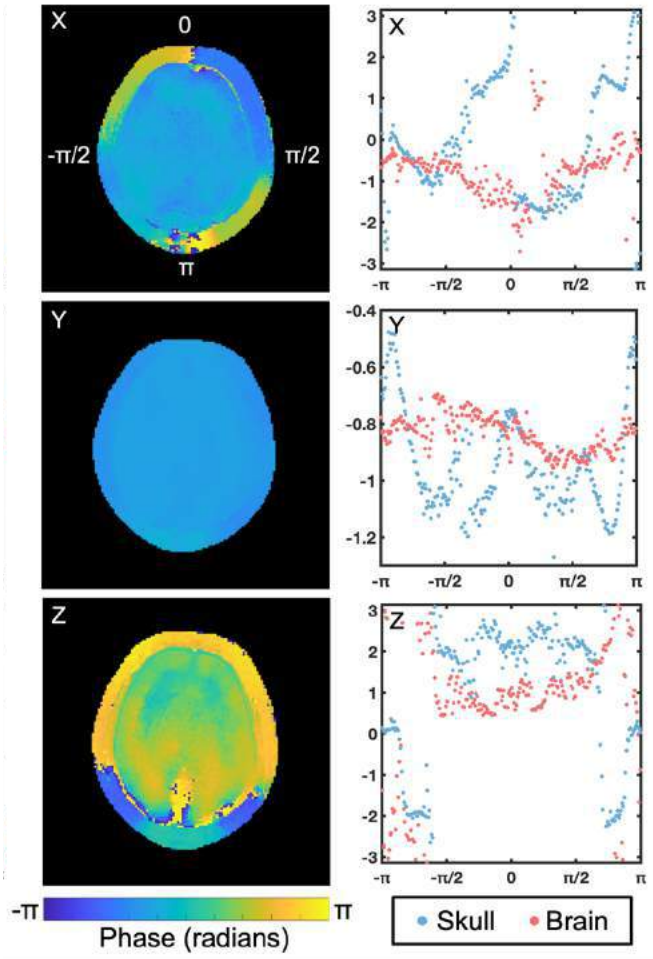


**Figure 3: Phase of x, y, and z motion at 50 Hz.**

## DISCUSSION

These preliminary results support the hypothesis that the brain moves out of phase with the skull as captured by our modified fat-water spiral MRE sequence. Further sequence developments will seek to optimize the skull signal and reduce artifacts caused by the scalp[6]. An increased range of actuation frequencies with multiple excitation directions will allow us to comprehensively quantify skull-brain transmission. Understanding this relationship will allow researchers to improve TBI models by accounting for the skull-brain interface and evaluate how this relative motion changes in patients with a history of mild TBI.


## ACKNOWLEDGEMENTS

This project was supported by NIH grant U01-NS112120, the Department of Defense in the Center for Neuroscience and Regenerative Medicine, and the NIH Bench-to-Bedside Award.


## REFERENCES


[1] Hyder, AA et al., *NeuroRehabilitation*, 22:341-353, 2007. [2] Nguyen, R et al., *J. Neurol. Sci.*, 43:774-785, 2016. [3]Yin, Z et al., *Magn. Reson. Med.,* 80:2573-2585, 2018. [4] Bayly, PV et al., *Ann. Biomed. Eng.,* 2021:1-16, 2021. [5] Badachhape, AA et al., *J. Biomech.,* 139:0510021, 2017. [6] Badachhape, AA et al., *J. Biomech.,* 73:40-49, 2018. [7] Johnson, CL et al., *Magn. Reson. Med.,* 70:404-412, 2013. [8] Sutton, BP et al., *IEEE Trans. Med. Imaging*, 22:178-188, 2003.

SB³C2022
Summer Biomechanics, Bioengineering and Biotransport Conference
June 20-23, Eastern Shore, MD, USA

# A NOVEL MATLAB SCRIPT FOR THE ANALYSIS OF MECHANICAL CHARACTERIZATION DATA

**Emily R. King (1), Michael T.K. Bramson (1), David T. Corr (1)**

(1) Biomedical Engineering, Rensselaer Polytechnic Institute, Troy, New York, USA

## INTRODUCTION

Mechanical characterization is an important component of biomedical research focused on the development of engineered tissues and biomaterials. Although a robust experimental design and data collection process is an important preliminary step, a robust data analysis process is also critical. Specifically, balancing objectivity and sensitivity within the data analysis process allows for meaningful conclusions to be drawn from the data. Thus, we sought to develop a MATLAB script to objectively identify key material and failure properties from tensile testing data, with the flexibility to enable characterization of a wide variety of material behaviors.

The aims of this project were (i) to develop a script that determines key material parameters from collected raw experimental data and sample geometries, and (ii) demonstrate its ability to extract key characterization parameters from tensile pull-to-failure data of mouse tendons, engineered tendon fibers, and engineered biomaterials exhibiting a range of characteristic behaviors [1, 2]. Eight parameters of interest were selected to be extracted from the experimental data: peak stress, failure strain, toe-in strain, toughness, pre- and post-yield modulus, and yield stress and strain.

## METHODS

Load-displacement-time data collected from uniaxial tensile pull-to-failure characterization experiments of engineered tendon fibers, mouse hind-limb tendons, and engineered biomaterials (i.e., Lipase-catalyzed Poly(Glycerol-1,8-Octanediol-Sebacetate; or PGOS) were used as input data for our analyses. Mechanical testing was performed using a materials testing system (TestResources Inc., MN) for mouse tendon and engineered biomaterials, and a custom tensile bioreactor system (Admet Inc., MA) for engineered tendon fibers. Force-displacement data were exported from the testing software as an Excel file. Sample geometries were acquired prior to testing.

When initialized, the program prompts the user to select the Excel data file for analysis, and loads the collected force-displacement data. The user is then prompted to input the sample geometries: gauge length and cross-sectional area, which the program uses to calculate values for strain and stress. Strain is then normalized by determining the strain that corresponds to the start of sample deformation, and subtracting this offset from the raw strain values to get an adjusted strain where zero corresponds to the start of tensile strain in the material. From this normalized data, peak stress is determined as the maximum stress value. The index corresponding to this peak stress is then used to define the failure strain. Toughness is determined as the integration of the stress-strain curve from the start of sample deformation until failure strain.

Determination of Young's elastic modulus is initiated through user input of upper and lower strain percentage boundaries, to accommodate a variety of material behaviors. These boundaries are used as the range over which the modulus is calculated, determined as the slope of the line of best fit via linear regression. Subsequently, a stress-strain plot of the data is generated with the range for modulus calculation highlighted (Figure 1A), for visual confirmation that the selected range captures the specimen's linear elastic response.

Should the selected range not reflect an appropriately-linear region, the user can select new strain boundary inputs, and run the code block again. A new figure will be generated to provide immediate visual feedback on the selected range for modulus determination. This process is mirrored for calculation of a post-yield modulus, as necessary.

Calculation of toe-in strain is accomplished by fitting the adjusted stress-strain data with a spline, from the onset of loading until sample failure. The first derivative of the spline fit is calculated, and the program iteratively compares values of the derivative to determine the strain at which it equals the modulus determined in the prior block. This approach identifies the transition between the strain-stiffening and linear regions, which is indicative of the toe-in strain. Noise within the

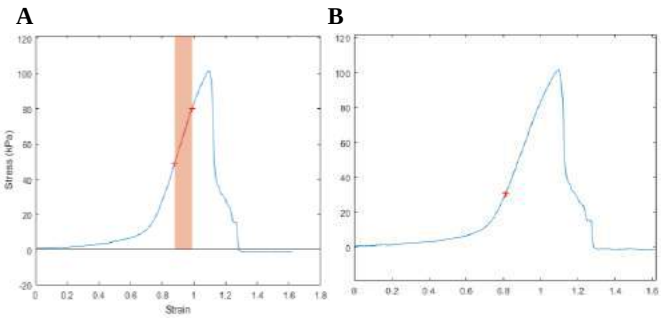


**Figure 1: A: Modulus is calculated from user-prescribed upper and lower strain boundaries, and plot provides visual confirmation. B: Representative image of stress-strain plot with toe-in region marked (red asterisk) for user verification.**

data, most notable in low-stress regions of smaller-scale samples (e.g., single fibers), creates the potential for the condition to be triggered prematurely within the initial strain-stiffening response. To account for and address this possibility, the program generates a plot with the calculated toe-in strain marked on the strain-strain curve with a red asterisk (Figure 1B). The user is prompted to verify (Y/N) that the toe-in strain appears reasonable, and reflects the transition from strain-stiffening to linear response. Should the user indicate no, the program undergoes another iteration, selects the next data point that satisfies this criterion, and generates a new figure. In this manner, the feedback loop allows the program to balance sensitivity with objectivity by accommodating for noise in the data while maintaining a numerical basis for the toe-in strain selection.

For materials that exhibit yield behavior, yield strain is determined by constructing linear equations from the pre- and post-yield moduli and determining their respective intersection point. The strain and stress corresponding with the index of this intersection defines the yield strain and the yield stress, respectively.

## RESULTS

Calculated values of interest and generated figures are exported automatically, including a figure with key values marked (Figure 3). When applied to experimental tensile data of engineered single tendon fibers and mouse tendons, which exhibit a characteristic strain-stiffening, linear response to failure, the MATLAB script was able to objectively identify the key parameters of interest, including the toe-in strain (Fig. 2). Additionally, this program was applied to pull-to-failure

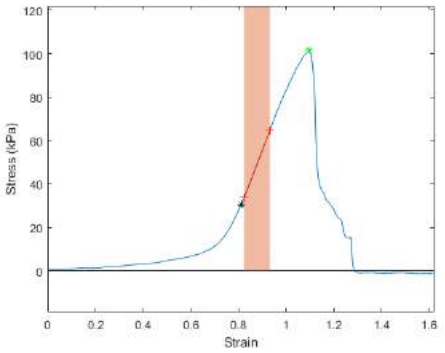


**Figure 2: Representative stress-strain curve of an engineered fiber, as generated by code. Modulus is the slope calculated within the red shaded region, and asterisks denote the end of the toe-in region (black) and point of failure (green).**

data of various engineered PGOS biomaterials exhbiting a wide range of tensile behaviors, demonstrating its ability to extract the key parameters of interst for tensile characterition from diverse material responses, including bilinearly-elastic, elastic-perfectly plastic, and elastic-softening, (Figure 3).

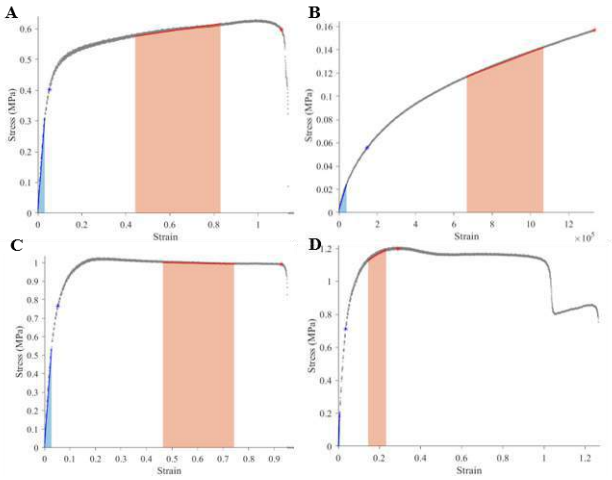


**Figure 3: Representative figures of engineered biomaterials exhibiting different characteristic behaviors. A, B: bi-linearly elastic C: elastic-perfectly plastic D: elastic-softening**

## DISCUSSION

This novel MATLAB script streamlines the process for mechanical characterization data analysis, and reduces subjectivity in parameter determination. Visualization of the data and extracted parameters during the analysis process creates a functional tool for objective analysis with visual confirmation, that can be applied across multiple length scales (engineered single tendon fibers vs. whole tendon and engineered biomaterials), and for a variety of material behaviors.

In the future, this code can be expanded to include additional parameters of interest and to accommodate other modes of mechanical characterization, such as viscoelastic parameters from stress-relaxation or creep testing.

## ACKNOWLEDGEMENTS

This project was supported, in part, by the Rensselaer Polytechnic Institute Undergraduate Research Program.

## REFERENCES

[1] Mubyana, K. and Corr, D., *Tissue Engineering*, 24:1808-1817, 2018.
[2] Lang, K et al., *Biomacromolecules*, 21:3197-3206, 2020.

SB³C2022
Summer Biomechanics, Bioengineering and Biotransport Conference
June 20-23, Eastern Shore, MD, USA

# PARAMETERS TO MODEL CARTILAGE AS OSTEOARTHRITIS PROGRESSES

**Xiaogang Wang (1), David M. Pierce (1,2)**

(1) Department of Mechanical Engineering, University of Connecticut, Storrs, CT, USA
(2) Department of Biomedical Engineering, University of Connecticut, Storrs, CT, USA

## INTRODUCTION

The remarkable mechanical function of healthy cartilage derives from interactions among proteoglycans, networked collagens (in three through-thickness zones: superficial, middle, and deep), and electrolytic fluid. Osteoarthritis (OA) is a pervasive disease involving failure of the synovial joint and deleterious changes in composition and micro-structure (e.g. loss of zones) of cartilage. Changes in cartilage properties correlate with tissue composition and thus with OA severity [1-3].

During normal movement, healthy cartilage provides load transfer between bones and near-frictionless joint articulation, compressing as much as 30% under pressures up to 20 MPa [1,4,5]. These large *in vivo* deformations of the tissue, where shear is critical in both failure and cell death, mean mechanical analyses of cartilage should employ large-strain, nonlinear mechanics. Moreover, research shows tensile properties of the collagen network dominate the shear response [1,6].

Finite element (FE) modeling plays a well-established and increasingly significant role in analyses of cartilage at organ, tissue, and cell scales. An accurate FE model requires an experimentally calibrated and validated constitutive model; however, research literature features few calibrated large-strain constitutive models for healthy human cartilage, and even fewer for osteoarthritic human cartilage [2,3].

We established a finite-strain constitutive model of cartilage addressing both solid (reinforcement) and fluid (permeability) dependence on the network of collagen fibers, and which admits patient-specific organizations of collagen via diffusion tensor MRI [7]. We also included osmotic swelling and the osmotically prestretched/prestressed state of cartilage determined from medical images [8]. In this study, we aimed to advance our constitutive model by leveraging our novel experimental data [9,10] to establish parameters with respect to structurally defined OA progression quantified by OARSI scoring [11].

## METHODS

*Experimental Evidence.* We previously harvested 106 3×3 mm, full-thickness specimens of healthy and progressively osteoarthritic cartilage from 17 donors [9,10]. Using standard histological scoring we determined the OARSI grade of each specimen [11]. Briefly, we applied cyclic simple-shear displacements at a rate of 75 μm/min for six cycles, and at maximum displacements corresponding to shear strains of 5%, 10%, 15%, 20%, and 25%. Many mechanical tests failed at 20% shear strain and we used data only up to 15%. We grouped specimens based on OARSI grade: Healthy ($n = 42$) contains healthy specimens with OARSI score of 0-1; OARSI-1 ($n = 11$) with OARSI grade $\in [0,2)$; OARSI-2 ($n = 20$) with OARSI grade $\in [2,3)$; OARSI-3 ($n = 17$) with OARSI grade $\in [3,4)$; and OARSI-4 ($n = 10$) with OARSI grade $\geq 4$.

*Constitutive Model.* We described cartilage as a biphasic continuum $\varphi = \varphi^{\mathrm{S}} + \varphi^{\mathrm{F}}$ of a porous solid phase $\varphi^{\mathrm{S}}$ saturated with a fluid phase $\varphi^{\mathrm{F}}$. We calculated the total Cauchy stress as [7,8]

$$\boldsymbol{\sigma} = -p\mathbf{I} + 2\rho^{\mathrm{S}}\mathbf{F}_{\mathrm{S}}\frac{\partial \Psi^{\mathrm{S}}}{\partial \mathbf{C}_{\mathrm{S}}}\mathbf{F}_{\mathrm{S}}^{\mathrm{T}} = -p\mathbf{I} + \boldsymbol{\sigma}_{\mathrm{E}}^{\mathrm{S}}, \tag{1}$$

where $p$ is the fluid pressure, $\mathbf{I}$ is the identity, $\rho^{\mathrm{S}}$ is the partial density of solid, $\mathbf{F}_{\mathrm{S}}$ is the solid deformation gradient, $\mathbf{C}_{\mathrm{S}} = \mathbf{F}_{\mathrm{S}}^{\mathrm{T}}\mathbf{F}_{\mathrm{S}}$, and $\boldsymbol{\sigma}_{\mathrm{E}}^{\mathrm{S}}$ is the effective Cauchy stress. We used an additive decomposition of the solid Helmholtz free-energy $\Psi^{\mathrm{S}}$ into contributions from Donnan osmotic pressure $\Psi_{\mathrm{OP}}^{\mathrm{S}}$, an isotropic matrix $\Psi_{\mathrm{IM}}^{\mathrm{S}}$, and a fiber network $\Psi_{\mathrm{FN}}^{\mathrm{S}}$ as [8]

$$\Psi^{\mathrm{S}} = \Psi_{\mathrm{OP}}^{\mathrm{S}}(J_{\mathrm{S}}) + (1-\nu)\Psi_{\mathrm{IM}}^{\mathrm{S}}(J_{\mathrm{S}}, I_1) + \nu\Psi_{\mathrm{FN}}^{\mathrm{S}}(\mathbf{C}_{\mathrm{S}}), \tag{2}$$

where $J_{\mathrm{S}} = \det\mathbf{F}_{\mathrm{S}}$, $\nu$ is the volume fraction of collagen to total solid, and $I_1 = \mathrm{tr}\mathbf{C}_{\mathrm{S}}$. We modeled the Cauchy stress from osmotic pressure as

$$\boldsymbol{\sigma}_{\mathrm{OP}}^{\mathrm{S}} = -R\Theta\left[\sqrt{4(\bar{c}_{\mathrm{m}})^2 + (c_{\mathrm{m}}^{\mathrm{fc}})^2} - 2\bar{c}_{\mathrm{m}}\right]\mathbf{I}, \tag{3}$$

where $R = 8.314 \times 10^3\,\mathrm{mJ/(K\cdot mol)}$, $\Theta$ is the absolute temperature, $\bar{c}_{\mathrm{m}}$ is the ion concentration of the external solution, and the concentration of the fixed charge depends on the deformation as [8]

$$c_{\mathrm{m}}^{\mathrm{fc}} = c_{0\mathrm{S}}^{\mathrm{fc}}\left(1 - n_{0\mathrm{S}}^{\mathrm{S}}\right)\left(J_{\mathrm{S}} - n_{0\mathrm{S}}^{\mathrm{S}}\right)^{-1}, \tag{4}$$

where $c_{0\mathrm{S}}^{\mathrm{fc}}$ is the initial concentration of fixed charge (within the tissue) and $n_{0\mathrm{S}}^{\mathrm{S}}$ is the initial solid volume fraction. We modeled the (largely)

proteoglycan solid matrix $\Psi^{S}_{IM}$ using a neo-Hookean function extended with compaction effects. We modeled the dispersed network of collagen $\Psi^{S}_{IM}$ using and orientation distribution function calibrated with diffusion tensor MRI. We considered the viscoelasticity of both the proteoglycan and collagen solids using two parameters: $\beta$ [-], a magnitude factor, and $\tau$ [s] the associated relaxation time, cf. [12].

*Inverse Finite Element Analyses.* We modeled the center slice of specimens under plane strain (**Fig. 1(a)**) using 20-node hexahedral elements to simulate the shear tests in FEBio (U. of Utah). We validated our mesh, using an *h*-refinement test [9,12]. In light of the available data we leveraged previous studies to establish some of the parameters (**Table 1**). We started the parameter optimization using a homogeneous constitutive model where we used $z^*$= 0.5 to obtain the averaged parameters and the diffusion tensor $\mathbf{D} = \mathbf{I}$ for an isotropic distribution of fibers. With this model we optimized the fiber stiffness parameter $k_1 \in$ [0.3,10], initialized with $k_1$= 3.0, using the "interior-point" algorithm. For healthy samples, we then fitted a heterogeneous model consisting of a superficial zone (SZ, 15%), middle zone (MZ, 55%), and deep zone (DZ, 35%) based on the tissue thickness (**Fig. 1(b)**) to refit $k_1$. To investigate the contribution of prestress resulting from Donnan osmotic pressure we repeated the parameter optimization without osmotic pressure and without the backward displacement method (BDM) to determine initial equilibrium [8].

*Statistical Analyses.* We tested whether the fitted $k_1$ was normally distributed by the Jarque-Bera test. We used the two-sample *t*-test to establish if two data sets were significantly different (with $p$ = 0.05).

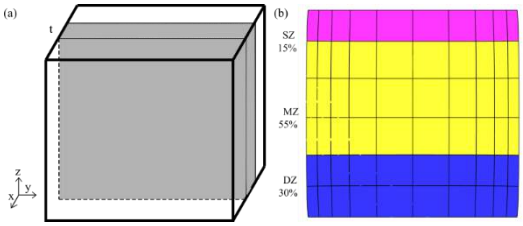


**Figure 1: FE model of the shear experiment: (a) schematic with center slice in plane strain; (b) mesh with three distinct zones.**

**Table 1: Model parameters from previous studies, where z* ∈ [0,1] is the normalized tissue thickness (zero refers to the articular surface and one to the interface with subchondral bone) [7,8].**

| Parameter | Value | Unit |
|---|---|---|
| $\boldsymbol{\Theta}$ | 310 | K |
| $\boldsymbol{\mu}$ | 0.23 | MPa |
| $\boldsymbol{k_2}$ | 8.0 | – |
| $\boldsymbol{\beta_{IM}, \beta_{FN}}$ | 2.7, 1.5 | – |
| $\boldsymbol{\tau_{IM}, \tau_{FN}}$ | 360, 1500 | s |
| $\boldsymbol{c^{fc}_{0S}}$ | $2.0 \times 10^{-7}$ | mol/mm$^3$ |
| $\boldsymbol{\bar{c}_m}$ | $1.5 \times 10^{-7}$ | mol/mm$^3$ |
| $\boldsymbol{n^{S}_{0S}(z^*)}$ | $0.15 + 0.15(z^*)$ | – |
| $\boldsymbol{\nu(z^*)}$ | $0.43(z^*)^2 - 0.60(z^*) + 0.85$ | – |
| $\boldsymbol{J^{S}_{cp}(z^*)}$ | $0.36 + 0.11(z^*)$ | – |
| $\boldsymbol{k_{0S}(z^*)}$ | $(1 - 0.9(z^*)) \times 10^{-3}$ | mm$^4$/(N · s) |
| $\boldsymbol{m(z^*)}$ | $3.0 + 5.0(z^*)$ | – |

## RESULTS

Fitting results of the healthy samples with both homogeneous and heterogeneous models are normal distributed. There is no significant difference between the bulk responses of the two models with the BDM approach. Without osmotic pressure and BDM, the optimal fiber stiffness parameter $k_1$ is larger in the homogeneous model **(Fig. 2(a))**. Starting from OARSI-1, $k_1$ decreased as OARSI grade increased. The most significant changes occurred between OARSI-1 and OARSI-2 in both BDM and Non-BDM approaches. Since OARSI-3 in BDM and OARSI-4 in both BDM and Non-BDM did not pass the JB-test, we show median and interquartile ranges for these three cases instead of mean and standard deviation **(Fig. 2(b))**. We also plot the bulk stress-strain response of representative specimens for comparison **(Fig. 3)**.

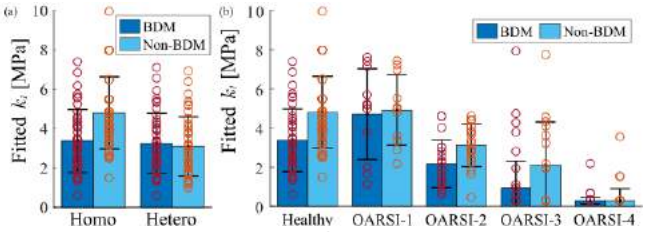


**Figure 2: Fitted fiber stiffness $k_1$: (a) healthy specimens with different methods and models, (b) specimens from OARSI grades.**

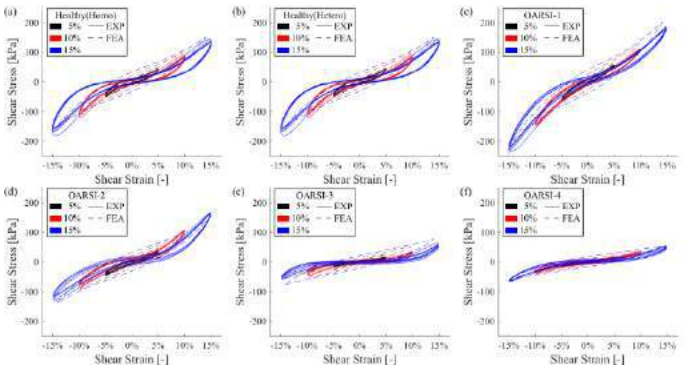


**Figure 3: Representative stress-strain responses of OARSI grades.**

## DISCUSSION

In this study, we calibrated our constitutive model with experimental data from healthy and progressively osteoarthritic human articular cartilage undergoing large-strain shear. Since many of the parameters we require are directly measureable and well established (e.g. the permeability of healthy cartilage) we focused our fitting under shear on the stiffness of collagen fibers, particularly since the properties of the collagen network dominate the shear response of cartilage. With advancing OA, the fiber stiffness parameter $k_1$ progressively reduces indicating progressive loss of collagen integrity. We can further improve our cartilage model by leveraging more experimental data.

We also established a general method to better calibrate our cartilage model using experimental data. Our methods can be expanded for fitting multiple parameters simultaneously or different constitutive models, or leveraging other types of experimental data. With our models and modeling methods, we hope to improve the fidelity of FE-based, patient-specific biomechanical simulations of joints and cartilage.


## ACKNOWLEDGEMENTS

NSF CAREER 1653358, NSF 1662429; N. Kamath, F. Maier.


## REFERENCES


[1] Mow, VC et al., *Basic Orthopaedic Biomechanics & Mechano-Biology*, 181-258, 2005. [2] Robinson, DL et al., *J Mech Beh Biomed Mat*, 61:96-109, 2016. [3] Nissinen, MT et al., *J. Biomech*, 126:110634, 2021. [4] Park, S et al., *J. Biomech.*, 36:1785-1796, 2003. [5] Bingham, JT et al., *Rheum*, 47:1622-1627, 2008. [6] Mow, VC et al., 1992. [7] Pierce, DM et al., *Biomech Model Mechno*, 15:229-244, 2016. [8] Wang, X et al., *J Mech Beh Biomed Mat*, 86:409-422, 2018. [9] Maier, F et al., *J Mech Beh Biomed Mat*, 65:53-65, 2017. [10] Maier, F et al., *Osteoarthritis Cartilage*, 27:810-22, 2019. [11] Pritzker, KPH. et al., *Osteoarthritis Cartilage*, 14:13-29, 2006. [12] Wang, X. et al., *J Mech Beh Biomed Mat*, 104150, 2020.

SB³C2022
Summer Biomechanics, Bioengineering and Biotransport Conference
June 20-23, Eastern Shore, MD, USA

# A NOVEL APPROACH FOR MAPPING 3D EXTRACELLULAR MATRIX MECHANICS AT THE CELLULAR SCALE USING MAGNETIC MICROPARTICLES

**Adil Khan (1), Jacopo Ferruzzi (1)**

(1) Department of Bioengineering, The University of Texas at Dallas, Richardson, TX, USA

## INTRODUCTION

Mechanical interactions between cells and their microenvironment have been shown to regulate important biological processes such as adhesion, proliferation, and migration [1]. However, cell-matrix mechanical interactions are neither simple nor unidirectional. As cells responds to biomechanical cues from the extracellular matrix (ECM), they actively restructure and remodel this surrounding micro-environment, thereby altering its mechanical properties [2]. Over the past several decades, there has been an increased effort towards understanding the complexity of cell-ECM dynamics, and the inherent role played by mechanical forces in regulating cell behavior. The ECM derives its tensile strength from collagen, its predominant protein constituent. Because collagen also provides the scaffolding for cell adhesion in vivo, it is often the substrate of choice for three-dimensional (3D) cell culture studies. Traditional characterization of collagen mechanics has either relied on global methods such as uniaxial tension, compression, and shear rheometry, or on nano- and micro-scale manipulation techniques such as atomic force microscopy [3]. While these tests have led to important insights on the impact of factors such as protein concentration on collagen network mechanics, they do not provide an accurate representation of the forces that are experienced by resident cells in a 3D ECM. In addition, they commonly fail to address spatial heterogeneities that emerge during the cell-driven remodeling of complex 3D fibrous networks.

In this study, we introduce a novel approach to characterize the mechanics of the ECM at a scale best representative of the cellular microenvironment. Our method uses ferromagnetic beads, embedded in collagen hydrogels during polymerization, which experience a torque from the application of two orthogonal magnetic fields. By measuring the deformation field in the fibril structure that surrounds these microscopic force probes, we quantify the local mechanical properties of the collagen network. While a similar technique has been used previously to capture changes in mechanical properties with changes in collagen concentration in two dimensions (2D) [4], our study is the first to use magnetic bead stimulation to explore spatiotemporal aspects of collagen mechanics in a full 3D setting.

## METHODS

Acellular networks of type I collagen (Corning), of concentrations between 1 and 4 mg/mL, were prepared using established protocols [5]. Custom ferromagnetic microparticles, with an average diameter of 8.37 μm and at a density of $10^6$ particles/mL, were distributed evenly throughout the gels during polymerization. Intrafibrillar and interfibrillar cross-links were generated by adding a solution of glutaraldehyde diluted in deionized water. Following the protocol of Doyle et al. [6], an Atto 488 NHS ester dye (Sigma-Aldrich) was used for fluorescent labeling of collagen fibrils. In brief, 2 moles of fluorescent dye per mole of collagen protein were added to a borate buffer solution and allowed to bind with fully polymerized collagen. The dye conjugated with collagen for 1 hour (at room temperature and protected from light), after which the solution was replaced with a 50mM TRIS buffer to quench the dyeing reaction. Finally, excess dye was washed out thrice with 1x PBS before testing.

The micro-structural organization of the collagen network around selected beads was assessed using a Nikon AX confocal microscope equipped with a 20× water immersion objective lens (0.95 N.A., 950 μm working distance). The unit for 3D magnetic twisting includes a microscope insert with three perpendicular coils [7]. The embedded microparticles were stimulated by the application of a strong magnetic pulse followed by a weak magnetic field in a perpendicular direction to generate a torque about one of the coordinate axes (*z*-axis in Figure 1). Confocal stacks were acquired both before and after magnetic stimulation. In order to capture how deformations propagate into the matrix surrounding the beads, the collagen network was imaged using

both reflection and fluorescence modes. An augmented Lagrangian digital volume correlation algorithm [8] was used to quantify the induced 3D deformation fields. These displacement maps were then recreated in an iterative finite element framework to estimate the unknown material parameters of the collagen network, which was modeled as a locally homogenous neo-Hookean material. To demonstrate the ability of the proposed approach to capture spatially and temporally evolving mechanical properties of remodeled ECMs, we monitored the local properties of gels surrounding highly contractile MDA-MB-231 breast cancer spheroids (Figure 1a).

## RESULTS

Ferromagnetic beads were found to localize around collagen fibrils, and to induce measurable deformations in the collagen matrix upon magnetic stimulation (Figure 1b). Experimental and simulated displacement fields show a pattern of deformation that is consistent with the twist of a spherical inclusion (Figure 1c-d). Radial profiles of absolute matrix displacement display decays that are sensitive to collagen concentration and degree of cross-linking. Iterative simulations allowed us to match experimental and computational displacement fields thereby extracting the unknown material parameters under the assumption of neo-Hookean material behavior (Figure 1e).

MDA-MB-231 post-metastatic breast cancer cells are highly contractile and are known to remodel the surrounding ECM as they invade either as single cells or as collective multicellular strands [9]. Embedded MDA-MB-231 spheroids actively remodel the collagen matrix, resulting in a characteristic increase in collagen density and alignment at the spheroid-ECM interface. These structural changes were captured by our mechanical measurements, thereby demonstrating the feasibility of quantifying the mechanical effects of remodeling due to cell-matrix interactions.

## DISCUSSION

Changes in ECM structure and mechanics via cell-mediated matrix remodeling have important implications for tissues in both physiological and pathological states. To understand the complex roles played by ECM remodeling in health and disease, accurate quantification of 3D tissue mechanics is of the essence, though not currently possible with high spatial and temporal resolution. Previous studies have used magnetic forces largely to study cytoskeletal mechanics of cells adhering to a 2D substrate [7, 10, 11]. The micromechanics of collagen gels has been analyzed using optical tweezers [12, 13], standard magnetic twisting cytometry [14], 2D optical magnetic twisting cytometry [5], and more recently using 3D twisting of magnetic micro-rods [15]. To the best of our knowledge, our study is the first to use magnetic forces to investigate the mechanics of collagen networks fully in a 3D setting, combining the effects of concentration and degree of cross-linking. The recent study by Asgeirsson et al. [15] proposed a similar framework but examined only the effect of collagen concentration and limited their analysis within the context of linear elasticity. Instead, our approach has the potential to define the local structure-function relationship in collagen networks by stimulating thousands of covalently bound microbeads at the same time via an external magnetic field, imaging local matrix displacements, and modeling ECM mechanics. Future work will focus on incorporating the nonlinear anisotropic properties of the fibrous ECM by means of a constitutive model that accounts for both structural and material features of collagen fiber networks.


## ACKNOWLEDGEMENTS

The authors acknowledge Professor Jeffrey J. Fredberg and Dr. Chan Y. Park (Harvard T.H. Chan School of Public Health) for their support with ferromagnetic beads, and Professor Christian Franck and Dr. Jin Yang (University of Wisconsin-Madison) for their expert assistance with Digital Volume Correlation.


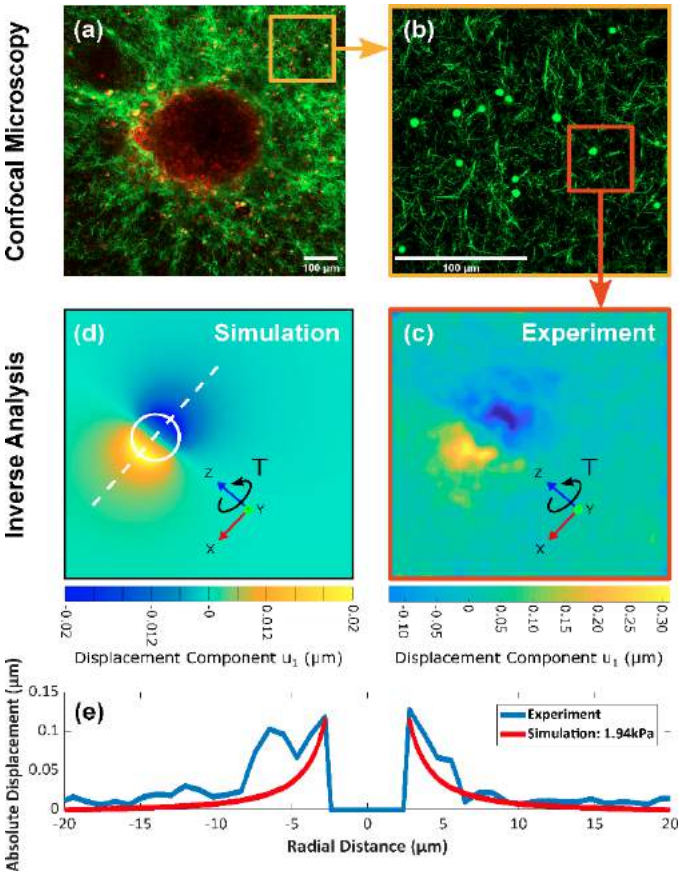


**Figure 1: A representative MDA-MB-231 tumor spheroid (red) invading into 3D collagen (green) after 48 hours of culture. (b) Ferromagnetic beads of 8.37 µm diameter are dispersed into collagen and are used as local force probes. (c) A torque T is applied about a specific axis (herein indicated as the z axis) and generates a displacement field that can be quantified by combining 3D confocal imaging and digital volume correlation. (d) Finite element simulations of a spherical inclusion embedded into a homogeneous neo-Hookean medium of fixed stiffness reproduce qualitatively the displacement field. (e) Iterative simulations are conducted to match experimental and computational displacements thereby estimating the micro-scale stiffness of the collagen network at 1.94 kPa.**

## REFERENCES


[1] Humphrey, J.D. et al., *Nat Rev Mol Cell Biol*, 15: 802–812, 2014.
[2] Cox, T.R. and Erler, J.T., *Dis Model Mech*, 4: 165–178, 2011.
[3] Ferruzzi J. et al., in *Multi-scale Extracellular Matrix Mechanics and Mechanobiology*, 343-387: 2020.
[4] Li H. et al., *ACS Biomater Sci Eng*, 3: 2815–2824, 2017.
[5] Ferruzzi J. et al., *Sci Rep*, 9: 17151, 2019.
[6] Doyle A.D. et al., *Nat Commun*, 6: 8720, 2015.
[7] Hu S. et al., *Am J Physiol Cell Physiol*, 287: C1184–91, 2004.
[8] Yang J. et al., *Exp Mech*, 60: 1205–1223, 2020.
[9] Kang W., Ferruzzi J. et al., *iScience*, 24: 103252, 2021.
[10] Fabry, B. et al., *J Appl Physiol*, 91: 986–94, 2001.
[11] Wei F. et al., *Nat Commun*, 11: 4902, 2020.
[12] Velegol, D. and Lanni, F., *Biophys J*, 81: 1786–92, 2001.
[13] Han Y.L. et al., *Proc Natl Acad Sci U S A*, 115: 4075–4080, 2018.
[14] Leung, L.Y. et al., *FASEB J*, 21: 2064–73, 2007.
[15] Asgeirsson D.O. et al., *Lab Chip*, 21: 3850–3862, 2021.

SB³C2022
Summer Biomechanics, Bioengineering and Biotransport Conference
June 20-23, Eastern Shore, MD, USA

# SIMULATION OF THROMBUS FORMATION IN MICROFLUIDIC CONSTRICTION AT SUPRAPHYSIOLOGIC SHEAR RATE

**R. Méndez Rojano, G. W. Rowlands, S. Schirmacher, J. F. Antaki**

Meinig School of Biomedical Engineering, Cornell University, Ithaca, NY, USA

## INTRODUCTION

Excessive blood clot formation, also known as thrombosis, is one of the leading causes of mortality worldwide accounting for one out of four deaths [1]. Thrombosis can impact the cardiovascular, neurovascular, and pulmonary systems. In addition, blood wetted medical devices are frequently affected by abnormal thrombus formation [2].

To better understand the hemostatic process that leads to thrombosis, microfluidic flow experiments and mathematical models have been developed over the past decades [3]. Microfluidic chambers are often designed to mimic a vascular injury and characterize thrombogenesis. This is achieved by coating surfaces with collagen, Tissue Factor (TF), or von-Willebrand Factor (vWF) to capture platelets and trigger coagulation reactions. While microfluidic experimental studies provide useful insight for thrombus formation dynamics, their data are limited to fibrin polymerization and platelet aggregation [4], and do not capture intermediate steps in the coagulation cascade. This is one of the motivations for mathematical models of thrombosis: to simulate the hemostatic steps at different spatial and temporal scales.

In the current study, a parallel plate microfluidic chamber with a constriction was developed to study the thrombus formation at supraphysiologic shear rate (>6000 s-1). Microfluidic experiments were conducted with healthy human whole blood. Commensurate numerical simulations were performed to reflect platelet and vWF activity. The main objective of this work is to replicate experimental observations with our multi-constituent thrombosis model.

## METHODS

An acrylic parallel plate flow chamber was constructed using a polydimethylsiloxane (PDMS) microfluidic chip with a constriction to generate large shear stresses (>6000 s-1.) The PDMS channel was sealed with a glass slide that was partially coated 1 mm downstream and upstream of the constriction with Collagen type 1 from calf skin to promote clotting. Flow was introduced via syringe pump. (See Fig 1A and 1B.)

The channel was passivated with 0.5 % Bovine Serum Albumin (BSA) solution for 10 minutes at a flow rate of 75 µL $min^{-1}$. Subsequently, citrated whole blood was perfused at 75 µL $min^{-1}$ for 10 minutes. Blood was collected from healthy adults, following the Helsinki declaration and approved by Cornell University IRB. Citrated blood collection tubes were used, the first tube was discarded to avoid introducing activated platelets to the channel from the venipuncture procedure. Hematocrit and platelet count were measured with a hematology analyzer. Hematocrit and platelet count were maintained at approximately 30-45% and 150,000-300,000 plt $\mu L^{-1}$ respectively. Platelets were labeled with a Phosphate-Buffered Saline-mepacrine solution in a 1:9 ratio. Platelet aggregation was observed with an inverted fluorescence microscope equipped with a. color CCD Camera at 10 fps.

Computational fluid dynamics was performed to estimate the scalar shear rate field, considering the blood as a Newtonian fluid. (See Fig. 1C.) The Reynolds number of the flow under these conditions was 8 considering the asymptotic value of the kinematic viscosity ($3.5\times10^{-6}\ m^2\ s^{-1}$), the bulk velocity before the constriction (0.2 m $s^{-1}$), and the constriction width as characteristic length (140 µm). This ensured the absence of recirculation downstream of the constriction. (See Fig. 1D.)

Thrombus formation was simulated using the mathematical models of Wu et al. [5] that considers platelet mechanical activation by shear, platelet chemical activation by thrombin, thromboxane (TxA2), and adenosine diphosphate (ADP). In addition, vWF activity and its effect on platelet recruitment and embolization is modeled following Zhussupbekov et al. [6]. Briefly, the Navier-Stokes (NS) are coupled with Convection-Diffusion-Reaction (CDR) equations for seven biochemical species involved in platelet activation and aggregation. As the thrombus grows, a resistance term is introduced in the conservation of momentum equations hindering the blood flow within the thrombus.

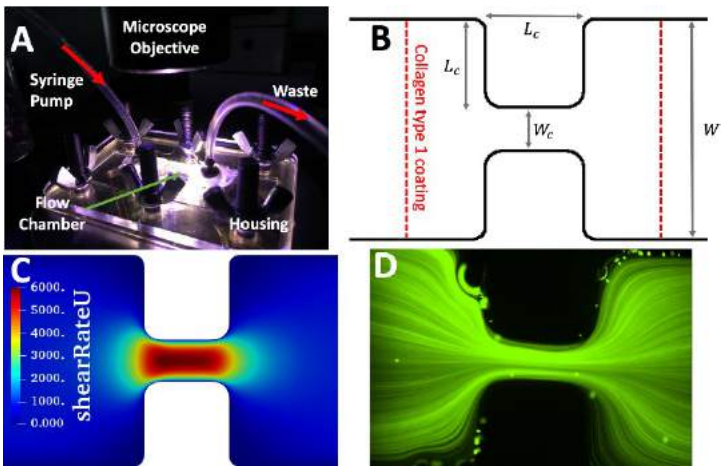


**Figure 1: A) Microfluidic experiment set up. B) Top view of chamber at constriction with dimensions ($W = 540\mu m, W_c = 140\mu m$ and $L_c = 200\mu m$) the depth is 180 µm. C) Shear rate field ($s^{-1}$.) D) Flow path lines visualized with fluorescent microspheres.**

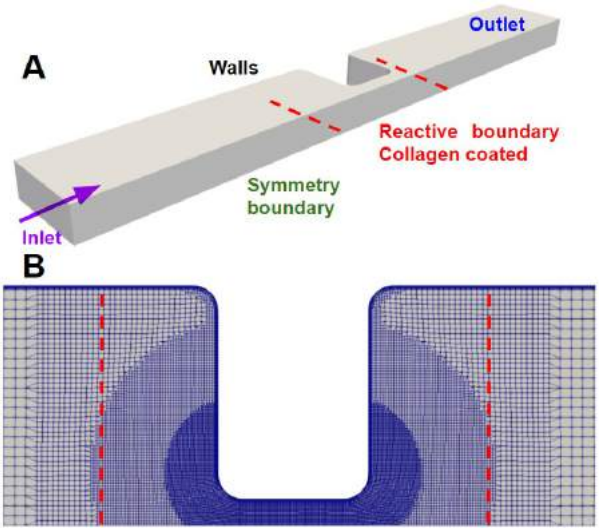


**Figure 2: A) Computational domain considered in the simulation. B) Mesh refinement near the constriction; red dashed lines indicate the regions where the reactive boundary conditions were applied (platelet deposition flux due to collagen.)**

## RESULTS

In both experiments and simulation, thrombus formed preferentially within the constriction of the channel, initiating along the lateral wall edges of the channel, growing towards the center of the constriction, and propagating downstream. (See Fig. 3.) In the experiment, embolization impeded occlusion of the channel, and large aggregates were observed downstream of the constriction. The location of the thrombus experimentally was somewhat variable, sometimes in the leading edge of the constriction and some others in the downstream edge; in contrast in the deterministic simulation, wherein the thrombus always forms in the downstream edge of the constriction. Figure 4, which presents the time course of the percent occlusion over 10 minutes, illustrates overprediction of the rate of occlusion by the numerical model, although the general trend was well captured with similar lag times and sigmoidal growth rate.

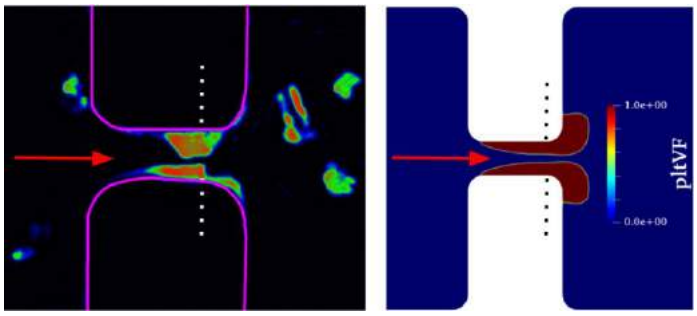


Experiment Thrombosis Simulation

**Figure 3: Thrombus formation for citrated human blood at 480s. Left: representative experimental result (colored by intensity.) Right: simulated platelet volume fraction.**

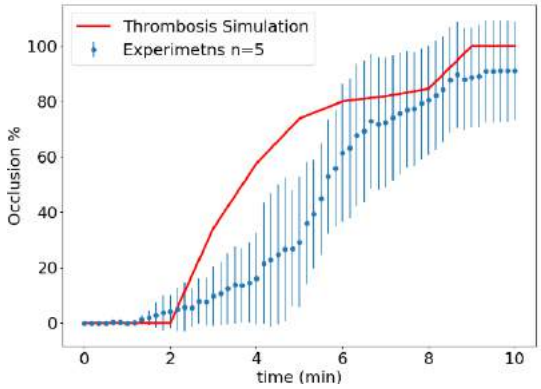


**Figure 4: Thrombus occlusion percentace evolution in time computed at the middel plane along the white and black dotted lines of Fig 3 for experiments n=5.**

## DISCUSSION

The current study presents both numerical and experimental results of thrombus formation under high shear rate conditions within a microfluidic constriction. The thrombosis model considers a mechanistic description of platelet aggregation and vWF activity. The model predicted reasonably well the thrombus formation at the constriction and the occlusion dynamics. The main limitation of the model was the omission of thrombus fracture and embolization. The present model represents embolization through a constant "shear cleaning" term as a function of the local shear rate, therefore does not capture the sudden and prevalent embolization of large platelet aggregates. Ongoing development of the model is incorporating fibrin production, which is important in capture of red blood cells – which may contribute significantly to the volumetric growth of a thrombus.

## ACKNOWLEDGEMENTS

This research was supported by NIH R01 HL089456 and NIH R01 HL086918.

## REFERENCES

[1] Wendelboe and Raskob G E, Circulation Research, 18: 1340-1347, 2016.
[2] Jaffer, I and Weitz, J I, Acta Biomaterialia, 94:2-10, 2019.
[3] Fogelson, A L and Neeves, K B, Annual Review of Fluid Mechanics, 47:377-403 2015.
[4] Schoeman, R M et al., Cellular and Molecular Bioengineering, 10:3-15, 2017.
[5] Wu, W et al., Scientific Reports 2017.
[6] Zhussupbekov, M, et al., Annals of Biomedical Engineering, 49: 2646-2658, 2021.

SB³C2022
Summer Biomechanics, Bioengineering and Biotransport Conference
June 20-23, Eastern Shore, MD, USA

# EVALUATION OF TACHYCARDIA PACING THERAPY RESPONSE IN A WHOLE HEART HFpEF MODEL: THERAPY DESIGN IMPLICATIONS

**Kevin L. Sack (1), Joshua Blauer (1), Richard Cornelussen (2), Troy Jackson (1)**

(1) Cardiac Rhythm Management, Medtronic, Mounds View, Minnesota, USA
(2) EMEA CS&T Therapy Innovation, Bakken Research institute, Medtronic, Netherlands

## INTRODUCTION

Heart failure with preserved ejection fraction (HFpEF), which affects over half of the patients diagnosed with heart failure [1], is a vast, underserved patient population. While pharmacological therapies are marginally useful, there is no approved therapy to lower cardiovascular morbidity and mortality. Tachycardia induced remodeling is a new therapy concept whereby high-rate pacing delivered by a dual-chamber pacemaker would promote remodeling and subsequent normalization of the diastolic failing heart. In recent preclinical studies, moderate to high increased heart rates (to 125/min and 175/min) could be used to increase left ventricular (LV) volumes and lower mass-to-volume ratios in concentrically hypertrophied LVs without reducing the EF [2]. This change in LV structure is reversible, can be titrated, and is not associated with HF. To burn down risk and identify optimal therapeutic protocols, finite element computer modeling was employed to simulate the effects of high pacing rates in virtual hearts and under a wide range of applicable conditions.

## METHODS

**Geometry:** CT scan data of a human subject were imported and processed in Simpleware ScanIP (Synopsys, Mountain View, USA). Detailed geometric segmentations of the atria and the ventricles at end diastole were created and meshed into 10-node tetrahedral elements.

**Myofiber orientation:** Myofiber orientation in the ventricular structure has been well described in the literature [3]. Accordingly, we assumed that the ventricular myofiber orientation could be represented through a linearly varying helix angle from −60° on the epicardium to +60° on the endocardium. Myofiber orientations of papillary structures and the extending pulmonary trunk were assigned manually to run parallel and circumferential to anatomical structures respectively. Myofiber orientations in the atria are characterized by overlapping, joining and separating fiber bundles that are critical for both electrical and mechanical function [4]. Accordingly, we assigned atrial myofibers aligned circumferentially with the native orifices and atrioventricular valve annuli. Distinct fiber bundles representing Bachman's bundle, pectinate muscle and atrial free wall were prescribed following the morphology of atrial anatomy.

**Constitutive properties:** The passive material response for myocardium is governed by an anisotropic hyperelastic description [5]. Contractile function is coupled to the solution of simulated electrophysiological activation, which is initiated when the calcium transients exceed a resting threshold. Active tension development following initiation is governed by a time varying elastance law [6].

**Excitation contraction coupling:** The electrical activation of the heart was simulated using CARPentry electrophysiology simulation software. The geometry was refined to a tetrahedral mesh with approximately 400 μm edge length resolution. The cardiac activation was simulated in a pseudo-bidomain mode for atrial and ventricular [7] cell models. The calcium transients for 4 consecutive cycles of activation at rates between 77-150 BPM were exported from the cell models to drive the timing of atria and ventricular contraction which was simulated in ABAQUS (Dassault Systèmes Simulia Corp, Providence, USA.)

**Circulatory system**: Our electromechanical four-chamber heart is coupled to a closed loop circulatory model adapted from simple lumped parameter representations of the cardiovascular system [8]. Unidirectional fluid exchange, driven by pressure difference between two connected chambers, allow for a meaningful representation of the entire circulatory system and the cyclic performance of a beating heart. To simulate natural baroreflex response of the systemic arteries, systemic vascular resistance was adjusted (i.e., resistance reduced with increasing rate to allow more flow in the system). This was done under the assumption that the mean arterial pressure (MAP) was maintained within 5% of values at baseline.

**Disease state modeling**: Severity of pathophysiology was simulated by adjusting myocardial constitutive properties and

circulatory parameters to produce graded deterioration of cardiac function representative of HFpEF. Ventricular myocardial stiffness was scaled linearly by a factor of 1.5, 2.0, 2.5 and 3.0 in HFpEF prototypes HF25, HF50, HF75 and HF100 respectively [9]. Lusitropic impairment, the inability of the myocardium to adjust contraction and relaxation with rate effects [9], is also considered by slowing the rate of active tension development and lengthening the relaxation of contractile function. Global contractility appears normal in HFpEF patients due to remodeling. When contractile properties are normalized by wall thickness [10] the contractile capacity (per unit volume) is diminished. To reflect this, all HFpEF prototypes have a peak contractile capacity set at 80% of normal. Normal physiological response to rate includes increased contractility (often referred to as "functional reserve"), which HFpEF patients lack to varying degrees. In HFpEF prototypes this reserve was diminished by degree of pathology (see **Table 1**). A prominent symptom of HFpEF is elevated left-sided pressure and pulmonary congestion. To simulate this, the circulatory parameters for the pulmonary circuit were raised to a higher-pressure state as part of new "pathological" initial conditions which creates higher LV preload, resulting in increased mean left atrial pressure (mLAP) and the LV end diastolic pressure (EDP) [11]. (see **Table 1**). The clear majority of HFpEF patients present with hypertension [11]. To represent this, elevated mean arterial pressure (MAP) was included to elevated degrees in the HFpEF prototypes by severity of pathology.

**Table 1: Summary of disease state modeling in the HFpEF prototypes compared with normal cardiac properties.**

| HF prototype | Normal | HF25 | HF50 | HF75 | HF100 |
|---|---|---|---|---|---|
| Myocardial stiffness | baseline | 150% | 200% | 250% | 300% |
| Peak tension capacity (kPa) | baseline | 80% | 80% | 80% | 80% |
| Lusitropic capacity | baseline | 79% | 53% | 26% | 0% |
| Contractility reserve | baseline | 75% | 50% | 25% | 0% |
| LV EDP (mmHg) | 9.3 | 17.3 | 21.7 | 27.5 | 30.7 |
| mLAP (mmHg) | 6 | 12 | 16 | 22 | 27 |
| MAP (mmHg) | 93 | 93 | 96 | 99 | 103 |

**Modeling scenarios:** Each patient prototype simulation was explored over a range of heart rates and atrioventricular intervals:

- Heart Rate (bpm) – 77, 90, 100, 110, 120, 130, 140, 150
- AV Interval (ms) – 80, 100, 120, 140, 160, 200 (over a reduced range of HRs: 77, 100, 110, 120 and 130)

The combination of 77 bpm and 120ms is considered the baseline (default) state of the patient.

## RESULTS

Over the full set of scenarios, the reduction of LV end diastolic pressure with increased heart rate was observed regardless of the AV delay. All HFpEF prototypes had significant unloading of the LV with increases in rate, with 130bpm being a general inflection point of diminishing unloading at higher rates. This achieved ~ 30% decrease in LV end diastolic pressure suggests that if unloading helps with remodeling, it can be established, at least acutely in all patient prototypes. Analysis of chamber wall stress also showed general improvements relative to the 77bpm baseline with increased rate in all prototypes. Maximum stress reduction of ~50% was achieved in some prototypes due to increased rates (22.0 vs 10.5 kPa, from 77 to 130bpm). However, with more severe pathology, adverse or undesirable wall stress results emerged as AV intervals extended to 160ms and beyond (see **Figure 1**).

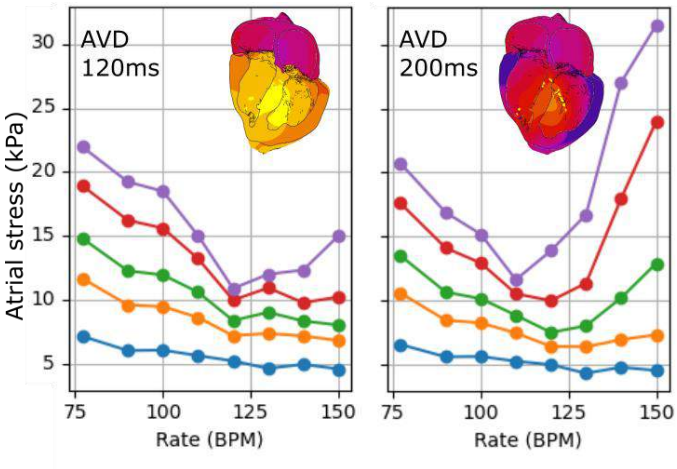


**Figure 1: Effects of rate and AV interval on LA stress at peak atrial activation. Colors of data represent the different patient prototypes of increasing severity: Normal, HF25, HF50, HF75, HF100. Colors across full heart model insert represent calcium transient concentration from high to low, illustrating AV delay.**

## DISCUSSION

Computational modeling of the interactions of rate and atrioventricular delay has provided mechanistic insight into the emerging therapy of high-rate induced remodeling. While there are unanswerable questions around tachycardia remodeling due to the lack of definitive concepts on the drivers of remodeling, the modeling effort has allowed us to systematically examine the therapy space. A key discovery was that AV delay could reduce and even reverse the positive effects of rate unloading (see **Figure 1**). Consequently, dual-chamber pacing modes with careful selection of AV interval may be needed to ensure patient safety and efficacy of future trial designs. These insights would otherwise have been impractical to obtain through clinical means, costing >$2M, spanning multiple years and with vastly limited operating procedures.

## ACKNOWLEDGEMENTS

Authors would like to acknowledge Joost Lumens and Tim van Loon for discussions on the subject.

## REFERENCES

[1] B. A. Borlaug, Nat. Rev. Cardiol., vol. 11, pp. 507–515, 2014.
[2] F. J. Klein, et al., Am. J. Physiol. - Heart. Circ. Physiol., vol. 311, pp. H1031–H1039, 2016.
[3] D. D. Streeter, et al., Circ. Res., vol. 24, pp. 339–347, 1969.
[4] J. Zhao, et al., Circ. Arrhythmia Electrophysiol., vol. 5, pp. 361–370, 2012.
[5] G. A. Holzapfel and R. W. Ogden, Philos. Trans. R. Soc. A Math. Phys. Eng. Sci., vol. 367, pp. 3445–3475, 2009.
[6] J. C. Walker, et al., Am. J. Physiol. - Heart. Circ. Physiol., vol. 289, pp. H692-H700, 2005.
[7] K. H. W. J. Ten Tusscher, et al., Am. J. Physiol. - Heart. Circ. Physiol., vol. 286, pp. H1573-H1589, 2004.
[8] K. L. Sack, et al., Front. Physiol., vol. 9, pp. 539, 2018.
[9] R. Wachter, et al., Eur. Heart J., vol. 30, pp. 3027–3036, 2009.
[10] B. A. Borlaug, et al., J. Am. Coll. Cardiol., vol. 54, pp. 410–418, 2009.
[11] M. R. Zile, et al., Circulation, vol. 124, pp. 2491–2501, 2011.

SB³C2022
Summer Biomechanics, Bioengineering and Biotransport Conference
June 20-23, Eastern Shore, MD, USA

# DENOISING AND SUPER-RESOLVING 4D FLOW MRI USING PHYSICS-GUIDED NEURAL NETWORKS

**Neal M. Patel (1), Emily R. Bartusiak (2), Hemanth Devarapalli (3), Sean Rothenberger (1), Amy J. Schwichtenberg (4), Edward J. Delp (1,2,5), Vitaliy L. Rayz (1)**

(1) Biomedical Engineering, Purdue University, West Lafayette, IN, USA
(2) Electrical and Computer Engineering, Purdue University, West Lafayette, IN, USA
(3) Mechanical Engineering, Purdue University, West Lafayette, IN, USA
(4) Health and Human Sciences, Purdue University, West Lafayette, IN, USA
(5) Psychological Sciences, Purdue University, West Lafayette, IN, USA

## INTRODUCTION

Patient-specific computational fluid dynamic (CFD) models have enabled a greater understanding of the role of fluid mechanics in various systems' physiology and pathophysiology. However, these models are limited by the segmentation of the patient geometries and the prescribed boundary conditions [1]. Time resolved 3D phase-contrast MRI (4D Flow MRI) can address these limitations by providing *in vivo* measurements of biofluid flow non-invasively [2]. While 4D Flow MRI has been applied to a range of vascular territories, recent work has extended its application to cerebrospinal fluid (CSF) flow in study patients with normal pressure hydrocephalus [3].

While 4D Flow MRI provides *in vivo* measurements of flow, there exist tradeoffs between acquisition time, resolution, field of view, and velocity-to-noise ratio. Given that CSF flow is slow moving and traverses through narrow passageways, *e.g.,* the cerebral aqueduct, the application of 4D Flow MRI can result in particularly noisy measurements. This high noise complicates deriving reliable flow metrics such as wall sheer stress (WSS) that rely on near-wall velocity gradients and may be related to pathologies in the cerebrospinal fluid systems.

Recently, Ferdian *et al.* proposed using convolutional neural networks for super-resolution and denoising of 4D Flow MRI data within aortic geometries [4]. This network uses a gradient-based loss constraint and a mean square error loss. Additionally, Rutkowski *et al.* proposed using convolutional neural networks for denoising 4D Flow MRI in cerebral aneurysms using a traditional mean square error loss function [5]. We extend on this work by (1) adapting a densely connected super-resolution network (DCSRN) architecture previously utilized for denoising MRI [6] to 4D Flow MRI data and (2) utilizing a divergence-based regularization constraint.

## METHODS

Herein, we assess the ability of a physics-guided neural network (PGNN) to super-resolve and denoise synthetically generated 4D Flow MRI within a stenotic pipe geometry. The velocity field in the stenotic pipe was simulated with an opensource software SimVascular [7]. Four simulations were run: (1) physiological pulse wave inflow with a peak Reynolds number ($Re_{peak}$) of 250, (2) physiological pulse wave inflow with $Re_{peak}$ equal to 500, (3) sinusoidal pulse wave inflow with $Re_{peak}$ equal to 250, and (4) sinusoidal pulse wave inflow with $Re_{peak}$ equal to 500. Each inflow condition had a period of one second and all simulations were run for four seconds with data from 1.0 – 4.0 seconds being utilized.

The velocity distributions computed in the four simulations were interpolated onto a high-resolution grid with isotropic voxels of 0.5 mm to serve as the network target data. To obtain synthetic 4D Flow MRI measurements, these data were converted to a complex MRI signal which was downsampled in space and time by a factor of 2 and 3 respectively. Gaussian noise of 10% and 20% was also added to the signal. The resulting synthetic MRI signal was then transformed back into a low-resolution velocity field with an isotropic voxel size of 1 mm. This created a total of eight full geometry paired high-resolution low-resolution datasets with 20 timesteps for each case. Each of the eight paired datasets was sub-divided into 72 patches to decompose the dominant flow features into smaller-scale flow features that may be conserved across varying geometries. The entire dataset included 11,520 patches. The dataset was split using a 6:1:1 ratio for training, testing, and validation. The physiological pulse wave inflow condition with a $Re_{peak}$ of 500 at 10% and 20% noise levels was reserved for testing and validation.

The neural network architecture, shown in Figure 1, is based on the DCSRN network architecture that was previously used for denoising MRI data [6]. The network was trained using the traditional mean square error loss function and a divergence regularization term. Pytorch was

used for implementation [8]. The Adam optimizer was used for training [9].

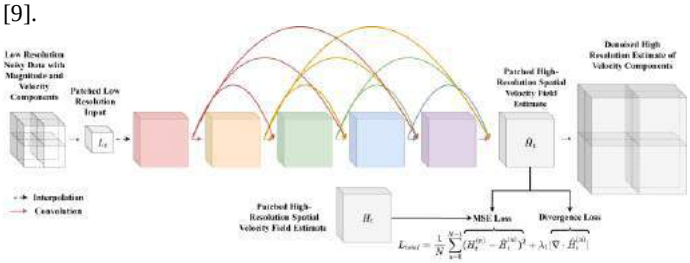


**Figure 1: Physics-guided neural network (PGNN) utilizing patching and a divergence-based regularization term.**

## RESULTS

For validation, we assessed the trained network's performance in the case of flow through a stenotic pipe with a physiological pulse wave resulting in a peak Reynolds number of 500. The synthetic 4D Flow MRI data with 10% noise and 20% noise was the input for the trained model. We observed a temporally averaged mean square error of 1e-4 between our network's reconstruction of the high-resolution velocity field and the high-resolution structured CFD data. Qualitative results are shown below in Figure 2 and illustrate the network's ability to resolve flow recirculation and near-wall velocities.

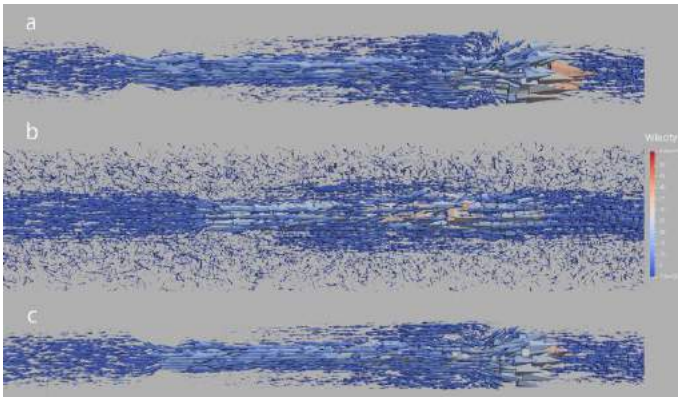


**Figure 2: PGNN shows the ability to denoise and super-resolve synthetic 4D Flow MRI. (a) High-resolution target data derived from CFD simulations, (b) synthetic 4D Flow MRI downsampled in time and space with 10% added noise, and (c) network estimation of the high-resolution, denoised velocity field.**

Upon examining the reduction of the mean square error and divergence error, we observed temporally dependent characteristics of the error terms. Figure 3 demonstrates the cumulative dimensionless divergence error increases as diastole progresses.

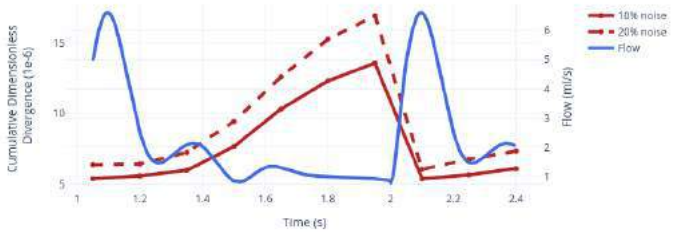


**Figure 3: Temporally dependent cumulative dimensionless divergence error with 10% added noise (solid red) and 20% added noise (dashed red) with the superimposed pulse wave (blue).**

## DISCUSSION

These preliminary results indicate that our physics-guided neural network can denoise and estimate the high-resolution velocity field for stenotic pipe flow. By using a divergence-based metric as a regularization term, the mass conservation of the flow is enforced, which aids in generating more physically consistent results. This will enable more reliable derivation of flow metrics including WSS. Interestingly, we observe a temporally dependent divergence and mean square error profile, which is in accordance with observations by Ferdian *et al.* [4]. Utilizing temporal dependence of the flow may enable greater performance and will be the focus of future work. Additionally, a dataset of CSF flow within varying cerebral ventricle geometries will be created and paired synthetic 4D Flow MRI with varying noise levels will be generated as performed in the current work. Once trained on CSF flow within the cerebral ventricles, we will apply this network to in-vivo and in-vitro 4D Flow MRI cases.


## ACKNOWLEDGEMENTS

Purdue Institute of Integrative Neuroscience, Grand Challenges in Neuroscience Grant (PI: Schwichtenberg).


## REFERENCES


[1] D. A. Steinman and V. M. Pereira, "How patient specific are patient-specific computational models of cerebral aneurysms? An overview of sources of error and variability," *Neurosurg Focus*, vol. 47, no. 1, p. E14, Jul 1 2019, doi: 10.3171/2019.4.FOCUS19123.

[2] G. Soulat, P. McCarthy, and M. Markl, "4D Flow with MRI," *Annu Rev Biomed Eng*, vol. 22, pp. 103-126, Jun 4 2020, doi: 10.1146/annurev-bioeng-100219-110055.

[3] S. Yamada *et al.*, "Cerebrospinal fluid dynamics in idiopathic normal pressure hydrocephalus on four-dimensional flow imaging," *Eur Radiol*, vol. 30, no. 8, pp. 4454-4465, Aug 2020, doi: 10.1007/s00330-020-06825-6.

[4] E. Ferdian *et al.*, "4DFlowNet: Super-Resolution 4D Flow MRI Using Deep Learning and Computational Fluid Dynamics," *Frontiers in Physics*, vol. 8, 2020, doi: 10.3389/fphy.2020.00138.

[5] D. R. Rutkowski, A. Roldan-Alzate, and K. M. Johnson, "Enhancement of cerebrovascular 4D flow MRI velocity fields using machine learning and computational fluid dynamics simulation data," *Sci Rep*, vol. 11, no. 1, p. 10240, May 13 2021, doi: 10.1038/s41598-021-89636-z.

[6] Y. Chen, Y. Xie, Z. Zhou, F. Shi, A. G. Christodoulou, and D. Li, "Brain MRI super resolution using 3D deep densely connected neural networks," in *2018 IEEE 15th International Symposium on Biomedical Imaging (ISBI 2018)*, 2018-04-01 2018: IEEE, doi: 10.1109/isbi.2018.8363679.

[7] A. Updegrove, N. M. Wilson, J. Merkow, H. Lan, A. L. Marsden, and S. C. Shadden, "SimVascular: An Open Source Pipeline for Cardiovascular Simulation," *Annals of Biomedical Engineering*, vol. 45, no. 3, pp. 525-541, 2017-03-01 2017, doi: 10.1007/s10439-016-1762-8.

[8] A. Paszke *et al.*, "PyTorch: An Imperative Style, High-Performance Deep Learning Library," 2019-12-03T22:06:05 2019.

[9] D. P. Kingma and J. Ba, "Adam: A Method for Stochastic Optimization," 2017-01-30T01:27:54 2017.

# PCR-BASED APPROACH TO MEASURE INTRAVASATION AND METASTASIS OF MOUSE CANCER CELLS IN THE CHICK CHORIOALLANTOIC MEMBRANE ASSAY

**Molly C. Brennan (1), Susan E. Leggett (1), Celeste M. Nelson (1,2)**

(1) Department of Chemical and Biological Engineering, Princeton University, Princeton, NJ, USA
(2) Department of Molecular Biology, Princeton University, Princeton, NJ, USA

## INTRODUCTION

Metastasis is responsible for the majority of cancer-related deaths. Understanding the risk of metastasis is necessary when determining a patient's prognosis and deciding upon the appropriate treatment. Animal models are often used to study the metastatic cascade. Tumor formation, intravasation, and metastasis can be studied in the chick chorioallantoic membrane (CAM) assay. When compared to other animal models, the CAM assay has several advantages, including the brevity of the assay and natural immunodeficiency in chick embryos. To measure intravasation, low numbers of cancer cells must be detected in samples from the lower CAM and various organs. Previously, PCR-based approaches using primers that bind to Alu repeat sequences have been used to amplify human DNA and detect human cancer cells in the CAM assay (*1*). However, many mouse cell lines are used in cancer research and, as Alu sequences are not present in the mouse genome, another method was needed to detect mouse cancer cells. Using primers that bind to B1 repeat sequences found in the mouse genome, we developed a quantitative PCR-based approach to measure intravasation and metastasis of mouse cancer cells in the CAM assay. As an application of this method, we are investigating the relative intravasation and metastasis of epithelial-like and mesenchymal-like populations derived from a mouse cancer cell line.

## METHODS

We performed PCR with primers that bind to the B1 repeat sequences in the mouse genome (*2, 3*) to detect 4T1 triple-negative mouse breast cancer cells in the CAM assay. A window was created above the upper CAM on embryonic day 3. On embryonic day 9, the mouse cancer cells were xenografted onto the upper CAM. On embryonic day 18, the embryo was sacrificed, and the tumors formed on the upper CAM were imaged. The areas of the tumors on the upper CAM were measured to determine tumor burden. A sample from the highly vascularized lower CAM was extracted and used to measure intravasation. Samples from the liver and lung were extracted to measure metastasis (**Figure 1**). Genomic DNA was isolated from the samples and processed for PCR.

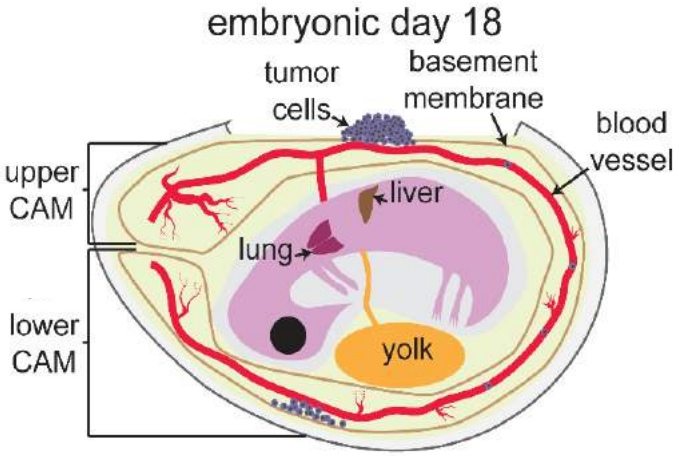


**Figure 1: Schematic of the chick CAM assay.**

## RESULTS

Using quantitative PCR, we were able to detect mouse cancer cells in samples from the lower CAM, liver, and lung. Primers bound to B1 repeat sequences in the mouse genome and amplified mouse DNA in the samples. The B1 repeat threshold cycle for each sample was then compared to a standard curve relating B1 repeat threshold cycles to the number of mouse cells per nanogram of DNA. The number of mouse cells per nanogram of DNA was used as a measure of relative intravasation and metastasis.

We have begun to investigate intravasation and metastasis by epithelial-like clonal populations, mesenchymal-like clonal populations, and mixes of clonal populations of 4T1 mouse breast cancer cells. Epithelial-like clonal populations (E1 and E2) and mesenchymal-like populations (A and M) were derived from single cells in the parental 4T1 cell population. The expression of E-cadherin and vimentin by these populations was measured to verify their phenotypes as epithelial-like and mesenchymal-like. Homogeneous clonal populations and a 1:1:1:1 mix of the populations were xenografted onto the chick embryo and samples were extracted on embryonic day 18 to measure relative intravasation and metastasis. All populations formed tumors on the upper CAM, and cancer cells from several populations could be detected in the lower CAM, liver, and lung. Relative metastasis was measured as the number of 4T1 mouse cancer cells detected per nanogram of DNA from the liver and lung (**Figure 2**).

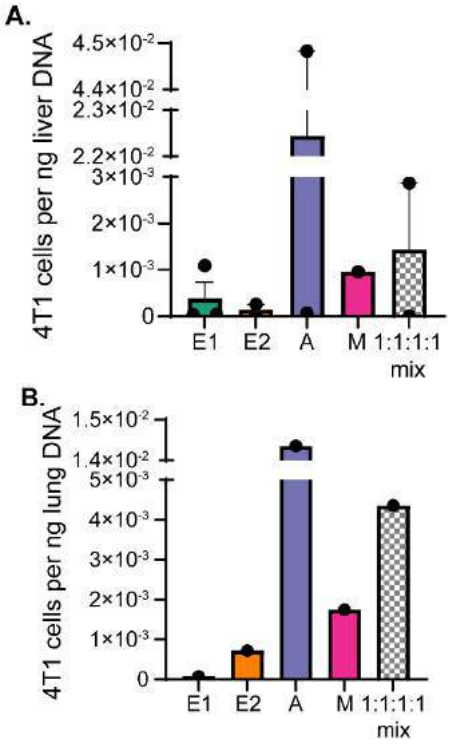


## DISCUSSION

Using quantitative PCR, we established a method that permits the use of mouse cancer cells in the CAM assay. Using primers that bind to B1 repeat sequences, the amplification of mouse DNA allows for the detection of low numbers of cancer cells in a sample. Mouse DNA detected in samples from the lower CAM is used to measure intravasation, while that from the liver and lung is used to measure metastasis.

This quantitative PCR-based method enables the use of the CAM assay to investigate metastasis of mouse cancer cells. For example, the relative intravasation and metastasis of epithelial-like, mesenchymal-like, and heterogeneous mixtures of mouse cell lines can be examined in this model. We have used this approach to investigate potential differences in intravasation and metastasis as a function of epithelial/mesenchymal phenotype. Overall, the quantitative PCR-based method enables researchers to use any of the many common mouse cancer cell lines in this animal model to study metastasis.


## ACKNOWLEDGEMENTS

This work was supported in part by grants from the National Institutes of Health (CA187692, CA214292) and a Faculty Scholars Award from the Howard Hughes Medical Institute. MCB was supported by a predoctoral fellowship from the New Jersey Commission on Cancer Research. SEL was supported by the New Jersey Alliance for Clinical Translational Science postdoctoral fellowship (NIH award: TR003019).


## REFERENCES


1. Kim, J. et al., *Cell*, **94**, 353-362, 1998.
2. Zhang, H. et al., *International Journal of Radiation Oncology, Biology, Physics*, **74**, 1592-1599, 2009.
3. Krayev, A. S. et al., *Nucleic Acids Research*, **10**, 7461-7475, 1982.

# RADIOFREQUENCY ABLATION OF THE MEDIAL NERVE FOR FACET JOINT PAIN ALTERS THE BIOMECHANICS OF THE SPINE - A COMPUTATIONAL STUDY

**Faris A. Almalki (1,2), Daniel H. Cortes (2)**

(1) Mechanical Engineering Department, University of Jeddah, Jeddah, Saudi Arabia
(2) Mechanical Engineering Department, Penn State University, State College, PA, USA

## INTRODUCTION

Lower back pain affects the lives of an increasing number of individuals, deteriorates their movement and lifestyle, and hinders their capability of performing daily-life tasks. Back pain is related to facet joint in approximately 31% of the cases [1]. The first line of treatment for facet joint pain is physical therapy. However, if physical therapy is not effective, radiofrequency ablation (RFA) of medial nerve is prescribed. Although RFA provides pain relief to the patients, it also denervates the multifidus muscle (MF). The multifidus is one of the most essential muscles for the stability of the lumbar spine [2]. By activating psoas major (agonist) and multifidus muscles (antagonist), stability is increased in lateral bending and torsion [3]. Multifidus contraction also influences intradiscal pressure in the lumbar joints [4]. Therefore, denervation of multifidus after RFA may affect the biomechanics of the spine. In fact, an increase in degeneration of the intervertebral disc has been reported after RFA [5]. However, the changes in spine biomechanics after RFA are not well known. The objective of this study is to quantify changes in joint angle and loading of the intervertebral disc after RFA of the medial nerve using computer simulations. We hypothesize that RFA ablation of the medial nerve affects the loading of the intervertebral joint in the different directions of reaction forces and joint angles.

## METHODS

This study used the force-dependent kinematics (FDK) module of AnyBody Modelling Software (Version 7.3, AnyBody Technology A/S, Aalborg, Denmark) that have been previously validated in different conditions [6,7]. Intervertebral joint forces (mediolateral, proximodistal and anteroposterior) and angles in the lumbar spine were calculated for the following movements: 50º flexion, 20º lateral bending, and 20º torsion. The range of motion for those body movements were chosen to represent common daily activities [8]. Both unilateral (MF Red Unil) and bilateral ablations (MF Red BiL) were compared to intact multifidus muscles (MF ON). The reduction of force production of the multifidus fascicles after RFA was simulated by reducing the physiological cross-sectional area (pCSA) of the fascicles similar to other studies [9]. The spine levels analyzed in this study were the L3L4-L4L5-L5S1 joints. The reduced cross-sectional area (rCSA) for each fascicle of the multifidus was calculated as:

$$rCSA = (\#\ joints\ spanned - \#\ joints\ ablated) / (\#\ joints\ spanned) \times pCSA$$

where # *joints spanned* is number of intervertebral discs between the proximal and distal insertion point of the fascicle, and # *joints ablated* corresponds to the number joints ablated within the insertion points.

## RESULTS

Figure 1 shows the joint angle and forces for different motions and treatments. As the flexion angle of the torso increased, the difference in disc joint angle between MF ON and MF Red UniL, and MF ON MF Red BiL also increased. The maximum differences among the joint angles were seen in the L5S1 disc: 1.4º for unilateral, and 2.93º for bilateral ablation. A similar change in the disc lateral bending angle of the disc was observed during lateral bending of the torso, with maximum differences of 1.7º and 2.07º in the L5S1 joint for unilateral and bilateral ablations respectively. Meanwhile in torsion, the maximum differences in the disc torsion angle (0.35º for unilateral, and 0.74º for bilateral RFA) were found in L4L5 joint.

The proximodistal reaction forces differences in flexion were highest between MF ON and MF Red UniL and MF Red BiL in the L5S1 disc (33.12 N and 59.75 N respectively). The general trends for lateral bending reaction forces showed that the largest absolute maximum difference for mediolateral force was in L3L4 in both unilateral (28.71 N) and bilateral reduction of MF (27.99 N). Regarding torsion, the absolute maximum difference for mediolateral reaction

forces where highest in L4L5 in unilateral (11.1 N) and bilateral reductions (14.73 N). Meanwhile, L4L5 had the highest difference anteroposterior reaction forces unilaterally (14.26 N) and bilaterally (31.26 N).

## DISCUSSION

The simulations of spine deformations shown differences in joint angles and forces after RFA. Some differences are more pronounced in the case of bilateral RFA compared to unilateral. For instance, the increase in joint angle in flexion as it changes from MF ON to unilateral then to the maximum mean in bilateral ablation. In this motion, the action multifidus from both sides of the spine is cumulative. Therefore, larger differences can be expected for bilateral ablation. However, for other motions like lateral bending and torsion, the fascicles of the multifidus from both sides of the multifidus experience different activation and elongation. Therefore, the differences between unilateral and bilateral ablation are not as pronounced.

There was considerable angular difference in flexion between the angle of L5S1 with intact and with bilateral reduction (maximum difference= 2.93º). Also, in lateral bending of the L5S1 joint, the maximum difference between intact and bilaterally reduced MF was 2.07º. These changes in disc angle can be considered large relative to the normal values (up to 30%) and can have significant effects in the mechanobiology of the spine. An increase in angles during flexion with bilateral ablation can lead to larger deformations in the intervertebral disc, which can lead to altered cell behavior and structural damage. Therefore, these changes may lead to the increase in disc degeneration after RFA reported in a previous study [5].

The largest absolute difference in proximodistal joint forces for flexion in the L5S1 joint (59.75 N) is relatively small compared to the total value of the force (~1400 N). This is expected since the contribution of the force generated by the multifidus is relatively small compared to the force generated by other muscle like the erector spinae and the weight of the upper body. The changes in reaction forces in lateral bending and torsion are also small (10-20 N), but represent a large percentage of the normal force.

Modification of pCSA have been used by other studies to change the force production of the spine muscles. For example, a previous study altered the pCSA of deep muscles to change the maximum force. This study found that joint shear forces were decreased with the increase of maximum force of the muscles. [9] Another study used different pCSA values of the transversus abdominis muscle to study their strength. They found that, by altering PCSA, the spinal loading was detrimentally affected by changing the strength of this muscle. [10]

One of the limitations of this study is that the model was only for the spine, not including arms and lower limbs, to simplify FDK calculations. Another limitation is that model represents an average size male body. However, it is expected that similar results would be obtained for bodies with other anthropometric characteristics.

It can be concluded that modifying the MF muscle by RFA leads to changes in loading and angles of intervertebral joints, leading to more susceptibility to disc degeneration and facet joint pain. The findings from this research can help in treating facet joint pain which is caused by load alteration.

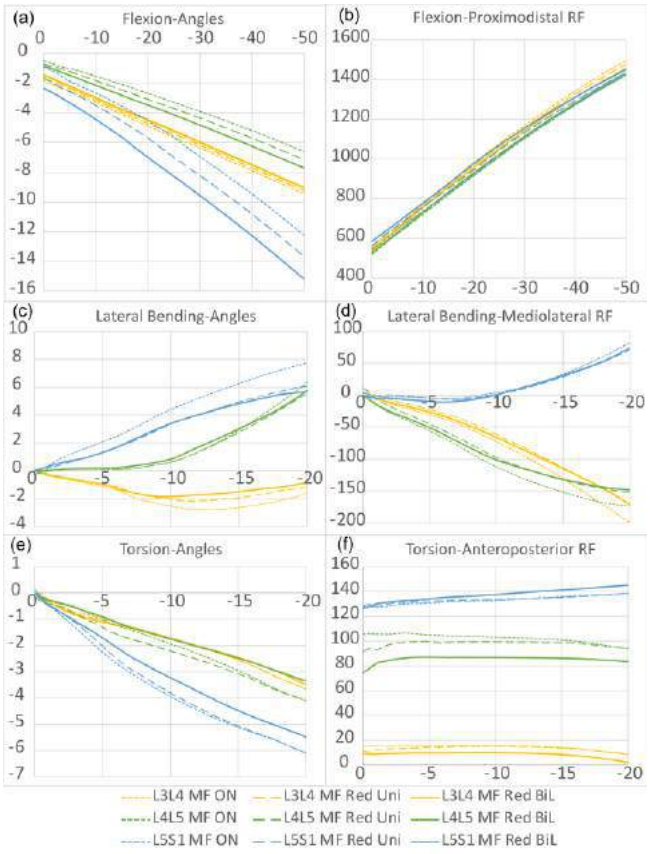


Figure 1. Joint angles in degrees in (a) flexion, (c) lateral bending, and (e) torsion. Joint reaction forces in Newtons for each degree of movement: (b) proximodistal reaction forces in flexion, (d) mediolateral reaction forces in lateral bending, and (f) anteroposterior reaction forces in torsion.


## ACKNOWLEDGEMENTS

This work is funded by the Saudi Cultural Mission, SACM and University of Jeddah, Jeddah, Kingdom of Saudi Arabia.


## REFERENCES


[1] Manchikanti L, et al., BMC Musculoskelet Disord, 28;5:15, 2004
[2] Wilke HJ, et al., *Spine*, 20(2): 192-198, 1995
[3] Quint U, et al., *Spine*. 15;23(18):1937-45, 1998
[4] Wilke HJ, et al., *J Biomech*, 29(4):549-55, 1996
[5] M. Smuck, et al., *Spine J.*, vol. 15, no. 6, pp. 1415–21, Jun. 2015.
[6] Damsgaard, M. et al., *Simulation Modelling Practice and Theory*, *14*(8), 1100-1111, 2006
[7] Bassani, T. et al., *Journal of biomechanics*, *58*, 89-96, 2017
[8] Ng, J. K, et al., *Spine*, *26*(1), 53-60. 2001
[9] Kim K, et al., *Proc Inst Mech Eng H*, 224(10):1165-74, 2010
[10] Nowakowska-Lipiec, K., et al., *Computer Methods in Biomechanics and Biomedical Engineering*, *23*(16), 1287-1296., 2020

# AI-ACCELERATED MULTISCALE MODELING FOR PLATELET ADHESION DYNAMICS AND MULTI-PLATELET AGGREGATION AT MILLISECOND AND MOLECULAR RESOLUTIONS

**Peineng Wang (1), Yicong Zhu (2), Jawaad Sheriff (1), Peng Zhang (2), Changnian Han (2), Yuefan Deng (2), Danny Bluestein (1)**

(1) Department of Biomedical Engineering
Stony Brook University
Stony Brook, New York, U.S.A.

(2) Department of Applied Mathematics and Statistics
Stony Brook University,
Stony Brook, New York, U.S.A.

## INTRODUCTION

Platelet adhesion to blood vessel walls and platelet-platelet aggregation in shear flow is essential in initiating the blood coagulation cascade and prompting clot formation in prosthetic cardiovascular devices and vascular disease processes. In adhesion and aggregation, which lead to thrombus formation, platelets undergo complex and rapid receptor-ligand binding such as GPIbα-von Willebrand factor (vWF) and αIIbβ3-Fg-αIIbβ3 bond association and breakage.

We have developed a combined Dissipative Particle Dynamics (DPD) - Coarse Grained Molecular Dynamics (CGMD) multiscale model (MSM) to continuously evolve platelet structures, to describe the platelet mechanotransduction process induced by blood flow and synergistically activate platelets, aggregate, and adhere to the blood vessel wall [1-2]. In addition to describing flipping and adhesion of a deformable platelet, we modeled a thrombus interacting with flowing platelets consisting of 250 platelets, the first of such effort to integrate multi-physics of thrombus formation at multi-scales [3].

Due to the vast spatial and temporal scales involved in this multi-component system, we developed a novel artificial intelligence (AI) inference algorithm that adaptively adjusts multiple timestep (MTS) sizes to underlying biophysical dynamics, with the overall modeling accuracy and speed are largely improved [4], achieving 500× speedup over fixed timestep sizes. To overcome a major challenge of analyzing flowing in vitro platelet images and generating accurate inputs for the MSM platelet simulations, we applied a semi-unsupervised learning system (SULS) [5], trained and fine-tuned with in vitro platelet morphological changes under flow shear. We describe the kinematics of platelet adhesion and thrombus formation, illustrate the implementation details of the AI-MTS algorithm, and summarize the biophysical insights our system provides.

## METHODS

Two simulation systems were used in this study. For platelet adhesion, we adapted our deformable CGMD multiscale platelet model to describe flipping over vWF in a channel with DPD particles at 30 dyne/cm$^2$ (Fig. 1A). The platelet's bilayer membrane has a total of 67,004 particles, with 16,751 particles designated as GPIbα receptors, with a particle density of 585/μm$^2$. The vWF, with 506/μm$^2$ density, is fixed on the blood vessel wall, binds to a platelet GPIbα receptor, and initiates platelet adhesion.

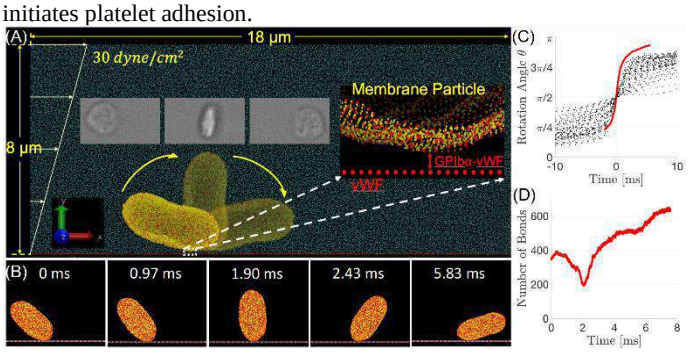


**Figure 1. (A) MSM platelet adhesion model. (B) Simulated platelet flipping. (C) Rotational angle of MSM platelet (red curve) and in vitro results (black dots) and (D) GPIb*α*-vWF bonds over time.**

Additionally, a large-scale multiscale system of a flow-mediated forming thrombus with 102 million particles, representing 70 flowing and 180 aggregating platelets under shear flow, was simulated and integrated with our AI-MSM framework (Fig. 2). A microchannel is simulated by a rectangular channel (302.3×21.3×19.9 μm), with periodic boundary conditions. Two thrombi are attached to the blood vessel wall, each consisting of 90 aggregated platelets and form a

stenosis of 14.3 μm in the microchannel. The blood vessel walls are modeled with a no-slip boundary conditions with a pressure-driven fully developed Poiseuille blood flow between the top and bottom plates.

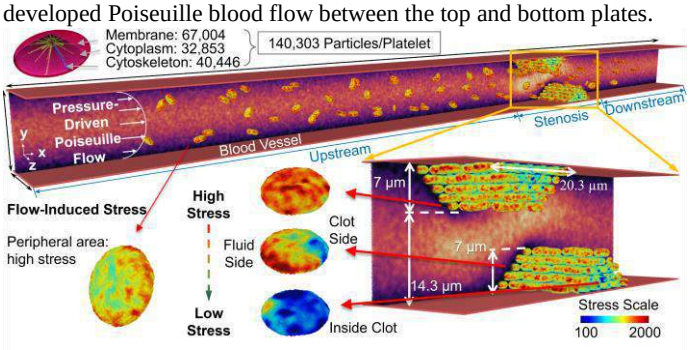


**Figure 2. Simulated thrombosis with 102,300,840 particles, involving 70 flowing platelets and 2 thrombi, each with 90 aggregated platelets.**

The force field between the platelet GPIbα receptor and the vWF ligand is described by a hybrid force field combing Morse and Hooke potentials:

$$E_{Adhesion} = E_{Morse} + E_{Hooke} \quad (1)$$

$$E_{Morse} = D_0\left(e^{-2\alpha(r_{ij}-r_0)} - 2e^{-\alpha(r_{ij}-r_0)}\right) \quad (2)$$

$$E_{Hooke} = k_1(r-r_b)^2 + k_2(r-r_b)^4 \quad (3)$$

The aggregation between receptors of the platelets is mediated by the membrane GPIIb-IIIa receptors and fibrinogen (Fg), governed by a force field [2]:

$$\boldsymbol{F}_{ij} = D_0\left(e^{-2\alpha(r_{ij}-r_0)} - 2e^{-\alpha(r_{ij}-r_0)}\right)\boldsymbol{e}_{ij} + f^A(t_{ij})\left(1-\frac{r_{ij}}{d_c}\right)\boldsymbol{e}_{ij} \quad (4)$$

The hybrid force field was parameterized, and the GPIbα receptor distribution was modified based on the curvature of the platelet, to reproduce flipping kinematics as the rotation angle $\theta$ during adhesion. We validated our numerical method by correlating simulations (Fig. 1B) and model predictions with in vitro results [6].

Our MTS algorithm splits the system into two subsystems based on the spatial scales of the underlying components [5]: the fluid at the macroscopic scale and the platelet at the microscopic scale. A three-level MTS time integrator is developed to handle the two subsystems and the interface using different timestep sizes. The characteristic $\Delta t_{\mathrm{f}}$ is employed to integrate the fluid subsystem aggressively, and a variable $\Delta t_{\mathrm{p}}$ attuning the dynamics is applied to the platelet subsystem for capturing molecular-level details while an intermediate $\Delta t_{\mathrm{m}}$, where $\Delta t_{\mathrm{f}} > \Delta t_{\mathrm{m}} \geq \Delta t_{\mathrm{p}}$, handles the fluid-platelet interface bridging the energy exchange. By collecting the multiple time series properties which describe the platelet dynamics, we were able to predict the adaptive timestep sizes and number of jumps by a deep learning framework consisting of (a) a 2-stage denoising by moving average and wavelet transform filters to cleanse high-frequency noise in raw data and (b) two RNN-based autoencoders to extract latent features.

## RESULTS

Our multiscale model successfully described the biophysical properties for platelet adhesion and thrombus down to *nm*-length and *ps*-time scales.

The progression of the simulated flipping angle $\theta$ during platelet adhesion follows the in vitro observations well, with slightly higher peak flipping speed – as compared with the ML-guided in-vitro analysis of the flipping (Fig. 1C). The model further distinguishes between the distinct lift-off and reattachment periods of the flipping. GPIbα-vWF bond number is variable during the flipping, ranging from 200 to 650 (Fig. 1D). The total GPIbα-vWF bonds force, ranging from 1 to 1.5 nN, primarily acts in the y-direction, and is positively correlated with the number of bonds. Ongoing simulations and in vitro experiments will expand our predictive capability over the 15-45 dyne/cm$^2$ range.

In the thrombus formation system, the position of individual platelets impacts the accumulation of flow-induced stresses: the closer to the blood vessels, the larger stress accumulation as expected (Fig. 2). The periphery zone of the platelets (red) experiences larger stresses than its central area (green/blue). Platelets that have aggregated have relatively larger stresses than those of flowing platelets. For the two thrombi, surface platelets exposed to flow experienced larger stresses than those at the core layers of the thrombus (Fig. 2). Fluid particles approaching the stenotic section strongly accelerated downward, the redirected upwards after passing the first thrombus, slowing down downstream of the stenotic section (Fig. 3). Shear stresses of blood flowing in this system corresponded to its velocity profile, where high shear stress was observed near the blood vessel wall and declined gradually in the center of the microchannel, with the highest stresses generally observed upstream of the thrombi.

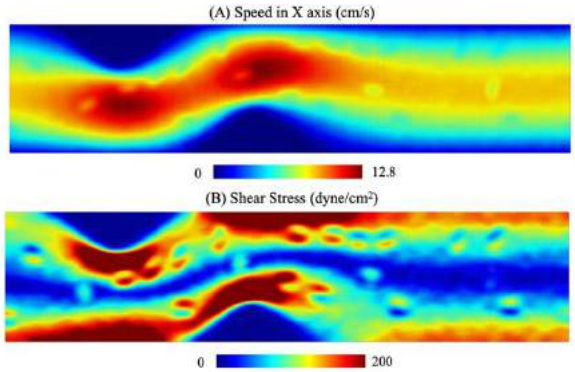


**Figure 3. (A) Flow speeds and (B) shear stress through the stenosis.**

## DISCUSSION

We simulated the adhesion process of a flowing marginated platelets in a flow channel, where our results converging towards high-fidelity prediction of flipping dynamics. We modeled a multi-physics MSM of flow- and platelet-mediated thrombus formation involving 102 million particles and integrated an AI-MTS algorithm for splitting the system and adapting timestep sizes to varying dynamics. This MSM approach enables computationally affordable, highly resolved, and validated granular studies of flow dynamics in stenoses, accumulated stress-induced platelet activation, platelet adhesion to vWF-coated vessels, and recruitment aggregation of flowing platelets with activated platelets adhered to the vessel walls. Nanoscale-level depictions of the biophysical properties of deformable platelets allows mapping of hemodynamic stresses on membrane and intra-platelet components. This approach will be expanded to simulate thrombosis processes involving several hundred platelets under pathological flow conditions.

## ACKNOWLEDGEMENTS

This project was supported by the NHLBI (5U01HL131052, DB) and the SUNY-IBM Consortium (FP00006445, YD), and computational resources on the AiMOS supercomputer.

## REFERENCES

[1] Zhang, P. et al., *J Biomech*, 50: 26-33, 2017.
[2] Gupta, P. et al., *Cell Mol Bioeng*, 12: 327-343, 2019.
[3] Zhu, Y. et al. in B.L. Chamberlain et al. (Eds.), *ISC High Performance 2021*, LNCS 12728: 237-254, 2021.
[4] Han, C. et al., *J Comput Phys*, 427: 110053, 2021.
[5] Zhang, Z. et al., *Comput Med Imaging Graph*, 89: 101895, 2021.
[6] Sheriff, J. et al. *Ann Biomed Eng*, 49: 3452-3464, 2021.

# SUBJETS WITH CAROTID WEBS EXHIBIT DIFFERENT HEMODYNAMIC FLOW PATTERNS THAN SUBJECTS WITH ATHEROSCLEROTIC LESIONS

**A. Sharifi (1), R. El Sayed (1,2), C. Park (2), D. Haussen (3), J. W. Allen (1,2,3), J. N. Oshinski (1,2)**

(1) Department of Radiology & Imaging Sciences Emory University, Atlanta, GA, USA.
(2) Department of Biomedical Engineering, Georgia Institute of Technology & Emory University, Atlanta, GA, USA.
(3) Department of Neurology, Emory University, Atlanta, GA, USA.

## INTRODUCTION

Carotid webs (CaWs) have previously been associated with stroke and they may account for up to one-third of cryptogenic strokes in younger patients between the ages 30-48 without vascular risk factors [1,2]. CaWs are intraluminal shelf-like projections in the internal carotid artery bulb that cause focal luminal narrowing of 20-50%. Unlike carotid atherosclerosis, CaWs are not characterized by inflammation, wall thickening, or plaque deposition. CaWebs are primarily characterized by intimal hyperplasia. The shelf/pyramidal shape of the CaW may result in significant hemodynamic disturbance resulting in flow separation, recirculation, stagnation, and ultimately thrombus formation. Understanding the hemodynamic alterations caused by CaWs is essential for determining the risk of thrombus formation and subsequent stroke. The ***goal*** of this study is to understand the effect of CaW geometry on local hemodynamic parameters, which may lead to the formation of clots.

Shear rate is considered an important hemodynamic parameter in clot formation, and low shear values have been linked to activation of the coagulation cascade [3,4]. We compared the area of low shear rate in the carotid bifurcation in subjects with CaW and subjects with mild atherosclerosis using computational fluid mechanics (CFD) simulations based on 3D patient specific imaging-based geometries. We ***hypothesized*** that CaWs will be associated with a larger area of low shear rate than mild atherosclerosic lesions.

## METHODS

This was an IRB-approved study. The study population included patients with CaWs (n=5, 4 female, age 48.3±10.8) with history of stroke or TIA and mild luminal narrowing near the web, and subjects with mild atherosclerosis (n=5, 2 female, age 71±14.60) with mild stenoses. All CaW subjects has computed tomography angiography (CTA) of the carotids available. All subjects were imaged on a 3T system (MAGNETOM Prismafit, Siemens Medical Solutions). Multi-slab, transverse, 3D time of flight (TOF) images were acquired to cover the bifurcation ($0.5mm^3$, TR=23ms, TE=3.1ms). 2D, ECG-gated, cine phase contrast (PCMR) images were acquired 10mm below and 10mm above the bifurcation (1x1x5mm3, VENC=80 cm/sec, TR=43.6, TE=7). Mimics and 3-Matics (Materialise, 2019) were used to create the smoothed 3D geometry based on segmentation of TOF images for subjects with atherosclerosis, and CTA images for patients with CaW. Fluent (ANSYS, 2021 R1) was then used to mesh the geometry and conduct transient flow simulations based on 2D PCMR at the inlet and constant pressure at the outlet with the assumption of rigid walls and the no-slip conditions. Outlet 2D PCMR data was used for validation of our CFD method (**Figure 1**).

Based on literature review, when the shear rate is below a value of 10 $s^{-1}$ it has been linked to coagulation and clot formation [3,4]. Therefore, the *fractional area of low shear rate* was quantified using the surface area of the computational domain that was below the threshold of 10 $s^{-1}$ divided by the surface area of the entire computational domain (carotid bifurcation starting from 10mm below the bifurcation to 10mm above the bifurcation). An unpaired t-test was performed for

statistical analysis comparing the areas of low shear between CaW subjects and atherosclerosis patients.

**RESULTS**

the *fractional area of low shear rate* was 0.33±0.24 for the 5 CaWs, and 0.05±0.05 for the 5 atherosclerotic lesions (**Table 1**). The difference was statically significant (p~0.05). The results are also presented visually (in **Figure 3**) with an example of each of the cases. The areas with low shear rate are shown with blue color. The results show that CaWs with similar degree of luminal narrowing to atherosclerosis are associated with a larger area of low shear rate and with more complex flow patterns.

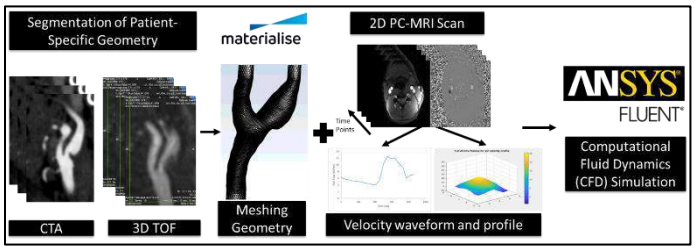


**Figure 1**.Overview of methods. Patient specific MRA geometry segmentation and smoothing using Materialize Mimics and 3-Matic. Fluent was used for the meshing and simulation of flow (ANSYS, 2021 R1). Velocity data from patient specific PCMR data.

**Table 1**. Area of low shear rate based on CFD in in patients with mild atherosclerosis and patients with CaW.

| ***Model*** | ***fractional area of low shear rate*** | ***Mean+/- std*** |
|---|---|---|
| Atherosclerosis case # 1 | 0.12 | 0.048 □0.0334 |
| Atherosclerosis case # 2 | 0 | |
| Atherosclerosis case # 3 | 0.07 | |
| Atherosclerosis case # 4 | 0.05 | |
| Atherosclerosis case # 5 | 0 | |
| CaW case# 1 | 0.21 | 0.332 ±0.215 |
| CaW case# 2 | 0.09 | |
| CaW case# 3 | 0.31 | |
| CaW case# 4 | 0.25 | |
| CaW case# 5 | 0.8 | |

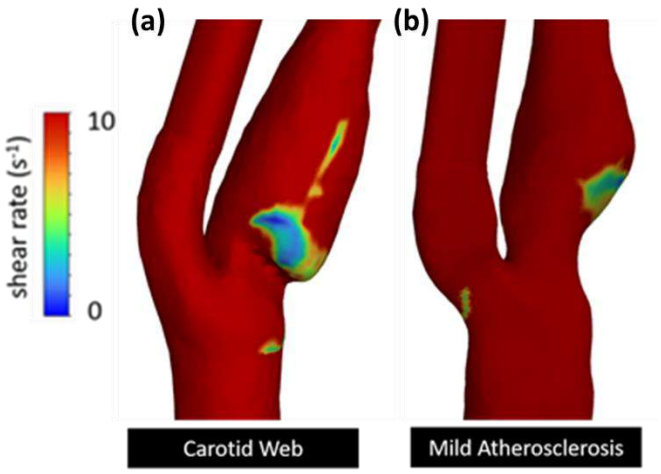


**Figure 3**. Area of low shear rate (<10 $sec^{-1}$) are shown in two example geometries: carotid web and mild atherosclerosis.

**DISCUSSION**

Carotid webs (CaWs) have been linked to cryptogenic strokes and therefore quantifying different hemodynamic parameters is essential to understand the mechanism of clot formation in patients. CFD modelling based on patient-specific geometry and PCMR inlet flow conditions was conducted on five subjects with CaWs and five subjects with mild atherosclerosis (with a similar degree of luminal narrowing. The total area within the carotid bifurcation that contained low shear rate values associated with clot formation is significantly larger in CaW subjects compared to subjects with atherosclerotic lesions or healthy subjects. The results indicate that CaW caused a greater degree of flow disturbance, recirculation, and stagnation in comparison to atherosclerosis with similar degree of stenosis.

In conclusion, CaWs showed a statistically significant larger area of area of low shear rate compared to atherosclerotic lesions and healthy carotid.

**ACKNOWLEDGEMENTS**

This project was supported by a grant from the National Institutes of Health (Allen/Oshinski), and NSF graduate Fellowship (El Sayed) and an American Heart Association (AHA) post-doctoral Fellowship (Sharfi).

**REFERENCES**

[1] Haussen DC, Grossberg JA, Bouslama M, et al. *Stroke,* 2017.
[2] Park CC, El Sayed R, Haussen DC, Risk BB, Oshinski JN, Allen JW, *The 59th Annual Meeting of the American Society of Neuroradiology*, 2021.
[3] Casa LD, Deaton DH, Ku DN. *J Vasc Surg.* 2015.
[4] Davie EW, Fujikawa K, Kisiel W. *Biochemistry*, 1991.

# Hemodynamics describing the localization of clot formation in patients with carotid web

**A. Sharifi (1), R. El Sayed (1,2), C. Park (2), D. Haussen (3), J. W. Allen (1,2,3), J.N. Oshinski (1,2)**

(1) Department of Radiology & Imaging Sciences Emory University, Atlanta, GA, USA.
(2) Department of Biomedical Engineering, Georgia Institute of Technology & Emory University, Atlanta, GA, USA.
(3) Department of Neurology, Emory University, Atlanta, GA, USA.

## INTRODUCTION

Carotid atherosclerosis is a leading cause of ischemic stroke and is characterized by inflammation, wall thickening, plaque build-up, stenosis, and thrombus formation. However, atherosclerosis is not the only cause of strokes as carotid webs (CaWs) account for up to one-third of cryptogenic strokes in younger patients without vascular risk factors [1]. CaWs are intraluminal shelf-like projections in the ICA bulb, which cause local lumen narrowing of only 20-50%, but can cause significant hemodynamic disturbance resulting in flow separation, recirculation, stagnation, and ultimately thrombus formation [2,3]. Low shear rate produces an environment enabling development of red clot that can embolize to produce strokes intracranially and this may occur distal to CaWs.

The ***goal*** of this study was to find the shear values in the thrombogenic areas where the specific area that a clot has formed in patients with CaWs. We identified a set of patients with CaWs who had a computed tomography angiography (CTA) scan *with a clot present* and another CTA study *without the presence of a clot*. Computational fluid dynamics (CFD) was used to simulate the blood flow in these patients *before* clot formation to determine a quantitative critical value for shear rate in the location that clot formed.

## METHODS

CTA images were acquired from six patients with CaWs with history of stroke or transient ischemic attack who had images *with* and *without* clot separated by less than one year. Images were segmented to create a smoothed 3D geometry using Mimics and 3-Matics (Materialise, 2019). As CTA is a static study without flow information, we conducted CFD simulations using the mean flow inputs from five patients with CaWs, who had undergone a 2D cine phase contrast magnetic resonance (PCMR) scan below and above the bifurcation. Fluent (ANSYS, 2021 R1) was used to mesh the geometry and conduct transient flow simulations based on 2D PCMR at the inlet and constant pressure at the outlet with the assumption of rigid wall and the no-slip condition. Outlet PCMR data was used for validation of our CFD method. Time averaged shear rate and particle residence time (PRT) over the cardiac cycle was determined for each case in the area where clot formed (**Figure 1**). The exact location of the formed clot was determined based on the images with the clot.

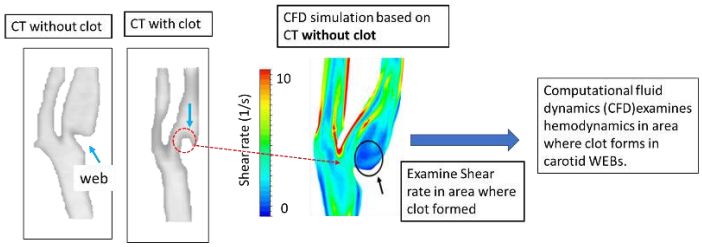


***Figure 1****. Overview of methods. Patient specific CTA geometry with and without clot. Examining the shear rate in the exact location of the formed clot shows the relation between the hemodynamic parameters in the Web patients and clot formation.*

## RESULTS

For the CaWs, the shear rate in the area inside the thrombogenic area is lower 10 $s^{-1}$. The areas with critical low shear rate are shown with blue color. It is known that low shear

rate values can cause red clot forming in some patients [2-4]. The other hemodynamic parameters including the particles residence time is also larger than 4 s in this section. (**Figure 2**). Moreover, the velocity values are very close to zero (stagnation) in the area of where the clot formed.

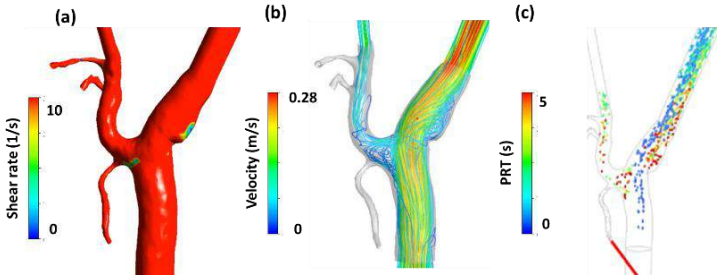


***Figure 2****. The hemodynamic parameters in a patient with CaW. (a) time averaged shear rate in a cardiac cycle, (b) streamlines during the systole, and (c) time averaged particle residence time in a cardiac cycle*

## DISCUSSION

While carotid webs (CaWs) have been associated with cryptogenic strokes, the mechanism of thrombosis is unknown. Therefore, we quantified different hemodynamic parameters such as shear rate directly in the area where a clot was known to have formed. Computational fluid dynamics (CFD) based on patient-specific geometry and PCMR inlet flow conditions was conducted on six subjects with CaWs. The area within the carotid bifurcation where the clot formed demonstrated low shear rate values (less than 10 $s^{-1}$), high PRT (longer than 4 cardiac cycle) and very low flow velocity (close to 0 m/s).

In conclusion, there exists and area of shear rate below 10 $sec^{-1}$ shear rate associated with the area of clot formation in CaW patients.

## ACKNOWLEDGEMENTS

This project was supported by a grant from the National Institutes of Health (Allen/Oshinski), an NSF Graduate Fellowship (El Sayed) and an American Heart Association (AHA) post-doctoral Fellowship (Sharfi)

## REFERENCES

[1] Haussen DC, Grossberg JA, Bouslama M, et al. *Stroke*, 2017.
[2] Park CC, El Sayed R, Haussen DC, Risk BB, Oshinski JN, Allen JW, *The 59th Annual Meeting of the American Society of Neuroradiology*, 2021.
[3] Casa LD, Deaton DH, Ku DN. *J Vasc Surg.* 2015.
[4] Davie EW, Fujikawa K, Kisiel W. *Biochemistry*, 1991.

SB³C2022
Summer Biomechanics, Bioengineering and Biotransport Conference
June 20-23, Eastern Shore, MD, USA

# ROLES OF POLARIZED MEMBRANE TRAFFICKING IN BREAST CANCER CELL MIGRATION

**Emily T. Chan (1), Yasaman Madraki (2), Jonathan W. Song (1,3), Comert Kural (1,2)**

(1) Interdisciplinary Biophysics Graduate Program, The Ohio State University, Columbus, OH, USA
(2) Department of Physics, The Ohio State University, Columbus, OH, USA
(3) Department of Mechanical and Aerospace Engineering, The Ohio State University, Columbus, OH, USA

## INTRODUCTION

Breast cancer is the most common malignancy and the leading cause of cancer-related death in women worldwide **[1]**. Triple-negative breast cancer (TNBC), which accounts for 10-20% of all breast cancers, is the most aggressive breast cancer subtype with an overall 5-year relapse of 40% owing to metastatic spread of cells from tumor sites **[2]**. As metastatic cancer cells detach from a tumor site and acquire a highly migratory phenotype **[2]**, their successful progression to distant organs relies, in part, on membrane trafficking pathways to uptake and secrete factors that assist them in navigating within their surroundings **[3]**. Notably, endocytic membrane trafficking, responsible for the cellular uptake of key cell migration-promoting factors, has been shown to be easily disturbed by tension at the plasma membrane **[4,5]**. While tension gradients assist in maintaining a front-to-rear polarity of the cell during migration **[6]**, recently it has been shown that these gradients create an asymmetry in endocytic dynamics across the plasma membrane **[4,5]**, termed as polarized membrane trafficking. However, questions remain about whether this asymmetry is intrinsic to migratory TNBC cells and what its role is in cell migration.

We aim to develop experimental and analytical approaches that will allow us to monitor clathrin-mediated endocytosis (CME) and the force required to deform the plasma membrane in migrating TNBC cells, which can be used to quantify membrane tension **[7]**. This involves utilizing a microfluidic platform that simultaneously allows the leading and trailing edge of a cell to be separately treated during migration and enables the application of inputs native to the cellular microenvironment. To establish the role of asymmetric membrane trafficking in cell migration, we will separately apply small molecule CME inhibitors at the leading and trailing edges of migrating TNBC cells. Here, we discuss initial results showing an inverse relationship between CME dynamics and the force required to deform plasma membrane in stationary TNBC cells and our optimization of the microfluidic platform.

## METHODS

Our TNBC cell line, SUM-159 was genome-edited to express a fluorescently tagged component of CME, AP2-EGFP. AP2-EGFP expressing SUM-159 cells were maintained in an enclosed glass slide in environmental-controlled conditions overnight. Endocytic dynamics were then captured with laser scanning confocal microscopy **(Fig 1A)** and the force required to deform the plasma membrane was measured with optical tweezers shortly after **(Fig 1B)**. Precise locations to perform force measurements were selected by noting the varying thicknesses of plasma membrane around a cell body via brightfield microscopy. Both microscopy modules and the optical tweezers apparatus were housed within the same system, allowing fast exchanges between the different cell analysis modules.

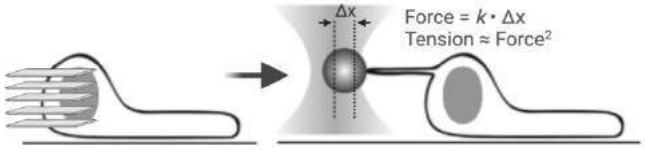


**Figure 1:** *Left*: Each cell is imaged for 7 min along 5 axial planes. *Right*: After an average delay of 3 minutes after confocal imaging, a tether is created at the plasma membrane 3 μm above the glass slide, where the force can be calculated from a bead's displacement, Δx and trap stiffness, *k*. Figure adapted from **[6]**.

Custom Python scripts were used to create the membrane tether and extract the force measurements performed on each cell. The maximum intensity projection of the imaged axial planes was processed for each cell over time with a custom MATLAB script to generate the slopes corresponding to the formation and dissolution of endocytic coats from the normalized fluorescence intensity curve of each endocytic event. These slopes were then used to obtain a distribution consisting of the rates of formation and dissolution of endocytic coat components during the entire timespan of cell tracking, termed the growth rate

distribution **(Fig 2)**. The smaller the standard deviation of the growth rate distribution, the larger the population of low magnitude slopes, or equivalently, the slower the formation and dissolution phases, and represents impeded endocytosis **[4,5]**.

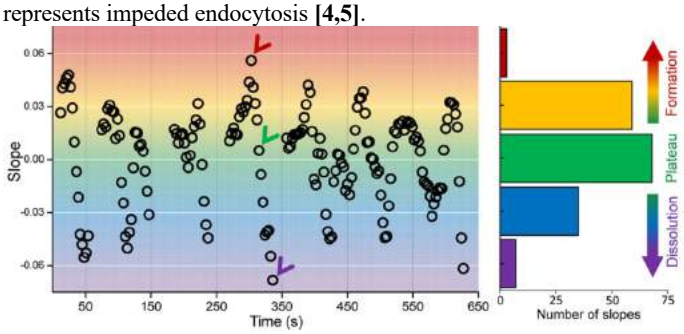


**Figure 2:** The growth rate distribution. *Left*: Slopes extracted from temporal windows centered at each timepoint of the fluorescence intensity curves of AP2-driven endocytic events. *Right*: Binning these slopes gives the growth rate distribution at a single AP2/CME hotspot over time. Figure adapted from **[5]**.

Our proposed microfluidic device will allow for unidirectional tracking of cells subject to mechanical stimulation by the microchannel walls and chemical stimulation by inducing steady-state gradients of epidermal growth factor (EGF) to induce chemotactic cell migration (*see Results section*). The device was designed with these considerations in AutoCAD and computationally modelled in COMSOL. FITC-dextran, a fluorescent molecule with a similar molecular weight to EGF, and its properties were used as input parameters. As activation of non-CME pathways is enhanced when high doses of EGF are used to induce chemotaxis compared to low EGF doses **[8]**, a low concentration (2 ng/ml) of FITC-dextran was additionally used as an input parameter in the simulations. A scalar mixing analysis was used to obtain the concentration distribution of FITC-dextran in the device by solving the steady-state Navier-Stokes and 1D advection-diffusion equations.

## RESULTS

Relating the tether force measured at areas of varying plasma membrane thickness to the standard deviation of the growth rate distribution obtained from the same SUM-159 cell, we find that the tether force is inversely related to CME efficiency **(Fig 3)**.

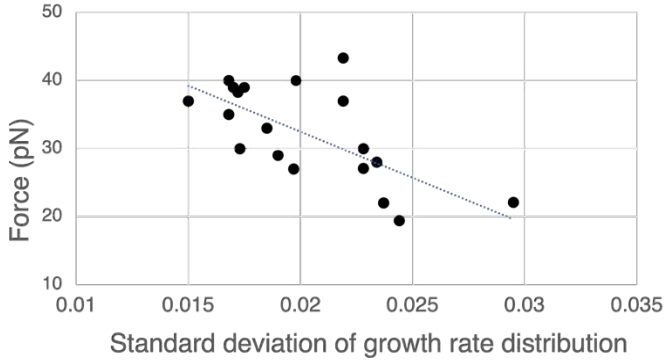


**Figure 3:** Inverse relationship between CME dynamics and the force required to deform plasma membrane in SUM-159 cells (n = 19).

The theoretical time for steady-state gradient establishment is 2.9 minutes (calculation not shown). In addition, endocytic dynamics may be recorded for periods up to 30 minutes without obvious signs of photoxicity. Thus, we concentrate our analysis of the computational model between the timespan of 3-30 minutes after introduction of FITC-dextran into the microchannels **(Fig 4A)**. We observe minimal loss of the gradient during this time **(Fig 4B)**, obtaining a maximum percent error in concentration differences between the 3- and 30-minute timepoints of 4% for a channel located at the edge of the device and 6% for a channel located in the middle of the device (at the location of each microchannel that is furthest from the FITC-dextran source).

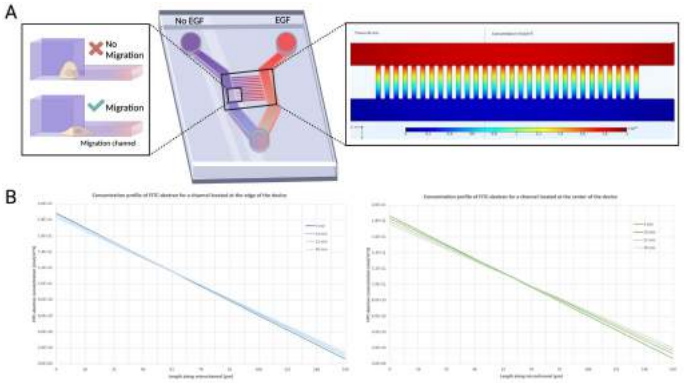


**Figure 4:** Simulated concentration profile of FITC-dextran, used to simulate the diffusive properties of EGF. **(A)** *Left:* Cells enter the microchannel only once they are well-spread i.e., less than 5 μm in height. *Right:* Concentration profile at 30 minutes. **(B)** Concentration profile along the distance of the microchannel for a channel located at the edge of the device (*left*) or at the center of the device (*right*).

## DISCUSSION

Although tether forces were performed on stationary, adherent cells, our results can be compared to force measurements performed on the plasma membrane of migrating cells, where membrane tension at the leading edge of cells is significantly greater than tension at the trailing edge **[4,6]**. As a cell polarizes towards a direction of migration, a heterogeneity in the thickness of the membrane becomes apparent, where the trailing edge of the cell appears thicker than the leading edge due to the localization of the nucleus to this area. We provide the first results connecting the spatial characterization of CME dynamics to the tether force, which may lead to the generalization that CME dynamics are reduced at leading edge with additional studies in migrating cells.

Fast establishment of a linear chemogradient and minimal loss of the gradient during the short timespan for measuring CME dynamics shown here will be desirable for future optimization, which will include experimental confirmation of the gradient by fluorescently imaging FITC-dextran (i) in the absence of cells and (ii) in the presence of cells with the addition of EGF. The completion of these studies will further allow us to connect the spatiotemporal distribution of endocytosis and membrane tension to the directionality of cell migration by performing force measurements and measuring endocytic dynamics in cell lines of varying levels of malignancy migrating in the microfluidic platform.

## ACKNOWLEDGEMENTS

This work was supported by funding from NIH T32 GM118291-04, NSF CBET-1752106, NSF Faculty Early Career Development Program (Award number: 1751113), and NIH R01GM127526.

## REFERENCES

**[1]** Lebert, JM et al., *Curr Oncol*, 25:142-150, 2018. **[2]** Koedoot, E et al., *Nat Commun*, 10:2983, 2019. **[3]** Khan, I et al., *Br J Cancer*, 124:66-75, 2021. **[4]** Djakbarova, U et al., *Biol Cell*, 113:344-373, 2021. **[5]** Ferguson, JP et al., *J Cell Biol*, 214:347-358, 2016. **[6]** Lieber, AD et al., *Biophys J*, 108:1599-1603, 2015. **[7]** Diz-Muñoz, A et al., *Trends Cell Biol*, 23(2):47-52, 2013. **[8]** Pascolutti, R et al., *Cell Rep*, 27:3049-3061, 2019.

# MICROBIOME METABOLIC NETWORK EXPANSION FOLLOWING MUSCADINE GRAPE EXTRACT INTERVENTION OF HYPERTENSIVE RATS

**Brian M. Westwood, Pooja D. Patil, E. Ann Tallant, Patricia E. Gallagher**

Hypertension and Vascular Research Center
Wake Forest University School of Medicine
Winston-Salem, NC, USA

## INTRODUCTION

The concerted expression of genes sets, cross-referenced with the expertly annotated Kyoto Encyclopedia of Genes and Genomes (KEGG), [1] can illuminate the influence of an intervention on both a host and its microbiome. KEGG BRITE hierarchy files list pathway-organized KEGG orthologs (denoted by KO identifier, aka K number) and corresponding NCBI-GeneID. Metabolic pathway modeling and complex microbiome mapping can be used to examine human disease through the lens of microbial circuitry. However, a simple visual method could provide succinct clarity. The KEGG Mapper Color Tool (KCMT) visualizes the extent of differentially expressed host genes and the affected microbiome.

Merging host and microbiome pathway maps in ImageJ can clarify the host and microbiome boundaries, with specific focus on treatment changes. The goal of this study was to assess hypertension-induced cardiac gene expression in association with microbiome alterations following treatment of hypertensive rats with a proprietary muscadine grape extract. The muscadine grape (*Vitis rotundifolia*) is native to the Southeastern United States and muscadine grape seed and skin products are marketed as dietary supplements, based upon their antioxidant properties. Bioactive phenolic compounds found in grapes can serve not only as signaling molecules but also as fuel sources for the endogenous microbiome.

## METHODS

Sprague-Dawley rats (male, 8 weeks old, n=8/group) were treated for four weeks with drinking water, muscadine grapeseed extract (MGE, 0.2 mg phenolics/mL in drinking water), angiotensin II (Ang II, 24 µg/kg/h via osmotic minipump) to induce hypertension, or both Ang II and MGE (Ang II/MGE). Heart and fecal samples were flash frozen to -80°C for RNA sequencing (RNA seq) and bacterial identification from sequenced 16Sv4 amplicons, respectively. Genus proportions [Operational taxonomic unit (OTU), n=122, Microbiome Insights; Vancouver, BC, Canada] or 32,754 RNA seq counts (Bioinformatics Shared Resource of the Wake Forest Baptist Comprehensive Cancer Center) for the control group 25th (Q1) and 75th (Q3) percentiles [limits for the interquartile range (IQR)] [2] were calculated. All subjects in the four groups scored 0 (within IQR), -1 (< Q1) or 1 (> Q3).

$$\text{IQR score} = n_0*(0) + n_{-1}*(-1) + n_1*(1) \qquad (1)$$

An IQR score of 4 and OTU control Q3 $\geq$ 100 ppm, or for RNA seq control counts Q3 $\geq$ 64 was needed to assert change for treatment group. Only Swiss-Prot genes were searched for rat heart. 6350 bacterial species existed on the KEGG site on at the time of study. Each gene (by K number) found in > 25% of the species of a genus was included for this analysis. For visualization purposes, OTU gene hits as well as cardiac RNA seq were combined for changes by Ang II alone and both Ang II and the combination of Ang II and MGE [A∪(A∩AM)]. Similar analysis was also performed for changes by MGE alone and both MGE and the combination of Ang II and MGE [M∪(M∩AM)]. All OTUs were considered as the baseline bridge. First to fifth neighbors, for 33 KEGG pathways were explored for receiver operator conditions to show the relationship between cardiac and bacterial microbiome genes regulated by [A∪(A∩AM)] or [M∪(M∩AM)] treatments [3].

To investigate the affected metabolome, SMILES (Simplified Molecular Input Line Entry System) and KEGG pathway memberships via cardiac [A∪(A∩AM)] gene-connected compounds and gut [M∪(M∩AM)] gene connected compounds were tabulated from 9 pathways (F-AUC-3) with a 1-specificity and sensitivity area under the curve (AUC) of at least 0.7 or F-measure (2/[1/precision+1/recall]) of

at least 0.7 and at least 3 directly adjacent compounds to (adjC) cardiac [AU(A∩AM)] genes were fifth neighbor to adjC microbiome [MU(M∩AM)] genes.

## RESULTS

**Figure 1** is the fifth neighbor map for arginine and proline metabolism KEGG pathway as a representative of the 33 KEGG metabolic pathways analyzed. For 4109 cardiac [AU(A∩AM)] genes detected, 1075 genes (orange) were identified in KMCT. For 240 cardiac [MU(M∩AM)] genes detected, 50 genes (purple) were identified in KMCT. A total of 5718 microbiome genes and 670 compounds (pink) were identified in KMCT. For 7 microbiome [AU(A∩AM)] genera, 2714 genes (magenta) and 9 microbiome [MU(M∩AM)] genera, 4368 genes (cyan) were identified in KMCT.

For F-AUC-3, contingency tests of specific SMARTS (SMILES arbitrary target specification) or not that specific SMARTS vs. rat network adjacent or bacterial network adjacent compounds was analyzed. Arenes were predominantly found adjacent to cardiac [AU(A∩AM)] genes (odds ratio [OR] = 7.941; Fisher exact [FE] $p < 0.0001$), and carbonyls were generally located adjacent to microbiome [MU(M∩AM)] genes (OR = 2.980; FE $p < 0.01$). The extent of the rat genome and connected compounds is found in **Figure 2** (depicted by green edges and nodes). Thirty-five (35) microbiome [MU(M∩AM)] gene adjacent compounds, that were carbonyl and not arene, were mapped on the KEGG metabolic pathway map in black.

Aggregate correlate summation (ACS) [4] clustering performed on all of the Euclidean distances between the 35 microbiome [MU(M∩AM)] gene adjacent compounds on the KEGG metabolic pathway map yielded an arginine and proline metabolism cluster (yellow ellipse, **Figure 2**) and a galactose metabolism cluster. The compounds related to putrescine degradation in the ACS cluster are components of the arginine and proline metabolism KEGG pathway. Six putrescine to 4-amino-butanoate gut genes found in species in the genus Escherichia were downregulated by MGE. Analysis of the other ACS cluster was further explored for the galactose metabolism KEGG pathway and showed similar gene alterations.

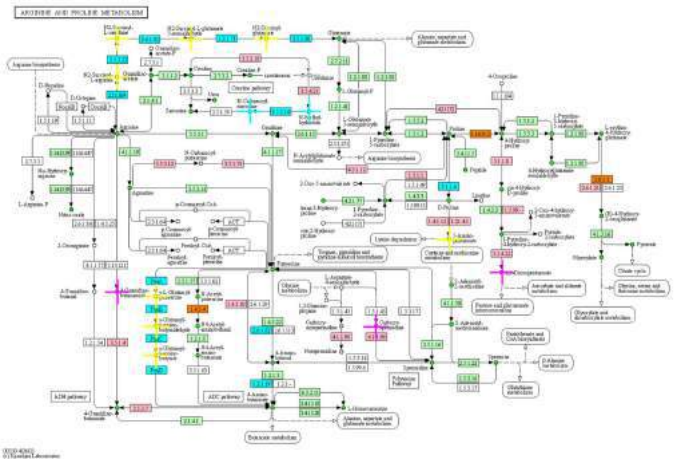

**Figure 1: Arginine and proline metabolism KEGG pathway; gene coloring- [AU(A∩AM)] cardiac (orange), ∉*i*[AU(A∩AM)] rat (green), [MU(M∩AM)] microbiome (cyan), ∉*i*[MU(M∩AM)] microbiome (pink).**

## DISCUSSION

The results of the ACS clustering suggest more scrutiny of arginine and proline metabolism KEGG pathway is warranted. Putrescine may be shunted toward spermidine in the host. Spermine and spermidine administration can be beneficial for general metabolic health and positively correlated to healthy clinical parameters in cardiac tissue, through reactive oxygen species scavenging. N-acetylputrescine is converted to N4-acetylaminobutanal amine oxidase [flavin-containing] A (MAOA) which is upregulated by Ang II in the rat heart, possibly shunting putrescine away from spermidine in cardiac tissue.

In galactose metabolism, D-glyceraldehyde 3-phosphate is processed through an open circuit via D-tagatose 6-phosphate to galactitol by gut genes found in species in genus Escherichia, which is downregulated by MGE. MGE could restrict galactitol to exploit the prebiotic properties of D-tagatose. Galactitol is converted to D-galactose by aldo-keto reductase family 1 member B, which is downregulated by both Ang II and Ang II/MGE in rat heart. Galactitol is toxic at high levels and is reduced during intermittent fasting. Reduced conversion of D-tagatose 6-phosphate to either D-tagatose or galactitol 1-phosphate and further to galactitol in MGE gut indicates that tagatose 6-phosphate levels may play a role in MGE beneficial effects.

The results of this analysis suggest that microbiome metabolic network expansion could provide a useful tool for the investigation of complex biological systems.

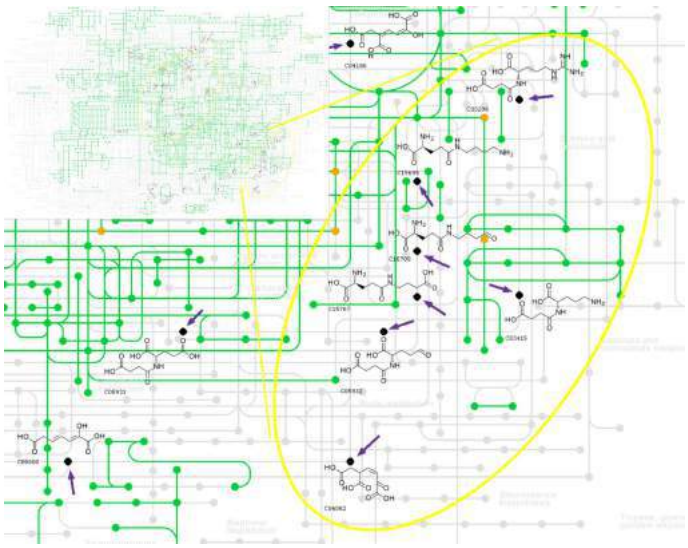

**Figure 2: KEGG metabolic pathway map; Arrows on KEGG map indicate amino acid metabolism compounds in purple.**


## ACKNOWLEDGEMENTS

This research was supported by the Chronic Disease Research Fund. We acknowledge the technical assistance of Mark Landrum, Valerie Payne, L. Tenille Shields, and Robert Lanning.


## REFERENCES


[1] Kanehisa et al. *Nucleic Acids Res*. 28, 27-30 (2000).
[2] Tukey. Exploratory Data Analysis. Addison-Wesley, 1977.
[3] Fawcett. *Pattern Recogn Lett*, 27 (2006), pp. 861-874.
[4] Westwood et al. *TMBIO '06*. ACM. p21–26.

SB³C2022
Summer Biomechanics, Bioengineering and Biotransport Conference
June 20-23, Eastern Shore, MD, USA

# DEVELOPMENT OF POROUS, MINERALIZED COLLAGEN-CHITOSAN SCAFFOLDS TO RECREATE THE 3D CANCELLOUS BONE MICROENVIRONMENT

**Sandra Stangeland-Molo (1), Kathryn L. Benedict (1), Jacqueline H. Cole (1)**

(1) Joint Department of Biomedical Engineering
University of North Carolina-Chapel Hill and North Carolina State University
Raleigh, NC, United States

## INTRODUCTION

Three-dimensional (3D) *in vitro* platforms (microdevices and on-a-chip systems) are becoming more common in research, as they allow decoupling of local and systemic effects on cell behavior, recapitulate cell microenvironments, are more physiologically relevant compared to 2D culture, and have fewer ethical concerns [1,2]. A limitation of current 3D *in vitro* platforms of bone microenvironments is that they do not provide a model for studying the cancellous bone environment [3,4]. Highly porous and load-directing, cancellous bone is particularly susceptible to mass loss during disease [5] and thus important for assessing utility of therapeutic interventions. A challenge in creating 3D *in vitro* cancellous bone is development of a scaffold to support the cells and provide cues that best recreate the microenvironment.

Cells behave more favorably when they are cultured on a substrate that is similar to their native extracellular matrix [6]. Cancellous bone is a highly porous composite of type I collagen and hydroxyapatite mineral. Previous work on bone scaffolds have prioritized either protein mineralization [7,8] or increasing porosity [9,10], despite both being key components of the cancellous bone environment. Previous mineralized collagen scaffolds have included chitosan to provide additional structural support to achieve a desired mechanical stiffness but were limited for this application by low porosity [8]. Previous porous bone scaffolds have either not contained any protein [9] or not incorporated mineralization [10]. The goal of this study was to create porous, mineralized collagen-chitosan scaffolds that promote mesenchymal stem cell activity.

## METHODS

Scaffold Fabrication. Commercially available type I collagen (3 mg/mL) and chitosan were homogenized in desired ratios (10:0, 8:2, and 6:4 wt% collagen:chitosan) and then mixed with 20 vol% phosphate buffered saline (10x). To create large pores, a two-step freeze-drying protocol was used. Protein solutions were pipetted into Teflon molds that were placed on a copper block chilled to below -30 °C to induce ice crystal formation and growth. Once frozen, pellets were removed from the mold and lyophilized to remove water, leaving a porous cylindrical protein scaffold. Scaffolds were crosslinked in a 2:1 molar ratio of EDC:NHS with 98% ethanol as solvent to prevent protein dissolution and covalently bind proteins to retain the porous structure. Two mineralizing solutions, modified simulated body fluid (mSBF) and polymer-induced liquid precursor (PILP), were made using methods described previously [7,11]. Crosslinked scaffolds were rinsed 3x in deionized water and submerged in 20 mL of mineralizing solution for 14 days. After mineralization, scaffolds were rinsed 3x in deionized water, lyophilized, and prepared for characterization.

Characterization. Scaffold pellet pore size distributions and approximate porosity were determined by thresholding scanning electron microscopy (SEM) micrographs (n=4 per collagen:chitosan/ mineralizing formulation) and measuring pore size in ImageJ. Scaffold composition was evaluated using Fourier transform infrared (FTIR) spectroscopy, labeling characteristic peaks for collagen and chitosan.

Biocompatibility. Scaffolds (n=3 per formulation) were trimmed to 1 mm thick, biopsy-punched to fit in a 96-well plate, and then sterilized in ethylene oxide. Scaffolds were placed in a 96-well plate and immersed in cell growth medium comprised of Dulbecco's Modified Eagle Medium supplemented with 10% fetal bovine serum and 1% penicillin-streptomycin. Bone-derived rat mesenchymal stem cells (rMSCs) were plated in growth medium in a separate 96-well plate and allowed to attach overnight. Beginning at experimental day 0, scaffold-conditioned media or control growth media was added to rMSCs with daily media changes for 6 days. Cell-conditioned media was collected on experimental days 0, 3, and 6 for fluorometric measures of alkaline phosphatase (ALP) activity to assess rMSC function. Live/dead staining and fluorescence imaging of rMSCs were performed as an endpoint measure on experimental day 6. For quantitative viability measurements, fluorescence images were

processed in ImageJ to remove background and converted to a greyscale image for thresholding. The processed images were then analyzed using the built-in particle analysis tool in ImageJ, in which number of counted particles were exported for both live and dead cells.

Statistics. Differences between formulations were assessed using one-way ANOVAs with Tukey tests for multiple comparisons ($\alpha$=0.05, Graphpad Prism 9).

## RESULTS

Characterization. The two-step freeze-drying protocol produced porous scaffolds that retained the bulk of their structure through the crosslinking and mineralization steps. Some protein dissolution was present, but over 80% of the protein remained. Pores for each formulation ranged 2-230 μm in size, with mean pore sizes of 30 ± 35 μm despite differing formulations. Approximate porosity measures indicated low surface-level porosity for each formulation, with 10% porosity near the outermost face of the scaffold pellets. Preliminary data of interior scaffold pore architecture suggest pore size distribution of 6-290 μm, mean pore size of 85 ± 75 μm, and approximate porosity of 50%. SEM micrographs showed mineral deposition, appearing as cuboid crystalline deposits between 1-2 μm in length, on the exterior scaffold surface and on surfaces within the pores. FTIR spectra for all scaffold formulations displayed strong peaks characteristic of collagen for amides A, B, I, II, and III at ~3300, 2900, 1650, 1550, and 1200 $cm^{-1}$, respectively. The 8:2 and 6:4 collagen:chitosan formulations also had the chitosan out-of-plane C-O bending peak at ~560 $cm^{-1}$.

Biocompatibility. Culturing rMSCs in scaffold-conditioned media was not detrimental to cell health, evidenced by no statistical differences in cell viabilities between the scaffold formulations and the control (**Figure 1A**). All groups had average viabilities above 70%, and 10:0 mSBF and both 6:4 formulations had viabilities of 84%. ALP activity was clustered around 2 mU/mL and did not differ between each scaffold formulation or compared to the control at each timepoint (**Figure 1B)**.

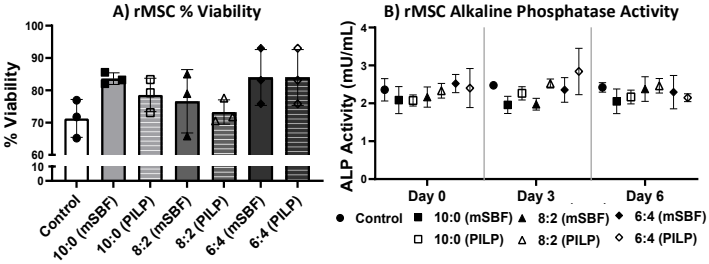


**Figure 1: A) % viability and B) alkaline phosphatase activity of rMSCs cultured for 6 days in scaffold-conditioned media.**

## DISCUSSION

The freeze-drying protocol was successful in producing porous collagen-chitosan scaffolds of varying wt% protein. The entire fabrication scheme produced mineralized biomimetic cancellous bone scaffolds that retained porosity through multiple processing steps. The varying weight % of collagen and chitosan proteins was reflected in FTIR spectra, which contained characteristic peaks for collagen and chitosan for the 8:2 and 6:4 ratio samples, in line with previous data [8]. While our mean scaffold pore sizes were lower than what has been reported previously for this freeze-drying method of unmineralized collagen:glycosaminoglycan scaffolds (150 μm, -40°C freezing temperature) [12], we presume that this is largely due to the location of our analysis. Measures in previous studies analyzed samples near the innermost region, while our initial analysis was taken from a more exterior location. Our preliminary data of interior scaffold porosity measures showed pore size distributions that skewed larger and a higher % porosity than the exterior measures. Further evaluation of interior scaffold porosity is ongoing. Additionally, we presume that the diminished pore architecture in our mineralized scaffolds relative to the previous study in unmineralized scaffolds is due in part to our fabrication method; when exposed to aqueous mineralization solutions, a small amount of protein dissolution likely occurs on the exterior scaffold surface, and this slow removal of uncrosslinked protein and subsequent scaffold drying likely leads to pore collapse. Despite the exterior protein loss and pore collapse, we are still able to retain pore structure and create mineralized biomimetic bone scaffolds.

Cell viabilities were not impacted by scaffold-conditioned media, and all formulations had average viabilities greater than or equal to 70%. The neutral effect of scaffolds on rMSC viability was not surprising and aligns with previous data [8]. Surprisingly, ALP activity was constant over the 6-day experimental window, and similar across all formulations and the control, indicating a lack of increased osteoblast differentiation. This finding differs from previous work showing higher ALP activity for mineralized scaffolds compared to controls [13]. ALP activity is usually measured for cells plated directly on the scaffolds, which likely is a key contributor to the differences in ALP activity observed here compared to past work. Cells are sensitive to the substrate they are cultured on and behave differently with varied stiffness and surface topology [6]. Since the rMSCs were cultured on treated tissue culture plastic and not the scaffolds, our results suggest that soluble factors in the scaffold-conditioned media are not sufficient to promote osteoblastic differentiation, at least on this timescale.

Limitations of this study include incomplete characterization of the mineral phase in scaffolds and plating of cells on tissue culture plastic rather than the scaffolds for biocompatibility analysis. Mineral composition and % mineralization are important metrics, as they influence the scaffold stiffness and cell responses [7,8]. Understanding cell responses when cultured on the scaffolds is also important, as their behavior is influenced by the substrate. While these metrics of mineral characterization and cell responses to culture on scaffolds were not included here, they are currently being collected as part of our study.

Overall, these results show that porous, mineralized biocompatible cancellous bone scaffolds can be fabricated using a two-step freeze-drying protocol and subsequent mineralization. This work is a first step in creating 3D *in vitro* environments to better study interactions within the cancellous bone niche.

## ACKNOWLEDGMENTS

Support was provided by Integrative Vascular Biology Training Fellowship (NIH T32 HL69768) and Functional Tissue Engineering Cross-Disciplinary Research Initiation Funding (NC State).

## REFERENCES

[1] Huh, D *et al.*, *Trends Cell Biol*, 21:745-754, 2011.
[2] Alépée, N *et al.*, *Altex*, 31:441-447, 2014.
[3] Chou, DB *et al.*, *Nat Biomed Eng*, 4:394-406, 2020.
[4] Hao, S *et al.*, *Small*, 14:1-10, 2018.
[5] Osterhoff, G *et al.*, *Injury*, 47(Suppl 2):S11-S20, 2016.
[6] Ghosh, K *et al.*, *Biomaterials*, 28:671-679, 2007.
[7] Li, Y *et al.*, *Biomacromolecules*, 13:49-59, 2012.
[8] Socrates, R *et al.*, *Mater Sci Eng C*, 99:357-366, 2019.
[9] Ye, X *et al.*, *Mater Sci Eng C*, 33:5001-5007, 2013.
[10] Lee, SJ *et al.*, *Biomaterials*, 27:3466-3472, 2006.
[11] Oyane, A *et al.*, *J Biomed Mater Res- Part A*, 65:188-195, 2003.
[12] Caliari SR *et al.*, *Biomaterials*, 32:5330-5340, 2011.
[13] Trivedi, S *et al.*, *Odontology*, 108:251-259, 2021.

SB³C2022
Summer Biomechanics, Bioengineering and Biotransport Conference
June 20-23, Eastern Shore, MD, USA

# AN IN VITRO MODEL OF THE TUMOR MICROENVIRONMENT SHAPED BY CANCER-ASSOCIATED FIBROBLASTS

**S. Shelton (1,2), B. Piel (2), T. Thai (2), H. Nguyen (1), J. Lorch (2), K. Sehgal (2) D. Barbie (2,3), R. Kamm (1,4)**

(1) Biological Engineering, Massachusetts Institute of Technology, Cambridge, MA, USA
(2) Medical Oncology, Dana-Farber Cancer Institute, Boston, MA, USA
(3) Belfer Center for Applied Cancer Science, Dana Farber Cancer Institute, Boston, MA, USA
(4) Mechanical Engineering, Massachusetts Institute of Technology, Cambridge, MA, USA

## INTRODUCTION

Our goal is to develop vascular models of the tumor microenvironment (TME) in microfluidic devices to observe interactions between multiple cell types in 3D and to investigate factors that drive tumor growth, metastasis, and resistance to therapy. In this study, we have focused on the role of cancer-associated fibroblasts (CAF) in shaping the phenotype of the TME. Many other groups have developed 3D organoid or microphysiological to replicate the TME more fully than in 2D culture, but the majority of these lack functional vasculature, making studies of angiogenesis and immune cell extravasation from circulation into the tissue impossible [1,2]. This work overcomes this limitation by using CAF to support self-assembled vascular networks in microfluidic devices. To this end, tissue was dissociated from thyroid and oral cavity cancer specimens, and CAF were expanded. CAF or normal fibroblasts (lung, dermal, thyroid) were embedded in microfluidic devices, either with endothelial cells applied as a monolayer to assess sprouting or co-mixed to generate vascular networks. In these studies, we have quantified several ways in which CAF remodel the TME: induction of angiogenesis, secretion of cytokines and chemokines, production of extracellular matrix, recruitment of immune cells, and immunosuppression.

CAF are a heterogeneous cell type, defined by their function, and generally classified as myofibroblast CAF (responsible for fibrosis and extracellular matrix (ECM) remodeling), inflammatory CAF (secrete immunogenic and immunosuppressive cytokines), or the newly identified "antigen-presenting CAF" [3]. Recent results by other groups using CAF from head and neck cancers showed they induced lymphangiogenesis in a microphysiological model [4]. However, the work described here focuses on vascular angiogenesis, the secreted factors and extracellular matrix (ECM) responsible for modifying the TME, as well as subsequent immunosuppression through recruitment and polarization of macrophages.

## METHODS

Under IRB approval, tumor resection specimens were dissociated into single cells, and fibroblasts were isolated and expanded. CAFs or normal fibroblasts (lung, dermal, thyroid) were embedded in microfluidic devices with a single hydrogel channel. Endothelial cells were either applied as a monolayer to assess sprouting or co-mixed to generate vascular networks. For sprouting experiments, fluorescent human umbilical vein endothelial cells (HUVEC) were applied as a monolayer and allowed to sprout into the fibroblast-laden gels for 4 days before imaging and quantification of sprout area, length, and density (in FIJI). To generate microvascular networks for immune cell recruitment experiments, endothelial cells and fibroblasts were combined in fibrinogen and injected into microfluidic devices. Over 7 days, microvascular networks self-assembled. Then, T cells and monocytes were fluorescently labeled with cytoplasmic dyes and perfused through the microvasculature for 1 hour before washing out unbound cells with fresh cell culture medium. All imaging was performed on a confocal microscope. Secreted factors were quantified using bead-based cytokine arrays, angiogenesis protein profiler arrays, and ELISA for VEGF and CAF. All microfluidic devices were maintained in endothelial-specific culture medium (Vasculife VEGF, Lifeline Cell Technology) changed daily.

## RESULTS

Endothelial cells sprouted more readily into gels with CAFs than those containing normal fibroblasts, with 2.35-fold higher sprouting area ($p = 3 \times 10^{-18}$) in CAF devices (see fig. 1). Cytokine arrays and ELISA revealed that secretion of VEGF ($p = 0.02$) and CCL5 ($p = 0.006$) by CAFs was much greater than by normal fibroblasts, and CCL5 exhibited a significant positive correlation with sprout area ($p = 0.003$, $R^2 = 0.74$). Treating devices with neutralizing antibodies against VEGF and CCL5 nearly eliminated sprouting. Figure 1 summarizes the experimental design for sprouting quantification, example images, plots

of sprouting area comparing normal fibroblasts vs CAF or CAF controls vs CAF + blocking antibodies, CCL5 production by normal fibroblasts vs CAF, and the correlation between CCL5 and sprouting area.

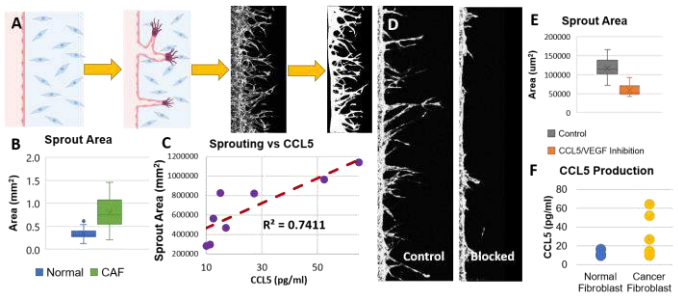


**Figure 1: A) Workflow to quantify angiogenic sprouting, B) sprout area in gels with normal fibroblast vs CAF, C) linear regression showed a positive correlation between sprouting and CCL5 concentration, D-E) sprouting is inhibited when VEGF and CCL5 are blocked with neutralizing antibodies, F) Secreted CCL5 in normal fibroblasts and CAF, quantified with ELISA.**

Additionally, CAFs supported generation of self-assembled microvascular networks, which were perfused with T cells and monocytes. The goal of this experiment was to observe their retention in the microvasculature to compare differential recruitment of these cell types in 3D microvascular culture systems mimicking healthy tissue or the TME. Perfusion of equal numbers of THP-1 monocytes and Jurkat T cells demonstrated that both cell types are retained more abundantly in microvascular devices containing CAF than in control devices made with fibroblasts from healthy tissue. Figure 2 shows example images of microvasculature from these devices shown in blue, with clear visible differences in the number of immune cells present in each case.

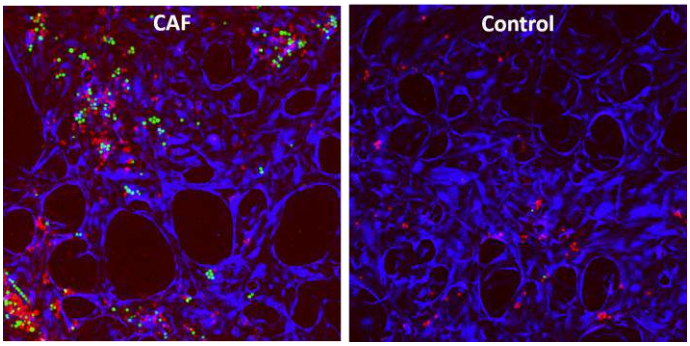


**Figure 2: Monocytes (red) and T cells (green) retained in microvascular networks (blue).**

The TME is typically immunosuppressive rather than immunogenic, despite the ability to recruit immune cells (as seen in figure 2). Therefore, we also examined the ability of CAF to polarize macrophages to the M2/tumor associated macrophage (TAM) phenotype. We generated non-polarized macrophages (M0) via differentiation from primary monocytes and M-CSF treatment for 6 days. M0 macrophages were then treated with CAF supernatant from 5 different patients, and RNA was collected for gene expression analysis with qPCR. Table 1 summarizes the relative expression of markers for M2 (CD206) and TAM (TGF-β) phenotype, as well as M1 (CD80) type. CAF from all five donors strongly polarized macrophages to the M2 type, and also generated significant expression of TGF-β, an immunosuppressive growth factor.

**Table 1: Gene expression of markers of M1/M2 polarization for macrophages incubated with CAF supernatant.**

| | M0-ctrl | CAF 1 | CAF 2 | CAF 3 | CAF 4 | CAF 5 |
|---|---|---|---|---|---|---|
| CD206 (M2) | 0.145 | 0.459 | 0.354 | 0.241 | 0.280 | 0.444 |
| TGF-b (TAM) | 0.116 | 0.170 | 0.179 | 0.130 | 0.152 | 0.150 |
| CD80 (M1) | 0.003 | 0.002 | 0.002 | 0.001 | 0.001 | 0.002 |

In addition to the stimulation of angiogenesis and the immunosuppression promoted by cancer associated fibroblasts, they are also involved in remodeling the extracellular matrix (ECM). Therefore, CAF promote metastasis both through direct interactions with tumor cells leading directed migration [5], as well as through pro-metastatic ECM modifications [3]. Devices were fixed with 4% paraformaldehyde and stained with an antibody for collagen 1 and a conjugate for hyaluronic acid, two ECM components related to CAF and the TME. See figure 3, below.

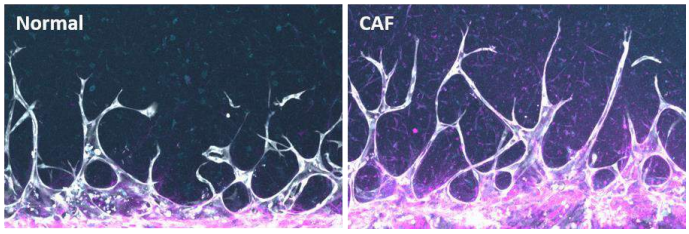


**Figure 3: Images of ECM in sprouting devices (normal vs CAF), with endothelial cells in gray, hyaluronic acid in cyan, and collagen 1 in magenta. Collagen 1 is notably more apparent in the device containing CAF, as expected.**

## DISCUSSION

This work represents the first demonstration of *in vitro* 3D microvascular networks formed with patient-derived cells for immuno-oncology studies. The overarching goal is to determine how CAF reshape the phenotype of the TME, including processes such as remodeling of the ECM, neovascularization via sprouting angiogenesis, secretion of cytokines and chemokines, recruitment of immune cells and subsequent polarization to immunosuppressive phenotypes. In this project, we generated vascular networks by combining cancer associated fibroblasts with endothelial cells, which allowed us to perfuse T cells and monocytes through the vasculature *in vitro*. In another configuration, sprouting was quantified by adding the endothelial cells as a monolayer on one side of the fibroblast gel and showed higher angiogenesis in devices containing CAF, likely due to VEGF and CCL5, which were identified to be secreted in significantly higher concentrations by CAF than by normal fibroblasts. Ongoing studies will increase the number of specimens included in this work, incorporate tumor spheroids, and quantify immune cell migration with primary and patient-derived immune cells.


## ACKNOWLEDGEMENTS

Supported by K00CA212227 (SS) and U01CA214381 (DB, RK).


## REFERENCES


[1] Truong, D et al. Cancer research 79:12:3139-3151, 2019.
[2] Nguyen, M et al. Cell reports 25.13:3884-3893, 2018.
[3] Sliker, B and Campbell P. *Vaccines* 9.6, 2021.
[4] Lugo-Cintrón, K et al. *EBioMedicine* 73, 2021.
[5] Labernadie, A et al. *Nature cell biology* 19.3:224-237, 2017.

# FABRICATION AND CHARACTERIZATION OF 3D-PRINTED ANISOTROPIC, HYDROGEL LATTICES

**Margrethe Ruding (1), Daniel Yoon (1), Charlotte A. Guertler (1), Annabella Mascot (1), Philip V. Bayly (1)**

(1) Mechanical Engineering & Materials Science, Washington University in St. Louis, St. Louis, MO, USA

## INTRODUCTION

Many fibrous biological tissues are structurally and mechanically anisotropic. Mechanical anisotropy plays an important role in normal tissue function and is affected by injury and disease. In modeling and fabricating synthetic biomaterials, it is thus important to include anisotropy [1-3]. Furthermore, fibrous materials may exhibit anisotropy in both tension and in shear. One way to incorporate anisotropy is via a reinforcing fiber network or lattice structure. Others have characterized isotropic 3D-printed lattices [4,5] but ignored anisotropy. This previous work has also focused on materials that are much stiffer than soft tissue.

The objective of this study is to design, 3D-print, and characterize isotropic and anisotropic hydrogel scaffolds of various lattice types. These 3D-printed, hydrogel lattices will allow us to create tunable, structures of desired shape, stiffness, and anisotropy (shear and tensile), to advance research in the field of soft biomaterials and biomechanics.

## METHODS

Lattice and sample design: Samples were designed using Rhino7 (Robert McNeel & Associates, Seattle, WA) [6] and plugins Grasshopper and Intralattice. (ADML, Montréal, QC) [6,7]. Unscaled (isotropic) and scaled (anisotropic) versions of three lattices (cubic, diamond, and vintile) were created. Unscaled lattices had a unit cell spacing of 1.25 mm; strut diameter was 0.4 mm for cubic and diamond lattices, 0.2 mm for vintile lattices. To create anisotropic lattices, the lattice was scaled by a ratio of 2 in one direction. In this abstract the direction of scaling (elongation) is denoted as the "X"-direction.

Samples for two mechanical tests: compression (cube, 10×10×10 $mm^3$) and dynamic shear testing (DST; disc 15 mm dia × 4 mm thick) were designed for each lattice, for a total of 12 samples (Table 1).

Sample fabrication: A LumenX+ bioprinter (CellInk, Boston, MA) stereolithography (SLA) was used to print samples. PEGDA Start™ (polyethylene (glycol) diacrylate < 2000 Da, CellInk), a photocurable bioink, was cured at 100-µm resolution at a light intensity of 20 $mW/cm^2$. Each slice was illuminated for 5 sec when in contact with the print bed; first and last layers were illuminated for 25 sec. CAD models and photographs of samples are shown in Figure 1.

**Table 1: Summary of 12 hydrogel lattice samples used in the study**

| y<br>x | Cubic | Diamond | Vintile |
|---|---|---|---|
| Unit Cell [8] |  |  |  |
| Compression (cube) 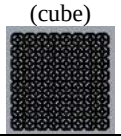 | Unscaled (isotropic) | Unscaled (isotropic) | Unscaled (isotropic) |
| | Scaled 2× in X direction | Scaled 2× in X direction | Scaled 2× in X direction |
| DST (disc) 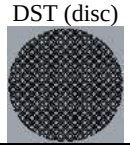 | Unscaled (isotropic) | Unscaled (isotropic) | Unscaled (isotropic) |
| | Scaled 2× in X direction | Scaled 2× in X direction | Scaled 2× in X direction |

Compression testing: Samples were tested in compression on an HR-20 rheometer (TA Instruments, New Castle, DE). The top platen (20 mm, flat) was lowered until contact was reached with an axial force of 0.05 N. A displacement ramp of 1 mm/min to 5% compression was then applied; axial load and displacement were recorded. For all tests, samples were held at ~23°C and submerged in DI water until testing. Each cubic sample was tested twice. Scaled samples were compressed parallel ("X") and perpendicular ("Y") to the scaling direction, unscaled samples were loaded in two arbitrary directions ("1", "2").

Shear testing: Disc samples were tested using DST procedures established previously [9]. Briefly, samples were placed in a chamber

on the platform of a flexure connected to a voice-coil actuator. A top platen instrumented with dynamic load cells was lowered until contact was achieved. Horizontal (shear) displacement of ~ 100 µm over a frequency range of 20-100 Hz was applied by driving the voice-coil actuators with a "chirp" signal. Shear testing was repeated at 4%, 8%, and 12% compressive strain, achieved by lowering the platen to the appropriate height. Each sample was tested twice. Scaled samples were sheared parallel ("X") and perpendicular ("Y") to the scaling direction (Fig. 2), unscaled samples were sheared in arbitrary directions (1 & 2).

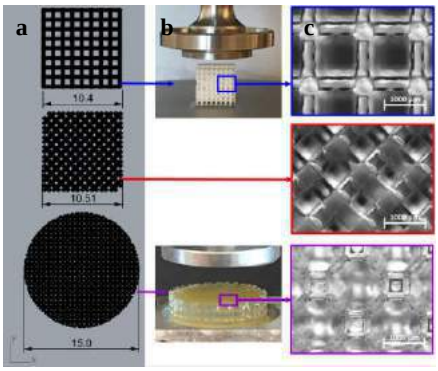


**Figure 1. (a) Cubic, diamond, and vintile lattices. (b) Compression (cube) and shear (disc) samples. (c) Photographs of samples at 2.5X (Scale bar: 1 mm).**

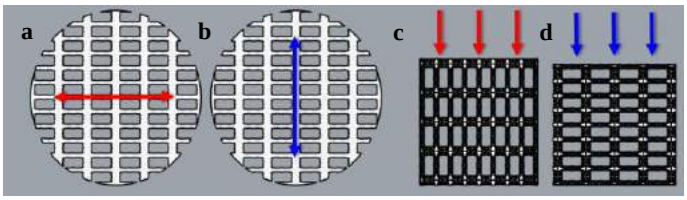


**Figure 2. (a) Diagram of scaled cubic lattice discs loaded in shear parallel to scaling direction (X) for DST; (b) Scaled sample loaded in shear perpendicular to scaling direction (Y); (c) Cube samples loaded in compression parallel to scaling direction (X); (d) Sample loaded in compression perpendicular to scaling direction (Y).**

## RESULTS

Compression: Stress was estimated from the ratio of force to sample area ($\sigma = F/A$) and strain from the ratio of displacement to sample height ($\varepsilon = \Delta L/L$). Apparent Young's moduli ($E$) were found by linear fits to stress-strain curves (Fig. 3) and summarized in Fig. 5.

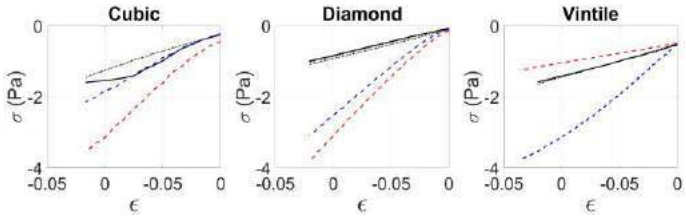


**Figure 3. Stress-strain curves for cube samples of cubic, diamond, and vintile lattices loaded in compression. Unscaled samples: black (solid: 1, dotted: 2). Scaled samples: dashed; red: X, blue: Y.**

Shear: Apparent shear modulus,$iG$, was estimated from the ratio of apparent shear stress (shear force/area; $\sigma = F/A$) to shear strain ($\varepsilon = \Delta X/h$, e.g.). Apparent shear moduli and ratios for 20-60 Hz at 8% normal strain are shown in Fig. 4, and summarized in Fig. 5.

Anisotropy: Ratios of apparent moduli are shown in Table 2. For isotropic (unscaled) lattices, the loading directions are denoted as 1 and 2, respectively. All scaled samples exhibited mechanical anisotropy. Unscaled diamond and vintile lattices exhibited similar moduli in different loading cases; the unscaled cubic lattice exhibited different moduli in each direction, possibly due to test order.

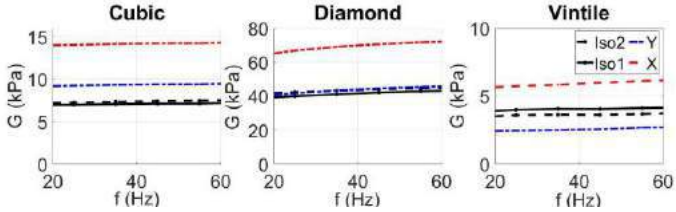


**Figure 4. Magnitude of apparent shear modulus, $G$, over 20-60Hz in different loading directions by DST at 8% normal compression, in unscaled lattices (Iso1 and Iso2) and scaled lattices (X, Y).**

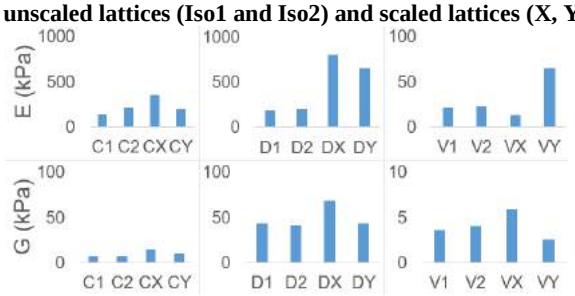


**Figure 5. Summary of apparent Young's modulus, $E$, and shear modulus, $G$, in cubic (C) diamond (D), and vintile (V) lattices under in loading in different directions (1, 2, X, Y).**

**Table 2. Ratios of apparent moduli in unscaled and scaled lattices.**

| | Cubic | | Diamond | | Vintile | |
|---|---|---|---|---|---|---|
| | C1/C2 | CX/CY | D1/D2 | DX/DY | V1/V2 | VX/VY |
| $E_X/E_Y$ | 0.65 | 1.80 | 0.98 | 1.22 | 0.93 | 0.21 |
| $G_X/G_Y$ | 1.04 | 1.52 | 1.05 | 1.59 | 0.90 | 2.31 |

## DISCUSSION

Geometrically scaled hydrogel lattices 3D-printed in tunable, soft biomaterial (PEGDA Start™) exhibited mechanical anisotropy in both tension and shear. The type of lattice strongly influenced the magnitude of effective Young's moduli and shear moduli, with the diamond lattice being the stiffest and vintile lattices the softest. The effects of scaling on anisotropy differed in different lattice types: the diamond lattice appeared stiffer in compression when loaded along the scaling axis (X), while the vintile lattice appeared softer when compressed along the scaling axis. Relative changes in lattice mechanical properties due to scaling were different in shear and in tension.

In future work, it will be important to increase sample numbers and to better characterize and control the properties of the PEGDA material. Future work will explore additional lattice types and scaling strategies.


## ACKNOWLEDGEMENTS

NIH Grant R01EB027577 and NSF Grant CMMI-1727412


## REFERENCES


[1] Guertler, C et al. *J Biomech Eng*, 142(3): 031001, 2020.
[2] Chatelin, S et al., *J Biorheology*, 26-37, 2012.
[3] Qin, E. C. et al, *J Magenetic Resonance Imaging*, 217-226, 2013.
[4] Egan, P et al. *3d Printing and Additive Manufacturing*, 73-81, 2019.
[5] Mekonen, K et al. *Intl J Adv Manuf Tech*, 1253-1265, 2020.
[6] Robert McNeel & Associates. *Rhinoceros*, 1993.
[7] Kurtz, A. *Intralattice*, 2013.
[8] Nsiempba, K et al.*Applied Sciences*, 3845, 2021.
[9] Okamoto, R et al. *Phys. Med. Biol*, 6379, 2011.

# DESIGN AND DEVELOPMENT OF IN VITRO MEDICAL INDUCTION HEATING SYSTEM

**R. Yasalonis* (1), J.Low* (1), A. Aiman (1), M. Abu-Ayyad (1), M. Garner (2), A. Attaluri (1)**

(1) Department of Mechanical Engineering, The Pennsylvania State University Harrisburg, Harrisburg, PA, United States
(2) Division of Orthopaedic Trauma, Milton S. Hershey Medical Center Penn State College of Medicine, Hershey, PA, United States

## INTRODUCTION

Each year, the number of orthopaedic implant-related procedures in the U.S. rises, as does implant associated infections [1]. Current standard treatments rely on a two-stage revision arthroplasty which involves surgery to remove the implant, followed by antibiotics to eradicate the bacteria [2]. While this approach has a high cure rate [3], it involves a highly invasive procedure with a significant effect on the patient's quality of life [1]. Furthermore, this treatment is very expensive [4], with a projected annual cost for patients in the U.S. at $1.6 billion in 2020 [5]. The primary obstacle to effective antibiotic treatment is the formation of biofilm, a thin (< 1 mm) [6] extracellular polymeric substances (EPS) layer, on the implant surface [7]. The EPS forms a barrier to the surrounding environment, rendering more resistance to antibiotics [8]. Inadequate biofilm eradication is the main reason for the standard procedure of replacing the infected implant [9]. A minimally invasive means of eradicating biofilm would be a positive step towards effective infection treatment. High frequency alternating magnetic fields (AMF) can generate heat on the surface (skin effect) of the metal implants [10] which provides a non-invasive approach for the eradication of biofilms on implanted devices. The goal of this project is to design a high throughput *in vivo* medical induction heating system to facilitate heating of multiple metal coupons simultaneously. The system should be able to uniformly heat multiple metal coupons.

## METHODS

### a. Induction Coil

To achieve uniform heating, the coils were custom designed to current system specifications. The coil must be able to hold and heat three metal coupons uniformly, reaching a target temperature of ≥ 85°C within 10 sec. Several coil designs were considered, and the design specifications were listed in a selection criteria table. Ultimately, an open coil design (pancake) and closed coil design (flat solenoid) were chosen (*Figure 1*) to facilitate a future monitoring and control system based on non-contact temperature measurement. The two designs were modelled in a 3D CAD design software (SOLIDWORKS®). Coil dimensions were optimized to hold three metal coupons.


**Figure 1: Models of (a) Flat solenoid coil, and (b) Pancake coil.**

### b. Finite Element Analysis (FEA)

A commercial finite element software, COMSOL Multiphysics, was used to evaluate the magnetic field and coupon temperatures for the flat solenoid and pancake coils. In the simulations, each coil holds three equally spaced metal coupons. The coupons were modelled following laboratory grade disc coupons for biofilm-related studies (12.7 mm diameter, 3.8 mm thickness). Three industry standard orthopaedic implant materials were tested–316L Stainless Steel, Cobalt Chromium, and Ti-6Al-4V Titanium–to compare heating performance. The thermophysical properties of the materials used in the simulations are as listed in Table 1.

**Table 1: Thermophysical Properties of Metal Coupons**

| Materials | k [W/mK] | σ [S/m] | c [J/kg.K] | ρ [kg/m3] | δ [μm] |
|---|---|---|---|---|---|
| 316L Steel | 15.0 | $1.32*10^6$ | 500 | 8050 | 0.875 |
| Cobalt Chromium | 9.4 | $1.18*10^6$ | 390 | 10000 | 0.925 |
| Ti64 | 7.2 | $2.38*10^6$ | 560 | 4450 | 0.652 |

The computer-generated simulations were used to help estimate and compare the magnetic field strength, surface temperature of the coupons and the heating performance of the pancake and flat solenoid coil on the various coupon materials. Based on our induction system's specification, the induction heating simulations were carried out at 200 A current and frequency of 315 kHz. The coupons were initialized at room temperature, 20°C.

## RESULTS

The magnetic field strength and distribution of the flat solenoid and pancake coil can be seen in Figure 2. The magnetic field amplitude is higher for the pancake coil based on simulation results. The magnetic flux streamlines in Figure 2 also indicate a uniform magnetic field around the coil and coupons on both coil designs.

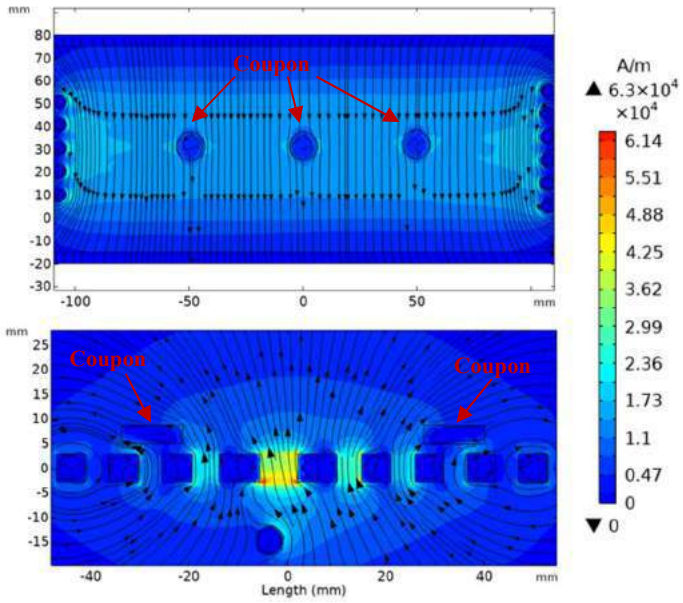


**Figure 2: FEA simulations of magnetic field strength of (a) Flat solenoid coil, and (b) Pancake coil with metal coupons.**

The temperature contour plots (*Figure 3*) and distribution with time (*Figure 4*) from the simulation results show the heating capability of the coils. The surface temperature of the metal coupons was measured at 10 sec. Both coils achieved similar temperatures (134°C) at 10 sec for the 316L stainless steel coupons that were used for the simulation results in Figure 3. The temperature distribution of each coupon material (*Figure 4a*) shows that the Ti64 coupon heats the quickest and achieves the highest surface temperature at 10 sec, which is consistent with its thermophysical properties. Equally spaced coupon placement on the pancake coil (*Figure 4b*) also helped with relatively uniform heating. Coupon #3 showed a higher temperature rise due to its coupon placement being slightly closer to the center of the pancake coil.

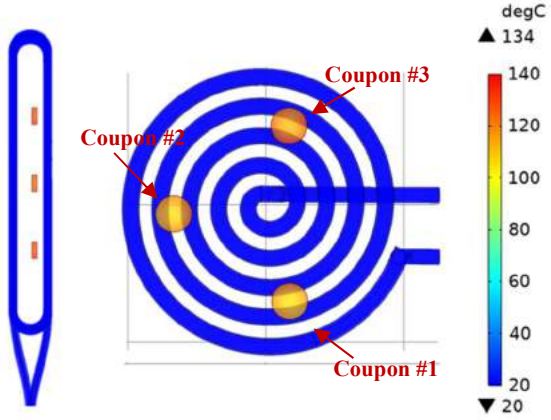


**Figure 3: FEA simulations of coupon surface temperature on (a) Flat solenoid coil, and (b) Pancake coil at 10 sec.**

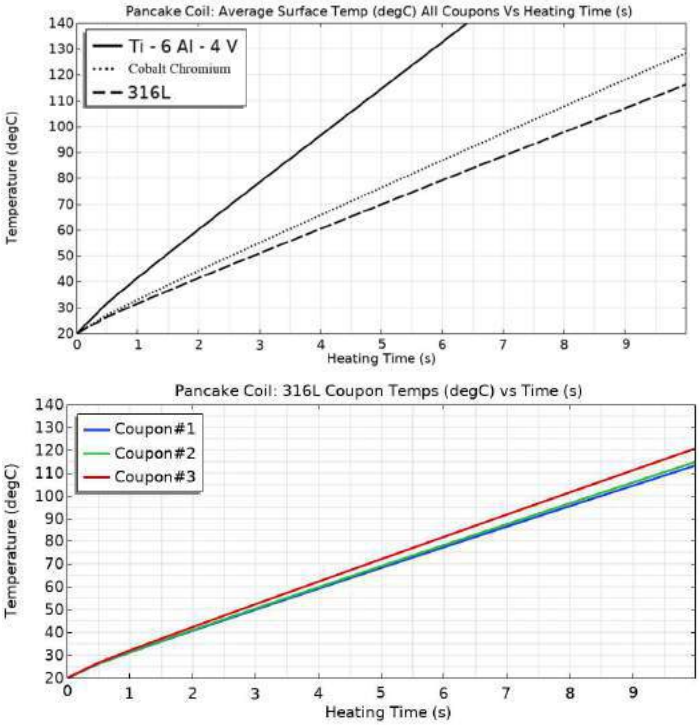


**Figure 4: Surface temperature with time of (a) Various coupon materials, and (b) Coupon placement of 316L on pancake coil.**

## DISCUSSION

The simulation results show that the flat solenoid and pancake coil can successfully heat the coupons to setpoint temperature within the specified time. The metal coupons models simulated at 200 A and 315 kHz for 10 sec resulted in surface temperatures of 134°C on both coils for the example 316L coupon test. Although the pancake coil displayed a higher magnetic field amplitude, the flat solenoid still managed to reach similar temperatures, showcasing the effectiveness of a closed coil design. Simulation results also show relatively uniform heating with proper coupon placement for the pancake coil. Future studies will explore more open coil designs, and a temperature controller to maintain coupon temperature at the target temperature.


## ACKNOWLEDGEMENTS

This project was made possible with the help of the project sponsors: Penn State College of Medicine Center for Medical Innovation and Penn State Center for Orthopaedic Research and Translational Science (CORTS) for financial support.


**Work was shared equally between the authors.*

## REFERENCES


[1] Kurtz, S et al., *Journal of Bone & Joint Surgery*, 89:780-785, 2007.
[2] Osmon, D et al., *Clinical Infectious Diseases*, 56:e1-e25, 2013.
[3] Gooding, C et al., *Clin Orthop Relat Res.*, 469:985-993, 2011.
[4] Bozic, K et al., *Clin Orthop Relat Res*, 468:45-51, 2010.
[5] Premkumar, A et al., *J Arthroplasty*, 36:1484-1489, 2021.
[6] Al-Ahmad, A et al., *J Biomed Mater Res B Appl Biomater*, 95B:101-109, 2010.
[7] Lei Tan, J et al., *Advanced Materials*, 30:1801808, 2018.
[8] Stewart. P et al., *The Lancet*, 358:135-138, 2001.
[9] Darouiche, R et al., *N Engl J Med*, 350:1422, 2004
[10] Chopra. R, *Sci Rep.*, 7520, 2017

SB³C2022
Summer Biomechanics, Bioengineering and Biotransport Conference
June 20-23, Eastern Shore, MD, USA

# EFFLUX OF CEREBROSPINAL FLUID THROUGH CERVICAL LYMPH VESSELS IS REDUCED IN AGED MICE

**Aditya Raghunandan (1), Ting Du (2), Virginia Pla Raquena (2), Yara Izhiman (2), Guojun Liu (2), Maiken Nedergaard (2,3), Douglas H. Kelley (1)**

(1) Mechanical Engineering, University of Rochester, Rochester, NY, USA
(2) Centre for Translational Neuromedicine, University of Rochester, Rochester, NY, USA
(3) Centre for Translational Neuromedicine, University of Copenhagen, Copenhagen, Denmark

## INTRODUCTION

Incidences of Alzheimer's disease (AD) and other dementias increase with age and are linked to the reduced clearance of the toxic waste products (such as amyloid-β (Aβ)) accumulating in the brain [1]. Cerebrospinal fluid (CSF) entering and leaving the brain is integral to this clearance. CSF is propelled into the brain along perivascular spaces, mixes with the brain's waste-laden interstitial fluid (ISF) and then drains these toxins predominantly via the cervical lymph vessels of the neck. This transport of fluid deteriorates with age, presumably because lymphatic function is compromised [1]. However, the dominant physiological mechanisms that drive cervical lymphatic flow (or fail in aging) remain unclear as most studies assess fluid transport using isolated lymph vessels. These conditions do not accurately represent physiological transport, where a network of vessels undergoes coordinated pulsations to transport fluid. In this talk, we present measurements of fluid flow in the cervical lymph vessels of mice in vivo. We use these first-of-their-kind measurements to explore the failure mechanisms impacting fluid clearance in mouse models of aging.

## METHODS

Intravital two-photon microscopy was used to visualize and quantify CSF flow in the cervical lymph vessels of both young (2-month) and aged mice (18 – 22-month, n>5). The mice were anaesthetized using ketamine/xylazine, and the cervical lymph vessels were surgically exposed. We simultaneously visualized vessel diameter fluctuations and the motion of 1 µm fluorescent microspheres (injected in the cisterna magna) flowing in the vessels. Detailed velocity measurements from particle motion and correlations to the changes in vessel diameter were performed using custom particle tracking and vessel wall detection algorithms in MATLAB [2]. All experiments were approved and conducted in accordance with the relevant guidelines and regulations stipulated by the University Committee on Animal Resources of the University of Rochester Medical Center, certified by the Association and Accreditation of Laboratory Animal Care.

## RESULTS

Figure 1 shows typical particle tracking measurements in lymph vessels. Particle tracking revealed significantly impaired clearance in the cervical lymph vessels of aged mice (Figure 2). The reduced speeds (Figure 2a) and lower volumes cleared (Figure 2c) were strongly correlated to the decrease in the contraction frequency (intrinsic rate, Figure 2b)) of the lymphatic vessels – the dominant driving force of fluid transport. Additionally, valve function is compromised in aged vessels, leading to stronger retrograde flows that reduce the net fluid volumes cleared.

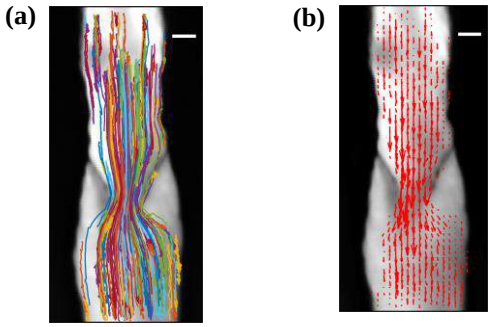


**Figure 1: In vivo particle tracking in cervical lymph vessels. (a) Rainbow colored lines represent the super-imposed tracks of the injected 1µm particles flowing in the lymph vessel. (b) The arrows represent the velocity vector field of the net particle motion. The downward pointing arrows indicate that net direction of fluid clearance away from the brain. Scale bars = 50 µm.**

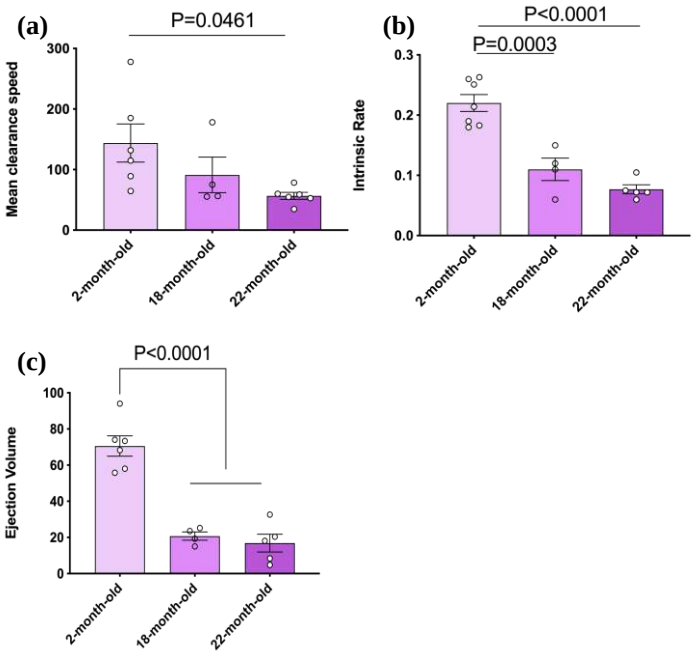


**Figure 2: Derived flow characteristics. (a) Mean clearance speed (µm/s) was calculated by first spatially averaging the measured speeds of particles flowing in the imaged lymphangion, and then performing a temporal average over one minute. (b) The intrinsic rate (Hz) represents the number of contractions per second in each of the data sets. The decrease in frequency with age indicates the weakening of the active pumping mechanism with age. (c) The volume flow rate (µL/min) was calculated as the product of the spatially averaged mean flow speed of particles exiting the vessel and cross-sectional area of the lymph vessel computed using a median value of the diameter.**

## DISCUSSION

The techniques and results presented here allow for the first in vivo investigation of fluid dynamics and vessel function in the cervical lymph vessels – a dominant exit pathway draining CSF from the brain. With simultaneous particle tracking and vessel contraction measurements, we present mechanistic evidence that the severely reduced volumes of CSF cleared through these vessels is strongly correlated to the decrease in vessel function with age. Our measurements bolster the hypothesis that the cervical lymph vessels are a bottleneck in the aged brain's fluid transport and restoring their function could be a powerful therapeutic target.

## ACKNOWLEDGEMENTS

This work was supported by the NIH/National Institute on Aging (grant RF1AG057575).

## REFERENCES

[1] Nedergaard, M., et al., *Science*. 2020, 370(6512).

[2] Kelley, D.H., et al., *Am. J. Phys.* 2011, 69, 267

# MODELING MACROPHAGE-REGULATED PULMONARY FIBROSIS WITH ENGINEERED MEMBRANEOUS LUNG MICROTISSUES

**Ying Xu (1), Ruogang Zhao (1)**

(1) Department of Biomedical Engineering, State University of New York at Buffalo, Buffalo, USA

## INTRODUCTION

Idiopathic pulmonary fibrosis (IPF) is a chronic, progressive disease that affects around 3 million people worldwide [1, 2]. The exact pathological mechanisms underpinning the initiation and progression of pulmonary fibrosis are poorly understood [3], but postmortem examination shows that IPF involves significant inflammatory cell infiltration, fibroblast activation and massive destruction of the normal alveolar structures. Despite the recent introduction of novel drugs that slow disease progression (namely pirfenidone and nintedanib), IPF remains a deadly disease, and the benefits of these new drugs differ markedly between patients [4,5]. A major roadblock in the understanding of IPF mechanism and the development of novel therapies is the lack of suitable in vitro models that can model the pathogenesis of the disease. Although existing Lung-on-chip devices can simulate flow-mediated inflammatory responses, the use of synthetic polymer (PDMS)-made membranes made it unsuitable for the study of tissue remodeling such as fibrosis induced alveolar destruction. Here we developed a co-cultured fibrotic microtissue system that can model macrophage-induced fibrogenesis of the lung interstitial tissue and tested the effect of fibroblast activation on tissue remodeling using a collagen-elastin (CE) fabricated alveolar-like thin membrane system.

## METHODS

To model macrophage-induced fibrosis initiation and progression, human peripheral blood mononuclear cell (PBMC) derived monocytes were isolated and polarized into profibrotic M2a macrophages (MΦ) using IL4 and IL13, then dropped onto a normal human lung fibroblasts (NHLF) - populated microtissue which was created on micropillar array (**Fig. 1A**) [6]. The co-cultured system was maintained for three days and was co-stained for the fibrotic marker α-smooth muscle actin (α-SMA) and macrophage marker CD206. To recapitulate the ECM remodeling and alveoli destruction found in progressive fibrotic disorders, a thin collagen-elastin membrane was fabricated on a gold mesh (250 μm hole diameter and 18-μm-thin) via surface tension to mimic the alveolar structures. NHLFs were seeded on the thin membrane and were treated with fibrosis inducer TGF-β to examine the effect of fibroblast activation on the remodeling of alveolar-like thin membraneous tissues.

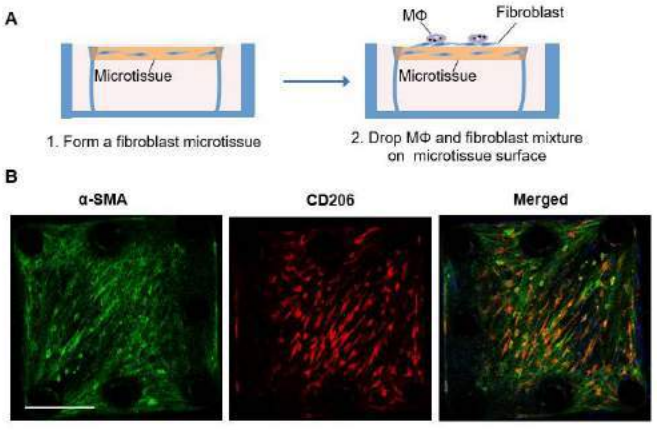


**Figure 1: Macrophage co-cultured lung microtissue model. (A) Schematic showing that lung fibroblasts and polarized M2a macrophages (MΦ) were directly dropped onto the 3D microtissue surface. (B) Representative immunofluorescence images of α-SMA (green) and CD206 (red) of the co-cultured microtissue. Note the macrophages became elongated and aligned with the fibroblasts along the diagonal direction of the microtissue. Scale bar is 200 μm.**

## RESULTS

Human PBMC derived monocytes were successfully polarized into M2a MΦs using IL4 and IL13, as characterized by the expression of CD206. After loading M2a MΦs onto the surface of NHLF- populated lung microtissue, M2 MΦs adhered well to the tissue surface in large numbers (**Fig. 1B**). After three days of co-culture, strong expression of α-SMA was observed in the co-cultured microtissue, indicating the differentiation of fibroblasts to myofibroblasts. There is significant alignment formation in the differentiated myofibroblasts along the diagonal direction of the microtissue, suggesting the generation of contractile forces. Surprisingly, the macrophages adopted an elongated morphology and aligned along the fibroblasts (**Fig. 1B**), implying the strong interaction between these two cell types that affected the morphology and phenotype of both cell types. Quantitative analysis of fluorescence intensity shows much higher expression of α-SMA in co-cultured microtissue as compared to mono-cultured fibroblast-populated microtissue, confirming myofibroblast differentiation.

Alveolar-like CE membrane was formed successfully on gold mesh. Macroscopic examination shows intact CE membrane with smooth surface. Phase contrast images showed that NHLFs distributed uniformly on the CE membrane and spread well, suggesting the good biocompatibility of the CE membrane. While quiescent NHLFs (untreated, **Fig. 2A)** didn't cause significant remodeling of the CE membrane, TGF-β treated NHLFs tore open many CE membrane units and caused significant destruction of the membrane with holes (**Fig. 2B)**. Since TGF-β has been shown to induce NHLF differentiation to myofibroblasts, the destruction of the CE membrane is likely caused by elevated contractile forces generated by differentiated myofibroblasts. Significant level of cell alignment was also observed in TGF-β treated condition, further confirming the generation of high contractile forces by the myofibroblasts.

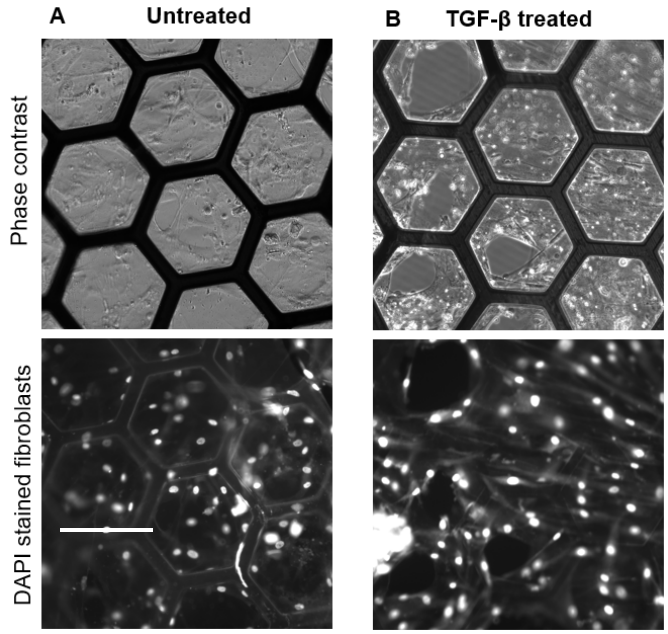


**Figure 2: Collagen-elastin (CE) membrane remodeling by activated lung fibroblasts. Phase contrast image and fluorescent image (DAPI stained) showed NHLF cultured on CE membrane formed on a gold mesh without (A) or with (B) the presence of TGF-β. Note significance tearing of the CE membrane in TGF-β treated condition. Scale bar: 200 μm.**

## DISCUSSION

In this work, we modeled MΦ induced lung fibrogenesis using a micropillar-based 3D microtissue system. PBMC-derived MΦs adhered well to the NHLFs, became elongated and aligned with the fibroblasts. With co-cultured MΦs, NHLFs differentiated to myofibroblasts. The simultaneous changes of phenotypes in both cell types suggest they interact and affect each other. Such interaction is likely facilitated by the close physical contact between the two cell types, as suggested in previous publications. Notably, the immunostaining results (**Fig. 1B**) demonstrated that a large number of M2a MΦs on the lung microtissue co-expressed MΦ marker (CD206) and myofibroblast marker (α-SMA), implying these MΦs acquired both myofibroblast and MΦ phenotypes. It is possible that these PBMC-derived MΦs underwent MΦ to myofibroblast transition in the current model system. Furthermore, since PBMC sub-populations such as fibrocytes have been reported to infiltrate fibrotic tissue and differentiate to the myofibroblast, fibrocytes can also contributed to the results observed in the current study. Compared with conventional 2D culture model, the force sensing capability of the microtissue system, contributed by the micropillar force sensors, allows measurement of the changes in tissue mechanics occurred during fibrosis progression. Together, this co-cultured model system provides a useful platform for the investigation of the disease mechanism of IPF including the MΦ-fibroblast interaction and the testing of potential anti-fibrosis drugs that targets inflammatory pathways.

Additionally, the CE membrane formed on the gold mesh recreated the structure, composition and mechanical properties of the alveolar tissue. Its membranous structure allows the modeling of alveolar destruction caused by the contractile myofibroblasts in the fibrotic tissue. Compared to the existing synthetic polymer based lung-on-chip devices, this model offers new opportunity to examine the mechanism of pathogenesis in the fibrotic lung. It is expected that the adoption of these new models in the field of pulmonary fibrosis will help the understanding of the disease mechanism and the development of novel anti-fibrosis therapies.

## ACKNOWLEDGEMENTS

This study was supported in part by National Institutes of Health (NIH) under grant R33HL154117 and American Lung Association Innovation Award IA-84300.

## REFERENCES

[1]. Martinez, F.J., et al., Idiopathic pulmonary fibrosis. Nature Reviews Disease Primers, 2017. 3(1): p. 17074.
[2]. Ogawa, T., et al., Macrophages in lung fibrosis. International Immunology, 2021.
[3]. Wuyts, W.A., et al., The pathogenesis of pulmonary fibrosis: a moving target. European Respiratory Journal, 2013. 41(5): p. 1207-1218.
[4]. Richeldi, L., et al., Efficacy and Safety of Nintedanib in Idiopathic Pulmonary Fibrosis. New England Journal of Medicine, 2014. 370(22): p. 2071-2082.
[5]. Noble, P.W., et al., Pirfenidone for idiopathic pulmonary fibrosis: analysis of pooled data from three multinational phase 3 trials. European Respiratory Journal, 2016. 47(1): p. 243-253.
[6]. Asmani, M., et al., Fibrotic microtissue array to predict anti-fibrosis drug efficacy. Nat Commun, 2018. 9(1): p. 2066.

# UNDERSTANDING THUMB JOINT MOVEMENT AND HOW AGE CONTRIBUTES TO ITS CHANGES

**Nicole D. Arnold (1), Adam J. Chrzan (1), Kevin Chan, MD (2), and Tamara Reid Bush, PhD (1)**

(1) Department of Mechanical Engineering, Michigan State University, East Lansing, MI, USA
(2) Department of Hand Surgery, Spectrum Health, Grand Rapids, MI, USA

## INTRODUCTION

Osteoarthritis (OA) of the hand is a debilitating musculoskeletal disease that can severely impact one's ability to carry out activities of daily living, such as opening a bottle or food packages. Almost 70% of women and 55% of men over the age of 55 will develop hand OA in at least one joint [1]. People diagnosed with thumb OA, regardless of severity, benefit from conservative treatment methods such as strengthening or stretching exercises, non-steroidal anti-inflammatory drugs, splinting, and/or corticosteroid injections [2,3]. Conservative treatment options can provide pain relief for a few days to several months. However, a limitation to all these treatments is that their effects weaken over time, and the disease may continue to progress to where surgery may be required to improve strength and function.

Clinical assessments (i.e., patient questionnaires and range of motion using goniometers) are not sufficient to quantify complex, dynamic motions. On the other hand, motion capture systems can obtain both standard clinically measured ranges of motion and more complex multi-planar motions, which provide an accurate assessment of joint motions [4]. Thus, motion capture systems can provide quantitative and comprehensive baselines of healthy function so that impairments and restoration of function during rehabilitation can be identified. The purpose of this research was to determine and compare the maximum flexion angles of the interphalangeal (IP) and metacarpophalangeal (MCP) joints of the thumb in populations of younger and older individuals to establish baselines of healthy function.

## METHODS

10 young healthy (YH) (5 female, 5 males, and ages 26 ± 4 years) and 10 older healthy (OH) participants (8 females, 2 males, ages 63 ± 10 years) were included in this study. All participants had no prior injury or disease (including osteoarthritis), were not pregnant, and were right hand dominant. Three-dimensional kinematic data of the thumb's movements were captured using three reflective marker pods attached to the distal phalange, proximal phalange, and metacarpal of the thumb (Fig. 1 left). Additionally, four single markers were attached to the sides of the wrist. (Note: Tracking movement of the thumb was our primary goal, but as seen in the figures, markers were also placed on the index finger to accommodate other tests not discussed in this abstract.) Participants sat in a chair with their hand and forearm resting in the testing device on a table (Fig. 2). This system prevented movement of the forearm and wrists permitting individuals to focus on thumb motions. Participants were instructed to flex their thumbs three times to the best of their ability. Thumb flexion was defined as increasing the angle between the two bones around the IP or MCP joints (Fig. 1 right).

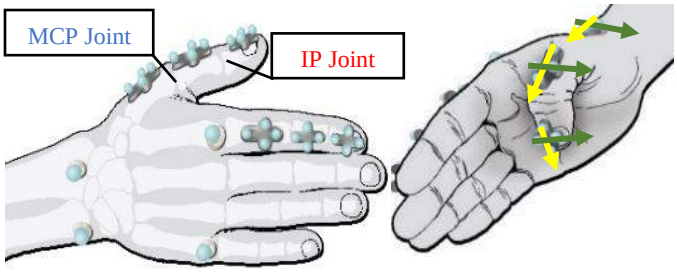


**Figure 1: Marker pods on the thumb and single markers located on the base of the 2nd and 5th metacarpophalangeal joints and the medial and lateral sides of the wrist (left). X- and Y -axes of the local coordinate systems on the distal, proximal, and metacarpal phalanges (right). Flexion of the IP and MCP joints occurs about the green axes.**

## RESULTS

The maximum flexion IP and MCP joint angles are presented in Table 1 and Figure 3. The averages of the maximum IP and MCP flexion values for the younger healthy group were 69º and 59º, respectively. The averages of the maximum IP and MCP flexion values for the older healthy group were 66º and 56º, respectively. Additionally, the averages for the flexion angles were reduced in the OH group by 4.3% for the IP joint and 5.1% for the MCP joint relative to the YH group.

**Figure 2: A participant's hand resting in the testing device performing maximum flexion of the IP and MCP joints**

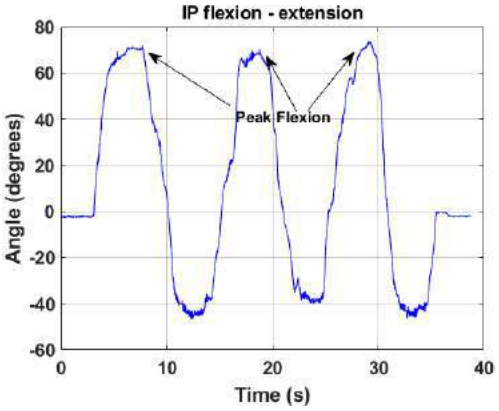


**Figure 3: IP thumb flexion, with maximum flexion identified at three time points for a single participant.**

## DISCUSSION

The goal of this study was to investigate IP and MCP ranges of flexion in the thumbs of young and old healthy groups. As expected, the older group had a reduction in the average ranges of flexion. On average, those older in age had a decrease of 4-5% range of motion of the IP and MCP joints. However, what has not been evaluated by other studies is the comparison of IP flexion to that of the MCP flexion. 70% of the YH participants had larger motion at the IP joint with the difference between the IP and MCP averaging 20º. However, in the OH group, the IP and MCP maximum flexion values had similar movement angles. The max IP and MCP flexions for 6 of 10 OH participants were less than 5º apart, and the average difference was only 11º. Similarly, the IP joint had the larger magnitude for most participants in the OH group, but as noted, it was only slightly larger than the MCP flexion. The similar contributions of the IP and MCP joints to thumb movements in the OH group relative to the YH group could be explained by several mechanisms. These mechanisms include inflammation, stiffness, strength loss, joint alignment changes, or muscle imbalance. All of these have been shown to be present in patients with doctor diagnosed OA. So, a question for future consideration is whether or not this decreased differential between IP and MCP flexion is a pre-cursor to OA. Further, if our OH participants sought out hand therapy now (prior to pain), could the contributions of the IP and MCP joints be restored to that of the YH group?

**Table 1: Maximum individual and group values of thumb IP and MCP flexion. n= 20 (10 younger and 10 older)**

| Subject | YH | YH | OH | OH |
|---|---|---|---|---|
| | Max IP (º) | Max MCP (º) | Max IP (º) | Max MCP (º) |
| 1 | 56 | 62 | 81 | 39 |
| 2 | 80 | 41 | 75 | 65 |
| 3 | 72 | 50 | 57 | 60 |
| 4 | 74 | 90 | 72 | 45 |
| 5 | 66 | 45 | 75 | 77 |
| 6 | 67 | 58 | 59 | 55 |
| 7 | 74 | 40 | 49 | 47 |
| 8 | 72 | 60 | 52 | 51 |
| 9 | 59 | 79 | 78 | 61 |
| 10 | 74 | 65 | 60 | 55 |
| Average | 69±7 | 59±15 | 66±10 | 56±10 |

Such reductions in joint ranges of motion have an impact on thumb function when carrying out activities of daily living. Examples of activities that require larger degrees of thumb joint flexion are buttoning and/or zipping up pants/shirt, putting on a shoe and tying shoelaces [5]. Because of the large range of motion needed to do these activities, they may be the first impacted by a reduction in range of motion. As a result, many individuals will experience a loss of independence to some degree. Our work suggests that these reductions in motion may appear prior to pain, or other signs of OA, and are occurring in our OH group.

This research provides information on the range of motion of healthy thumbs. Understanding healthy function is important when monitoring treatment effects or designing therapies for thumb OA and identifying when older individuals may need to seek out therapy. Our work indicates that even older individuals who are pain-free may benefit from hand therapy to preserve their ability to conduct daily activities.

These data from healthy thumbs will be used to define healthy baseline values for those treatments and therapies. Our future goals include testing participants with thumb OA pre- and post- surgery. It is important to quantify healthy movement of the thumb to further assess the deficits in those with OA.


## ACKNOWLEDGEMENTS

This work was supported by the Michigan State – Spectrum Alliance Grant.


## REFERENCES


[1] Dahaghin, et al., Ann Rheum Dis 2005;64:682–7.
[2] Dias, et al., Postgr Med J 2007;83:40–3.
[3] Estes, et al., J Hand Ther 2000;13:108-123.
[4] Kuo, et al., J Biomech 2002;35:1499–50.
[5] Gracia-Ibáñez, et al., J Hand Ther 2017;30:337–47.

SB³C2022
Summer Biomechanics, Bioengineering and Biotransport Conference
June 20-23, Eastern Shore, MD, USA

# MECHANICAL AND BIOLOGICAL MONITORING OF TISSUE STIFFNESS IN THREE-DIMENSIONAL FIBROBLAST CULTURE

**David Csordas[1], Junru Zhang[2], Julie Leonard-Duke[1], Paul DeCostanza[1], Blake Johnson[2], Shayn Peirce-Cottler[1]**

(1) Department of Biomedical Engineering, University of Virginia, Charlottesville, Virginia, United States
(2) Department of Industrial and Systems Engineering, Virginia Tech, Blacksburg, Virginia, United States

## INTRODUCTION

Fibrosis is a critical way in which a body heals itself from injury. While this is a necessary process, many diseases have an aspect of pathological fibrosis which can lead to long-lasting effects and organ damage. In the lung, fibrosis can be extremely debilitating and is seen in a range of diseases, such as Idiopathic Pulmonary Fibrosis (IPF) and in coronavirus infections of SARS-CoV2 (COVID-19)[1]. Lung fibrosis stiffens the otherwise malleable lung tissue and decreases the airspace that is necessary for gas exchange. It is well established that activated fibroblasts, or myofibroblasts, are critical for healing damaged tissue by secreting and remodeling extracellular matrix (ECM) proteins, such as collagen. However, if this process is unregulated, pathological fibrosis can ensue. The mechanisms that regulate fibroblast-to-myofibroblast transitions and aberrant ECM remodeling are active areas of research. Here, we have developed a novel method to quantify fibroblast activation and measure stiffness changes in the surrounding ECM. We present a 3-dimensional (3D) *in vitro* cell culture model that allows for histologic endpoint analysis of cell phenotypic transitions and allows us to dynamically measure physical stiffness of the matrix using a novel, sensor-based method[2,3].

## METHODS

We have developed a novel method to culture fibroblasts in a 3D type I collagen gel and visualize and quantify how they interact with and remodel their ECM over a period of days, while allowing the addition of pro-fibrotic stimulants, such as transforming growth factor beta (TGF-β), tumor necrosis factor alpha (TNF-α), and interleukin one beta (IL-1β). At the terminal endpoint of the study, cells can be labeled with NucBlue (nuclei), as well as immunostained for F-actin and alpha-smooth muscle actin (α-SMA) to assess fibroblast activation and fibroblast-to-myofibroblast phenotypic transitions. The cell-laden gel is also instrumented with a piezoelectric milli-cantilever sensor, which allows for real-time measurements of ECM stiffening (Fig 1a, 1b). Custom MATLAB software allows continuous tracking of the sensors' resonant frequencies and phase angles, which are then calibrated to provide the ECM storage modulus. The change in viscoelastic properties reported by the sensor over time correlate with the Young's modulus of the gel. We validated this *in vitro* culture system by seeding $3.5x10^5$ human lung fibroblasts (CCL-210 ATCC) per mL in 2.7 mL of type I collagen (from bovine skin) and in the presence or absence of transforming growth factor-beta (TGF-β), a growth factor known to induce fibroblast-to-myofibroblast differentiation and collagen synthesis and remodeling. 3.5 mm thick cell-laden collagen gels were cultured in 8-well and 12-well plates, and were fed with DMEM media supplemented with 10% fetal bovine serum for 55 hours and maintained in standard culture conditions (37 ºC, 5% $CO_2$). Negative control wells contained collagen gels without cells. Thirty hours after the initiation of the experiment, half of the wells containing cell-laden collagen gels were supplemented with exogenous TGF−β (20 ng/mL), while the other half were supplemented with vehicle (Fig 1c).

## RESULTS

Cells labeled with NucBlue were assessed for viability at 55 hours (Fig 1d). Immunohistochemical staining for F-actin and α-SMA enabled visualization of markers of fibroblast activation between TGF−β stimulated and un-stimulated groups (Fig 1e). Samples that received TGF−β stimulation exhibited increased levels of F-actin and α-SMA protein expression, indicating that more cells had undergone fibroblast-to-myofibroblast transitions. Additionally, collagen stiffness in each well was able to be quantified over time using our mechanical force sensor, and the sensors embedded in the cell-laden gels that received TGF−β stimulation reported altered stiffness values over time relative to cell-laden gels that received vehicle control or gels without cells.

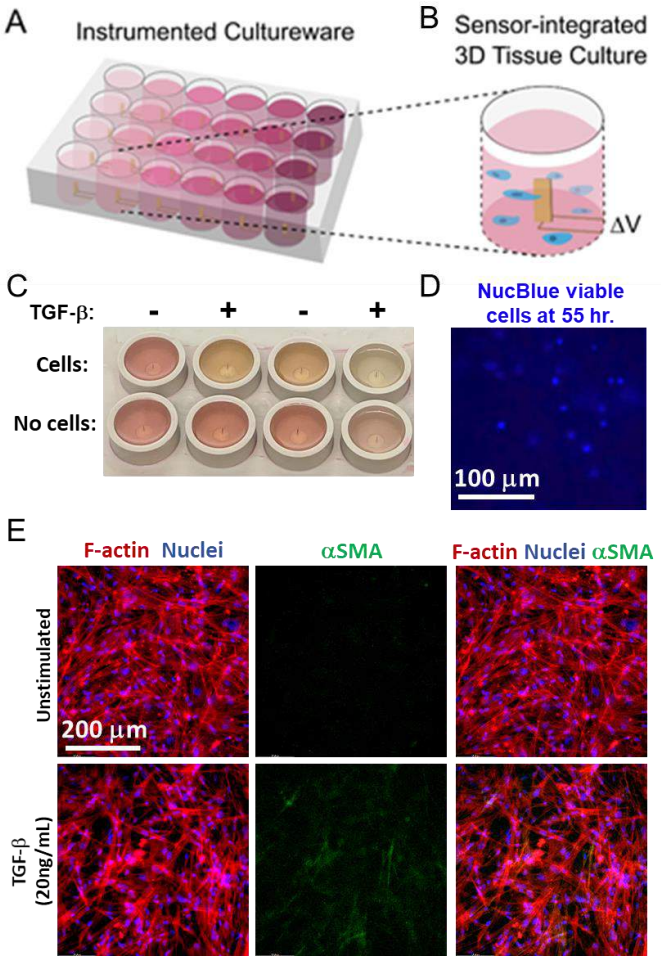


**Figure 1: Schematic of the multi-well culture plate (A) instrumented with a force sensor protruding from the bottom of the well containing the cell-laden gel (B). The sensor measures changes in voltages (ΔV) corresponding to changes in matrix stiffness. (C) Experimental image of cell-free and cell-laden gels with and without TGF-β in a custom-made tissue culture plate instrumented with sensors. (D) Cells labeled with NucBlue nuclei stain visualized at 55 hours to confirm viability. (E) Immunohistochemical staining of unstimulated fibroblasts in gels (top row) and fibroblasts in gels stimulated with TGF-β (bottom row) to visualize nuclei (blue), F-actin (red) and α-SMA (green).**

## DISCUSSION

Our novel fibroblast culture model incorporates a method for quantifying both cell phenotypic differentiation and the mechanical properties of the ECM in a real-time and non-destructive manner. To validate our model, we immunohistochemically assessed human lung fibroblast activation and differentiation, and quantified type 1 collagen matrix stiffening over time. Our model can be extended to interrogate how co-cultures of different cell types (e.g. endothelial cells and fibroblasts) interact with each other and impact the mechanical stiffness of the ECM. Other natural ECM constituents (e.g. fibronectin) and synthetic ECM mimics (e.g. elastin-like peptides[4]), in addition to collagen, can also be assessed in our system. Our model facilitates the incorporation of different biochemical activators of fibrosis (or inducers of other cell differentiation processes to a myofibroblast phenotype, such as Endothelial to Mesenchymal Transition (EndoMT)[5]), as well as the exploration of pharmaceutical agents to therapeutically alter these processes. Model systems that report metrics of both cell activation/differentiation and ECM remodeling non-destructively are not yet commonplace in fibroblast research, and studying them could inform new therapeutic intervention strategies for fibrotic diseases, such as lung fibrosis.

## ACKNOWLEDGEMENTS

This research was funded by NSF EAGER #2140549.

## REFERENCES

[1] Bazdyrev, E et al., *Pharmaceuticals*, 14, 807 (2021).
[2] Haring, AP et al., *Journal of Rheology*, 64, 837 (2020).
[3] Cesewski, E et al., *Journal of Applied Physics*, 128, 174502 (2020).
[4] Meco, E and Lampe, KJ, *Biomacromolecules*, 20, 1914-1925 (2019).
[5] Piera-Velazquez, S, Mendoza, FA, Jimenez, SA, *J Clin Med*, 5, 45 (2016).

SB³C2022
Summer Biomechanics, Bioengineering and Biotransport Conference
June 20-23, Eastern Shore, MD, USA

# FEATURE TRACKING MICROFLUIDIC ANALYSIS REVEALS DIFFERENTIAL ROLES OF VISCOSITY AND FRICTION IN SICKLE CELL BLOOD

**H. Szafraniec (1), J. Valdez (1), E. Iffrig (2), W. Lam (2), J. Higgins (3), P. Pearce (4), D. Wood (1),**

(1) Biomedical Engineering, University of Minnesota, Minneapolis, MN, US
(2) Department of Pediatrics, Emory University, Atlanta, GA, US
(3) Systems Biology, Harvard University, Cambridge, MA, US
(4) Applied Mathematics, University College London, London, UK

## INTRODUCTION

Sickle Cell Disease (SCD) is a hematological disorder affecting millions of people worldwide [1]. The disease can manifest in various vascular pathologies such as vaso-occlusions, acute chest syndrome and organ damage. As a result, patients experience a decreased life expectancy and reduce quality of life [2]. SCD is caused by a genetic mutation to the oxygen carrying hemoglobin molecule resulting in a sickle hemoglobin (HbSS) molecule which can polymerize under reduced oxygen conditions and subsequently cause changes in red blood cell properties and alter whole blood rheology [3,4].

Altered blood rheology has been defined as a driver of the pathophysiology and progression of the disease as seen by the increased likelihood of vaso-occlusive crisis with increased blood viscosity [5]. Therefore, therapies such as transfusions and anti-sickling drugs aim to prevent disease complications by restoring normal blood flow [6]. Thus, the main goal of this work is to further the understanding of the rheological properties of SCD blood as it relates to disease severity and therapeutic effectiveness. Previous studies have characterized macroscopic rheological properties of SCD blood such as average velocity or effective viscosity but blood is a complex suspension that exhibits non-Newtonian flow behavior such as shear-thinning and frictional effects arising from wall interactions, all of which depend on the properties of the red blood cells [7]. Therefore, a deeper understanding of the physical determinants of SCD blood rheology is needed.

Herein, we present a method which quantifies the unique properties of SCD blood as it flows in a microcirculatory geometry under reduced oxygen conditions by tracking individual red blood cell velocities in bulk blood flow. This approach allows us to quantitatively interpret the observed non-Newtonian rheological behavior and further investigate the role of frictional and viscous resistance on the overall effective fluid resistance while including oxygen dependent effects. This increased understanding of SCD blood rheology extends beyond previous macroscopic measurements and may provide insight into features of the disease to therapeutically target. Additional work will be aimed at assessing rheological properties of SCD blood prior to and following treatments to investigate therapeutic effects.

## METHODS

All studies were conducted using a bifurcating microfluidic device previously described [8]. Blood samples from healthy donors and donors with SCD were collected at the Massachusetts General Hospital under Institutional Review Board approved protocols (2006P000066). For all measurements, sample plasma was replaced with phosphate buffered saline (PBS) and the hematocrit was fixed at 25%.

To estimate red blood cell velocity using computer vision, the Kanade-Lucas-Tomasi (KLT) algorithm was used as a sparse feature-tracking method to identify object features such as corners and edges based on image intensity gradients [9]. The pixel coordinates of identified features were initialized and tracked among a set of consecutive frames and their positions saved. Using this method, red blood cell (RBC) velocity fields across the width of the microfluidic channel were reproduced from experimental image sets.

To quantify the non-Newtonian flow behavior, the observed RBC velocity profiles were modeled as an effective power-law fluid in which the velocity ($V$) depends on the distance from the channel center ($r$).

$$V(r, O_2) = V_{max} * \left(1 - \left(1 - \frac{V_{wall}}{V_{max}}\right) * \left|\frac{R}{W}\right|^B\right) \quad (1)$$

$V_{\text{wall}}$ is the slip velocity at the channel wall, $V_{\text{max}}$ is the maximum velocity, and $B$ is the bluntness index. $V_{\text{wall}}$ , $V_{\text{max}}$ and $B$ are fitted parameters to the empirical values for both $V$ and $r$ from the experimental setup, and $W$ is a fixed parameter based on measurements of the channel width.

We then calculated the frictional resistance and viscous resistance as follows

$$R_{friction} = {\Delta P}/{Q_{slip}} \quad (2)$$

$$R_{viscous} = {\Delta P}/{Q_{bulk}} \quad (3)$$

The pressure drop $\Delta P$ in the blood channel was found using a linear network model [10] . The flow rate $Q$ in the experimental channel was found using the average velocity and device geometry previously determined. The total flow rate was separated into a bulk component $Q_{bulk}$ and a slip component $Q_{slip}$ by conservation of mass.

## RESULTS

To characterize the effect of oxygen on SCD blood rheology, velocity profiles at a fixed pressure drop were sampled for both HbSS blood and healthy blood (HbAA) at different oxygen tensions. SCD blood demonstrated a strong dependence on oxygen compared to healthy blood as seen by the decrease in velocity with decreasing oxygen (Fig. 1A-B). Additionally, SCD blood exhibited both a change in red blood cell velocity near the channel walls along with a transition in the profile from parabolic to plug flow as oxygen decreased (Fig. 1A-B). These changes in physical properties were quantified using Eq. 1 and the results indicated a large RBC slip velocity factor (${V_{\text{wall}}}/{V_{\max}}$) and increased bluntness index ($B$) in response to hypoxia (Fig. 2E-H). Our results suggest that as oxygen decreases, SCD blood flow experiences a larger shear stress transition near the wall along with a more blunted flow profile; both of which describe the physical changes of SCD blood properties from that of healthy blood.

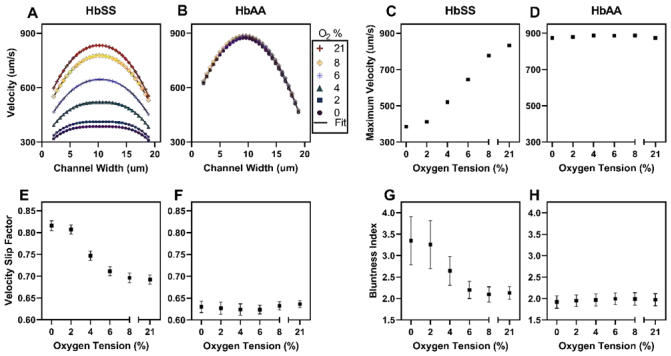


**Figure 1: Qualitative and quantitative oxygen dependence of representative samples of healthy (HbAA, n=1) and SCD (HbSS, n=1) blood flow.**

To gain a deeper understanding of how the macroscopic rheological properties of SCD blood differ from healthy blood for a cohort of patients, effective flow resistances were computed, and the results demonstrated statistically significant differences even at normoxic conditions (Fig 2A). Effective flow resistances were separated into their viscous and frictional parts (see Methods) to determine their contribution to the overall resistance (Fig. 2C-D). The results revealed sharp increases in effective viscous and frictional resistance at lower oxygen tensions in SCD blood which was consistently differentiable from healthy blood. The large increase in viscous resistance suggests that as SCD blood becomes more deoxygenated, the bulk viscosity increases. In contrast, the frictional resistance shows an oxygen dependent effect, but the magnitude is significantly less than the viscous resistance. This result suggests that the overall resistance of SCD blood at low oxygen tensions becomes increasingly dependent on frictional effects to maintain flow.

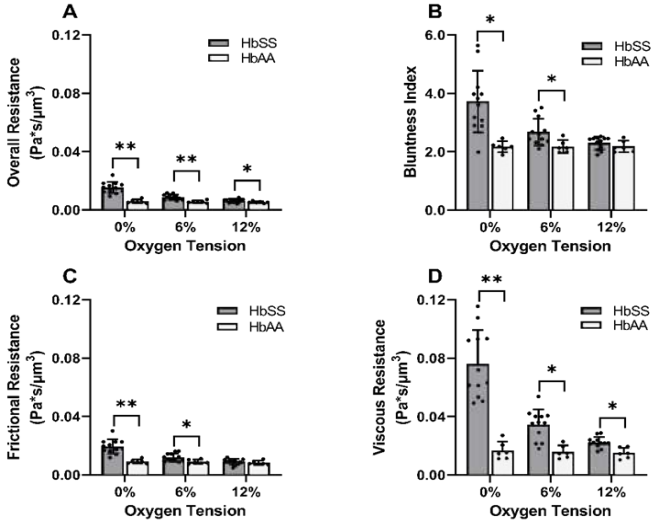


**Figure 2: Evaluation of effective material properties of SCD blood across a range of samples. 12 HbSS samples, 6 HbAA samples. P values correspond to p* < 0.05 and p** < 0.001 using a Mann-Whitney U test.**

## DISCUSSION

We have presented a new method that combines microfluidic, optical tracking, and modeling approaches that can quantify and decouple multiple macroscopic characteristics of SCD blood, including effective viscous and frictional resistances. It is not yet known how the combination of these resistances determines the risk of a vaso-occlusive crisis *in vivo*, and further work is needed to understand how heterogeneity in red blood cell properties determines these emergent properties. Future work will also be aimed at combining our results with clinical outcomes which will allow the determination of vaso-occlusive risk and the prediction of optimal transfusion ratios and treatment regimens that reduce acute and chronic pathology in SCD.


## ACKNOWLEDGEMENTS

Portions of this work were conducted in the Minnesota Nano Center, which was supported by the National Science Foundation through the National Nano Coordinated Infrastructure Network (NNCI) under Award No. ECCS-1542202. This work was supported by the NHLBI under Grant Nos. HL130818 and HL132906.


## REFERENCES


[1] Weatherall, DJ et al., *Blood*, 115:4331–4336, 2010.
[2] Piel, FB et al., *NEJM*, 376:1561–1573, 2017.
[3] Barabino, GA et al., *Annual Review of Biomedical Engineering*, 12:345–367, 2010.
[4] Nash, GB et al., *Blood*, 67:110–118, 1986.
[5] Embury, SH et al., *Microcirculation,* 11:101–113, 2004.
[6] Connes, P et al., *Blood Reviews*, 30:111–118, 2016.
[7] Popel, AS et al., *Annual Review of Fluid Mechanics*, 37:43–69, 2005.
[8] Valdez, JM et al., *APL Bioengineering*, 3:, 2019.
[9] Shi J, et al., IEEE Computer Society Conference on Computer Vision and Pattern Recognition, 593–600, 1994.
[10] Erlich, A et al., *Science Advances*, 5:1–9, 2019.

# ROLE OF THERMAL CONTACT RESISTANCE IN INDUCTION HEATING OF IMPLANTS

**A. Ahmad (1), N. Werkheiser (1), M. Abu-Ayyad (1), M. Garner (2), A. Attaluri (1)**

(1) Department of Mechanical Engineering, The Pennsylvania State University Harrisburg, Harrisburg, PA, United States
(2) Division of Orthopaedic Trauma, Milton S. Hershey Medical Center Penn State College of Medicine, Hershey, PA, United States

## INTRODUCTION

Preclinical studies have shown that non-contact induction heating can be a useful tool to eradicate biofilm infections[1-4]. Exposure to alternating magnetic field (AMF) induces eddy currents in the metal implants and causes the implant to heat up. One concern regarding this method is the heating of the bone which could cause tissue necrosis. Early studies are addressing patient safety and the overall viability of the treatment method[5]. Experimental data from previous test indicates limited heat conduction to the bone during induction heating of the implant[6]. We explore the role of thermal contact resistance between implant and bone in the context of patient safety.

## METHODS

### a. Finite Element Analysis of Thermal Contact Resistance

Figure 1 shows the 3D CAD model used in the thermal contact resistance analysis. The model was obtained from a CT scan of a cadaver that was sliced using 3DSlicer program and converted into a SOLIDWORKS(R) file.

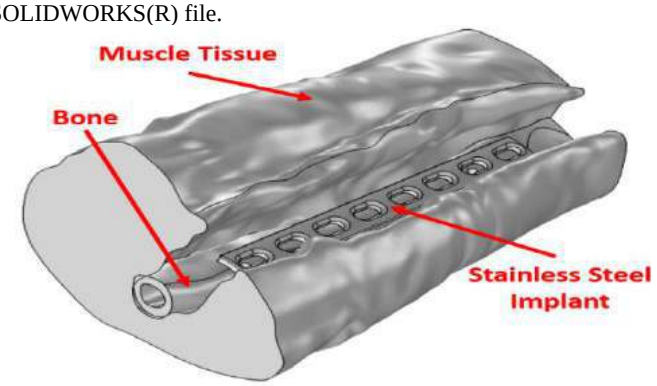


**Figure 1: Simplified CAD model of a cadaver used for thermal contact resistance simulation.**

The heat transfer analysis was done using a commercial finite element software, COMSOL Multiphysics. The model was situated inside and air domain at 20$^{O}$C while the muscle, bone, and implant were given an initial temperature of 37 $^{O}$C. The material properties are shown in Table 1.

**Table 1: Material properties used for bone, muscle, and implant for the thermal contact resistance analysis.**

| Properties | Bone | Muscle | Implant |
|---|---|---|---|
| **Heat Capacitance** | 1313 $\frac{J}{kg-K}$ | 3421 $\frac{J}{kg-K}$ | 500 $\frac{J}{kg-K}$ |
| **Density** | 1908 $\frac{kg}{m^3}$ | 1090 $\frac{kg}{m^3}$ | 7990 $\frac{kg}{m^3}$ |
| **Thermal Conductivity** | 0.32 $\frac{W}{m-K}$ | 0.49 $\frac{W}{m-K}$ | 16.2 $\frac{W}{m-K}$ |
| **Relative Permeability** | 1 | 1 | 1 |
| **Relative Permittivity** | 191 | 5230 | 1 |
| **Electrical Conductivity** | 0.0214 $\frac{S}{m}$ | 0.407 $\frac{S}{m}$ | 1.35E5 $\frac{S}{m}$ |

To simulate the heating condition of the implant from previous cadaver test, a temperature function was created using the step function shown in Figure 2. This condition was applied to the top surface of the implant.

A parametric sweep for the surface roughness was conducted for the values between 0.5 – 2 µm with an increment of 0.5 µm. A parametric study was also done on the contact pressure for the value of 100 – 1000 kPa with an increment of 100 kPa.

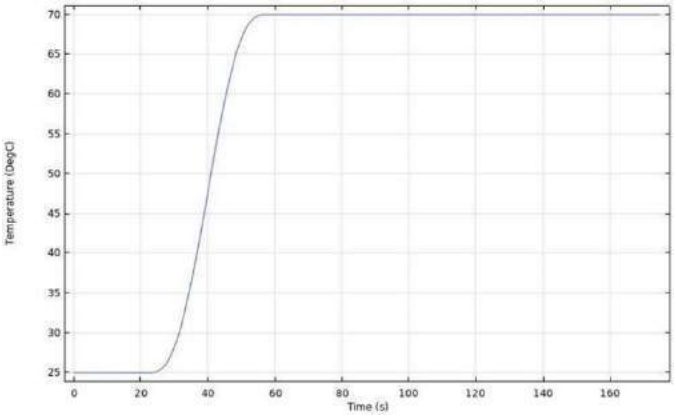


**Figure 2: Temperature function simulating the implant heating during the previous cadaver test.**

## RESULTS

Figure 3 shows the results of the implant and bone temperature for with and without thermal contact resistance. Contact pressure and surface roughness of 400 kPa and 1 µm respectively was assumed as it yielded similar results to previous experimental data[6].

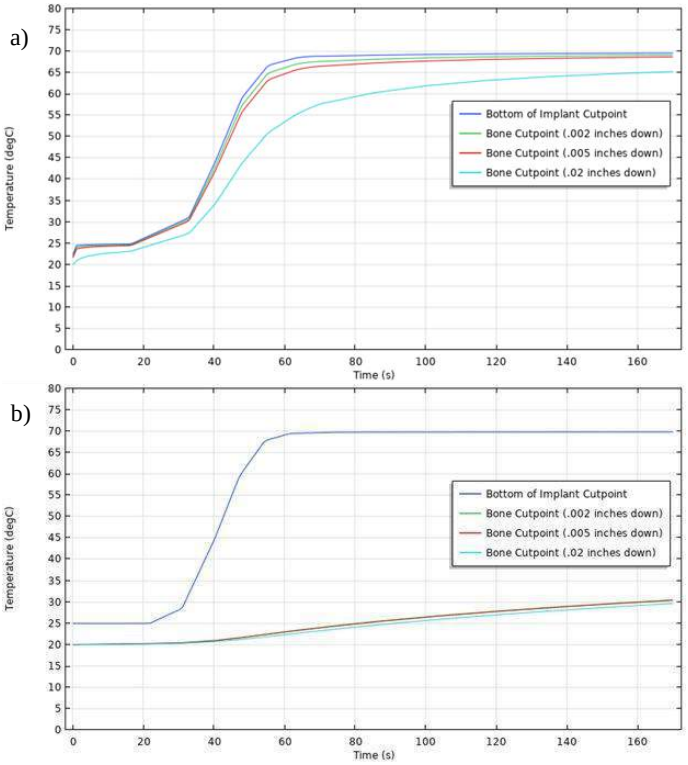


**Figure 3: Temperature of the bottom surface of the implant and the bone at different depth for without (a) and with (b) thermal contact resistance.**

Figure 4 shows the individual effect of surface roughness and contact pressure on the temperature of the bone. The relationship between surface roughness and bone temperature is inversely proportional while the relationship between contact pressure and bone temperature is directly proportional.

## DISCUSSION

Thermal contact resistance plays a crucial role in the heating of the bone. As seen in Figure 3a, the surface of the bone almost reached 70$^{O}$C. Even at a bone depth of 0.02 inches, the temperature rises to a harmful level. Modeling the thermal contact resistance, as seen in Figure 3b, the bone temperature is approximately 54% lower - well below the thermal damage threshold and safe for patients undergoing the treatment.

Note that the results from Figure 3 are specific to contact pressure and surface roughness of 400 kPa and 1 µm respectively. More studies must be done to determine the bone temperature based on different combinations of contact pressure and surface roughness.

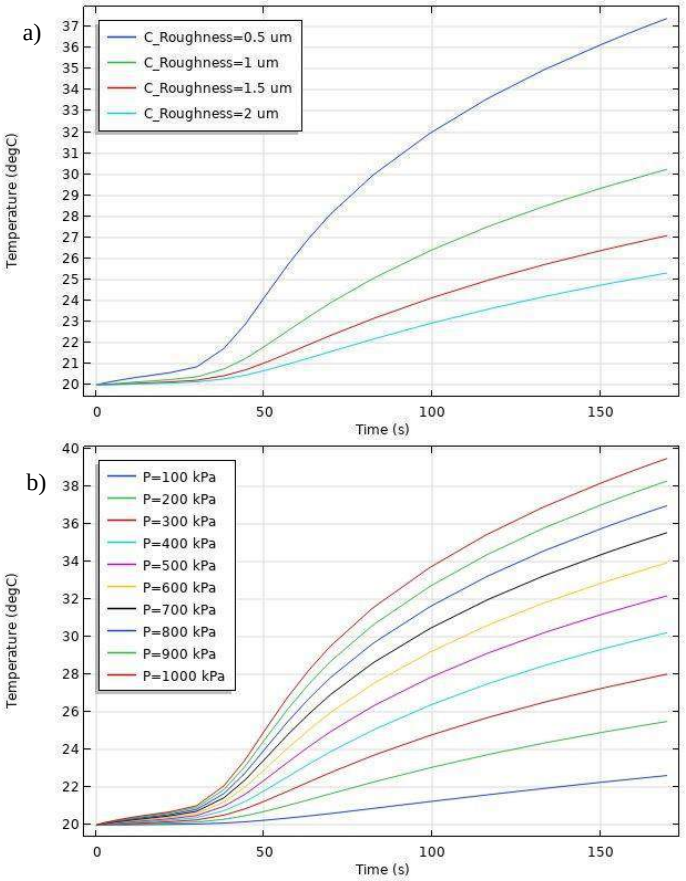


**Figure 4: a) Effect of varying surface roughness on bone heating at a depth of 0.002in assuming 400KPa for contact pressure. b) Effect of varying contact pressure on the bone heating at the same point and assuming surface roughness of 1µm.**


## ACKNOWLEDGEMENTS

This project was made possible with the help of the project sponsors: Penn State Harrisburg and Penn State Center for Orthopaedic Research and Translational Science (CORTS) for financial support.


## REFERENCES


[1] Pijls, B.G et al., *Bone Joint Res.* 2020;9(4):192-199.
[2] Kenneth, L et al., *The Journal of Arthroplasty*, 29:1128-1132, 2014.
[3] Chopra. R, *Sci Rep.*, 7520, 2017.
[4] Pijls, B.G et al., *Bone Joint Res.* 2018;7:609-619.
[5] Sadaphal, et al., *International Journal of Hyperthermia* 39:1 (2021): 81-96.
[6] Attaluri et al, ASME SB3C 2020, Abstract # 351.

# RECENT UPDATES ON THE GHBMC HUMAN HEAD FINITE ELEMENT MODEL – NEW VISCO-HYPERELASTIC BRAIN MATERIAL MODEL AND BRAIN STRAIN VALIDATION

**Ding Lyu (1), Runzhou Zhou (1), Liying Zhang (1)**

(1) Department of Biomedical Engineering, Detroit, MI, United States

## INTRODUCTION

In the United States, approximately 2.5 million Traumatic Brain Injury (TBI)-related emergency department visits, 280,000 TBI-related hospitalizations, and 56,000 TBI-related deaths occurs each year[(1)]. The postmortem human subjects (PMHS) experiments have been conducted to obtain the biomechanical responses relevant to injury production. The Finite Element (FE) model evolve in complexity and improve our understanding of mechanisms of brain injuries far beyond what could be learnt from experimentation. The Global Human Body Models Consortium (GHBMC) human body model is a well-developed FE model for predicting crash-induced injury in an effort to advance crash safety technology.

White matter injury is one of the key features of diffuse brain injury ranging from cerebral concussion to diffuse axonal injury (DAI) of various severities. A variety of experimental studies on the directional properties of gray and white matter tissues revealed transverse isotropy for some of the white matter structures, notably the brainstem, corpus callosum and internal capsules[(2,3)]. This work described the refinement of the GHBMC 50$^{th}$ percentile adult male (M50) head model by the development and incorporation of a new anisotropic hyper-elastic material into the white matter tissues. The material properties were then optimized to best correlate the prediction of brain strain response to the measured strain from PMHS tests. This improved head model v6.0 enables the model capability of predicting directional dependent responses and associated type and severity of the neurotrauma.

## METHODS

*Anisotropic hyper-elastic material model*

All prior versions of the GHBMC M50 head model including v5.0 defined the brain as an isotropic viscoelastic material. To model the anisotropic property of hyper-elastic material, the reinforced fiber may be embedded in the ground Mooney-Rivlin matrix. The strain energy of the material is formulated as:

$$\boldsymbol{W = C_1(I_1 - 3) + C_2(I_2 - 3) + F(\lambda) + \frac{1}{2}[Kln(J)]^2} \quad (1)$$

in which $C_1$ and $C_2$ are the Mooney-Rivlin coefficients; $I_1$ and $I_2$ are the two principal invariants of left Cauchy-Green deformation tensor; $F(\lambda)$ is the function to depict the mechanical properties of axonal fibers; $K$ is the effective bulk modulus of the material. The fiber is assumed to be unable to resist compressive loading and its mechanical behavior was described as

$$\frac{\partial \boldsymbol{F(\lambda)}}{\partial \boldsymbol{\lambda}} = \begin{cases} \boldsymbol{0} & \boldsymbol{\lambda < 1} \\ \boldsymbol{\frac{C_3}{\lambda}\left[e^{C_4(\lambda-1)} - 1\right]} & \boldsymbol{1 < \lambda < \lambda^*} \\ \boldsymbol{C_5 + C_6/\lambda} & \boldsymbol{\lambda > \lambda^*} \end{cases} \quad (2)$$

The deviatoric and volumetric decay coefficients $\beta_s$ and $\beta_p$ are introduced to present the viscoelasticity of soft tissue.

$$\boldsymbol{s_I^\nabla = s^\nabla - \beta_s s_I; \dot{p}_I = \dot{p} - \beta_p p} \quad (3)$$

where s and p can be understood as the deviatoric stress and pressure from the last iteration results. In this new version head model (v6.0), a transversely anisotropic material model (*MAT_SOFT_TISSUE) coupled with *MAT_ADD_INELASTICITY was developed and defined for subcortical white matter, corpus callosum, and brainstem (LS-DYNA R12.0). The direction of the neuronal fiber architecture in each of the structures was defined via MAT_COORDINATES and related to the location of the white matter elements.

*Brain Strain Validation and Optimization of Material Properties*

A multiple-objectives optimization model was built to find the optimal parameters of anisotropic material model for various brain

components in order to improve the validity of brain strain prediction by the model. Seven PMHS head impact cases (C380-T1, T2, T3, T4, T6, C288-T3, and C393-T3)[4, 5] were simulated. The average Green maximum principal strain (MPS) of 12 triad-elements simulated for each case were compared with the experimental curves to derive the validation score (Fig.1). To optimize the properties for test results, the optimization target score was defined as the averaged validation score from all 7 simulations. The higher the target score, the better the model was which reflecting the overall predictive ability of MPS response.

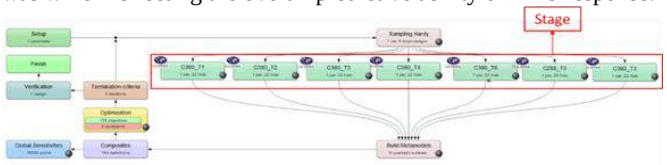


**Figure 1: The optimization model used to optimize the match of the MPS prediction with the PMHS experimental data**

*Intracranial Pressure Validation*

The GHBMC head model v6.0 was subjected to validation against intracranial pressure (ICP) measured from frontal head impact test[6] as well as ICP and ventricular pressure from facial impact[7].

*Facial and Skull Impact Validation*

The skin of the head model v6.0 was updated with a new Ogden material model consistent with the skin model used in other body regions. The model was validated against force-deflection (F-D) responses from 8 skull impacts (frontal, temporal, tempo-parietal, occipital)[8,9] and 6 facial impacts (nasal, zygomatic and maxilla)[10].

## RESULTS

*Brain Response Validation*

Overall, the simulated MPS curves matched well with the experimental curves (Fig. 2). The peak MPS of the experiment and model were 0.076±0.02 and 0.067±0.015, respectively. The average CORA (CORelation and Analysis, v4.0.4) rating was 0.58 (0.48 - 0.74).

The model predicted ICPs matched well to test data[6]. The phase of the simulated pressure curves showed the highest match to the test whereas the magnitude score was the least. The CORA score was 0.60 for coup ICP and 0.63 for contrecoup ICP.

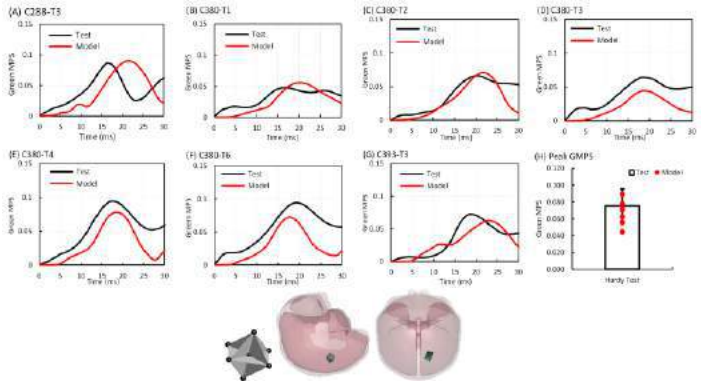

**Figure 2: Validation of time-histories and peak green MPS responses in the brain and 12 null-triad elements for MPS output**

*Skull and Facial F-D Response Validation*

The model predicted F-D, stiffness, and peak fracture force matched well with test results for various facial and skull impact (Fig. 3).

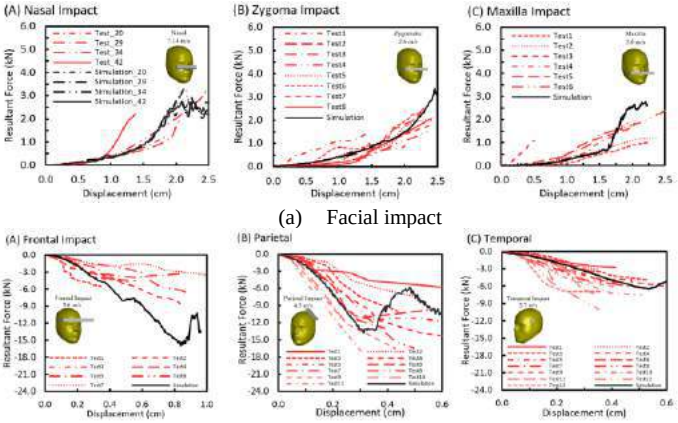


(a) Facial impact




(b) Skull impact

**Figure 3: Comparison of F-D responses in facial and skull impacts**

## DISCUSSION AND CONCLUSIONS

An advanced anisotropic material model was developed, optimized, and incorporated to improve bio-fidelity of the GHBMC M50 head model v6.0. These improvements enable the model to simulate directional properties of the white matter and predict realistic directional dependent impact response in the brain and associated injury severity. The head model v6.0 has been subjected to rigorous validations against a total of 60 PMHS experiments to ensure the accuracy of the model in predicting kinematic, kinetic, stress and strain responses in a variety of loading conditions. The current model showed good biofidity in MPS prediction. The error of peak MPS compared with the test data, was 15% in the current v6.0 model and was 31% in the head model published[5].

To the authors' best knowledge this is the first FE head model that has been rigorously validated against responses in the skull, face and the brain of various regions. This validated head model has been used to develop Crash-induced Injury Indices (CIIs) for predicting facial bone fracture, skull fracture, cerebral contusion, acute subdural hematomas and diffuse brain injury through the reconstructing PMHS and real-world injury cases and the findings are reported in a separate communication.


## ACKNOWLEDGEMENTS

The study was support by the GHBMC, LLC.


## REFERENCES


1. Taylor CA, Bell JM, Breiding MJ, Xu L. Traumatic brain injury–related emergency department visits, hospitalizations, and deaths—United States, 2007 and 2013. MMWR Surveillance Summaries. 2017;66(9):1.
2. Budday S, Sommer G, Birkl C, et al. Mechanical characterization of human brain tissue. Acta Biomaterialia. 2017;48:319-40.
3. Budday S et al. Fifty shades of brain: a review on the mechanical testing and modeling of brain tissue. Archives of Comput. Methods in Engg. 2019:1-44.
4. Hardy WN, Mason MJ, Foster CD et al. A study of the response of the human cadaver head to impact. Stapp Car Crash J. 2007;22-0002
5. Zhou Z et al. A reanalysis of experimental brain strain data: implication for finite element head model validation. Stapp Car Crash J. 2018;22-0007.
6. Nahum AM, Smith R, Ward CC. Intracranial pressure dynamics during head impact. SAE Paper 1977; 770922.
7. Trosseille X, Tarriére C, Lavaste F, et al. Development of a F.E.M. of the Human Head According to a Specific Test Protocol. SAE Paper 1992; 922527
8. Allsop DL et al. Force/Deflection and Fracture Characteristics of the Temporo-parietal Region of the Human Head. SAE Paper 1991; 912907.
9. Yoganandan N, Pintar FA, Sances A, et al. Biomechanics of skull fracture. J Neurotrauma. 1995;12(4):659-68.
10. Allsop DL et al. Facial Impact Response - A Comparison of the Hybrid III Dummy and Human Cadaver. SAE Paper 1988; 881719.

# EXPRESSION OF THE INJURY MARKER ACTIVATING TRANSCRIPTION FACTOR 3 AFTER EXPOSURE TO MMP-1 IS DECREASED IN A NEURON COLLAGEN CO-CULTURE WITH PHOSPHOLIPASE A2 INHIBITION

**Sagar Singh (1), Prabesh Ghimire (1), Beth A. Winkelstein (1,2)**

(1) Department of Bioengineering, University of Pennsylvania, Philadelphia, PA, USA
(2) Department of Neurosurgery, University of Pennsylvania, Philadelphia, PA, USA

## INTRODUCTION

Degeneration of the spinal facet joints is a primary cause of pain, and occurs with aging or trauma [1,2]. The capsular ligament that encases the facet joint is comprised of collagen fibers with afferents that innervate it and have their cell bodies in the dorsal root ganglion (DRG) [3]. After a ligament injury, a complex combination of biomechanical, biochemical, and inflammatory cascades alters the extracellular matrix (ECM) and initiates responses in the afferents, resulting in pain [4]. The matrix metalloproteinases (MMPs) are one such regulator and are responsible for modifying the ECM. The interstitial collagenase MMP-1, in particular, digests type I collagen fibers and has been implicated in pain by acting on neuronal receptors involved in nociception [5,6].

Phospholipase $A_2$ ($sPLA_2$) is involved in inflammation and is an enzyme that hydrolyzes glycerophospholipids, releasing active molecules that induce inflammation and tissue damage [7]. Although $sPLA_2$ is present at a basal level in joint tissue, it is upregulated in degenerated joints [8,9]. Thiotheramide-PC (TEA-PC) is a competitive inhibitor of $sPLA_2$ and has been shown to mitigate degeneration when introduced in the joint space [10]. Further, targeted TEA-PC loaded micelles mitigate neuronal injury in neuropathy, and attenuate spinal neuronal hyperexcitability and pain [11]. Although TEA-PC helps retain joint tissue and relieves pain, it is unclear whether or how that inhibitor alters neuronal activity and/or injury.

In this study an in vitro culture model of the facet capsular ligament was used to begin to evaluate the effect of the $sPLA_2$ inhibitor TEA-PC on neuronal dysfunction and injury following exposure to a collagen-digesting agent. Our neuron-collagen construct (NCC) that models the microstructural environment of the facet capsular ligament was exposed to MMP-1 to simulate the early effects of the degenerative cascade [1,6]. Calcium activity in the afferent DRG neurons was recorded in a time-lapse study before and after MMP-1 exposure and again after treatment with the inhibitor, to serve as a proxy for neuronal dysfunction. NCCs were also assayed for expression of activating transcription factor-3 (ATF-3) 24 hours after treatment to assess injury.

## METHODS

NCCs (n=4) were fabricated from a 2mg/mL collagen solution with dissociated DRG neurons ($3x10^5$cells/mL) from embryonic day 18 rats [12-14]. After plating, neurons were cultured with neurobasal medium supplemented by 1% GlutaMAX, 2% B-27, 1% fetal bovine serum, and 10ng/mL 2.5S nerve growth factor (ThermoFisher). On day in vitro (DIV) 2, neurons were transduced with an AAV expressing GCaMP6f in the media (1:5000), which causes them to transiently fluoresce at 488nm with calcium influx [15,16]. At DIV6, additional collagen (150µL) was added to encapsulate the NCC. At DIV9, NCCs were placed on glass-bottomed dishes in 1.2mL of culture media.

Gels were imaged on a Leica inverted spinning disc confocal microscope under a 20X water-immersion objective. Fields of view (FOVs; n=4) were selected for each NCC and their x-y stage positions were stored using the microscope software to enable making repeated measurements from the same FOV. Images were captured at 3 timepoints for each gel: baseline (BL) before any exposure to MMP-1, immediately after 20mins of exposure to MMP-1, and then 20mins after the treatment. Image series were captured (1024 x 1024 pixels$^2$) at each timepoint at 20fps for 60s to capture transient calcium events (Fig. 1). Baseline images were captured before replacing the culture media with human recombinant MMP-1 (30µg/mL; SRP3117; Sigma Aldrich) [5]. Gels were exposed to MMP-1 and the media was removed after 20mins. A subset of gels (n=2) received 1.2mL of culture media with 10mM of the $sPLA_2$ inhibitor, TEA-PC. The other subset of gels (n=2) received 1.2mL of the media only and served as a vehicle control. Images were taken again after 20mins of treatment and gels were transferred to fresh culture media supplemented with 1% penicillin/streptomycin. After

24hrs, they were fixed with 4% paraformaldehyde for 2hrs, transferred to 30% sucrose in saline solution, and stored at 4°C.

Fixed gels were triple-washed with 3X PBS and incubated with blocking buffer for 2hrs at room temperature. Gels were incubated at 4° overnight with primary antibodies ATF-3 anti-Rabbit (1:200) and collagen anti-Mouse (1:200). The next day, gels were washed with PBS and incubated for 2hrs at room temperature with secondary antibodies Goat-anti-Rabbit 555 (1:500) and Goat-anti-Mouse 647 (1:500). Gels were also labelled with DAPI (1:1000) for 10mins and washed again before being cover-slipped and stored at 4°C.

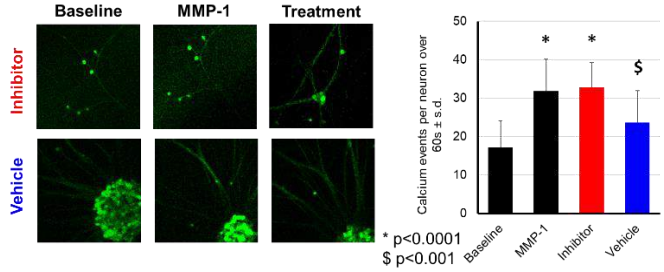


**Figure 1: Calcium activity was imaged before (baseline) and 20mins after exposure to MMP-1, and 20mins after treatment (inhibitor or vehicle). Calcium activity increases with MMP-1 exposure (*) but decreases with vehicle treatment ($).**

Neuronal activity was measured using the custom MATLAB script, FluoroSNNAP, to segment and quantify the number of calcium events for each neuron ($n_{inhibitor}$=122; $n_{vehicle}$=81) [16]. The same neurons were identified and segmented across timepoints using the images of each FOV. A grader blinded to the treatment and exposure time segmented each neuron by drawing around the soma. The frequency of calcium events for each neuron was captured by a template-matching algorithm [16,17]. The mean number of calcium events for each neuron at each timepoint was calculated and compared using a one-way repeated measures ANOVA, with treatment as the factor.

Gels were imaged on a Leica inverted spinning disc confocal microscope under a 20X water-immersion objective with12 FOVs (1024 x 1024 pixels$^2$) acquired for each gel. A separate set of labeled, unexposed gels was also imaged to serve as a control for basal ATF-3 expression levels. Images were analyzed in ImageJ and ATF-3 expression was quantified by measuring the average intensity of the pixels positive for ATF-3 signal, and compared between treatment groups using a t-test.

## RESULTS

Exposure to MMP-1 for 20mins increases the calcium activity from 17.2±6.8 events/min at baseline to 31.8±8.4 events/min in each neuron (p<0.0001) (Fig. 1). Of the two treatment groups, both groups have similar BL activity (18.7±6.4 inhibitor, 16.2±7.0 vehicle events/min/neuron; p=0.68) and activity after MMP-1 exposure (inhibitor 29.9±6.9, vehicle 33.1±9.1 events/min/neuron; p=0.76) but before treatment. Although treatment with TEA-PC does not lower calcium activity (32.8±6.5 events/min/neuron; p=0.925), exposure to culture media alone in the vehicle group does lower activity (23.6±8.3 events/min/neuron; p<0.001) (Fig. 1).

Contrary to the calcium activity responses at 20 minutes after treatment (Fig.1), ATF-3 expression at 24 hours later does appear to be reduced with TEA-PC treatment (Fig. 2). Expression of ATF-3 decreases (p=0.047) after treatment with the sPLA$_2$ inhibitor (25.7±10.3 pixel intensity units) compared to expression levels observed with the vehicle treatment (35.9±8.1 pixel intensity units). Both of these groups exhibited ATF-3 expression levels higher (p<0.01) than those in the control gels (16.8±4.9 pixel intensity units).

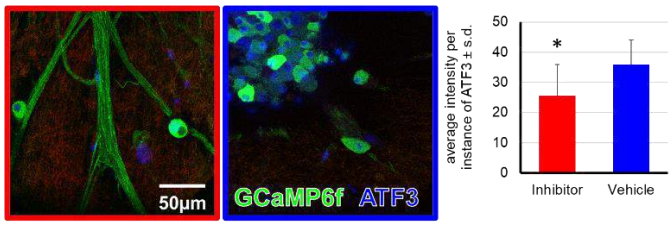


**Figure 2: ATF3 expression 24hrs after MMP-1 exposure and treatment decreases with inhibitor treatment (*p=0.047).**

## DISCUSSION

Although a 20min treatment with the sPLA$_2$ inhibitor, TEA-PC, following exposure to MMP-1 does not reduce neuronal calcium activity, it *does* reduce expression of the injury marker ATF-3 (Figs. 1 & 2), though not to control levels. In fact, ATF-3 levels were approximately 1.5-fold higher than control in the TEA-PC-treated gels. MMP-1 directly binds to protease-activated receptors (PARs), inducing signaling cascades that modulate the inflammatory cascade [18]. The fact that TEA-PC does not appear to fully return ATF-3 to normal suggests that the sPLA$_2$ inhibitor either acts on specific signaling pathways that attenuate, but not wholly prevent, downstream transcriptional changes [19], or that there is a temporal effect in which the TEA-PC is more effective hours after the initial insult.

TEA-PC loaded micelles (at a dose of 0.25 mg/mL) applied immediately after a painful nerve root injury to reduce neuronal hyperexcitability in vivo when injected at the injury site [11]. That concentration of TEA-PC is much higher than the one used in the current study (10mM; which is approximately 30-fold less), which could also explain why calcium activity after MMP-1 stimulation was not attenuated by the TEA-PC. Furthermore, in the micellar delivery the TEA-PC is retained for much longer due to the inhibitor's controlled release, which enables them to also sustain the absence of any pain - related behavior after injury [11]. MMP-1 inhibitors, such as tissue inhibitors of metalloproteinases (TIMPs), may be more effective in mitigating neuronal dysfunction and nociception from degeneration since they directly target the enzymes that are upregulated in the degenerative cascade and that contribute to neuropathic pain [20]. Nevertheless, although the sPLA$_2$ inhibitor does not alter neuronal dysfunction at the concentration used here, it does affect transcriptional changes that underlie neuronal injury and central sensitization [21].

## ACKNOWLEDGEMENTS

Funding from the NIH (R01NS100892) and Catharine Sharpe Foundation. We thank Carlos Aguila for culture and treatment prep.

## REFERENCES

[1] Gellhorn A et al, *Nat Publ Gr* 9(4):216–24, 2013. [2] O'Leary S et al, *Ann Rev Biomed Eng* 20(1):145–70, 2018. [3] Kallakuri S et al, *World J Orthop* 3(2):10, 2012. [4] Ita M et al, *J Orthop Sports Phys Ther* 47(7):450–61, 2017. [5] Ita M et al, *ORS Ann Mtg*, 2018. [6] Troeberg L & Nagase H, *Biochim Biophys Acta-Proteins Proteomics* 1824(1):133–45, 2012. [7] Leistad L et al, *Scand J Rheumatol* 40(4):308–16, 2011. [8] Biyani A & Andersson G, *J Am Acad Orthop Surg* 12(2):106–15, 2004. [9] Carabaza A et al, *Biochem Pharmacol* 45(3):783–86, 1993. [10] Wei Y et al, *Sci Adv* 7(15), 2021. [11] Kartha S et al, *ACS Nano*, 14(7):8103–15, 2020. [12] Zhang S et al, *J Biomech Eng* 138(021013–1):1–12, 2016. [13] Singh S & Winkelstein B, *8th WCB Mtg* p.1, 2018. [14] Singh S & Winkelstein B, *submitted*. [15] Chen T et al, *Nature* 499(7458):295–300, 2013. [16] Patel T et al, *J Neurosci Methods* 243:26–38, 2015. [17] Singh S & Winkelstein B, *SB3C Con*, 17–8, 2021. [18] Heuberger D & Schuepbach R, *Thromb J* 17(4):1–24, 2019. [19] Morioka N et al., *J Neurochem*, 80:989-97, 2002. [20] Ahmed M et al., *Ann Neurosci*, 18(4):162–67, 2011. [21] Kartha S et al., *Mol. Pain*, 17:174480692110662, 2021.

# USING A TISSUE-ENGINEERED MODEL TO INVESTIGATE THE IMPACT OF COLLAGEN ORIENTATION ON THE LOCAL MECHANICAL BEHAVIOUR OF ATHEROSCLEROTIC PLAQUE CAPS

**Hanneke Crielaard (1), Tamar B. Wissing (1,2), Su Guvenir Torun (1), Pablo de Miguel (1,3) Ranmadusha M. Hengst (1,3), Gert-Jan Kremers (4), Frank J.H. Gijsen (1,3), Kim van der Heiden (1,2), Ali C. Akyildiz (1,3)**

(1) Department of Biomedical Engineering, Erasmus Medical Center, Rotterdam, the Netherlands
(2) Department of Biomedical Engineering, Eindhoven University of Technology, Eindhoven, the Netherlands
(3) Department of Biomechanical Engineering, Delft University of Technology, Delft, the Netherlands
(4) Erasmus Optical Imaging Center, Erasmus Medical Center, Rotterdam, the Netherlands

## INTRODUCTION

Stroke is commonly initiated by rupture of the atherosclerotic plaque fibrous cap in a carotid artery. However, cap rupture mechanisms are not well understood yet. Collagen is the main load-bearing component in caps. [1] Understanding its impact on local cap mechanics may provide critical insights into plaque rupture. Various limitations within studying the real animal and human plaques in vivo and ex vivo highlight the need for additional methods to investigate rupture mechanics. Therefore, we created a tissue-engineered collagenous plaque cap analog model, with controllable collagen architecture, that can be imaged and mechanically tested [2]. In the current study, we present our pipeline for visualizing collagen orientation and obtaining local mechanical properties in these analogs to analyze the relation between collagen architecture and local cap mechanics.

## METHODS

*Development of fibrous cap analogs*

Ten cap analogs were created by seeding human vena saphena cells (HVSCs) in 1 x 1.5 cm-sized fibrin gels (Fig 1A).

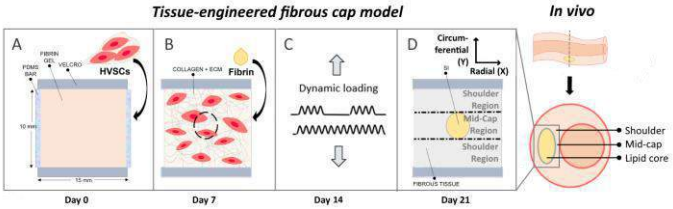


**Figure 1: Protocol for developing fibrous cap analogs.**

After seeding, the samples were cultured for 7 days under static loading, whereafter a 2 mm Ø soft inclusion (SI) was created by punching a hole in the center of each analog and filling this core with fibrin (Fig 1B). This fibrin inclusion mimics the soft lipid core of atherosclerotic plaques. The analogs were statically cultured for 7 more days, after which they were exposed to 7 days of dynamic loading (Fig 1C) using the Flexcell FX-4000T (Flexcell Int, 196 McKeesport, PA).

*Collagen imaging*

On day 21, the samples were exposed to multiphoton microscopy (MPM) with second harmonic generation (SHG) to visualize the collagen architecture. First, a tile scan was made of the entire sample (Fig 2A). From the tile scan, two horizontal lines of adjacent tiles were selected for further analysis. One line of the selected tiles overlaid the shoulder region of the sample while the other overlaid the mid-cap, including the soft inclusion (Fig 2B). For each tile, z-stack imaging in the depth direction was performed (728x728 µm, 512x512 pixels, 3-µm steps).

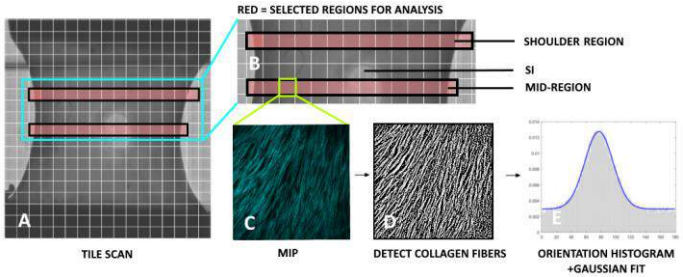


**Figure 2: Collagen imaging and fiber orientation analysis pipeline.**

After imaging, maximum intensity projection (MIP) images were created of each z-stack (Fig 2C). Finally, a MATLAB based fiber orientation analysis tool (FibLab) was used to calculate the orientation of individual collagen fibers in the MIP (Fig 2D). A Gaussian distribution was fit to the histogram of all detected collagen fiber orientations (Fig 2E). From this gaussian distribution, the predominant

fiber orientation (θ in degrees) and standard deviation (SD) of the fiber orientations in the tile, which indicates the degree of fiber anisotropy, were determined.

*Uniaxial tensile tests and DIC*

After imaging, the samples were mechanically tested. A speckle pattern for digital image correlation (DIC) was applied to the top surface of each sample using an airbrush and a tissue dye. After pre-stretch (15 mN) and preconditioning (10 cycles of 10% strain), the samples were uniaxially strained until complete failure at a speed of 100%/min. The samples were strained in the y-direction, which biologically corresponds to circumferential strain (Fig 1D). To obtain local strains (Green-Lagrange), DIC analysis was performed in MATLAB using the open-source software Ncorr [3].

## RESULTS

*Collagen imaging*

The predominant fiber angles (θ) and standard deviations within the tiles of a representative sample are presented in Fig 3. The figure shows that the fibers in both the shoulder and mid-cap region are mostly oriented in the y-direction. Similar results are found in the other samples. The average fiber orientation (θ ± SD) of the ten analyzed samples is 91±22° in the shoulder region and 89±22° in the mid-cap region.

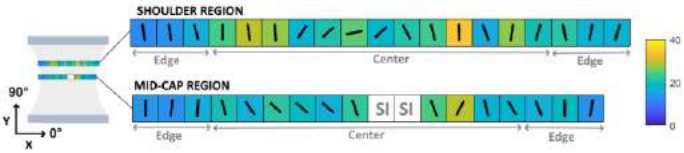


**Figure 3: Mean predominant fiber angle (black line) and SD (background color) in both the mid-cap and shoulder region of an analog. A larger SD indicates greater fiber dispersion. Z-stacks located in the SI were excluded from analysis.**

The figure also indicates that the fibers at the edges of the sample (defined as the 3 most left and right tiles) are oriented closer to the y-direction than the fibers in the center of the sample. This holds for both shoulder and mid-cap regions. The difference of the predominant fiber orientation with the y-axis (Δθ) averaged over the ten analyzed samples is 13° at the edges and 35° in the center. The minimum and maximum Δθ found in the ten samples are 0 and 54 at the edges and 0 and 89 in the center of the sample, respectively. Finally, the center sections indicate a more dispersed fiber distribution, indicated by the high SD values (background color in Fig 3), compared to the edge sections of the samples (Average SD values 10 samples: 24 vs 18).

*Uniaxial tensile tests and DIC*

Of the ten samples, five ruptured at the clamping site and were therefore excluded from further strain analysis. The rupture in all analyzed samples (n=5) initiated in the SI, in the mid-cap region (Fig 4A.1). After rupture initiation, the rupture propagated in a -slightly tilted-horizontal direction (Fig 4A.2). Once the rupture arrived at the SI-fibrous tissue interface, the rupture propagation paused for a short period (Fig 4A.3). Finally, the rupture propagated to the fibrous tissue, resulting in a crack over the full width of the analog (Fig 4A.4).

Fig. 4B shows the DIC-derived local strain measurements in the tensile direction ($E_{yy}$) at the time point of rupture initiation in the SI. The figure shows a region of elevated tensile strain near the rupture location. The maximum tensile strain ± SD found in this high-strain region averaged for all five analyzed samples is 60% ± 20%. This maximum strain is four times higher than the average tensile strain in the entire sample (15±5%). This clearly indicates that the average tissue strain commonly used for plaque tissue rupture characterization underestimates the real, local rupture strain.

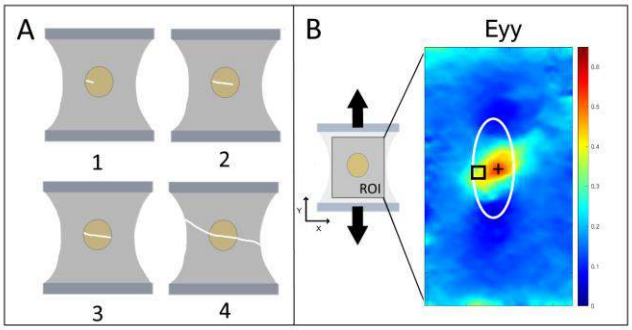


**Figure 4: A) Phases of rupture identified in cap analogs. B) DIC-derived local strains (tensile ($E_{yy}$)). The white oval shape marks the edge of the soft inclusion, the black rectangle the location of rupture initiation and the plus sign the maximum strain location.**

## DISCUSSION

We successfully created tissue-engineered collagenous plaque cap analogs to study the atherosclerotic plaque cap rupture characteristics. We used MPM with SHG to obtain information about the collagen architecture of these analogs and obtained local strain data using uniaxial tensile tests with DIC.

The results from MPM showed that the collagen fibers in the analogs are mainly oriented in the y-direction, which corresponds to the circumferential direction in the real plaque tissue. This predominant fiber orientation is in line with the predominant fiber orientation in human plaques [4]. Despite the overall circumferential orientation, MPM results demonstrated larger deviations of the predominant fiber orientation from the circumferential direction and indicate more dispersed fiber architecture in the center sections compared to the edges.

The DIC measurements showed elevated tensile strains in the SI, representing the necrotic core of the real plaques. Rupture initiated near this region of elevated tensile strains. The maximum strain found in this region is similar to the local rupture strain found in a previous DIC-analysis of ex vivo human plaque tissue [5]. After rupture initiation near the high-strain region within the SI, the rupture in the analogs propagated towards the luminal surface of the fibrous cap. The directionality (from SI to lumen) observed in this study differs from the hypothesis that proposes plaque rupture starts at the lumen.

As the next step, with a larger sample set, we will investigate the intra- and inter-sample variations in the fiber orientations in more detail and study the association of this local structural information to the rupture propagation path and to the local strain pattern. Furthermore, we will further study our new hypothesis proposing rupture initiation in the SI to gain better understanding of the underlying plaque rupture mechanisms.

## ACKNOWLEDGEMENTS

This research, HC, TBW and KvdH are funded by an NWO-Vidi grant 18360.

## REFERENCES

[1] Holzapfel GA et al. *J Biomech.* 47(4): 859-869, 2014 [2] Wissing TB et al. *BioRxiv.* Preprint 2021 doi:10.1101/2021.07.20.451997; [3] Blaber J et al. *Exp. Mech.*, 55: 1105-1122, 2015 [4] Akyildiz AC et al. *J Struct Biol.* 200(1): 28-35, 2017 [5] Guvenir, S. et al. *Proceedings book of SB³C2021*, 195, 2021

# HEAD ACCELERATION MEASUREMENT IN YOUTH FOOTBALL ATHLETES USING A MOUTHPIECE-BASED SENSOR

**Madison E. Marks (1,2), Ty D. Holcomb (1,2), N. Stewart Pritchard (1,2), Logan E. Miller (1,2), Joel D. Stitzel (1,2), Jillian E. Urban (1,2)**

(1) School of Biomedical Engineering and Sciences, Virginia Tech - Wake Forest University, Winston-Salem, NC, USA
(2) Department of Biomedical Engineering, Wake Forest University, Winston-Salem, NC, USA

## INTRODUCTION

Concussions continue to be a prevalent safety concern in contact sports due to their potential short-term and long-term neurodegenerative effects. Studies suggest that repetitive, non-concussive head impact exposure may lead to similar pathologies as those caused by concussion.[1,2] With approximately 3.5 million youth athletes (age 6-13) participating in football each year, it is essential to minimize head impact exposure to prevent future brain injury.[3-6] Football head acceleration data has been quantified using the Riddell Head Impact Telemetry (HIT) System. Advancements in sensor technology has allowed for head acceleration measurement with greater accuracy using mouthpiece-based sensors.[7,8] however, there is little information on head acceleration events in youth football with mouthpiece-based sensors.[9] Therefore, the objective of this study was to characterize head acceleration in middle school football using mouthpiece-based sensors.

## METHODS

Thirty athletes on two middle-school-level (ages 11-14) football teams were instrumented with a mouthpiece-based sensor, containing a gyroscope and tri-axial accelerometer. Mouthpieces were custom fit to each athlete's upper dentition using a TRIOS intraoral scanner (3Shape, Copenhagen, Denmark). The mouthpiece sensors were set to a threshold of 5g: if any axis exceeded 5g for at least 3 milliseconds, the mouthpiece would record an event for 15 ms pre-trigger and 45 ms post-trigger.[7] Head acceleration exposure was quantified by number of head acceleration events (n), linear acceleration (LA), rotational velocity (RV), and rotational acceleration (RA). Data were collected for each session (e.g., practice, scrimmage, game) during which a participating athlete was present. One time-synchronized camera was placed on the sideline at sessions to collect video data. Members of the research team were present to monitor all data collection.

All head acceleration events were individually video-verified by the research team so that false-positive events could be identified and excluded from analysis. True-positive events were categorized by several variables, including session type and impact type (Table 1). Analysis and results from athletes participating on one of the enrolled youth football teams (n=15 athletes) are presented herein.

**Table 2: Overall values for biomechanical parameters.**

| Impact Type | Description |
|---|---|
| Blocking | Collision with closing distance of <10 ft. |
| Running | Collision between athletes while running |
| Passing | Collision while attempting to catch/block a pass |
| Tackling | Athlete is taken to the ground by another player |
| Isolated Fall | Athlete falls without contact from external source |

## RESULTS

A total of 23,605 recordings were collected over 34 sessions (25 practices, 1 scrimmage, and 8 games). After video verification of individual recordings was completed, 21,773 false-positive events were excluded; the remaining 1832 recordings were determined to be true-positives, 752 (41%) of which exceeded 10g. False-positive recordings were often a result of an athlete interacting with their mouthpiece. The total number of head acceleration events (i.e., events) per athlete ranged from 7 to 436, with an average (± standard deviation) of 122±128 events (i.e., events) over the duration of the season. Summary statistics for peak resultant LA, RV, and RA for the sample are provided in Table 2.

**Table 2: Summary statistics for biomechanical parameters.**

| Event Threshold | Sensor Output | Mean ± St Dev | Median | 95$^{th}$ Percentile |
|---|---|---|---|---|
| ≥5g (n=1832) | LA (g) | 11.7 ± 10.2 | 8.9 | 28.2 |
| | RV (rad/s) | 8.9 ± 4.5 | 8.0 | 17.4 |
| | RA (rad/s$^2$) | 925.6 ± 1029 | 655.0 | 2477 |
| ≥10g (n=752) | LA (g) | 18.4 ±13.0 | 14.1 | 42.6 |
| | RV (rad/s) | 11.2 ± 4.91 | 10.3 | 20.1 |
| | RA (rad/s$^2$) | 1439 ± 1439 | 966.0 | 4231 |

All data, exceeding 5g, were analyzed by session type and impact type. Summary statistics of head acceleration data grouped by session type are provided in Table 3. Games had the greatest magnitude median LA, RV, and RA. Scrimmages had the lowest median LA, RV, and RA.

**Table 3: Biomechanical parameters by session type.**

| Session Type | Sensor Output | Mean ± St Dev | Median | 95th Percentile |
|---|---|---|---|---|
| Practice (n=1273) | LA (g) | 11.9 ± 11.3 | 8.8 | 30.0 |
| | RV (rad/s) | 8.8 ± 4.4 | 7.9 | 16.9 |
| | RA (rad/s$^2$) | 945.6 ± 1157 | 637.7 | 2770 |
| Scrimmage (n=110) | LA (g) | 10.6 ± 7.4 | 8.5 | 22.3 |
| | RV (rad/s) | 8.8 ± 4.7 | 7.6 | 17.3 |
| | RA (rad/s$^2$) | 825.4 ± 679.4 | 651.0 | 1836 |
| Game (n=449) | LA (g) | 11.2 ± 6.9 | 9.4 | 24.1 |
| | RV (rad/s) | 9.3 ± 4.6 | 8.5 | 18.3 |
| | RA (rad/s$^2$) | 893.4 ± 641.9 | 723.7 | 2006 |

Summary statistics of head acceleration data by impact type are provided in Table 4. Running collisions had the greatest median LA, RV, and RA. Isolated falls had the lowest median LA and RA. Blocking collisions had the lowest median RV. A sample running event collected by an instrumented athlete, engaging in helmet-to-helmet contact during a game, is shown in Figure 1.

**Table 4: Biomechanical parameters by impact type.**

| Impact Type | Sensor Output | Mean ± St Dev | Median | 95th Percentile |
|---|---|---|---|---|
| Blocking (n=1157) | LA (g) | 10.7 ± 8.9 | 8.6 | 20.8 |
| | RV (rad/s) | 8.1 ± 4.0 | 7.3 | 15.0 |
| | RA (rad/s$^2$) | 817.1 ± 916.6 | 601.7 | 1780 |
| Running (n=269) | LA (g) | 14.7 ± 11.7 | 11.3 | 33.9 |
| | RV (rad/s) | 10.7 ± 5.1 | 9.8 | 19.9 |
| | RA (rad/s$^2$) | 1210 ± 1146 | 857.8 | 3435 |
| Passing (n=21) | LA (g) | 13.4 ± 11.1 | 8.7 | 41.9 |
| | RV (rad/s) | 9.6 ± 4.3 | 9.3 | 15.6 |
| | RA (rad/s$^2$) | 1453 ± 1702 | 790.8 | 5937 |
| Tackling (n=319) | LA (g) | 13.1 ± 12.6 | 9.4 | 33.0 |
| | RV (rad/s) | 10.3 ± 5.0 | 9.3 | 20.8 |
| | RA (rad/s$^2$) | 1078 ± 1238 | 762.8 | 2770 |
| Isolated Fall (n=66) | LA (g) | 8.7 ± 6.1 | 6.8 | 18.0 |
| | RV (rad/s) | 9.0 ± 3.9 | 8.2 | 16.9 |
| | RA (rad/s$^2$) | 764.5 ± 549.0 | 598.2 | 1976 |

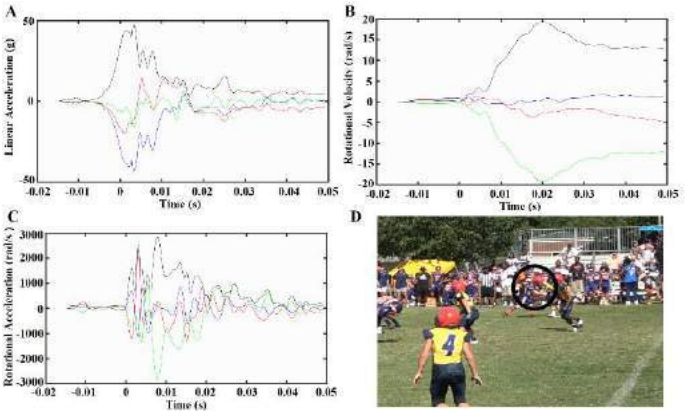


**Figure 1: Running event collected from an instrumented athlete. (A) LA plot, (B) RV plot, (C) RA plot, and (D) image of the event.**

## DISCUSSION

The objective of this study was to characterize head acceleration events in middle school football athletes using mouthpiece-based sensors. Events with LA greater than 10g generally had lower median LA values and higher RA values, when compared with past studies utilizing the HIT System.[5,7,9] This may result from differences in the coupling of sensors (i.e. mouthpiece, HIT System) to an athlete's skull.

All head acceleration data were categorized and analyzed by session type and impact type. Games had the greatest magnitude median LA, RV, and RA; however, two-thirds of the head acceleration events were attributed to practices. This aligns with prior youth football research with the HIT system.[6,9] The higher head acceleration events in games might result from athletes engaging in more intense contact than they would experience in practices. Practices involve repetitive contact across multiple days per week, resulting in a greater proportion of head acceleration events over the course of the season.

Running collisions had the highest magnitude LA. Higher LAs could result from athletes building up high speeds before the event. This is consistent with past studies, which found that events involving fast contact speeds had greater linear acceleration.[10] Running collisions also had the greatest median RV and RA. This might result from athletes running in from oblique field positions.

One limitation of this study was that several research team members completed video verification of acceleration events. To ensure consistency in film review, inter-rater-reliability was analyzed and determined to be acceptable. The results of this study represent a single football team and the results of this study may not be generalizable to every team youth football across the country. This research utilized mouthpiece-based sensors to collect head acceleration data in youth football and demonstrate kinematic differences by session and impact type. The data collected in this study will be utilized in the future development of an evidence-based intervention for youth football.


## ACKNOWLEDGEMENTS

The authors thank the youth football organizations for participating in this research. The authors also thank the project manager, Tina Strates, and the undergraduate interns for assisting with this study. NIH NICHD (K25HD101686) provided funding for this study.


## REFERENCES


[1] Stern, RA et al., *PM&R*, 3:S460-S467, 2011. [2] Stamm, JM et al., *Neurology*, 84(11): 1114-1120, 2015. [3] Guskiewicz, KM et al., *Am J Sports Med*, 28(5):643-650, 2000. [4] Powell, JW et al., *JAMA*, 282(10):958-963, 1999. [5] Daniel, RW et al., *Ann Biomed Eng*, 40(4):976-981, 2012. [6] Cobb, BR et al., *Ann Biomed Eng*, 41(12):2463-2473, 2013. [7] Rich AM et al., *Ann Biomed Eng*, 47(10):2109-2121, 2019. [8] Swenson AG, et al., *Res Sports Med*, 1-11, 2021. Gabler, LF et al., *Ann Biomed Eng*, 49(10):2760-2776, 2021. [9] Kelley, ME et al., *J Neurotrauma*, 34(11):1939-1947, 2017. [10] DiGuglielmo, DM et al., *J Appl Biomech*, 37(2):145-155, 2021.

# IMAGE-BASED TEMPORAL QUANTIFICATION OF AORTIC COARCTATION WITHIN THE RANGE OF SEVERITIES AND DURATIONS SEEN CLINICALLY

**Jamasp Azarnoosh (1), Arash Ghorbannia (1), John F. LaDisa Jr. (1,2)**

(1) Department of Biomedical Engineering, Medical College of Wisconsin and Marquette University, Milwaukee, WI, USA
(2) Departments of Pediatrics, Medicine and Physiology, Medical College of Wisconsin, Milwaukee, WI, USA

## INTRODUCTION

Coarctation of the aorta (**CoA**) is one of the most common congenital cardiovascular defects. CoA often presents at birth as a narrowing that is most frequently treated surgically [1], [2]. Even after successful treatment, life expectancy is still lower than normal due to long-term morbidity, most often caused by refractory hypertension (**HTN**) [3]. The contributors to persistent HTN in CoA after treatment are not well understood [1], which is the primary focus of our research. The current treatment guideline of a peak-to-peak blood pressure gradient (**$BPG_{pp}$**) ≤20 mmHg implemented clinically has revealed irreversible changes in arterial structure and function, yet revised $BPG_{pp}$ guidelines have not been proposed [4]. Prior studies of pathologic aortic remodeling have neglected the temporal evolution of mechanical stimuli at younger ages that may contribute to HTN in CoA [1], [3]–[5]. As a step towards quantifying temporal alterations in mechanical stimuli and changes in arterial properties for the range of CoA severities and durations seen clinically, the current study proposes a methodology using ultrasound images and magnetic resonance imaging (**MRI**) data to develop computational geometries of the aorta. Investigation into the temporal evolution of coarctation in human patients is technically challenging due to a relatively low number of heterogeneous patients at each center. Therefore, we used a novel rabbit model that has served as a clinically representative model of CoA in humans [4], [5].

## METHODS

Following IACUC approval, rabbits were exposed to $BPG_{pp}$ severities ≤10, 11-20, and >20 mmHg for 1, 3, or ~20 weeks by varying the severity and duration of coarctation using permanent (**CoA**), dissolvable (**dCoA**), and rapidly dissolvable (**RdCoA**) sutures tied around the aorta at the location CoA most often presents clinically [4], [5]. The CoA group replicates untreated condition while the coarctation is corrected in dCoA and RdCoA groups within 1 and 3 weeks, respectively. This rabbit model includes data from a control group and nine CoA groups that mimic the morphology seen clinically in humans with CoA.

The general approach to develop computational geometries over ages is shown in **Figure 1**. Bodyweight for the rabbits was measured during the experimental duration, which aligns with data from Masoud et al. [6] (**Figure 1A**). Data were fit to the allometric (power-law) equation, which is wildly used for scaling in biology [7], [8]. A subject-specific geometry was reconstructed using SimVascular (simvascular.github.io) from 3-D MRI at the final week (MRI week marked in **Figure 1A**) and used as the baseline to create geometries at younger ages. A series of ultrasound images across all regions from the proximal to distal aorta including the coarctation were collected during

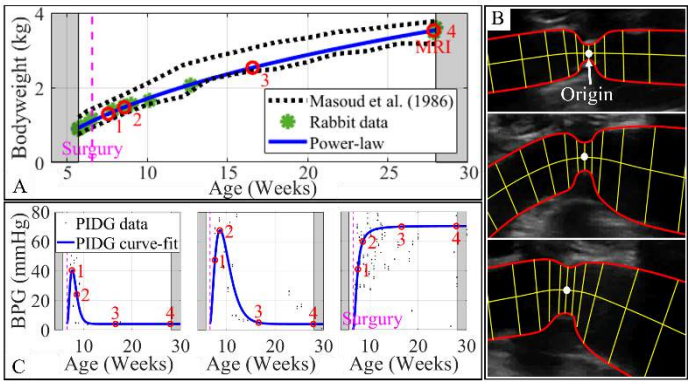


**Figure 1: (A) To replicate geometries at younger ages, MRI data are adjusted based on body size using allometric scaling (e.g. bodyweight vs. age for the dissolvable 20mmHg BPGpp rabbit at 4 time points). (B) A series of ultrasound images at the diastolic phase for three time points in a representative rabbit. (C) Temporal peak instantaneous Doppler pressure gradient (PIDG) for RdCoA, dCoA, CoA from left to right, respectively.**

the experimental duration. Images during the diastolic phase for all available series of ultrasound were imported for image processing (ImageJ) to quantify diameters. **Figure 1B** shows segmentations assigned perpendicular to the centerline to measure the temporal evolution of CoA shape from initial to final weeks. The longitudinal length of each segmentation was measured from the coarctation. Diameters and longitudinal length measurements were imported to MATLAB to predict the shape of the aorta using interpolation (Piecewise Cubic Hermite Interpolating Polynomial). The allometric equation was then used again to determine temporal changes of diameters at any longitudinal locations from proximal to distal. A similar procedure was performed during the systolic phase to determine arterial wall deformation (i.e. percentage radial strain) that will be used for quantifying elastic modulus in FSI simulations. The CoA shape based on longitudinal ultrasound images was determined at four time points of interest. The critical time points at younger ages are selected based on peak velocities seen in each group by Doppler-based estimates of BPG. Briefly, the first time point represents the age when peak BPG is observed in the rapid dissolvable group i.e. one week after surgery date (time point 1 in **Figure 1C**). Similarly, the second time point is two weeks after the surgery date when peak BPG occurs in the dissolvable group (time point 2 in **Figure 1C**). The third time point is the middle age of the rabbits (i.e. ~10 weeks after surgery date) to evaluate the evolution of mechanical stimuli at this age from early weeks (time point 3 in **Figure 1C**).

## RESULTS

**Figure 2** provides example results from the methods above by showing temporal changes in the CoA shape at four time points for a dissolvable CoA with the severity of 20 mmHg. **Figure 2A** shows diameter variation over ages at three selected locations (proximal, CoA, and distal), during the diastolic phase (solid black line) that was used to develop geometries and systolic phase (dotted blue line) used to determine arterial wall deformation for quantifying elastic modulus in future FSI simulations. Corresponding models for each time point are shown in **Figure 2B** with the final week reconstructed model from MRI. The other three time points scaled from the geometry of the final week based on the bodyweight curve shown in **Figure 1A** and the coarctation region adjusted corresponding to the shapes as depicted in **Figure 2C**.

Similar to the results presented in **Figure 2**, imaged-based quantification of computational geometries was conducted for other CoA groups as well as a control group. A complete summary of aortic deformation at four time points is presented in **Table 1**. The results in the control group indicate that radial strain seems to remain consistent with age (i.e. ~11%). In all CoA groups, radial strain in the proximal region above the coarctation was generally more than was seen in control measurements. Conversely, less deformation was seen distal to the coarctation as the severity and associated pressure drop across the coarctation increased. The proximal region of dissolvable CoA groups appeared to be exposed to smaller deformation with age compared with permanent CoA. The radial strain variation in the final week of dissolvable groups was similar between proximal and distal regions, but more pronounced in the rapid dissolvable groups since the suture dissolves in the first few weeks and the narrowing is enlarged with age.

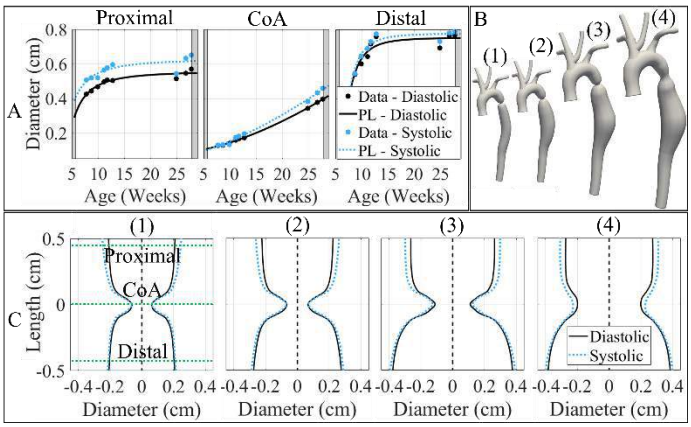


**Figure 2: (A) Diastolic and systolic diameters with age at proximal, CoA, and distal locations were measured and fit to the power-law model. (B) The 3-D geometries at four selected time points. (C) Temporal evolution of the CoA shape measured using longitudinal ultrasound images (e.g. dissolvable 20mmHg BPGpp at 4 time points) and incorporated into computational models.**

**Table 1: Temporal changes in radial strain at the proximal, CoA, and distal for control and 9 CoA groups. Values are in percentage.**

| | Proximal | | | | CoA | | | | Distal | | | |
|---|---|---|---|---|---|---|---|---|---|---|---|---|
| Group | 1 | 2 | 3 | 4 | 1 | 2 | 3 | 4 | 1 | 2 | 3 | 4 |
| Control | 11 | 11 | 12 | 12 | N/A | N/A | N/A | N/A | 11 | 11 | 12 | 12 |
| CoA5 | 10 | 10 | 11 | 11 | 0 | 0 | 0 | 0 | 11 | 10 | 9 | 7 |
| CoA10 | 13 | 12 | 10 | 10 | 0 | 0 | 0 | 0 | 10 | 9 | 5 | 4 |
| CoA20 | 12 | 12 | 12 | 10 | 0 | 0 | 0 | 0 | 5 | 5 | 5 | 6 |
| dCoA5 | 14 | 14 | 10 | 9 | 0 | 0 | 13 | 13 | 13 | 13 | 11 | 10 |
| dCoA10 | 10 | 10 | 9 | 8 | 0 | 0 | 12 | 12 | 8 | 8 | 8 | 7 |
| dCoA20 | 15 | 14 | 11 | 11 | 0 | 0 | 12 | 14 | 4 | 4 | 4 | 3 |
| RdCoA5 | 11 | 9 | 8 | 8 | 0 | 4 | 7 | 8 | 8 | 8 | 7 | 7 |
| RdCoA10 | 11 | 10 | 9 | 8 | 0 | 8 | 11 | 11 | 8 | 9 | 8 | 8 |
| RdCoA20 | 10 | 10 | 8 | 7 | 0 | 4 | 6 | 5 | 4 | 5 | 6 | 6 |

## DISCUSSION

The temporal evolution of aortic coarctation is absent in the literature. We proposed a novel approach to quantify image-based computational models of the aorta exposed to severities and durations seen clinically. This method provides quantitative information on the temporal evolution of regional aortic deformation (i.e. radial strain from the proximal to distal regions of the coarctation). Subject-specific geometries for nine CoA groups and a control group were developed at four time points that can now be used in FSI simulations to determine the range of mechanical stimuli that correlate with irreversible vascular impairment [4]. We will conduct longitudinal FSI simulations using the developed geometries and boundary conditions measured empirically for each group to characterize mechanical stimuli including blood flow velocity patterns, medial tension, and wall shear stress (WSS) indices. The radial strain across all regions (i.e. from proximal to distal) measured using longitudinal ultrasound images as well as 2-D phase-contrast magnetic resonance imaging (PC-MRI) sequences at the final week allows for quantification of elastic modulus at younger ages in the FSI simulation tuning process, which is our ongoing work.


## ACKNOWLEDGEMENTS

The authors acknowledge the support from the National Institutes of Health (NIH) Grant No. R01HL142955.


## REFERENCES


[1] LaDisa Jr., J. F. et al., *Congen Heart Disease*, 6(5):432–443, 2011.
[2] Cohen M. et al., *Circulation*, 80(4):840-845, 1989.
[3] Frydrychowicz A. et al., *J Cardiovas Magne Reson*, 10(1):30, 2008.
[4] Menon A., et al., *Am J Physiology*, 303(11):1304-1318, 2012.
[5] Menon A. et al., *J Pharm & Toxicol Methods*, 65(1)18-28, 2012.
[6] Masoud, F. et al., *J Orthopaedic Research*, 4(2) :221-231, 1986.
[7] Westerhof, N. et al., *Springer International Publishing*, 2019.
[8] Gayon, J. et al., *American Zoologist*, 40(5):748-758, 2000.

# A NOVEL BI-VENTRICLE MECHANICAL SUPPORT CONFIGURATION FOR THE FAILED FONTAN CIRCULATION

**Emrah Sisli (1), Canberk Yildirim (2), Ibrahim B. Aka (3), Osman N. Tuncer (4), Yuksel Atay (4), Mustafa Ozbaran (4), Kerem Pekkan (5)**

(1) Department of Cardiovascular Surgery, Osmangazi University, Eskisehir, Turkey
(2) Department of Biomedical Sciences and Engineering, Koc University, Istanbul, Turkey
(3) Department of Mechatronics Engineering, Istanbul Bilgi University, Istanbul, Turkey
(4) Department of Cardiovascular Surgery, Ege University Faculty of Medicine, Izmır, Turkey
(5) Department of Mechanical Engineering, Koc University, Istanbul, Turkey

## INTRODUCTION

Mechanical circulatory support devices (MCSDs) have been widely used to improve a patient's transplant candidacy and act as a bridge-to-heart transplantation for end-stage failing Fontan [1]. However, a healthy pulmonary circulation requires physiological pulsatility [2] while most of the standard MCSDs proposed for Fontan circulation are continuous flow [3]. Furthermore, due donor shortage novel approaches and devices are desired for this vulnerable patient population [4]. Therefore, a novel Fontan-support modification which can provide the desired pulsatile pulmonary flow is proposed in this study. It hypothesizes that in combination with a conventional left MCSD, sparing the native single ventricle (SV) for pulmonary circulation would result the physiological hemodynamics. Our previously developed multi-compartmental lumped parameter cardiovascular model (LPM) [5] was modified to simulate a realistic Fontan circulation to investigate the feasibility and performance of the proposed modification. The LPM was also validated via our established pediatric pulsatile *in vitro* Fontan mock-up flow loop [6].

## METHODS

*In silico* analyses were performed for an optimal Fontan circulation representing the baseline, i.e. the functional hemodynamic state, of the patient before the Fontan failure (*Case-1*). A ventricular dysfunction Fontan failure mode is simulated next (*Case-2*), which is treated through the proposed MCS configuration by delegating the SV to the right-side and a clinical ventricle assist device (VAD) (*Case-3*), Figure 1.

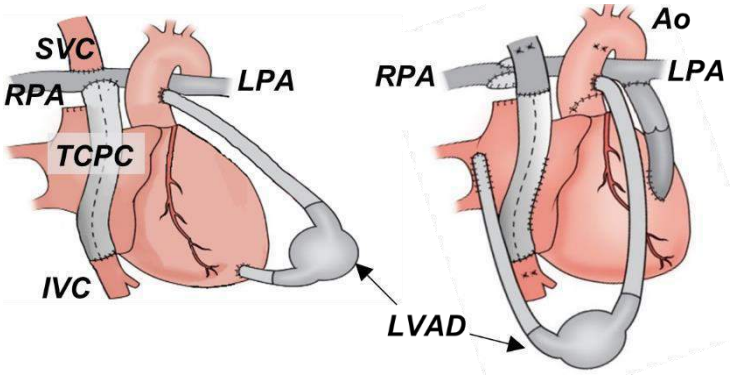


**Figure 1: *Left:* Conventional mechanical support of failed Fontan circulation with a left ventricle assist device (LVAD). *Right:* The proposed support alternative where the single-ventricle is spared as a right heart. Ao: aorta, IVC: inferior vena cava, SVC: superior vena cava, LPA: left pulmonary artery, RPA: right pulmonary artery TCPC: total cavopulmonary connection**

*Case-1* was reproduced based on the clinical data reported for optimal Fontan hemodynamics [7]. In *Case-2*, stroke volume was reduced by 40% to initiate the SV failure through decreasing ejection fraction (EF). In the proposed modification, a small portion of the common atrium is separated to form a posterior pulmonary venous (PV) chamber, while the remaining part serves as a right atrium. The systemic return was detached from the total cavopulmonary connection and directly connected to the newly created right atrium. Thus, systemic and pulmonary

circulations become parallel, similar to a native biventricular system. Finally, SV was connected to pulmonary arter (PA) to maintain the pulmonary circulation while the systemic circulation was governed by an MCSD. Its inlet was connected to the newly created posterior PV chamber and its outlet was placed to the aorta enabling it to act like a native left ventricle.

Numerical computations were validated through our *in vitro* Fontan mock-up loop. For both *in silico* and *in vitro* analyses as a clinical VAD the Heartware, HVAD (Medtronic)$^{TM}$ was used.

## RESULTS

***In vitro* Validation of LPM.** Mean values and percent differences between *in silico* and *in vitro* results for the selected clinical circulation states are provided in Table 1. It shows that LPM demonstrated acceptable agreement with the *in vitro* measurements in terms of compared hemodynamic parameters.

**Table 1: Difference between *in silico* and *in vitro* results for the key hemodynamic parameters. $P_{AO}$: aortic pressure, CI: cardiac index, $P_{SV}$: single ventricle pressure, $P_{CV}$: central venous pressure and $P_{PV}$: pulmonary venous pressure. *In silico* results of pressure and CI values in *Case-1* are given in *mmHg* and *l/min*, respectively**

| *Parameter* | *Case-1* | *Case-2* | *Case-4* |
|---|---|---|---|
| **$P_{AO}$ (70)** | No disparity | 1.5% | No disparity |
| **CI (4)** | No disparity | No disparity | 3% |
| **$P_{SV}$ (50.5)** | 1% | 6% | 5% |
| **$P_{CV}$ (16)** | 13% | 4% | 6% |
| **$P_{PV}$ (11.5)** | 11% | 8% | 3% |

**Ventricular Dysfunction Model.** In *Case-2*, reducing stroke volume decreased the EF from 44% to 26%, which led to a decrease in cardiac index (CI) and mean aortic pressure by 1.7 l/min/m$^2$ and 5 mmHg, respectively. The proposed modification was implemented in *Case-3* to support the failing SV. In systemic circulation, MCSD directly reflects the pulmonary flow. In pulmonary side, EF of the SV remained constant although the stroke volume was doubled. Mean SV pressure was simulated as 18.5 mmHg. Mean PA pressure increased from 10.7 mmHg to 17.5 mmHg (39%). Central venous pressure (CVP) was decreased by 2 mmHg (13%). As expected, MCSD suction caused a decrease in PV pressure to -1.2 mmHg, almost collapsing the chamber. Nevertheless, CI and aortic pressure increased by 1.7 l/min/m$^2$ (doubled) and 25 mmHg (38%), respectively, compensating the low EF as particularly aimed. Figure 2 shows the hemodynamic waveforms observed via implementation of proposed modification on ventricular dysfunction Fontan failure.

## DISCUSSION

In this study, a novel support modification for failing Fontan circulation states is proposed and investigated. In *Case-3*, mean PA pressure and flow waveforms were observed as very similar to a native pulmonary circulation. Additionally, simulated mean

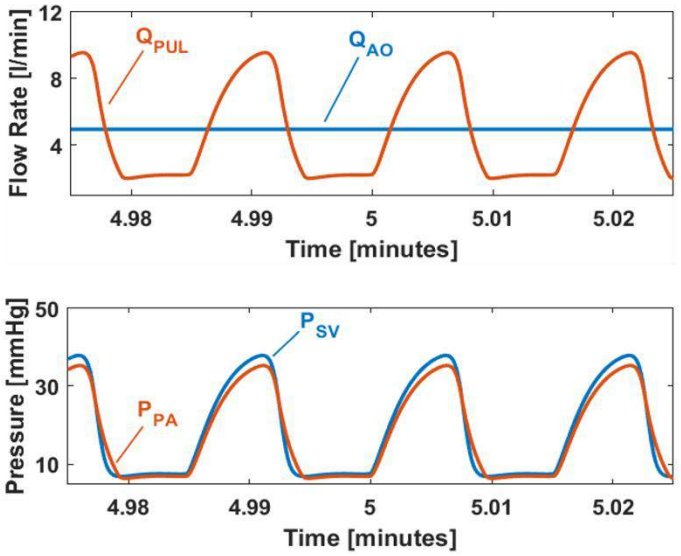


**Figure 2: Ventricular dysfunction Fontan failure with proposed modification (Case-3). Top: Aortic ($Q_{AO}$) and pulmonary ($Q_{PUL}$) flow waveforms. Bottom: Single ventricle ($P_{SV}$) and pulmonary artery ($P_{PA}$) pressure waveforms**

pressure value of the SV in pulmonary circulation was calculated to be very similar to a native right ventricle. As such, in addition to providing systemic support the proposed modification also assists the cavopulmonary connection through a decreased CVP. These observations showed that a failing SV, which might be insufficient to govern the systemic circulation can be enriched in the pulmonary side.

Only the ventricular dysfunction associated Fontan failure mode was analyzed in this study and the high pulmonary vascular resistance (PVR) failure mode will be presented during the meeting. Likewise, utilizing an SV having mildly reduced or normal EF may lead to pulmonary hypertension due to excessive stroke work over even a considerably high PVR, as previous studies demonstrated [2,3]. The hemodynamic benefit of the proposed modification likely to be more prominent for patients with severely failing SV. Considering the low resource settings with limited access to VAD systems, the proposed modification utilizing the native ventricle might lead to a novel perspective for MCSD implantation in failed Fontan patients.

## ACKNOWLEDGEMENTS

We acknowledge support of ERC-PoC 966765 BloodTurbine and Tubitak 2247a research grants.

## REFERENCES

[1] Bernstein, D et al., *Circulation*, 4:273-280, 2006.
[2] Dell'Italia, L J, *Cardiol Clin*, 2:167-187, 2012.
[3] Karimov, J H et al., *Ann Thorac Surg*, 2:651-658, 2016.
[4] Horne, D et al., *Semin Thorac Cardiovasc Surg Pediatr Card Surg Annu*, 1:17-24, 2015.
[5] Yigit, B et al., *Matern Health Neonatal Perinatol*, 5:5, 2019.
[6] Pekkan, K et al., *J Thorac Cardiovasc Surg*, 1:292-301, 2018.
[7] Ohuchi, H, *Korean Circ J*, 6:842-857, 2017.

SB³C2022
Summer Biomechanics, Bioengineering and Biotransport Conference
June 20-23, Eastern Shore, MD, USA

# TIME-DEPENDENT MATERIAL PROPERTIES OF NONPREGNANT AND PREGNANT HUMAN UTERUS UNDER SPHERICAL NANOINDENTATION

**Daniella Fodera (1), Shuyang Fang (2), Michelle Oyen (3), Kristin Myers (2)**

(1) Department of Biomedical Engineering, Columbia University, New York, NY, USA
(2) Department of Mechanical Engineering, Columbia University, New York, NY, USA
(3) Department of Biomedical Engineering, Washington University in St. Louis, St. Louis, MO, USA

## INTRODUCTION

The uterus plays a critical role in the establishment and maintenance of pregnancy, undergoing dramatic growth and remodeling from the time of embryo implantation to labor and birth. The uterus is composed of three distinct tissue layers: (i) the endometrium, the innermost mucosal layer that proliferates, differentiates and sheds throughout the menstrual cycle and transforms into the decidua in pregnancy, (ii) the myometrium, the middle smooth muscle layer, and (iii) the perimetrium, the outermost serosal layer (Fig.1a). Although the uterus performs critical biomechanical functions and is known to be mechanosensitive, remarkably few studies have investigated the mechanical and structural properties of the human uterus and how they change throughout pregnancy [1-3]. Yet, this knowledge is essential for developing physiologically accurate *in vitro* and *in silico* models of the uterus to better understand the pathophysiology of different gynecological and obstetric disorders.

Therefore, the purpose of this study is to characterize the spatial variance of time-dependent micromechanical properties of the human uterus across the endometrium, decidua and myometrium between nonpregnant and pregnant individuals, respectively. We then investigated how distinct viscoelastic and poroelastic mechanisms contribute to the time-dependent behavior of uterine tissues by evaluating the differences in individual versus combined model fits.

We therefore hypothesize that stiffness of the myometrium will be significantly greater than the endometrium and decidua in both nonpregnant and pregnant states, respectively. Furthermore, we expect the intrinsic permeability of the uterus to be greater in the endometrium than the myometrium and to increase in pregnancy.

## METHODS

In accordance with Columbia University Irving Medical Center (CUIMC) IRB approval, nonpregnant human uterine samples (n = 4) were collected from women undergoing hysterectomies, while pregnant samples were collected from biopsies of Caesarian sections (healthy, n = 2) and hysterectomies for abnormal placentation (placenta accreta, n = 2). Hysterectomy and biopsy samples were collected at the fundus and anterior regions of the uterus, respectively, and subsequently stored at -80°C. Prior to testing, samples were sectioned into myometrial and endometrial/decidual layers (Fig.1a) and subsequently thawed at 4ºC overnight in Opti-Free contact lens solution (Alcon, Fort Worth, TX, USA) and equilibrated at room temperature for 30 min. Spherical nanoindentation (Piuma, Optics11Life, Amsterdam, NL) was utilized to characterize the time-dependent mechanical properties of the samples at three distinct regions sized 1mm x 1mm with 200µm resolution between points and a probe radius of 57.5 $\pm$ 1 µm. Samples were indented to fixed depth of 4 µm, corresponding to a 5% strain rate, for 15s to achieve equilibrium load relaxation. Load relaxation curves were fit in Matlab (1) individually with a two-parameter viscoelastic model and poroelastic model, as described by Mattice et al. 2006 and Hu et al. 2010, respectively, and (2) with a combined poro-viscoelastic (PVE) model, described by Islam et al. 2021 [4-6]. Parameters of stiffness ($E_\infty$), viscoelastic ratio ($E_\infty/E_0$), and intrinsic permeability ($k$) were determined (Fig.1b) [4-6]. Normality of the data was first assessed with a Shapiro-Wilk normality test. The Mann-Whitney test was then utilized to analyze two groups of data with statistical significance of $p < 0.05$.

## RESULTS

Regardless of the time-dependent model employed for data analysis, uterine stiffness was determined to be in the range of $10^2 – 10^3$ Pa for all tissues evaluated (Fig.1c). Supporting our hypothesis, the myometrium is significantly stiffer than the endometrium for nonpregnant samples, however, surprisingly, no distinction in stiffness exists between decidua and myometrium layers in 3rd trimerster pregnancies (Fig.1c). Interestingly, the myometrium is significantly stiffer in placenta accreta patients as compared to healthy pregnancies, however additional samples are needed to confirm this trend (Fig.1c).

Viscoelastic ratio and permeability were subject to the greatest changes between the two models employed. Viscoelastic ratio ranges from 0 to 1, whereby 0 indicates a perfectly viscous material and 1 a perfectly elastic material. Measurements for viscoelastic ratio determined by the individual viscoelastic model yielded a larger degree of variation with many infinitesimally small values indicating a poor model fit (Fig.1d). This issue was subsequently resolved with the PVE model whereby the mean viscoelastic ratio increased from approximately 0.4 to 0.5 (Fig.1d). Viscoelastic ratio differed marginally across uterine layers for both nonpregnant and pregnant samples, suggesting all uterine tissues exhibit viscoelastic properties to an extent (data not shown).

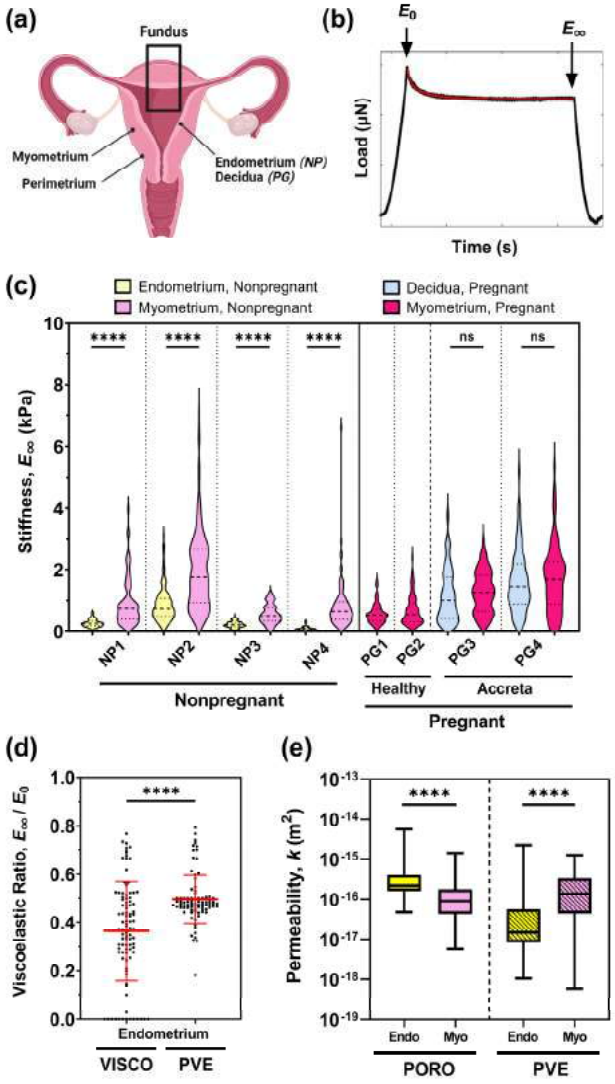


***Figure 1*: (a) Schematic of the human uterus. Nonpregnant (*NP*) endometrium / pregnant (*PG*) decidua, myometrium, and perimetrium are shown for the frontal plane. (b) Representative load versus time plot used for model fitting. (c) Stiffness of all patient matched endometrial, decidual, and myometrial layers determined by the combined PVE model. (d) Representative endometrial sample data analyzed with the viscoelastic and PVE models. (e) Representative patient-matched permeability measurements of the endometrium and myometrium analyzed with the poroelastic and PVE models.**

Interestingly, analysis with the poroelastic model reveals that the intrinsic permeability of nonpregnant endometrium is significantly greater than that of the myometrium, supporting our original hypothesis (Fig.1e). Notably, this distinct trend is not only eliminated, but reversed in the majority of nonpregnant samples when the same data in analyzed with the combined PVE model, exhibiting a greater degree of variability (Fig.1e). No clear distinctions exist across the pregnant decidual and myometrial tissues, which, contrary to our hypothesis, does not dramatically increase in relation to nonpregnant samples (data not shown). All samples had a mean permeability in the range of $10^{-17}$ to $10^{-14}$ $m^2$, corresponding to pore sizes on the nanometer scale.

## DISCUSSION

Here, a novel dataset representing the time-dependent mechanical properties of the human uterus at small length scales is presented, including the first reported measurements of uterine permeability and viscoelastic ratio, distinguishing between the endometrial, decidual and myometrial layers in nonpregnant and pregnant states. The data correspond to stiffness measurements previously reported in the literature as evaluated with AFM, spherical indentation, and small-strain tensile testing [2-3].

Fundamental differences in the evaluated time-dependent material properties exist between the individual and combined poroelastic-viscoelastic models, however this finding suggests that neither theories of viscoelasticity or poroelasticty alone are sufficient to fit the uterine nanoindentation data. Furthermore, given current understanding of uterine structure, it is likely that both poroelastic and viscoelastic mechanisms act in concert to yield the observed time-dependent behavior of these tissues, which can be confirmed using a similar approach employed by Wang et al. 2014 and Strange et al. 2013 [7-8]. The sensitivity of the permeability data to the two models further highlights the need for additional analysis to determine the exact contribution of poroelastic and viscoelastic mechanisms to the observed time-dependent response in nonpregnant and pregnant uterine tissue.

Key limitations of the current data set include the small sample size, inherent pathological nature of the nonpregnant hysterectomy samples, and the absence of the outermost layer of the uterus, the perimetrium. Moving forward, we plan to address these issues with the inclusion of additional samples.

Yet, despite these limitations, the data presented here yield key insights into the mechanobiology of the uterus, providing foundational knowledge for advancing models of pregnancy, particularly in relation to embryo implantation and placentation. Furthermore, the distinct differences in healthy and pathological uterine tissue at term reveals a fundamental question about the role mechanics plays in the initiation and progression of placenta accreta.


## ACKNOWLEDGEMENTS

We would like to thank Drs. Joy Vink, George Gallos, and Arnold Advincula from CUIMC for their assistance in the collection of uterine tissue. Research was supported financially by the NSF GRFP, Iris Fund, and Eunice Kennedy Shriver National Institute of Child Health & Human Development Grant (R01HD091153).


## REFERENCES


**[1]** Myers, K et al. *Wiley Interdiscip Rev Syst Biol Med*, 9(5), 2017. **[2]** Abbas, Y et al. *Hum Reprod.*, 34(10):1999-2008, 2019. **[3]** Fang, S et al. *Ann Biomed Eng*, 49(8):1923-1942, 2021. **[4]** Mattice, J et al. *J. Mater. Res*, 21(8):2003-2010, 2006. **[5]** Hu, Y et al. *Appl. Phys. Lett*, 96:121904, 2010. **[6]** Islam, M et al. *Experimental Mechanics*. 61:939-49, 2021. **[7]** Wang, Q et al. *Acta Mechanics Sinica*, 30:20–27, 2014. **[8]** Strange, D et al. *Appl. Phys. Lett*, 102:031913, 2013.

# INFLUENCE OF VASCULAR STASIS BASED BLOOD PERFUSION ON MAGNETIC NANOPARTICLES MIGRATION USING MODIFIED THERMAL DAMAGE MODEL: AN ILLUSTRATION OF THERMAL BY-STANDER EFFECT

**Manpreet Singh**

Department of Mechanical Engineering,
University of Maryland Baltimore County,
Baltimore, MD, USA

## INTRODUCTION

MicroCT imaging assisted *in-vivo* animal studies have suggested possible change in nanoparticle distribution after heating[1]. The redistribution of nanoparticles from the region of higher concentration to the region of lower concentration is described as *"Thermal By-Stander Effect"*[1,6].

One hypothesis[7] suggests the possibility of continuous regeneration of living human tissues due to meeting of oxygen demands through arterial blood. Hence, due to this regeneration process, the biological tissues shows an accelerated tissue repair and recovery with an evident rise in blood perfusion levels. Previous studies[2-3] implemented regeneration term into Arrhenius formulation; however, effect of hyperemic region through vascular stasis (non-linear perfusion change[4-5]) is missing for such regeneration based model.

This study incorporates vascular stasis based blood perfusion for magnetic nanoparticle assisted thermal therapy to model the thermal by-stander effect using modified thermal damage model with regeneration.

## METHODS

Pennes Bioheat Transfer Equation[6] (PBHTE) is used to compute the temperature field distribution in both the healthy, *h* and cancerous, *c* tissue domains respectively as per equations (1a) and (1b);

$$\rho_h c_h \frac{\partial \mathrm{T}_h}{\partial \mathrm{t}} = k_h \nabla^2 \mathrm{T}_h + \omega_{h,0} \rho_b c_b (\mathrm{T}_b - \mathrm{T}_h) + Q'''_{met,h} \quad (1a)$$

$$\rho_c c_c \frac{\partial \mathrm{T}_c}{\partial \mathrm{t}} = k_c \nabla^2 \mathrm{T}_c + \omega_{c,0} \rho_b c_b (\mathrm{T}_b - \mathrm{T}_c) + Q'''_{met,c} + Q'''_{source} \quad (1b)$$

Here, the subscripts *b* and *met* represents blood and metabolic heat generation respectively. The thermophysical properties for biological tissue domains are shown in Table-II. Contribution of heterogeneously distributed magnetic nanoparticles are extracted from MicroCT images from pixel value information known as Specific Absorption Rate (SAR) mapped at different tumour locations. This source term[6] is coupled with Concentration as $Q'''_{source}(x,y,z,t) = 2266.67 \times C(x,y,z,t)$. The governing equation for nanoparticle diffusion is given as;

$$\frac{\partial C(x,y,z,t)}{\partial t} = \nabla \cdot \left[ \phi D_n \nabla \left( \frac{C(x,y,z,t)}{\phi} \right) \right] \quad (2)$$

where, the diffusion coefficient $(D_n)$ relates to interstitial space $(\phi)$ and diffusion coefficient in unbound interstitial fluid $(D_{n,f})$ as;

$$D_n = D_{n,f} \left[ \frac{2\phi}{3-\phi} \right] \quad (3)$$

The interstitial space tends to increase with the cell-necrosis as;

$$\phi = \phi_o + (80\% - \phi_o)\left(1 - e^{-\Omega(\mathrm{x,y,z,t})}\right) \quad (4)$$

Spatio-temporal thermal cell-death, Ω (dimensionless) can be computed as per first-order traditional Arrhenius equation;

$$\Omega(x,y,z,\tau) = \int_0^\tau A e^{-E_a / R_u T(x,y,z,t)}\, dt \quad (5)$$

The Arrhenius kinetic rate equation is recently modified[1-3] to account for regeneration of healthy cells. The modified thermal damage is;

$$\frac{d\Omega(\mathrm{x,y,z,t})}{d\mathrm{t}} = A\left(1 - \Omega(x,y,z,t)\right) \exp\left(\frac{-E_a}{R_u T(x,y,z,t)}\right) - B\omega_{c,0}\Omega(x,y,z,t) \quad (6)$$

where, $R_u$ is the universal gas constant 8.314 J/(mol·K), $\tau$ is the duration of exposure(s), T is the temperature (K), B is a dimensionless coefficient[2] $(9 \times 10^{-3})$. The thermal damage parameter, $\Omega = 1$ represents 63.21% of denaturation of proteins sufficient to initiate coagulation. It should be noted that the induced thermal damage is zero before the onset of nanoparticle assisted heating.

It is well known that during heating, the blood perfusion rate, $\omega_{c,0}(t)$ first increases at hyperthermic temperature due to vasodilation of vessels and then starts decreasing due to total collapse of vasculature[5]. This phenomenon is known as "*degree of vascular stasis*" or "*vascular collapse*" or "*fractional injury*" or "*vascular stasis*". The functional dependence of $\omega_{c,0}(t)$ on VS is shown in fig. 2 and Eq. 7 as;

$$\omega_{c,0}(t) = \begin{cases} \omega_{b,o}(1 + 30 \cdot \mathrm{VS}); \text{if ori} 0 < \mathrm{VS} \leq 0.02 \text{if ori} \\ \omega_{b,o}(1.86 - 13 \cdot \mathrm{VS}); \text{if ori} 0.02 < \text{if VS} \leq 0.08 \\ \omega_{b,o}(0.884 - 0.79 \cdot \mathrm{VS}); \text{if ori} 0.08 < \text{if VS} \leq 0.97 \\ \omega_{b,o}(3.87 - 3.87 \cdot \mathrm{VS}); \text{if ori} 0.97 < \text{if VS} \leq 1.00 \\ \text{if} 0; \text{if ori VS} > 1.00 \text{if} \end{cases} \quad (7)$$

VS can be mathematically expressed as

$$\mathrm{VS}(x, y, z, t) = 1 - \exp(-\Omega(x, y, z, t)) \quad (8)$$

Here, the baseline value of blood perfusion, $\omega_{b,o}$ is extracted from the thermal infrared imaging by adjusting the metabolic heat generation rates and blood perfusion values using inverse heat transfer analysis[6]. The Arrhenius kinetic coefficients used to evaluate the vascular stasis (VS) and thermal damage ($\Omega$) are summarized in Table-I.

**Table-I**: Arrhenius coefficients considered in this study[1-5].

| Parameters | Symbol [Units] | Vascular Stasis | Thermal damage |
|---|---|---|---|
| Frequency factor | $A$ [$s^{-1}$] | $1.98 \times 10^{106}$ | $3.1 \times 10^{98}$ |
| Activation Energy | $E_a$ [$Jmol^{-1}$] | $6.67 \times 10^5$ | $6.28 \times 10^5$ |

*#bulk tissue consideration*.

**Table-II**: Thermophysical properties[6].

| Property | Symbol [Units] | Healthy Tissue | Cancerous Tissue | Blood |
|---|---|---|---|---|
| Thermal conductivity | $k$ [W/(mK)] | 0.5 | 0.5 | 0.55 |
| Density | $\rho$ [kg/m$^3$] | 1060 | 1060 | 1060 |
| Specific heat capacity | $c$ [J/(kgK)] | 3780 | 3780 | 3780 |
| Baseline blood perfusion | $\omega_b$ [m$^3$/(sm$^3$)] | 0.00285$^{\#}$ | 0.00111$^{\#}$ | – |
| Metabolic heat generation | $Q_{met}$ [W/m$^3$] | 9265$^{\#}$ | 3602$^{\#}$ | – |
| Porosity | $\phi$ [-] | – | 20% | – |
| Diffusion coefficient in unbound interstitial fluid | $D_{n,f}$ [m$^2$/s] | – | $9.57\times10^{-12}$ | |

*#extracted from thermal imaging using inverse heat transfer analysis*.

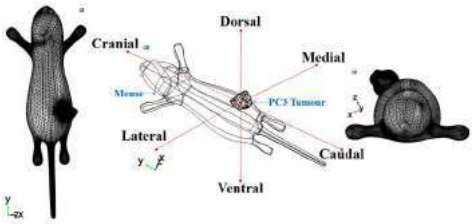


**Figure 1.** Wireframe and meshed model of mouse and PC3 tumour.

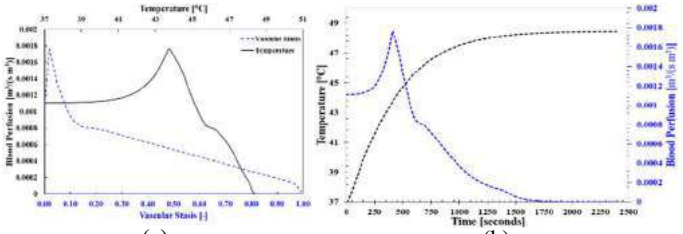


(a) (b)

**Figure 2.** Blood perfusion variation on vascular stasis and temperature at minimal temperature location.

## RESULTS AND DISCUSSION

Fig.1. shows the wireframe and meshed model of PC3 tumour attached to the flank position of mouse. In this problem formulation, the blood perfusion of cancerous lesion is defined as a piecewise function of vascular stasis as per equation 7 and pictorially represented in fig. 2(a). It can be inferred from fig. 2(a) that the maximum peak of perfusion is achieved at 43.5°C. From fig. 2(b), perfusion collapse occurs at minimal temperature location takes 1750 sec. Fig. 3 illustrates temperature ($T_{max}$=83.13°C, $T_{min}$=48.46°C, $T_{avg}$=67.23°C), modified thermal damage with healthy tissue regeneration ($\Omega_{modified}$=1), diffusion coefficient ($4.87\times10^{-11}$m$^2$/s), vascular stasis (VS=1), and porosity (80%) after 2400 sec. The probe is located at minimum temperature location to monitor these parameters. It is noticeable from fig. 3 that there is 39.62% increase in redistribution volumes of nanoparticles and five-fold increase in diffusion coefficient after heating of 2400 sec. The implementation of equation 4 is verified through fig. 3(e) that maximum interstitial space of 80% inside PC3 tumour can be achieved after thermal cell-death of 63.2%. The physical interpretation of this regeneration term implies that thermal damage would not propagate deep inside the healthy tissue fringes. Thus, it can inferred that regeneration phenomenon prevents and suppress the collateral thermal damage spread at the interface within bounds of $\Omega \leq 1$ which is in agreement with the findings of literature[3-5].The implication of this work would help design better heating protocol designs in future. However, more experimental exploration is needed in this context.

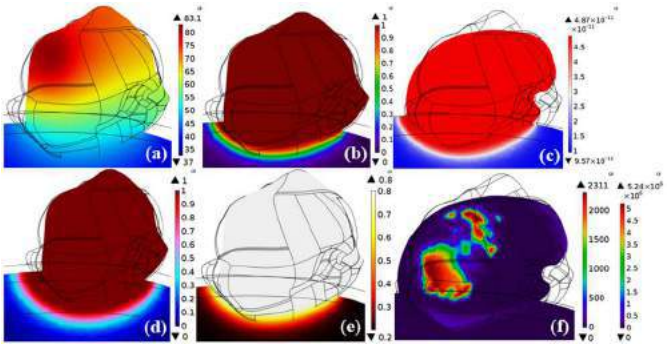


**Figure 3.** (a) Temperature [°C], (b) Modified thermal damage [-], (c) Diffusion coefficient [m$^2$/s], (d) Vascular stasis [-], (d) Porosity [-] at 2400 sec and (e) Initial concentration distribution [mol/m$^3$] and Nanoparticle heat generation rate [W/m$^3$].

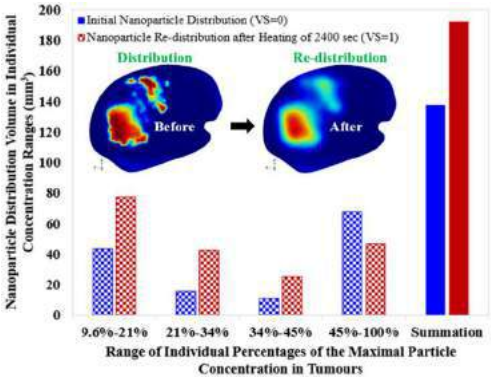


**Figure 4.** Nanoparticle distribution volumes in individual nanoparticle concentration ranges before heating-left patterned bars (VS=0) and after heating-right patterned bars (VS=1).


## ACKNOWLEDGEMENTS

The author would like to thank the Graduate School, UMBC for conferring the award of Dissertation Fellowship and the Department of Mechanical Engineering for the usage of computational facilities.


## REFERENCES


[1] Gu, Q et al., *ASME J. Heat Transf.,* 141:032402, 2019.
[2] Kumar, D, and Rai, KN, *J. Therm. Biol.,* 62:170-180, 2016.
[3] Liu, K-C, and Chen, T-M, *J. Therm. Biol.,* 98: 102907, 2021.
[4] Prakash, P, and Diederich, CJ, *Int. J. Hyperthermia,* 28:69-86, 2012.
[5] Schutt, DJ, and Haemmerich, D, *Med. Phys.,* 35: 3462, 2008.
[6] Singh, M et al., *Int. Comm. In Heat Mass Trans.,* 126:105393, 2021.
[7] Dombrovsky, L, et al., *Therm. Proc. Eng.,*7:24-36, 2015.

# PROGRESSIVE DISC AND BONE ADAPTATIONS DUE TO POSTEROLATERAL TETHERING IN A PORCINE MODEL OF SCOLIOSIS

**Axel C. Moore (1), Adriana Barba (2), Harrah R. Newman (1), Kyle D. Meadows (1), Benjamin P. Sinder (3), Alessandra Fusco (2), Rachel Hillard (2), Sriram Balasubramanian (4), Edward J. Vresilovic (1), Brian Snyder (5), Patrick J. Cahill (3), Thomas P. Schaer (2), Dawn M. Elliott (1)**

(1) Biomedical Engineering, University of Delaware, Newark, DE, USA
(2) Veterinary Medicine, University of Pennsylvania, Philadelphia, PA, USA
(3) Children's Hosp of Philadelphia, Philadelphia, PA, USA
(4) Biomedical Engineering, Drexel University, Philadelphia, PA, USA
(5) Boston Children's Hosp, Boston, MA, USA

## INTRODUCTION

Scoliosis is a multi-planar spine deformity that presents predominantly as a lateral curve in the coronal plane >10°. In children and adolescents the etiology of scoliosis is most often idiopathic. Stokes hypothesized that spinal deformities progress as a "vicious cycle" in which asymmetric stresses and strains applied to the growing spine induce deformity of both osseous and non-osseous tissues, causing growth modulation in agreement with the Hueter-Volkmann Principle (i.e., tension applied to the physis stimulates growth, compression inhibits growth) [1]. This concept was validated clinically, demonstrating that spine deformity progresses as a function of skeletal age: during periods of high growth, spine deformity evolves primarily through the intervertebral disc (IVD), whereas towards the end of growth, the deformity increases primarily through the vertebrae (VB) [2]. Interventions to correct scoliosis that preserve spinal growth and motion are based on predictably modulating spine growth. Currently, it is unknown how asymmetric loading alters the growth of IVD relative to the VB. The goal of this study is to identify progressive spinal deformity transitions (i.e., initiation of VB wedging and attenuation of IVD wedging) under asymmetric loading. In this proof-of-principle study we investigate the influence of mechanics in spinal deformity progression by applying a bending moment to a straight spine in an otherwise healthy, growing pig. Our long-term goal is to apply this controlled model of skeletal deformity to determine the effect of the mechanical environment on mechanotransduction through molecular and mechanical analyses and to evaluate clinical interventions for correcting the scoliotic spine.

## METHODS

With IACUC approval, 3 Yorkshire pigs were instrumented with a CoCr cable spanning the thoracolumbar junction and lumbar spine; this offset tether created a lateral bending moment and an initial scoliosis that progressed as the pig matured (**Fig 1**). Two un-instrumented Yorkshire pigs were used as controls. Anatomical changes to the IVD and VB as a function of time were measured with serial CT scans at -2, 0, 4, 6, 8, 12, and 19 weeks post-op and MRI at 5, 19, and 22 weeks post-op. CT scans were used to quantify lateral wedging and longitudinal growth along the line of curvature between the instrumented levels. Two MRI sequences were utilized, a T1-weighted FLASH sequence to evaluate IVD volume and a T2-weighted CPMG echo sequence to evaluate IVD T2 relaxation time. The T2 relaxation time, which is positively correlated with hydration

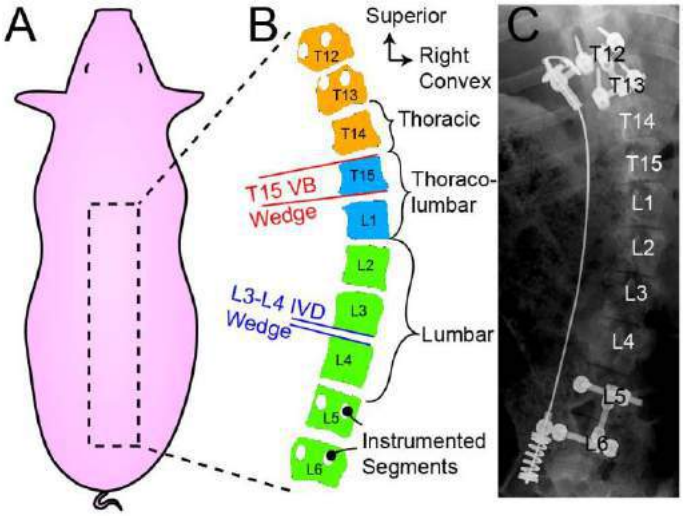


**Figure 1: (A) Pig model, (B) schematic, and (C) radiograph showing instrumentation and curvature at 6 weeks post-op. Avoiding instrumented levels, analysis was conducted from the inferior side of T13 to the superior side of L5. Color coding indicates the thoracic (orange), thoracolumbar junction (blue), and lumbar (green) regions.**

and is decreased in IVD degeneration, was calculated for the IVD nucleus pulposus.

## RESULTS

3D CT reconstructions demonstrate progression of spinal deformity and vertebral growth modulation due to the tether (**Fig 2**).

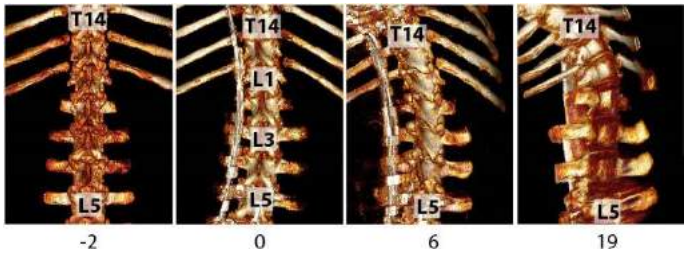


**Figure 2: CT reconstructions in weeks post-op demonstrating progressive curvature.**

At the time of surgery, a 17° Cobb angle was produced via IVD wedging (**Fig 3A,B**). At 6 weeks, deformity progression was approximately equally distributed between the thoracolumbar (45%) and lumbar (41%) regions (**Fig 3A**) with VB wedging accounting for 60% of the total deformity (**Fig 3B**). From 12 to 19 weeks post-op, the spine deformity transitioned from nearly equal contributions of IVD and VB to only VB (**Fig 3B**). At 19 weeks post-op, the spine developed a 41° Cobb angle.

The longitudinal growth of the VBs progressed overtime (**Fig 3C**) with tethering which is an important outcome as it demonstrates growth modulation rather than simply remodeling. However, the VB growth at 19 weeks post-op was less than the control at 18 weeks post-op indicating possible impaired growth. A larger sample size is required to confirm this observation. Reduced spinal height is a typical feature of scoliosis [3]. On the other hand, the IVDs did not undergo a clear change in the longitudinal growth between the instrumented levels or relative to the controls (**Fig 3C**). The IVDs did however grow in the lateral dimensions as demonstrated by an increase in IVD volume (**Fig 4**). When compared to the controls the volumetric growth is impaired. Despite this growth modulation of the IVDs, the T2 times (290 ± 40 ms) were similar to a control (340 ± 10 ms) suggesting that the tether did not induce degeneration over the time course assessed, but rather geometric alterations.

## DISCUSSION

In this preliminary study, asymmetric spine loading in a porcine model using a tether provoked asymmetric spine growth. Early-stage deformity was shared between the IVDs and VBs. However, from 12 to 19 weeks the deformity transitioned to be primarily located in the VBs. The growth of the IVDs and VBs appear to be impaired when compared to controls.

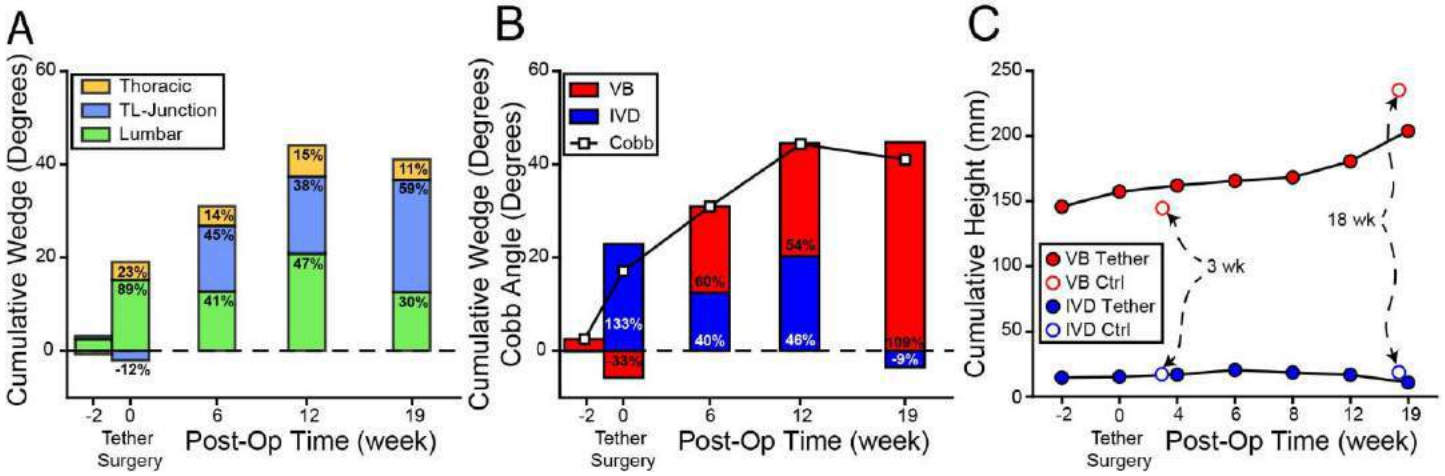


**Figure 3: Sum of segmental IVD and VB wedge angle by (A) anatomical region (see Fig 1) and (B) tissue type. Positive wedging = right curve. (C) Sum of VB and IVD height between instrumented segments. Controls at equivalent age are shown at 3- and 18-weeks post-op. Data from one representative pig shown.**

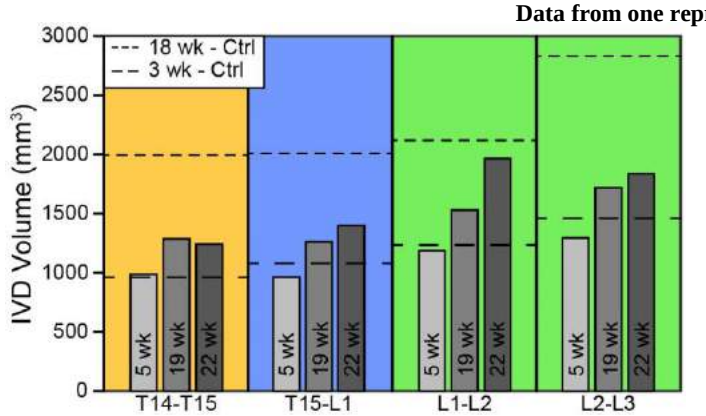


**Figure 4: IVD volume by level and post-op time. Control pigs at equivalent age are shown at 3- and 18-weeks post-op. Data from one representative pig shown.**

## SIGNIFICANCE

We have developed a clinically relevant in vivo animal model to mimic scoliosis. Serial CT and MRI imaging allowed differentiation of mechanical deformation of the soft tissues from modulated growth which manifest as changes in the composition, structure, and geometry. This model will allow biomechanical, biochemical, and biological adaptations to be studied. Moreover, this model is being developed to predictably apply corrective treatments for scoliosis.


## ACKNOWLEDGEMENTS

Wyss/Campbell Center for Thoracic Insufficiency Syndrome at Children's Hospital of Philadelphia and by the NIH.


## REFERENCES


[1] I. A. F. Stokes, *Eur. Spine J.*, 16:1621–1628, 2007. [2] Will, RE et al., *Spine* 2782–2786, 2009. [3] Schlager, B et al., *Biomechanics of the Spine*, 2018.

# COMPUTATIONAL MODELING OF CONNECTIVITY-DRIVEN CORTICAL SCALING AND FOLDING

**Xincheng Wang (1), Maria A. Holland(1,2)**

(1) Aerospace and Mechanical Engineering
(2) Bioengineering Graduate Program
University of Notre Dame
Notre Dame, Indiana, USA

## INTRODUCTION

The human brain is one of the most important and complex organs in our nervous system. It consists of an intricately folded outer layer of grey matter part and an inner white mater part saturated with axon tracts. It is also one of the most vulnerable organs in our body because it is affected by various neurological diseases and disorders, like Autism Spectrum Disorder, Anxiety Disorder, Alzheimer's Disease, etc. These neurological diseases and disorders are associated with abnormal white matter connectivity [1]. However, the complexity of the brain cortex and subcortex impeded the early diagnosis and treatment of brain diseases.

In recent years, there are renewed interests in assessing the axonal tension hypothesis [2]. From the biological perspective, Van Essen proposed that axon tension pulls surrounding tissue closer together. From a mechanistic standpoint [3], Holland suggested that the heterogeneous orientation of white matter connections leads to more physiological, less regular brain morphologies [4]. Garcia proposed that brain connectivity plays a significant role in inducing folding [5]. These recent discoveries draw our attention to connectivity-driven cortical folding.

Historically, many subcortical models have been based on a purely elastic subcortex and an isotropic stretch-driven growth model. These limitations conflict with the real distribution of axon tracts and the induced material heterogeneity. If the axon tracts are considered, there are still gaps to be filled. What's the level of tension provided by single axon tracts? How much of this level of tension affects the cortical morphology? Would this level of tension result in global wiring efficiency?

To address these questions, we built a novel computational model to explicitly simulate brain tissue growth with embedded axon tracts. We hypothesize that axonal tension could serve as a slight perturbation and trigger global tissue surface instability in the subcritical state.

## METHODS

We first build a bilayer system of an elastic thin film on a soft elastic substrate (Fig. 1). The top layer is the grey matter with a thickness of $h_g = 2\ mm$. The substrate is the subcortical white matter with a thickness of $h_w = 8\ mm$. The length of the system is $l = 20\ mm$. The simplified axon connectivity pattern located in the center, composed of three axon tracts.

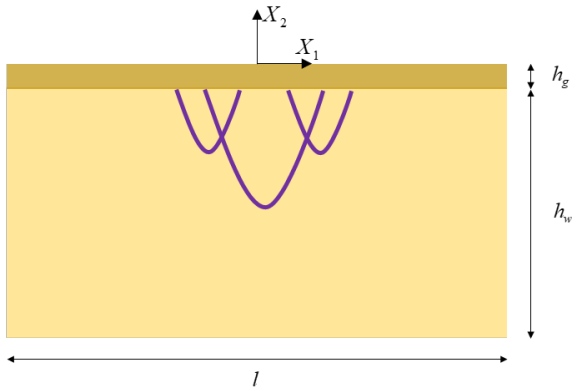


**Fig. 1 Schematics of the bilayer system**

We model brain development using the finite growth theory [6], with the deformation gradient $\boldsymbol{F}$ split into an elastic part $\boldsymbol{F^e}$ and volume growth part $\boldsymbol{F^g}$

$$\boldsymbol{F} = \boldsymbol{F^e F^g} \tag{1}$$

Next, we model the cortical growth as isotropic growth and assume a pure elastic normal response. The growth tensor is defined as

$$\boldsymbol{F^g} = \sqrt{\vartheta^g}\mathbf{1} + \left(1 - \sqrt{\vartheta^g}\right)\boldsymbol{n_R}\otimes\boldsymbol{n_R}, \quad (2)$$

where $\vartheta^g$ is the growth parameter and $\boldsymbol{n_R}$ is the unit vector normal to the surface [7].

The bilayer system is implemented numerically in the standard finite element package Abaqus by writing user-defined material subroutine (UMAT) [8]. Both the grey matter and the white matter substrate are modeled as compressible neo-Hookean materials. The energy density function is

$$\phi = \frac{G}{2}[tr(\boldsymbol{b}) - 3 - 2\ln(J^e)] + \frac{L}{2}\ln(J^e)\ln(J^e), \quad (3)$$

where $G$ and $L$ are Lamé constants, $\boldsymbol{b}$ denote left Cauchy-Green tensors. $J^e$ denote volumetric change due to the elastic deformation.

$$\boldsymbol{b} = \boldsymbol{F^e}\cdot\boldsymbol{F^{eT}},\ J^e = \det(\boldsymbol{F^e}). \quad (4)$$

The corresponding Kirchhoof stress $\tau$ is obtained as

$$\boldsymbol{\tau} = 2\frac{\partial\phi}{\partial\boldsymbol{b}}\cdot\boldsymbol{b} = [L\ln J^e - G]\boldsymbol{I} + G\boldsymbol{b}, \quad (5)$$

where $\boldsymbol{I}$ denotes the second-order unit tensor [9].

It was reported that neurites growing on the substrate generate substantial mechanical tension around 150 μdyn for 1μm diameter sensory neurons [2], with a relationship between force and length change. Scientists also model a typical axon fiber tract as an elastic spring with spring constants of 10-30 μdyn/μm [10].

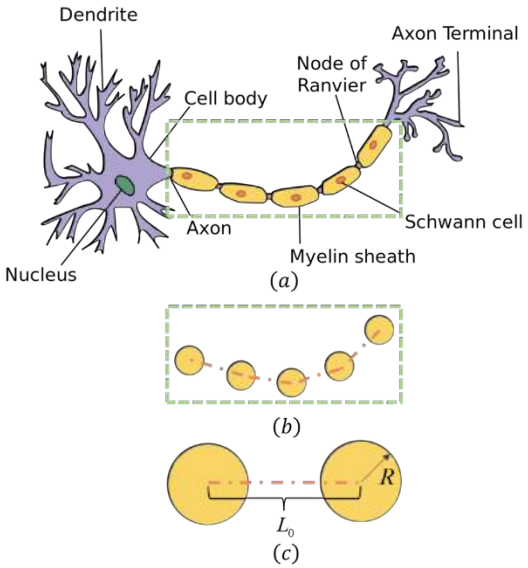


**Fig. 2 Schematics of simplified neuron and axon tracts. (a) Structure of neuron [11] (b) Connector element chain mimics the axon tracts (c) A connector element with two coupling nodes**

Axon is composed of multiple myelin sheaths connected with nodes of Ranvier(Fig. 2(a)). To explicitly model the axon fiber tracts in the Abaqus Standard [8], we adopt 1D connector elements with connection type Axial (Fig. 2(c)). We define the $n_{th}$ connector has an original length $L_0^n$ of 9.2e-3 mm and its reference length $L_r^n$ of 4.6e-3 mm. The generated axonal tension is

$$f_n = \boldsymbol{D}(L_0^n - L_r^n) \quad (6)$$

where $\boldsymbol{D}$ denote the axonal spring constant, and $f_n$ is the axonal tension on the $n_{th}$ connector element [8].

Each connector node is uniformly coupled with the subcortical substrate with an influence radius $R$ of 5e-4 mm. Together, these nodes from chains (Fig.2 (b)) of varying orientations.

## RESULTS

Fig. 3 shows the simulation results of bilayer brain tissue. The interaction between the isotropic tissue growth and anisotropic axon tensions leads to the progressive wrinkled surface. The global instability is induced by physical axon tension.

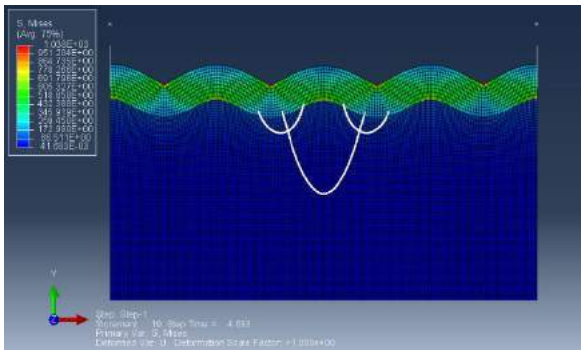

**Fig. 3 Deformed configuration and stress distribution in the brain slices**

## DISCUSSION

Here, we have established a connectivity-driven cortical folding model, which represents the heterogeneity in the subcortical region by incorporating the microstructure of varying axonal orientations. Our model suggests the axon tension leads to global instability by replacing the added imperfection perturbations in most finite element modeling of brain folding. Furthermore, the simulated surface becomes more physiological meaningful with different connectivity or tension levels. In the next step, we will study the influence of various densities of axon tracts and the effects of varied orientation and different levels of tensions on brain morphology. We also plan to fuse the experimental image data with our computational model to integrate a high-fidelity white matter simulation platform for helping the diagnosis and treatment of neurological disabilities.

## REFERENCES


[1] Ameis et al., *Cortex*, 62:158-181, 2015.
[2] Van Essen et al., *NATURE*, 385:313 -318, 1997.
[3] Van Essen et al., *Proc. Natl. Acad. Sci. U.S.A.*, 117:32868-32879, 2020.
[4] Holland et al., *Ann Biomed Eng*, 43.7:1640-1653, 2015.
[5] Garcia et al., *Nat. Commun*, 12.1:1-13, 2021.
[6] Rodriguez et al., *J. Biomech*, 27.4: 455-467, 1994.
[7] Wang et al., *Biomech Model Mechanobiol*, 20.2:555-567, 2021.
[8] Abaqus/Standard, Abaqus reference manuals. Dassault Systemes Simulia, Providence.
[9] Andreas et al., *Mech. Res. Commun*, 42:1-14, 2012.
[10] Dennerll et al., *J. Cell Biol*, 107.2:665-674, 1988.
[11] "Anatomy and Physiology",US National Cancer Institute's SEER Program.

SB³C2022
Summer Biomechanics, Bioengineering and Biotransport Conference
June 20-23, Eastern Shore, MD, USA

# Designing a Sustainable in-Clinic Protocol to Expand Postural Stability Data Collection

**Rita M. Patterson (1), Mai Dinh (2), Alec Doederlein (2), Shawn Kennedy (1), Rajesh Nayak (3), Sanya Gupta (3), Fan Zhang (1), David Mason (1), and Yein Lee (1)**

(1) Family and Osteopathic Manipulative Medicine, University of North Texas Health Science Center, Fort Worth, TX, USA
(2) Texas College of Osteopathic Medicine, University of North Texas Health Science Center, Fort Worth, TX, USA
(3) Data Analytics, University of North Texas Health Science Center, Fort Worth, TX, USA

## INTRODUCTION

Examining human movement and gait mechanics provides insight into the underlying mechanisms of injuries. For example, degenerative diseases, such as osteoarthritis, are thought to stem from asymmetrical loading in which one limb bears more load and moves differently than the other. This may result in changes in stability and balance that are crucial for reducing fall risk. Therefore, fundamental knowledge about movement allows us to create mobility solutions in our community to prevent disability and improve the integrity of care we provide by using a holistic and multi-disciplinary approach**.**

Balance is the ability to maintain the vertical line of gravity of the body within the base of support with minimal postural sway. It is a function of the vestibular, somatosensory and visual systems and provides insight into musculoskeletal mobility issues. Postural sway measurement may be a predictor of falls to identify those at risk for falling (1). Assessing postural stability aids in understanding underlying movement mechanisms that correlate to fall risk (2).

Previous research has consistently used small experiment populations to identify the conditions which cause excessive sway. Which often concludes with ambiguous or inconclusive data alluding to the presence of underlying mechanisms such as age, gender, race, and social/economics factors affecting sway outcomes.

To identify what, if any, known or unknown conditions are influencing postural sway, developing a large repository of human movement data is key. With a large data set we can begin to understand to how underlying factors affect the postural sway of diverse populations.

Therefore, an in-clinic data collection protocol was created, modified, and followed to achieve the purpose of expanding the dataset on this topic. The objective of this study was to design a sustainable data collection and analysis protocol to establish a new clinical vital sign as to better understand fall risk in the diverse populations surrounding the HSC community.

## METHODS

Sustainability Plan: Third year medical students rotating in the OMM clinic collected sway data for one half day during their month-long rotation. Data collectors were presented a video demo of the protocol and a didactic video explaining the importance of the visual, auditory, and proprioceptive systems in helping maintain balance before collecting data. Medical assistants (MA) in the clinic brought patients to students before the appointment time or when the patient's physician was seeing another patient, to avoid delays in clinic schedule. MAs roomed the patients afterwards. The total time for data collection is approximately 2 minutes.

Sway Data Collection: Postural sway was evaluated in patients seen in the Osteopathic Manipulative Medicine (OMM) clinic at University of North Texas Health Science Center between 6/7/2021 and 12/31/2021. Patients with mobility assist devices and children under 65 lbs. where excluded. Patients were instructed to take off their shoes and put on disposable shoe

covers. Patients then stood on footprints attached to the Bertec Force Plate (Bertec Columbus, Ohio). Patients were asked to stand straight, hands by their sides, body facing and looking at a target in front of them for 10 seconds with their eyes open (EO). Patients then repeated the same procedure on the Force Plate with their eyes closed (EC). Three trials of each condition were performed. A rest period of 3 seconds took place between each trial. Data was merged with the electronic medical record in a de-identified data warehouse and retrospectively analyzed from the clinic data collection (UNTHSC IRB# 2013-102)

## RESULTS

Sway Data: Postural sway variables were evaluated for 701 patient encounters (total of 511 patients) between June and December 2021. Figure 1 shows the positional trajectory of the center of pressure between the feed in a typical sway plot.

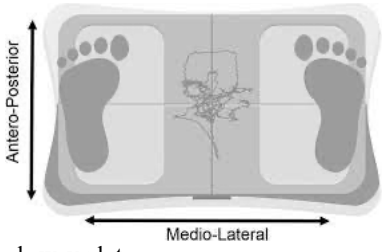


Figure 1 typical sway plot.

Dashboard creation: Data from the Bertec force plate were uploaded to a data warehouse and merged with the electronic medical record. Figure 2 shows the high-level data flow diagram. A Power BI dashboard (Figure 3) was created to visualize data characteristics.

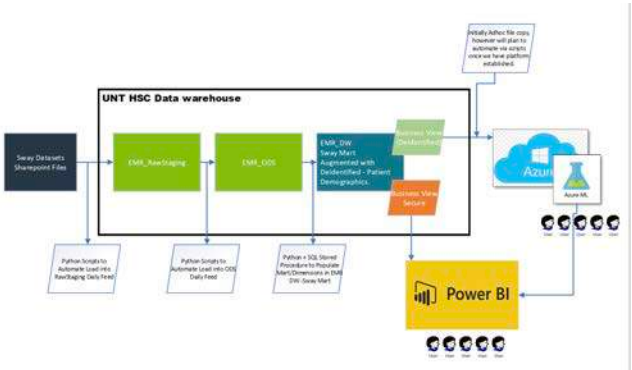


Figure 2 High level data flow diagram

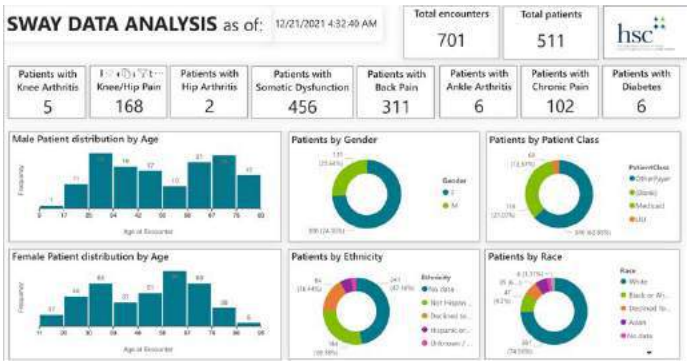


Figure 3 current dashboard of data collected.

## DISCUSSION

As a result of creating a sustainable data collecting model by incorporating third-year medical students in their rotations as data collectors, 701 postural sway measurements were achieved in approximately 7 months. This achievement was possible due to the continuous improvement of the protocol from the first week of data collection and onward. This improvement included a quality control protocol to assess human errors in data entry by matching patient encounter data with the electronic medical record demographic data. Further improvements will include placing students to collect data only on days with a higher patient census based on the past month's patient appointments. Additionally, this data collection protocol can be modeled in other clinics to further expand the database, such as UNTHSC's family medicine and internal medicine clinics.

Other future steps will be to allow healthcare providers secure access to their patient's data so they can discuss changes in sway with their patients during clinic visits. Furthermore, it is our goal to deliver the healthcare providers baseline sway data that is specific to possible differentiating factors (such as age, gender, race, socioeconomic factors) that can allow for more precise and targeted data for their clinical practice. For example, we may be able to provide precise fall prediction parameters that are more precisely designed for each patient encounter.

Finally, we are partnering with in-house experts in artificial intelligence and statistics to analyze sway parameters. Specifically, we will be focusing on machine learning through utilizing Microsoft Azure to analyze the repository to obtain information on human movement for diverse patient populations as to encourage Precision Medicine.

## ACKNOWLEDGEMENTS

We would like to thank HSC Health for providing space and access to their patient populations.

## REFERENCES

1.Johansson J, et al., *Human Movement Science*, 2019;66:117-123.
2. Roos PE, et al., *Human Movement Science*, 2013;32(5):984-996.

SB³C2022
Summer Biomechanics, Bioengineering and Biotransport Conference
June 20-23, Eastern Shore, MD, USA

# HANDRIM BIOMECHANCS AND WHEELCHAIR FIT MEASURES IN PEDIATRIC AND EMERGING ADULT MANUAL WHEELCHAIR USERS

**Samantha R. Schwartz (1), Alyssa J. Schnorenberg (1), Hannah R. Frank (1), Matthew M. Hanks (1), Shubhra S. Mukherjee (2), Brooke A. Slavens (1)**

(1) Rehabilitation Sciences and Technology, University of Wisconsin- Milwaukee, Milwaukee, WI, USA
(2) Shriners Hospital for Children- Chicago, Chicago, IL, USA

## INTRODUCTION

Approximately 124,000 people in the United States under the age of 21 primarily use manual wheelchairs for mobility [1], however, most studies of manual wheelchair users (MWU) focus on adult populations [2]. These studies contribute to the development of adult recommendations for manual wheelchair propulsion that aim to reduce pain and pathology development in the upper extremity [3]. Recommendations include minimizing force and rate of force application to the handrim of the wheel, maximizing time in the contact phase, and reducing push frequency. Importantly, these recommendations cannot be accurately scaled to children because children are not anthropometrically proportional to adults, are still developing their musculoskeletal system [4], and spend more of their lifetimes using a manual wheelchair.

Additionally, recommendations for wheelchair fit settings such as the position of the wheel axles with respect to the shoulder and elbow have been developed for adults [3], but not specifically for pediatric MWU. The implications of applying adult wheelchair fit recommendations to children have not been tested in an evidence-based clinical setting [5, 6]. Pediatric MWU have a difficult time following adult wheelchair fit recommendations due to rapid growth and the need to reassess fit and alter settings regularly with limited funding and insurance for clinic visits and obtaining new wheelchairs [6].

Because children cannot be treated as proportionally scaled down versions of adults, research on wheelchair fit settings and propulsion recommendations for younger MWU are warranted. The purpose of this study was to determine if pediatric and emerging adult MWU followed adult recommendations for wheelchair fit and handrim biomechanics during propulsion, as well as investigate correlations among wheelchair fit and biomechanics metrics.

## METHODS

**Participants:** This study was approved by the UW-Milwaukee Institutional Review Board. Ten pediatric and emerging adult manual wheelchair users (age range: 6-21yr, mean: 15.2yr, 5 females, 5 males) were recruited from Shriner's Hospital for Children- Chicago. All participants had a spinal cord injury at least 1 year prior (time since injury: 3-18yr, mean: 8.9yr, level of injury: T1-L3) and used a manual wheelchair for the majority of their mobility. Consent and/or assent forms were signed prior to data collection.

**Data Collection**: Reflective markers were placed on selected positions on the participant's personal wheelchair and on bony anatomical landmarks of the upper body. Three-dimensional (3D) marker positions were obtained in Vicon Nexus software using a 14-camera Vicon MX motion capture system (Vicon Motion Systems, Oxford, UK). Static trials were obtained of the participant seated in their wheelchair with their hands placed at the top dead center of the wheelchair handrim.

Next, a size matched SmartWheel (Outfront, Pasco, WA) replaced the wheel on one side of the participant's wheelchair to obtain the 3D forces applied to the handrim during propulsion. Participants propelled their wheelchairs along a 15m path at a self-selected speed for multiple trials. SmartWheel data were collected at 240 Hz while simultaneously, kinematic data were collected in Vicon Nexus at 120 Hz. The SmartWheel was then switched to the other side of the wheelchair and the process was repeated.

**Data Processing:** The SmartWheel and kinematic data were imported to custom MATLAB codes. The marker positions obtained during the static trials were used to calculate the elbow angle, and wheel axle position (Table 1). The SmartWheel data and kinematic data obtained during the dynamic trials were used to calculate the maximum resultant force, maximum rate of rise of resultant force, percent contact phase, frequency, and velocity during 10 stroke cycles, using 5 cycles from each side (Table 1). Force measurements were normalized by dividing by the participant weight. All handrim metrics were calculated per cycle and averaged for each subject.

Exploratory Spearman correlations were run on all wheelchair fit and handrim biomechanics metrics with significance set at $p < 0.05$.

**Table 1: Descriptions of wheelchair fit and handrim metrics**

| Metric | Description |
|---|---|
| Elbow angle (degrees) | Sagittal plane angle between ulnar styloid, olecranon process, and acromion while hand is positioned at the top of the handrim |
| Axle position (mm) | Fore (-)/aft (+) position of the wheel axle with respect to the acromion. |
| Maximum resultant force ($F_r$) (N/kg) | Maximum force applied to the handrim during stroke cycle divided by weight of participant. |
| Maximum rate of rise of $F_r$ (N/s/kg) | Maximum value of the derivative of the force applied to the handrim during the stroke cycle divided by weight of participant. |
| Percent contact phase (%) | The percent of the stroke cycle that the hand was in contact with the handrim. |
| Frequency (strokes/s) | Number of complete stroke cycles in one second. |
| Velocity (m/s) | Distance traveled in one second. |

## RESULTS

Wheelchair fit metrics are reported as the number of participants who did or did follow the adult recommendations and their resulting group averages (Table 2). Five participants had elbow angles between 100 and 115 degrees, which fall within the recommended range of 100-120 degrees for adults [3], while four had elbow angles smaller than recommended and one had an elbow angle greater than recommended. Axle position measurements were only processed for 9 of the 10 participants, but of these, only two had their wheelchair axle positioned anteriorly to the shoulder, as is recommended for adults [3]. No participants followed both of the adult recommendations for wheelchair fit and three followed neither of the adult recommendations. Average and range of values for the handrim biomechanics metrics, as well as values from the adult literature are presented in Table 3.

**Table 2: Wheelchair measure averages and number of participants who did and did not follow adult recommendations**

| | Followed Adult Rec. | | Did Not Follow Adult Rec. | |
|---|---|---|---|---|
| **Metric** | Number | Average | Number | Average |
| Elbow angle | 5 | 105.8° | 5 | 96.5° |
| Axle position | 2 | -26.5 mm | 7 | 97.2 mm |

**Table 3: Handrim Biomechanics Metrics for study participants and reference adult values from literature**

| | Pediatric & Emerging Adults | | Adults |
|---|---|---|---|
| **Metric** | Average | Range | Average |
| $F_r$ (N) | 61.2 | 16.7-133.4 | 67.3 [7] |
| Max rate of rise of $F_r$ (N/s) | 2602.7 | 941.9-5732.8 | 915.2 [7] |
| Percent Contact Phase (%) | 37.0 | 27.4-41.4 | 47.2 [8] |
| Frequency (strokes/s) | 1.3 | 0.78-2.0 | 0.84 [9] |
| Velocity (m/s) | 1.63 | 1.0-2.4 | 0.87-1.1 [8, 9] |

Preliminary results of the Spearman tests suggest the $F_r$ was highly correlated to normalized rate of rise of $F_r$ ($r = 0.964$, $p << 0.01$). Both the $F_r$ and the rate of rise of $F_r$ also had strong positive correlations with the propulsion frequency ($r = 0.891$ and $0.952$; $p = 0.001$ and $p < 0.001$, respectively) and velocity ($r = 0.770$ and $0.697$; $p = 0.009$ and $p = 0.025$). Additionally, frequency and velocity were moderately correlated ($r = 0.624$ and $p = 0.054$).

There was a moderate negative correlation between elbow angle and percent contact phase ($r = -0.624$ and $p = 0.054$) and a moderate correlation between the axle position and velocity ($r = 0.650$ and $p = 0.058$). Additionally, elbow angle and axle position were positively correlated ($r = 0.850$ and $p = 0.004$).

## DISCUSSION

Only 50% of participants had elbow angles that followed adult recommendations. Elbow angles between 100-120 degrees are recommended for adults to help increase time spent in the contact phase, which typically reduces push frequency and therefore reduces repetitive motion [3]. In this young population of MWU, however, only a moderate correlation was found between elbow angle and time spent in contact phase and no correlation with frequency, suggesting that this adult recommendation may not improve propulsion technique in children the same as it does in adults. Only two of nine participants followed adult recommendations to place the axle anterior to the acromion which has been shown to reduce rolling resistance and therefore reduce the force required to propel the wheelchair in adults. Interestingly, the participant who had the axle placed most anteriorly to the acromion also had the lowest normalized force, however the other who followed the recommendation was in the midrange of normalized force values. The lack of correlation between axle position and force may indicate that this adult recommendation does not perfectly translate to pediatric and emerging adult manual wheelchair users.

Overall, the average values of handrim metrics for our participants did not fall near adult averages. Notably, the maximum rate of rise of $F_r$ was more than twice the adult average reported in previous literature [7]. Reducing the rate of rise of $F_r$ is recommended for adult MWU because higher values have been associated with median nerve damage and carpal tunnel syndrome [7]. The average percent contact phase was more than 10 percentage points shorter than adult averages and even the participant with the largest percent contact phase did not meet the adult average [8]. Increased time in the contact phase is recommended to decrease the necessary frequency required to propel the wheelchair.

Current work is underway to collect data for more participants to investigate this question further. Currently, no strong correlations were found between wheelchair fit measures and handrim metrics. The wheelchair fit measures used in this study are derived from recommendations for adult manual wheelchair users that are intended to prevent pain and pathology development by providing ideal ergonomics and reducing repetitive joint dynamics of the upper extremity. Since no participants followed both adult recommendations, we cannot conclude that the recommendations do or do not work for pediatric and emerging adult MWU. It is important to continue to investigate this question to determine if the adult recommendations are applicable to younger MWU populations.

## ACKNOWLEDGEMENTS

The authors would like to thank Eunice Kennedy Shriver National Institute of Child Health and Human Development of the National Institutes of Health (1R01HD098698) and Kathryn Reiners at Shriners Hospital for Children- Chicago for recruitment.

## REFERENCES

[1] Brault, M. *U.S. Department of Commerce*. 2012.
[2] Slavens, Brooke A., et al. *Front Bioeng Biotechnol*. 3, 2015.
[3] PVA. *Consortium for Spinal Cord Medicine*. 2005.
[4] Schnorenberg, A. J., et al. *J Biomech*. 47:269-76, 2014.
[5] Krey, C. H., Calhoun, C. L. *J Spinal Cord Med*. 27, 2004.
[6] Krey, C. H. *Int J Ther Rehabil*. 12, 2005.
[7] Boninger, M.L., et al. *Arch Phys Med Rehabil*. 80:910-5, 1999.
[8] Symonds, A., et al. *J Rehabil Assist Technol Eng*. 3, 2016.
[9] Kwarciak, A. M., et al. *Spinal Cord*. 49:457-62, 2011.

# EFFECTS OF GEOMETRICAL AND MICROSTRUCTURAL REMODELING ON VENTRICULAR MECHANICS IN HYPERTROPHIC CARDIOMYOPATHY

**Joy Mojumder (1), Lei Fan (1), Thuy Nguyen (2), Julius Guccione (3), Theodore Abraham(2), Lik Chuan Lee (1)**

(1) Dept. of Mechanical Engineering, Michigan State University, East Lansing, Michigan, USA
(2) Dept. of Cardiology, University of California San Francisco, San Francisco, California, USA
(3) Dept. of Surgery, University of California San Francisco, San Francisco, California, USA

## INTRODUCTION

Hypertrophic cardiomyopathy (HCM) is a genetic heart disease that is associated with sudden cardiac death. This disease is often classified based on whether the left ventricle (LV) outflow tract is obstructed or not (non-obstructive). The clinical features associated with HCM include a reduction in longitudinal and circumferential systolic strains (shortening) in the LV, alterations in contractility, myofiber disarray and asymmetrical septal hypertrophy. While these features are well established in HCM, the contribution of each remodeling feature (such as a change in contractility and myofiber disarray) to LV dysfunction is not clear. Besides, it is also not clear how differences in remodeling between obstructive and non-obstructive HCM affect LV function. To address these issues, we developed patient specific computational LV models to investigate the isolated effects of myofiber disarray, contractility and asymmetrical hypertrophy in these two types of HCM.

## METHODS

Clinical data from 2 patients with obstructive and non-obstructive HCM and a control subject were acquired. These data include the blood pressures, global longitudinal strain estimated from 3D echocardiography and magnetic resonance (MR) images. Left ventricle cavity volume waveform of each subject was derived by segmenting the endocardial wall from the MR images over the cardiac cycle with MeVisLab (MeVis Medical Solutions AG). Together with the pressure waveforms of HCM patients reported in published data, we obtained the pressure-volume (PV) loop of each subject. Finite element (FE) LV geometry of each subject was reconstructed from the MR images associated with end-diastole (ED) (**Fig. 1a**). Regional thickness of each subject was measured from the reconstructed geometry (**Fig. 1b**),

In the LV, mean myofiber direction, $\boldsymbol{e}_{f_0}$ was prescribed to vary transmurally from $+60^0$ at endocardium to $-60^0$ at epicardium (**Fig. 1c**). Myofiber disarray was described by applying a structural tensor to the constitutive models of the cardiac tissue. The structure tensor, **H,** is defined as[1]

$$\boldsymbol{H} = \kappa \boldsymbol{I} + (1 - 3\kappa)\boldsymbol{e}_{f_0} \otimes \boldsymbol{e}_{f_0} \quad . \qquad (1)$$

This tensor describes a conical dispersion of myofibers about a mean direction $\boldsymbol{e}_{f_0}$. The degree of myofiber disarray is parameterized by a dispersion parameter $\kappa$, which varies between 0 (perfect alignment or no dispersion) to 1/3 (complete disarray).

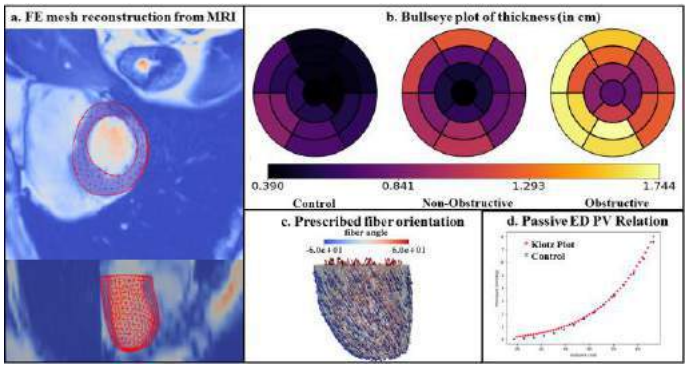


**Fig 1: Construction of LV Finite Element model.**

Left ventricular mechanics were described by an active stress formulation based on prescribed active and passive material laws. The passive mechanical behavior was described by the Holzapfel-Ogden constitutive model, whereas the active mechanical behavior was described using the Guccione model[2]. Simulation of LV mechanics in a cardiac cycle was performed in 2 steps for each subject-specific model. First, the unloaded LV geometry was estimated from the reconstructed ED LV geometry using a backward displacement

method, in which model parameters of the Holzapfel-Ogden model was calibrated so that the model-predicted end-diastolic pressure-volume relationship (EDPVR) matches the "Klotz" curve[3] that holds also in HCM (See **Fig. 1d** for the control subject). Following that, the unloaded LV FE model was coupled to a closed-loop lumped parameter model of the circulatory system to predict the cardiac hemodynamics and mechanics. Peak tension in the active contraction model, resistances and compliances in the circulatory model in each subject-specific model were first calibrated without myofiber disarray (i.e., $\kappa$ = 0) to match the corresponding measured LV PV loop, pressure and volume waveforms, blood pressure and longitudinal strain. Thereafter, based on published data of fractional anisotropy (FA), a different degree of myofiber disarray (i.e., $\kappa$ in **Eq. 1**) was determined, and was imposed globally into the HCM LV models. The peak tension in the active contraction model was adjusted to match results with the clinical data.

## RESULTS

The calibrated models' predictions were close to the measurements (see **Fig. 2a** for a representative case of the control subject). Left ventricular geometry and function were greatly different in the HCM patients compared to the control. Specifically, compared to the control subject, in both types of HCM patients end diastolic volume (EDV) were larger, whereas end systolic volume (ESV) was larger only in obstructive HCM patient (obstructive HCM: EDV 114.5 ml, ESV 37.9 ml; non-obstructive HCM: EDV 82.1 ml, ESV 12.1 ml vs. Control: EDV 63.1 ml, ESV 18.9 ml). Global longitudinal strain was reduced in the HCM patients: (obstructive HCM: 13%; non-obstructive HCM: 19% vs. Control: 20%). Thickness at septum was highest in the obstructive HCM patient (17.4 mm) followed by the non-obstructive HCM patient (12.3 mm) and the control (9.1 mm) (**Fig. 1b**).

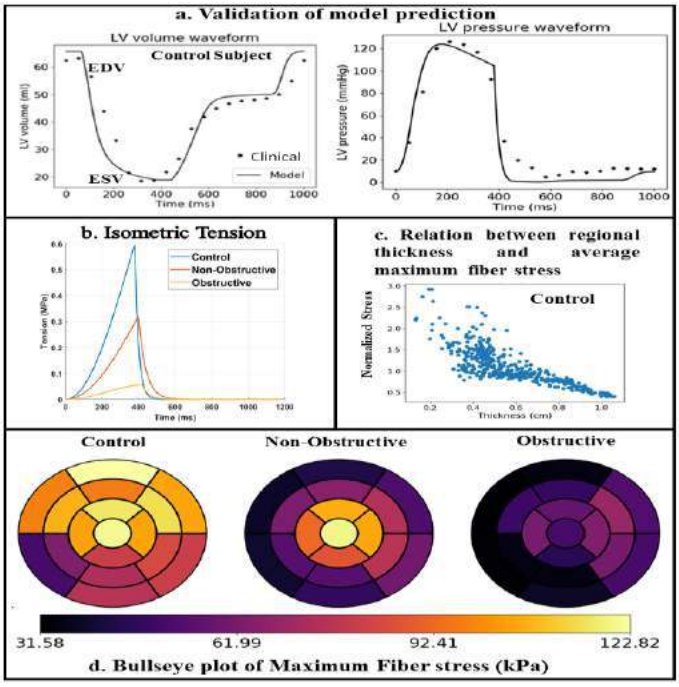


**Fig 2: Validation of hemodynamics results and prediction of mechanics data by model.**

Resultant isometric tension curve based on the calibrated active stress model parameters shows that the peak tension was lowest in the obstructive HCM patient (60 kPa) followed by the non-obstructive HCM patient (320 kPa) and the control (600 kPa) (**Fig. 2b**). Regional stress and stretch in the 3-material directions (i.e., fiber, sheet and sheet-normal) have good correlation with the regional thickness. The average maximum fiber stress showed a very good linear correlation with the variation in thickness in each subject (**Fig. 2c**). At the septum, maximum fiber stress was lowest in the obstructive HCM patient followed by the non-obstructive HCM patient and the control (**Fig. 2d**).

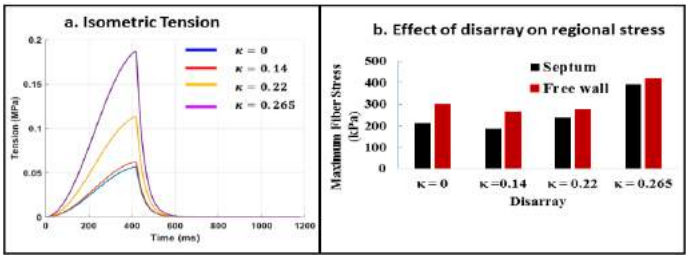


**Fig 3: Effect of myofiber disarray in Obstructive HCM**

With increasing $\kappa$, the resultant peak tension in the obstructive HCM patient needs to be increased to match the measured hemodynamics and strains. Specifically, when $\kappa = 0.265$ that is equivalent to a fractional anisotropy FA of 0.38, peak tension needs to be increased from 60 kPa (without disarray) to 200 kPa (**Fig 3a**). The increase in myofiber dispersion led to an increase in the maximum fiber stress at the septum and free wall. The change in fiber stress with respect to myofiber dispersion is monotonic (**Fig 3b**).

## DISCUSSION

Ventricular wall stress is an important determinant of myocardial oxygen consumption and ventricular remodeling. Because regional myofiber stress (or load on the myocytes) cannot be directly measured in the intact LV, we have estimated stress in HCM patients with different phenotypes (obstructive vs. non-obstructive) using computational modeling to gain insights of this disease.

We found that myofiber stress and contractility are all reduced in HCM patients compared to the control without consideration of myofiber disarray. The reduction is greatest in the obstructive HCM patient than the non-obstructive HCM patient. We also found that the reduction in myofiber stress is caused by the increased in wall thickness due to asymmetrical hypertrophy in the HCM patients. In the obstructive HCM patient, we found that an increase in myofiber disarray resulted in an increase in peak tension that is necessary to match the measured cardiac hemodynamics and function. With a substantially large degree of disarray FA = 0.38 that has been reported previously, peak tension of the myocyte, however, is still lower than that found in the control subject. This result suggests that it is likely that the myofiber contractility is reduced in HCM patient. __

There are some limitations associated with this study. First, the analysis was performed only on 2 HCM patients. Second, the degree of myofiber disarray is varied globally in this study. Future work on variation of the degree of myofiber disarray on non-obstructive HCM patient and incorporating spatial variation of disarray parameter will be helpful to understand the effect of different remodeling features in different HCM patients.

**References:**


1. Gasser, T. et al , J of Royal Society Interface (2006) 3(6):15-35
2. Fan, L. et al, Comput. Biol. Med. 105050 (2021).
3. Klotz, S. Am. J. Circ. Physiol. 291, H403-12 (2006).

SB³C2022
Summer Biomechanics, Bioengineering and Biotransport Conference
June 20-23, Eastern Shore, MD, USA

# SIMULATIONS OF CELLULAR GUIDANCE BY 3D MATRIX ORIENTATION AND ANISOTROPY VIA DEFORMABLE CONTINUOUS FIBRIL DISTRIBUTIONS

**Steven A. LaBelle (1,2), Steve A. Maas (1,2), Adam Rauff (1,2), Jeffrey A. Weiss (1,2)**

(1) Department of Biomedical Engineering, University of Utah, Salt Lake City, UT, USA
(2) Scientific Computing and Imaging Institute, University of Utah, Salt Lake City, UT, USA

## INTRODUCTION

Matrix fibril anisotropy and density are gaining recognition for their mechanoregulatory roles in cellular growth and guidance. During angiogenesis, for instance, matrix density contributes to durotaxis while fibril orientation contributes to haptotaxis in an anisotropy dependent manner. The configuration of matrix density and fibril alignment are thought to affect the success of establishing new vasculatures during pathologic and homeostatic angiogenesis [1]. Computational simulation is emerging as a tool to determine how the integrated effects of mechanical and biochemical stimuli coordinate cell guidance depending on the relevant matrix architecture. Current 3D frameworks generally calculate guidance cues from discrete vector fields which represent general orientation but fail to reflect the degree of alignment [2-4]. We propose a deformable continuous 3D ellipsoidal fibril distribution (EFD) representation of collagen fibril orientations during simulations of collective migration phenomena. Our simulations accounts for matrix anisotropy and realignment due to cellular traction. We find that a continuous distribution is needed to model strongly polarized guidance. Further, our distributions encode the local degree of alignment, which is known to affect a range of cellular behaviors.

## METHODS

*In vitro alignment studies of angiogenesis:* The effects of matrix anisotropy on microvessel guidance using rat fat microvessels were embedded in type I collagen. Collagen was stretched along the axial direction just before polymerization finished to induce low, medium, or high levels of anisotropy (n > 6 ea.). The gel edges were cut from stretch anchors and then gels were cultured free-floating for 10 days before fixation, staining, and imaging. Avascular gels were imaged via second harmonic generation (SHG) to extract collagen fibril orientation distribution functions (ODFs) as inputs to simulations.

*Simulations of microvascular guidance*: Finite element mechanical models in FEBio were coupled with AngioFE, a plugin that simulates neovessel growth from parent microvessels [4]. Our prior approach to neovessel guidance represented the local fibril direction at each finite element node as a discrete vector. In this work, we developed a new method that represents fibril ODFs as EFDs stored as symmetric positive-definite (SPD) tensors at the integration points. The SPD criteria are critical as it allows us to interpolate local ODFs using DT-MRI methods [5].

Certain deformations morph SPDs into asymmetric shapes. Thus, we developed a pseudo-deformed EFD, $\boldsymbol{P}$, that accounts for scaling and rotation while maintaining the SPD criteria:

$$\boldsymbol{P} = \boldsymbol{Q}\boldsymbol{D}\boldsymbol{Q}^{-1} \tag{1}$$

Here, $\boldsymbol{Q}$ is a 3x3 matrix whose columns contain the directions of the EFD semiprincipal axes rotated by $\boldsymbol{R}$ (the rotational component of the deformation gradient). $\boldsymbol{D}$ is a diagonal matrix containing the lengths of the semiprincipal axes scaled by the deformation gradient $\boldsymbol{F}$. This approach was tested using simulations of uniaxial extension of a biphasic, hyperelastic material containing initially isotropic fibril distributions.

The direction of fibril guidance, $\boldsymbol{\theta}$, is sampled from EFDs using a Monte-Carlo approach. A randomly sampled vector is accepted if it lies within the surface of the EFD given by:

$$\frac{x^2}{a^2}+\frac{y^2}{b^2}+\frac{z^2}{c^2}<1 \tag{2}$$

where $x$, $y$, and $z$ are the components of the random vector, and $a$, $b$, and $c$ are the lengths of the semiprincipal axes.

The new direction that a vessel grows, $\boldsymbol{\psi}_{new}$, depends on the persistence (prior) direction, $\boldsymbol{\psi}$, and the fibril guidance direction $\boldsymbol{\theta}$. This direction is calculated by partially rotating the persistence direction towards the fibril guidance direction via

$$\boldsymbol{\psi}_{new} = \boldsymbol{R}(\boldsymbol{\psi}, \boldsymbol{\theta}, \alpha)\boldsymbol{\psi} \quad (3)$$

where $\boldsymbol{R}(\boldsymbol{\psi}, \boldsymbol{\theta}, \alpha)$ is the matrix that completely rotates $\boldsymbol{\psi}$ to $\boldsymbol{\theta}$**.** The factor $\alpha$ scales the fibril contribution so that when $\alpha = 0$, directional control is governed by the persistence direction $\boldsymbol{\psi}$**,** while when $\alpha = 1$, directional control is governed by the fibril direction $\boldsymbol{\theta}$.

Simulations of guidance in low, medium, or highly anisotropic collagen were performed using both the discrete fibril and the continuous EFD approaches. Initial conditions and microvessel growth over time were prescribed based on in vitro data. Experimental collagen fibril ODFs were extracted from SHG images and fit to EFDs. Discrete fibril directions were sampled from a global EFD. A parametric study was performed on the fibril contribution scale $\alpha$ between 0 and 1 to determine how well each approach could simulate guidance for each level of anisotropy. A total of 10 simulations with unique initial random seeds (and thus initial conditions) were performed for each case. We focused on the 2D ODF in the XY plane was evaluated because the majority of collagen alignment was in this plane.

## RESULTS

Pseudo-deformed EFD fibril distributions undergo tension, compression, and shear while maintaining the qualities of an SPD (Fig **A**). This is crucial to allow approximation of the local ODF at all locations within the simulation domain.

A vector-field approach was unable to reproduce the experimentally measured 3D fibril guidance for medium and high anisotropy simulations (**Fig B,** blue lines). The continuous EFD approach, however, was able to replicate guidance to the degree seen experimentally (orange lines). These results are observable when comparing confocal imaging to simulation results (**Fig C**).

## DISCUSSION

In vitro and in vivo, cells continuously probe the matrix for cues. Discrete fibril approaches only sample the ODF once during model initiation while EFDs can be sampled as cells grow and move, much like is seen experimentally. Further, discrete fibril approaches are more sensitive to meshing constraints.

The contribution of fibril guidance required to match experimental data increased with anisotropy, which may reflect changes in the balance of persistence and guidance signaling.

Another crucial benefit of the continuous distribution approach is that it inherently encodes information about the degree of alignment. Anisotropy has previously been shown to affect cellular proliferation and growth rate, and may be mechanoregulatory in numerous other signaling pathways involved in homeostasis, healing, and pathology.

The presented approach is extensible to other guidance phenomena such as chemotaxis where cytokine gradients are anisotropically distributed.


## ACKNOWLEDGEMENTS

Funding from NIH R01HL131856, NIH R01GM083925, and NIH R01AR069297 are gratefully acknowledged. We would like to thank Elena Budko for her contribution to microvessel isolations and the Cell Imaging Core Facility at the University of Utah.


## REFERENCES


[1] McCoy, MG., et al., ACS Biomater, Sci.Eng. 4(8): 2967-76, 2018. [2] Barocas, VH. & Tranquilo, RT., J Biomech Eng. 119(2): 137-45, 1997. [3] Dallon, JC., et al., J Theor Biol. 199(4): 449-71, 1999. [4] Maas, SA., et al., Biophys J. 115(9): 1630-37, 2018. [5] Fletcher, PT. & Joshi, S., Signal Process. 87(2): 250-62, 2007.


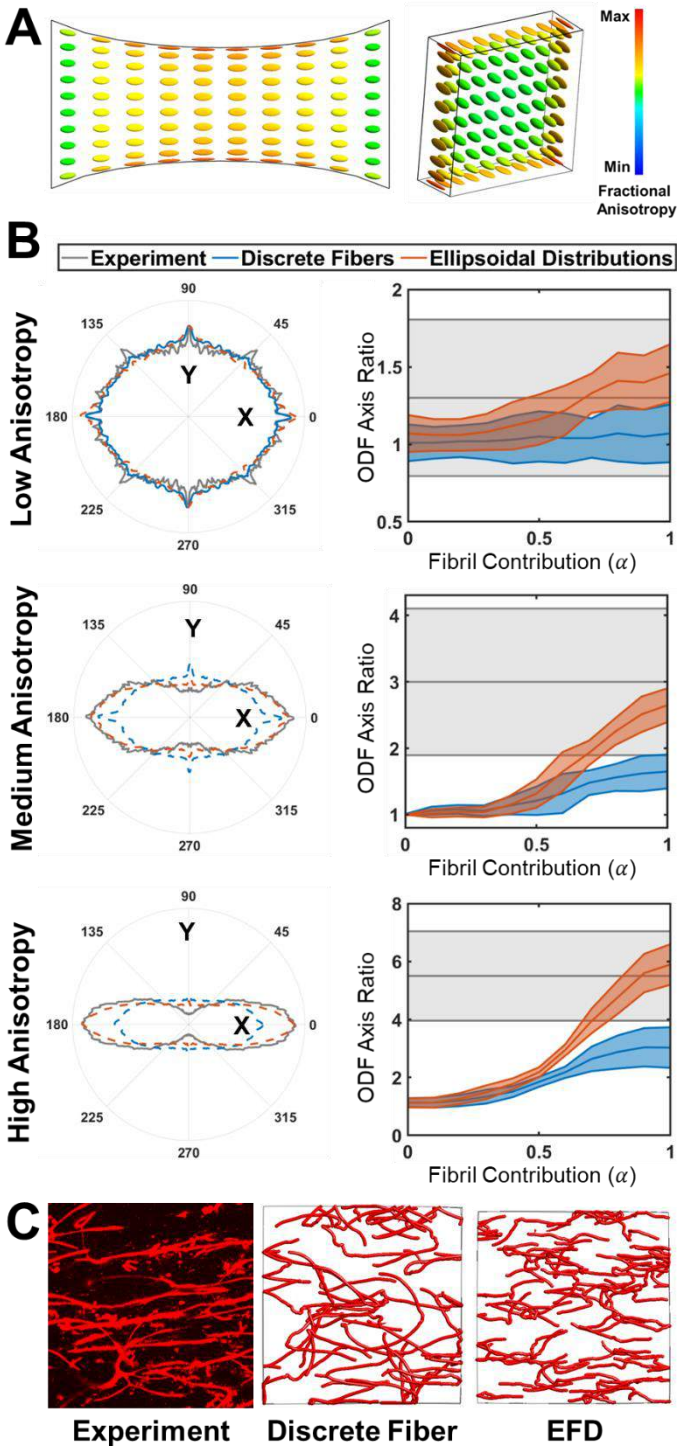


Figures. **A)** Glyphs indicating deformation of initially isotropic EFDs after uniaxial extension. **B)** Comparison of modeling results to experimental vessel guidance at increasing levels of anisotropy. Left: Experimental ODFs compared to the best-case ODF for each modeling approach. Right: Parametric study on fibril contribution ($\alpha$) and the resulting ratio of the ODF axis magnitudes. Mean ± std. **C)** Comparison of results for modeling approaches for guidance in highly aligned collagen to experiment. EFDs yield stronger vessel guidance.

SB³C2022
Summer Biomechanics, Bioengineering and Biotransport Conference
June 20-23, Eastern Shore, MD, USA

# MOLECULAR DESIGN OF POLYELECTROLYTE COMPLEX MICELLES FOR NUCLEIC ACID DELIVERY

**Alexander E. Marras (1), Jeffrey R. Vieregg (1), Matthew V. Tirrell (1)**

(1) Pritzker School of Molecular Engineering, University of Chicago, Chicago, IL, USA

## INTRODUCTION

Developing effective non-viral methods for delivery of nucleic acids and other macromolecular therapeutics is one of the most pressing challenges in nanomedicine. The immense potential of engineered nucleic acids as therapeutic agents is limited by the difficulty of overcoming physical and biological barriers. A solution to this critical problem is using hydrophilic charged block polymers to condense nucleic acids, driving nanoscale phase separation to form polyelectrolyte complex micelles (PCMs) (Figure 1A). These core-shell nanoparticles sequester and protect nucleic acids from nucleases and immune response. Still, few systematic studies have been conducted on how parameters such as nucleic acid backbone chemistry, polymer charge density and polymer length influence PCM properties, despite evidence that these strongly influence complexation behavior. Here, we present an investigation of the impact of physical and chemical properties on PCM assembly and stability.

## METHODS

We used light scattering, small angle X-ray scattering (SAXS), and electron microscopy to investigate the relationship between oligonucleotide PCM properties and the properties of the nucleic acids and block copolymers that form them. Materials were synthesized by aqueous reversible addition-fragmentation chain transfer (RAFT) polymerization [1] or ordered from Alamanda Polymers or Integrated DNA Technologies. PCMs were prepared using a salt-annealing method [2] where dissolved complexes in 1M NaCl are slowly dialyzed into low salt conditions. SAXS measurements were made at the Advanced Photon Source at Argonne National Laboratory and analyses were performed using the Irena software package for Igor Pro as detailed in Marras et al. [2]. PCMs were imaged using transmission electron microscopy (TEM) at University of Chicago. Phase and morphology of homopolymer complexes were observed by bright field optical microscopy. To assess the stability against salt, samples were titrated with NaCl and light scattering intensity was measured.

## RESULTS

We found the molecular details of the cationic charged group and nucleic acid backbone strongly influence complexation behavior and stability. Briefly, nucleic acid hybridization drives PCM shape, where single-stranded nucleic acids formed spheres and double-stranded formed cylinders [3,4]. DNA, RNA, and common chemically modified nucleic acids also exhibited drastically different assembly behavior (Figure 1B) and phosphorothioate backbone modifications radically increase complex stability (Figure 1C). Furthermore, polymer lengths in the block copolymer control size and aggregation number while nucleic acid length is independent of these physical properties [5]. Experimental scaling laws (Figure 1D) were developed for numerous physical parameters and show consistency with previous studies and theoretical predications [6].

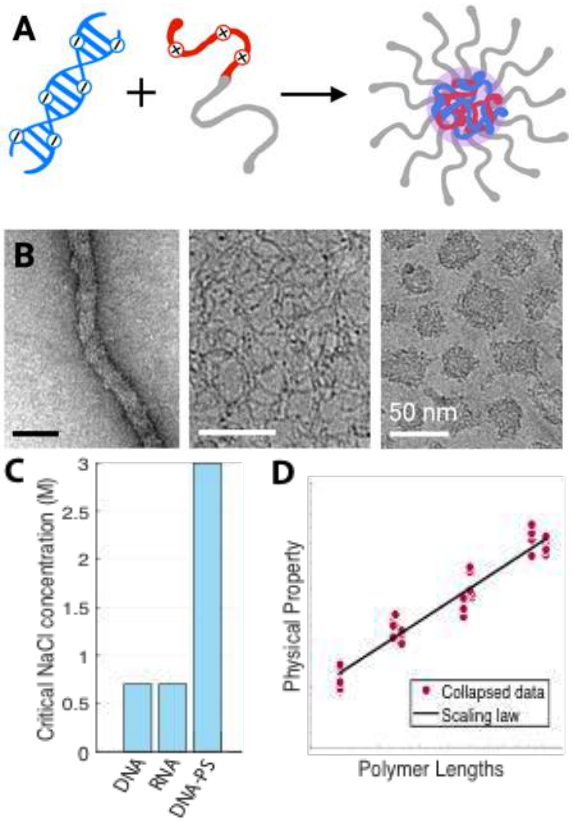


**Figure 1: (A) Charged polymers sequester therapeutic nucleic acids for protection and delivery. (B) Molecular details of both components control the shape, size, and stability of these particles. All scale bars = 50 nm. (C) Stability vs. NaCl show drastic differences with phosphorothioate (PS) modifications to nucleic acid backbones. (D) Scaling laws for physical parameters of PCMs were developed**

## DISCUSSION

Molecular details of nucleic acids and cationic polymers drastically influence PCM assembly and stability and should be considered when designing therapeutic delivery systems. These observations narrow the design space for tailored therapeutic micelles, promoting efficient design of delivery devices for therapeutic payloads.

## ACKNOWLEDGEMENTS

This work was supported by the National Institute of Standards and Technology (NIST), through the Center for Hierarchical Materials Design (CHiMaD) under award 70NANB14H012. This work used resources of the Advanced Photon Source, a U.S. Department of Energy (DOE) Office of Science User Facility operated for the DOE Office of Science by Argonne National Laboratory under Contract No. DE-AC02-06CH11357. Parts of this work were carried out at the Soft Matter Characterization Facility and the Advanced Electron Microscopy Facility of the University of Chicago. The authors thank Xiaobing Zuo for his assistance with the SAXS data acquisition and Tera Lavoie for assistance with electron microscopy.

## REFERENCES

1) Ting, J.M. et al., *ACS Macro Lett.* 2018; 7:726-733.
2) Marras, A.E. et al., *J Vis Exp*. 2020; e60894.
3) Marras, A.E. et al., *Polymers.* 2019; 11:83.
4) Lueckheide, M. et al., *Nano Lett.* 2018; 18:7111-7
5) Marras, A.E. et al., *Macromolecules*. 2021; 54:6585-6594
6) Marras, A.E. et al., J Chem Phys B. 2021; 125:7076-7089

SB³C2022
Summer Biomechanics, Bioengineering and Biotransport Conference
June 20-23, Eastern Shore, MD, USA

# CHANGES IN CD44 AND DRUG RESISTANCE IN OVARIAN CANCER CELLS WITH DIFFERING MECHANICAL PRESENTATIONS OF HYALURONIC ACID

**Maranda E. Tidwell (1), Gillian Huskin (1), Molly Buckley (1), Joel Berry (1,2), M.K. Sewell-Loftin (1,2)**

(1) Department of Biomedical Engineering, University of Alabama at Birmingham, Birmingham, Alabama, United States of America
(2) O'Neal Comprehensive Cancer Center, University of Alabama at Birmingham, Birmingham, Alabama, United States of America

## INTRODUCTION

Ovarian cancer is the deadliest and third most common gynecological cancer with a 5-year survival rate less than 30% [1]. However, little research has been done in understanding the role of the biomechanical tumor microenvironment (TME) in the metastasis of ovarian cancer. Previous studies have shown a link between hyaluronic acid (HA) in the TME and cancer progression and metastasis, through its receptor CD44 [2]. CD44 can activate many cell-signaling pathways including the cancer pathogenic pathway, Ras-MAPK. In the clinical setting, ovarian cancer is treated with surgical removal and chemotherapy, with cisplatin and paclitaxel being the primary drugs of choice. A higher presence of HA in the TME is associated with a more drug resistant phenotype of ovarian cancer and increases in CD44 levels in cancer cells correspond to more metastatic behaviors [3]. We hypothesize that biomechanical signaling in the HA-CD44 axis alters ovarian cancer growth and metastasis and increases chemo-resistance. The objective of this study was to evaluate changes in CD44 expression with differing presentations of HA. Further, the effects of HA and CD44 signaling on ovarian cancer cell response to cisplatin in 2D and 3D environments were quantified.

## METHODS

Human ovarian cancer cell line OVCAR8 was used as the model for the studies. OVCAR8 cells are non-serous and exhibit highly invasive behaviors [4,5]. HA (Sigma-Aldrich, 41897, 1MDa) was introduced to the cells in two methods: in the media as a soluble factor (SOL HA) or plated on tissue culture plastic (PLT HA). Concentration of HA was maintained across exposure groups at 1 μM. The HA plated dishes were made by coating HA to the tissue culture plastic with HA in HBSS overnight at 4C [6]. No treatment controls (0μM) only received HBSS. The cells were fed every 2-3 days and lysed after 7 days. Another study used collagen-I coated FlexCell plates coated with HA (FLX+PLT HA). OVCAR8 cells seeded on these plates and were allowed to adhere over night before straining at 10% and 0.3% Hz frequency for 24 hours. For analysis, all cells were lysed in RIPA buffer plus 1:100 HALT solution prior to a Western Blot for CD44 expression β-actin or GAPDH as a loading control. Densitometry was performed using FIJI, and CD44 expression was normalized first to the loading control, then to the appropriate no treatment control group.

For 3D studies, PDMS rings with an ID of 8mm and height of 1mm were used as microtissue models [7]. The rings were loaded with 25K cells in fibrinogen plus thrombin that quickly form a fibrin gel. The rings were fed with control media or 1 μM soluble HA (F+SOL HA). A separate set of samples were made with HA mixed in the fibrinogen (F+GEL HA). The rings were fed every 2 days for 7 days before the gels were digested with nattokinase; remaining cells were lysed for protein analysis as mentioned previously.

To evaluate the role of CD44 signaling in OVCAR8 chemo-resistance, we generated genetically-modified cell lines with lentivirus to knock down CD44 (shCD44) or a scramble was used as a control (shSCR). Knockdown was verified via Western Blot, and shCD44 cells show ~50% decrease in CD44 protein levels. These cells were seeded in fibrin only or F+GEL HA gels and treated with 50μM cisplatin (Cis) or vehicle (Veh) control for 24h. A live/dead imaging assay (ThermoFisher, L32250) was performed on the cells and co-stained with Hoescht 33342. For each gel, a 100um z-stack was collected and processed in FIJI.

## RESULTS

The results for the 2D experiments show that, CD44 expression decreased by ~30% in the SOL HA samples and increased by ~10% in the PLT HA samples compared to the no treatment controls (Figure 1). When the PLT HA samples were further mechanically stimulated in the

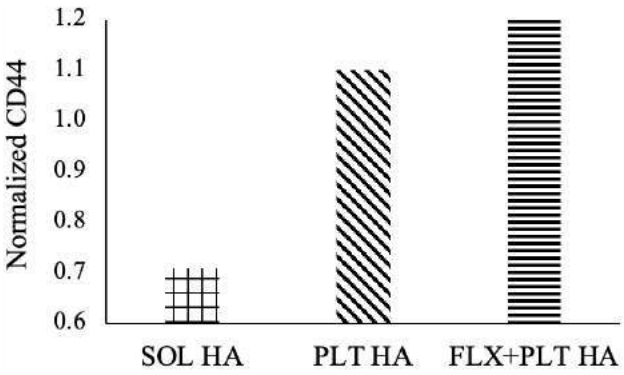


**Figure 1 Results from Western blot for 2D OVCAR8 with different exposures to HA. Values are double normalized first to a loading control protein, then to the appropriate no treatment control sample.**

FLX+PLT HA studies, CD44 increased by another 10% making the total increase ~20% compared to the no treatment control (Figure 1). We observed similar increases in CD44 when HA is incorporated into

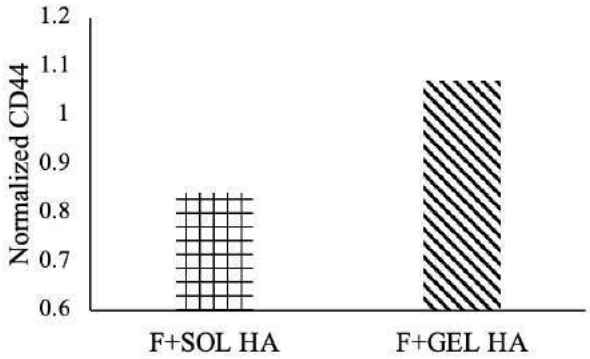


**Figure 2 Results from Western blot for 3D OVCAR8 with different exposures to HA normalized to 0 μM**

the 3D environment, compared to when it is supplied to OVCAR as a soluble factor in 3D studies. Overall, CD44 expression decreased by ~15% when the cells were presented with F+SOL HA (Figure 2). When the HA was incorporated in the gel in the F+GEL HA samples, CD44 was increased by ~7% (Figure 2).

The results from the chemosensitivity studies suggest that F+HA gels are somewhat protective for OVCAR8 cells with reduction in cell death for all lines when treated with cisplatin compared to cells grown in fibrin only gels (Figure 3). For cells with high levels of CD44 expression, WT and SCR, the effect is small. However, in the shCD44 cells there is a significant decrease in cell death for cisplatin-treated cells grown in the combination gels compared to fibrin only.

## DISCUSSION

The results show that the mechanical presentation of HA, whether in a 3D gel or coated on a 2D surface, increases CD44 expression more than when HA is a soluble factor in the media. This suggests a mechanobiological role for the HA-CD44 signaling pathway and could impact our understanding of ovarian cancer metastatic growth.

In our drug sensitivity studies, results indicate that HA embedded in the fibrin prevents or inhibits cell death compared to controls for cells treated with cisplatin. This effect was even observed in the shCD44 line which suggests the combination of HA in the matrix and limited CD44

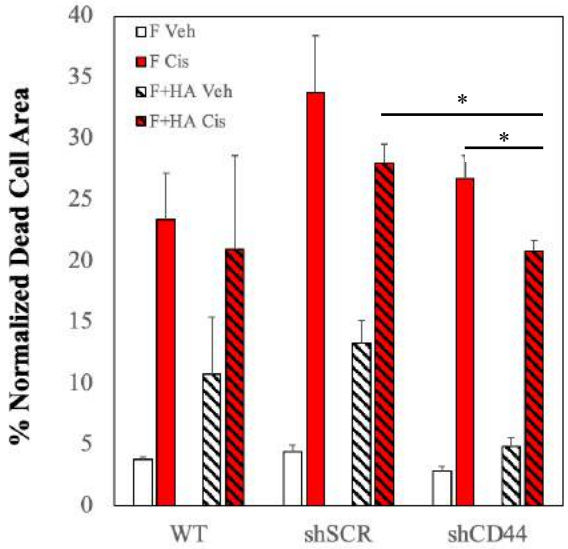


**Figure 3. Percentage of dead cells in 3D studies with OVCAR8 cell lines. All values are normalized to total nuclear area. Averages ± SEM; N=3-4. * p < 0.05.**

expression decreases the sensitivity of the cancer cells to cisplatin. Another potential explanation for this is that the large HA molecules in the microenvironment prevented the cisplatin from fully diffusing to cells; future studies will optimize delivery of chemotherapeutic agents in the 3D microtissues. Additionally, while the shRNA was designed to knockdown the standard splice variant of CD44, alternative splice variants such as CD44v6 may not be decreased in the shCD44 line. Studies are ongoing to evaluate the differential expression of CD44v6 in the shCD44 cells. Overall, our studies support that HA is associated with a worse prognosis of ovarian cancer and that this may be due to mechanobiological signaling.

Our studies demonstrate proof of concept that biomechanical stimulation of OVCAR8 cells with HA can cause changes in cell behaviors. We will further study this phenomenon by investigating factors downstream of CD44 such as Src And p38. Additionally, we will leverage 3D microtissue models developed in our lab to examine OVCAR8 migration and invasion in vascularized tissue mimics. These systems can also be used to evaluate how CD44 levels regulate response to cisplatin treatment. These proof-of-concept studies help explain the role HA plays in mechanically stimulating CD44. Ultimately, this project will help elucidate proliferation, metastasis, and drug resistance observed in ovarian cancer and open the doors for researching new diagnostics and therapeutics.

## ACKNOWLEDGEMENTS

The Authors would like to acknowledge funding for the project: Blazer Graduate Research Fellowship (MT): T32-EB023872 (MB): R00-CA2302022 (M.K.S.L.), IMPACT Award, O'Neal Comprehensive Cancer Center (M.K.S.L.)

## REFERENCES

[1] Momenimovahed, Z et al., *Int J Women's Health,* 11:287-299, 2019. [2] Yahya, R et al., *Clin. Lab*, 60(7):1115-1121, 2014. [3] Ween, M et al., *Int. J. Mol. Sci.* 12(2):1009-1029. [4] Hallas-Potts, A et al., *Sci. Rep.* 9:5515, 2019. [5] Haley, J et al., *Oncotarget* 7(22):32810-38220, 2016. [6] Hamann, K et al., *Immunol.* 154(8): 4073-4080, 1995. [7] Sewell-Loftin, M et al., *Sci. Rep*. 7:12574, 2017

# A HYBRID PARADIGM TO DEVELOP REGIONAL THORACO-ABDOMINAL CRITERIA FOR BEHIND ARMOR BLUNT TRAUMA

**Narayan Yoganandan (1), John Humm (1), Brian Stemper (1), Cameron Bass (2), Robert Salzar (3), B. Joseph McEntire (4)**

(1) Department of Neurosurgery, Medical College of Wisconsin, Milwaukee, WI
(2) Department of Biomedical Engineering, Duke University, Durham, NC, WI
(3) Department of Mechanical & Aerospace Engineering, University of Virginia, Charlottesville, VA
(4) Injury Biomechanics & Protection Group, US Army Aeromedical Research Laboratory, Fort Rucker, AL

## INTRODUCTION

Injury criteria are critical in the development of standardized tests and surrogates for evaluating injury risk and the efficacy of devices such as personal protective equipment (PPE), and to improve the overall safety of our Warfighters/Service Members. Protective body armor is ubiquitous to military and civilian law enforcement personnel. It reduces the risk of penetrating injury while decreasing the energy transferred to the body [1]. However, any deformation of the armor can lead to trauma to the underlying organs and tissues through momentum transfer. Tissue response, anatomy, geometry, and loading conditions all play a role in any resulting injuries, injury patterns, and injury mechanisms. The composition and mechanical properties such as stress-strain responses of cortical and cancellous bones of the ribcage and spinal column will lead to different injury responses. A similar analogy applies to the thoraco-abdominal organs because they are viscoelastic and loading rate sensitive. In addition, skin and subcutaneous fat plays a role. The heterogeneity of the human system anatomy should be considered during the development of biomedical injury criteria for behind armor blunt trauma (BABT). Many studies have been conducted using different types of animal models to develop injury metrics; however, the focus on regional tolerance differences is largely ignored in current injury assessment (residual clay penetration) [2]. The objective of this study is to examine the rationale for current clay-based injury criteria used in the military, identify recent studies and advancements in experimentation, analysis, and statistical modeling, and develop a hybrid paradigm that can be used to determine thoraco-abdominal regional injury criteria for BABT.

## METHODS

Studies focusing on live animal experiments to different body regions and metrics to develop current injury assessments and criteria were analyzed. Original studies conducted by the military that formed the basis of testing standards included impacts to goat thoraces (lungs) and liver [2]. Lethality in the former and liver injuries in the latter experimental model were used as the main injury outcome measures. Studies were also conducted using the swine and dog models with similar impacting locations and projectiles. Goat studies were used to develop the original probability curve for lethality using a binary regression model. Impacts to the midsternum were delivered to swine in another study that focused on heart impacts. Later studies used more sophisticated techniques for measuring deformations and adding other metrics such as viscous criterion, and post-mortem human subjects. A summary of some of these studies are presented to achieve the objectives of this project.

## RESULTS

Impacts were delivered to the lateral region of the thorax of goats with projectile diameters ranging from 40 to 63 mm, masses from 50 to 125 g, and velocities from 25.2 to 85.7 m/s in a group of 30 animals, out of which 12 resulted in fatal injuries. In another series of nine animals, a 63 mm diameter and 125 g projectile impacts resulted in four fatal injuries, with velocities ranging from 55.8 to 80 m/s. With diameters of 40 and 80 mm and masses of 50 and 200 g, respectively, none out of two and one out of five animal sustained fatal injuries, where velocities ranged from 78.3 to 82.1 m/s and 34.3 to 51.3 to 61.8 m/s, respectively. With diameters of 76.2 and 36.5 mm and mass of 132 and 210 g, respectively, none out of 15 and all 5 animals sustained fatal injuries. The velocities for this group ranged from 18.3 to 47.1 m/s and 24 to 28 m/s, respectively. Swine tests included 79 mm and 196 g impacts at 21.3 to 36 m/s with four out of six animals sustaining fatal injuries, and 27.7 mm and 11.7 g impacts resulting in three out of 15 animals sustaining fatalities, with velocities ranging from 21.3 to 36 m/s and 80.8 to 148.1 m/s, respectively. Dogs were subjected to 63 to 70 mm diameter and 43 to 382.2 g mass impacts with velocities from 18.9 to 80.2 m/s, and greater mass was associated with greater velocities.

**Table 1: Summary of thorax impacts to different animals.**
Fatal ratio refers to the percentage of animals in the specific group

| Animal | Dia. (mm) | Mass (g) | Velocity (m/s) | Specimen mass (kg) | Fatal Ratio |
|---|---|---|---|---|---|
| Goat | 36.8-80 | 43-210 | 18.3-85.7 | 27.8-52.8 | 23% |
| Swine | 79 | 196 | 21.3-36.0 | 13.1-17.4 | 67% |
| Swine | 27.69 | 11.7 | 80.8-148.1 | 12.6-18.2 | 20% |
| Dog | 70 | 63-383 | 18.9-80.2 | 14.8-23.1 | 21% |

Impacts were delivered to goat livers with projectile diameters from 40 to 63 mm and mass from 50 to 125 g in a group of 38 animals, out of which all sustained liver injuries, from velocities ranging from 44.8 to 81.2 m/s. In another group, projectile diameters of 36.5 and 63.5 mm with mass of 210 and 43 g, and velocities from 28 to 38 m/s and 50 to 80.8 m/s, resulted in liver injuries in 14 out of 16 animals and six out of 21 animals, respectively. In another group, projectile diameters from 83.9 to 90.7 mm with mass from 21.4 to 59.66 g, and velocities from 85.1 to 182.4 m/s and 50 to 80.8 m/s, resulted in no liver injuries in 14 animals and six out of 21 animals, respectively. As in the case of the thoracic impacts, greater mass was associated with greater velocities. In the swine model, projectile diameters of 79.4 and 27.8 mm with mass of 196 and 11.7 g, and velocities from 15.5 to 36 m/s and 58.2 to 147.2 m/s, resulted in liver injuries in one out of 13 animals and three out of seven animals, respectively. In the baboon model, projectile diameters from 76.2 mm and 132 g mass, and velocities from 16.3 to 52.3 m/s and 41.0 to 48.4 m/s, resulted in 13 and four liver injuries in 24 and four animals, respectively. In another series of tests, projectile diameters from 76.2 mm and 132 g mass, and velocities from 16.4 to 52.3 m/s and 41.0 to 48.4 m/s, resulted in 13 and four liver injuries in 24 and four animals, respectively (Table 2). Heart impacts using the swine model with a 140 g and 3.7 mm diameter impactor at velocities from 37 to 72 m/s produced cardiac injuries in 21 out 25 animals, whereby 20 to 34 m/s injured all six animals. The same study reported injuries to all six animals with a 10 mm diameter and 140 g impactor at velocities from 50 to 64 m/s.

**Table 2: Summary of liver impacts to different animals.**
(Injury ratio refers to the percentage of animals in the specific group)

| Animal | Dia. (mm) | Mass (g) | Velocity (m/s) | Specimen mass (kg) | Injury ratio |
|---|---|---|---|---|---|
| Goat | 40-80 | 50-200 | 44.8-85.7 | 26.4-46.8 | 100% |
| Goat | 36.5 | 210 | 28-38 | 45-68 | 93% |
| Goat | 63.5 | 43 | 50-80.8 | 28.8-46.4 | 29% |
| Swine | 79.4 | 196 | 15.5-36 | 13.1-17.4 | 92% |
| Swine | 27.7 | 11.7 | 58.2-147.2 | 13.6-17.0 | 43% |
| Baboon | 76.2 | 132 | 16.4-52.3 | 31.1-52.8 | 54% |
| Baboon | 76.2 | 132 | 41-48.4 | 19.0-25.6 | 100% |

## DISCUSSION

Studies incorporating body armor were specific to the type and design of the armor prevalent at the time testing, some dating to the 1970s. The Angora goat served as the baseline animal for which the mean lethality injury probability curve was developed based on the data from the impactor/indentor. The peak deflection metric was used in the logistic regression model. While numerical data were not reported for the mean/estimated risk curve and confidence intervals, indentor deformation depths of 44 and 50 mm were associated with 10% and 15% risk of fatal injuries in the original study [2]. The corrected analysis showed that the actual risk for soft armor for a 44 mm goat deformation is approximately 4% [3]. It should be noted that no animals sustained fatal injuries at this risk level. The current standard backface deformation (BFD) test is conducted with Roma Plastilina clay [3]. Based on clay and goat model tests at a velocity of 55 m/s, with a 200 g and 80 mm diameter solid hemispherical impactor, clay-goat response was linear, with a slope of 0.28 at deformations from 3 to 60 mm. This results in 56 and 44 mm for the clay corresponding to 44 and 34 mm for the goat model and associated with 10% and 4% risk of fatal injuries to the goat [3]. These data are based on impactor tests without body armor and is not region specific. Human cadaver studies have shown poor correlation ($R^2$=0.054) between penetration depth and velocity [1].

Based on subjective assessments from clinicians, the goat was justified in the original studies and was based on the assumptions that a 40 to 50 kg total body mass of the animal represents a typical 70 kg male, damage levels are similar between the goat and human, with both species experiencing the same course of ageing and disease process, etc. It should be noted that organ orientations in the goat are not the same as the axial anatomy in the human. While recognizing that no available animal model mimics the in vivo human in terms of anatomy, structure, and biomechanical response to impacts, swine models are extensively used in recent studies spanning from automotive to military. They include varying breeds, Sus Scrofa, Swedish Landrace, Yorkshire, cross between Yorkshire and Hampshire domestic breed, etc. The development of the swine model has been related to the onset of human puberty in the automotive safety field in the development of injury criteria. Human respiratory and circulatory systems are like the swine, as are human metabolic properties such as muscle perfusion. Studies have correlated/used swine anthropometry to thorax and organ injuries. Automotive injury biomechanics studies have shown that the responses between are comparable live and cadaver swine tests. From these perspectives, the swine is appropriate for BABT injury prediction and injury criteria research and development.

One important factor is the scaling between the animal and human. Subjecting live swine to BABT impacts yields important information on the resulting physiology and pathologies over time and allows the collection of biomedical and injury biomechanical measures; however, translating this information to the living human needs another set of experiments with the human as a surrogate. Because it is not ethical to apply potential injury producing impacts to any human subjects, human cadavers are required. Conducting matched pair tests with the human and swine cadavers, while not yielding pathophysiological outputs, allows structural scaling relationships to be developed for BABT scenarios. Equal stress-equal velocity and impulse momentum approaches are available [4]. Conducting parallel impact experiments with human and swine cadavers, and longitudinal live swine studies is an effective means to correlate injuries from the swine to human via scaling to develop human injury criteria. As impacts can be controlled with indentor designs that replicate the BFD and focused on regional areas of the human and swine anatomy, this hybrid paradigm can be effectively used to develop throacoabdominal region-specific BABT criteria.

From a statistical modeling perspective, the only risk curve reported is the mean/estimated curve with no associated confidence intervals. It is important to determine the confidence interval bounds, as an assessment can be made of the quality of the injury probability curve. Another issue is the use of the logistic regression model that ignores data censoring. More sophisticated methods such as parametric and Bayesian survival models are available to overcome this limitation [5]. They are used in recent military injury biomechanics studies for human injury criteria and developing advanced manikins. Thus, it is important to incorporate these developments to the outcomes from the hybrid paradigm using matched pair cadaver swine and human, and live swine experiments to develop improved BABT injury criteria and standards.

## ACKNOWLEDGEMENTS

This research was supported by the Department of Veterans Affairs Medical Research, Department of Neurosurgery at the Medical College of Wisconsin, and U.S. Army Medical Research and Development Command contract W81XWH-21-9-0015. This material is the result of work supported with the resources and use of facilities at the Zablocki VA Medical Center, Milwaukee, Wisconsin.

## REFERENCES

[1] C. R. Bass et al., Int. J. Occup. Safety. Ergonomics, 2006.
[2] R. Prather, et al., ARCSL-TR-77055, 1977.
[3] C. R. Bass, Chapter in Military Injury Biomechanics, 2017
[4] N. Yoganandan, et al. J Biomech, 2014.
[5] H. C. Cutcliffe, et al., Stapp Car Crash J, 2012.

SB³C2022
Summer Biomechanics, Bioengineering and Biotransport Conference
June 20-23, Eastern Shore, MD, USA

# REGULATION OF WHOLE-BODY ANGULAR MOMENTUM IN PERSONS WITH PARKINSON DISEASE WHEN TRANSITIONING FROM A REGULAR TO AN IRREGULAR SURFACE

**Nicholas G. Gomez (1), Kelton K. Gubler (1), Andrew S. Merryweather (1)**

(1) Department of Mechanical Engineering, University of Utah, Salt Lake City, Utah, USA

## INTRODUCTION

Whole-body angular momentum in relation to the body's center of mass (COM) is highly regulated in overground walking [1] and is invariant to walking speed in healthy adults [2-3]. These conclusions have been found to not be generalizable to other conditions beyond level, overground walking such as negotiating 90-degree turns [4] as well as stair ascent and descent [5]. Furthermore, it is unknown whether conclusions regarding regulation of whole-body angular momentum in healthy individuals extend to populations that are neurologically impaired, such as those with Parkinson disease (PD). A recent investigation found that in stair descent, persons with PD regulated whole-body angular momentum differently than a healthy control population [6]. This finding, in addition to the growing body of literature showing that Persons with PD alter their kinematics and kinetics in the presence of irregular terrain [7] as well as surface transitions [8], prompted us to investigate whether persons with PD regulate their whole-body angular momentum differently when transitioning from a regular surface to an irregular, potentially destabilizing surface compared to level, overground walking. Impaired regulation of whole-body angular momentum is significant because rotational momentum that is not cancelled can lead to the COM exceeding the base of support, and thus potentially leading to a fall [9].

This study seeks to determine how persons with PD and healthy, age-matched controls regulate their whole-body angular momentum when ambulating from a regular to an irregular surface compared to their normal, steady-state gait. We hypothesized that each health group would adjust their sagittal, frontal, and transverse whole-body angular momentum when overcoming a transition from regular to irregular terrain compared to level, overground walking. Furthermore, we also hypothesized that the Parkinson group would adjust their angular momentum when transitioning differently than the healthy group.

## METHODS

Ten persons that had been diagnosed by their primary treating neurologist with mild-to-moderate PD (6 male, 4 female; 67.7±6.7 years; 1.74±0.10m; 83.4±12.2kg) and five healthy, age-matched controls (2 female, 3 male; 66.6±6.8 years; 1.70±0.07m; 74.2± 13.0kg) were recruited for this study. This study was IRB-approved, and all participants provided informed consent. Participants wore tight-fitting clothes upon which 57 reflective markers were applied according to the Biomech 57 marker set [10,11]. The protocol asked participants to ambulate on a custom 9.75m long and 0.92m wide walkway that had two different surfaces, each covering half of the walkway: 1) Regular: oriented-strand board (OSB) covered in BEHR premium slate gray paint and premium NonSkid floor finish and 2) Irregular: OSB covered in faux rock panels (Model R3-RV-PN-MT, Regency River Rock, FauxPanels.com) (Fig. 1) until they expressed familiarity with the terrain. Once participants were comfortable, they ambulated from regular to irregular at least three times. A 14-camera motion capture system (OptiTrack; NaturalPoint Inc., Corvallis, OR) recorded marker trajectories at 120 Hz. Trajectory data were filtered using a 4$^{th}$ order, low-pass Butterworth filter at 6 Hz. The Parkinson group completed trials having taken their medication approximately 1 hour prior to data collection and expressed they felt to be in an "ON" medication state. A successful trial consisted of five consecutive steps (2 gait cycles) with the first two steps occurring on the regular surface and the final three steps occurring on the irregular surface. Following data collection with the surface transition present, participants ambulated on the same walkway with the surfaces removed as a control condition. Again, participants ambulated at least three times and the gait cycles used were those that began and ended at approximately the same start and end location on the walkway as if the transition had been present.

A 15-segment model was created for each participant (2 feet, 2 shanks, 2 thighs, pelvis, trunk, head, 2 arms, 2 forearms, 2 hands) in Visual3D (C-Motion Inc, Germantown, MD) to calculate the whole-body angular momentum about the three principal axes over the course

of a trial. The segmental contributions of inertia were summed together according to (1), where $\boldsymbol{L}$ is whole-body angular momentum, $\boldsymbol{I_i}$ and $\boldsymbol{\omega_i}$ are the moment of inertia and angular velocity of the i-th segment, respectively, $\boldsymbol{r_{COM}}$ is the distance from the body COM to the COM of the i-th segment, $m_i$ is the mass of the i-th segment, and $\boldsymbol{v_i}$ is the translational velocity of the i-th segment.

$$\boldsymbol{L} = \sum_{i=1}^{n}[\boldsymbol{I_i\omega_i} + \boldsymbol{r_{COM}} \times m_i\boldsymbol{v_i}] \quad (1)$$

We defined positive sagittal $\boldsymbol{L}$ as rotating forward, positive frontal $\boldsymbol{L}$ as rotating left with respect to the direction of travel, and positive transverse $\boldsymbol{L}$ as rotating left. All trials were normalized to participant body mass, height, walking velocity, and 100% of 2 gait cycles. Trials were reflected as necessary to have the left leg always lead across the transition and three trials from each participant for both the transition trials and control trials were averaged together to create an ensemble average. The results for sagittal, frontal, and transverse $\boldsymbol{L}$ were compared between surface conditions for each health group using non-parametric, two tailed, statistical parametric mapping paired t-tests. To compare health groups the sagittal, frontal, and transverse $\boldsymbol{L}$ for the transition condition were compared using a non-parametric, two tailed, two sample, statistical parametric mapping t-test (alpha=0.05).


**Figure 1: Overhead view of walkway, 5 steps used for analysis, and walking direction of trials. The control condition (not pictured) consisted of exposed, oriented-strand board.**

## RESULTS

The comparison between health groups for the transition condition revealed no significant differences in $\boldsymbol{L}$. When comparing each health group separately to the control condition, the healthy group did not exhibit significant differences between the transition and control condition while the Parkinson group did (Fig. 2). The Parkinson group significantly altered their sagittal $\boldsymbol{L}$ from 54-68% and 84-100% of the first gait cycle. They also altered their transverse $\boldsymbol{L}$ from 52-60% of the first gait cycle.

## DISCUSSION

This study provides evidence that persons with PD regulate their whole-body angular momentum differently than healthy, age-matched controls when transitioning from a regular surface to an irregular surface. Our study indicates that persons with PD adopt a distinct and consistent strategy to cross the surface transition. This strategy consisted of temporally arresting their sagittal $\boldsymbol{L}$ the step prior to the transition (25% Fig.2) followed by an immediate increase in sagittal $\boldsymbol{L}$ as the leading limb crossed the transition to step onto the irregular surface (50% Fig.2). The reduction was facilitated by early cancellation if the transverse $\boldsymbol{L}$ that began just prior to the second step of the trial (25% Fig.2). These findings coincide with the recent literature [8] that found persons with PD regulate their sagittal $\boldsymbol{L}$ differently than healthy, age-matched controls in alternative conditions, such as stair ascent and descent, but not in level, overground walking. Consequently, the results of this study support that investigations of momentum regulation in persons with PD should focus on scenarios and activities of daily living outside of level, overground walking to better understand where the impaired ability to regulate movement and gait in persons with PD may be most significant in terms of safety.

The present study has several strengths and limitations. It is the first to investigate regulation of whole-body angular momentum in persons with PD when ambulating from a regular to an irregular terrain. Furthermore, it investigated differences over two gait cycles, which gives a more complete picture of how momentum regulation changes over time. However, this study is limited by the small number of participants, which reduced the statistical power. We suspect this is why there were no significant differences between health groups even though the Parkinson group was significantly different than the control surface while the healthy group was not. Further work should investigate a larger study population as well as steady-state gait on different surfaces to confirm if the results we observed at the beginning and end of the trials are generalizable.

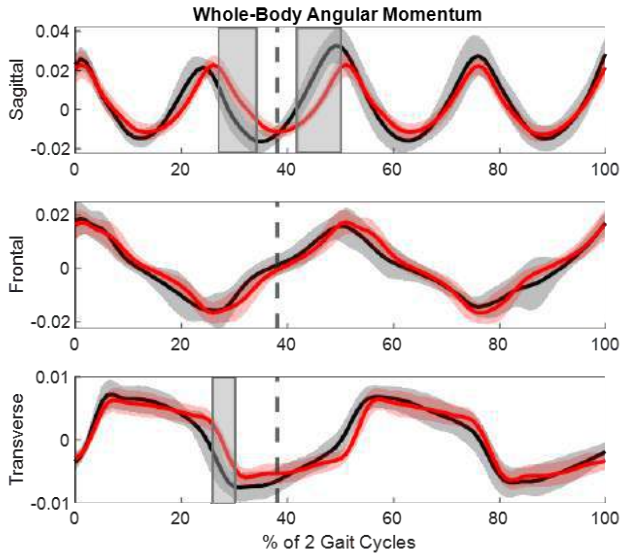


**Figure 2: Mean and standard deviation whole-body angular momentum results for the Parkinson group about the three principal axes for the Transition(BLACK) and Control(RED) conditions. Vertical dashed line represents when they crossed the transition and the grey boxes indicate significance at an alpha level of 0.05.**


## ACKNOWLEDGEMENTS

This work was financially supported by the National Science Foundation (NSF #1162131). The opinions, findings, and conclusions are exclusive to the author(s) and do not reflect the opinions and views of the NSF.


## REFERENCES


[1] Gu, J., *MIT(thesis)*, 2003.
[2] Bennett, B et al., *Hum Mov Sci*, 29:114-124, 2010.
[3] Herr, H et al., *J Exp Biol*, 211:467-481, 2008.
[4] Nolasco, L et al., *Gait Posture*, 70:12-19, 2019.
[5] Silverman, A et al., *Gait Posture*, 39:1109-1114, 2014.
[6] Li, W et al., *IEEE EMBC*, 2021.
[7] Xu, H et al., *Clin Biomech*, 57:93-98, 2018.
[8] Gomez, N et al., *J Appl Biomech*, 37:59-65, 2020.
[9] Chiovetto, E et al., *Sci Rep*, 8(1): 95, 2018.
[10] Leardini, A et al., *Clin Biomech*, 26:562-571, 2011.
[11] Leardini, A et al., *Gait Posture*, 26 :560-571, 2007.

SB³C2022
Summer Biomechanics, Bioengineering and Biotransport Conference
June 20-23, Eastern Shore, MD, USA

# DISTORTIONAL STRAIN DEFINITION FOR FINITE ELEMENT FRACTURE HEALING ALGORITHM

**George Morgan (1), Hana Fox (1), Lucas Low (1), Arul Ramasamy (1,2,3), Spyros Masouros (1)**

(1) Department of Bioengineering, Imperial College London, London, UK
(2) Royal Centre for Defence Medicine, Queen Elizabeth Hospital Birmingham, Birmingham, UK
(3) Academic Department of Trauma and Orthopaedics, Queen Elizabeth Hospital Birmingham, Birmingham, UK

## INTRODUCTION

Fracture healing is a complex process involving various mechanical and biological parameters, and failed or delayed healing can lead to additional surgeries and mortality risk. The ability to predict accurately fracture healing can inform surgical planning and fracture fixation device design. Fracture healing algorithms, such as the Ulm Fracture Healing Model [1], simulate healing times and outcomes and can be used to compare different fixation methods and configurations. These algorithms model callus ossification based on the mechanical strain environment at each location in the callus. Volumetric and distortional strains are used to represent the strain environment as each governs mostly separate biological processes. A finite-element (FE) model of the fracture and fixator calculates the strains due to expected external loading, and the healing algorithm calculates updated material properties for each callus finite element, and the simulation is repeated in an iterative process.

Despite the generally accepted good performance of healing algorithms when axial loading is applied, there is a significant limitation in the ability to predict the effect of torsional loading on healing; they often predict non-union even for low levels of torsion, for which the clinically observed outcome is usually delayed union [2]. Torsional loading creates high levels of distortional strain, which healing algorithms classify as 'destructive' levels, leading to the prediction of non-union. However, one variation of a healing algorithm successfully predicted delayed union under torsional loading by arbitrarily raising the threshold for 'destructive' distortional strain within the model [2].

Distortional strain is often defined in healing algorithms as octahedral shear strain (Equation 1) [1,2]. An alternative distortional strain definition (Equation 2) is derived similarly to von Mises equivalent stress and includes a dependence on material properties; this definition, therefore, is relevant in situations where material properties change over time, such as in fracture healing algorithms. The coefficient of the alternative strain definition is set such that the two strain definitions are equal at a Poisson's ratio of 0.3, representing the initial soft tissue callus [1]. However, as healing progresses and the callus differentiates into cartilage and bone, and as the Poisson's ratio increases, the alternative strain decreases, effectively raising the threshold for 'destructive' distortional strain.

$$\varepsilon_{oct} = \sqrt{\frac{1}{2}[(\varepsilon_1 - \varepsilon_2)^2 + (\varepsilon_2 - \varepsilon_3)^2 + (\varepsilon_3 - \varepsilon_1)^2]} \quad (1)$$

$$\varepsilon_{alt} = \frac{1.3}{1+\nu}\sqrt{\frac{1}{2}[(\varepsilon_1 - \varepsilon_2)^2 + (\varepsilon_2 - \varepsilon_3)^2 + (\varepsilon_3 - \varepsilon_1)^2]} \quad (2)$$

This study compares effect of octahedral and alternative strains, as well as an arbitrarily raised 'destructive' strain threshold, on fracture healing algorithms simulating torsional loading.

## METHODS

An FE model was developed in MSC.Marc (v2021, MSC.Software) of a simple transverse mid-diaphyseal tibial fracture secured with an intramedullary nail with a pre-defined callus region. The tibia was represented as a hollow cylinder 100 mm in length, with outer diameter and thickness of 17 and 3 mm, respectively, with a 3 mm fracture gap. The intramedullary nail was modelled as an axial-torsional spring [2]. A mesh of 151,628 linear tetrahedral elements was used with an average callus element size of 1 mm. The material properties for each tissue type in the model are given in Table 1 [1].

**Table 1: Material properties of model tissue types [1].**

| Tissue Type | Young's Modulus (MPa) | Poisson's ratio |
|---|---|---|
| Lamellar bone | 10,000 | 0.36 |
| Woven bone | 4,000 | 0.36 |
| Cartilage | 200 | 0.45 |
| Connective tissue | 3 | 0.30 |

A fracture healing algorithm was developed based on the Ulm Fracture Healing Algorithm [1], which assumes maximum callus perfusion [2]. The algorithm was run with: (a) a 400 N axial compressive load case, a combined axial-torsional load case with a 1 Nm moment about the medullary axis using the (b) octahedral and (c) alternative strain definitions, and (d) a combined axial-torsional load case using octahedral strain with an arbitrarily raised threshold for 'destructive' distortional strain. Each simulation was run for 30 iterations, representing 30 days.

Callus torsional rigidity was quantified at each iteration by removing the fixator from the FE model and applying a pure torsional load. Fracture healing progress was quantified by the torsional rigidity at each iteration normalized to the rigidity of a fully-ossified callus [2].

## RESULTS

The normalized torsional rigidity over 30 iterations for each of the cases (a-d) is shown in Figure 1. The number of iterations required to reach 20% normalized torsional rigidity was 20, 27, 27, and 26 iterations for cases a-d, respectively. The normalized torsional rigidities at iteration 30 were 40.4%, 28.6%, 29.1%, and 35.1%, for cases a-d, respectively.

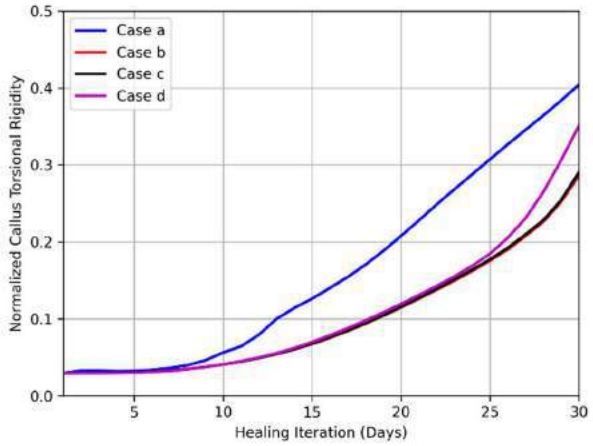


**Figure 1: Normalized callus torsional rigidity for healing algorithms with case: (a) axial loading and octahedral strain, (b) axial-torsional loading and octahedral strain, (c) axial-torsional loading and alternative strain, (d) axial-torsional loading and octahedral strain with a modified threshold for 'destructive' distortional strain.**

## DISCUSSION

The algorithm using an axial compressive load (case a) predicts the fastest fracture healing rate, as expected for an 'uncomplicated' loading regime. The algorithm with combined axial-torsional loading and an arbitrarily raised threshold for 'destructive' distortional strain (case d) predicts a delayed healing, as expected physiologically for low levels of torsional loading, and agreeing with similarly modified algorithms [2].

The algorithms using octahedral (case b) and alternative (case c) strain definitions with combined axial-torsional loading predicted the slowest healing rates and yielded the same healing rate at day 30. This is expected, as the two strain definitions are equivalent in the initial stages of healing when the callus is composed of connective tissue. However, as the torsional rigidities, and therefore the material properties, of the two cases diverge, the values of the two strain definitions will diverge, leading to a greater difference in algorithm outputs in the following iteration, thereby forming a positive feedback loop. Therefore, future works should examine the difference between these two strain definitions for simulations with a greater number of total iterations.

Elements with high distortional strains are primarily located at the bone-callus interface in the fracture gap region. This is caused by the glued contact model used at the bone-callus interface and the load transfer from a 'hard' material (cortical bone) to a 'soft' material (callus tissue). It is possible that a non-glued contact condition is more physiologically accurate and can reduce these distortional strain artifacts. Alternatively, a separate healing algorithm formulation could be used for a boundary layer model at the bone-callus interface.

This study compares an alternative definition for a distortional strain scalar against the commonly used octahedral shear strain for use in fracture healing algorithms. These results show minor differences between the strains in the outputs of the algorithm, however, a greater number of iterations in future simulations is likely to lead to greater differences between the two strain definitions.

## ACKNOWLEDGEMENTS

This research was supported by an EPSRC Doctoral Training Partnership.

## REFERENCES

[1] Simon, U et al., *Comp Meth Biomech Biomed Eng*, 2011; 14:79-93.
[2] Ren T & Dailey H, *Biomech Model Mechan*, 2020; 19:2307-2322.

# HOW SIGNAL-TO-NOISE RATIO IMPACTS THE APPARENT STIFFNESS OF BRAIN TISSUE IN MR ELASTOGRAPHY AT 7T

**Emily R. Triolo (1), Oleksandr Khegai (2), Jelle Veraart (3) Akbar Alipour (2), Priti Balchandani (2), Mehmet Kurt (1,2)**

(1) Department of Mechanical Engineering, University of Washington, Seattle, WA, USA
(2) The Biomedical Engineering and Imaging Institute, Icahn School of Medicine at Mount Sinai, New York City, NY, USA
(3) Center for Biomedical Imaging, Dept. Radiology, New York University Grossman School of Medicine, New York City, NY, USA

## INTRODUCTION

Magnetic resonance elastography (MRE) is a technique for determining the mechanical response of tissues using applied harmonic deformation and motion-sensitive MRI[1]. Studies using MRE to investigate the mechanical properties of the human brain are most commonly performed at conventional field strength (3 Tesla (T) or 1.5T), although there have been a few attempts at the ultra-high field strength, 7T[2,3]. Aiming for higher resolution scans of the human brain at 7T, MRE presents unique challenges of decreased signal-to-noise ratio (SNR) and lower shear wave motion sensitivity. Additionally, it has been shown that quantitative values of MRE, i.e., the magnitude of the complex shear modulus estimate (|G*|), are sensitive to changes in SNR[4], so 7T MRE can present a challenge of not only quality, but accuracy. While applying commonly-used filtering techniques (e.g., Gaussian, Median) to MRE phase data can increase SNR (to combat low SNR in high-resolution scans), this can also blur fine physiological features, decrease the effective resolution[5], resulting in artificially increased |G*|[4]. We increase the SNR of our MRE acquisition without comprising the anatomical accuracy and spatial resolution by utilizing a Marchenko-Pastur Principal Component Analysis (MP-PCA) denoising algorithm[5]. In this technique, we are exploiting the intrinsic redundancies in MRE acquisition to identify and remove noise-only principal components[5].

In the most recent studies comparing 1.5T, 3T, and 7T MRE of the human brain, MRE at 7T and 1mm resolution resulted in significantly lower stiffness values than MRE at 1.5T and 3T at 2mm resolution[3,6]. However, one study indicated that when down sampled to 2mm, the 7T MRE results matched the traditional MRE field strength results, but in a second study, the difference remained[3,6]. In the past, we have shown that changes in resolution and field strength do not inherently change the value of |G*| in a linear elastic phantom[7]. However, MRE of phantoms typically have very high SNR, even at high resolutions, so this decrease in SNR as resolution increases may not have a large effect on scans with inherently high SNR. For MRE of the human brain however, SNR drastically drops with increasing resolution, very likely causing an artificially low |G*| calculation.

In this abstract, we will be investigating the effect of SNR on calculated |G*| in both a linear elastic phantom and the human brain using 7T MRE. We will therefore also be investigating how increasing SNR using MP-PCA denoising will change |G*| in scans that have inherently high SNR (phantom) and scans that have low SNR (human brain).

## METHODS

Full brain coverage MRE was performed on one healthy human subject at 1.7mm, 1.3mm, and 1.1mm isotropic resolutions at 50Hz vibration frequency, using a 32-channel head coil (Nova Medical) on a 7T Siemens Magnetom MRI Scanner. MRE was also performed on a custom silicone MRE phantom (CIRS 049) at 2.5mm, 1.3mm, and 1.1mm isotropic resolutions. The designed MRE sequence was a modified single-shot multi-slice spin-echo 2D-EPI sequence with trapezoidal flow-compensated motion encoding gradients (MEGs)[8], synchronized with the pneumatic acoustic actuator (Figure 1)[7] by TTL triggering at the beginning of every TR (TR/slice=140ms, TE=65ms,

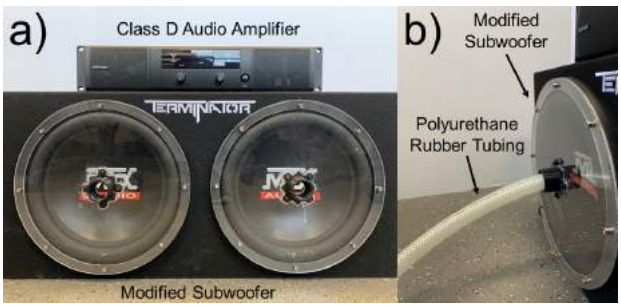


**Figure 1: Custom pneumatic actuator**

GRAPPA=3). Human brain images were masked using BET (Brain Extraction Tool) of FSL package[9] while phantom images were manually masked, denoised using a MP-PCA algorithm[5], and unwrapped using a Laplacian-based technique[10]. Curl filtering, Fourier decomposition, and a quartic smoothing kernel (scaled for resolution based on our previous investigation[7]) were used to acquire wavefield images, before Algebraic Inversion of the Helmholtz Equation was used to calculate the complex shear stiffness[11]. For the human brain, whole brain average stiffness was calculated (Figure 2), while for the phantom scans the mean of each stiffness map of five homogeneous slices per scan were calculated and compared using a one-way ANOVA. We then calculated the average octahedral shear strain-based SNR (OSS-SNR) for both original and denoised displacement data at each resolution[12].

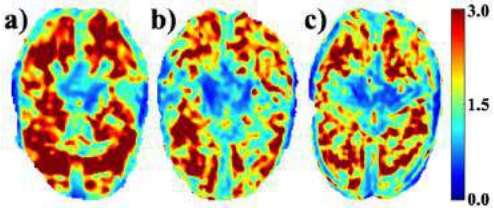


**Figure 2: Elastograms showing |G*| in kPa at (a) 1.7mm, (b) 1.3mm, and (c) 1.1mm isotropic resolution.**

## RESULTS

Looking at our average |G*| for the phantom results, we find no statistically significant difference between any resolution, nor between original and denoised. We also find that while denoising does increase the average OSS-SNR for a specific resolution, the average OSS-SNRs for all data sets are above 100 (Table 1).

**Table 1: Average |G*| and OSS-SNR in Phantom**

| | | 2.5mm | 1.3mm | 1.1mm |
|---|---|---|---|---|
| **|G*| (kPa)** | **Original** | 1.425±0.007 | 1.430±0.005 | 1.423±0.012 |
| | **Denoised** | 1.425±0.005 | 1.430±0.005 | 1.423±0.110 |
| **OSS-SNR** | **Original** | 953.7±248.1 | 195.8±39.8 | 115.9±23.9 |
| | **Denoised** | 980.6±274.5 | 247.5±50.0 | 153.7±20.9 |

For the human brain, on the other hand, average OSS-SNR ranges from 3.5 through 11.5. Once again, applying denoising increases the average OSS-SNR for each resolution. Also different from the phantom results, the average |G*| differ both between resolutions and between original and denoised data. Generally, |G*| increases with increasing OSS-SNR, but it appears to not be a perfectly linear relationship between resolutions (Figure 3).

## DISCUSSION

Based on the whole-brain stiffness estimates (|G*|) and SNR values, within-resolutions, denoising using the MP-PCA algorithm substantially increases the OSS-SNR and therefore increases |G*|. It also appears, based on the results of the phantom experiments, that increasing OSS-SNR only increases |G*| to a point, at which point additional increases in OSS-SNR using denoising will not significantly affect the |G*|. The benefit of using PCA-based denoising as opposed to other filtering techniques is that denoising maintains the physiological structures within the human brain and helps prevent over-smoothening/overfitting (Figure 4). This increased accuracy and sensitivity is of particular importance for smaller brain features, for example, the hippocampus when investigating changes due to Alzheimer's disease or dementia.

However, there appears to be a more complex relationship between OSS-SNR and |G*| between resolution likely due to the post-processing

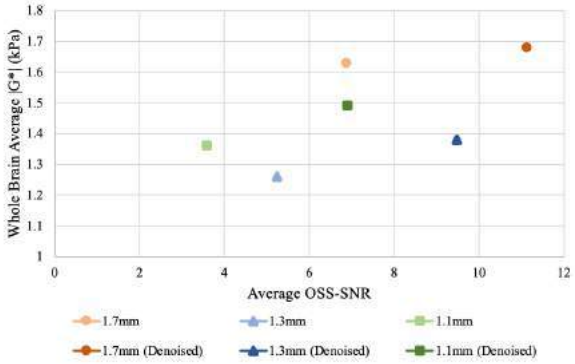


**Figure 3: The relationship between whole brain stiffness (kPa) and average OSS-SNR**

steps taken between displacement calculation and stiffness estimation. Additionally, the 1.7mm resolution scan appears to have an overall higher average |G*| than the 1.3mm and 1.1mm resolution scans, somewhat matching the increase in OSS-SNR values, which can be confirmed with further replicates. This potentially implies that additional fine viscoelastic features are detected at higher resolutions, decreasing the wavelength-based stiffness estimate, supporting the hypothesis of Barnhill, et al.[3]. Overall, to better understand these trends,

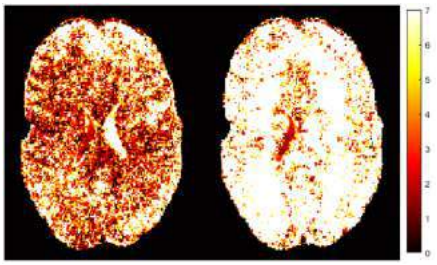

**Figure 4: OSS-SNR map comparison between original (left) and MP-PCA denoised (right) data at 1.1mm resolution**

we will continue to perform MRE at 7T on healthy human subjects at these three representative resolutions to better characterize the effects of both differing resolutions, change in field strength (3T versus 7T), and denoising on complex stiffness estimations of the human brain. Additionally, we will also implement a more complex segmentation algorithm to both investigate stiffness of specific subregions of the human brain.

In conclusion, our pilot study has shown a substantial increase in OSS-SNR after the use of MP-PCA denoising algorithm on the complex displacement data generated during MRE at 7T, and has shown a relationship between resolution, OSS-SNR, and |G*| that requires further investigation with a larger cohort of subjects.


## ACKNOWLEDGEMENTS

We acknowledge support from NSF CMMI 1953323 and NIH funding R21AG071179.


## REFERENCES


[1] Greenleaf, J *et al., IEEE Int Ultrason Symp,* 467-472, 1996 [2] Braun, J *et al., Neuroimage*, 90:308-314, 2014. [3] Barnhill, E *et al., ISMRM*, 2016. [4] Murphy, M *et al., PloS one,* 8:e81668, 2013. [5] Veraart, J *et al., Neuroimage*, 142:394-406, 2016. [6] Marshall, H *et al. ISMRM*, 2017. [7] Triolo, E *et al. BMES*, 2021. [8] Chaze, C *et al., NeuroImage Clin,* 22, 2019. [9] Woolrich, M *et al. NeuroImage*, 45:S173-86, 2009 [10] Herraez, M *et al., Applied Optics*, 41:7437-7444, 2002. [11] Oliphant, T *et al., Magn Reson Med,* 45:299-310, 2001. [12] McGarry, M *et al., Phys Med Biol*, 56, 2011.

# INTERVERTEBRAL DISC GEOMETRY AND HYDRATION ARE ALTERED FROM IN VIVO TO SEGMENT PREPARATION FOR MECHANICAL TESTS

**Harrah R. Newman (1), Natalie A. Thurlow (2), Kyle D. Meadows (1), Adriana Barba (3), Thomas P. Schaer (3), Edward J. Vresilovic (1), Dawn M. Elliott (1)**

(1) Biomedical Engineering, University of Delaware, Newark, DE, USA
(2) Biomedical Engineering, University of Florida, Gainesville, FL, USA
(3) School of Veterinary Medicine, University of Pennsylvania, Kennett Square, PA, USA

## INTRODUCTION

Numerous studies have quantified cadaveric intervertebral disc structure, composition, and mechanical behavior. Cadaveric disc mechanical tests are frequently interpreted in the context of *in vivo* disc function for research related to back pain, degeneration, surgery, implants, computational models, engineered discs, and mechanobiology. However, there are substantial differences in the physical constraints and boundary conditions between *in vivo* and *ex vivo* multiple and single segment discs, which alter disc size, shape, hydration, pressure, residual stress, and mechanical behaviors. In many *ex vivo* studies, segments are pre-loaded in an attempt to mimic *in vivo* axial compression and are kept in a buffered bath solution to mimic *in vivo* hydration and fluid exchange. However, the differences that arise between the *in vivo* and *ex vivo* conditions are unknown, limiting our ability to mimic them experimentally, and complicating our ability to interpret cadaveric study outcomes for the *in vivo* disc. The objective of this study is to assess geometric and hydration differences between *in vivo* and *ex vivo* conditions using repeated magnetic resonance imaging (MRI) in the porcine spine. The *in vivo* condition will be represented by the Physiological group and the *ex vivo* condition will be represented by the Multilevel group and Segment group (**Fig 1**).

## METHODS

Repeat 3T MRI were acquired at room temperature on the L1-L2, L3-L4, and L5-L6 discs from Yucatan minipigs in three conditions (**Fig 1**): P**hysiological** (intact torso within two hours of sacrifice, n = 4 pigs, 12 discs), **Multilevel** (fresh-frozen intact excised spine extending from mid-thoracic to caudal, n = 8 pigs, 24 discs), and **Segment** (fresh-frozen vertebra-disc-vertebra motion segments with facets intact, n = 8 pigs, 24 discs).

Following the MRI of Physiological condition, the spine was dissected out to the Multilevel condition. The sample was wrapped in PBS-soaked gauze and frozen. The Multilevel was thawed, imaged, then dissected down to the Segment condition. Each segment was wrapped in PBS-soaked gauze and frozen, then later thawed and imaged.

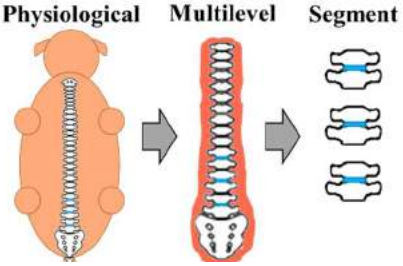


**Figure 1:** Spine condition groups shown with discs of interest in blue.

The variation in sample size, particularly for the Segment condition, required several changes for MRI acquisition. A methodology check was performed to ensure that changes in image resolution and MRI reception coil did not independently induce changes in $T_2$ relaxation time. Discs (n=2) were imaged across a variety of conditions (**Table 1**) in the same scanning session and the $T_2$ times were evaluated.

**Table 1:** T2 CPMG MRI changes between the Multilevel scan (#1) and Segment scan (#4). Change from previous case highlighted.

| # | Condition | MRI Coil | Image Resolution (mm) |
|---|---|---|---|
| 1 | Multilevel | Table/Spine | 0.47 x 0.47 x 3 |
| 2 | Multilevel | Table/Spine | 0.39 x 0.39 x 3 |
| 3 | Multilevel | Knee | 0.39 x 0.39 x 3 |
| 4 | Segment | Knee | 0.39 x 0.39 x 3 |

Two MRI sequences were used to evaluate differences between the conditions: a $T_1$-weighted FLASH sequence with in-plane resolution of at least 0.47 mm and slice thickness of 3 mm for assessing geometry, and a $T_2$-weighted CPMG sequence with in-plane resolution of 0.3-0.6

mm, TE = 13.6, 27.2, … 340 ms and TR = 3000 ms for quantifying $T_2$ relaxation time. Total scan time was less than an hour per condition.

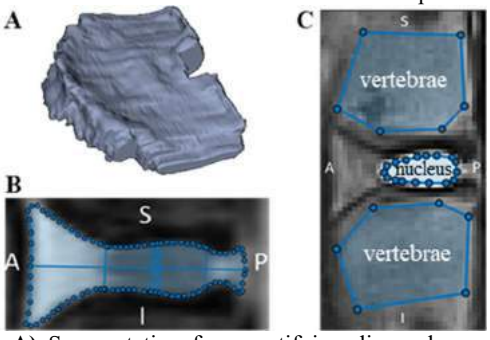


**Figure 2: A)** Segmentation for quantifying disc volume. **B)** MRI FLASH scan with outline for disc area, horizontal line for anterior-posterior disc width, and vertical lines for showing nucleus boundary and central vertical lines for calculating central NP height shown. **C)** MRI $T_2$ scan, nucleus and vertebrae ROIs shown.

The disc volume was calculated from segmentations of the $T_1$ images using ITK-SNAP (**Fig 2A**). The disc mid-sagittal height, anterior-posterior width, and area were calculated using a custom MATLAB code (**Fig 2B**). The $T_2$ relaxation times, which are positively correlated with hydration, were evaluated in the nucleus pulposus (NP) and adjacent vertebral bodies (VB). The $T_2$ times were calculated from the $T_2$-weighted echoes by fitting the intensity decay in the regions of interest (ROIs) to noise-corrected exponential fits [1] (**Fig 2C**). For statistical assessment, mixed model fits with fixed effect of condition, random effect of specimen, and post-hoc pair-wise Tukey tests were conducted. The significance was set at $p < 0.05$.

## RESULTS

From the altered scanning methods check, the $T_2$ relaxation time was within 10 ms for the nucleus ROIs and within 3 ms for the vertebrae ROIs (**Fig 3**), therefore the change in scanning coil and resolution did not impact study findings.

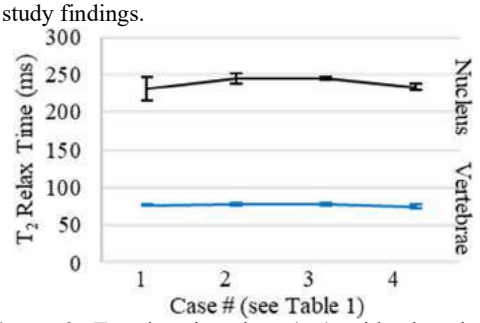


**Figure 3**: $T_2$ relaxation time (ms) with altered scan conditions. Average +/- standard deviation

For the conditions of interest, the disc volume increased 19% from Physiological to Segment (Fig 4A). The mid-sagittal NP height increased by 6% from the Physiological to Multilevel and by 17% from the Physiological to Segment (Fig 4B). The mid-sagittal width decreased 11% from Physiological to Segment (Fig 4C). There were no significant changes in mid-sagittal area (not shown). The NP $T_2$ time decreased by 7% from Physiological to Multilevel and by 13% from Physiological to Segment, while in the adjacent vertebrae the $T_2$ time increased 63% from Physiological to Multilevel and Segment (Fig 4D).

## DISCUSSION

Although a live, *in vivo* MRI was not performed, the Physiological condition is reasonably represented by the immediate post-mortem torso because *in vivo* MRI is generally performed in a relaxed supine position which minimizes axial load, and *in vivo* MRIs in animal models of the spine are performed under anesthesia which further eliminates active muscle contraction [2].

The Segment condition had substantially less surrounding tissue compared to the other conditions and required MRI scan modifications; however, they did not significantly alter the $T_2$ time of the NP (**Fig 3**).

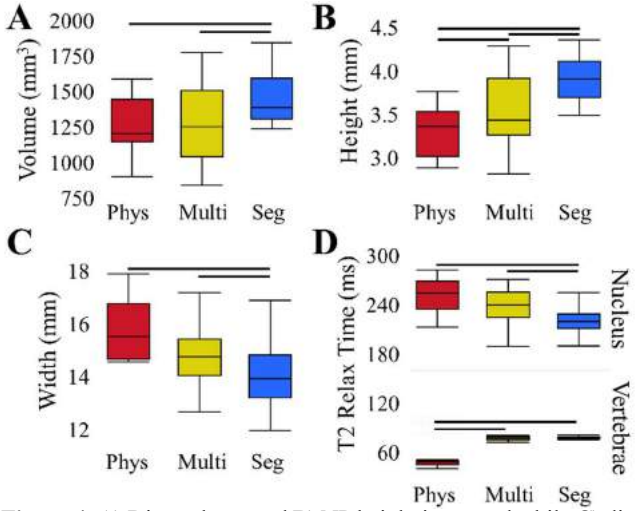


**Figure 4**: **A)** Disc volume and **B)** NP height increased while **C)** disc width decreased across conditions. **D)** NP $T_2$ time decreased but VB $T_2$ time increased across conditions.

*In vivo* spines are constrained and loaded by the surrounding muscles, ligaments, and body forces, causing pressurization and residual strain in the disc tissues. These *in vivo* constraints and loads are progressively removed when spines are dissected for *ex vivo* testing. This study showed that dissection alters disc geometry, leading to increased disc volume without changes in mid-sagittal area, increased mid-sagittal height, and decreased mid-sagittal anterior-posterior width. The driving cause of the significantly increased volume is likely the increased disc height resulting from a larger reduction of the loading constraints in the axial direction with soft tissue dissection. The reduced sagittal width could be related to release of annulus fibrosus circumferential residual strain. Future work will evaluate the changes between conditions in both the sagittal and coronal planes to enable a multi-dimensional perspective for understanding the geometric changes that arise between conditions. $T_2$ time is known to correlate with water concentration [1] and measurable changes in water content were not expected in the NP. This reduction in T2 time suggests a decrease in water concentration, likely from water redistribution within the larger volume disc. Alternatively, the disc could have lost water to the adjacent vertebrae, which had an increased $T_2$ time, though no previously understood mechanism underlying this fluid exchange is known. Collectively, these geometric and hydration changes will alter segment mechanical behaviors. While the effects of spinal dissection have been quantified here, further study is ongoing to restore cadaveric spinal segments to the *in vivo* state for testing and modeling.


## ACKNOWLEDGEMENTS

Funding for this research was provided by NIH/NIAMS R01 AR050052 and NSF REU Grant Award #1460757 (NAT).


## REFERENCES


[1] Meadows et. al. JOR Spine, 3:1-12, 2020. [2] Wilke et. al. J Biomech, 29:549-555, 1996.

# THE LONG HEAD OF THE BICEPS TENDON UNDERGOES MULTIAXIAL DEFORMATION DURING SHOULDER MOTION

**S. Cyrus Rezvanifar, PhD (1), JJ Lamb (2), Miles F. Wing (2), Arin M. Ellingson, PhD (1), Paula M. Ludewig, PhD (1), Victor H. Barocas, PhD (2)**

(1) Department of Rehabilitation Medicine, University of Minnesota, Minneapolis, MN, USA
(2) Department of Biomedical Engineering, University of Minnesota, Minneapolis, MN, USA

## INTRODUCTION

The shoulder joint is one of the most complex joints in the human body, and within this joint, the long head of the biceps tendon (LHBT, Figure 1) is a common source of injury and pain. In a study of 141 shoulders with complete rotator cuff tears, 36.1% also had LHBT pathology [1]. Despite LHBT common pathologies such as tendon rupture, tendinopathy, instability, and superior labrum anterior and posterior (SLAP) lesions and tears [2], diagnosis and treatment remain relatively poorly understood and controversial [1, 3]. While many shoulder and LHBT pathologies are thought to be symptomatic, a study of 21 asymptomatic Major League Baseball pitchers revealed that 11 pitchers had a rotator cuff tear, 10 had a SLAP tear, and it was unclear whether there were pitchers who had both [4]. Therefore, a deeper understanding of the LHBT mechanical environment and underlying mechanisms of its pathologies is of great importance. The purpose of this study was to develop a subject-specific finite element (FE) model of the shoulder joint to investigate the stress/strain response of the LHBT across the simulated range of motion.


**Figure 1. Demonstration of glenohumeral anatomy; LHBT passes under the THL and through the bicipital groove [5].**

## METHODS

*Geometry and mesh*

MRI scans of a right shoulder (48-year-old female) were reconstructed using Mimics (Materialise, Leuven, Belgium) to create the 3D model of the shoulder joint. An initial 3D mesh was assigned to the 3D models using HyperMesh (Altair, Troy, MI) and the humerus, scapula, LHBT, and transverse humeral ligament (THL) were imported into FEBio [6]. Four-node tetrahedral elements (TET4) were used for all bony and soft tissue components of the model (Figure 2).

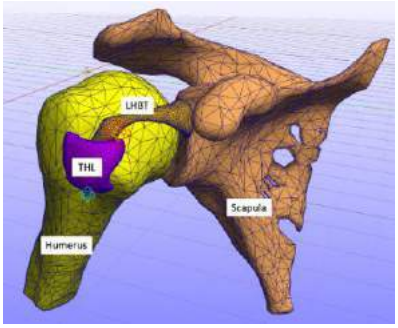


**Figure 2: Present FE model with bony and soft tissue structures**

*Boundary Conditions*

The scapula was fixed in place for all translational and rotational degrees of freedom, and all other motion happened relative to the scapula. The glenohumeral joint was defined via a "spherical joint rigid connector". The THL was fixed over the bicipital groove of the humerus. A frictionless sliding contact was defined between the LHBT and both the THL and the bicipital groove of the humeral surface to replicate in vivo conditions. The proximal end of the LHBT was rigidly connected to the superior rim of the glenoid, and a force with a

magnitude of 76.3 N was applied to the distal end of the LHBT to simulate native tension in the tissue.

*Material Properties*

The humerus and scapula were defined as rigid bodies, given the orders of magnitude greater stiffness compared to the soft tissues. The THL was modeled as a Neo-Hookean material with a bulk modulus of 600 MPa and a Poisson's ratio of 0.47. The material properties of the LHBT, as the tissue of focus in this study, was obtained by fitting a fiber-reinforced transversely isotropic Mooney-Rivlin model (Eq. 1) to previously published experimental data of uniaxial tensile tests on LHBT cadaveric tissues [7, 8].

$$W = C_1(I_1 - 3) + C_2(I_2 - 3) - 2(C_1 + 2C_2)\ln J + \frac{1}{2}k(\ln J)^2 + W_{fib} \quad (1)$$

where $C_1$, $C_2$, and k are material parameters, $I_1$ and $I_2$ are first two deviatoric invariants of the Cauchy Green deformation tensor (C), and J is the Jacobian of the deformation gradient tensor F [6]. The fiber contribution $W_{fib}$ is used to describe the mechanics in terms of three regimes (compressed, uncrimping, and uncrimped). Writing in terms of the first Piola-Kirchhoff stress $P_{fib}$,

$$P_{fib} = \begin{cases} 0 & \lambda_{fib} \le 1 \\ C_3\left(e^{C_4(\lambda_{fib}-1)} - 1\right) & 1 < \lambda_{fib} \le \lambda_{unc} \\ C_5\lambda_{fib} + C_6 & \lambda_{unc} < \lambda_{fib} \end{cases} \quad (2)$$

where $\lambda_{fib}$ is the fiber stretch ratio, the parameter $\lambda_{unc}$ is the stretch ratio at which the fiber is fully uncrimped, and the parameters $C_3$ - $C_6$ describe the mechanical behavior and are specified so that $P_{fib}$ is continuous and differentiable at $\lambda_{unc}$. The acquired material parameters were imported into FEBio software to study LHBT mechanical behavior during simulated glenohumeral motion.

*FE Simulated Motion*

In vivo joint kinematics during arm elevation acquired through our previous study [9] were used to drive the simulation. With the scapula fixed to the global reference frame, humeral motion started from a neutral arm position at side and ended at 90° of scapular plane abduction with 90° external rotation to represent a wider range of motion.

## RESULTS

The material properties obtained from the two curve fittings are listed in Table 1.

**Table 1. Results of curve fit for the Mooney-Rivlin Model**

| Parameter | Kolz [7] | McGough [8] |
|---|---|---|
| **$C_1$ (MPa)** | 1.00 | 1.00 |
| **$C_2$ (MPa)** | 1.00 | 1.00 |
| **$C_3$ (MPa)** | 0.0503 | 2.83 |
| **$C_4$ (unitless)** | 112.5 | 42.7 |
| **$C_5$ (MPa)** | 190.9 | 358.6 |
| **$C_6$ (MPa)** | -195.2 | -361.8 |
| **$r^2$ of model fit** | 0.999 | 0.998 |

Maximum von Mises (effective) stress occurred at nearly 70° of glenohumeral abduction, with magnitudes of 85.2 and 152.6 (MPa) with parameters from Kolz and McGough data, respectively. At this joint position, both sets of parameters resulted in von Mises strains of approximately 1.3, as demonstrated in Figure 3. Interestingly, a plateau (indicated by black arrow in Figure 3) was observed in the stress despite the continual increase in the strain measures.

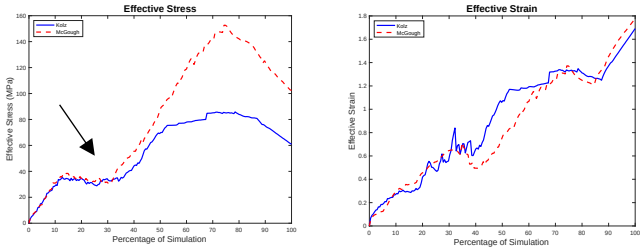


**Figure 3. Maximum von Mises stress (left) and strain (right) within the LHBT throughout the simulated range of motion**

Figure 4 demonstrates large stress and strain magnitudes occurring near the midpoint of LHBT where it is constrained with the THL and enters the bicipital groove.

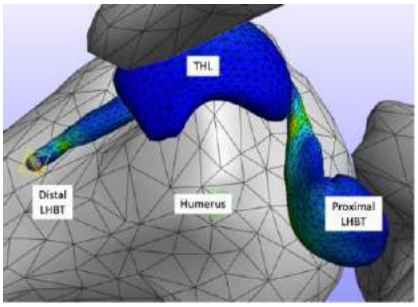


**Figure 4: Deformed LHBT near end range of motion.**

## DISCUSSION

This study was conducted to assess the viability of using uniaxial tension data to understand mechanisms of LHBT injury during FE simulated glenohumeral motion. The aforementioned plateau in stress concurrent with an increasing strain is evidence of complex multiaxial deformation within the LHBT during typical shoulder motion. Further experimental tests on cadaveric specimen, including bi-axial tension and combinations of tension and torsion, are needed to acquire realistic material properties. Our ongoing work will obtain and implement these material properties to provide a deeper understanding into the mechanisms of LHBT injury.

## ACKNOWLEDGEMENTS

The authors acknowledge the support from Carly Donahue for running and troubleshooting FE simulations.

## REFERENCES

[1] Desai, SS and Mata, HK, *Arthroscopy*, 33:11:1971-1976, 2017.
[2] Kim, TK et al., *J Bone Joint Surg Am*, 85:1:66-71, 2003.
[3] Ditsios, K et al., *Adv Orthop*, 405472, 2003.
[4] Lesniak, BP et al., *Am J Sports Med*, 41:9:2022-7, 2013.
[5] Earth's Lab, Glenohumeral Joint, Accessed 01/2022, URL.
[6] Maas, SA, et al., *J of Biomech Eng*, 134(1):011005, 2012.
[7] Kolz, CW et al., *Clin Biomech*, 30:9:940-5, 2015.
[8] McGough, RL et al., *KSSTA*, 3:4:226-9, 1996.
[9] Ludewig, PM et al., *J Bone Joint Surg*, 91(2):378, 2009.

# USING SMART PHONES TO SELECT HOUSEHOLD FABRIC FOR MAKING FACE COVERINGS: A CASE STUDY BY FDA, NIST AND HIGH SCHOOL STUDENTS

**Alexander Herman (1), Matthew Staymates (2), Salvatore Trupia (3), Victoria Guerrier (3), Glenda Garcia (3), Gloria Guerrier (3), and Suvajyoti Guha (1)**

(1) Division of Applied Mechanics, Office of Science and Engineering Laboratories, U.S. Food and Drug Administration (FDA), Silver Spring, MD, USA
(2) Material Measurement Science Division, National Institute of Standards and Technology (NIST), Gaithersburg, MD, USA
(3) West Hempstead High School (WHHS), West Hempstead, NY, USA

## INTRODUCTION

Face coverings are a critical tool in the fight against the spread of airborne pathogens such as SARS-CoV-2, the virus behind the COVID-19 pandemic [1]. These face coverings have been shown to reduce transmission of viral aerosol particles both in the laboratories as well as in clinical settings [2]. However, effectively testing these face coverings for filtration efficiency (FE) and breathability, as seen in most studies testing face coverings, require sophisticated aerosol instruments in the range of $10,000 - $100,000 or more. In addition, lack of consistency across techniques also precludes the user from making clear choices on fabrics they can use to make their own face coverings. Very few studies to date have offered simple, and cheap means of characterizing FE of fabrics [3, 4]. These studies, however, have still been conducted in controlled environments by experienced researchers. To our knowledge, no studies have been conducted in real world settings by non-experts for characterizing FE of fabrics. The objective of this study is to report a cost-friendly (< $1000) method to characterize the performance of household fabrics against viral droplets that can be accomplished using handheld cell phones and the expertise of sophomore-level high school students within a public school system and compare it to traditional quantitative particle counting techniques and semi-quantitative fog visualization system.

## METHODS

Three different experimental setups at the FDA, NIST and WHHS were developed. A quantitative setup was used at the FDA, and semi-quantitative fog visualization system at NIST & WHHS. Each of these setups tested the same three fabrics: silk, flannel, and cotton pillowcase (PC) materials.

**Quantitative Measurements.** The experimental testing for the quantitative measurement was performed by the researchers at the FDA and based of a study by Guha et al. [5]. To minimize protocol differences across the various institutes, some notable differences from the previous study included use of a heater coil (Nickel 200) with a cotton wick instead of a nebulizer and water was replaced with 1% glycerin water. The remaining equipment used, such as the Aerodynamic Particle Sizer (APS, Model # 3321, TSI Inc.), was the same. A schematic of the setup is shown in Figure 1. For consistency with NIST set up, the orifice was designed to achieve 42 cm/s fluid velocity across the material under test. The APS was set up for four scans per sample, with the droplet source triggered for 3 seconds at 18-20 Watts during the 2nd scan. This was done with and without a do-it-yourself (DIY) coupon in the holder.

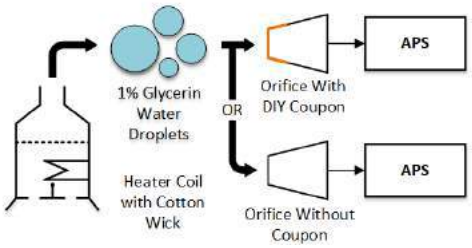


**Figure 1: Schematic of FDA's Lab experimental setup including the heater coil with wick and APS system.**

**Semiquantitative Measurements.** A pipe fog flow visualization system, shown in Figure 2, was developed at NIST to visualize fog droplets penetrating these fabrics. Specific details of this system can be found in Staymates [6]. High speed videography used to visualize fog droplets penetrating through various fabrics, and the video data was then processed with a custom image processing script in LabVIEW®. The experimental setup consisted of a 5 cm straight-walled pipe and a custom mounting flange. Flexible tubing connected the pipe system to a custom in-line fog generator that consisted of a cotton plug (soaked in an aqueous solution of 1% glycerin) wrapped with 20-gauge nichrome wire. A custom flow regulator system with 2 1.75 L accumulators controlled the flow to the fog generator. The particle size distribution of these droplets was measured with an APS (Model # 3321, TSI Inc.). A solid-state timer (Model # TMM-0999M-466, AMETEK Inc.) was used to pulse current into the fog generator for 2 seconds and provided a reasonably repeatable plume of fog droplets for each visualization experiment. Video data was collected with a high-speed camera (Model # NOVA S9, Photron USA, Inc.) at 125 frames per second.

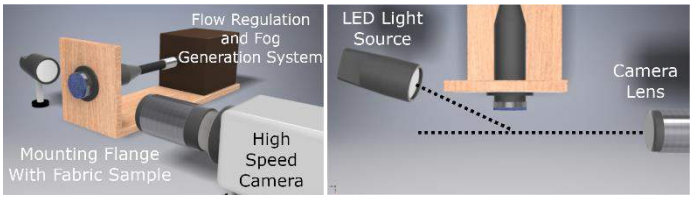


**Figure 2: Schematic diagram showing the NIST flow visualization system. (left) 3D rendering showing the highspeed camera, light source, flow regulation and fog generation system, and fabric mounting flange. (right)**

**High School Setup.** High school students in a sophomore-year science research class at WHHS built a set up like the NIST system (Figure 3 below). Water droplets were created with a commercially available ultrasonic nebulizer (Philips Respironics, InnoSpire Essence), while a light source (Model # Qualite 300, Impact Studio Lighting) was used to illuminate the droplets emerging through the fabric samples. A smartphone (Galaxy Note 20, Samsung Electronics Co., Ltd. and iPhone XR, Apple, Inc.) or digital single-lens-reflex (dSLR) camera (Model # T6i, Canon USA Inc.) was used to collect flow visualization footage. The fabric samples were tightly taped to the end of the 243mm tube connected to the ultrasonic nebulizer. The camera/phone was positioned such that the fabric sample was visible and located near the bottom of the field of view. A black curtain was used as a backdrop. The ultrasonic nebulizer was connected to a programmable timer (Model # AC 85V - 265V Cycle Timer Module, Pemenol) that ran the ultrasonic nebulizer for 4 seconds. Best results were obtained when the auto-exposure of the phone's camera was disabled.

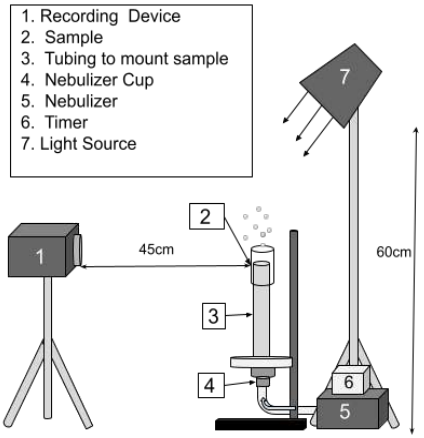


**Figure 3: Schematic diagram showing the High School flow visualization system.**

## RESULTS

**FDA Quantitative Analysis.** The size averaged FE shows the following order: Cotton PC > Flannel > Silk with the FEs aiming around 97.9%, 91.6%, and 65.4% respectively (Table 1). These results are consistent with prior findings for the same fabrics performed with water droplets [5].

**NIST and WHHS Semi-Quantitative Analysis.** When doing an image analysis of the data, all fabric samples produced smaller pixel intensities compared to the "open" scenario, so pixel intensity was normalized to the open case. Silk shows a roughly 20% decrease compared to open, the flannel shows a 60% reduction, and the pillowcase shows almost 90% reduction in pixel intensity. Qualitatively, when comparing the results from the 3 cameras from WHHS, the results show a similar trend in image intensity compared to the NIST data even in a less controlled environment (Figure 4).

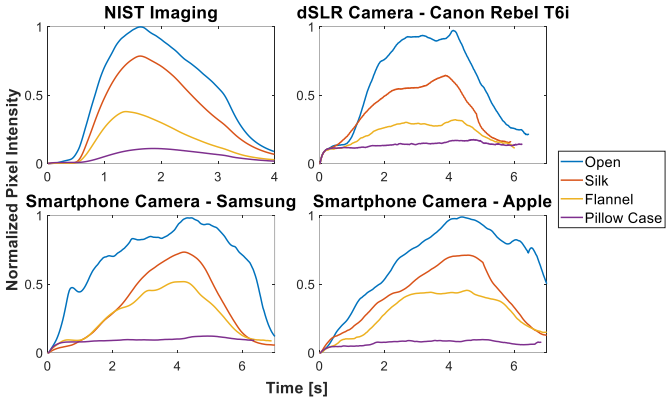


**Figure 4: Semi-quantitative image processing results from the WHHS and NIST flow visualization measurement system.**

An estimated FE can be derived by integrating the pixel intensity of each fabric and normalizing them to the pixel intensity with no sample (Open) and subtracting 1 from them (Table 1). There is a clear and observable trend between the correlation considering all the differences between experimental setups between the data sets (camera types, fog distributions, zoom, lighting, etc.) with no significant difference in the results between the visualization techniques (2 Factor ANOVA, $p<0.74$, $\alpha$-0.05). Inclusion of the FDA data into ANOVA analysis however, yielded $p<0.0233$ implying difference amongst the groups. The higher FEs reported with the FDA data across all three fabrics could have been because of electrical charges in the droplets at the time of aerosolization that may have enhanced dipole induced capture of the droplets on the fabrics, or from the over saturation of the smaller coupons used.

**Table 1: Estimated FE from the Image Analysis Data. Quantitative Data from the FDA shown as a comparison.**

| | *Cotton PC* | *Flannel* | *Silk* |
|---|---|---|---|
| NIST | 8□.0□ | 68.5□ | 2□.2□ |
| WHHS - dSLR | 77.0□ | 64.3□ | 38.4□ |
| WHHS - Samsung | 87.□□ | 61.7□ | 50.6□ |
| WHHS - Apple | □0.2□ | 55.□□ | 40.5□ |
| FDA (Actual FE) | □7.□□ | □1.6□ | 65.4□ |

## DISCUSSION

The flow visualization and imaging analysis method outlined here provides an easy and budget friendly method of determining the relative effectiveness of fabrics for homemade face masks, comparable to more professional methods. While there are significant differences in filtration efficiency values between the NIST and WHHS and laboratory FDA methods, the fabric-to-fabric trends overlap. These results suggest that anyone with a commercially available items that can be purchased for < $1000, can conduct these experiments and generate meaningful data that helps with the selection of fabrics for DIY face coverings and masks.

## ACKNOWLEDGEMENTS

**Disclaimer.** The Department Health and Human Services or NIST does not promote nor endorse any of the materials or instruments used here. The findings and conclusions of this paper are solely the authors' and do not represent the official position of the FDA or NIST.

## REFERENCES

[1] U.S. CDC, Press Release, *CDC calls on Americans to wear masks to prevent COVID-19 spread.* 2020.
[2] Howard et al., *Proc. Natl. Acad. Sci. U.S.A.*, 118(4): e20145641182021, 2021
[3] Neupane, B. et al., *PeerJ*, 8:e9647, 2020
[4] Fischer, E, P, et al., *Science Advances*, 6(36), 2020
[5] Guha, S. et al., *PLoSone*, 16(1):e0244626, 2021
[6] Staymates, M., *Phys. Fluids*, 32:111703, 2020

# EXERCISE THERAPY IMPROVES GLENOHUMERAL JOINT FUNCTION WHEN REACHING BEHIND THE BACK IN INDIVIDUALS WITH ROTATOR CUFF TEARS

**Luke T. Mattar (1), Rachel P. McLoughlin (1), Adam J. Popchak (3), William J. Anderst (2), Volker Musahl (1,2), James J. Irrgang (2,3), Richard E. Debski (1,2)**

(1) Department of Bioengineering, University of Pittsburgh, Pittsburgh, PA, USA
(2) Department of Orthopaedic Surgery, University of Pittsburgh, Pittsburgh, PA, USA
(3) Department of Physical Therapy, University of Pittsburgh, Pittsburgh, PA, USA

## INTRODUCTION

Individuals with rotator cuff tears are generally prescribed non-operative treatment to improve pain and their ability to complete activities of daily living including personal hygiene and dressing that require one to reach behind their back. A tear involving the supraspinatus tendon may cause pain during these activities as the hand behind the back position has been shown to maximally stretch the supraspinatus[1]. Furthermore, posterior capsule tightness commonly seen in individuals with rotator cuff tears may contribute to experienced pain as the capsule is stretched during internal rotation when reaching behind the back. In regard to joint motion, reaching behind the back is a complex movement involving motion at the scapulothoracic, glenohumeral and elbow joints, where it is believed that the majority of internal rotation at the shoulder complex occurs before reaching the sacrum in healthy individuals[2].

Due to the movement's complexity and pain experienced by individuals with rotator cuff pathology, it is important to understand the effects of exercise therapy on one's ability to reach behind the back. Thus, the objective of the study was to assess changes in glenohumeral kinematics and arthrokinematics during a reaching behind the back movement in individuals with isolated supraspinatus tears before and after a 12-week structured and individualized exercise therapy program.

## METHODS

Eighty-three individuals (60.2 ± 9.3 years of age, BMI 28.4 ± 5.0) with a symptomatic rotator cuff tear isolated to the supraspinatus tendon were recruited after providing IRB-approved written informed consent prior to performance of any research procedure. Each individual participated in a 12-week structured and individualized exercise therapy program focused on restoring range of motion and strengthening of the rotator cuff and scapular muscles. To assess function, the individuals were asked to perform a behind the back task. Individuals began with their hand placed on their thigh and reached as far as they could behind their back. No specific instructions were given resulting in the individuals completing the task in their own manner. Glenohumeral kinematics and arthrokinematics were measured using a previously described and validated model-based tracking technique with images acquired from a synchronized biplane radiography system at 50 images/second[3].

Individuals underwent a computed tomography scan of the involved shoulder, and images were segmented to create individual specific bone models of the humerus and scapula. Digitally reconstructed radiographs of the bone models were created from the known geometry of the biplane radiography system. The bone models were then manipulated to match the digitally reconstructed radiographs to the corresponding bones in the biplane radiographic images in all 6 degrees of freedom for each pair of synchronized images throughout the movement. The local coordinate system for each humerus was constructed based on the International Society of Biomechanics recommendations with the origin located at the center of the humeral head. The scapula coordinate system was modified to create a glenoid based system to describe humeral motion with respect to the center of the glenoid. A X-Z-Y Euler angle rotation sequence was used to quantify translation and rotations with accuracy of ± 0.4mm and ± 0.5° for dynamic motion[3].

For each data frame, a 3D distance map was calculated between the humeral head and glenoid surfaces. The centroid of the 3D distance map was then quantified as the weighted average of the closest 200mm$^2$ region between the humeral head and glenoid surfaces and acted as an estimate of the contact center location. A contact path length was calculated as the change in frame-by-frame position of the contact center providing a quantification of the distance the humeral head articulated on the glenoid surface during the movement. A larger contact path length may indicate less joint stability as there is more movement of the humeral head on the glenoid surface. Three trials of the reaching behind the back movement were performed before and after exercise therapy. The trial on each day where maximum glenohumeral internal rotation was attained was used for all analyses. To compare glenohumeral kinematics and arthrokinematics, the common range of motion within each individual between testing days was utilized.

Outcome parameters include maximum glenohumeral anterior-posterior and superior-inferior translations (normalized to glenoid width and height, respectively), maximum glenohumeral internal rotation, and contact path length (normalized to glenoid size). Paired t-tests of Wilcoxon Sign Ranked tests were utilized to determine changes in maximum glenohumeral translations, maximum glenohumeral internal rotation, and contact path length following exercise therapy. Significance was set at $p<0.05$.

## RESULTS

All individuals completed the 12-week structured and individualized exercise therapy program. Maximum glenohumeral internal rotation significantly increased by 3.2° (12.5% in respect to before treatment) after exercise therapy (Table 1, $p=0.001$). Contact path length significantly decreased by 6.0% glenoid size (13.6% in respect to before treatment) after exercise therapy ($p=0.018$). No changes in maximum anterior, posterior, superior, or inferior translations occurred after exercise therapy ($p>0.05$).

**Table 1: Glenohumeral kinematics and arthrokinematics before and after a 12-week exercise therapy program.**

| | Before | After | p |
|---|---|---|---|
| Max. Internal Rotation (°) | 25.7 ± 13.9 | 28.9 ± 13.3 | 0.001 |
| Max. Ant. Trans. (% glenoid width) | 3.3 ± 4.0 | 3.7 ± 4.8 | 0.333 |
| Max. Post. Trans. (% glenoid width) | 3.2 ± 3.6 | 3.3 ± 3.8 | 0.823 |
| Max. Sup. Trans. (% glenoid height) | 2.7 ± 2.6 | 2.4 ± 2.4 | 0.068 |
| Max. Inf. Trans. (% glenoid height) | 2.4 ± 2.9 | 2.1 ± 2.4 | 0.709 |
| Contact Path Length (% glenoid size) | 44.0 ± 24.5 | 38.0 ± 21.2 | 0.018 |

## DISCUSSION

The primary findings of the study were that a 12-week structured and individualized exercise therapy program led to 1) improvements in maximum glenohumeral internal rotation and 2) decreased contact path lengths when reaching behind the back. The first finding suggests that individuals may be able to reach further behind their back due to increases in internal rotation after exercise therapy. Increases in maximum internal rotation likely occurred due to the prescribed stretching and exercise targeting passive range of motion[4]. The second finding may suggest that individuals have more joint stability when reaching behind the back after exercise therapy due to more control of the humeral head on the glenoid surface. The observed decrease in contact path length most likely occurred due to increases in compensatory muscle strength of the infraspinatus, teres minor, and subscapularis which are components of the transverse and coronal plane force couples of the glenohumeral joint, which have been shown to maintain joint stability in the presence of an isolated supraspinatus tear[5].

A previous study investigating glenohumeral kinematics in 15 healthy individuals using a dual fluoroscopy system found that individuals utilized 29.5° of glenohumeral internal rotation to reach L4-L5 when reaching behind the back[6]. Following exercise therapy in the current study, individuals utilized 28.9° of glenohumeral internal rotation, indicating that exercise therapy improved these individuals' internal rotation to levels comparable to that of healthy individuals. It has also been reported that during a reaching behind the back movement the majority of internal rotation at the shoulder complex occurs before reaching the sacrum[2]. After reaching the sacrum, reaching up the back is mostly comprised of elbow motion. Thus, since the individuals' glenohumeral internal rotation in the current study were comparable to healthy individuals, exercise therapy may improve one's ability to reach behind and up their back.

During our protocol, quantitative data on how far behind or up the back the individuals reached was not collected. This data may be important as vertebral level reached is commonly evaluated clinically. However, the current study provides novel information regarding glenohumeral kinematics and arthrokinematics in individuals with isolated supraspinatus tears before and after a 12-week exercise therapy program. Future studies will aim to quantify how far behind and up the back individuals in the current study reached.

## ACKNOWLEDGEMENTS

Support from the National Institutes of Health grant 5R01AR069503 is gratefully acknowledged.

## REFERENCES

[1] Nishishita, S et al., *JSES*, 27:2242-2248, 2018.
[2] Wakabayashi, I et al., *JSES,* 15:306-310, 2006.
[3] Bey, MJ et al., *J Biomech Eng*, 128:604-609, 2006.
[4] Keramat, KU and Babur, MN, *BMJ Open Sport Exerc Med*, 6:e000805, 2020.
[5] Parsons, IM et al., *J Orthop Res*, 20:439-446, 2002.
[6] Hunter, J et al., ORS2021, Paper#1369.

# COMPUTATIONAL MODELING OF BRAIN BILAYER UNDER CEREBROSPINAL FLUID PRESSURE

**Fatemeh Jafarabadi (1), Maria A. Holland (1,2)**

(1) Aerospace and Mechanical Engineering, University of Notre Dame, Notre Dame, IN, USA
(2) Bioengineering Graduate Program, University of Notre Dame, Notre Dame, IN, USA

## INTRODUCTION

The cerebral cortex is folded in some mammals, in contrast to others with a smooth brain surface. Folding patterns are a significant feature associated with the functionality of the brain, especially in humans. Lissencephaly, polymicrogyria, and microcephaly are among the various abnormalities that have been observed in folding patterns. Furthermore, these folding malformations have been linked to many neurological disorders, such as schizophrenia and autism spectrum disorder. The folding process is mainly known to result from mechanical instabilities induced by compressive forces and mechanical stresses. Several theories explain the folding mechanisms with respect to internal and external factors [1].

Focusing on the extrinsic constraints, early on researchers hypothesized that cortical folding happens during the embryogenesis period because the skull adds a constraint over the brain, which resists the tangential growth of the cortex. However, after the experimental results of a 1950s study showed the brain continued to normally develop after removing a piece of a sheep's cranium, researchers have lost their interest in this theory [2]. Therefore, most models consider the brain tissue without any external constraint and model gray and white matter as an isolated bilayer system. This approach has led to a comprehensive understanding of internal factors which form the gyri and sulci and addressed the importance of cortical growth, cortical thickness, and stiffness ratio between gray and white matter in brain folding [3, 4].

However, excluding the skull, other external constraints might contribute to brain instability and influence folding patterns. Here, we will focus on the cerebrospinal fluid (CSF) pressure as a non-zero stress boundary condition over the brain surface. CSF is a body liquid that circulates in the space between the brain surface and meninges, protecting the brain from external damage. The normal CSF pressure is between 0.2 kPa to 0.8 kPa on an infant's brain and 1.3 kPa to 2 kPa on an adult brain. In severe abnormal cases, the pressure might increase up to 6 kPa. The effect of CSF pressure on brain development and function has been proved in various studies, but its influence on the gyrification process of the brain has been understudied [5, 6].

## METHODS

We used the commercial software ABAQUS/Explicit to implement a three-dimensional finite element model of a bilayer with non-zero stress boundary conditions on the top and front faces, as shown in Figure 1. The whole model is subjected to a uniform compression imitating the growth-induced forces from the right side. CSF pressure is added as a follower surface traction on the top surface of gray matter, and the front face of the two layers is subjected to an in-plane pressure, replicating the influence of neighboring tissue boundaries on the bilayer system. The remaining sides are fixed due to the symmetry of the problem [7].

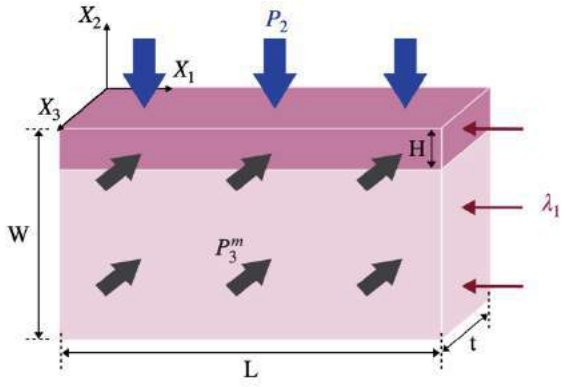


**Figure 1. Schematic of the bilayer system. The blue and black arrows imitate the CSF and the in-plane pressure, respectively, and the red arrows are uniform compression.**

Both gray and white matter are assumed to be nearly incompressible neo-Hookean hyperelastic materials with strain energy:

$$\Psi = \frac{1}{2}\lambda ln^2(J) + \frac{1}{2}\mu[tr(\mathbf{C}) - 3 - 2\ln(J)] \quad (1)$$

where $\mu$ and $\lambda$ are Lamé constants ($\lambda \gg \mu$) and $\mathbf{C}$ is the right Cauchy green tensor. We defined the stiffness ratio as the ratio between gray and white matter shear modulus, $\beta = \mu_f/\mu_s$, and the in-plane pressures are assumed to be a factor of surface pressure [8]:

$$P_3^f = 1.3P_2 \quad (2)$$

$$P_3^s = P_3^f/\beta \quad (3)$$

## RESULTS

We ran a total of 242 simulations, covering combinations of $\beta$ from 1.5 to 50 and CSF pressure from 0 to 2 kPa. The simulation results are presented, with an emphasis on the critical compressive strain and thickness variations. The critical buckling strain is identified by monitoring the total elastic strain energy in the cortex region; a sudden decrease in energy is assumed to indicate the buckling point. Then, the thicknesses of gyri and sulci regions are measured at this point and compared for multiple cases of pressure and stiffness ratios.

To investigate the effect of surface pressure on the stability of our bilayer system, we compared zero pressure cases for different stiffness ratios with non-zero pressure cases (Fig. 2). Adding pressure reduces the system's stability and makes the bilayer system buckle at smaller compressive strains, especially for stiffness ratios smaller than 4. Additionally, when we expand the range of stiffness ratios to $1.5 < \beta < 50$, the influence of applied pressure on the instability seems to vanish. This shows that the effect of pressure is only relevant for sufficiently low stiffness contrast, $\beta < 10$, and as the stiffness contrast between layers increases, it becomes very unstable regardless of the stress boundaries of surface pressure.

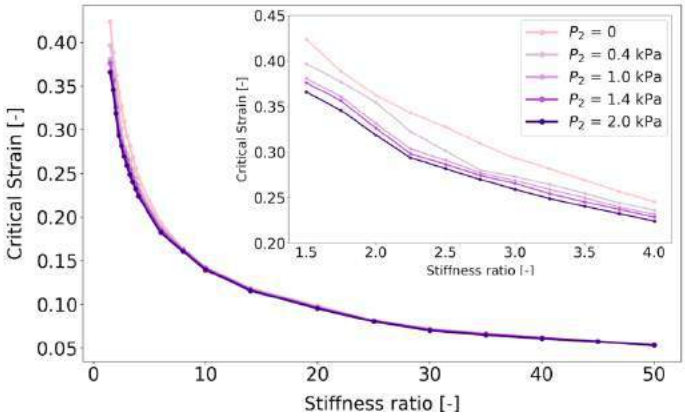


**Figure 2. Influence of pressure on stability for different stiffness ratios.**

Cortical thickness is a biomarker indicating the healthy and diseased condition of the brain. Generally, gyral regions are thicker than sulcal regions in the brain [9]. Here, we sought to find the influence of CSF pressure on thickness ratio throughout the folds of the brain. We compared the thickness of the cortex in gyrus and sulcus areas for four different pressure values, along with the zero-pressure case (Fig. 3). Here, we considered a region consisting of five elements along the between them. We defined the thickness ratio as the ratio between gyri and sulci thicknesses, $TR = t_g/t_s$, and measured the average ratio depending on the number of gyri and sulci for each simulation. We can see that adding surface pressure significantly influences thickness ratio, and when the amount of pressure is larger, the difference between sulcus and gyrus thicknesses increases. Also, we found that when the stiffness ratio between the layers increases, the thickness ratio decreases, which is in line with the previous data [9].

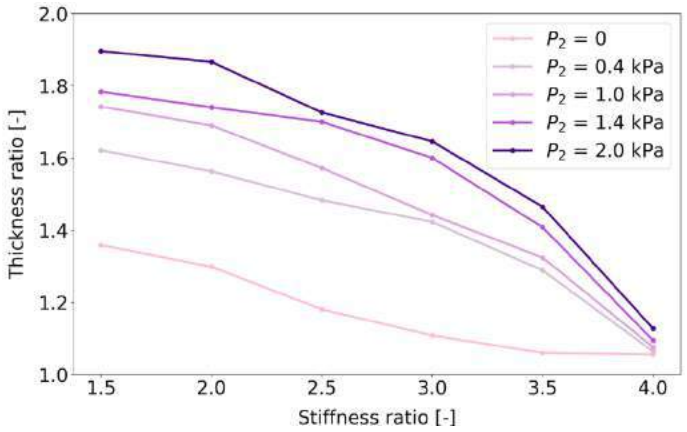


**Figure 3. Influence of pressure on thickness ratio for different stiffness ratios.**

## DISCUSSION

In this study, we investigated the wrinkling response of an inhomogeneous bilayer system, consisting of a dissimilar film and a substrate, under varying amounts of surface pressure. We focused on bilayer materials with similar mechanical properties to brain tissue, as we intended to investigate the influence of cerebrospinal fluid pressure on the instabilities of the brain. We showed that pressure plays a role in the system's instability, and a system under uniform compression with surface pressure is always more unstable. In our simulations, we could capture the instability behavior for stiffness ratios of 1.5 to 50, but our model could not converge for predicting buckling behavior of softer films, $\beta < 1$, which is closer to the brain tissue properties.

In the future, we plan to improve this study by incorporating tissue growth into our simulations, which would enable us to imitate the actual condition of brain tissue development. As the first step, we could repeat our simulations with an isotropic growth model and compare the results for both zero stress and non-zero stress boundary conditions. This will allow us to capture critical strain and thickness variations at the buckling point in a situation closer to the human brain.


## ACKNOWLEDGEMENTS

This work was supported by NSF Grant No. IIS1850102.


## REFERENCES


[1] Striedter, GF. et al., *Annu. Rev. Neurosci.* 38 (1): 291–307, 2015
[2] Barron, DH., *J of Experimental Zoology* 113(3): 553–581, 1950
[3] Holland, MA. et al., *J Mech and Phys Solids* 98:350–365: 2017.
[4] Budday, S. et al., *Sci Rep* 4 (1):5644, 2015
[5] Gafoor, V. et al., *Ann. Indian Acad. Neurol.* 20 (3): 220–224, 2017
[6] Lee, SCM. et al., *J of Neuro-Ophthalmology* 34 (3): 278–283, 2014
[7] Abaqus/Standard, Abaqus reference manuals. Dassault Systemes Simulia, Providence
[8] Darayi, M. et al., *Intl J. of Non-Linear Mech.* 127: 103589, 2020
[9] Holland, MA. et al., *Phys Review Letters* 121 (22): 228002, 2018

# THE LASSO STITCH: A NOVEL SUTURING TECHNIQUE FOR HIGH-TENSION WOUND REPAIR IN PLASTIC AND RECONSTRUCTIVE SURGERY

**Chung-Hao Lee (1), Colton J. Ross (1), Bradley Miyake (2), Henry Marsh (2), Parker Bryant (1), and Guilherme Barreiro (2,3,4)**

(1) Biomechanics and Biomaterials Design Laboratory, School of Aerospace and Mechanical Engineering, The University of Oklahoma, Norman, OK, USA
(2) Plastic and Reconstructive Surgery, Department of Surgery, The University of Oklahoma Health Sciences Center (OUHSC), Oklahoma City, OK, USA
(3) Plastic and Reconstructive Surgery, State University of Campinas, Brazil
(4) Plastic, Reconstructive, and Burn Surgery, State Institute for the Public Server's Health, São Paulo, Brazil

## INTRODUCTION

The skin is a three-layered structure consisting of the outer epidermis, the dermis (with a superficial and a deep component), and the subcutaneous layer. In the case of skin damage, surgical correction may be required. The optimum method of skin repair reduces the risk of adverse events and wound complications, such as wound dehiscence, infection or cosmetic scarring. Skin repair is often performed with staples, tissue adhesives, and sutures. With specific regard to sutures, there are several techniques that can be used.

The most commonly used suturing techniques include the simple interrupted (SI), vertical mattress (VM), horizontal mattress (HM), and deep dermal with a running subcuticular (i.e., "plastics stitch") (DDR) (**Fig. 1**) [1]. The ideal stitch is one that minimizes tension on the skin edges, is fast to perform, and, especially in the case of high-tension wound areas has a minimal risk of wound dehiscence. Previous research works have evaluated the various stitch patterns using uniaxial tensile testing of excised skin samples until suture failure. From these investigations, the following observations have been made: (i) the SI withstands greater tension than a subdermal stitch [2]; (ii) the VM can hold a greater load than the HM before failure [3]; (iii) the DDR is optimal for high-tension wound repair. Although these studies have elucidated the functional advantages of each pattern, there is still an emerging need for a stitch that is faster to perform and with a much better tensile strength.

In this study, we propose a new suturing technique for full thickness skin repair – the "Lasso" stitch (**Fig. 1**). This new method consists of a modified combined deep dermal and vertical mattress stitch, which has a superior mechanical strength and a faster time-to-repair than the existing suture patterns. If this new technique is used in the clinic, it could reduce the overall operating time and reduce wound complication rates due to dehiscence.

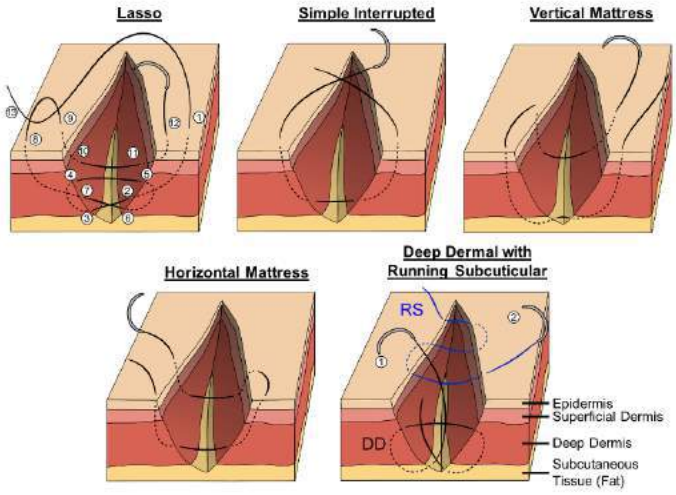


## METHODS

***Suture Procedure*:** The procedure to perform the proposed Lasso stitch is depicted in **Figure 1**, with the step breakdown herein. (Step 1) Starting 7 mm from the wound edge, a full thickness pass of the needle is performed, exiting at the dermal-subcutaneous fat transition. (Step 2) Going through the contralateral dermis, a complete deep-to-superficial pass is made, followed by a superficial-to-deep pass through the ipsilateral dermis. (Step 3) Starting at the contralateral dermal-subcutaneous fat transition, perform a full thickness pass, exiting the

skin 7 mm from the wound edge. (Step 4) A dermal-partial thickness pass is performed 4 mm from the wound edge, crossing the wound superficial to the buried deep dermal suture, and exiting 4 mm from the wound edge on the contralateral side. (Step 5) Finally, the tail end of the suture is pulled through the loop, the suture is made taut, and a knot is securely tied.

***Uniaxial Tensile Failure Mechanical Characterization*:** To characterize the tensile properties of the Lasso, we performed uniaxial load-to-failure testing of suture-repaired skin samples according to the previous literature [4-5]. Briefly, caprine skin was sectioned into 10x10 cm sections and further bisected to create a pseudo-wound. The divided skin specimens were then repaired with the Lasso, SI, VM, HM, or DDR stitch, and with either nylon (NYL) or polydioxanone (PDS) sutures, with 5 implanted sutures at a 1-2 cm spacing ($n$=6 for each subcategory). Thickness measurements were made for each specimen before mounting to a commercial uniaxial testing device (TestResources, Model #100-36) (**Fig. 2a**). Then, the specimens were loaded until suture failure, with the force and strain ε readings recorded throughout the test.

***Suture Operation Time Assessment*:** To assess the time-to-repair, we also enrolled $n$=6 medical residents to perform each of the five suture types on 10 cm wound incisions, and the time to repair with each stitch was recorded.

***Data and Statistical Analysis*:** For data analysis, the first Piola-Kirchhoff tissue stress $\sigma$ was calculated using the cross-sectional area of the specimen (from the measured thickness and width). Then, we determined the stresses and strains at the first suture rupture, and the stored elastic energy before the first suture rupture (**Fig. 2b**). For gaining better insights into the mechanical properties of the suture types, we also performed constitutive modeling of the stress-strain behaviors by prior to the first suture rupture using an exponential model form:

$$\sigma = \begin{cases} A(e^{B\varepsilon} - 1) & \text{for } \varepsilon \le \varepsilon_{ub} \\ A[(e^{B\varepsilon_{ub}} - 1) + Be^{B\varepsilon_{ub}}(\varepsilon - \varepsilon_{ub})] & \text{for } \varepsilon > \varepsilon_{ub} \end{cases}.$$

Herein, $A$ is a constant representing the material stiffness, $B$ represents the level of nonlinearity in the stress-strain behaviors, and $\varepsilon_{ub}$ is the upper bound of strain for the linearization of the stress-strain response.

For statistical analysis, a Kruskal-Wallis one-way analysis of variance was used with a Tukey's (normal data) or Dunn's (non-normal data) post-hoc test, and $p$<0.05 was considered statistically significant.

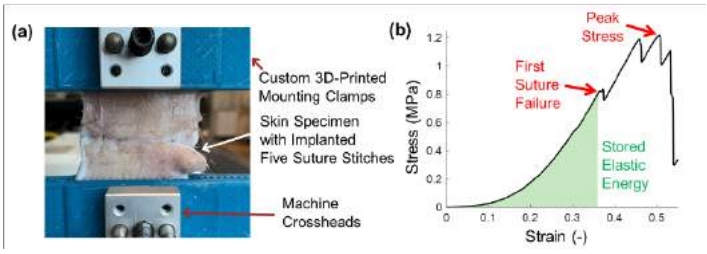


**Figure 2: (a) Uniaxial testing setup for the repaired skin samples. (b) Quantified failure mechanics from the stress-strain behaviors.**

## RESULTS

The results from the uniaxial failure testing of the sutures with the PDS and NYL materials are shown in **Figure 3**. In the PDS-repaired samples, for the first suture rupture stress, the Lasso reached a higher stress than all other patterns: 59% greater than SI ($p$=0.007), 51% greater than VM ($p$=0.022), 74% greater than VM ($p$=0.002), and 60% greater than DDR ($p$=0.039). This finding was further reflected in the stored elastic energy, where the Lasso outperformed all other patterns. Similar trends were also observed in the NYL-repaired specimens (bottom panel of **Fig. 3**). Additionally, from the time-based trials we found that the Lasso was significantly faster to perform than the DDR (264±21 s vs. 349±25 s, $p$=0.027); however, the SI (125±10 s), HM (164±16 s), and VM (182±18 s) were all significantly faster to perform than the DDR and Lasso stitches.

Finally, from the constitutive model fitting $\varepsilon_{ub}$ was largest for the Lasso specimens, indicating a longer low-tension regimen before transitioning into high-tensile behaviors. For the PDS-repaired specimens: $\varepsilon_{ub}$=0.33±0.16 (Lasso), 0.33±0.07 (SI), 0.29±0.08 (VM), 0.25±0.04 (HM), 0.24±0.04 (DDR), whereas similar trends in the estimated parameters were found with nylon sutures.

## DISCUSSION

In this work, we have shown that our proposed novel stitching technique was quantifiable demonstrated as superior or comparable to the suturing patterns classically employed in the clinic through uniaxial tensile testing and time-based operational trials. The Lasso is slower to perform than other traditional low-tension wound options such as the SI, VM, and HM, but provides a substantially superior tensile strength. Thus, it becomes clear that the choice of suturing pattern is a trade-off between a faster operational time and the suture strength, based on the requirements of the specific wound. Further, comparing the Lasso to the current standard for high-tension wound repair, the DDR, we have found that the Lasso has a superior first rupture stress and stored elastic energy with the PDS material, and comparable failure mechanics using the NYL material. These findings suggest the Lasso may have a lower rate of wound dehiscence. At the same time, the Lasso has a 28% faster time-to-repair than the DDR, which could lead to reduced operational times in the clinic for plastic and reconstructive surgeries.

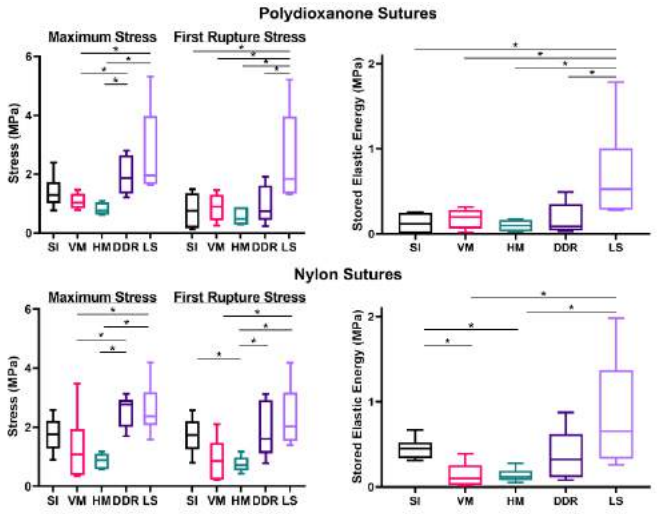


**Figure 3: Failure mechanics of the tested sutures with polydioxanone material (*top panel*) and nylon material (*bottom panel*). * denotes statistically significant difference, $p$<0.05.**


## ACKNOWLEDGEMENTS

We gratefully acknowledge Cody Dalton (M.D.), Thomas Kerestes (M.D.), Matthew Marr (M.D.), and Nasser Alamiri (M.D.) for their contributions in performing the time-based suturing studies.


## REFERENCES


[1] Regula, CG, *et al*., *Dematol Surg*, 41:S187-S200, 2015.
[2] Zellner, EM, *et al*., *J Am Vet Med*, 248(12):1377-1382, 2012.
[3] Post, WR, *et al*., *J Arthrosc Relat Surg*, 13(6):731-736, 1997.
[4] Annaidh, AN, *et al*., *J Mech Behav Biomed Mater*, 5(1):139-148, 2012.
[5] Yang, W, *et al*., *Nat Commun*, 6(1):6649, 2015.

SB³C2022
Summer Biomechanics, Bioengineering and Biotransport Conference
June 20-23, Eastern Shore, MD, USA

# PREDICTING JOINT TORQUE USING SEMG AND DEEP NEURAL NETWORKS

**Heath Boyea (1), J. Miles Canino, Ph.D. (2)**

(1) Mechanical Engineering, Rose-Hulman Institute of Technology, Terre Haute, Indiana, United States
(2) Mechanical Engineering, Rose-Hulman Institute of Technology, Terre Haute, Indiana, United States

## INTRODUCTION

According to the Center for Disease Control (CDC), 1 in 7 American adults are affected by disabilities that affect mobility [1]. Assistive devices, such as exoskeletons, may be able to assist affected individuals. Though these devices may be helpful, constant assistance can create dependence on the device. We hypothesize that an assist-as-needed control system can be developed to aid the wearer only when necessary. We hypothesize that an artificial neural network (ANN) can be used to predict user-intended torque outputs of joints. The user-intended torque can be compared to actualized torque outputs, with the difference of these torque values contributed by the assistive exoskeleton.

## METHODS

It has been shown by Coker et al. that future joint angles can be predicted from observing current joint angles, torques, and surface Electromyography (sEMG) data of pertinent muscle groups through the implementation of a Nonlinear Input-Output Time Series Neural Network [2]. We sought to evaluate the capability of this method in predicting knee joint angles and torques at varying walking speeds with a dataset supplied by the works of Moriera et al. [3].

This dataset is comprised of gait data for 16 subjects. Each participant performed 7 trials at 7 walking speeds: 1.0, 1.5, 2.0, 2.5, 3.0, 3.5, and 4.0 km/h. An 8-channel sEMG system, sampling at 2000 Hz, recorded EMG signals from four lower limb muscles, comprising the quadriceps and hamstring groups of both lower limbs. EMG signals were band-pass filtered using a 4$^{th}$ order Butterworth filter with cutoff frequencies at 20 Hz and 450 Hz. Motion capture information from the lower limb joints and pelvis were also sampled at 200Hz. Visual3D was used by the researchers to extrapolate joint angles and torques. Joint angle data was also low-pass filtered through a 4$^{th}$ order Butterworth filter with a 6 Hz cutoff frequency. 1001 EMG, joint angle, and torque measurements were logged for each stride [3].

For our purposes, 10 subjects were selected from this cohort (5 males, 5 females, with average age = 25 +/- 2 years, average height = 1.67 +/- 0.16 meters, average weight = 64.4 +/- 12.4 kg). Filtered quadriceps and hamstring sEMG data, X-axis knee joint angles, and X-axis knee torque measurements were extracted for each trial, individual leg, and stride of each participant. 1-in-7 trials were removed to produce a separate validation data set. The remainder were used as a training data set. A separate neural network was trained for each independent lower limb of each subject. To evaluate the networks' ability to predict joint mechanics, each network was trained to predict knee joint kinematics 50, 100, and 150 ms into the future. To obtain these time-shifted datasets, the entry offset was calculated (1).

$$\text{entry offset} = \frac{\text{time shift} * 100}{\text{stride time}} \quad (1)$$

The number of entries equal to the entry offset was then removed from the front of the matrix to be time-shifted and removed from the rear of the ground-truth matrix. This maintains equal matrix lengths and data synchronicity. One training set was produced for each person, limb, and time shift by horizontally concatenating the associated training data. Targets were set to the time-shifted joint angle and torque. A Nonlinear Input-Output Time Series Neural Network utilizing Bayesian Regularization, a singular hidden layer, and two delays was then trained for each set. 70% of the data was allocated for training, 15% for testing, and 15% for validation. A total of 60 networks were trained (10 subjects, 2 limbs, and 3 time shifts). Networks trained on left strides were trained on half as much data as networks trained on right strides. This was due to each trial containing 2 right strides and 1 left. All networks were validated by entering the validation data into the trained model and comparing the output to the ground-truth validation target. The Root Mean Squared Error (RMSE) was computed between the predicted knee

joint torque and the ground-truth, and the knee joint angle and ground-truth.

## RESULTS

The RMSE of the knee joint torques is shown in Table 1 and the RMSE of the knee joint angles is shown in Table 2.

**Table 1: RMSE of Predicted Knee Joint Torques (N-m)**

| | 50 ms | | 100ms | | 150ms | |
|---|---|---|---|---|---|---|
| Subject | Left (N-m) | Right (N-m) | Left (N-m) | Right (N-m) | Left (N-m) | Right (N-m) |
| 1 | 3.0018 | 2.3229 | 5.4527 | 4.5192 | 7.5845 | 6.4013 |
| 2 | 1.8135 | 1.7262 | 3.8986 | 3.8488 | 5.3251 | 5.6883 |
| 3 | 1.3801 | 1.4548 | 2.8054 | 2.9359 | 3.5711 | 5.6567 |
| 8 | 2.2311 | 1.4675 | 4.6335 | 4.5696 | 6.2067 | 5.0188 |
| 9 | 1.9617 | 2.1004 | 4.3709 | 4.6790 | 6.5095 | 4.1446 |
| 10 | 2.2165 | 2.3870 | 6.1208 | 5.3578 | 7.7621 | 6.4034 |
| 11 | 2.2095 | 2.0147 | 3.8053 | 3.6923 | 5.1819 | 7.3721 |
| 12 | 2.0811 | 1.9838 | 4.2189 | 3.9195 | 5.7380 | 4.5427 |
| 13 | 1.8866 | 1.9585 | 3.5044 | 3.5252 | 4.2837 | 7.1439 |
| 14 | 4.5115 | 1.8662 | 3.7765 | 4.2577 | 4.7780 | 4.9842 |
| Average | 2.3293 | 1.9282 | 4.2587 | 4.1305 | 5.6941 | 5.7356 |

**Table 2: RMSE of Predicted Knee Joint Angles (deg)**

| | 50 ms | | 100ms | | 150ms | |
|---|---|---|---|---|---|---|
| Subject | Left (deg) | Right (deg) | Left (deg) | Right (deg) | Left (deg) | Right (deg) |
| 1 | 1.8282 | 2.0503 | 3.3278 | 4.1263 | 5.6861 | 5.7360 |
| 2 | 1.7483 | 1.7429 | 4.1857 | 3.8520 | 5.8970 | 5.1469 |
| 3 | 2.0244 | 1.7405 | 4.3545 | 5.3600 | 5.2839 | 3.6910 |
| 8 | 1.4512 | 2.1675 | 3.2952 | 3.7357 | 5.3014 | 6.0310 |
| 9 | 1.3249 | 1.2519 | 3.0568 | 2.7714 | 4.5638 | 6.6518 |
| 10 | 1.6743 | 1.7126 | 4.2026 | 4.1058 | 6.3127 | 5.2424 |
| 11 | 2.4286 | 2.4970 | 5.0475 | 3.9368 | 6.4483 | 5.9241 |
| 12 | 1.6222 | 1.5239 | 3.6338 | 3.0996 | 4.7769 | 5.2960 |
| 13 | 1.8068 | 1.9775 | 3.3983 | 4.0182 | 5.1366 | 4.4932 |
| 14 | 2.9253 | 1.6462 | 6.9693 | 3.6557 | 5.5523 | 5.4481 |
| Average | 1.8834 | 1.8310 | 4.1472 | 3.8662 | 5.4959 | 5.3660 |

The average data is plotted in Figure 2, below. As one would expect, there is a consistent increase in error as our time shift increases and, interestingly, a slight increase in error as we compare right and left legs. It was also found that the right side has much lower standard deviation. These interesting observations were likely due to its much larger training data set available for the right side.

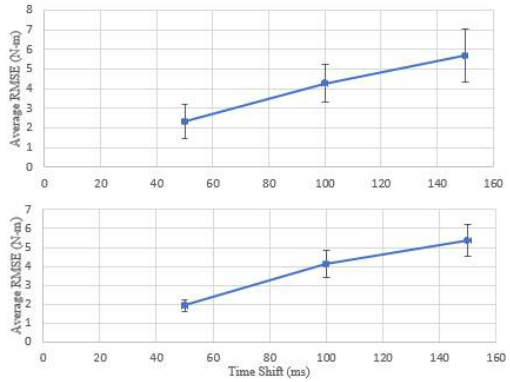


**Figure 2: Average RMSE of joint torque for left (top) and right (bottom) limbs across the three time shifts (50, 100, 150 ms).**

When predictions from our model are overlayed with the ground-truth, as in Figure3, it can be seen that future knee joint kinematics can be predicted with reasonable accuracy, even at a time shift of 100 ms.

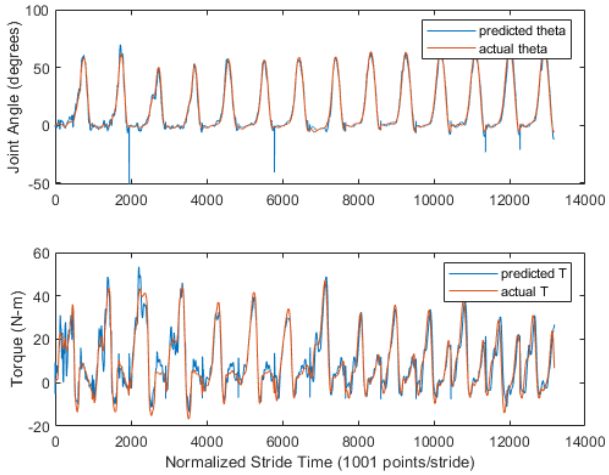


**Figure 3: 100 ms offset knee joint angle and torque prediction vs. ground-truth.**

## DISCUSSION

Similar work conducted by Coker et al. demonstrated lower RMSE for joint angle prediction at each of the time shift intervals [2]. This discrepancy is likely a result of our dataset having varying walking speeds for each subject, rather than a consistent walking speed.

Our work demonstrates an accurate system for estimating knee joint torque and knee joint angle out to at least 150 ms of offset. Networks were each trained on less than 100 strides and accurately predicted knee joint kinematics over various walking speeds. Such a robust system, that is easily trained, could be of substantial use for assist-as-needed exoskeleton devices. Future work conducted by this lab will explore the use of this neural network in the estimation of more complex upper limb joint kinematics, particularly of the hand and wrist.

This methodology could also be used in the post-acute injury rehabilitation setting, to assess functional recovery of patients with range of mobility impairment and better assess the efficacy of rehabilitation techniques being implemented.


## ACKNOWLEDGEMENTS

The researchers would like to thank Rose-Hulman Institute of Technology for their support of this project.


## REFERENCES


[1]Center For Disease Control, ”1 in 4 US Adults Live with a Disability”, 2018 https://www.cdc.gov/media/releases/2018/p0816-disability.html

[2] Coker, Jordan, Howard Chen, Mark C. Schall Jr., Sean Gallagher, and Michael Zabala. 2021. "EMG and Joint Angle-Based Machine Learning to Predict Future Joint Angles at the Knee" Sensors 21, no. 11: 3622.

[3] Moreira, L., Figueiredo, J., Fonseca, P. et al. Lower limb kinematic, kinetic, and EMG data from young healthy humans during walking at controlled speeds. Sci Data 8, 103 (2021).

# TRI-COMPARTMENT KNEE LOADING 3 MONTHS AFTER ACL RECONSTRUCTION

**Jack R. Williams (1), Kelsey Neal (1), Abdulmajeed Alfayyadh (2), Ashutosh Khandha (3), Kurt Manal (2,4), Lynn Snyder-Mackler (2,3,5), Thomas S. Buchanan (1,2,3)**

(1) Mechanical Engineering, University of Delaware, Newark, DE, USA
(2) Biomechanics and Movement Science, University of Delaware, Newark, DE, USA
(3) Biomedical Engineering, University of Delaware, Newark, DE, USA
(4) Kinesiology and Applied Physiology, University of Delaware, Newark, DE, USA
(5) Physical Therapy, University of Delaware, Newark, DE, USA

## INTRODUCTION

Osteoarthritis (OA) development after ACL reconstruction (ACLR) is well documented[1]. OA is commonly seen within the medial tibiofemoral compartment of the knee; however, recent evidence suggests that patellofemoral OA may be equally prevalent[2]. Medial compartment underloading within the involved limb 6 months after ACLR is associated with radiographic OA development 5 years after surgery[3]; suggesting a potential link between early knee loading after ACLR and eventual OA development. However, no one has examined loading within all three compartments of the knee (medial, lateral, and patellofemoral compartments) and few have examined loading prior to 6 months after surgery. Additionally, many have restricted their analyses of knee loading to specific points within the movement pattern (e.g., peak medial compartment force) creating the possibility of omitting relevant information about the mechanical variable analyzed. Thus, the purpose of this study was to examine loading within the medial tibiofemoral, lateral tibiofemoral, and patellofemoral compartments of the knee 3 months after ACLR over the entirety of the stance phase of overground walking.

## METHODS

48 individuals (20 female; age: 23 ± 7 years; BMI: 26 ± 4 kg/m$^2$) completed motion analysis during overground walking at a self-selected speed (1.5 ± 0.2 m/s) 3.1 ± 0.5 months after ACLR. Prior to walking, surface electromyography (EMG) electrodes were placed over seven muscles on each leg after shaving and cleaning the area over each muscle belly. These seven muscles included the rectus femoris, vastus medialis, vastus lateralis, medial gastrocnemius, lateral gastrocnemius, semimembranosus, and the long head of the biceps femoris. After electrode placement, each participant performed maximal voluntary isometric contractions (MVICs) which were used to normalize the EMG data collected during walking. All EMG data were collected at 1080 Hz. Following completion of the MVICs, retroreflective markers were placed bilaterally on bony landmarks (1$^{st}$ and 5$^{th}$ metatarsal heads, top and bottom heels, femoral epicondyles, greater trochanters, iliac crests) and rigid multi-marker shells were attached to the pelvis, thighs, and shanks. Motion data were recorded using an 8-camera infrared Vicon system at a sampling rate of 120 Hz. Ground reaction forces during walking were captured using a single embedded force plate at a sampling rate of 1080 Hz.

Three trials per leg were used for data analysis. Kinematic and kinetic variables were calculated via inverse dynamics (Visual3D). A SIMM model was anatomically scaled and used to estimate muscle-tendon lengths and moment arms. Each subject's EMG data were high-pass filtered at 30 Hz using a second-order Butterworth filter, rectified, low-pass filtered at 6 Hz, and then normalized to MVICs to create linear envelopes. Linear envelopes for the semitendinosus and short head of the biceps femoris were set equal to the those of the semimembranosus and long head of the biceps femoris, respectively. The linear envelope of the vastus intermedius was estimated as the average of the vastus medialis and vastus lateralis. These EMG signals were used in a validated, subject-specific neuromusculoskeletal model to calculate muscle forces[4]. Briefly, EMG signals were transformed into neural activations using a previously described discretized second-order differential equation to model muscle activation dynamics[4]. These neural activations were subsequently transformed into muscle activations after accounting for the non-linear relationship between muscle stimulation frequency and muscle force. Finally, these muscle activations were used in a Hill-type model of a muscle fiber in series with a tendon to calculate muscle force. The muscle force model was then tuned so that the net extensor moment from the forward dynamics model matched the net extensor moment from the inverse dynamics model. This was done by adjusting the parameters and coefficients involved in the prediction of muscle forces rather than directly altering the muscle forces themselves. These muscle forces, in combination with frontal plane moment arms, were utilized in frontal plane moment

balances to determine medial and lateral compartment forces (MCF and LCF, respectively)[5]. Both MCF and LCF were normalized by bodyweight (BW).

After calculation of muscle forces, a separate two-dimensional model, similar to those of Yamaguchi and Zajac[6] and Shelburne and Pandy[7], was utilized to determine patellofemoral contact force (PCF). Briefly, the 2D model was scaled to each subject's anthropometrics. Using Equation (1)[6,7] the PCF by quadriceps muscle force ratio from 0° to 90° of knee flexion was calculated at 5° intervals.

$$\frac{PCF}{QuadiForce} = i\frac{-\sin i(\theta_q+\beta)}{\cos i(\beta-\alpha)}i \quad (1)$$

Where $\theta_q$ is the angle of the quadriceps tendon with respect to the femur, β is the angle of the patellar ligament with respect to the y-axis of the femur, and α = the patellar flexion angle; all of which are functions of knee flexion angle. A fourth-order polynomial was fit to these data to provide a subject-specific equation for the PCF by quadriceps muscle force ratio as a function of knee flexion angle. Each subject's knee flexion angle throughout stance was then utilized in this equation to determine the PCF by quadriceps muscle force throughout stance. The forces from the vastus medialis, vastus lateralis, vastus intermedius, and rectus femoris were summed to determine the net quadriceps muscle force. Finally, the net quadriceps muscle force throughout stance was multiplied by the PCF by quadriceps muscle force throughout stance to determine PCF. PCFs were normalized by BW.

Statistical analyses were performed in MATLAB with statistical significance defined as α = 0.05. Statistical parametric mapping (SPM) was utilized to perform a two-tailed paired t-test (comparing the involved limb to the uninvolved limb) over the entirety of stance phase. A Bonferroni correction was utilized to account for multiple comparisons.

## RESULTS

Significant underloading of the medial tibiofemoral compartment was present in the involved limb (vs. uninvolved) during the loading response phase of stance (p = 0.016 from 11-21% of stance; max difference = 0.5 BW; **Figure 1A**). Peak MCF was 2.4 BW and 2.9 BW in the involved and uninvolved limbs, respectively. The patellofemoral compartment of the involved limb was underloaded (vs. uninvolved) during initial contact and into loading response (p < 0.001 from 4-38% of stance; max difference = 0.5 BW), and during terminal stance (p = 0.016 from 90-98% of stance; max difference = 0.2 BW) and was overloaded during midstance (p < 0.001 from 53-71% of stance; max difference = 0.1 BW; **Figure 1B**). Peak PCF was 1.1 BW and 1.6 BW in the involved and uninvolved limbs, respectively. LCF in the involved limb was underloaded (vs. uninvolved) during terminal stance (p = 0.044 from 91-94%; max difference = 0.2 BW; not shown); however, this was likely not meaningful given the small range over which it occurred. Peak LCF was 1.6 BW and 1.8 BW in the involved and uninvolved limbs, respectively.

## DISCUSSION

Asymmetries in loading were present in both the medial and patellofemoral compartments of the knee 3 months after ACLR, but not in the lateral compartment. The asymmetries in MCF early after ACLR seen here align well with previous work from our lab which saw asymmetries in MCF pre-surgery and 6 months after ACLR[3]. The PCFs seen here align well with reports of patellofemoral underloading following ACLR during running tasks after return-to-sport time points[8].

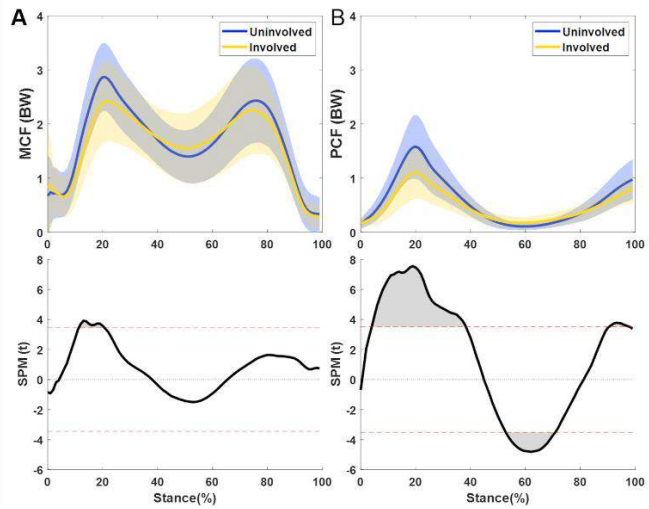


**Figure 1: Top: Average of loading variable in the involved (gold) and uninvolved (blue) limbs ± 1 SD during stance. Bottom: Two-tailed paired t-test test statistic over the entirety of stance. Dashed lines are the critical p-value (α = 0.05); shaded regions are areas of significant differences. (A) MCF (B) PCF.**

Both the medial compartment and patellofemoral compartment displayed reduced involved limb loading (vs. uninvolved) during the loading response phase of stance as the limb accepted load after contacting the ground. This is not surprising as many tend to adopt a stiffened knee gait strategy, typically consisting of reduced vertical ground reaction forces, quadriceps avoidance, and less knee flexion, within the involved limb early after ACLR[9]. These strategies can likely be attributed to reports of patients experiencing pain and Kinesiophobia[10]. Interestingly, the patellofemoral compartment experienced involved limb overloading (vs. uninvolved) during midstance. This, coupled with underloading during the loading response phase of stance, implies that the patellofemoral compartment experiences a much narrower range of forces in the involved limb during walking 3 months after ACLR (i.e., the difference between the peak during loading response and the peak during midstance is less in the involved limb [0.9 BW] vs. uninvolved limb [1.5 BW]). As cartilage is a highly mechanosensitive tissue[11], it may be that this reduction in range of forces applied to the medial and patellofemoral compartments may result in disruption of the biochemical environment of the knee and thus may be a mechanism for eventual OA development. Future work needs to investigate the long-term implications of these early loading asymmetries.


## ACKNOWLEDGEMENTS

NIH R01-HD087459; NASA 80NSSC20M0045


## REFERENCES


[1] Barenius, B et al., *Am J Sports Med*, 42:1049-1057, 2014.
[2] Culvenor, AG et al., *Br J Sports Med*, 47:66-70, 2013.
[3] Wellsandt, E et al., *A J Sports Med*, 44:143-151, 2016.
[4] Buchanan, TS et al., *J Appl Biomech*, 20:367-395, 2004.
[5] Manal, K et al., *J Biomech Eng*, 135:1-7, 2013.
[6] Yamaguchi, GT et al., *J Biomech*, 22:1-10, 1989.
[7] Shelburne, KB et al., *J Biomech*, 30:163-176, 1997.
[8] Sritharan, P et al., *Am J Sports Med*, 48:1711-1719, 2020.
[9] Davis-Wilson, HC et al., *Med Sci Sports Exerc*, 52:785-794, 2020.
[10] Zarzucki, R et al., *J Orthop Sports Phys Ther*, 48:968-973, 2018.
[11] Vincent, TL et al., *J Physiol*, 597:1271-1281, 2019.

# THE EFFECTS OF NEGATIVE PERIOCULAR PRESSURE ON BIOMECHANICS OF THE OPTIC NERVE HEAD AND CORNEA: A COMPUTATIONAL MODELING STUDY

**B. N. Safa (1), J. P. Berdahl, MD (2), C. R. Ethier (1)**

(1) Wallace H. Coulter Department of Biomedical Engineering, Georgia Institute of Technology/Emory University, Atlanta, GA, USA
(2) Vance Thompson Vision, Sioux Falls, SD, USA

## INTRODUCTION

Glaucoma is the leading cause of irreversible blindness worldwide, and elevation of intraocular pressure (IOP) is the most prominent risk factor for this disease. Clinical treatment of glaucoma seeks to slow or stop vision loss by decreasing IOP using medications, medical devices, and/or surgical procedures. The Multi-Pressure Dial system (MPD; Equinox Ophthalmic) is a medical device that lowers IOP non-invasively [1]. It consists of a pair of goggles connected to a programmable vacuum pump that delivers a negative periocular pressure (NPP), which results in increased ocular globe volume and concurrent IOP reduction. Despite experimental data [1] and lumped biomechanical analysis [2], there is no information about the effects of NPP on optic nerve head (ONH) and corneal biomechanics. Our objective was to evaluate the biomechanical effects of NPP on the ONH and cornea via finite element (FE) modeling.

## METHODS

*Geometry and FE mesh:* We generated a 3D axisymmetric (wedge) model of the eye (Figure 1) based on existing FE models and dimensions of the human eye [3]–[6]. Two planes containing the axis of symmetry bounded the wedge: the *y*-*z* plane, and an obliquely oriented plane having a 3º dihedral angle relative to the *y*-*z* plane. Key dimensions included: axial length = 24 mm; corneal radius = 7.8 mm; scleral radius = 11 mm; and thicknesses of cornea, sclera, retina and lamina cribrosa (LC) = 0.56 mm, 0.8 mm, 0.2 mm, and c. 0.2 mm, respectively. We modeled the extraocular muscles as a rigid body at the superior aspect of the globe. The geometry was meshed with conforming second-order tetrahedral elements (TET10) in Gmsh, and the model was solved in FEBio. The use of high-order elements was necessary to implement incompressible constitutive relations (see below).

*Constitutive modeling:* We modeled the tissues as incompressible neo-Hookean materials (Table 1), with material properties based on literature values [3], [4], [7], [8]. To account for the microarchitecture of the peripapillary sclera (ppSC), we included circumferential (along the x-axis; Figure 1) collagen fibers in the ppSC.

*Boundary conditions:* Nodes on the axis of symmetry were constrained to move along the z-axis. The nodes in the bounding planes of the wedge were constrained to move in-plane, so their displacement was radial relative to the axis of symmetry (Figure 1). The muscle attachment was constrained in all degrees of freedom except displacement along the y-axis ($u_y$), to allow expansion of the ocular globe (Figure 1).

Loads were applied in two configurations, denoted as "Reference" and "Goggle." The Reference configuration describes a normal eye without goggles and corresponded to the following pressures: IOP = 15.8 mmHg, NPP = 0, retrolaminar pressure (RLTP) = 8 mmHg. The Goggle configuration describes the same normal eye with the MPD goggles applied and corresponded to lowered IOP = 11.5 mmHg (based on

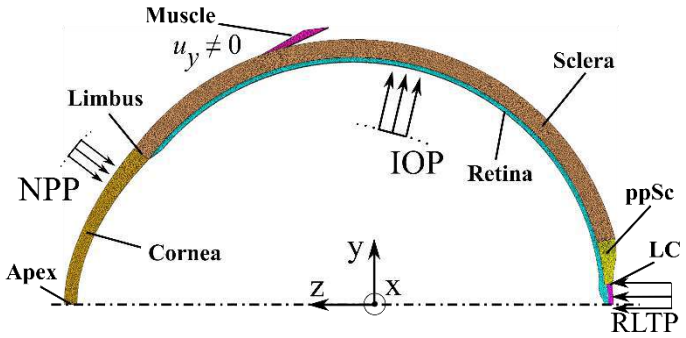


**Figure 1: The axisymmetric finite element model used in this study, showing the different regions of the corneoscleral shell (ppSC=peripapillary sclera; LC=lamina cribrosa), its attachment to extraocular muscle, and the boundary conditions, including intraocular pressure (IOP), negative periocular pressure (NPP), and retrolaminar tissue pressure (RTLP).**

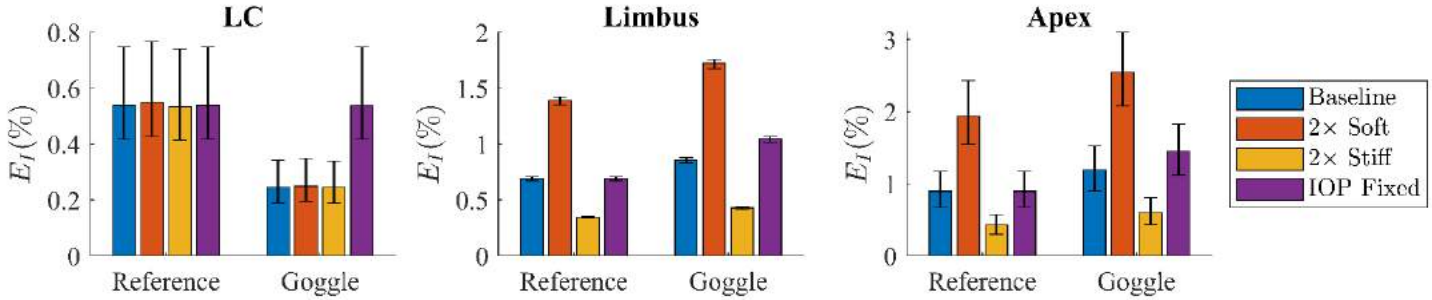


**Figure 2: The results of FE studies showing the volumetric distribution of the first invariant of the Lagrangian strain tensor ($E_1$) in the lamina cribrosa (LC) of the ONH, the limbus, and the apex of the cornea. The data are shown as median and interquartile range (IQR) within the region of interest. Note differing vertical axis scales between graphs**

experimental data [1]), NPP = -7.9 mmHg, and unchanged RLTP. For both configurations, IOP was uniformly applied on the interior surface of the corneoscleral shell, while the NPP was applied uniformly from the corneal apex to ~2.5 mm posterior to the limbus and then decreased linearly to zero near the edge of the ppSC.

*Model validation:* We computed the compliance of the corneoscleral shell as $C$ = d(IOV)/d(IOP) in the Reference configuration, where d(IOV) is the change in intraocular volume, i.e., the volume enclosed within the corneoscleral shell (Figure 1), in response to a change in IOP, d(IOP). The computed value of $C$ was compared to experimental data [9].

*Sensitivity studies and data analysis:* We denote the above FE model as the "Baseline case." We also considered the effects of changing material parameters and loads. Specifically, we evaluated the sensitivity of our results to material parameter values by changing the corneoscleral shell stiffness: we multiplied the sclera, ppSC matrix, and cornea stiffness by a factor of ½ ("2X Soft"), or 2 ("2X Stiff"). Finally, we also investigated the effects of scleral expansion alone by imposing NPP while holding IOP unchanged ("IOP fixed").

Our primary outcome measures were the volumetric median and interquartile range (IQR) of the nodal first principal Lagrangian strain ($E_1$) within the corneal apex (cornea nodes with $y$ = 0), limbus (nodes shared by cornea and sclera), and LC regions (Figure 1).

## RESULTS

*Model validation:* The compliance of the FE model was 3.1 µL/mmHg, which falls within the reported range of values for human eyes of 1.4-3.9 µL/mmHg [9].

*Baseline case*: NPP caused the median $E_1$ in the LC to decrease by 54.5%, from 0.54% [0.42%, 0.75%] (median [IQR]) to 0.25% [0.19%, 0.34%] (Figure 2). Conversely, $E_1$ in the limbus increased by 23.7%, from 0.69% [0.67%, 0.71%] to 0.86% [0.83%, 0.88%], and at the corneal apex by 33.1%, from 0.90% [0.66%, 1.17%] to 1.19% [0.91%, 1.52%].

*2X Soft and 2X Stiff cases:* LC strains were similarly decreased between the Baseline and the 2X Soft/Stiff cases. However, compared to the Baseline case, the strains at the corneal apex and limbus doubled in the 2X Soft case and halved for the 2X Stiff case (Figure 2).

*IOP fixed case:* NPP had a minimal effect on $E_1$ in the LC (-0.1% decrease) but increased limbal (51.2%) and corneal apex (61.5%) strains.

**Table 1: Summary of material parameter values (Baseline). The sclera and ppSC matrix stiffnesses were increased compared to literature values to match experimental ocular compliance.**

| Tissue | E (MPa) | Reference |
|---|---|---|
| Sclera | 4.50 | 1.5× Sigal *et al.* 2005 |
| ppSC matrix | 4.50 | 1.5× Sigal *et al.* 2005 |
| ppSC fiber | 41.83 | Grytz *et al.* 2014 |
| LC | 0.30 | Sigal *et al.* 2005 |
| Retina | 0.06 | Feola *et al.* 2016 |
| Cornea | 0.84 | Blacken *et al.* 2019 |
| Muscle | rigid | - |

## DISCUSSION

This study showed that negative periocular pressure (NPP) decreases strain on the ONH while increasing it on the cornea. The reduction of ONH strain is predicted to be beneficial for glaucoma patients. The predicted corneal straining was small and thus potentially benign (<1% strain; Figure 2).

The observed ONH strain lowering was slightly surprising, since increased globe volume due to NPP could be expected to increase ONH strain. However, this effect was outweighed by the effects of lowered IOP due to NPP. In fact, increased globe volume due to NPP occurred primarily in the anterior eye (data not shown) while the magnitude of scleral stretching in the ppSC region was small, which explains why changes in scleral stiffness did not affect ONH strains. To further understand this effect, it would be of interest to evaluate different boundary conditions to model the effects of the extraocular muscles, as well as different distributions of NPP.

A potential limitation of this study was the assumption that the IOP decrease due to NPP was unaffected by corneoscleral stiffness. In reality, we expect that corneoscleral stiffness will affect the magnitude of the IOP decrease; thus, as a future direction, it would also be worth extending the model to include blood flow and fluid-solid interactions [2].

In conclusion, this study provides novel insights into the biomechanical effects of NPP on the ONH and cornea. We showed that NPP decreases the deformation of key ONH tissues by reducing IOP while slightly straining the cornea and limbus. On balance, this suggests potential benefits of MPD for glaucoma patients.

## ACKNOWLEDGEMENTS

We acknowledge financial support from the Georgia Research Alliance (CRE). CRE has acted as a consultant to Equinox Ophthalmic, the developer of the MPD system. JPB is the founder/CEO of Equinox Ophthalmic and holds IP related to the MPD system.

## REFERENCES

[1] Swan *et al.*, *Transl Vis Sci Technol*, 9: 19, 2020.
[2] Ethier *et al.*, *Exp Eye Res*, 191: 107928, 2020.
[3] Sigal *et al.*, *Investigative Ophthalmology and Visual Science*, 46: 4189–4199, 2005.
[4] Feola *et al.*, *Investigative Ophthalmology & Visual Science*, 57: 1901–1911, 2016.
[5] Medeiros *et al.*, *Am J Ophthalmol*, 135: 131–137, 2003.
[6] Woo *et al.*, *Ann Biomed Eng*, 1: 87–98, 1972.
[7] Grytz *et al.*, *Journal of the Mechanical Behavior of Biomedical Materials*, 29: 602–617, 2014.
[8] Blackburn *et al.*, *Front Bioeng Biotechnol*, 7: 66, 2019.
[9] McEwen and Helen, *OPH*, 150: 321–346, 1965.

SB³C2022
Summer Biomechanics, Bioengineering and Biotransport Conference
June 20-23, Eastern Shore, MD, USA

# BIOHEAT TRANSFER BASIS OF HUMAN THERMOREGULATION:

# PRINCIPLES AND APPLICATIONS

**Laura H. Namisnak (1), Shahab Haghayegh (1,2), Sepideh Khoshnevis (1), Kenneth R. Diller (1)**

(1) Biomedical Engineering Department, University of Texas, Austin, TX, USA
(2) T.H. Chan School of Public Health, Harvard Medical School, Boston, MA, USA

## INTRODUCTION

Thermoregulation is a process that is essential to the maintenance of life for all warm-blooded mammalian and avian species. It sustains a stable core body temperature in the face of a wide array of environmental thermal conditions and intensity of physical activities that generate internal heat. A primary component of thermoregulatory function is the movement of heat between the body core and the surface via the circulation of blood. The peripheral vasculature acts as a forced convection heat exchanger between blood and local peripheral tissues throughout the body enabling heat to be conveyed to the skin surface where it may be transferred to and from the environment via conduction, convection, radiation, and/or evaporation of water as local conditions dictate. Humans have evolved a particular vascular structure in glabrous (hairless) skin that is especially well suited for heat exchange. These vessels are called arteriovenous anastomoses (AVAs) and can vasodilate to large diameters and accommodate high blood flow rates. We report herein a new technology based on a physiological principle that enables simple and safe access to the thermoregulatory control system to allow manipulation of thermoregulatory function via glabrous skin blood flow (GSBF) to AVAs. The technology operates by applying a small amount of local heating to control tissue on the body surface overlying the cerebral spine that upregulates AVA perfusion. This technology is called Selective Thermal Stimulation (STS). During STS heat exchangers can be applied to glabrous skin, preferably on the palms and soles, to alter the temperature of elevated blood flow prior to its return to the core, resulting in the ability to manipulate the internal body temperature on demand.

## METHODS

An important application of STS involves enhancing the onset and quality of sleep. The human thermoregulatory system operates on a circadian cycle in coordination with sleep. Physiological sleep data show that as late hours in the circadian cycle approach, there is a significant upregulation in GSBF, opening the primary heat exchange portal from the warmer core to the (usually) cooler environment. A subsequent drop in core temperature occurs via enhanced convection of blood to glabrous skin, facilitating the loss of core heat to the environment, with a time constant on the order of 2–3 h, and with sleep onset following thereafter in an additional 0.5 h. Absence of the normal nocturnal decline in core temperature by approximately 1°C can be associated with sleep-onset insomnia.

Another important benefit of AVA vasodilation during sleep is that the diminished terminal vascular resistance to blood flow results in a reduced sleep-time blood pressure that is increasingly recognized as protective against risk of cardiovascular diseases and major organ (kidney, eye, etc.) pathology [1]. An overnight dip in blood pressure has been identified as a significant contributing factor in lowering the occurrence of cardiovascular-derived events by as much as 40% or more, even when daytime blood pressure is elevated (hypertensive).

STS intervention was evaluated on a male subject who typically experiences difficulty falling asleep after going to bed and entering a productive sleep state. Two nights of data were acquired with continuous monitoring of GSBF on the foot sole via a laser Doppler perfusion probe, of core temperature via a sublingual thermocouple, and of mean arterial pressure via a pulse transit time monitor. STS was produced with a heated pillow maintained at 39°C for 30 minutes, after which it was turned off. The male subject was clothed in shorts and a tee shirt.

In another study STS intervention was also measured for being able to delay the onset of AVA vasoconstriction during body cooling by lowering the mean skin temperature with a water circulation suit. Four subjects underwent two trials each, with and without STS applied. The trial protocol consisted of an initial passive baseline period followed by lowering the suit water temperature to the point where there was no further vasoconstriction for the subject on that particular day. Next the suit water temperature was adjusted to 40°C and held for 30 min to

allow subjects to reach their personal maximum level of vasodilation on the trial day. If the experiment included STS, after the initial 15 min of warming a resistance heater was set to hold a temperature of 40°C on the skin surface overlying the cervical region of the spine. The STS heater remained energized for the duration of the experiment. Following 30 total minutes of warming, water bath temperature was decreased at 1°C/min until a state of maximum vasoconstriction was observed for 5 min. Each of our subjects underwent control and STS trials separated by at least 7 days.

## RESULTS

The results of the sleep study are shown in Fig. 1 with STS producing an immediate increase in GSBF (a), drop in core body temperature (b), and dip in MAP (c). Fig. 2 shows that STS enables maintenance of GSBF to substantially lower skin temperatures during body cooling. Heat exchangers may be applied to the palms and soles to add heat to blood circulating back to the core to facilitate the body's ability to defend against the dangerous perioperative hypothermia.

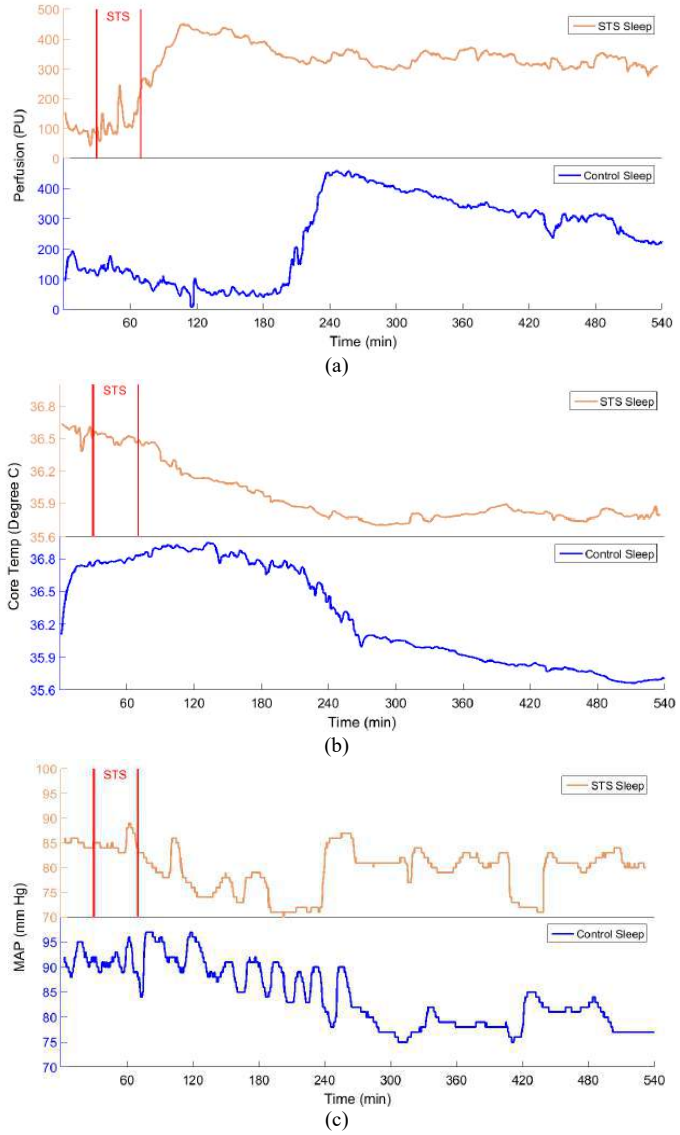


**Figure 1. Overnight physiological data measured on a subject who slept one control night without using (STS) (*lower blue plots*) and one night with STS applied for 30 min at bedtime (*upper orange plots*). (*a*) Blood flow to glabrous skin of the foot measured from an initial 20-min baseline period. (*b*) Core temperature measured with a sublingual probe. (*c*) Mean arterial blood pressure (MAP).**

## DISCUSSION

In Fig. 1, GSBF is induced by STS three hours earlier than in its absence, leading to more effective sleep onset. Simultaneously, the enhanced convective heat loss by greater blood flow to glabrous skin from the core directly produces an immediate decline in core temperature that is required for healthy sleep. Finally, STS induced vasodilation of AVAs reduces the systemic vascular resistance resulting in a healthy overnight dip in MAP and its associated health benefits.

During skin temperature cooling, for all 4 subjects GSBF was maintained with STS to a lower temperature by 2 - 4°C, meaning that STS will enable heat to be transported by blood flow to the core under conditions for which it would otherwise not be possible, thereby defending against the occurrence of perioperative hypothermia.

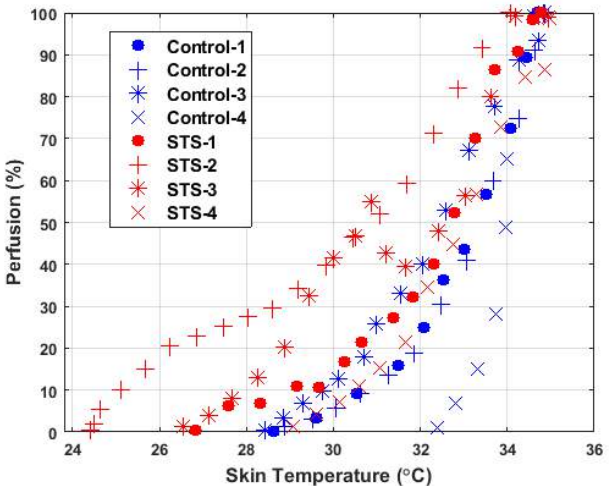


**Fig. 2. GSBF plotted as a function of mean skin temperature during active cooling induced vasoconstriction with and without STS applied. 0% and 100% perfusion represent the range of minimum and maximum perfusion values for individual subjects.**


## ACKNOWLEDGEMENTS

This research was sponsored in part by Small Business Technology Transfer (STTR) grant 2R42GM119871 awarded to Mercury Biomed, LLC (Cleveland, OH) and subcontracted to The University of Texas at Austin, and by the Robert and Prudie Leibrock Professorship in Engineering at the University of Texas at Austin. Kenneth Diller has an equity position in Mercury Biomedical, LLC, a corporation that holds a license from the University of Texas for STS technology. Dr. Diller has never received any direct financial compensation from Mercury Biomedical. Patents have been filed by The University of Texas for technologies described herein. The intellectual property is owned by The University of Texas, and all co-authors are co-inventors.

A complete version of this paper appears in the Journal of Heat Transfer in the Cravalho Memorial issue [2].


## REFERENCES


[1] Hermida, R.C., et al., *Euro Heart J,* 39(47):4159-4171, 2018.
[2] Namisnak, L, et al., *J Heat Trans*, 144(3):031203, 2022.

SB³C2022
Summer Biomechanics, Bioengineering and Biotransport Conference
June 20-23, Eastern Shore, MD, USA

# MATHEMATICAL MODEL FOR COMBINED EFFECTS OF HEAT TRANSFER AND PRESSURE IN CAUSING SOFT TISSUE INJURY

**Gary L. McGregor (1), Bruno V. Rego (2), Kenneth R. Diller (1)**

(1) Biomedical Engineering Department, University of Texas, Austin, TX, USA
(2) Department of Biomedical Engineering, Yale University, New Haven, CT, USA

## INTRODUCTION

Pressure and thermal injuries affect millions of lives every year. Typically, each injury mechanism is studied in isolation due to differences in the primary factors causing the trauma. The confluence of applied tissue deformation, inflammation, and ischemia combine over time to cause mechanically derived injury, whereas high or low-temperatures are independent causative factors for thermal injuries. Modeling and simulation analyses have been used to develop an understanding of both types of injury pathways to predict threshold conditions for the onset of damage and to develop methods of prevention. Although thermal and mechanical injury processes are often viewed separately, prior experiments have demonstrated that these two phenomena may have active cross-coupling. Temperature can act as prophylactic or accelerant to pressure injuries, depending on its magnitude, to radically alter the outcome. Our objective is to develop a finite element model to predict injury as a combined function of applied temperature and pressure, local blood perfusion and time. The model uses constitutive terms derived from experimental data that are relevant to physiological processes that govern injury occurrence.

In the mid-1990's Iaizzo, et al. conducted a well-designed large-scale study on a porcine model to investigate the relationship between temperature, mechanical loading, and time to graded injury causation [1,2]. The study covered six temperatures from 25–50°C, four pressures from 10-150 mm Hg, and three exposure times up to 10 hours at 840 sites in 70 animals. Injury was graded at three levels of severity at four tissue depths: epidermis, dermis, subcutaneous fat, and muscle. It stands as the largest and most comprehensive study of its kind, and (to the authors' knowledge) it has not been replicated since. The results document how temperature can modulate pressure ulcers (PU's) in view of the complex coupled relationship between temperature and pressure in injury causation. The study also showed that lowered temperature is prophylactic against mechanical loading injury. Conversely, elevated temperature may act as an accelerant to mechanical loading in PU formation. An ancillary observation of the study was that elevated local pressure increased the rate by which burns occurred. More recently Gefen and colleagues [3] have conducted an extensive series of experimental and modeling studies into the formation of PU's. This body of work has provided valuable guidance for the current research on pressure/temperature coupling in soft tissue injury etiology.

## METHODS

Even though the Iazzo data set embodied a large matrix of measurements, the actual density of the data was sparse, particularly for assessment of wound severity. Thus, our initial work was to fit a mathematical function to the data set to enable smooth interpolation for each independent variable to create a continuous set of injury outcomes. The model was formulated to include thermal and elastic stress distributions, local blood perfusion, and the kinetics of injury formation. Details of the models are published in a companion paper [4].

The evolution of cell viability (injury) over time was described using temperature and blood perfusion as quantitative predictors, with perfusion coupled directly to tissue mechanical stress. The injury model was fit to the survival data directly using least-squares regression based on Cox's proportional hazard model [5]. The baseline viability was represented as a Weibull distribution. Injury coefficients were determined by optimal fitting to the experimental data using the methodology described in [4].

## RESULTS

The model was applied to simulate the combined action of applied temperature, blood perfusion normalized from 100% at no applied pressure, to 0% for pressure in excess of the mean arterial pressure, and exposure time up to 10 hours. A three-dimensional representation of a simulation of the progressive loss of cell viability in a representative tissue system is shown in Fig. 2.

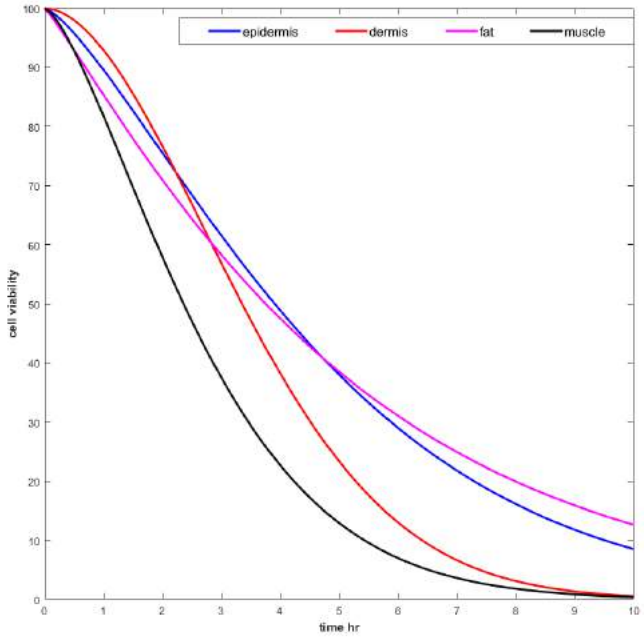


**Fig. 1. Predicted temporal cell viability in epidermis, dermis, fat and muscle for surface exposure to 40°C and 100 mmHg.**

Injury develops most rapidly in the superficial epidermis and dermis under the action of heat diffusion from the surface. Pressure is transmitted much more rapidly than heat diffusion deep into the tissue, but the kinetics of the development of pressure derived injury are slower resulting in a longer time constant to manifestation.

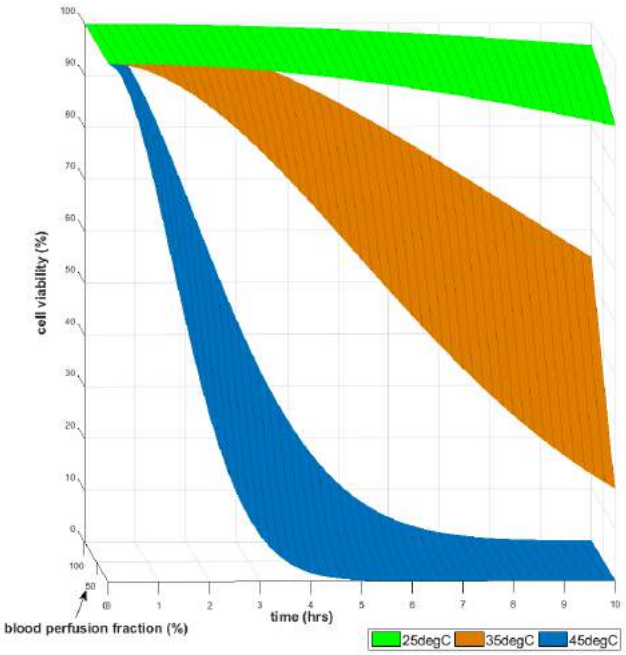


**Fig. 2. Injury model simulation of the combined effects of applied pressure and temperature over time in reducing viability of a representative cell line. Time and pressure effects are continuous plots at three incremental temperatures of 25°C, 35°C, and 45°C.**

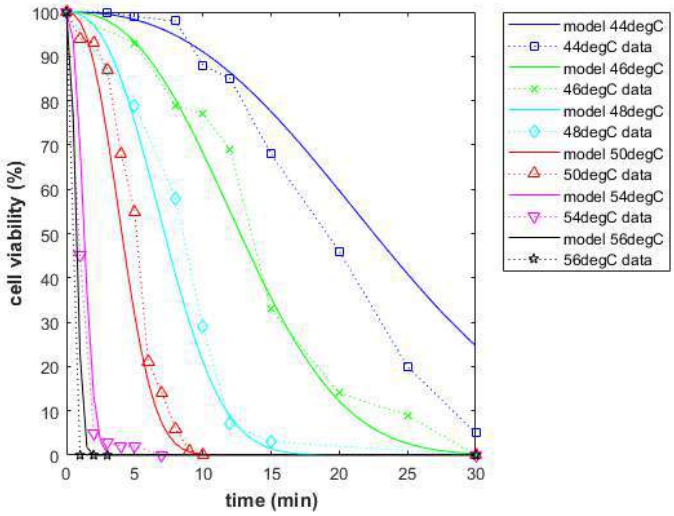


**Fig. 3. Comparison of the present injury model (continuous lines) with experimental data (symbols) for loss of viability during continuous heating of prostate cancer PC3 cells over the temperature range between 44 and 58°C [6]. The regression between the model and the data of $R^2 = 0.95$ demonstrates an effective capability for predicting thermal injury even in the range of low temperatures and long exposure times for which a traditional Arrhenius model has limited accuracy [7]**

## DISCUSSION

The differential influences of temperature and pressure in injury causation are seen in Fig. 1 as noted. Pressure dominates at greater depths, and temperature more superficially. Fig. 2 demonstrates the strong coupling between temperature and pressure in causing injury. Lower temperature is prophylactic against pressure injury. In contrast, higher temperatures accelerate the action of pressure in producing necrosis. Also, at intermediate pressures injury is less dependent on temperature coupling. The results plotted in Fig. 3 show that the current model can be used for pure thermal injury as well as for when pressure effects are also involved. At the lower temperature range close to the threshold for causing a burn, it is likely that the long exposure times allow enough time for expression of heat shock proteins that diminish the extent of injury, leading to over prediction of injury extent by traditional Arrhenius-based models.

## ACKNOWLEDGEMENTS

This research was sponsored in part by the Robert and Prudie Leibrock Professorship in Engineering at the University of Texas at Austin. We thank the current Iaizzo lab at the University of Minnesota for providing archival data from their original experiments that were crucial in the effort to build and validate our injury model.

## REFERENCES

[1] Iaizzo, P.A., et al., *Clin.Res.Pract*. 7(5):161-169, 1995.
[2] Kokate, J.L., et al., *Wounds*, 9(4):111-121, 1997.
[3] Gefen, A., *EWMA J*, 19(2): 7-13, 2018.
[4] McGregor, G.L., *J Heat Trans*, 144(3):2022.
[5] Cox, D.R., *J Roy Stat Soc, B*, 34(2):187-220, 1972.
[6] Rylander, M.N., et all, *Intl J Hypertherm*, 26(8):748-764, 2010.
[7] Pearce, J.A., *J Biomech Engr*, 137(12):1-7, 2009.

# TRANSCRANIAL BLOOD-BRAIN-TUMOR BARRIER MODULATION FOR ENHANCING DRUG DELIVERY TO GLIOBLASTOMA

**Qi Cai (1), Xiaoqing Li (2), Hejian Xiong (1), Xiaofei Gao (3), Ryan Margolis (2), Monica Giannotta (5), Kenneth Hoyt (2), Robert Bachoo (3,4,6), Zhenpeng Qin (1,2,7,8)**

(1) Department of Mechanical Engineering, University of Texas at Dallas, Richardson, TX, USA
(2) Department of Bioengineering, University of Texas at Dallas, Richardson, TX, USA
(3) Department of Internal Medicine, University of Texas Southwestern Medical Center, Dallas, TX, USA
(4) Harold C. Simmons Comprehensive Cancer Center, University of Texas Southwestern Medical Center, Dallas, TX, USA
(5) FIRC Institute of Molecular Oncology Foundation (IFOM), Milan, Italy
(6) Department of Neurology, University of Texas Southwestern Medical Center, Dallas, TX, USA
(7) Department of Surgery, University of Texas Southwestern Medical Center, Dallas, TX, USA
(8) Center for Advanced Pain Studies, University of Texas at Dallas, Richardson, TX, USA

## INTRODUCTION

Glioblastoma multiforme (GBM) is the most common and aggressive malignant brain tumor in adults. The major obstacle in GBM treatment is the presence of the blood-brain-tumor barrier (BBTB), which displays heterogeneous permeability to circulating drugs [1], and presents as a challenge for drug delivery across this barrier. Over the last decades, approaches for drug delivery to GBM have been investigated, such as convection enhanced delivery, intranasal delivery, intra-arterial delivery, and focused ultrasound with microbubbles. However, they have not yet led to a significant increase in survival for most patients with GBM due to their invasiveness, toxicity, and poor drug delivery efficacy to the brain [2]. Therefore, novel approaches to non-invasively modulate the BBTB for drug delivery are the unmet need in GBM treatment.

Entry of circulating molecules into the brain is strictly limited by the blood-brain barrier (BBB) that includes the endothelial tight-junction (TJ) complex and low rates of transcytosis. To safely and reversibly increase the BBB permeability, we have developed a method that non-invasively modulates the BBB with picosecond laser excitation of TJ-targeted plasmonic gold nanoparticles (AuNPs) [3]. In this approach, AuNPs were conjugated with the antibody BV11 (AuNP-BV11) to target JAM-A, which is a part of the TJ complex. Then the picosecond laser pulse excitation of AuNPs leads to the generation of mechanical wave that perturbs the TJ, and increases the BBB permeability without compromising normal brain function. This method allows the delivery of immunoglobulins, adeno-associated viral vectors, and liposomes to the brain parenchyma.

In this work, we successfully exploited this optical approach to modulate the BBTB (named optoBBTB technique). We demonstrated that optoBBTB can enhance the drug delivery to the tumor, suppress the tumor growth, and increase the survival rate of tumor-bearing mice. Our results also suggested that taxol is a potent anti-cancer drug in GBM treatment, which has not been used in the clinic previously due to its poor penetration ability across the BBB [4]. The optoBBTB paves a new way of drug delivery to treat glioma.

## METHODS

*Glioma model*: 73C glioma cells were used, which were generated in primary astrocyte cultures from neonatal mice and carried conditional mutations for $Pten^{f/f}$, $p53^{f/f}$, and $LSLBraf^{V600E}$. 90 µL of the cell suspension ($2\times10^5$ cells/µL) was transplanted into the left hemisphere of nude mice (Nu/J, stock no.002019, 7 weeks) at 500 µm depth.

*OptoBBTB and drug delivery for glioma treatment*: The molecular targeting nanoparticles AuNP-BV11 were prepared as reported [3]. At 4 days post injection (dpi), the glioma-bearing mice were randomly divided into 4 groups with 5 mice in each group: (1) vehicle control, (2) free taxol control, (3) optoBBTB+vehicle, and (4) optoBBTB+taxol. Specifically, taxol was dissolved in a vehicle of Cremophor EL: absolute ethanol (1:1 v/v) to 6 mg/mL and then diluted to 2 mg/mL with saline. To modulate the BBTB, 37 µg/g of the AuNP-BV11 was administrated by intravenous (i.v.) injection into the tumor-bearing mouse. 1 hour later, the mice were received either vehicle or taxol via i.v. injection. Then the mice received picosecond-laser excitation (40 $mJ/cm^2$, 1 pulse, pulse duration was 28 ps, and beam size was 6 mm) in the tumor area. The treatment was repeated every 4 days during 4-12 dpi. The tumor size was measured by 3T-MRI (T2-Weighted scan) at 3 and 15 dpi. To obtain the survival rate, similar treatment groups were used with 7 mice in each group.

## RESULTS

*Characterization and optimization of optoBBTB:* To modulate the BBTB in 73C glioma model, we i.v. injected AuNP-BV11, followed by applying a transcranial picosecond laser pulse after 1 hour. We then i.v. injected a fluorescent dye (Evans blue) to visualize the increase in BBTB permeability (Figure 1a). AuNP-BV11 was exploited in this study because it preferentially targeted the tumor area, as it showed doubled accumulation in the tumor than in the normal brain tissue as analyzed by ICP-MS (Figure 1b). By using laser fluence of 40 mJ/cm$^2$, the BBTB permeability can be successfully increased after single pulse laser excitation, indicated by the Evans blue extravasation from blood vessel to the brain parenchyma (Figure 1c).

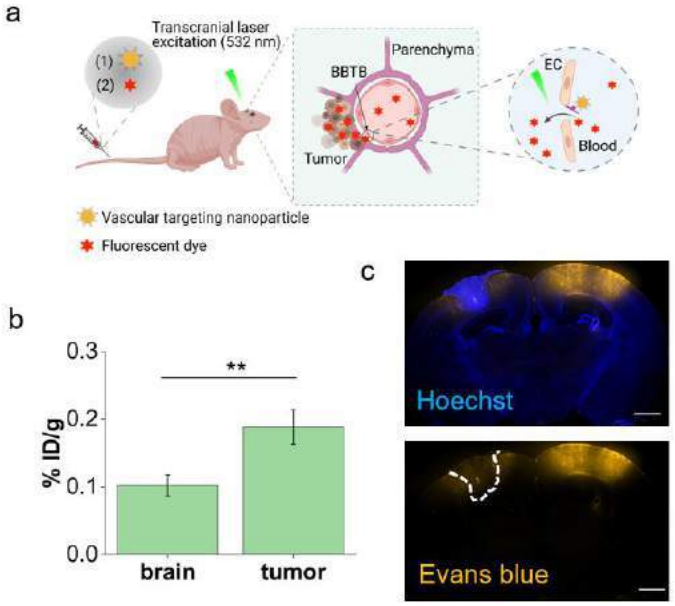


**Figure 1: Characterization and optimization of optoBBTB in 73c glioma model. (**a) Schematic illustration of optoBBTB. (b) The analysis of AuNP-BV11 accumulation in 73C tumor bearing mice. Student's t-test, n=3 mice, ** p<0.01. (c) Optimization of optoBBTB. Scale bar represents 1 mm.

We next investigated the feasibility of using optoBBTB to deliver anti-cancer drug taxol for 73C glioma treatment. We showed that optoBBTB enhanced the delivery of fluorescent taxol into the tumor core and margin, while it could not cross the intact BBTB at the early tumor stage (Figure 2a). The combination of optoBBTB and taxol showed great potential in 73C glioma treatment, and the tumor growth was suppressed significantly after 3 treatments (Figure 2b). The result was further supported by the significantly decreased tumor volume (i.e., 100 mm$^3$ in the control groups and 40 mm$^3$ in the optoBBTB+taxol group) measured by MRI (Figure 2c). More importantly, we also observed that optoBBTB and taxol increased the survival rate of the tumor-bearing mice, and the median survival time was increased from 16 to 24 days (Figure 2d).

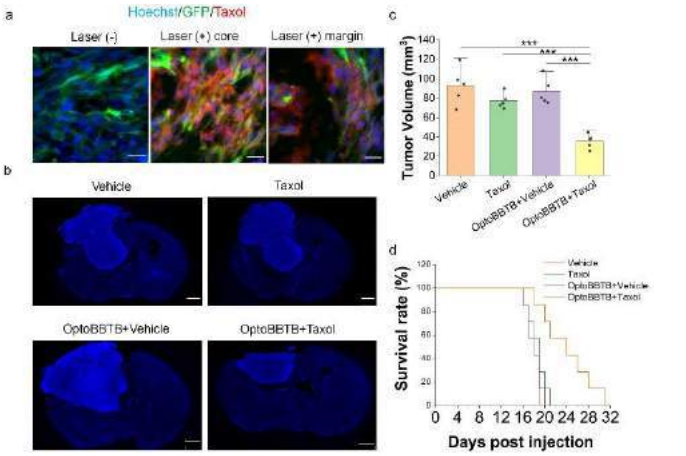


**Figure 2: Evaluation of optoBBTB for 73C brain tumor treatment.** (a) OptoBBTB facilitated the delivery of fluorescent taxol to the tumor. Scale bar represents 20 μm. (b) Tumor size indicated by fluorescent imaging at 15 dpi using Hoechst staining. Scale bar represents 1mm. (c) The analysis of tumor volume at 15 dpi. One way Anova, ***p<0.001, n=5 mice in each group. (d) Kaplan-Meier survival analysis, n=7 mice in each group.

## DISCUSSION

The standard of care for GBM is maximal safe resection followed by radiation and chemotherapy. However, since gliomas infiltrate into surrounding healthy brain tissue, unresected tumor margin is the primary cause of recurrence. Moreover, since the BBTB remains intact at the tumor margin, the chemotherapy drug concentration is much lower within the tumor margin than at the tumor core [5]. Therefore, GBM always results in poor patient prognosis, and there is an imperative need for the development of novel, targeted, and effective therapies for GBM.

This study shows that the BBTB permeability can be non-invasively enhanced using picosecond laser excitation of TJ-targeted AuNPs, which enjoys high spatial resolution. We demonstrated that, taxol, which has not been used in clinical due to its incapability of crossing the BBTB, could be delivered to tumor core and margin using optoBBTB technique, and it is actually a potent anti-cancer drug for glioma treatment. By using the combination of optoBBTB and taxol, the growth of 73C glioma can be significantly suppressed, and the median survival rate of the tumor bearing mice was increased by 50%. Therefore, optoBBTB is a novel, non-invasive and effective approach to increase local drug concentration for glioma treatment.

Future work will be focused on optimizing the optoBBTB modulation efficacy by using tumor specific targets, and test the optoBBTB in other infiltrative brain tumor models.

## ACKNOWLEDGEMENTS

This research was supported in part by award RP180670 from the Cancer Prevention and Research Institute of Texas (CPRIT) to establish the Small Animal Imaging Facility at the University of Texas at Dallas. This research was funded CPRIT grants RP190278 to Z.Q.

## REFERENCES

[1] Arvanitis, C et al., *Nature Reviews Cancer*, 20:26-41, 2020.
[2] Haumann, R et al. *CNS Drugs*, 34, 1121-1131, 2020.
[3] Li, X et al., *Nano Lett*, 21, 9805-9815, 2021.
[4] Zhang, D et al., *Clin Cancer Res*, 26, 477-486, 2020.
[5] Mainprize, T et al.,. *Sci Rep*, 9:321, 2019.

# PLASMONIC LAMP: HIGHLY SPECIFIC AND SENSITIVE DETECTION OF SARS-COV-2 BY PLASMONIC SENSING OF ISOTHERMALLY AMPLIFIED NUCLEIC ACIDS

**Haihang Ye (1), Chance Nowak (2,3), Yaning Liu (1), Yi Li (2,4), Tingting Zhang (1), Leonidas Bleris (2,3,4), Zhenpeng Qin (1,4,5,6)**

(1) Department of Mechanical Engineering, The University of Texas at Dallas, Richardson, TX, USA
(2) Center of Systems Biology, The University of Texas at Dallas, Richardson, TX, USA
(3) Department of Biological Sciences, The University of Texas at Dallas, Richardson, TX, USA
(4) Department of Bioengineering, The University of Texas at Dallas, Richardson, TX, USA
(5) Center for Advanced Pain Studies, The University of Texas at Dallas, Richardson, TX, USA
(6) Department of Surgery, University of Texas Southwestern Medical Center, Dallas, TX, USA

## INTRODUCTION

Loop-mediated isothermal amplification (LAMP) has emerged as an alternative to polymerase chain reaction and allow point-of-care testing without the need for thermal cycling.[1] Although simple, LAMP is susceptible to non-template amplification and its simple readout (e.g., based on pH change) cannot distinguish template versus non-templated amplification, resulting in false-positive results. Methods that mitigate this issue rely on the utilities of molecular beacons, strand displacement probes, and clustered regularly interspaced short palindromic repeats diagnostic methods. They provide additional sequence identification for improved specificity, however, extensive expertise in molecule design (i.e., primers and probes) is required to identify LAMP amplicons. Motivated by this challenge, we have developed an approach, termed as plasmonic LAMP, that utilizes oligonucleotide-labeled gold and silver (Au-Ag) nanoshells as plasmonic sensors and presents color change upon detecting amended amplicons via DNA hybridization (**Figure 1**).[2] Importantly, the detection specificity and sensitivity of plasmonic LAMP is significantly improved over commercially available LAMP kit and allows virus diagnosis at its early representation.

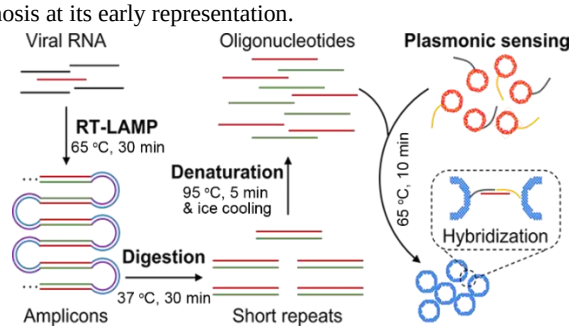


**Figure 1: Schematic illustration of the major steps for the proposed plasmonic LAMP single-molecule RNA detection.**

## METHODS

*Preparation of plasmonic nanoparticles.* In brief, ~50 nm gold-silver (Au-Ag) nanoshells were prepared via galvanic replacement reaction, where Ag templates were mixed with sodium citrate in deionized water and preheated at 95 °C, followed by the injection of $HAuCl_4$ solution using a syringe pump. The products were washed and collected by centrifuge and finally re-dispersed in water.

*RNA detection by plasmonic LAMP.* In brief, RNA sample was mixed with RT-LAMP master mix containing Warm Start RT-LAMP mix and primers for RT-LAMP reaction. The products were then subjected to restriction endonuclease digestion by HincII and EaeI and heat denaturation to form single-strand DNA for the plasmonic sensing using a set of Au-Ag shells-based probes.

## RESULTS

Due to the presence of sodium citrate in the reaction, the as-prepared Au-Ag nanoshells show thick and solid walls on the surface and a hollow interior (**Figure 2A**). In contrast, the absence of sodium citrate led to the formation of thin and porous Au-Ag nanocages. The energy-dispersive X-ray (EDX) mapping of an individual Au-Ag shell shows that the Au and Ag elements are distributed across the entire particle (**Figure 2B**) and thus confirms the alloyed structure, which is expected to improve the corrosion resistance of Au-Ag nanoshells. More importantly, the extinction peak of Au-Ag shells shows restricted shift from 392 nm to 530 nm (**Figure 2C**), while that of cages shifts to longer near-infrared wavelength (**Figure 2D**). To understand the optical change for the Au-Ag shells, we performed the simulation using boundary element method (BEM). The simulation result reveals that the formation of thick and solid walls during the shell growth is the key for the limited peak shift (**Figure 2E**). In addition, we found that the Au-Ag shells show a similar peak position at visible wavelengths and 4-times higher peak extinction over 50 nm Au counterparts at the same particle concentration.

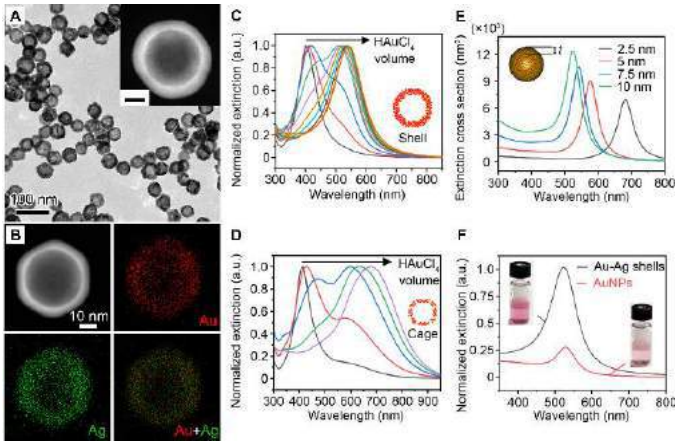


**Figure 2. Structural characterization and optical properties of Au-Ag nanoshells.** (A, B) Morphological and elemental analyses of Au-Ag shells. Scale bars in insets are 10 nm. (C, D) Spectral monitoring during the growth of Au-Ag shells and cages. (E) BEM simulation of Au-Ag shells. (D) Comparison of optical property between Au-Ag shell and AuNPs.

For the plasmonic LAMP, we first carried out the RT-LAMP (65 ºC, 30 min) for the amplicon production. The agarose gel image confirms the successful LAMP amplification in the presence of target SARS-CoV-2 RNA (red box of **Figure 3A**). The amplicon was then subjected to restriction endonuclease digestion by HincII and EaeI (37 ºC, 30 min), which recognize and cleave the conserved regions GTY/RAC and Y/GGCCR sites, respectively. As a result, the gel image (blue box of **Figure 3A**) reveals clean bands located below 200 base-pair (BP) length, confirming the effective and uniform digestion. Next, the reaction product was denatured into single-strand DNA (ssDNA) by heating to 95°C for 5 min and cooling on ice (2 min), followed by mixing with a set of shells-based probes and incubated at 65 ºC for 10 min or room temperature for 30 min. **Figure 3B** shows corresponding LSPR extinction spectra normalized at 537 nm. A linear relationship ($R^2$=0.99) was observed covering 3 logs from 1 to 1,000 copies/μL (**Figure 3C**). The limit of detection (LOD) was determined to be 1.3 copy/μL or 10 copies per reaction equivalent.

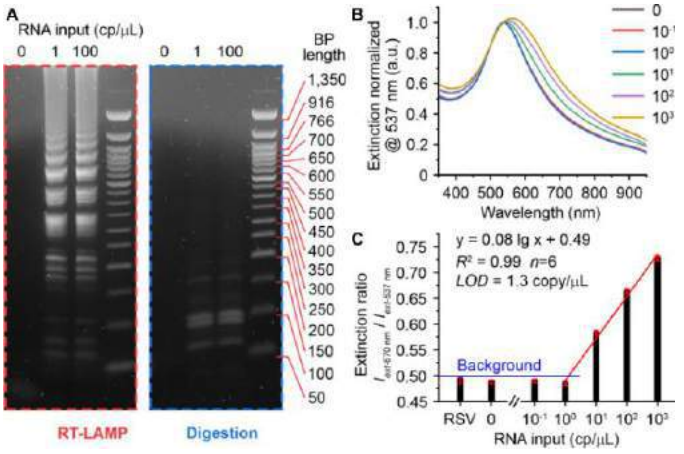


**Figure 3. Plasmonic LAMP for SARS-CoV-2 RNA detection.** (A) Gel images showing the LAMP amplicons before and after enzyme digestion at different RNA inputs. (B) SARS-CoV-2 RNA detection results recorded by spectral measurements. (C) Spectral analysis of the detection results by plasmonic LAMP.

## DISCUSSION

The plasmonic LAMP has two key features. First, it represents a significant step forward in sensor innovation with materials advances. Previous efforts in developing colorimetric plasmonic sensors mainly focused on Au and Ag nanoparticles (NPs), whereas AuNP has a weak plasmonic response and AgNP is not stable. Promising advances have been made on Au-Ag nanocages, but its near-infrared absorption is not suitable for naked-eye detection. We overcome this challenge by developing Au-Ag nanoshells with plasmonic peaks in the visible wavelengths (500-600 nm) and 4-times higher extinction intensity over AuNPs. Importantly, Au-Ag-shells-based sensors allow ~20 times improvement in the analytical sensitivity for the oligonucleotide detection compared with same-sized AuNPs (data not shown). As a result, the Au-Ag shells have the potential to be a class of highly sensitive plasmonic sensors.

Second, the plasmonic LAMP allows highly sensitive detection of nucleic acids with improved specificity. With restriction enzyme digestion and heat denaturation, the LAMP amplicons can be converted from concatemers into short repeats that are amendable for subsequent hybridization with plasmonic sensors (**Figure 1**). The dual sequence identification of plasmonic LAMP, enabled by the primers and plasmonic sensors, eliminates the contamination from non-template amplification and thus improves the detection specificity and sensitivity. Using SARS-CoV-2 RNA as an example, we demonstrate that the plasmonic LAMP approach detects a single RNA molecule per microliter with colorimetric readouts. Compared with the commercially available colorimetric RT-LAMP kit, the plasmonic LAMP has enhanced detection sensitivity and reduced false results (**Figure 4**).

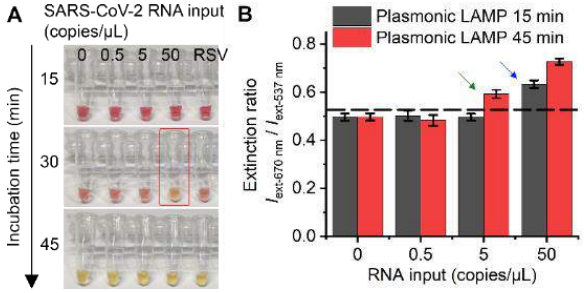


**Figure 4. Comparison of plasmonic LAMP and a commercially available colorimetric LAMP kit for SARS-CoV-2 RNA detection.** (A) Colorimetric LAMP kit. (B) Plasmonic LAMP.

Despite the superior detection performance, plasmonic LAMP suffers from the multistep operation and multiple temperature controls. We aim to optimize the protocol for further improving the detection sensitivity and simplifying the workflow. For example, we may adopt a longer LAMP reaction time to generate more amplicons and thereby detect lower analyte copies. Also, integrating a portable cartridge with pre-stored reagents and a heating dock (similar to the Accula™ SARS-CoV-2 Test, available at https://www.mesabiotech.com/) is a potential way to enable the plasmonic LAMP with a sample-to-answer workflow and a minimal hands-on time.


## ACKNOWLEDGEMENTS

This work was supported partially by NIH grant R01AI151374 (Z.Q.), U.S. DOD grant PR192581 (Z.Q.), NSF grant 1361355 (L.B.), and Cecil H. and Ida Green Endowment (L.B.).


## Reference:


[1] Notomi, T et al., *Nucleic Acids Res*, 28:e63, 2000.
[2] Ye, H et al., *Small*, Accepted, 2022.

SB³C2022
Summer Biomechanics, Bioengineering and Biotransport Conference
June 20-23, Eastern Shore, MD, USA

# PULMONARY ARTERY MECHANICS IN MURINE MODELS OF AGEING

**Abhay B. Ramachandra (1), Edward P. Manning (2,3), Jay D. Humphrey (1,4)**

(1) Department of Biomedical Engineering, Yale University, New Haven, CT, United States
(2) Pulmonary, Critical Care and Sleep Medicine, Yale School of Medicine, New Haven, CT, United States,
(3) VA Connecticut Healthcare System, West Haven, CT, United States
(4) Vascular Biology and Therapeutics Program, Yale University, New Haven, CT, United States

## INTRODUCTION

Ageing is used to describe a broad set of conditions that lead to impaired biologic function and vulnerability to death [1]. It includes changes at cell, tissue and organ levels. Vascular ageing, where changes in vascular cells and structure lead to impaired organ function, is an important aspect of ageing. Vascular ageing is a complex biological process and has multiple aspects to it including cell dysfunction, impaired signaling, stiffening of the blood vessels etc. [1]. With recent advances in mechanobiology, role of mechanics in ageing is being increasingly appreciated. Tissue mechanics influences local cell signaling as well as organ function. Alterations in tissue mechanics can be a cause as well as a consequence of ageing, but understanding this intricate biological process can be a challenge. Murine ageing models can provide more control over data collection and have proved very useful in studying changes to vascular mechanics with ageing. Prior efforts on quantifying vascular mechanics in ageing murine models have focused on systemic arteries [2,3]. Pulmonary artery mechanics remains relatively unexplored. Here, we quantify biaxial mechanics in the pulmonary arteries of three different mouse models of ageing and ascertain common underlying themes to vascular ageing from a mechanics perspective.

## METHODS

We report mechanics for four different groups of male mice – 12-week C57Bl/6J (C57-12wk; n=5) mice serve as controls while Fibulin5 knockout mice (Fib5 KO; n=6, ~ 20 weeks old), deficient in elastin associate glycoprotein fibulin5, serve as an accelerated model of ageing. Progeria mice (HGPS-168d; n=7, ~168days old), homozygous to $Lmna^{G609G/G609G}$, serve as a mouse model of the Hutchinson Gilford Progeria Syndrome (HGPS) – a devastating condition that accelerates many characteristics of aging in humans. Finally, 120-week old C57Bl6/J (n=5; C57-120wk) mice serve as a natural ageing group.

All animal protocols were approved by the Institutional Animal Care and Use Committee of Yale University. Tissue dissection, cleaning, and preparation for biaxial testing is similar to our previous work [4]. Briefly, pulmonary arteries were bluntly dissected out of euthanized and exsanguinated mice. Perivascular tissue and fat were gently cleaned and branch vessels were ligated. The right pulmonary artery, from the main pulmonary bifurcation up to the first branch into the parenchyma, was ligated on custom glass pipettes and mechanically tested using a custom computer-controlled biaxial testing device [5]. Biaxial protocols consisted of three pressure-distension tests at fixed stretches (5% above, 5% below and at *in vivo* stretch) and four axial force-extension tests at fixed pressures (fixed pressures of 5, 15, 25 and 40 mmHg). Pressure and force were measured using standard transducers, diameter was measured using a videoscope and length was controlled using a submicron resolution stepper motor.

Similar to prior work [4], biaxial data was modeled using a pseudo elastic constitutive formulation where vessel mechanical behavior is modeled using four 'Fung-like' exponential families of fibers along axial, circumferential, and two symmetric diagonal directions, and a neo-Hookean term to model elastin contributions. Constitutive parameters were determined from best-fits to experimental data using MATLAB's *lsqnonlin* function. Mechanical metrics of interest (e.g., stress, stiffness and stored energy) were computed at physiologically relevant conditions. A one-way ANOVA a one-way ANOVA with Tukey's post-hoc analysis was used to probe potential statistical differences between groups. A $p$ value less than 0.05 was the threshold for statistical significance.

## RESULTS

We report mechanical metrics of interest at a physiologically relevant, subject-specific axial stretch and a pressure of 25 mmHg. Axial stretch (Figure 1a) was significantly lower in the aged groups compared to control group suggesting a higher collagen to elastin ratio in the wall.

Consistent with this, stored energy (Figure 1b), a measure of energy available in the wall to augment diastolic flow, was significantly lower in the aged groups, with the HGPS-168d having the lowest stored energy. Similarly, circumferential and axial stress (Figure 1c and d) were significantly lower in the aged groups compared to the control. Fib5-KO group had significantly higher stresses (both circumferential and axial) and stored energy than the HGPS-168d groups. Notably, circumferential stiffness was comparable and not significantly different across groups (Figure 1e). Axial stiffness was significantly lower in C57-120wk and HGPS-168d groups (Figure 1f) compared to the control group. There were also significant differences in axial stiffness between Fib5 KO and C57-120wk, and Fib5 KO and HGPS-168d.

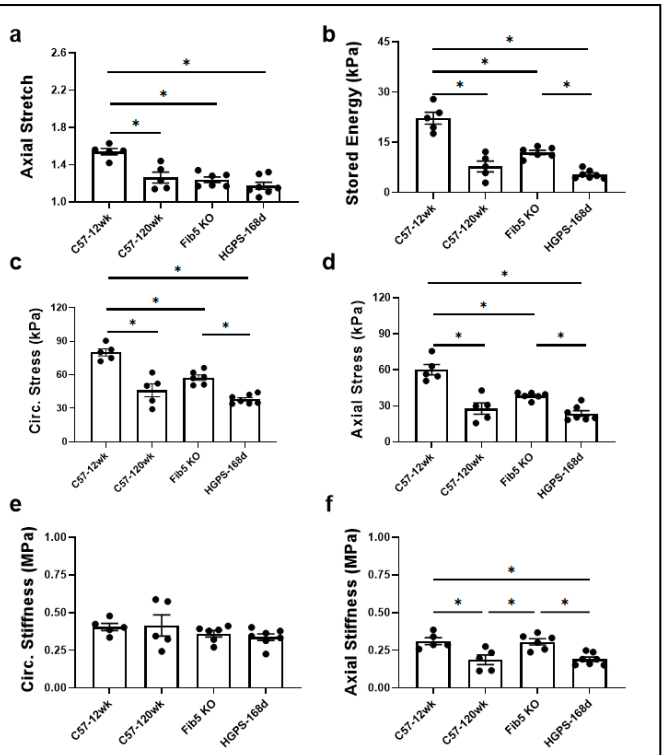


Figure 1 – Axial Stretch (a), Stored Energy (b), Circ. Stress (c) and Stiffness (e), Axial Stress (d) and Stiffness (f) in C57Bl/6J 12 weeks (C57-12wk; control), 120-week (C57-120wk), Fibulin-5 Knock out (Fib5 KO), Hutchinson Gilford Progeria Syndrome 168 days (HGPS-168d) groups. $p<0.05$ is significant (*). Results are reported at specimen-specific *in vivo* stretch and

## DISCUSSION

Murine models cannot phenocopy a human completely. But consistent findings across multiple murine models can yield insights into human health and disease. Here we show that all ageing models are associated with a reduced in vivo axial stretch, axial and circumferential stress and stored energy. Importantly, circumferential stiffness was preserved across multiple ageing models. Indeed, these findings are consistent with prior studies that have looked at ageing in the systemic arteries [2] with the exception of circumferential stiffness, which was significantly lower in the aged aorta of a Fib5-KO. These differences in mechanical metrics may be of relevance to ageing in human pulmonary arteries.

Lower axial in vivo stretch and a reduced stored energy suggest a higher collagen to elastin ratio in the wall. These findings will be confirmed using histology. Future efforts will also be directed towards quantification of lung function using pulmonary function test and cardiac function using echo [6]. This will enable understanding change in vascular mechanics within the context of remodeling in adjacent organs.

Major limitation of this study is only male mice were used. Challenges associated with breeding and maintaining mice up to 120 weeks for C57Bl/6J and 168 days for HGPS mice prevented us from achieving enough number of female mice for statistical tests. We will address this limitation in the future.


## ACKNOWLEDGEMENTS

Authors would like to acknowledge Dr. Sae-il Murtada's help in maintaining the mouse colonies.


## REFERENCES


[1]López-Otin, C. et. al., *Cell*, 153.6:1194-1217,2013
[2] Ferruzzi, J. et.al., *BMMB*, 17.5:1281-1295,2018
[3] Murtada, S-I et. al., *J. RSI*, 17.166,20200066, 2020
[4] Ramachandra &Humphrey, *J. Biomech.*, 84:18-26,2019
[5] Gleason, R. et. al., *J. Biomech.*, 126.6:787-795, 2004
[6] Ramachandra A., et al., *J. Biomech. Eng.*, Accepted, 2022

SB³C2022
Summer Biomechanics, Bioengineering and Biotransport Conference
June 20-23, Eastern Shore, MD, USA

# STATISTICAL SHAPE REPRESENTATION OF ASCENDING THORACIC AORTIC ANEURYSMS: ACCOUNTING FOR MAJOR BRANCHES OF THE AORTIC ARCH

**Hadi Wiputra (1), Shion Matsumoto (2), Jessica E. Wagenseil (3), Alan C. Braverman (4), Victor H. Barocas (1)**

(1) Department of Biomedical Engineering, University of Minnesota, Minneapolis, Minnesota, USA
(2) Department of Biomedical Engineering, University of Michigan, Ann Arbor, Michigan, USA
(3) Department of Mechanical Engineering & Materials Science, Washington University, St. Louis, Missouri, USA
(4) Department of Internal Medicine, Cardiovascular Division, Washington University, St. Louis, Missouri, USA

## INTRODUCTION

Computational methods have gained significant traction in the risk assessment for thoracic aorta aneurysm (TAA)[1]. However, the computational demand of such simulations is high, and there is a relative lack of large datasets to be used for training and testing. Thus, there is considerable interest in reduced-dimension representation of the aorta. Statistical shape models (SSMs) describe the geometry of semantically similar objects to recover morphological features. SSMs have been used previously to model geometric variations in TAA[2], but those SSMs considered only the parent vessel of the thoracic aorta and removed the branching head vessels of the aortic arch[2,3]. Branching flows introduce recirculation regions that could affect the observed wall shear stress and flow profile[4]. Therefore, we introduced and evaluated an SSM method that incorporates the head branches.

## METHODS

The general method follows a standard SSM framework with additional modelling of the head vessels included in the shape descriptor. First, 3D geometries of the ascending aorta were extracted from 33 patient scans, scaled, and aligned based on generalized Procrustes analysis. These geometries were then parameterized onto a cylindrical coordinate system, as described by the vessel radius (r), polar angle ($\theta \in [0,2\pi)$), normalized centerline length ($s \in [0,1]$), and centerline coordinates ($C$), such that any surface quantifiable values (e.g., $r$) can be described in a shared parametric space of (θ,s).

The presence of holes marking the location of branches would violate the cylinder homeomorphicity constraint. Instead, branching holes were defined by an implicit closed curve in (θ,s) space as:

$$f(\theta,s) = 2/\left(1+e^{-\frac{4G_{signed}(\theta,s)}{k}}\right) - 1 = L \qquad (1)$$

where $f$ is a logistic function of a signed geodesic distance function ($G_{signed}$) that classifies whether a point on the surface is found within a branch hole. This function is normalized by $k = |min(G_{signed})|$, and $L$ is a level set segmentation value, iteratively determined by an auto thresholding algorithm[5].

These parameterized variables were concatenated into a shape descriptor matrix ($M$), for each subject ($n$), up to N number of subjects. $M$ could be reconstructed by principal component analysis (PCA) as the summation of weights ($w$) for $N_{PC}$ number of basis vectors ($\overrightarrow{PC}$):

$$M = \begin{bmatrix} C^{(n)} & f^{(n)} \\ \vdots & i \\ C^{(N)} & f^{(N)} \end{bmatrix} \approx \begin{bmatrix} w_{n_{PC}}^{(n)} \cdots w_{N_{PC}}^{(n)} \\ \vdots \\ w_{n_{PC}}^{(N)} \cdots w_{N_{PC}}^{(N)} \end{bmatrix} \begin{bmatrix} \overrightarrow{PC}_{n_{PC}} \\ \vdots \\ \overrightarrow{PC}_{N_{PC}} \end{bmatrix} i \qquad (2)$$

Once the SSM had been generated, the ability of the model to represent the original branched geometry was assessed. Aside from a geometrical comparison by distance and curvature, CFD was also performed, using Simvascular[6], on all reconstructed geometries at $N_{PC} = 20$ and 3 cases at $N_{PC} = 5,10,15,20,25,30$. Each geometry was meshed with ~1 million tetrahedral elements, following a mesh convergence study. Boundary conditions were set to be subject-specific flow rate from PC-MRI at the inlet and three-element windkessels at the outlets, calibrated to match clinically measured flow split and pressure via differential evolution. Blood was modelled as Newtonian with viscosity 4cP and density 1.06g/cm$^3$, yielding similar results to its non-Newtonian counterpart[7]. CFD were run to the fifth cardiac cycle using 500 timesteps of ~0.002s per cycle.

## RESULTS

The first few $\overrightarrow{PC}$s have mainly vessel radius information, so radius errors decreased quickly at low $N_{PC}$ (Fig. 1a), with -3dB cutoff of the variance explained at $N_{PC} = 1$ (Fig. 1b). A spider plot of the first 3 $\overrightarrow{PC}$s illustrates their major effect on vessel geometry: $w_1$ affects primarily overall radius-to-centerline-length ratio, $w_2$ affects radial dilation near the aortic root, and $w_3$ affects constriction in the mid-aorta (Fig. 1c).

SB³C2022-312

The distribution of $f$ at low $\overrightarrow{PC}$ reflects the common location of the branches along the centerline. At low $N_{PC}$, many of the head branches were joined, but they were well separated at high enough $N_{PC}$ (Figure 1d) as high $\overrightarrow{PC}$ generated large gradients to distinguish the outlet holes. This effect explained the large $N_{PC}$ for geodesic distance to reach -3dB cutoff, at $N_{PC} = 9$ (Figure 1a). $\overrightarrow{PC}$ carried the least amount of centerline information, as the centerline hardly varied across the cases. Thus, the Euclidean distance error of the centerline starts small and decreases modestly with $N_{PC}$ (Figure 1b), with the -3dB cutoff being at $N_{PC} = 14$ (Figure 1a).

The time- and wall-surface-averaged pressure across $N_{PC}$ did not vary significantly from the original geometry ($p > 0.3$ by a paired, two-tailed t-test). The average pressure error was typically less than 4% and largely independent of $N_{PC}$ (**Figure 2**a) as flow impedances were mainly determined by the windkessel outflow parameters. At the same time, vessel resistance (as a function of radius and vessel length) was already well represented in the lower $N_{PC}$. Furthermore, while the lower $N_{PC}$ cases often had merged branches of the head vessels, if the windkessel parameters were also parallelly merged, the aberrant branching pattern hardly affected the surface averaged pressures.

Similar to pressure, the surface- and time-averaged wall shear stress (SA-TAWSS) did not differ significantly from the original geometry ($p > 0.3$, **Figure 2**a). In contrast, the distribution of WSS error was sensitive to local vessel geometry. While the surface-averaged value was similar, the wall shear stress pattern differed with $N_{PC}$. Further breakdown of distribution of WSS error along the surface at $N_{PC} = 20$ are shown in **Figure 2**b. The location of the highest wall shear stress error in the geometry was found where the vessel branched, as caused by a recirculation region found near the branches.

## DISCUSSION

In general, the branching pattern did not affect global measures, such as SAWSS and surface averaged pressure. Even when the branches were merged, if their lumped parameter models are properly combined, the resulting pressures were similar to the fully branched model. Aortic shape variations may indicate adaptation to abnormal changes in pressure[8], but they do not drive these changes. The diameter is, however, still an important metric that relates how these pressures translates into stress experienced by the wall via the law of Laplace.

Meanwhile, WSS is known to be sensitive to variation in geometry, however, the variations were highly localized, with the location of the highest WSS found near the branches, similar to other studies[9]. The locations of highest WSS error were also near the branches, which required high $N_{PC}$ for accurate representation. Despite high local errors, surface-averaged WSS was well captured with low $N_{PC}$. In a study correlating WSS obtained from 4D MRI and aorta's shape, the diameter and velocity were strongly associated with WSS value[10], such that the radius-dominant low $N_{PC}$ could be sufficient to represent the SAWSS. Other locations of WSS errors appear to be weakly correlated with the surface curvature error. The curvature of the aorta introduced secondary flow patterns that depend on aortic curvature (**Figure 2**c)[11], primarily because the curvature affects the angle of inflow boundary condition and therefore downstream flow profile. Therefore, low $N_{PC}$ may be sufficient to describe the average WSS, but a high $N_{PC}$ is required to obtain more accurate surface distribution.

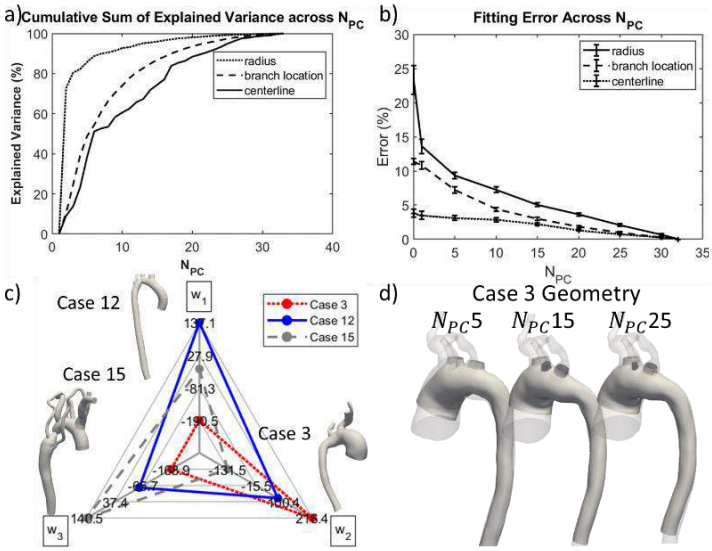


**Figure 1a) Cumulative sum of explained variance carried by the principal components across $N_{PC}$ and b) Fitting error (%) across different $N_{PC}$ for radius, branch location, and centerline. c) Spider plot of 3 cases to represent the effect of the first 3 $\overrightarrow{PC}$ on vessel radius. d) Evolution of geometry over $N_{PC}$, with transparent original geometry.**

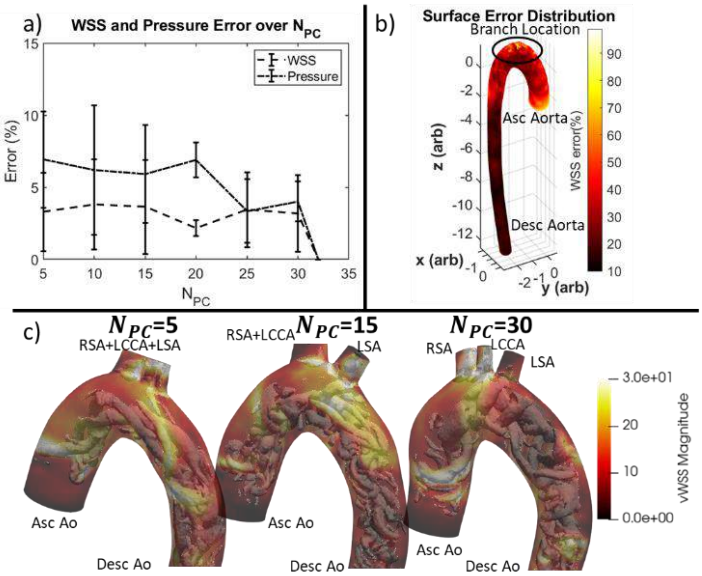


**Figure 2a) WSS and pressure error vs. $N_{PC}$. b) Wall shear stress error distribution on surface ($N_{PC} = 20$). c) WSS overlaid on visualized vortices for one case at different $N_{PC}$.**


## ACKNOWLEDGEMENTS

Funding provided by NIH grant U01-HL139471, computational resources were provided by Minnesota Supercomputing Institute.


## REFERENCES


[1] Ong, C.W. et al., *Ann. Vasc. Surg.*, 63:336-381,2020. [2] Liang, L. et al., *Biomech. Model. Mechanobiol.*,16(5):1519,2017. [3] Catalano, C., et al, *Appl*, 12(1): 394,2002. [4] Tsui, Y.Y., et al., *Int. J. Numer. Methods Fluids*,50(2):235,2006. [5] Ridler, T., et al., *IEEE trans syst Man Cybern*, 8(8): 630-632,1978. [6] Updegrove, A., et al., *Ann Biomed Eng*,45:525-541,2017. [7] Perktold, K., et al., *Biorheology*,26(6):1011-1030,1989. [8] Girardi,L.N.,et al., *J. Thorac. Cardiovasc. Surg.*,161(4):1193,2021. [9] Lantz, J., et al., *Med Eng Phys*, 34(8):1139-1148,2012. [10] Callaghan, F.M. and Grieve, S.M., *Am. J. Physiol. Heart Circ. Physiol.*,315(5):1174,2018. [11] Dean,W.,*Lond. Edinb. Dublin philos. mag. j. sci.*,5(30):673,1928.

SB³C2022
Summer Biomechanics, Bioengineering and Biotransport Conference
June 20-23, Eastern Shore, MD, USA

# MULTISCALE MODELING OF TISSUE GROWTH AND REMODELING COUPLED WITH MECHANOSENSITIVE CELL-SCALE SYSTEMS BIOLOGY

**Mohammadreza Soltany Sadrabadi (1), Seungik Baek (2), Mohammad R. K. Mofrad (3), Amirhossein Arzani (1)**

(1) Department of Mechanical Engineering
Northern Arizona University
Flagstaff, AZ, USA

(2) Department of Mechanical Engineering
Michigan State University
East Lansing, MI, USA

(3) Department of Bioengineering and Mechanical Engineering
University of California, Berkeley
Berkeley, CA, USA

## INTRODUCTION

Soft biological tissues respond to unprecedented stimuli (e.g., diseases) by adapting, repairing, and growth and remodeling (G&R). In most cases, these stimuli are sensed by certain receptors, and the related signals transduce chemically and mechanically, leading to alterations in cell behavior. These cellular changes often lead to changes in organ-scale geometry and function. These observations can be explained across the scales from cellular to tissue-scale levels [1].

Numerous studies highlight the role of continuum mechanics modeling in understanding the responses to these stimuli at the tissue-scale level [2]. For example, disease and aging-driven quantification of G&R improve our understanding of the interaction between tissue growth and mechanical forces [2,3]. Subsequently, knowing the underlying biochemistry of cell signaling pathways, a mathematical description could be developed to model a system of differential equations to represent the cellular level. These models, which are in two different scales are dependent on each other and studying them individually will give us imperfect information [4].

Coupling cell-scale biology and tissue-scale G&R models is challenging. Herein, we developed simple cases to illustrate different approaches to achieving this task. Particularly, one vs. two-way coupling between mechanics and biology, ordinary vs. partial differential equation approach for modeling the biology, and coupling to transient mechanics (elastodynamics) is investigated.

## METHODS

A cube and a cylinder (idealized aneurysm) were assumed as our test-case geometries. Systems of ordinary differential equations (ODEs) representing reactions between biochemicals (cell-scale level) were coupled (1-way and 2-way) with kinematic G&R (tissue-scale level). Also, for the cylinder, a system of partial differential equations (PDEs) model was implemented to smoothly model the spatial pattern of cell reactions.

**Cube (1-way coupling of ODEs with kinematic growth):** The geometry was discretized into 10000 quadratic tetrahedral elements. An idealized system of ODEs representing cell signaling of three species was implemented. These ODEs include three equations representing the reactions of three species A, B, and C:

$$if_i \rightarrow A \quad A + B \rightarrow C \quad where \quad = each \; node \tag{1a}$$

$$\frac{dy_j}{dt} = F(y_j) \quad where \quad y_j = A, B, C \tag{1b}$$

$f_i$ represents an arbitrary function for each computational node $i$ described as $f_i(x,y) = \frac{|x_i+y_i|}{2}$ and was used for the first species [A] as a source term driving its concentration. The initial conditions for species concentration [A] and [B] were set to one and for [C] was set to zero. Kinematic growth was used for the growth model at the tissue scale:

$$F_t = F_e F_g \quad \text{where} \quad F_g = I + \nu ik \otimes k \tag{2}$$

The growth rate ($\nu$) in each node was assumed as a function of the normalized output of the third species [C] in each timestep ($\nu = 0.01\frac{C}{C_0}$). The growth direction was in the z-direction. The cube was fixed at the bottom surface and was not pressurized.

**Cube (2-way coupling of ODEs with kinematic growth):** In this part, the source term for species A was modified to include the mechanical stress ($f_i(x,y,\sigma)\, i = \frac{|x_i+y_i|}{2} + \frac{|\mathrm{tr}(\sigma_i)|}{\sigma_0}$), where at t=0, $\sigma$ was assumed to be zero. The system of ODEs was solved,

and the growth rate was updated in each timestep. Next, by updating the stress from the G&R simulation, the source term for [A] was updated.

**Cylinder (1-way coupling of ODEs with kinematic growth):** A cylinder was modeled to represent an idealized artery. The geometry was meshed into 51000 quadratic tetrahedral elements. The aim was to study an idealized aneurysm growth (a common test case in the G&R literature). Cell signaling with a system of ODEs with five species was used from a previous study [5]. TGF-β, MAPK, Smad, MMP, and TIMP were the species featured in this model. A Gaussian distribution of the coordinates of the mesh was used as an input (source term) for the first species (TGF-β) and zero initial conditions were used. The growth rate $(\boldsymbol{v})\dot{\boldsymbol{\iota}}$was implemented as a function of MMP and was set in the radial direction. A pressure waveform was applied to the aneurysm wall during the G&R simulations.

**Cylinder (2-way coupling of ODEs with kinematic growth):** In this case, the TGF-β source term was defined as a function of stress and the aforementioned Gaussian distribution. Similar to the last 2-way coupling case, the stress value used in the systems biology model was updated based on the G&R simulations.

**Cylinder (1-way coupling of PDEs with kinematic growth):** In this case, the previous 1-way coupled model was extended to include diffusion terms, which were added to each equation of the system of ODEs to generate a system of unsteady reaction-diffusion PDEs.

## RESULTS

The displacement results for 1-way coupling and 2-way coupling of the ODE model with kinematic growth for the cube are shown in Figure 1. In the 1-way coupling case, more localized growth was observed at the tip of the cube, whereas in the 2-way coupling case the growth at the top surface was more homogeneous. Additionally, the stress induced by growth showed heterogeneous patterns with higher stress within the middle of the cube (results not shown).

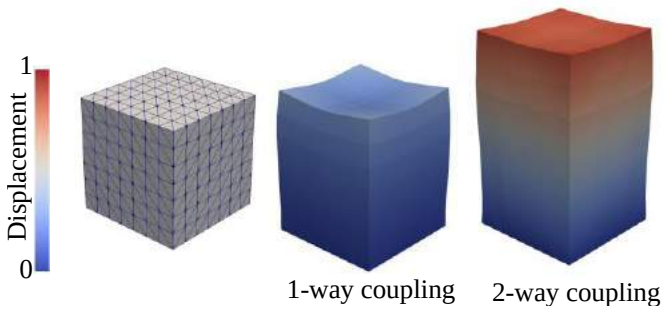


**Figure 1. Displacement results for 1-way coupling and 2-way coupling of the box.**

The displacement results for the cylinder case are shown in figure 2. The growth of the aneurysm in the 1-way coupling ODE model is consistent with the input of TGF-β. However, in the 2-way coupling cases, because of pressurizing the artery, the stress alters the growth to expand the artery more in the longitudinal direction. Finally, the results for 1-way coupling of the system of PDEs with kinematic growth indicate that the aneurysm length and diameter are altered slightly compared to the 1-way coupling of the system of ODEs.

## DISCUSSION

We modeled two different test case geometries representing an idealized tissue block and aneurysm to compare the results of 1-way and 2-way coupling strategies in modeling kinematic G&R coupled with systems biology. We observed the different growth patterns in both geometries between 1-way and 2-way coupling approaches. Additionally, we implemented a system of PDEs approach for modeling the systems biology and compared the results to the ODE approach. Our models were implemented in the open-source finite-element software FEniCS. The future release of our code will enable the implementation of flexible coupling strategies between systems biology and continuum mechanics models of G&R. In future work, we will implement the 2-way coupling of the system of PDEs. Additionally, we are currently implementing our framework to study calcific aortic valve disease growth based on our prior systems biology [6] and continuum [3] calcification models where we will study large deformation elastodynamics.

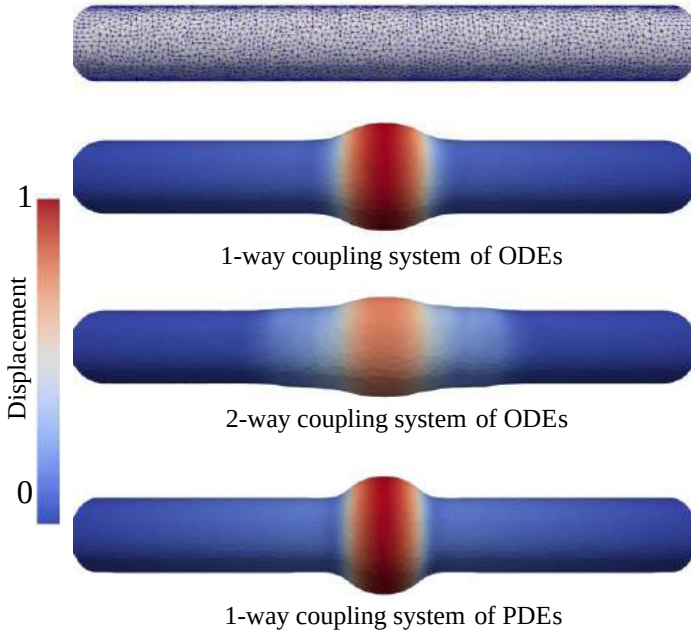


**Figure 2. Displacement results for 1-way coupling and 2-way coupling of the cylinder (aneurysm).**


## ACKNOWLEDGEMENTS

This work was supported by NSF grant No.~1947559.


## REFERENCES


[1] Saucerman, J. J., et. al. Nat.Rev. Cardiol. 16(6):361–378, 2019.
[2] Ambrosi, D et.al. J. R. Soc. Interface 16(157):20190233, 2019.
[3] Sadrabadi M. et. al. Journal of Biomechanics 128: 110773, 2021.
[4] Irons, L.,et. al. PLoS computational biology,16(8):e1008161, 2020.
[5] Irons, L. et. al. Annals of Biomedical Engineering, 1-15. 2021.
[6] Arzani, A. et. al. ACS biomaterials science & engineering, 2017.

SB³C2022
Summer Biomechanics, Bioengineering and Biotransport Conference
June 20-23, Eastern Shore, MD, USA

# ON-FIELD EVALUATION OF MOUTHPIECE- AND HELMET-MOUNTED SENSOR DATA FROM HEAD KINEMATICS IN FOOTBALL

**Ty D. Holcomb (1, 2), Madison E. Marks (1, 2), N. Stewart Pritchard (1, 2), Logan E. Miller (1, 2), Jillian E. Urban (1, 2), Joel D. Stitzel (1, 2)**

(1) School of Biomedical Engineering and Sciences Virginia Tech – Wake Forest University Winston-Salem, NC, USA
(2) Department of Biomedical Engineering Wake Forest University, Winston-Salem, NC, USA

## INTRODUCTION

Concussive and sub-concussive head impacts in contact and collision sports are of increasing concern as changes in cognition and neuroimaging associated with repeated head impact exposure (HIE) in football have been observed following a single season of play.[1,2] Helmet-mounted sensors have allowed researchers to measure the frequency and magnitude of head impacts experienced by athletes on-field; however, coupling of sensors has been questioned.[3,4] Advances in sensor technology have allowed for the development of mouthpiece-based sensors with improved kinematic measurement, in some load cases, with improved coupling;[5] however, evaluation of field variance between sensor systems in an on-field environment has been limited. Therefore, the objective of this study was to compare HIE measured from athletes dually instrumented with the Head Impact Telemetry (HIT) System and a mouthpiece-based sensor system.

## METHODS

A total of five high school football athletes (ages 15-18) were enrolled in this study, approved by the Wake Forest School of Medicine Institutional Review Board. Each player was fitted with either a Riddell Speed or Speed Flex football helmet containing a HIT System MxEncoder and simultaneously instrumented with a custom-fit mouth guard containing the mouthpiece (MP)-based sensor system[5]. The athletes were instrumented with the aforementioned sensors during a single spring football season. The HIT System was set to record at the default 10g threshold while the MP-based sensors were set to record when 5g was exceeded on any axis for at least 3 milliseconds. Trained researchers monitored the HIT System and MP-based sensors at all contact practices and games. Two cameras were used to capture time-synchronized film at each session with a camera placed at the end zone and on the sideline. Events from each sensor system were time-aligned and verified with video. The frequency and peak magnitude of video-verified head acceleration events (i.e., events) were compared across sensor systems. Peak resultant linear and angular acceleration was calculated for each recorded event and compared across sensor systems. Head acceleration events were paired between devices using the measured event recording time and the synchronized video time. Peak resultant linear and angular acceleration recorded on each sensor system was then compared for paired events by subtracting the HITS measurement from the MP-based sensor measurement and outliers were identified by evaluating the distribution of differences in peak magnitude between paired events.

## RESULTS

A total of 7189 events were collected with the MP-based sensor system and a total of 1523 events were collected with the HIT System throughout the season. Using video-verification, 6006 false-positive events (83.5%) were excluded from the MP-based sensors data and 817 (53.6%) false-positive events were excluded from the HIT System data. A false event was typically due to handing of the sensor off the field (e.g., removing helmet or mouthpiece). In total, 1183 true-positive head acceleration events (16.5%) were identified from the MP-based sensor data and 706 true-positive head acceleration events (46.3%) were observed from the HIT system sensor data. These events were then paired based on the time of the recorded event coincident with observed contact. 537 events were captured by both sensor systems. The analysis that follows refers to these paired events.

Figure 1 demonstrates the peak resultant linear acceleration recorded by each device for each paired event. The origin regression line represents the same linear regression calculation forced through the origin. Greater variation in the linear acceleration was observed as the linear acceleration measured by the sensor systems increased. A histogram of the difference in peak resultant linear acceleration between the sensor systems is provided in Figure 2. Approximately 78.8% of the paired events fell between ±20 g difference in peak resultant linear acceleration. Angular acceleration measured by each device is shown in

Figure 3 and angular acceleration difference in peak resultant is shown in Figure 4. Summary statistics for the peak resultant kinematics recorded by each sensor system are provided in Tables 1 and 2.

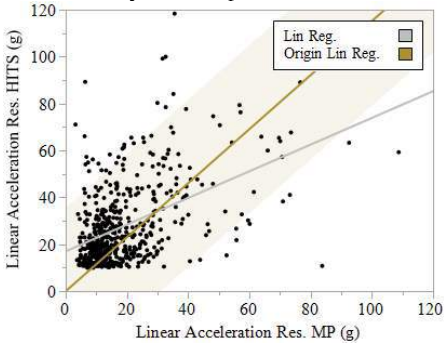


**Figure 1: Linear Acceleration MP vs. HITS**

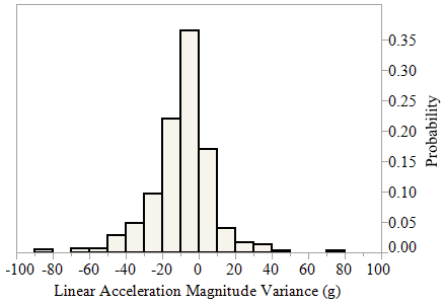


**Figure 2: Linear Accel Magnitude Variance (MP-HITS)**

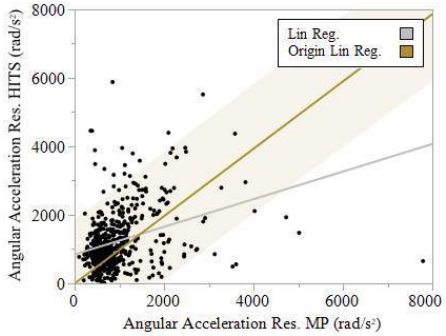


**Figure 3: Angular Acceleration MP vs. HITS**

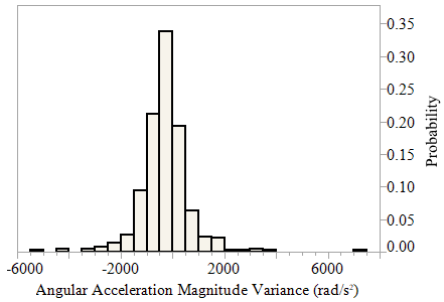


**Figure 4: Angular Accel Magnitude Variance (MP-HITS)**

**Table 1: Linear Acceleration Comparison MP vs. HITS**

| Lin Accel (g) | Mean | SD | Median | 95% | Max |
|---|---|---|---|---|---|
| MP | **19.0** | **13.9** | **14.5** | **46.4** | **108.8** |
| HIT System | **27.8** | **17.0** | **22.6** | **63.1** | **118.4** |
| Difference | **-8.6** | **16.2** | **-7.1** | **12.5** | **73.0** |

**Table 2: Angular Acceleration Comparison MP vs. HITS**

| Ang Accel (rad/s²) | Mean | SD | Median | 95% | Max |
|---|---|---|---|---|---|
| MP | **959** | **696** | **774** | **2132** | **7789** |
| HIT System | **1236** | **857** | **1008** | **2841** | **5884** |
| Difference | **-277** | **910** | **-275** | **1025** | **7135** |

Paired events were classified as outliers by evaluating the respective cumulative distribution function. 90% of paired events varied by less than 30g for linear acceleration or less than 1500 rad/s$^2$ for angular acceleration; therefore, >30g and >1500 rad/s$^2$ difference was used to categorize linear angular acceleration outliers respectively for a total of 88 events. These outliers were re-evaluated using the video-verification review process. The description of each impact was further evaluated. In 72 instances (82%), the MP-based sensor measurement appeared to be a more realistic and lower measurement compared to the HIT System, but this was subjectively determined from video.

## DISCUSSION `

The objective of this study was to compare HIE measured from athletes dually instrumented with the HIT System and a MP-based sensor system with improved skull coupling. The MP-based sensors recorded lower linear and angular acceleration magnitudes, on average, with an average difference in magnitude of 8.6g for peak resultant linear acceleration and an average difference in magnitude of 277 rad/s$^2$ for peak resultant angular acceleration. This could potentially be attributed to sensor coupling with the head of the athlete. Helmet fit plays a role in how well the HIT System is coupled to the head of an athlete, as the HIT System assumes the helmet and the skull move as a single rigid body [4,6]. The MP-based sensors are custom-fit and coupled to the roof of the mouth. The results of this study differ from those produced by Shah et al in that the MP collected more video-verified events than the HIT system most likely due to the difference in device impact threshold [7]. Approximately 10% of events had greater than 30g difference in peak resultant linear acceleration and 1500 rad/s$^2$ and were deemed outliers.

The limitations of this study include a small sample of size of 5 athletes, multiple film reviewers which has the potential to introduce human bias, the different trigger thresholds of 5g for the MP-based sensors and 10g for the HIT System, and that the data was collected from a single football team.

The results of this study demonstrate a difference in the HIT System and MP-based sensors. While the difference in peak resultant kinematics was, on average, -8.6g and -277 rad/s$^2$, greater differences in peak resultant magnitude were observed at higher magnitude events. The HIT System generally recorded higher acceleration measurements for outlier events than the MP-based sensors. The results of this study help to improve our understanding of the sensors utilized in the collection of head acceleration data and may inform interpretation of head acceleration data collected from different sensors.


## ACKNOWLEDGEMENTS

The authors would like to thank the Oak Grove High School Varsity Football Team for participating in this voluntary study along with Konstantina Strates, Alex Riddell, Brian Wexler, and Jess Towns.


## REFERENCES


[1] Bahrami, N et al, *Radiology*, 281(3):919-926, 2016. [2] Bazarian, JJ et al, *Magn Reson Imaging*. 30(2):171-80, 2012. [3] King, D et al, *Am J Sports Med*, 43(3): 614– 624, 2015. [4] Jadischke, R et al, *J Biomech*, 46(13):2310-5, 2013. [5] Rich, AM et al., *Ann Biomed Eng*, 47(10):2109-2121, 2019. [6] Broglio, SP et al., *Ann Biomed Eng*, 40(1):37-46, 2012. [7] Alok SS et al, IRCOBI Conference 2019, 2019.

# BATCH-PROCESS OPTIMIZATION OF KINK-RESISTANT VASCULAR GRAFTS WITH HIGH COMPLIANCE

**David Jiang (1), Andrew J. Robinson (2),**
**Elizabeth M. Cosgriff-Hernandez (2), Lucas H. Timmins (1,3)**

(1) Department of Biomedical Engineering, University of Utah, Salt Lake City, UT, U.S.A
(2) Department of Biomedical Engineering, University of Texas at Austin, Austin, TX, U.S.A
(3) Scientific Computing and Imaging Institute, University of Utah, Salt Lake City, UT, U.S.A

## INTRODUCTION

Each year ~1.4 million patients require arterial grafts in the US. Synthetic vascular grafts are required in ~10-20% of patients when autografts are unavailable; however, synthetic vascular grafts in small diameter applications (ID < 6 mm) have high failure rates. Synthetic grafts are associated with a 40-50% reduction in patency after 2 years and a 40% failure rate at 5 years [1]. This loss of patency due to intimal hyperplasia has been attributed, in part, to poor compliance-matching with native arterial tissue [2]. Data demonstrate that the high compliance of native vessels (e.g., coronary artery, 10-15 %/mmHg*$10^{-2}$) permits expansion and contraction during the cardiac cycle, whereas commercially available synthetic grafts have limited deformation at these pressure loads (e.g., ePTFE, 1-2 %/mmHg*$10^{-2}$). Notwithstanding the role of altered hemodynamics at the graft-tissue interface leading to neointimal hyperplasia, improved compliance matching between the graft and arterial tissue has been identified as a key determinant of long-term patency and graft success.

Advances in material chemistry and microfabrication strategies have allowed the manufacturing of polyurethane-based small diameter vascular graft with improved compliance matching [3]. Indeed, these grafts have been shown to reduce cellular markers for intimal hyperplasia, however, the increased compliance resulted in grafts that were prone to kinking. To improve kink-resistance, a polymeric coil was added, but the addition negatively impacted compliance [4]. The ideal graft (i.e., high compliance and high kink-resistance) requires a balance between multiple biomechanical properties that are in opposition (e.g., methods to increase graft kink-resistance reduce its compliance). Between geometric and material property tunability, the number of design parameter combinations for coil-reinforced graft manufacturing via a trial-and error approach is nearly limitless and prohibitively time-consuming. Herein, we develop and apply a novel computational biomechanics approach to inform graft design and identify mechanically-optimized tissue engineered candidate designs.

## METHODS

**Computational Geometry and Modeling:** The graft was modeled as an axisymmetric cylinder ($l = 40$ mm, $d_i = 4.74$ mm, $d_o = 4.94$ mm) with a reinforced coil wrapped helically around the outer surface (Fig. 1A). The graft and spiral coil were discretized with hexahedral and tetrahedral elements, respectively. Both the graft and coil were described as a nearly incompressible neo-Hookean solid with material properties derived from mechanical testing performed in our laboratory. Two computational simulations were performed for each coil-reinforced graft to quantify compliance and kink resistance (Fig. 1B-C). To quantify compliance ($C$, Eq. 1), the graft was inflated to a lumen pressure of 80 mmHg and 120 mmHg. Predicted inner diameters at these pressures were extracted and compliance was calculated as,

$$C = \frac{d_{i,120\ mmHg} - d_{i,80\ mmHg}}{d_{i,80\ mmHg} * 40\ mmHg} \quad (1)$$

To quantify kink-resistance, a 1° bend (i.e., imperfection) was applied to the central axis of the graft to facilitate buckling, as previously established [5]. The lumen was pressurized to 100 mmHg, and the graft was compressed axially by application of a displacement to initiate kinking. Kink-resistance was quantified as the axial displacement (mm) at which a kink forms in the graft (i.e., discontinuity in the geometry). For all models, symmetry boundary conditions were enforced on the graft to restrict rigid body motions in the circumferential and axial directions. A tied-elastic contact formulation was implemented between the outer graft surface and the spiral coil. Finite element analysis was performed using FEBio [6].

**Batch-Processing Scheme:** To advise and accelerate the graft design process, an optimization scheme was utilized to sweep the multi-dimensional design space to identify optimal parameter combinations for grafts with target compliance and kink-resistance. As an extension to the computational models, a batch processing scheme was implemented using GIBBON (open-source MATLAB toolbox) and

FEBio. [6,7] First, a parameter sweep analysis was used by selecting parameter sets from uniform distributions over the defined parameter ranges (Fig. 1D). Coil diameter ($d_{coil}$) ranged from 0.1 to 0.5 mm, and coil spacing (i.e., pitch; $P_{coil}$) ranged from 2 to 10 mm. The coil modulus ($G_{coil}$) was defined as either 8.13 MPa (Bionate® PCU 55D) or 2.93 MPa (Bionate® PCU 80A). Lastly, the graft modulus ($G_{graft}$ = 1.315 MPa) was chosen to match the compliance of native arterial tissue at physiologic pressure. The batch-processing algorithm automatically generated and solved 2 FEBio models (compliance and kink-resistance) for each of the 72 unique parameter combinations (144 models in total).

**Graft Optimization:** To balance the contribution of competing mechanical responses (i.e., compliance versus kink-resistance), an optimization function (φ) was defined and sought to be minimized across the parameter search space. For each combination of design parameters, the value φ was calculated as,

$$\varphi(d_{coil}, P_{coil}, G_{coil}, G_{graft}) = \alpha\left[\frac{C_{graft} - C_{artery}}{C_{artery}}\right]^2 + (1-\alpha)\left[\frac{K_{graft} - K_{ePTFE}}{K_{ePTFE}}\right]^2 \quad (2)$$

where $C_{graft}$ and $C_{artery}$ are the compliance values for the examined graft and artery tissue, respectively, $K_{graft}$ and $K_{ePTFE}$ are the kink-resistance values of the graft and ePTFE, respectively, and $\alpha$ is a weighting coefficient, which was defined as 0.5 (i.e., equal weight between compliance and kink-resistance). Note that a minimized $\varphi$ value indicated the modeled graft had a graft compliance and kink-resistance comparable to native arterial tissue and ePTFE grafts, respectively.

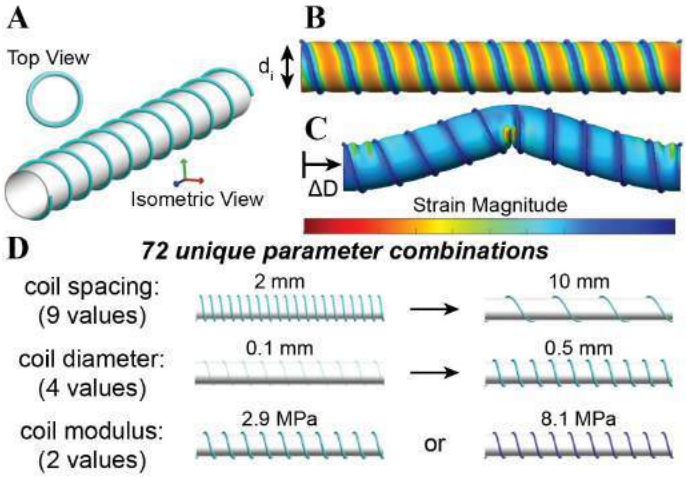


**Figure 1: A) Representative geometry of coil-reinforced graft at reference configuration. B) Compliance quantified via changes in inner diameter ($d_i$). C) Kink-resistance quantified via axial displacement distance (Δ$D$). D) Batch-generated coil-reinforced graft geometries via Gibbon.**

## RESULTS

Across the 72 parameter combinations (~9 days of computational time on 12-core, 4.4 GHz processor), graft compliance displayed a wide range of values. For example, the compliance values varied from 0.39 to 7.17 %/mmHg*$10^{-2}$ across the parameter space, and values were dependent on both coil diameter and coil spacing. Surprisingly, however, there were minimal changes to kink-resistance (i.e., prescribed axial displacement when kinking initiates) across the parameter space, except at coil spacings of 2 mm. More specifically, for coil spacings >2 mm the axial displacement that initiated kinking was 2.07 ± 0.12 mm, but values 3.58 ± 1.32 mm were observed for coil spacings of 2 mm (higher kink-resistance). Predicted compliance and kink-resistance values led to diverse values for the optimization function (Fig. 2). The minimum value of φ = 0.44 resulted from the combination of a coil diameter = 0.1 mm, coil spacing = 10 mm, and coil modulus = 2.93 MPa (Bionate® PCU 80A). For this parameter combination, the compliance and axial displacement were 7.10 %/mmHg*$10^{-2}$ and 2.08 mm, respectively. The maximum optimization value of φ = 0.88 had the combination of a coil diameter = 0.5 mm, coil spacing = 4 mm, and coil modulus = 8.13 MPa (Bionate® PCU 55D).

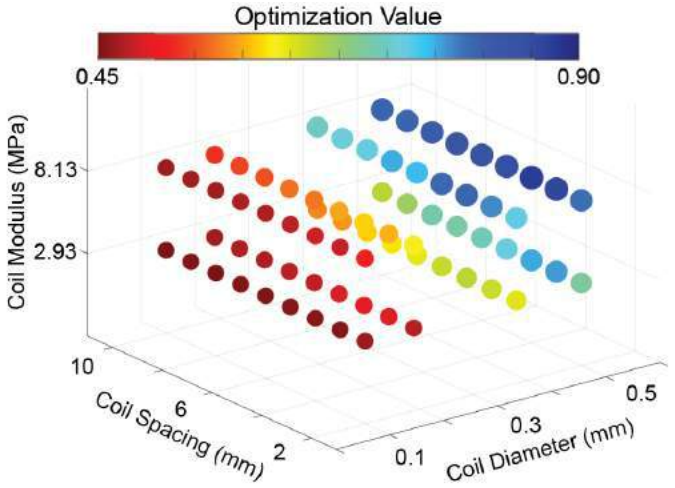


## DISCUSSION

Our investigation demonstrates the success in implementing an FE-batch processing framework to accelerate model-directed tissue engineered vascular graft design. Results suggests that smaller coil spacing improves kink-resistance of the graft but reduces compliance; whereas, compliance and kink-resistance are independent of coil moduli. Furthermore, the data suggests that coil spacings <2 mm should be explored to improve optimization values, but fabrication limitations may constrain this parameter space. Importantly, the optimization scheme successfully identified a graft with improved kink-resistance without sacrificing compliance. It should be emphasized that experimental fabrication and testing of 72 grafts would take 6-9 months. We anticipate that this model-directed design approach is expected to provide a kink-resistant graft with high compliance for small diameter vascular graft applications. Ultimately, these unique grafts have potential to improve clinical outcomes by addressing failures of current synthetic grafts.

## ACKNOWLEDGEMENTS

This research was supported, in part, by the National Institutes of Health (R01 HL150608). The authors thank DSM Biomedical for providing polyurethane samples for mechanical testing.

## REFERENCES

[1] Salacinski, HJ et al., *J Biomater Appl*, 15(3):241-278, 2001.
[2] Burkel, W. E., *Med Prog Technol*, 14(3-4):165-175, 1989.
[3] Post, A et al., *Acta biomater*, 89:84-94, 2019.
[4] Li, X., MS Thesis, University of California Los Angeles, 2018.
[5] Sanyal, A et al., *Biomed Eng Online*, 14(Suppl 1): S4, 2015.
[6] Maas, SA et al., *J Biomech Eng*, 134(1):011005, 2012.
[7] Moerman. KM et al., *J Open Source Softw,*3(22): 506, 2018.

# BIOMECHANICAL AND MICROSTRUCTURAL CHARACTERIZATIONS OF HUMAN HEALTHY AND HYPERTROPHIC SEPTAL TISSUES

**Katherine M. Copeland (1), Uday Chintapula (1), Alan M. Taylor (1), Yi Hong (1), Kytai T. Nguyen (1), Matthias Peltz (2), Pietro Bajona (2,3), Jun Liao (1)**

(1) Department of Bioengineering, University of Texas at Arlington, Arlington, TX 76010, USA
(2) Department of Cardiovascular and Thoracic Surgery, University of Texas Southwestern Medical Center, Dallas, TX 753□0, USA
(3) Allegheny Health Network-Drexel University College of Medicine, Pittsburgh, PA 15212, USA

## INTRODUCTION

Hypertrophic cardiomyopathy (HCM) is a genetic disease of the sarcomere that results in overgrowth of the left ventricular septum. This overgrowth often causes mitral valve regurgitation and additional stress on the heart. A fibrotic collagenous microenvironment is associated with HCM due to this altered stress condition [1]. Hypertrophy of the cells and the fibrotic environment contribute to the abnormal biomechanical properties of the septal tissues. Additionally, previous literature has shown that the circumferential myocardial shortening of ventricular muscle during contraction often occurs and is directly involved in the preservation of left ventricular systolic performance in HCM [2]. Reduced left ventricular strain, due to the thickening of the wall, has also associated with poor cardiac outcomes, which consequently result in heart failure and mortality [3]. In this study, we performed thorough microstructural and biomechanical characterizations on human septal tissues in both healthy condition and hypertrophic condition.

## METHODS

Hypertrophic septal samples were obtained from the surgical waste of clinical myectomy of the HCM patients (UTSW: IRB STU 082017-072). Patients include both male and female and range in age from 19 years to 71 years. Healthy human septal tissues were obtained from a tissue bank under the same IRB protocol. Septal tissues were then dissected for histology and uniaxial tensile testing. Samples prepared for uniaxial testing were aligned with the longitudinal direction of the septum. Tissue samples were then mounted onto the TestResources Universal Testing Machine (Shakopee, MN) and tested in 1X Phosphate Buffered Saline (PBS). After preconditioning, the sample were loaded until failure (tissue breakage). For histology, all samples were fixed in 10% neutral buffered formalin for 24 hours and were processed through a standard histological preparation protocol, including alcohol-dehydration and paraffin-embedment. 5 μm sections were cut and a standard Masson's trichrome staining protocol was performed. The Masson's trichrome protocol stained heart muscle red and collagen blue. Histological images were taken under bright light field using a Nikon Eclipse Ti Series Microscope (Nikon).

## RESULTS

The averaged uniaxial stress-strain curve of the healthy septal tissues showed a very typical nonlinear concave upward stress-strain relation (**Figure 1**). The HCM tissues, however, showed a stress-strain trend that was much less nonlinear. The HCM septal tissues had an initial modulus that was higher than healthy septal tissues, most likely due to the abundant fibrotic collagen associated with HCM. Very interestingly, we found that the healthy septal tissues had much higher mechanical strength than the HCM septal tissues, demonstrated by the failure stress (healthy: 2,561 ± 919 kPa vs HCM: 494 ± 206 kPa). In the high strain region, the healthy septal tissues were also stiffer than the HCM septal tissues, as shown by the maximum tensile modulus of the tissues. Overall, HCM septal tissues were stiffer at the initial phase of tissue loading, less nonlinear, less stiff in the linear region, and much weaker in mechanical strength. This is a very novel biomechanical finding of this disorganized,

hypertrophic, and fibrotic septal muscle tissue. Masson's trichrome staining revealed that the HCM septal tissue had hypertrophic cardiomyocytes that were significant larger and disarrayed when compared with the healthy cardiomyocytes (**Figure 2**).

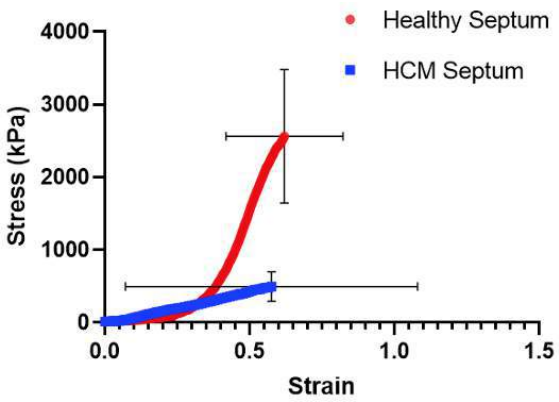


**Figure 1: Average stress-strain behavior of healthy (red) and HCM (blue) human septal tissues.**

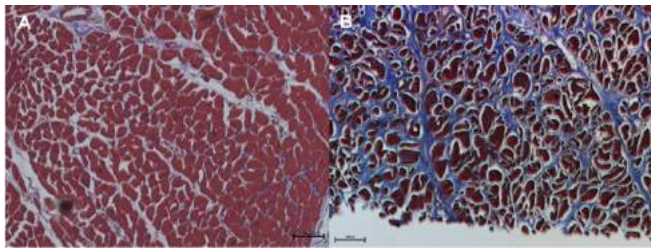


**Figure 2: Masson's trichrome images of healthy (A) and HCM (B) human septal tissues.**

## DISCUSSION

Uniaxial tensile stress-strain curves up to failure revealed that healthy human septal tissues were less stiff in the initial loading region, but was much stiffer in the linear region and had a much higher mechanical strength than the HCM human septal tissues. The healthy septal tissues took an optimal soft tissue biomechanical behavior, and the HCM septal tissues exhibited deteriorated mechanical behavior due to pathological structural alterations of HCM. Our biomechanical and microstructural data provide a strong foundation to understand tissue behavior of HCM septal tissues in relation to healthy septal tissues.

## ACKNOWLEDGEMENTS

R01EB022018, R15HL140503, and T32 HL134613 from NIH, and UT STARS.

## REFERENCES

[1] A. Varnava, P. Elliott, S. Sharma, W. McKenna, M. Davies, Hypertrophic cardiomyopathy: the interrelation of disarray, fibrosis, and small vessel disease, Heart 84(5) (2000) 476-482.
[2] J.A. Urbano-Moral, E.J. Rowin, M.S. Maron, A. Crean, N.G. Pandian, Investigation of global and regional myocardial mechanics with 3-dimensional speckle tracking echocardiography and relations to hypertrophy and fibrosis in hypertrophic cardiomyopathy, Circulation: Cardiovascular Imaging 7(1) (2014) 11-19.
[3] R. Hinojar, C. Fernández-Golfín, A. González-Gómez, L.M. Rincón, M. Plaza-Martin, E. Casas, A. García-Martín, M.A. Fernandez-Mendez, A. Esteban, J.J.J. Nacher, Prognostic implications of global myocardial mechanics in hypertrophic cardiomyopathy by cardiovascular magnetic resonance feature tracking. Relations to left ventricular hypertrophy and fibrosis, International journal of cardiology 249 (2017) 467-472.

# ASSESSING LOCAL DELIVERY CAPABILITY OF A NOVEL SEPTAL ABLATION SYSTEM VIA AN *EX VIVO* PIG HEART MODEL

**Katherine M. Copeland (1), Uday Chintapula (1), Joyita Roy (1), Yi Hong (1), Liping Tang (1), Matthias Peltz (2), Pietro Bajona (2,3), Kytai T. Nguyen (1), Jun Liao (1)**

(1) Department of Bioengineering, University of Texas at Arlington, Arlington, TX 76010, USA
(2) Department of Cardiovascular and Thoracic Surgery, University of Texas Southwestern Medical Center, Dallas, TX 753□0, USA
(3) Allegheny Health Network-Drexel University College of Medicine, Pittsburgh, PA 15212, USA

## INTRODUCTION

For inoperable hypertrophic cardiomyopathy (HCM), surgeons often inject pure alcohol into the septum via a septal perforator to destroy part of the septal muscle by triggering necrosis. This alcohol septal ablation (ASA) procedure is common but has risky complications (a periprocedural mortality rate of ~2%), including atrioventricular block, ventricular septal defect, ventricular fibrillation/tachycardia, and need for pacemaker, all due to the diffusive nature of alcohol (uncontrollable necrosis). To overcome ASA limitations, we have designed a novel collagenase-coated, doxorubicin-loaded nanoparticle (NP) ablation system to achieve a controllable, localized septal tissue shrinkage and hence a safe ablation [1]. To determine the localization patterns of our novel NP ablation system, we performed an *ex vivo* study using a pig heart model to measure the mean diffusion area of the injected ablation solution in the cardiac septum. With this *ex vivo* pig heart model, we were able to determine the localization capability of our NP ablation system.

## METHODS

Cy5 NPs were prepared by a standard double emulsion process. Briefly, 100 mg of PLGA (90% PLGA 50:50, 10% PLGA-NHS) was dissolved in 3 mL DCM. Cy5 was dissolved in dimethyl sulfoxide (DMSO) and was added dropwise to the PLGA solution on a stir plate at room temperature. After overnight stirring, the NPs were washed with deionized water and were collected by centrifugation and lyophilization. To conjugate collagenase (COL) to the surface of the Cy5 particles, 20 μg (per 10 mg of NPs) of COL were added to a NP solution in PBS (1 mg/mL). 1 mL of each COL-PLGA-Cy5 and PLGA-Cy5 solutions were injected *ex vivo* into the septum of fresh porcine hearts via the uppermost septal perforator of the left anterior descending coronary artery using a 21-gauge needle. Note that 1 mL of Cy5-Alcohol was used as a control. After injection, images were taken of the hearts using a custom-built fluorescent microscope. After the initial image, each heart was washed with PBS and reimaged to capture how the NPs could migrate under fluid flow. Quantitatively, we used the area of Cy5 signal on images of each group to assess whether the solution was diffusing from the injection site or staying close the injection site (localized delivery).

## RESULTS

As reported in literature, alcohol is not specifically localized to the septal tissue which results in alcohol diffusing and expanding into other regions. Our results confirmed that, when delivered via a septal perforator, alcohol signal covered a large anterior septal surface area (390±10 $cm^2$). PLGA-Cy5, on the other hand, covered 94 $cm^2$, while COL-PLGA-Cy5 covered the least amount of area (61±8.5 $cm^2$) (Fig. 1B,C). In short, PLGA-Cy5 and COL-PLGA-Cy5 appeared to localize close to the injection site, while alcohol dispersed downwards and outwards. In this study, the use of *ex vivo* healthy porcine heart model was a limitation; however, as a proof-of-concept study the reported results demonstrated a localized spatial distribution of NPs and formed a strong foundation for future validation using diseased tissues and *in vivo* model.

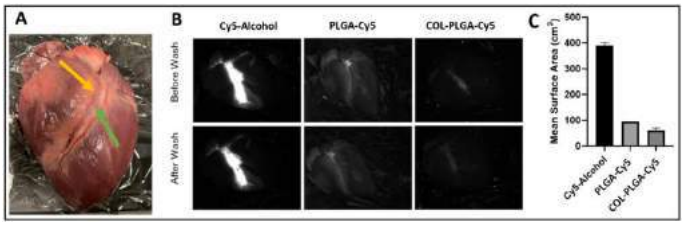


**Figure 1: (A) Injection site on a fresh porcine heart (orange arrow) and visible septal perforator (green arrow). (B) Anterior view following treatments with Cy5-Alcohol, PLGA-Cy5, and COL-PLGA-Cy5. (C) Mean surface area coverage after Cy5-alcohol, PLGA-Cy5, and COL-PLGA-Cy5 injections.**

## DISCUSSION

Using an *ex vivo* porcine heart model, we demonstrated that our targeted COL-PLGA NP ablation system had better localization capability than the treatment of alcohol, covering the least amount of septal area after the uppermost septal perforator injection.


## ACKNOWLEDGEMENTS

This study is in part supported by NIH 1R15HL140503 and T32 HL134613 and UT STARS.


## REFERENCES


[1] KC McGrath, et. al., BMES 2020 Virtual Annual Meeting, October 14-17, 2020

SB³C2022
Summer Biomechanics, Bioengineering and Biotransport Conference
June 20-23, Eastern Shore, MD, USA

# COMPARISON OF DISC DESIGNS AND OUTCOMES IN CERVICAL DISC ARTHROPLASTY USING MULTISCALE MODELING

**Yuvaraj Purushothaman, Jamie Baisden, Hoon Choi, Narayan Yoganandan**

Department of Neurosurgery
Medical College of Wisconsin
Milwaukee, WI

## INTRODUCTION

Cervical disc arthroplasty (CDA) is designed as a motion preserving technique to overcome the problems associated with anterior cervical discectomy and fusion (ACDF) used to treat cervical radiculopathy and myeloradiculopathy [1]. The CDA's have survived the noninferiority tests in comparison to ACDF but the ideal CDA has yet been determined. Clinical problems associated with ACDF are potential decrease in the range of motion and increase in adjacent segment degeneration, potentially requiring additional surgery. There have been multiple arthroplasty devices designed but only seven FDA has approved for commercial use [FDA.gov]. The inherent design features and biomaterials used affect cervical kinetics (loads and motions). Multiple models are needed to compare the responses of different devices, and a head-to-head evaluation using laboratory and clinical models is often the optimum choice. In this study a three-tiered multi-scale modeling approach was used to study the CDA's: longitudinal caprine model, human patient outcome analysis, and computational finite element modeling of different CDAs and ACDF.

## METHODS

**Animal Study: T**he study was approved by the institutional review boards (IRB), Institutional Animal Care and Use Committee at the VA, and sponsor. Eleven Alpine caprine (weight ranging from 36.4 to 72.2 kg) underwent anterior cervical discectomy fusion and plating in four animals, Mobi-C in four animals, and Prestige in three animals. All surgeries were done at the C3-C4 spinal level. The rationale for selecting the caprine is provided in the discussion. Pre- and immediate post-operative radiographs were taken to ensure the implant. Continuous monitoring of the animal was done in the Veterinary Medical Unit of the VA Medical Center. It included obtaining longitudinal x-rays until the six-months, after which time the animal was euthanized, and images were obtained after excision. Two neurosurgeons performed the procedure on every animal.

**Human Study:** A literature review was conducted with human data using the PubMed database. It covered 30 years for the five commonly used FDA approved CDA's: Prestige LP by Medtronics; Secure-C by Globus; Prodisc-C by Centinel Spine; Mobi-C by Biomet; and Bryan disc by Medtronic. Patient outcomes from our institution were examined after obtaining approvals from the local IRB and sponsor. Complications and outcomes were reviewed for each artificial disc.

**Finite element modeling study:** A previously validated three-dimensional osteoligamentous finite element model of the cervical column (C2-T1) was used [2]. The model simulated the vertebra of the body, posterior elements, intervertebral disc, and ligaments. Each vertebral body of the body consisted of a thin cortical shell, a softer cancellous bone, endplate, and a posterior bony structure. The cortical bone was modeled as a linear isotropic material of 0.5 mm thick shell surrounding the cancellous bone, and a 0.2 mm thick endplate was placed on the superior and inferior surfaces of the disc. The intervertebral disc was modeled composed of the nucleus pulposus, annulus ground substance, and annulus fibrosus. All major ligaments were included. Material properties from literature were used. Using standard surgical procedures, the intact spine was modified at the C5-C6 vertebral level to simulate the biomechanics of ACDF and two types of CDAs. One was a metal-on-metal (MOM) and the other one was a metal-on-polymer (MOP) type device. The anterior longitudinal ligament was removed at the surgical level in all cases. In the case of ADR, a cavity was created at the implanted level for the placement of the disc prosthesis. In the case of ACDF, the disc properties were altered at the surgical level to simulate the trabecular bone, and this simulated complete fusion. The plate was placed along the anterior surfaces from C5-C6 level, and four titanium screws were simulated. Figure 1 shows the coronal views of the finite element model for each case.

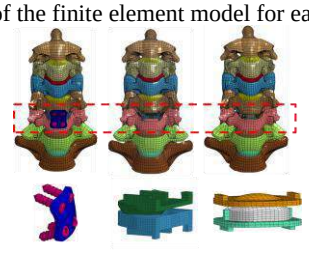

**Figure 1**: **Top row shows the coronal views of the spinal column and bottom rows show the ACDF, and MOM and MOP CDAs.**

All finite element models were fixed at the first thoracic vertebra in all degrees-of-freedom, and the load was applied at the superior endplate of the C2 vertebra. A follower load of 75 N and a bending moment of 2 Nm under flexion and extension and lateral bending were applied to the three groups, ACDF, MOM and MOP CDAs. The range of motion was measured at each level and across the C3-C7 levels. The variable moment loading protocol, also known as hybrid loading, was then applied [4]. The bending moment was varied until the ACDF, metal-on-metal and metal-on-polymer models responded with the same total C3-C7 range of motion. The range of motion and facet force were obtained at the index and adjacent segments under each loading mode.

## RESULTS

**Animal Study:** All four metal-on-polymer implants experienced anterior extrusion from the disc space and no additional animals were used to implant this device. Metal-on-metal implants experienced one anterior migration in six animals.

**Human study:** The kinematic responses were similar for all CDAs, i.e., improved range of motion and similar clinical risks/complications. The outcomes were mixed, however, with respect to the reported reduction in adjacent segment disease and need for additional surgeries.

**Finite element modeling study:** The metal-on-metal device had lower range of motion, lower facet forces at the index level and both adjacent levels compared to the metal-on-polymer device. The ACDF resulted in an increase in the range of motion at each spinal level except at the index level, and this was higher than the intact spine and both types of CDA's.

With respect to the intact spine, in flexion, the ACDF at C4-C5 and C6-C7 levels showed 27% and 16% increase in the range of motion. The metal-on-metal CDA had a decrease in the range of motion of 8% at the cephalad and 5% at the caudal level. The metal-on-polymer CDA responded with decreases of 5% and 14% at these levels, respectively.

In extension, for the ACDF, the increase in the range of motion at the cephalad and caudal levels were 34% and 21%, respectively. For the metal-on-metal CDA, the decrease in the range of motion was 7% at the cephalad level and 4% at the caudal level. For the metal-on-polymer CDA, the decrease was 12% and 13%, respectively.

In lateral bending, compared to the intact spine, for the ACDF, the increase in the range of motion at the cephalad and caudal levels were 19% and 10%, respectively. For the metal-on-metal CDA, the decrease in the range of motion was 8% at the cephalad level and 15% at the caudal level. For the metal-on-polymer CDA, the decrease was 5% and 15%, respectively.

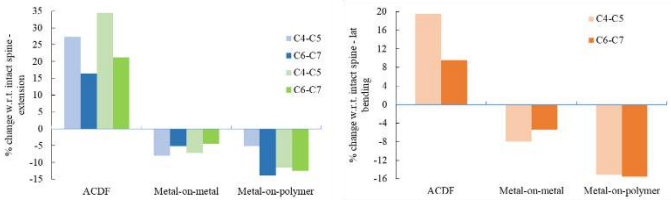


**Figure 2: Change in the range of motion at adjacent segments. Left chart shows the flexion (blue bars) and extension (green bars), and right chart shows the data for lateral bending.**

With respect to the intact spine, in the metal-on-metal CDA, facet forces decreased by 17% each at the cephalad and caudal levels. The increase in the facet force was 11% at the cephalad level and 12% at the caudal level in lateral bending. The metal-on-polymer CDA responded with a 34% decrease at the cephalad level and 27 % decrease at the caudal level in extension, and 18% decrease at the cephalad level and 7% decrease at the caudal level, in lateral bending.

At the index level, facet forces increased in both CDA's: 56% in extension and 20% in lateral bending for the metal-on-metal CDA and 174% in extension and 43% in lateral bending for the metal-on-polymer, while the ACDF responded with decreases of 85 and 90%, respectively.

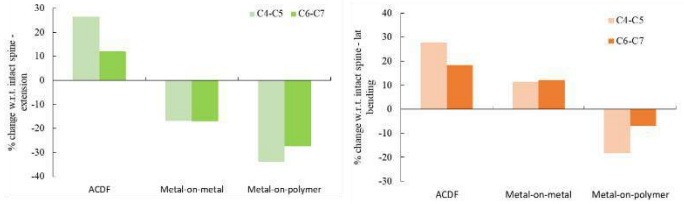


**Figure 3: Change in the fact force at adjacent segments. Left and right charts correspond to extension and lateral bending modes.**

## DISCUSSION

Differences in the range of motion and facet forces were noted within the CDA implants. This is attributed to the inherent design of the implant, i.e., material type and material properties of the CDA implant. The metal-on-metal implant exhibited less range of motion and less facet forces at the index/operative level compared to the metal-on-polymer implants that demonstrated greater motion and facet forces at the operative level and lower values at the adjacent segment levels. The differences in motion and facet forces between the metal-on-polymer CDA's infers that the intended design feature, i.e., the translational potential, and fixation of the implant to the adjacent endplates is responsible for these differences. This type of kinematic and load response would be theoretically predicted based on the proposed advantages of CDA over the ACDF but not necessarily observed in the clinical data as the determination of in vivo segmental loads are not possible. The potential advantage of CDA over the ACDF with respect to decreasing adjacent segment disease in humans has not been clinically confirmed and will require further studies. While the caprine model may be somewhat hypermobile, it was selected due to its striking similarities in the axial loading compared to the human, comparable size of the cervical vertebrae, and ability to accommodate the same FDA commercially available CDA implants used in patients, and the capacity tolerate the implantation surgery with a relatively quick recovery time. The hypermobility in the caprine with the most mobile CDA- metal-on-polymer correlated with anterior migration of the implant in all four animals. This is supported by the high facet force response elicited from the computational modeling study. Complications of human CDA's are somewhat difficult to quantify as anterior migrations may also be categorized as revision surgery non-specified in the human clinical literature.

## CONCLUSION

Distinct differences in the kinetics between metal-on-polymer and metal-on-metal CDAs were found in our multi-scale modeling that consisted of longitudinal patient outcomes, longitudinal animal surgical outcomes, and finite element modeling with a generic spinal column. Patient-specific models that accurately mimics patient anatomy, pain pattern, cervical pathology and occupation/ lifestyle risks should be used to select the optimal CDA to minimize patient risks, minimize the potential need for additional surgeries, and maximize patient outcomes. Such studies may have implications to military and civilian patients.

## ACKNOWLEDGEMENTS

This study was supported by the Office of the Assistant Secretary of Defense for Health Affairs, through the Broad Agency Announcement under Award No. W81XWH-16-1-0010 and VA Medical Center.

## REFERENCES

[1] Choi H, et al., *Eur. Spine.* J, 2019.
[2] Yoganandan N, et al., *Clin. Biomech.* 2020.
[3] John JD, et al., *J. Biomech. Eng.*, 2019.
[4] Patwardhan A, et al., *Spine*, 2001

# PORCINE NEONATAL HEART ECM-BASED HYDROGEL AS A CARDIAC INJECTABLE BIOMATERIAL

**Karla Perez (1), Alan Taylor (1), Jiazhu Xu (1), Diana Alatalo (3), Tam Nguyen (1), Rachel Claus (4), J. Ryan Butler (4), Pietro Bajona (2), Matthias Peltz (2), Fatemeh Hassanipour (3), Kytai T. Nguyen (1), Yi Hong (1), Jun Liao (1)**

(1) Department of Bioengineering, University of Texas at Arlington, Arlington, TX, USA
(2) Department of Cardiovascular and Thoracic Surgery, University of Texas Southwestern Medical Center, Dallas, TX, USA
(3) Department of Mechanical Engineering, University of Texas at Dallas, Richardson, TX, USA
(4) College of Veterinary Medicine, Mississippi State University, Mississippi State, MS, USA

## INTRODUCTION

Cardiac disease is the leading cause of death in the United States. Approximately 800,000 people suffer a heart attack each year, and the resulted myocardial infarction (MI) places a heavy burden on the healthcare. Hydrogels have emerged as a promising option for the treatment of MI. Injectable hydrogels can be delivered to the injured heart with minimally invasive procedures, such us catheter placement, which makes it an attractive approach as a new cardiac therapy. Several studies of adult cardiac ECM hydrogel have demonstrated benefits in the treatment of MI [1]. However, there has been no study that harnesses the regeneration potential of porcine neonatal heart extracellular matrix (ECM) and makes it a novel hydrogel platform. In this study, we aim to bridge this gap by developing a porcine neonatal heart ECM hydrogel (nhECM) that leverages the regenerative capacity of ECM microenvironment at the neonatal stage.

## METHODS

Neonatal porcine hearts were obtained from 0-day old piglets from a local farm (**Fig. 1A**). Each ventricle was visually inspected and followed by decellularization. A 1% SDS solution was used for decellularization, and the tissue was rinsed with DI water after full decellularization. The acellular nhECM was frozen overnight and then lyophilized. The obtained lyophilized nhECM was digested in 1 mg/ml HCL/pepsin solution. The mixture was then neutralized with NaOH and brought to pH at 7.4 PBS was added to achieve a final concentration of 10 mg/ml. The digested solution was then placed in a mold and incubated at 37 $^{o}$C for 30 minutes for gel formation. H&E staining was performed to verify decellularization. The nhECM hydrogel was characterized by SEM to assess microstructural morphology. Rheological properties were measured with a rheometer to obtain storage modulus, loss modulus, and gel dynamic behavior. Cell biocompatibility was assessed using MTS assay and Live/Dead staining.

## RESULTS

Thorough decellularization was achieved and confirmed by H&E staining. A white and opaque hydrogel could be obtained at 10 mg/ml concentration and 37$^{o}$C (**Fig. 1B**). SEM images of the nhECM hydrogel exhibited a typical porous structure of gel (**Fig. 1C**), which would allow cell growth and migration within. The MTS and Live/Dead results showed that the nhECM hydrogel had good cell compatibility with HL-1 cardiomyocytes, and allowed for HL-1 cell growth (**Fig. 1D**). The rheological measurement presents a storage modulus of approximately ~10 Pa in the linear viscoelastic region, and the nhECM hydrogel has the behavior of a gel-like structure.

## DISCUSSION

In this study, we have successfully developed an effective protocol to reliably fabricate porcine neonatal heart ECM hydrogel. The porcine nhECM hydrogel demonstrated excellent structural and mechanical integrity, a gel-like rheological behavior, and good cell compatibility. In short, our study proved the feasibility of porcine nhECM hydrogel as a potential cardiac injectable biomaterial. Further characterizations of the nhECM hydrogel system are ongoing, with an ultimate goal of developing new MI therapies.

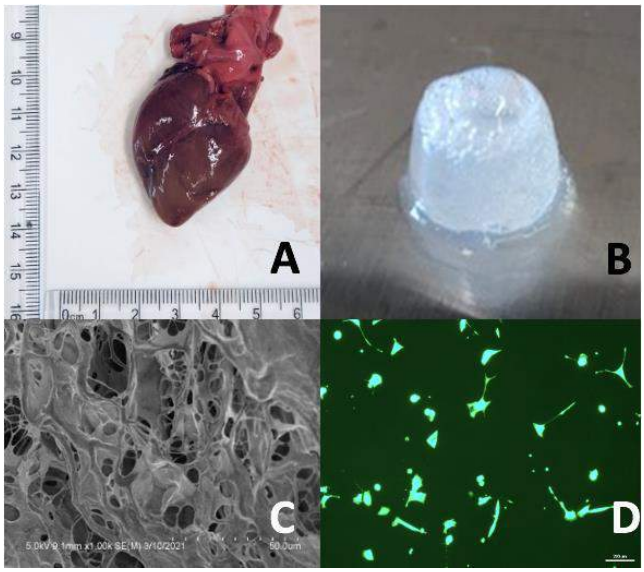


**Figure 1: (A) Neonatal porcine heart. (B) nhECM hydrogel. (C) Hydrogel microstructure observed by SEM. (D) Live/dead image of HL-1 cardiomyocytes seeded on the nhECM hydrogel at day 5.**

**ACKNOWLEDGEMENTS**

R15HL140503 and T32 HL134613 from NIH and UT STARS.

**REFERENCES**

[1] J.M. Singelyn, J.A. DeQuach, S.B. Seif-Naraghi, et al, Biomaterials 30(29) (2009) 5409-16.

SB³C2022
Summer Biomechanics, Bioengineering and Biotransport Conference
June 20-23, Eastern Shore, MD, USA

# SIMULATED PERFORMANCE OF A BIOPRINTED PULSATILE FONTAN CONDUIT

**Zinan Hu (1), Erica L. Schwarz (2), Jessica Herrmann (3), Mark Skylar Scott (2), Alison L. Marsden (2,4)**

(1) Department of Mechanical Engineering, Stanford University, Palo Alto, CA, USA

(2) Department of Medicine, Stanford University, Palo Alto, CA, USA

(3) Department of Pediatrics, Stanford University, Palo Alto, CA, USA

(4) Department of Bioengineering, Stanford University, Palo Alto, CA, USA

## INTRODUCTION

For patients born with univentricular hearts, the Fontan surgery, the final of three staged palliative surgical procedures, places the pulmonary and systemic circulations in series. Though it extends the life expectancy of patients significantly, survivors of the Fontan procedure tend to develop a state of circulatory inefficiency due to the lack of a subpulmonary ventricle. This inefficiency leads to an elevation in central venous pressure while simultaneously reducing pulmonary artery pressure and pulsatility in a condition known as the Fontan paradox [1]. Over time, the Fontan paradox may contribute to various morbidities, including early demise, arrythmias, and reduced exercise tolerance [2]. Years of research aimed at preventing or reversing the Fontan paradox have unfortunately produced limited clinical benefit. Replacement of the missing subpulmonary pump source has been proposed as a means to overcome the Fontan paradox. Mechanical circulatory pumps have received considerable attention, and remain promising, but are hindered by limitations of external battery supply and artificial materials. Thus, our group is exploring 3D bioprinted conduits as a possible replacement for traditional conduits which lack growth potential. Connecting the inferior vena cava (IVC) to the pulmonary arteries, bioprinted conduits could theoretically contract to provide a pulsatile energy source to the lungs.

Bioprinting of large-scale contractile materials is currently an expensive and complex procedure. Computational modeling provides a means to accelerate conduit design by allowing for efficient exploration of the design space and an assessment of how the hemodynamics of a Fontan patient changes in response to conduit design choices. In this study, we construct both a reduced order model and a 3D model of the pulsatile conduit to evaluate design parameters of interest. Using a closed-loop lumped parameter network (LPN), we show how valve placement, conduit geometry, and contractile properties change patients' hemodynamics, thus evaluating the functionality of the conduit. Using a 3D model, we evaluate mechanisms of contraction, combining electrophysiology and active contraction models. These models can provide a comprehensive means to evaluate bioprinted conduit designs and narrow the design space prior to printing in the lab.

## METHODS

We have developed a closed-loop LPN computational model of a Fontan patient based on work by Kung et al [3] (Fig. 1a). LPN parameters were tuned for a 6-month post-Fontan patient studied by Schwarz et al [4]. The proposed pulsatile Fontan conduit was designed in the Skylar-Scott laboratory at Stanford University. Briefly, the conduit will be 3D bioprinted using a combination of two printing techniques: freeform reversible embedding of suspended hydrogels [5] and sacrificial writing of functional tissues [6]. The myocardial walls will be manufactured using a cardiac organoid-laden bioink, while the valves will be printed with a collagen ink. The vasculature will be created by bioprinting a sacrificial gelatin ink into the myocardial walls and later evacuating the ink to yield perfusable channels (Fig. 1b). The conduit is designed to achieve a 5 mN/mm$^2$ active stress generation and is assumed to have a passive stiffness of 3 mN/mm$^2$.

We began by creating a 0D model of the pulsatile conduit. Having similar function as a ventricle, the 0D conduit model is simplified to be a time-varying elastance component of our LPN model of the Fontan circulation. The pressure of the conduit is governed by its volume and capacitance (Equation 1). The parameters of the conduit were tuned to achieve 30% volume amplitude, comparable to initial estimates of pulsatile conduit performance. We coupled the 0D valve model and simulated the situations with zero valve, one valve, and two valves.

$$P_{con} = i\frac{V_{con}-V_0}{C_{con}} + c_{con}(\exp(d(V_{con}-V_0)) - 1) \quad (1)$$

We further investigated how significantly these the initial radius, initial thickness, and activation function impacted the conduit design by creating a 1D model of the pulsatile conduit. The 1D model is a simplified cylinder with passive and active stress responses. Assuming contraction is purely circumferential and material is incompressible, we

derived the stress expression (Equation 2) and weak form of mechanical equilibrium (Equation 3) [7-8]. The inlet and outlet boundary conditions were prescribed with pressure waveforms at the inlet of 12-14mmHg and distal pressure of 7.5 mmHg. To find the conduit design providing maximum pressure and volume pulses, we performed parameter sweeps of the maximum active stress, thickness and radius. The maximum active stress ranged from 0 to $4 \cdot 10^4$ N/m$^2$, thickness from $1 \cdot 10^{-3}$ to $4 \cdot 10^{-3}$ m, and radius from 0.005 to 0.2 m.

$$\sum_y = 2(1 - C_{\sigma\sigma}^{-2})\left(\frac{dW}{J_1} + \frac{dW}{J_2}\right) + 2\frac{dW}{J_4} + i\sigma_{1D} + \eta(\dot{C} + C^{-4}) \quad (2)$$

$$\rho d_0 \ddot{y} + \frac{d_0}{R_0}\left(1 + \frac{y}{R_0}\right)\sum_y = C_{\sigma\sigma}^{1/2} P_{con} \quad (3)$$

Last, a full 3D finite element model was implemented combining the passive and active stresses from the myocardium fiber, and Purkinje fiber propagation of the cardiac action potentials. We used the Guccione model for myocardium fiber's material property, and tenTusscher-Panfilov model for the electrophysiology. These two models were one-way coupled and simulated in the svFSI finite element solver provide with the open-source software SimVascular [9]. The output action potential of Purkinje fibers from the electrophysiology simulation triggered the active contraction of the myocardium fiber. Boundary conditions were prescribed by hemodynamic pressure acted on the inner wall, and the outer wall was traction-free. Dirichlet boundary conditions were applied to top and bottom faces. Similar inlet and outlet pressure waveforms in the 1D simulation were used for this 3D conduit.

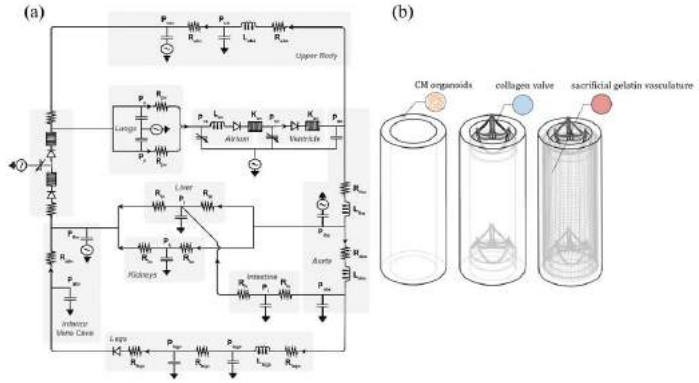


**Figure 1: (a) Layout of the post-Fontan LPN. (b) Conduit prototype and valve placement**

## RESULTS

We used the LPM model to compare conduit designs with zero, one or two valves and varying capacitances and frequencies. There was no significant change in pulmonary pressure or flow rate with or without valves. The one valve and zero valve cases were similar because there is relatively low backflow into the IVC due to the elevated IVC pressure. The implementation of two valves decreased the liver pressure from 16.38 to 15.23 mmHg, while the pressure of the conduit decreases from 11.17 to 9.87 mmHg. The capacitance of the system reduced the effects of the transient pressure reductions in the conduit. Higher elastance increased the volume amplitude from 29.4% to 48.77%. Increasing frequency of conduit induced a 15.0% reduction in liver pressure despite having roughly the same volume amplitude around 32.3%. Further, it better transfers pulsatility to the pulmonary junction.

Performing the parameter sweeps of the 1D model with two valves, we demonstrated that maximum stress and thickness were positively correlated with the volume and pressure pulses. At constant maximum active stress, thickness, and length, there is a radius that achieves the highest pressure pulse. Our results indicate that within certain constraints like conduit volume, the conduit design can be optimized to maximize performance metrics such as volume and pressure pulse.

The assumption of circumferential and simultaneous contraction is no longer applicable in 3D simulation which more accurately recapitulates the behavior of bioprinted tissue. Coupled with electronic propagation of Purkinje fiber, starting at the top end, the conduit is gradually activated over the first 4.85% of the cardiac cycle. Here, the maximum difference in active time is 38.8 ms and the isovolumetric contraction is assumed to last 100 ms. The volume pulse is 56.89% with an average ejection fraction during contraction of 38.98%. In contrast the case of simultaneous contraction over the conduit length produces a volume amplitude of 36.12%. We further investigated the role of fiber direction. We assign the fibers helically around the conduit with varying angles between fibers and the horizontal plane. The circularly oriented fiber gave a maximum volume pulse of 46.4%. With longitudinal orientation, the change in volume decreases to 20.82%. A conduit with mixed fiber directions resists volume changes and reduces the volume pulse to 15.38%. Multiple layers with different fiber directions in each layer generate 9.0% volume change.

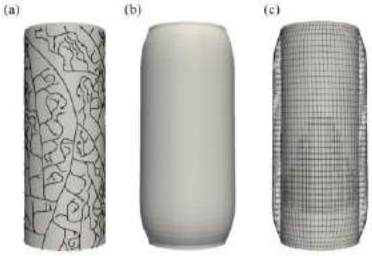


**Figure 2: (a) Illustration of Purkinje fibers. (b) Inflated conduit after prestress. (c) Maximum volume amplitude is 36.12% for the circumferential contraction.**

## DISCUSSION

We have developed 0D and 1D LPN models to explore how different pulsatile conduit designs can impact the hemodynamics and physiology of Fontan patients and possibly reverse the Fontan paradox. In our 0D LPN study, we showed that two valves are needed to optimally reverse the Fontan paradox. Increasing elastance is a way to increase volume amplitude and decrease central venous pressure, but increasing frequency can better increase the pulsatility of flow into the lung as well as reduce IVC pressure. The relation of geometry parameters and conduit performance was studied in our 1D model. The existence of a non-monotonic relationship between radius and conduit performance demonstrates the ability to use parameter-sweeping simulations to provide optimal design guidance prior to printing in the lab. 3D results demonstrate the importance of spatially varying activation and fiber direction. However, the clamping boundary conditions at the top and base faces may overcome the effects of longitudinal force. Future work should modify our approach to apply moving boundary conditions. We also plan to couple the full 3D model with the LPN framework to evaluate patients' hemodynamics and the effectiveness of the conduit in preventing or reversing the Fontan paradox.

## ACKNOWLEDGEMENTS

This study is supported by Additional Ventures Foundation Cures Collaborative Grant and the American Heart Association.

## REFERENCES

[1] de Leval, M R, *Pediatric cardiology*, vol. 19,4, 1998; [2] Gewillig M, et al., *Heart* 2016;102:1081-1086; [3] E. Kung, et al., *J Biomed Eng*, 136: 081007, 2014; [4] Schwarz, E.L. et al., *npj Regen Med* 6, 38, 2021; [5] Lee, A et al. *Science (N.Y.)* vol. 365,6452 (2019): 482-487; [6] M. A. Skylar-Scott, et al., *Sci. Adv*.5, eaaw 2459, 2019; [7] Caruel, M. et al., *Biomech Model Mechanobiol* 13, 897–914, 2014; [8] Sainte-Marie, J., et al., *Comput. Struct*. 84:1743–1759, 2006; [9] Updegrove, A et al, *A of biomedical eng* vol. 45,3, 2017: 525-541.

# CHARACTERIZATION OF PORCINE PANCREAS TISSUE PLASMONIC PHOTOTHERMAL HEATING AT 808 AND 1064 NM WAVELENGTHS

**F. Akhter (1), A. L. Smith (1), S. Manrique-Bedoya (1), C. Moreau (2), Y. Feng (3), K. M. Mayer (3), R. L. Hood (1, 4)**

(1) Mechanical Engineering, University of Texas at San Antonio, San Antonio, TX, USA
(2) Gastroenterology and Transplant, UT Health San Antonio, San Antonio, TX, USA
(3) Physics and Astronomy, University of Texas at San Antonio, San Antonio, TX, USA
(4) Graduate School of Biomedical Sciences, UT Health San Antonio, San Antonio, TX, USA

## INTRODUCTION

Pancreatic ductal adenocarcinoma (PDAC), a lethal and one of the most aggressive malignancies, has a five-year mean survival rate of around 10%[1]. Current treatment methods including surgery and different ablation techniques such as radiofrequency ablation and photodynamic therapy are lacking in improving the survival rate that could be attributed to advanced age, late-stage diagnosis, poor specificity, and adverse side effects[2]. Hence, innovative, selective therapeutic approaches for targeting and controlling the ablation volume are desperately needed. Plasmonic photothermal therapy (PPTT) utilizes different gold nanoparticles, i.e., gold nanorods (GNRs) to target tumor region followed by exposure to near-infrared light (NIR) to induce hyperthermia and tissue damage[3]. The advantage of using GNRs includes size and shape tunability, that would allow to utilize a specific light wavelength for achieving the surface plasmon resonance (peak absorption of photon by the GNRs)[4]. Literature review showed that biological tissue demonstrates lower light absorbance rate at ~800 nm wavelength that could be utilized for selectively heating of the GNRs[4]. In current study, a fiberoptic microneedle device (FMD, earlier developed by our group) was utilized for codelivering the GNRs and light to the targeted tissue volume through a silica-based light guiding capillary[5]. We hypothesized that local delivery of custom GNRs and ~800 nm range light via FMD into the targeted tissue volume would selectively heat the GNRs with minimum thermal damage to the healthy surrounding tissue. The aim of this study is to characterize the photothermal heating of *ex vivo* porcine pancreas tissue at two clinically important light wavelengths, 808 and 1064 nm. Light delivery was explored with both a collimated beam and through the FMD, both with and without the presence of GNRs. The effect of laser exposure time and GNRs concentrations were also investigated and reported.

## METHODS

Porcine pancreas tissue samples were collected from a USDA-approved abattoir and transported to the lab immediately (~30 min). Upon arrival, the samples were washed in phosphate-buffered saline (PBS) solution and sliced in a 3 × 3 $cm^2$ cross-section area using a scalpel. Samples used in different experiments had a thickness of approximately 1 ± 0.05 cm. GNRs were synthesized by a seed-mediated growth protocol described in the literature[6]. The optical absorbance of the nanorods was confirmed via UV-Vis spectroscopy (400–1100 nm) and their geometry (length, width, aspect ratio) was measured via SEM (scanning electron microscopy) imaging and analyzed in ImageJ. As-synthesized GNRs were utilized in this experiment where GNRs were suspended in CTAB solution (Cetyltrimethylammonium bromide).

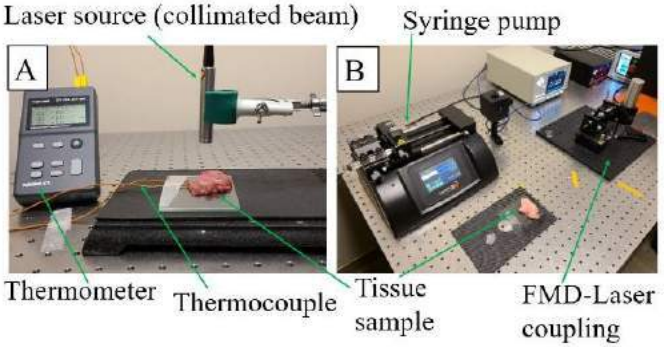


**Figure 1: Experimental setup for *ex vivo* porcine pancreas tissue photothermal heating via (A) collimated beam, (B) FMD.**

Two different continuous wave laser sources were utilized with collimated beam outputs at 808 nm and 1064 nm wavelengths. The tissue specimen was placed on a glass slide 4 cm beneath the laser

attached to an adjustable holder (Figure 1A). Two K-type thermocouples were inserted into the tissue at 5 mm below the tissue surface to measure the temperature at 5 Hz frequency. Laser exposure continued until the tissue temperature reached a steady state. In next set of experiments, FMD tips (365 µm diameter) were inserted horizontally (2–3 mm) into the tissue top surface for light delivery with/without GNRs (0.1-1 nM concentrations) (Figure 1B). Laser exposure continued for 60s followed by free convective cooling. Tissue temperatures were measured via a thermal camera (2 Hz). In both experiments, laser irradiations were set within 20-50 mW·mm$^{-2}$. The range was selected through preliminary tests to avoid tissue burning. All experiments started when tissue sample reached the room temperature (22°C). The tissue samples were discarded after each test. A single test was repeated five times (n = 5) for each laser irradiation and GNR concentration.

## RESULTS

SEM images of the GNRs were utilized to measure the average dimension of nanorods: length = 95.2 ± 4.7 nm and width = 24.8 ± 1.5 nm (Figure 2A). A spectrometric analysis showed the resonance wavelength (peak photon absorbance) of the GNRs to be 813 nm (Figure 2B). At 1064 nm, the GNRs' optical absorbance reduced to less than half of the peak absorbance.

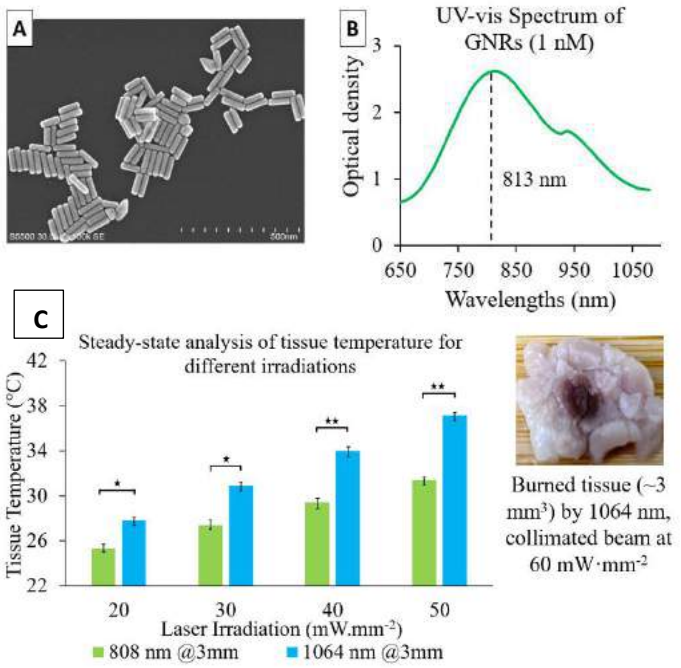


**Figure 2: (A) SEM image of GNRs, (B) UV-vis spectrum of GNRs, (C) Tissue temperature vs. Laser irradiation graph**

Preliminary tests demonstrated the threshold light intensity (≥ 60 mW·mm$^{-2}$ for 1064 nm and ≥ 80 mW·mm$^{-2}$ for 808 nm) that would induce tissue carbonization, an unwanted outcome to avoid during tissue photothermal heating. Analysis of the results (Figure 2C) showed that, at 808 nm, both tissue temperature increase (ΔT) and rate of temperature rise (ΔT/time) were 51.4 ± 5.5% and 87.7 ± 6.1% higher for 1064 nm, respectively. It implies that 808 nm will be less harmful than 1064 nm during plasmonic heating of pancreas tissue when paired with appropriate GNRs (peak resonance at ~800 nm).

Results from tissue photothermal heating by FMD+GNR (Figure 3) showed that the plasmonic heating of GNRs at 808 nm resulted in a sharp increase of porcine pancreas tissue temperature (~200% temperature rise than FMD only exposure, Figure 3A vs. 3C). GNRs absorbed maximum photon energy at 808 nm and dissipated heat, resulting in significant tissue temperature rise within a short time (60s). In contrast, 1064 nm laser increased the overall tissue temperature due to the higher photon absorption, which is not desired during selective tissue heating.

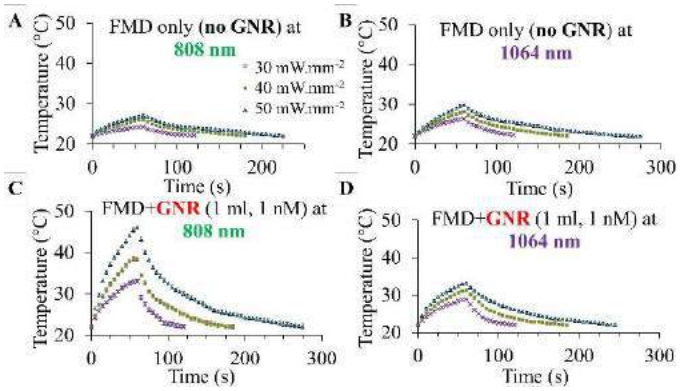


**Figure 3: *Ex vivo* porcine pancreas tissue plasmonic photothermal heating without GNRs at (A) 808 nm, (B) 1064 nm; and with locally infused GNRs (1 nM, 1 ml) at (C) 808 nm, and (D) 1064 nm.**

## DISCUSSION

808 nm demonstrated selective plasmonic heating capability of GNRs while being less lethal to the healthy pancreas tissue. However, laser intensity, exposure time, and GNR concentrations have direct impact on tissue plasmonic heating. Selective photothermal heating procedure can be controlled by manipulation of these parameters to achieve less tissue photothermal damage while ensuring high light to heat conversion of GNRs. A major limitation of this *ex vivo* study could be the tissue physiological condition as pancreas tissue degrades quickly over time which might affect the optical properties. This error was minimized by emphasizing on using fresh tissue samples in majority of the experiments. Custom GNRs utilized in this study can be functionalized through PEG (polyethylene glycol) coating to target the tumor tissue for future clinical application. Further investigation with human pancreas tumor tissue would bolster the hypothesis proven in this study.


## ACKNOWLEDGEMENTS

The funding source from the University of Texas at San Antonio is highly appreciated.


## REFERENCES


[1] Siegel RL et al., *CA: a cancer J. for clinicians*, 66(1):7-30, 2016
[2] Huang X et al., *Lasers in medical science*, 23(3):217, 2008
[3] Ali MRK et al., *International J. of nanomedicine*, 11:4849, 2016
[4] Jain PK et al., *The J. of physical chemistry B*. 110 (14):7238, 2006
[5] Akhter F. et al., *J. of the Mech. Behavior of Biomed. Mat.*, 112: 104042, 2020
[6] Nikoobakht B et al., *Chemistry of Materials*, 15(10):1957-1962, 2003

# A PREDICTIVE SIMULATION OF COREVALVE IMPLANTATION IN A PATIENT WITH THREE BIOPROSTHETIC AORTIC VALVES IN PLACE – A CASE STUDY

**Fateme Esmailie (1), Breandan Yeats (1), Huang Chen (1), Milad Samaee (1), Atefeh Razavi (1), Sri Krishna Sivakumar (1), Pradeep Yadav (2), Venkateshwar Polsani (2), Vinod Thourani (2), and Lakshmi Dasi (1)**

(1) Department of Biomedical Engineering
Georgia Institute of Technology
Atlanta, Georgia, United States

(2) Department of Cardiology
Piedmont Hospital
Atlanta, Georgia, United States

## INTRODUCTION

Aortic stenosis is the most common cardiovascular disorder, that may be treated with medication, valve repair, or valve replacement depending on the severity [1]. Aortic valve replacement is the replacement of the native aortic valve with a bioprosthetic valve either surgically or through transcatheter approaches. Transcatheter aortic valve replacement is a minimally invasive method that has been growing in recent years [2]. Bioprosthetic valves exhibit limited durability of 12-20 years due to structural valve deterioration. Therefore, younger patients undergoing aortic valve replacement with a bioprosthetic valve would need multiple interventions over the span of their lifetime [3]. Valve-in-valve transcatheter aortic valve replacement (ViV TAVR) is one possible solution for treating patients with failed prosthetic aortic valves who are too frail to undergo redo surgery [4, 5]. Coronary obstruction is one of the main problems related to the ViV TAVR procedure due to the proximity of the coronary ostium to the bioprosthetic leaflet and the supra-annular positioning of surgical bioprostheses [3]. Patient specific finite element simulations enable optimization of device selection and placement to reduce obstruction risk. The goal of this study is to demonstrate the role of computational modeling to reduce coronary obstruction risk in procedural planning of TAVR in a patient with one failed surgical valve, and two failed transcatheter heart valves in place.

## METHODS

A 78-year-old male with three bioprosthetic valves in place (a CoreValve 23, a Sapien 23, and an Edwards 3000 bovine pericardial valve) showing restricted motion of leaflets and mild calcification, was analyzed. Cardiac computed tomography (CT) images were imported to Materialise MIS (Leuven, Belgium). The aortic root and a portion of left ventricle were segmented using Mimics 24.0. CAD models of the

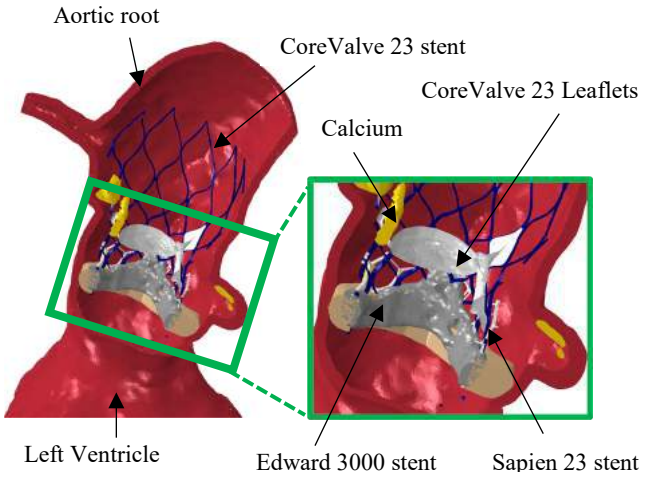


**Figure 1:** Patient segmentation including the aortic root and calcium and valve registration of the Edwards 3000 bovine pericardial valve, Sapien 23, and CoreValve 23**.**

CoreValve, Sapien, and the surgical valves were generated in Solidworks (Waltham, MA, USA) based on a microCT performed on the actual valves. To avoid significant blooming present in the CT images, the 3D models of the valves were registered and reconstructed using an in-house code (**Figure 1**). The bioprosthetic valve stents, aortic root, calcium, and leaflets were meshed in 3-Matic 15.0. ViV TAVR deployment for the CoreValve 23 and Sapien 23 were simulated using finite element method in Abaqus Explicit (Johnston, RI, USA). Sapien

23 was deployed by inflating a 23mm balloon using a fluid-cavity approach. CoreValve 23 was deployed by leveraging the shape-memory properties of the nitinol material model by crimping the stent then allowing it to expand [6]. The material properties for all components was derived from literature [7-10].

Coronary obstruction risk was evaluated by measuring the ratio of the distance from the bioprosthetic leaflet to the coronary ostium (DLC) by the diameter of the coronary (d) with a DLC/d of <0.7 considered to be representative of high risk of coronary obstruction [11].

## RESULTS

The patient had a prior coronary artery bypass graft surgery for the right coronary, and hence the right coronary is located much farther from the valve leaflets. As a result, the ratio of the distance from the coronary from bioprosthetic leaflet to the coronary ostium by the diameter of the coronary will be larger than 0.7. Thus, there is no concern of right coronary obstruction. The diameter of the left coronary in the widest region is 6.75 mm, and the distance of Sapien 23 leaflets from the coronary ostium is about 4.85 mm (see Figure 2 (a)), DLC/d = 0.71. The distance of CoreValve 23 leaflets from the coronary ostium is 9.79 mm, DLC/d = 1.45 (See **Figure 2** (b)). Therefore, the risk of coronary obstruction is lower for CoreValve 23. The results of the deployment simulation for both Sapien 23 and CoreValve 23 were presented to physicians and the CoreValve 23 was selected to be implanted in this specific case. The post-TAVR fluoroscopy image and the simulation results are illustrated in **Figure 3**. The comparison of the predicted final location of the valve and the post-TAVR fluoroscopy image, confirmed the predictive capabilities of the simulation (**Figure 3**).

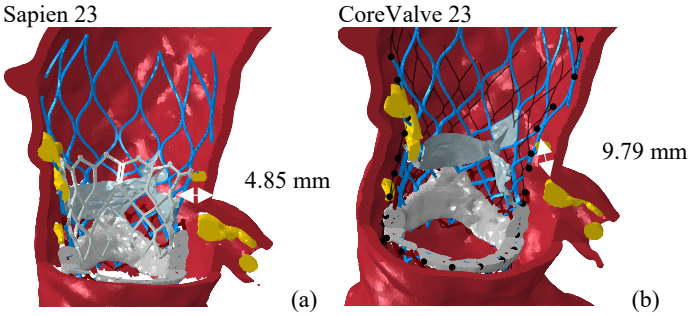


**Figure 2.** The distance from the bioprosthetic leaflet to the coronary ostium ($D_1$), (a) Sapien 23, (b) CoreValve 23.

## DISCUSSION

This study shows one application of computational modeling for pre-planning of ViV TAVR procedures in assisting physicians to predict and prevent possible complications. Due to the patient's condition, the post-TAVR CT imaging was a challenging task. Therefore, it was difficult to achieve enough data to validate the simulations results with CT images. Further studies are required, including performing computational fluid dynamics to quantify Post-TAVR pressure gradient, washout time, and resident time.

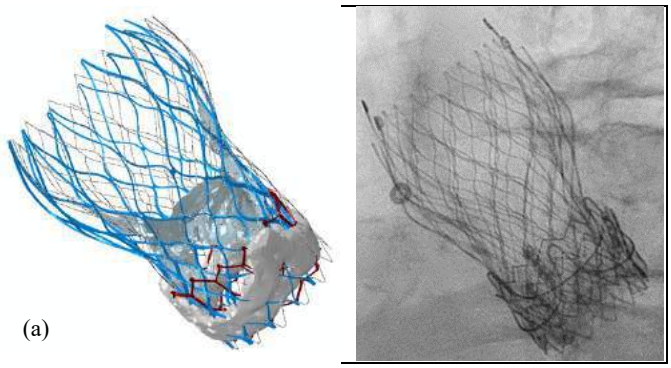


**Figure 3.** Simulation results after deploying CoreValve 23. (a) simulation results, (b) post TAVR fluoroscopy image.

## References


[1] Hinton, R. B. Current opinion in pediatrics, 26. 5: 546–552, 2014, https://doi.org/10.1097/MOP.0000000000000137

[2] Hemelrijck, V. M., et al. F1000Research, 7: 58. 2018, doi:10.12688/f1000research.11906.1

[3] Gąsior, T et al., Cor et Vasa, 59. 1: e35-e41, 2017, https://doi.org/10.1016/j.crvasa.2017.01.010.

[4] Deharo, P et al., Journal of the American College of Cardiology, 76. 5: 489-499, 2020. https://doi.org/10.1016/j.jacc.2020.06.010.

[5] Edelman, JJ, et al. Innovations. 14. 4:299-310. doi:10.1177/1556984519858020

[6] Zamtzis, S., et al., Medical Engineering and Physics 35. 1: 125-130, 2013

[7] Tzamtzis, S., et al., Medical engineering & physics, 35(1): 125-130, 2013

[8] Emendi, M., et al., Annals of Biomedical Engineering, 1-15, 2020

[9] Holzapfel, G.A., et al., J. Biomech. Eng., 126(5): 657-665, 2004

[10] Pham, Thuy, and Wei Sun, Journal of Biomedical Materials Research Part A, 102.8: 2692-2703 (2014)

[11] Heitkemper, M., et al., The Journal of Thoracic and Cardiovascular Surgery, 159. 3: 829-838.e3, 2020, https://doi.org/10.1016/j.jtcvs.2019.04.091.

SB³C2022
Summer Biomechanics, Bioengineering and Biotransport Conference
June 20-23, Eastern Shore, MD, USA

# EFFECTS OF COMPROMISED SYNOVIAL FLUID ON ARTICULAR CARTILAGE TRIBOLOGICAL REHYDRATION AND LUBRICATION

**Shamimur R. Akanda (1), David L. Burris (1), Christopher Price (1,2)**

(1) Mechanical Engineering, University of Delaware, Newark, DE, USA
(2) Biomedical Engineering, University of Delaware, Newark, DE, USA

## INTRODUCTION

Articular cartilage is the shock absorbing and lubricating tissue that allows near frictionless ($\mu$ ~0.002*)* joint articulation. Cartilage's phenomenal tribomechanical functions have predominately been ascribed to two mechanisms, interstitial and boundary lubrication.[1] Pressurization of cartilage's interstitial fluid allows it to carry nearly all applied stresses upon initial loading. This high fluid load support (FLS) shields the matrix from deformation and promotes exceptional lubricity.[1] However, under quasistatic contact stresses (which range from 0.2-2MPa *in vivo)*[2] time-dependent interstitial fluid exudation occurs, leading to elevated tissue strains and equilibrium friction coefficients (*~0.3*). Thus, mechanisms to minimize interfacial shear/friction forces appear necessary to mitigate the negative effects of fluid exudation on lubrication.

Synovial fluid (SF) is the native bathing solution of joints and contains constituents (hyaluronic acid (HA) & lubricin) thought to act as classical friction-reducing boundary lubricants. However, under very low (*i.e.*, zero) FLS and slow sliding speeds (≤1mm/s), rather unremarkable $\mu$ values (~0.2) have been observed for SF-lubricated cartilage; vs. ~0.3 for PBS.[3] To what degree such conditions replicate the *in vivo* sliding environment is also unclear. This fact is highlighted by our findings, using the convergent stationary contact area (cSCA) testing configuration, that cartilage can effectively combat load-induced interstitial fluid loss via articulation. Under sliding conditions consistent with average *in vivo* contact pressures (~0.25MPa) and sliding speeds (<30mm/s), interfacial sliding drives potent interstitial fluid recovery.[4-6] This 'tribological rehydration' robustly rescues tissue compression, FLS, and interstitial lubrication ($\mu$ ~0.02*)*—in the absence of SF.

Furthermore, when high-speed cSCA studies were performed in SF (and HA), an unanticipated lubrication synergy between sliding-driven fluid recovery and bath composition was observed. Tribological rehydration within SF-lubricated cartilage produced equilibrium friction coefficients ~10-fold lower than through tribological rehydration within PBS alone (0.002 for SF vs. 0.02 for PBS) with no concomitant benefit to hydration recovery.[7]

While the mechanisms underpinning this lubrication synergy are uncertain, a key question of clinical significance arises: *how might alterations in SF composition, including those seen in osteoarthritic disease, alter FLS recovery and lubricity in the presence of tribological rehydration promoting conditions?* On the one hand, the HA content of SF decreases with disease severity, resulting in decreased SF viscosity and 'boundary mode' lubricating capacity.[8] On the other hand, 'diseased' SF is more dilute than naïve SF (270mOsm vs. 450mOsm),[9] potentially altering tissue swelling responses. Either change could impact tribological rehydration and subsequent lubrication behaviors, and the study of their effects on cartilage could yield key insights into the natural tribomechanics of both healthy and diseased joints.

In the present study we investigated the tribological rehydration and lubrication behaviors of bovine cSCA explants, under both high- and low-speed sliding, in the presence of healthy SF vs. SF treated to model 'diseased state' compositions (*i.e.*, dilution by 25% or digestion with hyaluronidase). We hypothesized that if 'diseased' SF is a poor lubricant, then dilution and/or degradation of SF would generate significantly higher friction coefficients and a less lubricious sliding environment during both high and low cSCA sliding speeds. OwHo

## METHODS

19mm ϕ osteochondral cores were extracted from skeletally mature bovine femoral condyles using a coring bit, washed, and stored in 400mOsm phosphate buffered saline (sucrose was added to increase the osmolarity of 1x PBS). Pairwise tribological characterization of individual cSCA explants were performed on a reciprocating *in situ* tribometer in a compression matched manner for the following bathing solution combinations: i) 400 then 300mOsm PBS, ii) 100% bovine SF then 75% SF (diluted with di$H_2O$), or iii) naïve (100%) SF then SF digested for 2 hrs with 25ug/ml of hyaluronidase (Hyal). The tribological testing protocol comprised 20 min of compression at 5N

followed by 10 min of compression + sliding at 80 mm/s or 10 mm/s while bathed in the first solution (test 1; Fig. 1). Explants were then washed with 400mOsm PBS and allowed to free swell for ≥2 hrs in their second (test 2) bathing solution. Explants then underwent tribological testing in the second bathing solution; here, explants were statically loaded to the compression value reached during test 1 followed by 10 minutes of sliding. Separate explants were tested at each sliding speed.

Start- and end-of-sliding compression ($\delta$) and kinetic friction coefficients ($\mu$) were recorded via LABVIEW and analyzed in MATLAB. The effects of 'diseased' bathing solution were compared using paired *t*-tests (*, naive vs. diluted/digested), and the effects of sliding speed via *t*-tests (#) for each individual bathing solution; $p<0.05$.

## RESULTS

As seen previously in cSCA explants,[10] stereotypical sliding-speed-dependent compression (*i.e.*, tribological rehydration) and friction recovery behaviors (Fig. 1) were observed for all bathing solutions (Fig. 2). As reported previously, a potent lubrication synergy between tribological rehydration and synovial fluid presence at high sliding speeds[6] was observed (Fig. 2C). Contrary to our hypothesis that diluted and/or degraded SF is a 'poor' lubricant, we observed little to no effect of SF-dilution or enzymatic digestion on the lubrication responses of cSCA explants. There were no statistically significant pairwise differences in the friction behaviors of cSCA explants bathed in normal SF vs. either 25% diluted or Hyal-digested SF. Furthermore, dilution had no meaningful effect on compression recovery, while Hyal digestion produced a modest, statistically significant increase in high-speed compression recovery (Fig. 3).

Tribomechanical tests in 400 vs. 300mOsm PBS were conducted as controls to highlight the specific contributions of both SF presence and bath osmolarity changes on tribological rehydration and lubricity

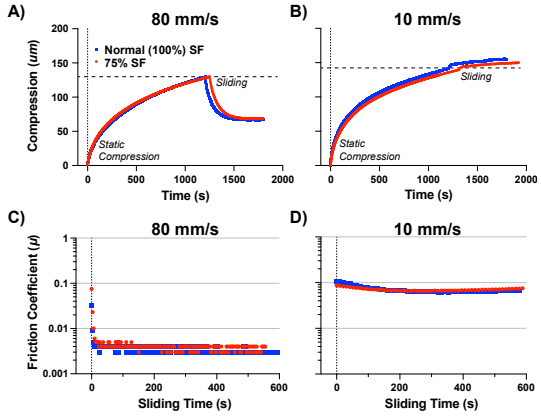


**Fig. 1 Representative compression and friction traces from two bovine cSCA explants slid at 80mm/s (A&C; sample 1) and 10mm/s (B&C, sample 2), respectively, in the presence of normal (100%; blue) vs. diluted (75%, red) synovial fluid (SF).**

## DISCUSSION

The present study highlights the unique additive lubrication benefit that interstitial fluid recovery, interstitial lubrication, and SF presence combined provide under high sliding speeds.[6] As expected, high-speed cSCA sliding led to compression recovery/tribological rehydration and friction suppression irrespective of bathing solution. In contrast, slow sliding resulted in continued interstitial fluid exudation and reduced lubricity under all bathing solutions.[3-6] Critically, SF promoted vanishingly low equilibrium friction coefficients at high speed (among the lowest values observed in benchtop studies; $\mu$ ~0.005 compared to ~0.02 in PBS), while disease-associated changes to SF composition (simulated through dilution/digestion) had no meaningful impact on

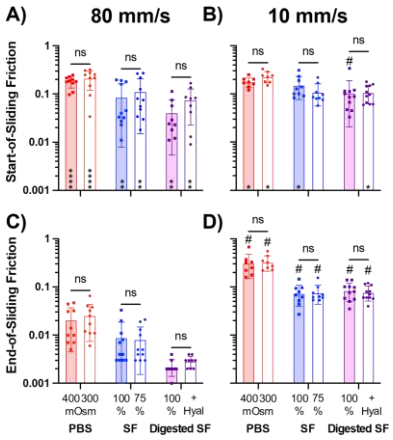


**Fig. 2 Start- (A, B) and end-of-sliding friction (C, D) outcomes for pairwise cSCA tests in the presence of 400 vs. 300mOsm PBS, 100% vs. 75% SF, or naïve vs Hyal digested SF at either 80 or 10mm/s.**

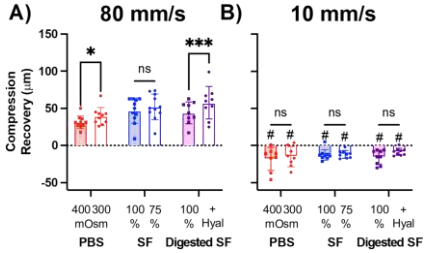


**Fig. 3 Compression recovery of cSCA explants slid in the presence of 400 vs. 300mOsm PBS, 100% vs. 75% SF, or naïve vs Hyal digested SF at either A) 80 or B) 10mm/s. Negative compression recovery indicates exudation.**

high- or slow-speed sliding frictional outcomes. Despite unaltered lubrication responses, SF degradation and dilution modestly enhanced high sliding speed-mediated compression recovery (*i.e.*, tribological rehydration) compared to naïve SF. These findings hint at a role for subtle changes in bathing solution osmolarity (such as those seen in the 400 vs. 300mOsm 1xPBS tests) on tribological rehydration magnitudes (and thus tissues strain), but not upon the lubrication synergy between SF and tribological rehydration.

Overall, these findings call into question the conventional wisdom that SF from osteoarthritic joints represents an inferior lubricating solution. Instead, when mechanisms that enable the active recovery and maintanence of tissue hydration, FLS, and interstitial lubrication are explicitly preserved during sliding tests, mimicking what we belief to be the predominate sliding environment experienced *in vivo*, both compromised and naïve SF appear equally effective in generating vanishingly low equilibrium interfacial frictions. Ongoing work seeks to characterize the mechanisms underlying these unanticipated lubrication synergies, as well as how they might influence and inform cartilage physiology/health. Such investigations will be critical to unlocking the true nature of the natural tribomechanics of both healthy and diseased joints.

## REFERENCES

[1] Ateshian, *J Biomech*, 2009. [2] Brand, *Iowa Orthop J.*, 2005 [3] Schimdt, *Arthritis Rheum*, 2007. [4] Burris, *OA&C*, 2017. [5] Burris, *Tribol Lett*, 2019. [6] Farnham, *JMBBM*, 2020. [7] Farnham, *Tribo Letters*, 2021. [8] Jebens, *J Bon Joint Surg*, 1959. [9] Shanfield, *Clin Orthop Relat Res*, 1988. [10] Kupratis, *Biotrib*, 2021.

# Comparative Study of Chemical and Nanomechanical Properties of Cat and Rat Vibrissae

**Davin Sim (1), Donna M. Ebenstein (1)**

(1) Biomedical Engineering, Bucknell University, Lewisburg, PA, USA

## INTRODUCTION

Known for their immense sensitivity to touch, vibrissae, or animal whiskers, can serve as a biomimetic model to enhance the functionality of the current mechanosensory mechanisms in robots [1]. Improved sensing mechanisms would enhance robot performance in many different applications – from pipeline inspection to non-invasive surgery [2]. Researchers have long been studying tactile sensing in rats for robotics applications [1]. However, these studies have primarily focused on the neural pathways involved in the sensing mechanisms, not on the whisker structure (internal or external) or considering rat whiskers in comparison to other species. Therefore, further understanding of the structure-property relationships of animal whiskers such as rats and cats may provide clues about how autonomous robots could improve their sensory capabilities by leading to enhanced design of the whiskers themselves.

Being predators, cats can protract and retract groups of whiskers to aid in hunting, while rats, as scavengers and prey, use active whisking to navigate in tight, dark spaces. Rat whiskers are more flexible than cat whiskers and differ from cat whiskers in both their external (e.g., length, diameter, tapering) and internal structure. For example, the center (medulla) of the cat whisker is filled compared to the rat medulla which is hollow (Fig. 1). To understand how the differences in structure and composition of different animal whiskers affect their function, the goal of this study was to characterize the chemical and mechanical properties of cat and rat whiskers using μRaman spectroscopy and nanoindentation. The results will help improve our understanding of structure-property relationship in animal whiskers, and hence better inform the design of bioinspired whiskers for robots.

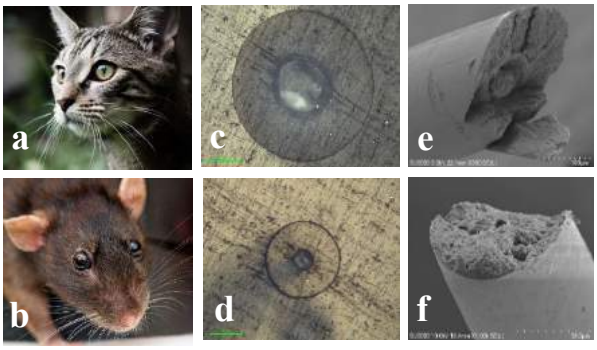


**Figure 1: Images of (a) cat and (b) rat whiskers. Optical microscope images of transverse sections of embedded and polished (c) cat and (d) rat whiskers. SEM images of cryofractured (e) cat and (f) rat whiskers.**

## METHODS

To prepare whiskers for chemical and mechanical analysis, whiskers from cats and rats were embedded in an epoxy resin and polished to reveal transverse or longitudinal sections.

Animal whiskers, like human hair, are made up of a protein called keratin, which can be chemically identified μRaman spectroscopy. Raman spectra were collected from each embedded whisker using a Horiba Xplora Plus spectrometer equipped with a 785-nm laser. Collected whisker spectra were compared to Raman spectra of pure keratin.

For mechanical analysis, nanoindentation was performed on each sample. Indents were performed to a depth of 1 micron using a TI-950 Triboindenter equipped with a Berkovich (3-sided pyramidal) tip (Fig. 2a). Unloading curves were analyzed to calculate a modulus ($E_r$) for each indent site [3]. Anisotropy ratios were calculated for cat and rat whiskers using Eq. (1),

$$A = 1 - \frac{E_{long}}{E_{trans}} \quad (1)$$

where $E_{long}$ and $E_{trans}$ are the mean reduced moduli for indents in the longitudinal and transverse sections, respectively.

## RESULTS

Spectral peaks found in cat and rat whiskers (Fig. 2a) are similar to peaks found in pure keratin, including disulfide Cys (S-S), symmetric ring breathing of Phe, and C-H stretching. The spectral peak area associated with disulfide bonds were more prominent in cat than rat whiskers (Fig. 2b).

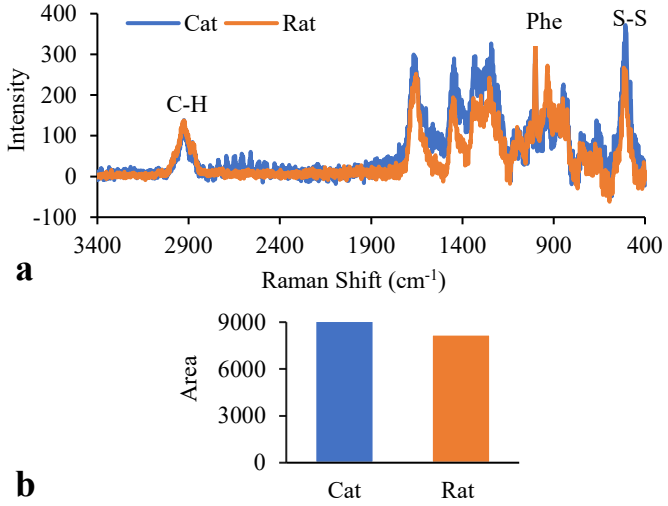


**Figure 2: (a) μRaman spectra of cat and rat whiskers were normalized to the C-H peak (~2900 cm$^{-1}$) and processed with baseline correction using LabSpec6 software. (b) Comparison of disulfide (S-S) bond peak areas from cat and rat spectra (cat area = 9074, rat area = 8204).**

Results from nanoindentation (Fig. 3) revealed that the mean modulus of cat whisker keratin in transverse sections (5.9±0.3 GPa) was significantly higher than the mean modulus in rats (5.0±0.3 GPa). Similarly, the mean modulus of cat whisker keratin in longitudinal sections (3.3±0.3 GPa) was significantly higher than in rats (2.6±0.1 GPa).

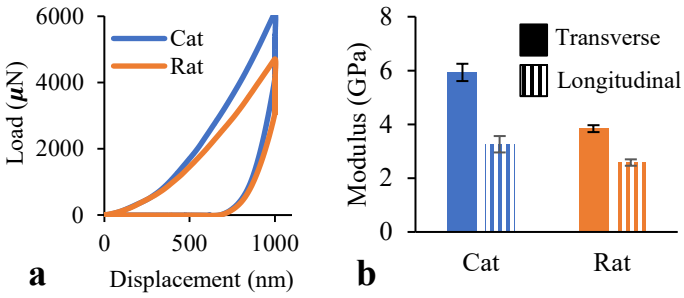


**Figure 3: (a) Representative load-displacement curves for indents in transverse sections of cat and rat whiskers and (b) a comparison of mean $E_r$ of cat and rat whiskers in transverse and longitudinal sections illustrate that cat whiskers are stiffer than rat whiskers. Error bars indicate one standard deviation.**

As the whisker keratin is stiffer in transverse than in longitudinal sections (Fig. 3b), whiskers were also found to be anisotropic. The anisotropy ratios of cat and rat whiskers were both approximately 4.0.

## DISCUSSION

Other studies have shown that an increase in disulfide bonding (Fig. 4a) is associated with increased keratin stiffness [4]. In this study, disulfide bond content is higher in cat than in rat whiskers. Therefore, cat whisker keratin is expected to be stiffer than rat whisker keratin. The results from nanoindentation support this conclusion from chemical analysis as cat whiskers had higher moduli than rat whiskers in both transverse and longitudinal sections. Hence, the increased flexibility of rat whiskers is due not only to having thinner, more tapered whiskers than cats (Fig. 4bc) but also due to differences in their chemical composition, and hence mechanical properties.

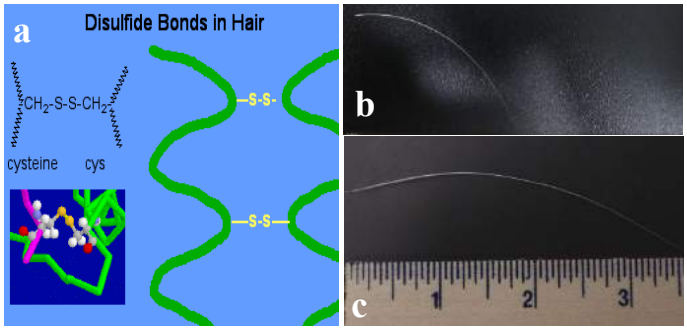


**Figure 4: (a) Cysteine S-S bonds in hair leads to crosslinking, folding, and stiffening of keratin [4]. Photographs of (b) a rat whisker and (c) a cat whisker showing that the cat whisker is longer, thicker, and less tapered than the rat whisker.**

The results of this study also demonstrated that cat and rat whiskers are both anisotropic, with anisotropy ratios (4.0) similar to results reported for spider silk fibers and bone [5]. This degree of anisotropy is consistent with the whisker microstructure, which shows keratin fibrils aligned along the long axis of the whisker (Fig. 1ef).

In the future, results from mechanical and structural analysis will be used as inputs for computational models to investigate how whisker microstructure and mechanical properties affect macroscale whisking mechanisms, and thus help further the development of bioinspired tactile sensors for robots.


## ACKNOWLEDGEMENTS

The authors would like to acknowledge Bucknell University's Program for Undergraduate Research and the Emmitt Memorial Chair in Biomedical Engineering for funding of this project.


## REFERENCES


[1] Habib M.K. et al., *IECON*, 143-8, 2007.
[2] A. E. Yang, et al., *IECON,* 1187-1192, 2018.
[3] W.C. Oliver and G.M. Pharr. *J MAT RES,* 7: 1564, 1992.
[4] Bornschlögl, T, et al. *PNAS*, 113: 5940, 2016.
[5] Ebenstein, D.M., et al., *J MAT RES*, 21: 2035, 2006.

# MULTISCALE ANALYSIS OF THE STRUCTURE-MECHANICS RELATIONSHIP OF MYCELIUM-BASED COMPOSITES

**Z. Qin (1), L. Yang (1)**

(1) Department Of Civil & Environmental Engineering, Syracuse University, Syracuse, NY, USA

## INTRODUCTION

Mycelium-based bio-composites materials have been invented and widely applied to different areas, including construction, manufacturing, agriculture, and biomedical [1]. As the vegetative part of a fungus, mycelium has the unique capability to utilize agricultural crop waste (e.g., sugarcane bagasse, rice husks, cotton stalks, straw, and stover) as substrates for the growth of its network, which integrates the wastes from pieces to continuous composites without energy input nor generating extra waste. Their low-cost and environmentally friendly features attract interest in its research and commercialization. For example, mycelium-based foam and sandwich composites have been actively developed for construction structures. It can be used as synthetic planar materials (e.g., plastic films and sheets), larger low-density objects (e.g., synthetic foams and plastics), and semi-structural materials (e.g., paneling, flooring, furniture, decking). Literature studies have shown that the material function of these composites can be further tuned by controlling the species of fungus, the growing conditions, and the post-growth processing method to meet a specific mechanical requirement in applications. Moreover, mycelium can be used to produce chitin and chitosan, which has the potential for biomedical applications. Given the strong potential and multiple advantages of such a material, we are working toward combining multiscale computational modeling with experimental synthesis and characterization in studying the composite mechanics.

## METHODS

### Preparation of Experimental Samples

**Figure 1** shows the 10-ton hydraulic press machine for performing the heat press test, which allows us to set different temperatures and pressure during sample preparation. In our experiment, we set three different temperatures including 80, 90, and 100°C. We also set the different applied press forces which are 1, 2, and 3 metric tons. Since the pressure gauge only shows the pressure, we convert the applied force to the pressure on the pressure gauge of the machine, as summarized in the different conditions in Fig. 2.

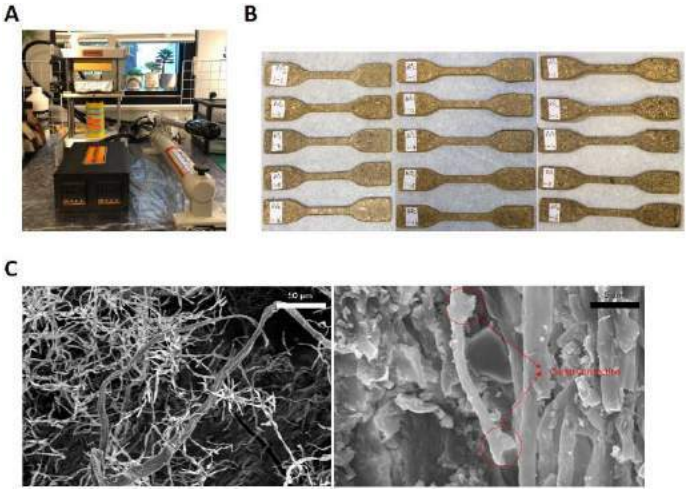


**Figure 1.** A. 10-ton hydraulic cylinder heat press machine with dual 3×5 inches heated plates. B. The dog bone shape samples (prepared under 80°C temperature and 6.75 MPa pressure baked for different times: 1, 2, 4, 8, 16 hours.) C. The SEM image of mycelium-based bio composite material at room temperature dried one month (left) and after the hot processing method (right).

For each of the different temperature-pressure combinations (9), we set the 5 different baking times including 1, 2, 4, 8, and 16 hours. Moreover, we take a piece from the sample that we processed hot press treatment to do the SEM image to compare with mycelium-based bio composites without hot processing (Fig. 1C).

### Tensile Test

The tensile tests were carried out at room temperature with a standard tensile testing machine (Instron 5966, USA). In each of the tensile tests, the dog bone sample was clamped to a pair of grips with the upper end

moved at a constant rate of 0.5 mm/min displacement. The sample was held by a force transducer and the reaction force was measured. The crosshead displacement was measured using a linear voltage displacement transducer mounted inside the actuator.

**Molecular Simulation of Cellulose-Chitin Interface**

Multiscale modeling starts with massively parallelized molecular dynamics (MD)[2] is used to characterize the structure-mechanics relationship of the cellulose-chitin interface at the nanoscopic scale. Large-scale MD models are a precise tool to investigate biological materials' mechanics and interfacial interaction by simulating their mechanical responses in different mechanical and environmental conditions. It reveals their nanomechanics and relates this characteristic to macroscopic material deformation, failure, and disease state[2–6]. Here, we investigate cellulose-chitin adhesion with varying orientations of crystal by using the CHARMM36 force field[7] with NAMD[2,8].

## RESULTS

We perform the tensile test with Instron for each sample to measure how the mycelium and environmental factors can affect the mechanical properties of the composite materials.

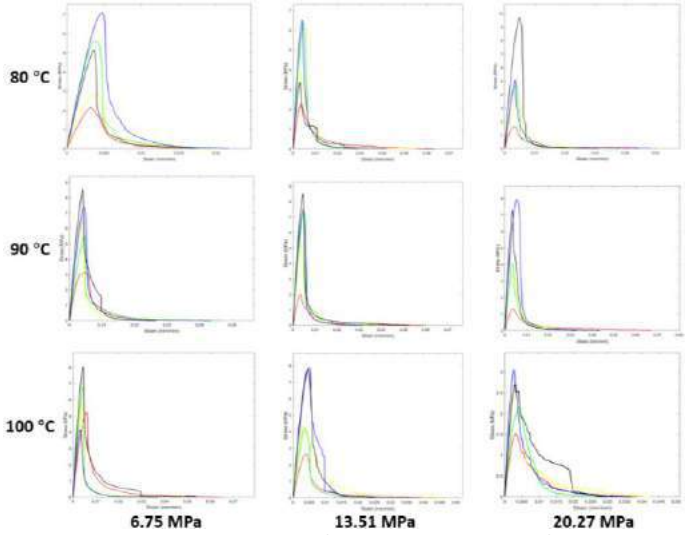


**Figure 2.** The stress-strain curve for dog bone samples of the mycelium composite as the mixture of hardwood with mycelium after heat press treatment under different temperatures, pressure, and baking time (1 hour-red, 2 hours-yellow, 4 hours-green, 8 hours-blue, 16 hours-black.)

It is shown that the existence of mycelium makes the composite slightly stiffer and stronger. Moreover, the higher temperature and pressure generally leads to materials of a higher density as well as a higher stiffness and strength. However, the toughness of the composite is not significantly affected by increasing the processing temperature and pressure.

To understand the effect of the mycelium on composite, we compare the naturally dried mycelium-based composite material at room temperature with the baked ones under 90 °C for an hour in SEM (**Fig. 1C**). We can see that under the condition of slowly losing water, all the mycelium become long flat strips and many of them are found to entangle with the wood fibers. The structure of mycelium after heat treatment is very different as the fibers break into smaller pieces and maintained a thicker rounded shape.

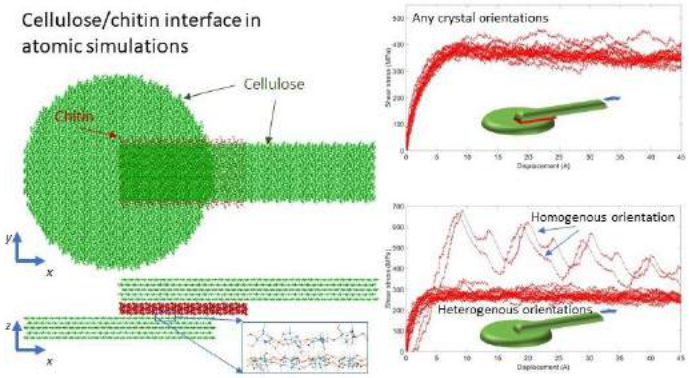


**Fig. 3** Chitin as a glue to enhance the interaction between cellulose: atomic simulations.

Using MD simulation, we investigate the cellulose-chitin adhesion with varying orientations of crystal (Fig. 3). We find that the chitin layer forms more hydrogen bonds (two times)[9] to a cellulose crystal than the pure cellulose-cellulose interface. Because of different lattice sizes, a chitin chain at the interface can form hydrogen bonds with 2~3 cellulose chains even they are overall parallel. Pure cellulose-cellulose interface with chains of same orientation yields a highest strength (~450 MPa) during the shear test. The interface of heterogeneous orientations is much weaker (~250 MPa). In contrast, the strength of the chitin-cellulose interface is much more consistent, with the consistent mechanical strength of ~375 MPa obtained for any crystal orientations.

## DISCUSSION

Our results suggest that the mycelium can enhance the stiffness and strength of the wood composite material. The elastic-plastic behavior of the chitin-cellulose interface at the nanoscale is very similar to the cellulose-cellulose interface[10], and the mechanism for energy dissipation is the stick-slip between polymers at the interface conjugate with breaking and reforming of hydrogen bonds. Further quantitatively studies include optimizing the processing conditions for composite with highest mechanical properties based on the experimental trials and coarse-grained models based on the atomic models to investigate the reinforcement mechanism of mycelium fibers at larger scales.

## REFERENCES


[1] L. Yang, D. Park, Z. Qin, *Front. Mater.* **2021**, *8*, DOI 10.3389/fmats.2021.737377.

[2] J. C. Phillips, R. Braun, W. Wang, J. Gumbart, E. Tajkhorshid, E. Villa, C. Chipot, R. D. Skeel, L. Kalé, K. Schulten, *J. Comput. Chem.* **2005**, *26*, 1781.

[3] A. F. Oberhauser, C. Badilla-Fernandez, M. Carrion-Vazquez, J. M. Fernandez, *J. Mol. Biol.* **2002**, *319*, 433.

[4] P. E. Marszalek, H. Lu, H. Li, M. Carrion-Vazquez, A. F. Oberhauser, K. Schulten, J. M. Fernandez, *Nature* **1999**, *402*, 100.

[5] M. Sotomayor, K. Schulten, *Science (80-. ).* **2007**, *316*, 1144.

[6] Z. Qin, M. J. Buehler, *J. Mech. Phys. Solids* **2014**, *62*, 19.

[7] K. Vanommeslaeghe, E. Hatcher, C. Acharya, S. Kundu, S. Zhong, J. Shim, E. Darian, O. Guvench, P. Lopes, I. Vorobyov, A. D. Mackerell, *J. Comput. Chem.* **2010**, *31*, 671.

[8] M. T. Nelson, W. Humphrey, A. Gursoy, A. Dalke, L. V. Kale, R. D. Skeel, K. Schulten, *Int. J. High Perform. Comput. Appl.* **1996**, *10*, 251.

[9] Z. Qin, M. J. Buehler, *Phys. Rev. E - Stat. Nonlinear, Soft Matter Phys.* **2010**, *82*, DOI 10.1103/PhysRevE.82.061906.

[10] J. Cui, M. Jiang, M. Nicola, A. Masic, Z. Qin, *Extrem. Mech. Lett.* **2021**, *49*, 101480.

SB³C2022
Summer Biomechanics, Bioengineering and Biotransport Conference
June 20-23, Eastern Shore, MD, USA

# PREDICTION OF DIABETES MELLITUS PROGRESSION USING SUPERVISED MACHINE LEARNING

**Apoorva S. Chauhan (1), Mathew S. Varre (2), Kenneth Izuora (3), Mohamed B. Trabia (1), Janet S. Dufek (2)**

(1) Department of Mechanical Engineering, University of Nevada Las Vegas, Las Vegas, NV, USA
(2) Department of Kinesiology and Nutrition Sciences, University of Nevada Las Vegas, Las Vegas, NV, USA
(3) Department of Internal Medicine, University of Nevada Las Vegas, Las Vegas, NV, USA

## INTRODUCTION

Diabetes Mellitus (DM) is a medical condition in which individuals are unable to produce enough or no insulin at all, or the body cannot use insulin correctly [1]. This condition can cause many complications, such as vision loss, heart disease, stroke, kidney failure, or the amputation of lower extremities. Neuropathy is a common complication that damages the nervous system, resulting in the degradation of nerves of extremities. This degradation, which leads to loss of sensation, can cause persons affected by it to apply elevated pressure on the affected plantar tissues, leading to plantar ulceration, which if left untreated can lead to limb amputation [2].

The most accessible methods to diagnose diabetic neuropathy include sensory testing with a 10-gram monofilament and a tuning fork. However, these tests are crude and highly subjective, which can lead to missing the early signs of neuropathy [3]-[5]. More reliable diagnostic tools, such as nerve conduction studies, are expensive and time consuming [5], [6]. A more cost-effective, reliable, and available method of diagnosing neuropathy has the potential to improve the accuracy and timeliness of detection, which can prevent further complications [5].

Studies have shown that static plantar pressure data of patients with DM were different from healthy participants [8]. Plantar pressure measurements taken during walking can show the tissue response to stress that correlates with ulceration. Supervised machine learning algorithms and dynamic plantar pressure parameters have been used to successfully classify individuals with diabetic neuropathy and DM from healthy individuals [9]. However, this study was unable to differentiate pre-diabetic patients from DM patients when compared to healthy individuals.

The aim of this research was to develop a diagnostic tool that can classify persons who have pre-diabetes, diabetes, or diabetes with neuropathy using supervised machine learning. Several plantar pressure features taken during walking, as well as patient-specific features would be used. The success of the proposed approach would be assess based on its classification efficacy to ensure that it is suitable for clinical use.

## METHODS

Data was collected from 110 participants, 19 with pre-diabetes, 62 with diabetes, and 29 with diabetes with neuropathy. Participants were fitted with Medilogic® pressure measuring insoles (60 Hz) and walked at their normal walking speed. Each participant performed three to five trials, with three to five steps occurring in the calibrated walking space, for a total of 1621 steps (observations). To allow granularization of the data, each foot was divided into three regions: rearfoot, midfoot, and forefoot, RF, MF, FF, respectively. The pressure data collected was used to calculate the peak plantar pressure (PPP), peak pressure gradient (PPG), and pressure time integral (PTI) for the fore-, mid-, and rearfoot during the support phase. Instead of including left and right feet, only left was considered along with the Asymmetry index (AI), which was calculated for each pressure feature in each region,

$$AI = \frac{|Right\ Foot - Left\ Foot|}{Left\ Foot} \quad (1)$$

In addition to these eighteen pressure features, the participants' age, mass, height, and HbA1c were also used as features for a total of twenty-one. Excluding HbA1c, features were tested in seven cases to assess the effect of combining features differently. Each combination was tested twice, with and without HbA1c for a total of fourteen cases. A variable sensitivity analysis was conducted to determine the five features with the greatest impact on classification. It was found out these features: age, mass, height, rearfoot PTI, and HbA1c. These five features were assessed in Case 15 while the first four were used in Case 16.

The K-Nearest Neighbors (KNN) classification algorithm was used, which classifies data points based on the classification of the K nearest data points to the point in question [10]. Each case was cross-validated using the holdout method where 20% of the data was randomly selected to be the test data and the remaining 80% was used

to train the model for twenty iterations. The average of these 20 trials was used to determine the overall efficacy of the algorithm's performance in each case. The average false negative rate for misclassifying participants was also recorded. To understand how accurately the algorithm is classifying DN participants only the average false negative rate for DN participants is reported.

## RESULTS

Table 1 lists the features in each tested case while Table 2 lists the cross-validated machine learning results. Case 15 was the best performing case had an accuracy of 99±0.59% and a false negative rate of 0.41% in diagnosing diabetic neuropathy. Including Case 15, cases 5, 6, and 13 produced accuracies greater than to 95%, with no false negative rates exceeding 0.5%.

## DISCUSSION

The results show that including many features does not necessarily produce good results. The four cases with the best performance included PTI of the rear foot, which suggests this feature may play a greater role in determining an individual's diagnosis than peak pressure gradient. When HbA1c was removed, cases only dropped approximately 1% in accuracy. However, when removing HbA1c from Case 15, there was a 26% drop in accuracy and significant rise in DN false negatives, which may indicate that a significant reduction in the number of pressure features may make the model unstable. The results suggest that PPG does not contribute to the prediction of diabetes for this sample of participants,

The presented research suggests that the KNN algorithm can be used to classify the progression of diabetes based on a combination of plantar pressure variables at different foot regions, along with patient-specific features. These findings indicate that this approach may be suitable for use in a clinical setting to inexpensively, quickly, and objectively classify individuals with diabetic neuropathy.

**Table 1: Features of Each Case in Addition to Age, Mass, and Height**

| Case | Features |
|---|---|
| 1 | $PPP_{LFF}$, $PPP_{LMF}$, $PPP_{LRF}$, $PPPAI_{FF}$, $PPPAI_{MF}$, $PPPAI_{RF}$, $PPG_{LFF}$, $PPG_{LMF}$, $PPG_{LRF}$, $PPGAI_{FF}$, $PPGAI_{MF}$, $PPGAI_{RF}$, $PTI_{LFF}$, $PTI_{LMF}$, $PTI_{LRF}$, $PTIAI_{FF}$, $PTIAI_{MF}$, $PTIAI_{RF}$, HbA1c |
| 2 | Same as Case 1 without HbA1c |
| 3 | $PPP_{LFF}$, $PPP_{LMF}$, $PPP_{LRF}$, $PPPAI_{FF}$, $PPPAI_{MF}$, $PPPAI_{RF}$, $PPG_{LFF}$, $PPG_{LMF}$, $PPG_{LRF}$, $PPGAI_{FF}$, $PPGAI_{MF}$, $PPGAI_{RF}$, HbA1c |
| 4 | Same as Case 3 without HbA1c |
| 5 | $PPP_{LFF}$, $PPP_{LMF}$, $PPP_{LRF}$, $PPPAI_{FF}$, $PPPAI_{MF}$, $PPPAI_{RF}$, $PTI_{LFF}$, $PTI_{LMF}$, $PTI_{LRF}$, $PTIAI_{FF}$, $PTIAI_{MF}$, $PTIAI_{RF}$, HbA1c |
| 6 | Same as Case 5 without HbA1c |
| 7 | $PPG_{LFF}$, $PPG_{LMF}$, $PPG_{LRF}$, $PPGAI_{FF}$, $PPGAI_{MF}$, $PPGAI_{RF}$, $PTI_{LFF}$, $PTI_{LMF}$, $PTI_{LRF}$, $PTIAI_{FF}$, $PTIAI_{MF}$, $PTIAI_{RF}$ HbA1c |
| 8 | Same as Case 7 without HbA1c |
| 9 | $PPP_{LFF}$, $PPP_{LMF}$, $PPP_{LRF}$, $PPPAI_{FF}$, $PPPAI_{MF}$, $PPPAI_{RF}$ HbA1c |
| 10 | Same as Case 19 without HbA1c |
| 11 | $PPG_{LFF}$, $PPG_{LMF}$, $PPG_{LRF}$, $PPGAI_{FF}$, $PPGAI_{MF}$, $PPGAI_{RF}$, HbA1c |
| 12 | Same as Case 11 without HbA1c |
| 13 | $PTI_{LFF}$, $PTI_{LMF}$, $PTI_{LRF}$, $PTIAI_{FF}$, $PTIAI_{MF}$, $PTIAI_{RF}$, HbA1c |
| 14 | Same as Case 13 without HbA1c |
| 15 | $PTI_{LRF}$ and HbA1c |
| 16 | $PTI_{LRF}$ |

**Table 2: Results for Cross-Validated Cases**

| Case | Average Accuracy (%) | Best Case Accuracy (%) | Average False Negative Rate for DN Participants (%) |
|---|---|---|---|
| 1 | 95 ± 1.2 | 97 | 1.28 |
| 2 | 95 ± 1.3 | 97 | 0.86 |
| 3 | 88 ± 1.2 | 91 | 8.21 |
| 4 | 85 ± 2.3 | 90 | 9.44 |
| 5 | 97 ± 0.94 | 99 | 0.46 |
| 6 | 96 ± 0.83 | 98 | 0.11 |
| 7 | 96 ± 1.1 | 98 | 0.87 |
| 8 | 95 ± 1.2 | 97 | 1.07 |
| 9 | 91 ± 1.7 | 93 | 4.34 |
| 10 | 88 ± 1.5 | 91 | 6.95 |
| 11 | 87 ± 1.7 | 90 | 6.69 |
| 12 | 82 ± 2.6 | 87 | 10.20 |
| 13 | 98 ± 0.83 | 99 | 0.41 |
| 14 | 97 ± 0.81 | 99 | 0.76 |
| 15 | 99 ± 0.59 | 100 | 0.41 |
| 16 | 73 ± 2.4 | 78 | 23.75 |

## REFERENCES


[1]American Diabetes Association, "Common Terms." https://www.diabetes.org/resources/students/common-terms.

[2] P. R. Cavanagh, G. G. Simoneau, and J. S. Ulbrecht, "Ulceration, unsteadiness, and uncertainty: the biomechanical consequences of diabetes mellitus.," *J. Biomech.*, vol. 26 Suppl 1, pp. 23–40, Jan. 1993, [Online]. Available: http://www.ncbi.nlm.nih.gov/pubmed/8505350.

[3] J. Dros, A. Wewerinke, P. J. Bindels, and H. C. Van Weert, "Accuracy of monofilament testing to diagnose peripheral neuropathy: A systematic review," *Ann. Fam. Med.*, 2009, doi: 10.1370/afm.1016.

[4] F. Wang *et al.*, "Diagnostic Accuracy of Monofilament Tests for Detecting Diabetic Peripheral Neuropathy: A Systematic Review and Meta-Analysis," *Journal of Diabetes Research*. 2017, doi: 10.1155/2017/8787261.

[5] D. Selvarajah *et al.*, "Diabetic peripheral neuropathy: advances in diagnosis and strategies for screening and early intervention," *The Lancet Diabetes and Endocrinology*. 2019, doi: 10.1016/S2213-8587(19)30081-6.

[6] G. Fuller, "How to get the most out of nerve conduction studies and electromyography," *Neurology in Practice*. 2005, doi: 10.1136/jnnp.2005.067355.

[7] D. Zou, M. Mueller, and D. Lott, "Effect of peak pressure and pressure gradient on subsurface shear stresses in the neuropathic foot," *J. Biomech.*, vol. 40, no. 4, pp. 883–890, 2007.

[8] F. S. Botros, M. F. Taher, N. M. Elsayed, and A. S. Fahmy, "Prediction of diabetic foot ulceration using spatial and temporal dynamic plantar pressure," *2016 8th Cairo Int. Biomed. Eng. Conf. CIBEC 2016*, pp. 43–47, 2017, doi: 10.1109/CIBEC.2016.7836116.

[9] C. C. Robinson, L. F. Balbinot, M. F. Silva, and M. Achaval, "Plantar Pressure Distribution Patterns of Individuals with Prediabetes," 2013, doi: 10.1177/193229681300700503.

[10] Knox, S. W. (2018). k-Nearest-Neighbor. In *Machine Learning: A Concise Introduction* (pp. 55–56). chapter, Wiley.

# THE CORRELATION STUDY OF BRAIN TISSUE BETWEEN MECHANICAL FREQUENCY PROPERTIES AND MICROSCOPIC STRUCTURES

**Suhao Qiu (1), Linghan Kong (1), Runke Wang (1), Fuhua Yan (2), Yuan Feng (1)**

(1) School of Biomedical Engineering, Shanghai Jiao Tong University, Shanghai, Shanghai, China
(2) Department of Radiology, Ruijin Hospital, Shanghai, Shanghai, China

## INTRODUCTION

It is known mechanical properties of brain tissues are important to understand its disease and development [1]. Many studies have used magnetic resonance elastography (MRE) to measure the biomechanical properties of brain in vivo [2]. Diffusion weighted imaging (DWI) provides important information of tissue structures in terms of water diffusion [3]. Studies have shown a strong correlation between diffusivity and elastic properties in liver [4]. However, the potential relationship between structural and biomechanical properties of brain is yet to be explored.

In this study, we used DWI and MRE to characterize the potential correlation between structural and biomechanical properties of brain. Apparent diffusion coefficient (ADC) and shifted ADC (sADC) values were estimated. The correlations between sADC and shear stiffness were analyzed for each of the specific brain region at 3 different actuation frequencies. A phenomenological model based on sADC and the shear stiffness was proposed.

## METHODS

A total of 43 healthy volunteers were recruited in this study. Among all the subjects, data from the 32 subjects were used for modeling and the rest 11 subject data were used for validation. MRE imaging was performed using a custom-built electromagnetic vibration actuator [5] (Figure 1). The measured was carried out using 4 actuation frequencies: 20, 40, 60 Hz for correlation analysis and 30 Hz for generalization validation of the model. Wave images of the brain were acquired using an echo planar imaging (EPI) based MRE sequence with three motion encoding directions. Shear modulus maps were calculated by using a three-dimensional local frequency estimation (LFE) method. For DWI, images were acquired with diffusion encoding along three axis. Among the 16 key b-values between 0 and 2500 s/mm2 acquired, we selected 2 optimized key b-values to calculate sADC, so that Gaussian and non-Gaussian diffusion effect was included. Both MRE and DWI scanning were performed on a 3T MR imager (uMR 790, United Imaging Healthcare, Shanghai, China).

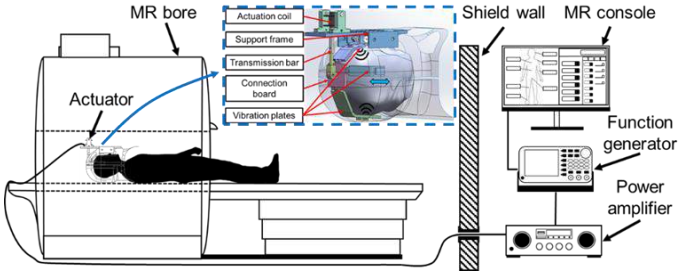


**Figure 1. A diagram of the custom-built electromagnetic MRE system. The vibration signal was generated by the function generator and amplified by the power amplifier before transmitted to the actuator. The MR console would synchronize the actuator vibration and MRE sequence scanning.**

All MRE and DWI images were registered to a common reference (MNI152 T1-weighted 2 mm brain atlas) by using Advanced Normalization Tools (ANTS) for later segmentation and correlation analysis. The whole brain was then segmented into frontal, occipital, parietal, and temporal lobe using the MNI template mask within the FMRIB Software Library (FSL).

Correlation between DWI and MRE registered results were calculated by using MATLAB with Pearson correlation coefficient. The linear correlation coefficient was quantified voxel by voxel at each frequency. All p values were corrected by the false discovery rate (FDR) method. Then the linear regression analysis between the mean values were performed. Finally, An appearance model were proposed based on the correlation results and was validated by the validation dataset.

## RESULTS

Based on the highest correlation between the shear stiffness and sADC at each frequency, we determined the 2 key b-vlaues as 200 s/mm2 and 2000 s/mm2. T1-weighted images, average shear stiffness, and average sADC values over the 32 subjects are shown in Figure 2. We observed the anatomical features of the brain structures such as white matter and ventricle regions could be identified base on the stiffness and sADC maps.

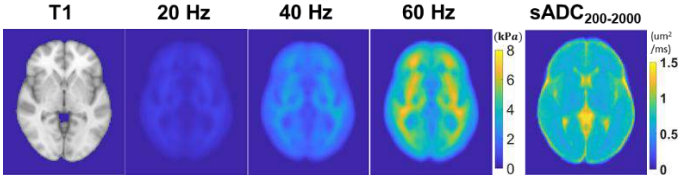


**Figure 2. Column 1 is the T1-weighted brain structure template. Column 2-4 are the mean values of shear stiffness from 32 volunteers at 20. 40, and 60 Hz, respectively. Column 5 is the mean sADC value from corresponding DWI results.**

Voxel correlation results along 3 equal spacing actuation frequencies are shown in Figure 3. The voxel with significant correlation had been indicated in color and large correlation regions for all 3 MRE frequencies were only observed in parietal lobe.

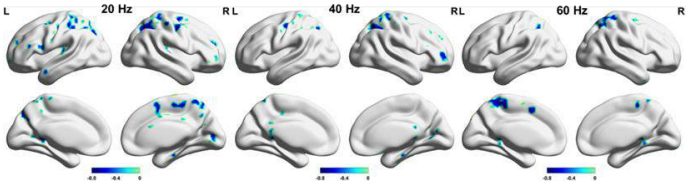


**Figure 3. The correlation results displayed on the cerebral cortex for all 3 experimental frequencies. Only the voxels with significant correlation relationship have been shown in color.**

The results from linear regression study confirmed the specificity of parietal lobe found in voxel correlation maps in Figure 3. The linear correlation was significant for all 3 frequencies in parietal lobe, while frontal lobe and occipital lobe only had significant result for 20 and 40 Hz, respectively. As for template lobe, there were no correlation existing at any frequency.

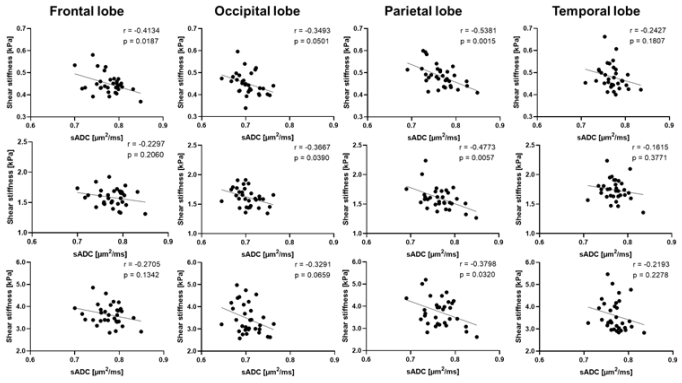


**Figure 4. The linear regression results of the 3 frequencies in the frontal, occipital, parietal, and temporal lobe. Only parietal lobe appeared linear relationship along all frequencies.**

Summarizing the correlation results in parietal lobe and we assumed that the shear stiffness, $\mu_f$, at each vibration frequency, $f$, could be estimated from the sADC as:

$$\mu_f = (\alpha_1 f^{\beta_1} + \gamma_1) \cdot sADC + (\alpha_2 f^{\beta_2} + \gamma_2) \quad (1)$$

where $\alpha_i$, $\beta_i$, and $\gamma_i$ are the model parameter and can be determined by data fitting.

The mean values of the 11 validation subjects using the proposed model and a traditional spring-spot model, standard linear solid (SLS), are shown in Figure 5(a). Comparing with measured data, the proposed results performed well similarity even at 30 Hz. Although the new model had similarity absolute error at 20 and 30 Hz comparing with the two traditional competitors (Figure 5(b)), around 50% prediction error decrease has been achieved for 40 Hz and 60 Hz.

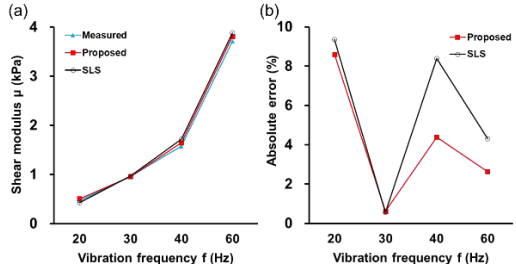


**Figure 5. (a) The comparison results between the measured mean values from measured validation dataset, the predicted values from the proposed model, and the SLS model, respectively. An validation frequency 30 Hz was added for generalization comparison. (b) The absolute error of proposed method and SLS model comparing with the measured results. Proposed model achieved better similarity, especially at 40 Hz and 60 Hz.**

## DISCUSSION

The previous simulation and experiment results have indicated that the biomechanical properties of human brains were related with their structures [6]. However, many traditional frequency response models lacked of structure information. Bihan, DL et al has observed the strong correlation between shear modulus and sADCs on human lives [7], but few similar studies have been applied on brains yet.

In this study, we proposed a phenomenological model for parietal lobe to describe the shear stiffness by sADC at multiple frequencies. The validation results highlighted the utility of the empirical model when comparing with traditional models such as the Maxwell. These results also demonstrated a strong correlation between mechanical properties and structural properties in parietal lobe.


## ACKNOWLEDGEMENTS

Funding support from grant 31870941 from National Natural Science Foundation of China (NSFC) and grant 19441907700 from Shanghai Science and Technology Committee (STCSM) are acknowledged.


## REFERENCES


[1] Hiscox, LV et al., *Phys Med Biol*, 61(24):R401-R437, 2016.
[2] Murphy, MC et al., *Neuroimage*, 187:176-183, 2019.
[3] Baliyan, V et al., *World J Radiol*, 8(9):785-798, 2016.
[4] Bihan, D et al., *Radiology*, 285(2):609-619, 2017.
[5] Qiu, S et al., *NMR Biomed*, e4592, 2021.
[6] Chatelin, S et al., *Bioheology*, 48(2):75-88, 2012.
[7] Bihan, DL et al., *Radiology*, 285(2):609-619, 2017.

SB³C2022
Summer Biomechanics, Bioengineering and Biotransport Conference
June 20-23, Eastern Shore, MD, USA

# EXPERIMENT-LED CONTINUUM MODELLING OF MICROSCALE BLOOD FLOW

**Simon Tupin (1), Stavroula Balabani (2), Joseph van Batenburg-Sherwood (1)**

(1) Bioengineering, Imperial College London, London, UK
(2) Mechanical Engineering, University College London, London, UK

## INTRODUCTION

Modelling blood flow is of great importance for both research and clinical applications. Blood in large vessels can be reasonably modelled using Newtonian or simple non-Newtonian models. For the smallest blood vessels (<30μm) the dynamics of individual red blood cells (RBCs) can be captured using methods such as Immersed Boundary and Dissipative Particle Dynamics (see e.g. reviews [1,2]). For arterioles and venules, the large microvessels (diameter 30-100μm), there are too many RBCs to model individually, but simple non-Newtonian methods are insufficiently detailed to capture the complex local blood rheology.

The rheology of blood is highly dependent on both shear rate and local concentration of RBCs (haematocrit), both of which vary considerably throughout the microvasculature, both between *and within* vessels. Continuum models for blood flow consider blood as a continuum fluid with shear- and haematocrit-dependent viscosity, with RBC motion modelled using a transport equation [3-5] (Figure 1).

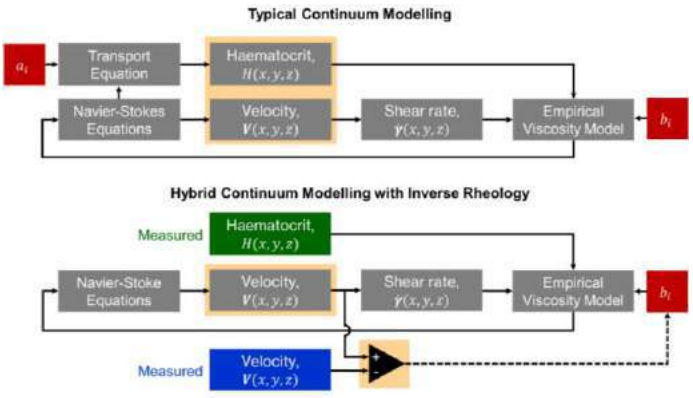


**Figure 1: Typical and proposed approaches to continuum modelling of microvascular blood flow [6].**

This approach is significantly more efficient than modelling individual cells, however, difficulties arise in

i. selecting appropriate transport equations terms and corresponding empirical parameters, $a_i$, to account for migration and margination of RBCs
ii. selecting an empirical viscosity model and corresponding parameters $b_i$, (typically derived in constant shear rheometers) to account for non-linear shear and haematocrit dependence
iii. validating that the modelled results actually represent the behaviour of blood

Irrespective of the modelling technique chosen, the reliance on typically 5-10 parameters and a range of available phenomenological models make the problem ill-defined, and proper validation requires high quality experimental data, which is scarce.

Here, we propose an approach to bypass these difficulties using a hybrid experiment-led approach (Figure 1). Firstly, we eliminate parameters $a_i$ using optical measurements of spatial distributions of haematocrit. Then, we use an iterative parameter optimisation process that we term 'inverse rheology' [7] to find the viscosity model parameters $b_i$ that minimise the error between modelled and measured velocity profiles.

In the present study, we demonstrate the methodology using experimental data of human blood flowing in a sequentially bifurcating microchannel to evaluate the model efficacy and the relative importance of RBC distribution and local shear rate.

## METHODS

### Experimental Methods

Experimental data was used from a previous study [8], comprising human blood samples at a feed haematocrit of 25% perfused through a sequentially bifurcating microchannel with a square cross section and side length 50μm. 38 experimental cases were captured with varying flow rates and flow splits between branches. RBC concentration distributions were calculated based on the light transmitted through the sample when averaged over time [8]. Velocity was measured using ensemble average micro-particle image velocimetry in each of the 5 branches in the region of interest of the channel [8] (see Figure 2 for channel layout). Three-dimensional distributions were estimated on the assumption of 4-fold symmetry in the inlet branch of the channel following a long, straight section.

### Viscosity Model

The Quemada viscosity model was used, with an additional empirical parameter Γ added for the inverse rheology process:

$$\mu = \mu_0/(1-0.5kH)^2$$
$$k = \left(k_0 + k_\infty/\Gamma\sqrt{|\dot{\gamma}|/\dot{\gamma}_c}\right)/\left(1+1/\Gamma\sqrt{|\dot{\gamma}|/\dot{\gamma}_c}\right) \quad (1)$$

where $\mu_0$ is viscosity of the suspending medium, $H$ is the haematocrit and $\dot{\gamma}$ is the shear rate. The parameters $k_0, k_\infty$ and $\dot{\gamma}_c$ were determined as functions of $H$ and $\dot{\gamma}$ from previously published data [9].

### Numerical Methods

Computational fluid dynamics was carried out using ANSYS CFX. For each of the 38 cases, boundary conditions were defined according to measured flow rates at 3 of the four branches with 0 pressure at the outlet. Experimental haematocrit data was mapped onto the mesh of ~2.4M elements and used to calculate the local viscosity using Equation 1 with $\dot{\gamma}$ calculated intrinsically. Velocity profiles at each of the 5 branches were extracted and normalised by the average velocity. The

Velocity Residuals, $e$, were calculated as the difference between the normalised experimental and numerical velocity. The relative error $E^*$ for each branch and case was determined as the root mean square of $e$, divided by the value calculated compaing the experimental data to a Newtonian fluid. $E^*$ thus defined varied between 0 (perfect match to experimental data) and 1 (equivalent to assuming a Newtonian fluid).

**Inverse Rheology Process**

To optimise the numerical model, we considered two parameters. Firstly, we varied the parameter Γ in Equation 1 between 1 and 5. This parameter increases the sensitivity if the local viscosity to shear rate and haematocrit. Secondly, we investigated different widths (0.3 to 2.7 µm) of the exclusion layer, the region of reduced time-averaged haematocrit that has a reduced haematocrit due to the finite size of the RBCs. 8 of the cases were selected to cover a range of flow rates and flow splits. 25 combinations of Γ and the exclusion layer width were simulated and the average $E^*$ for the 8 sample cases was calculated to find the combination that yielded the minimum error.

**Forward Modelling**

All 5 branches for all 38 cases (N=190) were considered for a number of different models. To evaluate the efficacy of the modelling approach, simulations were carried out for all cases using the baseline model, with no exclusion layer and $\Gamma = 1$. To investigate the advantages proffered by the inverse rheology process, simulations were carried with the optimised model. Finally, to evaluate the relative importance of haematocrit and shear dependence, additional simulations were carried out with either the shear rate or haematocrit was held constant.

## RESULTS

The baseline model yielded a mean $E^*$ of 0.38 [0.37,0.39] (mean [95%CI]), indicating a 60% reduction in error relative to a Newtonain model. From the inverse rheology process, $\Gamma = 3$ and an exclusion layer thickness of 1.5µm were found to minimise the averaged relative error. When the optimised model was applied to all data sets, the mean $E^*$ was further reduced by a third to 0.25 [0.24,0.26].

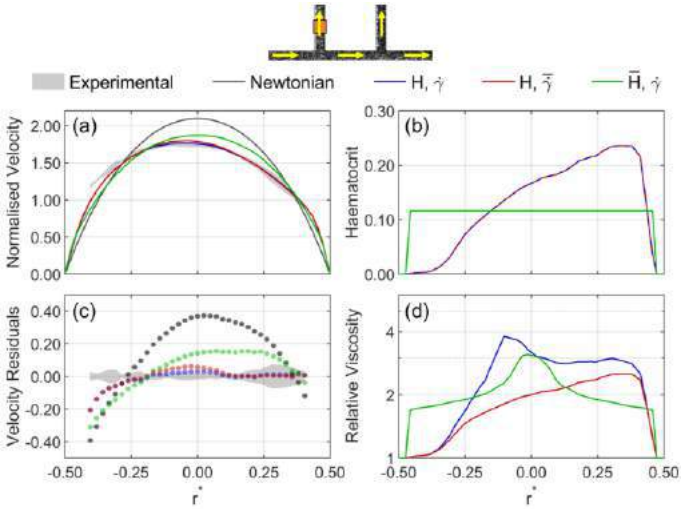


**Figure 2: Image shows channel, with yellow arrows indicating flow direction. (a) Sample velocity profiles, normalised by average velocity. Lines compare different models to experimental data in grey. (b) Haematocrit profiles. (c) Velocity residuals show model values minus experimental values. (d) Simulated relative viscosity.**

Figure 2 compares the results of the optimised ($H, \dot{\gamma}$, blue), constant shear ($H, \bar{\dot{\gamma}}$, red) and constant haematocrit ($\bar{H}, \dot{\gamma}$, green) models for a sample case in the first side branch (orange region in channel image). The normalised velocity profiles and residuals (Fig 2a,c) show that the model does a good job of recapitulating the experimental data when the haematocrit distribution is accounted for ($H, \dot{\gamma}$ and $H, \bar{\dot{\gamma}}$), but not when only the shear distribution is considered ($\bar{H}, \dot{\gamma}$).

The asymmetry in the velocity profile arises from the asymmetric haematocrit distribution, a common feature in branching channels on the scale of arterioles [8]. The different viscosity profiles (Fig 2d) demonstrate that the uniform haematocrit model fails to reproduce the asymmetry in the profile, while the constant shear model does not reproduce the peak in viscosity at the location of maximum velocity. Considering all cases, the uniform shear model had an average 0.47 [0.46,0.48], almost double that for the uniform shear model with 0.26 [0.25,0.27].

## DISCUSSION

The present study provided proof of principle that a continuum model is able to accurately model microscale blood flow when the local distribution of RBC is taken into account. This approach is considerably more efficient than modelling individual RBCs (minutes on a desktop computer, rather than weeks on a supercomputer) and is thus scalable.

The considerable asymmetry in the profiles of haematocrit, velocity and hence viscosity demonstrate the critical importance of evaluating and optimising such models in branching geometries, guided by experimental data. The results also demonstrated that local shear rate is considerably less important than local haematocrit in viscosity models, such that a simpler version of the viscosity model using $k = (k_0 + k_\infty\theta)/(1+\theta)$ may be sufficient.

Improvements to the experimental data include using round channels with different branching features and length scale, improved near-wall resolution and blood sample specific bulk viscosity data.

The next key step in the development of this approach is to incorporate transport modelling into the framework. This could be done using a similar data assimilation process in which the simulated velocity distributions from the inverse rheology are input into a transport model, and the results compared to the experimentally measured RBC distributions. Using such an approach, the model could be tuned for a specific blood sample in one geometry and then investigated in another geometry under different flow conditions.

Once validated, it will be possible to investigate how the model parameters and efficacy are affected by changes in the blood sample that occur in microvascular diseases, such as enhanced RBC aggregation or decreased RBC deformability. Although there is much to do to develop the model into a practical tool, the approach described in this study will provide a framework for this development and makes a step towards better incorporation of experimental and computational data in the study of microhaemodynamics.

## ACKNOWLEDGEMENTS

This project was supported by the Royal Academy of Engineering under the Research Fellowship Scheme (RF201617\16\18) and the Engineering and Physical Sciences Research Council (EP/T023155/1). Additional thanks to Prof James Moore and Prof Kim Parker for their valuable insights.

## REFERENCES

[1] Freund, JB, *Ann Rev Fluid Mech*, 46:67-95, 2014.
[2] Gompper G et al., *System Biol and Med*, 8:157–168, 2016
[3] Mansour MH, et al., *Biorheology* 47:73–934, 2010.
[4] Xu Z et al., *Biomech Model Mechanobiol* 18:99–110, 2019
[5] Schenkel T et al., Mathematics, 9(17):2100, 2021
[6] van Batenburg-Sherwood et al., *Biomech Model Mechanobiol*, 2021, online: doi.org/10.1007/s10237-021-01537-2
[7] Bandulasena HCH et al., *Measurement Sci Tech* 22:125402, 2011.
[8] Sherwood JM et al., *PLoS ONE* 9:e100473, 2014.
[9] Cokelet GR, In: *Handbook of Bioengineering*, *McGraw-Hill*, 1987.

# BIOLOGICAL RESPONSE OF RABBIT ANTERIOR CRUCIATE LIGAMENTS TO MECHANICAL LOADING IS SEX-SPECIFIC

**L. Paschall (1), A. Dhawan (2), S. Szczesny (1,2)**

(1) Department of Biomedical Engineering, Pennsylvania State University, University Park, PA, USA
(2) Department of Orthopaedics and Rehabilitation, Pennsylvania State University, Hershey, PA, USA

## INTRODUCTION

Anterior cruciate ligament (ACL) tears are one of the most common knee injuries and affect approximately 100,000 people a year in the USA[1,2]. Recent studies suggest that repetitive subfailure loading creates microtrauma and structural tissue damage, thereby predisposing the ACL to injury[3,4]. Similar fatigue-induced injury is observed in tendons, where structural damage from overloading initiates a degenerative (i.e., catabolic and inflammatory) cell response, which in turn, weakens the tendon[5]. Given the similarity between tendons and ligaments, it is possible that fatigue-induced degeneration also occurs in the ACL and contributes to ACL rupture. However, the biological response of the ACL to cyclic loading is unknown. Furthermore, it is unknown if there is a sex-specific response to loading, which may explain why ACL ruptures occur 2-8 times more often in female athletes than male athletes[6,7] To address these knowledge gaps, we developed a live tissue explant model that can cyclically load rabbit ACLs to a prescribed stress level and maintain cell viability[8]. The objective of this study was to use our explant model to compare the dose-dependent effect of cyclic loading on gene expression within ACL explants from male and female rabbits. We **hypothesized** that the female samples will exhibit an increased catabolic response to mechanical loading compared to male samples, which would be consistent with increased ACL rupture rates in women.

## METHODS

Following IACUC approval, ACLs were harvested from both knees of male and female New Zealand white rabbits and placed in a tensile bioreactor with culture media kept at 37°C and 5% $CO_2$. After 10 h of accumulating the ACLs to explant culture, the bioreactor cyclically loaded the samples to 2 MPa or 4 MPa at 0.5 Hz for 8 h. These stress levels are based on estimates of ACL loading in situ[9], and 8 h of loading was chosen based on previous explant studies of tendon[10]. Control samples were placed in the bioreactor under the same duration but under a minimal (0.1 MPa) static load. ACLs were immediately removed after loading, rinsed with ice cold RNase-free water and flash frozen in liquid nitrogen. Total RNA was extracted with RNeasy minicolumns, cDNA was synthesized from 10 ng of the total RNA, and real time-PCR was performed using Taqman probes to measure expression of anabolic (*COL1A1, COL1A2, LOX, COL3A1, TGFβ1 ACTA2*), catabolic (*MMP1. MMP2, MMP10, MMP13, TIMP1, TIMP3*), and inflammatory (*IL-1β, PTSG2*) genes with *ACTB* as a reference. Quantification of gene expression was performed via the delta-delta Ct method (after correcting for primer efficiencies) relative to the sex-specific statically loaded condition. For the 0.1 MPa data, the female group was compared relative to the male group. Single sample Wilcoxon tests were used to determine differential expression. Data are represented as box and whisker plots with whiskers representing the 10th and 90th percentile of data, and significance for all tests was set at $p < 0.05$.

## RESULTS

For the statically loaded samples, female ACLs (n = 6) exhibited an increased expression of anabolic (*COL1A2, COL3A1*), catabolic (MMP1, MMP2), and inflammatory genes (*IL-1β*, PTSG2) compared to the male samples ($p < 0.05$) (Fig. 1). For the cyclically loaded samples, female ACLs loaded to 2 MPa (n = 6) exhibited a decreased expression of *COL1A1, COL3A1,* and *MMP2* with an increased expression of *LOX* ($p < 0.05$) (Fig. 2). In contrast, there was no change in gene expression for female ACLs loaded to 4 MPa (n = 5); however, there was a trend toward differential expression of catabolic genes with potential downregulation of *MMP2* and *TIMP1* and upregulation of *MMP10* ($p = 0.063$) (Fig. 2). Male samples cyclically loaded to 2 MPa (n = 4-7) exhibited increased expression of anabolic genes *COL1A2* and *TGFβ1* ($p < 0.05$) (Fig. 3), whereas male samples cyclically loaded to 4 MPa (n = 6) exhibited increased expression of anabolic (*COL1A1, COL3A1,*

*LOX, TGFβ1)*, catabolic (*MMP2, TIMP1, TIMP3*), and inflammatory genes (*IL-1β*). ($p < 0.05$) (Fig. 3).

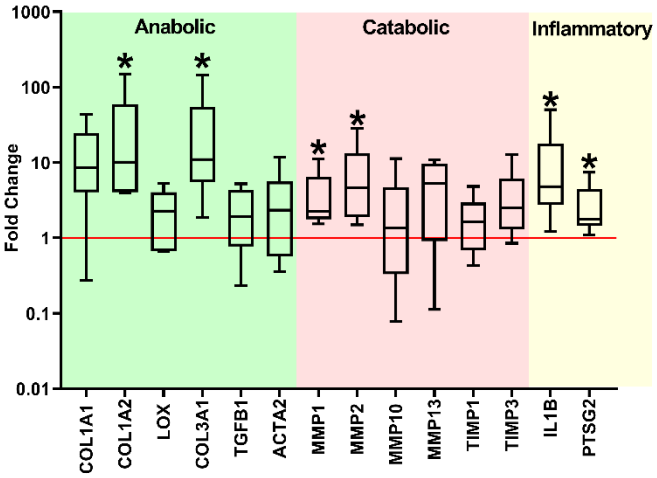


**Fig 1. Change in gene expression of female static control samples relative to males. ( * $p < 0.05$).**

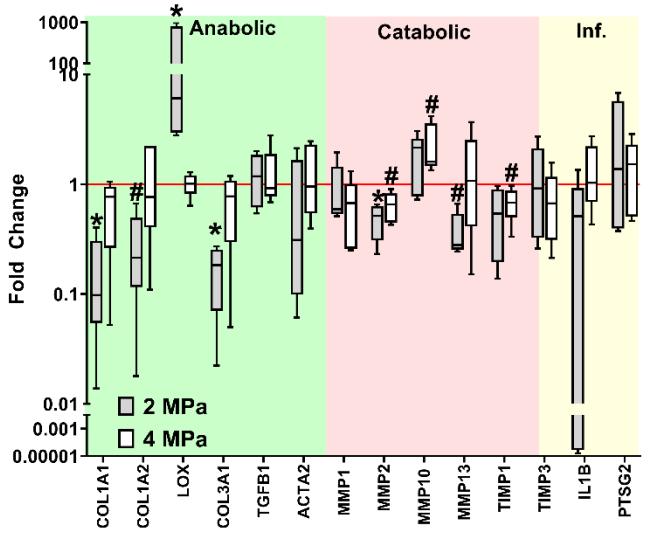


**Fig 2. Change in gene expression of female samples cyclically loaded to 2 or 4 MPa relative to a static control. ( * $p < 0.05$, # $p = 0.063$).**

## DISCUSSION

This study investigated how male and female rabbit ACLs respond to mechanical loading in a tissue explant model. We found that the biological response to mechanical loading was indeed sex dependent. Specifically, in the statically loaded samples, female ACLs exhibited an upregulation of anabolic, catabolic, and inflammatory markers compared to male samples. Upregulation of all gene categories suggests that, at baseline, female ACLs exhibit an increased level of tissue remodeling compared to males. Surprisingly, there was a mild downregulation in expression of anabolic and catabolic genes within female ACLs in response to loading. Note that while there was no statistically significant change with 4 MPa, this is likely due to an insufficient sample size ($p=0.063$). Furthermore, the 4 MPa data exhibited similar trends in gene expression as the 2 MPa data. In contrast, the male ACLs exhibited minimal changes in gene expression at 2 MPa but upregulated multiple anabolic, catabolic, and

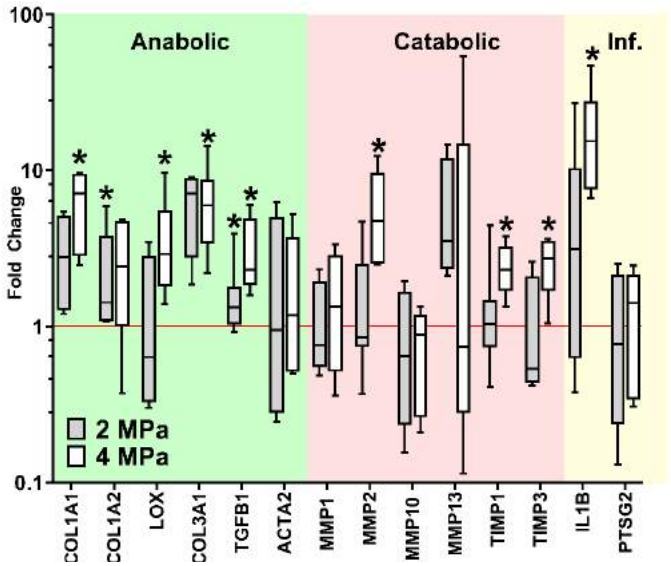


**Fig 3. Change in gene expression of male samples cyclically loaded to 2 or 4 MPa relative to a static control. ( * $p < 0.05$)**

inflammatory genes at 4 MPa, demonstrating that male rabbit ACLs are strongly mechanosensitive to increased loading. Together, these data suggest that male ACLs initiate active tissue remodeling with increased fatigue loading while female ACLs reduce tissue remodeling with loading. This lack of tissue remodeling with cyclic loading may inhibit the ability of female ACLs to repair fatigue damage, which offers insight into the increased rate of ACL injuries observed in women. A limitation to this study is that 8 h of loading is not sufficient to induce fatigue damage or changes in tissue structure/mechanics due to tissue remodeling. Future studies will investigate whether female ACLs have a reduced ability to repair fatigue damage by loading for a longer duration and measuring the change in mechanical properties.


## ACKNOWLEDGEMENTS

We would like to thank the Genomics Core Facility at Penn State for their assistance. Funding was provided by the Congressionally Directed Medical Research Program and the Orthopaedic Research and Education Foundation.


## REFERENCES


[1] Garrett, W et al., *J Bone Joint Surg. Am*, 88:660-667, 2006.
[2] Herzog, M et al., *JAMA Pediatr*, 171:808-810, 2017.
[3] Lipps, DB et al., *Am J Sports Med*, 41:1058-1066, 2013.
[4] Chen, J et al., *Am J Sports Med*, 47:2067-2076, 2019.
[5] Sun HB, et al., *Clin Orthop*, 466:1555-1561, 2008.
[6] Ardent, E. et al., *Am. J. Sports Med*. 23:694-701, 1995.
[7] Adachi, N et al., *Arch. Orthop. Trauma Surg*, 128:473-478, 2008.
[8] Paschall, L et al., *BMES Ann Meeting*, [Abstract], 2021.
[9] Papageorgiou, CD et al., *Am J Sports Med*, 29(5):620-6, 2001.
[10] Wang, T et al., *Biotechnol. Bioeng*. 110:1495-1507, 2013.

# FLOW DYNAMIC DIFFERENCES BETWEEN SELF-EXPANDING AND BALLOON EXPANDABLE TRANSCATHETER AORTIC VALVES

**H. Hatoum (1,2), M. Samaee (3), J. Sathananthan (4), S. Sellers (4), M. Kuetting (5), S. Lilly (6), A. Ihdayhid (7), P. Blanke (4), J. Leipsic (4), V. Thourani (8), and LP Dasi (3)**

(1) Department of Biomedical Engineering, Michigan Technological University, Houghton, MI
(2) Health Research Institute, Center of Biocomputing and Digital Health and Institute of Computing and Cybernetics, Michigan Technological University, Houghton, MI
(3) Department of Biomedical Engineering, Georgia Institute of Technology, Atlanta, GA
(4) St Paul's Hospital, University of British Columbia, Vancouver, Canada
(5) New Valve Technology, Hechingen, Germany
(6) Department of Cardiovascular Medicine, The Ohio State University, Columbus, OH
(7) Harry Perkins Institute of Medical Research, Perth, Western Australia
(8) Department of Cardiovascular Surgery, Piedmont Hospital, Atlanta, GA

## INTRODUCTION

Current commercially available transcatheter aortic valves (TAV) are either self- or balloon expandable. During the last two decades, tremendous improvements in TAV designs and materials took place to optimize valve performance and maximize its benefits[1]. Metals were replaced (stainless steel vs. cobalt chromium) to ensure stronger and more efficient anchoring, skirts were added and later modified to limit regurgitation, and valve profiles were altered to allow minimal interference with the downstream flow. Despite these improvements, the interaction of each TAV with the flow in the aortic root is associated with non-physiological flow properties compared to flow in a native annuli.

Clinical, in-vitro and in-silico studies have shown that TAV performance varies with valve type (self-expanding vs. balloon-expandable)[2,3], the unique design of each valve within the same type group[4,5], the deployment (axial and commissural)[6], and the surrounding patient-specific anatomy[7]. It is important to evaluate the flow downstream of the aortic valve, as it instructs directly on the performance parameters and ultimately durability (after sufficient follow-up). The turbulence of the flow downstream of the TAV informs on the pressure drop across the valve and explains some of the reasons behind differences in pressure recovery among different valves, as identified by different measurement modalities such as echocardiography and catheterization[2]. The turbulence of the flow downstream of the TAV also informs on the forces that the platelets and red blood cells undergo, in the context of general blood damage such as platelet activation, thrombus formation and hemolysis[8].

In this study, we aim to characterize the differences in the resulting flow dynamics and pressure recovery downstream of multiple self-expanding and balloon expandable TAVs.

## METHODS

The hemodynamic assessment of a 26mm Evolut, a 23mm SAPIEN 3, a small Acurate Neo and a 23mm Allegra transcatheter heart valves (THV) was performed in a left heart simulator under pulsatile physiological conditions. These sizes are equivalent in that they treat similar-sized annuli (20 – 23 mm). For the study, the TAVs were implanted into a rigid idealized test chamber. The aortic pressures ranged from 80 to 120 mmHg, the peak aortic pressure was set at 24 L/min, and the heart rate at 60 beats per minute. The fluid used in the experiments was a mixture of water-glycerin (60/40 by volume) with properties similar to those of blood (density of 1060Kg/m$^3$ and a kinematic viscosity of 3.5cSt). Flow data were acquired using ultrasonic flow probes (HXL, Transonic Inc., Ithaca, NY, USA), and pressures at all the measurement locations were measured with a Millar catheter (ADInstruments Inc., 2205 Executive Circle, Colorado Springs CO) along the centerline of the aortic valve chamber. Recordings of the pressure at every axial location along the ascending aorta with intervals of 5mm downstream of the valves and 1 mm inside the valves. Position 0 mm corresponds to the most upstream measurement (ventricular), and position 120 mm corresponds to the last measurement point in the measurement region of the chamber. Fifty consecutive cardiac cycles of aortic pressure, ventricular pressure, and flow rate data were recorded at a sampling rate of 100 Hz at every measurement location. The mean transvalvular pressure gradient (PG) is defined as the average of positive pressure difference between the ventricular and aortic pressure curves during forward flow.

Particle image velocimetry (PIV) experiments were performed to assess the flow downstream of each TAV. Time series recordings were acquired at a temporal resolution of 500Hz. Phase-locked recordings were acquired to calculate the resulting flow statistical parameters (Reynolds Shear Stress) over 250 images. The Reynolds Shear Stress (RSS), an established metric to evaluate turbulence and any associated blood damage potential, is a statistical quantity that is used to describe a turbulent flow field. The principal RSS and instantaneous viscous shear stress (VSS) were computed, and probability density functions (PDF) were calculated and plotted. The results are presented as mean standard deviations. Statistical analysis was performed using JMP Pro

version 15.2.0 (SAS Institute Inc, Cary, NC). All the data were distributed normally, and therefore, t-test for paired comparison between the vena contracta and recovery zone for each valve was performed along with Tukey test for unpaired comparison for vena contracta and recovery zone gradients of all valves.

## RESULTS

The maximal velocity at peak systole obtained with the Evolut R, SAPIEN 3, Acurate Neo and Allegra was found to be 2.12±0.19, 2.41±0.06, 2.99±0.10 and 2.45±0.08 m/s, respectively ($p<0.001$). Figure 1 shows the principal Reynolds Shear Stresses (RSS) at different phases in the cardiac cycle. The maximum RSS occurs during peak systole where the flow is maximal. The Acurate Neo and the Evolut R present the largest distributions of RSS in all 3 phases (acceleration, peak systole, and deceleration). The Allegra shows the minimal range of RSS magnitudes (up to 320 Pa), followed by the Evolut (up to 600 Pa) and then the Acurate Neo and SAPIEN 3 (up to 650 Pa). All the instantaneous VSS magnitudes obtained were lower than 10 Pa, a threshold associated with potential blood damage. The Evolut was shown to have the smallest magnitude range (up to 3.5 Pa), followed by the Allegra (up to 4.8 Pa), followed by the Acurate Neo (up to 5.5 Pa) and then the SAPIEN 3 (up to 6.2 Pa).

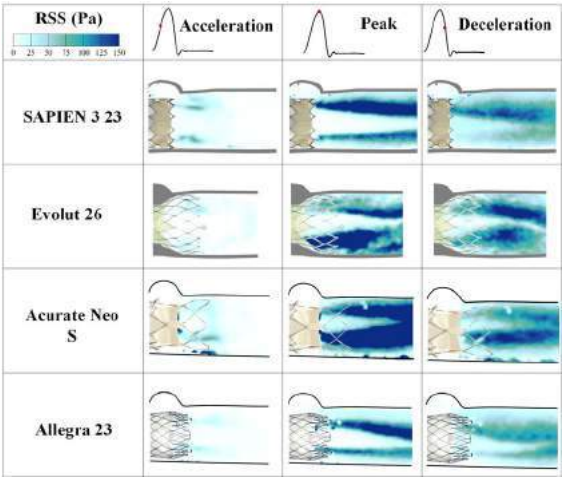


**Figure 1: Principal Reynolds shear stresses (RSS) at different phases in the cardiac cycle. The dark blue patches indicate an elevated RSS magnitude, and the more prevalent elevated RSS magnitudes are, the more turbulent the flow is considered to be.**

The importance of accounting for pressure recovery is that it permits identification of the true pressure gradient across the TAV and accordingly a more accurate assessment of performance. Figure 2 shows the variations of pressure gradients along selected locations in the aortic root with the 4 different valves. The largest pressure drop at the VC occurs with the S Acurate Neo TAV where the minimal pressure reaches 13.96±1.35 mmHg. The PG with the SAPIEN 3, Evolut and Allegra reach 10.54±0.51 mmHg, 10.64±0.38 mmHg, and 11.89±0.61 mmHg, respectively. The 23mm SAPIEN 3 showed the smallest pressure gradient at the VC. At 12 mm, in the recovery zone, the smallest pressure gradient was obtained with the Allegra (3.32±0.94 mmHg), followed by SAPIEN 3 (3.68±0.76 mmHg), then the Evolut R (4.77±0.87 mmHg) and the largest PG was obtained with the Acurate Neo (5±1.21 mmHg). Leaflet flutter was observed mostly with the Acurate Neo and the Evolut.

## DISCUSSION

In this study, we evaluated the hemodynamics downstream of 4 transcatheter aortic valves with variable leaflet position, 3 of which are self-expanding valves (26mm Evolut R, S Acurate Neo and 23mm Allegra) and 1 balloon expandable valve (23mm SAPIEN 3). We report findings on flow turbulence and its relationship to potential for thrombogenicity due to flow turbulence, and on pressure recovery along with its relationship to the assessment of overall valve performance. In literature, it was reported that a limit of 100 Pa to evaluate potential blood damage could be considered appropriate19. Any value that exceeds 100 Pa is considered elevated enough to be associated with blood damage potential. The Allegra TAV showed the smallest range of RSS indicating lowest turbulence levels compared with the other valves. This result was also accompanied by a small leaflet flutter frequency, that helped with the flow stabilization and with the reduction of RSS. The elevated leaflet flutter could be attributed to the supra-annular design of the leaflets and the location of the tip of the leaflet in the Evolut R and the Acurate Neo, in addition to the porcine pericardium material of the leaflets.

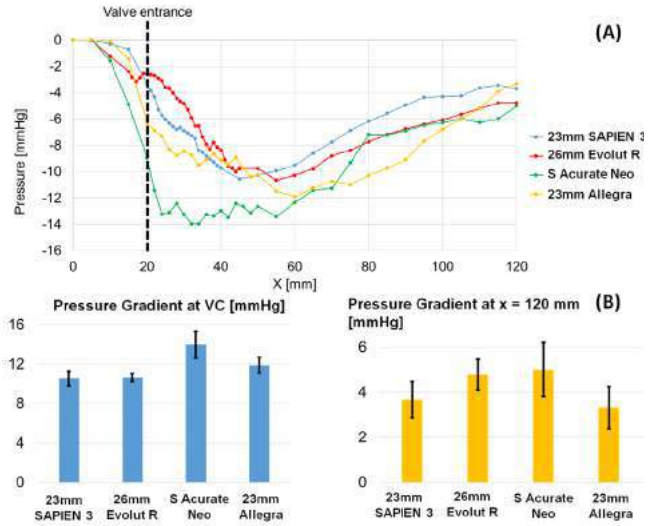


**Figure 2: (A) Variations of pressure gradients (PG) as a function of axial distance at selected location points during peak systole with the 23mm SAPIEN 3, 26mm Evolut R, S Acurate Neo, and 23mm Allegra TAVs. (B) Bar plot showing the pressure gradients at the VC and the recovery zone at x = 120 mm. The dark lines on the bar plots indicate the standard deviations.**

Pressure recovery is an important phenomenon that instructs on the performance of the implanted valve. As the jet expands downstream, its velocity starts decreasing and pressure is recovered depending on several factors such as turbulence, velocity of blood at the VC and the geometry of the aorta. Several clinical studies presented detailed comparative works between echo-based gradients (at the vena contracta) and catheterization-based gradients (in the recovery zone). Some of these studies highlighted that balloon-expandable valves are characterized by higher gradients at the VC and more elevated pressure recovery. Some of these studies were inconclusive. This study shows that pressure recovery is valve dependent, although it is hard to generalize the dependence on the self-expanding versus the balloon expandable type. With various valve types and designs, more experiments and more clinical outcomes are needed to assess the optimally performing valve type.

## REFERENCES

[1] Bui HT, et al. Advanced Healthcare Materials. 2021:2100115.
[2] Hatoum H, et al. JTCVS. 2018;156:1837-1848.
[3] Abdel-Wahab M, et al. JACC. 2020;13:1071-1082.
[4] Hatoum H, et al. JACC. 2021;77:1708-1708.
[5] Gonzálvez-García A, et al. JACC. 2019;74:B711-B711.
[6] Hatoum H, et al. The Annals of thoracic surgery. 2018;106:70-78
[7] Hatoum H, et al. JTCVS. 2019;157:540-549.
[8] Herrmann HC et al. CCI. 2021.

SB³C2022
Summer Biomechanics, Bioengineering and Biotransport Conference
June 20-23, Eastern Shore, MD, USA

# SEPSIS-DRIVEN INFLAMMATORY RESPONSES IN CARDIAC MICRO-TISSUES

**C. Virgile (1), E. Corbin (1, 2, 3)**

(1) Biomedical Engineering, University of Delaware, Newark, Delaware, United States
(2) Materials Science & Engineering, University of Delaware, Newark, Delaware, United States
(3) Department of Biomedical Research, Nemours/A.I. Dupont Hospital for Children, Wilmington, Delaware, United States

## INTRODUCTION

Heart failure and death due to sepsis is a growing concern in the medical community. Septic hospitalization rates have steadily increased, reaching a peak of almost 1,700,000 cases in the United States.[1,2] Sepsis is the result of an inappropriate immune response to an infection, where inflammatory cytokines are not kept in healthy concentrations. These inflammatory responses are thought to cause loss of contractility within the heart resulting in septic patients presenting with low blood pressure.[3] The weakened heart muscle tissue cannot overcome the increased end-diastolic volume thereby lowering the output pressure. Previous research has acknowledged that tumor necrosis factor α (TNF-α) and Interleukin (IL)-1β also are increased in individuals with sepsis and lead to reduction in cardiomyocyte lengths.[4] However, a number of other inflammatory factors (IL-6, -8, and -10) have demonstrated upregulation in septic serum and the collective septic inflammatory effects on heart muscle tissues remains to be understood. Therefore, we generated cardiac μtissues on soft lithography derived PDMS μ-pillar arrays to study the inflammatory and contractile responses of cardiac muscle tissue *in vitro*. Cardiac μtissues were dosed with individual inflammatory cytokines and assessed for their inflammatory response and tissue contractility properties. By understanding the effects of Sepsis on Cardiac muscle *in vitro*, we will help to inform future *in vivo* platforms of analysis and therapy.

## METHODS

Silicon wafers were designed and fabricated in a clean room environment and used as master molds for soft lithography polydimethhysiloxane (PDMS, Sylgard 184 DOW Corning) cantilever molding. Induced pluripotent stem cell-derived cardiomyocytes (iPSC-CMs), the primary cells that make up cardiac muscle tissues, and bone-marrow derived mesenchymal stem cells (MSCs) are encapsulated in collagen type I and cultured at 37.5 °C, 5% CO2. iPSC-CMs and MSCs self-assemble into spontaneously contractile cardiac μtissues within 48 hours. At 48 hours, μtissues are dosed with a vehicle (control), 2000 pg/mL, or 6000 pg/mL of TNF-α. An inverted microscope was used to record cantilever deflection every 3 hours for 24 hours. After 72 total hours, spent media is collected and μtissues are fixed and stained for DAPI, sarcomeric α-actinin, and connexin-43. An ELISA is used to analyze change in TNF-α levels after the 24-hour dosing.

## RESULTS

Cardiac μtissues present a positive feedback loop in response to dosages of inflammatory cytokines. TNF-α accumulation in spent media showed a significant increase in cardiac muscle release in response to a 2000 pg/mL dosage of TNF-α. ELISA results showed a 3-fold increase in TNF-α concentration after only 24 hours of culture for the 2000 pg/mL group (the 6000 pg/mL group had off-the-chart concentration readings at the time of study and thus have been left out of this data), as seen in **Figure 1A**.

Fluorescence staining of cardiac μtissues revealed continuous rearrangement of the cellular structure, including sarcomeres. In both 2-D and 3-D cultures with increasing amounts of TNF-α, iPSC-CMs stained for α-actinin and DAPI (and connexin-43 for the μtissues) had increasing amounts of misalignment (**Figure 2**) and cell death (**Figure 3**). Contractility studies are still ongoing.

These results confirm the danger of sepsis to the heart; when left untreated, cytokines will continuously self-upregulate in the blood. Unattended exponential growth of cytokines will lead to heart failure and other Sepsis related maladies.

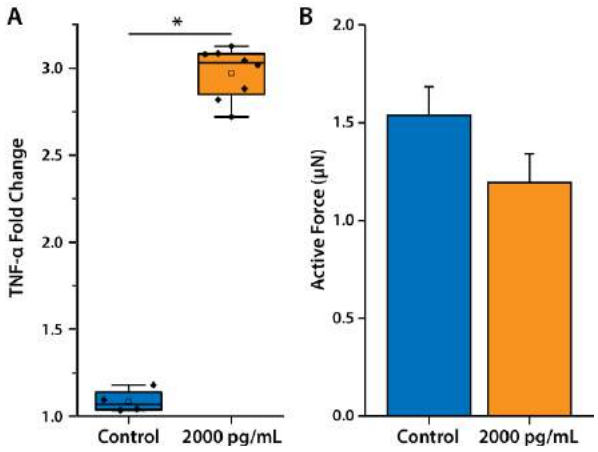


**Figure 1: TNF-α is upregulated in CMTs. In CMTs dosed with 2000 pg/mL of TNF-α, the cytokine is consistently produced to yield a higher concentration after 24 hours. Apparent trend of decreased contractility at 24 hours after TNF-α dosage.**

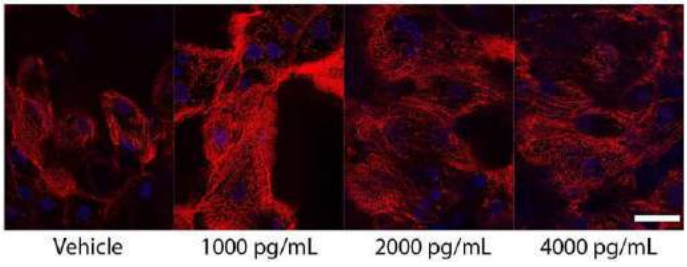


**Figure 2: Dosing iPSC-CMs with TNF-α in 2D monolayer. Representative images showing the degradation of sarcomere alignment (DAPI, Blue; α-Actinin, Red; scale bar is 200 μm).**

## DISCUSSION

The results of these experiments have demonstrated a positive feedback loop of TNF-α production in 3-D cardiac μtissues, consistent with the septic disease state. Additionally, the data show a dose-dependent response between sarcomere alignment and concentration of TNF-α. Lastly, the data show broad cell death over the course of 24 hours with increasing amount of TNF-α. Between sarcomere rearrangement and cell death, the contractility is likely decreasing over time, but further studies will be performed to confirm this hypothesis.

The mechanistic effects of sepsis on the heart are relatively unknown: researchers have theorized the molecular pathways and have performed post-mortem analysis on heart tissue. TNF-α has shown to regulate inducible nitric oxide production[5] and heat shock protein 72[6], two common cellular stress proteins. A critical piece missing is how sepsis affects heart mechanics and contractile properties. We have begun to show how individual septic cytokines can influence the inflammatory response in *in vitro* cardiac tissue. Our hope is to expand this research to include a range of cytokines, including IL-1β, -6, -8, and -10, and determine the contractile responses of septic serum dosing. Collectively, these data will help to drive future research into the relationship between heart muscle condition and sepsis

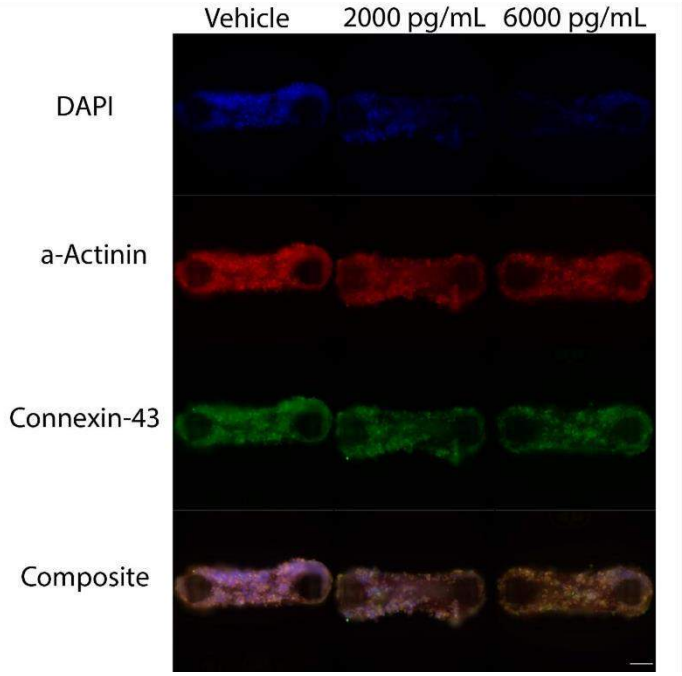


**Figure 3: Representative images showing continual cell death in cardiac micro-tissues dosed with TNF-α (scale bar is 200 μm).**


## ACKNOWLEDGEMENTS

Supported by a grant from NIH-NIGMS (P20 GM103446) and the State of Delaware.


## REFERENCES


1. Melamed, A et al., *Critical Care*, 12:1-8, 2009.
2. Sepsis Infographic. https://images.nigms.nih.gov/pages/DetailPage.aspx?imageid2=6536&utm_source=twitter&utm_medium=social&utm_campaign=Sepsis-Info.
3. Hunter, J. D. et al. *Br. J. Anaseth.*, 104:3-11, 2010.
4. Kumar, A. et al. *J. Exp. Med.*, 183:949-958, 1996.
5. Satoh, M. et al. *JACC*, 29:716-724, 1997.
6. Nakano, M. et al. *AJPHCP*, 270:1231-1239, 1996.

SB³C2022
Summer Biomechanics, Bioengineering and Biotransport Conference
June 20-23, Eastern Shore, MD, USA

# MICROFABRICATED ANISOTROPIC TISSUE BUNDLES FOR THE PRODUCTION OF 3D CARDIAC TISSUE AT SCALE

**Maggie E. Jewett (1), Amanda S. Bluem (1), Samuel J. DePalma (1), Brendon M. Baker (1,2)**

(1) Biomedical Engineering, University of Michigan, Ann Arbor, MI, USA
(2) Chemical Engineering, University of Michigan, Ann Arbor, MI, USA

## INTRODUCTION

Acute or chronic cardiac injuries, such as myocardial infarction or prolonged cardiac overload, cause irreversible damage to the heart[1]. Following myocardial infarction, tissue ischemia and resulting cardiomyocyte (CM) death initiate an inflammatory response and extracellular matrix (ECM) remodeling wrought by activated cardiac fibroblast (CF). This wound healing program results in permanent alterations to myocardial tissue composition, disruption of mechanical and electrical properties, and impaired function[2]. The field of cardiac tissue engineering aims to develop technologies to biomanufacture engineered tissues that could replace injured or diseased native myocardium and restore normal cardiac function for the patient.

Two features critical to healthy myocardial function are the ECM's high degree of structural anisotropy and the organization of resident cell populations (Fig. 1A). The key cell types that structurally compose the myocardium include cardiomyocytes and cardiac fibroblasts[3]. While incorporating these cell types in 3D structures has been well established[4], integrating distinct cell types with tissue-relevant organization and functionally maturing the resulting tissues both remain major challenges for the field. In particular, there is a critical need for new biomanufacturing technologies that can organize ECM and multiple, distinct cell types with microscale precision within tissue grafts of translationally relevant scale. Here, we propose a new method of microfabricating individual anisotropic myofiber bundle-like tissues that can be assembled into larger tissue grafts.

## METHODS

Microchannel devices ranging in channel height and width were designed in Solidworks and 3D printed using a Formlabs Form 3 SLA printer with Grey v4 resin. Sylgard 184 polydimethylsiloxane (PDMS) microchannels were cast from 3D printed molds and treated with 0.3% Pluronic-F127 for 1 hour, then placed channel side down on a 0.3% Pluronic-F127 treated PDMS coated glass coverslip. Channels were perfused with fibrin (20mg/mL fibrinogen with 1U/mL thrombin) containing up to 20M/mL GFP-expressing 3T3 fibroblasts and 2 vol% dextran-vinyl sulfone (DVS) electrospun fibers fabricated via previously described methods[6,7]. Tissues were gelled at 37°C for 30 minutes. Following gelation, PDMS molds were removed, and tissues were cultured in DMEM with 10% FBS and 1% pen/strep (Fig. 1B). Flow-induced alignment of DVS fibers was analyzed using the FibrilTool FIJI plugin to quantify the anisotropic index[8].

## RESULTS

To drive cell alignment, DVS fibers were added to the fibrin precursor solution as a synthetic ECM component and flow-aligned within microfabricated channels. Perfusion of fibrin containing DVS fibers and/or cells resulted in pronounced fiber alignment within formed tissues. Due to the geometry and boundaries of the microchannels, flow-induced alignment of DVS nanofibers within fibrin can be observed consistently across all five channel sizes (Fig. 1C). However, anisotropy of fiber alignment decreased with increasing channel size (Fig. 1D). The decrease in fiber alignment in larger channels is likely due to diminished mechanical boundary effects provided by channel walls. Additionally, fiber alignment varied more by depth within tissue constructs as width of the microchannel increased. While all sides of the gel interact with Pluronic treated PDMS, the surface roughness of 3D printed molds decreases flow-induced alignment. Thus, the top region of formed gels, which are in contact with a rough PDMS surface, were less anisotropic than bottom layers (Fig. 1E).

The inclusion of high-density cell suspensions in gel precursor solutions may influence flow rates and patterns due to changes in viscosity, in turn influencing the final alignment of incorporated fibers. To test whether tissue-relevant cell densities impaired fiber alignment, two cell densities, 10 and 20 M cells/mL, were compared to acellular gel precursor solutions (Fig 2A). Fibers were aligned in all microchannel sizes regardless of cell density (Fig. 2B). Therefore,

including high density cell suspensions in the tissues does not hinder the resulting anisotropy of the myofiber bundle-like tissues.

Upon PDMS mold removal, sustained culture of formed tissues is possible and tissues decreased in diameter due to cell-mediated contraction and proteolysis (Fig. 2C). Overall, these results display the feasibility of our method for producing anisotropic, myofiber-like tissue structures that can be combined to form larger, scalable tissue grafts.

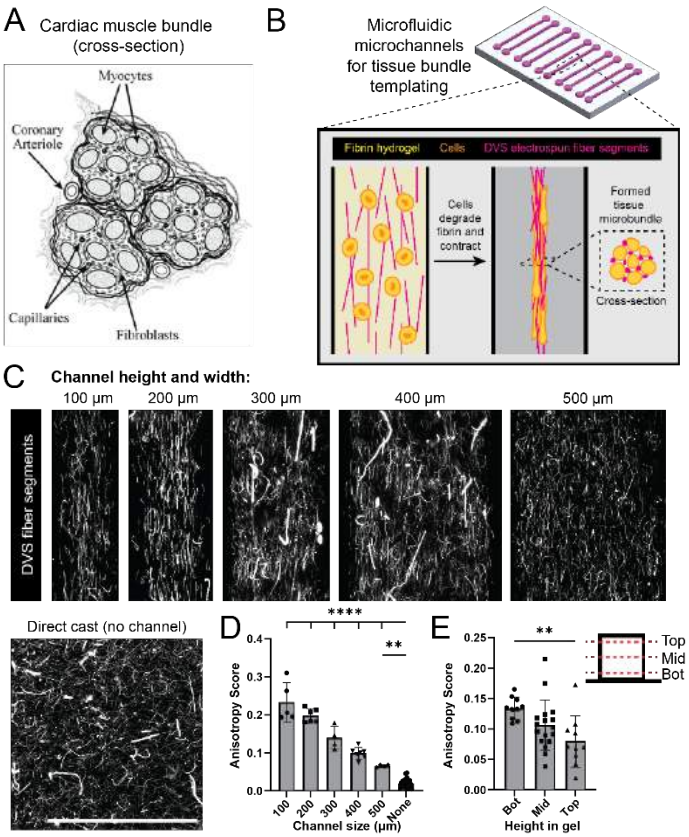


**Figure 1: (A) Diagram depicting a cross-section of myocyte bundles including containing myocytes, capillaries, and fibroblasts[5]. (B) Schematic of microfabricated channels for forming myofiber-like bundles. (C) Immunofluorescent images (scale bar: 500 µm) and (D) quantification of DVS fiber flow alignment via channels of varying sizes. (E) Anisotropy quantification of the bottom, middle, and top planes of formed tissues within all sizes of microchannels. **** p < 0.0001, ** p < 0.005.**

## DISCUSSION

In this study, we developed a microfabrication approach to produce anisotropic myofiber-like bundles using composites of naturally derived ECM and synthetic polymeric fibers that can be flow-aligned within microfabricated microchannels. We show that microchannel geometry controls the anisotropy of ECM-like matrix fibers and the resulting size of tissue bundles. This critical information along with our microfabrication approach allows us to fabricate unit cell tissue bundles of desired size and alignment that can be combined into a larger tissue construct for therapeutic applications. Although these studies were conducted using only fibroblasts, future studies will incorporate a co-mixture of iPSC-derived cardiomyocytes and cardiac fibroblasts. The inclusion of fibroblasts is critical for degrading the fibrin gel and contracting tissue bundles, and we anticipate a careful balance between cardiomyocyte and fibroblast constituents will be required to form cardiac tissue bundles with sufficient electrical and mechanical function characteristic of native cardiac tissues. These metrics will be measured by immunofluorescent imaging of cell-cell junction proteins, such as desmoplakin and connexin-43, and calcium imaging, respectively.

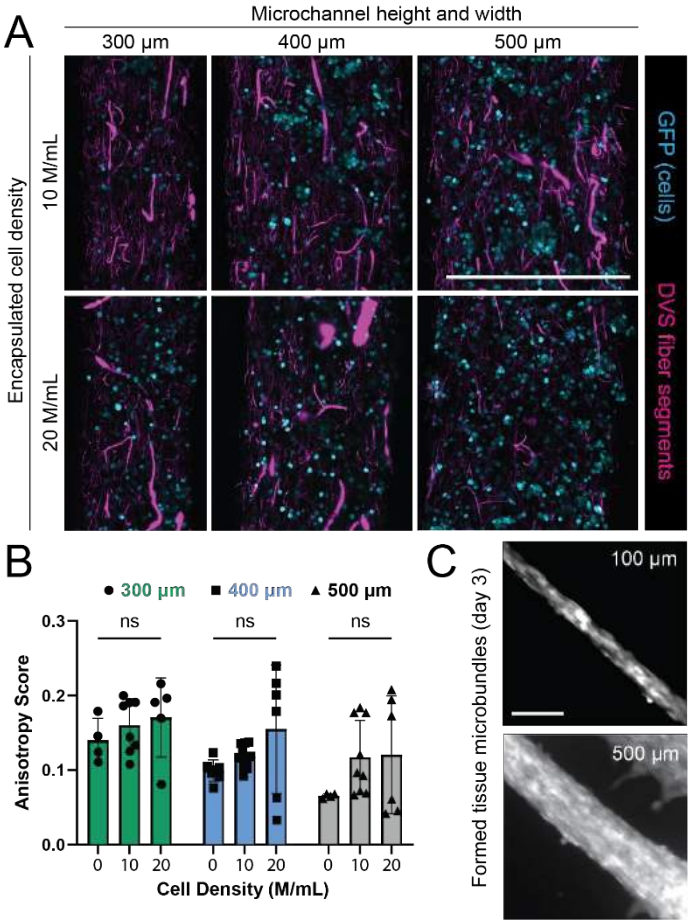


**Figure 2: (A) Immunofluorescent images of flow aligned fiber containing fibrin (scale bar: 500 µm). (B) Anisotropy score for acellular gels, and gels containing 10 and 20 M cells/mL for 300, 400, and 500 µm wide channels. (C) Fluorescent images of GFP-expressing fibroblast-laden tissues 3 days after mold removal and tissue contraction (scale bar: 500 µm). *** p < 0.0005.**


## ACKNOWLEDGEMENTS

This work was supported by the National Science Foundation (EEC-1647837, CBET-2033654) and Graduate Research Fellowship Program (DGE1256260). S.J.D acknowledges financial support from NIDCR of the NIH under T32DE007057.


## REFERENCES


[1] Schroer, AK+, *J of Cell Science*, 128:1865-1875, 2015. [2] Piek, A+, *Heart Failure Reviews*, 21:199-211, 2016. [3] Godier-Furnemont, AFG+, *Regenerating the Heart: Stem Cells and the Cardiovascular System,* Humana Press:443–475, 2011. [4] Ronaldson-Bouchard, K+, *Nature*, 556:239-243, 2018 [5] Gaetani, R+, *Studies in Mechanobiology, Tissue Engineering and* Biomaterials, 6:1-27, 2011. [6] Davidson, CD+, *Acta Biomaterials*, 105:78-86, 2020. [7] Matera, DL+, *Science Advances*, 5:1-31, 2020. [8] Burian, A+, *Nature Protocols*, 9:457-463, 2013.

SB³C2022
Summer Biomechanics, Bioengineering and Biotransport Conference
June 20-23, Eastern Shore, MD, USA

# SPATIAL GRADIENT IN FRONTAL LOBE STIFFNESS DURING BRAIN MATURATION

**Kyra E. Twohy (1), Grace McIlvain (2), Curtis L. Johnson (2)**

(1) Department of Mechanical Engineering, University of Delaware, Newark, DE, USA
(2) Department of Biomedical Engineering, University of Delaware, Newark, DE, USA

## INTRODUCTION

While the human brain develops dynamically from in utero to childhood, maturation is occurring through adolescence into adulthood [1]. Understanding how this development and maturation occurs and the driving mechanisms behind it has been a focus of brain research. One important factor is internal stresses that are critical in brain development and help drive processes such as cortical folding [1]. Measures of these mechanical factors *in vivo* are limited due to the invasive nature of many techniques [1]. A more accessible technique is magnetic resonance elastography (MRE), which leverage phase-contrast MRI to quantify the mechanical properties of brain tissue [2]. Analysis of these properties during late childhood and adolescent development is central to understanding the role internal stresses might play during maturation.

Quantitative values calculated from MRE, including shear stiffness, have been shown to be sensitive to the microstructure of brain tissue [2]. Use of MRE has shown significant changes in brain mechanical properties during aging [3]; however, the application of this technique during maturation is limited [4]. Microstructural changes occurring during maturating include myelination of neural pathways, reorganization and pruning of synaptic connections, and changes in white and gray matter densities [5], all of which are expected to affect brain mechanical properties [6]. MRE can be used to probe brain maturation and examining the distribution of properties spatially throughout the brain could improve understanding of factors supporting maturation. A particular area of interest is the frontal lobe, given its later and prolonged development compared to other areas of the brain [5]. This study aims to compare the spatial variation of shear stiffness in the frontal lobe from childhood to adulthood to understand how development affects the material properties of the brain.

## METHODS

13 children (age range: 5-7 years old, 8M/5F), 14 adolescents (12-14 years old, 8M/6F), and 14 young adults participated in this study (18-32 years old, 5M/9F). All participants completed an MRI protocol on a Siemens Prisma 3T MRI scanner. The MRE portion of the protocol used a custom 3D multiband, multishot spiral sequence with OSCILLATE acceleration to reduce scan time (TE: 76 ms, TR: 140 ms, field-of-view: 240x240 mm$^2$, gradient strength: 70 mT/m) [7]. Vibrations were applied at 50 Hz to the back of the head as shown in Figure 1 and the total MRE portion took 4.5 minutes. A T1-weighted MPRAGE (resolution: 0.9 x 0.9 x 0.9 mm$^3$) was also completed for anatomical segmentation.

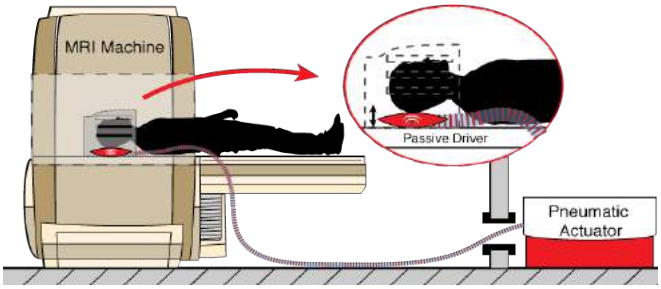


**Figure 1: MRE acquisition set up showing the passive pillow driver in red that applies the vibration.**

Displacement data was converted to shear stiffness using a nonlinear inversion algorithm (NLI) [8]. This defines complex shear modulus (G) by the storage (G') and loss (G") moduli as shown in Equation 1.

$$G = G' + iG'' \quad (1)$$

From complex shear modulus, shear stiffness (μ) can be calculated using Equation 2.

$$\mu = 2|G|^2/(G' + |G|) \quad (2)$$

For each subject, shear stiffness maps were converted into standard space for comparison between groups. The boundaries of the frontal lobe were defined using the WFU-Pick Atlas and the average frontal

lobe stiffness was calculated. To determine gradients in stiffness from the interior to the exterior of the frontal lobe, the stiffness values at each of the boundary points was identified and the gradients were calculated as

$$\frac{(\mu_e - \mu_i)}{d_{avg}}, \quad (3)$$

where $\mu_e$ is the average exterior boundary shear stiffness, $\mu_i$ is the average interior boundary stiffness, and $d_{avg}$ is the average distance between these two boundaries to account for subject specific geometry. This was completed for a middle slice of the frontal lobe. Statistical differences between groups in both frontal lobe stiffness and stiffness gradient were assessed using ANOVA in MATLAB. Additionally, stiffness gradients were correlated with age across all subjects.

## RESULTS

Shear stiffness over the entire frontal lobe was found to be 2.83 ± 0.14 kPa (child group), 2.92 ± 0.18 kPa (adolescent group), and 2.74 ± 0.10 kPa (adult group). Stiffness significantly differed between groups ($p = 0.010$), with significant *post hoc* group differences between the adolescent and adult groups ($p = 0.007$). The calculated average gradient for a middle slice is shown in Figure 2, below, ranging from a mean of -17.16 Pa/mm in the children to -11.42 Pa/mm in the adults. The stiffness gradient significantly differed between groups ($p = 0.035$), with significant *post hoc* group differences between the child and adult groups ($p = 0.031$). The largest magnitude stiffness gradient was found in the child group with the exterior of the brain being softer than the interior. Representative stiffness maps are included for each age group in Figure 2. These visually show that larger differences are found in the child group, but overall stiffness was higher in adolescents. When assessing the influence of age on the stiffness gradient, the gradient magnitude decreased with age ($p = 0.010$), shown in Figure 3.

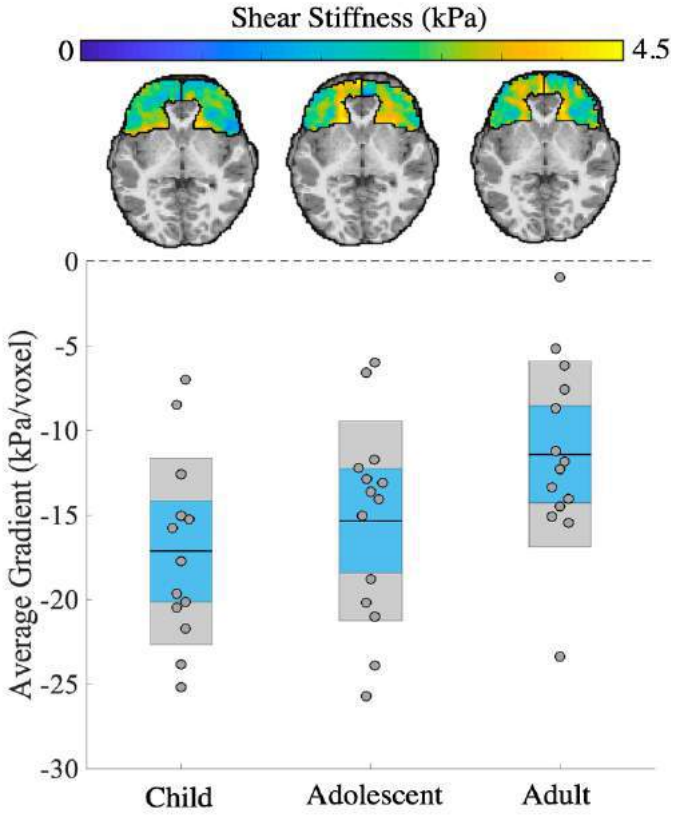


**Figure 2: Average gradient for each age group for a middle slice of the frontal lobe with representative shear stiffness maps shown above. Means are shown by the center line in the blue box, standard deviation by the entire blue box, and the 95% confidence interval identified in the light gray box.**

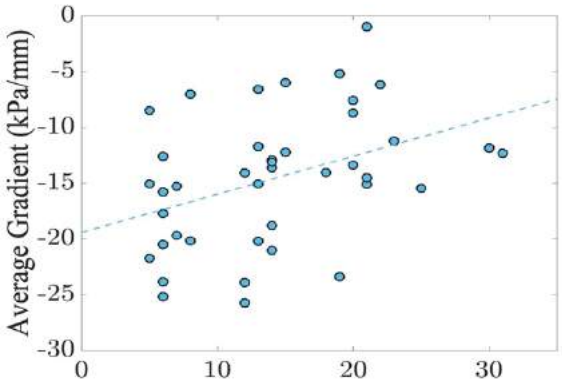


**Figure 3: Stiffness gradient as a function of age.**

## DISCUSSION

This study examined the spatial variation of shear stiffness during development using average stiffness gradients. Significant differences were found when comparing the stiffness gradient from the interior to the exterior of the frontal lobe, specifically between the child and adult groups. The exterior of the frontal lobe is softer than the interior, and across all groups the magnitude of the average gradient decreased with age, i.e., the exterior and interior stiffness became more similar. The sensitivity of this measure to age is likely due to the gradient reflecting maturational changes in the frontal lobe, likely due to microstructural changes in the cortex including myelination and synaptic pruning [5], both of which would impact material properties.

Although previous research comparing adolescent and adult average shear stiffness in the frontal lobe found no significant difference [4], this study found that adolescents had a significantly higher stiffness than adults. There were no statistical differences in average frontal lobe stiffness between the child and adult groups, even though significant structural changes likely occurred between those time points, as reflected in the stiffness gradient measure. Future work will include longitudinally assessing these gradients both in the frontal lobe and other areas of the brain.


## ACKNOWLEDGEMENTS

This work was supported in part by NIH grants R01-EB027577, R01-AG058853, U01-NS112120, F31-HD103361, and the Delaware INBRE program (P20-GM103446).


## REFERENCES


[1] Bayly, PV et al., J. Mech. Behav. Biomed. Mater., 29:568-581, 2014.
[2] Hiscox, LV et al., Phys. Med. Biol., 61:R401-R437, 2016.
[3] Hiscox, LV et al., Neuroimage, 232:117889, 2021.
[4] McIlvain, G et al., Dev. Cogn. Neurosci., 34:27-33, 2018.
[5] Blakemore, SJ, Neuroimage, 61:397-406, 2012.
[6] Johnson, CL et al., Dev. Cogn. Neurosci. 33:176-181, 2018.
[7] McIlvain, G et al., ISMRM, 2020.
[8] McGarry, MDJ et al., Med. Phys., 39:6388-6396, 2012.

# EFFECT OF RESIDUAL STRESSES ON RING-TEST MECHANICAL ANALYSIS

**Manoj Ghosh (1), Marissa Grobbel (1), Lik Chuan Lee (1), and Sara Roccabianca (1)**

(1) Department of Mechanical Engineering
Michigan State University
East Lansing, MI, United States

## INTRODUCTION

The existence of residual stress distributions is a peculiar characteristic of soft biological tissues, especially in the cardiovascular system [1]. The opening angle method is popularly implemented to estimate the residual stresses in left ventricle (LV) [1-2]. Furthermore, uniaxial tensile test on ring-shaped samples has been often used to estimate the mechanical properties of both arteries and the LV [3]. However, it is unclear how the existence and magnitude of a circumferential, auto-equilibrated, residual stress distribution may affect the estimation of mechanical properties via ring test. Using the data from experimentally quantified opening angles [4] paired with finite element analysis (FEA) we aim to understand the effect that residual stresses have on the stress distribution in the LV, associated with uniaxial mechanical testing.

## METHODS

Our approach can be outlined in two primary steps. First, we used the experimentally quantified opening angle from one representative sample as input for a continuum model to calculate the residual stress distribution, as outlined in [4]. The outputs of the model include the dimensions for the equilibrated closed configuration. Second, we used this geometric information as input for a FEA which includes the finite deformation associated with both the residual stress as well as the ring test [5].

The experimental protocol for the opening angle test as well as the description of the continuum model has been previously described in [4]. For this study, we have selected one representative sample form the isolated collagen experimental group from a healthy male rat (Sprague Dawley). Specifically, the experimental geometrical parameters for the open (after-cut) configuration are: inner and outer radius 4.08 mm 7.75 mm, respectively; and opening angle 96 [deg]. In the continuum model, we described the collagen fibers mechanical behavior employing the following strain energy function.

$$W = c(\exp k(I_1(\boldsymbol{C}) - 3) - 1). \quad (1)$$

Here $I_1(\boldsymbol{C})$ is the first invariant of right Cauchy-Green tensor $\boldsymbol{C} = \boldsymbol{F}^T\boldsymbol{F}$; and the material parameters are $c = 0.47i$Kpa and $k = 31.09$. The deformation gradient for the cut, stress free configuration $(R,\Theta,Z)$ to uncut traction free configuration $(\rho,\theta,z)$ is given by,

$$\boldsymbol{F} = diag\left(\frac{\partial\rho}{\partial R}; i\frac{\rho}{R}; i\frac{2\pi}{2\pi - \Phi}; i\Lambda_z\right). \quad (2)$$

Using this material description, the inner and outer radius for an equilibrated closed configuration was calculated. To understand the effect of the opening angle magnitude on the stress distribution during the opening angle test, we also considered an opening angle of 120 [deg] for the same sample.

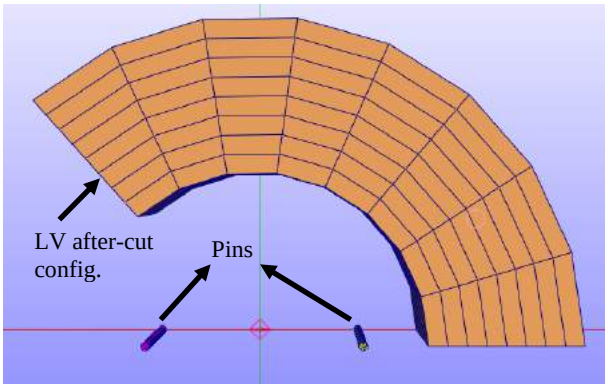


**Figure 1: Stress free ring model used for simulations. The tissue is shown in orange and pins are purple and yellow.**

The FEA was then carried out in two steps: closing the opening angle, first, and simulating the ring test by applying a displacement to the pins, second. A FE model of the after-cut, stress-free configuration of the representative LV was created (**Fig. 1**). For the FEA we used FEBio 3.0, as previously described in [5]. Briefly, the model was created using a solid arc tool, and the two pins used to pull the closed ring during the mechanical test were described as rigid bodies. A sliding node-on-facet contact was implemented between the pin surface and the inner surface of the sample. Both the sample and the pins were meshed using hex8 elements. The strain energy density was given by equation (1) and the material parameters used were the same as in the continuum model (i.e., $c = .47i$KPa and $k = 31.09$). The value of bulk modulus was 1000KPa to approximate the condition of incompressibility employed in the continuum model. For the first step (i.e., the residual stress calculation) the pins were fixed, and the deformation applied to close the model was the one calculated in the continuum model (to ensure an equilibrated condition). For the second step, a displacement of 2 mm was applied to one of the pins and the other one was fixed. We performed the simulation for an opening angle of 96 [deg] (as measured experimentally) and 120 [deg].

## RESULTS

**Fig. 2** represents the x-stress distribution calculated for an opening angle 96 [deg]. **Fig. 2a** shows the x-stress corresponding to the residual stress distribution, in the closed configuration. We can see that the stress distribution corresponds to a finite bending distribution (i.e., inner surface is in compression and the outer surface is in tension). The stress varies from -18.1 KPa to 13.9 KPa. In **Fig.2b**, we show the stress distribution after the ring test simulation, specifically after a 2 mm axial deformation is applied. The stress reaches a maximum tensile value of 28.4 KPa. **Fig. 3a** and **b** show the same set of results for a larger opening angle, namely 120 [deg]. Here, the stress varies from -38 KPa to 31.7 KPa after opening angle closer, and it reaches a maximum tensile value of 56 KPa during ring-test simulation.

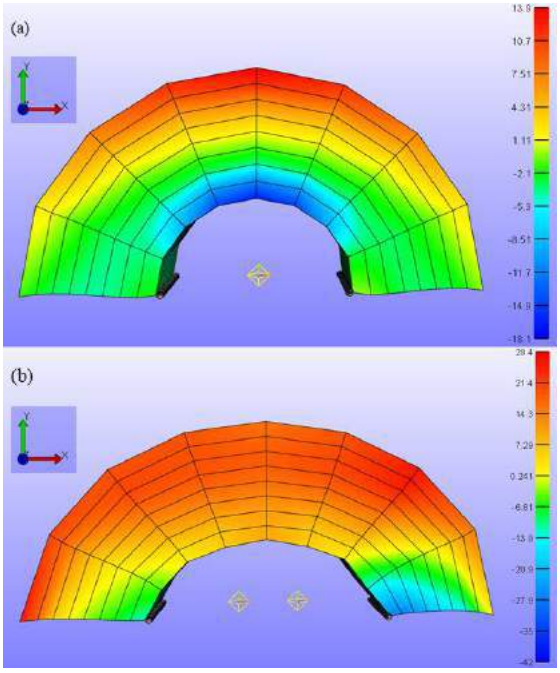


**Figure 2: Stress distribution along the ring after step 1(a) and 2mm pull after step 2(b) for opening angle $96^{\circ}$.**

Comparing the results from **Fig. 2** and **Fig. 3** it suggests that a larger opening angle will generate a larger value of tensile stress, for equal deformation, during the ring test simulation. Furthermore, after an identical axial displacement the change in pick values of the stress in the x direction is larger when the opening angle is larger. Specifically, it goes from 14.5 KPa to 24.3KPa, when increasing the opening angle from 96 [deg] to 120 [deg].

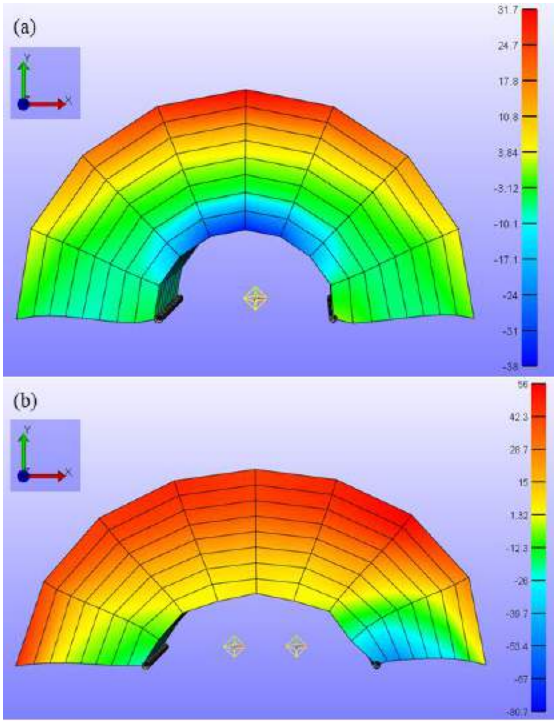


**Figure 3. Stress distribution along the ring after step 1(a) and 2mm pull after step 2(b) for opening angle $120^{\circ}$.**

## DISCUSSION

We performed a FEA to understand the effect of the opening angle magnitude on the maximum value of stress reached in a soft tissue during the ring-test. Our numerical simulations suggest that the opening angle plays a significant role in stress distribution in LV. From the results, we can see that the residual stress increases with a higher opening angle. In future, we will perform a parametric study to investigate the relationship between opening angle and stress distribution. The aim of this study is to understand if residual stresses should be included when estimating material parameters from the uniaxial ring test.


## ACKNOWLEDGMENTS

Projected funded by NSF CMMI GRANT #1933768 (SR).


## REFERENCES


[1] J.H. Omens et. al. Circulation Research, 1990
[2] C. J. Chuong, et. al. Frontiers In Biomechanics, 1986
[3] Shazly T,et. al. Exp Mech, 2015.
[4] M.R. Grobbel, et. al. *BMMB*, 2018.
[5] R.R. Mahutga et. al. Exp Mech 2021

# A NOVEL FIBROUS FINITE ELEMENT MODEL OF SOFT TISSUES

**Mohammad R. Islam (1), Fengting Ji (1,2), Manik Bansal (1), Yi Hua (1), Ian A. Sigal (1,2)**

(1) Department of Ophthalmology, University of Pittsburgh, Pittsburgh, PA, USA
(2) Department of Bioengineering, University of Pittsburgh, Pittsburgh, PA, USA

## INTRODUCTION

Soft connective tissues are characterized by a complex assembly of collagen fibers. Collagen forms three-dimensional (3D) fibrous structures where individual fiber exhibits strong geometric nonlinearities including tortuosity, entanglement, and preferential orientation. The tissue-specific fiber organization together with fiber-scale geometric complexities plays a central role in tissue's biomechanics. However, the fiber mechanics in soft tissues especially the effects of tissue-specific fibrous architecture remain poorly understood. Biomechanical models of soft tissues have been largely developed based on a continuum description which are limited in predicting fiber-scale deformation, and the contributions of fiber-fiber interactions and tissue-specific fiber architecture [1]. Although a few fiber-scale models have been developed recently, they are based on idealized architectures and do not represent tissue-specific fiber organization [1]. Therefore, the mechanistic links between tissue's fibrous structures and their emergent biomechanics cannot be fully understood from the existing models.

The objective of current work was to develop a fibrous finite element (FFE) model of soft tissues with tissue-specific fiber organization and fiber-level resolution, capable of establishing the direct association between tissue's fiber structure and mechanics. Specifically, we developed a FFE model of the peripapillary sclera (Fig. 1a) as a model system and investigated its mechanical behavior under elevated intraocular pressure (IOP). Using the high-fidelity FFE model (Fig. 1e), we examined the fiber-scale strain heterogeneity in the sclera and elucidated the geometric basis of its nonlinear mechanics.

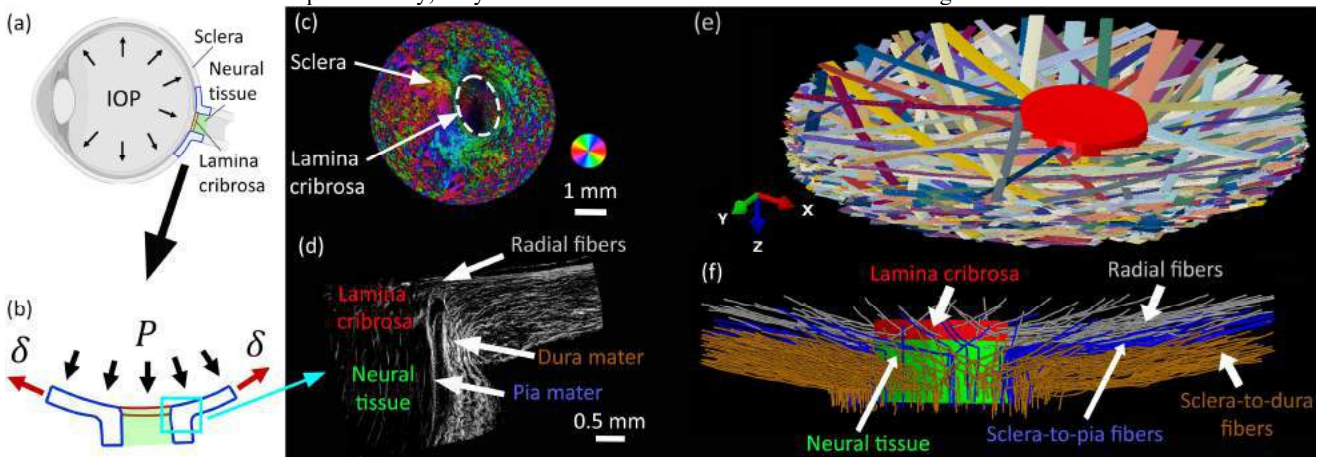


**Figure 1. (a) Schematic of eye cross-section with ONH region highlighted and (b) enlarged view of the region with boundary conditions. PLM images of (c) a coronal section with in-plane fiber orientation in color, and (d) a sagittal section corresponding to the region marked in (b). (e) 3D and (f) sagittal model views. (e) shows full bundle widths. (f) shows only bundle axes of selected fiber families colored according to (d).**

## METHODS

***Model geometry:*** An FFE model of sclera was developed based on highly detailed imaging data of a porcine eye from polarized light microscopy (PLM) [2]. In a coronal PLM image (Fig. 1c), sclera appears as a network of circumferential, isotropic, and radial fiber bundles [2]. The sagittal section (Fig. 1d) shows that a set of fibers merges into the lamina cribrosa (LC) and two other sets of fibers turn outward from sclera to pia mater and dura maters, respectively. To mimic this tissue-specific fiber organization, traces of fiber bundles with PLM-matched local orientation were generated for a stack of coronal images (Fig. 1c) and transformed into a curved assembly using in-house algorithms [3-4]. The circumferential fibers were not included, and collagen was modeled as homogenized fiber bundles.

***Constitutive properties:*** Fiber bundles were discretized with Timoshenko beams of ellipsoidal cross-section and linear elastic material properties ($E_b$). The bundle widths were sampled from the PLM images and a constant thickness of 20 μm was used. The LC and neural tissue (NT) were incorporated as boundary conditions for the sclera. Since the focus of the work is to understand the role of fibrous sclera, both LC and NT regions were modeled as linear elastic continuum solids ($E_{\mathrm{LC}} = 0.1i$MPa$i$, $E_{\mathrm{NT}} = 0.01i$MPa). A 3D illustration of the FE model is shown in Fig. 1e, whereas the sagittal fiber organization with LC and NT regions are depicted in Fig. 1f.

***Boundary conditions:*** The model was subjected to a pressure load ($P$ = 6.35 kPa) equivalent to IOP = 47.53 mmHg. A stretch ($\delta$=0.3 mm) was applied on the boundary to represent radial tension of the sclera due to IOP (Fig. 1b). The fiber-fiber interactions were incorporated using a surface-based contact algorithm and kinematic coupling was employed between the boundary of the solid regions and nearby sclera fibers. The solution was obtained using the FE solver Abaqus/Explicit.

***Parametric study:*** We studied the fiber-scale deformation processes of the sclera as a function of bundle stiffness ($E_b$). The model response was compared with an inflation experiment by calculating average surface strain ($\epsilon$) based on the displacement data of the surface fibers in the model mimicking the experiment [6].

## RESULTS

Fig. 2 compares the pressure-strain responses of the model for a soft ($E_b$= 30 MPa) and a stiff sclera ($E_b$= 100 MPa) with the experiment. The FFE model effectively captured the highly nonlinear response of porcine sclera observed experimentally. The stiff sclera model provided a better approximation compared to the soft sclera model. The nonlinear response predicted is a purely geometric effect since all the material parameters were linear elastic.

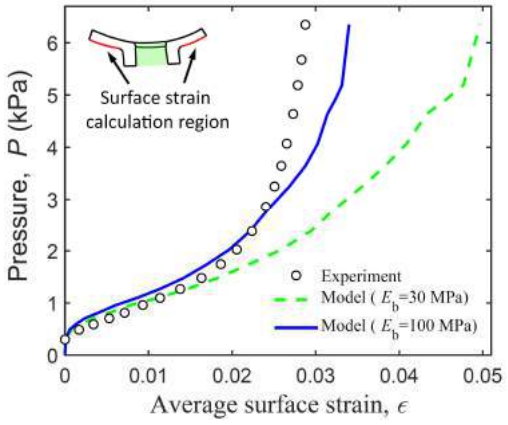


**Figure 2. Pressure-strain responses of the fibrous sclera model compared with the inflation test of a porcine eye [6]. The inset indicates the region used to calculate the average surface strain.**

Fig. 3a shows the heterogeneous strain distribution in the sclera ($E_b = i100i$MPa) at $P$ = 6.35 kPa. The principal strain varied from -2% to 5% where a majority of bundles showed tensile strains and some sclera-to-dura bundles showed compressive strains. Fig. 3b shows the large-scale uncrimping mechanism of a representative bundle with pressure. The extent of uncrimping was dominant for $P \leq 1.5$ kPa and the bundle was entirely uncrimped at P ~ 3.5 kPa.

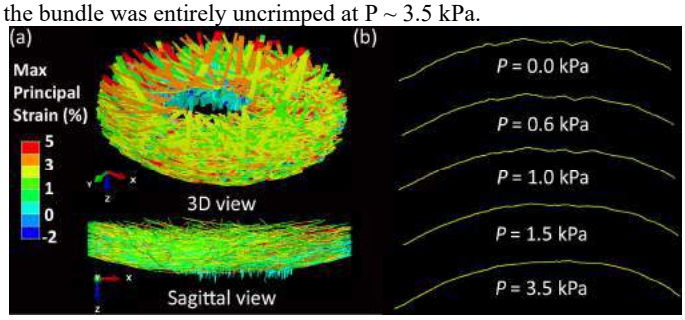


**Figure 3. (a) Strain contour plots of the stiff sclera model. (b) Example fiber bundle uncrimping with pressure ($P$).**

Out-of-plane model displacements are shown in Fig 4. Both soft and stiff sclera exhibited highly nonuniform displacement distribution with a broad range from -50 μm$i$ to 150 μm. The direction of the LC and NT displacements were sclera-dependent. They displaced posteriorly ($U_z > 0$) for the soft sclera and anteriorly for the stiff sclera ($U_z < 0$).

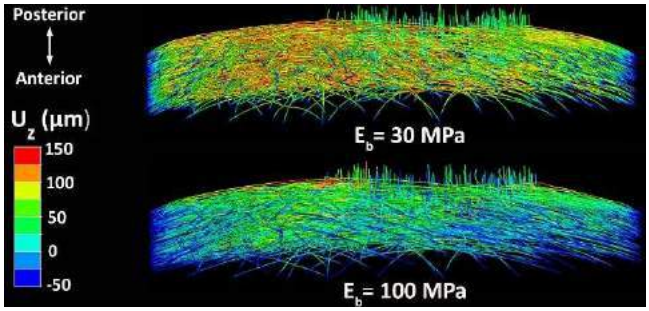


**Figure 4. Deformed configurations of a soft (top) and a stiff sclera (bottom) with z-displacement ($U_z$) contours at $P$ = 6.35 kPa.**

## DISCUSSION

We presented a novel FFE model of soft tissues and demonstrated its ability to reproduce the nonlinear tissue response geometrically from tissue-specific fiber organization and a single stiffness parameter ($E_b$). The FFE model allows for direct analysis of fiber-scale stress/strain distributions and uncrimping processes, which is critical to understand tissue remodeling and cell mechanobiology. Future work will investigate the role of other components in sclera, such as circumferential fibers, elastin and the extracellular matrix, fiber crosslinks and cells.


## ACKNOWLEDGEMENTS

Supported in part by National Institutes of Health R01-EY023966, R01-EY028662, P30-EY008098 and T32-EY017271 (Bethesda, MD), the Eye and Ear Foundation (Pittsburgh, PA), and Research to Prevent Blindness.


## REFERENCES


[1] Pissarenko, A. et al., *Acta biomater.*, 106, 208-224, 2020. [2] Gogola, A et al., *IOVS*, 59(12): 4763-4774, 2018. [3] Ji, F et al., *SB3C, 2021*, Abstract ID 109. [4] Islam, MR et al., *Comput. mater. sci.*, 125, 309-318, 2016. [5] Chung, CW et al., *IOVS*, 57(1): 236-245, 2016. [6] Murienne, BJ et al., *Acta biomater.* 12, 195–206, 2015.

# MICROENVIRONMENTAL STIFFNESS MODULATES MACROPHAGE RESPONSIVENESS AND COMMUNICATION WITH MESENCHYMAL STROMAL CELLS

**Sung Yeon Kim (1,2,3), Eddie D. Bonnevie (1,2,3), Carla R. Scanzello (3,4), Robert L. Mauck (1,2,3)**

(1) Department of Bioengineering, University of Pennsylvania, Philadelphia, PA, USA
(2) Department of Orthopaedic Surgery, University of Pennsylvania, Philadelphia, PA, USA
(3) Translational Musculoskeletal Research Center, Philadelphia VA Medical Center, Philadelphia, PA, USA
(4) Division of Rheumatology, University of Pennsylvania, Philadelphia, PA, USA

## INTRODUCTION

The synovial membrane envelopes the diarthodial joint and features two well-defined areas: (i) the lining layer (intima) composed of fibroblast-like synoviocytes (FLS) and macrophage-like synoviocytes (MLS) and (ii) a sublining layer (subintima) of vascularized loose connective tissue [1]. In healthy joints, the synovial cavity maintains a sterile environment and the interplay between FLS and MLS in the intimal lining contributes to synovial homeostasis. In the context of joint injury and/or osteoarthritis (OA), however, the synovial membrane undergoes marked structural and compositional changes, characterized by the infiltration of leukocytes, production of inflammatory cytokines, and fibrotic remodeling of the synovial extracellular matrix [2]. While soluble factors such as chemokines and cytokines are known to regulate the behavior of FLS and MLS during OA pathogenesis, less is known regarding how biophysical cues regulate the individual response and paracrine interactions between these two cell types during disease progression. Recent studies show that macrophages are mechanosensitive and tune their inflammatory phenotypes in response to altered microenvironmental mechanics [3,4]. The purpose of this study was therefore to test the hypothesis that stiffening of the synovial membrane during disease progression impacts the inflammatory secretome of synovial macrophages, which in turn modulates the behavior of FLS.

## METHODS

Assessment of Macrophage Polarization in Synovial Tissues: Following established protocols, paraffin sections of human synovial tissue [(n=4 healthy organ donors), (n=5 total knee arthroplasty (TKA) patients)] were stained for H&E or with DAPI, CCR7, CD68, PRG4, and p65. Synovial scoring of H&E sections was performed as in [2]. The mean intensity of each marker was quantified using ImageJ and CellProfiler as in [5].

Macrophage Secretome Analysis: Polyacrylamide (PA) gels of 5 and 55kPa were fabricated and functionalized with fibronectin as in [5] to create substrates of varying stiffness. THP-1 monocytes were differentiated for 48 hours with 20 nM PMA before being seeded onto PA substrates at a density of 300,000 cells/gel. Cells were cultured in RPMI with or without the addition of 50ng/mL TNF- α for 24 hours. RNA was isolated to measure inflammatory (M1) and pro-healing (M2) macrophage markers using qPCR.

Paracrine Co-culture Studies: Conditioned media from THP-1 macrophages cultured on 5 and 55 kPa substrates with and without TNF stimulation were collected and applied for 24 hours to human mesenchymal stem cells (hMSCs) cultured on tissue culture plastic (TCP). Here, hMSCs were used as a surrogate mesenchymal cell type to represent the FLS cells. RNA was isolated from hMSCs for qPCR analysis.

Statistical Analyses: Statistical significance for gene expression of M1/M2 markers was determined by two-tailed Student's t-test. One-way ANOVA with a Tukey post-hoc was used to evaluate qPCR results from the co-culture study.

## RESULTS

Marked structural differences were observed between synovial tissue derived from healthy organ donors (OD) and total knee arthroplasty (TKA) patients. Namely, TKA synovia

were highly fibrotic and enlarged with hyperplasia of the lining layer in comparison to OD synovia (**Fig 1A, B, C**). Interestingly, synovial histology scores for inflammation were predicted by the fibrosis scores, with a significant correlation coefficient ($r$ =0.65, $P$<0.03). This led us to assess the polarization of macrophages in OD and TKA synovia by staining for CCR7, a surface marker of M1 macrophages (**Fig 1D, E)**. TKA synovia exhibited higher fluorescence intensity for CCR7 than in TKA tissue, indicating greater activation and infiltration of M1 macrophages (**Fig 1F**).

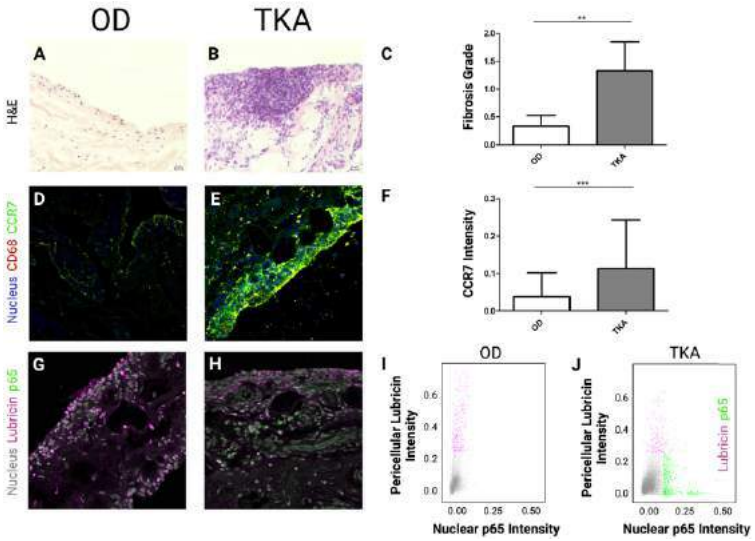


**Fig 1. Representative H&E histology of human synovium from an (A) OD and (B) TKA patient and their (C) fibrosis scores. (D) OD and (E) TKA synovium stained for CD68, DAPI, and CCR7. (F) Quantification of CCR7 fluorescent intensity. (G) OD and (H) TKA synoviums stained for DAPI, PRG4 and p65. Single-cell analysis of lubricin vs. nuclear p65 intensity in (I) OD and (J) TKA synovium. **P<0.01 and ***P<0.001**

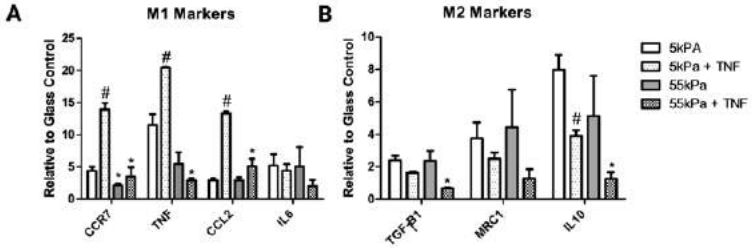


**Fig 2. Expression of (A) M1 and (B) M2 markers in THP-1 macrophages seeded on 5 or 55kPa polyacrylamide gels in the absence or presence of TNF-α. *P<0.05 when comparing substrates with the same soluble condition and #P<0.05 when comparing TNF-α to no TNF-α with the same substrate condition.**

Next, we probed the functional consequences of inflammatory signaling on FLS cells by staining for PRG4 (lubricin) and NF-$\kappa$B/p65 (**Fig 1G, H**). Single-cell analysis revealed that, in OD synovia, FLS cells stained positive for lubricin but not for p65 (**Fig 1I**). Conversely, in TKA synovia, nuclear translocation of p65 was apparent along with a marked decrease in lubricin expression (**Fig 1J**). Due to the fibrosis observed in TKA synovia, we next queried whether microenvironmental stiffness impacts the polarization of synovial macrophages. Here, THP-1 macrophages were used as analogues of synovial macrophages and were seeded on 5 or 55kPa PA gels in the presence/absence of TNF-α to simulate the stiffening and inflammatory signaling of the synovium in joint disease. Expression of M1 markers increased substantially for THP-1 macrophages on soft substrates in the presence of TNF-α (**Fig 2A**), demonstrating that macrophages integrate both chemical and biophysical cues to tune their inflammatory status. For M2 markers, IL-10 expression was significantly reduced on 55kPa compared to 5kPa in the presence of TNF-α (**Fig 2B**) indicating that these cells are generally more responsive to biochemical cues in soft environments. To investigate how macrophages communicate with surrounding cells, we collected conditioned media from THP-1 cells and applied this to hMSCs. Conditioned media from THP-1 cultured on 5kPa with TNF-α induced the greatest inflammatory activation of hMSCs (**Fig3A, B**), increasing the expression of the catabolic enzymes MMP13 and MMP3.

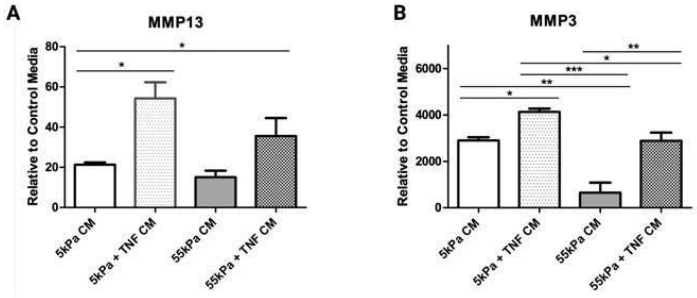


**Fig 3. Expression of (A) MMP13 and (B) MMP3 in hMSCs cultured in THP-1 conditioned media on 5 and 55 kPa with and without TNF stimulation. *P<0.05, **P<0.01 and ***P<0.001**

## DISCUSSION

Our data demonstrate that microenvironmental stiffness and biochemical signals integrate to modulate macrophage polarization, which in turn affects the way macrophages communicate with surrounding cells (i.e., MSCs and/or FLS). Here, we found that adhesion to soft hydrogels increases the inflammatory response of macrophages compared to to stiff substrates. Moreover, the secretome of macrophage cultured on soft substrates increased the catabolic and inflammatory activation of hMSCs. This finding sheds light on a possible feed-forward cascade of disease, where the changing biophysical environment promotes aberrant phenotypic changes.


## ACKNOWLEDGEMENT

This work was supported by the National Institutes of Health (R01 AR056624).


## REFERENCES


[1] Smith, M et al., *Open Rheumatol J*, 5:100-106, 2011. [2] Oehler, S et al., *Clin Exp Rheumatol,* 5:633-40, 2002. [3] Meli, V et al., *Sci Adv,* 6:49, 2020. [4] Jain, N et al., *Nat Mater,* 12:1134-1144, 2018. [5] Bonnevie, E et al., *Nat Biomed Eng,* 12:998-1008, 2019

SB³C2022
Summer Biomechanics, Bioengineering and Biotransport Conference
June 20-23, Eastern Shore, MD, USA

# THOUGH I WALK THROUGH THE SHADOW OF THE VALLEY OF DEATH… HARD LESSONS LEARNED THROUGH DEVELOPMENT OF THE DREEM MACHINES

**Alan W. Eberhardt**

Department of Biomedical Engineering
University of Alabama at Birmingham
Birmingham, Alabama, USA

## INTRODUCTION

The so-called "Valley of Death" in medical and rehab product development refers to the funding gap often seen at the translational and early clinical development stages. Figure 1 illustrates the phenomenon, where products may be discontinued due to cost overruns before they make sufficient revenues to sustain a viable business. The present abstract describes the author's experiences in the context of a new rehabilitation device, developed through a series of student projects at the author's institution.

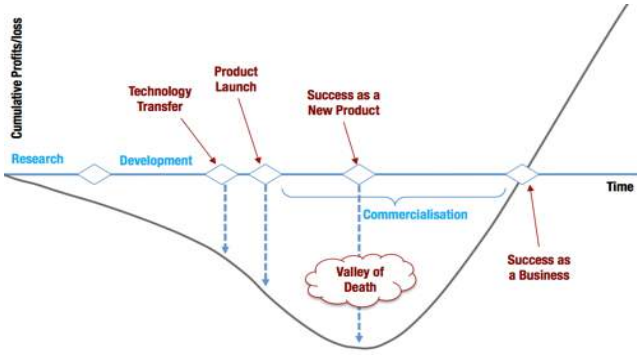


**Figure 1. The "Valley of Death" for new product development.**

For adults with post-stroke hemiparesis, physical activity may be extremely challenging. The resulting sedentary behavior often leads to secondary metabolic conditions that increase morbidity/mortality and reduce quality of life. Upright/mobile exercise is recommended to counter these conditions; however, those with hemiparesis are at high risk for musculoskeletal injury. Exercise machines, such as ellipticals, are rarely adjustable to allow users with musculoskeletal irregularities to enjoy full range exercise.

Our solution, the Differential Resistance Elliptical Exercise Machine (DREEM, Fig. 2a) is an adjustable, motorized elliptical machine that can safely vary resistive leg forces independently and thereby control the mechanical loading of a user's limbs. The DREEM takes advantage of adjustable lever arm mechanics to deliver differential workloads so that the paretic leg is compelled to work harder than the nonparetic leg. By providing variable resistance at variable speeds, user can approach appropriate aerobic workload levels. The value proposition is improved patient rehabilitation that is affordable, convenient, safe and effective for home use.

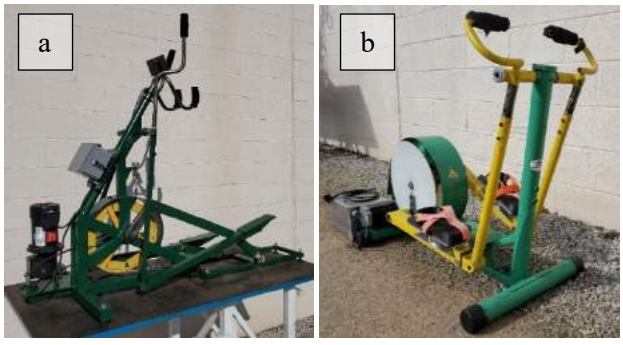


**Figure 2. The DREEM machines for a) adults and b) children**

## METHODS

The author led a student team to design, construct and test the original DREEM for a child with Level IV CP (Fig. 2b). A stepper motor joined to the main wheel of a commercial elliptical trainer provided motorized assistance, where pedals moved continuously or in a prescribed stepping pattern via an Arduino micro-controller. Foot pedal inserts with Velcro secured the user to the device. Safety was

verified by testing according to ASTM and IEC standards. Pilot user testing was completed at Lakeshore Foundation and United Ability (Birmingham, AL) on nine children with various mobility impairments following institutional review board approval (IRB-300003233). A commercial gait trainer (Rifton, NY) was found to be effective for body weight support and fall catch ability. Results from surveys on perceptions of user-friendliness, safety, functionality suggested the DREEM showed promise as an affordable device for home use.

Conversations with physical therapists revealed the need for the user to be able to drive the motion without motor assistance, and encounter resistance for aerobic and strength training. A "free-wheeling" gear system was added that permits the user to take control by pedaling faster than the motor drive. An adjustable band passed around the flywheel generates resistance, while differential resistance between legs is achieved by moving the pedal arm connection along the elliptical axis. These features (Fig. 3) were found to be directly applicable to persons post stroke and the adult DREEM machine was developed to include these features, along with multiple improvements.

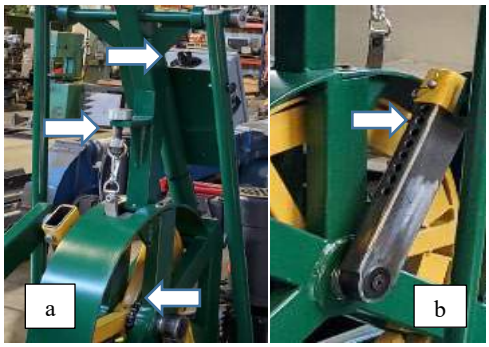


**Figure 3. a) Arrows indicate the speed controller, adjustable resistance belt, and freewheeling gear; b) Each crank arm connection (arrow) can be varied to change the resistance.**

Necessary steps for further product development and to achieve our ultimate goal of commercialization involve user testing to demonstrate that the device is safe and effective. In pursuit of funding for these activities, the author applied to the following programs and sponsors:

1. NSF Disability and Rehabilitation Engineering (DARE) - supports fundamental engineering research that will improve the quality of life of persons with disabilities through development of new technologies, devices, or software [1].
2. NIH Small Business Technology Transfer (STTR) - intended to stimulate technological innovation and increase private sector commercialization of innovations derived from federal research and development [2].
3. NSF Partnership for Innovation (PFI) - funds technology translation and development based on prior NSF-funded research projects from all science and engineering disciplines supported by NSF [3].

## RESULTS

None of the submitted proposals were funded. In the case of NSF DARE, there were concerns about a lack of advancement of scientific knowledge due to the lack of quantifiable kinematic metrics that were being assessed. There were concerns that the graduate student's focus on device construction would not help them develop into an independent researcher. The third aim was a business plan, which they stated would be more appropriate for an SBIR/STTR program.

Following the suggestion of the NSF reviewers, we submitted the NIH STTR, where reviewers identified weaknesses regarding a lack of expertise in rehabilitation devices, unclear milestones of success, questionable affordability, issues with sample size and inclusion criteria, a lack of the patient safety metrics and no discussion on biological variables.

Our most recent attempt was the NSF-PFI. In this case, the proposed applied research tasks were seen as incremental since the project focused only on testing and most of the development work had been done in previous projects. Innovation was deemed incremental and the expected revenue stream was not convincing.

## DISCUSSION

Our long-term goal is to commercialize the DREEM machines to provide a safe and affordable exercise option for home use that overcomes barriers that prevent people with disabilities from exercising. Users will make progress towards walking independently, thereby improving their quality of life. Parents and caregivers will reap the benefit of not having to travel to physical therapy sessions as frequently. Linking the device with telehealth exercise interventions may further increase the impact of exercise in populations where there is a significant need.

The challenges associated with crossing the Valley of Death and commercializing the DREEM machines are extensive. The technology is relatively simple, which was intentional in order to keep costs low and render the device affordable for home use. Competing devices that contain more sophisticated control systems (e.g., Innowalk Pro®, iCARE®) have price tags ranging from $15,000-$30,000. Unfortunately, our low tech, low cost solution was not seen as sufficiently innovative and did not excite reviewers at NSF. Our failure to provide a rigorous clinical evaluation strategy that included biological variables of gender and age as well estimations of appropriate sample sizes, led to poor reviews from the NIH.

Our most recent efforts have been to approach industry to gauge their interest in licensing the technology. Responses have been luke warm, noting the lack of demonstration of clinical efficacy and the need for application of design for manufacturing and assembly principles to develop the next level prototype. As funding is essential for the continuation of any project in academia, the likelihood of the DREEM machines passing out of the Valley of Death seems more and more unlikely.

## ACKNOWLEDGEMENTS

The authors gratefully acknowledge funding and intellectual input from Drs. David Brown (University of Texas Medical Branch, Galveston, TX) and James Rimmer (DHHS 90RE5009-02-00, UAB/Lakeshore Research Collaborative, Birmingham, AL). Special thanks go to Mr. Steven Thompson and the Design and Fabrication Center in the UAB School of Engineering for construction and testing. Dr. Drew Davis (Lakeshore Foundation), and Ms. Marlese Delgado (United Ability) provided the opportunity to perform user testing. Additional financial support was obtained through the University of Alabama Health Services Foundation, P.C., General Endowment Fund, Award #202043, the UAB Department of Orthopedic Surgery, and the UAB School of Engineering.

## REFERENCES

[1] https://beta.nsf.gov/funding/opportunities/disability-and-rehabilitation-engineering-dare-1.
[2] https://www.nigms.nih.gov/grants-and-funding/research-funding/small-business-research
[3] https://www.nsf.gov/pubs/2019/nsf19506/nsf19506.htm

SB³C2022
Summer Biomechanics, Bioengineering and Biotransport Conference
June 20-23, Eastern Shore, MD, USA

# A HYDRAULIC RESISTANCE MODEL FOR INTERSTITIAL FLUID FLOW IN THE BRAIN

**Helena E. Schreder (1), Jia Liu (1), Douglas H. Kelley (1), John H. Thomas (1), and Kimberly A. S. Boster (1)**

(1) Department of Mechanical Engineering, University of Rochester, Rochester, NY USA

## INTRODUCTION

Metabolic wastes may be cleared from brain tissue by the flow of water-like fluid through the interstitial spaces between cells, as proposed in the glymphatic model. However, measuring that *in vivo* flow directly is difficult, so models are essential. Here we use an analytic solution for Darcy flow in a porous medium to model the flow and calculate the hydraulic resistance (as a function of tissue permeability and fluid viscosity) for various arrangements of penetrating arterioles and ascending venules, since fluid is believed to flow from periarterial to perivenous spaces. We consider arrangements measured experimentally as well as idealized arrangements with simple geometry. We explore how the number of vessels, vessel density, arteriole-to-venule ratio, and vessel distributions affect hydraulic resistance. Our findings could enable future brain-wide models of glymphatic flow.

## METHODS

We modeled the flow of interstitial fluid as a two-dimensional viscous flow between line sources (representing periarterial spaces) and line sinks (representing perivenous spaces). We solved Darcy's equation and the continuity equation analytically, using superposition, to determine pressure and (superficial) velocity fields. To quantify the viscous opposition to flow, among many sources and sinks, we calculated the average two-dimensional hydraulic resistance

$$R = \frac{\bar{p}_{art} - \bar{p}_{ven}}{q},$$

where $\bar{p}_{art}$ and $\bar{p}_{art}$ are the average pressures in periarterial and perivenous spaces, respectively, and $q$ is the total volume flow rate per unit length. $R$ is an extensive measure of hydraulic resistance, in that it depends on the domain size, or equivalently, the number of periarterial spaces, $n_a$. $R$ also depends on the fluid viscosity μ and the permeability κ of the porous tissue between periarterial and perivenous spaces. Thus, we define an intensive quantity that depends on vessel arrangement but not μ, κ, or $n_a$:

$$\mathcal{R}_{art} = R n_a \kappa / \mu,$$

which we call the dimensionless resistance.

We required that the pressure be zero at infinity. The pressure diverges at a source or sink, so in the results below, we took each periarterial pressure to be the pressure 5.5 μm from the source itself, and we took each perivenous pressure to be the pressure 4.5 μm from the sink itself. $\mathcal{R}_{art}$ is independent of $q$, which cancels out when $\mathcal{R}_{art}$ is expressed as a superposition of line sources and line sinks (each driving a flow known analytically).

## RESULTS

Figure 1 shows the arrangement of periarterial and perivenous spaces in a region of one mouse's cortex, and the corresponding pressure and flow predicted on one slice through the cortex at constant depth $z$. As expected, streamlines connect periarterial spaces to perivenous spaces, and pressure decreases smoothly along streamlines. For this arrangement, $\mathcal{R}_{art} = 0.961$. Examining arrangements at many different cortical depths and in four different mice, we find that the median dimensionless resistance is $\mathcal{R}_{art} = 0.9563$.

Since venules outnumber arterioles by a roughly 3:1 ratio in murine cortex, we also studied an idealized, regular arrangement with an exact 3:1 ratio (Figure 2). By tiling the arrangement to create domains of varying size, we found that $\mathcal{R}_{art}$ converges to a constant value for large domains. In separate calculations (not shown), we observed convergence in *ex vivo* (not idealized) arrangements as well. Convergence is helpful for engineering models: when a large section of cortex is to be simulated, the exact positions of every vessel need not be considered, because $\mathcal{R}_{art}$ can be used instead, being insensitive to domain size and varying relatively little from one animal to the next.

We also considered variation of $\mathcal{R}_{art}$ with vessel density ρ, keeping the domain aspect ratio and the vessel ratio the same. We found that $\mathcal{R}_{art}$ decreases with density and is well-fit by

$$\mathcal{R}_{art} \approx a\, ln\left(1 - \frac{b}{\rho^{1/2}}\right),$$

where, for the idealized mouse arrangement, $a = 0.2204$ and $b = -1.402 \times 10^4$. Future models could use this fit with good accuracy.

To account for natural variation among animals, we went on to study how $\mathcal{R}_{art}$ varies when the idealized arrangement is perturbed, by changing some arterioles to venules and vice-versa, and/or by displacing vessels slightly. Variation (not shown) was relatively small, though more uniform arrangements had lower resistance. We also considered vessel arrangements measured *ex vivo* in primate cortex and corresponding idealized arrangements (not shown).

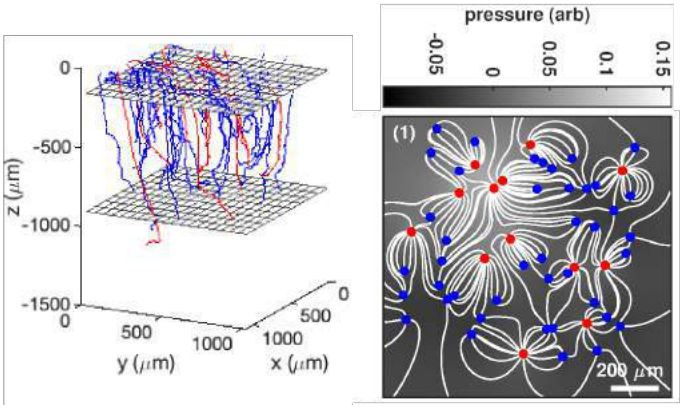


**Figure 1: Predicted interstitial flow among perivascular spaces in mouse cortex. *Left:* Paths of imaged penetrating arterioles (red) and ascending venules (blue) in a mouse cortex. Each vessel is surrounded by a perivascular space, and their paths are nearly parallel. From [1]. *Right:* By approximating each periarterial space as a line source and each perivenous space as a line sink, we calculate the interstitial fluid flow. White curves are streamlines.**

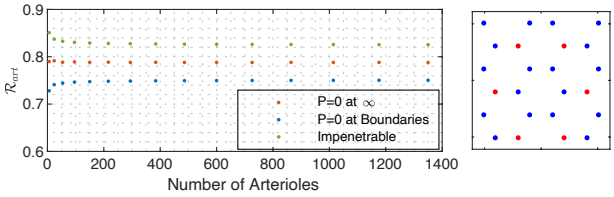


**Figure 2: The dimensionless resistance is an intensive quantity that converges to a constant value as the domain size (or arteriole count) increases, allowing accurate modeling for large domains. *Right:* An idealized arrangement of arterioles (red) and venules (blue). *Left:* Repeating that arrangement to create larger domains produces convergence, regardless of boundary condition (green: impenetrable boundary; red: zero pressure at infinity; blue: zero pressure at domain boundary).**

## DISCUSSION

Our findings could inform future numerical models of interstitial fluid flow in the brain. The convergence of $\mathcal{R}_{art}$ with size demonstrates the importance of calculating the resistance of an array of vessels, rather than isolated vessels. Dimensionless resistance decreases with density and depends non-monotonically on the ratio of arterioles to venules, consistent with another recent study [2]. Less-ordered vessel arrangements typically have higher resistance, all else being equal. However, the dimensionless resistance $\mathcal{R}_{art}$ does not account for flow changes due to variations in the permeability κ, which is highly uncertain; the accuracy of future models can be increased most by determining κ more precisely. More accurate models may be able to predict the relative importance of advection (driven by bulk flow flow) and diffusion for mass transport in brain tissue. That knowledge might facilitate drug delivery and interventions intended to assuage pathologies like stroke. More accurate models may also be able to estimate the pressure gradient necessary to drive physiological flow of interstitial fluid. Our findings were recently published [3].

## ACKNOWLEDGEMENTS

We thank Pablo Blinder for helpful conversations and for providing data on the mouse brain. This work was supported by the NIH/National Institute on Aging (grant no.RF1AG057575) and by the US Army Research Office (grant no. MURI W911NF1910280).

## REFERENCES

[1] P. Blinder, A. Y. Shih, C. Rafie, and D. Kleinfeld. Topological basis for the robust distribution of blood to rodent neocortex. *Proc. Nat. Acad. Sci. USA,* 107(28):12670–12675, 2010.

[2] Y. Qi and M. Roper. Control of low flow regions in the cortical vasculature determines optimal arterio- venous ratios. *Proc. Nat. Acad. Sci. USA,* 118(34), 2021.

[3] H. E. Schreder, J. Liu, D. H. Kelley, J. H. Thomas, and K. A. S. Boster. A hydraulic resistance model for interstitial fluid flow in the brain. To appear in *J. R. Soc. Interface,* 2022.

# CLINICAL IMAGING DERIVED AORTIC STIFFNESS AS AN AORTIC DISSECTION RISK STRATIFICATION METRIC

**Ronald N. Fortunato (1), Thomas G. Gleason, MD (2), David A. Vorp, PhD (1,3,4,5,6,7), Spandan Maiti, PhD (1,6,7)**

(1) Department of Mechanical Engineering and Materials Science, University of Pittsburgh, Pittsburgh, PA, USA
(2) Department of Surgery, University of Maryland, Baltimore, MD, USA
(3) McGowan Institute for Regenerative Medicine, Pittsburgh, PA, USA
(4) Department of Cardiothoracic Surgery, University of Pittsburgh Medical Center, Pittsburgh, PA, USA
(5) Department of Surgery, University of Pittsburgh Medical Center, Pittsburgh, PA, USA
(6) Department of Bioengineering, University of Pittsburgh, Pittsburgh, PA, USA
(7) Department of Chemical and Petroleum Engineering, University of Pittsburgh, Pittsburgh, PA, USA

## INTRODUCTION

Type A Aortic Dissection (TAAD), initiated by an intimal tear in the ascending aorta propagating through the aortic media, is a highly lethal event with a mortality rate of 1-2% per hour for the first 48 hours [1]. Current clinical guidelines for prophylactic surgical replacement of the ascending aorta to mitigate aortic dissection risk are based solely on dimensional characteristics and in rare cases for genetically triggered indices (e.g., Marfan syndrome) [2]. However, large retrospective series and data from the International Registry of Acute Aortic Dissection demonstrate that over 60% of patients with TAAD have aortic calibers less than the 5.5 cm diameter threshold [3] and yet most patients with aortic diameters less than 5.5 cm never dissect [4]. These data indicate that current risk adjudication metrics and clinical indices to intervene prophylactically are inadequate, thus, better dissection risk prediction metrics are needed to direct appropriate prophylactic aortic resection and reduce the risk of TAAD.

Prior work in our lab revealed overlap between intimal tear location and high longitudinal tensile stress in baseline CT angiography (CTA) scans from type A aortic dissection patients. In this work, we sought to create models to predict probability of dissection based on imaging-derived aortic stiffness as well as clinically measured parameters such as age, BMI, blood pressure, etc. with scrutiny of their specificity, sensitivity, and simplicity—*i.e.,* identify the lowest number of parameters that still yield a high predictability.

## METHODS

This study was performed with approval of the University of Pittsburgh Institutional Review Board and informed patient consent. Aortic dissection patients (dissected cohort) were chosen as the study group n=18. An aneurysmal control set of patients (non-dissected cohort) without aortic dissection but with statistically similar aortic diameter (46.17 ± 5.86 mm vs 47.19 ± 2.88 mm, p=0.31) was chosen for comparison (n=22). Patients in both the cohorts were of tricuspid aortic valve (TAV) phenotype. CTA and transthoracic echocardiograms (TTE) obtained **prior to** an aortic dissection event were evaluated.

Systolic (AoS) and diastolic (AoD) aortic diameters for each patient was assessed using the parasternal long axis window of two-dimensional TTE, measured 3 cm above the aortic valve. AoD was obtained at the peak of the R wave in the simultaneously recorded electrocardiogram, while AoS was measured at the initiation of the T wave. Patient specific aortic stiffness was estimated from these diameter measurements and knowledge of corresponding systolic (SBP) and diastolic (DBP) blood pressure [5]:

$$\text{Stiffness Index} = \frac{ln(SBP/DBP)}{AoS-AoD} AoD \quad (1)$$

Where *ln(SBP/DBP)* refers to the natural logarithm of the relative pressure. Blood pressure was measured at the time of echocardiography using a cuff sphygmomanometer. Phase 1 and Phase 5 Korotkoff sounds were used for SBP and DBP, respectively. All measurements were made by a single observer with 3 to 5 measurements per patient, all before the calculation of stiffness indices.

We used Prism (GraphPad, San Diego, CA) to develop single and multiple parameter logistic regression models and evaluate their predictability using the area under the receiver-operator curve (AUC). Receiver-operator curves are constructed to evaluate the true positive rate (Sensitivity) against the false positive rate (1-Specificity). Where the true positive rate is the ratio of the number of times a test result correctly indicates the condition, in this case dissection, to the number of real dissection cases from our database. Correspondingly, false positive rate is the ratio of the number of times a test result correctly indicates the absence of dissection to the number of non-dissection cases from our database. Finally, to increase the generality of our result we calculated AUC using leave-one-out cross validation implemented in RStudio (Boston, MA).

## RESULTS

Patients experiencing dissection at a time after the studied scans exhibited elevated baseline aortic stiffness (7.7 ± 2.3) relative to patients with similarly dilated aortas that did not go on to dissect (4.5 ± 1.56, $p<0.0001$) as shown in Figure 1 (a). A simple threshold model of Stiffness Index > 5 provided a sensitivity of 91% and specificity of 78%. Using aortic stiffness index in a single logistic regression model we calculated AUC of 0.90, ROC shown in Figure 1 (b), and associated odds ratio of 2.40 (95% CI: 1.73-3.63). Finally, we created a multiple parameter logistic regression model with age, gender, BMI, stiffness index, pulse pressure (PP=SBP-DBP), and aortic diameter. Each parameters' odds ratio is reported in Table 1 through a 95% confidence interval (CI) also reported in Table 1 is the corresponding AUC value.

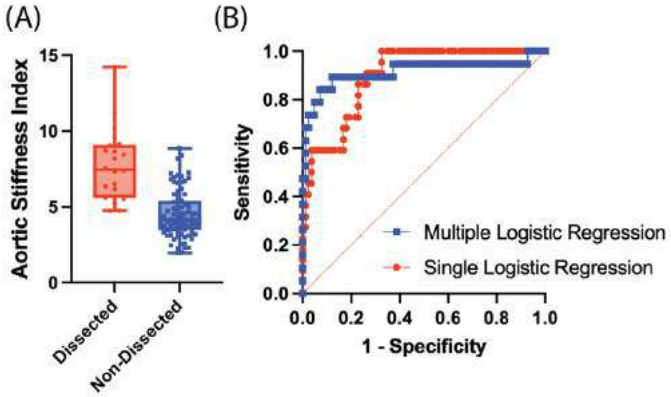


**Figure 1: A box and whisker plot of aortic stiffness index in the non-dissected and dissected cohort with raw data points (A). ROC for a single and multiple parameter logistic regression model with leave-one-out cross validation (B).**

**Table 1. Multiple Logistic Regression Results**

| Included Parameters | Odds Ratio (95% CI) | AUC |
|---|---|---|
| Age (years) | **(0.86-1.10)** | **0.92** |
| Gender | **(0.28-35.22)** | |
| BMI (kg/m$^2$) | **(0.87-1.02)** | |
| Stiffness Index | **(2.19-8.25)** | |
| PP (mmHg) | **(0.88-1.03)** | |
| Diameter (mm) | **(0.51-0.95)** | |

## DISCUSSION

We found that non-invasive TTE measurements were useful in predicting aortic dissection events. Starting at the simplest level we found a significant difference in stiffness among the dissected compared to the non-dissected cohorts (from TTEs done prior to a dissection event). A simple threshold should detect dissection, and indeed we found a high model accuracy with a threshold stiffness index of 5. To increase the accuracy, we went to the next level of complexity using logistic regression with a single parameter. Even with a single parameter, stiffness index demonstrated very strong predictability with the model (AUC of 0.90).

Introducing five additional parameters in the multiple logistic regression model led to a nominal increase in the AUC from 0.90 to 0.92. Review of the 95% confidence intervals of the multiple parameter logistic regression model demonstrate that most parameters do not have a significant impact over and above stiffness (95% CI contains the value of 1). Strikingly, for the parameter of diameter (the only parameter currently used clinically), the odds ratio interval does not contain one, and the interval is close enough to one such that its predictive value is distinctly inadequate.

Limitations of the work include its sample size, while our AUC was high, typical models used in clinical tools should be trained on very large datasets to increase robustness. Despite this limitation, the marked accuracy of the model generates enthusiasm to study the parameter of aortic stiffness more rigorously as measured by simple, serial noninvasive TTE testing as a biomechanically relevant metric for adjudicating the relative potential for aortic dissection in a patient-specific manner.


## ACKNOWLEDGEMENTS

Research in this work was supported by the National Institutes of Health under award numbers 5T32HL076124-12, R01HL109132, T32HL098036, T32HL076124. The content is solely the responsibility of the authors and does not necessarily represent the official views of the National Institutes of Health. The authors would like to thank Lauren V. Huckaby, MD and Leonid V. Emerel, MD for the collection of transthoracic echocardiography measurements.


## REFERENCES


[1] Hirst, A et al. Medicine 37(3): 217-79, 1958.
[2] Erbel, R et al. European Heart Journal 35(41): 2873-926, 2014.
[3] Pape, L et al. Circulation 116(10):1120-7, 2007.
[4] Kim, J. B. et al. JACC 68:1209-19, 2016.
[5] Emerel, L et al. JCTVS, 158(2): 355-363, 2019.

SB³C2022
Summer Biomechanics, Bioengineering and Biotransport Conference
June 20-23, Eastern Shore, MD, USA

# ACTOMYOSIN CONTRACTILITY CONTROLS ORGAN-SCALE BUCKLING IN THE DEVELOPING SMALL INTESTINE

**John F. Durel, Hyunjee Lim, Nandan L. Nerurkar**

Department of Biomedical Engineering
Columbia University
New York, NY, USA

## INTRODUCTION

Stress-strain, or constitutive, nonlinearity has been widely characterized in adult soft tissues, with particular focus on the compositional and microstructural basis of this material behavior. However, the emergence of constitutive nonlinearity during embryonic development has received less attention, primarily limited to connective tissues. Moreover, the potential morphogenetic consequences of nonlinearity have been largely unexplored during embryogenesis. The present study frames the question of constitutive nonlinearity in the context of looping morphogenesis of the small intestine.

Looping is the process by which the initially straight intestinal tube is deformed into its seemingly convoluted adult form. In fact, the intestine is precisely and stereotypically organized (Fig. 1) for a given species [1]. Errors in looping give rise to several devastating gastrointestinal birth defects [2], yet the molecular and cellular basis of this important morphogenetic process is poorly understood. From the mechanical standpoint, it is known that looping arises from an elastic instability established by differential growth as the intestinal tube elongates against the constraint of an attached tissue, the dorsal mesentery. The mesentery is stretched and in turn compresses the tube until it buckles into loops [1]. The mesentery has a pronounced constitutive nonlinearity, readily stretching to 100% strain before transitioning to the stiff linear response. This ability to accommodate stretch before stiffening is a key behavior in the looping process, as a shorter toe-region would result in excessive restriction of the elongating tube, leading to excessive buckling. On the other hand, a larger toe-region would reduce buckling, all else being equal. The present study aims to understand the potential cellular and molecular antecedents of constitutive nonlinearity in the mesentery, and the implications of this nonlinearity for intestinal buckling morphogenesis.


***Fig. 1*** *Looping of the chick small intestine. The small intestine begins as an approximately linear tube at embryonic day (E) 5, left, which forms several loops by E16, when the process is complete. At right, E16 intestines from three embryos demonstrate the precise stereotypy of looping across individuals of a given species [1].*

## METHODS

Fertilized chicken eggs were incubated to embryonic day (E) 16. Intestines were harvested and mesentery segments with gut tube attached at either end were isolated. Segments were treated with 0.1% DMSO (control), 25 μM Cytochalasin D (CD), or 30 nM Calyculin A (CA) for 2 hr at 37 ºC, followed by uniaxial tensile testing in a custom micromechanical tester [3]. Briefly, a fine tungsten cantilever (of known bending stiffness) was used as the force transducer, and displacement was applied to this cantilever at a rate of 0.5%/s. The free end of the cantilever was attached to the sample, and progressive deflection of the cantilever was used to calculate force. Fluorescent markers on the sample were tracked to calculate strain. The linear region modulus (E) and the transition strain ($\varepsilon_t$) from toe-region to linear-region were calculated from resulting stress-strain data using custom MATLAB scripts. For Second Harmonic Generation (SHG) imaging, fresh whole mesenteries were flattened under coverslips and exposed to 850 nm excitation from a 2-photon laser. Emission was detected around 425 nm using a 40X lens, and z-stacks were collected with 1 μm slices. Images were analyzed as maximum intensity projections.

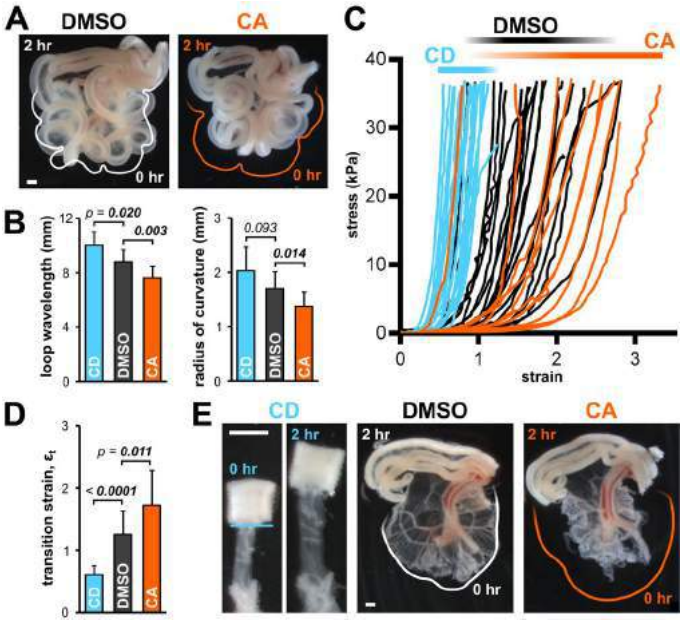


***Fig. 2*** *Cell contributions to mesentery mechanics. A) Treatment of E16 small intestines with 30 nM Calyculin A (CA) increased looping. B) Treatment with 25 μM Cytochalasin D (CD) (n=5) significantly reduced, and CA (n=10) significant increased, loop wavelength and radius of curvature vs. DMSO (n=13) C) Stress-strain curves from tensile tests of treated E16 mesentery. D) Treatment with CD (n=18) significantly reduced, and CA (n=10) significantly increased, the transition strain $\varepsilon_t$ vs. DMSO (n=20). E) Mesentery relaxes upon CD treatment and contracts upon CA treatment, indicative of an active pre-stress in the tissue. Colored lines show size prior to treatment. Scale bars represent 1 mm. p-values are from two-tailed unpaired t-tests.*

## RESULTS

To broadly test for an active cellular contribution to loop morphology, we treated whole small intestines with CD to disrupt the actin cytoskeleton (and by extension acto-myosin contractility) and with the myosin phosphatase inhibitor CA to induce contraction. Short term treatment resulted in significantly increased looping with increasing cell contractility (Fig. 2A, B), indicating that cell forces are sufficiently large to influence organ scale buckling of the intestine. To dissect the mechanics of this process, we subjected treated mesentery segments to tensile testing (Fig. 2C). Surprisingly, we noted that CD treatment to remove active cell contributions resulted in a significant reduction in the toe-region, while increasing cell contractility resulted in a significant increase in the toe region (Fig. 2D). This suggested, somewhat paradoxically, that removing cell contributions actually results in effective tissue stiffening. Measurement of sample length before and after CD (CA) treatment revealed that when cell contractility is inhibited (induced), the mesentery elongates (shortens), providing some explanation for the changes in transition strain (Fig. 2E).

We hypothesized that contracting cells may be modulating the extent of the soft toe-region by dynamically wrinkling extracellular matrix (ECM) fibers that must be decompressed by applied forces before these stiffer structural elements can be loaded (Fig. 3A). SHG imaging of fresh treated mesentery shows qualitatively increased fiber straightness with CD treatment (Fig. 3B). Preliminary quantification of fiber straightness indicates that relaxation of cellular forces significantly increases the straightness of mesentery ECM (Fig. 3C), in agreement with our proposed model.

## DISCUSSION

These results suggest that, unlike many well-studied adult tissues, constitutive nonlinearity of the embryonic mesentery is determined by active cell contraction, even in a mature tissue late in development. Interestingly, modulating contractility did not have a notable effect on the linear-region modulus. This suggests that the stiff linear-region behavior is dictated by ECM, but that the strain at which this stiff response begins is under cellular control. Based on these studies, we propose that cells of the mesentery act as a mechanical 'clutch,' providing compressive pre-stress on surrounding ECM. Consequently, as the mesentery is passively stretched by the elongating intestinal tube, contractile forces in the mesentery set its transition strain and, by extension, the compressive stresses that buckle the tube into loops.

Buckling has emerged as a core morphogenetic mechanism, laying the basic pattern of various organs during development, from intestinal villi [4] to airway branching [5] and folding of cortical sulci [6]. Despite the apparent ubiquity of buckling in morphogenesis, the underlying cell behaviors that control tissue mechanics to drive buckling have not been well characterized in most contexts. Here we show that cell contractility is central to setting the constitutive nonlinearity that drives buckling morphogenesis of the small intestine. Work is ongoing in the lab to identify the regulatory signals that tune mesentery cell contractility to ensure stereotyped morphogenesis of the small intestine.

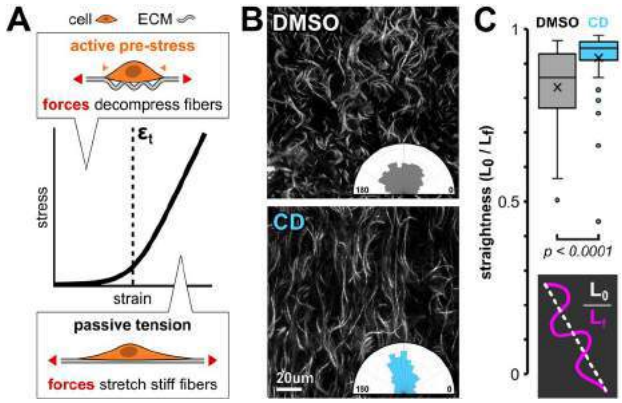


***Fig. 3*** *Cell contraction reorganizes mesentery ECM. A) Proposed model for cell control of nonlinearity: contraction pre-stresses ECM and fibers decompress as stretch is applied, leading to a stiff linear response as fibers are loaded. B) SHG images of DMSO and CD treated E16 mesentery; insets: fiber orientation distributions from 2D Fourier transform. C) Fiber straightness from SHG images. Straightness quantified as end-to-end length $L_0$ divided by contour length $L_f$; n=50-60 fibers, 2 embryos each. p-values are from two-tailed unpaired t-tests.*


## ACKNOWLEDGEMENTS

Work was carried out with the generous support of the Blavatnik Family Foundation (JFD), the Avery's Angels Gastroschisis Foundation (NLN), the NIDDK (JFD), the NICHD (NLN), and the NSF (NLN).


## REFERENCES


[1] Savin, T et al., *Nature*, 476(7358):57-62, 2011.
[2] Kluth, D et al., *Sem Ped Surg,* 12(4): 275-279, 2003.
[3] Nerurkar, N et al., *Proc Natl Acad Sci*, 114(9): 2277-2282, 2017.
[4] Shyer, A et al., *Science*, 342(6155): 212-218, 2013.
[5] Varner, V et al., *Proc Natl Acad Sci*, 112(30): 9230-9235, 2015.
[6] Tallinen, T et al., *Nature Phys*, 12: 588-593, 2016.

# EXAMINING THE EFFECTS OF LOCALIZED ACL DAMAGE ON THE NEIGHBORING LIGAMENTS OF THE KNEE VIA FINITE ELEMENT ANALYSIS

**Alexander M. Knapp (1), Lakiesha N. Williams (1)**

(1) Biomedical Engineering, University of Florida, Gainesville, Florida, USA

## INTRODUCTION

The anterior cruciate ligament (ACL) is a major structural component of the knee, thought to be primarily responsible for inhibiting anterior translation. Due to its role in maintaining stability within the foot it is particularly vulnerable to injury, which is a highly common occurrence in athletes, with approximately 200,000 injuries per year [1]. Once torn, be it partial or full, players are often removed from play, with minimal options for rehabilitation beyond surgical intervention as a result of poor vascularization in the knee joint. Damage, partial or full, is known to lead to joint instabilities, osteoarthritis, and increased risk of tear in the neighboring medial collateral, posterior cruciate, and lateral collateral ligaments (MCL, PCL, and LCL respectively).

While the consequences of a fully torn ACL on the neighboring ligaments are understood to some extent, the complications that may arise from a partially torn or partially compromised ACL are not. Therefore, the present work seeks to investigate the effects of localized damage to the ACL on the mechanics of the neighboring ligaments. This will be done using a novel continuum-damage approach for modeling the constitutive behavior of the ACL through the use of a finite element model of the knee. After inducing localized damage, the changes in stress contour and average stress within the neighboring ligaments will be characterized to gain new insights into the effects of localized ACL damage on the function of the knee joint.

## METHODS

To examine the effects of localized ACL damage on the neighboring ligaments, a continuum-damage constitutive model of the ACL was developed using the stress strain data obtained by Ristaneimi et al. [2]. To implement damage into the constitutive model, an incompressible modified Holzapfel strain energy density approach was developed as shown in Figure 1 [3].

$$\mathrm{W} = \mathrm{G}\left( (\mathrm{C}_1(I_1 - 3) + \frac{k_1}{k_2}\left( e^{k_2\left(k(I_1-3)+(1-3k)(I_4-1)\right)^2} - 1 \right) \right) \quad (1)$$

Here, $C_1$, $K_1$, and $K_2$ represent material parameters, $k$ is the fiber distribution parameter, assumed to be zero, $I_1$ and $I_4$ are the first and fourth invariants of the right Cauchy-Green deformation tensor, while G represents a damage function in the form first coined by Natali et al. that is a function of the maximum fiber stretch ($\lambda_{max}$) achieved such that

$$G(\lambda_{\max}) = \frac{1 - e^{\beta^2(\lambda_{max}^4 - \lambda_c^4)}}{1 - e^{\beta^2(\lambda_0^4 - \lambda_c^4)}} \quad (2)$$

Where $\beta$ represents a damage rate parameter and $\lambda_c$ and $\lambda_0$ represent fiber stretches at which damage completes and initiates, respectively [4]. Table 1 summarizes the final material parameters determined for the ACL. The damage model was implemented into the finite element software ABAQUS using the user defined field subroutine. The remaining ligaments were assigned the same properties as the ACL sans damage properties.

**Table 1. Summary of Material Parameters for ACL**

| C1 (MPa) | Q | $K_1$ (MPa) | $K_2$ | $k$ | $\lambda_0$ | $\lambda_c$ | $\beta$ |
|---|---|---|---|---|---|---|---|
| 5.0 | 1E -9 | 20.6 | 0.20 | 0 | 1.183 | 1.35 | 0.00019 |

To create the requisite finite element model, images obtained courtesy of the National Institutes of Health's Visible human Project were used [5]. These images were edited using thresholding techniques and stacked to develop the 3-D CAD geometry for the tibia, fibula, femur, ACL, MCL, PCL, and LCL, with the meniscus left out as early investigations indicated it played a minimal role in the loading cases

examined in this work. With the geometry developed, the models were imported to ABAQUS and meshed to an appropriate level using convergence studies to guide the meshing process.

To induce damage, a quadriceps force of 2000 N was applied to the tibia and removed (Figure 1A), similarly to DeMorat et al. [6].

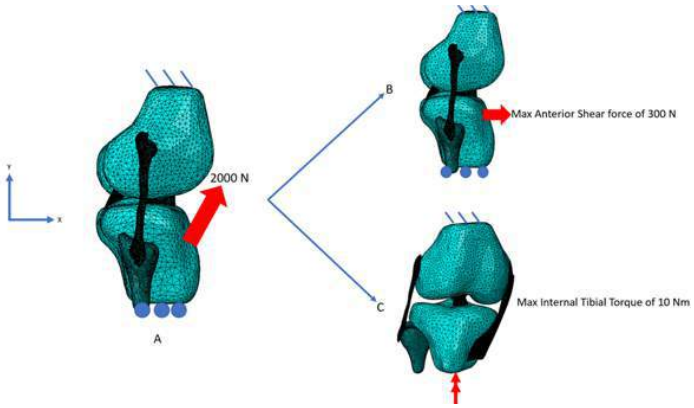


**Figure 1. Illustration of loading and boundary conditions. A) Illustration of loading to induce damage via quadriceps force loading. The simulation was then examined for loading cases of B) anterior shear forces or C) internal tibial torques**

Then, the effects of localized damage were studied under two loading cases, anterior shear loading of a maximum magnitude of 300 N and an internal tibial torque of up to 20 Nm, as shown in Figure 1B and 1C. The femur and tips of the ligaments were held fixed in all directions and the ligaments were attached to the tibia using tie constraints. In addition, to inhibit rotations in about the x axis the tibia was fixed in the y direction. Once the simulation was performed, the von Mises stress contours as well as the average mid-substance von Mises stresses were examined in the mid substance of the MCL, PCL, and LCL ligaments.

## RESULTS

Running the simulation for the prescribed loading cases yielded the following results. For each ligament, the von Mises contour plot changed significantly by altering the plots non-homogenously. One such example is shown in Figure 2, depicting the results for the MCL for the case of anterior shear forces (2A) and internal tibial torque (2B) post damage initiation.

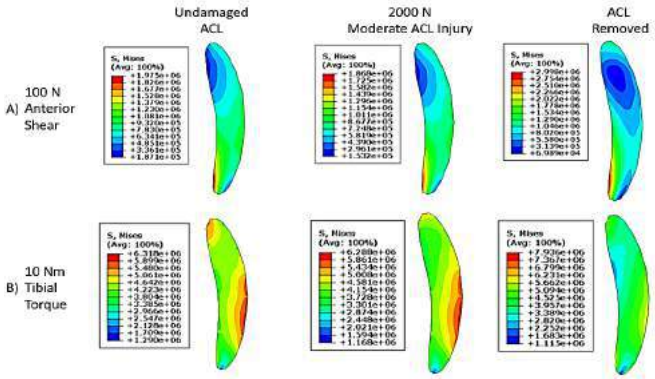


**Figure 2. Von Mises stress contour plots for the mid-substance of the MCL. A) Contour plot evolving under *anterior shear loading* between cases of no ACL damage, moderate ACL damage caused by quadriceps force loading, and for a fully torn ACL case. B) Presents the same trend for *tibial torque loadings* for the three damage cases.**

For both loading cases, the maxima and minima of the contour plot can be seen to shift following ACL damage, both partial and full. Similar trends were observed in the PCL and LCL (images omitted for brevity).

Similar shifts were observed in the average von Mises stress in the mid-substance of each ligament (images omitted for brevity). Under localized ACL damage and complete damage, it was found that the average stress generally increased in each ligament, with the dominant ligament changing as damage was induced.

## Discussion

The results of this study carry two major implications for the effects of localized ACL damage on the knee joint. First, the non-homogenous shifting of the von Mises indicates that under the effects of localized damage, non-homogenous morphological changes may occur in the neighboring ligaments. Over time, these changes may yield both degradations and increased stiffness in the ligaments, ultimately altering the load distribution in the joint, leading to instabilities. This finding is consistent with the minimal literature examining contour changes post damage [7]. With the alterations in load distribution, joint instabilities may be more likely to occur. The second major implication is that moderate localized ACL damage is also capable of inducing substantial shifts in the stress carrying capacity of each of the neighboring ligaments. As with the changing contours, this implies that with time shifts in the morphology of the ligaments will occur, with the dominant ligament (which itself can change based on the amount of damage) carrying more loading, leading to stress shielding effects in the other ligaments. Based on these results, it is therefore evident that moderate localized ACL damage may be sufficient to cause joint instabilities, giving evidence as to the need for early clinical diagnosis and intervention to circumvent these problems before they yield further injury and complications.

## ACKNOWLEDGEMENTS

The authors thank the UF Biomedical and Mechanical Engineering Departments for their support on this project.

## REFERENCES

[1] Laurencin, C. and Freeman, J., *Biomnaterials,* 26:7530-7535, 2005.
[2] Ristaneimi et al., *Journal of Biomechanics,*79:31-38, 2018.
[3] Gasser et al., *Journal of the Royal Society Interface,* 3:15-35, 2006.
[4] Natali et al., *Computer Methods in Biomechanics and Biomedical Engineering,* 6:329-336, 2003.
[5] National Institutes of Health, 2013
[6] DeMorat et al., *American Journal of Sports Medicine,* 32:477-483, 2004.
[7] Lujan et al., *Journal of Biomechanical Engineering, 129:386-392, 2007.*

SB³C2022
Summer Biomechanics, Bioengineering and Biotransport Conference
June 20-23, Eastern Shore, MD, USA

# PHOSPHORYLATION PATTERNS OF VASCULAR ENDOTHELIAL GROWTH FACTOR RECEPTOR-2 AND ANGIOGENESIS ARE DRIVEN BY BIOMECHANICAL FORCES

**Bronte Miller (1), Molly Buckley (1), McKenzie Johnson (1), Joel Berry (1,2), M.K. Sewell-Loftin (1,2)**

(1) Biomedical Engineering, University of Alabama at Birmingham, Birmingham, Alabama, United States of America
(2) O'Neal Comprehensive Cancer Center, University of Alabama at Birmingham, Birmingham, Alabama, United States of America

## INTRODUCTION

Blood vessel growth is a vital part of development; however, dysregulation of vascular structures is involved in various disease states such as arterial stiffening, ischemia, and cancer [1-3]. This process of new vessel growth from preexisting vasculature is known as angiogenesis, which is a key factor in tumor progression [4]. When small, a tumor can rely solely on diffusion to receive nutrients and oxygen, but in order to grow, a vascular network is required to deliver the increased nutrient supply [3, 5]. Tumors induce an angiogenic signaling cascade which causes nearby vessels to grow towards the mass [6]. Two major promoters of this process are vascular endothelial growth factor (VEGF) and VEGF receptor-2 (VEGFR-2). Cancer treatments targeting these factors have been employed clinically with the hope that inhibiting proangiogenic pathways will stop tumor growth [7, 8]. However, notwithstanding the critical role of VEGF and VEGFR-2 in angiogenesis, these therapies are often unable to stop tumor development [9].

One reason why anti-angiogenic therapies have proven ineffective may be because of VEGFR-2 mechanoactivation, which remains understudied in cardiovascular and cancer research [10]. Many cellular pathways can be activated by physical forces such as matrix stiffness, flow or shear stress, and compression, and several groups have shown VEGFR-2 activity to be affected by these forces, with various known mechanotransducers occurring downstream of this receptor [11-13]. Different VEGFR-2 tyrosine residues have shown varied phosphorylation patterns depending on mechanical cues, with non-soluble ligand stimulation causing prolonged Y1214 phosphorylation [14]. Furthermore, the tumor microenvironment (TME) often expresses altered mechanics such as stiffer matrices, increased interstitial fluid pressure, and irregular flow conditions [5, 15, 16]. Understanding how the mechanical environment surrounding a cell affects VEGFR-2 activation and angiogenesis is an important step in developing anti-angiogenic therapies that can effectively inhibit tumor growth. We hypothesize that endothelial cells exposed to biomechanical stimulation will express increased VEGFR-2 phosphorylation at the Y1214 residue and enhanced angiogenic activity. Results from these studies will be useful in addressing the knowledge gap related to mechanically-driven blood vessel regulation and possibly provide novel targets for anti-angiogenic therapeutic strategies.

## METHODS

To study expression and activity patterns of VEGFR-2, human umbilical vein endothelial cells (HUVECs) were seeded in EGM-2 (Lonza) media without VEGF for 24hr. Cells were then exposed to 150ng/ml VEGF for 0, 5, or 15 minutes, before lysing with RIPA buffer plus HALT solution for Western Blot analysis. The membrane was stained for phosphorylation of Y1054/Y1059 and Y1214 on VEGFR-2. HUVECs were also grown for four days in EGM-2 with 3μM SU5416, a VEGFR-2 inhibitor, or DMSO as a vehicle control. Blots were co-stained for YAP. Densitometry was performed using FIJI, and all expression levels were normalized to β-actin.

A custom-built, multi-microtissue microfluidic platform was utilized to determine the effect that mechanical stimulation has on angiogenesis [17]. The system has three separate chambers that can be loaded with matrix and cells, each with its own fluidic lines to permit control over interstitial flow. Tissue chambers were filled with 10mg/ml fibrin gels with the middle chamber filled with 1:1 HUVECs and normal human lung fibroblasts (NHLFs). The side chambers were filled with either thrombin-coated magnetic beads or cell-free fibrin gels. The magnetic beads permit mechanical stimulation of the microtissues without requiring stromal cells. Half of the devices were placed above a magnet on a rotating orbital shaker inside the incubator, while the other half were kept in a control incubator. Devices were fed with EGM-2 for 7 days, then were fixed and stained for VE-Cadherin, a blood vessel marker. Devices were then imaged and processed with AngioTool to quantify blood vessel growth in each of the chambers.

SB³C2022-342

## RESULTS

HUVECs exposed to soluble VEGF showed prolonged phosphorylation at Y1054/Y1059 at 15min, and phosphorylation at Y1214 dropped after 5min (Figure 1A). HUVECs that were exposed to the VEGFR-2 inhibitor SU5416 showed a ~69% decrease in pY1054/Y1059, while the inhibitor only caused a ~27% decrease in pY1214 (Figure 1B). Overall VEGFR-2 expression increased, likely due to decreased receptor activation. Furthermore, expression of YAP, a known mechanotransducer, decreased with VEGFR-2 inhibition.

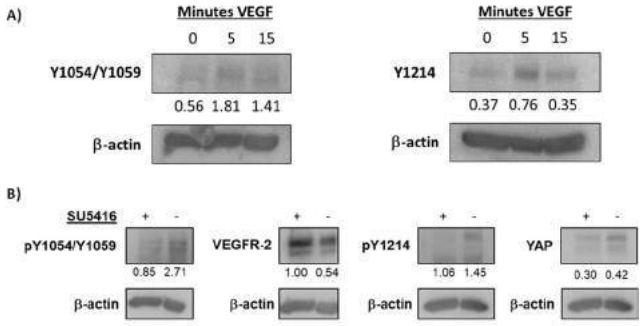


**Figure 1: Phosphorylation of VEGFR-2 in HUVECs. (A) HUVECs treated with soluble VEGF for 0, 5, or 15 minutes. Representative images of Western Blots quantifying VEGFR-2 pY1054/Y1059 and pY1214. (B) HUVECs grown in the presence of 3μM SU5416. Western Blot performed quantifying VEGFR-2 pY1054/Y1059, pY1214, and overall VEGFR-2 and YAP. All inset numbers are normalized to β-actin.**

Microfluidic devices were used to determine how angiogenesis is affected by mechanical strain. HUVECs and NHLFs in the center chamber effectively created a self-assembled, stable vascular network, with the left chamber gel containing magnetic beads (Figure 2A). Fluorescent images were successfully taken, showing sprouting vessels penetrating the side chambers, particularly in the devices exposed to the rotating magnet (Figure 2C,D). When total vessel length in each of the chambers was quantified and normalized to total vessel length in the center chamber, devices that experienced mechanical strain induced by the magnetic stimulation and magnetic beads showed increased angiogenesis in both side chambers compared to devices without the magnet (Figure 2B).

## DISCUSSION

Based on our studies, we have shown differential phosphorylation of tyrosine residues on VEGFR-2 when HUVECs are exposed to stimulation by the VEGF ligand or when treated with an inhibitor. VEGF displayed less prolonged phosphorylation at Y1214 compared to Y1054/Y1059. However, a VEGFR-2 inhibitor caused a larger drop in Y1054/Y1059 phosphorylation compared to Y1214. These results suggest that Y1054/Y1059 is more sensitive to soluble VEGF stimulation than Y1214, which is more resistant to SU5416. VEGF-independent mechanoactivation of VEGFR-2 could cause differential phosphorylation of Y1214. Total VEGFR-2 levels increased with SU5416 treatment, possibly due to the decrease in receptor activation which normally triggers VEGFR-2 endocytosis and degradation [13]. Further study of the effects of mechanical strain on Y1214 phosphorylation would provide deeper understanding of how the physical environment affects activity patterns of this residue and VEGFR-2 as a whole.

In a pilot study to test if magnetic mechanical stimulation could drive angiogenesis in a 3D microtissue model, we showed that there was a small increase in angiogenesis in chambers containing magnetic beads and cultured above a magnetic force. While some growth is seen in chambers without beads, further studies will focus on increasing mechanical strain and refining parameters used to quantify blood vessel development. Overall, this work suggests that mechanically-active environments result in increased angiogenesis, in line with previous results from our lab [17]. The TME can produce similar mechanical forces, which may be one reason why anti-angiogenic therapies have often proven ineffective in stopping blood vessel development in tumors. Understanding how the TME mechanically regulates angiogenesis is a critical area that requires further investigation in order to develop effective anti-angiogenic therapies.

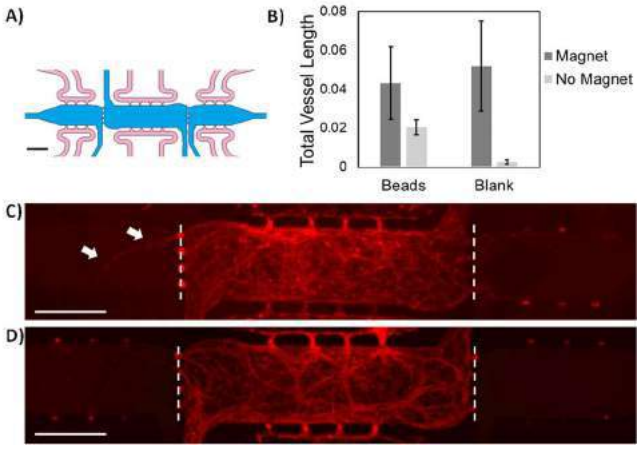


**Figure 2: Effects of mechanical strain on angiogenesis. (A) Schematic of the microfluidic device: blue represents tissue chambers, and pink represents fluidic lines. (B) Graph of angiogenesis in each of the side chambers. Total vessel length was quantified using AngioTool and normalized to total length in the center chamber. For Beads, n=3, and for Blank n=2. (C) Representative fluorescent images of a device with a rotating magnet and (D) without a magnet, stained for VE-Cadherin. White arrows point to blood vessels. Scale bars = 500μm.**


## ACKNOWLEDGEMENTS

The authors would like to acknowledge funding for this project: T32-EB023872 (M.B.); R00-CA230202 (M.K.S.L), IMPACT Award, O'Neal Comprehensive Cancer Center (M.K.S.L).


## REFERENCES


[1] Kohn, JC et al., *Front Genet,* 6:112, 2015. [2] Mitsos, S et al., *Angiogenesis,* 15:1-22, 2012 [3] Lugano, R et al., *Cell Mol Life Sci,* 77:1745-1770, 2020. [4] Fang, S et al., *J Mol Cell Cardiol,* 50:290-295, 2011. [5] Zanotelli, MR et al., *Adv Exp Med Biol*, 1092:91-112, 2018. [6] Carmeliet, P et al., *Nature*, 473:298-307, 2011. [7] Melincovici, CS et al., *Rom J Morphol Embryol,* 59:455-467, 2018. [8] Potente, M et al., *Cell,* 146:873-887, 2011. [9] Ribatti, D, *Oncotarget,* 7:46668-46677, 2016. [10] Miller, B et al., *Front Cardiovasc Med,* 8, 2022. [11] Matsuo, E et al., *Exp Cell Res*, 408:112835, 2021. [12] Jin, ZG et al., *Circ Res*, 93:354-363, 2003. [13] LaValley, DJ et al., *Converg Sci Phys Oncol,* 3, 2017. ]14] Chen, T et al., *J Cell Biol,* 188:595-609, 2010. [15] Padera, TP et al., *Nature*, 427:695, 2004. [16] Jain, RK et al., *Annu Rev Biomed Eng,* 16:321-346, 2014. [17] Sewell-Loftin, MK et al., *Lab Chip,* 20:2776-2787, 2020.

# ULTRASONIC ANALYSIS REVEALS LAYER-DEPENDENT SHEAR WAVE PROPAGATION IN THE PATELLAR TENDON AND SUPERFICIAL TISSUES

**Stephanie G. Cone (1), Lauren K.M. Welte (1), Darryl G. Thelen (1,2)**

(1) Mechanical Engineering, University of Wisconsin, Madison, WI, USA
(2) Biomedical Engineering, University of Wisconsin, Madison, WI, USA

## INTRODUCTION

Shear wave speed measurements have been employed to assess mechanical properties and dynamic loading in musculoskeletal tissues for many applications [1]. Traditional shear wave elastography employs an acoustic push and uses ultra-high frame rate ultrasound to track shear wave propagation within a region of interest [2]. In contrast, shear wave tensiometry [3] uses a mechanical tap and skin-mounted accelerometers to measure a single value for bulk shear wave speed in a superficial tendon. Each of these techniques have unique strengths and weaknesses. Ultrasonic measurements leverage a series of images to ascertain wave speeds within different tissues but are not suitable for high wave speeds or dynamic tasks. Tensiometry enables collections of time-varying wave speeds during dynamic tasks. However, further studies are needed to ascertain how wave propagation through the subcutaneous tissue and skin may differ from that in the underlying tendon.

To better understand the multi-layer implications of wave propagation, we implemented a high frame rate ultrasonic approach for measuring shear wave propagation induced via mechanical excitation. We then investigated the relationship between shear wave speeds near the skin over the patellar tendon and directly in the patellar tendon. This relationship was explored over a range of passive stretch and active loading about the knee. We anticipated finding an increase in shear wave speed both in the tendon and near the skin interface with active loading in knee extension, and little change due to passive stretch loading in the tendon.

## METHODS

For this study, 6 healthy young adults (2F/4M, ages (years): 27.8 ± 4.9, heights (meters): 1.79 ± 0.1, weights (kilograms): 80.0 ± 13.6) were recruited in an IRB approved study (University of Wisconsin IRB: 2018-0487-CP019). Shear waves were excited and measured in the left patellar tendon in static holds of the following conditions: relaxed or loaded with a voluntary knee extension moment, with the knee in 0° and 90° of flexion. Isometric flexion moments were measured via a handheld dynamometer (Mark 10) placed against the proximal tibia.

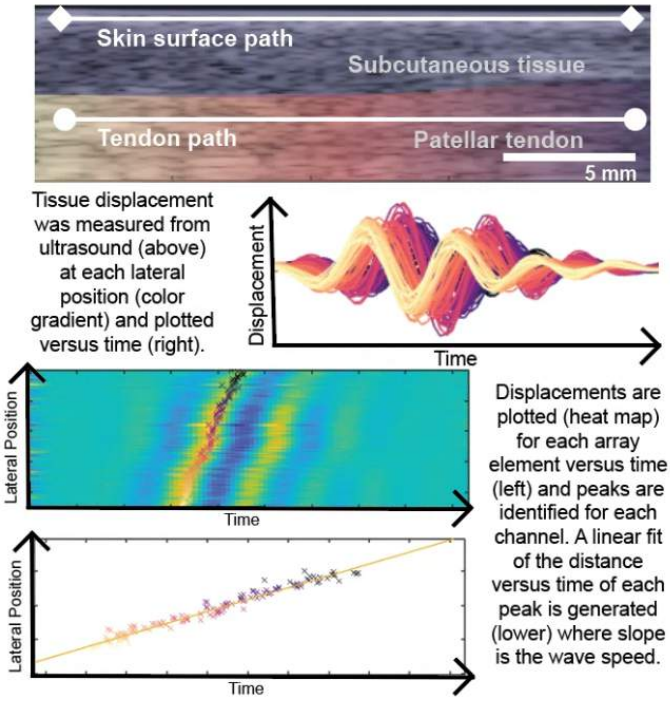


**Figure 1: Shear wave speeds are calculated within the patellar tendon in response to an external mechanical tap.**

Shear waves were excited via an electrodynamic mechanical tapping device described previously [3] placed at the proximal end of the superficial patellar tendon. High frame rate (20kHz) ultrasonic

images were captured of the central region of the patellar tendon using a commercially available programmable ultrasound system (Vantage 64LE, Verasonics) and a linear array transducer (Phillips CL 15-7). These images were exported into a custom MATLAB code for reconstruction and shear wave speed calculation (Figure 1). Briefly, the displacement of the tissue was measured for each pixel (0.18mm x 0.17mm) using a 2D autocorrelation algorithm [4]. The slope of a linear fit of time to peak displacement and the position along the line of interest measured shear wave speed. For the purposes of this study, a single measurement of the shear wave speed was taken over ~20 mm in the patellar tendon, with an example of the typical image shown in Figure 1. For each condition, the shear wave speed and the corresponding correlation coefficient ($R^2$ value) was recorded. Statistical analyses were performed in commercial software (JMP Pro 15) and consisted of one-way ANOVA tests for comparisons of loading conditions, postures, and tissue regions as independent factors ($p<0.05$) and individual subjects as a repeated measure.

## RESULTS

Shear wave speeds within the patellar tendon increased significantly (~4X, $p<0.005$) with active quadriceps loading (Table 1). Wave speeds near the skin tended to increase with loading ($p=0.07$), but to a lesser degree than increases seen in the tendon. Knee flexion did not consistently increase shear wave speeds in the unloaded tendon ($p=0.94$) or at the surface ($p=0.66$), suggesting that the loading due to passive muscle-tendon stretch were much less than the responses to active loading.

**Table 1: Extension torque about the knee, shear wave speeds (SWS) measured in the patellar tendon and at the skin surface, and correlation coefficients ($R^2$) for measurements in flexed (90°) and extended (0°) postures (mean ± standard deviation).**

| Knee Angle | Torque (Nm) | Tendon SWS (m/s) | Tendon $R^2$ | Surface SWS (m/s) | Surface $R^2$ |
|---|---|---|---|---|---|
| 90° | 13.3±4.8 | 40.3±28.5 | 0.67±1.2 | 20.5±16.6 | 0.67±0.2 |
| 90° | -- | 11.8±1.8 | 0.78±0.1 | 18.8±9.2 | 0.59±0.2 |
| 0° | 9.4±3.7 | 34.5±22.6 | 0.64±0.1 | 32.5±19.3 | 0.65±0.2 |
| 0° | -- | 9.8±4.1 | 0.60±0.2 | 12±7.5 | 0.50±0.2 |

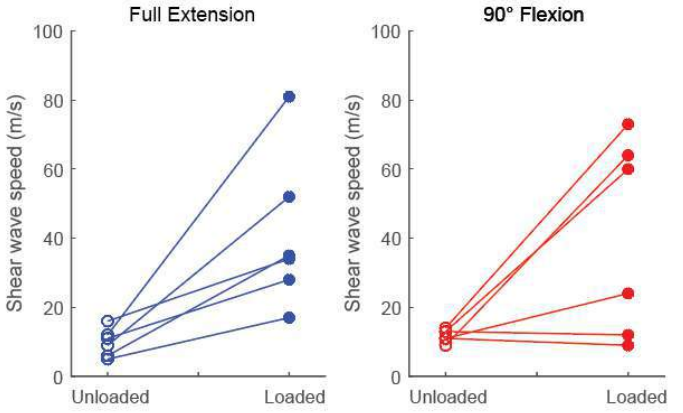


**Figure 2: Increased loading resulted in increased patellar tendon wave speeds across most subjects (individual data paired by lines).**

Within measurements taken in the patellar tendon tissue, a significant increase was seen in shear wave speed with the application of voluntary knee extension torque. These increases were seen in both the extended and flexed postures, with more consistent increases in the extended knee position (Figure 2). Comparisons of extension torque and shear wave speed revealed no significant relationship in either knee posture (0°: $p=0.12$, 90°: $p=0.84$).

Shear wave speed measurements differed between the skin and patellar tendon when participants actively loaded their knee joints (Figure 3). Interestingly, tendon measurements revealed greater magnitude increases with loading, improved correlation coefficients for wave speed calculations, and significant trends with loading compared to skin measurements.

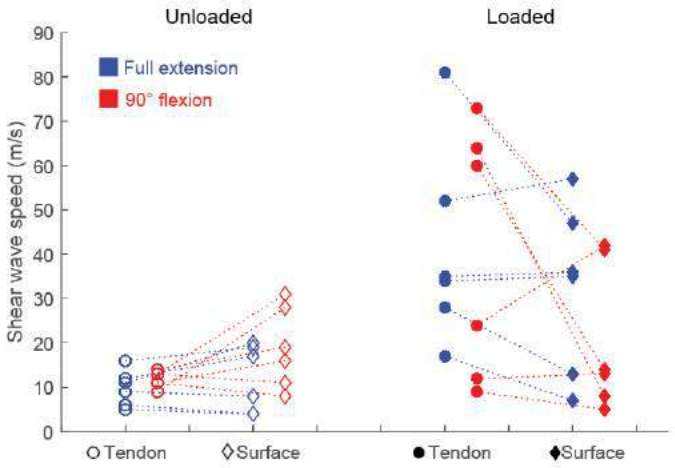


**Figure 3: Shear wave speed measurements are consistent across tendon and surface-based measurements in the unloaded knee, but are highly variable in the loaded state (tendon and surface data paired within individual images via dashed lines).**

## DISCUSSION

Tendon shear wave speeds increased with active muscle-tendon loading, and were higher than the wave speeds detected in layers of subcutaneous tissue near the skin surface. These wave speed increases were significant across subjects in this initial study only when measured directly in the tendon region, suggesting that this method varies in sensitivity across tissue layers in response to passive and active loading. Interestingly, the magnitude of patellar tendon responses to loading were subject-specific, suggesting potential differences in either the efficacy of mechanical taps or specific tissue loading between subjects following this protocol. Prior work in shear wave tensiometry has shown that bulk patellar tendon wave speeds modulate in proportion to the tendon load as ascertained from inverse dynamics [5]. This prior success in measuring patellar tendon wave speeds via shear wave tensiometry suggests that other experimental factors can amplify the load-dependent effects of wave speed measurements. While this study suggests potential challenges in measuring patellar tendon mechanics via skin-mounted sensors, experimental considerations such as interference pegs (allowing for deeper tissue measurement) and further modeling to understand the multi-layer effect may improve ongoing innovation in wearable sensors capable of tracking dynamic loading.


## ACKNOWLEDGEMENTS

This work was funded by the National Institutes of Health (NIH NIAMS F32 AR076267, NIH HD092697), the Stryker-ORS Women's Research Fellowship, and an NSERC Postdoctoral Fellowship.


## REFERENCES


[1] Blank+, *ABME,* in press; [2] Sigrist+, *Theranost,* 2017; [3] Martin+, *Nat Comm,* 2018; [4] Loupas+, *IEEE TUF*, 1995; [5] Ebrahimi+, *Gait & Pos,* 2021.

# INDEPENDENT AND SYNERGISTIC EFFECTS OF INTERSITIAL HYDRATION AND SYNOVIAL FLUID PRESENCE ON CARTILAGE LUBRICATION

**Emily P. Lambeth (1), Meghan E. Kupratis (1), David L. Burris (2), Christopher Price (1)**

(1) Biomedical Engineering, University of Delaware, Newark, DE, USA
(2) Mechanical Engineering, University of Delaware, Newark, DE, USA

## INTRODUCTION

Articular cartilage is the lubricious connective tissue that facilitates remarkably low friction during joint motion ($\mu$~0.002).[1] Several lubrication theories have been proposed for articular cartilage, including boundary and interstitial lubrication. In boundary lubrication, synovial fluid (SF) facilitates low friction through surface chemistry interactions.[2,3] In contrast, interstitial lubrication occurs through the pressurization of cartilage's interstitial fluid, allowing it to support >90% of the applied loads. Under high fluid load support (FLS), little stress is carried by the solid matrix, promoting low friction sliding.[4] Although these (and other) lubrication modes can be isolated and tested in *ex vivo* studies, no singular lubrication mode can recapitulate cartilage's true *in vivo* friction behavior on the benchtop (**Table 1**).

**Table 1: Minimum equilibrium friction coefficients ($\mu_{Eq}$) *in vivo* and under boundary (SF) & interstitial (PBS) lubrication regimes.**

| | ***in vivo*** | **boundary** | **interstitial** |
|---|---|---|---|
| $\mu_{Eq}$ | ~0.002[1] | ~0.02[5] | ~0.02[6] |

Recently, *ex vivo* studies using the convergent stationary contact area (cSCA) testing configuration have enabled the identification of a potent sliding-driven cartilage lubrication mechanism, termed tribological rehydration,[7] that finally permits facile replication of cartilage's truly remarkable *in vivo* lubricity on the benchtop. In the cSCA, and in the presence of PBS alone, sliding promotes speed-dependent, hydrodynamically-mediated recovery and maintenance of high FLS and low friction values ($\mu$~0.03).[7] When SF was introduced into high-speed cSCA sliding studies, vanishingly-small, *in vivo*-like equilibrium frictions ($\mu$~0.003) were recorded—a first for benchtop studies.[8] Presently, the mechanism(s) underlying (and the limits to) this un-anticipated lubrication synergy remain a mystery. Here, we explored friction mitigating interactions between interstitial lubrication (titrated through sliding speed-dependent tribological rehydration) and SF presence by comparing the tribomechanical response of PBS- and SF-lubricated cSCA cartilage contacts. Stribeck analysis was then used to inform the independent and synergistic effects of both interstitial lubrication and SF presence on the friction behaviors of cSCA explants.

## METHODS

19mm ϕ osteochondral explants (n=6) were extracted from the femoral condyles of skeletally mature bovine stifles. Explants were rinsed and stored in 1xPBS to which sucrose was added to match the osmolarity of synovial fluid (400mOsm; hereon referred to as PBS).[9]

A reciprocating tribometer[7] was used to statically compress each cSCA explant against glass at 7N (~0.25MPa) for 6 hours, to fully depressurize the contact, followed by sliding, in order, at 80, 60, 40, 30, 20, 10, 5, 1, & 0.5mm/s (**Fig. 1**). During this speed sweep, sliding speeds were changed when deformation rates <1µm/min and changes in friction coefficients <0.01/min (for $\mu$ >0.1) or <0.001/min (for $\mu$ <0.1) were achieved. Following initial characterization in PBS, explants free swelled in SF for >2hr, and were then tested in SF. Equilibrium compression ($\delta$) and kinetic friction coefficients ($\mu$) at each sliding speed were recorded in LABVIEW and analyzed in MATLAB.

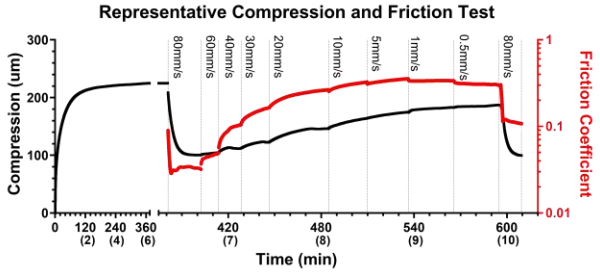


**Fig. 1: Representative tribomechanical test. This PBS-lubricated sample was statically compressed (7N) for 6 hrs followed by a speed iterative sweep (80-0.5mm/s, + 80mm/s run-out; under 7N).**

For Stribeck curve analysis,[3] Hersey's number ($\mathcal{H}$) was calculated as:

$$\mathcal{H} = i\frac{sv}{F_N} \quad (1)$$

where $s$ is sliding speed, $v$ is dynamic viscosity, and $F_N$ is normal force. For each sliding speed, shear-rate dependent SF viscosities ($v_{SF}$) were extrapolated from published data for various interfacial gap heights (0.8, 8, 80, & 800nm), corresponding to maximal shear rates of 100, 10, 1, & $0.1x10^6$ $s^{-1}$ respectively, at 80mm/s.[8,10] Repeated measure one-way ANOVAs or paired ratio $t$-tests were used to detect groupwise differences; significance was set at a multiplicity-adjusted $p < 0.05$.

## RESULTS

In a manner uniquely observable in the cSCA, the lowest equilibrium friction ($\mu_{Eq}$) values occurred at sliding speeds ≥30mm/s irrespective of bathing solution (**Fig. 2A**). SF significantly reduced $\mu_{Eq}$ at all speeds (**Fig. 2A**); however, the largest effects of SF on friction reduction (compared to paired PBS values) occurred at speeds ≤1mm/s & ≥30mm/s. Reduction in friction, calculated as the ratio of friction in PBS versus SF, was 11.8±3.2-fold at 0.5mm/s, only 1.7±0.6-fold at 10mm/s, yet 9.6±4.9-fold above 30mm/s (**Fig. 2B**).

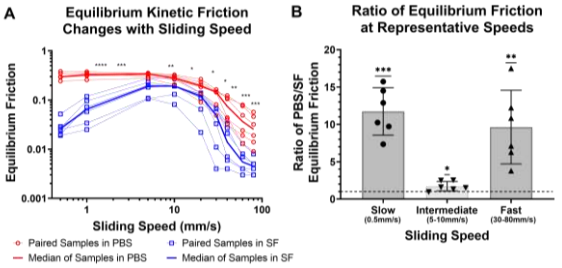


**Fig. 2: (A) Sliding speed-dependent $\mu_{Eq}$ for PBS-lubricated (red) and SF-lubricated (blue) explants. Thick lines indicate median responses for each lubricant. (B) Ratio of $\mu_{Eq}$ in PBS vs. SF at slow (0.5mm/s), intermediate (10mm/s), and fast (≥30 mm/s) sliding speeds. (* p<0.05, ** p<0.01, *** p<0.001, **** p<0.0001).**

Stribeck analysis identified noticeably different shaped PBS and SF cSCA curves (**Fig. 3A**; $v_{SF}$ estimated for a 80nm gap height, $v_{PBS}$ was fixed at 0.88mPa·s.). At intermediate Hersey numbers, PBS and SF-lubricated contacts exhibited similar overall friction behaviors (monotonically decreases with increasing $\mathcal{H}$. However, major differences between PBS and SF were observed at: (i) low and (ii) high Hersey numbers. At low Hersey numbers, PBS and SF generated distinctly different $\mu_{Eq}$ values (0.3 vs 0.03, respectively). At high Hersey numbers, both PBS and SF lubricated contacts exhibited remarkably low $\mu_{Eq}$ (<0.05), however, in SF, $\mu_{Eq}$ was an order of magnitude lower than in PBS (0.005±0.002).

Notably, the position of the SF Stribeck curve relative to PBS depended upon the gap height, and thus the shear-dependent SF viscosities, used to calculate $\mathcal{H}$ (**Fig. 3B**). When gap heights of 80 and 800nm (corresponding to $\nu_{min}$ 2.29 and 4.44mPa·s, respectively) were utilized, the resultant SF Stribeck curves fell to the right of the PBS curve. For a gap height of 8nm ($\nu_{min}$ 1.18mPa·s), the two curves largely overlapped at intermediate Hersey numbers, while for a 0.8nm gap ($\nu_{min}$ 0.61mPa·s), the SF curve fell entirely to the left of the PBS curve.

## DISCUSSION

The cSCA configuration, with its ability to titrate tissue hydration through sliding-speed dependent control of tribological rehydration, is uniquely suited to interrogate cartilage's frictional behaviors under both high and low FLS conditions. The rapid and robust recovery of tissue compression and lubricity by high-speed sliding after the complete (6hr) depressurization of cartilage highlights the robust ability of tribological

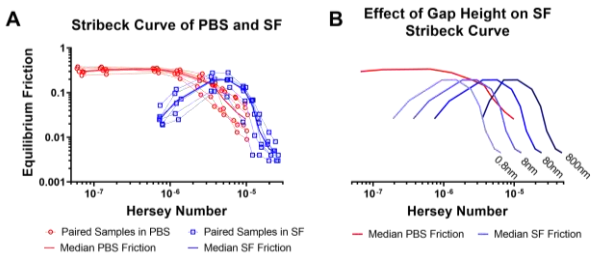


**Fig. 3: (A) Stribeck analysis of $\mu_{Eq}$ vs. Hersey number for paired samples in PBS (red) & SF (blue); SF viscosities predicted for an 80nm gap utilized. (B) Stribeck curves for PBS (red) & SF (blue), for SF viscosities predicted for gaps of 0.8, 8, 80, and 800nm.**

rehydration to drive interstitial fluid recovery. Our findings of maximal lubricity always accompanying the highest applied sliding speeds (and compression recoveries), irrespective of bathing solution, further confirms the importance of interstitial hydration (and its recovery) as a master regulator of cartilage lubrication.

However, SF presence did influence lubricity, and in ways that might not have been anticipated. The greatest relative changes in lubricity—but not the lowest absolute friction magnitudes—occurred at very low sliding speeds and low Hersey numbers. While these results confirmed the boundary lubricating function of SF at very slow speeds (<1mm/s) in fully-depressurized cartilage,[2-4] sliding speeds within joints are on the order of ~100mm/s during most activities[11] and it is unlikely that cartilage ever experiences near total fluid exudation/fluid loss *in vivo*.[12,13] Instead, our cSCA tests indicate that at modest sliding speeds (≥30mm/s), exceptional cartilage lubricity is promoted by the synergistic action of tribological rehydration and SF presence, supporting equilibrium friction coefficient values previously only observed in intact joints (~0.005).[1] Thus, while SF may act as a classical boundary lubricant under rather specific benchtop conditions, the lubrication of intact joints appears more likely to result from synergy between the active maintenance of interstitial hydration and FLS (fostered by tribological rehydration, bath exposure, and/or contact migration) and SF presence within rapidly articulated/slid contacts. Ongoing studies characterizing our samples after 'reducing' them to classical SCA sized contacts (~6mm ϕ), thereby explicitly eliminating their ability to sustain tribological rehydration, will serve to confirm the synergistic nature of FLS and SF supported lubrication.

Lastly, our parametric assessment of Stribeck curve behavior demonstrated that our SF and PBS curves only collapsed onto a single overlapping lubrication curve when shear-rate-dependent SF viscosities for a predicted interfacial gap height of ~8nm was utilized, corresponding to peak interfacial shear rates of $\sim 10x10^6$ $s^{-1}$ and a minimum $v_{SF}$ of ~1.2mPa·s (approximately that of water) at high sliding speed. This behavior again indicates that both interfacial $v_{SF}$ and gap heights are likely far smaller than previously anticipated.[8,10]

Overall, the present study highlights key additive effects of interstitial hydration and synovial fluid presence on cartilage lubrication. These insights further advance our objective of identifying the independent and combinatorial mechanisms governing the unmatched natural tribomechanics of articular cartilage *in vivo*.

## REFERENCES


[1] Clark et al, *J Lubricat Technol*, 1975; [2] Jones et al, *JOR*, 2007; [3] Bonnevie et al, *PLOS One*, 2015; [4] Caligaris & Ateshian, *OA&C*, 2008; [5] Irwin et al, *OA&C*, 2020; [6] Stotter et al, *JOR*, 2019; [7] Moore & Burris, *OA&C*, 2017; [8] Farnham et al, *Trib Let*, 2021; [9] Baumgarten et al, *J Bo Join Surg*, 1985; [10] Liao et al, *J Mech Behav Biomed Mat*, 2019 [11] Graham et al, *CTR*, 2020; [12] Krishnan et al, *JOR*, 2004; [13] Coleman et al, *J Biomech*, 2013.

SB³C2022
Summer Biomechanics, Bioengineering and Biotransport Conference
June 20-23, Eastern Shore, MD, USA

# FLUID STRUCTURE INTERACTION MODELING OF THE MIGRATION AND TRAPPING OF PHYSICALLY REALISTIC BLOOD CLOTS IN AN INFERIOR VENA CAVA FILTER

**Ebrahim M. Kolahdouz (1), Kenneth I. Aycock (2), Brent A. Craven (2), Boyce E. Griffith (3)**

(1) Center for Computational Biology, Flatiron Institute, New York, NY, United States
(2) Division of Applied Mechanics, Office of Science and Engineering Laboratories, Center for Devices and Radiological Health, US Food and Drug Administration, Silver Spring, MD, United States
(3) Department of Mathematics, University of North Carolina at Chapel Hill, Chapel Hill, NC, United States

## INTRODUCTION

Simulating the transport and fluid-structure interaction (FSI) of flexible and geometrically realistic blood clots in the circulation is critical to accurately modeling the performance of embolic protection devices like inferior vena cava (IVC) blood clot filters. IVC filters are cardiovascular devices that are implanted in the IVC, a large vein in the abdomen through which blood flow from the lower extremities returns to the heart. IVC filters capture clots before they can migrate to the lungs and cause a pulmonary embolism that is potentially fatal. Traditionally, non-clinical IVC filter clot trapping performance is evaluated through in vitro bench testing. Computational modeling has the potential to be used to complement or in lieu of experimental testing, however, if the simulations are rigorously verified and validated. To date, though, simulating the transport and trapping of realistic deformable blood clots in the circulation has been extremely challenging.

In this work, we use our recently developed sharp interface FSI framework [1,2] to simulate the migration and trapping of blood clots in the IVC, which is especially challenging due to the relatively large size of the clots that affects the local fluid dynamics, the large deformations that are generated, and the occurrence of contact between the clots, the vein wall, and the implanted device. The performance of the IVC filter in capturing realistic, flexible clots is investigated numerically and the results are compared with experimental data. It is important to note that in the literature, modeling realistic blood clots anywhere in the circulatory system (e.g., in the cerebral vasculature for predicting ischemic stroke), is currently restricted to either modeling rigid spherical clots or a small number of deformable clots, partly due to the computational expense of fully coupled FSI. Our sharp interface algorithm with features such as parallelized adaptive mesh refinement and multi-rate time-stepping is a significant improvement over alternative approaches, providing the capability to model large structural deformations of a number of deformable clots within complex patient-specific geometries.

## METHODS

Our numerical algorithm uses a partitioned approach to FSI with a sharp-interface immersed coupling strategy that resolves flow features up to the fluid-structure interface. It extends our recently developed rigid body immersed Lagrangian Eulerian (ILE) method for FSI [1] to models involving immersed flexible structures. The method combines a partitioned approach to FSI with an immersed coupling strategy. Like other partitioned formulations, the ILE approach uses distinct momentum equations for the fluid and solid regions. Unlike body-fitted arbitrary Lagrangian-Eulerian methods, our approach uses a non-conforming discretization of the dynamic fluid-structure interface that is "immersed" in the surrounding fluid and does not require any grid regeneration or mesh morphing to treat large structural deformations. We use a penalty approach to relax the kinematic constraint as well as a nearly incompressible solid mechanics formulation to relax the incompressibility constraint of the solid structure. Specifically, the penalty formulation uses two representations of the fluid-structure interface, including a thin surface mesh and a bulk volumetric mesh, that are connected by forces that impose kinematic and dynamic interface conditions. The dynamics of the volumetric mesh are driven by the accurate exterior fluid traction obtained from the sharp interface approach.

In our simulations, blood is modeled as a Newtonian fluid with a density of $\rho_f = 1.0\ \ \mathrm{g \cdot cm^{-3}}$ and dynamic viscosity of $\mu = 0.03\,\mathrm{g \cdot (cm \cdot s)^{-1}}$. The IVC filter used in this study is a new generic conical-type filter, referred to as the GENI (GEneric NItinol) filter, designed for research purposes by U.S. Food and Drug Administration (FDA) scientists and collaborators [3]. It resembles the support structure of an umbrella consisting of a central hub with 16 evenly spaced radial struts (Fig. 1). We first simulate the dynamics of clot transport and capture with the filter deployed in a rigid circular tube that is representative of the IVC vein. A realistic cylindrical blood clot with the length $L_{\mathrm{clot}} =$

2.0 cm and diameter $D_{\text{clot}} = 2.5$ mm is considered. The blood clot is modeled as a nearly incompressible hyperelastic material with Poisson ratio $\nu = 0.499$ and shear modulus $G_s = 2000$ dyn $\cdot$ cm$^{-2}$ and density $\rho_s = 1.2\rho_f$. In these initial simulations, we ignore the influence of gravity. The clot and the filter are deployed in a circular tube of length $L_{\text{tube}} = 6.4$ cm and diameter $D_{\text{tube}} = 2.8$ cm. A fully developed parabolic velocity profile with the maximum velocity of $U_{\max} = 15.0$ cm $\cdot$ s$^{-1}$ is imposed at the inlet of the tube at the bottom boundary ($y = -3.2$ cm), corresponding to the normal physiological flow conditions. Zero normal traction and tangential velocity conditions are imposed at the outlet of the tube at the top boundary. The boundary conditions along all the other parts of the Cartesian domain boundary are set to no-slip wall (zero velocity). Both the IVC filter and the circular tube are assumed to be rigid, stationary structures modeled by linear spring forces that tether the material coordinates of structural points to their initial positions. The surface of these structures is covered by two-dimensional bilinear quadrilateral surface elements. The mesh of the blood clot is discretized with trilinear hexahedral elements.

**Figure 1: Anatomical IVC model (left), generic IVC filter (middle), and cylindrical bovine blood clots (right). Adapted from [3].**

## RESULTS

A simulation of the transport and capture of a blood clot by the filter is demonstrated in Fig. 2. As time proceeds, the clot becomes more ensnared in the filter while undergoing deformations caused by the clot interacting with the local flow and because of contact with the filter and the tube wall. The overall dynamics of the clot's motion appear to be qualitatively similar to those observed in recent in vitro experiments using the same device [3].

## DISCUSSION

This study will advance the use of verification and validation (V&V) methods in computer modeling and simulation. We have previously performed simulations of flow in a realistic anatomical IVC model using our sharp interface algorithm and compared the simulated flow patterns with particle image velocimetry (PIV) measurements (Fig. 3). Our ongoing work is focused on further experimental validation of the simulated clot trapping physics with the IVC filter implanted in this anatomical IVC model. In each case, we are conducting a rigorous mesh convergence study to estimate the numerical uncertainty associated with the predictions. Our goal is to predict the statistical clot trapping performance of the GENI IVC filter for different clot sizes and vessel orientations and to validate the results by comparing with recent experimental data [3].

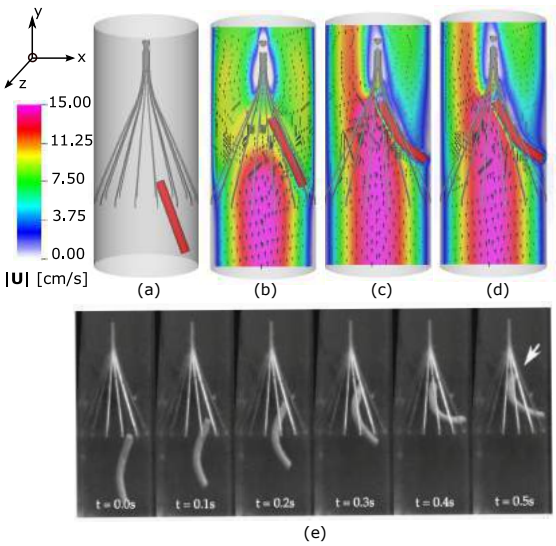


**Figure 2: Simulated capture of a cylindrical blood clot with the GENI IVC filter deployed in a rigid circular tube showing (a) the initial clot-filter-tube configuration and the dynamics of the clot deformation with contours of velocity magnitude and vectors on the x-z mid-plane at times: (b) t=0.3 s, (c) t=1.45 s, and (d) t=1.8 s. (e) Image sequence from high-speed videography during in vitro experiments with the same device and with a comparable blood clot showing similar clot trapping dynamics [3].**

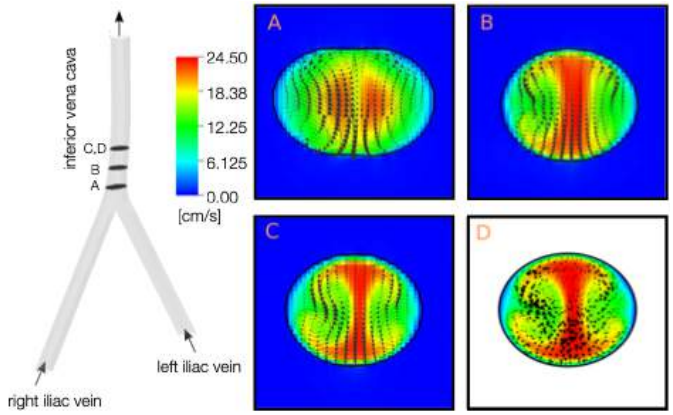


**Figure 3: Velocity magnitude with vorticity vectors for flow in an anatomical IVC model at exercise flow conditions using our sharp interface method (cross-sections A, B, and C) compared with a body fitted CFD simulation performed using OpenFOAM (cross-section D), adapted from [2].**


## ACKNOWLEDGEMENTS

This research was funded through NIH Awards HL117063 and HL143336, NSF Awards DMS 1664645, CBET 175193, OAC 1450327, OAC 1652541, and OAC 1931516, and the U.S. FDA Center for Devices and Radiological Health (CDRH) Critical Path program.


## REFERENCES


[1] Kolahdouz, EM et al., *J. Comput. Phys.,* 443:110442, 2021.
[2] Kolahdouz, EM et al., *J. Comput. Phys.,* 400:118854, 2020.
[3] Riley, JM et al., *J B Cardiovasc. Eng. Technol.*, 12:339–352, 2021.

SB³C2022
Summer Biomechanics, Bioengineering and Biotransport Conference
June 20-23, Eastern Shore, MD, USA

# THE RISK OF RECURRENT DISC HERNIATION FOLLOWING DECOMPRESSION SURGERY WITH SURGICAL DETACHMENT OF THE POSTERIOR EXTENSOR MUSCLES

**S. Rossman (1), E. Meyer (2), J. Isaza (3), S. Rundell (1)**

(1) Explico Engineering, Novi, MI, USA
(2) Biomedical Engineering Department, Lawrence Technological University, Southfield, MI, USA
(3) Spine Specialists of Louisiana, Baton Rouge, LA, USA

## INTRODUCTION

Disc bulging and herniation are two of the most frequently diagnosed low-back (lumbar) pathologies [1]. Herniations can compress the nerve roots and result in pain. If conservative treatment fails, surgery may be required. The most common low-back surgery performed in the United States is lumbar discectomy, which often includes facetectomy and laminotomy [2,3]. Recurrent disc herniations following surgical decompression has been reported in patients at rates between 5% and 21% and often require additional operations [4,5].

The facet joints and lumbar posterior extensor muscles (PEMs) help maintain proper spinal biomechanics, and decrease the risk for recurrent herniation [6,7]. Specifically, increased activation of the PEMs results in increased facet joint engagement and decreased disc pressure and posterior stresses [8]. Essentially, the facet joints assist the disc in carrying axial loads applied to the spine [9,10]. Engagement of the facet joints has the ability to reduce the loads carried by the discs, and thus, reduce the risk of herniation.

Lumbar discectomy can be performed through various techniques using open, microtubular, or endoscopic approaches to visualize the disc herniation. These techniques vary in invasiveness through the approach taken to access the herniation. Invasive surgical approaches, such as the posterior midline approach results in damage to the PEMs while minimally invasive approaches minimize muscular damage [11,12]. Surgical detachment of the PEMs during decompression surgery may limit the spine's ability to fully engage the facet joints and result in an increased risk of recurrent herniation.

Therefore, the objective of the current study was to evaluate the risk of herniation following bony decompression surgery with varying amounts of PEM detachment. We hypothesized that the removal of the facet joint (i.e., facetectomy) or detachment of the PEMs would result in a disc loading environment consistent with an increased herniation risk.

## METHODS

We previously developed and validated a finite element (FE) model of a lumbar motion segment that was then utilized for the current study [13]. Specifically, the model has been demonstrated to accurately predict disc herniation risk. Under the guidance of a spine surgeon, the FE model was surgically altered by either unilateral hemilaminotomy or unilateral facetectomy. PEM muscle detachment was simulated by reducing the muscle force. All other boundary conditions remained constant for each of the simulations. The following scenarios were simulated: unaltered; hemilaminotomy with no PEM detachment, partial unilateral PEM detachment, and complete unilateral PEM detachment; facetectomy with limited unilateral PEM detachment and complete unilateral PEM detachment.

Axial compression representative of body weight above the L4-5 motion segment for a 50$^{th}$ percentile male was applied anterior of the center of the L4 superior bony endplate to simulate forward bending. The location of the torso center of gravity was determined by an analysis utilizing a 3-Dimensional Static Strength Prediction Program. The inferior bony endplate of L5 was fixed rigidly in space. A surface-to-surface contact was established between the L4 and L5 posterior elements. The PEMs were modeled as two cable discrete beams attached between the spinous processes on bi-lateral sides of the model and four cable beams attached within each facet joint. Abdominal pressure force was represented by a force applied to a node constrained to the L4 superior bony endplate and located 8.4 cm anterior of the center of rotation of the vertebrae (Figure 1). The facet joint reaction forces, nuclear extrusion force, disc pressures, disc 1$^{st}$ principal stresses, and disc max shear stresses were recorded.

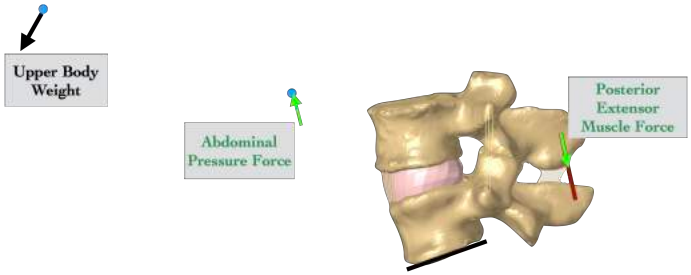


**Figure 1: Lateral view of the L4-5 motion segment FEM depicting the boundary conditions utilized to simulate forward bending.**

## RESULTS

The results for left and right hemilaminotomy and left and right facetectomy indicated similar trends. Therefore, only the results after right hemilaminotomy will be discussed. The interface contact force between the posterolateral circumference of the nucleus and inner annulus (i.e., NP extrusion force) ranged between 310 and 319 N for all scenarios with intact PEMs. The posterolateral NP extrusion force increased as the amount of PEM force was decreased (Figure 2).

There was an inverse relationship between facet joint contact force and disc pressure/stresses as the PEM force decreased. Specifically, after right hemilaminotomy, the peak disc pressures increased from 1.47 MPa to 2.12 MPa, and the facet joint contact force decreased from 746 N to 361 N as the amount of PEM force decreased from 2,376 N to 1,188 N (Figure 3). When the PEM was left intact, there were insignificant differences between the unaltered model and the surgically altered model. Similar trends were seen for peak disc 1st principal stress, peak disc max shear stress, and posterolateral NP extrusion force. Specifically, the peak disc 1st principal stress increased from 1.01 MPa to 2.65 MPa, the peak disc max shear stress increased from 1.12 MPa to 1.73 MPa, and the posterolateral NP extrusion force increased from 319 N to 355 N as the amount of PEM force decreased from 2,376 N to 1,188 N.

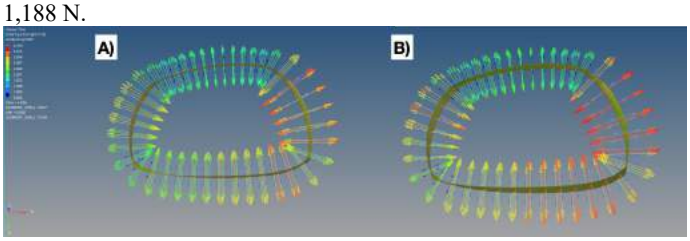


**Figure 2: NP extrusion force of the A) unaltered model compared to B) complete PEM detachment after right hemilaminotomy.**

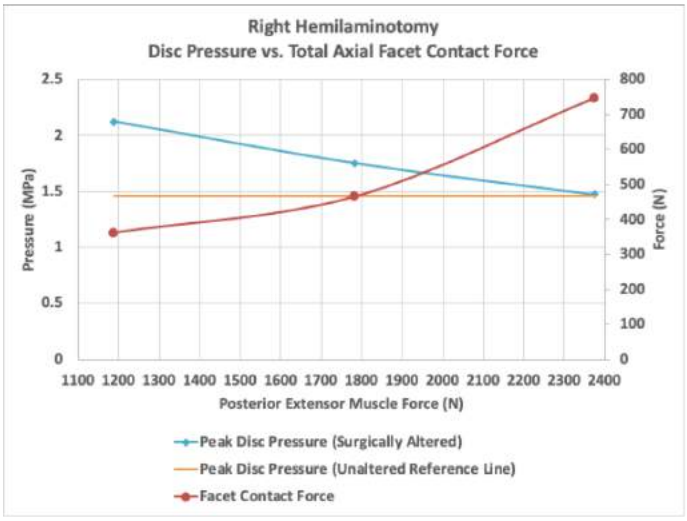


**Figure 3: Line graph showing the correlations between facet joint contact force, PEM force, and peak disc pressures following right hemilaminotomy.**

## DISCUSSION

Results of the current study partly confirmed the hypothesis that detachment of the PEM would reduce facet joint contact force and increase disc stresses. However, the hypothesis that removal of the facet joint would increase disc stress was not confirmed. Rather, the greatest risk for recurrent herniation occurred because of PEM detachment and not bone removal. Specifically, there was no significant change in the risk of recurrent herniation after hemilaminotomy or facetectomy when the muscles where left intact or when there was only limited muscle detachment. The highest magnitude of posterolateral NP extrusion force occurred on the right posterolateral aspect of the disc. These results are consistent with the literature which indicates that disc herniations are most common on the posterior or posterolateral aspect of the disc [14].

Previous studies have reported between 46% and 47% of subsequent operations were performed within 6 months of the original surgery regardless of whether endoscopic or open discectomies were performed [15,16]. These results suggest that the disc is most vulnerable immediately after surgery. This is consistent with decreased PEM activation either due to damage during surgery, atrophy, or poor bending and lifting techniques following surgery. These same studies show that the rate of recurrent surgery in the first 90 days after initial surgery following laminectomy was two times higher than for open or endoscopic discectomy alone. Since laminectomy may require full or partial detachment of the PEM, these clinical findings are consistent with the results from the current study. Regardless of the surgical technique utilized to treat the disc herniation, clinical data and the results of the current study suggest that PEM damage leaves the disc most vulnerable to recurrent herniation.

Results of the current study have clinical applications to surgeons who utilize techniques that require bone removal to gain access to the disc herniation during decompression surgery. Specifically, if removal of the laminae or facet joint is necessary, care should be taken to avoid detachment of the PEM from the vertebrae. However, if muscle detachment is unavoidable, post-surgical rehabilitation and care should be taken to minimize risk to the disc. Specifically, exercises that strengthen the remaining torso muscles and bending and lifting techniques that accentuate bending with a taught back should be emphasized. Additionally, establishing pre- and post-op methods for quantifying muscle strength may assist in determining an optimal recovery strategy.

## REFERENCES

[1] Gopalakrishnan, N et al., *JCDR*, 9(1):TC17-TC20, 2015.
[2] Sahrakar, K et al., *Medscape*, 2018.
[3] Chin, L et al., *Medscape*, 2015.
[4] Shin, E et al., *Inter. Orthopaedics*, 43(4):963-967, 2019.
[5] Chen, X. et al., *Eur Spine J*, 29(7):1752-1770, 2020.
[6] Bergmar, A. et al., *Acta Ortho Scandinavica*, 60(s230):1-54, 1989.
[7] Cholewicki, J. et al., *SPINE*, 22(19):2207-2212,1997.
[8] Rossman, S., Dissertation, Lawrence Tech Uni., 2021.
[9] Yang, K. and King A., *SPINE*, 9(6):557-565, 1984.
[10] El-bohy et al., *J Biomech*, 22(8-9):931-941, 1989.
[11] Raut, S. et al., *Ortho J of MP*, 27(1), 2021.
[12] Fu, C. et al., *Sci Rep*, 10(1):14635, 2020.
[13] Rossman, S. et al., *CMBBE*, DOI: 10.1080/10255842.2021.1922677, 2021.
[14] Wilke, H. et al., *SPINE*, 25L1363-1372, 2016.
[15] Cheng, J. et al., *Inter. Orthopaedics*, 37(8):1511-1517, 2013.
[16] Kim, C.H.. et al., *SPINE*, 38(7):581-590, 2013.

# VAGINAL BIOMECHANICAL FUNCTION AND COMPOSITION IN PREMENOPAUSAL WOMEN WITH AND WITHOUT PELVIC ORGAN PROLAPSE

**Qinhan Zhou (1), Benard Ogola (2), Jasmine Kiley (1), Shelby White (1), Lyndsey R. Buckner (3), Laurephile Desrosiers (4), Leise R. Knoepp (4), Sarah H. Lindsey (2), Kristin S. Miller (1)**

(1) Department of Biomedical Engineering, Tulane University, New Orleans, LA, United States
(2) Department of Pharmacology, Tulane University, New Orleans, LA, United States
(3) Department of Research, Ochsner Health System, New Orleans, LA, United States
(4) Department of Female Pelvic Medicine & Reconstruction Surgery, Ochsner Clinical School, New Orleans, LA, United States

## INTRODUCTION

Pelvic organ prolapse (POP) is the descent of the female pelvic organs, such as the uterus, bladder, and rectum, into the vagina. While the etiology of POP is not fully understood, loss of mechanical integrity of the vagina, uterosacral ligaments, and other muscular and connective tissues may contribute to POP development and progression [1]. While the incidence of POP is higher in postmenopausal women, 2.4‰ of premenopausal women require surgical intervention to restore normal anatomy and relieve symptoms such as voiding dysfunctions [2]. Previous biomechanical studies investigated the mechanical properties of premenopausal vaginal tissue by uniaxial tensile testing and suggested that the prolapsed vagina is stiffer than normal tissue; however, these protocols did not consider multiaxial loading or link mechanical changes to risk indexes [3,4]. The structural and compositional changes that dictate the loss of mechanical integrity are not fully understood, and research on vaginal tissue, especially in premenopausal women, is limited. The relationship between most mechanical properties, biochemical composition, and demographics in premenopausal vaginal tissue remains unknown.

Therefore, the objective of this study was to quantify biaxial mechanical behavior and biochemical content in vaginal tissue from premenopausal women with and without prolapse. Potential correlations between mechanical properties, protein content, and demographics were evaluated.

## METHODS

Samples were obtained from Ochsner Biobank following routine gynecological procedures as approved by the Ochsner Clinical School Institutional Review Board (2017.016A). De-identified demographic information including menopausal status, BMI, and age at surgery, etc. was collected from clinical records, and the POP stage and compartment during POP-Q examination was recorded. The inclusion criteria were female, older than 18 years old, and no prior pelvic floor reconstructive surgeries. The tissue was collected from either the apex or anterior wall of the vagina (Fig 1A) from women undergoing hysterectomy with no symptoms of POP (n=8) or symptomatic POP at stage 2 (n=5) or 3 (n=5). Samples were immediately snap-frozen and then stored at -80°C until the time of mechanical assessment.

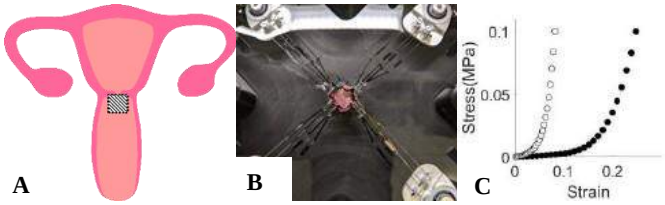


**Fig 1: (A) Tissue collected from apex or anterior wall (shadow). (B) Biaxial testing. (C) Directional difference in stress-strain behavior, circumferential (not filled) and axial (dark).**

For mechanical testing, samples were thawed at room temperature for one hour, and then planar biaxial testing was performed (Fig 1B) as described previously [5]. The specimen was preloaded to 0.1 N, followed by preconditioning from the preload to target stress of 0.1 MPa for at least ten tensile cycles. After a 10-minute re-equilibration period, samples were subjected to 5 displacement-controlled equibiaxial tensile tests, and the last loading cycle was used for data analysis. Data was analyzed using GOM correlate (GOM GmbH, Braunschweig, Germany) and the first image at the beginning of loading cycle was selected as reference configuration. Four points were optically tracked throughout the experiment and a custom MATLAB script was used to calculate the deformation gradient, the first Piola–Kirchhoff stress, and Green strain tensors from the displacements of reference points and real-time force (Fig 1C). The *lsqcurvefit()* function was used to fit the experimental data to a bilinear curve, and the linear modulus and peak strain were calculated as representative metrics of material stiffness and extensibility. Lilliefors test and Levene's test were implemented to evaluate the normality and homogeneity of variance of data error. A 2-way ANOVA or nonparametric alternative, Scheirer-Ray-Hare (SRH)

test, (direction, clinical group) followed by post-hoc Dunn & Sidák's approach assessed potential effects of direction and POP. Western blotting was performed to measure the content of collagen-I, collagen-III, fibulin-3, fibulin-5, and elastin in the tested specimens as described previously [6]. Protein content was calculated by dividing band intensity of each protein of interest by the band intensity of the selected control. A 1-way ANOVA or nonparametric alternative, Kruskal-Wallis (KW) test, followed by post-hoc Dunn & Sidák's approach evaluated the differences in protein content percentage among clinical groups. Pearson's correlation evaluated potential relationships between material stiffness, protein content, and demographics.

**RESULTS**

No significant correlations were identified with respect to age, BMI, parity, and gravidity between clinical groups. Vaginal material stiffness was normally distributed with equal variance; however, the peak strain was not normally distributed. Therefore, the 2-way ANOVA and SRH tests were used to evaluate vaginal stiffness and peak strain, respectively. The results showed that vaginal tissue was stiffer ($p=0.01$) and less extensible ($p=0.048$) in the axial than circumferential direction (Fig 2), however, no significant differences in material stiffness ($p=0.13$) or extensibility ($p=0.15$) were identified with POP. Moderate negative Pearson's correlations were identified between circumferential stiffness and gravidity ($R=-0.51$, $p=0.021$) and parity ($R=-0.54$, $p=0.029$). No other comparisons were statistically significant.

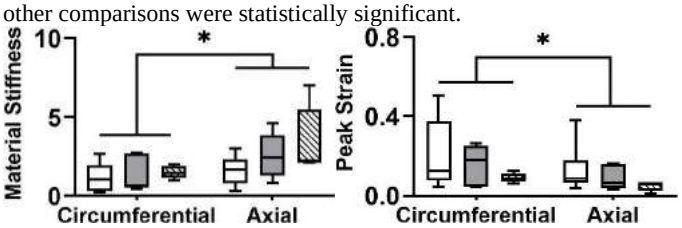


**Fig 2: (A) Vaginal stiffness and (B) extensibility between the control (n=8, not filled), POP-II (n=5, grey), and POP-III (n=5, shadow).**

Collagen-I and fibulin-5 content were normally distributed with the equal variance, and therefore were evaluated using a 1-way ANOVA. However, KW tests were used to evaluate collagen-III, fibulin-3, and elastin, and demonstrated that clinical group was significant factor for collagen-III content ($p=0.002$) (Fig 3). No significant difference was identified in collagen-I, fibulin-3, fibulin-5, or elastin content (Fig 3). Post hoc tests showed that the patients at POP stage 3 had a higher vaginal collagen-III content compared to non-POP control ($p=0.02$). A mild positive correlation was identified between axial stiffness and fibulin-3 content ($R=0.62$, $p=0.01$). Positive correlations were identified between elastin content and patient parity ($R=0.72$ and $p=0.002$) and gravidity ($R=0.63$ and $p=0.001$). No other comparisons were significant.

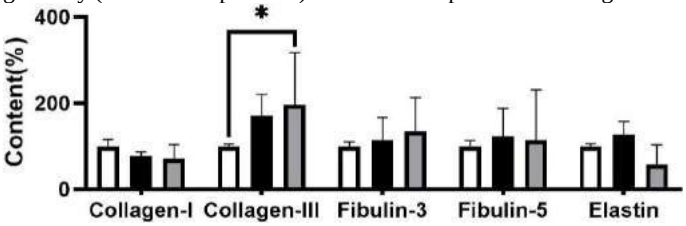


**Fig 3: Biochemical composition in control (n=8, not filled), POP-II (n=5, dark), and POP-III (n=5, grey).**

**DISCUSSION**

While no significant mechanical changes were observed with POP in premenopausal women, collagen-III content was higher in the POP-III group compared with controls, which is consistent with prior study [7]. Collagen-III plays a critical role in wound healing, and an increased production of collagen-III may occur during the tissue repair process after overstretching of the vaginal tissue [7], which occurs with POP. The increased vaginal stiffness with POP noted in previous studies was not identified herein. This may be due to the wide range of patient age (33 to 53 years old), limited sample size (n=5 in POP-II and POP-III), and the mixture of prolapse compartment or type (all cases diagnosed at least two of cystocele, rectocele, or uterovaginal prolapse). Cosson et al. showed that vaginal tissue exhibits high variability in function between patients [4], and age is both the main risk factor for POP and strongly influences mechanical properties of connective tissue [8].

We hypothesized that premenopausal vaginal tissue would be stiffer and less extensible in the circumferential compared to the axial direction, motivated by prior observations in women with POP and mice [5,6]. This may be due, in part, to collagen fiber orientation, however vaginal collagen fiber orientations with and without POP are not known. As for the correlations between direction stiffness and demographics, first, the circumferential stiffness mildly decreased as patients' parity and gravidity increased. An epidemiology study indicated the correlations between POP risk and patients' parity and gravidity [9], however, previous uniaxial studies on human vagina did not identify significant correlations between these indicators and tissue stiffness [3,4]. Therefore, it is possible that parity and gravidity predominantly influence circumferential vaginal stiffness, as prior work largely quantified uniaxial properties in the axial direction. Secondly, the mild correlation between axial vaginal stiffness and fibulin-3 content may offer insight into vaginal prolapse development and progression as mice deficient in fibulin-3 develop prolapse [10], however, more studies are needed to understand the functional contributions of fibulin-3. Further, the elastin content increased with patients' parity similar to prior work [11]. Both increased parity and gravidity may result in the vaginal distension during pregnancy to accommodate the growing fetus and in preparation for delivery, which may correlate to changes in elastin content.

While this study investigated the preliminary biomechanical and biochemical properties of the vagina, this study is not without limitations. One limitation is the wide range of patient ages, the mixture of POP compartments, and the limited sample size. In the future, optimized patient recruitment is needed for variability control. It is necessary to eliminate individual differences by recruiting more patients in each group and controlling for patient age and POP compartment, as variations in POP compartment likely lead to local variations in mechanical load and subsequent tissue remodeling. Consequently, a more comparable result will benefit the assessment of POP progression in vaginal tissue. Although sample variability hindered the identification of mechanical differences between tissues at different stages of POP, valuable information was obtained about mechanical and biochemical properties of the human premenopausal vagina. The directional mechanical properties and their correlations with fiber content identified in this study highlight the need for future investigations into the microstructure of vaginal tissue in the circumferential and axial directions. This will provide insight into the mechanical response of vaginal tissue during the development of POP.

**ACKNOWLEDGEMENTS** This work was supported by the Ochsner Clinical School (2017.016A).

**REFERENCES** [1] Ellerkmann, R+, *Am. J. Obstet. Gynecol.*, 185(6):1332-1338, 2001; [2] Shah, A+, *Int Urogynecol J*, 19(3):421-428, 2008; [3] Lei, L+, *Int Urogynecol J*, 18(6):603-607, 2007; [4] Cosson, M+, *Eur. J. Obstet. Gynecol*., 112(2):201-205, 2004; [5] Danso, E+, *Sci. Rep.*, 10(1):1-14, 2020; [6] Ogola, B+, *Front. Endocrinol.*, 10:586, 2019; [7] Moalli, P+, *Obstet. Gynecol.*, 106(5 Part 1):953-963, 2005; [8] Henry, F+, *J Am Geriatr Soc*,45:220–222, 1997; [9] Chow, D+, *Curr Opin Urol*, 23(4):293-298, 2013; [10] Rahn, D+, *Am. J. Pathol.*, 174(1):206-215, 2009; [11] Gunja-Smith, Z+, *Am. J. Obstet. Gynecol.*, 153(1):92-95, (1985).

# I-PREDICT: DEVELOPING A FULL HUMAN BODY MODEL IN FEBIO

**L. Frazer (1), D. Nicolella (1), B. Stemper (2), R. Salzar (3) N. Yoganandan (2), D. Bass (4), M. Davis (5), T. Bentley (6), Barry Shender (7)**

(1) Mechanical Engineering, Southwest Research Institute, San Antonio, TX, USA
(2) Biomedical Engineering, Medical College of Wisconsin, Milwaukee, WI, USA
(3) Center for Applied Biomechanics, University of Virginia, Charlottesville, VA, USA
(4) Biomedical Engineering, Duke University, Durham, NC, USA
(5) Elemance LLC. Clemmons, NC, USA
(6) Force Health Protection, Office of Naval Research, Arlington, VA, USA
(7) Naval Air Warfare Center Aircraft Division, Patuxent River, MD, USA

## INTRODUCTION

The Incapacitation Prediction for Readiness in Expeditionary Domains: An Integrated Computational Tool (I-PREDICT) program is designed to address the limitations of current human body models (HBMs) and provide the military with an advanced, state-of-the-art model that may be used to assess injury risk in various mission environments (Figure 1). For the last decade, the model has been developed in LS-DYNA and has primarily been used for high-rate loading events, such as pilot ejections and behind armor blunt trauma. Recently, other aviation and maritime risks have been considered, such as long-duration flight and spinal injuries occurring therein. To accommodate these new programmatic goals, a parallel I-PREDICT HBM has been developed in FEBio to leverage the unique tissue damage capabilities, active musculature, and other relevant functionalities that facilitate high-fidelity modeling. The following methods, results, and discussion provide an update on model development and recent implementations.

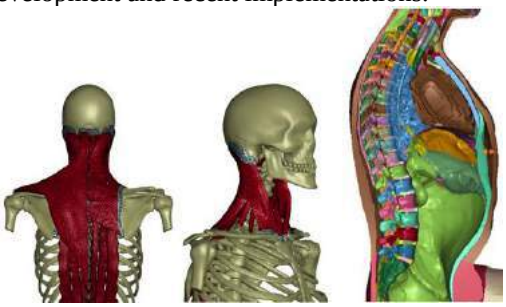

**Figure 1. Three perspectives of the I-PREDICT HBM torso, head, and neck to reveal model detail.**

## METHODS

### Overall Modeling Approach

The I-PREDICT HBM is a probabilistic model that accounts for uncertainty and variability in material properties, threats, model boundary conditions, etc. Moreover, the probabilistic approach guides model development. This is accomplished by distinguishing between epistemic and aleotric sources of uncertainty using probabilistic software (NESSUS, Southwest Research Institute). In situations where the output of interest is highly influenced by a variable with large epistemic variability (uncertainty arising from too few data points), experimental efforts are directed towards addressing this exposed variable. This underlying probabilistic approach taken with the I-PREDICT HBM allows for both a more accurate assessment of injury risk and a more efficient use of resources to improve model shortcomings.

### Anatomy

The I-PREDICT HBM anatomy was developed from Zygote 5.0 geometry of the 50$^{th}$ percentile male.

### Material Properties

Material properties are primarily derived from literature with in-house experimental testing saved for special tissues of interest and tissues identified as contributing high uncertainty to relevant outputs. One such tissue given special attention in the FEBio implementation of the model is the intervertebral disc. Since lumbar pain is a focal concern of this program, intervertebral disc degeneration may be a contributing factor. As such, porcine

annulus specimens have bene rigorously tested with non-damaging step-and-hold tensile loading in the circumferential direction, non-damaging cyclic tension in the circumferential direction, and damaging cyclic tension testing. Using FEBio and an external optimizer (DAKOTA, Sandia National Labs), inverse finite element analyses have been used to fit annulus properties to the experimental data. The annulus is modeled as a solid mixture of a ground matrix (Holmes-Mow) with two crossing fiber families (fiber-pow-linear). The fibers are modeled with reactive viscoelasticity and reactive damage mechanics. First, matrix properties have been taken from literature [1]. Next, using the non-damaging tensile loading, fiber properties are fit (both elastic parameters and reactive viscoelastic parameters). Next, these properties are held fixed and reactive damage mechanics parameters are fit to match the experimental damaging cyclic loading testing. Thus far, the elastic and reactive viscoelastic properties have been fit.

Active Musculature

Another tissue of special interest in this program is musculature. Muscles are modeled as 3D continuum and controlled with active contraction using the trans-iso-Mooney-Rivlin material. As a preliminary demonstration of the role of active musculature in spinal mechanics during a long-duration flight, an analysis was performed to compare a pilot slouching during flight and a pilot with an erect posture accomplished via contraction of the erector spinae muscles. A torque was placed on the C1 vertebra to slump the pilot forward with vibrational loading on the pelvis to simulate the flight boundary conditions. In the active contraction model, the torque was resisted via contraction of the muscles controlled by a PID controller with a target C1 vertebra rotation of zero.

Hierarchical Modeling

Solving a full, long-duration flight (greater than 4 hours) with a full human body model can take weeks, or even months. With a probabilistic modeling approach, hundreds of simulations are run per analysis, and the time constraint per simulation becomes mountainous. To address this limitation, we have developed a hierarchical modeling approach that uses OpenSim to generate relevant muscle forces over a full flight duration, the full HBM to generate boundary conditions in the spinal tissues, and then spinal component models that run for extended periods of time. After a set period of time, the component model is sent back to the full HBM, and a new muscle force is sampled from the OpenSim model. The process is then repeated.

## RESULTS

With annulus testing and inverse finite element analyses, fiber modulus was found to be 3.5±1 MPa. The toe exponent was 6.5±2, and the exponential decay time constant for reactive viscoelasticity was 30±22 s.

In the active muscle demonstration, the slouched posture resulted in high peak stresses occurring in the lumbar discs. With active contraction, peak stresses were reduced by ~40% and occurred in the thoracic and cervical discs. Average stresses were higher in the active contraction model.

The pipeline for hierarchical modeling has been developed and has been successfully demonstrated using a smaller, simple model. Results were similar between the hierarchical model and the full model ran for the full duration. A single python script controls the entire modeling loop.

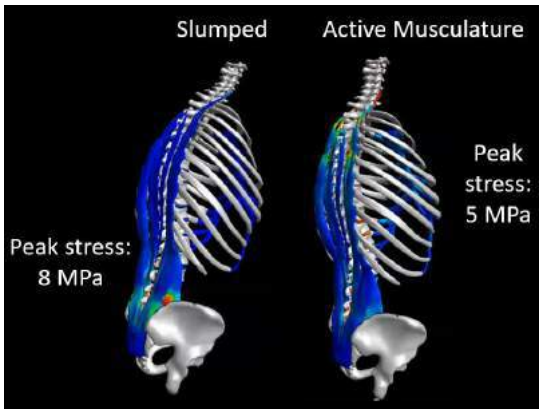


**Figure 2. Comparison between a slumped posture and an erect posture during long-duration flight.**

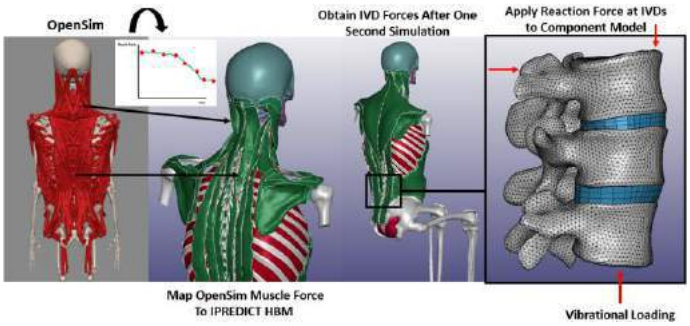


**Figure 3. I-PREDICT HBM Hierarchical modeling approach.**

## DISCUSSION

To the authors' knowledge, the I-PREDICT HBM is the first full-body finite element model implemented in FEBio. FEBio's unique constitutive modeling options tailored to biomechanics have provided the means for a novel approach to modeling the annulus fibrosis. Moreover, enabling 3D solid-element active musculature within the code provides physiologically consistent boundary conditions and response to load – an important consideration in injury risk. Lastly, we have developed the pipeline for a unique hierarchical modeling approach to speed the analysis of large computational models.

## ACKNOWLEDGEMENTS

This work is supported by MTEC-18-04-I-PREDICT-07.

## REFERENCES

[1] Jacobs, N et al., *J Biomech*, 47(11):2540-2546, 2014.

# MECHANICAL ANISOTROPY OF THE EQUATORIAL SCLERA DOES NOT CONCUR WITH THE PRIMARY COLLAGEN FIBER ORIENTATIONS

**Yi Hua (1), Samuel Salinas (3), Marissa Quinn (1), Fengting Ji (1,2), Rouzbeh Amini (3,4), Ian A. Sigal (1,2)**

(1) Department of Ophthalmology, University of Pittsburgh, Pittsburgh, PA, USA
(2) Department of Bioengineering, University of Pittsburgh, Pittsburgh, PA, USA
(3) Department of Bioengineering, Northeastern University, Boston, MA, USA
(4) Department of Mechanical and Industrial Engineering, Northeastern University, Boston, MA, USA

## INTRODUCTION

Collagen fibers provide the sclera with the mechanical strength to be the principal load-bearing component of the eye (**Figure 1**) [1]. Compared to the tissues at the front or back of the eye, such as the cornea, limbus, and peripapillary sclera, little is known about the biomechanics of equatorial sclera [2].

We set out to measure the equatorial sclera mechanical behavior and collagen fiber architecture, focusing on the anisotropies in stiffness and fiber orientation. The degree to which the tissues exhibit either anisotropy was unclear from the literature, and we did not have a defined expectation. Conversely, it has become standard in soft tissue biomechanics to assume that mechanical and structural anisotropies concur, and thus this was our expectation.

Specifically, we used biaxial tensile testing to characterize the stiffness in the circumferential and meridional directions and polarized light microscopy to quantify collagen fiber orientations.

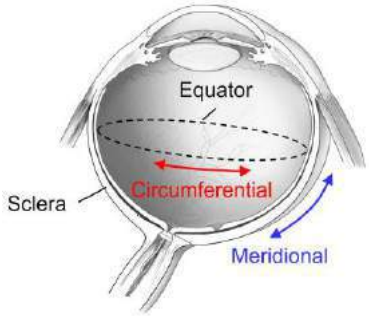


**Figure 1: Schematic cross-section through a human eye. The black dashed line indicates the equator of the eye. The red and blue arrows indicate the circumferential and meridional directions, respectively (consistent throughout the paper).**

## METHODS

*Biaxial tensile testing*. Five porcine eyes were obtained from a slaughterhouse within 24 h postmortem. Equatorial sclera samples (11 mm × 11 mm) were excised from each of four anatomical quadrants: nasal (N), superior (S), temporal (T), and inferior (I) (**Figure 2**). Each sample was mounted on a custom-built biaxial mechanical testing system [3], with the loading axes aligned with the circumferential and meridional directions of the sample. Four submillimeter glass markers were attached to the surface of the sample for optical tracking of tissue deformation (strain). The sample was then loaded under equal-biaxial stress control, with a maximum stress of 120 kPa. Each test consisted of ten loading/unloading cycles, and only data from the tenth cycle was used in the analysis. During the test, the sample was immersed in PBS. After testing, the samples were fixed overnight in 10% formalin [2].

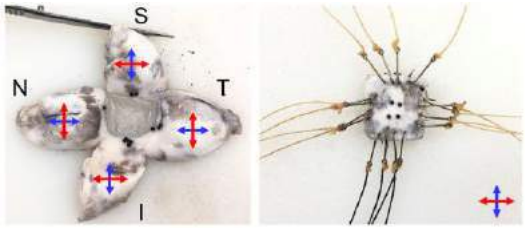


**Figure 2: (Left) Example of a dissected eye with cornea in the center and the four quadrants labeled. (Right) Example of a sample with hooks attached for biaxial testing.**

*Polarized light microscopy*. Four samples from three eyes were cryosectioned into 30-µm-thick sections. Sections were imaged using polarized light microscopy and collagen fiber orientations determined using a previously reported technique (**Figure 3**) [2]. Orientation maps were stacked, registered and analyzed to determine the fiber orientation distributions and the preferred orientation of each sample.

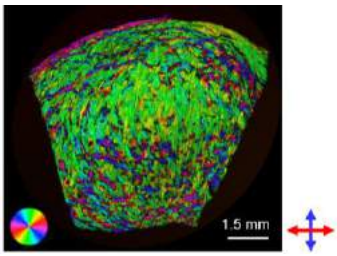


**Figure 3: Example orientation map of a section from the temporal quadrant obtained by polarized light microscopy. Colors indicate the orientations of fibers as shown in the color wheel.**

## RESULTS

Biaxial tensile testing showed that the superior and inferior quadrants had the highest anisotropy (**Figure 4, Left column**), with much higher stiffness along the circumferential direction (red) than along the meridional direction (blue). Microstructural analysis showed that all four quadrants were highly anisotropic (**Figure 4, Right column**), with clearly preferred fiber orientations in the meridional direction (or nearly meridional in the inferior quadrant).

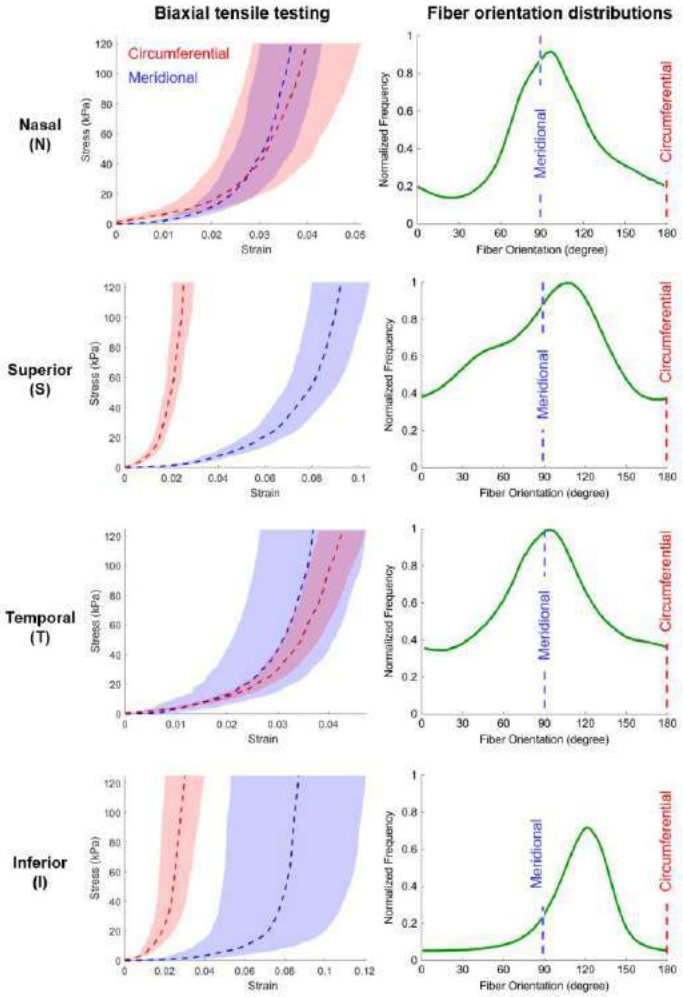


**Figure 4: (Left) Average stress-strain responses (N = 5) along circumferential and meridional directions as measured by the biaxial tensile testing. Shaded regions are standard error of the mean. (Right) Fiber orientation distributions obtained using polarized light microscopy of four samples.**

## DISCUSSION

The equatorial sclera is central to overall globe mechanics. Our goal was to quantify its mechanical and microstructural anisotropy. The superior and inferior quadrants of equatorial sclera were consistently mechanically anisotropic: stiffer in the circumferential direction. All four quadrants of equatorial sclera were microstructurally anisotropic: collagen fibers primarily oriented in the meridional direction. Altogether, the results show that equatorial sclera anisotropy did not concur with the primary collagen fiber orientations. Below we discuss the findings.

A sclera that is softer in the meridional direction may steer the eye to respond to loads by elongating longitudinally (or anteriorly-posteriorly), without increasing the equatorial diameter. This is consistent with previous MRI observations that the equatorial diameter of sheep eyes did not change as intraocular pressure increased from 0 to 40 mmHg [4]. This finding may relate to the mechanisms underlying myopia, in which the sclera undergoes a large degree of permanent stretching along the longitudinal axis [5].

The nasal, superior, and temporal quadrants had fibers clearly oriented in the meridional direction. In the inferior quadrant, the primary orientation was shifted about 30º, but it was still closer in orientation to meridional than circumferential. The inferior quadrant had the highest anisotropy. Despite variability section by section, overall orientation distributions were smooth and unimodal.

It was unexpected to find that the equatorial sclera mechanical anisotropy did not concur with the primary collagen fiber orientations. The contrast was most evident in the superior and inferior quadrants, but in all quadrants, there were clear differences. The origin for the observed discrepancy remains unknown. It may be that not all collagen fibers are equally stiff. For instance, it is possible that the collagen fibers in the meridional direction are more compliant than those in the circumferential direction. This could be if they are more crimped, and thus recruiting only at higher levels of stretch. The meridional fibers may also be more compliant if they are thinner or sparser, yet have a similar birefringence. Further analysis of the biaxial tests and of the orientation maps, including higher resolution imaging to measure fiber crimp, is necessary to identify the origin of the differences.

It is important to consider that we have only analyzed four of the tested quadrant samples so far, and it is unknown how common the discrepancy is. Nevertheless, we posit that a discrepancy between mechanical and microstructural anisotropy is potentially crucial even if it only occurs sporadically.

In summary, we quantified the mechanical and microstructural anisotropies of equatorial sclera. Quantitative anisotropy data is essential to understand the eye and to build accurate models. Further work to understand the origin of the apparent discrepancy between mechanics and microstructure is thus of great importance.

## ACKNOWLEDGEMENTS

This work was supported by National Institutes of Health R01-EY023966, R01-EY028662, P30-EY008098, and T32-EY017271; National Science Foundation (NSF CAREER 2049088); Eye and Ear Foundation (Pittsburgh, PA); Research to Prevent Blindness; BrightFocus Foundation; and Hillman exploratory grant.

## REFERENCES

[1] Boote, C et al., *Prog Retin Eye Res*, 74: 100773, 2020.
[2] Jan, NJ et al., *Invest Ophthalmol Vis Sci*, 58: 735-744, 2017.
[3] Salinas, SD et al., *J Biomech*, 98: 109462, 2020.
[4] Voorhees, AP et al., *Exp Eye Res*, 160: 85-95, 2017.
[5] Grytz, R et al., *Curr Opin Biomed Eng*, 15: 40-50, 2020.

SB³C2022
Summer Biomechanics, Bioengineering and Biotransport Conference
June 20-23, Eastern Shore, MD, USA

# REGIONAL MAXIMUM PRINCIPAL STRAIN RESPONSE OF AN ANATOMICALLY ACCURATE FINITE ELEMENT HUMAN BRAIN MODEL

**Tyler F. Rooks, Jamie L. Baisden, Narayan Yoganandan**

Department of Neurosurgery
Medical College of Wisconsin
8701 Watertown Plank Road
Milwaukee, WI 53226

## INTRODUCTION

Brain sensitivity to loading direction has been shown in animal [1–3] and finite element (FE) modeling [4–6] studies with increased susceptibility to injury (animals) and higher global strain responses (FE) for lateral than frontal impact. Additionally, computational models have shown that brain strains are dependent on the impact direction due to the involvement of the falx cerebri [7]. As the falx splits the brain laterally, it is not expected to influence anterior/posterior motion of the brain as much as lateral motion. This study was based on the hypothesis that strains increase, albeit nonuniformly, in all regions in lateral impact compared to frontal impact. The objective of the study was to determine the regional strains under both impact conditions to test the hypothesis.

## METHODS

The Medical College of Wisconsin-USAARL Head Impact Model (MUHIM) is a newly developed, anatomically accurate FE human brain model. The SIMon model was used as the baseline. Its solid elements were split into 8 equally sized elements and all shell elements were split into 4 equally sized elements, while maintaining the remaining element definitions. The refined mesh was overlaid with anatomical reference shells extracted from the *fsaverage* template [8]. Elements within the refined mesh corresponding to the reference anatomy were manually selected to create components defining the brain regions in the new model. In addition to the *fsaverage* template, the anatomical region location, volume, and shape were reviewed with a neurosurgeon. Upon review, the model was further refined to define the hypothalamus and midbrain structures, not segmented in the original *fsaverage* template. Anatomic regions of interest included the cerebrum grey matter, cerebrum white matter, corpus callosum, basal ganglia, pallidum, thalamus, midbrain, hypothalamus, hippocampus, amygdala, brain stem, and cerebellum. Additional structures included were the falx, tentorium, foramen magnum, meninges, cerebral spinal fluid, bridging veins, a rigid skull, and the 3rd, 4th, and lateral ventricles. Material properties were obtained from literature [9]. A summary is included in Table 1.

**Table 1: Summary of MUHIM material properties.**

| | Density (kg/m^3) | Bulk (GPa) | $G_0$ (GPa) | $G_\infty$ (GPa) | beta |
|---|---|---|---|---|---|
| **Corpus callosum / white matter** | 1060 | 0.2 | 3.75E-6 | 7.5e-7 | 0.2 |
| **Basal Ganglia / pallidum / hypothalamus / thalamus / cerebellum** | 1060 | 0.2 | 3e-6 | 6e-7 | 0.2 |
| **Grey matter / hippocampus / amygdala** | 1060 | 0.2 | 6e-6 | 6e-7 | 0.2 |
| **Brain stem / midbrain** | 1060 | 0.2 | 6e-6 | 1.2E-6 | 0.2 |
| **Ventricles / CSF** | 1040 | 0.2 | 5e-7 | 1e-7 | 0.2 |

The MUHIM model was driven using data from our laboratory experiments. Tests were performed with a rigid arm pendulum striking a helmeted head-neck system. The headform used for all tests was the Facial and Ocular CountermeasUres for Safety (FOCUS) headform [10]. The headform is an anthropomorphic test device (ATD) based on the anthropometry representative of male military aviators. The FOCUS headform was mounted to a H-III neck and fitted with an Advanced

Combat Helmet (ACH) for all tests. The Frankfurt plane of the head was maintained in a horizontal position for all tests. Impacts from tests conducted at two sites around the helmet, front, and left side, at a velocity of 6 m/s was used in the present modeling study.

The model was run using LS-DYNA (Livermore Software Technology Corporation, Livermore, CA). The 95th percentile of the Maximum Principal Strain (MPS) for each brain region was calculated for both exposure directions. Percent differences were calculated between the frontal and lateral loading directions.

## RESULTS

Regional MPS (rMPS) ranged from 0.14 to 0.36 for frontal and from 0.20 to 0.51 for lateral impacts (Figure 1). Percent difference in rMPS (Figure 2) between frontal and lateral impacts ranged from 0.4% (for the right Thalamus) to 59% (for the left cerebellum). Several brain regions responded with decreased rMPS for lateral impacts versus frontal (hippocampus: 8% and 46% reduction in the left and right hemispheres; grey Matter: 20% and 4% reduction in the left and right hemispheres; and amygdala: 4% reduction in the right hemisphere). The percent difference between the left and right hemisphere regions for frontal test was between -3% and 3%, while the percent difference between the left and right hemisphere regions for the lateral test was between -23% and 28%.

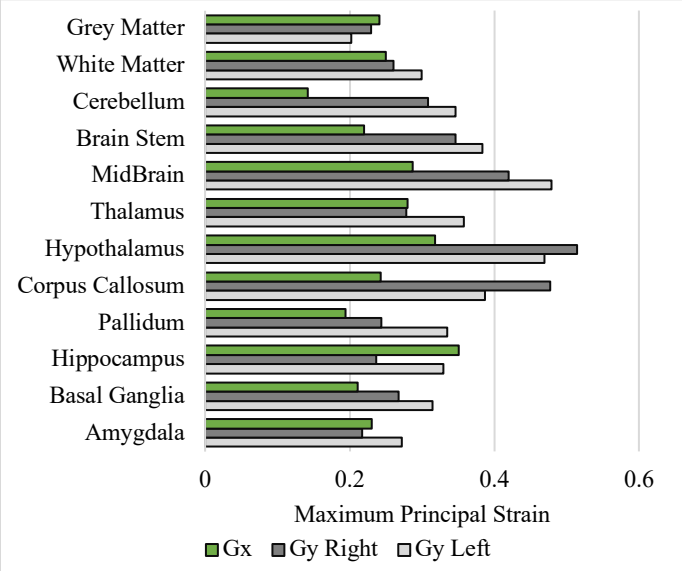


**Figure 1: Regional Maximum Principal Strain Response for the Frontal (Gx) test compared with the Lateral (Gy) test. Frontal (Gx) results are shown as the average of the left and right hemispheres.**

## DISCUSSION

These results showed a sensitivity of the human brain to loading direction. Further, not all regions showed increased MPS for the lateral versus frontal impact conditions. These results highlight the variability in the sensitivity for each brain region to impact direction. The reduction in MPS and the variability between the two hemispheres was unexpected and is under further investigation with additional impact severities and directions. Similar results with the MUHIM model have been seen previously in the regional CSDM response [11].

It is well known that neural functions are related to anatomical structures (e.g., hippocampus for memory, corpus callosum for interhemispheric communication, and basal ganglia and cerebellum for motor control). Understanding the regional response of the brain is important for an improved understanding of brain injury as well as informing clinicians of expected symptoms based on the damaged region. It may also assist in the development of advanced injury criteria for impact-induced brain injuries and applicable to sports and military environments.

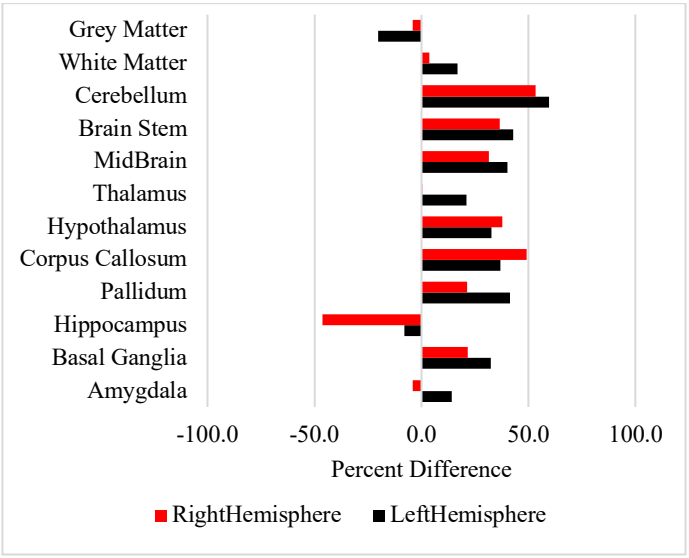


**Figure 2: Percent difference in regional Maximum Principal Strain Response between the lateral (Gy) and frontal (Gx) tests for the left (black) and right (red) hemispheres.**


## ACKNOWLEDGEMENTS

This work was supported by the Office of the Assistant Secretary of Defense for Health Affairs, through the Broad Agency Announcement under Award No. W81XWH-16-1-0010. The opinions, interpretations, conclusions, and recommendations are those of the authors and are not necessarily endorsed by the Department of Defense or other sponsors. The authors would like to thank the experimental and computational modeling teams at the Medical College of Wisconsin for their assistance with the work presented. Additionally, the authors would like to thank Dr. Carol Chancey of the U.S. Army Aeromedical Research Laboratory for her support of this work.


## REFERENCES


[1] Atlan, LS., et al., *J. Neurosci. Res.,* 2018.
[2] Gennarelli, T. A., et al., *SAE Transaction*., 1987.
[3] Sullivan, S., et al., *Biomech. Model. Mechanobiol*., 2015.
[4] Bian, K., and Mao, H., *Biomech. Model. Mechanobiol*, 2020.
[5] Elkin, B. S., et al., *Clin. Biomech*., 2019.
[6] Weaver, A. A., et al., *Ann. Biomed. Eng.*, 2012.
[7] Hernandez, F., et al., *Biomech. Model. Mechanobiol,* 2019.
[8] Fischl, B., *NeuroImage*, 2012.
[9] Mao, H., et al., J. *Biomech. Eng.* , 2013
[10] Crowley, J. S., et al., *Aviat. Space Environ. Med.* , 2009.
[11] Rooks, T.F., et al., *IMECE Proceedings*, 2021

# COMMUNITY BASED CAPSTONE DESIGN PROJECTS AT THE UNIVERSITY OF SOUTH FLORIA (USF)

**Stephanie L. Carey (1,2), Stephen Sundarrao (1), Rajiv Dubey (1)**

(1) Department of Mechanical Engineering, University of South Florida, Tampa, FL USA
(2) Department of Medical Engineering, University of South Florida, Tampa, FL USA

## INTRODUCTION

The Accreditation Board for Engineering and Technology (ABET) adopted a new definition for engineering design that went into effect with the 2019-2020 evaluation cycle[1]. The required student outcomes include an ability to 1) apply engineering design to produce solutions, 2) communicate effectively, and 3) recognize ethical and professional responsibilities in engineering situations. Recent articles suggest implementing industry engagement and real-world projects to meet the ABET requirements for engineering design[1]. The Capstone Design course in the Department of Mechanical Engineering at the University of South Florida (USF) meets these ABET student outcomes. The course has used real-world assistive design projects informally for over 15 years,[2-3] but has recently implemented a formal community-based engagement to motivate engineering students and increase soft skills such as communication, organization, collaboration, and critical thinking.

## METHODS

The community at USF includes local companies, government agencies such as the VA and NASA, nonprofit organizations that help the elderly and wounded warriors, and a vibrant interdisciplinary, innovative team on the academic campus. The Capstone Course at USF has two primary instructors and a liaison to assist with community engagement. Before the start of the semester, the liaison reaches out to the community to recruit real world-based projects. Potential community partners fill out a form that includes a project description, problem/need, design considerations, desired student skills, acceptable solutions or deliverables, and technical contact. This form also helps to set expectations and deliverables. At the beginning of the course, student teams are given options for real-world projects or create their topic within their group. Student teams communicate with their community contact to discuss and negotiate design considerations, budgets, expectations, and acceptable deliverables within the academic time frame. Before graduation, it gives students direct contact with possible users, manufacturers, or designers.

The real-world design projects give students a chance to recognize ethical and professional responsibilities in engineering situations. Student teams write a report and present the final design, a Solidworks and 3D printed model, a prototype, or a working product that is often delivered to the community partner representative. The community partners are invited to attend the presentations in person or via online streaming and ask questions and give comments.

## RESULTS

Students are engaged with various types of partners and motivated by the real-world application of designs and working with experts in multiple fields, as explained in the following example projects.

### Industry Partners

There are companies within the community that need well-skilled engineers. These companies may hire interns, which helps with hiring and recruitment. The Capstone Design course is another opportunity for companies to inform engineering students about their company and share the skills required to be a successful engineer. At USF, the community liaison for this course solicits projects from companies by tapping into the USF engineering alumni pool and engaging with the members of the Advisory Board. Companies such as General Electric, Top End, Jormac Aerospace, Tampa Electric, Sun Hydraulics, JTD Enterprises, and Jabil have sponsored student design projects at USF. Nearby tourist locations such as Busch Gardens, the Lowry Park Zoo, and the Victory Ship have also proposed design projects. Students seem motivated by completing these projects that are used around the community. A student design team worked with a local company, JTD Enterprises, to improve the efficiency of filling ballast bags used for sonobuoys often used by the U.S. Navy. The engineering students designed and fabricated a vibratory table

that helps with the dispersion of the ballast bag filler material and assists in the zip tying of the bags. The students delivered the product to the company CEO. This project also exposed students to the manufacturing chain in this case: the filler material company to the ballast bag filling company to the sonobuoy company to the U.S. Navy

### Government Agencies and Nonprofit Organizations

Government agencies such as the National Science Foundation (NSF) and NASA often deploy student design competitions that may be relevant and appropriate for a Capstone Design project. These contests come with design criteria, expectations, and acceptable deliverables already in place. These contests are often motivating to the students for their real-world nature and their competitiveness. Top teams may be rewarded with a trip to a NASA center, a visit with an astronaut, or a chance to travel to a conference to disseminate the results of their design project. Figure 1 shows a USF team awarded top honors at a NASA competition. The Tampa Bay area also has a large military and Veteran population. The recently formed Institute of Applied Engineering (IAE) at USF has agreements with SOFWERX, a venue operated under an agreement between the United States Special Operations Command (USSOCOM) and DefenseWERX. With these new collaborations in place, the Capstone Design students will soon have military-type design projects to tackle. The James A. Haley Tampa VA hospital is located across the USF's main Tampa campus. The collaboration with the Tampa VA generates design projects in the assistive technology and rehabilitation engineering realm.

**Figure 1: USF engineering students design a rock sampling device for NASA's competition**

Nonprofit organizations may also have design projects appropriate for Capstone Design students. Although these organizations may not have the funds to financially sponsor a project directly, they may have donors willing to provide financial assistance if required for the project budget. The Shriners Hospital for Children in Tampa has provided projects for teams such as a prosthetic knee for pediatric patients learning to walk and a prosthetic hand to play the violin.

### Campus Partners and Alumni

The rehabilitation engineers at the Center for Assistive, Rehabilitation & Robotics Technologies (CARRT) at USF often identify specific assistive device needs in the community to improve the lives of local persons with disabilities[2,3]. The Capstone Design course also receives projects from other departments and investigators on campus. Examples include a dance chair and an omnidirectional platform for the USF School of Theatre and Dance. Engineering students have designed a temperature sensor and a prosthetic kayak hand in collaboration with the USF School of Physical Therapy.

Recent graduates are appointed as Teaching Assistants (TA)s for the course as they pursue graduate studies at USF. Their recent experience in the Capstone Design course and having some entry level engineering experience allows the TAs to provide the students unique perspectives on managing projects and overcoming pitfalls. More experienced alumni provide projects, serve as mentors, and guest speak at lectures leading to informative discussions about career pathways and important qualities for a successful job search.

### Individuals

The students or faculty may also come across individuals in the community that have specific, personal, and unique design needs. For example, a team designed a specialized tray attached to a wheelchair for a student's brother with cerebral palsy. Another student designed an all-terrain wheelchair, so his father could visit the beach. A backpack retriever was designed for a student on campus that uses a wheelchair. Figure 2 shows the student design team's handcycle case design for an Army Veteran to transport his handcycle more effectively and safely.

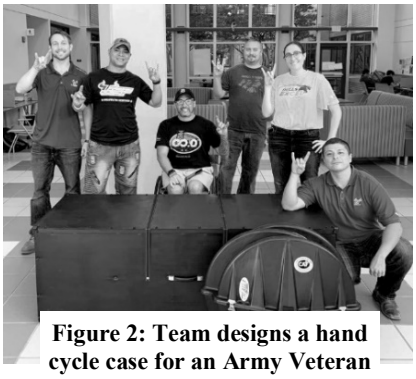

**Figure 2: Team designs a hand cycle case for an Army Veteran**

A recent student design team worked on a wrist hand orthosis that is currently being further developed. A USF employee has requested designs for assistive devices to help her granddaughter with cerebral palsy.

## DISCUSSION

These real-world projects from the community of industry partners, government agencies, nonprofit organizations, alumni and needs on campus inspire students and provide the necessary skills to become successful engineers. Direct collaborations between engineering students and these community partners will be mutually beneficial during the recruitment and hiring process. Anecdotal evidence has shown that student groups are more motivated by community-based projects. It has been seen by the time and care put into the projects and the outcomes.

Although the USF Capstone Design Course team has been informally engaging the community to help with real-world project ideas, a new formal approach will better track and assess the benefits to the students and the community. The project suggestion form is on the various USF websites. Still, there are plans to solicit more community engagement through more in-person meetings such as lab tours and increase the online and social media presence of the student project successes and community needs. The USF College of Engineering also is planning an interdisciplinary approach to these design projects by forming student teams from multiple engineering departments. The student outcomes such as motivation, communication skills, and critical thinking will be tracked and assessed.

## REFERENCES


[1] Fergus JW, "Approaches to Addressing ABET Engineering Design Requirements," *JOM*, Vol 70, No.9, 2018, pp. 1362-1362. https://doi.org/10.1007/s11837-018-3017-7

[2] Dekker D, Sundarrao S, and Dubey R, "Capstone Design and Rehabilitation Engineering: A Great Team," *Capstone Conference*, Boulder, CO June 2007.

[3] Dekker D, Sundarrao S, and Dubey R, "Integrating Rehabilitation Engineering into the Mechanical Engineering Capstone Design Course at the University of South Florida, *Capstone Conference*, Rochester, NY, June 2018.

SB³C2022
Summer Biomechanics, Bioengineering and Biotransport Conference
June 20-23, Eastern Shore, MD, USA

# DEVELOPMENT OF AN IN VITRO EXPERIMENTAL MODEL TO STUDY ENDOTHELIAL DYSFUNCTION FROM COARCTATION OF THE AORTA

**Dylan J. Schock (1), Hilda Martinez Ramirez (1), Joy Lincoln (2,3), Abdel A. Alli (4) and John F. LaDisa Jr. (1,2,3)**

(1) Department of Biomedical Engineering, Marquette University and the Medical College of Wisconsin, Milwaukee, WI, USA
(2) Department of Pediatrics, Medical College of Wisconsin, Wauwatosa, WI, USA
(3) Section of Pediatric Cardiology, Herma Heart Institute, Children's Wisconsin, Wauwatosa, WI, USA
(4) Department of Physiology and Functional Genomics, University of Florida, Gainesville, FL, USA

## INTRODUCTION

Coarctation of the aorta (CoA) is one of the most commonly occurring congenital heart defects (5,000 to 8,000 births annually) and is characterized as the constriction of the descending thoracic aorta[1]. This constriction results in elevated mechanical forces such as blood pressure (BP), wall stress, and strain on the aortic tissue proximal to the coarctation (**Fig 1**). Early surgical intervention is the preferred treatment option due to positive short-term outcomes in restoring normal blood pressure and flow. However, long-term studies of post-operative patients report higher risks of cardiovascular (CV) complications, among the most prevalent being systemic hypertension (HTN)[2].

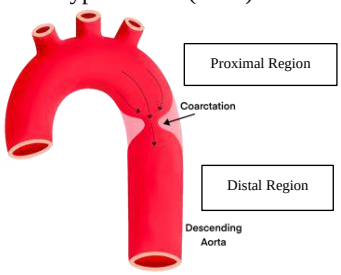


**Figure 1. Coarctation of the aorta (CoA) is characterized by a constriction of the descending thoracic aorta, often near the left subclavian artery. CoA results in altered mechanical stimuli in the region proximal to the coarctation.**

The mechanistic development of HTN associated with CoA is not yet completely understood. Identifying specific mechanisms in humans is difficult due to confounding variables such as age of repair, severity of coarctation, genetic variability, and the presence of other congenital CV defects. Studies done with clinically representative rabbit models of CoA (20 mmHg BP gradient) and treatment have shown that altered endothelial function is associated with pathologic strain and deformation and persists after treatment[3]. Moreover, RNA sequencing of aortic tissue collected from humans with CoA has shown downregulation of natriuretic peptide receptor C (NPR-C; aka NPR3) in the proximal sections exposed to elevated BP[4]. Complimentary microarray analysis of proximal aortic tissue from the in vivo rabbit model showed a similar downregulation of NPR-C in the proximal section[4]. The functional ramifications of altered NPR-C activity have been associated with decreased intracellular calcium concentration ($[Ca^{2+}]_i$) activity in response to application of C-type natriuretic peptide (CNP) in the intact artery sections from the proximal section of the rabbit model. Use of this model to further probe the mechanisms of hypertension from coarctation induced stiffening and endothelial function is not tractable due to the experimental duration and limitations on the long-term usefulness of the tissue ex vivo. The objective of the current work was to develop an in vitro experimental CoA model to study the endothelial dysfunction seen with the previously developed in vivo model by inducing cyclic strain on cultured cells using a mechanically active bioreactor.

## METHODS

Primary human aortic endothelial cells (HAECs) from Cell Biologics were cultured with the manufacture recommended human endothelial cell medium supplemented with 5% fetal bovine serum, 10mL/L of L-Glutamine and Antibiotic-Antimycotic, and 1mL/L of VEGF, HEPARIN, EGF, and FGF. The cultures were maintained in a humidified incubator at 37°C and atmosphere of 5% $CO_2$-95% air. Cells were received frozen at passage 3 and initially seeded onto a T25 cell culture flask where they were passaged in a 1:3 ratio every 5-6 days. All culture flasks were coated with the manufacture recommended Gelatin-Based Coating Solution (Cell Biologics) prior to seeding. At passage 7, the cells were split at a 1:2 ratio onto a T75 culture flask. Once >80% confluent, the cells were either frozen for later experiments or then transferred from a single T75 flask onto a six-well Bioflex plate coated with Collagen I (FlexCell International Corporation). All experiments were conducted at passage 8.

Once >90% confluent, the cultured HAECs in the Bioflex plate were transferred to the FX-6000T Tension System (FlexCell International), which is a pneumatic bioreactor that induces equibiaxial

tension on cultured cells in monoculture. Tension was set to be applied cyclically for twelve hours using a triangular waveform pattern, with a duty cycle of 33% to replicate the physiologic pattern of strain experienced by the aortic wall over a cardiac cycle. Maximum strain conditions were derived from measurements of the CoA rabbit model, with a 12% elongation being the physiologic Control condition and 17% elongation designated as the pathologic CoA condition.

Average HAEC calcium transients ($[Ca^{2+}]_i$) were recorded (n=5 cells/well) during experimentation using an upright Olympus Fluoview FV1000 microscope equipped with Ti:sapphire lasers set to a wavelength of 810nm and imaged with a 25X water-immersion objective lens (XLPL25XWMP, Olympus). Prior to imaging, cells were loaded with Fluo-4AM (3.8uM, Invitrogen) using 0.02% Pluronic acid (Pluronic F-127, Invitrogen) in serum-free media for one-hour. Afterwards, the flexible silicone Bioflex membranes containing the cells were carefully sectioned from the Bioflex plate and pinned down in a silicone-coated 35mm imaging dish containing a $Ca^{2+}$ buffer solution (2mM). Continuous image acquisition settings were set to capture every 1.644s for a maximum duration of 200 frames (328.5s). Upon starting experiments, 30 frames were allowed to pass to establish a baseline intensity. At frame 30, 1.5e-6M of CNP was diluted into the imaging dish. This dose was chosen to balance the response to the agent with cellular toxicity[4].

The HAEC response to CNP application was also quantified after preloading a Control group with 10µM of NPR3-specific inhibitor, M372049 (AstraZeneca)[5], in serum-free media for 45 minutes. The treated media was then replaced with fresh media and loaded into the bioreactor. Tension was induced and the cells were imaged as previously described.

Image stacks were quantified using the Loci tool plugin in Fiji (National Institute of Health). Regions of interest (ROIs) were identified over five different cells and the Measurement option within the Analyze tool was employed to record the mean intensity, among other features to describe intensity distribution and cellular morphology across all frames. The resulting intensities were then normalized to the background and to their respective baselines.

## RESULTS

Preliminary two-photon imaging of the Control HAECs (n=3 six-well plates) after undergoing physiologic in vivo strain conditions reveals a rapid decrease in cytosolic $[Ca^{2+}]_i$ in response to CNP **(Fig 2)**. In comparison, the CoA HAECs (n=3 six-well plates) exposed to pathologic strain conditions show a decreased response to CNP when applied under the same conditions.

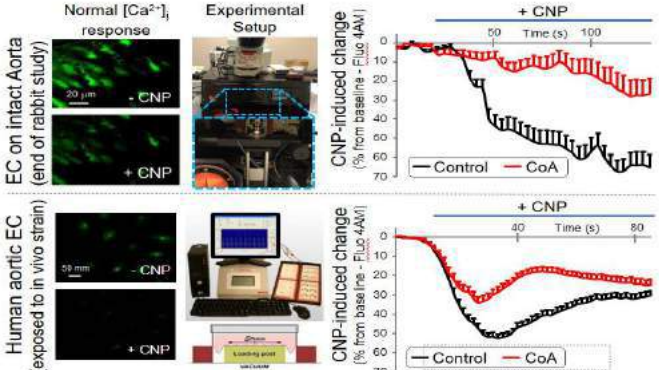


**Figure 2. Preliminary two-photon imaging results of HAECs after undergoing Control and CoA strain conditions and their associated experimental setups. The $[Ca^{2+}]_{in}$ results from the intact artery (in vivo) model are shown for comparison.**

Initial interrogation of Control HAECs (n=3 wells) that have been pretreated with an NPR3 inhibitor reveals that the response to CNP diminishes as compared to the group without the inhibitor (**Fig 3**).

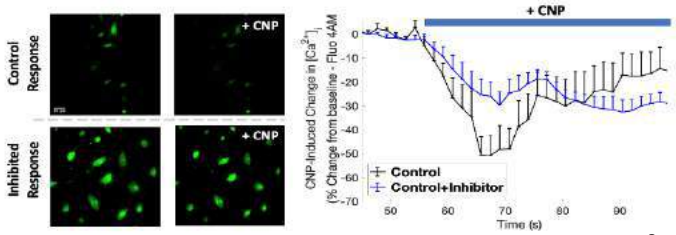


**Figure 3. Comparison of the CNP-induced change in $[Ca^{2+}]_i$ between a Control group and HAECs pretreated with NPR3 inhibitor, M372049 (AstraZeneca)**

## DISCUSSION

The objective of this study was to develop an in vitro experimental model using cultured cells and a mechanically active bioreactor to recapitulate the altered endothelial function that has been shown to develop in a previously established in vivo rabbit model of CoA. Preliminary data shows that when HAECs undergo pathologic levels of cyclical tension their cytosolic $[Ca^{2+}]$ response to CNP diminishes as compared to cells that undergo normotensive strain conditions. This general CNP response between the two strain conditions correlates with the results of the in vivo CoA study (**Fig 2**), suggesting this model's usefulness in recreating the environment and dysfunction of the intact CoA endothelium, however further study is needed to establish the robustness and reproducibility of the model. Current limitations of this study include the small data set, however additional experiments are planned to validate the Control and CoA CNP response as well as more testing with the NPR-C inhibitor to further compliment and validate against the available data from the in vivo model[4]. Furthermore, variable-selection techniques (*i.e.*, machine learning) will be applied to study and correlate specific cellular features that best predict functionally relevant responses to CNP application.


## ACKNOWLEDGEMENTS

The authors acknowledge the support from the National Institutes of Health (NIH) Grant No. R01HL142955.


## REFERENCES


[1] Cohen M, et al. Coarcation of the aorta. Long-term follow-up and prediction of outcome after surgical correction. Circulation. 1989; 80(4):840-5.

[2] Hager A, et al. Coractation Long-term Assessment (COALA): significance of arterial hypertension in a cohort of 404 patients up to 27 years after surgical repair of isolated coarctation of the aorta, even in the absense of restenosis and prosthetic material. J Thorac Cardiovasc Surg. 2007; 134:738-745

[3] Menon A, et al. Altered hemodynamics, endothelial function, and protein expression occur with aortic coarctation and persis after repair. Am J Physiol Heart Circ Physiol. 2012; 303:H1304-H1318

[4] LaDisa JF, et al. Human genotyping and an experimental model reveal NPR-C as a possible contributor to morbidity in coarctation of the aorta. Physiol Genomics. 2019; 51:177-185

[5] Veale CA, et al. The discovery of non-basic atrial natriuretic peptide clearance receptor antagonists. Part 1. Bioorg Med Chem Lett. 2000; 10:1949-1952

# ASSESSMENT OF BLADDER BIOMECHANICS USING MRI

**Juan Pablo Gonzalez-Pereira (1,2), Cody J. Johnson (2), Wade A. Bushman (3), Shane A. Wells (2), Alejandro Roldan-Alzate (1,2,4)**

(1) Mechanical Engineering, University of Wisconsin-Madison, Madison, Wisconsin, United States
(2) Radiology, University of Wisconsin-Madison, Madison, Wisconsin, United States
(3) Urology, University of Wisconsin-Madison, Madison, Wisconsin, United States
(4) Biomedical Engineering, University of Wisconsin-Madison, Madison, Wisconsin, United States

## INTRODUCTION

Lower urinary track symptoms (LUTS) generally progress with age. Existing methods to evaluate the lower urinary tract are invasive and provide limited information. Importantly, these tests do not offer dynamic anatomical evaluation of the lower urinary tract (LUT)[1]– [3] and specifically the bladder. Previous studies have demonstrated that MRI can provide both static and dynamic high fidelity 3D images of the bladder, prostate, and urethra[4]. Therefore, the aim of this study is to implement an MRI urodynamics protocol for the comprehensive assessment of the bladder biomechanics during voiding.

## METHODS

In this HIPAA compliant, IRB-approved study, 5 healthy males and 1 BPH patient were recruited equipped with a condom catheter and instructed to void in the MRI scanner. All scans were completed on a clinical 3T scanner (Premier, GE Healthcare, Waukesha, WI), using a high-density flexible surface coil array (AIR Coil, GE Healthcare). A dynamic acquisition was performed using 3D Differential Subsampling with Cartesian Ordering (DISCO) with a temporal resolution of 3.7 seconds, generating a total of 40 time steps. 15 minutes prior to the MRI scans, 1/3 of a single weight-based dose (0.1 mmol/kg) of gadolinium-based contrast was hand injected intravenously into each subject to enhance the visualization of bladder deformation, volumetric displacement over time, bladder wall thickness, bladder neck funneling, post void residual (PVR) and total voided volume (TVV). Images were imported into MIMICS (Materialise, Leuven, Belgium), where bladder wall and lumen were segmented to obtain 3D renderings of the bladder lumen and bladder wall (Figure 1 and 2). Two critical points during the voiding event were determined from the 3D segmentations, pre-void phase and maximum flow rate phase.

Bladder lumen volumes are then used to calculate volumetric flow rate throughout the voiding event by calculating the volume change over time. Median Bladder wall thickness was calculated by importing the bladder wall segmentation into 3-Matic (Materialise, Leuven, Belgium) and using the "Create Wall Thickness Analysis" tool.

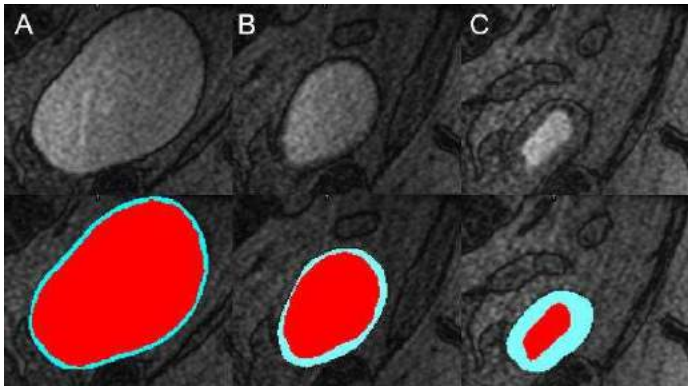


**Figure 1: Sagittal cut of 3D renderings of the wall and lumen of the bladder at the critical points a) pre-void, b) maximum flow rate, c) post-void.**

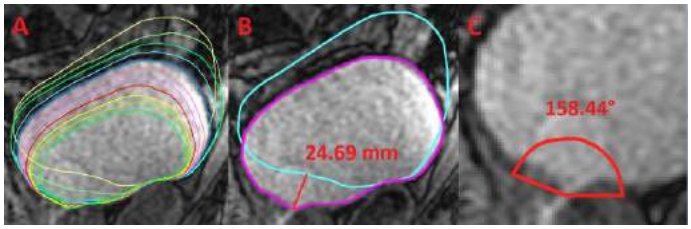


**Figure 2: a) Contour lines of bladder lumen segmentations though the voiding event. b) Bladder emptying prolapse distance and c) EBNA at maximum flow rate for P1.**

Bladder neck funneling was measured with the change of the external bladder neck angle (EBNA). EBNA was taken at all critical points of each voiding event as observed in figure 1c). This angle is measured at the internal urethral sphincter.

Alongside the angle measurements, maximum emptying prolapse was measured as the distance between the lowest internal sphincter to the other internal sphincter locations at the critical points.

## RESULTS

A methodology to evaluate and characterize biomechanics of the bladder during voiding in human subjects was successfully implemented. Figure 3 shows the flow rate and bladder wall thickening for obtained for all 6 subjects.

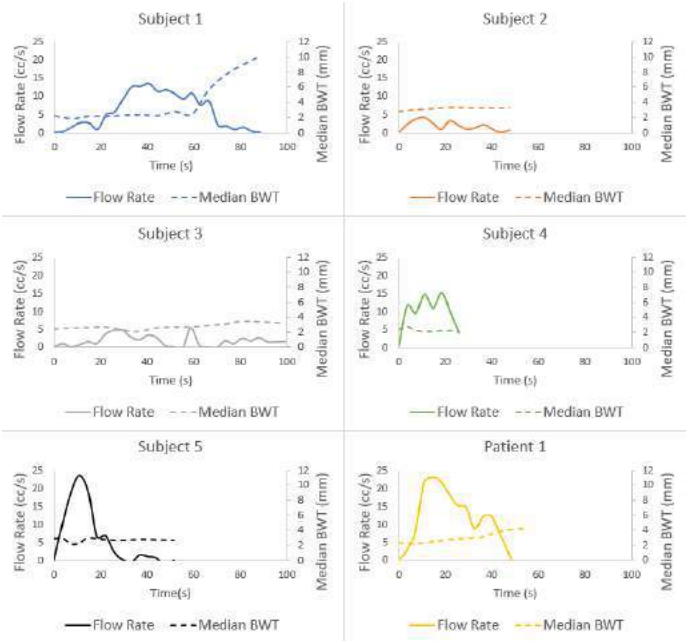


**Figure 3: Flow rates and BWT over the voiding events**

A wide range of voiding rates (Q), voiding times, TVVs, and PVRs were found as shown in Table 1.

| *Subject* | *TVV (ml)* | *PVR (ml)* | $Q_{max}$ *(ml/s)* | $Q_{avg}$ *(ml/s)* |
|---|---|---|---|---|
| ***S1*** | 521.78 | 9.63 | 13.53 | 5.9 |
| ***S2*** | 91.23 | 598.77 | 4.13 | 1.92 |
| ***S3*** | 186.83 | 277.65 | 5.33 | 1.88 |
| ***S4*** | 379.49 | 361.33 | 15.21 | 14.76 |
| ***S5*** | 315.74 | 263.33 | 23.59 | 6.16 |
| ***P1*** | 596.94 | 104.79 | 22.91 | 11.05 |

**Table 1: Calculated bladder micturition metrics**

During the pre-void (resting) phase, all healthy subjects displayed EBNA between 130° and 170°, while P1 had EBNA of 209.98° indicating prostate protrusion. At maximum flow rate, P1 had an EBNA decrease of at least double of any other healthy subject at 51.54°. Subject 2, which voided less than 150 cc and had the lowest flow rate, showed an increase in EBNA between these critical points. Subjects with the highest flow rates show the highest variations in EBNA between pre-void and maximum flow phases. Also observed between pre void and maximum flow was the bladder prolapsing between 3 mm and 25 mm for all 6 subjects.

## DISCUSSION

To our knowledge, biomechanics of the bladder has not been possible to evaluate during a voiding event non-invasively, and current diagnostic methods fail to completely characterize voiding mechanics. This non-invasive, novel MRI–based technique, allows for the quantitative assessment of the bladder during a voiding event. Correspondingly, measurements of volumetric flow rate, BWT, TVV, PVR and EBNA were able to be obtained during these voids. BWT, EBNA and bladder emptying prolapse displayed similar characteristics between subjects. BWT increased significantly only in patients that voided more than 500 cc. EBNA decreased in every patient that voided over 150 cc. EBNA measurements are also affected by prostatic protrusion into the bladder. For bladder emptying prolapse, as flow rate increases, the bladder neck descends towards the lower pelvis to potentially assist the funneling of the bladder neck, favoring the urine flow until it reaches a maximum flow rate. When the flow rate starts to decrease the bladder retracts to its resting position as the void comes to an end. These bladder's emptying prolapse measurements allow us to understand the motion of the bladder as the bladder neck funnels and how adjacent structures like the rectal cavity, lower pelvic muscles and plexi around the bladder behave at critical points during the voiding event.

In our results, flow rates, TVV and PVR varied largely between all 6 subjects. This shows the ability of this novel methodology to characterize diverse bladder biomechanics during any voiding event. For example, subject 2's voided volume wouldn't have qualified for urodynamic studies as it voided less than 150 cc. Nevertheless, our methodology allows us to analyze low volume voids. Appropriately, EBNA shows an increase between pre-void and maximum flow phase, during which the bladder only prolapsed 3 mm. These are characteristics opposite to ones displayed by the other 5 subjects. This proves the necessity for patient specific methodologies to analyze bladder biomechanics.

In summary, MRI is an invaluable imaging modality that can be used to characterize anatomical and functional information of the LUT throughout the voiding cycle in a safe, accurate, and reproducible way. Future advancements in this study will be aimed at using the data acquired to further deepen the comprehension of the bladder voiding events and how they get affected by different diseases.

## ACKNOWLEDGEMENTS

The authors would like to acknowledge GE Healthcare and support from the NIH (R01 DK126850-01).

## REFERENCES

[1] R. Pewowaruk et al., *PLoS ONE*, 15(11), 2020, doi: 10.1371/journal.pone.0238404.

[2] J. S. Engelsgjerd and C. M. Deibert, *Cystoscopy*, 2022nd ed. Treasure Island: StatPearls Publishing;, 2021.

[3] W. Verla et al., *BioMed Research International*, 2019. Hindawi Limited, 2019. Doi: 10.1155/2019/9046430.

[4] L. E. Anzia *et al.*, *Abdominal Radiology*, vol. 46, no. 4, 2021, doi: 10.1007/s00261-020-02808-9.

# THE STRAIN RESPONSE OF THE HUMAN LAMINA CRIBROSA FROM INTRAOCULAR PRESSURE DECREASE

**Cameron A. Czerpak (1), Michael Saheb Kashaf (2), Brandon K. Zimmerman (3), Harry A. Quigley (3), Thao D. Nguyen (1)**

(1) Mechanical Engineering, Johns Hopkins University, Baltimore, MD, United States
(2) Ophthalmology, University of California San Diego, San Diego, CA, United States
(3) Ophthalmology, Johns Hopkins University, Baltimore, MD, United States

## INTRODUCTION

The lamina cribrosa (LC) is a connective tissue that forms part of the eyewall covering the optic nerve head (ONH). It is composed of a stack of perforated plates that appears as a network of beams and pores when viewed in the transverse plane. The LC acts as the primary structural support for the axons of the retinal ganglion cells (RGC) exiting the eye, astrocytes, and other glial cells that provides physiological support to the axons [1,2]. Glaucoma is a progressive neurodegenerative disease marked by dysfunction and injury of the RGC axons at the level of the LC. Glaucoma damage is associated with intraocular pressure (IOP), thus it is important to understand the deformation response of the LC to IOP.

Recent advances in ophthalmic imaging using optical coherence tomography (OCT) have allowed researchers to track the motion of structural features *in vivo* in response to changes in IOP [3.4]. However, the motion of structural features, such as change in the anterior LC depth (ALD), may not predict the strain response of the LC. We previously measured the change in ALD to an IOP decrease from trabeculectomy and found that the anterior LC surface could move either into the eye (anterior) or outward (posterior) [3].

More recently, our group developed a method using digital volume correlation (DVC) to accurately calculate the strain field in OCT images [5]. We acquired 24 radial OCT scans of patients immediately before and 20 minutes after laser suturelysis surgery after trabeculectomy, and applied DVC to correlate the natural speckle patterns of the two image pairs to calculate the three-dimensional strain field in visible LC volume [5]. We estimated the baseline and displacement correlation errors and found that on average, the baseline and correlation errors for the displacement components were less than 0.25 pixels and the average error for all the strain components was less than 0.37%. In this study, we applied the method to measure the strain response and ALD change response in the LC from IOP decrease after suturelysis surgery. We analyzed for possible correlations between the ALD and the strain components. We also evaluated whether the degree of glaucoma damage was related to the change in ALD or strain responses.

## METHODS

Twenty-nine suturelysis procedures were performed on 27 eyes from 26 patients. The average age was 67.7 +/-8.5 years old with an average IOP decrease of 11.9+/- 8.9 mmHg and mean deviation (MD) range of -0.17 to -29.2 dB.

Twenty-four radial scans by spectral domain, optical coherence tomography (SD-OCT) of the optic nerve were captured using Heidelberg Spectralis (Heidelberg, Germany, Heidelberg Engineering) immediately before and 20 minutes after suturelysis laser surgery [5]. IOP was measured using the iCare rebound tonometer right before each set of imaging. The contrast of the images was enhanced using contrast limited adaptive histogram equational (CLAHE) and Gamma correction was used to reduce noise in areas with low signal (Fig. 1). The anterior lamina surface and Bruch's membrane opening were marked manually on each radial scan, and a parallel curve was drawn 250 μm posterior to the anterior lamina surface to segment the anterior portion of the LC.

DVC was applied to correlate the natural speckle patterns of the OCT images taken before and after suturelysis to calculate

the strains caused by the decrease in the intraocular pressure (Fig. 1). Linear regression was used to analyze for relationships between the tissue-averaged ALD and the strain components; between the strains/ALD and the IOP, between strains/ALD and functional measurements of glaucoma severity, i.e. MD and visual field index (VFI), and structural measurements of glaucoma severity, i.e., retinal nerve fiber layer (RNFL) thickness. The strain components, ALD, and RNFL thickness were also averaged in the 4 quadrants (nasal, temporal, inferior, superior) of the LC to analyze for regional variations in the relationship between strain and ALD.

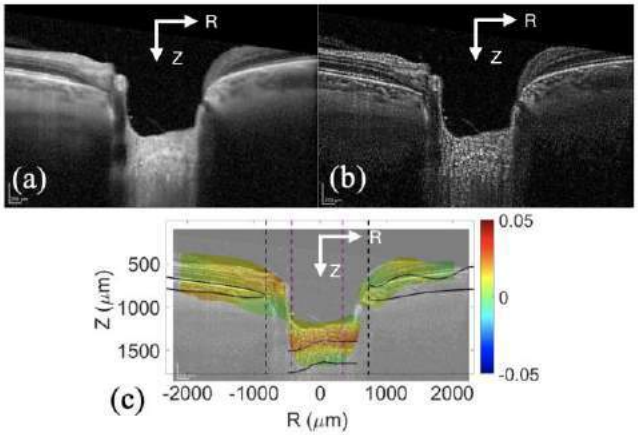


**Figure 1: Slice 1 of a) the original OCT image, b) contrast enhancement, and c) the $E_{max}$ outcome.**

## RESULTS

A larger IOP decrease produced larger tensile strain in the anterior-posterior direction ($E_{zz}$), maximum principal strain ($E_{max}$), and maximum shear strain ($\Gamma_{max}$) ($p<0.01$). The tissue-averaged ALD change ranged from -20 μm to 15 μm and was not statistically significantly different than zero. However, ALD was significantly associated with the torsional shear strain $E_{\theta z}$ ($p=1e\text{-}6$) and $\Gamma_{max}$ ($p=0.01$). A more anterior ALD change produced a larger, more positive $E_{\theta z}$ (clockwise twist) and a larger $\Gamma_{max}$. However, the tissue-averaged ALD was not associated with the normal strain components nor with $E_{max}$. Analyzing the quadrant averages showed a more nuanced relationship between strain and ALD. A more posterior ALD change produced greater $E_{zz}$ and $E_{rr}$ in the clock hours of the nasal quadrant ($p<0.05$). In contrast more anterior ALD change produced greater $E_{max}$ and $\Gamma_{max}$ in the inferior and temporal quadrants, and greater $E_{rr}$ in the inferior quadrant ($p<0.05$).

Compliance of the strain or ALD response was defined as the strain or ALD, respectively, divided by the IOP change. Eyes with a thinner RNFL had a more compliant tissue-averaged $E_{max}$, $\Gamma_{max}$, and $E_{\theta z}$ response to IOP change ($p<0.04$) (Fig. 2a). A more complaint $E_{max}$, $E_{\theta z}$, $E_{rz}$ response was found with worse (more negative) MD ($p<0.05$) (Fig. 2b). Likewise, a more compliant $E_{\theta z}$, and $E_{rz}$ response was associated with worse VFI ($p<0.05$). We also found borderline significant results showing a more compliant $\Gamma_{max}$ response for worse MD ($p=0.08$) and a more compliant $E_{max}$ response for worse VFI ($p=0.08$). A thinner RNFL had a more complaint $E_{max}$ response in the nasal quadrant and a more compliant $\Gamma_{max}$ response in the nasal and inferior quadrants ($p<0.05$).

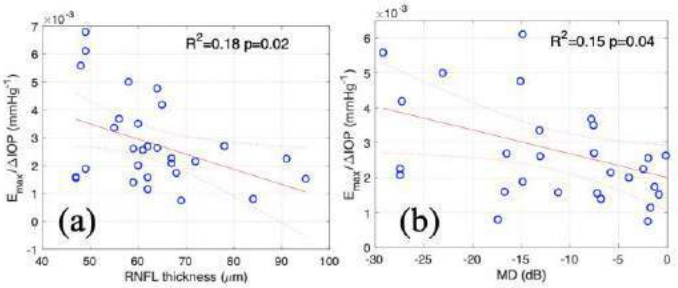


**Figure 2: The relationship between compliance, RNFL, and MD using linear regression. A more compliant $E_{max}$ response was found with a) a thinner RNFL, and b) worse MD.**

## DISCUSSION

IOP decrease produced on average tensile $E_{zz}=0.9\% \pm 1.2\%$ ($p=.0002$), compressive $E_{rr}=-0.2\% \pm 0.3\%$ ($p=.004$), and clockwise twist $E_{\theta z}=0.2\% \pm 0.5\%$ ($p=0.07$). Surprisingly the maximum shear strain $\Gamma_{max}$=5.0% ± 3.4% was larger than the maximum tensile strains $E_{max}$=2.8% ± 2.0%. IOP did not produce a significant average ALD change = $1.33\ \mu m \pm 6\ \mu m$ ($p=0.26$). While the tissue-averaged $E_{zz}$, $E_{max}$ and $\Gamma_{max}$ increased with IOP ($p\leq0.002$), ALD change did not vary significantly with IOP. The average ALD change was predictive of shear strains $E_{\theta z}$ and $\Gamma_{max}$, but not normal strains. However, analyzing quadrant averages, we found significant correlations between the ALD change and normal strains, but the correlations could be positive or negative depending on the quadrant. These results showed the complex relationship between ALD change and the strains.

The LC of eyes with more severe glaucoma damage (thinner RNFL, worse MD, and lower VFI), had a more compliant strain response overall and in the inferior and nasal quadrants. These findings may result from progressive LC remodeling with glaucoma damage into a more curved structure or may represent baseline LC biomechanics prone to damage.


## ACKNOWLEDGEMENTS

Supported by National Institutes of Health Grant EY02120, and National Science Foundation Grant CMMI-1727104


## REFERENCES


[1] Burgoyne, CF et al., Prog Ret Eye Res. 24:39–73, 2005.
[2] Sigal, IA et al., Exp Eye Res. 88:799–807, 2009.
[3] Quigley, H et al., Invest. Opthalmol Vis. Sci. 58, 2566, 2017.
[4] Rhodes LA et al., Invest Ophthalmol Vis Sci. 55:8123–8133, 2014.
[5] Midgett, DE et al., Acta Biomater. 96:385-399, 2019.

SB³C2022
Summer Biomechanics, Bioengineering and Biotransport Conference
June 20-23, Eastern Shore, MD, USA

# DESIGN AND MECHANICAL TESTING OF A SHOULDER-ASSISTIVE EXOSUIT

**Kaleb Burch (1), Cara McKenna (2), Michael McIntire (2), Jill Higginson (1,2)**

(1) Mechanical Engineering, University of Delaware, Newark, DE, USA
(2) Biomedical Engineering, University of Delaware, Newark, DE, USA

## INTRODUCTION

Nearly 800,000 Americans suffer a stroke each year [1], and 66% of these people will consequently experience upper extremity impairments [2]. These impairments often pose consequences such as reduced independence and compromised ability to perform activities of daily living [3].

Prior work has suggested that mechanical assistance can improve post-stroke arm function by increasing reachable workspace and reducing required muscle activity [4,5]. Early assistive devices [4] were stationary and could not assist patients during daily life, but recently wearable assistive devices, or exosuits, have been developed to meet this need while at home and not just in rehabilitation clinics [5-7].

We developed an exosuit that uses a cable to assist shoulder motion. In order to benchmark and optimize device performance, we conducted quasi-static mechanical testing to quantify the cable forces required to lift the arm over a range of flexion angles. Furthermore, theoretical cable forces were estimated by modeling the arm as a pendulum subject to gravity in order to evaluate experimental results.

## METHODS

The exosuit used in this study (Figure 1A&B) was developed using a shoulder brace (ZENKEYZ) with custom 3D-printed cable attachment points sewn in as well as a custom elbow wrap. A cable (braided nylon twine) was affixed to the elbow wrap and routed through the attachment points on the shoulder brace.

In order to evaluate the exosuit, it was placed on a mannequin. We conducted a quasi-static test to quantify cable forces required to lift the arm. Starting with the mannequin arm resting at the side (approximately 0˚ flexion), the cable was slowly pulled to lift the arm to approximately 90˚ flexion, and then slowly released to lower the arm back to 0˚ flexion. During this motion, data was recorded at 2,000 Hz using a load cell (ATO-LC-TC01, 50kg capacity, ATO, Diamond Bar, CA, USA) affixed to the end of the cable (Figure 1A). Retroreflective markers were placed on the mannequin (Figure 1A&B) and on cable attachment points on the exosuit. Motion capture (Oqus, Qualysis AB, Gothenburg, Sweden) was then used to track arm movement and positions of the cable attachment points at a rate of 100 Hz.

Marker positions and load cell forces were lowpass filtered using zero phase shift 4th order Butterworth filters with 6 Hz and 1 Hz cutoff frequencies, respectively.

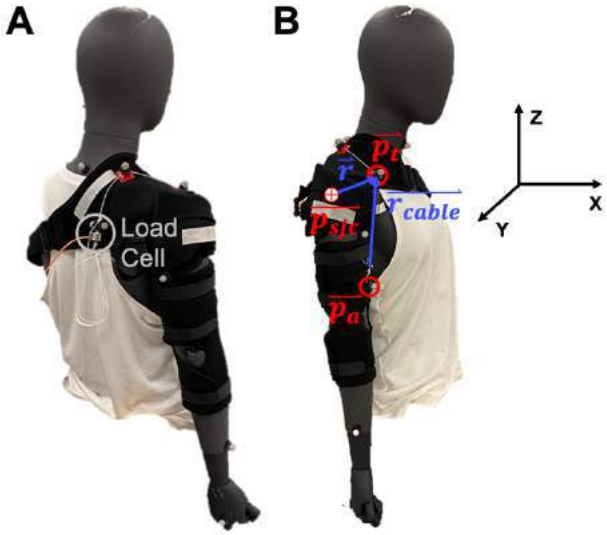


**Figure 1: Back (A) and front (B) view of the experimental test setup of the exosuit placed on the mannequin with markers and load cell attached. Variables used in the model are overlaid, with the positions of attachment points and shoulder joint center in red and vectors between positions shown in blue.**

Inverse kinematics was used to compute shoulder elevation angle based on a model of the arm developed in Visual3D software. Markers on cable attachment points enabled definition of cable position and orientation.

These data were input into a custom MATLAB script which computed theoretical cable forces at each arm position. First, gravitational moment, $M_g$, about the shoulder was computed for each arm position according to equation 1.

$$M_g = mgl_{com}\sin(\theta) \quad (1)$$

In the above equation, $m$ represents arm mass, $g$ represents acceleration due to gravity, $l_{com}$ represents arm center of mass position, and $\theta$ represents flexion angle.

Instantaneous attachment point positions were estimated based on their positions at the beginning of the trial and then simulating their movement assuming they are rigidly fixed to the corresponding bodies. Consequently, $\vec{p}_t$, the position of the attachment point on the torso in Figure 1B, remains fixed in place, while $\vec{p}_a$, the position of the attachment point on the arm in Figure 1B, rotates with the arm. This motion can be computed using $\theta$ to define a rotation, $R_y(\theta)$, about the shoulder joint center $\vec{p}_{sjc}$ according to equation 2:

$$\vec{p}_a = R_y(\theta)\left(\vec{p}_{a,initial} - \vec{p}_{sjc}\right) + \vec{p}_{sjc} \quad (2)$$

Then, the cable moment arm about the shoulder, $\vec{r}_{ma}$, was computed based on positions $\vec{p}_{sjc}$, $\vec{p}_t$, and $\vec{p}_a$, according to equations 3-6.

$$\vec{r}_{cable} = \vec{p}_t - \vec{p}_a \quad (3)$$
$$\vec{r}_{loa} = \vec{r}_{cable}/\|\vec{r}_{cable}\| \quad (4)$$
$$\vec{r} = \vec{p}_t - \vec{p}_{sjc} \quad (5)$$
$$\vec{r}_{ma} = proj_{XZ}(\vec{r}) \times proj_{XZ}(\vec{r}_{loa}) \quad (6)$$

In the above equations, $\vec{r}_{cable}$ represents the orientation of the cable between attachment points (Figure 1B), $\vec{r}_{loa}$ represents the unit vector describing the cable's line of action, $\vec{r}$ represents the vector from the shoulder joint center to the torso attachment point ($\vec{p}_{sjc}$ to $\vec{p}_t$, Figure 1B), and the notation $proj_{XZ}$ indicates a projection onto the XZ plane within which shoulder flexion occurs. Finally, theoretical cable force was computed using equation 7 to solve for the force required to balance the gravitational moment given the magnitude of the cable moment arm, $\|\vec{r}_{ma}\|$.

$$F_c = M_g/\|\vec{r}_{ma}\| \quad (7)$$

## RESULTS

The mechanical testing demonstrated that cable forces up to 91.6 N are required to balance the arm against gravity. This maximum experimental cable force was 2.2 times greater than the theoretical maximum cable force (41.7 N). Flexion angle at maximum force was comparable between theoretical results (96.4˚) and experimental results (90.6˚).

In general, experimental forces were higher than theoretical forces during the elevation phase of the motion (Figure 2). The largest instantaneous cable force error in this phase was 52.8 N. During the descent phase, experimental forces were generally lower than theoretical forces. Furthermore, experimental forces matched theoretical forces more closely during the descent phase at arm angles below 90˚. Experimental forces were within 17.4 N of the tracked theoretical force during this phase of the motion.

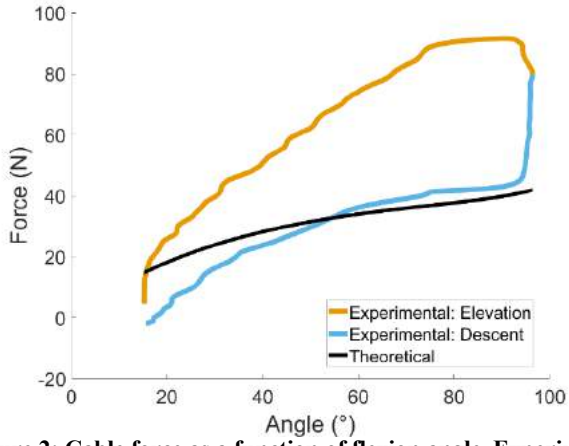


**Figure 2: Cable force as a function of flexion angle. Experimental forces during the elevation phases (before maximum angle has been reached) are shown in orange; experimental forces during the descent phase are shown in blue. Theoretical cable forces are shown in black.**

## DISCUSSION

This study benchmarked cable forces required for a shoulder-assistive exosuit. Required cable forces were larger than predicted to counteract gravitational moments alone, and therefore this basic model requires further development. These discrepancies can be reduced by accounting for friction forces or attachment point movement in the model. Alternatively, these factors can be mitigated by improving the design of the device.

The results of this study were comparable to prior studies. Kesner et al., 2011 developed a cable-driven shoulder-assistive exosuit that required cable forces of approximately 80 N at arm angles near 80˚ to lift a robotic arm with the same mass as the mannequin's arm in this study (1.6kg). The exosuit in this study also exhibited significant hysteresis, similar to prior cable-driven shoulder exosuits [6,7]. This hysteresis is likely due to friction at the cable attachment points.

The choice to conduct mechanical testing on a mannequin posed both benefits and limitations. Benefits of this approach include a repeatable test setup and the ability to restrict arm movement to a single degree of freedom. Limitations of the mannequin include evaluation of only a single body size and shape, not representing the mechanical effect of body tissues interfacing with the exosuit, and not representing the mass of the body.

This study demonstrated that this exosuit exhibits comparable mechanical behavior to prior exosuits. The mechanical performance data measured in this study also provided a reference to guide future design iterations and establish requirements for actuation.


## ACKNOWLEDGEMENTS

UNIDEL Foundation, Inc


## REFERENCES


[1] Benjamin, E et al., *Circulation*, 143(8):254-743, 2021.
[2] Sunderland, A et al., *J. Neurol. Neurosurg. Psych.*, 52(11):1267-1272, 1989.
[3] Lai, S. M. et al., *Stroke*, 33(7):1840-1844, 2002.
[4] Sukal, T M et al., *Exp. Brain Res.*, 183(2): 215-223, 2007.
[5] Simpson, C., et al., *IEEE Trans. on Med. Rob. and Bionics*, 2(3): 474-484, 2020.
[6] Kesner et al., *33rd Ann. Int. Conf. IEEE EMBS*, 8130-8134, 2011.
[7] Asgari et al., *42nd Ann. Int. Conf. IEEE EMBC*, 4926-4929, 2020.

SB³C2022
Summer Biomechanics, Bioengineering and Biotransport Conference
June 20-23, Eastern Shore, MD, USA

# MITRAL VALVE PARAMETERIZATION

**Shelley C. Gooden (1), Mani A. Vannan (2), Konstantinos D. Boudoulas (3), Vinod H. Thourani (2), Pradeep K. Yadav (2), Lakshmi P. Dasi (1)**

(1) Department of Biomedical Engineering, Georgia Institute of Technology, Atlanta, Georgia, US
(2) Marcus Valve Center, Piedmont Heart Institute, Atlanta, Georgia, US
(3) Division of Cardiovascular Medicine, Wexner Medical Center, Columbus, Ohio, US

## INTRODUCTION

The mitral valve is an essential component of the left heart and is composed of an annulus, the anterior and posterior mitral leaflets (AML and PML), chordae tendinea, and two papillary muscles. The PML most commonly shows all three scallops, where the P2 scallop is in the center scallop and the P1 and P3 scallops surround P2. However, anatomical features of the mitral valve vary from patient to patient.

In assessing mitral valve therapies, there is a need to parameterize the mitral valve during diastole for a geometry resembling the human mitral valve that is not patient specific.

Although others have parameterized the mitral valve as a representative model, these models are highly idealized and do not faithfully capture human mitral leaflet morphology [1, 2, 3]. For example, in 2017, Shen et. al. [4] developed a parameterized mitral valve. While key dimensions characterizing the mitral valve model fell within known ranges, the final geometry did not resemble a human mitral valve; the annulus was fully planar, the leaflets were perpendicular to the annulus, and the leaflets were over-simplified as a semi-ellipse lying perpendicular to the annular plane.

The objective of this study is to develop a framework for parameterizing the human mitral valve with a goal of simplifying without over-simplifying.

## METHODS

The mitral valve was segmented using Materialize Mimics in diastole from four patient CT scans with no known mitral lesion, and points were extracted to form the annulus, AML free-edge, and PML free-edge.

Of these, key points for parameterization were selected to define the annulus and leaflets. For the annulus, these points included the two commissures, the center of the anterior annulus, and the center of the posterior annulus.

For the AML, key points included the connection between the AML and PML, the corner of the AML, and the central tip of the AML. For the PML, key points included the connection between the AML and PML, the P1/P3 length, the connection between P1/P3 to P2, the corner of P2, and the P2 length.

Figure 1 shows an example of the mitral valve geometry with overlayed points (red) and key points for measurement (black).

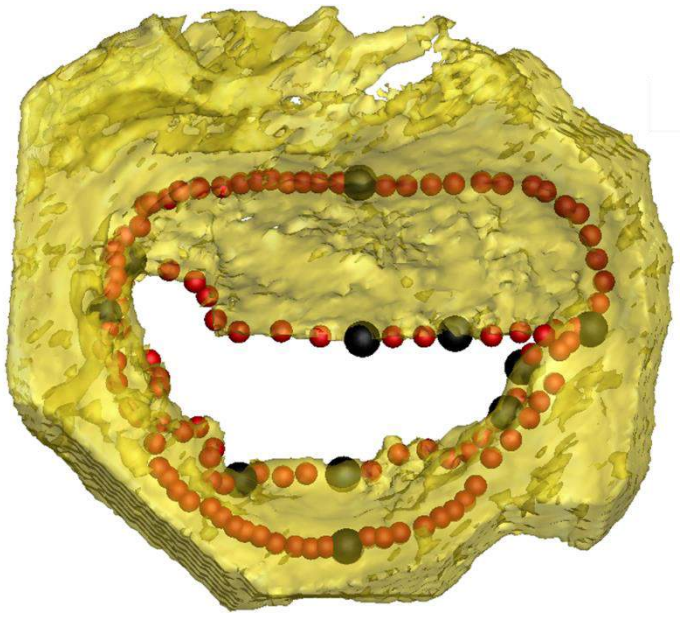

**Figure 1: Mitral Valve Geometry (yellow) with Overlayed Points (red) and Key Points (black)**

To parameterize the valve, the annular commissural and septolateral dimensions as well as the angle between the anterior and posterior annulus segments were calculated, assuming a symmetric valve, and each segment was defined as a partial ellipse. The leaflet free-edge curvature was defined using the Modified Amika interpolation.

## RESULTS

The raw points and parameterized mitral valve points are shown for one patient in Figure 2.

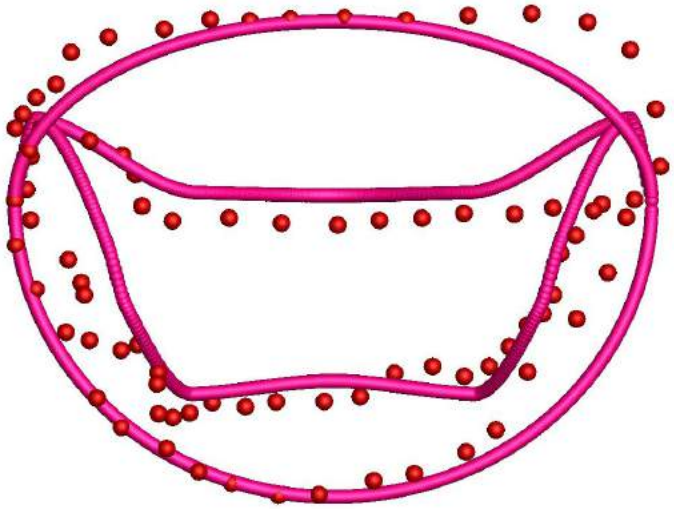

**Figure 2: Raw and Parameterized Mitral Annulus, Anterior Leaflet, and Posterior Leaflet**

To assess the fit of the parameterized model, root mean square error (RMSE) was calculated as in Eq 1, where $p_i - \hat{p}_i$ is the distance between the raw point $p_i$ and the closest parameterized point $\hat{p}_i$.

$$RMSE = \sqrt{\frac{\sum_{i=1}^{N}(p_i - \hat{p}_i)^2}{N}}i \quad (1)$$

RMSE values for each patient are noted in Table 1 for the annulus, AML, and PML.

**Table 1: Root Mean Square Error for Each Patient**

| Patient | Annulus [mm] | Anterior Leaflet [mm] | Posterior Leaflet [mm] |
|---|---|---|---|
| 1 | 1.45 | 2.93 | 1.94 |
| 2 | 1.25 | 4.28 | 4.20 |
| 3 | 1.88 | 4.39 | 6.98 |
| 4 | 2.40 | 4.39 | 2.98 |

RMSE for the annulus was 1.45 mm, 1.25 mm, 1.88 mm, and 2.40 mm for patients 1, 2, 3, and 4, respectively. RMSE for the AML was 2.93 mm, 4.28 mm, 4.39 mm, and 4.39 mm for patients 1, 2, 3, and 4, respectively. RMSE for the PML was 1.94 mm, 4.2 mm, 6.98 mm, and 2.98 mm for patients 1, 2, 3, and 4, respectively.

## DISCUSSION

Looking at the RMSE values, parameterization for the annulus had the best match for each patient compared to the leaflets. The AML and PML had more variability between the patient anatomy and the smoothed geometry, reaching up to 6.98 mm for patient 3's PML. This is likely because the valve was assumed to be symmetric, and the annulus has a simpler, more symmetric geometry while the AML and PML have more asymmetry and variability.

However, deviation of the parameterized geometry and patient geometry is expected because the goal is to parameterize without adding too many points, which would instead lead to recreation of the patients' individual anatomy.

Results from this study expand the current parametric modeling of mitral valves to better incorporate the leaflet free-edge curvature and allow for simplification of the mitral annulus and leaflets while being representative of the patients' anatomy.

Limitations to address in continuing work on this model include that the assumption that the mitral valve is symmetric. The annulus was defined using only four points, and the shape can better match patient geometry if more points were used. Only seven points were used to define the leaflet free-edge curvature, which should be expanded to better capture leaflet features, perhaps with an alternative interpolation function. Lastly, this model focused on the mitral valve and leaflet free-edge and does not yet include curvature of the leaflet belly.

Improvement of this model along with normalization can provide a representative mitral valve geometry for which mitral therapies can be assess, whether by computation simulations or *in vitro* testing.


## ACKNOWLEDGEMENTS

This research was supported by National Institutes of Health (NIH) under Award Number R01HL119824.


## REFERENCES


[1] Kunzelman, K. S. et al., *J Heart Valve Dis*, 3(5):491-496, 1994.
[2] Goode, D. et al., *J Med Eng & Tech*, 44(6):346-353, 2020.
[3] Jolley, M.A. et al., *J Am Soc Echocardiogr*, 30(6):561-571, 2017.
[4] Shen, X et al., *PLOS One*, 12(8):e0183362, 2017.

SB³C2022
Summer Biomechanics, Bioengineering and Biotransport Conference
June 20-23, Eastern Shore, MD, USA

# EFFECT OF SMOOTH MUSCLE TONE AND AGE ON BIAXIAL MECHANICS OF THE MURINE VAGINA

**Shelby White (1), Qinhan Zhou (1), Kristin Miller, Ph.D. (1)**

(1) Biomedical Engineering, Tulane University, New Orleans, Louisiana, USA

## INTRODUCTION

Increased age is associated with higher risk of vaginal tearing during childbirth [1]. While the etiology of the increased risk is not known, remodeling of the vaginal extracellular matrix (ECM) may contribute. The ECM is comprised of collagen and elastic fibers, which provides tensile strength and recoil, respectively. In addition to vaginal contractions, smooth muscle cells (SMCs) provide structural and functional integrity to the vaginal wall. Biaxial extension-inflation protocols are useful tools to evaluate SMC responses, including the baseline contractile potential in the absence of external stimuli (basal tone) as well as the behavior of the vagina without tone wherein the collagen and elastic fibers are the main contributors of the mechanical properties. Towards this end, our prior work showed that vaginal stiffness increases with age [2] and that the 4–6-month murine vagina demonstrates increased stiffness in the absence of SMC tone [3]. However, it is unknown if SMC basal tone contribution changes with reproductive aging, which may be important to delineate potential structural processes that may contribute to increased vaginal tear risk [4]. Therefore, the objective of this study was to quantify the biaxial mechanical properties of the vagina with increasing age and smooth muscle tone. We hypothesized that the vagina materially stiffens in the absence of SMC tone, and with increased reproductive age. Additionally, we hypothesized that the vagina is materially stiffer in the circumferential direction.

## METHODS

A total of n=32 CD-1 mice aged 2-3 months (n=8), 4-6 months (n=8), 7-9 months (n=8), and 10-14 months (n=8) were utilized within this study (Tulane IACUC approved) (Figure 1A) [5]. Mice at estrus were weighed using a digital scale and euthanized via guillotine without anesthesia. Vaginal tissue was dissected from the cervovaginal complex and cannulated onto an extension-inflation device (Danish MyoTechnololgy, Denmark) [3]. The extension-inflation device was filled with active Krebs Ringer Buffer (KRBs), which allowed for smooth muscle cells to maintain contractile function (tone). A water bath heated the KRBs testing media at 37 degrees Celsius throughout the test and aerated the media with 95% oxygen and 5% carbon dioxide to maintain pH near 7.4. The unloaded configuration was identified as previously described, followed by determining the physiologic length wherein the transducer-measured axial force remained constant over an increasing range of pressure [6] (Figure 1B). After a 10-minute equilibration period, the vagina was subjected to cyclic pressure diameter protocols over a range of physiologic pressures (0-15 mmHg) at the physiologic length and about -2% and +2% of the length. Smooth muscle tone was removed by adding 2 mM of a calcium-chelating agent, egtazic acid (EGTA), to the organ bath. The organ was then incubated for 30 minutes. The KRBs solution was replaced with passive KRBs, which does not contain calcium and therefore limited the contractile function of smooth muscle cells. After smooth muscle tone was removed, pressure-diameter testing was then conducted as described above (Figure 1C). The material stiffness in both the circumferential and axial direction were calculated by using the MATLAB polyfit linear function to define the region from the lower physiologic bound (LPB) and upper physiologic pressure boundary (UPB), which corresponded to +/- 1 standard deviation of the physiologic pressure (Figure 1D, Figure 1E). Statistics were performed using R software (version 3.6.2). To ensure normality, Shapiro-Wilks tests were completed for each data set. Separate 3-way ANOVAs (age, direction, tone) evaluated potential differences in the material stiffness and physiologic stress of the vagina in both the circumferential and axial directions. Data reported as mean +/- standard error of mean herein.

## RESULTS

**Material stiffness:** A 3-way ANOVA (age, direction, tone) observed significant differences in material stiffness with respect to age ($p<0.001$) and direction ($p<0.001$). The interaction between age and direction was also statistically significant ($p<0.001$).

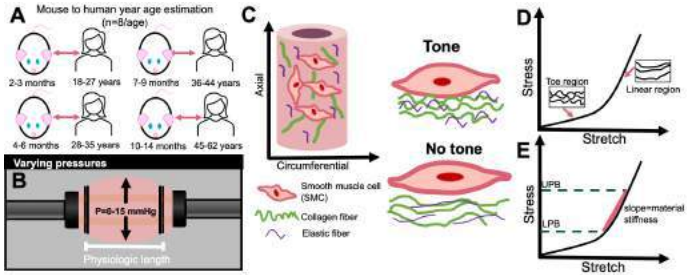


**Figure 1: A total of 32 female CD-1 mice at estrus were used (A; human year age correlations) [5]. Extension-inflation protocols were employed to characterize the vagina with smooth muscle tone (B; basal conditions) and without tone (passive). Further, it was hypothesized that the two conditions will be statistically different due to potential SMC contractile function (C). When SMCs relax (no tone), it was hypothesized that the load during mechanical testing transferred to collagen and elastic fibers and results in subsequent uncrimping or straightening of the fibers. This change in fiber geometry may contribute to material stiffening of the vagina with no tone, which was assessed using stress-stretch curves (D). The material stiffness was determined as the slope between the physiologic pressure range (UPB, LPB), which corresponded to +/- 1 standard deviation of the physiologic pressure (E).**

Post-hoc tests were not performed due to the significant interaction between age and direction. In both the circumferential and axial direction, the material stiffness increased with increased reproductive age (Figure 2A, 2C). Further, the material stiffness was greater in the circumferential direction (Figure 2A) than that of the axial direction (Figure 2C). Smooth muscle tone demonstrated a statistical trend although was not statistically significant (p=0.1). **Physiologic stress**: A 3-way ANOVA (age, direction, tone) identified statistical differences in the physiologic stress with respect to age (p<0.001), tone (p=0.004), and direction (p<0.001). Further, the interaction between age and direction was statistically significant (p<0.001). Post-hoc tests were not performed due to the significant interaction. In both the circumferential and axial direction, the physiologic stress increased with the removal of smooth muscle tone (Figure 2B, 2D). Furthermore, the stress values increased with increased reproductive age.

## DISCUSSION

The contribution of smooth muscle tone to the physiologic stress was statistically significant. Without SMC contraction, the initial load is likely born by collagen fibers, which may result in a decrease of collagen undulation, thus increasing the resistance to loading and subsequent calculated tissue stress in the passive state or the conditions without smooth muscle tone [4]. Further, similar findings were reported in the arterial wall and thought to be the result of smooth muscle cells transferring the load to the fibrous components of the extracellular matrix [4]. Herein, the smooth muscle tone contribution to vaginal material stiffness was identified as a statistical trend. However, a power analysis suggested a sample size of 14 mice would be needed to provide statistical significance for the role of basal tone.

Reproductive age as well as an interaction between age and direction were observed to be statistically significant in the material stiffness and physiologic stress of the vagina. Similarly, our prior work reported that material stiffness in the passive conditions increased with reproductive age [2]. In both conditions, the increased material stiffness may result from changes in the microstructural composition or organization of the vagina with aging. Similar findings were denoted in human cadaveric pelvic floor samples due to accumulation of collagen and advanced glycation end products [7]. To date, changes in the vaginal ECM content and organization that occurs during reproductive aging remain unknown.

Further, direction was observed to be a statistically significant factor for vaginal material stiffness and physiologic stress. This anisotropic behavior may be due to the fibrous ECM components and SMCs organization as well as the direction specific innervations of the vagina [8]. Clark et al detailed that in the C57BL/6 mouse, the elastic fiber area fraction was greater in the axial plane as compared to the circumferential and that collagen fibers were highly aligned towards the circumferential plane [3]. Thus, the vaginal composition likely contributes to the anisotropic characterization, though further work is needed to confirm the vaginal organization in the circumferential and axial planes in the CD-1 mouse.

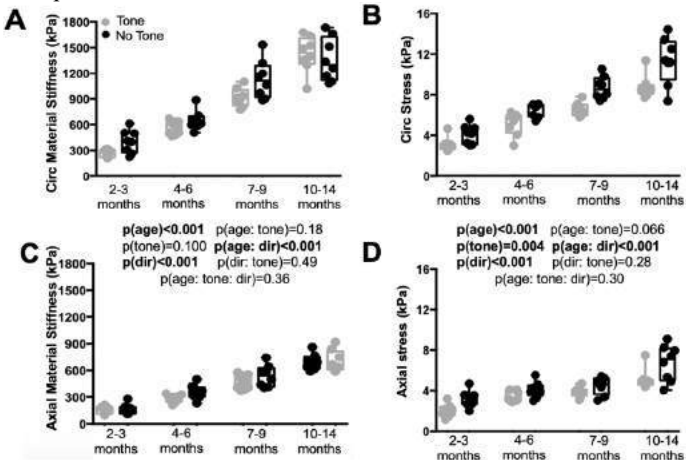


**Figure 2: The material stiffness in the circumferential (A) and axial (C) direction under smooth muscle tone (grey) and no tone (black) conditions for each age group. The 3-way ANOVA (age, direction, tone) observed statistical differences among age (p<0.001), direction (p<0.001), but not tone (p=0.10). Post-hoc analysis was not performed due to significant interactions among age and direction (p<0.001). Additionally, the physiologic stress of the vagina was assessed with tone and without tone in the circumferential (B) and axial direction (D). A 3-way ANOVA (age, direction, tone) observed that age (p<0.001), direction (p<0.001), and tone (p=0.004) were all statistically significant. Post-hoc tests were not performed due to significant interactions (p<0.001) among age and direction.**

**Conclusion**: Characterizing the direction-dependent mechanical properties of the vagina as a function of increasing reproductive age and tone may provide insight to how structural changes alter the functional integrity of the vagina. Future experiments for this study include investigation of how the vagina remodels with age during postpartum healing as well as immunostaining of the vagina to better elucidate the biochemical underpinnings of the biomechanical findings. Such studies are crucial towards developing therapeutics to better aid older mothers during childbirth or other age-related reproductive pathologies.


## ACKNOWLEDGEMENTS

We acknowledge funding from the NSF (CMMI-#1947770; KSM)



**REFERENCES**: [1] Rahmanou et al Am J Obstet 215(4), 2016 [2] White, S et al., *J Biomech* ,2022 (accepted); [3] Clark et al., *Interface Focus*, 9(4), 2019; [4] Kelly and Chowienczy *Cambridge University Press*, 2002 [5] Dutta et al., *Life Sci*, 152, 2016. [6] Akintunde et al*., J Biomech Eng* 2018; [7] Burnett, L et al., Psychol Methods 16(2), 2011

SB³C2022
Summer Biomechanics, Bioengineering and Biotransport Conference
June 20-23, Eastern Shore, MD, USA

# ROLE OF MICROTUBULES IN RIGHT VENTRICLE ANISOTROPIC VISCOELASTICITY WITH PULMONARY HYPERTENSION DEVELOPMENT

**Kristen E. LeBar (1), Wenqiang Liu (2), Kellan Roth (1), Matt Ahern (1,2), Erith Evans (1,2), Jassia Pang (4), Jessica Ayers (4), Adam Chicco (2,3), Zhijie Wang (1,2)**

(1) Department of Mechanical Engineering, Colorado State University, Fort Collins, CO, USA
(2) School of Biomedical Engineering, Colorado State University, Fort Collins, CO, USA
(3) Department of Biomedical Sciences, Colorado State University, Fort Collins, CO, USA
(4) Laboratory Animal Resources, Colorado State University, Fort Collins, CO, USA

## INTRODUCTION

Heart failure (HF) is the leading cause of death in both the US and worldwide. The nonlinear, anisotropic elasticity of the ventricular wall directly impacts the diastolic function [1]. But the ventricle is viscoelastic, which means that two types of resistant forces exist during diastole: elastic and viscous resistance [2]. Viscous resistance originates from the sliding of molecular bonds and works as a 'damper' to cause a delay between the force and deformation, which leads to strain- and time-dependent behavior. However, current studies of ventricular biomechanics mainly focus on the elastic property and the viscous behavior is less known. Moreover, the anisotropic viscoelasticity of right ventricle (RV) has not been studied despite an increasing awareness of the importance of this organ. Therefore, our overall goal was to investigate the viscoelastic behavior of the RV tissue in healthy and diseased states.

Microtubules in the cardiomyocytes (CM) are key elements contributing to myofiber viscoelasticity, and destabilizing microtubules reduces CM viscoelasticity [3,4]. Microtubules are increased in HF progression including the RV failure. However, prior studies investigated CM or myofiber viscoelasticity in 1D, at the cellular level. How exactly the microtubules affect entire tissue's anisotropic viscoelasticity is unclear. The aim of this study was to investigate the role of microtubules in RV anisotropic, viscoelastic behavior in healthy and failing RVs induced by pulmonary hypertension (PH). We hypothesize that the PH leads to increased viscoelasticity of the RV only in the longitudinal direction, and the microtubules contribute significantly in RV tissue elasticity but not viscosity.

## METHODS

All procedures were approved by Colorado State University IACUC. Adult male Sprague-Dawley rats were treated with single monocrotaline (MCT) (60 mg/kg) injection and then housed in normal condition for 3 weeks to induce PH, and intact healthy rats served as control (CTL). RV function was quantified by echocardiography and in vivo pressure-volume (PV) measurements as described previously [5]. After euthanasia, RV free wall, was placed and dissected in cardioplegic solution (CPS) and then placed in a 30mM 2,3-butanedione monoxime (BDM) bath at body temperature (37C) for 30 minutes to remove the active contraction of the myocardium. The RV underwent equibiaxial stress relaxation testing to obtain passive, biaxial viscoelastic behavior of the tissue. The tissue was stretched at 20% of strain and with physiological stretch rates (ramp speeds) of 5 and 8Hz to mimic resting and exercised heart rates, using an in-house biaxial tester. Preconditioning and tissue relaxation were included before and after data collection. The tissue was then treated by colchicine (0.3mM) for 30 minutes and the same mechanical tests were performed. Relaxation modulus and normalized stress at 0.01 s after reaching peak stress were derived to quantify RV elasticity and viscosity, respectively. These methods were established previously [6]. Student t test was performed.

## RESULTS

***RV Failure Establishment in MCT rats***

In vivo RV function measurements showed the development of PH and RV failure in the MCT rats (**Table 1**). Marked RV dilation and decreased fractional shortening confirmed the development of RV failure (n=8/group). PV loop measurements with fewer samples (n=3/group) also implied declines in cardiac output, load-independent contractility (Ees) and ventricular-vascular coupling (Ees/Ea).

***PH led to increased viscoelasticity in longitudinal direction only***

In the intact RVs (at baseline), PH development led to a trend of increased relaxation modulus (**Fig. 1A**) and significantly increased normalized stress (**Fig. 2A**) in the longitudinal direction. There was no change of viscoelasticity in the circumferential direction, though (**Figs. 1B&2B**).

***Colchicine affects RV anisotropic viscoelasticity differently in healthy and failing RVs***

We firstly examined the effect of colchicine on RV elasticity (**Fig. 1**). We observed a significant decrease in elasticity after colchicine treatment in healthy RVs in the longitudinal direction, but not the circumferential direction. In the failing RVs, though, there were significant decreases in elasticity after colchicine treatment in both directions. The percent reduction in elasticity after colchicine treatment was similar between groups and between directions, indicating a similar contribution of microtubules to RV anisotropic elasticity.

Next, we examined the effect of colchicine on RV viscosity (**Fig. 2**). Unexpectedly, we did not observe significant changes in viscosity after colchicine treatment in either group or in either direction, although there was a trend of increasing viscosity in the circumferential direction in the MCT RVs (p=0.07). As a result, the MCT RVs exhibited significantly higher viscosity than CTL RVs after colchicine treatment (**Fig. 2B**). Alternative to the elasticity, the percent changes in viscosity between groups or between directions were marginal and the trends were inconsistent. This suggests an insignificant contribution of microtubules to RV viscosity in both healthy and diseased states.

**Table 1: Function Measurements in Healthy and MCT RVs.**

| **RV Function (Echocardiography)** | **CTL** | **MCT** |
|---|---|---|
| End-Diastolic Diameter (cm) | 0.18 ± 0.03 | 0.30 ± 0.06 * |
| End-Systolic Diameter (cm) | 0.11 ± 0.01 | 0.21 ± 0.05 * |
| Fractional Shortening (%) | 40.11 ± 4.54 | 28.31 ± 9.39 * |
| AT (second) | 0.03±0.002 | 0.02±0.002 * |
| ET (second) | 0.05±0.002 | 0.08±0.006 * |
| AT/ET | 0.68±0.09 | 0.23±0.03 * |
| **RV Function (PV loop)** | **CTL** | **MCT** |
| End-Systolic Pressure (mmHg) | 46.2 ± 6.0 | 74.1 ± 9.1 * |
| End-Diastolic Pressure (mmHg) | 2.4 ± 0.2 | 5.7 ± 1.1 * |
| Cardiac Output (mL/min) | 80.0 ± 5.9 | 48.1± 10.4 * |
| Ea (mmHg/μL) | 0.2 ± 0.01 | 0.5 ± 0.11 |
| Ees (mmHg/μL) | 1.08 ± 0.5 | 0.645 ± 0.1 |
| Ees/Ea | 5.5 ± 2.5 | 1.5 ± 0.5 |

AT: Acceleration Time, ET: Ejection Time, Ea: Effective Arterial Elastance, Ees: End-Systolic Pressure-Volume Relation. *<0.05 vs. control.

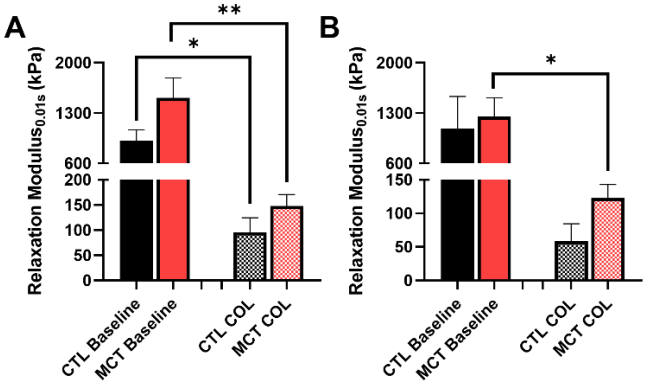


**Fig 1:** Relaxation modulus of CTL and MCT RVs before (baseline) and after colchicine (COL) treatment in the (A) longitudinal direction and (B) circumferential direction. N=4-5 per group. *<0.05, **<0.01.

## DISCUSSION

To our knowledge, this study is the first to quantify passive, anisotropic viscoelasticity of RV tissue by biaxial stress relaxation tests. A critical setting that we applied in the tests is to match the ramp speed to represent the diastolic stretch-rate in the rat species. This protocol will enable us to observe more physiologically relevant viscoelastic behavior of the RV. The equibiaxial mechanical test allows us to obtain anisotropic viscoelastic behavior of the RV, which is impossible for the 1D myocyte or myofiber force-length tension curve measurement.

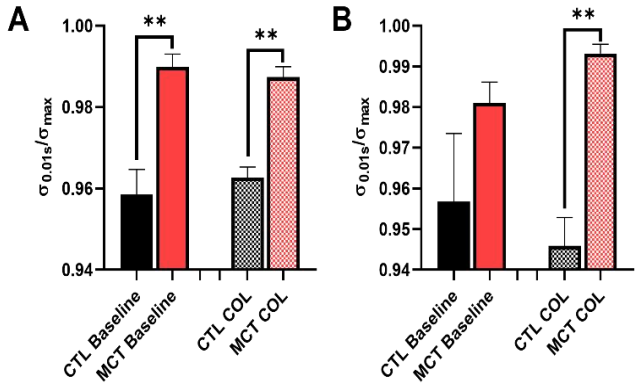


**Fig 2:** Normalized stress of CTL and MCT RVs before (baseline) and after colchicine (COL) treatment in the (A) longitudinal direction, and (B) circumferential direction. N=4-5 per group. *<0.05, **<0.01.

Firstly, we observed that the PH development did not result in equal changes in the viscoelasticity in both directions. Instead, the increases in elasticity and viscosity in the MCT group were more pronounced in the longitudinal direction than the circumferential direction. Like in the discussions on cardiomyocyte hypertrophy, it is yet unclear if the mechanical changes of ventricles are an adaptation or maladaptation of the RV. The implications of anisotropic viscosity in RV function awaits further investigation.

Second, our results from colchicine treatment demonstrated a significant impact of microtubules on RV elasticity but only marginal effect on RV viscosity. In isolated CM studies, it is found that colchicine treatment reduced viscosity and elasticity significantly [3,5], suggesting a role of microtubules in CM viscoelasticity. But the contribution at cell level seems to not translate to the tissue level. Microtubule depolymerization caused no change in healthy RV viscosity but a trend of increased viscosity in the circumferential direction in the failing RV. This suggests that microtubules do not play a major role in RV viscosity at the tissue level. Other components are contributing more greatly to tissue viscosity than cardiomyocytes, especially in diseased RV.

Additionally, our findings suggest that microtubules are contributing significantly to RV tissue elasticity. The marked drop (~90%) in elasticity after colchicine treatment suggests that microtubules (or cardiomyocytes) rather than other components (e.g., titin, collagen) play a major role in RV elasticity. This finding is consistent with prior studies on hyperelastic behavior of myocardium that shows the myofibers are dominant factors in determining tissue stiffness than collagen fibers. Further study with a larger sample size is needed to confirm these findings.

In summary, in this work we measured the anisotropic viscoelastic property of RV in healthy and diseased states. The role of microtubules in these RVs was examined and distinct impacts on elasticity and viscosity were observed. These findings will deepen the understanding of biomechanical mechanism of RV failure.

## REFERENCES

[1] B. GL et al., *Eur. J. Cardiothorac. Surg*, 604– 610 2006.
[2] Caporizzo, M et. al., *Front. Physiol*., 2021.
[3] Caporizzo, M et. al., *Circulation*, 902–915, 2020.
[4] Cooper, G. *Am. J. Phys.*, 1003-1014, 2006.
[5] Schmuck, E.G. et. al., *Am. J. Phys.*, 1005-1013, 2019.
[6] Liu, W. et. al., *Bioengineering.*, 2021.

# OVERSTRETCH-INDUCED SOFTENING IS INDEPENDENT OF STRAIN RATE IN CEREBRAL ARTERIES

**Noah R. Pearson (1), Gregory M. Boiczyk (2), Kenneth L. Monson (1,2)**

(1) Mechanical Engineering, University of Utah, Salt Lake City, UT, USA
(2) Biomedical Engineering, University of Utah, Salt Lake City, UT, USA

## INTRODUCTION

Mechanical damage is common in arteries following both trauma and surgical intervention. This damage is considered to primarily affect the collagen fibers [1], consistent with various histologic examinations demonstrating structural damage in the collagen [2]. We previously characterized mechanical softening following quasi-static (QS) overstretch of cerebral arteries [3] and used a collagen-hybridizing peptide (CHP) [4] to identify denatured tropocollagen following such overstretch [5]. We then predicted the amount of tropocollagen denaturation from mechanical softening data in a continuum damage model [6]. Further, we showed that high strain rate vessel rupture significantly reduces the amount of tropocollagen denaturation relative to QS failures [7].

Similar rate-dependent shifts in tropocollagen damage patterns have been previously observed in tendon (e.g. [8-10]). Furthermore, rate-induced changes in the ratio of fibril to tissue strain have been identified in tendon [11, 12]. These rate-changes in microstructure mechanics have been attributed, in part, to the interfibrillar proteoglycans [12, 13].

Given the apparent rate-dependent shift in collagen damage mechanisms, and the importance of collagen fibers in the mechanical response of arteries, we speculate that the rate of subfailure overstretch may affect the subsequent mechanical response, including softening, of tissue. Additionally, with the theory of interfibrillar proteoglycan damage, we hypothesize that high strain rate overstretch affects the subsequent high-rate response of a vessel more severely than its QS response, and conversely, that QS overstretch softens the subsequent QS response of the tissue more than its high-rate response. In the present work, we characterize the baseline rate-stiffening response of cerebral arteries, overstretch them to various magnitudes over a range of strain rates, and then recharacterize their rate-stiffening baseline response.

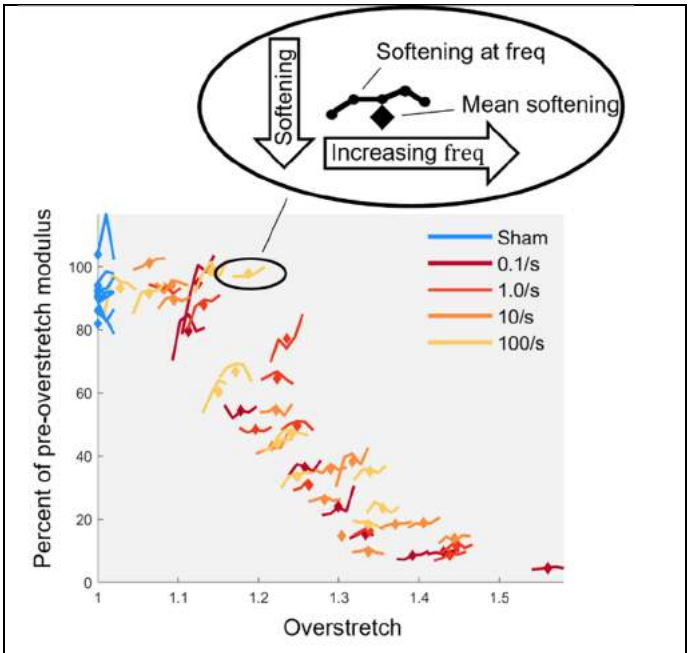


**Figure 1 Softening (characterized as reduction of dynamic modulus) at each characterization frequency as a function of overstretch (x-axis) and overstretch rate (color). For interpretation, each set of data corresponds to one sample. As the accompanying schematic illustrates, if each dataset is likened to a bird, the bird's body represents the mean extent of softening (over all characterization frequencies), while its wings, from left to right, correspond to softening values at increasing characterization frequencies.**

## METHODS

Göttingen minipigs (24-26 weeks old) were euthanized by Beuthanasia under the approval of the University of Utah Animal Care and Use Committee. The brains were removed from the skull, and the middle cerebral arteries (MCAs) were resected from the brain. Side branches were ligated, and rings were cut from either side of the sample and imaged to provide a reference cross-sectional area. Samples were then mounted onto cannulas on the testing apparatus. Vessels were preconditioned by oscillating luminal pressure between 50 and 150 mmHg five times at incrementally increasing axial stretch levels up to the *in vivo* length, defined as the axial stretch where changes in luminal pressure did not change axial force. A final preconditioning cycle was applied at 1.05 times the *in vivo* length.

The baseline rate-stiffening response of the vessels was evaluated using axial stretch cycles conducted at five different frequencies (giving maximum strain rates of 0.1, 0.31, 1.0, 3.1, and 10 $s^{-1}$) around three mean stretch values ($\lambda_{IV}$ = 0.95, 1.00, 1.05). Samples were then overstretched, with a single ramp, at strain rates ranging from 0.1 to 100 $s^{-1}$ to a maximum stretch value ranging from 1.1 to 1.4 times the *in vivo* stretch. Sham vessels were not overstretched. Following overstretch, the rate-stiffening baseline response was recharacterized.

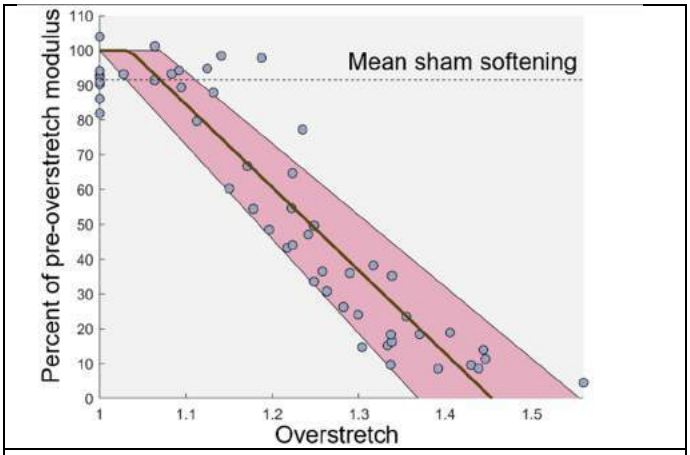


**Figure 2 Mean softening data as a function of overstretch magnitude. A regression line with 95% confidence intervals is plotted over the softening data.**

First Piola-Kirchoff stress was used to define stress, and stretch was calculated as the suture-to-suture stretch ratio. Dynamic modulus at each characterization frequency, calculated as the peak-to-valley stress divided by peak-to-valley strain, was used to define rate-stiffening response. Post-overstretch dynamic moduli were divided by pre-overstretch moduli at corresponding frequencies to quantify softening as a function of overstretch rate, overstretch magnitude, and characterization frequency.

Final overstretch magnitudes did not fall neatly into the targeted bins, preventing the use of discrete statistical techniques such as ANOVA. We thus used linear regression to evaluate the effect of the independent variables on the observed softening in the samples. A p-value assessing the difference between each variable's scaling coefficient and zero was calculated to determine statistical significance.

## RESULTS

As in our previous work, Figure 1 shows a clear pattern of increased softening with overstretch, but we did not find any effect of overstretch rate or characterization frequency on softening. This is presented visually in Figure 1, where softening values are plotted as a function of overstretch, overstretch rate, and characterization frequency. These visual observations are reinforced by the linear regression model, where only the scaling parameters on overstretch and the intercept were significantly different than zero.

Based on these initial observations that overstretch rate and characterization frequency did not affect softening, we performed another linear regression wherein the mean (all frequencies) softening values were predicted entirely by overstretch (Figure 2). In this case, we find good agreement between the overstretch and the amount of softening. We thus conclude that softening is independent of both the rate of overstretch and the rate of characterization.

As noted in Figure 2, sham vessels softened (between the baseline characterization and the recharacterization) to an average of 91.5%, indicating that a certain level of inelasticity was induced by the characterization process.

## DISCUSSION

The objective of this study was to examine the influence of overstretch rate and characterization frequency on extent of cerebral artery softening. Results show that while overstretch influences vessel softening, neither overstretch rate nor characterization frequency does.

These findings run counter to our hypothesis and seem to be inconsistent with the previously identified rate-induced reduction in molecular-level collagen damage [7]. While the implications of this are not yet fully understood, there are several points worthy of discussion. The first is that the present results appear to challenge the effect of tropocollagen denaturation on mechanical softening implied by our previous work with Marino *et al.* [6]. Tropocollagen denaturation may not directly cause softening, though it is clearly correlated with it following QS overstretches. While there is a paucity of research on fibril-to-tissue stretch ratio in arteries, this ratio has been shown to be on the order of 3.75% of the total tissue strain [14]. The collagen fibrils themselves thus do not actually account for much of the global tissue stretch in arteries. The non-collagenous interfibrillar matrix can be expected to contribute substantially to the mechanics of the tissue, perhaps reinforcing our present findings.

The present results also suggest that strain rate may be used as a design parameter to target damage in different parts of the ECM while maintaining the desired softening of the tissue. This could prove to be useful in angioplasty, wherein softening of the vessel is desirable, yet post-intervention inflammation is unwanted.

## ACKNOWLEDGEMENTS

Funding was provided by HJF contract number W81XWH-17-2-0008 and NSF CMMI 2027367.

## REFERENCES

[1] Weisbecker, H. et al., J Biomech, 46(11), pp. 1859-1865, 2013.
[2] Zollikofer, C. et al., 153(2), pp. 369-374, 1984.
[3] Bell, E. D. et al., Front Bioeng Biotechnol, 3(2), p.p. 2, 2015.
[4] Li, Y. et al., PNAS, 109(37), pp. 14767-14772 2012.
[5] Converse, M. I. et al., Acta Biomater, 67, pp. 307-318, 2018.
[6] Marino, M. et al., J Mech Behav Biomed Mater, 97, pp. 254-271, 2019.
[7] Pearson, N. et al., Proc. SB3C, 2020.
[8] Willett, T. L. et al., 35(11), pp. 1961-1972, 2007.
[9] Willett, T. L., et al., J. Orthop. Res., 26(12), pp. 1605-1610, 2008.
[10] Chambers, N. C. et al., J. Orthop. Res., 2018.
[11] Puxkandl, R. et al., Phil. Trans. R. Soc. Lond, 357(1418), pp. 191-197, 2002.
[12] Bonner, T. et al., J Mech Behav Biomed Mater, 41, pp. 261-270, 2015.
[13] Christian Gasser, T., Acta Biomater, 7(6), pp. 2457-2466, 2011.
[14] Schmid, F. et al., J. Synchrotron Radiat., 12(6), pp. 727-733, 2005.

SB³C2022
Summer Biomechanics, Bioengineering and Biotransport Conference
June 20-23, Eastern Shore, MD, USA

# IN-SITU BONE FRACTURE MECHANICS ASSESSED BY 3D-XRAY MICROSCOPY

**G. Gallaway (1), R. K. Surowiec (2, 3), M. R. Allen (2, 3), J. W. Wallace (3), L. J. Pyrak-Nolte (4), T. Siegmund (1)**

(1) School of Mechanical Engineering, Purdue University, West Lafayette, IN, USA
(2) Dept. of Anatomy, Cell Biology & Physiology, Indiana University School of Medicine, Indianapolis, IN, USA
(3) Dept. of Biomedical Engineering, Indiana University Purdue University of Indianapolis, Indianapolis, IN, USA
(4) Department of Physics and Astronomy, Purdue University, West Lafayette, IN, USA

## INTRODUCTION

Age related fractures are an increasing challenge in terms of healthcare costs and quality of life. In this study, a method is described for evaluating fracture mechanics in bone using in-situ three-point bend testing in a 3D X-ray microscope. The microstructure of bone is composed of layers of mineralized collagen fibrils with elongated tubular voids that result in a condition where crack growth deviates from an idealized planar crack. Studies on fracture of human and animal bones have used optical imaging and scanning electron microscopy (SEM) imaging to determine crack length during loading, yet this limits crack measurements to the surface [1]. Bone fractures have also been investigated with synchrotron imaging, yet this requires access to a central beamline which can prove challenging for use with fresh human bone tissue [2]. We investigated an alternative experimental approach that permits in-situ analysis of fracture mechanics by combining loading and imaging. We employed a mechanical loading state (CT5000 Deben) within a 3D X-ray microscope (XRADIA Zeiss). To date, evaluations of post-loading 3D crack geometry with this instrumentation have occurred following loading, but the combination of in-situ loading and imaging applied to cortical human bone has not been previously documented.

## METHODS

Sample Preparation. Human femur bones were obtained from unembalmed cadavers through the Indiana University School of Medicine body donation program. Femurs were kept frozen at -20 ºC until processing. The femurs were cut into 35 mm sections from the diaphysis and then processed into 4 x 4 x 33 mm beams using a low-speed saw under irrigation with Phosphate Buffered Saline (PBS) (Buehler Isomet, Sigma Aldrich). Frozen beams were transported wrapped in PBS-soaked gauze on dry ice for scanning. Beams were stored at -20 ºC; Prior to an experiment, bone tissue was thawed at 4 ºC overnight. Samples were notched by hand using a 0.02 mm thick saw. A pre-crack was created at the root of the notch using a repeated motion with a razor blade. All notching was done under irrigation of 0.2 µm diamond slurry (Buehler).

Loading and Imaging. Beams were kept in PBS-soaked gauze until immediately before testing. A Deben CT5000 displacement-controlled load rig fitted with a three-point bending fixture (Deben UK Ltd) was assembled in a Zeiss XRADIA Versa 510. Bone beams are loaded into the Deben fixture with the notch centered under the middle rod. The system was brought to a 5 N touch load to set all X-ray parameters. Loading was conducted at a displacement rate of 0.1 mm/min with a data sample rate of 100 ms. During loading, 2D through thickness X-ray images were taken in succession at 80 kV, 7 W, with a pixel size of 5 µm, and 1 s exposure time. After crack instability but retaining the applied displacement of the load rig, a 3D X-ray scan of the beam under load was performed with 80 kV, 7 W, with a pixel size of 5 µm, 5 s exposure time, and 2401 projections.

Post-Processing. Images were reconstructed using the XRM Data Explorer, and then exported as tiff files. Fiji was used to analyze all X-ray images [3]. Window leveling techniques with a greyscale threshold intensity, $I$, were used to determine crack tip location. Crack lengths were correlated with load, $F$, and stress intensity factors, $K(a)$, were calculated following ASTM methods [4]. Using the crack extension, $\Delta a = a - a_0$, and stress intensity factor, $K$, crack growth resistance curves, $K(\Delta a)$, are determined. From these plots, the blunting onset, $K_b$, the slope of the blunting line $T_b$, the crack initiation toughness $K_{ini}$, and tearing modulus $T_t$ can be obtained. During blunting, irreversible deformation processes in the tissue cause deformation of the initial (sharp) crack. Tearing occurs when continuous tissue is separated by the crack propagation. 3D image segmentation was conducted in Dragonfly (Object Research Systems); region of interest (ROI) tools were used to segment the crack and analyze geometry. In this abstract, one representative experiment is described; work on a larger number of samples is ongoing.

SB³C2022-360

## RESULTS

Changes in the X-ray attenuation properties of virgin and damaged bone tissue enable visualization of the processes (blunting and material separation) at the crack tip by using changes in the pixel intensity. Figures 1 and 2 contain 2D through thickness X-ray images obtained during the in-situ experiment. 2D X-ray images (Figure 1A-C) taken at several instances during loading visualize an effective, through thickness, crack advance. Differences in X-ray attenuation properties, as void-spaces are formed by fracture propagation, are thereby translated into changes in pixel intensity (Figure 2). This in turn enables the measurement of the crack propagation path within the beam. The resulting crack growth resistance curves (Figure 3) distinctly depict the blunting onset, blunting, crack initiation and tearing: $K_b$=4.9 MPa√m, $T_b$=201 x $10^3$ MPa/√m, $K_{ini}$ = 13.90 MPa√m, and $T_t$=40.2 x $10^3$ MPa/√m. Full details of the crack geometry are obtained from full 3D scans of the specimen while under load. Figure 4 depicts sections of a complete 3D reconstruction of the sample after crack instability but still under load. Image segmentation is used to highlight the crack path. The effective crack path obtained from the 2D x-ray (Figure 2B) is comparable to that of the specimen interior (Figure 4B). Images of the surface (Figures 4A,C) provide only limited information of the effective crack advance.

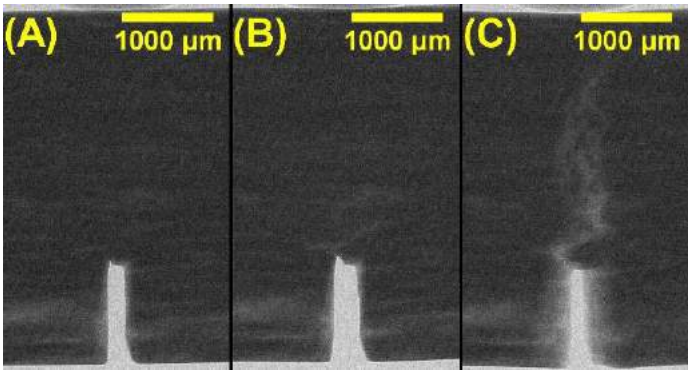


**Figure 1: 2D x-ray images through bone at (A) start of load, (B) immediately before crack instability, and (C) after instability.**

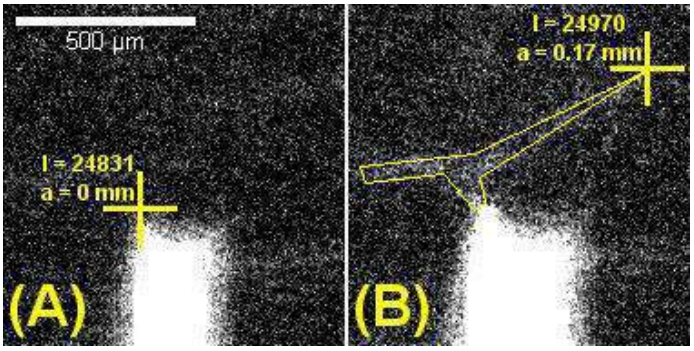


**Figure 2: 2D x-ray images of bone under loading at (A) beginning of load and (B) after stable crack growth. Markers depict crack tip identification via intensity (*I*).**

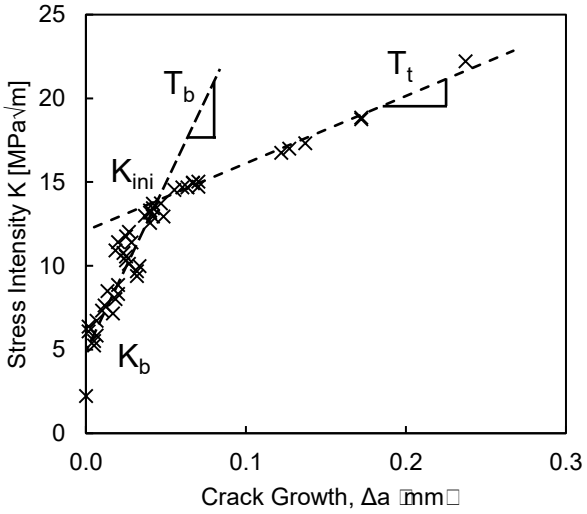


**Figure 3: Crack growth resistance curve.**

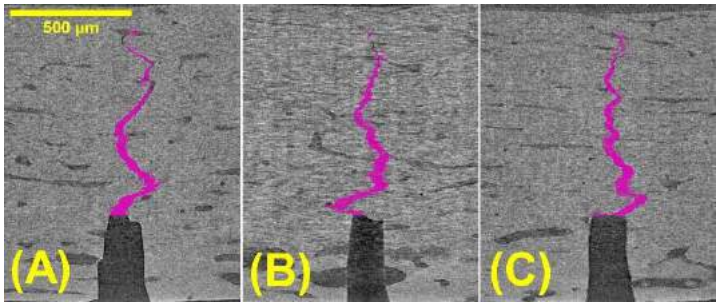


**Figure 4: Crack geometry at (A) front surface, (B) At a section 1.76 mm from front surface, and (C) back surface. 3D image acquired after crack instability at an applied displacement of 0.325 mm.**

## DISCUSSION

We demonstrate the use of a 3D X-ray microscope with an in-situ load rig for the evaluation of bone fracture behavior of human cortical bone. We thereby, can measure both an effective crack advance (by use of 2D through thickness x-rays) as well as the full 3D-shape of the crack under load. In particular, using the 2D-xray images we are able to provide distinct measurements of the blunting and tearing resistance of a cortical bone tissue. We show that imaging in an X-ray microscope used in combination with in-situ loading allows for visualization of the complex fracture geometry within bone tissue.


## ACKNOWLEDGEMENTS

Supported by NSF Award 1952993 and an NSF-GRF (G.G.).


## REFERENCES


[1] Launey, M. E. et al., *Acta Biomaterialia*, 6:1505-1514, 2010.
[2] Zhai, X. et al., *Journal of the Mechanics and Physics of Solids* 131:358-371, 2019.
[3] Schindelin, J. et al., *Nature Methods*, 9:676-682, 2012.
[4] ASTM D5045-14, 2014

# MEASURING THE ANISOTROPIC MECHANICAL PROPERTIES OF SINGLE NEONATAL MOUSE CARDIAC MYOCYTES

**Taylor M. Rothermel (1), Patrick W. Alford (1)**

(1) Department of Biomedical Engineering, University of Minnesota – Twin Cities, Minneapolis, MN, USA

## INTRODUCTION

Congenital heart defects and subsequent surgical interventions alter the loading conditions on the heart muscle.[1] Biomechanical models of congenital heart defects are useful for understanding disease progression and aiding clinicians in planning treatment. In order to formulate the most predictive tissue and organ level biomechanical models, the mechanical properties of the individual components must also be elucidated. In order to fully understand the mechanical properties of the heart, the mechanical properties of cardiac myocytes, the force generating cells in the heart muscle, must also be characterized. Cardiac myocytes play an important role in remodeling of the heart muscle and are sensitive to mechanical stimuli.[2-3] As cardiac myocytes exist in a dynamic mechanical environment and have a highly organized cytoskeletal architecture, there is a need to understand how complex mechanical loading conditions influence the cell's anisotropic mechanical properties. Here, we measure the stress-strain behavior of cardiac myocytes in response to biaxial loads.

## METHODS

**Substrate Fabrication and Cell Culture.** Neonatal mouse ventricular myocytes (NMVMs) were isolated from one-day-old mouse pups using standard methods.[4] As previously described,[5] NMVMs were micropatterned in an elongated architecture (aspect ratio 7:1 and an area of ~2250 μm$^2$) on a fluorescent-bead-doped polyacrylamide (PA) gel with a Young's modulus of 13.5 kPa bonded to an elastomer membrane (Fig. 1A).

**Cellular Micro-Biaxial Stretching (CμBS).** CμBS experiments were performed using a custom-built microscope-mounted device to perform traction force microscopy experiments on cells exposed to biaxial stretching (Fig. 1B). Four straining protocols were applied to the micropatterned NMVMs: axial tension, axial compression, transverse tension, and transverse compression, where the axial direction is parallel to the long axis of the cell and the transverse direction is parallel to the short axis of the cell (Fig. 1C). Strains were evaluated in 5% increments to a maximum of 15% for all protocols. NMVMs were paced at 1 Hz using an Ionoptix MyoPacer to induce contraction (Fig. 2A). High temporal resolution (100 Hz) images of the fluorescent bead layer were acquired to capture the full contraction of the cell and used to calculate traction forces of the cardiac myocytes at each applied strain. Traction forces at each stretch were calculated using standard methods.[5] First Piola-Kirchhoff (PK1) stresses, represented by $P_x = f_x/(2A_x)$ and $P_y = f_y/(2A_y)$, where $f$ is the total traction force and $A$ is the undeformed cross-sectional area of the cell, were calculated at the mid-plane of the cell (Fig. 1D). The cross-sectional areas of micropatterned NMVMs were estimated to be $A_x = 19$ μm$^2$ and $A_y = 131$ μm$^2$.[6] Sarcomere spacing during stretching was measured using a fast Fourier transform (FFT) on bright field images of the contracting NMVMs in which the sarcomere structures are visible.

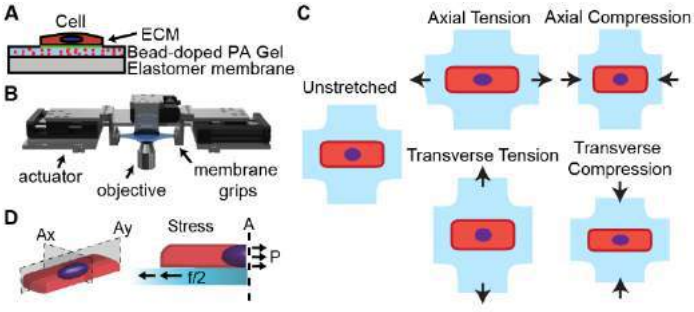


**Figure 1: CμBS device and methods for measuring cell stress. (A) Schematic of cell patterned on PA gel.[5] (B) CμBS device.[5] (C) Schematic of a cell under axial tensile, axial compressive, transverse tensile, and transverse compressive strains. (D) Relationship between the cell's cross-sectional area, traction force, and PK1 stress.**

## RESULTS

Traction forces of the NMVMs during contraction were measured and were greatest along the long axis of the cell (Fig. 2B-C), which is consistent with the underlying sarcomeric architecture. Using FFT, the sarcomere spacing prior to stretch was measured to be ~1.97 μm, which is consistent with measurements from fluorescently stained cells (Fig. 2D) and literature values.[7] When the NMVMs were exposed to axial tensile strains, the spacing between sarcomere subunits increased with stretch (Fig. 2E).

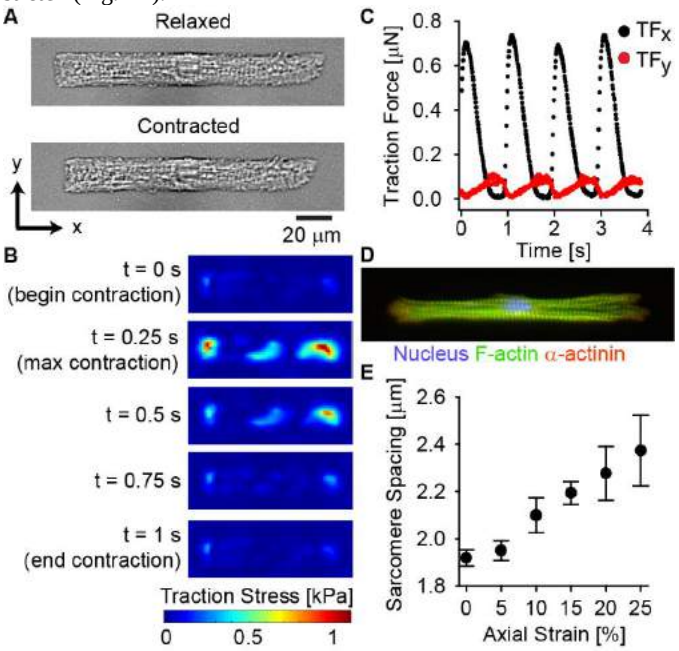


**Figure 2: NMVMs are compatible for use with CμBS. (A) Representative images of a contracting micropatterned NMVM (B) Traction stress heat maps during contraction. (C) Trace of the traction forces in a micropatterned NMVM. (D) Micropatterned NMVM stained for nuclei, F-actin and α-actinin. (E) Sarcomere spacing of NMVM stretched to 25% applied axial strain.**

NMVMs were extended or compressed using CμBS and PK1 stresses were calculated in the direction of the long axis (axial stress, $P_X$) and the short axis (transverse stress, $P_Y$) for each deformation. To determine the effect of biaxial stretch on the functional contractility of the NMVMs, passive and active cell stresses were calculated, where the passive stress was defined as the stress in the cell when the cell is not contracting and the active stress is defined as the difference in cell stress between the fully contracted and non-contracted states. During axial stretching (Fig. 3A), the active $P_X$ (Fig. 3B) of the contracting myocytes decreased as the cell was compressed and initially increases as the cell is extended before decreasing at the larger strains. This is consistent with previous understanding of the length-tension relationship in striated muscle.[8] The passive stress and the stress in the short axis of the cell, $P_Y$ (Fig. 3C), remained relatively unchanged under both axial tension and compression compared to the active stress in the long axis. Under transverse stretching (Fig. 3D), the active $P_X$ stress decreased with increasing stretch (Fig 3E) and the active $P_Y$ stress increased with increasing stretch (Fig 3F). This could also be due to inhibiting the interactions of the acto-myosin lattice by altering the lattice spacing in the micropatterned cells similar to what is described by the length-tension curve.[9] Passive stresses remained relatively unchanged. These data suggest that biaxial loads affect NMVM functional contractility.

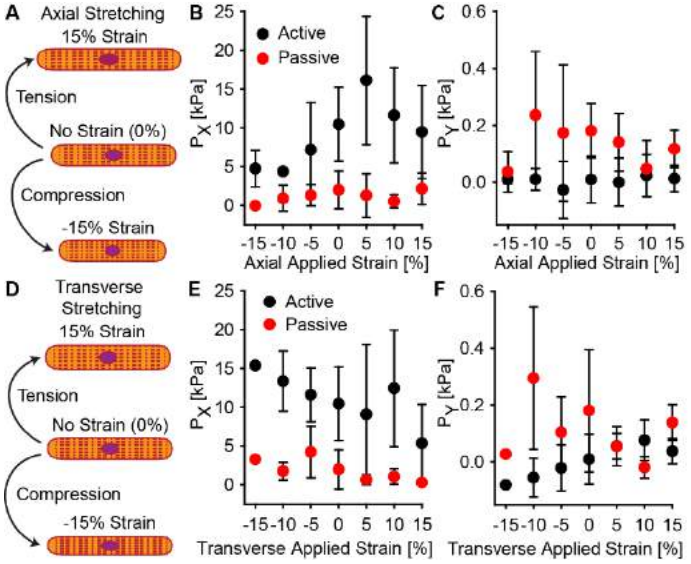


**Figure 3: Stress-strain measurements for NMVMs. Axial Stretching (A-C). (A) Schematic of a cell exposed to axial tensile and compressive strains, (B) axial direction PK1 stress, and (C) transverse direction PK1 stress. (For strains from -15% to 15%, n = 5, 3, 9, 25, 13, 13, 21). Transverse Stretching (D-F). (D) Schematic of a cell exposed to transverse tensile and compressive strains, (E) axial direction PK1 stress, and (F) transverse direction PK1 stress. (n = 1, 2, 4, 25, 4, 4, 3).**

## DISCUSSION

To develop the best tissue and organ level biomechanical models of the heart, the mechanical properties of the cardiac myocytes must be understood. The length-tension relationship is fundamental in understanding striated muscle contraction and has been characterized in cardiac muscle.[8] However, it is not well-understood on the single-cell level in cardiac myocytes. Thus, there is a need to fully characterize the anisotropic mechanical properties of cardiac myocytes. In this study, we used CμBS to measure the stress-strain behavior of NMVMs under biaxial loads. We found that in the axial direction, the stress-strain behavior is similar to what is described by the length-tension relationship of striated muscle in which changing the sarcomere spacing from an ideal distance decreases the force the cell is able to generate.[8] Additionally, we found that strains applied in the transverse direction altered cell stress as the active stress appeared to decrease with applied tensile strain. This could be due to inhibiting the interactions of the acto-myosin lattice in the micropatterned cells similar to the axial stretching. Future work includes expanding the stretching protocols to include equi-biaxial tension and characterizing the measured cell stresses with a strain energy density function. Overall, our results suggest that complex loads affect the functional contractility of NMVMs.


## ACKNOWLEDGEMENTS

We acknowledge financial support from the National Science Foundation (CMMI-1553255) and the American Heart Association (Pre-doctoral Fellowship).


## REFERENCES


[1] Petko, C. et al. *J. Am. Soc. Echocardiogr*., 24:1226-1232, 2011. [2] Taber, L. et al. *Dev. Dyn.*, 203:42-50, 1995. [3] Ribeiro, A. et al. *Proc. Natl. Acad. Sci*., 112:12705-12710, 2015. [4] Sakurai, T. et al. *JoVE*, 88:1-9, 2014. [5] Win, Z. et al. *J. Biomech. Eng.*, 139:1-10, 2017. [6] Geisse, N. et al. *In Vitro Cell. Dev. Biol. Animal*, 45:343-350, 2009. [7] Mansour, H. et al. *Circ. Res*., 94:642-649, 2004. [8] Allen, D. et al. *J. Mol. Cell. Cardiol.*, 17:821-840, 1985. [9] Williams, C. et al. *Proc. Royal Soc. B*, 280:1766, 2013.

# VASCULAR SMOOTH MUSCLE CELLS UPREGULATE GLYCOLYTIC AND CONTRACTILE PHENOTYPE GENES IN THE PRESENCE OF GLUTAMINE

**Pattie S. Mathieu (1), Alisa M. Clyne (1)**

(1) Fischell Department of Bioengineering, University of Maryland College Park, Maryland, USA

## INTRODUCTION

Vascular disease is the leading cause of death in the western world. Many vascular diseases are caused by vascular smooth muscle cell (VSMC) proliferation that narrows the vascular lumen. VSMC proliferation occurs during a shift in phenotype from a contractile to a synthetic phenotype. Contractile VSMC express proteins such as α-smooth muscle actin (αSMA), calponin, SM22α, and smooth muscle myosin heavy chain (SM-MHC), while synthetic VSMC proliferate and secrete extracellular matrix proteins.

VSMC phenotype may also be linked with metabolism. *In vitro*, increased VSMC proliferation has been linked with increased glycolytic flux and mitochondrial oxygen consumption.[1] When VSMC change from a contractile to a synthetic phenotype, they also become more glycolytic.[2,3] One study showed that increasing glutamine concentration increases VSMC proliferation and decreases contractile protein expression.[4] Glutamine metabolism is linked to glucose metabolism through the tricarboxylic acid (TCA) cycle since glutamine can be converted to α-ketoglutarate (αKG). However, no work has been done to understand how glutamine affects VSMC glycolysis.

To further understand the effects of glutamine on VSMC, we performed RNA sequencing on VSMC grown with or without glutamine, then confirmed the phenotypic changes through proliferation and protein expression. We hypothesized that the absence of glutamine would increase VSMC gene expression of glycolytic enzymes as well as gene transcription and protein expression of contractile markers.

## METHODS

*Cell Culture* Human coronary artery smooth muscle cells were cultured in smooth muscle growth medium (Lonza) with 10% FBS, 1% penicillin/streptomycin, and 2mM L-glutamine. For experiments, cells were switched to glutamine-free DMEM with 10% FBS and 1% penicillin/streptomycin, with increasing L-glutamine added to the media. In some experiments, medium was supplemented with 7 mM dimethyl-α-ketoglutarate (αKG), the cell soluble form of the molecule.

*RNA Sequencing* Total RNA for RNA sequencing was isolated using RNeasy Mini kit (Qiagen). RNA was sequenced by Novogene using the NovaSeq 6000 with 150-bp paired end reads. Data were cleaned and assessed in Galaxy and visualized in Advaita iPathway.

*Western Blot* Cells were lysed in cold RIPA buffer. Protein was quantified by BCA assay and equal concentrations of protein were run on NuPage 4-12% Bis-Tris gels and then transferred to a nitrocellulose membrane. Proteins were probed using 1:1000 primary antibody in 1% BSA in PBS-T overnight at 4°C. Membranes were incubated in HRP-conjugated secondary antibodies (1:2000 in 1% BSA in PBS-T) for 2 hours at room temperature. Membranes were treated with Western Lightning Chemiluminescence Substrate and then imaged on an Alpha Innotech Fluorochem Q gel imager. Western blot intensity was normalized to the average intensity of the samples cultured in media with glutamine.

*Immunostaining* Cells were fixed in 4% PFA for 20 minutes and blocked and permeabilized with 5% BSA and 0.2% Triton X-100 in PBS for 40 minutes. Antibody solutions were made in 0.5% BSA and 0.2% Triton X-100 in PBS. Primary antibody was diluted 1:200, and cells were incubated for one hour at room temperature. Secondary antibody was diluted 1:1000 with 1:1000 DAPI and cells were incubated for one hour at room temperature. Cells were imaged using Nikon Eclipse Ti2-E at 10x, taking five random images of three wells each. Total nuclei and Ki67+ nuclei were counted in Image J.

*Statistics* Differential expression of sequenced RNA was assessed using the EdgeR function in Galaxy with a Benjamini-Hochberg p-value correction. Genes with an adjusted p-value of less than 0.05 and a log fold change of at least 0.5 were identified as being significant. Western blots and proliferation results were analyzed using a one- or two-way ANOVA both in GraphPad Prism.

## RESULTS

VSMC cultured with or without 2mM glutamine for 24 hours showed differential expression of 4144 genes, with 2022 upregulated

and 2122 downregulated in the presence of glutamine (Figure 1A). Of note, 15 genes involved in glycolysis were upregulated, while three were downregulated in VSMC cultured with glutamine. (Figure 1B).

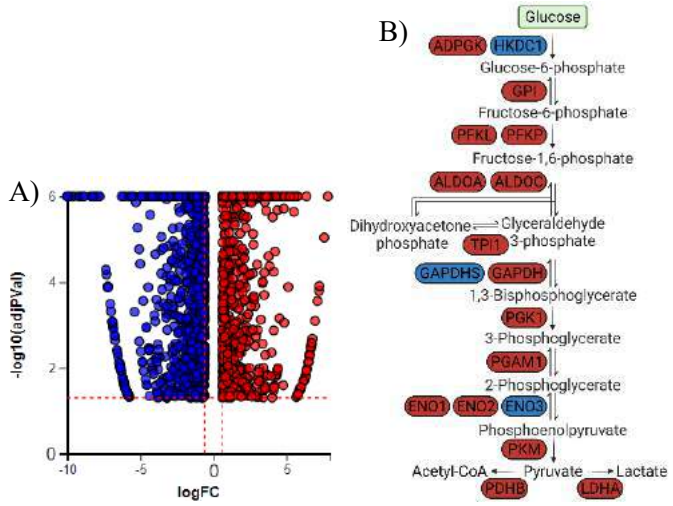


**Figure 1: A) Volcano plot showing genes that were significantly differentially expressed in response to 2mM glutamine. B) Glycolytic genes that were differentially regulated. Red = upregulated with glutamine; blue = downregulated with glutamine.**

VSMC differentially expressed genes involved in the VSMC contractile phenotype, with genes for αSMA(ACTA2), Calponin (CNN1, CNN2), and SM22α (TAGLN) all showing greater expression in the presence of glutamine. (Table 1)

| Gene | LogFC | p-value |
|---|---|---|
| ACTA2 | 3.170 | 1.000e-6 |
| CNN1 | 3.322 | 1.000e-6 |
| CNN2 | 2.044 | 1.000e-6 |
| TAGLN | 2.441 | 1.000e-6 |

**Table 1: Genes indicating contractile phenotype were significantly upregulated in the presence of 2mM glutamine.**

Culturing VSMC without glutamine decreased glycolytic enzymes phosphofructokinase-1 (PFK) and pyruvate kinase isozyme M2 (PKM) and contractile proteins αSMA, and calponin. Replacement with αKG restored PFK partially, PKM fully and contractile proteins partially at 4 days, and completely by 10 days. After 4 days, VSMC showed increasing cell proliferation as glutamine increased (Figure 3).

## DISCUSSION

Prior work suggested that glutamine promotes a synthetic VSMC phenotype. However, our RNA sequencing data shows that the presence of glutamine results in the upregulation of both glycolytic genes and contractile genes and proteins. While a previous paper showed a decrease in contractile VSMC markers in the presence of glutamine in pulmonary artery VSMC,[4] our experiments using coronary artery VSMC showed upregulation of contractile genes and proteins in the presence of glutamine. Conversely, increased glycolysis is associated with a synthetic phenotype in VSMC.[2,3] Therefore, the role of glutamine may be more complex than making VSMC more "contractile" or more "synthetic" as it promotes markers of both phenotypes.

A signaling pathway that might explain the glycolytic gene changes is the HIF-1 pathway. The gene HIF1A is shown to be upregulated with a log fold change of 1.111 in cells with glutamine compared to cells without glutamine. In cancer cells, the presence of glutamine increases HIF1α protein expression,[5] which in turn increases glycolytic enzymes.[6] However, HIF1α has also decreases contractile proteins in VSMC,[7] so glutamine likely affects other pathways involved in contractile protein expression that will need to be further investigated.

This study highlights the importance of glutamine for VSMC and indicates the further need for study on glutamine's effects on VSMC phenotype and glycolysis. Furthermore, it will need to be confirmed that the changes in glycolytic gene transcription and protein expression ultimately change VSMC glucose metabolism.

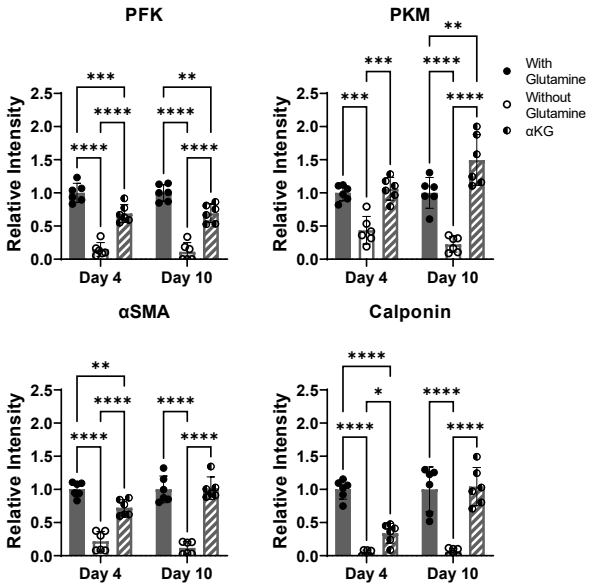


**Figure 2: VSMC treated without glutamine for 4 or 10 days show decreased PFK, PKM, αSMA, calponin, expression. αKG enabled partial or total recovery of these proteins. n=6 *p<0.05, **p<0.01, *** p<0.001, **** p<0.0001**

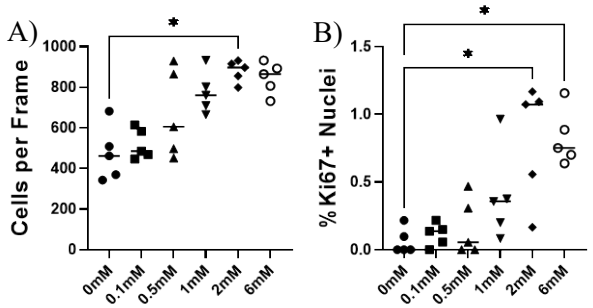


**Figure 3: VSMC show increasing A) cell number and B) actively dividing cells as indicated by nuclear Ki67 after 4 days of culture as glutamine concentration increases. n=5 *p<0.05**


## ACKNOWLEDGEMENTS

This research was funded by NSF CMMI 1916814, NSF CBET 1916997, NIH R21EB028466 and NIH T32HL007698-25.


## REFERENCES


[1] Perez, J. et al., *Biochem J*, 428(2): 255-267, 2010
[2] Butler, T.M.et al. *Annu Rev Physiol*, 47: 629-643, 1985
[3] Werle, M. et al. *J Biomed Sci,* 12: 827-834, 2005
[4] Zhang, C.Y. et al. *LifeSci*, 277:119365, 2021
[5] Kappler, M. et al. *Int J Mol Sci,* 20(19): 4742, 2019
[6] Webster, K.A. *J Exp Biol* 206(17): 2911-2922, 2003
[7] Liu K. *Oncotarget* 8(20): 33343-33352, 2017

SB³C2022
Summer Biomechanics, Bioengineering and Biotransport Conference
June 20-23, Eastern Shore, MD, USA

# REDUCED ORDER MODELING FRAMEWORK FOR RAPID SIMULATIONS OF TRANSCATHETER AORTIC VALVE REPLACEMENT PROCEDURES

**I. Shah (1,2), M. Samaee (1), A. Razavi (1), F. Esmailie (1), A. Veneziani (2,3), L. Dasi (1)**

(1) Wallace H. Coulter Department of Biomedical Engineering, Georgia Institute of Technology, Atlanta, GA, USA
(2) Department of Mathematics, Emory University, Atlanta, GA, USA
(3) Department of Computer Science, Emory University, Atlanta, GA, USA

## INTRODUCTION

Transcatheter aortic valve replacement (TAVR) has become a viable alternative for patients with severe aortic stenosis who are unable to undergo traditional surgical treatments. Within the TAVR pre-procedural planning pipeline, there is a need for accurate assessment of potential complications that may arise post-TAVR., such as coronary obstruction, paravalvular leakage, and leaflet thrombosis [1]. Computational modeling has become a critical tool that can be used to visualize the deployment behavior of transcatheter heart valves (THV) in patient-specific TAVR procedures, and help predict the likelihood of post-TAVR complications [2]. In the context of TAVR deployment analysis, the finite element (FE) method is the most commonly used computational modeling technique, where the THV stent frame and leaflets, as well as the patient-specific aortic root, native leaflets, and calcium deposits are all incorporated into the model. Due to the intrinsic geometrical and mechanical complexities of these components, the modeling process quickly becomes computationally expensive.

A common approach to introduce significant computational advantages is the customization of the FE basis functions from a *data-driven paradigm*, within the general idea of "Model Order Reduction" [3]. The reduced order model (ROM) here can be divided into two primary stages, the *offline* and *online* stages. In the offline stage, all computationally expensive full order model (FOM) simulations are performed for a specific set of parameters to create a library of solutions or *snapshots*. This is followed by a prompt recycling of the snapshots in the online stage for a rapid reduced order solution. Although ROMs have been employed in various biomedical engineering applications previously, the application of ROMs in TAVR modeling has not yet been studied.

The primary objective of this study is to develop a ROM framework based on the Proper Orthogonal Decomposition (POD) approach for the structural deformation of the 29 mm Medtronic CoreValve. Specifically, the focus here is on the use of POD for significantly reducing the computational costs of simulating the deformation of the CoreValve in response to defined sets of applied loads that mimic *crimping* and *expansion* of the THV stent frame. The framework serves as the first step towards real-time simulations of the entire TAVR deployment procedure which will allow for rapid identification of potential post-operative complications.

## METHODS

As an initial step towards creating the ROM framework, a linear elastic constitutive law is assumed where the problem considered reads as: find *u(x)* such that

$$\nabla \cdot \sigma = \mathrm{F}, \quad x \in \Omega \tag{1}$$

$$\sigma = \lambda(\nabla \cdot u)\mathrm{I} + 2\mu\varepsilon \tag{2}$$

$$\varepsilon = \frac{1}{2}(\nabla u + \nabla u^T) \tag{3}$$

where σ is the Cauchy stress tensor, $\varepsilon$ is the strain tensor, $I$ denotes the identity tensor, $F$ is an external volume force, and $\lambda$ and $\mu$ are the Lame' constants. The prescribed boundary conditions (BC) over the domain $\partial\Omega$ is split into three parts. First, the displacement was set as $u = 0$ at the lower and upper edges of the stent frame. Second, it was assumed that the normal stress was given at a set of 15 points, i.e. $\sigma \cdot n(P_i) = d_i$ for $i = 1, 2, \dots, 15$, where $n$ is the outward normal vector. All possible pairs among the 15 points were selected and $d_i$ was defined as a vector that was oriented along the line connecting the two end points of each pair. These "force pair" BCs idealize the loads applied from the native aortic wall and leaflets onto the CoreValve stent frame, as well as mimic crimping and expansion of the stent frame. For the remaining BCs, homogenous Neumann BCs were applied, i.e., $\sigma \cdot n = 0$.

In the offline stage of the ROM framework, a series of FE simulations of (1) with the parameterized force pair BCs are performed. The 3D geometry utilized was a model of the 29 mm Medtronic CoreValve stent frame without the leaflets included, allowing us to solely focus on the stent deformation. The CoreValve stent frame was

modeled with linear elastic material properties with a Young's modulus of 50 GPa and Poisson's ratio of 0.33. With the 15 nodes used to parametrize the BCs, a total of 105 offline stage simulations were run. Crimping and expansion of the stent frame was simulated at three planes P1, P2, and P3 via force pairs (Fig. 1) to form a *snapshot* library.

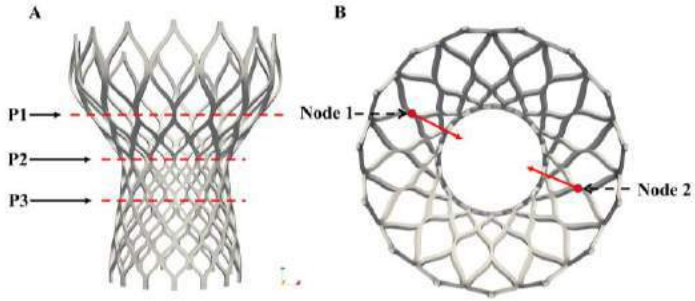


**Figure 1. Model of the CoreValve stent frame.**

To filter out the redundancy from the snapshot library, the *Singular Value Decomposition* (SVD) is employed, from which the singular values were analyzed. A rapid decay in the singular values indicates high redundancy in the snapshot library, and that the key features of the matrix can be captured by a linear combination of those left eigenvectors associated with the largest singular values. These eigenvectors form the reduced basis functions, such that the ROM solution reads as follows, where $W$ is the reduced order matrix, and the coefficients $c$ are found by solving the reduced problem.

$$u_{ROM} = \sum_{i=1}^{n_{ROM}} c_i W_i = Wc \qquad (4)$$

After discretization of the problem, the FOM from (1) leads to the solution of a linear system in the following form, where $u$ is the vector of displacements, $A$ is the stiffness matrix, and $b$ is the forcing terms.

$$Au = b \qquad (5)$$

Using the POD approach, an approximate form of (4) is created and after plugging in (5), the following reduced order system is obtained.

$$W^T AWc = W^T b \qquad (6)$$

In (6), $W^T AW$ is a matrix featuring a size in the range of tens or hundreds of rows. Using (6) with the vector $b$ incorporating new BCs in the online stage, the vector $c$ can be found from (4), from which the final reduced order solution can be solved for. The savings in computational costs becomes evident when comparing the size of $A$ (thousands or millions of rows) to the reduced order matrix $W^T AW$.

All offline stage simulations were performed using an in-house solver built in *FEniCS*, an open-source FE library, followed by a manual model reduction using the above approach in *MATLAB* [4]. The entire framework presented above was then also implemented into the *FEniCS*-based library *RBniCS*, an open-source model reduction library, which allowed us to combine the offline stage simulations, model reduction, online reduced order solutions, and speed-up analysis all into a single solver [3]. Results were visualized and analyzed in *ParaView*.

## RESULTS

Crimping and expansion of the CoreValve stent frame simultaneously at planes P1, P2, and P3 is shown in Fig. 2. Maximum deformation in the ROM and FOM simulations was 3.985 mm for crimping (Fig. 2A), and 3.981 mm for expansion (Fig. 2B). The degrees of freedom required for the FOM was 227,511, which was reduced to 15 when performing the model reduction. This led to the FOM requiring an average of 122.28 seconds to simulate, while the online phase of the ROM taking only an average of 2.14 seconds, a 98.25% reduction in computational time.

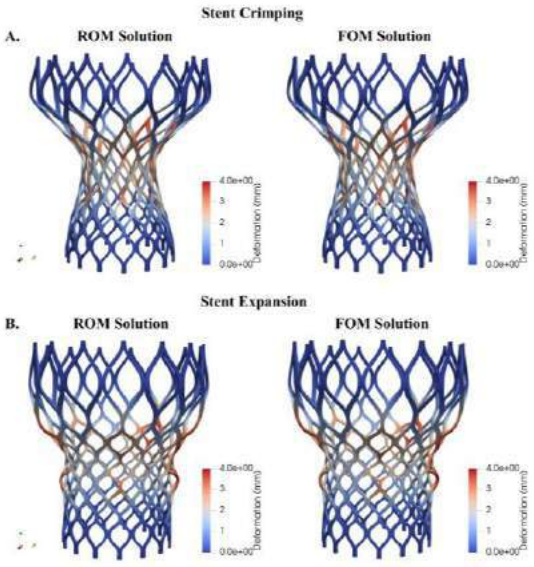


**Figure 2. Comparison of ROM and FOM solutions for stent crimping (A) and expansion simulations (B).**

The computational details for the ROM and FOM simulations are summarized in Table 1 below.

**Table 1. Summary of computational details.**

| Mesh Size | Number of Snapshots Computed | FE Degrees of Freedom | Number of Reduced Basis | Avg. Computational Time (s) | | |
|---|---|---|---|---|---|---|
| | | | | FE Simulation | ROM Offline | ROM Online |
| 257671 | 105 | 227511 | 12, 13, and 15 (depending on crimping/expansion plane) | 122.28 | 2654.39 | 2.14 |

## DISCUSSION

In this study, we introduce a ROM framework applied towards rapidly simulating the structural deformation of the Medtronic CoreValve. Utilizing the POD approach in the online phase of the ROM resulted in a reduced order solution that was identical to the FOM simulations with similarly applied BCs. The ROM solutions also required significantly less computational time, which suggests that the POD-based ROM results in an accurate and computationally efficient solution. Enhanced computational efficiency using this framework suggests a significant role of the ROM in segregated algorithms for solid-solid interaction simulations in TAVR. One limitation of this study is that the stent was modeled as a linear elastic material, while the self-expandable nitinol frame would be more accurately modeled as a superelastic alloy. A constitutive model for hyperelasticity (Generalized Neo-Hookean) is proposed as an initial step to capture the nonlinear properties of the stent. The basic POD approach also requires linear differential operators, and thus the Empirical Interpolation Method will be applied to perform model reduction for nonlinear problems.

In conclusion, the POD based ROM framework significantly reduces the computation time required to simulate crimping and expansion of the CoreValve stent frame, while retaining the accuracy from FOM models. Further refinements are underway to incorporate the nonlinear nature of the stent frame, as well as to rapidly and accurately simulate the entirety of the TAVR deployment process.


## ACKNOWLEDGEMENTS

Research was supported by the NSF 2012286 (PI: A. Veneziani).


## REFERENCES


[1] Kodali, S. K., et al. *New England J of Medicine*, 366:1686, 2012.
[2] Bianchi, M. et al. *Biomech & Model in Mechanobio*, 18:435, 2019.
[3] Hesthaven, J. et al. *Cert Reduced Basis Meth for PDEs*, 590, 2016.
[4] Logg, A., et al. *The FEniCS Book*, Vol 84, Springer Science, 2012.

# COMPUTATIONAL MODELING OF IPSC-DERIVED ENGINEERED CARDIAC MICROTISSUES

**Jason W. Lo (1), Javiera Jilberto (1), Samuel J. DePalma (1), Brendon M. Baker (1), David A. Nordsletten (1,2,3)**

(1) Department of Biomedical Engineering, University of Michigan, Ann Arbor, MI, USA
(2) Department of Cardiac Surgery, University of Michigan, Ann Arbor, MI, USA
(3) School of Biomedical Engineering and Imaging Sciences, King's College London, London, UK

## INTRODUCTION

Heart disease is one of the leading causes of mortality within the US, causing about 1 in every 4 deaths [1]. One of the reasons for this high prevalence is the lack of regenerative capabilities of the myocardium [2]. One option to tackle this problem is through engineered heart tissues (EHT) constructed using induced pluripotent stem cell-derived cardiomyocytes (iPSC-CMs). These EHTs can be used to better understand the mechanisms for heart regeneration on a cellular level and can be used to engineer tissues for transplantation. Creating EHTs that are similar in function and structure to adult heart tissues remains a challenge, in part due to our incomplete understanding of the mechanobiology of iPSC-CMs. Modifications to the mechanical environment of EHTs have been shown to influence cardiomyocyte organization and structure [3]. However, how factors like extracellular matrix stiffness and alignment (see Fig. 1) influence the local micromechanical environment remains poorly understood. Further, while the function of EHTs is usually measured globally (e.g. total force generation), the local mechanical environment for cardiomyocytes is usually unknown. In this work, we implemented a computational model that integrates the global data of an experimental setup to quantify and study how the local mechanics determine iPSC-CMs maturation and organization.

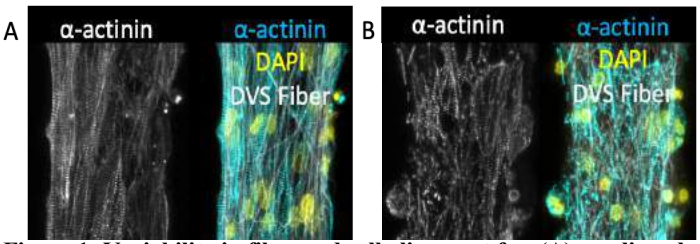


**Figure 1: Variability in fiber and cell alignment for (A) an aligned fiber matrix and (B) a random fiber matrix.**

## METHODS

We considered EHTs made of dextran vinyl sulfone (DVS) fibers suspended between PDMS posts and seeded with iPSC-CMs. The EHT fiber scaffolds investigated were either aligned or non-aligned between the posts (Fig. 1) and varied in stiffness via photoinitiator concentration (0.1, 1.0, and 5.0 mg/mL) of lithium phenyl-2,4,6-trimethylbenzoylphosphinate (LAP) [3].

**Geometric Model Development:** To characterize the ETs, tissue-specific continuum models were developed for each sample using 20x magnified tissue images (Fig. 2A). The images were then segmented using localized adaptive thresholding in MATLAB to produce a fiber mask. The mask was used to calculate a continuum field representing the fiber density and alignment for use within a finite element model (Fig. 2B). The tissue-specific mesh consisted of 2D quadratic quadrilateral elements.

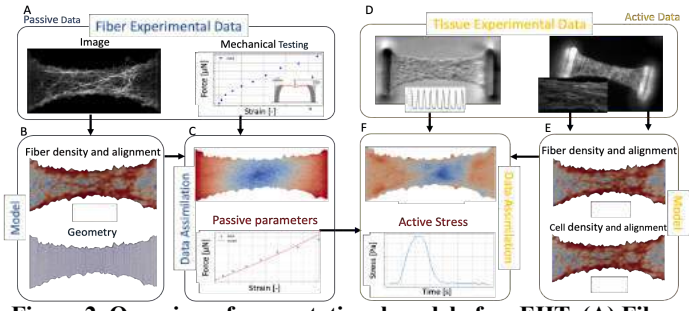


**Figure 2. Overview of computational model of an EHT. (A) Fiber structure and indentation test data. (B) Homogenized field of fiber density and alignment obtained from (A). (C) Passive stiffness parameterization from indentation test (D) EHT with iPSC-CMs and force quantification from post deflection. (E) Homogenized cell density and alignment for active data assimilation. (F) Active stress parameterization from force measurements**

**Passive Data Characterization:** The EHTs fibers were modeled by a modified neofiber material law where the strain energy function is given by

$$\Psi = \frac{\gamma C_1}{4}\left(I_{C_f} - 1\right)^2 + \frac{\gamma C_2}{2}(I_{\hat{C}} - 3) \quad (1)$$

where $I_{C_f} = C{:}\, f_0 \otimes f_0$ is the first invariant of the right Cauchy-Green tensor $C$ in the reference fiber direction $f_0$ and $I_{\hat{C}} = J^{-1}C{:}\, I$ is the first invariant of the isochoric component of $C$ and $J$ its determinant. $C_1$ and $C_2$ are material parameters representing the fiber and isotropic stiffness respectively [5] and $k_b$ regulates the compressibility penalty. The ratio of $C_1$ and $C_2$ was optimized based on explicit fiber meshes, enabling the homogenized models to be parameterized by a single scaling constant, $\gamma$. To find this value, we follow a similar approach to the one presented in [4], where Lagrange multipliers constrain a mechanics problem to meet the known boundary conditions and solve for the unknown displacement field and parameters. Experimentally, indentation tests were conducted to measure the passive stiffness of the different fiber conditions where iPSC-CMs were seeded on (Fig. 2C). From this experiment, the force $F(t)$ and displacement $d(t)$ at the post were obtained for the different permutations, and the passive forward problem and parameterization can be written as: Given the tissue domain $\Omega$ with the post boundary denoted by $\Gamma_b$, find $u, \lambda, \gamma \in X$ such that,

$$\int_\Omega \sigma(u,\gamma){:}\,\nabla\omega\, d\Omega + \int_{\Gamma_b} \lambda \cdot w d\Gamma + \int_{\Gamma_b} \left(u - d(t)\right) \cdot v d\Gamma + \int_{\Gamma_b} \lambda \cdot e_x q\, d\Gamma - \frac{F(t)}{t_t} \cdot e_x q = 0 \quad (2)$$

for all $w, v, q \in X$ where $X$ denotes the appropriate finite element spaces, $\sigma$ is the Cauchy stress and $e_x$ is a unitary vector perpendicular to the boundary and $t_t$ is the tissue thickness.

**Active Data Assimilation:** The fibers samples are then seeded with contractile iPSC-CMs and allowed to culture for 7 days to mature. From the videos, displacement of the tissue at the boundary of the EHT at varying time points were obtained (Fig 2D). We consider the active stress of the fibers as shown in Equation 3.

$$\sigma_a = \alpha f_c \otimes f_c \quad (3)$$

where $\alpha$ is a parameter that represents the active stress that the cells exert to contract and $f_c$, the deformed cell alignment direction (Fig. 2E). Using the $\gamma$ value solved in the passive data problem and the boundary displacement $d_a(t)$ obtained from the videos, we can find $\alpha(t)$ and the tissue displacements by solving: find $u(t), \lambda(t), \alpha(t) \in X$ such that,

$$\int_\Omega \sigma(u,\gamma){:}\,\nabla\omega\, d\Omega + \int_{\Gamma_b} \lambda \cdot w d\Gamma + \int_{\Gamma_b} \left(u - d_a(t)\right) \cdot v d\Gamma + \int_{\Gamma_b} \lambda \cdot e_x q\, d\Gamma - \frac{k d_a(t)}{t_t} \cdot e_x q = 0 \quad (4)$$

for all $w, v, q \in X$, with $k$ post stiffness.

## RESULTS

Both passive and active data assimilation tests were conducted on CHeart [6]. The proposed pipeline to characterize the tissue data is robust and allowed us to characterize myocyte function under the varying permutations of the tissue microenvironment (changes in fiber-matrix stiffness, post stiffness, matrix alignment). For each EHT model, we obtained the material parameters that characterize the experimental observations and the internal displacement fields (Fig. 3A). The method allows us to study the impact that the different stiffness and alignment conditions produce on material parameters (Fig. 3C). Using the material parameters found, the active data assimilation allows us to look at the deformed configuration (Fig. 3B) due to the contraction of the cells and quantify estimated active stresses that the cells are generating internally. For example, we note that aligned fiber matrices generate higher cellular stress (Fig. 3D). Importantly, this approach allows us to estimate the internal activity of the EHTs under varying micromechanical conditions, providing estimates of iPSC-CM function throughout the EHT.

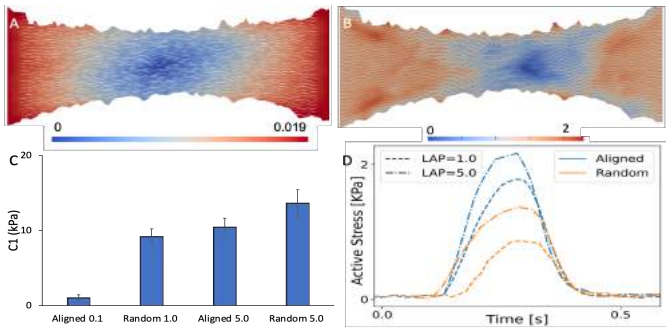


**Figure 3: Resulting displacement field for (A) indentation test and (B) contracting EHTs. (C) C1 value and (D) active stress for different fiber alignment and LAP concentration**

## DISCUSSION

In this work, we present a data-driven tissue-specific modeling pipeline to study how the mechanical environment of cardiac EHTs influence the function of iPSC-CMs throughout the tissue. This approach represents an advance with respect to the general measurements usually used in the tissue engineering field to assess EHT biomechanics, allowing us to differentiate between tissue-scale and cell stresses across varied microenvironments. For example, it is possible to study the effects of anisotropy and fiber stiffness on the contractility of the cells and tissue organization. We can also develop higher throughput data *in silico* by adding variation to fiber alignment and stiffness to suggest promising permutations that can then be tested experimentally. This work shows how combining experimental and computational approaches can shed light on the mechanical cues that determine the assembly and function of EHTs. This work serves as an important step towards the goal of generating better and more mature engineered cardiac tissues that can be used in clinical applications.

## ACKNOWLEDGEMENTS

This work was supported by the National Science Foundation (EEC-1647837, CBET-2033654). J.J acknowledges financial support from the Becas Chile-Fulbright BIO Fellowship. S.J.D acknowledges financial support from NIDCR of the NIH under T32DE007057. D.N acknowledges funding from Engineering and Physical Sciences Research Council (EP/R003866/1).

## REFERENCES

[1] Murphy, S et al., NCHS Data Brief, no. 328. National Center of Health Statistics. 2018.
[2] Frangogiannis NG. *Circulation Research*. 119:1049–51, 2016
[3] DePalma, S. J. et al., *Biomaterial Science*, 9:93-107, 2021
[4] Miller, R. et al., *Frontiers in Physiology*, 12:1-19, 2021
[5]Hadjicharalambous, M. et al., *Biomechanics and Modeling in Mechanobiology*, 14:807-828, 2015
[6] Lee, J et al., *SIAM Journal on Scientific Computing*, 38:C150-C178, 2016

SB³C2022
Summer Biomechanics, Bioengineering and Biotransport Conference
June 20-23, Eastern Shore, MD, USA

# EFFECT OF RENAL DENERVATION ON THE BIOMECHANICAL PROPERTIES OF COMMON CAROTID ARTERIES IN RATS

**Anastasia Gkousioudi (1), Margherita Razzoli (2), Jesse D. Moreira (3), Gianluca Harbert (2), Richard D. Wainford (3), Katherine Y. Zhang (1,2,4)**

(1) Department of Mechanical Engineering, Boston University, Boston, MA, USA
(2) Department of Biomedical Engineering, Boston University, Boston, MA, USA
(3) School of Medicine, Boston University, Boston, MA, USA
(4) Division of Materials Science & Engineering, Boston University, Boston, MA, USA

## INTRODUCTION

Hypertension (HT) affects approximately 1 billion people worldwide and its prevalence increases with age [1, 2]. Resistant HT manifests when the conventional antihypertensive therapy fails to control blood pressure. Uncontrolled HT carries a mortality risk to resistant hypertensive patients who are more likely to develop irreversible damage in end-organs such as the kidneys and brain [3]. Several studies have reported the role of the renal sympathetic nervous system, comprised of both afferent and efferent nerves, as a regulatory mechanism for blood pressure through modulation of electrolyte balance, renin production and renal blood flow [4]. Renal denervation (RDN) has emerged as a potential therapeutic approach to resistant HT by selectively removing the renal nerves and therefore attenuating or even inhibiting the activity of the renal sympathetic nervous system [5]. However, the effect of RDN on the microstructure and biomechanical response of elastic arteries is not understood.

This study focuses on investigating the alterations in mechanical properties and microstructure of rat common carotid arteries (CCAs) following RDN. Biaxial extension-inflation tests were performed on CCAs from the 3-month-old (3mo), 8mo, and 8mo denervated groups. Structural changes of the underlying extracellular matrix (ECM) were investigated through multi-photon microscopy.

## METHODS

Renal denervation: All animal experimental procedures were approved by the Institutional Animal Care and Use Committee (IACUC) of Boston University. Sprague Dawley (SD) male rats were used in the study. Spontaneous HT is developed in the 8mo group with mean arterial pressure (MAP) of 136 ± 3 mmHg, when compared to the 3mo group with MAP of 123 ± 3 mmHg. RDN attenuated HT in 8mo rats (MAP 126 ± 3 mmHg). The kidneys from SD rats were exposed by flank incisions and complete RDN was performed by stripping of all visible renal nerve bundles and painting the renal vein and artery with 10% phenol in ethanol [5] prior to closing of the incision. Rats were left to recover for 2 weeks before tissue harvesting.

Biomechanical testing: CCAs were excised from the 3mo, 8mo, and 8mo denervated groups (n=9) and carefully cleaned from surrounding connective tissue and fat. Segments of approximately 5 mm were cannulated and secured to a pressure myograph (110P DMT, Denmark) while being immersed in a PBS bath at room temperature throughout the mechanical testing. After preconditioning, the *in vivo* stretch ratio of each artery was estimated [6]. Arteries were then subjected to biaxial inflation-extension tests, at the *in vivo* axial stretch ratio, from 0 to 140 mmHg with 10 mmHg increments and a loading rate of 5 mmHg/sec. The axial force, outer diameter and pressure were recorded. After the testing, the unloaded arterial dimensions were measured by imaging arterial rings of ~0.5 mm in length. The images were then imported into FIJI (http:/Fiji.sc/Fiji, Ashburn, VA). The outer and inner circumference were manually traced, and the corresponding diameters were calculated. Under thin wall assumption, Cauchy stresses in circumferential and longitudinal direction can be calculated as [7]:

$$\sigma_\theta = \frac{Pr_i}{h} \quad \text{and} \quad \sigma_z = \frac{f + P\pi r_i^2}{\pi h(2r_i + h)} \tag{1}$$

where $P$ is the transmural pressure, $f$ is the axial force, $r_i$ is the deformed inner radius and $h$ is the deformed thickness.

Multi-photon imaging: CCA segments were mounted into a custom-built tissue stretching-inflation chamber which can subject the artery to physiological loading while being imaged using a Carl Zeiss LSM 710 NLO microscope system equipped with a tunable femtosecond IR pulse laser (Coherent Chameleon Vision-S) [8]. Samples were stretched to *in vivo* stretch ratio and imaged under a set of pressure values (0, 30, 60, 90 and 120 mmHg). An excitation wavelength of 810 nm was used to generate two-photon fluorescence (500/550 nm) from elastin and second harmonic generation (395/415 nm) from collagen. Arterial samples were imaged to a depth of ~100 μm with a 1 μm spacing and a field of view of 425 × 425 μm using a

water immersion objective (20×, NA 1.0, W Plan-Apochromat, Zeiss). Z-stack images of elastin and collagen were acquired at every pressure level.

## RESULTS

Figures 1A and 1B show the response of CCAs under pressurization for the three experimental groups. The axial force needed to maintain the CCAs at their *in vivo* stretch increased for the 8mo group (Figure 1A). After RDN, the axial force decreased to the values of the 3mo arteries. On the other hand, the outer diameter (Figure 1B) showed a rightward shift at 8 months which remained about the same after RDN.

Cauchy stresses were calculated under an intraluminal pressure of 100 mmHg and are presented in Figures 1C and D. Arteries responded with an increased wall stress from 109.91 ± 15.71 kPa to 146.99 ± 16.16 kPa in longitudinal direction (Figure 1C) and from 49.84 ± 5.06 kPa to 78.73 ± 5.9 kPa ($p < 0.05$) in circumferential direction (Figure 1D) due to maturation from 3mo to 8mo. RDN restored stresses to values similar to the 3mo arteries, with a significant decrease to 98.58 ± 5.5 kPa and 61.92 ± 4.4 kPa in longitudinal and circumferential direction, respectively ($p < 0.05$).

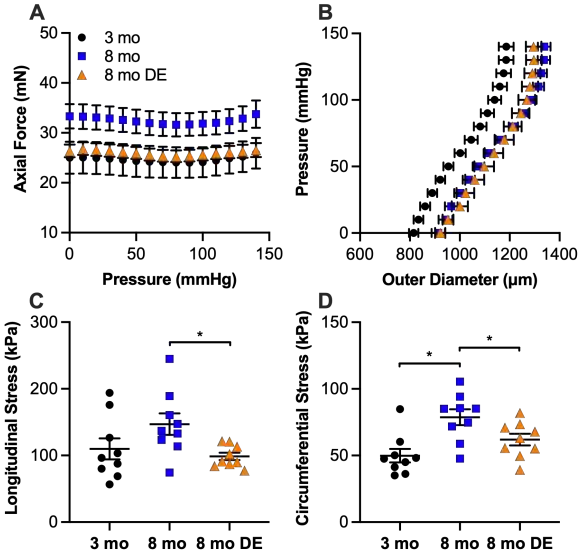


**Figure 1: Biomechanical response of rat carotid arteries under pressurization. Average (mean ± SEM) axial force – pressure (A) and pressure – outer diameter (B) response, Cauchy stress at 100 mmHg in longitudinal (C) and circumferential (D) direction as a function of age and renal denervation.**

Representative multi-photon images of collagen and elastic fibers are shown in Figure 2. The CCA from 3mo appeared to have a denser external elastic lamella at the adventitia-media interface (Figure 2A). On the other hand, the 8mo and 8mo denervated CCAs seem to be sparse with more straightened and disorganized elastic fibers (Figures 2C, E). Collagen fibers in the adventitia of the 3mo CCAs appear to be undulated (Figure 2B). Straightening of the collagen fibers at 8mo with the presence of thicker collagen bundles was observed, while after RDN a mixture of undulated and straight collagen fibers present in the adventitia (Figures 2D, F).

## DISCUSSION

Here we studied the structure and biomechanical response of CCAs after RDN using a rat model. Our results suggest that sustained elevated blood pressure resulted in arterial remodeling which was manifested as a significant increase in stresses after 8 months. In addition, RDN had a favorable impact on CCAs with a reverse of stresses in values similar to the 3-month-old ones. Multi-photon images indicated structural alterations of the main ECM components which possibly affecting arterial biomechanical response.

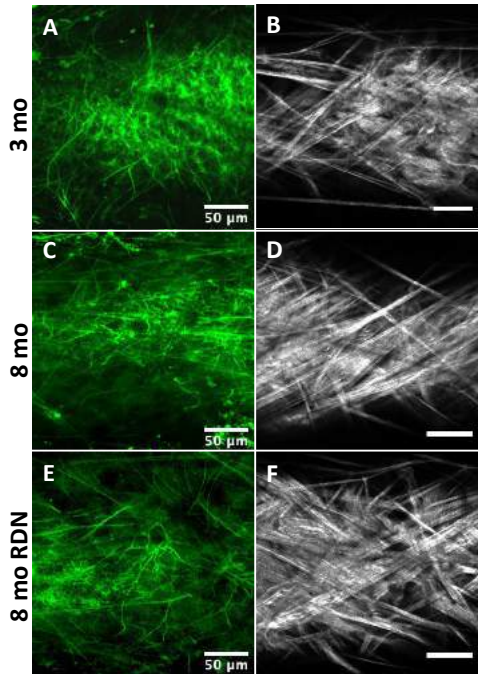


**Figure 2: Representative multi-photon images of elastic (A, C, E) and collagen (B, D, F) fibers of CCAs at 90 mmHg pressure.**

Vascular remodeling is known to be associated with HT [1]. Using a rat model of spontaneous HT, our results show an enlargement of the deformed outer diameter at 8 months which remained after RDN (Figure 1B). In addition, the sparse elastic fiber network in conjunction with the straight collagen fiber bundles (Figures 2C, D) indicated that there is a shift of the load bearing to the stiffer collagen fibers, which could explain the increase in stresses of the 8mo CCAs [2]. Even though deformed diameter remained about the same for the 8mo denervated, multi-photon images revealed a remodeling of ECM components with similarly disrupted elastic fiber network as the 8mo, as well as the presence of undulated collagen fibers (Figure 2E, F). Given that arterial wall stresses decreased, this finding indicates that RDN result in changes in ECM components, and possibly cells, which in turn effectively reversed the biomechanical behavior of CCA.

Effect of RDN on large elastic arteries and HT remain to be understood. Future studies to quantify the ECM structural changes and include RDN in older rat groups could provide more insight on understanding the effectiveness of RDN in the aged group.

## ACKNOWLEDGEMENTS

This research is supported by funding from NIH (2R01 HL098028 to YZ and R01AG062515-A1 to RW).

## REFERENCES

[1] Sun Z. *Hypertension* 65: 252–256, 2015.
[2] Arribas SM, *Pharmacol Ther* 111 (3): 771-91, 2006.
[3] Iliescu R, *Am J Physiol Renal Physiol* 309: F583–F594, 2015.
[4] Frame AA, *Current Hypertension Reports* 18: 69, 2016.
[5] Foss JD, *Am J Physiol Regul Integr Comp Physiol 308:* R112-R122,2015.
[6] Weizsäcker HW, *Journal of Biomechanics* 16: 703–715, 1983.
[7] Ferruzzi J, *Annals of Biomedical Engineering* 41: 1311–1330, 2013.
[8] Yu X, *Journal of The Royal Society Interface* 15: 20180492, 2018.

SB³C2022
Summer Biomechanics, Bioengineering and Biotransport Conference
June 20-23, Eastern Shore, MD, USA

# SHEAR WAVE SPEED AS A MEASURE OF REGIONAL TENDON STRESS

**Jonathon L. Blank (1), Darryl G. Thelen (1,2), Matthew S. Allen (3), Joshua D. Roth (1,4)**

(1) Department of Mechanical Engineering, University of Wisconsin-Madison, Madison, WI, USA
(2) Department of Biomedical Engineering, University of Wisconsin-Madison, Madison, WI, USA
(3) Department of Mechanical Engineering, Brigham Young University, Provo, UT, USA
(4) Department of Orthopedics and Rehabilitation, University of Wisconsin-Madison, Madison, WI, USA

## INTRODUCTION

Tendons undergo complex region-dependent mechanics when loaded physiologically [1][2]. Currently, researchers rely on inverse finite element modeling to infer regional stress from measured strain patterns. However, it remains challenging to ascertain the veracity of model-based stress estimates because there is a paucity of techniques for direct measurements of regional stress. Researchers would benefit from a technique to directly measure regional soft tissue stress to enhance analyses of physiological soft tissue behavior.

Shear wave tensiometry is a measurement technique to gauge loading in tendons [3] and ligaments [4] directly based on the shear wave speed in the loaded tissue, where the shear wave speed squared is proportional to the axial stress. Tensiometry measurements are usually used to infer bulk tissue stress. However, computational studies [5] suggest that the shear wave speed varies regionally with the axial tissue stress when there is a load gradient across the tissue cross-section. If correct, then measurements of regional shear wave speeds could be used to evaluate regional variations in axial tissue stress.

This study empirically investigated relationships between regional shear wave speed and axial stress using multipoint laser Doppler vibrometry to track variations in shear wave profiles across a tendon surface. The objective of this study was to determine how well regionally measured shear wave speeds predict regional axial stress. Our hypothesis was that regional shear wave speeds would track regional stress according to the tensioned beam model underlying shear wave tensiometry.

## METHODS

***Mechanical testing procedure:*** Three porcine digital flexor tendons were loaded into a uniaxial testing system (Acumen 3, MTS, Eden Prairie, MN) with the tendon oriented longitudinally (y-direction, Fig. 1). Specimens were first preconditioned for 100 cycles from 0 to 5% strain in a uniformly loaded reference configuration (0°) [6]. We loaded the specimens using a ramp to 5% grip-to-grip strain at a strain rate of 0.5/s. This loading ramp was performed both in the reference configuration and with the proximal end of the tendon rotated 10° (determined using a digital protractor) within the grip of the MTS to generate a nonuniform strain gradient across the tendon width. The tendons were kept moist with 0.9% saline during the testing procedure.

***Shear wave speed measurement:*** Shear waves were excited over the entire width of the tissue cross-section using a piezoelectric tapper (20 micron ramp over 0.62 ms, PK4JQP1, Thorlabs Inc, Newton, NJ) on the back of the tendon. The tissue's transverse surface motion (x-direction, Fig. 1) was recorded at 15 locations (5 locations each on left, middle, and right sections of the front of the tendon, Fig. 1) using a multi-point laser Doppler vibrometer system (MPV-800, Polytec Inc., Irvine, CA). The surface of the tendon at the measurement locations was

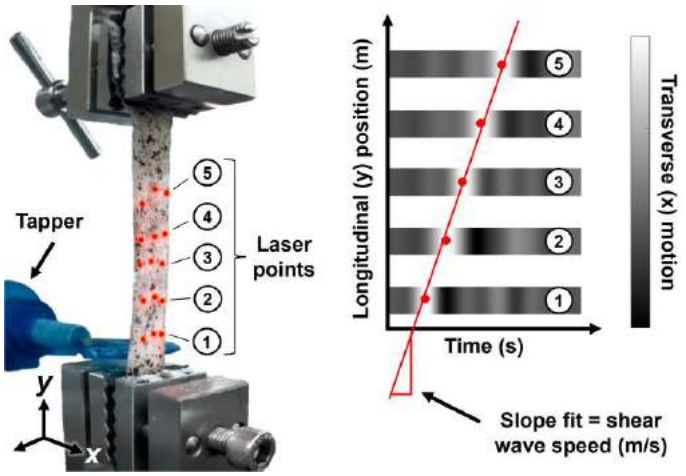


**Figure 1: Tendons were loaded longitudinally, and the shear wave speed was computed as the slope between the laser location and the wave arrival times at each laser location.**

lightly coated with titanium dioxide to enhance surface reflectivity. The distance between laser locations was determined using ImageJ (NIH, Bethesda, MD). Shear wave speed (in m/s) was computed as the linear fit of the wave arrival time vs laser location for the five laser locations within a section (Fig. 1). Outlier exclusion of the shear wave speeds was performed using a Hampel filter [7].

***Digital image correlation (DIC):*** Specimens were speckled with black India ink prior to mechanical testing. During the loading ramp for the 0° and 10° configurations, the deformation of the speckle pattern on the tissue surface was recorded with two cameras (Raspberry Pi 4 with HQ camera, 25 fps). The longitudinal 2D strain in each measurement region was computed using an open-source DIC toolbox [8].

***Analysis and statistical methods:*** Regional axial stress was estimated for the 10° rotated condition using the regional strain from the 10° rotated condition loading ramp and the bulk axial stress-strain relationship from the 0° reference configuration loading ramp for a particular region on the tissue (Fig. 2). We performed a linear regression between the estimated axial stress (dependent variable) and squared shear wave speed (independent variable) to calibrate the slope and intercept (i.e., density and shear modulus, Fig. 2, Eq. 1) for each tendon in the 0° configuration. We then used that slope and intercept to predict the regional stress from regional wave speed in the 10° configuration.

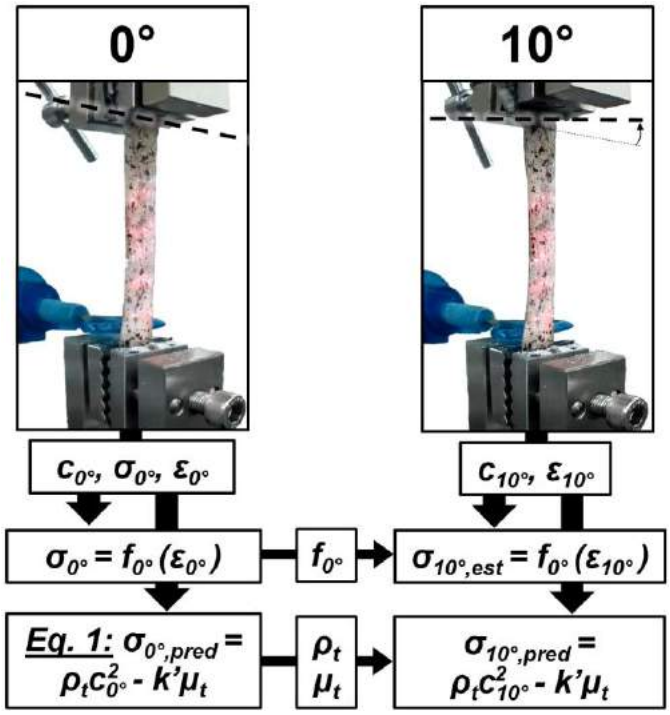


**Figure 2: The stress-strain relationship from the 0° loading ramp ($f_{0°}$), the tendon density ($\rho_t$), and the tendon shear modulus ($k'\mu_t$) were used to estimate regional stress ($\sigma_{est}$) in the 10° configuration from the regional strain ($\varepsilon$) and predict regional stress ($\sigma_{pred}$) using the shear wave speed ($c$) measured in each region.**

## RESULTS

Measured shear wave speeds increased with increasing regional strain, and the tissue strain increased monotonically with axial loading. The squared shear wave speed and estimated regional axial stress during the loading ramp demonstrated strong linear relationships for each specimen in both the 0° reference configuration (average $r^2 = 0.93 \pm 0.07$) and the 10° configuration (average $r^2 = 0.81 \pm 0.19$) for all measurement regions. On average, we could predict axial stress from shear wave speed within 0.17-1.01 MPa for the 0° configuration, and within 0.22-1.59 MPa for the 10° configuration when using tendon-specific analytical model fits (Fig 2).

**Table 1: Errors in predicting regional stress (in MPa) for the left, middle, and right sections of each tendon using shear wave speed (predicted value) and regional strain (estimated true value).**

| Tendon | Config. | Left | Middle | Right |
|---|---|---|---|---|
| 1 | 0° | [b]-1.01 ± 0.44 | [a]0.27 ± 0.65 | [b]0.72 ± 0.99 |
| | 10° | -1.37 ± 1.12 | [b]-0.40 ± 0.07 | [a]0.26 ± 0.33 |
| 2 | 0° | [a]0.27 ± 0.71 | [a]0.17 ± 0.30 | [b]-0.47 ± 0.28 |
| | 10° | -0.68 ± 0.19 | -0.58 ± 0.05 | -1.59 ± 0.84 |
| 3 | 0° | [b]0.52 ± 0.59 | [a]-0.20 ± 0.34 | [a]-0.30 ± 0.35 |
| | 10° | -0.60 ± 0.15 | -1.27 ± 0.12 | [b]-0.22 ± 0.20 |

[a]0-10% of max observed stress, [b]10-20% of max observed stress

## DISCUSSION

The objective of this study was to determine whether regionally measured shear wave speeds could predict regional axial stress. We found that relationships between regional shear wave speeds and estimated regional stress are highly linear. We also found that, in select trials, regional stress predicted using shear wave speed corresponded to regional stress estimated using regional strain.

Shear wave speeds measured regionally using the slope fit of five vibrometer points were in range of bulk shear wave speeds measured previously in flexor tendons using a normalized cross-correlation between two vibrometer points [9]. Regional strains measured using DIC were less than the global grip-to-grip strain, which is in accordance with previous DIC studies [10]. We found that shear wave speeds are proportional to estimated axial stress at every location across the tendon width. However, there was variability in the slope and intercept (i.e., density and shear modulus, Fig. 2, Eq. 1) of the linear fit between shear wave speed squared and estimated axial stress across measurement locations and loading configurations (0 and 10°) across tendons. This variability contributed to errors in predicting axial stress using shear wave speed. These regional variations in slope and intercept should be accounted for to make more accurate regional stress predictions.

This study has limitations to consider when interpreting the results. First, we used the bulk stress-strain relationship in the tendon to estimate regional axial stress. An inverse FE model could better account for variations in tendon geometry and material properties and is a focus on our ongoing work. Second, regional strains were determined using 2D DIC. In the future, we plan to perform 3D DIC to capture out of plane strain and thus a more representative measure of the tendons' deformation state during loading.

The findings of this study suggest that increases in regional shear wave speed are proportional to increases in estimated regional stress in porcine digital flexor tendons. These observations suggest that it may be viable to predict regional stress from spatial shear wave speed measurements. Variability between specimens remains a challenge and may be best considered by using inverse finite element models to better account for both material and morphological factors.


## ACKNOWLEDGEMENTS

NSF GRDP DGE-1747503, NIH R21 EB024957, University of Wisconsin-Madison Department of Animal Sciences.


## REFERENCES


[1] Gardiner, *J. Orthop. Res.*, 21:1098-1106, 2003. [2] Robinson, *J. B. Jt. Surg.*, 5:674-681, 2004. [3] Martin, *Nat. Commum.*, 9:2-10, 2018. [4] Blank, *J. Mech. Beh. Biomed. Mat.*, 105:103704, 2020. [5] Blank, *Orthopaedic Research Society*, 2020. [6] Schatzmann. *K. Surg. Sport. Tr. A.*, 6:56-61, 1998. [7] Hampel, *J. Am. Stat. Assoc.*, 69-346:383-393, 1974. [8] Blaber, *Exp. Mech.*, 55:1105-1122, 2015. [9] Martin, *J. Biomech.*, 90:9-15, 2019. [10] Mallet, *Acta Biomater.*, 56:44-57, 2017.

SB³C2022
Summer Biomechanics, Bioengineering and Biotransport Conference
June 20-23, Eastern Shore, MD, USA

# REAL-TIME SHAPE OPTIMIZATION OF THE TOTAL CAVOPULMONARY CONNECTION IN FONTAN SURGICAL PLANNING VIA REDUCED ORDER MODELING

**I. Shah (1,4), L. Dasi (1), T. Iliescu (2), O. San (3), A. Veneziani (4,5)**

(1) Wallace H. Coulter Department of Biomedical Engineering, Georgia Institute of Technology, Atlanta, GA, USA
(2) Department of Mathematics, Virginia Tech, Blacksburg, VA, USA
(3) School of Mechanical & Aerospace Engineering, Oklahoma State University, Stillwater, OK, USA
(4) Department of Mathematics, Emory University, Atlanta, GA, USA
(5) Department of Computer Science, Emory University, Atlanta, GA, USA

## INTRODUCTION

The Fontan operation is the culmination of a staged surgical procedure for children with congenital single ventricle defects such as hypoplastic left heart syndrome. During the operation, venous return from the inferior vena cava (IVC) is rerouted to the pulmonary arteries (PA) using a surgical graft, resulting in the formation of the total cavopulmonary connection (TCPC). The TCPC prevents mixing of oxygenated and deoxygenated blood in the malfunctioning ventricle, which in general results in favorable short-term outcomes for patients. However, long-term complications are still prevalent, such as pulmonary atriovenous malformations (PAVMs) and limited exercise capability of the heart. Previous studies have shown the importance of optimizing pulmonary flow and TCPC hemodynamics to significantly reduce the likelihood of these long-term complications.

Surgical planning via computational modeling has allowed for pre-operative examination of a wide range of potential patient-specific morphologies for the TCPC, typically by varying the placement of the IVC with respect to the superior vena cava (SVC) and the left and right PAs. This represents a shape optimization problem, where differences in the anatomical connection between the IVC, SVC, and PAs result in unique hemodynamics and flow distributions. Hemodynamic factors such as hepatic flow distribution (HFD) and power loss (PL) can be numerically quantified, and thus aid clinicians in choosing the optimal morphology. HFD has been an apparent target for optimization, as the absence of hepatic flow from the IVC has been previously linked to the development of PAVMs in patients [1]. PL due to the collision of colliding fluid fronts in the TCPC may also cause turbulent flow dynamics, leading to potential blood damage and viscous shear losses.

However, due to the intrinsic numerical complexities required to discretize and linearize the time-dependent Navier-Stokes equations (NSE) that govern flow dynamics, the computational costs of modeling these surgical planning cases become extremely high, especially for repetitive testing of various patient-specific TCPC geometries in a trial-and-error fashion [2-3]. Therefore, there is a need for rapid and accurate predictive models that can optimize patient-specific TCPC geometries, and thus allow for real-time Fontan surgical planning.

Reduced order models (ROMs) are a common *data-driven paradigm* used to simplify full order models (FOMs) to their dominant components, thus significantly reducing the required computational resources. ROMs can be divided into two stages: the *offline* stage, where computationally expensive simulations are offloaded, and the *online* stage, where these simulations are promptly recycled for a rapid reduced order solution [4]. Although ROMs have been employed in previous fluid dynamic studies, the application of ROMs towards real-time shape optimization of the TCPC has not yet been studied.

In this preliminary study, we introduce a ROM framework using the Proper Orthogonal Decomposition (POD) Galerkin approach for rapidly assessing hemodynamics through idealized models of the TCPC. Specifically, the proposed POD approach allows for a significant reduction in the computational costs of simulating blood flow dynamics in 2D TCPC geometries. This framework serves as a first step towards real-time shape optimization simulations of the TCPC, which will allow for rapid identification of the optimal TCPC morphology.

## METHODS

We began by developing a reference geometry of an idealized 2D TCPC geometry where specific nodes of the TCPC were parameterized, as indicated by $\mu_0 \dots u_5$ (Fig. 1). Each of the variables $\mu_0 \dots u_5$ were parameterized within a certain range as shown in Fig. 1. This geometrical parameterization resulted in the formation of different TCPC morphologies, each with varying offsets between the IVC and SVC, as well as varying inlet diameters for both the IVC and SVC. In each case, parabolic velocity boundary conditions were enforced at the SVC and IVC ($v_{max} = 100 icm/s$ at the SVC, and $v_{max} = 50 icm/s$ at the IVC). At the right pulmonary artery (RPA) and left pulmonary artery (LPA), pressure boundary conditions were enforced ($P_{RPA} = 200 iPa$, $P_{LPA} = 1000 iPa$).

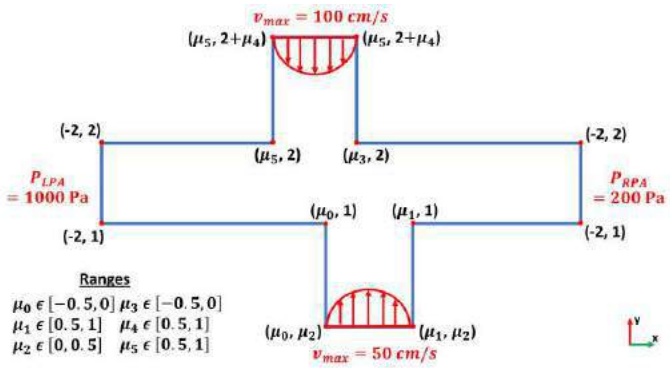


**Figure 1: Reference geometry for idealized 2D TCPC.**

A total of 100 computational fluid dynamics (CFD) simulations were performed with the parametrized TCPC geometries in the offline stage of the ROM framework, from which a *snapshot* library was created. Specifically, these simulations were performed with the steady NSE after discretization with the finite element (FE) method.

The online stage of the ROM framework began with filtering out redundancy from the snapshot matrix via the *Singular Value Decomposition* (SVD), and the resultant singular values were analyzed. A rapid decay in the singular values indicates that the snapshot library can be well approximated by utilizing a select few of those eigenvectors associated with the largest singular values. Using these eigenvectors, the POD-Galerkin approach was implemented to create the reduced basis functions. This was done by first representing the FOM as a linear system obtained after FE discretization, as shown below.

$$Au = b \tag{1}$$

Here, $A$ is the *stiffness matrix* extracted from the FE simulations featuring a size in the range of thousands or millions of rows, $u$ is the resultant solution, and $b$ is a matrix containing the applied boundary conditions. Using the POD-Galerkin approach, the solution $u$ to the differential problem can be rewritten as

$$u_{ROM} = W\underline{c}. \tag{2}$$

Here, $\underline{c}$ is a vector of unknown coefficients, and $W$ is a matrix formed from the eigenvectors obtained from the SVD analysis. Plugging in Eq. (2) into Eq. (1) and multiplying both sides by $W^T$ results in the final reduced order problem, which reads as

$$W^T AW\underline{c} = W^T b. \tag{3}$$

From Eq. (3), $W^T AW$ is a matrix that features a size in the range of tens or hundreds of rows. When compared to the size of the stiffness matrix $A$, the savings in computational costs become evident.

The ROM framework described above was implemented in an open-source model reduction library known as *RBniCS*, which allows for all offline stage simulations, model reduction, and online phase calculations to be combined into a single solver [4]. In the online phase, new geometrical parameters different from those used to generate snapshot library were applied, and the resulting reduced order solution was simulated. Visualization of all results was done in *ParaView*.

## RESULTS

Velocity streamlines and pressure contours for the ROM and FOM solutions are shown in Fig. 2. The ROM solutions were in strong agreement with the FOM CFD simulations with regards to resultant pressure drops and contours, velocity streamlines, and flow dynamics. Peak velocities in the ROM and FOM solutions were identical (99.91 cm/s), while peak pressures were 5408.32 and 5407.14 Pa in the ROM and FOM solutions, respectively. The ROM was also able to accurately capture unique regions of flow separation (corner between the SVC and LPA) that occur due to an adverse pressure gradient from the nonlinear term of the NSE. In terms of computational costs, the FOM required an average of 153.46 seconds to simulate, while the ROM reduced this to 27.48 seconds, an 82.09% decrease in computational time.

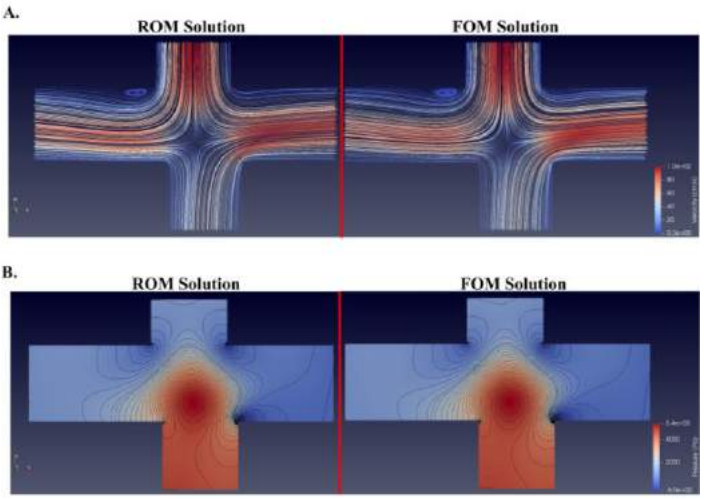


**Figure 2: Comparison between resultant velocity streamlines (A) and pressure contours (B) from ROM and FOM solutions.**

## DISCUSSION

In this study, we introduce a POD-based ROM framework applied towards real-time fluid dynamic simulations in idealized 2D TCPC geometries. The ROM framework resulted in a significant decrease in the computation time required to simulate blood flow dynamics through the TCPC morphology, all while providing identical hemodynamic results as compared to the FOM simulations. Although this framework shows promise in rapidly simulating TCPC flow dynamics, further refinements are underway to fully incorporate the shape optimization problem and thus allow for real-time assessment of the optimal TCPC geometry in 2D scenarios. The optimization criteria will rely on the previously mentioned HFD and PL. Using these quantities, a possible function can be formed to use in the optimization problem, which reads

$$J_{TCPC} = \frac{\alpha_1}{2} PL^2 + \frac{\alpha_2}{2} (HFD_{RPA} - 0.5)^2, \tag{4}$$

where $\alpha_1$ and $\alpha_2$ are user-defined parameters that minimize the PL ($\alpha_1$) and maximize the HFD to the LPA ($\alpha_2$). If $b$ are the geometrical parameters that define the TCPC, then the shape optimization can be formalized as follows: find a value $b$ that minimizes $J_{TCPC}$ under the constraints of the NSE. This optimization problem will be implemented into the in-house solver using the Karush-Kuhn-Tucker (KKT) conditions. A significant limitation of this preliminary investigation is the use of idealized 2D geometries to model the TCPC. Moving forward, the ROM framework will be adapted to parametrize 3D models of the TCPC. This will require the use of advanced techniques such as radial basis functions (RBFs) that allow for adaptive mesh morphing.

In conclusion, the POD-based ROM framework presented here significantly reduces the computational costs of simulating flow dynamics through 2D TCPC geometries. Further refinements of the ROM framework are underway to incorporate the shape optimization problem, as well as to transition towards 3D TCPC morphologies.

## ACKNOWLEDGEMENTS

Research was supported by the NSF Project 2012254 (T.I.)-2012255 (O.S.)-2012286 (A.V.).

## REFERENCES

[1] Pike, N. A., et al. *Ann Thorac Surg*, 78(2):678-679, 2004.
[2] Siallagan, D., et al. *J of Thorac Cardio Surg*, 155(4):1734, 2018
[3] Yang, W., et al. *J of Thorac Cardio Surg*, 143(5):1086-97, 2012
[4] Hesthaven, J. et al. *Cert Reduced Basis Meth for PDEs*, 590, 2016

SB³C2022
Summer Biomechanics, Bioengineering and Biotransport Conference
June 20-23, Eastern Shore, MD, USA

# DEVELOPMENT OF A 3D MICROFLUIDIC LIVER CONSTRUCT MODEL FOR ASSESSING THE EFFECT OF PUFA DIETS

**N. Hauser (1), L. Madison Kirk (1), E. Rahbar (1)**

(1) Department of Biomedical Engineering, Wake Forest School of Medicine, Winston-Salem, NC, United States

## INTRODUCTION

Three dimensional (3D) cell culture for *in-vitro* studies has existed since the 1980's. In the decades since, 3D cultures have gained increasing popularity and have demonstrated increased physiological relevancy when compared to 2D cultures due to the ability for cells to spatially arrange, extracellular matrix (ECM) interactions, and a closer material approximation to native tissue. However, 3D cell cultures still lack critical factors found to have a noticeable impact on cell phenotype such as shear stress or other mechanical conditions (1).

Cell culture within a microfluidic chip offers an opportunity to create more relevant microphysiologic systems. Through the addition of fluid flow, mechanical forces simulating physiologic factors such as flow or shear and strain can be introduced (2). Additionally, the introduction of highly controlled fluid movement allows for the ability to connect varying cultured organ systems in an organized manner which enables precise control of nutrient and metabolite flow within the cultured systems. Specifically, for this study we are looking to examine the downstream effects of omega-3 (n-3) and omega-6 (n-6) dietary polyunsaturated fatty acids (PUFAs). These dietary fatty acids are metabolized by the liver into long chain PUFAs, which are precursors to bioactive lipid mediators including prostaglandins, leukotrienes, thromboxanes, and specialized pro-resolving mediators (SPMs). Omega-3 PUFAs have been shown to play a role in resolving various acute and chronic inflammatory diseases within animal models, but translation of these findings into humans has been difficult. We postulate that genetic variability in humans and their PUFA metabolism may be contributing to this challenge and there is a need for further examination into the mechanisms of human PUFA metabolism within the liver (3).

In this abstract, we leverage microfluidics and 3D cell culture to create a highly controllable and physiologically relevant liver model for use in assessing the effects of dietary PUFAs. We aim to create liver-like constructs that recapitulate structures and cell populations within the liver and to allow for a simulated nutrient exchange like those in the hepatic portals. This is accomplished by incorporating three distinct cell types found within the liver into each construct: hepatocytes, stellate cells, and liver sinusoidal endothelial cells. Through the inclusion of these cells in a layered organization (Figure 1) we aim to closely simulate the process through which dietary PUFA's are processed within the body. This design also allows for the selective removal of different cell types to determine their importance in PUFA metabolism.

Another, a key feature of this microfluidic chip is the two distinct flow channels only bridged by the hepatic constructs. By introducing nutrients of interest to the endothelial side we can determine that any change in the lumen channel from baseline is due to metabolic processing through the hepatic-like structure. Once the model is tested, we aim to be able to use these liver chips as a plug-and-play system to work with similar microfluidic chips modeling other organ systems both upstream (intestinal models) and downstream (lung, heart, brain) with the goal of viewing the effects of PUFA metabolism in a more complete system than just hepatic constructs alone.

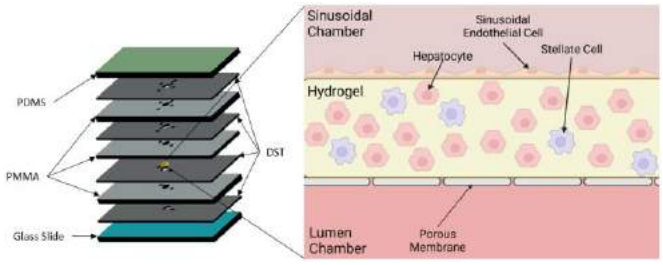


**Figure 1: Illustration of microfluidic chip architecture (exploded view) and hepatic culture cross section**. (This figure was partially created with BioRender.com).

## METHODS

The microfluidic chips used in this study were constructed from stacked layers of double sided adhesive tape (DST) and poly-methyl-methacrylate (PMMA). A laser cutter was used to cut channels and fluid wells into the materials and then they were sandwiched together as shown in Figure 1 to create a microfluidic chip with two separate fluid chambers and a liver construct suspended between them. A PDMS cap was placed as the last layer to fully enclose the chip.

The constructs within the microfluidic chips were made using commercially available methacrylated gelatin (GelMa) hydrogel (Advanced Biomatrix #5272). HepG2 and Lx-2 cells were suspended in a 5% GelMa and lithium phenyl-2,4,6-trimethylbenzoylphosphinate (LAP), a photocrosslinker, prepared according to the manufacturer's specifications. The cells were suspended at a concentration of 20 million cells/mL and with a 3:1 ratio of HepG2 to Lx-2 cells. Linear RGD peptide was then added to create a 1mM solution. 12.5 µL of hydrogel is then pipetted onto the membranes suspended within each microfluidic channel. The constructs were then crosslinked using 365nm UV light for 7 seconds to photo-polymerize the hydrogel. 200,000 EA.hy926 cells were then seeded onto the apical surface to create the endothelial monolayer.

Hepatic constructs were maintained for 24 hours in static conditions before being attached to microfluidic flow. The flow rate used to maintain the constructs was 9.5 µL/min. Cultures were then maintained with regular media changes for up to 14 days.

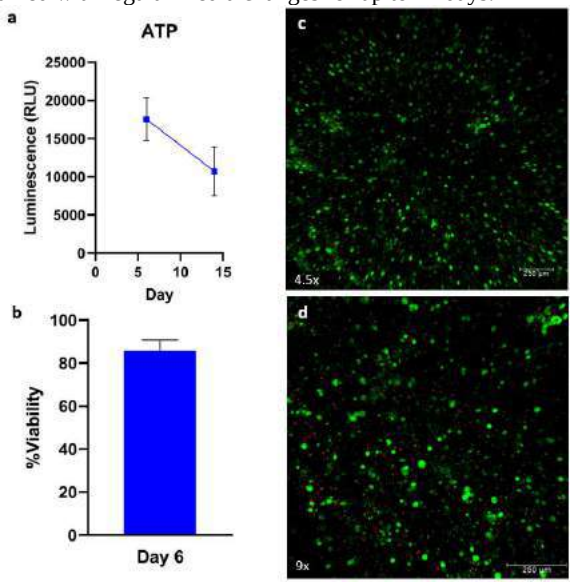


**Figure 2: (a) ATP measures of hepatic cultures over time. (b) ImageJ cell count of living vs dead cells. (c, d) LIVE/DEAD macroconfocal images of HepG2+Lx2 constructs after 6 days in culture, scale bars are 250µm**

## RESULTS

Currently, we have determined that the constructs remain fairly viable out to one week with a moderate reduction (~30%) in metabolism at the two week margin (Figure 2) based on ATP output. Confocal imaging using LIVE/DEAD staining reinforces these findings. Notably, the constructs here demonstrate a uniform viability throughout the entire structure indicating that there is no necrotic core formation, a common problem in larger static construct cultures.

Based on confocal imaging (Figure 3) it was determined that the stellate and hepatocyte cells within the constructs were evenly distributed. Examination of the Lx2 stellate cells (Figure 3a) shows a more rounded morphology compared to 2D cultures of these cells which is associated with a non-fibrotic state. Figure 3d demonstrates the capability to seed an endothelium onto these constructs.

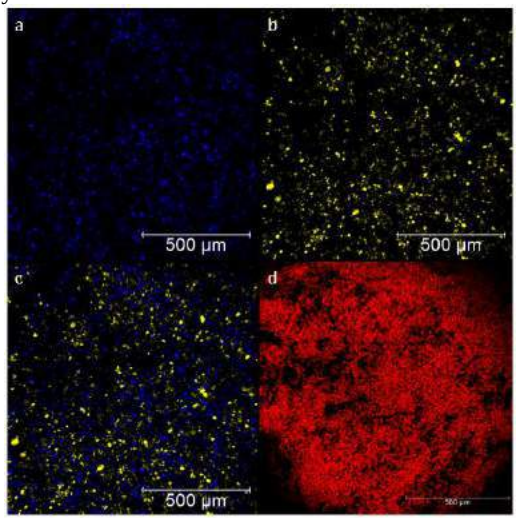


**Figure 3: Cell membrane dye tracking. (a) DiD(blue) tagged Lx2 stellate cells. (b) DiO(yellow) tagged HepG2 cells. (c) Merged image of (a) and (b). (d) EA.hy926 cells tagged with DiL(red) as a monolayer 6 hours post seeding.**

## DISCUSSION

The overall goal of this chip is the creation of a microfluidic construct system for use in multi-organ PUFA dietary studies. The first step to establishing that system is ensuring that the cell populations required to simulate physiological liver activity are both viable and functional within the constructs. Here, we have shown the potential to create liver constructs stable out to at least two weeks using commonly available liver cell lines. This time period is long enough to examine the acute effects within the liver and body of varying PUFA diets. Specifically, this timeframe would be useful for examining the use of PUFA's for treating acute inflammatory conditions after traumatic injuries including concussions, TBI, and ALI/ARDS.

The next step will be examining the metabolic function of these constructs over time by looking at CYP expression, FADS expression and urea and albumin production. Following that would be the inclusion and use of primary human hepatocytes to further increase this model's physiological relevance. Finally, the primary evaluation for this model will be PUFA feeding studies where various blends of n-3 and n-6 PUFAs are introduced via the sinusoidal channel and gene expression, as well as downstream metabolic outputs will be measured from the lumen channel. We expect that the presence of flow in conjunction with a modeled endothelium will increase the metabolic activity of these constructs compared to static models.


## ACKNOWLEDGEMENTS

Funding for this study was provided by Dr. Rahbar's laboratory start-up funds, NIH K25 HL133611 and HL13361-04S1 and NSF REU Award #1950281. HepG2 and Lx-2 cell lines were provided by Dr. Shay Soker.


## REFERENCES


[1] Duval, K et al, *Physiology*, 32:266-277, 2017
[2] Hegde, M et al, *Lab on a Chip*, 14:2033-2039, 2014
[3] Kirk, LM et al, *PLOS1*, 10.1371, 2022.

SB³C2022
Summer Biomechanics, Bioengineering and Biotransport Conference
June 20-23, Eastern Shore, MD, USA

# VERIFICATION OF BIPHASIC MATERIAL PARAMETER IDENTIFIABILITY BY FULLY AUTOMATED SENSITIVITY ANALYSIS AND ERROR CHECKING

**John M. Peloquin (1), Harrah R. Newman (1), Dawn M. Elliott (1)**

(1) Biomedical Engineering, University of Delaware, Newark, DE, USA

## INTRODUCTION

Recent work in biomechanics increasingly relies on structural material models because they provide clear physical interpretations and, potentially, predictive validity. They naturally complement the widely-held structure-function hypothesis that tissue organization and composition reflects its health and physiologic role [1]. Despite the expectation that tissue organization is linked with mechanical function, experiments often find structure or composition to be uncorrelated with material parameters [2]. Accordingly, there is growing interest in scrutinizing the methods used to quantify material parameters.

A range of potential inadequacies in material parameter quantification have been described, including specimen preparation, test protocols, and parameter estimation via model fitting [3–5], but these findings unfortunately had limited impact on common practice. Estimating material parameters from data is a multi-stage process (Fig 1). Consequences from a flaw in the test protocol design are often hidden until after data collection when parameter estimation is attempted; then, the root cause is obscured in the muddle of all prior choices. Here, we focus on evaluating the capacity of a test protocol to constrain a material parameter estimate; i.e., whether all parameters in a chosen material model will be *identifiable* from a test protocol's data.

The objectives of this work were: (1) develop software to assess parameter identifiability for any chosen protocol that is suitable for use across research groups, and (2) evaluate a practically significant protocol, confined compression of the intervertebral disc (IVD) cartilaginous endplate (CEP). Endplate permeation is an important transport pathway for the IVD and accurate CEP properties are needed for continued development of IVD FEA models with predictive validity.

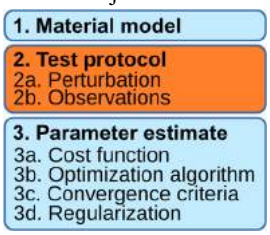


**Figure 1: Decisions in fitting material parameters to data**

## METHODS

Global sensitivity analysis was used because it can evaluate a test protocol prior to data collection, without knowledge of which parameter values are correct. FEBio was used for the simulations due to its flexibility and widespread adoption. A template FEA model was created to represent a CEP specimen (Fig 2). The material model was a biphasic mixture of a Holmes–Mow elastic solid, Holmes–Mow strain-dependent permeability, and Donnan equilibrium swelling (10 parameters total). Each material parameter was varied using full factorial sampling with 3 equally spaced levels spanning best estimates of the 95% confidence intervals for human CEP [6–8], generating 59,049 cases. The need for 3 levels was confirmed by comparison to a 2-level analysis (1,024 cases).

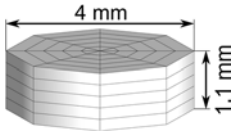


**Figure 2: Simulated confined compression specimen geometry**

Confined compression for each case was simulated consistent with a confined compression test protocol with prior and ongoing use [6,9], consisting of isometric swelling followed by three 10% strain incremental stress relaxation periods in a 0.15 M PBS bath (Fig 3a). The bottom surface was free-draining. In a physical experiment, the CEP is already swollen with unknown strain at t = 0 s, and this preswelling strain was parameterized as $f_s$. Axial compression force, $Fz$, was tabulated for all cases as the test protocol's output variable (Fig 3a).

Parameter effects at each time point were quantified by Pearson correlation coefficient (r) between the parameter and $Fz$. Similarity (redundancy) in the parameter effects was quantified by hierarchical cluster analysis, similar to its use in genetic analysis. A new Python package, "spamneggs", was written to automatically create and run cases, check output for errors, and tabulate and plot results. All computation took < 48 h on a standard office PC.

## RESULTS

$Fz$ was affected most strongly by intrinsic permeability ($k0$), fixed

charge density (FCD), and preswelling strain fraction ($f_s$) (Fig 3b, magnitude of correlation coefficients, r). $E$, $\phi$, $M$, and α had moderate to weak effects on $Fz$. However, decomposition of total variance via Sobol analysis (not shown) revealed that M and α, which govern permeability's strain-dependence, had strong effects due to parameter interactions or nonlinear effects not captured by Pearson correlation.

The distinctiveness of each parameter's effects on $Fz$ ranged from unique to redundant (Fig 3b, correlation patterns and clusters). $\phi$, $k0$, and β had unique correlation patterns with $Fz$. However, $E$ and ν were fully redundant with each other, as were FCD and Φ. Redundancy in a pair of parameters implies that at least one is non-identifiable. $f_s$ was similar to FCD and Φ but, fortunately, not entirely identical.

Parameters can have mutually redundant effects in combinations of 3 or more, not only pairwise. Therefore, the identifiability provided by the entire protocol was quantified using the eigenvalues of the matrix of all correlation coefficients (i.e., normalized covariance). Two eigenvalues were ≈ 0, reflecting the two fully redundant pairs noted above, and six eigenvalues were ≥ 1% of the total normalized variance (Fig 4). Thus, data from this protocol provides enough information to constrain ~ 6 of this material model's 10 parameters.

Unexpectedly, the automated error checks provided important information. 20% of cases had one or more output errors (Fig 5a). Only 1/3 of errors were reported by FEBio; the rest were detected by custom error checks, the most important of which were for protocol errors (boundary conditions not enforced) and pore collapse (pore volume ≤ 0, a violation of biphasic theory's assumptions) (Fig 5b). Cases with errors were excluded from quantification of each parameter's effects above;

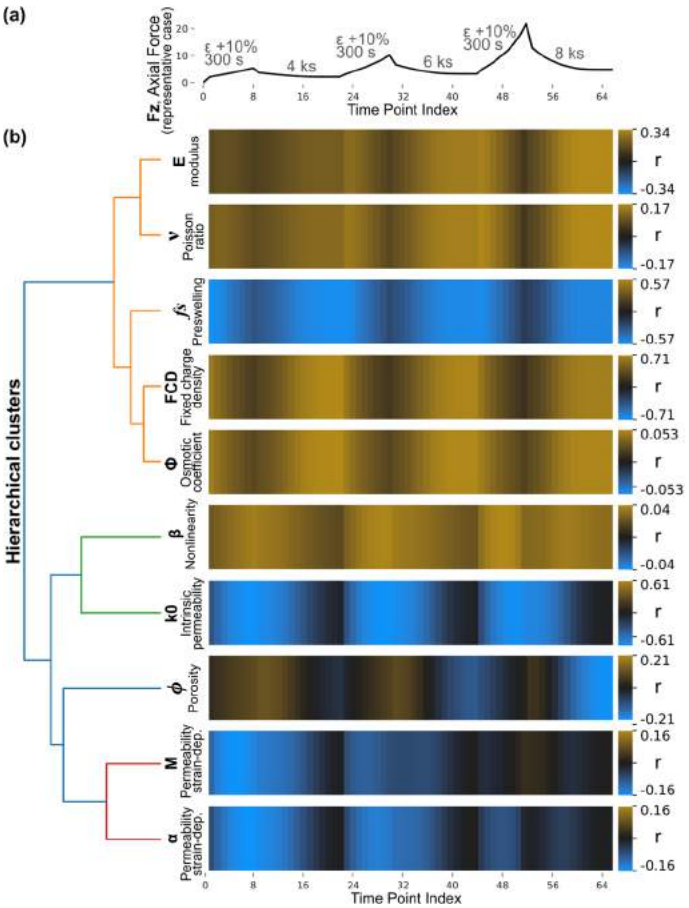


**Figure 3: (a) Test protocol; (b) Parameter effects (correlation coefficients, r, between the parameter and Fz across time).**

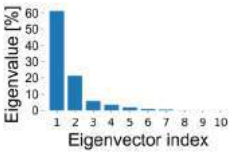


**Figure 4: Eigenvalues of the parameter correlation matrix**

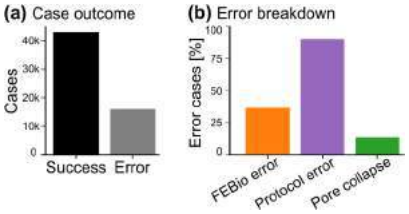


**Figure 5: Error counts and proportions**

without these checks, parameter effects were severely distorted.

## DISCUSSION

Automated global sensitivity analysis was successfully performed for an IVD CEP confined compression test protocol and nonlinear biphasic material model that is also applicable to cartilage and other soft tissues. Due to redundant parameter effects, only ~ 6 parameters are identifiable by model fitting, *if* the remainder can be constrained by other methods.

Selection of constraints should be based on the parameter effects (Fig 3). Only one parameter in each of the redundant pairs can be fit. Φ is already assumed [6,8], and ν = 0 could be assumed (treating $E$ like an aggregate modulus). FCD can be measured by DMMB assay [6], and usually is; $\phi$ can be measured [7]; and $f_s$ can be calculated from $E$, ν, β, and FCD at equilibrium [6]. To consistently achieve equilibrium, the protocol duration must be extended. Because assay errors are uncorrelated with the major axes of a model fit's solution domain, small direct measurement errors tend to cause an outsized reduction in model accuracy [10]. We recommend using direct measurements only to regularize (softly constrain) FCD, $\phi$, and $f_s$. These 2 hard constraints and 3 soft constraints should provide parameter identifiability when fitting the model. Alternatively, confined compression could be exchanged for indentation, as was done for fitting linear elastic constant-permeability biphasic models [3], to hopefully provide better data for model fitting.

Simulation errors were frequent but were successfully managed by an additional layer of automated error checking. These checks were critical to obtain valid results and would also be necessary when fitting a model to experimental data, as optimization algorithms will not function correctly when 10–20% of the model evaluations are incorrect. These results reveal that parameter estimation for a biphasic model involves identifying both the feasible region as well as the parameters themselves. This dual task is under-studied; many optimization algorithms accept parameter bounds but these must be chosen up front.

Importantly, the software we developed for this study is general-purpose. It can operate on any FEBio model, and tables and figures are produced automatically, adapting to the chosen material parameters and output variables. Given a template FEBio model, and assuming the automated error checks remain adequate, the corresponding sensitivity analysis takes < 1 h of human time. The software is published at https://github.com/jpeloquin/spamneggs. We therefore expect that these methods will provide practical assistance during experimental protocol design, making material parameter estimation easier and more reliable.


## ACKNOWLEDGEMENTS

NIH R01AR050052, P20GM139760, R01AR054620.


## REFERENCES


[1] Lanir, Y. J Elasticity, 129, 7–48, 2017.
[2] Zhou, M. J Biomech Eng, 142, 030302, 2020.
[3] Mow, V. C. Int J Solids Structures, 35, 4945–62, 1998.
[4] Hartmann, S. Arch Appl Mech, 88, 3–26, 2018.
[5] Wale, M. J Biomech Eng, 143, 011011, 2021.
[6] Cortes, D. J Biomech, 47, 2088–94, 2014.
[7] Wu, Y. Spine, 42, E1002–9, 2017.
[8] Yang, B. Acta Biomaterialia, 100, 61–74, 2019.
[9] DeLucca, J. J Orthop Res, 34, 1410–17, 2016.
[10] Gutenkunst, R. PLoS Comput Biol, 3, e189, 2007.

SB³C2022
Summer Biomechanics, Bioengineering and Biotransport Conference
June 20-23, Eastern Shore, MD, USA

# ENTHESIS MECHANICAL PROPERTIES AND COMPOSITION ARE DEPENDENT ON MOVEMENT AND DEVELOPMENT

**Kaitlin P. McCreery (1,2), Olivia R. Tonti (2), Callan M. Luetkemeyer (1), Corey P. Neu (1,2), Sarah Calve (1,2)**

(1) Paul M. Rady Department of Mechanical Engineering, University of Colorado Boulder, Boulder, CO, USA
(2) Biomedical Engineering Program, University of Colorado Boulder, Boulder, CO, USA

## INTRODUCTION

Developing musculoskeletal tissues consist of a dynamically changing extracellular matrix (ECM) that can directly and indirectly regulate cell behavior. Tissue mechanical properties and composition activate and control key cellular processes through reciprocal cell-matrix interactions. Researchers have been unable to capitalize on these instructive cues for tissue engineering scaffold design due to limited knowledge of the cell microenvironment during musculoskeletal ontogeny [1]. Furthermore, while research efforts are usually concentrated on tissue-specific development, how these vastly different structures and functions become integrated remains unclear.

Skeletal muscle transmits forces to the skeleton through the enthesis, a strong interface between tendon and bone. This interface effectively attaches mechanically dissimilar tissues by providing stress and strain reduction via splayed collagen microfibrils [2]. Because these fibrous tissues do not regenerate, the only time that a strong, functional attachment forms is during initial tissue assembly [3]. The migration and stabilization of enthesis progenitors relies on postnatal muscle loading, resulting in a mineralized and mechanically strong tissue gradient [4]. The dynamics of the developing enthesis in prenatal development, however, has been underexplored.

The objective of this study is to define how mechanical properties and proteome of the assembling enthesis change as a function of development and motility. Specifically, we investigate the Achilles enthesis at the pre-osteogenic calcaneus in murine embryonic and postnatal timepoints. Furthermore, we investigate the impact of muscle forces on enthesis development using the *muscular dysgenesis* (*mdg*) murine model in which skeletal muscles lack excitation-contraction coupling due to a mutation in the calcium channel subunit Cacna1s [5].

## METHODS

To investigate the influence of muscle contractions on enthesis development, mice heterozygous for Cacna1s$^{mdg}$ were paired to generate wildtype controls (+/+), normal-appearing littermates (+/mdg), and homozygous (*mdg*/*mdg*) paralyzed mutants for testing. Homozygous mice do not survive postnatally, so these studies were conducted at embryonic day (E) 18.5. To investigate the influence of development on enthesis formation, adolescent wild-type mice (C57B6/J) were obtained postnatal day (P) 21. Cacna1s$^{+/mdg}$ mice were combined with mice expressing Scleraxis-GFP (Scx-GFP) to visualize tendon progenitors and identify the enthesis *ex vivo*. Cacna1s$^{+/mdg}$ and Scx-GFP mice were provided by R. Schweitzer at OHSU.

Tissue specimens were collected and analyzed the same day via atomic force microscopy (AFM) while still viable, confirmed with EthD-1 staining. AFM tests were conducted while tendon/entheses tissues were undeformed. A Keysight 5500 AFM system facilitated mapping of micromechanical properties of the ECM in tendon, enthesis, and cartilage tissues. Tissues were characterized with a cantilever equipped with a 5µm borosilicate glass sphere (NovaScan), pre-calibrated to be 0.07 N/m. The tissue was identified optically and then indented at 1.2µm/s until the setpoint force of ~12nN was reached, and the probe was retracted. AFM was performed over the approximate area of the cell microenvironment 15x15µm, with 16 or 64 independent indentations as technical replicates. The indentation curves were fit to a two-parameter model developed by Fung to extract an initial stiffness modulus and a strain-stiffening, nonlinear parameter [7]. Two-way ANOVA was used to calculate significant interactions between ECM stiffness, genotype, and developmental timepoint, and Tukey or simple effects post-hoc tests were conducted for independent comparisons.

To identify ECM composition in developing cartilage, tendon, and enthesis tissues, liquid chromatography-tandem mass spectrometry (LC-MS/MS) was utilized. At E18.5 and P21, tissues from the Achilles enthesis (tendon, calcaneus, and interface) were isolated and tissues were mechanically homogenized with 8M urea, 100mM ammonium bicarbonate, and 10mM DTT following [8]. Protein concentrates were sent to the Mass Spectrometry facility at CU Boulder for analysis.

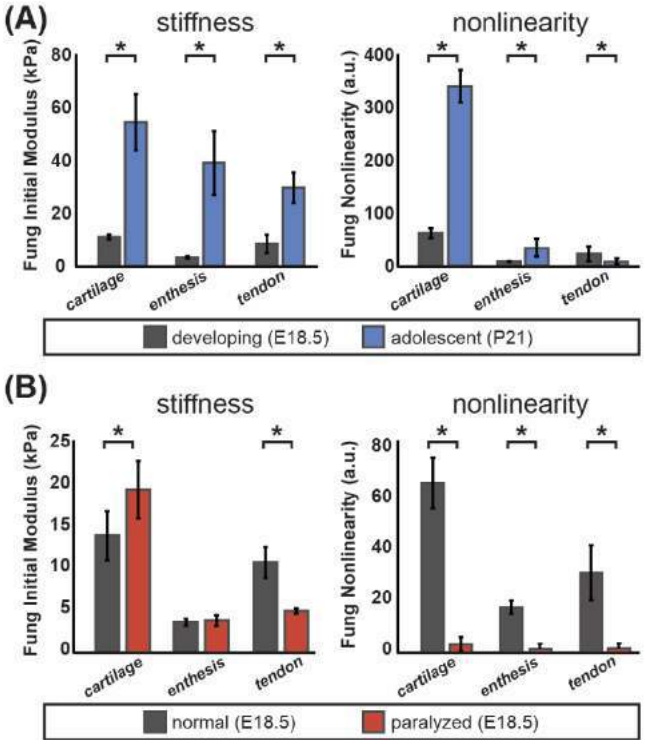


**Figure 1: Stiffness and nonlinearity significantly change with postnatal development (A) and embryo motility (B).**

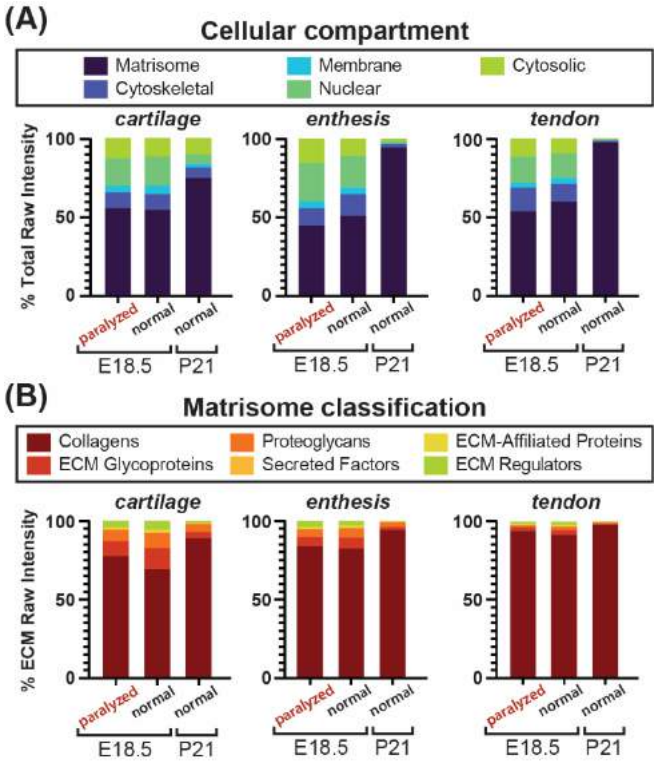


**Figure 2: Distribution of proteins identified by LC-MS/MS. Raw intensities of tissue compartment (A) and matrisome classification (B) were plotted as a percent of total raw intensity.**

Proteins were annotated as cytosolic, nuclear, membrane, cytoskeletal, or matrisome based on a list of cellular compartments derived from The Matrisome Project [6].

## RESULTS

Two-factorial ANOVA identified a significant interaction between the effect of embryo motility on tissue stiffness ($p<0.05$). A follow-up test for simple effects detected significant differences between each tissue type both as a function of motility ($p<0.05$) and developmental timepoint ($p<0.05$). While we did not identify a significant interaction between stiffness and developmental timepoints ($p=0.12$), Tukey post-hoc tests were significant between tissue types within each developmental stage ($p<0.05$). Significant differences of nonlinearity were detected between developing and adolescent timepoints ($p<0.05$), and as a function of embryo motility.

Comparison of the proteome of developing tissues (normal vs. paralyzed) and adolescent tissues (wildtype only) showed that the effect of ECM category was significant between tissues ($p<0.0001$). The proteomic makeup divided into cellular compartments showed little change as a function of embryo movement; however, relative abundance of collagens decreased in paralyzed embryos, particularly in developing cartilage. The relative abundance of ECM regulators increased at the onset of movement during development, then decreased in adolescence.

## DISCUSSION

We measured mechanical properties of the ECM cell microenvironment and characterized the ECM proteome in the enthesis as a function of development and embryo movement. The initial stiffness of each region in embryonic tissue did not demonstrate a linear gradient, but rather a bimodal characteristic where the enthesis is the least stiff between tissues. Interestingly, by the time the hindlimb is routinely loaded at P21, a stiffness gradient was observed. These results support the hypothesis that the mechanical gradient of the enthesis is established during postnatal loading/walking. Postnatal activity may be responsible for the nonlinearity of cartilage and functional grading of the tendon interface. Preliminary data of the proteome in the developing enthesis suggests that embryonic motility potentially stimulates ECM production and diversity in matrisome composition, particularly levels of collagens and ECM regulators. Possibly, collagens contribute to the linear stiffness parameter providing tissues with structural integrity. On the other hand, collagen-based biopolymers exhibit a nonlinear strain stiffening response to applied shear stress, providing inherent stability to connective tissues under tenson [9].

This is the first study to measure the mechanical properties of the enthesis during embryogenesis and compare the tissue composition of enthesis and neighboring tissues as a function of embryonic movement and developmental timepoint. The study is currently limited to correlational comparisons. However, not only does this work define mechanical and proteomic changes in enthesis development, but it can also form a basis for design of synthetic ECM networks for tissue engineering. Future work will investigate enthesis matrix organization and validation of unique protein identifications, and reductionist experimentation will be applied to identify ECM networks responsible for linear vs. nonlinear mechanical properties.

## ACKNOWLEDGEMENTS

This work was supported by NIH grant R01 AR071359.

## REFERENCES

[1] McCreery+, *Conn Tiss Res*, 2020; [2] Rossetti+, *Nat Mater.*, 2017; [3] Lu & Thomopoulos, *Annu. Rev. Biomed. Eng*, 2013 [4] Thomopoulos+, *J Orthop Res.*, 2007; [5] Pai+, *Dev Biol.*, 1965; [6] Lin+, *Biomech Model Mechanobiol.*, 2009; [7] Naba+, *Mol Cell Proteomics*; 2012 [8] Jacobson+, *J. Proteome Res.*, 2020. [9] Licup+, *PNAS*, 2015.

# EXPLORING 3D PRINTED SCAFFOLD DESIGNS FOR MENISCAL REPLACMENT

**Kevin Eckstein (1), Lawrence Smith (1), Robert MacCurdy (1), Virginia L. Ferguson (1), Kristine M. Fischenich (2)**

(1) Department of Mechanical Engineering, University of Colorado Boulder, Boulder, CO, USA
(2) Department of Orthopedics, University of Colorado Anschutz Medical Campus, Aurora, CO, USA

## INTRODUCTION

Knee osteoarthritis affects around 16% of the global population[1] and meniscal tears are among the most common knee injuries[2]. The menisci are C-shaped fibrocartilaginous tissues that distribute 60% of the load from the upper body[3] and are critical to healthy knee function. The meniscus, however, is avascular and struggles to heal when damaged. Repair approaches have limited success[4] and tissue graft demand exceeds supply. Thus, tissue-engineered alternatives are desired to replace damaged menisci.

Tissue engineered meniscal scaffolds are often fabricated though molding techniques, bioprinting, or electrospinning. These fabrication techniques, however, have limited design options and struggle to fully restore load distribution. Designing a meniscal replacement is further complicated by trying to balance the need for load support with a pore size that supports cellular infiltration.

Our group has designed a tissue-engineered system that uses additive manufacturing. To improve mechanical properties while enabling tissue regeneration, we propose fabricating stiff structures using a commercially available liquid deposition printer (Stratasys® Polyjet™), and then infilling these structures with a degradable hydrogel cell scaffold. This composite approach may enable scaffolds that distribute physiological loads while providing a suitable volume fraction for a cell-laden hydrogel infill.

The objective of this study was to establish a structural design, evaluated via computational modeling, that bears physiologically relevant loads, maximizes structural efficiency, and maintains a total volume fraction under 0.4 to allow for a cell-laden hydrogel infill. We hypothesize that scaffold designs that help to transmit load radially and circumferentially will outperform the more basic lattice structure.

## METHODS

**Structure Designs and Outcome Measures:** All scaffolds were designed to fit an idealized circular shape with wedge-shaped cross-sections (Figure 1). All designs had a diameter of 10 mm, inner diameter of 3 mm, and a radius of curvature of 7 mm which is comparable to native rabbit menisci[5]. Structures were limited to volume fractions ($V_f$) less than 0.4 to allow future infilling of a cell-laden hydrogel. Three designs were evaluated with finite element (FE) modeling (Figure 1B-C): a classic square lattice ($V_f$ = 0.35), a truss frame ($V_f$ = 0.30) meant to direct loads radially, and a circumferentially reinforced truss frame ($V_f$ = 0.37) which provides additional circumferential support. A solid-material design ($V_f$ =1) was also modeled for comparison (Figure 1A).

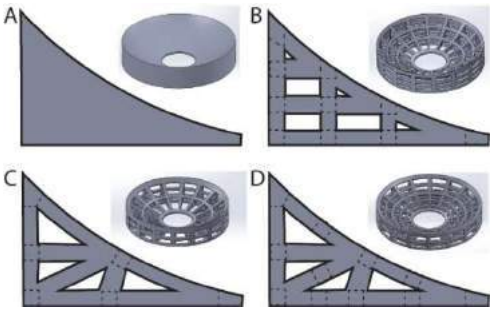


**Figure 1: Cross section and overview of scaffold designs (dashed lines in cross section represent circumferential components). A) solid B) classic square lattice C) truss frame and D) circumferentially reinforced truss frame**

Outcome measures included local strain in the articular cartilage at physiological load (20 N), structural efficiency (Table 1), and von Mises stress distributions at 10% local strain (Figures 2 and 3). We defined local strain as the indentation depth of the femoral condyle divided by articular cartilage thickness. Physiological load (20 N) was determined from gait analysis of skeletally mature (4-5kg) New Zealand White rabbits, suggesting the mean intersegmental axial knee force is 40%

body weight[6]. Structural efficiency was calculated as load divided by displacement divided by material volume; high structural efficiency indicates that a design optimizes load bearing capability while retaining a low enough volume fraction to infill with a cell-laden hydrogel.

**Simplified Femoral Condyle-Meniscus-Articular Cartilage 3D FE Model:** We used FE analysis in Abaqus to model the femoral condyle (rigid sphere) indenting to a depth of 10% of the thickness of the tibial plateau articular cartilage (simplified as a flat substrate). The outcome measure "Strain at 20 N load" was interpolated from the results. Each model was simplified to a 1/16 sector of their full designs using cyclic symmetry (Figure 3A). Both the structure and articular cartilage were modeled as linear elastic materials with $\nu = 0.45$. Elastic modulus for the structure ($E$ = 50 MPa) was estimated from shore hardness provided by Stratasys for material FLX9130-DM. The elastic modulus for cartilage ($E$ = 10 MPa) assumed near-instantaneous loading[7]. All parts interacted with frictionless sliding contact. Analyses were static and considered nonlinear geometric effects.

The mesh for the articular cartilage substrate used 1,375 quadratic hybrid hexahedral elements (C3D20H) and 389 quadratic hybrid tetrahedral elements (C3D10H). Meshes for the meniscal structures used between 2.5–15k linear hybrid incompatible mode hexahedral elements (C3D8IH). Mesh refinements verified that results converged with decreasing mesh size. Final meshes featured at least four elements across the smallest features of the frame.

We verified our implementation of cyclic symmetry and spherical indentation by comparing a sub-model to Hertz' analytical solution for spherical indentation of a half-space. Our sub-model of pure indentation used a 100 mm thick substrate and was within 3% of the Hertz solution.

**3D Printing:** A "truss frame" prototype structure was fabricated using Stratasys Polyjet printer and Agilus30Clear material.

## RESULTS

Regardless of design, peak stress was observed in the inner third of the meniscal construct (Figure 2). Circumferential beams in all designs were loaded in tension and had higher stress than radial and vertical features (Figure 3A). Of the three structure designs, the circumferentially reinforced truss frame resulted in the least local articular cartilage strain (5.25%) while having the highest structural efficiency at 6.66 N/mm/mm$^3$ (Table 1). However, the circumferentially reinforced truss frame design also had the highest $V_f$ at 0.37. The less dense truss frame ($V_f$ = 0.30) allowed more strain than the square lattice design but improved upon structural efficiency (Table 1).

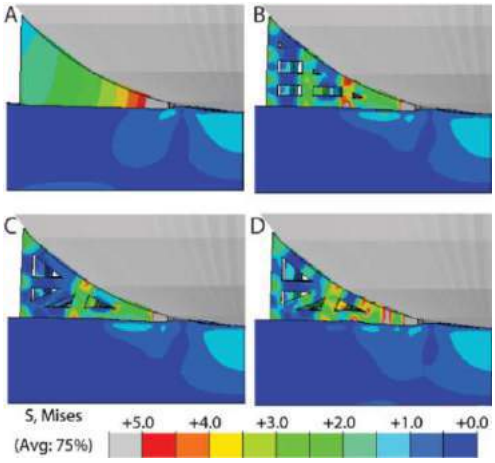


**Figure 2: Von Mises stress at 10% local strain for each design: A) Solid B) classic square lattice C) truss frame and D) circumferentially reinforced truss frame.**

**Table 1: Measured Outcomes.**

| | Solid | Square lattice | Truss frame | Circum. reinforced |
|---|---|---|---|---|
| **Volume fraction, $V_f$** | 1.00 | 0.35 | 0.30 | 0.37 |
| **Strain at 20 N load** | 2.6% | 5.97% | 6.74% | 5.25% |
| **Structural Efficiency** | 4.99 $\frac{\text{N/mm}}{\text{mm}^3}$ | 6.18 $\frac{\text{N/mm}}{\text{mm}^3}$ | 6.36 $\frac{\text{N/mm}}{\text{mm}^3}$ | 6.66 $\frac{\text{N/mm}}{\text{mm}^3}$ |

We printed a proof-of-concept "truss frame" to scale (10 mm dia.) with Agilus30Clear material (Figure 3B). Degradable support material enabled all truss features, including horizontal overhangs, to be printed.

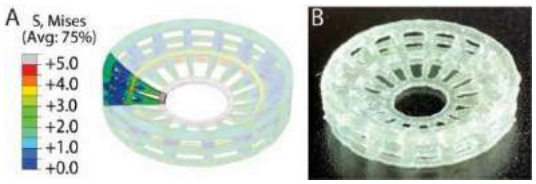


**Figure 3: A) Stress field of truss frame visualized from cyclic symmetry of 1/16 sector; B) 3D printed truss frame design**

## DISCUSSION

Additive manufacturing has enabled the design of complex load-bearing structures for tissue scaffolds. However, existing meniscus designs are limited to overlayed bio-ink lattices or a classic square lattice design (Figure 1B)[8]. This study showed that a more complex truss design (Fig. 1C) could reduce material volume by almost 15% while increasing structural efficiency by 3%. Our models revealed how circumferential features in these structures experience the greatest stress. Acting on this insight, we improved upon structural efficiency in our circumferentially reinforced design (Fig. 1D) at the cost of an increased volume fraction. When infilling a scaffold with a hydrogel, it is critical that enough space remains for complete infill, cell infiltration, and new extracellular matrix production. For this reason, we concluded that the truss frame was preferred because it balanced a lower $V_f$ with high structural efficiency. We then demonstrated the design was feasible to 3D print (Figure 3B). However, future prints should use a stiffer material like FLX9130-DM to better match our models.

It is not surprising that the circumferential features experienced the highest stresses. In the native tissue, circumferential collagen fibers help to resist lateral expansion and convert axial loads to circumferential hoop stresses. Future designs may be optimized by reducing the volume of radial features while reinforcing circumferential features.

This study highlights how scaffold design can impact structural efficiency and how 3D printing enables more complex designs. While our current study idealized the shape of the meniscus to reduce computational complexity, this same approach can be implemented into more accurate meniscal shapes obtained from medical imaging. Overall, our findings here may inform future implant designs that effectively recapture the meniscus' native mechanical function.

## ACKNOWLEDGEMENTS

This work (project number 20-204) was supported by a grant from the ON Foundation, Switzerland.

## REFERENCES

[1] Cui, A et al., *EClinicalMedicine*, 29-30:100587, 2020. [2] Adams, BG, et al., *Sports Med Arthrosc*, 29(3):e24-e33, 2021. [3] Zhang, K et al., *J Orthop Surg Res*, 14(1):1-12, 2019. [4] Goble, EM et al., *Scand J Med Sci Sports,* 9(3):146-157, 1999. [5] Proffen, BL et al., *Knee*, 19(4):493-499, 2012. [6] Gushue, DL et al., *J Orthop Res,* 23(4):735-742, 2005. [7] Li, LP et al., *J Biomech Eng* 125:161-168, 2003. [8] Zhang, Z-Z et al., Am J Sports Med 45:1497-1511 (2017)

# Targeting of Immune Cell Mechanotransduction

# Improves Healing and Prevents Fibrosis

Kellen Chen[1], PhD; Michelle Griffin[1], MD; Dominic Henn[1], MD; Clark A Bonham[1], BS; Katharina Fischer[1], MD; Dharshan Sivaraj[1], BS; Geoffrey C Gurtner[1], MD

[1]Hagey Laboratory for Pediatric and Regenerative Medicine, Division of Plastic and Reconstructive Surgery, Department of Surgery, Stanford University, Stanford, CA 94305, USA

## Background

Repair after tissue injury involves a dynamic interplay among not just tissue resident cells (e.g., fibroblasts)[1], but also cells recruited from the circulation. Myeloid cells, such as monocytes and macrophages, are derived from hematopoietic precursors and migrate to sites of injury where they play a role in modulating all stages of wound healing and scar formation[2]. There is mounting evidence that mechanical stimuli are also able to modulate monocyte and macrophage response during tissue healing, but the exact mechanisms behind this "mechano-immunomodulation" remain incompletely understood[3].

## Methods

We attached a mechanical strain device to the mouse dorsum to initiate a uniform and consistent strain profile across an incisional wound to create hypertrophic scar (HTS) formation in mice[4]. These devices are steel palatal expanders with rod extender arms that are attached to the backs of the mice using skin adhesive and staples to allow for a uniform strain profile. We waited 4 days after the incision to mount the device, allowing the wound to close. Next, we extended the device every other day for a 14-day time period.

To analyze the scar tissue, we took photos of the scars before we explanted. Then, once we explanted the scar tissue, we stained it using picrosirius red, a type of staining that magnifies collagen formation and structure. With the stained tissue, we were able to use CurveAlign and CT-Fire collagen architecture algorithms[5]. CurveAlign quantifies all fiber angles within the given image, while CT-Fire analyzes individual fiber measurements.

To investigate mechano-responsive immune cells, we performed parabiosis of wildtype (WT) and GFP+ mice, allowed the mice to develop a shared blood circulation, initiated HTS formation in the WT mouse, and analyzed the cells using single cell RNA sequencing (scRNA-seq), fluorescent-activated cell sorting (FACS), and immunofluorescent staining.

We then specifically bred mice to knockout focal adhesion kinase (FAK, encoded by *Ptk2*) signaling in either fibroblasts (*Col1a2 Cre, Ptk2-flox*) (n=3) or myeloid cells (*Lyz2-Cre, Ptk2-flox*) (n=3), We used the HTS model on both breeds of mice, along with WT mice. Of a total of 18 WT mice, (n=2) received an incision but no device (control); (n=10) received an incision with mechanical strain (HTS); (n=6) were treated with FAK inhibitor (FAKI) hydrogels in conjunction with mechanical strain (S+FAKI)[6].

## Results

Utilizing these devices created scars in wildtype mice with increased levels of fibrotic tissue and highly aligned collagen as compared to the control wildtype mice without extension. Mechanical modulation significantly upregulated the presence of inflammatory subtypes within the healing tissue, characterized by an increase in infiltrating GFP+ immune cells from 5.4% to 12.2%. In the GFP+ circulating immune cells, mechanical strain directly increased the proportion of fibrotic myeloid cells, primarily defined by the monocyte marker *Ly6c2* as well as the TGFB responsive and macrophage activating gene *Thbs1* (which codes for the protein Thrombospondin 1). Mechanical strain also increased the proportion of inflammatory myeloid cell populations, defined by *Ccl* and *Il6* chemoattractants, and *Cd74*+ migratory myeloid cells.

SB³C2022-372

With gross photography, we took measurements of both the length and width of the scars to compare the fibroblast and myeloid FAK KO scars with wildtype HTS scars. We observed that both knockout strains generated visually less scarring than in wildtype mice. Furthermore, FAKI treated wounds also improved healing and reduced fibrosis compared to HTS groups.

Using picrosirius red staining, we observed that the HTS collagen fibers were also significantly longer and more highly aligned than FAKI treated and FAK KO scars, as well as unwounded skin.

Using scRNA-seq, we found that FAK inhibition inhibition reduced the proportion of *Thbs1+/Ly6c2+* fibrotic cells and *Ccl+/Il6+* inflammatory myeloid cells within the healing murine wound and instead promoted a unique subset of regenerative myeloid cells. Regenerative myeloid cells primarily upregulated anti-inflammatory myeloid markers *Mrc1*, *Cd163,* and *Selenop*, as well as *Egr1* (encoding early growth response protein 1). We have previously demonstrated that *Egr1* signaling in fibroblasts is promoted by FAK inhibition, mediated by Akt signaling, and associated specifically with regenerative phenotypes that suppress fibrosis[1].

Using immunofluorescent staining, we confirmed that the scars in the HTS mice had significantly elevated levels of a pro-fibrotic extracellular matrix marker Thrombospondin1 compared to FAKI treated and KO scars. We also confirmed an upregulation of Selenoprotein P (encoded by *Selenop*) with FAK modulation.

## Conclusions

Tissue injury activates a cascade of signaling pathways to recruit and orchestrate various cell types during healing. Our study indicates that modulating mechanical stress directly affects myeloid cell phenotypes and interactions with other cell types in the complicated, multicellular milieu of wound healing. This principle has been previously unexplored in the context of fibrosis and regeneration, with most previous studies focused on fibroblast heterogeneity and transcriptional profiles. To our knowledge, this is the first study to directly investigate the effects of modulating mechanotransduction on immune cell response at the single cell level utilizing parabiosis and wound healing. Collectively, we demonstrate that mechano-immunomodulation of the “early responders” of healing can trigger a cascade of downstream regenerative healing.

## References


1 Chen, K. *et al.* Disrupting biological sensors of force promotes tissue regeneration in large organisms. *Nat Commun* **12**, 5256, doi:10.1038/s41467-021-25410-z (2021).

2 Gurtner, G. C., Werner, S., Barrandon, Y. & Longaker, M. T. Wound repair and regeneration. *Nature* **453**, 314-321, doi:10.1038/nature07039 (2008).

3 Adams, S., Wuescher, L. M., Worth, R. & Yildirim-Ayan, E. Mechano-Immunomodulation: Mechanoresponsive Changes in Macrophage Activity and Polarization. *Ann Biomed Eng* **47**, 2213-2231, doi:10.1007/s10439-019-02302-4 (2019).

4 Aarabi, S. *et al.* Mechanical load initiates hypertrophic scar formation through decreased cellular apoptosis. *The FASEB Journal* **21**, 3250-3261, doi:10.1096/fj.07-8218com (2007).

5 Bredfeldt, J. S. *et al.* Computational segmentation of collagen fibers from second-harmonic generation images of breast cancer. *J Biomed Opt* **19**, 16007-16007, doi:10.1117/1.JBO.19.1.016007 (2014).

6 Wong, V. W. *et al.* Focal adhesion kinase links mechanical force to skin fibrosis via inflammatory signaling. *Nat Med* **18**, 148-152, doi:10.1038/nm.2574 (2011).

# HEMODYNAMIC IMPACT OF ANTERIOR LEAFLET LACERATION IN TRANSCATHETER MITRAL VALVE REPLACEMENT

**Keshav Kohli (1), Zhenglun Alan Wei (2), Vahid Sadri (1), Andrew Siefert (1), Philipp Blanke (3), Emily Perdoncin (4), Adam Greenbaum (4), Jaffar Khan (5), Robert Lederman (5), Vasilis Babaliaros (4), Ajit Yoganathan (1), and John Oshinski (1,4)**

(1) Department of Biomedical Engineering, Georgia Tech and Emory University
(2) Department of Biomedical Engineering, University of Massachusetts, Lowell
(3) Department of Radiology, St. Paul's Hospital and University of British Columbia
(4) Emory University School of Medicine
(5) Cardiovascular Branch, Division of Intramural Research, National Heart, Lung and Blood Institute, National Institutes of Health

## INTRODUCTION

Left ventricular outflow tract (LVOT) obstruction is a prevalent and potentially fatal complication of transcatheter mitral valve replacement (TMVR) caused by displacement of the anterior leaflet towards the ventricular septum. Laceration of the Anterior Mitral leaflet to Prevent Outflow Obstruction (LAMPOON) is a catheter-based technique designed to alleviate the risk of obstruction by mimicking surgical anterior leaflet resection [1]. The optimal result of the LAMPOON procedure is a complete midline laceration of the anterior leaflet which, following TMVR, exposes open cells of the transcatheter valve. These exposed cells are thought to permit additional blood flow through the LVOT and decrease the risk of obstruction.

Despite the growing clinical experience with this technique, a controlled clinical trial comparing the outcomes of patients undergoing TMVR with versus without LAMPOON has never been designed nor conducted. It would be *impossible* to conduct such a trial in which the control intervention (i.e., TMVR without LAMPOON) would be anticipated to cause immediate LVOT obstruction following valve implantation. Thus, while the LAMPOON technique has been shown to be safe and feasible, its impact on left ventricular outflow tract hemodynamics has never been investigated.

Therefore, the *goal* of this computational (*in silico*) controlled study was to compare the hemodynamics of TMVR with LAMPOON versus TMVR without LAMPOON. We *hypothesized* that LAMPOON improves flow dynamics through the LVOT in patients with a small residual LVOT (neo-LVOT).

## METHODS

LAMPOON Trial Dataset: De-identified subject data from the LAMPOON investigational device exemption trial (NCT03015194) were retrospectively evaluated under an Institutional Review Board approved protocol [1]. All subjects in that trial (N=30) were considered at prohibitive risk for TMVR-related LVOT obstruction based on a predicted end-systolic neo-LVOT area of <200 $mm^2$. Subjects underwent a valve-in-ring or valve-in-mitral annular calcification procedure with the SAPIEN 3 valve (Edwards Lifesciences, Irvine, CA) with retrograde LAMPOON prior to valve implantation.

Selection of Study Cohort: Inclusion criteria for this study were: (1) the availability of a post-procedure, multi-phase CT scan with contrast-enhancement, and (2) a splayed anterior leaflet that was visible on post-procedure CT and exposed cells of the implanted transcatheter valve. Of the thirty subjects in the LAMPOON investigational device exemption trial, eight subjects were selected for the present study.

3D Models Created for Each Subject: Contrast-enhanced, multi-phase CT scans were acquired after the procedure, either pre-discharge or within 30-days of follow-up. CT images were reconstructed in 10% intervals over the cardiac cycle within <1.0-mm slice thickness. Mimics 20.0 (Materialise, Leuven, Belgium) image post-processing software was used to generate 3-D models of the left ventricle and aorta using conventional segmentation techniques.

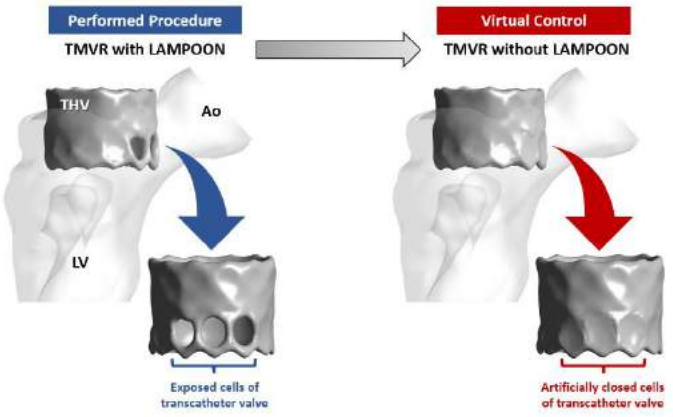


**Figure 1: 3D anatomical models created for each subject**

Two different 3D models were created for each subject. The first model represented 'TMVR with LAMPOON'. In this model, the *actual* implanted transcatheter valve and splayed anterior leaflet were reconstructed in 3D from the post-procedure CT (**Figure 1**, left). The second model represented 'TMVR without LAMPOON'. In this model, the exposed cells of the transcatheter valve were *artificially closed*, mimicking a completely intact anterior leaflet geometry (**Figure 1**, right). Since the model of 'TMVR with LAMPOON' mimicked the performed interventional procedure, the model of 'TMVR without LAMPOON' was considered to mimic a 'virtual control'.

Computational Fluid Dynamics (CFD) Simulations: We utilized a validated workflow for generating patient-specific CFD simulations of left ventricular outflow which has been previously reported in detail [2]. Patient-specific CFD simulations were performed for both modeled conditions (TMVR with and without LAMPOON) for each subject. For each 3D model, an inlet was placed at the left ventricular apex, and an outlet was placed at the sino-tubular junction. The time-varying left ventricular volume curve (obtained from the post-procedure CT dataset) was used to calculate a peak systolic flow rate, which was then prescribed as the inlet boundary condition. The CT phase which most closely coincided with the peak systolic flow rate was selected for creating a volumetric mesh using ANSYS Fluent Meshing (Ansys, Inc. Canonsburg, Pennsylvania). This mesh included polyhedral elements with an edge length of 0.5 mm, and a prismatic boundary layer mesh which was applied on the left ventricular wall. The outlet boundary condition was set to a zero-reference pressure. Transition-to-turbulence characteristics in the flow field were accounted for using the scale-adaptive simulation turbulence model. All structures were assumed to be rigid and non-permeable, and a no-slip condition was applied at the walls. Blood was modeled as a single-phase Newtonian fluid with a density of 1060 kg/m$^3$ and dynamic viscosity of 0.0034 poise. The 3D Navier-Stokes equations were solved in ANSYS Fluent 19.0.

Obtaining Simulated Hemodynamics: Hemodynamic metrics were extracted from each CFD simulation, including the peak outflow velocity ($V_{peak}$), peak LVOT pressure gradient ($\Delta P_{peak}$), and peak LVOT effective orifice area ($EOA_{peak}$). To calculate $\Delta P_{peak}$, the ventricular pressure was derived from an average pressure across the model inlet (LV apical plane), and the aortic pressure was derived from an average pressure across the model outlet (sino-tubular junction plane). $EOA_{peak}$ was calculated as the ratio of the peak volumetric flow rate ($Q_{peak}$) to the peak outflow velocity ($V_{peak}$).

Data Analysis: All data analyses were performed with the MedCalc statistical software package (MedCalc, Ostend, Belgium). Simulated hemodynamics for each subject were compared between the two modeled conditions using the paired samples t-test or Wilcoxon test for parametric and non-parametric data, respectively. Statistical significance was defined as $p<0.05$.

## RESULTS

Across all subjects, simulated hemodynamics were improved for TMVR with LAMPOON compared to TMVR without LAMPOON (**Figure 2**). As compared to TMVR without LAMPOON, TMVR with LAMPOON resulted in lower $V_{peak}$, lower $\Delta P_{peak}$, and higher $EOA_{peak}$ by 14±7% (p=0.006), 31±17% (p=0.01), and 17±9% (p=0.002), respectively. Following LAMPOON, $V_{peak}$ decreased from 2.6±1.1 m/sec to 2.2±0.9 m/sec, $\Delta P_{peak}$ decreased from 17.5±19.6 mmHg to 10.0±8.8 mmHg, and $EOA_{peak}$ increased from 1.6±0.6 cm$^2$ to 1.8±0.7 cm$^2$ ($p<0.05$ for all comparisons).

LAMPOON was most effective in improving hemodynamics in subjects who had a small post-procedure neo-LVOT area (**Figure 3**). The largest hemodynamic improvement with LAMPOON was observed in the subject who had the smallest post-procedure neo-LVOT area across all subjects (49 mm$^2$). This subject experienced a 32 mmHg reduction in the simulated LVOT gradient following LAMPOON. As the post-procedure neo-LVOT area increased beyond 250 mm$^2$, LAMPOON began to demonstrate a smaller hemodynamic effect.

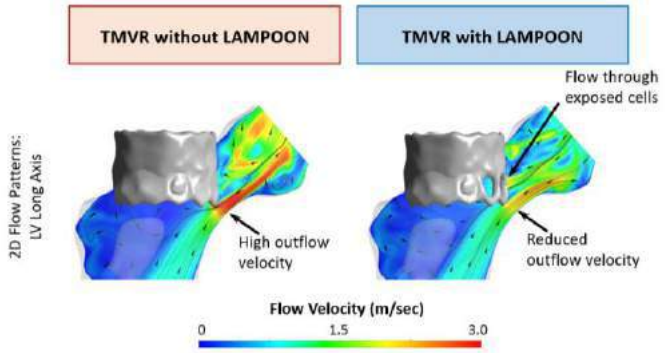


**Figure 2: Effect of LAMPOON on left ventricular flow patterns in a representative subject.**

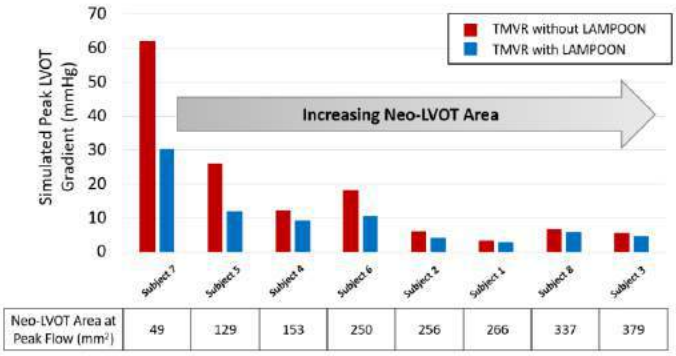


**Figure 3: Relationship between residual LVOT (neo-LVOT) area and the hemodynamic impact of LAMPOON**

## DISCUSSION

A controlled *in silico* study was performed to investigate the hemodynamic impact of LAMPOON in TMVR. LAMPOON achieved a critical increment in outflow area which resulted in a consistent improvement in hemodynamic outcomes and flow patterns following TMVR. Patients with a smaller post-procedure neo-LVOT area experienced a greater hemodynamic improvement with LAMPOON. Importantly, in this study, the TMVR without LAMPOON condition could not be conducted *in vivo* due to prohibitive patient risk. Furthermore, only an *in silico* study could be used to examine the hemodynamic effects of LAMPOON. This study highlights the growing potential for *in silico* studies to evaluate procedures virtually which may improve cost-effectiveness and patient safety as compared to a conventional clinical trial.


## ACKNOWLEDGEMENTS

ANSYS software was provided through an Academic Partnership between ANSYS, Inc. and the CFM Lab at Georgia Tech. This study was supported by an American Heart Association pre-doctoral fellowship (20PRE35200392) and NIH grant (R01EB027774).


## REFERENCES


[1] Khan et al., Journal of the American College of Cardiology, 2019
[2] Kohli et al., Annals of Biomedical Engineering, 2021

SB³C2022
Summer Biomechanics, Bioengineering and Biotransport Conference
June 20-23, Eastern Shore, MD, USA

# SHEAR PROPERTIES OF COLLAGEN CROSSLINKED PROCINE CORNEA

**H. Hatami-Marbini, M.E Emu**

(1) Mechanical and Industrial Engineering, University of Illinois at Chicago, Chicago, Illinois, USA,
Email. hatami@uic.edu

## INTRODUCTION

The cornea is the outer transparent part of the eye which provides structural integrity and contributes vastly to refract light. The tissue acts as a protective layer for internal contents of the eyeball and its structural properties are important for proper vision. The optical properties of the cornea include transmission and refraction of the light. The cornea is subjected to intraocular pressure from the inside and could be subjected to external forces caused by eye rubbing, for example. The mechanical properties of the cornea are altered in several diseases such as keratoconus, which is an eye disease changing the corneal microstructure. Keratoconus affects about one in 2000 individuals and causes the cornea thins and gradually becomes a cone-like bulge. Any change in the shape of the cornea interferes with its optical properties and causes the vision to become blurry and distorted. At initial stages of the disease, eyeglasses or lenses can be used to correct for vision abnormalities. However, keratoconus is a progressive disease making the cornea to bulge more. Thus, the vision of individuals significantly decreases if no medical intervention is done.

The corneal collagen cross-linking procedure has been shown to be effective in halting or at least slowing the progression of keratoconus. In this procedure, the corneas are soaked in riboflavin solution and crosslinks are created in the corneal stroma by shining ultraviolet (UV) light. It has been shown that corneal structural properties improve because of this procedure, the progression of the disease stops, and individuals may not need corneal transplants. The strengthening effects of the collagen crosslinking treatment procedure have been commonly investigated by performing uniaxial tensile experiments [1-2]. For example, we have shown that corneal collagen cross-linking resulted in a significant increase of tensile stress–strain response which is dependent on the hydration of the samples [3]. The primary objective of the present work was to conduct shear experiments in order to determine how corneal collagen crosslinking procedure influences shear properties of corneal samples in vitro. For this purpose, we used porcine corneas and used the Dresden crosslinking protocol to create crosslinks in vitro. We then performed oscillatory shear experiments to characterize the dynamic modulus of treated and untreated samples.

## METHODS

Fresh porcine eyes were collected from an abattoir and brought to the laboratory. Corneal samples with a scleral rim were prepared after removing epithelial and endothelial layers from the samples. We divided the samples into two groups. The samples in the first group were crosslinked using photosensitizer riboflavin solution. In order to prevent excessive swelling of the specimens, we used 20% dextran in the riboflavin solution. All samples were initially soaked in the riboflavin dextran solution for 30 minutes in order to ensure proper penetration of riboflavin inside the specimens. Then, the samples were irradiated with UV light (370 nm, 3 mw/cm$^2$) for 30 minutes. During this period, we continued instilling drops of riboflavin dextran solution every 5 minutes on the samples. Following crosslinking the samples, we used a biopsy punch to obtain corneal disks from the center of the samples.

A rheometer (DHR-2, TA instruments, Delaware) was used to perform the shear mechanical experiments. These tests were done using

the protocol that we have used before [4]. Briefly, the samples were mounted in the rheometer and the chamber was filled with PBS solution, Figure 1. In order to avoid samples to slip during the experiments, sand papers were glued to the machine. The upper geometry was then brought down and both shear frequency and strain sweep experiments were performed. The strain sweeps were performed using oscillating strains ranging from 0.01% to 10% at the frequency of 1 Hz. Furthermore, frequency sweep experiments were performed at constant oscillating strain of 0.02% and with frequencies between 0.01 HZ and 2 Hz. The storage modulus ($G'$) and loss modulus ($G''$) were calculated using the experimental measurements. The one-way ANOVA was used to compare the behavior of treated and untreated groups. The significance level of 0.05 was used in the statistical analysis.

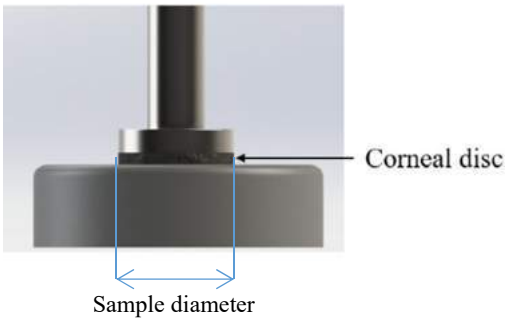


**Figure 1. A schematic plot of the dynamic torsional experimental setup. The samples were placed between the top and bottom platens and sand papers were used to avoid slippage. Furthermore, all experiments were done inside the PBS solution.**

## RESULTS

The storage and loss moduli of the samples in the collagen crosslinked group and the untreated group are shown in Figure 2 as function of the applied shear strain. It is seen that the shear modulus of crosslinked samples is significantly larger than the storage modulus of untreated samples. This figure also shows the range of linear viscoelasticity is almost the same in both groups, i.e. crosslinking of the samples does not have any effect on the overall shear viscoelastic response of the cornea.

## DISCUSSION

The main goal of this study was to characterize the effects of corneal collagen crosslinking on shear properties of porcine corneas. The experimental measurements clearly showed that the corneal collagen crosslinking significantly increased the shear modulus of the samples. We did not see any significant difference in the characteristic curves between both groups, i.e., the linear viscoelastic region for both crosslinked and untreated groups was found to be the same. The range of linear viscoelasticity and the shear modulus of untreated samples were consistent with previous findings [4]. The possible reason for the improvement in the shear properties of the crosslinked cornea could be the crosslinks that are formed in the collagen proteoglycan matrix. This is an important finding because although collagen fibers are important in tensile properties of the samples, shear properties of the samples are determined from the interaction of collagen fibers with the proteoglycan matrix.

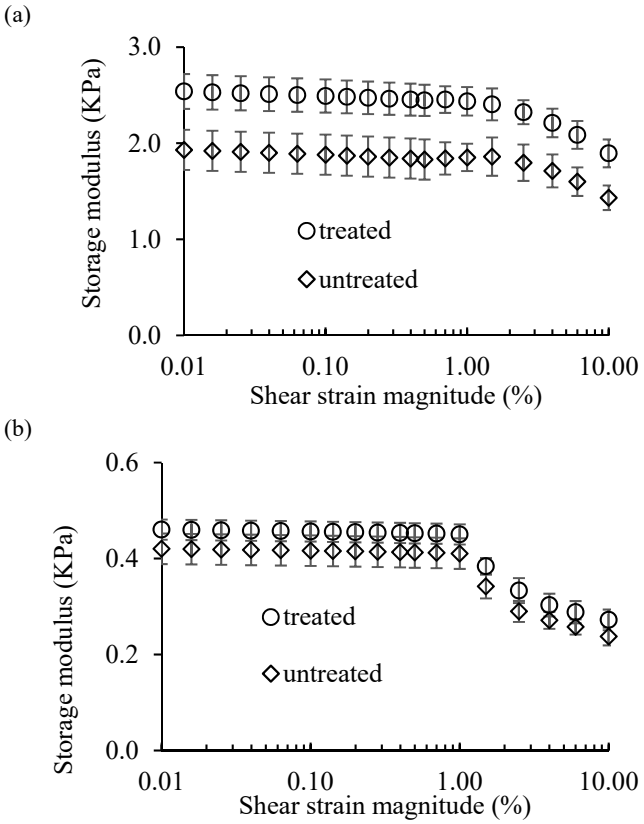


**Figure 1: (a) storage modulus and loss modulus of crosslinked and untreated porcine corneas. The symbols denote the average of experimental measurements and the error bars indicate standard deviation.**


## ACKNOWLEDGEMENTS

This work has been supported in part by grants from the National Science Foundation (1636659) and the National Institutes of Health (R21 EY030264).


## REFERENCES


*[1] G. Wollensak, E. Spoerl, and T. Seiler, Stress-strain measurements of human and porcine corneas after riboflavin–ultraviolet-A-induced cross-linking, J. Cataract Refract. Surg., vol. 29.9, 1780–1785, 2003.*

*[2] H. Hatami-Marbini, and A. Rahimi. Stiffening effects of riboflavin/UVA corneal collagen cross-linkingis hydration dependent. Journal of biomechanics 48.6, 1052-1057, 2015.*

*[3] H. Hatami-Marbini, and A. Rahimi. Interrelation of hydration, collagen cross-linking treatment, and biomechanical properties of the cornea. Current eye research 41.5, 616-622, 2016.*

*[4] H. Hatami-Marbini,Viscoelastic shear properties of the corneal stroma." Journal of biomechanics 47.3, 723-728, 2014.*

H. Hatami-Marbini, *J. Biomech.*, vol. 47, no. 3, pp. 723–728, 2014, doi: 10.1016/j.jbiomech.2013.11.019.

# MITRAL VALVE LEAFLET COAPTATION IN THE POST-MYOCARDIAL INFARCTION HEART

**Natalie T. Simonian (1), Hao Liu (1), Alison M. Pouch (2), Joseph H. Gorman, III (2), Robert C. Gorman (2), Michael S. Sacks (1)**

(1) James T. Willerson Center for Cardiovascular Modeling and Simulation, The Oden Institute and the Department of Biomedical Engineering, University of Texas at Austin, Austin, TX, USA
(2) Gorman Cardiovascular Research Group, Smilow Center for Translational Research, Department of Surgery, Perelman School of Medicine, University of Pennsylvania, PA, USA

## INTRODUCTION

Mitral regurgitation (MR) is the most common valvular disease in the United States with a prevalence of over 2% of the entire population, and is a major prognostic factor of mortality [1, 2]. Ischemic mitral regurgitation (IMR) is a subtype of MR characterized by the insufficiency of an otherwise healthy MV, occurring secondary to myocardial infarction (MI) as the left ventricle (LV) dilates in response to the impaired contractility of an infarcted region [3]. IMR is particularly deadly: five-year mortality after MI with IMR is 62% [4].

Undersized ring annuloplasty (URA) is currently the preferred treatment and reduces the annular orifice area to better approximate the leaflets based on Carpentier's principle that increased coaptation results in a more durable repair [5, 6]. However, long-term patient outcomes remain unpredictable, suboptimal, and poorly understood; six months after URA repair, up to 30% of patients experience recurrent MR [7]. Thus, there is an urgent need to deepen understanding of MR to develop durable IMR treatments to improve long-term patient outcomes.

Given that poor coaptation is the mechanistic driver of IMR, restoring normal coaptation is an important objective in MV repair. However, the full coaptation zone is difficult to visualize using real-time 3D echocardiography (rt-3DE) due to signal loss near the free edge of the leaflets in the systolic position. Consequently, coaptation is generally quantified indirectly or as a one-dimensional length index using 2D echocardiography [8]. Using our state-of-the-art, extensively validated noninvasive image-based modeling approach, we are able to directly quantify the full coaptation area and also resolve this zone into its subregions, providing a more nuanced understanding of the closing behavior of the regurgitant MV.

## METHODS

Rt-3DE images of the MV from 14 IMR patients were obtained from an extant database from a previous study on MV leaflet strain pre- and post-URA repair [9]. 7 showed no recurrence of MR six months after repair, while 7 had recurrence. These images were segmented and processed to produce 3D medial surface representations of each valve in the fully open and fully closed states, before and after repair.

In order to build direct material point correspondence between the open and closed state and to recover the full coaptation zone, we morphed the open state MV mesh to its corresponding closed shape using a hyperelastic shape morphing technique in a finite element (FE) framework [10]. The simulation was conducted in the commercial FE software Abaqus by applying an annular displacement boundary condition, a physiological ventricular pressurization, and a downward chordal-mimicking force. After the leaflets have initially coapted, a local corrective pressure field was applied to penalize any mismatch between the simulated geometry and the true closed-state rt-3DE reconstruction. Using this technique, we can achieve a close match between the simulated geometry and the imaged closed state (Fig. 1).

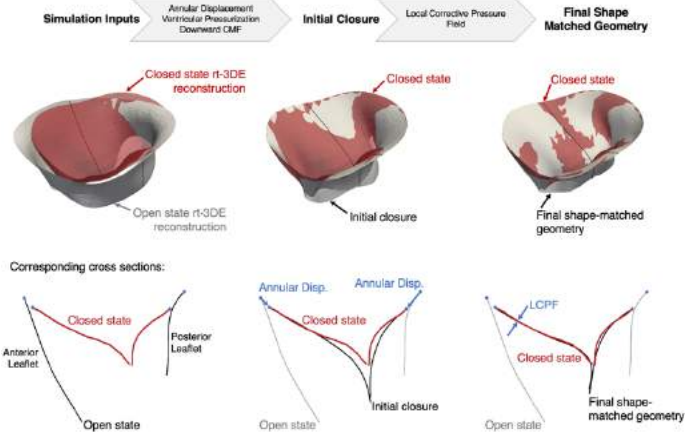


**Figure 1: The progression of the FE-based closure simulation from the open state to the final, shape-matched closed state.**

The coaptation zone of the MV was subdivided into the contact region, the region where the two leaflets are in direct contact, and the redundant region, the portion of the leaflet which hangs below the free edge of the opposing leaflet (Figure 2). Contacting elements are defined as those with centroids within 0.8 mm (the voxel resolution) of each other and with nearly antiparallel outward normals, such that

$$\boldsymbol{t}_a \cdot \boldsymbol{t}_b \leq -0.98, \quad (1)$$

where $\boldsymbol{t}_a$ and $\boldsymbol{t}_b$ are the respective outward normals for any two elements *a* and *b*. Redundant region elements were selected manually in ParaView (Kitware Inc.) by visualizing the valve from the positive and negative y axes and extracting all elements that were visible below the free edge of the other leaflet. Any elements which were identified as both contact and redundant were assigned to the contact set. To determine which elements corresponded to the anterior and posterior leaflets, the outward normal of each element was dotted with the unit y-normal vector; a positive dot product corresponds with the anterior leaflet, and a negative dot product with the posterior leaflet. Finally, the areas of the elements in each set were calculated and summed to compute the total area of that region.

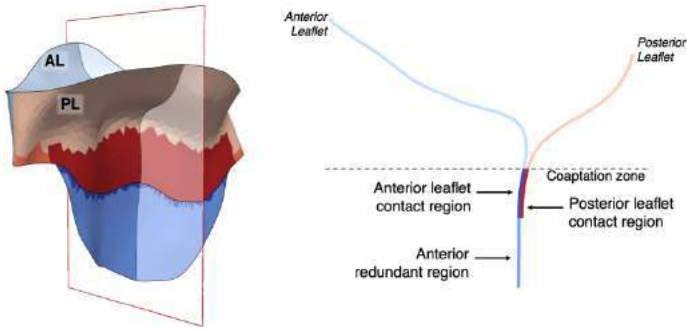


**Figure 2: A cross section of a representative recurrent MV illustrating the coaptation zone and sub-regions on each leaflet.**

## RESULTS

First, the shape-matching technique recovered the full coaptation zone, which is ordinarily not visible in part or in full on rt-3DE. This area was recovered in the final simulated geometry as the open state reconstruction is morphed to shape of the closed state (Figure 3).

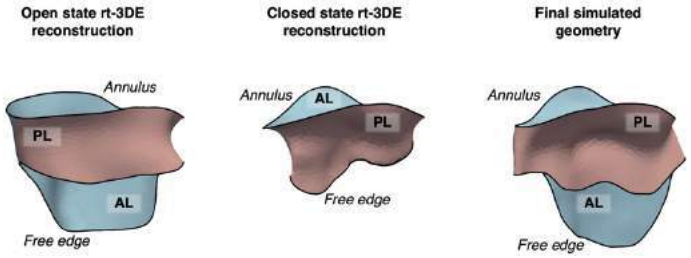


**Figure 3: The open and closed geometries, as well as the simulation output, for a representative recurrent MV.**

Furthermore, this method was able to resolve the coaptation zone into its subdivisions, a distinction which is otherwise impossible to achieve using modern echocardiographic imaging data alone (Figure 2). This more precise insight into the closing behavior of the MV in both the diseased state and after URA repair will deepen our understanding on the impact of the ring on the MV and may help contextualize the divergent clinical outcomes among patient groups. Total systolic leaflet surface area decreased following surgical repair in both the nonrecurrent and recurrent valves ($p < 0.05$). Contact area increased more post-surgically in the recurrent group (Fig. 4A; $p = 0.0203$, $p > 0.05$ for nonrecurrent), a trend which held even when normalized to total systolic leaflet area to account for generally larger recurrent valves (Fig. 4B; $p = 0.0080$, recurrent; $p = 0.0401$, nonrecurrent). The redundant region also increased post-surgically in recurrent valves ($p = 0.0050$, recurrent; $p > 0.05$, nonrecurrent), and again when normalized ($p = 0.0022$, recurrent; $p > 0.05$, nonrecurrent). A general increase in contact area is expected in the context of URA repair; however, it is important to note that MVs with recurrence of MR at six months showed *greater* normalized contact immediately after repair.

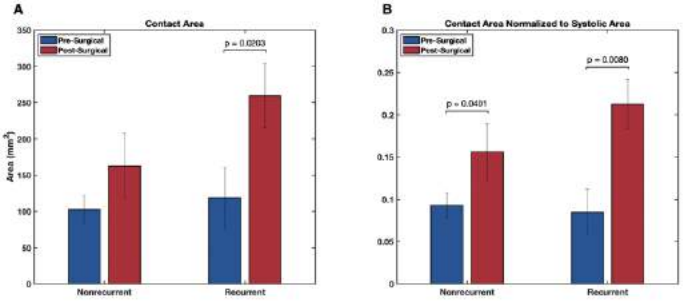


**Figure 4: A: Contact region area in nonrecurrent and recurrent valves before and after URA repair. B: Contact region area normalized to total systolic leaflet area.**

## DISCUSSION

We found that in patients who develop recurrent MR six months after URA repair, the contact area immediately after repair was greater than that of patients who did not have recurrent MR at the same time point. Moreover, the contact area normalized to total systolic leaflet area increased more for recurrent MVs compared to nonrecurrent MVs. This trend could be explained by the fact that recurrent valves tend to have more dilated pre-surgical annuli than nonrecurrent valves, and therefore experience a greater percent change in annulus reduction post-repair [9]. As a result, more leaflet tissue is shunted into the coaptation zone, increasing both contact and redundant region area for the recurrent subset. Importantly, this finding suggests that greater coaptation area alone may not necessarily indicate a more durable repair in the long-term, especially in patients whose LV dilatation is more pronounced. Therefore, improved contact alone may not be a reliable metric for determining durability of the repair. In this study, we have also demonstrated the capability of our shape-matching technique in recovering the full coaptation zone, which can be underestimated in rt-3DE. Moreover, we were able to further resolve this zone into its subregions, which will allow us to refine our understanding of MV coaptation behavior in MR as well as the functional consequences of available repair techniques.


## ACKNOWLEDGEMENTS

The authors gratefully acknowledge funding NIH from R01 HL073021.


## REFERENCES


[1] Benjamin, EJ et al., *Circulation* 137:e67-e492, 2018.
[2] Messika-Zeitoun, D et al., *J Am Heart Assoc,* 9(15), 2020.
[3] Perrault, L et al., *J Thorac Cardiovasc Surg,* 143:1396-1403, 2012.
[4] Crabtree, TD et al., *Ann Thorac Surg,* 85(5):1537-1543, 2008.
[5] Nishimura, RA et al., *Circulation,*129:e521-e643, 2014.
[6] Bouma, W et al., *Ann Thorac Surg,* 100(4):1300-1306, 2015.
[7] Bouma, W et al., *Ann Thorac Surg,* 101(2):567-575, 2016.
[8] Cobey FC et al., *Ann Thorac Surg,* 97(6): 1998-2004, 2014.
[9] Narang, H et al., *Ann Biomed Eng,* 49(12):3711-3723, 2021.
[10] Rego, BV et al., *Int J Biomed Eng,* 101(2):567-575, 2018.

SB³C2022
Summer Biomechanics, Bioengineering and Biotransport Conference
June 20-23, Eastern Shore, MD, USA

# EFFECTS OF SCAFFOLD DEGRADATION BEHAVIOR ON TISSUE ENGINEERED VASCULAR GRAFT GROWTH AND REMODELING

**Jason M. Szafron (1), Yuichi Matsuzaki (2), Stephanie E. Lindsey (3), Christopher K. Breuer (2), Jay D. Humphrey (4), Alison L. Marsden (1)**

(1) Department of Pediatrics, Stanford University, Stanford, CA, USA
(2) Center for Regenerative Medicine, Nationwide Children's Hospital, Columbus, OH, USA
(3) Department of Mechanical Engineering, University of California San Diego, San Diego, CA, USA
(4) Department of Biomedical Engineering, Yale University, New Haven, CT, USA

## INTRODUCTION

Tissue-engineered vascular grafts (TEVGs) offer hope for improved long-term functionality in congenital heart surgeries due to their abilities to grow with native vessels and limit long-term complications from the permanent presence of synthetic material [1]. The ability of cells infiltrating the TEVG to alter their gene expression and matrix production or degradation kinetics in accordance with variations in mechanical stimuli allows for adaptation in maturation or changing hemodynamic loading. However, early TEVG remodeling is also dictated by the foreign body response to the polymeric scaffold. Variations in the material properties or microstructure of the scaffold can mediate changes in the phenotypes of the immune cells responsible for removing the scaffold and replacing it with new extracellular matrix [2]. Furthermore, timing of acidic products generated by the hydrolytic degradation of commonly used ester-containing polymers lead to different inflammatory responses [3]. As such, there is a complex interplay between the mechanobiological and immunobiological aspects of remodeling that determines the success or failure of implants.

Our group previously examined the link between the formation of early stenosis in TEVGs and the immune response, which demonstrated that narrowing could reverse with resolution of inflammation and the inhibition of new matrix deposition by mechanobiological cues [4, 5]. Scaffolds used in these studies consisted of a knitted polyglycolic acid (PGA) mesh enclosed in a porous sealant of caprolactone and lactic acid co-polymers (PCLA). Earlier work on TEVG design had replaced the PGA knit with a poly-L-lactide (PLLA) knit for a subgroup of a clinical trial that showed no long-term differences in outcome between the two different knitted polymers [6]. However, the differences in initial remodeling were not well characterized between PGA and PLLA knitted TEVGs.

In this work, we sought to predict potential differences in TEVG evolution for scaffolds made with these different materials. To that end, we utilized a computational model of TEVG growth and remodeling (G&R) that has been shown to capture geometric and mechanical changes of the remodeling time course [7]. We developed novel constitutive relations that relate the scaffold degradation time course to inflammatory kinetics and simulated perturbations to the degradation behavior of the PGA knitted grafts to understand potential changes to the severity and persistence of stenosis. These simulations suggested that delaying degradation beyond the initial foreign body response could reduce stenosis severity.

## METHODS

A constrained mixture theory G&R framework was used to simulate the evolving composition and geometry of the TEVG through one year of implantation in an ovine model of the Fontan procedure [4]. Briefly, each of the structurally significant constituents was prescribed constitutive relations for material behavior, production kinetics and degradation behavior. The neotissue was assumed to consist of collagen and smooth muscle cells produced according to both mechanobiological and immunological stimuli, where different behavior was used for constituents produced due to each stimulus. Polymeric constituents were present initially and degraded over time with a sigmoidal behavior

$$\varepsilon^p(s) = \frac{1+\exp(-k^p\zeta^p)}{1+\exp\left(k^p(s-\zeta^p)\right)}\varepsilon_0^p \qquad (1)$$

where $\varepsilon^p(s)$ is the surviving volume fraction of polymeric constituent $p$ with original volume fraction $\varepsilon_0^p$, $k^p$ is the degradation rate parameter, and $\zeta^p$ is the offset to rapid degradation. Effects of changing $k^p$ and $\zeta^p$ are shown below (**Fig. 1A and B**). Neotissue production $m^i(s)$ for inflammatory constituents $i$ was prescribed as a sum of two stimulus functions tailored by a decaying windowing function $w^i(s)$, written as

$$m^i(s) = m_h^i\left(K_\rho^i\Upsilon_\rho^i + K_{\rho'}^i\Upsilon_{\rho'}^i\right)w^i(s) \qquad (2)$$

with basal production rate $m_h^i$. The first stimulus function depends on the presence of the foreign body response-inducing scaffold

$$\Upsilon_\rho^i = \sum \varepsilon^p(s)/\sum \varepsilon_0^p \qquad (3)$$

which decreases monotonically as the polymer degrades. The second stimulus is a function of the rate of change of polymer mass

$$\Upsilon^i_{\rho\prime} = \sum \varepsilon^{p\prime}(s)/(\sum \varepsilon^{p\prime}(\zeta^p) \sum \varepsilon^p_0) \quad (4)$$

where $\varepsilon^{p\prime}(s) = d\varepsilon^p/ds$ and the stimulus increases during periods of rapid scaffold degradation.

In vitro degradation experiments informed the degradation parameters $k^p$ and $\zeta^p$ for each of the polymers used in this study [5]. Geometry and thickness data from implants using scaffolds with PGA knitted fibers were captured to provide parameters for neotissue production and removal [4]. The parameters $k^p$ and $\zeta^p$ were then varied parametrically to examine the potential differences in TEVG evolution for knitted fibers that had different degradation profiles.

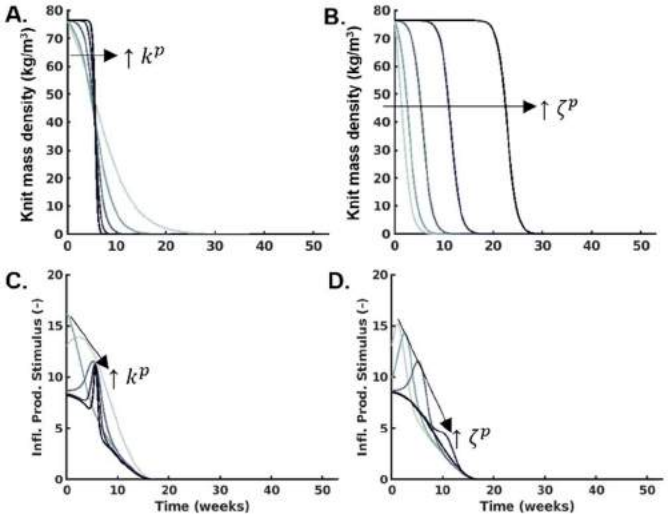


**Figure 1. Parametric studies of knitted scaffold degradation rate $k^p$ (A) and degradation offset $\zeta^p$ (B) and their corresponding effects on the inflammatory production stimulus for neotissue deposition (C, D), respectively. Darker lines and arrows indicate results for increasing parameter values.**

## RESULTS

For increasing values of $k^p$, the rate of mass loss during rapid degradation increased (**Fig. 1A**), while increasing $\zeta^p$ shifted the period of rapid degradation rightward to occur later in the time course (**Fig. 1B**). The inflammatory production stimulus for increasing $k^p$ showed a sharper peak at higher values of $k^p$ for shorter durations, but total inflammatory matrix production first increased and then decreased (**Fig. 1C**). For increasing $\zeta^p$, the time to peak inflammatory matrix production shifted rightward and decreased in magnitude as the decaying window function reduced immune activity (**Fig. 1D**).

We then examined changes in the inner radius (**Fig. 2A and B**) and thickness (**Fig. 2C and D**) for corresponding changes in the scaffold degradation parameters to determine how the potential for stenosis is affected by the resulting inflammatory stimuli. Total inflammatory matrix produced determined the degree of narrowing and thickening as increased areas under the inflammatory production stimuli curves (**Fig. 1C and D**) resulted in lower values of radius and higher values of thickness (**Fig. 2**). However, peak narrowing and thickening did not necessarily occur at the time of peak inflammatory matrix production, as, for example, the simulation with the lowest value of $k^p$ had its highest production value within the first simulated week but did not reach peak narrowing until 9 weeks (**Fig. 1C and Fig. 2A**). Changes in inflammatory stimuli with both degradation parameters produced non-monotonic changes in radius and thickness. Substituting the degradation parameters for those of a scaffold with PLLA knitted fibers that degrade slower and with a lower degradation rate than PGA suggested that scaffolds made with PLLA would tend to exhibit less stenosis than those made with PGA knitted fibers.

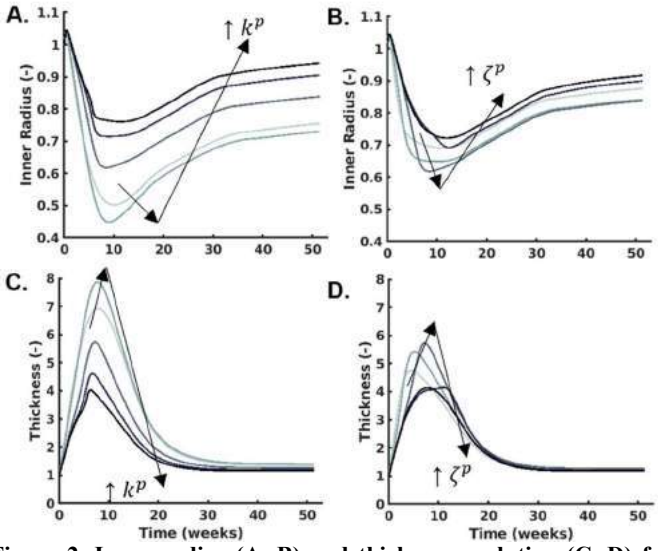


**Figure 2. Inner radius (A, B) and thickness evolution (C, D) for corresponding variations in $k^p$ (A, C) and $\zeta^p$ (B, D) from Figure 1. Quantities are normalized by their implantation values. Darker lines and arrows indicate results for increasing parameter values.**

## DISCUSSION

Computational models of scaffold evolution have been used to guide the design of subsequent design iterations [8, 9]. Here, we take this approach to understand potential changes in TEVG outcomes by changing the degradation properties of the scaffold components. As scaffolds with PLLA knitted fibers had been fabricated with a similar microstructure and mechanical behavior as those with PGA knitted fibers used in preclinical studies [1, 4], G&R simulations offered the chance to predict differences in evolution between designs based purely on the difference in degradation behavior. Therefore, we adapted our G&R framework to account for differences in inflammation caused by the presence of a foreign body and the accumulation of acidic degradation products. Parametric variation of the degradation rate and onset of rapid degradation demonstrated benefits to delaying the onset of rapid degradation beyond the initial foreign body response to the scaffold. Non-monotonic changes to the degree of narrowing and thickening with variations in degradation behavior highlight the utility of computational simulations to determine parameter ranges with improved outcomes. Though the novel constitutive relations require additional validation with implantation of PLLA scaffolds, these simulations suggest that delayed degradation of the knitted fibers can reduce stenosis and will be compared against future experimental data.


## ACKNOWLEDGEMENTS

The authors are grateful for support from NIH R01HL139796.


## REFERENCES


[1] Brennan, M.P., et al., *Ann Surg*, 248(3):370-377, 2008.
[2] Garg, K., et al., *Biomater*, 34(18):4439-4451, 2013.
[3] Grayson, C.R., et al., *J. Biomater Sci,* 15(10):1281-1304, 2004.
[4] Drews, J.D., et al., *Sci Trans Med,* 12(537), 2020.
[5] Blum, K.M., et al., *Commun Med,* 2(1), 2022.
[6] Hibino, N., et al., *J Thorac Cardiovasc Surg,* 139(2):431-436.
[7] Szafron, J.M., et al., *Ann Biomed Eng*, 46(11):1938-1950.
[8] Emmert, M.Y., et al., *Sci Trans Med*, 10(440), 2018.
[9] Szafron, J.M., et al., *Tissue Eng Part C*, 25(10):561-570, 2019.

SB³C2022
Summer Biomechanics, Bioengineering and Biotransport Conference
June 20-23, Eastern Shore, MD, USA

# RELATIONSHIPS BETWEEN ATHLETIC PERFORMANCE MEASURES AND HEAD KINEMATICS IN YOUTH ICE HOCKEY

**Abigail G. Swenson (1), N. Stewart Pritchard (2,3), Logan E. Miller (2,3), Chesney S. Oravec (4), Jason P. Mihalik (5), Jillian E. Urban (2,3), Joel D. Stitzel (2,3)**

(1) Dept. Neuroscience, Wake Forest School of Medicine, Winston Salem, NC, USA
(2) Dept. Biomedical Engineering, Wake Forest School of Medicine, Winston Salem, NC, USA
(3) Virginia Tech-Wake Forest School of Biomedical Engineering & Sciences, Winston Salem, NC, USA
(4) Dept. Neurological Surgery, Wake Forest School of Medicine, Winston Salem, NC, USA
(5) Dept. Exercise & Sport Science, University of North Carolina at Chapel Hill, Chapel Hill, NC, USA

## INTRODUCTION

Nearly 1 million athletes under the age of 20 participate in ice hockey each year.[1] The sport is characterized by frequent player-to-player contact and has a high rate of concussion;[2-3] however, most impacts hockey athletes experience are subconcussive (i.e., not acutely symptomatic). Subconcussive head impact exposure (HIE) poses a risk to brain health, as evidence from other contact and collision sports suggest subconcussive HIE may lead to neurologic sequelae observed even after a single season of youth sport participation.[4-5] Therefore, it is critical to understand factors influencing HIE to inform evidence-based strategies to reduce head impacts in youth hockey. While several studies have characterized hockey HIE,[6-8] none have investigated the relationship between sport-specific skills (broadly referred to as athletic performance) and HIE. Well-developed, hockey-specific skills may allow athletes to better avoid collisions with opponents. Interventions aimed at improving skills may be one avenue to reduce injury, as evidence from other sports suggests refining sport-specific skills reduces HIE.[9] Thus, this study assessed relationships between HIE and hockey-specific athletic performance assessments.

## METHODS

Youth ice hockey players (n=42 boys; ages 9-16) from a single organization participated in a preseason athletic performance combine event to assess sport-specific skills. Athletic performance in hockey was evaluated using a series of on- and off-ice tasks to assess speed, agility, power, and stick-handling.[10-11] On-ice tasks separately measured included stick-handling, cornering S-turn, acceleration & sprint skating, and modified Reed repeat sprint skating (Fig 1). Off-ice ("dry land") tasks included vertical jump, 30 meter sprint, and 5-10-5 yard agility shuttle. Two trials were completed for each task. Each athlete's mean times across trials were recorded for sprinting and skating tasks; mean number of times the athlete crossed the puck over a line on the ice was recorded for stick-handling; mean maximum jump heights were recorded for vertical jump.

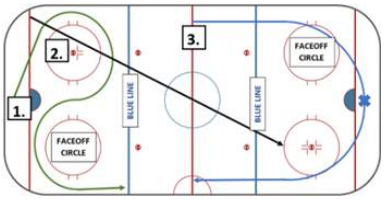


**Figure 1. The on-ice assessment components. 1) S-turn, 2) Accel. & sprint skating, 3) Reed repeat skating (not pictured: stick-handling).**

A subset of these participants (n=12, ages 12-14) consented to wear a custom-fit instrumented mouthpiece in the ensuing hockey season; mouthpiece data were excluded from analyses for goaltenders or if an athlete did not participate in the combine (n=4). The mouthpiece used a 5 g threshold to measure frequency and magnitude of head acceleration events (i.e., events).[12] Raw data were processed as described previously.[12-13] Mouthpiece events were then paired to time-synchronized video collected from 24 games during the ongoing season to characterize on-ice events by contact characteristics (e.g., head contact) using a custom MATLAB graphical interface (MathWorks, Natick, MA).

Preliminary statistical analyses examining relationships between preseason performance measures and head kinematic metrics were completed in SAS using generalized linear regressions (Cary, NC). For all regressions, Cook's distance was calculated and outliers were removed using a threshold of 4/n.

## RESULTS

Summary statistics for on- and off-ice combine assessment components are provided in Tables 1 and 2. A total of 304 visually-verified contact scenarios were collected from 12 youth athletes during 24 games. Following exclusion of the goaltenders and those that did not participate in the combine (n=4 athletes), 236 visually-verified contact scenarios recorded by the mouthpiece from 8 athletes were analyzed.

Number of contact scenarios per athlete ranged from 12 to 56; proportion of head impacts (i.e., number of contact scenarios with head contact / total number of contact scenarios) ranged from 0.21 to 0.55. Median (95th percentile) peak linear acceleration (PLA), rotational velocity (PRV), and rotational acceleration (PRA) for all verified contact scenarios were 8.09 (26.44) g, 6.63 (16.4) rad/s, and 549.4 (1565) rad/s$^2$, respectively.

**Table 1. Pooled mean [standard deviation; SD] preseason scores for on-ice tasks.**

| | S-turn | Accel & Sprint Skate | | Reed Skate | Stick-handling |
|---|---|---|---|---|---|
| | Time (s) | Accel time (s) | Total time (s) | Time (s) | # Crosses |
| Instrumented athletes (n=8) | 10.53 [1.60] | 2.16 [0.22] | 7.42 [0.85] | 11.23 [1.85] | 58.8 [10.60] |
| All athletes (n=42) | 10.68 [1.54] | 2.09 [0.31] | 7.41 [0.85] | 11.24 [1.47] | 57.00 [11.45] |

**Table 2. Pooled mean [SD] preseason scores for off-ice tasks.**

| | Vertical Jump | | 30 m Sprint | Agility Shuttle |
|---|---|---|---|---|
| | Standing Height (in) | Jump Height (in) | Time (s) | Time (s) |
| Instrumented athletes (n=8) | 83.35 [4.72] | 97.95 [5.73] | 5.21 [0.33] | 5.60 [0.36] |
| All athletes (n=42) | 81.05 [6.72] | 94.86 [9.14] | 5.51 [0.55] | 5.89 [0.53] |

Several notable relationships between preseason performance and head kinematic metrics were observed. Namely, athletes with faster mean completion times on skating tasks had significantly lower median PLA [S-turn (p=.02, $r^2$=.65), acceleration skate (p<.01, $r^2$=.76), sprint skate (p<.01, $r^2$=.71), Fig 2A, B)].

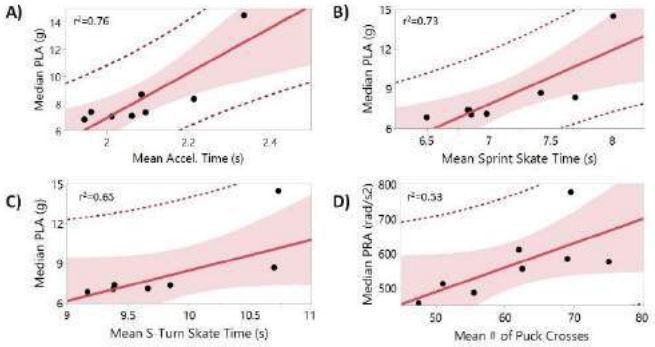


**Figure 2. Significant relationships between median PLA & A) mean accel. skate time, B) mean sprint skate time, C) S-turn skate time; D) median PRA and # of puck crosses during stick-handling.**

Additionally, faster mean completion time for the Reed skating task and S-turn skating task were associated with lower proportion of head impacts [S-turn (p=.03, $r^2$=.55) Reed skating (p=.03, $r^2$=.63)]. Greater stick-handling skill (i.e., greater number of puck crosses) was associated with higher median PRA (p=.04, $r^2$=.53). There were no significant associations between off-ice tasks and head kinematic metrics or between 95th percentile kinematics and performance on any task. In general, better performance scores correlated with decreases in head kinematic metrics, particularly for on-ice tasks.

## DISCUSSION

This study sought to examine preliminary relationships between measures of ice hockey athletic performance both on- and off-ice and head kinematic metrics using accepted measures of performance adopted from literature.[11-12,14] Previous literature from other collision sports such as football has indicated higher levels of physical performance correlate with greater HIE metrics;[14] however, this study hypothesized the opposite trend would be observed in hockey athletes, as increased hockey-specific skills such as skating and stick-handling would better allow athletes to avoid opponents and unnecessary body collisions on ice.

Findings from this study indicate that greater performance measures are associated with lower median PLA, particularly for skating tasks measuring speed and agility. Interestingly, we did not observe the same relationship between off-ice measures of speed and agility (5-10-5 yd. agility shuttle, 30 m sprint) and median PLA. This may be because there are differences between on- and off-ice forward motion[10] and that head accelerations in ice hockey may be more influenced by sport-specific characteristics than raw measures of speed or agility alone.

We additionally found greater stick-handling skill was associated with higher median PRA. It is possible that the stick-handling task as designed is not sensitive enough to accurately measure stick-handling ability. Athletes during this task may have directed their attention downwards to the puck, while in real gameplay would be focused on their surroundings rather than keeping their head down. This supports a possible methodological change to consider for future studies whereby this task should be completed with the athlete looking forward instead of down during task completion. This revised method has translational significance as previous literature has demonstrated that poor body positioning and collision anticipation (i.e., athlete keeps their head down) result in more severe head impacts than good body positioning and anticipation.[7] Refining this task may better elucidate relationships between stick-handling ability and HIE.

This study was limited in several areas. Firstly, the sample of athletes with both combine data and biomechanics data was small. As such, the statistical analyses may not be sufficiently powered. Expanding our sample size will reduce this limitation, as will continued biomechanics data collection as the current season continues. This study also only investigated preseason performance and does not reflect performance or skill degradations, or improvements that may occur during the season or measured post-season. The latent period between regular hockey season end (early spring) and the preseason combine (late summer) may also reduce discernable differences in performance between athletes due to lack of practice. We aim to host a post-season combine to innovatively understand the influence of performance level changes on HIE across the span of the season.

This preliminary study investigated relationships between athletic performance metrics and exposure to head acceleration events in boys' hockey athletes. While there have been studies characterizing HIE in youth ice hockey, and studies of ice hockey performance measures, this is the first study to assess how performance influences measured head kinematics. Our findings support the notion that ice hockey HIE is influenced by hockey-specific performance measures, with better performance corresponding to decreased exposure. This is an important addition to the literature, as it may support evidence-based skill-development strategies to reduce HIE and head acceleration events among youth hockey athletes, improving sport safety.


## ACKNOWLEDGEMENTS

We thank the Triad Hockey Alliance for their participation and coaches, students, and staff for their assistance with data collection. Childress Institute for Pediatric Trauma provided support for this study.


## REFERENCES


[1] International Ice Hockey Federation. Survey of Players. 2020. [2] Kontos et al., *Pediatrics*. 2016. [3] Emery et al., *JAMA*. 2006. [4] Talvage et al., *J Neurotrauma* 2014. [5] Davenport et al., *J Neurotrauma* 2014. [6] Mihalik et al., *Ann Biomed Eng*. 2019. [7] Mihalik et al., *Pediatrics*. 2010. [8] Swenson et al., *Research Sports Med*. 2021. [9] Kerr et al., *Ortho J Sport Med*. 2015. [10] Dominik et al., *J Sport Med Sci*. 2019. [11] Farlinger et al., *J Strength Cond Res*. 2007. [12] Miller et al., *J Biomech Eng*. 2018. [13] Rich et al., *Ann Biomed Eng*. 2019. [14] Kelley et al., *Med Sci Sports Exerc*. 2020. [15] Biro wet al., *J Pediatrics*. 1995.

# IMPLEMENTATION OF A LOW-COST OFF-AXIS LOADING FIXTURE (OALF) TO ADD SPINE BENDING TO A UNIAXIAL COMPRESSION DEVICE

**Axel C. Moore (1), Harrah R. Newman (1), Raith Nowak (1), Sean Magee (1), Gabriela Carlisle (1), Imani Carter (1), Justin Bouyer (1), Edward J. Vresilovic (1), Dawn M. Elliott (1)**

(1) Biomedical Engineering, University of Delaware, Newark, DE, USA

## INTRODUCTION

The primary function of the spine is to support and distribute large loads in all six degrees of freedom (DOF). Clinical disorders, such as degeneration or scoliosis, alter the structure and mechanical properties of spine tissues, subsequently changing the six DOF spine mechanical behavior. However, effectively isolating tissue-level changes in a coupled system such as the spine requires several careful considerations. First, multi-axial loading is needed to simulate all the degrees of mechanical function. Second, axial compression needs to be added to rotational loadings, such as lateral bending or flexion, to mirror physiological conditions (e.g., musculature and mass of the upper body). Therefore, mechanical evaluation of the spine should be capable of controlled multi-axial loading. Third, any applied loading introduces off-axis forces and moments that need to be accounted for and ideally minimized [1].

Single- and dual-axis testing platforms are widely used to measure compression and compression-torsion spine segment mechanics [2]. These systems are widely available in many biomechanics labs, but unfortunately are not readily adapted for flexion or bending conditions that are important for assessing spine function. Multi-axis testing platforms that integrate multiple linear and rotary motors, hexapod platforms, and serial arm robots have been used to quantify all six DOF spine segment mechanics [1], [3], [4]. While these are highly effective solutions, they involve significant equipment costs ($200k+) and are therefore not as accessible for spine researchers.

The objective of this study was to design an off-axis loading fixture (OALF) that is comparatively low-cost (~$10k) and can apply off-axis lateral bending or flexion-extension in combination with axial compression, on an existing uniaxial test frame. Here we use a TA Electroforce 3510, but similar test frames can be found in many materials research facilities. The OALF can be easily installed and

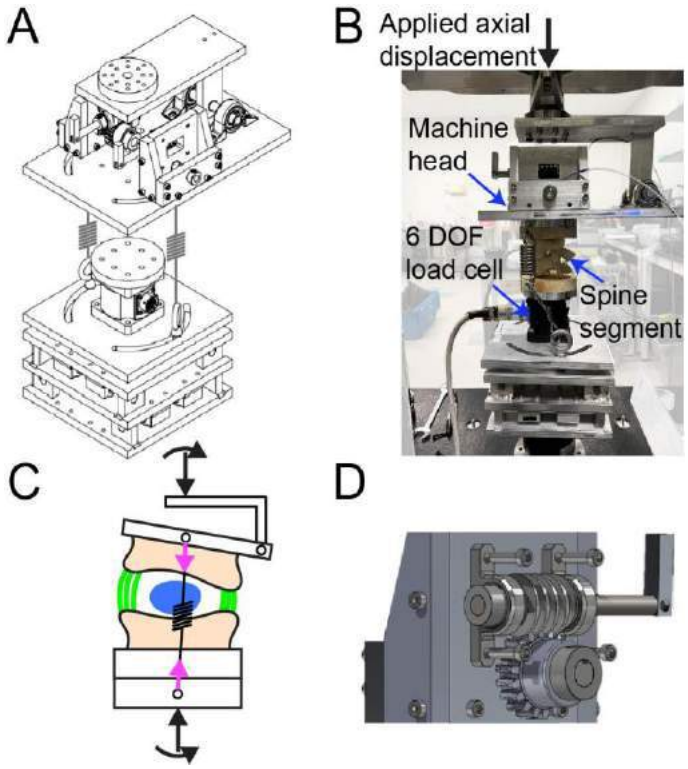


**Figure 1: (A) OALF design schematic showing the upper and lower assemblies. (B) OALF is bolted to a uniaxial test frame with a simulated spine segment. (C) Free body diagram. (D) Machine head assembly.**

removed in a single testing period. Preliminary data is presented demonstrating proof-of-concept.

## METHODS

The OALF was constructed to interface with an existing TA Electroforce 3510 uniaxial test frame (**Fig 1A**). The OALF enabled the axial displacements imposed by the Electroforce test frame to be transformed into angular displacements through a lever arm attached to the spinal motion segment (**Fig 1B**). The design allows for axial compression and one axis of rotation (lateral bending or flexion-extension) **(Fig 1C**) while minimizing shear forces.

Axial compression was applied through a guitar inspired machine head assembly (**Fig 1C(pink spring),D**). The machine head was used to apply tension to two wire stays which axially compressed the spine segment. Inline tension springs were installed to enable fine tuning of the resulting compressive force. A 6 DOF load cell (AMTI MC3A-500) was placed below the OALF fixture (**Fig 1A,B**). The total cost of design is approximately $10,000 which includes $2,000 for materials and machining and $8,000 for the load cell.

A single functional spinal unit (bone-disc-bone) from a Yucatan minipig was used in this proof-of-concept study. The facets were removed and the superior and inferior vertebrae were fixed in PMMA (polymethyl methacrylate) bone cement and bolted into the OALF. The disc was wrapped in phosphate buffered saline (PBS)-soaked gauze throughout testing to prevent tissue dehydration.

Three cycles of lateral bending (±4 degrees [1]) were applied to the spine segment [5]. To achieve this target rotation a ±11.18 mm axial displacement was imposed at 0.05 Hz via the Electroforce linear actuator. To demonstrate the addition of physiological compression, the test was repeated with a 100 N axial compression load. Forces and moments in six DOF were measured throughout the test, and the neutral zone and linear region stiffness were calculated.

## RESULTS

Applying a displacement to the OALF resulted in the expected lateral bending moments (**Fig 2**), with a neutral zone of ±2 degrees and a stiffness of 0.25 Nm/degree. The addition of a 100 N axial load led to a larger neutral zone of ±3 degrees and larger lateral bending stiffness of 0.50 Nm/degree (**Fig 2**). The axial force variation induced by the OALF converting axial displacement to bending was less than 15 N (**Fig 3C,D**). The off-axis coupled shear forces were negligible **(Fig 3C,D**) and the coupled flexion moments were small (**Fig 3A,B**). However, a large coupled torsional moment of similar magnitude to the lateral bending occurred during unloaded testing, but was mitigated with the addition of axial compression (**Fig 3A,B**). This limitation will be addressed in future work, as described below.

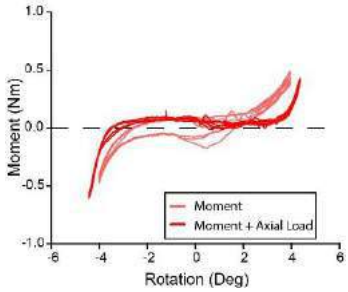


**Figure 2: The moment produced during lateral bending with and without a 100 N axial load.**

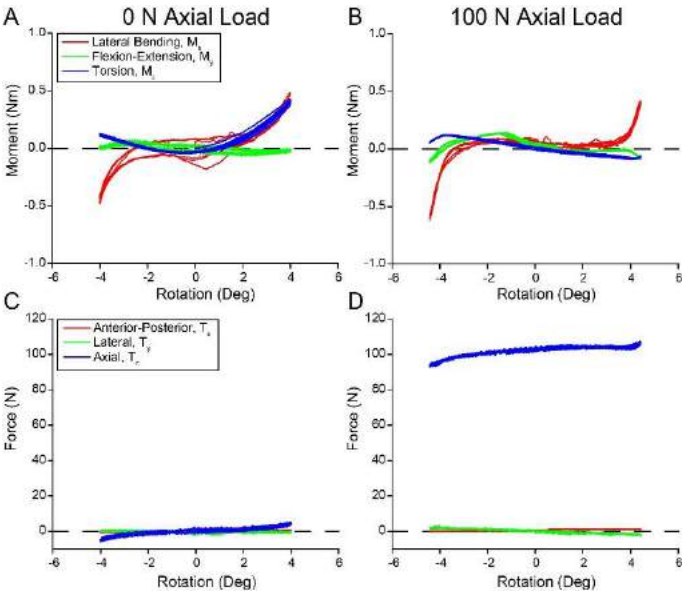


**Figure 3: Measured (A,B) moments ($M_{x,y,z}$) and (C,D) forces ($T_{x,y,z}$) for lateral bending. The axial compressive load was set at (A,C) 0 and (B,D) 100 N.**

## DISCUSSION

We have developed an off-axis loading fixture, OALF, which enables combined lateral bending (or flexion-extension, not shown) with axial compression and measures all six DOF (force and moments). The device is low-cost when compared to existing multi-axis testing platforms such as hexapods and serial arm robots.

Developing this low-cost solution led to several design constraints. The first design limitation is the fluctuation in axial force (**Fig 3**), as axial force drives the bending moment of the system. This variation is minimized as the line of action for the tension springs approximate the center of rotation for the spine segment. With the addition of physiological compression loads, this fluctuation is ~15% of the applied compression. While we successfully minimized off-axis shear forces, the second limitation was the substantial torsional coupling, which was not anticipated (**Fig 3A**). A thrust bearing will be added to address this limitation. In conclusion, we have implemented a low-cost system to apply off-axis loads to spine segments; ongoing work will quantify system capabilities and apply OALF to quantify multi-axial spine biomechanics in human and animal spine studies.


## ACKNOWLEDGEMENTS

The authors acknowledge support for this research from the NIH (R01AR050052). The authors also thank Dr. Jennifer Buckley for her support and mentorship of the senior design team.


## REFERENCES


[1] J. F. DeLucca, et al., *JOR SPINE*, 2:e1047, 2019. [2] J. J. Costi, et al., *JOR Spine*, 4:1–25, 2021. [3] D. B. Amin, et al., *J. Biomech.*, 49:3407–3414, 2016. [4] I. A. Stokes, et al., *J. Biomech.*, 35:517-521, 2002. [5] H. J. Wilke, et al., *Front. Bioeng. Biotechnol.*, 8:1–11, 2020.

SB³C2022
Summer Biomechanics, Bioengineering and Biotransport Conference
June 20-23, Eastern Shore, MD, USA

# INJURY CRITERIA: DEFINING MECHANICAL THRESHOLDS FOR COLLAGEN IN SOFT TISSUES

**Callan M. Luetkemeyer (1), Kaitlin P. McCreery (1,2), Kathryn R. Jacobson (3), Corey P. Neu (1,2), Sarah Calve (1,2,3)**

(1) Paul M. Rady Department of Mechanical Engineering, University of Colorado Boulder, Boulder, CO, USA
(2) Biomedical Engineering Program, University of Colorado Boulder, Boulder, CO, USA
(3) Interdisciplinary Life Sciences Program, Purdue University, West Lafayette, IN, USA

## INTRODUCTION

Injuries to soft tissues like ligaments, intervertebral discs, and cartilage are debilitating, costly, and common [1]. Because injuries are the result of excessive mechanical deformation, computational methods like finite element analysis are an ideal means by which to study injury risk and prevention in a systematic and deterministic way. However, predictive computational models require accurate, experimentally-derived models of tissue mechanical behavior. To this end, progress has been made to model the stress-deformation relationship for soft tissues [2]. Yet, methods for characterizing the deformation thresholds for injury are lacking. Such models are critical for informing computational studies on injury risk, as well as for directly assessing how material differences – i.e., extracellular matrix composition (ECM) and organization – affect injury susceptibility.

We propose a method for defining injury criteria (multimodal mechanical thresholds) for soft tissues [2]. In this work, we focus on molecular-level collagen damage, which can be spatially mapped using collagen hybridizing peptide (CHP) [3]. The objectives of this study were (1) to develop a method to identify molecular-level collagen injury criteria for soft tissues that accounts for multimodal and spatially heterogeneous deformation and (2) to examine the effect of fibrosis and disorganized ECM on injury risk by comparing injury criteria for medial collateral ligaments (MCLs) from *Fbn1*$^{Tsk}$ (Tsk) heterozygous mice [4] – a fibrillin-1 (Fbn1) knock-in mutation that results in hyperplasia of connective tissues – and wild-type (WT) controls. Results demonstrate that mechanically-induced collagen denaturation can be driven by multiple modes of tissue-level deformation. Moreover, the Tsk mutation appears to increase the influence of shear strain on thresholds for collagen denaturation.

## METHODS

Hindlimbs from 10-14 week old WT and Tsk mice (obtained and euthanized in accordance with CU Boulder IACUC regulations) were isolated, and the skin, tendons, muscles, and fascia around the knee joint were removed. Specimens were stained with Ghost Dye (Tonbo Biosciences), which binds to amine groups, and NucBlue (ThermoFisher Scientific), which stains cell nuclei, for 3 hours at 4 ºC in 1× PBS to provide trackable image texture for deformation mapping from confocal images.

All remaining soft tissues were then removed except for the MCL. Both bones were potted in custom grips with heat-set polystyrene, and the grips were secured to a custom loading chamber in a 1× PBS bath mounted under an upright confocal microscope (Leica STELLARIS). A 0.1 N pre-load was used to define the reference state.

The PBS in the bath was exchanged for a 5 µM solution of CHP for 15 minutes. Following CHP staining, samples were imaged at 10× magnification (2.14 µm resolution) to provide a sample-specific baseline from which to map mechanical deformation and collagen damage. Samples were imaged in 3 deformed configurations, defined by actuator displacements of 250–1000 µm in the longitudinal/fiber direction. After each deformation, samples were returned to the reference state, stained again with CHP for 15 minutes, and reimaged.

Surface voxels were used to create 2D projections of each specimen. 2D displacement fields were estimated using composite Ghost Dye and NucBlue reference and deformed images with Matlab's *imregdemons* function, from which Lagrange strain fields were estimated. Pixels were considered to have significant collagen denaturation if its CHP image intensity was above the following threshold:

$$\gamma_i = \mu_i + 3\sigma_1 \quad (1)$$

Where $\gamma_i$ is the CHP image intensity threshold for the $i^{\text{th}}$ reference image, $\mu_i$ is the mean CHP intensity of the $i^{\text{th}}$ reference image, and $\sigma_1$ is the standard deviation in CHP intensity of the original reference image. From the strain fields and binary damage maps, injury criteria were developed using logistic regression (Matlab) to determine the strain thresholds for collagen denaturation.

## RESULTS

The proposed damage mapping method demonstrated an ability to distinguish between increased image intensity resulting from additional stain time versus collagen damage. With additional stain time on a static specimen, CHP image intensity histograms shift, but there is little effect on the standard deviation or the number of pixels above the threshold (Eq. 1). However, following deformations and additional staining, distributions widen and the proposed method identifies a greater number of pixels above the damage threshold.

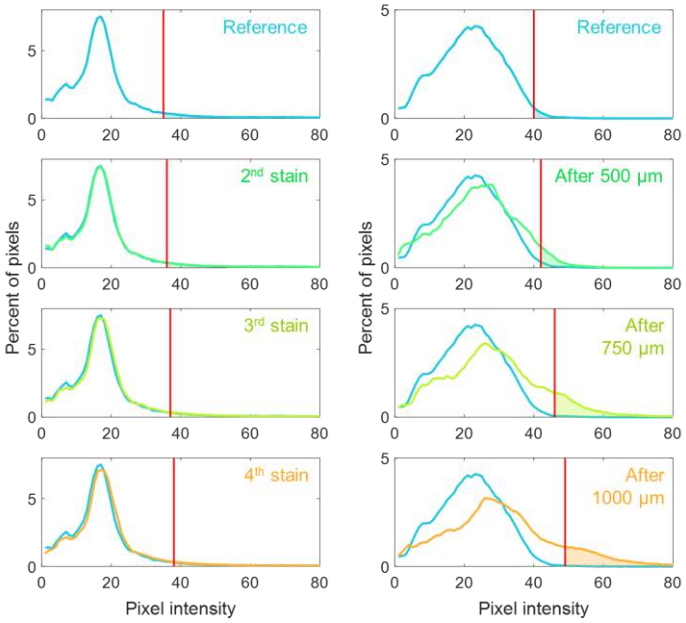


**Figure 1: CHP image intensity histograms shift with stain time in a static specimen (left), but the number of pixels above the damage threshold (red line, Eq. 1) increase only after deformation (right).**

Deformation fields and damage maps were spatially inhomogeneous (Fig. 2). In general, collagen denaturation most closely correlated with $E_{11}$ (strain in the mean collagen fiber direction), but $E_{22}$ (transverse strain) was also consistently an important predictor of damage (Fig. 3A).

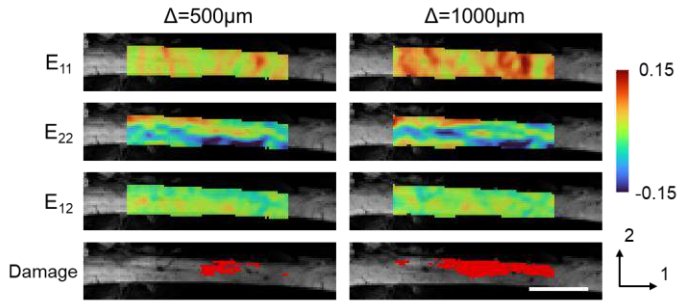


**Figure 2: Lagrange strain fields and damage maps (damage in red) after 500 and 1000 µm applied displacements reveal spatial heterogeneity in deformation and damage (scale bar = 500 µm).**

Comparing MCLs from one male Tsk mouse to a male WT (littermate) control, we saw no significant differences in injury criteria in the $E_{11}$-$E_{22}$ plane (Fig. 3A). However, shear strain ($E_{12}$) was a significant predictor for collagen damage in the Tsk MCL, while shear strain did not affect the injury criterion for the WT MCL (Fig. 3B).

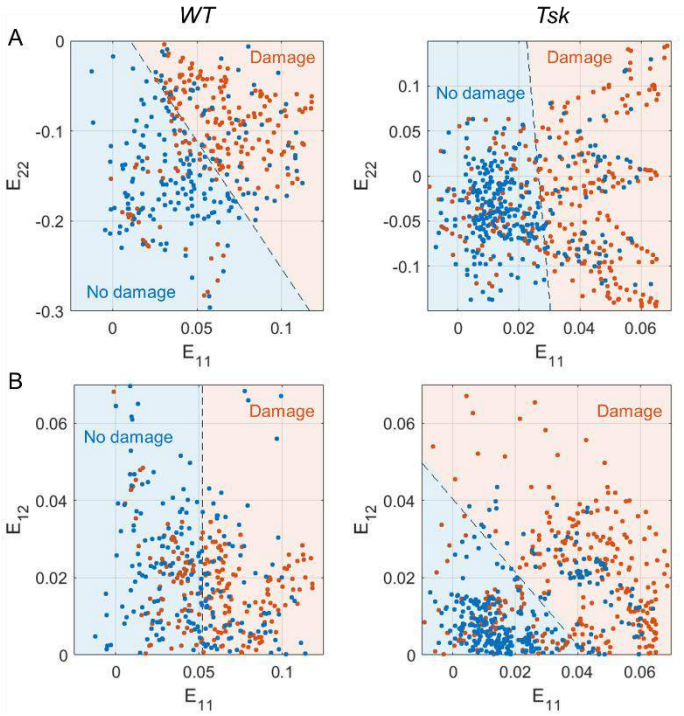


**Figure 3: Collagen injury criteria in the $E_{11}$-$E_{22}$ plane (A) and $E_{11}$-$E_{12}$ plane (B) for MCLs from WT (left) and Tsk (right) mice indicate deformation thresholds are multimodal.**

## DISCUSSION

We developed a method for defining injury criteria for collagen molecules in soft tissues. The method is robust to shifts in CHP image intensity that result from staining a specimen multiple times (Fig. 1) and it accounts for spatial heterogeneity and multimodal strain (Fig. 2). Our findings demonstrate that, in the normal MCL, mechanically-induced collagen denaturation depends on tissue-level tensile strains in the longitudinal and transverse directions (Fig. 3A). Furthermore, preliminary data comparing MCLs from Tsk and WT mice suggest that the Tsk MCL is also susceptible to damage from shear strain (Fig. 3B). This finding suggests that fibrotic ligaments with more disorganized ECM [5] are at higher risk of collagen damage and failure.

This is the first study to model the multimodal, tissue-level mechanical thresholds for collagen denaturation. Limitations include noisy image-based strain field estimates, 2D surface measurements, and linear strain thresholds identified by logistic regression. Still, the utility of the proposed method is readily demonstrated by the difference observed in injury criteria for the Tsk MCL and WT control. Future work will use these findings to inform multi-scale damage models with which to study injury in a computational framework.


## ACKNOWLEDGEMENTS

This work was supported by the Schmidt Science Fellowship (CML), NIH R01 AR071359 (CPN), and NIH DP2 AT009833 (SC).


## REFERENCES


[1] Asahara, H et al., *JBMR*, 32(9): 1773-1782, 2017.
[2] Luetkemeyer, CM et al., *JMPS*, 156:104577, 2021.
[3] Zitnay, JL et al., *Nat Comm*, 8(1):1-12, 2017.
[4] Saito, S. et al., *Mol Med*, 6:825-36, 2000.
[5] Abate, et al., *Arthritis Res Ther*. 11(3):235, 2009.

# INTRAOCULAR PRESSURE-INDUCED LAMINA CRIBROSA DEFORMATIONS ARE LARGER AND MORE INHOMOGENEOUS BETWEEN QUADRANTS IN AN EXPERIMENTAL GLAUCOMA EYE THAN IN HEALTHY EYE

**Bingrui Wang (1), Fuqiang Zhong (1), Junchao Wei (1), Yi Hua (1), Juan Reynaud (3), Brad Fortune (3), Ian A. Sigal (1,2)**

(1) Department of Ophthalmology, University of Pittsburgh, Pittsburgh, PA, USA
(2) Department of Bioengineering, University of Pittsburgh, Pittsburgh, PA, USA
(3) Devers Eye Institute, Legacy Health Research, Portland, OR, USA

## INTRODUCTION

Elevated intraocular pressure (IOP) is a primary risk factor for the development and progression of glaucoma [1]. However, the mechanisms by which the elevated IOP leads to neural tissue damage remain unclear [2]. A leading hypothesis is that the mechanical loads of IOP cause deformations and remodeling of the lamina cribrosa (LC), such as stretch, compression, and shear, and that these deformations act as mechanical stimulus to the astrocytes and retinal ganglion cell axons at the LC, triggering or contributing to mechanisms of axon degeneration, and thus loss of vision [3, 4]. Evaluating this hypothesis requires a better understanding of the effects of elevated IOP on the LC deformations.

Our goal was to measure in-vivo the IOP-induced LC deformations in experimental glaucoma and healthy eyes. Specifically, we analyzed the stretch, compression, and shear in four anatomical quadrants of the LC: temporal, superior, nasal, and inferior.

## METHODS

The optic nerve head of a rhesus macaque monkey with unilateral experimental glaucoma was imaged using optical coherence tomography (OCT) (**Figure 1**). [5] For this study we compare images of the right eye, the control eye, obtained at baseline, with images of the left eye, the experimental glaucoma eye, obtained at glaucoma onset. In each session, OCT images were acquired at controlled IOPs of 10, 20, 30, 40, 50, and 60 mmHg. A high-accuracy digital volume correlation method was used to analyze the OCT image sets for displacement field [6]. From the displacement results relative to 10 mmHg, we calculated the maximum principal strain (stretch), the minimum principal strain (compression), and the maximum shear strain (shear) of the LC region.

The LC region was marked manually and divided into four quadrants (**Figure 2**): temporal (T), superior (S), nasal (N), and inferior (I). All the strains in each quadrant were extracted and compared.

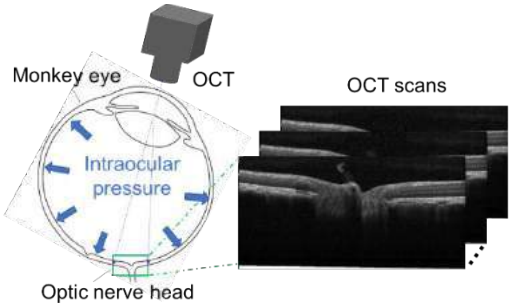


**Figure 1: Optical coherence tomography volumes of the lamina cribrosa were acquired using raster scanning.**

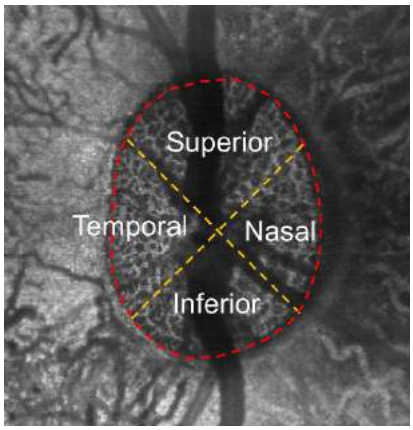


**Figure 2: C-mode view of an LC illustrating the quadrants.**

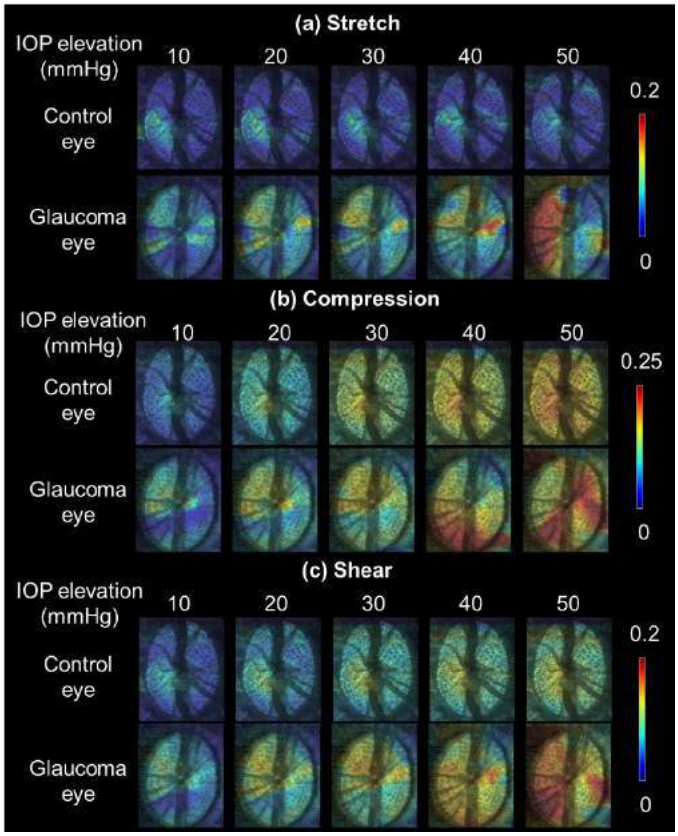


**Figure 3: Both eyes exhibited substantial deformations as IOP increased. Deformations were larger in the glaucoma eye. Shown are deformations from the baseline IOP of 10 mmHg.**

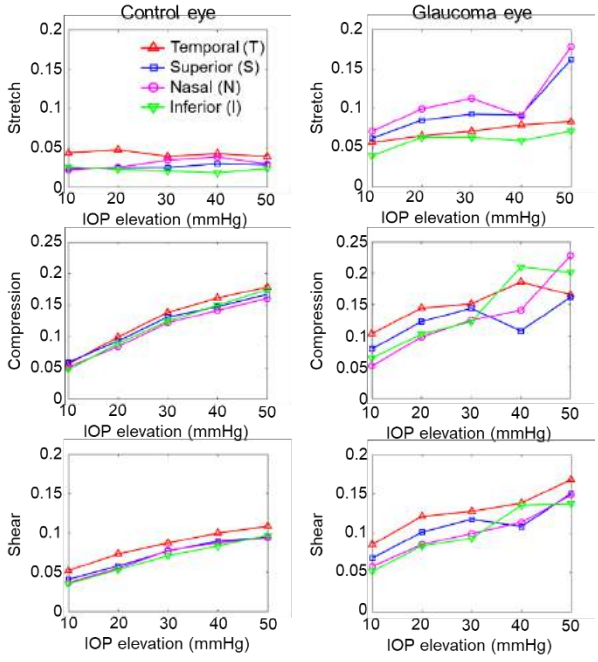


**Figure 4: The median values of stretch (first row), compression (second row), and shear (third row) in four quadrants for both control eye (left column) and glaucoma eye (right column).**

## RESULTS

Strain plots of the LC region at different elevated IOPs were obtained (**Figure 3**). When the IOP increased from 10 mmHg to 20 mmHg, the differences of stretch, compression and shear between both eyes were small. However, with further IOP increases, the glaucoma eye had larger strain compared to that of the healthy eye. For example, when IOP increased from 10 mmHg to 60 mmHg, shear in the glaucoma eye doubled compared to that in the control eye (0.2 vs. 0.1).

The median values of stretch, compression, and shear in four quadrants of both eyes are shown in **Figure 4**. In the control eye, the values of stretch, compression, and shear in all four quadrants were fairly homogeneous in contrast with the inhomogeneous values obtained in the glaucoma eye. In addition, in the control eye, the temporal quadrant had a larger deformation compared to others. In the glaucoma eye, the nasal and superior quadrants had a larger stretch than the other two quadrants. Specifically, when IOP increased from 10 to 60 mmHg, the stretch in nasal and superior quadrants is almost three times larger than those in the temporal and inferior quadrants.

## DISCUSSION

Our goal was to measure in-vivo the IOP-induced LC deformations in healthy and glaucoma eyes. Three main findings arise from this work. First, as IOP increased, the LC deformations of the glaucoma eye were larger than those of the healthy eye. Second, the LC strain distribution in the glaucoma eye was inhomogeneous across the four quadrants, whereas the healthy eye strain distribution was relatively homogeneous. Third, in the glaucoma eye, the stretch in the nasal and superior quadrants was larger than in the temporal and inferior quadrants, especially at very high IOPs. Below we discuss each of the main findings in detail.

We found that the IOP-induced LC deformations of the glaucoma eye were larger than those of the healthy eye. A possible explanation could be that tissues in the glaucoma eye are more compliant at this early stage, resulting in larger deformations as IOP increases. These large deformations may contribute to retinal ganglion cell axon damage in the LC leading to vision loss.

We also found that the LC strain distribution in the glaucoma eye was inhomogeneous throughout the four quadrants, a phenomenon that we did not observe in the healthy eye. It is possible that as glaucoma develops, tissue remodeling in the LC is not uniform, resulting in the non-uniform compliance of tissues in the LC.

We further found that in the glaucoma eye, the stretch in the nasal and superior quadrants were larger than that in the temporal and inferior quadrants, especially at very high IOPs. This may help explain the region-dependent axon damage commonly observed in glaucoma eyes.

In summary, we have measured in-vivo the IOP-induced LC deformations in glaucoma and healthy eyes. Results from this study are essential to understanding the mechanisms of the IOP-induced retinal ganglion cell axon damage in glaucoma. Efforts to expand the measurement of LC deformation to more eyes are currently underway.

## ACKNOWLEDGEMENTS

NIH R01-EY023966, R01-EY025011, R01-EY030590, R01-EY031708, P30-EY008098 and T32-EY017271, Eye and Ear Foundation (Pittsburgh, PA), Research to Prevent Blindness

## REFERENCES

[1] Quigley HA, *IOVS*, 46: 2662-2670, 2005.
[2] Yang H et al., *Prog. Retin. Eye Res.*, 59:1-52, 2017.
[3] Sigal IA et al, *IOVS*, 55:1-15, 2014.
[4] Campbell IC, *J. Biomech. Eng.*, 136(2), 021005, 2014.
[5] Fortune B et al, *IOVS*, 54(8): 5653–5661, 2013.
[6] Zhong F et al, *bioRxiv*, 08.07.455176, 2021.

# CALIBRATION OF CARDIOPULMONARY AND SYSTEMIC CIRCULATION MODELS IN PULMONARY ARTERIAL HYPERTENSION AND CARDIAC TRANSPLANT SUBJECTS

**Christopher Tossas-Betancourt (1), Nathan Y. Li (2), Sheikh M. Shavik (3), Adam L. Dorfman (4), Seungik Baek (5), Lik C. Lee (5), C. Alberto Figueroa (1,6)**

(1) Department of Biomedical Engineering, University of Michigan, Ann Arbor, MI, USA
(2) Department of Pharmaceutical Sciences, University of Michigan, Ann Arbor, MI, USA
(3) Department of Mechanical Engineering, Bangladesh University of Engineering and Technology, Dhaka, Bangladesh
(4) Department of Pediatrics, University of Michigan, Ann Arbor, MI, USA
(5) Department of Mechanical Engineering, Michigan State University, East Lansing, MI, USA
(6) Department of Surgery, University of Michigan, Ann Arbor, MI, USA

## INTRODUCTION

Pediatric pulmonary arterial hypertension (PAH) is a complex disease, characterized by functional and structural changes that can lead to right ventricular (RV) failure. While ventricular-arterial interactions between the RV and pulmonary vasculature are well established [1], interactions between the left ventricle (LV) and RV are less understood [2]. To broaden our understanding of PAH, there is a need to identify metrics of ventricular-arterial and interventricular interactions.

The aims of this work were to: (A) construct high-resolution (3D) arterial and ventricular computational models to study cardiopulmonary mechanics and hemodynamics, using a workflow previously developed by our group [3]; (B) calibrate the models to match prospectively acquired clinical data on two patient cohorts (PAH patients and control subjects); and (C) derive functional and structural metrics from clinical data and computational models to compare these patient cohorts.

## METHODS

**Clinical Data**. Clinical data was prospectively acquired in two pediatric patient cohorts: 12 PAH patients and 14 cardiac transplant patients, who serve as control subjects. Magnetic resonance imaging (MRI) was performed to acquire data on cardiac and vascular anatomy. Phase-contrast MRI was performed to obtain dynamic data of luminal area changes and blood flow velocity. LV and RV volume waveforms were generated by segmenting endocardial surfaces using software packages CVI42 (Circle Cardiovascular Imaging, Calgary, Canada) and MeVisLab (www.mevislab.de). Pressure waveforms were acquired via invasive right heart catheterization.

**Arterial Modeling.** Patient-specific closed-loop 3D fluid structure interaction (FSI) models were constructed from anatomical data using the CRIMSON software [4] (**Fig. 1A**). Clinical data were used to inform arterial wall properties, inflow, and outflow boundary conditions (BC). Dynamic luminal area and pressure waveforms were used to derive spatially-varying arterial wall stiffness [5]. Resistance and compliance of the distal vasculature was described using lumped-parameter three-element Windkessel models (**Fig. 1A**). The heart was described using a lumped-parameter network of models that represent the atria, ventricles, and valves [6].

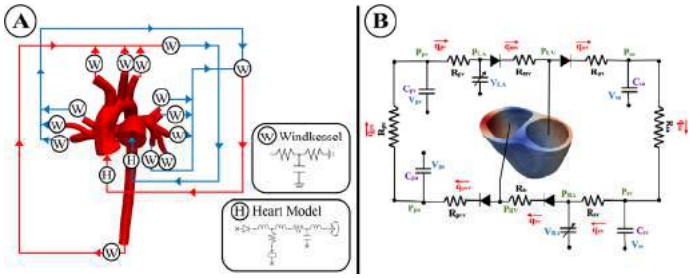


**Figure 1. (A) Arterial model has high-resolution (3D) models of the large arteries, and low-resolution (0D) models of the heart and veins. (B) Ventricular model contains a 3D biventricular model, and 0D models of the vasculature, atria, and valves.**

**Ventricular Modeling.** Finite-element (FE) models of the LV and RV were constructed using the open-source modeling platform FEniCS (www.fenicsproject.org). This biventricular model was coupled to closed-loop lumped parameter circuits of the systemic and pulmonary circulations [7] (**Fig. 1B**). Passive constitutive model [8], active contraction model [9] and lumped-parameter model values were tuned to match clinically-acquired ventricular pressure-volume (PV) loops and arterial pressure waveforms. RV end-systolic pressure volume relationship (ESPVR), a contractility metric, was estimated in a fully-calibrated model by varying preload and calculating the slope between maximum end-systolic elastance values (**Fig. 2**).

## RESULTS

We present results for one representative subject for each group – a PAH patient and a control.

**Arterial Modeling.** Simulated mean flow rates at the MPA and ascending aorta were matched within 3% of clinically-measured data; systolic, diastolic, and mean pressures were matched within 5% (**Fig. 3**).

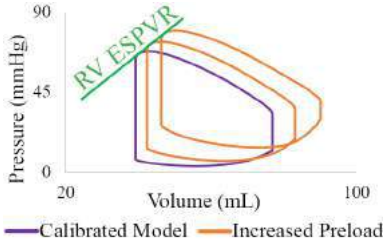


**Figure 2. RV ESPVR estimation**

**Ventricular Modeling.** Closed-loop 3D ventricular models successfully reproduced the clinically-measured PV loops of the LV and RV and pressure waveforms at the MPA and aorta (**Fig. 4**).

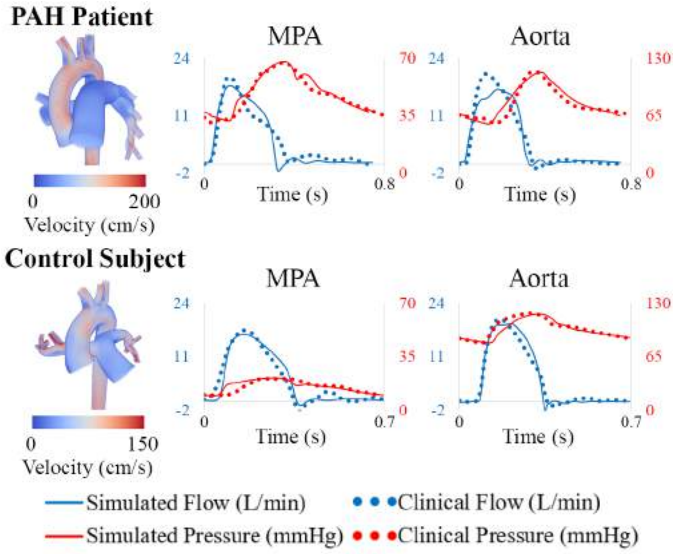


**Figure 3. Left: Peak systolic velocity maps in a PAH and control subject. Right: Comparison between clinically measured (dots) and simulated hemodynamics (solid lines) at the inlets of the main pulmonary artery (MPA) and aorta.**

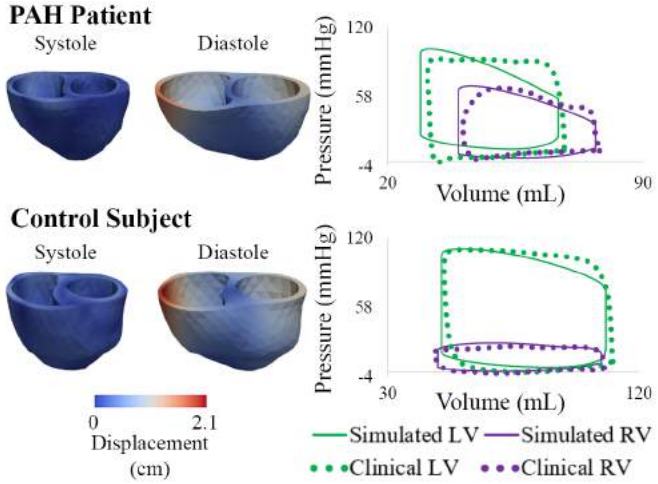


**Figure 4. Anatomical ventricular models with maps of maximum fiber stress (left) and displacement (middle). Right: Comparison of clinically-measured (dots) and simulated (solid lines) PV loops.**

**Metric Comparison.** As expected, all pulmonary pressures (mean, systolic, diastolic, pulse) and MPA stiffness were higher in the PAH patient than in the control subject (**Fig. 5**). However, while systemic pulse arterial pressure was higher in the PAH patient, systemic mean arterial pressure was surprisingly lower. Both subjects had healthy RV ejection fractions (≥ 55%), and similar end-systolic, end-diastolic, and stroke volumes (**Fig. 5**). RV ESPVR was found to be higher in the PAH patient (1.63 mmHg/mL) than in the control subject (0.43 mmHg/mL).

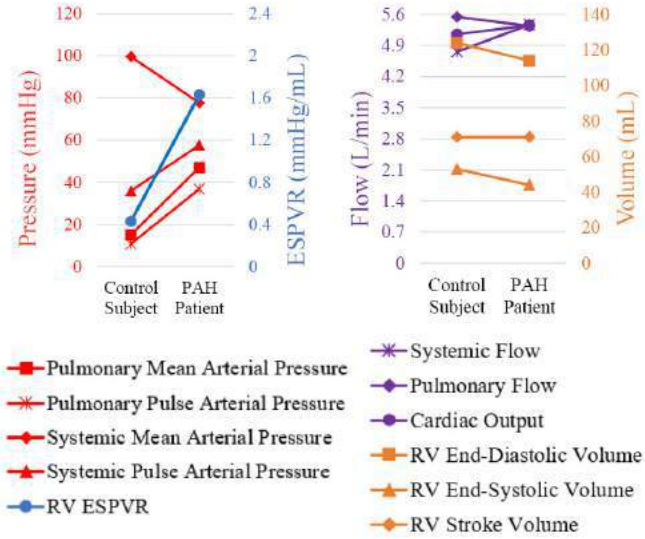


**Figure 5. Comparison of various hemodynamic parameters between PAH patient and control subject models.**

## DISCUSSION

We developed a framework that combines ventricular and arterial computational models to study hemodynamics in PAH and control subjects. We successfully matched clinically-acquired hemodynamic data and used the model to derive functional and structural metrics to compare these subjects. While the cardiac output and ventricular volumes were similar, pressures were drastically different in the cardiopulmonary circulation, cementing the complexity in the presentation of this disease.

Given the choice of active contraction model and the outlined calibration process, we can estimate ESPVR by varying preload. Our modeling results show that the PAH patient has a higher RV ESPVR than the control subject, which suggests that the PAH patient's RV and septum may have undergone remodeling to compensate for the increased pulmonary arterial pressures. This RV and septal remodeling could alter LV function [2] and therefore systemic hemodynamics.

While these results are based on a PAH and a control subject, future work will be focused on constructing models for all subjects in the PAH cardiac transplant control subjects in the study. This will help us provide a better description of functional and structural PAH metrics.


## ACKNOWLEDGEMENTS

The study was supported by the NIH (U01 1HL135842), NSF GRFP (DGE1256260), and the UM Rackham Merit Fellowship. Computing resources were provided by the NSF [Grant 1531752].


## REFERENCES


[1] Tonelli , AR et al., *Am J Respir Crit Care Med*, 188(3): 365-9, 2013.
[2] Marcus, JT et al., *Chest*, 119: 1761-65, 2001.
[3] Tossas-Betancourt, C et al., *SB3C Podium Presentation*, 2020.
[4] Arthurs, CJ et al., *PLoS Comput Biol*, 17(5), e100881, 2021.
[5] Hirai, T et al., *Circ*, 80(1): 78-86, 1989.
[6] Mynard, JP et al., *Int J Numer Biomed Engng,* 28: 626-641, 2011.
[7] Shavik, SM et al., *Mech Res Commun*, 97: 101-11, 2019.
[8] Guccione, JM et al., *J Biomech Eng*, 113(1): 42-55, 1991.
[9] Guccione, JM et al., *J Biomech Eng*, 115(1): 82-90, 1993.

# NOVEL PATIENT-SPECIFIC COMPUTER MODELLING OF STENT RETRIEVER THROMBECTOMY

**S. Mostafa Mousavi J. S. (1,2), Danial Faghihi (1), Muhammad Waqas (2,3), Andre Monteiro (2,3), Ciprian Ionita (2,4), Elad I. Levy (2,3), Adnan H. Siddiqui (2,3), and Vincent M. Tutino (1,2,3,5)**

(1) Department of Mechanical and Aerospace Engineering, University at Buffalo, Buffalo, NY, USA
(2) Canon Stroke and Vascular Research Center, Buffalo, NY, USA
(3) Department of Neurosurgery, University at Buffalo, Buffalo, NY, USA
(4) Department of Biomedical Engineering, University at Buffalo, Buffalo, NY, USA
(5) Department of Pathology and Anatomical Sciences, University at Buffalo, Buffalo, NY, USA

## INTRODUCTION

Stent Retriever Thrombectomy (SRT) for Acute Ischemic Stroke (AIS) aims to physically remove the occlusive clot. The main goal of SRT is the restoration of blood flow in one treatment pass. However, only ~30% of treatments are successful in the first pass [1], while the rest need to undergo more attempts that are associated with added mortality and mobility. Computer simulation of SRT can help understand underlying factors in unsuccessful cases and create a testbed for developing safer, more effective devices.

To date, few SRT computer models have been developed, but none can realistically simulate the complex stent-clot interactions, especially in failed cases. Finite element analysis (FEA) and XFEA based models were tested for patient specific models [2,3], but these models were not able to show the clot fragmentations or embolus dissection from the clot1's mass. Moreover, most previous computer models were developed for ideal geometries which do not consider the effect of the patient's vessel geometry [4].

Recently, we developed a method to accurately model the clot behavior in interaction with stent wires, which was even able to simulate clot fragmentation and embolus creation in failed cases [5]. In order to consider the vessel geometry in our simulation, we are expanding our method for patient specific vasculature and proposing a new workflow to model the SRT. Our new workflow is capable of accurately addressing two major problems faced in previous studies. Firstly, our clot model, which uses a hybrid FEA-SPH technique, realistically simulates the tissue's behavior in failed cases where an embolus could be created or the clot does not get retrieved at all. Secondly, it is implemented in patient specific vasculature geometries to accurately capture the effect of parent vessel geometry and Circle of Willis configuration.

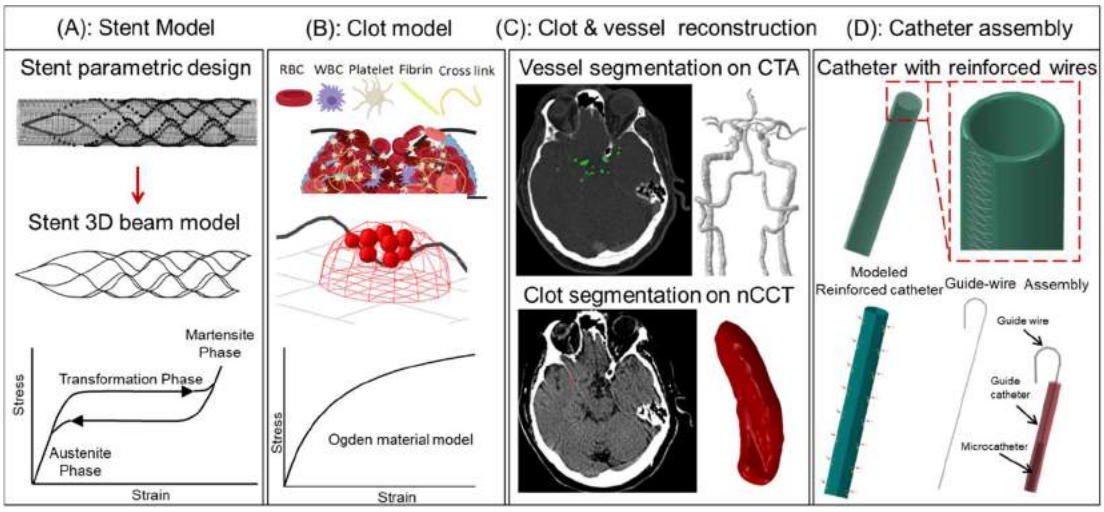


**Figure 1: Modeling Workflow. A).** The stent parametric geometry and nitinol superelastic behavior. **B).** The clot's hybrid FEA-SPH model and hyperelastic material behavior. **C).** Reconstruction of the patient's cerebral vessels and clot geometry from nCCT and CTA. **D).** The catheterization device assembly including microcatheter, guide-wire and guide catheter are also modeled to capture pre-deployment and retrieval steps.

## METHODS

In our method, all the parts involved in a thrombectomy procedure were modeled assuming that the blood flow is arrested. The major modeled components include the stent, clot, vessel, and wire-guided catheter. To model different parts, considerations for each portion of the device are applied individually to assure the accuracy of the simulation. Our workflow is illustrated in Figure 1.

*Stent model:* The stent model follows a parametric design procedure as detailed in [5] in which different parameters are modifiable like cell size and shape, stent length and diameter, overlapping edges distances, working length versus nonworking length ratios. After having stent's geometry, Timoshenko beam elements and superelastic material behavior of nitinol was assigned to the stent's wires.

*Clot model:* The hybrid FEA-SPH model for clot was developed and explained in details in our previous work [5]. In this method, a combination of grid-based FEA and meshless SPH methods was implemented. In the beginning, clot is in FEA mode and as it deforms under the loading, elements which their strain passes a threshold convert to more flexible and separable particles.

*Vessel and clot reconstruction:* The realistic geometry of vessel was reconstructed from CTA images of real patients (UB institutional review board study 00002092). Also, the geometry of the same patient's clot was reconstructed from nCCT.

*Catheter assembly modeling:* Catheterization to deliver the stents to a clot's site include using a guideare, guidecather and microcather in combination. Real Microcather and guidecathers are reinforced with embedded wires, to model them we used shell elements for both catheters with rebar reinforcement. Guide wire was modeled as J-shape with beam elements and modified material properties to consider its multi-structure and maneuverability.

## RESULTS

Figure 2 shows the results for a failed case in which the clot was not retrieved. As seen, in this workflow, all five steps of a real thrombectomy procedure were successfully simulated: (1) placing the stent into a packager, (2) deploying the microcatheter to pass the clot, (3) delivering the stent to the clot site, (4) deploying the stent across the clot so it can engage the tissue (done by holding the push wire and unsheathing the catheter), (5) attempted retrieval of the clot by pulling the stent through the cerebral vessels. As it can be seen, the stent was not able to hold the clot after cavernous curve, and failed to retrieved it.

## DISCUSSION

We developed a workflow that was able to accurately capture the real behavior of clot and stent in a thrombectomy procedure. Since catheter deployment and its positioning against clot is a driving factor in the deployment of a stent into the clot mass, we also modeled the catheter deployment procedure. In the example case, we showed that our model simulates different behaviors of different parts in a thrombectomy procedure accurately including passing a catheter from clot, penetration of stent wires into a clot and engaging with it, fragmentation of clot under the stent's load, and the separation of the clot from stent. The clot's FEA-SPH solver accurately simulated the dynamic clot behavior throughout, as it was deflected and moved by the wire and catheter, began breaking, and then dissociated from the stent.

This workflow represents a significant advance compared to previous models that have been unable to model failed SRT cases (e.g. clot fragmentation during retrieval). In the future, we will implement our method on larger cohorts of patient-specific cases to study how different factors, such as like vessel tortuosity, clot material and mechanical behavior, , catheter deployment and stent retrieval techniques, contribute to successful or unsuccessful SRTs.

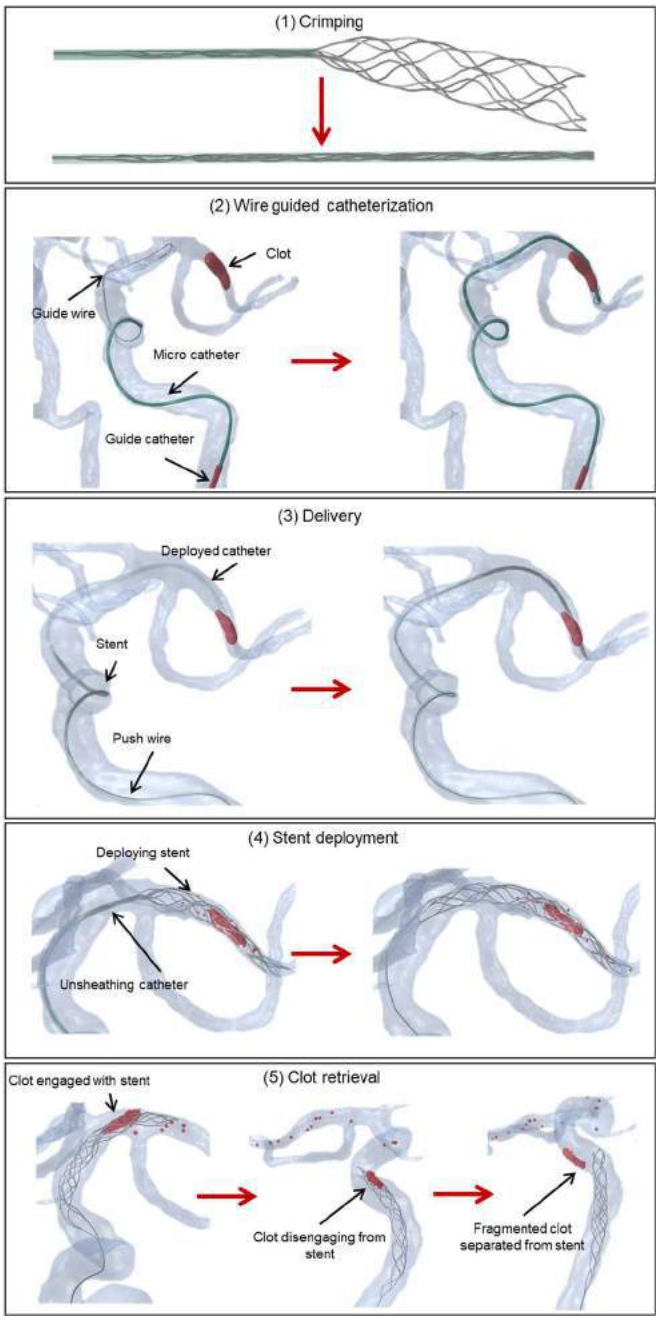


**Figure 2: A Patient-Specific SRT Case.** All components of SRT are modeled, including stent packaging, wire manipulation and microcatheter deployment, clot interaction with the stent, and retrieval. As seen here, SRT was unsuccessful in retrieving the clot past the cavernous ICA region.

## REFERENCES

[1] Ducroux, C et al, *J. Neurointerv. Surg.,* 386–391, 2020
[2] Luraghi, G et al, *Interface Focus.,* 20190123, 2021
[3] Luraghi, G et al, *J. Biomech.,* 110622, 2021
[4] Gu, X et al, *J. Med. Devices,* 021001-1, 2017
[5] MJ Sarayi, SM et al, *J. R. Soc. Interface,* 20210583, 2017

SB³C2022
Summer Biomechanics, Bioengineering and Biotransport Conference
June 20-23, Eastern Shore, MD, USA

# SIMULATIONS OF THE GRAVID HUMAN UTERUS AND CERVIX FOR PATIENTS AT HIGH- AND LOW-RISK FOR PRETERM BIRTH

**Erin Louwagie (1), Mirella Mourad (2), Michael House (3), Ronald Wapner (2), Kristin Myers (1)**

(1) Mechanical Engineering, Columbia University, New York, NY, USA
(2) Obstetrics and Gynecology, Columbia University Irving Medical Center, New York, NY, USA
(3) Obstetrics and Gynecology, Tufts Medical Center, Boston, MA, USA

## INTRODUCTION

Preterm birth (PTB), defined as delivery before 37 weeks gestation, occurred in 10.1% of deliveries in the United States in 2020 [1]. Globally, complications arising from PTB are the leading cause of death for children under five years of age, and infants who survive are at an increased risk of short- and long-term health problems [2]. The current gold standard for predicting PTB is the ultrasonic measurement of cervical length, where a cervical length of less than 25 mm is considered at increased risk for PTB [3]. However, this method of PTB risk assessment has only moderate ability to predict PTB, even in populations considered at high risk for PTB (those with a history of PTB) [4,5]. Many patients with short cervices also present with cervical funneling, where the fetal membranes protrude into the cervical canal, which is also thought to increase the risk of PTB [4]. To improve preterm birth prediction, we sought to achieve a better understanding of how the cervix and other reproductive tissue are loaded throughout gestation in order to identify loading patterns that could cause these tissues to fail mechanically. We present patient-specific computational models of patients at high- and low risk for PTB in this work.

Because studying the *in-vivo* gravid environment poses both ethical and practical obstacles, *in-silico* methods have been pursued which rely on medical images for patient geometry. Though MRI and 3D ultrasound provide high-fidelity patient-geometry, these imaging modalities are not frequently used in prenatal care [6,7]. Therefore, parametric patient-specific modeling methods based on 2D ultrasound, standard in prenatal care, have been implemented to study the gravid environment [8,9]. This research aims to generate hypotheses on what causes cervices to funnel and identify patterns of loading that will ultimately lead to PTB. Finite element analysis (FEA) is conducted for patients at high- and low risk for PTB, including patient-specific geometry and cervical tissue stiffness. The pattern and magnitude of strain in the proximal cervix are compared across cohorts.

## METHODS

Two cohorts of patients were recruited at Columbia University Irving Medical Center. The first cohort is patients considered at high-risk for PTB based on a sonographic cervical length of less than 20mm and typically presented with cervical funneling, with no prior history of PTB. This cohort was recruited at and underwent their first research examination at 16-24 weeks gestation. High-risk patients underwent a second research examination at 26-30 weeks gestation. The second cohort is patients considered at low-risk for PTB based on screening to exclude subjects with known risks. These patients were recruited in the first trimester (before 14 weeks gestation) and underwent the first of four research exams at the time of recruitment. The other research exams were conducted at 18-20 weeks, 24-26 weeks, and 34-36 weeks gestation. In both cohorts, the research exam included the collection of ultrasonic measurements characterizing the overall size and shape of the maternal uterus and cervix and the measurement of cervical stiffness. Cervical stiffness was measured using the Pregnolia system (Pregnolia AG, Switzerland), a device that captures *in-vivo* cervical tissue stiffness.

To compare the simulations of the high- and low-risk cohorts, we used measurements taken in the 16-24 week window for the high-risk patients (n = 12) and 18-20 week window for the low-risk cohort (n = 12) to ensure overlapping gestational ages between groups. Using our established parametric modeling workflow, we automatically generated patient-specific geometry from the ultrasonic measurements in Solidworks 2019 (Dassault Systemes, Vélizy-Villacoublay, France) [9]. We used a reference cervical length for the high-risk cohort to simulate the loading on their cervices before cervical funneling. A fetal membrane and supporting abdomen were included in each model, and a quarter model geometry used for computational efficiency. The geometries were imported in Hypermesh 2021 (Altair Engineering Inc., Troy, Michigan), where they were discretized into finite element models. The meshed models were imported into FEBio studio (v1.3.0) for model setup and simulation [10].

SB³C2022-384

The material properties, boundary conditions, and contact conditions were assigned in FEBio. The cervix, uterus, and fetal membranes were given material properties based on existing literature [11-13]. Inverse FEA was used to determine patient-specific fiber stiffness from the cervical stiffness measurements [14]. The abdomen was assigned nearly incompressible neo-Hookean material properties. Physiologically inspired contact conditions were set between tissues, and the model was fixed in the normal direction on the superior, inferior, and anterior surfaces, as well as in the sagittal cut plane. A gestationally determined intrauterine pressure was applied to the inner membrane surface [15]. Levels and patterns of strain in the proximal cervix were compared across cohorts.

## RESULTS

The high-risk cohort has higher magnitudes of 1st principal Lagrange strain at the internal os (opening of the cervical canal into the intrauterine cavity) and the uterocervical than the low-risk cohort (Fig. 1).

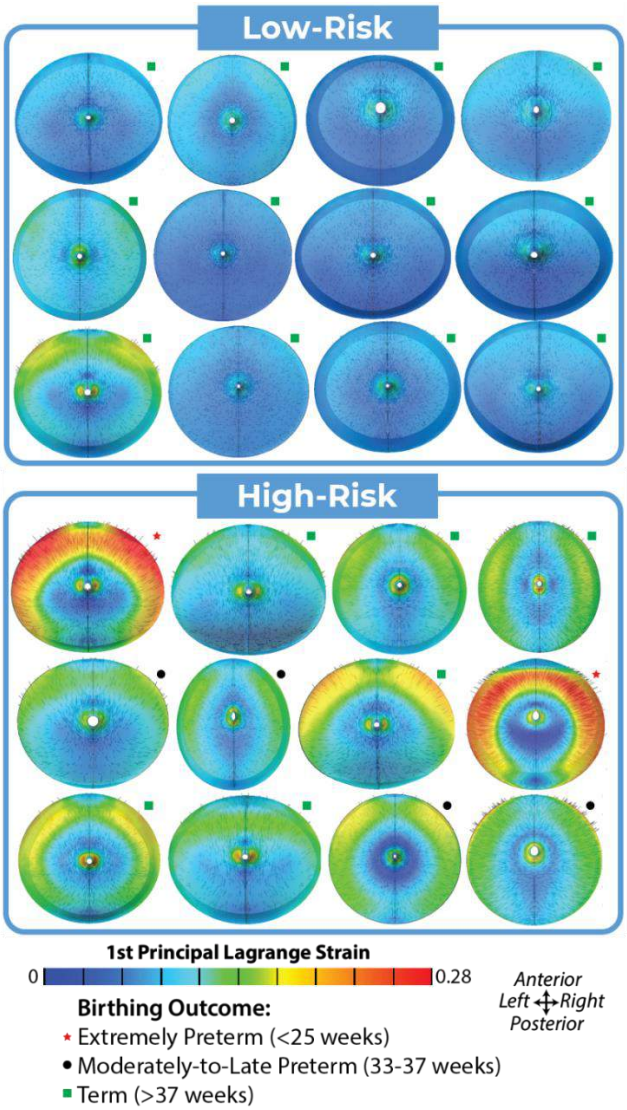


**Figure 1: Heat maps of 1st Principal Lagrange strain in the proximal cervix for subjects at high- and low-risk for preterm birth, with strain direction noted by black lines within the heat map. Birthing outcome is noted on the top-right of each cervix.**

Across cohorts, the direction of the 1st principal Lagrange strain is conserved at the internal os, where it is aligned circumferentially, and at the uterocervical junction, where it is aligned radially (Fig. 1). In the high-risk cohort, two patients delivered extremely preterm (before 28 weeks gestation). These patients have the highest magnitude 1st principal Lagrange strain at the uterocervical junction and the lowest cervical stiffnesses measured by cervical aspiration.

## DISCUSSION

A distinct strain pattern is shown in the FEA results for the high-risk cohort. The high-risk subjects tend to have larger magnitudes of 1st principal Lagrange strain at the internal os and uterocervical junction than the low-risk subjects. Because the high-risk subjects clinically presented with cervical funneling, we believe this strain pattern in the proximal cervix uncovers the possible mechanism by which cervical funneling initiates and propagates, where membranes push into the cervical canal, causing high levels of circumferential strain at the internal os. The uterocervical junction also pulls the cervix open, shown by the high levels of radial strain between the uterus and cervix. We believe these higher tensile strain levels between the uterus and cervix are associated with extremely preterm birth.

A primary limitation of this work is the geometries are built using measurements of the uterus and cervix in a loaded state, excepting the reference cervical length used for high-risk subjects. Thus, the reference configuration in these geometries is not in a stress-free state. Additionally, patient-specific uterine and fetal membrane tissue properties and intrauterine pressure are unknown, and the FEA results have no *in-vivo* loading results to be compared. Thus, the degree to which the FEA results provide a true measure of strain in the cervix is unknown. However, the results thus far are promising and warrant further investigation.

## ACKNOWLEDGEMENTS

This work is supported by the Eunice Kennedy Shriver National Institute of Child Health & Human Development of the National Institutes of Health under award number 1R01HD091153-01. The content is solely the responsibility of the authors and does not necessarily represent the official views of the National Institutes of Health.

## REFERENCES

[1] Centers for Disease Control, “Preterm Birth”, 2021.
[2] World Health Organization, “Preterm Birth”, 2018.
[3] “Prediction and Prevention of Spontaneous Preterm Birth: ACOG Practice Bulletin, Number 234”, *Obstet Gynecol*, 138(2):e65-e90, 2021.
[4] Berghella, *Contemporary Ob/Gyn*, 49:26-34, 2004.
[5] Crane, J & Hutchens, D, *Ultrasound Obstet Gynecol*, 31(5):579-587, 2008.
[6] House, M et al., *Clin Anat*, 26: 97-104, 2013.
[7] Fernandez, M et al., *Comput Methods Biomech Biomed Engin*, 19:404-417, 2016.
[8] Westervelt, A et al., *J Biomed Eng*, 139:051004, 2017.
[9] Louwagie, E et al., *PLOS ONE*, 16(1):e0242118, 2021.
[10] Maas, S et al., *J Biomech Eng*, 134(1):011005, 2012.
[11] Myers, K et al., *J Biomech*, 48:1533-1540, 2015.
[12] Conrad, Jet al., *Am J Ob Gynecol*, 96:1055-1059, 1966.
[13] Bürzle, Wand Mazza, E., *J Biomech*, 46:1777–1783, 2013.
[14] Badir, Set al., *Prenat Diagn*, 33:737-741, 2013.
[15] Fisk, N et al., *BJOG*, 99(1):18-22, 1992.

# PROBING MOLECULAR DIFFUSION IN THE BRAIN AND TUMOR EXTRACELLULAR SPACE BY THE FAST RELEASE FROM PLASMONIC NANOVESICLES

**H. Xiong (1), B. A. Wilson (1), A. Naik (2), S. Hrabetova (2), R. Bachoo (3,4,5), Z. Qin (1,6,7,8)**

(1) Department of Mechanical Engineering, University of Texas at Dallas, Richardson, TX, USA
(2) Department of Cell Biology, SUNY Downstate Health Sciences University, Brooklyn, NY, USA
(3) Department of Internal Medicine, University of Texas at Southwestern Medical Center, Dallas, TX, USA
(4) Harold C. Simmons Comprehensive Cancer Center, University of Texas at Southwestern Medical Center, Dallas, TX, USA
(5) Department of Neurology, University of Texas Southwestern Medical Center, Dallas, TX, USA
(6) Department of Bioengineering, University of Texas at Dallas, Richardson, TX, USA
(7) Center for Advanced Pain Studies, University of Texas at Dallas, Richardson, TX, USA
(8) Department of Surgery, University of Texas Southwestern Medical Center, Dallas, TX, USA

## INTRODUCTION

Diffusion in the tumor extracellular space (ECS) is extremely important for the delivery of intravenous or directly injected therapeutics to tumor cells. Once in the brain, the diffusion is governed by the geometry of ECS and the extracellular matrix. Glioblastoma is the most common and aggressive malignant brain tumors among adults. Although several studies have investigated the molecular diffusion in glioma by real-time iontophoretic method[1] and photobleaching measurements[2], the diffusion properties of glioma are only moderately understood. The challenge is the lack of reliable method and complexity of tumor microenvironment.

In this work, we developed a new optical method based on the fast release from **P**lasmonic n**A**novesi**C**l**E**s (PACE v1.0) to measure the molecular diffusion in the normal brain and tumor ECS. Fluorescent dye calcein could be encapsulated in the plasmonic nanovesicles and released within sub-second under the stimulation of near-infrared laser pulses. The bolus of released calcein worked as a point diffusion source and the diffusion was recorded by a two-photon microscope with tight spatial and temporal resolution. We validated the PACE technique by successfully measuring the calcein diffusion *in vitro* and in different mouse models. Importantly, we found that the diffusion is faster in tumor than that in tumor margin in a 73C glioma model.

## METHODS

*Nanovesicles preparation:* Gold-coated calcein-loaded liposomes (Au-nV-Cal) were prepared by the thin-film rehydration method reported previously.[3]

*Animal and brain slice preparation:* 400 μL of tdTomato-labelled 73C cell suspension ($2\times10^5$ cells/μL) was transplanted into the left hemisphere of the Nu/J mice at 500 μm depth. After 4 weeks, acute brain slice with a thickness of 400 μm was prepared in artificial cerebrospinal fluid continuously bubbled with a mixture of 95% $O_2$ and 5% $CO_2$. Hyaluronan-deficient brain model was established by intraventricular injection of 4 μL of 20 mg/mL hyaluronidase two days before the diffusion measurement. To induce the brain ischemia, 1 mL of 1M KCl was administrated intracardially to cause the immediate cardiac arrest. Finally, 20 nL of Au-nV-Cal were stereotaxically injected to 0.2% agarose gel and above brain samples by a nanoinjector at 1 nL/s.

*Diffusion measurement:* Au-nV-Cal were imaged at 920 nm and stimulated at 720 nm (75 or 100 mW) to trigger calcein release by a multi-photon laser scanning microscope (FVMPE-RS, Olympus).

*Data analysis:* A Point-source paradigm was used to analyze the calcein diffusion. The concentration $C(r,t)$ with respect to location $r$ (distance from the source) and time $t$ is given by Eq. 1. The fluorescence intensity in the two-photon images can be mapped to the shape of Eq. 1 by a two-parameter ($E$ and $\gamma$) Gaussian function (Eq. 2). Images at each time point are fitted to this 2D Gaussian function by non-linear fitting with the Nelder-Mead algorithm (Eq. 2). The acquired $\gamma^2$ increases linearly with time ($t$) (Eq. 3), which is further linearly fitted to estimate the diffusion coefficient.

$$C\ (r,\mathrm{t}) = \frac{Q}{\alpha}\cdot\frac{\lambda^3}{(4D\pi t)^{1.5}}\cdot\exp\left(-\frac{\lambda^2 r^2}{4Dt}\right) \quad (1)$$

$$\Delta F\ (r) = E\ \cdot\ \exp\left(-\frac{r^2}{\gamma^2}\right) \quad (2)$$

$$\gamma^2 = 4\ D\ (t + t_0) \quad (3)$$

where $Q$ is the total molecule number from the source; $\alpha$ is the volume fraction of brain ECS; $D$ is the diffusion coefficient.

## RESULTS

To test the feasibility of the PACE technique, we first demonstrated measuring the diffusion properties of fluorescent dye calcein both *in vitro* and in mouse cortex. Gold-coated nanovesicles packed with calcein dye (Au-nV-Cal) were injected into 0.2% diluted

agarose gel, which can be considered as "free" medium (**Figure 1a**).[4] In the nanovesicles, calcein fluorescence is self-quenched due to the high concentration (75 mM). The photo-stimulation releases the calcein dye and the dilution increases its fluorescence (ΔF) before the fluorescence decreases as the dye diffuses away. Thus, the stimulated nanovesicles can be considered as the point source for calcein diffusion. Representative image sequences after laser stimulation clearly show the hindered diffusion for calcein dye in mouse cortex compared with that in agarose gel (**Figure 1b**). The ΔF in each pixel was fitted by a 2D Gaussian model (Eq. 2), resulting in a time-dependent parameter γ. The diffusion coefficient was acquired by the linear fitting $\gamma^2$ versus $t$ (**Figure 1c**). The effective diffusion coefficient of calcein ($D^*$) is 3.4-fold lower than the free diffusion coefficient ($D$) in the diluted agarose, suggesting the slow diffusion in the brain ECS (**Figure 1d**). The measured values by PACE are close to the results from a traditional method, integrative optical imaging (IOI). We further investigated the $D^*$ in a hyaluronan-deficient brain model (Hyase) and an ischemic brain model. The $D^*$ is 2-fold higher in Hyase group than that of normal cortex. It suggests that the diffusion is faster in hyaluronan-deficient brain because diffusion becomes less hindered when long-chained hyaluronan is reduced in brain ECS. The $D^*$ under brain ischemia decreased to 8% of its normoxic value due to the swelling of brain cells.[4] Taken together, we demonstrate that the PACE is reliable and robust for molecular diffusion measurement at different contexts.

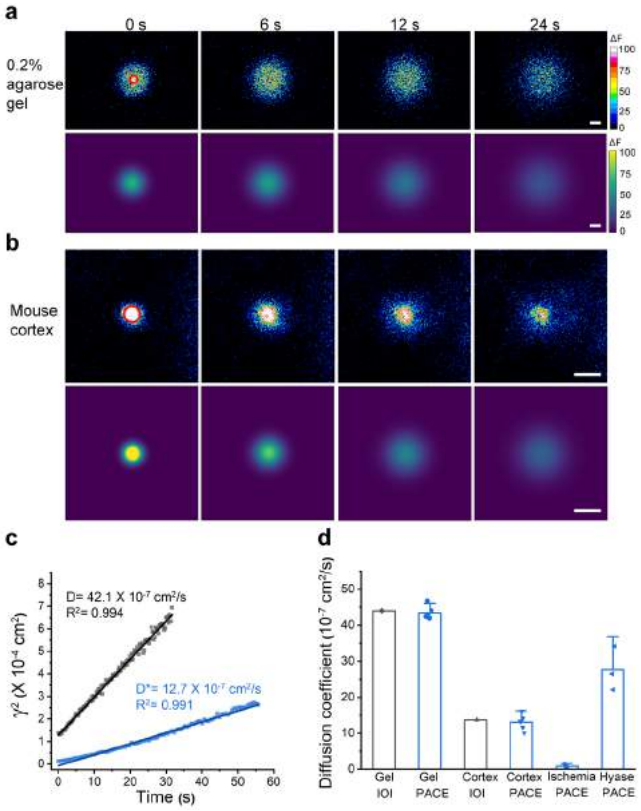


**Figure 1. Calcein diffusion in 0.2% agarose gel and mouse cortex.** (a, b) Two-photon fluorescent images (upper panel) and 2D Gaussian fitted images (lower panel) of calcein diffusion in (a) 0.2% agarose gel and (b) in mouse cortex. 75-μm-diameter and 60-μm-diameter tornado scans (red circle) were performed on Au-nV-Cal for 0.1 s before the diffusion recording in (a) and (b), respectively. Scale bar (a,b): 100 μm. (c) Linear fitting of $\gamma^2$ versus $t$ to get the diffusion coefficient. (d) Measured diffusion coefficients at different conditions compared with the results from integrative optical imaging (IOI) method.

Next, we measured the calcein diffusion in the astrocyte-derived 73C glioma model (*BRAF*$^{V600E}$; *Pten*$^{-/-}$; *p53*$^{-/-}$),[5] which expresses td-Tomato for bioimaging. Since there is negligible binding or uptake of calcein by the cells in the brain, we can image the brain ECS by incubating calcein with glioma slice. **Figure 2a** shows that the interstitial space between brain cells was filled with calcein. In the tumor, glioma cells take up of most of the space and the gaps between the cells are clearly observed, while the density of glioma cells is low, and the gaps are too narrow to be captured in the tumor margin. The PACE was performed at these two areas to measure calcein diffusion. The $D^*$ of calcein in the tumor is 2.3-fold higher than that in the tumor margin (**Figure 2b**), which is consistent with the wider ECS in the tumor. This is probably due to the enlarged ECS resulted from degradation of extracellular matrix and neuronal death in the tumor.[1]

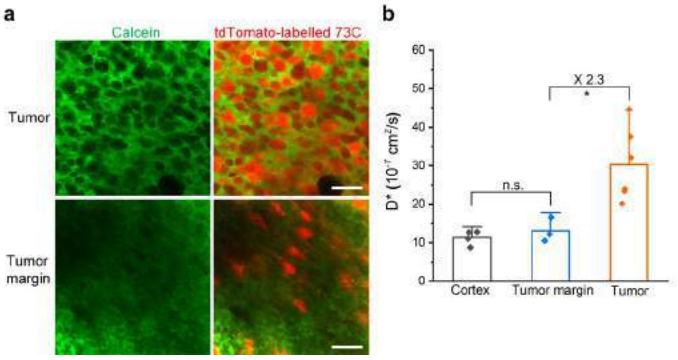


**Figure 2. Calcein diffusion in glioma slice.** (a) Two-photon fluorescent image of calcein and tdTomato-labelled 73C glioma cells at a depth of 50 μm. 50 μM of calcein was incubated with glioma slice for 5 minutes. Scale bar: 20 μm. (b) Comparison of calcein diffusion coefficient ($D^*$) in cortex, tumor margin and tumor. Statistical analysis was performed by Student's t-test in Origin. Single asterisk (*) indicates $p < 0.05$.

## DISCUSSION

The diffusion of anticancer drugs in ECS determines their distribution and therapeutic effects after the entry into brain parenchyma. Taking advantage of the fast release from plasmonic nanovesicles, we successfully developed a PACE technique to measure the molecular diffusion both in normal brain and glioma. Our measurements suggest that the calcein diffusion is faster in tumor than that in the tumor margin, which indicates that tumor margin could be the main obstacle and new target for glioma treatment. Since there are nearly no neuronal structures in the core of 73C glioma, the diffusion measurement is ongoing in a highly invasive glioma model, in which most of the brain parenchyma elements are present. The diffusion measurements in these gliomas will advance our understanding the tumor microenvironment and facilitate the new strategy for cancer treatment.


## ACKNOWLEDGEMENTS

We acknowledge funding support from NIH under award number RF1NS110499 (Z.Q.), NSF under award number 2123971 (Z.Q.) and CPRIT under award number RP190278 (Z.Q.).


## REFERENCES


[1] Vargova, L et al., *Glia*, 42: 77-88, 2003.
[2] Verkman, A S, *Phys Biol*, 10: 045003, 2013.
[3] Li, X et al., *Adv Funct Mater*, 27: 1605778, 2017.
[4] Thorne, R G et al., *Proc Natl Acad Sci*, 103: 5567-5572, 2006.
[5] Gao, X et al., *Cell Rep*, 30: 2489-2500, 2020.

SB³C2022
Summer Biomechanics, Bioengineering and Biotransport Conference
June 20-23, Eastern Shore, MD, USA

# NON-DESTRUCTIVE EVALUATION OF REGIONAL CELL DENSITY WITHIN TUMOR AGGREGATES FOLLOWING DRUG TREATMENT

**Cassandra L. Roberge (1), Ling Wang (2), Margarida Barroso (2), and David T. Corr (1)**

(1) Department of Biomedical Engineering, Rensselaer Polytechnic Institute, Troy, NY USA
(2) Department of Molecular and Cellular Physiology, Albany Medical College, Albany, NY USA

## INTRODUCTION

Tissue-engineered tumor aggregate models are gaining increasing utility for *in vitro* study of cancer progression and drug discovery. Once grown to volumes of 0.03-0.5 $mm^3$, these relatively simple avascular constructs mimic key aspects of *in vivo* tumors, such as 3D structure and pathophysiological gradients [1], [2]. Critical insight can be gained by characterizing aggregate model behavior during development and in response to drug; however, their requisite size drastically limits the tools that can be used, particularly for non-destructive assessment.

Previously, our lab has used Optical Coherence Tomography (OCT) structural imaging and Imaris image analysis for rapid, non-destructive, and label-free quantitative measurement of 3D tumor model morphology [3], [4]. We also utilized Imaris to count the number of cell-sized objects present in each scan, which, when normalized to the measured aggregate volume, provided a systematic estimation of total cell density within the aggregate [3]. Additionally, this technique accurately measured the number of live cells present within drugged tumor aggregates, thus establishing a non-destructive approach to longitudinally measure cell viability over a full drug timecourse within a 3D tumor aggregate.

Herein, we present an extension of this technique for regional cell density quantification in multicellular aggregates; assessing cellularity within the outer, inner, and core regions of a given aggregate. We also apply this technique to drugged samples, non-destructively tracking regional cell death throughout the depth of these samples over a 5-day timecourse.

## METHODS

In our established method [3, 4], OCT imaging is performed to obtain a 3D volume scan of an aggregate, which is then imported into Imaris software (Bitplane, UK) for image analysis. Following intensity thresholding to isolate the aggregate, the "spots" function within Imaris is used to count the number of cell-sized objects present in each scan, providing an estimation of total cell density within the aggregate.

To extend this technique to measure local cell densities, we use OCT-Imaris to count cells within small defined zones (i.e., regions of interest), at sequential radial depths throughout an aggregate. These zones, or "regional plugs", provide indications of the local cell density, akin to a virtual biopsy at each selected radial depth. To begin this analysis, we identify the aggregate center and radius, then add reference frames within the software to the center point, midpoint (radius ÷ 2), and outer point (radius location - 50 μm) of the sample, along a single axis. The file statistics for that aggregate may then be exported, and the number of objects within 100 μm of each reference frame can be calculated. The resulting value corresponds to the number of cells in that 100-μm diameter regional plug. This value is then divided by the volume of the plug to obtain local cell density, which we assume to serves as a representative measure of the cell density at that depth within the aggregate. For more detailed studies, this analysis can be adapted to include more reference frames (e.g., every 100 μm) to provide a more spatially-refined measure of local density throughout the aggregate.

To establish the fidelity of this technique, we investigated regional cell densities in multiple cell lines, selecting MDA-MB-231 triple negative breast cancer cells and AU565 HER2+ breast cancer cells. Liquid overlay (L.O.), the current gold standard method for aggregate production [5], was used to form aggregates from each cell line. Cells were seeded (2.5 $x10^4$ cells/well) in non-adherent U-shaped 96-well plates and cultured for 4 days until maturity, either with or without the addition of 2.5% Matrigel, to explore aggregates of different morphologies. Matrigel is solubilized basement membrane derived from mouse sarcoma and is well-documented to aid in cell aggregation [6]. OCT imaging was performed on day 4, and the Imaris-based regional assessment described above was performed to quantify cell density at the central core, midpoint, and outer zones of each aggregate.

Next, we wanted to apply this technique to explore potential regional differences in drug response, as well as possible indications of drug penetration. Focusing on HER2+ samples, AU565 L.O. samples prepared with Matrigel were drugged on Day 4 with Trastuzumab (TZM), a clinically-used chemotherapeutic, at a dose concentration of 50 µg/mL. Samples were continuously exposed to the drug for 5 days, and OCT imaging was performed longitudinally; immediately prior to addition of the drug (t = 0), and at 24 hours and 120 hours (5 days) post-addition. Cell density was quantified following drugging within progressively deeper 100−$\mu$m zones using the detailed approach described above. This analysis was performed at each timepoint, ***within each individual aggregate,*** throughout the drug timecourse.

## RESULTS

Qualitatively, AU565 aggregates grown with liquid overlay were quite flat, while those grown with Matrigel became thicker and more disk-like (**Figure 1, lower row insets**). MDA-MB-231 aggregates were disk-like when grown without Matrigel and grew to be spherical when Matrigel was added (**Figure 1, upper row insets**). Despite these morphologic changes, Matrigel addition did not affect the number of cells in the aggregate. For all observed morphologies, we found that cell density was substantially higher in the core of the spheroid than in the middle and outer layers, for both cell types (**Figure 1**). This trend was most prominent in the samples prepared with Matrigel, suggesting that Matrigel does not affect proliferation but does redistribute cell density, promoting core compaction and decreasing cell density in outer layers.

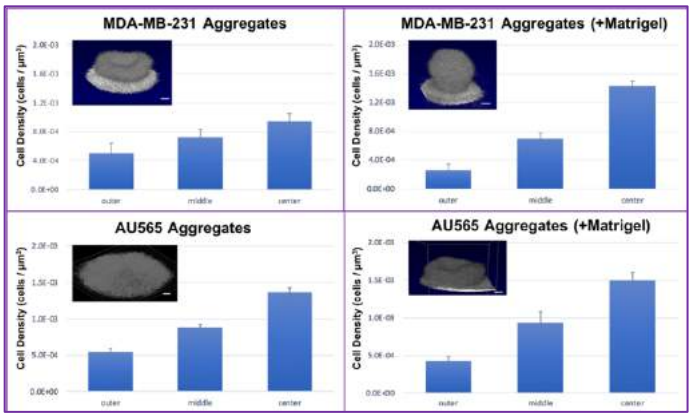


**Figure 1: Matrigel addition redistributes cell density in multiple cancer cell lines, decreasing density in outer zone and increasing compaction in center (n=3). Image scale bars = 100 µm.**

Next, we sought to use this regional approach to non-destructively track cell death in drugged AU565 aggregates. These aggregates were relatively large, with radii of approximately 700 µm on day 4. The diameter of the central plugs was held constant at 100 µm while the outer was allowed to fluctuate in diameter corresponding to changing aggregate size. We observed only minor fluctuations in cell density over time in the inner 500 µm of each aggregate, indicating minimal cell death (**Figure 2**). Indeed, the majority of cell death occurred in the outer 200 µm of each aggregate, particularly in the outer 100 µm, which disappeared by the 120h timepoint for all three aggregates analyzed.

## DISCUSSION

Our goal was to establish a technique to non-destructively assessthe regional cell density within matured multicellular aggregates. We also sought to apply this technique to longitudinally track regional cell viability within drugged aggregates. Our data show that cell density increases towards the aggregate center, regardless of aggregate morphology or cell type (for those tested herein). This result indicates compaction in the model core after 4 days, which agrees well with literature that has well-documented the increased hypoxia in this region as the deeper cells fight for limited oxygen [7]. This trend was exacerbated in samples prepared with Matrigel, an exogenous

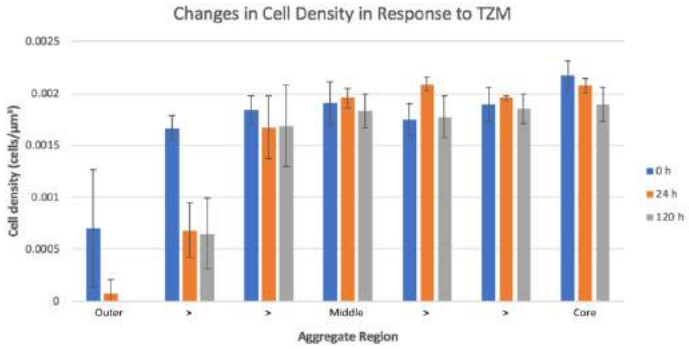


**Figure 2: Cell viability in response to drug (TZM), as a function of aggregate radial depth. The inner core was kept constant at 100 µm diameter, while the outer zone was allowed to fluctuate with changing aggregate size. Cell death was largely constrained to the outer 200 µm, particularly the outermost 100 µm, which disappeared completely after 120 hours of treatment. The inner 500 µm thickness of the aggregates saw little change in cell viability (n=3).**

additive which is poorly characterized, yet known to promote aggregation. This finding provides valuable insight into the physical mechanisms by which Matrigel enables cell aggregation. To our knowledge, this is the first method to non-destructively quantify regional cell density within dense, cellular tissues.

When we applied our technique to drugged samples, we saw different cell behaviors at different depths within the three samples tested. The density within the inner 400 µm of all aggregates remained fairly stable over 5 days. The zone 300 µm deep (3rd cluster of data from left, **Figure 3**) saw larger fluctuations in density over the timecourse than the inner layers. Predictably, much of the cell death observed was constrained to the outer 200 µm of the aggregate, the layers that experienced either direct drug exposure or a relatively short diffusion of the drug inwards (< 200 µm). Given these results, this technique holds great potential as a tool to measure regional cell viability *non-destructively.* This approach also provides an indirect measure of drug penetration without the need for sample fixing and staining, enabling live, continuous drug screening with cell-scale information.


## ACKNOWLEDGEMENTS

This work was funded, in part, by NIH R01 BRG CA207725 (MB/DTC) and NIH R01 CA233188 (MB/DTC).


## REFERENCES


[1] Hirschhaeuser F *et al.*, *J. Biotechnol*. 148 3–15, 2010.
[2] Mueller-Klieser W, *J Cancer Res Clin. Oncol.* 113 101–22, 1987.
[3] Roberge C L *et al.*, *Acta Biomater*. 117 322–34, 2020.
[4] Kingsley D M *et al., Acta Biomater*. 95 357–70, 2019.
[5] Nagelkerke A *et al*., *Anal. Biochem*. 437 17–9, 2013.
[6] Badea M A et al., *SLAS Discov*., 24:5 563–578, 2019.
[7] Groebe K and Mueller W, *Eur. Biophys. J*., 19: 4 169–181,1991.

# COMPUTATIONAL FRAMEWORKS TO INVESTIGATE AGING AND DISEASE IN ELASTIC TISSUES AT THE NANOSCALE

**Anna Tarakanova (1)**

(1) Department of Mechanical and Biomedical Engineering, University of Connecticut, Storrs, CT, USA

## INTRODUCTION

Biological aging, as well as many age-related diseases including diabetes mellitus and atherosclerosis, is characterized by compromised elastic tissue function, which significantly impacts human morbidity and mortality. A number of debilitating diseases of genetic origin, e.g. cutis laxa, Williams Syndrome and supravalvular aortic stenosis, present similar properties and modified mechanical function in elastic tissue. In this work we investigate the molecular origins that drive changes in elastic tissue function, by considering the behavior of its nanoscale building blocks, from the bottom up. Elastin is the dominant building block of elastic fibers in the extracellular matrix that impart structural integrity and elasticity to a range of elastic tissues, including the lungs, blood vessels and the skin. The elastin polymer is assembled from its molecular precursor tropoelastin. Historically, elastin's dynamic nature has precluded traditional approaches such as X-ray crystallography to understand its detailed features. In this work we present a series of experimentally-validated computational models to probe elastin's structure, origins of its mechanical function, and changes to its function as a result of modifications associated with disease.

## METHODS

We use atomistic and coarse-grained models based on a particle dynamics approach, as detailed in the references.

## RESULTS

We propose a molecular model to describe elastin's atomistic structure, self-assembly, mechanics and dynamic interactions with other components of elastic fibers and the extracellular environment. We further use the models to probe the functions of key molecular regions, investigate disease etiology — associated with mutations in the elastin gene, as well as with aging-linked physicochemical modifications that alter elastin's structure and function, and explore implications for hierarchical assembly, coupling these to a suite of experimental studies for validation.

## DISCUSSION

This research pioneers novel nanoscale insight into mechanical degeneration of elastic tissue under the presence of genetic mutations and physicochemical stress associated with aging and aging-linked diseases, by establishing a new validated in silico framework, calibrated from experiment, for investigating multifactorial modifications to elastin at multiple length scales, and leverages models to elucidate molecular mechanisms on mechanical function.

## ACKNOWLEDGEMENTS

This work utilized the Extreme Science and Engineering Discovery Environment (XSEDE), which is supported by National Science Foundation grant number ACI-1548562 (83). XSEDE resources Stampede 2 and Ranch at the Texas Advanced Computing Center and Bridges at the Pittsburg Supercomputing Center through allocation TG-MCB180008 were used.

## REFERENCES

[1] Tarakanova, A.; Yeo, G. C.; Baldock, C.; Weiss, A. S.; Buehler, M. J., Molecular model of human tropoelastin and implications of associated mutations. *PNAS* **2018,** *115* (28), 7338-7343.
[2] Tarakanova, A; J.Ozsvar; A.S.Weiss; M.J.Buehler, Coarse-grained model of tropoelastin self-assembly into nascent fibrils. *Materials Today Bio* **2019,** *3*.
[3] Ozsvar, J; Tarakanova, A; Wang, R; Buehler, MJ; Weiss, A. S., Allysine modifications perturb tropoelastin structure and mobility on a local and global scale. *Matrix Biology Plus* **2019,** *2* (100002).
[4] Tarakanova, A.; Huang, W.; Weiss, A. S.; Kaplan, D. L.; Buehler, M. J., Computational smart polymer design based on elastin protein mutability. *Biomaterials* **2017,** *127*, 49-60.

[5] Tarakanova, A.; Yeo, G. C.; Baldock, C.; Weiss, A. S.; Buehler, M. J., Tropoelastin is a Flexible Molecule that Retains its Canonical Shape. *Macromol Biosci* **2019,** *19* (3), e1800250.
[6] Yeo, G. C.; Tarakanova, A.; Baldock, C.; Wise, S. G.; Buehler, M. J.; Weiss, A. S., Subtle balance of tropoelastin molecular shape and flexibility regulates dynamics and hierarchical assembly. *Sci Adv* **2016,** *2* (2), e1501145.
[7] Ozsvar, J.; Wang, R.; Tarakanova, A.; Buehler, M. J.; Weiss, A. S., Fuzzy binding model of molecular interactions between tropoelastin and integrin alphaVbeta3. *Biophysical Journal* **2021**.
[8] Lockhart-Cairns, M. P.; Newandee, H.; Thomson, J.; Weiss, A. S.; Baldock, C.; Tarakanova, A., Transglutaminase-Mediated Cross-Linking of Tropoelastin to Fibrillin Stabilises the Elastin Precursor Prior to Elastic Fibre Assembly. *J Mol Biol* **2020,** *432* (21), 5736-5751.

# COMPARISON OF VELOCITY AND FLOW-BASED METHODS TO CALCULATE WALL SHEAR STRESS FROM 4D FLOW cMRI DATA

**Elliott R. Hurd (1), Elizabeth Iffrig (2,3), John N. Oshinski (3,4), Lucas H. Timmins (1,5)**

(1) Department of Biomedical Engineering, University of Utah, Salt Lake City, Utah, USA
(2) Department of Medicine, Emory University School of Medicine, Atlanta, Georgia, USA
(3) Department of Biomedical Engineering, Georgia Institute of Technology and Emory University School of Medicine, Atlanta, Georgia, USA
(4) Department of Radiology and Imaging Sciences, Emory University School of Medicine, Atlanta, Georgia, USA
(5) Scientific Computing and Imaging Institute, University of Utah, Salt Lake City, Utah, USA

## INTRODUCTION

Four-dimensional flow cardiac magnetic resonance imaging (4D flow cMRI) is a non-invasive, non-ionizing radiation-based imaging tool that can interrogate the *in vivo* blood flow environment. This imaging modality has shown promise as a diagnostic and prognostic tool to evaluate and quantify complex flow patterns in the setting of several vascular pathologies. For example, studies have demonstrated the utility of 4D flow cMRI in distinguishing between normal and pathologic flow patterns associated with aortic valve disease and associated secondary aortopathy [1]. In addition, methods have been developed to quantify wall shear stress (WSS) from these image data and highlight its clinical value [2,3]. Importantly, however, the methods used to calculate WSS from 4D flow cMRI data have yet to be validated.

Various methods have been established to calculate WSS directly from 4D flow cMRI data. The most commonly applied approach seeks to quantify the gradient in the 4D flow-derived velocities at the wall and calculate WSS by taking the product between the velocity gradient and the fluid (blood) viscosity (Fig. 1) [4]. However, the limited spatial resolution of MRI, and particularly the inability to capture the gradient within the fluid boundary layer, and image noise can impact determining the near-wall velocity gradient. A more recently developed approach utilizes the 2D phase-contrast MRI-derived volumetric flow waveform constrained by the Womersley solution for pulsatile flow in a cylinder to calculate WSS [5]. Briefly, image data are divided into $i$-sectors, temporal flow waveforms are determined in each sector ($Q_i$), and waveforms are decomposed into harmonics to calculate WSS via the Womersley solution (Fig. 1). As this method only utilizes through-plane velocities (i.e., axial component), it is limited in only calculating the axial component of the WSS vector. This method, too, has yet to be validated for accuracy.

Thus, the goal of this study was to extend the application of the flow-based method to 4D flow cMRI data and examine the accuracy (i.e., validate) of the velocity and flow-based methods to calculate WSS.

## METHODS

**Generation of Synthetic 4D flow cMRI Data.** To compare the 4D flow-derived values of WSS against exact solutions, synthetic MRI data were created from the analytical solutions of the Navier-Stokes equations for steady (Poiseuille) and pulsatile (Womersley) flow in a straight tube (Fig. 2). The fluid was described as Newtonian ($\mu$ = 3.5 cP, blood) with flow rates in the physiologic domain. Data were generated to include variations in tube radius (2.4-4.2 mm), fluid velocity (0.1-100 cm/s), and image signal-to-noise ratio (SNR; 20-80). Two-dimensional flow profiles derived from the analytical solutions were down-sampled to a resolution of 1.2 × 1.2 mm to represent acquired 4D flow cMRI data. To provide a more complex and anatomically representative geometry to examine 4D flow-derived WSS calculation accuracy, WSS values were also derived from a patient-specific fluid-structure interaction (FSI) computational model of the carotid bifurcation. Briefly, the FSI model was taken from the FEBio repository (Fig. 3) [6].

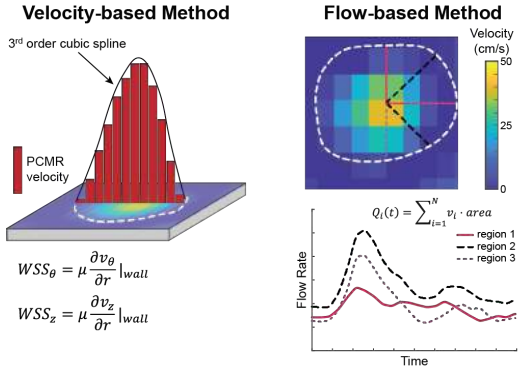


**Figure 1: Illustration of the velocity and flow-based methods to calculate WSS from 4D flow cMRI data.**

The model simulated pulsatile flow of a Newtonian fluid through a two-layered vascular structure, with unique material properties for each layer described by a microstructurally-motived strain energy function. Predicted velocity field data were extracted at the location of the carotid bulb and down-sampled to a resolution of 1.2 × 1.2 mm.

**Methods to Calculate WSS from 4D Flow Data.** Synthetic image data derived from the analytical solutions and FSI model were processed using both the velocity and flow-based methods to calculate WSS. All image data were segmented with the exact known position of the wall boundary. For the velocity-based method, image data were upsampled to an isotopic in-plane resolution of 0.75 mm using weighted nearest-neighbor interpolation. A cubic spline was fit to the 4D flow derived velocity values across the full diameter, and the derivate of the spline was calculated to determine the velocity gradient and WSS value (Fig. 1). Values were determined at 256 points around the circumference, and data were averaged within 12 sectors (central angle of 30°). For the flow-based method, flow waveforms were determined in 80 overlapping 90°-regions around the circumference (Fig. 1). Each flow waveform was reconstructed with 10 Fourier harmonics. WSS values were calculated via the Womersley solution and defined at the central angle for each overlapping region. Values were averaged over 12 sectors.

**Statistical Analysis.** Accuracy in the velocity and flow-based methods were determined by taking the difference between the analytical or model-predicted WSS value and each 4D flow cMRI method. A two-tailed paired Student's *t*-test was used to evaluate statistical significance.

## RESULTS

Across all cases using the exact solutions for calculating WSS, the flow-based method demonstrated greater accuracy than the velocity-based method for determining WSS directly from 4D flow cMRI data. For example, variations in steady fluid velocity showed that on average the flow-based method was ~13% more accurate than the velocity-based method (Fig. 2a). Moreover, the flow-based values were significantly different from the velocity-based values. Similar observations were seen with changes in tube radius and image SNR with the flow-based method being ~13% and ~12% more accurate on average, respectively, than the velocity-based method. Notably, data from the steady flow cases also demonstrated that the flow-based method was less sensitive to changes in the location of wall boundary (i.e., segmentation) than the velocity-based method. For the flow-based methods, changes in the wall boundary of ±20% resulted in WSS deviations <16%, whereas the velocity-based method had changes exceeding 75%. Results from the pulsatile flow cases demonstrated comparable results, whereby the flow-based method showed greater accuracy across all cases examined. Whether examining time-averaged WSS or peak WSS, values derived from the flow-based were closer to the analytical solution across changes in tube radius or inlet velocity (Fig. 2b).

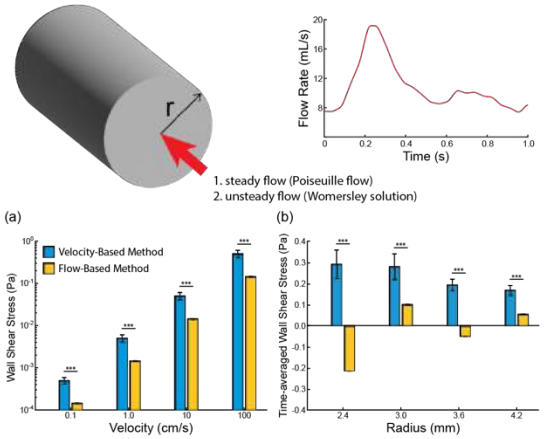


**Figure 2: Analytical solution geometry and flow conditions. Differences between analytical solution and 4D flow-derived values of WSS under (a) steady flow with changes in velocity and (b) pulsatile flow with changes in radius (*r*). *** indicates $p<0.001$.**

Comparing FSI predicted WSS values to those calculated with the velocity and flow-based methods further demonstrated the improved accuracy of the flow-based method. At the carotid bulb, for example, the velocity and flow-based methods exhibited averaged differences in time-averaged WSS (TAWSS) values from the FSI predictions of 0.22 and 0.07 Pa, respectively, across the 12 sectors (Fig. 3). In addition, peak TAWSS occurred in sector 8 in the FSI model and from flow-based calculations, whereas the peak TAWSS value from the velocity-based calculations occurred in sector 6.

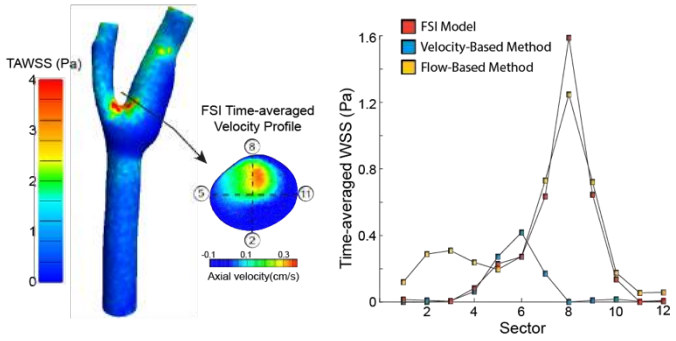


**Figure 3: Time-averaged WSS values derived from velocity and flow-based methods versus FSI predictions in a patient-specific carotid bifurcation at the carotid bulb (dashed line).**

## DISCUSSION

Herein, we present data from a study examining the accuracy of two distinct methods (velocity and flow-based) to calculate WSS from 4D flow cMRI data. Using synthetic MRI data generated from flow profiles calculated from analytical solutions of the governing equations of fluid flow, we observed that the flow-based method showed increased accuracy over the velocity-based method for calculating WSS when compared to analytical values (i.e., ground-truth values). Furthermore, these observations persisted when comparing against predicted WSS values from an FSI simulation of a patient-specific carotid bifurcation. It is important to highlight that while both methods are impacted by the limited spatial resolution of MRI, the flow-based method is more accurate and robust to changes in image quality (SNR). In addition, the flow-based method is more stable to inaccuracies in lumen boundary detection. It is recognized that the full potential of the flow-based method will require application and integration into the clinical setting; however, these data provide confidence in the *in vivo* quantification of an important mechano-biologic metric.


## ACKNOWLEDGEMENTS

This research was supported by the National Institutes of Health (R21 NS114603; JNO).


## REFERENCES


[1] Garcia, J. et al., *J. Am. Coll. Cardiol. Img.*, 12(2):252-266, 2019.
[2] Barker, A.J. et al., *Circ. Cardiovasc. Imaging*, 5:457-466, 2012.
[3] Soulat, G. et al., *J. Am. Coll. Cardiol. Img.*, 15(1):33-42, 2022.
[4] Stalder, A.F. et al., *Magn. Reson. Med.*, 60(5):1218-1231, 2008.
[5] Iffrig, E. et al., *J. Biomech. Engr.*, (under review).
[6] Shim, J.J. et al., *J. Biomech. Engr.*, 141(5):0510101-5, 2019.

# A STAND-ALONE MODULE TO INTRODUCE MEDICAL IMAGE SEGMENTATION INTO THE BME CURRICULUM

**Donna M. Ebenstein (1), James W. Baish (1), Christine M. Buffinton (2)**

(1) Department of Biomedical Engineering, Bucknell University, Lewisburg, PA USA
(2) Department of Mechanical Engineering, Bucknell University, Lewisburg, PA USA

## INTRODUCTION

Clinical practice has long made use of medical images for diagnosis and treatment planning. With the recent advances in 3D digital imaging technology, the need for biomedical engineering (BME) students to learn the basics of extracting specific anatomical features from the images, a process called segmentation (Fig. 1), has grown significantly. The trend towards patient-specific healthcare provides many examples of the need to segment a region from clinical imaging data and create a model that can be 3D printed or imported into a CAD program for further processing. For example, printed models are especially useful in orthopaedics for understanding the anatomy of bones and joints, manufacturing customized orthotics and implants, surgical planning, teaching, and research [1]. Commercial enterprises have also developed to offer customized hip, shoulder, and cranio-maxillofacial replacements using a combination of clinical imaging data and CAD software (e.g., KLS Martin WORLD, Tuttlingen, Germany; LOGEEKs Medical Systems, Novosibirsk, Russia; Materialise, Leuwen, Belgium). Patient-specific, 3D printed models are also well-suited for diagnosis and treatment planning for congenital heart disease, helping to clarify the complicated anatomy of the heart, great vessels, and coronary arteries before intervention [2]. To highlight these current clinical and industry applications of CAD and 3D printing, a stand-alone class module was developed to teach BME students the principles of medical image segmentation and its interface with CAD post-processing.

## METHODS

The introductory medical image segmentation stand-alone module was developed for a biomechanics course, and further refined for biomedical engineering courses in both imaging and fabrication. It uses ITK-SNAP, a free, open-source application designed to segment structures in 3D medical images [3]. ITK-SNAP provides semi-automatic segmentation using active contour methods, and had the best combination of cost, ease of use, and industry adoption when compared to other available image-processing software packages.

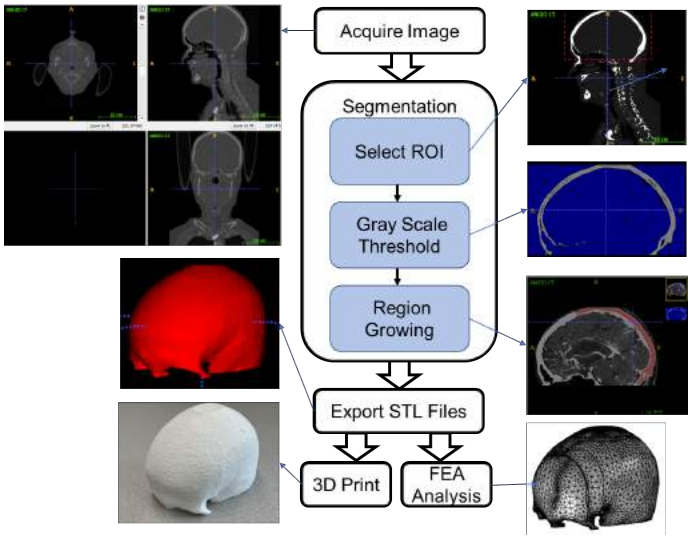


**Figure 1: The process of image segmentation applied to a set of CT images to extract part of the skull using the software ITK-SNAP. The exported STL file was 3D-printed and converted to a finite element modeling (FEM) mesh in COMSOL.**

The module consists of an introduction, a tutorial that guides students through a step-by-step process to extract a skull from a provided set of CT data, and a culminating assignment where students use the same software program to extract a different body part from clinical imaging data.

To introduce the module, the instructor provides basic background on how CT scans work and an explanation of the clinical relevance of image segmentation, often using videos. The instructors have found that showing videos of specific patients who were treated using these techniques can be an effective way to motivate students.

The tutorial document provides students with background information on image segmentation, instructions on how to install ITK-SNAP, and step-by-step instructions on how to extract a portion of the skull from a provided DICOM dataset of the head and neck with 460 CT slices of 512x512 pixels [4]. These step-by-step instructions include screen captures along with written instructions on how to perform each step. Three different methods of segmentation are introduced in the tutorial background section (threshold-based, edge-based, and region-growing), and two of the three are implemented in the tutorial.

While completing the tutorial, students load the image series, adjust the contrast, select a region of interest, and try auto-segmentation with the Snake Tool to extract a portion of the skull from the CT data (Fig. 1). Custom thresholding is applied to refine the selection and the students then explore different combinations of seed point quantity and size. After segmentation, students export files suitable for 3D printing or import into a CAD program.

The culminating assignment varies by instructor and course, but in all classes has included tasking the students with extracting a different body part from clinical imaging data using ITK-SNAP. In addition to this base task, some instructors have included additional components in the culminating assignment, such as having the students 3D print their extracted body part and evaluate the outcome, reflect on the challenges of segmenting different anatomical structures, or place images of the extracted body part into a portfolio to share with potential employers.

## RESULTS

This module has been implemented in approximately two courses per year since it was developed in 2016, impacting more than 150 students. Students complete the tutorial exercise in an 82-min class and then independently segment regions of their own choice from the provided images or another publicly available data. The primary learning objective for this module, "Students will be able to perform segmentation from a set of medical images," can be assessed directly from student completion of the culminating assignment in the module, since all faculty have required students to independently extract a new anatomical feature from clinical imaging data. 100% of students have successfully achieved this learning objective. As shown in Figure 2, students were able to segment a wide variety of mineralized and soft tissues from the provided or publicly available datasets. Most datasets were CT scans, but some body parts were extracted from MRI data.

The students engage well with this assignment and appreciate its clinical relevance. Students showed interest and excitement about segmenting their own choice of images/body parts, and particularly about 3D printing to obtain a physical object of their own creation. In reading student reflections on this activity, a few themes emerge. Students typically found the software to be easy to learn and user-friendly, even when independently applying the software to segment soft tissue. They also found it easy to 3D print a model using the exported segmentation file, although some students noted that "small details do not print accurately". Most of the challenges identified by the students were related to seed placement and propagation during region growing, and issues with file size. Students noted that if you used too many seed points, or seed points that were too large, the software might crash or freeze up. File size was an issue both when seeking other datasets to use for image extraction (many datasets students found on their own were too large for ITK-SNAP), and when slicing the exported file for 3D printing.

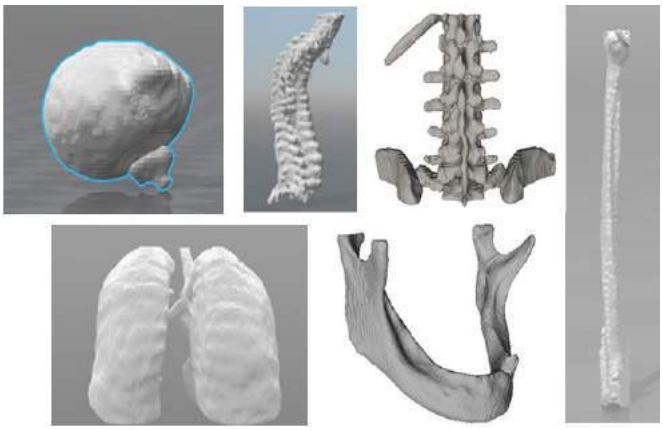

**Figure 2. Examples of extracted body parts from culminating assignments.**

## DISCUSSION

Successful completion of the tutorial and culminating assignment, particularly the ability of students to segment soft tissues on their own after only being trained to segment a mineralized tissue, showed that it is possible for students to sufficiently master the image segmentation technique in ITK-SNAP using the provided tutorial. In addition, instructors have observed that students often apply these skills independently in later courses, such as senior design and independent research projects. Several of our BME students have also landed internships or jobs at companies that create patient-specific implants using image segmentation.

Five different faculty members have utilized this learning module. Instructors previously unfamiliar with the technique were able to learn the package well enough for demonstration to students through completion of the tutorial. In addition to being easy to learn, this module is low-cost to implement. The software is free, and the module introduction and tutorial require less than 2 hours of classroom time to complete (even with troubleshooting of student computer issues). Hence, this module would be easy to incorporate into a variety of lecture and lab classes. So far, the stand-alone module has been successfully implemented in a biomechanics elective, a medical imaging elective, and a biomedical fabrication core course. It has been taught to sophomores, juniors, and seniors, and would also likely also be successful in a first-year course as it requires no pre-requisite material.

In conclusion, this stand-alone module provides a low-cost, flexible way to bring the clinical and industry trends combining medical image segmentation, CAD, and 3D printing into the undergraduate BME curriculum, and provide students with a concrete skill to market when applying for summer internships, jobs, or graduate school.


## ACKNOWLEDGEMENTS

The authors would like to thank Tyler Chlebowski, a Bucknell student ('16) who helped develop the original body part extraction exercise in collaboration with CMB. The authors would also like to acknowledge that initial development of ITK-SNAP was funded by NIH grant R01 EB014346 and was a collaboration between PICSL at U Penn and SCI at the University of Utah, and that PICSL maintains the software.


## REFERENCES


[1] Ejnisman, L et al., *Curr Rev Musculoskelet Med*, 14:1-8, 2021.
[2] Vukicevic, M et al., *JACC Cardiovasc Imaging*, 10:171-184, 2017.
[3] ITK-SNAP.. http://www.itksnap.org. Accessed 21 Jan 2022.
[4] DICOM Image Library. http://www.osirix-viewer.com/datasets/ Accessed 21 Jan 2022.

SB³C2022
Summer Biomechanics, Bioengineering and Biotransport Conference
June 20-23, Eastern Shore, MD, USA

# NON-MUSCLE MYOSINS ARE CRITICAL REGULATORS OF SKELETAL AND CONNECTIVE TISSUE FORMATION

**Mary K. Evans (1), Tonia K. Tsinman (1), Xi Jiang (1), Ellie J. Ferguson (1), Joel Boerckel (1), Lin Han (2), Eiki Koyama (3), Robert L. Mauck (1), Nathaniel A. Dyment (1)**

(1) Department of Orthopaedic Surgery, University of Pennsylvania, Philadelphia, PA, USA
(2) School of Biomedical Engineering, Drexel University, Philadelphia, PA, USA
(3) Orthopaedic Biomedical Research, Children's Hospital of Philadelphia, Philadelphia, PA, USA

## INTRODUCTION

The site where tendons insert into bone is known as the enthesis, which acts to mitigate stress concentrations between stiff bone and compliant tendon and is essential for the efficient transfer of muscle generated forces to bone, enabling skeletal motion. Tendon entheses often insert into bone eminences (i.e, tuberosities) which are protrusions on the ends of long bones that increase the mechanical advantage during ambulation. Tuberosities and the entheses attached to them develop in a biphasic process where cells specify into a distinct progenitor population that co-express Scleraxis (Scx) and Sox9. This is followed by a growth and differentiation phase where these progenitors proliferate to grow the eminence and then differentiate into tuberosity chondrocytes or enthesis fibrochondrocytes [1]. Studies have shown that both biophysical and biochemical cues are critical to enthesis development at each of these stages, as the disruption of key signaling pathways (TGFβ and BMP4) in the limb mesenchyme, ablation of Sox9 in Scx lineage cells, and the absence of muscle contraction all attenuate tuberosity formation [2]. Since cells sense mechanical stimuli and translate them into biochemical signals through their cytoskeleton via actomyosin contractility, studies have looked at the role of this process in directing cell differentiation and matrix production. However, studies thus far have been limited to *in vitro* experiments that fail to recapitulate the complex interaction of tendon and bone at the enthesis. While it is clear that applied (external) loading is critical for enthesis development, the role of cell-mediated (internal) forces generated via actomyosin contractility, is largely unknown. In order to disrupt cell-mediated contractility, we chose to ablate non-muscle myosin II, which interacts with actin filaments to initiate critical cell functions, such as cytoskeletal rearrangement, cell migration, and cell proliferation. NMII is encoded by the Myh9 (NMIIA), Myh10 (NMIIB), and Myh14 (NMIIC) genes; however, Myh14 expression is limited to a small set of differentiated tissues [3]. Therefore, to determine the extent to which actomyosin contractility governs tissue formation at this interface between tendon and bone, we ablated NMIIA and NMIIB in either all limb mesenchyme or targeted to tendinous tissue. We hypothesized that NMII ablation in both mesenchymal cells and tendinous tissues would disrupt enthesis and tuberosity formation and maturation.

## METHODS

All animal work was approved by the UPenn IACUC. Mouse Models: $Myh9^{f/f}$;$Myh10^{f/f}$ mice were crossed with either Prrx1Cre or ScxCre to target all limb mesenchyme or to restrict ablation to dense connective tissues, respectively. Because homozygous double knockouts did not appear with the Prrx1Cre driver at birth, suggesting embryonic lethality, we analyzed Prrx1Cre;$Myh9^{f/wt}$;$Myh10^{f/f}$ (Prrx1Cre $Myh9^{HET}$ $Myh10^{KO}$) and Prrx1Cre;$Myh9^{f/f}$;$Myh10^{f/wt}$ (Prrx1Cre $Myh9^{KO}$ $Myh10^{HET}$) mice. The ability of a single allele of either gene to rescue embryonic lethality reinforced previous findings that Myh9 and Myh10 are mutually compensatory; therefore, we only analyzed ScxCre;$Myh9^{f/f}$;$Myh10^{f/f}$ double knockouts (ScxCre dKO). Micro-CT: Prrx1Cre $Myh9^{HET}$ $Myh10^{KO}$, Prrx1Cre $Myh9^{KO}$ $Myh10^{HET}$, and ScxCre dKO mice were sacrificed at 5 weeks of age along with Cre-negative littermate controls (n=3 per genotype) and tissues were scanned at 10μm resolution. Skeletal Preparations: Prrx1Cre $Myh9^{HET}$ $Myh10^{KO}$ (n=1) and Cre-negative littermate control (n=3) mice were sacrificed at P0, stained with Alcian blue and Alizarin red, and cleared. Histology Sample Preparation: Knees, ankles, and shoulders from ScxCre dKO (n=3) and Cre-negative littermate control mice (n=2) were harvested, fixed in formalin, cryo-embedded, and serially sectioned in the longitudinal plane. Staining: Sections were stained for alkaline phosphatase (AP) activity with ELF97 endogenous phosphatase fluorescent substrate, counterstained with Hoechst-33342 (nuclei), and imaged by brightfield and polarized light microscopy.

## RESULTS

Non-muscle myosin is critical for appendicular skeletal

development. To assess the roles of NMIIA and NMIIB in appendicular skeletal development we conditionally ablated Myh9 and Myh10 with Prrx1Cre. Physical examination of Prrx1Cre Myh9$^{HET}$ Myh10$^{KO}$ mice at 5 weeks of age revealed a marked shortening of the forelimbs coinciding with impaired mobility. Interestingly, these limb shortening and ambulation defects were less severe in Prrx1Cre Myh9$^{KO}$ Myh10$^{HET}$ mice, indicating that NMIIB is more dominant than NMIIA in limb formation. Micro-CT reconstruction showed severe abnormalities in the Prrx1Cre Myh9$^{HET}$ Myh10$^{KO}$ mutants (**Fig. 1**) including, a subluxed patella (P), missing trochlear groove (TG), unfused tibia and fibula (T), and missing third trochanter in the hindlimb (100% penetrance). These abnormalities are also present in the hindlimb of Prrx1Cre Myh9$^{KO}$ Myh10$^{HET}$ mice; however, these mice display some, albeit incomplete fusion of the tibia and fibula. In the forelimb of Prrx1Cre Myh9$^{HET}$ Myh10$^{KO}$ mice, the deltoid tuberosity (DT) was missing, the humeral head and scapula were misshapen, and the spine of the scapula (S) was absent. In the Prrx1Cre Myh9$^{KO}$ Myh10$^{HET}$ mice, the humeral head, scapula, and spine of the scapula appeared normal and the deltoid tuberosity was present; however, it was severely misshapen. This led us to question if the absence of the deltoid tuberosity in the Prrx1Cre Myh9$^{HET}$ Myh10$^{KO}$ mutants was due to a lack of tuberosity initiation, or a failure of mineralization. P0 skeletal preparations revealed that the deltoid tuberosity absence was due to lack of initiation (**Fig. 2**).

Non-muscle myosin regulates tuberosity development and mineralization. To target non-muscle myosin ablation more in the tendon than the adjacent cartilage anlagen, we created ScxCre dKO mice. These mice display a strikingly similar shoulder phenotype to the Prrx1Cre Myh9$^{KO}$ Myh10$^{HET}$ mice, with a misshapen tuberosity, despite no other apparent skeletal defects (**Fig. 3**). Further investigation into the mineralization of several tendon entheses demonstrated a severe lack of mineral apposition at the tibial tuberosity enthesis (**Fig. 4**), with disorganized mineralization in the Achilles and supraspinatus tendons.

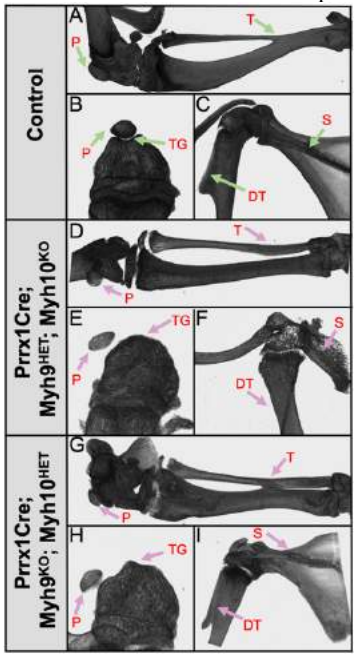


**Figure 1: NMII is critical to long bone and tuberosity formation. 3D µCT renderings of the hindlimb (A), frontal view of the knee (B), and shoulder joint (C) of control samples with arrows denoting important skeletal features that are lacking or abnormal in the Prrx1Cre Myh9$^{HET}$ Myh10$^{KO}$ (D-F) and Prrx1Cre Myh9$^{KO}$ Myh10$^{HET}$ (G-I) mutants. P: patella, TG: trochlear groove, T: tibia-fibula fusion, DT: deltoid tuberosity, S: spine of scapula.**

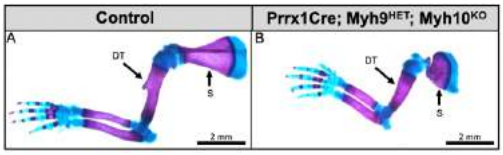


**Figure 2: Skeletal preparations of P0 control (A) and Prrx1Cre Myh9$^{HET}$ Myh10$^{KO}$ (B) mice illustrating the absence of the deltoid tuberosity in mutant mice. DT: deltoid tuberosity, S: scapula.**

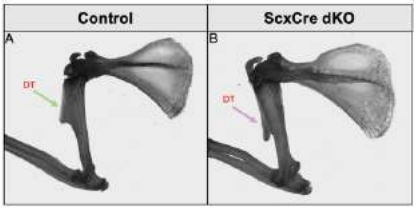


**Figure 3: µCT images illustrating the misshapen deltoid tuberosity (DT) in ScxCre Myh9$^{KO}$ Myh10$^{KO}$ (B) compared to controls (A).**

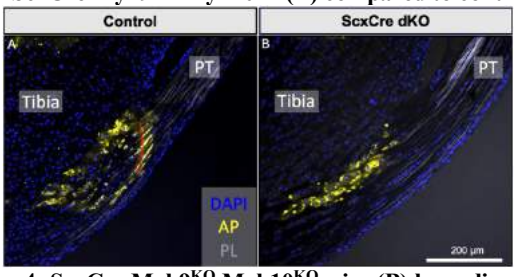


**Figure 4: ScxCre Myh9$^{KO}$ Myh10$^{KO}$ mice (B) have disrupted mineral deposition within the distal patellar tendon enthesis as seen by reduced AP activity compared to controls (A). PT: patellar tendon, AP: Alkaline phosphatase, PL: Polarized light. Tide mark (red line).**

## DISCUSSION

Despite the well-known role of applied (external) loading in the development of the enthesis, the role of cell-mediated (internal) forces in enthesis development is unknown. Here we show that mice retaining a single copy of either Myh9 or Myh10 in limb mesenchyme demonstrate similar, yet less severe, abnormalities to mice lacking skeletal muscle contraction. The differences in skeletal defects observed depending on which gene remains active, highlights the differential roles of Myh9 and Myh10 in tuberosity and bone formation. Additionally, we show that NMII ablation in tendons disrupts deltoid tuberosity formation and yielded markedly reduced mineral apposition in the distal patellar tendon enthesis. Interestingly, ScxCre dKO mice phenocopy the deltoid tuberosity defects found in Prrx1Cre Myh9$^{KO}$ Myh10$^{HET}$ mice but are less severe than Prrx1Cre Myh9$^{HET}$ Myh10$^{KO}$ mice. Therefore, we will investigate allele dosages in Scx Cre mutant mice to determine the cell autonomous roles of NMIIA and NMIIB in enthesis development. These results also raise the question of whether defects in tuberosity development are due to disrupted transduction of applied loads to the cells or rather loss of actomyosin contractility which alters cell patterning during tuberosity initiation and growth. Future studies will investigate these important questions.


## ACKNOWLEDGEMENTS

Work was supported by NIH R00AR067283, P30AR069619, R01AR075418, T32AR007132, and VA IK6 RX003416.


## REFERENCES


1. Blitz, Developmemt, 140(13):2680-90, 2013; 2. Zelzer, Birth Defects Res C Embryo Today, 102(1): 101–112, 2014;
3. Shutova, Biokhimiia, 506(2):394-402, 2018

SB³C2022
Summer Biomechanics, Bioengineering and Biotransport Conference
June 20-23, Eastern Shore, MD, USA

# MODELING VENTRICULAR MECHANICS IN PATIENTS WITH OBSTRUCTIVE HYPERTROPHIC CARDIOMYOPATHY (HOCM)

**Lei Shi (1), Hiroo Takayama (2), Vijay Vedula (1)**

(1) Department of Mechanical Engineering, Columbia University, NY, USA
(2) New York Presbyterian Hospital/Columbia University Irving Medical Center, NY, USA

## INTRODUCTION

Hypertrophic obstructive cardiomyopathy (HOCM) is an inherited cardiac disease where the left ventricle (LV) myocardium thickens abnormally around the basal plane, dynamically obstructing the flow into the aorta. Affecting 14-35 million people worldwide [1], HOCM can increase the risk of heart failure which leads to sudden cardiac death. Septal myectomy, an open-heart procedure, is the current gold standard to treat HOCM patients that involves removing excess myocardial tissue. However, the procedure relies heavily on the surgeon's expertise and may lead to repeat interventions [2]. Patient-specific modeling of cardiac mechanics in HOCM patients provides a viable myectomy planning tool by virtually predicting the mechanical response of the myocardium before and after performing the surgery.

Cardiac mechanics is composed of a passive component and an active contraction component. The primary step for simulating cardiac mechanics is to obtain the passive material parameters of the myocardium and the stress-free reference configuration. In this work, we developed an inverse finite element analysis (iFEA) framework to estimate the passive material parameters and the stress-free reference configuration of the ventricular myocardium in a HOCM patient. We plan to further extend the framework by including electrophysiology modeling and active contraction to analyze the myocardial mechanics during the entire cardiac cycle, before and after performing myectomy. Such a modeling framework, coupled with optimization, may find clinical utility in planning myectomy for optimized cardiac performance, thereby leading to improved patient outcomes.

## METHODS

A schematic of the workflow for patient-specific characterization of myocardial material parameters is shown in Figure 1. Briefly, we obtained high-resolution dynamic CT (3D+time) data for three HOCM patients from the database at Columbia University Medical Center (CUMC). We used our previously developed workflow to segment the ventricular myocardium at four phases during diastole ($t_{n,\ n=1\text{-}4}$, typically between 45%R-R and 100%R-R), to create FEA-ready models [3]. Optimization is subsequently applied to not only characterize the myocardial material parameters but also determine the stress-free configuration using the augmented inverse Sellier's method [4], described next (Figure 2).

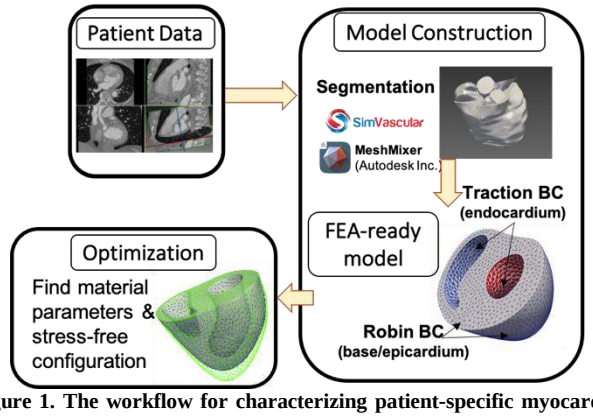


**Figure 1. The workflow for characterizing patient-specific myocardial properties and stress-free configuration in HOCM patients using finite element analysis (FEA) and optimization.**

The basic idea of the algorithm (Figure 2) was to iteratively update the reference configuration based on the result of each forward FEA to reduce the difference between the image-based configuration $\mathbf{X}_{imag}$ and the loaded reference configuration $\boldsymbol{\psi}_{p_1}(\boldsymbol{X})$ predicted by the FEA at pressure $p_1$. Here, $\psi(\boldsymbol{X})$ is the standard mapping between the reference configuraton $(\boldsymbol{X})$ and the deformed configuration $\boldsymbol{x} = \psi(\boldsymbol{X})$ in nonlinear continuum mechanics. During the update, we apply Aitken's relaxation to accelerate convergence [5]. Meanwhile, the material parameters of the constitutive model were optimized by reducing the

difference between the `measured' and the predicted diastolic pressure-volume ($p$-V) profiles at all the acquired phases ($t_{n,\ n=1\text{-}4}$). Since pressure data is not routinely acquired for these patients, we approximate the diastolic $p$-V relation using an exponential profile, characterized by two constants $p_0$ and $k_0$. These constants are determined using a Python-based Levenberg-Marquardt algorithm such that the diastolic pressures are bound within empirically determined clinical data (8-20mmHg).

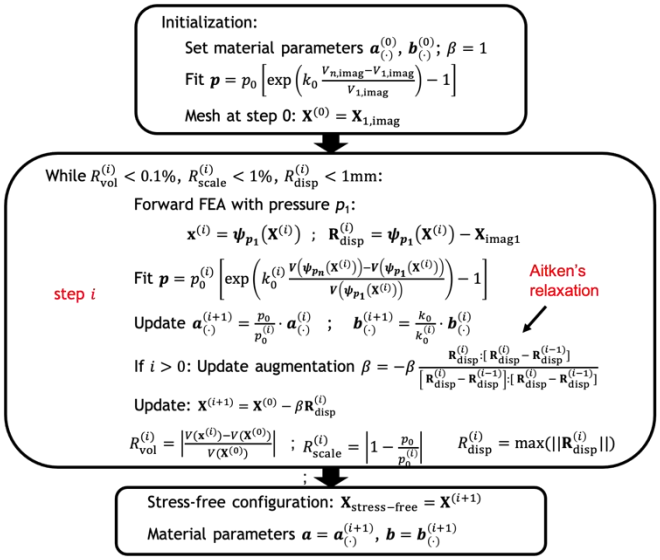


**Figure 2. Algorithm to find the stress-free configuration and parameters of the Holzapfel-Ogden constitutive model for the myocardium.**

We begin our algorithm with the ventricular configuration at the beginning of the diastole (or end-systole ~45%R-R). The forward FEA is then performed by applying pressure boundary conditions on the endocardium such that the pressure on the RV endocardium is about 1/5$^{th}$ of the pressure on the LV endocardium (~8mmHg at beginning of diastole) [6]. We employ the open-source multiphysics finite element solver, svFSI, and the myocardium is modeled using the Holzapfel-Ogden (HO) orthotropic constitutive model with initial values for the parameters extracted from Pfller et al. [7]. The fiber directions of the myocardium were determined using a rule-based method [7]. The top surface was fixed and a Robin boundary condition was applied on the epicardium surface to model the effects of the pericardium [7]. The process is iterated until the errors in myocardial volume ($R_{\text{vol}}$), maximum displacement ($R_{\text{disp}}$), and material parameter scaling ($R_{\text{scale}}$) are within acceptable ranges.

## RESULTS

The parameter estimation process converges in less than 6 steps for all the three patients with $R_{\text{disp}}$=0.7±0.2mm, $R_{\text{vol}}$=0.49±0.43%, and $R_{\text{scale}}$=0.81±0.15%. The optimized reference configuration of a representative patient is shown in Figure 3a, where the green mesh is the image-based configuration at the beginning of the iterative process (beginning of diastole), and the gray surface is the optimized stress-free reference configuration. When loaded with a mid-diastolic pressure (14.15mmHg), that corresponds to 80%R-R, there is a reasonable agreement between the deformed reference configuration (Figure 3b, gray) and the image-based model (Figure 3b, green) with a slight mismatch near the basal plane of the ventricular free-wall. The LV cavity volumes of both the image-based and the predicted models are within 3.3% for all four diastolic pressure loads (Table 1), while the optimized passive material parameters of the HO model for the three HOCM patients are given in Table 2.

**Table 1: Comparison of the image-based and predicted LV cavity volumes (ml) during diastole for the three HOCM patients**

| Phase | | Patient #1 | | Patient #2 | | Patient #3 | |
|---|---|---|---|---|---|---|---|
| (%R-R) | p(mmHg) | $V_{\text{imag}}$ | $V_{\text{pred}}$ (%diff) | $V_{\text{imag}}$ | $V_{\text{pred}}$ (%diff) | $V_{\text{imag}}$ | $V_{\text{pred}}$ (%diff) |
| 45% | 8 | 74.3 | 74.8 (0.7) | 114.3 | 115.2 (0.8) | 71.2 | 71.2 (0.0) |
| 70% | 11.25 | 90.3 | 87.3 (3.3) | 130.9 | 129.6 (1.0) | 91.3 | 88.6 (3.0) |
| 80% | 14.15 | 101.7 | 99.3 (2.4) | 148.9 | 145.6 (2.2) | 100.4 | 98.1 (2.3) |
| 99% | 20 | 118.6 | 118.5 (0.1) | 167.5 | 166.9 (0.4) | 111.4 | 111.7 (0.3) |

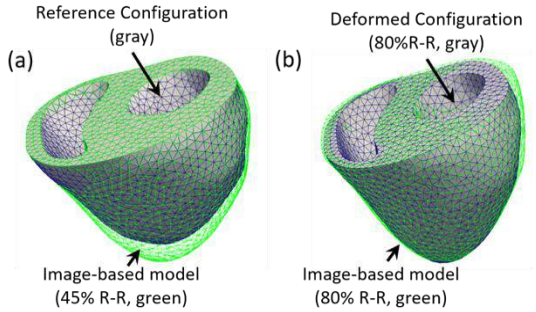


**Figure 3. (a) The optimized stress-free reference configuration (gray) superposed on the image-based model at the beginning of the iteration (45%R-R, green). (b) Comparison of the deformed configuration (gray), obtained by loading the reference configuration with an LV $p$=14.15 mmHg, and the image-based model at 80%R-R (green).**

**Table 2: Material parameters of the Holzapfel-Ogden (HO) constitutive model for the myocardium of the 3 HOCM patients.**

| Parameter | $a$ (Pa) | $b$ | $a_f$ (Pa) | $b_f$ |
|---|---|---|---|---|
| Value | 27±15 | 1.6±0.4 | 8339±4679 | 3.1±0.7 |
| Parameter | $a_s$ (Pa) | $b_s$ | $a_{fs}$ (Pa) | $b_{fs}$ |
| Value | 1120±628 | 2.2±0.5 | 97±55 | 2.2±0.5 |

## DISCUSSION

We developed an inverse FEA-based framework (Figures 1, 2) to determine the passive material parameters and the stress-free reference configuration of a patient-specific HOCM myocardium. The framework has been applied on three patients and shows reasonable agreement between the FEA-based model and image-based ventricular myocardium (Figure 3, Table 1). Next, we will establish the complete cardiac mechanics model of a HOCM patient by including electrophysiology modeling and active contraction in the current framework. We will first apply the integrated model on a preoperative HOCM patient with the myocardial parameters estimated during diastole using inverse FEA. We will then perform virtual myectomy using post-operative CT data as reference and assess the effect of myectomy on the cardiac mechanics. Validation will be performed by comparing CT-based image data and ECG waveforms pre- and post-myectomy. Our long-term goal is to couple the framework with topology optimization leading to a myectomy planning tool for optimal cardiac performance.


## ACKNOWLEDGEMENTS

We acknowledge computing resources from Columbia University's Shared Research Computing Facility – Ginsburg HPC.


## REFERENCES


[1] R. Nishimura, et al. Circulation research, 121(7), (2017): 771-783. [2] Minakata K, et al. Ann Thorac Surg. 2005;80(3):851-856. [3] Vedula, Vijay, et al. PLoS Comp. Bio. 13.10 (2017). [4] L. Marx, et al. arXiv preprint arXiv:2101.04411 (2021). [5] M. Genet, et al. J biomechanics 48.10 (2015): 2080-2089. [6] S. Göktepe et al. Int. J. Num. Mthd Biom. Eng. 27, no. 1 (2011): 1-12. [7] M. Pfaller et al. Bio. & Model. Mecha. 18, no. 2 (2019): 503-529.

SB³C2022
Summer Biomechanics, Bioengineering and Biotransport Conference
June 20-23, Eastern Shore, MD, USA

# A NOVEL MODEL FOR PASSIVE MYOCARDIUM THAT INCORPORATES COMPLETE DIFFUSION TENSOR INFORMATION

**Christian L. Goodbrake (1), Kenneth L. Meyer (2), Michael S. Sacks(1,2)**

(1) 1 James T. Willerson Center for Cardiovascular Modeling and Simulation, Oden Institute for Computational Engineering and Sciences and the Department of Biomedical Engineering, University of Texas, Austin, Texas, USA
(2) Department of Computational Engineering, University of Texas, Austin, Texas, USA

## INTRODUCTION

Cardiac tissue is traditionally modeled as a pseudo-elastic anisotropic material using the language of nonlinear solid mechanics. Different models represent this anisotropy in different ways, but all require some manner of translating tissue structure into the mathematical formalism. At their simplest, models such as these may locally identify a preferred fiber direction, and then construct a transversely isotropic strain energy density from that direction using strain invariants and pseudo-invariants. Other more complex models may define fiber, sheet, and normal directions as an orthonormal frame, and then build an orthotropic material model based on this data. One challenge that faces all of these models is the difficulty in connecting model anisotropy to the actual structure of the tissue.

Diffusion Tensor Magnetic Resonance Imaging (DTMRI) is a convenient way to noninvasively locally measure the structure of fibrous biological tissues like axonal tissue and myocardium. Despite this, current models based on DTMRI measurements only incorporate secondary quantities derived from the positive definite diffusion tensor field **D**. For example, **D**'s eigenvectors may be extracted to determine local orientation without regard for the strength of the anisotropy; there is currently no material model that fully incorporates **D**, which contains rich structural information embedded within it. We introduce a material model that directly incorporates **D**, resolves degeneracy conditions and singularities, and is easily modified to suit other fibrous biological materials.

## METHODS

**Structural DTMRI Data.** Ex-vivo DTMRI data was densely mapped on 1 $cm^3$ cubes of passive ovine myocardium (Figure 1). The diffusion tensor **D** is a quantity that relates the gradiant in osmotic pressure ρ to fluid flux J within tissue.

$$J = -\boldsymbol{D}\nabla\rho \qquad (1)$$

The diffusion tensor **D** is a positive definite symmetric tensor, meaning that it possesses a spectral representation.

$$\boldsymbol{D} = \sum_{i=1}^{3} \lambda_i \boldsymbol{n_i} \otimes \boldsymbol{n_i} \qquad (2)$$

There are several natural symmetries of such data, namely that permuting the eigenvalues of **D** is locally indistinguishable from a material rotation. Additionally, whenever two or three of these eigenvalues are equal, the corresponding set of eigenvectors ceases to be uniquely defined.

We demanded that our model respect these symmetries, in that it gives the same physical predictions for materials that only differ by these symmetry transformations. This lets it reduce to the degenerate symmetry cases of transverse isotropy and isotropy whenever the DTMRI data itself adopts these symmetries. Because this does not completely determine the model form, we make further simplifying assumptions to obtain a particular model form. We distinguish between necessary functional forms induced by the inherent symmetries of the diffusion tensor, and the particular functional choices we make in this specific model, demonstrating the generality of this approach, and making clear where modification can be freely made without losing the desirable symmetry features of the model.

**Model Form.** Our model is a pseudo-elastic material model, so we define a strain energy density Ψ depending on the Lagrange strain tensor $\mathbf{E}=(\mathbf{F}^T\mathbf{F}-\mathbf{I})$.

We adopt an exponential polynomial form in accordance with earlier work [1], drop odd order terms to ensure convexity, and enforce major and minor symmetries on $Q_2$ and $Q_4$ because of the symmetric action on **E** and the symmetry of **E**. In terms of the spectral basis $\{\mathbf{n}_i\}$, and utilizing Einstein summation, this energy takes the form

$$\Psi = e^{\left(Q_0 + Q_2^{ABCD} E_{AB} E_{CD} + Q_4^{ABCDEFGH} E_{AB} E_{CD} E_{EF} E_{GH}\right)} \qquad (3)$$

SB³C2022-392

In this basis, we compute the components of $Q_2$ and $Q_4$, and enforce symmetry conditions. The major symmetries of $Q_2$ and $Q_4$ require that pairs of indices can be arbitrarily permuted, while their minor symmetries require that the indices within each pair can be swapped.

**Symmetry Conditions.** Because the permutation of the eigenvalues of **D** is indistinguishable from certain rotations of **D**'s eigenvectors as shown in Figure 1, we want to ensure that our model's dependence on **D** is insensitive to this distinction. To enforce this, we permute the eigenvalues, and then apply the rotation that places the eigenvectors back in their original orientation. This is a nontrivial transformation on the components of the strain energy, which yields a set of functional equations that must be satisfied by the different components of our model's energy.

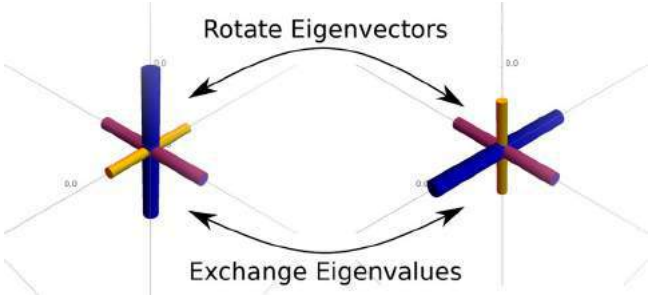


**Figure 1: Cubic rotations of the diffusion tensor's eigenvectors are indistinguishable from permutations of the diffusion tensor's eigenvalues.**

These symmetries reduce $Q_0$ to be a symmetric function of DT's eigenvalues, the components of $Q_2$ to be determined by three underlying functions, and the components of $Q_4$ to be determined by ten underlying functions. Furthermore, because our model must become transversely isotropic or isotropic when **D** does, these functions are not arbitrary, but must satisfy functional equations at particular values of the eigenvalues. If these underlying functions are linear combinations of simple functions, these functional equations become linear, and can be explicitly solved to obtain a set of independent free parameters.

## RESULTS

We nondimensionalize the eigenvalues of **D** so that the sum of their squares is 1. Taking the remaining free components of $Q_0$, $Q_2$, and $Q_4$ to be linear in these projectivized eigenvalues $\{\widetilde{\lambda}_i\}$, we obtain a model with

$$Q_0 = q_0 + q_1\left(\widetilde{\lambda}_1 + \widetilde{\lambda}_2 + \widetilde{\lambda}_3\right), \quad (4)$$

$$Q_2 = Q_2\left[f_{shear}, f_{couple}, f_{normal}\right], \quad (5)$$

with

$$f_{shear}(l,e) = \mu_{00} + \mu_{10}\, l + \mu_{01}\, e, \quad (6)$$

$$f_{couple}(l,e) = \nu_{00} + \nu_{10}\, l + \nu_{01}\, e, \quad (7)$$

$$f_{normal}(l,e) = \nu_{00} + 2\mu_{00} + \left(\nu_{10} + 2\mu_{10}\right)e + \left(2\,\nu_{01} - \nu_{10} + 4\,\mu_{01} - 2\,\mu_{10}\right)l, \quad (8)$$

l and e being different linear combinations of the projectivized eigenvalues, and $Q_4$ similarly depending on 10 underlying functions involving 10 parameters $a_{00}$, $a_{10}$, $a_{01}$, $c_{000}$, $c_{100}$, $c_{010}$, $c_{001}$, $i_{00}$, $i_{10}$, and $i_{01}$, these 18 parameters being the structural sensitivities.

Applying our model to extant data from [2], we obtain an inhomogeneous anisotropic material model with fixed global parameters, the inhomogeneity and anisotropy being induced by the diffusion tensor field itself (Figure 2). We perform inverse modeling in FEniCS to find values for model parameters that best capture the behavior of our samples. The parameters appearing in our model reflect the sensitivity of the material's stiffness in particular deformation modes to its diffusivity in different directions.

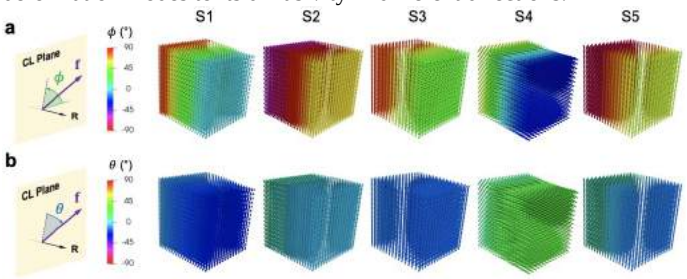


**Figure 2: a) In-plane fiber angle φ of each specimen. b) Out-of-plane fiber angle θ for each sample.**

## DISCUSSION

Using these structural stiffnesses instead of fiber, normal, and sheet moduli eliminates the need to manually identify which DT eigenvector field corresponds to which material direction, since all three eigenvector fields are used along with their respective eigenvalues. This is especially useful in regions where two the diffusion tensor's eigenvalues are close since in these regions small variations in the diffusion tensor's components can lead to rapid changes in eigenvector orientation, which is only exacerbated by noise in data. Because we incorporate the relative strengths of these orientations, rapid changes in orientation due to nearly equal eigenvalues is attenuated by the nearly equal eigenvalues themselves, leading to nearly transversely isotropic behavior. This approach also allows us to describe both healthy and diseased tissue with a single material model when the disease is primarily manifested structurally, since the local DTMRI data captures this structural defect through **D**.

While the overall form of our model is very similar to previous models, being exponential polynomial, the work we have done ensures that the structure of the DTMRI data is preserved by the final model exactly. By incorporating dense diffusion tensor mappings, we capture the subtle effects of material structure. For example, our model captures twisting and shearing due to transmural fiber variation that a homogenous model cannot.

In summary, we have developed a flexible material model for myocardium and any other 3D soft tissue that directly incorporates D in a robust manner. This model is inhomogeneous, yet relies on a set of fixed global parameters, and automatically reduces to the degenerate symmetry cases of transverse isotropy and isotropy whenever the diffusion tensor's eigenvector fields become ill-defined or degenerate. Furthermore, our derivation is easily modified for application to other fibrous biological tissue, and produces sample-specific material models.

## ACKNOWLEDGMENTS

NIH grant no. R01 HL073021 and R01 103723 awarded to MSS. We thank the Gorman Cardiovascular Research Group for their assistance and collaboration with mechanical testing and sample preparation.

## REFERENCES

[1] Zhang W. et al. JMBBM. 2019 Jan; 89:168-198.
[2] Li, DS et al., J Mech Behav Biomed Mater, 2020, 103, 103508

# AORTIC COARCTATION ASSESSMENT – IN VITRO 4D FLOW MRI APPROACH

**James P. Rice (1,2), Labib Shahid (1,2), Haben Berhane (3,5), Cynthia K. Rigsby (4), Joshua D. Robinson (4), Lindsay M. Griffin (4), M. Markl (3,5), A. Roldán-Alzate (1,2)**

(1) Department of Mechanical Engineering, University of Wisconsin-Madison, Madison, WI, USA.
(2) Department of Radiology, University of Wisconsin-Madison, Madison, WI, USA.
(3) Department of Biomedical Engineering, Northwestern University, Evanston, IL, USA.
(4) Department of Medical Imaging, Lurie Children's Hospital of Chicago, Chicago, IL, USA.
(5) Department of Radiology, Northwestern University Feinberg School of Medicine, Chicago, IL, USA.

**INTRODUCTION:**

Coarctation of the aorta is a common congenital heart defect (5-8%), presenting as a narrowing of the proximal descending aorta [1]. COA can be discrete or more complex and associated with severe secondary complications such as diffuse arch hypoplasia and descending aortic aneurysm. The most common therapy is to restore normal aortic blood flow thus, understanding pre- and post-interventional COA hemodynamics is crucial [1-4].

4D flow MRI shows promise in assessing 3D aortic hemodynamics in patients with COA [2-3]. 4D flow MRI data are acquired with velocity encoding sensitivity ($V_{enc}$), set above the expected maximum velocity in the vessel of interest. High $V_{enc}$ is necessary to capture high velocity regions without aliasing, like in the stenosis in COA. However, noise in velocity measurements is directly proportional to $V_{enc}$ and increasing $V_{enc}$ leads to difficulties in distinguishing low velocities from noise, like in an aortic aneurysm (slow vortex flow) [4-5]. This complicates 4D flow MRI measurements in complex flow regimes.

Pulsatile in vitro flow models allow for systemic evaluation of 4D flow MRI performance by providing a way to produce anatomically accurate, patient-specific geometries that can be analyzed with higher resolution flow methods [6-7]. The goal of this study was to develop an accurate and reproducible modeling framework using in vitro models and 4D flow MRI to evaluate the hemodynamics of three different clinical presentations of COA, pre- and post- intervention.

**METHODS:**

In this HIPAA compliant study, three pediatric patients underwent standard-of-care cardiothoracic MRI pre- and post-COA repair following an IRB approved protocol (Table 1). MR imaging included aortic 4D flow MRI and 3D contrast-enhanced (CE)-MR angiography (MRA), which was used to segment aortic geometries and construct two in vitro, patient-specific models per patient using additive manufacturing [8]. The models were connected to a pulsatile flow circuit and scanned on a 3.0T MRI scanner (Signa Premier, GE, Waukesha, WI). 3D flow dynamics were measured using the 4D flow MRI sequence PC-VIPR [9]. Scan parameters were 1.3mm isotropic spatial resolution, TR=6.1ms, flip angle=8°, 320 mm FOV, and 160 cm/s $V_{enc}$. Heart rate was simulated to 60 beat/min and a 35% systolic cardiac waveform was prescribed resulting in mean inlet aortic flow of 2.0 liters/min. ECG gating was achieved via signal output from the pump. A blood mimicking solution of water and glycerol (42:58 by weight) was used in the flow loop.

**RESULTS:**

The Study cohort is outlined in Table 1. The cohort included three patients (mean age 10 ± 4 years) with a median follow-up duration of 5 ± 3 years (2 males). Figures 1-3 depict the 4D flow MRI data obtained at peak systole in the pre- and post-intervention cases for patients 1-3, respectively. For patients 1 and 2, high velocity jets extending into the descending aorta are observed in pre-interventional models in the COA location. For both patients, it is evident that COA-interventions reduced peak velocity at the site of the repair. Similar consistencies are seen in the flow maps depicted for patient 3 in Figure 3, which shows improvement in flow profiles between pre- and post-cases despite prior stenting, suggesting re-intervention improved aortic hemodynamics. For patient 1, full-field flow visualization is achieved in the pre-repair aortic aneurysm, which is not available in the in-vivo dataset (Figure 1). The same is true for the stented region in patient 3, where in-vitro flow information fills the void seen in the in-vivo flow map (Figure 3). Pre- and post-repair peak velocities at the location of the coarctation and results of volumetric flow analysis are summarized in Table 1.

**Table 1:** Demographic and procedure information for patient cohort. 4D Flow MRI obtained peak velocities pre- and post-intervention and results from volume flow analysis for validation of 4D flow MRI data (* indicates patient underwent reintervention for COA).

| Patient | Intervention Strategy | Gender | Case | Age | Peak Velocity [m/s] | Inflow [ml/cycle] | Outflow [ml/cycle] | Error [%] |
|---|---|---|---|---|---|---|---|---|
| 1 | COA repair and pseudoaneurysm resection with placement of 16mm gel weave interposition graft | Female | Pre | 6 | 1.17 | 35.8 | 31.8 | 11.2 |
| | | | Post | 8 | 0.414 | 52.2 | 57.2 | 9.49 |
| 2 | Ebstein anomaly and dysplastic mitral valve. Repair with interposition graft. | Male | Pre | 14 | 0.927 | 33.8 | 30.2 | 10.8 |
| | | | Post | 20 | 0.414 | 37.8 | 35.0 | 7.34 |
| 3* | Reintervention with 16mm gel weave end-to-end interposition graft | Male | Pre | 10 | 0.769 | 38.6 | 34.5 | 10.5 |
| | | | Post | 15 | 0.743 | 39.2 | 40.9 | 4.41 |

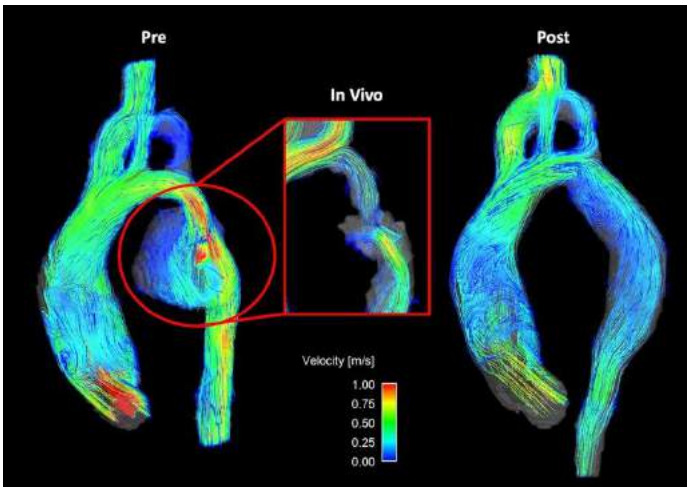


**Figure 1:** Comparison of pre- (left) and post-repair (right) in vitro model flow fields derived from 4D flow MRI for patient 1. Highlighted is a comparison of the in vitro and in vivo flow profiles in the aneurysm region of the descending aorta. In vitro modeling enhances slow, recirculating flow that is lost in the in vivo acquisition.

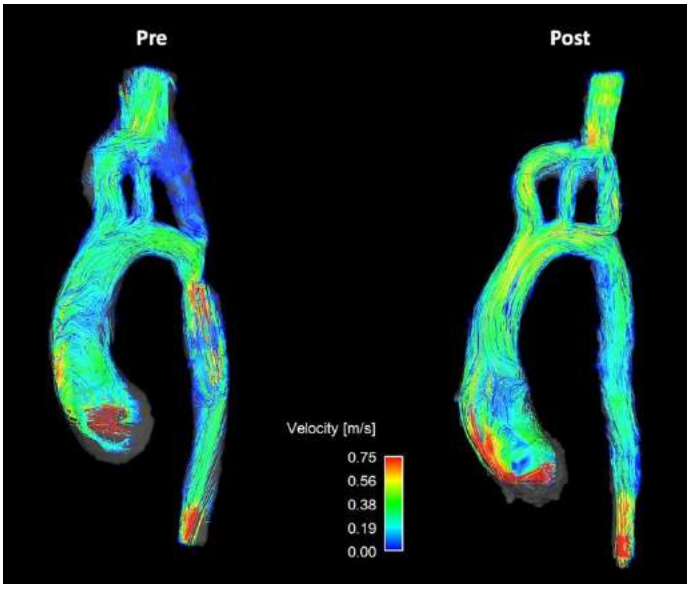


**Figure 2:** Comparison of pre- (left) and post-repair (right) in vitro model flow fields derived from 4D flow MRI for patient 2. High velocity COA jet observed in pre-repair case is relieved with repair.

**DISCUSSION:**

This study utilized patient-specific, in vitro models and 4D flow MRI for hemodynamic analysis of different presentations of COA. In cases where narrowing is observed (patient 1 and 2), velocities in the stenosis are shown to reduce after intervention. This agrees with expectations for treatment, suggesting in vitro modeling can shed light on the effect of surgical intervention on post-repair hemodynamics. Imposing the same inlet flow induced similar model inflow conditions for comparison of the effect of presentation on overall COA hemodynamics. It is noted that this does not reflect in vivo flow conditions. Comparisons to in vivo 4D flow MRI datasets are necessary and prescribing patient-specific inflow rates must be carried out in the future. Another aspect of interest is the ability to analyze flow in regions typically inaccessible with in vivo PC-MR imaging: areas that contain both high and low velocity flow (patient 1, aortic aneurysm) and regions with high susceptibility to MR artifact (patient 3, stent). This is seen in the flow fields for patient 1 and 3, respectively. These results hint that in vitro modeling can be used in other cases where flow information is lost due to a high $V_{enc}$ setting or medical device influence. Results from volumetric flow analysis yielded an average difference between in- and out-flow of 8.95%, agreeing with previously published studies validating the consistency of 4D flow MRI [9].

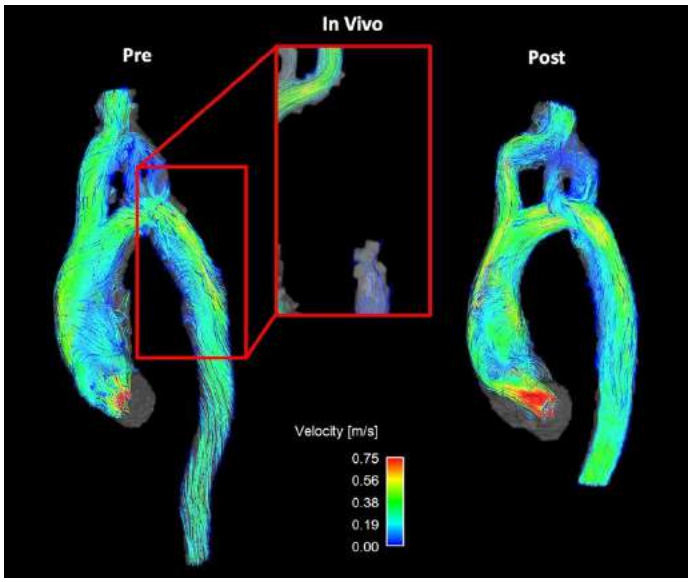


**Figure 3:** Comparison of pre- (left) and post-repair (right) in vitro model flow fields derived from 4D flow MRI for patient 3. Highlighted is a comparison of the in vitro and in vivo flow profiles in the stent, where velocity information is clearly missing in the in vivo dataset.

**ACKNOWLEDGEMENTS:**

The authors acknowledge grant support by the American Heart Association (AHA) 19TPA34850066 and GE Healthcare, which provides research support tot UW-Madison.

**REFERENCES**

[1] Rao P. *Curr Cardiol Rep*. 2005; 7(6):425-434.
[2] Hope M, et al. *J Magn Reson Imaging*. 2005;31(3):711-718.
[3] Frydrychowicz, et. al. *Investigative Radiol.* 2011;46(5):317-325.
[4] Dyverfeldt P, et al. *J Cardiovasc Magn Reson.* 2015;17(72).
[5] Markl M, et al. *J Magn Reson Imaging.* 2021;36(5):1015-1036.
[6] Rutkowski D, et al. *J Biomech Eng.* 2019; 141(12):121004.
[7] Medero R, et al. *Ann Biomech Eng.* 2020;48:2484-2493.
[8] Ruedinger K, et al. *Cardiovasc Eng Technol, 2019;*10(3):500-507.
[9] Johnson K, et al. *Magn Reson Med.* 2008;60(6):1329-1336.
[10] Roldán-Alzate A, et al. *J Magn Reso Imaging.* 2013;37(5):1100-8.

# A COMPARTIVE STUDY OF BONE TISSUE GROWTH BETWEEN BIOINSPIRED AND SQUARE SCAFFOLDS

**Marco A. Fielder (1, 2), Arun K. Nair (1, 2)**

(1) Materials Science and Engineering, University of Arkansas, Fayetteville, AR, USA
(2) Institute for Nanoscience and Engineering, University of Arkansas, Fayetteville, AR, USA

## INTRODUCTION

Several studies have investigated combining tissue scaffolds with ultrasound stimulation to enhance bone growth [1-4]. However, one challenge that remains is designing a scaffold with a high porosity to enable more tissue ingrowth without compromising structural integrity of the scaffold is to withstand the necessary mechanical loads [5]. A study by Gu et al. showed that a bioinspired scaffold derived from the atomic structure of hydroxyapatite was more resistant to deformation compared to a scaffold with uniform square pores [6]. A recent study also found that this bioinspired scaffold structure allows a higher transmission of ultrasound wave energy than the square pore scaffolds [7]. Our study hypothesizes that the bioinspired scaffold from Gu et al. can additionally maintain a level of cell growth compared to the square pore scaffold of the same porosity when subjected to ultrasound stimulation. This would be useful for addressing the issue of designing a scaffold structure with a high structural integrity that also does not impede tissue growth while being stimulated by ultrasound. Our study also hypothesizes that the initial distribution of mesenchymal stem cells (MSCs) in the scaffold can significantly affect the growth and differentiation of the tissue. Figure 1 shows the two scaffolds studied.

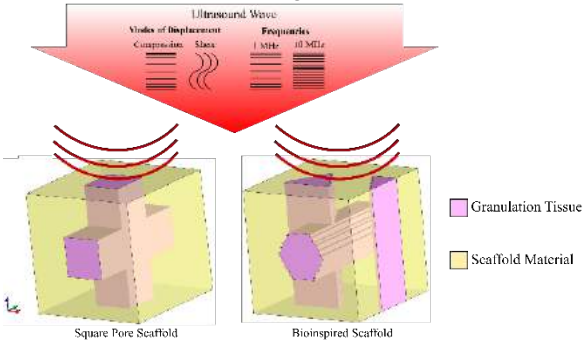


**Figure 1: Ultrasonically stimulated tissue scaffolds**

## METHODS

The finite element method (FEM) simulations of the scaffolds were performed using FEBio [8]. The pores of the scaffold, whose diameters are 400 μm, are filled with granulation tissue and the structure undergoes ultrasound stimulation from the top of the scaffold with the wave propagating in the negative *y*-direction with an amplitude of 0.1 μm, as seen in Figure 1. We test the effect of ultrasound frequencies of 1 MHz and 10 MHz on the tissue growth, as well as the ultrasound wave type between compression and shear waves. The scaffold is modeled as an isotropic solid while the granulation tissue is modeled as a biphasic material of an isotropic solid and Newtonian fluid. Table 1 shows the material properties used in the FEM simulations.

**Table 1: Material Properties of the Finite Element Models**

| Material | Scaffold | Granulation Tissue |
|---|---|---|
| Elastic Modulus, $E$ (MPa) | 1000 | 0.2 |
| Poisson's Ratio, $\nu$ | 0.3 | 0.167 |
| Solid Density, $\rho_{solid}$ (kg/m$^3$) | 400 | 300 |
| Fluid Density, $\rho_{fluid}$ (kg/m$^3$) | NA | 997 |
| Solid Volume Fraction | NA | 0.2 |
| Permeability, (m$^4$/N/s) | NA | constant, 1 x $10^{-14}$ |

The tissue growth algorithm used is from Byrne et al. [9] and is written in MATLAB [10]. Initially, the granulation tissue is randomly seeded at 1% with mesenchymal stem cells (MSCs). These stem cells can then proliferate or differentiate into fibroblasts (fibrous tissue), chondrocytes (cartilage), or osteoblasts (bone) based on the mechanical stimulus. We test the effect of initial MSC distribution on the tissue growth by testing a second random initial MSC distribution, and by localizing random MSCs to be randomly distributed near the bottom of the bioinspired scaffold. Visualization of the differentiated tissue distributions is done using Paraview [11].

## RESULTS

Figure 2 (a) shows the maximum bone tissue growth after 60 days for the bioinspired and square pore scaffolds. Increasing the wave frequency from 1 MHz to 10 MHz increases the amount of bone formation. A compression wave also produces more bone compared to a shear wave for both scaffolds. Overall, the square scaffold produces more bone than the bioinspired scaffold. From Figure 2 (b) this is likely due to more cartilage and fibrous tissue in the bioinspired scaffold. For a compression ultrasound wave of 10 MHz frequency, the calculated percent difference in bone tissue formation between the two scaffolds is 4.7%.

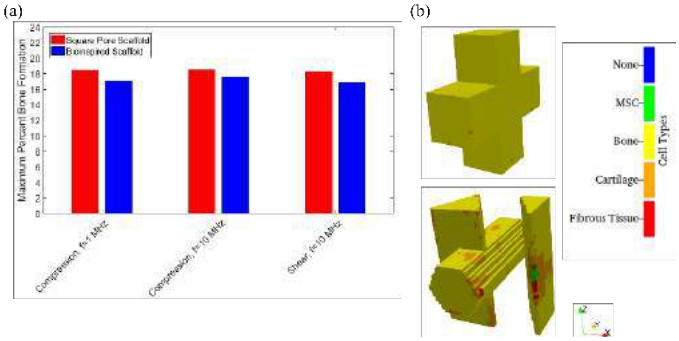


**Figure 2: Square pore and bioinspired scaffolds: (a) Maximum bone formation, (b) Tissue distribution for stimulation by compression wave ultrasound with f = 10 MHz**

Figure 3 shows the maximum bone formation rate for the two scaffolds. For all ultrasound parameters the bioinspired scaffold has a lower maximum bone formation rate than the square pore scaffold. For a compression ultrasound wave of 10 MHz frequency, the calculated percent difference in maximum bone tissue formation rate between the two scaffolds is 41.2%.

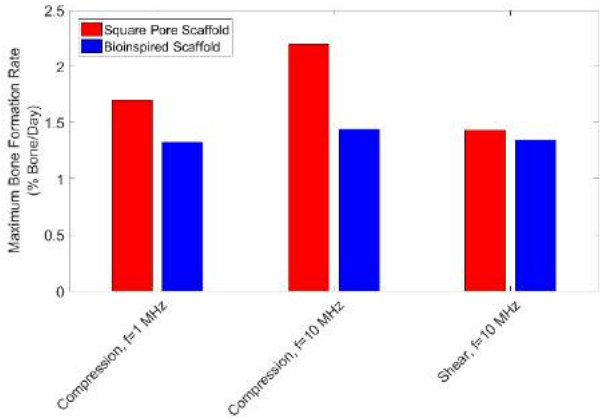


**Figure 3: Maximum bone formation rate for square pore and bioinspired scaffolds**

Figure 4 shows the effect of the initial MSC distribution on bone growth in the bioinspired scaffold stimulated by a compression ultrasound wave with a frequency of 1 MHz. The two random MSC distributions have a negligible difference in maximum growth rate and bone formation. In contrast, localizing the MSC distribution significantly reduces the maximum growth rate and percent bone formation. Between the localized and random MSC distributions there is a calculated percent difference of 178.3% in maximum growth rate and 128.7% in maximum percent bone formation. This is likely due to the amount of space available for the MSCs to proliferate, and the level of mechanical stimulation they receive to differentiate, as can be seen in the tissue distributions in Figure 4 (c).

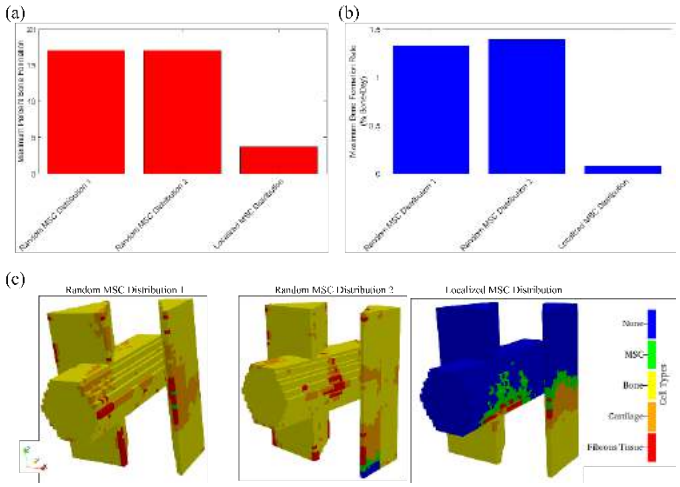


**Figure 4: Effect of MSC distribution: (a) Maximum bone formation, (b) maximum bone formation rate, (c) tissue distribution**

## DISCUSSION

This study demonstrates that, while the bone tissue growth in the bioinspired scaffolds is slower, it can produce amounts of bone tissue comparable to the square pore scaffold. Previous studies show the bioinspired scaffold also has a higher fracture resistance and ultrasound wave transmission than the square pore scaffold, making the bioinspired structure ideal for ultrasonically stimulated tissue scaffolds to enhance cell growth. Our study further shows that the initial MSC seeding of the tissue scaffolds can significantly affect the growth rate and amount of tissue formation. This warrants further computational and experimental study on controlling MSC seeding of tissue scaffolds, and optimal seeding patterns to maximize tissue growth rate amount.


## ACKNOWLEDGEMENTS

MF and AKN would like to thank support from the 21st Century Professorship grant from Department of Mechanical Engineering, University of Arkansas, and the resources from the Arkansas High Performance Computing Center.


## REFERENCES


[1] Loving, J., Fielder, et al., *J Nondestructive Eval*, 37:43, 2018.
[2] Zhao, L., et al., *Applied Acoustics*, 153:102-109, 2019.
[3] Grabec, T., et al., *Wave Motion*, 92:102417, 2020.
[4] Aliabouzar, M., et al., *Biomed Mater*, 13. 2018.
[5] Zhang, S., et al., *J of Biomed Mater Research Part B: Applied Biomaterials*, 107:1329-1351. 2019.
[6] Gu, Y., et al., *Comp Methods in Biomech and Biomed Eng*, 21:703-711. 2018.
[7] Fielder M., and Nair A. K., *J of the Mech Behavior of Biomed Mater*, 105065. 2021.
[8] Maas, S.A. et al., *J Biomech Eng-T Asme*, 134:011005, 2012.
[9] Byrne, D.P., et al., *Biomaterials*, 28:5544-5554, 2007
[10] 1. MATLAB. version 9.1 (R2016b). Natick, Massachusetts: The MathWorks Inc.; 2016.
[11] Ahrens, James, Geveci, Berk, Law, Charles, ParaView: An End-User Tool for Large Data Visualization, Visualization Handbook, Elsevier, 2005, ISBN-13: 978-0123875822

# VESEEL WALL ENHANCEMENT IS ASSOCIATED WITH INCREASED WALL STRESS IN INTRACRANIAL ANEURYSMS

**Sricharan S. Veeturi (1,2), S. Mostafa Mousavi J. S (1,2), Ammad A. Baig (2,3), Andre Monteiro (2,3), Adnan H. Siddiqui (2,3), Vincent M. Tutino (1,2,3,4,5)**

(1) Department of Mechanical and Aerospace Engineering, University at Buffalo, Buffalo, NY, USA
(2) Canon stroke and vascular research center, Buffalo, NY, USA
(3) Department of Neurosurgery, University at Buffalo, Buffalo, NY, USA
(4) Department of Biomedical Engineering, University at Buffalo, Buffalo, NY, USA
(5) Department of Pathology and Anatomical Sciences, University at Buffalo, Buffalo, NY, USA

## INTRODUCTION

Vessel wall enhancement has emerged as a potential imaging biomarker for risk stratification of intracranial aneurysms (IAs). This is a phenomenon wherein the presentation of the aneurysm wall on contrast-enhanced MRI (CE-MRI) exhibits markedly higher signal intensity as compared to its presentation on the baseline or non-enhanced MRI (NE-MRI). Vessel wall enhancement (VWE) of the aneurysm wall has been correlated with inflammation in the IA, as well as growth and rupture [1]. However, the underlying tissue mechanobiology in regions of high VWE, which could be related to rupture, remain poorly understood.

Stress in the aneurysm wall tissue could be related to the VWE phenomenon, as aneurysm growth and remodeling are thought to be driven, in part, by vascular smooth muscle responses to abnormal arterial stresses [2]. To measure mechanical stress in the IA wall, finite element analysis (FEA) is a particularly useful tool. Previous studies have shown that IAs exhibiting VWE had a significantly higher 95$^{th}$ percentile wall tension as compared to IAs that did not, showing a potential correlation between mechanical forces in the aneurysm wall and VWE [3]. However, their model used generic assumptions about the internal pressure as well as the IA wall thickness. Variations in thickness and pressure could influence stress distributions in the IA.

In this preliminary study, we investigate the effect of using patient specific internal pressure as well as patient specific wall thickness on the potential correlation between VWE and the Von-mises stress in the aneurysm wall.

## METHODS

In the current study, approved by the IRB (Study 00004370), we collected patient specific 3D Time of flight TOF-MRA image as well as T1 weighted NE-MRI and CE-MRI. The MRA image was used to segment and generate 3D stereolithographic (STL) geometry file for the aneurysm. We then used OpenFOAM V6 to perform hemodynamics as described in previous studies [3]. Assuming the time-averaged inlet pressure to be 90 mm Hg, we generated pressure maps on the IA wall, which were used as loads in FEM simulations.

We then used the NE- and CE-MRI to manually reconstruct the aneurysm wall. This was then used as a point cloud in an in-house MATLAB code (R2021) to generate thickness for each triangulated surface on the STL file. The reconstructed volume of the aneurysm wall was used as input for the FEA simulation. We assumed a location based uniform thickness of 0.58 mm for the parent artery [5].

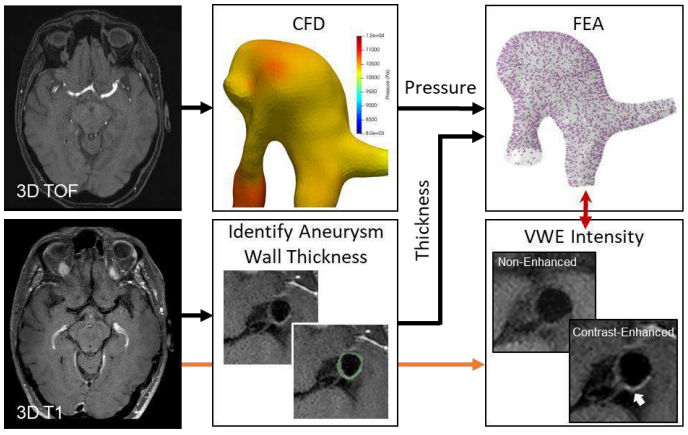


**Figure 1: Modeling Workflow.** From 3D TOF images we reconstruct aneurysm geometry, find blood flow characteristics using CFD, and implement variable pressure on the geometry. From 3D T1 imaging, we find aneurysm thickness and map it on aneurysm geometry. Also, from latter imaging modality we find VWE and compare it to FEA results.

We used Abaqus CAE/2019 to perform FEA models on the aneurysm in four different models: (1) uniform thickness and uniform pressure of 90 mm Hg (UTUP) (2) patient-specific thickness and uniform pressure (PTUP) (3) uniform thickness and patient-specific pressure (UTPP) (4) patient-specific thickness and patient-specific pressure (PTPP). Aneurysm wall was modeled as shell elements. Material models follow a nonlinear hyperelastic model describe previously [6]. For the variable pressure cases, average pressure of one cardiac cycle at different coordinates of aneurysm wall was withdrawn from CFD analysis and implemented on the inside of aneurysm wall. For the uniform pressure, we used the values from a previous study [7]. To map the variable thickness, nodal distribution was used.

Finally, we used previously established method to map the MRI signal intensity in CE-MRI onto the aneurysm wall [8]. We used the intensity at the genu of corpus callosum for normalization of MRI signal intensity ($CC_{ratio}$). Enhancing regions in the sac were defined as areas with $CC_{ratio}>1$. We performed univariate analysis to investigate the differences in Von-Mises stress in enhancing and non-enhancing regions in all the 4 FEA models after isolating the aneurysm sac manually. Furthermore, we also evaluated the potential correlation between $CC_{ratio}$ and Von-mises stress in all the models.

## RESULTS

The aneurysm sac was 8.3 mm in size and was located at the middle cerebral artery. The thickness map generated is shown in figure 3A. We observed that enhancing regions had a significantly higher wall thickness as compared to non-enhancing regions ($p<0.001$) which is also shown in previous literature.

In our FEA analysis, we found that enhancing regions had significantly higher Von-Mises stress as compared to non-enhancing regions ($p<0.001$) in all the models. Qualitatively, we observe that the type of pressure loading used has negligible effect on the stress contours ($R^2>0.99$) in both fixed thickness as well as variable thickness models. However, using aneurysm specific thickness values does indeed have an effect on the stress distributions ($R^2=0.54$) as shown in figure 2.

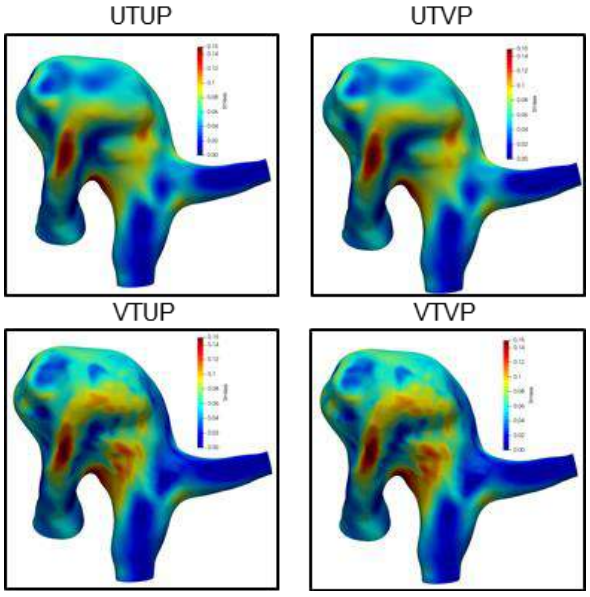


**Figure 2: Contours of Von-Mises stress distribution across different models.** We observed no noticeable change in the stress values when varying pressure was used across the aneurysm as compared to generic uniform pressure loading. However, we do find changes in stress values when varying values of wall thickness are used.

We also found that enhancing regions had significantly higher stress values than non-enhancing regions as was found by previous studies [3]. However, we found that there was only a weak linear correlation between $CC_{ratio}$ values and Von-mises stress in all the models. The correlation of intensity and stress values for different models was as follows: UTUP: 0.094, UTPP: 0.096, PTUP: 0.139 and PTPP: 0.14.

## DISCUSSION

In this study we developed a pipeline for investigation of the potential relationship between aneurysm wall stress and the vessel wall enhancement phenomenon. We found that enhancing regions in the aneurysm had a significantly higher stress than non-enhancing regions. VWE is an indication of inflammatory cell infiltration and neovascularization which have been associated with aneurysm instability and rupture. Hence, it is possible that the regions that have high stress and exhibit enhancement could indicate a damaged wall which is under high stress. Eventually, these regions may degrade further and cause an imbalance in forces which could lead to rupture of the aneurysm. Additionally, we also observed that thickness of the aneurysm has an effect on the stress distributions and using varying pressure does not. Thus, using patient specific aneurysm thickness is advised when possible.

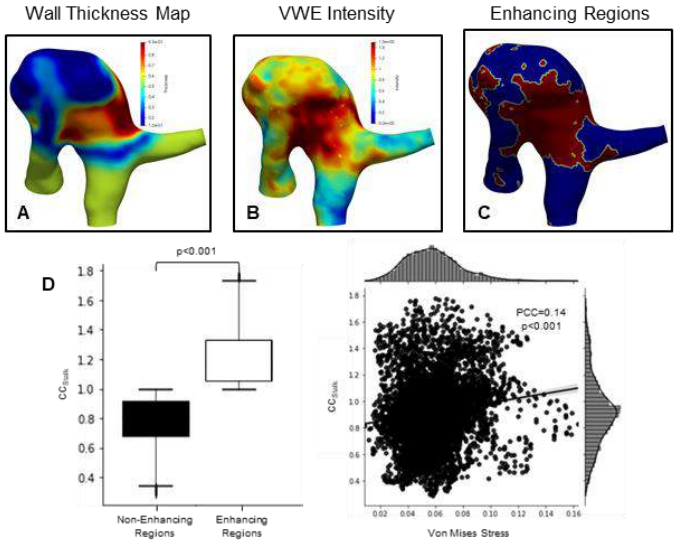


**Figure 3: Contours of wall thickness, VWE mapped intensity and enhancing regions. A).** Heat map of wall thickness. We observed higher thickness in enhancing regions. **B).** Heat maps of mapped vessel wall intensity ($CC_{ratio}$) across the aneurysm. **C).** Visualization of enhancing and non-enhancing regions in the aneurysm. **D).** Univariate analysis and correlation plots of stress values in enhancing and non-enhancing regions.

## REFERENCES

[1] Edjlali, M et al., *Neuroradiology*, 289:181-187, 2018.
[2] Frosen, J et al., *Stroke*, 35:2287-2293, 2004
[3] Galloy, A et al., *Frontiers in Neurology*, 12, 2021
[4] Veeturi, SS et al., *Royal society Open Science*, 8, 2021
[5] Hartevald, A et al., *Data in Brief*, 19: 6-12, 2018
[6] Shang, EK et al., *Circulation*, 128: S157-S162, 2013
[7] Steinman, DA et al., *Journal of Biomechanical Engineering*, 135, 2013
[8] Veeturi, SS et al., *Diagnostics*, 11: 1742, 2021

SB³C2022
Summer Biomechanics, Bioengineering and Biotransport Conference
June 20-23, Eastern Shore, MD, USA

# AN ULTRASOUND BASED ONE-DIMENSIONAL MODELING FRAMEWORK FOR THE ASSESSMENT OF PERIPHERAL ARTERIAL DISEASE

**Milan Gillissen (1), Frans N. van de Vosse (2), Marc R.H.M van Sambeek (1,3), Richard G.P. Lopata (1)**

(1) Laboratory for Photoacoustics and Ultrasound, University of Technology, Eindhoven, Noord-Brabant, The Netherlands
(2) Cardiovascular Biomechanics group, University of Technology, Eindhoven, Noord-Brabant, The Netherlands
(3) Catharina Hospital, Eindhoven, Noord-Brabant, The Netherlands

## INTRODUCTION

Cardiovascular diseases (CVDs) are a leading cause of death, representing an estimated 32% of all global deaths in 2019. It is a group of diseases that involve the heart and the circulatory system, including peripheral artery disease (PAD) which affects over 230 million people worldwide. With atherosclerosis the most common underlying mechanism, lower extremity peripheral arterial occlusive disease (PAOD) is an increasingly common condition in all countries. Currently, the length of the occlusion is used as criteria for endovascular therapy or surgical bypass [1]. However, main challenges of endovascular therapy include the durability of stents in the femoro-popliteal region where the artery is very mobile and the more typical restenosis, which can occur within six to twelve months [2]. Several studies have shown that finite element analysis (FEA) can predict restenosis regions in different arteries [3, 4]. Despite promising results, these patient-specific models are not used in the clinical setting yet. The current computed tomography (CT) or magnetic resonance (MR) approaches suffer from several drawbacks, e.g. ionizing radiation and high cost. Moreover, patient-specific material properties are unavailable in these approaches. The most important drawback of US, besides the low contrast compared to CT and MR, is the limited field-of-view (FOV). An in-house developed framework is demonstrated, which segments US images automatically, and meshes the geometries obtained for computational fluid dynamics (CFD) analysis. We propose a framework based on time-resolved two-dimensional ultrasound (US), which tackles the aforementioned disadvantages as well as acquire the vessel's motion during the cardiac cycle. Furthermore, a reduced order model is created based on the segmented geometries which provides more information about the circulatory system outside the bounds of the obtained US images.

## METHODS

Ultrasound (US) scans were made using a MyLab70 scanner (Esaote Europe B.V., Maastricht, The Netherlands). The images were automatically segmented by an in-house developed framework, created in Matlab (2020b, Mathworks Inc., Natick, MA, USA). These segmentations were extended to ensure flow was fully developed at the measured inlet. The final coordinates encapsulating the geometry were imported into Python (3.7, Python Software Foundation, Wilmington, DE, USA) where the Visualisation Toolkit (8.1.2, Kitware Inc., Clifton Park, NY, USA) was used to construct a surface from the scattered coordinates. Finally, the extended geometry was converted to a 3D tetrahedral volume mesh in Ansys (Fluent 19.2, Ansys Inc., Canonsburg, PA, USA) by using the built-in Fluent meshing tool.

To create the reduced order, one-dimensional (1D), model the cross-sectional area from the segmented geometry was used. The minimum calculated area, along with the mean of the healthy in- and outlet areas were used to define a one-dimensional stenosis element which is based on the work of Heinen et al. [5]. This element was placed in the Boileau model [6], in the middle of the scanned vessel. The full Boileau model can be seen in Figure 1. The pressure waveform resulting from the one-dimensional model was used to define two new parameters, the stenosis-brachial index (SBI, Equation 1) and the ankle-stenosis index (ASI, Equation 2). These parameters provide insight of the rest of the circulatory system and any other possible anomalies. The pressure at positions 1 and 2 are represented by the peak systolic pressure, proximal to the stenosis and distal to the stenosis respectively.

$$SBI = p_1/p_{brachial} \quad (1)$$

$$ABI = p_{ankle}/p_2 \quad (2)$$

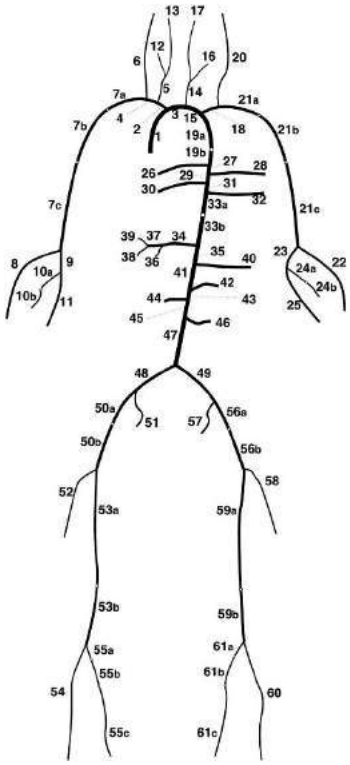

**Figure 1: Topology of the Boileau [5] model.**

## RESULTS

Preliminary results (Table 1) show that the calculated pressure drop in 1D is not in the same order as the calculated pressure drop from a three-dimensional computational fluid dynamics simulation. The proximal pressure is high for the 3D model with respect to the 1D model. The distal pressure is in the same order for both models. Furthermore, the newly introduced SBI and ASI are calculated and displayed. The SBI is high for the 3D model, and within acceptable range for the 1D model. The ABI values are in acceptable range for both models.

## DISCUSSION

Although these first results of the models do not coincide proximal to the stenosis, it does show the feasibility of the technique in an ideal geometry. The high $p_1$ and resulting SBI value for the 3D model could be due to the of the rigidness of the model, a smoothed flow waveform or a parabolic velocity waveform which all will be addressed in the near-future. The ASI values for both models indicate that there are no other stenotic areas in the distal circulatory system. This coincides with the fact that only one stenosis has been implemented in this example.

**Table 1: Preliminary results of both the three-dimensional model as the one-dimensional model. Pressures and pressure drop are in mmHg. SBI, ASI en ABI are dimensionless.**

| Model | $p_1$ | $p_2$ | $\Delta p$ | SBI | ASI | ABI |
|---|---|---|---|---|---|---|
| 3D | 352 | 89 | 263 | 2.82 | 0.82 | 0.58 |
| 1D | 150 | 76 | 74 | 1.20 | 0.97 | 0.58 |

## REFERENCES


[1] Victor Aboyans, Jean-Baptiste Ricco, Marie-Louise E.L. Bartelink, Martin Björck, Marianne Brodmann, Tina Cohn-ert, Jean-Philippe Collet, Martin Czerny, Marco De Carlo, Sebastian Debus, Christine Espinola-Klein, Thomas Kahan, Serge Kownator, Lucia Mazzolai, A. Ross Naylor, Marco Roffi, Joachim R¨other, Muriel Sprynger, Michal Tendera, Gunnar Tepe, Maarit Venermo, Charalambos Vlachopoulos, Ileana Desormais, Document Reviewers, Petr Widimsky, Philippe Kolh, Stefan Agewall, Héctor Bueno, Antonio Coca, Gert J. De Borst, Victoria Delgado, Florian Dick, Cetin Erol, Marc Ferrini, Stavros Kakkos, Hugo A. Katus, Juhani Knuuti, Jes Lindholt, Heinrich Mattle, Piotr Pieniazek, Massimo Francesco Piepoli, Dierk Scheinert, Horst Sievert, Iain Simpson, Jakub Sulzenko, Juan Tamargo,Lale Tokgozoglu, Adam Torbicki, Nikolaos Tsakountakis, Jos´e Tu˜n´on, Melina Vega de Ceniga, Stephan Windecker, and Jose Luis Zamorano. Editor's Choice – 2017 ESC Guidelines on the Diagnosis and Treatment of Peripheral Arterial Diseases, in collaboration with the European Society for Vascular Surgery (ESVS).European Journal of Vascular and Endovascular Surgery, 55(3):305–368, March 2018. ISSN 10785884. doi: 10.1016/j.ejvs.2017.07.018. URL https://linkinghub.elsevier.com/retrieve/pii/S1078588417304549.

[2] Dario Buccheri, Davide Piraino, Giuseppe Andolina, and Bernardo Cortese. Understanding and managing in-stent restenosis: a review of clinical data, from pathogenesis to treatment. Journal of Thoracic Disease, 8(10), October 2016.ISSN 2077-6624, 2072-1439. doi: 10.21037/jtd.2016.10.93. URL https://jtd.amegroups.com/article/view/10071.Publisher: AME Publishing Company.

[3] Nicolas Benard, Robert Perrault, and Damien Coisne. Flow through a stented coronary artery: CFD prediction of restenosis regions. Journal of Biomechanics - J BIOMECH, 39, December 2006. doi: 10.1016/S0021-9290(06)85542-9.

[4] Jonathan Murphy and Fergal Boyle. Predicting neointimal hyperplasia in stented arteries using time-dependant computational fluid dynamics: A review. Computers in Biology and Medicine, 40(4):408–418, April 2010. ISSN0010-4825. doi: 10.1016/j.compbiomed.2010.02.005. URL https://www.sciencedirect.com/science/article/pii/S00104825100002X

[5] Etienne Boileau, Perumal Nithiarasu, Pablo J. Blanco, Lucas O. M¨uller, Fredrik Eikeland Fossan, Leif Rune Hellevik, Wouter P. Donders, Wouter Huberts, Marie Willemet, and Jordi Alastruey. A benchmark study of numerical schemes for one-dimensional arterial blood flow modelling: BENCHMARK OF NUMERICAL SCHEMES FOR 1D BLOOD FLOW MODELLING. International Journal for Numerical Methods in Biomedical Engineering, 31(10):e02732, October 2015. ISSN 20407939. doi: 10.1002/cnm.2732. URL https://onlinelibrary.wiley.com/doi/10.1002/cnm.2732.

[6] S. G. H. Heinen, D. A. F. van den Heuvel, J. P. P. M. de Vries, F. N. van de Vosse, T. Delhaas, and W. Huberts. A geometry-based model for non-invasive estimation of pressure gradients over iliac artery stenoses. Journal of Biomechanics, 92:67–75, July 2019. ISSN 0021 9290. doi: 10.1016/j.jbiomech.2019.05.030. URL https://www.sciencedirect.com/science/article/pii/S002192901930362 8

SB³C2022
Summer Biomechanics, Bioengineering and Biotransport Conference
June 20-23, Eastern Shore, MD, USA

# RADIATION CYSTITIS RESULTS IN COMPROMISE URINARY FUNCTION AND DECREASED BLADDER DISTENSIBILITY

**Bernadette M.M. Zwaans[1,2], Marissa R. Grobbel[3], Laura E. Lamb[1,2], Sara A. Roccabianca[3]**

(1) Department of Urology, Beaumont Health System, Royal Oak, MI
(2) Oakland University William Beaumont School of Medicine, Rochester, MI
(3) Department of Mechanical Engineering, Michigan State University, East Lansing, MI

## INTRODUCTION

Radiation cystitis (RC) is a chronic bladder condition characterized by frequent urination, nocturia, urinary incontinence, pelvic pain, and hematuria. RC is the result of radiation therapy used to treat pelvic cancers. such as prostate, cervical, colorectal, and ovarian cancer. Approximately 10% of cancer survivors treated with pelvic radiation therapy will develop RC [1]. Current treatment options are focused on arresting bleeding, however, no therapies are currently available to treat other symptoms of RC, like urinary frequency and nocturia [2-4].

We previously developed a preclinical RC model that mimics the human condition [5,6]. In this model, we have shown that radiation exposure results in increased deposition of collagen (i.e., fibrosis) within the bladder detrusor muscle. In irradiated bladders, the extracellular matrix (ECM) consists of a higher concentration of collagen type I and III fibers when compared to controls. By 12 months post-irradiation, radiation exposure still resulted in increased expression of collagen I in comparison to littermate controls, supporting the notion that RC is a progressive condition [5].

It has been suggested that bladder fibrosis alters bladder compliance, resulting in lower urinary tract symptoms such as urinary frequency and nocturia [7]. However, no study has been done to investigate changes in mechanical properties of the bladder in response to radiation. This study aims to identify alterations to the mechanical behavior of urinary bladder tissue following radiation exposure in a murine model. Specifically, we aim to characterize these changes through mechanical testing and analysis, by employing a continuum mechanics model to estimate material parameters.

## METHODS

*Radiation cystitis mouse model.* This study was performed, in compliance with the NIH Guide for the Care and Use of Laboratory Animals. RC was induced in the mouse bladder as previously described by our group [5] (untreated mice were also anesthetized for a consistent amount of time). Forty 8-week old female C57Bl/6 mice were purchased from Charles River (Wilmington, MA). Mice were randomly assigned to an irradiated or control treatment group (n = 20/group). Radiation was delivered to the mouse bladder using the Small Animal Radiation Research Platform (SARRP) using a two-beam approach. Mice received a single dose of 40 Gy, evenly divided over the two beams, using a 5 x 5 collimator.

*Void Spot Assay.* Bladder function was assessed at baseline, and 3- and 6 months post irradiation using the Void Spot Assay [5]. In short, mice were singly housed for 4 hours in a cage lined with thick filter paper. After 4 hours, the filter paper was collected and urine spots were visualized under TransUV light. Using Fuji Software, urine spots were counted, and total and average void volumes were calculated. Statistical significance was determined through 2-way ANOVA followed by Bonferroni's post-hoc multiple comparison test.

*Mechanical testing.* At the same time points, animals were euthanized, bladders collected and cut into ring-shaped samples. After decellularization [8], we performed uniaxial mechanical stretch test. Cyclic loading, adapted from a previously published protocol [9], was applied to the samples as follows (all at a strain rate of 0.01 s-1): 5% stretch for 10 cycles (preconditioning), 10% stretch for 5 cycles, 15% stretch for 5 cycles, and 20% stretch for 5 cycles. Before each set of cycles, a pre-load of 2 ± 0.25g was placed onto the sample. Samples were assumed to be incompressible and isotropic, resulting in a deformation gradient of $\boldsymbol{F} = diag\left[\lambda; {}^{1}/_{\sqrt{\lambda}}; {}^{1}/_{\sqrt{\lambda}}\right]$ where $\lambda$ is the stretch in the direction of testing (i.e., circumferential).

*Constitutive modeling framework.* For each tested sample, the final loading curve of the last loading cycle (i.e., target stretch of 20%) was used for mechanical analysis. Tissue mechanical behavior was described employing a two-parameter, exponential constitutive model [10]

$$W = c\{exp[k(I_1(\boldsymbol{C}) - 3)] - 1\}$$

where $c$ and $k$ are material parameters ($c$ has the dimension of a stress and $k$ is nondimensional), $\boldsymbol{C}$ is the right Cauchy-Green deformation tensor defined as $\boldsymbol{C} = \boldsymbol{F}^{\boldsymbol{T}}\boldsymbol{F}$, and $I_1(\boldsymbol{C}) = tr(\boldsymbol{C})$ is $\boldsymbol{C}$ first invariant. Following, the definition of Cauchy stress for an incompressible material is:

$$\boldsymbol{T} = -p\boldsymbol{I} + 2\boldsymbol{F}\frac{\partial W}{\partial \boldsymbol{C}}\boldsymbol{F}^{\boldsymbol{T}}$$

where $p$ is a Lagrange multiplier and $\boldsymbol{I}$ is the identity tensor.

## RESULTS

At 3 months post-radiation, there were no significant differences between the untreated and irradiated tissues mechanical behavior (**Fig. 1A**). At 6 months, the stress-stretch curve showed an upward shift between irradiated and untreated tissue, indicating a decrease in distensibility of the ECM induced by radiation (**Fig. 1B**).

The material parameters estimated support this finding. While there were no changes to parameter $c$ (**Fig. 2A**), parameter $k$ was higher in the irradiated tissue compared to untreated tissue (**Fig. 2B**). This result was slight at the 3 months timepoint ($P < 0.1$) and significant at the 6 months timepoint ($P < 0.05$). An increase in $k$ is consistent with an increase in tissue stiffness for larger values of stretch/stress.

To determine if irradiation-induced bladder stiffness alters bladder function, we performed Void Spot Assays. Over a four-hours period, mice exposed to irradiation had an increased number of urine spots (**Fig. 3A**) accompanied by a decrease in voided volume per spot (**Fig. 3B**) in comparison to littermate controls. The change in micturition behavior started at 3-months post-irradiation ($P < 0.1$) and became significant by 6-months ($P < 0.05$).

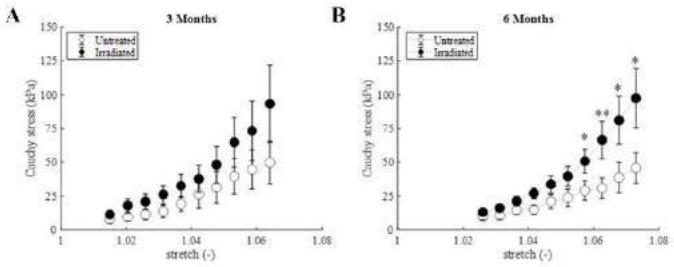


**Figure 1: Average ± SE stress-stretch curves for bladders ECM from untreated (empty) and irradiated (filled) animals at 3- (A) and 6-months (B) post-treatment; *P < 0.1, **P < 0.05 when comparing untreated and treated animals at each time point.**

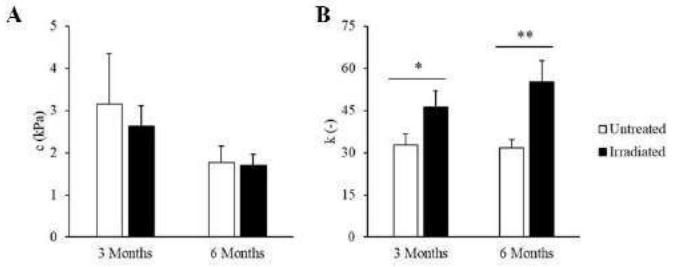


**Figure 2: Average ± SE constitutive model parameters, $c$ (kPa) and $k$ (-), calculated for irradiated and untreated animals at (A) 3- and (B) 6-months post-treatment; *P < 0.1, **P < 0.05 when comparing untreated and treated animals at each time point.**

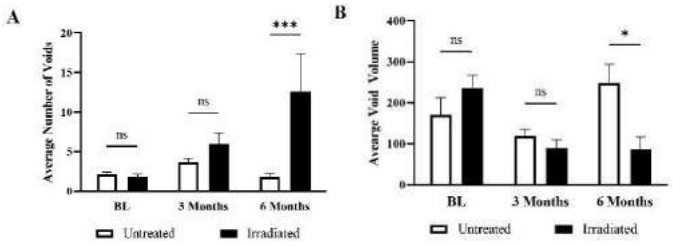


**Figure 3: Average ± SE of (A) number of voids and (B) void volume in untreated and irradiated at 3- and 6-months post-treatment; *P < 0.1, **P < 0.05 when comparing untreated and treated animals at each time point.**

## DISCUSSION

Radiation treatment can impact bladder function and induce lower urinary tract dysfunction in pelvic cancer survivors [1-4]. We sought to determine if radiation altered the mechanical properties of the bladder in response to stretch in a murine model. This study specifically examined ECM remodeling and mechanical behavior of the bladder ECM. To do so, we measured several mechanical and physiological parameters.

Average stress-stretch curves of the irradiated animals showed overall lower distensibility as compared to untreated (**Fig. 1 and 2**). This was accompanied by the constitutive model parameters analysis, which showed no changes to parameter $c$, which dominates mechanical behavior in the low-stiffness region, and at the same time highlighted an increase of the parameter $k$ in irradiated tissues, which dominates behavior in the high-stiffness region. Overall, these results indicate that RC causes a progressive increase in stiffness in the ECM of the bladder that is focused on the upper-end of the stress-stretch curve, when the bladder would be nearing maximum distension from urine filling.

This type of alteration to the stress-stretch behavior of the ECM could be indicative of a decreased bladder capacity, a common hallmark of RC [11], as the tissue is reaching maximum in vivo stress at a much lower stretch. This is supported in that the irradiated mice also voided smaller volumes of urine per void event, without significantly changing their total urine output (**Fig. 3B**).

This study is the first to show the mechanical properties of the bladder, as well as bladder function, are altered after irradiation. Radiation, and subsequent changes in ECM content, significantly increases the stress on bladder tissue as the bladder fills with urine and subsequently stretches, resulting in potentially reduced functional bladder capacity and more frequent urination.


## ACKNOWLEDGEMENTS

Funding: NIH K01DK114334 (BMMZ) and by NIH P20DK127554 (BMMZ, SR).


## REFERENCES


[1] Martin, SE et al., *Urology*, 131:190-195, 2019.
[2] Zwaans, BMM et al., *Int Urol Nephrol*, 50(10):1745-1751, 2018.
[3] Smit, SG et al., *Nat Rev Urol*, 7(4):206-214, 2010.
[4] Mendenhall, WM et al., *Am J Cli. Oncol*, 38(3):331-336, 2015.
[5] Zwaans, BMM et al., *Phys reports*, 8(4):e14377, 2020.
[6] Zwaans, BMM et al., *Adv Radiat Oncol*,1(4):333-343, 2016.
[7] Ikeda, Y et al., *Neurour Urodyn*, 37(8):2441-2451, 2018.
[8] Grobbel, MR et al.,*Biomech Model Mechanob*,17(4):985-999, 2018.
[9] Grobbel, MR et al., *Experimental Mechanics*, 61(1); 191-201, 2021.
[10] Delfino, A et al., *J of Biomech*, 30(8):777-786, 1997.
[11] Wit, EM et al., *Nat Rev Urol*, 11(2):110-117, 2014.

SB³C2022
Summer Biomechanics, Bioengineering and Biotransport Conference
June 20-23, Eastern Shore, MD, USA

# ANALYSIS OF UPPER AIRWAY FLOW DYNAMICS IN INFANTS WITH ROBIN SEQUENCE USING 4-DIMENSIONAL COMPUTED TOMOGRAPHY AND COMPUTATIONAL FLUID DYNAMICS MODELING

**Michael Barbour (1), Clare Richardson (2,3), Michael Bindschadler (4), Seth Friedman (5), Randall Bly (2,3), John P. Dahl (2,3), Alberto Aliseda (1)**

(1) Department of Mechanical Engineering, University of Washington, Seattle, WA, USA
(2) Department of Otolaryngology-Head and Neck Surgery, University of Washington, Seattle, WA, USA
(3) Division of Pediatric Otolaryngology, Seattle Children's Hospital, Seattle, WA, USA
(4) Department of Radiology, Seattle Children's Hospital, Seattle, WA, USA
(5) Center for Clinical and Translational Research, Seattle Children's Hospital, Seattle, WA, USA

## INTRODUCTION

Patency of the upper airway (UA) is required for critical functions such as breathing and speech production. Under healthy conditions, minimal effort is required to drive airflow through the UA, but even minor obstructions can significantly increase breathing resistance [1]. Robin Sequence (RS) is a congenital craniofacial anomaly characterized by small mandible, posteriorly displaced tongue, and subsequent upper airway obstruction (UAO). This is associated with significant morbidity and mortality in up to 11% of patients [2].

Reliable localization of UAO and characterization of UAO severity are critical to determine clinical airway management strategies [2]. Currently, there is no gold-standard for severity assessment and, therefore, severity is based on subjective evaluations of available diagnostic studies. Additionally, severity is typically assessed from anatomic features characterized via static imaging modalities which do not accurately represent the highly dynamic respiratory cycle [3] and provide no quantitative information on airflow dynamics.

Computational fluid dynamics provides a means of investigating and quantifying the airflow in healthy and diseased airways [1,4]. Four-dimensional computed tomography (4DCT) obtains multiple 3D images throughout the respiratory cycle, resolving the time-evolution of the airway's caliber. In this study, we combine 4DCT and CFD to analyze airflow dynamics in RS infants. By quantifying the fluid mechanics environment of RS patients, we provide a method for quantitative assessment of UAO severity, which is used to identify locations of maximum obstruction and risk-stratify patients. We hypothesize that these advanced modeling tools will improve the clinical understanding and management of UAO in RS patients.

## METHODS

Airflow dynamics were analyzed in five infants with RS, between the ages of 0-6 months. 4DCT scans were obtained with 3D reconstructions performed every 0.1s (SOMATOM Force Dual SourceCT, Siemens, Germany). Between 1 and 3 respiratory cycles were obtained for each patient, and each 3D image was segmented to obtain airway geometries extending through the upper trachea.

An idealized sinusoidal breathing waveform was generated for each patient using a tidal volume based on weight at the time of the scan and the respiratory period, calculated from the 4DCT image sequences. The point of peak exhalation in the idealized respiratory cycle was synchronized with the location of maximum oropharynx volume [5]. Quasi-steady CFD simulations of peak inhalation and peak exhalation were run to evaluate conditions of maximum respiratory resistance [6]. Second-order, unsteady RANS simulations were performed in StarCCM+ (v16, Siemens, PLM Software, Plano, TX, USA) with a K-$\omega$ SST model. Polyhedral meshes with approximately 2.5 million cells were generated for each patient at the airway geometries corresponding to peak inhalation and exhalation. Mass flowrates are prescribed at the trachea based on values computed from the respiratory waveform timepoints corresponding to peak inhalation and exhalation. Unsteady simulations were carried out for 0.15s with a dt of 5E-5s. Computed airflow metrics were averaged over the last 0.075s.

For each patient, breathing resistance ($R = \Delta P \,/\, Q$), where $\Delta P$ and $Q$ are the inlet-to-outlet pressure drop and flowrate respectively, maximum velocity, and viscous dissipation ($\Theta$) were computed. Viscous dissipation is defined as:

$$\Theta = 0.5\,\mu_t \int S : S\, dV + \int \rho\epsilon\, dV \qquad (1)$$

Where $\boldsymbol{S}$, the stress tensor, is defined as $[\boldsymbol{\nabla u} + \boldsymbol{\nabla u^T}]$, $\boldsymbol{\mu_t}$ is the effective viscosity, $\boldsymbol{\rho}$ is the fluid density and $\boldsymbol{\epsilon}$ is the turbulent dissipation rate. Additionally, local resistance and the rate of energy flux ($\boldsymbol{E_f}$) are computed along the airway centerline. Energy flux, is defined as:

$$E_f = \int (P + 0.5\rho|u|^2)(u \cdot \mathrm{n})dA \qquad (2)$$

where P is the local pressure, $u$ is the velocity field, and n is the normal vector of the extracted plane. Subtracting the energy flux at each point

along the centerline from the energy flux at the airway inlet provides the energy loss along the airway. The airway cross sectional area (CSA) is also measured at each centerline point.

Clinical metrics including hospital status, level of respiratory support, and blood CO2 levels were also obtained for each patient.

## RESULTS

Breathing resistance, viscous dissipation, maximum velocity, and minimum CSA are shown for all 5 patients in Figure 1, with patients organized from left to right in order of severity based on metric magnitude. Ranking is consistent regardless of metric or breathing condition chosen. A significant range is seen across the patients for all three computed airflow metrics, with Patient A (most severe) presenting 40x, 20x, and 6x greater values than patient E (least severe) for breathing resistance, viscous dissipation, and maximum velocity, respectively. The minimum CSA follows an inverse trend to the computed airflow metrics with the minimum CSA increasing as resistance decreases, although the differences are less differentiating.

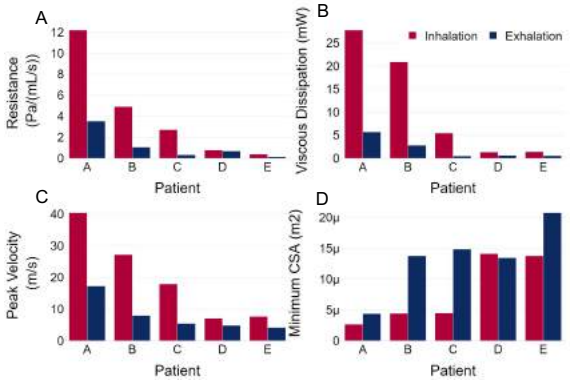


**Figure 1: Breathing resistance (A), viscous dissipation (B), maximum velocity (C), and minimum CSA (D) plotted for each patient at peak inhalation and exhalation**

In Figure 2 the flow field of the patients with the lowest and greatest values of airway resistance, E and A respectively, are highlighted via contours of velocity magnitude extracted along the centerline (3D image) and centerline computed values of respiratory resistance and accumulated energy loss (line graphs). For both patients, sharp increases in breathing resistance (blue curves) are found at local minimums of airway CSA (locations are highlighted by red spheres). A typical laryngeal jet is shown to exist downstream of the larynx in patient E, while in patient A, the dominant jet feature of the airway is found within the tongue base and has significantly higher velocity. As air accelerates through these constrictions, energy dissipation increases due to increased shear at the airway walls and internally as jet breakdown occurs downstream. The energy loss curves show that the dominant flow constriction at the larynx in patient E adds a minor increase to the overall dissipation, while in patient A, a significant increase in dissipation is generated through the tongue base constriction. This mechanism explains the large differences in airway resistance and suggests that the severity of UAO for patient E is minor compared to that of patient A.

At the time of scan, all patients, with the exception of patient E, were hospitalized for critical airway status and respiratory monitoring. Patient E required no respiratory support and was breathing room air. Patients C and D required extreme positioning maneuvers, patient B required high flow oxygen, and patient A required placement of a nasopharyngeal airway stent, the most severe non-invasive level of support. CO2 was elevated above normal values in all patients except patient E.

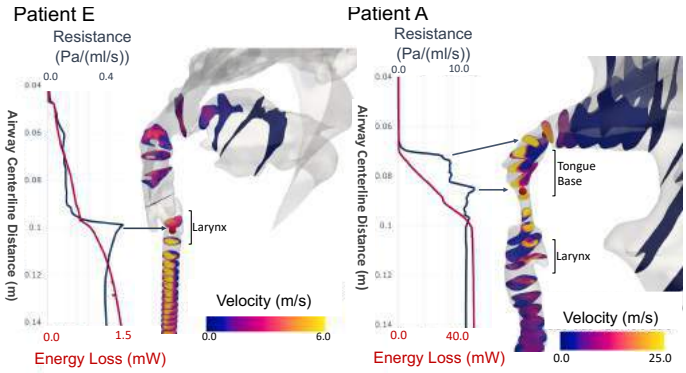


**Figure 2: Energy loss (red) and resistance (blue) computed along the airway centerline (line graphs) and contours of velocity magnitude (3D plot) for patient E and patient A.**

## DISCUSSION

This is the first study to combine 4DCT and CFD to analyze airflow dynamics in RS infants. CFD simulation results were used to retrospectively risk-stratify patients and identify the anatomic features primarily responsible for airway resistance. Large differences in computed airflow metrics were found between patients with airway resistance values ranging from those reported for healthy infant airways [7] to severe sleep apnea patients [8]. The dramatic range in airflow resistances across RS patients is due to the non-linear dependence on CSA and subsequent shear generation from accelerated flow, and a risk-stratification based solely on CSA would be less distinct (figure 1, panel D). CFD results also highlight that the location of maximum resistance is not always localized to the same anatomic subsite, suggesting that surgeries and interventions may need to be tailored specifically to meet the needs of each individual patient.

From a clinical perspective, airway resistance, peak velocity, and viscous dissipation all correlated with the severity of respiratory status defined by the level of intervention support. The patient with the most severe airflow resistance (patient A) also required the highest level of respiratory support. Patients who demonstrated obstruction at the tongue base had elevated blood levels of CO2, indicating their respiratory gas exchange was compromised by the UAO. Conversely, the patients who demonstrated maximum obstruction at the level of the larynx (patient E) required minimal respiratory support. The larynx represents the standard narrowest point in the upper airway, indicating this patient was functioning closer to what is physiologically normal.

The significant differences in airflow metrics and locations of obstruction highlight the variability in UAO in RS patients and the need for quantitative assessments of severity that include airflow dynamics. 4DCT and CFD has the potential to provide the quantitative metrics that lead to individualized surgical and medical treatment for RS patients.


## ACKNOWLEDGEMENTS

This research was supported by a T-32 training grant from the National Institute on Deafness and Other Communication Disorders.


## REFERENCES


[1] Bates, A. Et al, *Clinical Biomech,* 66, 88-96, 2019
[2] Evans, K. et al, *Pediatrics*, 127, 936-948, 2011
[3] Lam, A. el al, *J Otolaryngology-Head N,* 165, 905-908, 2021
[4] Faizal,W. et al.,*Comp Methods Program Biomed*,196:105627, 2020.
[5] Shwab, R. Et al, *Am Rev Respir Dis,* 148, 1385-1400, 1993
[6] Xu C. Et al, *J of Biomechanics*, 39, 2043-2054, 2020
[7] Wootton D. Et al, *J of Applied Physiol*, 116, 104-112, 2014
[8] Mason E. et al. *J of Petriatrics*, 238, 324-328, 2021

# FLOW AND PRESSURE CALIBRATION OF POLYVINYLIDENE FLUORIDE POLYMER FOR BIOSENSOR APPLICATIONS

**Matthew J. Danley (1), Jack T. Kloster (2), Ping Zhao (3), Victor K Lai (1)**

(1) Department of Chemical Engineering, University of Minnesota Duluth, Duluth, MN, USA
(2) Advanced Material Sciences, University of Minnesota Duluth, Duluth, MN, USA
(3) Department of Mechanical & Industrial Engineering, University of Minnesota Duluth, Duluth, MN, USA

## INTRODUCTION

The Transcatheter Aortic Valve Replacement (TAVR) is a minimally invasive procedure that has been performed at higher rates than in the past, yet certain complications still persist, for example the 90-day mortality rate is higher than surgical replacement procedures for Medicare beneficiaries [1]. The cause of this trend is unknown, and the underlying mechanisms have not been well studied. Some possible reasons for this trend include wear and tear on the aortic artery or even stresses caused by the implanted valve. To study the underlying mechanisms in vitro, our group is designing a 3D printed silicone model of the aorta artery with flow and pressure sensors surrounding the area of interest. The sensors will be made of polyvinylidene fluoride (PVDF).

PVDF is a piezoelectric material that has applications as an implantable biomedical device [2]. PVDF has been used to track changes in blood flow and pressure in various settings. For example, McLaughlin used PVDF as a non-invasive sensor to measure peripheral arterial pressure pulse wave velocity in humans [3]. Using a derivative of PVDF, PVDF-TrFE, Sharma was able to design a system to measure pressure around a catheter in a vascular testing model [4].

While PVDF has been used as a biosensor, there are few studies that show that PVDF being used to detect changes in blood flow and pressure in the aortic artery, which is necessary for our application. Specifically, PVDF needs to be subjected to conditions that similar to the aortic artery. These conditions include pressures peaking around 120mmHg in a healthy adult, and flow rates around 330mL/s [5]. Creation of an environment under these conditions in necessary to design the optimal sensor for investigating the TAVR procedure complications. The goal of this study is to design a flow chamber that mimics the environment of the aortic artery and to calibrate a PVDF sensor to those conditions.

## METHODS

Aortic Artery Model:

A flow chamber was designed and built to mimic the dimensions of the aortic artery. The section of interest of the aorta artery is around 12” in length and 1” in diameter [6], and clear tubing was used as the aortic segment for the purpose of testing the PVDF biosensor in this apparatus. A 12” portion was cut from clear PVC tubing (Abbot Rubber Company, Elk Grove Village, IL), and two copper wires were inserted into the walls of the clear tube to act as electrodes for the sensor.

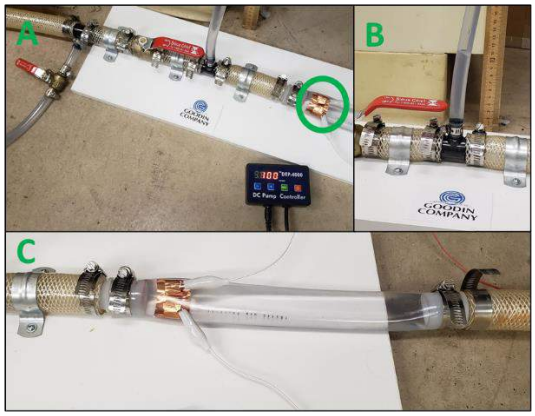


**Figure 1: A) Flow chamber for measuring PVDF response to changes in pressure and flow from a DEP-4000 water pump. The PVDF sensor, covered in copper tape is circled. B) Manometer used to measure head of fluid at various flow rates C) Aorta section of the flow chamber.**

A vertical tube manometer was connected right before the tube section to measure the head of fluid in the flow chamber. A bypass before the manometer and tube segment allows flow to be directed away

from the tube segment to determine if the sensor was detecting vibrations of the pump without water flowing through the segment. A Uniclife DEP-4000 submersible pump was used to vary the flow rates.

Flow rate of water was determined by collecting and weighing the water exiting the setup after 2 seconds. The pressure was determined by measuring the head of fluid in cm $H_2O$, later converted to mmHg, the standard measurement for blood pressure. The flow chamber and measurement of head of fluid can be seen in figures 1A and 1B.

Signal Acquisition:

A 1"x1" square was cut from the PVDF membrane (PolyK Technologies, State College, PA) and copper tape was placed on either face. The sensor was then placed in the flow chamber, with the copper tape touching the copper wire electrodes (figure 2A). The voltage from the PVDF sensor was collected using a National Instruments cDAQ-917 and 9215 Voltage Input module at a rate of 1,000Hz. Data acquisition would start with the flow of water running through the bypass, which was redirected to the aorta tube with PVDF sensor after two seconds.

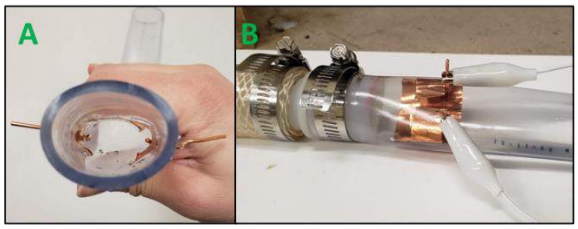


**Figure 2: A) PVDF Sensor held in place from copper wire electrodes. B) The PVDF sensor in flow chamber**

## RESULTS

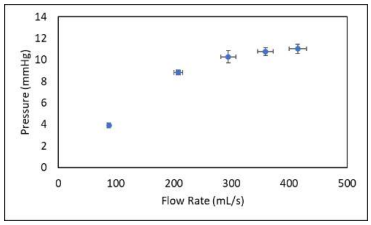


**Figure 3: Flow and Pressure in aortic heart model flow chamber. Figure 3 shows the flow rate and pressure from the Uniclife DEP-4000 pump. The error bars represent standard deviation of each replicate trial (n=3 for pressure, n=5 for flow rate).**

Figure 3 shows the relation between pressure and flow in the aorta. As the flow rate increases, the pressure increases nonlinearly. However, the rate of pressure increase drops with increasing flow rate, as observed by the gradual plateauing of pressures.

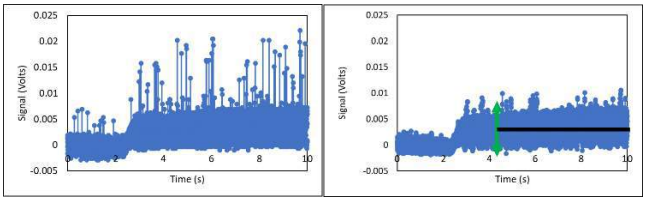


**Figure 4: Signal from PVDF sensor in Flow Chamber. The plot on the left shows the raw voltage from the sensor. The plot on the right is the voltage filtered through a 7-point Savitzy-Golay fit.**

Figure 4 shows the raw and filtered voltage from the PVDF sensor. The calculated signal was determined by taking the average voltage value from the 4 second mark to 10 second mark from the signal that had been filtered using a 7-point Savitzy-Golay [8] fit, after the flow was directed from the bypass to the flow chamber, as shown by the black line, with the signal amplitude shown in green.

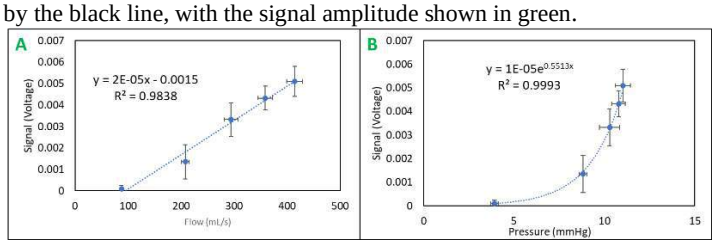


**Figure 5: A) Signal from PVDF sensor at various head pressure. B) Signal from PVDF sensor at various flow rates. The error bars designate standard deviation from triplicate data acquisitions.**

Figure 5 shows the signal generated from the PVDF sensor under various pressure and flow conditions in the aorta flow chamber. Figure 5A shows that as the pressure increases in the flow chamber, the corresponding voltage from the PVDF sensor increases. This is expected, as the force applied to the piezoelectric material increases, the corresponding signal should increase as well. The voltage from the sensor increases exponentially with increased pressure. The signal generated from the PVDF sensor also increases with higher flow rates. This follows a linear trend rather than the exponential trend seen with the increase in pressure.

## DISCUSSION

The flow chamber that was built to mimic the aortic artery did create an environment adequate for testing a sensor for use in studying the TAVR procedure. The flow rates generated from the Uniclife pump are in range of blood flow in the aorta. The pressure generated from the pump is a lot lower than expected, but since the PVDF sensor generated signal that was differentiable at these lower pressures, it is still useful for our application. One possible complication from the TAVR procedure is that the replacement valve could leak around the diseased valve. This could cause small changes in pressure relative to human blood pressure. The PVDF in the current set up is able to detect changes in pressure between 8-10mmHg, which could hypothetically detect leakages in the replacement valve.

The current flow chamber and biosensor set up presumably capture all the deformations which include fluid pressure and flow shear stress. In a native aorta, cyclic distension from pulsatile flow of blood will add to the complexity of the deformations on the aorta. These will have to be decoupled using our flow setup to fully understand the actual changes in the mechanical microenvironment around the TAVR implant as tracked by the PVDF sensor.

## ACKNOWLEDGEMENTS

I would like to thank Mike Danley, Master Plumber, for assistance in designing the flow chamber and George Behr, Goodin Company, for gathering parts and materials for the flow chamber.

## REFERENCES

[1] Culler, S et al, *The Annals of Thoracic Surgery*, 4:1137-1143, 2018
[2] Mao, Y et al., *Adv. Energy Mater.* 4:1301624, 2014
[3] McLaughlin, J et al., *Physiol. Meas*. 24:693–702, 2003.
[4] Sharma, T et al, *Annals of Biomed. Engineering*, 41:744-751, 2013
[5] American Heart Assoc., *Understanding Blood Press. Readings*,2022
[6] Hoffman, M, *Picture of the Aorta*, 2020
[7] Gabe, I et al, *Circulation*, 40:603-614, 1969
[8] Savitzy, A et al, *Anal. Chem.*, 36 (8): 1627-1639, 1964

# DEVELOPMENT OF A MULTI-TIMESTEP APPROACH FOR MICROPARTICLE AND ERYTHROCYTE IMAGE VELOCIMETRY

**Simon Tupin (1), Joseph van Batenburg-Sherwood (1)**

(1) Bioengineering, Imperial College London, London, UK

## INTRODUCTION

Numerical modelling techniques for simulating blood flow in microvessels have advanced significantly in recent years, but advances in experimental methods have been limited. Experimental measurements of microscale blood flow are needed to provide insight into blood behavior in the microcirculation, particularly in cases where the properties of the red blood cells are altered in complex ways, such as malaria and diabetes. While numerical models can make predictions, experimental data is required for optimisation and validation [1]. However, high quality experimental data is scarce.

Using microfluidics, it is straightforward to fabricate channels that mimic idealised sections of the microvasculature. The velocity in such branching networks is characterised by a wide range of velocities. For a given branch, the velocity increases from 0 at the wall to a peak value near the channel centre. As the network bifurcates, the peak velocity and the velocity in the important near wall region decrease. Accurately capturing this wide range of velocities is challenging.

Micro particle image velocimetry (µPIV) can be used to measure velocities with high spatial resolution in such microchannels [2]. Image correlation is then used to calculate the most likely displacement of the particles in a region of the image between two frames, separated by timestep $\Delta t$ (typically ~0.1-10 ms). A velocity vector can then be calculated for that region using the displacement and $\Delta t$. A limitation of this approach is that the accuracy of the measurement is dependent on the number of pixels that particles move between images. If particles move by one pixel or less between images, a strong correlation peak will be identified, but small differences in sub-pixel resolution can lead to large errors in the estimated velocity. Conversely, if particles move by too many pixels between frames, the correlation will struggle to identify the same group of particles and there will many spurious vectors.

The same difficulties arise in macro PIV in flow fields that include large velocity gradients. To address this problem, a number of authors have proposed multi-$\Delta t$ PIV algorithms. [3,4] In these approaches, image pairs are captured in a sequence of increasing $\Delta t$ values and indices of the signal to noise ratio are used to select the optimal $\Delta t$ for each vector. In the present study, we extend these approaches to µPIV acquisition of flow in branching networks that mimic an ideaslised section of an arteriolar network. First, we consider µPIV, with fluorescent particles suspended in a glycerol solution. We then apply the approach to brightfield illuminated images of erythrocytes flowing in the same branching microchannel.

## METHODS

### Fluidics

Standard techniques were used to fabricate microchannel masters with SU8-based photolithography, and PDMS microchannels were cast and bonded to glass coverslips. The channels had a 50µm square cross section throughout and featured two sequential branches inclined at 45° and on alternating sides of the main channel. A pressure controller (OB1 MK3+, Elveflow) was used to perfuse either 0.5µm diameter fluorescent particles suspended in glycerol solution (PS-FluoRed-PEG/Fi142-1, microParticles GmbH) or human erythrocytes suspended in an Optiprep (Sigma Aldrich) and phosphate-buffered saline solution at a haematocrit of 25%.

### Image Acquisition

A custom µPIV system designed specifically for microscale blood flow experiments was developed. The setup comprises an inverted microscope (IX73, Olympus) equipped with two illumination methods: a dual head pulsed Nd:Yag laser (532nm, NanoPIV, Litron) to image fluorescent microparticles and a red LED (623nm, Solis-623C, Thorlabs) to image erythrocytes (Fig 1).

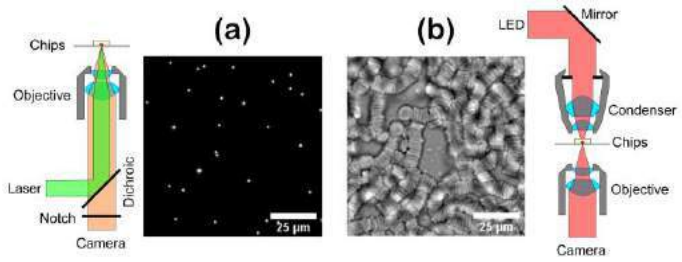


**Figure 1: Optical system schematics and typical image of (a) microparticles and (b) red blood cells.**

An sCMOS camera (Zyla 5.5, Andor) was used to record pairs of images at a resolution of 0.325 µm/px with a 20X objective (UPLXAPO20X, Olympus). The system is controlled using a custom LabVIEW program that enables interleaved recording of images pairs with multiple $\Delta t$ values. For the particle data, 5 values of $\Delta t$ = 0.1, 0.2, 0.5, 1 and 2 ms were acquired, for 50 image pairs at each $\Delta t$. For the demonstratin with erythrocytes, three timesteps ($\Delta t$ = 0.5, 1 and 5 ms) were sufficient to reconstruct the flow field (the different range of $\Delta t$ corresponds to lower flow rates).

**PIV processing**

Velocity magnitude fields for each $\Delta t$ were measured using the ensemble average algorithm implemented in PIVlab [5]. For each $\Delta t$, a two-pass algorithm was implemented. For the particle images, we used 48px then 24 px interrogation windows (IW), with 50% overlap, yielding a final spatial resolution of 3.9µm. For erythrocyte images, 32 then 16 px IWs were used, yielding a spatial resolution of 2.6 px, enabled due to the nature of the erythrocyte images offering more features that can be correlated in smaller IWs.

A method for selection of $\Delta t$ for each vector location was implemented based on the general PIV principle that optimal particle displacement between frames should be ~ IW/4 [6]. For each vector, the $\Delta t$ that yielded the highest displacement that was ≤ IW/4 was selected. We refer to the resulting vector field as 'optimised'.

In addition, the correlation (C) signal-to-noise ratio (SNR) was evaluated by measuring the peak to correlation energy (PCE) [7], defined as:

$$PCE = \frac{|C_{max}|^2}{\int_{-\infty}^{\infty}|C|^2 dx} \quad (1)$$

**RESULTS**

Figure 2a shows the optimised velocity field, with velocity magnitudes that vary by more than a decade. The selected $\Delta t$ values are shown in Figure 2b, and vary both between and within branches. Figure 2c presents the percentage differences between the optimised velocities and those calculated using the shortest $\Delta t$ (0.1ms). The latter approach led to a significant underestimation of >20% in the lower velocity regions, including near the wall. Use of longer $\Delta t$ values performed comparably better in such regions, but failed in higher velocity regions (Figure 2d).

The signal-to-noise ratio (PCE) field was found to be maximal when using the shortest $\Delta t$ throughout the domain, despite the fact that the displacement between frames was less than 1 pixel in the low velocity regions, indicating it is not appropriate for the present application.

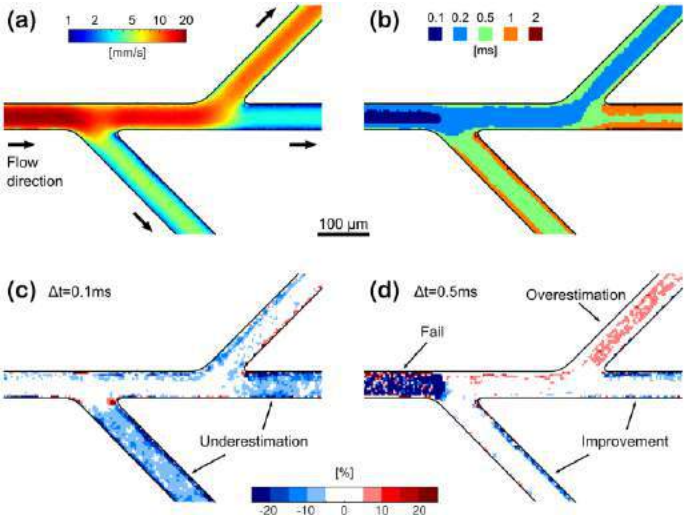


**Figure 2: Multi-timestep approach applied to the microparticle experiment: (a) optimised velocity field, (b) local $\Delta t$ selection. Percentage difference in velocity between the optimised field and (c) $\Delta t$ =0.1ms, (d) $\Delta t$ =0.5ms.**

The developed framework was then applied to erythrocytes (Figure 3). The velocities varied significantly throughout the channel, with clear asymmetries that arise due to asymmetric haematocrit distributions [1]. The inset demonstrates the high resolution with which the velocity was measured.

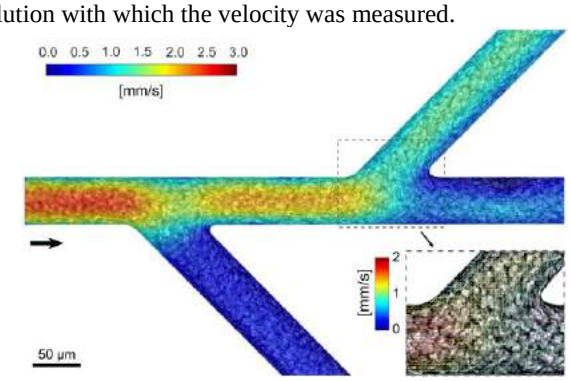


**Figure 3: Multi-timestep approach applied to the erythrocytes experiment.**

**DISCUSSION**

The multi-timestep approach developed in this study was found to be effective for the velocity measurement in branching geometries exhibiting large velocity gradients. Optimisation of the local timestep allows maintenance of an ideal displacement between frames, which improves the accuracy throughout the network. The accuracy of the near wall velocity was notably improved, which is particularly important when estimating the shear stress acting on the channel walls, or the endothelium for vascularised channels.

The proposed method was found to be more efficient than the correlation SNR in the selection of the local timestep. SNR values were high even when the particle displacement was small, as a strong correlation peak is identified, but the corresponding outcomes were not accurate. A larger displacement is demonstrated here to achieve a higher accuracy in the velocity estimation.

The current results demonstrate proof-of-principle, but further work is required to validate the reconstructed velocity field. For a range of input velocities and flow splits between branches, the accuracy of the approach will be determined by evaluating conservation of mass errors at each bifurcation, and by measuring the flow rates for each branch for direct comparison.

Once validated, this approach will be applied to the simultaneous velocity measurements of particles and erythrocytes. This multiphase characterisation will better describe the complex blood behavior in the microcirculation.

**ACKNOWLEDGEMENTS**

This project was supported by the Royal Academy of Engineering under the Research Fellowship Scheme (RF201617\16\18) and the Engineering and Physical Sciences Research Council (EP/T023155/1). Additional thanks to Dr. Christopher Rowlands for his valuable help in the optical system design.

**REFERENCES**

[1] van Batenburg-Sherwood J et al., *Biomech Model Mechanobiol*, 2021, online: doi.org/10.1007/s10237-021-01537-2
[2] Sherwood JM et al., *PLoS ONE*, 9:e100473, 2014.
[3] Hain R and Kähler CJ, *Exp Fluids*, 42:575–587, 2007.
[4] Bouillot P et al., *Exp Fluids*, 55:1746, 2014.
[5] Thielicke W and Sonntag, R., *J. Open Res. Softw.*, 9:12, 2021.
[6] Keane RD and Adrian RJ, *Meas. Sci. Technol.*, 1:1202, 1990.
[7] Xue Z et al., *Meas. Sci. Technol.*, 25:115301, 2014.

# HEMODYNAMIC CHANGES IN THE AORTIC ROOT UPON TRANSCATHETER AORTIC VALVE (TAV) IMPLANTATION

**Hunter Tashman (1), Mia Bonini (1), Marc Hirschvogel (2), Yunus Ahmed (3), G. Michael Deeb (3,4), Stanley J. Chetcuti (3,4), Nicholas Burris (4), David Nordsletten (1,2,3)**

(1) Department of Biomedical Engineering, University of Michigan, Ann Arbor, MI, United States
(2) School of Biomedical Engineering and Imaging Sciences, King's College London, London, United Kingdom
(3) Department of Cardiac Surgery, University of Michigan, Ann Arbor, MI, United States
(4) Department of Radiology, University of Michigan, Ann Arbor, MI, United States

## INTRODUCTION

Aortic stenosis (AS), the most common type of valvular heart disease, is characterized by a narrowing (stenosis) of the aortic valve (AV) orifice caused by progressive calcification and restricted opening of the aortic valve leaflets [1-2]. This results in significant obstruction of blood flow from the left ventricle outflow tract (LVOT) across the aortic valve into the ascending aorta and amplifying the ventricular pressures required to maintain normal cardiac output. If untreated, this obstruction can cause life-threatening complications such as cardiac arrhythmias, heart failure, and stroke. The primary treatment for AS is aortic valve replacement. The surgical aortic valve replacement (SAVR) procedure has been the gold standard for treating symptomatic AS. However, the transcatheter aortic valve replacement (TAVR), a procedure in which a stented valve is deployed into the aortic valve position via arterial catheter, introduced a novel, less invasive option for at-risk patients.

Although TAVR procedures have quickly become the standard of care for many patient subgroups [3], hemodynamic alterations in the aortic root induced by TAVR implant are not fully understood. Several prior studies have investigated this topic [4-5], however, there remains a need for an end-to-end pipeline for computational modeling of pre- and post-TAVR hemodynamics which is validated against clinical data.

The aims of this research are twofold: elucidate hemodynamic changes in the aortic root after TAV implantation by developing a patient-specific modeling pipeline that enables the simulation of fluid flow through a model of the aortic root; and validate these data against clinical patient data. Specifically, we examine the ability of our pipeline to non-invasively estimate measures of relative pressure and flow pre-operatively (under stenotic conditions) as well as post-operatively (after TAVR implantation). Understanding and predicting local hemodynamic changes within the aortic root upon TAV implantation provides a powerful tool for surgical planning and the clinical treatment of AS patients.

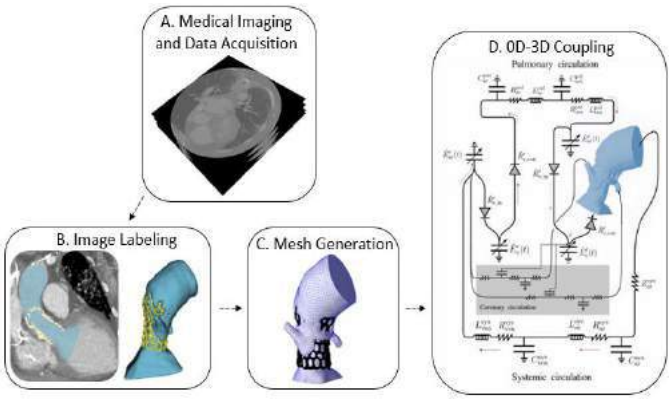


**Figure 1: Novel aortic root modeling pipeline. (A) Pre- and post-TAVR CT images and echocardiogram data is collected. (B) The aortic root is segmented (blue) and the TAVR (yellow) is subtracted from the segmented volume. (C) The remaining blood volume of the aortic root is meshed (blue) in SimModeler. (D) The 3D model (blue) is coupled to a closed loop 0D model and patient specific data is integrated into the CFD model**

## METHODS

In order to predict hemodynamic outcomes post TAVR, we developed a novel pipeline to create patient-specific computational fluid dynamic models of the aortic root. Computed tomography (CT) images were collected for each patient pre- and post- TAV implantation (Fig. 1a). The aortic root blood volume was segmented in 3DSlicer with the anatomic aortic valve orifice area (AVOA) defined from the CT and doppler flow data (Fig. 1b). Segmented models were imported into SimModeler for smoothing, inflow and outflow boundary generation, tetrahedral mesh generation, and the creation of a 3D boundary layer (Fig. 1c). Newly smoothed and meshed 3D models were coupled to a

closed loop 0D model (Fig. 1d) that represents the remaining vasculature and that provides continuous feedback to the 3D model [6]. Heart rate (HR), volumetric flow from the left ventricle, AVOA, and stroke volume (SV) provide the data for model assimilation using direct constraints on the 0D model. The finite element-based solver *CHeart* was used to perform CFD simulations of aortic root flow [7].

This pipeline (Fig.1) was used to analyze six different models: a pre-TAVR and post-TAVR aortic root model for three different patient-specific geometries.

**Pre-TAVR Models.** This modeling pipeline can be used to model the diseased state of patients with AS. For these models the location and orientation of the AV was determined from segmenting the preoperative CT images, however poor image resolution convoluted the process of obtaining a reliable AVOA. The AVOA was adjusted such that the area approximated the ratio of maximum left ventricle (LV) volumetric flux into the aortic root (calculated from dynamic CT images) to peak velocity across the valve plane.

**Post-TAVR Models.** Postoperative imaging and echocardiogram measurements allowed for assessment of patient hemodynamics post-TAVR. A TAV (composed of valve stents and skirt) and an aortic root model were created from the CT images. The valve skirt, which is not visible in the CT images, was manually segmented using stent landmarks. The TAV model was subtracted from the aortic root model to generate a post-TAVR aortic root blood volume. The AVOA was defined similarly to the pre-TAV case, however no dynamic post-operative CT data was available to calculate a maximum LV volumetric flux. Instead, the pre-TAV volumetric flux was adjusted such that the SV of the LV corresponded to the post-operative SV registered in the patient chart.

CFD results are validated using data taken directly from the patient's pre-procedural echocardiogram and their echocardiogram taken 24-48 hours post-TAV implantation.

## RESULTS

Figure 2 depicts the velocity field for a representative case across the aortic valve at peak systole for both pre- and post-TAVR models. At peak systole, the pre-TAVR model has a peak velocity magnitude of 4.7 m/s (compared to 4.1 m/s measured by doppler). The post-TAVR model has a peak velocity magnitude of 2.6 m/s (compared to 2.9 m/s measured by doppler) which is a 55.3% decrease in velocity magnitude after TAV implantation.

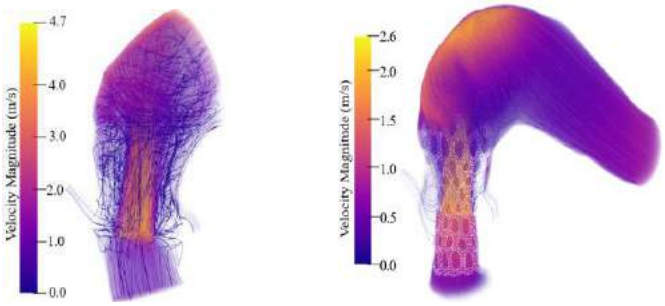


**Figure 2: Velocity field of aortic root models at peak systole. The pre-TAVR model (left) has a high velocity, centralized jet crossing the valve plane. The post-TAVR model (right) has a lower velocity, decentralized jet crossing the valve plane and into the ascending aorta. Extension of the ascending aorta included in order to highlight uniform flow patterns past the valve plane.**

Important hemodynamic parameters are shown in Table 1. The pre-TAVR model had a peak aortic valve pressure gradient, mean aortic valve pressure gradient, and peak velocity measurement percent errors of 8.21%, 3.86%, and 14.6%, respectively. The post-TAVR model had a peak aortic valve pressure gradient, mean aortic valve pressure gradient, and peak velocity measurement percent errors of 5.76%, 16.5%, and 10.0%, respectively. These results show good agreement between the CFD data generated *in silico* and the invasively measured patient data for both pre- and post-TAVR models of the representative case (Table 1).

**Table 1: CFD simulation data validation for representative case.**

| **Pre-TAVR** | | | | | |
|---|---|---|---|---|---|
| | *Data for constraining CFD model* | | *Data for model validation* | | |
| | HR (bpm) | SV (mL) | Peak AV pressure gradient (mmHg) | Mean AV pressure gradient (mmHg) | Peak velocity (m/s) |
| Patient Data | 71 | 85.6 | 67 | 44 | 4.1 |
| CFD Output | 71 | 85.6 | 72.5 | 45.7 | 4.7 |
| **Post-TAVR** | | | | | |
| | *Data for constraining CFD model* | | *Data for model validation* | | |
| | HR (bpm) | SV (mL) | Peak AV pressure gradient (mmHg) | Mean AV pressure gradient (mmHg) | Peak velocity (m/s) |
| Patient Data | 80 | 81.3 | 33 | 17 | 2.9 |
| CFD Output | 80 | 81.3 | 31.1 | 19.8 | 2.61 |

## DISCUSSION

In this study, we developed a novel modeling pipeline whose output includes a 0D-3D coupled patient-specific model that can be used in CFD simulations and the TAVR procedure. The predictive results of these simulations were then validated against velocity and pressure measurements.

Given the close agreement between hemodynamics measured by CFD and the patient specific data, we conclude that the computational modeling methods undertaken in this study are suitable to simulate aortic root hemodynamics pre- and post-TAV implantation. This outcome is supported by the conclusion of previous work which highlights the predictive information that is acquired from patient-specific computational models after device implantation [8].

A limitation of this work is that post-TAVR anatomies were taken from CT images rather than directly simulating the TAV implantation. Future work includes expanding this methodology to allow for investigation into the hemodynamic effects of implant depth and rotation orientation (e.g., commissural alignment) with valve types. Furthermore, we plan to expand this modeling framework to examine the hemodynamic effects of a repeat TAVR procedure (TAV-in-TAV) considering the growing need for advanced procedural planning techniques for such procedures due to patients outliving the durability of the original transcatheter valve [9].

## ACKNOWLEDGEMENTS

We would like to acknowledge funding from the Engineering and Physical Sciences Research Council (EP/R003866/1).

## REFERENCES

**[1]** Carità, P et al., *J Geriatr Cardiol*, 13:489-498, 2016. **[2]** Czarny, M. J. and Resar, J. R., *Clin Med Insights Cardiol*, 8:15–24, 2014. **[3]** Hu, P et al., *J Am Coll Cardiol*, 60:483-492, 2012. **[4]** Sirois, E et al., *Cardiovasc Eng Technol*, 2:186-195, 2011. **[5]** Bianchi, M et al., *Biomech Model Mechanobiol*, 18:435-451, 2019. **[6]** Hirschvogel, M et al., *Int J Numer Method Biomed Eng*, 33:e2842, 2017. **[7]** Lee, J et al., *SIAM Journal on Scientific Computing*, 38:C150-C178, 2016. **[8]** Schoenhagen, P et al., *J Cardiovasc Transl Res*, 4:459-469, 2011. **[9]** Landes, U et al., *J Am Coll Cardiol*, 77:1-14, 2021.

# ROLE OF MIDLEVEL CONSTRAINT IN REDUCING MIDFLEXION LAXITY AFTER ADDITIONAL DISTAL FEMORAL RESECTION IN POSTERIOR STABILIZED TKA

**S. Elmasry (1), B. Chalmers (2), C. Kahlenberg (2), P. Sculco (2), T. Wright (1), M. Cross (2), D. Mayman (2), G. Westrich (2), C. Imhauser (1)**

(1) Department of Biomechanics
Hospital for Special Surgery
NYC, NY, USA

(2) Adult Reconstruction and Joint Replacement Service
Hospital for Special Surgery
NYC, NY, USA

## INTRODUCTION

Surgeons resect additional distal femur during primary posterior-stabilized (PS) total knee arthroplasty (TKA) to correct for flexion contracture [1]. We previously demonstrated that utilizing this approach to alleviate a 10° flexion contracture, which elevates the joint line, induces significant increase of coronal laxity in the mid-flexion ranges, and, therefore, may contribute to knee instability; a common cause of patient dissatisfaction and revision surgery [2]. It has been postulated that a midlevel constrained (MLC) insert, an insert compatible with TKA implant components, provides more coronal stability than a PS insert due to a thicker and wider post [3]. However, the effect of MLC on tibiofemoral kinematics in the presence of joint line elevation is not well understood. Therefore, the goal of this study was to determine whether an MLC insert reduces mid-flexion laxity after additional resection of the distal femur in TKA.

## METHODS

Six computational knee models were developed via 3D reconstructing of bony geometries for the tibia and femur from CT scans of six cadaveric knees. A measured resection TKA was conducted and a standardized capsular and collateral ligament properties that produces a balanced knee at full extension were incorporated to the model (Fig. 1.a) [4]. PS and MLC inserts were subsequently installed on each of the six models (Optetrak Logic®, Exactech, FL, USA) (Fig. 1.b). A compliant contact formulation between the articulating surfaces of the femoral component and the polyethylene insert was defined [4]. A 10° flexion contracture was modeled by reducing the slack in the spring elements representing the posterior capsule while simulating a standard clinical exam of knee extension [5]. Additional bone resections of the distal femoral of +2 mm and +4 mm were simulated with the PS and MLC models (Fig. 1.c).

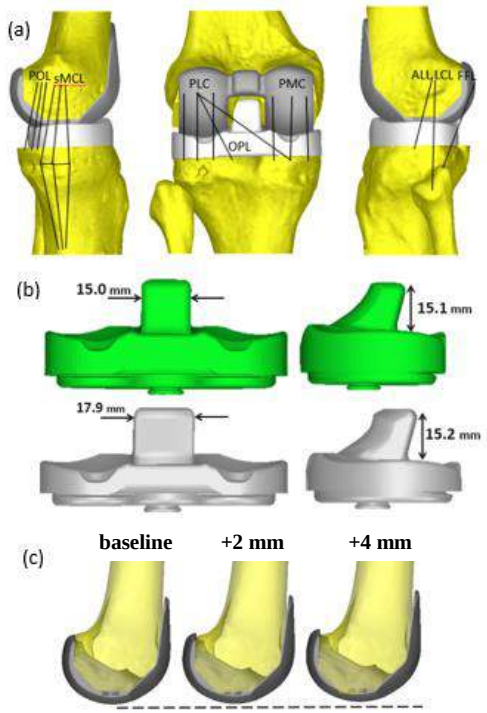


**Figure 1:** (a) The TKA model included 20 ligament fibers representing the collateral ligaments and posterior capsule. (b) The geometry of the PS insert (green) and the MLC insert (gray). (c) Three bone resections Subsequently, varus and valgus (VV) moments of ±10 Nm under 50 N of compression were applied to the tibia as the knee was flexed from 0°

Subsequently, varus and valgus (VV) moments of ±10 Nm under 50 N of compression were applied to the tibia as the knee was flexed from 0° to 90° at baseline (i.e., no additional resection) and after additional distal resections of +2 mm and +4 mm. The coronal laxity, defined as the sum of VV angulations in response to the VV moments, and coupled axial rotation, defined as the sum of coupled internal and external rotation in response to the VV moments, were measured at 30°, 45°, and 60° of flexion and compared between PS and MLC using RM-ANOVA with α set to 0.05.

## RESULTS

At 30° of flexion, the coronal laxities with the PS insert at the +2 mm and +4 mm resections averaged 7.9 ±0.5° and 11.3 ±0.6°, respectively. With the MLC insert, the coronal laxity decreased by 0.8° (p= 0.06) and 1.0° (p= 0.07) with the +2 mm and +4 mm resections, respectively (Fig. 2 and Table 1). With the PS insert, the coupled axial rotation at the +2 mm and +4 mm resections averaged 11.1 ±3.9° and 12.5 ±4.6°, respectively. With the MLC insert, the coupled axial rotation decreased by 5.6° (P= 0.01) and 7.1° (P=0 .02), respectively, (Fig. 3 and Table 2). Similar patterns were observed at 45° and 60° of flexion (Tables 1 & 2).

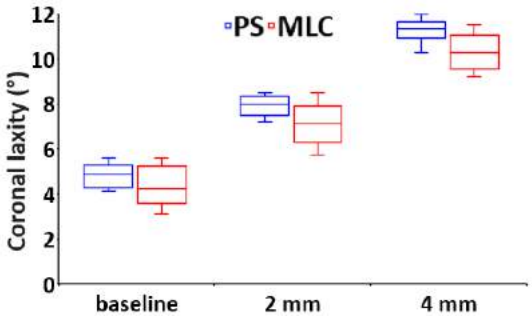


**Figure. 2**: Coronal laxity in PS and MLC models at the baseline, +2 and +4 mm of additional resections at 30° of flexion.

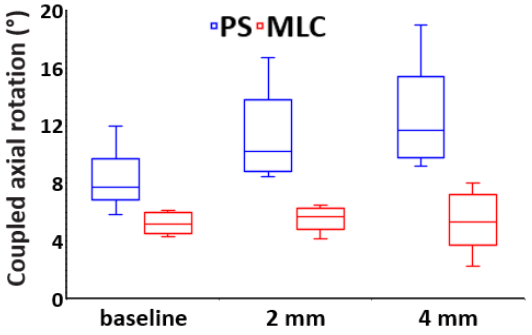


**Fig. 3**: Coupled axial rotation in PS and MLC models at the baseline, +2 and +4 mm of additional resections at 30° of flexion

## DISCUSSION

We found that with additional resections of the distal femur resulting in joint line elevation in primary TKA, utilizing an MLC insert reduced coupled axial rotation (up to 7.1°) but had a minimal impact on coronal laxity (only up to about 1.0°) in mid-flexion compared to that occurring with a PS insert. Midflexion instability could be attributed not only to increased primary motions, like coronal laxity, but also coupled rotations of the knee at midflexion [6]. Compared to the natural knee, the coupled axial rotations predicted by the model with joint line elevation were greater than those of the native knee in mid-flexion, which averaged at most 5° in valgus [7]. Our findings might suggest that MLC insert could contribute to reducing the incidence of midflexion

**Table 1:** Comparing coronal laxity in PS and MLC via RM-ANOVA

| Flexion angle (°) | Bone resection | PS (°) | MLC (°) | Mean Δ | P-value |
|---|---|---|---|---|---|
| 30 | Baseline | 4.8 ±0.6 | 4.3 ±1.0 | 0.5 | 0.14 |
| | 2 mm | 7.9 ±0.5 | 7.1 ±1.0 | 0.8 | 0.06 |
| | 4 mm | 11.3 ± 0.6 | 10.3 ±0.9 | 1.0 | 0.07 |
| 45 | Baseline | 5.0 ±0.9 | 4.6 ±1.2 | 0.4 | 0.17 |
| | 2 mm | 7.7 ±0.9 | 6.9 ±1.4 | 0.8 | 0.07 |
| | 4 mm | 10.5 ±1.1 | 9.7 ±1.3 | 0.9 | 0.09 |
| 60 | Baseline | 5.4 ±1.4 | 5.0 ±1.6 | 0.3 | 0.17 |
| | 2 mm | 7.4 ±1.6 | 6.8 ±1.8 | 0.6 | 0.08 |
| | 4 mm | 9.5 ±1.8 | 8.8 ±1.9 | 0.7 | 0.11 |

**Table 1:** Comparing coupled axial rotation in PS and MLC via RM-ANOVA

| Flexion angle (°) | Bone resection | PS (°) | MLC (°) | Mean Δ | P-value |
|---|---|---|---|---|---|
| 30 | Baseline | 8.2 ±0.6 | 5.2 ±1.0 | 3 | 0.03 |
| | 2 mm | 11.1 ±0.5 | 5.5 ±1.0 | 5.6 | 0.01 |
| | 4 mm | 12.5 ±0.6 | 5.4 ±0.9 | 7.1 | 0.02 |
| 45 | Baseline | 7.5 ±0.9 | 4.5 ±1.2 | 2.9 | 0.02 |
| | 2 mm | 10.7 ±0.9 | 5.2 ±1.4 | 5.5 | <0.01 |
| | 4 mm | 12.2 ±1.1 | 5.5 ±1.3 | 6.7 | 0.02 |
| 60 | Baseline | 6.8 ±1.4 | 3.9 ±1.6 | 3 | <0.01 |
| | 2 mm | 9.7 ±1.6 | 5.1 ±1.8 | 4.6 | <0.01 |
| | 4 mm | 11.3 ±1.8 | 5.8 ±1.9 | 5.5 | 0.02 |

instability by reducing the coupled axial rotation induced with the PS insert. However, the increased constraint provided by the post in MLC may also increase the mechanical burden on the bone-implant interface. Therefore, understanding the trade-offs between constraint, joint-level stability, and bone-implant loading are critical considerations when selecting the insert design. Importantly, MLC design differs among manufacturers, so these findings are specific to the simulated implant system. In conclusion, with additional resections of the distal femur in primary TKA to alleviate a flexion contracture, utilizing an MLC insert substantially reduced coupled axial rotation but had a minimal impact on coronal laxity compared to PS insert. These findings may help guide surgeons for the indications and potential kinematic impact of joint line elevation and utilization of MLC inserts.


## ACKNOWLEDGEMENTS

Shady Elmasry was supported from the NCATS of the NIH, Award No. TL1TR002386.


## REFERENCES


[1] Liu, DW et al., *J Arthroplasty*, 31:98-102, 2016
[2] Chalmers, B et al, *J Bone Joint Surg Am*, 103: 87-93, 2021
[3] Kahlenberg, C et al., *J Knee Sur*, 2021
[4] Elmasry, SS et al., *J Arthroplasty*, 34: 981-86, 2019
[5] Elmasry, SS et al., *J Biomech*, 120: 110367, 2021
[6] Leitze, Z et al., *Clin Orthop Relat Res*, 436: 229-36, 2005
[7] Gladnick, BP et al., *Knee*, 23: 387-92, 2016

# A TIMESCALE-GUIDED MICROFLUIDIC SYNTHESIS OF HYDROPHOBIC DRUG NANOPARTICLES WITH METAL-PHENOLIC NETWORK COATINGS

**Y. Shen (1), S. Yuk (2), Y. Yeo (2,3), B. Han (1,3)**

(1) School of Mechanical Engineering, Purdue University, West Lafayette, IN 47907, USA
(2) Department of Industrial and Physical Pharmacy, Purdue University, West Lafayette, IN 47907, USA
(3) Purdue University Center for Cancer Research, West Lafayette, IN, 47907, USA

## INTRODUCTION

Nanoparticle (NP) formulations have been extensively studied as a carrier of poorly water-soluble drugs[1]. However, many formulation schemes[2-5] are typically developed in a drug-specific manner, it is still challenging to adapt NP formulation schemes for a wide variety of hydrophobic drugs.

In this context, metal-phenolic network (MPN), a supramolecular structure formed by the rapid coordination between metal ions and polyphenols[6], has been considered a promising coating scheme because it can be easily deposited on various substrates with different sizes, shapes and compositions[7]. The MPN can adhere to aggregates of hydrophobic drugs and suppress their Ostwald ripening[8, 9] to produce NPs with high drug loading capacity. In addition, the MPNs display unique features such as pH and redox responsiveness, which can facilitate drug release control and combination therapy[10]. The MPN shell is also conducive to conjugation of biofunctional molecules via diverse molecular interactions; thus, tannic acid (TA)-$Fe^{III}$ nanocapsules, one of the MPNs, has been used to immobilize an endotoxin adsorbent for systemic use[11]. However, the application of MPN coating on different hydrophobic drug types needs empirical adjustment and optimization of synthesis parameters. Mechanistically designed manufacture schemes are essential to diversify the application of NP formulation with MPN coating.

In this study, a mechanistic guideline is proposed to synthesize NP with TA-$Fe^{III}$ coating for various hydrophobic drugs using hydrodynamic flow focusing (HFF) on a microfluidic platform. This method is based on a hypothesis that the drug NP with TA-$Fe^{III}$ coating can synthesized by controlling the mixing time scale of HFF as illustrated in Figure 1. Specifically, if the mixing time scale is shorter than the induction time scale of hydrophobic drug, small and uniform size NP with TA-$Fe^{III}$ coating will be formed. We test this hypothesis by investigating the NP formulation of several drugs with varying water solubility.

## METHODS

*Selection of drugs*.

We investigated the effects of flow conditions of HFF on the synthesis of NPs of several hydrophobic drugs with varying water solubility. These include vitamin D ($VD_3$) (< 1 ng/mL), curcumin (CM) and paclitaxel (PTX) (> 1 μg/mL).

*Microfluidics of HFF*.

As illustrated in Figure 1A, HFF is the crucial step of the microfluidics which controls the subsequent step of solvent exchange for NP formation. Drug and TA in the organic solvent is introduced to the central channel, and $FeCl_3$ in water is introduced to both side channels. The central organic stream is squeezed by the outer aqueous stream which flows at higher flow rates. Figure 1B shows HFF enables short diffusion length, leading to shorter mixing time scale ($\tau_m$) than the induction time scale ($\tau_i$) of a given hydrophobic drug. This leads to the formation of drug NPs with TA-$Fe^{III}$ coatings with small and uniform size.

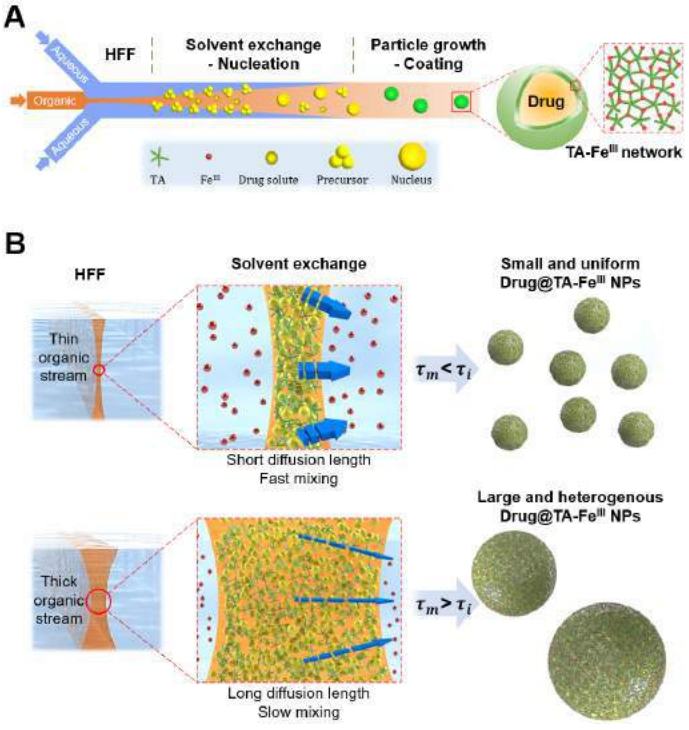


**Figure 1. Schematic illustration of the microfluidic synthesis method of hydrophobic drug NPs with TA-$Fe^{III}$ coating.**

*Characterization of NPs.*
The synthesized TA-$Fe^{III}$ network coated drug NPs of curcumin, paclitaxel and vitamin D are characterized by dynamic light scattering (DLS) measurement, the transmission electron microscopy (TEM) imaging, as well as the HPLC analysis of the drug loading contents.

## RESULTS

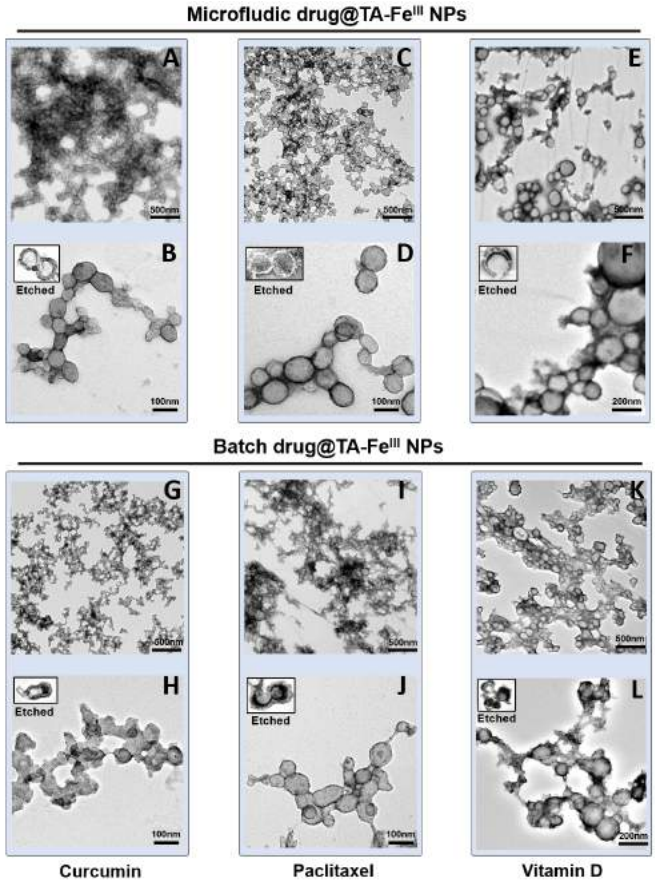


**Figure 2. Transmission electron microscopy images of drug NPs with TA-$Fe^{III}$ coatings synthesized by microfluidic and batch methods**.

Following our timescale-guided microfluidic method for the continuous production of drug NPs with TA-$Fe^{III}$ network coatings, we can produce size-controlled NPs of CM, PTX and $VD_3$. TEM images of the microfluidic NPs are shown in Figures 2A – 2F. Figures 2A, 2C and 2E show the low magnification TEM images of CM, PTX and $VD_3$ NPs, respectively, which were generally uniform in morphology and size. $VD_3$ NPs are significantly larger than CM or PTX NPs. More clearly exhibited in the high magnification TEM images in Figures 2B, 2D and 2F, $VD_3$ NPs are around 200 nm in diameter while CM and PTX NPs are around 100 nm in diameter. In the images (inserts) of the etched NPs, TA-$Fe^{III}$ coatings are clearly visible. Compared to the TEM images of the batch NPs in Figures 2G - 2L, the microfluidic NPs have more regular shapes.

According to the DLS measurement, microfluidic CM NP has the mean diameter of 140 ± 5 nm with the polydispersity index PDI of 0.1 ± 0.05, microfluidic PTX NP 121 ± 10 nm (PDI of 0.15 ± 0.03), and microfluidic $VD_3$ NP 233 ± 11 nm (PDI of 0.19 ± 0.03). Batch CM NP has the mean diameter of 199 ± 5 nm (PDI of 0.07 ± 0.02), batch PTX NP 166 ± 2 nm (PdI of 0.1 ± 0.03) and batch $VD_3$ NP 228 ± 7 nm (PDI of 0.08 ± 0.01). The DLS data agree reasonably well with the TEM images of microfluidic PTX and $VD_3$ NPs but overestimate the microfluidic CM NP size by approximately 30%. Figure 2B indicates that microfluidic CM particles are less spherical than microfluidic PTX or $VD_3$ particles, which results in a relatively large interfacial area between the particles, making the microfluidic CM particles more prone to aggregation during the DLS measurement. Similarly, the DLS data overestimate the size of batch NPs by more than 50%.

According to the HPLC analysis, for the microfluidic synthesis, CM, PTX and $VD_3$ are encapsulated with a loading content of 44 ± 7.2 wt%, 61 ± 8.4 wt%, 70 ± 9.9 wt%, respectively, and by comparison, these are 35 ± 10 wt%, 44 ± 0.2 wt%, 34 ± 3.7 wt%, respectively, for the batch synthesis. The NP production yield of the microfluidic synthesis is approximately 10 mg/hr, 9 mg/hr and 7 mg/hr for CM, PTX and $VD_3$, respectively, equivalent to approximately 5 mg/hr for all three drugs, which is comparable to or higher than the production yield of the batch synthesis.

## DISCUSSION

This work expands the proof of principle to the mechanistic study explaining the size control of the NP with a drug core – MPN shell structure, which provides a guideline for the future application to various hydrophobic drugs. We demonstrated the efficiency of this method via the synthesis of different drug NPs of CM, PTX and $VD_3$ with well controlled sizes of 100-200 nm and high drug loadings of 40-70%. Our microfluidic method enables continuous production of the MPN coated drug NPs at a relatively high yield of 7-10 mg/hr for these three drugs to facilitate scale-up efforts. Our work on this new microfluidic method lays the foundation for the well-controlled continuous production of MPN-coated NPs for a large variety of hydrophobic drugs.

## ACKNOWLEDGEMENTS

This work was partially supported by grants from the National Institutes of Health (U01 HL143403, R01 CA254110 to BH; R01 CA232419, R01 CA258737 to YY) and National Science Foundation (MCB-2134603 to BH). YS was partially supported by the Purdue University Center for Cancer Research (P30 CA023168) and a Program Grant from Purdue Institute of Drug Discovery.

## REFERENCES

[1] S. V. Jermain et al, *International journal of pharmaceutics* **2018**, *535*, 379.
[2] Y. Chen et al, *International Journal of Pharmaceutics* **2021**, *602*, 120650.
[3] P. Liu et al, *ACS Applied Materials & Interfaces* **2020**, *12*, 53654.
[4] Y. Liu et al, *Scientific reports* **2017**, *7*, 1.
[5] F. Taemaitree et al, *Molecular Crystals and Liquid Crystals* **2020**, *706*, 116.
[6] M. Zhao et al, *Small Methods* **2017**, *1*, 1600030.
[7] H. Ejima et al, *Science* **2013**, *341*, 154.
[8] J. Chen et al, *ACS nano* **2019**, *13*, 11653.
[9] G. Shen et al, *ACS nano* **2016**, *10*, 5720.
[10] M. S. Taha et al, *Nano letters* **2019**, *19*, 8333.
[11] S. A. Yuk et al, *Science Advances* **2021**, *7*, eabj1577.

SB³C2022
Summer Biomechanics, Bioengineering and Biotransport Conference
June 20-23, Eastern Shore, MD, USA

# DIFFERENCES IN PORCINE ACL MORPHOLOGY AND FUNCTION ARE MINOR BETWEEN BOARS AND BARROWS AT EARLY ADOLESCENCE

**Jacob D. Thompson (1), Danielle Howe (1), Lauren V. Schnabel (2), Matthew B. Fisher (1,3)**

(1) Joint Department of Biomedical Engineering, North Carolina State University and University of North Carolina at Chapel Hill, Raleigh, NC, USA
(2) Department of Clinical Sciences, North Carolina State University, Raleigh, NC, USA
(3) Department of Orthopaedics, University of North Carolina at Chapel Hill, Chapel Hill, NC, USA

## INTRODUCTION

There are an ever-increasing number of pediatric athletes through middle and high school sports, accompanied by an increase in pediatric anterior cruciate ligament (ACL) injuries [1]. Furthermore, there is a stark difference during adolescence in the rate of ACL injuries between males and females, with females being 3 times more likely to tear their ACL [2]. Several groups attribute this difference to aspects of puberty, including spikes and cycles of sex hormone serum concentrations of estradiol and progesterone in females [3,4]. Despite several groups showing correlations between estradiol and progesterone concentrations and overall joint laxity, there is still much debate over the effect of these sex hormones on changes within specific tissues, like the ACL [3]. Even less information exists on the influence of testosterone, the primary male sex hormone, on the developing male ACL. Surgical castration is known to drastically decrease total serum testosterone values, and there is some evidence that testosterone may play a protective role in ligament function [5]. One study showed that castrated rats had significantly less testosterone and similar-sized ACLs as intact rats, yet the ACL had a lower load to failure and ultimate stress [6]. Currently, there are no large animal models that have looked at the influence of surgical castration on the developing male ACL, which will be useful in identifying effects in the ACL, specifically, as opposed to overall joint laxity. Our group has also shown that the size of the porcine ACL diverges in males and females near the point of sexual maturity [7], similar to humans [8], suggesting the pig as a good model to study changes during adolescence. Therefore, the objective of this study was to use an established porcine animal model for the human ACL to determine how castration influences the structure and function of the male ACL during adolescence.

## METHODS

Twenty-four male Yorkshire crossbreed pigs were raised to 4.5 months (pre-puberty) or to 6 months (early puberty). Half of each age group were left sexually intact (boars), while the other half were castrated (barrows) at an early age (n=6 animals/age/treatment; Fig. 1A). All animals were bred at the North Carolina State University Swine Education Unit, and all experimental protocols were approved by the NC State University IACUC. Following euthanasia, hind limbs were removed, and the stifle (knee) joints were stored at -20°C in saline-soaked gauze. To determine structural data, stifle joints were thawed and imaged using a 7.0-T Siemens Magnetom MRI scanner (Siemens Healthineers) using a double-echo steady-state sequence (DESS, flip angle: 25°, TR: 17ms, TE: 6s, voxel size: 0.42 x 0.42 x 0.4mm). Joint size data, including bicondylar width, anterior-posterior (AP) tibial width, and cross-sectional areas (CSA) of the anteromedial (AM) and posterolateral (PL) bundle of the ACL, were recorded after segmentation using a commercial software (Simpleware ScanIP, Synopsys) and processing using MATLAB scripts (Fig. 1B).

Then, stifle joints (with the exception of two 4.5 month barrows) were biomechanically tested using a 6 degree-of-freedom force sensing robotic testing system (Kuka, SimVitro) as previously described [7]. AP loads of 80 N and 100 N for the 4.5 month and 6 month joints, respectively, were applied at 60° of flexion in force control mode and the kinematic paths were recorded. The kinematic paths were then repeated after removing the AM and PL bundles of the ACL to determine tissue-specific contributions during anterior drawer under the principle of superposition [9]. Normalized joint laxity was calculated as AP tibial translation divided by AP tibial width. ACL stiffness values were calculated as the slope of the linear region of the AP force-translation curve. Two-way ANOVAs were used to determine overall effects of age and castration on bicondylar width, CSA, joint laxity, ACL stiffness, and ACL bundle contributions. Sidak post-hoc tests were used for multiple comparisons between boars and barrows ($\alpha$=0.05). Data presented as mean ± 95% CI as each point representing an animal.

## RESULTS

Both age (p=0.002) and surgical castration (p=0.03) had significant effects on overall knee joint size (Fig. 1C). The average boar and barrow bicondylar width increased by nearly 9% from 4.5 to 6 months. Between boars and barrow, there was no significant difference at 4.5 months, but the barrows at 6 months had an 8% smaller width (adjusted p=0.04).

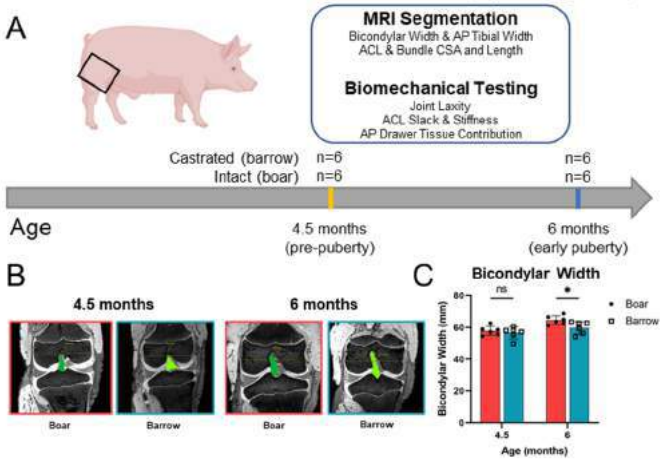


**Figure 1: (A) Joints were collected from boars and barrows at 4.5 or 6 months. (B) Representative MRI scans of joints. (C) Bicondylar width data. *indicates adj p<0.05 from post-hoc test.**

Raw ACL and AM bundle CSA values averaged 13% and 20% smaller in the barrows across both ages (ACL: p=0.08; AM: p=0.07; Fig. 2A-C). Raw PL bundle CSA values showed no differences between the boars and barrows across the ages (p=0.94). Once the raw CSA values were normalized to the bicondylar width, these minor size differences largely disappeared (ACL: p=0.79; AM: p=0.23; PL: p=0.77; Fig. 2D-F). Age, however, has a significant effect on all three CSA values, which persisted after normalizing to the bicondylar width (ACL: p=0.008; AM: p=0.008; PL: p=0.003).

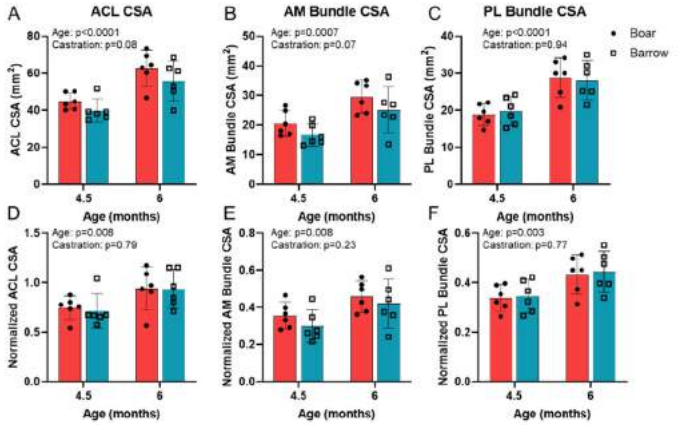


**Figure 2: Cross-sectional area of the (A) ACL, (B) AM bundle, and (C) PL bundle. Cross-sectional area normalized to bicondylar width of the (D) ACL, (E) AM bundle, and (F) PL bundle. P-values shown for main age and castration effects.**

Biomechanical analysis revealed that normalized joint laxity did not significantly differ between age (p=0.06) or castration status (p=0.94; Fig. 3A). There was no significant main effect of castration on ACL stiffness (p=0.55), although mean values were higher in the barrows at 6 months, but not 4.5 months (Fig. 3B). The AM bundle resisted the majority of the anterior drawer applied to the tibia in both the barrows (72%) and boars (88%) across 4.5 and 6 months (Fig. 3C). The difference in bundle contribution (Fig. 3D) did not significantly change because of castration (p=0.06), but the boars did have slightly higher bundle difference than the barrows (76% vs. 45%).

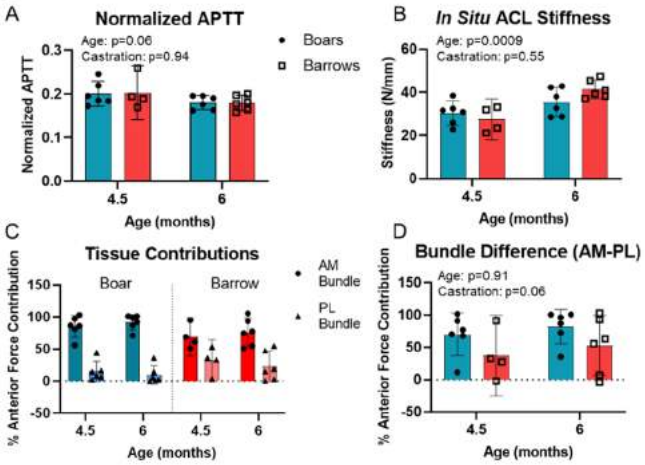


**Figure 3: (A) Normalized APTT and (B) *In situ* ACL stiffness. (C) AM and PL percent contribution to resisting anterior drawer. (D) Difference between AM and PL bundle contributions.**

## DISCUSSION

This study found that while surgical castration influenced overall joint size, it had only minor effects on ACL size and morphology as well as on mechanics. When looking at ACL CSA, these results are in agreement with other groups who have shown that surgical castration in rats does not change ACL size [6]. Raw structural values did show some minor differences, but these were mainly a result of smaller joints in the barrow groups. There were some interesting differences between boars and barrows when looking at function, though. After the point of sexual maturity (5-6 months) [10] the barrows had slightly stiffer ACLs that were not present pre-puberty. A possible explanation may be that there are less active muscle forces surrounding the knee in castrated animals that typically stabilize the knee joint. This might then result in greater force transmission in the ligaments and thus, stiffer ACLs via remodeling. When looking at load distribution between the AM and PL bundles, the boars seemed to be more AM-dependent, whereas the barrows have more variable load distribution between the bundle, which more closely resembles data in female pigs [7]. A larger sample size, older ages, and testosterone levels are necessary to fully tease out these effects. This and future work will help determine the role of sex hormones on ACL structure and function across development.


## ACKNOWLEDGEMENTS

We would like to thank Laboratory Animal Resources (NC State) and the Biomedical Research Imaging Center (UNC-CH) for their contributions to this work. Funding provided by NIH (R01 AR071985) and NSF (DGE-1746939).


## REFERENCES


[1] Beck, N et al., *Pediatrics,* 139:e20161877, 2017. [2] Gupta, A et al., *Orthop J Sports Med,* 8(5):2325967120919178, 2020. [3] Schultz, S et al., *Med Sci Sports Exerc,* 36:1165-1174, 2004. [4] Park, S et al., *Am J Sports Med,* 37:588-598, 2009. [5] Brunius, C et al., *Vaccine,* 29:9514-9520, 2011. [6] Romani, W et al., *Knee,* 23:1069-1073, 2016. [7] Howe, D et al., *J Orthop Res,* 1-12, 2021. [8] Cone, S et al., *J Orthop Res,* 1-8, 2021. [9] Rudy, T et al., *J Biomech,* 29:1357-1360, 1996. [10] Reiland, S, *Acta radiologica. Supplementum*, 358:15–22, 1978.

SB³C2022
Summer Biomechanics, Bioengineering and Biotransport Conference
June 20-23, Eastern Shore, MD, USA

# AN EXPERIMENTAL APPROACH TO QUANTIFY THE PRE-STRAINS OF THE TRICUSPID HEART VALVE LEAFLETS

**Devin W. Laurence (1) and Chung-Hao Lee, Ph.D. (1,2)**

(1) Biomechanics and Biomaterials Design Laboratory, School of Aerospace and Mechanical Engineering, The University of Oklahoma, Norman, Oklahoma, USA
(2) Institute for Biomedical Engineering, Science, and Technology, The University of Oklahoma, Norman, Oklahoma, USA

## INTRODUCTION

The importance of pre-strains in soft biological tissues was first emphasized by Dr. Y.C. Fung and colleagues in the 1980s [1,2]. Their seminal works showed that the pre-strains within the arteries are heterogeneous and influence the *in vivo* stress and strain distributions of the tissue. These findings sparked interests in this important topic over the past three decades, and our understanding of the topic has improved accordingly. For example, *in-silico* approaches have been employed to understand how pre-strains influence the behavior of thin membranes (e.g., heart valve leaflets) [3], how to best implement pre-stresses into simulations of abdominal aortic aneurysms [4], and the role of growth and remodeling in the formation of pre-strains in the left ventricle [5].

Despite the significant advancements in the topic of pre-strains since Dr. Fung's fundamental arterial studies, much remains to be further explored. This is especially true for the heart valve leaflets that have received considerably less attention in this topic compared to arterial or ventricular tissues. One key area of improvement is the experimental methodologies to quantify the pre-strains of these soft biological tissues. Exemplary investigations oftentimes involve some type of opening angle experiment. However, opening angle experiments are only easily performed on cylindrical tissues (e.g., arteries) and may not be directly applicable when considering planar tissues, such as the heart valve leaflets. Researchers have overcome this limitation by using fiducial markers to track configurational changes of the tissue following removal from the *in vivo* configuration, including the work by Amini *et al*. [6] that experimentally captured the central region pre-strains of the mitral valve leaflets. Although this has provided the foundation for our current understanding of heart valve leaflet pre-strains, experimental data that demonstrate the essential microstructural [7] and mechanical [8] heterogeneities suggest that these pre-strains are also heterogeneous. Thus, the objective of this study is to establish an experimental approach that provides a novel, rich, spatial description of the pre-strain to inform heart valve leaflet tissue biomechanics.

## METHODS

***Heart Retrieval and Preparation*:** Five porcine hearts ($n$=5) were acquired fresh from a local slaughterhouse (Chickasha Home Meat Co., Chickasha, OK) and promptly transported to the laboratory. Upon arrival, the right auricle was removed, and the right ventricle was opened by cutting along the posterior-septal leaflet commissure to the apex of the heart. The tricuspid valve (TV) leaflets were then briefly rinsed and visible coagulated blood was removed from the heart. Finally, a surgical pen was used to apply approximately 100 fiducial markers in a uniform unstructured grid on the leaflet surface.

***Stereo Image Acquisition and TV Excision*:** Following fiducial marker application, the heart was placed beneath two cameras arranged in a calibrated stereo configuration. The cameras were then used to capture two images (**Fig. 1**) of the valve in the *ex vivo* configuration for 3D registration. Following image acquisition, the TV was carefully dissected from the heart while maintaining the native annulus and chordae attachments. This dissected valve was floated in a bath of phosphate buffered saline and placed under the stereo camera for imaging of the explanted configuration.

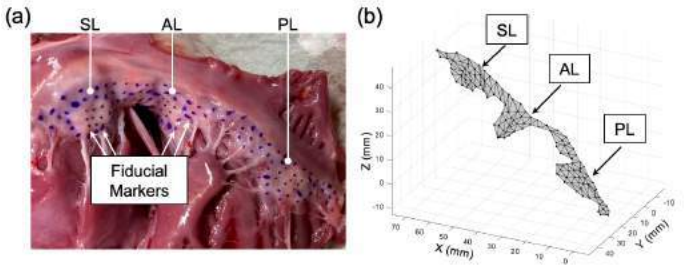


**Figure 1. (a) Representative image, and (b) 3D-registered leaflet surface. (SL: septal, AL: anterior, PL: posterior leaflets)**

***3D Fiducial Marker Registration via Discrete Linear Transform*:** The two sets of images of the valve in the *ex vivo* configuration were imported into MATLAB (MathWorks, Natick, MA). Next, the pixel locations of each fiducial marker in both images were manually determined using the `drawpolygon()` function. The two sets of pixel locations for each fiducial marker were then used with the calibrated discrete linear transformations of each camera according to [9] to determine the physical 3D marker locations. This process was repeated with the two offset images of the valve in the explanted configuration.

***Computation and Evaluation of Pre-Strains*:** The overhead view of the 3D fiducial marker locations were used with the MATLAB `delaunay()` function to construct a triangular mesh of the *ex-vivo* (reference) and explanted (deformed) leaflet surfaces. For each element, both the reference and deformed nodal coordinates were shifted so the centers of geometry were at the origin and rotated so each element's normal vector aligned with the +*Z*-axis. The 2D nodal displacements for each node $(u_i, v_i)$ were then used to compute the deformation gradient

$$\mathbf{F} = \mathbf{I} + \begin{bmatrix} \sum_{i=1}^{3} B_{Xi} u_i & \sum_{i=1}^{3} B_{Yi} u_i \\ \sum_{i=1}^{3} B_{Xi} v_i & \sum_{i=1}^{3} B_{Yi} v_i \end{bmatrix}. \quad (1)$$

Herein, **F** is the deformation gradient, **I** is the 2nd-order identity tensor, and $B_{Xi}$ and $B_{Yi}$ are the derivatives of the shape functions in the *X*- and *Y*-directions, respectively. The deformation gradient was then used to compute the Green-Lagrange strain $\mathbf{E} = 0.5(\mathbf{F}^T\mathbf{F} - \mathbf{I})$. Next, the principal strains were determined and classified as the circumferential or radial principal strain based on their principal orientations. These principal strains were finally rotated back to the undeformed configuration for visualization purposes.

## RESULTS

***TV Leaflet Residual Strains are Heterogeneous*:** The circumferential and radial principal residual strains for one representative heart are provided in **Figure 2**. These results clearly show the pre-strains vary across the tricuspid valve leaflets in both principal directions. However, the septal leaflet and posterior leaflet generally have positive circumferential and radial principal strains, respectively. In addition to the quantified principal pre-strains, these vectors within the visualizations show the how aligned the principal strains are near the circumferential direction (**Fig. 2a**) or the radial direction (**Fig. 2b**). These orientations are generally consistent across the three leaflets.

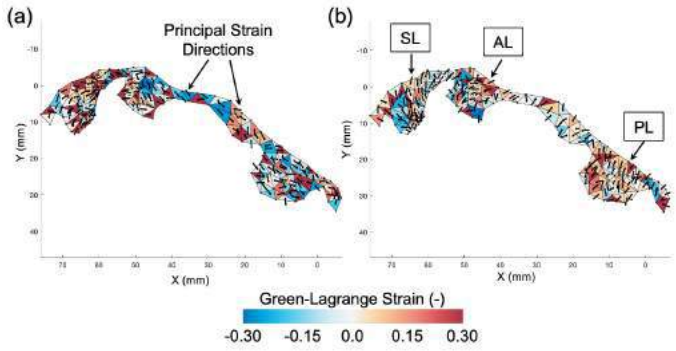


**Figure 2. Computed principal pre-strains and directions for a representative TV in the (a) circumferential, (b) radial directions.**

***Comparisons of the Average Leaflet Pre-Strains*:** The average principal pre-strains for each leaflet are shown in **Fig. 3**. These results indicate large variations across the three TV leaflets, further suggesting that the pre-strains are *leaflet-specific* and could be stemmed from the microstructural differences in the leaflets. Among the three leaflets, the posterior leaflet (PL) appears to exhibit the greatest variability while the anterior leaflet (AL) has the smallest variability in the radial direction.

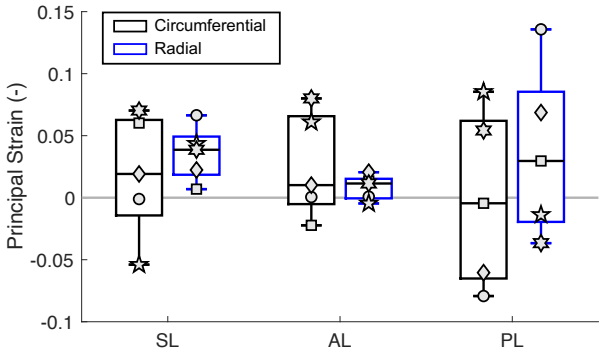


**Figure 3. Average circumferential and radial pre-strains for each TV leaflet. The individual heart is indicated with a unique symbol.**

## DISCUSSION

This study has provided the first experimental characterization of the TV leaflet pre-strains. This new approach allows us to determine the 3D configurational changes in the tricuspid valve following excision from the heart. As a result, we can obtain a rich description of the tricuspid valve leaflet pre-strains that was previously unobtainable. Our analysis has shown the pre-strains are heterogeneous and but generally align with the two anatomical directions – the circumferential direction and the radial direction. Furthermore, these pre-strains were found to be leaflet-specific, which agrees with the previous microstructural and mechanical observations in the literature [7-8].

One key extension of the present work is the incorporation of the quantified pre-strains into *in-silico* simulations of the TV [10]. By considering the accurate pre-strains, we can acquire more realistic predictions of the tricuspid valve behavior. Further, the acquired pre-strain information can be compared to information acquired from polarized spatial frequency domain imaging [11] to relate the quantified strains to the underlying collagen fiber architecture. This would be an important first logical step to establish the mechanics-microstructure relationship as well as the underlying growth and remodeling [5].

## ACKNOWLEDGEMENTS

Funding supports from the AHA Scientist Development Grant (16SDG27760143), Presbyterian Health Foundation, American Heart Association Predoctoral Fellowship (Award #821298), and National Science Foundation Graduate Research Fellowship (GRF 2019254233) are greatly appreciated. We would like to also thank Colton Ross, Kevin Pham, and Daniel Fitzpatrick for their help with the data acquisition.

## REFERENCES

[1] Chuong, CJ and Fung, YC, *J Biomech Eng*, 108:189-192, 1986.
[2] Liu, SQ and Fung YC, *J Biomech Eng*, 110:82-84, 1988.
[3] Rausch, MK, *et al*., *J Mech Phys Solids*, 61:1955-1969, 2013.
[4] Gee, MW, *et al*., *J Biomech*, 42(11):1732-1739, 2009.
[5] Genet, M, *et al*., *J Biomech*, 48(10):2080-2089, 2015.
[6] Amini, R, *et al*., *Ann Biomed Eng*, 40:1455-1467, 2012.
[7] Meador, WD, *et al*., *Acta Biomater*, 102:100-113, 2020.
[8] Laurence, DW, *et al*., *J Biomech*, 83:16-27, 2019.
[9] Smith, DB, *et al*., *Ann Biomed Eng*, 28:598-611, 2000.
[10] Laurence, DW, *et al*., *Int J Num Meth Biomed Eng*, 36(7):e3346, 2020.
[11] Jett SV, *et al*., *Acta Biomater*, 102:149-168, 2020.

SB³C2022
Summer Biomechanics, Bioengineering and Biotransport Conference
June 20-23, Eastern Shore, MD, USA

# ANALYSIS OF TRACHEAL AIR FLOW DYNAMICS IN INFANT TRACHEAL STENOSIS BEFORE AND AFTER SLIDE TRACHEOPLASTY USING 3D PRINTING AND COMPUTATIONAL FLUID DYNAMICS MODELING

**Clare Richardson (1,2), Michael Barbour (3), Seth Friedman (4), Randall Bly (2,3), John Dahl (1,2), Kaalan Johnson (1,2), Alberto Aliseda (3)**

(1) Department of Otolaryngology-Head and Neck Surgery, University of Washington, Seattle, WA, USA
(2) Division of Pediatric Otolaryngology, Seattle Children's Hospital, Seattle, WA, USA
(3) Department of Mechanical Engineering, University of Washington, Seattle, WA, USA
(4) Center for Clinical and Translational Research, Seattle Children's Hospital, Seattle, WA, USA

## INTRODUCTION

Tracheal stenosis is a rare congenital anomaly that most commonly occurs due to improperly formed tracheal cartilage rings.[1] It generally presents with long segment airway narrowing that leads to respiratory restriction as an infant. It is estimated that only 10-17% of patients can be managed with observation, while most undergo surgery.[2] Slide tracheoplasty (ST) is the preferred option for long segment tracheal stenosis (LSTS) due to its high success rates.[3] The procedure itself is technically challenging and involves complete transection and reconstruction of the trachea.

Due to relatively low surgical volumes and a heterogeneous patient population, it is difficult to study outcomes and compare techniques in ST. Prior anatomic studies have shown that all types of ST increase the diameter and volume of the stenosis, and that a beveled tracheal transection incision as opposed to a straight incision results in a longer post-operative tracheal length.[4] From a physiological perspective, little is understood about how surgery changes tracheal airflow. There are no studies examining pre- and post-operative airflow after ST. While increased length is optimal from a surgical and healing perspective, it is unknown how varying surgical techniques affects airflow.

Computational fluid dynamics (CFD) has been increasingly used in the past decade to investigate and quantify airflow dynamics in healthy and diseased airways [5,6]. In this study, we use 3D printed trachea models and CFD to analyze the airflow dynamics before and after ST and compare airflow between different surgical techniques. By leveraging these advanced modeling tools, we aim to improve the clinical understanding of LSTS and demonstrate which surgical technique yields the optimum anatomy and airflow physiology.

## METHODS

A high-resolution (0.357x0.357x 0.6mm slice thickness) computed tomography (CT) imaging scan was obtained (SOMATOM Force Dual Source CT, Siemens Healthineers, Erlangen Germany) from a two-year-old patient with complete tracheal rings and LSTS. Data from this scan was converted to a stereolithographic (STL) file and the lumen, cartilage, and soft tissue were modeled in Mimics/3-Matics (Materialise, Leuven Belgium). Model printing was performed on a Stratasys J750 digital anatomy printer (Stratasys Ltd., Rehovot Israel) using multi-materials (Agilus 30 for the wall, Structural-Frame 4 [pre-set] for cartilage rings, and Gel-matrix for the lumen). ST was performed on the models by a single pediatric airway surgeon using a combination of surgical technique variables. The main surgical variable was the type of tracheal transection incision angle (90º [straight], 45º anterior-superior to posterior-inferior bevel [AP bevel], and 45º posterior-superior to anterior-inferior bevel [PA bevel]. After transection, ST was completed on the models using standard instruments and suture. Post-operative CT scans of the models were obtained for analysis. Luminal surfaces were analyzed by single rates to derive measures of length, area, and volume measures.

For each surgical technique (straight, AP bevel, PA bevel) and the pre-treatment control, quasi-steady CFD simulations of peak inhalation were run to evaluate conditions of maximum respiratory resistance. Unsteady RANS simulations were performed in StarCCM+ (v16, Siemens, PLM Software, Plano, TX, USA) with a K-omega SST model. Polyhedral meshes with approximately 1 million cells are generated from the CT scans of each condition. Flow extensions equal to 20x the airway branch diameter were added to the trachea and bronchi. To model inspiratory flow, a mass flow boundary condition was applied at the trachea equal to 100 mL/s, and a flow-split ratio of 0.32:0.62 is applied at the R:L bronchus, respectively. The inflow rate is based on an estimated tidal volume for a patient of this age and the bronchi flow-splits were derived from the volume ratio of the patients segmented right and left lung. Simulations were run for 0.15s with a dt of 5e-5s. Computed airflow metrics are averaged over the last 0.075s.

For each surgical technique, we computed the total airway resistance, ($R = \Delta Pi/iQ$), where $\Delta Pi$ and $Q$ are the inlet-to-outlet

pressure drop and flow-rate respectively, maximum and average velocity, and viscous dissipation (Θ). Viscous dissipation is defined as:

$$\Theta = 0.5\,\mu_t \int \boldsymbol{S} : \boldsymbol{S}\, dV + \int \rho\epsilon\, dV \qquad (1)$$

Where $\boldsymbol{S}$, the stress tensor, is defined as $[\nabla \boldsymbol{u} + \nabla \boldsymbol{u}^{\boldsymbol{T}}]$, $\mu_t$ is the effective viscosity, ρ is the fluid density and $\epsilon$ is the turbulent dissipation rate.

## RESULTS

Nine STs were performed including three replicates of each incision. Pooling all combinations, ST decreased total tracheal length by 36% ($p<0.0001$), decreased the length of the stenotic segment by 43% ($p<0.001$), increased cross-sectional area at the midpoint of the stenosis by 397% ($p<0.0001$), and increased total tracheal volume by 53% ($p=0.003$). Comparing all beveled incisions to all straight incisions, beveled incisions resulted in a longer final trachea by an average of 3.9mm (95% CI: 2.7-5.0), corresponding to about 9.5% of total post-operative tracheal length ($p<0.0001$).

CFD simulations of peak inspiratory flow were performed for each surgical technique and the pre-operative control (Table 1, Figure 1)

**Table 1: Computed airflow metrics for each surgery condition. For each metric, both the value and percentage change as compared to the control condition are shown.**

| | Total Airway Resistance (Pa/(mL/s)) | Maximum Velocity (m/s) | Average Velocity (m/s) | Viscous Dissipation (mW) |
|---|---|---|---|---|
| Control | 2.3 | 19.9 | 5.1 | 14.2 |
| Straight | 0.8 (64%) | 11.2 (44%) | 3.9 (24%) | 4.2 (70%) |
| AP Bevel | 0.9 (60%) | 13.2 (34%) | 42 (18%) | 5.2 (63%) |
| PA Bevel | 0.9 (57%) | 14.0 (30%) | 4.0 (20%) | 5.5 (61%) |

**Figure 1: Velocity streamlines (top row) and pressure contours (bottom row) of the pre-operative condition and each surgical technique. Colormap ranges are identical for all operated models, but different from the control.**

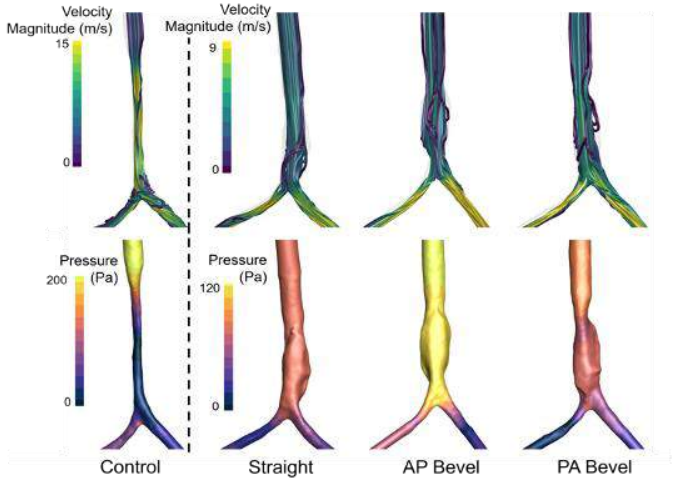


Each of the three surgeries was shown to reduce total airway resistance, maximum and volume averaged velocity, and viscous dissipation compared to the pre-operative condition with median reductions of each metric of 59%, 34%, 21%, and 63%, respectively. Relative differences between of each of the three surgeries was not significant.

The velocity streamlines and pressure contour maps (Figure 1) highlight the accelerated flow and pressure-drop through the primary tracheal stenosis. The flow conditions of each of the surgically repaired models exhibit similar behavior with a significant reduction of velocity and pressure-loss along the trachea, as compared to the pre-operative condition. The locations of maximum velocity and contributions to overall breathing resistance moved to the mainstem bronchi, representing a change to a more physiologically normal location.

## DISCUSSION

This is the first study to use CFD to analyze respiratory airflow changes in tracheal stenosis before and after ST. Additionally, it is the first to use CFD to analyze differences in ST surgical technique. As previously demonstrated, a beveled tracheal transection incision increased post-operative tracheal length and volume as compared to straight incisions.[4] There were no statistically significant CFD differences between surgical techniques, including straight incision compared to bevel, or between differing directions of incision bevel (45º AP versus PA). ST overall significantly decreased tracheal airflow pressure drop, velocity, and resistance. Computed energy expenditure during breathing decreased by 63% after surgery. These results mirror the clinical benefit observed from ST, reiterating it as a helpful treatment for patients suffering respiratory compromise from LSTS.

From a surgical technique standpoint, improving post-operative tracheal length without compromising airflow has important clinical implications. Due to the length preserved with improved tissue conservation, beveled incision tracheal segments require less distance to slide and therefore have less tension at the site of repair than straight incision tracheal segments. Relieving tension wherever possible may result in lower rates of complications such as anastomotic dehiscence, granulation, and re-stenosis, which can be life threatening.[7,8]

This study also represents the first reported use of 3D printed tracheal models used in combination with CFD. These models provide several advantages. They eliminate the variability that exists in the heterogeneous LSTS patient population. Using the same model for all procedures allows for direct comparison of simulated surgical variables on a single patient, which cannot be done in an in vivo model. Utilizing 3D printed models also allows for study of morphological and physiological changes immediately before and after surgery. Live comparisons rely on patient-based imaging or procedures, which can have inconsistent timing and are often avoided when possible in the pediatric population.

Overall, 3D modeling is an easy and safe way to study surgical variables in airway surgery. Adding CFD analysis allows for a more comprehensive understanding of the physiological changes introduced in tracheal stenosis after surgery. Our data show that a beveled tracheal incision has the added benefit over a straight incision of preserved tracheal length and does not compromise physiological airflow improvements. Taking these factors into consideration, we conclude that a beveled incision is the optimal surgical technique for ST.

## REFERENCES

[1] Ho A., et al., *Oto Clin N Am*, 41, 999-1021, 2008.
[2] Wilcox L., et al, *Otolaryngol Head Neck Surg*, 58, 729-735, 2018.
[3] Wertz A., et al, *J Ped Otorhinolaryngol*, 130:109814, 2020.
[4] Richardson C., et al, *Laryngoscope*, online ahead of print, 2021.
[5] Bates, A., et al, *Clin Biomech*, 66, 88-96, 2019.
[6] Shwab, R, et al, *Am Rev Respir Dis*, 148, 1385-1400.
[7] Chen S, et al., *Ann Thor Surg*, 108, 138-145, 2019.
[8] Holder T, et al., J Ped Surg, 8, 840, 1973.

# 3-DIMENSIONAL IMAGING OF THE MURINE VAGINA USING TO-PRO-3 IODIDE AND EOSIN WITH DUAL INVERTED SELECTIVE PLANE ILLUMINATION MICROSCOPY

**Jasmine X. Kiley (1), Mari J.E. Domingo (1), Guang Li (1), Diego R. Gatica (1), J. Quincy Brown, Ph.D. (1), Kristin S. Miller, Ph.D. (1)**

Department of Biomedical Engineering, Tulane University, New Orleans, Louisiana, United States

## INTRODUCTION

Pelvic floor disorders, such as pelvic organ prolapse (POP), and increased trauma risk are associated with increasing age and loss of elastic fibers [1]. While the etiology of pelvic floor disorders is not fully understood, disruption of elastic fibers and changes in the vaginal microstructure likely contribute. In clinical practice, the standard stain for two-dimensional (2-D) vaginal imaging is Hematoxylin and Eosin (H&E), which allows quantification of basic metrics such as layer thickness, collagen content, and elastin content [2]. However, 2-D histology involves sectioning three-dimensional (3-D) tissues into thin 2-D slices, limiting the ability to identify critical spatial relationships and orientations of extracellular matrix (ECM) components found in native tissues that are critical for tissue structural integrity and function.

Towards this end, dual-view inverted selective plane illumination microscopy (diSPIM) enables 3-D imaging of large samples with high resolution, more accurate cellular quantification, and increased image detail [3,4]. Similar approaches have been used to image human prostate tissue [4,5] and *C. elegans* embryos [6], utilizing stains such as TO-PRO-3 Iodide and Eosin (T&E). To date, how the 3-D vaginal architecture changes with pregnancy and other biological processes is not well defined. Further, it is unknown whether T&E stained vagina tissues are direct analogs of tissues stained with H&E.

Therefore, this study first sought to investigate the validity of T&E as an analog to H&E in murine vaginal tissue. In addition, T&E staining was utilized in diSPIM imaging to visualize vaginal morphology before and after pregnancy. It was hypothesized that pseudo-colored images from T&E fluorescent images would be analogous to H&E images and that diSPIM imaging with T&E staining will allow visualization of the 3-D architecture of the vagina. If successful, 3-D diSPIM imaging of the vagina will be an integral component of understanding changes in vaginal microstructure during pregnancy, aging, and POP.

## METHODS

**Stains.** TO-PRO-3 Iodide (Thermo Fisher Scientific, Waltham, MA) was dissolved to [0.1% v/v] solution with PBS and [0.2% v/v] Triton X-100. The tissue was stained with TO-PRO-3 Iodide, dehydrated, stained with Eosin Y, then optically cleared with Ethyl Cinnamate. Stains were applied directly to tissue sections without further modification.

**Animal Use.** A total of n=12 mice were used in this study. For H&E and T&E comparison, n = *9* nulliparous Fibulin-5 C57BL/6 x 129 SvEv female mice were used (IACUC approved). The mice comprised three different genotypes: wildtype (*Fbln5* ), haploinsufficient (*Fbln5* ), and deficient (*Fbln5* ) with n = 3/group. To evaluate the feasibility of 3-D imaging, three female CD-1 mice aged 2-3 months were used with nulliparous (n=1), day 18 gestation (n=1), and five days postpartum (n=1) (IACUC approved).

**2D Verification of Fluorescent Analog T&E.** Mice were euthanized via carbon dioxide inhalation, and the vagina was dissected. The vagina was then perfusion fixed in 10% formalin at the physiologic length and mean *in vivo* pressure for 24 hours. Physiologic length and *in vivo* pressure values were obtained from previous work [7]. Next, tissue samples were embedded in paraffin. 4μm thick sections were obtained in the circumferential plane and randomly allocated for either standard H&E or fluorescent T&E staining. To resemble H&E, the dual-channel fluorescent images were then pseudo-colored through a MATLAB algorithm.

**3-D diSPIM Imaging.** Mice were euthanized by guillotine without anesthesia and vaginas were extracted and stained as described above. The vagina was then mounted and imaged using lasers with wavelengths of 488 nm (eosin) and 640 nm (TO-PRO-3). The diSPIM imaging process was adapted from prior work [8]. The resulting images were pseudo-colored to resemble H&E. After 3-D diSPIM imaging, vaginal samples were sectioned (4 μm) and stained for H&E. The 2-D

slices were obtained at matched depths from the 3-D samples to identify key structures within the tissue.

**Data Analysis.** For the 2-D T&E images, qualitative analysis was performed by comparing key structures with the corresponding H&E tissue slice (Figure 2). Additionally, 3-D diSPIM images were viewed with Amira (Thermo Fisher Scientific) software. 2-D cross-sections were extracted to visualize morphological features before and after pregnancy (Figure 3).

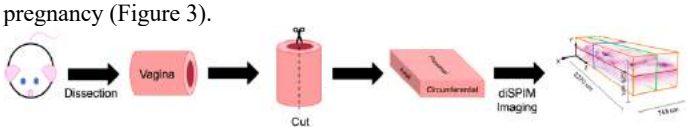


**Figure 1. Dissection and preparation of murine vaginas to obtain 3-D diSPIM images. Vaginas were cut axially and unrolled from cylindrical to rectangular geometry before mounting onto the diSPIM system [8].**

## RESULTS

A qualitative comparison between images stained with H&E versus T&E showed similar structures using both stains on FFPE tissue sections (Figure 2). Epithelial rugae were observable in the proximal view of the vagina in both the nulliparous (Figure 3A) and five days postpartum (Figure 3B) samples. Layer identification was possible in the cross-sectional images extracted from the 3-D diSPIM images (Figure 3A and Figure 3B). Upon qualitative observation, muscularis layer thickness was greater in the circumferential and axial views of the five days postpartum sample compared to the nonpregnant sample.

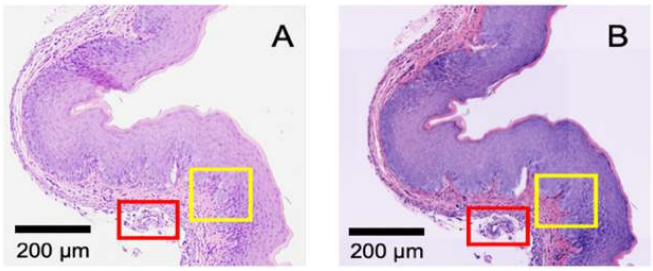


**Figure 2. Representative H&E (A) and T&E (B) images of Fibulin 5. demonstrated that fluorescent analog T&E was similar to the standard H&E stain. Specific regions of interest, including epithelial rugae (yellow) and a large vessel in the adventitia (red) showed further similarities between stains.**

## DISCUSSION

The qualitative and quantitative comparisons demonstrated that T&E staining was a high fidelity H&E analog (Figure 2). By applying the pseudo-color process within MATLAB, the same morphological features were visualized in both H&E and T&E images. This finding agreed with prior work that validated DRAQ5 and Eosin against H&E as a fluorescent analog [9].

The destructive nature and limited sampling frequency of standard 2-D histology techniques limits ability to identify spatial relationships and orientation of important ECM components such as collagen and elastic fibers. Volumetric histological imaging with the diSPIM system permitted visualization of T&E-stained vaginal tissue with easy sample mounting and isotropic resolution in three dimensions, thus enabling the analysis of structural relationships between cells and ECM components. Upon qualitative observation, the muscularis in the postpartum sample was thicker than the nulliparous sample. This observation was in agreement with findings in ovine samples [10].

Further imaging of multiple samples at both time points is needed to account for individual variation in vaginal morphology. A limitation to T&E was the inability to differentially stain collagen and elastin, which are proteins of high interest in the vagina. Further studies are needed to validate a fluorescent stain specific to these proteins compatible with diSPIM. To employ T&E's use in 3-D imaging of the vagina using the diSPIM system, future investigations include identifying changes in vaginal morphology throughout pregnancy, postpartum healing, and prolapse progression.

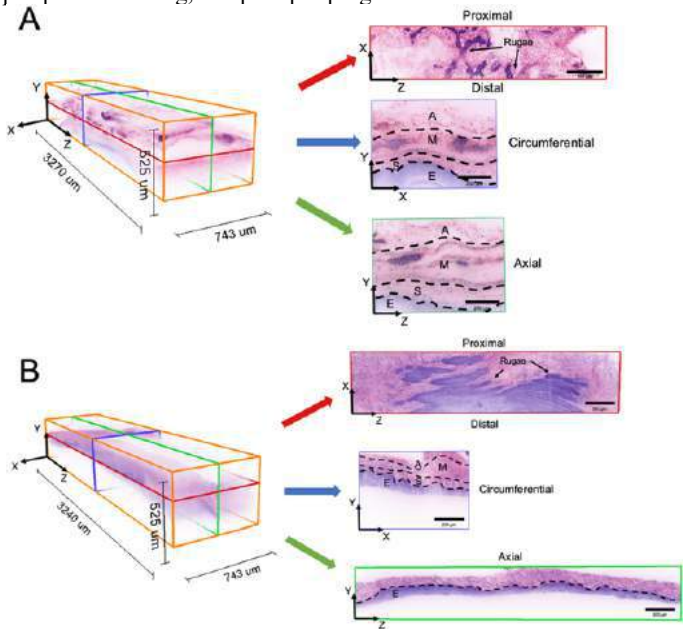


**Figure 3. XZ, XY, and YZ orthoslices extracted from 3-D diSPIM volumetric images of the nulliparous (A) and 5 days postpartum (B) vaginal samples. The XZ plane represented the vaginal plane from the proximal to the distal section. In this plane, the rugae of the epithelial layer was identifiable according to the purple staining of the nuclei of the epithelial cells (A, B). Along the Y direction from top to bottom of the sample, the rugae observed first in the XZ planes signify a section of epithelium which was thicker than other adjacent sections. The next observable layer along the Y direction was the sub-epithelial layer, which indicated that these rugae are "penetrating" into the sub-epithelium. The XY plane represented the circumferential plane of the vagina after being cut, and the vaginal layers were outlined as follows: E=epithelium, S=subepithelium, M=muscularis, A=adventitia, (A, B). The YZ plane represented the axial plane of the vagina across sample depth and the nulliparous vaginal layers were outlined (A), while the 5 days postpartum sample showed an identifiable epithelial layer (B).**


## ACKNOWLEDGEMENTS

We acknowledge funding from NSF CAREER (CMMI BMMB #1751050; KSM).


## REFERENCES


[1] Pandit L et al., *AJMS*, *314*(4), 228–231, 1997 . [2] Fischer AH et al., *Cold spring harbor protocols* pdb. Prot4986, 2008. [3] Huisken J et al., *Science* 305:1007-9, 2004 .[4] Power RM et al., *Nature methods* 14:360-73, 2017. [5] Glaser AK et al., *Nat Biomed Eng* 1:0084, 2017. [6] Duncan LH et al., *J Vis Exp*:10.3791/59533, 2019 . [7] Clark-Patterson GL et al., Sci Rep 11:20956, 2021. [8] Hu B et al., *Biomed Opt Express* 10:3833-46, 2019. [9] Elfer KN et al., *PLoS One* 2016 [10] Ulrich D et al., *PloS One* vol. 9,4 e93172, 2014.

# DESIGN AND INITIAL OPTIMIZATION OF A CENTRIFUGAL LEFT VENTRICULAR ASSIST DEVICE

**Huang Chen (1), Shweta Ashishkumar Karnik (1), Jeyan Kirtay (1), Lakshmi Prasad Dasi (1)**

(1) Department of Biomedical Engineering, Georgia Institute of Technology, Atlanta, GA

## INTRODUCTION

Left Ventricular Assist Device (LVAD) is used as an effective treatment for end-stage heart failure patients. However, severe complications, including thrombosis, stroke, and bleeding, are common. Past studies have shown that the blood damage associated with the supraphysiologic shear stress [1, 2] in the device is the cause for those complications. The mechanical forces generated by the rotating components destroy blood cells, leading to hemolysis; and activate platelets, causing thrombus formation. It is crucial to optimize the LVAD design to achieve minimal blood damage. In this work, we first designed a parametric centrifugal LVAD model and built a computational framework to assess blood damage. Subsequently, preliminary design optimization was carried out. Results from two models are compared and discussed.

## METHODS

An experimental parametric centrifugal LVAD has been developed at Georgia Tech (Fig.1a), based on the industry-proven design concept [3]. A Matlab script was used to generate the LVAD blade profile and the volute shape with different parameters. As illustrated in Fig.1b, the parameters that control the geometry and their ranges are: inlet diameter ($D_1$=10-15mm), rotor diameter ($D_2$=20-35mm), leading-edge angle ($\beta_1$=5-30°), trailing edge angle ($\beta_2$=10-60°), number of blades (z=3-8), blade thickness (d=1-4mm), blade tip gap size (distance between the blade tip and cutwater) (h=1-4mm), blade wrap angle ($\varphi$=30°-200°), and outlet diameter ($D_3$=10-20mm). Current optimization has been focused on the rotor, and the targeted quantity is the hemolysis index, a measure for blood damage, at the design condition of 5L/min and 3000 RPM. Three sample blade profiles generated by the code are shown in Figure 2. The rotors are named by their leading-edge angle followed by the trailing-edge angle ($\beta_1$-$\beta_2$). The inlet/outlet diameters are $D_1$=10mm and $D_2$=30mm, respectively. The initial design (20-60) is shown in Figure 2a, while

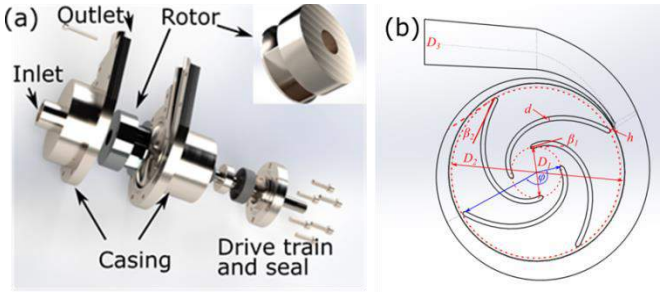


**Figure 1: (a) The experimental LVAD model and (b) design parameters.**

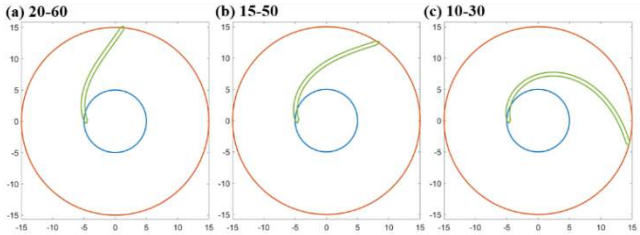


**Figure 2: Parametric rotor blade profiles.**

Figure 2c shows the rotor after optimization (10-30). There are four blades per rotor and the magnet attached to the top of the rotor was omitted in this initial optimization study.

A CFD model was developed in Ansys Fluent (Canonsburg, PA) to assess the performance and blood damage using the mesh motion method. The rotor and casing are defined as separate domains, and the interface between them slides freely to create the rotating motion. The 3D mesh was generated with mostly unstructured tetrahedral elements in Ansys Meshing. Boundary layer mesh was created by inflating the surface mesh, and the inner mesh layers were able to resolve the

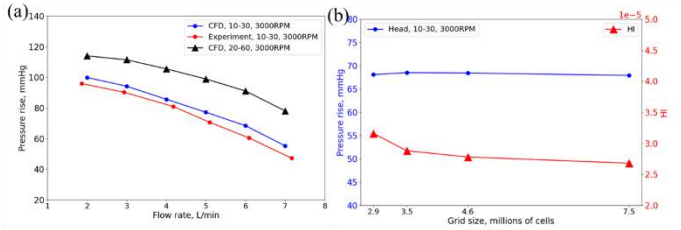


**Figure 3: (a) Performance comparison between experiments and CFD simulations. (b) Head rise and HI computed on different mesh grids.**

viscous sublayer. Blood was modeled as a Newtonian fluid with a density of 1060kg/m$^3$ and a viscosity of 3.5cP. Turbulence was modeled by the *k-ω* SST model. The reported quantities were the average of 3 consecutive rotor revolutions. A benchtop hydrodynamic testing was carried out to validate the CFD simulation. The results in Figure 3a have shown good agreementbetween the CFD and experiment for the 10-30 rotor at 3000RPM.

A hybrid Lagrangian/Eulerian hemolysis model was used, which is described in [4] as the model $C_E$. The hemolysis index (HI) is defined by the ratio of free hemoglobin to the total hemoglobin ($H_b$), $\mathrm{HI}(\bar{\tau}, it) = \Delta H_b / H_b$. The scalar stress $\bar{\tau}$ is defined by Eq1, where $\sigma$ is the stress tensor.

$$\bar{\tau} = [\frac{1}{6}\sum_{i,j}(\sigma_{ii} - \sigma_{jj})^2 + \sum_{i,j}\sigma_{ij}\sigma_{ij}]^{0.5} \quad (1)$$

The HI is calculated by a power law that includes the scalar stress and exposure time as defined in Eqn.2. The constants (a, b, c) are defines as (0.77, 3.075, $3.31\times10^{-6}$) following [5].

$$\mathrm{HI}(\bar{\tau}, it) = c\bar{\tau}^a t^b \quad (2)$$

Note that these constants and relations are empirical, and Reynolds stresses are not considered. Although the model might not provide the exact results, it is sufficient for the current optimization purpose. The HI is reported as the mass-weighted average at the outlet. A mesh independence study was carried out, and the results are shown in Figure 3b. The performance predicted by the CFD model is not affected much by the mesh size, while HI is very sensitive to it. In the following study, a mesh size of around 5 million was used.

## RESULTS

The current optimization step focuses on the blade leading and trailing edge angles, and two models: the original rotor design (20-60) and the optimized rotor (10-30), are compared. The head rise curve (Figure 3a) has shown the performance of the 20-60 rotor is much higher throughout the entire flow rate range. However, the 10-30 rotor causes much less blood damage (Figure 4), especially at low flow rates. For both models, HI is high at a low flow rate and decreases drastically at around 5L/min before rising again at high flow rates. The trend seems to be consistent with that for the efficiency, which peaks around 5L/min for both models. However, if HI and efficiency are compared across the models, higher efficiency does not suggest lower blood damage. For example, at 2L/min, both models have similar efficiency, but the 10-30 rotor causes much less blood damage.

The contours of velocity magnitudes (in the stationary reference frame) and HI at 5L/min are shown in Figure 5. This cross-section is located at the center of the rotor span. The vectors in the rotating reference frame have shown large recirculating regions for the 20-60 rotor (Figure 5a). HI is high in the recirculation region (Figure 5c) due to the long exposure time. While for the optimized rotor, the flow follows the blade profile without separation (Figure 5b). As a result, there is much less associated blood damage (Figure 5d). The velocity near the casing wall is high for the 20-60 rotor (Figure 5a), which is consistent with the higher performance for the model. However, the HI near the casing is significantly higher for the 20-60 rotor (Figure 5c) when compared with the optimized one (Figure 5d).

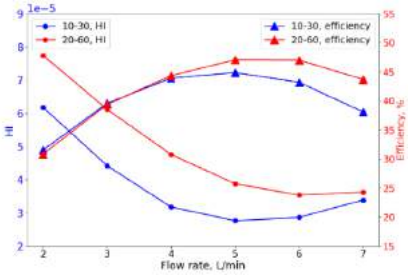


**Figure 4: HI and efficiency comparisons between the initial design and the optimized rotor.**

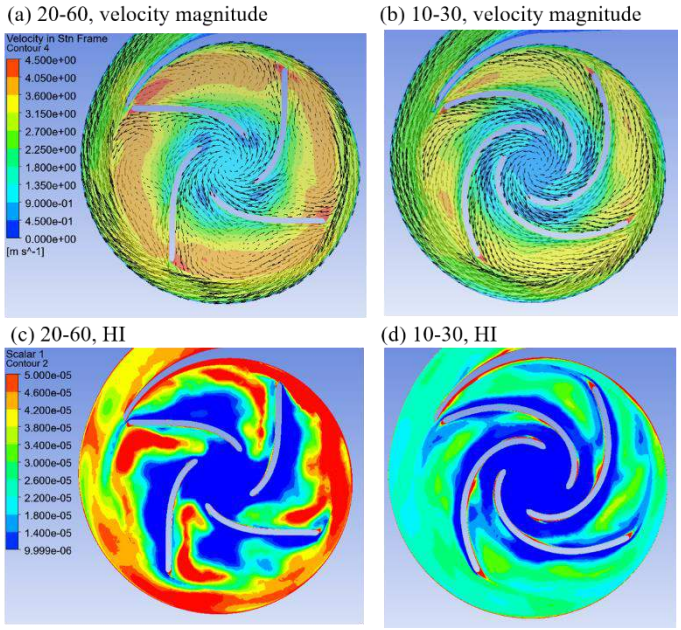


**Figure 5: (a, b) Flow and (c, d) HI comparisons between (a, c) the initial design and (b, d) the optimized rotor at 3000RPM and 5L/min. The color contour in (a, c) are computed in the stationary reference frame and the unit is m/s. The vectors in the rotor domain are plotted in the rotating reference frame.**

## DISCUSSION

A parametric LVAD model was design at Georgia Tech and initial optimization aimed at reducing the hemolysis has been carried out. Results have shown that the performance predicted by the CFD model matches well with experiments. It was found that the hemolysis index is very sensitive to the mesh grid size through a mesh independence study. The increase in blade angles increased both the performance and HI. The high HI is caused by the higher velocity near the casing and the large-scale separation in the rotor passage for the original rotor. The optimized rotor eliminates the flow separation thereby reducing the blood damage. Future work will focus on using advanced machine learning strategies to optimize the LVAD design.

## REFERENCES

[1] Chiu WC et al., *J Biomech Eng*. 2014;136:021014.
[2] Eckman PM et al., *Circulation*. 2012;125:3038-47.
[3] Gülich J. *Centrifugal Pumps*. Berlin Heidelberg: Springer-Verlag 2010.
[4] Yu H et al., *Artif. Organs*. 2017;41(7):603-621
[5] Bellofiore et al., *Ann Biomed Eng*, 2011;39(9):2417-2429

# AN IN-VITRO STUDY OF THE FLOW PAST A TRANSCATHETER AORTIC VALVE USING TIME-RESOLVED 3D PARTICLE TRACKING

**Huang Chen (1), Yasaman Farsiani (1,2), Lakshmi Prasad Dasi (1)**

(1) Department of Biomedical Engineering, Georgia Institute of Technology, Atlanta, GA
(2) Nationwide Children's Hospital, Columbus, OH

## INTRODUCTION

Three-dimensional flow field downstream of a transcatheter aortic valve was studied using time-resolved 3D particle tracking velocimetry. A fully refractive index matching imaging setup allows for unobstructed optical access downstream of the valve. Around 4,000 particles are tracked through three cardiac cycles. Velocity fields in a Cartesian mesh are obtained and analyzed by implementing a constrained interpolation algorithm.

## METHODS

An idealized aortic root model with three sinus lobes was made by cast PDMS. The wall thickness is at least 10mm to ensure minimal deformation during the cardiac cycle. A 26mm Edwards SAPIEN 3 (Edwards Lifesciences, Irvine, CA) transcatheter aortic valve was mounted inside the aortic chamber, with commissures aligned with the sinuses. The aortic root model was placed in the vertical left heart pulse duplicator flow loop shown in Figure 1. The model was tested under physiological conditions of 60 beats per minute, 120/80 mmHg, and an averaged cardiac output of 5 L/min. The working fluid was a mixture of water, glycerin, and urea, matching the viscosity of blood and the refractive index of the PDMS silicone. Undistorted optical access was achieved in the aortic root. The aortic flow rate was measured by a Transonic ultrasonic flow probe (Transonic Inc., Ithaca, NY) upstream to the aortic valve chamber. Aortic pressures were monitored across the valve using two Deltran transducers (DPT-200, Utah Medical) to ensure physiological conditions. The pulsatile pump used in this flow loop was a custom-built pneumatic bladder pump connected to a compressed air supply and controlled by a LabVIEW program.

Time-resolved 3D-PTV was used to measure the trajectories of the tracer particles in a 3D volume covering the entire aorta model downstream of the valve stent. The model was placed in a chamber filled with the same working solution (Figure 1). Four Phantom high-

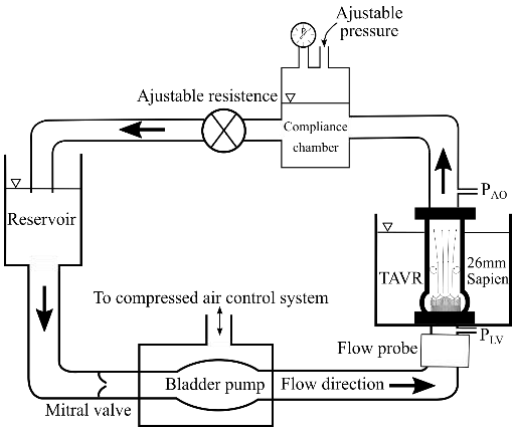


**Figure 1: Sketch of the pulsatile left heart simulator with the aortic root model.**

speed cameras (VEO 440l, 2560×1600 Pixels, 10μm pixel size) with 60mm Nikon lenses were used to record the particle images through four optical windows (Figure 2). The inner two cameras were separated by 60 degrees, while the outer two were separated by 140 degrees, satisfying 3D imaging conditions. The aorta was illuminated by a thick laser volume, expanded by a series of optics from a high-speed Nd:YLF double cavity laser beam. Scheimpflug adapters were used to ensure proper focus was achieved throughout the entire field of view. The imaging system and the laser were synchronized by a programmable timing unit (LaVision GmbH) and controlled by a desktop computer. The flow was seeded with fluorescence particles, and corresponding band-pass filters were used to filter out unwanted reflections. The data was acquired at 1,100 frames per second, and the flow in 3 consecutive cardiac cycles was recorded. The imaging

system was carefully calibrated in a two-step calibration process. First, rough calibrations of the cameras were obtained by placing a 3D

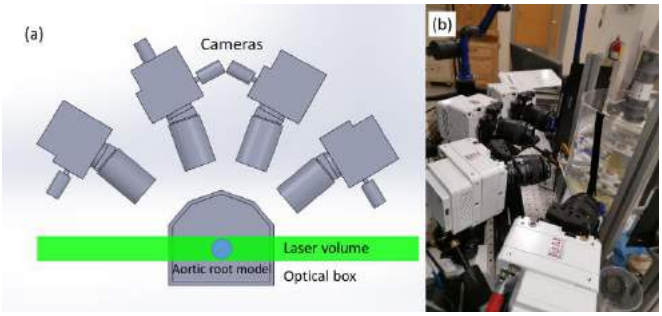


**Figure 2: 3D PTV experimental setup**

calibration target at the center of the laser volume. Second, a fine volume self-calibration [1] was carried out to reduce the residual calibration error to below 0.2 pixels. The optical transfer function (OTF) was calculated and used in subsequent particle detection algorithms [2]. Particles were tracked throughout the entire flow field by the Shake-the-box algorithm [3] implemented in DaVis 10 (LaVision GmbH). The tracking error of a single particle can be as low as 0.1px, much more accurate than the cross-correlation-based particle image velocimetry

## RESULTS

Around 4,000 individual particles were tracked in the $30\times30\times50mm^3$ volume. Two sample snapshots of the particle tracks are shown in Figure 4, representing the early systole (Figure 4a) and diastole phases (Figure 4b), respectively. The shear layer between the forward aortic jet and the surrounding fluid is clearly visible.

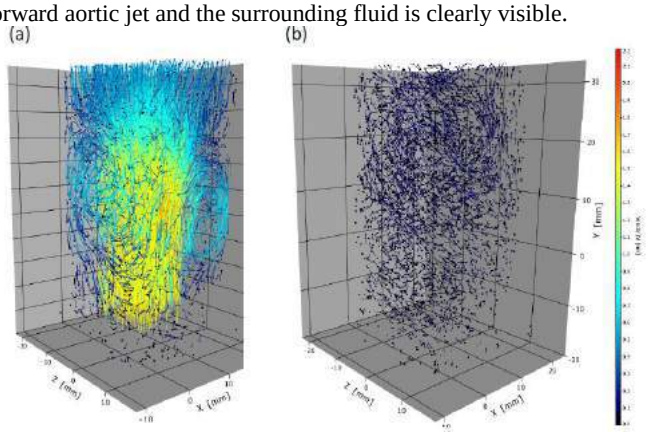


**Figure 3: Sample particle tracks color-coded by instantaneous velocity magnitude at (a) early systole and (b) diastole phases.**

The discrete velocity fields from the particle tracking were interpolated onto regular Cartesian grids using the second-order constrained cost minimization method described in [4]. The final 3D grid spacing is 0.8mm. Figure 4 shows the flow field at peak systole. At this phase, the flow field is dominated by a strong aortic jet, whose peak velocity exceeds 1.5m/s. Strong shear exists between the jet and the ambient fluid. The star-shaped jet shown in Figure 4b resembles the valve opening geometry. While the jet is developing downstream, it entrains the fluid surrounding it. This entrainment process is shown more clearly in the cross-section view (Figure 4b), where the velocity vectors are pointing from the wall towards the jet. Apart from the antegrade aortic jet, there is a strong retrograde flow near the wall, whose magnitude can reach 0.5m/s. The flow is driven by the positive pressure gradient associated with the attachment of the aortic jet at the wall downstream. The retrograde flow eventually enters the sinus region of the valve, contributing to the washout there.

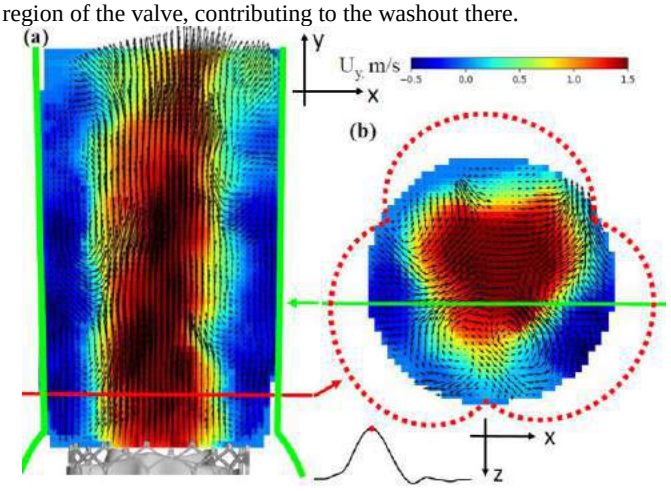


**Figure 4: In-plane vectors over $U_y$ contour at peak systole.**

The flow on the same plane at diastole is shown in Figure 5. The magnitude of the aortic jet has decreased significantly but is still entraining the surrounding fluid (Figure 5b). The scale and the magnitude of the retrograde flow increase, and it is still entering the sinus regions of the valve. However, this fluid has been in the aorta and might already be exposed to high shear associated with the jet. As a result, its contribution to thrombosis formation on the leaflets needs further investigation.

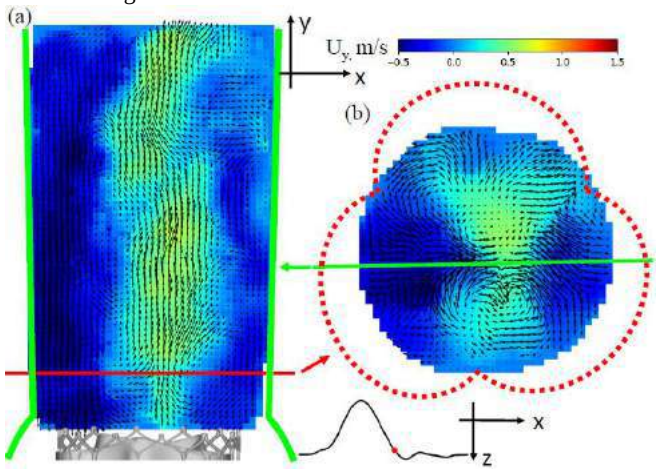


**Figure 5: In-plane vectors over $U_y$ contour at diastole.**

## DISCUSSION

Time-resolve 3D PTV was used in this study to quantify the particle trajectories and flow downstream of a transcatheter aortic valve. Detailed 3D flow features of the aortic jet were obtained and discussed. Future work will quantify the particle residence time and use it to study the effects of the retrograde flow on the washout in the sinus

## REFERENCES

[1] Wieneke B, *Exp. Fluids*, 45:549-556, 2008.
[2] Schanz D, et al., *Meas Sci Technol*, 24(2):024009, 2012
[3] Schanz D, et al., *Exp. Fluids*, 57(5):1-27, 2016
[4] Agarwal K, , et al., *Exp. Fluids*, 62(4): 1-20, 2021

# CARTILAGE MECHANICAL PROPERTIES OF DEVELOPMENTAL DYSPLASIA OF THE HIP IN A PORCINE MODEL

**Kate J. Benfield (1), Amevi M. Semodji (1), Vidyadhar V. Upasani (2), Christine L. Farnsworth (2), Derek Q. Nesbitt (1), Erin M. Mannen (1), Trevor J. Lujan (1)**

(1) Department of Mechanical & Biomedical Engineering, Boise State University, Boise, ID, USA
(2) Rady Children's Hospital San Diego, CA, USA

## INTRODUCTION

Developmental dysplasia of the hip (DDH) is a biomechanical disease of infancy that is the leading cause of early-onset hip osteoarthritis in people >50 years of age.[1] DDH occurs when the femoral head and/or acetabulum is developing incorrectly, requiring intervention in 2 of 1000 infants. Early diagnosis and treatment with a Pavlik harness is used to encourage proper hip development in babies with DDH; however, 20% of these treatments fail, requiring surgery and increasing the likelihood of lifelong complications. Despite the prevalence of DDH and the lasting negative impact on some patients, there are few pre-clinical models that can be used to investigate innovative treatment strategies. Dodds et al. previously developed a knee-stifling technique to study hip instability in a porcine DDH model,[2] but the potential tissue-level changes to the hip joint induced by the stifle were not quantified. In order to understand the localized effect of DDH on tissue remodeling, and to select appropriate constitutive models for future pre-clinical computational studies, the mechanical behavior of the articulating surfaces must be characterized. The objective of this study is to the quantify viscoelastic mechanical properties at the hip between DDH-induced limbs and controls in distinct regions of the acetabulum and femoral head.

## METHODS

*Specimen Preparation*: Articular cartilage was harvested from two pigs: one farm pig that was induced with DDH (3 months old), and one healthy juvenile Yucatan micro-pig (12 months old). The DDH pig had the right knee stifled with a screw for 6 weeks prior to harvest resulting in outcomes consistent with hip dysplasia (e.g., reduced acetabular coverage).[2] After dissection, a 4-mm biopsy punch was used to extract cylindrical cartilage plugs in anatomical regions of the acetabulum and femoral head specified by Athanasiou et al. **(Fig 1A)**[3]. Three plugs were excised per region within the superficial zone of the cartilage for 21 specimens per pig (42 total). Custom-made tooling was used to trim and level the deep surface of the plug to produce a uniform thickness of approximately 0.8 mm (0.79 ± 0.04 mm) (**Fig. 1B**). Specimens were stored in 0.9% saline solution and frozen. On the day of mechanical testing, each sample thawed for 30 minutes and then equilibrated for approximately one hour in a 0.9% saline solution bath (21°C). The diameter of each specimen was measured using ImageJ (4.2 ± 0.1 mm).

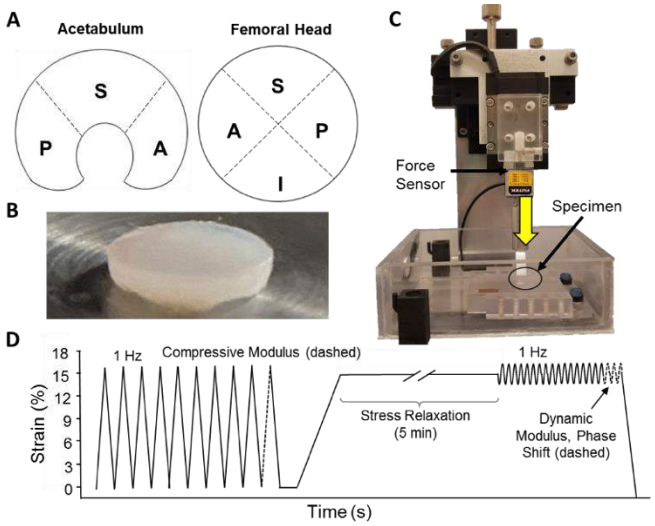


**Figure 1: Mechanical characterization protocol. A) Testing regions (A = anterior, P = posterior, S = superior, I = inferior) for B) porcine cartilage. C) A mechanical test system was used to compress the samples with D) a dynamic loading profile.**

*Mechanical Testing:* A custom mechanical testing system (**Fig. 1C**) applied unconfined compression tests with dynamic mechanical

analysis (**Fig. 1D**). Each of the forty-two cartilage plugs were placed between an acrylic platform and impervious platen (**Fig. 1C**). A preload of 0.05 N was applied to measure the reference thickness after soaking (0.92 ± 0.09 mm). The preload was followed by a preconditioning protocol of ten sinusoidal waves targeted to 16% strain at 0.5 Hz and a ramp to 14.4 ± 0.7% strain at a rate of 1%/s, followed by 5 minutes of stress relaxation. This strain level has been used to characterize articular cartilage in porcine and bovine studies[4,5], and the 5 minutes stress relaxation allowed the force response to equilibrate prior to dynamic testing.[6] Cyclic compression at 1% peak-to-peak amplitude was then applied for 20 cycles at 0.5 Hz.[6] The specimens were saturated with saline solution during mechanical testing but were not submerged. The compressive linear modulus was measured as the slope of stress-strain curve during the final preconditioning cycle. The equilibrium modulus was measured as the ratio of stress to strain at the end of the stress relaxation period. The dynamic modulus was calculated by fitting the last three sinusoidal compression cycles of the stress-time and strain-time data to a four-parameter sine wave function ($R^2 = 0.92 \pm 0.09$). The phase shift was determined by subtracting the fitted phase parameters from the stress-time and strain-time data.[6] The effect of treatment (DDH vs healthy), hip structure (socket vs head), and region on the mechanical properties were measured using MANOVAs in SPSS ($p < 0.05$) with a Bonferroni correction for multiple comparisons.

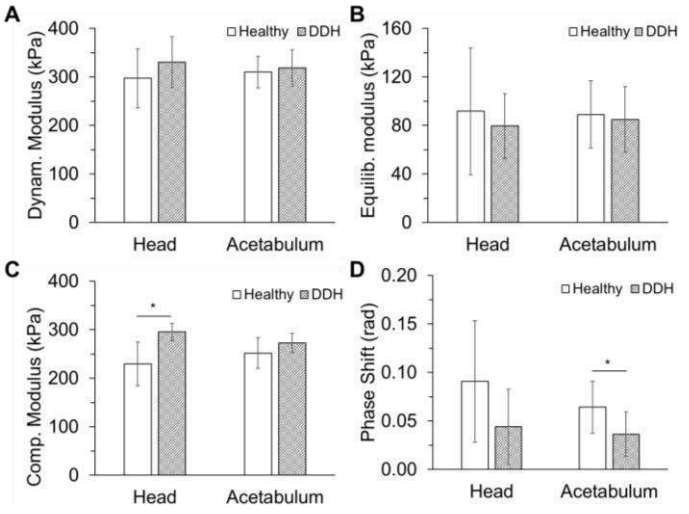


**Figure 2. Compressive properties of DDH and Healthy hip cartilage. No differences were observed in: A) Dynamic modulus, and B) equilibrium modulus, but DDH did have a higher C) compression linear modulus and a lower D) phase shift.**

## RESULTS

Mechanical properties of the cartilage specimens were shown to be similar for healthy and DDH hips (**Fig. 2**). No significance was found between the healthy and DDH hips for both dynamic modulus and equilibrium modulus (**Fig. 2A-B**), although the dynamic modulus for the DDH femoral head was 10% greater than the healthy pig ($p = 0.185$). The compressive modulus of the DDH femoral head was 22% greater than the healthy pig (**Fig. 2C;** $p = 0.01$). The DDH head and acetabulum had 52% and 43% less phase shift than the healthy pigs, respectively, although only the difference in the acetabulum was significant ($p = 0.024$) **(Fig. 2D)**. No significance was detected between regions on both the femur and acetabulum for the healthy and DDH hips. Additionally, no interaction was detected between treatment and region, nor between treatment and hip structure.

## DISCUSSION

This study characterized articular cartilage viscoelastic mechanical properties of DDH within a porcine model using unconfined compression testing. We were surprised to find that the superficial layer of cartilage in the infant DDH hip had mechanical properties similar to a juvenile healthy pig. When excising the cartilage plugs, the DDH hips had notably thicker cartilage and less subchondral bone than the healthy juvenile hips. Nevertheless, the superficial layer (0.8 mm thickness) had similar compressive properties that were largely unaltered in the DDH pig, with the exception of the compressive modulus in the femoral head. We did observe a decrease in the phase shift between the two pigs, which indicates that the DDH pig is less viscous and may suggest a reduction in aggrecan. It was also interesting to find that the mechanical properties did not have significant regional variations within the DDH hip. The acetabulum in the DDH hip experiences posterosuperior elongation,[7] and therefore we would have expected to see structural and mechanical changes within this region. However, the posterior and superior regions had compressive properties that were on average only 3% - 10% different than the other regions. These findings indicate that the structural changes in the hip socket observed in the DDH pig (e.g. reduction in acetabular coverage; data not shown) are not associated with alterations in cartilage mechanical properties. It is important to limit the interpretation of this data to the superficial zone, as we may have measured mechanical differences if cartilage plugs were drilled past the subchondral bone, since the older juvenile pigs experience greater ossification.

The compressive properties found in this study were compared to values reported in the literature. The average equilibrium modulus for the porcine specimens (86.2 ± 35.2 kPa) was about 70-80% less than published values for bovine and human cartilage using unconfined compression.[4,8] One reason for the mechanical differences is likely due to the bovine and human studies using on average thicker plugs (~1.5 mm). The phase shift for the pig specimens (0.060 ± 0.047 rad) was less than the reported phase shift for human articular cartilage (0.17 - 0.26 rad),[4] but was consistent with materials primarily comprised of collagen (0.06 rad).[4] The fact our results are closer to 0.06 rad seems reasonable since the superficial layer of cartilage is composed primarily by tightly packed collagen fibers.[9]

A principal limitation to the current study is that the forty-two experiments we conducted were from two porcine hips. Additionally, the contralateral DDH hip was excluded from this study based on a prior imaging analysis which found that the contralateral limb did not develop as a normal hip; therefore, it would not have served as a healthy control. Future experiments are planned with a greater sample size to calculate material parameters that are representative of a greater population of DDH and healthy porcine infant hips.

This study has established a baseline characterization of the cartilage mechanical behavior in a DDH induced porcine model and has provided new insight into the mechanobiology of DDH. Data from this study will be used for the calibration and validation of a finite element model for DDH hips that can serve as an investigative tool to encourage clinical advancement in this understudied disease.

**ACKNOWLEDGEMENTS**: This work was funded by NSF 1554353 and NIAMS 1R15AR075314-01.

## REFERENCES

[1] Gala et al., *JBJS*, 2016 [2] Dodds et al., *J Pediatr Orthop*, 2008 [3] Athanasiou, *J Ortho R*, 1995 [4] Little et al., *Tis. Eng.*, 2011 [5] Dilsilvestro et al, 2001 *J Biomech* [6] Yocham et al., *Adv Eng Mat*, 2018 [7] Greenhill et al., *J. Ped. Orth.* 1995 [8] Korhonen et al, 2002 *J* 2009 [9] *Biomech.* Fox et al., *Sports Health*

SB³C2022
Summer Biomechanics, Bioengineering and Biotransport Conference
June 20-23, Eastern Shore, MD, USA

# WHY DON'T BATS TEAR THEIR ROTATOR CUFFS DESPITE REPETITIVE OVERHEAD MOTION?

**Iden Kurtaliaj (1), Jennifer Kunes (1) Michael K. Rowley (2,3), Lynn Ann Forrester (1), Mikhail Golman (1), Guy M. Genin (4), Sharon M. Swartz (2), Stavros Thomopoulos (1)**

(1) Department of Biomedical Engineering, Columbia University, New York, NY, USA
(2) Department of Ecology, Evolution, and Organismal Biology, Brown University, Providence, RI, USA
(3) Department of Kinesiology, California State University East Bay, Hayward, CA, USA
(4) Department of Mechanical Engineering and Materials Science, Washington University, St. Louis, MO, USA

## INTRODUCTION

Rotator cuff tears often arise when humans exert substantial forces during repeated overhead motions. Such tears are common in humans, affecting more than 50% of patients over the age of 65 and resulting in pain and loss of shoulder function [1]. Yet, these tears are apparently uncommon in bats, which perform repetitive overhead motions during flight. Despite improvements in surgical techniques and postoperative rehabilitation, restoring glenohumeral joint stability after rotator cuff repair remains a clinical challenge [2]. To gain insight into strategies that might inform improved treatment, we therefore investigated the structure and function of the bat rotator cuff.

Bats and humans share a common quadrupedal ancestor, but evolutionary adaptations likely compromised human glenohumeral stability as posture changed from pronograde to orthograde. Stable glenohumeral joints, with mobility largely restricted to the sagittal plane, evolved into the less stable joints that allow bipedal primate shoulders to rotate and move in the coronal plane [3]. Bats, however, evolved a balance between glenohumeral mobility and stability, enabling a large, multiplanar, overhead range of motion [4]. In this study, we performed comparative anatomy to better understand the functional advantages of the bat shoulder versus that of the mouse, a similarly-sized quadrupedal animal. We hypothesized that the anatomy of the bat glenohumeral joint would differ from that of the mouse in ways that are consistent with improved stability. Results supported the hypothesis, and provided potential insight into techniques for surgical repair of the human rotator cuff.

## METHODS

Sample preparation: All animal procedures were approved by the Columbia and Brown University Institutional Animal Care and Use Committees. Shoulders harvested from adult (12 weeks) C57BL6/J mice (n=5) and *C. perspicillata* bats (n=5) were dissected then fixed in three different positions: full shoulder extension ("P1"), intermediate ("P2"), and full shoulder flexion ("P3"). To consistently identify the angle between the scapular spine and the humerus for each fixation position, gait (mouse) and flight (bat) analyses were used. Species-specific 3D-printed fixtures were used to fix samples at each position. *MicroCT Imaging:* Samples were scanned at 55 kV peaks with 145 mA intensity, and 19.3 μm resolution (Skyscan 1272, Bruker). *Anatomical Measurements:* Images were reconstructed (NRecon, Skyscan), and bone parameters measured (Skyscan CT Analyzer). The scapular linear index was determined as the ratio of scapular width to length. Supraspinatus and infraspinatus linear indices were calculated using the length from the medial aspect of the spine to the superior or inferior angle. Glenoid retroversion was measured via the anterior facing angle between the body of the scapula and the glenoid face on the axial cross section. Supraspinatus outlet area was measured as the area posterior to the coracoid, inferior to the acromion, and within the acromial arch. Supraspinatus clearance, measured as the vertical distance between the humeral supraspinatus insertion and the bottom face of the acromion, was measured for each sample at each of the three positions. Glenoid curvature was measured using the circle tool in ImageJ to create the best fit circle. The arc length of the glenoid was calculated using the angle from the anterior to the posterior glenoid rim. *Modeling:* Using a mathematical model based upon our imaging of the bony anatomy at the enthesis of mouse and bats, we predicted how strength, stiffness and toughness of the tendon enthesis would vary with loading direction and the bony ridge abutting the enthesis [9]. Simulations considered 20 linear elastic, brittle fibers of thickness $w$ = 10 μm and spacing $s/w$ = 1.5 abutting a cylindrical bone ridge of aspect ratio $B/A$=1 (mouse) or $B/A$=0.4 (bat). Strength, stiffness, and toughness were normalized against idealized scenario where tightly packed fibers ($s/w$ = 1) were pulled to failure uniaxially at 90° (Fig. 3). *Statistical Analysis:* All data are shown as mean ± standard deviation. Statistical analysis was performed for all experiments using unpaired t-tests with Welch's

correction (GraphPad Prism 7). The threshold for statistical significance was defined at $p < 0.05$.

## RESULTS

The scapular index and infraspinatus index were both significantly larger in bats than in mice, while the supraspinatus index did not differ (Fig. 1a). Supraspinatus-acromion clearance increased when moving from full shoulder flexion to extension (i.e., from P3 to P2 to P1) in both bats and mice. However, the supraspinatus outlet area was significantly greater in bats compared to mice (Fig. 1b). The glenoid was retroverted in bats and anteverted in mice (Fig. 2a). Glenoid curvature and arc length were significantly higher in bats than in mice (Fig. 2b). Simulations suggested that the strength and stiffness of the supraspinatus tendon attachment are greater for the bat's flatter humeral head for the mouse's more circular mouse humeral head (Fig. 3). The higher strength associated with the bat is maintained over a broad range of loading angles, while toughness was slightly reduced, particularly at very low abduction angles.

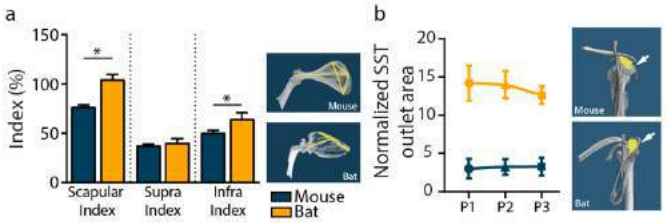


**Figure 1. (a) Scapular, supra and infra indices (b) Supraspinatus outlet area (yellow) normalized by attachment area.**

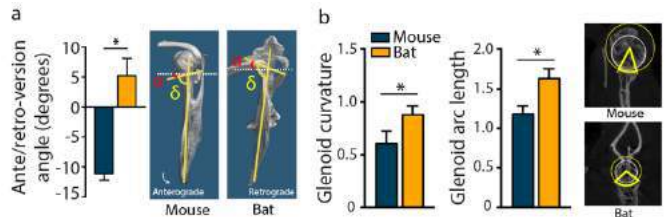


**Figure 2. (a) Glenoid ante/retroversion (α angle; α=δ-90) for mouse and bats. (b) Glenoid curvature and arc length for mouse and bats.**

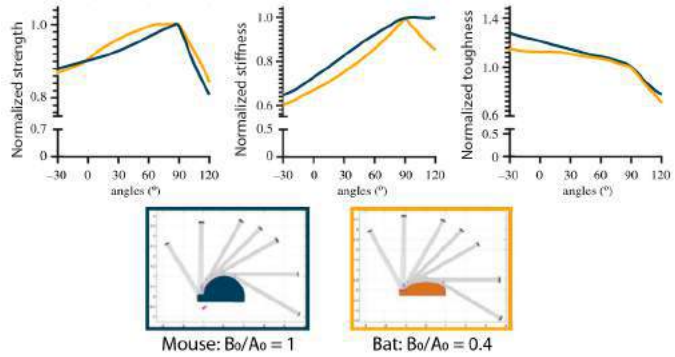


**Figure 3. Mathematical modeling suggested that the flatter bat humeral head may increase strength and stiffness relative to the mouse, across a broad range of abduction angles. This comes at the expense of reduced toughness.**

## DISCUSSION

Comparison of the glenohumeral joints of two similarly-sized species (i.e., bats and mice) suggested functional adaptations of bat shoulder anatomy in relation to the demands of flight.

***Evolutionary perspective.*** From the evolutionary perspective, the bat's enlarged scapular and infraspinatus indices imply changes to muscle size and orientation. The supraspinatus index, however, was conserved across species. Because the infraspinatus and supraspinatus stabilize quadrupedal gait, the bat's enlarged infraspinatus index suggests a larger role for the infraspinatus in the bat's glenohumeral stability. This also hints at adaptation to relieve stress on the supraspinatus, as does the observation that the larger supraspinatus outlet in the bat, providing more space for the supraspinatus to pass under the coracoacromial arch to prevent the supraspinatus shoulder impingement commonly seen in overhead-throwing athletes [5]. Although the glenoid is anteverted in mice, it is retroverted in bats, analogous to the retroverted glenoids reported in high-level overhead-throwing athletes [6]. This may enable more rotation of the joint while limiting capsular tension. The bat glenoid is more concave, encapsulating more of the humeral head when compared to mice. In addition, the bat has a larger glenoid arc length and articulating surface area with the humeral head, thus providing more stability while maintaining mobility.

***Insight from quantitative analysis of the data.*** The idea of the bat's deeper glenoid providing more stability is consistent with shoulder instability patients, who present with loss of glenoid concavity and a flatter glenoid morphology [8]. Our modeling revealed potential reasons why the humeral head shape at the supraspinatus tendon attachment may affect stability. The models suggested that flatter attachment in bats relative to mice lead to increased strength over a wide range of motion, enabling bats to perform high stress flight by optimizing strength over a wider range of motion than needed for walking. The mechanical energy needed to dislocated the humeral head increases with concavity of the glenoid and stiffness of the rotator cuff tendons: compression of the convex humeral head into the concave glenoid fossa stabilizes the shoulder. Dislocation requires displacing the humeral head laterally over the glenoid lip, with a force that increases with tendon stiffness. The energy required for this displacement is thus directly related to the shape of the glenoid. In bat's case, where the glenoid is deeper and more concave, more energy is required for shoulder dislocation.

***Implications for rotator cuff repair.*** From the clinical perspective, adaptations in the bat provide insight into reshaping of the anatomy in surgical repair. Features of bat shoulder anatomy, such as a larger infraspinatus fossa, a larger supraspinatus outlet area, a retroverted and concave glenoid, and the flattened shape of the humeral head attachment may contribute to increased stability of the glenohumeral joint at the extremes of range of the repetitive overhead motions of flight. Bone reshaping to increase the height of the glenoid lip may improve stability, and bone reshaping to increase the area of the supraspinatus outlet may reduce impingement. Future studies of the bat rotator cuff muscles and tendons will further test these hypotheses about passive stabilization of the shoulder and rotator cuff repair techniques to decrease supraspinatus stress.


## ACKNOWLEDGEMENTS

This work was supported by NIH (R01-AR055580).


## REFERENCES


[1] Sher, J et al., *J Bone Joint Surg Am,* 77(1):10-5, 1995 [2] Galatz, L et al., *J Bone Joint Surg Am,* 86-A:219-24, 2004 [3] Martorelli, J et al., *Ecol Evol,* 9(1): 703–722, 2019 [4] Bahlman, J et al., *Bioinspir. Biomim*., 8 016009, 2013 [5] Smith, C et al., *J Am Osteopath Coll Radiol*, 7(3):5-14, 2018 [6] Borsa, P et al., *Sports Med,* 38(1):17-36, 2008 [7] Willems, W. et al., *J. Normal and Pathological Anatomy of the Shoulder* 3–14, 2015. [8] Di Giacomo, G. et al., *Shoulder & Elbow* 10.1302/2058-5241.3.180028, 2018. [9] Golman, M. et al., *J R Soc Interface* 18(185):20210421, 2021.

SB³C2022
Summer Biomechanics, Bioengineering and Biotransport Conference
June 20-23, Eastern Shore, MD, USA

# EFFECTS OF INTERFACE MATERIAL ON CARTILAGE FLUID LOAD SUPPORT IN THE MIGRATING CONTACT AREA

**Jamie M. Benson (1) and David L. Burris (1,2)**

(1) Department of Biomedical Engineering, University of Delaware, Newark, DE, USA
(2) Department of Mechanical Engineering, University of Delaware, Newark, DE, USA

**INTRODUCTION:** The unique ability of cartilage to withstand contact stresses (0.5-10 MPa) that exceed its modulus (0.1-1 MPa) with minimal strains and friction coefficients is largely attributed to fluid load support (FLS) through interstitial pressurization via the migrating contact area (MCA). According to the MCA theory, cartilage achieves and maintains maximum fluid load support if the contact migrates across the cartilage surface faster (*Pe>>1*) than the fluid can escape [1].

Based on our recent experimental and analytical modelling we have found that not only is FLS dependent on speed, it is also dependent on range of motion [2]. In order to maintain maximum FLS the range of motion, or migration length, needs to be at least 10 times the contact diameter. However, cartilage can sustain non-zero FLS when migration lengths are smaller than the contact diameter—suggesting that small movements (i.e., fidgeting, drifting) can mitigate fluid loss during prolonged period of standing. Our previous work utilized smooth spherical glass probes as the contacting interface between bovine osteochondral explants. This allowed for a well-controlled and idealized experimental environment that allowed us to isolate the interfacial mechanics in each sample. However, this setup is not representative of the joint.

The objective of this study was to replicate our previous study using a cartilage-on-cartilage setup to determine: 1) FLS in an in-vitro setup and 2) if the glass-cartilage setup accurately describes the in-vitro interfacial contact mechanics.

**METHODS:** *Sample extraction:* Full thickness Ø 19 mm (N = 5) and Ø 6 mm (N = 1) osteochondral plugs were extracted along the centerlines of the medial and femoral condyles from 3 adult bovine stifle joints. Samples were rinsed in phosphate buffered saline (PBS) and stored in protease inhibitor solution at 4ºC. All tests were performed within 24hr of extraction to minimize the risk of enzymatic digestion-induced changes in material properties.

*In-situ characterization:* Samples were mounted to a reciprocating stage on a custom tribometer (Fig. 1A) and lubricated in 1X PBS. Normal force ($F_N$) and indentation depth ($\delta$) data were quantified first, under static conditions using a Ø 6.35 mm borosilicate glass probe to obtain sample specific material properties, then during sliding in the migrating contact area (MCA) configuration. Our previous in-situ observations with cartilage [3] showed that the contact geometry is best described by Hertzian mechanics, which we used to relate the contact

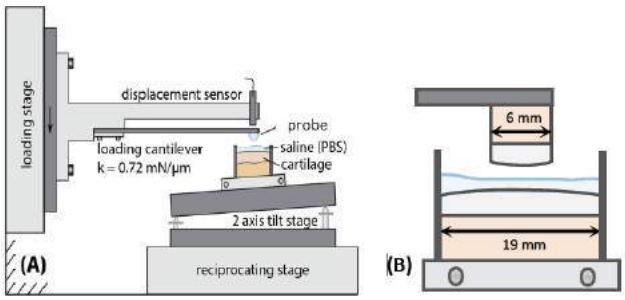


**Figure 1: (A) Schematic of custom tribometer and experimental setup. (B) Cartilage-on-cartilage experimental setup.**

radius ($a$) to the known probe radius ($R$) and the measured indentation depth ($\delta$) with Eq. (1).

$$a = \sqrt{\delta_s \cdot R} \quad (1)$$

The effective contact modulus ($E_c$), which depends on the material properties and sliding speed among other variables, is quantified experimentally with measured/known values of load ($F_N$), equilibrium tissue deformation ($\delta_s$), and probe radius ($R$), as described in Eq. (2):

$$E_c = \frac{3}{4}\frac{F_N}{R^{0.5}\cdot\delta_s^{1.5}} \quad (2)$$

At equilibrium under static contact conditions, load is supported entirely by osmotic pressure. With Eq. (2), the equilibrium contact modulus ($E_{c0}$) can be quantified by the force or deformation response during **static equilibrium** contact. During sliding, interstitial pressurization increases $E_c$ and reduces friction. At **dynamic equilibrium,** interstitial pressure, the fluid load fraction, the effective contact modulus, and the friction coefficient depend on material properties and the sliding conditions. We quantify the magnitude of fluid load support using the fluid load fraction (*FLS*), which varies between 0 and maximum fluid load fraction ($FLS_{max}$). As we have shown in a previous paper [3], fluid load support can be quantified experimentally based on $E_c$ and $E_{c0}$ using Eq. (3):

$$FLS = \frac{E_c - E_{c0}}{E_c} \quad (3)$$

*Tribological testing*: Each sample was first indented with the borosilicate glass sphere to a target load under static conditions until reaching equilibrium. Following equilibration, the next minute of data was used with Eq. (2) to determine the mean and standard deviation of the equilibrium modulus. Following static equilibration, the borosilicate glass probe was replaced with the Ø 6 mm osteochondral plug, as depicted in Fig 1B. Each sample was indented again to a static equilibrium in the cartilage-on-cartilage setup. Immediately following static equilibrium, a lateral stage began reciprocating at 1.5 mm/s ($Pe > 100$) over a maximum migration length ($S = 5$ mm) to establish the large Pe number and long migration length baseline ($FLS_{max}$). Reciprocation continued until a dynamic equilibrium was reached, which is defined < 0.3 $\mu$m/min change in indentation depth. Following dynamic equilibration, the migration length was reduced to $S = 2$ mm until the system reached a new dynamic equilibrium. This procedure was repeated for $S = 1$, 0.5, 0.2 and 0.1 mm in that order.

*Analysis and theoretical framework*: Methods for data analysis are described in depth in our previous publication [2]. Briefly, fluid load support was quantified across each migration length (*FLS*). To remove any sample specific material effects the relative *FLS* ($F^*$) was calculated by normalizing the FLS at each migration length by the maximum $FLS_{max}$ for that sample. Similarly, the relative migration length ($S^*$) was calculated by normalizing the migration length ($S$) by the contact diameter ($d$). The results were fit to our previously derived model equation, Eq. (4).

$$F^* = \frac{FLS}{FLS_{max}} = \frac{S^*}{S^* + \frac{\pi}{4}R^*} \quad (4)$$

We propose that the relative *FLS* ($F^*$) varies between 0 and 1 as a sigmoidal function of the relative migration length ($S^*$). *FLS* reaches 0.5 at a critical migration length, at which the rate of fluid exudation equals the rate of fluid recovery, which we define as the exudation ratio ($R^*$) in Eq. (5).

$$R^* = \frac{R_{exudation}}{R_{recovery}} \quad (5)$$

The relative *FLS* ($F^*$) and relative migration length ($S^*$) for each sample were plotted to obtain the exudation ratio ($R^*$). $F^*$, $S^*$, and $R^*$ values were compared with the values from our previous publication [2] using one-way ANOVAs where significance was determined by $p<0.05$.

**RESULTS:** Raw time-dependent force and indentation depth measurements from a representative cartilage on cartilage sample are plotted in Figure 2 with a representative glass on cartilage sample from our previous publication. Tissue deformation increased and normal force decreased similarly for both datasets starting at static equilibration throughout dynamic MCA testing. At the start of sliding across a S = 5 mm migration track, the system recovered a significant amount of fluid (decreased deformation) until dynamic equilibrium (fluid exudation rate = fluid recovery rate), as illustrated in Figure 2. Additional systematic fluid loss (increased deformation) was observed as the migration lengths

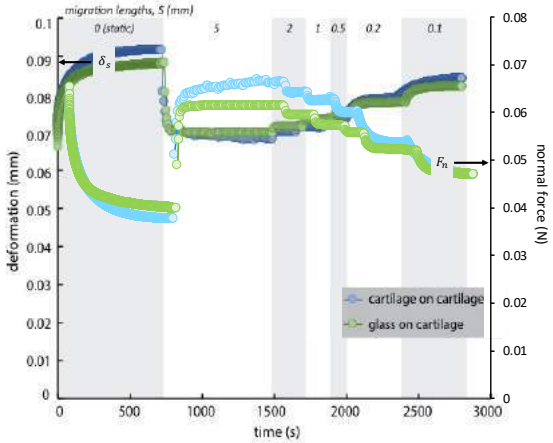


**Figure 2: Raw deformation (left y-axis) and normal force measurements (right y-axis) measurements vs. time for representative cartilage-on-cartilage (blue) and glass-on-cartilage (green) MCA experiments.**

were reduced. The relative *FLS* ($F^*$) vs. relative migration length ($S^*$) for each representative sample is plotted in Figure 3. Similarly, $F^*$ increased when $S^*$ increased for both samples. Using Eq. 4 from our previously described model [2], the exudation ratio ($R^*$) was calculated to be 0.102 and 0.101 for the cartilage-on-cartilage and glass-on-cartilage samples, respectively. There was no significance ($p>0.5$) in $F^*$, $S^*$ and $R^*$ values between the cartilage-on-cartilage setup and the glass-on-cartilage setup.

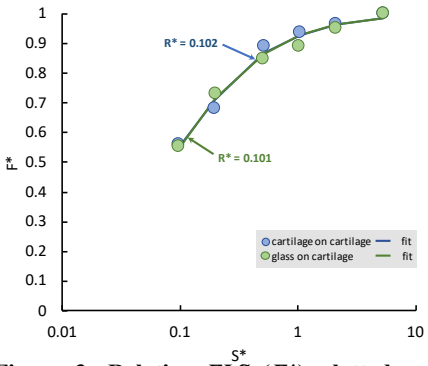


**Figure 3: Relative *FLS* ($F^*$) plotted vs. relative migration length ($S^*$) for representative cartilage-on-cartilage and glass-on-cartilage samples. Each dataset was fit to Eq. 4 to obtain the respective exudation ratios ($R^*$).**

**DISCUSSION:** This study demonstrates that the use of glass on cartilage setups in small-scale MCA experiments is an accurate experimental model of in vitro cartilage mechanics. More importantly, this work suggests that the use of the glass-cartilage setup can be more beneficial than the cartilage-cartilage setup. Unlike the stiff, impermeable glass probe, the cartilage probe was soft, porous and possessed material properties unique to that specific sample. During the cartilage-on cartilage testing, both surfaces were deforming and recovering fluid at different rates—making it impossible to separate the contributions made by each surface. Thus, mechanical properties can only be quantified for the system rather than independently for each surface. While the cartilage-on-cartilage system still provides valuable information, it doesn't allow the ability to isolate 1) the mechanisms driving fluid recovery and 2) which surface is dominant. Furthermore, glass on cartilage setups enable the ability to isolate key variable parameters (i.e. load/BMI, contact stress, etc.) that are vital in order to develop cartilage replacement materials and treatments for OA.

**ACKNOWLEDGEMENTS:** This work is supported by the NSF-EAGER (#1937493) and the STLE Jeanie S. McCoy Scholarship.

**REFERENCES:** [1] Ateshian+ J Biomech, 1995, [2] Benson+ Osteoarthr. Cartil, 2020, [3] Bonnevie+ J Biomech, 2012, [4] Moore+ J Biomech, 2014

SB³C2022
Summer Biomechanics, Bioengineering and Biotransport Conference
June 20-23, Eastern Shore, MD, USA

# IDENTIFICATION OF INTRAMURAL STRESS DISTRIBUTION IN CEREBRAL ANEURYSMS USING PATIENT SPECIFIC WALL THICKNESS MAPS

**Ronald N. Fortunato (1), Piyusha Gade (1), Juan Cebral (2), Anne M. Robertson (1,3), Spandan Maiti (1,3,4)**

(1) Department of Mechanical Engineering and Materials Science, University of Pittsburgh, Pittsburgh, PA, USA
(2) Department of Bioengineering, George Mason University, Fairfax, VA, USA
(3) Department of Bioengineering, University of Pittsburgh, Pittsburgh, PA, USA
(4) Department of Chemical and Petroleum Engineering, University of Pittsburgh, Pittsburgh, PA, USA

## INTRODUCTION

Rupture of intracranial aneurysms (IAs) is a catastrophic clinical event with a fatality rate of 45% [1]. Published models of rupture risk are based on patient and aneurysm characteristics discernable from current imaging modalities (e.g. aneurysm size and aspect ratio). From a biomechanics point of view, IA wall rupture is the mechanical failure of the wall tissue in the presence of wall stresses in excess of the tissue strength. However, accurate computation of aneurysm wall stress fields requires patient specific wall thickness measurements. Such data are rarely available from clinical imaging data for aneurysm patients due to the resolution of clinical scanners as well as the imaging modality. Wall thickness fields can be obtained ex-vivo from excised tissue and are reported to range from 16 um-550 um [2,3]. In this work, we leverage ten cases in our database for aneurysm patients that includes aneurysm specimens, surgical videos and pre-operative clinical images of the aneurysm and surrounding vasculature. Using high resolution micro-CT, we obtain a 3D model of each specimen, which is then mapped back to 3D model of the aneurysm and surrounding vasculature to create a patient specific 3D model. We then obtain for the first time, patient specific stress distributions in cerebral aneurysms, using the finite element method. We then compare normalized stress distributions to those obtained using constant wall thickness models.

## METHODS

Aneurysm tissue was harvested after surgical clipping from 22 patients with cerebral aneurysm from Allegheny General Hospital, Pittsburgh, USA, Helsinki University Hospital Helsinki, Finland and University of Illinois Hospital, Chicago, USA. Informed consent was signed by the patient before surgery and all study protocols were approved by the Institutional Review Board at both the University of Pittsburgh and respective sites. Before surgery, clinical imaging of the patient was taken, using 3-D rotational angiography (3DRA) or computed tomography angiography. During surgery an intraoperative video was obtained. Following harvest, the aneurysm specimen was kept in a dedicated cooled transport container submerged in HypoThermosol (Biolife Solutions, Bothell, WA), a preservation media, and transported to the University of Pittsburgh. After fixation in using 4% paraformaldehyde or 3% glutaraldehyde the specimen was scanned at a resolution of 6 μm using a micro-CT scanner (Skyscan 1272, Bruker, Belgium). The same protocol was followed for the samples from Helsinki except they were snap-frozen in the operating room and transported to Pittsburgh after fixation in 10% formalin. After 45 minutes of scanning, a stack of 3D images was reconstructed using NRecon reconstruction software (Bruker, Belgium). A series of image processing operations, including thresholding, Gaussian smoothing, and connected components filtering, were performed to clean up the segmentation mask in NRecon. Triangular surface meshes were then generated from the segmentation masks. Finally thickness of the triangular surface meshes were calculated in 3Matics Research (Materialise, Leuven, Belguim). Patient specific luminal surface geometries were created from 3DRA images using MIMICS (Materialise, Leuven, Belguim) [4-5].

Using Paraview (kitware, Clifton Park, NY) the surface mesh from microCT was aligned with the luminal surface mesh from 3DRA. Out of 22 aneurysm samples that were scanned under microCT, 10 samples could be mapped to the vasculature surface with the aid of surgical videos and intraoperative agreement. The thickness map generated from the microCT mesh in 3Matics was then mapped onto the luminal surface mesh using a custom algorithm implemented in both Paraview and MATLAB (Mathworks, Natick, MA). With the exception of one fusiform aneurysm, obtained during bypass surgery, the IA specimens were obtained following clipping and therefore only a subset of the aneurysm tissue was harvested. In the region surrounding the specimen region, a constant thickness of 200 um was prescribed and a two-ring smoothing algorithm was applied to the thickness field variable to remove artificially large gradients in the regions connecting measured

and prescribed thicknesses. Intramural stress values were reported for the region of the IA specimen. The thickness map on the current triangular luminal surface mesh was then mapped onto a quad surface mesh using a custom MATLAB (Mathworks, Natick, MA) script and Trelis (Coreform, Orem, UT). Finally, another custom code was used to extrude volumetric hexahedral elements from the quad luminal mesh for patient specific wall thickness maps. For each patient specific wall model, a second model was created with constant wall thickness by extruding a 200 um thickness volumetric hexahedral mesh from the same quad surface mesh. The IA wall was modeled as an isotropic, homogeneous hyperelastic material- a two constant power law neo-Hookean model, [6]. Material constants ($\alpha$=455 kPa and $\beta$=531 kPa) were regressed from previous uniaxial tests on unruptured aneurysms [7]. Finally, a custom finite element code was used to calculate maximum and minimum principal stresses, directions of principal stresses, and ratio of principal stresses under 120 mmHg of pressure applied on the luminal surface. Nodal values of the maximum principal stress were normalized by the respective sample average of the maximum principal stress. The 95$^{th}$ percentile values of the normalized stress were compared between patient specific and constant wall thickness models. The 95$^{th}$ percentile rather than absolute maximum was chosen to reduce artifacts from spuriously high nodal stress values.

## RESULTS

Average sample wall thickness ranged from 50 um to 800 um with a mean and standard deviation of 310 um ± 180 um, respectively. The average sample thickness was not normally distributed, with 77% of samples less than 300 um. The sample average maximum principal stress varied from 40 kPa to 240 kPa. Contour plots of normalized maximum principal stress for three samples and corresponding wall thickness maps are shown in Figure 1. Normalized 95$^{th}$ percentile

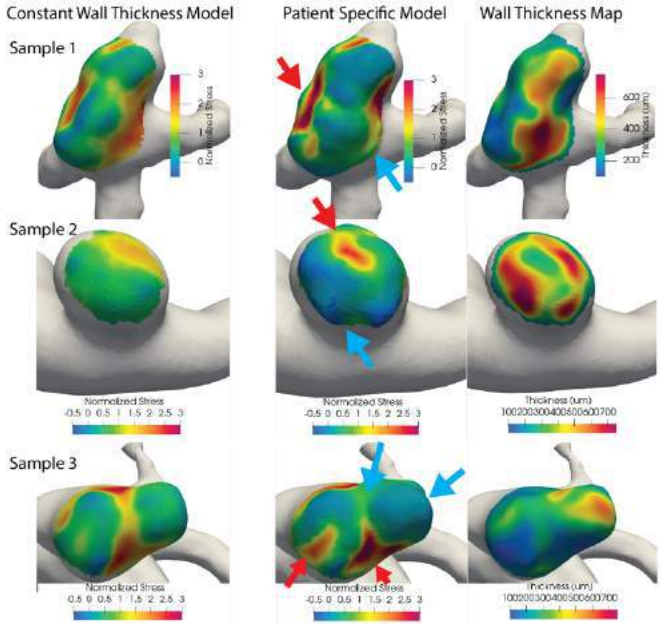


**Figure 1. Normalized maximum principal stress for constant and patient specific wall thickness models for three representative cases, columns 1 and 2. The wall thickness field for the patient specific model is shown in column 3. Blue arrows indicate locations of decreased stress and red arrows indicate locations of increased stress in the mapped versus uniform thickness model. Regions away from region of aneurysm specimen are shown in gray.**

maximum principal stress for each sample is shown in Figure 2. The 95$^{th}$ percentile of the normalized principal stress was elevated in the patient specific wall thickness model for nine out of ten samples, compared with constant wall thickness models (mean value of 2.03 vs 1.64, average difference of 39.79%).

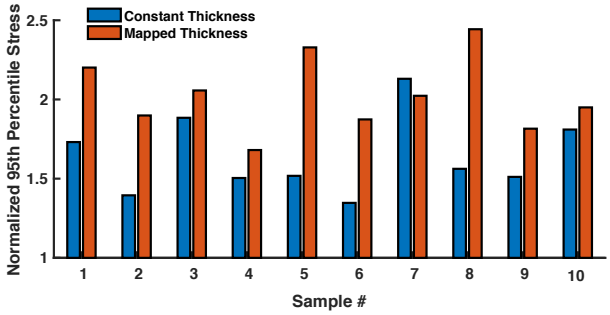


**Figure 2: Bar plot of 95$^{th}$ percentile of the normalized (by sample average) maximum principal stress.**

## DISCUSSION

We leveraged our data base for human aneurysms to calculate for the first time, the intramural stress in human cerebral aneurysms using patient specific values of wall thickness fields. The heterogeneous sample thickness was obtained using high resolution micro-CT analysis of the physical samples harvested during open brain surgery and mapped onto 3D reconstructions of the patient vasculature. As for other works, we found the wall thickness to be highly heterogenous. In this database, wall thickness ranged from 10 um - 1.2 mm and could increase by an order of magnitude within samples. We found the 95$^{th}$ percentile of the maximum principal stress ranged from 90 to 310 kPa. Prior work reported Cauchy failure stress in uniaxial testing for vulnerable aneurysm samples to range from 630 to 730 kPa, while in robust samples to be from 1.2 to 2.2 MPa [7].

Given the larger range in wall thickness in IA samples, in the absence of patient specific wall thickness values, biomechanical studies cannot provide reliable estimates of intramural stress. Here we explore the possibility that such models can provide reliable values of stress ratios (here, normalized stresses). The constant wall thickness model did capture many of the hot spots, Figure 1. However, the constant wall thickness models generally underestimated the intensity of the hot spot, red arrows in Figure 1. This finding is also reflected in results for the 95$^{th}$ percentile stress, which was nearly always higher in the patient specific model due to the existence of thinner regions that were not present in the constant wall thickness model.

There were limitations in this study. The IA sample was, with one exception, a subset of the IA sac and had to be merged to a constant wall thickness region. In the future, we can investigate the sensitivity of the solutions to this choice of wall thickness in the surrounding region.


## ACKNOWLEDGEMENTS

Research in this work was supported by the National Institutes of Health under award R01-NS097457-01 and 5T32HL076124-12.


## REFERENCES


[1] Kelly, P et al., Stroke, 32(2):530-534, 2001
[2] MacDonald, D. J. et al, Ann Biomed Eng 28:533-542, 2000
[3] Suzuki, J. et al, JNS, 48 (4): 505-514, 1978
[4] Cebral, J. et al., A J of Neuro, 26(10): 2550-2559, 2005
[5] Zeng, Z. et al., J Biomech Eng, 132(9): 2010
[6] Raghavan, M et al. J Biomech 33(4) 475-82, 2000
[7] Robertson, A. M. et al, Ann Biomed Eng 43:1502-15, 2015

# SIMULATION OF MURINE BRAIN DEFORMATION DURING CHIMERA IMPACTS

**C. Bradfield (1,2), K. McInnes (3), T. Cheng (4), L. Voo (1,2), K.T. Ramesh (1,2)**

(1) The Applied Physics Laboratory, The Johns Hopkins University, Laurel, MD, USA
(2) Dept. of Mechanical Engineering, The Johns Hopkins University, Baltimore, MD, USA
(3) Dept. of Mechanical Engineering, University of British Columbia, Vancouver, BC, Canada
(4) Dept. of Pathology and Laboratory Medicine, University of British Columbia, Vancouver, BC, Canada

## INTRODUCTION

The mechanisms responsible for Traumatic Axonal Injuries (TAI) are poorly understood. Mouse models are commonly used together with blunt impact experiments to understand the pathologies and neurophysiological deficits related to TAI [1], but the relationship between the initial impact, the subsequent motion of the mouse head and the brain tissue distortion is not well established. To address this gap, this study leverages a previously validated biomechanical model of the mouse brain to simulate recent CHIMERA (Closed Head Impact Model of Engineered Rotational Acceleration) mouse experiments [1,2]. The benefit of this approach is that the model's calculated strains in specific brain regions can be readily compared to pathological findings of axonal injury in living mice undergoing the same mechanical insult from head impacts. Results from such an analysis can also be compared to tissue-based thresholds of axonal injury taken from previous laboratory testing with different species, such as non-human primate, porcine and human biomechanical models [3]. This will help the biomechanics community gain insight into how TAI develops during injurious events such as a fall or automotive accident, and how mouse models can be leveraged to better understand the neuropathology for similar loading scenarios across multiple species.

## METHODS

In order to simulate the loading condition from the previous mouse CHIMERA experiments [1,2], two different finite element models (FEMs) were used. Each FEM serves a distinct purpose. The first FEM was based on coarsened segmented anatomy from a whole mouse body computed tomography imaging, and was used to simulate the initial skull deflection as the impactor struck the skull. Taking the kinematics of the interface between the skull and brain from this coarse FEM, the rigid body motion was subtracted, which allowed us to estimate the localized skull bending at the impact site over the frontal skull bone.

The second FEM consisted of high-resolution mouse brain anatomy derived from a diffusion tensor imaging atlas. Although this second FEM did not contain a skull, its brain strain response has been previously validated against experimental strain data, thus ensuring a realistic strain field response for dynamic head rotations in the sagittal plane up to 200 rad/s. Taking the skull deflection motion data from the first FEM of the whole mouse body, along with the experimental head marker motion data from the mouse impact experiments [2], the combined motion was applied to the boundary of the high-resolution mouse brain FEM. Brain strains were calculated for each time point of the simulation, with an element size of 125 μm.

Taking the skull motion from the whole-body mouse model (1st FEM) and applying it to the brain atlas model (2nd FEM) allowed for multiple tissue deformation metrics such as Maximum Principal Strain (MPS), strain rate (MPSR) and strain times strain rate (MPSxSR) to be calculated and readily compared to the simulation results of other species for Wu and colleagues [3].

## RESULTS

Figure 1 shows the high speed video of the CHIMERA mouse experiments from McInnes et al. [2], and the corresponding brain/skull kinematics calculated from the whole body FEM (first and second rows of Figure 1). Here, the whole body FEM simulated the initial skull deflection upon impact and the subsequent motion of the head. When the motion at the skull/brain interface was applied as boundary conditions to the high-resolution brain atlas FEM, the MPS distribution varied over time and by brain region. Observing the third row of Figure 1, the bottom left image shows the MPS distribution during the initial impact (t = 0.1 ms) due to skull flexure while the bottom right image shows the MPS distribution due to the subsequent head motion (t > 1 ms). During impact with the piston, the brain shows localized strain near impact location of the skull due to skull bending. As the head continues to move upwards, the strains in other parts of the brain begin

to increase, suggesting that the rapid head rotation following impact produces more severe brain tissue distortion.

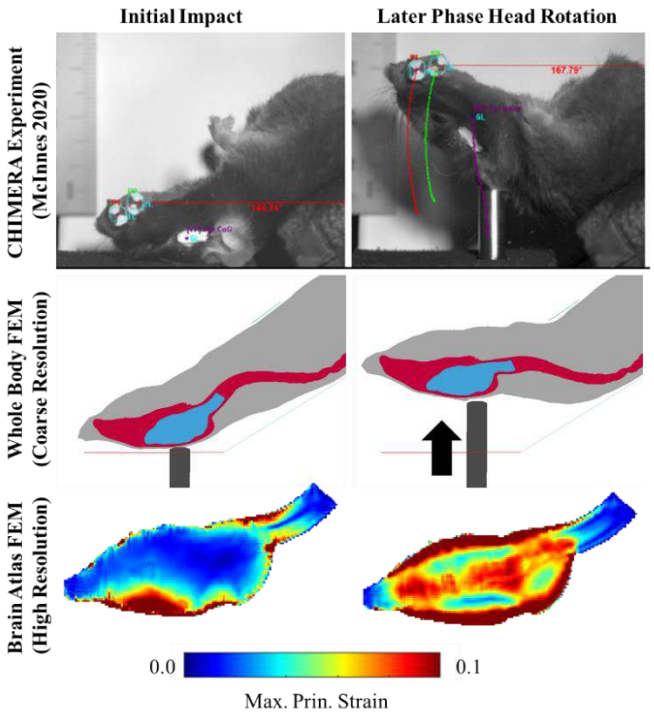


**Figure 1: Top row: High speed camera images CHIMERA experiments [2]. Middle row: whole body FEM simulating the skull deflection during impact. Bottom row: Strain distributions calculated by the high-resolution brain atlas FEM**

When the mouse FEM's 95$^{th}$ percent highest peak MPS, MPSR and MPSxSR values were compared to the non-human primate, human and pig FEM simulations from Wu et al [3], the results were mixed. Figure 2 shows the three deformation metrics from the mouse model (black circles) compared to the distribution of 25$^{th}$, 50$^{th}$ and 75$^{th}$ percentiles of the other species' mild traumatic brain injury FEM datasets (grey box plots). Here, the mouse strains (MPS95) are lower than the Wu 2021 results. However, the peak strain rates are higher than the other species FEM while the product of strain and strain rate (MPSxSR95) were comparable to the primate and pig simulations.

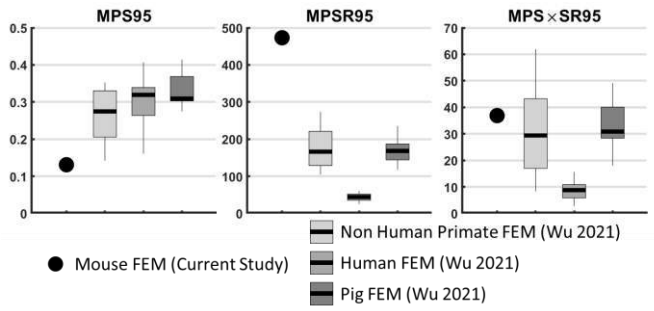


**Figure 2: Brain tissue deformation metrics compared between mouse (current study), non-human primate, human and pig simulation results from [3]**

## DISCUSSION

The simulation results presented here have implications for comparing the biomechanical response of the mouse brain during impact experiments to other species, including humans. The first implication is that the brain strain is localized at the site of blunt impact due to skull flexure. As the head begins to accelerate upwards and rotate into flexion, the majority of the brain tissue experiences increased strain. According to the MPS calculations in the current study, the accelerative head rotation is the primary mechanism responsible for increased brain tissue distortion, and thus cellular injury. The diffuse strain patterns calculated by the high-resolution FEM reflect the pattern of axonal pathology examined in the live mouse experiments, where TAI was found in different regions across the entire mouse brain, rather than limited near the impact location of the skull.

The second implication of the current study is that the tissue deformation responses calculated during the CHIMERA simulation of mTBI in the mouse had mixed results when compared to other species. In the Wu study [3], the approximate MPS value of 0.3 was consistent across the three types of species. In the current study simulating mild traumatic brain injury in the mouse, the corresponding MPS was 0.13, which is approximately half the MPS associated with injury from the Wu study. On the other hand, the strain rate from this study was much greater than those in Wu's study (Figure 2). There could be several reasons why the current mouse results potentially differ from the other species. One reason could be the smaller size of the mouse brain which could respond quicker (higher brain strain rate) to a head motion but limit its development of strain magnitude. The porcine and non-human primate FEMs had larger brain masses, but experience similar angular velocities as the mouse during CHIMERA impacts [3]. Given the similar peak angular velocities between the two studies, the larger mass of the pig and primate brains might contribute to the difference in tissue strain experienced during loading.

While the mouse brain tissue strains are lower than those in the other species, the strain rates from the CHIMERA experiments were higher, which may result from differences in tissue material properties between the various species, as well as the mouse head potentially experiencing higher rotational accelerations those reported in [3]. The rate sensitivity of axonal stretching has been previously studied in the biomechanics community, but there is still a lack of consensus about the appropriate threshold for inducing TAI. In summary, the current study is a first step in investigating the mouse brain deformation response during CHIMERA experiments, and the implications for comparison to other species for a more comprehensive understanding of traumatic brain injury. This study adds to the body of knowledge for TBI research using animal models to gain insight for human TBI mechanisms where the having the tissue level equivalences across different species is important for biomechanical understanding and quantification.


## ACKNOWLEDGEMENTS

The National Health Mission Area at the Johns Hopkins Applied Physics Laboratory provided funding for this study as part of an internal research and development project. KTR was supported in part by the Hopkins Extreme Materials Institute during this effort.


## REFERENCES


[1] Namjoshi, D et al., Experimental Neurology, 292:80-91, 2017
[2] McInnes, K et al., J Biomech Eng, 142(8):084503, 2020
[3] Wu, T et al., J of Neurotrauma, 38:1879–1888, 2021

# A PERFORMANCE COMPARISON OF A NOVEL ENDOTRACHEAL TUBE SYSTEM AND CURRENT CLINICAL STANDARD ENDOTRACHEAL CUFF

**C. N. Bedolla (1), J. C. White (1), R. De Lorenzo (2), D. Restrepo (1), R. L. Hood (1-2)**

(1) Department of Mechanical Engineering, The University of Texas at San Antonio, San Antonio, Texas, USA
(2) Department of Emergency Medicine, The University of Texas Health Science Center at San Antonio, San Antonio, Texas, USA

## INTRODUCTION

Endotracheal intubation (ETI) is the gold standard for the life-saving intervention of securing a patient's airway. In a combat setting, assessing the patient's airway is the second in priority when determining treatment. In a clinical setting, there is a large learning curve for clinicians to conduct proper intubations [3]. Additionally, the current clinical standard is a generic polymer endotracheal tube (ET) with significant drawbacks that has not had any substantial design advancements beyond materials used in almost 125 years [3]. Patients undergoing prolonged intubations, those being maintained on mechanical ventilation (e.g., en route care), or in prolonged field care, frequently experience health complications such as tracheal stenosis, pneumonia, and necrosis of the tracheal tissue [3]. Most of these complications arise from the current design of the ET tube. The current design is a mass-produced, large, inflexible, fixed-diameter, polyvinylchloride ventilation tube. Sizing is determined through patient's size and age. The current ET utilizes a thin filmed, pneumatically inflated cuff to secure the airway. This cuff is recommended to be inflated to a recommended pressure range of 20-30 $cmH_20$ and exerts radial pressure to the tracheal wall [3]. The current ET is not designed to be in place for more than 24 hours, although in practice it is frequently required by clinical need. The shape and actuation of the donut-shaped pneumatic cuff creates a relatively narrow ring-shaped interface with the trachea and concentrates most of the tissue pressure (and mechanical sealing) in a small annular anatomic area, which has been demonstrated to cause downstream complications [1-2]. Our research proposes a redesigned ET that replaces the standard ET cuff with a novel expanding cylindrical lattice enclosed in a thin silicone sheathing tube. The lattice removes the need for multiple sizes since it can expand through the entire range of adult standard ETs sizes. We hypothesize that this will enable the same fluid tight seal necessary to secure the airway with a lower maximum pressure due to more distributed contact forces.

## METHODS

The expanding lattices were made from an array of individual strips combined into a planar lattice that is rolled into a cylinder [3]. All lattices are composed of two sets of strips that are attached utilizing annular snap-fitting elements that secure the lattice while allowing actuation of the mechanism, which is radial expansion during axial contraction. Small ring shuttles are attached to the middle of the lattice by going over both sets of strips. The lattices were designed in SolidWorks and 3D printed using FormLabs Form 2 printer with their Durable Resin. Sheathing material was casted utilizing Ecoflex 00-20 silicone to have a thickness of 0.5 mm. The lattice is mounted onto a flexible, hollow aluminum rod by guiding the rod through the ring shuttles. A fishing line is run inside the aluminum rod and tied onto the top end of the lattice, creating a pulley system. The lattice is then actuated by applying tension to the fishing line.

A series of leak and pressure tests were conducted with the prototype lattice and the standard ET. For these tests, size 8 Shiley ETs were used for testing. Leak tests were conducted by inflating the ET cuff to a pressure of 20, 25, and 30 $cmH_20$ inside of 20 ml syringes for 10 trials conducted over a 1-hour period, as previously done in Mariyaselvam et. al. Once inflated, 4 ml of water was added on top of the seal and water was collected at the bottom after the hour period. The prototype was also inserted into 20 ml syringes and actuated to match the seal performance of the standard ET using an Instron 3345 Universal Tensile Tester. The experimental setup for both leak tests is shown in Figure 1. Fresh swine tracheas were chosen as pre-clinical models to examine the pressure applied by the lattice. Digital Image Correlation (DIC) was used to evaluate the forces exerted by the lattices and standard ET on the swine trachea. Strain measurements of the external surface of the phantom was collected and used to relate to internal pressure applied. The prototype and the standard ET were submerged into a phosphate-buffered saline (PBS) bath in a 4x4 in. acrylic container, as shown in Figure 2.

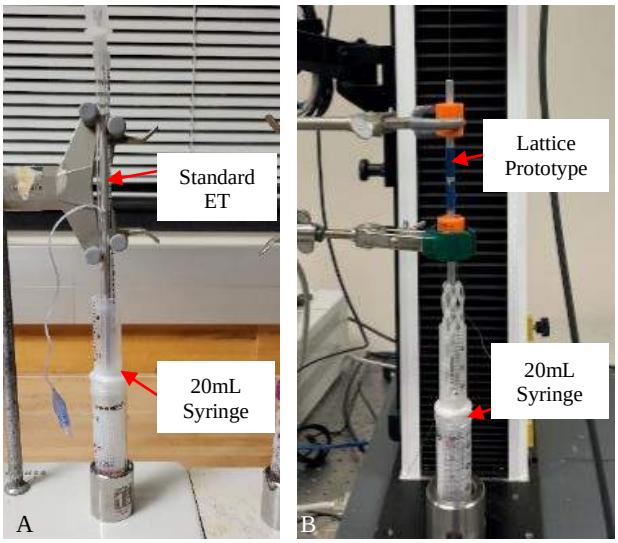


**Figure 1: Experimental setup for leak tests. A) Standard ET, B) Prototype Lattice.**

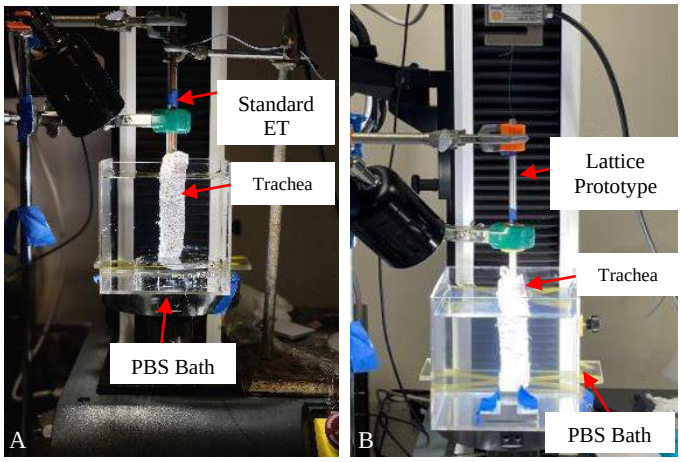


**Figure 2: Experimental setup for DIC experiment. A) Standard ET, B) Prototype Lattice.**

## RESULTS

From the leak tests, it was observed that the standard ET did not create a proper seal at the recommended range of 20-30 $cmH_20$. Utilizing the prototype, the leak performance was then evaluated by actuating to the tension needed to create a proper seal. The prototype was then expanded inside the tracheas by matching the tension needed to create a proper seal. The strain map results from the DIC experiments showed concentrated regions of deformation in the trachea as shown in Figure 3.

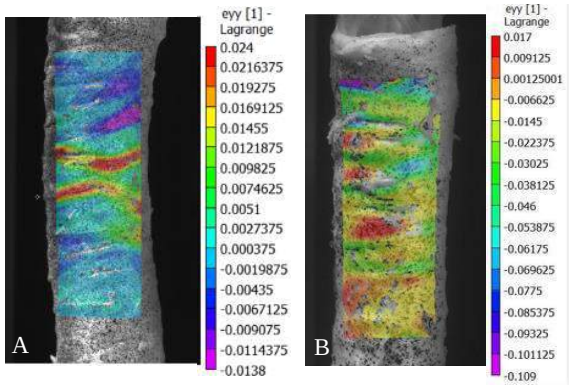


**Figure 3: Strain maps ($e_{yy}$) results from DIC experiments. A) Standard ET, B) Prototype Lattice.**

## DISCUSSION

The leak results observed using the standard ET does not match previous studies. Thus, the lattice prototype was not possible to accurately match the leak performance of the standard of care. These results may need to be further evaluated in order to make a proper comparison between the lattice prototype and standard ET. Previous studies showed small leaks for other brands while the results in this study show a complete leak. This might be due to using a different brand that has not been evaluated in previous studies.

The strain map results showed concentrated regions of pressure in the trachea for both devices. In the case of the standard ET cuff, the pressure is seen in a small, concentrated region. This supports previous studies where it has been described that this concentrated pressure may cause complications to the patient in prolonged intubations. In the case of the prototype lattice, the strain concentrations are distributed along a wider surface area. Different tracheas were used for each device, which could account to some small discrepancies in our results due to the different trachea sizes and geometries.

These results are insufficient to fully evaluate our hypothesis due to the discrepancies between the leak results in this study and previous studies. Future works will further examine the leak tests to assess the differences between our results and previous studies. Other brands of standard ETs will be tested to further compare the lattice prototype. However, this study shows that the novel expanding lattice has the potential to reduce the maximum pressure required to achieve a fluid-tight seal by distributing forces over a wider area. Due to the experimental issues encountered, additional studies will be necessary to properly assess this potential.

## ACKNOWLEDGEMENTS

This grant was funded in part by the San Antonio Medical Foundation. The authors would also like to extend thanks to Robert Brothers, Isaac Trevino, and Darnell Campbell for their support in the prototype development and background research of this work.

## REFERENCES

[1] Cooper, J.D., *Thorac Surg Clin*, 28:139-144. 2018.
[2] Gaynor, E.B. et. al. *Laryngoscope*, 95:1461-7. 1985.
[3] Berard D et. al. *Journal of the Mechanical Behavior of Biomedical Materials, 114*, 2020.
[4] Mariyaselvam, M. Z et. al. *BMC anesthesiology*, 17:1-9, 2017.

# A COMPUTATIONAL RULE-BASED SEMI-AUTOMATIC METHOD FOR CREATING LEFT ATRIAL FIBER ARCHITECTURE

**Simone Rossi (1), Laryssa Abdala (1), Boyce E. Griffith (1,2,3)**

(1) Department of Mathematics, University of North Carolina, Chapel Hill, North Carolina, United States
(2) Applied Physical Sciences, University of North Carolina, Chapel Hill, North Carolina, United States
(3) Biomedical Engineering, University of North Carolina, Chapel Hill, North Carolina, United States

## INTRODUCTION

With an aging population, atrial fibrillation (AF) affects 2.7 million to 6.7 million people in the United States. [1] Although, the $CHA_2DS_2VASC$ score is the most used risk-stratification scoring system to guide AF treatment, the measurement lacks personalization. To overcome this limitation, many researchers have started creating patient-specific computer simulations of AF. [2,3]

One of the challenges faced in the creation of patient-specific computational models of AF is the complexity of the atrial muscle arrangement.[4] While some studies have proposed rule-based models, others have created atlas-based models that require data mapping among anatomies.[5-8]

This work proposes a semi-automated rule-based algorithm for left atrial (LA) myofiber construction. The main fiber LA bundles are created in two layers: the endocardium, and the epicardium. The notable advantage of our approach is the ability to capture the main LA fiber bundles while solving only seven harmonic fields, leading to a straightforward and reproducible approach.

## METHODS

The anatomical regions and muscle fiber were created using seven harmonic fields, solutions of the partial differential equation:

$$-\Delta\phi_i = 0 \text{ on } \Omega \quad (1)$$

$$\phi_i = g \text{ on } \Gamma_D \quad (2)$$

$$\frac{\partial \phi_i}{\partial \boldsymbol{n}} = 0 \text{ on } \partial\Omega. \quad (3)$$

In which $i = 1, \dots, 7$; and $\Gamma_D$ is a side set. The side sets include landmarks such as lines (e.g., pulmonary vein, mitral valve), and points (e.g., the tip of the left atrial appendage, a point on the fossa ovalis). **Figure 1** shows the solutions of Equations (1)-(3) for a patient-specific geometry.

Given these seven harmonic fields, we construct an algorithm that subdivides the left atrium into subregions. To achieve the final region segmentation, we introduce thresholds that are used to control the extent of each subdomain. In the following, we use the gradients of the fields to define a local frame of reference, denoted as {**f**, **s**, **n**}, for each point in $\Omega$.

To compare the resulting fiber field **f** with other models available in the literature, we perform electrophysiology simulations. More specifically, we solve the monodomain equations:

$$\chi\left(C_m \frac{\partial V}{\partial t} + I_{ion}(\boldsymbol{y}, V) + I_{stimulus}\right) = \nabla(\sigma \nabla V), \quad (4)$$

$$\frac{d\boldsymbol{y}}{dt} = g(\boldsymbol{y}, V, t), \quad (5)$$

in which $\chi$ is the surface-to-volume ratio of cells, $I_{ion}$ is the transmembrane current density, $\sigma$ is the conductivity tensor and $C_m$ is the specific membrane capacitance. $I_{ion}$ is defined by a system of nonlinear ordinary differential equations, g, that depends on state variables $\boldsymbol{y}$. More specifically, Equation (5) is characterized by the Cherry-Ehrlich-Nattel-Fenton [9] human atrial ionic model.

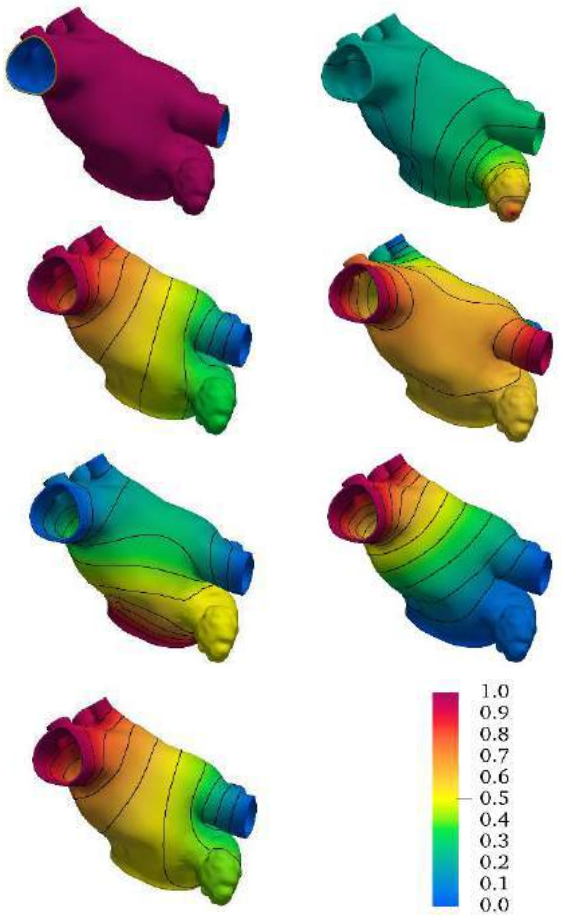


**Figure 1: Harmonic fields for a patient-specific anatomy.**

## RESULTS

The resulting fiber field on the endocardial and epicardial surfaces is shown in **Figure 2.** The interface between them is continuous and smooth.

**Figure 2: Endocardial fiber field (left panel), and epicardial fiber field (right panel) for a patient-specific anatomy.**

The electrophysiology simulation uses an activation function to initialize the signal. The support of this function lies on the anterior wall of the LA, and is defined by the intersection of a sphere centered at (-0.31, 3.35, 3.65) with radius 0.4 and the domain $\Omega$. **Figure 3** shows the comparison between local activation times using the fiber structure presented in this work and more complex fiber architecture developed by Fastl et al. [5]

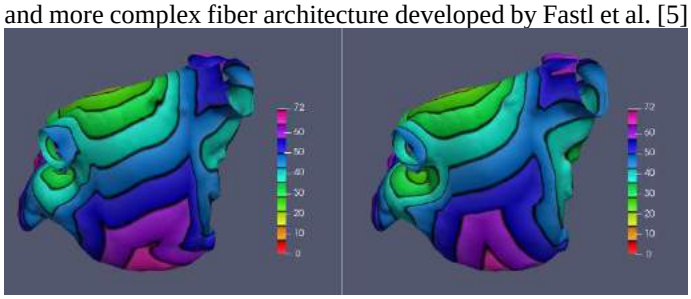

**Figure 3: Local activation times (milliseconds) for using the fiber model by the Fastl et al. [5] (left panel) in comparison to our approach (right panel).**

## DISCUSSION

This work developed a semi-automated rule-based method for fiber construction on left atrial anatomies. To compare our novel algorithm with those currently available, we simulated the propagation of the action potential using the monodomain model. Transmural fibers produced by our algorithm generate similar electrical activation patterns compared to the patterns generated using the more complex model by Fastl et al.[5]

Current approaches for defining the orientation of the atrial fiber bundles either require the definition of hundreds of landmarks or are overly simplistic. The notable advantage of our approach is the ability to capture the main LA fiber bundles while solving only seven harmonic fields, leading to a straightforward and reproducible approach.

Common approaches are well defined for common atrial geometries with four distinct pulmonary veins. However, most patients with AF do not fall in this category and have different pulmonary vein configurations. Our method extends to these scenarios easily.

## ACKNOWLEDGEMENTS

Partial support for RA Laryssa Abdala is gratefully acknowledged from the National Science Foundation, award NSF-DMS-1929298 to the Statistical and Applied Mathematical Sciences Institute.

## REFERENCES

[1] Du, X et al, *J Am Coll Cardiol*., 69(15):1968-1982, 2017.
[2] Boyle, P et al., *Nature biomedical engineering*, 3:870-879, 2019.
[3] Aslanidi, O et al., *Progress in biophysics and molecular biology* 107:156-168, 2011.
[4] Ho, S., Sanchez-Quintana, D., *Clinical Anatomy: The Official Journal of the American Association of Clinical Anatomists and the British Association of Clinical Anatomists* 22:52-63, 2009.
[5] Fastl, T et al, *Medical Image Analysis*, 47:180–190, 2018.
[6] Roney, C et al., *Med Image Anal*., 55:65-75, 2019.
[7] Roney, C et al., *Ann Biomed Eng*., 49:233-250, 2021.
[8] Piersanti, R et al., *Comput Methods Appl Mech Eng*., 373:113468-113501, 2021.
[9] Cherry, E et al, *Heart rhythm*, 4:1553-1562, 2007.

SB³C2022
Summer Biomechanics, Bioengineering and Biotransport Conference
June 20-23, Eastern Shore, MD, USA

# PERTURBED CYCLIC STRAIN IN CARDIAC FIBROBLAST CULTURES RESULTS IN A MECHANICALLY-INDUCED SENESCENT PHENOTYPE

**Stephanie E. Schneider (1), Adrienne K. Scott (1), Corey P. Neu (1,2)**

(1) Mechanical Engineering, University of Colorado Boulder, Boulder, CO, U.S.
(2) Biomedical Engineering Program, University of Colorado Boulder, Boulder, CO, U.S.

## INTRODUCTION

Though initially characterized as an arrest in cell cycle, the cellular senescence phenotype has become more complex as we begin to understand the induction of senescence. Extrinsic factors such as oncogene disruption, irradiation, chemotherapy, developmental cues, and tissue damage have been shown to generate a new form of senescence, stress-induced senescence [1]. With exposure to these stresses, the cell will express an array of biomarkers intended to promote regeneration and repair. However, if the stress continues a senescent phenotype emerges, often characterized by cell cycle arrest, morphological changes, chromatin reorganization, and secretion of proinflammatory factors. This phenotype is linked with disease states such as cancer, osteoarthritis, and cardiac disease [1-3]. Furthermore, disease states often lead to changes in both biochemical and mechanical environments in the tissue. While the biochemical effects that induce a premature-stress senescent state are currently under significant exploration [2], the influence of how mechanical perturbations in disease states might influence this induction are still unclear.

Our objective of this study was to examine if perturbed strain magnitudes similar to those described with cardiac disease could induce a premature senescent-like state. In cardiac disease, cardiac fibroblasts (CFs) are one of the main cell types involved in the adaptive response to environmental cues in heart tissue. CFs regulate the remodeling and repair process, and the balance between healthy or fibrotic tissue [4]. To study how changes in the mechanical environment influence the CF, we chose a model system in which the cells have been shown to have immediate strain-dependent response. Studies have estimated heart contractility at 8% strain with decrease contractility to approximately 2% strain with injured or stiffened tissue [5]. Our simplified model examines the cardiac fibroblast phenotype during the mechanical transition observed in cardiac pathology with established senescent markers for biophysical alterations (i.e. nuclear area and Lamin B expression), cell cycle arrest, and cellular damage response [1,2]. For comparison, we used ROS (reactive oxygen species)-induced senescent CFs to investigate a premature senescent phenotype in stretched cells.

## METHODS

***Cell Culture***: Primary cardiac fibroblasts (CFs) were harvested from wild type *Lmna* mice (Jackson Lab #009125) between 4-8 wks old. Minced perfused tissue was digested with CollagenaseP with DNaseI for 30 mins at 37°C. Cells were filtered, RBC lysed, and then plated in petri dishes for 2 hrs. After 2hrs, dishes were washed in warmed DPBS to remove any nonadherent cells, and D10 (DMEM/F12 + 10% FBS + 1X Pen/Strep) medium was added. CFs were grown to confluency and then plated on Geltrex-coated CellScale MCFX membranes at 4 x $10^3/cm^2$. Cells were allowed to adhere for 12 hrs prior to treatment for

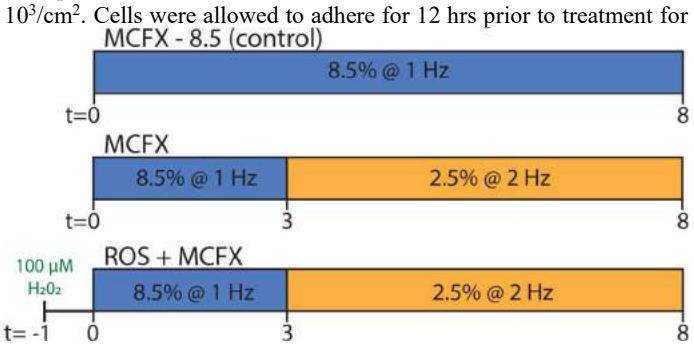


**Figure 1. Cardiac fibroblasts (CFs) loading protocol. A) CFs received uni-axial strain for 8 days in a CellScale MCFX device. Controls for the mechanical stretch treatment were stretched cyclically for 8 days at 8.5% strain at 1 Hz (MCFX-8.5) where time (t) is in days. The two treatment groups, MCFX and ROS + MCFX, had the same cyclic loading protocol. At time t=0, cells were stretched for 3 days at 8.5% strain at 1 Hz. At time, t=3, the loading scheme was changed to 2.5% strain at 2 Hz for 5 days. ROS + MCFX CFs received 100µm $H_20_2$ for 24 hrs prior to stretching.**

both chemical and stretch. Tissue culture plastic (TCP) controls were plated at the same density and allowed to grow to 95% confluency before fixing (4% PFA in DPBS). ***Mechanical Stretch***: Cells received cyclic uni-axial stretched for a total of 8 days in a CellScale MCFX device with daily medium changes (see **Figure 1** for stretch protocols) in a 37°C incubator. On day 8 *in vitro*, cells were fixed for imaging or lysed for RNA (Qiazol). ***ROS treatment:*** Cells plated on TCP received 300µm $H_20_2$ in D10 for 2 hrs at 37°C, and were washed in DPBS prior to replacing the D10 medium. After 24 hours, cells were passaged and replated. Four days after the first dose, the cells received a second dose of 300µm $H_20_2$ for 2 hrs. Plates were observed for increased confluency (typically 5-7 days) before fixation or RNA collection. ***Immunofluorescence/Microscopy***: Cells were stained with DAPI (405nm), Phalloidin Texas-Red (561nm), Lamin B1 (640nm), mounted and imaged with NIKON A1R confocal 60x oil objective. ***Image Analysis***: Images were process in ImageJ and analyzed using a custom MATLAB code for morphological feature extraction (i.e. nuclear area). ***Gene Expression***: RT-qPCR was used for gene expression analysis with targets: p16, p19, p53, and p21 [2]. Expression was first normalized to reference genes *Actb* and *Gapdh*, prior to calculating the fold change compared to treatment controls.

## RESULTS

We first confirmed the senescent phenotype by comparing ROS-induced senescent CFs to CFs plated on TCP. We found ROS-induced senescent CFs showed decreased Lamin B intensity and an inconsistent ring around the nucleus (Fig. 2A). Similarly, CFs which experienced MCFX or ROS + MCFX treatment showed a decrease in Lamin B fluorescent intensity and a discontinuous Lamin B ring around the nuclear periphery compared to control, MCFX–8.5 (Fig. 2A). Additionally, nuclear envelope wrinkling was visualized through Lamin B in ROS + MCFX CFs.

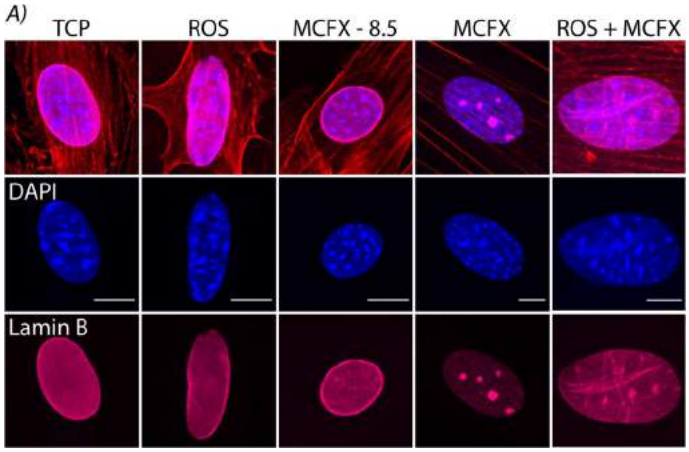


**Figure 2: MCFX and ROS + MCFX loading treatments results in altered Lamin B expression. A) Representative images of CFs from controls (TCP or MCFX – 8.5) and chemical or stretch treatments. ROS-induced senescent CFs have a non-uniform Lamin B ring around the nuclear periphery compared to TCP. MCFX and ROS + MCFX CFs show decreased Lamin B fluorescence and nuclear wrinkling, respectively, compared to MCFX–8.5. Scale bar = 10µm.**

Examining nuclear area, ROS-induced senescent CFs showed no increase in nuclear area compared to TCP (Fig. 3A). However, preliminary data from MCFX and ROS + MCFX CFs show an increased nuclear area compared to CFs which received continuous 8.5% strain (MCFX - 8.5, Fig. 3B). Further assessment of a senescent phenotype was examined with genes upregulated in cell cycle arrest, *Cdkn2A* (p16 and p19), and cellular damage response activation, *Cdkn1a* (p21) and

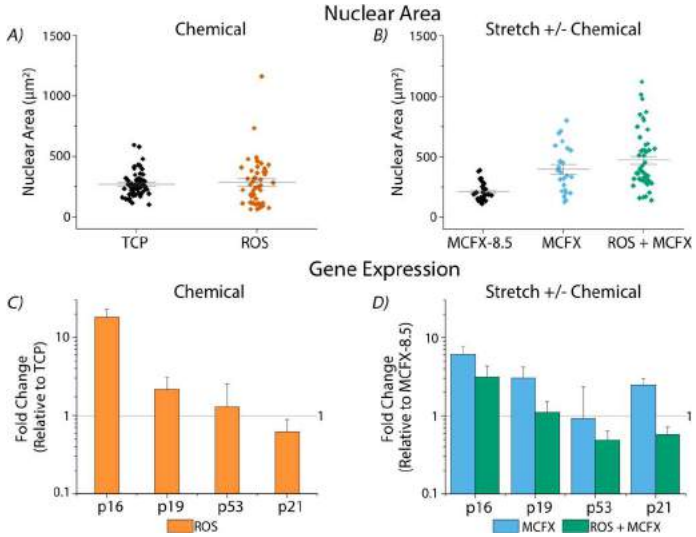


**Figure 3: Biophysical features and gene expression of stretched CFs have senescent-like phenotype. A) ROS-induced senescent CFs do not show increased nuclear area compared to TCP controls. B) MCFX and ROS + MCFX CFs show modest increase in nuclear area compared to constant MCFX – 8.5. C) Gene expression of ROS-induced CFs for cell cycle markers and damage response marker, p53, are increased compared to TCP controls. D) Compared to MCFX-8.5 CFs controls, MCFX and ROS + MCFX CFs have increased expression of cell cycle arrest and damage response marker, p21. N=1-2 animal(s)/treatment, n= 25 nuclei/treatment. All error bars = s.e.m.**

*Tp53* (p53). ROS-induced senescent CFs had upregulated expression of p16, p19, and p53 compared to TCP controls (Fig. 3C). Similarly, preliminary data showed MCFX and ROS + MCFX CFs had increased expression of p16, p19, and p21 compared to MCFX-8.5 CFs (Fig. 3D).

## DISCUSSION

In our work, we show preliminary evidence that perturbing strain in an *in vitro* model to study CFs in cardiac pathology induced a senescent-like phenotype. Compared to ROS-induced CFs, MCFX and ROS + MCFX CFs displayed similar biomarkers of senescence. This premature mechanically-induced senescent phenotype shows increased nuclear area, increased expression of cycle cell arrest, and damage response markers with perturbed cyclic strain compared to continuous strain. While this preliminary evidence demonstrates the importance of maintaining homeostasis of the tissue microenvironment, there are several limitations of this simplified *in vitro* model. One caveat is the length of time the cells spend in the device stretching. This long culture duration could be "prematurely aging" the cells, especially in a 2D environment. Additionally, while 2% strain is reported in the literature with tissue stiffening, this change occurs gradually allowing cellular adaption [5]. Future work will further examine the DNA damage response pathways and potential mechanisms which might induce the transformation observed in this study.


## ACKNOWLEDGEMENTS

This work was supported by funding from NIH, NSF, and Biophysics Training Grant T32


## REFERENCES


[1] Rodier, F et al., *J Cell Biol*, 192(4):547-556, 2011. [2] Gualda-González, E et al., *FEBS J*, 288(1):56-80, 2021. [3] Childs, B et al., *J Clin Invest*, 128(4):1217-1228, 2018. [4] van Putten, S et al., *J Mol Cell Cardiol*, 93:133-142, 2016. [5] Ugolini, G et al., *eLife,* 6 (3), 2017.

# EFFECT OF HELMET SIZE AND VELOCITY ON CERVICAL SPINE SEGMENTAL RESPONSES UNDER REAR IMPACT ACCELERATION

**Yuvaraj Purushothaman, Hoon Choi, Narayan Yoganandan**

Department of Neurosurgery
Medical College of Wisconsin
Milwaukee, WI

## INTRODUCTION

Numerous studies have been conducted to determine the biomechanics of impact loading to the cervical spine under postero-anterior accelerations, and this rear impact loading vector is used in civilian and military for advancing injury criteria and occupant safety. Experiments with whole-body human cadavers and isolated head-neck complexes are used as validation tools to develop computational models as they can determine parameters such as the range of motion at each segment of the cervical spine and, also extract spinal loads at each level [1]. The advantage of the former metric is its applicability to clinical measures as motions in radiographs are a hallmark for treatment. Experimental studies have been limited to cadaver studies without the use of the head supported mass (HSM), typical in military use. Any data obtained from human cadaver studies should be modulated to delineate the effect of the head supported mass, example, army combat helmet used by Soldiers during operational activities. The objective of this study was to determine the effect of different sizes of the head supported mass (miliary helmets) on male cervical spine responses under two different impact velocity severities.

## METHODS

Our mid-size male head-neck finite element model was used in the study. The cervical spine included the seven vertebrae from the axis to the first thoracic level, intervening discs that consisted of the nucleus and anulus fibers and ground substance, and the ligaments, i.e., anterior and posterior longitudinal, capsular, interspinous, and flavum at each vertebral level. The trabecular bone, cortical bone, and endplates were included for each vertebra. The anterior and posterior regions of the disc consisted of sixteen and eight layers, mimicking the human intervertebral component of the neck. The material properties of the components were obtained from literature. The anulus fibers were defined using membrane elements with tension-only directional fibers embedded in the ground substance. The fibers in the anterior annulus were defined in a crisscross manner, while fibers in the posterior region were defined in the vertical direction. The head to axis structure was attached to the subaxial cervical column. The head center of mass was located using coordinate system based on the location of the occipital condyles. The spinal musculature was simulated using the respective anatomical origin-insertion locations and expressed as one-dimensional beam elements. A coordinate measuring machine was used to describe the geometry of the three different helmets. A collection of coordinates was registered at each point of contact of the probe with the external component surface. The inner component of the helmet was lined with seven foam pads. The helmet and inner foam were modeled as solid hexahedral elements, and the material properties were based on literature studies [1]. The size and mass of the helmet are shown in the Table 1 [2].

**Table 1:** Size and mass of the helmet used in the study.

| Helmet Size | Length (mm) | Width (mm) | Height (mm) | Weight (Kg) |
|---|---|---|---|---|
| Small | 246.38 | 231.14 | 177.80 | 1.33 |
| Medium | 261.62 | 236.22 | 177.80 | 1.40 |
| Large | 266.70 | 241.30 | 177.80 | 1.50 |

**Figure 1: Head-neck finite element models without HSM on the left and with HSM on the right.**

The helmet model was strapped using a chinstrap, modeled using solid elements. Automatic surface-to-surface contact was defined between the head and helmet. The models were exercised under rear impact ($G_x$ accelerative loading) by inputting pulses at velocities of 1.8 and 2.6 m/sec to the T1 vertebra, and these pulses were also used in the experimental validation studies [3]. The input pulses are shown (Figure 2). The model without helmet were validated with the experimental data at both velocities for segmental motions at all levels. The range of motion data from the helmeted models were normalized with respect to the no HSM case to quantify the effect of helmet, and with respect to the low velocity to quantify the effect of impact pulse on the change dur to HSM use. Helmet and HSM are used synonymously.

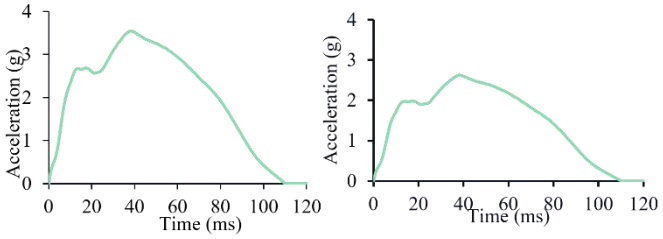


**Figure 2: Input acceleration-time histories for the high (left) and low (right) impact severity simulations for four cases: no-HSM, and small, medium, and large size HSM finite element models. All segmental motions were validated for the first case with human cadaver experimental results.**

## RESULTS

The finite element model without the presence of any HSM was validated using kinematics data from human cadaver tests conducted in our laboratory [3]. The model-predicted range of motion at each subaxial segment was within the mean ±1 standard deviation corridors of experimental motions, at both impact velocities. Segmental motions increased with increase in velocity at all segments of the spine. Angulations ranged from 1.3 deg to 10.3 deg at the higher and from 0.9 deg to 9.3 deg at the lower velocity for the no HSM case. For the small size HSM, they ranged from 1.7 deg to 11.6 deg and 1.4 deg to 10.4 deg, respectively. For the medium size HSM, they ranged from 1.9 deg to 12.3 deg and 1.5 deg to 11.1 deg, respectively. For the large size HSM, angulations ranged from 2.3 deg to 13.2 deg, and 1.7 deg to 11.7 deg, respectively. The maximum increase was at the C5-C6 segment in all cases with the exception of the no HSM case that had a slight increase at the C6-C7 segment. These results are shown in Figure 3.

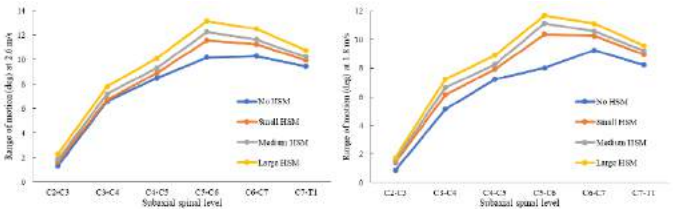


**Figure 3: Segmental angulations for the four cases, without and with different size HSM at the high (left) and low (right) impacts.**

## DISCUSSION

The objective of the study was to determine the effect of HSM on the range of motion of the cervical column for military applications. Three helmet sizes chosen in the study represented Army Combat Helmets [2]. It is customary to validate any computational model with matched pair experimental data. This was accomplished in this study with the model that did not have any HSM, i.e., no helmet condition. This because human cadaver tests with HSM under the accelerative loading vector used in the study is not published in literature; however, matched pair tests without the HSM were available. The range of motion at all segmental levels were within the experimentally determined mean plus/minus one standard deviation corridors, demonstrating that the model was validated at both impact velocities.

This model was then used to add different size HSM to evaluate the size/mass of on neck motions, indirectly considering the addition of HSM as parametric. As expected, increasing velocity increased spinal motions and this was true for all three HSM conditions. Under each HSM condition, as described in the results section, motions increased from the axis to the C5-C6 level and then decreased, and this was true for both impact velocities. The motion was the greatest with the large HSM, and this was expected as the large helmet has greater mass, greater inertial properties, reflecting an anterior shift in the center of gravity of the head from its original non-HSM center of mass. Because large size helmets are a better to fit large size Soldiers, the increased motions may be better tolerated with the change in the spinal anthropometry, although this issue was not specifically addressed in this study. Simulating necks with small, medium, and large anthropometries may be needed to clearly delineate these effects, and this should be pursued in the future.

The increase in the motion at the C5-C6 level with any HSM may have clinical implications. For example, this is the most common site of spinal disorders such as spondylosis/pain in military patients, and some receive surgical treatment with conventional fusion and or arthroplasty [4,5]. From this perspective, the use of a larger HSM than necessary may predispose to the added mobility of the spine under this mode, and to the C5-C6 segment, in particular. The second most common level for surgery in military patients is the C6-C7 level [5,6]. This is also borne out by this study as it is the segment with the second highest increased motion regardless of helmet size.

In summary, the lower cervical spinal region appears to sustain greater motions at both velocities and in an increasing magnitude with the use of the small to medium to large HSM. Common cervical spine disorders in military populations as reported in clinical studies appear to connect increased motion with the disorder. The use of HSM affects spinal responses and increased motions may contribute to clinical observations of neck pathology in the lower spine.


## ACKNOWLEDGEMENTS

This research was supported by the Department of Veterans Affairs Medical Research, Department of Neurosurgery at the Medical College of Wisconsin, and W81XWH-16-01-0010. This material is the result of work supported with the resources and use of facilities at the Zablocki VA Medical Center, Milwaukee, Wisconsin. The last author (NY) is an employee of the VA Medical Center, Milwaukee, WI.


## REFERENCES


[1] Palta. E, et al., *Int. J. Impact Eng*. 2018.
[2] Department of the Army, *Technical manual for ACH*, 2008.
[3] Stemper, BD, et al., *AAAM*, 2004.
[4] Choi, H, et al, *Euro. Spine J*., 2019.
[5] Tumialen, et al., *Neurosurg.*, 2019.
[6] Tumialen, et al., *Neurosurg. Focus*, 2010.

SB³C2022
Summer Biomechanics, Bioengineering and Biotransport Conference
June 20-23, Eastern Shore, MD, USA

# ESTIMATION OF MYOCARDIAL MATERIAL PARAMETERS IN DEVELOPING ZEBRAFISH USING INVERSE FINITE ELEMENT ANALYSIS

**Aaron L. Brown (1), Lei Shi (2), Vijay Vedula (2), Tzung K. Hsiai (3), Alison L. Marsden (4)**

(1) Department of Mechanical Engineering, Stanford University, Stanford, CA, United States
(2) Department of Mechanical Engineering, Columbia University, New York, NY, United States
(3) Departments of Medicine and Bioengineering, UCLA, Los Angeles, CA, United States
(4) Departments of Pediatrics and Bioengineering, Stanford University, Stanford, CA, United States

## INTRODUCTION

The zebrafish is a widely used model for studying cardiac development due to its optical transparency, fast development in culture, and ease in applying genetic modifications or pharmacological treatments. Bulk cardiac performance metrics, such as cardiac output and stroke work have recently been obtained for the developing zebrafish [1], but the material properties of the zebrafish heart that underlie these metrics are less studied. Due to the small size of the zebrafish heart, traditional experimental techniques for material characterization are challenging to apply. Experimental characterization of the zebrafish myocardium is limited, and existing work has for the most part studied only the passive mechanical response of *ex vivo* hearts or hearts in otherwise non-physiological states [2], [3]. In this work, we apply an inverse finite element analysis (FEA) to estimate the passive material parameters of the zebrafish ventricle under physiological conditions. This pipeline provides a means for researchers to connect pharmacological and genetic treatments to changes in myocardial material properties during development, potentially revealing new links between cell-level processes and bulk cardiac performance.

## METHODS

Our framework uses 4D light-sheet images of developing zebrafish acquired at 5 days post fertilization (dpf). We use the open-source SimVascular framework (www.simvascular.org) to manually segment the zebrafish myocardium at a single cardiac phase (mid-diastole) and construct a computational model of the ventricle. We then use deformable image registration to extract myocardial displacements and morph the initial segmentation to create a computational model of the beating heart [4]. This approach efficiently and robustly yields a segmentation of the myocardium for each time step, minimizing manual user input. This "moving" segmentation of the ventricular myocardium derived from light-sheet images constitutes the ground truth for the calibration process, and we henceforth denote this data the *"in vivo* configurations."

We model the zebrafish ventricular myocardium as an incompressible, hyperelastic material using our recently developed unified variational multiscale method for incompressible solid mechanics [5]. In this study, we explore multiple material models for developing ventricular myocardium, including the commonly-used Guccione model [6], Ogden model, and Gent model [7]. We were inspired to explore the latter two models because of an unusual diastolic ventricular pressure-volume relationship during development [1], discussed later.

We perform a quasi-static inflation simulation of the ventricle, applying diastolic pressure load measured *in vivo* from previous experiments [1] to a computational model at mid-diastole. We then calibrate the material parameters of each constitutive model such that the FEA loaded configuration matches the *in vivo* configuration at a given pressure load. We compare two calibration procedures. In the first, we seek only to match the volumes of the FEA loaded configuration and the *in vivo* configuration at a given pressure and employ a simple iterative algorithm to estimate material parameters. In the second, we seek to minimize the sum squared differences in nodal point positions between the FEA loaded configuration and the *in vivo* configuration and employ the derivative-free surrogate management framework to achieve this.

## RESULTS

The modeling pipeline produces realistic ventricular displacements that match the collected imaging data as well as volume vs. time data from previous studies (Fig. 2). These agreements serve to validate the process used to construct the ground truth *in vivo* computational models.

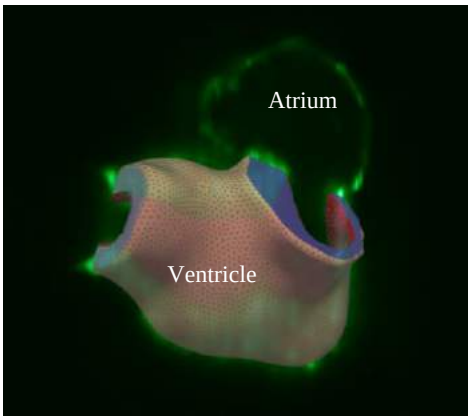


**Figure 1: Computational model of zebrafish ventricular myocardium overlaying one slice of raw light-sheet image.**

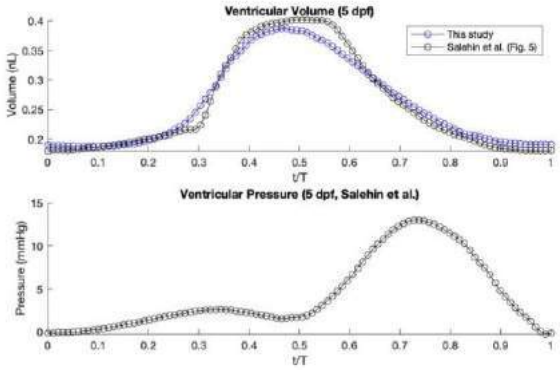


**Figure 2: Ventricular volume vs. time (normalized to cardiac cycle). In this study, volume was calculated from the *in vivo* configurations [4]. In Salehin et al., volume was calculated from manual segmentations at each time point. We note the qualitative agreement in volume vs. time curves. Additionally, pressure vs. time from Salehin et al. is reproduced here.**

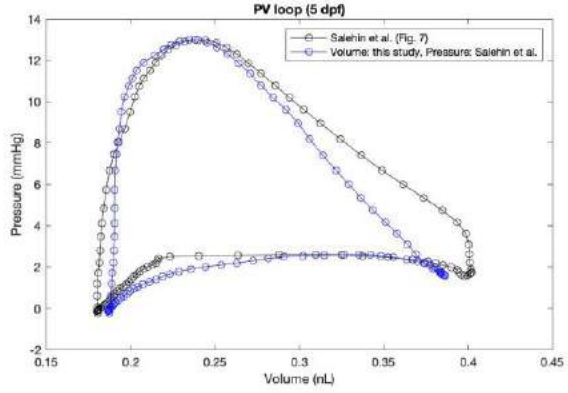


**Figure 3: Pressure-volume loops. The PV loop in blue was obtained by synchronizing pressure data from Salehin et al. to volume data obtained via our modeling pipeline. Note the atypical behavior of the filling curve (lower portion of the loop): pressure initially increases with volume, then plateaus, and finally decreases.**

The simpler volume-based calibration algorithm determines the material parameters such that the pressure-volume relation from the FEA matches the desired diastolic pressure-volume relation (Fig. 3), obtained using the volume of the *in vivo* configurations, synchronized with pressure data from [1]. Synchronization was performed as described in [1]. Since the second calibration procedure is more demanding (imposes nodal point agreement), we expect it to be more accurate for the transversely isotropic Guccione model.

We apply the above framework to estimate myocardial parameters in multiple wild type zebrafish ($N \geq 5$) acquired at 5dpf. In a follow-up study, we discuss the extension of this technique to other stages during zebrafish development (2dpf – 5+dpf) and conduct an analysis of changes in myocardial material properties in response to genetic and pharmacological interventions.

## DISCUSSION

We present an inverse finite element modeling approach for estimating zebrafish myocardial material properties under physiological conditions, using light-sheet imaging that is commonly used to study zebrafish cardiac development. Our approach will allow researchers to study not only the bulk changes in cardiac morphology and function associated with genetic mutations or drug treatments, but also the underlying changes in material properties. Such an added dimension to studying zebrafish development has the potential to reveal new links between cellular biology and tissue mechanics during cardiac morphogenesis.

In addition, we explore the validity of several different material models for the ventricular myocardium of developing zebrafish. While the Guccione model has been used successfully to model the myocardium across many species [6], [8], recent experimental studies on the developing zebrafish suggest a significantly different behavior. Specifically, in the diastolic pressure-volume relationship presented in [1], the myocardium appears to become more compliant with increasing strain, to the point that the pressure plateaus and eventually decreases with volume (Fig. 3). In the "typical" diastolic pressure-volume relation, pressure increases linearly or weakly exponentially with volume [9]. The filling curve in Figure 3 is reminiscent of the so-called "limit-point instability," a phenomenon observed in some rubber-like pressure vessels in which there is a maximum in pressure as a function of volume. The existence of this phenomenon depends on the chosen constitutive model and values of the constitutive parameters, as well as the geometry [7]. This study evaluates the applicability of different material models to zebrafish ventricular myocardium, particularly as it relates to capturing this behavior.

## ACKNOWLEDGEMENTS

I would like to thank the National Institutes of Health (R01HL129727) and the National Science Foundation (1663671) for grant funding for this project, and the members of the Cardiovascular Biomechanics Computation Lab at Stanford for many helpful discussions.

## REFERENCES

[1] Salehin, N et al., *Annals Biomed Eng*, 49(9):2080-2093, 2021.
[2] Yu, JK et al., *Sci* Rep 8, 15661, 2018.
[3] Gendernalik, A et al., *Ann Biomed* Eng 49(2):834-845, 2021.
[4] Vedula, V et al., *PLoS Comput Biol* 13(10): e1005828, 2017.
[5] Liu, J et al., *Comp. Methods for App Mech Eng* 337:549-597, 2018.
[6] Guccione, JM et al., *J Biomech Eng*, 113(1):42-55, 1991.
[7] Goriely A et al., *Quart J Mech App Math* 59(4):615-630, 2006.
[8] Wang VY et al., *Medical Image Analysis* 13(5):773-784, 2009.
[9] Zhang, W et al., *Am J Physiol. Heart Circ Physiol* 294(6): H2750-60, 2008.

# VIT-FNO; A ROBUST MODEL FOR TRACKING MOTION IN 4D-MRI

**A. Chopra (1), A. Pionteck (2), J. Abderezaei (2), M. Kurt (2)**

(1) Department of Computer Science, Stevens Institute of Technology, Hoboken, NJ, USA
(2) Department of Mechanical Engineering, University of Washington, Seattle, WA, USA

## INTRODUCTION

The primary objective in this experiment is to develop a novel deep learning-based image registration algorithm that can accurately and efficiently extrapolate displacement fields for 4D MRI sequences while being robust against landmark changes and flow related artifacts that hamper the usability and generalizability of these algorithms for clinical applications. The networks presented here have been trained to be applied to brain motion tracking. However, the network architecture can be adapted to track motion in a wide variety of clinical cases that involve 4D sequences. For example, the network parameters can be adjusted to match new image modalities for cardiac movements.

The development of the algorithm was done in 2 steps: 1) by iteratively modifying and evaluating existing state-of-the-art 3D UNet [1] algorithms [Fig. 1] and 2) using insights from these results to develop a novel algorithm, the ViT-FNO [Fig. 2], that performs part of the calculations in the frequency domain instead of the traditional temporal only approach, in combination with Convolution-Transformer hybrid architecture, allowing for a much efficient and robust image registration pipeline.

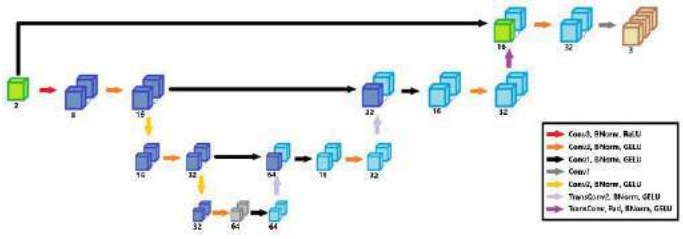

**Figure 1: Modified 3D UNet architecture.**

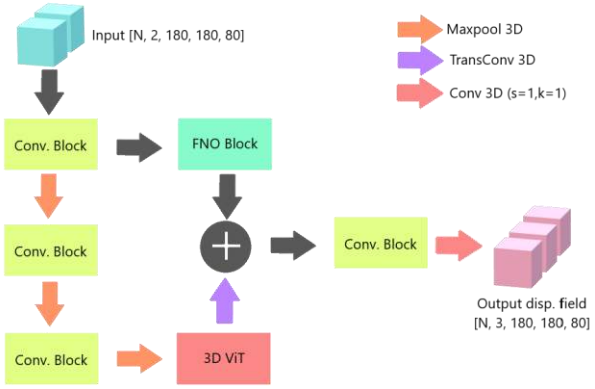


**Figure 2: ViT-FNO architecture.**

Recently, Vision Transformer and Convolution based hybrid models such as the ViT VNet [2] have shown promising results in outperforming traditional Convolution only architectures such as the 3D UNet. But training such models can be quite tedious and often plagued with overfitting for niche tasks where training data is limited. Our proposed model, the ViT-FNO, combines the architecture of ViT VNet with a modified Fourier Neural Operator [3] such that the resulting model is much simpler and more resilient to overfitting.

## METHODS

We generated the training dataset with data from 10 patients. Each patient dataset was made of a series of 3D MRIs volumes, each volume corresponding to a timestep of an MRI cine-sequence. For each patient, the reference image was extracted from the first timestep (t=0) of the sequence, and for each time step from t=1, the displacement field was extracted by a conventional method such as the Demons registration algorithm. These displacement fields were filtered, resized, and used to

deform the other patient's reference images by warping. The process was repeated for all patient sequences, generating approximatively a thousand deformed images with known displacement field and initial image. We split each patient sequence by pairing each timestep to its corresponding reference frame to generate the final dataset used for training and validation. The training set contains data from 8 patients while the remaining 2 patient data is reserved for validation of the models. The data is randomly augmented (rotated in random directions by random amounts) during training.

We iteratively trained a 3D UNet model with Huber Loss and modified the architecture by identifying possible architectural improvements to the previous model by comparing the predicted displacement fields against the ground truth displacement fields using Structural Similarity Index (SSIM).

Finally, drawing from these insights, we propose a novel architecture, ViT-FNO [Fig. 2.] to address some of the pitfalls of the 3D UNet techniques. The ViT-FNO network contains several subunits. Namely, 1) Convolution blocks, that consist of 3 Convolution operations with kernel size of 3 and stride of 1, each followed by a ReLU nonlinearity and batch normalization. 2) FNO block, that consists of first transforming the data into the frequency domain, picking the first 3 modes, applying the weights and biases, transforming back to the time domain, and lastly applying ReLU nonlinearity and batch normalization. 3) 3D ViT block that first encodes the features into 4x4x4 patches unrolled to a single dimension and then passes these vectors to a vision transformer. The data is then reshaped back into the 3D domain and passed through a ReLU nonlinearity and batch normalization function. A Convolution operation of kernel size of 3 and stride of 1 is applied followed by ReLU and batch normalization. 4) Maxpool operation that is used to down sample the data and has kernel and stride size of 2. 5)Transposed Convolution that up samples the data followed by padding to get to the same size as the FNO output. The FNO and Transposed data are concatenated and passed through another padding function such that the resulting final Convolution block output is of the desired size. A final convolution is applied with kernel and stride size of 1 and the output channel size is set to 3 to construct the predicted displacement fields.

## RESULTS

For the Validation set, the average SSIM score was 0.763 and the Loss was 0.0169, while the training Loss was in the range of $10^{-5}$. Our final 3D UNet variant appears to overfit on the training dataset.

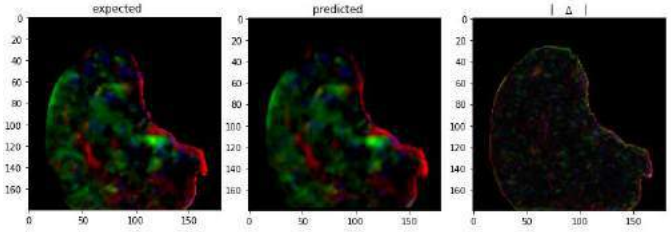


**Figure 3: Displacement field for relatively healthy sample.**

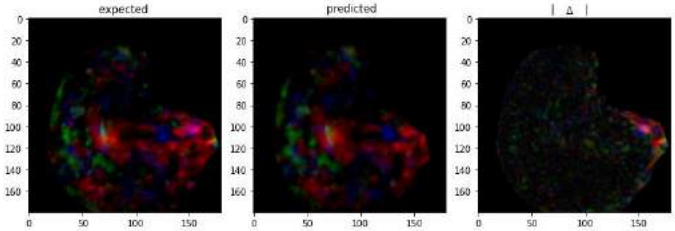


**Figure 4: Displacement field for structural abnormality.**

## DISCUSSION

Although Fig. 3 shows a prediction produced by our 3D UNet model that is almost equal to the ground truth, in Fig. 4, we observe that the same 3D UNet model does not produce a reliable displacement field for a sample with some prominent structural abnormality. This is one of the biggest issues with the 3D UNet model that depends heavily on the training data landmarks to construct reliable displacement fields. This issue could be a biproduct of overfitting.

Reducing model complexity can be one way to minimize overfitting but this may not be an ideal solution in many real-world scenarios. To address this issue, our proposed model, ViT-FNO, will be significantly more robust than previous state-of-the art models while achieving similar performance at a fraction of the computational overhead. Since we transform the paired data into the frequency domain at the FNO block and only apply the nonlinear transformation to the first 3 modes, we can infer that the FNO block is able to accurately extrapolate coarse features such as the structural changes and major landmark changes between the reference frame and the timestep t-frame. Corollary, we suspect that the 3D ViT block can extrapolate features related to much finer details and motions, depending on the patch size. The final block should combine these features and produce the desired displacement field. This novel architecture should be able to produce more reliable displacement field estimations for samples with prominent malformations and other structural abnormalities. Since the model is significantly smaller than traditional algorithms, training should be much faster and vanishing gradient problem should also be minimized, improving performance, and further improving training times. The implications of the proposed ViT-FNO model need to be validated by further testing on the dataset.

## ACKNOWLEDGEMENTS

This work was partially supported by the NIH Grant 1R21NS111415-01 and the NSF Grant CMMI 1826270.

## REFERENCES

[1] Çiçek, Ö., Abdulkadir, A., Lienkamp, S. S., Brox, T., & Ronneberger, O. (2016, October). 3D U-Net: learning dense volumetric segmentation from sparse annotation. In International conference on medical image computing and computer-assisted intervention (pp. 424-432). Springer, Cham.

[2] Chen, J., He, Y., Frey, E. C., Li, Y., & Du, Y. (2021). ViT-V-Net: Vision Transformer for Unsupervised Volumetric Medical Image Registration. arXiv preprint arXiv:2104.06468.

[3] Li, Z., Kovachki, N., Azizzadenesheli, K., Liu, B., Bhattacharya, K., Stuart, A., & Anandkumar, A. (2021, May 17). Fourier neural operator for PARAMETRIC partial differential equations. arXiv.org. Retrieved August 1, 2021, from https://arxiv.org/abs/2010.08895

# FRICTIONAL FORCES DO NOT CAUSE WEAR IN HUMAN ARTICULAR CARTILAGE

**C.V. Sise (1), Courtney A. Petersen (2), Brenna Carbone (1), Clark T. Hung (1), Gerard A. Ateshian (1,2)**

(1) Biomedical Engineering, Columbia University, New York, New York, USA
(2) Mechanical Engineering, Columbia University, New York, New York, USA

## INTRODUCTION

Osteoarthritis (OA) is a multi-tissue joint disease that affects more than 32 million adults in the United States [1, 2]. It is characterized by the degeneration of articular cartilage and causes joint pain, inflammation, and permanent alteration of the cartilaginous structure. Changes to the structure of the joint can adversely affect load distribution and cause mechanically-mediated advancement of the disease. Understanding the mechanical breakdown of articular cartilage would lend insight into the progression of the disease.

OA is often attributed to wear associated with aging or as the pathological response to acute damage to the cartilage. The exact mechanisms by which stress results in tissue degeneration has yet to be elucidated. Disruption of the extracellular matrix (ECM) compromises the integrity of the tissue and promotes degeneration via mechanical aggravation [3].

Few studies have been conducted to determine the initiating factors of structural wear in human cartilage. In the biotribology literature, the friction coefficient ($\mu$) has often served as a proxy for understanding wear in cartilage, with an abrupt change in $\mu$ possibly indicating a loss of cartilage integrity [4]. In previous studies from our lab, Durney et al. [5] and Oungoulian et al. [6] showed that in immature bovine cartilage, $\mu$ for cartilage-on-cartilage contact and cartilage-on-glass remained low over sustained frictional sliding in a migrating contact area configuration, despite the emergence of delamination wear. In the porcine model, Vazquez et al. found that cyclic compression loading in cartilage-on-cartilage contact can cause tissue softening and damage [7]. Regarding human articular cartilage, Weightman reported early signs of fibrillation following cyclic compressive loading [8]. Additionally, Kaplan found that human articular cartilage plugs under cyclic unconfined compression testing resulted in loss of thickness and integrity of the ECM [9]. Other studies have reported fatigue failure in human articular cartilage during tensile cyclic loading [10, 11, 12].

In this study we explored the hypothesis that wear of human articular cartilage could be initiated under reciprocal frictional sliding, using testing conditions that promote loss of interstitial fluid pressurization to exacerbate reciprocal frictional forces on the cartilage extracellular matrix. We hypothesized that applying a supra-physiological contact pressure under static loading and reciprocal sliding for 24 hours leads to wear from delamination of the superficial zone, as observed by Oungoulian et al. in immature bovine cartilage [6].

## METHODS

Sample Preparation: Three fresh frozen human knee joints were obtained from a tissue bank (31-48 y.o., 485 - 756 N, female, two right knees and one left knee) and dissected to expose the articular cartilage on the distal femur. The knee joints were sectioned into medial condyle (MC) and lateral condyle (LC) samples of approximately 50 mm length and 25 mm width, producing five samples. No joints showed visual evidence of cartilage degeneration. Condyles were mounted in custom cylindrical acrylic holders and the bony end was fixed in dental cement (Buff Stone, Whip Mix), leaving the femoral articular cartilage exposed (Fig. 1).

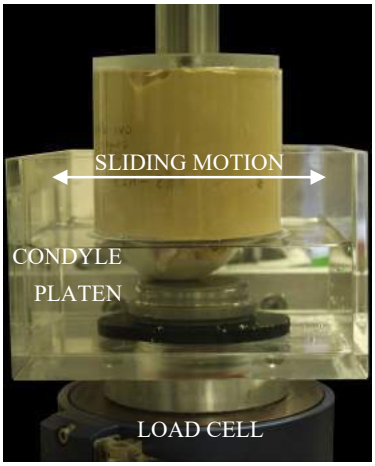


**Fig. 1: Femoral condyle mounted in dental stone articulates against a stainless steel platen.**

Friction Testing: The fixed samples were mounted on a custom testing device described earlier [13] sliding against a stainless steel platen mounted on a 6-axis load cell (JR3, Inc.; Fig. 1). A constant contact force of 439 ± 12 N load was applied under load control. Sliding was prescribed under displacement control with a 5 mm stroke length at 5 mm/s (4 s/cycle) for a duration of 24 hours (21,600 cycles). Samples were immersed in phosphate buffered saline with 0.04% isothiazolone-base biocide (Proclin 950, Sigma-Aldrich) and 0.1% protease inhibitor (0.05 M ethylenediaminetetraacetic acid, EDTA, Sigma-Aldrich) for the duration of the test. Before and after the test, samples were submerged in the same solution, kept at 4 ˚C, and refreshed daily.

Experimental Measurements: Prior to friction testing surface scans were obtained of the samples for topological assessment using a Keyence Profilometer (LJ-V7080), which captured a dense point cloud of 50,000 points/cm$^2$. Additional scans were taken immediately after loading, and again after a 120 hour recovery period. Pressure-sensitive film (Fujifilm, prescale 4LW; 0.05 – 0.2 MPa) was used to determine the average contact area under the 439 N load.

## RESULTS

Friction Testing: The friction coefficient $\mu$ increased over time, from a minimum value of 0.009 ± 0.004 to a final value of 0.095 ± 0.013 after 24 h (Fig. 2A). The final creep deformation across all samples was 1.03 ± 0.09 mm (Fig. 2B).

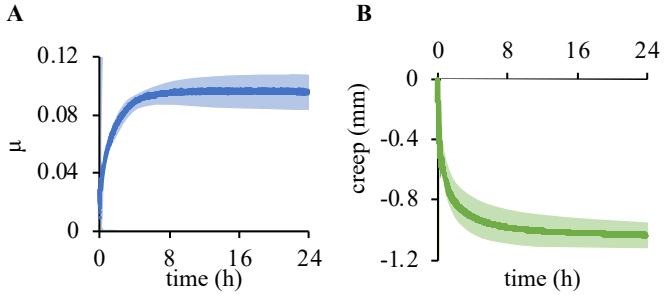


**Fig. 2: Mean and standard deviation of (A) friction coefficient and (B) creep displacement for all five samples**

Experimental Measurements: The mean cartilage thickness was measured with a needle probe to be 1.49 ± 0.30 mm. After 120 h recovery, samples recovered to an average of 99.3% ± 2.34% of their original thickness. Representative photos and scans of a sample before, immediately after, and 120 h after friction testing are shown in Fig. 3.

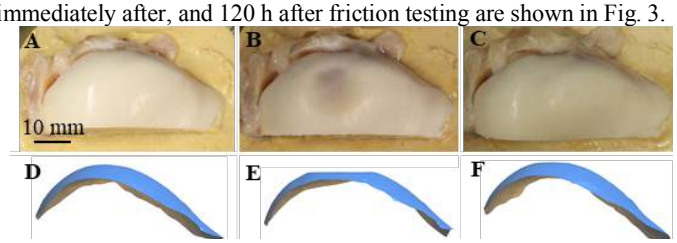


**Fig 3: Photos (A-C) and scans (D-F) of one representative sample before friction testing (left), immediately after the 24 hour test (middle), and after 120 hours of recovery (right).**

The average contact area before the 24 h test, immediately after the test, and after 120 h recovery was 69.0 ± 12.8 mm$^2$, 124 ± 33.3 mm$^2$, and 85.1 ± 13.1 mm$^2$ respectively. Thus, the mean contact pressure during the test decreased from 6.51 ± 1.29 MPa to 3.79 ± 1.05 MPa. At test completion there was no histological evidence of superficial zone delamination or fibrillation in any of the samples (Fig. 4).

**Fig 4. Representative Safranin-O and Fast Green staining of tested sample after 120 h recovery, showing no evidence of wear**

## DISCUSSION

This study tested the hypothesis that supra-physiologic contact pressures sustained statically for 24 h under reciprocal frictional sliding would induce delamination wear in human articular cartilage due to sustained frictional forces resulting from loss of interstitial fluid pressurization. Temporal responses showed that steady friction coefficients $\mu$ and creep displacements were achieved over the test duration (Fig. 2), confirming loss of interstitial fluid pressurization [14] and relatively elevated values of $\mu$ consistent with prior reports [6]. Creep deformation was supra-physiologic as cartilage was compressed nearly to the bone in all cases (Fig. 3B,E), but recovered significantly each time (Fig. 3C,F). Despite these harsh testing conditions, no evidence of delamination wear was observed from histology (Fig. 4). These results strongly suggested that reciprocal frictional forces are not responsible for initiating fatigue wear in articular cartilage. Thus, we must consider alternative mechanisms for understanding mechanically-induced tissue degradation.

In our previous work on immature bovine articular cartilage, Durney et al. reported surface delamination to the tibial cartilage strips, which were articulated against opposing femoral condylar plugs [5]. The condylar plugs did not have delamination. While the tibial cartilage strips and the condylar plugs both underwent frictional cyclical forces, the compressive forces were cyclical for the tibial strips and static for the condylar plugs. This prior result, when taken in conjunction with the current study and [7,8], suggests that delamination wear is induced by fatigue due to cyclical compressive forces, rather than cyclical frictional forces.

We conclude from our study that human articular cartilage is resilient to reciprocal sliding and that cyclical friction alone does not cause delamination. Moving forward, we will modify our experimental design to test the hypothesis that delamination wear in human articular cartilage is mediated by cyclic compressive loading.


## ACKNOWLEDGEMENTS

National Institutes of Health, R01 AR073289, R01 GM083925


## REFERENCES


[1] CDC (website), https://www.cdc.gov/arthritis/basics/osteoarthritis.htm. [2] CDC & Arthritis Foundation, *National Public Health Agenda for OA*, 2020. [3] Dijkgraaf, L.C., J. Oral Maxillofac. Surg. 53:1182–1192, 1995. [4] Ateshian, G.A., Mow, V.C. In: Basic ortho. biomech. & mechano-biology. V. C. Mow, & R. Huiskes, (Eds.). Lippincott Williams & Wilkins, Philadelphia, Pa.; London. [5] Durney, K M., et al. J. Biomech., 107:109852, 2020. [6] Oungoulian, S R., et al. J. Biomech., 48:10:1957–64, 2015. [7] Vazquez, K J et al. J Mech Behav Biomed Mater. 98:262-267, 2019. [8] Weightman, B., et al. Nature, 244:303-4, 1973. [9] Kaplan, JT., et al. J Mech Behav Biomed Mater, 65:734–42, 2017. [10] Weightman, B. J Biomech, 9:4:193–200, 1976. [11] Weightman, B., et al. Ann. Rheum. Dis., 37:1:58–63, 1978. [12] Bellucci, G., et al. Rheumatology, 40:12:1337–45, 2001. [13] Jones, B.K., et al. J Biomech, 48:3945-9, 2015. [14] Krishnan, R. et al. J Ortho Res, 22:565-70, 2004.

SB³C2022
Summer Biomechanics, Bioengineering and Biotransport Conference
June 20-23, Eastern Shore, MD, USA

# LAYER-SPECIFIC AORTIC ANEURYSM BIOMECHANICS SUGGEST RELATIONSHIP BETWEEN MEDIAL STIFFNESS AND INTERFACIAL STRENGTH IN PATIENTS WITH BICUSPID AORTIC VALVE

**L. Neave (1,2), T. Sigaeva (3) P.W.M. Fedak (2,4), E.S. Di Martino (1,2)**

(1) Biomedical Engineering, University of Calgary, Calgary, AB, Canada
(2) Libin Cardiovascular Institute of Alberta, University of Calgary, Calgary, AB, Canada
(3) Department of Systems Design Engineering, University of Waterloo, Waterloo, ON, Canada
(4) Department of Cardiac Sciences, University of Calgary, Calgary, AB, Canada

## INTRODUCTION

Bicuspid aortic valve (BAV) patients make up 1-2% of the population and present more frequently with aortic disease than the general population. Among these diseases, a common one, ascending aortic aneurysm (AsAA), often precedes the onset of potentially fatal complications such as aortic dissection or rupture [1]. Despite the severity of these outcomes, the cause and progression of BAV-associated aortic disease is not well understood, which has motivated research into the biomechanics and microstructure of BAV-AsAA tissue. This research has shown that certain properties of AsAA tissue vary regionally, suggesting that the tissue degeneration and remodeling that is widely associated with aortic aneurysms does not occur homogenously throughout all areas of the aneurysm [2,3]. These studies, however, have generally considered the aortic wall as a homogenous material, even though the three layers of the wall – intima, media, and adventitia – have been known to exhibit significantly different mechanical properties and microstructural composition [4]. Considering that aortic dissection initiates as a tear in the inner layer of the aortic wall followed by propagation of the dissection between the layers, it becomes important to consider the heterogeneity of the aortic wall layers and their individual contributions to the composite wall. It is possible that tissue remodeling processes are not homogenous through the wall thickness, but rather vary in severity and effect for individual layers or at layer interfaces. Studying the individual layers of the composite aortic wall in BAV-AsAA may provide new insight into the mechanisms of AsAA disease progression and its associated complications.

This study proposes to investigate layer-specific and inter-layer biomechanical properties of BAV-AsAA tissue to further explore the heterogenous nature of aortic tissue degeneration and remodeling. Specifically, exploring the relationship between the primary load-bearing layers – the media and adventitia - and their interfacial strength.

## METHODS

Whole aneurysms were removed from ten BAV patients undergoing elective surgery. Aneurysms were cut first into regions (greater curvature, lesser curvature, posterior, and anterior), and then further divided into specimens based on region size. From each specimen, one circumferential (11) and one longitudinal (22) test strip was removed for delamination testing. The remainder of the specimen was separated into two layers - media (including intima), and adventitia - using the methods described in [4] for biaxial tensile testing.

Delamination testing was conducted using a uniaxial tensile testing device (CellScale Biomaterials Testing, Waterloo, ON) with a 10N load cell. The unloaded width and thickness of the specimen was measured using digital calipers. Layer separation was initiated manually, and the free flaps were attached vertically in the grips of the testing device as per the methods in [5]. The sample was submerged in a PBS bath warmed to a temperature of 37°C, and uniaxial elongation was imposed at a rate of 1 mm/min for a duration of 10 minutes or until full delamination was achieved. The data was processed into delamination tension, which is the recorded tensile load divided by the unloaded width of the specimen. From this, delamination strength was found as the average value of delamination tension after the initial peak [5].

Biaxial tensile testing was conducted using a four-motor biaxial testing system (ElectroForce Systems, TA Instruments, Springfield, MO) with two 22N load cells. The adventitia and media were tested separately, subjected to a series of displacement-controlled test protocols (1:1, 1:0.75, 1:0.5, 1:0.2, 0.2:1, 0.5:1, 0.75:1), where 1 indicates the maximum defined displacement in the circumferential or longitudinal direction based on the original specimen dimensions. These test protocols were carried out in a PBS bath warmed to 37°C, first to a maximum 60% displacement, followed by a maximum 80% displacement if the specimen survived all 60% displacement protocols. Local tissue deformation was recorded through camera tracking of five dots placed in the center of the specimen, and force was recorded in both

SB³C2022-423

directions. Finally, global force, local deformation, and initial specimen dimensions were used to calculate the Cauchy stress and stretch for each specimen. This data was further processed for biomechanical descriptors to compare behaviour across specimens. Specifically, the stress-stretch curve for each sample was plotted and analyzed for a low-strain tangential modulus (LTM), a high-strain tangential modulus (HTM), and the stress and strain values at the transition zone onset and end points, which mark the start and end points of the non-linear portion of the stress-stretch curve (*Figure 1*). These values were obtained for both circumferential and longitudinal directions. Methods for data processing and analysis were performed as in [6].

The biaxial and delamination properties were then matched by specimen location and compared to determine if there was any relationship between the performance of the individual layers and their strength at the interface.

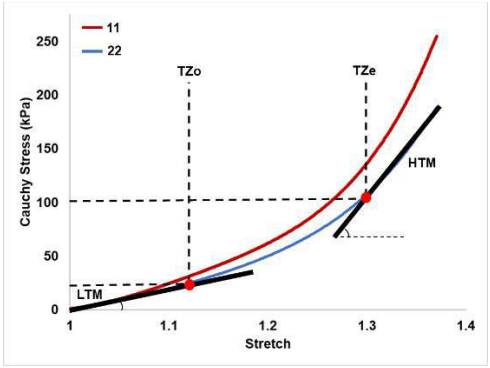


**Figure 1: Example of biaxial tensile test analysis for biomechanical properties including low-strain tangential modulus (LTM), non-linear transition zone onset and end points (TZo, TZe), and high-strain tangential modulus (HTM).**

## RESULTS

Initial results were found based off a subset of seven patients, from which 30 specimens were tested. From these specimens, 50 delamination tests, 29 adventitial biaxial tests, and 22 medial biaxial tests were completed successfully. No significant relationship was found between the LTM of the media and adventitia, or between the LTM of either layer and delamination strength. A paired t-test showed significant difference between the LTM's of the layers in the circumferential direction, but not in the longitudinal. The most noticeable difference was in the HTM's of the layers, where the media and adventitia were significantly different in both directions (*Figure 2*).

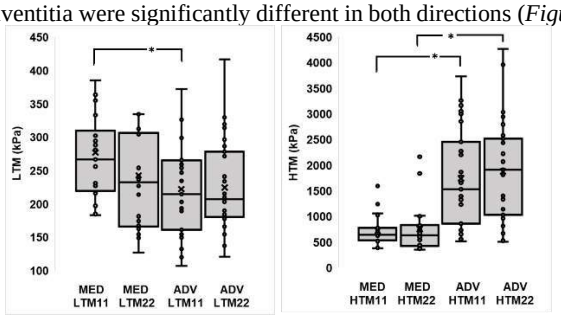


**Figure 2: Comparison of LTM between the layers showed difference in the circumferential direction (p<0.01) (LEFT) and significant difference between the HTM's of the layers in both directions (p<0.001) (RIGHT).**

A positive correlation was found between delamination strength in the circumferential direction and the intima-media HTM in both directions (Pearson's r = 0.774 p < 0.001 for HTM-11; Pearson's r = 0.489, p = 0.039 for HTM-22) (*Figure 3)*. A similar relationship was found for delamination strength in the longitudinal direction, again showing positive correlation with medial HTM in both directions (Pearson's r = 0.715, p <0.01 for HTM-11; Pearson's r = 0.568, p = 0.027 for HTM-22) (*Figure 3*). Delamination strength in both directions was also positively correlated with the biaxial transition zone end point (TZe) stresses in the media but had no correlation with adventitial biaxial properties.

Adventitial HTM and medial HTM were found to be positively correlated in both directions (Pearson's r = 0.484, p = 0.049 for HTM-11; Pearson's r = 0.792, p <0.001 for HTM-22). However, when comparing delamination strength to the ratio of adventitia and media properties, no correlation was found, suggesting that delamination properties are more strongly associated with the condition of the media.

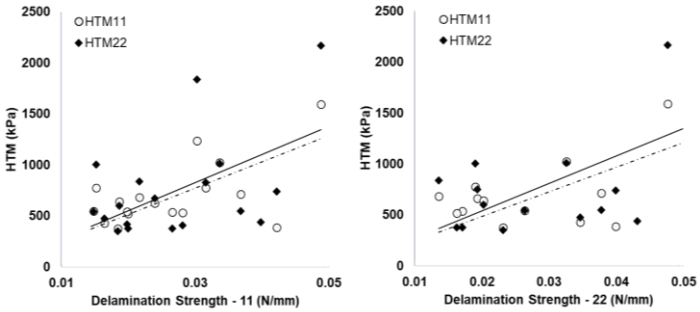


**Figure 3: Delamination strength had a positive correlation with media HTM11 and HTM22. This relationship was seen in both the circumferential delamination strength (LEFT) and the longitudinal delamination strength (RIGHT).**

## DISCUSSION

The present study is one of few that has investigated the heterogenous characteristics of the aortic wall layers and interface. Preliminary results confirm findings that adventitial and medial properties are significantly different in high-strain conditions, however this is the first study to realize a possible relationship between medial stiffness and interfacial strength that appears to be independent of adventitial behaviour. However, the significance of the preliminary findings is currently limited by sample size, preventing statistical analysis that can account for inter-patient and inter-region variability.

Previous literature findings cite the importance of studying aortic wall delamination strength and layer-specific properties to better understand the heterogenous wall remodeling process in AsAA [4,5]. The distinct mechanical behaviour found in each of the layers can be largely attributed to their unique structure and composition, which also strengthens the idea that layers may have independent remodeling or degeneration characteristics. Future investigation of the biomechanical properties in partnership with microscopy or histology may help further our understanding of the mechanisms behind AsAA tissue degeneration.

## ACKNOWLEDGEMENTS

We acknowledge support from the US National Institutes of Health (NIH HL133504) and the NSERC Discovery Programme.

## REFERENCES

[1] Fedak, PWM et al., *Circulation*, 106: 900-904, 2002.
[2] Choudhury, N et al., *Cardiovasc Pathol*, 18:83-91, 2009.
[3] Tsamis, A et al., *J Thorac Cardiovasc Surg*, 151:1718-1728, 2016.
[4] Sokolis, DP et al., *Med Biol Eng Comput*, 50:1227-1237, 2012.
[5] Angouras, DC et al., *J Mech Behav Biomed Mater*, 98:58-70, 2019.
[6] Forneris, A et al., *Appl Sci*, 11:3485, 2021.

# BIOPROSTHETIC LEAFLET STRESS FOLLOWING TRANSCATHETER AORTIC VALVE REPLACEMENT IN BICUSPID AORTIC VALVES

**Breandan Yeats (1), Aniket Venkatesh (1), Milad Samaee(1), Pradeep Yadav (2), Venkateshwar Polsani (2), Vinod Thourani (2), and Lakshmi Dasi (1)**

(1) Biomedical Engineering, Georgia Institute of Technology, Atlanta, GA, United States
(2) Cardiology, Piedmont Hospital, Atlanta, GA, United States

## INTRODUCTION

Bicuspid aortic valve (BAV) disease is the most common congenital heart defect present in 2-4% of the general population and is associated with calcific aortic valve disease [1]. Historically, BAV patients have been treated with surgical replacement however, patients are transitioning to transcatheter aortic valve replacement (TAVR) which is a minimally invasive alternative. Currently, long-term durability in BAV patients is unknown due to the lack of long-term clinical data. Due to the elliptical shape and often high volume of calcium in BAV patients the transcatheter aortic valve (TAV) stent is often elliptical and underexpanded and is hypothesized to impact durability.

Bioprosthetic leaflet stress has not been measured in a cohort of BAV patients which is not possible in the clinical setting. However, this is possible through computational methods. Additionally, the impact of various TAVR strategies including balloon filling volume has not been evaluated in its impact on bioprosthetic leaflet stress in patient specific anatomies. Lastly, it is unknown how bioprosthetic leaflet stress relates to anatomical characteristics. This study aims to quantify bioprosthetic leaflet stress in BAV patients treated with TAVR with varying balloon expansion volumes and compare stress with calcium volume and the shape of the native valve opening through computational techniques.

## METHODS

10 CT scans taken of patients being evaluated for TAVR with BAV and calcific aortic valve disease were analyzed. The aortic valve including leaflets and calcium nodules, ascending aorta, and part of the left ventricle were segmented in Materialise Mimics (Leuven, Belgium) (**Figure 1A**). The total calcium volume in the landing zone for the TAV stent was measured. The angle between the free edges of the two leaflets was measured to quantify the shape of the opening. An angle closer to 120 degrees signifies a tricuspid-like shape and an angle closer to 180 degrees signifies bicuspid-like shape (**Figure 1B**). Finite element analysis (FEA) models of the Edwards SAPIEN balloon-expandable TAV were created for the 23, 26, and 29 mm sizes and were performed in Abaqus (Johnston, RI, USA). Each stent was generated from microCT measurements in Solidworks (Waltham, MA, USA) of the actual device and meshed in Hypermesh (Powell, OH, USA) (**Figure 2**). A balloon was then generated and meshed from benchtop measurements of the actual balloons. Verification of each TAV size was performed by crimping the stent and balloon followed by a volumetric expansion of the balloon until the stent reached the manufacturer specified diameter (**Figure 2C**). Stent deployment was validated previously in a post-TAVR CT scan to reasonable agreement [2].

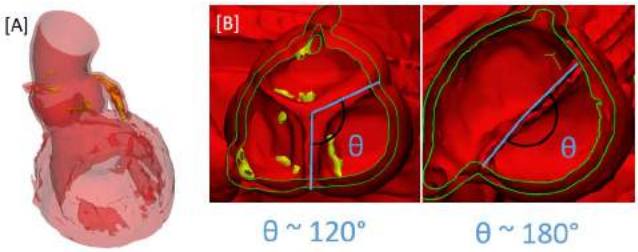


**Figure 1:** Reconstruction of the aortic valve including leaflets and calcium nodules, ascending aorta, and left ventricle (A) and free edge angle measurement depicting tricuspid-like (120°) and bicuspid-like (180°) BAV anatomical shapes (B).

The SAPIEN FEA model was deployed in each anatomy using the manufacturer recommended size. Following deployment of the stent, the bioprosthetic leaflets were mapped onto the stent by displacing the sutured edge of the leaflets to match the sutured edge of the deformed stent. They were then pressurized under peak diastolic physiological pressure and the maximum principal stress was recorded. This process was repeated in various balloon volume scenarios consisting of

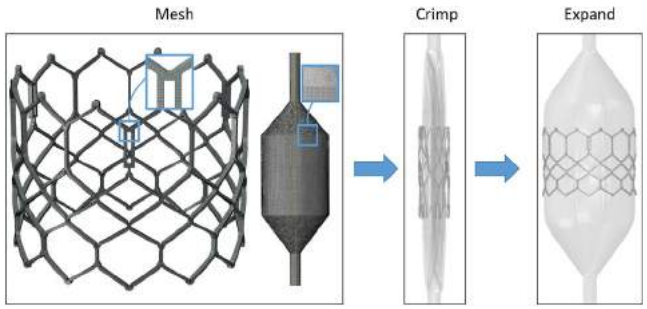


**Figure 2:** Process of developing the SAPIEN FEA 23, 26, and 29 mm models including meshing of the stent and balloon, crimping, and expansion to the manufacturer specified diameter.

underexpansion, nominal expansion, and overexpansion. Material properties used for the native tissues and TAV were extracted from previous studies [3-6]. Statistical analysis consisted of regression analysis between stress and anatomical variables and comparison between means of stresses between expansion configurations with statistical significance considered when $p < 0.05$.

## RESULTS

Geometry of the TAV deployment at nominal expansion and the bioprosthetic leaflet stress under physiological loading for two anatomies, one with high calcium volume (490 mm^3) and one with low calcium volume (58 mm^3) are shown (**Figure 3**).

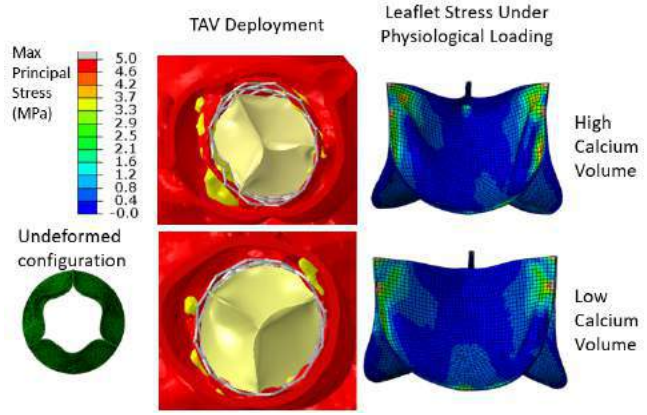


**Figure 3:** TAV deployment geometry (left) and bioprosthetic leaflet stress under physiological loading (right) in an anatomy with high calcium volume (top) and an anatomy with low calcium volume (bottom).

Increased stent ellipticity, increased leaflet stress, and leaflet folding near the commissural points are observed in the anatomy with high calcium volume. The peak stress from each anatomy with nominal expansion was compared to the total calcium and was found to have statistical significance ($R^2 = 0.53$, $p = 0.017$) (**Figure 4**). The free edge angle was also compared to leaflet stress but did not have statistical significance ($R^2 = 0.25$, $p = 0.137$).

The average peak leaflet stress values were 2.26, 2.34, and 2.49 MPa for the nominal expansion, overexpansion, and underexpansion deployments but their differences were not found to be statistically significant. Qualitatively, the leaflets were observed to have increased rates of folding and pinwheeling in the underexpansion deployments.

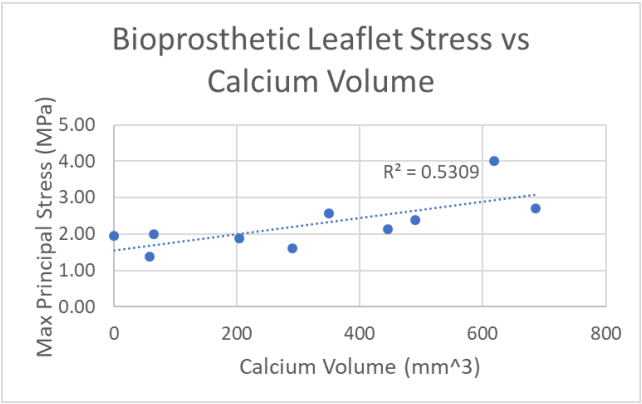


**Figure 4:** Bioprosthetic leaflet stress vs calcium volume with $R^2 = 0.5309$ and statistical significance ($p = 0.017$).

## DISCUSSION

The goal of this study was to investigate the bioprosthetic leaflet stress following balloon-expandable TAV deployment in BAV patients with severe calcific aortic valve disease. Calcium volume was shown to have a statistically significant correlation to the bioprosthetic leaflet stress ($p = 0.017$). The shape of the native valve, quantified by the angle between the free edges of the two leaflets, was not found to have a statistically significant correlation to leaflet stress. Underespansion of the TAV was seen to increase the stress on the leaflets on average however, did not have statistical significant differences from the nominal and overexpansion states.

These results indicate calcium to be the dominant controller of bioprosthetic leaflet stress. This is likely due to calcium high stiffness resisting the uniform deployment of the stent thus causing the leaflets to be deformed increasing their stress under diastolic loading. Other anatomical factors likely also contribute but require a larger patient cohort to find statistical significance. The results also show changes in balloon volume, which is controlled by the operator, does not impact leaflet stress however, qualitative observations of leaflet folding and higher average stress in the underexpanded configuration indicate significance may be found with a larger patient cohort.

The main limitations of this study are the lack of patient specific material properties due to it being difficult to extract from medical imaging alone and validation of the bioprosthetic leaflet stress which currently cannot be measured in a clinical setting. Future directions include investigating the impact of other deployment strategies on leaflet stress. This includes altering the deployment depth and commissural alignment with the native commissures. Additionally, the results of this FEA model can be used in a computational fluid dynamics model to assess for paravalvular regurgitation which is a concern in heavily calcified BAV patients.

## REFERENCES

[1] SC Siu et al. J Am Coll Cardiol. 2010;55:2789-2800.
[2] B Yeats, et al. American College of Cardiology Conference. 2021.
[3] B Bosmans, et al. J Biomech. 2016;49:2824-2830.
[4]GA Holzapfel, et al. J Biomech Eng. 2004;126:657-665.
[5] S Tzamtzis, et al. Med Eng Phys. 2013;35:125-130.
[6] W Mao, et al. Cardiovasc Eng Technol. 2016;7:374-388.

SB$^3$C2022
Summer Biomechanics, Bioengineering and Biotransport Conference
June 20–23, Eastern Shore, MD, USA

# IN SILICO INVESTIGATION OF CONTRALATERAL EMBOLIC STROKE RISKS FROM CAROTID ARTERY DISEASE

**Ricardo Roopnarinesingh[1], Debanjan Mukherjee[1]**

[1]Department of Mechanical Engineering
University of Colorado Boulder
Boulder, CO, USA

## INTRODUCTION

Stroke is one of the leading causes of death worldwide. Embolic stroke accounts for a majority of all ischemic stroke patients, and a significantly large proportion are categorized as Embolic Stroke of Undetermined Source (ESUS) [1]. Identifying embolic stroke etiology is a critical step in improving treatment efficacy and reducing incidence of recurring stroke events [1]. However, the ability to definitively identify embolus source based on occlusion location remains limited. One critical source of emboli are the carotid arteries, where build up of vulnerable atherosclerotic plaques can generate thromboemboli that move into the cerebral arteries. While the prevailing notion is that carotid emboli directed into the Circle of Willis (CoW) cause ipsilateral cerebral embolic events only, there are many reported instances of non-intuitive contralateral embolic strokes in patients with prominent carotid disease lesions. Despite such contralateral events being less frequent, they comprise a critical category of cases owing to the inherent difficulty in disambiguating stroke etiology and the disproportionately severe adversities in terms of treatment outcomes. There is a lack of proper understanding of how emboli released from the left and right carotid arteries intermix across the hemispheres into the CoW; whether particles originating from the left carotid will flow into the right hemisphere of the CoW and vice versa. This inspires a comprehensive investigation of how carotid emboli travel to the six major cerebral arteries, as function of CoW anatomy, embolus size, and laterality of release. Here, we present an in silico study addressing this question, using a custom patient-specific embolic stroke model outlined in several prior works [3, 4].

## METHODS

**Image-Based Modeling of Anatomy:** A patient-specific model from the aortic arch to the cerebral arteries connected at the CoW was created using artery lumen segmentation from patient CT images using SimVascular [3, 5]. Starting from a patient model with a compete CoW, five common variations in CoW anatomy were modeled by removing the absent artery in that variation from the complete CoW model [3]. The anatomical variants include an absent anterior communicating artery (AcoA), absent left or right posterior communicating arteries (LComm and RComm), and absent left or right P1 connectors (LP1 and RP1). Together with the complete CoW variant, a total of six different variations were used in this study, as illustrated in Figure 1.

**Hemodynamics simulation:** Hemodynamics across the aorta-CoW model was simulated using a stabilized finite element method for incompressible Navier-Stokes equations in SimVascular [5]. Blood was assumed to be a Newtonian fluid with a bulk density of 1.06 g/cc, and viscosity of 4.0 cP. At the aorta inlet, a validated pulsatile flow profile is specified over a cardiac cycle spanning 0.83 seconds [6]. Resistance based boundary conditions were applied to the outflow arteries to account for downstream vascular beds. These resistance values were acquired by calculating a total arterial resistance and allocating this resistance proportionally to each outflow artery based upon target flow divisions. 65% of the the flow was set to exit the descending aorta [7]. The six cerebral artery outflows were accordingly split based upon data reported in [8]. The remainder fraction of flow was assigned to the subclavian and external carotid arteries based on their cross-sectional area [9].

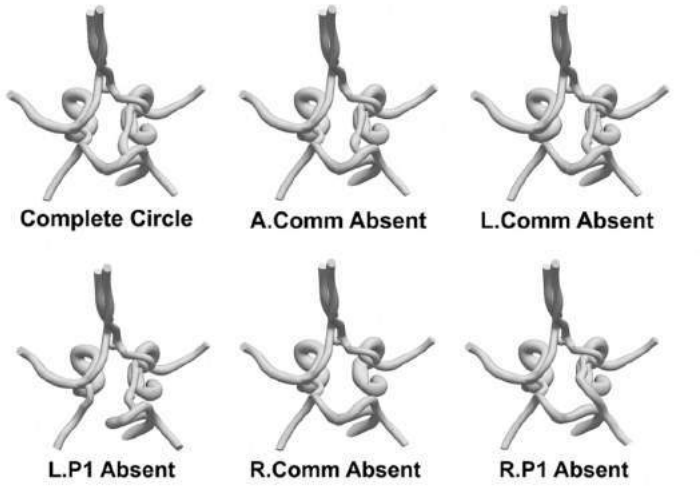


**Figure 1: The six patient-specific CoW models. The absent structures of the CoW are shown for each variation. Each variation model is based upon a modified patient-specific model with complete CoW anatomy to properly represent each variation [3].**

**Embolus Transport:** Embolus transport was modeled using a custom modified version of the Maxey-Riley equation [10]. These modifications included incorporating near-wall shear gradient lift forces, particle collisions with the walls of arteries, and elastohydrodynamic effects near-wall [3]. The emboli were assumed to be spherical particles with a one-way coupled fluid interaction in which the fluid affects the particle but the particle does not affect the fluid. Particles were assigned the mechanical properties of thrombo-emboli [4] and three embolus sizes of 1000$\mu$m, 750$\mu$m, and 500$\mu$m were considered to gain a range of insight on travel. For each model, approx. 12,000 emboli were released along artery wall (mimicking release from plaque wall) around the left and right carotid bifurcation. Resulting embolus distribution data spanning 36 simulations including 432,000 emboli were synthesized to illustrate contralateral trans-

port of carotid emboli into the brain.

## RESULTS

Embolus transport was quantified as the percentage of particles that reached each of the six major cerebral arteries, and the resulting distribution of emboli for each embolus size and each CoW anatomical variant have been presented in Figure 2. The data supports the notion that majority of left/right carotid emboli distribute ipsilaterally into the left/right cerebral arteries. Specifically, the middle cerebral arteries receive the highest proportion of carotid emboli across all sizes and anatomical variants . This is expected owing to the anatomical route of the internal carotid arteries into the middle cerebral arteries. However, when aggregated across all CoW variants, we observed an increased probability of emboli exiting the anterior and posterior cerebral arteries as emboli sizes reduced. This was associated with greater mobility of the emboli across the communicating arteries of the CoW. While the majority trend of ipsilateral carotid embolus distribution was observed as expected, we also observed that across all CoW variants, a smaller but non-zero proportion of emboli crossed hemispheres to distribute contralaterally from their carotid release site. Figure

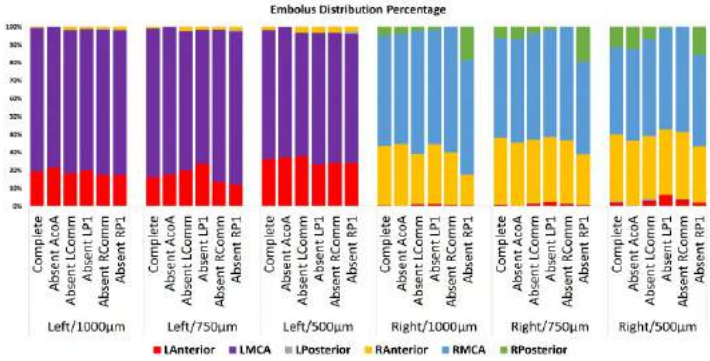


**Figure 2: Percentage of embolic particles moving through the six cerebral output arteries for each variation. Output percentage is given for combinations of both carotid arteries and the three particle sizes.**

3 presents the distribution of emboli that crossover contralaterally into the opposite hemisphere of the CoW with respect to the left or right carotid release. The data illustrates that small fractions of contralateral crossover occurs for all sizes and CoW anatomical variants considered, providing evidence that left carotid artery disease can lead to right cerebral hemisphere embolic events and vice versa. Furthermore, availability of detailed embolus trajectory data enabled viewing the route taken by these contralaterally traveling emboli. A snapshot for the ensemble of 12,000 emboli for the absent RComm CoW variant studied here illustrates that the communicating arteries of the CoW provide the conduit for a small fraction of emboli to move contralaterally into the left cerebral arteries, while the majority remains ipsilaterally distributed into the right cerebral arteries as can be seen in Figure 4 with the usage of the AcoA.

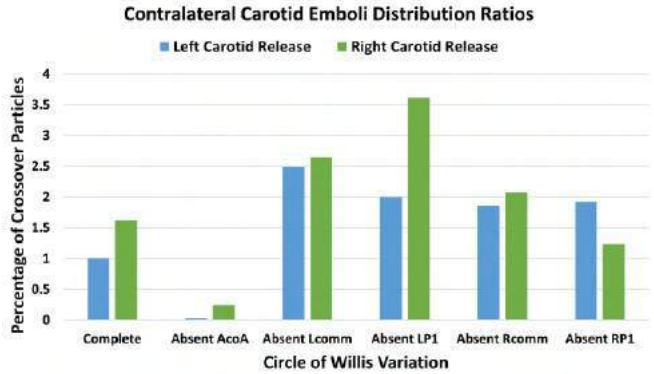


**Figure 3: Percentage of embolic particles that have contralateral movement for both carotid release areas and all six CoW variations.**

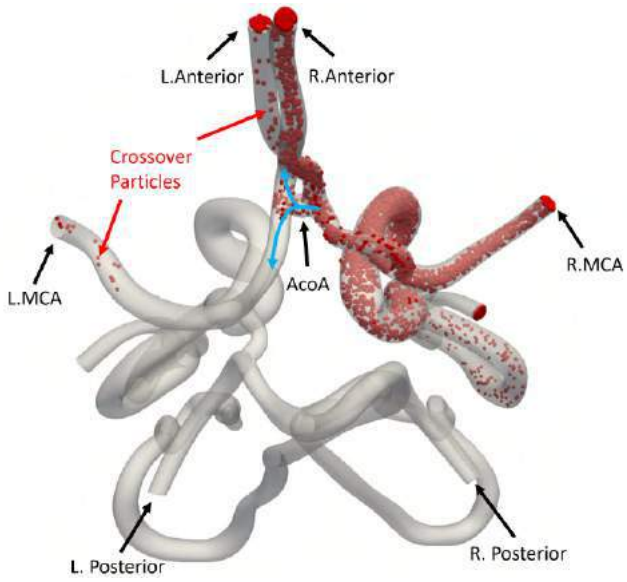


**Figure 4: The simulated movement of embolic particles into the absent R.Comm CoW variation released from the right carotid. The embolic particles are shown in red and a small amount of particles can be seen moving into the left hemisphere heading towards the left anterior and left middle cerebral artery outlets. The blue arrow indicates emboli routing through the AcoA and into left hemisphere arteries.**

## DISCUSSION

Using a patient-specific embolus transport model for stroke, we were able to obtain quantitative data on how particles travel contralaterally from the left and right carotid arteries to the cerebral arteries to cause embolic stroke. We considered systematic simulations including 6 CoW anatomical variations, 3 thromboembolus sizes, and an ensemble of 432,000 embolus samples. The findings are of high clinical relevance, as it enables disambiguating embolus source-destination relationship for contralateral carotid artery disease sites. Despite their lower occurrence as also seen here, such contralateral cases are of high importance as the etiology is difficult to establish and treatment can be adversely impacted. In continuing work, we seek to further characterize the occurrence risks and trends for such contralateral cases by considering more patient anatomy models. Furthermore, this study provides additional evidence on CoW anastomosis and its role in stroke. Specifically, the communicating arteries of the CoW are known to play a key role in determining proximal collateral capacity in occlusive cerebrovascular events such as stroke. Here, we illustrate that this network of vessels can play a secondary role in routing emboli across destination cerebral artery beds, thereby enabling the contralateral conduit for left/right carotid emboli to crossover and reach right/left cerebral arteries.

## ACKNOWLEDGMENTS

This work is supported by the NIH award R21EB029736. This work utilized resources from the CU Boulder Research Computing Group, which is supported by NSF (awards ACI-1532235 and ACI-1532236), CU Boulder, and Colorado State University.

## REFERENCES

[1] Ntaios, G., *J. Am. Coll. Cardiol.*, 75(3):333-340, 2019.
[2] Alpers, B.J., and R.G. Berry. *Arch. Neurol,-Chicago*, 8(4):398–402, 1963.
[3] Mukherjee, D., et al., *Ann. Biomed. Eng.*, 46(8):1128–1145, 2018.
[4] Mukherjee, D., et al., *J. Biomech. Eng.*, 138(8):081008, 2016.
[5] Simvascular. *http://simvascular.github.io/*, 2020.
[6] Olufsen, M.S., et al., *Ann. Biomed. Eng.*, 28(11):1281–1299, 2000.
[7] Carr, I.A.et al., *Am. J. Physiol.-Heart C*, 305(5):H732–H739, 2013.
[8] MacDonald, M.E., et al., *Physiol. Meas.*, 36(7):1517–1527, 2015.
[9] Zamir, M. et al., *J. Biomech.*, 25(11):1303–1310, 1992.
[10] Maxey, M.R.and J.J. Riley., *Phys. Fluids*, 26(4):883–889, 1983.

# MATHEMATICAL MODELING OF PAR2 SIGNALING AND RECEPTOR PHOTOINACTIVATION WITH MOLECULAR HYPERTHERMIA

**Blake A. Wilson (1), Chen Xie (1), Xiaoqian Ge (1), Peiyuan Kang (1), Theodore J. Price (2,3), Zhenpeng Qin (1,3,4,5)**

(1) Department of Mechanical Engineering, The University of Texas at Dallas, Richardson, TX, USA
(2) Department of Neuroscience, The University of Texas at Dallas, Richardson, TX, USA
(3) Center for Advanced Pain Studies, The University of Texas at Dallas, Richardson, TX, USA
(4) Department of Bioengineering, The University of Texas at Dallas, Richardson, TX, USA
(5) Department of Surgery, The University of Texas Southwestern Medical Center, Dallas, TX, USA

## INTRODUCTION

Protease-activated receptor type 2 (PAR2) is a G-protein coupled receptor involved in inflammation and pain sensitization [1]. It is canonically activated by irreversible proteolytic cleavage of its N terminus by proteases such as thrombin and tryptase [2]. Importantly, PAR2-mediated calcium response can further sensitize transient receptor potential vanilloid (TRPV) receptor ion channels such as TRPV1 and TRPV4 [1,3], and thereby induce sustained inflammatory response and hyperalgesia. As such, interrupting PAR2 activation and signaling can yield therapeutic relief of protease pain sensitization and inflammation.

Recently, our lab demonstrated that PAR2 could be selectively and remotely photoinactivated in live cells by molecular hyperthermia (MH) [4], which was induced by optical stimulation of gold nanoparticles with ultrashort nanosecond laser pulses. When gold nanoparticles are stimulated by an ultrashort nanosecond laser pulse they act as nano heaters with a nanoscale localized heat distribution that denatures nearby proteins. Although MH treatment was able to significantly reduce cellular calcium response to a PAR2-specific agonist, it's unclear what proportion of each cell's receptors were targeted and photoinactivated by the treatment.

In this work, we use mathematical modeling of the PAR2-mediated calcium signaling cascade to quantify the proportion of receptors photoinactivated by MH and understand how it affects the downstream calcium response (**Figure 1**). From the model we found that the calcium response for a given PAR2 agonist concentration decreased non-linearly with the proportion of photoinactivated PAR2 and provide new insight into how receptor photoinactivation by MH modulates intracellular calcium response to a PAR2 activating stimulus.

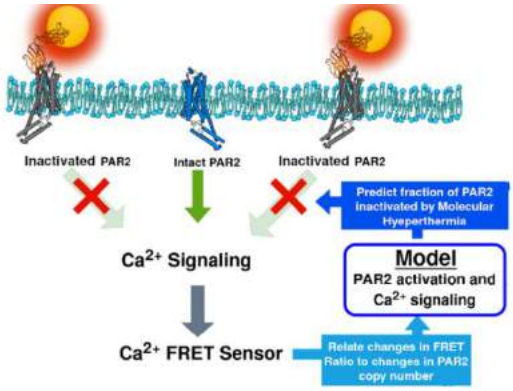


**Figure 1: Schematic depicting how the PAR2 signaling model is used to relate changes in Förster resonance energy transfer (FRET) signal during PAR2-mediated calcium signaling to PAR2 photoinactivation.**

## METHODS

To model PAR2 signaling we created a rule-based ordinary differential equation model of the PAR2 activation-mediated calcium signaling cascade (github.com/NTBEL/PARM). The model was encoded as a Python program module using the PySB framework [5], and it incorporates key elements of the PAR2-mediated calcium signaling cascade including PAR2 activation, PAR2 coupling with and activation of G-protein alpha, and calcium signaling via the phospholipase C and IP3 pathway (**Figure 2**), as well as the Förster resonance energy transfer (FRET) ratio signal generated by a genetically encoded calcium sensor to allow for direct comparison to experimental data. Unknown model parameters were inferred using Bayesian parameter estimation with the PyDREAM software [6], calibrating the model against previously published dynamic calcium

FRET sensor signal from PAR2 expressing HEK293 cells in response to different concentrations of the PAR2 agonist aminothiazol-4-yl-LIGRL-$NH_2$ (2AT) [4].

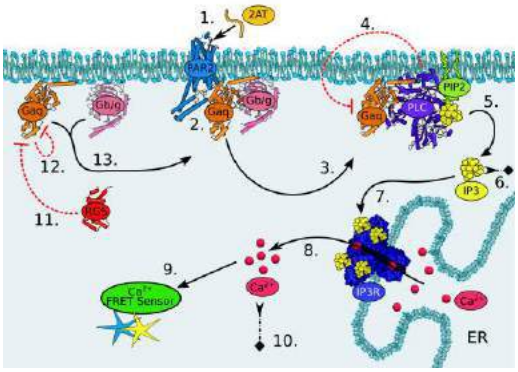


**Figure 2: Schematic of PAR2 activation and calcium signaling.**

*Model calibration:* DREAM$_{(ZS)}$ sampling was executed via PyDREAM with 4 chains and 50000 sampling iterations. The first 25000 iterations were taken as sampler burn-in, leaving a total of 100000 posterior samples (before any sample thinning). Each posterior sample corresponds to a parameter set that fits the calibration data reasonably well. Convergence of the posterior distribution was monitored using the Gelman-Rubin diagnostic.

## RESULTS

To quantify the relationship between PAR2 photoinactivation and changes to the calcium response the PAR2 signaling model was simulated with a wide range of PAR2 copy number values (number of receptors per cell) and the corresponding peak FRET signal in response to 330 nM 2AT agonist was computed for each case (**Figure 3**).

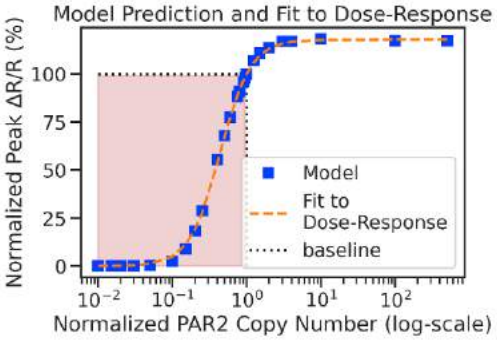


**Figure 3. Dose-response curve relating the normalized PAR2 copy number to the normalized peak FRET signal (ΔR/R) in response to 330 nM 2AT agonist; the quantities were normalized relative to the value of PAR2 copy number estimated by model calibration and the corresponding peak FRET signal at 330 nM 2AT. The dotted lines show the normalized baseline values of 1 and 100% for the PAR2 copy number and FRET signal, respectively. The orange dashed line shows the fit to Equation 1. The region shaded in red corresponds to cases where a fraction of the receptors is inactivated.**

The model results were then fit to a sigmoidal dose-response function:

$$E = iE_{max}/(1 + (EC_{50}/N_{PAR2})^n) \quad (1)$$

where $E_{max}$ is the maximum normalized peak FRET signal response, $EC_{50}$ is the dose at half-maximal response, and $N_{PAR2}$ is the normalized PAR2 copy number which is the dose in this case, and n is the Hill coefficient. The parameters determined when fitting Equation 1 to the model data were then used to map reductions in the normalized peak FRET signal to the percentage of inactivated receptors corresponding to that reduction in calcium response (Equation 2).

$$I_{PAR2} = i100\% - iEC_{50}/\left(1 + i(E_{max}/E)^{1/n}i\right) \quad (2)$$

where $I_{PAR2}$ is the percentage of inactivated PAR2 for any given normalized peak FRET signal $E \leq 100\%$. The percentage of inactivated PAR2 deviated from a linear response relationship (**Figure 4**), decreasing non-linearly with reductions in the peak FRET signal response from calcium signaling.

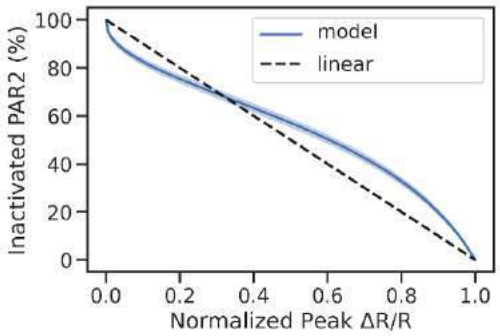


**Figure 4: Predicted relationship of the amount of inactivated PAR2 to the peak FRET signal (ΔR/R) determined from Equation 2 after fitting Equation 2 to the model responses. The dashed line shows a linear relationship for comparison.**

## DISCUSSION

Our results suggest calcium signal in response to a fixed agonist concentration decreases non-linearly with the proportion of photoinactivated PAR2. This result contrasts with enzyme systems which exhibit a linear reduction in the reaction rate with the proportion of enzyme photoactivated by MH [7], providing new insight into the relationship between PAR2 activation and calcium signaling. One current limitation of the model is that the experimental cellular expression level (protein per cell) of PAR2 is unknown. If the actual expression level is significantly different than the model value, the simulated results for the sensitivity of the FRET response to changes in PAR2 may be inaccurate. As a first step, we have experimentally quantified the number of gold nanoparticles that bind to each cell to help explain the fraction of inactivated PAR2. Going forward, we will incorporate this new data into our model analysis and better constrain the PAR2 number per cell. We are also working towards estimating an overall efficiency for MH-induced PAR2 photoinactivation on the cell surface.


## ACKNOWLEDGEMENTS

Research reported in this work was supported by the National Institutes of Health under award number R35GM133653.


## REFERENCES


[1] Tillu, D V et al., *Pain*, 156(5):859-867, 2015.
[2] Heuberger, D M et al., *Thrombosis Journal*, 17(4), 2019.
[3] Poole, D P et al., *Journal of Biological Chemistry*, 288(8):5790-5802, 2013.
[4] Kang, P et al., *ACS Nano*, 13:12487-12499, 2019.
[5] Lopez, C F et al., *Mol. Syst. Biol.*, 9(646), 2013.
[6] Shockley, E M et al., *Bioinformatics*, 34:695-697, 2018.
[7] Kang, P et al., *Small*, 1700841, 2017.

# THE IMPACT OF STIFFNESS GAIN ON SPINE STABILITY

**Valerie R. Jardon (1), Sara E. Wilson (1,2)**

(1) Bioengineering Graduate Program, University of Kansas, Lawrence, KS, USA
(2) Department of Mechanical Engineering, University of Kansas, Lawrence, KS, USA

## INTRODUCTION

Low back pain and injury are costly health conditions that are prevalent in our society. Consequently, researchers have developed trunk models to investigate the functions and behaviors of the spine, focusing specifically on spine stability.

After the onset of a perturbation, it is crucial that the muscles adequately respond to assist in the stabilization of the spine and that the system return to equilibrium. If the system is unable to reach equilibrium after a perturbation, this may result in injury.

While intrinsic stiffness of the muscles has proven to be satisfactory for stability of many loading conditions on the spine, Franklin *et al.* [1] determined that there may be loading conditions that cannot be stabilized by only this mechanism, and reflex stiffness is necessary to achieve stability.

Models examining spine stability require representation of short-range muscle stiffness. Bergmark's model for short-range muscle stiffness (Equation 1) has been utilized by many researchers to model the spring-like behavior of the muscle crossbridges [2]:

$$K = q\frac{F}{L_o} \tag{1}$$

where $F$ is the muscle force, $L_o$ is the neutral length of the muscle and $q$ is the stiffness gain.

Panjabi and Crisco [3] defined a range of 0.5 to 42 for the stiffness gain ($q$), with an average value of 10. Correspondingly, the stiffness gain $q$ utilized has varied between research studies (Table 1).

**Table 1: Dimensionless Stiffness Gains in Key Literature**

| | q |
|---|---|
| Bergmark [2] | 40 |
| Cholewicki *et al.* [5] | 30 |
| Franklin *et al.* [1] | 10 |
| Granata & Wilson [8] | 5 |
| Stokes & Gardner-Morse [9] | 5 |

This investigation focuses on the influence that the stiffness gain has on stability and how this potentially affects our ability to adequately model the behavior of the lumbar spine.

## METHODS

To continue our investigation of the impact of stiffness gain on spine stability, a model based on the work of Franklin *et al.* has been developed and utilized [1]. This 18 degree-of-freedom trunk model consists of a fixed pelvis, a rigid body representing the cervical and thoracic regions of the spine, and a rigid body for each of the lumbar vertebrae. There are 90 Hill-type muscle fascicles [4] with curved paths based on Cholewicki *et al.* [5]. The muscle model consists of a damper, spring and contractile element in parallel (Equation 2):

$$F_m = F_{CE} + K_{PE}x + B\dot{x} = f_{max} * \alpha + \left(\frac{q * f_{max} * \alpha}{x_o}x(t)\right) + \left(\frac{b * f_{max} * \alpha}{x_o}\dot{x}(t)\right) \tag{2}$$

where $K_{PE}$ is the stiffness coefficient, $B$ is the damping coefficient, $x$ is the muscle length, $\dot{x}$ is the muscle stretch rate, $f_{max}$ is the maximum muscle force, $q$ is the stiffness gain, $b$ is the damping gain, $x_o$ is the equilibrium muscle length and $\alpha$ is the muscle activation.

The muscle activation can incorporate both the steady-state muscle activation and the reflex activation, with the reflex activation similar to a PD controller providing feedback (Equation 3):

$$\alpha(t) = \alpha_o + \alpha_r = \alpha_o + \alpha_o * \left(G_P * \frac{x(t-\tau) - x_o}{x_o} + G_D * \frac{\dot{x}(t-\tau)}{x_o}\right) \tag{3}$$

where $G_p$ is the proportional gain, $G_d$ is the differential gain and $\tau$ is time delay.

After linearizing the system, with the assumption $\tau = 0$ if reflex activation is included, a constrained optimization was performed to solve for the muscle activations that minimized metabolic power while

requiring that the system is stable and in equilibrium. The total metabolic power utilized is determined through use of Equation 4 from Anderson [6] with an equivalent magnitude of fast and slow twitch fibers:

$$P = \sum_{n=1}^{90} \frac{m_n * 74}{2} * \sin\left(\frac{\alpha * \pi}{2}\right) + \frac{m_n * 111}{2} * \left(1 - \cos\left(\frac{\alpha * \pi}{2}\right)\right) \quad (4)$$

where $m$ is muscle mass and $\alpha$ is steady-state muscle activation.

For a simulation with reflexes, the eigenvalues of the Jacobian matrix and the method by Chen [7] can be used to determine the time delay in which the system becomes unstable. A nonlinear verification procedure was then performed to ensure that the linearized system adequately predicted the behavior of the nonlinear system.

Simulations were completed for q=5, 10, 15, 20, 25, 30, 35, 40 for the following loading conditions: 0 N and 200 N vertical load applied to T4. The resulting metabolic power and muscle force required to stabilize the spine was determined for each simulation. Initial simulations did not include the incorporation of reflexes (i.e $G_p$=$G_d$=0). Reflexes were included in the model and nonlinear analyses were performed if intrinsic stiffness alone was not sufficient for stability of a trial ($G_p$=20, $G_d$=0).

## RESULTS

The resulting metabolic power and muscle force required to stabilize the spine for each of the simulations are provided in Figure 1 and 2. As shown in Figure 1, for both loading tasks, as the stiffness gain ($q$) increases, the necessary metabolic power decreases. Additionally, at smaller stiffness gains, the difference between the metabolic power from one gain to the next was greater. As the gain increases in magnitude, there is less of a decrease in metabolic power between gains. These trends can also be seen for the muscle force required to stabilize the system (Figure 2).

For the stiffness gain magnitude of 5 and 10, the system was unstable with the applied external load of 200 N (Figure 2). When reflexes were included and these simulations were run again, the resulting delay margins were 0.102 and 0.1015 seconds for the stiffness gain of 5 and 10 respectively (Table 2). The resulting metabolic power for the stiffness gain of 5 was 39.8 Watts and 38.1 Watts for the stiffness gain of 10 (Table 2).

**Figure 1: Metabolic Power vs. Stiffness Gain**

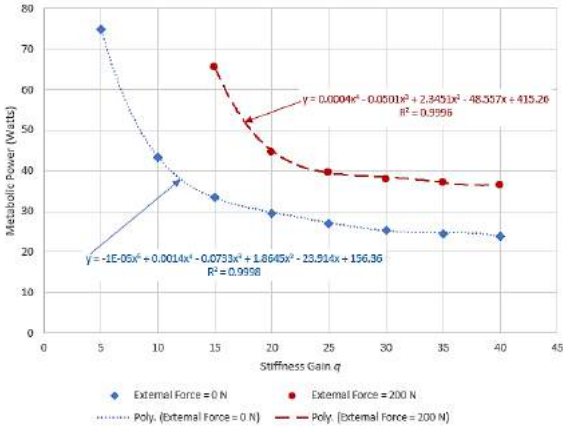


**Table 2: Simulation Results with Reflexes**

| Stiffness Gain | Time Delay (sec) | Metabolic Power (Watts) |
|---|---|---|
| 5 | 0.102 | 39.8 |
| 10 | 0.1015 | 38.1 |

**Figure 2: Muscle Force Required to Stabilize vs. Stiffness Gain**

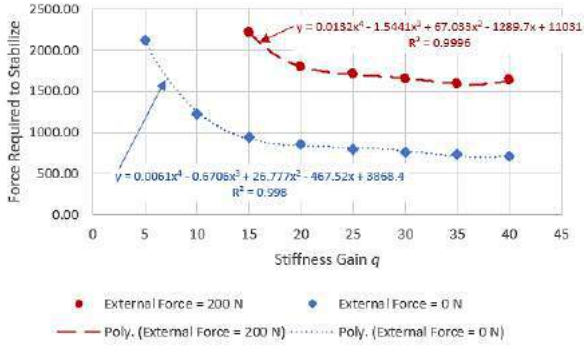


## DISCUSSION

It is evident from Equation 2 that an increased stiffness gain would result in a greater muscle force than a muscle with the same activation and a lesser stiffness gain. Based on this relationship, it makes sense that more metabolic power and force would be required to stabilize the system for muscles with smaller stiffness gains. In order to stabilize the system with the smaller gain, more muscles would need to be activated or have increased activation to generate the force needed to stabilize the system. Additionally, it is important to notice the difference between the predictions made at q=5 and q=40. It is crucial to know that based on the stiffness gain used, the results may differ between studies. This would be important for validation of results. Additionally, the results in this study can be used as guidance for which results can be compared reasonably.

For the simulations with reflex stiffness, the calculated delay margins were greater than 0.06 seconds [9], the minimum physiological time delay of reflexes. This indicates that the reflexes would be able to reasonably act at this time to stabilize the system. Using the state variables and through the calculation of their displacement from equilibrium, we determined that that the system was approaching equilibrium in the simulation, verifying the linear analysis results.


## ACKNOWLEDGEMENTS

This publication was made possible by grant number R01AR046111 from the National Institute of Arthritis and Musculoskeletal and Skin Diseases (NIAMS) at the National Institutes of Health. Its contents are solely the responsibility of the authors and do not necessarily represent the official views of NAIMS.


## REFERENCES


[1] Franklin TC, Granata KP. *J Biomech*. 2007;40(8):1762-1767.
[2] Bergmark A. *Acta Orthop Scand Suppl.* 1989;230:1-54.
[3] Crisco, JJ, Panjabi, MM. *Spine* 1991;16: 793–799.

[5] Cholewicki J, McGill SM. *Clin Biomech*. 1996;11(1):1-15.
[6] Anderson,F.C. (1999) A dynamic optimization solution for a complete cycle of normal gait. Ph.D. Dissertation, Univ Texas, Austin.
[7] Chen, J. *IEEE Transactions on Automatic Control* 1995; 40(6):1087-1093.
[8] Granata KP, Wilson SE. *Clin Biomech*. 2001;16(8):650-659.
[9] Stokes IA, Gardner-Morse M. *J Biomech*. 2001;34(6):733-740.
[10] Reeves NP. *J Electromyogr Kinesiol.* 2005;15(1):53-60.

SB³C2022
Summer Biomechanics, Bioengineering and Biotransport Conference
June 20-23, Eastern Shore, MD, USA

# THE INTERPLAY BETWEEN ELASTIN AND PROTEOGLYCANS AND THEIR EFFECT ON ASCENDING AORTIC ANEURYSMAL BIOMECHANICS

**Miriam Nightingale (1,2), Amy Bromley (3), Jehangir J Appoo (4), Elena S Di Martino (1,2)**

(1) Department of Biomedical Engineering, University of Calgary, Calgary Canada
(2) Libin Cardiovascular Institute, University of Calgary, Calgary, Canada
(3) Department of Pathology & Laboratory Medicine, University of Calgary, Calgary Canada
(4) Department of Cardiac Sciences, University of Calgary, Calgary, Canada

## INTRODUCTION

The biomechanics of ascending aortic aneurysmal tissue are primarily dictated by the content and arrangement of the extra-cellular matrix [1]. While the fragmentation and decrease of elastin has long been established a sign of disease progression, the role of proteoglycans in this process has remained elusive [2]. Previous research into the role of proteoglycan in vascular disease paints a complex picture, with both positive and negative effects attributed. Specifically, for aortic aneurysms, it has been shown that in abdominal aneurysms there is a reduction in proteoglycan content in aneurysmal vs. healthy tissue, suggesting a positive regulative role associated with healthy tissue functioning [3]. From the negative side, it has been theorized that the structure of proteoglycans themselves may be associated with disease progression; increasing stress concentrations and reducing tensile strength when accumulated/pooled [4]. This study attempts to shed some light on this complex relationship by examining the effects of proteoglycan content and pooling on the mechanical and histopathological properties of ascending aortic tissue.

## METHODS

Tissue samples from the anterior region of the aorta were collected from 28 patients undergoing elective ascending aortic replacement surgery. Inclusion criteria included: greater than 18 years of age, tricuspid (TAV) or bicuspid aortic valve (BAV), no known or suspected connective tissue disorders, and no previous aortic dissections or ruptures. The sample were subjected to planar biaxial testing to assess mechanical properties such as low strain tangent moduli (physiological stiffness) and energy loss. These methods have been described previously [5]. For this study, a displacement-controlled protocol with a maximum displacement of 60% of the edge length of effective testing area of the sample for both the circumference and axial direction was used. The mechanical behavior of the tissue was characterized by the 2nd Piola-Kirchhoff stress and Green strain both locally at the center of the specimen (through optically measured dot-displacement) and globally (through displacements measured through the testing device) in both directions via a MATLAB Program. Aortic mechanical behaviors were determined under the assumption of homogeneity and incompressibility. A combination of testing methods and post-processing data selection ensured the shear stress on tested samples was low and could be considered negligible in the analysis. The histopathology evaluation of proteoglycan accumulation, elastin fragmentation, and collagen alteration was completed by a pathologist, in accordance with the consensus statement from Society for Cardiovascular Pathology [6]. The samples also underwent a quantitative histopathological analysis to determine proteoglycan and elastin content in the media. A subset of samples was subjected to uniaxial testing until failure to determine tissue strength

For statistical analysis, the normality of continuous variables was assessed through the Shapiro-Wilk Test. The Pearson correlation (if a normal distribution) or Spearman rank correlation (if a non-normal distribution) were used to assess the relationship between continuous variables. Categorical variables were assessed for equivalence of variance through the Levene test. An ANOVA (normal distribution), Mann-Whitney test (non-normal, two categories) or Kruskal-Wallis test (non-normal, > 2 categories) were used to assess the relationships between categorical and continuous/categorical variables. The significance threshold for all tests was set to 0.05.

## RESULTS

Proteoglycan content and accumulation showed a significant inverse relationship ($p=0.002$) where overall content decreased while areas/severity of accumulation increased. This interplay was seen in

both the mechanical and histopathological properties. Both Elastin and collagen were seen to be significantly associated with proteoglycan content and accumulation. Decreased elastin content was significantly associated with decreased proteoglycan content (Figure 1A: $p<0.001$, rho=0.91) and severe proteoglycan accumulation (Figure 1B: $p=0.029$). While increased elastin fragmentation was significantly related to a decreased PG content ($p<0.001$). Proteoglycan content was also seen to significantly decrease in the presence of collagen alteration ($p=0.019$).

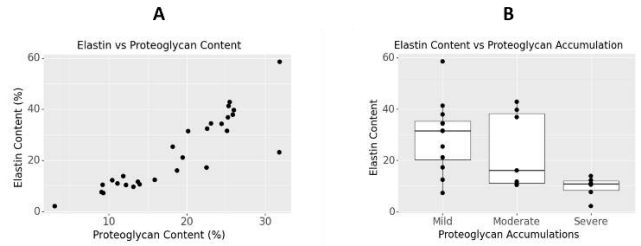


**Figure 1: Scatterplots and boxplots showing the significant associations between elastin content and proteoglycan content/arrangement. Elastin content vs Proteoglycan content (A), Elastin content vs Proteoglycan Accumulation (B)**

A decrease in physiological stiffness was found to be significantly associated with a decrease in both proteoglycan content (Figure 2A: $p=0.038$, rho=0.39) and elastin content ($p=0.041$, rho=0.38). While severe proteoglycan accumulation also led to a significant decrease in physiological stiffness (Figure 2B: $p=0.034$). A trend was also found to be associated with increased elastin fragmentation and decreased physiological stiffness ($p=0.089$). A decrease in proteoglycan content also significantly correlated with increased energy loss ($p<0.001$, rho=-0.61). For decreased elastin content, a trend was associated with increased energy loss ($p=0.065$, rho=-0.35). Both severe proteoglycan accumulation and elastin fragmentation were significantly associated with an increase in energy loss ($p=0.001$ and $p=0.03$ respectively). Finally decreased proteoglycan content was seen to significantly correlated with a reduction in strength ($p=0.032$, rho=0.43). Severe proteoglycan accumulation and collagen alteration were also significantly associate with a reduction in strength ($p=0.023$ and $p=0.016$ respectively).

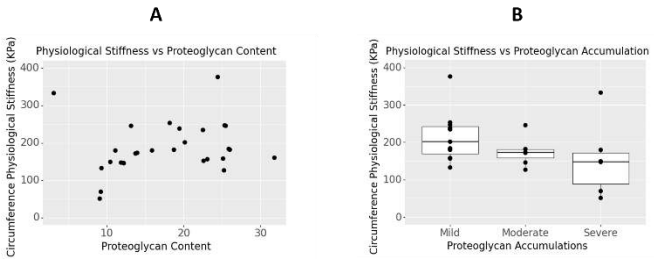


**Figure 2: Scatterplots and boxplots showing the significant associations between physiological stiffness and proteoglycan content/arrangement. Physiological Stiffness vs Proteoglycan content (A), Physiological Stiffness vs Proteoglycan Accumulation (B)**

## DISCUSSION

The media/middle layer of the aortic wall is thought to be the main contributor to the overall mechanical properties [1]. It is composed of equally spaced elastin lamellae, with each lamella perpendicularly connected by elastin as well [1]. Smooth muscle cells and collagen are interspaced between the elastin layers [1]. The elastin lamellae structure is supported by ground substance consisting mostly of Mucopolysaccharides (usually referred to as proteoglycans) [7]. Proteoglycans are thought to be associated with intercellular communication and regulating homeostasis in the aortic wall [7].

These results suggest a complex interplay between proteoglycans and histopathologic and mechanics changes associated with aneurysmal disease progression. High proteoglycan content appears to be associated with healthy tissue functioning, significantly associating with high elastin content, low elastin fragmentation, low collagen alteration, higher physiological stiffness, lower energy loss and higher strength – all histological and mechanical properties previously associated with healthier tissue structures and mechanics [8]. Conversely, proteoglycan accumulation was associated with weakening tissue: low elastin content, high elastin fragmentation, high collagen alteration, lower physiological stiffness, higher energy loss, and lower strength [8] – all histological and mechanical properties previously associated with disease progression.

These results reinforce the interconnection between proteoglycans and elastin and collagen as well as the effect these proteins have on aortic biomechanics. Interestingly, the localized accumulation of proteoglycan appears to be a mechanism separate from the fluctuations of proteoglycan content, existing simultaneously with an overall reduction of proteoglycans within the tissue. These results corroborate previous research illustrating a positive role being associated with content and a negative role being associated with accumulation [1,2]. Increased proteoglycan accumulation alongside decreased content could potentially be utilized as sign of disease progression and weakening.

Several limitations exist for this study. There were no measurements taken from normal aortic tissue to function as controls. Though we included both BAV and TAV patients, we did not have enough samples to determine differences between the two patient populations. Finally, as with all ex-vivo approaches, this study is limited to the passive mechanical properties, missing any changes associated with the interactions of living cells (such smooth muscle cells).


## ACKNOWLEDGEMENTS

This work was supported through the Natural Sciences and Engineering Research Council (NSERC) Discovery grant RGPIN/07178-2019, the NIH grant 1 R01 HL133504-01A1, the Libin Cardiovascular Institute of Alberta, and the Biomedical Engineering Graduate Program at the University of Calgary.


## REFERENCES


[1] Bergmann, G et al., *J Biomech*, 34:859-871, 2001.
[1] Wolinsky, H et al, *Circ Res*, 20:99-&, 1967.
[2] Okamoto, RJ et al, *J Thorac Cardiovasc Surg*, 126:842-850, 2003.
[3] Theocharis, AD et al., *Atherosclerosis*, 145:359-368, 1999.
[4] Humphrey, JD, *J Vasc Res*, 50:1-10, 2013.
[5] Forneris, A et al, *Appl Sci*, 11:3485, 2021.
[6] Halushka, MK et al, *Cardiovasc Pathol*, 25:247-257, 2016.
[7] Emmott, A et al, *J Thorac Cardiovasc Surg*, 156:503-512, 2018.
[8] Nightingale, M et al, *JTCVS Open*, In press, 2022.

# COMPARING IN-PERSON BIOMEDICAL ENGINEERING LABORATORY TEACHING TO VIRTUAL REALITY TEACHING APPROACH

**Anita Singh (1), Sriram Balasubramanian (2)**

(1) Biomedical Engineering, Widener University, Chester, PA, USA
(2) School of Biomedical Engineering, Science and Health Systems, Drexel University, Philadelphia, PA, USA

## INTRODUCTION

Biomedical Engineering laboratories are designed to create hands-on experience that help student's ability to design an experiment while applying engineering principles. They learn to perform data acquisition, analysis while considering safety aspects and apply required engineering standards. They also learn to apply modern technical skills, perform teamwork, and develop communication skills practice [1,2]. Several new teaching modalities resulted from recent COVID-19 pandemic limitations and there is a need to investigated them for their continued implementation in enhancing engineering educational experience and learning . Our team has previously reported the efficacy of virtual reality (VR) videos in explaining the lab procedures. This modality has resulted in enhanced student learning of experimental protocol when compared to the standard online modality that uses traditional 2D videos. In this study, we aim to directly compare the efficacy of VR videos when compared to the in-person lab session.

## METHODS

A total of 18 Junior-level biomedical engineering (BME) students enrolled in BME 303: Biomedical Engineering Lab 1 participated in this study. During a bone-biomechanics lab, students were asked to watch a VR video of the lab and then take a quiz (Figure 1). The instructor then demoed that lab for the students and the students were asked to take another quiz. The questions in the two quizzes were shuffled between the two takes among these students. They were also asked to provide feedback on the ease of use of VR videos and their preference between VR sessions and in-person sessions.

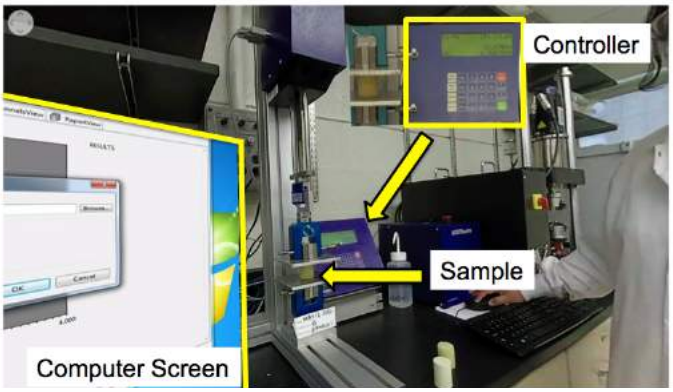


**Figure 1: Bone compression lab with zoomed controller and computer screen display in VR.**

## RESULTS

Student's quiz scores after VR video followed by in-person lab demo were slightly higher than after watching VR video only and before the in-person lab demo (Figure 2). However, no significant differences were reported. This confirms that between the two teaching modalities (VR versus in-person), the student learning attained was comparable. Student feedback also reported VR glasses to be user-friendly. However, students did prefer in-person sessions over VR-only sessions. They highly supported the VR videos as a critical supplemental learning tool since the videos could be watched even after the in-person lab session as they prepared their lab reports.

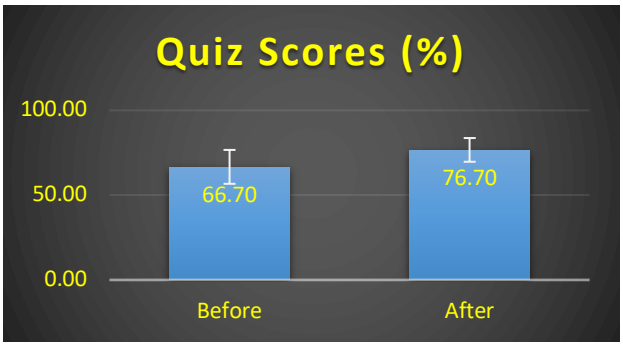


**Figure 2: Quiz scores after watching VR videos only and after watching VR videos followed by in-person lab demo.**

## DISCUSSION

The benefits of using VR technology in teaching biomedical engineering labs exist and it should further be explored as a supplemental teaching tool. It is also noteworthy that while in-person sessions were the preferred format of hands-on experience, the student learning was not different between the VR videos and in-person learning modalities.

## ACKNOWLEDGEMENTS

The research reported in this publication was supported by the National Institute of Biomedical Imaging and Bioengineering of the National Institutes of Health under Award Number R25EB023857.

## REFERENCES

[1] Trumbower, R.D et al., *IEEE EMBS*, 101-110, 2003.
[2] Foulds, R.A et al., *IEEE EMBS*, 92-100, 2003.

SB³C2022
Summer Biomechanics, Bioengineering and Biotransport Conference
June 20-23, Eastern Shore, MD, USA

# RAMAN SPECROSCOPIC PROBE ASSESSMENTS OF CARTILAGE COMPOSITION AND FUNCTIONAL MECHANICAL PROPERTIES

**M Kazemi (1), D Mehrotra (1), J Zhang (1), C Yu (1), D Desai (1), MW Grinstaff (1), BD Snyder (2), MS Bergholt (3), MB Albro (1)**

(1) College of Engineering, Boston University, Boston, MA, USA
(2) Department of Orthopaedics, Beth Israel Deaconess Medical Center, Boston, MA, USA
(3) Center for Craniofacial & Reversative Biology, King's College London, London, UK

## INTRODUCTION

Articular cartilage is a highly specialized tissue that lines the ends of long bones. Cartilage mechanical performance is highly dependent on its biochemical and structural properties: the extracellular matrix (ECM) is comprised of water and highly sulfated anionic glycosaminoglycans (GAG) constrained by fibrous network of type-II collagen that provide tribological material properties essential to supporting applied joint loads and maintaining a nearly frictionless shear interface between articulating joint surfaces. Osteoarthritis (OA), a painful, chronic, condition that damages diarthrodial joint function, is characterized by initial depletion of GAG, loss of collagen organization, and accompanying tissue softening, followed by more severe erosion of the collagen matrix. Promising therapies to treat OA include disease modifying drugs that mitigate or reverse cartilage degeneration and chondroregnerative tissue engineering platforms that recapitulate the composition and structure or healthy hyaline cartilage. The R+D pipeline for assessing the efficacy of treatments consists of a hierarchy of model systems: *in vitro* cartilage organ culture, *in vivo* preclinical animal studies, and randomized clinical trials. However, measurement of the effectiveness of therapies to preserve or regenerate cartilage is burdened by a lack of standardized biomarkers that can be applied across the spectrum of testing platforms. Evidence-based evaluations of the utility of OA therapies should be predicated on measuring biomarkers that reflect OA pathophysiology and portray the structure and composition of regenerated or neo-cartilage repair tissue relevant to its function. Arthroscopic-based cartilage grading systems (Outerbridge) and MRI (dGEMRIC, T1rho, T2*) are only moderately correlated with quantitative assessments of the tissue's material properties [1]. Therefore, robust methods capable of measuring changes in the functional properties of damaged cartilage are requisite for advancing OA treatment.

Raman spectroscopy is an inelastic optical light scattering technique that can provide a quantitative, point-wise optical fingerprint of a tissue's molecular building blocks (amides, sulfates, carboxylic acids, and hydroxyls), thus allowing recognition of the predominant molecular constituents of articular cartilage: GAG, collagen (COL), and $H_2O$. In our prior work, we developed a Raman arthroscopic needle probe and real-time spectral analysis platform capable of measuring ECM-specific compositional biomarkers of hyaline cartilage over the hierarchy of tissue model systems—*in vitro* analysis of enzymatically degenerated cartilage explants and *in vivo* ovine cartilage analysis via intraarticular Raman arthroscopy measures [2]. In this work, we aim to further advance this platform by investigating the capability of our Raman probe to assess the composition and material properties of cartilage in health and disease using ex vivo bovine and human osteochondral specimens over a range of degenerative states.

## METHODS

**Tissue specimens**: Bovine specimens were harvested from the medial femoral condyles (N=5). The first four knees (J1-J4) had no macroscopic degeneration on any of the articular surfaces (Outerbridge grade (OB0) (Fig 1A). The last knee (J5) exhibited a ~∅15mm focal chondral lesion (OB2) within the medial condyle load bearing (LB) region, but no macroscopic degeneration (OB0) in the surrounding LB and non-load bearing (NLB) cartilage (Fig 1B). Specimens were further harvested from the condyles of two cadaveric human knees (NDRI; age/sex: 32/M, 65/F). The 32/M exhibited no macroscopic degeneration (OB0, Fig 1C). The 65/F joint exhibited severe degeneration

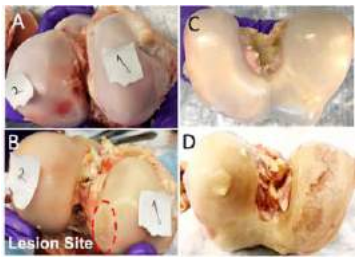


**Fig 1: (A) Healthy and (B) chondral lesion afflicted bovine femoral condyles. (C) Healthy (32yr) and (D) OA (65yr) human femoral condyles.**

(OB4) on the medial condyle, but grossly intact lateral condyle cartilage (OB0, Fig 1D). For both bovine and human models, rectangular osteochondral blocks (~5x5x5mm) were sectioned from the LB and NLB regions for analysis. **Raman analysis**: The Raman platform consisted of an NIR diode laser (ex=785nm, 500mW, B&W Tek), fiber-coupled spectrograph (QEPro, Ocean Optics), and needle probe with a 2mm sapphire ball lens (Fig 2)[2]. Raman spectra were acquired with the probe lens in gentle contact with the chondral surface over 30s acquisition time. The spectral fingerprint range (800-1800cm$^{-1}$) was preprocessed and subjected to a multivariate least-squares linear regression model to decomposition of Raman spectra to calculate the relative contribution of the predominant cartilage constituents (GAG, COL and $H_2O$) to the composite cartilage Raman spectra (Equation 1).

$$\mathbf{Cartilage_{spectra}} = GAG_{score}*(\mathbf{GAG_{REF}}) + COL_{score}*(\mathbf{COL_{REF}}) + H_2O_{score}*(\mathbf{H_2O_{REF}}) \quad (1)$$

where $GAG_{REF}$, $COL_{REF}$, and $H_2O_{REF}$ are the component spectra of purified reference chemicals for each ECM constituent.

**Property measures**:
The elastic modulus of the chondral layer for each tissue block was derived by indentation using a ∅3mm spherical indenter and the slope of the loading curve (Hertzian). The central ∅3mm chondral core of each block was sub-punched and GAG content determined by DMMB assay.

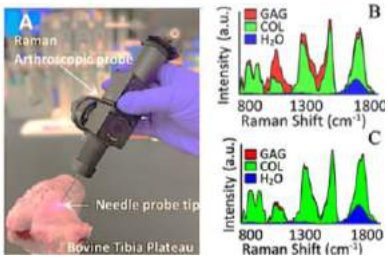


**Fig 2: (A) Raman needle probe in direct contact with cartilage surface. Representative 2D stacked area plot showing cumulative contribution of GAG, COL, $H_2O$, to composite Raman spectra of (B) healthy and (C) degenerative bovine cartilage.**

## RESULTS

The multivariate regression model accounted for 91±1.5% of the variation in composite Raman spectra (Fig 2B&C). Compared to healthy bovine specimens (J1-J4), tissue from the J5 specimen was degraded as evidenced by significantly reduced GAG content and elastic modulus within both the focal lesion (OB2) and surrounding tissue (OB0) (p<0.001; Fig 3A-B).

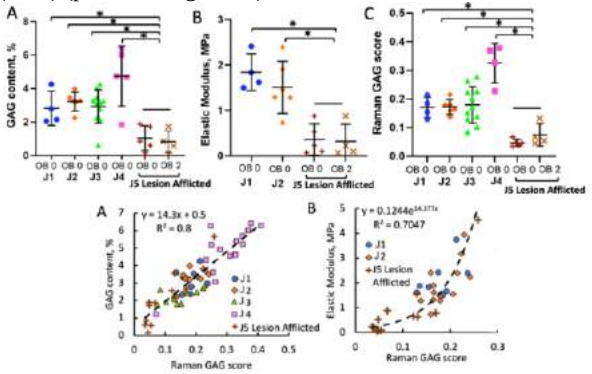


**Fig 3: (A) GAG content, (B) elastic modulus, and (C) Raman GAG scores for cartilage from LB regions of healthy (J1-J4) and lesion-afflicted (J5) bovine tissue blocks. Regression Raman GAG score vs. (D) DMMB-assay GAG content, and (E) elastic modulus for bovine blocks (n=59) * p<0.001: significant differences.**

Similarly, Raman derived biomarkers revealed significantly lower Raman GAG scores in both the lesion and surrounding tissue (p<0.001; Fig 3C). For all bovine specimens, results demonstrated that Raman GAG scores predicted 80% of the variation in GAG content (Fig 3D) and 70% of the variation in elastic modulus (Fig 3E). For the human model, specimens from both condyles of the 65/F-OA were degraded as evidenced by significantly reduced elastic modulus within the OB 4 and intact (OB 0) specimens (p<0.001; Fig 4A). Significantly lower Raman GAG scores were also measured in specimens from both condyle regions of the 65/F-OA joint compared to the 32/M (p<0.001; Fig 4B). For all human specimens, Raman GAG scores predicted 70% of the variation in elastic modulus (Fig 4C).

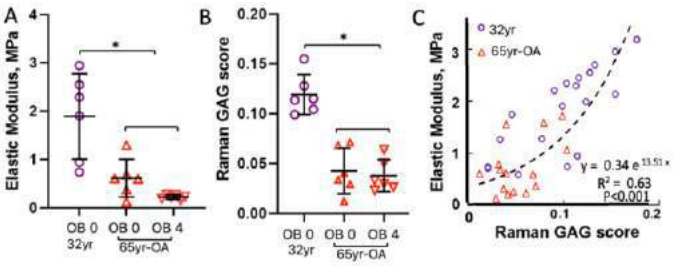


**Fig 4: (A) Elastic modulus and (B) Raman GAG score in LB regions of 32/M and 65/F human tissue blocks. (C) Regression Raman GAG score vs elastic modulus for all human tissue blocks (n=34). * p<0.001: significant differences.**

## DISCUSSION

GAG "scores" derived from multivariate regression spectral analysis represent the relative contribution of GAG to the composite Raman spectra of cartilage acquired in real-time, using Raman probe platform. The GAG score accounted for 80% of the variation in the measured GAG composition and predicted 60-70% of the variation in the elastic modulus of cartilage specimens over a range of cartilage morphologies including intact (OB 0), focal chondral lesion (OB 2), and severely degraded cartilage (OB 4). Raman GAG scores revealed depleted GAG composition and diminished tissue stiffness in regions where there was no visual macroscopic degeneration: "intact" cartilage from human 65/F and tissue surrounding the focal lesion in bovine J5. These outcomes support the feasibility of developing a Raman-based needle probe that maps real-time non-uniform and reduced sGAG distribution within the lesion and peripheral cartilage that was otherwise visually normal. Therefore, Raman spectroscopy of the joint can show molecular signatures of damaged tissue, even if it is invisible to the eye. Raman spectroscopy can "optically biopsy" cartilage and quantify the relative contribution of key biochemical constituents that serve as biomarkers for determining cartilage composition, structure, and material properties in normal and pathological tissue and in response to chondroprotective and/or chondroregenerative treatments. This work supports the use of Raman spectroscopy as a research platform to objectively assess the efficacy of emerging OA therapies across the hierarchy of in vitro, in vivo, and clinical model systems. In the future, Raman arthroscopy can serve as a transformative clinical platform for discrimination of healthy versus degraded tissue, diagnosing early OA, and guiding clinical treatment courses.


## ACKNOWLEDGEMENTS

This work is supported by the Arthritis Foundation, Musculoskeletal Transplant Foundation, and Boston University Materials Science & Engineering Innovation Award.


## REFERENCES:


[1]. Hayashi, D et al., J *Ann Phys Rehab Med*, 59:161-9, 2016.
[2]. Kroupa, K et al., *JOR*, 2021.

# INVESTIGATING STRUCTURAL CHANGES OF NEONATAL BRACHIAL PLEXUS POST-STRETCH

**V. Orozco, MS (1), R. Magee, MS (1), M. Sahni, MD (2), S. Balasubramanian, PhD (1), A. Singh, PhD (3)**

(1) School of Biomedical Engineering, Sciences and Health Systems
Drexel University
Philadelphia, PA, USA

(2) Sunrise Children's Hospital, Pediatric Medical Group,
Las Vegas, NV, USA

(3) Department of Biomedical Engineering
Widener University
Chester, PA, USA

## INTRODUCTION

The brachial plexus (BP) is an intricate network of nerves responsible for providing motor and sensory innervation to upper extremities [1]. A common BP nerve injury in infants is neonatal brachial plexus palsy (NBPP) [2]. NBPP is defined as over-stretching of BP during complicated birthing scenarios [3]. Despite obstetric care improvements, NBPP continues to significantly impact infants' lives, with a worldwide incidence of 1 to 4 per 1000 live births [3, 4]. Current available treatment strategies for infants who do not fully regain function by three months after BP injury during a complicated delivery is surgical intervention, such as nerve transplantation surgery [2, 3]. However, surgical intervention remains controversial since timing and type of surgery highly rely on understanding structural changes observed after a neonatal BP injury [3]. Therefore, objective of this study was to relate structural changes at varying degrees of stretch of neonatal BP using a neonatal large animal model.

## METHODS

Ten neonatal piglets (3-5 days old) were anesthetized and BP was exposed using an axillary approach per approved procedures by Institutional Animal Care and Use Committee (IACUC). *Biomechanical Studies*: A custom-built mechanical testing device was used to perform *in vivo* stretch at a displacement rate of 500 mm/min to predetermined strains of <15% and >15% to represent mild and severe stretch injury, respectively (Fig. 1A). BP nerve segments were cut and anchored at the distal end. Three to five black acrylic paint markers were placed along the length of nerve segment and a stereo-camera (ZED Mini) was positioned above to measure real-time strain (Fig. 1B). Load and displacement data was acquired at a sampling rate of 1000 Hz. Images were captured at 100 frames/s.

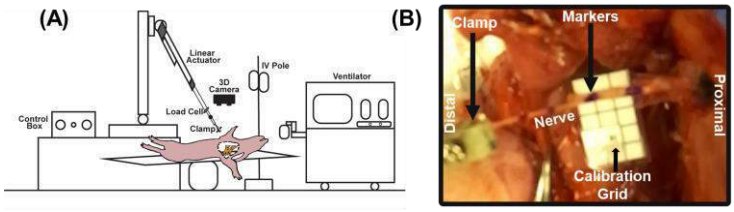


**Figure 1.** (A) Schematic of mechanical testing set-up. (B) A BP terminal nerve branch was clamped and stretched to failure at a rate of 500mm/min. A camera was placed above the BP along with a calibration grid for 3D strain analysis.

*Histology*: BP nerves were harvested post-stretch and OCT-embedded. Ten-µm-thick serial longitudinal sections were stained with Hematoxylin-Eosin (H&E) and neurofilament (NF) immunofluorescence. Using Leica DMI 4000 B microscope, stained slides were imaged at 10x along nerve length. Each image was scored by an independent-blinded observer for vascular damage and fiber disruption using an adaptive scoring system for each. Vascular damage was scored on scale of 0-2 (0-no damage, 1-torn vessel, 2-scattered blood cells) (Table 1).

**Table 1.** Blood Vessel Scoring System

| Score Value | Definition | Staining Method | Notations |
|---|---|---|---|
| | | Hematoxylin–Eosin | |
| 0 | None to minimal damage | 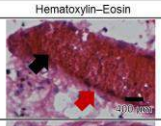 | Intact blood vessel wall (**black arrow**); compact RBCs (**red arrow**) |
| 1 | Moderate damage | 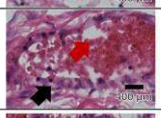 | Intact blood vessel wall with spacing (**black arrow**); minimal scattered RBCs (**red arrow**) |
| 2 | Severe damage | 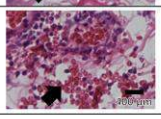 | Broken blood vessel wall with scattered RBCs (**black arrow**) |

RBCs: Red Blood Cells

Fiber damage was scored on a scale of 0-4 (0-no to minimal damage, 1-straightening, 2-increased spacing, and 3 and 4-torn to scattered fiber disruption, respectively) (Table 2).

**Table 2.** Fiber Damage Scoring System

| Score Value | Definition | Staining Method | Notations |
|---|---|---|---|
| | | Neurofilament Immunofluorescence | |
| 0 | Normal/Control | 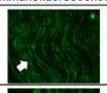 | The fibers hold their wavy pattern (**white arrow**) with no increase in space or breakage |
| 1 | Straightening of fibers | 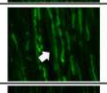 | The uniform wavy pattern begins to straighten (**white arrow**), while fibers remain intact |
| 2 | Increased spacing | 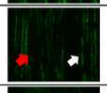 | The fibers are still intact, with loss of wavy pattern (**white arrow**) and increased amount of spacing (**red arrow**) |
| 3 | Fiber disruption | 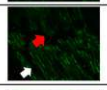 | The fibers begin to fragment (**red arrow**) while the spacing increases (**white arrow**) |
| 4 | Complete disruption | 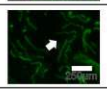 | The fibers are no longer intact and there is more space between them (**black arrow**) |

Extent of fiber disruption was measured at thickest fascicle by binarizing image and measuring area of a 100x100 pixel region of interest.

## RESULTS

Using the modified scoring systems, vascular damage (**Fig. 2A**) and fiber damage (**Fig. 2B**) increased with increasing stretch.

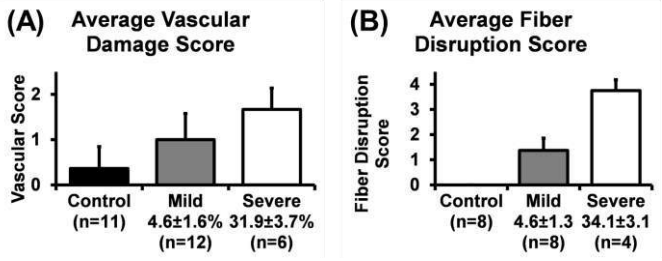


**Figure 2.** Bar graphs of average (A) increasing vascular damage, (B) increasing fiber damage, with increasing stretch.

Extent of fiber disruption decreased with increasing stretch (**Fig. 3**).

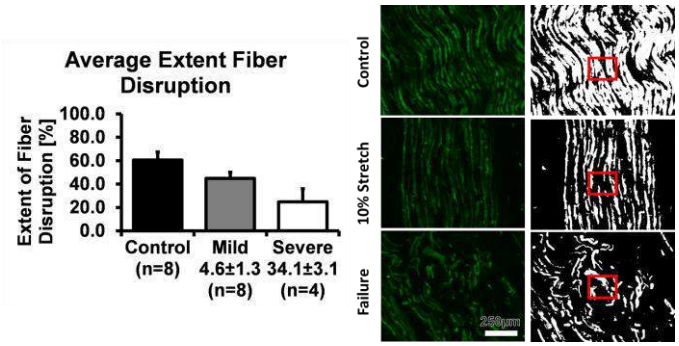


**Figure 3.** Bar graphs of average decreasing extent of fiber disruption with increasing stretch with representative images.

## DISCUSSION

The current study is a novel contribution to understanding the neonatal BP structural response to a stretch injury that may aid the understanding of injury thresholds in human neonatal BP because neonatal piglet BP and neonatal human BP share anatomical similarities [5]. This study is the first to report structural changes of neonatal BP with respect to varying degrees of stretch. Characterizing structural changes as a result of stretch injury is of importance to understand the extent of injury. Future functional studies may further contribute to the understanding of NBPP injury mechanism.


## ACKNOWLEDGEMENTS

This project was supported by the Eunice Kennedy Shriver National Institute of Child Health and Human Development of the National Institutes of Health (R15HD093024) and NSF CAREER grant Award #1752513.


## REFERENCES


1. Abid, A. *Brachial plexus birth palsy: Management during the first year of life.* Orthopaedics & Traumatology: Surgery & Research. 2016. **102**(1, Supplement): p. S125-S132. DOI: 10.1016/j.otsr.2015.05.008.
2. Mehlman, C.T., *Neonatal Brachial Plexus Palsy*, in *The Pediatric Upper Extremity*, J.M. Abzug, S.H. Kozin, and D.A. Zlotolow, Editors. 2015, Springer New York: New York, NY. p. 589-605.
3. Abzug, J.M.M.D. and S.H.M.D. Kozin. *Current Concepts: Neonatal Brachial Plexus Palsy.* Orthopedics (Online). 2010. **33**(6): p. 430-5. DOI: 10.3928/01477447-20100429-25.
4. Johnson, E.O., T. Troupis, A. Michalinos, J. Dimovelis, and P.N. Soucacos. *Obstetrical brachial plexus palsy: Lessons in functional neuroanatomy.* Injury. 2013. **44**(3): p. 293-298.
5. Hanna, A.S., D.J. Hellenbrand, D.T. Schomberg, S.M. Salamat, M. Loh, L. Wheeler, B. Hanna, B. Ozaydin, J. Meudt, and D. Shanmuganayagam. *Brachial plexus anatomy in the miniature swine as compared to human.* J Anat. 2022. **240**(1): p. 172-181. DOI: 10.1111/joa.13525.

SB³C2022
Summer Biomechanics, Bioengineering and Biotransport Conference
June 20-23, Eastern Shore, MD, USA

# AUTOMATED 4D MESHING OF EX-VIVO FILLING OF THE MURINE URINARY BLADDER

**Eli Broemer (1), Sara Purdue (1), Pragya Saxena (2), Nathan Tykocki (2), Sara Roccabianca (1)**

(1) Mechanical Engineering, Michigan State University, East Lansing, MI, USA
(2) Pharmacology & Toxicology, Michigan State University, East Lansing, MI, USA

## INTRODUCTION

The urinary bladder is a highly distensible organ capable of expanding to over twice its initial volume while accommodating urine volume increases at low pressures. For mechanical analysis, the bladder is often modeled as an idealized spherical pressure vessel. In reality, the shape of the bladder is closer to an ellipsoid. Indeed, in the clinical setting, bladder volume is often approximated by measuring the 3 major axes via ultrasound [1]. However, even this is a simplifying proposition, and the true shape changes throughout filling due to the anisotropic and heterogeneous material properties of the soft tissue. The bladder has been shown to have different material properties in the apex-to-base vs circumferential directions [2] as well as distinctive contractility between the dome, bladder wall, and trigone (i.e., top, sides, and lower neck) [3]. This is all to say, the urinary bladder has complex mechanical characteristics that drive a constantly shifting geometry during filling. Accurately modeling the shape of the bladder during filling is necessary to better understand the unique mechanical features of this organ.

In this study, a novel method has been developed for reconstructing accurate 3D geometries/meshes from *ex-vivo* bladder filling experiments, with a time resolution of 0.1 sec (4D). The method is highly automated and utilizes open-source software. 4D meshing of the bladder, as shown here, provides a vectorized organ representation from empty to full capacity. These techniques will be used to further study the anisotropic mechanical behavior of the urinary bladder.

## METHODS

*EXPERIMENTAL SETUP* A mouse bladder was extracted, cleaned, and mounted on a cannula connected to a pump and pressure transducer. A custom testing device was built to allow multiple views (i.e. top, left, right, front, & back views) of the organ to be imaged throughout filling (**Figure 1**). The bladder was empty when mounted, submerged in 37°C saline, and then filled at a rate of 30 µL/min until a measured inner pressure of 25mmHg was reached.

A camera captured the bladder throughout the pressurization. Camera and pressure recordings were synchronized, so that images and pressure measures were collected at the same instant. The output was a video of the experiment at 10 frames/sec, and a spreadsheet of bladder pressure where each measure corresponds to a frame in the video.

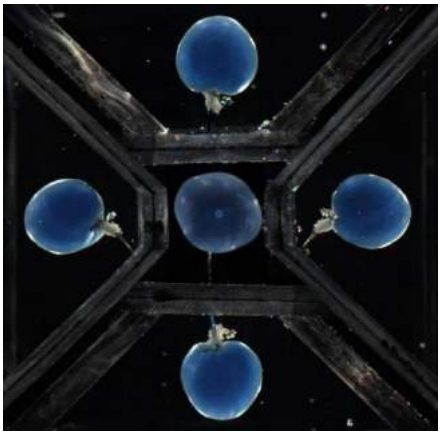

**Figure 1: Experiment setup. Bladder is mounted in the center (viewed from the top), and is surrounded by 4 mirrors which show front, back, left, & right views of the tissue.**

*IMAGE PROCESSING* The data was processed with python. Custom code locates tissue boundaries and segments bladder silhouettes from the top, left, and front views (**Figure 1**) in each frame. First, a region of interest was selected in the final frame with the Paint.NET software. This task creates a window for the code to search for exact tissue boundaries, and takes ~1 minute to perform by a researcher for each sample. The region of interest and the experiment video are then passed into the code, and no more input is needed from the researcher.

SB³C2022-432

Within the region of interest, a Canny algorithm [4] is used to locate the tissue boundaries of each view (**Figure 2A**). In short, the brighter soft tissue in contrast to the dark background creates a sharp gradient along its edge—this gradient is detected, some smoothing and continuity is enforced, and the result is a line denoting the bladder edge.

The edge line is not guaranteed to be a closed curve (**Figure 2A**), so an Open Curve Filling algorithm was developed [5]. This algorithm seeds a pixel at the center of the bladder view, and then pixels "grow" outwards in all directions until an edge is hit. In directions which are open (i.e., no edge will be found) the algorithm draws a connection between the two nearest edges. The result is a solid silhouette of the bladder view (**Figure 2B**). These silhouettes are used to generate a 3D reconstruction of the bladder at each time point in the experiment (4D).

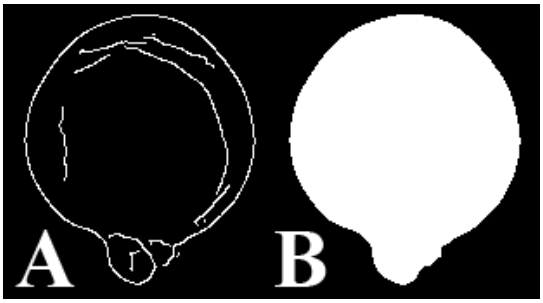


**Figure 2: Segmentation of bladder front view. A) Output of Canny edge detection. B) Output of Open Curve Fill algorithm.**

*MESHING* A 3D solid shape is created by the space carving method [6]. The method begins with a primitive rectangular prism, and then the two side views (**Figure 1**) are used to cut away from the primitive in the direction normal to their plane. These first two carves produce a bicylinder-like shape (intersection of 2 cylinders). The top view is then used to form the final shape by carving in the Z direction (**Figure 3 left**). However, in this case, for each unit in the Z direction, the top silhouette is scaled to fit the rectangular slice of the bicylinder. Phrased another way, the top-down view is mapped along the entire height of the bladder. If this technique was not used, a tricylinder would be obtained instead, and the final bladder shape would have sharp corners. This is an approximation of the actual bladder 3-dimensional volume, yet it is necessary given the type of experimental data available.

Finally, the voxel (3D pixel) representations of the tissue, obtained from space carving, were transformed into surface meshes (**Figure 3 right**). The marching cubes algorithm [7, 8] was employed for this step. Each mesh was verified to be defect-free and watertight, and then smoothed. The final result gave a set of bladder meshes at every time point imaged, which have a corresponding internal pressure measure that may be used for mechanical analysis.

## RESULTS

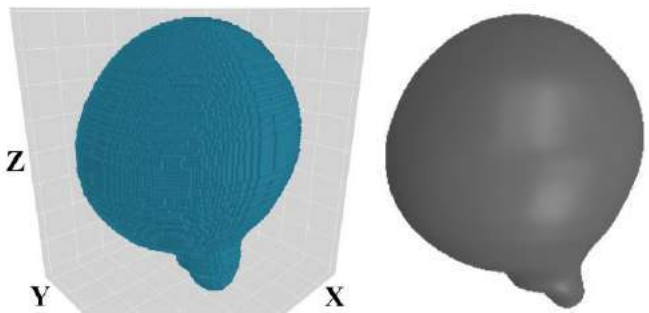


**Figure 3: Left) Voxellized bladder. Right) Meshed bladder.**

Accuracy of automated segmentation was validated by comparing the volume result to a manual segmentation at points throughout the experiment (**Figure 4**). Both manual and automated segmentation produced a linear volume increase correlating to the constant fill rate.

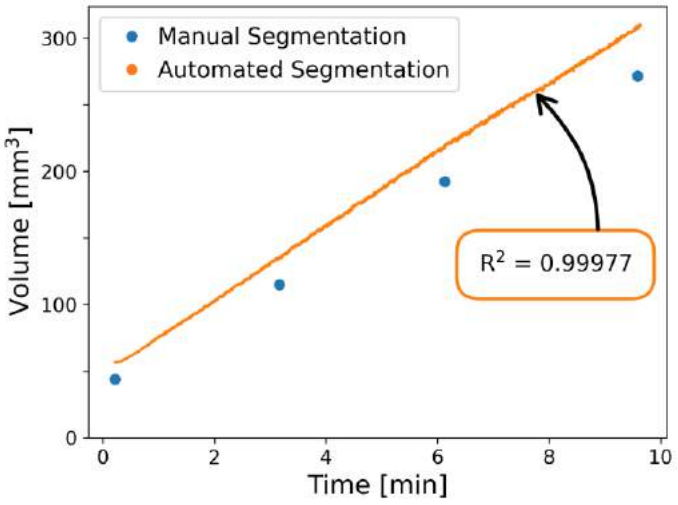


**Figure 4: Bladder volume comparison between fully automated segmentation (Figure 2) and a comparable manual method in which the bladder was isolated from background by a researcher (not shown).**

## DISCUSSION

The methods described here were shown to generate accurate 3D bladder volumes in either voxel or mesh forms. Effort to automatize this process allowed these geometries to be easily rendered at all time points captured during filling. Volumes were compared to a manual method, and the automated process was shown to over-estimate (**Figure 4**). This discrepancy is likely due to the inclusion of the bladder neck, which was removed during manual segmentation. Steps are being made to exclude the neck from automated geometries by obscuring it in the experimental setup. The source code for all image processing and meshing described here is publicly available for use [5].

The work shown here is a step towards fully describing the unique and transient shape of the urinary bladder during filling. Future work will develop more techniques so that bladder deformations in these volumes can be quantified to study the anisotropic behavior of this tissue.

## ACKNOWLEDGEMENTS

Thanks to Sara Purdue for the manual segmentations, and Pragya Saxena for performing the experiments. This work was supported by the National Institutes of Health (grant numbers K01DK103840, R01DK119615, NIH P20DK127554).

## REFERENCES

[1] Araklitis, G et al., *Neurol and Urodyn*, 38(4):1100-1105, 2019.
[2] Gilbert, TW et al., *Biomaterials*, 29(36):4775-4782, 2008.
[3] Pagala, MK et al., *J Urol*, 166(2):721-727, 2001.
[4] Canny, J, *IEEE Trans Pattern Analysis*, 8:679-714, 1986.
[5] Broemer, E, *Github Inc*., github.com/broemere/ccarvv, 2021.
[6] Kutulakos, KN et al., *Int J Comput Vision*, 38(3):199-218, 2000.
[7] Lewiner, T et al., *J Graphics Tools*, 8(2):1-15, 2003.
[8] Lorensen WE & Cline, HE, *SIGGRAPH '87: Proceedings of the 14th Annual Conference on Computer Graphics*, 163-169, 1987.

# CHARACTERIZATION OF BIOENGINEERED TISSUES BY DIGITAL HOLOGRAPHIC VIBROMETRY AND MACHINE LEARNING

**Colin Hiscox (1), Juanyong Li (2), Ziyang Gao (3), Dmitry Korkin (3), Cosme Furlong(1), Kristen Billiar (2)**

(1) Mechanical Engineering Department, Worcester Polytechnic Institute, Worcester, MA, USA
(2) Biomedical Engineering Department, Worcester Polytechnic Institute, Worcester, MA, USA
(3) Department of Computer Science, Worcester Polytechnic Institute, Worcester, MA, USA

## INTRODUCTION

Mechanical properties are critical and often overlooked factors defining the quality of bioengineered tissues. Current tests used to measure the physical properties of engineered tissues, such as uniaxial tensile tests and nanoindentation, tend to be invasive and destructive and thus not applicable for in-process quality control, requiring aseptic non-destructive assessment.

The goal of this work is to develop a noncontact nondestructive method to measure the properties of bioengineered tissues during production. We apply acoustic vibration to Apligraf living skin substitute and measure the modes and displacements of vibration of the entire surface of the tissue within its packaging. We then utilize Finite Element Methods (FEM) and supervised machine learning algorithms to relate the measured vibrations to the mechanical properties.

## METHODS

Our methodology used three components to measure important information of the sample: optical coherence tomography (OCT), digital holographic vibrometry (DHV), and nanoindentation. All measurements and experiments were performed on samples of Apligraf generously donated by Organogenesis Inc. [1]

First a sample was measured with OCT (Telesto SD-OCT, Thorlabs). A b-scan taken at multiple points was used to estimate the thickness of each layer of the Apligraf nondestructively.

DHV, the primary tool, uses a speaker and a holographic sensor to induce and measure vibrations [2]. The sensor (Fig. 1) uses a 532 nm light to illuminate the sample while it is still in its packaging. In DHV, a subwoofer placed above the sample outputs single tone frequencies and sweeps between 70 Hz and 500 Hz. We identified vibrational modes of the $0^{th}$ order and imaged the sample at 12 equidistant points within a single vibration curve by modifying the phase of camera strobing for image acquisition. This gave a full-field-of-view video with 12 frames that showed the nm-scale waveforms oscillating in the sample.

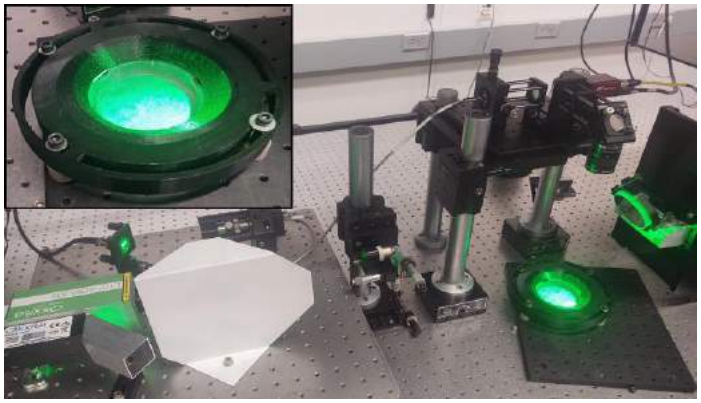

**Figure 1: DHV sensor with inset of tissue during measurement [3]**

Samples were also measured with nanoindentation at 4 multiple random points with a 51 μm-radii probe on a 3.45 N/m stiffness cantilever (Chiaro, Optics 11). During indentation, the sample was covered by a lid with a small opening to minimize evaporation. The epidermis was measured then peeled back with a scalpel and forceps, and the tissue's dermis was measured the same way. This was used to validate the modulus of the epidermal and dermal layers to compare to simulated results and to algorithm predictions.

To demonstrate the utility of the method, two experiments were performed. In the first experiment, a single sample was measured with nanoindentation then with DHV. Four different speaker volumes were measured at each mode, measuring different pressures applied by the acoustic waves to the sample, to test for linearity of the tissue response.

For the second experiment, the sample was subjected to controlled drying to change the thickness and/or stiffness of the sample and measure the resulting change in frequency of vibrational modes over time. Due to the destructive nature of the drying, two different samples from the same production batch were used for nanoindentation and

DHV. Each sample was dried for 90 minutes in a 23 °C oven (Isotemp, Fisher Scientific) for controlled humidity and temperature, and measured at several time points: 0, 3, 6, 10, 15, 30, 60 and 90 minutes. Each sample was put back into the oven with an open lid after measurement until the next time interval is reached.

To integrate future machine learning algorithms into the methodology, we developed a composite linear-elastic Finite Element (FE) model in Ansys APDL. The model includes three layers: the epidermis, dermis, and porous plastic membrane on which they sit. A modal analysis was performed in which the stiffness and thickness of the epidermal and dermal layers were modified across a range of expected values. This model output the frequencies of several modes for each combination of stiffness and thickness values.

## RESULTS

The maximum positive displacement measured at the first four vibration modes for four different acoustic forces applied by the speaker show roughly linear relationships (Fig. 2) indicating that the tissue is within the linear region at these low displacements. For these analyses, the largest displacement is taken from the point in the 12-image set of measurements that reflects the top of the sinusoidal curve.

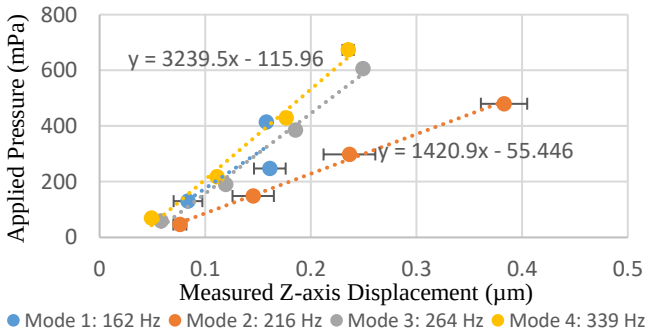


**Figure 2: Amplitude of tissue displacement for multiple applied pressures during vibration [3]**

In the second experiment, OCT measurements of thickness for both epidermal and dermal layers of the Apligraf tissue decreased with drying time (Fig. 3).

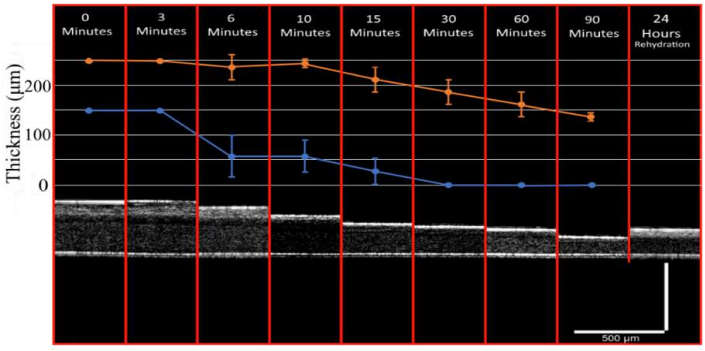


**Figure 3: OCT measurement of tissue thickness during drying [3]**

The frequencies at which each of the 1st four modes of vibration occur decrease monotonically with drying (Fig. 4). The modal FEA in which the layer thickness was decreased to match the measured data show the opposite trend in frequency of the fundamental mode (Fig. 5). This result indicates that it is more likely that the increase on modulus with drying dominates the vibratory behavior.

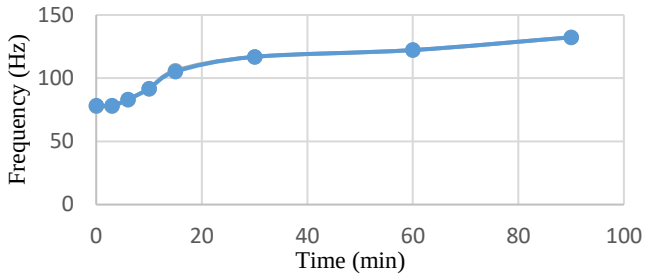


**Figure 4: Expected frequency of vibration from FEM [3]**

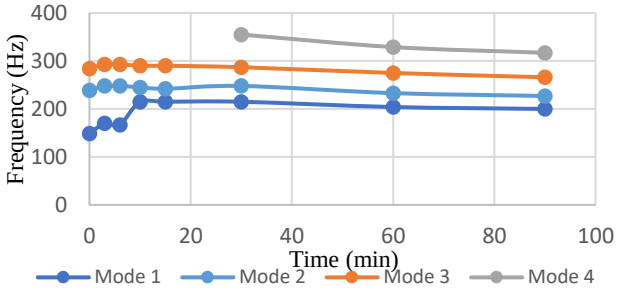


**Figure 5: Frequency location for each mode during drying [3]**

## DISCUSSION

This study demonstrates the ability to measure the full-field surface displacements of engineered skin tissue nondestructively and aseptically within its packaging using stroboscopic holographic vibrometry. By utilizing multiple acoustic pressures, the linearity of the tissue behavior was confirmed. Drying the tissue demonstrated the ability of the system to detect changes in the physical properties, and the FE analysis indicates that the changes in modal frequencies are due to stiffening of the tissue. However, due to the complexity of the layered system which includes the agar and stiff membrane on which the tissue is grown, it is not currently possible to extract the precise mechanical properties of the Apligraf layers from vibrometry alone. Further, the interferometric images output from the holographic system are very large and complex and can take multiple hours to analyze. Machine learning models are being constructed to relate finite element results to experimentally measured results and to more quickly analyze the full-field surface displacement data to predict the mechanical properties.

Once completed, this non-invasive measurement technique and associated analysis method would likely take around 5 minutes allowing for in-line measurement during production. This QC assay has the potential to enable identification of faulty batches before the full growth time is reached, increasing efficiency of manufacturing.

## ACKNOWLEDGEMENTS

This work was supported by the NSF (CMMI 1761432) and ARMI BiofabUSA (T0137). We would also like to thank Kate Faria and Organogenesis for providing the Apligraf tissue used in this research.

## REFERENCES

[1] Faria, K., *Personal Communications*, Organogenesis Inc., 2021
[2] Kuppers, J. et al., Proc. SPIE 6293, Interferometry XII: Applications, 629309, 2006
[3] Hiscox, C., MS Thesis, ME Department WPI, 2022

# QUANTIFYING TISSUE-SPECIFIC DIFFERENCES IN COMPRESSIVE MATERIAL BEHAVIOR OF PORCINE GASTROINTESTINAL TISSUE

**Samantha J. Barr (1), Alexander J. McGuigan (1), Caroline Karczewski (1), Alexander W. Caulk (1)**

(1) Surgical Innovations, Medtronic Inc., North Haven, Connecticut, United States

## INTRODUCTION

Surgical stapling is a common intervention used in gastro-intestinal (GI) applications to resect and repair damaged or diseased tissue. Despite significant technological advancements in surgical stapling, rates of adverse postoperative outcomes such as anastomotic leak remain high in some applications [1]. Clinicians and medical device manufacturers alike remain interested in design improvements to surgical staplers which may aid in improving postoperative outcomes. One key design parameter of interest is identification of the optimal compression profile of tissue which is highly dependent on tissue geometry and material properties. Currently, staplers compress tissue to a predetermined thickness, and manufacturers offer a variety of stapling products with differing final compression thicknesses to provide surgeons the opportunity to account for different tissue characteristics during stapling procedures. However, the opportunity remains to further improve device performance through design enhancements which better account for patient- and tissue-specific differences in compressive material properties of tissue.

*Ex vivo* mechanical characterization of GI tissues has been performed extensively in tension. While compressive properties of some GI tissues have been reported in minimal contexts [2], there remains a pressing need to perform material testing of GI tissues which adequately supports constitutive modeling and material parameter estimation in applications which recapitulate the large compressive strains commonly imposed during surgical stapling.

In the present study, porcine GI tissues were subjected to uniaxial compressive testing to evaluate loading and stress relaxation behavior. We focused on GI tissues which are commonly subjected to procedures involving surgical stapling: colon, small bowel, and stomach.

## METHODS

*Tissue harvest and preparation.* Fresh porcine colon, small bowel, and stomach were obtained from Animal Technologies (Tyler, TX). All tissues were tested within 72 hours of harvesting. Samples were cut into 1 $cm^2$ pieces and secured to a standard material testing device (Electropuls Model E3000, Instron, Norwood, MA, USA) using sandpaper (220 grit) and tissue glue to minimize slipping during testing. Reference thickness was determined by applying a load of 0.01 lbs. to the tissue. After reference thickness was determined, the entire fixture was submerged in a 37°C saline bath.

*Mechanical testing.* For all tissues, each sample was preconditioned for 3 loading and unloading cycles to the target strain. Target strains were chosen for each tissue type to reach sufficiently high stress without inducing structural damage as defined by a decrease in the stress-strain curve. Colon was compressed to 75%, small bowel to 71%, and all stomach samples to 45% strain. The protocol for small bowel included remeasurement of reference thickness after preconditioning, which was not performed for other tissues. Target strain was calculated based on the remeasured thickness, but to facilitate comparison with other tissues, strain was recalculated based on the original thickness, which introduced variation in the target strain ($\epsilon = 0.71 \pm 0.025$). Stomach tissue was further divided into anatomical region (i.e., fundus, body, antrum) based on preliminary testing and literature reports of significant material heterogeneity across regions; however, an applied strain of 45% was implemented across all regions to facilitate data comparison. Preliminary testing suggested minimal regional differences within colon and small bowel.

All testing was performed at 0.5%/sec. In the fourth cycle, the sample was compressed to the tissue-specific target strain and held for 600 seconds before unloading to quantify the relaxation response of the tissue.

*Data analysis.* Stress and strain were calculated according to Equations 1 and 2,

$$\sigma = \frac{F}{A} \tag{1}$$

SB³C2022-434

$$\epsilon = 1 - \frac{h}{H} \quad (2)$$

where $\sigma$ is the 1st Piola Kirchoff stress, $F$ is the applied load, $A$ is the reference cross-sectional area, $\epsilon$ is the strain (noting a positive sign convention for compression to aid in visual interpretation), $h$ is the current or deformed thickness, and $H$ is the reference thickness.

Stresses during loading were compared at a common strain value of 0.45 ($\sigma_{\epsilon=0.45}$) to aid in interpretation of differences in stiffness. To quantify the stress relaxation response, stress during the 600 second relaxation period of cycle 4 was normalized to the peak stress, i.e., the stress developed in the tissue at the maximum applied strain, and normalized values were compared at the 600 second time point.

*Statistics.* A one-way ANOVA with a Tukey's post hoc significance test was performed across groups for all metrics to determine statistical significance, defined as $p < 0.05$. All data are presented as mean ± SEM.

## RESULTS

Material metrics for all tissues are reported in Table 1. Small bowel was significantly thinner than colon (0.071 ± 0.004 in. vs. 0.116 ± 0.014 in., respectively, $p < 0.05$), but both tissues exhibited similar material behavior in compression at a strain of 0.45 (Table 1).

**Table 1.** Material metrics derived from mechanical tests for porcine GI tissue. Data are presented as mean ± SEM.

| | Small bowel (n = 6) | Colon (n = 5) | Stomach | | |
|---|---|---|---|---|---|
| | | | Fundus (n = 3) | Body (n = 3) | Antrum (n = 2) |
| $h$ (in) | 0.071 ± 0.004 | 0.116 ± 0.014 | 0.139 ± 0.008* | 0.166 ± 0.016* | 0.134 ± 0.009* |
| $\sigma_{\epsilon=0.45}$ (psi) | 6.2 ± 2.2 | 1.9 ± 1.0 | 55 ± 5.6 | 83 ± 17 | 88 ± 34 |
| $\sigma_{relax\|600s}$ (%) | 26 ± 2.1 | 9.2 ± 4.0 | 6.6 ± 2.2 | 10 ± 4.1 | 5.3 ± 0.2 |

Notably, the small bowel exhibited qualitatively stiffer behavior overall, which was not evident at strain of 0.45 but was apparent at strains nearing 0.60 (Figure 1). All regions of the stomach were thicker than small bowel ($p < 0.01$), but only the body region was statistically thicker than colon ($p < 0.05$). All regions of the stomach were stiffer than colon and small bowel, defined as higher stresses at a common strain of 0.45 ($p < 0.05$). Regional differences within the stomach were observed, with the fundus being more compliant, but these differences were not statistically significant, possibly due to low sample sizes.

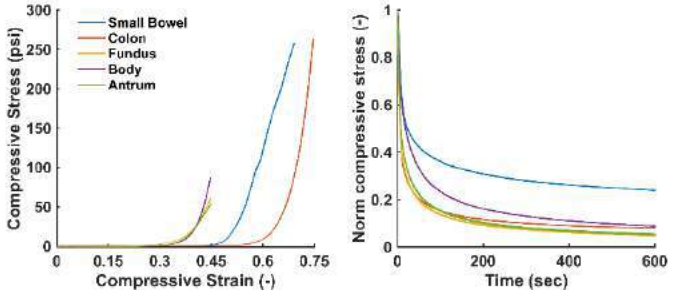


**Figure 1:** (Left) Representative curves of compressive loading to target strain for each tissue type. (Right) Representative curves of normalized stress relaxation for each tissue type at target strain.

All tissues exhibited a remarkable degree of relaxation despite a low strain rate of 0.5%/sec. Stress relaxation profiles were similar across all groups except small bowel, which exhibited less relaxation than colon and fundus ($p < 0.001$). As stress relaxation was observed following compression to different strains, it is difficult to assert whether differences in small bowel are due to inherent tissue-specific differences or differences in testing protocol. The body exhibited less relaxation than other regions, but this was not statistically significant, possibly due to low sample sizes. Further stress relaxation testing should be performed for all tissues at equivalent target strains to facilitate further comparison.

## DISCUSSION

Quantifying tissue-specific material properties in compression is of critical importance in surgical stapling. Though various models of surgical staplers are designed for different tissue thicknesses to prevent ischemia and tissue damage, these models do not inherently account for differences in tissue material properties between tissue types or patient characteristics (e.g., sex, age, disease state). Thus, beginning to understand and characterize compressive tissue mechanics for each tissue type can inform future design parameters in surgical stapling in pursuit of improving patient outcomes through patient-specific treatment of tissue.

An optimal compression profile may be defined not only by intraoperative metrics such as minimization of structural damage, but also postoperative metrics such as reduction of maladaptive tissue remodeling. Previous studies have demonstrated increasing inflammation and apoptosis in GI tissue with increasing applied load [3], suggesting a link between mechanics and postoperative tissue remodeling. Proper understanding of tissue-specific material properties in compression may better inform critical thresholds of applied loads which can prevent undesired mechanobiological responses and thus adverse tissue remodeling.

These data were obtained in unconfined uniaxial compression, but applied loads in surgical stapling are significantly more complex. Future studies may include combinatorial loading in compression and shear [4], which can better inform clinically relevant loading scenarios. Such data may also inform constitutive modeling for studies implementing finite element analyses for more detailed analyses of spatial differences in loads which develop during surgical stapling. The data presented herein provide the foundation necessary for beginning to develop a robust understanding of tissue-specific differences in material properties under clinically relevant scenarios for surgical stapling. Further testing is necessary to increase sample sizes, adapt protocols to facilitate comparisons in stress relaxation data, and expand to additional tissue types (e.g., esophagus, liver, pancreas).

In conclusion, these results demonstrate clear differences in viscoelastic compressive properties of different organs of the GI system. These results can inform necessary design parameters in surgical stapling to improve intraoperative performance of staplers and postoperative clinical outcomes.

## ACKNOWLEDGEMENTS

This work was internally funded by the Surgical Innovations unit of Medtronic plc.

## REFERENCES

[1] McDermott F.D. et al., *BJS*, 102 :462-479, 2015.
[2] Rosen J. et al., *J Biomech Eng*, 130(2):021020, 2008.
[3] De S. et al., *Int J Rob Res*, 26(11-12):1159-1171, 2007.
[4] Budday S. et al., *Acta Biomater*, 48:319-340, 2017.

# TEXAS TRIVALVE 1.0 : A REVERSE-ENGINEERED, OPEN MODEL OF THE HUMAN TRICUSPID VALVE

**Mrudang Mathur (1), William D. Meador (2), Marcin Malinowski (3,4), Tomasz Jazwiec (3,5), Tomasz A. Timek (3), Manuel K. Rausch (2,6,7)**

(1) Department of Mechanical Engineering, UT-Austin, Austin, TX, USA
(2) Department of Biomedical Engineering, UT-Austin, Austin, TX, USA
(3) Cardiothoracic Surgery, Spectrum Health, Grand Rapids, MI, USA
(4) Department of Cardiac Surgery, Medical University of Silesia School of Medicine, Katowice, Poland
(5) Department of Cardiac Surgery, Silesian Centre for Heart Diseases, Zabrze, Poland
(6) Department of Aerospace Engineering and Engineering Mechanics, UT-Austin, Austin, TX, USA
(7) Oden Institute for Computational Engineering and Sciences, UT-Austin, Austin, TX, USA

## INTRODUCTION

The tricuspid valve ensures the unidirectional flow of blood between the right atrium and the right ventricle of the heart. However, nearly 1.6 million Americans suffer from clinically significant leakage, or regurgitation, in the valve. In most patients, the origin of regurgitation is extrinsic to the valve itself and occurs as a result of right ventricular (RV) remodeling. RV remodeling displaces the papillary muscles and dilates the tricuspid annulus thereby distorting the shape and disrupting the dynamics of the normal valve. Notably, current repair strategies for regurgitant tricuspid valves have a significant rate of failure. As such, almost 10-30% of patients redevelop leakage within a few years [1].

We submit that an incomplete understanding of tricuspid valve mechanics is, in part, responsible for this shortcoming in treatment. Highly-detailed computer models of the tricuspid valve may be critical tools to better understand the valve. Specifically, they may be used to uncover the etiology of the valve's morphology and structure. Furthermore, they may be used to optimize medical devices and surgical procedures. Existing models of the valve are often based on idealized or population-averaged geometries. Furthermore, they often employ material and structural properties from other subjects or species. Additionally, existing models of the human tricuspid valve have not been made publicly available as a research tool.

In this study, we seek to overcome these shortcomings of existing models. Namely, our goal is to build an openly-available, high-fidelity, subject-specific model of the human tricuspid valve.

## METHODS

Towards building a highly detailed subject-specific model of the human tricuspid valve we developed an extensive pipeline to combine ex vivo and in vivo measurements from a healthy, beating human heart, see **Figure 1**. Briefly, we reperfused and electrically paced a donor heart in an organ preservation system (TransMedics, Andover, MA). This heart was rejected for clinical transplantation but deemed otherwise structurally sound. In the beating heart, we recorded tricuspid annular dynamics via sonomicrometry crystals (Sonometrics Inc., London, Ontario) over multiple cardiac cycles. Additionally, we measured right atrial and ventricular pressures via miniaturized pressure sensors. Moreover, we recorded epicardial echo images of the tricuspid valve in the beating heart.

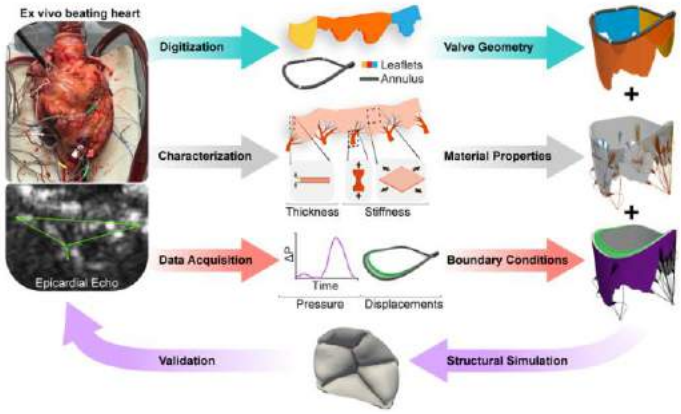


**Figure 1: The reverse-engineering pipeline. We combine measurements from an ex vivo beating human heart with in vitro material characterization to build a highly-detailed, subject-specific finite element model of the human tricuspid valve. We then simulate valve closure with boundary conditions derived from ex vivo data. Finally, we validate our predictions against echo images of the tricuspid valve in the same beating heart.**

Upon conclusion of the ex vivo experiments, we arrested the heart and explanted the tricuspid valve apparatus. Next, we made an incision

in the valve annulus at the postero-setpal commissure and laid the valve on a calibrated grid. We then took detailed photographs of the atrial and ventricular surfaces of the valve. Subsequently, we biaxially tested the valve leaflets and uniaxially tested the chordae. We modelled the constitutive behaviour of the leaflets via a hyperelastic material model as suggested by Kamensky et al [2]. Similarly, we model the hyperelastic response of the chordae using the Ogden model.

To recreate the model geometry, we first fit a 3D cubic spline to the annulus sonomicrometry data. Next, we used a custom MATLAB code (MathWorks, Natick, MA) to digitize leaflet geometry from photographs taken previously. We then non-rigidly transform the leaflet geometry onto the reconstructed 3D annulus to rebuild the valve in a stress-free state. To assemble the sub-valvular apparatus, we inform chordal insertion sites through in vitro images and existing literature [3]. Furthermore, we fix papillary muscle positions from sonomicrometry data. Additionally, we iteratively adjust chordae lengths to achieve leaflet coaptation similar to Kong et al [4].

We subsequently discretized the valve leaflets and chordae tendineae with C3D8R hexahedral elements and T3D2 linear elements, respectively. We then imported the models into Abaqus/Explicit (Dassault Systemes, Velizy-Villacoublay, France) where we assigned subject-specific material properties to all three leaflets and their chordae tendineae based on in vitro measurements. Furthermore, we assigned transvalvular pressure gradients and annular displacements, measured ex vivo, as Neumann and Dirichlet boundary conditions to our model, respectively. Note, we modeled contact between the valve leaflets using the kinematic predictor-corrector algorithm in Abaqus.

To showcase the predictive capabilities of our model, we use it to examine disease- and repair-induced changes to valve mechanics. To this end, we first create a regurgitant tricuspid valve by non-uniformly dilating the valve annulus, tethering the chordae tendineae, and applying pathological pressures to the ventricular surface of the leaflets. We then virtually repair the valve using two different techniques: ring-annuloplasty and clip-based repair.

## RESULTS

To validate our model, we quasi-statically loaded the valve to the end-systolic state. Our model faithfully captures the deformation of the leaflets when compared to echocardiographic images of the tricuspid valve in the beating heart, see **Figure 2**.

We then demonstrate the utility of our model through two virtual case studies. We observe that disease induces greater stresses the valve

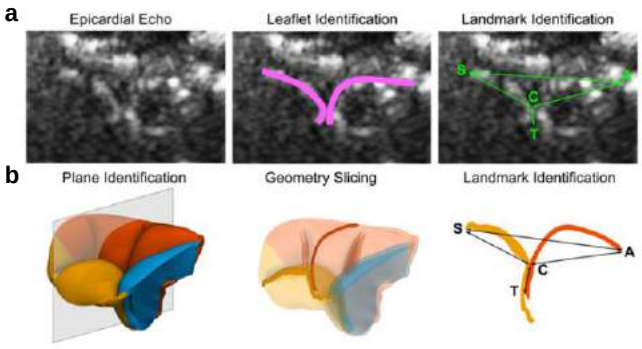


**Figure 2: Model validation against beating heart echocardiography. (a) We measure distances between anatomic landmarks: the anterior (A) and septal (S) leaflet hinge points, coaptation point (C), and coaptation length (T). (b) We then identify the corresponding plane in the valve model and compare distances between those same landmarks.**

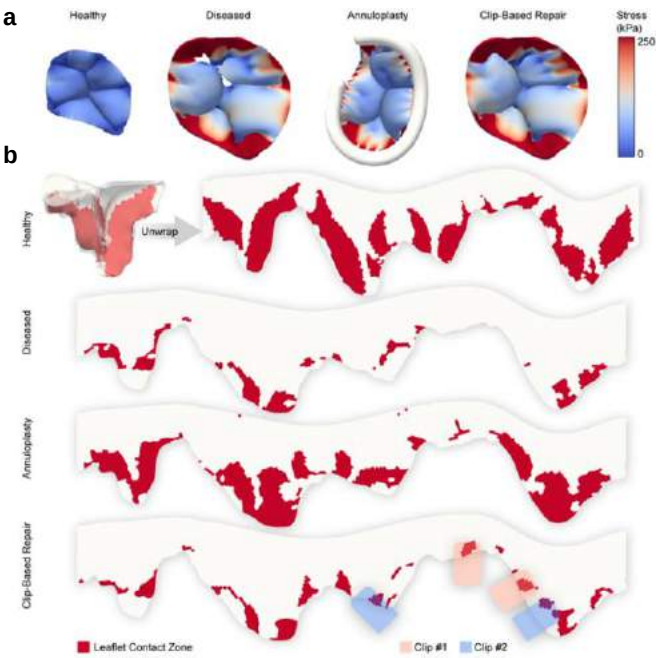


**Figure 3: Outcomes of simulated valve repair strategies. (a) Neither annuloplasty nor clip-based repair can completely resolve stress increases induced by disease. (b) Leaflet contact areas (in red) projected onto a 2D representation of the valves at end-diastole show the loss in coaptation area under disease. While annuloplasty restores this, clip-based repair is unable to.**

leaflets in comparison to the healthy valve (**Figure 3a**). While ring-annuloplasty and clip-based repair reduce these stresses, they are unable to restore the valve to its original stress state. Additionally, we observe a sizeable loss of leaflet contact area in the diseased valve leading to leakage (**Figure 3b**). Ring-annuloplasty restores this lost contact area to a large extent. In contrast, clip-based repair provides only modest gains in contact area.

## DISCUSSION

In our current work, we present a validated, openly-available, high-fidelity model of the human tricuspid valve informed by subject-specific geometries, material properties, and boundary conditions. Furthermore, we showcase the utility of our model through two virtual case studies. Models such as ours may be crucial in future efforts to optimize medical devices and improve patient outcomes.

## DATA AVAILABILITY

The Abaqus input files for all models are available at https://github.com/SoftTissueBiomechanicsLab/Texas_TriValve.git

## ACKNOWLEDGEMENTS

We appreciate support from the AHA via awards 18CDA34120028 and 902502, and from the NIH via awards 1R21HL181632-01 and F31HL145976. We would also like to thank the Living Heart Team at Abaqus for their courtesy software license.

## REFERENCES

[1] Wang, H et al., *J Thorac Dis*, 8(11):3087–3095, 2016
[2] Kamensky, D et al, *CMAME*, 330: 522–546., 2018
[3] Silver, MD et al, *Circulation*, 43(3):333-48, 1971
[4] Kong, F et al., *Ann Biomed Eng*, 46(8):1112-1127, 2018

# CREATING A PLATFORM TO STUDY HEADBANGING PATTERNS IN A VIRTUAL HEAVY METAL CONCERT ENVIRONMENT

**A. Pionteck (1), D. Stein (2), J. Abderezaei (1), L. Wu (3), M. Kurt (1)**

(1) Department of Mechanical Engineering, University of Washington, Seattle, WA, USA
(2) Department of Mechanical Engineering, Stevens Institute of Technology, Hoboken, NJ, USA
(3) Department of Mechanical Engineering, University of British Columbia, Vancouver, BC, Canada

## INTRODUCTION

The headbanging first started in 1968 when Led Zeppelin played a set at the Boston Tea Party on their first US tour [1,2]. Currently, headbanging is mostly referred to the rhythmic shaking of the head synchronous with the music, most commonly heavy metal and rock music [3]. It comes with many different styles such as the up-down, the circular swing, the full body, and the side-to-side motion [4]. Even though headbanging in its current form has been around for a few decades, there is still no consensus whether this level of head shaking could carry any minor brain injury implications. Despite being considered by some as a routine and daily activity, the biomechanical and neurological consequences of headbanging is largely unknown, mainly due to a lack of data in this field.

Even though, several health issues including traumatic aneurysm of cervical vertebral artery or subdural hematoma [3, 5, 6] have been reported to be possibly related to headbanging, little research has been conducted on this phenomenon so far. Previous works have analyzed the kinematics of voluntary head motion by instrumenting subjects with sensor-laden mouthguards and measuring six-degree-of-freedom head accelerations for rapid voluntary head rotations [7]. Baseline and post-experiment neurological tests revealed no significant deficits, and the authors suggested that high velocity, low-acceleration rotational inputs are unlikely to cause concussion in the subjects [7]. In another study, the effects of vigorous voluntary head shaking was analyzed on the head and neck motion [8]. Subjects were asked to vigorously shake their heads 5–10 times in a completely unconstrained manner, while recording the kinematics and kinetics of their head and neck [8]. The subjects shook their heads at self-selected tempos ranging from 1.9–4.7 Hz over a 20–91º range of motion, which resulted in low peak head accelerations of 4.3 ± 1.1 g and 250 ± 103 rad/s2 for men, 3.0 ± 0.9 g and 182 ± 58 rad/s2 for women [8]. Even though, these new studies have analyzed the voluntary head motion and the vigorous head shaking [7,8], not many studies have analyzed the kinematics of the head during headbanging in a concert event. In this work, we created a platform to study headbanging patterns in a concert environment and tested it during a simulated heavy metal/hard rock virtual concert. In short, this platform was designed to study the effect of 1) the song's tempo, 2) participant's familiarity with the song, and 3) the type of headbanging with associated head kinematics.

## METHODS

The aim of this study was to create a protocol to record and compare the different head kinematics involved in different headbanging patterns during a concert. The study was deceptive, as participants were not aware of the true objectives of the experiment prior to participation, i.e., the study of headbanging. The protocol was validated by an IRB board.

First, volunteers were selected based on their response to a prescreening form based on their heavy metal/hard rock music listening and concert habits, and to ensure that they have no history of neurological or neck injuries or allergies. Participants were encouraged to participate with friends to create an atmosphere conducive to dance and headbanging demonstrations. However, sessions were limited to 3 people to meet social distancing requirements due to the COVID-19 pandemic.

During the concert, volunteers wore instrumented mouthguards which needed to be custom fit for each subject. Instrumented mouthguard devices are made of a soft plastic material and fit onto the upper teeth of participants [10], who were invited in the days preceding the experiment to obtain their dental impressions. The custom fit provided a conforming, rigid coupling to the participant's skull through the maxillary (upper) dentition. Mouthguards were instrumented to record 6 degrees-of-freedom (DOF) translational and rotational head kinematics. Each mouthguard sensor board were equipped with a tri-axial accelerometer (ST H3LIS331), a tri-axial gyroscope (Invensense ITG-3500A) measuring rotational velocity in

the coronal, sagittal, and horizontal planes, and a digital proximity sensing module for near-field proximity sensing (AMS TMD2771).

Simulated concert sessions of 60 minutes were organized during which head kinematics were tracked with the mouthguard. A series of concert footage were collected and merged to simulate a live concert session and to cover a range of 90 to 180 BPM. Sessions were video recorded to classify the different headbanging patterns into the categories defined below. The real conditions of a concert were simulated as best as possible, including lighting and sound system, and the concert footage were projected on a giant screen.

Instructions were given to the participants to replicate their usual behavior when attending hard rock/heavy metal concerts. No mention was made of headbanging to avoid encouraging this behavior and introducing bias into the study. Mouthguard acquisition and camera recording were synchronized by performing a series of flicks on the mouthguard in front of the cameras.

Before starting the session and after the end of the concert, the participants were asked to perform neurocognitive testing. The Sports Concussion Assessment Tool-5 (SCAT5) was used to determine if the headbanging induced temporary neurocognitive changes. After the session, participants received a debriefing document revealing the true purpose of the experiment, the study of headbanging, and asking for their consent to participate in the study with knowledge of these new conditions. Participants also completed a postscreening form to assess their familiarity with the various music tracks to verify if the occurrences and intensity of headbanging were higher when subjects were familiar with the songs played, as reported in [11].

The video recordings were detailed to classify the different types of head motion. The different types of headbanging were classified as:

1. up and down: it is the most common style, and consists in shaking the head up and down in the sagittal plane
2. circular swing: swinging the head in a circular motion, approximately in the coronal plane
3. full body: swinging backwards and forwards from the waist, in sagittal plane
4. side-to-side: shaking the head from side to side, rotating around the longitudinal axis
5. random style: head moving in random directions

## RESULTS

10 participants were selected based on their response to the prescreening form. All participants were successfully fitted with instrumented mouthguards and no issues were encountered during the recording of the sessions. Preliminary results showed a great heterogeneity of behavior and dancing intensity among the volunteers, but only one of them did not show any motion that could be considered as headbanging. All types of headbanging were successfully identified, but a majority of up and down shaking was observed. Preliminary results of one volunteer were analyzed in detail and showed high velocity and acceleration values, with peaks reaching 5 rad/s for rotational velocity in the sagittal plane and linear acceleration of 8g along the superior-inferior axis (Figure 1). This volunteer also demonstrated synchronization with the music, with his headbanging patterns adopting the tempo of the song being played. In addition, the amplitude of the movement was greater when the volunteer indicated the track as being known and/or appreciated.

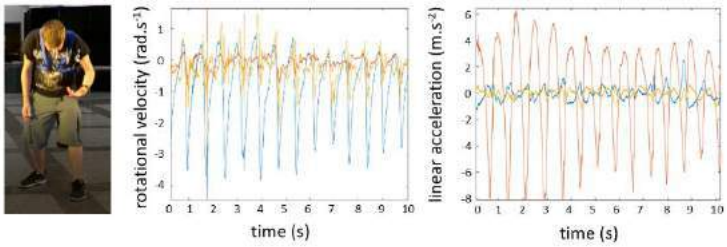


**Figure 1: Portion of the head kinematics data corresponding to an up and down movement, video recording (a), rotational velocity (b) and linear acceleration (c). The blue line corresponds to the rotation around the left-right axis for rotational velocity, or to the acceleration along the same axis for the linear acceleration. The yellow line corresponds to the antero-posterior axis, and the red line to the superior-inferior axis.**

## DISCUSSION

The developed platform was successfully tested during simulated concerts and allowed us to acquire the head kinematics of 10 volunteers, as well as the data necessary for the study of the effects of familiarity with the sound and tempo. Detailed analysis of the results for one volunteer showed that acceleration and velocity values were below the brain injury thresholds. The results of the corresponding SCAT5 test did not show any degradation after the session. However, these first results have already revealed the effects of tempo and familiarity with the sound on the intensity of headbanging. Since this preliminary study showed promising results with the developed testing platform, in the future, we can consider the implementation of this testing protocol on a larger scale, in the context of a real concert for example.

## REFERENCES

[1] Lewis D, Pallett S. Led Zeppelin: the concert file. London: Omnibus Press, 1997.

[2] Spheeris P.Wayne's World. United States, Paramount Pictures, 1992.

[3] Neyaz Z, et al. 'Head banging' during rock show causing subdural hematoma. Neurology India 2006;54:319-20.

[4] Patton, D. et al. (2008). Head and neck injury risks in heavy metal: Head bangers stuck between rock and a hard bass. Bmj, 337.

[5] Basham D. Bassist Jason Newsted leaves Metallica. 2001, www.mtv.com/news/articles/1438016/20010117/metallica.jhtml

[6] Egnor MR, et al. Vertebral artery aneurysm: a unique hazard of head banging by heavymetal rockers. J PediatricNeurosurgery 1991;17:135-8

[7] Hernandez, F. et al. (2019). Voluntary head rotational velocity and implications for brain injury risk metrics. Journal of neurotrauma, 36(7), 1125-1135.

[8] Funk, J. R. et al. (2015). Kinematics and kinetics of vigorous head shaking. Journal of applied biomechanics, 31(3), 170-175.

[9] Kivlin, J. D. et al. (2000). Shaken baby syndrome. Ophthalmology, 107(7), 1246-1254.

[10] D. Nasti et al. "Characterizing the Dynamics of Soccer Heading Scenarios with a Custom Instrumented Mouthguard", BMES, OCT 14-17th 2020, Virtual

[11] Swarbrick, D. et al. (2019). How live music moves us: head movement differences in audiences to live versus recorded music. Frontiers in psychology, 9, 2682.

SB³C2022
Summer Biomechanics, Bioengineering and Biotransport Conference
June 20-23, Eastern Shore, MD, USA

# AUTOMATED VASCULAR DESIGN AND SIMULATION FOR 3D BIOPRINTING

**Zachary Sexton (1), Jessica Herrmann (2), Andrew Hudson (3), Jonathan Pham (4), Mark Skylar-Scott (1,5), Adam Feinberg (3), Sean M. Wu (5,6), Alison L. Marsden (1,6)**

(1) Department of Bioengineering, Stanford University, Stanford CA, USA
(2) School of Medicine, Stanford University, Stanford CA, USA
(3) Department of Biomedical Engineering, Carnegie Mellon University, Pittsburgh PA, USA
(4) Department of Mechanical Engineering, Stanford University, Stanford CA, USA
(5) Cardiovascular Institute, School of Medicine, Stanford University, Stanford CA, USA
(6) Department of Pediatrics, Division of Cardiovascular Medicine, Stanford University, Stanford CA, USA

## INTRODUCTION

Incorporating perfusable vascular networks within engineered tissues and organs remains a grand challenge and precludes advancement towards artificial tissues at clinically relevant scales. Recent techniques in 3D biofabrication demonstrate the ability to manipulate living matter at resolutions and speeds necessary for viable tissues. However, there are currently no comprehensive algorithms to generate, model, and simulate biomimetic vascular networks for tissues of varying shape, vascular complexity, and perfusion conditions. Without a unified approach, efforts to vascularize tissues rely on simplified perfusion networks which poorly recapitulate pressure and flow distributions of native vasculature. To address these limitations, we present a unified framework through the open-source software package, SimVascular (simvascular.org), and validate predicted flow behavior in 3D printed bioreactors[1].

## METHODS

Our framework extends previous methods in constrained constructive optimization (CCO) by partially binding local optimization routines and triaging vessel collision repair to ensure efficient, accurate vascular generation for multiple vascular trees Fig1. Further, new methods for implicit volume reconstruction are presented to efficiently vascularize nonconvex tissue and organ shapes with and without cavities using a based on the Duchon's function (1) and variational point set surfaces[2]. We implement this reconstruction procedure as a partition of unity to avoid memory and complexity reported in literature for global approaches[3]. Resulting vascular networks

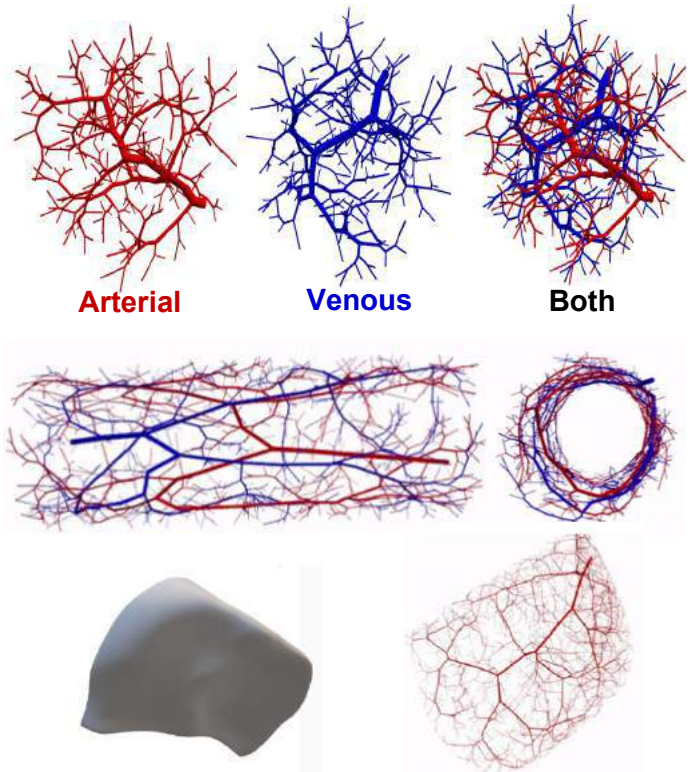


**Figure 1: Arterial (top left), venous (top middle), and arterial-venous circuit (top right) are CCO constructed collision-free for a cube volume. Arterial-venous network approximating the vasa vasorum (middle). Liver hepatovenous segment IV requiring perfusion (bottom left) and arterial network (bottom right)**

are exported for SWIFT and FRESH 3D bioprinting as well as multiscale (0D, 1D, 3D) hemodynamic simulations[4,5].

**Duchon Interpolant**

$$f(\boldsymbol{x}) = \sum_{i}^{N} a_i \phi_1(||\boldsymbol{x} - \boldsymbol{x_i}||) + \sum_{i}^{N} \boldsymbol{b_i^T} \frac{\partial}{\partial \boldsymbol{x_i}} \phi_1(||\boldsymbol{x} - \boldsymbol{x_i}||) + \boldsymbol{c^T x} + d$$

**Subject to**: $\sum_i a_i = 0, \sum_i a_i \boldsymbol{x_i} + \sum_i \boldsymbol{b_i} = 0$ (1)

Networks are constrained to meet desired bioreactor perfusion specifications (i.e. time-average wall shear stress, inlet/outlet diameters) and printing limitations (>100μm vessel spacing) for each technique. Geometric integrity of printed networks is assessed through optical coherence tomography and epifluorescence imaging which obtain 3D reconstructions. Flow splits, pressure distribution, and wall shear stress characteristics are simulated before and after printing using model and reconstructed geometries to determine flow deviations between ideal and printed networks. Experimentally, flow splits and diffusion are measured via fluorescence particle tracking and 10-70kDa dextran perfusion assuming a Darcy law relation. In addition to soft (hydrogel) type material, models are 3D printed using stereolithography a rigid, plastic resin to ensure wall assumptions are satisfied for the underlying assumptions of homogeneous, incompressible, fully-developed, steady, laminar, axisymmetric blood flow in rigid-walled cylinders. These assumptions are necessary for CCO methods but not necessarily subsequent CDF simulations which may better match physical systems given known material behaviors.

## RESULTS

Computational complexity of collision detection verifies that simple sphere proximity checks can decrease the average number of oriented bounding box (OBB) evaluations to 1 or 2

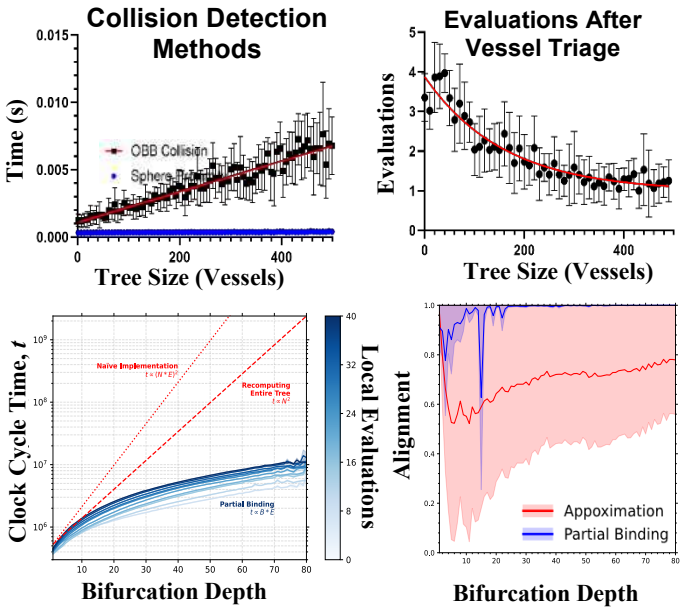


**Figure 2: Comparison of collision detection methods (top right) and performance from triaging detection with sphere proximity. Computational complexity (CPU clock cycles) for local bifurcation optimization (bottom left) alignment performance against finite difference ("ground truth") compared to previous literature[6].**

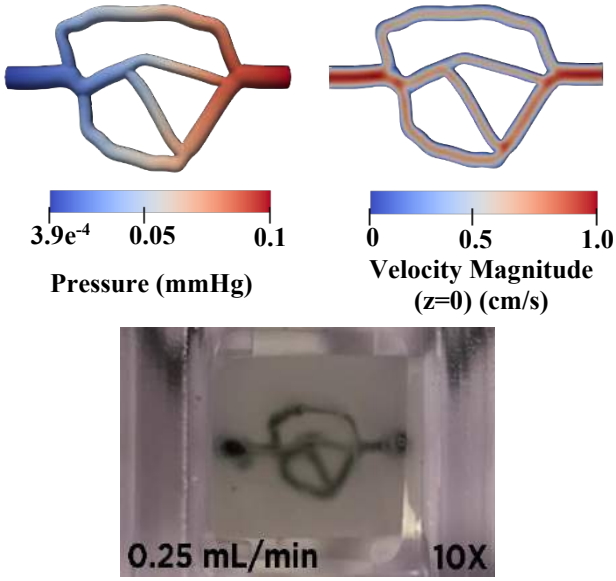


**Figure 3: Pressure (top left) and velocity magnitudes (top right) obtained during hemodynamic analysis and 3D FRESH bioprint in collagen (bottom) generated from the same 3D model file. Generic dye shown flowing through patent vessels.**

per vessel addition as trees extend into hundreds of vessels. Partial binding similarly accelerates CCO vascularization while increasing accuracy of bifurcation placement Fig2 with logarithmic scaling of bifurcation depth over more expensive implementations scaling on number of vessels[6]. Steady-state hemodynamic simulations show uniform pressure distribution through vascular circuits with qualitatively uniform flow splits which are also observed in 3D bioprints Fig3 which serve as an initial validation of this fully automated pipeline in rational vascular design, simulation, and fabrication.

## DISCUSSION

Our unified framework enables effective, efficient vascularization of engineered tissues and simulation of flow behavior within 3D bioprinted networks. Preliminary experimental bioprinting results provide initial validation of this framework for rapid vascular design from first principals of mammalian vasculature. Further work is needed to account for variability of bioinks when approximating wall deformability and permeability for nutrient considerations of metabolically active engineered tissues approaching significant functional densities.


## ACKNOWLEDGEMENTS

This work was supported by the National Science Foundation Graduate Research Fellowship Program, Additional Ventures Cures Collaborative, and Stanford EDGE Program.


## REFERENCES


[1] Updegrove et al. *Ann Biomed Eng.* 45(3):525-541. 2017
[2] Duchon. Constructive Theory of Functions of Several Variables. Lecture Notes in Mathematics, vol 571. 1977.
[3] Huang et al. *ACM Trans. Graph.* 38(4):1-13 2019.
[4] Hinton et al. *Sci. Adv.* 1(9) 2015.
[5] Skylar-Scott et al. *Sci. Adv.* 5(9). 2019.
[6] Guy et al. *IEEE Trans Biomed Eng.* 67(6):1650-1663. 2019

SB³C2022
Summer Biomechanics, Bioengineering and Biotransport Conference
June 20-23, Eastern Shore, MD, USA

# HIGH-FAT DIET CONCURRENTLY ALTERS BONE MICROSTRUCTURE AND NANOSTRUCTURE

**Yoshihiro Obata (1), Neha S. Dole (2), Claire Acevedo (1,3), Tamara Alliston (2)**

(1) Department of Mechanical Engineering, University of Utah, Salt Lake City, UT, USA
(2) Department of Orthopaedic Surgery, University of California, San Francisco, San Francisco, CA, USA
(3) Department of Biomedical Engineering, University of Utah, Salt Lake City, UT, USA

## INTRODUCTION

Bone quantity (bone mass) is the clinical indicator for risk of fracture; however, this metric explains less than half of bone fragility fractures. In diseases such as type 2 diabetes mellitus (T2DM), bone mass can be normal, if not slightly elevated, while risk of fracture is higher compared to the risk of the healthy population. This elevated risk of fracture points to the role of bone quality in addition to bone quantity when determining fracture risk.

Bone quality, an admittedly broad term, describes many aspects of bone health outside of bone quantity that contribute to the unique mechanical properties of bone. Common aspects of bone quality include bone's matrix and collagen properties as well as its multiscale hierarchical structure. At the microstructural scale, canals are vascular porosities responsible for transporting nutrients throughout the bone. Osteocytes, the most abundant cell in bone, are intricately connected to canals and each other via a dense, nanoscale network of dendritic processes called canaliculi. This network of osteocytes and canaliculi is known as the lacunocanalicular network (LCN).

One process by which bone quality is maintained is known as perilacunar/canalicular remodeling (PLR). This process involves osteocyte cells resorbing and replacing bone matrix directly surrounding the LCN. PLR is not only a response to metabolic stress and disease, but also a hallmark of healthy bone homeostasis. The effects of PLR are seen in the bone matrix and osteocyte lacunae, which are voids in the bone matrix that osteocyte cells reside within.

PLR performed by osteocytes is signaled by transforming growth factor beta (TGF-β). Ablation of TGF-β signaling in osteocyte cells is known to induce bone fragility while maintaining bone mass [1]. Furthermore, circulating TGF-β is significantly elevated in obese and high-fat diet (HFD) induced obese mice or humans and is associated with insulin resistance [2]. While recent work has elucidated the role of TGF-β in signaling osteocytes to orchestrate PLR, a critical gap in knowledge remains in determining whether T2DM and obesity impact osteocyte-intrinsic TGF-β signaling in bone.

To address whether T2DM and obesity impact TGF-β signaling in osteocytes to reduce bone's mechanical properties, we tested the hypothesis that HFD-fed mice possess exacerbated osteocytic-TGF-β signaling. We also hypothesize that with an osteocyte-intrinsic inhibition of TGF-β receptor type II, this exacerbated TGF-β signaling can be downregulated in the HFD mice.

## METHODS

**Study Design and Mouse Model.** This work was performed in collaboration with the Alliston Lab at the University of California, San Francisco. To determine whether HFD-induced obesity adversely affects bone quality and to determine whether inhibiting TGF-β signaling will impact bone quality, two genotypes of mice are considered: a control, wild-type (WT) mouse model and a TGF-β receptor type II gene knockout ($T\beta RII^{ocy-/-}$) mouse model. To begin, WT and $T\beta RII^{ocy-/-}$ mice are raised to an age of 12 weeks, where they will take on a diet challenge. Mice from each genotype were randomly assigned to a HFD or a control, low-fat diet (LFD). Following 18 weeks of diet treatment, the mice were sacrificed and mice tibia were extracted for synchrotron radiation tomography and silver nitrate stain imaging.

**Synchrotron Radiation Micro-Computed Tomography (SRμT).** SRμT image acquisition was performed at beamline 8.3.2 at the Advanced Light Source. SRμT is an imaging modality that captures micro-scale internal morphology and material composition using high-flux x-rays. Mouse tibia were mounted on a rotating stage and transmission radiographs were taken over a range of 180°. A beam energy of 18 keV with 1313 projections and a 500 ms exposure time was used to acquire images. Full 3-dimensional (3D) image volumes were reconstructed at a final resolution of 1.3μm/pixel using open-source python code Tomopy.

Following image reconstruction and segmentation, the size and density (#/bone volume) of canals and lacunae were calculated in Dragonfly (ORS) to compare the genetic model and diet models. All statistics compared each group to each other using an ANOVA with a Tukey multiple comparison test. The distribution of mineralization in each bone was calculated from ImageJ by directly converting image grayvalues to a volumetric tissue mineral density (vTMD) using a relationship with beam energy.

**Ploton Silver Nitrate Stain.** Silver nitrate staining of the LCN was used to visualize canaliculi and osteocytes as described by Jáuregui et al [3]. For this study, four sections from each mouse were analyzed. Canalicular length and number were measured individually using ImageJ. Average LCN area was calculated by thresholding grayscale images of silver-stained bone sections. The resulting LCN area is then normalized per osteocyte cell in the image.

## RESULTS

**Canals and Canaliculi are Concurrently Altered with High-Fat Diet and TβRII$^{ocy-/-}$.** Alterations to canal morphology were observed with both HFD and TβRII$^{ocy-/-}$ (Figure 1). HFD treatment tended to increase canal diameter compared to LFD groups for both WT and TβRII$^{ocy-/-}$ genotypes. Additionally, canal diameter tended to increase in TβRII$^{ocy-/-}$ groups when compared to WT groups. These effects together resulted in a significant increase in canal diameter between WT-LFD and TβRII$^{ocy-/-}$-HFD groups ($p < 0.01$). Canal density tended to increase with HFD compared to LFD in WT groups but not with TβRII$^{ocy-/-}$. As such, TβRII$^{ocy-/-}$-HFD possessed a Ca.Dn similar to that of the LFD groups. The WT-HFD group possessed significantly higher Ca.Dn than the TβRII$^{ocy-/-}$-LFD group ($p < 0.05$).

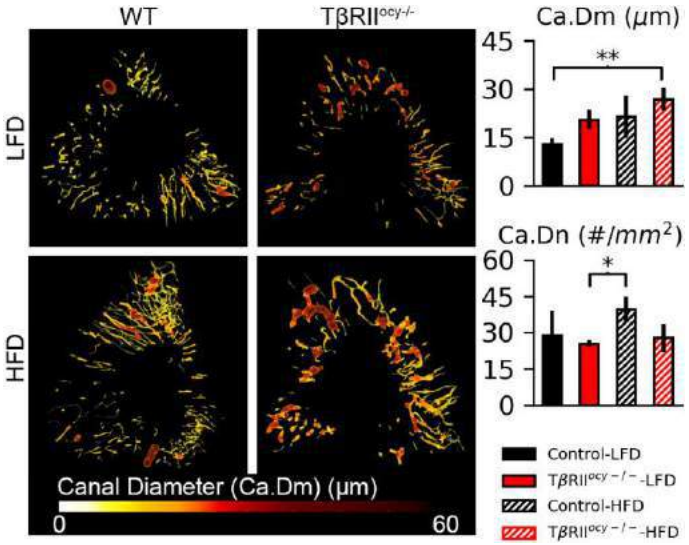


**Figure 1: Representative SRμT canal volumes (left), average canal diameter (top right), and average canal density (bottom right). Error bars denote one standard deviation.**

Silver nitrate staining and quantification of the LCN revealed that changes in the LCN occur in parallel with changes to canals (Figure 2). LCN area demonstrated a similar trend to Ca.Dn, with HFD tending to increase LCN area and TβRII$^{ocy-/-}$ tending to decrease LCN area. Canalicular number and length tended to remain constant with each respective diet model but decreases with TβRII$^{ocy-/-}$.

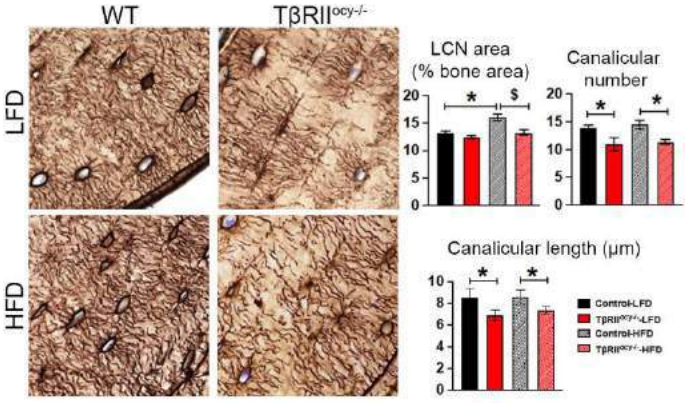


**Figure 2: Silver nitrate staining (left) reveals that TβRII$^{ocy-/-}$ decreases LCN area, canalicular number, and length (right). Error bars denote one standard deviation.**

**High-Fat Diet Induces Hypomineralization in Wild-Type Mouse Bone.** Hypomineralization is present in high-fat diet mice compared to low-fat diet mice (data not shown for brevity). In this study, mineralization in bone tissue was analyzed in four quantile ranges to capture low and high regions of mineralization. These quantile ranges were 1300-1660, 1660-2015, 2015-2375, and 2375-2725 mgHA/cm$^3$. The WT-HFD group possessed a significantly higher percentage of bone in the lowest region of mineralization (1300-1660 mgHA/cm$^3$) than all groups ($p < 0.05$). The WT-HFD bone model still possessed more bone in the second-lowest region (1660-2015 mgHA/cm$^3$) of mineralization than the WT-LFD group ($p < 0.05$). Other groups in each mineralization quantile were not significantly different.

## DISCUSSION

Because canal diameter at the microscale increased with both HFD and TβRII$^{ocy-/-}$, it is possible that both these alterations reflect an increase in the need to transport nutrients or perform PLR. Similar changes in LCN area and canalicular number and length may indicate that transport systems at both microscale and nanoscale are simultaneously influenced by diet and TβRII$^{ocy-/-}$. Because Ca.Dn, LCN area, canalicular number, and canalicular length follow similar tendencies with genotype and diet, it may follow that ablation to osteocyte-intrinsic TGF-β signaling affects the transport system at all length scales through the mechanism of PLR.

Furthermore, hypomineralization in the WT-HFD group indicates bone is being remodeled, with new bone material possessing lower vTMD [4]. Per quantile in each group, mineralization follows the trend of Ca.Dn and LCN area, where TβRII$^{ocy-/-}$ tends to "recover" the HFD model to levels akin to LFD groups. Both SRμT data and histology images point to the phenomena of PLR exacerbation in HFD, as well as to potential recovery of PLR exacerbation with TGF-β receptor II inhibition.

The effect of HFD-induced obesity on the transport system, LCN, and mineralization in bone tends to be mitigated with TβRII$^{ocy-/-}$. These metrics of PLR suggest potential protection of bone quality with TβRII$^{ocy-/-}$ in HFD mice. Although inhibition of TGF-β receptor II shows promising results in recovering the effects of HFD-induced obesity, further investigation of PLR through a comprehensive analysis of lacunar volume is necessary to completely illustrate the effect of HFD and TβRII$^{ocy-/-}$ in this mouse model. Additionally, a correlation between the impact of PLR and mechanical properties of bone remains to be fully examined, though salient mechanical properties have been obtained and will be analyzed in the context of data presented here. Despite these current limitations, present results indicate that PLR may indeed be exacerbated, as shown in histological data, placing a burden on microscale transport systems (canals). TGF-β receptor II inhibition shows promise in reducing the negative impact of HFD on osteocyte-intrinsic TGF-β signaling.


## ACKNOWLEDGEMENTS

We would like to acknowledge the Advanced Light Source at Lawrence Berkeley National Lab for assistance in SRμT data acquisition at beamline 8.3.2. – microtomography.


## REFERENCES


[1] Dole, N. S. et al., *Cell Reports*, 21:2585-2596, 2017
[2] Yadav, H. et al., *Cell Metabolism*, 14:67-79, 2011
[3] Jáuregui, E. J. et al., *Bone*, 89:7-15, 2016
[4] Grynpas, M. *Calcified Tissue International*, 53:S57–S64, 1993

# EVALUATION OF PRESSURE DROP ACROSS AORTIC COARCTATION: A COMPARISON OF ZERO-DIMENSIONAL AND THREE-DIMENSIONAL MODELS

**Priya J. Nair (1), Martin R. Pfaller (2), Seraina A. Dual (3), Daniel B. Ennis (3), Doff B. McElhinney (4), Alison L. Marsden (1,2)**

(1) Bioengineering, Stanford University, Stanford, CA, USA
(2) Pediatric Cardiology, Stanford University, Stanford, CA, USA
(3) Radiology, Stanford University, Stanford, CA, USA
(4) Cardiothoracic Surgery, Stanford University, Stanford, CA, USA

## INTRODUCTION

Coarctation of the aorta (CoA) is a congenital defect characterized by a constriction of the aorta, typically just beyond the left subclavian artery, which accounts for 6-8% of congenital heart defects[1]. The narrowing of the aorta causes a drop in blood pressure (BP) across the stenosis region which can be alleviated using surgical approaches or catheter-based interventions using stents. The current guideline for treatment is a BP gradient $\geq$ 20 mmHg at rest.

Computational fluid dynamics (CFD) simulations are used to characterize local hemodynamics in patients with CoA. Previous studies have showed the capability of three-dimensional (3D) simulations in modeling aortic coarctation and predicting the trans-coarctation pressure gradient.[2,3] However, 3D simulations are computationally expensive and time-intensive which can prevent them from being used routinely in clinical applications. Reduced-order models, in our case zero-dimensional (0D) models, that are less expensive, therefore become crucial for patient-specific applications of cardiovascular flow simulations. 0D circuit analogy models have no spatial dependency; they only depend on time but can be evaluated at different locations along the cardiovascular system by creating models comprising multiple circuit elements.

The objective of this study was to non-invasively predict the pressure drop across the coarctation, comparing patient-specific CFD simulations to 0D models. Both 0D and 3D simulations were performed using the open-source software SimVascular. The pressure drops measured across the coarctation using both models were compared and validated using invasive cardiac catheterization measurements.

## METHODS

**Acquisition of Patient Data:** 4D-Flow MRI datasets were acquired for two patients with CoA who thereafter underwent a catheter intervention and stent placement. Invasive measurements of pressure via cardiac catheterization in the ascending and descending aorta were also acquired, in addition to BP measured using a sphygmometer cuff within 48 hours of the catheterization.

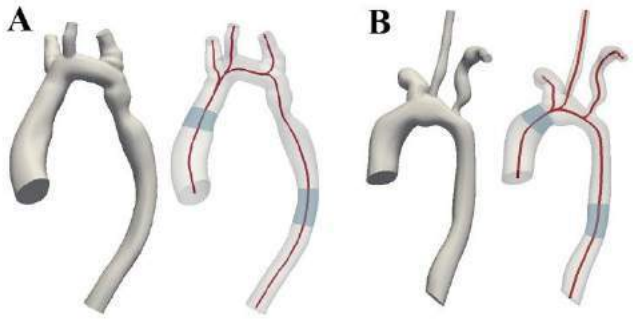


**Figure 1. 3D geometry (left), with centerlines (right) for Patient A and Patient B. Blue shaded regions in the ascending and descending aorta indicate where pressure was measured.**

**Anatomic Model Generation:** MRI magnitude images were imported into SimVascular (simvascular.org)[4] and manually segmented to generate 3D geometries of the aorta and branches arising from the aortic arch: brachiocephalic trunk, left carotid artery, and left subclavian artery. Centerlines were automatically extracted from the 3D geometry for use in creating the 0D model which consists of individual lumped-parameter elements (resistors and capacitors) that connect to form a complex lumped parameter network. The 3D volume was meshed using tetrahedral elements and contained ~1.5 million elements. A boundary layer mesh consisting of three layers was also incorporated to resolve large velocity gradients at the wall.

**Boundary Conditions:** Boundary conditions were tuned using 4D-Flow MRI and cuff BP measurements. Eddy-current corrected images from the 4D-Flow MRI dataset were analyzed to measure 2D time-resolved flow at the inlets and outlets using Arterys (Arterys, San

Francisco, USA). A patient-specific temporally varying parabolic flow profile was prescribed to the inlet of the 0D and 3D models. Flow from the brachiocephalic trunk, left carotid artery, left subclavian artery and descending aorta were used, along with BP data, to tune outflow boundary conditions. A three-element Windkessel model (proximal resistance $R_p$, capacitance C, distal resistance $R_d$) was imposed at each of the outlets. Total resistance ($R_p + R_d$) for each of the branches was calculated using the cuff BP and the flow split determined from MRI. 0D simulations were performed first and used to fine-tune the prescribed boundary conditions. An approximate value of $10^{-4}$ for C was used as a starting point. The value of C, along with $R_p/R_d$ ratio, were adjusted to fine-tune the boundary conditions until the calculated pressures matched the patient's systolic and diastolic cuff BP within 5 mmHg.

**0D and 3D simulations:** For the 0D simulation, the value of each of the lumped-parameter elements was determined from the geometric and material properties of the blood and blood vessel: fluid density 1.06 g/cm$^3$, viscosity 4cP, Young's modulus 3 MPa[5] and thickness of the vessel defined as 20% of the radius of the vessel.. Simulations were run for ten cardiac cycles to reach a periodic state of the solution. Inclusion of a stenosis model did not affect results. Results from the last time step of the 0D simulation were projected onto the model's 3D mesh and this was used as the initial condition for the 3D simulation[6].

3D simulations were performed using a coupled-momentum method using the same boundary conditions as the 0D simulation. Deformable walls with Young's modulus 3 MPa, Poisson ratio 0.5 and shear correction factor 0.8333 were used. Simulations were run for ten cardiac cycles until a periodic state of the solution was reached.

Pressure along the centerline before and after the coarctation were measured at peak systole in both the 0D and 3D models. The drop in pressure was calculated as the difference in pressure between the mean of the pressure measured in a region defined by 80% of the length to 100% of the length of the ascending aorta, and the mean of the pressure measured in a region defined by 50% of the length to 70% of the length of the descending aorta, shown in Figure 1. This drop was compared to the invasively acquired measurements during cardiac catheterization.

## RESULTS

Anatomy and hemodynamics reflective of coarctation were observed and captured in the simulation. Figures 2 and 3 show a comparison of the pressure obtained from the 0D simulation to that of the 3D simulation over the normalized vessel path for the inlet and some outlets for Patient A and B respectively.

The non-invasively computed peak-to-peak pressure drop was lower using 0D than using 3D (10 mmHg vs. 15 mmHg). The 0D estimate correctly estimated pressure drop and 3D estimate overestimated pressure drop compared to the catheter-based measurement of 10 mmHg for Patient A.

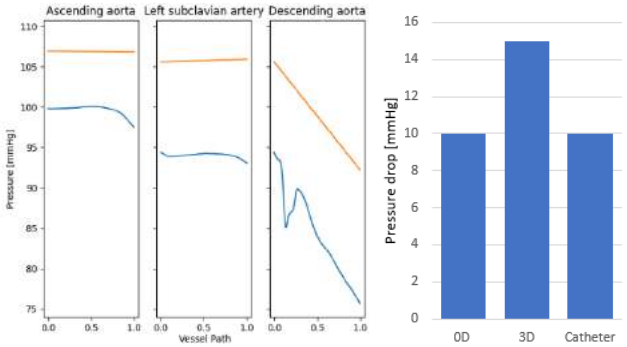


**Figure 2: Pressure over the vessel path (scaled with the length of the vessel) for 3D (blue) and 0D (orange) simulations of Patient A's geometry (left). Comparison of pressure drop measured using 0D, 3D and catheter (right)**

In Patient B, since the coarctation is located in a junction region, the 0D model estimate (7 mm Hg) was a poor estimate of the pressure drop measured using the catheter (30 mmHg). The 3D model estimate (31 mmHg) slightly overestimated the pressure drop compared to the catheter-based measurement of 30 mmHg for Patient B.

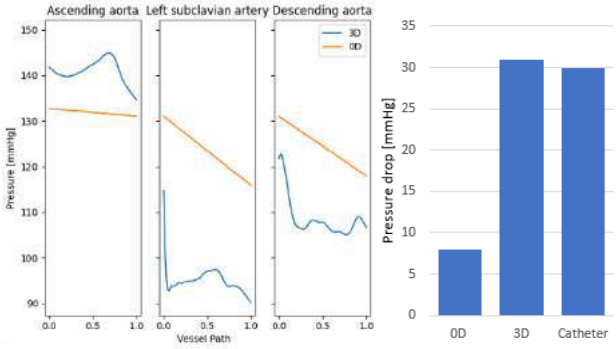


**Figure 3: Pressure over the vessel path (scaled with the length of the vessel) for 3D (blue) and 0D (orange) simulations of Patient B's geometry (left). Comparison of pressure drop measured using 0D, 3D and catheter (right)**

## DISCUSSION

This study demonstrates the capability of 0D models constructed automatically from 3D models in computing flow and pressure in a patient-specific model of aortic coarctation. Pressure drop measured from 0D and 3D simulations validated using invasive catheter measurements showed that the 0D and 3D model estimated pressure gradient within 5 mmHg in the case where the coarctation was located in a non-junction region, as seen in Patient A.

The significantly lower computational time of the 0D models makes them more feasible to use in a clinical setting. 0D models, however, currently cannot resolve flow and pressure when the coarctation is located at the junction of two vessels (as seen in Patient B) which reduces the number of patients that this model can be applied to. A limitation with validation using catheter measurements is that the specific location at which the pressure was measured clinically is unknown. This would be of interest since the location at which the pressure is measured in the simulation is sensitive and can alter results.

This study is currently being extended to include more patients with aortic coarctation. Future studies can explore the prediction of the trans-coarctation gradient before and after stent intervention, as well as in exercise conditions.

## ACKNOWLEDGEMENTS

This work is funded by a National Science Foundation Graduate Research Fellowship and by the National Library of Medicine (award R01LM013120).

## REFERENCES

1. Singh, S. *et al. Heart. Lung Circ.* **24**, 110–118 (2015).
2. LaDisa, J. F. *et al. J. Biomech. Eng.* **133**, (2011).
3. Saitta, S. *et al. J. Biomech.* **94**, 13–21 (2019).
4. Updegrove, A. *et al. Ann. Biomed. Eng.* **45**, 525–541 (2017).
5. Beller, C. J. *et al. J. Med. Eng. Technol.* **32**, 167–170 (2008).
6. Pfaller, M. R. *et al. Ann. Biomed. Eng.* **49**, 3574–3592 (2021).

SB³C2022
Summer Biomechanics, Bioengineering and Biotransport Conference
June 20-23, Eastern Shore, MD, USA

# LEARNING WHOLE HEART MESH GENERATION FROM PATIENT IMAGES FOR COMPUTATIONAL SIMULATIONS

**Fanwei Kong and Shawn C. Shadden**

Department of Mechanical Engineering
University of California, Berkeley
Berkeley, California, USA

## INTRODUCTION

Patient-specific cardiac modeling combines geometries of the heart derived from medical images and biophysical simulations to simulate various aspects of cardiac function. It can provide useful physiological information non-invasively to facilitate understanding, diagnosis and treatment planning of cardiac diseases for individual patients [1]. However, generating simulation-suitable meshes of the heart from patient image data often requires complicated procedures and significant human efforts, limiting clinical translations. We are thus motivated to develop fast and automated methods to construct simulation-ready meshes of the heart from medical images.

Deep learning methods can train neural networks from existing data to automatically process medical images and generate whole heart reconstructions. While most prior deep learning methods have focused on image segmentation, our recent approaches directly reconstructed surface meshes from patient image data [2-3]. By deforming a surface mesh template, our previous methods eliminate the intermediate segmentation step that sometimes introduce extraneous regions containing topological anomalies that are unphysical and unintelligible for simulation-based analyses [2]. We have also combined free-form deformation (FFD) with deep learning to predict the displacement of a control point grid to deform the space enclosing a simulation-ready whole heart template, thus enabling direct reconstruction of simulation-ready meshes from image data [3].

However, since FFD has limited capability for complex shape deformation, our prior method requires a dense control point grid including thousands of control point to achieve acceptable whole heart reconstruction accuracy [3]. Here we propose a new deep-learning approach that leverage biharmonic coordinates to deform the whole heart template to fit the target image data with higher accuracy and using far less control points. We also introduce a few effective learning biases as objective functions to produce meshes that better satisfy the modeling requirements for computational simulation of cardiac flow.

## METHODS

**Dataset**: We trained our method with 87 contrast-enhanced CT images and 41 MR images that cover the whole heart [3]. 15 CT images and 6 MR images were used for validation. The final performance of our model was evaluated on the MMWHS held-out test dataset that contains 40 CT and 40 MR images [4], as well as time-series CT images.

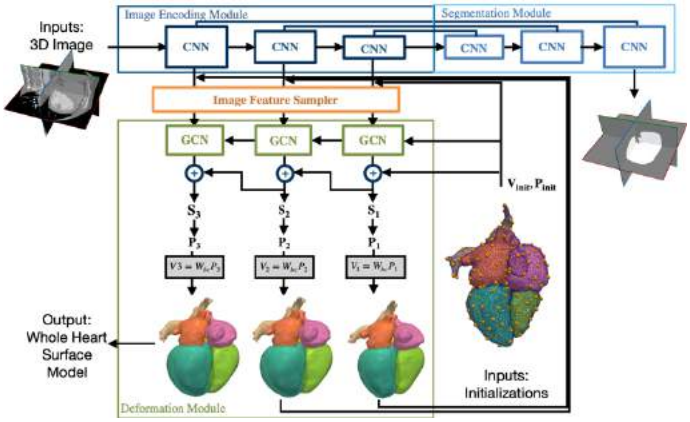


**Figure 1: Proposed automatic whole heart reconstruction approach**

**Shape Deformation Using Biharmonic Coordinates**: Our approach constructs whole heart meshes by deforming a pre-defined whole heart mesh template. We parameterize the deformations with the translations of a small set of deformation handles uniformly sampled from the mesh template. Given a set of mesh vertices $V \in R^{n\times 3}$ and a set of control points $P \in R^{c\times 3}$, we compute the biharmonic coordinates $W \in R^{n\times c}$, which is a linear map, $V = WP$. $W$ is pre-computed by minimizing a quadratic deformation energy function while satisfying the handle constraints with linear precision [5].

**Neural Network Architecture**: As shown in Fig 1, our framework

first uses an image encoding module that extracts and encodes image features. These features are used as inputs to graph convolutional layers to predict the displacements of mesh vertices ($S \in R^{n\times 3}$) from their previous locations. We then select control handles ($P \in R^{c\times 3}$) from the updated mesh vertex locations to deform the template. The shape deformation module consists of three deformation blocks that progressively deform mesh templates, using increasing number of control handles (75, 150 and 600, respectively). We also use a segmentation module that predict a binary segmentation map to enable additional supervision using ground truth annotations.

**Neural Network Optimization**: 3D ground truth meshes of the whole heart extracted from manual segmentations were used to supervise the training of the neural network model. We used point and normal consistency losses to supervise the geometric consistency between the prediction and the ground truth. In contrast to [2], which uses edge length and Laplacian regularization losses, the smoothness of the mesh prediction is naturally constrained by the biharmonic coordinates used to deform the template. For CFD simulation of cardiac flow, the inlet and outlet vessel geometries need to be trimmed to have planar faces orthogonal to the vessel walls. We thus applied a co-planar loss on the cap that penalizes the L2 differences of surface normal vectors among mesh vertices on the caps. For mesh vertices that are on the vessel walls near the caps, we minimize the absolute value of the dot products between their surface normal vectors and the surface normal vector of the caps to encourage orthogonality. As geometries of inlet vessels are important to the accuracy of CFD results, we applied a higher weight of the geometric consistency loss on mesh vertices that are located on vessel walls near the inlets.

## RESULTS

We compare the performance of whole-heart reconstructions from our method against two mesh reconstruction methods, HeartFFDNet [3] that learns FFD to deform mesh template of the heart, MeshDeformNet [2] that learns to predict displacements from sphere mesh templates, as well as two segmentation methods, 2D UNet [6] and a modified 3D UNet [7].

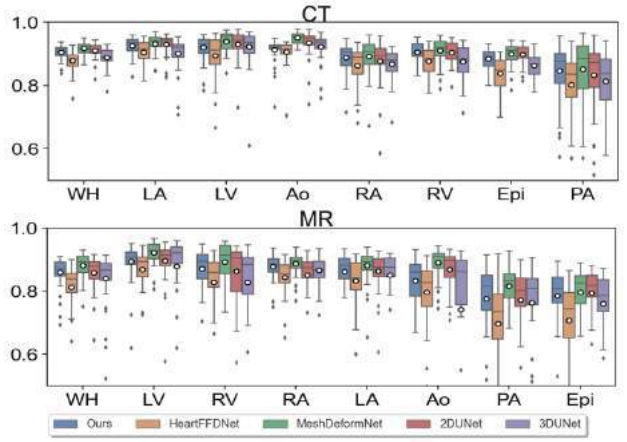


**Figure 2: Dice scores of different methods on MMWHS test set**

Figure 1 shows the average Dice score (a similarity index) of the reconstruction results of both the whole heart and individual cardiac structures for the MMWHS test dataset. For both CT and MR data, our method consistently outperformed HeartFFDNet and 3D UNet and achieved comparable performance with MeshDeformNet and 2D UNet. Figure 3 compares the reconstructed whole heart geometries from different methods for time-series CT images. From end-diastole to end-systole, mesh-based methods produced more anatomically and temporally consistent geometries than segmentation-based methods (the UNets). MeshDeformNet is prone to gaps between adjacent cardiac structures since it deforms uncoupled spheres to represent separate structures. Our method avoids this issue by deforming a realistic whole heart template. Compared with HeartFFDNet, we used far less control points (600 vs 4096) and achieved better accuracy.

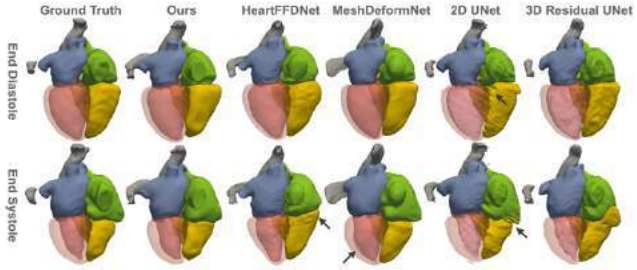


**Figure 3: Qualitative comparisons for time-series CT images**

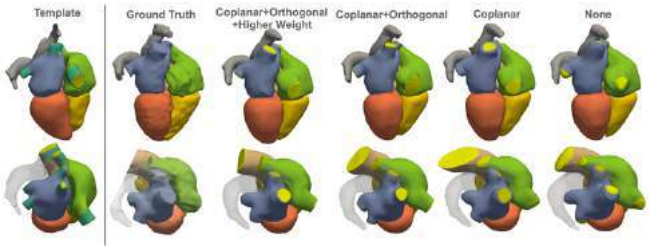


**Figure 4: Contribution of different loss components on vessel inlet geometries. 1st column shows the template mesh with caps tagged in yellow and walls tagged in turquoise.**

Figure 4 demonstrates the effect of adding individual loss components on the predicted inlet and outlet geometries (pulmonary veins, vena cava, and aorta). The coplanar loss and the orthogonal loss succeeded in producing planar cap geometries that are orthogonal to vessel walls. Applying a higher weight on the inlet mesh vertices in the geometric consistency loss improved the accuracy of inlet geometries.

## DISCUSSION

Automated image-based reconstruction of cardiac meshes is important for computational simulation of cardiac physiology. We have demonstrated a novel approach for automated image-based cardiac model reconstruction that is generally more geometrically accurate than our prior approach [4] while at the same time better satisfying modeling requirements for cardiac flow simulations. Our approach can automatically construct whole heart meshes within seconds on modern desktop computers. Once being trained on the whole heart template, the network can deform alternative template meshes that represent a subset of the geometries in the template to accommodate different modeling requirements, by interpolating the biharmonic coordinates onto new template meshes. Future work will focus on validating the reconstructed meshes for CFD simulation of cardiac flow.


## ACKNOWLEDGEMENTS

This work was supported by the NSF, Award #1663671.


## REFERENCES


[1] Prakosa et al., *Nature Biomed Eng*, 2(10), Oct, pp. 732–740, 2018.
[2] Kong et al., *Medical Image Analysis* 74 (1), 102222, 2021.
[3] Kong et al., *MICCAI*, *Springer* pp. 550-559, 2021
[4] Zhuang et al., *Med Image Analysis*, 58, 101537, 2019.
[5] Wang et al., *ACM Transactions on Graphics* 34(4), 2015.
[6] Ronneberger et al., *MICCAI*, *Springer*, pp 234-241, 2015.
[7] Isensee et al., *MICCAI*, *Springer* pp. 287–297, 2017.

# IMAGE-BASED 3D ANATOMICAL MODELS FOR CHARACTERIZATION AND SURGICAL PLANNING OF BIATRIAL DRAINAGE AND SINUS VENOSUS ATRIAL SEPTAL DEFECTS

**R. Hang (1), J. Bracamonte (2), N. Roberts (2),
U. Truong (3), S. Gullquist (3), T. Yeh (4), J. Soares (2)**

(1) Department of Biomedical Engineering, Virginia Commonwealth University, Richmond, VA, USA.
(2) Department of Mechanical and Nuclear Engineering, Virginia Commonwealth University, Richmond, VA, USA.
(3) Department of Pediatrics, Division of Cardiology, Virginia Commonwealth University School of Medicine, Richmond, VA, USA.
(4) Department of Surgery, Virginia Commonwealth University

## INTRODUCTION

Surgical intervention for congenital heart diseases (CHD) remains a significant challenge for cardiothoracic surgeons because of the wide variation of anatomy and physiology. Traditional methods for presurgical planning involve multimodality imaging methods and interdisciplinary consultations. Current standard imaging still fails to fully reflect the actual intraoperative inspection of the open and cardioplegic heart, particularly with respect to anatomical distortion of the non-physiologic condition, spatial orientation, and dimensional perception. Previous studies have shown that it is possible to use modern visualization software to recreate 3D anatomical models of the heart with different degrees of fidelity [1]. Understanding the complex anatomy and hemodynamic patterns of each CHD is critical to making clinical decisions involving surgery and post-operative treatment.

To further support the translation of 3D models into clinical decision-making, we report prospective and retrospective modeling efforts in patient-specific models of two different presentations of atrial septal defects (ASDs). The two specific variations of ASD studied herein are sinus venosus atrial septal defect (SVASD) and biatrial drainage of the superior vena cava (SVC). SVASD comprises about 10% of all ASDs, and embryologically originates as a deficient inward folding of the atrial wall that forms the posterior wall of the SVC and upper right pulmonary veins; in such presentations, the pulmonary veins drain into the right atrium (RA) at the root of the SVC instead of the left atrium (LA) [2]. ASDs with biatrial drainage of the SVC is a very similar defect but is distinct from SVASD in that biatrial drainage does nmot have a true interatrial shunt; that is the defect is superior to allow shunting from one atrium to the other [3].

In this work, we applied 3D modeling to compare the anatomy of the two types of ASDs to justify the choice between deploying a cardiac stent-graft shunting the SVC into the RA with minimally invasive methods versus implementing a cardiac baffle draining the pulmonary veins through the ASD into the LA with open-heart surgery.

## METHODS

**Data Collection.** Anonymized datasets were provided by the team of cardiologists and surgeons at the Children's Hospital of Richmond (CHoR) acquired prior to surgical intervention for clinical purposes as part of the follow-up of each patient. Each imaging dataset consisted on several MRI series comprising 3D angiograms with and without contrast, long and short axis planes with cine MRI, and several 2D and 3D phase-contrast MRIs (Figure 1).

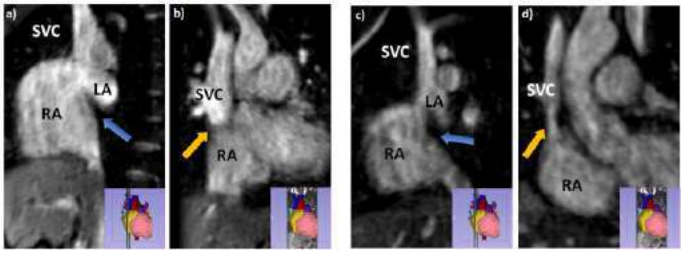


**Figure 1.** Multiplanar Magnetic Resonance Angiography (MRA) of SVASD a) Sagittal view, b) Coronal view, and Biatrial Drainage c) sagittal view, d) coronal view. (blue arrows: atrial septal wall, yellow arrows: junction between the SVC and RA) Location of each plane within the entire 3d anatomical model is shown in small insert in the bottom right.

**3D anatomical model generation.** Slicer3D software and 3D angiograms were used to segment and model the blood pools and walls of the major heart chambers and vessels. Cine3D planar views and feedback from CHoR collaborators were used to refine and ensure the anatomical precision of the models (Figure 2). Since the surgical intervention is focused around the SVC-RA junction and how the right pulmonary veins connect to the heart, we selected the anterior quadrant of the heart containing the SVC, right-sided pulmonary veins, and portions of the RA, left atria and right ventricle as our region of interest (Figure 3). The finished models were 3D-printed with acrylonitrile

butadiene styrene (ABS) to demonstrate the differences between their respective interventions and assist in physician understanding of the anatomical differences.

Additionally, the 3D models were uploaded into an augmented reality platform to further facilitate the model exploration and use for didactic and teaching purposes (Figure 4).

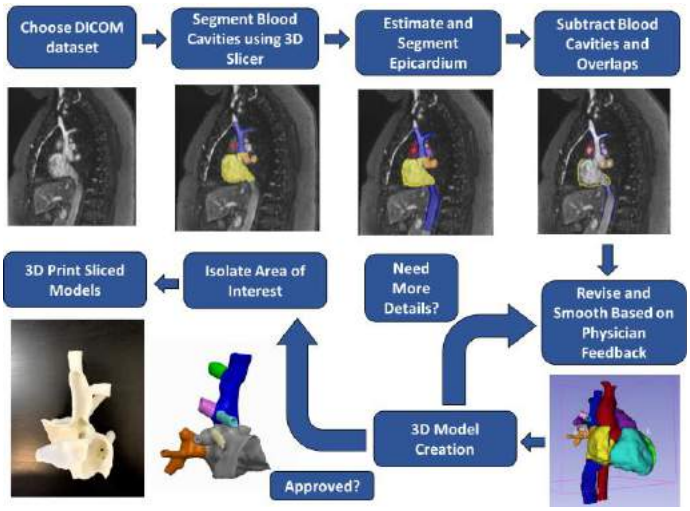


**Figure 2.** Medical imaging processing and 3D modeling pipeline.

**Assessment of modeling impact on treatment planning.** The models were then presented at the Pediatric Cardiology Conference at CHoR and a survey to assess the efficacy of 3D modeling in clinical decision making was distributed among its members.

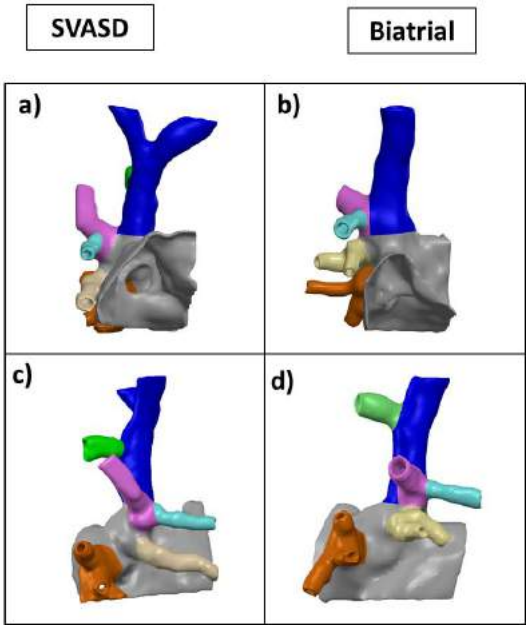


**Figure 3.** Four Panel Cut Model 3D Rendering, blue: SVC, pink: upper right pulmonary vein, turquoise: middle right pulmonary vein, green: azygous vein, beige: lower right pulmonary vein, orange: normal pulmonary veins draining into LA.

## RESULTS

Two 3D computational heart models were created, showcasing the subtle differences between the two CHD cases. The biatrial drainage ASD showcased an anteriorly tilted septal wall which caused a stenotic channel into the right atrium. This narrowing justified the choice of minimally invasive repair with a stent-graft placement, which could be deployed and expanded to properly anchor it distally shunting the SVC into the narrowing entrance of the RA. Additionally, computational modeling allowed the surgical team to realize that enough clearance would remain underneath the proximal placement of the stent-graft in the SVC to allow for proper drainage of pulmonary veins into the left atria. The SVASD heart showcased anatomy more appropriate for surgical repair with a patch closing the ASD and Warden procedure transecting the SVC connecting to the RA appendage. Both surgeries proceeded successfully. Eighty-six percent (86%) of physicians surveyed reported that the models "helped immensely" in their understanding of the differences between the two types of CHDs.

## DISCUSSION

3D models of two distinct CHDs have been created and shown to positively aid in pre-surgical planning and justifying a stent placement with a minimally invasive procedure rather than the deployment of a cardiac baffle with open-heart surgery in one of the cases that demonstrated biatrial drainage ASD. In addition to aiding in clinical decision-making, these models can serve as powerful educational tools for healthcare professionals. Current limitations include accounting for the movement of the vessels during the heart cycle and improving the semi-automatic processing pipeline in which these models are constructed. In future studies, 4D-Flow MRI data can be extracted and be used to estimate hemodynamic parameters, like wall shear stress (WSS), which can aid in understanding the onset and progression of cardiovascular disease.

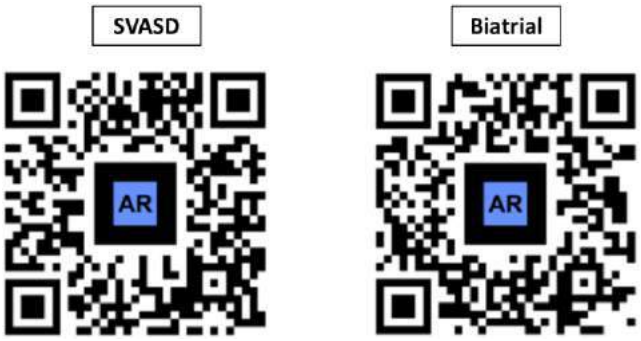


**Figure 4.** 3D-models in augmented reality platform. These QR codes can be used with any cell-phone with AR capabilities to inspect the 3D-models.

## ACKNOWLEDGEMENTS

We thank Anthony Gonella, Lindsay Jordan and VCU College of Engineering Dean's Undergraduate Research Initiative. We also thank the Children's Hospital of Richmond.

## REFERENCES

[1] S.J. Yoo, T. Spray, E.H. Austin, T.J. Yun, G.S. van Arsdell, Hands-on surgical training of congenital heart surgery using 3-dimensional print models, J. Thorac. Cardiovasc. Surg. 153 (2017) 1530–1540. https://doi.org/10.1016/J.JTCVS.2016.12.054.

[2] J.H. Hansen, P. Duong, S.G.M. Jivanji, M. Jones, S. Kabir, G. Butera, S.A. Qureshi, E. Rosenthal, Transcatheter Correction of Superior Sinus Venosus Atrial Septal Defects as an Alternative to Surgical Treatment, J. Am. Coll. Cardiol. 75 (2020) 1266–1278. https://doi.org/10.1016/J.JACC.2019.12.070.

[3] M.D. Patel, S. Balasubramanian, A.L. Dorfman, A. Joshi, J.C. Lu, M.G. Mahani, P.P. Agarwal, Biatrial drainage of the right superior vena cava: Imaging findings, Radiol. Cardiothorac. Imaging. 2 (2020). https://doi.org/10.1148/RYCT.2020200414/ASSET/IMAGES/LARGE/RYCT.2020200414.FIG7C.JPEG.

# RECENT UPDATES ON THE GHBMC HUMAN HEAD FINITE ELEMENT MODEL – DEVELOPMENT OF CRASH INJURY INDEX FOR MULTIPLE BRAIN INJURIES

**Ding Lyu (1), Shirin Phadke (1), Abhijeet Kumbhare (1), Liying Zhang (1)**

(1) Department of Biomedical Engineering, Detroit, MI, United States

## INTRODUCTION

Each year, an estimated 1.5 million Americans sustain a Traumatic Brain Injury (TBI). Motor vehicle crashes are the leading cause of TBI resulting in hospitalization. Mathematic modeling of a traumatic event has become a powerful tool to study biomechanical processes of head injuries that are difficult to investigate experimentally on living human subjects. The Global Human Body Modelling Consortium (GHBMC) 50$^{th}$ percentile human adult male head model (M50) based on the Finite element (FE) technique has been developed and validated extensively. Most recently, GHBMC M50 head model was updated with an anisotropic hyperelastic brain model to enable its capability to predict axonal injury in various white matter structures and identify the impact direction-dependent injury risk. This updated GHBMC head model v6.0 was rigorously validated against 63 head impact experiments conducted on Postmortem Human Subject (PMHS) to ensure the accuracy of the prediction of the kinematic, kinetic, stress and strain responses as experienced by the human head from a variety of loading conditions.

To utilize the FE model's predictive power to delineate the injury process and predict injury severity by relating types of injury to material failure of tissues, tissue level predictors based on model parameters need to be established. Previously, FE head model simulation of 56 helmet impacts involving concussed and non-concussed American Football players suggested that the local brain response in the form of maximum principal strain (MPS) and product of MPS and maximum principal strain rate (MPSR) were predictors that corelated better to neurological symptoms, memory impairment and return to play than the HIC15 (Head Injury Criterion) and rotational acceleration alone[2,3,4]. FE reconstruction of limited real-world vehicle crashes involving brain injuries implied that MPS was a potential injury parameter for AIS 4+ diffuse brain injury while the intracranial pressure (ICP) and bridging vein (BV) strain were predictive for brain contusion and ASDH[5].

The objective of this study was to develop Crash-Induced Injuries indices (CIIs) for the GHBMC M50 head model v6.0 based on tissue response measures for predicting multiple brain injuries, skull fractures and facial fractures.

## METHODS

The GHBMC M50 head model v6.0 was applied to reconstruct a total of 49 PMHS impact tests and real-world injury cases (Table 1). The correlation of the model parameters for various injuries were determined according to logistic regression and Weibull survival analysis or the overall average values.

**Table 1: Cases reconstructed to determine various CIIs**

| CIIs (Test | Parameter | Injury, Noninjury |
|---|---|---|
| Facial Fractures[6,7] | MPS / MPST# | 6 fractures |
| Skull Fractures[8,9] | MPS / MPST | 9 fractures |
| Cerebral | ICP in ROI | 8 injuries, 5 noninjuries |
| ASDH[12] | BV Strain | 6 injuries, 9 noninjuries |
| Diffuse Brain | MPS, MPS × MMPSR | 4 injuries |

#MPST: Maximum principal stress

Development of CIIs for Facial and Skull Fracture of Various Regions

A series of cadaveric facial and skull impacts on the nasal, maxilla, zygomatic, frontal, temporal, and parietal bones were simulated[6,7,8,9]. To predict fractures of the cortical and spongy bones, the MPS and MPST failure limits were specified respectively to initiate the fracture predictions by using *MAT_ADD_EROSION (LS-DYNA R12.0). The final failure thresholds were determined while all resulting fracture forces fell well within the reported range of experimental results.

Development of CIIs for Various Brain Injuries

A set of frontal head impact tests[11,12] were simulated to determine the ICP for cases with and without cerebral contusion. Eighteen occipital head impacts were simulated to determine the ASDH[12]. The logistic regression and Weibull survival analysis were conducted to develop the injury risk curves of cerebral contusion and ASDH. The injury threshold

for diffuse brain injury was based on the simulation results of four real-world crash accidents which covers a range of different levels of head injuries (AIS0, AIS4, AIS5, and MAIS5)[5].

## RESULTS

CIIs for Fractures

For skull impact, the model predicted fracture forces for frontal, temporal and temporal-parietal bones were 5.09, 6.39, and 7.52 kN, respectively and were comparable to the experimental data in the corresponding regions. The predicted fracture force in the facial bones were 1.78, 1.88 and 0.97 kN for nasal, zygomatic and maxilla impact, respectively and fell well within the range of experimental results (Figure 1). 0.88 MPS and 0.78 MPS were the fracture CIIs for the outer/inner tables and facial cortical bone, respectively. 20 MPa MPSR was the CII for both skull diploe and facial spongy bone.

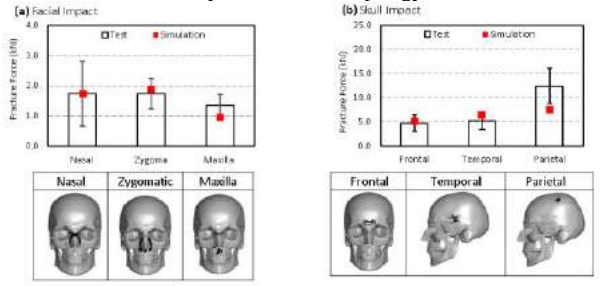


**Figure 1: Comparison of fracture forces and predicted facture location (a) facial impact and (b) skull impact**

CIIs for Cerebral Contusion

The cerebral contusion injury risk functions based on ICP were determined in equations (1) and (2) from Logistic regression and Weibull survival analysis:

$$P(Contusion)_{Logistic} = \frac{1}{1 + e^{-0.02394 \times coup + 3.8606}} \quad (1)$$

$$P\ Contusion\ _{Weibull} = 1 - e^{-\ coup/244.92\ ^{5.29}} \quad (2)$$

Receiver Operating Characteristic (ROC) curves were reconstructed and the Area Under the ROC Curve (AUC) was 0.8 for both models indicating excellent discrimination of the model (Figure 2). Based on logistic regression model, the peak ICP values at 50% and 5% risk of contusion were 161kPa and 38 kPa, respectively.

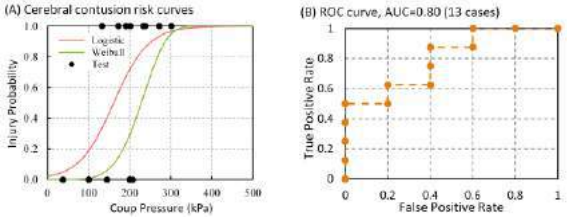


**Figure 2: (A) Cerebral contusion risk curves and (B) AUC**

CIIs for ASDH

The strain in the BV was highly related to the occurrence of ASDH based on the AUC of 0.82 (Figure 3) evaluated for both injury risk functions. The ASDH injury function based on Logistic regression and Weibull survival analysis are described in equations (**3**) and (**4**):

$$P(ASDH)_{Logistic} = \frac{1}{1 + e^{-9.184 \times stretchiratio + 4.195}} \quad (3)$$

$$P(ASDH)_{Weibull} = 1 - e^{-(stretchiratio/0.6181)^{5.3232}} \quad (4)$$

The BV strained at 0.46 and 0.14 would respectively result in 50% and 5% risk of BV rupture leading to ASDH according to the Logistic regression function.

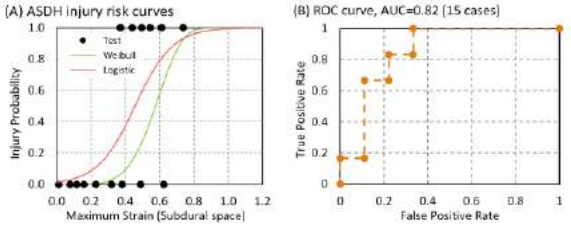


**Figure 3: (A) ASDH risk curves and (B) AUC**

CIIs for Diffuse Brain Injury

The MPS was the averaging of the top 10 elements with highest MPS. The MPSR was the derivative of MPS time-histories. The peak product of the MPS and MPSR was obtained by multiplying MPSR by MPS curves. The peak MPS, MPSR, and MPS × MPSR responses from brainstem, corpus callosum, and subcortical white matter were averaged to predict the risk of diffuse brain injury for AIS 2 and AIS 4+ injury. It appeared that MPS×MPSR had better predictability than MPS alone for differentiating serious diffuse brain injury from concussion.

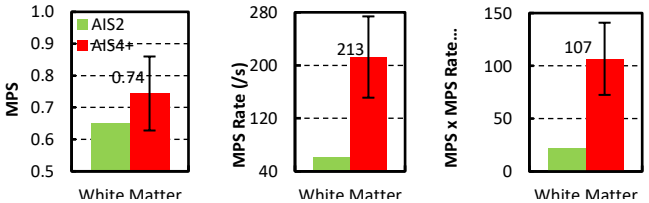


**Figure 4: Diffuse brain injury CIIs based on (a) MPS, (b) MPSR, and (c) MPS x MPSR in the white matter**

## DISCUSSION AND CONCLUSIONS

The CIIs of the GHBMC M50 head model in all prior versions for predicting various brain injuries were based on an average value of the predictions from injury cases. In this study, the risk functions were developed for assessing the probability of cerebral contusion and ASDH injuries. For diffuse brain injury, it was found that the product of strain and strain rate in the white matter might be a more sensitive injury predictor than the strain alone, consistent with the finding from previous studies[3,4]. For skull/facial fractures, established strain and stress limits at failure enables the model to simulate tensile failure of the compact bone as well compressive failure of the cancellous bone. All CIIs show improved capability over previous versions of the GHBMC M50. The authors believe that this tool can be used for testing of various hypothesis advanced as the mechanisms of brain injuries, prediction of injuries and developing countermeasures to reduce risk of injuries in many environments, e.g., falls, transportation, sports and military.


## ACKNOWLEDGEMENT

The funding was support by the GHBMC, LLC.


## REFERENCES


(1) Mao H et al. 2013. J Biomechanical Engineering, 135(11), 111002.
(2) Zhang L et al, 2001. Stapp Car Crash J 45: 369-394
(3) King A et al. 2003. Proc. IRCOBI Conference. Aldman Lecture.
(4) Viano D et al. 2005. Neurosurgery 57:891-916.
(5) Franklyn M et al. 2005. Stapp Car Crash J 49: 2005-22-0001
(6) Nyquist G et al. 1986. SAE Transactions, 95, 850-871.
(7) Allsop D et al. 1988. SAE Transactions, 97, 1224-1240.
(8) Allsop D et al. 1991. SAE Transactions, 100, 2009-2018
(9) Yognandan N et al. 1995. J Neurotrauma 12(4): 659-668.
(10) Nahum A et al. 1977. SAE Technical Paper 770922.
(11) Nahum A and Smith R. 1976. SAE Technical Paper 760825.
(12) Depreitere B et al. 2006. J Neurosurgery 104(6): 950-956.

# ANALYSIS OF THE SHORT-TERM EFFECTS OF INHALED NITRIC OXIDE ON PULMONARY ARTERY HEMODYNAMICS BY TIME-RESOLVED 1D AND 3D PHASE-CONTRAST MAGNETIC RESONANCE IMAGING

**J. Bracamonte (1), N. Roberts (1), R. Hang (2), D. Grinnan (3), E. Sonntag (3), J. Pinson (3), U. Truong (4), J. Soares (1)**

(1) Department of Mechanical and Nuclear Engineering, Virginia Commonwealth University, Richmond, VA, USA.
(2) Department of Biomedical Engineering, Virginia Commonwealth University, Richmond, VA, USA.
(3) Department of Pulmonology, Virginia Commonwealth University School of Medicine, Richmond, VA, USA.
(4) Department of Pediatrics, Division of Cardiology, Virginia Commonwealth University School of Medicine, Richmond, VA, USA.

## INTRODUCTION

Pulmonary artery hypertension (PAH) is a progressive pulmonary vascular remodeling disease and increased pulmonary vascular resistance leading to right ventricular dysfunction. The introduction of medications, such as calcium channel blockers and endothelin reception antagonists, has significantly improved the treatment and prognosis of PAH. [1] An acute vasodilator challenge is performed to assess a patient's responsiveness to these treatments. This is conventionally performed by right heart catheterization (RHC) whereby pressure, cardiac output, and vascular resistance are measured in response to a short-acting vasoactive agent such as inhaled nitric oxide (iNO). RHC is an invasive and relatively expensive procedure with inhered risks, making this method's serial characterization of pulmonary artery hypertension a challenging task. [2]

Phase-contrast magnetic resonance imaging (PC MRI) is a non-invasive technique that allows the resolution of blood flow and its velocity. As with any other MRI sequence, it poses no radiation exposure and unlike RHC, does not require vascular instrumentation. Originally, PC MRI was applied for the time-resolved assessment of through and in-plane blood velocity components at a given MRI slice; the technique has now evolved to allow time-resolved 3D resolution of blood velocity components (4D Flow MRI) by sacrificing some of the voxel size resolutions. Herein, we study the hemodynamics of patients with PAH undergoing an acute vasodilator challenge with inhaled nitric oxide by the analysis of both 2D through-plane PC MRI and 4D Flow MRI data of pulmonary artery hemodynamics. This study aims to explore the capacities of non-invasive MRI techniques to assess the vasoreactivity of PAH patients, which could eventually decrease the costs and risks associated with the characterization, diagnosis, and treatment of PAH.

## METHODS

**Data collection.** Retrospective anonymized data from ten adult patients with PAH undergoing the iNO vasodilator challenge. Each dataset consisted of respiratory-gated phase-contrast MRI for time-resolved 2D cross-sections (~1.5 mm/px) of the ascending aorta (AA), the proximal main, left, and right pulmonary artery (MPA, LPA, and RPA, respectively), and a thoracic 4D Flow MRI with a voxel size of 2.5 x 2.5 x 2.5 before and after 10 minutes of iNO administration. Typical sequence parameters were as follows: echo times, 2.4 to 2.6 ms; repetition times, 4.2 to 5.0 ms; flip angle, 10°; temporal resolution, 38 to 48 ms, and VENC set at 150 cm/s.

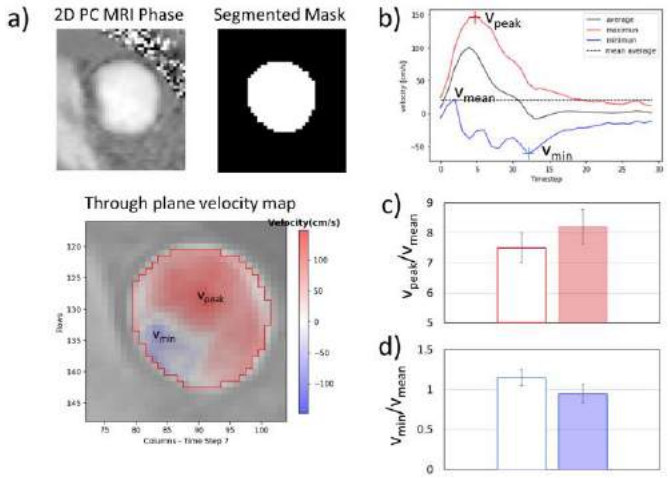


**Figure 1.** a) PC MRI data and processed velocity map. b) time resolved velocity metrics, c) statistics of peak over mean velocity ratio, and d) statistics of peak backflow velocity over mean velocity ratio.

**Image Processing.** Phase data offset error was corrected following the method proposed by Lankhaar et al. [3] assuming this error to be time-dependent and varying linearly within each scanned slice. Time-resolved segmentation masks were built semi-automatically with

custom-developed segmentation pipelines with ImageJ for planar PC MRI scans by two independent observers, and a fixed volumetric mask at systolic configuration was generated with Slicer3D for each 4D Flow dataset.

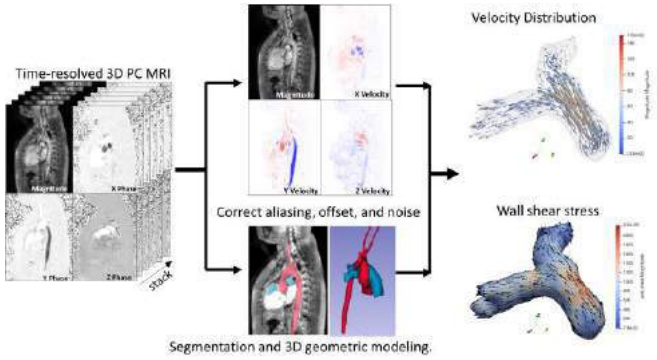


**Figure 2.** 4D Flow processing pipeline.

**PC MRI Postprocessing.** 2D PC MRI pixel-wise data was integrated to generate time-resolved area and flow curves that were smoothed with Python Scipy library tools. Smoothed data was used to generate the following hemodynamic parameters: Ratio of Area Change (RAC), peak and average net flow, peak retrograde flow, peak-net to peak retrograde flow time delay, onset time of retrograde flow, ejection time, acceleration time, acceleration volume, and volumetric-flow branch distribution (Figure 1). Pulse-wave velocity (PWV) was estimated with the slope of the flow vs. area curve at early stages of systole as proposed by Vullieamoz et al. [4]

**4D Flow Postprocessing.** A smooth surface was generated from 3D segmentation mask at systole, surface spatial information and voxel-wise 4D Flow data was used to generate time-resolved wall-shear stress distribution using the B-spline method proposed by Potter et al.[5] Wall shear stress has been previously shown to be significantly lower in pulmonary arteries of PAH patents compared to normal controls [6]. Then, voxel-wise data was exported to Paraview in .vtk format files and a 3D Delaunay mesh was generated with offset and α parameters set to 0.1mm and 2 respectively (figure 2). The Delaunay mesh was used to estimate velocity gradients and estimations of time-resolved vorticity. Paraview filters were applied to identify magnitude and location of regions with highest wall shear stress and vorticity.

**Statistics.** Statistics were performed with JMP® Pro 15.1.0 (SAS Institute Inc.) and assumed a significance level of $p^* < 0.05$. Standard ANOVA was used to study the effect of treatment, location, case and observer on hemodynamic parameters. Then a case paired Student t-test was applied to explore the effect of iNO treatment on hemodynamic parameters.

## RESULTS

Resulting velocity distributions and derived hemodynamic parameters showed good agreement with previous studies on PAH on adults. Notably, PWV estimations were $4.3 \pm 0.3 \dot{m}/s$, $3.2 \pm 0.4 \dot{m}/s$, and $1.7 \pm 0.3 \dot{m}/s$ at the MPA, LPA and RPA respectively. Blood flow is distributed in the pulmonary branch such that $55 \pm 10\%$ of the volume is directed to the LPA.

For all cases studied, PC MRI suggests that normal peak forward velocity normalized to the mean time-averaged velocity is on average 10% larger at the MPA after iNO inhalation, and 40% larger at the LPA, a trend that requires further study to explore potential statistical significance ($p<0.2$). Retrograde peak velocity normalized to mean time-averaged velocity was 20% lower at the MPA after iNO inhalation, a difference that approached statistical significance ($p=0.12$). However, statistical analysis showed that, for the cases studied here, iNO treatment does not affect PC MRI derived measurements of area change, net blood flow, retrograde flow, blood flow distribution or pulse wave velocity. These results were on agreement with findings from 4D Flow MRI data, that revealed that peak velocity and wall shear stress were on average 15% and 10%, respectively, larger after iNO inhalation (figure 3). Peak velocities were found on consistently within the MPA. Wall shear stress peaked at the superior wall of the MPA product of the interaction with the flow ejected from the right atrium, and at the posterior side of the main pulmonary branching.

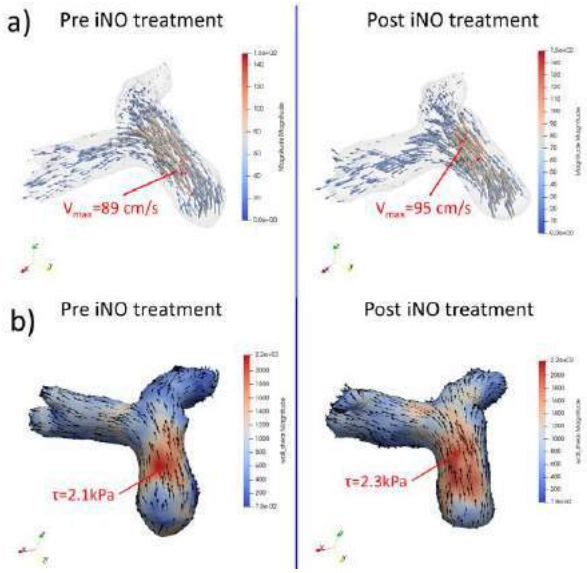


**Figure 3.** a) Velocity distribution b) Wall shear stress distribution.

## DISCUSSION

PC MRI and 4D Flow MRI are useful tools to quantitatively, and qualitatively assess patient-specific pulmonary artery hemodynamics in PAH. Herein, these tools were applied to explore potential effects of iNO inhalation for vasoreactivity tests on pulmonary artery hemodynamics. The method did show differences on velocity and velocity-gradient distributions, suggesting that iNO inhalation treatment reduces the intensity of retrograde flow velocity, wall shear stress, and flow vorticity. The statistical analysis showed that case-to-case variability dominated over the effects of iNO treatment. Nevertheless, the trends found here motivate us to pursue future studies with a larger cohort of recruited patients to further explore the effects of iNO treatment on PAH hemodynamics. The developments of non-invasive tools to assess PAH severity and responsiveness to vasoactive agents has the potential to reduce costs of diagnosis and treatment of this disease, with a positive impact on patients quality of life.


## ACKNOWLEDGEMENTS

This work was supported by the American Heart Association and the D.C. Women's Board (award number 834649/2021), and the National Institute of Health (grant number NIH NHLBI K23HL135352). We also thank Jenna Gaspar and the VCU College of Engineering DURI Dean's Undergraduate Research Initiative Program.


## REFERENCES


**[1]** Hunt, J.M. et al. Pulm. Circ. 4 (2014) 103. https://doi.org/10.1086/674880. **[2]** M. Schäfer, B.S. J. Am. Heart Assoc. 10 (2021) 20548. https://doi.org/10.1161/JAHA.120.020548. **[3]**Lankhaar, J.-W. Reson. Imaging. 22 (2005) 73–79. https://doi.org/10.1002/jmri.20361 **[4]**Vulliémoz, S. Reson. Med. 47 (2002) 649–654. https://doi.org/10.1002/MRM.10100. **[5]** Potters, W. J. Magn. Reson. Imaging. 41 (2015) 505–516. https://doi.org/10.1002/jmri.24560. **[6]** Truong, U. Cardiovasc. Magn. Reson. 15 (2013) 81. https://doi.org/10.1186/1532-429X-15-81.

# EFFECT OF BULGING SINUS ON HEMODYNAMIC PERFORMANCE OF POLYMERIC RV-PA CONDUIT FOR PEDIATRIC AND ADULT PATIENTS

**Srujana S. Joshi (1), Hieu T. Bui (1), Milad Samaee (1), Susan P. James (2), Lakshmi P. Dasi (1)**

(1) The Wallace H. Coulter Department of Biomedical Engineering, Georgia Institute of Technology, Atlanta, GA, USA
(2) Department of Mechanical Engineering, Colorado State University, Fort Collins, CO, USA

## INTRODUCTION

Congenital heart defects (CHD) are among the most common birth defects in the United States and a leading contributor to infant mortality rates across the globe. In 2017, CHD caused about 181,000 deaths in infants, accounting for 70% of the total CHD mortality rate worldwide[1]. A right ventricle to pulmonary artery (RV-PA) conduit is often used in procedures for various congenital heart defects such as pulmonary atresia, Tetralogy of Fallot, truncus arteriosus and right ventricle outflow tract reconstruction. This device helps restore the pulmonary blood flow from the heart. Currently available conduit options include homografts, decellularized allografts, commercial xenografts (Contegra and Hancock by Medtronic), prostheses made from expanded polytetrafluoroethylene (ePTFE) and/or polyethylene terephthalate (PET) that are hand sewn intraoperatively, and a newly developed tissue engineering conduit, the Xeltis pulmonary valve[2-6]. The challenges with these existing conduits include thrombus formation, calcification, stenosis, regurgitation and sternal compression, which affects the device's longevity leading to surgical reinterventions[7]. Therefore, there is a critical need to investigate biocompatible materials, optimize the design for these conduits, and introduce geometrical modifications that can alleviate these issues.

Our group has demonstrated the use of a novel biomaterial made of an interpenetrating polymeric network of hyaluronan (HA) and linear low density polyethylene (LLDPE) for cardiovascular devices, owing to its biocompatibility, anti-calcific and anti-thrombotic properties[7,8]. In addition to these advantages, HA-LLDPE has good hemodynamic performance due to low bending stiffness, high tear and tensile strengths, as well as excellent handling characteristics, and is inexpensive. Therefore, the objective of this pilot project is to demonstrate the potential of the HA-LLDPE conduit for pediatric and adult populations to address many of the drawbacks of the available options. We will look at HA-LLDPE conduit as an alternative to existing options and understand the difference in hemodynamics post geometrical modifications. Particularly, we will investigate the introduction of a bulging sinus ad its effect on the conduit's performance characteristics.

## METHODS

### Conduit Design

LLDPE conduits of diameters 14 mm and 26 mm were designed with and without a sinus, having the same leaflet geometry as shown in Figure 1. In order to incorporate the sinus geometry, the correlation between body surface area (BSA) and sinus of Valsalva, which is 26.79  6.59 mm/m$^2$ (r – 0.886, p < 0.001) when BSA is between 0.5 and 1.0 m$^2$, was used[9]. Equation 1 gives the relationship between the main pulmonary artery (MPA) and body surface area (BSA)[10]:

$$MPA=(1.653)(BSA0.5)+0.033\text{MPA}=1.653\text{BSA}0.5+0.033\ldots \quad (1)$$

Based on the above relationship, the sinus diameter for each of the designs was calculated and incorporated into their respective designs.


**Figure 2: Top view and side view of valved conduit (A) With bulging sinus and (B) Without bulging sinus**

**Valve Fabrication and Conduit Assembly**

LLDPE (80um thick) sheet was mounted on a vacuum former, preheated for 30 seconds, and vacuum formed into a valve using a 3D printed mold. The process was repeated with another LLDPE sheet thermoformed around a tubular mold that it mounted on the valve, which created the conduit. Further heating of the valved conduit along its wall fused two LLDPE layers together. In order to incorporate a sinus geometry into the valve, the molds used to create the valved conduits will be altered. Figure 1 shows the two conduit designs after thermoforming.

***In vitro* Hemodynamic Assessment**

LLDPE valved conduits, with and without a sinus of Valsalva, of two diameters (14 and 26 mm) were fabricated and mounted in an in-vitro model as shown in Figure 2 and tested under pulsatile flow conditions (8/25 mm Hg diastolic/peak systolic pressure). The 14 mm and 26 mm conduit were tested at pediatric and adult conditions, respectively. A working fluid of 60/40 water to glycerin (99% pure glycerin) was used as a blood analog to provide required density and kinematic viscosity of 1060 kg/m$^3$ and 3.5 x 10-6 m$^2$/s, respectively. Pressure gradient and flow waveform were collected. From this data, mean transvalvular pressure gradient (ΔP), peak transvalvular pressure gradient (peak ΔP), effective orifice area (EOA), and regurgitant fraction (RF) were computed for each of the valved conduits.

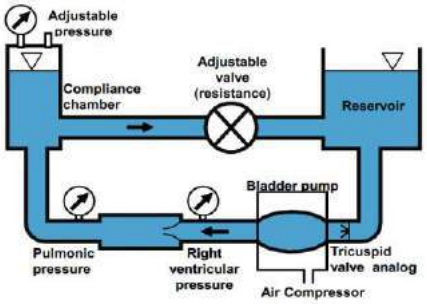


**Figure 2: Schematic of physiological right heart simulator**

**RESULTS**

The ΔP, peak ΔP, and RF for the 14 mm and 26 mm straight conduits without a sinus are shown in Table 1. The EOA for all samples is close to the minimum device performance required value for the appropriate valve size, between 1.45 cm$^2$ for 26 mm ID and approximately 0.47 cm$^2$ for 14 mm ID as extrapolated from the ISO 5840. Additional data for the 14 mm and 26 mm conduits with bulging sinus is being generated for the presentation.

**Table 1: Hemodynamic data and in-vitro setting of the LLDPE pulmonary valved conduit**

| Size (mm) | ΔP (mmHg) | | Peak ΔP (mmHg) | | (RF) (%) | |
|---|---|---|---|---|---|---|
| | mean | std | mean | std | mean | std |
| 14 | 13.6 | ±0.72 | 24.9 | ±1.17 | 2.83 | ±0.74 |
| 26 | 18.1 | ±0.25 | 24.7 | ±0.28 | 9.53 | ±0.49 |

**DISCUSSION**

The HA-LLDPE valved conduits proposed in this study will be a positive step towards developing a biocompatible conduit that has excellent hemodynamics and durability. The pressure gradients of the LLDPE conduits are comparable to that of Contegra bovine jugular conduits[10]. The incorporation of a bulging sinus can improve the overall hemodynamic performance characteristics of the conduit, increasing the longevity of the device. Thus, the development of this conduit would help in the treatment of various complex congenital heart defects.

**ACKNOWLEDGEMENTS**

We would like to thank the staff at Georgia Tech's biomedical engineering machine shop for their equipment and insights.

**REFERENCES**

1. GBD 2017 Congenital Heart Disease Collaborators, Lancet Child Adolesc Health. 2020 Mar;4(3):185-200.
2. Corno, A. F. et al, Ann. Thorac. Surg. 78, 1382–1388 (2004).
3. Ootaki, Y. et al, Ann. Thorac. Surg. 105, 843–850 (2018).
4. Yamamoto, Y. et al, Semin. Thorac. Cardiovasc. Surg. 32, 990–999 (2020).
5. Prodan, Z. et al, Semin. Thorac. Cardiovasc. Surg. (2021)
6. Carreon, C. K. et al, J Thorac Cardiovasc Surg. 157, 342-350 (2019)
7. Prawel, D. A. et al, Cardiovasc. Eng. Technol. 5, 70–81 (2014).
8. Heitkemper M. et. al, Novel Hyaluronan Enhanced Polymeric Transcatheter Aortic Valve Replacement: A proof of concept. in (2018).
9. Paytoncu, Ş, J. Cardiovasc. Med. 7, 126–132 (2019).
10. Sfyridis, P. G. et al,. J. Cardiol. 52, 501–508 (2011).

# PERFORMANCE OF THE BALLOON-EXPANDABLE VALVE IN A SELF-EXPANDING VALVE AT DIFFERENT IMPLANTATION HEIGHTS

**Milad Samaee (1), Huang Chen (1), Pradeep Yadav (2), Vinod Thourani (2), Lakshmi Prasad Dasi (1)**

(1) Biomedical Engineering, Georgia Institute of Technology, Atlanta, GA, USA
(2) Department of Cardiovascular Surgery, Piedmont Heart Institute, Atlanta, GA, USA

## INTRODUCTION

Transcatheter aortic-valve (TAV) replacement (TAVR) is currently approved for all risk categories of patients [1]. Following the use of TAVR at younger ages, the life expectancy may go beyond the durability of the TAVs [2], which have been raised by the structural heart community. As a result, implantation of a second TAV inside a prior TAV (which is known as redo TAVR or TAV-in-TAV) procedure may be considered to treat patients with failed TAVs due to regurgitation, stenosis, or a combination of the two. However, depending on the patient anatomy (such as coronary access due to risk of coronary obstruction) and the initial TAV status and characteristics, the second TAV's selection and implantation height will be crucial. Moreover, the second TAV performance, such as leaflet fluttering, pinwheeling, effective orifice area (EOA) size, and the downstream flow pattern can be affected by the implantation height compared with the initial TAV. The current in vitro study investigates the effects of the second TAV implantation height in a TAV-in-TAV procedure by comparing the hemodynamics and performance of the second TAV at different implantation heights.

## METHODS

A 26 mm SAPIEN 3 Ultra (Edwards Lifesciences, Irvine Calif) was deployed in a 29 mm Evolut PRO+ (Medtronic Inc, Irvine, Calif) within a transparent distensible aortic chamber at four different heights ($H_1$ = 24.5mm, $H_2$ = 20.5mm, $H_3$ = 16mm, and $H_4$ = 12.5mm) as shown in **Figure 1**. The aortic chamber was implanted in a left heart simulator, which was designed and used in our previous studies [3]. The flow loop imposed physiological hemodynamics (peak aortic flow = 25±0.2 L/min; heart rate = 60 bpm; systolic/diastolic aortic pressure = 120/80±1 mmHg) in all four sets of experiments. 60 consecutive cardiac cycles were recorded for calculating hemodynamic parameters, namely EOA and regurgitant fraction (RF). EOD and RF percentage were calculated as Equitation 1 and Equation 2, respectively.

$$RF = \frac{Regurgitant\ Volume\ [ml]}{Stroke\ Volume\ [ml]} \times 100 \quad (1)$$

where regurgitant volume was the sum of closing volume and leakage volume; stroke volume was considered as forward flow volume.

$$EOA = \frac{Q\ [cm^3/s]}{51.6\sqrt{PG\ [mmHg]}} \quad (2)$$

where Q represents the root mean square aortic valve flow and PG is the mean transvalvular aortic pressure gradient in a cardiac cycle.

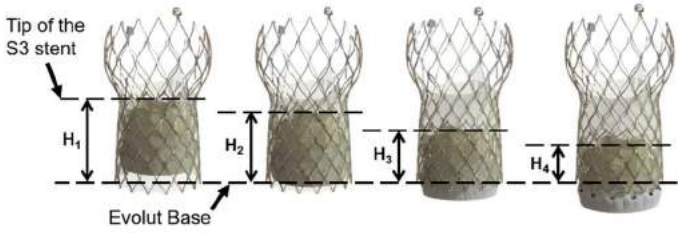


**Figure 1: Deploying a 26 mm SAPIEN 3 Ultra in a 29 mm Evolut PRO+ at four different heights**

En face images were recorded using a 1 kHz frame rate high-speed camera. Geometric orifice area (GOA) and pinwheeling index (PI) were calculated using the en face images. PI was calculated as Equation 3.

$$PI = \frac{L_{actual} - L_{ideal}}{L_{ideal}} \times 100 \quad (3)$$

where $L_{actual}$ and $L_{ideal}$ represent the deflected and unconstrained free edge of the leaflet, respectively. Fluid flow patterns downstream of the TAV were assessed using high spatial and temporal resolution particle image velocimetry (PIV). 200 consecutive image pairs were acquired at 3 time points: mid acceleration, peak systole, and mid deceleration.

Velocity vector field, vorticity dynamics, and Reynolds shear stress (RSS) were also evaluated distal to the TAV.

## RESULTS

The obtained mean pressure gradients (PG) for four conditions was 11.84±0.27 mmHg, 11.61±0.48 mmHg, 12.46±0.52 mmHg, and 12.26±0.47 mmHg for $H_1$, $H_2$, $H_3$, and $H_4$, respectively, which is comparable to each other. The RF for all cases is shown in **Figure 2**.

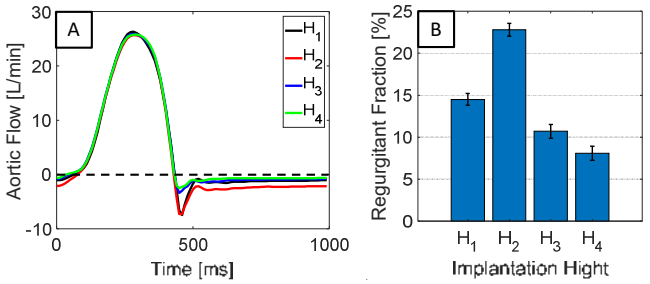


**Figure 2: Aortic Flow and regurgitant fraction Comparison between different implantation heights**

Similarly, calculated EOAs were comparable with all cases (1.72±0.02 $cm^2$, 1.57±0.03 $cm^2$, 1.55±0.06 $cm^2$, and 1.69±0.04 $cm^2$) for $H_1$, $H_2$, $H_3$, and $H_4$, respectively. The en face view of the valve at peak systole and during diastole for different implantation heights are shown in **Figure3**. As shown in **Figure 3**, PI cannot be calculated for $H_3$ and $H_4$ since the Evolut valve is fully closed during diastole and blocks the SAPIEN 3 en face view. The PI values for $H_1$ and $H_2$ were 12.42% and 18.31%, respectively.

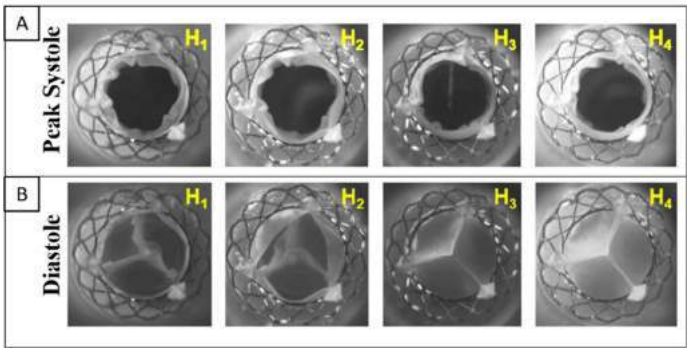


**Figure 3: En face view of TAV at A) peak systole and B) diastole**

RSS and velocity vector fields overlaid with z-vorticity contours at peak flow and acceleration phase are plotted as shown in **Figure 4**. Results for the mid-decelerations will be presented.

## DISCUSSION

With the highest implantations of SAPIEN 3 in Evolut ($H_1$) the stent frame of the SAPIEN 3 pushes the Evolut leaflets and generates a neo-skirt. Therefore, the Evolut leaflets stay fully open during diastole and may cause a coronary obstruction that needs further investigation. Evolut leaflets remain half-open in $H_2$ during diastole and fully closed in lower implantation heights, $H_3$ and $H_4$. Therefore, PGs were lower in $H_1$ and $H_2$ than $H_3$ and $H_4$ since both SAPIEN 3 and Evolut leaflets need to be open in early systole in $H_3$ and $H_4$.

The closing volume and leakage volume are reduced in lower heights of implantation ($H_3$ and $H_4$) due to having two valves closing in series, unlike those higher implantation heights ($H_1$ and $H_2$). This result can be beneficial from the fluid mechanical point of view; however, the clinical aspects need to be justified.

The RSS looks very high in $H_1$ and shows the lowes in $H_3$. A vortex ring is generated in $H_3$ and $H_4$ during the acceleration phase (early systole), which is due to having the closed Evolut leaflets opening and will be beneficial for mixing fluid flow.

Another important point that needs to be investigated is incorporating the stiffness of the Evolut valve in this study. The TAV-in-TAV is usually proposed to be performed on a calcified TAV. The stiffness of the Evolut will play an important role in the amount of pressure gradients and will be highly dependent on the implantation heights. Therefore it seems to be beneficial to open up the Evolut valve ($H_1$ or $H_2$), but at the same time can cause coronary obstructions. Another important future study is washout investigations in the sinus area since the geometry of the neo-sinus is highly dependent on the implantation height.

Results suggest that the implantation height in TAV-in-TAV is an important factor. A detailed hemodynamics comparison between cases will be discussed.

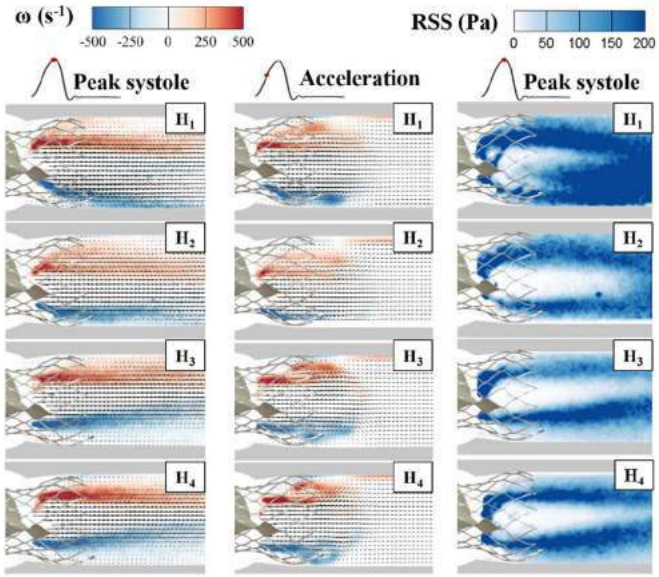


**Figure 4: En face view of TAV at A) peak systole**

## Reference:


[1] Tang, GHL et al., *JACC Cardiovasc Interv*, 13(9): p 1030-1042, 2020.

[2] Popma JJ et al., *N Engl J Med*, 380(18): p. 1706-1715, 2019.

[3] Hatoum, H. et al., *Ann Biomed Eng*, 47(4): p. 1116-1128, 2019.

# CHANGES IN THE IN-VIVO FUNCTIONAL STATE OF THE MITRAL VALVE IN PERCUTANEOUS MITRACLIP REPAIR

**Hao Liu (1), Natalie Simonian (1), Sneha Vakamudi (3), Mark Pirwitz (3), Joseph H. Gorman III (2), Robert C. Gorman (2), and Michael S. Sacks (1)**

(1) James T. Willerson Center for Cardiovascular Modeling and Simulation, The Oden institute and the Department of Biomedical Engineering, University of Texas at Austin, Austin, Texas, USA
(2) Gorman Cardiovascular Research Group, Department of Surgery, University of Pennsylvania, Philadelphia, Pennsylvania, USA
(3) Department of Internal Medicine, University of Texas at Austin, Austin, Texas, USA

## INTRODUCTION

Mitral regurgitation is the most common valvular disease in the United States affecting over 2% of the population and is expected to double by 2030 due to population aging [1, 2]. The preferred treatment strategy for MR is undersized ring annuloplasty (URA), but the long-term outcomes of this repair are mixed [3, 4]. Recently, minimally invasive edge-to-edge leaflet clipping methods (e.g the MitraClip) have been of great clinical interest as the technique is generally effective, particularly for patients at high surgical risk with no suitable alternatives [5]. However, outcomes as compared to other treatment options have been unclear, as well as long-term outcomes (>5 years) after surgical procedures. Furthermore, the details of the procedure (the number, size, and placement of the clips) are dependent on the clinician's experience, and these configurations are adjusted heuristically in real-time during the procedure until maximum reduction of MR grade on echo has been achieved. Therefore, there is clearly an urgent need for quantitative, patient-specific treatment optimization. In particular, we seek to develop models which consolidate the highly variable clinical metrics of each individual into predictive factors of future repair efficacy.

In this study, we focused on the MitraClip percutaneous edge-to-edge repair (Abbott Inc.) used to correct ischemic mitral valve regurgitation (IMR). Our long-term objective is to develop an understanding of the functional consequences of minimally invasive edge-to-edge leaflet approximation methods using clinically available imaging data to accurately assess and predict the efficacy and longevity of MitraClip procedure for individual patients. In the present study, as a first step we examined the leaflet deformation patterns of pre- and post-surgical post-IMR state mitral valves (MV) to develop an improved understanding of how point loads generated by the MitralClip affect both the local and more distant leaflet deformation patterns.

## METHODS

Real-time three-dimensional echocardiography (rt-3DE) images of 20 patients before and after MitraClip procedure were performed and 3D volume data was then converted to the Cartesian coordinates system. MitraClip devices were clearly visible in rt-3DE images using ITK-snap software (Figure 1).

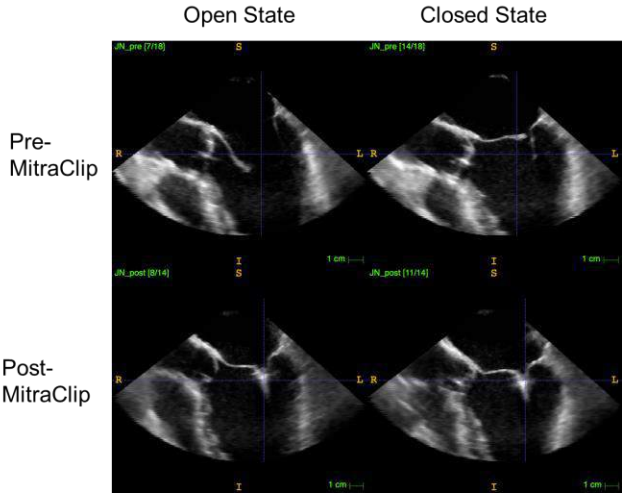


**Figure 1: 3D echocardiography (parasternal long-axis view) of one patient in pre- and post- MitraClip state**

Then, these rt-3DE images were segmented with our previous established segmentation pipeline in MATLAB [6, 7] (details are shown in Figure 2). Afterwards, in-vivo strain estimation of pre-MitraClip state was analyzed using our extensively validated pipeline [6, 7] (Figure 3A). The simulation was conducted in the commercial FE software Abaqus by applying an annular displacement boundary

condition, a physiological ventricular pressurization, and a downward chordal-mimicking force. After the leaflets have initially coapted, a local corrective pressure field was applied to penalize any mismatch between the simulated geometry and the true closed-state rt-3DE reconstruction. For post-MitraClip state simulation, we improved the in-vivo strain estimation pipeline by introducing axial and beam connectors which are functionally equivalent to the MitraClip (Figure 3B). First, six axial connectors were created by connecting the anterior and posterior leaflets where MitraClip located. Secondly, two nodes on each connector were activated to minimize its distance to zero similar to MitraClip actuation. Next, the axial connectors were replaced with beam connectors to fix these points of leaflets and the same shape-matching technique as in the pre-MitraClip state was utilized to generate the global radial and circumferential strain fields.

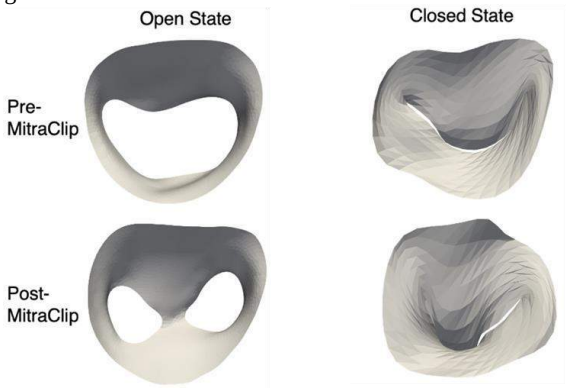


**Figure 2: rt-3DE Image segmentation of a patient MV before and after percutaneous repair. In the open state, the double orifice and pinching of two leaflets is clearly visible, and in the closed state, the excessive posterior distension of the anterior leaflet is delineated by the mesh element edges**

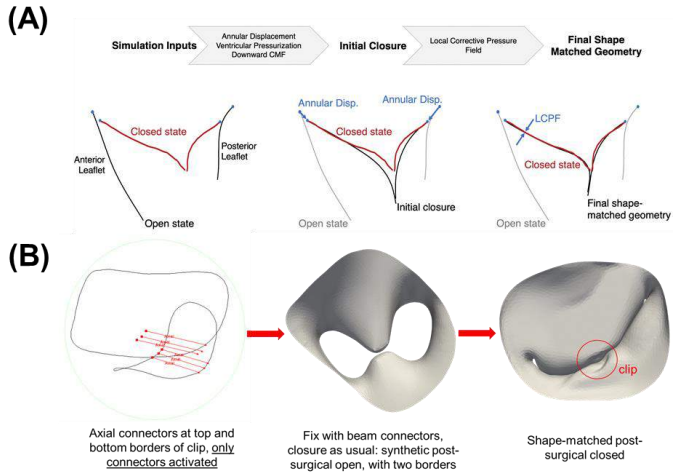


**Figure 3: (A) Shape matching method for pre-surgical simulation: starting from MV open state geometry, annular motion and transmural pressure were applied to have a transitional state. Then, local corrective pressure forces were implemented to match MV closed state geometry; (B) Improved shape matching technique by introducing axial and beam connectors as MitraClip device in post-MitraClip cases**

## RESULTS

Results firstly demonstrated a clear distortion in leaflet geometry due to leaflet edge-edge repair. The anterior leaflet was dramatically displaced towards posterior side which is confirmed with notable increase in radial strain of anterior leaflet. In the meantime, the posterior leaflet moved towards the posterior side and induced a decrease of radial direction of posterior leaflet. An increase of circumferential strain was observed around free edge area mainly due to the grippers of the MitraClip grabbing the leaflets. However, circumferential strain in the belly area had an overall decrease after repair (Figure 4, left panel).

Then, we compared the stress distributions between pre-surgical and post-surgical states. Clearly, stress concentration in both circumferential and radial directions were observed and locations were confirmed with where dramatic change of strain occurred (Figure 4, right panel).

## DISCUSSION

Application of the MitraClip was shown to clearly induce major alterations in MV leaflet strain and stress behaviors. This work confirms that such techniques dramatically alter the MV functional behaviors, which may elucidate the underlying reasons long-term MV remodeling occurs in response to the observed stress concentrations, possibly leading to limited repair durability. We are currently conducting analyses on 20 patients to: (1) establish the pre-operative state of MV across the mitral regurgitation spectrum and (2) elucidate overall consequences of MitraClip on MV leaflet geometry, behavior, and remodeling. This study will allow us to develop an anatomically faithful patient specific model of MV apparatus to predict post-surgical outcomes strictly from pre-surgical information. Such studies are critical since clinical long-term outcomes of MV repair are quite poor, yet our knowledge on how to improve surgical outcomes is very limited. Our long-term goal is to inform the optimal treatment for each patient, including of repair or replacement is the best treatment of choice.

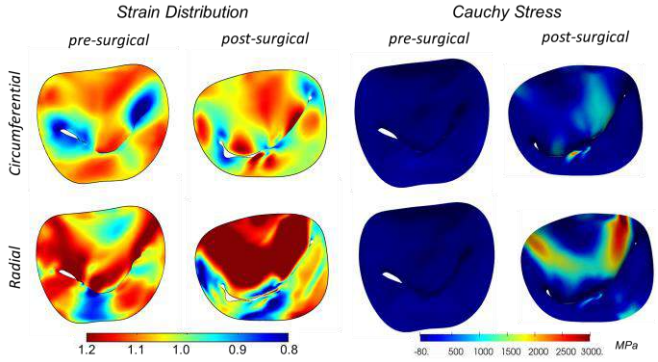


**Figure 4: In-vivo strain and Cauchy stress estimation of pre-surgical and post-surgical states: an increase of radial strain on anterior leaflet and a decrease of radial strain on posterior leaflet due to excessive posterior distention for both leaflets; an increase of circumferential strain around contact area and a decrease in the belly area; stress concentration were captured where dramatic changes of MV strain occurred.**


## ACKNOWLEDGEMENTS

The authors gratefully acknowledge funding from NIH R01 HL073021


## REFERENCES


[1] Benjamin EJ et al., Circulation, 2018; 137:e67—e492
[2] Nkomo VT et al, Lancet. 2006; 368(9540): 1005-1011
[3] Perrault, L. et al., JTCVS. 143(6), pp. 1396-1403
[4] Whitlow, P.L et al., JACC. 59(2), 2012. 130-139
[5] Brouwer, H.J et al,. EHJCI 2019. 20(3), 307-313
[6] Rego B.V. et al,. IJNMB 2018 34. 12: e3142
[7] Narang H. et al,. ABME 2021: pp 1-13

# DRUG DISCOVERY FOR SELECTIVE TARGETING OF PANCREATIC CANCER CELLS USING MICROFLUIDIC TUMOR-STROMA MODEL

**Hye-ran Moon (1), Mark R. Kelley (2,3), Melissa L. Fishel (2,3), Bumsoo Han (1,4)**

(1) School of Mechanical Engineering, Purdue University, West Lafayette, IN, USA
(2) Department of Pediatrics and Herman B Wells Center for Pediatric Research, Indiana University School of Medicine, Indianapolis, IN, USA
(3) Indiana University Simon Comprehensive Cancer Center, Indiana University School of Medicine, Indianapolis, IN, USA
(4) Purdue Center for Cancer Research, Purdue University, West Lafayette, IN, USA

## INTRODUCTION

Pancreatic ductile adenocarcinoma (PDAC) is a dismal disease whose 5-year survival rate is only 10%. [1] PDAC comprises a complex and heterogeneous tumor microenvironment (TME) with a strong desmoplastic stroma, including cancer-associated fibroblast, which causes inherent resistance to anti-cancer therapy. Among stromal cells, cancer associated fibroblast (CAFs) play a central role in PDAC progression and drug resistance, but their interplay with pancreatic cancer cells (PCCs) remains elusive. [2] Specifically, CAFs can also hinder drug delivery to PDAC tumors and escalate therapeutic resistance. [3] Therefore, it is essential to have a reliable tumor model that allows for the systematic study of the complex disease to make advances in anti-cancer therapeutic strategies.

In the present study, we used a tumor microenvironment on-chip (T-MOC) model, which reconstitutes PCC and CAFs in the 3D perfused TME context, to discover the efficacy of drug candidates targeting the redox function of Ref-1 in PDAC. The Ref-1 has been recognized as a redox signaling protein regulating redox metabolic activity of cancer in hypoxia, known to induce drug resistance and metastasis. [4] The inhibition of the redox activity has been recognized as effective in reducing PDAC tumor growth. Our group already synthesized multiple analogs of Ref-1 inhibitors [4]. Here, we investigated the efficacy of the Ref-1 inhibition on PCC in the presence of CAFs by using the T-MOC model to test its capability of screening the drug efficacy difference between the cell types. The results are analyzed to test whether the T-MOC model can provide a reliable testbed to study the potential cancer-selective targeting drugs for the complex and heterogeneous TME in a controlled manner.

## METHODS

The tumor-microenvironment-on-chip (T-MOC) is a 3D *in vitro* microfluidics platform composed of three channels – an interstitial and two side channels. The 1mm-wide interstitial channel includes cells embedded in the 3D extracellular matrix (ECM), sided with two 300μm-wide channels allowing for drug perfusion mimicking the actual interstitial transport in PDAC TME. The microfluidic platform was fabricated by soft-lithography techniques using PDMS. Details of fabrication and preparation were described previously. [5] The interstitial channels were filled with cell-collagen mixture fulfilling the 3D culture condition. We used a human pancreatic cancer cell line (Pa03C, transfected with Td-tomato) and cancer-associated fibroblast cell line (CAF19, transfected with GFP) for the model. [4] The cell-collagen mixture was composed of Pa03C and CAF19 cells, and 6 mg/ml of type I collagen with 10X PBS, NaOH, HEPES buffer, FBS, Glu, P/S, and cell culture grade distilled water. PCCs (Pa03C) and CAFs (CAF19) were mixed into the cell-collagen mixture at a 1:1 cell ratio. The initial cell concentration was $2 \times 10^6$ cells/mL for each cell type. After loading, the chips were incubated at 37°C for 1 hour for collagen polymerization. Then, the culture medium was introduced through the side channels. The loading process was controlled by pressurizing channels.

To assess drug efficacy, we followed the experiment timeline shown in **Fig 1**. The PDAC T-MOC were cultured for 48 hours before the experiments. Then, the drugs were perfused through the side channels (DAY0). We initially applied a pressure difference between two side channels to ensure the drug perfusion to cells encapsulated by the collagen matrix. The pressurization was achieved by varying a medium level in the side channel reservoirs. The drug solutions were prepared in the culture medium as 0 μM (control), 3, 10, and 30 μM for APX2009 (Ref-1 inhibitor). On day 3, the channels were washed with a drug-free medium and re-perfused with the same drug-containing medium. On day 6, we finalized the treatment and measured drug efficacy.

Drug efficacy was analyzed in two ways, cell growth and cell survival. Cell growth was determined by quantifying the fluorescent cell area. Fluorescence of transfected Pa03C (Td-tomato) and CAF19 (GFP)

was measured with an inverted microscope (Olympus IX71, Japan) with TRITC and FITC filter on days -2, 0, 3, and 6. Cell growth was analyzed by normalizing the corresponding fluorescent pixel counting by day 0.

$$\text{Cell growth} = \frac{[\text{Fluorescent area of cells}]_{\text{DAY } n}}{[\text{Fluorescent area of cells}]_{\text{DAY0}}} \quad (n = 0, 3, \textit{and } 6)$$

Cell survival was determined by evaluating cell viability at the end of the experiment. The cell survival was defined as the cell growth at day 6 of drug treatment groups normalized by the cell growth of the control groups (absence of drug) as following:

$$\text{Cell survival} = \frac{[\text{Cell growth}]_{treatment}}{[\text{Cell growth}]_{control}}$$

## RESULTS

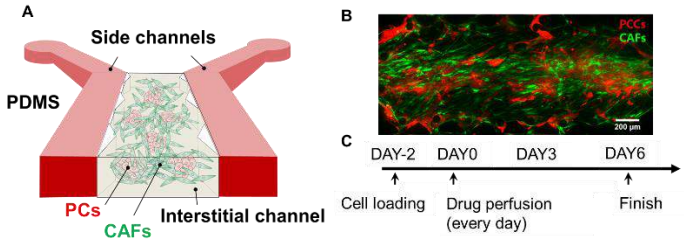


**Figure 1: (A) Schematic of functional structures of PDAC T-MOC (B) Fluorescent microscopic observation of PCCs (red) and CAFs (green) in PDAC T-MOC (C) Experimental timeline**

To assess the potential effect of Ref-1 inhibition as a cancer-selective target drug, the PDAC T-MOC model was utilized with co-culture of Pa03C and CAF19 cells. (**Fig.1A**) The T-MOC platform was developed to reconstitute the heterogeneity in the tumor microenvironment as described in our previous publication. [5] In the present study, we integrated the human PCCs with CAFs in the T-MOC platform. [4] Each cell type was transfected, having distinguishable fluorescence. The red fluorescent PCCs were clearly distinguished over the green fluorescent CAFs as shown in **Fig.1B**, highlighting the capability of T-MOC to capture the cell-cell interactions *in vitro*. The treatment schedule was also designed to mimic an animal treatment schedule (**Fig.1C**).

We tested the efficacy of Ref-1 inhibitor (APX 2009) for Pa03C (red fluorescence) and CAF19 (green fluorescence) co-cultured in tumor-stroma PDAC T-MOC to compare the differential response to the drug. Representative fluorescence micrographs of the T-MOC samples during the experiment are shown in **Fig. 2A**. In the control group (0μM), both cell types grew significantly over time, as indicated by the increasing red and green fluorescence. On the other hand, the treatment groups showed a differential effect of the APX 2009 between Pa03C and CAF19. The Pa03C cells treated by APX 2009 proliferated significantly slower than CAF19 from 3μM. The red fluorescence indicating Pa03C notably diminished over time, whereas no notable fluorescence change in green fluorescence of CAF19 even at the higher concentration of 30μM. We confirmed our observations by quantifying the cell growth and survival. (**Fig. 2B**) In terms of cell growth, the cancer cell growth treated by APX 2009 started to be slightly slower than the control from DAY3. On Day6, a significantly notable difference was observed in cancer cell growth among the experimental groups ($p<0.05$). The cell survival at DAY6 showed the cancer cell growth was suppressed as 0.48 in the 3μM treatment group while the control group was denoted as 1. For the CAF growth rate, no difference was noted among the experimental groups even at the 30μM treatment group. The resulting survival confirms that the efficacy of the combination treatment is notably high on PCC but not for CAF, indicating the tumor-selective targeting potential of the Ref-1 inhibition.

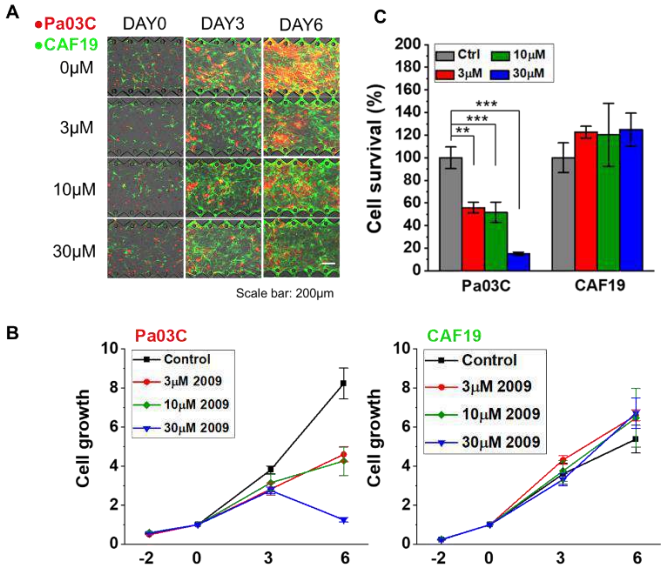


**Figure 2: (A) Fluorescent microscopic observation of Pa03C (red) and CAF19 (green) in PDAC T-MOC for APX 2009 treatment (B) Cell growth of Pa03C and CAF19 for APX2009 treatment (0, 3, 10, and 30μM) (C) Cell survival at the end of the experiment (DAY6); n≥3. Dots and bars; mean ± S.E. *: p<.05 (Tukey *post hoc* in ANOVA).**

## DISCUSSION

The present results demonstrate the capability of the T-MOC platform. We investigated the effect of the Ref-1 inhibitor as a potential tumor-selective targeting therapeutics by reconstituting the tumor-stroma TME in T-MOC. The results confirmed that the Ref-1 inhibition suppressed cancer cell growth whereas CAF growth was consistent even at the high concentration of 30μM APX 2009. The T-MOC platform provides a unique testbed to mimic the TME and pharmacokinetics and bridge high throughput spheroid models and *in vivo* animal models. In fact, most previous *in vitro* tumor models have not demonstrated distinct tumor microenvironment features. Both 2D monolayers and 3D spheroid tumor models inadequately recapitulate biophysical interactions in the complex TME. Animal models, including the complex feature of TME, are cost-ineffective and limited to control the biophysical and biochemical interactions in the complex TME. In this sense, the microfluidic technique has an advantage in bridging the conventional models with their controllability and easy accessibility.


## ACKNOWLEDGEMENTS

This work was partially supported by grants from the National Institutes of Health (U01 HL143403, R01 CA254110), the Purdue University Center for Cancer Research (P30 CA023168) and a Program Grant from Purdue Institute of Drug Discovery.


## REFERENCES


[1] Siegel RL, et al., *CA Cancer J Clin*. *2019*, 69:7–34, 2019.
[2] Öhlund D, et al., *J Exp. Med*, 211:1503-23, 2014.
[3] Han B, et al., *Cancer Letters* 380:319-29, 2016.
[4] Gampala et al., *J Exp Clin Cancer Res*, 40:251, 2021.
[5] Moon HR, et al., *Lab Chip*. 20:3720–32, 2020.

SB³C2022
Summer Biomechanics, Bioengineering and Biotransport Conference
June 20-23, Eastern Shore, MD, USA

# EVALUATION OF SHEAR STRESS VARIABILITY ALONG CAPILLARIES IN ANGIOGENIC RAT MESENTERIC MICROVASCULAR NETWORKS

**N. Hu (1), B. Lomel (1), P. Balogh (2), W. L. Murfee (1)**

(1) J. Crayton Pruitt Family Department of Biomedical Engineering, University of Florida, Gainesville, Florida, U.S.A.
(2) Mechanical and Industrial Engineering, New Jersey Institute of Technology, Newark, New Jersey, U.S.A.

## INTRODUCTION

Shear stress is commonly implicated in angiogenesis, defined as the formation of new vessels from existing vessels. The role of shear stress as a regulator of endothelial cell dynamics during capillary sprouting is supported by the influences on cell phenotype, proliferation and function [1,2]. For example, exposure of endothelial cells to 10-30 dyne/cm$^2$ laminar shear stress *in vitro* can result in the secretion of angiogenic growth factors (i.e. bFGF) and the upregulation of growth factor receptors (i.e. VEGF-R2) [3,4]. The appreciation of the physiological relevance of these models, however, is challenged by not knowing the actual shear stress values along vessels in an angiogenic microvascular network. Computational modeling based estimates in quiescent, adult microvascular networks suggest that shear stresses in individual capillary segments can range from 0.1 to over 500 dyne/cm$^2$ [5]. The potential heterogeneous distribution suggests that the range of relevant shear stresses might be different from those commonly used in *in vitro* studies and motivate critical questions. What is the shear stress experienced by endothelial cells along capillaries? Do all capillaries experience similar shear stress magnitudes? Can variations in shear stress along different capillary segments explain vessel-specific responses? The objective of this project was to estimate shear stress values in regions of angiogenic microvascular networks using measurements from real networks and a network segmental flow model.

## METHODS

**Angiogenic Microvascular Network Stimulation and Vessel Specific Measurements** Rat mesenteric tissues were harvested from adult male Wistar rats post the stimulation of angiogenesis via 48-80 mast cell degranulation. Microvascular networks were identified by perfusion of a 40kDa fixable dextran prior to harvesting and immunolabelling for PECAM. Dextran presence identified perfused segments along the hierarchy of microvascular networks, which were characterized by increased vessel density indicative of angiogenesis. Three representative network regions with arteriole input and venule output vessels were selected for analysis. Vessel segments were defined by nodes, branch order position, and the measurements of lengths and diameters.

**Computational Modeling** A network segmental flow model was used to computationally estimate vessel-specific shear stresses and velocities similar to previous studies [5,6]. Using the boundary conditions (i.e. input arteriolar pressure and output venular pressure), our segment measurements (length (L), diameter (D), and nodal pressures, segmental flows were estimated assuming a modified Poiseuille Flow relationship. An apparent viscosity per vessels was defined based on empirical data derived from the rat mesenteric microcirculation [5]. Initially, vessel viscosity ($\mu$) was set to 4 cP. Then conductance, C, was calculated per segment using equation (Eq. 1):

$$C = \frac{\pi D^4}{128 \mu L} \qquad (1)$$

With the segmental conductances and assuming 75 mmHg inlet pressures and 10 mmHg outlet pressures, the nodal pressure (P) and the flow going through each node (Q) was calculated using the following matrix equation: **CP = Q**. The discharge hematocrit (HD) was set to 0.45 at first and then be updated with the segmental flow, flow fraction ($\psi$) and cell flux ($\varphi$) entering a daughter segment, the diameter of parent segment (D) and daughter segments ($D_1, D_2$), based on an empirical red blood cell distribution law (Eq. 2-3) [6]:

$$A = -\frac{6.96 l \frac{D_1}{D_2}}{D}, \quad B = 1 + \frac{6.98(1-HD)}{D}, \quad X_0 = \frac{0.4}{D} \qquad (2)$$

$$\log it \varphi = B \log it \frac{\psi - X_0}{1 - 2X_0} + A, \quad \log it x = \ln \frac{x}{1-x} \qquad (3)$$

The updated hematocrit was then used to calculate segmental viscosity based on (Eq. 4-6) [6]:

$$C = (0.8 + e^{-0.075D})\left(-1 + \frac{1}{1 + 10^{-11}D^{12}}\right) + \frac{1}{1 + 10^{-11}D^{12}} \quad (4)$$

$$\mu^* = 6e^{-0.85D} + 3.2 - 2.4e^{-0.06D^{0.645}} \quad (5)$$

$$\mu = \{1 + (\mu^* - 1)\frac{(1-HD)^C - 1}{(1-0.45)^C - 1}(\frac{D}{D-1.1})^2\}(\frac{D}{D-1.1})^2 \quad (6)$$

With the updated segmental-specific viscosity, the segmental conductance, nodal pressure, and segmental flow was re-calculated, leading to another updated viscosity and a calculation loop. The calculation loop was stopped upon meeting the conversion requirement defined as total ratio of nodal pressure difference from previous iteration being less than 1%.

## RESULTS

Three angiogenic microvascular regions with clearly identified arteriole inputs and venule output vessels, as well as the loop connected by the arterioles and venules were selected for analysis (Fig. 1). For region 1, shear stresses along capillaries ranged from 0.3 to 708 dyne/cm$^2$ (average = 73± 98 dyne/cm$^2$). For region 2, shear stresses along capillaries ranged from 0.2 to 1509 dyne/cm$^2$ (average = 91± 120 dyne/cm$^2$). For region 3, shear stresses along capillaries ranged from 0.1 to 1645 dyne/cm$^2$ (average = 127± 178 dyne/cm$^2$). For the three regions, the maximum shear stress along capillary segments was greater than the maximum shear stress in the initial arterial branches.

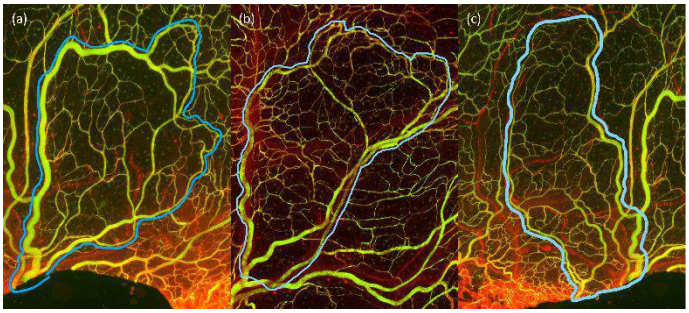


**Figure 1: Angiogenic Microvascular Network Regions. Perfused vessels were identified by perfusion of a 40kDa fixable dextran prior (Green). PECAM immunolabelling identifies all vessels (RED). (a) Region. 1 (b) Region 2. (c) Region 3.**

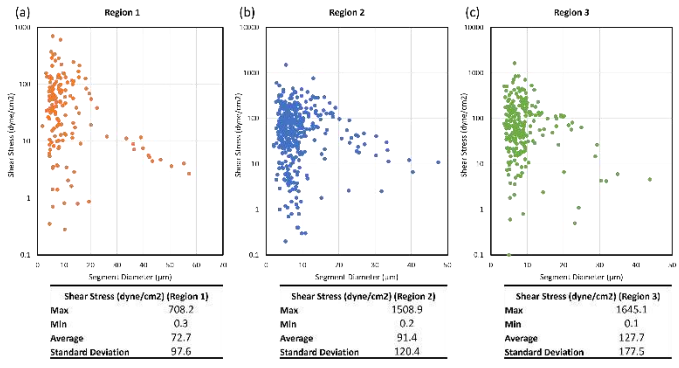


**Figure 2: Segment-Specific Shear Stress Estimates per Network Region. (a) Region 1 (b) Region 2 (c) Region 3.**

Vessel specific estimates allowed for comparing of shear stresses values for different vessel locations within the region. The maximum shear stresses in proximal capillary segments connecting the high-pressure arterial sides to the lower pressure venous sides in a network were increased compared to stresses for segments in more distal network regions. In order to evaluate the sensitivity of the vessel specific estimates to different network pressure drops, the shear stress distribution was evaluated for different pressure boundary conditions. Inlet vessel pressures were varied from 45 mmHg to 105 mmHg with the same outlet vessel pressure of 10 mmHg. Shear stress distributions per pressure scenario displayed a similar trends with high variability at the capillary level (Fig. 3).

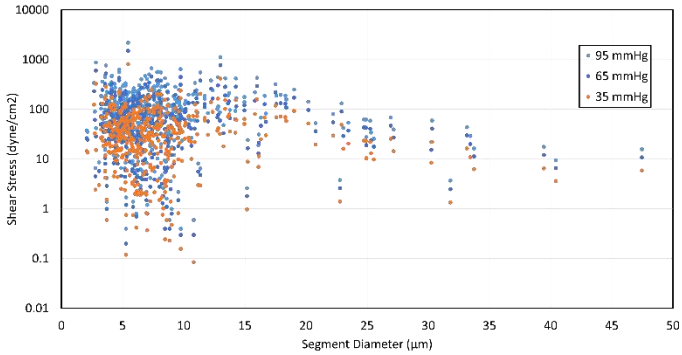


**Figure 3: Segment-Specific Shear Stress Estimation for Region 1 per Different Pressure Drop Scenarios. Inlet pressures were equal to 105 mmHg, 95 mmHg, and 45 mmHg. Outlet pressures were equal to 10 mmHg for each scenario.**

## DISCUSSION

The main contribution of this study is the estimate of vessel specific shear stress values in angiogenic microvascular networks. Consistent with previous cauterization, angiogenic remodeling in the 48-80 stimulated networks was supported by increased vessel density and capillary branching [7]. In the context of understanding the role of shear stress as a regulator of endothelial dynamics involved in capillary sprouting and to make sense of effects reported in the literature based on *in vitro* studies, we need to know the relevant shear stresses experienced *in vivo*. The results of this study highlight the potential heterogeneity of shear stresses at the capillary level in angiogenic microvascular networks and provoke questions related to how vessel-specific hemodynamic environments regulate endothelial cell function.


## ACKNOWLEDGEMENTS

This work was supported by the funding from the National Institute of Aging (Grant number R01AG049821).


## REFERENCES


[1] Murfee, WL, *Mechanobiology of the Endothelium*, 166-184, 2015.
[2] Stapor, PC et al., *Cardiovascular Engineering and Technology*, 2(2): 124-136, 2011.
[3] dela Paz, NG et al., *Journal of cell science*, 125(4), 831-843, 2012.
[4] Gloe, T et al., *Journal of Biological Chemistry*, 277(26), 23453-23458, 2002.
[5] Pries, AR et al., *American Journal of Physiology - Heart and Circulatory Physiology*, 281(3), H1015-H1025, 2001.
[6] Yang, M et al., *Medical & biological engineering & computing*, 50(6), 585-593, 2012.
[7] Sweat, RS et al., *Lymphat Res Biol*, 10(4):198-207, 2012.

# FABRICATION OF POLYMERIC HEART VALVES THROUGH ADDITIVE MANUFACTURING

**Hieu T. Bui (1), Adam S. Verga (1), Srujana S. Joshi (1), Scott J. Hollister (1), Lakshmi P. Dasi (1)**

(1) The Wallace H. Coulter Department of Biomedical Engineering, Georgia Institute of Technology, Atlanta, GA, USA

## INTRODUCTION

Approximately 30 million people are affected by valvular heart disease in the United States. About 182,000 heart valve replacements are conducted each year. Current solutions include replacing the native heart valve with either a mechanical valve or a bioprosthetic valve, both of which have significant downsides. For the mechanical valves, the major problem arises due to thrombogenicity, whereas for the bioprosthetic valves, issues arise because of the immune rejection by the host and low durability which reduces the longevity of the device and may require surgical reinterventions in the future.

In recent years, 3D printed heart valves are being developed to overcome these drawbacks [1]. With the help of 3D printing, intricate geometries representing the anatomy of native leaflets can be incorporated into the valve design to create patient-specific valves. Some of the advantages of customized valves are improved hemodynamic performance, higher durability and ease of surgical implantation. In addition to this, the recent advancements made in additive manufacturing techniques can enable printing leaflet materials with anisotropic mechanical properties, which mimic the properties of the native leaflets. This pilot study is the first attempt to design, manufacture and test 3D printed heart valves. Different 3D printed materials and leaflet thickness were investigated.

## METHODS

### Valve Design

The valve design is based on works described in the literature [1]. Computer-aided design (CAD) (Solidworks) was used to create valves. Figure 1 shows the fabrication process. Figure 2 shows an example of a valve leaflet with heterogeneous thickness. The valve assembly is presented in figure 3.

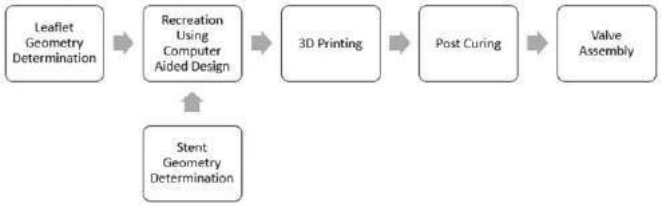


**Figure 1:** Flowchart of valve design and manufacturing process

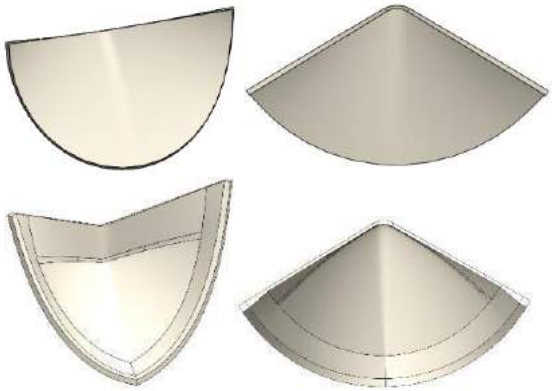

**Figure 2:** Isometric (top left) and top (top right) views of a leaflet with a low profile and homogenous thickness of 300 um. Isometric ( bottom left) and top views ( bottom right) of a leaflet with varying thickness where 1.5 mm radial outer portion is 500-um while the inner portion is 200 µm thick. The top and bottom leaflets were made in the v4 and v5 valves, respectively.

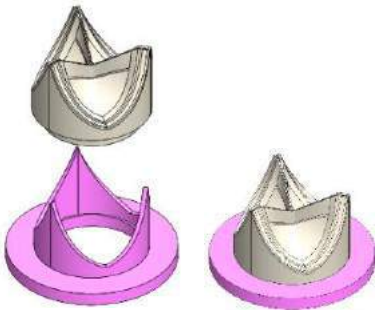

**Figure 3:** rendering of 3D printed valve assembly where the leaflet portion (beige) can be easily mounted on top of the frame (purple).

### Valve Production and Assembly

Valve prototyping was conducted using 3D printers and materials purchased from Stratasys. Shore-A materials are composed of mixes, in varying proportions, of soft Agilus material and rigid Vero material. Leaflets composed of shore-A materials and frames composed of pure Vero material were printed, as full assemblies, on a Stratasys J750 polyjet printer. Leaflets composed of polyurethane were printed on a Stratasys F370 FDM printer and assembled by hand, utilizing cyanoacrylate adhesive, to Vero frames printed on the J750.

### Pulsatile Flow Test

Valve samples were tested under pulsatile flow conditions (80/10 mm Hg diastolic/peak systolic pressure, 1.5 L/min cardiac output). A working fluid of 60/40 water to glycerin (99% pure glycerin) was used as a blood analog to provide required density and kinematic viscosity of 1060 kg/m$^3$ and 3.5 10-6 m$^2$/s, respectively. The average simulated cardiac output was 5 L/min, and the heart rate was 60 bpm. The mean systolic gradient (ΔP), effective orifice area (EOA), and a regurgitant fraction (RF) were calculated. ΔP is the transvalvular pressure gradient across the valve during systole. The EOA was calculated using the Gorlin equation, the recorded systolic gradient, and the flow rate. RF is the fraction of backflow over forwarding flow volume [2].

## RESULTS

Figure 4 shows the various valve designs and their 3D printed counterparts. The hemodynamic data can be found in Table 1. The gradient was lowest with the v4 design using Agilus to make leaflets. The EOA was also highest with a valve made from Agilus. The effect of valve design is evident when comparing the v4 and v5 valves, each printed with the shore-A 70 leaflet material. The significantly higher RF of v5 indicates more undesirable leakage than the v4. The v6 design was printed with polyurethane, and the valve was deemed too rigid during in vitro testing, as the leaflets barely opened during the systolic phase. Overall, the 3D printed valves have higher ΔP and lower EOA than native human aortic valves, though RF is comparable.

**Figure 4:** The CAD models of heart valves with different geometry (top row) and the 3D printed counterparts (bottom row). Designs were labeled (from left to right) as v4, v5, and v6.

**Table 1:** Results from the pulsatile flow test.

| Leaflet | Design | Gradient (mmHg) | Effective Orifice Area | Regurgitant Fraction (%) |
|---|---|---|---|---|
| Shore-A 85 | v4 | 30.6 | 0.95 | 4.26 |
| Shore-A 70 | v4 | 36.2 | 0.9 | 3.36 |
| Shore-A 70 | v5 | 34.7 | 0.87 | 21.9 |
| Shore-A 30 | v4 | 30 | 1.08 | 7.78 |
| Physiological | physiological | < 5 | 0.95 | < 15 |

## DISCUSSION

The results show that heart valves can be fabricated with variable performance using additive manufacturing. A more comprehensive study will be conducted to compare all the valve designs and 3D printed material. Although further optimization is needed to ensure comparable performance with the native heart valves, the results reveal that hemodyanmics can be manipulated easily through valve design and material selection. In addition to implantable devices, additive manufacturing can be used for disease modeling for surgical practice or the testing of other devices. Future work could involve replicating patient-specific aortic roots with complex geometry and simulating valve diseases such as the presence of calcium nodules, bicuspid aortic leaflets, and aortic insufficiency.

## REFERENCES

[1] Gardin C et.al, *Cells*, 2020
[2] Thubrikar M, *The Aortic Valve*, 2011.
[3] Saikrishnan N et.al, *Circulation*, 129:244–253, 2014

SB³C2022
Summer Biomechanics, Bioengineering and Biotransport Conference
June 20-23, Eastern Shore, MD, USA

# HEMODYNAMICS AND VASCULAR WALL MECHANICS OF THE PULMONARY ARTERY IN PATIENTS WITH PULMONARY HYPERTENSION AND ARTERIOVENOUS FISTULA

**Fatemeh Bahmani (1), Daniel Pearce (2), Ali Vahdati (1), Veeranna Maddipati (3), and Stephanie M. George (1)**

(1) Department of Engineering, East Carolina University, Greenville, NC, USA
(2) Department of Biomedical Engineering, University of Wisconsin-Madison, Madison, WI, USA
(3) Internal Medicine, Brody School of Medicine, East Carolina University, Greenville, NC, USA

## INTRODUCTION

Pulmonary hypertension (PH) is the increased pressure in the vessels that carry blood from the heart to the lungs. This disease may be inherited or can be developed because of other illnesses. Patients with chronic kidney disease (CKD) and end stage renal disease (ESRD) may develop pulmonary hypertension. The presence of pulmonary hypertension in patients with CKD and ESRD is linked to increased mortality rate [1]. The prevalence of pulmonary hypertension in end stage renal disease is reported to be between 30-60% based on echocardiography measurements [2]. The pathophysiologic mechanism underlying development of pulmonary hypertension in ESRD patients is still an open question and according to WHO pulmonary hypertension classification, is categorized in group 5 (miscellaneous effects) [2]. This uncertainty comes from the fact that patients with CKD and ESRD often have other coexisting diseases that might be the cause of developing pulmonary hypertension. Cardiac dysfunction, fluid overload, endothelial dysfunction due to increased oxidative stress, increased venous return and increased cardiac output due to arteriovenous fistula placement and vascular calcification are suggested as the possible mechanisms of pulmonary hypertension development in CKD patients although not confirmed by clinical studies [3, 4].

Computational fluid dynamics (CFD) is used to assess the blood flow through the cardiac system. Images from magnetic resonance imaging (MRI) or computed tomography (CT) from patients can be used in software to produce the geometry and inlet velocity waveforms. The fluid flow and structural equations are solved to compute parameters of interest over these geometries.

There are several studies in which the fluid-structure interaction problem of blood flow in pulmonary arteries were investigated. Kong et al. studied the unsteady problem of blood flow interaction with the arterial wall in pulmonary arteries with a Newtonian fluid assumption [5]. It is shown in the CFD analysis of pulmonary arteries by Tang et al. [6] that wall shear stress is decreased over the pulmonary arterial walls in PH patients. Their approach does not include the effect of vasculature wall deformation. Zambrano et al. [7] also developed a fluid-structure interaction model of pulmonary artery hypertension. The primary goal of this study is to perform the fluid-structure interaction analysis and characterize blood flow in the pulmonary arteries of patients diagnosed with pulmonary hypertension and who are undergoing arteriovenous fistula hemodialysis.

## METHODS

The data acquisition from patients was approved by East Carolina University Internal Review Board (UMCIRB 19-000708). Due to the pandemic restrictions, the MRI data was acquired from one patient who was a 41-year-old African American male with PH diagnosed through right heart catheterization and undergoing hemodialysis with arteriovenous fistula.

The MR imaging was performed using a Siemens Aera 1.5 T scanner which uses a gradient echo (GR) imaging sequence. The subject's pulmonary artery geometry was reconstructed using 22 slices with 8 mm thickness from short axis cine scan. The echo time of 1.34 ms and the repetition time of 289.5 ms was used for image acquisition. Pixel spacing was given to be 1.61 mm. The transient velocity waveform of the cardiac cycle just past the leaflets of the pulmonary artery was obtained using phase-contrast magnetic resonance imaging (PCMRI). The blood flow rate through the pulmonary artery and vessel diameter were calculated from PCMRI images.

The 3D geometry of the vessel was then reconstructed in Mimics 20.0 (Materialise, Inc.; Plymouth, MI) using the image segmentation techniques. The thresholding segmentation method identifies the pixel

values below a specified threshold in order to separate the anatomical structure from its background. The 3D geometry of the pulmonary artery was reconstructed using the "calculate 3D" feature of Mimics. It was then further trimmed in Solidworks 2017 (Dassault Systemes; Waltham, MA) to generate the solid shell with a defined thickness. The fluid domain was created in SpaceClaim using the 'volume extract' feature.

The transient linear fluid-structure interaction model (ANSYS, Inc.; Canonsburg, PA) was used to model the coupled blood flow and vessel wall mechanics. The fluid domain was discretized using 557559 elements of size 1 mm while the solid domain consisted of 55768 elements of size 2 mm. Both the fluid and solid domain have been examined for mesh convergence. The mesh created for fluid and solid domains is depicted in Figure (1)

The blood was taken to be a non-Newtonian fluid with a variable viscosity modeled using the Carreau model and a density of 1200 kg/m$^3$. The solid domain was modeled as a linear elastic material with E= 2 MPa and Poisson's ratio ν=0.48 [5, 7]. The transient velocity waveform in Figure (2) was implemented at the inlet boundary and the outlets were taken to be zero gauge pressure outlets. In the structural model the inlet and outlets were assumed to be fixed.

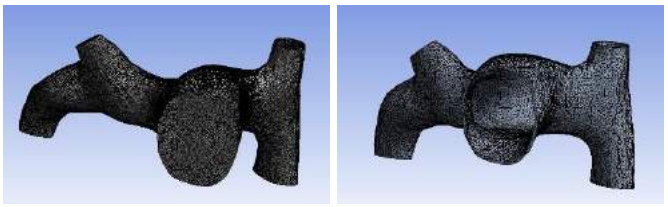

(a) (b)

**Figure 1: (a) Fluid domain meshing (b) Solid domain meshing**

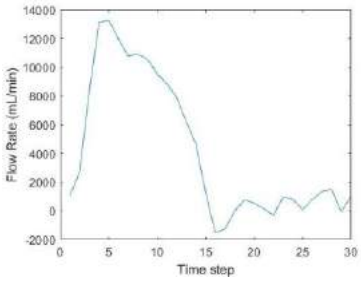


**Figure 2: Inlet fluid flow rate waveform calculated from MRI data**

## RESULTS

The contours of wall shear stress and velocity at peak systole are shown in Figure (3). The maximum velocity is found to be 0.714 m/s and the maximum wall shear stress to be 33.3 Pa. The contour of total deformation is shown in Figure (4). The structural analysis yields the value of maximum deformation to be 0.01 mm, maximum stress to be 0.03 MPa and maximum strain to be 0.0013 at peak systole.

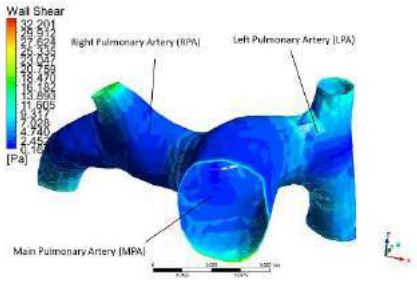


(a)

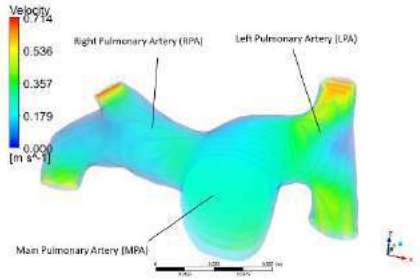


(b)

**Figure 3: (a) Wall shear stress (b) Flow velocity at peak systole**

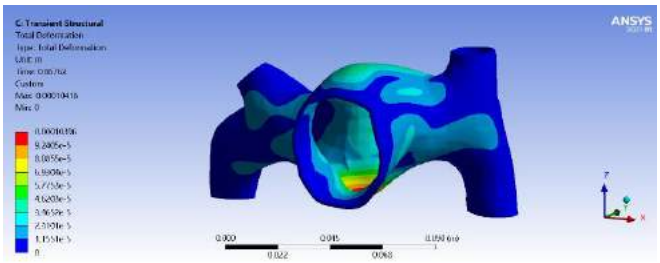


**Figure 4: Contours of total deformation at peak systole**

These values are in good agreement with the data reported in the previous studies for different PH populations.

## DISCUSSION

The coupled analysis of blood flow and vasculature wall mechanics has been conducted in the pulmonary artery of a patient with pulmonary hypertension undergoing arteriovenous fistula hemodialysis. Clinical data from more patients should be acquired to perform better analysis and reach strong conclusions. The application of other wall mechanical models will be explored and compared with the results from linear elastic model. In the future, the outcome of this research may provide clinicians with data to monitor the function of pulmonary artery and intervene to prevent the incidence of pulmonary hypertension. Early diagnosis of PH development in ESRD patients will improve the patients' quality of life, outcome of healthcare procedure, and potentially prevent the patients' removal from the kidney transplant list.


## ACKNOWLEDGEMENTS

The authors would like to thank Constantin B. Marcu, MD for image acquisition. This work was supported in part by the Division of Research, Economic Development, and Engagement, East Carolina University.


## REFERENCES


[1] Thenappan, T., Pulmonary circulation, 7(3), 567-568, 2017.

[2] Kawar, B et al., American journal of nephrology, 37.3: 281-290, 2013.

[3] Agarwal, R., Nephrology Dialysis Transplantation, 27(10), 3908-3914, 2012.

[4] Gazda, Alexander J et al., Heart & lung: the journal of critical care 50.1: 232-233, 2021.

[5] Kong, F et al., International journal for numerical methods in biomedical engineering 35.7: e3208, 2019.

[6] Tang, Beverly T et al., Pulmonary circulation 2.4: 470-476, 2012.

[7] Zambrano, Byron A et al., Journal of biomechanics 68: 84-92, 2018.

# EFFECT OF BREAKING CALCIFICATION ON THE COMPLIANCE OF CORONARY ARTERIES

**Yasamin Seddighi (1), Aleksandra Gruslova (2), Drew Nolen (2), Deborah Vela (3), L. Maximilian Buja(3), Marc Feldman (2), Hai-Chao Han (1)**

(1) Department of Mechanical Engineering, The University of Texas at San Antonio, San Antonio, TX, USA
(2) Department of Medicine, University of Texas Health at San Antonio, San Antonio, TX, USA
(3) Texas Heart Institute, University of Texas Health Science Center at Houston, Houston, Texas

## INTRODUCTION

Atherosclerosis leads to coronary artery disease (CAD) which is one of the leading causes of death in the United States. Calcified atherosclerotic plaque is common in CAD and hinders therapeutic interventions such as balloon angioplasty and stenting. Intravascular Lithotripsy has been used to break calcifications [1, 2]. Breaking the plaque and calcification to increase vessel compliance is crucial for effective therapeutic interventions.

Therefore, the objective of this study was to determine the effect that cracks in calcification and intimal tear had on the compliance of heavily calcified arteries.

## METHODS

Calcified cross-sections were created in SOLIDWORKS® based on a histology image of a calcified coronary artery segment (Fig. 1a) and the 2D cross-sections were extruded for 3 mm to create 3D models. The pre-cracking intact cross-section was created by artificially "healing" the cracks and breakage in the calcification and plaque. Both arterial wall and atherosclerotic plaque were assumed to be isotropic, incompressible, hyperelastic material with reduced polynomial strain energy density function:

$$W = C_{10}(\bar{I}_1 - 3) + C_{20}(\bar{I}_1 - 3)^2 + C_{30}(\bar{I}_1 - 3)^3 + C_{40}(\bar{I}_1 - 3)^4 + C_{50}(\bar{I}_1 - 3)^5 + C_{60}(\bar{I}_1 - 3)^6 \quad (1)$$

Where $I_1$ is the first invariant of deformation tensor and $C_{10}$ to $C_{60}$ are the material constants are given in Table 1. Density of the arterial wall and stiff plaque (calcification) were assumed to be the same and equal to 1120 kg/m³ [3].

Pressurized inflations of the calcified arteries were simulated using commercial FEA package ABAQUS®. Arterial wall and atherosclerotic plaque were meshed using eight-node linear brick reduced integration (C3D8R) elements. A uniform pressure up to 15 kPa was gradually applied to the lumen mimicking balloon expansion. Both ends of the artery were free to expand radially but fixed in other directions to prevent free movement as a rigid body. Additionally, tie constraint was defined to eliminate the relative motion between arterial wall and atherosclerotic plaque.

In addition to the pre- and post-cracking models, more models with different number of cracks in calcifications and intimal tears were simulated to determine how they would affect arterial compliance.

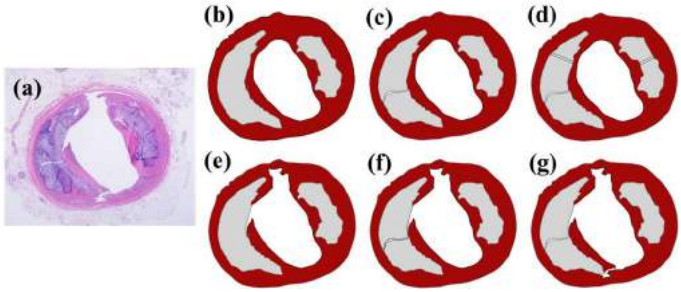


**Figure 1: Cross-sectional image of a coronary artery post cracking and 6 corresponding models. (a) Histology image, (b) intact model, (c) intact tissue+ 1 Ca crack, (d) intact tissue + 3 Ca Crack. (e) 2 intimal tears+ intact Ca. (f) 2 intimal tears+ 1 Ca crack. (g) 3 intimal tears + 1 Ca crack.**

**Table 1: Material coefficients for arterial wall and calcified plaque [3]. Units of all constants are in kPa.**

| | C10 | C20 | C30 | C40 | C50 | C60 |
|---|---|---|---|---|---|---|
| Arterial Wall | 6.52 | 4.90 | 9.26 | 760 | -430 | 87.0 |
| Calcification | 12.1 | 1540 | 2190 | 2.14E5 | -3.35E6 | 1.34E8 |

## RESULTS

A total of 6 different models with intact and cracked calcification and intimal tears were analyzed (Figure 1). The changes in the lumen area of the middle cross section of the calcified coronary artery were calculated and plotted as functions of lumen pressure to illustrate vessel compliance (Figure 2).

Our results showed that the compliance of the artery with either crack in calcification or intimal tear is higher than the intact artery. However, cracked calcification with intact tissue has an insignificant effect on vessel compliance, even when multiple cracks were added to the calcification. In contrast, intimal tears significantly increased the compliance of the artery (Figure 2).

## DISCUSSION

The effect of calcification and tissue lasing on the compliance of the coronary artery were investigated. Our results showed that cracking calcification, while keeping tissue intact, has little effect on improving the compliance of the artery. Cracking the surrounding plaque tissue increased the compliance significantly. Combining intimal tears and cracks in calcification would further increase the compliance of the artery.

There are a few limitations in this study. First, variation of the calcification and arterial wall along the length of the artery were not considered. Second, the arterial wall was assumed to be homogenous and isotropic though the arterial is anisotropic [4,5].

While limitations exist, these results shed light on how lithotripsy of calcification and plaque affects the compliance of the artery and provides guidance for targeted treatment.

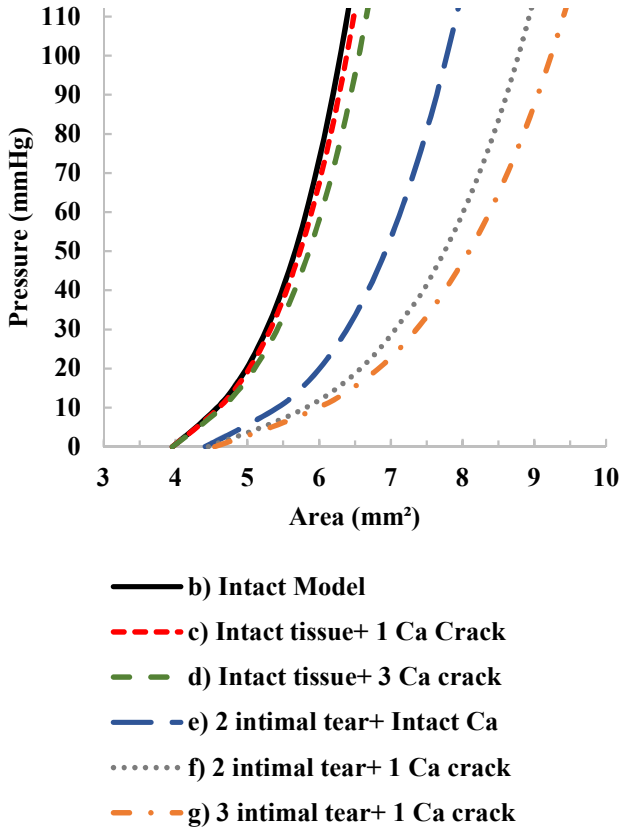


**Figure 2: Lumen pressure plotted as functions of lumen area of the 6 calcified coronary artery models.**


## ACKNOWLEDGEMENTS

This study was partially supported by the Clayton Foundation for Biomedical Research.


## REFERENCES


[1] Nakahara, T., et al., *JACC Cardiovasc Imaging*, **10**(5): p. 582-593, 2017.

[2] Hill, J.M., et al., *J Am Coll Cardiol*, **76**(22): p. 2635-2646, 2020.

[3] Chiastra, C et al., *J Biomech*, **49**(11):p.2102-2111, 2016.

[4] Wang, L., et al., *Front Physiol* 12:721195, 2021.

[5] Fung, Y. C., *Biomechanics: Mechanical Properties of Living Tissues*. New York, Springer Verlag. 1993.

# MAPPING STRAIN AMPLIFICATION IN LUNG CANCER: A GEOMETRIC MODEL TO TEST HOW ALTERED MECHANICS COULD PROMOTE TUMOR PROGRESSION

**Rebecca G. Zitnay (1,3), Keith R. Carney (2,3), Michael R. Herron (1,4), Jeffrey A. Weiss (1,4), Michelle C. Mendoza (2,3)**

(1) Biomedical Engineering, University of Utah, Salt Lake City, Utah, United States
(2) Oncological Sciences, University of Utah, Salt Lake City, Utah, United States
(3) Huntsman Cancer Institute, University of Utah, Salt Lake City, Utah, United States
(4) Scientific Computing and Imaging Institute, University of Utah, Salt Lake City Utah, United States

## INTRODUCTION

Lung cancer is the primary cause of cancer related death worldwide. Even when detected early, the 5-year survival is poor (1). To improve patient outcomes, a better understanding of the factors that drive early lung tumor progression is needed.

Lung cancer progression is driven by both biochemical and mechanical signals. Cancer initiates from mutations in lung epithelial cells that line the alveoli to cause aberrant proliferation and survival. As the transformed cells grow into tumors that fill the alveoli, additional mutations and alterations in the tumor microenvironment contribute to the tumor's progression to invasive cancer. Signals from local fibroblasts and the deposition of new extracellular matrix correlates with and promotes progression toward invasive and metastatic cancer (2). The fibrotic remodeling associated with late stage lung cancer is similar to that observed in other solid tumors, in which increased tumor stiffness promotes metastasis (3).

In addition to the alterations associated with tumorigenic remodeling, lung cancer is also subjected to the mechanics of cyclic expansion during respiration. During normal respiration alveoli expand 5-20% (4), with a change in surface area at total lung capacity of ~50% (5). *In vitro*, lung epithelial cells subjected to strain exhibit increased proliferation, differentiation, and growth factor production (6). Lung fibroblasts also exhibit strain-sensitive proliferation, myofibroblast differentiation, and matrix production (7). While mechanotransduction associated with abnormal forces has been recognized in many cancers, strain is a previously unappreciated mechanical signal in early lung cancer lesions.

We aimed to map the strain in the early lung tumor environment and probe its contribution to tumor progression. Understanding the role of mechanical signaling in lung cancer is challenged by the lack of good experimental models that capture early tumorigenesis. The direct measurement of strain in lung tissue during respiration and tumor heterogeneity pose additional challenges. To address this, we adapted previous models of the lung that incorporated the stress-strain behavior (8) and architecture (9) to develop a model that predicts the strain in the local tissue when a tumor modifies the architecture.

## METHODS

We created an idealized geometric finite element model of the lung. A mesh was prepared in MATLAB as a hexagonal lattice of 100 units horizontally and vertically that mimics the alveolar architecture in the lung (Fig. 1A). Each measured ~100 μm in diameter, which represents the approximate size of alveoli in the human lung, twice the size of mouse lung (Fig. 1B, C). To account for variability in lung architecture, a randomization algorithm was applied to the initial geometry, followed by simulated annealing through energy minimization (9). The randomized lattice was imported into FEBio and modeled with z-height of 30 μm. Shell elements were used to represent alveolar walls, 10 μm in width. A neo-Hookean constitutive model was used for the lung matrix and the modulus was set by parameter optimization using FEBio to match the behavior of a constitutive model previously reported to for bulk lung tissue (8). The resulting optimized modulus for the alveolar walls was 35 kPa with a Poisson's ratio set to 0.25. A simulated rigid body indentation experiment using a 30 μm thick volume assigned the bulk lung constitutive model confirmed that the modulus is consistent with atomic force microscopy (AFM) measurements the of lung tissue, ~1.8 kPa (10).

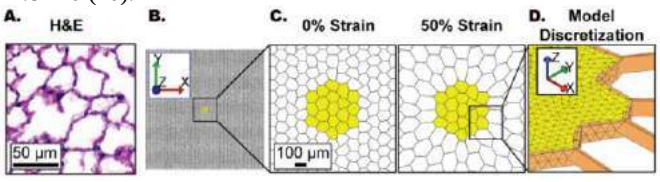


**Figure 1: A) Normal mouse lung tissue, inflated before fixation, and stained with hematoxylin and eosin (H&E). B) A zoomed-out**

**view of the human lung model. C) Inset to visualize tumor and adjacent matrix under 0% and 50% globally applied strain. D) Discretization of the lung model. The lung matrix is represented by shell elements. The tumor is discretized using tetrahedral elements with a surrounding material layer of triangular elements.**

A tumor was incorporated as 20 filled alveolar units in the center of the lattice and discretized as solid 4-noded tetrahedral elements (Fig. 1C, D). The tumor was represented as neo-Hookean with a Poisson's ratio of 0.49 (3) and the tumor modulus was varied parametrically. Early tumor was modeled with modulus of 1 kPA, matching the normal lung. Late tumor with fibrotic stiffening was represented with a modulus of 35 kPA, and this base value was varied between 0.2 kPa and 350 kPa to represent the range for tumor or fibrotic tissue (3, 11). Using FEBio, the final discretized mesh was subjected to 50% biaxial prescribed elongation to mimic respiration with plane strain boundary conditions (Fig. 1C and D). We considered the amplification at 5%, 20% and 50% to represent the baseline lung, the strain associated with normal respiration, and the strain expected at total lung capacity.

## RESULTS

In order to understand strain in the early lung tumor environment, we calculated the strain expected during lung expansion in normal lung and around a lung tumor. In the normal lung, at 20% globally applied strain we observed a relatively homogenous strain distribution in the alveolar walls (Fig. 2A, Normal lung). To assess how the lung model amplifies strain, we calculated the strain ratio [1st principal strain/globally applied strain] (Fig. 2B, normal lung). We found strain amplification increased with applied strain. Around the tumor, strain was largest directly adjacent to the tumor and increased with increasing stiffness (Fig. 2A). Strain was amplified adjacent to the tumor in both early (1 kPa) and fibrotic (35 kPa) tumor conditions; however, the amount of strain amplification was dependent on both distance from the tumor and tumor stiffness, with the highest amplification associated with the stiffer tumor and greater applied strain (Fig. 2B).

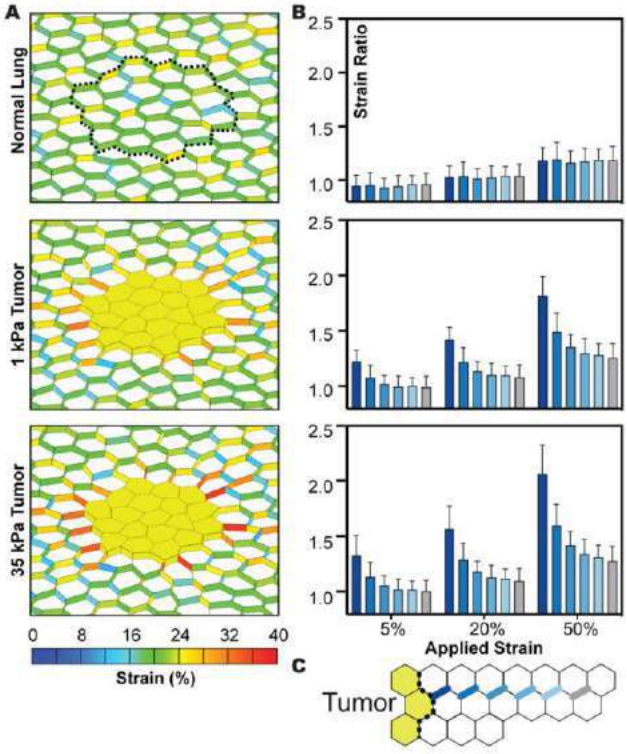


**Figure 2: A) 1st principal strain in alveoli walls surrounding the tumor at 20% applied strain for normal lung and tumors with 1 and 35 kPa modulus. B) The strain amplification ratio at 5%, 20%, and 50% applied strain, showing amplification in matrix shell elements in normal and tumor lung model as a function of distance from the tumor boundary. The schematic, (C) indicates the distance from the tumor where line color corresponds to the shell layer indicated. Strain ratio = globally applied strain / 1st principal shell strain. Error bars are SD of all elements at the indicated distance.**

## DISCUSSION

Our results demonstrated that the strain experienced by alveolar walls near the tumor is larger than that experienced in healthy lung tissue. The model predicts that tumor stiffening associated with tumor progression will lead to additional strain amplification that would exacerbate the altered mechanical environment.

Our modeling approach represents the first geometric tissue scale model of a tumor in a lung matrix. This model design allowed us to test the magnitude of change and spatial distribution of strain in lung tissue. We selected geometries that reflected our observations from mouse models of lung cancer and human histopathology. By applying an established constitutive model of normal lung tissue to our geometric model, we mapped the amplification of strain associated with the presence of a small early tumor and stiffened late tumor.

The poor prognosis of lung adenocarcinoma, even when caught small and seemingly localized, suggests that early tumor cells invade away from the tumor and metastasize. Our finding of strain amplification at even the earliest stage of lung cancer suggests that mechanical signaling may contribute to early tumorigenesis and invasion. Strain amplification directly adjacent to the tumor would be sensed by tumor cells at the invasive front. Thus, the epithelial cell proliferation and growth factor production response to strain observed in vitro may occur in vivo at the tumor edge. Additionally, fibroblasts at the tumor edge may respond to changes in strain and stiffness with increased matrix production to further promote progression.

This model underscores the importance of future research to interrogate how strain influences mechanotransduction in lung cancer. Future adaptations of the model can be used to test the role of other mechanical changes in the tumor microenvironment, such as matrix remodeling and tumor growth, contribute to changes in stiffness, tumor progression, and invasion.


## ACKNOWLEDGEMENTS

This research was supported by American Cancer Society RSG CSM130435 to MCM, NIH #2R01GM083925 and U24EB029007 to JAW, and by the Huntsman Cancer Foundation and the National Cancer Institute of the NIH under Award Number P30CA042014.


## REFERENCES


[1] Siegel, R.L., *Cancer J. Clin.* 69:7–34, 2019. [2] Gocheva, V., *Proc. Natl. Acad. Sci.* 114:E5625–E5634, 2017. [3] Acerbi I., *Integr. Biol.* 7:1120–1134, 2015. [4] Perlman, C.E., *J. Appl. Physiol.* 103:1037–1044, 2007. [5] Gil, J., *J. Appl. Physiol. Respir. Environ. Exerc. Physiol.* 47:990–1001, 1979. [6] Waters, C.M., *Compr. Physiol.* 2:1–29, 2012. [14] Breen, E.C., *J. Appl. Physiol.* 88:203–209, 2000. [8] Birzle, A.M., *J. Mech. Behav. Biomed. Mater.* 94:126–143, 2019. [9] Cavalcante, F.S.A., *J Appl Physiol.* 98:672–679, 2005. [10] Sicard, D., *Am. J. Physiol. Cell. Mol. Physiol.* 314:L946–L955, 2018. [11] Liu, F., *J. Cell Biol.* 190:693–706, 2010.

SB³C2022
Summer Biomechanics, Bioengineering and Biotransport Conference
June 20-23, Eastern Shore, MD, USA

# COMPUTATIONAL ANALYSIS OF PAPILLARY MUSCLE APPROXIMATION FOR FUNCTIONAL MITRAL REGURGITATION REPAIR

**Gediminas Gaidulis (1,2), Daisuke Onohara (1,2), Muralidhar Padala (1,2)**

(1) Structural Heart Research and Innovation Laboratory, Carlyle Fraser Heart Center at Emory University Hospital Midtown, Atlanta, GA, USA
(2) Division of Cardiothoracic Surgery, Emory University School of Medicine, Atlanta, GA, USA

## INTRODUCTION

Functional mitral regurgitation (FMR) is a heart valve lesion that perturbs mitral valve (MV) geometry resulting in inadequate closure and backward leakage of the valve. It is a common complication of myocardial infarction, which develops in approximately 50% of patients [**1**]. In such condition, the MV leaks because of distortion of its geometry by the dysfunctional and dilated left ventricle which tethers the valve. The constant pulmonary venous return, when combined with the mitral regurgitant volume, increases total blood volume that fills the left ventricle and thus causes a volume overloaded state. Wall stresses are elevated, and ventricular dysfunction ensues, altogether accelerating heart failure hospitalizations and doubling mortality [**2**].

It is now well established through randomized controlled trials that correcting FMR can reduce both heart failure hospitalizations and mortality, and significantly improve the functional capacity in these patients [**3**]. Papillary muscle approximation (PMA) is a novel surgical technique that aims to restore the configuration of subvalvular apparatus by drawing papillary muscles (PMs) together and subsequently relieving tethering forces and improving mobility of the MV leaflets [**4**] (**Figure 1**). Our recent bench work on FMR repair demonstrated that PMA not only relieves tethering forces in the chordae, but it also preserves the twisting motion of the left ventricle, thus improving the ventricular mechanics [**5**].

Patient-specific computational simulations of the MV behavior before and after surgical repair can be extremely useful in procedure planning. Such approach is particularly valuable while investigating the impact of novel treatment strategies since computational simulations can help surgeons to assess interventional outcomes. However, up to date, only a single simplified 2D computational study was performed to investigate PMA and its impact on the MV function [**6**]. Therefore, in this study, we present patient-specific PMA simulations performed using realistic 3D computational MV models that allow to assess the outcomes of PMA and therefore can aid in surgical planning.

## METHODS

Two patient-specific computational models of the MV affected by FMR were created from 3D epicardial echocardiography data obtained in two pigs that received a myocardial infarction via percutaneous occlusion of the left circumflex artery, and as a result developed FMR. The modeling workflow used in this study was based on the approach developed and validated previously in our lab, which allows to create a realistic computational model of the MV with subvalvular apparatus.

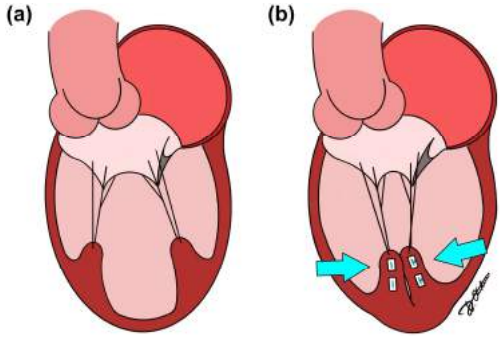


**Figure 1: Schematic of MV before (a) and after (b) PMA.**

For each case, a geometry of the MV annulus, leaflets, and PMs in diastole was reconstructed from echo images. Each MV model was completed by adding a branched network of chordae, connecting the MV leaflets to the PMs. To create FMR state of the MV, the PMs were displaced further from the annular plane, thus stretching the chordae and imposing a pre-strain on both chordae and MV leaflets (**Figure 2a**). By adjusting this pre-strain, we were able to simulate the restricted motion of the leaflets and obtain a realistic systolic configuration of the valve for both MV models used in this study.

To simulate the MV closure before the repair, physiologic transvalvular pressure gradient was applied to the leaflets, and patient-specific annular contraction and movement of the PMs were prescribed as kinematic boundary conditions. For each model, explicit dynamic simulation was performed and pre-repair peak systolic configuration of the MV was obtained. PMA repair was achieved by bringing the PMs together laterally and fixing them in diastole (**Figure 2b**). The simulations were repeated and for each model post-repair peak systolic configuration of the MV was obtained. In addition, the following parameters were calculated: stress distribution on the leaflets, tension forces in the chordae, reaction forces on the PMs, and coaptation area of the leaflets. Moreover, to investigate the mobility of the leaflets, tenting height, tenting area, and tenting angles for both MV leaflets were computed. Post-repair systolic results were compared with pre-repair values.

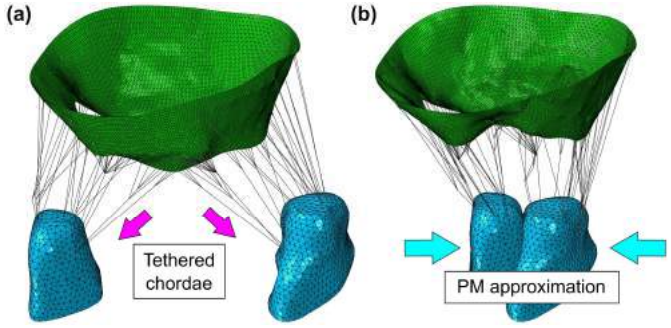


**Figure 2: MV model with FMR (a) and after PMA (b) in diastole.**

## RESULTS

Simulation results for both investigated cases are presented in **Table 1**, while stress distribution across the MV leaflets in peak systole for each model is shown in **Figure 3**. In both pre-repair models, regurgitant gaps at A1-P1 and A3-P3 segments of the leaflets were noticed, while high stress distribution areas were observed near the insertion sites of the strut chordae. After PMA, the elimination of regurgitant gaps was seen, and high stresses were abolished in both post-repair models. Similarly, the overall chordal tension forces were greatly reduced, as shown by the decrease of reaction forces acting on the PMs. In addition, a reduction of tenting height, tenting area, and tenting angles was observed after PMA, whereas leaflet coaptation area increased significantly.

**Table 1: Simulation results in peak systole.**

| | Case 1 | | Case 2 | |
|---|---|---|---|---|
| | **FMR** | **PMA** | **FMR** | **PMA** |
| Max stress AL (MPa) | 0.79 | 0.85 | 5.32 | 1.04 |
| Max stress PL (MPa) | 2.04 | 0.64 | 1.56 | 1.32 |
| Max strut force (N) | 2.82 | 1.96 | 6.62 | 1.80 |
| Max marginal force (N) | 0.60 | 0.89 | 1.25 | 1.09 |
| Max basal force (N) | 0.72 | 0.42 | 0.37 | 0.74 |
| APM force (N) | 11.26 | 8.38 | 13.26 | 8.71 |
| PPM force (N) | 10.77 | 7.39 | 14.95 | 8.75 |
| Coaptation area ($mm^2$) | 105.0 | 189.1 | 133.0 | 191.9 |
| Tenting height (mm) | 10.4 | 5.0 | 11.4 | 6.8 |
| Tenting area ($mm^2$) | 166.1 | 79.7 | 166.3 | 98.4 |
| Tenting angle AL (deg) | 24.8 | 12.3 | 29.9 | 21.0 |
| Tenting angle PL (deg) | 48.4 | 29.6 | 51.1 | 30.5 |

**AL**, anterior leaflet; **PL**, posterior leaflet; **APM**, anteroposterior PM; **PPM**, posteromedial PM.

## DISCUSSION

In this study, we presented an application of computational modeling approach, used to create a realistic patient-specific MV model and simulate the outcomes of PMA. The bench work recently done in our lab demonstrated that in the presence of FMR there is an increase in MV tethering forces and leaflet tenting parameters [**5**]. The simulation results of FMR affected MV function showed similar trend: high leaflet stresses and chordal tension forces, as well as increased tenting height, tenting area, and tenting angles for both leaflets were observed. After PMA, these elevated values were greatly reduced, relieving leaflet and chordal tethering, and enabling better leaflet mobility and coaptation.

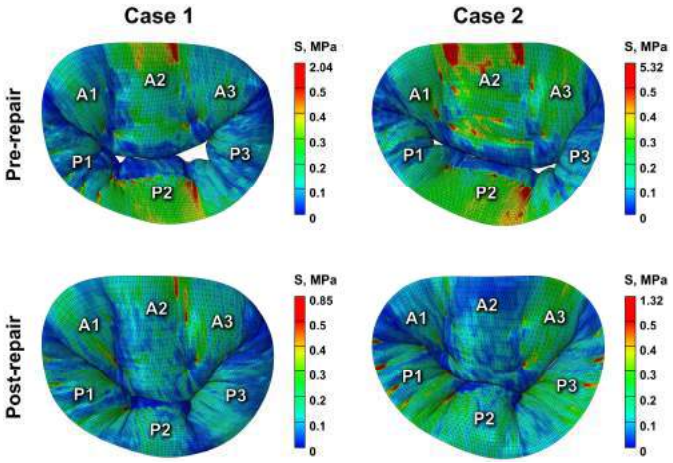


**Figure 3: Stress distribution on MV leaflets in systole.**

In post-repair models, both leaflet stresses and chordal tension forces decreased. While a slight increase of maximum stress value was observed on the anterior leaflet in case 1, high stress areas on the posterior leaflet were abolished, and more even stress distribution across the whole surface of the leaflets was achieved, thus showing the overall relief of leaflet tethering. Similarly, a slight force increase was noticed in marginal (case 1) and basal (case 2) chordae. Still, the overall chordal tension forces were greatly reduced, as shown by the reduction of reaction forces acting on the PMs. Thus, a more even force distribution across the whole chordal network was achieved.

In addition, increased leaflet mobility after PMA was observed. The values of tenting parameters (tenting height, area, and angles) in pre-repair models were elevated, if compared to the data on healthy valves recently measured in our lab [**7**]. In general, the increased tenting parameters show reduced leaflet mobility, which leads to insufficient leaflet coaptation. After PMA, all tenting parameters were greatly reduced, thus leaflet mobility and coaptation were increased.

To sum up, patient-specific PMA simulations performed using realistic 3D computational MV models showed that PMA was effective in not only improving coaptation but also in reducing leaflet stresses and chordal tension forces. Our computational results indicate that PMA could be an effective technique to repair FMR.

## REFERENCES

[1] Vajapey, R et al., *Cardiovasc Diagn Ther*, 11(3):781-792, 2021.
[2] Baskett, RJ et al., *Can J Cardiol*, 23(10):797-800, 2007.
[3] Pascual, I et al., *J Clin Med*, 9(6):1792, 2020.
[4] Nappi, F et al., *J Am Coll Cardiol*, 67(20):2334-2346, 2016.
[5] Zhan-Moodie, S et al., *J Thorac Cardiovasc Surg*, 7:91-104, 2021.
[6] Nappi, F et al., *Materials (Basel)*, 12(9):1518, 2019.
[7] Onohara, D et al., *J Cardiovasc Transl Res*, 2021. Epub ahead of print.

SB³C2022
Summer Biomechanics, Bioengineering and Biotransport Conference
June 20-23, Eastern Shore, MD, USA

# REPLACEMENT HEART VALVE SIMULATIONS USING A NEURAL NETWORK FINITE ELEMENT SURROGATE MODEL

**Shruti Motiwale (1,2), Christian L. Goodbrake (1), Wenbo Zhang (1), Michael S. Sacks (1,2)**

(1) James T. Willerson Center for Cardiovascular Modeling and Simulation, Oden Institute and the Department of Biomedical Engineering, University of Texas at Austin, Austin, Texas, USA
(2) Department of Mechanical Engineering, University of Texas at Austin, Austin, Texas, USA

## INTRODUCTION

Our understanding of heart valve structure and function, though still limited, has advanced significantly over the past decade. With the advances in computation power we are now able to perform robust heart valve simulations, addressing such problems as longterm cyclic loading to estimate replacement heart valve structural degradation over time. Such simulations can account for detailed features such as fiber distributions, through thickness variations, coupling between material phases etc. However, even with the latest computational resources, the computation times are still too slow for extensive parametric studies, let alone being conducted in a clinically relevant time frame for patient specific applications. We thus need to develop computational methods that can run thousands of simulations within a very short time.

Neural networks (NN), in their capacity as universal function approximators, can serve as a useful tool as 'surrogate' models for finite element simulations. NN have been trained to represent parametric PDEs using either a data-driven approach or a physics-informed approach [1-3]. Our group has developed a hybrid approach that couples a neural network to a differentiable finite element domain map to create a neural network finite element (NNFE) surrogate model [4].

In this work, we have developed a NNFE surrogate model of a tri-leaflet heart simulation model under valve quasi-static loading. The neural network is directly trained using a potential function corresponding to the parametric PDE, and thus does not require any 'training dataset' in the form of experimental data or other simulation results. Although neural networks can be computationally expensive to train, a trained model takes a few seconds at most to provide simulations results. Thus, our approach effectively shifts the computational expense offline, allowing for rapid simulations in clinical settings. Such a model paves the pathway for bridging the gap between computational research and real clinical applications in this field.

## METHODS

The NNFE surrogate model can be specified as

$$\mathcal{N}(\mathbf{u}(\mathbf{x}); \mathbf{m}) = 0 \qquad (1)$$

where, $\mathcal{N}$ represents a differentiable surrogate model, $\mathbf{u}(\mathbf{x})$ represents the displacement function, and $\mathbf{m}$ represents the boundary condition. The NN takes parametrized boundary conditions as inputs and provides control points and weights of the displacement function as output

$$\hat{\boldsymbol{u}} = f_{NN}(\mathbf{m}) \qquad (2)$$

where, $f_{NN}$ represents the neural network, and $\hat{\boldsymbol{u}}$ are the control points and weights of the NURBS displacement function. The Dirichlet boundary conditions are strongly imposed by replacing the corresponding control points and weights. The updated control points and weights $\hat{\boldsymbol{u}}$ along with the NURBS basis functions are used to obtain the solution $\mathbf{u}(\mathbf{x})$. Once $\mathbf{u}(\mathbf{x})$ is obtained, its gradient is computed using automatic differentiation, which is then used to calculate the potential function used for minimization in the neural network training algorithm (Fig 1). The neural network is developed to be a fully differentiable model and is coded using JAX python library [5].

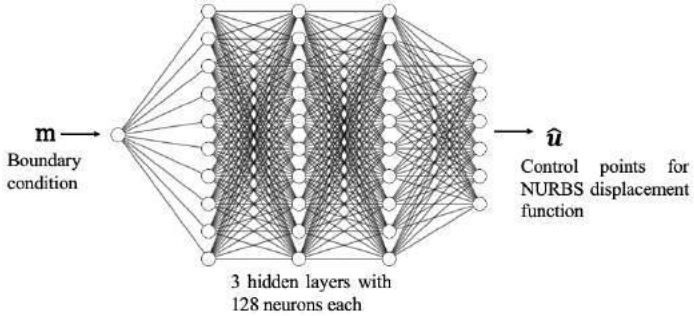


**Figure 1: Neural network surrogate model mapping boundary condition to displacement control points and weights**

The network parameters were trained using the gradient descent algorithm with momentum [6]. Assuming a pressure boundary condition, the cost function for training is given by the total potential

$$\Pi(\mathbf{u}) = \Pi_{int} - \Pi_{ext} = \int_{\Omega_0} \Psi \, d\Omega - p \int_{\Delta\Omega} dV \qquad (3)$$

where, $\Pi_{int}$ and $\Pi_{ext}$ are the internal energy and work done by external forces respectively, $\Psi$ is the strain energy of the domain and describes its material behavior, p is the pressure acting on the surface, and $\Delta\Omega$ represents the displaced volume. As an initial study, we trained a NNFE surrogate model to simulate a pressurized membrane with fixed edges. We modeled the membrane geometry as a flat square sheet (1 cm x 1 cm x 1 mm) with solid elements and linear basis functions. The strain energy was modeled using a neo-Hookean material model. We trained the model for a fixed geometry under a range of pressures from p=0 to p=50 MPa.

As the next step, we trained a NNFE surrogate model to simulate a tri-leaflet heart-valve geometry for varying pressures. We used a full structural model that accounts for fiber architecture to represent the internal potential energy. The strain energy for the heart valve leaflet is given by

$$\Psi = \phi_{\mathrm{m}}\Psi_m + (1 - \phi_{\mathrm{m}})[\Psi_c + \Psi_{int}] - p(J - 1) \qquad (4)$$

where $\Psi_m, \Psi_c, \Psi_{int}$ are the strain energies of the matrix, collagen fibers and their interactions respectively and $\phi_{\mathrm{m}}$ is the volume fraction of the matrix. The material model is described in further detail in our previous publication [7]. The heart valve geometry is represented as shell elements using 2nd order NURBS basis functions (Fig. 4a inset). We developed a custom method to simulate contact between the leaflets using related energy potential function.

## RESULTS

We evaluated the trained NNFE surrogate model for the pressurized membrane at different pressure values and compared the results against results from FE simulations done in FEniCS (Fig 2).

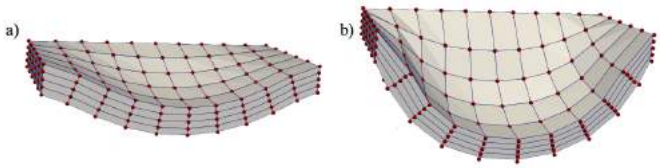


**Figure 2: Cut-section view of a pressurized membrane with fixed edges. Solid elements represent the NNFE surrogate model results and red dots represent FEniCS results. a) p=10 MPa b) p=50 MPa. The maximum displacement error among all nodes was < 1%.**

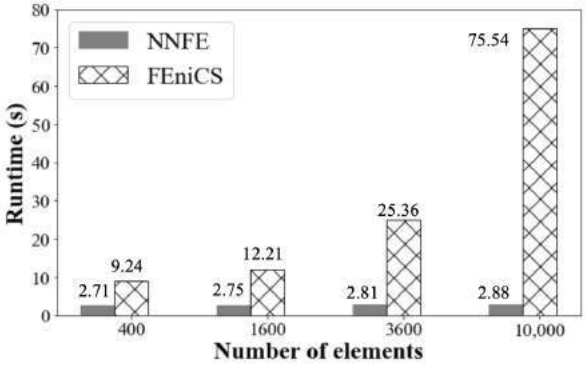


**Figure 3: Simulation time comparison between FEniCS and NNFE surrogate model for pressurized membrane.**

The pressurized membrane NNFE surrogate model took 25 min for training. However, once trained, the surrogate model took only 2-3 secs to simulate a problem irrespective of the number of elements, whereas FEniCS took 26x longer to run a simulation consisting of 10,000 elements (Fig 3). We also evaluated the results of the tri-leaflet heart valve NNFE surrogate model against the results published previously [8] and found that it gives visually indistinguishable results (Fig 4). Even with the greater model size in this problem, the NNFE computational times did not increase, whereas the FE solutions increased to ~20 minutes on the same computer.

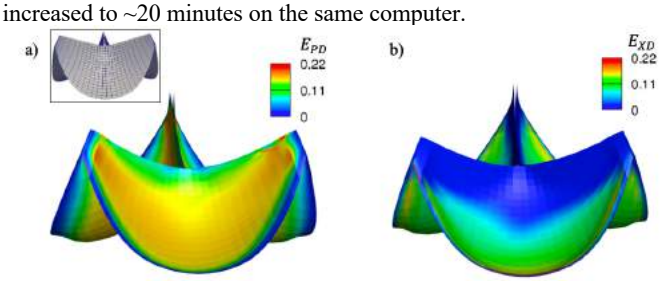


**Figure 4: Strain in the a) preferred and b) cross-preferred fiber direction obtained from replacement heart valve simulations for a fiber splay of $\sigma = 30°$ with the NNFE surrogate model.**

## DISCUSSION

We have demonstrated that we can develop neural network finite element surrogate models that can simulate heart valves within a few seconds with no loss of accuracy or related limitations due the use of aggressive approximation methods. Furthermore, these models are trained on the potential function describing the physical laws of the problem, and not on any experimental or simulated data. The material model used for training takes detailed fiber architecture information into account. Thus, these models are extremely high-fidelity and obey the physical principles within the training range.

The use of NURBS for both the geometric descriptions and NNFE basis functions provide two key advantages. First, they allow for exact representation of heart valve geometry without any discretization errors. This is also a crucial advantage for solving contact problems. Secondly, they allow for quick modifications to the geometry that is important for parametric studies. While we have used shell elements in the model presented here, we are currently developing the solid element model. The use of solid elements can allow us to capture through thickness variation of material properties that evidently exists in heart valves. In this work, we have considered a fixed fiber distribution. However, we are extending our approach to include fiber distribution data as an additional input to the neural network. In the future, we would also like to include geometry information as inputs to the neural network. With regards to the material model, we have only considered elastic effects in the model at this stage. However, our goal is to extend the model to also include plasticity effects [9] and simulate time-evolving behavior of the native and replacement heart valve under long-term conditions.


## ACKNOWLEDGEMENTS

NIH grant nos. R01 HL073021 and HL142504.


## REFERENCES


[1] Zhu, Y et al., *J Comput Phys*, 394:56-81, 2019.
[2] O'Leary-Rooseberry, T et al., *Comput Methods Appl Mech Eng*, 388:114199, 2022.
[3] Sheriffdeen, S. et al., Accelerating PDE-constrained inverse solutions with deep learning and reduced order models, 2019.
[4] Zhang, W et al., *Int Conf Func Imag Model Heart,* 11:416-424, 2021.
[5] Bradbury, J et al. http://github.com/google/jax, 2018.
[6] Polyak B, *USSR Comp Math Math Phys*, 4:1–17, 1964
[7] Sacks, M et al., *Interface focus*, 6.1:20150090, 2016.
[8] Zhang, W et al., *Int J Numer Meth Biomed Eng*, 37.4:e3438, 2021.
[9] Zhang, W et al., *J Mech Behav Biomed Mater*, 123:104745, 2021.

# SUPERFICIAL ZONE CHONDROCYTES CAN GET COMPACTED UNDER PHYSIOLOGICAL LOADING: A MULTISCALE FINITE ELEMENT ANALYSIS

**Kimberly R. Kroupa (1), Katherine A. Spack (2), Lianna R. Gangi (2), Nadeen O. Chahine (3), Clark T. Hung (2,3), Gerard A. Ateshian (1,2)**

(1) Department of Mechanical Engineering, Columbia University, New York, NY, USA
(2) Department of Biomedical Engineering, Columbia University, New York, NY, USA
(3) Department of Orthopedic Surgery, Columbia University, New York, NY, USA

## INTRODUCTION

Articular cartilage is a specialized tissue lining diarthrodial joints in the body, where it serves to reduce friction while sustaining contact forces for over 108 million cycles of loading in a 60-year lifespan. As with any mechanical system, cartilage must experience some normal 'wear and tear' over normal activities of daily living. This routine damage initiates in the superficial zone (SZ) of cartilage tissue [1,2], where its resident chondrocytes have been shown to die even under normal physiologic loading conditions [3, 4, 5]. This counter-intuitive observation suggests that there must exist a cell replenishment mechanism in diarthrodial joints, most likely from the synovium lining [6]. The objective of the current study is to better understand mechanical factors that may lead to SZ chondrocyte death, as part of a broader effort of understanding the mode of repair of normal 'wear and tear'.

The SZ is known to exhibit lower compressive and shear moduli compared to the middle and deep zones (MZ, DZ) of the articular layer [7], likely resulting in excessive SZ compaction under physiological loading. Such compaction may wring out the interstitial fluid of SZ chondrocytes, significantly altering their fluid transport properties and possibly causing their death. Chahine et al. [8] showed that SZ chondrocytes died after sustained 12-hour compaction of live cartilage explants by 50-80% strain. Using suitable control experiments they reported that SZ chondrocyte were more vulnerable to loading than their MZ and DZ counterparts.

Albro et al. [9] showed that chondrocytes can survive a volume loss of 50%, induced by hyperosmotic loading, for a short period of time (up to 1 h). However, lasting changes in cell volume can affect the ability of the cell to regulate its volume via ion channel transport, significantly affecting its homeostasis and viability [10]. Tissue compaction, especially of the pericellular matrix (PCM), and reduced cytoplasm permeability as fluid volume is lost, may also decrease diffusivity of glucose, insulin, other nutrients, and waste products between the cell and the synovial fluid, harming cell metabolism and potentially resulting in cell death.

In this study we performed a multiscale finite element analysis of articular contact to understand the fate of a SZ chondrocyte, by tracking the temporal evolution of its interstitial fluid pressure, hydraulic permeability, and volume change under physiologic loading conditions.

## METHODS

A multiscale finite element model was constructed in the open-source FE software FEBio (www.febio.org). A model by Zimmerman et al. [11] of biphasic frictional sliding contact between a cartilage plug and strip, accounting for symmetry, was modified by replacing one element in the cartilage strip SZ with a finite element domain containing an embedded 15×15×5 μm [12] ellipsoidal chondrocyte (Fig. 1). The finite element mesh of the strip, plug, and PCM + cytoplasm respectively included 7743, 3780, and 9728 8-node hexahedral elements; the cell membrane consisted of 384 4-node porous shell elements [13] (Fig. 1).

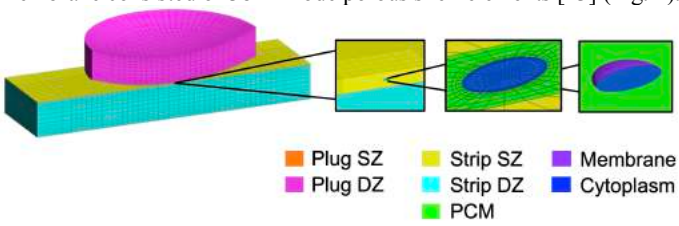


**Figure 1. Multiscale model of a cartilage plug in contact with a cartilage strip, containing a chondrocyte in the strip SZ.**

The properties of the cartilage matrix were described previously [11]. The cell cytoplasm was modeled as a biphasic material with a solid volume fraction of 0.4 [9], porous neo-Hookean solid matrix with E=0.78 kPa [13], and a Holmes-Mow strain dependent hydraulic permeability ($k=0.002$ mm$^4$/N·s [13], $M=2.2$, $\alpha=2$), to account for decreasing permeability as the cytoplasm gets compacted. The cell membrane was assigned a thickness of 10 nm. Its elasticity was

modeled with a Mooney-Rivlin solid with a shear modulus of 0.5 kPa and bulk modulus of 2.5 MPa. Its hydraulic permeability was set to $7\times10^{-10}$ mm$^4$/N·s [13]. The PCM kept the same properties as the SZ.

The model was subject to the following two loading conditions: Migrating Contact: Reciprocal displacement of the cartilage plug with an amplitude of 10 mm at 6 mm/min was prescribed for 15 minutes under a constant prescribed compressive load of 3.15 N and an equilibrium friction coefficient $\mu_{eq}$=0.201 [11]. This model ran for 12 hours (wall clock) on a high-performance cluster. Static Contact: A static compressive load of 3.15 N was prescribed on the plug for 3 hours. This model ran for 7 h (wall clock).

## RESULTS

The cell volume relative to its reference state (t=0) was recorded as a function of time (Fig. 2a). In both loading configurations, the cell volume decreased steadily throughout loading, following the same trend. In the stationary contact model, after 30 minutes of loading, a cell volume loss greater than 20% and a PCM volume loss of ~10% were observed (Fig. 2b, center). After 3 hours of stationary contact loading, the cell volume had reduced to 50% of its initial value, indicating that almost all the cytoplasmic fluid had left the cell. The PCM volume decreased by 20%, but notably remained higher in regions directly adjacent to the cell membrane (Fig. 2b, right).

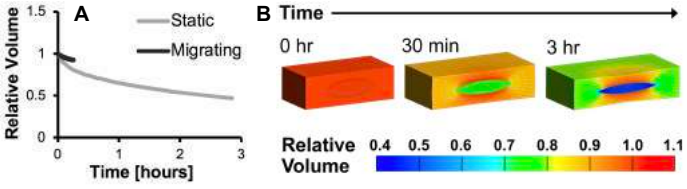


**Figure 2. (a) Relative volume of the cytoplasm versus time (b) Visualization of cell and PCM compaction in the stationary contact model, at time 0, after 30 minutes, and after 3 hours of loading**

The fluid pressure in the cytoplasm decreased as fluid flowed out of the cell and the tissue. (Fig. 3a). The cytoplasm progressively became compacted, decreasing its hydraulic permeability (Fig. 3b). In the stationary contact model, permeability decreased by four orders of magnitude over the loading duration due to compaction.

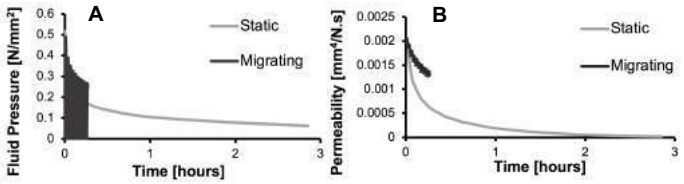


**Figure 3. (a) Fluid pressure in the cytoplasm versus time (b) Minimum principal permeability in the cytoplasm versus time**

As interstitial fluid flowed out of the tissue, its pressure decreased and the stresses were transferred to the solid matrix, exhibiting significant creep deformation (Fig. 4).

## DISCUSSION

This study showed that loading articular cartilage under physiological conditions and durations resulted in significant changes in the volume of SZ chondrocytes (Fig. 2), producing cell compaction and considerable reduction in the fluid transport properties (Fig. 3b). The drastic decrease in permeability of the cell cytoplasm and the creep deformation of the soft SZ also support the hypothesis that compressive loading may reduce the diffusivity of nutrients from the synovial fluid to the cell. Durney et al. [2] demonstrated that culturing explants with physiologic levels of the metabolic mediators found in synovial fluid, including glucose, cortisol, insulin, and ascorbic acid, is critical in maintaining tissue homeostasis. Further, Cigan et al. [14] showed that insulin and ascorbic acid are essential for chondrocyte viability in engineered construct culture, and that glucose has a dose-dependent effect on cell metabolism and proliferation. Together these results support our premise that access to nutrients at the proper dosage is critical to maintaining cell function. Reduced transport of these nutrients during loading may cause SZ cell death. DZ and MZ chondrocytes may be less sensitive to changes in nutrient transport, as they are accustomed to low nutrient access and may be more phenotypically mature. Thus, the results of this study provide a cogent hypothesis for the normal occurrence of SZ chondrocyte death reported in prior *in vitro* and *in vivo* studies [3,4,5].

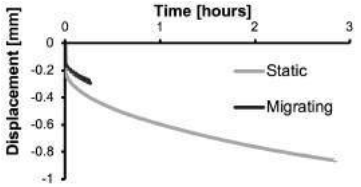


**Figure 4. Creep deformation of the cartilage tissue versus time**

It should be noted that intrinsic differences in cell properties, metabolism, or other mechanobiological signaling pathways in response to loading are other possible causes for the vulnerability of SZ cells to normal loading. Understanding these mechanisms may elucidate how OA initiates and progresses, possibly providing therapeutic targets.

Several factors influence the compaction time of SZ chondrocytes due to loss of interstitial fluid. In addition to the tissue material and transport properties, the most significant factor is the path length for the pressurized fluid to escape the loaded regions of the articular layer. In a contact configuration this means that the size (radius) of the contact area influences the compaction time, with larger contact areas requiring longer times. In this study the contact radius increased from 2.7 mm to 5.0 mm over 3 hours of loading. In the experimental study of Guilak et al. [12], loaded cartilage explants with a radius of 1.5 mm required only 20 minutes to produce steady-state values for their chondrocyte volume. These outcomes are self-consistent in the context of porous media mechanics and interstitial fluid transport.

A potential limitation of this computational analysis was the inability to compute the response to migrating contact for more than 15 minutes of loading. Though migrating contact is more representative of physiological loading, the computational challenge of solving this configuration was apparent from the disparity in the wall clock solution times between the two models. However, since both contact configurations led to consistent changes in cell volume (Fig. 2), fluid pressure and permeability (Fig. 3) and creep deformation (Fig. 4), it is reasonable to assume that the conditions achieved under stationary contact loading would be reproduced under migrating contact at later times, while remaining consistent with loading durations for activities of daily living (~ 8 hours).

## ACKNOWLEDGEMENTS

The authors acknowledge support from NIH R01 GM083925.

## REFERENCES

[1] Oungoulian et al., *J Biomech,* 47:694-701, 2014. [2] Durney et al., *J Biomech Eng,* 141:02100-1, 2019. [3] Chen et al., *Trans Orthop Res.* 26:259, 2001. [4] Bonnevie et al., *J Biomech.* 74:72-8, 2018. [5] Horisberger et al., *Clin Biomech.* 27:292-8, 2012. [6] Kurth et al., *Arthritis Rheum.* 63:1289-300, 2011. [7] Schniagl et al., *J Orthop Res.* 15:499-506, 1997. [8] Chahine et al., *Biomechan Model Mechanobiol,* 6:103-11, 2007. [9] Albro et al., *Biophys,* 97:2886-2893, 2009. [10] Kittl et al., *Front Cell Dev Biol.* 8:583131, 2020. [11] Zimmerman et al., *J Biomech Eng,* 144:021008, 2002. [12] Guilak et al., *J Orthop Res,* 13:410-21, 1995. [13] Hou et al., *J Biomech Eng,* 140, 2018. [14] Cigan et al., *Tissue Eng,* 19:1941-8, 2013.

SB³C2022
Summer Biomechanics, Bioengineering and Biotransport Conference
June 20-23, Eastern Shore, MD, USA

# NUCLEAR MORPHOLOGY OF VALVE INTERSTITIAL CELLS IN THE PRESENCE AND ABSENCE OF NATIVE ELASTIN IN PORCINE TRICUSPID VALVE ANTERIOR LEAFLET

**Samuel D. Salinas (1), Julia Clarin (1), Rouzbeh Amini (1,2)**

(1) Department of Bioengineering, Northeastern University, Boston, MA, USA
(2) Department of Mechanical Engineering, Northeastern University, Boston, MA, USA

## INTRODUCTION

Residing within the heart valve leaflets, the valvular interstitial cells (VICs) are at the center of maintaining valve competency. The primary role of VICs revolves around the production and remodeling of the extracellular matrix (ECM). The two primary constituents of the ECM, i.e., collagen and elastin fibers, function in synergy to provide the mechanical integrity necessary for the valve to handle physiological loads. The expression and remodeling of the ECM is mediated through the mechano-transduction of the VICs. The ability to sense their environment and any deviation allows VICs to alter their protein expression [1]. Repeated high cyclic strain, for example, is known to increase collagen production in aortic valves [2].

Certain genetic mutations pose a risk to a structurally sound ECM, nevertheless. Marfan syndrome (MFS), for example, is characterized by having fragmented elastin fibers in the ECM heart valves among other tissues. Because collagen and elastin fiber configuration depend on one another, MFS has the potential to result in a cellular morphology that differs from native ECM when the ECM micro-architecture is compromised.

aim was to characterize the nuclear aspect ratio of VICs of native leaflets and those of leaflets devoid of elastin across the thickness of the tricuspid valve leaflets. To establish an initial baseline, this study focused on anterior leaflet specimens in a stress-free state. This approach offered an insight into how cellular morphology was affected as a result of MFS. We hypothesized that leaflets devoid of elastin would display a higher nuclear aspect ratio, a result of a relaxed collagen fiber configuration.

## METHODS

Porcine hearts were acquired from a slaughterhouse and delivered to our laboratory within 24 hours after the animal was sacrificed. The anterior leaflet was carefully excised. The leaflet was then trimmed to a 7.6-mm small square. A small fiducial marker was attached at a specified location on the atrial surface of the leaflet such that the orientation of the leaflet could be recalled after the tissue was trimmed.

Fixation took place in 10% formalin overnight in a no-load state. After fixation, tissue specimens were embedded in paraffin before obtaining 20-µm-thick sections along the transmural-circumferential direction. Sectioned specimens were then deparaffinized and permeabilized with Triton-X, at a concentration of 1:1000, for 25 minutes. Next, the VIC nuclei were stained with SYTOX Green (Thermo Fisher Scientific, Cat: S7020), at a concentration of 1:2000, for 15 minutes before finalizing mounting with Fluoromount-G (Thermo Fisher Scientific, Cat: 00-4958-02).

Imaging on the processed sections was performed on a Zeiss LSM 880 NLO using a 10x objective with a field of view sufficient to cover the entire thickness of the specimen. Stained VICs were imaged using 488 nm as an excitation wavelength. The acquired z-stacks were then segmented using in Imaris (Bitplane, Zurich, Switzerland), as seen in Fig. 1A.

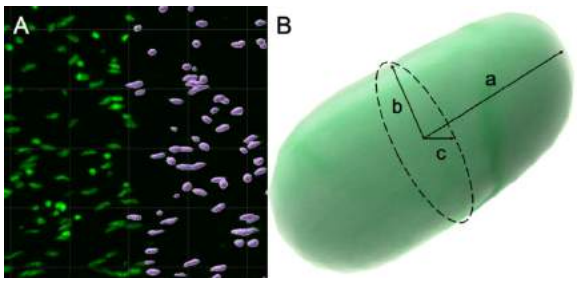


**Figure 1: (A) Representative ellipsoid fit of a VIC where axes a, b and c, are the three semi-axes lengths calculated using Imaris. (B) Stained (green) and segmented (purple) VIC images of a representative sample. Segmentation performed in Imaris.**

The abovementioned procedure was repeated for two groups: the control group (n=3) and the elastase-treated group (n=3). Similar to a previous study, elastase at a concentration of 7.5 U/ml for 20 minutes was used in the elastase-treated group [3].

Segmentation took place for a region of interest which was located in the center field of view of the acquired z-stack. An average number of X nuclei was segmented per each sample. The semi-axes for each fitted ellipsoid (corresponding to each segmented VIC, see Fig. 1B) were obtained in addition to the number of total segmented VICs in each sample and the nuclear aspect ratio (NAR) for each segmented VIC was obtained by dividing the major semi-axis a, by the minor semi-axis c.

To evaluate the overall morphology pertinent to each imaged sample, the average NAR was calculated across every sample along the entire transmural-circumferential thickness of the leaflet. For statistical testing, a two-sample *t*-test was performed to detect any significance of NAR in between the total segmented VICs of both groups.

## RESULTS

Figure 3 shows that the nuclear aspect ratio of the VIC increased in the specimens that were treated with elastase. The mean value of NAR for the control group was 2.44, whereas the mean value for the elastase-treated group was 2.63. Further, the calculated standard error of the mean was higher in the elastase-treated group (±2.70%) than that of the control group (±1.51%).

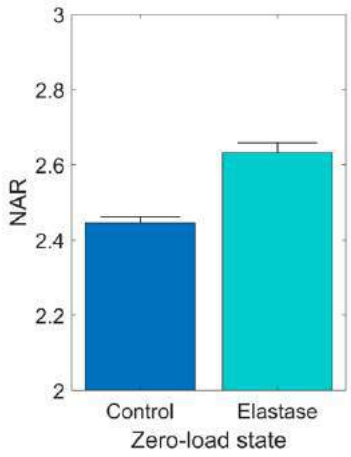


**Figure 3: Average NAR for Control and Elastase-treated groups. Error bars represent standard errors of the mean.**

Because of the inherent presence of variation across specimens, the thicknesses of each sample varied. In particular, the control samples were thicker than the elastase-treated samples. As such, the total VIC nuclei count in the control group was 2360, whereas 1297 nuclei were identified in the elastase-treated group. A significant difference was observed between the NAR values of the control and elastase-treated groups ($p < 0.01$, two-sample *t*-test).

## DISCUSSION

The purpose of this study was to understand how the landscape of VICs are modified when there is a degradation of native elastin fibers. The NAR in the control group represent the VICs that are residing within a native micro-structural environment of the leaflet. It is important to note that through focal adhesions, said VICs are connected to the extra cellular matrix (ECM) and have a "sense of mechanical awareness" of their residing environment [4]. Further, while the tricuspid valve leaflets undergo dynamic deformation, the main load-bearing constituents of the ECM (i.e., elastin and collagen) provide coupled responses, intrinsic to the mechanical response of leaflet [4].

When native tissue is treated with elastase, the original ECM micro-architecture is clearly altered as collagen undulation is reduced (Fig. 4). With the shift in ECM landscape coupled with focal adhesions of the VICs, one would expect that VICs morphology would also alter. As shown in Fig. 3, we noticed a significant increase of 7.78% in the elastase-treated NAR from that of the native tissue, suggesting a close link between collagen fibers micro-architecture (including reduced fiber crimp) and VIC nuclear morphology once elastase was applied. Using two-photon microscopy, we have previously observed the effect that elastase has on decreasing the undulation of collagen fibers in the tricuspid valve anterior leaflet (Fig. 4).

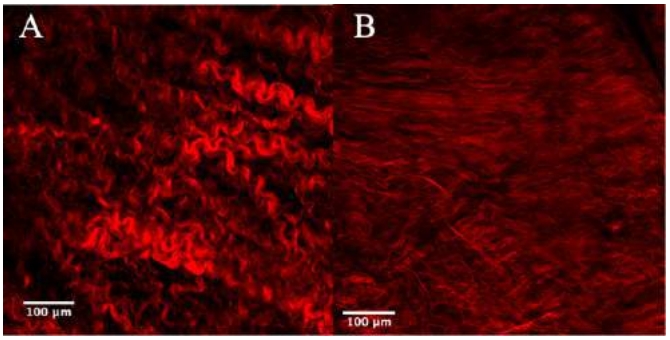


**Figure 4: Two-photon images of collagen fibers obtained from (A) a native tricuspid valve anterior leaflet as compared with (B) less-undulated collagen fibers in an elastase-treated sample.**

Nevertheless, to establish a trend between the NAR of control and elastase groups future investigation would have to include further load ranges. While results presented are for a zero-load state, additional loading protocols would include biaxial loads that concentrate mostly in the lower stress ranges which offer a wider strain range as seen in previous publication from our research group [6]. It should be noted that MFS, and its detrimental effects to elastin occur over a longer timeline than what is simulated in our investigation, as such, remodeling of the ECM may vary compared to what has been demonstrated here.

In summary, to simulate the effects of MFS on native tricuspid valve anterior leaflet tissues, the NAR of zero-load native specimens were calculated and compared with that of elastase-treated specimens. The average NAR, across all three samples per group, were 2.44 and 2.63 for the control and elastase-treated groups, respectively. The increase in NAR, was statistically significant at the zero-load state.

## ACKNOWLEDGEMENTS

Support for this work was provided by the National Science Foundation (NSF CAREER award 2049088). We also thank the Institute for Chemical Imaging of Living Systems at Northeastern University for consultation and imaging support.

## REFERENCES

[1] Ng, C et al., *J Clin Invest*, 114:1586-1592, 2004.
[2] Ku, C et al., *Cardiovasc Res*, 71:548-556, 2006.
[3] Ferruzi, J et al., *Cardiovasc Res,* 92:287-295, 2011.
[4] Butcher, J et al., *Phil. Trans. R. Soc. B,* 362:1145-1457, 2007.
[5] Visely, I, *J Biomech*, 31:115-123, 1997.
[6] Khoiy, K et al., *J Biomech*, 138:104504, 2016.

# DYNAMIC IN-VIVO MOTION OF THE MOUSE AORTIC HEART VALVE

**Xinzeng Feng (1), Daniel P. Gramling (2), Aletea L. vanVeldhuisen (2), David McComb (3), Christopher K. Breuer (4), Craig, Goergen (2), Michael S. Sacks (1)**

(1) James T. Willerson Center for Cardiovascular Modeling and Simulation, The Oden Institute and Department of Biomedical Engineering, The University of Texas at Austin, Austin, Texas, USA
(2) Weldon School of Biomedical Engineering, Purdue University
West Lafayette, IN, USA
(3) Center for Electron Microscopy and Analysis, The Ohio State University
Columbus, OH, USA
(4) Tissue Engineering and Surgical Research, Nationwide Children's Hospital
Columbus, OH, USA

## INTRODUCTION

Mouse animal models are attractive for their ability to perform genetic studies of the disease process and test potential pharmaceutical treatments. While mouse models have been used for cellular level studies of heart valve disease, their small size and fast heart rates has hindered our ability to utilize them for tissue and organ level studies. We have recently developed a novel small animal imaging technique based on high-frequency four-dimensional ultrasound (4DUS) [1]. Using this method, we have developed a pipeline for reconstructing, for the first time, the *in vivo* geometry of the mouse aortic valve (mAV). This method was guided and validated using high-resolution µCT images of *ex vivo* mouse mAV geometric modeling.

## METHODS

**Data acquisition.** A Vevo 3100 (FUJIFILM VisualSonics) instrument with MX550D linear array transducer (Fig. 1) was used to acquire 4DUS images of the aortic valve of three C57BL/6J mice (healthy, male, 3 months old) with spatial voxel size and temporal resolution to be 40µm$^3$ and 2ms, respectively. Segmentation was performed using an in-house MATLAB GUI in which the imaging volume was first oriented orthogonal to aortic valve opening to ensure true short axis (SAX) view and then rotated to ensure that the right and left coronary cusp (RCC/LCC) were on the left and right side of the image, and non-coronary cusp (NCC) pointing downward. To overcome the motion of mAV within chest cavity and isolate leaflet motion, the center of the mAV was tracked throughout the cardiac cycle, and motion was offset across time in three axes. At each time point, the following geometric features were manually segmented (Fig. 2) including points along the free edges $\mathbf{P}_{FE}$ (black squares) including the commissure points, the midpoints of the basal attachment $\mathbf{P}_{BA,mid}$ (green squares), the lowest points of each leaflet $\mathbf{P}_{lowest}$ (red squares) along the SAX, and the horizontal cross sections of each leaflet at the height of the triple point ($\boldsymbol{\ell}_{triple}$).

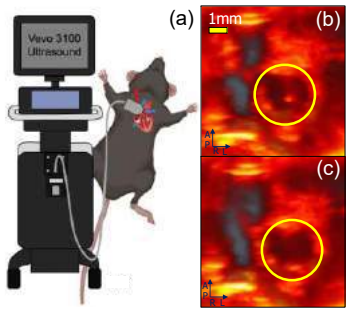


**Figure 1: 4DUS images of mAVs (highlighted) were acquired at fully closed (b) and open (c) states.**

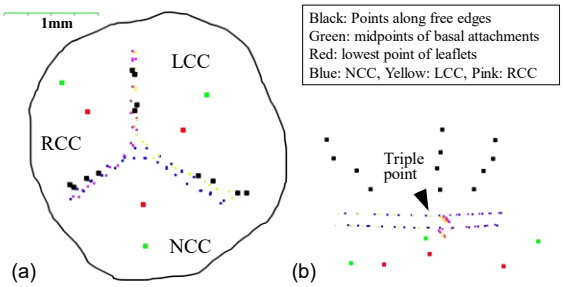


**Figure 2: Top (a) and side (b) views of the 4DUS-segmented geometric features of a mAV at the closed state. The contour represents a slice of the aortic wall.**

A Thermo Scientific Heliscan µCT instrument was used to obtain the *ex vivo* images of the aortic valve of a C57BL/6J mouse (healthy, male, 10 months old). The mAV was excised and fixed at the closed state under 100 mmHg. This was achieved by elevating a reservoir of solution to a

height relative to the mAV [2]. The polyethylene pressure monitor tubing was anastomosed to the aorta with polyamide sutures. Transvalvular hydrostatic pressure was applied from the arterial side with saline solution initially to ensure proper pressurization of the aortic trunk. Segmentation of the µCT images was performed using Synopsys' Simpleware ScanIP software (Version 2018.12-SP2).

**In vivo closed-state surface reconstruction.** To reconstruct the *in vivo* closed-state geometry, we used a generic NURBS-based geometric model (Fig. 3) to fit the 4DUS-segmented geometric features. The geometric model used 33 independent parameters to control the position of a grid of NURBS control points with which the size and shape of the midsurface geometry was determined. The controlling geometric parameters include but not limited to the valve height, leaflet span angle, position of the triple point, etc. A two-step fitting scheme was then adopted to ensure proper fitting to the segmented features. In the first step, only $\mathbf{P}_{FE}$ and $\mathbf{P}_{BA,mid}$ of all leaflets were fitted which set the size and rigid body translation of the mAV from the model to the lab coordinate. In the second step, $\mathbf{P}_{lowest}$ and $\ell_{triple}$ were included to further characterize the profiles of the free edge and belly curve.

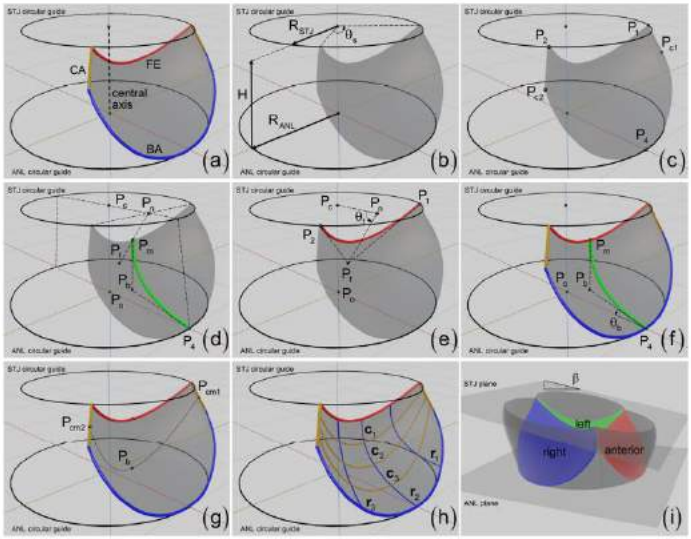


**Figure 3: NURBS-based geometric model was used to fit the *in vivo* closed-state geometry of mAV.**

**In vivo open-state surface reconstruction.** The *in vivo* open-state geometry was developed by morphing the control points of the closed-state geometry to match the 4DUS-segmented geometric features at the open state. The morphing process was governed by the displacement vectors of control points at the two commissure lines $\mathbf{u}_{comm,line1}$, $\mathbf{u}_{comm,line2}$, the midpoints of the basal attachment $\mathbf{u}_{BA,mid}$ and free edge $\mathbf{u}_{FE,mid}$. In particular, for a control point associated with NURBS parameter $(\xi,\eta)$, $0 \le \xi \le 1$, $0 \le \eta \le 1$, the following displacement vector $\mathbf{u}$ was introduced to morph the geometry from the closed-state to the open-state:

$$\begin{aligned}\mathbf{u}(\xi,\eta) = {} & (1-\eta)^2 \mathbf{u}_{comm,line1} + \eta^2 \mathbf{u}_{comm,line2} + \\ & 4(1-\xi)\eta(1-\eta)\mathbf{u}_{BA,mid} + \\ & \alpha\xi\eta(\eta-c)(\eta-1+c)(\eta-1)\mathbf{u}_{FE,mid}\end{aligned} \quad (1)$$

Here, $\xi$ and $\eta$ are the coordinates of the NURBS parametric domain along the radial and circumferential directions, respectively.

## RESULTS

In both states, the final *in vivo* geometry was rendered as volumes by assigning µCT-measured thickness to the fitted midsurface with a uniform thickness value to the belly region and a realistic thickness model to the nodulus position (Fig. 5). It was found that the limited segmented geometric features were sufficient to characterize the geometry at both states indicating that the geometric model could substantially lower the amount of segmentation load in reconstruction. Compared with the *ex vivo* geometry, the reconstructed *in vivo* closed-state mAV geometry showed reasonably good agreement (Fig. 4a and Fig. 5b, d). Particularly, the *in vivo* and *ex vivo* mAV geometry indicated similar dimensions and dipping profile of the free edges, a characteristic seen in mouse heart valves [2] but not in bioprosthetic heart valves [3]. By morphing the control points of the closed state, we also reconstructed the geometry at the open state although no µCT counterpart was available at this stage (Fig. 5a, c).

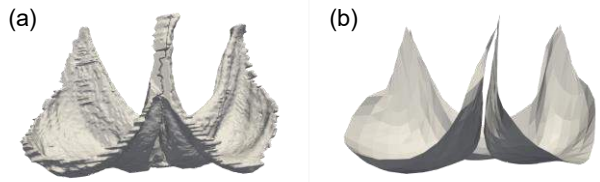


**Figure 4: The *ex vivo* µCT-segmented geometry (a) and reconstruction of the midsurface using the geometric model (b), which was used to guide the *in vivo* geometric model form.**

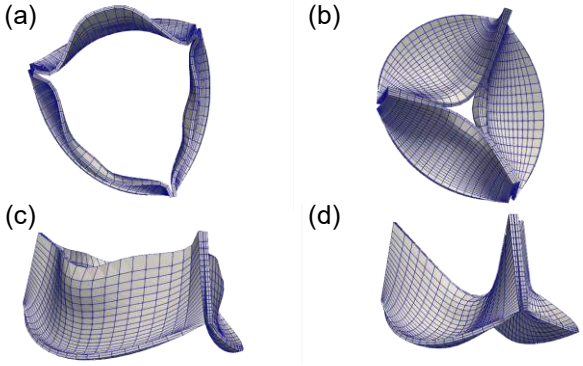


**Figure 5: Final reconstructed *in vivo* mAV geometry at open (a, c) and closed (b, d) states.**

## DISCUSSION

In this work, we have demonstrated the ability to use high-frequency 4DUS to reconstruct *in vivo* mAV geometry. *To our knowledge, this is the first time such reconstruction was ever achieved*. By using a geometric model based on µCT data, we were able to reconstruct mAV geometry given limited amount of 4DUS segmentation data. Looking forward, we are working on increased number of frames to develop a more accurate picture of mAV motion over the cardiac cycle. This will allow for longitudinal characterization of mouse models of aortic heart valve disease in long-term mechanistic studies.


## ACKNOWLEDGEMENTS

The authors give special acknowledgement to Dr. Felix Liu, Dr. Frederick W. Damen for their help, and NIH grant R01 HL142504 for funding.


## REFERENCES


[1] Damen, Frederick W., et al., *Tomogr* 3.4, 2017.
[2] Liu, Yifei, et al., *Sci. Rep.*, 2021.
[3] Hsu, Ming-Chen, et al., Comput. Mech, 2014.

SB³C2022
Summer Biomechanics, Bioengineering and Biotransport Conference
June 20-23, Eastern Shore, MD, USA

# CYSTEINE CHEMICAL MODIFICATIONS AS THE REGULATORY RESPONSE TO DIMETHYL SULFOXIDE EXPOSURE

**N. Ghousifam (1), M. Rezaeeyazdi (1), C. L. Riley (2), D. Romanovicz (1), M. N. Rylander (1), and M. Uden (3)**

(1) Department of Mechanical Engineering, The University of Texas, Austin, TX, United States
(2) Department of Molecular Biosciences, The University of Texas, Austin, TX, United States
(3) Department of Psychology, The University of Texas, Austin, TX, United States

## INTRODUCTION

Cysteine is a key amino acid in proteins with a chemical composition of three functional groups - amino, carboxyl, and thiol - all highly abundant among different organisms [1]. Specifically, the presence of highly reactive thiol group and its structural feature to form disulfide bonds under oxidative conditions makes cysteine an ideal compound for investigation of oxidation induced chemical modifications in biologically relevant models [2-4]. On the other hand, dimethyl sulfoxide (DMSO) is a low molecular weight cell permeating compound that is widely used in the pharmaceutical industry as a solvent, and it is a very well-known cryoprotective agent that is routinely used to preserve cells at cryogenic temperatures. Particularly, DMSO is the major component of many vitrification solutions [5-7] due to its ideal property of eliminating ice formation and preventing freezing damage during organ transplantation; however, organ transplantation is currently hindered due to cell death that occurs during the cryopreservation process. Therefore, in this work, we proposed to identify whether DMSO exposure modulates cysteine properties as part of its cytotoxicity effect. Various parameters, such as the number of free thiol groups, were assessed following immediate exposure of cysteine to DMSO and upon treatment with a reducing agent Dithiothreitol (DTT) post removal of DMSO using a series of designed ad hoc ideally simplified experiments. The observed chemical modifications of cysteine after DMSO treatment indicate that DMSO would irreversibly alter the activity and function of many proteins in signaling pathways consequently affecting the ultimate cell survival rate.

## METHODS

L-Cysteine (Sigma-Aldrich, 30089) solution was prepared in phosphate buffer saline (Sigma-Aldrich, P5368) and exposed to 30% v/v DMSO to the final concentration of 2 mM, followed by 1 hour incubation at 37 °C. Then, DMSO was diluted out to 0.5% v/v and samples were second incubated with 150 µM DTT for another hour at 37 °C. The number of free thiol groups were quantified at the end of the first and second incubation steps using Ellman's reagent (Thermo Scientific, 22582) according to the manufacturer's protocol and reading absorbance at 412 nm. All experiments were performed in triplicates to determine the mean ± standard deviation (SD) of each group. Student's t-test was used to evaluate the significantly different groups among pairs. p value of $< 0.05$ was considered significant.

## RESULTS

The absorbance values obtained from Ellman's reagent-based colorimetric assay for cysteine samples exposed to DMSO is shown in Figure 1. Total number of free thiol groups decreased significantly (50%, $p < 0.05$) compared to the cysteine untreated group. Control and DMSO exposed samples were then diluted and second incubated with DTT to investigate the effect of a reducing agent on the DMSO induced cysteine modifications. The absorbance data is shown in the same Figure 1. Interestingly, the reducing agent did not change the number of available thiol groups compared to the DMSO exposed alone samples, which suggests that the nature of chemical modifications that DMSO induces is unlike the formed intramolecular disulfide bridges upon oxidation when the thiol group is exposed to the traditional oxidizing agents, such as hydrogen peroxide.

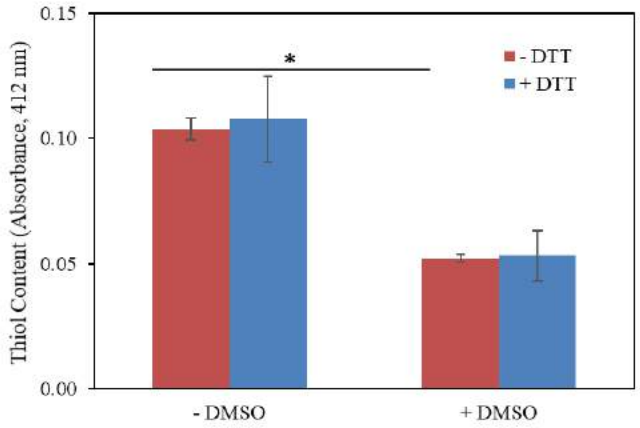


**Figure 1: Thiol content of cysteine samples post exposed to (+) DMSO and (+) DTT using Ellman's reagent-based colorimetric assay. Negative control samples are shown as (-) indicating no exposure to DMSO or DTT. Values are presented as mean ± SD of n = 3, $p < 0.05$.**

## DISCUSSION

The loss of free thiol groups, which is shown by the significant reduction of absorbance of the treated samples, indicates that cysteine directly interacts with DMSO. The observed chemical modification suggests that the thiol groups of the cysteine solution may have been oxidized by DMSO, which might have induced the formation of disulfide bonds. This phenomena along with the fact that the interaction was not reversed with the reducing agent, DTT, lead to the conclusion that maybe the toxic effect of DMSO on cells is caused by exerting extensive severe damage to proteins' cysteine content and ultimately irreversibly disturbing major oxidative signaling pathways/mechanisms during organ cryopreservation for transplantation purposes.

## ACKNOWLEDGEMENTS

This is a Plan II SAWIAGOS project.

## REFERENCES

1. Miseta, A. and P. Csutora, *Relationship between the occurrence of cysteine in proteins and the complexity of organisms.* Molecular Biology and Evolution, 2000. **17**(8): p. 1232-1239.
2. Daher, B., M. Vučetić, and J. Pouysségur, *Cysteine depletion, a key action to challenge cancer cells to ferroptotic cell death.* Frontiers in Oncology, 2020. **10**.
3. Banjac, A., et al., *The cystine/cysteine cycle: a redox cycle regulating susceptibility versus resistance to cell death.* Oncogene, 2008. **27**(11): p. 1618-1628.
4. Chalker, J.M., et al., *Chemical modification of proteins at cysteine: opportunities in chemistry and biology.* Chemistry – An Asian Journal, 2009. **4**(5): p. 630-640.
5. Fahy, G.M., et al., *Improved vitrification solutions based on the predictability of vitrification solution toxicity.* Cryobiology, 2004. **48**(1): p. 22-35.
6. Fahy, G.M., et al., *Cryopreservation of organs by vitrification: perspectives and recent advances.* Cryobiology, 2004. **48**(2): p. 157-178.
7. Taylor, M.J., Y.C. Song, and K.G.M. Brockbank, *22 Vitrification in tissue preservation: new developments*. 2004. p. 603-641.

# A DEEP LEARNING APPROACH TO INVESTIGATE THE HIDDEN LINKS BETWEEN CANNABIS AND CARDIOVASCULAR HEALTH

**Joseph C. E. Messou (1), Francis Oparaocha (2), Hasan Imanli (3), James A. Perry (4), Timm-Michael L. Dickfeld (4), Jean Jeudy (5), Eleonora Tubaldi (2, 4)**

(1) Department of Electrical and Computer Engineering, University of Maryland, College Park, MD, USA
(2) Department of Mechanical Engineering, University of Maryland, College Park, MD, USA
(3) University of Maryland Medical Center, University of Maryland, Baltimore, MD, USA
(4) Department of Medicine, University of Maryland, Baltimore, MD, USA
(5) Department of Diagnostic Radiology, University of Maryland, Baltimore, MD, USA

## INTRODUCTION

While cannabis has been legalized in many U.S. states, its impact on cardiovascular health is still unclear and remains to be explored. On one hand, some studies have shown that no association could be made between cannabis use and cardiovascular diseases [1,2], but on the other hand other studies have suggested a negative correlation between the two. A study conducted in the United States by Desai et al. [3] using the National Inpatient Sample (NIS) database has shown that 0.23% of cannabis users were admitted for acute myocardial infarction (AMI) while non-users had a lower frequency of admission for the same disease (0.14%). Overall, the current literature is still divided on the impact of cannabis on cardiovascular health. In this work, we take a step towards a better understanding of the issue by exploring a potential correlation between cannabis use and cardiovascular magnetic resonance (CMR) images.

Cardiovascular magnetic resonance (CMR) imaging is a non-invasive imaging technique used to diagnose different cardiovascular diseases such as congenital heart disease and myocarditis [4]. While most cardiovascular disease (CVD) studies use long-axis and short-axis image sequences displaying the heart during a cardiac cycle [5], some studies focus on another sequence of CMR images that measures relaxation time of myocardial tissue: native T1 mapping images [6]. Here, we take a similar approach in order to build a fast model that only uses a single T1 mapping image instead of a stack of long-axis and short-axis images.

To explore the potential correlation between cannabis use and CMR images, we used the UK Biobank platform [7], a large-scale biomedical database containing both CMR images and cannabis use information obtained through a survey. In this survey, volunteers were given the option to report if they have used cannabis in the past, how often, and the last age at which they used it.

In this work, (1) we explore the UK Biobank and identify individuals with CMR data and cannabis use information, (2) we segment T1 mapping images of regular cannabis users and non-users, and (3) we train and test a deep learning model to distinguish T1 mapping images of regular cannabis users and non-users.

## METHODS

Before investigating the correlation between cannabis use and T1 mapping images, we first explore the UK Biobank dataset. To avoid extracting features that might be related to a particular disease and focus on the correlation between cannabis use and T1 mapping images, we remove individuals with 96 common diagnoses (diagnoses that affect more than 1% of the dataset) and other cardiovascular diagnoses (dilated cardiomyopathy, cardiomyopathy, preexcitation syndrome, heart failure, and cardiomegaly). We then select the cohort of individuals that would be classified as regular cannabis users. As shown in Figure 1, we define regular cannabis users as individuals who have used cannabis at least 100 times, once a week or more, and with a most recent use no longer than 1 year before taking the survey.

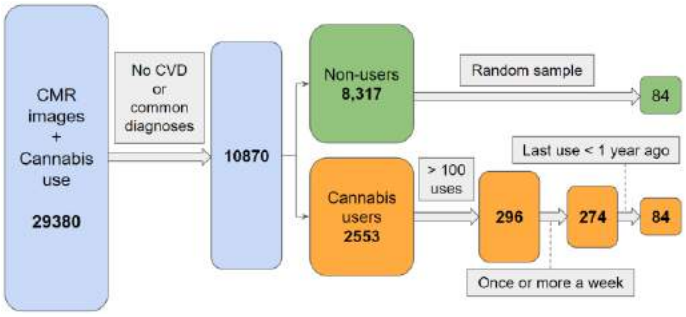


**Figure 1: UK Biobank cannabis use exploration**

After obtaining the final dataset consisting of 168 T1 mapping images, with 84 images from regular cannabis users and 84 images from "healthy" non-users, each image is manually segmented as seen in Figure 2 by identifying pixels belonging to the LV myocardium and the RV.

We then split the 168 T1 mapping images coupled with their segmentations into a 60:15:25 split, yielding 100 training images, 26 validation images, and 42 test images. To avoid training issues due to class imbalance, the splits are done for each class individually before putting the data back together.

After exploring different architectures available in PyTorch [8], we choose ResNet18 [9], a deep learning model widely used for image classification, and change the last fully connected layer to output 2 predictions. We finetune the hyperparameters on the validation set and finally select a batch size of 16 and an initial learning rate of 0.01 that is divided by 10 every 30 epochs. With these parameters fixed, we then select for the inputs shown in Figures 2.B and 2.D the 3 fully-converged models that perform the best using 5-fold cross validation.

## RESULTS

Figures 2.B and 2.D show the different types of input used during training and testing depending on the model. Figure 2.A is the full T1 mapping image and Figure 2.C is its corresponding heatmap. Figure 2.B is obtained by changing all the positive values of the manually segmented mask to 1 and multiplying the result with Figure 2.C. Figure 2.D is obtained using a similar process where only the mask of the left ventricle (LV) myocardium is kept.

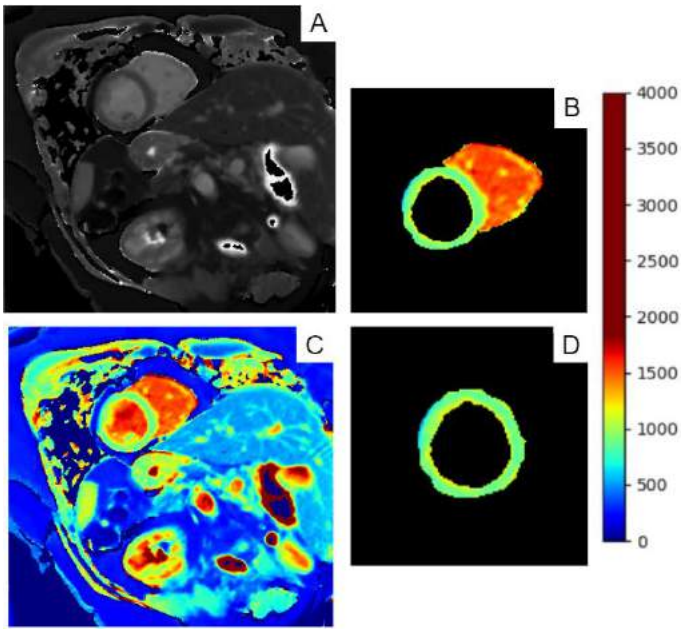


**Figure 2: (A) T1 mapping image; (B) Segmented Left Ventricle (LV) myocardium + Right Ventricle (RV); (C) T1 mapping heatmap; (D) LV myocardium**

Figure 3 shows the results obtained on the test set. Since our validation set is small and might not be fully representative of the test set despite 5-fold cross validation, for each type of input, we select the 3 models that converged and performed the best on the validation set.

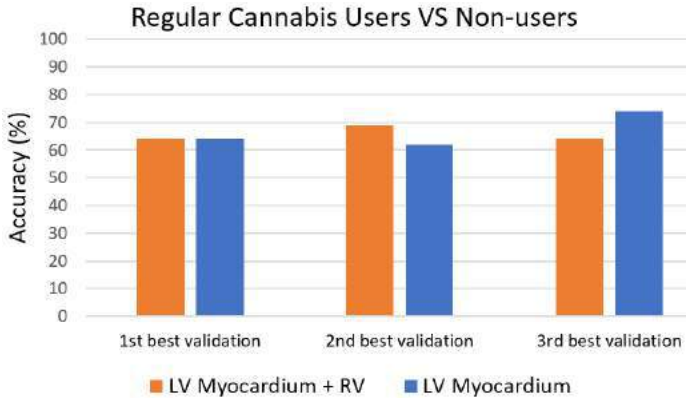


**Figure 3: Test set classification accuracy for each type of input**

## DISCUSSION

Figure 3 shows that the model trained on the LV myocardium performs the best (73.8%), which is well above a random binary classification of 50%. This result aligns with most methods that analyze T1 mapping images using global and regional T1 values of the LV myocardium [6]. While adding the RV allows the network to see more pixels, it seems that it cannot leverage this extra information, including the location of the septum to give a better classification accuracy. Overall, our experiments show that the LV myocardium in T1 mapping images could be used with a deep learning model to distinguish between the T1 mapping images of some regular cannabis users and non-users.

One limitation of our study is the limited number of available images to train our deep learning model. With only 26 validation images, our validation results do not directly transfer to our test set. To avoid selecting a model biased towards the validation set, we select the best 3 models for each input type and report their results on the test set. With more images, we could train a more robust model that could handle outliers. Since the UK Biobank is continuously accruing data, we hope to address this issue as more data becomes available.

While the impact of cannabis use on cardiovascular health is still unclear, this preliminary study shows that deep learning algorithms might be used to distinguish between T1 mapping images of regular cannabis users and non-users. This useful tool for non-invasive image-based diagnostics might help shading some lights on potential hidden links between cannabis use and major cardiovascular events.

## ACKNOWLEDGEMENTS

E.T. would like to acknowledge the UMD Start-up grant for supporting this work.

## REFERENCES

[1] Auer, R. et al., *Addiction*, 113:845-856, 2018.
[2] Adegbala, O. et al. (2018). *The American journal of cardiology*, 122:129-134, 2018.
[3] Desai, R. et al. *Medicina*, 55:438, 2019
[4] Pennell, D. J., *Circulation*, 12:692-705, 2010
[5] Bai, W. et al., *Journal of Cardiovascular Magnetic Resonance*, 20:65, 2018
[6] Puyol-Antón, E.M. et al., *Journal of Cardiovascular Magnetic Resonance*, 22:1-15, 2020
[7] Littlejohns, T. J. et al., *European heart journal*, 40:1158-1166, 2019
[8] Paszke, A. et al., *Advances in neural information processing systems*, 32:8026-8037, 2019
[9] He, K. (2016). *Proc. IEEE CVPR*, 770-778, 2016

# THE INFLUENCE OF PERSONAL PROTECTIVE EQUIPMENT ON MALE AND FEMALE SPINAL LOADS IN VERTICAL IMPACT

**Sagar Umale (1), Prashant Khandelwal (1), John R. Humm (1), Narayan Yoganandan (1,2)**

(1) Department of Neurosurgery, Medical College of Wisconsin, Milwaukee, WI, USA
(2) Neurosurgery Research, VA Medical Center, Milwaukee, WI, USA

## INTRODUCTION

Mounted Soldiers are subjected to vertical loads, transmitted from the seat to the pelvis to the torso regions during underbody blast events. The use of personal protective equipment (PPE) adds to the weight of the torso, influencing the load transmission within the vertebral column. Due to the loading direction and proximity to the seat, during blast events, the thoracolumbar spine is at a higher risk of injury, and injuries to this region are reported in clinical literature [1]. With increase in the female population, and with the acknowledgment that this group has different biomechanical injury tolerance limits, the objective of the present investigation was to determine the forces and sagittal bending moments in male and female spines with the PPE and head supported mass using human body finite element models.

## METHODS

The detailed Global Human Body Models Consortium (GHBMC) mid-sized male [2] and the small female model [3] were used in the study. The simulation environment consisted of the human body model, a rigid seat, and a footrest. As the models represented the posture of automotive occupants, to mimic the posture of a seated soldier, the male and female occupants were seated close to the seat and were then settled under the 1 g acceleration along the z (vertical) and x (antero-posterior) directions. The final postures of the two models were extracted from the positioning simulations such that the models represented an upright seated soldier in a military vehicle (Figure 1).

The positioned models were restrained in the seat with a five-point seatbelt, typical of a military harness. They were updated with PPE, which consisted of a 1.4 kg military Army Combat Helmet and 11 kg body armor vest. The vest consisted of carrier plates (3.6 kg) with arms protective inserts (5 kg) and side ballistic inserts (2.4 kg) [4]. Cross-sectional sets along the transverse axis were defined at the L5 and T12 mid-intervertebral bodies to obtain loads in the spine at the lumbar and thoracic end, termed distal and proximal regions [5]. Three acceleration ($G_z$) pulses with peak velocities of 4.8 m/s, 6.5 m/s and 7.9 m/s, termed as low, medium, and high severity) were derived from acceleration pulses. They were applied to the seat and the footrest to determine the effect of impact severity on spine loads. A total of twelve cases were simulated for the two models (with and without PPE) and three severities. The peak forces and moments were extracted at the proximal and distal regions of the spine for the low, medium, and high severity impacts.

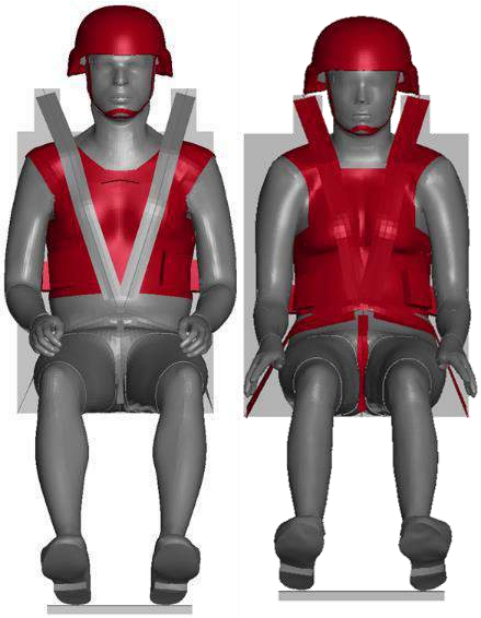

**Figure 1: The male (left) and female (right) models positioned in the seat with PPE (body armor and army combat helmet).**

## RESULTS

The kinematic analysis showed that the thoracic and lumbar spines responded with compression-flexion in both male and female models, and this was true for with and without PPE cases.

*Effect of impact severity:* The increasing severity of impact increased forces more in males than females. For PPE cases, compared with the low severity, at the proximal and distal regions, force increased by 31% and 36% for the male spine while for the female spine the increase was 18% and 20%, for high severity respectively. At the medium severity, increases in the male spine were 25% and 28%, and in the female spine they were 24% and 26%, respectively. Compared with the low severity, at the proximal and distal regions, moments increased by 34% and 36% for the male spine while for the female spine the increase was 20% and 21%, for high severity respectively. At the medium severity, increases in the male spine were 25% and 30%, and in the female spine they were 27% and 26%, respectively. These results for with and without PPE increase in force are shown in Figure 2.

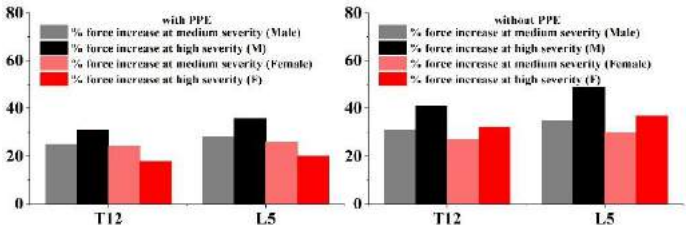


**Figure 2: The % increase in force for medium and high severity velocity compared to low severity.**

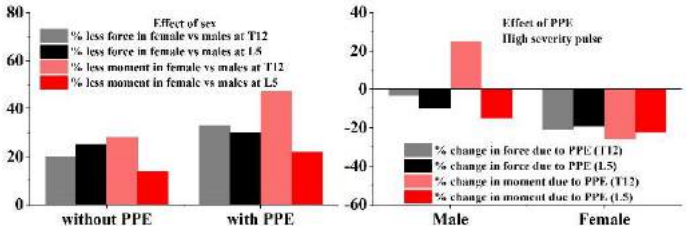


**Figure 3: The effect of sex (left) and PPE (right) on spinal loads.**

*Effect of sex:* With the use of the PPE, forces in the female spine were lower than those in male spine. Across the three impact severities, on average, forces were lower by 33% at the proximal and 30% at the distal regions, and moments were lower by 47% and 22%, respectively. As a comparison, without PPE the female spines had lower changes than with PPE. These results for without and with PPE are shown in Figure 3 (left).

*Effect PPE:* With PPE the forces decreased in both spines: up to 10% at the distal region in the male spine and up to 21% at the proximal region in the female spine. Bending moments decreased by 26% and 22% for the female spine at the distal and proximal regions, and in the male spine, moments decreased by 15% at the distal and increased by 25% at the proximal regions (Figure 3 - right).

## DISCUSSION

In this study, male and female human body models were used to determine the thoracolumbar spine kinetics simulating underbody blast loading, and three impact severities were used. Because the original models were developed for automotive occupants, and the currently intended application is for Soldiers, PPE was added to each torso, and in addition, the posture was altered. The PPE simulated in the models represented the equipment currently used in the military. A head supported mass was added, and it simulated the midsize Army Combat Helmet. These changes rendered the modeling and output responses more realistic and are considered as a first step in the analysis of spinal kinetic for vertical loading from underbody blast events.

From an overall kinematics perspective, both male and female spines responded similarly, as expected; however, the internal load transmissions were different, and these metrics depended on the type of the metric, force versus moment, spinal region, distal versus proximal, and male versus female. The kinematic patterns showed that the mechanism of loading was compression combined with flexion. This mode of loading parallels injuries such as wedge compression fractures in military environments [6]. While not the focus of the present study, similar kinematics and mechanism without PPE is applicable to the civilian automotive environments, as similar inferences have been reported from field data [7]. Thus, the results based on the overall kinematics indicate that the present analysis is applicable to both automotive and military scenarios.

As expected, increase in impact severity increased spinal loads at both regions; however, the use of the PPE reduced forces in both spines. Bending moments were reduced with PPE in the female spine at both regions. Whereas in the male spine, they reduced at the distal and increased at the proximal region, suggesting that the PPE is more effective in female. The increase in the bending moment at the proximal region may predispose the male spine to compression-flexion injures.

Spinal loads were lower in the female spine than the male spine. This is largely due to the size effect. The vertebral column length, depth breadth along the antero-posterior direction, and intervertebral disc depths along the superior-inferior direction are lower in the female spine than the male spine [8]. Although not investigated here, curvature also plays a role in the load transmission. They are different between men and women, and the female pelvis anatomy orients the dorsal spine differently in women in a seated position. The male vertebral body cross-sectional areas are 20% greater on an average [9]. The female vertebral body cross-sectional areas in the present model were 43% lower at T12 and 20% at L5 than the male model. These parameters contributed to the differences in the force and moment pattern changes between the male and female spines.

The present human body modeling study showed that increase in vertical impact velocity increased spinal forces and moments for both PPE cases, the PPE decreased the spinal force and moments, except the bending moment at thoracolumbar junction in the male spine, and the spinal loads in males were greater than females. These results delineate the effects of PPE, male-female, sex and impact severity on proximal and distal spinal forces and moments under simulated underbody blast loading.


## ACKNOWLEDGEMENTS

This research was supported by the Department of Veterans Affairs Medical Research, Department of Neurosurgery at the Medical College of Wisconsin, and W81XWH-16-01-0010. This material is the result of work supported with the resources and use of facilities at the Zablocki VA Medical Center, Milwaukee, Wisconsin. The authors thank the GHBMC for providing the models. The last author (NY) is an employee of the VA Medical Center, Milwaukee, WI.


## REFERENCES


[1] Freedman, B.A., et al., Arch Orthop Trauma Surg, 2014.
[2] GHBMCManual. Version 5.1.1 Users' Manual, Feb 2020.
[3] Davis ML, et al., STAPP Car Crash J, 2016.
[4] US Government Accountability Office, 2017.
[5] Yang, K.H., et al., Basic FEM. Academic Press.
[6] Spurrier, E.G., et al., Spine, 2016.
[7] Pintar, F.A., Ann Adv Automot Med, 2012.
[8] Gilsanz, V., et al, Radiology, 1994.
[9] Bruno, A.G., et al., *J Bone Miner Res*, 2014.

# 3D MICROFLUIDIC CELL ARRAYS WITH RECIRCULATION AND TUMOR-STROMA INTEACTIONS FOR THE DEVELOPMENT OF IMMUNOTHERAPEUTIC DRUG

**Chun-Wei Chi (1), Yeh-Hsing Lao (2), A.H. Rezwanuddin Ahmed (1), Kam W. Leong (2) and Sihong Wang (1)**

(1) Department of Biomedical Engineering, CUNY– City College of New York, New York, NY, USA
(2) Department of Biomedical Engineering, Columbia University, New York, NY, USA

## INTRODUCTION

Recent studies have demonstrated cancer immunotherapy's feasibility in treating triple-negative breast cancer, the most aggressive breast cancer type with worse survival, as two of immune checkpoint blockades have received FDA approval. Since there are many checkpoint proteins involved in adaptive immunity, and more candidates of inhibitory receptors being discovered, more and thorough studies are warranted to explore and validate their clinical potentials.[1] However, generation of a proper murine model to mimic human tumor microenvironment (TME) for immunotherapy validation is difficult, costly, and complicated. There is therefore an unmet need for novel approaches to replicate TME for pre-screening these drug candidates. Moreover, several studies have demonstrated that the immune response observed in 2D monolayer culture is significantly different from that in 3D culture. [2, 3] Microfluidic platforms further provide a spatial control of cell distribution as well as the TME construction, thereby allowing a more precise flow control to better mimic the transport conditions *in vivo*.

We previously developed a three-layer microfluidic cell array (μFCA) to reconstruct the physiologically spatial structure of tumor microenvironment by co-culturing cancer cells with microvascular endothelial cells (EC) in two compartments, separated by a thin layer with patterned pores.[4, 5] Cancer-associated fibroblasts (CAFs), the most abundant stromal cells in TME, were cocultured with cancer cells in Matrigel to reconstruct more physiologically relevant TME. Compared with conventional 2D *in vitro* assays, in our platform, the spatial configuration of endothelial monolayer on the top channel represents an EC barrier against lymphocyte infiltration to mimic the *in vivo* scenario occurring during the cancer immunotherapy treatment. Continuous flow in the endothelial channel provides nutrient supply as well as waste removal in TME. It also mimics the mechanical and chemical stimulations of bloodstream. Indeed, evidence has shown shear stress affects lymphocyte attachment and migration across endothelium through mediating the expression of E-selectin and ICAM-1 in endothelium.[6] In this study, we further develop a recirculation circuit to enable the on-chip immune cell circulation with unidirectional flow by a syringe pump with functions of infusion and withdraw. With these designs, we are able to study effects of tumor-endothelium and tumor-stroma interactions in cancer drug responses and kinetics in a scenario close to real physiological conditions. The observation of the $CD8^+$ T cell infiltration and cytotoxicity to the cancer cells on this platform further demonstrates this platform's potential for prescreening cancer immunotherapy candidates in a high throughput manner.

## METHODS

**Figure 1A** illustrated our μFCA platform configuration and the recirculation circuit constructed by microfluidic check valves. Both were fabricated by standard soft lithography techniques. Briefly, the selective bonding in the region of check valves was carried out by transferring PDMS residual oligomers from a PDMS stamp to the stopper region of an oxidized bottom layer before bonding with the bonded top and middle layers. The feasibility of recirculation circuit was firstly evaluated by the viability of human monocytes circulated in the system using calcein AM and ethidium homodimer-1.

For the T cell infiltration experiment, GFP-expressing MDA-MB-231 breast cancer cells and CAFs, differentiated from human MSC by culturing with cancer-conditioned media for 30 days, were encapsulated in Matrigel and introduced to the bottom chambers of our µFCA. ECs were then seeded on the top channels on the second day, and a continuous flow of media was given 5 h after. On the fourth day, the recirculation circuit was connected to the cell array, and CellTracker CM-DiI stained cytotoxic T cells (TALL-104) were introduced to the platform. At the end of experiment, cells were incubated with 2µM NucView®405 Caspase-3 substrate for 1 h and then fixed with 4% paraformaldehyde for 60 min. The Z-stacked images for monitoring T cell infiltration and/or caspase-3 activity were captured by an epi-fluorescent microscope (Zeiss AxioObserver) and/or a confocal microscope (Zeiss LSM800).

## RESULTS

As shown in **Figure 1B**, human monocytes could follow the flow direction guided by check valves in the recirculation circuit. In addition, there was no negative effect on their viability after 3-day recirculation in the microfluidic platform. Thus, we further circulated human $CD8^+$ T cells with this design to investigate T cell infiltration into regenerated micro-tumors and their cytotoxicity in different coculture conditions.

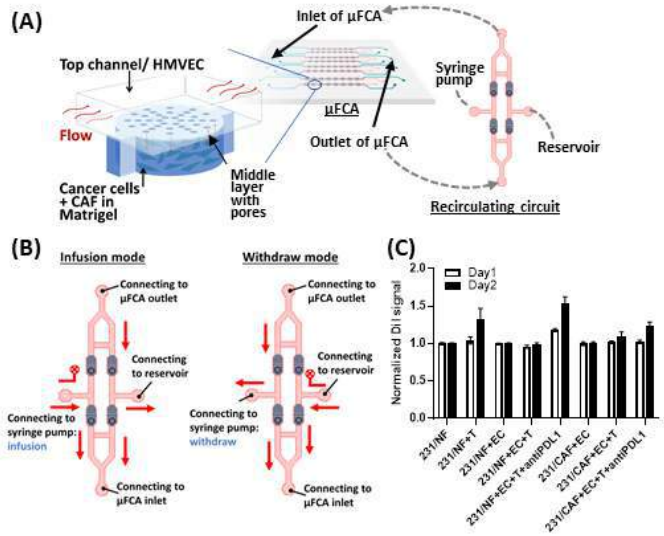


**Figure 1. Microfluidic cell array (µFCA) integrated with tumor-stroma microenvironment and recirculating circuit for studying T cell infiltration and cytotoxicity. (A)** Scheme of the connection between µFCA and the recirculating circuit. **(B)** Working mechanism of the recirculation circuit **(C)** DiI-stained T cell infiltration in the tumor chamber.

As shown in **Figure 1C**, T cell infiltration could be observed after one-day recirculation, and the difference between culture conditions became more significant after a two-day recirculation. Compared with the coculture of MDA-MB-231 and normal fibroblasts with endothelial cells (231/NF+EC+T), the condition with the absence of endothelial cell (231/NF+T) had a significant DiI signal increase in the bottom chamber, indicating that the endothelial monolayer in the µFCA hampered the T cell infiltration. Anti-human PD-L1 antibody treatment increased T cell infiltration and even overcame the interference from the endothelial monolayer, resulting in the highest DiI signal in the coculture with normal fibroblasts among all conditions. We further analyzed the caspase-3 activity in the tumor chamber of our µFCA via fluorogenic caspase-3 substrates (data not shown). The caspase-3 activity in the coculture with normal fibroblast was higher than the one with CAF. Although T cell alone did not lead to significant cytotoxicity, additional anti-PD-L1 treatment increased the caspase-3 activity. However, the enhancement by anti-PD-L1 in coculture with CAFs cannot reach the same level of caspase-3 activity in coculture with normal fibroblasts without any treatment.

## DISCUSSION

In this study, a microfluidic cell array, which reconstructs tumor-stroma microenvironment and is integrated with a recirculation circuit, has been developed for studying T cell infiltration and cytotoxicity. The recirculation circuit provides unidirectional flow in µFCA, primarily through manipulation of flow from a reciprocating syringe pump coupled with check-valves; immune cells directly travelling in this recirculation circuit retain uncompromised viability. Furthermore, this design enables to study the dynamics of cytotoxic T cells in continuous flow with a more physiologically relevant TME. The reconstructed endothelium plays a role as a barrier to the T cell infiltration into the tumor compartment. Blockade of anti-human PD-L1 enhances T cell infiltration and even overcomes the interference from the endothelial monolayer. The tumor stroma strongly influences $CD8^+$ T cell infiltration and cytotoxic activity. Compared with the coculture with normal fibroblasts, the CAF coculture attenuates T cell infiltration and leads to lower caspase-3 activity. Treatment of anti-PD-L1 enhances the caspase-3 activity but is not enough to compensate the influence from CAFs, when compared with the normal fibroblast coculture conditions without any treatment. Collectively, these results reveal that our µFCA could serve as an *in vitro* tool for studying cancer immunotherapeutic strategies with precisely mimicked TME, paired with a high throughput adaptation.


## ACKNOWLEDGEMENTS

The authors acknowledge the instrumental support from the nanofabrication facility at CUNY-Advanced Science Research Center. This work is supported by Pershing Square Sohn Cancer Research Alliance (S.W.) and NIH (K.W.L., UG3/UH3TR002151).


## REFERENCES


1. Freeman, G. J.; Sharpe, A. H., *Nat Immunol* **2012,** *13* (2), 113-5. DOI 10.1038/ni.2211.
2. Busse, A.; Letsch, A.; Fusi, A.; Nonnenmacher, A.; Stather, D.; Ochsenreither, S.; Regenbrecht, C. R. A.; Keilholz, U., *Clin Exp Metastas* **2013,** *30* (6), 781-791. DOI 10.1007/s10585-013-9578-5.
3. Dangles, V.; Validire, P.; Wertheimer, M.; Richon, S.; Bovin, C.; Zeliszewski, D.; Vallancien, G.; Bellet, D., *Int J Cancer* **2002,** *98* (1), 51-56. DOI 10.1002/ijc.10140.
4. Chi, C. W.; Lao, Y. H.; Ahmed, A. H. R.; Benoy, E. C.; Li, C.; Dereli-Korkut, Z.; Fu, B. M.; Leong, K. W.; Wang, S., *Adv Healthc Mater* **2020**, e2000880. DOI 10.1002/adhm.202000880.
5. Dereli-Korkut, Z.; Akaydin, H. D.; Ahmed, A. H. R.; Jiang, X. J.; Wang, S. H., *Anal Chem* **2014,** *86* (6), 2997-3004. DOI 10.1021/ac403899j.
6. Cinamon, G.; Shinder, V.; Alon, R., *Nat Immunol* **2001,** *2* (6), 515-22. DOI 10.1038/88710.

# EFFECT OF STATURE AND LORDOSIS ON FEMALE LUMBAR SPINE LOADS IN VERTICAL IMPACT

**Sagar Umale (1), Prashant Khandelwal (1), John R. Humm (1), Narayan Yoganandan (1,2)**

(1) Department of Neurosurgery, Medical College of Wisconsin, Milwaukee, WI, USA
(2) Neurosurgery Research, VA Medical Center, Milwaukee, WI, USA

## INTRODUCTION

It is well known that female spines are different from male spines although clinical options do not have specific targets for the surgical treatment of traumatic injuries. The lumbar spines of women are generally smaller in terms of parameters such as column length, disc height, and vertebral anteroposterior depth than men spines. The stature, sitting height, and body mass of men and women for the same anthropometric definitions (mid-size male versus mid-size female, for example) are also different [1]. A clinical measure of the spine is the curvature, defined as the Cobb angle between various vertebrae of the lumbar spine, e.g., the angle formed between L1 and L5 endplates in the midsagittal plane [2]. As the lumbar spine responds to the external loading via interaction within the various joints of the column, and with the aforementioned differences between men and women, it is expected that the load carrying capacity and hence, tolerance of female spines are lower than men [3]; specifically, for the same categorization such as equivalent stature and curvature, forces and moments will be lower than the male spine. The share of the forces and moments load also depends on the external mechanical load vector. The objective of this study is the parametrically determine the loads on the female spines.

## METHODS

A validated finite element model of the human lumbar spinal column was used in the study [4]. The T12-S1 model consisted of three-dimensional hexahedral solid elements representing the cancellous bone, intervertebral disc (annulus and nucleus), spinous process, transverse process, and facet joints at each vertebral level. The two-dimensional quadratic shell elements represented the cortical bone, endplates, and annulus fibers at each level. One-dimensional beam elements were used to represent the anterior and posterior longitudinal ligaments, ligamentum flavum, interspinous ligament, transverse ligaments, and supraspinous ligaments. The model consisted of 273 beam elements, 98,978 shell elements and 289,586 solid elements. The mapping blocks/hex-boxes technique was used to develop the mesh [5]. To incorporate the variation in the length and curvature, the hex boxes were converted to morphing boxes. The range for the variation of length and curvature parameters was obtained from the literature [6,7]. The morphing of the model for these parameters was automated using the Latin Hypercube Sampling parametrization technique in the LS-Dyna software. A routine was developed in LS opt using the ANSA software and the models were solved using LS-Dyna. The spine model was constrained at the T12 level by constraining all nodes, and displacement was applied to S1 in a vertically upward direction. The displacement pulse corresponding to 6.5 m/s was applied to the sacrum [8]. One-hundred finite element 100 models were simulated, and the vertical forces and moments were extracted using pre-defined cross-sectional planes defined at the mid-vertebral body level of L1.

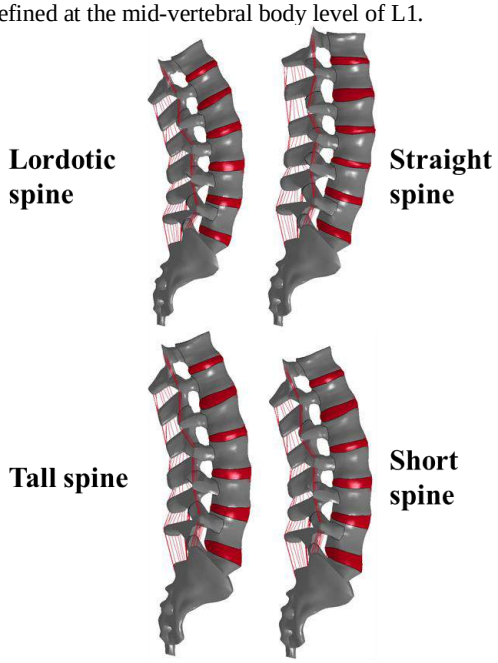


**Figure 1: Lordotic, straight, tall and short spine models generated by morphing using the developed technique.**

## RESULTS

The overall length of the 100 lumbar spines ranged from 158 to 193 mm. The overall lumbar lordosis defined as the Cobb angle ranged from 34 to 65 deg, where the less value represents higher lordosis, and the greater value represents less lordosis, i.e., inverse relationship to angle. The peak force, moment for the shortest and tallest spine was 5.6 kN, 82.1 Nm and 4.1 kN, 82.4 Nm. The overall spine forces decreased, and moments remained the same with increase in stature. Independent of the stature, the peak L1 force, moment for the most lordotic and straight spine was 4.3 kN, 73.7 Nm and 5.7 kN, 110.2 Nm. Thus, with the increase in lordosis, the spinal forces and moments decreased.

The models were analyzed based on two groups, spinal column length representing the short and tall population, and curvature representing the lordotic and straight spine configurations. For the short and tall groups, the spinal column length ranged from 158 to 176 mm and 176 to 193 mm, respectively. For the short population models, the lordotic spine Cobb angles ranged from 42 to 49 deg, and for the straight spine ranged from 49 to 62 deg. For the tall population models, the lordotic spine Cobb angles ranged from 34 to 56 deg and the straight spine ranged from 56 to 65 deg. The breakup was done such that all subgroups had equal number of finite element simulations under the same vertical loading. The average and standard deviation of the spinal loads for each group were calculated (Figure 2).

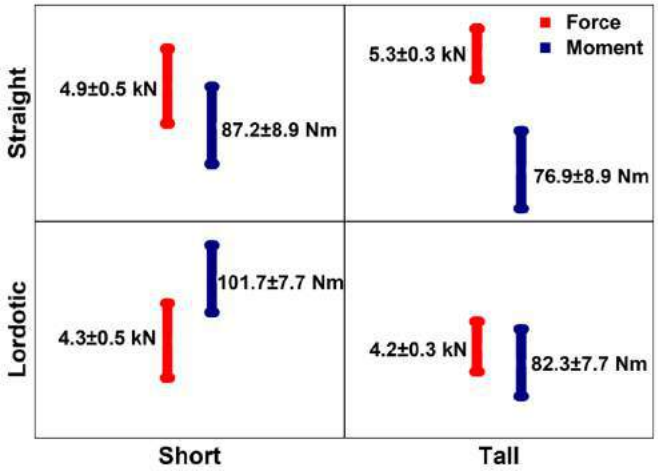


**Figure 1: Female lumbar spine loads based on stature and lordosis.**

Comparing the stature, the forces for lordotic spine were marginally (2%) decreased from short to tall females. Whereas, for straight spine, the forces for the tall stature were 8% higher. The moments were greater for short stature compared to the tall stature (23% for lordotic and 13% for straight spine), irrespective of the lordosis. The lordotic spine forces were lower for both short (14% lower) and tall (26% lower) stature spines, whereas the moments were higher (16% for short and 7% for tall).

## DISCUSSION

In this study, a validated lumbar spine model was used to investigate the effect of stature and lumbar lordosis in females [4]. The model was validated under all physiological modes. A parameterized morphing technique was used to generate 100 models to cover a wide range in the anatomical spectrum of female lumbar spines. An initial study was conducted to determine the most sensitive geometrical parameters on spinal loads and the Pearson's correlation coefficients between the parameters and the spinal forces were determined. Results while not shown indicated that the curvature and column length were sensitive parameters. The Pearson's correlation values for L1 force with lumbar lordosis and column length were -0.87 and 0.75.

The models were simulated for vertical impact from the seat to the spine via pelvis, representing underbody blast loading. The spinal loads were extracted at the cranial end of the column, representing the transmitted biomechanical metrics, reflecting the energy absorption of the structural system. Individual investigation of stature and lordosis demonstrated that forces decreased, while moments were less variant with an increase in stature, whereas with an increase in lordosis both force and moments decreased.

Further, the spinal loads were grouped based on short and tall stature and lordotic and straight spines. Decrease in lordosis increased spinal forces. It can be attributed to the lack of shearing in the straight spine and resulting in more axial force, and this fits well with the Euler theory of columns. The greater moments in the straight spine compared to the lordotic spine may be due to the selected distribution in the stature subgroups. Straight models in short and tall subgroups were marginally longer than the lordotic models, and perhaps a further subdivision between the two stature and or between the angular ranges may shed light on this observation. This is a future study. The lumbar spinal forces increased with stature for straight spine, and it can be attributed to the lordosis bias in the tall spine models. The moments decreased with increase in stature. As stated above, further subdivisions in these parameters for additional understanding is a future study.

In summary, this finite element modeling study provides a range of spine loads that a female spine experiences during vertical loading simulating underbody blast impacts, and data were grouped on the external anthropomorphic metric, i.e., stature, and clinical measure of Cobb angle, i.e., curvature. As the study is specific to females, these results are applicable to this group of our population, and as the loading is vertical, it is applicable for the military scenarios [9] and civilian events such as falls and vehicle crashes [10,11]. The results may be useful to develop independent women injury criteria for the lumbar spine. A comparison between male spines can be made with the present approach of simulating male-specific stature and curvature to delineate the response differences between male and female spines.

## ACKNOWLEDGEMENTS

This research was supported by the Department of Veterans Affairs Medical Research, Department of Neurosurgery at the Medical College of Wisconsin, and W81XWH-16-01-0010. This material is the result of work supported with the resources and use of facilities at the Zablocki VA Medical Center, Milwaukee, Wisconsin. The last author (NY) is an employee of the VA Medical Center, Milwaukee, WI.

## REFERENCES

[1] Fryar, C.D. et al., National Health Statistics Reports, 2018.
[2] Hay, O. et al., PLOS ONE, 2015.
[3] Firouzabadi, A., Front Bioengg Biotech, 2021.
[4] Umale, S. et al. JMBBM, 2020.
[5] John, J.D. et al. TIP, 2018.
[6] Been, E. et al., Spine, 2010.
[7] Zhou, S.H. et al., Eur Spine J, 2000.
[8] Yoganandan, N. et al., JMBBM. 2020.
[9]Kang, D.G. et al., The Spine J, 2012.
[10] Kannus, P, et al., Arch Intern Med, 2000.
[11] Muller, C.W., et al., Acc Ana Prev, 2014.

# CHARACTERIZATION OF CELLULAR RESPONSE TO ENDOVASCULAR ABLATIVE THERAPIES

**S. Brocklehurst (1), D. Stolley (2), N. Ghousifam(1), E. Cressman(2), D. Fuentes(2), M.N. Rylander(1)**

Mechanical Engineering, University of Texas at Austin, Austin, Texas, USA (1)
M.D. Anderson Cancer Center, Houston, Texas, USA (2)

## INTRODUCTION

Curative therapies are not available to greater than 80% of the patient population with hepatocellular carcinoma (HCC). There is a well-recognized need for novel methods that can intricately balance (1) treatment of the disease extent with (2) preservation of liver function and minimize the risk of recurrence and metastasis. Ablation and embolization are the two most common minimally invasive methods used in treating unresectable HCC. These are established therapies with a known survival advantage [1]. Thermally ablative therapies include radiofrequency ablation (RFA) and microwave ablation (MWA) and utilize thermal energy to destroy the disease. Embolization techniques utilize a direct injection of a chemotherapeutic agent or radiation into the hepatic artery with or without lipiodol and a procoagulant material to promote intratumoral retention. Thermoembolization (TE) provides a novel conceptual endovascular approach in which a bolus of acid chloride dissolved in an inert oily solvent delivers an exothermic chemical reaction. Recent investigations of TE indicate that it might offer unique advantages versus current techniques [2]. This approach is unique and combines the benefits of embolic and thermal- and chemical-ablative therapy modalities. The target tissue and vascular bed are subjected to simultaneous hyperthermia, ischemia, and acidic environments in a single procedure.

These complex conditions caused by the injection of acid chloride into the target tissue must be understood thoroughly in order to develop techniques to effectively destroy the intended cancerous tissue without negatively affecting the surrounding parts of the body. Accurate predictions of cell death are important towards these goals, and we have developed and calibrated preliminary mathematical models of the TE procedure using *in vitro* platforms that mimic vascularized liver. Validated cell damage models will accurately estimate the cellular damage as a function of hyperthermia, ischemia, and low pH stress that occurs during TE. The work presented in this paper focuses on the evaluation of how the conditions in the target tissue affect cells in order to develop an appropriate cell damage model.

## METHODS

To understand the independent contribution of hypothermia, ischemia, and acidic environments that work in concert during TE, we first isolated the decrease in local pH and localized hyperthermia to determine their individual impact *in* vitro for computational model development. These conditions were later combined to identify any synergistic effects between them. Normal human dermal fibroblasts were cultured in flasks and then passaged and seeded into 96-well plates for use in experiments. Each plate had 20-25 wells with a confluent monolayer of adherent cells coating their bottom surfaces. Cell survival ratios were determined 24 hours after exposure to hyperthermia and diminished ph using Cell-Titer blue assays. Additional unexposed control plates were measured alongside the exposed samples. The survival ratio was calculated as the ratio of absorbance between exposed and unexposed samples after subtracting the background absorbance observed from an acellular plate.

A temperature-controlled water bath was used to expose cells to hyperthermia. Cell culture media was removed from cell-seeded plates, and it was replaced with only 40 µL of media per well to reduce heating times. The plastic skirt of the plates was broken with pliers in 6 places around the circumference to allow water to flow under and cover the bottom surface without trapped air. At the start of the experiment, plates were taken from the incubator and placed directly into the water bath, and held down with aluminum plates at the same temperature as the water. One cell-bearing plate was tested simultaneously with a second, acellular plate with the same fluid volumes and a thermocouple placed in the bottom of one well. Temperatures were recorded throughout the exposure, and water bath settings were adjusted to maintain the target temperature within the plates. At the end of the experiment, plates were removed and shaken upside-down to remove the warm media rapidly,

then fresh media was added, and the plates were stored in an incubator. Cells were exposed to temperatures of 43, 45, 47, and 50 $^{o}$C for 10 to 60 minutes.

Phosphate-buffered saline (PBS) solutions with added glacial acetic acid were used to expose cells to acidic pH. Solutions with a pH of 6.00, 6.25, 6.50, 6.75, and 7.00 were prepared and passed through sterile filters. Media was removed from each well of a plate, then a timer was started, and 150 µL of acidified PBS was added to each well. The plate was kept in an incubator for between 10 and 60 minutes, then the acid solutions were removed in the same order they were added. A small pH probe was used to record the pH over time in identical cell-bearing plates. Combined pH and hyperthermia testing were performed using the pH exposure protocol listed above with heated solutions, then placing the plates into cell culture incubators set to 43 or 45 $^{o}$C.

Arrhenius damage models are used to provide a first-order estimate of the cell death resulting from the thermal and acidic pH exposure. Cell kill as a function of exposure to temperature is known to approximately follow an Arrhenius rate process [3]. Here, parameters of the Arrhenius damage model will be considered dependent on the presence of the acid as well. Arrhenius parameters are calibrated to the pathology response observed from *in vitro* cell damage testing. The Arrhenius parameters follow a log-linear relationship [4]. Regardless of the type of damage process being examined, a plot of the activation energy versus the log of the frequency factor that defines the Arrhenius model approximately follows a straight line. This empirical relationship has been measured independently by Wright[5] and He[6] and is used to constrain the damage model under variations in temperature and acidic ph exposure. A constrained optimization formulation is numerical solved to fit model parameters to the cell viability data. The parameters corresponding to the temperature-only data are recovered first. The parameters corresponding to pH are then recovered given the known Arrhenius parameters that fit temperature.

## RESULTS

Preliminary *in vitro* testing results have been applied toward the creation of cell death models based on exposure to hyperthermia and acidic solutions. As seen in Figure 1, a steady decline in cell survival was observed for acidic solutions, with the rate of death increasing with lower pH and longer exposure times.

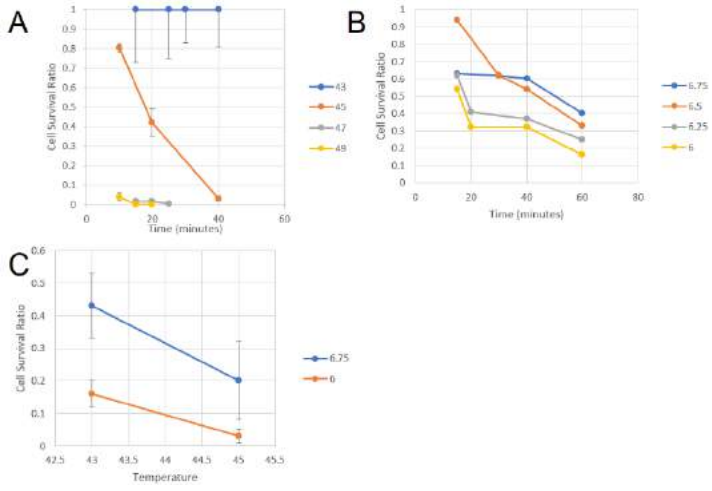


**Figure 1 – Experimental viability. A – Hyperthermia exposure B – Acidic pH exposure C – Combined hyperthermia and acidic pH**

Cell death was gradual during hyperthermia, until temperatures rose above 46 $^{o}$C after which cellular death was rapidly accelerated. Similar results were observed when hyperthermia and acidic solution exposure were combined in the same experiments under various conditions, with the combined cell death greater than each condition separately. These results further confirm the benefit of the combined effect of multiple mechanisms of cell injury implicity to TE.

Numerical optimization of cell damage model fits to viability data recovered an Arrhenius activation energy of 1.99e5 [J/mol] with a linear correction for pH as .994e4 [J/mol/pH] and frequency factor of 1.18e30 [1/s] as shown in Figure 2. The model fit of the predicted damage vs. measured damage achieves an $R^2$ values of .42.

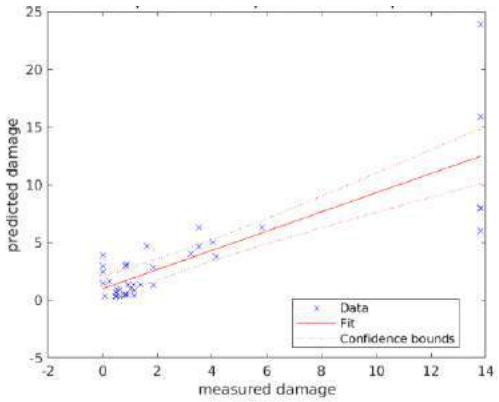


**Figure 2 – Fitting of Arrhenius model to viability data**

## DISCUSSION

The work presented in this abstract has successfully broken down the conditions present in the target tissue during TE in separate and combined experiments to observe the resulting cell death. In this way, the contribution of each variable to the therapeutic effect of TE can be quantitatively studied, and the synergistic interactions between multiple conditions can be identified. Initial results demonstrate the feasibility of calibrating a temperature and pH-dependent cell damage model to the observed viability data. Further studies will cross-validate the results to study the prediction accuracy of our cell damage modeling approach.

The results from this study will enable the development and calibration of mathematical models to understand and predict the independent and synergistic effects of hyperthermia and acidic environments caused by TE. Deeper insight into effective delivery of this new therapy will provide valuable knowledge applicable to the treatment of other cancers (e.g. renal cell, soft tissue sarcomas, metastatic colorectal, and neuroendocrine), immunotherapies, and other diseases beyond cancer

## ACKNOWLEDGEMENTS

Resources for cell studies were supported by the MD Anderson-Oden Institue-Texas Advanced Computing Center pilot project.

## REFERENCES

[1] Jean-Charles Nault et. al. Journal of hepatology, 68(4):783– 797, 2018.
[2] David Fuentes et. Al. International Journal of Hyperthermia, 37(1):356–365, 2020.
[3] Mark W et. al. International Journal of Hyperthermia, 19(3):267–294, 2003.
[4] John A Pearce et. al .International Journal of Hyperthermia, 29(4):262–280, 2013.
[5] Neil T Wright et. al. Journal of biomechanical engineering, 125(2):300–304, 2003.
[6] Xiaoming He et. al. Critical Reviews in Biomedical Engineering, 31(5&6), 2003.

SB³C2022
Summer Biomechanics, Bioengineering and Biotransport Conference
June 20-23, Eastern Shore, MD, USA

# CHARACTERIZING THE MECHANICAL RESPONSE OF CORNEA USING BIAXIAL TESTS

**M.E Emu, H. Hatami-Marbini**

Mechanical and Industrial Engineering, University of Illinois at Chicago, Chicago, Illinois, USA,
Email. hatami@uic.edu

## INTRODUCTION

The cornea is a transparent tissue that covers the front of the eye and has unique mechanical properties. The cornea and sclera protect internal parts of the eye globe, i.e., iris, pupil, and lens. The cornea is a tissue that is exposed to the outside environment; thus, it could undergo significant amount of external pressure that is, for example, caused by eye rubbing and sudden injuries. The cornea is composed of five layers, i.e. epithelium, Bowman's layer, stroma, Descemet's membrane, and endothelium. The stroma is its thickest layer and comprises about 90 percent of the corneal thickness. The corneal stroma is mainly composed of water, collagen fibers, and proteoglycans that are found in the form of many superimposed lamellae. The uniform diameter and regular arrangement of collagen fibers in the corneal stroma are essential for its transparency and unique optical properties. In addition, the stromal layer is responsible for the structural properties of the cornea.

The mechanical behavior of the cornea has been mainly investigated using the in vitro uniaxial tensile testing method and inflation method [1-3]. In the tensile experiments, uniaxial tensile force or displacement is applied to cornea strips for investigating their stress-strain behavior. In the inflation testing method, the deformation of corneal samples subjected to posterior pressure is determined. These testing techniques showed that the cornea has a rate-dependent and anisotropic mechanical behavior. However, the exact relationship between the corneal microstructure and anisotropic mechanical properties has not yet been fully characterized. The ability to understand and predict anisotropic corneal response is of significant importance for developing a proper material model that is able to accurately capture the corneal mechanical response. The biaxial tensile test is an experimental testing method that has been used to characterize the mechanical properties of biological tissues; however, it has not been commonly employed to investigate corneal biomechanics. The biaxial testing is particularly useful for characterizing the mechanical response of anisotropic materials, i.e. it could determine the influence of collagen fiber orientation on the mechanical response of a material. It is known that collagen fibers in the healthy human cornea have two preferred orientations orthogonal to each other, i.e. they are primarily in the horizontal (nasal-temporal) and vertical (inferior-superior) directions. The primary objective of the present work was to conduct biaxial tensile experiments to determine the anisotropic biomechanical response of the corneal samples.

## METHODS

Five porcine eyes were brought to the laboratory and corneal rings with sclera were dissected carefully from the eyeballs. A square sample was then prepared from the center part of each cornea-scleral ring. The samples were allowed to air–dry or were allowed to swell in solution until their thickness was about 800 um. A pachymeter (DGH Technology Inc., Pennsylvania) was used to measure the thickness of

specimens. The samples were mounted into the planar biaxial machine (ElectroForce TestBench), Figure 1. The samples were stretched along the nasal-temporal (NT) and superior-inferior (SI) directions at a stretch ratio of 1:1 with a displacement rate of 2 mm/min. A tare force was initially applied to remove slack, and ensure the firm grip of samples, and have a complete contact with the specimens. The samples were then strained up equally in each direction. The stress was defined as the measured force divided by the initial cross-sectional area of the samples in order to determine the stress-strain curves. The data was reported as mean ± standard deviation and one-way ANOVA with a significance level of 0.05 was used for the statistical analysis.

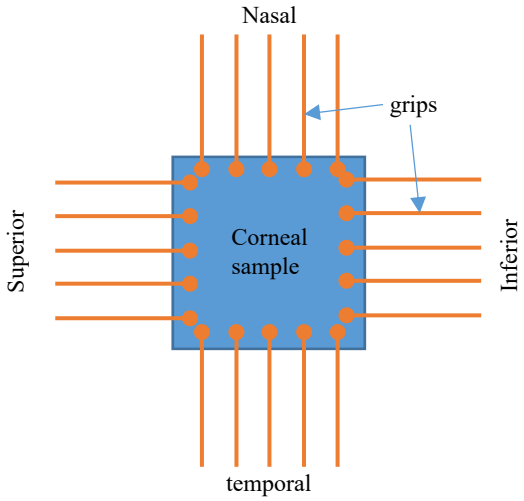


**Figure 1:** *The corneal specimens were gripped into the planar biaxial machine such that nasal-temporal (NT) and superior-inferior (SI) directions were aligned in the vertical and horizontal axes, respectively.*

## RESULTS

The experimental stress-strain curves are shown in Figure 2. From the stress-strain curves, the elastic modulus at 6% strain was calculated. The mean maximum stress was 0.09 MPa and 0.07 MPa in NT and IS directions, respectively. The variation in the maximum stress of NT and SI directions was statistically significant but the variation in the elastic modulus was not statistically significant.

## DISCUSSION

The primary purpose of this study was to characterize the anisotropic mechanical response of porcine cornea using the biaxial tensile testing method. A different nonlinear stress-strain curve was observed for each direction (Fig. 2). The collagen fibril orientations and arrangements inside the corneal stroma are responsible for the observed variation in tensile stress-strain curves.

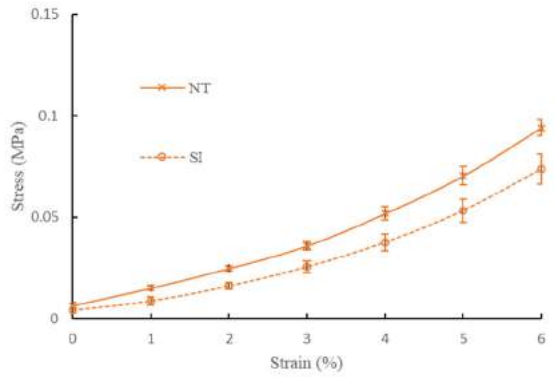


**Figure 2:** *Stress-strain curve of porcine corneal samples obtained from the biaxial experiments. The symbols show the average response and the error bars indicate one standard deviation.*

Previous imaging studies have shown a clear preferential orientation of collagen fibrils in the vertical and horizontal directions [4-5]. The mechanical measurements of the present study can be used along with these imaging results to relate the macroscopic response of the cornea in terms of its microstructure. The biaxial testing has a number of limitations. For example, the specimens were initially curved and they had variable thickness. The number of samples used in the present study was also small and future experiments are undergoing in our laboratory to decrease the variability in the measurements. Despite these limitations, the present work showed that biaxial experiments could be used to characterize the nonlinear anisotropic mechanical response of the corneal samples.

## ACKNOWLEDGEMENTS

This work has been supported in part by grants from the National Science Foundation (1636659) and the National Institutes of Health (R21 EY030264).

## REFERENCES

[1] A. Elsheikh, K. Anderson. Comparative study of corneal strip extensometry and inflation tests Journal of Royal Society – Interface 2, 177-185, 2005.

[2] B. Boyce, J. Grazier, R. Jones, D. Nguyen. Full-field deformation of bovine cornea under constrained inflation conditions. Biomaterials. 29. 3896-904, 2004.

[3] H. Hatami-Marbini, and A. Rahimi. Interrelation of hydration, collagen cross-linking treatment, and biomechanical properties of the cornea. Current eye research 41.5, 616-622, 2016

[4] K.M. Meek, T. Blamires, G.F. Elliot, T.J. Gyi, C. Nave, The organization of collagen fibrils in the human corneal stroma: a synchroton x-ray distraction study. Current Eye Research, 6:841-846, 1987

[5] K.M. Meek KM, R.H. Newton, Organization of collagen fibrils in the corneal stroma in relation to mechanical properties and surgical practice. Journal of Refractive Surgery, 15(6):695-
699, 1999.

SB³C2022
Summer Biomechanics, Bioengineering and Biotransport Conference
June 20-23, Eastern Shore, MD, USA

# PRECISE MEASUREMENT OF MICROPARTICLE VISCOELASTIC PROPERTIES USING A MICROFLUIDIC EXTENSIONAL FLOW DEVICE

**S. Ghanbarpour Mamaghani, J.B. Dahl**

Department of Engineering, University of Massachusetts Boston, Boston, Massachusetts, USA

## INTRODUCTION

Several studies have shown the clinical potential of mechanophenotyping or grouping of cells based on mechanical properties, for disease diagnostics and therapeutics. However, accuracy and precision of these measurements needs to improve before reliable clinical products are possible. Comparing measured cells stiffnesses across studies is challenging due to lack of standard calibration procedures, and uncertainty in the experiment parameters, namely the force that deforms cells [1]. Many microfluidic platforms that measure the mechanical properties of suspended single cells rely on approximations and empirical calibration due to complicated cell deformations and viscous stresses arising from close proximity to or contact with channel walls [2,3]. Our objective here is to develop accurate microfluidic mechanical measurement techniques using non-contact hydrodynamic deforming forces along with validation checks to confirm that experimental conditions closely match the mechanical model.

This work builds off our published proof-of-principle study demonstrating the first use of extensional flow device to measure average cell mechanical properties from the maximum observed stretch [4]. Here we improve our technique to measure single cell mechanical properties from an elongation test that captures the transient stretching and the steady-state strain plateau. We also use particle trajectory information to check that the suspended particle is entrained in the fluid and experiencing the viscous forces assumed in the mechanical model.

## METHODS

A microfluidic extensional flow device, commonly called a cross-slot, consists of two channels that intersect at 90 degrees, generates a linear planar extensional flow field. The initially spherical microparticles elongate into prolate ellipsoids in the extensional flow region that has a uniform extensional strain rate (Fig. 1a). Channel dimensions are 300 µm wide and 165 µm deep.

Agarose microparticles are fabricated using an emulsion technique from 0.5% (w/v) low melting point agarose. The agarose hydrogels are spherical and isotropic. The average particle diameter is approximately 45 µm. For microfluidic experiments, particles are suspended in aqueous 0.97% (w/v) methylcellulose ($\mu \sim 81.9$ mPa·s)

To measure mechanical properties, microparticles are observed stretching in the extensional flow region of the cross-slot. Videos are captured in phase contrast at 10x (Zeiss Axiovert 200 M) using a high-speed camera (JetCam, 9000 fps). In this study, two fluid flow rates are used, 10 and 15 mL/hr. Microparticle deformation and trajectories are analyzed using a custom MATLAB (MathWorks) analysis code. Microparticle strain over time is measured from ellipses fitted to detected particle edges. Kelvin-Voigt viscoelastic parameters for individual microparticles are obtained by fitting the mechanical model (described below) to the strain history (Fig. 1b).

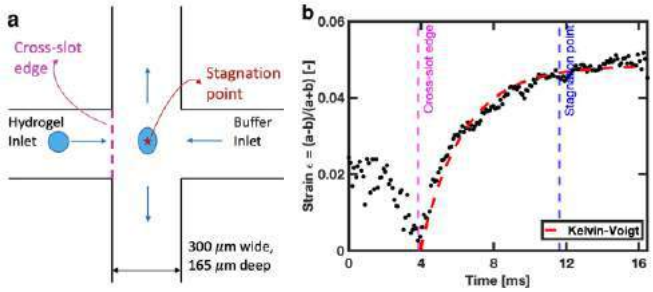


**Figure 1: a) Schematic of the extensional flow experiment to measure microparticle viscoelastic properties. b) An example of hydrogel deformation analysis. For this hydrogel, the fitted model yields $G_0$ = 1.519 kPa and $\tau$ = 0.0023 s**

Using the viscoelastic correspondence principle [5], the Laplace-transformed viscoelastic solution of a sphere deforming in planar extensional flow is obtained directly from the corresponding elastic

solution [6]. The result for a viscoelastic sphere is obtained upon taking the inverse Laplace transform:

$$\varepsilon(t) = \frac{5}{2}\frac{\mu\dot{\varepsilon}}{G_0}(1 - \exp i(-\frac{t}{\tau})) \quad (1)$$

Here we employed the Kelvin-Voigt constitutive model for a viscoelastic solid. $\varepsilon = (a-b)/(a+b)$ is the strain of the stretched microparticle where $a$ and $b$ are the long and short axes, respectively, of an ellipse fitted to the outer edge of the microsphere. $\dot{\varepsilon}$ is the extensional strain rate, $G_0$ is the relaxation modulus, and $\tau$ is the retardation time.

The actual extensional strain rate experienced by a particle could be different from what is expected based on flow rate and channel geometry, possibly due to subtle pressure fluctuations or a particle being too close to a wall. At midchannel height, deep cross-slot devices produce planar extensional flow with a stagnation point located at $(x_{sp}, y_{sp})$ has a velocity defined as:

$$\mathbf{v} = i\dot{\varepsilon}(-(x - x_{sp})\hat{\mathbf{x}} + (y - y_{sp})\hat{\mathbf{y}}) \quad (2)$$

By integrating the velocity components $u = \frac{dx}{dt} = -\dot{\varepsilon}(x - x_{sp})$ and $v = \frac{dy}{dt} = \dot{\varepsilon}(y - y_{sp})$, we obtain equations that relate the strain rate to the microparticle trajectory points ($x$, $y$) as it flows through the extensional flow region:

$$\ln\left(\left|\frac{x-x_{sp}}{x_0-x_{sp}}\right|\right) = -\dot{\varepsilon}t, \qquad \ln\left(\left|\frac{y-y_{sp}}{y_0-y_{sp}}\right|\right) = \dot{\varepsilon}t \quad (3)$$

$x_0$ and $y_0$ are the initial hydrogel coordinates at the video start. With Eq. 3, the extensional strain rate around the suspended particle can be computed from the linear regression slope of these functions of particle $x$ and $y$ coordinates vs. time.

## RESULTS

The box plots in Fig.2 shows similar distributions of relaxation moduli and retardation times for 0.5% w/w agarose microparticles stretched at two flow rates that differ by a factor of 1.5. We expect these parameters to be in close agreement between the two flow rates because the same concentration of agarose is used. However, inherent variation in small particle mechanical properties is expected due to slight differences in how they were polymerized.

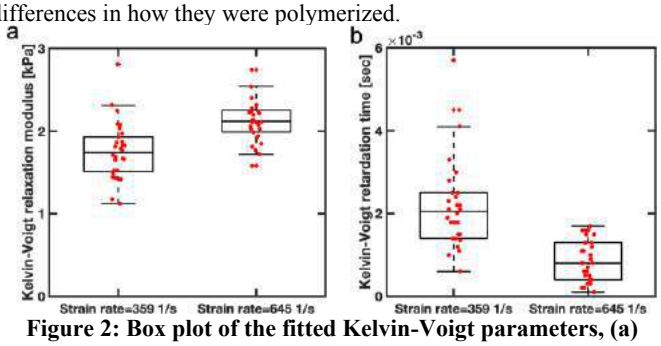


**Figure 2: Box plot of the fitted Kelvin-Voigt parameters, (a) relaxation modulus $G_0$ and (b) retardation time ($\tau$) for 0.5% w/w agarose microparticles at two strain rates. $N = 30$ hydrogels were analyzed for each experiment.**

To confirm the accuracy of the results, we compared the extensional strain measured from the microparticles' trajectories to the expected flow field in this device. Guillou et al. [4] and Foster et al. [7] have indicated that the strain rate inside the cross-slot is proportional to the average velocity ($U$) in the straight channels and inversely proportional to the channel's width ($w$):

$$\dot{\varepsilon} \approx \frac{2U}{w} \quad (4)$$

Fig. 3a shows the computing extensional strain rate experimentally using $x$ coordinates (orange line), and y coordinates (blue line) of one microparticle's trajectory. Both coordinates resulted in similar strain rate. The measured strain rates measured are in good agreement with the strain rates computed using the theoretical Eq. 4 (Fig. 3b). This agreement means that the particle is entrained in the fluid and flowing at midchannel height and experiencing the forces that we assume in the mechanical model used to extract the Kelvin-Voigt parameters.

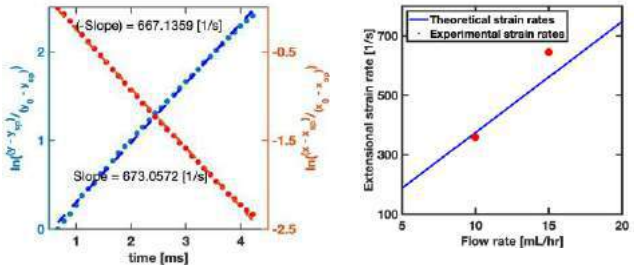


**Figure 3: a) Strain rate computed experimentally using the $y$ coordinates and $x$ coordinates of one hydrogel trajectory. Strain rate is obtained from the slope of the line of best fit. b) Comparison of strain rates computed theoretically using Eq.4 (blue line) and experimentally using microparticles' trajectory.**

## DISCUSSION

Our agarose microparticle mechanical property results agree with other non-contact microfluidic devices in which particle are deformed by hydrodynamic forces only and do not contact walls. Mietke et al. [8] measured an average modulus of 2.15 kPa for 0.5% w/w agarose microparticles. We measured an average relaxation modulus of 1.75 kPa, and 2.12 kPa in two experiments with different strain rates microparticles made of the same 0.5% w/w agarose formulation.

Accuracy of microfluidic measurement techniques can be improved by confirming that all controllable experimental parameters are the same values used in mechanical model that extracts mechanical properties from the observed deformation. That means independently measuring these parameters and quantifying the precision of control as opposed to relying on theoretical predictions or calibrations. Here we are used auxiliary particle kinematic information to confirm that the particles are entrained in the fluid and experiencing the extensional strain rate that we expect the device to generate. We will continue to validate our technique by independently measuring flow velocities with particle image velocimetry to further confirm extensional strain rates. We will also compare our viscoelastic property measurement technique to traditional methods on bulk agarose (rheometer) and agarose microparticles (atomic force microscopy). These comparisons will help us further prove our technique's ability to reproduce the standard creep test at the microscale and at high-throughput.

In addition to the creep test performed in this work on particles approaching the stagnation point, cross-slot microfluidic devices can perform relaxation test as particles leave the stagnation point. Next we will measure microparticle relaxation as they exit the extensional flow region towards the outlet channels.

## REFERENCES


[1] Girardo, S., et al., *J. Mater. Chem. B.* vol. 6, pp. 6245–6261, 2018.
[2] Armistead, F. J. et al., *Scientific Reports*, vol. 10, pp. 3254, 2020.
[3] Nyberg, K.D., et al., *Biophys. J.*, vol. 113, pp. 1574–1584, 2017
[4] Guillou, L., Dahl, J.B., et al., *Biophys. J*, 111: 2039–2050, 2016.
[5] Christensen, RM, *Theory of Viscoelasticity*, New York: Academic Press, Inc. 1982.
[6] Murata, T., J Phys Soc Jpn, 50(3):1009-1026, 1981.
[7] Foster, K. M. et al., *Cells*, vol. 10, no. 9, p. 2352, 2021.
[8] Mietke, A. et al., *Biophys. J.*, vol. 109, pp. 2023–2036, 2015.

SB³C2022
Summer Biomechanics, Bioengineering and Biotransport Conference
June 20-23, Eastern Shore, MD, USA

# COMPUTATIONAL ASSESSMENT OF STRESS DISTRIBUTION IN THE BRAIN: BIOMARKERS OF WHITE MATTER LESION FORMATION

**Tyler C. Diorio (1), Kevin G. McIver (2), Noah J. Mehringer (1), Sean E. Bucherl (2), Eric A. Nauman (3), Yunjie Tong (1), Vitaliy L. Rayz (1,2)**

(1) Weldon School of Biomedical Engineering, Purdue University, West Lafayette, IN, USA
(2) School of Mechanical Engineering, Purdue University, West Lafayette, IN, USA
(3) Department of Biomedical Engineering, University of Cincinnati, Cincinnati, OH, USA

## INTRODUCTION

Vascular contributions have been implicated with numerous disease states including cancer, heart failure, and neurodegenerative diseases, such as Alzheimer's Disease (AD). With each heartbeat, our distensible arterial system and circulating cerebrospinal fluid (CSF) within the brain act to dampen an otherwise damaging pulse wave. Studies have demonstrated that in disease states, the transmission of excess energy from cardiac pulsations to the cerebral microvasculature can lead to the formation of white matter lesions or hyperintensities (WMH) observable on T2-weighted MRI[1]. WMH have been linked to neurodegenerative disease states including dementia, Parkinson's disease, and AD. Further, WMH have proven to be better indicators of preclinical AD than any other conventional evaluation method[2]. Critical insight into the formation of WMH, as well as their early detection and risk mitigation could provide clinicians with a window of opportunity to treat aging individuals.

The presence of a sensitive microvasculature in the brain makes it particularly susceptible to damage. The established correlation of the lateral ventricle wall movement with the cardiac cycle suggests that this serial contraction/expansion elicits biomechanical stress within the periventricular white matter. Brain tissue is a highly organized, anisotropic material with viscoelastic properties that dissipates energy across each cardiac pulse and requires a delicate biomechanical balance of forces to maintain healthy brain clearance. Additionally, the unique shape of the ventricular system makes a 3D modeling analysis necessary for capturing true *in vivo* behavior.

We have developed a modeling pipeline to quantify stress in the brain over each cardiac cycle by employing a computational model informed by patient-specific anatomy and spatiotemporally resolved lateral ventricle wall movement. Using information obtained across multiple scales and modalities, we hope to provide insight into the biomechanical progression of WMH and enable early risk stratification.

## METHODS

### Imaging

MRI data was obtained for a healthy volunteer with temporally resolved motion of the lateral ventricle walls assessed using a single slice, fast echo-planar imaging (EPI) sequence (Siemens Prisma 3T scanner). This sequence provided spatial resolution of 1.97x1.97x4mm with a repetition time of 86ms, resulting in 1500 frames of dynamic lateral ventricle movement from the 129s scan. Wall movement was assessed by extracting an intensity profile across the parenchyma and ventricles. Additionally, structural MRI (T1- and T2-weighted) sequences were used to obtain high spatial resolution images of the brain tissue, 1x1x1mm, for segmentation.

### 2D Computational Modeling

T1-weighted images were used to generate image segmentations at the widest level of the lateral ventricles using ITK-SNAP. Following surface geometry creation in Geomagic (3D Systems), finite element meshes were generated and simulations were conducted using an in-house python code incorporating DOLFIN and the FEniCS open-source software[3]. Viscoelastic properties of human white matter were obtained from literature sources with homogenous conditions of Poisson ratio of 0.48, short term modulus of 0.25 kPa, long-term modulus of 1.5 kPa, and viscosity parameter of 3.87 kPa-s[4]. CSF was also modeled as a soft, viscoelastic solid with a Poisson's Ratio of 0.48 and constant Modulus of 0.2 kPa and viscosity parameter of 0.1 kPa-s to mimic fluid-like distension. 2D modeling boundary conditions include (1) Neumann boundary condition assigned to the inner wall facets of the lateral ventricle – simulations were iteratively repeated to produce spatiotemporally varying displacement fields most similar to EPI-measured displacement fields; (2) zero displacement Dirichlet boundary condition prescribed on the facets of the outer dura - to represent fixation of the skull.

## 3D Computational Modeling

We have also implemented a previously developed 3D brain modeling pipeline that enables construction of patient-specific geometries and accounts for 3D anisotropic properties using Diffusion Tensor Imaging (DTI)**.** The in-house pipeline shown in Figure 1 automatically processes T1-weighted and DTI scans to generate the following patient-specific outputs: (1) 3-label tissue segmentation, (2) 133-label deep brain labeling, (3) whole-brain tractography, (4) 3D nested geometry including idealized skull and skin layers using in-house MATLAB/Python code, and (5) whole-head finite element mesh with embedded fiber orientations using a combination of commercial meshing software and in-house MATLAB/Python code. This modeling pipeline is currently being extended to conduct automatic finite element analysis in 3D. A transversely isotropic hyperviscoelastic 3D material model will be informed by patient-specific fiber orientations and published values of relevant parameters. Boundary conditions will seek to replicate in-vivo brain loading as informed by time-resolved MRI.

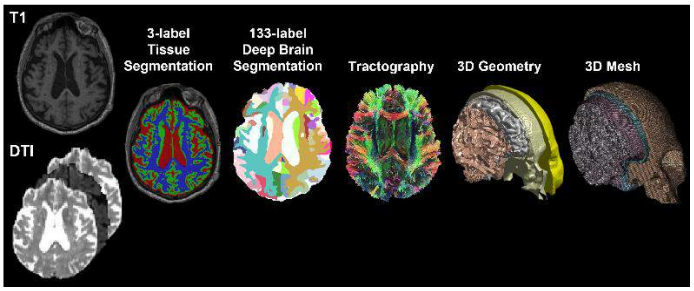


**Figure 1:** Patient-specific 3D Modeling pipeline. Inputs of T1-weighted and Diffusion Tensor Magnetic Resonance Imaging are used to generate segmentations, tractography, nested geometry, and finite element mesh with embedded fiber orientations and idealized skull.

## RESULTS

Preliminary results of the 2D model demonstrated stress clustering around the horns of the lateral ventricles, as shown in Figure 2. These locations align with commonly reported locations of periventricular WMH formation. The 3D modeling pipeline has demonstrated the ability to process large cohorts of patients from T1-weighted and DTI scans through generation of a finite element mesh with embedded fiber orientations.

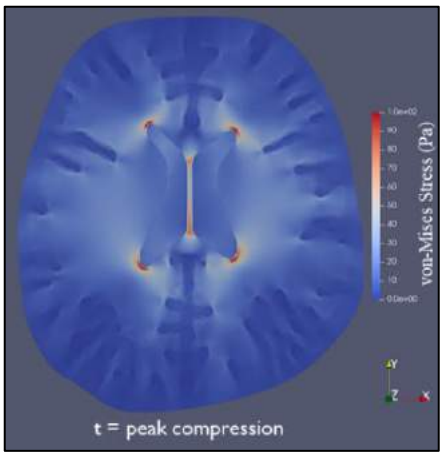


**Figure 2:** Normalized von-Mises stress at peak compression showing regions of elevated stress around the horns of the lateral ventricles.

## DISCUSSION

The effect of the cardiac pulse on highly anisotropic brain tissue depends on subject-specific brain geometry which can vary greatly across individuals. Our modeling pipeline allows to maximize patient-specificity and account for anisotropic, variable brain volumes based on T1-weighted and DTI scans. Preliminary data has demonstrated that there is merit in further investigating the underlying biomechanical drivers of tissue damage that lead to neurodegeneration. This modeling methodology provides the fundamental groundwork required for a larger scale study seeking to identify biomarkers of WMH formation in a cohort of neurodegenerative and aging individuals.

The 2D approximations of biomechanical stress distribution in a healthy volunteer represent a significant simplification made in the current study. 2D computational models of the brain fail to capture the non-symmetric 3D organization of the brain which is likely to reduce the model's predictive capability. We are extending our modeling approach to simulate various degrees of disease and neurodegeneration in 3D. Additionally, modeling patient-specific fiber orientations will allow for new computational parameters, such as axonal strain, to be incorporated along with more accurate material models.

Combining a multimodality imaging approach with state-of-the-art computational modeling, will allow us to elucidate the biomechanical mechanisms by which mid-life cardiovascular disease promotes degeneration of periventricular white matter in late-life, as well as and develop clinical risk stratification metrics.

## ACKNOWLEDGEMENTS

The authors would like to acknowledge funding from NIH 1R21AG068962-01A1 for biomechanical risk assessment. The authors would like to thank the Alfred P. Sloan Foundation through the Sloan Indigenous Graduate Partnership program at Purdue University, and the Chickasaw Nation Higher Education Foundation, the GEM Consortium, and the Association for Computing Machinery's Special Interest Group on High-Performance Computing who supported this research through graduate fellowships and scholarships. Partial support for this work was provided by Army Research Labs.

## REFERENCES

1. Budday et al. 2015. *J. Mech. Behav. Biomed. Mater.* 46:318–330
2. Hase et al. 2018. *J. Neurochem. 144:617–633.*
3. Kandel et al. 2016. *Alzheimer's Dement. Diag., Assess..* 4:18–27
4. Alnaes et al. 2015. *Archive of Numerical Software 3.*

# MECHANICAL ANCHORING DRIVES STEM CELL DIFFERENTIATION AND TISSUE MATURATION IN TISSUE ENGINEERED LIGAMENT-TO-BONE ENTHESES

**M. Ethan Brown (1), Sophia Murphy (1) Lais Morandini (1), Rene Olivares-Navarrete (1), Jennifer L. Puetzer (1,2)**

(1) Biomedical Engineering, Virginia Commonwealth University, Richmond, VA, USA
(2) Orthopaedic Surgery, Virginia Commonwealth University, Richmond, VA, USA

## INTRODUCTION

Ligament-to-bone attachments, or entheses, are structurally complex tissues that transfer load from elastic ligament to stiff bone via a compliant fibrocartilage region with gradients in organization, composition, and cell phenotype. These gradients are not restored in healing, repair, or in engineered replacements, resulting limited repair options and high failure rates [1]. Previously, we developed a novel culture system that guides anterior cruciate ligament (ACL) fibroblasts to form postnatal-like ligament-to-bone entheses via a zonal tensile-compressive culture environment [2]. Specifically, compressive restrains at the edge of the constructs produce a tensile-compressive environment which guides cells to produce 3 unique zones of organization and composition, with zone specific cell morphologies, recapitulating early postnatal enthesis properties [2]. While these engineered entheses are promising replacements, ACL fibroblasts are not an optimal clinical cell source. Human mesenchymal stem cells (hMSCs) are more clinically relevant; however, it remains a challenge to guide hMSCs to form the complex zonal and cellular gradients necessary for functional entheses [1]. The objective of this study was to investigate if the tensile-compressive nature of our culture system is sufficient to drive zonal differentiation of stem cells and produce zonal ligament-to-bone entheses similar to ACL fibroblast seeded constructs.

## METHODS

Engineered constructs were made by individually mixing human MSCs (hMSCs) from 3 donors or bovine immature ACL fibroblasts with rat tail type I collagen to form 20 mg/mL sheet gels at $5x10^6$ cells/mL as previously described [2]. Rectangular constructs (30x8 mm) were cut from the sheet gels and cultured in our clamping device (Fig 1A) for up to 4 weeks. At completion of culture, constructs were cut into half-samples for analysis of organization and mechanics or middle (M), transition (T), and clamped (C) regions for analysis of matrix composition and gene expression (Fig 1A). Zonal collagen organization was analyzed via confocal reflectance. DNA, glycosaminoglycans (GAGs), and collagen content were measured via Picogreen, DMMB, and hydroxyproline assays. Quantitative RT-PCR was performed on 4 week hMSC constructs to measure gene expression of types I and X collagen, Ihh, Gli1, Runx2, ALPL, Scx, and Sox9, normalized to GAPDH. Mechanical testing was performed across the transition zone via tensile tests at 0.75% strain/sec to failure. All data are expressed as mean ± SD. Significance was determined by 2-way ANOVA and 2-way repeated measures ANOVA with Tukey's post-hoc ($p < 0.05$).

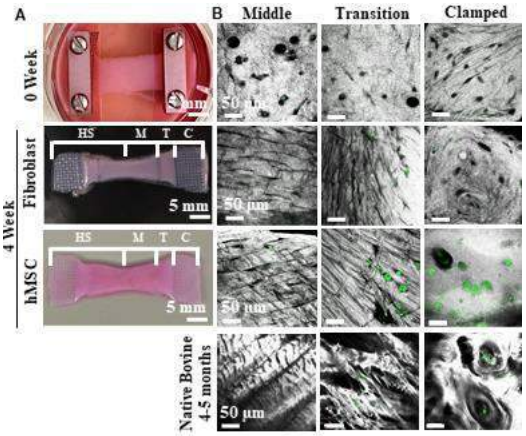


**Figure 1: A) Clamping device and constructs at 0 & 4 weeks with analysis regions depicted. B) Confocal reflectance of zonal collagen organization. Collagen = grey, cells = green.**

## RESULTS

Confocal imaging revealed samples begin as unorganized matrix for both hMSC and ACL fibroblast seeded constructs. By 4 weeks, ACL constructs develop early postnatal-like zonal collagen organization with aligned parallel fibers in the mid-section, perpendicular fibers in the transition, and unorganized collagen under the clamp. hMSC constructs developed similarly, however had accelerated zonal organization by 2 weeks (data not shown), and by 4 weeks fibers in the transition shifted

from perpendicular alignment to more direct insertions, indicative of more mature organization and later stage development (Fig 1B, [3]).

Analysis of zonal matrix composition revealed hMSC constructs had no changes in zonal DNA concentration throughout culture, while ACL constructs had significant increases in DNA content in the middle and transition regions by 4 weeks (data not shown). Both hMSC and ACL constructs maintained steady collagen content across all regions at ~60% of native tissue throughout culture (data not shown) [4]. Finally, hMSC constructs had significantly increased GAG/DNA in all regions by 4 weeks with significantly more GAG accumulation in the clamped region, while GAG/DNA remained constant in all zones for ACL constructs (data not shown).

Tensile tests across the transition region revealed hMSC constructs significantly increased the elastic modulus of the enthesis region to ~5.5 MPa by 4 weeks, while ACL constructs remained under 2 MPa throughout culture (Fig 2A). Additionally, hMSC constructs had a 2-3 fold significant increase in toe modulus, ultimate tensile strength (UTS), and transition stress (Fig 2A-B). There were no differences in strain properties between hMSC and ACL constructs by 4 weeks (Fig 2C).

Gene expression analysis of 4 week hMSC constructs revealed that key genes associated with enthesis development such as Ihh, Gli1, Scx, Sox9, and type X collagen were upregulated in all regions in relation to day 0 cell controls (data not shown). Normalizing zonal gene expression to the middle region revealed zonal differences at 4 weeks with clamped regions having significantly upregulated expression of Indian Hedgehog (Ihh), Gli1, Runx2, and type I and X collagen compared to middle regions (Fig 3). Additionally, ALPL expression was trending in upregulation compared to middle ($p$ = 0.06) and transition ($p$ = 0.08).

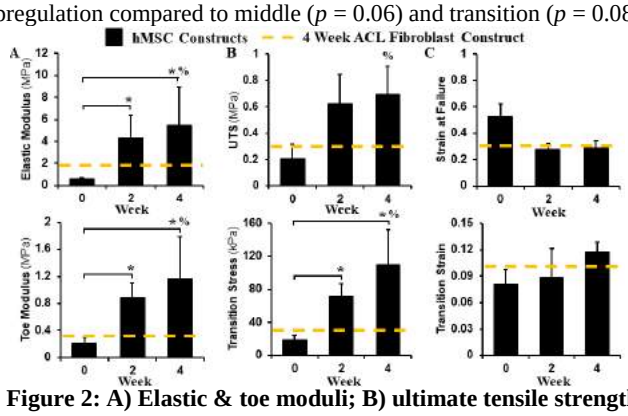


**Figure 2: A) Elastic & toe moduli; B) ultimate tensile strength (UTS) and stress at toe to linear region transition; and C) strain at failure and transition. *Significance to bracket, %Significance to 4 week ACL construct mechanics ($p$<0.05). N=2-3 donors, n=3-4.**

## DISCUSSION

Four weeks of static tensile-compressive culture hMSC seeded high density collagen gels resulted in enhanced zonal collagen organization, zonal composition, and significantly increased mechanical properties compared to ACL constructs, as well as zonal expression of key enthesis developmental markers. Both hMSC and ACL constructs developed similar collagen organization in the middle and clamped regions, mirroring immature native tissue organization; however, hMSC constructs demonstrated a marked shift in collagen organization from perpendicular fiber alignment in the transition to more direct fiber insertions. This shift in organization resembles more mature enthesis organization where fibers shift from being perpendicular to the ligament to more parallel with the ligament, while maintaining a degree of disorganization [3]. This organization in mature entheses is critical for proper mechanical function and reduction of stress concentrations [5]. Previously, we have observed similar organizational shifts in the transition region after 10 days of dynamic

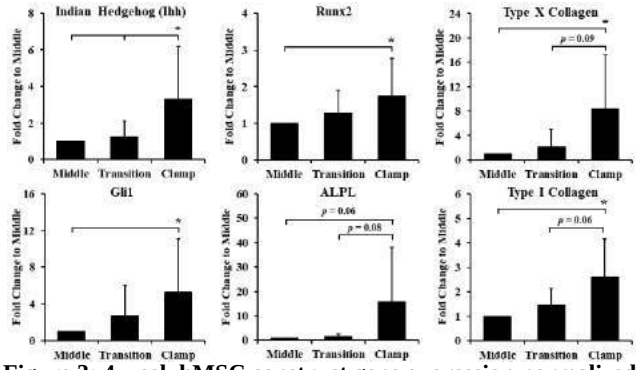


**Figure 3: 4 week hMSC construct gene expression normalized to middle region for enthesis markers Ihh and Gli1, mineralization markers Runx2 and ALPL, and matrix markers type X and I collagen. *Significance to bracket ($p$<0.05). N=2 donors, n=3-4.**

mechanical stimulation in ACL constructs [6]. These organizational changes in ACL constructs also resulted in a significant 2-3 fold increase in moduli and stress properties [6]. Interestingly, while ACL constructs require further mechanical stimulation to reach this level of maturation, hMSC constructs develop these properties with simple static clamping, suggesting mechanical forces of the clamping system may be sufficient to drive hMSC differentiation into appropriate cell phenotypes that can more readily facilitate these changes.

Interestingly, only hMSC constructs had zonal GAG/DNA changes throughout culture, with significantly increased GAG/DNA under the clamp compared to the middle region. This indicates that the compressive environment under the clamp drives the hMSCs to shift to a more chondrocyte-like phenotype similar to that observed in early postnatal enthesis fibrocartilage [3,7]. Mirroring compositional changes, hMSC constructs also had zonal gene expression differences for key enthesis developmental markers. In particular, significant upregulation was observed under the clamp for Ihh and Gli1, known to be critical for proper development of the fibrocartilage regions of the enthesis [8,9]. Additionally, markers commonly associated with mineralization of the fibrocartilage tissue, such as Runx2, ALPL, and type X collagen, were upregulated in the clamp region as well [8]. Collective upregulation of these key markers under the clamp suggests zonal differentiation of hMSCs into fibrochondrocytes or hypertrophic fibrochondrocytes, cells known to populate the fibrocartilage regions of late postnatal entheses [1,2]. Evaluation of gene expression at 0 and 2 weeks, and evaluation of zonal types I, II, and X collagen accumulation are ongoing. This study provides insight into how tensile-compressive culture conditions can drive zonal hMSC differentiation and tissue maturation in engineered ligament-to-bone tissues, ultimately producing the complex gradients of the enthesis. These constructs hold great promise as ACL replacements and provide an *in vitro* model to investigate driving stem cell regeneration for ligament-to-bone repair.


## ACKNOWLEDGEMENTS

We thank AR$^3$T, supported by NIH NICHD & NIBIB, for funding this work (P2CHD086943).


## REFERENCES


[1] Lu, H et al., *Annu Rev Biomed Eng*, 15:201-226, 2013. [2] Brown, E et al., *Acta Biomat*, 2021. [3] Wang, I et al., *J Orthop Res*, 24:1745–1755, 2006. [4] Puetzer, J et al., *Biomaterials*, 2020. [5] Boys, A et al., *ACS App Mat & Int*, 11(30):26559-26570. [6] Brown, E et al., *SB3C*, 2021. [7] McCorry, M et al., *Stem Cell Res & Ther*, 7:1, 2016. [8] Dyment, N et al., *Dev Biol*, 405(1):96-107, 2015. [9] Schwartz, A et al., *Development*, 142(1):196-206, 2015.

# DIRECT NUMERICAL SIMULATION OF BLOOD FLOW WITH CELLS IN RETINA VASCULAR NETWORK

**Kacper Ostalowski (1), Jifu Tan (1)**

(1) Department of Mechanical Engineering, Northern Illinois University, DeKalb, IL, USA

## INTRODUCTION

Blood flow in capillary network is important for delivery of oxygen, water, nutrient, and removal of waste substance. Modeling the blood flow in capillary network is important for both fundamental understanding the multiphase flow and clinic applications. However, it is challenging because of the complex network structure with branches and loops and deformable cells, which needs to be explicitly considered due to the size of cells is comparable to capillary vessel. Previously, Balogh et al. presented the first direct numerical simulation of 3D cellular-scale blood flow in physiologically realistic microvascular networks using the finite volume method coupled with finite-element method[1]. Bernabeu et al. coupled the lattice Boltzmann method (LBM), finite element method, and immerse boundary method to study the hematocrit in cancer vascular network and found uneven hematocrit split in the downstream branching point[2]. However, these works either did not consider the heterogeneous blood cell suspensions in vascular network or did not study the blood cell transport in vessel blockage in vascular network. This paper tried to bridge the gap in studying the transport of cells in the complex vascular network and with stenosis. To the best of authors' knowledge, this is the first time to simulate blood cell transport in a patient-specific vascular network with stenosis.

## METHODS

In this work, the multiphase flow in a patient-specific retina capillary network, as shown in Figure 1(a)Figure 1, was simulated by the LBM coupled with particle-based cell membrane models through the immersed boundary method. Both the red blood cells (RBCs) and white blood cells (WBCs) were modeled as cell membranes.

Briefly, the LBM was used to approximate the incompressible fluid flow with governing equations

$$\nabla \cdot \boldsymbol{u} = 0 \quad (1)$$

$$\frac{\partial \boldsymbol{u}}{\partial t} + \boldsymbol{u} \cdot (\nabla \boldsymbol{u}) = -\frac{1}{\rho}\nabla p + \nu \nabla^2 \boldsymbol{u} + \boldsymbol{g} \quad (2)$$

where $\boldsymbol{u}$ is the velocity, $t$ is time, $\nu$ is the kinematic viscosity, $\boldsymbol{g}$ is the external body force. The LBM solver was based on open source packages Palabos (Parallel lattice Boltzmann solver)[3].

The cell membranes are made of interactive particles with potentials resisting stretching, bending, area/volume changes.

$$U = U_{stretch} + U_{bend} + U_{area} + U_{volume} \quad (3)$$

The membrane nodal forces are calculated from potential functions, and the position are updated based on the Newton's law of motion. The detailed potential forms can be found in our previous publication and others[4], [5]. The membrane model was implemented in LAMMPS (large-scale atomic/molecular massively parallel simulator) [6].

The coupling between the cell and the flow was done through the immersed boundary method where the cell interpolated velocity from fluid, and the fluid feel the existence of the cell through spreading the restoring force through the body force term in Eqn (2). Details on the implementation and validations can be found in Ref.[4], [7].

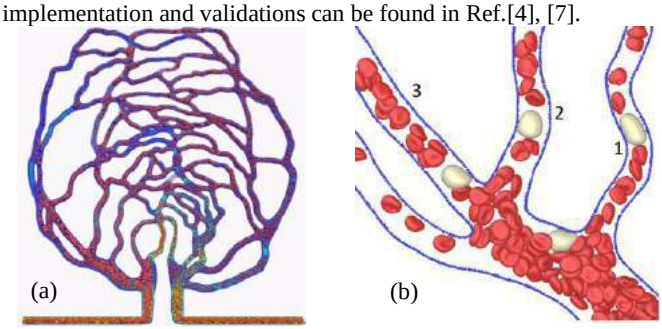


**Figure 1: (a) Snapshot of RBCs in a patient specific retina vascular network. The background color shows the velocity. (b) the zoom-in view of the simulation with both RBCs (red) and WBCs (white).**

## RESULTS

### Dynamic stalling of flow in the network

The complex geometry of the curved vessels and bifurcations can lead to cells temporarily being stuck at the vessel wall near flow stagnation regions. The aggregated cells will increase the size of the stagnation region and change local flow. E.g., RBCs were found to accumulate and create a blockage at a T-shaped bifurcation as seen in Figure 2(a).

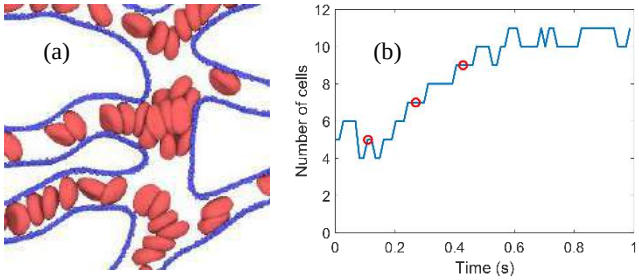


**Figure 2: (a) The aggregation of cells in the T-junction of the vessel network. (b) The growth of the cell aggregation in flow.**

A large stagnation zone was created where the mass of cells built up which remains for the entire duration of the simulation. The size of the blockage varied over time and eventually stabilized during our simulation, see Figure 2(b). At its largest, flow was significantly reduced at the upstream vessel and through the bifurcation region. As a result, the downstream vessel experienced reduced hematocrit compared to surrounding vessels. The cell blockage can affect local flow rate and hematocrit distributions.

The simulation with mixed RBCs and WBCs showed that the flow rate reduced significantly when a WBC was squeezing through the vessel (Data not shown here, a snapshot of the simulation can be found in Figure 1(b)Figure 1). It is expected that the large size of WBC would increase the resistance of the vessel.

### RBCs oscillation in the network with partial blockage

The growth of plaque may narrow the blood vessel, which leads to the investigation of RBC transport in a partially blocked blood vessel. In the simulation, 50% of the cross section in a vessel was blocked, as shown in Figure 3(a). Flow with RBC suspensions was simulated through the partially blocked network. Interestingly, oscillatory flow was observed in a vessel near the obstruction. The cells oscillating in the vessel were shown in different colors in the dashed box in **F**igure 3(b).

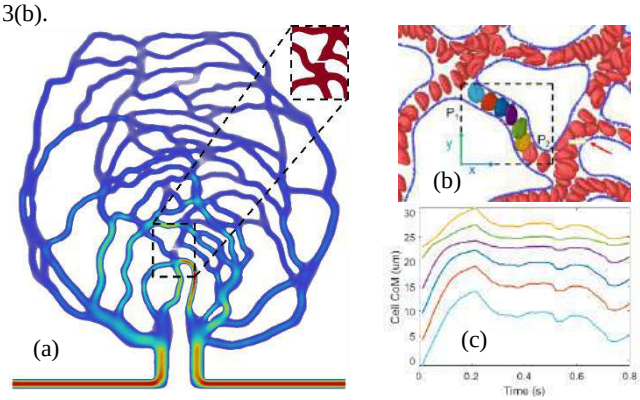


**Figure 3. (a) Simulation of blood flow with a stenosis in one of the blood vessels in the center region, as indicated by the inset. (b) The oscillating cells trapped in the vessel bounded by a dashed box. (c) the oscillating center of mass for each trapped cell.**

The partial blockage reduced the flow in the oscillating vessel by changing the pressure gradient. The pressure at both ending points (P1 and P2 in Figure 3(b)) showed fluctuations (data not shown here). In general, the inclusion of RBCs through the vasculature had a small effect on the pressure distribution, but the effect can be significant near vessels where the pressure gradient was already low. The oscillations in flow direction in a vessel was most likely caused by variations in the local hematocrit at either end of the vessel. The supply of oxygen would be interrupted since no new cells enter the vessel. Indeed, the time history of the center of mass of the six trapped cells in x direction further confirmed the oscillation of cells, as shown in Figure 3(c).

## DISCUSSION

The simulation showed that dynamic stalling can happen in a vascular network with explicit cells in certain branched regions. Without cells, the fluid flow in the retina network is steady without any fluctuations. However, the multiphase nature of blood flow due to cells in the vessel change the flow to be unsteady with fluctuating velocities, see Figure 1(a). In some branched vessel, there is no cell entry due to the plasma skimming effect in capillaries. On the other hand, simulation results with partial blockage showed that cells may be trapped in certain blood vessel due to the narrowing of other vessels. In such cases, the supply of oxygen may be stalled. This could be fatal if the stalling lasts for a long time for cerebral capillaries due to the high metabolic demand of continuous oxygen in brain tissue. In addition, the blood flow rate was reduced significantly when a WBC squeezed into a capillary lumen due to the large size of WBC. Similar results were reported in experimental work too. E.g, the dynamic stalling was observed in cerebral capillary network by obstructing WBCs in experimental strokes[8]. In their work, the adhesion between WBCs and the injured vessel wall contributed to the obstruction. In another study, even in a healthy mouse brain, about 7.5% of ~200 capillaries had at least one stall in awake mice with chronic widows during a 9 min observation under observation[9]. The similar oscillating of RBCs were also reported in a mouse retina vessel network [10]. All these experimental studies confirm that our model can capture blood transport at cell size scale in capillaries including dynamic stalling. The model will provide tools for future investigation of stalling events in capillary pathologies.

Note that the current study only considered the mechanical effect of cells in the flow. The pulsative nature of the flow was not considered, which was shown to affect the RBC flux in capillaries[10]. In capillary networks, the obstruction in blood flow will trigger vasodilation to restore the flow. Further improvement of the model is needed to include chemical signaling to study the mechanobiology in capillaries.


## ACKNOWLEDGEMENTS

We acknowledge the parallel computing support from Gaea at NIU and Theta at Argonne national laboratory.


## REFERENCES


[1] Balogh et al, *Biophys. J.*, vol. 113, no. 12, pp. 2815–2826, 2017.
[2] Bernabeu *et al.*, *Proc. Natl. Acad. Sci.*, vol. 117, no. 45, pp. 27811–27819, 2020.
[3] Latt *et al.*, "*Comput. Math. Appl.*, vol. 81, pp. 334–350, 2021,
[4] Tan, et al, *J. Comput. Sci.*, vol. 25, pp. 89–100, Mar. 2018
[5] Fedosov, et al, *Biophys. J.*, 98 (10), pp. 2215–2225, 2010.
[6] Thompson *et al.*, *Comp Phys Comm*, 271:108171, 2022,
[7] Tan, et al, *Biomicrofluidics*, vol. 13, no. 6, p. 064105, 2019.
[8] Rolfes *et al.*, *Brain. Behav. Immun.*, vol. 93:322–330, 2021
[9] Erdener *et al.*, *J. Cereb. Blood Flow Metab.*, 39(5):886–900, 2019.
[10] Guevara-Torres, et al, *Biomed. Opt. Express*, 7 (10):4228, 2016.

SB³C2022
Summer Biomechanics, Bioengineering and Biotransport Conference
June 20-23, Eastern Shore, MD, USA

# HETEROGENEITY IN CELL DISTRIBUTION DUE TO COLLECTIVE ORGANIZATION LEADS TO LOCALIZED HIGHER STRESSES.

**M. Jebeli (1), S. P. Lopez (1), Q. Wen (2), K. Billiar (1)**

(1) Biomedical Engineering, Worcester Polytechnic Institute, Worcester, Massachusetts, USA
(2) Physics, Worcester Polytechnic Institute, Worcester, Massachusetts, USA

## INTRODUCTION

Collective cell behavior drives many crucial biological phenomena including morphogenesis, tissue repair, and cancer metastasis. These behaviors arise from cell interactions in addition to individual cell behavior [1], as it has been shown that an individual cell's behavior differs when in communication with other cells [2]. Previous studies on collective cell behavior have focused mainly on epithelial monolayers showing that cells are relatively uniform throughout the monolayer and cells are extruded when the layer become dense. Further, when cultured on protein islands which provide geometrical constraint, non-uniform patterns of proliferation more on edges, and cell alignment emerge due to gradients in mechanical stresses and contact guidance at the edges [3, 4]. Cell-cell transmission and build-up of stresses within these monolayers and constrained cell aggregates have been estimated with computational models since they cannot be directly measured. The models suggest symmetric stress distribution in circular aggregates, higher on the edges and lower in the center yet they assume uniform cell properties.

In our observations of valvular interstitial cells (VICs), we noticed more heterogeneity of cell distribution than reported with other types of cells on micro contact printed islands regardless of the shape. VICs crowd in the middle, yet, in contrast to epithelial cells, they do not extrude as single cells. Rather densification occurs at the center of aggregates which leads to apoptosis, likely driven by collective cell behavior and reduction of stress in the center which is predicted by our computational models when radially varying modulus or contractility are included [5]. We have also observed heterogeneity in the cell distribution and formation of multicellular bands spanning the 200 µm circular 2D aggregates [5]. Further, rather than high tractions around the edge of each pattern, we observed hotspot tractions associated with the cells spanning the aggregates.

We hypothesize that the heterogeneity observed in traction force maps is due to the formation of bands with more elongated cells at the endpoints and the formation of local hyperconfluent regions with rounded cells within constrained cell aggregates. To quantify the mechanical state of the cells within the aggregates, we measure the collective forces that cells apply to the substrate using traction force microscopy (TFM). Further, we utilize relatively large 400 µm diameter microcontact printed circular islands to increase the homogeneity of the cell behaviors and minimize the ability of single cells to span the pattern.

## METHODS

Substrate preparation

Circular collagen patterns of 400 µm were printed onto 19.2 kPa polyacrylamide (PA) gels. We used the size of micropatterns of 400 µm to minimize single cell spanning of the pattens and increase the homogeneity of the collective behavior i.e., obtain a more clear differentiation between edge and center of the cell islands.

The surface of each substrate was sandwiched between glass coverslips coated with fluorescent micro-beads to transfer fluorescent displacement tracking beads to the surface of the gel which were prepared per [5]. To analyze the displacement of the beads, a custom MATLAB code was used[5].

Direct microcontact printing

To form microcontact printed protein islands, collagen was directly printed on the previously described PA gels per [5].

Cells and media

Porcine aortic VICs, isolated per [6] from a heart obtained from a local abattoir (Blood Farm, Groton, MA), were chosen as a primary fibroblastic cell type; porcine VICs are commonly used for CAVD research due to the similarity to human VICs. Cells were cultured in DMEM with 10% FBS and 1% Antibiotic/Antifungal at 37 °C in 10% CO2.

Experimental design

VICs were seeded at passage 3-6 at 12,500 cells per $cm^2$ [7] on microcontact printed substrates. 24 hours post-seeding, the aggregates

were imaged with phase contrast and red fluorescent channels; then utilizing trypsin, the cells were detached from the substrate and a red fluorescent image was captured again. Two red fluorescent images, with cells attached and after cells detachment, were analyzed using the customized MATLAB code, to calculate the displacement on the surface of the PA gel.

## RESULTS

Heterogeneity of cell distribution in microcontact printed aggregates

Despite the large size of the protein islands, we observed heterogeneity in cells distribution and formation of multicellular bands spanning across the protein island diameter. Figure 1 shows a four-day time-series images in which a clear multi-cellular band is formed. From observations of many aggregates, it appears that banding occurs over time when cells have more affinity with lining up with each other than forming symmetric rings due to contact guidance around the edges. The bands do not disappear, rather they strengthen over time. This banding is not predicted by existing computational models and the mechanisms driving this behavior are unclear.

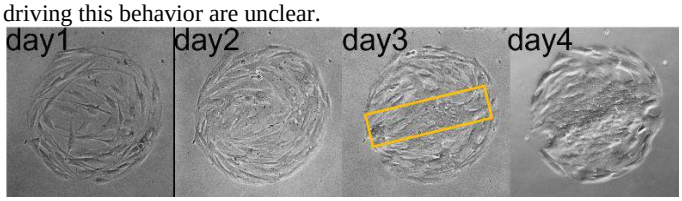


**Figure 1. Phase images of an aggregate of 400 µm over 4 days, showing the heterogeneity of the cell distribution and formation of band crossing over the aggregate surface, yellow rectangle showing the cells alignment and band formation.**

Hyper-confluency and banding changes the mechanical state of the cells in aggregate

Rather than generate high traction stresses uniformly around the circumference of the patter as is observed for epithelial cells, the calculated traction forces for the VICs is significantly higher at the endpoints of the bands (Fig. 2).

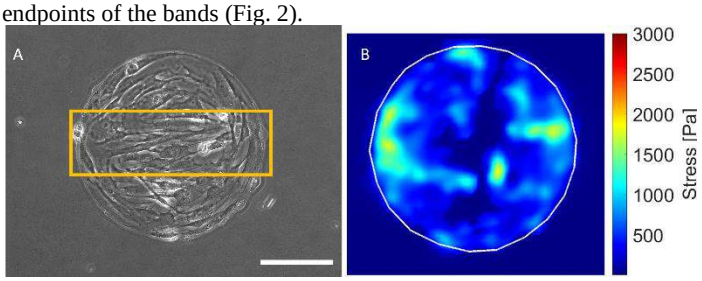


**Figure 2. TFM demonstrates that the cells apply higher forces to the substrate at the endpoints of the bands, shown by yellow rectangle, collectively. A) Phase image of a sparse aggregate. B) TFM analysis of the aggregate in sparse stage. Scale bar = 200 µm.**

Further, to quantify the forces cells apply to the substrate in local hyper-confluent areas, we have imaged a hyper-confluent aggregate, with a clear local hyper-confluent region, Figure 3. In the TFM image, Fig 3B, it is evident that the cells in hyper-confluent regions, even though very high in number and density, apply significantly lower forces to the substrate compared to the endpoints of bandings and the areas with elongated cells.

## DISCUSSION

Multicellular banding creates heterogenous stress patterns

We hypothesized that with the larger protein islands, we would observe more uniform traction force patterns with high stress on the outer circumference and low tractions in the center. Indeed, single cells were no longer able to span the islands; however, we still observed substantial heterogeneity in the traction force maps. To our surprise, large multicellular bands formed across the patterns rather than forming radially symmetric patterns with predominantly circumferentially cell orientation. We observed that the traction stresses were clearly higher at the endpoints of the bands. Interestingly, in the center of the bands the cell density is very high, which is correlated with low stress and increased rates of apoptosis.

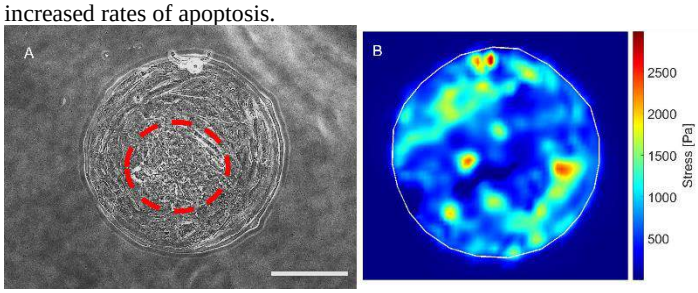


**Figure 3. TFM shows that in hyper-confluent regions, shown by red dotted circle, the cells apply significantly lower forces to the substrate collectively. A) Phase image of a hyper-confluent aggregate. B) TFM analysis of the aggregate in hyper-confluent stage. Scale bar = 200 µm.**

Asymmetric mechanical state

Previous studies have shown that cells require a homeostatic tension to survive; for example, states of low cell stress initiate apoptosis [8, 9]. Furthermore, indicators of high cell tension are localized to the edges of aggregates [10], while indicators of low cell tension are found in central regions [5]. Here we showed that these signals are not symmetric with primary mesenchymal cells and change with heterogeneity in confluency levels; we showed heterogeneity in cell distribution, which leads to asymmetric traction forces, which are higher at the two endpoints and not uniform around the edges.


## ACKNOWLEDGEMENTS

This work was funded by the AHA (20AIREA35120448) and NSF (CMMI 1761432).


## REFERENCES


[1] B. Ladoux and R.-M. Mège, *Nature Reviews Molecular Cell Biology*, vol. 18, no. 12, pp. 743-757, 2017/12/01 2017.

[2] B. A. Camley and W.-J. Rappel, *J Phys D Appl Phys*, vol. 50, no. 11, p. 113002, 2017.

[3] S. J. Streichan, C. R. Hoerner, T. Schneidt, D. Holzer, and L. Hufnagel, *Proceedings of the National Academy of Sciences of the United States of America*, vol. 111, no. 15, pp. 5586-5591, 2014.

[4] S. He, C. Liu, X. Li, S. Ma, B. Huo, and B. Ji, *Biophysical journal*, vol. 109, no. 3, pp. 489-500, 2015.

[5] Z. E. Goldblatt *et al.*, *Biophysical Journal*, vol. 118, no. 1, pp. 15-25, 2020/01/07/ 2020.

[6] R. A. Gould and J. T. Butcher, *J Vis Exp*, no. 46, p. 2158, 2010.

[7] H. A. Cirka, J. Uribe, V. Liang, F. J. Schoen, and K. L. Billiar, *Lab Chip*, vol. 17, no. 5, pp. 814-829, Feb 28 2017.

[8] M. Egerbacher, S. P. Arnoczky, O. Caballero, M. Lavagnino, and K. L. Gardner, *Clin Orthop Relat Res*, vol. 466, no. 7, pp. 1562-1568, 2008.

[9] J. D. Humphrey, E. R. Dufresne, and M. A. Schwartz, *Nat Rev Mol Cell Biol*, vol. 15, no. 12, pp. 802-812, 2014.

[10] B. Li, F. Li, K. M. Puskar, and J. H. Wang, *J Biomech*, vol. 42, no. 11, pp. 1622-7, Aug 07 2009.

# MECHANICAL REMODELING OF MURINE THORACIC AORTA DURING PREGNANCY

**Ana I. Vargas (1), Samar Tarraf (1), Rouzbeh Amini (1,2), Chiara Bellini (1)**

(1) Department of Bioengineering, Northeastern University, Boston, MA, USA
(2) Department of Mechanical and Industrial Engineering, Northeastern University, Boston, MA, USA

## INTRODUCTION

The maternal body undergoes multiple physiological changes in the cardiovascular system during pregnancy [1]. During normotensive pregnancy, cardiac output, arterial compliance, and heart rate increase, causing vascular resistance and blood pressure (BP) to decrease [2, 3]. The drop in vascular resistance caused by vasodilation are indicators of increased arterial distensibility [4]. However, attenuations of these physiological changes in maternal cardiovascular system, have been linked to the pathogenesis of maternal cardiovascular disease and mortality [5].

Aortic and hemodynamical properties during pregnancy are commonly evaluated using non-invasive methods in humans or rats, by measuring pulse-wave velocity and augmentation index (AIx), both of which are indicators of structural stiffness [6, 7]. However, the changes in aortic mechanical properties that are responsible for the functional changes in the cardiovascular system during pregnancy are largely unknown. To address this question, we aimed to investigate the structural and functional properties of the thoracic aorta in C57BL7/6 pregnant and virgin female mice. We hypothesized that the mechanical response of the murine thoracic aorta adapts during pregnancy.

## METHODS

*Sample groups.* Pregnant C57BL/6 mice at gestation day 17 (N=2) were purchased from the Jackson Laboratories (Bar Harbor, Maine) and were used for the late-gestation experimental group. Nulligravida female C57BL/6 mice (N=2) at 10 weeks of age served as nonpregnant, age-matched controls.

*Blood Pressure.* Blood pressure measurements were collected on each mouse using a non-invasive tail-cuff system (CODA; Kent Scientific) before sacrifice.

*Sample collection and preparation.* Mice were euthanized and a ~5mm sample of the descending thoracic aorta (DTA) was excised. Samples were cleaned from excess perivascular tissues and fat. Lateral branches on the tissue were tied with 9-0 nylon sutures. DTA specimens were cannulated on the proximal and distal end onto custom-made glass micropipettes. Ring samples were taken from either end of each specimen to measure unloaded thickness.

*Biaxial Mechanical testing.* Prepared samples were mounted onto a custom-made biaxial testing system which is controlled by a computer (Fig. 1) [8]. The outer diameter of the vessel was measured using a camera. Linear actuators controlled the axial stretch, and a load cell measured the axial force. Luminal pressure and axial length were set through a custom LabView Program. Samples were acclimated, pre-conditioned, and their axial stretch was estimated. Cyclic pressure-diameter and force-length tests were done on each sample. Following mechanical testing, a nonlinear regression was implemented to fit a four-fiber family constitutive model to the experimental data. Estimated material parameters were used to predict mechanical variables, including biaxial Cauchy stress, biaxial linearized stiffness and aortic distensibility [8].

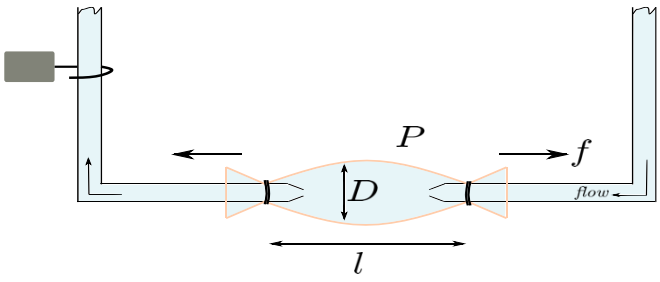


**Figure 1: Biaxial Testing Schematics. DTA sample is connected to glass capillary tubes on both ends. D denoted the diameter of the tubal tissue, l denotes its length, P is the applied pressure, and f denotes the axial force that is applied on both ends of the tubal tissue.**

## RESULTS

Preliminary data on blood pressure measurements suggested a decrease in systolic and diastolic measurements during pregnancy (Fig. 2), with mean values of 119 and 96 mmHg for control mice, and 102 and 75 mmHg for pregnant mice, respectively.

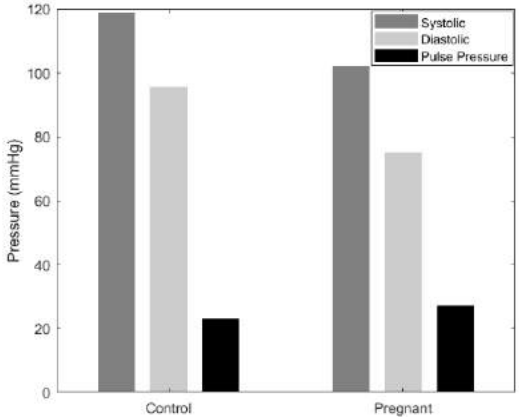


**Figure 2: Measured blood pressure in pregnant mice and age-matched control group**

Figure 3 shows the results of the experimental gathered dring biaxial testing and fitted to the mathematical model. While the focus of this premilinary work was not quantifying the mechanical properties, the excersise of fitting the data demonstrated the feasibility of using such models in further analysis of the experimental data when more samples becomes available.

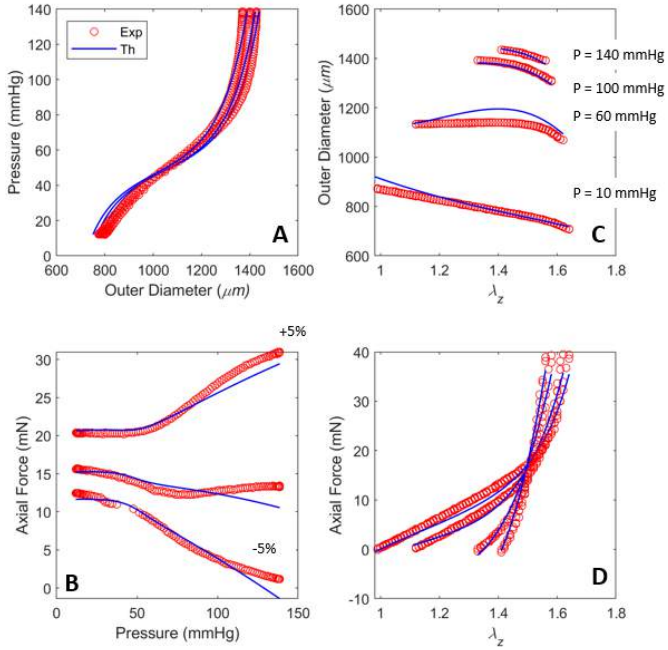


**Figure 3: Results of a typical experiment in the control group shown in red hallow cricles and the mathematical model in blue lines. In (A) and (B) the intitial axial stretch was kept constant for each experimental protocol and the pressure increased whereas in (C) and (D) the pressrure for each protocol was kept constant and the axial stretch ($\lambda_z$) was increased.**

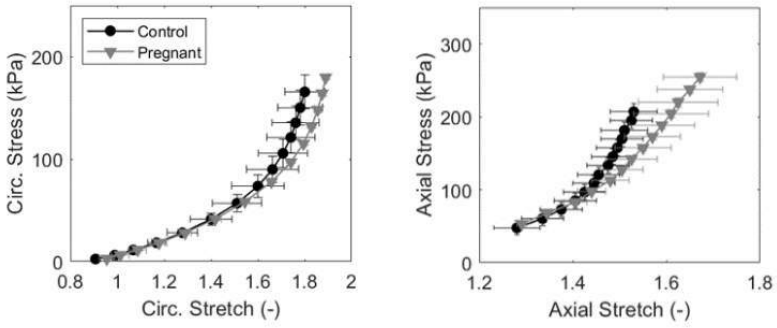


**Figure 4: DTA biaxial stresses for pregnant and age-matched control C57BL/6 mice: (A) circumferential direction, and (B) axial direction**

Stress vs. stretch response of aortic tissues in the circumferential and axial direction is shown in Figure 4. Again, due to the limited number of experiments, a rigorous statistical analysis was deemed impossible at this stage. However, visual examination of the data showed a nonlinear behavior of the tissue consistent with previous observations in murine DTA and other species (including human). In addition, anisotropic response was observed, especially in the control samples. Finally, the pregnant groups seemed to be more compliant at higher levels of mechanical stress.

## DISCUSSION

With cardiovascular disease being one of the major causes of maternal mortality [9], we are motivated to understand the changes in cardiovascular function during pregnancy. In the reported study, we presented our observation and initial analyses of the passive mechanical responses of the descending thoracic aorta in nulligravida and late-gestation pregnant mice.

Preliminary data (N=2 for each group) suggested an increase in circumferential distensibility and axial extensibility in pregnant mice. Our ongoing research is focused on increasing sample size for DTA specimen as well as performing biaxial mechanical testing on the ascending thoracic aorta (ATA) for both groups. We expect to elucidate the changes in the intrinsic stiffness of tissues during pregnancy and to provide insights into the changes in axial and circumferential stretch, the relationship between the thickness of the aortic wall, and the changes in the stored elastic energy of the thoracic aorta, which are all important factors in biomechanical assessment of aortic tissue in health and disease.

## ACKNOWLEDGEMENTS

Support for this work was provided by the National Science Foundation (NSF CAREER award 204088).

## REFERENCES

[1] Sanghavi M. et al., *Circulation*, 130 :1003–1008, 2014.
[2] Soma-Pillay, P. et al., *Cardiovasc. J. Afr*, 27:89, 2016.
[3] Macedo, M.L. et al., *Hypertension*, 51 :1047–1051, 2008.
[4] Van Bortel, L. M. et al., *Hypertension*, 26:531–534, 1995.
[5] epigenetic
[6] Hart, M. V. et al., *Am. J. Obstet. Gynecol.*, 154:887–891, 1986.
[7] Ulusoy, R. E. et al., *Heart Vessels*, 21:38–41, 2006.
[8] Bellini, C. et al., *J. Biomech.*, 49:2383, 2016.
[9] Bersi, M. R. et al., *Hypertension*, 67:890–896, 2016.
[10] Mocumbi, AO, et al., *Cardiovasc. J. Afr*, 27:84, 2016.

# DEVELOPMENT OF FIBER OPTIC PROBES TO DETECT VISCERAL ARTERIES FOR *IN SITU* FABRICATION OF STENT-GRAFTS

**Timothy K. Chung (1), Nicholas P. Lagerman (1), Cyrus J. Darvish (1), Mohammad H. Eslami (4), David A. Vorp (1,2,3,4,5,6,7)**

(1) Department of Bioengineering, University of Pittsburgh, Pittsburgh, Pennsylvania, USA
(2) Department of Mechanical Engineering and Materials Science, University of Pittsburgh, Pittsburgh, Pennsylvania, USA
(3) McGowan Institute for Regenerative Medicine, University of Pittsburgh, Pittsburgh, Pennsylvania, USA
(4) Department of Surgery, University of Pittsburgh, Pittsburgh, Pennsylvania, USA
(5) Department of Chemical and Petroleum Engineering, University of Pittsburgh, Pittsburgh, Pennsylvania, USA
(6) Department of Cardiothoracic Surgery, University of Pittsburgh, Pittsburgh, Pennsylvania, USA
(7) Clinical and Translational Sciences Institute, University of Pittsburgh, Pittsburgh, Pennsylvania, USA

## INTRODUCTION

Abdominal Aortic Aneurysm (AAA) is a common cardiovascular disease, causing irreversible enlargement of the lower part of the aorta by more than 50%. An aneurysm can continue to grow and lead to eventual rupture, the 13th leading cause of death in the US [1]. However, surgical intervention can be performed to stabilize an aneurysm using two methods: high-risk open surgical repair (up to 12% mortality) or minimally invasive endovascular repair (~2% mortality). Open surgery requires opening the abdominal cavity and resecting the diseased portion of the abdominal aorta with a graft. Endovascular aneurysm repair (EVAR) involves making a small incision in the femoral artery and deploying a stent-graft using a catheter. The stent-graft in turn would protect the aneurysm by reducing the forces it experiences due to systolic blood pressure. EVAR has become more prevalent due to its lower mortality rate during operation [2].

Complex geometry aneurysms pose significant compatibility issues with traditional endovascular approaches because of their short neck (superior to the aneurysm sac to the lowest inferior renal artery). To accommodate complex geometry aneurysms, a fenestrated EVAR (FEVAR) approach was introduced to overcome the challenges of placing a traditional stent graft superiorly that would block visceral arteries (renal, celiac, and superior mesenteric arteries). Surgeon modified or custom prefabricated endografts are required to restore blood flow to visceral arteries and allow for the placement of bridging stent-grafts.

Currently, there is only one FDA-approved fenestrated stent-graft on the market, the Cook Zenith graft (Cook Medical LLC, Bloomington, Indiana). This prefabricated stent-graft requires a medical image for the placement of fenestrations (up to 8 weeks for custom manufacturing) and can cost up to three times more than a traditional endograft. The lead time for delivery of the customized stent-graft poses a potential for rupture to occur for patients that are in need of immediate repair. Katsarygyris et al. reported that nearly 2% of patients experienced a rupture before a fenestrated stent-graft operation could take place [3].

To alleviate the extended costs and wait times for customized devices, a novel system was introduced to perform *in situ* fabrication of stent-grafts. The proposed system begins with placing a point source on a guidewire into the visceral arteries with a separate device that detects the point source prior to fenestration. The purpose of this study is to develop a prototype that can visualize visceral arteries in an *in vitro* test bench through stent-graft material (woven polyester fabric), a first step in realizing a medical device to perform *in situ* fenestration of stent-grafts.

## METHODS

*Summary:* The feasibility of the sensing device will be determined by its ability to detect an artery from white light imaging. The device consists of a bundle of fiber optic cables for transmitting light and a camera for real-time visualization of the light. A light-emitting diode (LED) connected to an Arduino (Arduino LLC, Boston, MA) is placed into the lumen of a visceral artery of a 3D printed aorta model. A 400 µm, 0.50 numerical aperture – Thorlabs (Thorlabs, Inc. Newton, New Jersey) fiber optic cable bundle was used to retrieve light waves from the visceral artery point source. Fiber optic cables consist

of slim strands of glass that are used to carry information in the form of light. For this experiment they are a means for carrying light a short distance for real-time visualization. A separate MATLAB (Mathworks, Inc. Natick, Massachusetts) script was used for visualization.

*Experimental Setup:* Two models of an aorta with visceral arteries was created using Solidworks (Dassault Systemés, Vélizy-Villacoublay, France) 3D printed using the Form 3 SLA printer (Formlabs, Inc. Somerville, MA) with grey and elastic resin. A 3D model was cut in half through its longitudinal axis in Solidworks to allow for visualization of the probe position while the second model remained intact (**Figure 1A**). A piece of a Zenith stent-graft was cut and placed onto the aorta model. A single LED was placed in the lumen of a visceral artery for emitting white light. The LED was connected to a potentiometer connected to the 5V power source from the Arduino. The experiment was conducted in the air with two different custom-designed and 3D printed probe tips with fiber optics bundles.

*Quantitative Fiber Optic Measurements:* A five fiber-bundle probe (**Figure 1C**) was used along with a custom printed circuit board (PCB) to retrieve analog sensor values emitted from a LED. The PCB had five photoresistors record the amount of light the fiber optic bundle transmitted. The data was recorded using a live data stream connected to MATLAB and the data was post-processed and visualized (**Figure 1B**).

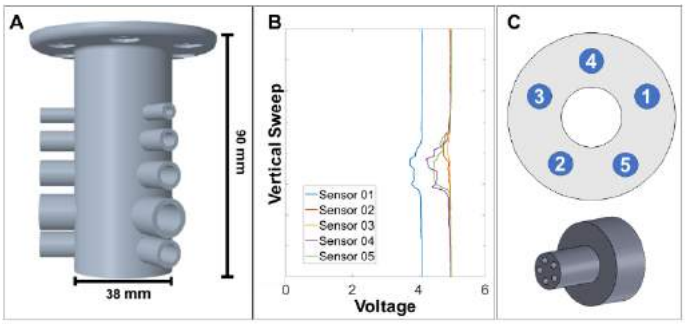


**Figure 1: A) 3D printed experimental test bench with a stent graft placed inside. B) Analog sensor values when the visceral artery was detected. C) Position of fiber optic wire corresponding to sensor values and the CAD rendering of the probe tip.**

*Fiber Optic Visualization:* A probe was designed to hold fourteen fiber optic cables on Autodesk Inventor (Autodesk, San Rafael, CA) and 3D printed. The fiber optic cables were arranged in two circular patterns, an inner and outer ring. The outer ring is 4.8 mm in diameter with 8 fiber optic cables. The inner ring is 2.5 mm in diameter with 6 fiber optic cables, for a total of 14 cables (**Figure 2C**). The cables were cut to 1.5 feet in length each and attached to a block with holes arranged in the same pattern as the probe. The half-cut test bench was used for this experiment to visualize the boundary of the visceral artery (**Figure 2A)**. The fiber optic probe was placed on the North, South, East, West, and center of the artery opening (**Figure 2B**). A video stream taken of fiber optic bundle end was converted to an 8-bit grayscale image ranging from 0 to 255. An image was created using 14 unique gray value points when detecting light. Finally, bicubic interpolation was performed on the 14 fiber bundle to resize the image in MATLAB for visualization (**Figure 2B**).

## RESULTS

Two experiments were successfully developed by designing and 3D printing test benches, probes, and a PCB to record data. The first experiment reported the voltage changes due to the detection of the orifice of a visceral artery where the point source was located. The voltage decrease (percent change) when an orifice was detected was 8.47 ± 2.55%. The results from the second experiment exhibited expected behavior. When the probe was placed on the center of each edge (NSWE), it was found that the fibers receiving light were brighter than when an individual fiber did not detect light.

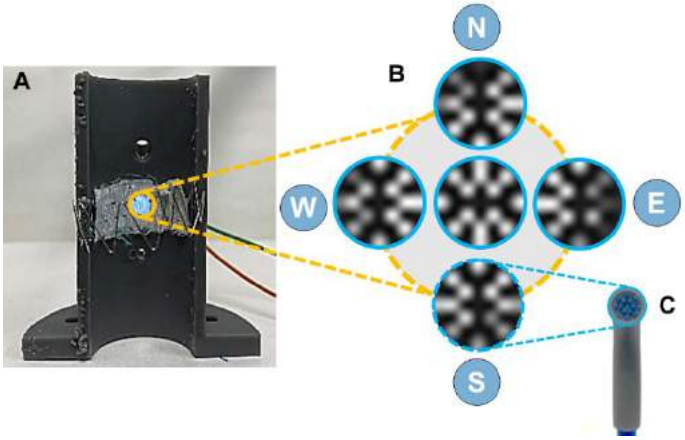


**Figure 2: A) Half-cut test bench with the stent-graft materials placed in front of the opening of the visceral artery. B) Visualization of the probe tip in the NSWE and center positions. C) probe tip with a 14-fiber bundle for visualization.**

## DISCUSSION

Several fiber-optic probes were constructed that had the ability to detect white light with either a photoresistor or a camera to visualize light intensity. Quantitative measurements of the voltage were achieved but did not have accurate spatial information of the probe tip in relation to the opening of the orifice. The half-cut test bench allowed for real-time visualization and accurate placement of the probe tip in several positions. Although the probe exhibited expected behavior, it is unclear whether the grayscale images are sufficient to detect the visceral artery when deployed. The ability to detect the edge of the visceral artery is an important step towards the development of *in situ* fabrication of stent-grafts. Future research and development will include testing the system in chelated sheep blood, testing the reliability of sensor-based measurements vs. camera visualization, and developing a puncturing mechanism to create fenestrations in the stent-graft material.

## ACKNOWLEDGEMENTS

We would like to thank the Michael G. Wells Pitch Competition hosted by the Innovation Institute at the University of Pittsburgh for funding for prototype development.

## REFERENCES

[1] Vorp, D., *J. Biomech*, 40(9), 1887-1902, 2007.
[2] Greenhalgh, RM., *THE LANCET*, 364(9437), 843-848, 2004.
[3] Katsargyris, A., et al. Eur J Vasc Endovasc Surg, vol. 60, no. 1, pp. 44-48, Jul 2020

SB³C2022
Summer Biomechanics, Bioengineering and Biotransport Conference
June 20-23, Eastern Shore, MD, USA

# PREDICTIVE MODELING OF CORONARY ARTERY OCCLUSION DURING TRANSCATHETER AORTIC VALVE REPLACEMENT

**Sri Krishna Sivakumar (1), Breandan Yeats (1), Atefeh Razavi (1), Ignacio A. Santos (2), Susan O'Neil (3), Scott Lilly (3), Pradeep Yadav (4), Venkateshwar Polsani (4), Vinod Thourani (5), Lakshmi Prasad Dasi (1)**

(1) Department of Biomedical Engineering, Georgia Institute of Technology, Atlanta, Georgia, USA
(2) Department of Cardiology, Valladolid University Clinical Hospital, Valladolid, Spain
(3) Department of Cardiology, The Ohio State University Wexner Medical Center, Columbus, Ohio, USA
(4) Department of Interventional Cardiology, Piedmont Heart Institute, Atlanta, Georgia, USA
(5) Department of Cardiovascular Surgery, Piedmont Heart Institute, Atlanta, Georgia, USA

## INTRODUCTION

Patients with severe aortic stenosis undergo aortic valve replacement (AVR) through surgical or transcatheter approaches to prevent heart failure. Transcatheter AVR has emerged as an alternative mode of AVR for patients deemed high risk to undergo surgical AVR based on age and comorbidities. Transcatheter devices and methods have progressed vastly over the last two decades, showing similar or better outcomes compared to surgical AVR. However, TAVR has its shortcomings as well, with adverse procedural outcomes such as coronary obstruction (1-3% of all cases), aortic root rupture (1-2%), paravalvular leak (20-40%) etc., being reported [1-2]. Understanding the biomechanics of TAVR is crucial to prediction and prevention of such events.

Coronary obstruction (CO) is a procedural complication of TAVR that has been observed in 0.7% of all TAVR cases, and up to 2.3% in valve-in-valve TAVR cases [3]. In the event of CO during TAVR, the failed aortic valve leaflets get displaced and obstruct one or both coronary arteries, thus occluding coronary perfusion, leading to myocardial infarction. Coronary obstruction is associated with a high 30-day mortality rate of 40-50%. Currently, pre-procedural computed tomography (CT) is the imaging modality used to make decisions on valve type, sizing and in the assessment of risk of adverse events. Based on a multicenter registry study, coronary artery height (h) and sinus of Valsalva diameter (SOVd) were derived to be predictors of coronary obstruction with cutoffs of h<12mm or SOVd < 30mm**.** However, given the severity of the complication, these predictors are insufficient in accurately identifying patients at high risk of CO, with reported sensitivity and specificity of only 78% and 66% respectively.

Therefore, the goal of this study is to use high-fidelity computational simulations to overcome the limitations posed by clinical guidelines based on cardiac imaging and develop a highly accurate patient specific predictive tool for coronary obstruction after TAVR.

## METHODS

Pre-procedural cardiac CT images of a patient cohort (n=50) deemed to be at risk of coronary obstruction based on clinical guidelines (h<12mm or SOVd <30mm) was collected retrospectively from multiple TAVR centers. Patient specific aortic root, valve leaflets and calcification were segmented and meshed in Materialise Mimics (Figure 1) (Leuven, Belgium). Geometries for both the balloon expandable Edwards SAPIEN and self-expanding Medtronic Evolut valves were created using Solidworks (Dassault Systems, Concord, MA, USA). Aortic root, leaflets and calcification were meshed with 4-node tetrahedral elements to retain patient specific features and the mesh density ranged from 100K-200K elements per model. Transcatheter heart valve (THV) stent models are meshed using 6-node hexahedral elements in Hypermesh maintaining 4 elements across the stent thickness (Altair, Powel, OH, USA). ABAQUS Explicit (Dassault Systems, USA) was chosen as the finite element solver for this work.

*Material modeling*

The SAPIEN stent was modeled using an elasto-plastic model with a Young's modulus of E = 193 GPa, $\sigma_{yield}$ (0.2%) = 340 MPa, $\sigma_u$ (48%) = 670 MPa and a Poisson's ratio, $\nu$ = 0.29 with a density of $\rho$ = 7760 kg/m$^3$ [4]. The Evolut valve stent was modeled using superelastic nitinol properties and the material model was employed in ABAQUS using a user defined subroutine [5]. The aortic root was modeled using a hyperelastic neo-Hookean material model with the strain energy function represented in equation (1).

$$\varphi = \frac{\mu}{2}(\bar{I}_1 - 3) + \frac{k}{2}(J-1)^2 \qquad (1)$$

$\bar{I}_1$ is the first invariant of the right Cauchy-Green tensor $\bar{C} = J^{-2/3}I_1$ where $J = detF$, $F$ being the deformation gradient tensor. $\mu$ represents the shear modulus in which 0.5 MPa was used and $k$ represents the bulk modulus in which 5 MPa was used to allow compressibility of the material [6].

*FE Simulations*

A quasi-static approach was adopted with a cone propping open the failed native valve leaflets to position the crimped THV in place prior to deployment. The balloon and crimped SAPIEN stent were positioned coaxially inside the aortic root and a fluid-cavity based approach was employed to inflate the balloon and deploy the stent. The Evolut stent was crimped and released inside the native valve by leveraging the shape-memory properties of nitinol. Scaled penalty contact was prescribed for the stent-balloon and stent-AV interactions.

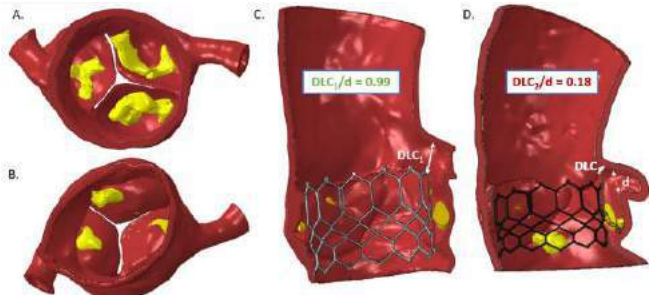


**Figure 1. Patient specific aortic root, leaflets, yellow calcific nodules in aortic and ventricular views (A, B). DLC/d measured in an unobstructed (C) and obstructed case (D).**

TAVR was virtually simulated in these patients based on the corresponding valve type and size received by the patient. The closest distance between the native aortic valve leaflet and the tip of the left coronary ostium is then measured (DLC) and the ratio of this distance to the diameter of the coronary artery (d) is considered as a representative measure of the fraction of occlusion [7] (Figure 1).

## RESULTS

Visualization of the final THV configuration after simulation of TAVR and the measurement of DLC and d was done through post-processing in ABAQUS. Out of the 50 patients in the study, 39 patients received a TAVR without CO and 11 patients underwent TAVR with CO. Mean values of the predictors of CO in the successful and unsuccessful cohorts is presented in Table 1.

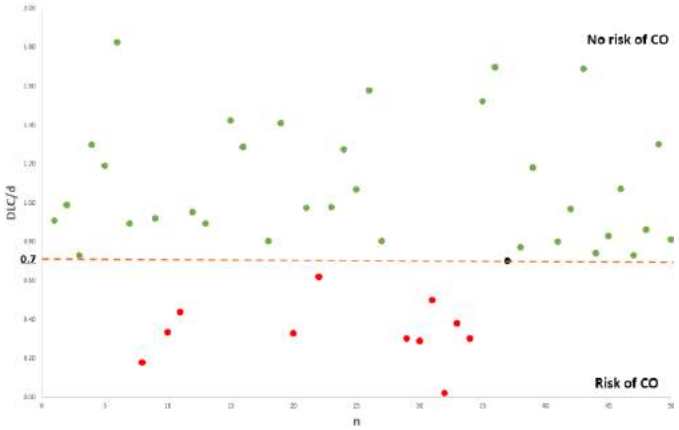


**Figure 2. Study population characterized by DLC/d to predict coronary artery obstruction. Green dots represent patients who successfully underwent TAVR without coronary obstruction, red dots represent patients who had CO after TAVR, and the black dot represents the 1 patient who underwent TAVR successfully but had DLC/d <= 0.7.**

A DLC/d cutoff of 0.7 predicted the occurrence of coronary obstruction accurately in 11/11 confirmed cases (100% sensitivity) and predicted no occurrence of CO accurately in 38/39 cases (97.8% specificity), improving significantly over current clinical guidelines (Figure 3). In comparison, coronary height (h) showed sensitivity and specificity of 72% and 41% respectively in the same cohort.

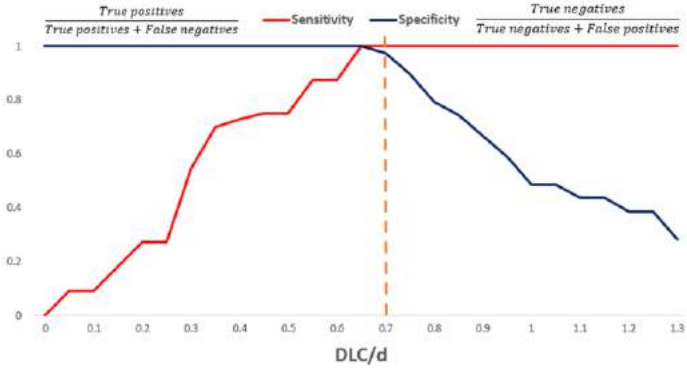


**Figure 3. Sensitivity & Specificity plots for the predictor DLC/d based on TAVR outcomes in 50 retrospective cases.**

**Table 1: Predictors of coronary obstruction in study population**

| Predictors | Successful (n=39) | Unsuccessful (n=11) |
|---|---|---|
| **DLC/d** | **1.23 ± 0.54** | **0.34 ± 0.15** |
| **Coronary height** | **11.33 ± 2.69mm** | **10.82 ± 2.17mm** |
| **Sinus diameter** | **30.09 ± 3.22mm** | **29.32 ± 3.61mm** |

## DISCUSSION

Coronary obstruction after TAVR, despite its low reported incidence, is a catastrophic complication that presents a very high mortality rate. Due to the fatal nature of coronary obstruction, candidacy for TAVR is often dependent on the risk of CO assessed in procedural planning. Therefore, a less sensitive/specific predictor can lead to low CO-risk patients not receiving TAVR and vice versa. In this study, DLC/d derived from computational modeling showed much better stratification between patients who successful and unsuccessful TAVR cases (Table 1) than h or SOVd. The complex interaction between the THV and the aortic root influences the final configuration of the THV as well as aortic valve leaflets, as demonstrated by the superior predictability shown by DLC/d. With TAVR expanded to all patients with AS, there is a need for accurate patient selection to prevent adverse events while improving TAVR accessibility. Computational patient specific modeling of TAVR can lead to better patient selection through accurate assessment of risk of fatal complications such as CO.


## ACKNOWLEDGEMENTS

We would like to thank Dr. Gerdisch from Franciscan Health and our collaborators at Mount Carmel Health System for providing us with deidentified patient data used in this study.


## REFERENCES


[1] Pasic, M et. al., *JACC: Cardio Interv*, 8:1-9, 2015.
[2] Genereux, P., et. al., *JACC*, 61:1125-1136, 2013.
[3] Ribeiro, H.B., et.al., *JACC*, 62: 1552-62, 2013.
[4] Tzamtzis, S., et al., *Med. Eng Phy*, 35: 125-130, 2013.
[5] Auricchio, F, Taylor R.L., *Comp Meth Appl Mech Eng*., 143:175-194, 1997.
[6]Bosmans, B., et al., *J Biomech*, 49: 2824-2830, 2016.
[7] Heitkemper, M et.al., *JTCVS*, 159: 829-838, 2020.

SB³C2022
Summer Biomechanics, Bioengineering and Biotransport Conference
June 20-23, Eastern Shore, MD, USA

# REGIONAL DIFFERENCES IN PERIVASCULAR ADIPOSE TISSUE FOLLOWING ANGIOTENSIN II-INDUCED HYPERTENSION

**Yujun Xu (1), J. Caleb Snider (1), Niyousha Karbasion (1), Matthew R. Bersi (1)**

(1) Department of Mechanical Engineering and Materials Science
Washington University in St. Louis
St. Louis, Missouri, USA

## INTRODUCTION

Hypertension, also known as high blood pressure, is a prevalent condition that is associated with many adverse cardiovascular events such as stroke, aneurysm, and end-organ damage. Along these lines, the renin-angiotensin-aldosterone system (RAAS) is an important mediator of hypertensive arterial remodeling, as shown by the ability of angiotensin-II (AngII) to modulate renal function and peripheral resistance while promoting excessive vascular inflammation, which leads to the development and persistence of chronic hypertension [1].

Previous work using an AngII infusion mouse model of hypertension has revealed the existence of spatio-temporal relationships between mechano- and immune-mediated aortic remodeling [2]. Namely, in response to an early increase in blood pressure and mechanical loading of the aortic wall, the thoracic aorta experienced excessive fibrotic remodeling and structural stiffening while the abdominal aorta experienced less remodeling and minimal adventitial fibrosis. Additionally, the amount of remodeling in each region was found to correlate with the extent of immune cell expression in the adventitia and perivascular space [3].

Though geometric and anatomical differences may contribute to the regional variations in hypertensive remodeling between the thoracic and abdominal aorta, there are also variations in the structure and function of perivascular adipose tissue (PVAT) depots along the length of the aorta. Given that PVAT is known to secrete cytokines that regulate vascular contractility, signaling, and inflammation [4], and can be activated by external mechanical stimulation [5], we hypothesize that regional PVAT may contribute to the observed differences in hypertensive vascular remodeling. Using a combination of histology, gene expression, and co-culture analysis, the current study is focused on the mechanobiology of regional PVAT. Our findings reveal that thoracic PVAT (tPVAT) and abdominal PVAT (aPVAT) respond differently to AngII-induced hypertension and that thoracic PVAT secretes factors that lead to changes in fibroblast phenotype *in vitro*.

## METHODS

**Animal Models.** Male wild-type C57BL/6J mice were housed in standard conditions with food (normal chow) and water available *ad libitum*. At ~8 weeks of age, animals received either saline or AngII (490 ng/kg/min) delivered via subcutaneous mini-osmotic pumps (Alzet) for a period of two weeks. Following AngII infusion, mice from each group were euthanized and the descending thoracic aorta (DTA) and infrarenal abdominal aorta (IAA) were isolated with PVAT in-place [6]. For studies on regional PVAT, tissues were separated from the DTA or IAA prior to storage in -80°C for further experimentation.

**Histological Analysis.** Vascular tissues containing PVAT were fixed in formalin overnight at 4°C prior to embedding, freezing, and sectioning at a thickness of 8 μm. Sections were washed with phosphate-buffered saline (PBS) for at least 10 min prior to staining with Oil Red O solution (ORO; Abcam) overnight at room temperature to label adipocytes. PVAT area was quantified from brightfield images of ORO-stained sections using a custom image-processing algorithm (Matlab). For all quantification, a minimum of three sections per sample with a total of five biological replicates per group were analyzed.

**RNA Extraction and Analysis.** Total RNA was extracted from isolated thoracic PVAT and abdominal PVAT using the Qiagen RNeasy mini kit. RNA quantity and purity was measured using a Nanodrop spectrophotometer (ThermoScientific). cDNA synthesis and real-time quantitative PCR (qPCR) were performed using SuperScript IV VILO Master Mix. Expression of genes related to PVAT phenotype (*Ucp1*, *Lep*) and immune cell activity (*Ccl2*, *Mmp2*) were measured.

**Fibroblast-PVAT Co-culture.** To assess the impact of PVAT on fibroblast phenotype, we performed a co-culture of thoracic PVAT and 3T3 fibroblasts in a 0.4 μm pore 24-well transwell setup (Costar). Fibroblasts were seeded ($0.05\times10^6$ cells/well) one day prior to placement of 5 mg of thoracic PVAT in the insert. For a subset of groups, 1mM AngII was added to the media to isolate the effect PVAT

and AngII on the observed phenotypic changes. Together, this resulted in four experimental groups – 3T3, 3T3+PVAT, 3T3+AngII, and 3T3+PVAT+AngII. All cells were cultured at 37°C and 5% $CO_2$ in DMEM supplemented with 10% FBS and 1% penicillin/streptomycin antibiotic. Experiments were performed in triplicate.

**Immunofluorescence Analysis.** Following 48 hours of co-culture, cells were fixed at room temperature in 4% paraformaldehyde and 0.1% Triton X-100 for 10 min prior to staining with a conjugated antibody to α-smooth muscle actin (1:200; Sigma-Aldrich). Staining intensity was quantified for each group using a custom image analysis code (Matlab).

**Statistical Analysis.** Data are presented as means ± SEM. Normally distributed groups were compared with a Student's *t* test and a value of $p < 0.05$ was considered statistically significant. All data points are mean values of at least two technical replicates.

## RESULTS

Given that adipose tissue – and in particular PVAT – has been shown to alter its structure and cellular composition in response to obesity and hypertension [7], we first wanted to confirm if tPVAT and aPVAT are responsive to AngII infusion. Indeed, after two weeks of AngII-induced hypertension we observed an increase in PVAT area in each region. While the increase in aPVAT was not statistically significant, we found that tPVAT increased by ~20% relative to saline control ($p < 0.05$; **Fig.1**). The increase in PVAT area, as shown by ORO positive staining, is consistent with adipocyte proliferation and suggests a hypertension-driven remodeling. Notably, the changes in aortic PVAT are consistent with prior observations of excessive vascular remodeling in the thoracic aorta but not in the abdominal aorta suggesting PVAT may play a role in regional hypertensive vascular remodeling.

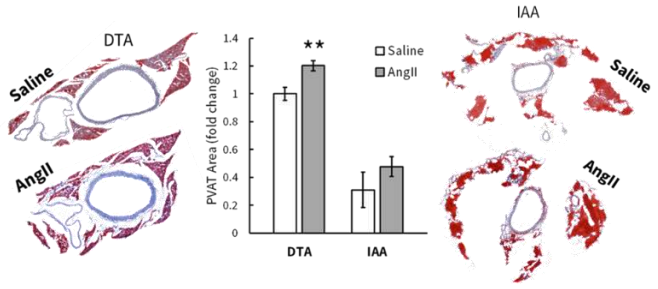


**Figure 1: PVAT is significantly increased around the DTA (tPVAT) and marginally increased around the IAA (aPVAT) after AngII infusion. Red indicates adipocytes labeled by ORO stain.**

Based on the differences in PVAT remodeling, we next investigated the transcriptional differences between tPVAT and aPVAT in response to AngII-induced hypertension. Using canonical genetic markers of fat phenotype, we observed high expression of the brown fat marker *Ucp1* in tPVAT as measured by qPCR ($p < 0.01$, **Fig.2A**), whereas aPVAT had higher expression of leptin (*Lep;* $p < 0.05$, **Fig.2A**) a marker of white fat phenotype. Such phenotypic differences in PVAT may suggest the potential for disparate responses to systemic hypertension. Indeed, gene expression of *Ccl2* – a general marker of immune regulation and inflammatory processes – was increased in tPVAT ($p < 0.01$, **Fig.2B**) and expression of the matrix enzyme *Mmp2* was increased in aPVAT ($p < 0.01$, **Fig.2B**). Together, this suggests a higher immune cell recruitment to tPVAT and increased extracellular matrix turnover in aPVAT, both of which may contribute to the observed levels of vascular remodeling and fibrosis.

Based on the altered transcription between regional PVAT depots, and our observations of regional vascular remodeling, we next hypothesized that tPVAT may alter the phenotype of fibroblasts to promote fibrotic remodeling. To investigate the impact of PVAT on

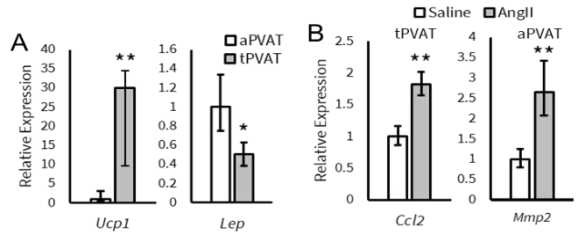


**Figure 2: Gene expression analysis of regional PVAT depots reveals differences in fat phenotype and response to AngII.**

fibroblast phenotype, we performed a co-culture of 3T3 fibroblasts with multiple combinations of PVAT and AngII treatments *in vitro*. Quantification of alpha-smooth muscle actin (αSMA) immunostaining revealed increased staining intensity in cells cultured with PVAT (**Fig.3**). PVAT-treated cells also showed apparent changes in cell morphology (**Fig.3**). Using αSMA as a proxy for a myofibroblast phenotype, this suggests tPVAT can alter fibroblast phenotypes *in vitro* and may promote fibrotic remodeling *in vivo*.

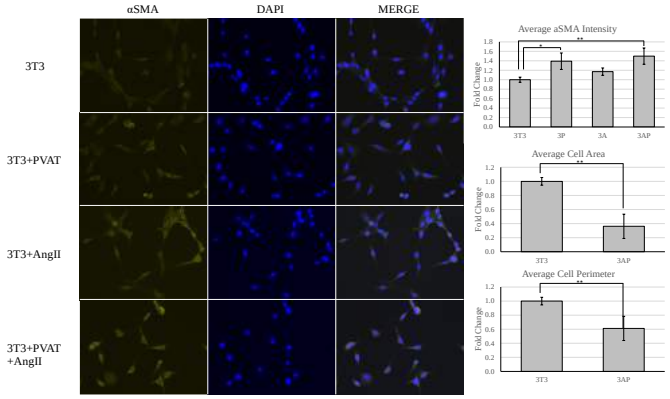


**Figure 3: PVAT-treated cells have an altered shape and increased expression of the contractile protein αSMA, relative to control.**

## DISCUSSION

In this study, we demonstrate that at a tissue, protein, and transcriptional level, aortic PVAT responds differently to hypertension depending on its anatomical location. The regional variations in PVAT phenotype and gene expression, combined with our observations of PVAT area change, suggest a potential relationship to our previously reported regional variations in vascular remodeling. Indeed, higher expression of immune cell recruitment genes and area change in tPVAT is consistent with marked wall thickening and adventitial fibrosis of the DTA in response to AngII-induced hypertension [3]. Our co-culture studies suggest PVAT can alter fibroblast phenotype indirectly. Future work will focus on PVAT secreted factors and specific immune cell populations (macrophages or T cells) as drivers of vascular remodeling. Altogether, this study identifies regional differences in aortic PVAT and highlights the potential of PVAT to regulate vascular remodeling via immune cell recruitment and effector adipokine secretion.


## ACKNOWLEDGEMENTS

This work was supported, in part, by NIH grant R00 HL146951 to MRB


## REFERENCES


[1] Benigni A, et al. *EMBO Mol Med*, *2*(7), 247–257 (2010). [2] Bersi MR, et al. *Hypertens* **67**, 890–896 (2016). [3] Bersi MR, et al. *J R Soc: Interface* 14: 20170327 (2017). [4] Horimatsu T, et al. *Front Phys*, 8, 969 (2017). [5] Hu H, et al. *Antiox & Redox Signal*, *34*(9), 736–749. (2021). [6] Ye M, et al. *Cell Mol Life Sc.* **76,** 777–789 (2019). [7] Guzik TJ, et al. *Cardiovasc Res.* **113,** 1009-102 (2017).

# BIOMECHANICAL ANALYSIS OF LOCAL MURAL DEFECTS IN ANGIOTENSIN-II-INDUCED THORACIC AORTOPATHIES

**Dar Weiss (1), Aaron S. Long (1), George Tellides (2,3), Stéphane Avril (4), Jay D. Humphrey (1,3), Matthew R. Bersi (5)**

(1) Department of Biomedical Engineering
Yale University
New Haven, Connecticut, USA

(2) Department of Surgery
Yale School of Medicine
New Haven, Connecticut, USA

(3) Vascular Biology and Therapeutics Program
Yale School of Medicine
New Haven, Connecticut, USA

(4) Mines Saint-□tienne, Université de Lyon,
INSERM, U105□ SainBioSE,
F-42023 Saint-□tienne, France

(5) Department of Mechanical Engineering and Materials Science
Washington University in St. Louis
St. Louis, Missouri, USA

## INTRODUCTION

Thoracic aortic aneurysms and dissections (TAADs) are vascular pathologies responsible for significant morbidity and mortality. While there is a complex network of cellular, molecular, and genetic factors that render the aorta susceptible to TAAD formation, it is ultimately biomechanical factors – such as blood pressure, wall stress, and wall strength – that lead to material and structural failures of the aortic wall [1]. Thus, a better understanding of evolving aortic vulnerability and the biomechanical mechanisms that promote dissection and rupture is needed to develop viable therapeutic strategies for TAAD management.

The ongoing discovery of genetic mutations that predispose the aorta to lesion formation has led to the development of models for TAAD in the mouse. Studies in these models have revealed critical insights into the underlying molecular mechanisms, cell pathobiology, and tissue-level changes in microstructure associated with TAAD [2]. In addition to genetic approaches, previous work has shown that chronic infusion of the pro-inflammatory vasoconstrictor angiotensin-II (AngII) can similarly promote the formation of local mural defects in the ascending thoracic aorta (ATA) of the mouse [3]. Using this approach, the current study seeks to measure the local biomechanical properties of AngII-treated thoracic aortic samples with a specific focus on quantifying the behavior of regions with measurable mural defects.

Herein, we combine a sophisticated ex vivo mechanical testing pipeline – biaxial biomechanical testing (for identification of axial loads), panoramic digital image correlation (pDIC; for identification of surface deformation), and optical coherence tomography (OCT; for identification of wall thickness) – with quantitative histological image analysis [4]. This allowed us to develop spatial correlations between the evolving local microstructural composition, mural defects, and mechanical properties of the ATA over the duration of AngII infusion.

## METHODS

**Animal models.** Hypertension was induced in male, apolipoprotein-E null (*ApoE*$^{-/-}$) mice by Ang II infusion (1000 ng/kg/min) via subcutaneous mini-osmotic pump for up to 28 days. A subset of mice were euthanized at weekly experimental time points of 0, 7, 14, 21, or 28 days of infusion, and the ascending thoracic (ATA) was gently excised and prepared for mechanical testing and analysis.

**Biomechanical phenotyping.** Isolated ATA segments were cleaned of excess perivascular tissues and sutures were placed around the left carotid artery, left subclavian artery, and distal aortic arch to allow for pressurization. Samples were cannulated at each end through the aortic root and the brachiocephalic artery and were placed in a custom computer-controlled extension-inflation biaxial mechanical testing system [5]. Following preconditioning, the *in vivo* axial stretch was estimated based on the axial force-pressure relationship and multiple cyclic pressurization and axial extension protocols about the *in vivo* axial stretch were used to characterize the material response.

**Optical coherence tomography imaging.** Following biomechanical phenotyping, samples were recannulated onto a custom needle composite and high-resolution OCT images (ThorLabs, Inc.) were acquired at a series of fixed pressure and axial stretch values. This not only provides a measurement of the wall thickness profile over the entire ATA [4], but it also enables the identification local mural defects that would otherwise only be detectable using destructive methods.

**Panoramic digital image correlation.** Following OCT imaging, a random speckle pattern of black and white India ink was applied to the outer adventitial surface of the ATA. Speckled samples were then mounted in the center of a concave conical mirror and subjected to the same series of fixed pressure and axial stretch values. Using optics-

based techniques – such as digital image correlation, direct linear transformation, and ray tracing – a discrete grid of points defining the ATA surface was defined, tracked through all deformed configurations, and reconstructed in 3D [6]. Calibration of the conical mirror as well as the pDIC image processing and analysis was performed in Matlab.

**Material property estimation.** A finite element mesh of the ATA (FEBio) was generated from OCT images and displacement boundary conditions on the outer adventitial surface were imposed based on the measured pDIC deformation. The ATA surface was subdivided into 1000 patches and material properties were identified using an inverse analysis based on the principal of virtual power [7]. Using the virtual fields method, and an appropriate hyperelastic constitutive model, material parameters were iteratively identified for each surface patch.

**Histological analysis.** Following the multi-step testing, vessels were fixed overnight in a 10% neutral buffered formalin and stored in 70% ethanol at 4°C prior to paraffin embedding, sectioning, and staining with Movat's pentachrome for proteins of interest (elastin, collagen, etc.). Custom image analysis was developed to isolate constituents based on colorimetric analysis and subdivide images into evenly spaced circumferential segments for spatial correlation with material properties [4]. Localization of histological images was determined based on registration to the OCT dataset using a normalized thickness profile.

## RESULTS

Chronic infusion of AngII resulted in adventitial fibrosis, thickening, and aneurysmal dilatation of the ATA. A *k*-means clustering analysis of the 17 samples included in the current study resulted in the classification of three groups based on diameter: no dilatation (n=3), modest dilatation (n=7), and marked dilatation (n=7) (**Fig.1A**). Identification of mural defects in OCT images revealed some degree of mural degeneration in each AngII-treated sample (**Fig.1B**) and showed that mural defect area tended to increase linearly with the degree of dilatation (**Fig.1C**). This suggests that the energy release associated with elastin fragmentation and mural damage may contribute to aneurysmal dilatation.

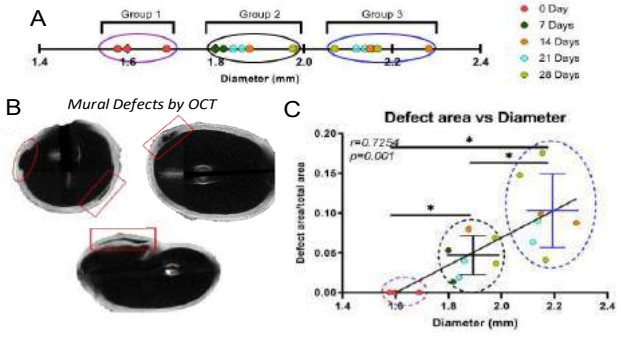


**Figure 1: (A) ATA samples was clustered into three groups and (B) OCT images were used to identify mural defects which were (C) linearly related to the extent of aneurysmal dilatation.**

By combining OCT and pDIC data for each sample, we were able to investigate biomechanical differences between the regions of the ATA that did or did not present with mural defects (**Fig.2A**). While there was substantial sample-to-sample variation in the magnitude of the identified material properties – i.e., stored energy and material stiffness – within each classification group, several trends emerged. Namely, defect regions tended to have reduced stored energy (**Fig.2B**) and increased circumferential material stiffness compared to non-defect regions. These trends held within each ATA sample as well as at a population level across all samples within each classification group.

Finally, spatial correlations between the identified full-field material properties and quantitative histological analysis (**Fig.2C**) revealed

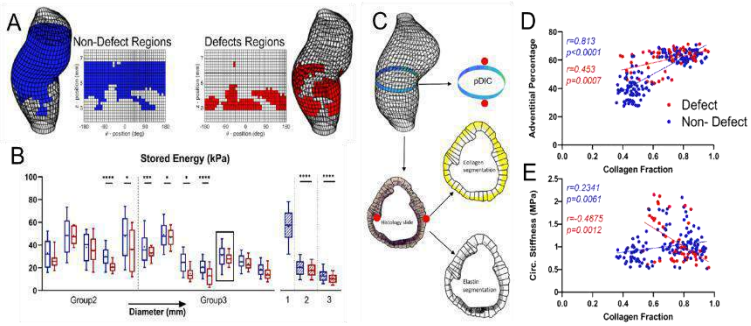


**Figure 2: (A) Spatial maps of defect vs. non-defect regions derived from OCT images allow for (B) biomechanical assessment of mural defects. (C) Spatial correlations with quantitative histological image analysis reveals (D) local collagen content and (E) relationships between collagen and material stiffness in areas with and without mural defects.**

several interesting local structure-function relationships. As mural defects were often associated with medial damage and elastin fragmentation, regions associated with mural defects tended to have higher collagen content and adventitial percentage (**Fig.2D**). Additionally, while non-defect regions showed a nearly constant relationship between circumferential stiffness and collagen content, defect regions appeared to have a negative correlation between stiffness and collagen (**Fig.2E**). Similarly, defect regions had little elastin – and thereby stored energy – compared to non-defect regions. Independent of defect or non-defect region, there was a nearly linear relationship between elastin and stored energy, consistent with the notion that elastin is responsible for providing the elastic recoil associated with diastole.

## DISCUSSION

Using a multi-step experimental biomechanical testing pipeline, we show for the first time that the local mechanical properties of defect regions found in AngII-treated thoracic aortic samples are distinct from non-defect regions in the mouse. While the extent of mural defects are linearly related to aneurysmal dilation of the ATA, they typically present as regions of marked medial damage and elastin fragmentation following AngII infusion. The excessive medial damage is spatially correlated with low levels of elastin area fraction and elastically stored energy. Conversely, defect areas are highly collagenous but tend to have a negative correlation with material stiffness. This suggests that collagen orientation and integrity are critically important aspects of maintaining native tissue stiffness of the ATA, even in extreme cases of remodeling as seen with instances of mural degeneration associated with TAAD [8]. Together, the results from this study indicate that 1) TAAD is a geometrically and materially complex vascular pathology and 2) local collagen reinforcement may be a viable therapeutic option for the management of TAAD and aneurysmal dilatation.


## ACKNOWLEDGEMENTS

This work was supported, in part, by NIH grants P01 HL134605, U01 HL142518, and R01 HL146723.


## REFERENCES


[1] Koullias G, et al., *J Thorac Cardiovasc Surg*, 130:677.e1-e9, 2005. [2] Pinard A, et al., *Circ Res*, 124:588-606, 2019. [3] Rateri DL, et al., *American J Path*. 184(9):2586-2595, 2014. [4] Bersi MR, et al., *Biomech Model Mechanobiol*, 18(1):203-218, 2018. [5] Gleason RL, et al., *J Biomech Eng*, 126(6):787, 2004. [6] Genovese K, et al. *Exp Mech*, 61(9):1455–1472, 2021. [7] Bersi MR, et al., *J Biomech Eng*, 138(July):1-15, 2016. [8] Iliopoulos DC, et al., *J Thorac Cardiovasc Surg*, 137:101-109, 2009.

# INFANT SKULL FRACTURE PATTERN CHARACTERISTICS FROM LOW-HEIGHT FALLS

**Yousef Alsanea (1), Tagrid Ruiz-Maldonado (2), Brittany Coats (1)**

(1) Mechanical Engineering, University of Utah, Salt Lake City, Utah, USA
(2) Pediatrics, University of Utah, Salt Lake City, UT, USA

## INTRODUCTION

Approximately 686,000 children are victims of abuse and neglect every year. The highest percentage are children between birth and 1 year of age, and are more likely to experience a recurrence of maltreatment if the abuse is not identified. Accidental falls are the leading cause of non-fatal injury in infants and the most common explanation given by caretakers suspected of abuse. Thus, distinguishing a truthful history of a fall from a false one proves to be a difficult but important task for a clinician.

Skull fracture is a common finding for both accidental falls and abusive injuries, and may provide insight into head impact direction and impact energy. Unique fracture patterns, such as biparietal fractures, may be even more distinctive in their application and provide better insight into the validity of the provided history. The objectives of this study were (1) to determine how child age, fall height, impact surface, and impact location influence skull fracture patterns in infants, and (2) to gain insight into the mechanism and locations of occipital impact that lead to biparietal fracture in infants.

## METHODS

All studies were approved by the University of Utah and Primary Children's Hospital IRB. Infants <12 months of age with skull fracture from a low height fall between 2014-2019 and associated 3D CT reconstruction were retrospectively reviewed. 201 subjects with well-characterized falls, suitable imaging for analysis, and no significant concern for inflicted injury, as determined by a child abuse pediatrics team, were selected for this study. A semi-automated MATLAB routine was created to segment fractures and quantify the Euclidean distance between fracture endpoints (**Fig. 1**), the true line length, and the nonlinearity (true length divided by Euclidean distance). In cases with multiple fractures, each fracture was evaluated individually. The nonlinearity was averaged and true length summed across all the fractures. Fractures spanning multiple bones were excluded from this analysis and will be evaluated at a later date.

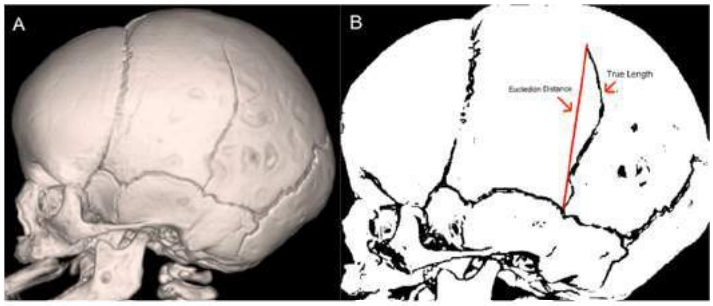


**Figure 1: (A) 3D CT reconstruction of infant skull fracture. (B) segmentation of fracture and calculation of length and linearity**

In each subject, the mechanism of the fall (e.g., fall from bed, drop from arms), impact surface, bone fracture location (parietal, occipital, frontal), and fall height were collected. Fall heights were estimated by 3 independent reviewers based on the mechanism of fall and medical record history. A least squares linear regression was used to evaluate the effect of child age, impact surface, bone fracture location, and fall height on fracture nonlinearity and length.

In the data set, 12 infants had biparietal fracture, 10 that were not aligned across the sagittal suture. Of these fractures, 3 had evidence of soft tissue swelling (all located on the occiput). A parametric finite element analysis was performed to identify the mechanism and occipital location by which biparietal fracture could occur.

Using an infant skull finite element model developed and validated by Coats et al. (2007), and later further validated by Hajiaghamemar et al. (2018), we simulated 1.45m falls onto a rigid surface with 13 different impact locations on the occipital bone (**Fig. 2**). The locations were selected based on the regions of soft tissue swelling identified from the medical history and were arranged symmetrically about the

ossification center of the occipital. The geometry of the model was based off CT images of a 1.5-month-old infant. Therefore, the skull had non-uniform thickness and was asymmetric about the midsagittal plane. The presence of fracture was defined by a stress threshold of 25 MPa across an approximately 10x10 mm localized region of elements (Coats et al. 2007; Hajiaghamemar et al. 2018).

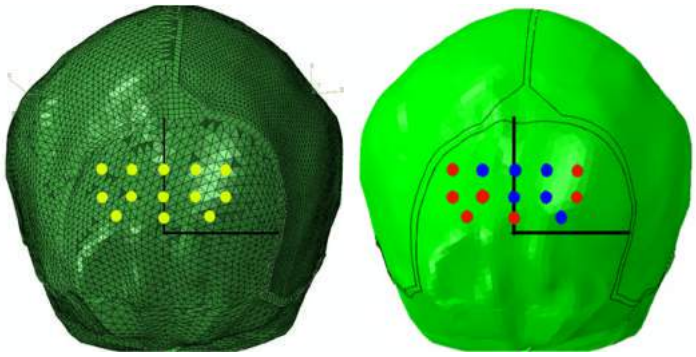

**Figure 2: Thirteen occipital impact locations were selected for the biparietal parametric study. Six of those locations (blue in right image) resulted in biparietal fracture**

## RESULTS

Fall heights averaged 1.0m, with 122 (60.7%) falls between 0.3-0.9 m, and 78 (38.8%) between 0.9 and 1.8 m. Least squares regression revealed a significant increase in fracture nonlinearity with younger infants ($p<0.001$) and with impacts to the frontal or occipital bones ($p=0.032$). Fracture length significantly decreased with increasing age of the child ($p=0.028$), lower fall heights ($p=0.035$), and with impacts to the frontal and occipital bones ($p=0.016$). Increasing nonlinearity with increasing height was also seen (**Fig. 3**), but was only significant in parietal fractures of older infants ($p=0.038$).

Out of the 13 points, 6 points predicted biparietal fractures based on the 25 MPa threshold. Due to the asymmetry of the skull and the non-uniform skull thickness, these points were not symmetric around the ossification center. Points further away from the vertical ossification center axis predicted fracture only on one parietal bone. Points that were near the horizontal axis and below did not predict biparietal fracture. The asymmetry resulted in an asymmetric stress distribution (**Fig. 4**).

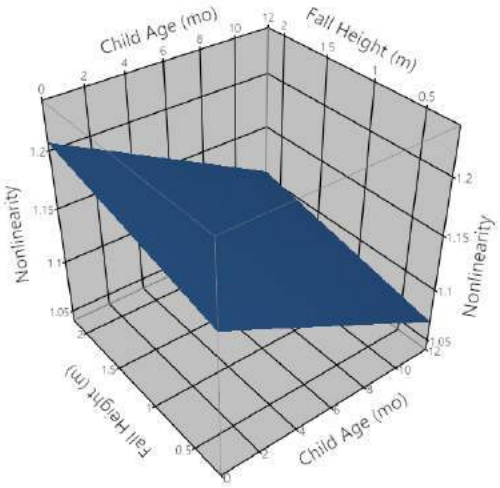


**Figure 3: Surface plot illustrating the linear relationship between child age (mo), fall height (m), and nonlinearity**

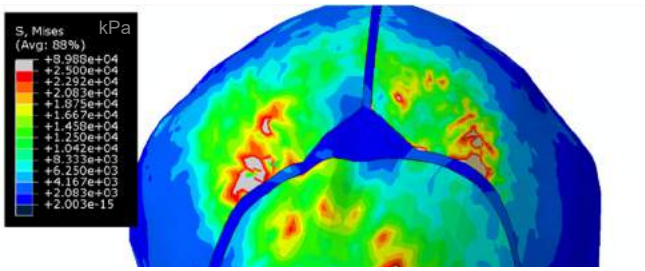


**Figure 4: Stress contour plot of impact to the top of the occiput in the middle**

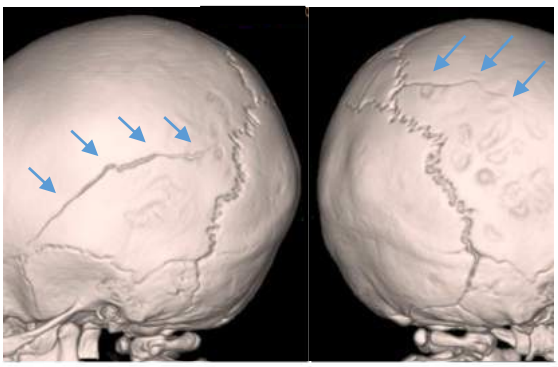

**Figure 5. Asymmetric length of biparietal fracture (arrows) in 7-month old infant**

## DISCUSSION

Fracture characteristics in this large dataset confirm previous computational simulations by our group that fracture length and nonlinearity increase with fall height (He et al.). However, the present study found that younger infants had approximately 10% more nonlinearity compared to older infants. Infant skull is highly transversely anisotropic and begins to become more isotropic with age. The increased anisotropy may contribute to the increased nonlinearity. Frontal and occipital bones exhibited decreased fracture length and nonlinearity, likely due to the greater curvature and thicker structure compared to parietal bones.

We predicted the presence of biparietal fracture in several of our impact locations, particularly those closer to the vertex of the skull and laterally located around the ossification center. The parietal stress was not caused by direct impact to the plate, but was rather due to contact with the occipital bone. The asymmetry of the skull and variability in the skull thickness resulted in asymmetric stress distribution which resulted in one bone having a larger stress field than the other. This would result in a larger fracture on one side, a common finding in the clinical data set (**Fig. 5**). These data highlight the contribution of anatomical variability in skull fracture patterns. Future work will evaluate the effect of skull thickness variability on skull fracture predictions and investigate more complicated fracture patterns.


## ACKNOWLEDGEMENTS

This research was supported by 2016-DN-BX-0160 and 2020-75-CX-0014 provided by the National Institute of Justice. The opinions, findings, and conclusions are those of the authors and do not necessarily reflect those of the Department of Justice.


## REFERENCES


[1] Coats B. et al. *Stapp Car Crash J.* 51:1-15, 2007
[2] Hajiaghamemar M et al. *Int J Leg Med* 133:1-16, 2018
[3] He J. et al. Biomech Model Mechanobiol, 19:1595-1605, 2020

# AN ITERATIVE APPROACH TO ASSIGN TUMOR-SPECIFIC FLOW BOUNDARY CONDITIONS FOR LIVER CANCER USING MULTI-MODAL IMAGE ANALYSIS

**S. Andrews (1), P. Trivedi (2), D. Mukherjee (3)**

(1) Paul M. Randy Mechanical Engineering, University of Colorado Boulder, Boulder, CO, USA
(2) Department of Radiology, University of Colorado Anschutz Medical Campus, Denver, CO, USA

## INTRODUCTION

In 2020, liver cancer was the sixth most common form of cancer, and the third leading cause of cancer-related mortality [1]. Transarterial embolization (TARE), a prominent treatment for unresectable hepatic tumors, utilizes a guided microcatheter to deliver radioactive particles intra arterially to a tumor. Undesirable clinical outcomes of TARE, which may be fatal [2,3], can be attributed to unwanted particle delivery to healthy tissue via the hepatic arterial network. Angiogenesis stimulated by tumor growth ultimately alters local flow dynamics, pulling more blood into the tumor, lending to the efficacy of embolization treatments. Flow dynamics are also altered at the site of drug administration and may influence final drug distributions [4]. However, flow information under pathological conditions and during TARE are poorly characterized *in vivo*. Pretreatment planning relies on surrogate tracer particles to predict drug distribution, but these particles differ morphologically and in size compared to treatment particles, limiting pretreatment accuracy [5]. Computational methods offer a more accurate and less invasive approach to dosimetry and treatment planning, but few models have incorporated pathologic and patient-specific flow information in their distribution predictions. Here, we devise a multi-modal imaging-based framework for determining tumor specific flow conditions that can be used to create high resolution *in silico* models for tumor embolization therapy.

## METHODS

**Image based vascular modeling:** Computed tomography angiography (CTA) images were used to create a 3D patient-specific model of the descending aorta and hepatic arteries, using planar 2D segmentation technique as employed in SimVascular (Fig. 1A) [6]. The tumor and its surrounding vessels were located by intersecting the 3D vascular model with CTA images, and cross referencing with cone beam CT imaging of the hepatic tumor vasculature.

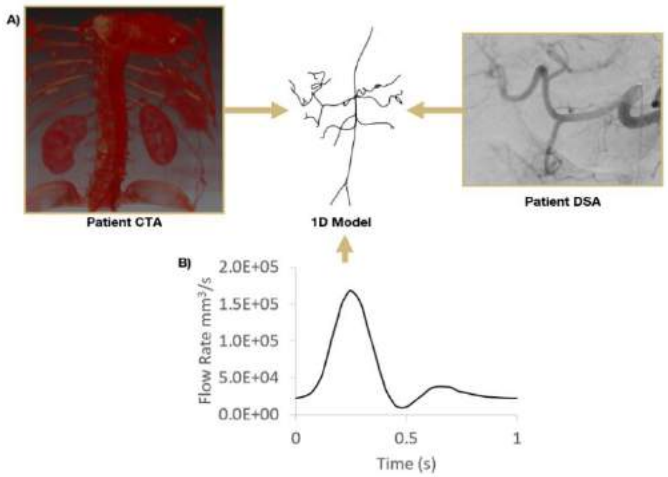


**Figure 1: (A) Patient specific 1D model creation from CTA imaging data, with implementation of DSA based outlet conditions. (B) Aortic inlet flow waveform used as an inlet boundary condition.**

**Image-based quantification of tumor's influence on flow:** Arteries feeding the tumor were located on pretreatment mapping digital subtraction angiography (DSA) images, by aligning the DSA images with a combination of cone beam CT images and patient CTA scans. Contrast intensities from DSA scans were used to quantify preferential flow into the tumor. An affine registration technique was used to stabilize the DSA image stack, and account for patient breathing and movement during the DSA acquisition. Vessels injected with contrast agent were segmented to record contrast intensity over time for key sections of the hepatic arterial network (Fig. 2). The raw intensity values were normalized with respect to the cross-sectional area of the

respective vessels. The ratio of flow rates through the tumor-feeding artery and healthy artery was estimated in terms of the time averaged contrast intensity ratio for these same vessels. This ratio served as a target flow rate ratio for tuning a tumor-specific boundary condition.

**Tuning of resistance boundary conditions:** A numerical framework to tune the boundary conditions was devised using the DSA target flow ratio and a reduced order 1D vascular model as implemented in SimVascular (see 1D model, Fig. 1A). A pulsatile waveform (Fig. 1B) was prescribed at the aorta inlet. The tuning started with baseline vascular resistance values prescribed at the vessel outlets, which were estimated as:

$$R_v\, i = i\frac{MAP}{Q_v} \quad (1)$$

where MAP is the mean arterial pressure (derived from literature [7]), and Qv is the flow rate through the respective vessel outlet. The flow rate was assumed to proportional to the cross-sectional area of the vessel outlet

$$Q_v\, i = ikA_v \quad (2)$$

where the proportionality constant, k, was derived from the time averaged flow ratio of the inlet waveform (Fig. 1B) and the sum of the outlet areas. For subsequent iterations of the tuning algorithm, the resistance of the tumor-feeding vessel was iteratively lowered by increments of 0.01 g/mm$^4$s, and subsequent ratio of flow rates through the tumor-feeding and healthy vessels were compared to the target DSA-derived flow ratio. The segments analyzed in the 1D simulation were taken from corresponding visual portions of the DSA, before either vessel bifurcates (Fig. 2). This process was repeated until the flow distribution ratio from the 1D simulation matched the DSA-derived ratio.

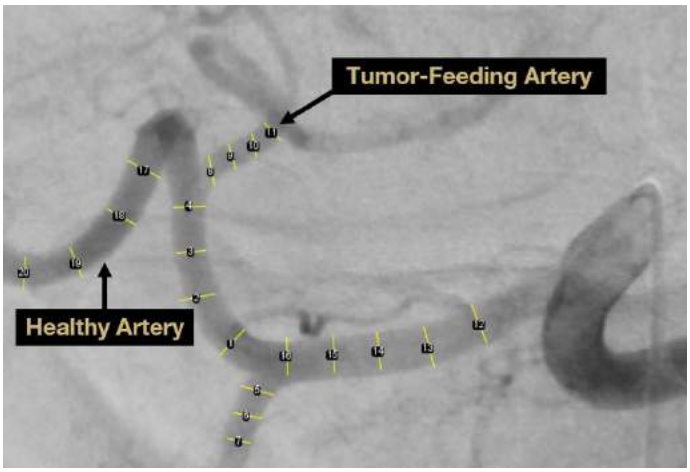


**Figure 2: DSA image of the common hepatic artery (segments 1-4), right hepatic artery (segments 17-20), and left hepatic artery (segments 8-11).**

## RESULTS

The DSA intensity values from the stabilized image processing workflow over time are shown in Figure 3. The normalized intensity values in the tumor-feeding artery (time averaged, μ = 0.98) were greater than the intensity values of the non-tumor artery (μ = 0.64). The tumor to non-tumor intensity ratio is 1.54, which was subsequently used as the target flow ratio to demonstrate the efficacy of proposed approach. The baseline resistance value calculated for the tumor-feeding vessel was 18.96 g/mm$^4$s. Using our tuning framework, the tumor resistance was lowered to a value of 2.78 g/mm$^4$s; for which the computed flow rate ratio between the tumor-feeding artery and healthy artery matched the target DSA ratio. Two sets of reduced order simulations of the entire arterial network leading into the tumor were conducted. One assumed baseline boundary condition values, the other assumed tuned boundary condition values. The resulting flowrates into the tumor-feeding and healthy vessels are presented in Figure 4.

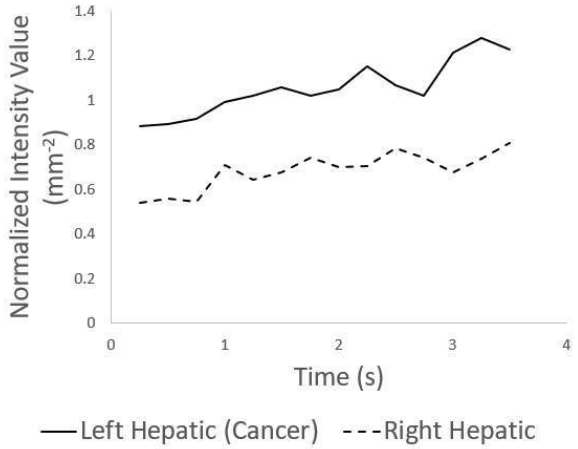


**Figure 3: Vessel intensities normalized to cross-sectional area versus time. DSA scans were captured at 4 frames per second.**

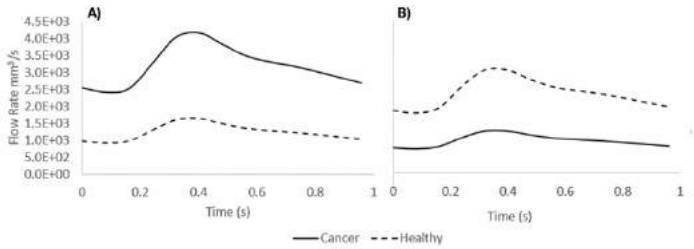


**Figure 4: Comparison of flow rates at outlets of vessels feeding the tumor and healthy tissue for (A) tuned boundary conditions and (B) baseline boundary conditions.**

## DISCUSSION

Here we have presented a systematic numerical approach to incorporate the preferential flow into the tumor into tumor-specific boundary condition for *in silico* modeling of the hepatic arterial network for liver cancer cases. Our approach integrates the multiple modalities of imaging (CTA, cone beam CT, DSA) that are standard-of-care in liver cancer embolization therapy. This enables precise characterization of *in vivo* flow conditions in *in silico* models. We did not consider catheter effects on contrast flow rates in the DSA images, which could potentially alter flow rates. Additionally, this methodology assumes that contrast intensity is a direct quantification of flow rate, but future work can explore a more mathematical relationship between contrast diffusion in the bloodstream and flow.

## REFERENCES

[1] Cancer today. *http://gco.iarc.fr/today/home,* 2020.
[2] Sangro, B et al., *Cancer*, 112(7):1538–1546, 2008.
[3] Leung, TW et al., *Int J Radiat Oncol Biol Phys*, 33(4)919–924, 1995.
[4] Braat, A et al., *J Nucl Med*, 56(7):1079-1087, 2015.
[5] Garin, Y et al., *Eur J Nucl Med Mol Imaging*, 43:559-575, 2016.
[6] SimVascular. *http://simvascular.github.io/*, 2020.
[7] Steele BN et al., *Comput. Methods Biomech. Biomed Engin.*, 10(1):39-51, 2007.

# ELUCIDATING THE IMPACT OF PLASMONIC NANOPARTICLE SHAPE ON INFECTIOUS VIRUS DIAGNOSIS

**Y. Liu (1), H. Ye (1), T. Zhang (1), Q. Cai (1) H. Huynh (2), J. Kahn (2), Z. Qin (1, 3, 4, 5)**

(1) Department of Mechanical Engineering, University of Texas at Dallas, Richardson, Texas 75080, U.S.
(2) Department of Pediatrics & Microbiology, University of Texas Southwestern Medical Center, Dallas, TX 753□0, U.S.
(3) Department of Bioengineering, University of Texas at Dallas, Richardson, Texas 75080, U.S.
(4) Center for Advanced Pain Studies, University of Texas at Dallas, Richardson, Texas 75080, U.S.
(5) Department of Surgery, University of Texas Southwestern Medical Center, Dallas, Texas 753□0, U.S.

## INTRODUCTION

Respiratory infectious viruses have burdened millions of people as evidenced by the ongoing COVID-19 pandemic. Simple and sensitive detection of pathogens is critical to screen potential patients and combat infectious diseases spread. Homogeneous immunoassays have simple operation and generate analyte-specific signals without the need of immobilization, separation, and washing, and thus are promising for point-of-care (POC) diagnostics. With unique localized surface plasmonic resonance (LSPR) and coupling properties, gold nanoparticles (AuNPs) have been widely used in homogeneous assays.[1] Upon identifying analytes, they can form aggregates and change color, resulting from the interparticle distance change. Despite the visual recognition and rapid readouts, conventional AuNPs-based homogeneous assays suffer from the low sensitivity as confined by the weak optical response of the AuNPs.[2] As a result, they oftentimes are inadequate to be a standalone diagnostic tool. Previous efforts in enhancing the assay sensitivity focused on the strategies including coupling with dynamic light scattering and metallic enhancement.[3] The requirements of instrumentations and addition operation add complexity to the homogeneous assays. Therefore, it remains an unmet and urgent need for improving the detection performance of AuNP-based homogeneous assay.

Driven by this need, we systematically investigated the effect of AuNP shape on the homogeneous immunoassay with the goal to substantially improve the detection sensitivity. Particularly, antibody-conjugated gold nanosphere (AuNSs), nanorods (AuNRs), and nanourchins (AuNUs) were prepared for the evaluation (**Figure 1**). Using respiratory syncytial viruses (RSV), we demonstrated that AuNUs have the lowest detection limit compared to that of AuNSs and AuNRs. Our simulation based on the boundary element method revealed that the Au urchins have the most significant change in the extinction cross-section upon plasmonic coupling, resulting in more sensitive detection.

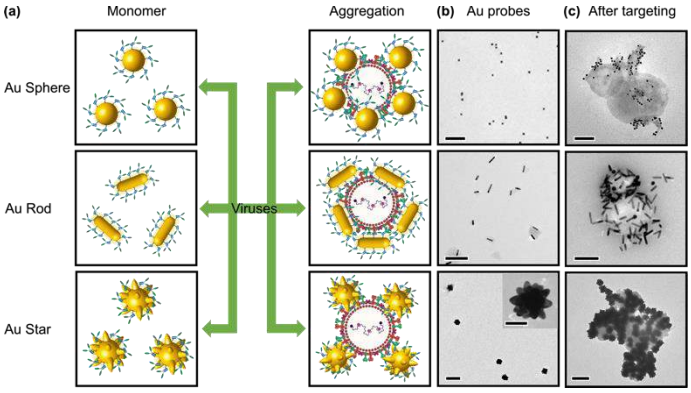


**Figure 1: Concept of the plasmonic coupling assay for diagnosis of infectious viruses.** (a) Antibody-conjugated AuNP probes with different morphologies aggregated on virus' surface due to specific antigen recognition. (b-c) TEM images confirmed the binding of AuNP probes on RSV. Scale bar =200 nm. Inset scale bar = 50 nm.

## METHODS

*RSV detection by AuNPs probes.* Antibody functionalized AuNP probes were prepared and incubated with RSV and other close relative respiratory viruses (e.g., influenza type A virus (IAV), human metapneumovirus viruses (hMPV), and parainfluenza viruses (PIV)) as controls in a volume ratio of 2:1. The extinction of the assay solutions was monitored after 30 minutes.

*BEM simulation of plasmonic coupling properties of AuNPs-based sensors.* Three models of AuNPs (i.e., AuNSs, AuNRs, and AuNUs) were embedded in water as surrounding dielectric environment. The dielectric functions of gold used in the simulations were obtained from Johnson and Christy.[4] All simulations were conducted via the MNPBEM toolbox in MATLAB (version 2021b).[5]

## RESULTS

We first analyzed the extinction spectra monitored for RSV detection using AuNSs, AuNRs, and AuNUs as probes, respectively (**Figure 2a-c**). Obviously, the extinction peak of the measured solution has decreased intensity with increasing RSV concentrations. To quantify the detection results, a ratiometric method was used. Taking AuNSs as an example, we generated the calibration curve by plotting the extinction intensity ($I_{ext}$) ratio of 700 nm to 532 nm against the viral titers (**Figure 2d**). A linear relationship ($R^2$ = 0.98) was observed in the range of 10,000-200,000 PFU/mL (**Figure 2d inset**). The limit of detection (LOD) was determined to be 8,000 PFU/mL by calculating the concentration corresponding to a signal that is 3 times the standard deviation above the blank control calibrator. Same applied to other AuNPs-based sensors (**Figure 2e** for AuNRs and **Figure 2f** for AuNUs). The linear detection range was determined to be 10,000-100,000 PFU/mL and 2,500-50,000 PFU/mL for AuNRs and AuNUs, respectively. Their corresponding LOD was then calculated to be 4,360 PFU/mL and 1,402 PFU/mL, which was about 1.8 and 5.7-times lower than that of AuNSs, respectively. Apparently, AuNUs probes provide the most sensitive detection for RSV.

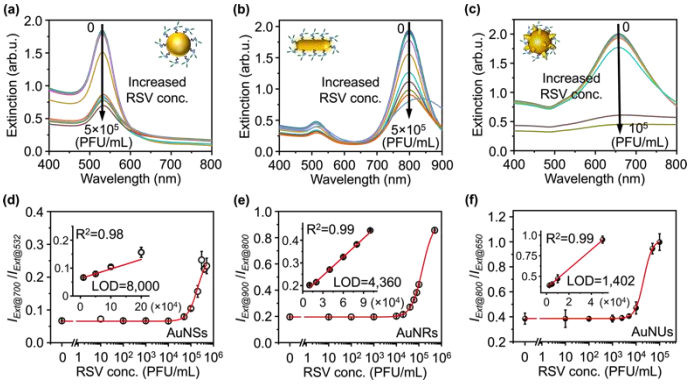


**Figure 2. Plasmonic coupling assay for diagnosis of RSV.** Spectra measurements (a-c) and ratiometric quantification (d-f) for colorimetric detection using AuNSs (a, d), AuNRs (b, e), and AuNUs (c, f).

Next, we performed computational modeling and simulation and aimed to provide optical insights in the plasmonic coupling effect. We applied boundary element method due to its ability to provide simple and fast simulation for AuNPs with complex geometries. As colorimetric assays essentially measure the extinction change of the AuNPs-based probes upon aggregating on the target, we calculated the extinction cross-section area as an index to present the plasmonic activities for all AuNPs of different shapes. For simplicity, we only calculated the plasmonic coupling strength between two coupled AuNPs. We built three sets of models of two identical AuNPs with varied interparticle distance ($d$ = 1-10 nm, **Figure 3a, b, c**). Using a single AuNP as a reference, we calculated the change of extinction cross-section area ($\Delta Ext_{@SPR}$) and peak shift ($\Delta\lambda$). **Figure 3d, e** show the $\Delta Ext_{@SPR}$ and $\Delta\lambda$ of two coupled AuNSs with different sizes. Basically, decreasing the interparticle distance leads to the increase of the extinction cross-section area and a red shift in the plasmonic peak, regardless of the particle size. Nevertheless, larger particle shows higher $\Delta Ext_{@SPR}$ and $\Delta\lambda$. Notably, for d > 5 nm, the $\Delta Ext_{@SPR}$ becomes close for 50 nm and 100 nm AuNSs. This suggests that further increasing AuNP size does not necessarily improve the plasmonic coupling, hence the assay performance. While for AuNRs, two representative coupling models (i.e., side-to-side, STS, and edge-to-edge, ETE) were considered for the simulation. **Figure 3f, g** show $\Delta Ext_{@SPR}$ and peak shift of the coupled rods against that of a single particle. Notably, both STS and ETE modes of two closely coupled AuNRs ($d$ = 0) induce the blue shift of the peaks as compared to a single AuNR. While ETE mode initially develops an increase in $\Delta Ext_{@SPR}$, STS mode shows a decrease on the contrary. Further increasing the $d$ (>1 nm) leads to the increase of $\Delta Ext_{@SPR}$ and peak shift for STS and decrease of $\Delta Ext_{@SPR}$ and peak shift for ETE. Attractively, ETE mode holds higher $\Delta Ext_{@SPR}$ values than the STS mode, regardless of the coupling gap. Lastly, we constructed the model for Au urchins, where the tip number ($n$ = 14), tip length ($L$ = 20 nm), and core size ($D$ = 50 nm) based on the TEM imaging. **Figure 3h, i** show the $\Delta Ext_{@SPR}$ and $\Delta\lambda$ against the $d$, where we found that the interparticle distance barely affects the peak shift but is of great importance for $\Delta Ext_{@SPR}$ in two coupled Au urchins. Under experimental conditions, the interparticle distance is typically larger than 10 nm due to surface conjugation with antibodies (e.g., the size of antibodies ~10 nm).[6] When setting $d$ at 10 nm, AuNUs dimer possesses the highest value of $\Delta Ext_{@SPR}$ among three simulated cases, which is consistent with the best detection sensitivity in the experimental section.

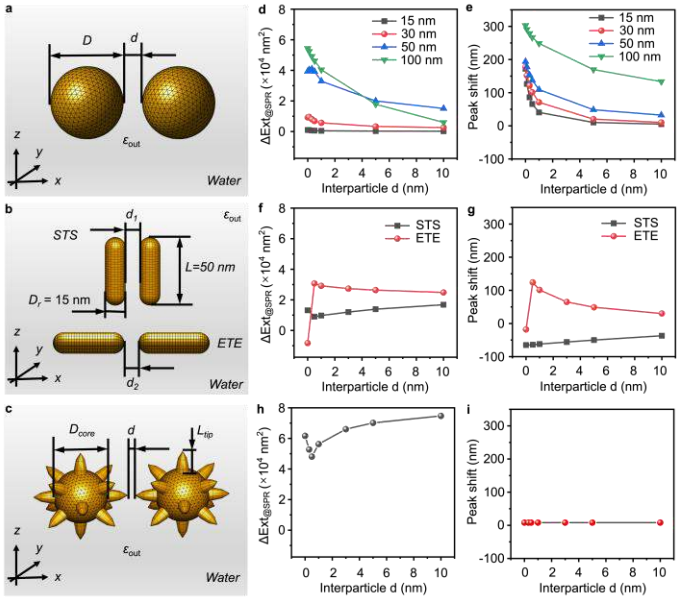


**Figure 3. BEM simulation of plasmonic coupling properties for Au nanosensors with different shapes.** Models built for two coupled AuNSs (a), AuNRs (b), and AuNUs (c). The simulated $\Delta Ext_{@SPR}$ and peak shift as a function of interparticle distance for coupled AuNSs (d, e), AuNRs (f, g), and AuNUs (h, i).

## DISCUSSION

In summary, we have systematically studied the impacts of particle shape on the detection sensitivity of AuNP-based homogeneous immunoassay. Our experimental results suggest Au nanourchins achieve a detection limit of 1,402 PFU/mL for RSV and provide the most sensitive detection compared with nanorods and nanospheres. With BEM simulation, we found that Au urchins have the largest extinction cross-section area change that contribute to the sensitivity enhancement over the other counterparts. Our study advances our understanding of nanoparticle design for rapid pathogen detection.


## ACKNOWLEDGEMENTS

Research reported in this manuscript was partially supported by National Institutes of Health (NIH) grants R21AI140462 and R01AI151374, and CDMRP grant PR192581.


## Reference:


[1] Godakhindi, V.S., et al. *ACS Sens*. **2017**, *2*, 1627-1636.
[2] Xie, X., et al. *Acc. Chem. Res*. **2012**, 45, 1511-1520.
[3] Huiqiao, L., et al., *Theranostics*. **2016**, 6, 54-64.
[4] Johnson, P. B., et al. *Physical Review B*. **1972**, 6, 4370-4379.
[5] Hohenester, U., et al. *Comput. Phys. Commun.* **2012**, 183, 370-381.
[6] Shaw, A., et al. *Nat. Nanotechnol*. **2019**, 14, 184-190.

SB³C2022
Summer Biomechanics, Bioengineering and Biotransport Conference
June 20-23, Eastern Shore, MD, USA

# MYOSIN AND MYOFIBRIL DYNAMICS DRIVE HYPERTROPHIC CARDIOMYOPATHY DISEASE MECHANISMS

**Alison S. Vander Roest (1), Kathleen M. Ruppel (2), James A. Spudich (2), Beth L. Pruitt (3), Daniel Bernstein (1)**

(1) Pediatrics (Cardiology), Stanford University School of Medicine, Stanford, CA, USA
(2) Biochemistry, Stanford University, Stanford, CA, USA
(3) Mechanical Engineering, University of California Santa Barbara, Santa Barbara, CA, USA

## INTRODUCTION

Heart disease is the leading cause of death in the developed world and is often characterized by changing contractile mechanics and subsequent cellular remodeling. Hypertrophic cardiomyopathy (HCM) is the most common inherited form of heart disease and is the leading cause of sudden cardiac death in young adults. This condition is characterized by hypercontractility and cardiomyocyte hypertrophy that can obstruct the outflow tract and contribute to heart failure [1].

Approximately one third of known HCM mutations are found in beta-cardiac myosin, the motor protein responsible for contraction in human ventricles. Given the known hypercontractile phenotype of HCM in patients, our biochemical studies have investigated how these mutations alter kinetic rates of myosin function and myosin regulation. Ensemble measurements of myosin interactions with actin as well as single molecule measurements of myosin binding events have revealed a surprising heterogeneity of effects of different myosin mutations (some mutations increase while others decrease or cause no change to rates of myosin activity – Table 1)[2-5]. The ability of myosin to form a super-relaxed state (SRX) associated with folded conformation is important for energy conservation, and is also disrupted by many HCM mutations, including the pediatric mutations P710R and H251N [4,5].

New therapies targeting these properties of myosin regulation and function are currently in clinical trials to assess how changes observed in vitro in molecular assays translate to the more complex in vivo context of the heart. Mavacamten was originally discovered for its inhibitory effect on ATPase rates, but has been shown to alter SRX% and is effective in reducing symptoms, hypercontractility, and hypertrophy in patients with obstructive cardiomyopathy [6]. Omecamtiv Mercabil (OM) is a myosin activator that can potently affect myosin function and muscle contractility in vitro, but its effects in patients experiencing heart failure were less clear [1]. Understanding how these drug and other related compounds affect contraction and cellular responses could accelerate the development of new therapies for cardiac patients. When the effects of mutations and drugs have been well defined, they can be incorporated into computational models that link measurements across scales and predict outcomes and targets.

Studying the impact of specific mutations in primary cardiomyocytes is challenging (especially for rare mutations associated with pediatric onset HCM). Human induced pluripotent stem cell derived cardiomyocytes (hiPSC-CMs) provide a powerful platform for investigating the particular effects of heterozygous mutations in human cells. While these cells are immature compared to adult cardiomyocytes, the use of patterning and engineered environments can improve the functional maturity of these cells and allow for measurement of force production and intracellular organization with various perturbations [7].

## METHODS

We have previously assessed the effects of HCM mutations and myosin targeting therapeutics on myosin function using purified recombinant human β-cardiac myosin protein constructs. The load-dependent detachment rates ($k_{det}$) and step size of wild type and mutant myosin molecules were measured in a dual-beam optical trap using the harmonic force spectroscopy (HFS)[2,5]. Motility measurements and actin-activated ATPase assays of WT, H251N, and P710R assess the motor function of active myosin [3-5]. Additional ATPase assays and single turnover experiments were used to compare the activity of WT and mutant versions of two-headed human ß-cardiac myosin constructs to assess the percentage of myosin in an SRX state [4-5].

To assess the impact of these mutations in living cells, heterozygous mutations (P710R and H251N) were introduced using Crispr/Cas9 gene editing in hiPSCs generated from healthy patients, and these healthy lines were used as isogenic controls. We have previously reported an increase in traction force generation, and cell size, and myofibril disruption in cells with the P710R mutation [5], and treated these cells with mavacamten for 3 weeks to determine its affect on cell hypertrophy. The H251N mutation was edited onto a healthy

SB³C2022-479

background line with a GFP-tagged alpha actinin protein to allow for live cell tracking of cardiac differentiation, cell size, and sarcomeric contraction. These cells were differentiated into cardiomyocytes following established protocols manipulating beta catenin signaling and grown for 30 to 60 days [5]. Some H251N cells were replated onto patterned substrates at day 30 and the remainder replated onto unpatterned coverslips at day 60 and fixed and stained for cardiac troponin after 48 hours. H251N cells plated on patterned glass were imaged before, immediately after and 24 hours after treatment with 300 nM OM, and patterns of sarcomere lengths during contraction was visualized with Kymograph plots generated in ImageJ. We then quantified cell spread area and beta myosin expression.

We have also modified a computational model to incorporate exponential force sensitive detachment rate and fit cellular traction force measurements from representative control and P710R cells. We assessed the sensitivity of predicted force to different muscle properties, and have made preliminary predictions of the expected force generation of cells with the H251N mutation or OM.

## RESULTS

Molecular measurements have revealed a surprising heterogeneity of effects on ATPase rate, unloaded motility, SRX%, basal detachment rate ($k_0$) and the exponential force sensitivity term of the detachment rate ($\delta$) caused by mutations, mavacamten and OM (Table 1).

**Table 1: Molecular measurements of the biomechanics of myosin with HCM mutations and myosin targeting therapeutics.**

| Mutation/ drug | Vel. | $k_{cat}$ | $k_0$ | $\delta$ | Step size | SRX % |
|---|---|---|---|---|---|---|
| **P710R** | -60% | -40% | -15% | -60% | -60% | -50% |
| **H251N** | +40% | +30% | +50% | +10% | +20% | -45% |
| **Mava** | -50% | -50% | ? | ? | ? | +90% |
| **OM** | -80% | -80% | -80% | -85% | -90% | ? |

Our multiscale assessment of the P710R mutation in cells revealed a significant increase in cell traction force generation, in addition to changes in myofibril organization and cell size [5]. Incorporation of measured myosin parameters into a computational model enabled fitting the cell force and predicting the individual effects of the measured changes to myosin function as well as the predicted range in forces that moderate changes in cross bridge density would cause (Figure 1). Our analysis confirmed the significance of the SRX state as a therapeutic target for this mutation and the importance of myofibril organization.


**Figure 1: Model incorporates myosin metrics to predict force.**

The presence of a GFP-tagged alpha actinin in the H251N cells and their isogenic controls enabled live assessment of the sarcomere contraction dynamics in spontaneously beating cells (Figure 2). Initial sarcomere kymographs showed more coordinated motion and more distinct diastolic rest periods in Control cells compared to H251N. Immediately after the addition of OM, both cell types experienced longer duration contractions with no clear relaxed phase and showed evidence of overextension of sarcomeres at sporadic points along the myofibril, especially in the H251N cells. After 24 hours, the magnitude of sarcomere displacements were significantly reduced in both cells, and we observed some evidence of myofibril remodeling and confirmed beta myosin expression via immunostaining.

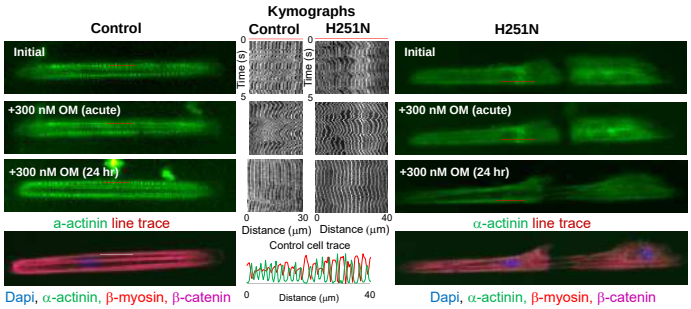


**Figure 2: Analysis of sarcomere structure and contraction in patterned hiPSC-CMs before and after treatment with OM**

Treatment with a moderate dose of mavacamten (0.3 uM) reduced cell area of P710R cells to the level of Control cells. In contrast to cells with the P710R mutation, cells with the H251N mutation had significantly lower baseline cell spread area at day 62, but both patterned and unpatterned H251N cells treated with OM for 24 hours were not significantly different from control cells (Figure 3).

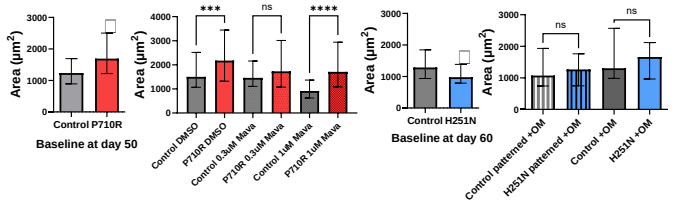


**Figure 3: Median cell spread area varies with different mutations, mavacamten and OM treatment.**

## DISCUSSION

These results confirm the surprising heterogeneity in phenotypes caused by HCM mutations in myosin across scale and highlights the benefits of an integrated, multiscale approach to assess myosin biomechanics and mechanobiology. Analysis of the sensitivity of predicted force generation to model parameters highlighted the importance of both the SRX state and the density of crossbridges, which can be affected by myofibril density and structure. Analysis of myofibril and sarcomere dynamics in control and H251N cells before and after perturbing their homeostasis with OM treatment revealed differences in myofibril structure exacerbated by acutely increased force that may contribute to the myofibril disarray and adverse remodeling which occurs in HCM. Future experiments will determine if inhibiting myosin activity with mavacamten in the H251N cells rescues sarcomeric organization and cell spreading. The ability to predict how different mutations and therapeutics affect contractile function and cellular hypertrophy could provide important clinical insights for personalized medicine and treatment plans, especially for pediatric patients.


## ACKNOWLEDGEMENTS

We gratefully acknowledge funding from the NIH (K99HL153679 to AVR, and 1RM1GM131981), AHA (AHA20POST35211011), and Stanford MCHRI and CVI.


## REFERENCES


[1] Nag S et al., eLife 2021;10:e63703
[2] Liu C et. al., *Nat Struct Mol Biol* **25**, 505-514, 2018.
[3] Adhikari AS et al., *Cell Rep* **17**, 2857-2864, 2016.
[4] Adhikari AS et al., *Nat Commun* **10**, 2685, 2019.
[5] Vander Roest AS et al., *PNAS*, 118 (24) e2025030118, 2021.
[6] Sabieri S et al., *Circulation* 2021;143:606-8.
[7] Ribiero A et al., PNAS **112**, 12705-12710 (2015).

# EVALUATION OF A CARRAGEENAN–BASED HYDROGEL CONFINEMENT APPROACH TO INCREASE COLLAGEN DEPOSITION FOR IN VITRO TISSUE DEVELOPMENT

**Joseph Krebs (1), Alyssa Brown (1), Samuel Stealey (1), Silviya P. Zustiak (1,2), Natasha Case (1)**

(1) Biomedical Engineering Program, School of Engineering, Saint Louis University, St. Louis, MO, USA
(2) Department of Physiology and Pharmacology, School of Medicine, Saint Louis University, St. Louis, MO, USA

## INTRODUCTION

Tissue models grown from cell monolayers can be used for screening of pharmacologic agents, for evaluation of stem cell differentiation potential, and for wound healing and regenerative medicine scenarios including skin, subcutaneous connective tissue, adipose tissue, and periosteum [1]. Connective tissues in the body contain fibrillar collagen. However, achieving an abundant, collagen-rich extracellular matrix (ECM) during *in vitro* culture is challenging, due in part to insufficient assembly and retention of fibrillar collagen.

In comparing the physiological extracellular space where tissues grow in the body to the *in vitro* culture environment, one critical difference is the lack of biological macromolecules within the *in vitro* environment. Macromolecules are a ubiquitous component of all fluid compartments within the body, with some macromolecules moving freely in solution and others present within an interconnected, insoluble, hydrophilic network permeated by the aqueous solvent. These macromolecules, through repulsive interactions, reduce the volume of solvent within which transport, interactions, and reactions of solutes can occur [2]. The effects of macromolecules to influence solute transport and reactions in fluid media through excluded volume effects are generally described by the biophysical concepts of macromolecular crowding and confinement. Crowding applies to fluid environments where macromolecules freely moving in solution are present at a high total volume fraction, while confinement applies to fluid environments in which structural obstacles to solute transport exist [2].

Macromolecular crowding has been shown to enhance the processing of type I procollagen, leading to significant increases in fibrillar collagen assembly and accumulation during *in vitro* culture of a variety of cell types [3]. The confinement approach, while more difficult to implement within the *in vitro* culture environment, has the advantage of avoiding any interactions with the growing tissue layer. Additionally, the "confined" environment can be more easily controlled than the "crowded" environment, since the confinement approach is based upon a macromolecular barrier rather than macromolecules in solution. Limited evidence suggests that a confinement approach can be used to improve *in vitro* collagen deposition [4]. In this study, we developed a carrageenan-based hydrogel confinement approach, evaluated the effectiveness of this approach to increase collagen accumulation by the human MG-63 bone cell line, and characterized the stability of the carrageenan hydrogel in the culture system. Additionally, computational modeling of oxygen transport within the confinement culture model was performed to complement the experimental results.

## METHODS

A modified culture system was developed for the hydrogel confinement approach. A polyethylene washer (2.4 mm thickness) was affixed to the base of a 6-well tissue culture plate, and cells were seeded on the surface inside the washer. The MG-63 bone cell line was used as an immature human osteoblast model to evaluate confinement effects on type I collagen deposition. A sterilized and presoaked CR gel (thickness range of 2 – 3 mm) was placed on top of the washer to provide a confinement barrier, and a medium layer was added above the gel (1.2 mm thickness). For preparation of the CR gels, a kappa-CR or kappa/lambda-CR solution (5% w/v) was prepared with stirring at 100 °C until homogeneous. The solution was cast into layers, with individual gels punched from the layers. Gels were replaced every two days along with replacement of the culture medium. After 7 days in medium containing ascorbic acid-2-phosphate -/+ a CR gel, MG-63 cultures were enzymatically digested and evaluated for hydroxyproline and DNA content, which were used as indirect measures of deposited collagen and cell number, respectively.

To directly measure CR hydrogel degradation, a release experiment was performed. Hydrogels (50 µL) were incubated in 4 mL of PBS/37ºC on a rocking platform. At specified time points, 500 µL of release buffer was collected and replaced with fresh PBS. CR released from hydrogels was quantified by measuring absorbance at 500 nm. Hydrogel mechanical properties were also measured using a rheometer

on CR slabs (1 x 20 mm) following incubation in PBS/37 ºC for 1, 2, or 3 days. Storage modulus, *G'*, and loss modulus, *G"*, were measured as a function of angular frequency from 1 – 10 rad/s. To evaluate whether material released from the CR hydrogels influenced cell viability, MG-63 cultures were incubated in medium that had been in contact with CR gels for 2 days, and a resazurin assay was used to indirectly assess cell viability of the cultures after 48 hours of exposure to the medium.

To determine if hydrogel degradation could influence diffusivity of solutes in the culture medium above the cell layer, fluorescence correlation spectroscopy (FCS) was performed utilizing RNase A fluorescently labeled with Atto 655-NHS ester. Buffer samples were taken from CR hydrogels incubated in PBS/37 ºC for 1, 2, or 3 days. FCS samples were prepared (1 µg/mL final protein concentration in hydrogel releasate or PBS) and loaded (40 µL) into capped perfusion chamber gaskets adhered to #1.5 coverslip for measurements (180 s; 640 nm ps pulsed laser; ~11.4 µW optical power; n≥6 per sample). An autocorrelation function was determined for each measurement and normalized to the initial time point. The effective tracer diffusion coefficient for RNase A in each solution was then calculated.

A computational model of steady-state axial transport of oxygen within the culture model for Fickian diffusion of a dilute species was developed (COMSOL, V5.6). A constant concentration boundary of 0.185 mol/m$^3$ of oxygen was applied to the upper medium surface based upon exchange between the aqueous medium and humidified air at 37 ºC. Oxygen consumption by the cell layer at the lower surface of the model was represented as a flux boundary based upon Michaelis-Menten kinetics and using values for osteoblasts defined in [5]. There was no oxygen flux through any surface of the culture well or the washer. Oxygen diffusivity in both the culture medium and CR hydrogel were approximated as that of oxygen in water. A constant gel thickness of 2.5 mm was used.

## RESULTS

Given the thermoreversibility of CR hydrogels, the initial focus of the study was to determine a CR concentration that would support survival of the hydrogels for 2-3 days in culture at 37°C. We found that a 5% weight per volume concentration of either kappa-CR or a CR mixture of kappa and lambda isoforms produced a hydrogel that remained intact and could be handled after a culture period of three days.

The kappa-CR and kappa/lambda-CR confinement barriers supported a 1.65-fold and 1.25-fold increase, respectively, in collagen deposition compared to the level deposited by control cultures in the absence of a gel overlay. However, both gel conditions significantly decreased the total cell number by about 50% compared to the control cultures without a gel overlay.

A direct measurement of hydrogel degradation was performed using UV-vis spectroscopy. Hydrogel degradation led to a release of polymer molecules, thereby affecting absorbance values. Following six days of incubation, kappa/lambda CR hydrogels showed 14% release, while kappa-CR hydrogels released 10% of original hydrogel concentration. Rheology was used as an indirect measurement of hydrogel degradation. Hydrogel stiffness, *G'*, decreased for both types of CR hydrogels between Day 1 and Day 3 (31% and 43% decrease for kappa and kappa/lambda, respectively). Although hydrogel degradation occurred, it was found that viability of MG-63 cultures exposed to gel-conditioned medium for 2 days was not different from control cultures that received medium only based upon assessment of metabolic activity using a resazurin assay.

FCS was used to assess potential effects of hydrogel degradation on diffusivity of solutes within the culture medium above the cell layer. Both types of CR hydrogel releasates showed slowed diffusivity of Rnase A between Day 1 and Day 3, as expected. A rightward shift of the normalized autocorrelation function was observed in the presence of the releasates, indicating hindered diffusion of protein molecules caused by release of carrageenan molecules into solution. The diffusivities of Rnase A in the hydrogel releasates were quantified and normalized by the diffusion coefficient of the protein in PBS. Kappa/lambda CR solutions showed a 1.45-fold decrease in diffusivity from Day 1 to Day 3, while kappa-CR diffusivity was reduced 1.21-fold.

To complement the cellular experiments, oxygen transport in a steady-state axial model of the confinement culture system was modeled. Because the MG-63 cell line does not exhibit contact inhibition during adherent culture, the transport model included effects of increasing cell number within the oxygen consumption boundary condition. Under baseline conditions in the absence of any hydrogel degradation, the oxygen concentration in contact with the cell layer was found to vary from 0.162 to 0.023 mol/m$^3$ for cell densities ranging from 40,000 to 320,000 cells/cm$^2$, respectively. In additional simulations, oxygen diffusivity was reduced within the culture medium directly above the cell layer to represent the effects of carrageenan macromolecules present in this medium due to hydrogel degradation. Under these conditions, a 10-25% reduction in oxygen diffusivity led to reductions in oxygen concentration for the higher densities, while only larger reductions (75 – 90%) led to reductions at the lower densities.

## DISCUSSION

This study demonstrated the potential for a confinement barrier to enhance collagen deposition in a developing 2D tissue model for a bone cell line. Degradation of the CR hydrogels was characterized by both direct and indirect measurements, with similar levels of degradation found in both types of hydrogels. The degradation of the hydrogels could lead to accumulation of carrageenan macromolecules within the culture medium located above the cell layer. This accumulation could support a localized crowding effect, as indicated by the reduced diffusivities measured with FCS in the hydrogel releasates. Given this consideration, the observed increase in collagen deposition cannot be exclusively associated with confinement effects from the hydrogel barrier. Reductions in cell number were found over the course of a 7-day culture period. An assessment of viability following exposure to gel-conditioned medium suggested that hydrogel degradation products did not have adverse effects on the MG-63 cells. The computational model indicated that the continued growth of the bone cells, coupled with a possible reduction in oxygen diffusivity due to the presence of carrageenan molecules within the medium following degradation, would lead to reduced oxygen available to the cell layer that likely contributed to the reduction in cell number that occurred when the CR gels were used. Future studies evaluating the confinement approach will utilize a stable hydrogel formulation and will evaluate a more in-depth characterization of the developing tissue layer.

## ACKNOWLEDGEMENTS

Funding, including a graduate fellowship for Samuel Stealey, was provided by the Parks College of Engineering, Aviation and Technology. Use of FCS instrumentation was kindly provided by Dr. Nicola Pozzi at Saint Louis University.

## REFERENCES

[1] Nam, K et al., *J Lab Autom*, 20:201-215, 2015.
[2] Kutnetsova, I et al., *Molecules*, 20:1377-1409, 2015.
[3] Chen, C et al., *Adv Drug Deliv Rev*, 63:277-290, 2011.
[4] Etheredge, L et al., *Matrix Biology*, 29:519-524, 2010.
[5] Burova, I et al., *J Tissue Eng*, 10:1-14, 2019.

# A case study to evaluate pediatric gait speed and effects of Chiari Malformation

**T Streat-Ricchiuti (1), Dr. D Wajda (1) and Dr. B Davis (1)**

(1) Cleveland State University, Cleveland, OH, USA

## INTRODUCTION

The distinction between normal and abnormal gait in growing children is complicated by a number of factors. The formation of characteristic gait patterns is influenced by musculoskeletal growth, central nervous system maturation, and learning capacity. Furthermore, changes in gait characteristics are linked to changes in walking speed and subjects' statures. While the literature is extensive when it comes to gait patterns that are characteristic of cerebral palsy and other pediatric conditions, there is a paucity of information related to gait parameters in Chiari Malformation pediatric patients.

Chiari Malformation (CM) is a condition that affects the skull-spine junction and is linked to the cerebellum protruding into the top of the spine, obstructing the passage of cerebrospinal fluid. Headaches, dizziness, trouble swallowing, muscle weakness, and loss of neuromuscular coordination arise as a result of this increased pressure (Curone, 2017).

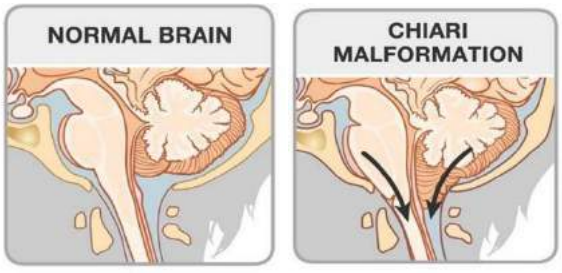


**Figure 1: Diagram of normal neurological and Chiari malformation development in patients (Shah, 2017)**

Our understanding of the functional implications of CM and how it affects gait and posture is hampered by these knowledge gaps. A better knowledge of neuromuscular function will aid neurologists, neurosurgeons devising surgical therapies, and physiotherapists developing pain reduction and rehabilitative balancing approaches. This abstract analyzes walking data collected on 10 control subjects and pediatric CM patient.

Type 2 Chiari Malformation has been diagnosed in the CM patient. The cerebellar tonsils, inferior vermis, fourth ventricle, and brain stem, as well as a small posterior fossa, are herniated in Chiari-Type 2 (Cotes, 2015).

The goal of this research is to analyze the increase in gait velocity in growing children in comparison to CM children. Even though loss of stability and difficulty walking are common symptoms in CM patients, no previous research has investigated these issues.

## METHODS

This study was approved by the Cleveland State University Institutional Review Board. Our Chiari subject was a 14 year old male and 172 centimeters in height. Our control 10 subjects were male and female ranging from 12 to 17 years old, and 60 to 178 centimeters in height. The kinematic parameters of walking, including as gait speed and step/stride parameters, were determined using a 6.1m electronic Zeno walkway (Protokinetics Inc., Havertown, PA). Individual footfalls were distinguished, and spatiotemporal aspects of the subject's gait were quantified using pressure sensors on the Zeno walkway. Participants were told to take four walks: two at their normal walking pace and two at a faster tempo without running. The subjects were instructed to walk as fast as safely possible for the fast walk trial.

**Figure 2: Control patient normal walking trial**

**Figure 3: Chiari patient normal walking trial. Yellow refers to a step that was removed because it was partially off the walkway.**

Gait trials were processed removing any uncompleted steps. Stride velocity for both variation of walking were analyzed to establish the relationship between walking velocity and height.

**Table 1: Heights, walking speed variations, and speed vs height ratio for all subjects. Chiari subject data is indicated in the green highlighted row.**

| Height (cm) | Fast walk mean (cm/sec) | Regular walk mean (cm/sec) | Fast Walking Speed/Ht | Regular Walking Speed/Ht |
|---|---|---|---|---|
| 64 | 188.4 | 125 | 2.94 | 1.95 |
| 172 | 180 | 119 | 1.05 | 0.69 |
| 163 | 181 | 127 | 1.11 | 0.78 |
| 162 | 191 | 108 | 1.18 | 0.67 |
| 161 | 182 | 120 | 1.13 | 0.75 |
| 60 | 189 | 153 | 3.15 | 2.55 |
| 156 | 219 | 167 | 1.40 | 1.07 |
| 178 | 191 | 141 | 1.07 | 0.79 |
| 156 | 192 | 140 | 1.23 | 0.90 |
| 149 | 197 | 130 | 1.32 | 0.87 |
| 158 | 163 | 113 | 1.03 | 0.72 |

## RESULTS AND DISCUSSION

When comparing the Chiari individual to the control data, there was a substantial difference for the speed/height ratio for both fast ($p = 0.035$) and regular walking ($p = 0.034$). The fast walking pace was 67 percent of the expected value for a subject of Chiari's stature, and 63 percent for the ordinary self-selected speed.

Our understanding of the functional implications of CM and how it affects gait and posture is hampered by a variety of factors, including (i) degree of tonsillation at the base of the cerebellum, (ii) presence or absence of syringomyelia, (iii) height, gender and weight influences, (iv) effects of age, (v) medication usage, and (vi) surgical history. A better knowledge of each of these factors and how they influence neuromuscular function will aid neurologists, neurosurgeons devising surgical therapies, and physiotherapists developing pain reduction and rehabilitative balancing approaches.

## CONCLUSION

The Chiari subject displayed slower walking speeds for a person of his stature. This is likely due to lack of stability in his gait. Whilst this is a case study, ongoing research will ascertain the degree to which this is consistent for all pediatric Chiari patients, and the degree to which gross motor control changes over time.

## REFERENCES

[1] Beck, R. J et al, *The Journal of bone and joint surgery. American volume*, *63*(9), 1452–1457, 1981.

[2] Cotes, C. et al, *The neuroradiology journal*, *28*(3), 238–253, 2015.

[3] Curone, M. et al, *Neurological sciences: official journal of the Italian Neurological Society and of the Italian Society of Clinical Neurophysiology*, *38*(Suppl 1), 91–93, 2017.

[4] Shah, A. H. et al, *Journal of craniovertebral junction & spine*, *8*(4), 297, 2017.

## ACKNOWLEDGEMENTS

This work is supported by a grant from the American Syringomyelia Alliance Project.

SB³C2021
Summer Biomechanics, Bioengineering and Biotransport Conference
June 20-23, Eastern Shore, MD, USA

# Development of 3D Brain Structures from Histology Images

**John Sayut (1), Maria A. Holland (1,2)**

(1) Aerospace and Mechanical Engineering
(2) Bioengineering Graduate Program
University of Notre Dame
Notre Dame, Indiana, USA

## INTRODUCTION

Abnormal morphological brain development is a symptom of some neurological diseases. For example, a unique cortical folding pattern is known to be a symptom of schizophrenia [1]. Mammalian brain images are important for studying such abnormal development in the brain because it shows how the brain folds into different thicknesses and shapes while unaffected by pathology, providing insight that can untangle the root causes of neurological disorders where abnormal folding is a symptom. A common tool for studying brain shape is magnetic resonance imaging (MRI). MRI captures the 3D gross morphologies. However, standard MRI brain scans do not consistently have an adequate resolution for analyzing cortical thickness and laminar thickness in mammalian brain scans, especially in smaller animals and in brains with a high degree of foldedness [2]. Stained tissue slices of a brain give a higher resolution picture of the white and gray matter of a brain than what is currently available through MRI. However, these images do not typically capture 3D information, and 3D geometry is known to affect thickness [3]. A 3D reconstruction would provide the necessary resolution and structure for highly accurate measurement of common brain folding parameters such as cortical thickness. Additionally, it would enable researchers to study unique brains that are solely found as serial tissue sections. In a step towards full three-dimensional reconstruction of the brain geometry, we segmented the white and gray matter from histology images of serial sections of a manatee brain using the software ImageJ, and wrote a script to align each slice to the adjacent one. The next step is to convert the connected slices into a 3D structure. This pipeline will build 3D structures of given mammalian brains. We determined that the given histology images can be processed, analyzed appropriately, and further developed into 3D models of mammalian brains.

## METHODS

For this study we utilized histology images from the University of Wisconsin and Michigan State Comparative Mammalian Brain Collections (CMBC) [4]. The CMBC has stained brain images from over 100 species in its archive. We selected the manatee brain for development of the automation pipeline because it is relatively large, making it well-defined - this will help us in identifying issues with the pipeline for ideal brains, and then the pipeline can be tailored for more difficult one. Additionally, it is less folded than a human brain, meaning it has implications for the study of human brain diseases involving lissencephaly. During collection, the CMBC sliced the mammal brains into 25-40 micron sections, with every 20th slice available on the CMBC website [4]. The resolution is comparable to the .5 mm cube resolution of an MRI scan, and the resolution in the slice plane is much higher than an MRI scan.

We used the NIH-funded image analysis software platform ImageJ to build an analysis pipeline for the histology slices [5]. The exact goal of this pipeline code is to convert the histology slices into separate 3D structures of white and gray matter. Currently, we are able to align single slices relative to each other, and have developed an ImageJ-based segmentation process that can be implemented automatically. First, we remove the text from the histology images that identifies the slice and scale of the image (Fig. 1A). We use ImageJ's color thresholding tool to separate the white and gray matter, developing masks for both tissues. Next, we make a separate binary mask of the whole brain to use to execute the alignment code. Through this process, we are able to create three separate images - a binary mask of the white matter, a binary mask of the gray matter, and a binary mask of both tissues for use in the alignment code (Fig. 1B). Finally, the binary brain slices are aligned using an optimization algorithm to minimize the differences between slices (Fig. 1C). Once

this is repeated sequentially over many pairs of images, the pipeline can use the displacements calculated from the binary images to build a 3D model of the gray matter, white matter, and whole brain (Fig. 1D).

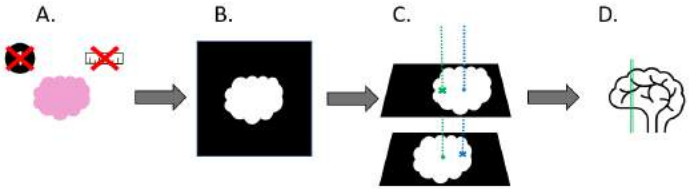


**Figure 1: Summary of pipeline code steps**

The alignment code developed through this research seeks to match two adjacent histology images of a sliced brain so that the centers of the images are aligned as they were in the original 3D brain. The displacement of each brain image from the biological center of the brain must be determined. To do this, we assume that the best alignment of adjacent brain images is the position with the least difference between the two images. The code quantifies the difference between the images by calculating the mean squared error between them. In this case, the variable $n$ represents the number of pixels in each image, and $x_i$ and $y_i$ represent the value of the pixel at each point where the variable $x$ is one binary image and $y$ is the other.

$$MSE = \frac{1}{n}\sum_{i=1}^{n}(x_i - y_i)^2 \quad (1)$$

The slices are roughly centered in the images, so the displacement necessary to align adjacent slices should only be a few pixels. The code loops through displacements for the second image from (-20,-20) to (20,20) pixels and evaluates the mean squared error between the images for each displacement. This code identifies the lowest error displacement, aligning the images. This will allow the user to create a 3D shape from any set of sequential histology images.

## RESULTS

The code's performance can be illustrated by considering a single slice (Fig. 2A) and examining the difference between it and its adjacent slice for different displacements (Fig 2B and 2C). When the images are subtracted from each other, there is a slight mismatch, which we minimize through the alignment code. The fewer yellow pixels in the second image illustrate how the difference between images is minimized through displacement, although not completely eliminated.

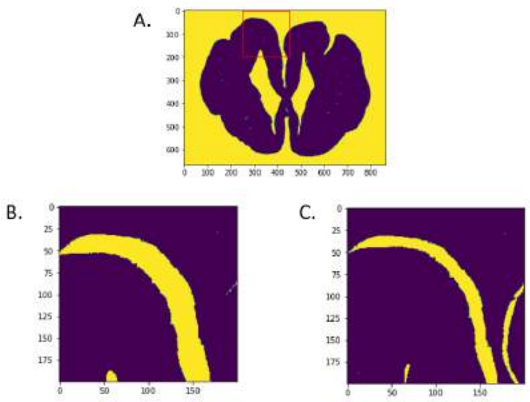


**Figure 2: (A) Brain slice #880 with the detailed portion highlighted in red. (B and C) Detail of slice difference between slice #880 and #900 for displacements [0,0] in B and [12,-9] in C. Yellow pixels indicate unique values between images.**

Our script evaluates the alignment between two sequential images via the mean squared error as a function of relative displacement (Fig. 3). The alignment of the brains is not sensitive to small displacements of a few pixels in any direction from this optimal position. However, differences of more than 5 pixels generate poor alignment.

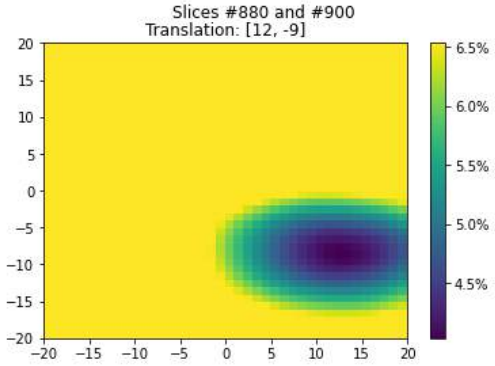


**Figure 3: Heatmap of mean squared error between slices #880 and #900 for displacements in *x* and *y*.**

## DISCUSSION

In this study we develop a code that can determine the optimal displacement between two adjacent brain histology images. Our results indicate that the alignment code can converge on an optimal displacement by minimizing the mean squared error resulting from different displacements. This means that a three-dimensional file of highly detailed gray and white matter can be developed from these images. We note that our script minimizes error between images but cannot completely eliminate it. Further development work will allow for the generation of many such 3D files that compile the highly detailed histology images of rare brains.


## ACKNOWLEDGEMENTS

This work was supported by NSF CMMI 214412.


## REFERENCES


[1] Wisco, J. et al., *Schizophrenia Research*, 2007.
[2] Mota, B et al., *Proceedings of the National Academy of Sciences*, 2019.
[3] Demirci, N. and Holland MA, *Hum Brain Mapp*, 2022.
[4] http://neurosciencelibrary.org/index.html
[5] Broeke, J et al., *Packt Publishing open source*, 2015.

# Development of a Sensor-Imbedded Transmetatarsal Foot Amputation Prosthetic (TMAP)

**Jenna M. Munshi[1,2,3], Vinod Rangaprasad[1,2,3], Simon Hasik[1,2,3]**

**1 - Purdue University**
**2 - Purdue Medical Innovation, Networking, and Design**
**3 - West Lafayette, IN, USA**

## ABSTRACT

Diabetes and peripheral arterial disease are two prevalent chronic medical conditions afflicting the global population. Lower extremity disease secondary to diabetic microvascular and peripheral vascular disease often result in transmetatarsal foot amputation (TMA). Management after TMA requires extensive rehabilitation, often with the aid of prosthetics. Current prosthetics lack the comfort and suspension patients required; they do not adequately support gait, balance, proprioception, and can negatively impact post-amputation limb health. To address these drawbacks, our team designed a Transmetatarsal Foot Prosthetic (TMAP) that enhances proprioception, balance and gait while improving limb health. The new prosthetic is integrated into a compression sock with contractible strings placed within the sock acting as tendons to distribute the patient's weight evenly as they walk. As the patient steps forward, placing weight on the prosthetic results in the "tendons" extending to redistribute the weight across the foot. Placing weight on the back of the foot results in retraction of the tendons. The prosthetic is flexible and utilizes an elastic band to aid in weight distribution. Sensors embedded in the insoles detect changes in weight distribution across both feet. Heart rate/pulse oximetric sensors within the compression sock monitor the health of the limb. Data is collected and stored in real time on a mobile app, to be retrieved by therapists during scheduled appointments. The prototype, currently in its developmental phase, will be completed by early March. In conclusion, the TMFP will improve gait and balance, increase comfort and proprioception, and improve limb health post-amputation.

## INTRODUCTION

The transmetatarsal foot amputation is one of the most common procedures for patients suffering from diabetes and peripheral neuropathy. Current solutions do not focus on the patient's health and safety, but rather on convenience. Our prosthetic is designed to monitor the patient's biometric data and account for balance and gait. This gives the patient the ability to return to their daily life with ease. Our prosthetic works in conjunction with a mobile app. This allows physicians and physical therapists to see the patient's data (heart rate, blood pressure, etc) and assign the necessary exercises or procedures that will most benefit the patient. It provides individualized care with easy transmission of data from patient to doctor. TMAP would be considered a Class I medical device as it is an improvement of similar prosthetics, while using elements of modern design: sensors and improved comfort for the user. A 510(k) or PMA would likely not be needed. TMAP would follow FDA's General Controls in ensuring safety and effectiveness through provisions regarding adulteration, misbranding, device registration, keeping records, and standard manufacturing practices. The market for TMAP is on the increase. As more and more people acquire comorbidities like diabetes and peripheral neuropathy disease, the TMA will become more common. Our modern

SB³C2022-483

and holistic prosthetic will be the ideal solution to this issue.

**PROBLEM STATEMENT**

The transmetatarsal foot amputation (TMA) is common in patients with diabetic neuropathy, ulcers, and peripheral artery disease. Partial foot amputations such as TMA are the most common type of amputation in the United States, and affects over 600,000 individuals. As the prevalence of diabetes and vascular diseases increase over time, experts say the frequency of TMA could double by 2050. While it is a viable option for limb salvage, TMA is an especially difficult wound to heal. Approximately 15 to 45% of partial foot amputation patients undergo a secondary amputation[1]. One factor in this is post-amputation skin breakdown and subsequent ulceration. Prosthetics can be used as a solution to promote healing and preserve function with respect to weight-bearing and ambulation. Current solutions lack suspension, impair limb health, and do not allow for proper proprioception of users. Our prosthetic is designed to take into account gait and balance, and provide a safer, more comfortable way of walking.

**SOLUTION STATEMENT**

The objective of this prosthetic is to provide a comfortable and safe way for Transmetatarsal foot amputation patients to heal and ambulate again. The sensors in the insoles of the prosthetic detect changes in weight distribution across not only the partially amputated foot, but also the healthy foot. This allows the prosthetic to normalize the patient's gait and ensure that they are walking as they once did. The compression sock contains sensors that take basic biometric data to monitor the limb health. The data is then stored in a mobile app and can be analyzed each time the patient has an appointment with the physical therapist or primary care doctor. This is invaluable because it provides day by day documentation of the patient's progress, allowing therapists and doctors to see each piece of data necessary to assess the patient and recommend the right medication, exercise, or activity with specificity.

SB³C2022
Summer Biomechanics, Bioengineering and Biotransport Conference
June 20-23, Eastern Shore, MD, USA

# *IN VITRO* HUMAN LUNG FIBROBLAST-TO-MYOFIBROBLAST TRANSITION FROM PROFIBROTIC GROWTH FACTOR STIMULATION

**Catherine S. Sano (1), Julie Leonard-Duke (2), Shayn M. Peirce-Cottler (2)**

(1) Department of Chemical Engineering, University of Virginia, Charlottesville, Virginia, United States
(2) Department of Biomedical Engineering, University of Virginia, Charlottesville, Virginia, United States

## INTRODUCTION

Idiopathic pulmonary fibrosis (IPF) is a terminal disease characterized by uncontrolled extracellular matrix (ECM) production mediated by fibroblast and myofibroblast activity in the lung.[1] The complex lung microenvironment poses challenges to determining the mechanisms of IPF progression. There are currently only two FDA-approved antifibrotic drugs, Nintedanib and Pirfenidone, which can slow the rate of fibrosis but do not halt it.[2] Fibroblasts have cell surface protein receptors called integrins that bind to the ECM allowing them to sense their environment, a process called mechanosensing.[3] Thy-1, a cell surface glycoprotein, blocks the binding of integrins with the ECM and regulates this mechanosensing.[3] The loss of Thy-1 increases susceptibility to external mechanical stimuli, as the integrin-ECM binding is uninhibited, and triggers the excessive and pathological fibrotic response in IPF.[3]

Fibroblasts additionally respond to signaling molecules in the lung microenvironment, specifically inflammatory cytokines and growth factors, such as TGF-$\beta$, inducing their differentiation into myofibroblasts.[4] Myofibroblasts are characterized by an increase in size, α-smooth muscle actin ($\alpha$-SMA) upregulation, and elevated collagen I production, which increase the stiffness of the lung, reducing compliance and impairing gas exchange, and is exacerbated by increased mechanosensing from Thy-1 loss in IPF.[5] Fibroblasts also produce and secrete additional inflammatory cytokines and profibrotic growth factors, such as TGF-$\beta$, which causes a reduction in their Thy-1 expression levels and further perpetuates the pro-fibrotic pathways and fibroblast-to-myofibroblast transition.[6] **The objective of this study was to quantify the impact of TGF-$\beta$ stimulation on human lung fibroblast f-actin and α-SMA expression, and determine whether the lung fibroblasts can be stimulated to exhibit a myofibroblast phenotype *in vitro*.**

## METHODS

To determine myofibroblast transformation, human lung fibroblast cells were stimulated with the growth factor, TGF-$\beta$, and the expression of characteristic myofibroblast markers were quantified using immunofluorescent staining. Commercially available human lung fibroblasts (CCL-210) were initially plated on a 24-well glass plate in 0.5mL standard culture media, DMEM-F12 with 1% Penicillin-Streptomycin and 10% fetal bovine serum (FBS), at a density of 50,000 cells/well to allow for proliferation and adherence to the wells. The media was changed to media without FBS the following day and the experimental groups were be stimulated with 20ng/mL of TGF-$\beta$. The media without FBS prevents binding of the treatment to factors in the serum, allowing uptake of TGF-$\beta$ by the cells. Additionally, a control group without treatment received media without FBS. Three days after the media change, the cells were fixed and immunostained.

Cells were stained with different colored fluorescent markers to image nuclei (DAPI stain), $\alpha$-SMA (monoclonal antibody), and F-actin (Phalloidin stain). Five representative microscopic images of each well of the culture plate were acquired using a Leica Thunder microscope and a 20x objective. ImageJ software was used to quantify cell numbers and sizes according to DAPI and Phalloidin stains, respectively, as well as the relative fluorescence intensity of the stains for $\alpha$-SMA and Thy-1. The five representative images were cropped to 500x500µm images, which were separated into three images: blue (DAPI), red (Phalloidin), and green ($\alpha$-SMA). The colored images were grey-scaled and each pixel was quantified on a scale from 0-255, proportional to the fluorescence. The median grey values for the Phalloidin and $\alpha$-SMA stains were averaged for the unstimulated and stimulated groups and percent change in the averaged median grey values were calculated. Error was determined by standard error of mean and standard error propagation with a total of 10 images analyzed per experimental group.

SB³C2022-484

## RESULTS

Upon stimulation of the human lung fibroblast cells with TGF-$\beta$ the cells exhibited elevated f-actin and $\alpha$-SMA expression, demonstrated by the percent increase in fluorescence from the Phalloidin and $\alpha$-SMA monoclonal antibodies that bind to those proteins (Figure 1).

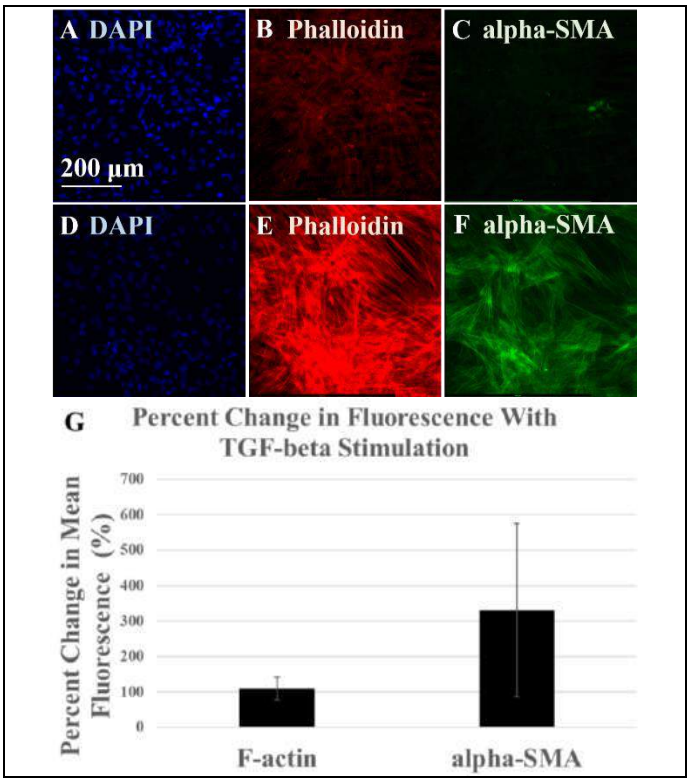


**Figure 1 Stimulation of fibroblasts with TGF-$\beta$ results in cytoskeleton remodeling. A-F: Immunofluorescent images without stimulation (A-C) and with TGF-$\beta$ stimulation (D-F). G: Percent change in mean fluorescence (from multiple wells and fields of view) of Phalloidin stain (109.9±32.1%) and stain for $\alpha$-SMA (330.6±245%) with TGF-$\beta$ stimulation.**

## DISCUSSION

Increased expression levels of f-actin and $\alpha$-SMA are consistent with previous work by Rikard et al. from the Peirce-Cottler lab, where human cardiac fibroblast cells similarly exhibited heightened f-actin and $\alpha$-SMA upon stimulation with TGF-$\beta$.[7] Elevated expression of both f-actin and $\alpha$-SMA indicates enhanced growth of the fibroblasts and contractility in the lung consistent with the myofibroblast phenotype.

Limitations of the study include the small sample size: a total of 20 images were analyzed, 10 stimulated and 10 unstimulated, which likely contributed to the large error in percent increase of $\alpha$-SMA expression. Further repetitions of the experiment should be performed to corroborate these results. Future experiments will test for other myofibroblast marker expressions, such as Thy-1, collagen, and inflammatory cytokines, upon stimulation with combinations of inflammatory cytokines and growth factors. Additional protein expression measurement methods, including qRT-PCR, ELISA, and western blot will also be used to support myofibroblast character.

The results of this experiment are evidence of myofibroblast transition upon uptake of the growth factor present in the lung microenvironment naturally and in greater numbers from the pathological response in IPF. This phenotypic shift, thus likely contributes to the reduced respiration and ventilation as a result of impaired alveolar expansion and contraction in IPF, demonstrating the pathological interaction of lung fibroblasts with growth factor signaling molecules in IPF. Determining how specific intersecting molecular signaling pathways drive pathological fibroblast behaviors has the potential to suggest new treatments that more comprehensively address the interplay between lung fibroblasts and their environment in IPF, as well as other diseases characterized by lung fibrosis, such as long-COVID-19.


## ACKNOWLEDGEMENTS

This research was funded by NIH R01HL155143.


## REFERENCES


[1] Kendall, R et al., *Frontiers in Pharmacology*, 5:123, 2014.
[2] Barratt, S et al., *Journal of Clinical Medicine*, 7:201, 2018.
[3] Hu, P et al., *Frontiers in Cell and Developmental Biology*, 7:22, 2019.
[4] Liu, Y et al., *Scientific Reports*, 6 : 32231, 2016.
[5] Baum, J et al., *Journal of Cardiovascular Pharmacology*, 57:376-379, 2011.
[6] Hannan, R et al., *ACS Biomaterials Science & Engineering*, 4:1223-1232, 2018.
[7] Rikard, M et al., *Frontiers in Physiology*, 10:1481, 2019.

SB³C2022
Summer Biomechanics, Bioengineering and Biotransport Conference
June 20-23, Eastern Shore, MD, USA

# 3D ULTRASOUND IMAGING OF THE MURINE CERVIX DURING PREGNANCY USING PRETERM BIRTH MODELS

**Riley L. Holloway (1), Jennifer L. Anderson (1), Craig J. Goergen (1)**

(1) Weldon School of Biomedical Engineering
Purdue University
West Lafayette, Indiana, USA

## INTRODUCTION

Preterm birth (PTB) is defined as birth before 37 weeks gestation in humans and affects 1 in 10 babies in the United States [1]. These babies face higher morbidity and mortality rates due to their underdeveloped organs. One cause of preterm birth is cervical insufficiency or cervical incompetence that affects every 1 in 100 pregnancies in the U.S. Cervical insufficiency is defined as the inability of the cervix to remain closed until gestation is complete [2][3]. It is widely known that as gestation progresses, the cervix length decreases. This is known as cervical ripening, a normal process of softening and opening of the cervix before labor starts. Premature or extreme remodeling or ripening of the cervix can cause cervical insufficiency and lead to preterm birth.

The current tool to diagnose an incompetent cervix is a uniaxial ultrasound measurement at routine checkups. The ultrasound measurement method utilizes a uniaxial view of the cervix, which does not account for the three-dimensional complexity of the organ. This can lead to incomplete or inaccurate measurements of the cervix. For example, one study found that out of 56.3% of subjects whose cervixes decreased in length between gestation weeks 24-28, only 4.2% gave birth preterm [4]. Other studies have assessed the cervix in a non-pregnant state or have failed to assess the cervix longitudinally over time [5]. This lack of data on the geometric remodeling of the cervix and an assumed uniaxial ultrasound measurement can lead to both over and underdiagnosis, and a larger number of preterm births. Our study aims to capture two and three-dimensional longitudinal ultrasound images of the cervix so that a better understanding of the complex remodeling process can be made.

There are two established mouse models of PTB: one by an inflammatory process, and one by the premature withdrawal of progesterone (P) activity through the administration of lipopolysaccharide (LPS) and RU486, respectively. LPS is an endotoxin derived from the *e. coli* pathogen. RU486 (or mifepristone) blocks progesterone which is needed to keep the embryo attached to the uterine lining. These animal models allow us to study the distinct pathways driving premature cervical remodeling [6]. To address these challenges, our group induced both models of PTB to assess changes in murine cervical geometry and mechanics throughout gestation via *in vivo* ultrasound assessment.

## METHODS

For this study, a similar experimental protocol was used as with previous three-dimensional ultrasound studies that measured the cervix [7]. Five nulligravida female C57BL/6J mice, ages 8-12 weeks were used (initial body mass = 21.6g ± 1.0 g). The mice were anesthetized using 1-3% isoflurane, depilatory cream was used on the pelvic area to remove hair and ultrasound conductive gel was placed on the lower abdomen. Three-dimensional ultrasound images of the murine cervix were acquired before and during pregnancy using a high-frequency ultrasound system (Vevo3100 Imaging system, FUJIFILM VisualSonics, Inc., Toronto, ON, Canada). To take a three-dimensional ultrasound image, a stepper motor was used to acquire successive ECG and respiration-gated B-mode images with a step size of 0.08 mm from the vaginal canal through the bifurcation of the uterine horns. The female mice were then paired with male mice and checked every 3-4 days for pregnancy using standard two-dimensional ultrasound images. Dating of pregnancy was determined by of the appearance of the decidual reaction, gestational sacs, and other features seen in early gestation. Three-dimensional ultrasound was repeated at this pregnancy check (typically gestational stage e6.5), and then again at days e12.5, e15.5, and e16.5.

Between timepoints e15.5 and e16.5, the preterm birth intervention was implemented - either via the inflammatory process from LPS (inflammation group, n = 2), or the premature withdrawal of progesterone via RU486 (non-inflammation group, n = 1). For the inflammation model, we administered 250 μg of LPS (Escherichia coli

serotype 055:B5, Sigma) dissolved in 30 uL sterile water intravaginally [8]. For the non-inflammation model, we administered 0.5 mg of RU486 (Sigma) dissolved in 50 µL of ethanol and brought up in 150 µL of glycerol trioleate (Sigma) subcutaneously [9]. Sham groups used the vehicle, (30 uL sterile water injected intravaginally for the inflammation model and 50 µL of ethanol and 150 µL of glycerol trioleate injected subcutaneously for the non-inflammation model) as a control (inflammation, n = 1; non-inflammation, n = 1).

Three-dimensional volumetric renderings (see Figure 1) were created using SimVascular [10] and analyzed in Python (v3.8.2) and Blender (v2.79b) using the NeuroMorph toolset (v2.0) [11]. Cervical area and height were calculated at all timepoints from the volumetric renderings. At e16.5, the mice were euthanized via isoflurane overdose and cervical dislocation. Upon euthanasia, the intact uterus and cervix were removed and weighed.

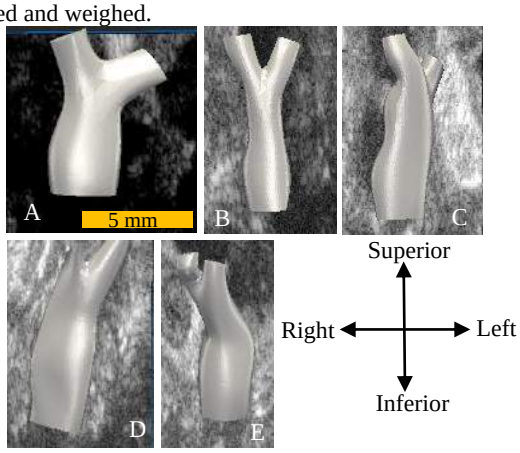


**Figure 1: Three-dimensional volumetric rendering of the murine cervix in the non-inflammation model. (A) Non-pregnant state. (B) Gestational age e6.5. (C) Gestational age e12.5. (D) Gestational age e15.5. (E) Gestational age e16.5.**

## RESULTS

Our results suggest cervical length increases and cervical area decreases after LPS introduction which occurs after e15.5 (Figure 2). In the non-inflammation model, cervical length decreases and cervical area increases after injection of RU486, also occurring after e15.5.

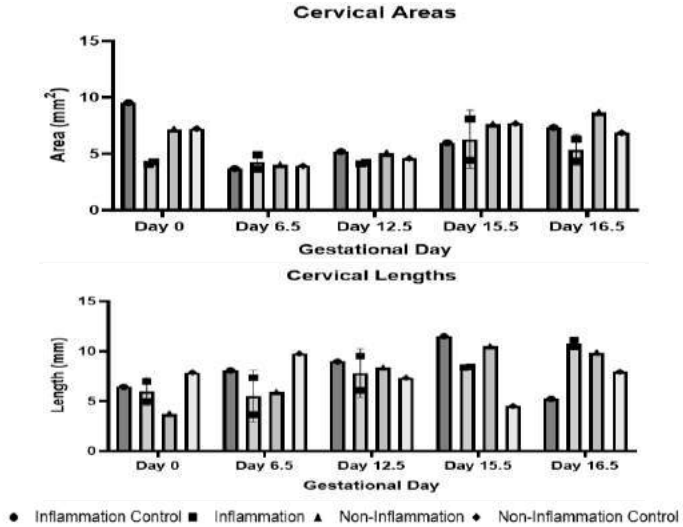


**Figure 2: Cervical area (top) and length (bottom) at multiple gestational timepoints.**

## DISCUSSION

In a typical pregnancy as gestation progresses, cervical length decreases, and cervical area increases. While the non-inflammation model follows this expectation, the inflammation model results do not. This could be because of our very small group sizes or be a potential indicator of differences between groups in respect to how the cervix remodels. Additionally, external factors such as the administration route - intravaginally versus subcutaneously - could affect cervical remodeling. More data is needed to investigate these findings, with work in progress to add additional animals to each group. Future work could also assess both cardiac remodeling and histologic changes associated with both models.


## ACKNOWLEDGEMENTS

We would like to acknowledge the Clinical and Translational Sciences Institute (Funder ID: 10.13039/100006975, funded in part by Award No. UL1TR002529 from the National Institutes of Health, National Center for Advancing Translational Sciences, Clinical and Translational Sciences Award), the Purdue Women's Global Health Institute, and a Bill and Melinda Gates Foundation Global Grand Challenges Exploration Grant (OPP1182739; Funder ID:10.13039/100000865). The content is solely the responsibility of the authors and does not necessarily represent the official views of the National Institutes of Health. Jennifer L. Anderson acknowledges the National Science Foundation for support under the Graduate Research Fellowship Program (GRFP) under grant number DGE-1842166.


## REFERENCES


[1] Quinn, J.A., et al. (2016). Preterm Birth: Case Definition & Guidelines for data collection, analysis, and presentation of Immunization Safety Data. Vaccine, 34(49), 6047–6056.

[2] M. Thakur and K. Mahajan, "Cervical Incompetence," StatPearls Publishing, 2019.

[3] World Health Organization, Make every mother and child count. Geneva, 2005.

[4] Iams, J. D., et al., "The Length of the Cervix and the Risk of Spontaneous Premature Delivery," The New England Journal of Medicine, vol. 334, no. 9, p. 6, 1996.

[5] Yoshida, K. *et al.*, "Material properties of mouse cervical tissue in normal gestation," *Acta Biomaterialia*, vol. 36, pp. 195–209, May 2016.

[6] Gonzalez, J. M., et. al., (2011). Complement activation triggers metalloproteinases release inducing cervical remodeling and preterm birth in mice. The American Journal of Pathology, 179(2), 838–849.

[7] Conway, C. K., et al., (2019). Biaxial biomechanical properties of the nonpregnant murine cervix and uterus. Journal of Biomechanics, 94, 39–48.

[8] Yoshida, K., et al., (2019). Mechanics of cervical remodelling: Insights from rodent models of pregnancy. Interface Focus, 9(5), 20190026.

[9] Holt, R., Timmons, et al., (2011). The molecular mechanisms of cervical ripening differ between term and preterm birth. Endocrinology, 152(3), 1036–1046.

[10] Updegrove, A. *et al.*, " SimVascular: An Open Source Pipeline for Cardiovascular Simulation" *Ann Biomed Eng*, vol. 45, no. 3, pp. 525–541, Mar. 2017.

[11] Jorstad, A., Blanc, J., & Knott, G. (2018). NeuroMorph: A software toolset for 3D analysis of neurite morphology and connectivity. Frontiers in Neuroanatomy, 12.

SB³C2022
Summer Biomechanics, Bioengineering and Biotransport Conference
June 20-23, Eastern Shore, MD, USA

# TENSILE STIFFNESS OF SKELETAL MUSCLE UNDER UNIAXIAL VERSUS BIAXIAL STRETCH

**Minhaj U. Bhuiyan (1), Benjamin B. Wheatley (2)**

(1) Biomedical Engineering, Bucknell University, Lewisburg, PA, United States
(2) Mechanical Engineering, Bucknell University, Lewisburg, PA, United States

## INTRODUCTION

Skeletal muscle provides the necessary functions required for human locomotion. Computational models – such as musculoskeletal or finite element simulations – are often utilized in clinical settings for a variety of purposes, such as rehabilitative strategies, prosthetic and orthotic device fitting, and determining at-risk groups for certain injuries [1,2]. In most models, muscles are treated as one-dimensional elements that only exert force in a single line of action. However, research has shown that force is transmitted both laterally within skeletal muscle and between surrounding muscles [3,4]. Such findings also highlight the importance of passive properties such as anisotropic stiffness, which allow the force generated by the muscle cells to be transmitted throughout the skeletal system and induce movement [5]. Passive muscle properties are also crucial to proper function, as many neuromuscular impairments can manifest through increased passive stiffness. While this lateral force transmission is known to exist, there is not much information on the specifics - such as when and how much force transmission occurs. Recent studies also show that stretching muscle biaxially may enact certain passive mechanisms relating to force transmission, such as dispersed collagen fibers, that are hidden during uniaxial stretch [6].

Therefore, we conducted biaxial tensile testing to study the stiffness of muscle tissue under uniaxial versus biaxial tensile stretch and hypothesized that skeletal muscle will be stiffer in biaxial stretch. The data gained from this study can help improve future musculoskeletal and finite element models by developing a more comprehensive understanding of lateral force transmission in skeletal muscle. This may drastically alter the assumptions used to drive such simulations.

## METHODS

Fresh porcine skeletal muscle was obtained for experimentation on the day of sacrifice from a local abattoir. No live animal handling was performed by any researchers for this study. Tissue was harvested from the semimembranosus and biceps femoris using standard dissection techniques and prepared into cruciform shapes. The samples were speckled with graphite powder and fitted into a planar biaxial tensile testing machine with integrated digital image correlation. The samples each underwent three tensile tests, including uniaxial stretch in each direction and biaxial stretch. Specifically, the muscle was stretched longitudinally while being allowed to naturally compress in the transverse direction due to the Poisson effect. Similarly, it was also stretched in the transverse direction while being allowed to compress naturally in the longitudinal direction. Finally, the muscle was stretched biaxially at a ratio of 1:1. The testing order was randomized, and all three tests were conducted at a strain rate of 0.5% until 20% nominal strain. Testing was performed on n=25 samples.

Image data was collected and analyzed with VIC2D (Correlated Solutions, Inc.), where engineering strains were calculated and exported into MATLAB along with the raw force and displacement data from the tensile machine. A custom script was written to extract, filter, and smooth the data to obtain stress-strain relationships for all three tests for each sample. The stress-strain curves were plotted, and a mean curve for each testing type and direction was calculated to allow for a visual representation of the stiffness of the muscle. The individual curves were then fit to an exponential equation with parameters a, correlating to stiffness, and b, correlating to nonlinearity, to characterize the general tissue stiffness between testing conditions. These data were exported to Excel and used to a run a statistical analysis, specifically a t-test assuming unequal variance, to determine whether the parameters were significantly different or not. Some tests, due to the nature of the stretching, yielded parameters with very poor fit; these samples, all with a goodness of fit value below 0.8, were omitted from the statistical analysis to achieve a more representative p-value.

## RESULTS

The stress-strain curves for the longitudinal biaxial test and longitudinal uniaxial test can be seen in Figure 1. The p-value for the unpaired t-test was 0.219 and 0.193 for parameters a and b, respectively, indicating that neither of these values were statistically significant from each other.

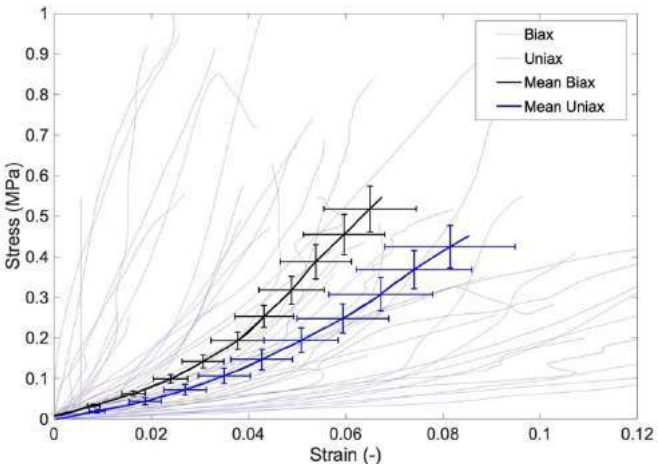


**Figure 1: Stress-strain curve of samples (n=25) under longitudinal biaxial and uniaxial stretch with stress and strain data calculated from force and displacement data, respectively.**

The stress-strain curves for the transverse biaxial test and transverse uniaxial test can be seen in Figure 2. The p-value for the unpaired t-test was 0.191 and 0.039 for parameters a and b, respectively, indicating that the former coefficients were not statistically significant while the latter coefficients were.

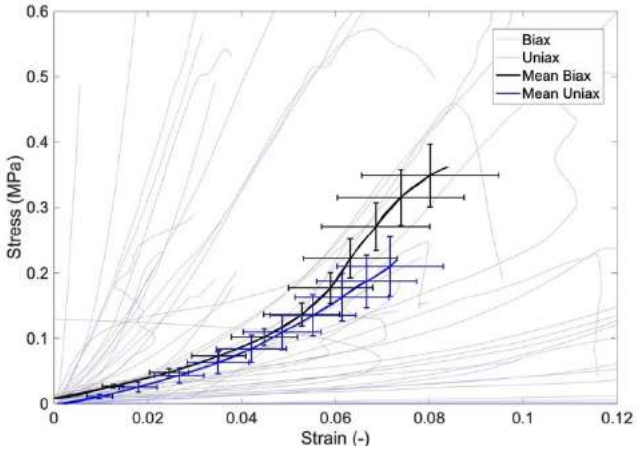


**Figure 2: Stress-strain curve of samples (n=25) under transverse biaxial and uniaxial stretch with stress and strain data calculated from force and displacement data, respectively.**

## DISCUSSION

This study presents, to the best of our knowledge, a direct comparison of uniaxially and biaxially stretched skeletal muscle for the first time. From this novel data, we conclude that there is no statistical significance in the stress-strain relationships in the longitudinal direction when fit with an exponential function (Figure 1); this indicates that there is limited functional difference in the stiffness when experiencing uniaxial versus biaxial stretch. The results of Figure 2 indicate that there was a significant difference in coefficient b, the exponent of the exponential function, which shows that the nonlinearity of the muscle varies between the two testing types in the transverse direction; judging by the two curves, the tissue experienced a marginally greater stiffness under biaxial stretch than it did in uniaxial.

Although the statistical significance can be determined via the analyses presented here, the biological significance of these results was not evaluated in this study. Biaxial stretch may be a better representation than uniaxial stretch, but our results suggest it may not cause considerable differences in observed stiffness. In order to fully see the consequences of uniaxial versus biaxial stretch, constitutive modeling should be implemented to better understand the results in the context of muscle structure and function. The exponential fit applied here, although a simple and effective method, did not capture the interaction between the longitudinal and transverse directions. The stress calculated was not an accurate simulation of the cruciform shape and the true stress experienced by the center of the muscle sample. Overall, the tests performed here are only a small representation of an attempt to characterize the deformative behaviors of skeletal muscle and can be expanded upon much farther with more advanced experimentation and computational analysis.

Our results correlate to previously published data that observed a greater stiffness in the transverse direction of passively stretched muscle; however, there have also been studies that have found the stiffness to be greater in the longitudinal direction [7,8]. The similarities in stiffness of both directions in our data indicate the variability of muscle tissue and how many factors can affect the apparent mechanical properties. In addition, there are other methods of evaluating stiffness outside what was done in this study, such as comparing tangent moduli and inverse finite element analysis that may be of interest.

The results show that biaxial stretch may be a more accurate way of characterizing the stiffness of muscle. The information gleaned from this study can be implemented into musculoskeletal models to evaluate the effect on its behaviors. One application of these models includes surgical planning for hamstring lengthening for cerebral palsy patients [9]. In this condition, the hamstring contracts into an extremely tight state that prevents full range of motion in the leg; in order to treat it, the tendons in the hamstring are either elongated or fully cut to let the muscle stretch out and prevent poor force transmission. The choice can be unclear at times, and computational tools such as musculoskeletal simulations, which could benefit from the work done here, can be used to guide such procedures by estimating hamstring lengths and forces.

Our main takeaways from this study are that skeletal muscle tissue is slightly stiffer under biaxial stretch, with more similarity in the longitudinal direction, but that the stiffness may not be functionally significant. Future work on the collection of biaxial tensile data and implementation into various models can verify these findings.


## ACKNOWLEDGEMENTS

The authors would like to thank the Costa Healthcare Research and Design Funds at Bucknell University for funding this study.


## REFERENCES


[1] Rajagopal, A et al., *IEEE*, 63:2068-2079, 2016.
[2] Hicks, J et al., *J Biomech*, 137:209-233, 2015.
[3] Huijing P, *J Biomech*, 32:394-345, 1999.
[4] Maas H, *J ApplPhysio*, 126:1465-1473, 2019.
[5] Leiber R et al., *J ApplPhysio*, 126:1492-1501, 2019.
[6] Wheatley B, *FPhys*, 11:1021-1036, 2020.
[7] Takaza M et al., *J MechBehav*, 17:209-220, 2012.
[8] Morrow D et al., *J MechBehav*, 3:124-129, 2009.
[9] Arnold A et al., *Ann BME*, 29:263-274, 2011

SB³C2022
Summer Biomechanics, Bioengineering and Biotransport Conference
June 20-23, Eastern Shore, MD, USA

# THE RELATIONSHIP BETWEEN INTRAMUSCULAR PRESSURE AND COMPRESSION OF SKELETAL MUSCLE

**Sabrina S. Lorza (1), Pierre-Yves Rohan (2), Mark A. Seeley (3), Benjamin B. Wheatley (1)**

(1) Department of Mechanical Engineering, Bucknell University, Lewisburg, PA, USA
(2) Institut de Biomécanique Humaine Georges Charpak, Arts et Métiers, Paris, FR
(3) Department of Pediatric Orthopedics, Geisinger Medical Center, Danville, PA, USA

## INTRODUCTION

There are over 600 skeletal muscles in the human body, and each plays a specific role in generating and transmitting force. Skeletal muscle is considered bi-phasic, consisting of solids (such as collagen, contractile constituents, etc.) and liquids (interstitial fluid and cellular fluid). Muscle tissue is approximately 70-80% fluid, yet fluid is largely ignored when considering the mechanical function of skeletal muscle. However, recent work has shown that fluid could play a key role in force generation and transmission [1].

Intramuscular pressure (IMP) is the pressurization of skeletal interstitial fluid during active contraction and passive deformation [2]. While much work has been done to characterize the relationship between contractile force and IMP, fluid pressurization as a phenomenon is poorly understood under compressive conditions. Specifically, it is unknown how the solid and fluid phases of muscle contribute to compressive stiffness. The goal of this project is to determine the relationship between fluid pressure and compressive stress of skeletal muscle under semi-confined, passive compression conditions. We developed and employed an experimental protocol to measure fluid pressure during semi-confined compression. We hypothesized that fluid pressure and compressive stress would be correlated during compression, but that fluid pressure would remain between 50-100% of compressive stress.

## METHODS

Four porcine hind limbs were obtained from a local abattoir. No live animal handling was performed by researchers involved in this study. Following standard dissection procedures, the gracilis and semitendinosus muscles were isolated. These muscles were stored in a refrigerator at 4ºC immediately after dissection. Between 24-48 hours post-mortem, testing samples were isolated from the refrigerated muscles. The desired specimen sizes were 30x30x20 mm rectangular cuboids, cut with a custom specimen slicer. Rectangular cuboid samples had an average length and standard deviation of 30.24 ± 0.89 mm for two sides with an average height and standard deviation of 20.08 ± 0.43 mm as measured using a digital caliper.

Compression tests were conducted on a planar biaxial material testing system custom fabricated by ADMET (Norwood, MA). Force data was collected by a 50 lbf (222 N) load cell collected at 100 Hz. In semi-confinement, specimens were compressed uniaxially and confined in one direction with the third direction free from boundary conditions. All testing was completed with samples submerged in 10% phosphate buffered saline. A compression rate of 0.33 %/s was used to 30% compressive strain (0.7 stretch), followed by a 300 second relaxation period post-compression. A total of n=13 samples were used for this study. Engineering stress and engineering strain were calculated from initial sample dimensions, load cell force data, and displacement data.

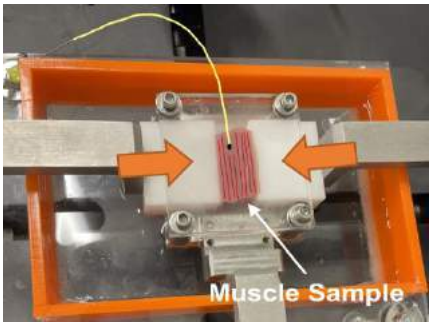


**Figure 1. Image of the experimental setup. Orange arrows denote the direction of compression. The midbelly sensor location is represented with the yellow line and black sensor tip. Muscle samples were restricted with platens in the vertical direction and free of boundary conditions in the lateral direction.**

Fluid pressure data was collected using a fiber-optic pressure microsensor (diameter 0.46 mm and ± 3 mmHg accuracy) inserted transverse to the compression direction for each sample [2] (FISO Technologies). Prior to sensor insertion, 400 µL of hyaluronic acid (HA) was placed near the needle tip, to create a stable aqueous area [3]. Muscle fibers were mounted parallel to sensor insertion and

perpendicular to the direction of compression (Figure 1). Fiber direction was established by visual inspection.

Linear regression analysis was performed for fluid pressure versus engineering stress values at 0.1, 0.2, and 0.3 compressive engineering strain levels and at 50 and 300 seconds into the relaxation period with significance set at $p<0.05$ to determine the correlation between intramuscular fluid pressure and tissue stress.

## RESULTS

Muscle tissue exhibited nonlinear stiffness in compression (Figure 2) and relaxation (Figure 3). Fluid pressure followed a similar, but inverted, pattern to engineering stress, with increases during the compression phase (Figure 2), and decreases during relaxation (Figure 3). As the skeletal muscle reaches 30% compression, fluid pressure and engineering stress exhibit a near 1:1 ratio (Figure 4). This near ratio becomes more exact in the relation period (Figure 4). Across all engineering strain and relaxation levels, fluid pressure was positively correlated with tissue engineering stress ($R^2>0.86$, $p<0.001$ for 10%, 20%, and 30% compressive engineering strain and at 50 and 300 seconds of relaxation).

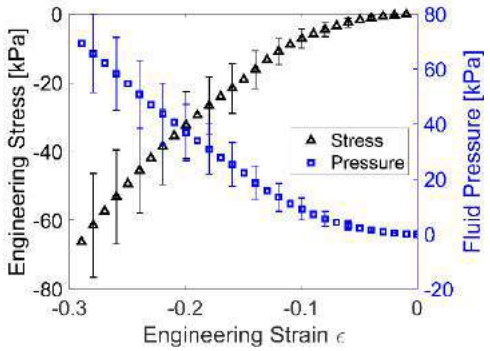


**Figure 2. Engineering stress (black triangles) and intramuscular fluid pressure (blue squares) versus compressive stretch with standard error bars).**

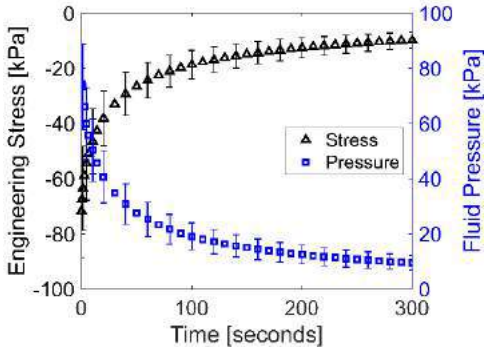


**Figure 3. Engineering stress (black triangles) and intramuscular fluid pressure (blue squares) versus time during the relaxation period. Data presented with standard error bars.**

## DISCUSSION

This work presents the first experimental study of the effect of compression on intramuscular pressure. We used a pressure microsensor and custom materials testing setup to perform semi-confined compression on porcine muscle tissue, as semi-confinement is likely to be more representative of *in vivo* conditions than fully confined or unconfined states [4]. The nonlinear stiffness and nonlinear relaxation of muscle tissue under compression agrees with previous materials testing studies of skeletal muscle [4].

Our results show that tissue engineering stress and fluid pressurization exhibit a nearly 1:1 inverse relationship, particularly under semi-confined conditions. This finding suggests that fluid pressurization plays a key role in the compressive stiffness of muscle tissue. However, further experimentation and modeling is needed to test this hypothesis more rigorously. While we hypothesized that fluid pressure would correlate to tissue stress but remain between 50-100% of stress, our data suggests slightly higher fluid pressurization during compression (Figure 4).

This work can be used to better understand how various constituents contribute to muscle stiffness in compression, and thus how the conditions such as a deep tissue injury (DTI) develop. For example, while interstitial fluid is present in all muscle, impaired or injured tissue may have altered interstitial fluid flow or pressurization. Such a case could cause mechanical damage to muscle fibers due to bearing a larger fraction of the compressive load. Future studies to investigate this potential phenomenon, particularly with computational modeling, would benefit the field.

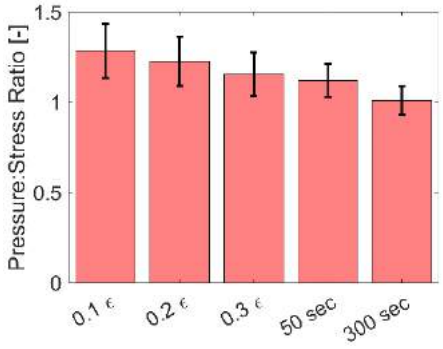


**Figure 4. Intramuscular fluid pressure:engineering stress ratio versus compressive engineering strain and relaxation points with standard error.**

## CONCLUSIONS

This study suggests that interstitial fluid may be a key contributor to muscle stiffness in compression. Previous studies have largely ignored the role of fluid pressure in muscle mechanics, with the exception of some work during elongation and contraction [1]. We employed an experimental approach to measure tissue stress and intramuscular pressure during semi-confined compression. Our results show that during compression, tissue stress and fluid pressure are highly correlated (Figures 2-4). Future work to investigate the role of interstitial fluid in various ages could be a significant contribution to the biomechanics field. Such work could be completed by performing simulations, such as a finite element modeling, to relate experimental data to tissue physiology.


## ACKNOWLEDGEMENTS

We would like to acknowledge the Clare Boothe Luce Research Program for Women in STEM and the Department of Mechanical Engineering at Bucknell University for funding.


## REFERENCES


[1] Sleboda, et al., *PNAS*, 2020, doi.org/10.1073/pnas.1914433117
[2] O'Connor, et al., *ABE*, 2021, doi.org/10.1007/s10439-020-02633-7
[3] Go, et al., *ABE*, 2017, doi.org/10.1007/s10439-016-1703-6
[4] Vaidya, et al., *JMBBM,* 2019, doi.org/10.1016/j.jmbbm.2019.103526

SB³C2022
Summer Biomechanics, Bioengineering and Biotransport Conference
June 20-23, Eastern Shore, MD, USA

# THE EFFECT OF PREGNANCY ON MECHANICAL INJURY CRITERIA IN MURINE UTEROSACRAL LIGAMENTS

**Catalina Bastías (1), Lea M. Savard (2), Kathleen Connell (3), Sarah Calve (1, 2, 4), Virginia L. Ferguson (1, 2, 4), Callan M. Luetkemeyer (2)**

(1) Biomedical Engineering Program, University of Colorado, Boulder, CO, USA
(2) Department of Mechanical Engineering, University of Colorado, Boulder, CO, USA
(3) Department of Obstetrics and Gynecology, University of Colorado Anschutz, Aurora, CO, USA
(4) BioFrontiers Institute, University of Colorado, Boulder, CO, USA

## INTRODUCTION

Worldwide, about 50% of adult women are affected by pelvic organ prolapse (POP), which is characterized by the descent of any or all the pelvic floor organs: bowel, uterus, and bladder. Only 12.6% of women suffering from POP are eligible to undergo corrective surgery, which only has a ~30% success rate [1]. Multiple factors are associated with POP, such as age, body weight, pregnancy, and the number of vaginal births, which are thought to affect the mechanical integrity of pelvic floor tissues, including the uterosacral ligament (USL) [1]. USLs are critically important supportive structures for the uterus and vagina, and tether the cervix to the sacrum [2]. Pregnancy and vaginal childbirth are known to impose additional mechanical strain on the USLs, potentially causing injury and increasing the chances of developing POP [3]. Type I collagen is known to be a major tensile load-bearing protein, and therefore likely to be involved in USL failure and POP. However, mechanical thresholds (i.e., injury criteria) for collagen in the USL are unknown. Defining injury criteria for USLs before, during, and after pregnancy will inform computational models of pelvic floor injury, improve our understanding of injury risk, and guide injury prevention efforts.

In this study, we employ a murine model to investigate the effect of pregnancy on the susceptibility of USLs to mechanical injury. Murine and human anatomy are similar; USLs in both species have similar anatomical landmarks and intersection points with the uterus, cervix, and sacrum, as well as similar composition and histology [4]. Here, we develop a methodology to spatially map mechanical strain and collagen damage in the murine USL, construct multimodal injury criteria from this full-field data, and compare the injury criteria for USLs from virgin and pregnant mice. Preliminary results indicate that pregnancy-related changes may protect the USL from major collagen damage by reducing the injurious potential of strains transverse to the primary collagen fiber direction.

## METHODS

Female mice (one virgin and one pregnant at day 19 of gestation) were obtained and euthanized according to the University of Colorado Boulder's Animal Care and Use Committee. For each sample, we isolated the pelvic bone structure, a single USL, and the cervix. The cervical end of the USL was tied with a 5-0 polyglactin suture, and the uterus was cut away, leaving a section of the cervix to act as an anchor and prevent the USL from sliding out of the suture loop. The second USL was completely removed, so that only one USL was mechanically tested. The sample was then placed in a custom staining well with a solution of Ghost Dye 780 (Tonbo Biosciences) and NucBlue Reagent (ThermoFisher Scientific) in 1× PBS for 2 hours at 4 °C on a rocker.

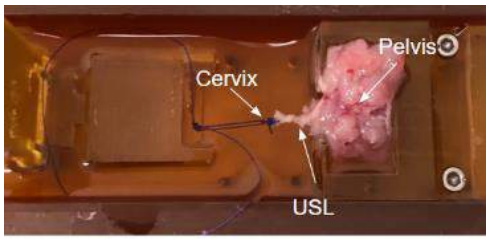


**Figure 1. Murine USLs were mechanically tested in a custom loading device.**

The sample was attached to two custom 3D printed (Objet Polyjet) grips (Fig. 1). The pelvis was secured onto a fixed grip, and the cervical attachment grip was connected to a movable Femtotools actuator. The sample was tested in a custom loading chamber with a bath of 1× PBS under a confocal microscope (Leica STELLARIS), attached to a Futek in-line 10 N load cell. The actuator was displaced until the slack in the USL was removed to determine the reference state.

Collagen hybridizing peptide (CHP) was used to determine regions with significant collagen denaturation [5]. Prior to mechanical testing, the PBS bath was replaced with a 10 µM solution of CHP for 15 minutes. This staining procedure was repeated after each deformation step to monitor changes in collagen damage. The samples were imaged at 10× magnification (2.14 µm pixel resolution) before, during, and after deformation. Deformed configurations were prescribed by actuator displacements of 1000, 2000, 3000, and 4000 µm. For each volume image, max intensity projections were created. 2D displacement fields were estimated using composite Ghost Dye and NucBlue images of reference and deformed states with MATLAB's *imregdemons* function, from which, Lagrange strain fields were derived. A moving threshold was used to determine pixels with significant collagen damage,

$$\gamma_i = \mu_i + 3\sigma_1 \quad (1)$$

Where $\gamma_i$ is the CHP image intensity threshold for the $i^{\text{th}}$ reference image, $\mu_i$ is the mean CHP intensity of the $i^{\text{th}}$ reference image, and $\sigma_1$ is the standard deviation in CHP intensity of the original reference image. This thresholding method is robust to increases in image intensity resulting from multiple stain times. Injury criteria were developed from damage maps and corresponding strain fields using logistic regression (MATLAB) to determine the strain thresholds for collagen denaturation.

## RESULTS

Ghost Dye and NucBlue composite images provided a trackable pattern for deformation mapping, and there was an increase in CHP image intensity following increased applied displacement (Fig. 2).

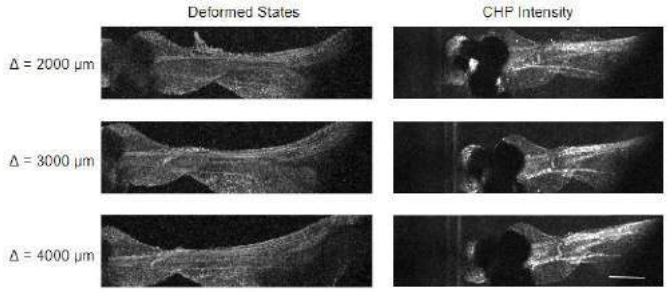


**Figure 2. Raw images of a USL from a virgin mouse at applied displacements of 2000, 3000 and 4000 µm and respective CHP images following deformation (scale bar = 500 µm).**

Computed deformation fields and collagen damage maps were inhomogeneous (Fig 3). Axial strains ($E_{11}$) increased as the applied deformation increased. This strain is along the orientation of the collagen fibers, and as predicted, damage increased with axial strain.

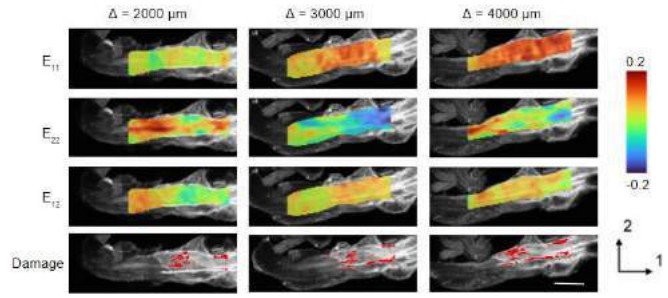


**Figure 3. Lagrange strain fields and damage maps after 2000, 3000 and 4000 µm displacements for a USL from a pregnant mouse (scale bar = 500 µm).**

Comparing collagen injury criteria for USLs from a virgin mouse and a pregnant mouse (gestation day 19), we saw a slight increase in $E_{11}$ thresholds: 0.08 vs. 0.085, respectively (Fig. 4). However, the biggest difference in injury criteria was observed in transverse strain ($E_{22}$). $E_{22}$ was a significant predictor of collagen damage for the virgin USL, but did not have a pronounced effect on collagen damage in the pregnant USL. Shear strain ($E_{12}$) did not correlate with collagen damage in either case.

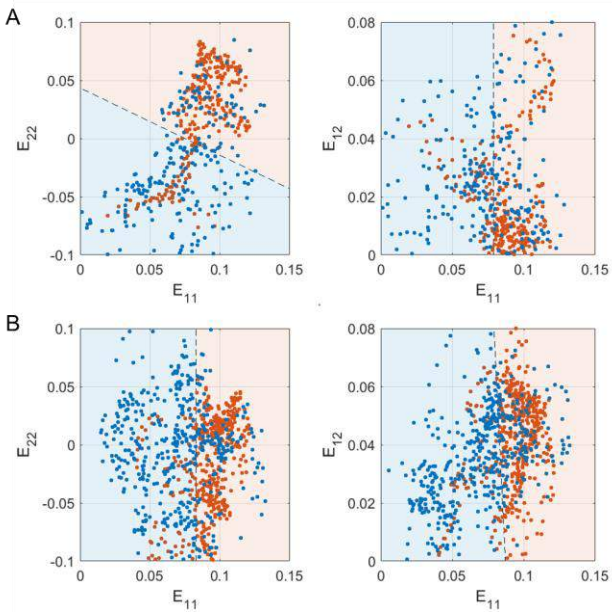


**Figure 4. Collagen injury criteria in $E_{11}$-$E_{22}$ and $E_{11}$-$E_{12}$ planes for USLs from virgin (A) and pregnant (B) mice.**

## DISCUSSION

We present a method to determine collagen injury criteria for the murine USL, accounting for spatial inhomogeneity and multi-directional strains. Our findings demonstrate that axial strain is a significant predictor of collagen damage in the USL (determined by logistic regression analysis), as has been assumed. However, transverse strain also appears to be a significant predictor of collagen damage in USLs from virgin mice. This result may indicate a decrease in collagen crosslinking in late pregnancy, which has been demonstrated in the cervix by Yoshida et al. [6].

This is the first study to model the mechanical thresholds for collagen damage in the USL. The method is limited to 2D, and more data is needed to confirm the present results. Nevertheless, the data suggest there are pregnancy-related changes in the relationship between deformation and collagen damage in the USL.


## ACKNOWLEDGEMENTS

This work was supported by the NSF Graduate Research Fellowship (LS), the Schmidt Science Fellowship (CL), the University of Colorado Innovative Grant Program, and the Anschutz Boulder Nexus Seed Grant.


## REFERENCES


[1] Barber, MD et al., *Int Urogynecol J*, 24(11): 1783-90, 2013.
[2] Donaldson, K et al., *Ann Biomed Eng*, 49: 1788-1804, 2021.
[3] Blomquist, JL et al., *JAMA*, 320: 2438, 2018.
[4] Iwanaga, R et al., *Int Urogynecol J*, 27: 1697-1704.
[5] Zitnay, JL et al., *Nat Comm*, 8(1): 1-12, 2017.
[6] Yoshida, H et al., *PloS One*, 9(11), 2014.

SB³C2022
Summer Biomechanics, Bioengineering and Biotransport Conference
June 20-23, Eastern Shore, MD, USA

# 4D Flow MRI Comparison of Surgical Grafts for Correction of Pulmonary Artery Aneurysms□A Case Study

**Téa J. Cohen (1), Melody L. Dong (1), Arshid Azarine (3,7), Francois Haddad (4), Olaf Mercier (5,6,7), Alison L. Marsden (1,2)**

(1) Bioengineering, Stanford University, Stanford, CA, USA
(2) Pediatric Cardiology, Stanford University, Stanford, CA, USA
(3) Department of Radiology, Groupe Hospitalier Paris Saint-Joseph, Paris, France
(4) Division of Cardiovascular Medicine, Stanford University, Stanford, CA, USA
(5) Biomedical Engineering Lab, Groupe Hospitalier Paris Saint-Joseph, Paris, France
(6) Department of Thoracic Surgery, Université Paris-Saclay, Marie Lannelongue Hospital, Le Plessis Robinson, France
(7) INSERM UMR-S □□□, Pulmonary Hypertension□Pathophysiology and Novel Therapies, Marie Lannelongue Hospital, Le Plessis Robinson, France

## INTRODUCTION

A pulmonary artery aneurysm (PAA) is a rare condition (~1 out of 14,000) defined by dilation of all three layers of the vessel wall (intima, medial, adventitia) and can lead to dissection or be fatal if ruptured (50-100% mortality).[1,2] Patients with a PAA have a dilated main pulmonary artery (MPA) diameter more than 1.5 times the normal value, with the normative MPA diameter estimated to be 2.89 cm in males and 2.69 cm females.[3] Although most PAAs are managed conservatively, other PAAs require surgical intervention to prevent future rupture or dissection or to alleviate symptoms (chest pain, dyspnea, palpitations, syncope).[4,5] Proximal PAAs are treated surgically by replacement of the native dilated vessel with a graft – either synthetic or biological. Synthetic dacron grafts are made of woven or knitted polyester while biological grafts may be either xenogeneic (animal origin) or allogeneic (from a human donor) and are decellularized using tissue engineering techniques to prevent immune response. However, we have a limited understanding of optimal treatment.

4D-flow magnetic resonance imaging (4DMRI) provides non-invasive comprehensive assessment of anatomic and blood velocity features in a time-resolved 3D velocity field.[6] Visualization and quantitative velocity metrics from 4DMRI has shown promise in evaluating hemodynamics in several diseases.[7] Although previous studies have analyzed pulmonary artery (PA) hemodynamics using 4DMRI, these have primarily been focused on characterizing pulmonary arterial hypertension (PAH) and not PAAs.[8]

In this case study, we evaluate the MPA hemodynamics using 4D Flow MRI in two patients with a PAA before and after surgical correction with a dacron graft and an aortic homograft from donor tissue to understand the extent to which different surgical replacement grafts aid in restoring healthy hemodynamics.

## METHODS

We obtained time-resolved 4DMR scans with 20-30 cardiac frames from two patients with a PAA from the Marie Lannelongue Hospital in France before and after they received surgical corrections. Patient 1 had a PAA located in the MPA and received a synthetic dacron graft (woven polyester) to replace the dilated PA trunk. Patient 2 had PAH with a PAA in the MPA and the right PA (RPA) and received a bilateral lung transplant attached distally to the left and right lobar branches as well as a donor aortic homograft to replace the dilated PA trunk and RPA in a valve-sparing procedure.

4DMR scans were downloaded from the medical imaging cloud platform, Arterys (Arterys Inc., San Francisco, CA, USA) where phase offsets and background corrections were applied. To isolate 4DMR velocity in the PAs, we created patient-specific 3D models of the PAs (beginning at the pulmonary valve and ending at the left and right PAs) using the open-source software SimVascular (simvascular.org). To account for movement of the PAs throughout the cardiac cycle, patient-specific models were created at two timepoints in the cardiac cycle when the PAs were minimally deformed and maximally deformed with dilation and lateral movement. The shape analysis registration algorithm from the open-source software Deformetrica was used to interpolate geometries throughout the cardiac cycle, specifically between the minimum and maximum deformed timepoints, and then back down to the minimum. These interpolated geometries were visually checked and adjusted to match the magnitude 4DMR images. 4DMR velocity was resampled onto a discretized tetrahedral element mesh for all PAs at all timepoints in the cardiac cycle.

We compared blood flow in the preoperative and postoperative state for both patients by visualizing velocity streamlines. Additionally, we computed the fractional area of reverse flow (RF) for a cross-sectional slice taken in the middle of the MPA to capture recirculating and reverse flow using **Equation 1:**

$$FractionaliAreaiRF = \frac{A_{\vec{u}\cdot\vec{n}\leq 0}}{A_{total}} \quad (1)$$

where $A_{total}$ is the total area of the slice and $A_{\vec{u}\cdot\vec{n}\leq 0}$ is the area of the slice with reverse flow as defined by the dot product of $\vec{u}$, the velocity, and $\vec{n}$, the surface normal, less than or equal to 0. We also calculated the spatially and temporally averaged velocity through a cross-sectional slice taken at the most proximal portion of the MPA, parallel to the pulmonary valve (PV).

## RESULTS

We found that both patients' preoperative hemodynamics were characterized by a large area of recirculation in the MPA, the result of the systolic jet from the PV hitting the MPA wall opposite to it. We found an initial drop in the fractional area of RF (**Equation 1**) in the MPA during early systole due to the onset of the systolic jet. Although the fractional area of RF remained high during systole preoperatively, indicating larger regions of inefficient reverse flow, it remained low during postoperative systole in both patients (**Figure 1**). This indicates a large percent of recirculation flow in the pre-op MPA as opposed to the more forward and laminar flow seen postoperatively. Furthermore, we found that the fractional area of RF during systole is greater in the patient with the aortic homograft than in the patient with the dacron graft. In the postoperative aortic homograft MPA, there were more regions of lower velocity recirculation, specifically two separate regions at the native valve annulus.

Additionally, both patients had greater MPA velocity postoperatively, but the patient with the dacron graft had higher post-op velocities than the aortic homograft patient (**Figure 2**). Further, both the Dacron and aortic homograft patients postoperatively had vortices to the right and left of the MPA bifurcation as well as near the valve annulus.

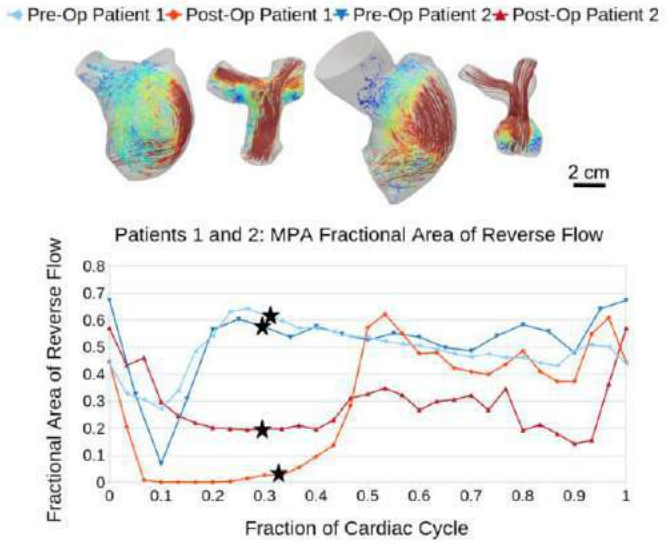


**Figure 1: Fractional Area of RF in a cross-sectional middle MPA slice. Patient 1 (Dacron) and Patient 2 (Aortic Homograft). Fractional Area of RF is low during post-op systole and high during most of pre-op systole apart from the onset of the systolic jet.**

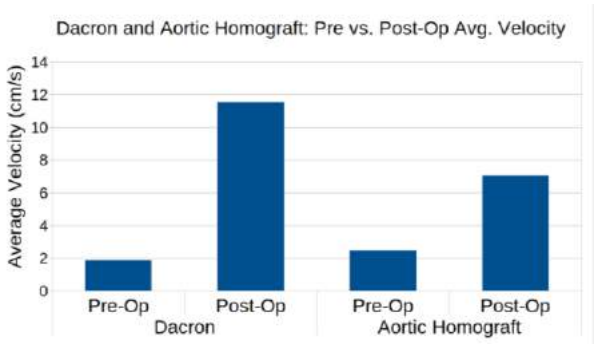


**Figure 2: Average Velocity (cm × $s^{-1}$) through a slice parallel to the pulmonary valve is low preoperatively. Dacron graft restored high velocity flow to greater extent than Aortic homograft.**

## DISCUSSION

In two PAA patients, we compared the 4DMRI-derived PA hemodynamics between a dacron graft and an aortic homograft pulmonary trunk replacement before and after surgical correction. We found both grafts recovered healthy hemodynamic phenotypes postoperatively but saw slight differences between the grafts in the laminar flow and velocity at the valve annulus and in the MPA.

Specifically, we found that preoperative MPA hemodynamics in PAA patients were characterized by a large area of recirculating flow which became more laminar after surgical replacement of the aneurysms with grafts. Because laminar blood flow is associated with more efficient transport of blood, the grafts in patients 1 and 2 improved PA hemodynamics leading to more desirable blood flow.[9]

Though both patients' grafts improved and restored a healthier flow, the aortic homograft yielded postoperative hemodynamics with lower velocity flow and more areas of recirculation near the valve annulus than the synthetic dacron graft, indicating greater inefficient flow and likely due to the native MPA geometry. However, a more direct comparison of the performance of different graft types with more patients is needed to understand the long-term PA hemodynamics and longevity across graft types.

This case study provides insights from 4DMRI into the changing PA hemodynamics before and after correction of a PAA using a dacron graft and an aortic homograft. These insights show promise in evaluating the performance of different graft types for PAA correction to aid in the surgical decision-making process.


## ACKNOWLEDGEMENTS

De-identified 4DMR data was obtained from the Marie Lannelongue Hospital. 4DMR post-processing was conducted using high-performance computing resources from Sherlock as part of the Stanford Research Computing Center.


## REFERENCES


[1] Duijnhouwer, AL et al., *Congenital Heart Disease*. 11:102-109, 2016.
[2] Park, HS et al., *Cardiovasc Diagn Ther*. 8(3): 350–361, 2018.
[3] Truong, QA et al., *Circulation: Cardiovascular Imaging*. 5:147–154, 2012.
[4] Theodoropoulos, P et al., *Int J Angiol*. 22(3): 143–148, 2013.
[5] Kreibich, M et al., *Circulation*. 131:310–316, 2015.
[6] Stankovic, Z et al., *Cardiovasc Diagn Ther*. 4(2): 173–192, 2014.
[7] Azarine, A et al., *RadioGraphics*. 39(3): 632-648, 2019.
[8] Pillalamarri, NR et al., *Annals of Biomedical Engineering*. 49:3465-3480, 2021.
[9] Chiu, JJ, Chien, S, *Physiol Rev*. 91(1), 2011.

SB³C2022
Summer Biomechanics, Bioengineering and Biotransport Conference
June 20-23, Eastern Shore, MD, USA

# ESTABLISHING AN OPTIMIZED ANNULOPLASTY RING TYPE USING *IN VIVO* AND *EX VIVO* BIOMECHANICAL ANALYSES

**Katelynne A. Berland (1), Sanchita S. Bhat (1), Andrew W. Siefert (1), Maeve Janecka (1), Shelley C. Gooden (1), Beatrice E. Ncho (1), Takayuki Kawashima (2), Mori Kazuki (2), Satoshi Kozaki (2), Robert C. Gorman (2), Joseph H. Gorman III (2), Ajit P. Yoganathan (1)**

(1) The Wallace H. Coulter Department of Biomedical Engineering, Georgia Institute of Technology, Atlanta, GA, USA
(2) Perelman School of Medicine, University of Pennsylvania, Philadelphia, PA, USA

## INTRODUCTION

The purpose of the heart's mitral valve (MV) is simple. It aims to maintain unidirectional flow from the left atrium to the ventricle while preventing the backflow of blood during ventricular contraction. Diseases can alter MV function. Most diseases render the valve unable to close and result in mitral regurgitation (MR). In MR, blood that is normally pumped to the body is reversed through the unsealed mitral leaflets, into the left atrium, and then onto the lungs, for which the extra work with time tires the heart's muscles, leading to heart failure.

Worldwide, MR is the most common heart valve dysfunction whose prevalence and severity increase with age. When left untreated this disease results in excess morbidity and mortality. Open heart surgery is the established treatment of choice. The most common type of surgery is MV repair, where a prosthetic annuloplasty ring is sutured into the tissue surrounding the MV orifice. By constraining the MV's orifice to a comparably smaller ring, the shape and size of the valve orifice is reduced to force the MV leaflets into a state of closure [1].

Ring annuloplasty is effective in most patients but failures can occur. The most common surgical failure is suture dehiscence where the sutures securing the ring to the MV tear out of their underlying tissue. Mechanistically, *this occurs when the forces on each suture exceed the holding strength of the underlying tissue.* In review of historical clinical findings, suture dehiscence more frequently is reported with completely rigid annuloplasty rings and occurs more frequently in one region of the mitral valve orifice (posterior region) [1-3].

To build understanding for these clinical observations and develop further insight for clinical translation, our group developed sensors to measure the forces in each suture used to secure an annuloplasty ring to the MV in the beating heart of sheep. To understand the effect of ring stiffness, two differing rings were tested (full rigid vs. fully flexible). To understand why suture dehiscence seems regionally dependent, suture pull-out force testing was completed and compared to the beating heart suture force measurements.

## METHODS

### *Force Sensors and Annuloplasty Ring Selection*

Miniature, strain-gage based force sensors were designed and fabricated (**Figure 1A**). The spring element of each sensor was rapid prototyped from 316L stainless steel. Half-bridge strain gages were adhered and protected on each spring element. Each sensor was calibrated and then attached to an annuloplasty ring (**Figure 1B**). As demonstrated in **Figure 1C**, forces applied to a suture result in the bending of the spring element's upper arm, creating a moment arm to deform the cantilever beam for which the strain gages are adhered. The strain gages deform with the measurement arm, resulting in changes to the gauge's electrical resistance. Through calibration, changes in electrical output are correlated to known forces providing the ability to measure cyclic suture forces in the beating heart of animals.

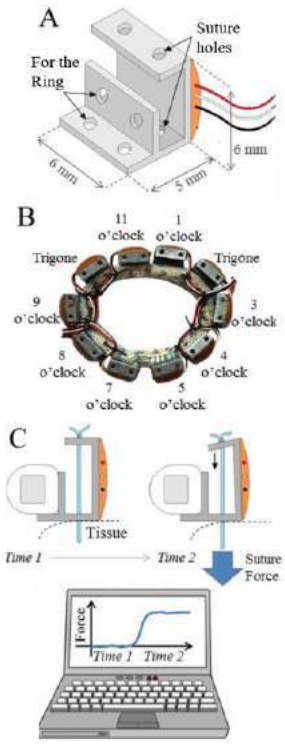


Two ring types were instrumented with force sensors. Completely rigid (Medtronic Profile 3D™) and completely flexible (fabricated to the same dimensions as the Profile 3D™ rings). Multiple sizes of each ring were instrumented and made ready for each animal experiment.

### *Animal Experiments*

A diseased large animal model was utilized for this study. This model creates MR in sheep. Fourteen healthy sheep (~90 kg) were subjected to a coronary artery occlusion which blocks blood flow to ~20% of the left ventricular wall, including the posteromedial papillary muscle. Following occlusion, the animals were recovered, and their MR allowed to develop over a 6-8 week period. At the completion of this period, an open-heart ring annuloplasty procedure was completed using the force sensor instrumented annuloplasty rings.

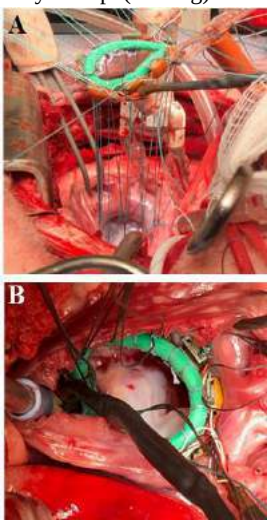


**Figure 2**

Open heart surgeries were completed (**Figure 2A-B**), implanting the instrumented rings using the same exact methods used clinically. Seven animals were implanted with the fully rigid ring and remaining animals implanted with the fully flexible ring (**Figure 2**). Following implantation, each animal was weaned from cardiopulmonary bypass, stabilized, and cyclic suture force measurements recorded for cardiac cycles reaching a peak left ventricular pressure of 125 mmHg to approximately match left ventricular pressures in humans. All suture force data was recorded using LabView and analyzed in MATLAB.

### *Suture Pull-Out Testing*

Following each animal experiment, each heart was removed, left atrium opened, and rings removed so that the sutures remained within the annular tissue. The mitral valves were then excised and secured to a fixture to conduct suture pull-out testing using an 858 MiniBionix (MTS, Eden Prairie, MN) (**Figure 3**). Each suture was pulled perpendicularly to the plate until it tore through the tissue. The maximum force was recorded for each suture position.

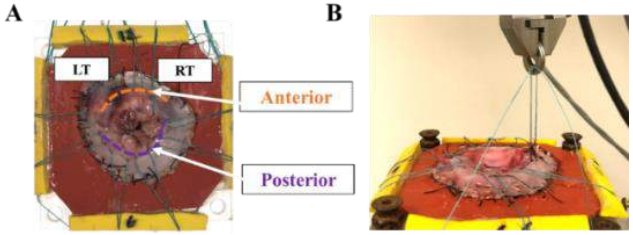


**Figure 3.**

## RESULTS

At the time of ring implantation, each animal exhibited MR and incomplete leaflet closure. Ring implantation successfully eliminated MR in all animals. The mean cyclic suture forces measured for both ring types by ring position are reported in **Figure 4**. The flexible ring experienced greater suture loading at the anterior positions, especially at 1 o'clock, compared to the posterior positions. Compared to the posterior region of the rigid rings, suture loading in the posterior region of the flexible rings were lower.

Suture pull-out testing (**Figure 5**) demonstrated differences in suture holding strength between suture positions and regions. The highest suture pull-out forces were observed along the anterior region (Left Trigone, 11'oclock, 1 o'clock, and Right Trigone). Overall, the anterior positions had greater holding strength than the posterior regions, with the lowest being in the 5 and 7 o'clock regions.

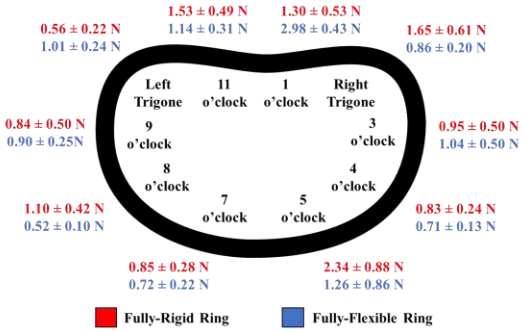


**Figure 4. Cyclic Suture Force Measurements**

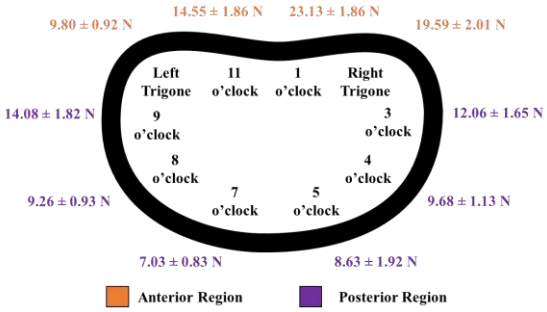


**Figure 5. Suture Pull-out Force Data**

## DISCUSSION

Preliminary results in fourteen animals with MR demonstrate regional differences in suture force loading between ring types. The flexible ring experienced lower posterior suture loading compared to the rigid ring, which suggests that reduced ring stiffness may redistribute the loads to the more robust anterior region, where suture holding strength is greater. Pull-out testing revealed suture holding strength was less in the posterior region, correlating well with clinical reports detailing suture dehiscence to occur in this region more commonly.

This data is currently limited to fourteen animals that were selected by weight. Each ring was selected to 'undersize' the mitral valve by 2 sizes, as done clinically. As part of the procedural protocol, there were no controls for the force for with which the surgeon tied the sutures into the underlying tissue. This was done to reflect real-world conditions at the cost of experimental control. The effect sizes between the ring types may have been reduced but may improve with further experiments.

Initial findings suggest rigid rings may as a whole elevate suture forces, and the posterior region of the annulus exhibits lower suture force holding capacity. These initial data, with their further expansion and study, provide possibility and promise for further serving the large MR patient population by improving knowledge for the effect of ring selection and regional holding strength, to further reduce the potential for surgical repair failures.


## ACKNOWLEDGEMENTS

This study was partially supported by the National Heart, Lung and Blood Institute (R01HL147256-01).


## REFERENCES


[1] Madukauwa-David, I et al., *Biomech Model Mechanobiol*, 18(2):291-299, 2019.

[2] Ncho, B et al., *J Thorac Cardiovasc Surg*, 159(5):1766-1774, 2020.

[3] Pierce E et al., *Ann Thorac Surg*, 102(2):518-526, 2016.

# VISUAL CHARACTERIZATION OF APONEUROSIS MICROSTRCUTURE

**Olivia L. Dyer (1), Mark A. Seeley (2), Benjamin B. Wheatley (3)**

(1) Cell Biology/Biochemistry, Bucknell University, Lewisburg, PA, USA
(2) Department of Pediatric Orthopedics, Geisinger Medical Center, Danville, PA, USA
(3) Mechanical Engineering, Bucknell University, Lewisburg, PA, USA

## INTRODUCTION

Aponeurosis is a tendinous sheath-like tissue found in many muscle-tendon units that covers the muscle belly and transitions into tendon. The sheath-like structure of aponeurosis is thinner towards the muscle belly and thicker near the tendon. Unfortunately, not much else is known about the structure-function mechanics of aponeurosis tissue, especially in comparison to other musculoskeletal tissues such as tendon and ligament. Previous work has shown that the mechanical properties of the aponeurosis tissue vary depending on whether it is a thinner portion of the tissue near the muscle or the thicker portion near the tendon [1]. Little research has been done to understand how collagen fiber microstructure contributes to aponeurosis stiffness.

The mechanical function of musculoskeletal soft tissues is often driven by collagen microstructure, such as orientation, waviness, and dispersion. While the mechanical properties of aponeurosis tissue have been studied, it remains unclear how the collagen fiber morphology – such as collagen crimping – change in response to stretch. Evaluating how the structure of the aponeurosis tissue changes in relation to its observed functional characteristics will enable a better understanding of how aponeurosis functions in the human body. These data can enable the improvement of computational models that include aponeurosis as a component of muscle-tendon units and improve our understanding of how aponeurosis tissue may accumulate damage as a result of injury. The goal of this work was to use scanning electron microscopy to characterize the microstructure of aponeurosis tissue be comparing waviness values measured in unstretched and stretched tissue. It is hypothesized that the waviness of the collagen fibers will decrease after tissue has been stretched.

## METHODS

Porcine shoulder tissue, obtained from a local abattoir, was dissected to obtain 40x10 mm specimens that include the transition from thick to thin aponeurosis tissue. Long and steady cuts using sharp dissection blades were used to ensure minimal damage to the aponeurosis (Figure 1A). As much muscle tissue as possible was removed without tearing or damaging the aponeurosis [2,3]. All samples were kept moist by applying 10% phosphate buffered saline throughout the dissection process and before testing [2,3].

Unstretched samples (n=10) were fixed in a 1:20 volume to fixative ratio of 10% formaldehyde for 24 hours at 4 C, while stretched samples (n=10) were similarly fixed in a custom fixing stretcher at five percent strain (Figure 1B).

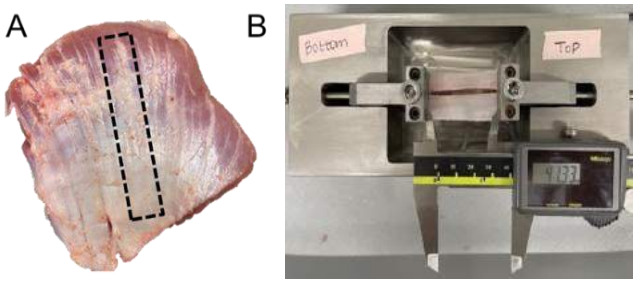


**Figure 1: (A) Sample aponeurosis tissue showing the transition from thick to thin tissue. (B) Sample of aponeurosis tissue in uniaxial material testing setup.**

Both the stretched and unstretched samples were then subject to a series of graded ethanol soakings that included 15min in 30% ethanol. 15min in 50% ethanol, 15min in 70% ethanol, 15min in 90% ethanol, 15min in 100% ethanol, and finally 30min in 100% ethanol. In preparation for dehydration, samples were placed in the fume hood and soaked in a 1:2 solution of HMDS to ethanol for 20min followed by 20min in 2:1 solution of HMDS to ethanol. Samples were then dehydrated in two 20min soakings in 100% HMDS. The final HMDS was poured off to just cover the top of the samples and left in a fume

hood to evaporate overnight. After 24 hours, all samples were fully dried and prepared for SEM.

Once all the samples were fully dehydrated 24-48hrs later they were sputter coated with gold and stored in an airtight container until they were imaged with the SEM. Images were taken at 50, 100, 1k, and 3.5k magnification at 6 equally spaced points along the entire 40mm length of the aponeurosis with the Hitachi SU5000 Field Emission Gun Microscope. Waviness was determined using the NeuronJ plugins for Fiji/ImageJ, a free image analysis tool [4]. Waviness of the stretched and unstretched aponeurosis was quantified as the ratio of the true length of the collagen fiber to the tangent of two endpoints of that same collagen fiber [5]. Approximately 3 fibers were measured for each image at 50 and 100 magnification and waviness values were calculated based on these measurements. An unpaired two-way t-test was run to determine if the waviness values of the stretched tissue was greater than the waviness values of the unstretched tissue.

## RESULTS

Scanning electron microscopy of aponeurosis tissue showed that it exhibited a hierarchical structure, similar to that of tendon or ligament, with collagen-rich fascicles (75μm to 200μm diameter), fibers (50μm to 20μm diameter), and fibrils (10-300nm) (Figure 2). Waviness in the collagen fibers was observed at lower magnifications (100 μm), while at higher magnifications the sheet-like structure of the collagen fibrils was seen (1,000 μm). At lower magnifications, the collagen fibers exhibited some degree of alignment, while at higher magnifications the fibrils appeared to be more randomly organized in the collagen sheet (Figure 2). The unstretched collagen fibers had an average waviness value of 1.174 ± 0.211 The stretched collagen fibers had waviness values ranging from 1.051 ± 0.064 (Figure 2). The p-value was 6.615e-08, which shows there is a statistically significant difference in the waviness values of stretched and unstretched tissue.

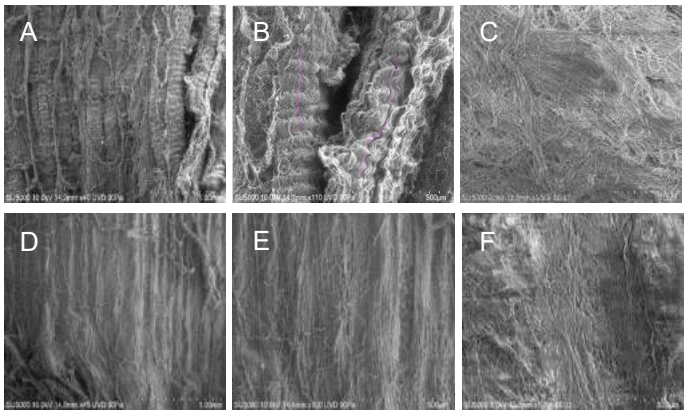


**Figure 2: Porcine triceps brachii aponeurosis SEM images at increasing magnifications. Unstretched samples at (A) 40x magnification, (B) 100x magnification, and (C) 1,000x magnification. Stretched samples at (D) 40x magnification, (E) 100x magnification, and (F) 1,000x magnification.**

## DISCUSSION

SEM imaging was used to characterize aponeurosis microstructure and determine how waviness changed in stretched and unstretched tissue. Aponeurosis tissue appeared to have a similar hierarchal structure comprised of fascicles, fibers, and fibrils similar to tendon tissue. This is unsurprising as aponeurosis tissue is largely an extension of tendon. Additionally, unstretched tissue exhibits a high degree of waviness and there is observed collagen crimp. Tissue that has been fixed under a five percent stretch appeared to have a lower degree of collagen waviness and less collagen crimp compared to the unstretched tissue. This is unsurprising because as the tissue is stretched the collagen fibers stretch out making them straighter and less wavy. This also supported by the transition out of the toe-region to the linear elastic region of the stress-strain curves for aponeurosis tissue, which occurs at approximately five percent stretch [1].

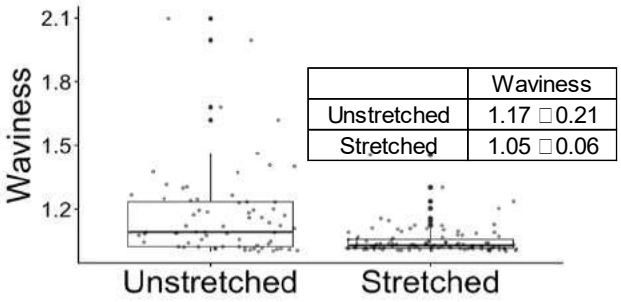


**Figure 3: Comparison of unstretched and stretched aponeurosis collagen fiber waviness values. The average waviness value of unstretched aponeurosis is greater than the average waviness value of stretched aponeurosis ($p < 0.05$).**

The hierarchical structure of aponeurosis tissue can be implemented to develop better musculoskeletal simulations and modeling efforts, which will allow for more accurate analysis of how muscle forces are transmitted to tendon. All analysis was performed on undamaged tissue, and it is unclear how damage affects aponeurosis mechanics. Improved modeling efforts can inform how collagen structures change in response to load and how the tissue becomes damaged so better protocols on how to help heal injuries more quickly can be developed. Future work will include comparing how waviness values of stretched and unstretched tissue compare depending on the location of the aponeurosis tissue, closer to the muscle belly or closer to the tendon.

## CONCLUSION

Aponeurosis exhibits a similar hierarchical structure similar to tendons that is composed of fascicles, fibers, and fibrils. Additionally, when the tissue is stretched the fibers become less wavy which is agrees with stress strain curves that show around five percent stretch the tissue becomes linearly elastic [1]. Using these data, better musculoskeletal simulations can be developed to improve clinical care of injuries and impairments that affect muscle-tendon units.

## ACKNOWLEDGEMENTS

This work was supported in part by The John P. & Mary Jane Swanson Professorship in Engineering & the Sciences and the Program of Undergraduate Research (PUR) at Bucknell University.

## REFERENCES

[1] Tully, E., et al. Location Dependent Mechanical Behavior of Aponeurosis Tissue Under Uniaxial Tensile Stretch. SB3C 2021.
[2] Azizi, E. Integr Comp Biol 49.1: 51-58, 2009
[3] Shan, X. PLoS ONE 14.2: 1-18, 2019
[4] J. Schindelin, I, et al. Nat. Methods, 2012, vol. 9, pp. 676-682
[5] Mohammadkhah, Melika, et al. J Mech Behav Biomed Mater, 2018, vol. 77, pp. 734–744.

SB³C2022
Summer Biomechanics, Bioengineering and Biotransport Conference
June 20-23, Eastern Shore, MD, USA

# CHARACTERIZING THE MECHANICAL HETEROGENEITY OF PORCINE CAROTID ARTERY BIFURCATIONS

**Claire L. Westman (1), Carly L. Donahue (1), Victor H. Barocas (1)**

(1) Department of Biomedical Engineering, University of Minnesota —Twin Cities, Minneapolis, Minnesota, United States

## INTRODUCTION

Arterial bifurcations serve as important regulators in the distribution of blood throughout the body. Due to their anatomy, bifurcations experience a heterogeneous distribution of stresses from the blood pressure and wall shear stress. Because arteries are known to remodel in response to mechanical load [1], we expect that bifurcations would have a heterogeneous distribution of mechanical properties.

The carotid artery (Fig. 1A) has been widely characterized using both *in vivo* and *ex vivo* techniques [2,3]. However, the local material heterogeneity that arises in healthy bifurcations has been less explored. Using a combination of uniaxial tensile testing and digital-image-correlation-based displacement tracking, this study characterized the stiffnesses in different regions of porcine carotid bifurcations.

## METHODS

**Dissection and Sample Preparation:** Strips of tissue were cut from three different regions of healthy porcine carotid arteries. Each carotid artery either yielded two samples, the outer side of the interior and exterior carotid [Fig. 1B], or one sample from the apex of the bifurcation [Fig. 1C]. In addition to samples from the three regions of interest, a control sample was also tested that was from the common carotid artery.

Each sample was cut to a width of 5.29 mm ± 1.23 mm (mean ± SD). The thickness for each sample ranged from 0.5 mm to 1 mm and was consistent along the length of the samples. Samples were tested within 48 hours of tissue harvest and were kept refrigerated and suspended in 1X Phosphate Buffered Saline before and after dissection. Testing was performed at room temperature.

**Uniaxial Tensile Testing:** The rectangular samples were loaded into the grips of a Q Series Test Resources uniaxial mechanical tester equipped with 10lbf load cells. The measured gauge length was 10.48mm ± 2.47mm (mean ± SD). Each sample was pre-conditioned to 50% engineering strain for 5 cycles at a controlled displacement rate of 3 mm/min, followed by extension to failure at the same rate. Both tests were videorecorded from above for digital image correlation (DIC).

**Strain Tracking and Analysis:** Once the testing was complete, the data from the tests and the videos were uploaded and analyzed. Quasi-static analysis of the load-cell data allowed the determination of the tissue stress throughout the test. An existing DIC and strain-tracking program [4] was used to determine the local strain on the tissue. Strain field graphics were generated using TecPlot.

Stress-strain curves were made by taking an average of the strain for three different regions within a sample for each frame. Strain data were removed on both ends of the sample to eliminate error that could occur from proximity to the grips. The stress is assumed to be uniform across the sample for each time frame.

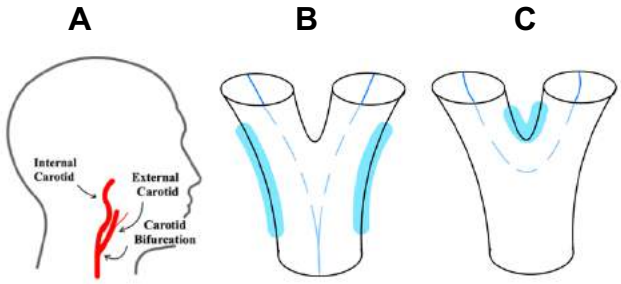


**Figure 1: A) Anatomical location of the carotid bifurcation and its internal and external daughter branches. B) Dissection diagram highlighting the regions of interest on the outer wall of the bifurcation. C) Dissection diagram highlighting the apex of the bifurcation.**

## RESULTS

The experimental results are summarized in Fig. 2-5. For the apex sample [Fig. 2], there was slightly more strain farther from the bifurcation region, especially at large strains. For the strip taken from the interior branch [Fig. 3], there was a clear gradient in strain, with the largest strains occurring in the distal segment (i.e., that which is in the internal carotid rather than the common carotid artery); no such gradient was seen in the exterior branch [Fig. 4] or the control sample [Fig. 5]. The measured stresses were much higher in the apex and interior samples than in the exterior and control samples.

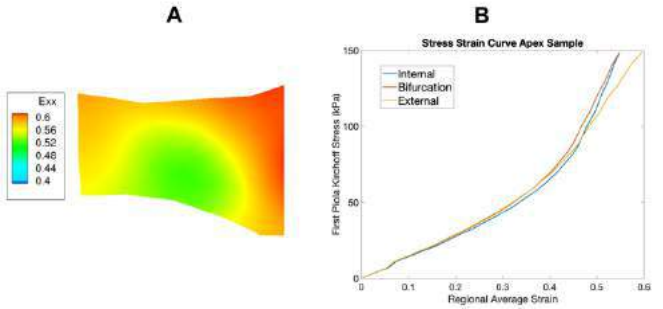


**Figure 2: A) Local strains along the bifurcation apex at 50% grip strain. B) Stress-strain curves showing material heterogeneity in different regions of the sample.**

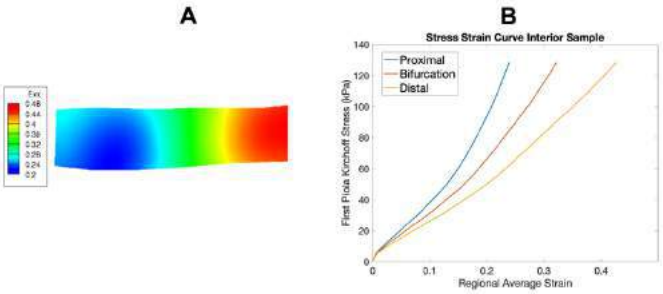


**Figure 3: A) Local strains along the wall of the bifurcation between the common carotid and the interior carotid at 50% grip strain. B) Stress-strain curves showing material heterogeneity in different regions of the sample.**

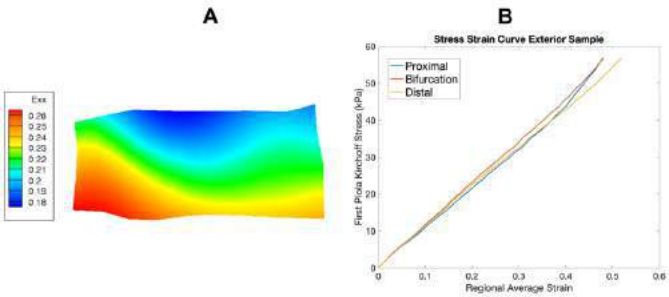


**Figure 4: A) Local strains along the wall of the bifurcation between the common carotid and the exterior carotid at 50% grip strain. B) Stress-strain curves showing material heterogeneity in different regions of the sample.**

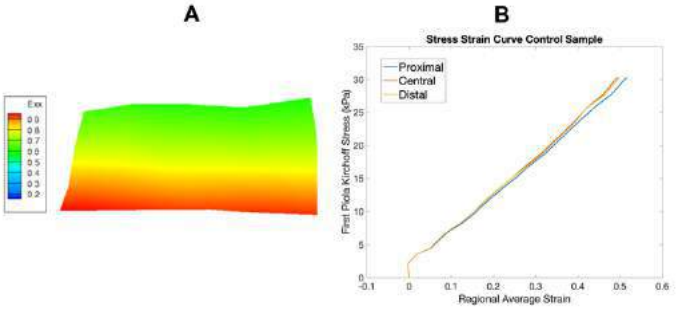


**Figure 5: A) Local strains along the common carotid artery at 50% grip strain. B) Stress-strain curves showing material heterogeneity in different regions of the sample.**

## DISCUSSION

The common carotid artery, the control, experienced the least amount of stress of any of the samples. This is expected because it has been found that the principal stresses arising in the apex and walls of the bifurcation are higher than the principal stresses of the carotid artery. [5]. A control was used to validate the tensile testing procedure.

The apex of the bifurcation exhibited greater longitudinal stiffness than the surrounding vessel wall, which may be the a result of remodeling in respoinse to the heterogeneous loading experienced by the bifurcation. From finite element studies, it has been seen that the wall thickness of the parent artery affects how much stress the apex experiences [6]. In [6], it was found that when the apex and external transition have a normalized wall thickness of 0.5, the stress of the apex is about 200% of the stress of the external transition. Those estimates are consistent with our results.

Previous studies of carotid heterogeneity are largely focused on atherosclerotic plaque lesions [7]. However, it is also important to characterize heterogeneity resulting from the arterial remodeling process in healthy tissues as well.

While this work expands on our current understanding of the material behavior of arterial bifurcations, there were some limitations that should be considered, including that the samples were only tested in the axial direction. Future work will involve testing the arteries circumferentially, expanding the number of samples tested, and studying heterogeneity in other healthy arterial bifurcations in the body. This work contributes to our understanding of the arterial remodeling process in complex anatomical structures.

## ACKNOWLEDGEMENTS

We thank the Visible Heart Lab for providing the tissue used in this project. This work was supported by the National Institutes of Health (U01-HL139471, T32-HL139431).

## REFERENCES

[1] Fung, Y. et al., *J of Applied Physiology*, 70:2455-2470, 1991.
[2] Boekhoven R., et al., *Ultrasound in Med. & Biol*, 2:574-585, 2016.
[3] Luo X., et al., *BMC Medical Imaging*, 19:2-7, 2019.
[4] Raghupathy, R., *University of Minnesota*, 36-39, 2011.
[5] Hariton, I, et al., *J Theor Biol*, 248:460-465, 2007.
[6] Delfino, A. et al., *J Biomech*, 30:777-782, 1997.
[7] Paritala, P. et al., *Cerebrovascular Dis*, 50:510-519, 2021.

# BLOOD CLOT REMOVAL PRESSURES IN AN EXPERIMENTAL MODEL OF ASPIRATION THROMBECTOMY

**Nicole J. Beautz (1), Noah P. Robison (1), Michael T. Froehler (2), Bryan C. Good (1)**

(1) Mechanical, Aerospace, and Biomedical Engineering
University of Tennessee
Knoxville, TN, USA

(2) Department of Neurology
Vanderbilt University Medical Center
Nashville, TN, USA

## INTRODUCTION

Blood clots form in many places throughout the body and often break off and lodge in downstream locations within the vasculature. One such instance is acute ischemic stroke (AIS), which results from embolic occlusion of a cerebral artery. This obstruction of normal blood flow prevents nutrients and oxygen from getting to the brain, and brain cells can begin to die within minutes [1]. Without early action to restore blood flow, major complications can occur for the patient including paralysis, loss of muscle movement, difficulty talking, and cognitive losses [2].

A common method to treat AIS is aspiration thrombectomy, which utilizes a guidewire to navigate an aspiration catheter to the proximal face of the lodged clot and remove it via suction [3]. Different factors have been shown to influence the effectiveness of aspiration thrombectomy, including the clot's length and composition [4]. The goals of this study are therefore to determine the relationships between the aspiration pressures required to remove lodged blood clots and their length and composition, specifically their hematocrit. With an improved understanding how clots of varying geometry and hematocrit respond to thrombectomy, we can establish a relationship between the removal pressures and clot properties. The knowledge gained from this study could be utilized to improve surgical recanalization techniques and devices, with the goal of achieving complete reperfusion on the first pass with decreased rates of clot fragmentation.

## METHODS

*Part I: Embolus Analog Preparation and Flow Loop Set-Up*

Bovine blood was collected in CPDA-1 anti-coagulated bags (Lampire Biologic) and separated into its components (plasma and red blood cells (RBC)) using a centrifuge before being recombined in specific hematocrit ratios. Blood was reconstituted in increments of 20% hematocrit over a range of 0-80%. Coagulation was initiated by the addition of $CaCl_2$ to a 20 mM concentration in the reconstituted blood. Roughly 7 mL of the coagulating blood was drawn into a section of 0.25" inner-diameter (ID) PVC tubing before being placed into a Chandler loop and allowed to clot dynamically for 1-2 hours under physiologically flow rates and temperatures. The resulting embolus analogs (EAs) were refrigerated and stored in PBS for 1 week after their creation to maintain their physical properties before use.

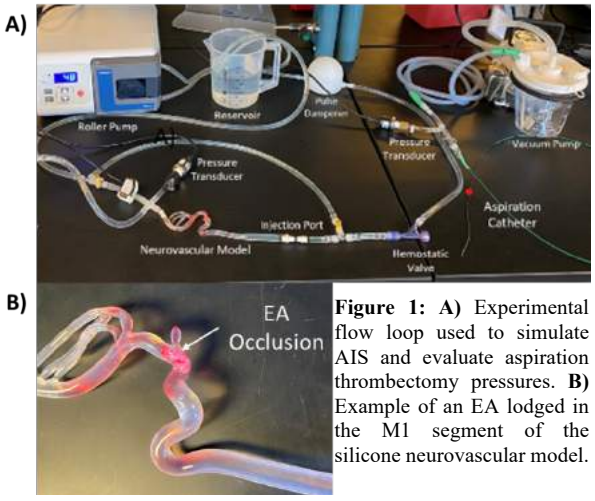


**Figure 1: A)** Experimental flow loop used to simulate AIS and evaluate aspiration thrombectomy pressures. **B)** Example of an EA lodged in the M1 segment of the silicone neurovascular model.

An experimental flow loop was built to model the physiological environment of AIS (**Fig. 1A**) and consisted of a peristaltic pump pushing fluid from a reservoir through 0.25" ID PVC tubing. A flow dampener was included downstream to minimize flow oscillations from the pump before entering a silicon middle cerebral artery (MCA) model (United Biologics). EAs were introduced into the loop through a connection upstream of the neurovascular model and subsequently lodged in the MCA model. A rotating hemostatic valve upstream of the MCA model was used to insert the aspiration catheter for each experimental test. The fluid used in the loop was a mixture of water and baby shampoo to mimic the physiological resistance of the catheters being guided through the cerebral vasculature.

*Part II: EA Lodging and Catheter Aspiration*

Cylindrical EAs of varying hematocrit created in the Chandler loop were cut to be approximately 10 mm in length but varied between 8-15 mm. Each EA was measured using digital calipers prior to its injection into the flow loop. After EA insertion, the samples would flow into the silicone cerebral model and lodge in the M1 segment of the MCA, seen in **Fig. 1B**. After allowing approximately 15 minutes for the EAs to lodge, distal pressures were measured and compared to baseline data to determine how lodging altered the system conditions. A React 68 aspiration catheter (Medtronic) was then inserted into the flow loop through the hemostatic valve and guided to the proximal end of the EA. Using a VC-701B medical aspiration pump (Cliq Medical), vacuum pressure was applied via the catheter to the EA to dislodge it from the model. Starting at 200 mmHg, the aspiration pressure was increased in increments of 50 mmHg and an aspiration thrombectomy pass was attempted the EA with the catheter, similar to standard surgical techniques. A second pressure transducer was connected to the proximal end of the catheter base and used to measure the pressures being applied by the catheter. If EA removal was unsuccessful after two passes, the pump pressure was increased by 50 mmHg and the process was repeated. The final recanalization pressure as well as the fate of the clot (i.e., ingestion into catheter, clean removal, or fragmentation) were recorded.

## RESULTS

Analysis of the experimental pressures data revealed a positive correlation between EA length and the magnitude of aspiration pressure required to dislodge it (**Fig. 2**).

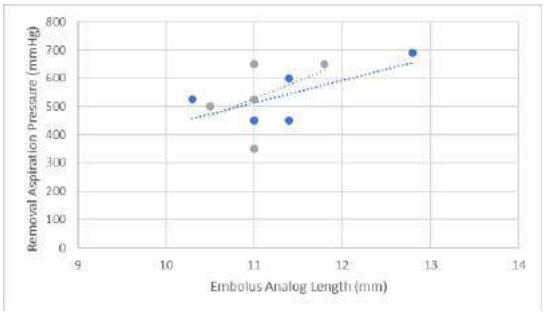


**Figure 2:** Correlations between aspiration removal pressure and EA length (0% hematocrit EAs in gray and 40% in blue).

For both 0% (gray markers) and 40% (blue markers) EAs, removal pressure increased with EA length. The smaller EAs, approximately 10 mm in length only needed 500 mmHg of pressure to remove while the longest 13 mm EAs needed nearly 700 mmHg of pressure. Similarly, a negative correlation was observed between EA hematocrit and the magnitude of removal pressure (**Fig. 3**). The platelet rich 0% hematocrit EAs were the hardest to remove and required aspiration pressures between 500-675 mmHg. As EA hematocrit increases, the amount of pressure for removal decreased with the 80% hematocrit EAs requiring only about 300 mmHg of aspiration pressure.

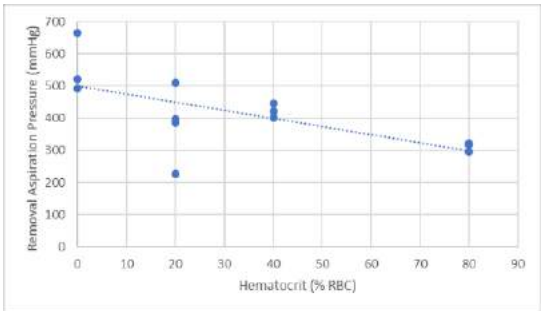


**Figure 3:** Correlation between EA hematocrit and the aspiration pressure required for their removal.

Fragmentation of the EAs occurred about 25% of the time, with little consistency in terms of length, hematocrit, or removal aspiration pressure. However, it most often occurred after multiple unsuccessfully removal attempts at lower pressures.

## DISCUSSION

A positive relationship was found between EA length and vacuum removal pressure. This is most likely due to longer EAs having increased contact area, and ultimately increased friction, between the EA and the MCA walls. It was also found that a negative relationship exists between EA hematocrit and vacuum removal pressure. It has been shown in several other experimental studies that RBC rich clots (higher hematocrit) are softer compared to platelet rich (lower hematocrit) clots and could contribute to their easier removal. Softer clots under higher pressures may also have an increased tendency to fragment and result in micro-emboli downstream of the initial clot location. If a clot's size and composition can be determined through pre-surgical imaging data, this information could be leveraged as part of surgical planning and enable clinicians to remove the clots more effectively by knowing the optimal vacuum pressures to apply. By analyzing the behavior of EAs of varying size and composition experimentally, we can potentially improve the surgical techniques used clinically to optimize recanalization.

## ACKNOWLEDGEMENTS

We thank Dr. Michael Froehler of the Vanderbilt University Medical Center for providing the catheters used in this study.

## REFERENCES

[1] Hui, W, et al., *AHA Journals*, 51:2026-2035, 2020.
[2] Pérez, MA, et al., *Journal of NeuroInterventional Surgery*, 2011.
[3] Luraghi, G, et al., *Journal of Biomechanics*, 127, 2021.
[4] Benson, JC, et al., *Journal of NeuroInterventional Surgery*, 12:38-42, 2020.

SB³C2022
Summer Biomechanics, Bioengineering and Biotransport Conference
June 20-23, Eastern Shore, MD, USA

# PHYSIOCHEMICAL MECHANISMS OF BONE DISSOLUTION PLAY A SIGNIFICANT ROLE IN REGULATING BONE COMPOSITION AND FUNCTION IN ACIDOSIS

**Margaret E. Easson (1), Stephanie Wong (1), Mikayla M. Moody (1), Tannin A. Schmidt (1), Alix Deymier (1)**

(1) Department of Biomedical Engineering, School of Dental Medicine, University of Connecticut Health Center, Farmington, CT, USA

## INTRODUCTION

Metabolic Acidosis (MA) is a condition characterized by reduced blood pH and bicarbonate levels and affects millions of people annually. [1]. A healthy body is able to maintain a homeostatic pH level near 7.4 by removal of carbon dioxide and excretion of hydrogen ions through the lungs and kidneys, respectively. However, the skeletal system, which is the largest ionic reservoir in the body, also helps regulate the body's pH. When pH levels decrease, bone dissolution releases buffering ions from bone mineral returning the body to pH homeostasis, but it also in turn causes bone loss and increases fracture risk [2, 3]. Previous work indicates that this process of bone dissolution during acidosis is a 2-part mechanism that involves cell-mediated resorption and physiochemical bone dissolution. Although these two mechanisms have been identified, the relative contributions of each remain unknown [4]. The current consensus points to cell-mediated dissolution as the primary cause of bone loss/modification [5]. However, the physiochemical response of bones to acid remains largely unstudied. Therefore, the goal of this study was to determine the effects of cell-free acid exposure on bone composition and mechanics in comparison to established in vivo acidosis data.

## METHODS

The shin bones, tibia and fibula, and forearm bones, radius and ulna, were excised from 4-5-month-old male CD-1 Wild Type Mice. Groups of one shin and one forearm were incubated in 1x Phosphate Buffered Saline (PBS) at an initial pH ($pH_i$) of 5.5 (as seen in cancerous environments), 7.0 (clinical acidosis), or 7.4 (physiological) for 5 days at 5°C. Controls included bones not exposed to solution and each of the PBS solutions at the varying pH's without the bones. Each condition was performed in triplicate. Over the course of the 5-day exposure, pH testing was performed at 0, 1, 3 and 6 hours followed by every successive 24 hours using a pH probe. Changes in calcium, phosphorus, potassium, and sodium of the solutions post exposure were measured by Inductively Coupled Plasma Optical Emission Spectroscopy (ICPOES). The tibia/fibula complex was mechanically tested via 3-point bend on a Biomomentum Mach-1 system. The samples were loaded at a rate of 0.1 mm/s until failure. Force-displacement curves were used to calculate structural mechanical properties. Stress-strain plots were calculated from the bone cross-sectional area and the span of the 3pt bend setup. The cross-sectional areas were determined by measuring the distance between bone facets using calipers. Raman spectroscopy was used to determine compositional changes in the exterior and interior of the tibia after solution exposure and fracture. The bone exterior was measured at 5 points along the anterior facet starting at the distal end to the point of fracture. The interior was measured using six points, one at each apex of the triangular cross section and one at the medial point of each facet. The measurements were taken using Witec alpha 300 Raman Spectrometer with a 785 nm laser at a power of ~60 mW. A 50X long range objective was used for both the interior and exterior regions of the bones with an acquisition time of 5 x 30s. Each Spectra was fit using Lorentzian curves to fit 8 peaks of interest. One-Way ANOVA, was used to measure statistical differences between controls and samples with significance set at $p<0.05$.

## RESULTS

The pH of the $pH_i$ 7.0 and 7.4 solutions remained relatively constant over the 5-day exposure. However, the $pH_i$ 5.5 solution showed a significant increase in pH at all timepoints of exposure. Furthermore, ICPOES data showed an increase in calcium and phosphate in all solutions when exposed to bones as compared to controls. The increase was much greater at pH 5.5 than at pH 7 or 7.4 for calcium. While the solution phosphate showed similar increases at $pH_i$ 5.5 and 7.0 but smaller changes at pH 7.4.

Raman spectroscopy indicated a significant decrease in mineral to matrix content in both the interior and exterior of the bone between pH 7.4 and 5.5, but not relative to the control. There was also a significant

decrease in mineral to matrix content on the exterior only between pH 7.4 and pH 7.0 (Fig 1A).

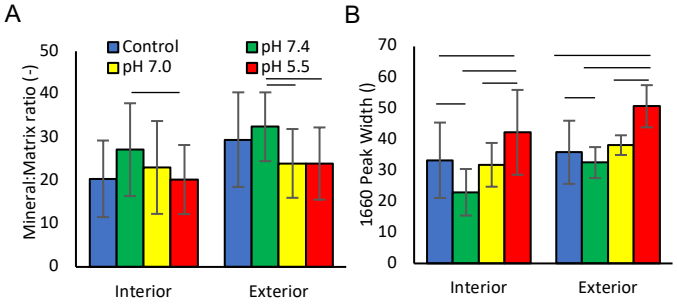


**Figure 1: A. Raman values of mineral:matrix and B. 1660 amide I peak width on the bone interior and exterior after acid exposure. Bars indicate p<0.05**

There were also significant differences in the collagen peaks after solution exposure. Specifically, the 1670/1640 peak on the exterior showed a significant increase between control and pH 5.5 and an increase between pH 7.0 and pH 5.5. This was accompanied by an increase in the width of the joint 1660 peak (Fig 1B). The width of the 1660 peak on the interior had a significant decrease between control and pH 7.4, and a significant increase between control and pH 5.5. On the exterior the width of 1660 had a significant increase between control and 5.5. In addition, the 1000/1660 ratio also showed a significant decrease between control, pH 7.4 and pH 7.0 versus 5.5.

Mechanical testing on the tibia-fibula complex after exposure showed no significant change in structural mechanical parameters. However, it showed a significant increase in material toughness of 91.6% and 91.7% for pH 7.0 and 5.5 compared to controls (Fig 2).

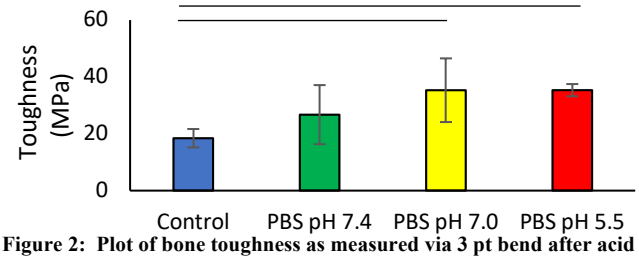


**Figure 2: Plot of bone toughness as measured via 3 pt bend after acid exposure. Bars indicate p<0.05**

## DISCUSSION

The current research suggests that bone loss during acidosis is mainly mediated by cellular responses. However, this work points to physiochemical acid exposure as a significant cause of compositional, and mechanical changes to bone. Mineral dissolution during solution exposure was indicated by a significant increase in solution pH as well as calcium and phosphate levels in all solutions. This is similar to the pH change and calcium release seen with biomimetic apatite mineral crystals in solution [6] suggesting that bone mineral, even at neutral pHs, releases buffering anions and cations into solution via dissolution or ion exchange. At pH 5.5, the solution had a significantly higher pH increase as well as calcium and phosphate levels than at the higher initial pH's suggesting greater ion release. The solutions Ca/P ratio at pH 5.5 is 1.97, indicating stoichiometric dissolution [7], while that at 7.0 and 7.4 falls around 0.7, suggesting a preferential ion exchange. This predicted dissolution is measureable in the Raman derived mineral:matrix ratio which is significantly decreased at pH 5.5 compared to pH 7.4 throughout the bone. Interestingly, mineral levels are also decreased at pH 7.0 on the bone surface compared to 7.4 suggesting that the measured ion release is causing mineral loss even at neutral pHs associated with physiological acidosis. One must note that the decreased mineral:matrix ratios are only significant relative to pH 7.4 and not control. This may be an indication of mineral accumulation or crystallization despite the ionic releases at physiological pH in conjunction with mineral loss at pH 7 and 5.5.

In addition to the changes in mineral content in the bone, there were also significant changes to the collagen structure throughout the bone as measured by Raman. Collagen has been shown to be pH sensitive with lower pH levels causing denaturation and collagen uncoiling [8]. The measured increase in the 1670/1640 ratio as well as the increased width of the combined 1660 peak both indicate an increase in collagen disorder, possibly caused by denaturation [9,10]. These results indicate that bone collagen is also significantly affected by exposure, even at acidosis associated pH's. These results are similar to those recently measured in bones exposed to in vivo acidosis [data not shown].

We expected that the combination of decreased mineral content and changes in collagen structure would likely cause significant changes to the bone's mechanical properties. 3-point bend tests showed that exposure led to a significant increase in toughness at both pH 7.0 and pH 5.5 compared to control. Toughness, defined as the amount of stress needed for failure, is controlled by many structural and compositional factors. Studies have shown that collagen denaturation causes a decrease in toughness suggesting that collagen changes are not responsible for our measured mechanical changes. Instead, we hypothesize that the reduced mineral:matrix ratio, which has been shown to increase tissue toughness [11], may be responsible for our measured changes.

## CONCLUSION

Acidosis-induced bone loss is caused by both cell-mediated resorption and physiochemical dissolution; however, the relative contributions of these mechanisms remain unknown. The data presented here shows that exposure of cell-free *ex vivo* bones to pathological pH's results in pH regulation via ion release, decreased whole bone mineral content, increased collagen denaturation, and increased toughness. This suggests that physiochemical acid exposure may play a more significant role that previously expected in structural, compositional, and mechanical changes of bone in acidosis.


## ACKNOWLEDGEMENTS

We acknowledge the UConn Institute of Materials Science for the use of the XRD and FTIR systems. The UConn Center for Environmental Science and Engineering for the ICP-OES data. Funding was provided by Dr. Deymier's startup funds and NSF CAREER grant #2044870 as well as Dr. Schmidt's UConn Health startup funds.


## REFERENCES


[1] Kraut, J.A., et al. Nature Reviews Nephrology. 6: 274-285. 2010. [2] Peterson, A.K., et al. Acta Biomaterialia. 121:484-496. 2021. [3] Frassetto, L., et al. Nutrients. 10:517. 2018. [4] Krieger, N.S., et al. Current opinion in nephrology and hypertension. 13: 423-436. 2004. [5] Meghji, S., et al. American Journal of Physiology - Endocrinology and Metabolism. 280:E112-E119. 2001. [6] Moynahan MM, et al. PLoS ONE 16: e0250822, 2021. [7] Pellegrino, R.M., et al. Nature. 219:1261-1262. 1968 [8] T. Hayashi, Y. Nagai, J. Biochem.73:1006, 1973. [9] Uquillas, J.A., et al. J Mech Behav Biomed Mater. 15:176-189. 2012. [10] Bailey, A.J., et al. Radiation Research. 22:606-621. 1964. [11] Launey, M.E., et al. Annual Review of Materials Research. 40:23-53. 2010.

# DYNAMIC HAND BRAKE FOR MANUAL WHEELCHAIRS

**J. Coombs (1), N. Johnson (1), N. Oram (1), S. Osterhout (1), Z. Sun (1), N. Tenney (1)**

**Faculty Advisor(s)**

**A. Merryweather (1)**

(1) Mechanical Engineering, University of Utah, Salt Lake City, Utah, USA

## INTRODUCTION

Nearly 5.5 million people use manual wheelchairs as an integral part of their daily lives [1]. Users self-propel their wheelchairs by pushing on the wheel rims or tires and they stop by creating friction on these surfaces with their hands. Existing brakes used to lock the wheels and are not suitable for dynamic braking. When wheelchair users need to actively control the speed of their wheelchair, their hands become dirty, calloused, burned or even severely injured because they are being used as brake pads. Braking is especially difficult for individuals with low hand or wrist motor function, such as those with tetraplegia. This population has greater potential for losing control of their wheelchairs, especially on an incline. A dynamic brake device on the wheelchair could improve the safety and controllability of a manual wheelchair during daily life activities.

Currently, only a few dynamic braking systems exist on the market that partially satisfy this need. The ADI Disk Brake System [2] does not have a suitable user interface for users with low grip ability, adds significant weight, and is prohibitively expensive (> $1000 USD).

A mechanical engineering senior design team at the University of Utah has developed a dynamic braking system that is lightweight, adjustable, and inexpensive (Figure 1).

## PRODUCT DESIGN

The dynamic hand brake shown in Figure 1 is designed to be an ergonomic interface between the user's hands and the wheelchair tire. The brake provides friction to the tire without damaging the user's hands. This hand brake system will aid wheelchair users in slowing and stopping under various circumstances, including rolling downhill. This brake will serve as a mobility aide for manual wheelchair users by giving them safer control over their speed.

The brake system is comprised of four main parts: fender, sliding base, T-bracket, and collar. The fender is the portion users push down with their hand, fist, or forearm to activate the brake, as shown in Figure 2. It is ergonomically designed to reduce interference during self-propulsion.

The sliding base holds the pivot point for the lever mechanism, which is held at a neutral position with a torsion spring to keep the brake off the wheel when not being pressed. This part interfaces with the T-bracket to create anterior-posterior adjustability and the T-bracket slides into the collar's T-slot for up and down adjustability. Both lock in place with a set screw. The collar attaches the system to the wheelchair's frame using four bolts.

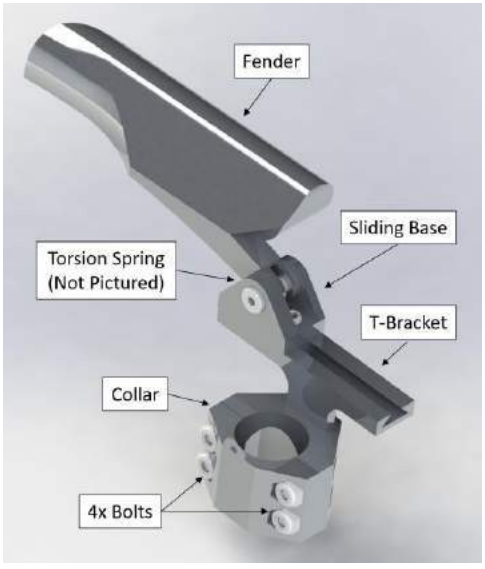


**Figure 1: Rendered aluminum model of right-side dynamic hand brake prototype. Labeled are the main parts of the prototype: Fender, Sliding Base, Torsion Spring, T-Bracket, Collar, and 4 Bolts.**

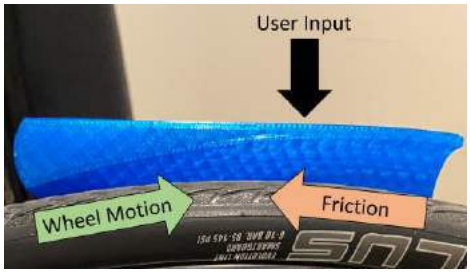


**Figure 2: Side view of right-side dynamic hand brake 3D printed prototype. Noted are the direction of user input (down), wheel motion (clockwise), and friction force (counterclockwise).**

The full assembly will be manufactured using 6061 Aluminum. It will weigh approximately 0.2 kg per side, or 0.4 kg total for a pair of hand brakes. This would add approximately 2% mass to a 18 kg wheelchair.

This design meets user needs by providing a simple, but effective dynamic hand brake system for manual wheelchairs. The system is intuitive to use, lightweight, and inexpensive.

## TESTING

Exploratory brake material testing determined 11 N input force on a plastic or metal hand brake would provide sufficient deceleration for the wheelchair. This metric meets the requirements of ISO 7176-3:2012 [3] where hand-activated wheelchair brakes require no more than 13.5N of input force.

User feedback testing indicated the current prototype, shown in Figures 2 and 3, meets user needs for form, fit, and function of the hand brake system. The fender profile is easy to push down, provides effective proportional braking, and does not impede users' natural self-propulsion motions.

**Figure 3: Front view of dynamic hand brake 3D printed prototype used for exploratory testing.**

Usability evaluations conducted with 3 individuals with a spinal cord injury indicated they would like additional adjustability for placement along the wheel and something that could replace static parking brakes. The team is currently working to implement these features.

Functional testing was performed on the 3D printed prototype (Figures 2 and 3) by able-bodied participants to show proof-of-concept when travelling downhill. The 3D-printed prototype successfully slowed down and stopped users when in use. Further testing will be performed to determine how much force is required to stop a wheelchair using this hand brake.

## BUDGET & MARKET ANALYSIS

The University of Utah Spinal Cord Injury Acute Rehabilitation Program sponsored the project with $2000 and two donated manual wheelchairs. Student fees for the University of Utah contributed an additional $600 for a total of $2600 for the project budget. The budget plan is listed in Table 1. The team expects to use $1800 of this budget on prototyping and testing through April 2022.

**Table 1: Prototyping Budget**

| | |
|---|---|
| Prototyping | $1300 |
| Test Equipment | $500 |
| **Total Expenses** | **$1800** |

The North America wheelchair market size was $940 million in 2020 and is expected to reach $ 1.7 billion by 2028. Around 60% of this market is dominated by manual wheelchairs [4]. The market share for manual wheelchairs was estimated at $564 million in 2020. As an add-on for manual wheelchairs, this hand brake system would occupy a small percentage of the market share. Table 2 demonstrates the potential profits, expenses, and ROI over 3 years.

**Table 2: 3-Year Startup Profits, Expenses, and ROI**

| | **Year 1** | **Year 2** | **Year 3** |
|---|---|---|---|
| Units Sold | 1,000 | 2,500 | 5,000 |
| Cost Per Unit | $124 | $114 | $104 |
| Projected Sales Price | $250 | $250 | $250 |
| **Sales Profit** | **$126,000** | **$340,000** | **$730,000** |
| Engineering | $100,000 | $100,000 | $100,000 |
| Tooling | $100,000 | $10,000 | $10,000 |
| Yearly Profit | ($74,000) | $230,000 | $620,000 |
| **ROI** | **($74,000)** | **$156,000** | **$776,000** |

Over three years, hand brake system could yield an estimated $776,000 return on investment. The current prototype (provisional patent pending) meets the weight, cost, and functional needs of users and further iterations will only improve these metrics. This hand brake has the potential to improve the lives of many people who use manual wheelchairs.

## ACKNOWLEDGEMENTS

We would like to acknowledge Dr. Jeffery P. Rosenbluth, MD and his team at the Spinal Cord Injury Acute Rehabilitation program at the University of Utah for funding support and expert knowledge. His team has been critical in ensuring this design meets the needs of individuals with various spinal cord injuries who use manual wheelchairs.

## REFERENCES

[1] Taylor, Danielle M. Americans with Disabilities: 2014. United States Census Bureau. [Online] November 29, 2018. https://www.census.gov/library/publications/2018/demo/p70-152.html.

[2] ADI Disk Brake System. ADI Stealth Products. [Online] https://adi.stealthproducts.com/disc-brake-systems/.

[3] Wheelchairs — Part 3: Determination of Effectiveness of Brakes. 2012. ISO 7176-3.

[4] Grand View Research. North America Wheelchair Market Size, Share & Trends Analysis Report by Application (Hospitals, Homecare, ASCS), by Product (Manual, Electric), by Category Type, By Country, and Segment Forecasts, 2021-2028. s.l. : Research and Markets, 2021.

# CONFIDENCE EXPRESSION IN PERSONAL STATEMENTS FROM A BIOMEDICAL ENGINEERING REU SITE

**E. Reed (1), D. Cotto (2), and S. M. George (3)**

(1) Department of Psychology, East Carolina University, Greenville, NC, USA
(2) Department of Sociology, East Carolina University, Greenville, NC, USA
(3) Department of Engineering, East Carolina University, Greenville, NC, USA

## INTRODUCTION

Mastery experience, vicarious experience, and verbal persuasions all play a role in self-efficacy development [1]. It has been found that women's self-efficacy is most informed by verbal persuasions and vicarious experiences, whereas men's self-efficacy is most informed by mastery experiences [2]. Investigating how these elements of self-efficacy are reflected in student writing may be revealing of impactful experiences of students in STEM, thus giving insight into how to better build student confidence in STEM environments. Additionally, how they choose to write about these experiences may be revealing of student attitudes and values, in turn providing insight on how students may portray confidence.

As part of an application, students may use personal statements to convey confidence. Previous work analyzed personal statements from before and after completion of the Biomedical Engineering in Simulations, Imaging, and Modeling (BME-SIM) Research Experiences for Undergraduates (REU) program [3]. Quantitative writing measures were compared to self-reported confidence in research abilities. The relationship between elements of writing – most notably noun variation – and self-reported confidence differed between men and women. Women's self-reported confidence was found to have a moderate positive relationship with noun variation, while men's self-reported confidence was found to have a weak negative relationship; additionally, these relationships seemed to change between pre- and post-program statement groups [3]. This raised questions on how students may choose to reflect confidence in personal statements.

This investigation aims to explore what experiences students choose to discuss, how they choose to discuss these experiences, and how these choices may relate to self-reported confidence.

## METHODS

This study was approved by the Institutional Review Board at ECU and informed consent was received by all participants. The BME-SIM program is a 10-week residential summer program providing students with research experiences, professional development, workshops on written and verbal communication, and mentoring opportunities [4]. Students are asked to submit personal statements before and after the program, detailing their goals, experiences, personality, and accomplishments. Surveys were also administered before and after program completion, assessing students' mastery of knowledge and skills on a 10-point Likert scale. This investigation utilized self-reported confidence in research abilities from survey results and personal statements from before and after program completion.

A subset of students' (n=16) personal statements from before and after program completion were coded in NVivo by two student readers and analyzed through the Linguistic Inquiry and Word Count (LIWC2015) software to explore the types of words students were using and how these word choices may relate to different social and psychological states [5]. The LIWC2015 takes specific words and sorts them into a variety of different categories, then determines what percentage of total words used in the personal statement fall into that category [5]. This study utilized the categories of positive emotion, negative emotion, tentativeness, certainty, achievement, power, and reward. Examples of words categorized by the LIWC2015 can be found in Table 1.

**Table 1: Examples of LIWC2015 Word Categorizations**

| Categorization | Examples |
|---|---|
| Positive Emotion | Determined, loved, success, graciously, etc. |
| Negative Emotion | Problem, defense, pain, traumatic, etc. |
| Tentativeness | Any, question, most, maybe, perhaps, etc. |
| Certainty | Specific, exact, true, particularly, etc. |
| Achievement | Best, lead, successful, recovery, etc. |
| Power | Mentor, honors, bigger, help, etc. |
| Reward | Got, opportunity, best, won, etc. |

NVivo will be used to analyze personal statement content through categorizing themes and topics within the personal statements, revealing common ideas throughout personal statements. A ground-up approach will be used to organize and interpret findings. Coding with NVivo is still being conducted. Once data from the LIWC2015 was collected, categorization percentages between overall, pre-, and post-program statement groups were compared among all students and between genders. Differences between groups were analyzed using a student's *t-test* to determine if students differed in LIWC2015 categorization frequencies between pre- and post-program statement groups. Correlations between self-reported confidence and categorization percentages were also investigated to gauge how frequencies of types of words may relate to self-reported confidence. Correlation coefficients of ± 0.3 and less were classified as no relationship, ± 0.31-0.49 as a weak relationship, ± 0.5-0.69 as a moderate relationship, and ± 0.7 and above as a strong relationship.

## RESULTS

No significant differences were found in the self-reported confidence in pre- or post-program evaluations between genders [3]. No significant differences were found between all students' pre- and post-program statements among any LIWC2015 categorization. No significant differences were found in any LIWC categorization between men and women's pre- nor post-program statements. When investigating how self-reported confidence related to differing LIWC2015 categorizations, multiple relationships arose.

Among all students, achievement had a moderate negative relationship to self-reported confidence in both pre- and post-program statements. Self-reported confidence was found to have moderate relationships with positive emotion, negative emotion, tentativeness, certainty, power, and reward among post-program statements. In all students' post-program statements, tentativeness and power were both moderate and positive, while positive emotion, negative emotion, certainty, and reward were all moderate and negative. All correlations between self-reported confidence and LIWC2015 categorizations can be found in Table 2.

**Table 2: Comparison of Correlations Between LIWC2015 Categorizations and Self-Reported Confidence**

| | All Students | | Women | | Men | |
|---|---|---|---|---|---|---|
| | **Pre** | **Post** | **Pre** | **Post** | **Pre** | **Post** |
| Positive Emotion | 0.06 | -0.67 | -0.38 | -0.51 | 0.34 | -0.77 |
| Negative Emotion | -0.46 | -0.62 | -0.59 | -0.49 | 0.19 | -0.75 |
| Tentativeness | 0.26 | 0.62 | -0.37 | 0.36 | 0.39 | 0.90 |
| Certainty | -0.38 | -0.68 | 0.49 | -0.67 | -0.40 | -0.69 |
| Achievement | -0.54 | -0.58 | -0.59 | -0.44 | -0.54 | -0.66 |
| Power | 0.18 | 0.67 | 0.64 | 0.42 | -0.31 | 0.81 |
| Reward | -0.29 | -0.62 | -0.51 | -0.18 | -0.32 | -0.82 |

Moderate negative relationships were found between negative emotion, achievement, and reward and self-reported confidence in women's pre-program statements. A moderate positive relationship was found between women's self-reported confidence in pre-program statements and power. Moderate negative relationships were found between women's post-program self-reported confidence in positive emotion and certainty.

A moderate negative relationship was found between achievement and self-reported confidence in men's pre-program statements. In men's post-program statements, moderate negative relationships were found between certainty and achievement. Strong negative relationships were found in men's post-program self-reported confidence and positive emotion, negative emotion, and reward. Strong positive relationships with self-reported confidence in men's post-program statements in tentativeness and power.

## DISCUSSION

Previous research has found that STEM environments tend to value agentic, assured communication styles [2]; additionally, other research has found that men tend to use more boosters, or words exemplifying power, sureness, and success [6]. This investigation found that men seemed to feel most confident while using tentative language rather than language expressing certainty, and both genders used less certainty-related words as their confidence increased. Additionally, all students' self-reported confidence had either no relationship or negative relationships with both positive and negative emotion categorizations. Given that STEM fields tend to value objectivity [2], students may feel the need to present their experiences rather than their feelings around their experiences. This may show an additional need to evaluate specific experiences discussed in these personal statements.

Additionally, research has found that genders may alter their communication styles based on the environment they are in [7]. Reward had a negative relationship with self-reported confidence among multiple groups. In women's pre-program statements, this negative relationship could be due to fear of promoting oneself in STEM environments or altering their communication styles to remain object about their experiences. In men's post-program statements, this may be due to emphasizing objectivity about their experiences. Moreover, other research has found that men tend to use more boosters, or words exemplifying power, sureness, and success [6]; however, no significant differences were found between the percentages of power-related words that men and women were using. This may fall back to male communication styles favoring dominance, while women's communication styles seem to value community [2, 6]. Men may feel most confident when they are abiding by these norms. Women's relationship between self-reported confidence and power between pre- and post-program statements may be explained by the feeling to need to 'prove' oneself in STEM environments [1, 2]. Following program completion, the need to use power-related language to prove oneself may seem unneeded as they have gained confidence in the area.

While the LIWC2015 has given some insight into the types of language students are using and how it may relate to self-reported confidence, investigating the context of these words would be more revealing of student values that may inform their confidence.

## ACKNOWLEDGEMENTS

Funding provided by National Science Foundation (NSF) EEC-1359183, EEC-1659796 and East Carolina University's Undergraduate Research and Creative Activity Award.

## REFERENCES

[1] Rittmayer, A.D. and Beier, M.E. *Assessing Women and Men in Engineering,* 10:1-12, 2009.
[2] Sobieraj, S. and Kramer, N. C. *Frontiers in Psychology,* 1-16, 2019.
[3] Reed, E., Kain, D., and George, S. *Journal of Biomechanical Engineering: Annual Education Issue*, 143(12), 2021.
[4] George, S. M. and Domire, Z. J. *Journal of Biomechanical Engineering,* 142(11), 2020.
[5] Pennebaker, J.W., Booth, R.J., Boyd, R.L., & Francis, M.E. Linguistic Inquiry and Word Count: LIWC2015, 2015.
[6] Nasri, M., Biri, R., & Karimi, M. *International Journal of Applied Linguistics & English Literature,* 7(3), 2018.
[7] Babal, J. C., Gower, A. D., Frohna, J. G., & Moreno, M. A. *BMC Medical Education,* 19(392), 2019.

SB³C2022
Summer Biomechanics, Bioengineering and Biotransport Conference
June 20-23, Eastern Shore, MD, USA

# THE ROLE OF ACTIN CORRALLING IN THE FORMATION OF CELL-CELL ADHESIONS

**Payton J. Thomas, Tamara C. Bidone**

Biomedical Engineering, University of Utah, Salt Lake City, UT, USA

## INTRODUCTION

E-cadherins are single-pass transmembrane glycoproteins that create cell-cell adhesions in epithelial tissues [1]. Dysregulation of E-cadherins may cause reduced tissue permeability, and metastatic initiation [2-3]. Understanding how E-cadherins form cell-cell adhesions is necessary for the study of tissue development and repair, as well as the for the development of new cancer therapeutics.

During cell-cell adhesions assembly, E-cadherins transit across molecular states: monomers, dimers (*trans*-associated), and *cis*-associated E-cadherins. *Trans*- associated E-cadherins embedded in the membranes of neighboring cells exist in a stable 'S-dimer' state which they enter by transiting through an unstable 'X-dimer' state (Fig. 1A). Once in the S-dimer state, E-cadherins form lateral *cis*- associations with E-cadherins in the same membrane (Fig. 1A).

In cell-cell adhesions, the number and size of E-cadherin clusters vary [6-7]. This variance may be attributed to E-cadherin concentration, association with the actomyosin cytoskeleton through α- and β-catenin, and the spatial arrangement of the actin filaments. It has been reported that the mesh formed by cytoskeletal actin filaments regulates the movement of E-cadherins by corralling them into clusters [8-9]. However, it remains unknown whether an actin mesh either increases the fraction of E-cadherins that interact laterally (*cis*-interactions), increases the overall number of clusters, or both. This is due, in part, to the difficulty in experimentally tracking the molecular state of E-cadherins in relation with cytoskeletal arrangements. However, these properties may be probed *in silico*, where clustering can be measured in relation with actin mesh properties such as size and permeability. Here, we extended our computational model of E-cadherin clustering [10] by incorporating a mesh of actin filaments that form regular spaces in which E-cadherins can freely diffuse. We used the model to evaluate the transitions of E-cadherins between monomers, *trans*-dimers and *cis*-associated proteins at different mesh sizes and at different values of cytoskeletal force.

Our results collectively indicated that actin mesh size controls both the amount of laterally associated E-cadherins and the number of clusters. Interestingly, mesh permeability did not affect the distribution of E-cadherin molecular states.

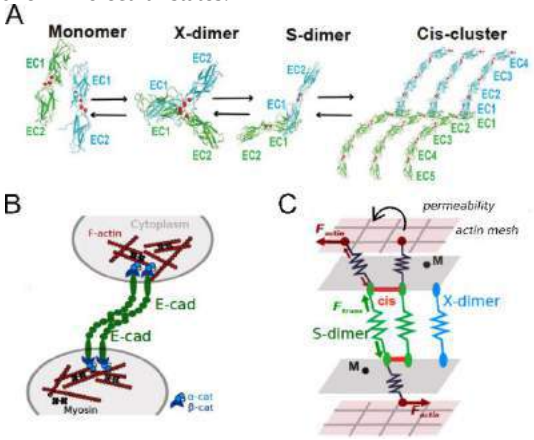


**Figure 1 E-cadherin molecular states during clustering** (A) Ribbon representation of E-cadherin molecular states. (B) Illustration of two E-cadherin *trans*-dimers that interact laterally and associate with the cytoskeleton. (C) Schematic diagram of our 3D, including E-cadherin state transitions (adapted from [10]).

## METHODS

A 3-dimensional simulation domain composed of four different layers was used: two internal layers represented the plasma membranes of neighboring cells, and two external layers mimicked the actin cytoskeleton. E-cadherins were represented as single point particles on the plasma membranes that switch between molecular states according to previously determined rate constants [10], and the actin mesh was

represented using a regular grid, in which free diffusion of E-cadherins was allowed within the grid spaces and hopping between the spaces was determined by the permeability. Simulations were performed with Euler's method on the Langevin Equation under a low-Reynold's number assumption (Eq. 1).

$$F_i - \varepsilon_i \frac{dr_i}{dt} + F^T{}_i = 0 \qquad (1)$$

Where $r_i$ is the position vector of the i-th E-cadherin, $\varepsilon_i$ is the 2-dimensional drag coefficient corresponding to the diffusion coefficient $D = 0.028\ \mu m^2/s$, and $F_i$ and $F^T{}_i$ are net deterministic and stochastic force, respectively. Deterministic force was the sum of forces due to actin association and cadherin *trans*- association, both of which were approximated to be Hookean (Eq. 2).

$$F_i = k_{actin}(l - l_{actin,0}) + k_{trans}(l - l_{trans,0}) \qquad (2)$$

Where $k_{actin} = 2$ pN/μm, $k_{trans} = 2$ pN/μm, $l_{actin,0} = 10$ nm, and $l_{trans,0} = 20$ nm [12]. Stochastic force was applied only to cadherins outside of clusters, which were assumed to be diffusive. Stochastic force was modeled according to the fluctuation-dissipation theorem (Eq. 3):

$$\langle \boldsymbol{F_i^T}(t)\boldsymbol{F_j^T}(\boldsymbol{t})\rangle = \frac{2k_B T\varepsilon_i\delta_{ij}}{dt}\boldsymbol{\delta i} \qquad (3)$$

where $k_B$ is the Boltzmann constant, $T$ is the temperature, $\delta_{ij}$ is the Kronecker delta, and $\boldsymbol{\delta}$ is a unit second-order tensor.

Mesh size was systematically varied from 0.1 μm to 1μm, a value corresponding to the side dimension of our 3-dimensional domain and indicating the absence of actin corralling. The probability of hopping between neighboring grid spaces was varied systematically between 0-1 (permeability). Force from E-cadherin interactions with actin, $F_a$, was systematically varied between 0-50 pN. As outputs, we evaluated cluster size, in terms of number of E-cadherins per cluster, proportion of E-cadherins in *cis*-interactions, and number of clusters at steady state.

## RESULTS

Analysis of our simulation results showed that the number of clusters increases with increasing mesh size up to about 22/μm$^2$ (Fig. 2A). The increase in cluster number with mesh size is due to an increase in the fraction of E-cadherins that interact laterally (Fig. 2B). Increasing force magnitude reduces the fraction of E-cadherins involved in *cis*-interactions (Fig. 2B), and thus reduces cluster numerosity (Fig. 2A).

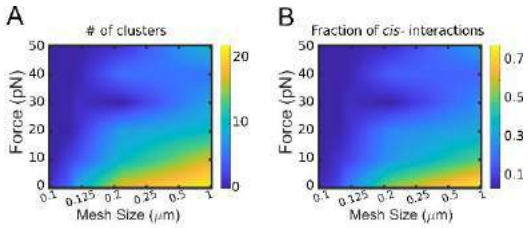


**Figure 2 Cluster numerosity and E-cadherin molecular states.** (A) Mean number of clusters as a function of actin corralling (mesh size) and $F_a$, using permeability of … (B) Mean proportion of E-cadherins in the S-state as a function of actin corralling (mesh size) and $F_a$, using permeability of 0.5. Data are extracted between 20-30 s of simulations.

Using mesh permeability of 0.4, cytoskeletal force $F_a = 30\,pN$ and mesh size 0.25 $\mu m$, about 50 % of the clusters contain between 1-5 E-cadherins and 60% of the cluster contain between 6-10 E-cadherins, without larger clusters due to the limited mesh size. In these conditions, about 20% of E-cadherins are involved in cis-interactions at steady-state and the majority of E-cadherins present as monomers (Fig. 3A). The relative fractions of E-cadherins in the different states are comparable for lower permeability, with about 20% *cis*- E-cadherins and about 80% monomers (Fig. 3C). This suggests that inhibition of E-cadherin diffusion from decreased mesh permeability does not affect the molecular state of E-cadherins.

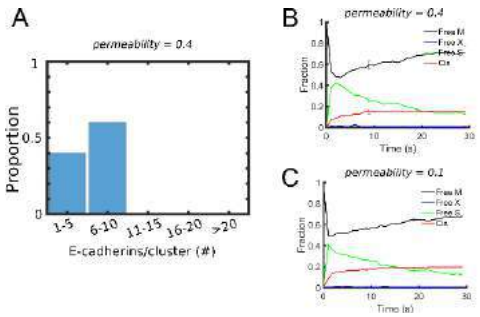


**Figure 3 Effect of mesh permeability on E-cadherin clustering and molecular states.** (A) Distribution of cadherin cluster sizes with a permeability of 0.4. mesh size of 0.25 μm, and $F_a$ = 30 pN. Data are extracted between 20-30 s of simulations. (B and C) Time evolution of proportion of E-cadherins in each state as permeability varies. Error bars indicate the standard error.

## DISCUSSION

Here, we extended our computational model of E-cadherin clustering in order to evaluate the effects actin corralling on the assembly of cell-cell adhesions with varying degrees of cytoskeletal tension. Consistent with our previous results [10], force reduces the number of clusters (Fig. 2A) by decreasing the fraction of E-cadherins that interact laterally (Fig. 2B). Actin mesh size promotes clustering to different extends, depending on cytoskeletal force, with overall less clusters at high force (Fig. 2). This is consistent with previous experiments suggesting that binding of E-cadherins to cytoskeletal filaments guide clustering [8-9]. Here, however, we provide insights that actin mesh size promotes clustering while actin force reduces it because of it changes E-cadherin molecular states. Interestingly, actin mesh permeability does not impact the molecular state of E-cadherins (Fig. 3). It will be interesting to test, in the future, if variations in permeability affects cluster size and number.


## ACKNOWLEDGEMENTS

This work was supported by the National Science Foundation grant NSF BMMB 2044394 to T.C.B. and the University of Utah Undergraduate Research Opportunities Program (UROP).


## REFERENCES


[1] Lodish, H et al., *Molecular Cell Biology*, Cambridge University Press, Cambridge, 2019.
[2] Lobos-Gonzalez, L et al., *Pigment Cell Mel. Res.*, 26:555-570, 2013.
[3] Liu, X et al., *Tissue Barriers*, 2:e969112, 2014.
[6] Harrison, OJ et al., *Structure*, 19:244-256, 2011.
[7] Adams, CL et al., *Curr. Opin. Cell Biol.*, 10:572-577, 1998.
[8] Hong, S et al., *J. Cell Biol.*, 201(1):131-143, 2013.
[9] Sako, Y et al., *J Cell Biol.*, 140(5):1227-1240, 1998.
[10] Chen, Y et al., *Biophys. J.*, 120:4944-4954, 2021.

# OPEN-SOURCE SYSTEM FOR REAL-TIME FUNCTIONAL ASSESSMENT OF ENGINEERED MULTICELLULAR FILTRATION BARRIERS

**Tess K. Fallon (1,2), Alan D. Stern (2), Nanditha Anandakrishnan (3), Ilse S. Daehn (2), Evren U. Azeloglu (2,3)**

(1) Electrical Engineering, Columbia University, New York, NY, USA
(2) Nephrology, Icahn School of Medicine, New York, NY, USA
(3) Pharmacological Sciences, Icahn School of Medicine, New York, NY, USA

## INTRODUCTION

One goal of precision medicine is to develop patient-derived tissue analogs that enable faster and more accurate drug screening and discovery. Others[1] and we have developed various kidney organoid and organ-on-chip systems that aim to recapitulate the physiological functions of the kidney (Figure 1), most importantly selective filtration, which is an important function of the kidney. Malfunction of selective filtration is associated with acute kidney injury and chronic kidney disease (CKD), which affects 37 million people in the US alone. Recently, organ-on-chip models have been proposed to study kidney dysfunction that results in altered filtration characteristics, and use this metric as a surrogate parameter to evaluate drug candidates for treatment of kidney disease. To test applicability of such model systems, we need a quantitative assay that can evaluate the filtration status of these tissue analogs in real-time.

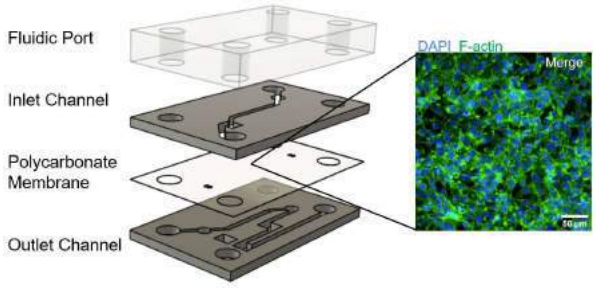


**Figure 1: Microfluidic kidney-on-chip seeded with mouse glomerular endothelial cells**

Current methods use absorbance or enzyme-linked immunosorbent assay (ELISA) to determine the presence of biomarkers.[2] Looking at absorbance is not physiologically applicable and limited since quantitative evaluation of more than one molecule at a given time is challenging. Additionally, perfused media must be removed from the microfluidic device. Repeated removal of medium can damage cells, preventing continuous monitoring of filtration status over time. Non-invasive methods use regenerating electrochemical or physical sensors within the microfluidic device to track target molecules.[3,4] Regeneration of sensors takes up to 4 hours, limiting the ability to continuously measure biomarkers within the regeneration time frame using a single chip.[5] Additionally, if there is a sudden increase in biomarker levels, sensors can immediately saturate and values above the saturation range can be missed. In the case of kidney selective filtration, detecting sudden increases is important for detecting potential cellular damage.

Here, we report a non-invasive, open-source fluorescence-based sensor system that can simultaneously track real-time filtration of human serum albumin (HSA) and inulin, two molecules used to estimate kidney function.

## METHODS

Working with a simple epifluorescent light path and a dual-bandpass filter set, we developed a 3D printable sensor that tracks the filtration status of a kidney-on-a-chip system. The model used for the purposes of this paper was a retrofitted Thermo-Fischer Countess II™ system.

For our first prototype, we used the optical path of Countess II in combination with 3D printed materials (Figure 2a). Organ-on-chip was mounted on a custom-built stage and secured using magnets (Figure 2b). The objective was a 0.1 NA 4X Olympus Plan Achromat (Part #RMS4X). The three optical components of the light cube, namely excitation, emission, and beam-splitter, were obtained from Chroma (59010x, 59010m, and 69015bs, respectively). This filter combination allowed simultaneous imaging of both fluorescein isothiocyanate (FITC) and Texas Red dye conjugates, and it was mounted on a custom filter cube (Figure 2c). An amber 595nm LED (Luxeon-C) was

used to excite Texas Red and 490nm MCPCB LED (Thor Labs) was used for FITC.

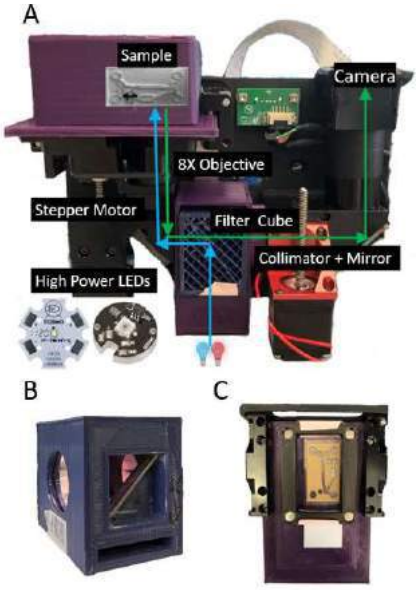


**Figure 2: Custom (A) light path, (B) filter cube, and (C) sample mount**

The sensor was automated using Raspberry Pi™ and Arduino™ UNO. Stage movement was automated with a Haydon-Kerk™ linear actuator stepper motor, allowing focus control. A circuit was designed to give user control over LED brightness and stage height (Figure 3a). A Raspberry Pi™ HQ Camera was used to acquire 8-bit-depth images at 507x380pixel resolution, binned eight times relative to the initial camera resolution. A graphical user interface (GUI) was designed for basic user controls and the live-streaming (Figure 3b).

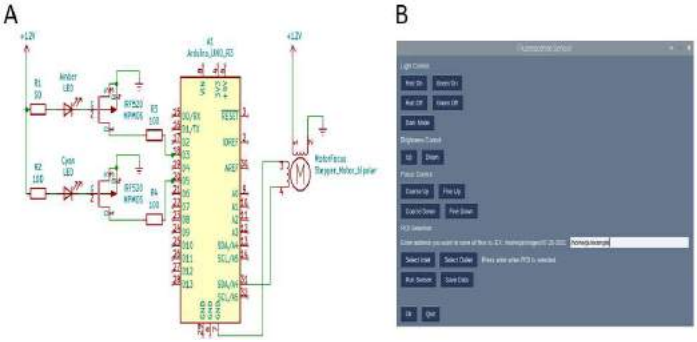


**Figure 3: (A) Electronics circuit diagram and (B) the user interface**

Media containing HSA-Texas Red and inulin-FITC was perfused into the inlet. Over a user-specified length of time, the sensor can acquire data with FITC excitation followed by Texas Red excitation. We then quantified the concentration of HSA and inulin in both the inlet and the outlet by comparing the pixel intensity values of each case. Higher intensity indicated higher concentrations of dye. In healthy kidneys, HSA is selectively retained while inulin is selectively filtered; we therefore expect equivalent concentrations of inulin at both inlet and outlet, while only low levels of HSA at the outlet. Thus, comparing pixel intensity values of the two species over time can allow continuous evaluation of the functional status of the selective filtration barrier.

## RESULTS

Several quality control assays were performed to verify the sensitivity and precision of the sensor. We confirmed that only one target molecule was excited at each time, by placing inulin-FITC in the left chamber and HSA-Texas Red on the right and selectively turning on the LEDs in different combinations (Figure 4a-d). We also ensured image consistency by placing 1 mg/mL of each solution and taking timelapse images at 15-minute intervals (Figure 4e). Finally, we found the linear sensitivity region of pixel intensities as a function of target molecule concentration (Figure 4f). The linear sensitivity region for inulin-FITC was found to be between 0.01mg/mL and 1mg/mL.

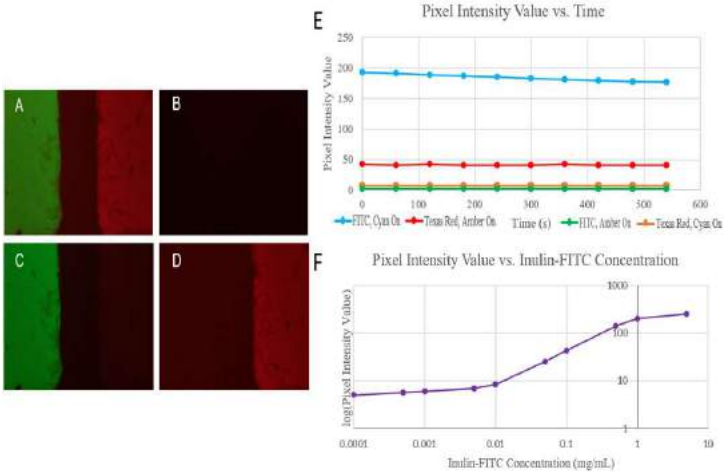


**Figure 4: Visual verification with (A) both LEDs on (B) both LEDs off (C) only cyan on (D) only amber on and quantified verification for (E) consistency over time and (F) sensor sensitivity.**

## DISCUSSION

We present an economical system for real-time, quantitative and non-invasive assessment of filtration status in engineered kidneys using off-the-shelf components. The final prototype will be available through a CC BY 4.0 open-access license. Unlike complicated electrochemical sensors, our design can be implemented by those without a technical background for their own engineered systems. We plan on using this sensor to compare filtration function of healthy and diseased kidney cells differentiated from patient-derived induced pluripotent stem cells.


## ACKNOWLEDGEMENTS

We acknowledge support from NIH R25 DK124917 for the Multidisciplinary Engineering and Renal Research for Innovation of Technology (MERRIT) Program and W81XWH-20-1-0837 from Department of Defense. We thank Jacob Wright and Stefanie DeFronzo for their technical assistance.


## REFERENCES


[1] Hosic, S et al., *ACS Biomaterials Science & Engineering* 7(*7*): 2949-2963 (2021)

[2] Petrosyan, A et al., *Nat Commun* 10: 3656 (2019)

[3] Zhang Y S et al., *Proc Natl Acad Sci USA* 114(*12*): E2293-E2302 (2017)

[4] Aleman, J et al. *Nat Protoc* May; *16*(5): 2564-2593 (2021)

SB³C2022
Summer Biomechanics, Bioengineering and Biotransport Conference
June 20-23, Eastern Shore, MD, USA

# MECHANICAL IMPROVEMENT AND HAPTIC QUANTIFICATION OF DIGITAL EXTENDERS INTUBATION DEVICE

**Tristan Arias (1), R. Lyle Hood (2), Emma Treadway (1)**

(1) Engineering Science, Trinity University, San Antonio, Texas, United States
(2) Mechanical Engineering, University of Texas at San Antonio, San Antonio, Texas, United States

## INTRODUCTION

There currently exist several methods of performing endotracheal intubation on an individual. One is to use a laryngoscope to depress the patient's tongue and guide the endotracheal tube into their trachea. Another, called Digital Intubation (DI), consists of the same actions performed with the provider's own fingers. While direct laryngoscopy is considered the gold standard of airway management, DI can be more advantageous in field scenarios when the glottal opening cannot be visualized with the laryngoscope, either due to obstruction by tissues or fluids or when the patient's injuries prevent the necessary head and neck tilt tied to laryngoscopy performance [1]. In these cases, use of DI enables a haptic, tactile performance of intubation that does not require visual data nor the patient positioning necessary for laryngoscopic intubation [2]. However, DI is generally discouraged as it can be dangerous, to both the caregiver and patient, as well as unsanitary. If the patient is even partially conscious, they can reflexively bite down, damaging the medical provider's fingers, and the insertion of natural digits can introduce contaminants into the patient's system [1].

Hernandez-Hinojosa et al. [3] designed a device to extend the reach of a user's digits with two-joint robotic digits. While it was shown these Digital Extenders (DEs) could perform intubation while decreasing both the quantity of necessary applied force and duration over which this force was applied to complete the procedure, there were significant disadvantages and shortcomings associated with their use. Greater head and neck tilt were seen with the use of DEs compared to other methods, hypothesized as due to a decreased ability to visually confirm procedure performance as the platform visually obstructs the oral cavity. It was suggested that the lack of haptic feedback that might be present in standard DI may have contributed to this issue [3].

The objective of this research was to compare control of force applied with the Digital Extenders to force applied with natural digits, in order to quantify the useful haptic forces exerted on the user by the device.

## METHODS

### Prototype Fabrication and Mechanical Changes

First, a single digit of the Digital Extenders was fabricated, with minor design changes in most areas (Figure 1) relative to previous work. An Arduino microcontroller measures the deflection of the trigger (via a potentiometer) and uses that to command the rotation of the servo (ANNIMOS DS3225MG). Red, low-strength parts were made on an Ultimaker S5 FDM printer using Ultimaker Tough Red PLA ($S_{ut}$=37 MPa, E=1.8 GPa, $E_{flex}$=2.5 GPa). Blue, high-strength parts were made on a Formlabs Form 3 SLA printer using Formlabs Tough Resin V, cured with a Formlabs Form Cure for 60 minutes at 60°C ($S_{ut}$=55.7 MPa, E=2.7 GPa, $E_{flex}$=1.6 GPa).

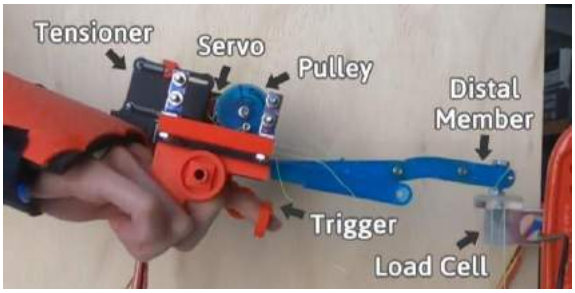


**Figure 1: Digital extenders prototype**

The major improvement upon the original design was the incorporation of an adaptive line tensioner, which employs springs to keep the lines threaded along the top and bottom of the Digital Extender digits from developing slack. This decreased the amount of time during which the servo motor delayed actuating the members while it collected slack, thus resulting in more immediate and intuitive response to user trigger movement. The dark grey tensioner components made on a Markforged Onyx One FDM printer using Onyx composite with Fiberglass reinforcement ($S_{ut}$=37 MPa, E=2.4 GPa, $E_{flex}$=3.0 GPa).

### Control and Haptic Feedback Testing

A human-participant experiment was performed to quantify forces exerted at the fingertips and on the back of a user's hand under a protocol approved by the Trinity University Institutional Review Board. During the experiment, each of two participants (21yr old F, right-handed; 20yr old F, right-handed) was asked to apply target forces to a load cell (Transducer Techniques LSP-10), either with the DE fingertip, or with their own fingertip, the finger held flat against the load cell pad in either case. The inclusion of natural digit data allowed a comparison in some manner parallel to Digital Intubation, while NoVis trials allowed a measurement of the helpfulness of non-visual feedback to control operation.

Data was taken under four conditions: DEs with visual feedback (DE/Vis), DEs with no visual feedback (DE/NoVis), natural digits with visual feedback (ND/Vis), and natural digits with no visual feedback (ND/NoVis). In each condition, three trials were performed where, during each trial, the participant was asked to apply 5 target forces to the load cell, presented in a randomized sequence for 5 seconds each. The two Vis condition trial sets were each performed before their respective NoVis condition trial sets, to allow the participant to become accustomed to whatever data might exist without visual feedback. During the Vis condition, the participant was allowed to view their proximity to the target force on a graph, while during the NoVis condition, the participant was shown the target and their

they tried to achieve it. At the end of the target, they were allowed to view how close they had gotten to the goal after the five seconds had expired to allow them to adjust their correlation of force output to any received data. Applied forces were mapped to a linear 1-5 scale for display to the user through a MATLAB Simulink scope window, with 0 being the approximate resting weight of the DEs and participant's hand on the load cell and 5 being the maximum recorded exertable force by the DEs.

In our analysis, the best three seconds of each target in terms of mean absolute percentage error (MAPE) of applied force relative to target force were averaged:

$$MAPE = \frac{100\%}{n}\sum_{i=1}^{n}\frac{|A_i - T|}{T}, \quad (1)$$

where, $n$ is the number of datums averaged, $i$ is an indexer, $T$ is the target force, and $A_i$ is the actual measured force. An average MAPE per condition was calculated.

To quantify the inherent force feedback available to the user, we mounted two resistive pressure sensors under the DE hand cover, with one located closer to the participant's knuckles and the other positioned closer to the participant's wrist. The applied force data was scaled to the approximate range of the haptic force data and plotted together to observe any potential relationship.

## RESULTS

The MAPE (represented by the shaded regions of Figure 2) was no greater than 8.6% for any given condition. Average performance for each of the four conditions is summarized in Table 1. As expected, both participants performed better in the Vis condition than in the NoVis condition for both ND and DE. In the NoVis conditions, both participants performed better with DEs than with ND.

The maximum normal force exerted by the device on the load cell during the trials was recorded as 4.97 N, compared with the median maximum force of 17.0 N recorded in Hernandez-Hinojosa et al. [3].

## DISCUSSION AND CONCLUSIONS

We found the accuracy of force-matching with the DEs surprising, especially in the NoVis condition. There was only a 0.4% difference between the average DE/Vis and ND/Vis accuracies, and only 2.6% difference between the average DE/Vis and DE/NoVis accuracies. Additionally, the DE/NoVis condition had on average 2.9% less error than the ND/NoVis condition. This could be due to the relatively lower noise in force profiles applied with the DEs as compared to ND, which can be observed in Figure 2.

These results indicate a high level of Digital Extender control relative to natural digits and suggest the existence of useful haptic feedback inherent in the device, which allowed participants to maintain some level of accuracy in the absence of visual feedback, even outperforming ND accuracy in the case of NoVis. This conclusion is supported by measurements taken with the pressure sensors under the hand cover, shown in Figure 3, which demonstrate a correlation between the forces applied to the load cell and those felt where the device is worn.

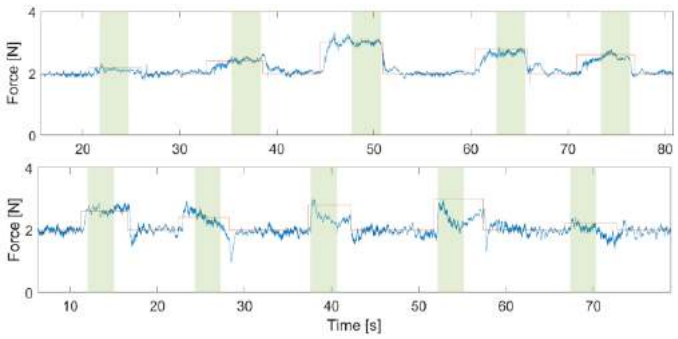


**Figure 2: Sample force accuracy trials for one participant, with target (red) and measured forces applied to the load cell (blue): NoVis/DE Trial 3 (Top), and NoVis/ND (Bottom). Green bars indicate best 3 seconds for MAPE calculation.**

**Table 1: MAPE to Target Force (Best 3s Averages)**

| | Vis | NoVis | Avg |
|---|---|---|---|
| Digital Extenders (DE) | 3.1% | 5.7% | 4.4% |
| Natural Digits (ND) | 2.7% | 8.6% | 5.6% |
| Avg | 2.9% | 7.2% | |

However, these conclusions come with some limitations worth discussing. In some cases, participants did not achieve a steady-state force-application before the 5 seconds for one target had expired, which could be addressed in future work by extending the time for each target force. Additionally, these conclusions are limited to the low range of forces exerted, namely between 2-5 N. This range is distinctly lower than expected from previous work. While the exerted forces were similar to those seen during intubation in [3], the conditions under which that force was exerted, namely the digit angles, were not replicated. Future work will investigate losses, as well as endeavor to pursue testing under conditions that conform to the higher flexion state seen in intubation to investigate the holding of these conclusions in such a condition.

The existence of haptic feedback has been confirmed, but the exact relationship between the magnitude and nature of this feedback and the accuracy of DE control has not been established. Users' reliance on haptic feedback could have been obfuscated by the availability of auditory feedback, which we plan to address in future work by employing noise-cancelling headphones.

Finally, this experiment contained a limited dataset from two participants, which future work will need to expand on in order to make more meaningful conclusions to the application of improved intubation. Neither participant in this study had any training in performing intubation, and it would be valuable to see how medical professionals trained in intubation compare in their fine motor control and use of the DEs. Future work should include expert participants and investigate the utility of haptic feedback in applied intubation settings, extending beyond simple force control.

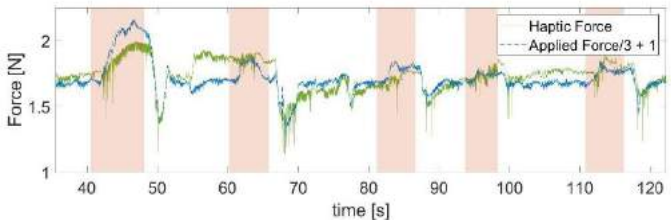


**Figure 3: Load cell force scaled to range of pressure sensor for ease of interpretation**


## ACKNOWLEDGEMENTS

The advice, expertise, and insight of Ernesto Hernandez-Hinojosa was instrumental in the production of this work.


## REFERENCES


[1] Hardwick, W. C., Bluhm, D. (1984). Digital intubation. *The Journal of Emergency Medicine*, *1*(4), 317-320. https://doi.org/10.1016/0736-4679(84)90159-8

[2] Young, S. E., Miller, M. A., Crystal, C. S., Skinner, C., Coon, T. P. (2006). Is digital intubation an option for emergency physicians in definitive airway management? *Am J Emerg Med*, *24*(6), 729-732. https://doi.org/10.1016/j.ajem.2006.03.001

[3] Hernandez-Hinojosa, E., Nawn, C. D., Abbott, C., Astorga, D., Jain, P., Restrepo, D., Hood, R. L. (2020). Bioinspired robotic exoskeleton for endotracheal intubation. *Journal of Materials Research and Technology*, *9*(6), 12167-12176. https://doi.org/10.1016/j.jmrt.2020.08.071

SB³C2022
Summer Biomechanics, Bioengineering and Biotransport Conference
June 20-23, Eastern Shore, MD, USA

# MODELING OF ORGAN-SPECIFIC TUMOR MICROENVIRONMENTS TO ANALYZE CELL-TO-CELL INTERACTIONS

**Morgan C. Connaughton (1), Mahsa Dabagh (2), (1,2)**

(1) Biomedical Engineering Department, University of Wisconsin-Milwaukee, Milwaukee, Wisconsin, United States
(2) Biomedical Engineering Department, University of Wisconsin-Milwaukee, Milwaukee, Wisconsin, United States

## INTRODUCTION

Cancer is one of the leading causes of deaths worldwide and in 2020 alone, it accounted for about 10 million deaths. Various organ-specific cancers have a higher chance of being properly treated and even cured if caught in the early stages, which is typically more difficult to diagnose and can even be misdiagnosed entirely.

The tumor microenvironment (TME) seen within the extracellular matrix (ECM), consists of stromal cells (fibroblasts) and is highly complex. The ECM, itself, is a type of non-cellular structure that regulates most cellular functions of tissue and organs, which overall, determines cell behavior, which includes, cell proliferation, polarity, differentiation, migration, and adhesion [1]. Mechanical properties, such as cell elasticity and stiffness, of single cells are important factors for many different biological processes, and this includes cancer. Elasticity plays a huge role in determining a cells resistance to deformation and the stiffness will determine the rigidity of a material in response to the stress imposed onto it. Cancer cells are different than the surrounding normal cells by their high elasticity and have even been shown to have a lower Young's modulus (E), which indicates a higher elasticity.

There has been a great deal of effort directed toward developing novel therapeutics for different cancer types in the laboratories that do not reach the clinic. The main reason for current limited success in cancer treatment is lack of biologically relevant *in vitro* or *in vivo* models resembling the complexity and heterogeneity of the TME. The purpose of the present study is to develop a novel computational model of tumor tissue. Our main goal is to build an investigational platform to study the crosstalk between cancer cells (CCs), stroma cells (SCs), and ECM.

## METHODS

The TME and ECM were created using COMSOL Multiphysics. The model consisted of a structure of singular cells surrounded by the ECM. The cells consisted of stromal cells (fibroblasts) and one singular cancer cell. The Young's modulus and Poisson ratio of the cells and the organ-specific ECM were obtained through a short literature review. Six different cancer cell lines were used throughout the present study, which included two breast cancer cell lines (MCF-7 and T-47D), two kidney cancer cell lines (ACHN and A-498), and two pancreas cancer cell lines (PANC-1 and MIA PaCa-2).

The cancer cell was placed either within the singular cell structure, not directly in contact with the ECM or on the outside of the singular cell structure, so directly in contact with the ECM. A boundary load was added to the model to represent both high (160 mmHg) and normal blood pressure (80 mmHg). This load acted on the ECM, therefor the surrounding TME. The data was then exported to MATLAB to evaluate and process the data computed from the model.

## RESULTS

Our results show that there is an interaction between the CC and SC from the given mechanical properties of the ECM and cells. Figure 1 depicts the CC that is directly in contact with the ECM and shows how the stress is impacting the CC and the surrounding SC on the x-axis with a boundary load of 160 mmHg (~21,332Pa), whereas Figure 2. depicts how the stress is impacting the CC and surrounding SCs on the y-axis, with a boundary load of 160 mmHg (~21,332Pa). The CC lines with a higher Young's modulus behave differently than its organ-specific counterpart. For example, on Figure 1 both pancreatic cancer cell lines, PANC-1, and MIA PaCa-2 both behave similarly, but then behave differently at 30 $\mu$m. The only mechanical property that is different between the two is the Young's modulus. The Young's modulus for PANC-1 was 2.4 kPa, which was higher than the Young's modulus of MIA PaCa-2, which was 1.7 kPa. This is also seen in the CC's with a

higher Young's modulus with the breast cancer cell lines and the kidney cancer cell lines.

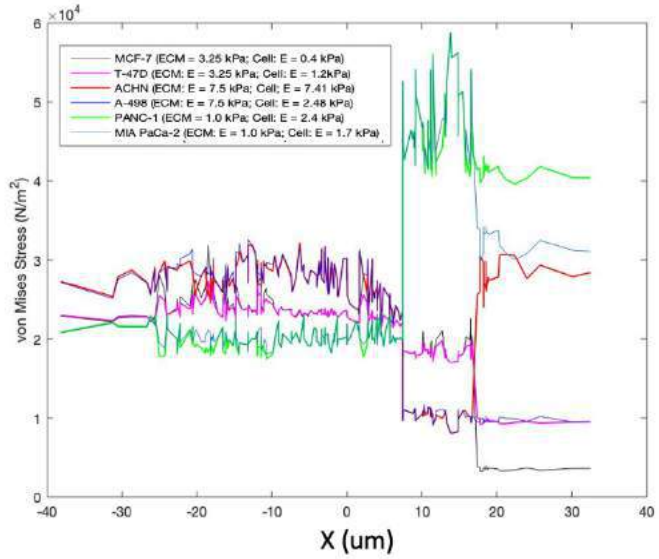


**Figure 1:** Cancer cell line that is directly in contact with the ECM on the x-axis with a boundary load of 160 mmHg (breast cancer cell lines, MCF-7 and T-47D; kidney cancer cell lines, ACHN and A-498; Pancreatic cancer cell lines, PANC-1 and MIA PaCa-2).

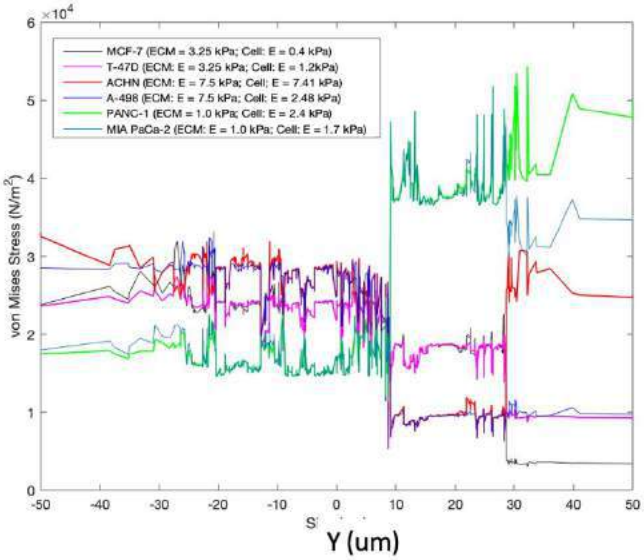


**Figure 2:** Cancer cell line that is directly in contact with the ECM on the y-axis with a boundary load of 160 mmHg (breast cancer cell lines, MCF-7 and T-47D; kidney cancer cell lines, ACHN and A-498; Pancreatic cancer cell lines, PANC-1 and MIA PaCa-2).

## DISCUSSION

Our results show that heterogeneity of CCs, SC, and ECM properties, representing different organ-specific biological condition, impact the stresses that the cells and ECM exert on each other. These CCs are leading to higher stress within the ECM and surrounding SCs, which can allow for the growth of tumors to become easier. This is because the cells are then pushing on the TME and allowing for further turmeric growth. This impacts CC competition because these cells are winning because of the structure of the ECM and SCs. Our study reveals that cell competition can be controlled by forces exposed on cancer cells by their TME. To our knowledge, this is the first study done on this type of work and it will serve as an important first step in understanding the mechanisms of cell competition, a process controlling preferential elimination of one cell by another through apoptosis.


## ACKNOWLEDGEMENTS

We thank Support for Undergraduate Research Fellows (SURF) for supporting this work.


## REFERENCES


[1] Kusindarta, D. L., & Wihadmadyatami, H. (2018). The Role of Extracellular Matrix in Tissue Regeneration. In (Ed.), Tissue Regeneration. IntechOpen. https://doi.org/10.5772/intechopen.75728

SB³C2022
Summer Biomechanics, Bioengineering and Biotransport Conference
June 20-23, Eastern Shore, MD, USA

# The Impact of Disturbed Flow Induced Arterial Stiffness on Mechanotransduction in Endothelial cells

**Andrea Alonso, Mahsa Dabagh**

Biomedical Engineering, University of Wisconsin, Milwaukee, WI, United States

## INTRODUCTION

Atherosclerosis prone regions of the vasculature are exposed to disturbed flow where low and oscillatory wall shear stress affect endothelia cell (EC) functions such as proliferation, apoptosis, migration, permeability, cell alignment and mechanical properties. ECs transduce fluid shear stress resulting from blood flow into intracellular signals whereas the response of subcellular structures to hemodynamic forces play a significant role in vascular health and disease. In this project, we are developing a multiscale, multicomponent model of endothelial cells and intra/inter-cellular organelles to explore how the mechanotransduction in subcellular structures of endothelial cells are influenced under exposure to the disturbed flow. Moreover, we take into account the impact of disturbed flow induced arterial stiffness on mechanotransduction. Our model includes adheres junction, glycocalyx, cytoskeleton, focal adhesions, nucleus, cytosol, and apical layer. In our study, we hypothesize that disturbed flow induced stiffness of the arterial wall will significantly impact the activation of mechanosensors relative to unidirectional flow applied on straight regions of the vasculature. Our results show that changes in the stiffness promotes the activation of mechanosensors in cells exposed to disturbed flow while it doesn't have same influence in ECs exposed to unidirectional flow. Our study quantifies the forces on integrins, adherence junctions, filaments and other substructures in the range that activate mechanotransduction. Our results provide insight into mechanisms underlying the progress of atherosclerosis and identifies new pathways that may lead to novel therapies to suppress the disease progression.

## METHODS

In this study, a three-dimension multi-structural model was used to interpret EC seven cells layers(figure 1): where each EC consists of the following major subcellular load-bearing structures: the apical glycocalyx layer with thickness that is in direct contact with fluid flow; the apical cortex layer with thickness; the cytosol, respectively; the nucleus at the center of each EC is located above the cell base taken as an ellipsoid with maximum radius along x-axis minimum radius along y-axis, and maximum height along z-axis ; the cytoskeleton linking the apical plasma membrane to FAs or the nucleus or intercellular junctions FAs providing the contact points with the extracellular matrix and ADJs binding ECs together across their lateral boundaries, The base of the EC is made of hexagonal cells.EC located in pro-athero-sclerosic region of the arteries/aorta. In this case the apical plasma membrane/cortical cytoskeleton layer and the glycocalyx layer with a smaller thickness are located over the cytosol. In the process of the research there is a deliberation between the in vitro and in vivo of the thickness of the denser inner layer that can have a mechanically signific. It's have shown that the thickness of the culture cells has consist firm and uniform on the cells which at the given point has not been exposes to the shear stress. It can be observed that EC cell changes within minutes of shear exposure, keeping in mind that unfortunately in this model the reflection of the biomolecular responses of the cell are not

captured in this model. The nucleus is located at the center of each EC and within them the cell base. The cytoskeleton network in this model is characteristic of a cell upon initial exposure to shear stress. The EC's do not have a preference in orientation.

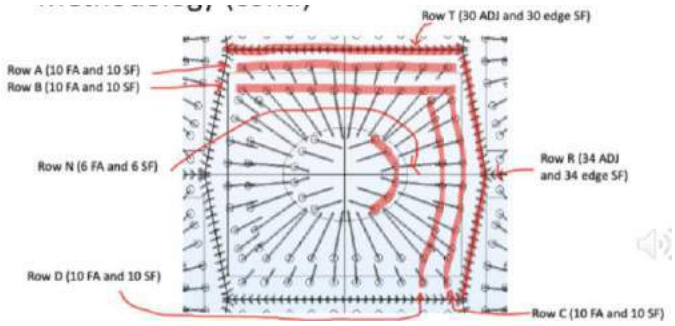


Figure1. A close- up of the model, displaying the individual rows of components through the cell to be analyzed

**Equations:**

$$U = C_{10}(\lambda_1^2 + \lambda_2^2 + \lambda_3^2 - 3), \quad (1)$$

$$\sigma_{VM} = \left\{\tfrac{1}{2}[(\sigma_{xx} - \sigma_{yy})^2 + (\sigma_{xx} - \sigma_{zz})^2 + (\sigma_{yy} - \sigma_{zz})^2 + 6(\sigma_{xy}^2 + \sigma_{xz}^2 + \sigma_{yz}^2)]\right\}^{\frac{1}{2}}. \quad (2)$$

$$\varepsilon = \frac{L_1 - L_0}{L_0}. \quad (3)$$

**RESULTS**

In this specify study the focused was particularly on how the EC, Focal Adhesions(FA), Stress Fibers(SF), and the Adherens junction with particular parameter. In this case there where 7 different cases that where sun to be able to compare the data obtained. The parameters where flow over the endothelium cells disturbed or unidirectional, ECM Properties young module, relaxation time in EMC and the behavior of ECM (viscoelastic). The thickness was keeping the same for all cases. In this particular the behavior of adherens junction through all cases showed that the data collected from a multidirectional flow have a similar behavior despite their difference in parameter. (figure2).

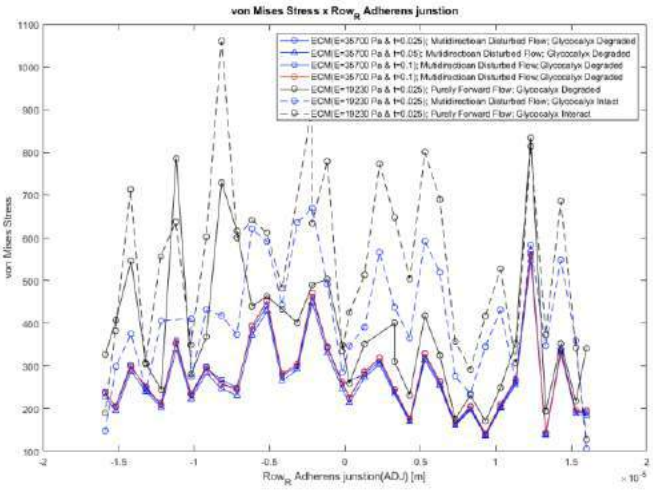


Figure 2: Von Mises Stress from rowR ADJ

**DISCUSSION**

In this study a three-dimensional mutli-strucutal model composed of, glycocalyx, apical cortex layer, cytoskeleton, stress fiber and adhesion junctions (ADJ), focal adhesion, nucleus, and cytosol to investigate mechanotransmission in the epithelial cells (ECs), expose to the distributed flow over time at the aorta. This model allowed to be compare Adhesions (FA), Stress Fibers(SF), and the Adherens junction through a period of ten seconds through different parameters. This can allow us to better understand the behavior that the aorta understanding of the complex anatomy and physiology of the aorta

**REFERENCES**


Mahmoud, Marwa, et al. "Glycocalyx Core Protein Glypican 1 Protects Vessel Wall Endothelial Cells from Stiffness-Mediated Dysfunction and Disease." *OUP Academic*, Oxford University Press, 9 July 2020, https://academic.oup.com/cardiovascres/advance-article-abstract/doi/10.1093/cvr/cvaa201/5869525.

Thanassoulis, George, and Mehdi Afshar. "Atherosclerosis - Heart and Blood Vessel Disorders." *Merck Manuals Consumer Version*, Merck Manuals, 7 Feb. 2022, https://www.merckmanuals.com/home/heart-and-blood-vessel-disorders/atherosclerosis/atherosclerosis.

Venugopal, Nishanth. *Fabrication of a Dual-Layer Cell ... - Iopscience.iop.org*. 28 July 2020, https://iopscience.iop.org/article/10.1088/1758-5090/abf995/meta.

Warboys, Christina M, et al. "The Role of Blood Flow in Determining the Sites of Atherosclerotic Plaques." *F1000 Medicine Reports*, Faculty of 1000 Ltd, 2011, https://www.ncbi.nlm.nih.gov/pmc/articles/PMC3096883/.

# PEDIATRIC HEART ASSIST DEVICE MONITOR

**Rachel M. Hillner (1), Luke Perry (1), Yuzhong Gong (1), Abdulaziz Khayat (1)**

**Faculty Advisor(s)**

**Dr. Venkat Keshav Chivukula (1)**

(1) Biomedical Engineering, Florida Institute of Technology, Melbourne, Florida, United States

## INTRODUCTION

Heart failure among pediatric patients remains a relevant area of concern throughout the medical field with 11,000 to 14,000 new cases occurring annually in the United States alone[1]. However, there is currently only one FDA approved device on the market for treatment: the Berlin Heart EXCOR[2]. The EXCOR is composed of two separate chambers: an air chamber and a blood chamber, which are divided by a flexible membrane. Thrombosis, or clot formation, in the blood chamber is a prevalent area of concern and is the leading cause of death associated with the EXCOR with 29% of patients experiencing a neurological injury[2]. A thrombus within the device would affect the movement of the membrane, causing it to deform in an unnatural fashion. Therefore, clinicians are required to perform a qualitative assessment of the membrane motion every four hours to ensure proper functioning[3]. Due to the rapid motion of the membrane (often greater than 120 bpm), clinicians record a video and qualitatively inspect the movement of the membrane frame by frame. The next steps for the patient are based on the clinician's judgment. This method can be time consuming for clinicians and is prone to subjectivity. Developing an accurate method to monitor the functioning of the device towards detecting a thrombus is of the utmost importance in order to reduce thrombogenic risk and improve patient outcomes. Our goal is to design a smartphone application that provides a tool for clinicians to perform a quantitative assessment of the EXCOR in a timely fashion, within 30 minutes, whilst maintaining high accuracy.

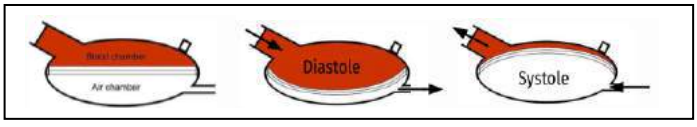


**Figure 1: The EXCOR is divided into two regions, blood and air chambers, separated by a flexible membrane. During diastole, the membrane is pulled down allowing blood to fill. During systole the membrane is pushed up and blood exits the device.**

## PRODUCT DESIGN

The PHADM (Pediatric Heart Assist Device Monitor) utilizes computer vision and machine learning to quantitatively assess the performance of the EXCOR based on the relation between membrane deformation and device functionality. The front end of PHADM will be in the form of an user-friendly smartphone application. An outline of the application can be seen in Figure 2 and 3. The first page of the mobile application will allow the clinician to determine the method of data collection: to upload a previously recorded file from files or to record a video in app. If selecting a previously recorded file, then the clinician will be asked to select a recording and ensure its quality. If recording in app, they will be directed to a camera application with directions detailing how to record a quality video. Afterword they will be asked to review the video. Lastly, after inputting patient specifications such as expected bpm and patient ID, the clinician can proceed to analysis. While the algorithm is evaluating membrane motion, a progress bar with expected completion time will appear. Once complete, a notification will be sent to the clinician from which the results can be viewed.

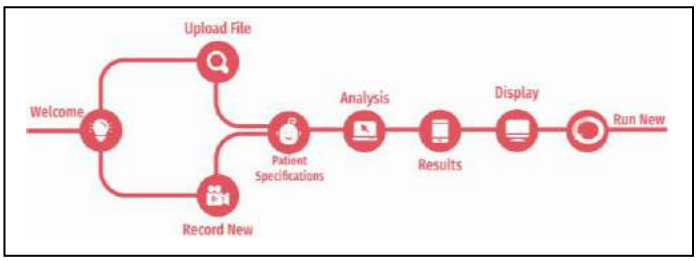


**Figure 2: Outline of Application Design**

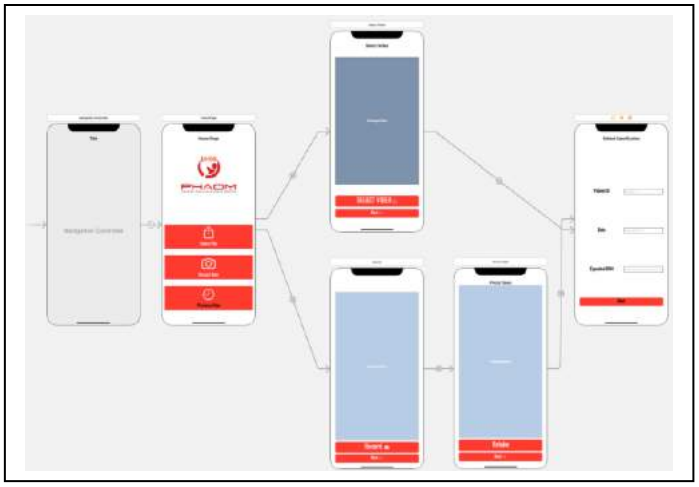

**Figure 3: Current Application Display. Application is under construction.**

Membrane movement will be quantified through the use of a computer vision algorithm, HOG (Histogram of Oriented Gradients). HOG quantifies the change in pixel intensity of neighboring pixels; large differences in pixel intensity are indicative of membrane deformation and small changes represent a smoother membrane. HOG is solely applied to the membrane region of the EXCOR through the process of background subtraction. In doing so, noise will be greatly reduced, thus amplifying the signal produced from the movement of the membrane. HOG is calculated for every pixel in a given frame and summed such that each frame can be represented by a single HOG value. The corresponding HOG values are then normalized and features are extracted from this signal. Peak prominence and time between peaks are the two features most telling of membrane performance. Peak prominence is calculated from the difference between maximum and minimum HOG values for a given time frame. Time between peaks is calculated as the difference in time from $peak_n$ and $peak_{n+1}$. The HOG of the membrane motion is capable of clearly indicating the smoothed and deformed phases of membrane movement. Small changes in membrane deformation may suggest that the membrane is not completely smoothing as it should and would be flagged. In addition, increased time between identified smooth points suggests that the membrane is not completely smoothing twice during each cardiac cycle as shown in Figure 4. Both features will be used in order to accurately assess the functioning of the EXCOR in a quantitative manner. Based on preliminary results, PHADM is able to successfully identify slight deviations in membrane movement that could easily be missed by the human eye. When analyzing an EXCOR functioning at 120 bpm, good filling would result in a smooth point occurring at a mean of every 0.25s. It was found that diastole takes longer than systole, approximately 0.31s compared to 0.19s respectively. When plotted with a playback speed 1/8 of real time, a cardiac cycle is 4s (2.5s diastole, 1.5s systole). This information is helpful when identifying at what stage the EXCOR is malfunctioning. Figure 4, point D was identified to be abnormal through the usage of peak prominence and time between peaks. The peak was minimal and the time between peaks was greatly increased, ~3.7s plotted at 1/8 real speed or 0.46s real time, and occurred during systole.

Preliminary testing using pre-recorded patient data from clinical collaborators at the University of Iowa suggest that PHADM is highly accurate in quantifying membrane movement as well as identifying cardiac phase (systole vs diastole), as shown in Figure 4. More testing will be conducted using additional pre-recorded data from clinical collaborators. A mock flow loop with an EXCOR will be used to investigate clinically relevant EXCOR scenarios in a controlled manner. Finally, the smartphone application will be made available to clinicians for beta testing in the near future.

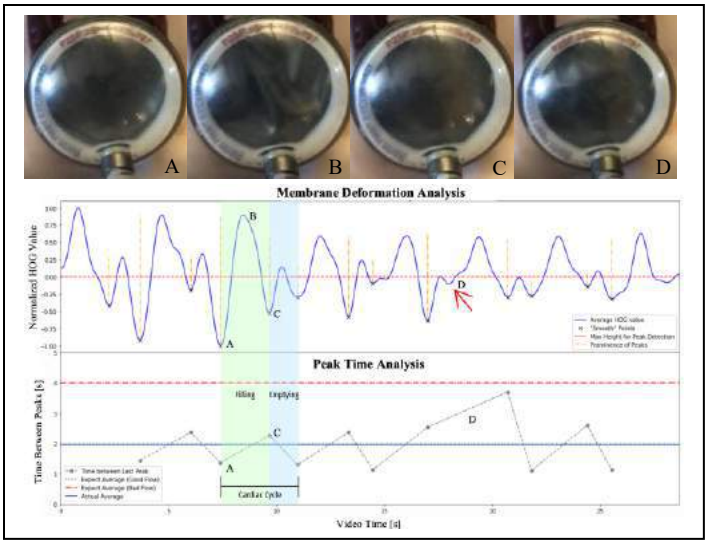


**Figure 4: Membrane Deformation & Peak Time Analysis with Respect to Cardiac Cycle where blue line represents membrane movement: (A) Minimal HOG value representative of a smooth membrane; (B) Maximum HOG value representative of increased membrane deformation; (C) Second smooth point of the cardiac cycle; (D) Point that did not completely smooth indicated by the red arrow and minimal peak prominence representative of abnormal membrane deformation.**

## BUDGET & MARKET ANALYSIS

The current budget is $99. This project is primarily a software based design from which free IDEs such as XCode and JupyterLab are utilized. The sole expense associated with the maintenance of this app is a $99/year fee to keep PHADM on the Apple App Store. Future expenses such as further app development, i.e. hiring of a software engineer, may ensue, however, such expenses won't be relevant until future years. Regardless, PHADM will be sold with a subscription plan from which a hospital will pay a base fee for the software, then an additional fee for each device added the account. Subscription plans will start at $110/year for a single device. An additional $22/year will be charged for each new device added to an account.


## ACKNOWLEDGEMENTS

Dr. Aditya Badheka, University of Iowa


## REFERENCES


[1] Das, Bibhuti B. "Current State of Pediatric Heart Failure." Children (Basel, Switzerland) vol. 5,7 88. 28 Jun. 2018, doi:10.3390/children5070088

[2] Jordan, Lori C., et. al. "Neurological Complications and Outcomes in the Berlin Heart EXCOR® Pediatric Investigational Device Exemption Trial." Journal of the American Heart Association, doi:10.1161/JAHA.114.001429.

[3] Badheka, Aditya, and Veerajalandhar Allareddy. "IPhone in the Management of the Berlin Heart EXCOR Ventricular Assist Device." ASAIO Journal, 2018, doi:10.1097/MAT.0000000000000708.

SB³C2022
Summer Biomechanics, Bioengineering and Biotransport Conference
June 20-23, Eastern Shore, MD, USA

# INVESTIGATING THE ROLE OF ASPIRIN ON THE GEOMETRIES AND MECHANICAL PROPERTIES OF EXPERIMENTAL BLOOD CLOTS

**Nolan Corbitt (1), Bryan C. Good (1)**

(1) Mechanical, Aerospace, and Biomedical Engineering
University of Tennessee
Knoxville, TN, USA

## INTRODUCTION

An acute ischemic stroke (AIS) occurs when a blood clot occludes a vessel in the brain, causing a lack of oxygen and nutrients being delivered to downstream regions of the brain [1]. In 2016, the American Heart Association and National Institute of Health reported the stroke mortality rates in patients aged 65 or older to be 271.4 per 100,000 [2]. In many countries, stroke is the second or third largest cause of death, and one of the highest causes of adult disability [3]. One way to treat patients that are at risk for an AIS is to administer medication like aspirin to reduce or prevent clot formation. However, AIS's can still occur in these patients, and it is unclear how their clots may differ from those of untreated patients. The mechanical properties and size of AIS patient clots have also been shown to affect successful recanalization via mechanical thrombectomy. To improve patient outcomes in these procedures, the effects of medication on the geometries and mechanical properties of AIS blood clots should be further investigated to determine how they can be used in combination with thrombectomy devices.

## METHODS

To determine the effects of aspirin on embolus analog (EA) geometries and mechanical properties, two experimental protocols were utilized to create EAs. In both protocols, EAs were created *in situ* from bovine blood collected in CPDA-1 anticoagulated bags (Lampire Biologic). The blood was first centrifuged to separate the red blood cells (RBCs) and platelet rich plasma (PRP). The RBCs were then further centrifuged to separate the platelet poor plasma (PPP) from the RBCs. For all solutions, the blood was reconstituted to a hematocrit of 40%, modeling typical human blood. To add aspirin into the blood, acetylsalicylic acid powder was diluted with a HEPES buffer solution and pH adjusted to 7.4 [4]. To separately investigate the effect of the buffer solution on EA properties, three solutions were used: blood with no buffer or aspirin solution added (H=40), blood incubated with only the buffer solution (HEPES), and blood incubated with the aspirin-buffer solution (ASP).

For the first experimental protocol, the effect of aspiration incubation time was also investigated to determine its role on EAs. Following reconstitution to a 40% hematocrit, the blood was put into one of five groups: 1) H=40 blood, HEPES incubated with blood for 2) 24 and 3) 48 hours, and ASP incubated with blood for 4) 24 and 5) 48 hours. Each solution was recalcified using a 1:25 ratio of $CaCl_2$ to blood, drawn into ¼" diameter PVC tubing, and inserted into a Chandler Loop system (**Fig. 1A**). The tubing was submerged in a water bath at body temperature and was rotated to achieve velocities observed in the carotid artery. After 1-2 hours of clotting, the EAs were removed from the Chandler Loop and their length and mass measured with calipers and a balance, respectively.


**Figure 1: A)** Chandler Loop system used to create EAs and **B)** Instron mechanical tester used for measuring EA mechanical properties.

The second experimental protocol was used to determine the mechanical properties of the EAs. 6-well cell culture plates were filled with the same three blood solutions (H=40, HEPES, or ASP) and allowed to mix for 24 hours on an orbital shaker. The blood was then recalcified at a 1:25 ratio with $CaCl_2$ to blood and mixed on the orbital shaker for another 1-2 hours to coagulate. After coagulation, the EAs were removed, and uniaxial compression testing was performed with a single-column mechanical tester and 50 N load cell (Instron) (**Fig. 1B**). The EAs were cylindrical in shape with thicknesses and diameters of approximately 10 mm and 34 mm, respectively. All EAs were compressed at a rate of 10 mm/min and their stress and strain curves output for further analysis.

## RESULTS

The Chandler loop experimental system led to the formation of consistent cylindrical EAs with 1-2 hours of dynamic clotting. Examples of these EAs can be seen in **Fig. 2**.

**Figure 2:** Examples of ¼" diameter cylindrical EAs taken from Chandler Loop under varying experimental conditions.

EAs formed from whole blood, blood incubated with HEPES, and blood incubated with aspirin were all measured and weighed after their removal from the Chandler loop tubing. Decreases in EA length (**Fig. 3A**) was observed from the HEPES EAs to the ASP EAs for both the 24- and 48-hour incubation groups with average lengths decreasing by approximately 7 and 4 mm, respectively.

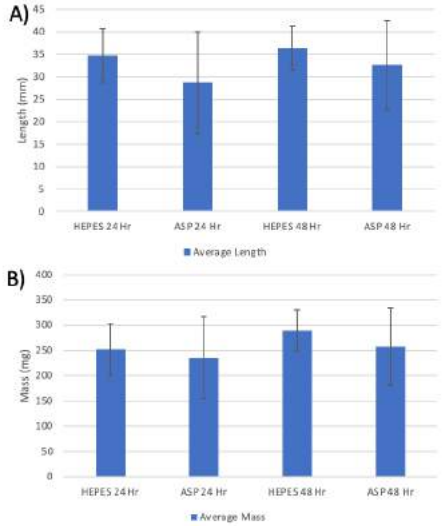


**Figure 3:** Averaged **A)** length and **B)** mass for EAs taken from Chandler loop.

The average EA masses (**Fig. 3B**) followed a similar trend, with the ASP EAs weighing less than the corresponding incubation time HEPES EAs, (decreases of approximately 10 and 30 mg, respectively). While both length and mass parameters decreased from the HEPES to ASP EAs, indicating that the addition of aspirin is playing a role in EA formation, the results were not statistically significant.

The mechanical testing results are shown in **Fig. 4**, and H=40, HEPES, and EA stress values were compared at strains of 10, 20, 30, and 40%. At all strains, there was a large decrease in resultant EA stress in both the HEPES and ASP EAs compared to the H=40 EAs. Additionally, there was a further decrease with the addition of aspirin compared to the EAs with only buffer added. Similar to the EA geometric data, the differences between the HEPES and ASP EA mechanical properties were not statistically significant but clear trends were observed that point to the role of aspirin in modifying the EAs.

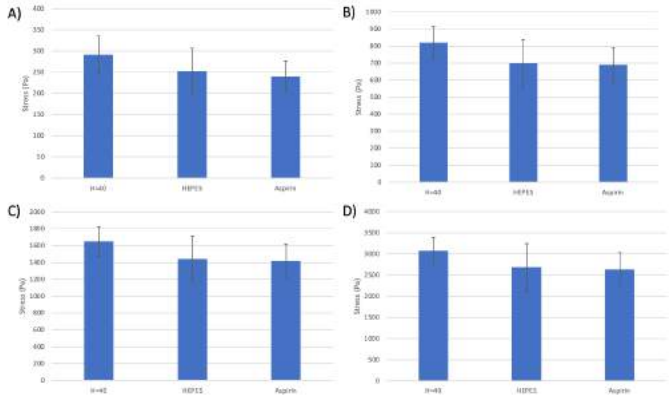


**Figure 4:** Averaged EA stresses at strains of **A)** 10%, **B)** 20%, **C)** 30%, and **D)** 40%.

## DISCUSSION

The trends of decreasing EA length, mass, and stiffness between the HEPES and ASP test groups suggest that the addition of aspirin is playing a role in clotting. This is likely due to the role aspirin plays in lowering platelet activity, causing decreased coagulation. The decrease in EA stiffness upon the addition of the HEPES buffer could be due to the buffer solution diluting the coagulation factors in blood plasma and effecting the EA structure compared to H=40 EAs. These experiment protocols will be applied in future experiments with other therapeutic drugs including blood thinners, like Warfarin, and thrombolytic drugs, like tissue plasminogen activator (tPA). Additionally, one of the risks of any drug that affects the mechanical properties of EAs is that they can soften the EAs too much and cause fragmentation during mechanical thrombectomy and distal embolization. Further experiments will focus on EA failure using a lap-shear test setup on the Instron mechanical tester to determine the role these same therapeutic drugs play.

## REFERENCES


[1] Randolph, S., *Workplace Health & Safety*, 64(9). 2016.
[2] Virani, S., et al. *Circulation*, 143(8). 2021
[3] Langhorne, P, et al., *The Lancet*, 377(9778). 2011.
[4] Marciniak Jr., S., *Thrombosis and Haemostasis*, 87. 2002.

# SILENT SPEECH INTEFACE FOR AUGMENTED REALITY DEVICES

**Tania Rivas (1), Gianna R. Distefano (2)**

**Faculty Advisor(s)**

**Victor Huayamave, PhD. (1), Cristine Dailey Walck, PhD. (2)**

(1) Mechanical Engineering, Embry Riddle Aeronautical University, Daytona Beach, FL, USA

## INTRODUCTION

Silent speech is defined as communication through biosignals when no acoustic means is outputted or received. Many applications for silent speech interfaces (SSIs) have risen over the years including aiding those with communication and/or movement disorders in multiple areas such as rehabilitation therapy, training for jobs where bulky equipment was previously required and entertainment. The beginning of this project involved using electromyography (EMG) sensors to collect subvocalization data from four neck muscles activated during the speech production process to train and test a 1-dimensional convolutional neural network (CNN) that works as a classifier to categorize the six command words in the current library. This is to eventually be integrated into an augmented reality (AR) device to be controlled solely by subvocalizations. The team explored the unique characteristics of EMG signals from various neck muscles, experimented with post-processing the data filtration and expanded the datasets. While preliminary testing accuracies show promising results, the process of applying the sensors themselves has proven to be cumbersome. Each EMG sensor requires two pieces of double-sided medical grade adhesive and separate positioning of the reference sensor and sensor head. This current method exhausts resources concerning time, finances, and energy from the user. The team posits a hardware design that can house all four sensors simultaneously and override the need for the tape to streamline the sensor application process.

## PRODUCT DESIGN

The hardware design idea is centered on the contour of the reference electrode since ensures only material that is absolutely needed is being used. Initially, a spider like design was envisioned where a main block with four extrusions to hold four flexible conduits to house the EMG sensors would be placed on the side of the neck. This idea was discarded because of the bulky design and inconvenient placement. Eventually, the team decided to house only the reference electrodes and add some type of flexible housing for the wires that would be sturdy enough to hold up the sensor heads as well. It was decided a short wall would surround the sensors as it would offer enough traction around all sides to ensure a safe and sturdy placement and provide a small face to attach the future wiring housing to hold the sensor heads. Two curves were cut through on the back side of the apparatus to maximize the flexibility to best fit the contour of the neck. It was decided the apparatus would be 3D printed out of thermoplastic polyurethane because of its low density, flexibility, affordability, and machinability. The current reference sensor housing, Figure 1, design highlights the goal of finding a balance between maximizing structural flexure by reducing the material used and maintaining structural integrity by lodging the sensors with the aid of friction.

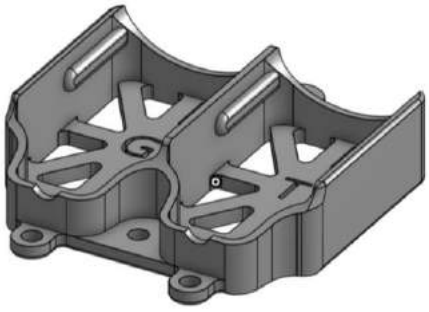

**Figure 1: Complete reference sensor housing CAD.**

The software design of the SSI began with experimenting with sensor placement. The placement selection was determined through an amplitude qualities and characteristic waveform comparison during the speech production process. Sensors with poor signal to noise ratios were excluded as they were considered low quality. A healthy 22-year-old Caucasian male, 20-year-old Hispanic female, 23-year-old Caucasian female, and 18-year-old Caucasian male with no speech impairments in a controlled lab environment were prompted to subvocalize command words from a library of six words: Up, Down, Left, Right, Yes, and No. To ensure high accuracy rates while reducing potential error from differences within individual subvocalizations, the subject was prompted to subvocalize commands forty times. Preliminary subvocalization data was collected using EMG sensors applied to the Digastric, Sternohyoid, Stylohyoid, and Cricothyroid and their respective reference muscles, as seen in Figures 2 and 3. Then, data was filtered to remove environmental noise that could potentially interfere with the recognition model. According to the sensor manufacturer, the EMG electrodes have a bandwidth of 10 – 450 Hz establishing the value of a band-pass filter to remove high and low frequency noise from the

signal at a window of 10 – 400 Hz. Applying the filter allowed the band of frequencies describing the subvocal activity to be isolated. Individual command words were parsed from the EMG signal data and placed into individual training datasets. A one dimensional, seven layered CNN was created with the Keras library in Python. Important characteristics of this model are the two dropout layers integrated to reduce overfit by randomly compensating for small training datasets and reduce the model's dependency on the current training data while simultaneously improving the accuracy of unseen data.

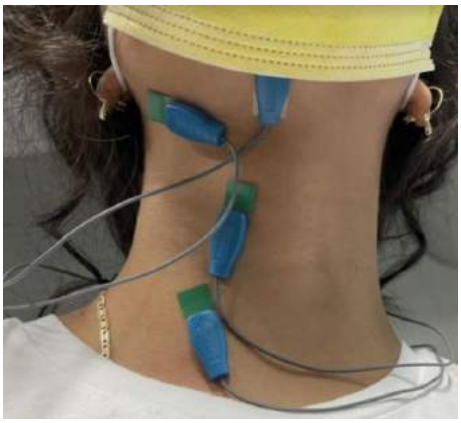

**Figure 2: The EMG sensor heads applied to neck muscles of interest.**

**Figure 3: The EMG reference sensors applied to stationary neck muscles.**

## BUDGET & MARKET ANALYSIS

The American Speech, Language and Hearing Association reports 7.5 million Americans have communication disorders and the University of Michigan's medical department reports another 40 million have movement disorders [1]. Integrating silent speech and AR, creates opportunities for those with disabilities to recover ranges of motion, expand their career choices and even immerse themselves into dynamic entertainment. By easing the process of sensor application, constraints for those opportunities minimize even further.

Potential market size initially would be kept to the 38,800 clinics in America providing physical, occupational and speech therapy. They have an average annual receipt (per clinic) of $886,000 and have a 14.6% net profit gain [2]. Included in the price of the product would be the Delsys EMG sensors themselves, the price of the 3D printed sensor housing, the soldering wire, as well as overhead costs. The design budget $4,007.73. Expected manufacturing/testing/overhead, including engineering and tooling price of the sensors, cost comes out to $1,162.73, and the product would be sold for $3,463.00 resulting in a profit of $2,208.00. Below in Figure 3 the budget breakdown, without the price of the sensors and licenses, can be seen. Since wire and 3D printing are low in price the shoelaces used to tie the apparatus together is taking up the majority of the budget.

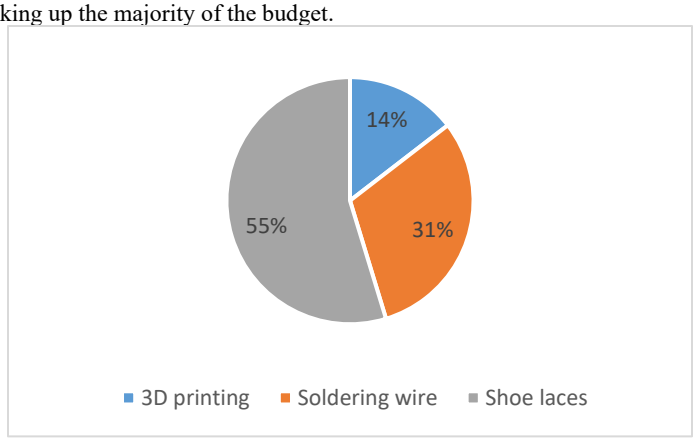


**Figure 3: Budget Breakdown by Percentages (sensor prices excluded)**


## ACKNOWLEDGEMENTS

Special thanks to Embry-Riddle Aeronautical University's biomedical laboratory facilities and management, which is supported by the Mechanical Engineering Department


## REFERENCES


[1] Regents of the University of Michigan, "Neurosciences: Movement Disorders," 2021. [Online]. Available: https://www.uofmhealth.org/conditions-treatments/brain-neurological-conditions/movement-disorders.

[2] LaRosa, John,"U.S. Physical Therapy Clinics Constitute a Growing $34 Billion Industry," 1 July 2019. [Online]. Available: https://blog.marketresearch.com/u.s.-physical-therapy-clinics-constitute-a-growing-34-billion-industry

# THE ANALYSIS OF URTHERAL BIOMECHANICS DURING VOIDING USING MRI

**Maxwell C. Kounga (1,2), Cody J. Johnson (1), Juan P. Gonzalez-Pereira(1,3), Shane. A Wells (1), Wade A. Bushman (4), Alejandro Roldán-Alzate (1,2,3)**

(1) Radiology, University of Wisconsin Madison, Madison, WI, USA
(2) Biomedical Engineering, University of Wisconsin Madison, Madison, WI, USA
(3) Mechanical Engineering, University of Wisconsin Madison, Madison, WI, USA
(4) Urology, University of Wisconsin Madison, Madison, WI, USA

## INTRODUCTION

Lower urinary tract symptoms (LUTS) are costly and contribute to lower urinary tract dysfunction [1]. The investigation of biomechanics during voiding, with respect to the urethra, may provide some insight into the function of the LUT. Current diagnostic methodologies, such as cystoscopy, retrograde urethrography, and multichannel urodynamics with fluoroscopic imaging, are invasive and limited in the information they provide [2, 3]. In contrast, magnetic resonance imaging (MRI) can provide anatomical and functional information of the LUT as shown in previous studies [4, 5] in a non-invasive manner. Building upon those previous studies, we examine the potential for MRI to deliver a non-invasive methodology to acquire anatomical and biomechanical information of the urethra throughout the voiding process.

## METHODS

This study was HIPAA-compliant, IRB approved, and was performed after informed consent. All scans were completed on a clinical MRI 3T scanner (Premier, GE Healthcare, Waukesha, WI), with a high-density flexible surface coil array. (AIR Coil, GE Healthcare). Four healthy adult males ages 29, 55, 62, 74 were recruited for this study. The subjects were instructed to drink copious amounts of fluids before testing and to not void prior to the study. 15 minutes prior to the MRI scans, 1/3 of a single weight-based dose (0.1 mmol/kg) of gadolinium-based contrast was hand injected intravenously into each subject to enhance the visualization of urethral change during the voiding process. Subjects were equipped with a condom catheter and instructed to void whilst in the MRI scanner. A dynamic acquisition was performed using 3D Differential Subsampling with Cartesian Ordering (DISCO) Flex, with a temporal resolution of 3.7 seconds. After urination, the subjects were given the remaining 2/3 of the contrast. A static acquisition was then performed using a fast-spin echo T2-weighted axial sequence with an in-plane resolution of .625mm, to get anatomical reference images of the prostate.

The resulting images were imported into Mimics (Materialise, Leuven, Belgium). At each point of the dynamic imaging, the internal and external urethral sphincter (IUS, EUS) diameters, urethral length, prostatic urethral angles were measured, while the prostatic, membranous, and penile urethra were segmented (Figure 1a). Using these segmentations, 3D renderings of the urethra were calculated (Figure 1b) at each point of the dynamic imaging.

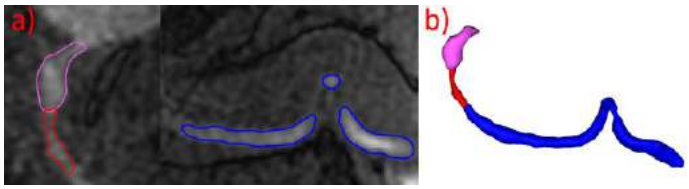


**Figure 1: a) Segmentation of the prostatic (purple), membranous (red), and penile (blue) urethras. b) 3D renderings of those segmentations**

Using the centerline tool, centerlines were created for each urethral segment at each time point during the voiding event, and the corresponding average best-fitted diameter were calculated. From the 3-D rendering, the urethral volumes were also calculated. The prostate volume was determined by creating 3D renderings using segmentations from the anatomical reference images.

From an affiliated study done by this lab, voided volume, and flow rates of urine from the bladder into the urethra were calculated and used in this study. The IUS and EUS diameters were correlated with these flow rates, and an $R^2$ were calculated.

## RESULTS

This novel MRI-based technique was successfully implemented to characterize the anatomy and biomechanics of the urethra during voiding. The anatomical dimensions of the prostate and urethra at listed in Table 1.

**Table 1: Observed dimensions of the prostate and urethra.**

| | PV (cc) | Largest Urethral length (cm) | Largest Urethral Volume (cc) | Post-void urethral residual (cc) |
|---|---|---|---|---|
| Subject 1 | 22.4 | 23.5 | 13.2 | 0.18 |
| Subject 2 | 36.2 | 22.6 | 19.1 | 12.6 |
| Subject 3 | 49.4 | 22.2 | 11.1 | 0 |
| Subject 4 | 16.6 | 23.2 | 13.2 | 4.85 |

The average IUS across the voiding process was significantly larger than the average EUS ($p < 0.05$) for all four subjects.

As displayed in Figure 2, the EUS correlated with flow rate ($R^2$ = 0.8 - 0.91), while the IUS showed no correlation ($R^2$ = 0.03 - 0.3).

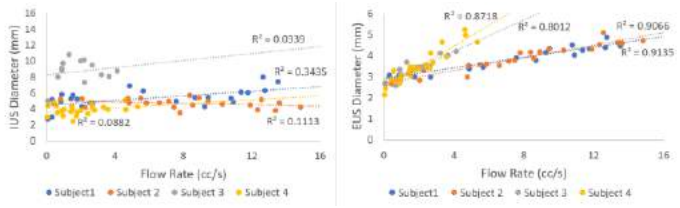


**Figure 2: IUS and EUS diameter over flow rate with each respective $R^2$ value.**

The biomechanical changes of the membranous urethra showed to be consistently smaller than both the Prostatic and Penile across the voiding cycle, as shown in Figure 3.

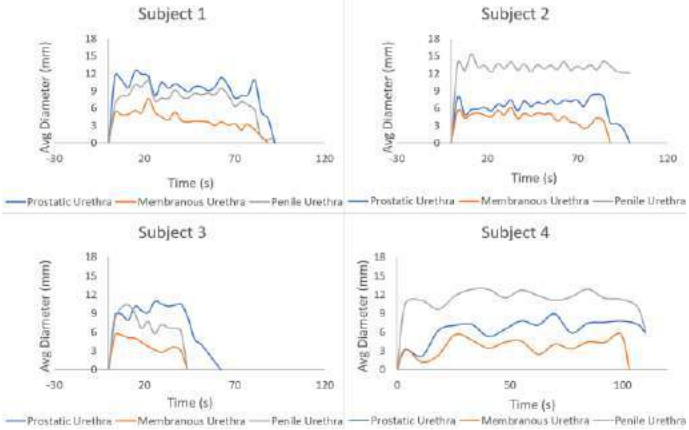


**Figure 3: Average diameter of prostatic (blue), membranous (orange), and penile (grey) urethra during the voiding process.**

During the resting phase, the subjects displayed average prostatic angle of 41.1 degrees. During voiding the prostatic urethra straightened by 19.1 degrees.

## DISCUSSION

Prior studies have signaled that the LUT and urological diseases create anatomical changes in the body [6, 7]. Current methodologies to medically examine these anatomical changes in the urethra is to invasively instill fluid into the urethra to get comprehensive imaging [8]. Such methodologies inhibited researchers from collecting information about the biomechanical function of the urethra during the voiding process. However, advancements in dynamic MRI can be used to inspect the LUT during the voiding process. In this MRI based study, we introduce a novel technique for the non-invasive quantitative and qualitative analysis of urethral anatomy and biomechanics during the voiding process.

MRI is a noninvasive imaging tool used primarily to analyze soft tissue, much like that found in the LUT. With this novel technique we can image the urethra throughout the duration of the voiding process at a variety of urethral capacities. This unique ability enables for the investigation of urethral dynamics at various stages and for those dynamics to be compared for the duration of the voiding process. Thus, providing a level of information detail, unique to this technique.

In this study, we obtain measurements of urethral length, prostatic urethral angle, IUS and EUS diameter, and region-specific diameter (Prostatic, Membranous, Penile). The EUS diameter showed a strong positive correlation with flow rate for all 4 subjects. The IUS diameter, however, showed no correlation to the flow rate. This difference in trends of the EUS indicate that the EUS plays a large active role in determining flow rate when compared to IUS**.** The prostatic urethral angles straightened during voiding suggesting a potential tactic to decrease resistance.

As observed in our study, our technique can be applied to a wide variety of subjects with diverse physiological and anatomical differences. For instance, subject 3 and 4 voided 91.23 and 186.83, respectively. Despite these, comparatively low voids we were still able to obtain an in depth quantitative and qualitative analysis of their urethral anatomy and biomechanical function during the voiding process. Such analysis could be used to investigate voiding disfunction and signs for urological diseases. Furthermore, it is also clear that the data obtained yields varied information from subject to subject. This suggests that the technique can discern between anatomical and physiological diversity and reflect this diversity in the data produced. The technique's ability to differentiate between diverse voiding processes, introduces a significant amount of specificity in the observed results, which can be utilized to quickly gage the extent to which a subjects anatomical and biomechanical characteristics deviate from the norm.

In summary, the new methodology presented here, which uses MR imaging to obtain quantitative and qualitive data about the LUT can give specific and varied informational about anatomy and biomechanics during the voiding process in a safe, accurate and reproducible way. Further investigations into this technique will focus on establishing a healthy baseline for the biomechanics of LUT. This information can then be compared with patients with conditions involving LUTS and lead to earlier diagnosis and more specific treatment which is informed directly by their anatomical and biomechanical characteristics.


## ACKNOWLEDGEMENTS

The authors would like to acknowledge GE Healthcare and support from the NIH (R01 DK125850-01).


## REFERENCES


[1] Wei, J et al., (2005). *The Journal of Urology*, 173(4), 1256–1261.
[2] Verla, W et al., (2019). *BioMed research international*
[3] Engelsgjerd, J et al., (2021). *StatPearls Publishing*
[4] Anzia, L et al., (2021). *Abdominal radiology* 46(4), 1670–1676.
[5] Pewowaruk, R et al., (2020). *PloS one*, 15(11), e0238404.
[6] Güzel, Ö, et al., (2015). *Urology*, 86(3), 439–444.
[7] Mirone, V, et al., (2007). *European Urology*, 51(1), 57–66.
[8] Cox, J, et al., (1994). *International journal of radiation oncology, biology, physics*, vol. 29,5: 1119-23.

# OPTIMIZATION OF ECM/GELATIN SOLUTION IN A NEAR FIELD ELECTROSPINNING SYSTEM FOR ENGINEERING TENDON

**Aasim F. Hussain (1), Zachary G. Davis (1,3), Matthew B. Fisher (1,2,3)**

(1) Department of Biomedical Engineering, University of North Carolina-Chapel Hill and North Carolina State University, Raleigh, NC, USA
(2) Department of Orthopaedics, University of North Carolina-Chapel Hill, NC, USA
(3) Comparative Medicine Institute, North Carolina State University, Raleigh, NC, USA

## INTRODUCTION

Tendon injuries are one of the most pervasive injuries and a leading cause of mobility issues with tendons involved in ~50% of musculoskeletal injuries [1]. Yet, the full complexity of the injury and subsequent healing is not well understood, including cell-matrix interactions in these processes. To understand such interactions, three-dimensional (3D) *in vitro* models such as fibrous scaffolds have grown in use, as an alternative to animal models. More recently, electrospinning has grown as a technique for creating fibrous scaffolds that mimic the structural nature of the extracellular matrix (ECM) [2]. Electrospinning, through the manipulation of an electric field and a fine nozzle, actively converts polymer solutions into a random sheet of nanofibers, however, individual fiber control is limited [2]. The overall orientation and alignment are essential in creating a scaffold as it greatly influences the efficacy of cells on the scaffold in terms of function and growth [1,2]. 3D additive manufacturing methods, such as fused deposition modeling can be used to create singular fibers, however, the size of the fibers range in the 100-400 µm range whereas collagen fibers are in the range of 1-20 µm. Direct-write, near-field electrospinning (DWNFE) is a computer-guided, single fiber deposition method for creating 3-D structures on a collagen fiber scale. DWNFE, though more widely known for its use within synthetic polymers, more recently has shown promise with natural polymers such as collagen and gelatin [2]. DWFNE can produce fibers that can match natural collagen size and allow for fine fiber orientation, allowing control of specific aspects of tendon behavior within engineered tissues in vitro [2].

Gelatin is a natural, biodegradable, and biocompatible polymer that is obtained from the partial hydrolysis of collagen [3,4]. Gelatin is known to be a more cost-effective alternative to collagen. Compared to synthetic polymers, gelatin can provide a better environment for cell attachment, growth, and proliferation. Previous work in the lab showed success with the use of a gelatin-acetic acid solution within a DWNFE system whilst being able to control fiber morphology and fiber diameter [2]. Further incorporation of ECMs into this system will allow for more tissue-specific bioactivity and specific proteins that can impact cell behavior. Currently, the use of ECM in DWNFE systems is limited, though its use within bioinks illustrates the feasibility of ECM-based solutions in fabricating constructs with the beneficial, bioactive nature needed to elicit a more innate response. Objective**:** To demonstrate the feasibility of using gelatin-acetic acid solution as a carrier for decellularized tendon extracellular matrix (dECM) within the DWNFE process.

## METHODS

Equine superficial digital flexor tendon was obtained from 3 specimens and decellularized, digested, neutralized, and powdered following *Wolf et al* (Figure 1) [5]. To determine the optimal ratio of dECM to gelatin, 625 mg/mL dECM/gelatin solute concentration solutions in 70 v/v% acetic acid were mixed at 0%, 10%, 15%, and 25% dECM. Solutions were mixed for 2 days at 40°C. Afterward, the solutions were stored at 4°C. As viscosity has a direct impact on fiber diameter and fiber morphology for electrospinning, solution viscosities, and shear stress were measured with a rheometer over a two-ramp sweep across a shear rate of 0.1 to 1000 (1/s). Each of the groups was printed using a custom DWNFE system following the protocol established in Davis et al [2]. The fibers were then printed in crosshatches with a length of 10 mm and a width of 30 mm. The pressure was set to 0.1 psi, stage speed of 75 mm/s, spacing of 0.5 mm for both horizontal and vertical fibers, a working distance of 1.0 mm, and an accelerating voltage was set at 3 kV with an ambient humidity of 50-55%. The values for the DWNFE were designated by a custom MATLAB script and were converted to GCODE for printer recognition following previous work in the lab [2]. Fibers were printed onto a noncharged glass microscope slide with a blunt 22 G metal needle. An n=3 solution was made for each concentration, and n=10 scaffolds were fabricated for each solution. To qualify the presence of collagen and glycosaminoglycans (GAGs) for the 25% dECM solution, picrosirius red and alcian blue stains were used to determine the presence of collagen and GAGs respectively, after crosslinking with 10:1 1-ethyl-3-

(3-dimethyl aminopropyl) carbodiimide (EDC)/N-hydroxysuccinimide (NHS) for 24 hours.

Brightfield imaging was used to measure fiber diameter and an inverted microscope was used to visualize staining. Fiber diameters were derived with ImageJ. Outliers were removed for scaffolds with the ROUT method and a Q=1%. A Mann-Whitney t-test was used to compare each dECM to the 0% dECM control (α=0.05).

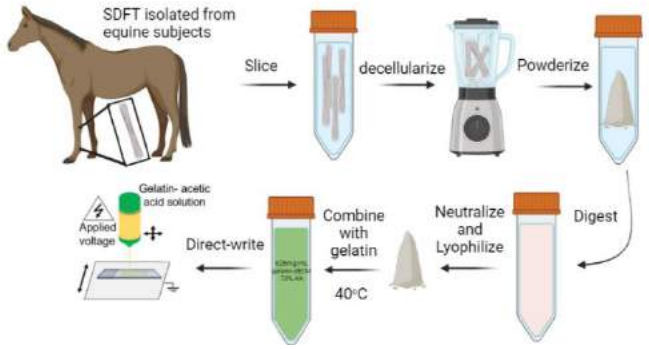


**Figure 1: Schematic for DWNFE dECM/gelatin solution preparation**

## RESULTS

The dECM/gelatin hybrid solutions were successfully produced with a total concentration of 625 mg/mL and varied dECM concentrations from 0 to 25 w/w%. The mean viscosity for the 0, 10, 15, and 25% dECM was 13.8, 17.7, 8.0, and 22.8 Pa*s respectively (Figure 2).

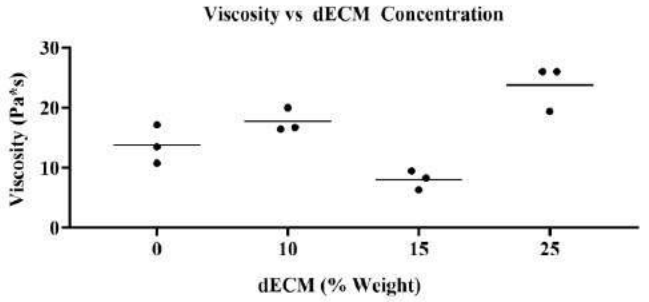


**Figure 2: Average viscosity of the 0, 10, 15, and 25 percent dECM over linear region for shear rates 0.1-100 [1/s]. Dots represent individual solution viscosity. Bars represent mean viscosity with dots representing solution viscosities**

The median fiber diameters for 0, 10, 15, and 25% were 3.0, 3.9, 3.1, and 6.0 µm with an interquartile range (IQR) of 2.5-3.5, 2.4-7.4, 2.5-3.9, and 4.0-10.4 µm respectively (Figure 3B). The Mann-Whitney t-tests showed statistically significant differences from each group to the 0% dECM (Figure 3B). However, the lowest difference was seen by the 15% dECM in comparison to the 0% with a mean difference of 0.3±1.1 µm whilst the 10% and 25% showed a mean difference of 2.2±3.4 and 4.9±4.9 µm respectively (Figure 3C). Picrosirius red and Alcian blue stains showed the presence of collagen and GAGs in the ECM fibers (Figure 4).

## DISCUSSION

We successfully produced tendon ECM that can be incorporated with gelatin and successfully direct-written with fibers similar to gelatin only fibers in diameter and morphology. Davis et al found median fiber diameter for gelatin only fibers to be 2.3 µm with an IQR of 1.7-3.0 µm [2]. The fibers presented here are slightly larger, even for the similar 0%

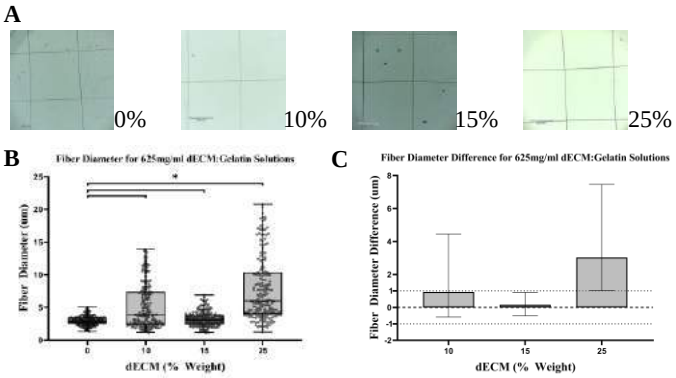


**Figure 3: Impact of dECM on DWNFE fibers. (A) Representative scaffold images for the dECM groups [Scale bar: 220 um]. (B) DWNFE fiber diameters with 20 fibers from 10 scaffolds for each concentration of dECM. (C) Fiber diameter difference to 0% dECM. Bar graph represents normalized median with interquartile range.**

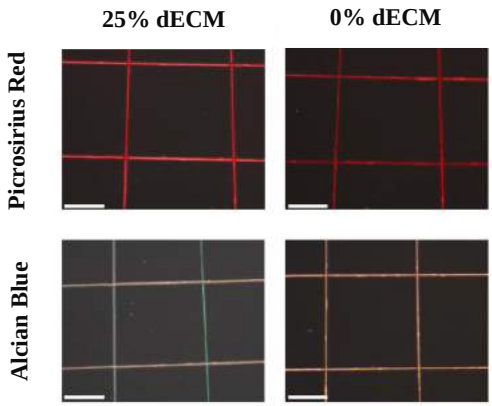


**Figure 4: DWNFE fibers written with 25 and 0% dECM with picrosirious red or alcian blue stain [Scale bar: 110 µm]**

dECM fibers with a median fiber diameter of 3.0 µm. This difference could be due to slightly altered ambient humidity [2]. Fiber diameter for the 0% and 15% dECM showed the highest similarity with a mean difference of 0.3±1.1 µm, though statistically different. Picrosirius red illustrated collagen networks being retained in both scaffolds. Alcian blue illustrated GAGs in the 25% dECM, showing retention of dECM content. Additional concentrations of dECM needs to be examined across multiple scaffolds to establish the repeatability of the approach. We also need to further analyze the protein content of the dECM/gelatin fibers to better understand what components of the ECM are retained, and a cell study is needed to investigate how the addition of the dECM impacts cell behavior. This process shows the validity of a new technique for fabricating scaffolds for applications like tissue-on-a-chip models.

## ACKNOWLEDGEMENTS

We acknowledge the NC State Office of Undergraduate Research, NC State/UNC-Chapel Hill Abrams Scholars Program, and all Translational Orthopaedic Research Lab members for their support and expertise.

## REFERENCES

[1] Lim WL, Liau LL, Ng MH, Chowdhury SR, Law JX. *Tissue Eng Regen Med*. 2019. [2] Davis ZG, Hussain AF, Fisher M. *Biomed Mater*. 2021. [3] Thorpe CT, Screen HRC. *Adv Exp Med Biol*. 2016. [4] Campiglio CE, Contessi Negrini N, Farè S, Draghi L. *Materials (Basel)*. 2019. [5] Wolf MT, Daly KA, Reing JE, Badylak SF. *Biomat*. 2012.

# SIXTH SENSE – A HANDS FREE AND HAPTIC FEEDBACK NAVIGATION TOOL FOR THE VISUALLY IMPAIRED

**Alyssa N. Taylor (1), Joseph H. Lahmann (1)**

**Faculty Advisor(s)**

**J. Miles Canino (1)**

(1) Department of Mechanical Engineering, Rose-Hulman Institute of Technology, Terre Haute, IN, USA

## INTRODUCTION

According to the Center for Disease Control and Prevention (CDC) approximately 12 million people 40 years and older in the United States suffer from visual impairment [1]. A 2018 survey conducted by the National Health Interview Survey (NHIS) found that 994,000 people above the age of 18 admitted being legally blind. Legal blindness is defined as corrected eyesight no better than 20/200 for either eye or a restricted field of vision of less than 20 degrees wide [5]. Only 2 to 8% of the visually impaired population utilize the common white cane, with the majority relying on guide dogs or sighted guides [3].

While white cane and guide dogs are the most common visual impairment aids, Electronic Travel Aides (ETAs) have been adopted by very few visually impaired individuals. ETAs are largely avoided due to impracticality of use, specifically the need for the user to repetitively scan the environment manually [2], low reliability, and little feedback [4]. We believe our design addresses these drawbacks and creates a compelling ETA that intuitively addresses the needs of the visually impaired population.

## PRODUCT DESIGN

The Sixth Sense device is a hands-free haptic-feedback device that has two main components: a sensor module designed to be clipped to pants at the waist and a haptic feedback belt that is worn in direct-skin contact of the torso. The current prototype consists of a 3rd housing for the motor control unit, though this will be consolidated in subsequent designs. Figure 1 depicts all 3 modules of the current prototype.

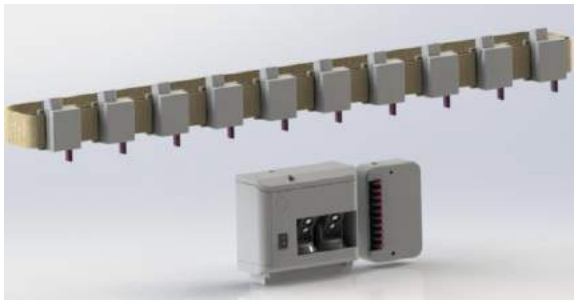

**Figure 1: Complete scanning housing and secondary housing for motor driver with haptic feedback belt.**

The main sensor module consists of two LIDAR sensors that continually scan the environment in front of the user. They are geared together on rotating spindles, driven by a servo. This housing also features a power switch, internal battery bank, and removable top panel, allowing access to the internal components. Figure 2 shows the internals of the main sensor module.

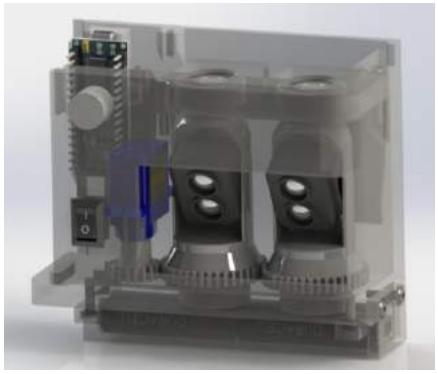

**Figure 2: Main housing for the lidar scanners and microcontroller.**

The haptic feedback belt consists of an array of 10 micro high torque DC motors. Each of these motors has a small, ribbed rubberized end effector that contacts the skin, as shown in Figure 3.

**Figure 3: Sensory feedback belt units with rubberized end effectors.**

This motor-skin interfacing imparts a gentle shear force on the skin, allowing for enhanced perception compared to traditional vibratory feedback. The magnitude and location of this skin-shear effect can be directly correlated to the proximity of adjacent objects, allowing for an intuitive and immersive perception of an individual's surroundings. The belt holding the motors is built with easy donning, doffing, and adjustment in mind. The belt features a robust parachute-buckle clasping mechanism and easily adjustable strap lengths for holding the belt, and motors, firmly against the user's torso. The main sensor module and motor control unit can be easily clipped onto the user's pants or affixed to a lanyard system if pants are not worn.

At startup, the device calibrates to the height of the user. The LIDAR sensors continually scan the environment in a sweeping motion, translating the surroundings to the motors in the belt. The initial prototype refreshes at an average frequency of ~2.5 Hz.

## BUDGET & MARKET ANALYSIS

Our team has prototyped this project as a self-funded endeavor. Table 1 details the major costs associated with this prototype and anticipated costs of a final production model.

**Table 1: The cost of primary components of our current prototype.**

| Component | Qt | USD/ Unit | Total | Production USD/Unit | Production Total |
|---|---|---|---|---|---|
| Elegoo Nano | 1 | 6.60 | 6.60 | 0.25 | 0.25 |
| Tf-Luna Lidar Sensor | 2 | 24.50 | 49.00 | 16.50 | 33.00 |
| PCA9685 16 Channel PWM/Servo Driver | 1 | 14.95 | 14.95 | 3.60 | 3.60 |
| 608RS Bearing | 4 | 0.66 | 2.64 | 0.03 | 0.12 |
| 9161C Micro Planetary Reducer DC Motor | 10 | 1.78 | 17.80 | 0.75 | 7.50 |
| IRLZ34N MOSFET | 10 | 0.50 | 5.00 | 0.15 | 1.50 |
| 5V DC Buzzer | 1 | 0.95 | 0.95 | 0.12 | 0.12 |
| 9g Micro Servo | 1 | 2.50 | 2.50 | 1.00 | 1.00 |
| Diodes x10 | 1 | 2.10 | 2.10 | 0.07 | 0.07 |
| Resistors x10 | 1 | 0.60 | 0.60 | 0.04 | 0.04 |
| Misc* | - | - | 20.00 | - | 20.00 |
| **TOTAL** | **-** | **-** | **$122** | **-** | **$67.20** |

* Includes plastics for housing, wires, heat shrink wrap.

As seen in Table 1, it is anticipated that the production model will cost less than 50% of the prototype. Components purchased in bulk, coupled with mass-manufacturing techniques, would reduce the manufacturing cost to around 60 USD. With a conservative profit in mind, we anticipate an MSRP of around $140 before any regulatory costs. Section 201(h) of the Food, Drug and Cosmetic Act appears to indicate that our product could be considered a medical device [6], and as such could be subject to regulatory costs that increase the price. The only item of note that could be a safety concern are the LIDAR modules, which are classified as Class 1 lasers. However, this classification is considered non-hazardous and does not require even a warning label [7]. Because our device is low risk, promotes mobility and reduces the impact of a chronic condition, we believe our device would constitute a General Wellness Product and thus not be actively regulated by the FDA [8].

Table 2 details the cost of other mobility aides in comparison to the projected cost of our proposed device.

**Table 2: The cost of other assistive solutions and products for the visually impaired.**

| Assistive Solution | Description/Notes | Cost (USD) |
|---|---|---|
| White Cane | - | $20-$60 |
| Buzzclip | A small ultrasonic sensor and buzzer that alerts the user to nearby obstacles. | $250 |
| Mini Guide | A hand-held ultrasonic sensor that correlates vibratory feedback to distance. | $500 |
| Guide Dogs | Training costs are $40,000-$60,000 and require a huge number of volunteers and donations. | Free |
| Sixth Sense | Projected costs | ~$140 |

Our device provides numerous advantages at a projected widely affordable price point. It is unique and competitive against traditional mobility solutions in its hands-free application, quality of feedback provided and discretion. It will also outperform other market ETAs due to its usage of LIDAR sensors which boast a higher resolution and reliability when compared to widely used ultrasonic sensors. Ultimately we believe our device is potentially a feasible and valuable mobility tool for the visually impaired to live with minimal impact from their disability.

## REFERENCES


[1] "Basics of Vision and Eye Health." *Centers for Disease Control and Prevention*, Centers for Disease Control and Prevention, 10 Aug. 2021,

[2] *Sensory Substitution Glove*. National Institutes of Health

[3] "What's With the White Cane." *Metrolina Association for the Blind*, 12 Nov. 2021.

[4] R. Pyun et al., *2013 IEEE 13th International Conference on Rehabilitation Robotics (ICORR)*, 2013, pp. 1–6.

[5] Zuckerman, Diana M. "Blind Adults in America: Their Lives and Challenges." *National Center for Health Research*, 22 Jan. 2018.

[6] "How to Determine if Your Product is a Medical Device" *U.S Food and Drug Administration.* 16 Dec. 2019.

[7] "Laser Products and Instruments" *U.S Food and Drug Administration.* 26. Mar. 2021.

[8] "General Wellness: Policy for Low Risk Devices" *U.S. Food and Drug Administration*. 27 Sept. 2019.

# A MEASURE OF PLATELET ACTIVATION AND AGGREGATION ACROSS TWO FLOW REGIMES TO MINIMIZE THROMBOEMBOLIC EVENTS IN BLOOD PUMPS

**H. Sturgis (1), N. Tobin (1), K. Manning (1,2)**

(1) Department of Biomedical Engineering
The Pennsylvania State University
University Park, PA, USA

(2) Department of Surgery
Penn State Hershey Medical Center
Hershey, PA, USA

## INTRODUCTION

Cardiovascular disease (CVD) is the leading cause of death for men and women in the United States. The significant number of individuals suffering from CVD has created a clinical need for mechanical blood pumps that have provided numerous benefits and life-saving solutions to patients. Despite these advantages, however, their function is burdened by thromboembolic complications due to the non-physiologic blood flow induced by the device geometry. The design of the device can create instability and stagnation in blood flow, leading to mechanical activation of platelets and thrombus formation [1]. Anticoagulation therapies can reduce the occurrence of clotting; however, such treatment can be complex and increase hemorrhagic risk [2]. The prevalence of blood clotting has driven research focused on blood damage and chronic platelet activation occurring in devices. Platelet activation is an important step in coagulation and thrombus formation and can therefore be measured and used to study device-induced thrombosis [2].

This study modeled platelet activation in blood pumping devices with the use of a rotating cylinder system. The purpose of this study was to investigate platelet activation upon exposure to high and low shear stress conditions induced by a rotating cylinder system. The findings from this study provide insight into platelet activation upon exposure to shear stress, independent of plasma protein activation agonists for the optimization of device design to minimize mechanical platelet activation and reduce the occurrence of thrombosis.

## METHODS

Investigation of the specific effects of flow-induced stress on platelet activity was studied using human blood obtained from healthy volunteers at the Pennsylvania State University Noll Laboratories in accordance with the Penn State Institutional Review Board. The developed protocol involved centrifugation of whole blood to obtain platelet-rich plasma (PRP). The PRP was then filtered on a Sepharose-2B gel column to purify the platelets from plasma proteins. Gel-filtered platelets (GFP) eluted from the column and were collected into Tyrode's buffer. Filtration of the platelets allowed for the study of platelet activation specific to flow-induced stress and independent from plasma proteins in the coagulation cascade. Platelet counts were recorded in this study using a hemocytometer, and the GFP samples were fixed to a standard concentration of 10,000 platelets/µl.

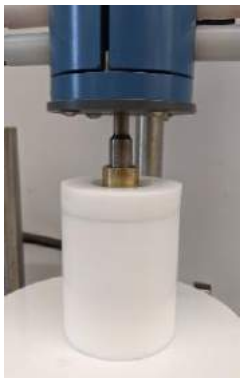

Figure 1. Cylindrical rheometer used to stress GFP.

A cylindrical rheometer consisting of a 2.4-cm diameter titanium cylinder submerged in a cylindrical vessel (depicted in Figure 1) was used to simulate the dynamic flow conditions platelets are exposed to in blood pumping devices. The GFP were subjected to constant low and high shear stress conditions at 60 rpm with a Reynolds number of 900, and 4000 rpm with a Reynolds number of 5000, respectively. The average shear stress across the gap in the 60-rpm case was 0.06 dyne/cm$^2$, while the 4000-rpm case had an average shear stress of 50 dyne/cm$^2$. The GFP were contained in a vessel for the duration of cylindrical rotation. A vessel with a 1.2 cm gap was used to stress the GFP at 60 rpm, and a vessel with a 1 mm gap was used to stress the GFP at 4000 rpm.

Experiments were run for 30 minutes, and a GFP sample was collected from the vessel every five minutes during rotation to measure platelet activation. Platelet activation was measured using a BD LSR-Fortessa Flow Cytometer. The activation of the whole blood samples, PRP, and GFP were measured throughout the protocol to ensure the protocol was conducted with low levels of platelet activation at each step. Initial low levels of activation were necessary to accurately

simulate physiological blood conditions and measure the impact of shear stress on platelet activation. Each of the samples were stained to measure expression of CD62P (for activation) and CD61 (to identify platelets) to be analyzed for activation using flow cytometry. Adenosine diphosphate (ADP) was used as an activation positive control for the whole blood and GFP samples.

Platelet aggregation was also measured using flow cytometry to determine the level of aggregation in the GFP exposed to high shear stress conditions. Half of the GFP sample was stained with CD61 antigen conjugated with PE and the remaining half was stained with CD61 antigen conjugated with APC. Platelet aggregates were then quantified as flow cytometer events that expressed both PE and APC.

## RESULTS

Samples of the whole blood, PRP obtained from centrifugation of the whole blood, and GFP after elution from the gel column were collected, stained, and measured for activation during the protocol. Activation of samples from a total of 13 experiments was measured and analyzed, and the average activation and standard error of the mean (SEM) for the samples are summarized in Table 1. Both whole blood and ADP are also reported with positive controls. The activation levels in the GFP are depicted for both the low-stress and high-stress conditions over time in Figure 2.

**Table 1. Average platelet activation of collected samples**

| Sample | Average Activation (%) ± SEM |
|---|---|
| Whole blood | 2.54 ± 1.43 |
| Whole blood + ADP | 37.86 ± 6.03 |
| PRP | 1.40 ± 0.31 |
| GFP | 2.53 ± 1.00 |
| GFP + ADP | 39.69 ± 6.30 |

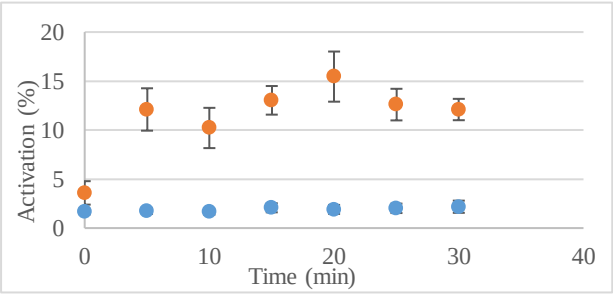


**Figure 2**. Average gel-filtered platelet activation at high (4000 rpm) and low (60 rpm) shear stress conditions. The error bars represent standard error of the mean.

Aggregation was measured for the GFP samples exposed to 4000 rpm in the rotating cylinder system. Aggregation was also measured in the GFP and ADP-stimulated GFP samples. Aggregation levels are reported in Table 2.

**Table 2. Average platelet aggregation at 4000 rpm.**

| | Sample | Average aggregation (%) |
|---|---|---|
| | GFP | 23.79 |
| | GFP + ADP | 24.90 |
| **4000 rpm** | t=0 | 16.58 |
| | t=5 | 18.53 |
| | t=10 | 18.54 |
| | t=15 | 18.03 |
| | t=20 | 17.27 |
| | t=25 | 14.03 |
| | t=30 | 12.54 |

## DISCUSSION

Low levels of activation in the whole blood and PRP were successfully maintained throughout the protocol, with an average percent activation of 2.54% and 1.40%, respectively. Recording platelet activation at various steps throughout the protocol ensured the gel-filtered platelets could be tested in the rotating cylinder without any previous activation or stress exposure. The average GFP activation at 4000 rpm at zero minutes (t=0) was 3.59%. After five minutes of rotation (t=5), platelet activation significantly increased to 12.10%. Significance was determined between t=0 and t=5 using a two-tailed t-test with a 95% confidence interval and an alpha value of 0.05. The initial exposure to flow stress modified the motion, collision, and contact of the platelets, resulting in a statistically significant increase in activation [3]. There was no significant increase in activation from t=5 through t=30. The flow conditions simulated at 4000 rpm exposed the GFP to turbulence similar to conditions induced by recirculating devices.

Data at 60 rpm showed no significant increase in activation throughout the 30 minutes of stress exposure, which suggests the platelets were not exposed to a high enough level of stress to induce activation [3].

The results of this experiment are in line with those of *Soares et al.* [4]. Researchers used a hemodynamic shearing device (HSD), a cone-and-plate rheometer, to induce platelet activation. Platelets were exposed to varying levels of constant shear stress ranging from 1 to 70 dyn/cm$^2$ for two minutes, followed by an extended period of low shear stress. The results showed that levels of shear stress similar to those in the 4000 rpm case (50 dyn/cm$^2$) were associated with increased levels of platelet activation within the first two minutes, while low stress levels showed little to no activation over time. Although a different geometry was used in this study, the results of *Soares et al.* [4] show similar trends to those depicted in Figure 2 with an increase in activation occurring upon initial exposure to high shear stress.

Supported by the results in Figure 2, exposure to high levels of shear stress can lead to mechanical activation of platelets. Upon activation, platelets form aggregates as part of the coagulation cascade leading to thrombus formation. Aggregation was measured for the GFP samples exposed to 4000 rpm in the rotating cylinder system and no significant increase in levels of aggregation were found, as reported in Table 2. Previous studies have found that platelet aggregation occurrs in response to stress exposure and activation only with platelet counts of approximately 200,000 platelets/µl, much higher than the levels in the current study [5].

The findings from this study provide insight into platelet activation upon exposure to shear stress, independent of plasma protein activation agonists. The results from this study can be incorporated into a computational model to optimize the geometry and flow patterns induced by blood recirculating devices with the goal of decreasing thrombogenic events.

## ACKNOWLEDGEMENTS

The work was supported, in part, by NHLBI R01HL136369, and supported through an REU Supplement to NSF CMMI-2017805.

## REFERENCES

[1] Jaffer, H et al., *Acta Biomaterialia*, 94:2-10, 2019.
[2] Alemu, Y et al., *Artificial Organs*, 31:677-688, 2007.
[3] Rubenstein et al., *J Thromb Thrombolysis*, 30:36-45, 2010.
[4] Soares et al., *Biomech Model Mechanobiol*, 12(6):1127-1141, 2013.
[5] Schulz-Heik K et al., *Pathophysiol Haemos Thromb*, 34:255-262, 2005.

SB³C2022
Summer Biomechanics, Bioengineering and Biotransport Conference
June 20-23, Eastern Shore, MD, USA

# IPSC-DERIVED BRAIN MICROVASCULAR ENDOTHELIAL CELLS INCREASE GLYCOLYSIS AND GLUCOSE TRANSPORT IN HYPERGLYCEMIA

**Sophia M. Zic (1), Callie M. Weber (1), Alisa Morss Clyne (1)**

(1) Fischell Department of Bioengineering
University of Maryland
College Park, MD USA

## INTRODUCTION

Of the 6.2 million Americans currently living with Alzheimer's disease (AD), an estimated 37% have type 2 diabetes mellitus (T2DM) [1]. The increased AD incidence in patients with T2DM may relate to hyperglycemia, a common pathological feature of T2DM [2]. Human studies have shown acute hyperglycemia leads to increased brain glucose uptake [3], while long-term hyperglycemia leads to decreased brain glucose uptake. Hyperglycemic nonobese diabetic mice also decreased expression of the predominant glucose transporter in the brain, GLUT1 [4]. Thus, chronic hyperglycemia may result in downstream brain glucose hypometabolism [5]. A decrease in glucose metabolism in the brain leads to cognitive impairment and is a marker of AD [6]. Brain microvascular endothelial cells (BMEC) line blood vessels in the brain and form the blood-brain barrier (BBB), which tightly regulates glucose influx into the brain. However, little is known about BMEC glucose transport in hyperglycemia, and its specific contribution to AD development and progression.

BMECs derived from induced pluripotent stem cells (iPSCs) provide a powerful tool to study neurodegenerative diseases such as AD *in vitro* [7]. In this study, we investigated glucose and lactate metabolism using a BMEC Transwell model in normal and high glucose conditions. We hypothesized that acute hyperglycemia will increase iPSC-derived BMEC glucose uptake and transport, while chronic hyperglycemia will decrease iPSC-derived BMEC glucose uptake and transport. These data could contribute to our understanding of how hyperglycemia in T2DM increases the risk of AD.

## METHODS

**Cell culture:** Human IMR90 iPSCs were differentiated into BMECs (hiBMECs) following previously established protocols [7]. Briefly, iPSCs were cultured in TeSR-E6 basal medium for 4 days, with a daily medium change. On day 4, the medium was changed to human endothelial serum free medium (heSFM) with 0.1% retinoic acid (RA), 0.01% basic fibroblast growth factor (bFGF), 0.25% GlutaMAX, and 2% B27 supplement. On day 6, hiBMECs were subcultured onto Transwell filters (0.4 µm pore) coated with collagen IV and fibronectin for metabolite concentration quantification, or hiBMECs were subcultured onto a 96-well Agilent Seahorse XF Cell Culture Microplate coated with collagen IV and fibronectin for the Seahorse XF Cell Mito Stress Test. hiBMECs were compared to primary human BMECs (hpBMECs), which were cultured in microvascular endothelial cell growth medium until confluent and then subcultured onto Transwell filters (0.4 µm pore) coated with collagen IV and fibronectin.

**Metabolic Analysis:** 24 hours after subculture onto Transwells, BMECs were washed with PBS and given Dulbecco's Modified Eagle Medium containing 4.5 mM glutamine, 2% B27 supplement, and either 5.5 mM glucose (NG) in both the top and bottom Tranwell compartments or 25 mM glucose (HG) in the top compartment and 5.5 mM glucose with 19.5 mM mannitol (osmotic control) in the bottom compartment. 200 µl media samples were then taken from the top and bottom Transwell compartments at 0- and 24- hours. Medium glucose and lactate concentrations were measured using a YSI 2950 Bioanalyzer. A Seahorse XF Cell Mito Stress Test was conducted through the addition of oligomycin (1.5 µM), carbonyl cyanide-4 (trifluoromethoxy) phenylhydrazone (FCCP; 0.5 µM), and rotenone/antimycin A (0.5 µM). Oligomycin inhibits ATP synthetase, FCCP ends the inhibition of electron flow in the electron transport chain to maximize oxygen consumption, and rotenone/antimycin A shuts down mitochondrial respiration. Extracellular acidification rate (ECAR), which relates to glycolysis, was measured. Cells in the Seahorse assay were treated in DMEM containing 4.5 mM glutamine, 1 mM pyruvate, and either 5 mM glucose or 25 mM glucose.

**Statistical Analysis:** Data were analyzed using a Mann-Whitney Test in GraphPad Prism. $p<0.05$ was considered significant. For the Seahorse XF Cell Mito Stress Test, the third time point of the basal glycolytic rate was analyzed.

## RESULTS

hiBMECs preferentially localized glucose basolaterally and lactate apically (Fig 1A-B). Basolateral media contained more glucose than apical media. In contrast, apical media contained more lactate than basolateral media. This same trend was observed in hpBMECs (Fig 1C-D), as basolateral hpBMEC media contained more glucose than apical media, and apical hpBMEC media contained more lactate than basolateral media.

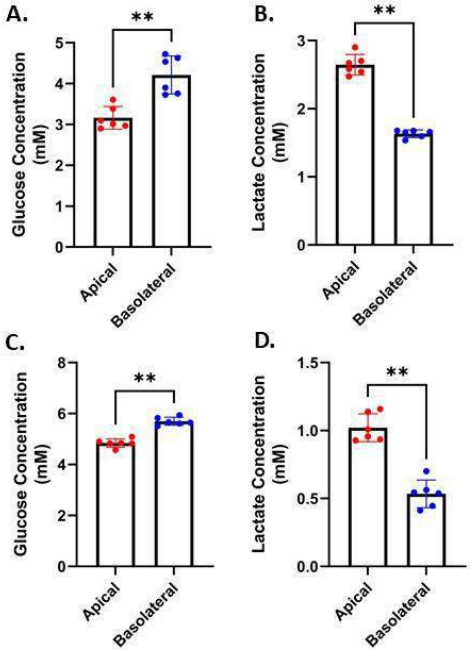


**Figure 1: hiBMECs and hpBMECs localize extracellular glucose basolaterally and lactate apically. A-B) Glucose and lactate concentrations of hiBMECs in the apical and basolateral media. C-D) Glucose and lactate concentrations of hpBMECs in the apical and basolateral media. Measured by YSI Bioanalyzer. **p<0.01**

Basal glycolytic metabolic rate trends toward being higher in hiBMECs cultured in high glucose for 24 hours as compared to cells cultured in normal glucose (p=0.0517; Fig 1A). Apical glucose uptake was higher in hiBMECs cultured in high glucose compared to cells cultured in normal glucose for 24 hours (Fig 2B). In contrast, basolateral glucose concentration was higher in high glucose hiBMECs than normal glucose hiBMECs, indicating increased glucose transport from the apical side of the hiBMECs to their basolateral side (Fig 2C). Lastly, lactate concentration was higher in both the apical and basolateral media in high glucose hiBMECs, supporting the Seahorse data suggesting higher glycolytic rate in cells cultured in high glucose (Fig 2D-E).

## DISCUSSION

Since hiBMEC and hpBMEC glucose distributions were similar, hiBMECs can act as a model of glucose and lactate localization across the brain endothelium. We originally thought that the 24-hour time point would show decreased glucose transport, as observed in long-term hyperglycemia; however, increased glucose transport was observed instead. Thus 24 hours may represent acute rather than chronic hyperglycemia. The increase in basolateral glucose in hyperglycemia is greater than the increase in glycolytic rate in hyperglycemia. Excess glucose transport across BMECs in hyperglycemia may lead to harmful effects on the brain.

We will continue to investigate glucose transport and metabolism in hiBMECs in hyperglycemic culture. We will quantify metabolite concentrations at shorter and longer times. We will also co-culture hiBMECs with astrocytes to determine how additional BBB cells affect BMEC glucose metabolism and transport. To identify the transport mechanism, we plan to label high and normal glucose hiBMECs for the glucose transporter GLUT1 and tight junction-associated protein ZO1.

Here we illustrate that hiBMECs on Transwell inserts can be used as a model of glucose and lactate polarization in the BBB. These studies improve our understanding of how T2DM induced hyperglycemia increases a patient's risk of developing AD. Eventually, hiBMECs could be used in a patient-specific manner.

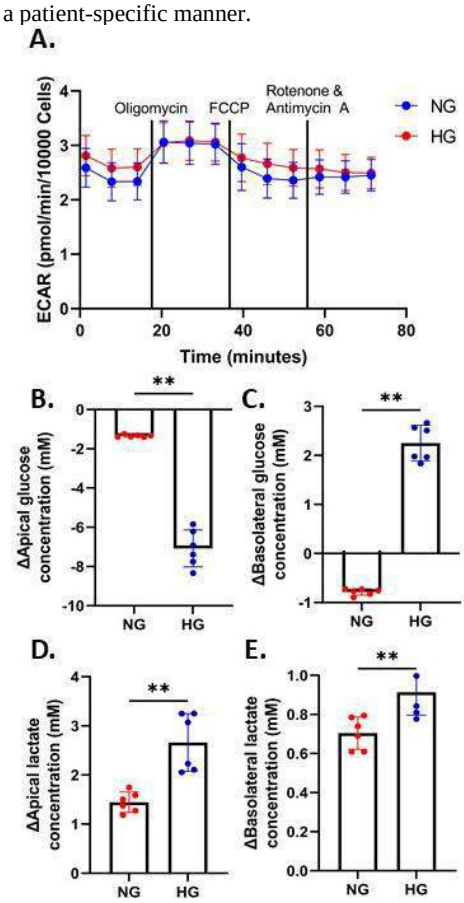


**Figure 2: In high glucose, hiBMECs increase glucose transport to their basolateral side and increase glycolytic rate. A) Glycolytic rates in hiBMECs after 24 hours of normal or high glucose culture, as measured by a Seahorse XF Cell Mito Stress Test. B-C) Apical and basolateral media glucose and D-E) lactate after 24 hours of normal or high glucose culture. Measured by YSI Bioanalyzer. **p<0.01**


## ACKNOWLEDGEMENTS

This research was supported by an ASPIRE Scholarship to SMZ, NSF-GRFP DGE 1840340 to CMW, NIH R01HL140239 to ASMC, and a University of Maryland Brain Behavior Institute seed grant.


## REFERENCES


[1] 2021 Alzheimer's Disease Facts and Figures Report [2] Garcia-Serrano, AM, Duarte, JMN, *Front Neurosci*, 14:229, 2020. [3] Hwang, JJ et al., *JCI Insight*, 2(20):e95913, 2017 [4] Cornford, EM et al., *Neurochem Res*, 20(7):869-73, 1995 [5] Teo, E et al., *eLife*, 8:e50069, 2019. [6] Cunnane, SC et al., *Front Mol Neurosci*, 9:53, 2016. [7] Neal, EH et al., *Stem Cell Rep*, 12(16):1380-1388, 2019.

# COMPUTATIONAL MODELING OF ARTERIOVENOUS FISTULA HEMODYNAMICS IN PULMONARY HYPERTENSION PATIENTS

**Kaitlin M. Southern (1), Fatemeh Bahmani (1), Veeranna Maddipati (2), Stephanie M. George (1)**

(1) Department of Engineering, East Carolina University, Greenville, NC, US
(2) Internal Medicine, Brody School of Medicine, East Carolina University, Greenville, NC, US

## INTRODUCTION

Over 37 million Americans suffer from chronic kidney disease (CKD), which is a gradual loss of kidney function over time [1]. If not treated properly, CKD can eventually progress to end stage renal disease (ESRD), which is a life-threatening and progressive condition characterized by severely impaired renal function, anemia, and the development of various cardiovascular diseases [2]. Treatments for ESRD include replacement therapy by hemodialysis, with the creation of an arteriovenous fistula (AVF), peritoneal dialysis, and kidney transplant [2].

The brachiocephalic AVF is the most clinically used, due to its ease of creation, high flow rates, and high rate of maturation. Even though this form of treatment is effective for blood filtration and treating ESRD, recent studies have suggested connections between fistula creation (size and shape) and the development of pulmonary hypertension (PH) in this patient population [3]. ESRD patients, who develop PH, are automatically removed from the kidney transplant list.

The objective of this research is to develop a protocol for creating subject-specific computational fluid dynamics (CFD) models of fistulas in patients with PH. A better understanding of the trends between fistula creation and pulmonary hypertension will lead to more improved risk monitoring and offer physicians evidence for earlier intervention.

## METHODS

The first step of the project was to obtain approval from the East Carolina University Internal Review Board (UMCIRB19-000708). Inclusion criteria for this study are as follows: patients must be over the age of 18, have an arteriovenous fistula actively being used for dialysis, have been diagnosed with PH by right heart catheterization (RHC), have no contraindications for MRI, have not been diagnosed with connective tissue disease, and do not have advanced left heart disease.

Magnetic resonance (MR) imaging was performed, with a Siemens Aera 1.5 Tesla MR machine. Scans were completed of the fistula to obtain geometry and velocities in the proximal arterial and venous segments. A total of 22 images, with a slice thickness of 8 mm and pixel spacing of 1.61 mm, were captured. Time varying velocity data, captured through the midplane (Figure 1) of the AVF while the patient was in supine position, was gathered using phase-contrast (PC) scans at 30 time points along the cardiac cycle. During the same imaging session, similar data were acquired for the pulmonary artery, as well as clinically standard cardiac measures. Patient identifiers were removed from image files prior to processing.

MR images were imported into Mimics 20.0 (Materialise, Belgium) for model creation. A thresholding technique was used to segment the anatomical geometry captured in each MR slice and the "Calculate 3D" function was used to create a three-dimensional model of the highlighted region. The smooth, three dimensional AVF created in Mimics is shown in Figure 1.

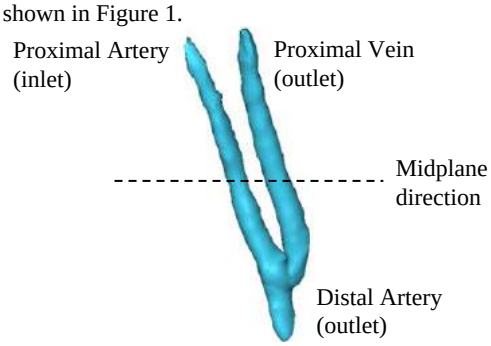


Figure 1: A smoothed, three-dimensional AV fistula model created in Mimics 20.0.

The model was then exported to 3-matic 12.0 where models were trimmed to define inlets and outlets, with perpendicular cross-sectional cuts. The 3-matic files were uploaded into ANSYS Workbench 19.1 (ANSYS Inc., USA), where they were discretized. Metrics such as

orthogonal quality and skewness were used to assess mesh quality and any necessary improvements were made accordingly [4].

Blood was characterized as an incompressible, non-Newtonian fluid with viscosity, 3.2 cP, and density, 1060 kg/m$^3$. The distal artery and proximal vein were assigned pressure-based outlets. The inlet, or the proximal artery, boundary condition was defined by the patients-specific flowrate waveform from the MR data. The MRI waveform was created using in house MATLAB file to crop and isolate cross sections of the AVF from the MRI, to segment the AVF cross sections across 30 timesteps in the cardiac cycle, and lastly to multiply the segmented AVF cross section images with the phase part of the images to calculate fluid velocity. Output parameters included fluid flowrate, mass flowrate, artery diameter, and artery diameter across all 30 points.

A double precision, second order, transient flow pressure-based solver was used during CFD analysis. A total number of 624 timesteps was used, with a single time step durations of 0.0038221 s. Times steps for each subject were calculated by multiply the RR interval, which is the times elapsed between two consecutive R waves of a QRS signal from an ECG, by three to achieve three full cardiac cycles. Residual values were set to default, $1 \times 10^{-4}$.

Post-processing included velocity streamline plots, velocity volume rendering, wall shear stress (WSS) contours, all visualized using CFD Post. These measurements were compared using maximum and minimum velocities, maximum and minimum WSS values.

## RESULTS

The results to date only include one patient. The maximum WSS was 903 Pa, and the minimum WSS was found to be 0.935 Pa. These can be shown in Figure 2.

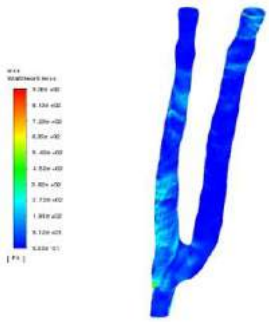

Figure 2: Wall shear stress contour for the AV fistula CFD model.

The maximum velocity of the transient CFD model was 6.58 m/s, which occurs at the distal artery. The peak velocity is significantly greater than the maximum inlet velocity in the velocity waveform utilized for the transient model (approximately 0.298 m/s). Velocity measurements are seen to be greater at the proximal vein and distal artery outlets than the proximal artery inlet.

## DISCUSSION

Over 15% of adults in the United States are affected by chronic kidney disease, which can overtime progress to end stage renal disease if not treated properly. While hemodialysis, with the surgical creation of an arteriovenous fistula provides patients with effective kidney filtration, there has been recent evidence suggesting a correlation between hemodialysis, increased pulmonary artery pressures, and the development of pulmonary hypertension [5]. The development of PH for ESRD patients removes them from the kidney transplant list, leaving them with hemodialysis and disease management treatments.

The patient analyzed in the present study had a mean AVF flow rate, mean pulmonary arterial pressure (mPAP), and pulmonary capillary wedge pressure (PCWP) of 1.97 L/min, 46.5 mmHg, and 19 mmHg, respectively. This flow rate is higher than the hypothesized limit for an AVF flow rate that is both effective for dialysis and does not overload the heart, which is currently believed to be approximately 1.5 L/min. A recent study by Tudoran et al. found significantly higher average AVF flow rates in PH patients when compared to normotensive patients [6]. This study also found a strong correlation between sPAP and the amount of time spent on dialysis as well as AVF flow rates. The areas of low wall shear stress, seen in the model may indicate disturbed flow within the AVF, which is supported by the elevated CFD resulted velocity at the distal artery and the confirmed diagnosis of PH for the retrospective patient.

There are many limitations to this study. The most apparent is the patient sample size. Due to the COVID-19 pandemic, patient recruitment was more difficult. The results presented include data from only one patient which limits interpretation of results. Furthermore, the computational approach relies on several assumptions including a rigid vessel wall. The inlet arterial velocity was modeled as a blunt profile which is not physiologically accurate. Future work could examine the impact of the shape of the velocity profile on simulation results. Despite these limitations, an in silico approach may reduce the need for in vivo or in vitro experiments and enable subject-specific predictions.

Overall, the creation of an AVF is seen to exacerbate pre-existing pulmonary arterial pressure conditions by elevating cardiac output. With the inclusion of additional patients, metrics from this study may offer insight to physicians about AVF monitoring which may lead to early surgical interventions to prevent the development of pulmonary hypertension. This improvement would cause fewer incidences of pulmonary hypertension and overall enhance the quality of life for those suffering with this condition.

## ACKNOWLEDGEMENTS

The authors would like to thank Constantin B. Marcu, MD for image acquisition. This work was supported in part by the Division of Research, Economic Development, and Engagement and Undergraduate Research and Creative Achievement Award, East Carolina University.

## REFERENCES

[1] Webster, Angela C, Associate Prof *et al*, "Chronic Kidney Disease," *The Lancet (British Edition)*, vol. 389, *(10075)*, pp. 1238-1252, 2016;2017;.

[2] M. Yigla *et al*, "Pulmonary Hypertension in Hemodialysis Patients: An Unrecognized Threat: PULMONARY HYPERTENSION IN HEMODIALYSIS PATIENTS," *Seminars in Dialysis*, vol. 19, *(5)*, pp. 353-357, 2006.

[3] K. B. Quencer and M. Arici, "Arteriovenous Fistulas and Their Characteristic Sites of Stenosis," *American Journal of Roentgenology (1976)*, vol. 205, *(4)*, pp. 726-734, 2015.

[4] P. D. Morris et al, "Computational fluid dynamics modelling in cardiovascular medicine," *Heart (British Cardiac Society)*, vol. 102, (1), pp. 18-28, 2016.

[5] G. Acarturk *et al*, "The relationship between arteriovenous fistula blood flow rate and pulmonary artery pressure in hemodialysis patients," *International Urology and Nephrology*, vol. 40, *(2)*, pp. 509-513, 2008.

[6] M. Tudoran, T. Ciocarlie, A. Mates, S. A. Pescariu, A. Abuawwad, and C. Tudoran, "Pulmonary Hypertension in Patients with End Stage Renal Disease Undergoing Hemodialysis," *Niger. J. Clin. Pract.* ¦, vol. 23, no. 2, 2020, doi: 10.4103/njcp.njcp_278_19.

SB³C2022
Summer Biomechanics, Bioengineering and Biotransport Conference
June 20-23, Eastern Shore, MD, USA

# THE INFLUENCE OF EMBOLI SIZE AND DENSITY ON THEIR TRANSPORT IN A CARIOPULMONARY BYPASS FLOW LOOP

**Amy E. Chandler (1), Bryan C. Good (1)**

(1) Mechanical, Aerospace, and Biomedical Engineering
University of Tennessee
Knoxville, TN, USA

## INTRODUCTION

Cardiopulmonary bypass (CPB) is essential for a variety of open-heart surgeries in order to create a bloodless and motionless field for the surgeon to work. Roller pumps are commonly used for CPB and are composed of two rollers on opposite sides of a rotating arm which compress a section of tubing, pushing blood flow forward [1]. Consequently, roller pumps are a major attributing factor to blood clotting as their compressive function can induce damage to blood components and provoke an inflammatory response while a patient is on CPB [2]. These emboli can cause a range of issues including stroke and it is critical to understand their delivery to the cerebral arteries to help minimize postoperative complications. Previous experimental transport studies in the aorta have shown that embolus trajectory paths are proportional to the flow rate split within aortic branches during normal flow conditions [3]. However, no studies have looked into the role CPB plays in emboli distribution. To minimize the risk of embolism and potential stroke while on CPB, a better understanding of emboli delivery to the cerebral arteries must be understood.

## METHODS

To study the flow trajectories of emboli through the branches of an aortic arch under CPB conditions, a flow loop was constructed as displayed in **Fig. 1**. The flow loop consisted of a Sorin Stockert Roller Pump (10-10-00 CAPS Module 10H) with plasticized polyvinyl chloride (PVC) tubing used throughout the loop. A generalized aortic arch model was 3D printed out of polylactic acid (PLA) tubing connectors and included the four primary branches: the brachiocephalic artery (BCA), the left common carotid artery (LCCA), the left subclavian artery (LSCA), and the descending aorta (DA). Benim *et. al*. previously determined that the percentage distribution of aortic blood flow through each branch is as follows: 15.80% in the BCA, 7.89% in each the LCCA and LSCA, and 68.42% in the DA [4]. To achieve these flow splits experimentally in each branch, downstream metal tubing clamps were used to change their resistance, and a flow meter (Transonic) was used to measure the resultant flow rates in liters per minute in each branch. Water served as a substitute for blood as the densities are nearly equivalent at 1 g/cm$^3$ [5].

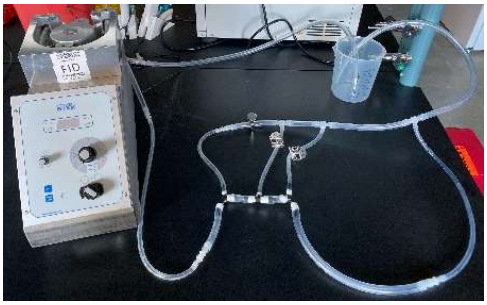

**Figure 1:** Experimental setup of model CPB flow loop on roller pump.

To represent emboli generated in the CPB system, 1/16” and 3/32” diameter Nylon and Delrin beads were individually sent through the flow loop. For the Delrin beads, a range of CPB pump flow rates (1-5 LPM) were prescribed and the aortic branch flow rates adjusted accordingly. A second set of studies were performed with the Nylon beads at a single flow rate of 3 LPM to compare between emboli of different density.

The calculated densities of the large and small Nylon beads were found to be 1.12 g/cm$^3$ and 1.17 g/cm$^3$ respectively. These densities were less than the Delrin beads which were calculated to be 1.27 g/cm$^3$ for the larger size and 1.36 g/cm$^3$ for the smaller size. After the introduction of each bead into the flow loop, their paths through the chosen aortic branch were recorded. For each bead size and type, the total number of beads through each branch was divided by the total number of beads to calculate the percentage of distribution to each branch. This resulted in separate percentages for each trial in terms of small and large Delrin beads and small and large Nylon beads.

## RESULTS

The emboli distribution of Delrin beads at various flow rates was observed and compared as displayed in **Fig. 2**. The percent distributions between each bead size (1/16" and 3/32") and flow rate followed closely to the percent flow distributions within each aortic branch regardless of the pump flow rate.

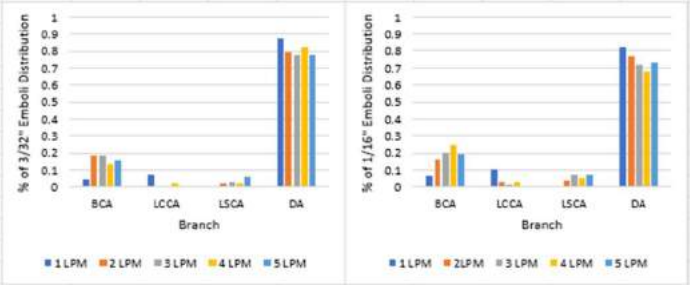


**Figure 2:** Distribution of 3/32" and 1/16" Delrin Beads Through the Aortic Arch Branches at 1, 2, 3, 4, and 5 LPM.

When flow rate was set to 3 LPM, Delrin and Nylon beads followed a similar trend in branch trajectory that aligned with the flow distribution within the CPB flow loop (**Table 1**).

**Table 1: Bead distribution from each experimental trial at 3 LPM**

| | Branch | BCA | LCCA | LSCA | DA |
|---|---|---|---|---|---|
| 3/32" Nylon | Number of beads | 9 | 0 | 2 | 95 |
| | Sum of all beads | | | | 106 |
| | Percentages | 0.0849 | 0 | 0.0189 | 0.8962 |
| 1/16" Nylon | Number of beads | 18 | 2 | 2 | 84 |
| | Sum of all beads | | | | 106 |
| | Percentages | 0.1698 | 0.0189 | 0.0189 | 0.7925 |
| 3/32" Delrin | Number of beads | 20 | 1 | 3 | 84 |
| | Sum of all beads | | | | 108 |
| | Percentages | 0.1852 | 0.0093 | 0.0278 | 0.7778 |
| 1/16" Delrin | Number of beads | 14 | 1 | 5 | 50 |
| | Sum of all beads | | | | 70 |
| | Percentages | 0.2 | 0.0143 | 0.0712 | 0.7143 |

As seen in **Fig. 3**, a majority of Delrin beads (77.78% of 3/32" and 71.43% of 1/16") flowed through the DA. The next most common pathway was the BCA for both sized beads while the least likely for any Delrin beads were the LCCA or LSCA. Similarly, in **Fig. 4**, the largest percentage of Nylon beads flowed to the DA. While the Nylon and Delrin beads followed the same trends their distributions in the other aortic branches, the higher density Delrin beads more commonly traveled through the BCA compared to the lower density Nylon beads. For the BCA, 8.49% of the 3/32" and 16.98% of the 1/16" Nylon beads entered while 18.52% of the 3/32" and 20% of the 1/16" Delrin beads entered. For all bead types and sizes, it was rare for the beads to flow through the LCCA and LSCA branches.

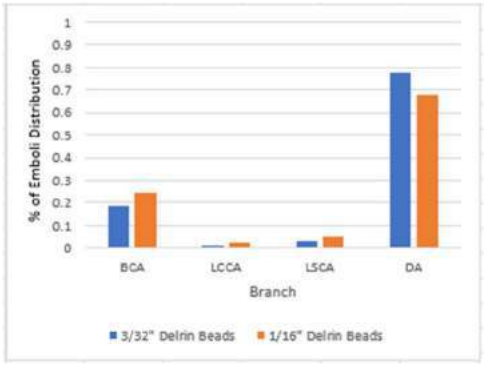


**Figure 3:** Distribution of 3/32" and 1/16" Delrin Beads Through the Aortic Arch Branches at 3 LPM.

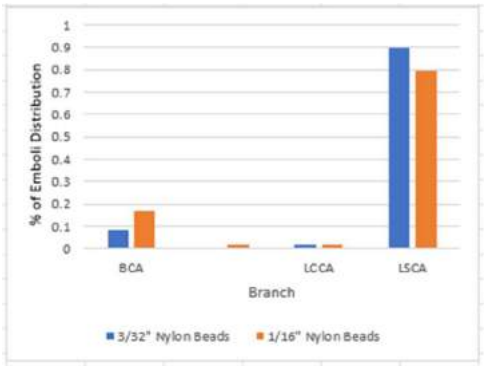


**Figure 4:** Distribution of 3/32" and 1/16" Nylon Beads Through the Aortic Arch Branches at 3 LPM.

## DISCUSSION

The results of these experimental studies indicate that emboli generated in CPB roller pumps with densities like blood (Nylon beads) are most likely to travel through the DA leading to the abdomen and lower body. This is due to the majority of blood flow leaving through the DA. The similar density allows the emboli to follow the flow of blood without deviating from the fluid. Inversely, emboli with densities greater than blood (Delrin beads) have a greater possibility of traveling through the BCA which delivers blood to the right arm and right side of the brain. Emboli traveling through this branch increases a patient's risk of stroke which can be life threatening or severely impair the patient due to lack of oxygen supply to the brain. Further experiments in this field are necessary to understand how emboli travel to the brain during CPB and what can be done to minimize this. Factors such as intraoperative hypothermia to decrease metabolism and heparin to increase activated clotting time affect blood viscosity from a range of 1.5 to 3.5 cP. To further study these results as blood's viscosity is adjusted throughout CPB, emboli traveling in this flow loop with fluids of varying viscosities and densities will be investigated.

## REFERENCES


[1] Sarkar, M et al., *Indian Journal of Anesthesia*, 760-767, 2017.
[2] Morgan, I et al., *European Journal of Cardio-thoracic Surgery*, 1998.
[3] Malone, F et al., *Journal of Biomechanical Engineering*,2019
[4] Benim, A et al., *Applied Mathematical Modeling,* 2011.
[5] Vitello, D et al., *Journal of Veterinary Medicine,* 2015.

# DEVELOPMENTAL DYSPLASIA OF THE HIP PEDIATRIC MEDICAL TRAINER

**Seth B. Eaby (1), Sheridan C. Perry (1), Joseph S. Sauerbrun (1)**

**Faculty Advisor**

**Victor A. Huayamave (1)**
**Charles T. Price M.D. (2)**

(1) Mechanical Engineering, Embry-Riddle Aeronautical University (ERAU), Daytona Beach, Florida, USA
(2) International Hip Dysplasia Institute, Orlando, Florida, USA

## INTRODUCTION

Developmental dysplasia of the hip (DDH) or hip instability is a serious medical condition occurring in 14% of infants and is the most common abnormality in neonates [1]. This congenital malformation is characterized by a ball and socket hip joint that is not fully formed and/or a hip joint that exhibits excessive laxity, resulting in instability or dislocation. Early diagnosis via physical examination or a hip ultrasound and prompt treatment of DDH is critical to ensure the best possible outcomes and avoid chronic disability. If left undiagnosed or improperly treated, DDH can result in abnormal gait and function, low strength, and early degeneration of the hip and knee, including early-onset osteoarthritis [2]. In a registry study in Norway, neonatal hip instability doubled the risk of early onset osteoarthritis and hip arthroplasty before age 40 [3]. Nearly 50% of total hip arthroplasty surgeries for patients under 50 are attributed to hip dysplasia [4].

Physical screening for DDH in infants relies on two manipulative tests developed by Thomas Barlow [5] and Marino Ortolani [6]. The Barlow and Ortolani maneuvers, have become the "gold standard" techniques to assess hip stability on 3 months old infants or younger. The Ortolani procedure is performed by gently abducting the leg with the hips flexed at 90° and applying an upward force through the greater trochanter. An Ortolani positive test will feature a palpable "clunk" sensation representing the reduction of the dislocated hip. In general, a positive Ortolani test indicates a reducible dislocation while a negative Ortolani test indicates an irreducible dislocation. On the other hand, the Barlow procedure is performed by adducting the leg with the hips flexed at 90° and gently pushing the knee. A Barlow positive test will feature a palpable "clunk" sensation and will force the femoral head out of the acetabulum confirming hip dislocation.

Unfortunately, these physical tests are highly subjective and depends greatly on the competence and experience of the examiner [7]. The actual technique with which the manipulation of the joint is carried out is poorly standardized, and the mechanical features of a successful test are not understood in detail. Current training models that closely simulate a range of different hip pathologies cost between $700-$1,200. The existing models are not intuitive for new examiners to use and do not allow visual assessment of the pathological hip as seen in Figure 1

*Figure 1: Laerdal Model*

Figure 1 shows a model known as the "Hippy Baby" created by Laerdal Medical. The model was designed to train residents in the Barlow and Ortolani techniques with each hip designed with a generic setup for residents to dislocate and reduce the hip. Unfortunately, despite a unique design it has numerous flaws that have resulted in it not being effective at mimicking the Barlow and Ortolani maneuvers.
Hippy Baby's downsides include a high cost between $700-$1,200, opaque surface preventing residents from being able to visualize what the maneuvers are doing beneath the skin to the bones, ligaments. The model is composed of a rubber-like material, resulting in more force being needed to dislocate and reduce the hips. This increased force could be disastrous if a resident attempts to apply the same amount of force to an infant during an examination as it could severely damage the infant's skeletal system.

## PRODUCT DESIGN

Figure 2 shows new DDH models using various 3D printed pelvis.

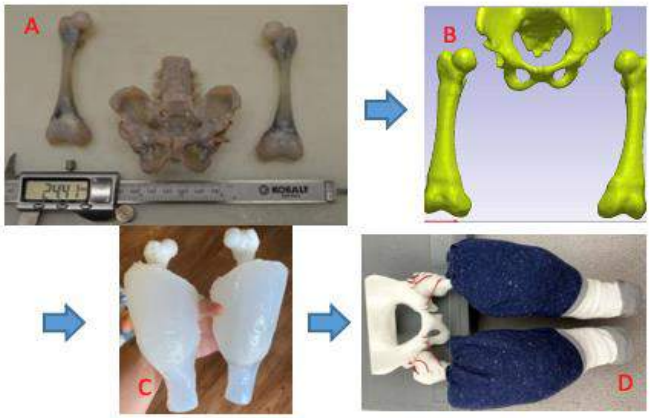


*Figure 2: Development of Hip Models*

The goal of the team while developing the new trainer was to address the major issues with the existing Laerdal model. Develop a model that allows the examiner to apply the Barlow and Ortolani techniques, and simultaneously visualize the effects of those techniques. The new model would also need to better represent the infant's softness to prevent excessive force while training residents.

The first step to developing the new model was to create a 3D model of a DDH afflicted pelvis and femora. The CT scans used were provided by the University of Padua from Dr. Marino Ortolani's collection (see Figure 2-A). The model used was that of a healthy infant that was heavily post-processed and altered which allowed for the most realistic form of the Barlow and Ortolani techniques. The model was developed and augmented in Synopsys's SimpleWare ScanIP before being exported to Dassault Systèmes Solidworks (see Figure 2-B).

The bones were initially printed on a modified Creality Ender 3 using the slicing software of Ultimaker Cura. The ligaments were also 3D printed after dissecting one of the Hippy Baby models and observing its design. The team used a combination of SimpleWare and Solidworks to create Thermoplastic Polyurethane (TPU) ligaments as well as anchor points in the form of pegs on the surface of the femur and pelvis. The team finally cast the legs of the model to simulate an infant's weight (see Figure 2-C for legs and Figure 2-D for full model).

The team then chose to use a combination of a transparent silicone skin and foam to hold the skeletal geometry in place instead of ligaments. They also acquired an Ultimaker S5 and FlashForge Creator Max 2 3D printers to improve the print quality and reduce production time of the bones The first prototype was created using a dissected Laerdal Model to create an initial prototype and gain a better understanding of the end goal.

Next steps for the project will be to create a mold of the Laerdal model and using that mold along with the custom pelvis and femora to create a similar model with different materials. The goal would then be to refine the model and prepare it for market.

## BUDGET & MARKET ANALYSIS & BUDGET

The projected price for the 3D printed hippy baby will be around $300 to $400 and it will be developed in collaboration with the International Hip Dysplasia Institute in Orlando, FL. At this price point and with the additional features that make it more useful, there are many opportunities for this product in the medical training market. Target customers are primarily medical educators while end-users are students.

The market for medical trainers as of 2021 is approximately 1.7 billion dollars. There are 210 pediatric residency programs in the USA and 27 in Canada. The potential market for that group is 2 per program every three years. Additional opportunities for sales include orthopedic residencies, osteopathic and nursing programs, educational workshops at medical conferences, and European or South American medical education programs. Projected sales of an affordable, effective model would be likely to approach 200 per year for the first three years.

Additionally, some pediatricians or pediatric orthopedic surgeons may use models in their offices for patient education. Patient education may add to the market size an additional 100 per year.

The team applied for an Ignite grant via the ERAU Office of Undergraduate Research and received a grant of $4300. Figure 3 shows the largest expenses are the 3D printer and design of a production ready prototype through a third-party 3D printing company.

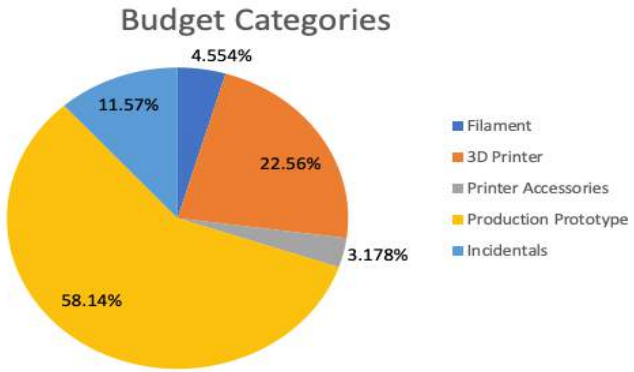


*Figure 3: Project Budget*

This group proposes licensing to a large well-established producer/seller of orthopedic training models (Pacific Research Labs in the USA and its subsidiary Sawbones Europe). The model can also be manufactured by us and then distributed through Pacific Research Labs. They currently do not have a hip dysplasia teaching model for diagnosis although they have bone models for surgical practice

The global impact has enormous potential. Newborn examination is the best way to detect infant hip dislocations that occur in approximately 1/500 infants globally [9]. Exams currently fail to detect 20% of cases in North America [10]. Far greater numbers are undetected in less developed countries. Early detection allows simple non-surgical correction with bulky diapers, harnesses, or splints, but late detection leads to surgery or disability. Improved education for diagnosis by examination has proven to dramatically decrease the incidence of late detection. A better teaching model is essential to decreasing the burden of this common infant condition. Furthermore, the design and concept of the team's models can be adapted to model other pediatric pathologies, vastly expanding the market.


## ACKNOWLEDGEMENTS

Office of Undergraduate Research Ignite Grant, ERAU


## REFERENCES


[1] Laborie, L.B. et al, Pediatr Radiol **44**(8): 410-424, 2014
[2] Woodacre, T. et al, J Child Orthop., 2014. **8**(4): p. 325-332.
[3] Engesaeter, I.O. et al, Acta Orthopaedica, 2008. **79**(3): p. 321-326.
[4] Clohisy, J.C. et al, JBJS, 2011. **93**(Supplement_2): p. 292-301.
[5] Barlow, T., JBJS, British Volume, 1962. **44**(2): p. 292-301.
[6] Ortolani, M., La lussazione congenita dell'anca: nuovi criteri diagnostici e profilattico-correttivi. 1948: Cappelli.
[7] Chow, Y. et al, Med Eng. Phys. 1994. **16**(3): p. 181-187
[8] Aronsson, D.D. et al, Pediatrics, 1994. **94**(2): p. 201-208
[9] Mulpuri, K. et al, Clinical Orthopaedics and Related Research®,, 2016. 474(5): p. 1131-1137
[10] Harper, P. et al, J Child Orthop., 2020. **40**(8): p.408

SB³C2022
Summer Biomechanics, Bioengineering and Biotransport Conference
June 20-23, Eastern Shore, MD, USA

# VASCULAR SMOOTH MUSCLE CELLS ALIGNMENT ON MICROPATTERNS ALTERS GLUCOSE METABOLISM

**Yusuf M. Mastoor (1), Pattie S. Mathieu (1), Alisa M. Clyne (1)**

(1) Fischell Department of Bioengineering, University of Maryland, College Park, MD, USA

## INTRODUCTION

In healthy conditions, vascular smooth muscle cells (vSMCs) circumferentially align around the blood vessel lumen. This alignment is integral for modulating vascular tone, as it allows vSMCs to efficiently contract and dilate to alter blood vessel diameter in response to mechanical and biochemical stimuli[1]. vSMCs aligned on micropatterned substrates also have reduced proliferation and migration, mimicking healthy vSMC phenotype[2,3]. In diseased states, such as atherosclerosis, vSMCs rapidly proliferate and migrate. These synthetic vSMCs also metabolize more glucose through glycolysis[4]. However, the effect of vSMC alignment on glucose metabolism has not been measured.

Micropatterns can be used to align vSMCs on a variety of substrates including polydimethylsiloxane (PDMS) and hydrogels. We previously showed that the inherent ridges created during fused deposition modeling (FDM) can be used to topographically pattern substrates and align vSMCs[5]. In the current study, we hypothesized that vSMCs aligned along micropatterned ridges will exhibit decreased proliferation and glucose metabolism.

## METHODS

**Cell Culture:** Human coronary artery smooth muscle cells between were cultured in SmGM-2 (Lonza) supplemented with 10% fetal bovine serum, 1% penicillin-streptomycin, and 2mM l-glutamine.

**PDMS Patterning and Mold Fabrication:** 150μm ridges were patterned in polydimethylsiloxane (PDMS) using 3D printed stamps as previously described[5]. PDMS elastomer base and curing agent were mixed in a 10:1 ratio and added to each well in a six-well plate. 3D printed molds were placed on top of uncured PDMS and cured at 80°C overnight. After the mold was removed, imprinted PDMS was plasma treated for 1 minute and coated with 50 μg/mL collagen overnight at 37°C. $10^5$ cells were added to each well in 2mL of SmGM-2.

**Immunofluorescent Imaging and Quantification:** Cells were washed with cold PBS, fixed with 4% paraformaldehyde for 20 minutes, and permeabilized with 0.2% Triton X-100 for 40 minutes. Non-specific binding was blocked with 5% bovine serum albumin (BSA). Cells were labelled with a Ki-67 primary antibody (1:200, Abcam, ab15580) overnight at 4°C. After washing with PBS, cells were labelled an Alexa Fluor 488 conjugated secondary antibody (1:1000), rhodamine phalloidin (1:80), and Hoechst (1:2000). Actin fiber alignment was quantified using MatFiber software[6].

**Glycolytic Rate:** Glucose and lactate concentrations were measured in vSMC conditioned media using a YSI biochemical analyzer 2950. The differences in glucose or lactate concentration at 48 hours were then normalized to cell number, which was determined by labelling nuclei Hoechst and counting nuclei using ImageJ.

**Western Blotting:** Cells on patterned and unpatterned PDMS were scraped and lysed in ice-cold RIPA buffer. Samples were normalized to total protein content, separated using SDS-PAGE on a 4-12% Bis-Tris gel, and transferred to a nitrocellulose membrane. Non-specific binding was blocked using 5% BSA. Membranes were treated with primary antibodies for hexokinase I (HXK1), phosphofructokinase-1 (PFK1), lactate dehydrogenase (LDH; all 1:1000) overnight at 4°C, followed by horseradish peroxidase conjugated secondary antibodies (1:2000) for two hours at room temperature. Protein bands were imaged using an Enhanced Chemiluminescence Substrate in a Fluorchem digital imager.

**Statistics:** Statistical significance was analyzed using a two-way Student's t-test.

## RESULTS

vSMCs seeded on patterned PDMS aligned in the ridge direction, while vSMCs on unpatterned PDMS did not align in any direction (Fig. 1A-D). Furthermore, cells on the patterned substrates trended towards less proliferation as compared to those on the unpatterned substrates, as quantified by the percentage of Ki-67 positive nuclei (Fig. 1E-F).

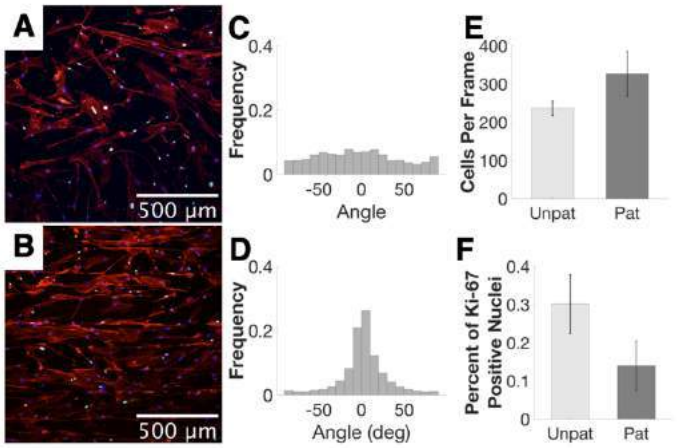


**Figure 1: vSMCs aligned on 3D patterned PDMS. Representative images of vSMCs labelled for nuclei (Hoechst, blue), actin (phalloidin, red), and Ki-67 (green) on (A) unpatterned PDMS and (B) patterned PDMS. Alignment of actin fibers on (C) unpatterned and (D) patterned PDMS. (E) Average number of cells per frame and (F) percentage of Ki-67+ cells.**

Cells on patterned PDMS consumed significantly less glucose and produced less lactate compared to cells on unpatterned PDMS (Fig. 2A-B). For every one molecule of glucose metabolized, vSMC produced three lactate molecules (Fig. 2C). To determine if decreased glycolysis was related to glycolytic enzymes, the relatives amounts of HXK1, PFK1, and LDH were compared in cells on patterned versus unpatterned PDMS. There were no significant differences in the amounts of these key glycolytic proteins in cells on patterned versus unpatterned PDMS (Fig. 3)

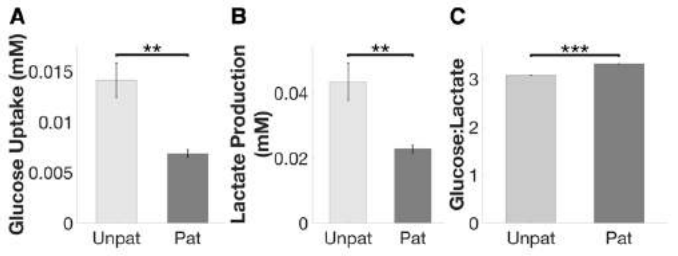


**Figure 2: vSMCs on patterned PDMS have decreased glucose uptake and lactate production. (A) Glucose uptake and (B) lactate production normalized to average cell number. (C) Glucose to lactate ratio. ** p < 0.01, ***p < 0.001.**

## DISCUSSION

In this study, we investigated how vSMCs aligned along micropatterned PDMS ridges changed proliferation and glucose metabolism. Similar to previous studies, we found that aligned vSMCs had lower proliferation[2,3]. We further found decreased glucose uptake for vSMCs on patterned PDMS. Thus aligned vSMC are more similar to contractile healthy vSMCs, whereas non-aligned vSMC are more similar to unhealthy synthetic vSMC[7].

After glucose is taken up by the cell, it can be processed into two molecules of lactate via glycolysis. We found that vSMCs on both patterned and unpatterned PDMS produced three lactate molecules per one glucose molecule, indicating that the cell is generating lactate from a non-glucose source. Since glycolytic enzyme quantity did not change in vSMC on patterned and unpatterned PDMS, the functional changes in glucose metabolism may related to regulatory glycolytic proteins such as 6-phosphofructo-2-kinase/fructose-2,6-biphosphatase 3 (PFKFB3) or to glycolytic reaction inhibition by metabolites. We will elucidate the mechanism behind the decreased glucose metabolism in aligned vSMCs via metabolic mass spectrometry.

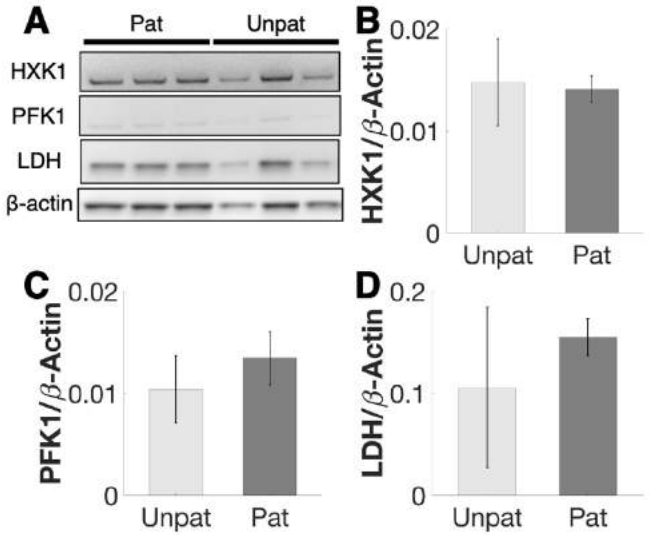


**Figure 3: vSMC glycolytic protein expression did not change in cells on patterned and unpatterned PDMS**

In conclusion, we showed that micropatterns created by 3D printed molds can be used to align vSMCs decreasing their proliferation and glucose metabolism. Understanding the mechanism by which vSMCs alter their glucose metabolism on patterned PDMS will help us develop tissue engineered blood vessels which both look like and act like healthy human blood vessels.


## ACKNOWLEDGEMENTS

This research was supported by an NSF REU supplement to YM and NIH R01HL140239, NIH R21EB028466, and NSF CMMI 1916814 to ASMC. 96(8):3423-32


## REFERENCES


1. Li Y, et al. *Biotechnol Adv*. 32 (2):347-65,2014.
2. Chang S, et al. *PloS one*. 9(2):e88089, 2014.
3. Thakar RG, et al. *Biophys J*. 96(8):3423-32, 2009
4. Werle M, et al. *J Biomed Sci*. 12(5):827-34, 2005.
5. Vo J, et al. *Biomed Eng Adv*. 100001, 2021
6. Fomovsky GM, Holmes JW. *Am J Physiol Heart Circ Physiol*. 298(1):H221-8 , 2010.
7. Shi J, et al.. *Am J Physiol Heart Circ Physiol*. 319(3):H613-H631, 2020.

# DYNAMIC ANKLE BRACE FOR ANKLE SPRAIN RECOVERY

**Amulya Bajracharya (1), Caitlin Brumley (1)**

**Faculty Advisor(s)**

**Dr. Victor Huayamave**

(1) Mechanical Engineering Department, Embry Riddle Aeronautical University, Daytona Beach, FL, USA

## INTRODUCTION

Ankle injuries are a common problem one will experience in their lifetime. Whether it is simply stepping incorrectly on your feet or through excessive strain on the ligaments through sports or other activities, these types of injuries are an unfortunate part of life. 65.6% of all injuries that occur in men's soccer happen to the lower limbs with 25.3% being ligament sprains [1]. Of those ligament sprains, 12.2% occur in the ankle representing a large amount of injury to this location [1]. The most common sprains of this nature are lateral sprains where there is an over-inversion of the ankle joint on the lateral collateral ligaments. These sprains are categorized into mild, moderate and severe sprains and can increase the chances of reinjury tremendously depending on the severity of injury. To help prevent injury and reinjury, external ankle supports are key with ankle braces proving better than taping or casts [2]. Athletic taping is common for injury prevention and stability though they tend to be one time use items and require professionals to properly taping up individuals. Ankle braces are reusable and can typically be put on by the injured person. Common types of braces on the market are straps, lace ups, stirrups, or some combination of the 3. Straps are adjustable and comfortable though only provide mild support, lace ups provide more support though they are bulkier and are difficult to place in shoes, and provide great support due to their rigidity, but greatly reduce a person's inversion and eversion motions. The ankle brace designed by the team seeks to be a combination of the different types of braces to provide maximum support while still being able to fit comfortably inside a shoe. The end goal is to allow this brace to be used during competitions to help prevent ankle injury while allowing users full range of motion. Specifically, this product was originally designed for soccer players and hopes to tap into the professional market to allow ankle braces to become as commonplace as athletic taping.

### PRODUCT DESIGN

**Figure 1: First and third design prototypes stitched onto compression socks**

The current brace model is constructed using an ultimaker S5 3D printer. The brace is made of TPU and currently there are five different types of ankle brace designs. Each print is sewn onto a compression sock and has holes for laces to ensure a conformed fit to the user. Elastic straps are attached to the bottom of the foot and behind the lower calf and heel.

The first design consists of a triangular geometric pattern with a solid outline for sewing on to a compression sock. The lacing holes are grouped towards the top of the brace.

The second design is a solid print with a thin solid outline for easier sewing. The lacing holes are also grouped towards the top of the brace.

The third design is a solid print with no thin outline. The lacing holes are the same number but spread evenly across the arc of the brace.

The fourth design is a combination of solid and mesh. There are three thin layers. The base layer is solid, the middle is triangular geometry, and the top layer is solid. The lacing holes are again, evenly spread out along the arc of the brace.

The fifth design combines the two prints into one print, making a rainbow shape. The goal is to eliminate the need for silicone straps and ensure the brace stitching will stay intact after each use.

The main benefit to these TPU braces is that they are thin, easy to put on, fit comfortably inside shoes, flexible enough to allow range of motion and yet supportive enough to help prevent injury. In addition, these braces are machine washable meaning they can be reused unlike taping.

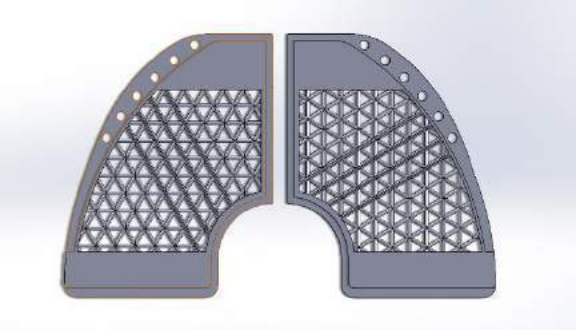

**Figure 2: Triangular geometry design**

## BUDGET & MARKET ANALYSIS

The budget for developing, printing and using these ankle braces is a projected 5,000 USD. This cost includes the purchase of the ultimaker 3D used, TPU filament, compression fabric, and lacing used for the braces. The ultimaker is an investment cost as it is an industry grade printer that should last for years and provide accurate prints. It uses TPU ranging from 50 to 70 USD for a 750 g roll with printing time of about 8 hours. The average cost to produce one ankle brace is 10 USD predicted to retail for 60 USD. The most popular ankle braces sell between 20 to 100 USD so these braces are within normal price ranges. With the resurgence of the sport industry after initial shutdowns due to the pandemic, the demand for support devices is increasing. The braces are intended to be sold to sports departments through online ordering. Initial prototypes for a brace are one size fit all though research and development is being made to create different sizing options for customers. This way, the brace is not only a preventative and rehabilitative device, but also highly customizable to suit the needs of each wearer.

## ACKNOWLEDGEMENTS

Dr. Victor Huayamave, Embry-Riddle Aeronautical University
Elizabeth A. Payne, Office of Undergraduate Research, Embry Riddle Aeronautical University
Wesley F. Lewis, Office of Undergraduate Research, Embry Riddle Aeronautical University
Sophie E. Brundin Jr., SIQ Engineering LLC

## REFERENCES

[1] NCAA. *Men's Soccer Injuries*. Datalys Center for Sports Injury Research and Prevention, https://www.datalyscenter.org/sites/datalyscenter.org/files/NCAA_M_Soccer_Injuries_HiRes.pdf.

[2] Philip J. van der Wees, Anton F. Lenssen, Erik J.M. Hendriks, Derrick J. Stomp, Joost Dekker, Rob A. de Bie, Effectiveness of exercise therapy and manual mobilization in acute ankle sprain and functional instability: A systematic review, Australian Journal of Physiotherapy, Volume 52, Issue 1, 2006, 27-37, ISSN 0004-9514, https://doi.org/10.1016/S0004-9514(06)70059-9. (https://www.sciencedirect.com/science/article/pii/S0004951406700599)

# RESTRUCTURING OF THE ENDOTHELIAL GLYCOCALYX AFTER PNEUMONECTOMY

**Taylor M. Paradis (1,2), Natasha J. Cruz-Calderon (1), Lydia B. Masse (1), Gillian R. Miller (1), Samantha G. Raskind (1)**

**Faculty Advisor(s)**

**Aaron B. Waxman, PhD. (3), Solomon A. Mensah PhD. (1,2,4)**

(1) Department of Biomedical Engineering, Worcester Polytechnic Institute, Worcester, Massachusetts, United States
(2) Department of Mechanical Engineering, Worcester Polytechnic Institute, Worcester, Massachusetts, United States
(3) Department of the Pulmonary Vascular Disease Program, Brigham and Women's Hospital (BWH), Boston, Massachusetts, United States
(4) Department of Biomedical Engineering, Northeaster University, Boston, Massachusetts, United States

## INTRODUCTION

A pneumonectomy is a surgical procedure during which one entire lung is removed from a patient and the connective vessels are sealed off [1]. Postpneumonectomy pulmonary edema is one of the most prevalent fatal complications resulting from the procedure, affecting nearly 2.5-5% of patients that undergo this procedure with an 80-100% mortality rate [2]. Our study aims to explore the effect of changes in blood flow after pneumonectomy. This is modeled by controlled flow through a macrofluidic cell chamber modeling the geometry of the pulmonary arteries to depict vascular changes after pneumonectomy.

The glycocalyx is a cell coating composed of proteoglycans, glycosaminoglycans, and plasma proteins. The endothelial glycocalyx forms an interface between blood vessels walls and circulating blood [3]. The glycocalyx protects the endothelial cells and in doing so helps maintain cellular homeostasis [4]. The glycocalyx is regulated by the shear stress blood flow creates, and changes in flow can impair its ability to function. The disruption of this layer can lead to cardiovascular disease which can be fatal in many cases. [5]. Our study will examine how this component might be affected in a pneumonectomy by measuring how components of this layer such as heparan sulfate are affected by increases in shear stress after a pneumonectomy.

## METHODS

To mimic the conditions that endothelial cells and the glycocalyx experience after a pneumonectomy a flow chamber was developed as seen in Figure 1. There are four main components that make up the 2D flow chamber. The bottom plate has cut outs for culture media to flow through. This flow path was created to accurately mimic the anatomical features of the pulmonary arteries as the diameters and angels of the pulmonary arteries are accurately displayed here [3]. A Teflon gasket sits along the edges of the flow path to prevent leaking and give the required height needed for shear stress. Seven glass slides sit in the flow path at data collection points so cells can be seeded to them. Finally, a top plate screws into the bottom plate and has an opening that introduces the flow into the system. This model allows different shear stresses to be applied on the cultured endothelial cells through fluid flow changes through the system. Using Solidworks, the flow chamber was created to include the main pulmonary artery, the left pulmonary artery, and the right pulmonary artery.

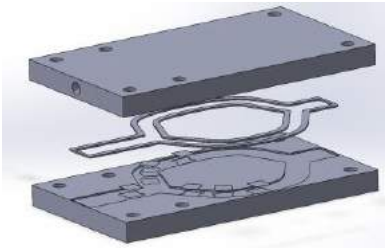

**Figure 1: Solidwork model of the 2D flow chamber. Parts include a bottom plate, glass slides, a gasket, and a top plate.**

Using Solidworks, flow simulations were run to confirm the increased shear stress that would be experienced on the cells by introducing an input volume flow rate of 5 L/min similar to the rate that the heart pumps blood through the pulmonary arteries to the lungs [3].

## RESULTS

Fluid flow simulations were performed on the 2D CAD model to compare the shear stress produced along the pulmonary artery with or without a pneumonectomy. These simulations revealed that the shear stress produced by the single pulmonary artery remaining after a pneumonectomy was significantly higher than the regular shear stress experienced by the pulmonary artery without undergoing a pneumonectomy.

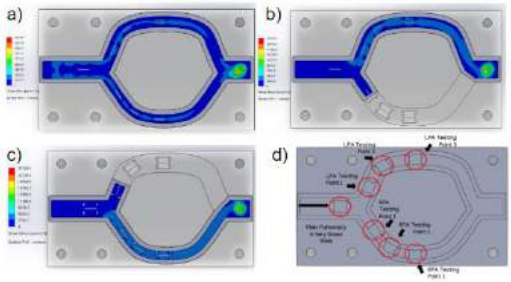


**Figure 2: Flow simulations of shear stress completed on solidworks. a) no pneumonectomy model b) right pneumonectomy model c) left pneumonectomy model d) shows the seven testing points where shear stress is being measured**

Shear stress was measured in seven different locations which is where the glass slides were placed. Figure 2 displays the shear stress overly throughout the model due to the flow for the three different models.

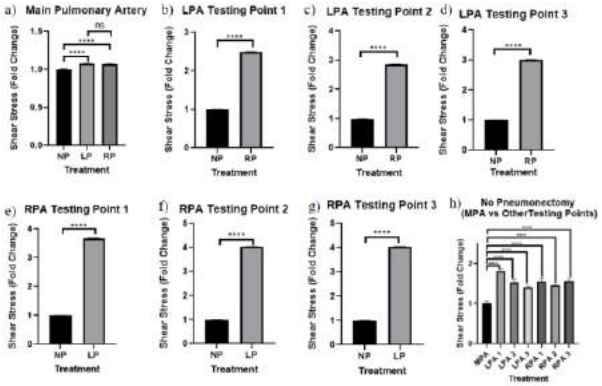


**Figure 3: Statistical analysis of difference in shear stress for the seven different testing points in the three different models (no pneumonectomy (NP), left pneumonectomy (LP), and right pneumonectomy (RP). a) Anova analysis comparison between the three models at the main pulmonary artery testing point. b) T-test analysis between the NP and RP models at LPA testing point 1. c) T-test analysis between the NP and RP models at LPA testing point 2. d) T-test analysis between the NP and RP models at LPA testing point 3. e) T-test analysis between the NP and LP models at RPA testing point 1. f) T-test analysis between the NP and LP models at RPA testing point 2. g) T-test analysis between the NP and LP models at RPA testing point 3. h) Anova analysis for the NP model comparing the MPA testing point against all other testing points. For all statistical testing there was strong significance found.**

Statistical analysis (including Anova analysis & t-tests) were used to determine if there was statistical significance in the shear stress between the no pneumonectomy model and the two pneumonectomy models. As seen in figure 3, the shear stress observed at all 7 testing points during either type of pneumonectomy, when compared to the no pneumonectomy model, had very high significance.

## DISCUSSION

With the flow simulations showing an almost 300% increase in shear stress after a pneumonectomy, the amount of shear stress on the endothelial glycocalyx is nearly triple what it would normally be. This data and information can be critical in helping reduce the mortality rate of patients with complications post-pneumonectomy. Furthermore, the results show a significant increase in shear stress depending on which lung is removed. Using the data from the flow simulations, a left pneumonectomy had a higher shear stress result than the right pneumonectomy.

The future direction of this project is to test the model with Human Lung Microvascular Endothelial Cells and measure the effect of exposure to shear stress for longer periods of time in each condition. By increasing the flow by sectioning off one side of the arteries represented in the chamber, the shear stress will increase. Imaging and staining analysis tools will further allow us to examine how increased shear stress affects these cells, modeling how the endothelial glycocalyx is affected after a pneumonectomy.

Other future work for this project includes designing a 3D model that will hopefully confirm what was found in the 2D model for shear stress on the cells. The 3D model will be more anatomically correct, including the diameters, lengths, and angles of the pulmonary arteries, following the actual shape of the pulmonary arteries. This will allow for a more accurate representation of the pulmonary arteries and how the cellular components of the endothelial glycocalyx are affected by increased shear stress resulting from a pneumonectomy or increased blood flow.

## ACKOWLEDGEMENTS

The authors would like to Dr. Aaron Waxman and Dr. Solomon Mensah for the valuable support, direction, and discussions, and the Biomedical Engineering Department at Worcester Polytechnic Institute, and by the WPI Provost Startup funds awarded to Solomon A. Mensah for funding.

## REFERENCES

[1] Chae, E. J., Seo, J. B., Kim, S. Y., Do, K.-H., Heo, J.-N., Lee, J. S. Song, K. S., Song, J. W., & Lim, T.-H. (2006). Radiographic and CT findings of thoracic complications after pneumonectomy. *RadioGraphics*, *26*(5), 1449–1468. https://doi.org/10.1148/rg.265055156

[2] Hall, D. R. (1974). Regional lung function after pneumonectomy. *Thorax*, *29*(4), 425–431. https://doi.org/10.1136/thx.29.4.425

[3] Kandathil, A., & Chamarthy, M. (2018). Pulmonary Vascular Anatomy & Anatomical variants. *Cardiovascular Diagnosis and Therapy*, *8*(3), 201–207. https://doi.org/10.21037/cdt.2018.01.04

[4] Townsley, M. I. (2012). Structure and composition of pulmonary arteries, capillaries, and veins. *Comprehensive Physiology*, 675–709. https://doi.org/10.1002/cphy.c100081

[5]Rancan, L, *et al.* (2018) Glycocalyx Degradation after Pulmonary Transplantation Surgery. *European Surgical*

# TEMPERATURE ASSESSMENT ENABLED SIMULATION MANNEQUIN

**Emily Eisele (1), Mason Klaus (1,2), Jessica Guarino (1), Amelia Wellmon (1), Sean Blade (1)**

**Faculty Advisor(s)**

**Dr. Ria Mazumder (1)**

**(1) Department of Biomedical Engineering, Widener University, Chester, PA, USA**
**(2) Department of Mechanical Engineering, Widener University, Chester, PA, USA**

## INTRODUCTION

More than 80% of medical schools and 87% of nursing schools have integrated high-fidelity human simulation mannequin-based training into their curriculum [1]. Simulation mannequins provide an immersive learning environment by mimicking real-life clinical scenarios that healthcare workers will potentially encounter in the field. These realistic education opportunities allow students to enhance their skills and competencies in a controlled and risk-free environment.

While today's high-fidelity human simulation mannequins are equipped with multiple intricate features, there is still a lack in the ability to replicate several essential, clinically relevant attributes that improves the realism of simulations. One attribute is the ability to realistically assess body temperature from the mannequin. Human body temperature can serve as an early warning sign of infection, illness, and injury. As a result, it is one of the first vital measurements taken during a clinical assessment to determine a treatment plan. During the COVID-19 pandemic, the importance of proper temperature assessment escalated as part of the effort to identify potential carriers of the virus. Temperature measurements were taken in more locations than ever before, including, but not limited to, hospitals, schools, workplaces, and airports.

Given the reliance on temperature, it has become essential that medical professionals, such as nurses, should have temperature assessment integrated into their simulation regimes, so they can practice taking human body temperature and evaluating the potential causes of a patient's elevated temperature. Therefore, there is a need to incorporate a temperature assessment component into existing simulation mannequins that can accurately portray the qualitative and quantitative components of human body temperature.

The prototype proposed by our team will have two components; (i) a qualitative component that will allow tactile assessment of the mannequin's temperature and (ii) a quantitative component that will allow the user to directly measure temperature from the mannequin's surface. As in all simulation set-ups, the instructor will predetermine the simulation mannequin's temperature based on the clinical scenario, and then configure both the qualitative and quantitative components prior to the simulation lab experience. Overall, this project will result in a prototype that will enhance the realism of simulation-based education and better prepare medical professionals for real-world clinical experiences.

## PRODUCT DESIGN

After careful consideration of the input from the expected users and discussion to identify constraints and need, several design criteria were considered for this project. The most significant criteria of those criteria are safety, ease of use, interchangeable between mannequins, low cost, minimal maintenance, temperature-controlled, and realistic, in terms of temperature assessment and appearance. Additionally, it is important to keep manufacturing standards in mind for the eventual production and sale of this device.

Based on the design criteria to address the quantitative objective of this project we are building a radio frequency identification (RFID) temperature measurement system which focuses on high precision and realistic measurements of temperature. As shown in Figure 1, the system features an RFID chip containing stickers with unique IDs and a device that mimics the role of the thermometer (scanner). The scanner's main components are an RFID scanning element, microprocessor, LCD display, and various buttons for operation. These components of the scanner will be housed in an in-house 3D printed case that will resemble a typical thermometer present in a mobile stand for vital signs measurement.

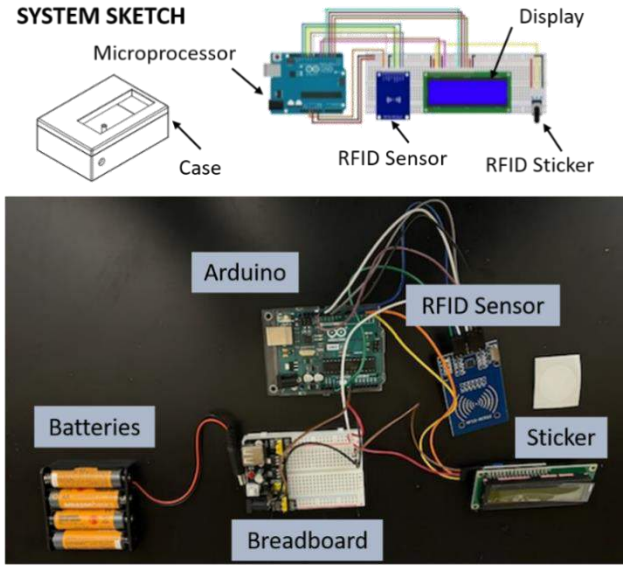


**Figure 1: Current layout of the quantitative component**

Prior to simulation, an instructor will be required to place the RFID stickers on the mannequin in reasonable locations for measurement sites, for example the oral cavity. The instructor will then preset the

output value that resembles the desired temperature for the simulation scenario. For student use, they simply need to operate the scanner like a contact tip thermometer, placing the probe element near the stickers and the device registers the ID causing the LCD screen to display the corresponding temperature. The provision for students to measure temperature in the aforesaid manner is an important aspect of realism that has been integrated into this prototype.

The major benefits to the users of this device are the precise, controllable temperature read-out and the realistic motion needed to operate it. Additionally, different cases can be programmed to fit the needs of the simulation: such as an increase in temperature in order to simulate hyperthermia or a drop in temperature in order to simulate hypothermia. The device is easy to operate and transferable between mannequins making it a robust standalone design. The major drawback to this design is that it lacks a tactile assessment component, I.e., it does not produce heat. We sought to mitigate this issue by incorporating a second component that meets the qualitative objective of the project since tactile assessment was determined to be equally as beneficial to the simulation as the quantitative assessment.

The qualitative component (shown in Figure 2), that addresses surface heat sensation, consists of a band heater that sits on top of a resistive base, with a layer of skin colored material on top of the band heater. A piece of Velcro allows the device to be strapped onto the forehead/forearm. The resistive base prevents heat conduction to the underlying mannequin and the skin-colored material on top resembles human skin. An attached controller allows the instructor to set the desired temperature output based on the simulated scenario requirements. The temperature is maintained using a thermocouple. This controller and the band heater are powered by rechargeable batteries. These electrical components are designed to be tucked away below the simulation bed so that it is not in the way during the simulation.

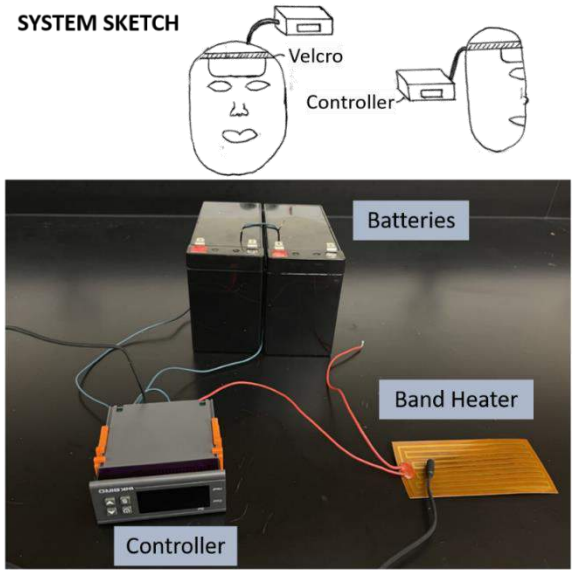


**Figure 2: Current layout of qualitative component**

The main benefit of this design is that it is mobile and reusable. This design can easily be moved between mannequins and, since it is battery powered, the simulation mannequin can be moved from one location to another without having to disconnect the device. The batteries also prevent extra wires from being present in the simulation and avoid the need for a nearby outlet power source. Constructing the device is simple because it can be easily assembled from a series of preexisting electronic components.

The proposed final design is a combination of the two described components, envisioned to be housed in one organized tower. This tower will contain the electrical components of the qualitative design, the controller, batteries, and wiring, with a storage location for the heated portion when not on the mannequin's forehead. It will also have a system to hold the quantitative mock thermometer realistic to true hospital probe placement techniques. This tower will condense the two components and be reasonably sized to fit next to the mannequin's bed without interfering with the simulation.

## BUDGET & MARKET ANALYSIS

The budget for this project is $550. This budget includes building and testing the prototype, and a contingency. So far, $247.45 has been spent to develop both the quantitative and qualitative components of the design. The next steps are to test the qualitative component that has been built, program the quantitative component, and purchase casing materials for both components. Given the forecasted work and remaining materials that need to be purchased, it is predicted that the proposed final design will cost, at most, $450 to develop.

Based on the "Mannequin-Based Simulation - Global Market Trajectory & Analytics" report [2], the global market for mannequin-based simulation estimated at US$1.2 Billion in the year 2020, is projected to reach a revised size of US$5 Billion by 2027, growing at a CAGR of 22% over the period 2020-2027. Given that our product is a standalone system, it not only has potential in the newly manufactured mannequin market, but could also be integrated into the existing mannequins, resulting in a very large market for the product. Additionally, since the product is easily interchangeable between different mannequins (irrespective of size, functionality, manufacturer), individual institutions do not need to acquire independent products for all their mannequins. This cost-effective option makes the product a lucrative investment for institutions. As mentioned earlier, the potential market size for this device branches to schools that utilize human simulation mannequins in their clinical simulations which includes 87% of nursing schools and 80% of medical schools [1].

Based on this need and the current growing market for human simulation-based mannequins, we could be considering selling about 150,000 temperature assessment units a year (100K for existing mannequins and 50K for newly manufactured mannequins). After developing the initial prototype, the forecasted price to build a single device is $345.65 and the projected sell price is $1000 per unit the net gain on one unit at this price would be $654.35. This gain would be used in for marketing the product, renting lab space, employing engineers for mass production and in other relevant expenses related to manufacturing. After all the expenditures we still envision to make an approximate profit of 25% on the selling price of each device.

## ACKNOWLEDGEMENTS

We would like to extend our thanks to Widener University's School of Nursing for allowing us access to their simulation lab and providing us with feedback. We would also like to thank David Leuter, Tyler Hoikins, Dr. Syed Ali Hamza, and Dr. Piotr Hryniewicz for their assistance in the development of our prototype.

## REFERENCES

[1] Vyas, D., et al., *Am. J. Pharm. Educ*, 73(3), 53-55, 2013.
[2] *Mannequin-Based Simulation – Global Market Trajectory & Analytics*, (2021)

# A NOVEL, PORTABLE, NONELECTRONIC, AND VERSATILE OXYGENATING PERFUSION SYSTEM FOR MULTI-ORGAN PRESERVATION

**S. Salazar (1), A. Fasci (1), J. Oseghale (2), M. Garcia (1), A. Khalil (1), B. Wearden (1), L. Muenchow (3), J. Gonzalez (1), C. Villareal (2), D. Portillo (1)**

**Faculty Advisor(s)**

**R.L. Hood (1,2)**

(1) Department of Mechanical Engineering, The University of Texas at San Antonio, San Antonio, TX, USA
(2) Department of Biomedical Engineering, The University of Texas at San Antonio, San Antonio, TX, USA
(3) Department of Biology, The University of Texas at San Antonio, San Antonio, TX, USA

## INTRODUCTION

There are currently over 100,000 people on the national transplant waiting list [1]. In 2020, only 39,000 people were able to receive the life-saving procedure [1]. Lack of efficient preservation methods is one of the leading reasons as to why only 30% of the people on the transplant list are able to receive the transplant procedure. The current gold-standard method of preservation is known as static cold storage (SCS), although hypothermic machine perfusion (HMP) has been discovered to provide better perfusion pressures and oxygenation rates [2]. There are six major competitors within the organ preservation market: Paragonix Tecnhologies, Inc; 21st Century Medicine, Inc; Essential Pharmaceuticals LLC, Organ Recovery Systems, Inc; and Preservation Systems, Inc; and Transmedics, Inc. [3]. Unfortunately, the systems produced by these companies are all organ specific, electrically powered, and either only provide static cold storage or provide perfusion but are prohibitively expensive to purchase and operate. Due to these issues, hospitals are required to have a variety of organ preservation devices on hand. Many of them are non-portable, which eliminates them from use when the donor and recipient are not at the same hospital.

The proposed device to sufficiently versatile to preserve a variety of organs and tissues, is pneumatically powered, and has a streamlined design with fewer moving parts which is intended to lead to a substantially reduced price point. We have named this device the multi-organ preservation system (MOPSY) [4]. The MOPSY device was designed to be portable and easy to use while providing the necessary components to effectively transport a variety of organs that range from hypothermic to normothermic temperature ranges making it more versatile than various organ preservation devices because that can only manage hypothermic machine perfusion or normothermic machine perfusion. In addition to that, other devices do not supply oxygen to the organ but it has been shown that oxygenation of the perfusion solution increases the quality of preservation which the MOPSY device does. For battlefield usage, the device being small and lightweight are key benefits due to space constraints in field hospitals, as well as the need to transport between the donor and recipient. The device being nonelectric allows it to be in settings out on the field where power may not be as easily accessible.

## PRODUCT DESIGN

The MOPSY device is composed of two main chambers: the pump chamber and organ storage chamber. Figure 1 shows the 6 total components: the top cap, the silicone tubing, the fastening lid, the tube casting, the organ chamber, and the base cap. The top chamber consists of the top cap, the silicone tubing, and the fastening lid. The silicone tubing is positioned in helical coils for optimal effectiveness and can be bought to fit the specification of the device. The organ storage chamber is the lower half of the device; it contains the base cap and the organ chamber which is made out of acrylic and has the capacity needed to store a human sized kidney, liver, heart, pancreas, or forelimb. The chamber has threads machined on the out end which allows other components, specifically the pump cover and the base cap, to be easily fastened to it. The top cap, pump chamber, fastening lid, and base cap are machined out of 6061 aluminum. Both chambers of the device are filled with a perfusion solution.

Compressed oxygen inflates and deflates the silicone tubing causing circulation of the perfusion solution to occur through two separate one way valves. In the organ chamber, a catheter could be directly connected from the pump chamber to the organ through a perfusion point allowing the perfusion to circulate through the organ. After circulating, the

perfusion solution exits the organ and mixes with the perfusion solution that organ is immersed in. In turn, this forces the perfusion solution from the organ chamber back into the pump chamber through the perfusion return port.

Currently, the device is set up to conduct tests regarding various viscosities and silicone tubing lengths. Aspects that make the device novel include it ability to preserve multiple organs entirely free of electronics, while being lightweight and easily transportable. The addition of a pneumatic circuit allows the device to be free of electronics, and it operates by having two valves that work synchronously. Within each of the valves, there is a piston that has two positions that gets turned on and off through the compressed oxygen that is provided. When one valve is open, the other valve is in the closed position, and their outputs feed into each other's inputs, ultimately providing pulsatile flow. The device so far has proved to be technically feasible from the approximate 200 hours of total data collected.

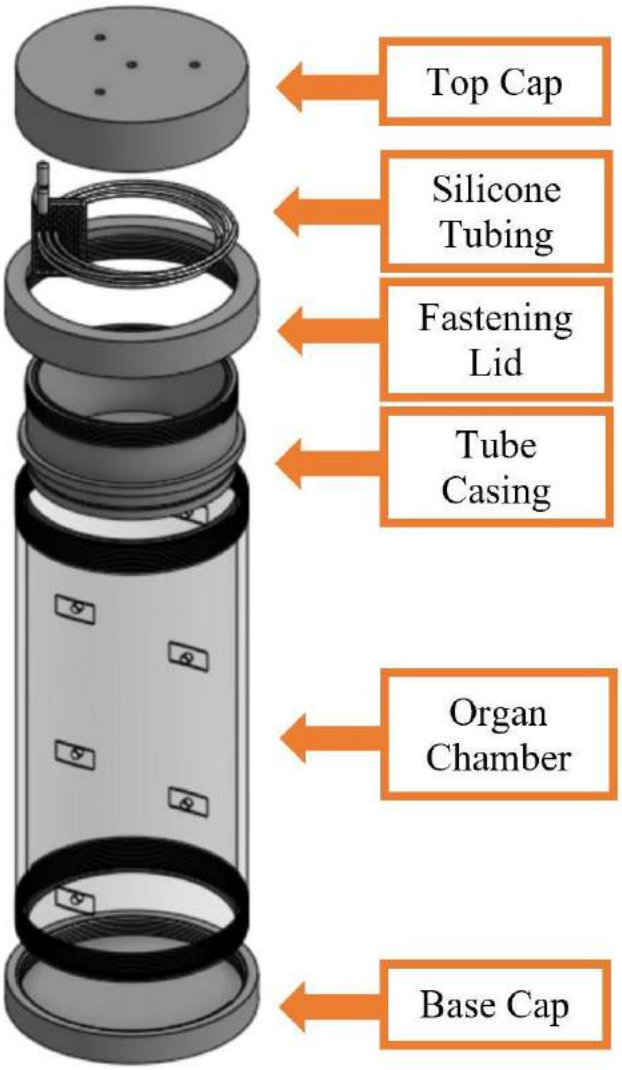


**Figure 1: MOPSY Device**

## BUDGET & MARKET ANALYSIS

The organ preservation market it forecasted to grow nearly 6.3% within the time period of 2018-2026 [3]. This initial investment of engineering and tooling is a one-time purchase for design purposes. According to the U.S. Bureau of Labor and Statistics, the average labor cost of designing a device is roughly $35 per hour (U.S. Bureau of Labor Statistics, 2020), and $22-26 per hour for testing and machining (U.S. Bureau of Labor Statistics, 2020). Within the research department there has been over 140 hours of design, machining, and testing the device, if valuating the volunteer hours towards the average labor cost would translate to $27.6 per hour at 140 hours equating to $3,850 labor. The material cost for a singular device is approximately $650 using acrylic, silicone tubing, aluminum, and the pneumatic circuit. Thus, the initial prototype development is approximately $4,500, which includes the labor and material costs ($3,850 and $650, respectively). Those costs could change depending on different manufacturing processes and specifications to optimize material and machining cost, but will not be addressed in this discussion.

There are approximately 36,000 transplants per year, including kidneys, livers, hearts, and pancreases. Since the MOPSY device has been shown to achieve perfusion parameters for all of those organs, there is a large market pool. Pricing the device at $5,000 for consumers covers the initial costs for the device as well as $1,150 in profit per device sold. That market price would be extremely competitive, as competitors' disposable packages cost roughly $10,000 (not including the device itself). The profit margin could be further increased with possible alternatives due to manufacturing costs and materials used. In addition to the reduced cost, this device offers the versatility to be utilized for a non-specified organ preservation method. In the event that 36,000 units are sold per year at a price point of $5,000 each, the yearly gross income would be $180,000,000. That estimation does not account for the potential to increase the donor pool and number of organ donations, as this technology presents the opportunity to be used for various organs, rather than buying multiple different devices.


## ACKNOWLEDGEMENTS

This work was funded through a Department of Defense PRMRP; Award Number: W81XWH-18-1-0640. The authors would like to thank Dr. Ender Finol and Dr. Chris Combs for providing data acquisition equipment. The authors would also like to thank David Kuenstler for assisting with the fabrication of the device.


## REFERENCES


[1] Organ donation statistics. (n.d.). Retrieved January 10, 2022, from https://www.organdonor.gov/learn/organ-donation-statistics

[2] Guibert, Edgardo E et al. "Organ Preservation: Current Concepts and New Strategies for the Next Decade." *Transfusion medicine and hemotherapy: offizielles Organ der Deutschen Gesellschaft fur Transfusionsmedizin und Immunhamatologie* vol. 38,2 (2011): 125-142. doi:10.1159/000327033

[3] *Organ preservation market growth: Industry outlook (2022 - 27) - mordor intelligence*. Organ Preservation Market Growth | Industry Outlook (2022 - 27) - Mordor Intelligence. (n.d.). Retrieved February 12, 2022, from https://www.mordorintelligence.com/industry-reports/organ-preservation-market

[4] Portillo, Daniel J., et al. "Characterizing and Tuning Perfusion Parameters Within an Innovative, Versatile Oxygenating Perfusion System." *Annals of Biomedical Engineering* 49.12 (2021): 3154-3164.

# THE IMPACT OF HYPERGLYCEMIA AND OVARIECTOMY ON HOST RESPONSE TO VAGINAL PROLAPSE MESH IMPLANTS

**A. Fisk (1), G. King (2), K. Weber (2), R. Liang (2),**

(1) Department of Bioengineering, University of Pittsburgh, Pittsburgh, Pennsylvania, United States of America
(2) Department of Obstetrics, Gynecology, & Reproductive Sciences, University of Pittsburgh, Pittsburgh, Pennsylvania, United States of America

## INTRODUCTION

Pelvic organ prolapse (POP), a common pelvic floor disorder in menopausal women, is often treated with surgical repairs. Compared to native tissue repair which has high failure rate (~70% at 6 years), mesh augmented surgeries are related to better outcomes. However, the use of mesh is associated with several mesh related complications such as mesh erosion through the vaginal cavity and chronic pain [1]. These complications hamper the use of mesh in urogynecologic surgeries.

Diabetes, which affects 1 in 10 women in the US, has been associated with higher rates of mesh related complications and has been identified as an independent risk factor by previous literature [2]. Mechanisms which increase the risk of mesh complications in diabetic patients are unknown. The hypothesis is that impaired wound healing caused by hyperglycemia dysregulates the mesh associated inflammation (MAI) and therefore causes higher rates of mesh complications within this group of patients.

In addition, previous literature has shown that the significant decrease in estrogen following menopause has adverse effects on cell functioning and tissue [3]. Recently site-specific hormonal treatments have been popularized for the management of mesh complications. As many women with diabetes undergoing mesh augmentation surgeries are also postmenopausal, the objective of this study is to compare the mesh associated inflammatory response under hyperglycemic and normoglycemic conditions with/without ovariectomy. As both conditions have potential impact on the vaginal tissue integrity, this study also examines the effects of both factors on vaginal muscularis in the context of mesh implantation.

## METHODS

Diabetes was induced in 18 rats with 19 nondiabetic rats being used as controls. Two weeks following the development of hyperglycemia, a polypropylene mesh was implanted on the anterior and posterior vagina via sacrocolpopexy after a supracervical hysterectomy with or without a bilateral ovariectomy (OVX). Nondiabetic rats underwent the same procedures. At 42 days (OVX diabetic n = 9 & nondiabetic n=10 and non-OVX groups, diabetic n = 9 & nondiabetic n =9) post-surgery, mesh-grafted vaginal tissues were collected for gross morphology and histology analysis**.**

Harvested tissue was cryosectioned and stained using a Hematoxylin & Eosin (H&E) and Masson's Trichrome staining protocol. Three indexes of inflammation were quantified. The overall area of MAI (fibrosis capsule + granuloma area) and foreign body giant cell (FBGC) formation was quantified in H&E-stained samples. In Trichrome stained samples the area of the granuloma was also quantified (figure1).

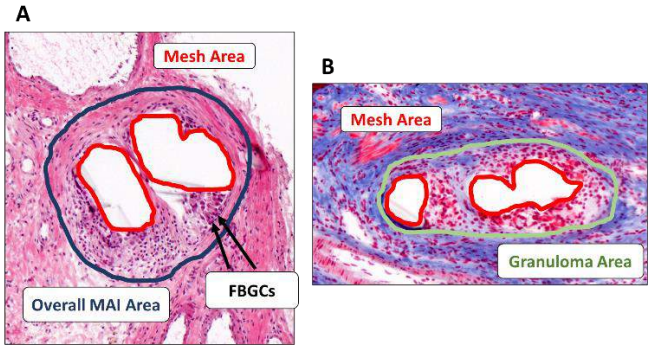


**Figure 1. Shows quantified gross morphology of the three indexes of inflammation in H&E samples (A) and Trichrome samples (B).**

In Trichrome stained samples the SM wall thickness was measured at intervals of approximately 100 μm. SM wall measurements were spilt into two groups: SM wall without mesh impact, and SM wall impacted by mesh. SM wall impacted by mesh was defined as the SM wall

adjacent to the mesh fibers and areas within a 100 μm ratio horizontally from the mesh fibers (figure 2).

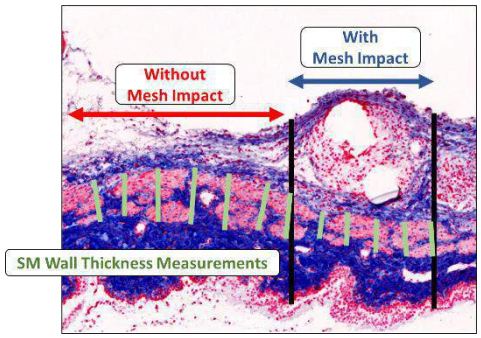


**Figure 2. Shows SM wall thickness quantification method in areas with mesh impact and areas without mesh impact.**

JMP pro was used to preform comparative analysis between the diabetic & nondiabetic groups and the OVX & non-OVX groups. All comparisons were made using Kruskal-Wallis tests. Significance for all analysis was set at $\alpha = 0.05$.

## RESULTS

Positive correlations were found between mesh fiber area and each index of inflammation, overall MAI, granuloma area, and FBGC formation, under normoglycemic conditions ($p < .01$ for all groups). Similar trends were observed under hyperglycemic conditions.

Without OVX, overall MAI, granuloma area, and FBGC formation were all significantly increased in diabetic rats ($p = 0.0031$, $p = 0.0274$, $p = 0.0022$). With OVX, granuloma area and FBGC formation significantly increased under hyperglycemic conditions compared to normoglycemic conditions ($p = 0.0014$, $p = 0.0086$) while overall MAI was not found to be significantly changed despite an increase by 60 % in diabetic rats (figure 3). OVX was not found to significantly affect inflammatory response when comparing rats with OVX and without OVX under both glycemic conditions.

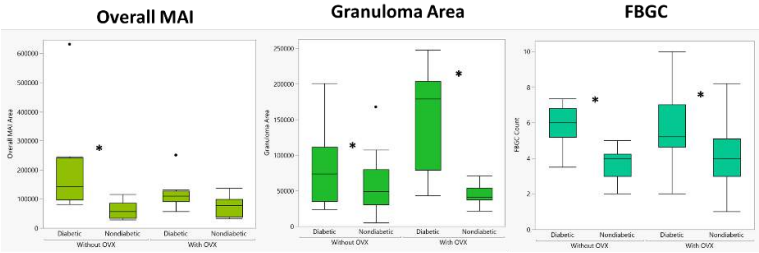


**Figure 3. Shows comparisons of diabetic and nondiabetic rats relating to the three indexes of inflammation.**

Smooth muscle wall thickness was significantly decreased in areas impacted by mesh fibers when compared to areas not impacted by mesh fibers in both diabetic and nondiabetic rats without OVX ($p = 0.0469$, $p = 0.0284$) (figure 4).

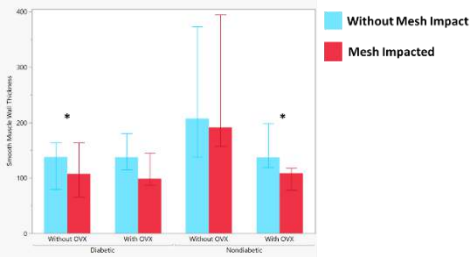


**Figure 4. Median SM wall thickness in areas both impacted by mesh and areas without mesh impact.**

OVX was found to significantly decrease smooth muscle wall thickness in areas adjacent to mesh fibers under normoglycemic conditions ($p = 0.0014$). However, no significant difference was found between the smooth muscle wall thickness in OVX and non OVX samples under hyperglycemic conditions.

Further, SM wall thickness was significantly decreased in diabetic rats when compared to nondiabetic rats without OVX in areas impacted by mesh fibers ($p = 0.0274$) (figure 5).

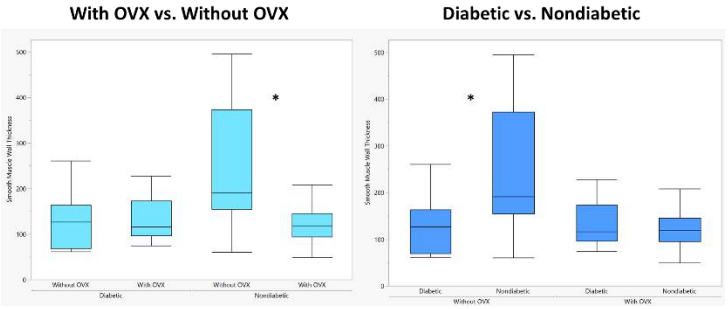


**Figure 5. Shows comparisons of SM wall thickness in OVX vs. non-OVX groups and diabetic vs. nondiabetic groups**

## DISCUSSION

Quantification of the mesh associated inflammatory response shows that inflammation is dysregulated under hyperglycemic conditions at a long-term time frame, which may contribute to the increased risk of mesh complication. The dysregulation of inflammation in diabetic samples occurs independent of estrogen levels.

While estrogen does not seem to have a significant effect on inflammation the presence of surgical menopause significantly decreases the smooth muscle wall thickness in areas impacted by mesh fibers. Hyperglycemia also has a significant effect on the SM wall thickness but only without postmenopausal conditions. This could indicate that the effect of hyperglycemia on SM wall thickness is increased without estrogen withdrawal. Another possibility is that under postmenopausal conditions smooth muscle wall thickness is too dysregulated to show any significant differences between diabetic and nondiabetic samples. While this could be hypothesized further research on SM wall dysregulation is needed to confirm the observations made in this study.

Data from this study also suggests that as mesh fiber area increases inflammation increases. This supports previous literature which supports the use of stable mesh configurations which decrease the risk of shrinking and buckling.

This study highlights several components of a dysregulated host response under hyperglycemic conditions. The exact molecular mechanisms causing dysregulation should be examined in future work. Targeting both MAI and SM wall formation could have the potential to develop effective therapeutic strategies for the management of mesh complications in patients with diabetes.

## ACKNOWLEDGEMENTS

I would like to acknowledge the R21HD099549 NIH funding for this research and the support from the TRLU research group on this project.

## REFERENCES

[1] Maher C. Int Urogynecol J Pelvic Floor Dysfunct. 17:195-201 2006
[2] Yung-Wen Cheng, Taiwanese Journal of Obstetrics and Gynecology, 56:184-187 2017
[3] Taylor HS J Clin Endocrinol Metab, 96:255–264 2011

SB³C2022
Summer Biomechanics, Bioengineering and Biotransport Conference
June 20-23, Eastern Shore, MD, USA

# DESIGN AND VALIDATION OF A BIOREACTOR FOR DYNAMIC BIAXIAL MECHANICAL STIMULATION OF ENGINEERED TISSUE VASCULAR GRAFTS

**Luke L. Dague (1,2), Hayden Nothacker (1), Sarah K. Saunders (1), Johane Bracamonte (1), Joao S. Soares (1)**

(1) Department of Mechanical and Nuclear Engineering,
Virginia Commonwealth University, Richmond, VA, USA
(2) Department of Biomedical Engineering,
Georgia Institute of Technology, Atlanta, GA, USA

## INTRODUCTION

Cardiovascular disease remains as the leading cause of death worldwide, with mortality strongly correlated with coronary artery disease and commonly observed as stenosis or occlusion of blood vessels leading to myocardial infarction. Engineered tissue vascular grafts (ETVGs) promise an attractive alternative option to autologous grafts typically employed in coronary artery bypass grafting surgery.[1] In theory, ETVGs hold many advantages such as relieving supply limitations, the ability to grow and repair in vivo, and lacking the need of either using the internal mammary artery or harvesting the saphenous vein. However, more research is necessary before this technology can reach clinical application. The main hurdles lie in achieving similar mechanical properties of native vessels as compliance mismatch is a strong factor correlating with grafting success. It is known that mechanical conditioning of engineered tissues during incubation improves their properties and physiological function; specifically, biaxial loading of ETVGs has been shown to improve vascular mechanics.[2] However, there is a lack in systematic understanding of the parameters driving ETVG growth and remodeling during in vitro incubation and the resulting patency of the ETVG once deployed in vivo. Therefore, more research is necessary in determining the ideal protocols of mechanical stimulation to produce viable ETVGs. Unfortunately, access to bioreactors capable of providing this stimulation is a limiting factor in the field due to complexity and cost.[3] A low-cost, automated, robust, and reproducible method for experimenting with in vitro culture of ETVGs is needed to progress the field through systematic collection of data for model generation. Here, we propose and validate a custom designed dynamic biaxial bioreactor to meet these criteria.

## METHODS

Axial Stimulation. The bioreactor is designed to accept four electrospun PCL scaffolds of 2mm diameter, 3cm length, and 200μm thickness suitable for deployment as an aortic interposition graft in rats. A novel scaffold mounting system and associated fixturing procedures were developed to grip the scaffolds. The scaffolds are attached to stainless steel cannulas at both ends, and these cannulas are gripped by collets that hold the scaffold and stretch it between two spaced brackets made of stainless steel. The system ensures consistent mounting results while minimizing leakage and scaffold damage at mounting points. Axial stretch on the scaffolds is achieved through the use of a linear actuator acting on one of the brackets through a linear bearing system with minimal resistance. The use of a single linear actuator simplifies the bioreactor design, yet it retains the capability of providing uniform axial displacement to four scaffolds simultaneously.

Circumferential Stimulation. A closed bioreactor flow system was developed to provide cell media circulation through the scaffolds as well as control over the pressure and velocity of the fluid, and it serves as an analogic fluid level sensor on the culture chambers. The system utilizes a single multi-channel pump and a four-channel pinch valve placed downstream to regulate the pressure in the loop. Circumferential strain is controlled by coordinating the controls of the pump and pinch valve via software to achieve predetermined pressure levels in the scaffolds. To prevent cross-talk and possible cross-contamination, each scaffold has an independent flow loop with an isolated bioreactor chamber and cell media reservoir.

Bioreactor Design and Construction. The bioreactor was designed in Solidworks. The main body with 4 separate ETVG chambers was developed with 3D printing constraints in mind, specifically for FDM manufacturing with ABS thermoplastic. The remaining pieces of the bioreactor system are primarily off-the-shelf parts and electronics. While some of the brackets are custom, they were designed for reproducibility and ease of manufacture. Overall, the design is not technologically demanding, and the construction can be easily and quickly performed with basic tools. Sterility during seeding and incubation is another integral design feature. A custom room-

temperature-vulcanizing silicone gasket was developed, which was formed and cured in a 3D printed mold; this method is simple to recreate and could be easily scaled. The gasket provides an air-tight seal for the lid of the incubator to avoid contamination in culture. The linear bearing system and the inlets and outlets of the flow system were also designed to prevent exposure of the inner chamber of the bioreactor to the incubator environment.

Software Control. A custom user interface was developed to control the bioreactor system in LabView. The user can adjust all inputs to control the pump velocity, axial stretch magnitudes and frequencies, max pressure, time to hold pressure, number and duration of cycles, etc. The fine control over these parameters allows for future experimentation with different mechanical stimulation procedures on the scaffolds. Additionally, a single Texas Instruments data acquisition board controls all the electronic components of the bioreactor. The entire assembly can easily be transported in a single tray and placed on an incubator shelf with the possibility being able to run 2 bioreactors simultaneously in a standard 160L incubator.

Validation of Mechanical Stimulation. A computer vision program was implemented for tracking the circumferential and axial strain response of the scaffolds. Grayscale-based edge tracking of the scaffold reports changes in the diameter. For the axial component, three dots are drawn on the scaffolds and the distances between them are used to compute axial stretch. Additionally, a pressure sensor was added to the flow system to measure luminal pressure inside the ETVG. Test scaffolds were produced by casting silicone around a brass rod of 2mm diameter to match the desired scaffold dimensions. After curing, the thin silicone tubes were pulled off the rod and cut to length for use in validation of the axial and circumferential strain feedback in the bioreactor flow loop. Impermeable silicone model scaffolds were a useful tool for prototyping the pressure system and the actuation for axial stretch by providing repeatable strain values from the various inputs.

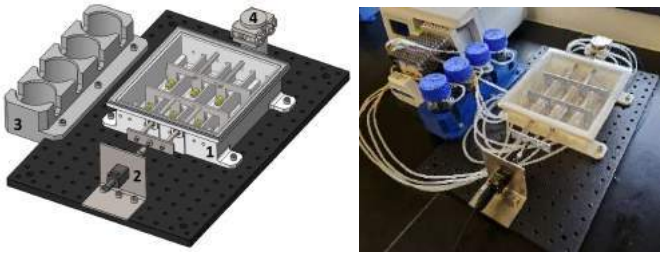


**Figure 1: Final 3d-CAD assembly (left) and constructed bioreactor (right). Legend: 1) Bioreactor Chambers, 2) Linear Actuator, 3) Reservoir Fixture, 4) Pinch Valve.**

## RESULTS

The custom-designed ETVG bioreactor (Figure 1), was demonstrated to be effective in producing axial and circumferential stretch on small-diameter tubular scaffolds. The control programs and hardware effectively delivered the desired inputs to the bioreactor, and outputs could be measured with sufficient accuracy. The computer vision measurement system was capable of recording deformations less than 0.1mm in the scaffolds. We were able to prescribe any type of combination of axial and circumferential stretches. Circumferential stretch is achieved with a three-phase cycle (Figure 2) that involves a sequential activation of pump driving flow with pinch valve closing downstream to build luminal pressure. We found a linear correlation between time and pressure/diameters achieved, which could then be held for any duration until valve opens and initial diameter is recovered. Axial strain implementation was also validated; we found that displacement of the linear actuator applied strain directly and uniformly to the scaffolds as expected. We were able to reproducibly impart axial strains of ~10% and circumferential strains of ~4%, which are typical values of physiological strains observed in vivo due to pulsatility.[2] These results were met while maintaining a low cost for the bioreactor. In total, the system costs about $450 in hardware and $5,800 in electrical components, most of which are standard laboratory equipment that may already be available.

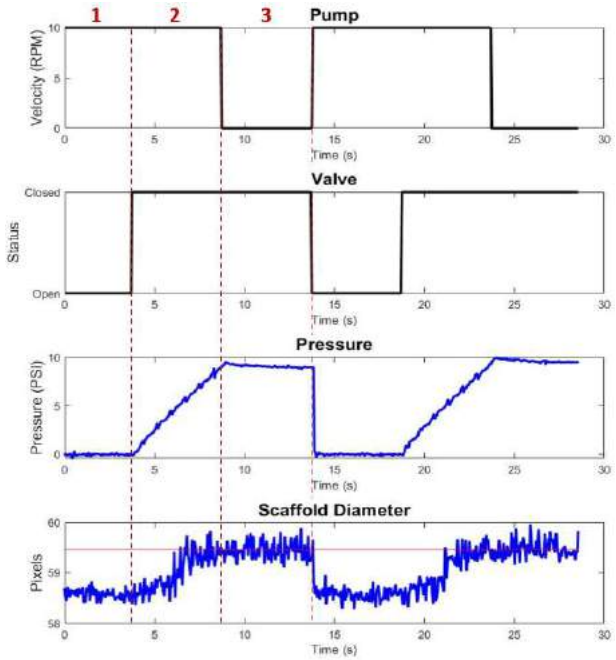


**Figure 2: Cyclic circumferential strain data from bioreactor operation. Inputs are shown in black and outputs in blue. Vertical red dashed lines show different phases of the pressure cycle.**

## DISCUSSION

3D printing holds many advantages as a manufacturing process in this application.[4] First, it allows the bioreactor to remain low-cost relative to commercial alternatives. Additionally, 3D printing allows for rapid prototyping of the bioreactor, making it simple to perform future design iterations if desired. The technology is also easily accessible, which contributes to the reproducibility of the design. Increased availability of bioreactor technology for dynamic mechanical stimulation of engineered tissues during their incubation will enable systematic experimentation of ETVG development and determination of ideal mechanical stimulation protocols. Additionally, the bioreactor is easily scaled; a sample size of n=8 can be achieved with two bioreactors in one standard-size incubator. Due to its low cost, reliable results, and ease of manufacture and assembly, the proposed dynamic biaxial bioreactor holds potential for broader impact in the field of small-diameter vascular graft tissue engineering.

## ACKNOWLEDGEMENTS

This research was funded by the NSF and VCU through the Mechanobiology REU program. The work was guided and supported by the members of the ETM[3] laboratory.

## REFERENCES

[1] Isenberg, B.C. et al., *Principles of Regenerative Medicine (Second Edition)*, 853-875, 2011. [2] Huang, A.H. et al., *Tissue Eng. Part C: Methods*, 22:524-533, 2016. [3] Avci-Adali, M. et al., *J Biomed. Materials Research Part B: Applied Biomaterials*, 101B:1061-1068, 2013. [4] Putame, G. et al., *J Healthcare Eng*., 3957931, 2019.

SB³C2022
Summer Biomechanics, Bioengineering and Biotransport Conference
June 20-23, Eastern Shore, MD, USA

# ESTIMATION OF FLOW DATA FROM ANGIOGRAPHIC TIME SERIES

**Noah C. Stevens (1), Kritika Iyer (1), Brahmajee K. Nallamothu (2), C. Alberto Figueroa (1,3)**

(1) Biomedical Engineering, University of Michigan, Ann Arbor, MI, USA
(2) Cardiovascular Medicine, University of Michigan, Ann Arbor, MI, USA
(3) Surgery, University of Michigan, Ann Arbor, MI, USA

## INTRODUCTION

Coronary artery disease (CAD) is one of the most widespread causes of heart disease, accounting for over 20% of adult mortality in the US [1]. CAD is characterized by a buildup of plaque in the coronary arteries known as stenosis. The condition is diagnosed using X-ray angiography, in which dye is injected into the patient's bloodstream to estimate diameter reduction of the arteries. While diameter reduction is useful for informing clinical management of the disease, functional metrics such as Fractional Flow Reserve (FFR) lead to better patient outcomes [2]. FFR, defined as the ratio of distal and proximal coronary pressures, provides a quantitative measure of stenosis severity. Traditionally, FFR is measured via an invasive pressure guidewire which is pulled through the stenosed artery to record pressures proximal and distal to the stenosis. However, this technique presents several risks to CAD patients and has great inter-operator variability [3].

To eliminate these drawbacks, patient specific computational fluid dynamics (CFD) simulations of coronary blood flow can be used to derive FFR. A major challenge of these simulations is determining patient-specific boundary conditions, particularly since the flow and pressure in each vessel are not typically measured clinically. In this work, we developed an algorithm to extract patient-specific flow information from an angiographic time series. Previous work on angiographic velocity extraction has preliminarily explored comparison of extracted flow to simulation results or doppler measurements using techniques such as spline fitting [4, 5]. However, this is the first implementation of a flow estimation algorithm that tracks changes in 2-D planar vessel area in an angiographic time series compared against simulation results, ultimately with the goal of creating patient-specific flow boundary conditions.

## METHODS

We generated synthetic angiography data based on patient-specific blood flow simulations performed using CRIMSON [6] to evaluate the accuracy of our flow-extraction algorithm in controlled conditions (no cardiorespiratory motion, steady flow, known ground truth flow in each branch of the coronary tree. We extracted flow in each branch of two models: one healthy right coronary tree and one containing a stenosis (Fig. 1A).

The 3D geometry of the right coronary artery (RCA) was reconstructed from computed tomography angiography (CTA) images. Boundary conditions were assigned to the model as follows: a steady flow of 0.1 L/min was assigned at the inlet, resistances were assigned to the outlets, and no slip was applied at the walls. Resistances were tuned until the flow in each branch matched literature values [7]. A scalar species—angiography dye—was introduced at the inlet with a constant concentration of 200 mol/mm$^3$, and the position of the dye was tracked over time. The results of 3D scalar transport were converted into a binary angiographic time series (Fig. 1B) by projecting the dye onto manually chosen image planes at several time steps. We chose viewing angles where the distal branches were most clearly visible to minimize error due to foreshortening (Fig. 1C). The procedure was repeated in the same model, but with a 92% stenosis added to the medial RCA.

Once the angiographic time series was generated, an algorithm based on that of Khanmohammadi *et al.* [5] was used to automatically extract velocity. For each frame, a Euclidean distance transform was used to compute the radius along the centerline in the vessel of interest; the area was approximated as the vessel diameters summed along the centerline. The difference in area per branch between consecutive frames was plotted as a function of time. The flow in each branch was calculated using the area as a function of time and vessel radius as

$$\mathrm{Q(t)} = \frac{\frac{\mathrm{d}}{\mathrm{dt}}(A(t))}{2R} \cdot \pi R^2 \qquad (1)$$

where $Q(t)$ is the flow [mm$^3$/s], $A(t)$ is the area of the vessel as a function of time [mm$^2$], and $R$ is the mean radius of vessel [mm].

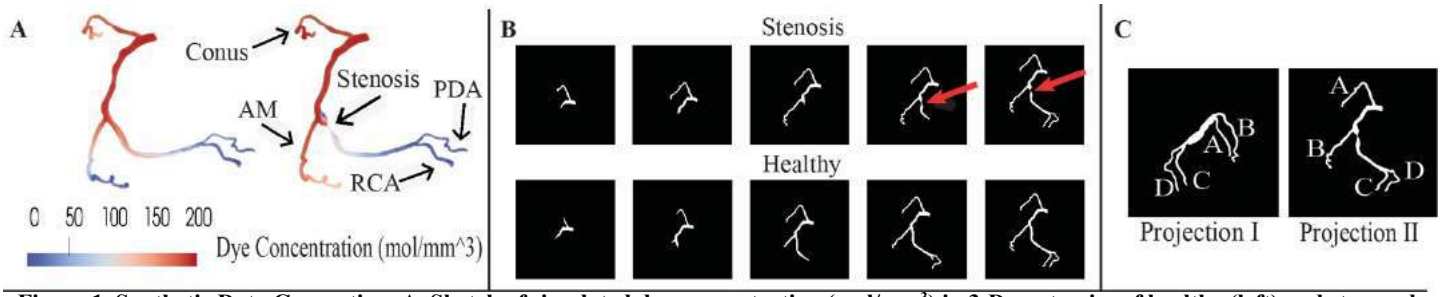


**Figure 1. Synthetic Data Generation. A. Sketch of simulated dye concentration (mol/mm$^3$) in 3-D anatomies of healthy (left) and stenosed (right) coronary trees. B. Simulated angiographic time series for the stenosed (top) and healthy (bottom) trees, used to extract flow data. C. Two projections depicting the PDA (D), the RCA (C), the AM (B), and the conus (A).**

Percent flow in each branch was calculated by dividing its flow by the flow at the inlet of the right coronary tree.

Flow was calculated for each of the four branches of interest—the posterior descending artery (PDA), the right acute marginal (AM), the conus, and the distal main RCA. The relative flow in each branch was averaged between two projection angles to mitigate the error due to foreshortening or magnification from projecting a 3-D structure onto a 2-D plane.

## RESULTS

Figure 2 compares the ground truth flow in healthy and stenosed coronary trees with the estimated flows from our flow extraction algorithm. The mean percent error between the simulation values and the algorithm values is 21.5±6.29% in the healthy coronaries and 15.2±5.69% in the stenosed coronaries. Plots of the estimated flow vs time in each branch for both the healthy and stenosed model are presented in Figure 3.

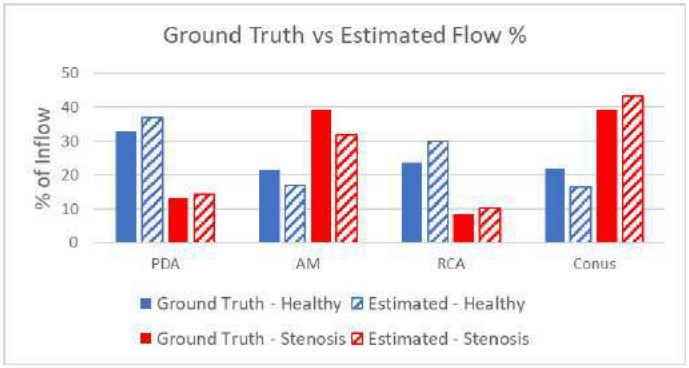


**Figure 2 - Percent flow values of healthy and stenosed coronaries, including both simulation and algorithm flow values.**

## DISCUSSION

The flow estimation algorithm successfully distinguished the change in relative flow values in each branch between the healthy and stenotic models. According to the ground truth simulations, the addition of the medial RCA stenosis leads to decreased flow in the branches distal to the stenosis (PDA, distal RCA), while the proximal branches (AM and conus) would have an increased flow compared to the non-stenotic geometry. This is depicted in our measured values, as the PDA changed from 36.8% flow to 14.4% flow with the stenosis. Similarly, the RCA changed from 29.9% without the stenosis to 10.3%. with the stenosis. Both the AM and conus flow percentages increased as well, going from 16.9% and 16.5% to 31.8% and 43.4% respectively.

Relative to the ground truth data, the estimated values of percent flow were similar in most branches. The largest error was a 26.7% percent error between the estimated and ground truth distal RCA flow in the healthy model. Discrepancies in relative flow (in both the healthy and stenosed models) could be due to the choice of projection angles. Projection angle I is oriented such that the PDA and RCA are in closer proximity to the viewer, while the AM and conus branches are more distant. Not only will the radius of the AM and conus branches appear smaller, but the dye will also appear to move at a slower rate due to being angled out of the image plane. These artifacts of the projections directly contribute to the error in flow computation. In the future, we can minimize these errors by incorporating the true distance and radius values from the 3-D geometry of the vessel tree.

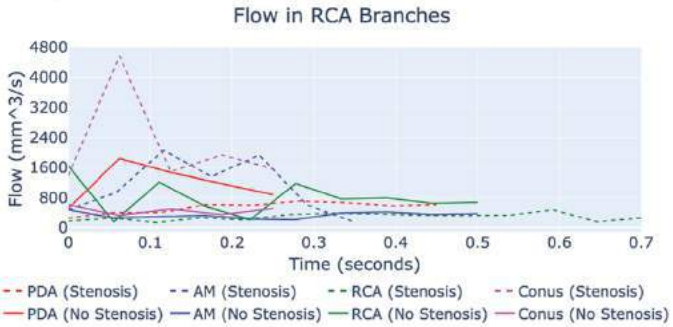


**Figure 3 - Flow in coronary branches as a function of time in healthy (solid) and stenotic (dashed) models using Projection I data.**


## ACKNOWLEDGEMENTS

This work is supported by the National Science Foundation GRFP (DGE1841052).


## REFERENCES


[1] M. W. Russell, et al., 1998. doi:10.1016/S0002-9149(98)00136-2.
[2] W. F. Fearon, 2013. doi:10.3904/kjim.2013.28.1.1
[3] R. Petraco, *et al.*, 2013. doi:10.1016/j.jcin.2012.10.014
[4] S. Y. Sokolov, *et al.*, 2019. doi:10.1134/S1054661819040163
[5] M. Khanmohammadi, *et al.,* 2019. doi:10.3389/fcvm.2019.0000
[6] C. J. Arthurs, et al., 2021. doi:10.1371/journal.pcbi.1008881
[7] S. Sakamoto *et al.*, 2013. doi: 10.1016/J.AMJCARD.2013.01.290.

# THE EFFECT OF DEVELOPMENT SLOW ELONGATION IN DRIVING HEIRARCHICAL COLLAGEN FIBER FORMATION IN ENGINEERED TISSUES

**Kelly R. Ott (1), Jennifer L. Puetzer (1,2)**

(1) Biomedical Engineering, Virginia Commonwealth University, Richmond, Virginia, USA
(2) Orthopaedic Surgery, Virginia Commonwealth University, Richmond, Virginia, USA

## INTRODUCTION

Hierarchical collagen fibers are the primary source of strength and function in tendons, ligaments, and menisci. Injuries to these tissues disrupt collagen organization, resulting in loss of function, and over 1.6 million surgeries in the US each year [1,2]. Current treatment strategies fail to restore the structure or function of native tissue. It remains a challenge to form the hierarchical collagen fibers essential for long term mechanical success in engineered replacements or *in vivo* after injury [2]. Previously, we developed a novel culture system that guides anterior cruciate ligament (ACL) fibroblasts to produce aligned collagen fibrils at 2 weeks, which mature into native-sized fibers and fascicles by 4 and 6 weeks (Fig 1A)[2]. These are some of the largest hierarchical collagen fibers produced to data, however, further maturation is needed to be clinically relevant. Mechanical cues, such as slow growth and rapid cyclic muscle loading, are critical for fiber development *in vivo* and if not present tissues fail to mature [3,4]. However, this environment is complex and it is unknown how each type of load effects fiber formation. In particular, growth rates of the ACL can vary more than 10 fold between embryonic to early postnatal stages [5]. The objective of this study was to investigate whether slow stretch at rates similar to neonatal and postnatal ACL growth rates differentially drive hierarchical collagen fiber development in our system and whether the effect of load varies at different levels of collagen organization.

## METHODS

Engineered constructs were created by mixing immature bovine ACL fibroblasts with rat tail type I collagen to form 20 mg/mL sheet gets at $5x10^6$ cells/mL [2]. Rectangular constructs (30x8 mm) were cut from the sheet gels and cultured in our static clamping device (Fig 1A) or in a modified CellScale tensile bioreactor. Two experiments were performed to evaluate the effect of prolonged and temporal slow stretch. To evaluate the effect of prolonged slow stretch (Fig 1B), constructs were continuously stretched for up to 3 weeks at 0.1 mm/day to mirror ACL postnatal growth rates[5] or at 1 mm/day to mirror neonatal growth rates[3] (Fig 1B). To determine the temporal effect of load and whether the effects of stretch vary for different levels of collagen organization, constructs were clamped for 0, 2 or 4 weeks and then loaded at 0.1 mm/day or 1 mm/day for 1 week to evaluate load applied to unorganized collagen and at the fibril or fiber level (Fig 1C). Post culture, constructs were weighed and sectioned for analysis of organization, composition, and mechanics. Confocal reflectance was performed to analyze collagen organization. DNA, glycosaminoglycans (GAGs), and collagen content were measured via Picogreen, DMMB, and hydroxyproline (hypro) assays. All data were normalized to wet weight and multiplied by construct weight to determine composition per construct to account for differences in size from stretch. Mechanical properties were analyzed by tensile tests at 0.75% strain/sec to failure. Statistical analysis was performed by two-way ANOVA with Tukey's post-hoc ($p$<0.05).

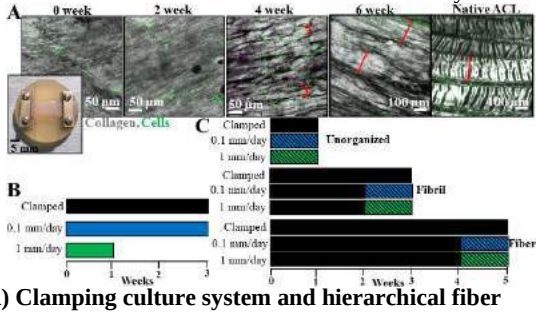


**Figure 1: A) Clamping culture system and hierarchical fiber development over 6 weeks (brackets denote fibers and fascicles). Slow stretch B) duration and C) temporal experimental set up.**

## RESULTS

In the first experiment we evaluated the effect of prolonged slow stretch on cell driven hierarchical fiber development. While constructs exposed to 0.1 mm/day stretch could be cultured for up to 3 weeks, constructs cultured at 1 mm/day began to rupture by 1 week. One week of stretch at 1 mm/day resulted in increased collagen and cell alignment

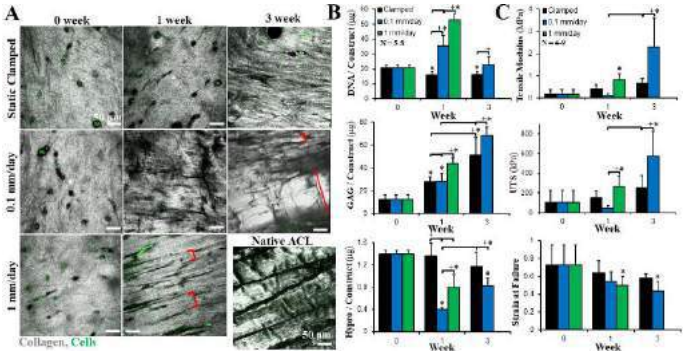


**Figure 2: Effect of slow stretch over extended culture on A) collagen organization, B) matrix composition, & C) mechanics. Significance compared to *0 week & +bracket**

(Fig 2A), significantly increased DNA and GAG content (Fig 2B), and significantly increased tensile modulus, ultimate tensile strength (UTS), and decreased strain at failure (Fig 2C). Interestingly, cell free constructs loaded at 1 mm/day did not have increased mechanics at 1 week (data not shown), suggesting changes in matrix mechanics are cell driven. Constructs cultured with 0.1 mm/day stretch had more aligned fibrils by 1 week in comparison to clamped controls, and developed larger fibers and fascicles by 3 weeks (Fig 2A). Similar to 1 mm/day constructs, 0.1 mm/day constructs had significantly improved DNA and GAG content, and significantly increased tensile modulus, UTS, and decreased strain at failure, however these changes primarily occurred at 3 weeks, rather than 1 week (Fig 2B-C). Both 0.1 and 1 mm/day constructs had decreased collagen (hypro) content compared to static clamped constructs after one week of loading, however collagen content did later increase after 3 weeks of 0.1 mm/day stretch (Fig 2B).

In the second experiment we evaluated whether the two stretch rates had differential effects when applied for 1 week in unorganized collagen (0 weeks) or after collagen had organized into aligned fibrils (2 weeks) or fibers (4 weeks). Regardless of timing or stretch rate, loading increased degree of collagen organization resulting in larger collagen fibers compared to clamped controls (Fig 3A). It appeared 1 mm/day constructs had larger, more organized collagen fibers than 0.1 mm/day constructs at each timepoint, and both rates of stretch resulted in more wavy or crimped collagen fibers when load was applied at 4 weeks once fibers had formed (5 week timepoint, Fig 3A). Regardless of timing of load, both stretch rates resulted in significantly increased DNA, in a dose dependent fashion, compared to clamped constructs (Fig 3B). While 1 mm/day load applied to unorganized collagen resulted in significantly increased GAG content at 1 week, this effect was lost at the fibril and fiber level, with both stretch rates accumulating similar

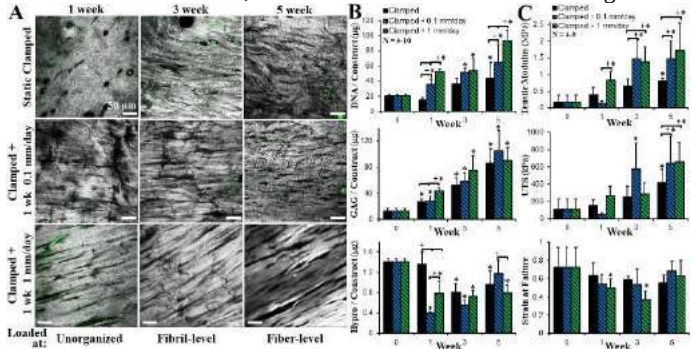


**Figure 3: Temporal effect of load applied to unorganized collagen or at the fibril or fiber level on A) collagen organization (collagen = grey, cells = green), B) matrix composition, & C) mechanical properties. Significance compared to *0 week and +bracket.**

GAG as clamped constructs at 3 and 5 weeks. Further, while both rates of stretch in unorganized collagen resulted in significantly decreased collagen (represented by hydroxyproline content) compared to clamped constructs at 1 week, this effect was lost at higher levels of organization (Fig 3B). Particularly, both rates of stretch at the fibril level resulted in similar collagen content as clamped constructs at 3 weeks, and at the fiber level 0.1 mm/day constructs had significantly more collagen in comparison to 1 mm/day constructs by 5 weeks (Fig 3B). Finally, both rates of stretch resulted in significantly increased tensile moduli when applied at the fibril and fiber level and UTS when applied at the fiber level (Fig 3C). Interestingly, while 1 mm/day stretch reduced the tissue failure strain at 1 and 3 weeks, this effect was lost by 5 weeks when load was applied at the fiber level.

## DISCUSSION

Collectively, in this study we found that slow stretch that mirrors neonatal and early postnatal growth rates increases collagen organization, DNA and GAG accumulation, and tissue mechanics in a dose and duration dependent manner. Further, these stretch rates have differential effects when applied at different levels of collagen organization. Specifically, we found that slow stretch increased cell proliferation regardless of collagen organization, as evident by the increase in DNA with load. Further, 1 mm/day stretch increased GAG content in unorganized collagen, however this effect was lost at later timepoints. Interestingly, by 5 weeks, all constructs had reached GAG concentrations that match native immature ACL tissue [2](data not shown), thus cells may differentially regulate GAG synthesis in response to stretch depending on tissue organization or tissue GAG concentration. Additionally, both rates of stretch appeared to differentially affect cellular collagen synthesis depending on the degree of collagen organization. Previously, we have found the largest turnover of collagen in our device is in the first two weeks when cells reorganize the collagen from unorganized to aligned fibrils [2]. During this period, it appears slow stretch may increase the rate of collagen turnover, resulting in significantly lower collagen concentrations and more organized aligned fibrils by 1 week. However, once cells are on aligned collagen, with altered tissue mechanics, they will most likely sense these stretch rates differently, possibly account for altered GAG and collagen production at 3 and 5 weeks.

Both rates of stretch resulted in increased collagen fiber organization, and increased tensile moduli and ultimate strength, regardless of the timing of load. However, both rates of stretch resulted in increased waviness or crimp-like formation and increased strain properties when applied at 4 weeks. Collagen crimp plays an important role in force transduction, absorbing initial load and reducing the load applied directly to fibers [6]. While it is not completely understood how crimps form, it is believed to be due to a mechanobiological response [6], thus slow stretch applied once fibers form may drive cells to start to form crimp. Overall, this study provides new insight into how different rates of growth during development effect hierarchical fiber formation and cellular response. A better understanding of how mechanical cues regular collagen fiber formation could help to develop better rehabilitation protocols to drive repair and help engineer replacements.

## ACKNOWLEDGEMENTS

This work is supported by NSF CAREER #2045995 (CMMI)

## REFERENCES

[1] Patel S. et al., *JOR*, 36(4):1069, 2018; [2] Puetzer J et al., *Biomat*, 2021; [3] Kalson N et al. *Dev Dyn* 240: 2520, 2011; [4] Connizzo B *Matrix Bio* 32: 1006, 2013; [5] Cone, S et al., *J Bone Jt Surg*, 7(6):e8, 2019. [6] Lavagnino M et al, *JOR*, 35(3):573, 2017.

SB³C2022
Summer Biomechanics, Bioengineering and Biotransport Conference
June 20-23, Eastern Shore, MD, USA

# THE-FRANNY

Zahin A. Akif (1), Ryan Jose (2), Lazaros Papa (3), Francisca Vallejo (4), Winston Yuen (5)

**Faculty Advisor(s)**

**Parisa Saboori (1)**

(1) Mechanical Engineering, Manhattan College, New York City, NY, USA

## INTRODUCTION

The population ratio of elders who are 65 years or older is growing at approximately 860,000 people per month (Henry). The main objectives to consider for the assistive devices such as walker frames are the guaranteed safety and comfortability of use from the user. The most basic walking frame is the Zimmer walking frame. The Zimmer frame assists its users with walking at the cost of long-term back strain, pain, and compromising support. Using static FEA analysis to identify stresses and strains present in the erector spinae muscles, we determined that conventional walkers tend to induce poor posture. An introduction to a modern and effective assistive walking device is pivotal step towards the solution of this problem. After our market research, we determined that there is a need for a high-end upper walker that has all the features that are present in its competitors while incorporating a modern lens. To achieve this optimization, we used our engineering discipline to redesign the most popular walker that is out in the market and create our walker named “The-Franny”.

## PRODUCT DESIGN

The-Franny is a modernized mobility aid that will be used to assist the senior citizen population with walking while ensuring user safety, comfortability, and ease of transportation. The overall height, width, and length of the device, as shown in Figure 2, is 41.7, 42, and 21, inches respectively. The-Franny is a walker that takes the safety and comfortability of a bulky and expensive upper walker and brings it to the conventional Zimmer Frame while maintaining a lightweight and compactable frame through aluminum tubing and a linked bar folding mechanism. Designed with the intention of reducing lower back strain while promoting an upright posture, this device features elbow rests, vertical handle/brake bars, and a set of 5-inch casters. In addition, it provides storage and a retractable seat for when the user needs to rest. Finally, a heart rate sensor as shown in Figure 1 is to be located at the handles of the walker, recording orthostatic vital signs to be accessible by the user and healthcare professionals.

This device will be designed and manufactured using CAD, 3D Printing, and laser cutting software. Using the engineering department and university resources, all necessary materials will be ordered while meeting budgetary restraints. The equipment and machinery necessary for tube bending, welding, fabrication, and assembly will be provided.

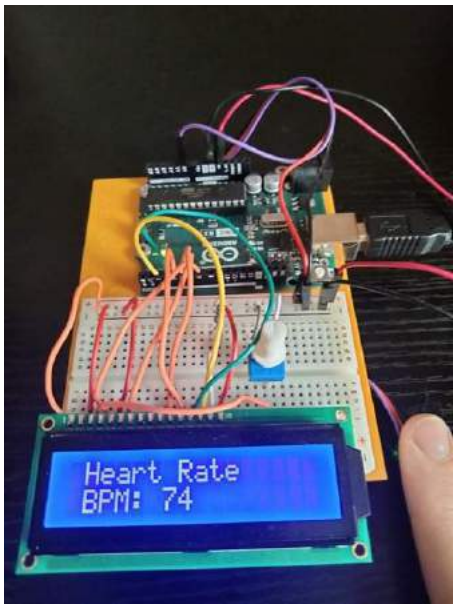

**Figure 1: Built Heartbeat Sensor (With Current Finger Reading) to be Incorporated Towards Final Build of The-Franny**

**Figure 2: Isometric View of The-Franny on SOLIDWORKS**

## BUDGET & MARKET ANALYSIS

The total design utilized a budget of $500. The total cost is dependent primarily on the build of The-Franny for the prototype. A lot of components for the walker were 3D-printed making effective use of the budget and resources available.

Walkers are used by nearly 5 million people in the United States alone. The expected manufacturing cost, when meeting this demand of walkers is dependent on the type of contracts made on bulk order basis, but the general high-end walker is sold for $700. If The-Franny is sold for $600 per walker, the end user would save 14% compared to what is available on the market, and the product would have a 20% profit margin. An important aspect of the cost to consider is that the user will not usually be paying for the full price of the walker, but a portion after insurance. When designing The-Franny, the design team never intended to create the device for profit. Everyone who needs a walker should have access to an affordable walker fitting for the 21st century. Therefore, the 20% profit margin is a figure that is a variable that can go lower when considering the greater mission of the design team.


## ACKNOWLEDGEMENTS

The project has received funding from the Grove School of Engineering at the City College of New York.


## REFERENCES


Hardwood, S., & Saboori, P. (2020). Zimmer Frame Design and Back Strain. ASME 2020 International Mechanical Engineering Congress and Exposition, 1–5.

Henry, Derrick. “Study Warns of Hazards for Elderly Using Walking Aids.” The New York Times, The New York Times, 29 June 2009, www.nytimes.com/2009/06/30/health/30fall.html#:~:text=%E2%80%9CIt%20gives%20them%20greater%20independence,and%2012%20percent%20involved%20canes.

Kevin Kinsella and Wan He" An Aging World: 2008 International Population Reports" U.S. Department of Health and Human Services and U.S. Department of Commerce, Issued June 2009.

Williams, B. (n.d.). Normal human range of motion. livestrong.com. Retrieved November 16, 2021, from https://www.livestrong.com/article/257162-normal-human-range-of-motion/.

Ming, Dong & Bai, Isabella & Liu, Xiuyun & Qi, Hongzhi & Cheng, Longlong & Wan, Baikun & Hu, Yong & Wong, Yatwa & Luk, Keith & Leong, John. (2009). A gait stability investigation into FES-assisted paraplegic walking based on the walker tipping index. Journal of neural engineering. 6. 066007. 10.1088/1741-2560/6/6/066007.

NASA. (n.d.). Anthropometry and Biomechanics. NASA. Retrieved November 7, 2021, from https://msis.jsc.nasa.gov/sections/section03.htm#Figure%203.3.1.3-1.

Shin, Eunji et al. “Analysis of walker-aided walking by the healthy elderly with a walker pocket of different weights attached at different locations.” Journal of physical therapy science vol. 27,11 (2015): 3369-71. doi:10.1589/jpts.27.3369

# GADOLINIUM-INFUSED SILICONE: A NEW MATERIAL FOR CYCLICALLY DEFORMING MRI PHANTOMS

**A. Baldassarre (1), C. Buckley (1), S. Ardila (1), F. Loth (1, 2), J. Oshinski (3), R. Amini (1,2)**

(1) Department of Mechanical and Industrial Engineering, Northeastern University, Boston, Massachusetts, USA
(2) Department of Bioengineering, Northeastern University, Boston, Massachusetts, USA
(3) Department of Radiology and Imaging Sciences, Emory University, Atlanta, Georgia, USA

## INTRODUCTION

Rigorous assessment and verification of biomechanical measurements obtained from existing magnetic resonance imaging (MRI) techniques are clinically important. In particular, the development of diagnostic tools for conditions characterized by subtle pulsatile motion and deformation, such as Chiari malformation, could benefit from such validated clinical approaches. Our group has recently developed a method to examine the accuracy of displacement encoding with stimulated echoes (DENSE) MRI technique for measurements of rigid body displacement that is within the range of brain motion in vivo [1]. However, unlike the brain, the phantom used in the abovementioned study does not undergo any deformation. To better understand the behavior of biological tissues experiencing small-scale deformations (<5% strain) a proprietary imaging phantom that can be deformed cyclically is necessary. The purpose of this study was to develop such a phantom that (a) can be easily detected in MRI scans, and (b) deforms in a controlled manner to produce physiologically relevant strains. In this study, for the first time, we examined gadolinium (a typical contrast agent for MR imaging)-infused silicone as a potential candidate for the MRI strain phantom. We hypothesized that gadolinium-infused silicone is detectable in MRI and the addition of gadolinium to silicone does not alter its mechanical properties.

## METHODS

Three different Smooth-On Sorta Clear$^{TM}$ molding silicones were acquired with Shore A 12, 18, and 37 hardness values. Consequently, three different concentrations of gadolinium were chosen – 100μg/mL silicone, 200μg/mL silicone, and 300μg/mL silicone – so that nine different gadolinium infused silicone samples were examined in total. The samples were made by dissolving the appropriate amount of gadolinium in one milliliter of water and then mixing the solution with a small sample of the corresponding silicone. These samples were then cured in a vacuum chamber to reduce bubble concentration. Each sample was "biopsied" wherein a piece was removed and pared down to a small piece for later mechanical testing. The samples were cured with a segment of toothpick in it to act as a fiducial marker. The number of toothpick segments corresponded to the sample number (one toothpick in sample 1, two toothpicks in sample 2, and so forth). These markers appeared as black dots along the edge of the sample (Figure 1).

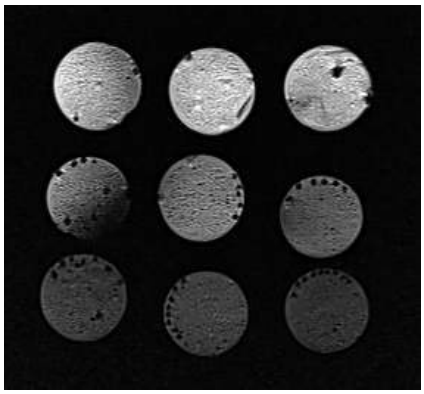

**Figure 1: Sample materials viewed with phase-sequence MRI. Each row has a different material hardness, each column has a different gadolinium concentration as described above.**

Biaxial mechanical testing was subsequently performed on the gadolinium-infused silicone. The setup involved applying load in X- and Y-dimensions to cause deformation. The samples for testing were manually shaped with a scalpel to approximately 11mm by 11mm by 1mm. From there, black markers were attached to the face of the sample in a square pattern and cables with hooks were embedded in the edges

of the sample. The sample was then pulled by means of a linear actuator attached to a series of pullies and hooks. A camera was used to track the markers and an internally developed software was used for calculation of stresses and strains, as described previously [2].

## RESULTS

The results of MRI scans are shown in Figure 1. The quality of the signal for these samples greatly exceeded expectation when compared to materials currently being used. It was determined that the relationship between the concentration of gadolinium in silicone samples and the subsequent MR visibility was non-linear. More surprisingly, it was observed that there was an optimal gadolinium density in a material sample after which increasing the gadolinium concentration led to a decline in MR visibility. Because sample 2 provided the greatest quality of signal, it was selected for the final prototype.

The results of biaxial mechanical testing of a representative sample are shown in Figure 2. The material behaved in a linear manner with little difference between the responses of the two axes, indicating an isotropic response. Based on the biaxial mechanical testing, and with the assumption of a linear elastic model, the elastic modulus of the gadolinium-infused silicone medium was determined to be 554kPa (Figure 2).

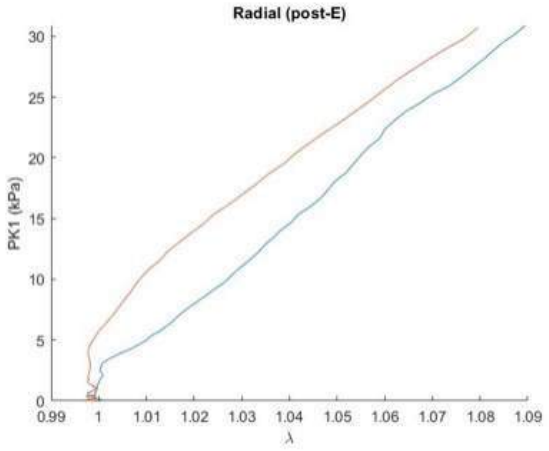


**Figure 2: Stress-stretch curve from biaxial testing showing a largely linear and isotropic relationship. The blue line and red line represent two different directions of the deformation.**

A finite element model of a phantom was subsequently developed in ANSYS Workbench with the assumption of linear elastic properties on the silicone encasement and embedded balloon with an internal pressure of 1960 Pa. There were fixed boundary conditions on all walls of the medium encasement as well as the two spherical ends of the balloon. The other boundary conditions were defined from the pressure and displacement relationship along the balloon boundary. The model confirmed that the phantom can produce small strain values comparable to those produced in the brain due to in-vivo pulsatile motions (Figure 3). The MRI displacement values from DENSE will ultimately be compared directly to the FEA results to verify the MRI outputs and to validate intracranial strains.

## DISCUSSION

Based on the results obtained, the most important takeaway was the ability to visualize silicone with MRI by way of infusing dissolved gadolinium into the material. Without gadolinium, silicone is an invisible medium in standard MRI practices, which may explain why it has yet to be used in phantom studies. The signal obtained from the samples tested, on the other hand, proved that gadolinium-infused silicone was a viable option for MRI phantoms. The clear relationships between silicone hardness and gadolinium volume for optimal signals are yet to be determined.

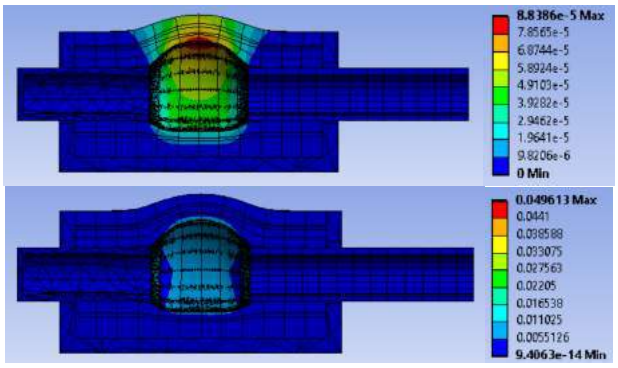


**Figure 3: Finite element simulations produced in ANSYS of pulsations occurring due to a balloon embedded within a volume of silicone. This simulation maps strain (top) and stress (bottom) of the balloon assuming rigid sides and bottom, and exposed top surface.**

The preliminary mechanical testing of the gadolinium-infused silicone proved that the dissolved gadolinium produced less than 0.1% change in the measured material properties of the silicone rubber, which falls well within the typical range for silicone rubber [3]. This finding is key to predicting behavior of potential future silicone samples, as it demonstrates the known mechanical properties of silicone are preserved. Such a finding is extremely valuable for the small-scale deformations that are associated with Chiari malformation and the ongoing research to properly diagnose diseases with DENSE MRI.

Our design was not without limitations. For one thing, the processing of the material needs to be improved to ensure repeatability and complete and even diffusion of gadolinium. In addition, the relationships between the volume of gadolinium and signal strength remains unclear.

In summary, we determined that that gadolinium-infused silicone provided excellent signal in MRI. Additionally, we observed that the infusion of gadolinium does not demonstrably influence the mechanical properties of silicone.

## ACKNOWLEDGEMENTS

The authors would like to thank the Northeastern University capstone program, in particular Bridget Smyser and Andrew Gouldstone for their championing of undergraduate research. Additionally, the help from Samuel Salinas is acknowledged.

## REFERENCES

[1] Nwotchouang, B et al., *Annals of Biomedical Engineering*, 49(6):1462-1476, 2021.

[2] Khoiy, Keyvan Amini, et al., *Journal of the mechanical behavior of biomedical materials* 78 (2018): 154-163.

[3] O'Hara, G, US Army Armament Research and Development Center, 1983.

[4] Khoiy, K., Amini, R., *Journal of biomechanical engineering* 138.10 2016

[5] Ghadimi, S et al., *Journal of Cardiovascular Magnetic Resonance: official journal of the Society for Cardiovascular Magnetic Resonance, 23*(1) 20, 2021.

SB³C2022
Summer Biomechanics, Bioengineering and Biotransport Conference
June 20-23, Eastern Shore, MD, USA

# LOW-INTENSITY VIBRATIONS INDUCE CHANGES IN MICROTUBULE DYNAMICS IN VITRO

**Chase A. Crandall (1), Nina Nikitina (2), Gunes Uzer (3)**

(1) Mechanical and Biomedical Engineering, Boise State University, Boise, Idaho, U.S.A
(2) Mechanical and Biomedical Engineering, Boise State University, Boise, Idaho, U.S.A
(3) Mechanical and Biomedical Engineering, Boise State University, Boise, Idaho, U.S.A

## INTRODUCTION

Microtubules are cytoskeletal filaments responsible for many vital cellular processes. They align to form the spindle during cell division, making them an important target for cancer therapeutics. They maintain intracellular organelle organization and enable the movement of intracellular components throughout the cell. These diverse functions are made possible by the ability of microtubules to rapidly grow and shrink—an activity termed "dynamic instability."[1] Dynamic instability also enables microtubules to respond to mechanical signals. Positive tensile forces in the form of positive strain result in increased microtubule mass, while compression forces in the form of negative strain result in decreased microtubule mass[2]. However, it's currently unknown how microtubules respond to vibration forces. Because low-intensity vibrations (LIV) are known to cause an increase in the actin cytoskeleton[3] and microtubules are known to respond to other mechanical signals, we hypothesize that the polymerization dynamics of microtubules will be affected by LIV. In this study, we apply LIV to mouse mesenchymal stem cells (MSCs) and use centrifugal separation and Western blot analysis to determine its effect on the amount of polymerized microtubules.

## METHODS

**Experimental Design** Mouse MSCs were plated, then starved in adipogenic media before applying LIV. Lysates were collected at 0 hours, 1 hour, and 3 hours after LIV. They were immediately centrifuged at low speed to pellet out large microtubules—this pellet is referred to as the "low-speed pellet" (LSP). The supernatant was centrifuged at ultra-high speed to pellet out small microtubules—this pellet is referred to as the "high-speed pellet" (HSP). The resulting supernatant contains the free tubulin protein—this sample is referred to as the "high-speed supernatant" (HSS). Western blot analysis was used to determine the relative abundance of tubulin in the LSP, HSP, and HSS.

For each treatment, the absorbance of each sample (e.g. LSP) was divided by the sum of the absorbances of all the tubulin samples in the treatment and multiplied by 100 to obtain the % sample (see Equation 1) to determine the fraction of cellular tubulin present in the form of large microtubules, small microtubules, and free tubulin. The LIV and control treatments were compared by calculating the difference between their respective percentages of each sample for each timepoint. An ANOVA test was used to determine if differences between control and LIV treatments were significant.

**Equation 1: Calculating % LSP**

$$\%\, LSP = \frac{LSP}{(LSP+HSP+HSS)} \times 100 \qquad (1)$$

The experiment was repeated multiple times with an increasing number of vibrations until 6 rounds of LIV became the standard. 6 rounds of LIV were used because it yielded samples with the greatest difference between control and LIV (compared with fewer rounds) and performing more rounds was logistically difficult.

**Mesenchymal Stem Cell Culture** MSCs were plated at 100K/well in 6-well plates and cultured using 10% FCS, 1% P/S Iscove's Modified Dulbecco's Medium (IMDM). After ~30 hours, the medium was changed to IMDM with 2% serum, 1% P/S, 5 ug/mL Insulin, 0.1 uM Dexamethasone, 50 uM Indomethacin. Cells remained in this media for ~12 hours before the start of vibration.

**Application of LIV** LIV was applied 6 times. For each round, plates were placed on a machine at room temperature that vibrated them at 90 Hz, 0.7 xg for 20 minutes (see Figure 1). Control plates were not vibrated, but they were also kept at room temperature during vibrations. Plates were incubated for 60 minutes at 37 ℃ between each dose. Samples were taken down at the following time points: immediately after LIV (0H), 1 hour after (1H), and 3 hours after (3H).

**Figure 1: Apparatus with subwoofers underlying 4 platforms fitted for 6-well plates used for LIV application.**

**Collection of Cell Lysates** The "Microtubules/Tubulin In Vivo Assay Kit" from Cytoskeleton.com (Cat. # BK038) was utilized to take down cell lysates, separate large microtubules from small microtubules from free tubulin, and quantify their abundance with Western blot. Protocol was done as per the manufacturer's instructions. Briefly, lysates were taken down into a microtubule stabilizing buffer. The lysates were homogenized and centrifuged at 1000 xg for 5 minutes at 37 ℃ to obtain the LSP. 100 uL of the supernatant from each sample was centrifuged at 100,000 xg for 60 minutes at 37 ℃ to obtain the HSP and HSS (see Figure 2). To ensure band visibility on the Western blot, lysates from at least two wells were combined for each treatment before the first centrifugation. Samples were run on Western blots.

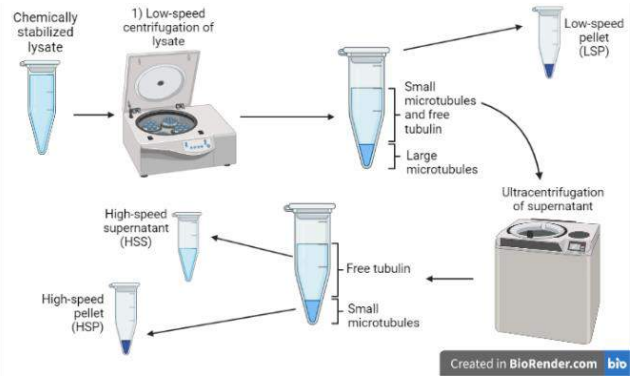


**Figure 2: Centrifugal separation of the LSP, HSP, and HSS.**

## RESULTS

The experiment was repeated 3 times using 6 rounds of LIV. Western blots revealed a trend: 3 hours after LIV. LIV treatments diminished the LSP was by 9.8 percentage points (p=0.16) and the HSS was increased by 12.4 percentage points (p=0.26), signifying a lower amount of large microtubules and larger amount of free tubulin (see Figure 3). One-way ANOVA tests were used to determine p values.

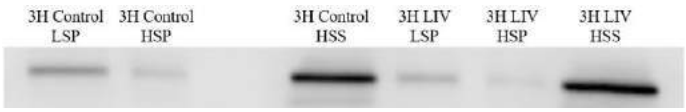


**Figure 3: Western blot showing LSP, HSP, and HSS for 3H control and LIV treatments. The LSP is diminished and the HSS is increased in the LIV treatment.**

## DISCUSSION

LIV results in a trend of depolymerization of large microtubules and thus increasing the number of smaller microtubules. The trend is not statistically significant, so we are performing more experiments to increase the sample size. Based on our inter-group variations, power calculations indicate that a sample size of 5/group will be sufficient to

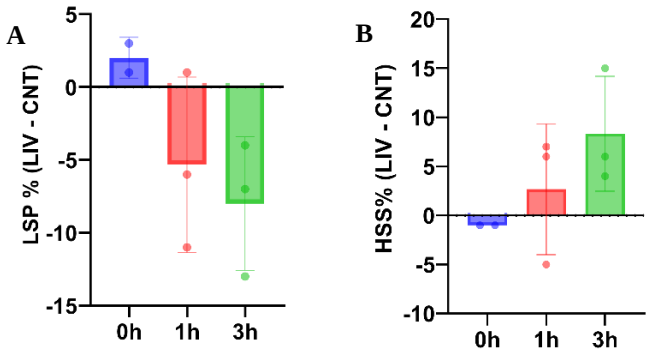


**Figure 4: A) Difference between % LSP between the LIV and control samples. At 3 hours, LSP is diminished in the LIV treatment by 9.8 percentage points (p=0.16). B) Difference between % HSS between the LIV and control samples. At 3 hours, HSS is increased in the LIV treatment by 12.4 percentage points (p=0.26).**

detect significant differences at the 3-hour timepoint. Past studies examining microtubule response to large mechanical signals (±10% strain) showed that tensile strain increases microtubule growth while compression decreases it.[2] Additionally, microtubule response is known to dominate over actin response in higher magnitude strain[4]. Thus, since vibration exerts a dynamic and oscillating force with relatively small magnitude, if we find that LIV does not affect microtubule dynamics, it may indicate that that the tension-compression environment may not be a suitable regulator of microtubule growth or LIV-induced forces may not be sufficient in magnitude to drive microtubule dynamics.

If the trend towards lower polymerization levels in the LIV treatment proves to be significant with a larger sample size, this finding would be more in agreement with the literature. We have reported that LIV increase F-actin contractility[3]. In this case, the cell might be responding to mechanical signals by shifting towards less polymerized microtubules in response to changes in F-actin forces.

Regardless, the assay used in this study is a global indicator of microtubule polymerization. To further characterize the results, we will use immunohistochemistry and confocal imaging to determine spatial changes in the microtubule cytoskeleton. whether there are microtubule changes localized to a particular region of the cell.

Ultimately this study will help understand whether microtubule dynamics can be regulated by low intensity high frequency vibrations.

## ACKNOWLEDGEMENTS

This study was supported in-part by NIH AG059923, NSF 1929188 and NSF 2025505. We acknowledge support from COBRE, INBRE, the Institutional Development Awards (IDeA) from the NIGMS Grants #P20GM103408, P20GM109095, and *1C06RR020533*. We also acknowledge support from The Biomolecular Research Center with funding from the NSF Grants #0619793 and #0923535; the M. J. Murdock Charitable Trust; Lori and Duane Stueckle, and the Idaho State Board of Education.

## REFERENCES

[1] Desai, A., et al., *Annual Review of Cell and Developmental Biology*, 13:83-117, 1997.
[2] Putnam, A.J., et al., *American Journal of Physiology-Cell Physiology-Cell Physiology*, 280:C556-564, 2001.
[3] Uzer, G., et al., *Stem Cells*, 33:2063-2076, 2015.
[4] Kubitschke, H., et al., *New Journal of Physics*, 19:093003, 2017.

SB³C2022
Summer Biomechanics, Bioengineering and Biotransport Conference
June 20-23, Eastern Shore, MD, USA

# LABORATORY AND ON-FIELD EVALUATION OF A PADDED FOOTBALL HELMET SHELL COVER

**AA Callan (1), NJ Cecchi (1), Y Liu (1), LP Watson (1), Xianghao Zhan (1), GA Grant (2), MM Zeineh (3), DB Camarillo (1,2,4)**

(1) Department of Bioengineering, Stanford University, Stanford, CA, USA
(2) Department of Neurosurgery, Stanford University, Stanford, CA, USA
(3) Department of Radiology, Stanford University, Stanford, CA, USA
(4) Department of Mechanical Engineering, Stanford University, Stanford, CA, USA

## INTRODUCTION

Concussion and repeated head impacts are frequent in contact sports, particularly in American football [1]. This head trauma can lead to both acute and long-term deterioration of brain health and function [2]. To address safety concerns related to brain injury, protective helmets were introduced in American football over a century ago and have since evolved significantly in their appearance, materials, and efficacy in attenuating impact energy.

One recent advance in helmet technology includes the addition of a layer of padding material fashioned to fit over the exterior of a helmet shell [3,4,5]. A variety of these padded helmet shell covers have been designed and tested, with some becoming commercially available to athletes and rapidly gaining popularity. While previous evaluations of these technologies have been conducted, they have been limited to either laboratory test methods that cannot assess both linear and angular head kinematics [3] or evaluations of prototypes [4] or products that are not readily available to the general public [5]. Further, no peer-reviewed data exists that describes the on-field efficacy of these products.

The objective of this study was to evaluate the efficacy of a commercially available padded helmet shell cover in attenuating linear and angular head kinematics both in the lab and on the field.

## METHODS

Laboratory Testing: A linear impactor (Biokinetics and Associates Ltd.; Ottawa, Ontario, Canada) was used to impact a 50$^{th}$ percentile male Hybrid III headform mounted on a sliding table. The headform was equipped with three helmets individually: the Riddell Speedflex Diamond, Xenith X2E+, and Schutt Vengeance Pro LTD. These helmets represented a range of high-, middle-, and low-performing helmets according to the National Football League (NFL) helmet rankings. Each helmet was impacted at four helmet shell locations described in the NFL Helmet Test Protocol (Side, Oblique Rear, Side Upper, Oblique Front) and three velocities (3.5, 5.5, 7.4 m/s). Each helmet-location-velocity combination was repeated three times. Then, both the face of the linear impactor and a new helmet of the same model was equipped with a commercially available padded helmet shell cover (Guardian Cap, Guardian Sports; Peachtree Corners, GA) and subjected to the identical test procedure (Fig. 1).

To explore if the efficacy of the padded helmet shell cover deteriorated after repeated impact exposure, we ran a second set of laboratory tests in which we impacted a Riddell Speedflex Diamond helmet 100 times, with both the helmet and impactor equipped with a padded helmet shell cover. All impacts were performed at the oblique front location at 3.5 m/s, the average closing velocity for a professional football head impact. Approximately 80 seconds separated each impact while the test equipment was reset.

The headform was equipped with a six-degree-of-freedom sensor package including three DTS A64C accelerometers and three DTS ARS PRO-8k gyroscopes (Diversified Technical Systems; Seal Beach, CA). For each impact, linear acceleration and angular velocity in the X, Y, and Z directions was captured and used to calculate the Head Acceleration Response Metric (HARM) [5].

On-field Testing: Using the Stanford Instrumented Mouthguard (MiG2.0) [1], we captured athlete head kinematics during official practices of the Stanford University football team. Seven linebackers were equipped with MiG2.0 mouthguards that recorded a 200 ms time window of angular velocity and linear acceleration in the X, Y, and Z directions when linear acceleration in any of the X, Y, or Z directions exceeded a threshold of 10 g. Peak linear and angular accelerations were saved from this data for each impact. Data was collected in the 2019 season, when all instrumented athletes wore bare helmets, and the 2021 season, when instrumented athletes wore helmets fitted with Guardian Caps. Video footage of all team practices was captured and two of the authors reviewed and verified each impact.

We focused specifically on linebackers in practices only and only examined helmet-to-helmet impacts. Helmet-to-helmet impacts were

SB³C2022-528

classified as any impact where the helmet of one player contacted the helmet of another player. All impacts which did not feature a bare helmet striking another bare helmet, or a helmet with a Guardian Cap striking another helmet with a Guardian Cap, were discarded.

Data Analysis: Three separate two-way ANOVAs were used to test for differences in HARM between bare helmet impacts and padded helmet shell cover impacts for the three helmets in the lab experiments. Mann-Whitney tests were used to test for differences in peak linear acceleration and peak angular acceleration between bare and padded helmet impacts in the on-field dataset.

## RESULTS

In the lab, the use of a padded helmet shell cover was found to reduce HARM compared to the bare helmet impacts at all impact locations in all helmets at 3.5 m/s (Fig. 2). The same was true at 5.5 m/s, with the exception of the Schutt Vengeance Pro LTD at the Side Upper location. HARM was not decreased in any helmet equipped with the padded helmet shell cover at the Side Upper 7.4 m/s velocity impact condition. HARM reduction decreased with increasing impact velocity, a trend that was common among all three helmet models tested. The association between the number of repeated impacts and magnitudes of peak linear acceleration and peak angular acceleration met statistical significance (p=0.04), but the increase in magnitude with increasing impact count was very small (Fig. 3).

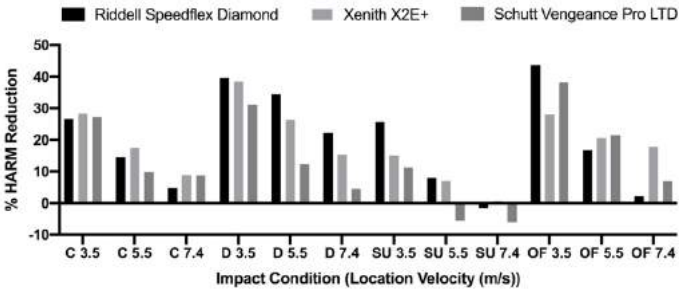


**Fig. 2 Laboratory efficacy of the padded helmet shell cover stratified by impact condition. Results shown in percentage of HARM reduced when comparing to bare helmet control (averaged across three repeat trials for each condition).**

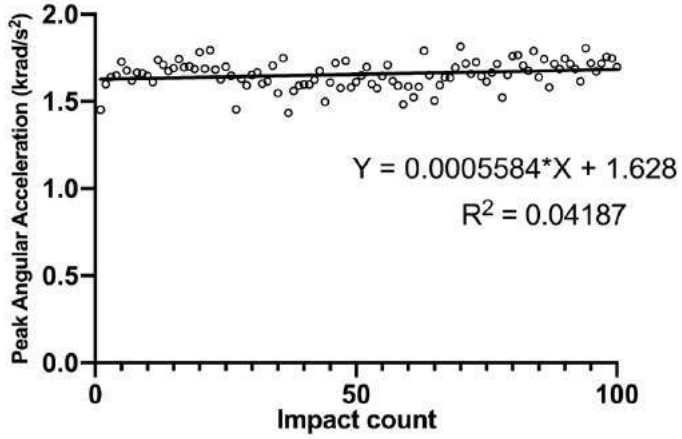


**Figure 3: Peak angular acceleration for repeated, consecutive impacts delivered to a Riddell Speedflex Diamond helmet equipped with a padded helmet shell cover. Impacts were performed at the Oblique Front location at 3.5 m/s.**

On the field, there was no significant difference between the peak head kinematics of the bare helmet impacts and padded helmet shell cover impacts (Fig. 4).

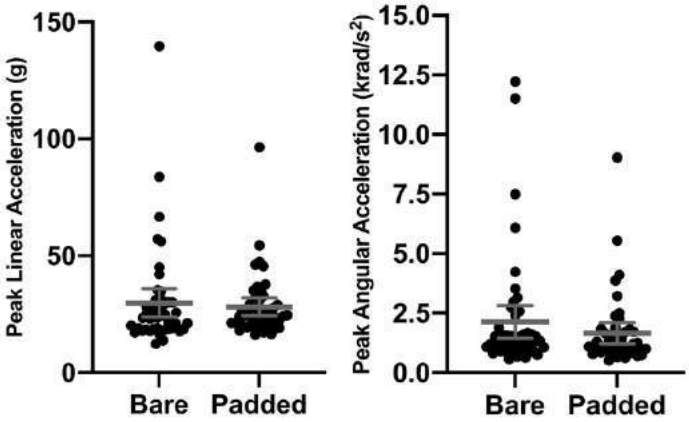


**Figure 4: Comparison of peak head accelerations of on-field helmet-to-helmet impacts with bare helmets and helmets equipped with a padded helmet shell cover. Solid gray lines and error bars represent mean values and 95% confidence intervals, respectively.**

## DISCUSSION

The present study is the first to assess the ability of the standard, commercially available Guardian Cap for reduction of brain injury metrics based on both linear and angular head kinematics and the first study to evaluate the attenuation capabilities of a padded helmet shell cover both in the lab and on the field. Several previous studies have utilized laboratory testing experiments to evaluate the efficacy of padded helmet shell coverings, with some finding effectiveness of these technologies in linear impactor tests [4,5], and others finding limited efficacy in standardized drop tests. We found the padded helmet shell cover to effectively attenuate values of HARM, a brain injury metric derived from both linear and angular head kinematics, at most impact conditions in the lab. We also observed minimal changes in peak head kinematics after repeated impact testing, suggesting the padded helmet shell cover can endure extended use without reduced performance.

Despite the ability of the Guardian Cap to reduce head kinematics in the lab, on-field reductions in peak head accelerations did not reach statistical significance. Two possible explanations for this include the small sample of on-field impacts and the inclusion of facemask impacts in our on-field dataset. As these technologies only cover the shell of a helmet, it is likely that facemask-to-facemask impacts would not be attenuated by their use. However, other studies have similarly found no difference in on-field head kinematics between helmets that significantly differed in performance in the lab [1], suggesting that more helmet testing methodology can still be improved to accurately replicate on-field football head impacts.


## ACKNOWLEDGEMENTS

This study was supported by the Taube Stanford Children's Concussion Initiative and the Pac-12 Conference's Student-Athlete Health and Well-Being Initiative.


## REFERENCES


[1] Cecchi et al., *Ann Biomed Eng,* 49(10):2814-2826, 2021.
[2] Montenigro et al., *J Neurotrauma,* 34(2), 328-340, 2017.
[3] Breedlove, K et al., *J Athl Train,* 52(9):802-808, 2017.
[4] Zuckerman et al., *J. Neurosurgery*, 130(5):1634–1641, 2018.
[5] Bailey, A et al., *Ann Biomed Eng,* 49(10):2747-2759, 2021.

SB³C2022
Summer Biomechanics, Bioengineering and Biotransport Conference
June 20-23, Eastern Shore, MD, USA

# ASSESSMENT OF PRESSURE GRADIENT AND RECOVERY FOLLOWING TRANSCATHETER AORTIC VALVE REPLACEMENT IN BICUSPID AORTIC VALVES

**Aniket Venkatesh (1), Breandan Yeats (1), Atefeh Razavi (1), Pradeep Yadav (2), Venkateshwar Polsani (2), Vinod Thourani (2), and Lakshmi Dasi (1)**

(1) Biomedical Engineering, Georgia Institute of Technology, Atlanta, GA, United States
(2) Cardiology, Piedmont Hospital, Atlanta, GA, United States

## INTRODUCTION

Calcific aortic stenosis (AS) is the thickening, due to calcium buildup, of the aortic valve leaflets in the heart, which control blood flow from the left ventricle into the aorta to be distributed to the rest of the body [1]. Most common risk factors that lead to AS include old age, congenital defects such as bicuspid aortic valve (BAV), and several others. Currently, the most common treatment option is transcatheter aortic valve replacement (TAVR), with more than 100,000 procedures performed annually in the US compared to 50,000 open-heart surgeries [2]. TAVR is a minimally invasive interventional procedure where bioprosthetic leaflets are attached to a stent, which is delivered through a catheter delivery system to the site of AS and deployed to expand the diseased valve, allowing the prosthetic valve to "replace" it [3].

The primary method of assessing TAVR's efficacy in treating AS is to examine the transvalvular pressure gradient (PG) post-TAVR. Current techniques to measure PG include the noninvasive Doppler echocardiography and invasive percutaneous cardiac catheterization [4]. However, studies have shown that both techniques report discordant PG measurements due to the phenomenon of pressure recovery (PR), or reconversion of kinetic energy from blood flow velocity past the vena contracta (VC) into potential energy (pressure) [5]. Neither PG nor PR have been thoroughly studied in BAV patients. Additionally, prosthetic valvular orientation during initial deployment, including implantation depth and rotational configuration, have shown to affect eventual clinical outcomes [6], but its effect on pressure recovery has not been thoroughly explored. Therefore, the main objective of this study is to quantitatively assess PG and PR following TAVR on BAV patient-specific aortic geometry, with the capability of assessing different deployment orientations. It also aims to assess the feasibility of computational methods such as Finite Element Analysis (FEA) and Computational Fluid Dynamics (CFD) in determining PG and PR post-TAVR.

## METHODS

**Valve Selection and Deployment:** A 79-year-old male with severe AS and BAV received a 29 mm Edwards Lifesciences SAPIEN 3 balloon-expandable TAV to replace the stenosed native valve. Computed Tomography (CT) images prior to and following the TAV deployment were obtained under IRB approved protocols. The patient's three-dimensional aortic root geometry was segmented and meshed using pre-TAVR CT images in Materialise Mimics (Leuven, Belgium) (**Figure 1A**).

**Finite Element Analysis:** Using the post-TAVR CT images, the stent was oriented appropriately, and its expansion was simulated using FEA in Abaqus CAE (Johnston, RI, USA). A meshed 29 mm SAPIEN 3 prosthetic leaflets model was displaced to fit the deformed post-FEA stent model in Abaqus CAE (**Figure 1B**) by tracking the displacement of contacting nodes on the meshed stent. The prosthetic leaflets were configured to simulate the motion of an aortic valve throughout a cardiac cycle by applying a time-varying pressure load to the internal surface of each leaflet. The values for the pressure load were obtained by extracting data points from an aortic and ventricular pressure vs time curve [7] using WebPlotDigitizer (Notre Dame, IN, USA), then calculating the pressure difference across the valve. To simulate peak systolic flow, the fully open prosthetic leaflets were exported along with the post-FEA stent, aortic root, and calcium nodules to Materialise Mimics to create a meshed internal fluid domain (**Figure 1C**). 300 mm extensions were added on the inlet and outlet faces to ensure fully developed flow through the aortic root.

SB³C2022-529

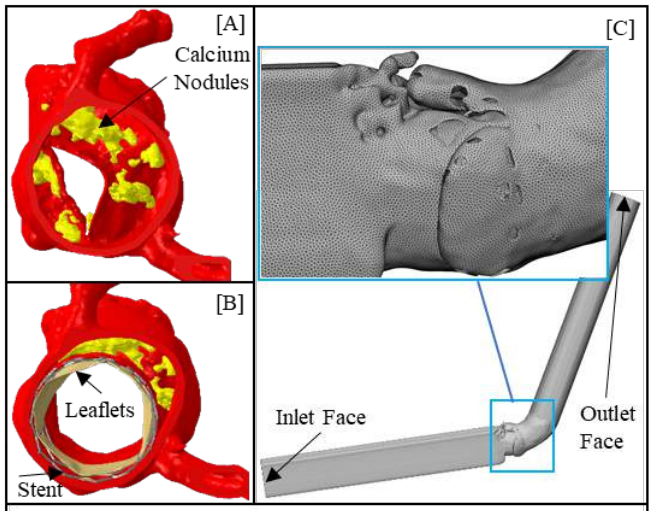


**Figure 1:** Pre-FEA segmented aortic valve with calcium nodules highlighted (A), post-FEA stent and prosthetic leaflets deployment during peak systole (B), and meshed internal fluid domain with extensions created from post-FEA geometry for CFD simulations (with inlet and outlet faces used for boundary conditions highlighted) (C).

**Computational Fluid Dynamics:** The fluid domain geometry was imported to ANSYS Fluent (Canonsburg, PA, USA) to simulate blood flow using CFD. The continuity equation and Reynolds averaged Navier–Stokes equations with a shear stress transport transitional (SST-Trans) model were used to describe 3D incompressible flow [8]. A 120-mmHg peak systolic aortic pressure was applied at the inlet face and a target peak systolic volumetric flow rate of 25 L/min was applied at the outlet for computational calculation of outlet pressures. The CFD simulation was executed under steady conditions and the pressure and velocity contours, and velocity streamlines were plotted. Planes were created on the aortic orifice and the aortic root end, and the average pressures at the inlet face, aortic root orifice, and the aortic root end were determined for calculation of mean PG and PR.

## RESULTS

Velocity streamlines and velocity and pressure contours of peak systolic blood flow through the post-TAVR aortic geometry are shown (**Figure 2**).

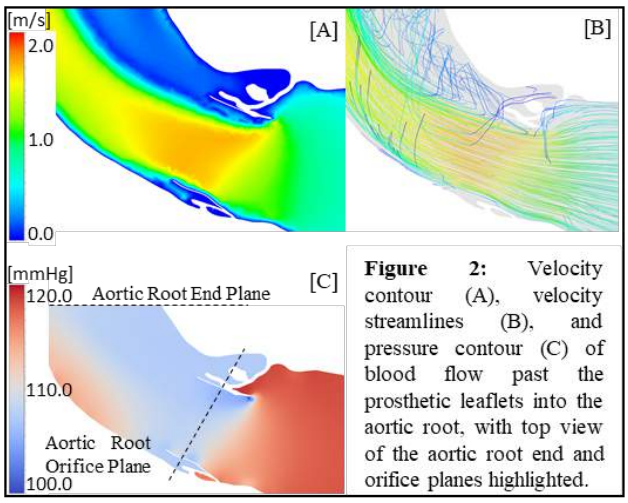


**Figure 2:** Velocity contour (A), velocity streamlines (B), and pressure contour (C) of blood flow past the prosthetic leaflets into the aortic root, with top view of the aortic root end and orifice planes highlighted.

The average pressure on the inlet face, aortic root orifice plane, and aortic root end plane were found to be 118.4 mmHg, 107.7 mmHg, and 110.0 mmHg, respectively. From the measurements above, the mean PG through the prosthetic leaflets was calculated to be 10.7 mmHg and the recovered pressure was calculated to be 2.3 mmHg, hence giving a net PG throughout the aorta of 8.4 mmHg and a PR of 21.5%. The average velocity of blood flow across the inlet face, aortic root orifice plane, and aortic root end plane were found to be 0.63 m/s, 0.74 m/s, and0.70 m/s, respectively. Low velocity recirculation zone is observed in the stenosed sinus with large calcium deposits.

## DISCUSSION

The goal of this study was to visualize changes in blood flow pressure and velocity through a BAV patient specific post-TAVR anatomy, and quantitatively assess mean PG and PR. The calculated mean PG through the aortic orifice falls within the 5-25 mmHg aortic valve mean gradient range [9], indicating the effectiveness of TAVR in reducing AS-induced high gradients. However, this calculation does not consider the recovered 2.3 mmHg of pressure downstream of the aortic orifice, which gives a mean PG closer to the normal aortic valve mean gradient range of under 5 mmHg [9]. This study therefore demonstrated the discrepancy between the mean PG readings that would be obtained if this patient underwent Doppler echocardiography and percutaneous cardiac catheterization. Since Doppler estimates the maximum pressure drop through the aortic valve using the maximum flow velocity recorded [5], it will overestimate the net gradient across the entire aorta measured through catheterization.

This study indicated the capability of patient specific CFD analysis in determining hemodynamic characteristics post-TAVR. The findings, once validated and tested in a larger cohort, can be used to assess the device hemodynamic performance. For the future study, we plan to include the impact of the stent orientation, deployment height and the degree of alignment of the prosthetic leaflets with respect to native commissure on PG, PR, as well as the sinus washout.

## REFERENCES:

[1] Lindman, B et al., *Nat Rev Dis Primers*, 2, 16006, 2016.
[2] Makkar, R et al., *N Engl J Med*, 382:799-809, 2020.
[3] Dasi, L et al., *Ann Biomed Eng*, 45(2), 310–331, 2017.
[4] Yogesh, N et al., *J. Am. Heart Assoc.*, 10(19), 2021.
[5] Pibarot, P et al., *Circulation*, 127(10), 1101–1104, 2013.
[6] Hatoum, H et al., *Ann Thorac.*, 106(1), 70–78, 2018.
[7] Gharaie, S et al., *Int J Artif Organs*, 38(5), 259–270, 2015.
[8] Singh-Gryzbon, S et al., *Ann Biomed Eng*, 48(10), 2400–2411, 2020.
[9] Zhang, Y et al., *Eur. Heart J*, 6(12), 999–1005, 1985.

SB³C2022
Summer Biomechanics, Bioengineering and Biotransport Conference
June 20-23, Eastern Shore, MD, USA

# EXERCISE THERAPY DOES NOT ALTER KINEMATIC REPEATABILITY IN INDIVIDUALS WITH ROTATOR CUFF TEARS WHEN REACHING BEHIND THE BACK

**Rachel P. McLoughlin (1), Luke T. Mattar (1), Adam J. Popchak (3), William J. Anderst (2), Volker Musahl (1,2), James J. Irrgang (2,3), Richard E. Debski (1,2)**

(1) Department of Bioengineering, University of Pittsburgh, Pittsburgh, PA, USA
(2) Department of Orthopaedic Surgery, University of Pittsburgh, Pittsburgh, PA, USA
(3) Department of Physical Therapy, University of Pittsburgh, Pittsburgh, PA, USA

## INTRODUCTION

Rotator cuff tears affect over 20% of the general population, where prevalence increases with age[1]. Exercise therapy is typically prescribed as the initial treatment for individuals with rotator cuff tears who present with pain and inability to complete activities of daily living. Numerous studies have found a correlation between abnormal glenohumeral kinematics and shoulder pain[2,3]. It has also been shown that individuals with shoulder pain employ movement adaptations related to kinematics, which suggests that individuals experiencing shoulder pain may not complete provocative motions in a consistent manner[4].

One particularly painful movement commonly utilized during personal hygiene tasks such as bathing and dressing is reaching behind the back. Prior research attributes the problematic nature of this movement to a large required range of motion, sizeable shoulder moments, and maximum supraspinatus stretching[5,6]. Further, reaching behind the back is a complex movement involving motion at the scapulothoracic, glenohumeral, and elbow joints. Consequently, individuals with rotator cuff tears may vary techniques used to reach behind the back in an effort to mitigate pain.

Exercise therapy has been shown to improve patient reported outcome scores and glenohumeral kinematics[7]. Patient reported outcome score forms often include questions designed to quantify pain, indicating that exercise therapy improves pain levels for individuals with rotator cuff tears. Therefore, following exercise therapy, individuals may complete the behind the back movement in a more consistent manner with respect to glenohumeral kinematics. Thus, the objective of this study was to assess changes in kinematic repeatability during a reaching behind the back movement following a 12-week structured and individualized exercise therapy program.

## METHODS

Seventy-two individuals (59.9 ± 9.2 years of age, 28.1 ± 5.0 BMI) with a symptomatic rotator cuff tear isolated to the supraspinatus tendon were recruited after providing IRB-approved written informed consent prior to performance of any research procedure. All individuals participated in a 12-week structured and individualized exercise therapy program focused on restoring range of motion and strengthening the rotator cuff and scapular muscles. The individuals were asked to perform a behind the back task three times to assess glenohumeral joint function. To complete this task, each individual began seated with their affected-side hand placed on their thigh and reached as far as they could behind their back. No specific instructions were given, so each individual completed the task in their own manner.

Glenohumeral kinematics were measured using a previously described and validated model-based tracking technique with images acquired from a synchronized biplane radiography system at fifty images/second[8]. Individuals underwent a computed tomography scan of the involved shoulder, and images were segmented to create individual specific bone models of the humerus and scapula. Digitally reconstructed radiographs of the bone models were created from the known geometry of the biplane radiography system. The bone models were then manipulated to match the digitally reconstructed radiographs to the corresponding bones in the biplane radiographic images in all six degrees of freedom for each pair of synchronized images throughout the movement. The local coordinate system for each humerus was constructed based on the International Society of Biomechanics recommendations with the origin located at the center of the humeral head. The scapula coordinate system was modified to create a glenoid based system to describe humeral motion with respect to the center of the glenoid. An X-Z-Y Euler angle rotation sequence was used to quantify translation and rotations with accuracy of ± 0.4 mm and ± 0.5° for dynamic motion[8]. In this sequence, X rotations represented glenohumeral elevation, Y rotations represented glenohumeral flexion-extension, and Z rotations represented glenohumeral internal-external rotation.

Kinematic outcome parameters included glenohumeral elevation, glenohumeral flexion-extension, and glenohumeral internal-external rotation. To begin calculating kinematic repeatability, each rotational degree of freedom was plotted for all three movement trials on a given test day (Figures 1,2,3). As a means of standardization, the same number of points were used for analysis of each curve. Because prior biomechanical movement studies have validated the root mean square error as a measure of repeatability, the root mean square error was then calculated between curves for trials one and two, trials two and three, and trials one and three[9]. The average of these values was taken as the final root mean square error for the given test day. This process was performed both pre-therapy and post-therapy. Because all data was non-normally distributed, Wilcoxon Signed Rank tests were used to compare root mean square errors for the three pre-therapy degrees of freedom to those for the three post-therapy degrees of freedom. Significance was set at $p < 0.05$.

## RESULTS

All individuals completed the 12-week structured and individualized exercise therapy program. No statistically significant differences were found between pre- and post- exercise therapy average root mean square error values ($p > 0.05$, Table 1). Glenohumeral elevation root mean square error values ranged from 1.4° to 13.2° pre-therapy and from 1.4° to 7.8° post-therapy (Table 1). Glenohumeral flexion-extension root mean square error values ranged from 1.1° to 17.8° pre-therapy and from 1.1° to 13.6° post-therapy (Table 1). Glenohumeral internal-external rotation root mean square error values ranged from 1.8° to 32.7° pre-therapy and from 1.4° to 22.8° post-therapy (Table 1).

**Table 1: Kinematic repeatability measured as root mean square error before and after a 12-week exercise therapy program.**

| | | Elevation (°) | Flexion-Extension (°) | Internal-External Rotation (°) |
|---|---|---|---|---|
| Before | Minimum | 1.4 | 1.1 | 1.8 |
| | Mean ± SD | 4.5 ± 2.5 | 5.2 ± 3.5 | 7.9 ± 5.9 |
| | Maximum | 13.2 | 17.8 | 32.7 |
| After | Minimum | 1.4 | 1.1 | 1.4 |
| | Mean ± SD | 3.8 ± 1.5 | 4.7 ± 2.5 | 7.5 ± 4.7 |
| | Maximum | 7.8 | 13.6 | 22.8 |
| p | | 0.08 | 0.90 | 0.75 |

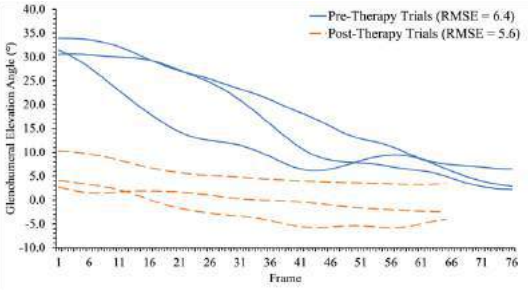


**Figure 1. Representative glenohumeral elevation angle curves before and after a 12-week exercise therapy program.**

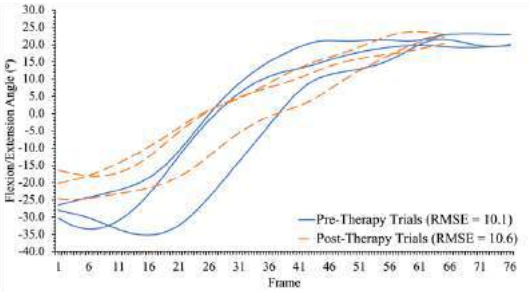


**Figure 2. Representative glenohumeral flexion/extension angle curves before and after a 12-week exercise therapy program.**

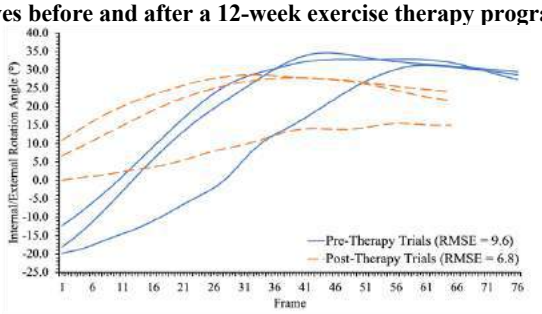


**Figure 3. Representative glenohumeral internal/external rotation angle curves before and after a 12-week exercise therapy program.**

## DISCUSSION

The primary finding of the study was that a 12-week structured and individualized exercise therapy program did not lead to changes in kinematic repeatability related to glenohumeral elevation, glenohumeral flexion-extension, or glenohumeral internal-external rotation when reaching behind the back. This suggests that glenohumeral joint motion repeatability was not affected by exercise therapy.

One potential explanation for this finding is that all individuals included in the study had isolated supraspinatus tears, which may allow for some conservation of normal joint function. This result is further supported by the fact that education has been shown to improve development of standardized clinical examination techniques[10]. Individuals in our study were not educated on the behind the back movement, which may explain why uniform motion techniques were not observed following exercise therapy.

During our protocol, overall changes in glenohumeral kinematics that may hint at adaptive motion strategies were not studied—only repeatability related to these parameters was analyzed. Future studies will aim to determine the effects of exercise therapy on glenohumeral kinematics and the relationship between patient reported outcomes and kinematic repeatability during the behind the back movement.


## ACKNOWLEDGEMENTS

The NIH grant 5R01AR069503 is gratefully acknowledged.


## REFERENCES


[1] Yamamoto, A et al., *JSES*, 19:116-120, 2010.
[2] Ludewig, PM et al., *PT & Rehab J*, 80:276-291, 2000.
[3] Yamaguchi, K et al., *JSES*, 9:6-11, 2000.
[4] Dupuis, F et al., *Physiol Rep*, 9, 2021.
[5] Hall, LC et al., *Clin Biomech,* 26:579-584, 2011.
[6] Nishishita, S et al., *JSES*, 27:2242-2248, 2018.
[7] Miller, RM et al., *JSES*, 25:641-649, 2016.
[8] Bey, MJ et al., *J Biomech Eng*, 128:604-609, 2006.
[9] Cossin, M et al., *J Sport Eng & Tech*, 232:225-235, 2018.
[10] Naendrup, JH et al., *Knee Sur Sport Tra Arth*, 27:3418–3425, 2019.

# EMG ANALYSIS OF VASTUS LATERALIS AND VASTUS MEDIALIS WITH DIFFERENT BICYCLE CRANK LENGTHS, PEDALING RATE, AND PEDAL SPEED

**Jackson C. Crovella (1), Karoline M. Wucherer (2), Christiane R. O'Hara (1)**

(1) Department of Kinesiology and Public Health California Polytechnic State University San Luis Obispo, CA, USA
(2) Department of Mechanical Engineering California Polytechnic State University San Luis Obispo, CA, USA

## INTRODUCTION

As cycling gains popularity as a sport, exercise modality, and rehabilitative tool, there is growing interest in optimizing the bicycle to meet health and performance demands. One method of optimization is the adjustment of bicycle crank length (CL). Commercial CLs are between 170-175 mm in length. However, CLs are often adjusted according to cyclist preference. These adjustments may have health and performance implications. Little research has looked at the effects of CL on lower leg muscle activation [1, 2]. Of this research, there has been no analysis on the activation of both the vastus lateralis (VL) and vastus medialis (VM) muscles. The relationship between the relative activation of these muscles is important in preventing patellofemoral joint pain (PFP). In cycling, it is common for long term overcompensation of the VL to pull the patella laterally. Lateral malalignment of the patella is a major cause of PFP [3]. It is possible that CL alters the relative activation of VL and VM, potentially increasing the risk of lateral malalignment of the patella and further PFP.

The purpose of this study is to examine the effects of two different CLs (155 and 185 mm) at a constant pedal rate (70 rpm) and constant pedal speed (1.47 m/s) and the resulting muscular activation of the vastus lateralis (VL) and vastus medialis (VM). Hypotheses were (H1) VL and VM muscle activation would not change with CL, and (H2) muscle activation would increase with an increase in pedal speed.

## METHODS

Twenty-six non-cyclists (12M, 14F, aged 18-55) participated in a single blind randomized cross-over experiment with four CL (155, 165, 175, and 185 mm). CLs 155 mm and 185 mm were analyzed for comparison. Fifteen participants were excluded from statistical analysis due to EMG signal error and sensor inaccuracy. Participant characteristics are shown in Table 1.

**Table 1. Participant Characteristics, Mean ± SD shown.**

| Participants | N = 11 |
|---|---|
| Age (years) | 28.0 ± 11.9 |
| Height (cm) | 170.7 ± 8.5 |
| Weight (kg) | 64.6 ± 11.8 |
| BMI (kg/m$^2$) | 22.0 ± 2.6 |
| Weekly Training (hrs/week) | 6.4 ± 3.4 |

A 12-camera 3D motion analysis system with Cortex software (Motion Analysis Corp., CA, USA) was used to capture crank angle. A stationary bike (SRM IndoorTrainer, Germany) with adjustable cranks was used for trials. Delsys Trigno EMG sensors were placed on target muscles of the right leg to collect electromyographic data. Electrodes for VL were placed 2/3 from the ASIS to the lateral side of the patella. Electrodes for VM were placed 4/5 between the ASIS and the joint space in front of the medial ligament. Participants performed a 3-minute warm-up for each CL at 1.5 W/kg and 70 rpm. 4x1 minute experimental trials were conducted at 2 W/kg. The first two trials were conducted at a constant cadence of 70 rpm. The second two trials were conducted at a constant pedal speed of 1.47 m/s (rpm = 90, 85, 80, 76 rpm with respect to CL). Adjusted rpm values were determined by Equation (1). There were 10 seconds of rest between trials and 5 minutes of recovery between each condition. Saddle and handle height was adjusted for each condition to maintain the same height for corresponding crank length.

**Equations:** $$\text{rpm} = (1.47 \text{ m/s} \times 60)\,(2\pi \times \text{CL})^{-1} \quad (1)$$

EMG data for each one minute trial was trimmed to 30 seconds, then averaged into one 360 degree crank cycle in MATLAB. Averaged EMG signals were rectified and filtered with a 4th order Butterworth low-pass filter, with a 20 Hz cut off frequency. A threshold value of 20% of the maximum voltage was applied to determine periods of muscular activation for each trial. Using the threshold value, total activation time (TON) and total deactivation time (TOFF) were

recorded to measure the duration of muscle activation in a 360 degree crank cycle. Average voltage (AV) and maximum voltage (MV) of the EMG signals were recorded to quantify muscle excitation. Area under the curve (AUC) was recorded to estimate total muscular activity [2]. Two-sample t-tests at 95% confidence were used to compare measures across CLs (155 and 185 mm) and cadences (70 rpm and 1.47 m/s).

## RESULTS

The five measures of muscles activation (AV, MV, AUC, TON, TOFF) for VL and VM are outlined in Figure 1. The means and SDs of each measure for each condition are shown in Table 2 and Table 3. For VL and VM, there were no significant differences between CLs at 70 rpm or between CLs at 1.47 m/s ($p>0.05$ for all measures). This supports H1. For VL and VM, there were no significant differences between the 70 rpm and 1.4 m/s trials for 155 mm or 185 mm ($p>0.05$ for all measures). This does not support H2.

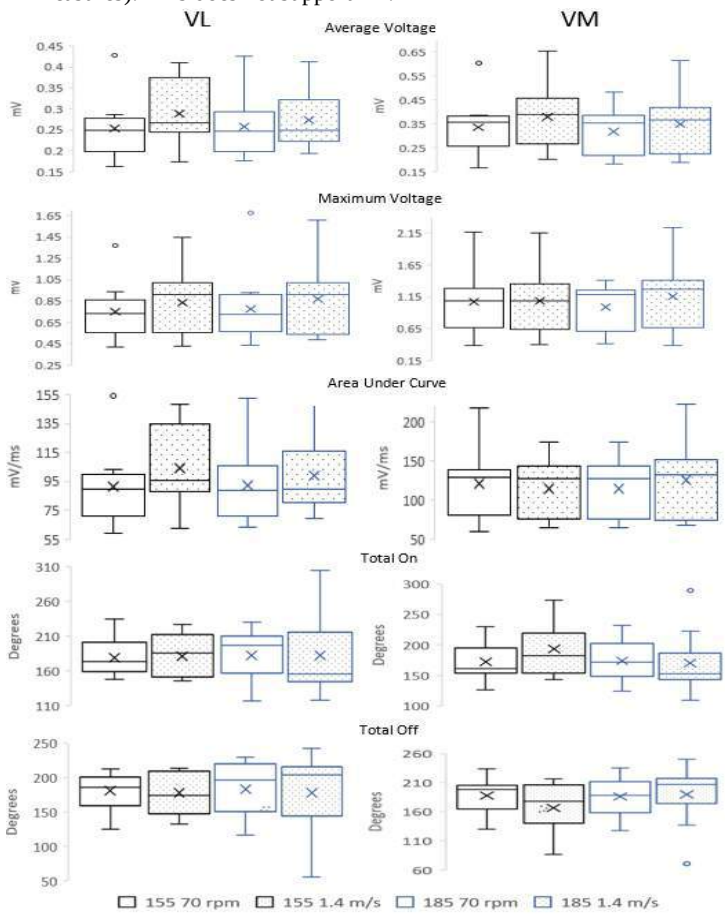


**Figure 1: Measures of muscular activation (AV, MV, AUC, TON, TOFF) of VL and VM at 70 rpm and 1.47 m/s for 155 and 185 mm CL. No significant differences in these measures.**

**Table 2: Vastus Lateralis Measures, Mean ± SD shown.**

| Trial | AV (mV) | MV (mV) | AUC (mV/ms) | TON (degrees) | TOFF (degrees) |
|---|---|---|---|---|---|
| 155 70 | 0.2529 ± 0.0708 | 0.750 ± 0.273 | 91.0 ± 25.6 | 179.0 ± 26.5 | 181.0 ± 26.6 |
| 155 1.47 | 0.2894 ± 0.0745 | 0.835 ± 0. 317 | 104.1 ± 26.8 | 181.8 ± 29.8 | 178.2 ± 29.8 |
| 185 70 | 0.2575 ± 0.0704 | 0.775 ± 0.342 | 92.6 ± 25.9 | 182.8 ± 36.6 | 182.8 ± 36.5 |
| 185 1.47 | 0.2745 ± 0.072 | 0.869 ± 0.347 | 98.8 ± 25.4 | 182.3 ± 60.7 | 177.7 ± 60.7 |

**Table 3: Vastus Medialis Measures, Mean ± SD shown.**

| Trial | AV (mV) | MV (mV) | AUC (mV/ms) | TON (degrees) | TOFF (degrees) |
|---|---|---|---|---|---|
| 155 70 | 0.336 ± 0.127 | 1.072 ± 0.536 | 120.8 ± 45.5 | 172.4 ± 32.6 | 187.6 ± 32.6 |
| 155 1.47 | 0.379 ± 0.139 | 1.085 ± 0.531 | 114.6 ± 37.6 | 193.4 ± 47.9 | 166.6 ± 47.9 |
| 185 70 | 0.319 ± 0.104 | 0.987 ± 0.384 | 114.6 ± 37.6 | 173.9 ± 37.6 | 186.1 ± 37.6 |
| 185 1.47 | 0.348 ± 0.134 | 1.161 ± 0.567 | 125.4 ± 48.3 | 170.2 ± 53.1 | 189.8 ± 53.1 |

## DISCUSSION

There were no significant differences between any of the measures at different CLs and pedal speed/rate. These results suggest that CL may not have a significant of an effect on muscle activation. Therefore, cyclists focused on performance, general knee health, or rehabilitation should not be overly concerned by the CL they use. There is no perfect formula for determining optimal CL for an individual. There is some evidence to show that optimal CL depends on leg length [4]. However, due to the amount of variability between individual people, a holistic approach that considers an individual's anthropometric dimensions, limb dynamics, health history, personal preference, and other factors will likely lead to a best suited CL.

These results may also be useful in rehabilitative contexts with stationary bicycles. While CL showed no effect on muscle activity, smaller CLs reduce range of motion (ROM) in the hip and knee joints. In addition, constant pedal speed trials at 1.47 m/s produce lower peak knee compressive forces across CLs compared to 70 rpm trials [5]. Therefore, the purpose of adjusting CL and cadence in a rehabilitation setting should be to restore ROM and reduce compressive forces. CL should not be considered as a tool for altering muscular activation in rehabilitation.

This study has several limitations. First, the number of participants used was low. Fifteen participants were excluded from statistical analysis due to EMG signal error and sensor inaccuracy. Poor EMG data was likely a result of signal noise caused by sweating and clothing. Software complications further limited the data pool for analysis. Second, although collected, onset and offset times were not analyzed in this research. While there was no significant difference in total activation time, it is possible that there were shifts in activation periods that were not accounted for.

Future research with this data will analyze a larger sample of participants across all four CLs. The research will include analysis of tibialis anterior, gastrocnemius (lateral head), and biceps femoris, as well as onset and offset times for all five muscles.


## ACKNOWLEDGEMENTS

This research was supported by the Bill and Linda Frost Fund. Students are Frost Research Fellows and recipients of the Bill and Linda Frost Undergraduate Student Research Award. The authors acknowledge Reymil Fernandez, Avery Newman, Melodie Leroudier, Michael Liang, and Chaitanya Adiga for their contributions.


## REFERENCES


[1] Mileva, K., Turner, D., *Exp Brain Res*, 152:393–403, 2003.
[2] Watanabe, K. *Eur. J. Appl. Physiol*, 120:697–706, 2020.
[3] Cerny, K. *Phys Ther*, 75:672-683, 1995.
[4] Inbar, O., et al., *Ergonomics*, 35(14):1328-1335, 1983.
[5] Newman, A., et al., *SB³C*, 2021.

# COMMODE FOR NEUROGENIC BOWEL: A MECHANISM FOR ACHIEVING THE SQUATTING POSITION

**John D. Bates (1), Chastity C. Chavez (1), Madison L. Lang (1), Alexander J. Rivera (1), Camila Ruiz Vega (1)**

**Faculty Advisor(s)**

**Amy Lerner (1), Scott Seidman (1), Richard Waugh (1)**

(1) Department of Biomedical Engineering, University of Rochester, Rochester, New York, USA

## INTRODUCTION

For individuals with neurogenic bowel (NB), performing a bowel movement can be a tedious and time-consuming process. NB is the neurological loss of normal bowel function and affects many individuals with acute spinal cord injuries and other neurological conditions such as multiple sclerosis, spina bifida, and others.

There are existing posture modification devices (PMD) that facilitate the bowel movement process such as the 'Squatty Potty,' a footstool that the user rests their feet on during defecation to produce a desired hip-flexion angle of 22.5°-35° [1]. These PMDs bring the legs up, which replicates a squatting position and straightens the colon to allow for easier passage of the bowel movement [2]. Studies have shown the effectiveness of PMD-facilitated hip flexion in reducing the time and strain involved with performing a bowel movement [1]. However, these current defecation PMDs target individuals with a full range of motion and are not suited for achieving and sustaining hip flexion for individuals with NB.

Achieving a bowel movement may take several hours for an individual with NB, putting them at risk of developing pressure ulcers. Therefore, our goal is to create a posture modification device that allows an individual with NB to safely achieve a squatting position for the duration of their bowel care program.

Our approach to creating a device capable of sustaining the squatting position is by means of an accessory item for the shower/commode chair rather than redesigning the commode chair itself. We are currently developing our device specifically for the HOMCOM Commode Shower Transport Wheelchair [3]. Nonetheless, our design process involves considerations for adjustable dimensions to cater to a range of commode chairs in the medical device industry.

## PRODUCT DESIGN

The design of our device takes a novel leaning forward approach to assist in posture modification during bowel care as depicted in Figure 1. Our design will support the user's torso to achieve the desired hip flexion angle and sustain it for the duration of their bowel care procedure. A key aspect to this novel leaning forward design is the pressure relief from the ischial tuberosities. Current PMD's achieve hip flexion by raising the knees from behind the knee, which concentrates pressure to the ischium, increasing the risk for developing pressure ulcers.

**Figure 1: General concept of the torso-lean mechanism to achieve the hip flexion angle.**

Early in our design process, we conducted a thorough literature review and met with a variety of voice of customers (VoC) to create a list of customer needs as the basis for our device. Listed in Table 1 are the goal metrics for the most crucial needs.

**Table 1: Summary analysis of customer needs**

| Needs | Goal Metrics |
|---|---|
| Support Hip Flexion Angle | 22.5º-35º [1] |
| Sustain Desired Hip Flexion Angle | 2-3 hours [3] |
| Support User Weight | 300-400 lbs |
| Provide Low User Contact Pressure | 0 to 33 mmHg per 15 to 20 minutes [4] |

The support user weight capacity was determined by HOMCOM's commode chair weight capacity and factor of safety listed by specifications of components (locking mechanism) for our device available online.

The device serves as an accessible attachment to current shower/commode chairs on the market. The interface location provides users easy access to the perianal region from the front and sides during bowel care. Our design is composed of a noncorrosive aluminum frame with adjustable dimensions to accommodate variable user demographics as shown in Figure 1. The device to commode interface consists of compatible constriction clamps to secure the device in place and adjust to variations in commode sizes

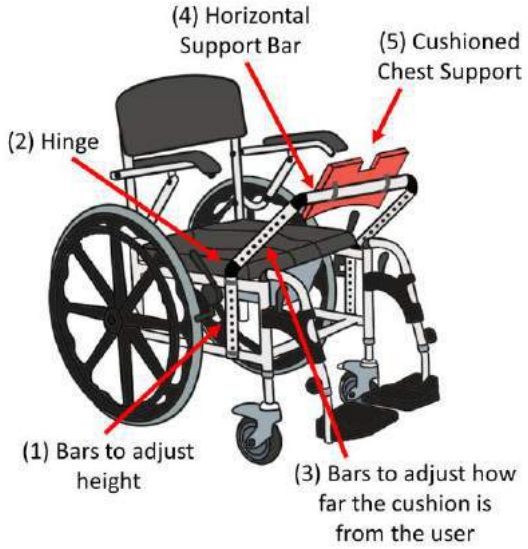


**Figure 2: Labeled schematic of the torso-lean attachment piece to the HOMCOM shower/commode chair.**

At the start of bowel care the user will need to transfer into their commode. Our design facilitates this process by incorporating a swivel mechanism to rotate the torso rest away from the user's intended path. The user can securely lock the torso rest back into place while preparing for positioning. The device can easily be adjusted and locked via a release button into the user's desired hip flexion angle through a heavy-duty aluminum hinge system. The user can then lean forward onto the torso support to sustain their hip flexion positioning throughout their bowel care procedure.

The torso support rest consists of a vinyl covered high density foam with a high-density polyethylene base for comforted support. After the user is finished with bowel care they can go right into a shower to get cleaned up and can continue to keep the device on their commode for extra support. These materials along with the lightweight aluminum frame are similar to current commode/shower chair materials providing for sufficient bathroom environmental compatibility as well as feasible manufacturability.

## BUDGET & MARKET ANALYSIS

Based on data from 1993-2012, the estimated incidence for acute spinal cord injury (SCI) was 54 cases per 1 million population, which would result in ~6 million Americans in 2022 [6]. Of those, 75% experience some degree of constipation and fecal incontinence [7]. This results in ~4.5 million Americans with NB. Commode chairs are a necessity for an individual with an SCI, and our device is designed to be used in conjunction with an existing commode rather than be a replacement. Therefore, this provides us with our rough market size and relevant demographic. As per our caregiver VoC, commodes and related devices are typically replaced in the 4–6-year range, however the material selection and nature of our device may lend itself to a slightly longer lifespan.

Below is the list of components we may need for any additional prototyping as we build towards our final device. Each category represents the overall anticipated cost for the device's subsystems. Additionally, prototyping may be necessary to test the viability of the device and help us get a preliminary sense of whether our hinge mechanism will support the load of the person's upper body and whether our device can be successfully clamped to the commode chair. Most of the materials for prototyping are found in our engineering department's design lab. We expect any additional prototyping would take 2-3 hours of our time to complete.

**Table 2: Overview of budget for prototyping.**

| Category | Cost |
|---|---|
| Torso support cushion: materials and fabrication | $72.68 |
| Locking components | $298.75 |
| Structural/stability framework | $92.44 |
| Miscellaneous (machining, screws, delivery, etc.) | $50.00 |

Therefore, the final monetary cost for our device is estimated to be approximately $514 for our device. The hinges make up a large fraction of these costs ($204/$514), so we are looking into cheaper alternatives that provide the same structural support. Our current plan is to discuss with a mechanical fabrication specialist to potentially fabricate our own hinges. The prices may also vary slightly depending on whether we choose the swivel ball joints or the split collar telescoping tube lock. Upcoming efforts will be dedicated towards deciding which mechanism to pursue and fabricating our final product.

## ACKNOWLEDGEMENTS

We would like to thank the nurse manager and the occupational therapists at The University of Rochester Medical Center Department of Physical Medicine and Rehabilitation, the specialists at Numotion, and members of Rochester Spinal Association for their continuous support and feedback, and for sharing their knowledge/experiences with us. We would also like to thank our customer, Dr. Sara Salim at The University of Rochester Medical Center Department of Physical Medicine and Rehabilitation, for providing us with our engineering design project, and our supervising TA, Lucas Lassinger, for providing detailed feedback throughout our design progress.

## REFERENCES

[1] Sakakibara et al, Influence of Body Position on Defecation in Humans. *LUTS: Lower Urinary Tract Symptoms*, 2(1), pp.16-21, 2010.
[2] The Squatty Potty Story, *Squatty Potty USA LLC*, 2012.
[3] Amazon, HOMCOM Accessibility Commode Wheelchair, Rolling Shower Wheelchair, 2022.
[4] Stiens, *Archives of Physical Medicine and Rehabilitation,* 1997.
[5] Agrawal, *Indian Journal of Plastic Surgery,* 2012.
[6] Jain, NB et al., *Journal of the American Medical Association*, 313(22):2236-2243, 2015.
[7] Emmanuel, A, *F1000 Research*, 8:1800-1803, 2019.